様式 C－１８

太陽系外惑星の新機軸：地球型惑星へ

New Frontiers of Extrasolar Planets: Exploring Terrestrial Planets

２３０２

平成２３年度～平成２７年度科学研究費助成事業（科学研究費補助金）（新学術領域研究（研究領域提案型））研究成果報告書

平成２９年６月

領域代表者　林　正彦
自然科学研究機構・国立天文台台長

目次

はしがき

この冊子は、平成２３年度～平成２７年度科学研究費助成事業（科学研究費補助金）（新学術領域研究（研究領域提案型））「太陽系外惑星の新機軸に関する総合的研究」（領域番号２３０２）の研究で得られた成果をまとめた研究成果報告書である。

本領域研究では、天文学と惑星科学の密接な連携・融合によって、我が国において「系外惑星」という学術領域を確立して世界的リードを狙い、当該分野における我が国の学術水準を向上･強化することを目的とした。本領域は、惑星の検出と分光（Ａ０１）、系外惑星大気のモデリング（Ａ０２）、原始惑星系円盤の観測（Ｂ０１）、惑星形成理論（Ｂ０２）という４つの計画研究からなっている。

計画研究Ａ０１では、すばる望遠鏡を用いて、木星の４倍の質量をもち、表面温度が５１０Ｋの「第二の木星」とも呼べる惑星の直接撮像に成功した。また新たに高コントラスト赤外線分光器等（SCExAO＋CHARIS）を開発し、予定より１年遅れたが平成２８年度には系外惑星大気を直接分光することに成功した。重力マイクロレンズ法等の間接的観測手法を用いた地球型惑星の検出も推進し、地球型惑星１個、海王星型惑星１０個を含む、合計３６個の惑星を検出した。

計画研究Ａ０２の系外惑星大気の研究においては、地球型惑星が形成される最終段階で生じる高温水蒸気大気について、その冷却進化過程を理論的に求めた。その結果、惑星に対する日射量がある閾値を超えると、高温状態が長期間持続しやがて水蒸気がほぼすべて失われるが、閾値未満の場合には水蒸気が地表に凝結し、惑星表層に液体の水が半永久的に保持されることを明らかにした。

計画研究Ｂ０１の原始惑星系円盤の観測に関しては、すばる望遠鏡を用いて多数の原始惑星系円盤を撮影し、ギャップや渦巻き構造の存在を明らかにした。またＡＬＭＡによる観測では、近傍の若い星 HD142527 に付随する原始惑星系円盤で、星から 160 天文単位の位置でダストがガスに比べて著しく濃集している領域があることを発見し、ここが岩石惑星（コア）の効率的な形成場所となっている可能性を指摘した。

計画研究Ｂ０２の惑星形成理論では、円盤内の氷ダストの合体成長･空隙率進化・軌道進化を無矛盾に考慮した進化シミュレーションを実施した。その結果、成長していく集積ダストの空気力学的特性が、高空隙率化に伴って変化することにより、ある時点で急な収縮を起こして微惑星へと成長することが分かった。これは、氷ダストが中心星に落下する前に氷微惑星が形成されることを、世界で初めて示したものである。

こうした５年間（繰越も入れると６年間）の研究は、国際的に競争の激しい分野にも

かかわらず、新たに２個の恒星周囲の惑星系の撮像に成功することに加え、公募研究も含めた約２００編の査読論文、新聞記事・雑誌特集などのメディア報道に結実されている。なお、本領域の成果に関して、研究終了以後の事後評価において科学研究費補助金審査部会から、「A（研究領域の設定目的に照らして、期待どおりの成果があった)」という所見をいただいた。

文末になりましたが、この新学術領域研究を進めるにあたり、評価委員の方々をはじめとして、多くの皆様からのご尽力を賜われたことに、深く感謝の意を表します。

研究組織

＜領域代表者および総括班研究代表者＞

総括班 X00：太陽系外惑星の新機軸：地球型惑星へ

林　正彦（自然科学研究機構・国立天文台台長）

＜領域および総括班評価者＞

観山正見（広島大学特任教授）

松井孝典（千葉工業大学・惑星探査研究センター所長）

山田　亨（国立研究開発法人 宇宙航空研究開発機構 宇宙科学研究所・教授）

【計画研究】

計画研究 A01：ガス惑星の直接撮像・分光と地球型惑星の検出

研究代表者：林　正彦（自然科学研究機構・国立天文台台長）

研究分担者：住　貴宏（大阪大学・理学研究科・准教授）

研究分担者：高遠　徳尚（国立天文台・ハワイ観測所・准教授）

研究分担者：左近　樹（東京大学・大学院理学系研究科・助教）

研究分担者：藤原　英明（国立天文台・ハワイ観測所・RCUH 職員）

研究分担者：Guyon Olivier（国立天文台・ハワイ観測所・RCUH 職員）

連携研究者：須藤　靖（東京大学・理学系研究科・教授）

連携研究者：佐藤　文衛（東京工業大学・グローバルエッジ研究院・准教授）

連携研究者：伊藤　洋一（兵庫県立大学・自然･環境科学研究所・教授）

連携研究者：本田　充彦（久留米大学・医学部・助教）

連携研究者：森野　潤一（国立天文台・光赤外研究部・助教）

計画研究 A02：系外惑星大気の数値モデリングと形成進化論

研究代表者：倉本　圭（北海道大学・理学研究科・教授）

研究分担者：はしもと　じょーじ（岡山大学・自然科学研究科・准教授）

研究分担者：林　祥介（神戸大学・理学研究科・教授）

研究分担者：関根　康人（東京大学・理学系研究科・准教授）

研究分担者：阿部　豊（東京大学・理学系研究科・准教授）

計画研究 B01：円盤から惑星へ

研究代表者：百瀬　宗武（茨城大学・理学部・教授）
研究分担者：深川　美里（国立天文台・チリ観測所・特任准教授）
研究分担者：尾中　敬（東京大学・理学系研究科・教授）
研究分担者：田中　秀和（北海道大学・低温科学研究所・准教授）
研究分担者：山本　哲生（北海道大学・低温科学研究所・名誉教授）
研究分担者：荒川　政彦（神戸大学・理学研究科・教授）
研究分担者：相川　裕理（筑波大学・計算科学研究センター・教授）
研究分担者：武藤　恭之（工学院大学・基礎・教養教育部門・准教授）
研究分担者：塚越　崇（茨城大学・理学部・助教）
連携研究者：片坐宏一（宇宙航空研究開発機構・宇宙科学研究所・准教授）
連携研究者：和田浩二（千葉工業大学・惑星探査研究センター・主席研究員）
連携研究者：村川幸史（大阪産業大学・工学部・講師）
研究協力者：金川和弘（シュチェチン大学・研究員）
研究協力者：木村宏（名古屋大学・理学研究科・研究員）
研究協力者：谷川享行（一関高専・准教授）
研究協力者：樋口あや（理化学研究所・研究員）
研究協力者：安井千香子（国立天文台・TMT 推進室・助教）
研究協力者：ロ・スニョン（ウルサン大学・研究員）

計画研究 B02：ハビタブル地球型惑星の形成理論

研究代表者：井田　茂（東京工業大学・地球生命研究所・教授）
研究分担者：長澤　真樹子（久留米大学・医学部・准教授）
研究分担者：野村　英子（東京工業大学・地球惑星科学系・准教授）
研究分担者：渡邊　誠一郎（名古屋大学・環境学研究科・教授）
研究分担者：中本　泰史（東京工業大学・地球惑星科学系・教授）
研究分担者：奥住　聡（東京工業大学・地球惑星科学系・准教授）
研究分担者：犬塚　修一郎（名古屋大学・理学研究科・教授）
研究分担者：生駒　大洋（東京大学・理学系研究科・准教授）
研究分担者：小久保英一郎（国立天文台・理論研究部・教授）

【公募研究】

＜平成２４年度～２５年度＞

公募 A01：セグメント型望遠鏡のための共通光路シアリングナル干渉計の開発

研究代表者：村上　尚史（北海道大学・工学系研究科・助教）

公募 A01：地球型惑星検出を目指した視線速度測定近赤外線分光器のためのファイバー較正法の確率

研究代表者：西山　正吾（国立天文台・研究員）

連携研究者：西川　淳　（国立天文台・助教）

連携研究者：周藤　浩士（国立天文台・アストロバイオロジーセンター・助教）

公募 A02：深部対流を考慮した系外ガス惑星表層大気運動形態の多様性の研究

研究代表者：竹広　真一（京都大学・数理解析研究所・准教授）

公募 A02：太陽系外惑星の内部構造モデル構築に向けた レーザー高圧物性実験からのアプローチ

研究代表者：佐野　孝好（大阪大学・レーザーエネルギー学研究センター・助教）

公募 B01：新たなダスト発生機構：微惑星衝撃波による微惑星蒸発の検討

研究代表者：田中　今日子（北海道大学・低温科学研究所・研究員）

公募 B01：巨大ガス惑星と原始惑星系円盤の共進化：インナーホール形成モデル

研究代表者：谷川　亨行（北海道大学・低温科学研究所・研究員）

公募 B01：サブミリ波を用いた原始惑星系円盤の進化段階の観測的解明

研究代表者：塚越　崇（茨城大学・理学部・研究員）

＜平成２６年度～２７年度＞

公募 A01：可視高精度分光撮像測光による系外惑星大気の研究

研究代表者：土居　守（東京大学・大学院理学系研究科・教授）

公募 A01：可視・近赤外線６バンド同時精密トランジット観測で探る 太陽系外惑星の大気組成
研究代表者：永山　貴宏（鹿児島大学・理工学域理学系・准助教）

公募 A01：視線速度法による地球型惑星のための超広帯域光周波数コムの開発
研究代表者：小谷　隆行（国立天文台・太陽系外惑星探査プロジェクト室・助教）
連携研究者：黒川　隆志（東京農工大学・教授）
連携研究者：柏木　謙　（東京農工大学・助教）
連携研究者：田村　元秀（東京大学・理学系研究科・教授）
連携研究者：西川　淳　（国立天文台・助教）

公募 A02：深部対流モデルによる系外惑星大気連動運動の多様性の数値的研究
研究代表者：竹広　真一（京都大学・数理解析研究所・准教授）

公募 B01：原始惑星系円盤の多波長輻射平衡モデルの構築
研究代表者：花輪　知幸（千葉大学・先進科学センター・教授）

公募 B01：円盤ギャップ内のダストサイズ分布の決定： 観測と直接比較可能な数理モデルの構築
研究代表者：金川　和弘（北海道大学・低温科学研究所・研究員）

公募 B02：形成過程から探る低温度星回りの短周期スーパーアースの 大気および内部組成の起源
研究代表者：堀　安範（国立天文台・太陽系外惑星探査プロジェクト室・特任助教）

公募研究　計１４件

＜研究領域全体に係るデータ＞

（1） 研究者数

種別		平成 23		平成 24		平成 25		平成 26		平成 27	
		計画	公募	計画	公募	計画	公募	計画	公募	計画	公募
研究組織	研究代表者	4	0	4	7	4	7	4	7	4	7
	研究分担者又は連携研究者	33	0	36	7	38	7	38	19	39	19
	研究協力者	4	0	8	1	7	1	12	0	14	0
	合計	41	0	48	15	49	15	54	26	57	26
	うち　若手研究者（～39 歳）※1	11	0	16	5	25	5	19	15	18	15
	うち　外国人研究者	1	0	1	0	1	0	1	0	2	0
ポスドク（本科研費での雇用者）※2		3	0	8	1	9	1	10	1	9	1
ＲＡ等　（本科研費での雇用者）※2		1	0	3	0	6	0	2	0	1	0

＊　1：各年年度末で３９歳以下の場合を指す。

＊　2：上段の研究組織に参画している場合でも重複して計上。

（2） 領域に関与したポスドク・RA 等・若手研究者（～３９歳*3）の就職状況

種別	平成 23 年度（人数）	平成 24 年度（人数）	平成 25 年度（人数）	平成 26 年度（人数）	平成 27 年度（人数）
研究職（常勤）	0	1	9	3	10
研究職（非常勤）	0	1	2	0	9
研究職以外	0	0	3	1	6

＊３：各年度末時点で３９歳以下の場合を指す。

交付額（配分額）（金額単位：円）

(金額単位：円)

	直接経費	間接経費	合　計
平成23年度	144,100,000	43,230,000	187,330,000
平成24年度	244,700,000	73,410,000	318,110,000
平成25年度	244,300,000	73,290,000	317,590,000
平成26年度	188,810,000	56,643,000	245,453,000
平成27年度	123,718,709	37,115,613	160,834,322
平成28年度	57,471,291	17,241,387	74,712,678
総　計	1,003,100,000	300,930,000	1,304,030,000

研究発表

（1） 雑誌論文

査読論文のみ、研究計画間で重複するものは一方を省略した。

研究代表者：二重下線　研究分担者：下線　研究協力者：下点線

計画研究 A01：ガス惑星の直接撮像・分光と地球型惑星の検出

1. Rich, E. A., Wisniewski, J. P., Mayama, S., Brandt, T. D., Hashimoto, J., Kudo, T., Kusakabe, N., Espaillat, C., Abe, L., Akiyama, E., Brandner, W., Carson, J. C., Currie, T., Egner, S., Feldt, M., Follette, K., Goto, M., Grady, C. A., Guyon, O., Hayano, Y., Hayashi, M., Hayashi, S. S., Henning, T., Hodapp, K. W., Ishii, M., Iye, M., Janson, M., Kandori, R., Knapp, G. R., Kuzuhara, M., Kwon, J., Matsuo, T., McElwain, M. W., Miyama, S., Morino, J., Moro-Martin, A., Nishimura, T., Pyo, T.-S., Qi, C., Serabyn, E., Suenaga, T., Suto, H., Suzuki, R., Takahashi, Y. H., Takami, M., Takato, N., Terada, H., Thalmann, C., Tomono, D., Turner, E. L., Watanabe, M., Yamada, T., Takami, H., Usuda, T., Tamura, M., 2015, Near-IR Polarized Scattered Light Imagery of the DoAr 28 Transitional Disk, The Astrophysical Journal, Volume 150, Issue 3, article id. 86, 9 pp , DOI: 10.1088/0004-6256/150/3/86
2. Momose, M., Morita, A., Fukagawa, M., Muto, T., Takeuchi, T., Hashimoto, J., Honda, M., Kudo, T., Okamoto, Y. K., Kanagawa, K. D., Tanaka, H., Grady, C. A., Sitko, M. L., Akiyama, E., Currie, T., Follette, K. B., Mayama, S., Kusakabe, N., Abe, L., Brandner, W., Brandt, T. D., Carson, J. C., Egner, S., Feldt, M., Goto, M., Guyon, O., Hayano, Y., Hayashi, M., Hayashi, S. S., Henning, T., Hodapp, K. W., Ishii, M., Iye, M., Janson, M., Kandori, R., Knapp, G. R., Kuzuhara, M., Kwon, J., Matsuo, T., McElwain, M. W., Miyama, S., Morino, J., Moro-Martin, A., Nishimura, T., Pyo, T.-S., Serabyn, E., Suenaga, T., Suto, H., Suzuki, R., Takahashi, Y. H., Takami, M., Takato, N., Terada, H., Thalmann, C., Tomono, D., Turner, E. L., Watanabe, M., Wisniewski, J., Yamada, T., Takami, H., Usuda, T., Tamura, M., 2015, Detailed structure of the outer disk around HD 169142 with polarized light in H-band, Publications of the Astronomical Society of Japan, Advance Access.16 pp , DOI: 10.1093/pasj/psv051
3. Tamura, Y., Kawabe, R., Shimajiri, Y., Tsukagoshi, T., Nakajima, Y., Oasa, Y., Wilner, D., Chandler, C., Saigo, K., Tomida, K., Yun, M., Taniguchi, A., Kohno, K., Hatsukade, B., Aretxaga, I., Austermann, J., Dickman, R., Ezawa, H., Goss, W., Hayashi, M., Hughes, D., Hiramatsu, M., Inutsuka, S., Ogasawara, R., Ohashi, N., Oshima, T., Scott, K., Wilson, G. W., 2015, Extremely Bright Submillimeter Galaxies beyond the Lupus-I Star-forming Region, The Astrophysical Journal, Volume 808, Issue 2, article id. 121, 14 pp, DOI: 10.1088/0004-637X/808/2/121
4. ALMA Partnership, Fomalont, E., Vlahakis, C., Corder, S., Remijan, A., Barkats, D., Lucas, R., Hunter, T., Brogan, C., Asaki, Y., Matsushita, S., Dent, W., Hills, R., Phillips, N., Richards, A., Cox, P., Amestica, R., Broguiere, D., Cotton, W., Hales, A., Hiriart, R., Hirota, A., Hodge, J., Impellizzeri, C., Kern, J., Kneissl, R., Liuzzo, E., Marcelino, N., Marson, R., Mignano, A., Nakanishi, K., Nikolic, B., Perez, J., Pérez, L., Toledo, I., Aladro,

R., Butler, B., Cortes, J., Cortes, P., Dhawan, V., Di Francesco, J., Espada, D., Galarza, F., Garcia-Appadoo, D., Guzman-Ramirez, L., Humphreys, E., Jung, T., Kameno, S., Laing, R., Leon, S., Mangum, J., Marconi, G., Nagai, H., Nyman, L., Radiszcz, M., Rodón, J., Sawada, T., Takahashi, S., Tilanus, R., van Kempen, T., Vila Vilaro, B., Watson, L., Wiklind, T., Gueth, F., Tatematsu, K., Wootten, A., Castro-Carrizo, A., Chapillon, E., Dumas, G., de Gregorio-Monsalvo, I., Francke, H., Gallardo, J., Garcia, J., Gonzalez, S., Hibbard, J., Hill, T., Kaminski, T., Karim, A., Krips, M., Kurono, Y., Lopez, C., Martin, S., Maud, L., Morales, F., Pietu, V., Plarre, K., Schieven, G., Testi, L., Videla, L., Villard, E., Whyborn, N., Zwaan, M., Alves, F., Andreani, P., Avison, A., Barta, M., Bedosti, F., Bendo, G., Bertoldi, F., Bethermin, M., Biggs, A., Boissier, J., Brand, J., Burkutean, S., Casasola, V., Conway, J., Cortese, L., Dabrowski, B., Davis, T., Diaz Trigo, M., Fontani, F., Franco-Hernandez, R., Fuller, G., Galvan Madrid, R., Giannetti, A., Ginsburg, A., Graves, S., Hatziminaoglou, E., Hogerheijde, M., Jachym, P., Jimenez Serra, I., Karlicky, M., Klaasen, P., Kraus, M., Kunneriath, D., Lagos, C., Longmore, S., Leurini, S., Maercker, M., Magnelli, B., Marti Vidal, I., Massardi, M., Maury, A., Muehle, S., Muller, S., Muxlow, T., O'Gorman, E., Paladino, R., Petry, D., Pineda, J., Randall, S., Richer, J., Rossetti, A., Rushton, A., Rygl, K., Sanchez Monge, A., Schaaf, R., Schilke, P., Stanke, T., Schmalzl, M., Stoehr, F., Urban, S., van Kampen, E., Vlemmings, W., Wang, K., Wild, W., Yang, Y., Iguchi, S., Hasegawa, T., Saito, M., Inatani, J., Mizuno, N., Asayama, S., Kosugi, G., Morita, K., Chiba, K., Kawashima, S., Okumura, S., Ohashi, N., Ogasawara, R., Sakamoto, S., Noguchi, T., Huang, Y., Liu, S., Kemper, F., Koch, P., Chen, M., Chikada, Y., Hiramatsu, M., Iono, D., Shimojo, M., Komugi, S., Kim, J., Lyo, A., Muller, E., Herrera, C., Miura, R., Ueda, J., Chibueze, J., Su, Y., Trejo-Cruz, A., Wang, K., Kiuchi, H., Ukita, N., Sugimoto, M., Kawabe, R., Hayashi, M., Miyama, S., Ho, P., Kaifu, N., Ishiguro, M., Beasley, A., Bhatnagar, S., Braatz, J., Brisbin, D., Brunetti, N., Carilli, C., Crossley, J., D'Addario, L., Donovan Meyer, J., Emerson, D., Evans, A., Fisher, P., Golap, K., Griffith, D., Hale, A., Halstead, D., Hardy, E., Hatz, M., Holdaway, M., Indebetouw, R., Jewell, P., Kepley, A., Kim, D., Lacy, M., Leroy, A., Liszt, H., Lonsdale, C., Matthews, B., McKinnon, M., Mason, B., Moellenbrock, G., Moullet, A., Myers, S., Ott, J., Peck, A., Pisano, J., Radford, S., Randolph, W., Rao Venkata, U., Rawlings, M., Rosen, R., Schnee, S., Scott, K., Sharp, N., Sheth, K., Simon, R., Tsutsumi, T., Wood, S. J., 2015, The 2014 ALMA Long Baseline Campaign: An Overview, The Astrophysical Journal Letters, Volume 806, Issue 1, article id. L10, 6 pp, DOI: 10.1088/2041-8205/806/1/L10

5. de Leon, J., Takami, M., Karr, J., Hashimoto, J., Kudo, T., Sitko, M., Mayama, S., Kusakabe, N., Akiyama, E., Liu, H., Usuda, T., Abe, L., Brandner, W., Brandt, T., Carson, J., Currie, T., Egner, S., Feldt, M., Follette, K., Grady, C., Goto, M., Guyon, O., Hayano, Y., Hayashi, M., Hayashi, S., Henning, Th., Hodapp, K., Ishii, M., Iye, M., Janson, M., Kandori, R., Knapp, G., Kuzuhara, M., Kwon, J., Matsuo, T., McElwain, M., Miyama, S., Morino, J., Moro-Martin, A., Nishimura, T., Pyo, T.-S., Serabyn, E., Suenaga, T., Suto, H., Suzuki, R., Takahashi, Y., Takato, N., Terada, H., Thalmann, C., Tomono, D., Turner, E., Watanabe, M., Wisniewski, J., Yamada, T., Takami, H., Tamura, M., 2015, Near-IR High-resolution Imaging Polarimetry of the SU Aur Disk: Clues for Tidal Tails?, The Astrophysical Journal Letters, Volume 806, Volume 806, Issue 1, DOI: 10.1088/2041-8205/806/1/L10

6. Akiyama, E., Muto, T., Kusakabe, N., Kataoka, A., Hashimoto, J., Tsukagoshi, T., Kwon, J., Kudo, T., Kandori, R., Grady, C., Takami, M., Janson, M., Kuzuhara, M., Henning, T., Sitko, M., Carson, J., Mayama, S., Currie, T., Thalmann, C., Wisniewski, J., Momose, M.,

Ohashi, N., Abe, L., Brandner, W., Brandt, T., Egner, S., Feldt, M., Goto, M., Guyon, O., Hayano, Y., Hayashi, M., Hayashi, S., Hodapp, K., Ishi, M., Iye, M., Knapp, G., Matsuo, T., Mcelwain, M., Miyama, S., Morino, J., Moro-Martin, A., Nishimura, T., Pyo, T., Serabyn, G., Suenaga, T., Suto, H., Suzuki, R., Takahashi, Y., Takato, N., Terada, H., Tomono, D., Turner, E., Watanabe, M., Yamada, T., Takami, H., Usuda, T., Tamura, M., 2015, Discovery of a Disk Gap Candidate at 20 AU in TW Hydrae, The Astrophysical Journal Letters, Volume 802, Issue 2, article id. L17, 5 pp , DOI: 10.1088/2041-8205/802/2/L17

7. Newman, K., Guyon, O., Balasubramanian, K., Belikov, R., Jovanovic, N., Martinache, F., Wilson, D., 2015, An Achromatic Focal Plane Mask for High-Performance Broadband Coronagraphy, The Astronomical Society of the Pacific, DOI: 10.1086/681242
8. Fukui, A., Gould, A., Sumi, T., Bennett, D., Bond, I., Han, C., Suzuki, D., Beaulieu, J., Batista, V., Udalski, A., Street, R., Tsapras, Y., Hundertmark, M., Abe, F., Bhattacharya, A., Freeman, M., Itow, Y., Ling, C., Koshimoto, N., Masuda, K., Matsubara, Y., Muraki, Y., Ohnishi, K., Philpott, L., Rattenbury, N., Saito, T., Sullivan, D., Tristram, P., Yonehara, A., MOA Collaboration; Choi, J., Christie, G., DePoy, D., Dong, S., Drummond, J., Gaudi, B., Hwang, K., Kavka, A., Lee, C., McCormick, J., Natusch, T., Ngan, H., Park, H., Pogge, R., Shin, I., Tan, T., Yee, J., μFUN Collaboration; Szymański, M., Pietrzyński, G., Soszyński, I., Poleski, R., Kozłowski, S., Pietrukowicz, P., Ulaczyk, K., Wyrzykowski, Ł.; OGLE Collaboration; Bramich, D., Browne, P., Dominik, M., Horne, K., Ipatov, S., Kains, N., Snodgrass, C., Steele, I., RoboNet Collaboration, 2015, OGLE-2012-BLG-0563Lb: A Saturn-mass Planet around an M Dwarf with the Mass Constrained by Subaru AO Imaging, The Astrophysical Journal, Volume 809, Issue 1, article id. 74, 16 pp , DOI: 10.1088/0004-637X/809/1/74
9. Ranc, C., Cassan, A., Albrow, M., Kubas, D., Bond, I., Batista, V., Beaulieu, J., Bennett, D., Dominik, M., Dong, S., Fouqué, P., Gould, A., Greenhill, J., Jørgensen, U., Kains, N., Menzies, J., Sumi, T., Bachelet, E., Coutures, C., Dieters, S., Dominis Prester, D., Donatowicz, J., Gaudi, B., Han, C., Hundertmark, M., Horne, K., Kane, S., Lee, C., Marquette, J., Park, B., Pollard, K., Sahu, K., Street, R., Tsapras, Y., Wambsganss, J., Williams, A., Zub, M., Abe, F., Fukui, A., Itow, Y., Masuda, K., Matsubara, Y., Muraki, Y., Ohnishi, K., Rattenbury, N., Saito, T., Sullivan, D., Sweatman, W., Tristram, P., Yock, P., Yonehara, A., 2015, MOA-2007-BLG-197: Exploring the brown dwarf desert, The Astrophysical Journal, Volume 580, id.A125, 16 pp , DOI: 10.1051/0004-6361/201525791
10. Itoh, Y., Fukagawa, M., Shibai, H., Sumi, T., Yamamoto, K., 2015, MOA-2007-BLG-197: Study of infrared excess from circumstellar disks in binaries with Spitzer/IRAC, Publications of the Astronomical Society of Japan, Advance Access., 17 pp , DOI: 10.1093/pasj/psv071
11. Jeong, J., Park, H., Han, C., Gould, A., Udalski, A., Szymański, M., Pietrzyński, G., Soszyński, I., Poleski, R., Ulaczyk, K., Wyrzykowski, Ł.; OGLE Collaboration; Abe, F., Bennett, D., Bond, I., Botzler, C., Freeman, M., Fukui, A., Fukunaga, D., Itow, Y., Koshimoto, N., Masuda, K., Matsubara, Y., Muraki, Y., Namba, S., Ohnishi, K., Rattenbury, N., Saito, T., Sullivan, D., Sweatman, W., Sumi, T., Suzuki, D., Tristram, P., Tsurumi, N., Wada, K., Yamai, N., Yock, P., Yonehara, A., MOA Collaboration; Albrow, M., Batista, V., Beaulieu, J., Caldwell, J., Cassan, A., Cole, A., Coutures, C., Dieters, S., Dominik, M., Dominis Prester, D., Donatowicz, J., Fouqué, P., Greenhill, J., Hoffman, M., Huber, M., Jørgensen, U., Kane, S., Kubas, D., Martin, R., Marquette, J., Menzies, J.,

Pitrou, C., Pollard, K., Sahu, K., Vinter, C., Wambsganss, J., Williams, A., PLANET Collaboration; Allen, W., Bolt, G., Choi, J., Christie, G., DePoy, D., Drummond, J., Gaudi, B., Hwang, K., Jung, Y., Lee, C., Mallia, F., Maoz, D., Maury, A., McCormick, J., Monard, L., Moorhouse, D., Natusch, T., Ofek, E., Park, B., Pogge, R., Santallo, R., Shin, I., Thornley, G., Yee, J., µFUN Collaboration; Bramich, D., Burgdorf, M., Horne, K., Hundertmark, M., Kains, N., Snodgrass, C., Steele, I., Street, R., Tsapras, Y., RoboNet Collaboration, 2015, Reanalyses of Anomalous Gravitational Microlensing Events in the OGLE-III Early Warning System Database with Combined Data, The Astrophysical Journal, Volume 804, article id. 38, 11 pp, DOI: 10.1088/0004-637X/804/1/38

12. Skowron, J., Shin, I., Udalski, A., Han, C., Sumi, T., Shvartzvald, Y., Gould, A., Dominis Prester, D., Street, R., Jørgensen, U., Bennett, D., Bozza, V., Szymański, M., Kubiak, M., Pietrzyński, G., Soszyński, I., Poleski, R., Kozłowski, S., Pietrukowicz, P., Ulaczyk, K., Wyrzykowski, Ł.; OGLE Collaboration; Abe, F., Bhattacharya, A., Bond, I., Botzler, C., Freeman, M., Fukui, A., Fukunaga, D., Itow, Y., Ling, C., Koshimoto, N., Masuda, K., Matsubara, Y., Muraki, Y., Namba, S., Ohnishi, K., Philpott, L., Rattenbury, N., Saito, T., Sullivan, D., Suzuki, D., Tristram, P., Yock, P., MOA Collaboration; Maoz, D., Kaspi, S., Friedmann, M., Wise Group; Almeida, L., Batista, V., Christie, G., Choi, J., DePoy, D., Gaudi, B., Henderson, C., Hwang, K., Jablonski, F., Jung, Y., Lee, C., McCormick, J., Natusch, T., Ngan, H., Park, H., Pogge, R., Yee, J., µFUN Collaboration; Albrow, M., Bachelet, E., Beaulieu, J., Brillant, S., Caldwell, J., Cassan, A., Cole, A., Corrales, E., Coutures, C., Dieters, S., Donatowicz, J., Fouqué, P., Greenhill, J., Kains, N., Kane, S., Kubas, D., Marquette, J., Martin, R., Menzies, J., Pollard, K., Ranc, C., Sahu, K., Wambsganss, J., Williams, A., Wouters, D., PLANET Collaboration; Tsapras, Y., Bramich, D., Horne, K., Hundertmark, M., Snodgrass, C., Steele, I., RoboNet Collaboration; Alsubai, K., Browne, P., Burgdorf, M., Calchi Novati, S., Dodds, P., Dominik, M., Dreizler, S., Fang, X., Gu, C., Hardis; Harpsøe, K., Hessman, F., Hinse, T., Hornstrup, A., Jessen-Hansen, J., Kerins, E., Liebig, C., Lund, M., Lundkvist, M., Mancini, L., Mathiasen, M., Penny, M., Rahvar, S., Ricci, D., Scarpetta, G., Skottfelt, J., Southworth, J., Surdej, J., Tregloan-Reed, J., Wertz, O., MiNDSTEp Consortium, 2015, OGLE-2011-BLG-0265Lb: A Jovian Microlensing Planet Orbiting an M Dwarf, The Astrophysical Journal, Volume 804, Issue 1, article id. 33, 12 pp, DOI: 10.1088/0004-637X/804/1/33

13. Calchi Novati, S., Gould, A., Udalski, A., Menzies, J., Bond, I., Shvartzvald, Y., Street, R., Hundertmark, M., Beichman, C., Yee, J., Carey, S., Poleski, R., Skowron, J., Kozłowski, S., Mróz, P., Pietrukowicz, P., Pietrzyński, G., Szymański, M., Soszyński, I., Ulaczyk, K., Wyrzykowski, Ł., OGLE Collaboration, Albrow, M., Beaulieu, J., Caldwell, J., Cassan, A., Coutures, C., Danielski, C., Dominis Prester, D., Donatowicz, J., Lončarić, K., McDougall, A., Morales, J., Ranc, C., Zhu, W., PLANET Collaboration; Abe, F., Barry, R., Bennett, D., Bhattacharya, A., Fukunaga, D., Inayama, K., Koshimoto, N., Namba, S., Sumi, T., Suzuki, D., Tristram, P., Wakiyama, Y., Yonehara, A., MOA Collaboration, Maoz, D., Kaspi, S., Friedmann, M., Wise Group; Bachelet, E., Figuera Jaimes, R., Bramich, D., Tsapras, Y., Horne, K., Snodgrass, C., Wambsganss, J., Steele, I., Kains, N., RoboNet Collaboration, Bozza, V., Dominik, M., Jørgensen, U., Alsubai, K., Ciceri, S., D'Ago, G., Haugbølle, T., Hessman, F., Hinse, T., Juncher, D., Korhonen, H., Mancini, L., Popovas, A., Rabus, M., Rahvar, S., Scarpetta, G., Schmidt, R., Skottfelt, J., Southworth, J., Starkey, D., Surdej, J., Wertz, O., Zarucki, M., MiNDSTEp Consortium; Gaudi, B., Pogge, R., DePoy, D., µFUN Collaboration, 2015, Pathway to the Galactic Distribution of Planets: Combined Spitzer

and Ground-Based Microlens Parallax Measurements of 21 Single-Lens Events, The Astrophysical Journal, Volume 804, Issue 1, article id. 20, 25 pp, DOI: 10.1088/0004-637X/804/1/20

14. Sai, S., Itoh, Y., Fukagawa, M., Shibai, H., Sumi, T., 2015, Near-infrared image of the debris disk around HD 15115, Publications of the Astronomical Society of Japan, Volume 67, Issue 2, Issue 2, id.2010 pp DOI: 10.1093/pasj/psu152
15. Maeda, K., Hattori, T., Milisavljevic, D., Folatelli, G., Drout, M., Kuncarayakti, H., Margutti, R., Kamble, A., Soderberg, A., Tanaka, M., Kawabata, M., Kawabata, K., Yamanaka, M., Nomoto, K., Kim, J., Simon, J., Phillips, M., Parrent, J., Nakaoka, T., Moriya, T., Suzuki, A., Takaki, K., Ishigaki, M., Sakon, I., Tajitsu, A., Iye, M., 2015, Type IIb Supernova 2013df Entering into an Interaction Phase: A Link between the Progenitor and the Mass Loss, The Astrophysical Journal, Volume 807, Issue 1, article id. 35, 10 pp DOI: 10.1088/0004-637X/807/1/35
16. Honda, M., Maaskant, K., Okamoto, Y., Kataza, H., Yamashita, T., Miyata, T., Sako, S., Fujiyoshi, T., Sakon, I., Fujiwara, H., Kamizuka, T., Mulders, G., Lopez-Rodriguez, E., Packham, C., Onaka, T., 2015, High-resolution 25 μ Imaging of the Disks around Herbig Ae/Be Stars: A Link between the Progenitor and the Mass Loss, The Astrophysical Journal, Volume 804, Issue 2, article id. 143, 8 pp DOI: 10.1088/0004-637X/804/2/143
17. Ishizuka, S., Kimura, Y., Sakon, I., 2015, In Situ Infrared Measurements of Free-flying Silicate during Condensation in the Laboratory, The Astrophysical Journal, Volume 803, Issue 2, article id. 88, 6 pp DOI: 10.1088/0004-637X/803/2/88
18. Norris, B., Schworer, G., Tuthill, P., Jovanovic, N., Guyon, O., Stewart, P., Martinache, F., 2015, The VAMPIRES instrument: imaging the innermost regions of protoplanetary discs with polarimetric interferometry, Monthly Notices of the Royal Astronomical Society, Volume 447, Issue 3, p.2894-2906, DOI: 10.1093/mnras/stu2529
19. Konishi, M., Shibai, H., Sumi, T., Fukagawa, M., Matsuo, T., Samland, M., Yamamoto, K., Sudo, J., Itoh, Y., Arimoto, N., Kajisawa, M., Abe, L., Brandner, W., Brandt, T., Carson, J., Currie, T., Egner, S., Feldt, M., Goto, M., Grady, C., Guyon, O., Hashimoto, J., Hayano, Y., Hayashi, M., Hayashi, S., Henning, T., Hodapp, K., Ishii, M., Iye, M., Janson, M., Kandori, R., Knapp, G., Kudo, T., Kusakabe, N., Kuzuhara, M., Kwon, J., McElwain, M., Miyama, S., Morino, J., Moro-Martín, A., Nishimura, T., Pyo, T.-S., Serabyn, E., Suenaga, T., Suto, H., Suzuki, R., Takahashi, Y., Takami, H., Takato, N., Terada, H., Thalmann, C., Tomono, D., Turner, E., Usuda, T., Watanabe, M., Wisniewski, J., Yamada, T., Tamura, M., 2015, Indications of M-dwarf deficits in the halo and thick disk of the Galaxy, Publications of the Astronomical Society of Japan, Volume 67, Issue 1, id.113 pp, DOI: 10.1093/pasj/psu125
20. Grady, C., Fukagawa, M., Maruta, Y., Ohta, Y., Wisniewski, J., Hashimoto, J., Okamoto, Y., Momose, M., Currie, T., McElwain, M., Muto, T., Kotani, T., Kusakabe, N., Feldt, M., Sitko, M., Follette, K., Bonnefoy, M., Henning, T., Takami, M., Karr, J., Kwon, J., Kudo, T., Abe, L., Brandner, W., Brandt, T., Carson, J., Egner, S., Goto, M., Guyon, O., Hayano, Y., Hayashi, M., Hayashi, S., Hodapp, K., Ishii, M., Iye, M., Janson, M., Kandori, R., Knapp, G., Kuzuhara, M., Matsuo, T., Miyama, S., Morino, J.-I., Moro-Martín, A., Nishimura, T., Pyo, T.-S., Serabyn, E., Suenaga, T., Suto, H., Suzuki, R., Takahashi, Y. H., Takato, N., Terada, H., Thalmann, C., Tomono, D., Turner, E. L., Watanabe, M., Yamada, T., Takami, H., Usuda, T., Tamura, M., 2015, The outer disks of Herbig stars from the UV to NIR, Astrophysics and Space Science, Volume 355, pp.253-266, DOI:

10.1007/s10509-014-2214-2

21. Hashimoto, J., Tsukagoshi, T., Brown, J. M., Dong, R., Muto, T., Zhu, Z., Wisniewski, J., Ohashi, N., Kudo, T., Kusakabe, N., Abe, L., Akiyama, E., Brandner, W., Brandt, T., Carson, J., Currie, T., Egner, S., Feldt, M., Grady, C. A., Guyon, O., Hayano, Y., Hayashi, M., Hayashi, S., Henning, T., Hodapp, K., Ishii, M., Iye, M., Janson, M., Kandori, R., Knapp, G., Kuzuhara, M., Kwon, J., Matsuo, T., McElwain, M. W., Mayama, S., Mede, K., Miyama, S., Morino, J.-I., Moro-Martin, A., Nishimura, T., Pyo, T.-S., Serabyn, G., Suenaga, T., Suto, H., Suzuki, R., Takahashi, Y., Takami, M., Takato, N., Terada, H., Thalmann, C., Tomono, D., Turner, E. L., Watanabe, M., Yamada, T., Takami, H., Usuda, T., Tamura, M., 2015, The Structure of Pre-transitional Protoplanetary Disks. II. Azimuthal Asymmetries, Different Radial Distributions of Large and Small Dust Grains in PDS 70, The Astrophysical Journal, Volume 799, Issue 1, article id. 43, 12 pp, DOI: 10.1088/0004-637X/799/1/43
22. Follette, K. B., Grady, C. A., Swearingen, J. R., Sitko, Michael L., Champney, E. H., van der Marel, N., Takami, M., Kuchner, M. J., Close, L. M., Muto, T., Mayama, S., McElwain, M. W., Fukagawa, M., Maaskant, K., Min, M., Russell, R. W., Kudo, T., Kusakabe, N., Hashimoto, J., Abe, L., Akiyama, E., Brandner, W., Brandt, T. D., Carson, J., Currie, T., Egner, S. E., Feldt, M., Goto, M., Guyon, O., Hayano, Y., Hayashi, M., Hayashi, S., Henning, T., Hodapp, K., Ishii, M., Iye, M., Janson, M., Kandori, R., Knapp, G. R., Kuzuhara, M., Kwon, J., Matsuo, T., Miyama, S., Morino, J., Moro-Martin, A., Nishimura, T., Pyo, T.-S., Serabyn, E., Suenaga, T., Suto, H., Suzuki, R., Takahashi, Y., Takato, N., Terada, H., Thalmann, C., Tomono, D., Turner, E. L., Watanabe, M., Wisniewski, J. P., Yamada, T., Takami, H., Usuda, T., Tamura, M., 2015, SEEDS Adaptive Optics Imaging of the Asymmetric Transition Disk Oph IRS 48 in Scattered Light, The Astrophysical Journal, Volume 798, Issue 2, article id. 132, 17 pp, DOI: 10.1088/0004-637X/798/2/132
23. Brandt, Timothy D.,… Guyon, O.,…Hayashi, M.,…Takato, N., ... Brandt, T. D., McElwain, M. W., Turner, E. L., Mede, K., Spiegel, D. S., Kuzuhara, M., Schlieder, J. E., Wisniewski, J. P., Abe, L., Biller, B., Brandner, W., Carson, J., Currie, T., Egner, S., Feldt, M., Golota, T., Goto, M., Grady, C. A., Guyon, O., Hashimoto, J., Hayano, Y., Hayashi, M., Hayashi, S., Henning, T., Hodapp, K. W., Inutsuka, S., Ishii, M., Iye, M., Janson, M., Kandori, R., Knapp, G. R., Kudo, T., Kusakabe, N., Kwon, J., Matsuo, T., Miyama, S., Morino, J.-I., Moro-Martín, A., Nishimura, T., Pyo, T.-S., Serabyn, E., Suto, H., Suzuki, R., Takami, M., Takato, N., Terada, H., Thalmann, C., Tomono, D., Watanabe, M., Yamada, T., Takami, H., Usuda, T., Tamura, M., 2014, A Statistical Analysis of SEEDS and Other High-contrast Exoplanet Surveys: Massive Planets or Low-mass Brown Dwarfs?, The Astrophysical Journal, Volume 794, Issue 2, article id. 159, 25 pp, DOI: 10.1088/0004-637X/794/2/159
24. Pyo, T.-S., Hayashi, M., Beck, T., Davis, C., Takami, M., 2014, [Fe II] Emissions Associated with the Young Interacting Binary UY Aurigae, The Astrophysical Journal, Volume 786, Issue 1, article id. 63, 8 pp, DOI: 10.1088/0004-637X/786/1/63
25. Brandt, T., Kuzuhara, M., McElwain, M., Schlieder, J., Wisniewski, J., Turner, E., Carson, J., Matsuo, T., Biller, B., Bonnefoy, M., Dressing, C., Janson, M., Knapp, G., Moro-Martín, A., Thalmann, C., Kudo, T., Kusakabe, N., Hashimoto, J., Abe, L., Brandner, W., Currie, T., Egner, S., Feldt, M., Golota, T., Goto, M., Grady, C., Guyon, O., Hayano, Y., Hayashi, M., Hayashi, S., Henning, T., Hodapp, K., Ishii, M., Iye, M., Kandori, R., Kwon, J., Mede, K., Miyama, S., Morino, J., Nishimura, T., Pyo, T.-S., Serabyn, E., Suenaga, T., Suto, H.,

Suzuki, R., Takami, M., Takahashi, Y., Takato, N., Terada, H., Tomono, D., Watanabe, M., Yamada, T., Takami, H., Usuda, T., Tamura, M., 2014, The Moving Group Targets of the SEEDS High-contrast Imaging Survey of Exoplanets and Disks: Results and Observations from the First Three Years, The Astrophysical Journal, Volume 786, Issue 1, article id. 1, 25 pp, DOI: 10.1088/0004-637X/786/1/1

26. Guyon, O., Hinz, P. H., Cady, E., Belikov, R., Martinache, F., 2013, High Performance Lyot and PIAA Coronagraphy for Arbitrarily shaped Telescope Apertures, The Astrophysical Journal, accepted for publication, (2013arXiv1305.6686G)
27. Guyon, O., Eisner, J. A., Angel, R., W., Neville, J., Bendek, E. A., Milster, T. D., Ammons, S. M., Shao, M., Shaklan, S., Levine, M., Nemati, B., Martinache, F., Pitman, J., Woodruff, R. A., Belikov, R., 2013, Simultaneous Exoplanet Characterization and Deep Wide-field Imaging with a Diffractive Pupil Telescope, The Astrophysical Journal, ApJ, 767, 11
28. Carson, J., Thalmann, C., Janson, M., Kozakis, T., Bonnefoy, M., Biller, B., Schlieder, J., Currie, T., McElwain, M., Goto, M., Henning, T., Brandner, W., Feldt, M., Kandori, R., Kuzuhara, M., Stevens, L., Wong, P., Gainey, K., Fukagawa, M., Kuwada, Y., Brandt, T., Kwon, J., Abe, L., Egner, S., Grady, C., Guyon, O., Hashimoto, J., Hayano, Y., Hayashi, M., Hayashi, S., Hodapp, K., Ishii, M., Iye, M., Knapp, G., Kudo, T., Kusakabe, N., Matsuo, T., Miyama, S., Morino, J., Moro-Martin, A., Nishimura, T., Pyo, T., Serabyn, E., Suto, H., Suzuki, R., Takami, M., Takato, N., Terada, H., Tomono, D., Turner, E., Watanabe, M., Wisniewski, J., Yamada, T., Takami, H., Usuda, T., Tamura, M., 2013, Direct Imaging Discovery of a "Super-Jupiter" around the Late B-type Star κ And, Astrophys. J., Letter, 76, L32, DOI: 10.1088/2041-8205/763/2/L32
29. Thalmann, C., Janson, M., Buenzli, E., Brandt, T. D., Wisniewski, J. P., Dominik, C., Carson, J., McElwain, M. W., Currie, T., Knapp, G. R., Moro-Martín, A., Usuda, T., Abe, L., Brandner, W., Egner, S., Feldt, M., Golota, T., Goto, M., Guyon, O., Hashimoto, J., Hayano, Y., Hayashi, M., Hayashi, S., Henning, T., Hodapp, K. W., Ishii, M., Iye, M., Kandori, R., Kudo, T., Kusakabe, N., Kuzuhara, M., Kwon, J., Matsuo, T., Mayama, S., Miyama, S., Morino, J.-I., Nishimura, T., Pyo, T.-S., Serabyn, E., Suto, H., Suzuki, R., Takami, M., Takato, N., Terada, H., Tomono, D., Turner, E. L., Watanabe, M., Yamada, T., Takami, H., Tamura, M., 2013, Imaging Discovery of the Debris Disk around HIP 79977, Astrophys. J., Letters, 763, L29, DOI: 10.1088/2041-8205/763/2/L29
30. Grady, C. A., Muto, T., Hashimoto, J., Fukagawa, M., Currie, T., Biller, B., Thalmann, C., Sitko, M. L., Russell, R., Wisniewski, J., Dong, R., Kwon, J., Sai, S., Hornbeck, J., Schneider, G., Hines, D., Moro Martín, A., Feldt, M., Henning, T., Pott, J.-U., Bonnefoy, M., Bouwman, J., Lacour, S., Mueller, A., Juhász, A., Crida, A., Chauvin, G., Andrews, S., Wilner, D., Kraus, A., Dahm, S., Robitaille, T., Jang-Condell, H., Abe, L., Akiyama, E., Brandner, W., Brandt, T., Carson, J., Egner, S., Follette, K. B., Goto, M., Guyon, O., Hayano, Y., Hayashi, M., Hayashi, S., Hodapp, K., Ishii, M., Iye, M., Janson, M., Kandori, R., Knapp, G., Kudo, T., Kusakabe, N., Kuzuhara, M., Mayama, S., McElwain, M., Matsuo, T., Miyama, S., Morino, J.-I., Nishimura, T., Pyo, T.-S., Serabyn, G., Suto, H., Suzuki, R., Takami, M., Takato, N., Terada, H., Tomono, D., Turner, E., Watanabe, M., Yamada, T., Takami, H., Usuda, T., Tamura, M., 2013, Spiral Arms in the Asymmetrically Illuminated Disk of MWC 758 and Constraints on Giant Planets, Astrophys. J., 762, 48, DOI: 10.1088/0004-637X/762/1/48
31. Shimonishi, T. ... Sakon, I. ... v, 2013, AKARI Infrared Camera Survey of the Large Magellanic Cloud. II. The Near-infrared Spectroscopic Catalog, Astron. J., 145, 2, DOI:

10.1088/0004-6256/145/2/32
32. Street, R. A., Choi, J.-Y., Tsapras, Y., Han, C., Furusawa, K., Hundertmark, M., Gould, A., Sumi, T., Bond, I. A., Wouters, D., Zellem, R., Udalski, A., RoboNet Collaboration, Snodgrass, C., Horne, K., Dominik, M., Browne, P., Kains, N., Bramich, D. M., Bajek, D., Steele, I. A., Ipatov, S., MOA Collaboration, Abe, F., Bennett, D. P., Botzler, C. S., Chote, P., Freeman, M., Fukui, A., Harris, P., Itow, Y., Ling, C. H., Masuda, K., Matsubara, Y., Miyake, N., Muraki, Y., Nagayama, T., Nishimaya, S., Ohnishi, K., Rattenbury, N., Saito, To., Sullivan, D. J., Suzuki, D., Sweatman, W. L., Tristram, P. J., Wada, K., Yock, P. C. M., OGLE Collaboration, Szymański, M. K., Kubiak, M., Pietrzyński, G., Soszyński, I., Poleski, R., Ulaczyk, K., Wyrzykowski, Ł., µFUN Collaboration, Yee, J., Dong, S., Shin, I.-G., Lee, C.-U., Skowron, J., De Almeida, L. Andrade, DePoy, D. L., Gaudi, B. S., Hung, L.-W., Jablonski, F., Kaspi, S., Klein, N., Hwang, K.-H., Koo, J.-R., Maoz, D., Muñoz, J. A., Pogge, R. W., Polishhook, D., Shporer, A., McCormick, J., Christie, G., Natusch, T., Allen, B., Drummond, J., Moorhouse, D., Thornley, G., Knowler, M., Bos, M., Bolt, G., PLANET Collaboration, Beaulieu, J.-P., Albrow, M. D., Batista, V., Brillant, S., Caldwell, J. A. R., Cassan, A., Cole, A., Corrales, E., Coutures, Ch., Dieters, S., Dominis Prester, D., Donatowicz, J., Fouqué, P., Bachelet, E., Greenhill, J., Kane, S. R., Kubas, D., Marquette, J.-B., Martin, R., Menzies, J., Pollard, K. R., Sahu, K. C., Wambsganss, J., Williams, A., Zub, M., MiNDSTEp, Alsubai, K. A., Bozza, V., Burgdorf, M. J., Calchi Novati, S., Dodds, P., Dreizler, S., Finet, F., Gerner, T., Hardis, S., Harpsøe, K., Hessman, F., Hinse, T. C., Jørgensen, U. G., Kerins, E., Liebig, C., Mancini, L., Mathiasen, M., Penny, M. T., Proft, S., Rahvar, S., Ricci, D., Scarpetta, G., Schäfer, S., Schönebeck, F., Southworth, J., Surdej, J., 2013, MOA-2010-BLG-073L: An M-dwarf with a Substellar Companion at the Planet/Brown Dwarf Boundary, Astrophys. J., 763, 67
33. Bensby, T., Yee, J. C., Feltzing, S., Johnson, J. A., Gould, A., Cohen, J. G., Asplund, M., Meléndez, J., Lucatello, S., Han, C., Thompson, I., Gal-Yam, A., Udalski, A., Bennett, D. P., Bond, I. A., Kohei, W., Sumi, T., Suzuki, D., Suzuki, K., Takino, S., Tristram, P., Yamai, N., Yonehara, A., 2013, Chemical evolution of the Galactic bulge as traced by microlensed dwarf and subgiant stars. V. Evidence for a wide age distribution and a complex MDF, Astron & Astrophys, 549, A147, DOI: 10.1051/0004-6361/201220678
34. Mayama, S., Hashimoto, J., Muto, T., Tsukagoshi, T., Kusakabe, N., Kuzuhara, M., Takahashi, Y., Kudo, T., Dong, R., Fukagawa, M., Takami, M., Momose, M., Wisniewski, J. P., Follette, K., Abe, L., Akiyama, E., Brandner, W., Brandt, T., Carson, J., Egner, S., Feldt, M., Goto, M., Grady, C. A., Guyon, O., Hayano, Y., Hayashi, M., Hayashi, S., Henning, T., Hodapp, K. W., Ishii, M., Iye, M., Janson, M., Kandori, R., Kwon, J., Knapp, G. R., Matsuo, T., McElwain, M. W., Miyama, S., Morino, J.-I., Moro-Martin, A., Nishimura, T., Pyo, T.-S., Serabyn, E., Suto, H., Suzuki, R., Takato, N., Terada, H., Thalmann, C., Tomono, D., Turner, E. L., Watanabe, M., Yamada, T., Takami, H., Usuda, T., Tamura, M., 2012, Subaru Imaging of Asymmetric Features in a Transitional Disk in Upper Scorpius, Astrophys. J., Letters, 760, L26, DOI: 10.1088/2041-8205/760/2/L26
35. Dong, R., Hashimoto, J., Rafikov, R., Zhu, Z., Whitney, B., Kudo, T., Muto, T., Brandt, T., McClure, M. K., Wisniewski, J., Abe, L., Brandner, W., Carson, J., Egner, S., Feldt, M., Goto, M., Grady, C., Guyon, O., Hayano, Y., Hayashi, M., Hayashi, S., Henning, T., Hodapp, K. W., Ishii, M., Iye, M., Janson, M., Kandori, R., Knapp, G. R., Kusakabe, N., Kuzuhara, M., Kwon, J., Matsuo, T., McElwain, M., Miyama, S., Morino, J.-I., Moro-Martin, A., Nishimura, T., Pyo, T.-S., Serabyn, E., Suto, H., Suzuki, R., Takami, M.,

Takato, N., Terada, H., Thalmann, C., Tomono, D., Turner, E., Watanabe, M., Yamada, T., Takami, H., Usuda, T., Tamura, M., 2012, The Structure of Pre-transitional Protoplanetary Disks. I. Radiative Transfer Modeling of the Disk+Cavity in the PDS 70 System, Astrophys. J., 760, 111

36. Hashimoto, J., Dong, R., Kudo, T., Honda, M., McClure, M. K., Zhu, Z., Muto, T., Wisniewski, J., Abe, L., Brandner, W., Brandt, T., Carson, J., Egner, S., Feldt, M., Fukagawa, M., Goto, M., Grady, C. A., Guyon, O., Hayano, Y., Hayashi, M., Hayashi, S., Henning, T., Hodapp, K., Ishii, M., Iye, M., Janson, M., Kandori, R., Knapp, G., Kusakabe, N., Kuzuhara, M., Kwon, J., Matsuo, T., Mayama, S., McElwain, M. W., Miyama, S., Morino, J.-I., Moro-Martin, A., Nishimura, T., Pyo, T.-S., Serabyn, G., Suenaga, T., Suto, H., Suzuki, R., Takahashi, Y., Takami, M., Takato, N., Terada, H., Thalmann, C., Tomono, D., Turner, E. L., Watanabe, M., Yamada, T., Takami, H., Usuda, T., Tamura, M., 2012, Polarimetric Imaging of Large Cavity Structures in the Pre-transitional Protoplanetary Disk around PDS 70: Observations of the Disk, Astrophys. J., Letters, 758, L19, DOI: 10.1088/2041-8205/758/1/L19
37. Kusakabe, N., Grady, C. A., Sitko, M. L., Hashimoto, J., Kudo, T., Fukagawa, M., Muto, T., Wisniewski, J. P., Min, M., Mayama, S., Werren, C., Day, A. N., Beerman, L. C., Lynch, D. K., Russell, R. W., Brafford, S. M., Kuzuhara, M., Brandt, T. D., Abe, L., Brandner, W., Carson, J., Egner, S., Feldt, M., Goto, M., Guyon, O., Hayano, Y., Hayashi, M., Hayashi, S. S., Henning, T., Hodapp, K. W., Ishii, M., Iye, M., Janson, M., Kandori, R., Knapp, G. R., Matsuo, T., McElwain, M. W., Miyama, S., Morino, J.-I., Moro-Martin, A., Nishimura, T., Pyo, T.-S., Suto, H., Suzuki, R., Takami, M., Takato, N., Terada, H., Thalmann, C., Tomono, D., Turner, E. L., Watanabe, M., Yamada, T., Takami, H., Usuda, T., Tamura, M., 2012, High-contrast Near-infrared Polarization Imaging of MWC480, Astrophys. J., 753, 153, DOI: 10.1088/0004-637X/753/2/153
38. Muto, T., Grady, C. A., Hashimoto, J., Fukagawa, M., Hornbeck, J. B., Sitko, M., Russell, R., Werren, C., Curé, M., Currie, T., Ohashi, N., Okamoto, Y., Momose, M., Honda, M., Inutsuka, S., Takeuchi, T., Dong, R., Abe, L., Brandner, W., Brandt, T., Carson, J., Egner, S., Feldt, M., Fukue, T., Goto, M., Guyon, O., Hayano, Y., Hayashi, M., Hayashi, S., Henning, T., Hodapp, K. W., Ishii, M., Iye, M., Janson, M., Kandori, R., Knapp, G. R., Kudo, T., Kusakabe, N., Kuzuhara, M., Matsuo, T., Mayama, S., McElwain, M. W., Miyama, S., Morino, J.-I., Moro-Martin, A., Nishimura, T., Pyo, T.-S., Serabyn, E., Suto, H., Suzuki, R., Takami, M., Takato, N., Terada, H., Thalmann, C., Tomono, D., Turner, E. L., Watanabe, M., Wisniewski, J. P., Yamada, T., Takami, H., Usuda, T., Tamura, M., 2012, Discovery of Small-scale Spiral Structures in the Disk of SAO 206462 (HD 135344B): Implications for the Physical State of the Disk from Spiral Density Wave Theory, Astrophys. J., Letters, 748, L22, DOI: 10.1088/2041-8205/748/2/L22
39. Sasada, M., Uemura, M., Fukazawa, Y., Kawabata, K., Itoh, R., Sakon, I., Fujisawa, K., Kadota, A., Ohsugi, T., Yoshida, M., Yasuda, H., Yamanaka, M., Sato, S., Kino, M., 2012, Multi-Wavelength Photometric and Polarimetric Observations of the Outburst of 3C 454.3 in 2009 December, Publications of the Astronomical Society of Japan, 64, 58
40. Martinache, F., Guyon, O., Clergeon, C., Blain, C., 2012, Speckle Control with a Remapped-Pupil PIAA Coronagraph Publications of the Astronomical Society of the Pacific, 124, 1288-1294
41. Boccaletti, A., Schneider, J., Traub, W., Lagage, P., Stam, D., Gratton, R., Trauger, J., Cahoy, K., Snik, F., Baudoz, P., Galicher, R., Reess, J., Mawet, D., Augereau, J., Patience,

J., Kuchner, M., Wyatt, M., Pantin, E., Maire, A., Vérinaud, C., Ronayette, S., Dubreuil, D., Min, M., Rodenhuis, M., Mesa, D., Belikov, R., Guyon, O., Tamura, M., Murakami, N., Beerer, Ingrid M. 2012, SPICES: spectro-polarimetric imaging and characterization of exoplanetary systems. From planetary disks to nearby Super Earths, Experimental Astronomy, 34, 355-384, DOI: 10.1007/ s10686-012-9290-5

42. Kawahara, H., Matsuo, T., Takami, M., Fujii, Y., Kotani, T., Murakami, N., Tamura, M., Guyon, O., 2012, Can Ground-based Telescopes Detect the Oxygen 1.27 μm Absorption Feature as a Biomarker in Exoplanets? Astrophys. J., 758, 113
43. Garrel, V., Guyon, O., Baudoz, P.A., 2012, Highly Efficient Lucky Imaging Algorithm: Image Synthesis Based on Fourier Amplitude Selection, Pub. of the Astron. Soc. of the Pacific, 124, 918, 861-867
44. Guyon, O., Bendek, E., Eisner, J., Angel, R., Woolf, N., Milster, T., Ammons, S., Shao, M., Shaklan, S., Levine, M., Nemati, B., Pitman, J., Woodruff, R., Belikov, R., 2012, High-precision Astrometry with a Diffractive Pupil Telescope, Astrophys. J., Supplement, 200, 1, DOI: 10.1088/0067-0049/200/2/11
45. Dong, R., Rafikov, R., Zhu, Z., Hartmann, L., Whitney, B., Brandt, T., Muto, T., Hashimoto, J., Grady, C., Follette, K., Kuzuhara, M., Tanii, R., Itoh, Y., Thalmann, C., Wisniewski, J., Mayama, S., Janson, M., Abe, L., Brandner, W., Carson, J., Egner, S., Feldt, M., Goto, M., Guyon, O., Hayano, Y., Hayashi, M., Hayashi, S., Henning, T., Hodapp, K., Honda, M., Inutsuka, S., Ishii, M., Iye, M., Kandori, R., Knapp, G., Kudo, T., Kusakabe, N., Matsuo, T., McElwain, M., Miyama, S., Morino, J., Moro-Martin, A., Nishimura, T., Pyo, T.-S., Suto, H., Suzuki, R., Takami, M., Takato, N., Terada, H., Tomono, D., Turner, E., Watanabe, M., Yamada, T., Takami, H., Usuda, T., Tamura, M., 2012, The Missing Cavities in the SEEDS Polarized Scattered Light Images of Transitional Protoplanetary Disks: A Generic Disk Model, Aatrophys. J., 750, 161
46. Bachelet, E., Fouqué, P., Han, C., Gould, A., Albrow, M., Beaulieu, J., Bertin, E., Bond, I., Christie, G., Heyrovský, D., Horne, K., Jørgensen, U., Maoz, D., Mathiasen, M., Matsunaga, N., McCormick, J., Menzies, J., Nataf, D., Natusch, T., Oi, N., Renon, N., Tsapras, Y., Udalski, A., Yee, J., Batista, V., Bennett, D., Brillant, S., Caldwell, J., Cassan, A., Cole, A., Cook, K., Coutures, C., Dieters, S., Dominik, M., Dominis Prester, D., Donatowicz, J., Greenhill, J., Kains, N., Kane, S., Marquette, J., Martin, R., Pollard, K., Sahu, K., Street, R., Wambsganss, J., Williams, A., Zub, M., PLANET Collaboration, Bos, M., Dong, S., Drummond, J., Gaudi, B., Graff, D., Janczak, J., Kaspi, S., Kozłowski, S., Lee, C., Monard, L., Muñoz, J., Park, B., Pogge, R., Polishook, D., Shporer, A., Fun Collaboration, Abe, F., Botzler, C., Fukui, A., Furusawa, K., Hearnshaw, J., Itow, Y., Korpela, A., Ling, C., Masuda, K., Matsubara, Y., Miyake, N., Muraki, Y., Ohnishi, K., Rattenbury, N., Saito, T., Sullivan, D., Sumi, T., Suzuki, D., Sweatman, W., Tristram, P., Wada, K., Moa Collaboration, Allan, A., Bode, M., Bramich, D., Clay, N., Fraser, S., Hawkins, E., Kerins, E., Lister, T., Mottram, C., Saunders, E., Snodgrass, C., Steele, I., Wheatley, P., Robonet-Ii Collaboration, Bozza, V., Browne, P., Burgdorf, M., Calchi Novati, S., Dreizler, S., Finet, F., Glitrup, M., Grundahl, F., HarpsøE, K., Hessman, F., Hinse, T., Hundertmark, M., Liebig, C., Maier, G., Mancini, L., Rahvar, S., Ricci, D., Scarpetta, G., Skottfelt, J., Southworth, J., Surdej, J., Zimmer, F., Mindstep Consortium 2012, A brown dwarf orbiting an M-dwarf: MOA 2009-BLG-411L, Astron & Astrophys., 547, A55, DOI: 10.1051/0004-6361/201219765
47. Bennett, D. P., Sumi, T., Bond, I. A., Kamiya, K., Abe, F., Botzler, C. S., Fukui, A.,

Furusawa, K., Itow, Y., Korpela, A. V., Kilmartin, P. M., Ling, C. H., Masuda, K., Matsubara, Y., Miyake, N., Muraki, Y., Ohnishi, K., Rattenbury, N. J., Saito, To., Sullivan, D. J., Suzuki, D., Sweatman, W. L., Tristram, P. J., Wada, K., Yock, P. C. M., MOA Collaboration, 2012, Planetary and Other Short Binary Microlensing Events from the MOA Short-event Analysis Astrophys. J., 757, 19, DOI: 10.1088/0004-637X/757/2/119

48. Choi, J.-Y., Shin, I.-G., Han, C., Udalski, A., Sumi, T., Gould, A., Bozza, V., Dominik, M., Fouqué, P., Horne, K., Szymański, M. K., Kubiak, M., Soszyński, I., Pietrzyński, G., Poleski, R., Ulaczyk, K., Pietrukowicz, P., Kozłowski, S., Skowron, J., Wyrzykowski, Ł., OGLE Collaboration, Abe, F., Bennett, D. P., Bond, I. A., Botzler, C. S., Chote, P., Freeman, M., Fukui, A., Furusawa, K., Itow, Y., Kobara, S., Ling, C. H., Masuda, K., Matsubara, Y., Miyake, N., Muraki, Y., Ohmori, K., Ohnishi, K., Rattenbury, N. J., Saito, To., Sullivan, D. J., Suzuki, D., Suzuki, K., Sweatman, W. L., Takino, S., Tristram, P. J., Wada, K., Yock, P. C. M., MOA Collaboration, Bramich, D. M., Snodgrass, C., Steele, I. A., Street, R. A., Tsapras, Y., RoboNet Collaboration, Alsubai, K. A., Browne, P., Burgdorf, M. J., Calchi Novati, S., Dodds, P., Dreizler, S., Fang, X.-S., Grundahl, F., Gu, C.-H., Hardis, S., Harpsøe, K., Hinse, T. C., Hornstrup, A., Hundertmark, M., Jessen-Hansen, J., Jørgensen, U. G., Kains, N., Kerins, E., Liebig, C., Lund, M., Lunkkvist, M., Mancini, L., Mathiasen, M., Penny, M. T., Rahvar, S., Ricci, D., Scarpetta, G., Skottfelt, J., Southworth, J., Surdej, J., Tregloan-Reed, J., Wambsganss, J., Wertz, O., MiNDSTEp Consortium, Almeida, L. A., Batista, V., Christie, G., DePoy, D. L., Dong, Subo, Gaudi, B. S., Henderson, C., Jablonski, F., Lee, C.-U., McCormick, J., McGregor, D., Moorhouse, D., Natusch, T., Ngan, H., Pogge, R. W., Tan, T.-G., Thornley, G., Yee, J. C., µFUN Collaboration, Albrow, M. D., Bachelet, E., Beaulieu, J.-P., Brillant, S., Cassan, A., Cole, A. A., Corrales, E., Coutures, C., Dieters, S., Dominis Prester, D., Donatowicz, J., Greenhill, J., Kubas, D., Marquette, J.-B., Menzies, J. W., Sahu, K. C., Zub, M., PLANET Collaboration, 2012, A New Type of Ambiguity in the Planet and Binary Interpretations of Central Perturbations of High-magnification Gravitational Microlensing Events, Astrophys. J., 756, 48, DOI: 10.1088/0004-637X/756/1/48

49. Bozza, V., Dominik, M., Rattenbury, N. J., Jørgensen, U. G., Tsapras, Y., Bramich, D. M., Udalski, A., Bond, I. A., Liebig, C., Cassan, A., Fouqué, P., Fukui, A., Hundertmark, M., Shin, I.-G., Lee, S. H., Choi, J.-Y., Park, S.-Y., Gould, A., Allan, A., Mao, S., Wyrzykowski, Ł., Street, R. A., Buckley, D., Nagayama, T., Mathiasen, M., Hinse, T. C., Novati, S. Calchi, Harpsøe, K., Mancini, L., Scarpetta, G., Anguita, T., Burgdorf, M. J., Horne, K., Hornstrup, A., Kains, N., Kerins, E., Kjærgaard, P., Masi, G., Rahvar, S., Ricci, D., Snodgrass, C., Southworth, J., Steele, I. A., Surdej, J., Thöne, C. C., Wambsganss, J., Zub, M., Albrow, M. D., Batista, V., Beaulieu, J.-P., Bennett, D. P., Caldwell, J. A. R., Cole, A. A., Cook, K. H., Coutures, C., Dieters, S., Prester, D. Dominis, Donatowicz, J., Greenhill, J., Kane, S. R., Kubas, D., Marquette, J.-B., Martin, R., Menzies, J., Pollard, K. R., Sahu, K. C., Williams, A., Szymański, M. K., Kubiak, M., Pietrzyński, G., Soszyński, I., Poleski, R., Ulaczyk, K., DePoy, D. L., Dong, Subo, Han, C., Janczak, J., Lee, C.-U., Pogge, R. W., Abe, F., Furusawa, K., Hearnshaw, J. B., Itow, Y., Kilmartin, P. M., Korpela, A. V., Lin, W., Ling, C. H., Masuda, K., Matsubara, Y., Miyake, N., Muraki, Y., Ohnishi, K., Perrott, Y. C., Saito, To., Skuljan, L., Sullivan, D. J., Sumi, T., Suzuki, D., Sweatman, W. L., Tristram, P. J., Wada, K., Yock, P. C. M., Gulbis, A., Hashimoto, Y., Kniazev, A., Vaisanen, P., 2012, OGLE-2008-BLG-510: first automated real-time detection of a weak microlensing anomaly - brown dwarf or stellar binary?, Mon. Not. R. Astron. Soc., 424,

902-918

50. Yee, J. C., Shvartzvald, Y., Gal-Yam, A., Bond, I. A., Udalski, A., Kozłowski, S., Han, C., Gould, A., Skowron, J., Suzuki, D., Abe, F., Bennett, D. P., Botzler, C. S., Chote, P., Freeman, M., Fukui, A., Furusawa, K., Itow, Y., Kobara, S., Ling, C. H., Masuda, K., Matsubara, Y., Miyake, N., Muraki, Y., Ohmori, K., Ohnishi, K., Rattenbury, N. J., Saito, To., Sullivan, D. J., Sumi, T., Suzuki, K., Sweatman, W. L., Takino, S., Tristram, P. J., Wada, K., MOA Collaboration, Szymański, M. K., Kubiak, M., Pietrzyński, G., Soszyński, I., Poleski, R., Ulaczyk, K., Wyrzykowski, Ł., Pietrukowicz, P., OGLE Collaboration, Allen, W., Almeida, L. A., Batista, V., Bos, M., Christie, G., DePoy, D. L., Dong, Subo, Drummond, J., Finkelman, I., Gaudi, B. S., Gorbikov, E., Henderson, C., Higgins, D., Jablonski, F., Kaspi, S., Manulis, I., Maoz, D., McCormick, J., McGregor, D., Monard, L. A. G., Moorhouse, D., Muñoz, J. A., Natusch, T., Ngan, H., Ofek, E., Pogge, R. W., Santallo, R., Tan, T.-G., Thornley, G., Shin, I.-G., Choi, J.-Y., Park, S.-Y., Lee, C.-U., Koo, J.-R., μFUN Collaboration, 2012, MOA-2011-BLG-293Lb: A Test of Pure Survey Microlensing Planet Detections, Astrophys. J., 755, 102, DOI: 10.1088/0004-637X/755/2/102
51. Bachelet, E., Shin, I.-G., Han, C., Fouqué, P., Gould, A., Menzies, J. W., Beaulieu, J.-P., Bennett, D. P., Bond, I. A., Dong, Subo, Heyrovský, D., Marquette, J.-B., Marshall, J., Skowron, J., Street, R. A., Sumi, T., Udalski, A., Abe, L., Agabi, K., Albrow, M. D., Allen, W., Bertin, E., Bos, M., Bramich, D. M., Chavez, J., Christie, G. W., Cole, A. A., Crouzet, N., Dieters, S., Dominik, M., Drummond, J., Greenhill, J., Guillot, T., Henderson, C. B., Hessman, F. V., Horne, K., Hundertmark, M., Johnson, J. A., Jørgensen, U. G., Kandori, R., Liebig, C., Mékarnia, D., McCormick, J., Moorhouse, D., Nagayama, T., Nataf, D., Natusch, T., Nishiyama, S., Rivet, J.-P., Sahu, K. C., Shvartzvald, Y., Thornley, G., Tomczak, A. R., Tsapras, Y., Yee, J. C., Batista, V., Bennett, C. S., Brillant, S., Caldwell, J. A. R., Cassan, A., Corrales, E., Coutures, C., Dominis Prester, D., Donatowicz, J., Kubas, D., Martin, R., Williams, A., Zub, M., PLANET Collaboration, de Almeida, L. Andrade, DePoy, D. L., Gaudi, B. S., Hung, L.-W., Jablonski, F., Kaspi, S., Klein, N., Lee, C.-U., Lee, Y., Koo, J.-R., Maoz, D., Muñoz, J. A., Pogge, R. W., Polishook, D., Shporer, A., μFUN Collaboration, Abe, F., Botzler, C. S., Chote, P., Freeman, M., Fukui, A., Furusawa, K., Harris, P., Itow, Y., Kobara, S., Ling, C. H., Masuda, K., Matsubara, Y., Miyake, N., Ohmori, K., Ohnishi, K., Rattenbury, N. J., Saito, To., Sullivan, D. J., Suzuki, D., Sweatman, W. L., Tristram, P. J., Wada, K., Yock, P. C. M., MOA Collaboration, Szymański, M. K., Soszyński, I., Kubiak, M., Poleski, R., Ulaczyk, K., Pietrzyński, G., Wyrzykowski, Ł., OGLE Collaboration, Kains, N., Snodgrass, C., Steele, I. A., RoboNet Collaboration, Alsubai, K. A., Bozza, V., Browne, P., Burgdorf, M. J., Calchi Novati, S., Dodds, P., Dreizler, S., Finet, F., Gerner, T., Hardis, S., Harpsøe, K., Hinse, T. C., Kerins, E., Mancini, L., Mathiasen, M., Penny, M. T., Proft, S., Rahvar, S., Ricci, D., Scarpetta, G., Schäfer, S., Schönebeck, F., Southworth, J., Surdej, J., Wambsganss, J., MiNDSTEp Consortium, 2012, MOA 2010-BLG-477Lb: Constraining the Mass of a Microlensing Planet from Microlensing Parallax, Orbital Motion, and Detection of Blended Light, Astrophys. J., 754, 73, DOI: 10.1088/0004-637X/754/1/73
52. Kubas, D., Beaulieu, J. P., Bennett, D. P., Cassan, A., Cole, A., Lunine, J., Marquette, J. B., Dong, S., Gould, A., Sumi, T., Batista, V., Fouqué, P., Brillant, S., Dieters, S., Coutures, C., Greenhill, J., Bond, I., Nagayama, T., Udalski, A., Pompei, E., Nürnberger, D. E. A., Le Bouquin, J. B., 2012, A frozen super-Earth orbiting a star at the bottom of the main

sequence, Astron & Astrophys, 540, A78, DOI: 10.1051/0004-6361/201015832
53. Cassan, A., Kubas, D., Beaulieu, J.-P., Dominik, M., Horne, K., Greenhill, J., Wambsganss, J., Menzies, J., Williams, A., Jørgensen, U. G., Udalski, A., Bennett, D. P., Albrow, M. D., Batista, V., Brillant, S., Caldwell, J. A. R., Cole, A., Coutures, Ch., Cook, K. H., Dieters, S., Prester, D. Dominis, Donatowicz, J., Fouqué, P., Hill, K., Kains, N., Kane, S., Marquette, J.-B., Martin, R., Pollard, K. R., Sahu, K. C., Vinter, C., Warren, D., Watson, B., Zub, M., Sumi, T., Szymański, M. K., Kubiak, M., Poleski, R., Soszynski, I., Ulaczyk, K., Pietrzyński, G., Wyrzykowski, Ł., 2012, One or more bound planets per Milky Way star from microlensing observations, Nature, 481, 7380, 167-169, DOI: 10.1038/nature10684
54. Kiriyama, Y., Ishihara, D., Nagayama, T., Kaneda, H., Oyabu, S., Onaka, T., Fujiwara, H., 2012, Debris Disks Explored by AKARI and IRSF, Publications of The Korean Astronomical Society, 27, 181-182, DOI: 10.5303/PKAS.2012.27.4.181
55. Honda, M., Maaskant, K., Okamoto, Y. K., Kataza, H., Fukagawa, M., Waters, L. B. F. M., Dominik, C., Tielens, A. G. G. M., Mulders, G. D., Min, M., Yamashita, T., Fujiyoshi, T., Miyata, T., Sako, S., Sakon, I., Fujiwara, H., Onaka, T., 2012, Mid-infrared Imaging of the Transitional Disk of HD 169142: Measuring the Size of the Gap, Astrophys. J., 752, 143, DOI: 10.1088/0004-637X/752/2/143
56. Thalmann, C., Janson, M., Buenzli, E., Brandt, T. D., Wisniewski, J. P., Moro-Martín, A., Usuda, T., Schneider, G., Carson, J., McElwain, M. W., Grady, C. A., Goto, M., Abe, L., Brandner, W., Dominik, C., Egner, S., Feldt, M., Fukue, T., Golota, T., Guyon, O., Hashimoto, J., Hayano, Y., Hayashi, M., Hayashi, S., Henning, T., Hodapp, K. W., Ishii, M., Iye, M., Kandori, R., Knapp, G. R., Kudo, T., Kusakabe, N., Kuzuhara, M., Matsuo, T., Miyama, S., Morino, J.-I., Nishimura, T., Pyo, T.-S., Serabyn, E., Suto, H., Suzuki, R., Takahashi, Y. H., Takami, M., Takato, N., Terada, H., Tomono, D., Turner, E. L., Watanabe, M., Yamada, T., Takami, H., Tamura, M., 2011, Images of the Extended Outer Regions of the Debris Ring around HR4796A, Astrophys. J., Letters, 743, L6-L6, DOI: 10.1088/2041-8205/743/1/L6

計画研究 A2: 系外惑星大気の数値モデリングと形成進化論

1. Massol, H., Hamano K., Tian F., Ikoma M., Abe, Y., Chassefière E., Davaille A., Genda H., Güdel M., Hori Y., Leblanc F., Marcq E., Sarda P., Shematovich, V. I., Stökl, A. and Lammer H., 2016, Formation and Evolution of Protoatmospheres, Space Science Reviews, 1-59. DOI: 10.1007/s11214-016-0280-1
2. Genda, H, Fujita, T., Kobayashi, H., Tanaka, H, and Abe, Y., 2015, Resolution dependence of disruptive collisions between planetesimals in the gravity regime, Icarus, Volume 262, p.58-56 DOI: 10.1016/j.icarus.2015.08.029
3. Kodama, T., Genda, H., Abe, Y., and Zahnle, K. J., 2015, Rapid Water Loss Can Extend the Lifetime of Planetary Habitability, The Astrophysical Journal, Volume 812, article id. 165, 11 pp. DOI:10.1088/0004-637X/812/2/165
4. Hamano, K., Kawahara, H., Abe, Y., Onishi, M., and Hashimoto, G.. L., 2015, Lifetime and Spectral Evolution of a Magma Ocean with a Steam Atmosphere: Its Detectability by Future Direct Imaging, The Astrophysical Journal, Volume 806, article id. 216, 17 pp. DOI: 10.1088/0004-637X/806/2/216
5. Iwagami, N., Hashimoto, G. L., Ohtsuki, S., Takagi, S., and Robert, S. 2015, Ground-based IR observation of oxygen isotope ratios in Venus's atmosphere, Planetary and Space Science, Volume 113, p. 292-297. DOI: 10.1016/j.pss.2014.10.004
6. Satoh, T., Ohtsuki, S., Iwagami, N., Ueno, M., Uemizu, K., Suzuki, M., Hashimoto, G., Sakanoi, T., Kasaba, Y., Nakamura, R., Imamura, T., Nakamura, M., Fukuhara, T., Yamazaki, A., Yamada, M., 2015, Venus' clouds as inferred from the phase curves acquired by IR1 and IR2 on board Akatsuki, Icarus, Volume 248, p. 213-220. DOI: 10.1016/j.icarus.2014.10.030
7. Harada, M., Tajika, E., and Sekine, Y., 2015, Transition to an oxygen-rich atmosphere with an extensive overshoot triggered by the Paleoproterozoic snowball Earth, Earth and Planetary Science Letters, Volume 419, p. 178-186. DOI: 10.1016/j.epsl.2015.03.005
8. Sekine, Y., T. Shibuya, F. Postberg, H-.W. Hsu, K. Suzuki, Y. Masaki, T., Kuwatani, M. Mori, P.K. Hong, M. Yoshizaki, S. Tachibana, S. Sirono, 2015, High-temperature water-rock interactions and hydrothermal environments in the chondrite-like core of Enceladus, Nature Communications, 6: 8604, 1-8, doi: 10.1038/ncomms9604.
9. Yamashita, T., Odaka, M., Sugiyama, K., Nakajima, K., Ishiwatari, M., Nishizawa, S., Takahashi, Y. O. and Hayashi, Y. 2016, A Numerical Study of Convection in a Condensing CO2Atmosphere under Early Mars-Like Conditions, Journal of the Atmospheric Sciences, 73, 4151-4169, doi:10.1175/JAS-D-15-0132.1
10. Matsui, H., Hayashi, Y. (16 番目), 他 35 名 2016, Performance benchmarks for a next generation numerical dynamo model, Geochemistry, Geophysics, Geosystem, 17, 1586-1607, doi:10.1002/2015GC006159
11. Nishizawa, S., Odaka, M., Takahashi, Y. O. Sugiyama, K. Nakajima, K., Ishiwatari, M., Takehiro, S., Yashiro, H., Sato, Y., Tomita, H. and Hayashi, Y., 2016, Martian dust devil statistics from high-resolution large-eddy simulations, Geophysical Research Letters, 43, 4180-4188, DOI:10.1002/2016GL068896
12. Noda, S., Ishiwatari, M., Nakajima, K., Takahashi, Y. O., Takehiro, S., Onishi, M., Hashimoto, G.. L., Kuramoto, K., and Hayashi, Y.-Y. 2017, The circulation pattern and day-night heat transport in the atmosphere of a synchronously rotating aquaplanet: Dependence on planetary rotation rate, Icarus, 282, 1-18, DOI: 10.1016/j.icarus.2016.09.004.
13. Genda, H, Fujita, T., Kobayashi, H., Tanaka, H, and Abe, Y., 2015, Resolution dependence of disruptive collisions between planetesimals in the gravity regime, Icarus, Volume 262,

p.58-56 DOI: 10.1016/j.icarus.2015.08.029
14. Kodama, T., Genda, H., Abe, Y., and Zahnle, K. J., 2015, Rapid Water Loss Can Extend the Lifetime of Planetary Habitability, The Astrophysical Journal, Volume 812, article id. 165, 11 pp. DOI: 10.1088/0004-637X/812/2/165
15. Hamano, K., Kawahara, H., Abe, Y., Onishi, M., and Hashimoto, G.. L., 2015, Lifetime and Spectral Evolution of a Magma Ocean with a Steam Atmosphere: Its Detectability by Future Direct Imaging, The Astrophysical Journal, Volume 806, article id. 216, 17 pp. DOI: 10.1088/0004-637X/806/2/216
16. Kamata, S., Sugita, S., Abe, Y., Ishihara, Y., Harada, Y., Morota, T., Namiki, N., Iwata, T., Hanada, H., Araki, H., Matsumoto, K., Tajika, E., Kuramoto, K., Nimmo, F., 2015, The relative timing of Lunar Magma Ocean solidification and the Late Heavy Bombardment inferred from highly degraded impact basin structures, Icarus, Volume 250, p. 492-503 DOI: 10.1016/j.icarus.2014.12.025
17. Iwagami, N., Hashimoto, G.. L., Ohtsuki, S., Takagi, S., and Robert, S. 2015, Ground-based IR observation of oxygen isotope ratios in Venus's atmosphere, Planetary and Space Science, Volume 113, p. 292-297. DOI: 10.1016/j.pss.2014.10.004
18. Satoh, T., Ohtsuki, S., Iwagami, N., Ueno, M., Uemizu, K., Suzuki, M., Hashimoto, G., Sakanoi, T., Kasaba, Y., Nakamura, R., Imamura, T., Nakamura, M., Fukuhara, T., Yamazaki, A., Yamada, M., 2015, Venus' clouds as inferred from the phase curves acquired by IR1 and IR2 on board Akatsuki, Icarus, Volume 248, p. 213-220. DOI: 10.1016/j.icarus.2014.10.030
19. Harada, M., Tajika, E., and Sekine, Y.., 2015, Transition to an oxygen-rich atmosphere with an extensive overshoot triggered by the Paleoproterozoic snowball Earth, Earth and Planetary Science Letters, Volume 419, p. 178-186. DOI: 10.1016/j.epsl.2015.03.005
20. Sekine, Y., T. Shibuya, F. Postberg, H-.W. Hsu, K. Suzuki, Y. Masaki, T., Kuwatani, M. Mori, P.K. Hong, M. Yoshizaki, S. Tachibana, S. Sirono, 2015, High-temperature water-rock interactions and hydrothermal environments in the chondrite-like core of Enceladus, Nature Communications, 6: 8604, 1-8, doi: 10.1038/ncomms9604.
21. Tsumura, K., Arimatsu, K., Egami, E., Hayano, Y., Honda, C., Kimura, J., Kuramoto, K., Matsuura, S., Minowa, Y., Nakajima, K., Nakamoto, T., Shirahata, M., Surace, J., Takahashi, Y., Wada, T., 2014, Near-infrared Brightness of the Galilean Satellites Eclipsed in Jovian Shadow: A New Technique to Investigate Jovian Upper Atmosphere, The Astrophysical Journal, Volume 789, Issue 2, p. 492-503 DOI: 10.1016/j.icarus.2014.12.025
22. Sugiyama, K., Nakajima, K., Odaka, M., Kuramoto, K., and Hayashi, Y.-Y. 2014, Numerical simulations of Jupiter's moist convection layer: Structure and dynamics in statistically steady states, Icarus, Volume 229, p. 71-91. DOI: 10.1016/j.icarus.2013.10.016
23. Sekine, Y., Genda, H., Muto, Y., Sugita, S., Kadono, T., and Matsui, T., Impact chemistry of methanol: Implications for volatile evolution on icy satellites and dwarf planets, and cometary delivery to the Moon, Icarus, Volume 243, p. 39-47. DOI: 10.1016/j.icarus.2014.08.034
24. Hamano, K., Abe, Y., and Genda, H., 2013, Emergence of two types of terrestrial planet on solidification of magma ocean, Nature, 497, 607–610 (筆頭著者は本計画研究 PD)
25. Kuramoto, K., Umemoto, T., and Ishiwatari, M., 2013, Effective hydrodynamic hydrogen escape from an early Earth atmosphere inferred from high-accuracy numerical simulation, Earth Planet. Sci. Lett., accepted for publication

26. Komatsu, G., Kumar, P.S., Goto, K., Sekine, Y., Giri, C., and Matsui T., 2013, Drainage systems of Lonar Cater, India: Contributions to Lonar Lake hydrology and crater degradation, Planet. Space Sci., accepted for publication
27. Sekine, Y., Takano, Y., Yano, H., Funase, R., Takai, K., Ishihara, M., Shibuya, T., Tachibana, S., Kuramoto, K., Yabuta, H., Kimura, J., and Furukawa, Y., 2013, Exploration of Enceladu' water-rich plumes toward understanding of chemistry and biology of the interior ocean, 29th Proc. of ISTS, accepted for publication
28. Ishiwatari, M., Toyoda, E., Morikawa, Y., Takehiro, S., Sasaki, Y., Nishizawa, S., Odaka, M., Otobe, N., Takahashi, Y. O., Nakajima, K., Horinouchi, T., Shiotani, M., Hayashi, Y. -Y. and Gtool development group, 2012, "Gtool5": a Fortran90 library of input/output interfaces for self-descriptive multi-dimensional numerical data, Geosci. Model Dev., 5, 449-455
29. Kamata, S., Sugita, S., and Abe, Y., 2012, A new spectral calculation scheme for long-term deformation of Maxwellian planetary bodies, J. Geophys.Res, 117, E02004
30. Matsui, H., Iwagami, N., Hosouchi, M., Ohtsuki, S., and Hashimoto, G. L., 2012, Latitudinal distribution of HDO abundance above Venus' clouds by ground-based 2.3 um spectroscopy, Icarus, 217, 610-614
31. Nakajima, K., Yamda, Y., Ishiwatari, M., and Hayashi, Y. -Y., 2012, Dependence of equatorial precipitation activity on the vertical profile of radiative cooling in an aqua-planet, Nagare Multimedia 2012
32. Sekine, Y., and Genda, H., 2012, Giant impacts in the Saturnian system: a possible origin of diversity in the inner mid-sized satellites, Planet. Space Sci. 63-64, 133-138,
33. Taguchi, M., Fukuhara, T., Futaguchi, M., Sato, M., Imamura, T., Mitsuyama, K., Nakamura, M., Ueno, M., Suzuki, M., Iwagami, N., and Hashimoto, G.. L., 2012, Characteristic features in Venus' nightside cloud-top temperature obtained by Akatsuki/LIR, Icarus, 219, 502-504
34. Ishimaru, R, Sekine, Y., Matsui, T., Mousis, O., 2011, Oxidizing proto-atmosphere on Titan: constraint from N2 formation by impact shock, Astrophys. J. Lett., 741, L10, 1-6
35. Sekine, Y., Suzuki, K., Senda, R., Goto, K.T., Tajika, E., Tada, R. Goto, K., Yamamoto, S., Ohkouchi, N., Ogawa, N.O., Maruoka, T., 2011, Osmium evidence for synchronicity between a rise of atmospheric oxygen and Palaeoproterozoic deglaciation, Nature Comm., 2:502, 1-6

計画研究 B1: 円盤から惑星へ

1. Konishi, M., Matsuo, T., Yamamoto, K., Samland, M., Sudo, J., Shibai, H., Itoh, Y., Fukagawa, M., Sumi, T., Kudo, T., Hashimoto, J., Kuzuhara, M., Kusakabe, N., Abe, L., Akiyama, E., Brandner, W., Brandt, T. D., Carson, J. C., Feldt, M., Goto, M., Grady, C. A., Guyon, O., Hayano, Y., Hayashi, M., Hayashi, S. S., Henning, T., Hodapp, K. W., Ishii, M., Iye, M., Janson, M., Kandori, R., Knapp, G. R., Kwon, J., McElwain, M. W., Mede, K., Miyama, S., Morino, J.-I., Moro-Mart´ın, A., Nishimura, T., Oh, D., Pyo, T.-S., Serabyn, E., Schlieder, J. E., Suenaga, T., Suto, H., Suzuki, R., Takahashi, Y. H., Takami, M., Takato, N., Terada, H., Thalmann, C., Turner, E. L., Watanabe, M., Wisniewski, J. P., Yamada, T., Takami, H., Usuda, T., & Tamura, M., 2016, "A substellar companion to Pleiades HII 3441", PASJ, Vol.68, 92 (doi: 10.1093/pasj/psw083)
2. Iino, T., Ohyama, H., Hirahara, Y., Takahashi, T., & Tuskagoshi, T., 2016, "Submillimeter Observation of Jupiter's Stratospheric Composition: Detection of Carbon Monosulfide (J=7-6) 19 Years After the Cometary Impact", AJ, Vol.152, 179 (doi: 10.3847/0004-6256/152/6/179)
3. Buragohain, M., Pathak, A., Sarre, P., Onaka, T., & Sakon, I., 2016, "Mid-infrared vibrational study of deuterium-containing PAH variants", Planetary and Space Science, Vol.133, 97 (doi: 10.1016/j.pss.2016.05.001)
4. Kataoka, A., Tuskagoshi, T., Momose, M., Nagai, H., Muto, T., Dullemond, C. P., Pohl, A., Fukagawa, M., Shibai, H., Hanawa, T., & Murakawa, K., 2016, "Submillimeter Polarization Observation of the Protoplanetary Disk around HD 142527", ApJL, Vol.831, L12 (doi: 10.3847/2041-8205/831/2/L12)
5. Walsh, C., Juh´asz, A., Meeus, G., Dent, W. R. F., Maud, L. T., Aikawa, Y., Millar, T. J., & Nomura, H., 2016, "ALMA Reveals the Anatomy of the mm-sized Dust and Molecular Gas in the HD 97048 Disk", ApJ, Vol.831, 200 (doi: 10.3847/0004-637X/831/2/200)
6. Imai, M., Sakai, N., Oya, Y., L´opez-Sepulcre, A., Watanabe, Y., Ceccarelli, C., Lefloch, B., Caux, E., Vastel, C., Kahane, C., Sakai, T., Hirota, T., Aikawa, Y., & Yamamoto, S., 2016, "Discovery of a Hot Corino in the Bok Globule B335", ApJL, Vol.830, L37 (doi: 10.3847/2041-8205/830/2/L37)
7. Tuskagoshi, T., Nomura, H., Muto, T., Kawabe, R., Ishimoto, D., Kanagawa, K. D., Okuzumi, S., Ida, S., Walsh, C., & Millar, T. J., 2016, "A Gap with a Deficit of Large Grains in the Protoplanetary Disk around TW Hya", ApJL, Vol.829, L35 (doi: 10.3847/2041-8205/829/2/L35)
8. Onaka, T., Mori, T., Sakon, I., & Ardaseva, A., 2016, "AKARI Near-infrared Spectroscopy of the Extended Green Object G318.05+0.09: Detection of CO Fundamental Ro-vibrational Emission", ApJ, Vol.829, 106 (doi: 10.3847/0004-637X/829/2/106)
9. Lomax, J. R., Wisniewski, J. P., Grady, C. A., McElwain, M. W., Hashimoto, J., Kudo, T., Kusakabe, N., Okamoto, Y. K., Fukagawa, M., Abe, L., Brandner, W., Brandt, T. D., Carson, J. C., Currie, T. M., Egner, S., Feldt, M., Goto, M., Guyon, O., Hayano, Y., Hayashi, M., Hayashi, S. S., Henning, T., Hodapp, K. W., Inoue, A., Ishii, M., Iye, M., Janson, M., Kandori, R., Knapp, G. R., Kuzuhara, M., Kwon, J., Matsuo, T., Mayama, S., Miyama, S., **, M**., Morino, J.-I., Moro-Martin, A., Nishimura, T., Pyo, T.-S., Schneider, G. H., Serabyn, E., Sitko, M. L., Suenaga, T., Suto, H., Suzuki, R., Takahashi, Y. H., Takami, M., Takato, N., Terada, H., Thalmann, C., Tomono, D., Turner, E. L., Watanabe, M., Yamada, T., Takami, H., Usuda, T., & Tamura, M., 2016, "Constraining the Movement of

the Spiral Features and the Locations of Planetary Bodies within the AB Aur System", ApJ, Vol.828, 2 (doi: 10.3847/0004-637X/828/1/2)

10. Tanaka, K. K., Tanak,H., Ang´elil, R., & Diemand, J., 2016, "Reply to "Comment on 'Simple improvements to classical bubble nucleation models'"", Physical Review E, Vol.94, 026802 (doi: 10.1103/PhysRevE.94.026802)
11. Ohta, Y., Fukagawa, M., Sitko, M. L., Muto, T., Kraus, S., Grady, C. A., Wisniewski, J. P., Swearingen, J. R., Shibai, H., Sumi, T., Hashimoto, J., Kudo, T., Kusakabe, N., Momose, M., Okamoto, Y., Kotani, T., Takami, M., Currie, T., Thalmann, C., Janson, M., Akiyama, E., Follette, K. B., Mayama, S., Abe, L., Brandner, W., Brandt, T. D., Carson, J. C., Egner, S. E., Feldt, M., Goto, M., Guyon, O., Hayano, Y., Hayashi, M., Hayashi, S. S., Henning, T., Hodapp, K. W., Ishii, M., Iye, M., Kandori, R., Knapp, G. R., Kuzuhara, M., Kwon, J., Matsuo, T., McElwain, M. W., Miyama, S., Morino, J.-I., Moro-Mart´ın, A., Nishimura, T., Pyo, T.-S., Serabyn, E., Suenaga, T., Suto, H., Suzuki, R., Takahashi, Y. H., Takami, H., Takato, N., Terada, H., Tomono, D., Turner, E. L., Usuda, T., Watanabe, M., Yamada, T., & Tamura, M., 2016, "Extreme asymmetry in the polarized disk of V1247 Orionis*", PASJ, Vol.68, 53 (doi: 10.1093/pasj/psw051)
12. Shimonishi, T., Onaka, T., Kawamura, A., & Aikawa, Y., 2016, "The Detection of a Hot Molecular Core in the Large Magellanic Cloud with ALMA", ApJ, Vol.827, 72 (doi: 10.3847/0004-637X/827/1/72)
13. Lin, S.-J., Shimajiri, Y., Hara, C., Lai, S.-P., Nakamura, F., Sugitani, K., Kawabe, R., Kitamura, Y., Yoshida, A., Tatei, H., Akashi, T., Higuchi, A. E., & Tuskagoshi, T., 2016, "The Intrinsic Abundance Ratio and X-factor of CO Isotopologues in L 1551 Shielded from FUV Photodissociation", ApJ, Vol.826, 193 (doi: 10.3847/0004-637X/826/2/193)
14. Ohsawa, R., Onaka, T., Sakon, I., Mori, T., Matsuura, M., Yamamura, I., & Kaneda, H., 2016, "Near-infrared views of dust in planetary nebulae: AKARI/IRC NIR spectral atlas of Galactic PNe", Journal of Physics Conference Series, Vol.728, 072010 (doi: 10.1088/1742-6596/728/7/072010)
15. Onaka, T., 2016, "Organic dust in galaxies", Journal of Physics Conference Series, Vol.728, 062001 (doi: 10.1088/1742-6596/728/6/062001)
16. Kanagawa, K. D., Muto, T., Tanak,H., Tanigawa, T., Takeuchi, T., Tuskagoshi, T., & Momose, M., 2016, "Mass constraint for a planet in a protoplanetary disk from the gap width", PASJ, Vol.68, 43 (doi: 10.1093/pasj/psw037)
17. Ono, T., Muto, T., Takeuchi, T., & Nomura, H., 2016, "Parametric Study of the Rossby Wave Instability in a Two-dimensional Barotropic Disk", ApJ, Vol.823, 84 (doi: 10.3847/0004-637X/823/2/84)
18. Tazaki, R., Tanak,H., Okuzumi, S., Kataoka, A., & Nomura, H., 2016, "Light Scattering by Fractal Dust Aggregates. I. Angular Dependence of Scattering", ApJ, Vol.823, 70 (doi: 10.3847/0004-637X/823/2/70)
19. Walsh,C., Loomis, R.A., Oberg, K.I., Kama, M., van't Hoff, M.L.R., Millar, T.J., Aikawa, Y., Herbst, E., Widicus Weaver, S. L., & Nomura, H., 2016, "First Detection of Gas-phase Methanol in a Protoplanetary Disk", ApJL, Vol.823, L10 (doi: 10.3847/2041-8205/823/1/L10)
20. Tanigawa, T., & Tanak,H., 2016, "Final Masses of Giant Planets. II. Jupiter Formation in a Gas-depleted Disk", ApJ, Vol.823, 48 (doi: 10.3847/0004-637X/823/1/48)
21. Yasui, C., Kobayashi, N., Saito, M., & Izumi, N., 2016, "Low-metallicity Young Clusters in the Outer Galaxy. II. Sh 2-208", AJ, Vol.151, 115 (doi: 10.3847/0004-6256/151/5/115)

22. Baba, S., Nakagawa, T., Shirahata, M., Isobe, N., Usui, F., Ohyama, Y., Onaka, T., Yano, K., & Kochi, C., 2016, "Revised wavelength and spectral response calibrations for AKARI near-infrared grism spectroscopy: Cryogenic phase", PASJ, Vol.68, 27 (doi: 10.1093/pasj/psw013)
23. Egusa, F., Usui, F., Murata, K., Yamashita, T., Yamamura, I., & Onaka, T., 2016, "Revised calibration for near- and mid-infrared images from ∼4000 pointed observations with AKARI/IRC", PASJ, Vol.68, 19 (doi: 10.1093/pasj/psv135)
24. Okuzumi, S., Momose, M., Sirono, S.-i., Kobayashi, H., & Tanak,H., 2016, "Sintering-induced Dust Ring Formation in Protoplanetary Disks: Application to the HL Tau Disk", ApJ, Vol.821, 82 (doi: 10.3847/0004-637X/821/2/82)
25. Liu, H. B., Lai, S.-P., Hasegawa, Y., Hirano, N., Rao, R., Li, I.-H., Fukagawa, M., Girart, J. M., Carrasco-Gonz´alez, C., & Rodr´ıguez, L. F., 2016, "Detection of Linearly Polarized 6.9 mm Continuum Emission from the Class 0 Young Stellar Object NGC 1333 IRAS4A", ApJ, Vol.821, 41 (doi: 10.3847/0004-637X/821/1/41)
26. Honda, M., Kudo, T., Takatsuki, S., Inoue, A. K., Nakamoto, T., Fukagawa, M., Tamura, M., Terada, H., & Takato, N., 2016, "Water Ice at the Surface of the HD 100546 Disk", ApJ, Vol.821, 2 (doi: 10.3847/0004-637X/821/1/2)
27. Sakai, N., Oya, Y., L´opez-Sepulcre, A., Watanabe, Y., Sakai, T., Hirota, T., Aikawa, Y., Ceccarelli, C., Lefloch, B., Caux, E., Vastel, C., Kahane, C., & Yamamoto, S., 2016, "Subarcsecond Analysis of the Infalling-Rotating Envelope around the Class I Protostar IRAS 04365+2535", ApJL, Vol.820, L34 (doi: 10.3847/2041-8205/820/2/L34)
28. Takami, M., Wei, Y.-J., Chou, M.-Y., Karr, J. L., Beck, T. L., Manset, N., Chen, W.-P., Kurosawa, R., Fukagawa, M., White, M., Galv´an-Madrid, R., Liu, H. B., Pyo, T.-S., & Donati, J.-F., 2016, "Stable and Unstable Regimes of Mass Accretion onto RW Aur A", ApJ, Vol.820, 139 (doi: 10.3847/0004-637X/820/2/139)
29. Ohsawa, R., Onaka, T., Sakon, I., Matsuura, M., & Kaneda, H., 2016, "AKARI/IRC Near-infrared Spectral Atlas of Galactic Planetary Nebulae", AJ, Vol.151, 93 (doi: 10.3847/0004-6256/151/4/93)
30. Sakatani, N., Ogawa, K., Iijima, Y.-i., Arakawa, M., & Tanaka, S., 2016, "Compressional stress effect on thermal conductivity of powdered materials: Measurements and their implication to lunar regolith", Icarus, Vol.267, 1 (doi: 10.1016/j.icarus.2015.12.012)
31. Kataoka, A., Muto, T., Momose, M., Tuskagoshi, T., & Dullemond, C. P., 2016, "Grain Size Constraints on HL Tau with Polarization Signature", ApJ, Vol.820, 54 (doi: 10.3847/0004-637X/820/1/54)
32. Currie, T., Grady, C. A., Cloutier, R., Konishi, M., Stassun, K., Debes, J., van der Marel, N., Muto, T., Jayawardhana, R., & Ratzka, T., 2016, "The Matryoshka Disk: Keck/NIRC2 Discovery of a Solar-system-scale, Radially Segregated Residual Protoplanetary Disk around HD 141569A", ApJL, Vol.819, L26 (doi: 10.3847/2041-8205/819/2/L26)
33. Nomura, H., Tuskagoshi, T., Kawabe, R., Ishimoto, D., Okuzumi, S., Muto, T., Kanagawa, K., D., Ida, S., Walsh, C., Millar, T. J., & Bai, X.-N., 2016, "ALMA Observations of a Gap and a Ring in the Protoplanetary Disk around TW Hya", ApJL, Vol.819, L7 (doi: 10.3847/2041-8205/819/1/L7)
34. Kondo, T., Ishihara, D., Kaneda, H., Nakamichi, K., Takaba, S., Kobayashi, H., Ootsubo, T., Pyo, J., & Onaka, T., 2016, "Modeling of the Zodiacal Emission for the AKARI/IRC

Mid-infrared All-sky Diffuse Maps", AJ, Vol.151, 71 (doi: 10.3847/0004-6256/151/3/71)
35. Yasui, C., Kobayashi, N., Tokunaga, A. T., Saito, M., & Izumi, N., 2016, "Low-metallicity Young Clusters in the Outer Galaxy. I. Sh 2-207", AJ, Vol.151, 50 (doi: 10.3847/0004-6256/151/3/50)
36. Liu, H. B., Takami, M., Kudo, T., Hashimoto, J., Dong, R., Vorobyov, E. I., Pyo, T.-S., Fukagawa, M., Tamura, M., Henning, T., Dunham, M. M., Karr, J. L., Kusakabe, N., & Tsuribe, T., 2016, "Circumstellar disks of the most vigorously accreting young stars", Science Advances, Vol.2, e1500875 (doi: 10.1126/sciadv.1500875)
37. Iino, T., Hirahara, Y., Hidemori, T., Tuskagoshi, T., Nakajima, T., Nakamoto, S., & Kato, C., 2016, "Observational constraint on Pluto's atmospheric CO with ASTE", PASJ, Vol.68, L1 (doi: 10.1093/pasj/psv120)
38. Yasui, C., Kobayashi, N., Hamano, S., Kondo, S., Izumi, N., Saito, M., & Tokunaga, A. T., 2016, "Herbig Ae/Be Candidate Stars in the Innermost Galactic Disk: Quartet Cluster", ApJ, Vol.817, 181 (doi: 10.3847/0004-637X/817/2/181)
39. Sakon, I., Sako, S., Onaka, T., Nozawa, T., Kimura, Y., Fujiyoshi, T., Shimonishi, T., Usui, F., Takahashi, H., Ohsawa, R., Arai, A., Uemura, M., Nagayama, T., Koo, B.-C., & Kozasa, T., 2016, "Concurrent Formation of Carbon and Silicate Dust in Nova V1280 Sco", ApJ, Vol.817, 145 (doi: 10.3847/0004-637X/817/2/145)
40. Kobayashi, H., Tanak,H., & Okuzumi, S., 2016, "From Planetesimals to Planets in Turbulent Protoplanetary Disks. I. Onset of Runaway Growth", ApJ, Vol.817, 105 (doi: 10.3847/0004-637X/817/2/105)
41. Furuya, K., van Dishoeck, E. F., & Aikawa, Y., 2016, "Reconstructing the history of water ice formation from HDO/H_2O and D_2O/HDO ratios in protostellar cores", A&A, Vol.586, A127 (doi: 10.1051/0004-6361/201527579)
42. Doney, K. D., Candian, A., Mori, T., Onaka, T., & Tielens, A. G. G. M., 2016, "Deuterated polycyclic aromatic hydrocarbons: Revisited", A&A, Vol.586, A65 (doi: 10.1051/0004-6361/201526809)
43. Shimonishi, T., Dartois, E., Onaka, T., & Boulanger, F., 2016, "VLT/ISAAC infrared spectroscopy of embedded high-mass YSOs in the Large Magellanic Cloud: Methanol and the 3.47 μm band", A&A, Vol.585, A107 (doi: 10.1051/0004-6361/201526559)
44. Muto, T., Tuskagoshi, T., Momose, M., Hanawa, T., Nomura, H., Fukagawa, M., Saigo, K., Kataoka, A., Kitamura, Y., Takahashi, S. Z., Inutsuka, S.-i., Takeuchi, T., Kobayashi, H., Akiyama, E., Honda, M., Fujiwara, H., & Shibai, H., 2015, "Significant gas-to-dust ratio asymmetry and variation in the disk of HD 142527 and the indication of gas depletion", PASJ, Vol.67, 122 (doi: 10.1093/pasj/psv098)
45. Ohsawa, R., Onaka, T., & Yasui, C., 2015, "Impact of the initial disk mass function on the disk fraction", PASJ, Vol.67, 120 (doi: 10.1093/pasj/psv094)
46. Tsujido, S., Arakawa, M., Suzuki, A. I., & Yasui, M., 2015, "Ejecta velocity distribution of impact craters formed on quartz sand: Effect of projectile density on crater scaling law", Icarus, Vol.262, 79 (doi: 10.1016/j.icarus.2015.08.035)
47. Genda, H., Fujita, T., Kobayashi, H., Tanak,H., & Abe, Y., 2015, "Resolution dependence of disruptive collisions between planetesimals in the gravity regime", Icarus, Vol.262, 58 (doi: 10.1016/j.icarus.2015.08.029)
48. Shimajiri, Y., Sakai, T., Kitamura, Y., Tuskagoshi, T., Saito, M., Nakamura, F., Momose, M., Takakuwa, S., Yamaguchi, T., Sakai, N., Yamamoto, S., & Kawabe, R., 2015, "Spectral-line Survey at Millimeter and Submillimeter Wavelengths toward an

Outflow-shocked Region, OMC 2-FIR 4", ApJSS, Vol.221, 31 (doi: 10.1088/0067-0049/221/2/31)
49. Currie, T., Cloutier, R., Brittain, S., Grady, C., Burrows, A., Muto, T., Kenyon, S. J., & Kuchner, M. J., 2015, "Resolving the HD 100546 Protoplanetary System with the Gemini Planet Imager: Evidence for Multiple Forming, Accreting Planets", ApJL, Vol.814, L27 (doi: 10.1088/2041-8205/814/2/L27)
50. Furuya, K., Aikawa, Y., Hincelin, U., Hassel, G. E., Bergin, E. A., Vasyunin, A. I., & Herbst, E., 2015, "Water deuteration and ortho-to-para nuclear spin ratio of H_2 in molecular clouds formed via the accumulation of H I gas", A&A, Vol.584, A124 (doi: 10.1051/0004-6361/201527050)
51. Buragohain, M., Pathak, A., Sarre, P., Onaka, T., & Sakon, I., 2015, "Theoretical study of deuteronated PAHs as carriers for IR emission features in the ISM", MNRAS, Vol.454, 193 (doi: 10.1093/mnras/stv1946)
52. Yasui, M., Matsumoto, E., & Arakawa, M., 2015, "Experimental study on impact-induced seismic wave propagation through granular materials", Icarus, Vol.260, 320 (doi: 10.1016/j.icarus.2015.07.032)
53. Itoh, Y., Fukagawa, M., Shibai, H., Sumi, T., & Yamamoto, K., 2015, "Study of infrared excess from circumstellar disks in binaries with Spitzer/IRAC", PASJ, Vol.67, 88 (doi: 10.1093/pasj/psv071)
54. Momose, M., Morita, A., Fukagawa, M., Muto, T., Takeuchi, T., Hashimoto, J., Honda, M., Kudo, T., Okamoto, Y. K., Kanagawa, K. D., Tanak,H., Grady, C. A., Sitko, M. L., Akiyama, E., Currie, T., Follette, K. B., Mayama, S., Kusakabe, N., Abe, L., Brandner, W., Brandt, T. D., Carson, J. C., Egner, S., Feldt, M., Goto, M., Guyon, O., Hayano, Y., Hayashi, M., Hayashi, S. S., Henning, T., Hodapp, K. W., Ishii, M., Iye, M., Janson, M., Kandori, R., Knapp, G. R., Kuzuhara, M., Kwon, J., Matsuo, T., McElwain, M. W., Miyama, S., Morino, J.-I., Moro-Martin, A., Nishimura, T., Pyo, T.-S., Serabyn, E., Suenaga, T., Suto, H., Suzuki, R., Takahashi, Y. H., Takami, M., Takato, N., Terada, H., Thalmann, C., Tomono, D., Turner, E. L., Watanabe, M., Wisniewski, J., Yamada, T., Takami, H., Usuda, T., & Tamura, M., 2015, "Detailed structure of the outer disk around HD 169142 with polarized light in H-band", PASJ, Vol.67, 83 (doi: 10.1093/pasj/psv051)
55. Kokusho, T., Nagayama, T., Kaneda, H., Ishihara, D., Lee, H.-G., & Onaka, T., 2015, "A study of iron and dust in the supernova remnant IC 443", Planetary and Space Science, Vol.116, 92 (doi: 10.1016/j.pss.2015.04.009)
56. Onaka, T., Mori, T. I., & Okada, Y., 2015, "Dust processing in the Carina nebula region", Planetary and Space Science, Vol.116, 84 (doi: 10.1016/j.pss.2015.03.025)
57. Hammonds, M., Mori, T., Usui, F., & Onaka, T., 2015, "Variations in the 3.3 μm feature and carbonaceous dust in AKARI data", Planetary and Space Science, Vol.116, 73 (doi: 10.1016/j.pss.2015.05.010)
58. Shalima, P., Wada, K., & Kimura, H., 2015, "Ejecta curtain radiative transfer modeling for probing its geometry and dust optical properties", Planetary and Space Science, Vol.116, 39 (doi: 10.1016/j.pss.2015.03.017)
59. Senshu, H., Kimura, H., Yamamoto, T., Wada, K., Kobayashi, M., Namiki, N., & Matsui, T., 2015, "Photoelectric dust levitation around airless bodies revised using realistic photoelectron velocity distributions", Planetary and Space Science, Vol.116, 18 (doi: 10.1016/j.pss.2015.03.009)
60. Kimura, H., Kolokolova, L., Li, A., Augereau, J.-C., Kaneda, H., & J¨ager, C., 2015,

"Cosmic Dust VII", Planetary and Space Science, Vol.116, 1 (doi: 10.1016/j.pss.2015.03.002)
61. Kimura, H., Wada, K., Senshu, H., & Kobayashi, H., 2015, "Cohesion of Amorphous Silica Spheres: Toward a Better Understanding of The Coagulation Growth of Silicate Dust Aggregates", ApJ, Vol.812, 67 (doi: 10.1088/0004-637X/812/1/67)
62. Aso, Y., Ohashi, N., Saigo, K., Koyamatsu, S., Aikawa, Y., Hayashi, M., Machida, M. N., Saito, M., Takakuwa, S., Tomida, K., Tomisaka, K., & Yen, H.-W., 2015, "ALMA Observations of the Transition from Infall Motion to Keplerian Rotation around the Late-phase Protostar TMC-1A", ApJ, Vol.812, 27 (doi: 10.1088/0004-637X/812/1/27)
63. Nakagawa, T., Shibai, H., Onaka, T., Matsuhara, H., Kaneda, H., & Kawakatsu, Y., 2015, "The Next-Generation Infrared Astronomy Mission SPICA Under the New Framework", PKAS, Vol.30, 621 (doi: 10.5303/PKAS.2015.30.2.621)
64. Oberg, K. I., Furuya, K., Loomis, R., Aikawa, Y., Andrews, S. M., Qi, C., van Dishoeck, E. F., & Wilner, D. J., 2015, "Double DCO^+ Rings Reveal CO Ice Desorption in the Outer Disk Around IM Lup", ApJ, Vol.810, 112 (doi: 10.1088/0004-637X/810/2/112)
65. Tanaka, K. K., Tanak,H., Ang´elil, R., & Diemand, J., 2015, "Simple improvements to classical bubble nucleation models", Physical Review E, Vol.92, 022401 (doi: 10.1103/PhysRevE.92.022401)
66. Ang´elil, R., Diemand, J., Tanaka, K. K., & Tanak,H., 2015, "Homogeneous SPC/E water nucleation in large molecular dynamics simulations", Journal of Chemical Physics, Vol.143, 064507 (doi: 10.1063/1.4928055)
67. Kataoka, A., Muto, T., Momose, M., Tuskagoshi, T., Fukagawa, M., Shibai, H., Hanawa, T., Murakawa, K., & Dullemond, C. P., 2015, "Millimeter-wave Polarization of Protoplanetary Disks due to Dust Scattering", ApJ, Vol.809, 78 (doi: 10.1088/0004-637X/809/1/78)
68. Aikawa, Y., Furuya, K., Nomura, H., & Qi, C., 2015, "Analytical Formulae of Molecular Ion Abundances and the N_2H^+ Ring in Protoplanetary Disks", ApJ, Vol.807, 120 (doi: 10.1088/0004-637X/807/2/120)
69. Yamagishi, M., Kaneda, H., Ishihara, D., Oyabu, S., Onaka, T., Shimonishi, T., & Suzuki, T., 2015, "Systematic Variations in CO_2/H_2O Ice Abundance Ratios in Nearby Galaxies Found with AKARI Near-infrared Spectroscopy", ApJ, Vol.807, 29 (doi: 10.1088/0004-637X/807/1/29)
70. Onozato, H., Ita, Y., Ono, K., Fukagawa, M., Yanagisawa, K., Izumiura, H., Nakada, Y., & Matsunaga, N., 2015, "A study on the mid-infrared sources that dramatically brightened", PASJ, Vol.67, 39 (doi: 10.1093/pasj/psv008)
71. Kanagawa, K. D., Muto, T., Tanak,H., Tanigawa, T., Takeuchi, T., Tuskagoshi, T., & Momose, M., 2015, "Mass Estimates of a Giant Planet in a Protoplanetary Disk from the Gap Structures", ApJL, Vol.806, L15 (doi: 10.1088/2041-8205/806/1/L15)
72. Kimura, H., 2015, "Interstellar dust in the Local Cloud surrounding the Sun", MNRAS, Vol.449, 2250 (doi: 10.1093/mnras/stv427)
73. Honda, M., Maaskant, K., Okamoto, Y. K., Kataza, H., Yamashita, T., Miyata, T., Sako, S., Fujiyoshi, T., Sakon, I., Fujiwara, H., Kamizuka, T., Mulders, G. D., Lopez-Rodriguez, E., Packham, C., & Onaka, T., 2015, "High-resolution 25 μm Imaging of the Disks around Herbig Ae/Be Stars", ApJ, Vol.804, 143 (doi: 10.1088/0004-637X/804/2/143)
74. Pilleri, P., Joblin, C., Boulanger, F., & Onaka, T., 2015, "Mixed aliphatic and aromatic composition of evaporating very small grains in NGC 7023 revealed by the 3.4/3.3 μm

ratio", A&A, Vol.577, A16 (doi: 10.1051/0004-6361/201425590)

75. Sai, S., Itoh, Y., Fukagawa, M., Shibai, H., & Sumi, T., 2015, "Near-infrared image of the debris disk around HD 15115", PASJ, Vol.67, 20 (doi: 10.1093/pasj/psu152)
76. Oberg, K. I., Guzm´an, V. V., Furuya, K., Qi, C., Aikawa, Y., Andrews, S. M., Loomis, R., & Wilner, D. J., 2015, "The comet-like composition of a protoplanetary disk as revealed by complex cyanides", Nature, Vol.520, 198 (doi: 10.1038/nature14276)
77. Kadono, T., Suzuki, A. I., Wada, K., Mitani, N. K., Yamamoto, S., Arakawa, M., Sugita, S., Haruyama, J., & Nakamura, A. M., 2015, "Crater-ray formation by impact-induced ejecta particles", Icarus, Vol.250, 215 (doi: 10.1016/j.icarus.2014.11.030)
78. Mousis, O., Chassefi`ere, E., Holm, N. G., Bouquet, A., Waite, J. H., Geppert, W. D., Picaud, S., Aikawa, Y., Ali-Dib, M., Charlou, J.-L., & Rousselot, P., 2015, "Methane Clathrates in the Solar System", Astrobiology, Vol.15, 308 (doi: 10.1089/ast.2014.1189)
79. Favre, C., Bergin, E. A., Cleeves, L. I., Hersant, F., Qi, C., & Aikawa, Y., 2015, "Evidence for DCO^+ as a Probe of Ionization in the Warm Disk Surface", ApJL, Vol.802, L23 (doi: 10.1088/2041-8205/802/2/L23)
80. Akiyama, E., Muto, T., Kusakabe, N., Kataoka, A., Hashimoto, J., Tuskagoshi, T., Kwon, J., Kudo, T., Kandori, R., Grady, C. A., Takami, M., Janson, M., Kuzuhara, M., Henning, T., Sitko, M. L., Carson, J. C., Mayama, S., Currie, T., Thalmann, C., Wisniewski, J., Momose, M., Ohashi, N., Abe, L., Brandner, W., Brandt, T. D., Egner, S., Feldt, M., Goto, M., Guyon, O., Hayano, Y., Hayashi, M., Hayashi, S., Hodapp, K. W., Ishi, M., Iye, M., Knapp, G. R., Matsuo, T., Mcelwain, M. W., Miyama, S., Morino, J.-I., Moro-Martin, A., Nishimura, T., Pyo, T.-S., Serabyn, G., Suenaga, T., Suto, H., Suzuki, R., Takahashi, Y. H., Takato, N., Terada, H., Tomono, D., Turner, E. L., Watanabe, M., Yamada, T., Takami, H., Usuda, T., & Tamura, M., 2015, "Discovery of a Disk Gap Candidate at 20 AU in TW Hydrae", ApJL, Vol.802, L17 (doi: 10.1088/2041-8205/802/2/L17)
81. Kanagawa, K. D., Tanak,H., Muto, T., Tanigawa, T., & Takeuchi, T., 2015, "Formation of a disc gap induced by a planet: effect of the deviation from Keplerian disc rotation", MNRAS, Vol.448, 994 (doi: 10.1093/mnras/stv025)
82. Shimajiri, Y., Kitamura, Y., Nakamura, F., Momose, M., Saito, M., Tuskagoshi, T., Hiramatsu, M., Shimoikura, T., Dobashi, K., Hara, C., & Kawabe, R., 2015, "Catalog of Dense Cores in the Orion A Giant Molecular Cloud", ApJSS, Vol.217, 7 (doi: 10.1088/0067-0049/217/1/7)
83. Tuskagoshi, T., Momose, M., Saito, M., Kitamura, Y., Shimajiri, Y., & Kawabe, R., 2015, "First Detection of [C I] $^3P_1$-$^3P_0$ Emission from a Protoplanetary Disk", ApJL, Vol.802, L7 (doi: 10.1088/2041-8205/802/1/L7)
84. Konishi, M., Shibai, H., Sumi, T., Fukagawa, M., Matsuo, T., Samland, M. S., Yamamoto, K., Sudo, J., Itoh, Y., Arimoto, N., Kajisawa, M., Abe, L., Brandner, W., Brandt, T. D., Carson, J., Currie, T., Egner, S. E., Feldt, M., Goto, M., Grady, C. A., Guyon, O., Hashimoto, J., Hayano, Y., Hayashi, M., Hayashi, S. S., Henning, T., Hodapp, K. W., Ishii, M., Iye, M., Janson, M., Kandori, R., Knapp, G. R., Kudo, T., Kusakabe, N., Kuzuhara, M., Kwon, J., McElwain, M. W., Miyama, S., Morino, J.-I., Moro-Mart´ın, A., Nishimura, T., Pyo, T.-S., Serabyn, E., Suenaga, T., Suto, H., Suzuki, R., Takahashi, Y. H., Takami, H., Takato, N., Terada, H., Thalmann, C., Tomono, D., Turner, E. L., Usuda, T., Watanabe, M., Wisniewski, J. P., Yamada, T., & Tamura, M., 2015, "Indications of M-dwarf deficits in the halo and thick disk of the Galaxy", PASJ, Vol.67, 1 (doi: 10.1093/pasj/psu125)

85. Aota, T., Inoue, T., & Aikawa, Y., 2015, "Evaporation of Grain-surface Species by Shock Waves in a Protoplanetary Disk", ApJ, Vol.799, 141 (doi: 10.1088/0004-637X/799/2/141)
86. Grady, C., Fukagawa, M., Maruta, Y., Ohta, Y., Wisniewski, J., Hashimoto, J., Okamoto, Y., Momose, M., Currie, T., McElwain, M., Muto, T., Kotani, T., Kusakabe, N., Feldt, M., Sitko, M., Follette, K., Bonnefoy, M., Henning, T., Takami, M., Karr, J., Kwon, J., Kudo, T., Abe, L., Brandner, W., Brandt, T., Carson, J., Egner, S., Goto, M., Guyon, O., Hayano, Y., Hayashi, M., Hayashi, S., Hodapp, K., Ishii, M., Iye, M., Janson, M., Kandori, R., Knapp, G., Kuzuhara, M., Matsuo, T., Miyama, S., Morino, J.-I., Moro-Mart´ın, A., Nishimura, T., Pyo, T.-S., Serabyn, E., Suenaga, T., Suto, H., Suzuki, R., Takahashi, Y. H., Takato, N., Terada, H., Thalmann, C., Tomono, D., Turner, E. L., Watanabe, M., Yamada, T., Takami, H., Usuda, T., & Tamura, M., 2015, "The outer disks of Herbig stars from the UV to NIR", ApSS, Vol.355, 253 (doi: 10.1007/s10509-014-2214-2)
87. Hashimoto, J., Tuskagoshi, T., Brown, J. M., Dong, R., Muto, T., Zhu, Z., Wisniewski, J., Ohashi, N., kudo, T., Kusakabe, N., Abe, L., Akiyama, E., Brandner, W., Brandt, T., Carson, J., Currie, T., Egner, S., Feldt, M., Grady, C. A., Guyon, O., Hayano, Y., Hayashi, M., Hayashi, S., Henning, T., Hodapp, K., Ishii, M., Iye, M., Janson, M., Kandori, R., Knapp, G., Kuzuhara, M., Kwon, J., Matsuo, T., McElwain, M. W., Mayama, S., Mede, K., Miyama, S., Morino, J.-I., Moro-Martin, A., Nishimura, T., Pyo, T.-S., Serabyn, G., Suenaga, T., Suto, H., Suzuki, R., Takahashi, Y., Takami, M., Takato, N., Terada, H., Thalmann, C., Tomono, D., Turner, E. L., Watanabe, M., Yamada, T., Takami, H., Usuda, T., & Tamura, M., 2015, "The Structure of Pre-transitional Protoplanetary Disks. II. Azimuthal Asymmetries, Different Radial Distributions of Large and Small Dust Grains in PDS 70", ApJ, Vol.799, 43 (doi: 10.1088/0004-637X/799/1/43)
88. Follette, K. B., Grady, C. A., Swearingen, J. R., Sitko, M. L., Champney, E. H., van der Marel, N., Takami, M., Kuchner, M. J., Close, L. M., Muto, T., Mayama, S., McElwain, M. W., Fukagawa, M., Maaskant, K., Min, M., Russell, R. W., Kudo, T., Kusakabe, N., Hashimoto, J., Abe, L., Akiyama, E., Brandner, W., Brandt, T. D., Carson, J., Currie, T., Egner, S. E., Feldt, M., Goto, M., Guyon, O., Hayano, Y., Hayashi, M., Hayashi, S., Henning, T., Hodapp, K., Ishii, M., Iye, M., Janson, M., Kandori, R., Knapp, G. R., Kuzuhara, M., Kwon, J., Matsuo, T., Miyama, S., Morino, J.-I., Moro-Martin, A., Nishimura, T., Pyo, T.-S., Serabyn, E., Suenaga, T., Suto, H., Suzuki, R., Takahashi, Y., Takato, N., Terada, H., Thalmann, C., Tomono, D., Turner, E. L., Watanabe, M., Wisniewski, J. P., Yamada, T., Takami, H., Usuda, T., & Tamura, M., 2015, "SEEDS Adaptive Optics Imaging of the Asymmetric Transition Disk Oph IRS 48 in Scattered Light", ApJ, Vol.798, 132 (doi: 10.1088/0004-637X/798/2/132)
89. Wagner, K. R., Sitko, M. L., Grady, C. A., Swearingen, J. R., Champney, E. H., Johnson, A. N., Werren, C., Whitney, B. A., Russell, R. W., Schneider, G. H., Momose, M., Muto, T., Inoue, A. K., Lauroesch, J. T., Hornbeck, J., Brown, A., Fukagawa, M., Currie, T. M., Wisniewski, J. P., & Woodgate, B. E., 2015, "Variability of Disk Emission in Pre-main Sequence and Related Stars. III. Exploring Structural Changes in the Pre-transitional Disk in HD 169142", ApJ, Vol.798, 94 (doi: 10.1088/0004-637X/798/2/94)
90. Shinozaki, K., Mizutani, T., Fujii, T., Onaka, T., Nakagawa, T., & Sugita, H., 2015, "Thermal Property Measurements of Critical Materials for SPICA Payload Module", Physics Procedia, Vol.67, 270 (doi: 10.1016/j.phpro.2015.06.086)
91. Ang´elil, R., Diemand, J., Tanaka, K. K., & Tanak,H., 2014, "Bubble evolution and properties in homogeneous nucleation simulations", Physical Review E, Vol.90, 063301

(doi: 10.1103/Phys-RevE.90.063301)
92. Iino, T., Mizuno, A., Nakajima, T., Hidemori, T., Tuskagoshi, T., & Kato, C., 2014, "Search for sulfur-bearing species as remnant of cometary impact on Neptune", Planetary and Space Science, Vol.104, 211 (doi: 10.1016/j.pss.2014.09.013)
93. Wakelam, V., Vastel, C., Aikawa, Y., Coutens, A., Bottinelli, S., & Caux, E., 2014, "Chemical modelling of water deuteration in IRAS16293-2422", MNRAS, Vol.445, 2854 (doi: 10.1093/mn-ras/stu1920)
94. Currie, T., Muto, T., Kudo, T., Honda, M., Brandt, T. D., Grady, C., Fukagawa, M., Burrows, A., Janson, M., Kuzuhara, M., McElwain, M. W., Follette, K., Hashimoto, J., Henning, T., Kandori, R., Kusakabe, N., Kwon, J., Mede, K., Morino, J.-i., Nishikawa, J., Pyo, T.-S., Serabyn, G., Suenaga, T., Takahashi, Y., Wisniewski, J., & Tamura, M., 2014, "Recovery of the Candidate Protoplanet HD 100546 b with Gemini/NICI and Detection of Additional (Planet-induced?) Disk Structure at Small Separations", ApJL, Vol.796, L30 (doi: 10.1088/2041-8205/796/2/L30)
95. Ohashi, N., Saigo, K., Aso, Y., Aikawa, Y., Koyamatsu, S., Machida, M. N., Saito, M., Takahashi, S. Z., Takakuwa, S., Tomida, K., Tomisaka, K., & Yen, H.-W., 2014, "Formation of a Keplerian Disk in the Infalling Envelope around L1527 IRS: Transformation from Infalling Motions to Kepler Motions", ApJ, Vol.796, 131 (doi: 10.1088/0004-637X/796/2/131)
96. Diemand, J., Ang´elil, R., Tanaka, K. K., & Tanak,H., 2014, "Direct simulations of homogeneous bubble nucleation: Agreement with classical nucleation theory and no local hot spots", Physical Review E, Vol.90, 052407 (doi: 10.1103/PhysRevE.90.052407)
97. Currie, T., Burrows, A., Girard, J. H., Cloutier, R., Fukagawa, M., Sorahana, S., Kuchner, M., Kenyon, S. J., Madhusudhan, N., Itoh, Y., Jayawardhana, R., Matsumura, S., & Pyo, T.-S., 2014, "Deep Thermal Infrared Imaging of HR 8799 bcde: New Atmospheric Constraints and Limits on a Fifth Planet", ApJ, Vol.795, 133 (doi: 10.1088/0004-637X/795/2/133)
98. Takami, M., Hasegawa, Y., Muto, T., Gu, P.-G., Dong, R., Karr, J. L., Hashimoto, J., Kusakabe, N., Chapillon, E., Tang, Y.-W., Itoh, Y., Carson, J., Follette, K. B., Mayama, S., Sitko, M., Janson, M., Grady, C. A., Kudo, T., Akiyama, E., Kwon, J., Takahashi, Y., Suenaga, T., Abe, L., Brandner, W., Brandt, T. D., Currie, T., Egner, S. E., Feldt, M., Guyon, O., Hayano, Y., Hayashi, M., Hayashi, S., Henning, T., Hodapp, K. W., Honda, M., Ishii, M., Iye, M., Kandori, R., Knapp, G. R., Kuzuhara, M., McElwain, M. W., Matsuo, T., Miyama, S., Morino, J.-I., Moro-Martin, A., Nishimura, T., Pyo, T.-S., Serabyn, E., Suto, H., Suzuki, R., Takato, N., Terada, H., Thalmann, C., Tomono, D., Turner, E. L., Wisniewski, J. P., Watanabe, M., Yamada, T., Takami, H., Usuda, T., & Tamura, M., 2014, "Surface Geometry of Protoplanetary Disks Inferred From Near-Infrared Imaging Polarimetry", ApJ, Vol.795, 71 (doi: 10.1088/0004-637X/795/1/71)
99. Kimura, H., Senshu, H., & Wada, K., 2014, "Electrostatic lofting of dust aggregates near the terminator of airless bodies and its implication for the formation of exozodiacal disks", Planetary and Space Science, Vol.100, 64 (doi: 10.1016/j.pss.2014.03.017)
100. Kaneda, H., Ishihara, D., Kobata, K., Kondo, T., Oyabu, S., Yamada, R., Yamagishi, M., Onaka, T., & Suzuki, T., 2014, "AKARI observations of interstellar dust grains in our Galaxy and nearby galaxies", Planetary and Space Science, Vol.100, 6 (doi: 10.1016/j.pss.2014.01.017)

101. Kimura, H., Kolokolova, L., Li, A., Inoue, A. K., & J¨ager, C., 2014, "Cosmic Dust VI", Planetary and Space Science, Vol.100, 1 (doi: 10.1016/j.pss.2014.02.009)
102. Nagasawa, M., Tanaka, K. K., Tanak,H., Nakamoto, T., Miura, H., & Yamamoto, T., 2014, "Revisiting Jovian-resonance Induced Chondrule Formation", ApJL, Vol.794, L7 (doi: 10.1088/2041-8205/794/1/L7)
103. Yen, H.-W., Takakuwa, S., Ohashi, N., Aikawa, Y., Aso, Y., Koyamatsu, S., Machida, M. N., Saigo, K., Saito, M., Tomida, K., & Tomisaka, K., 2014, "ALMA Observations of Infalling Flows toward the Keplerian Disk around the Class I Protostar L1489 IRS", ApJ, Vol.793, 1 (doi: 10.1088/0004-637X/793/1/1)
104. Yasui, C., Kobayashi, N., Tokunaga, A. T., & Saito, M., 2014, "Rapid evolution of the innermost dust disc of protoplanetary discs surrounding intermediate-mass stars", MNRAS, Vol.442, 2543 (doi: 10.1093/mnras/stu1013)
105. Sakai, N., Oya, Y., Sakai, T., Watanabe, Y., Hirota, T., Ceccarelli, C., Kahane, C., Lopez-Sepulcre, A., Lefloch, B., Vastel, C., Bottinelli, S., Caux, E., Coutens, A., Aikawa, Y., Takakuwa, S., Ohashi, N., Yen, H.-W., & Yamamoto, S., 2014, "A Chemical View of Protostellar-disk Formation in L1527", ApJL, Vol.791, L38 (doi: 10.1088/2041-8205/791/2/L38)
106. Nakamura, F., Sugitani, K., Tanaka, T., Nishitani, H., Dobashi, K., Shimoikura, T., Shimajiri, Y., Kawabe, R., Yonekura, Y., Mizuno, I., Kimura, K., Tokuda, K., Kozu, M., Okada, N., Hasegawa, Y., Ogawa, H., Kameno, S., Shinnaga, H., Momose, M., Nakajima, T., Onishi, T., Maezawa, H., Hirota, T., Takano, S., Iono, D., Kuno, N., & Yamamoto, S., 2014, "Cluster Formation Triggered by Filament Collisions in Serpens South", ApJL, Vol.791, L23 (doi: 10.1088/2041-8205/791/2/L23)
107. Walsh, C., Juh´asz, A., Pinilla, P., Harsono, D., Mathews, G. S., Dent, W. R. F., Hogerheijde, M. R., Birnstiel, T., Meeus, G., Nomura, H., Aikawa, Y., Millar, T. J., & Sandell, G., 2014, "ALMA Hints at the Presence of two Companions in the Disk around HD 100546", ApJL, Vol.791, L6 (doi: 10.1088/2041-8205/791/1/L6)
108. Furuya, K., & Aikawa, Y., 2014, "Reprocessing of Ices in Turbulent Protoplanetary Disks: Carbon and Nitrogen Chemistry", ApJ, Vol.790, 97 (doi: 10.1088/0004-637X/790/2/97)
109. Kataoka, A., Okuzumi, S., Tanak,H., & Nomura, H., 2014, "Opacity of fluffy dust aggregates", A&A, Vol.568, A42 (doi: 10.1051/0004-6361/201323199)
110. Bottinelli, S., Wakelam, V., Caux, E., Vastel, C., Aikawa, Y., & Ceccarelli, C., 2014, "CH in absorption in IRAS 16293-2422", MNRAS, Vol.441, 1964 (doi: 10.1093/mnras/stu700)
111. Leliwa-Kopystynski, J., & Arakawa, M., 2014, "Impacts experiments onto heterogeneous targets simulating impact breccia: Implications for impact strength of asteroids and formation of the asteroid families", Icarus, Vol.235, 147 (doi: 10.1016/j.icarus.2014.03.012)
112. Tanaka, K. K., Diemand, J., Ang´elil, R., & Tanak,H., 2014, "Free energy of cluster formation and a new scaling relation for the nucleation rate", Journal of Chemical Physics, Vol.140, 194310 (doi: 10.1063/1.4875803)
113. Yasui, M., Hayama, R., & Arakawa, M., 2014, "Impact strength of small icy bodies that experienced multiple collisions", Icarus, Vol.233, 293 (doi: 10.1016/j.icarus.2014.02.008)
114. Morbidelli, A., Szul´agyi, J., Crida, A., Lega, E., Bitsch, B., Tanigawa, T., & Kanagawa, K., 2014, "Meridional circulation of gas into gaps opened by giant planets in three-dimensional low-viscosity disks", Icarus, Vol.232, 266 (doi:

10.1016/j.icarus.2014.01.010)
115. Kimura, H., 2014, "The organic-rich carbonaceous component of dust aggregates in circumstellar disks: Effects of its carbonization on infrared spectral features of its magnesium-rich olivine counterpart", Icarus, Vol.232, 133 (doi: 10.1016/j.icarus.2014.01.009)
116. Okuzumi, S., Takeuchi, T., & Muto, T., 2014, "Radial Transport of Large-scale Magnetic Fields in Accretion Disks. I. Steady Solutions and an Upper Limit on the Vertical Field Strength", ApJ, Vol.785, 127 (doi: 10.1088/0004-637X/785/2/127)
117. Shimajiri, Y., Kitamura, Y., Saito, M., Momose, M., Nakamura, F., Dobashi, K., Shimoikura, T., Nishitani, H., Yamabi, A., Hara, C., Katakura, S., Tuskagoshi, T., Tanaka, T., & Kawabe, R., 2014, "High abundance ratio of ^{13}CO to C^{18}O toward photon-dominated regions in the Orion-A giant molecular cloud", A&A, Vol.564, A68 (doi: 10.1051/0004-6361/201322912)
118. Sakai, N., Sakai, T., Hirota, T., Watanabe, Y., Ceccarelli, C., Kahane, C., Bottinelli, S., Caux, E., Demyk, K., Vastel, C., Coutens, A., Taquet, V., Ohashi, N., Takakuwa, S., Yen, H.-W., Aikawa, Y., & Yamamoto, S., 2014, "Change in the chemical composition of infalling gas forming a disk around a protostar", Nature, Vol.507, 78 (doi: 10.1038/nature13000)
119. Tanaka, K. K., Kawano, A., & Tanak,H., 2014, "Molecular dynamics simulations of the nucleation of water: Determining the sticking probability and formation energy of a cluster", Journal of Chemical Physics, Vol.140, 114302 (doi: 10.1063/1.4867909)
120. Mori, T. I., Onaka, T., Sakon, I., Ishihara, D., Shimonishi, T., Ohsawa, R., & Bell, A. C., 2014, "Observational Studies on the Near-infrared Unidentified Emission Bands in Galactic H II Regions", ApJ, Vol.784, 53 (doi: 10.1088/0004-637X/784/1/53)
121. Yamamoto, T., Kadono, T., & Wada, K., 2014, "An Examination of Collisional Growth of Silicate Dust in Protoplanetary Disks", ApJL, Vol.783, L36 (doi: 10.1088/2041-8205/783/2/L36)
122. Tuskagoshi, T., Momose, M., Hashimoto, J., Kudo, T., Andrews, S., Saito, M., Kitamura, Y., Ohashi, N., Wilner, D., Kawabe, R., Abe, L., Akiyama, E., Brandner, W., Brandt, T. D., Carson, J., Currie, T., Egner, S. E., Goto, M., Grady, C., Guyon, O., Hayano, Y., Hayashi, M., Hayashi, S., Henning, T., Hodapp, K. W., Ishii, M., Iye, M., Janson, M., Kandori, R., Knapp, G. R., Kusakabe, N., Kuzuhara, M., Kwon, J., McElwain, M., Matsuo, T., Mayama, S., Miyama, S., Morino, J.-i., Moro-Martín, A., Nishimura, T., Pyo, T.-S., Serabyn, E., Suenaga, T., Suto, H., Suzuki, R., Takahashi, Y., Takami, H., Takami, M., Takato, N., Terada, H., Thalmann, C., Tomono, D., Turner, E. L., Usuda, T., Watanabe, M., Wisniewski, J. P., Yamada, T., & Tamura, M., 2014, "High-resolution Submillimeter and Near-infrared Studies of the Transition Disk around Sz 91", ApJ, Vol.783, 90 (doi: 10.1088/0004-637X/783/2/90)
123. Miura, H., & Yamamoto, T., 2014, "A New Estimate of the Chondrule Cooling Rate Deduced from an Analysis of Compositional Zoning of Relict Olivine", AJ, Vol.147, 54 (doi: 10.1088/0004-6256/147/3/54)
124. Malinen, J., Juvela, M., Zahorecz, S., Rivera-Ingraham, A., Montillaud, J., Arimatsu, K., Bernard, J.-P., Doi, Y., Haikala, L. K., Kawabe, R., Marton, G., McGehee, P., Pelkonen, V.-M., Ristorcelli, I., Shimajiri, Y., Takita, S., Tóth, L. V., Tuskagoshi, T., & Ysard, N., 2014, "Multiwave-length study of the high-latitude cloud L1642: chain of star formation", A&A, Vol.563, A125 (doi: 10.1051/0004-6361/201323026)

125. Walsh, C., Millar, T. J., Nomura, H., Herbst, E., Widicus Weaver, S., Aikawa, Y., Laas, J. C., & Vasyunin, A. I., 2014, "Complex organic molecules in protoplanetary disks", A&A, Vol.563, A33 (doi: 10.1051/0004-6361/201322446)
126. Ang´elil, R., Diemand, J., Tanaka, K. K., & Tanak,H., 2014, "Properties of liquid clusters in large-scale molecular dynamics nucleation simulations", Journal of Chemical Physics, Vol.140, 074303 (doi: 10.1063/1.4865256)
127. Bonnefoy, M., Currie, T., Marleau, G.-D., Schlieder, J. E., Wisniewski, J., Carson, J., Covey, K. R., Henning, T., Biller, B., Hinz, P., Klahr, H., Marsh Boyer, A. N., Zimmerman, N., Janson, M., McElwain, M., Mordasini, C., Skemer, A., Bailey, V., Defr`ere, D., Thalmann, C., Skrutskie, M., Allard, F., Homeier, D., Tamura, M., Feldt, M., Cumming, A., Grady, C., Brandner, W., Helling, C., Witte, S., Hauschildt, P., Kandori, R., Kuzuhara, M., Fukagawa, M., Kwon, J., Kudo, T., Hashimoto, J., Kusakabe, N., Abe, L., Brandt, T., Egner, S., Guyon, O., Hayano, Y., Hayashi, M., Hayashi, S., Hodapp, K., Ishii, M., Iye, M., Knapp, G., Matsuo, T., Mede, K., Miyama, M., Morino, J.-I., Moro-Martin, A., Nishimura, T., Pyo, T., Serabyn, E., Suenaga, T., Suto, H., Suzuki, R., Takahashi, Takami, M., Takato, N., Terada, H., Tomono, D., Turner, E., Watanabe, M., Yamada, T., Takami, H., & Usuda, T., 2014, "Characterization of the gaseous companion κ Andromedae b. New Keck and LBTI high-contrast observations", A&A, Vol.562, A111 (doi: 10.1051/0004-6361/201322119)
128. Onaka, T., Mori, T. I., Sakon, I., Ohsawa, R., Kaneda, H., Okada, Y., & Tanaka, M., 2014, "Search for the Infrared Emission Features from Deuterated Interstellar Polycyclic Aromatic Hydrocarbons", ApJ, Vol.780, 114 (doi: 10.1088/0004-637X/780/2/114)
129. Johansen, A., Blum, J., Tanak,H., Ormel, C., Bizzarro, M., & Rickman, H., 2014, "The Multifaceted Planetesimal Formation Process", Protostars and Planets VI, 547 (doi: 10.2458/azu_uapress_9780816531240-ch024)
130. Fukagawa, M., Tuskagoshi, T., Momose, M., Saigo, K., Ohashi, N., Kitamura, Y., Inutsuka, S.- i., Muto, T., Nomura, H., Takeuchi, T., Kobayashi, H., Hanawa, T., Akiyama, E., Honda, M., Fujiwara, H., Kataoka, A., Takahashi, S. Z., & Shibai, H., 2013, "Local Enhancement of the Surface Density in the Protoplanetary Ring Surrounding HD 142527", PASJ, Vol.65, L14 (doi: 10.1093/pasj/65.6.L14)
131. Akiyama, E., Momose, M., Kitamura, Y., Tuskagoshi, T., Shimada, S., Koyamatsu, S., & Hayashi, M., 2013, "An Observational Study of the Temperature and Surface Density Structures of a Typical Full Disk around MWC 480", PASJ, Vol.65, 123 (doi: 10.1093/pasj/65.6.123)
132. Aikawa, Y., 2013, "Interplay of Chemistry and Dynamics in the Low-Mass Star Formation", Chemical Reviews, Vol.113, 8961 (doi: 10.1021/cr4003193)
133. Seok, J. Y., Koo, B.-C., & Onaka, T., 2013, "A Survey of Infrared Supernova Remnants in the Large Magellanic Cloud", ApJ, Vol.779, 134 (doi: 10.1088/0004-637X/779/2/134)
134. Furuya, K., Aikawa, Y., Nomura, H., Hersant, F., & Wakelam, V., 2013, "Water in Protoplanetary Disks: Deuteration and Turbulent Mixing", ApJ, Vol.779, 11 (doi: 10.1088/0004-637X/779/1/11)
135. Egusa, F., Wada, T., Sakon, I., Onaka, T., Arimatsu, K., & Matsuhara, H., 2013, "Interstellar Dust Properties of M51 from AKARI Mid-infrared Images", ApJ, Vol.778, 1 (doi: 10.1088/0004- 637X/778/1/1)
136. Wada, K., Tanak,H., Okuzumi, S., Kobayashi, H., Suyama, T., Kimura, H., & Yamamoto, T., 2013, "Growth efficiency of dust aggregates through collisions with high mass ratios",

A&A, Vol.559, A62 (doi: 10.1051/0004-6361/201322259)
137. Currie, T., Burrows, A., Madhusudhan, N., Fukagawa, M., Girard, J. H., Dawson, R., Murray-Clay, R., Kenyon, S., Kuchner, M., Matsumura, S., Jayawardhana, R., Chambers, J., & Bromley, B., 2013, "A Combined Very Large Telescope and Gemini Study of the Atmosphere of the Directly Imaged Planet, β Pictoris b", ApJ, Vol.776, 15 (doi: 10.1088/0004-637X/776/1/15)
138. Noble, J. A., Fraser, H. J., Aikawa, Y., Pontoppidan, K. M., & Sakon, I., 2013, "A Survey of H_2O, CO_2, and CO Ice Features toward Background Stars and low-mass Young Stellar Objects Using AKARI", ApJ, Vol.775, 85 (doi: 10.1088/0004-637X/775/2/85)
139. Kimura, H., 2013, "The Reincarnation of Interstellar Dust: The Importance of Organic Refractory Material in Infrared Spectra of Cometary Comae and Circumstellar Disks", ApJL, Vol.775, L18 (doi: 10.1088/2041-8205/775/1/L18)
140. Aota, T., Inoue, T., & Aikawa, Y., 2013, "Thermal Instability behind a Shock Wave in H I and Molecular Clouds", ApJ, Vol.775, 26 (doi: 10.1088/0004-637X/775/1/26)
141. Shimajiri, Y., Sakai, T., Tuskagoshi, T., Kitamura, Y., Momose, M., Saito, M., Oshima, T., Kohno, K., & Kawabe, R., 2013, "Extensive [C I] Mapping toward the Orion-A Giant Molecular Cloud", ApJL, Vol.774, L20 (doi: 10.1088/2041-8205/774/2/L20)
142. Kataoka, A., Tanak,H., Okuzumi, S., & Wada, K., 2013, "Fluffy dust forms icy planetesimals by static compression", A&A, Vol.557, L4 (doi: 10.1051/0004-6361/201322151)
143. Yamamoto, K., Matsuo, T., Shibai, H., Itoh, Y., Konishi, M., Sudo, J., Tanii, R., Fukagawa, M., Sumi, T., Kudo, T., Hashimoto, J., Kusakabe, N., Abe, L., Brandner, W., Brandt, T. D., Carson, J., Currie, T., Egner, S. E., Feldt, M., Goto, M., Grady, C., Guyon, O., Hayano, Y., Hayashi, M., Hayashi, S., Henning, T., Hodapp, K., Ishii, M., Iye, M., Janson, M., Kandori, R., Knapp, G. R., Kuzuhara, M., Kwon, J., McElwain, M., Miyama, S., Morino, J.-I., Moro-Martin, A., Nishikawa, J., Nishimura, T., Pyo, T.-S., Serabyn, E., Suto, H., Suzuki, R., Takami, M., Takato, N., Terada, H., Thalmann, C., Tomono, D., Turner, E. L., Wisniewski, J., Watanabe, M., Yamada, T., Takami, H., & Usuda, T., 2013, "Direct Imaging Search for Extrasolar Planets in the Pleiades", PASJ, Vol.65, 90 (doi: 10.1093/pasj/65.4.90)
144. Diemand, J., Ang´elil, R., Tanaka, K. K., & Tanak,H., 2013, "Large scale molecular dynamics simulations of homogeneous nucleation", Journal of Chemical Physics, Vol.139, 074309 (doi: 10.1063/1.4818639)
145. Yamagishi, M., Kaneda, H., Ishihara, D., Oyabu, S., Onaka, T., Shimonishi, T., Suzuki, T., & Minh, Y. C., 2013, "Difference in the Spatial Distribution between H_2O and CO_2 Ices in M 82 Found with AKARI", ApJL, Vol.773, L37 (doi: 10.1088/2041-8205/773/2/L37)
146. Janson, M., Brandt, T. D., Moro-Mart´ın, A., Usuda, T., Thalmann, C., Carson, J. C., Goto, M., Currie, T., McElwain, M. W., Itoh, Y., Fukagawa, M., Crepp, J., Kuzuhara, M., Hashimoto, J., Kudo, T., Kusakabe, N., Abe, L., Brandner, W., Egner, S., Feldt, M., Grady, C. A., Guyon, O., Hayano, Y., Hayashi, M., Hayashi, S., Henning, T., Hodapp, K. W., Ishii, M., Iye, M., Kandori, R., Knapp, G. R., Kwon, J., Matsuo, T., Miyama, S., Morino, J.-I., Nishimura, T., Pyo, T.-S., Serabyn, E., Suenaga, T., Suto, H., Suzuki, R., Takahashi, Y., Takami, M., Takato, N., Terada, H., Tomono, D., Turner, E. L., Watanabe, M., Wisniewski, J., Yamada, T., Takami, H., & Tamura, M., 2013, "The SEEDS Direct Imaging Survey for Planets and Scattered Dust Emission in Debris Disk Systems", ApJ, Vol.773, 73 (doi: 10.1088/0004-637X/773/1/73)

147. Takami, M., Karr, J. L., Hashimoto, J., Kim, H., Wisniewski, J., Henning, T., Grady, C. A., Kandori, R., Hodapp, K. W., Kudo, T., Kusakabe, N., Chou, M.-Y., Itoh, Y., Momose, M., Mayama, S., Currie, T., Follette, K. B., Kwon, J., Abe, L., Brandner, W., Brandt, T. D., Carson, J., Egner, S. E., Feldt, M., Guyon, O., Hayano, Y., Hayashi, M., Hayashi, S., Ishii, M., Iye, M., Janson, M., Knapp, G. R., Kuzuhara, M., McElwain, M. W., Matsuo, T., Miyama, S., Morino, J.-I., Moro-Martin, A., Nishimura, T., Pyo, T.-S., Serabyn, E., Suto, H., Suzuki, R., Takato, N., Terada, H., Thalmann, C., Tomono, D., Turner, E. L., Watanabe, M., Yamada, T., Takami, H., Usuda, T., & Tamura, M., 2013, "High-contrast Near-infrared Imaging Polarimetry of the Protoplanetary Disk around RY TAU", ApJ, Vol.772, 145 (doi: 10.1088/0004-637X/772/2/145)
148. Kaneda, H., Nakagawa, T., Ghosh, S. K., Ojha, D. K., Ishihara, D., Kondo, T., Ninan, J. P., Tanabe, M., Fukui, Y., Hattori, Y., Onaka, T., Torii, K., & Yamagishi, M., 2013, "Large-scale mapping of the massive star-forming region RCW38 in the [CII] and PAH emission", A&A, Vol.556, A92 (doi: 10.1051/0004-6361/201321614)
149. Suzuki, A. I., Nakamura, A. M., Kadono, T., Wada, K., Yamamoto, S., & Arakawa, M., 2013, "A formation mechanism for concentric ridges in ejecta surrounding impact craters in a layer of fine glass beads", Icarus, Vol.225, 298 (doi: 10.1016/j.icarus.2013.03.027)
150. Hara, C., Shimajiri, Y., Tuskagoshi, T., Kurono, Y., Saigo, K., Nakamura, F., Saito, M., Wilner, D., & Kawabe, R., 2013, "The Rotating Outflow, Envelope, and Disk of the Class-0/I Protostar [BHB2007]#11 in the Pipe Nebula", ApJ, Vol.771, 128 (doi: 10.1088/0004-637X/771/2/128)
151. Lee, H.-G., Moon, D.-S., Koo, B.-C., Rahman, M., Eikenberry, S. S., Gruel, N., Onaka, T., Kim, H.-J., Chun, W.-S., Raymond, J., Raines, S. N., & Guzman, R., 2013, "Wide Integral-field Infrared Spectroscopy of the Bright [Fe II] Shell in the Young Supernova Remnant G11.2-0.3", ApJ, Vol.770, 143 (doi: 10.1088/0004-637X/770/2/143)
152. Spezzano, S., Bru¨nken, S., Schilke, P., Caselli, P., Menten, K. M., McCarthy, M. C., Bizzocchi, L., Trevin˜o-Morales, S. P., Aikawa, Y., & Schlemmer, S., 2013, "Interstellar Detection of c-C_3D_2", ApJL, Vol.769, L19 (doi: 10.1088/2041-8205/769/2/L19)
153. Suzuki, T., Kaneda, H., & Onaka, T., 2013, "AKARI view of star formation in NGC 1313", A&A, Vol.554, A8 (doi: 10.1051/0004-6361/201220294)
154. Kataoka, A., Tanak,H., Okuzumi, S., & Wada, K., 2013, "Static compression of porous dust aggregates", A&A, Vol.554, A4 (doi: 10.1051/0004-6361/201321325)
155. Kokusho, T., Nagayama, T., Kaneda, H., Ishihara, D., Lee, H.-G., & Onaka, T., 2013, "Large-area [Fe II] Line Mapping of the Supernova Remnant IC 443 with the IRSF/SIRIUS", ApJL, Vol.768, L8 (doi: 10.1088/2041-8205/768/1/L8)
156. Siudek, M., Pollo, A., Takeuchi, T. T., Ita, Y., Kato, D., & Onaka, T., 2013, "Infrared composition of the Large Magellanic Cloud", Earth, Planets, and Space, Vol.65, 229 (doi: 10.5047/eps.2012.09.001)
157. Kohyama, T., Shibai, H., Fukagawa, M., & Sumi, T., 2013, "A New Galactic Extinction Map in High Ecliptic Latitudes", PASJ, Vol.65, 13 (doi: 10.1093/pasj/65.1.13)
158. Tanaka, K. K., Yamamoto, T., Tanak,H., Miura, H., Nagasawa, M., & Nakamoto, T., 2013, "Evaporation of Icy Planetesimals Due to Bow Shocks", ApJ, Vol.764, 120 (doi: 10.1088/0004-637X/764/2/120)
159. Carson, J., Thalmann, C., Janson, M., Kozakis, T., Bonnefoy, M., Biller, B., Schlieder, J., Currie, T., McElwain, M., Goto, M., Henning, T., Brandner, W., Feldt, M., Kandori, R., Kuzuhara, M., Stevens, L., Wong, P., Gainey, K., Fukagawa, M., Kuwada, Y., Brandt, T.,

Kwon, J., Abe, L., Egner, S., Grady, C., Guyon, O., Hashimoto, J., Hayano, Y., Hayashi, M., Hayashi, S., Hodapp, K., Ishii, M., Iye, M., Knapp, G., Kudo, T., Kusakabe, N., Matsuo, T., Miyama, S., Morino, J., Moro-Martin, A., Nishimura, T., Pyo, T., Serabyn, E., Suto, H., Suzuki, R., Takami, M., Takato, N., Terada, H., Tomono, D., Turner, E., Watanabe, M., Wisniewski, J., Yamada, T., Takami, H., Usuda, T., & Tamura, M., 2013, "Direct Imaging Discovery of a "Super-Jupiter" around the Late B-type Star κ And", ApJL, Vol.763, L32 (doi: 10.1088/2041-8205/763/2/L32)

160. Shimonishi, T., Onaka, T., Kato, D., Sakon, I., Ita, Y., Kawamura, A., & Kaneda, H., 2013, "AKARI Infrared Camera Survey of the Large Magellanic Cloud. II. The Near-infrared Spectroscopic Catalog", AJ, Vol.145, 32 (doi: 10.1088/0004-6256/145/2/32)
161. Fujiwara, H., Ishihara, D., Onaka, T., Takita, S., Kataza,, H., Yamashita, T., Fukagawa, M., Ootsubo, T., Hirao, T., Enya, K., Marshall, J. P., White, G. J., Nakagawa, T., & Murakami, H., 2013, "AKARI/IRC 18 μm survey of warm debris disks", A&A, Vol.550, A45 (doi: 10.1051/0004-6361/201219841)
162. Grady, C. A., Muto, T., Hashimoto, J., Fukagawa, M., Currie, T., Biller, B., Thalmann, C., Sitko, M. L., Russell, R., Wisniewski, J., Dong, R., Kwon, J., Sai, S., Hornbeck, J., Schneider, G., Hines, D., Moro Mart´ın, A., Feldt, M., Henning, T., Pott, J.-U., Bonnefoy, M., Bouwman, J., Lacour, S., Mueller, A., Juh´asz, A., Crida, A., Chauvin, G., Andrews, S., Wilner, D., Kraus, A., Dahm, S., Robitaille, T., Jang-Condell, H., Abe, L., Akiyama, E., Brandner, W., Brandt, T., Carson, J., Egner, S., Follette, K. B., Goto, M., Guyon, O., Hayano, Y., Hayashi, M., Hayashi, S., Hodapp, K., Ishii, M., Iye, M., Janson, M., Kandori, R., Knapp, G., Kudo, T., Kusakabe, N., Kuzuhara, M., Mayama, S., McElwain, M., Matsuo, T., Miyama, S., Morino, J.-I., Nishimura, T., Pyo, T.-S., Serabyn, G., Suto, H., Suzuki, R., Takami, M., Takato, N., Terada, H., Tomono, D., Turner, E., Watanabe, M., Yamada, T., Takami, H., Usuda, T., & Tamura, M., 2013, "Spiral Arms in the Asymmetrically Illuminated Disk of MWC 758 and Constraints on Giant Planets", ApJ, Vol.762, 48 (doi: 10.1088/0004-637X/762/1/48)
163. Tanii, R., Itoh, Y., Kudo, T., Hioki, T., Oasa, Y., Gupta, R., Sen, A. K., Wisniewski, J. P., Muto, T., Grady, C. A., Hashimoto, J., Fukagawa, M., Mayama, S., Hornbeck, J., Sitko, M. L., Russell, R. W., Werren, C., Cur´e, M., Currie, T., Ohashi, N., Okamoto, Y., Momose, M., Honda, M., Inutsuka, S.-i., Takeuchi, T., Dong, R., Abe, L., Brandner, W., Brandt, T. D., Carson, J., Egner, S. E., Feldt, M., Fukue, T., Goto, M., Guyon, O., Hayano, Y., Hayashi, M., Hayashi, S. S., Henning, T., Hodapp, K. W., Ishii, M., Iye, M., Janson, M., Kandori, R., Knapp, G. R., Kusakabe, N., Kuzuhara, M., Matsuo, T., McElwain, M. W., Miyama, S., Morino, J.-i., Moro-Mart´ın, A., Nishimura, T., Pyo, T.-S., Serabyn, E., Suto, H., Suzuki, R., Takami, M., Takato, N., Terada, H., Thalmann, C., Tomono, D., Turner, E. L., Watanabe, M., Yamada, T., Takami, H., Usuda, T., & Tamura, M., 2012, "High-Resolution Near-Infrared Polarimetry of a Circumstellar Disk around UX Tau A", PASJ, Vol.64, 124 (doi: 10.1093/pasj/64.6.124)
164. Boyd, R. N., Kajino, T., & Onaka, T., 2012, "Stardust, supernovae, neutrinos and the chirality of the amino acids", Journal of Physics Conference Series, Vol.403, 012032 (doi: 10.1088/1742-6596/403/1/012032)
165. Aota, T., & Aikawa, Y., 2012, "Phosphorus Chemistry in the Shocked Region L1157 B1", ApJ, Vol.761, 74 (doi: 10.1088/0004-637X/761/1/74)
166. Ohsawa, R., Onaka, T., Sakon, I., Mori, T. I., Miyata, T., Asano, K., Matsuura, M., & Kaneda, H., 2012, "Unusual Carbonaceous Dust Distribution in PN G095.2+00.7", ApJL,

Vol.760, L34 (doi: 10.1088/2041-8205/760/2/L34)
167. Currie, T., Debes, J., Rodigas, T. J., Burrows, A., Itoh, Y., Fukagawa, M., Kenyon, S. J., Kuchner, M., & Matsumura, S., 2012, "Direct Imaging Confirmation and Characterization of a Dust-enshrouded Candidate Exoplanet Orbiting Fomalhaut", ApJL, Vol.760, L32 (doi: 10.1088/2041-8205/760/2/L32)
168. Mayama, S., Hashimoto, J., Muto, T., Tuskagoshi, T., Kusakabe, N., Kuzuhara, M., Takahashi, Y., Kudo, T., Dong, R., Fukagawa, M., Takami, M., Momose, M., Wisniewski, J. P., Follette, K., Abe, L., Akiyama, E., Brandner, W., Brandt, T., Carson, J., Egner, S., Feldt, M., Goto, M., Grady, C. A., Guyon, O., Hayano, Y., Hayashi, M., Hayashi, S., Henning, T., Hodapp, K. W., Ishii, M., Iye, M., Janson, M., Kandori, R., Kwon, J., Knapp, G. R., Matsuo, T., McElwain, M. W., Miyama, S., Morino, J.-I., Moro-Martin, A., Nishimura, T., Pyo, T.-S., Serabyn, E., Suto, H., Suzuki, R., Takato, N., Terada, H., Thalmann, C., Tomono, D., Turner, E. L., Watanabe, M., Yamada, T., Takami, H., Usuda, T., & Tamura, M., 2012, "Subaru Imaging of Asymmetric Features in a Transitional Disk in Upper Scorpius", ApJL, Vol.760, L26 (doi: 10.1088/2041-8205/760/2/L26)
169. Kato, D., Ita, Y., Onaka, T., Tanab´e, T., Shimonishi, T., Sakon, I., Kaneda, H., Kawamura, A., Wada, T., Usui, F., Koo, B.-C., Matsuura, M., & Takahashi, H., 2012, "AKARI Infrared Camera Survey of the Large Magellanic Cloud. I. Point-source Catalog", AJ, Vol.144, 179 (doi: 10.1088/0004-6256/144/6/179)
170. Imanishi, M., Nakagawa, T., Shirahata, M., Ohyama, Y., & Onaka, T., 2012, "Akari IRC Infrared 2.5-5 #13211 Spectroscopy of Nearby Luminous Infrared Galaxies", PKAS, Vol.27, 271 (doi: 10.5303/PKAS.2012.27.4.271)
171. Ohsawa, R., Onaka, T., Sakon, I., Mori, T. I., Yamamura, I., Matsuura, M., Kaneda, H., Bernard-Salas, J., Berne, O., & Joblin, C., 2012, "Investigation of PAHs in Galactic Planetary Nebulae with the Akari/irc and the Spitzer/irs", PKAS, Vol.27, 259 (doi: 10.5303/PKAS.2012.27.4.259)
172. Kondo, T., Kaneda, H., Oyabu, S., Ishihara, D., Mori, T., Yamagishi, M., Onaka, T., Sakon, I., & Suzuki, T., 2012, "The Central Region of the Barred Spiral Galaxy NGC 1097 Probed by Akari Near-Infrared Spectroscopy", PKAS, Vol.27, 257 (doi: 10.5303/PKAS.2012.27.4.257)
173. Egusa, F., Sakon, I., Onaka, T., Matsuhara, H., Arimatsu, K., Suzuki, T., Wada, T., & IRC Team, 2012, "Interstellar Dust in M51 from IRC Images", PKAS, Vol.27, 253 (doi: 10.5303/PKAS.2012.27.4.253)
174. Yamagishi, M., Kaneda, H., Oyabu, S., Ishihara, D., Onaka, T., Shimonishi, T., & Suzuki, T., 2012, "Systematic Study of Interstellar Ices in Nearby Galaxies", PKAS, Vol.27, 249 (doi: 10.5303/PKAS.2012.27.4.249)
175. Suzuki, T., Kaneda, H., & Onaka, T., 2012, "Observations of Star Formation Induced by Galaxy-Galaxy and Galaxy-Intergalactic Medium Interactions with Akari", PKAS, Vol.27, 243 (doi: 10.5303/PKAS.2012.27.4.243)
176. Kaneda, H., Ishihara, D., Onaka, T., Sakon, I., Suzuki, T., Kobata, K., Kondo, T., Yamagishi, M., & Yasuda, A., 2012, "Processing of Interstellar Dust Grains in Galaxies", PKAS, Vol.27, 237 (doi: 10.5303/PKAS.2012.27.4.237)
177. Siudek, M., Pollo, A., Takeuchi, T. T., Ita, Y., Kato, D., & Onaka, T., 2012, "Infrared Composition of the Large Magellanic Cloud", PKAS, Vol.27, 223 (doi: 10.5303/PKAS.2012.27.4.223)
178. Mouri, A., Kaneda, H., Ishihara, D., Oyabu, S., Kondo, T., Suzuki, S., Yasuda, A., &

Onaka, T., 2012, "a Study of the Galactic Center Regions Using the Improved Data of the Mid-Infrared All-Sky Survey", PKAS, Vol.27, 217 (doi: 10.5303/PKAS.2012.27.4.217)

179. Sakon, I., Onaka, T., Mori, T. I., Ohsawa, R., Doi, Y., Okada, Y., Kaneda, H., & Ootsubo, T., 2012, "Akari mid- to Far-Infrared Observations of Diffuse Galactic Emission", PKAS, Vol.27, 213 (doi: 10.5303/PKAS.2012.27.4.213)
180. Mori, T. I., Sakon, I., Onaka, T., Umehata, H., Kaneda, H., & Ohsawa, R., 2012, "Near- to Mid-Infrared Slit Spectroscopic Observations of the Unidentified Infrared Bands in the Large Magellanic Cloud", PKAS, Vol.27, 209 (doi: 10.5303/PKAS.2012.27.4.209)
181. PLANCK Collaboration, Giard, M., Berne, O., Doi, Y., Ishihara, D., Joblin, C., Kaneda, I., Marshall, D., Nakagawa, T., Ohsawa, R., Onaka, T., Sakon, I., Shibai, H., & Ysard, N., 2012, "Is the Anomalous Microwave Emission due to the Rotation of Interstellar Pahs? Planck Results: PLANCK - AKARI Project", PKAS, Vol.27, 195 (doi: 10.5303/PKAS.2012.27.4.195)
182. Onaka, T., 2012, "Akari Observations of the Interstellar Medium", PKAS, Vol.27, 187 (doi: 10.5303/PKAS.2012.27.4.187)
183. Kiriyama, Y., Ishihara, D., Nagayama, T., Kaneda, H., Oyabu, S., Onaka, T., & Fujiwara, H., 2012, "Debris Disks Explored by Akari and Irsf", PKAS, Vol.27, 181 (doi: 10.5303/PKAS.2012.27.4.181)
184. Shimonishi, T., Onaka, T., Kato, D., Sakon, I., Ita, Y., Kawamura, A., & Kaneda, H., 2012, "Akari Infrared Observations of Embedded YSOs in the Magellanic Clouds", PKAS, Vol.27, 171 (doi: 10.5303/PKAS.2012.27.4.171)
185. Ita, Y., Kato, D., Onaka, T., & AKARI/LMC Survey Team, 2012, "AKARI IRC Survey of the Large Magellanic Cloud: AN Overview of the Survey and a Brief Description of the Point Source Catalog", PKAS, Vol.27, 165 (doi: 10.5303/PKAS.2012.27.4.165)
186. Ishihara, D., Kaneda, H., Mouri, A., Kondo, T., Suzuki, S., Oyabu, S., Onaka, T., Ita, Y., Matsuura, M., & Matsunaga, N., 2012, "Lifecycle of the Interstellar Dust Grains in Our Galaxy Viewed with Akari/mir All-Sky Survey", PKAS, Vol.27, 117 (doi: 10.5303/PKAS.2012.27.4.117)
187. Yasui, M., Arakawa, M., Hasegawa, S., Fujita, Y., & Kadono, T., 2012, "In situ flash X-ray observation of projectile penetration processes and crater cavity growth in porous gypsum target analogous to low-density asteroids", Icarus, Vol.221, 646 (doi: 10.1016/j.icarus.2012.08.018)
188. Aikawa, Y., Wakelam, V., Hersant, F., Garrod, R. T., & Herbst, E., 2012, "From Prestellar to Protostellar Cores. II. Time Dependence and Deuterium Fractionation", ApJ, Vol.760, 40 (doi: 10.1088/0004-637X/760/1/40)
189. Caselli, P., Keto, E., Bergin, E. A., Tafalla, M., Aikawa, Y., Douglas, T., Pagani, L., Y´ıld´ız, U. A., van der Tak, F. F. S., Walmsley, C. M., Codella, C., Nisini, B., Kristensen, L. E., & van Dishoeck, E. F., 2012, "First Detection of Water Vapor in a Pre-stellar Core", ApJL, Vol.759, L37 (doi: 10.1088/2041-8205/759/2/L37)
190. Fujiwara, H., Onaka, T., Takita, S., Yamashita, T., Fukagawa, M., Ishihara, D., Kataza,, H., & Murakami, H., 2012, "The Absence of Cold Dust around Warm Debris Disk Star HD 15407A", ApJL, Vol.759, L18 (doi: 10.1088/2041-8205/759/1/L18)
191. Yamaguchi, T., Takano, S., Watanabe, Y., Sakai, N., Sakai, T., Liu, S.-Y., Su, Y.-N., Hirano, N., Takakuwa, S., Aikawa, Y., Nomura, H., & Yamamoto, S., 2012, "The 3 mm Spectral Line Survey toward the Lynds 1157 B1 Shocked Region. I. Data", PASJ, Vol.64, 105 (doi: 10.1093/pasj/64.5.105)

192. Hashimoto, J., Dong, R., Kudo, T., Honda, M., McClure, M. K., Zhu, Z., Muto, T., Wisniewski, J., Abe, L., Brandner, W., Brandt, T., Carson, J., Egner, S., Feldt, M., Fukagawa, M., Goto, M., Grady, C. A., Guyon, O., Hayano, Y., Hayashi, M., Hayashi, S., Henning, T., Hodapp, K., Ishii, M., Iye, M., Janson, M., Kandori, R., Knapp, G., Kusakabe, N., Kuzuhara, M., Kwon, J., Matsuo, T., Mayama, S., McElwain, M. W., Miyama, S., Morino, J.-I., Moro-Martin, A., Nishimura, T., Pyo, T.-S., Serabyn, G., Suenaga, T., Suto, H., Suzuki, R., Takahashi, Y., Takami, M., Takato, N., Terada, H., Thalmann, C., Tomono, D., Turner, E. L., Watanabe, M., Yamada, T., Takami, H., Usuda, T., & Tamura, M., 2012, "Polarimetric Imaging of Large Cavity Structures in the Pre-transitional Protoplanetary Disk around PDS 70: Observations of the Disk", ApJL, Vol.758, L19 (doi: 10.1088/2041-8205/758/1/L19)
193. Furuya, K., Aikawa, Y., Tomida, K., Matsumoto, T., Saigo, K., Tomisaka, K., Hersant, F., & Wakelam, V., 2012, "Chemistry in the First Hydrostatic Core Stage by Adopting Three-dimensional Radiation Hydrodynamic Simulations", ApJ, Vol.758, 86 (doi: 10.1088/0004-637X/758/2/86)
194. Ormel, C. W., Ida, S., & Tanak,H., 2012, "Migration Rates of Planets due to Scattering of Planetesimals", ApJ, Vol.758, 80 (doi: 10.1088/0004-637X/758/2/80)
195. Shimaki, Y., & Arakawa, M., 2012, "Low-velocity collisions between centimeter-sized snowballs: Porosity dependence of coefficient of restitution for ice aggregates analogues in the Solar System", Icarus, Vol.221, 310 (doi: 10.1016/j.icarus.2012.08.005)
196. Suzuki, A., Hakura, S., Hamura, T., Hattori, M., Hayama, R., Ikeda, T., Kusuno, H., Kuwahara, H., Muto,, Y., Nagaki, K., Niimi, R., Ogata, Y., Okamoto, T., Sasamori, T., Sekigawa, C., Yoshihara, T., Hasegawa, S., Kurosawa, K., Kadono, T., Nakamura, A. M., Sugita, S., & Arakawa, M., 2012, "Laboratory experiments on crater scaling-law for sedimentary rocks in the strength regime", Journal of Geophysical Research (Planets), Vol.117, E08012 (doi: 10.1029/2012JE004064)
197. Currie, T., Fukagawa, M., Thalmann, C., Matsumura, S., & Plavchan, P., 2012, "Direct Detection and Orbital Analysis of the Exoplanets HR 8799 bcd from Archival 2005 Keck/NIRC2 Data", ApJL, Vol.755, L34 (doi: 10.1088/2041-8205/755/2/L34)
198. Kusakabe, N., Grady, C. A., Sitko, M. L., Hashimoto, J., Kudo, T., Fukagawa, M., Muto, T., Wisniewski, J. P., Min, M., Mayama, S., Werren, C., Day, A. N., Beerman, L. C., Lynch, D. K., Russell, R. W., Brafford, S. M., Kuzuhara, M., Brandt, T. D., Abe, L., Brandner, W., Carson, J., Egner, S., Feldt, M., Goto, M., Guyon, O., Hayano, Y., Hayashi, M., Hayashi, S. S., Henning, T., Hodapp, K. W., Ishii, M., Iye, M., Janson, M., Kandori, R., Knapp, G. R., Matsuo, T., McElwain, M. W., Miyama, S., Morino, J.-I., Moro-Martin, A., Nishimura, T., Pyo, T.-S., Suto, H., Suzuki, R., Takami, M., Takato, N., Terada, H., Thalmann, C., Tomono, D., Turner, E. L., Watanabe, M., Yamada, T., Takami, H., Usuda, T., & Tamura, M., 2012, "High-contrast Near-infrared Polarization Imaging of MWC480", ApJ, Vol.753, 153 (doi: 10.1088/0004-637X/753/2/153)
199. Suyama, T., Wada, K., Tanak,H., & Okuzumi, S., 2012, "Geometric Cross Sections of Dust Aggregates and a Compression Model for Aggregate Collisions", ApJ, Vol.753, 115 (doi: 10.1088/0004-637X/753/2/115)
200. Kaneda, H., Yasuda, A., Onaka, T., Kawada, M., Murakami, N., Nakagawa, T., Okada, Y., & Takahashi, H., 2012, "Properties of dust at the Galactic center probed by AKARI far-infrared spectral mapping. Detection of a dust feature", A&A, Vol.543, A79 (doi: 10.1051/0004-6361/201219238)

201. Honda, M., Maaskant, K., Okamoto, Y. K., Kataza,, H., Fukagawa, M., Waters, L. B. F. M., Dominik, C., Tielens, A. G. G. M., Mulders, G. D., Min, M., Yamashita, T., Fujiyoshi, T., Miyata, T., Sako, S., Sakon, I., Fujiwara, H., & Onaka, T., 2012, "Mid-infrared Imaging of the Transitional Disk of HD 169142: Measuring the Size of the Gap", ApJ, Vol.752, 143 (doi: 10.1088/0004-637X/752/2/143)
202. Okuzumi, S., Tanak,H., Kobayashi, H., & Wada, K., 2012, "Rapid Coagulation of Porous Dust Aggregates outside the Snow Line: A Pathway to Successful Icy Planetesimal Formation", ApJ, Vol.752, 106 (doi: 10.1088/0004-637X/752/2/106)
203. Ootsubo, T., Kawakita, H., Hamada, S., Kobayashi, H., Yamaguchi, M., Usui, F., Nakagawa, T., Ueno, M., Ishiguro, M., Sekiguchi, T., Watanabe, J.-i., Sakon, I., Shimonishi, T., & Onaka, T., 2012, "AKARI Near-infrared Spectroscopic Survey for CO_2 in 18 Comets", ApJ, Vol.752, 15 (doi: 10.1088/0004-637X/752/1/15)
204. Uchiyama, Y.-i., Arakawa, M., Okamoto, C., & Yasui, M., 2012, "Restitution coefficients and sticking velocities of a chondrule analogue colliding on a porous silica layer at impact velocities between 0.1 and 80 m s^{-1}", Icarus, Vol.219, 336 (doi: 10.1016/j.icarus.2012.03.008)
205. Kondo, T., Kaneda, H., Oyabu, S., Ishihara, D., Mori, T., Yamagishi, M., Onaka, T., Sakon, I., & Suzuki, T., 2012, "The Central Region of the Barred Spiral Galaxy NGC 1097 Probed by AKARI Near-infrared Spectroscopy", ApJL, Vol.751, L18 (doi: 10.1088/2041-8205/751/1/L18)
206. Yamagishi, M., Kaneda, H., Ishihara, D., Kondo, T., Onaka, T., Suzuki, T., & Minh, Y. C., 2012, "AKARI near-infrared spectroscopy of the aromatic and aliphatic hydrocarbon emission features in the galactic superwind of M 82", A&A, Vol.541, A10 (doi: 10.1051/0004-6361/201218904)
207. Kaneda, H., Ishihara, D., Mouri, A., Oyabu, S., Yamagishi, M., Kondo, T., Onaka, T., Fukui, Y., Kawamura, A., & Torii, K., 2012, "Processing of Polycyclic Aromatic Hydrocarbons in Molecular-Loop Regions near the Galactic Center Revealed by AKARI", PASJ, Vol.64, 25 (doi: 10.1093/pasj/64.2.25)
208. Dohi, K., Arakawa, M., Okamoto, C., Hasegawa, S., & Yasui, M., 2012, "The effect of a thin weak layer covering a basalt block on the impact cratering process", Icarus, Vol.218, 751 (doi: 10.1016/j.icarus.2012.01.018)
209. Shimaki, Y., & Arakawa, M., 2012, "Experimental study on collisional disruption of highly porous icy bodies", Icarus, Vol.218, 737 (doi: 10.1016/j.icarus.2012.01.021)
210. Fujiwara, H., Onaka, T., Yamashita, T., Ishihara, D., Kataza,, H., Fukagawa, M., Takeda, Y., & Murakami, H., 2012, "Silica-rich Bright Debris Disk around HD 15407A", ApJL, Vol.749, L29 (doi: 10.1088/2041-8205/749/2/L29)
211. Tanaka, M., Nozawa, T., Sakon, I., Onaka, T., Arimatsu, K., Ohsawa, R., Maeda, K., Wada, T., Matsuhara, H., & Kaneda, H., 2012, "A Search for Infrared Emission from Core-collapse Supernovae at the Transitional Phase", ApJ, Vol.749, 173 (doi: 10.1088/0004-637X/749/2/173)
212. Muto, T., Grady, C. A., Hashimoto, J., Fukagawa, M., Hornbeck, J. B., Sitko, M., Russell, R., Werren, C., Cur´e, M., Currie, T., Ohashi, N., Okamoto, Y., Momose, M., Honda, M., Inutsuka, S., Takeuchi, T., Dong, R., Abe, L., Brandner, W., Brandt, T., Carson, J., Egner, S., Feldt, M., Fukue, T., Goto, M., Guyon, O., Hayano, Y., Hayashi, M., Hayashi, S., Henning, T., Hodapp, K. W., Ishii, M., Iye, M., Janson, M., Kandori, R., Knapp, G. R., Kudo, T., Kusakabe, N., Kuzuhara, M., Matsuo, T., Mayama, S., McElwain, M. W.,

Miyama, S., Morino, J.-I., Moro-Martin, A., Nishimura, T., Pyo, T.-S., Serabyn, E., Suto, H., Suzuki, R., Takami, M., Takato, N., Terada, H., Thalmann, C., Tomono, D., Turner, E. L., Watanabe, M., Wisniewski, J. P., Yamada, T., Takami, H., Usuda, T., & Tamura, M., 2012, "Discovery of Small-scale Spiral Structures in the Disk of SAO 206462 (HD 135344B): Implications for the Physical State of the Disk from Spiral Density Wave Theory", ApJL, Vol.748, L22 (doi: 10.1088/2041-8205/748/2/L22)

213. Rho, J., Onaka, T., Cami, J., & Reach, W. T., 2012, "Spectroscopic Detection of Carbon Monoxide in the Young Supernova Remnant Cassiopeia A", ApJL, Vol.747, L6 (doi: 10.1088/2041-8205/747/1/L6)
214. Walsh, C., Nomura, H., Millar, T. J., & Aikawa, Y., 2012, "Chemical Processes in Protoplanetary Disks. II. On the Importance of Photochemistry and X-Ray Ionization", ApJ, Vol.747, 114 (doi: 10.1088/0004-637X/747/2/114)
215. Nakamura, F., Miura, T., Kitamura, Y., Shimajiri, Y., Kawabe, R., Akashi, T., Ikeda, N., Tuskagoshi, T., Momose, M., Nishi, R., & Li, Z.-Y., 2012, "Evidence for Cloud-Cloud Collision and Parsec-scale Stellar Feedback within the L1641-N Region", ApJ, Vol.746, 25 (doi: 10.1088/0004-637X/746/1/25)
216. Aikawa, Y., Kamuro, D., Sakon, I., Itoh, Y., Terada, H., Noble, J. A., Pontoppidan, K. M., Fraser, H. J., Tamura, M., Kandori, R., Kawamura, A., & Ueno, M., 2012, "AKARI observations of ice absorption bands towards edge-on young stellar objects", A&A, Vol.538, A57 (doi: 10.1051/0004-6361/201015999)
217. Enya, K., Yamada, N., Imai, T., Tange, Y., Kaneda, H., Katayama, H., Kotani, M., Maruyama, K., Naitoh, M., Nakagawa, T., Onaka, T., Suganuma, M., Ozaki, T., Kume, M., & Kr¨odel, M. R., 2012, "High-precision CTE measurement of hybrid C/SiC composite for cryogenic space telescopes", Cryogenics, Vol.52, 86 (doi: 10.1016/j.cryogenics.2011.10.004)
218. Seok, J. Y., Koo, B.-C., & Onaka, T., 2012, "Detection of the 3.3 μm Aromatic Feature in the Supernova Remnant N49 with AKARI", ApJ, Vol.744, 160 (doi: 10.1088/0004-637X/744/2/160)
219. Mori, T. I., Sakon, I., Onaka, T., Kaneda, H., Umehata, H., & Ohsawa, R., 2012, "Observations of the near- to Mid-infrared Unidentified Emission Bands in the Interstellar Medium of the Large Magellanic Cloud", ApJ, Vol.744, 68 (doi: 10.1088/0004-637X/744/1/68)
220. Tanak,H., Wada, K., Suyama, T., & Okuzumi, S., 2012, "Growth of Cosmic Dust Aggregates and Reexamination of Particle Interaction Models", Progress of Theoretical Physics Supplement, Vol.195, 101
221. Arakawa, M., & Yasui, M., 2011, "Impact crater formed on sintered snow surface simulating porous icy bodies", Icarus, Vol.216, 1 (doi: 10.1016/j.icarus.2011.08.018)
222. Yamaguchi, T., Takano, S., Sakai, N., Sakai, T., Liu, S. -Y., Su, Y.-N., Hirano, N., Takakuwa, S., Aikawa, Y., Nomura, H., & Yamamoto, S., 2011, "Detection of Phosphorus Nitride in the Lynds 1157 B1 Shocked Region", PASJ, Vol.63, L37 (doi: 10.1093/pasj/63.5.L37)
223. Usui, F., Kuroda, D., Mu¨ller, T. G., Hasegawa, S., Ishiguro, M., Ootsubo, T., Ishihara, D., Kataza,, H., Takita, S., Oyabu, S., Ueno, M., Matsuhara, H., & Onaka, T., 2011, "Asteroid Catalog Using Akari: AKARI/IRC Mid-Infrared Asteroid Survey", PASJ, Vol.63, 1117 (doi: 10.1093/pasj/63.5.1117)
224. Akiyama, E., Momose, M. Hayashi, H., & Kitamura, Y., 2011, "Thermal Structure of a

Protoplanetary Disk around HD 163296: A Study of Vertical Temperature Distribution by CO Emission Lines", PASJ, Vol.63, 1059 (doi: 10.1093/pasj/63.5.1059)

225. Kobayashi, H., Kimura, H., Watanabe, S.-i., Yamamoto, T., & Mu¨ller, S., 2011, "Sublimation temperature of circumstellar dust particles and its importance for dust ring formation", Earth, Planets, and Space, Vol.63, 1067 (doi: 10.5047/eps.2011.03.012)
226. Lee, H.-G., Moon, D.-S., Koo, B.-C., Onaka, T., Jeong, W.-S., Shinn, J.-H., & Sakon, I., 2011, "Far-Infrared Luminous Supernova Remnant Kes 17", ApJ, Vol.740, 31 (doi: 10.1088/0004-637X/740/1/31)
227. Ishihara, D., Kaneda, H., Onaka, T., Ita, Y., Matsuura, M., & Matsunaga, N., 2011, "Galactic distributions of carbon- and oxygen-rich AGB stars revealed by the AKARI mid-infrared all-sky survey", A&A, Vol.534, A79 (doi: 10.1051/0004-6361/201117626)
228. Kobayashi, H., Tanak,H., & Krivov, A. V., 2011, "Planetary Core Formation with Collisional Fragmentation and Atmosphere to Form Gas Giant Planets", ApJ, Vol.738, 35 (doi: 10.1088/0004-637X/738/1/35)
229. Arimatsu, K., Onaka, T., Sakon, I., Oyabu, S., Ita, Y., Tanab´e, T., Kato, D., Egusa, F., Wada, T., & Matsuhara, H., 2011, "Characterization and Improvement of the Image Quality of the Data Taken with the Infrared Camera (IRC) Mid-Infrared Channels on Board AKARI", PASP, Vol.123, 981 (doi: 10.1086/661201)
230. Kato, E., Fukagawa, M., Perrin, M. D., Shibai, H., Itoh, Y., & Ootsubo, T., 2011, "Near- and Mid-Infrared Imaging Study of Young Stellar Objects around LkHα 234", PASJ, Vol.63, 849 (doi: 10.1093/pasj/63.4.849)
231. Yasui, M., & Arakawa, M., 2011, "Impact experiments of porous gypsum-glass bead mixtures simulating parent bodies of ordinary chondrites: Implications for re-accumulation processes related to rubble-pile formation", Icarus, Vol.214, 754 (doi: 10.1016/j.icarus.2011.05.012)
232. Wada, K., Tanak,H., Suyama, T., Kimura, H., & Yamamoto, T., 2011, "The Rebound Condition of Dust Aggregates Revealed by Numerical Simulation of Their Collisions", ApJ, Vol.737, 36 (doi: 10.1088/0004-637X/737/1/36)

計画研究B02：ハビタブル地球型惑星の形成理論

1. Taki, T. Fujimoto, M., Ida, S., 2016, Dust and Gas Density Evolution at a Radial Pressure Bump in Protoplanetary Disks, The Astrophysical Journal, in press
2. Ma, S., Mao, S., Ida, S., Zhu, W., Lin, D. N. C. 2016. Free-floating planets from core accretion theory: microlensing predictions, *MNRAS,* 461, p.L107-L111
3. Ida, S., Guillot, T. & Morbidelli, A. 2016. The radial dependence of pebble accretion rates: A source of diversity in planetary systems. I. Analytical formulation, *Astronomy & Astrophysics*, 591, id.A72(12pp)
4. Homann, H., Guillot, T., Bec, J., Ormel, C. W.. Ida, S., Tanga, P. 2016, Effect of turbulence on collisions of dust particles with planetesimals in protoplanetary discs, *Astronomy & Astrophysics*, 589, id.A129(15pp)
5. Hosono, N., Saitoh, T., Makino, J., Genda, H. & Ida, S. 2016, The Giant Impact Simulations with Density Independent Smoothed Particle Hydrodynamics. *Icarus*, 271, 131-157
6. Sato, T., Okuzumi, S., Ida, S., 2016, On the water delivery to terrestrial embryos by ice pebble accretion, Astronomy & Astrophysics, 589, id.A15(19pp)
7. Okuzumi, S., Momose, M., Sirono, S., Kobayashi, H., Tanaka, H., 2016, Sintering-induced Dust Ring Formation in Protoplanetary Disks: Application to the HL Tau Disk, The Astrophysical Journal, 821, 82(24pp)
8. Honda, M., Kudo, T., Takatsuki, S., Inoue, A., Nakamoto, T., Fukagawa, M., Tamura, M., Terada, H., Takato, N., 2016, Water Ice at the Surface of HD 100546 Disk, The Astrophysical Journal, 821, 2(6pp)
9. Miyake, T., Suzuki, T. K. & Inutsuka, S., 2016, Dust Dynamics in Protoplanetary Disk Winds Driven by Magneto-Rotational Turbulence: A Mechanism for Floating Dust Grains with Characteristic Size, Astrophysical Journal, 821, 3(8pp)
10. Nomura, H., Tsukagoshi, T., Kawabe, R., Ishimoto, D., Okuzumi, S., Muto, T., Kanagawa, K.D., Ida, S., Walsh, C., Millar, T.J.; Bai, X.-N., 2016, ALMA Observations of a Gap and a Ring in the Protoplanetary Disk around TW Hya, Astrophys. J. Letter, 819, L7, 7pp,
11. Shibaike, Y., Sasaki, T. & Ida, S. 2016, Excavation and Melting of the Hadean Continental Crust by Late Heavy Bombardment, *Icarus*, 266, 89–203
12. Sato, B. … Ida, S. (21st in 21 authors) A Pair of Giant Planets around the Evolved Intermediate-Mass Star HD 47366: multiple circular orbits or a mutually retrograde configuration, *Astrophysical J.*, 819, article id.59(11pp)
13. Harakawa, H. … Ida, S. …. (6th in 16 authors) (2015) Five New Exoplanets Orbiting Three Metal-rich, Massive Stars: Two-planet Systems Including Long-period Planets and an Eccentric Planet, *Astrophysical J.*, 806, article id.5(11pp)
14. Mori, S., Okuzumi, S., 2015, Electron Heating in Magnetorotational Instability: Implications for Turbulence Strength in the Outer Regions of Protoplanetary Disks, The Astrophysical Journal, Volume 817, Issue 1, article id. 52, 16 pp, DOI:10.3847/0004-637X/817/1/52
15. Tomida, K., Okuzumi, S., Machida, Masahiro N. 2015, Radiation Magnetohydrodynamic Simulations of Protostellar Collapse: Non-ideal Magnetohydrodynamic Effects and Early Formation of Circumstellar Disks, The Astrophysical Journal, Volume 801, Issue 2, article id. 117, 20 pp, DOI:10.1088/0004-637X/801/2/117
16. Okuzumi, S., Inutsuka, S., 2015, The Nonlinear Ohm's Law: Plasma Heating by Strong

Electric Fields and its Effects on the Ionization Balance in Protoplanetary Disks, The Astrophysical Journal, Volume 800, Issue 1, article id. 47, 19 pp., DOI:10.1088/0004-637X/800/1/47

17. Matsumoto, Y., Nagasawa, M., Ida, S., 2015, Eccentricity Evolution Through Accretion of Protoplanets, The Astrophysical Journal, Volume 810, Issue 2, article id. 106, 10 pp, DOI: 10.1088/0004-637X/810/2/106
18. Lewis, K. M., Ochiai, H., Nagasawa, M., Ida, S., 2015, Extrasolar Binary Planets II: Detectability by Transit Observations, The Astrophysical Journal, Volume 805, Issue 1, Volume 805, Issue 1, article id. 27, 13 pp, DOI: 10.1088/0004-637X/805/1/27
19. Matsumura, S., Brasser, R. & Ida, S. 2015, Effects of Dynamical Evolution of Giant Planets on the Delivery of Atmophile Elements During Terrestrial Planet Formation, Astrophysical J. 818: article id 15(18pp).
20. Miguel, Y. & Ida, S. 2015, A semi-analytical model for exploring Galilean satellites formation from a massive disk. ***Icarus***, 266, pp.1-14
21. Higuchi, A. & Ida, S. 2015, Temporary Capture of Asteroids by a Planet: Dependence of Prograde/Retrograde Capture on Asteroids' Semimajor Axes. *Astrononimcal J.,* 151, article id 16 (9pp)
22. Citron, R. I., Genda, H., Ida, S. 2015, Formation of Phobos and Deimos via a giant impact. ***Icarus,*** 252, pp. 334-338
23. Lewis, K. M., Ochiai, H., Nagasawa , M. & Ida, S. 2015, Extrasolar Binary Planets. II: Detectability by Transit Observations, *Astrophysical J,.* 805: article id 27, pp.
24. Tian, F. & Ida, S. Water contents of Earth-mass planets around M dwarfs, Nature Geoscience, 8, 177–180, 10.1038/NGEO2372
25. Muto, T., Tsukagoshi, T., Momose, M., Hanawa, T., Nomura, H., Fukagawa, M., Saigo, K., Kataoka, A., Kitamura, Y., Takahashi, S.Z., Inutsuka, S., Takeuchi, T., Kobayashi, H., Akiyama, E., Honda, M., Fujiwara, H., Shibai, H. 2015, Significant gas-to-dust ratio asymmetry and variation in the disk of HD 142527 and the indication of gas depletion, Publications of the Astronomical Society of Japan, 67, 122, 28pp, DOI: 10.1093/pasj/psv098 (2015)
26. Aikawa, Y., Furuya, K., Nomura, H., Qi, C. 2015, Analytical Formulae of Molecular Ion Abundances and the N2H+ Ring in Protoplanetary Disks, Astrophys. J., 807, 120, 19pp, DOI:10.1088/0004-637X/807/2/120
27. Ogihara, M., Kobayashi, H., Inutsuka, S. & Suzuki, T. K., 2015, Formation of terrestrial planets in disks evolving via disk winds and implications for the origin of the solar system's terrestrial planets, Astronomy & Astrophysics, 579, A65
28. Tanaka, Y., Suzuki, T. K. & Inutsuka, S. 2015, Atmospheric Escape by Magnetically Driven Wind from Gaseous Planets. II. Effects of Magnetic Diffusion, The Astrophysical Journal, Vol. 809, 125(12pp)
29. Genda, H., Kobayashi, H., Kokubo, E., 2015, Warm Debris Disks Produced by Giant Impacts during Terrestrial Planet Formation, The Astrophysical Journal, 810, 136(8pp), DOI:10.1088/0004-637X/810/2/136
30. Kikuchi, A., Higuchi, A., Ida, S., 2014, Orbital Circularization of a Planet Accreting Disk Gas: The Formation of Distant Jupiters in Circular Orbits Based on a Core Accretion Model, Volume 797, Issue 1, article id. 1, 13 pp, DOI: 10.1088/0004-637X/797/1/1
31. Guillot, T., Ida, S. & Ormel, C. W. On the filtering and processing of dust by planetesimals. I. Derivation of collision probabilities for non-drifting planetesimals. Astronomy &

Astrophysics, 572: id.A72, 2014, 10.1051/0004-6361/201323021
32. Ochiai, H., Nagasawa, M. & Ida, S. 2014, Extrasolar Binary Planets. I. Formation by Tidal Capture during Planet-Planet Scattering Astrophysical J,. 790: article id 92, 2014, 10.1088/0004-637X/790/2/92
33. Brasser, R., Ida, S. & Kokubo, E. 2014, A dynamical study on the habitability of terrestrial exoplanets - II The super-Earth HD 40307g. Monthly Notices of the Royal Astronomical Society, 440: 3685-3700, 2014, 10.1093/mnras/stu555
34. Kurosaki, K., Ikoma, M., Hori, Y., 2014, Impact of photo-evaporative mass loss on masses and radii of water-rich sub/super-Earths, Astronomy & Astrophysics, 562, id.A80, 14pp: 10.1051/0004-6361/201322258
35. Kataoka, A., Okuzumi, S., Tanaka, H., Nomura, H.Opacity of fluffy dust aggregates, 2014Astron & Astrophys, 568, A42, 15pp, DOI:10.1051/0004-6361/201323199 (2014)
36. Ono, T. Nomura, H., Takeuchi, T. 2014, Rotational Instability in the Outer Region of Protoplanetary
Disks, Astrophys. J., 787, 37, 7pp, DOI:10.1088/0004-637X/787/1/37 (2014)
37. Walsh, C., Millar, T.J.; Nomura, H., Herbst, E., Widicus Weaver, S., Aikawa, Y., Laas, J.C., Vasyunin, A.I., 2014, Complex organic molecules in protoplanetary disks, Astron & Astrophys, 56, A33, 35pp, DOI: 10.1051/0004-6361/201322446
38. Okuzumi, S. & Ormel, C. W., 2013, The Fate of Planetesimals in Turbulent Disks with Dead Zones. I. The Turbulent Stirring Recipe., Astrophys. J., 771, 43(14pp)
39. Takahashi, S. Z., Machida, M. N. & Inutsuka, S. 2013. A Semi-Analytical Description for Formation and Gravitational Evolution of Protoplanetary Disks. Astrophys. J. 770, 71(10pp)
40. Kataoka, A., Tanaka, H., Okuzumi, S. & Koji, W. 2013. Static compression of porous dust aggregatesAstron. Astrophys. 554, A4 (12pp)
41. Ormel, C. W. & Okuzumi, S., 2013, The Fate of Planetesimals in Turbulent Disks with Dead Zones. II. Limits on the Viability of Runaway Accretion, Astrophys. J., 771, 44(15pp)
42. Matsumura, S., Ida, S. & Nagasawa, M., 2013, Effects of Dynamical Evolution of Giant Planets on Survival of Terrestrial Planets, Astrophys. J., 767, 129(14pp)
43. Brasser, R., Ida, S. & Kokubo, E., 2013, A dynamical study on the habitability of terrestrial exoplanets - I. Tidally evolved planet-satellite pairs, MNRAS, 428, 1673-1685
44. Ida, S., Lin, D. N. C. & Nagasawa, M. 2013. Toward a Deterministic Model of Planetary Formation. VII. Eccentricity Distribution of Gas Giants, *Astrophys. J.,* 775, article id. 42, 25 pp.
45. Hasegawa, Y. & Ida, S., 2013, Do Giant Planets Survive Type II Migration? *Astrophys. J.,* 774, article id. 146, 9 pp.
46. Dwyer, C. A., Nimmo, F., Ogihara, M. & Ida, S. 2013. The Influence of Imperfect Accretion and Radial Mixing on Ice:Rock Ratios in the Galilean Satellites. *Icarus,* 767, 390-402.
47. Matsumura, S., Ida, S. & Nagasawa, M. 2013. Effects of Dynamical Evolution of Giant Planets on Survival of Terrestrial Planets. *Astrophys. J.*, 767, article id. 129, 14 pp.
48. Takahashi, S. Z., Machida, M. N. & Inutsuka, S., 2013, A Semi-Analytical Description for Formation and Gravitational Evolution of Protoplanetary Disks, Astrophys. J., 770, 71(10pp)
49. Kataoka, A., Tanaka, H., Okuzumi, S. & Koji, W., 2013, Static compression of porous dust

aggregates, Astron, Astrophys, 554, A4 (12pp)
50. Sato, B. …, Nagasawa, M. … Ida, S. …Sato, B., Omiya, M., Wittenmyer, R., Harakawa, H., Nagasawa, M., Izumiura, H., Kambe, E., Takeda, Y., Yoshida, M., Itoh, Y., Ando, H., Kokubo, E., Ida, S., 2013, A Double Planetary System around the Evolved Intermediate-Mass Star HD 4732, Astrophys. J., 762, 9(7pp)
51. Walsh, C., Millar, T. J., Nomura, H., 2013, Molecular Line Emission from a Protoplanetary Disk Irradiated Externally by a Nearby Massive Star, Astrophys. J., 766, L23 (8pp)
52. Kurokawa, H. and Nakamoto, T., 2013, Mass-Loss Evolution of Close-In Exoplanets: Evaporation of Hot Jupiters and the Effect on Population, Astrophys. J., 783, 54 (11 pp)
53. Umebayashi, T., Katsuma, S., Nomura, H., 2013, Effects of Dust Growth and Settling on the Ionization by Radionuclides. I. Formulation and Results in a Quiescent State of Protoplanetary Disks, Astrophys. J., 764, 104(21pp)
54. Maruyama, S., Ikoma, M., Genda, H., Hirose, K., Yokoyama, T., & Santosh, M. 2013. The Naked Planet Earth: Most Essential Pre-requisite for the Origin and Evolution of Life. Geoscience Frontiers 4, 141-165.
55. Narita, N., Fukui, A., Ikoma, M. 他 19 名: 2013. Multi-Color Transit Photometry of GJ 1214b through BJHKs-Bands and a Long-Term Monitoring of the Stellar Variability of GJ 1214. Astrophys. J. Submitted
56. Fukui, A., Narita, N., Kurosaki, K., Ikoma, M. 他 14 名: 2013. Optical-to-Near-Infrared Simultaneous Observations for the Hot Uranus GJ3470b: A Hint for Cloud-free Atmosphere. Astrophys. J. 770, 95.
57. Narita, N., Nagayama, T., Suenaga, T., Fukui, A., Ikoma, M., Nakajima, Y., Nishiyama, S., & Tamura, M.: 2013. IRSF SIRIUS JHKs Simultaneous Transit Photometry of GJ 1214b. PASJ 65, 27.
58. Tanaka, K. K., Yamamoto, T., Tanaka, H., Miura, H., Nagasawa, M., and Nakamoto, T. 2013. Evaporation of Icy Planetesimals Due to Bow Shocks. Astrophys. J. 764, 120(11pp)
59. Walsh, C., Nomura, H., Millar, T. J., Aikawa, Y., 2012, Chemical Processes in Protoplanetary Disks. II. On the Importance of Photochemistry and X-Ray Ionization, Astrophys. J., 747, 114(19pp)
60. Kurokawa, H. and Nakamoto, T., 2012, Effects of Atmospheric Absorption of Incoming Radiation on Radiation Limit of the Troposphere. J., Atmospheric Sciences, 69, 403 – 413
61. Matsumoto, Y., Nagasawa, M. & Ida, S., 2012, The orbital stability of planets trapped in the first-order mean-motion resonances, Icarus, 221, 624-631
62. Kobayashi, H., Ormel, C. W. & Ida, S., 2012, Rapid Formation of Saturn after Jupiter Completion, Astrophys. J., 756, 70(17pp)
63. Takeuchi, T. & Ida, S., 2012, Minimum Dust Abundances for Planetesimal Formation via Secular Gravitational Instabilities, Astrophys. J., 749, 89(8pp).
64. Kato, M. T., Fujimoto, M. & * Ida, S., 2012, Planetesimal Formation at the Boundary between Steady Super/Sub-Keplerian Flow Created by Inhomogeneous Growth of Magnetorotational Instability, Astrophys. J., 747, 11(10pp)
65. Ogihara, M. & Ida, S. 2012. N-body Simulations of Satellite Formation around Giant Planets: Origin of Orbital Configuration of the Galilean Moons, *Astrophys. J.* 753, article id. 60, 17 pp.
66. Genda, H., Kokubo, E. & Ida, S., 2012, Merging Criteria for Giant Impacts of Protoplanets, Astrophys. J., 744, 137(8pp)

67. Takeuchi, T., Muto, T., Okuzumi, S., Ishitsu, N. & Ida, S., 2012, Induced Turbulence and the Density Structure of the Dust Layer in a Protoplanetary Disk, Astrophys. J., 744, 101(16pp)
68. Michikoshi, S., Kokubo, E., & Inutsuka, S., 2012, Secular Gravitational Instability of a Dust Layer in Shear Turbulence, The Astrophysical Journal, 746, 35(12pp)
69. Inutsuka, S., 2012, Present-Day Star Formation – From Molecular Cloud Cores to Protostars and Protoplanetary Disks, Prog. Theor. Exp. Phys., 1, 01A307-331
70. Muranushi, T., Okuzumi, S. & Inutsuka, S. 2012. Interdependence of Electric Discharge and the Magnetorotational Instability in Protoplanetary Disks. Astrophys, J. 760, 56(14pp)
71. Takamoto, M., Inoue, T. & Inutsuka, S. 2012. Enhanced Dissipation Rate of Magnetic Field in Striped Pulsar Winds by the Effect of Turbulence. The Astrophysical Journal 755, 76(6pp)
72. Muto, T., …, Inutsuka, S., et al, 2012, Discovery of Small-scale Spiral Structures in the Disk of SAO 206462 (HD 135344B): Implications for the Physical State of the Disk from Spiral Density Wave Theory, The Astrophysical Journal, 748, L22(7pp)
73. Ikoma, M. & Hori, Y., 2012, In Situ Accretion of Hydrogen-rich Atmospheres on Short-period Super-Earths: Implications for the Kepler-11 Planets., Astrophys. J., 753, 66(6pp)
74. Oka, A., *Inoue, A. K., Nakamoto, T., and Honda, M. 2012. Effect of Photodesorption on Snow
Line at the Surface of Optically Thick Circumstellar Disks around Herbig Ae/Be Stars. Astrophysical Journal 747, 138(12pp)
75. Kokubo, E., Ida, S., 2012, Dynamics and Accretion of Planetesimals. Progress of Theoretical and Experimental Physics, 01A, 308 (23pp)
76. Sato, B.,…, Kokubo, E., Ida, S. 2012. Substellar Companions to Seven Evolved Intermediate-Mass Stars. Publications of the Astronomical Society of Japan 64, 1-14
77. Nagasawa, M. & Ida, S., 2011, Orbital Distributions of Close-in Planets and Distant Planets Formed by Scattering and Dynamical Tides, Astrophys. J., 742, 72 (16pp)
78. Kunitomo, M., Ikoma, M., Sato, B., Katsuta, Y. & Ida, S. 2011. Planet Engulfment by ~1.5-3 M_sun Red Giants. Astrophys. J. 737, 66(8pp).
79. Muto, T., Takeuchi, T. & Ida, S.. 2011. On the Interaction between a Protoplanetary Disk and a Planet in an Eccentric Orbit: Application of Dynamical Friction. Astrophys. J. 737, 37(23pp).
80. Fujii, Y., Okuzumi, S. & Inutsuka, S., 2011, A Fast and Accurate Calculation Scheme for Ionization Degrees in Protoplanetary and Circumplanetary Disks with Charged Dust Grains, Astrophys. J., 743, 53 (9pp)
81. Hori, Y. & Ikoma, M., 2011, Gas giant formation with small cores triggered by envelope pollution by icy planetesimals, MNRAS., 416, 1419-1429.
82. Oka, A., Nakamoto, T. & Ida, S., 2011, Evolution of Snow Line in Optically Thick Protoplanetary Disks: Effects of Water Ice Opacity and Dust Grain Size, Astrophys. J., 738, 141 (11pp)

（２）学会発表

計画研究 A01：ガス惑星の直接撮像・分光と地球型惑星の検出

高遠　徳尚　　南極ドームふじ基地 TwinCam による系外惑星探査
日本天文学会 2011 年秋季年会　2011 年 09 月 21 日　鹿児島大学、鹿児島県

高遠　徳尚　　南極大陸での可降水量調査
日本天文学会 2011 年秋季年会　2011 年 09 月 22日　鹿児島大学、鹿児島県

住　貴宏　　Recent Results from Gravitational Microlensing
Extreme Solar System II　2011 年 09 月 12 日　Jackson Lake Ledge, USA

住　貴宏　　Free-Floating Planets may be Common
日本天文学会 2011 年秋季年会　2011 年 09 月 21 日　鹿児島大学、鹿児島県

左近　樹　　赤外線観測に基づく Wolf-Rayet 連星系周囲に形成されたダストの性質
日本地球惑星科学連合 2011 年度連合大会　2011 年 05 月 23 日　幕張メッセ国際会議場、千葉県

左近　樹　　SPICA搭載中間赤外分光撮像装置(MCS)中分散分光部(MRS)の基本仕様と系内・系外銀河中の星間物質の化学的循環の理解への寄与
日本天文学会 2011 年秋季年会　2011 年 09 月 21 日　鹿児島大学、鹿児島県

左近　樹　赤外線継続観測に基づく新星 V1280Sco 周囲でのダスト形成史
日本天文学会 2012 年春季年会　2012 年 03 月 21 日　龍谷大学、京都府

左近　樹　　SPICA 搭載中間赤外線分光撮像装置の中分散分光部(MRS)の主要開発項目の進捗
日本天文学会 2012 年春季年会　2012 年 03 月 21 日　龍谷大学、京都府

左近　樹　　あかり衛星 Phase3 における近赤外分光データの性質評価と解析ソフトウェア開発への応用　日本天文学会 2012 年春季年会　2012 年 03 月 21 日　龍谷大学、京都府

高遠徳尚　　Deployment of Astronomical Instruments at Dome Fuji
XXXII SCAR　2012 年 07 月 18 日　Hilton Portland, Portland, USA

住　貴宏　　Space Microlensing Exoplanet Survey with WFIRST
The 220th AAS(American Astronomical Society) meeting　2012 年 06 月 13 日　Anchorage, Alaska, USA

住　貴宏　　Current and Future of Microlensing Exoplanet Search
IAU XXVIII General Assembly　2012 年 08 月 27 日　China National Convention Center, Beijing, China

住　貴宏　　MOA-II による系外惑星探査：2012 年の経過報告
日本天文学会秋季年会　2012 年 09 月 20 日　大分大学旦野原キャンパス、大分県

住　貴宏　　WFIRST/Euclid
すばる HSC サーベイによるサイエンス　2012 年 09 月 27 日　国立天文台、東京都

住　貴宏　　MOA-II による系外惑星探査：2012 年の結果
日本天文学会春季年会　2013 年 03 月 22 日　埼玉大学、埼玉県

藤原　英明　　AKARI and Spitzer Observations of Warm Debris Disks
Formation and Evolution of Planet 2012　2012 年 09 月 03 日　Ludwig-Maximilians-University Mnchen, Munich, Germany

Guyon, Olivier　　"Anybody out there ? Optical tricks to look for life around nearby stars"
Caltech　2013 年 02 月 25 日　Caltech, California, USA

Guyon, Olivier　　How Extremely Large Telescopes (ELTs) will Acquire the First Spectra of Rocky Habitable Planets
American Astronomical Society, AAS Meeting #221, #419.05　2013 年 01 月 23 日　Long Beach, USA

Guyon, Olivier　　Optical Tricks to image Habitable Planets around nearby Starts
Frontiers in Optics（招待講演）　2012 年 10 月 18 日　Rochester, NY, USA

Guyon, Olivier　　Direct Imaging of Habitable Planets with Extremely Large Telescopes
University of California Los Angeles (UCLA)　2012 年 10 月 10 日　University of California Los Angeles (UCLA), USA

高遠徳尚　　高アルベドヒルダ群小惑星の可視光スペクトル
日本天文学会 2013 年秋季年会　2013 年 09 月 10 日　東北大学、宮城県

高遠徳尚　反射スペクトルから見た木星の小衛星とヒルダ群・トロヤ群小惑星との関係
日本惑星科学会 2013 年秋季年会　2013 年 11 月 22 日　東北大学、宮城県

Guyon Olivier　Coronagraphy - From State of the Art to the Near Future
Search for Life Beyond the Solar System 2014（招待講演）　2014 年 03 月 20 日　Tucson, Arizona, USA

Guyon Olivier　LOWFSC & PSF for Exoplanets
NASA JPL　2014 年 02 月 26　NASA Jet Propulsion Laboratory, California, USA

Guyon Olivier　On-sky wavefront correction with a 2048 actuator MEMS
SPIE Photonics West 2014　2014 年 02 月 06 日　SPIE Photonics West, San Francisco, USA

住　貴宏　Exoplanet search via gravitational microlensing
Medium-Size Telescope Science Workshop　2013 年 06 月 22 日　Dianchi Hotel, 昆明、中国

住　貴宏　MOA-II による系外惑星探査：2013 年の経過報告
日本天文学会秋季年会　2013 年 09 月 11 日　東北大学、仙台、宮城県

住　貴宏　Current and Future of Microlensing Exoplanet Search
The 5th Subaru International conference　2013 年 12 月 12 日　Sheraton Kona Resort and Spa at Keauhou Bay, Kona, Hawaii, USA

住　貴宏　可視光赤外衛星計画 Euclid/WFIRST/WISH
理論懇シンポジウム　2013 年 12 月 26 日　東京大学柏キャンパス、千葉県

住　貴宏　WFIRST Wide-Field Infra-Red Survey Telescope
2020 年代の銀河サーベイ計画とすばる望遠鏡とのシナジー　2014 年 01 月 11 日　国立天文台、東京都

住　貴宏　The Microlensing Event Rate and Optical Depth Toward the Galactic Bulge from MOA-II, 18th International Conference on Microlensing　2014 年 01 月 20 日
The Canary Hotel, Santa barbara, USA

住　貴宏　MOA-II の重力マイクロレンズによる銀河系バー構造の解明
日本天文学会春季年会　2014 年 03 月 20 日　国際基督教大学、東京都

藤原　英明　Dust in Debris Disks

The Life Cycle of Dust in the Universe: Observations, Theory, and Laboratory Experiments（招待講演） 2013 年 11 月 18 ASIAA, Taipei, Taiwan

藤原 英明 Warm Debris Disks Probed by Mid-Infrared Observations
Japan Geoscience Union Meeting 2013 (Session P-CG32; New frontier of chronology of the Solar System)（招待講演） 2014 年 05 月 19 日
Makuhari Messe, Chiba, Japan

Guyon Olivier Imaging exoplanets with MKIDs on Subaru Telescope
Institute for Astronomy University of Hawaii Tech Talk 2014 年 04 月 17 日 Hilo, HI, USA

Guyon Olivier Low-order Wave-front Sensing and Control, and Point-spread-function Calibration, for Direct Imaging of Exoplanets
Exo-PAG 2014 年 06 月 06 日 Boston, MA, USA

高遠 徳尚 Design and performance of a F/#-conversion microlens for prime focus spectrograph at Subaru Telescope
SPIE 2014 年 06 月 23 日 モントリオール、カナダ

藤原 英明 Warm Debris Disks Proved by AKARI Observations
THE UNIVERSE IN THE LIGHT OF AKARI and Synergy with future Large Space Telescopes 2014年07月09 Oxford University, Oxford, UK

藤原 英明 Warm Debris Disks
JCMT Science Workshop 2014（招待講演） 2014 年 09 月 01 日 National Astronomical Observatory of Japan, Tokyo, Japan

Guyon Olivier Exoplanets
HawaiiCon 2014 2014 年 09 月 14 日 Kona, HI, USA

Guyon Olivier Optical Tricks to find and study Exoplanets Optical Society of America Student Leadership Chapter（招待講演） 2014 年 09 月 19 日 Tucson, AZ, USA

左近 樹, 尾中 敬, 佐藤一輝, 森珠実, 木村勇気, 中村正人, 市 村淳, 小川奈々子, 大河内直彦, 木村誠, 和田節子
実験室および ISS 軌道上実験に基づく未同定赤外バンドの担い手の理解
日本天文学会 2014 年秋季年会 2014 年 09 月 11 日 山形大学、山形県

住　貴宏　　MOA-2013-BLG-605Lb:晩期 M 型矮星に付随する海王星質量惑星
日本天文学会 2014 年秋季年会　2014 年 09 月 12 日　山形大学、山形県

住　貴宏　　MOA-II による系外惑星探査
名古屋大学南半球宇宙観測研究センター研究会（招待講演）　2014 年 10 月 03 日　名古屋大学、愛知県

左近　樹　　Quest for the Compositional identification and Chemical evolutional understanding of the interstellar carbonaceous dust based on the experiment using JEM/ExHAM on the ISS
Workshop on Interstellar Matter 2014　2014 年 10 月 16 日　北海道大学、北海道

Guyon Olivier　　Searching for Habitable Worlds and Life in the Universe with Optics 50 yr anniversary of the college of optical sciences special lecture（招待講演）　2014 年 10 月 23 日
University of Arizona, USA

左近　樹　　Exposure experiment of carbonaceous solids using JEM/ExHAM on the International space station International Conference on Interstellar Dust, Molecules and Chemistry 2014（招待講演）　2014 年 12 月 15 日　Tezpur University, India

住　貴宏　　WFIRST Wide-Field Infra-Red Survey Telescope
宇宙科学シンポジウム　2015 年 01 月 06 日　宇宙科学研究所、神奈川県

住　貴宏　　MOA-2013-BLG-605Lb:The Neptune Analog
19th International Conference on Microlensing　2015 年 01 月 20 日
The Maryland Inn-Historic Inns of Anapolis, USA

藤原　英明　　Warm Debris Disks Proved by AKARI Observations
East Asian Young Astronomers Meeting 2015　2015 年 02 月 09 日
Academia Sinica, Taipei, Taiwan

藤原　英明　　Multi-Band Mid-Infrared Observation of Saturn's Rings
Ground and space observatories: a joint venture to planetary science
2015 年 03 月 02 日　Santiago, Chile

左近 樹, 尾中 敬, 木村誠二, 和田節子, 木村勇気, 中村正人, 市村淳, 小川奈々子, 大河内直彦, 稲富裕光, 佐藤一輝, 島本早也佳, 渡辺英幸, 赤城弘樹,佐巻義昭
ISS「きぼう」日本実験棟 ExHAM を利用したダストの宇宙曝露実験計画
日本天文学会 2015 年春季年会　2015 年 03 月 18 日　大阪大学、大阪府

住　貴宏　重力マイクロレンズ探査で探る天の川銀河構造
天の川銀河研究会（招待講演）2015 年 03 月 23 日　東京大学、東京都

T. Sumi et al., “ MOA-2013-BLG-605Lb: The Neptune analog”, IAU XXIX General Assembly, 2015/8/3, Honolulu, HI, USA

T. Sumi, “Exoplanet Microlensing Context”, IAU XXIX General Assembly, WFIRST Splinter Session, 2015/8/9, Honolulu, HI, USA

T. Sumi, “マイクロレンズ探査とトランジット”, TESS と地上望遠鏡等との連携で広がる多様なサイエンス, NAOJ, 2015/11/26

T. Sumi, "Microlensing exoplanet search toward the solar system analog”, International Workshop on "Exoplanets and Disks: Their Formation and Diversity III” 2016/2/23, Ishigaki, Japan

T. Sumi et al., “海王星に似た惑星: MOA-2013-BLG- 605Lb の公転軌道”, 天文学会春季, 2016/3/16, 首都大学東京、東京都

藤原　英明　L05c　小天体の含水鉱物探査にむけた MIMIZUKU 近赤外線分光機能の検討
上塚貴史,臼井文彦,宮田隆志,酒向重行,大澤亮,岡田一志,内山允史,毛利清(東京大学),長谷川直(JAXA),高遠徳尚(NAOJ)　日本天文学会 2015 年秋季年会、甲南大学、兵庫

藤原　英明　V236a　地球型惑星検出のためのすばる赤外線ドップラー分光 IRD の開発: 10
小谷隆行他　日本天文学会 2016 年春季年会、首都大学東京、東京

藤原　英明　V216a　地球型惑星検出のためのすばる赤外線ドップラー分光 IRD の開発: 11
小谷隆行他日本天文学会 2016 年春季年会、首都大学東京、東京

計画研究 A02：系外惑星大気の数値モデリングと形成進化理論

林 祥介, 2015:「ビッグデータ時代の将来展望」,
2015 年公開気象講演会, 2015 年 5 月 24 日, つくば国際会議場、茨城県

杉山耕一朗, 小高正嗣, 中島健介, 高橋芳幸, 西澤誠也, 乙部直人, 林祥介, はしもとじょーじ, 長谷川晃一, 榊原篤志, 坪木和久
火星探査のための表層環境評価: 雲解像モデル CReSS の火星大気への適用, 2015 年日本気象学会春季大会, 2015 年 5 月 22 日, つくば国際会議場 (講演番号 P238) 、茨城県

高橋芳幸, 荻原弘尭, 西澤誠也, 原旅人, 石渡正樹, 林祥介, 2015:
惑星大気大循環モデルの構築 -- 鉛直一次元設定での数値実験.
2015 年 5 月 22 日, つくば国際会議場 (講演番号 P239) 、茨城県

大西将徳, はしもとじょーじ, 倉本圭, 高橋芳幸, 石渡正樹, 高橋康人, 林祥介, 2015: 水蒸気大気の圏界面の推定とハビタブルゾーンの内側境界,
2015 年 日本気象学会春季大会, 2015 年 5 月 23 日, つくば国際会議場 (講演番号 P305) 、茨城県

杉山耕一朗, 中島健介, 小高正嗣, 倉本圭, 林祥介, 2015: 木星型惑星大気の雲対流の数値実験, 日本気象学会春季大会, 2015 年 5 月 23 日, つくば国際会議場 (講演番号 D309) 、茨城県

佐々木洋平, 竹広真一, 石岡圭一, 中島健介, 林祥介, 2015:
高速に回転する薄い球殻内の熱対流により引き起こされる表層縞状構造の消滅,日本気象学会春季大会, 2015 年 5 月 23 日, つくば国際会議場 (講演番号 D310) 、茨城県

成田 一輝、倉本 圭:生命保有可能系外惑星 GJ667Cc の気候モデリング
2015 年 5 月 24 日日本地球惑星科学連合 2015 年大会 幕張メッセ、千葉県

渡辺 健介、倉本 圭:GJ1214b 大気の流体力学的散逸
2015 年 5 月 24 日日本地球惑星科学連合 2015 年大会 幕張メッセ、千葉県

齊藤 大晶、倉本 圭:原始太陽系星雲中で成長する火星の混成型原始大気の熱的構造
2015 年 5 月 24 日日本地球惑星科学連合 2015 年大会 幕張メッセ、千葉県

杉山 耕一朗、中島 健介、小高 正嗣、倉本 圭、林 祥介:
木星型惑星を想定した雲対流の数値計算, 2015 年 5 月 26 日
日本地球惑星科学連合 2015 年大会 幕張メッセ、千葉県

倉本 圭、荒井 朋子、小林 直樹、杉田 精司、橘 省吾、寺田 直樹、並木 則行、松本 晃治、渡邊 誠一郎
「惑星科学／太陽系科学 研究領域の目標・戦略・工程表」の概要
2015 年 5 月 25 日日本地球惑星科学連合 2015 年大会 幕張メッセ、千葉県

大西 将徳、はしもと じょーじ、倉本 圭、高橋 芳幸、石渡 正樹、高橋 康人、林 祥介
水蒸気大気の圏界面の推定とハビタブルゾーンの内側境界
2015 年 5 月 25 日日本地球惑星科学連合 2015 年大会 幕張メッセ、千葉県

高橋 康人、はしもと じょーじ、石渡 正樹、高橋 芳幸、杉山 耕一朗、大西 将徳、倉本 圭
The radiative cooling and the solar heating in Jovian troposphere
2015 年 5 月 26 日日本地球惑星科学連合 2015 年大会 幕張メッセ、千葉県

杉山耕一朗, 小高正嗣, 中島健介, 高橋芳幸, 西澤誠也, 乙部直人, 林祥介,
はしもとじょーじ, 長谷川晃一, 榊原篤志, 坪木和久,
火星探査のための表層環境評価: 雲解像モデル CReSS の火星大気への適用
日本地球惑星科学連合 2015 年大会. 2015 年 5 月 28 日 幕張メッセ国際会議場、千葉県

高橋芳幸, 荻原弘尭, 西澤誠也, 原旅人, 石渡正樹, 林祥介,
惑星大気大循環モデルの構築 - 鉛直一次元設定での数値実験
日本地球惑星科学連合 2015 年大会.
2015 年 5 月 27 日 幕張メッセ国際会議場、千葉県

石渡正樹, 増田和孝
同期回転水惑星大気循環の惑星半径依存性に関する数値実験
日本地球惑星科学連合 2015 年大会、2015 年 5 月 24 日 幕張メッセ国際会議場、千葉県

佐々木洋平, 竹広真一, 石岡圭一, 中島健介, 林祥介
高速に回転する薄い球殻内の熱対流により引き起こされる表層縞状構造の消滅.

日本地球惑星科学連合 2015 年大会.
2015 年 5 月 25 日　幕張メッセ国際会議場、千葉県

濱野景子, 河原創, 阿部豊, 大西将徳, はしもとじょーじ
水蒸気大気におおわれたマグマオーシャンの寿命と放射スペクトル進化
連合大会 2015/5/25　幕張メッセ、千葉県

阿部 豊, 新田 光, 阿部 彩子, 大石 龍太, 高尾 雄也
不均質な表面をもつ惑星で暴走温室効果を引き起こす気候不安定について
連合大会 2015/5/25　幕張メッセ, 千葉県

中山陽史, 阿部豊
地球型惑星が持つ水量が惑星表層環境に与える影響の検討:高圧氷と炭素循環
日本地球惑星科学連合 2015 年大会　　2015 年 5 月　幕張メッセ、千葉県

Sekine, Y., K. Kodama, S. Obata, T. Kobayashi, N.O. Ogawa, Y. Takano, N.Ohkouchi, K. Saiki, T. Sekine.
Impact-induced alterations of planetary organic and ice simulants
Asian Oceania Geosciences Society meeting, 2015.
2015 年 8 月 2 日―7 日、Suntec Singapore Convention & Exhibition Centre, シンガポール

関根康人　比較惑星海洋学とハビタビリティ
日本地球化学会年会 2015 年度　2015 年 9 月 16 日、横浜国立大学、神奈川県

佐々木洋平, 竹広真一, 石岡圭一, 中島健介, 林祥介,
高速回転する薄い球殻内の熱対流により引き起こされる表層縞状構造の消滅.
2015 年日本流体力学会年会,2015 年 9 月 26 日東工大大岡山キャンパス、東京都

齊藤 大晶、倉本 圭:原始太陽系星雲散逸期の火星形成:
熱史と大気－内部間発性物質分配
2015 年 10 月 14 日日本惑星科学会 2015 年度秋季講演会 東京工業大学 東京都

三上 峻, 高橋康人, 倉本 圭:周惑星ガス円盤内で形成する巨大氷衛星が獲得する原始大気, 2015 年 10 月 14 日日本惑星科学会 2015 年度秋季講演会 東京工業大学 東京都

大西 将徳, はしもとじょーじ, 倉本 圭, 高橋 芳幸, 石渡 正樹, 高橋 康人, 林祥介

放射対流平衡モデルによる水蒸気大気の圏界面温度の推定
2015 年 10 月 14 日 2015 年 10 月 14 日日本惑星科学会 2015 年度秋季講演会
東京工業大学 東京都

高橋康人, はしもとじょーじ, 石渡正樹, 高橋芳幸, 杉山耕一朗, 大西将徳, 倉本圭
木星大気放射冷却に対する雲対流の寄与 2015 年 10 月 14 日
2015 年 10 月 14 日日本惑星科学会 2015 年度秋季講演会 東京工業大学 東京都

杉山耕一朗, 小高正嗣, 中島健介, 今村剛, 林祥介,
金星雲層を想定した鉛直対流の 3 次元数値計算 日本惑星科学会 2015 年 秋季講演会
2015 年 10 月 14 日～ 10 月 16 日東京工業大学 地球生命研究所, 東京都

関根康人、玄田英典、舟津太郎
冥王星の黒いクジラ模様はカロン形成巨大衝突の痕跡か？
日本惑星科学会 秋季講演会 2015 年 10 月 14 日、東京工業大学、東京都

濱野景子, 阿部豊, 大西将徳
水素-水蒸気大気をもつ地球型惑星の海洋形成条件
惑星科学会秋季講演会 2015/10/14 東京工業大学, 東京都

日本気象学会秋季大会
樫村博基, 杉本憲彦, 高木征弘, 大淵済, 榎本剛, 高橋芳幸, 林祥介,
簡易金星版 AFES 高解像度計算における運動エネルギーの波数間収支
2015 年日本気象学会秋季大 2015 年 10 月 30 日京都テルサ, 京都府

杉山耕一朗, 小高正嗣, 中島健介, 今村剛, 林祥介
金星雲層を想定した鉛直対流の 3 次元数値計算
2015 年日本気象学会秋季大会 2015 年 10 月 30 日京都テルサ, 京都府

A massive primordial-atmosphere on proto-Titan formed in a cold circum-planetary disk
T. Mikami, Y. Takahashi, and K. Kuramoto, EPSC2015, La Cité des Congrès, 2015 年 10 月 30 日, Nantes, France

高橋芳幸, 林祥介,
惑星大気大循環モデル DCPAM を用いた火星大気中の水蒸気分布の計算.
第 138 回 SGEPSS 総会および講演会 2015 年 11 月 3 日 東京大学, 東京都

安藤紘基, 杉山耕一朗, 小高正嗣, 中島健介, 今村剛, 林祥介,
金星重力波の2次元数値実験 第 138 回 SGEPSS 総会および講演会
2015 年 11 月 3 日 東京大学, 東京都

Hiroaki Saito; Kiyoshi Kuramoto
Thermal History and Volatile Partitioning between Proto-Atmosphere and Interior of Mars Accreted in a Solar Nebula, American Astronomical Society, DPS meeting #47, 2015 年 11 月 11 日, National Harbor, MD, Washington DC, USA

Takahashi, Yasuto; Hashimoto, George L.; Ishiwatari, Masaki; Takahashi, Yoshiyuki O.; Sugiyama, Ko-ichiro; Onishi, Masanori; Kuramoto, Kiyoshi: Theoretical estimation of the radiative cooling rate in the Jovian troposphere, American Astronomical Society, , 2015 年 11 月 13 日, DPS meeting #47, Washington DC, USA

Yutaka Abe, Evolution of the steam atmosphere and ocean formation ISSI Workshop on the delivery of water to proto-planets, planets and satellites, 2016/1/14, ISSI, Switzerland

Keiko Hamano, Hajime Kawahara, Yutaka Abe, Masanori Onishi, and George L. Hashimoto Lifetime and Spectral Evolution of a Magma Ocean with a Steam Atmosphere Extreme Solar Systems III, 2015/11/29-2015/12/04 ポスター Waikoloa beach Marriotto Resort & Spa, USA

Nakayama, A., Y. Abe, Effects of Water Amount on the Surface Environment of Terrestrial Planets: High Pressure Ice and Carbon Cycle Extreme Solar Systems III, 2015 年 12 月 ポスター, Waikoloa Beach Marriott Resort & Spa, USA

K. Sugiyama, K. Nakajima, M. Odaka, K. Kuramoto, and Y.-Y. Hayashi：Extreme intermittency of moist convection on the giant planets", Joint Juno/Cassini Jupiter-Saturn Atmospheric Dynamics Meeting, 2015/12, San Francisco Marriott Marquis, San Francisco, USA

Sugiyama, K., Kawabata, T., Odaka, M., Ishiwatari, M., Nakajima, K., Imamura, T., Hayashi, Y.-Y., Numerical modeling of convection in Venus' cloud layer. AGU Fall Meeting, 2015 年 12 月 15 日, Moscone Center, San-Francisco, USA

Sekine, Y., H. Genda, T. Funatsu, Can a Charon-forming giant impact produce enlongated dark areas on Pluto? American Geophysical Union, 2015 fall meeting2015 年 12 月 18 日, Moscone

Center, USA

International Workshop on "Exoplanets and Disks: Their Formation and Diversity III", 2016 年 2 月 23 日, Hotel Nikko Yaeyama, 沖縄県

Yuta Kawai, Y. O. Takahashi, M. ishiwatari, S. Nishizawa, S. Takehiro, K. Nakajima, H. Tomita, Y. Hayashi: Development of a coupled atmosphere-ocean-seaice modelto explore aquaplanet climates, International Workshop on "Exoplanets and Disks: Their Formation and Diversity III", 22th February 2016, Hotel Nikko Yaeyama, 沖縄県

Y. O. Takahashi and collaborators: Development of a general circulation model for shallow planetary atmospheres, International Workshop on "Exoplanets and Disks: Their Formation and Diversity III", 23th February 2016, Hotel Nikko Yaeyama, 沖縄県

Ishiwatari, M. and collaborators: GCM experiments on the occurrence condition of the runaway greenhouse state on Earth-like exoplanets. International Workshop on "Exoplanets and Disks: Their Formation and Diversity III", 23th February 2016, Hotel Nikko Yaeyama, 沖縄県

Masanori Onishi, George L. Hashimoto, Kiyoshi Kuramoto, Yoshiyuki O. Takahashi, Masaki Ishiwatari, Yasuto Takahashi, Yoshi-Yuki Hayashi: Development of a general circulation model for shallow planetary atmospheres, International Workshop on "Exoplanets and Disks: Their Formation and Diversity III", 23th February 2016, Hotel Nikko Yaeyama, 沖縄県

Sugiyama, K., Nakajima, K., Odaka, M., Kuramoto, K., Hayashi,Y.-Y.: Numerical Modeling of Moist Convection in Saturn's and Uranus' atmospheres, International Workshop on "Exoplanets and Disks: Their Formation and Diversity III", XX February 2016, Hotel Nikko Yaeyama, 沖縄県

Takehiro, S., Takahshi, Y. O., Nakajima, K., Hayashi,Y.-Y.: Diversity of atmospheric circulations of tidally locked gas giant planets -- dependence on the intrinsic heat flux strength. International Workshop on "Exoplanets and Disks: Their Formation and Diversity III", 23th February 2016, Hotel Nikko Yaeyama, 沖縄県

Keiko Hamano, Yutaka Abe, Hajime Kawahara, Masanori Onishi:Thermal history and atmospheric evolution of terrestrial planets after giant impacts, Exoplanets and Disks: Their

Formation and Diversity III, 2016/2/23　　口頭, ホテル日航八重山, 沖縄県

Nakayama, A., Y. Abe, Effects of Water Amount on the Surface Environment of Terrestrial Planets: High Pressure Ice and Carbon Cycle on Ocean Planets, Exoplanets and Disks: Their Formation and Diversity III, 2016 年 2 月, ポスター, ホテル日航八重山, 沖縄県

日本気象学会 2016 年春季大会
佐々木洋平, 竹広真一, 石岡圭一, 中島健介, 林祥介,
高速回転する薄い球殻内の熱対流により引き起こされる表層縞状構造の消滅
2016 年日本天文学会春季大会, 2016 年 3 月 15 日 首都大学東京, 東京都

石渡正樹, 納多哲史, 中島健介, 高橋芳幸, 竹広真一, 林祥介,
暴走温室状態の発生条件に関する大気大循環モデル実験.
2016 年日本天文学会春季大会, 2016 年 3 月 15 日,首都大学東京, 東京都

林祥介, 汎惑星気象・気候シミュレーションに向けて.
2016 年日本天文学会春季大会, 3 月 15 日,首都大学東京南大沢キャンパス, 東京都

計画研究 B01: 円盤から惑星へ

T. Onaka, ``SPICA update", FIR Surveyor Workshop, 2015/6/3-5., Pasadena, USA

T. Onaka, “AKARI near-infrared spectroscopy of interstellar ices" (Focused Meeting 12, Bridging Laboratory Astrophysics and Astronomy, IAU General Assembly, 2015/8/3-5, Honolulu, Hawaii, USA

T. Onaka, ``Organic dust in galaxies" (The 11th Pacific Rim Conference on Stellar Astrophysics, Physics and Chemistry of the Late Stages of Stellar Evolution, 2015/12/14-17, Hong Kong, China

武藤恭之，「原始惑星系円盤の力学と直接撮像観測」 (日本惑星科学会 2015 年度秋季講演会, 2015 年 10 月 16 日, 東京工業大学、東京都

T. Muto, ``Connecting Disk Theory with High Resolution Observations, East Asia ALMA Science Workshop" 2015 年 12 月 9 日　大阪府立大学、大阪府

武藤恭之，「原始惑星系円盤における力学過程と詳細構造の観測」（理論懇シンポジウム 2015「宇宙における天体形成から生命まで」 2015 年 12 月 23 日～25 日　大阪大学、大阪府

M. Momose, ``Long baseline observations with ALMA: Impact by the image of HL Tau" （ALMA/45m/ASTE/Mopra Users Meeting, 2015.10.21, 国立天文台三鷹、東京都

百瀬宗武，「ALMA 高解像度撮像が明かしつつある惑星形成過程」（理論懇シンポジウム 2015「宇宙における天体形成から生命まで」　2015 年 12 月 23 日～25 日　大阪大学、大阪府

百瀬宗武，``HL Tau: a revolution in the study on the formation of planetary systems" （日本天文学会春季年会特別セッション, 2016.3.14, 東京都立大学、東京都

Y. Aikawa, ``Astrochemical models of water in molecular clouds and protoplanetary disks'', Focus Meeting 15, International Astronomical Union General Assembly XXIX, Aug. 3-5, 2015, Honolulu, HI, USA

Y. Aikawa, ``Chemistry in the Forming Disks'', Workshop, ALMA-Cycle 4, Astrochemistry as a diagnostic of Star and Planet Formation, Jan.12-13, 2016, Observatoire de Bordeaux, France

Y. Aikawa, ``Chemistry in the disk formation'', Workshop on Astrochemistry in Star and Planet Formation, Feb.16, 2016, Riken, Japan

相川祐理, ``Astrochemistry in star forming cores and protoplanetary disks'' (研究会「星形成の諸階層－銀河から惑星まで－」, 2015 年 9 月 14 日～16 日, フォレスト箱根、神奈川県

相川祐理, 「星・惑星系形成領域の星間化学：モデルと ALMA 観測」（日本地球化学会第 62 回年会, 2015 年 9 月 16 日～18 日, 横浜国立大学、神奈川県

相川祐理, 「星・惑星系形成領域における有機物：理論と観測の現状」（理論懇シンポジウム 2015「宇宙における天体形成から生命まで」2015 年 12 月 23 日～25 日, 大阪大学, 大阪府

百瀬宗武　Observations of Protoplanetary Disks with ALMA
East Asia ALMA Science Workshop 2014
2014 年 07 月 17 日～2014 年 07 月 17 日、Phoenix Island, Jeju, Korea

樋口あや　Science case with ALMA archive
East Asia ALMA Science Workshop 2014
2014 年 07 月 17 日～2014 年 07 月 17 日、Phoenix Island, Jeju, Korea

塚越崇　電波望遠鏡で探る原始惑星系円盤の詳細構造
第 1 回 DTA シンポジウム星形成領域および星団環境での惑星の形成と進化
2014 年 09 月 29 日～2014 年 09 月 29 日、国立天文台、東京都

百瀬宗武　原始惑星系円盤研究の現状と展望～ALMA を中心に～
名古屋大学南半球研究センター研究会「惑星から大質量星の形成までを俯瞰する」
2014 年 10 月 03 日～2014 年 10 月 03 日、名古屋大学、愛知県

尾中敬　Processing of the Interstellar Medium as Divulged by AKARI
THE UNIVERSE IN THE LIGHT OF AKARI and Synergy with future Large Space Telescopes, 2014 年 07 月 09 日～2014 年 07 月 11 日, Oxford, UK

尾中敬　Lifecycle of dust grains in the interstellar medium
The 7th meeting on Cosmic Dust, 2014 年 08 月 04 日～2014 年 08 月 08 日　大阪産業大学、大阪府

尾中敬　Dust processing in the interstellar medium
International Conference on Interstellar Dust, Molecules and Chemistry 2014
2014年12月15日～2014年12月18日, Tezpur, India

相川裕理　Gas-Grain Chemical Models in the Star- and Planetary System Formation
Icy Grain Chemistry for Formation of Complex Organic Molecules:From Molecular Clouds to Protoplanetary Disks, Comets andMeteorites
2015年03月05日～2015年03月07日，東京工業大学、東京都

相川裕理　Water in Protoplanetary Disks
Transformational Science with ALMA: From Dust to Rocks to Planets
2013年04月07日～2013年04月14日、コナ、ハワイ州、USA

相川裕理　原始惑星系円盤の化学進化と ALMA の成果
惑星科学と生命科学の融合　第4回研究会
2013年12月21日～2013年12月23日　湘南国際村、神奈川県

尾中敬他4名　Cryogenic silicon carbide mirrors for infrared astronomical telescopes: lessons learned from AKARI for SPICA, SPIE Optical Engineering + Applications 2013, Conference 8837, 2013年08月26日～2013年08月28日　San Diego, USA

武藤恭之　原始惑星系円盤の愉しみ
第43回天文・天体物理学若手夏の学校
2013年07月29日～2013年07月29日　宮城蔵王ロイヤルホテル、宮城県

武藤恭之　原始惑星系円盤における力学過程と円盤直接撮像観測
原始惑星系円盤研究, 2013年08月19日～2013年08月19日　国立天文台三鷹、東京都

武藤恭之　連星・円盤・惑星の相互作用
連星天文学研究会, 2014年02月10日～2014年02月10　京都大学、京都府

深川美里　Current understanding of young circumstellar disks
From Exoplanets to Distant Galaxies: SPICA's New Window on the Cool Universe
2013年06月18日～2013年06月21日　東京大学、東京都

深川美里　Star and Planet Formation; High Angular Resolution Study of Protoplanetary Disks
Thirty Meter Telescope Science Forum 2013
2013年07月22日～2013年07月23日　コナ、ハワイ州, USA

深川美里　原始惑星系円盤の高解像度観測
原始惑星系円盤研究会　2013年08月19日～2013年08月19日, 国立天文台、東京都

百瀬宗武　Planet Formation and Exoplanets
EA ALMA Development Workshop 2013, 2013年07月08日～2013年07月08日　国立天文台、東京都

百瀬宗武　Observations of Protoplanetary Disks with ALMA
日本天文学会2014年春季年, 2014年03月21日～2014年03月21日　国際基督教大学、東京都

相川祐理 Chemistry in Protoplanetary Disks
第8回太陽系外惑星大研究会 2012年04月18日～2012年04月20日 熱海、静岡県

相川祐理 他4名 From Prestellar to Protostellar Cores
COSPAR 2012年07月14日～2012年07月22日, Narayana Murthy Centre of Excellence, India

相川祐理 Chemical Models of Star Forming Cores
New Trends in Radio Astronomy in ALMA Era, 2012年12月03日～2012年12月08日 箱根、神奈川県

田中秀和 Growth of Dust Aggregates in Protoplanetary Disks and Reexamination of Particle Interaction Models, Dust and Grains in Low Gravity and Space Environment
2012年04月03日～2012年04月03日, ESA/ESTEC, Noordwijk, The Netherlands

百瀬宗武 Observations of Protoplanetary Disks with ALMA
ALMA East Asian Workshop in KOREA
2012年09月13日～2012年09月13日, Korean Astronomy and Space Science Institute, Daejeon, Korea

深川美里 撮像観測で探る若い星周円盤のダストの性質
日本地球惑星科学連合2012年度連合大会
2012年05月20日～2012年05月25日 幕張、千葉県

深川美里 High-Angular-Resolution Infrared Observations of Protoplanetary Disks
New Trends in Radio Astronomy in ALMA Era 2012年12月05日～2012年12月05日
箱根、神奈川県

百瀬宗武 Survey of star-forming cores and protoplanetary disks with the ASTE and Nobeyama 45-meter telescopes
Large Aperture Millimeter / Submillimeter Telescopes in the ALMA Era
2011年09月11日 大阪府立大学、大阪府

尾中敬　3rd Subaru International Conference, the 1st NAOJ Symposium,　Galactic Archaeology: Near-Field　Cosmology and the Formation of the Milky Way　Dust life cycle and processing in the interstellar medium, 2011年11月01日　修善寺、静岡県

尾中敬　Infrared Spectroscopy of the Unidentified Infrared Bands in the Galaxy and External Galaxies　International Conference on Interstellar Dust, Molecules and　Chemistry
2011年11月23日　Pune, India

尾中敬　Dust life cycle and processing in the interstellar medium The second AKARI conference: Legacy of AKARI: A　Panoramic View of the Dust Universe
2012年02月27日, Jeju, Korea

田中秀和　Molecular dynamics simulation of mechanical interaction between sub-micron spherical particles, Nonequilibrium Dynamics in Astrophysics and Material Science,
2011年11月02日, Yukawa Institute for Theoretical Physics, Kyoto, Japan

相川祐理　Ice observation towards low-mass edge-on YSOs and background stars
あかりによる我々の銀河系及び系外銀河の星間物質の研究会
2011年12月05日　東京大学、東京都

相川裕理　Chemistry in star-forming cores
International Conference on Interstellar Dust, Molecules and　Chemistry
2011年11月21日　Pune University, India

相川裕理　星形成コアにおける分子組成進化:星なし高密度コアから原始星コアまで
第4回アストロバイオロジーワークショップ　2011年11月27日　神戸大学、兵庫県

相川裕理　Chemistry in the formation of stars and planetary systems　Germany-Japan Round Table From the early universe to the　evolution of life　2011年11月30日
Heidelberg, Germany

相川裕理　Chemistry in Star-Forming Cores Formation of Stars　&　Planets 2011
2011年10月03日　石垣島、沖縄県

計画研究 B02: ハビタブル地球型惑星の形成理論

中本泰史　Bright Galilean Satellites in Jovian Shadow: Light Scattering by Jovian Upper Atmosphere
The 2014 German-Japanese meeting on Exo-Planets and their formation
2014年11月04日～2014年11月07日, ハイデルベルク, ドイツ

中本泰史　他9名　Three-Dimensional External Shape and Internal Structure of Chondrules in Allende CV3 Chondrite
Annual Meeting of Meteoritical Society, 2014年09月08日～2014年09月12日　カサブランカ, モロッコ

中本泰史　他10名　アエンデ隕石中コンドリュールの3次元外形と内部組織の分析
日本惑星科学会秋季講演会　2014年09月24日～2014年09月26日、東北大学、宮城県

奥住聡　Electric-field heating of plasmas and its effect on magnetorotational turbulence in protoplanetary disks
The 2014 German-Japanese meeting on Exo-Planets and their formation
2014年11月04日～2014年11月07日　ハイデルベルク, ドイツ

奥住聡　Magnetic Turbulence and Dust Evolution in Protoplanetary Disks　US-Japan Workshop on Magnetic Reconnection
2014年05月20日～2014年05月24日　東京大学、東京都

生駒大洋　Formation of the nebular-captured protoatmosphere　Workshop on the Disk in Relation to the Formation of Planets and Their Protoatmospheres
2014年08月26日～2014年08月28日　北京、中国

井田茂　Impacts of observed statistical properties on our understanding of planetary formation
Exoplanetary Science
2014年04月17日～2014年04月19日　Quy Nhon, Vietnam

小久保英一郎　Exploring Planet Fromation by N-Body Simulations　Stellar N-Body Dynamics　2014年09月08日～2014年09月12日　Sexten Center for Astrophysic, Italy

野村英子　原始惑星系円盤における複雑な有機分子生成モデル
日本地球惑星科学連合 連合大会 2014年大会
2014年04月28日～2014年05月02日　パシフィコ横浜、神奈川県

生駒大洋　Composition and origin of short-period low-mass planets: The importance of observation of their atmospheres Exoplanets and Disk: Their Formation and Diversity II
2013年12月09 Hawaii, USA

奥住聡　The fate of planetesimals in turbulent protoplanetary disks
Exoplanets and Disks: Their Formation and Diversity II　2013年12月09　Hawaii, USA

犬塚修一郎　From Magnetized Dense Molecular Cloud Cores to Protostars and Protoplanetary Disks Magnetic Fields from Cloud Cores to Protostellar Disk
2013年05月22日　Heidelberg, Germany

小久保英一郎　The Basic Dynamical Model of Terrestrial Planet Formation
The 1st COSPAR Symposium　2013年11月13日　Bangkog, Thailand

野村英子　Water and Organic Molecules in Protoplanetary Disks
Astronomy in the TMT Era　2013年10月16日、東京都

井田茂　Planet population synthesis
Protostars and Planets VI　2013年07月19日　Heidelberg, Germany

小久保英一郎　The Basic Dynamical Model of Terrestrial Planet Formation
IAU Symposium 293: Formation, Detection, and Characterization of Extrasolar Habitable Planets
2012年08月27日～2012年08月31日、中国

生駒大洋　On the impact of protoplanetary disk properties on the accretion of super- Earths' atmospheres.
Revealing Evolution of Protoplanetary Disks in the ALMA Era"Workshop
2012年05月09日　京都大学、京都府

犬塚修一郎　The Formation and Early Evolution of Protostars and Protoplanetary Disks
The Labyrinth of Star Formation　2012年06月18日、ギリシャ

前島直彦, 渡邊誠一郎　中心星加熱円盤における惑星のタイプI軌道移動の数値計算
日本惑星科学会2012年秋季講演会　2012年10月26日　幕張メッセ、千葉県

中本泰史　他3名　A Correlation among Shape, Composition, and Texture of Cosmic Spherules
European Geosciences Union　2012年05月17日、オーストリア

井田茂　Theoretically predicted distributions of mass and orbital elements of exoplanets
The origins of stars and their planetary systems　2012年06月11日、カナダ

野村英子　Water in Protoplanetary Disks
IAU Symposium 293: Formation, Detection, and　Characterization of Extrasolar Habitable Planets
2012年08月27日～2012年08月31日、中国

小久保英一郎　The Final Stage of Terrestrial Planet Formation
The First Kepler Science Conference　2011年12月08日、米国

生駒大洋　Accumulation of hydrogen- rich atmospheres of nebular origin on short- period super- Earths:
Implications for Kepler- 11 Planets
The First Kepler Science Conference　2011年12月08日、米国

犬塚修一郎　The Formation and Evolution of Filamentary Molecular Clouds
Formation of Stars & Planets 2011　2011年10月03日、イタリア

中本泰史　他1名　Refraction of Light in Exoplanet Atmosphere
The First Kepler Science Conference　2011年12月08日、米国

長澤真樹子　Orbital Evolution of Exoplanets Caused by Scattering and Tides
Extreme Solar System II　2011年09月13日、米国

井田茂　Predictions from Population Synthesis – Comparison with Obs. & Constraints on Theory
Extreme Solar System II　2011年09月17、米国

国際研究集会の開催実績

種別		平成 23 年		平成 24 年		平成 25 年		平成 26 年		平成 27 年	
		（件）	（人）	（件）	（人）	（件）	（人）	（件）	（人）	（件）	（人）
国内開催	国内からの参加	0	0	3	171	1	30	2	82	2	145
	海外からの参加		0		53		10		3		22
海外開催	国内からの参加	0	0	0	0	1	181		0	0	0
	海外からの参加		0		0		77		0		0

受賞・招待講演・基調講演等

種別		平成 23 年	平成 24 年	平成 25 年	平成 26 年	平成 27 年
受賞	国際的な賞	0	0	0	0	0
	国内学会等	0	0	0	2	1
	国内財団等	0	0	0	1	2
国際学会における招待講演		17	11	15	18	15
国際学会における基調講演		0	1	1	3	0

（３）図書

計画研究 A01：ガス惑星の直接撮像・分光と地球型惑星の検出

「生命の星の条件を探る」、阿部豊、文藝春秋、２０１５年

地球と宇宙の化学事典、左近樹 (分担執筆)、朝倉書、２０１２年

「南極からの天文学」（平成２４年理科年表）、高遠徳尚、丸善出版 （国立天文台編）２０１２年

計画研究 A02：系外惑星大気の数値モデリングと形成進化理論

「土星の衛星タイタンに生命がいるー地球外生命を探す最新研究」、関根康人、２０１３年小学館

計画研究 B01：円盤から惑星へ

新版　雪氷辞典、日本雪氷学会編（分担執筆)、古今書院、２０１４年

計画研究 B02: ハビタブル地球型惑星の形成理論

「系外惑星の事典」、井田茂 ・田村元秀 ・生駒大洋 ・関根康人、朝倉書店、２０１６年

「地球外生命—われわれは孤独か」、井田茂、長沼毅　岩波書店、２０１４年

「宇宙と生命の起源２ - 素粒子から細胞へ」、小久保英一郎、嶺重慎、岩波書店、２０１４年

「惑星形成の物理」、井田茂（中本泰史氏と共著)、共立出版、２０１５年

「地球外生命」、井田茂（長沼毅氏と共著)、岩波新書、２０１５年

「系外惑星 - 宇宙と生命のナゾを解く」、井田茂　ちくまプリマー新書、２０１２年

「スーパーアース」、井田茂、ＰＨＰサイエンス・ワールド新書、２０１１年

（4）新聞紹介記事・WEB

計画研究 A01: ガス惑星の直接撮像・分光と地球型惑星の検出

林　正彦
- WEB　太陽系外惑星が作る「腕」の検出に成功　すばる望遠鏡 HP、2014 年
- WEB　偏光観測で見えた惑星材料物質の成長　すばる望遠鏡 HP、2014 年
- WEB　重い恒星の巨大な惑星､すばる望遠鏡が直接観測で発見　すばる望遠鏡 HP、2014 年
- WEB　若い太陽のまわりの惑星誕生現場に見つかった巨大なすきま ~複数の惑星が誕生している現場か?~　すばる望遠鏡 HP、2014 年
- WEB　原始惑星系円盤に小さな渦巻き構造を発見 ― 密度波理論で探る惑星形成の現場　すばる望遠鏡 HP、2014 年
- WEB　ガリレオ衛星が「月食」中に謎の発光？ すばる望遠鏡とハッブル宇宙望遠鏡で観測　すばる望遠鏡 HP、2014 年
- WEB　アルマ望遠鏡が見つけた巨大惑星系形成の現場　すばる望遠鏡 HP、2014
- WEB　系外惑星の直接撮像の成果　すばる望遠鏡 HP、2013 年

計画研究 A02：系外惑星大気の数値モデリングと形成進化理論

阿部　豊
- 新聞（人物紹介）毎日新聞 2015 年 9 月 20 日，朝日新聞 2015 年 10 月 22 日

計画研究 B01: 円盤から惑星へ

田中　秀和
- WEB　惑星の種はすき間だらけ～「ダストから微惑星への成長の謎」を解明～　北海道大学 HP、　2013 年
  https://www.hokudai.ac.jp/news/131004_pr_lowtem.pdf
  https://www.soken.ac.jp/news/962/

百瀬　宗武
- WEB　形成しつつある惑星の兆候を捉えた―すばる望遠鏡による新たな発見、 茨城大学 HP、 2012 年 3 月 18 日
  http://stars.sci.ibaraki.ac.jp/~momose/kaisetu/asj2012march/

深川　美里
- WEB 国立天文台プレスリリース「アルマ望遠鏡が見つけた巨大惑星系形成の現場」2014 年 1 月 17 日
  http://alma.mtk.nao.ac.jp/j/news/pressrelease/201401177290.html

尾中　敬
- WEB　"宇宙の氷"で大マゼラン雲を探る～天の川銀河との違いが明らかに～ 2016 年 3 月 1 日
  http://www.s.u-tokyo.ac.jp/ja/info/4543/
  http://www.sci.tohoku.ac.jp/news/20160301-7724.html

塚越　崇

- WEB 国立天文台プレスリリース(2016 年 9 月 14 日)「巨大氷惑星の形成現場を捉えた ―アルマ望遠鏡で見つけた海王星サイズの惑星形成の証拠－」(Tsukagoshi et al. 2016、ApJL、Vol.829、L35 関係)
  http://alma.mtk.nao.ac.jp/j/news/pressrelease/201609148022.html

- 日本天文学会 2016 年秋季年会合同記者発表(2016 年 9 月 13 日)「巨大氷惑星の形成現場を捉えた ―アルマ望遠鏡で見つけた海王星サイズの惑星形成の証拠－」（塚越崇他）

- TW Hya 関係 (日本天文学会 2016 年度秋季年会，Tsukagoshi et al. 2016、ApJL、Vol.829、L35 関係)
  「愛媛大で天文学会秋季年会　きょうから」　愛媛新聞　2016 年 9 月 14 日
  「巨大氷惑星　形成の証拠とらえた」　しんぶん赤旗　2016 年 9 月 14 日
  「巨大氷惑星の形成現場を捉えた」　あいテレビお昼のニュース　2016 年 9 月 14 日

武藤　恭之

- SAO206462 関係(Muto et al. 2016、ApJL、Vol.829、L35 関係)
  「若い星の周りに渦巻き構造」　しんぶん赤旗　2012 年 4 月 12 日
  「原始惑星系円盤に小さな渦巻き構造」　科学新聞　2012 年 4 月 13
- WEB 国立天文台プレスリリース「太陽系外惑星が作る「腕」の検出に成功」2013 年 2 月 7 日
  http://subarutelescope.org/Pressrelease/2013/02/07/j_index.html
- WEB 国立天文台プレスリリース「若い太陽のまわりの惑星誕生現場に見つかった巨大なすきま ～複数の惑星が誕生している現場か？～」2012 年 11 月 8 日
  http://subarutelescope.org/Pressrelease/2012/11/08/j_index.html
- WEB 国立天文台／工学院大学プレスリリース「原始惑星系円盤に小さな渦巻き構造を発見 ― 密度波理論で探る惑星形成の現場」2012 年 4 月 11 日
  http://subarutelescope.org/Pressrelease/2012/04/11/j_index.html
- NHK BS2 コズミックフロント 出演　「スパイラル・ミステリー　５つの渦がひもとく宇宙の謎」2014 年 5 月 8 日放送

Raymond Angelil

- WEB 北海道大学プレスリリース(2013/9/5)「過飽和気体における核生成過程の大規模分子動力学計算：はじめて室内実験との直接比較を実現！」(Angelil et al. 2013 Journal of Chemical Physics、Vol.139、074309 関係)
  http://www.hokudai.ac.jp/news/130905_pr_lowtem.pdf
- WEB 北海道大学プレスリリース(2015/8/19)「水の凝縮核生成の大規模分子動力学シミュレーション－室内実験レベルの低生成率での凝縮核生成の再現に成功－」(Angelil et al. 2015 Journal of Chemical Physics、Vol.143、064507 関係)
  http://www.hokudai.ac.jp/news/150819_lowtem_pr.pdf

Juerg Diemand

- WEB 科学サイト Phys.org が沸騰分子動力学計算に関する我々の研究を紹介（2015/3/24）(Diemand、J et al. 2014 Physical Review E、Vol.90、0524070; Angelil et al. 2014 Physical Review E、Vol.90、63301 関係)
  Improving the theory of phase transitions with supercomputers
  http://phys.org/news/2015-03-theory-phase-transitions-supercomputers.html

下西　隆

- WEB 東北大学･東京大学プレスリリース(2016/9/5)「銀河系ホットコアを初検出」(Shimonishi et al. 2016、ApJ、Vol.827、72 関係)
  http://www.tohoku.ac.jp/japanese/2016/09/press20160905-01.html
  http://www.s.u-tokyo.ac.jp/ja/press/2016/4996/

片岡　章雅

- WEB 国立天文台プレスリリース(2016 年 12 月 5 日)「アルマ望遠鏡、惑星の種の成長に迫る」(Kataoka et al. 2016、ApJL、Vol.831、L12 関係)
  http://alma.mtk.nao.ac.jp/j/news/pressrelease/201612058078.html

計画研究 B02: ハビタブル地球型惑星の形成理論

小久保英一郎

- WEB
  Exploring the universe with supercomputing、iSGTW、2015
  シーズン・インタビュー、光村チャンネル、2012 年
  系外惑星の発見とシミュレーション天文学、WEBRONZA+、2011 年
- 雑誌
  宇宙の「素朴な謎」に迫る 5 つの質問 三浦しをん VS.小久保英一郎、週刊朝日 2014 年 1 月 24 日号、28
  宇宙をめぐる物語、週刊朝日 、2012 年 8 月 17-24 日号、118.
  学者男子、an・an 、2012 年 4 月 4 日号、27.
  夢のかなえかたを大人に聞いてみました、DreamNavi 、2012 年 5 月号、6
- テレビ番組出演
  「News ザップ!」BS スカパー!、2016.2.18
  「コズミックフロント」NHK BS プレミアム、2015.12.24 ; 2015.10.1 ; 2015.7.30 ; 2015.6.25; 2014.11.13 ; 2013.2.14 ; 2012.1.31 ; 2011.9.20
  「News ザップ!」BS スカパー!、2015.8.20
  「デザインの梅干」NHK 教育、2015.3.19
  「探検バクモン」NHK 総合、2013.9.1
  『NHK 高校講座地学基礎』NHK 教育，2013.5.15 OA
  『エル・ムンド』NHKBS1，2013.2.18 OA
  『Futurescape』Fm yokohama 84.7、2012.6.2 OA
- 新聞
  未知に迫る科学の力、読売新聞、2015.8.19、14 面
  駆ける、読売新聞、2014.11.20、夕刊 9 面

井田茂

- 雑誌
  地球中心主義からの解放、ユリイカ、2016 年 1 月号
  週刊『地球 46 億年の旅』創刊号「太陽と地球の起源」、2 号「ジャイアント・インパクトと月の誕生」、朝日新聞社、2014 年
- 対談
  井田茂×東浩紀「系外惑星から考える――太陽系は唯一の可能性か」2015 年
  『人類滅亡を避ける道―関野吉晴対論集』東海教育研究所、2013 年

- テレビ番組出演
  「コズミックフロント」NHK BS プレミアム、2014.6.5
- テレビ監修
  モーガン・フリーマン 時空を越えて「第 1 回 宇宙人との遭遇 そのとき人類は」2015 年
- プラネタリウム監修
  『GOODNIGHT GOLDILOCKS』~太陽系外惑星の世界 (五藤光学研究所) 2012 年
- WEB
  系外惑星の深すぎる海と砂漠 ―地球のような惑星は低質量星のまわりではなく、やはり太陽型星のまわりにある？、東京工業大学 HP、2015 年

中本泰史
- 雑誌
  『45 億年をさかのぼり「地球形成」の謎を解明する』，私立中高進学通信 2013 年 8 月号

メディア報道一覧 （件数）

種別		平成 23 年	平成 24 年	平成 25 年	平成 26 年	平成 27 年
国内	新聞	0	2	5	1	3
	雑誌	2	3	7	5	5
	テレビ	2	3	3	3	7
	その他の媒体	1	4	1	0	1
海外	新聞	0	0	0	0	0
	雑誌	0	0	0	0	0
	テレビ	0	0	0	0	0
	その他の媒体	0	0	0	1	0

（５）ホームページ

【新学術領域研究ウェブサイト】（本領域のホームページ）

http://exoplanets.astron.s.u-tokyo.ac.jp/index.php
に新学術領域研究ウェブページを製作し、同時に英文ページの製作も行った。最新の成果の紹介や研究会案内、公募研究案内等を、当ホームページを通じてリアルタイムに広く周知できるよう、更新作業を行いながら努めた。

（６）主催研究会

総括班 X00: 太陽系外惑星の新機軸：地球型惑星へ

平成２７年度「系外惑星」国際研究会
平成２８年２月２０日（土） ～ ２４日（水）
日航ホテル、石垣島、沖縄県

平成２６年度 系外惑星大研究会
平成２７年３月２日（月） ～ ３日（火）
東京大学 情報学環 福武ホール (本郷キャンパス)、東京都

第３１回 Grain Formation Workshop
平成２７年１月７日（水）午後 ～ ９日（金） 午後
文部科学省共済組合箱根宿泊所 強羅静雲荘、神奈川県

Exoplanets and Disks: Their Formation and Diversity II
平成２５年１２月８日（日） ～ １２日（木）

シェラトンコナリゾート＆スパ、ハワイ、米国

計画研究 B01: 円盤から惑星へ

平成 25 年度
「原始惑星系円盤研究会」国立天文台　（一部の旅費を補助）
平成 25 年 8 月 19 日(水)〜22 日(金)
国立天文台三鷹キャンパス講義室　http://th.nao.ac.jp/MEMBER/kataoka/disk2013/

平成 26 年度 北海道大学低温科学研究所共同研究集会
「ALMA を活用した原始惑星系円盤に関する研究の新展開」（北大低温研との共同開催）
平成 26 年 7 月 31 日(木)13:30〜8 月 2 日(土)15:00
北海道大学低温科学研究所講堂
http://www.lowtem.hokudai.ac.jp/symposium/201407312.pdf

（7）アウトリーチ活動

計画研究 A02：系外惑星大気の数値モデリングと形成進化理論

倉本　圭

- 市民講座：『地球惑星学入門』 NHK 文化センター新札幌校：『楽しく学ぶ宇宙と惑星学』 道新文化センター札幌校：ともに月一回開講、2011～継続中
- 高校教員対象セミナー講師：『第二の地球は存在するか』，北海道高教研物理部会，札幌市、 2012 年 1 月 12 日：『同』惑星科学研究センター第一回惑星科学最前線セミナー，神戸市，2012 年 3 月 15 日：『同』物理教育学会札幌支部，札幌市，2012 年 6 月 9 日：『系外惑星におけるハビタビリティ』惑星科学研究センター第二回惑星科学最前線セミナー，神戸市，2012 年 12 月 22 日
- テレビ番組出演：『頭がしびれるテレビ』NHK，2012.6.3 OA

阿部　豊

- テレビ番組出演：『コズミックフロント』NHK BS，2013.4.4 OA，『おはよう日本』NHK 地上波，2015.9.3OA

はしもとじょーじ

- 地球科学分野若手会講座講師：『多様な惑星の気象学と気候学』，第 23 回日本気象学会夏期特別セミナー(若手会夏の学校)，愛知県民の森(愛知県新城市)，2011 年 9 月 5 日
- 小学生対象授業講師：『空気であそぶ』、おもしろ理科実験教室，むかわ町役場穂別総合支所(北海道勇払郡むかわ町), 2013 年 1 月 8 日,『地球の外から落ちてきた石』，富内小学校(北海道勇払郡むかわ町)，2014 年 9 月 2 日，穂別小学校(北海道勇払郡むかわ町)，2015 年 9 月 15 日.

市民講座：『宇宙パラシュート』，むかわ町惑星講座，穂別小学校，2016 年 3 月 15 日

計画研究 B01: 円盤から惑星へ

武藤恭之

- 田園調布学園中等部高等部　土曜プログラム
  「大型望遠鏡とコンピュータで探る惑星形成の物語～「第二の地球」は存在するか？」 2015 年 10 月 17 日
- 自然科学カフェ講演
- 「惑星の作り方　～最新観測と理論計算で見えてきた惑星形成のシナリオ」
  2015 年 7 月 4 日
- Newton 別冊『最新研究による太陽系の成り立ち　誕生からの 1 億年』編集協力
  2015 年 3 月発行
- 「Newton」2014 年 7 月号 『太陽系 誕生と進化』編集協力
- 平塚市博物館　夏期特別展「ぼくたちはひとりぼっち？～地球の外に生命を探して」関連講演会「紙と鉛筆とコンピュータで探る惑星の作り方」
  2014 年 8 月 30 日　平塚市博物館
- 朝日カルチャーセンター横浜教室連続講座「ペンとコンピュータで挑む宇宙の謎—理論天文学最前線」分担
  「紙と鉛筆とパソコンで惑星誕生の謎に迫る」2013 年 6 月 15 日

塚越　崇

- アカデミストジャーナル・ウェブコラム「アルマ望遠鏡で 175 光年先の星を観る –惑星形成のメカニズム解明を目指して」 2016 年 1 1 月 1 1 日
  - ✓ https://academist-cf.com/journal/?p=2503

- 国立科学博物館上野・第 834 回天文学普及講演会（百瀬宗武）
  - ✓ 「アルマで探る惑星系の誕生」2016 年 8 月 20 日
- 茨城県高等学校文化連盟・自然科学部・冬季合同天体観測合宿@プラトーさとみ講演（百瀬宗武）「アルマで探る惑星系の誕生」2016 年 12 月 3 日

計画研究 B02: ハビタブル地球型惑星の形成理論

中本泰史

- 高校生向け講演「夢ナビライブ」講師：『生命を宿す星は宇宙のどこにあるだろうか？』，2011 年 6 月 4 日，名古屋市； 『同』，2011 年 7 月 16 日，東京ビッグサイト； 『同』，2012 年 7 月 14 日，東京ビッグサイト； 『同』，2012 年 12 月 15 日，静岡市； 『宇宙のどこに生命はいるだろうか？』，2015 年 7 月 11 日，東京ビッグサイト
- 惑星科学分野若手講座講師：『星・惑星系の形成過程入門』，惑星科学フロンティアセミナー，北海道むかわ町，2012 年 9 月 10 日-13 日

アウトリーチ活動一覧（件数）

種別	平成 23 年	平成 24 年	平成 25 年	平成 26 年	平成 27 年
広報誌・パンフレット	0	0	0	0	0
一般向け講演会・セミナー	16	14	13	13	13
小・中・高向け授業・実験・実習	3	3	2	4	9
サイエンスカフェ	1	4	2	2	4
イベント参加・出展	0	0	3	0	1
プレスリリース	1	5	4	1	3

（8）受賞

平成２４年度

Olivier Guyon: 2012 年度・マッカーサー賞（The John D. and Catherine T. MacArthur Foundation）

平成２５年度

奥住聡: 2013 年度・日本惑星科学会・最優秀研究者賞
片岡章雅：2013 年度・日本惑星科学会・最優秀発表賞
Kataoka et al. (2013、A&A、554)"Static compression of porous dust aggregates"　highlight paper 選出
Kataoka et al. (2013、A&A、557)"Fluffy dust forms icy planetesimals by static compression" highlight paper 選出

平成２６年度

相川祐理: 2014 年度・日本地球惑星科学連合・地球惑星科学振興西田賞
武藤恭之: 2014 年度・日本惑星科学会・最優秀研究者賞
片岡章雅：2014 年度・総合研究大学院大学・長倉研究奨励賞
Diemand et al. (2014、Phys. Rev. E、90)　"Direct simulations of homogeneous bubble nucleation:Agreement with classical nucleation theory"　Phys. Rev. E の Editors' Suggestion

平成２７年度

奥住聡: 2015 年度・日本天文学会・研究奨励賞
田崎亮：2015 年度・　日本惑星科学会・最優秀発表賞
Angelil et al. (2015、J. Chem. Phys. 143)"Homogeneous SPC/E water nucleation in large molecular dynamics simulations"　J. Chem. Phys.の Editors' Choice

平成２８年度

関根康人: 2016 年度・文部科学大臣若手科学者賞

（９）　共同研究の実施状況　（件数）

種別		平成 23 年	平成 24 年	平成 25 年	平成 26 年	平成 27 年
大学・研究機関	国内	20　(26)	12　(42)	17　(30)	19　(36)	13　(44)
	海外	5　(32)	9　(34)	8　(36)	16　(45)	12　(39)
企業等	国内	0　0(0)	0　0(0)	0　0(0)	0　0(0)	0　0(0)
	海外	0　0(0)	0　0(0)	0　0(0)	0　0(0)	0　0(0)

（○：契約書を交わしている件数、●：契約書を交わしていない件数（括弧書き））

（１０）研究成果による産業財産権の出願・取得状況　　該当せず

総括班評価者による評価

本研究領域では、観山正見（広島大学・特任教授・理論天体物理学)、松井孝典（千葉工業大学・惑星探査研究センター所長・惑星科学）山田亨（JAXA 宇宙科学研究所・教授・観測天文学）の 3 氏に統括班の評価担当を依頼している。これらの評価者には、毎年開催する大研究会に都合のつく限り出席してもらい、本領域の成果の全貌把握に努めていただくと同時に、個別に興味あるテーマの進捗については随時報告して評価していただいているところである。

【観山正見教授】

本研究領域は、近年急速に発展している「系外惑星」研究をさらに一歩進め、「宇宙の中に存在する地球型惑星」の探索と、その形成過程・存在頻度に関する理解を深めることを目指している。この目的を達成するためには、天文学と惑星科学という「二つの手法の融合」という方向性と、系外惑星の母胎と系外惑星自身の性質という「二つの対象を繋げる」という方向性とで、それぞれ大きな飛躍が望まれる。ここではこのような視点から、これまでの領域全体の成果を踏まえつつ評価を試みる。

まず「手法の融合」という側面からは、「系外惑星の更なる発見」という天文学上の進展と、「系外惑星パラメータ分布の再現」という惑星科学上の進展とが相まって進んでいる点に注目したい。具体的には、すばる望遠鏡によって大きな軌道半径をもつ巨大ガス惑星の直接検出に 2 例成功したことや、重力マイクロレンズ法によって地球型惑星 1 個を含む 36 個の惑星の間接検出がなされた（A01 班)。一方で、N 体計算とモンテカルロ法を組み合わせた惑星軌道離心率分布の再現や巨大惑星の重力散乱による影響に関する研究が進捗している（B02 班)。これらは、天文学的手法による「系外惑星の完全な探索へ向けた努力」と、惑星科学的（惑星形成理論も含む）手法による「系外惑星系の進化系列の全貌解明」とが両輪となって、宇宙における系外惑星の包括的な姿を解明するチャレンジングな試みである。また最近観測がスタートした ALMA からは、円盤の自己重力不安定によって惑星が形成されてもおかしくないような現場が見つかった（B01 班)。このような新たな発見とシミュレーションによって、上述した手法の融合による系外惑星の研究が進展した。特に、惑星形成の多様性という側面からもこの度の研究は大きな展開が図られたと考える。

一方、系外惑星とその母胎となる円盤という「二つの対象を繋げる」という側面から特に注目されるのは、円盤中に含まれるミクロンサイズの固体微粒子（ダスト）から、

キロメートル・サイズへの微惑星へと至る過程が、一貫した計算により世界で初めて再現された成果である（B01、B02 班)。ダストから微惑星へと至る道筋については、太陽系形成論が 1980 年代に確立された後も、長らく論争になっていた問題である。それに関して、初めて説得力ある方向性を示したことは、この問題を大きく解決に導く鍵を与えた成果として評価したい。ただし、微惑星形成過程については、今後、世界的な評価を受けてその方向性が確立していくものと思われる。また、この方向性を今後さらに発展させるためには、すばるや ALMA といった大型観測装置で得られる観測情報も踏まえ、原始惑星と円盤との相互作用も含めた検討が必要となろう。すでにグループ内でそのような動きが具体化しているので、本領域は今後の系外惑星研究のさらなる発展へ繋がると期待できる。

また、円盤と惑星との相互作用という観点から、もう一つ忘れてはならないのは、円盤物質がいかにして惑星物質、特に惑星大気や、地球型惑星を特徴付けている海に取り込まれるのかという問題である。この面においても、天文学の立場（A01、B01 班）からは星間化学で確立された手法が、惑星科学の立場（B02、A02 班）からは比較惑星学で確立された手法が、それぞれ応用され、精密なモデル化が順調に進んだと評価できる。また、これらモデルの検証をめざした新観測装置（SCExAO や CHARIS）の開発が進んだ。CHARIS については、製作工程の遅れのため期間内に惑星大気の分光観測が開始できなかったのは残念だが、装置はすでに完成しているので、領域終了後の成果に期待したい。

以上を総括すると、本新学術領域では研究題目にある「地球型惑星」に様々な手法で着実に迫っており、その起源の詳細と多様性を理解していく上で多彩な成果が実現できたと評価する。

【松井孝典所長】

計画研究 A02 を中心に評価を行った。本計画研究で開発を進めた大気循環と大気放射の数値モデルは、観測データの豊富な太陽系惑星大気の循環と構造について良好な再現性を得るに至っている。これらを駆使し、系外地球型惑星表層における水の安定性について、母星からの距離、表層水量、自転要素等に対する依存性を系統的に調べ、陸惑星における液体の水の両極域への局在化や、同期回転湿潤惑星における対流雲アルベドの増大など、ハビタブルゾーンを拡大させるメカニズムを新たに見出した。また複数の凝結成分を組み込んだ木星型惑星の雲対流のシミュレーションを世界に先駆け成功させ、積乱雲の発生サイクルと大気中の重元素濃度の関係や、動的に決まる物質分布の放射過

程への影響を明らかにした。高温状態から出発する地球型惑星の進化について、マグマオーシャンが長期間保持される場合と、大部分の水蒸気が速やかに凝結し海洋が形成する場合に類別されることを提唱した理論は世界的な注目を集めるとともに、各進化段階における惑星熱放射の観測可能性を定量的に示すなどの発展を見せている。新規開発装置による系外巨大惑星の直接分光観測が期間内に実現しなかったのは残念だが、将来の観測研究との融合を目指したモデリング研究が進んだことは高く評価できる。

【山田亨教授】

本新学術領域は、「太陽系外惑星」という新しい融合分野について、その探査とキャラクタリゼーション、および原始惑星系円盤における惑星形成論の観点から、光赤外および電波など多様な手法での観測、原始惑星系円盤・惑星形成・惑星大気についての理論、そして数値シミュレーションなどの多角的な方法により、非常に活発な研究が進められた点について、高く評価できる。

計画研究 A01 については、すばる望遠鏡 SEEDS プログラムでのガス惑星の系統的な観測の成果が着実に出ており、もっとも「第二の木星」と呼ぶに近い惑星の検出をはじめ、同プログラムでは直接の科学成果の創出に加え、若手研究者の国際共同研究への積極的かつ主体的な参加の機会、周辺分野との連携にも大きな成果を挙げた。高コントラスト赤外線分光器の開発も、多少の遅れは出たものの着実に進んだ。この装置は現時点で完成してハワイにあるので、今後のすばる望遠鏡による観測に期待ができる。また重力マイクロレンズレンズ法による地球質量、海王星質量の惑星探査は着実な成果を挙げた。

計画研究 A02 については、大気循環についての 3 次元惑星大気シミュレーションの構築も進められ、ハビタブルゾーン付近の惑星の温室効果についての知見が得られた。また、大気進化については、惑星の固化と初期大気の進化は、大気による温室効果や中心星の極紫外線による水蒸気の散逸と結びついているという、新たな知見に基づくモデルを構築し、地球と金星との相違を説明しうる理論を提唱するなど大きな成果を挙げた。今後、これらの理論・モデルをどのように検証してゆくか、と言う観点でも将来的な研究の発展に期待したい。

計画研究 B01 では、まず ALMA による円盤研究の着実な成果が挙げられる。SEEDS プロジェクトをはじめとした、すばる望遠鏡による円盤の散乱光観測などとの相補的発展も進み、原始惑星系円盤における惑星形成の観測的な検証を進めた。一方、円盤内固体物質の成長については実験・理論の構築が進んだ。

計画研究 B02 では、原始星の形成過程、およびその直後に始まる原始惑星系円盤の形成過程のシナリオを構築して、新たな描像を得るなどの成果を挙げた。また、氷惑星の形成過程についても、高空隙率化に伴う塵の空気力学的特性の変化が、氷の塵の急速な合体成長を引き起こし氷惑星が形成されるという、新たな描像を得る成果も挙げた。惑星形成の理論的研究が様々な面から進められており、高く評価される。

観測・理論両面で多岐にわたる成果を上げていることは、本研究課題の充実を示しているが、とくに惑星大気研究分野と系外惑星研究分野の融合的な発展、また、ALMA による高解像度観測と円盤・惑星形成モデルの精密な比較などの融合的研究については、本課題の成果を基礎としての今後のさらなる発展を期待したい。

さらに、計 14 件の公募研究の実施、国内・国際研究会の主催など、活発な研究交流の実施、PD 雇用による若手研究者の教育・研究機会の提供など、当研究領域を活性化させるための活動性も高く評価される。

研究紹介

（１）研究の目的及び概要

本領域では、天文学と惑星科学の密接な連携・融合によって、我が国において「系外惑星」という新たな学術領域を確立して世界的リードを狙うことで、当該分野における我が国の学術水準を飛躍的に向上・強化することを目的とした。

その中心となったのは、直接的・間接的観測手法を用いた太陽系外惑星の検出である。木星型惑星については、すばる望遠鏡を用いて直接検出を目指し、地球型惑星については、重力マイクロレンズ法による間接検出を推進した。また、新たに高コントラスト赤外線分光器等を開発して、系外惑星大気を直接分光することにより、系外惑星を分光学的に特徴づける（キャラクタリゼーション)ことを目指した。

惑星系形成の研究については、すばる望遠鏡や、運用を開始したばかりのアタカマ大型ミリ波・サブミリ波干渉計（ＡＬＭＡ）を用いた原始惑星系円盤の観測を推進した。またシミュレーションや室内実験も併用して、円盤内で固体微粒子（ダスト）が成長して岩石コア（地球型惑星）の形成へといたる過程や、巨大惑星によるギャップ形成などを明らかにし、惑星系の形成と進化の研究を推進することを目指した。

これらの観測を、日本の独創的分野である地球型惑星の形成理論や惑星大気理論と密接に連携・融合させることで、地球型および木星型惑星の起源と形成を解明し、系外惑

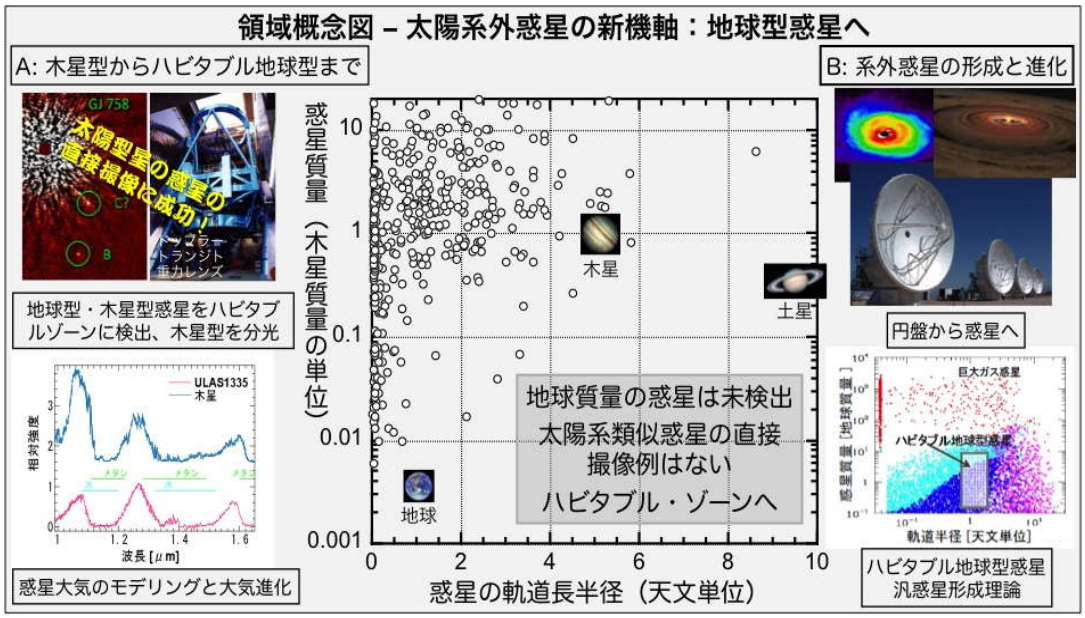

星における生命の議論にまで至ることを総合的な目標とした(前ページ図参照)。

これによって、天文学や惑星科学のみならず、地球科学や生物科学への多面的・学際的波及効果を期待した。また、本領域には多数の若手が参画し、天文学・惑星科学の融合する新たな学術領域を担う第一線の研究者の育成を進めた。

『応募領域の着想に至った経緯：天文学と惑星科学の密接な連携』

１９９５年の太陽以外の恒星を周回する惑星（以下、系外惑星）の発見以来、系外惑星は宇宙論と並んで天文学における最重要課題となっている。その理由は、これらの研究は人類の根源的な問い「我々はどこから来たのか、我々は何者なのか、我々はどこに行くのか」（ゴーギャン）に科学的に答えようとしているからである。人類が長年かけて発見してきた太陽系内の８個の惑星に対し、わずか 20 年のあいだに 2000 個以上の系外惑星が発見された。このような状況のなか、本研究開始時に「直接撮像・分光」と「地球型惑星」を重要なマイルストーンとして位置づけた。

我が国は、太陽系の起源の研究において、天文学と惑星科学の密接な連携関係を培い、世界をリードする成果を挙げてきた。系外惑星に関しても、両分野の研究者が非常に大きな関心を寄せており、また本研究に先立つ特定領域研究（平成１６～２０年度）では、非常に高い評価（A^+）を得た。しかしながら、系外惑星の研究をめぐる世界的競争は非常に激しく、我が国においても、本研究により両分野の連携・融合を一層強化し、系外惑星の研究をさらに発展させることが喫緊の課題であった。

『これまでの研究成果の飛躍的発展：直接撮像・分光による惑星のキャラクタリゼーション』

これまでに発見された系外惑星のうち、大部分はドップラー法やトランジット法（惑星の主星面通過）で検出されており、ごく限られた範囲だが惑星大気の情報も得られるようになった。これらの手法では、主星近傍の系外惑星に検出バイアスがかかり（6ＡＵまで調べるには約 15 年かかる；1AU は地球–太陽間の距離）、また太陽型ではあるが若いために活動性が高い恒星（Ｔタウリ型星）には適用できない。一方、直接観測では、そのような若い恒星を周回する若い惑星を検出し、分光することが可能となる。惑星系の内側の多様性が明らかになった現在、スノーラインを超えた外側領域（＞４ＡＵ）の多様性や、円盤から形成されたばかりの初期状態としての若い惑星に迫るには、直接観測が不可欠なのである。さらに、直接分光まで行えば、ドップラー法やトランジット法では得られない惑星の色、光度、スペクトル、従って、温度や大気組成の情報まで手

に入れることができ、単なる検出を超えた惑星系の特徴づけ(キャラクタリゼーション)が可能になる。

また、平成23年度からALMAが稼働を開始した。日米欧が対等に参画するこの国際観測施設が目指すテーマは、まさに惑星系形成であり、すでに重要な研究成果が出ている。我が国では、この研究に取り組む研究者数は欧米に比して少ないが、天文学・惑星科学の研究者の連携・融合によるオールジャパン体制を築ける点が優れており、本領域研究はそれを強く推進するための役割を担った。

『全体構想：研究期間内に何をどこまで明らかにしようとするのか』

5年にわたる本領域の研究期間において、我々は以下の四つの研究項目の実現を目指した。

Ａ０１）木星型惑星を直接検出し、また様々な手法を用いた地球型惑星の間接検出を推進する。また高コントラスト赤外線分光器を開発して、木星型惑星を直接分光し、その特徴を明らかにする　(キャラクタリゼーション)。

Ａ０２）直接分光によって得られたスペクトルを解釈し、惑星大気の化学的性質や進化を明らかにするための、汎惑星大気理論を構築する。

Ｂ０１）ＡＬＭＡやすばるを用いた原始惑星系円盤の観測や、ダストの成長実験を推進し、円盤物質から地球型惑星が形成されていく過程を解明する。

Ｂ０２）ハビタブル地球型惑星を含む惑星形成理論を展開し、直接・間接観測から得られる系外惑星の統一的描像との比較を通して、汎惑星系形成理論を構築する。

『目的達成に向けての取り組み、発展方法』

上記の達成のために、本研究では、天文学・惑星科学の両分野にわたる日本の代表的研究者が、オールジャパン体制で連携・融合して研究を推進した。本領域の研究分担者・連携研究者は、全国の様々な大学・機関の研究者を含み、また若手も多く含んでいる。本領域では、これらの研究者間の共同研究の推進に積極的に取り組み、天文学・惑星科学にこだわらず分野横断的に研究員等を雇用し、新たな学術領域を担う人材育成に取り組む。このような取り組みを通して、5年後には世界をリードする人材が育成され、当該領域が継続的に発展する状況を作り出すことを目指した。

（２）各研究項目と連携状況

本領域では、研究項目として下図のように４件の計画研究を設定し、それぞれが研究代表者のもとに組織化されている。また、公募研究もこれに対応して計画研究ごとに配置した。

４件の研究項目（計画研究）は、

A01: 系外惑星の観測研究

A02: 惑星大気のモデリング研究

B01: 惑星系形成の観測研究

B02: 惑星系形成の理論研究

からなっており、これらの相互関係は明確である。すなわち、系外惑星本体の研究と惑星系形成の研究という２項目に対して、それぞれの観測及び理論という形で４件をなしている。そのため、各研究項目において研究が深く掘り下げられると同時に、必然的にこれらの項目間で活発な連携が行われるという組織となっている。実際、以下で具体的に述べるように、これらの項目間では盛んに研究連携が行われた。また総括班では年１回の領域大研究会（うち２回は国際会議）を開催することで、本領域の参加者及び興味を持つ内外の研究者に対して、公募研究も含めた領域全体の研究の進展を俯瞰し、連携を促進する機会を設けた

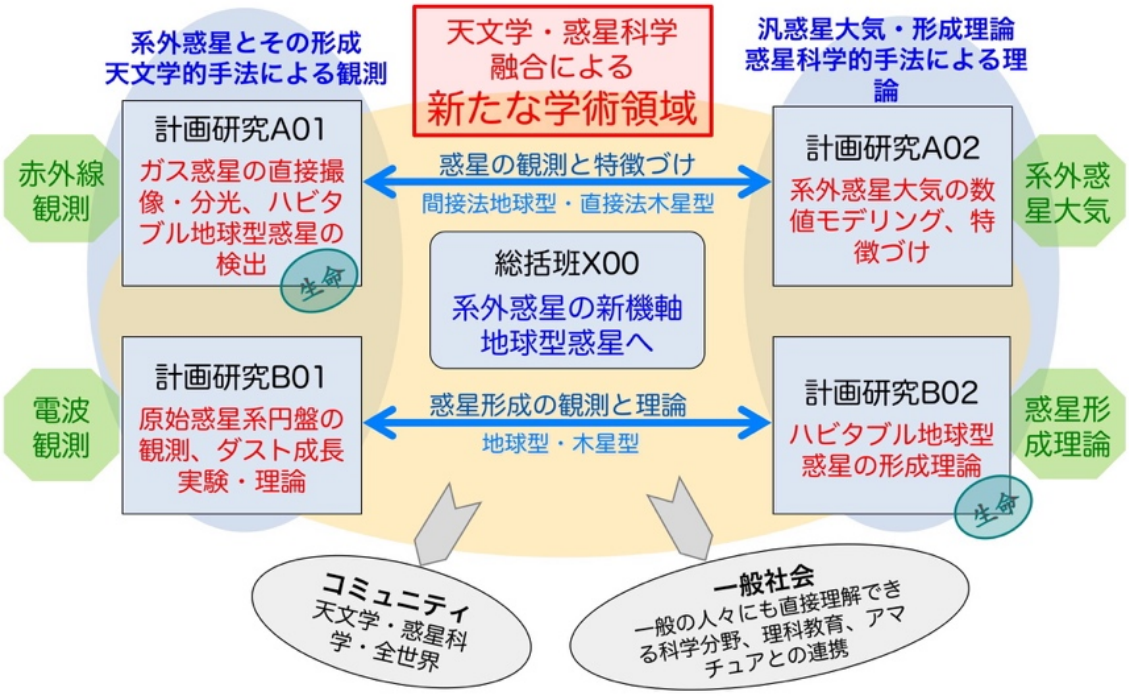

【研究項目Ａ０１】

研究項目 A01 で用いた直接撮像法では、中心星から数十天文単位の距離にあるガス惑星を２例検出した。これは、ドップラー法やトランシット法などの間接的惑星検出法が、中心星に近い惑星を選択的に検出するバイアスがあるのに対し、直接撮像法は中心星から離れた惑星を選択的に検出するバイアスがあるためである。このため、この２例の直接検出も含めて、木星の数倍から十倍程度の質量をもつ惑星がいくつも発見されるに至り、研究項目 B02 で進めている惑星系の形成理論との連携が進んだ。具体的には、このようなガス惑星の起源として、中心星近傍でコア集積によって形成されたガス惑星が、重力散乱の結果数十天文単位の遠方に飛ばされた可能性があることが研究項目 B02 によって示された。

また、赤外線による直接撮像法では若い星の周囲に円盤が検出されることが多いが、この点で研究項目 B01 とは常時相補的な連携関係のもとで研究を実施した。

なお、５年の期間中には高コントラスト赤外線面分光器を用いた実際の観測には至らなかったが、これは同装置のプリズム材料としてより高性能なものを使用する判断をしたことによって、工程が遅れたためである。新たなプリズム材は、近赤外線の広い波長域にわたって均質な分散を有するため、当初の設計に比較してより高品質の分光データを得られる予定であり、研究項目 A02 のモデリング結果との精密な比較が、当初の想定以上のレベルで可能となる。

【研究項目Ａ０２】

研究項目Ａ０１の目指す中心的観測対象である小質量星周りの同期回転惑星のハビタビリティ、木星型惑星の大気構造・ダイナミクスと分光スペクトルの関係等について重点的にモデリング研究を進め、観測量の予測を行った。またＢ０１およびＢ０２が明らかにした惑星形成論の最新の描像を反映し、大気形成と進化のモデリングを進めた。公募研究には木星型惑星の深部対流に関するテーマを採択し、大気モデリングの強化を図った。

【研究項目Ｂ０１】

研究項目 B01 は ALMA による原始惑星系円盤の高解像度観測を中核に据え、それと関連する赤外線観測、ダストの理論・実験、ガス化学モデリングを広く束ねた体制をとった。研究全般で研究項目 B02 と連携し、また赤外線観測では研究項目 A01 と連携しつつ、本研究項目では特に ALMA によるデータから得られる情報を効率良く抽出し、

最新理論モデルの観測データへの素早い適用を可能とする役割を担った。これらALMAやすばるの高解像度観測で得られた原始惑星系円盤の詳細構造に関する情報は、他の研究項目に速やかに提供した。結果的に、円盤中に惑星が作るギャップ構造やHL Tau円盤でのリング構造の起源などで多くの論文を発表した他、B02が研究対象とする系外惑星系の多様な姿や、A01やA02がメインテーマとする系外惑星大気の起源をさらに深く理解していくための、重要な手がかりを与えた。

研究項目B01の企画によって、研究交流の場において、電波観測になじみのない理論・実験研究者を対象にしたデータ解析講習会を実施した。一例は、平成26年度の北大低温研・共同研究集会「ALMAを活用した原始惑星系円盤に関する研究の新展開」である。このような機会を通じて、他の研究項目や計画研究の当事者との交流を促進するだけでなく、天文観測データの正しい取り扱い方の習得や、手法が異なる研究者間のコミュニュケーション促進に大いに貢献した。

【研究項目Ｂ０２】

研究項目B02は惑星形成理論、理論モデリングを主題としており、急速に進展する観測を通して、他の研究項目と連携した。

原始惑星系円盤については、ALMAによって撮像された原始惑星系円盤（HL Tau）の驚きのリング構造に対して、研究項目B02と共同で、その構造の起源を多角的に議論し、原始惑星系円盤内のダストの成長・移動・焼結による破壊モデル、円盤永年重力不安定性、存在している惑星による円盤ガスの構造形成などの論文を何本も発表した。また、さらに研究項目B01と共同でALMAに観測プロポーザルを出して採択され、他の円盤でも同様の円盤構造を発見した。

他にも、円盤の詳細な化学反応及び輻射輸送計算による、円盤中の有機分子の生成過程と彗星内の有機分子との関連や、そのALMAによる観測可能性の議論や、スノーラインの位置をALMAやTMT、SPICAを用いた水輝線の観測により求める議論なども、研究項目B01と密接に連携して実施した。

また短周期スーパーアースの大気の観測も進み、地球型惑星大気のモデリングも精力的に行い、トランジット惑星に対して岡山観測所で大気の透過光分光観測も行った。この研究および、ハビタビリティの議論を研究項目A02と行った。研究項目A01とは、ホット・ジュピターの形成を引き起こす巨大ガス惑星の重力散乱の結果として、遠方に散乱される巨大ガス惑星もあることを示し、それを予測することで、直接観測の指針をたてる議論で協力した。

（３）経費の使用状況

【総括班Ｘ００】

領域全体の円滑な運営を行うため、事務支援員１名を雇用して東京大学に配置した。それ以外の経費の大部分は、本領域が主催・共催する国際研究会の開催経費等に使用した。また、特に若手研究者に優先的に旅費を補助して成果発表の場を提供するなど、若手が研究交流を図れる機会を増加させるために研究費を効果的に役立てた。

【研究項目Ａ０１】

研究費の大部分は、高コントラスト観測装置の開発・製作に使用した。これには、前置光学系としての超高次波面補償光学装置 SCExAO と、赤外線面分光器 CHARIS が含まれる。SCExAO は国立天文台ハワイ観測所にて、研究分担者の Guyon を中心に開発した。また CHARIS は、プリンストン大学との共同研究として開発し、平成２８年にハワイ観測所に納入されて観測を開始し、系外惑星のスペクトル取得に成功した。

また、SCExAO の開発や重力マイクロレンズ法による低質量惑星の間接検出観測においては、それぞれ研究員として若手を雇用した。

【研究項目Ａ０２】

研究経費のほとんどを、ポスドク雇用経費と地理的に分散する拠点間をつなぐ旅費に割り当て、密接な共同研究を促進した。エアロゾル生成・分光実験装置によるデータは、惑星大気のモデリングに反映されている。大容量ディスクは、大気大循環シミュレーション等の大規模数値計算のデータ格納に用いた。

【研究項目Ｂ０１】

神戸大学においては、二段式軽ガス加速装置とこの装置の試料チャンバー全体を-15℃の氷点下に冷却するウォークイン型プレハブ式冷凍室を導入した。複数回の衝突を経た氷小天体の衝突破壊強度や、砕屑岩構造を持つラブルパイル天体の衝突破壊強度を決定する成果を得た。東京大学においては、中間赤外線分光装置に必要な高次の回折光を除去する干渉フィルター及び波長を分けるビームスプリッタの開発を行った。これら素子の極低温における波長感度特性の測定を行い、目標とする仕様値を満たす光学素子の製作を行い、将来の地上あるいは衛星望遠鏡搭載観測装置開発につながる基礎技術を確立する成果を得た。大阪大学・宇宙科学研究所にてモニター観測用に開発した可

視・近赤外同時撮像カメラは、研究期間内にファーストライトを迎えた。惑星形成の兆候が見られる原始惑星系円盤について、地球型惑星の形成が期待される内側領域のモニター観測を数年に渡って遂行し、一部の結果は ALMA による観測立案に活用した。また、系外惑星のトランジット観測にも使用した。北海道大学に導入した並列計算機コンピュータクラスタ、及び茨城大学に導入したハイパフォーマンスコンピュータは、それぞれ、ダスト付着モデル数値実験や ALMA データ解析の中核的設備として活用された。

【研究項目Ｂ０２】

研究項目 B02 の主な研究手法は、計算機シミュレーションを使った理論研究である。研究費の大半は、若手研究者の雇用および大学院生を含む若手研究者の旅費といった若手育成、国際共同研究促進のための研究代表者および研究分担者の海外渡航旅費に使用した。個人個人の研究者の旅費だけではなく、国際研究集会や合宿研究会を主催するための旅費として有効活用した。

その成果は、１６０編以上の国際ジャーナルへの論文発表として現れている。海外研究者との共同研究による理論の論文も多数あり、観測プロジェクトに理論研究者として参加した論文も多く、国際共同研究の推進、観測チームとの共同は順調に進んだ。

設備は、2011 年度に名古屋大学に設置した PC クラスター（リアルコンピューティング社製）と国立天文台に設置した重力多体問題専用計算機 GRAPE シリーズの最新機 GRAPE-9 であり、理論研究を支えた。

（４）関連学問分野への貢献度

【研究項目Ａ０１】

木星型ガス惑星の直接撮像においては、現在発見されている６個の恒星に付随する９個の惑星のうち、２個の恒星のそれぞれに付随する惑星を新たに検出し、今後キャラクタリゼーションが重要となる系外惑星、及び惑星大気の研究に向けて、対象となる天体数を有意に増やした。特に、そのうち１個（GJ504b）については、質量が木星の４倍、表面温度が 510 K、年齢 1.6 億歳であり、「第二の木星」と呼ぶことのできる天体の直接検出として、当該及び関連分野に大きな影響を与えた。

重力マイクロレンズ法による系外惑星の間接検出については、スノーラインの外側において多数の惑星を検出し、うち１例は地球型惑星１個の検出に成功した。

高コントラスト赤外線面分光器の開発については、工程の遅れから期間内に観測を開始するに至らなかったが、平成２８年９月にはすばる望遠鏡に搭載して、系外惑星のスペクトルの取得に成功し、系外惑星のキャラクタリゼーションに向けて大きく前進した。

【研究項目Ａ０２】

液体の水が安定に存在できるための惑星軌道（中心星放射量）、惑星年齢、H_2O 量、自転パラメータ等に対する依存性を浮き彫りにし、当該分野における地球型惑星の大気形成と進化の理解を大きく前進させた。特に、巨大衝突後の原始水蒸気大気とマグマオーシャンの共進化の二分性の解明（Nature、2013）は、地球型惑星の大気の多様性を整理し、また将来の観測を予測する新しいフレームワークとして広く受け入れられつつある。また本研究で開発した大気循環数値モデルは、地球大気大循環のシミュレータ間国際比較実験への参加などを通じて、将来の地球環境変動の数値予測の向上にも貢献する一方、仏フランス気象力学研（LMD）の大気モデリングチームとの連携により金星や火星などの大気シミュレーションモデルの高度化にも用いられ、わが国の進める太陽系探査のデータ解釈や立案に貢献しつつある。

また、生命存在の条件についての一般書「生命の星の条件を探る」（阿部著、文藝春秋、2015 年）を著した。

【研究項目Ｂ０１】

ALMA 観測を軸に、理論・実験の研究者を結集した研究グループ構成をとった。本科研費の活動を通じて、この分野における手法の違いを超えた共通の研究基盤が確固として確立し、その結果として手法間の共同研究に基づく多くの成果を輩出した。

ALMA やすばるの高解像度観測では、原始惑星系円盤には、非軸対で動径方向に局在化した柱密度分布が普遍的に存在していることが明らかになった。さらに、年齢が百万年を切るような若い星である HL Tau で惑星形成の兆候が捉えられた。これらは、円盤の初期条件として軸対称で動径方向にべき乗の密度分布を仮定し、約一千万年かかって惑星が形成されるとする古典的太陽系起源論とは、全く異なる状況である。すなわち、太陽系外の惑星系形成には多様なモードが存在することを示し、今後の惑星系形成の研究に質的な変革を促すものと位置づけられる。さらに、系外惑星系の多様な姿や系外惑星大気の起源を、今後さらに深く理解していくための、重要な手がかりを与えるものと位置づけられる。

【研究項目Ｂ０２】

惑星形成理論、理論モデリングを主題としていたが、地球型惑星の形成モデルにおいては、系外惑星系における生命を宿す環境を備えた惑星（ハビタブル惑星）の議論に大いに寄与した。質量、軌道半径だけで言えば、地球と似た環境の惑星が存在する確率は太陽型星の数十％に登ることを、本研究項目で解明した基礎プロセスを組み込んだモンテカルロ惑星生成モデルによって示したことは、アストロバイオロジー分野、地球科学分野、および一般の人々に大きなインパクトを与えた。ここのモンテカルロ惑星生成モデルは、学部学生向けの教科書『惑星形成の物理』（井田・中本著、共立出版、2015年）に解説した。また、系外のハビタブル惑星における生命についての議論は一般書『地球外生命』（長沼・井田著、岩波新書、2014）に著した。

ALMA による円盤構造に対する理論モデルや観測は、原始惑星系円盤という天体にダストとガスの相互作用やダストの成長というミクロ・プロセスが重要な役割を果たすという点で、天文学における新しい可能性を切り開くものとなった。

他方、プラズマ加熱による磁気乱流の安定化の議論は固体微粒子を含むプラズマ（ダストプラズマ）の物理現象としても興味深く、物理学にも影響を与えている。

（５）若手研究者の成長状況

【研究項目Ａ０１】

A01 班には、研究開始当時 39 歳以下だった 4 名の若手研究者が研究分担者として含まれている。それぞれの研究者が独自の研究を伸ばす取組を行った結果、各研究者とも高い評価を受ける研究成果を挙げた。たとえば Olivier Guyon 氏（開始当時 36 歳）は、本研究を開始して翌年 MacArthur Fellow (https://www.macfound.org/fellows/866/) に選ばれた。これは合衆国在住の優秀な研究者に、5 年間にわたって総額 50 万ドルの給付金（使途を問わない）を支給する制度であり、同氏の高コントラスト撮像分野における卓越した業績が評価されたものである。同氏は、本領域終了後も、国立天文台ハワイ観測所の主任研究員かつアリゾナ大学助教授として活躍を続けている。また住貴弘氏（開始当時 37 歳）は、重力マイクロレンズ現象を利用して多数の系外惑星を検出し、地球型惑星の検出にも成功した。同氏は、名古屋大学助教から大阪大学准教授に昇任し、同大学にて系外惑星研究をリードしている。この他に、左近樹氏が星間ダストの性質の研究において、また藤原英明氏は原始惑星系円盤の観測研究において業績を挙げた。

【研究項目Ａ０２】

専門の異なる若手２名をポスドクとして雇用した。大気モデル開発のミーティングをＴＶ会議で毎週行う一方、年に一度、系外惑星大気ＷＳを開催し、会合企画に加わることを通じてポスドクに研究分野全体の把握を促すとともに、大学院生を含め研究へのアドバイスを行い、相互交流を深める場を提供した。専門性の異なるポスドクの共同研究により、スペクトル観測から系外地球型惑星の進化段階を決定する可能性を定量的に示す成果を得た。若手の国際性を向上させるために、ポスドクと大学院生の国際学会や研究会への参加を積極的にサポートした。代表者と分担者に実質的に指導し、本計画研究の一部をなす研究を行った博士後期課程大学院生は９名（北大５（高橋・三上・斉藤・わたけん・荻原）東大３（小玉、中山、こう）神戸１（河合））である。うち１名が学位取得後、他科研費のポスドクに着任している。また５名が２０１６年度に学位を取得する見込みである。ポスドクの１名は学振特別研究員として、もう一名は他科研費のＰＤとして研究を継続している。また連携研究者の博士研究員１名が、高専の准教授（パーマネント）に異動した。

【研究項目Ｂ０１】

大規模なデータ解析や数値シミュレーションを実施するために、多くの若手研究者を研究員として雇用した。彼らは多くの論文成果を自身で挙げたほか、研究代表者・分担者や他研究項目の研究者との共同研究を通じて、領域全体の活性化に大きく貢献した。

その結果として、研究員として雇用した若手研究者の多くが、常勤職（谷川享行氏が産業医科大学助教に、塚越崇氏が茨城大学理学部助教(任期付)に、安井千香子氏が国立天文台助教に)、あるいは海外を含む研究機関で新たなポスドクの地位（金川和弘氏がポーランドの University of Szczecin、樋口あや氏が理研、ロ・スニョン氏が韓国の Ulsan National Institute of Science and Technology）を得ており、原始惑星系円盤や惑星系形成分野を支える若手研究者となっている。研究分担者として一翼を担った武藤・深川も、若手研究者を対象とする賞を受賞（日本惑星科学会最優秀研究者賞、自然科学研究機構若手研究者賞）した上で准教授に昇進し。さらに、相川・田中も教授へと栄転し、それぞれ今後この分野のリーダーとしての活躍が期待される。

【研究項目Ｂ０２】

主な研究手法は理論研究であり、研究費の大半は、若手研究者の雇用および大学院生を含む若手研究者の旅費といった若手育成、国際共同研究促進のための研究代表者および研究分担者の海外渡航旅費、国際研究集会や合宿研究会を主催するための旅費として活用した。

結果として、研究員として雇用した若手研究者は次々に、常勤職やより上のレベルのポストに移行し、今後の系外惑星研究を支える若手研究者となっている（奥住は５年の間に、博士課程学生から東工大の准教授までステップアップした)。また、大学院生を積極的に海外に送り出し、日本で開催した国際会議に出席させたことにより、多くの大学院生の国際化を促し、何人もの大学院生が国際共同研究を開始させている。多数の学振特別研究員(DC、PD)にも採用され、日本惑星科学会秋季講演会の若手最優秀発表賞（２名)、東工大の博士論文賞（手島精一記念研究賞)、名古屋大学研究科長賞など、学会や大学などでの受賞も多い。

研究成果

（１）計画研究

Ⅰ.【計画研究 A01】

１. 目標とその達成度

「ガス惑星の直接撮像・分光と地球型惑星の検出」においては、研究期間内に主として以下の２点を達成することを目標としていた。すなわち、
① 太陽系の惑星系と同程度の軌道（1–40 AU、スノーライン近傍とその外側）にある系外惑星を直接撮像すると同時に、種々の間接的手法により地球型惑星の検出を進める。
② 世界最高レベルの波面補償光学やコロナグラフを用いた高解像度の高コントラスト赤外線面分光器を開発し、系外惑星の大気を分光して特徴づけ（キャラクタリゼーション）を行う。

目標①については、この５年間にすばる望遠鏡等を用いた観測が順調に進み、新たに3 個の木星型惑星を直接撮影することに成功した（これを含めて、これまでに直接撮影された惑星はまだ 9 個しかない）。このうち GJ504b は、主星から約 30 天文単位の距離にあり、質量が木星の約 4 倍、表面温度が 510K、年齢が 1 .6 億歳のガス惑星であり、まさに「第二の木星」と呼ぶにふさわしい。また、間接的手法による検出では、重力マイクロレンズ効果を用いた観測によって、研究期間中に合計 36 個の系外惑星を検出した。その内訳は、木星型惑星が 25 個、海王星型惑星が 10 個、地球型惑星が 1 個だった。これらはすべて、スノーラインの外側に位置する冷たい惑星である。

目標②については、高コントラスト装置のうち、前置光学系として用いる超高次波面補償装置 SCExAO が完成し、既存の赤外線撮像装置と組合せて試験観測を行って性能を確認した。図（次ページ参照）は、その性能を既存の波面補償光学装置（AO188）と比較したものである。SCExAO を使用した画像では、主星周囲のノイズ（補償されない高次波面誤差によって生じるスペックル）が著しく低減されているのが分かる。SCExAO と組合せて、惑星のスペクトルを観測するのに用いる高コントラスト赤外線分光器 CHARIS については、製作途中で分光素子をより高性能のものに交換する必要

が生じたこと等の理由により、工程に遅れが生じた。この装置は、プリンストン大学での製作を終了し、ハワイ観測所に納入され、平成２８年７月から観測を開始している。

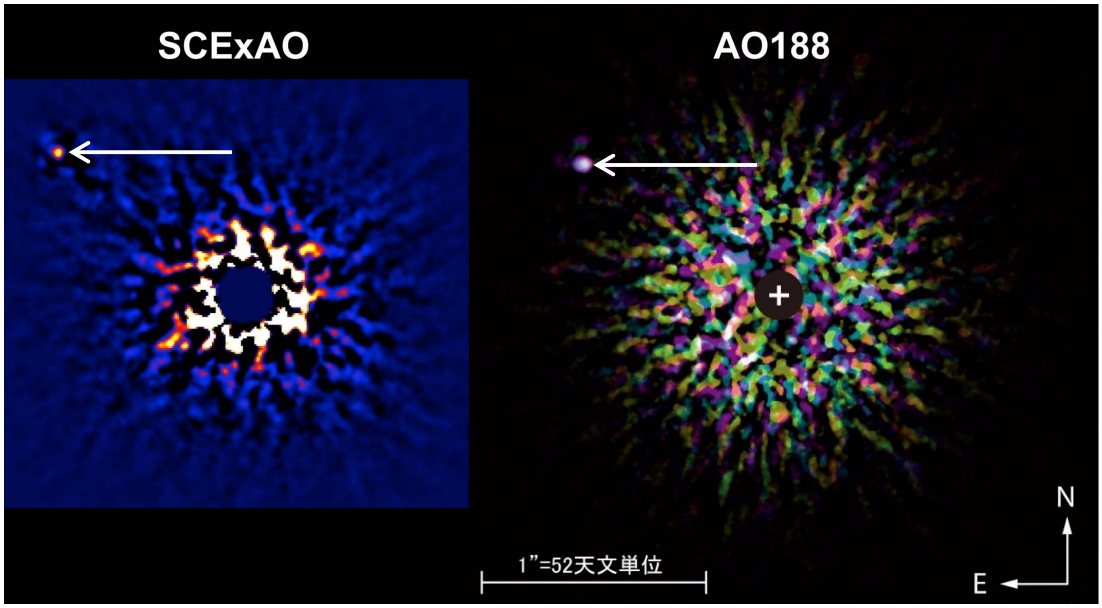

図：κ And 星に付随する惑星の画像（矢印）。前置光学系として左は SCExAO を、右は AO188 を使用。

２．研究成果

① すばる望遠鏡によるガス惑星や円盤の直接撮像観測

本計画研究によるガス惑星撮像の成果としては、2個の恒星周囲にそれぞれ1個、合計で2個の惑星を直接検出したことである。これも含めて、現在までに直接撮像された惑星は、6個の恒星周囲に9個しかない。ひとつはκ And星に付随する惑星（上図）で、質量は木星の13倍、表面温度は1700K、中心星から55天文単位離れている。もうひとつはGJ504星に付随する惑星GJ504b（次ページ図）で、質量は木星の4倍、表面温度は510K、中心星から44天文単位離れている。この惑星は直接撮像された惑星のなかでは最も低質量で低温であり、「第二の木星」と呼ぶにふさわしい。

またB01班との連携により、多数の原始惑星系円盤の直接撮像にも成功している（B01班の記述を参照）。

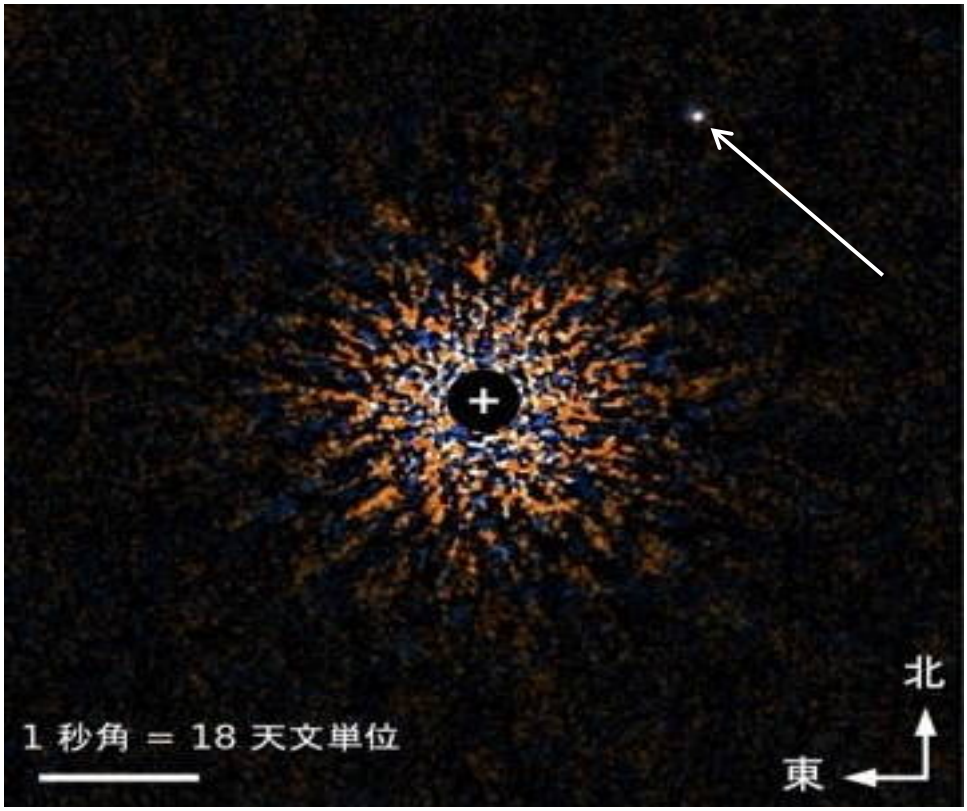

図：直接撮像した惑星 GJ504b（矢印で示した点）。

② ガス惑星の直接分光観測を目的とした専用装置群の開発・製作

すばる望遠鏡に搭載してガス惑星の分光を行うための装置として、高コントラスト赤外線面分光器（CHARIS）と超高次波面補償光学装置（SCExAO）の開発・製作を行った。SCExAOは完成し、前置光学系として本格的な高コントラスト観測に利用されている（図7-2）。これまでの波面補償光学装置AO188を使用した場合に比較して、SCExAOを前置光学系として用いるとコントラストが１０倍改善されていることが分かる。

またプリンストン大学と共同開発したCHARISについては、製作途中でより良い分光素子材が使用可能と分かり、これを利用するために設計変更と低温試験を行なったことで製作工程に遅れが出たが、最終的に完成した装置が平成28年5月にすばる望遠鏡に搬入されて、7月から観測を開始している（次ページからの図を参照）。

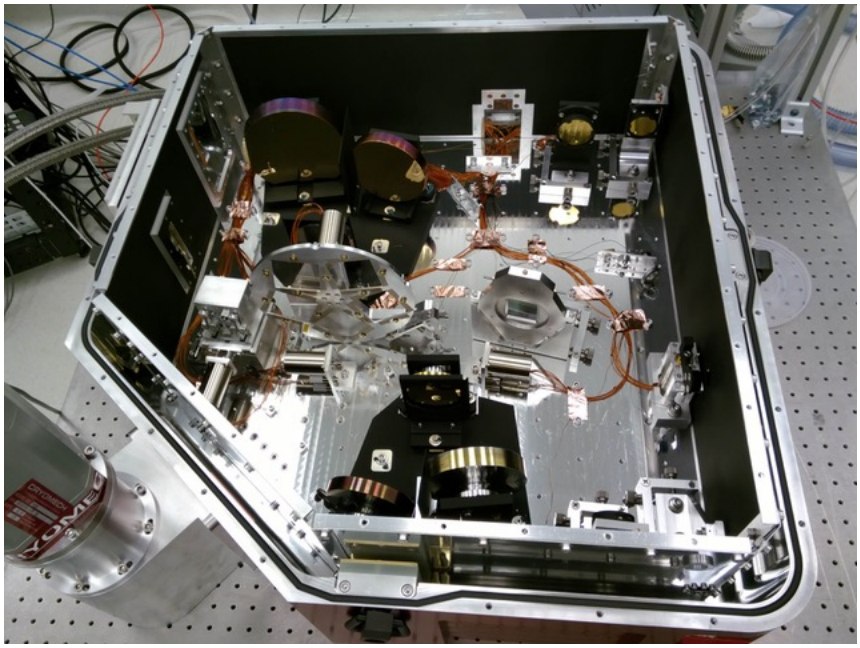

図：CHARISの光学系

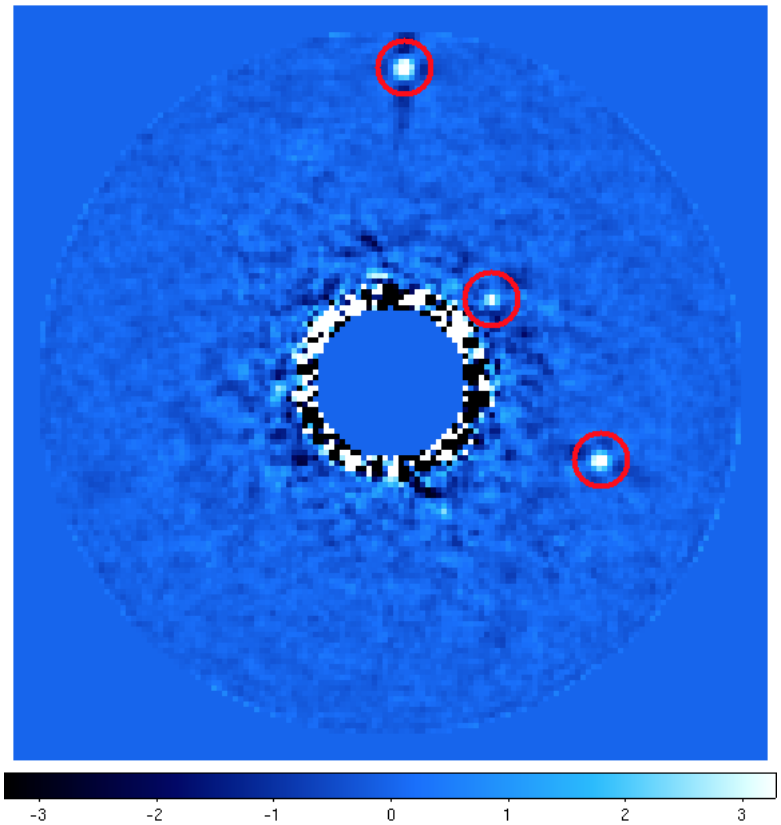

図：CHARISの試験観測で得られた系外惑星HR８７９９c（上）,d（右下）,e（中央右）の画像。２２分の露出時間による観測から達成されたコントラストは、5×10^{-6} (0″.9)、1×10^{-5} (0″.6)、5×10^{-5} (0″.4) だった。

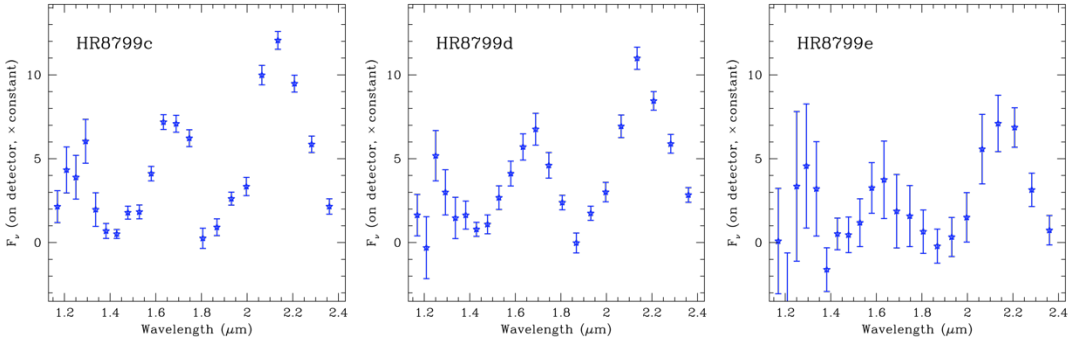

図：試験観測で得られた系外惑星HR8799c,d,eのスペクトル

図：プリンストン大学のCHARIS開発チーム

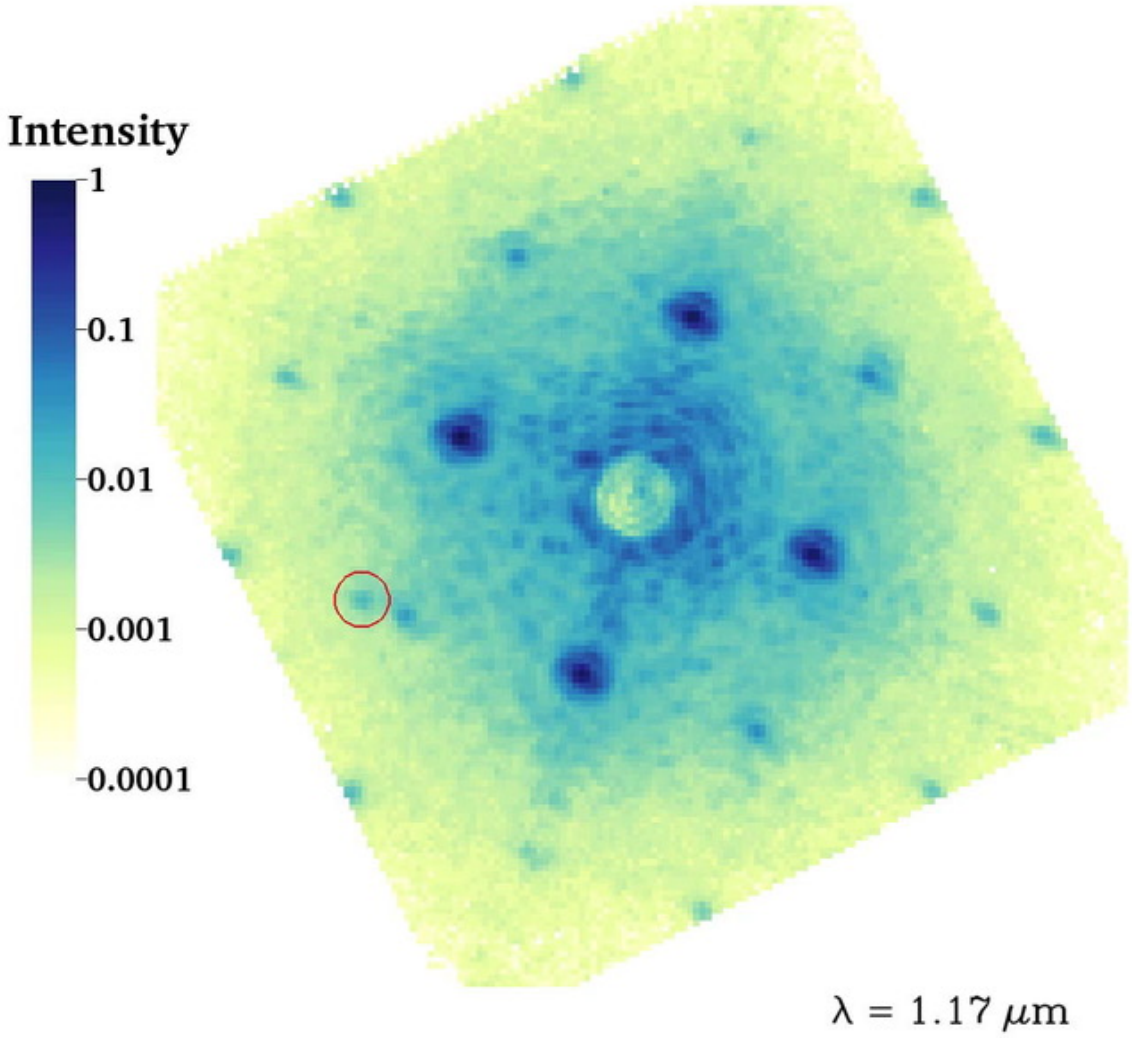

図：CHARISの試験観測で取得した褐色矮性HD1160Bの画像（左の丸印）。中心の主星から0″.78（85au）の距離にある。

③ 地球型惑星の間接検出

重力マイクロレンズ法による系外惑星の間接検出については、木星型ガス惑星25個、海王星型惑星10個、地球型惑星1個の検出に成功した。これらはスノーラインの外側に位置する冷たい惑星である。

Ⅱ.【計画研究 A02】

Ⅰ. 目標とその達成度

A02 においては、直接分光によって得られたスペクトルを解釈し、惑星大気の化学的性質や進化を明らかにするための、汎惑星大気理論を構築することを当初の目的とした。

惑星大気の多様性と進化経路の解明、それと連動した理論スペクトル予測について、想定を超える成果を得ている。巨大衝突による大規模融解状態から出発した地球型惑星の大気進化を初めて解明し、中心星からの距離に応じ、マグマオーシャンに覆われた暴走温室状態を持続する場合と、地表へ水蒸気凝結が生じ、その後安定に海洋が保持される場合に二分され、前者の継続時間が紫外線による水蒸気分解・散逸速度に支配されることを示した。

さらに、惑星年齢と中心星からの距離の関数として惑星スペクトルを予測し、マグマオーシャン保有惑星と水惑星の観測可能性を定量的に明らかにした。海洋の安定性や大気組成を制御する重要な素過程である水素散逸過程について、散逸効率が先行研究の推定よりもきわめて高いこと、また大規模大気散逸を経て大気質量が減少した後に水が両極域に局在化し、表層に液体の水を保持可能な惑星の軌道と年齢の条件が、著しく広がる可能性があることを明らかにした。

今後多数の検出が期待される同期回転地球型惑星について、大気大循環シミュレーションを実施し、雲によるアルベド上昇を考慮すると暴走温室効果の発生が抑制される（日射量にして２割増まで耐える）こと、またハビタブルゾーン内にある場合には、恒星直下点における活発な湿潤対流により全球炭素固定率が著しく上昇し、貧二酸化炭素大気を保有する可能性があることを明らかにした。

新分光器による系外木星型惑星大気分光データの取得の前に研究期間が終了したが、最も重要な参照天体である木星について、世界初となる全凝結可能種の雲生成を同時に解く流体力学モデルと、水素豊富大気の放射モデルを構築し、雲生成の間歇性、雲対流による物質分布の決定機構、大気層の放射伝達と可視・熱放射域それぞれの全球スペクトルを支配する因子を明らかにした。

２．研究成果

① 系外惑星の大気循環と熱収支の解明と予測

片方の半球に中心星放射が固定される同期回転地球型惑星について、雲放射過程の導入など高度化した大気大循環シミュレーションを実施した。その結果、雲による日射の反射により、暴走温室効果の発生に必要な日射量が抑制されることを明らかにした。他方、より弱い日射を与えた場合、恒星直下点での高温化と活発な降水により、化学風化による全球炭素固定率が著しく上昇し、大気二酸化炭素濃度が低く抑えられる傾向にあることを見出した。また世界初となる木星型惑星大気における複数の凝結成分を考慮した雲対流モデルの構築と拡張を進め、雲生成の間歇性の原因を明らかにし、大気中の物質分布を定量的に推定した。これらの循環数値モデル群はその最新版をインターネット上に無償公開している（http://www.gfd-dennou.org/library/dcmodel/）。

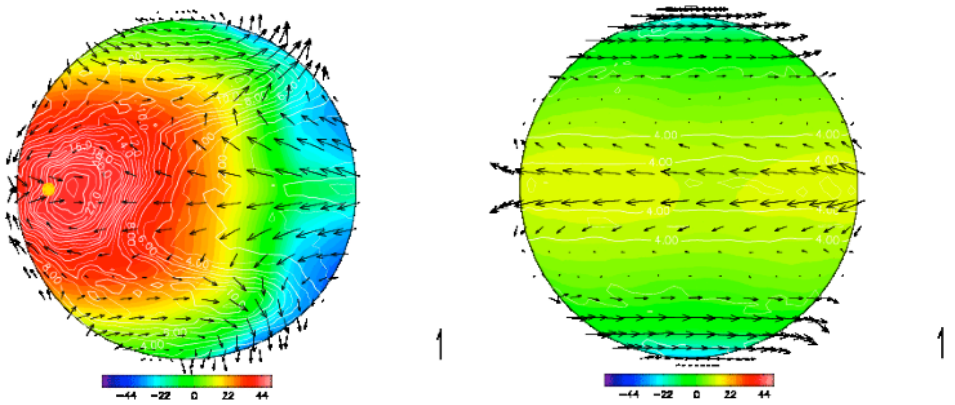

図：シミュレーションによって得られた、同期回転惑星(左)と地球条件惑星(右)の時間平均した表面気温分布と風速場（矢印)。同期回転惑星では対流活動が太陽直下点(黄丸)付近に集中し、そこで常時生じる雲が日射の反射に強く寄与する。

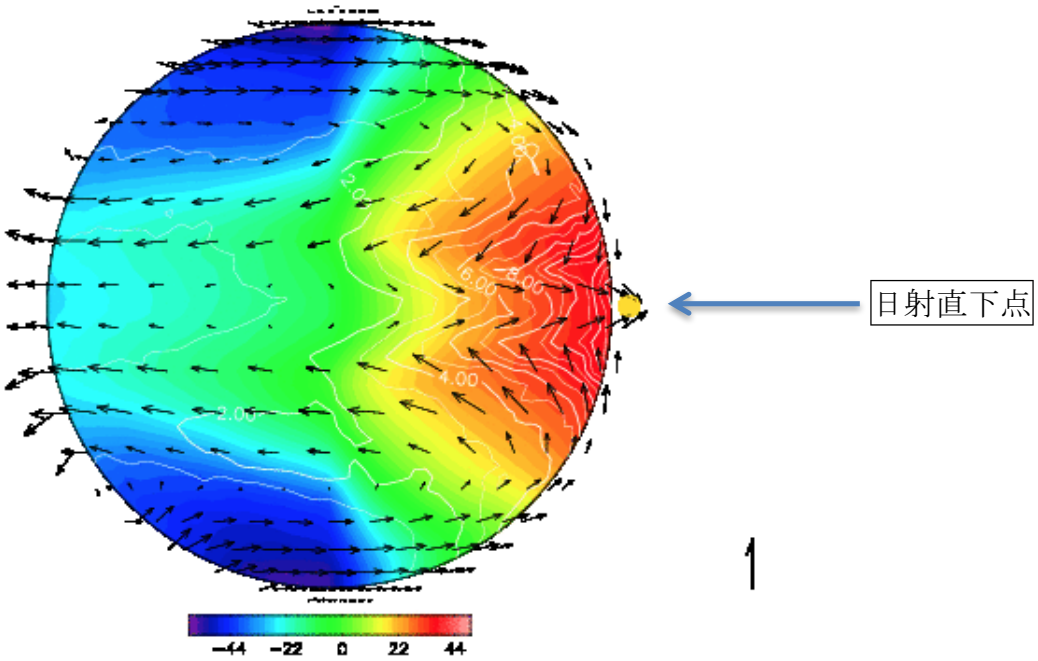

図：同期回転水惑星の３D 大気循環シミュレーション。カラーは温度（℃）、等高線は雨量（mm／day）、矢印は地表風速を表す。

② 系外惑星の大気進化の多様性の解明

巨大衝突による大規模融解後の地球型惑星の大気進化を初めて解明した。結果は、中心星からの距離に応じ、マグマオーシャンに覆われた暴走温室状態が長期間持続する場合と、水蒸気が地表へ凝結し速やかに海洋が形成される場合に大分される。前者の継続時間が紫外線による水蒸気分解・散逸速度に支配されることを示した。また、海洋の安定性や大気組成を制御する重要な素過程である水素散逸過程について、散逸効率が先行研究の推定よりもきわめて高いことを示した。大規模大気散逸によって大気を失うことにより、両極域に液体の水が局在化し、ハビタブルな惑星環境が長期的に維持されるような進化経路が存在することを明らかにした。

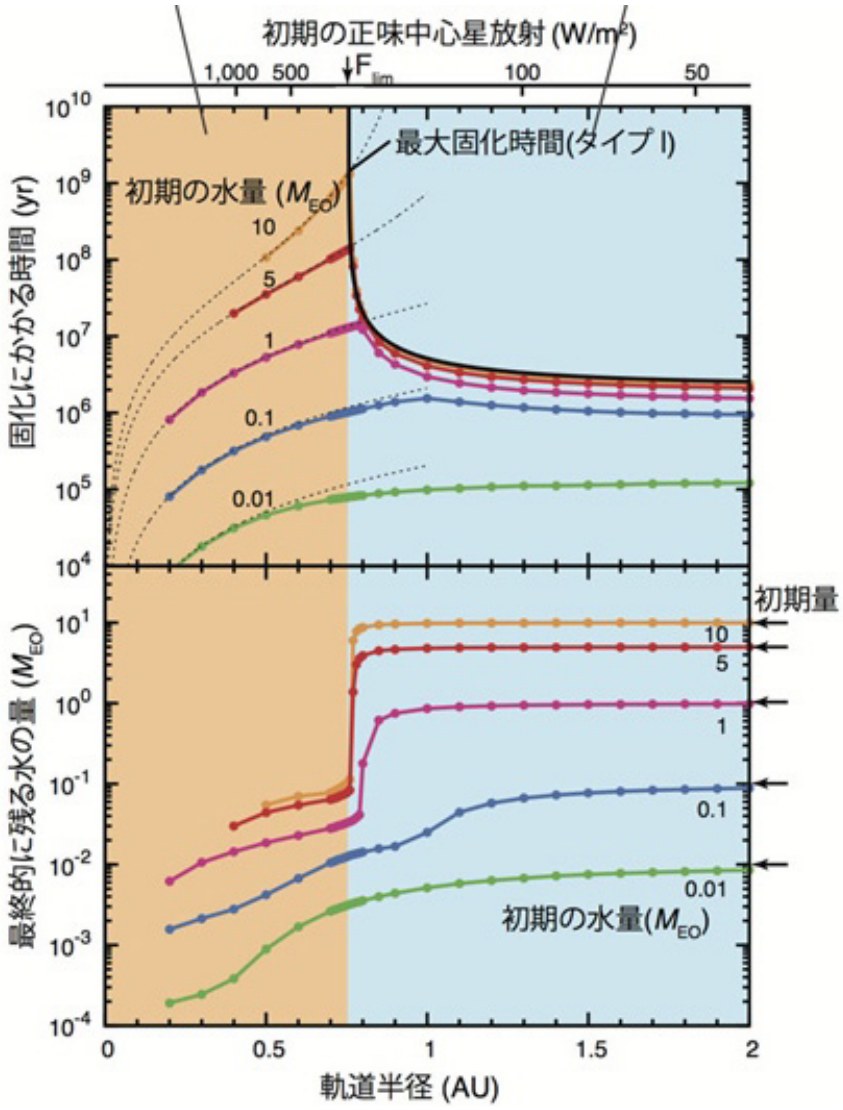

図：中心星からの距離に応じて、地球型惑星の大気進化と海洋形成の有無を示す。

③ 系外惑星のキャラクタリゼーションと解釈

木星型惑星大気について、雲対流モデルに加え放射伝達モデルを構築し、雲生成の間歇性、雲対流による物質分布の決定機構、可視・熱放射域それぞれの全球スペクトルを支配する因子を系統的に明らかにした。特に雲が赤外放射に及ぼす影響はよくわかっていなかったが、木星のような低温で放射冷却率の小さな惑星においては、雲粒よりも主成分の H_2 や放射活性な NH_3、CH_4 などのガス分子による吸収の効果が卓越する傾向にあることが明らかになった。さらに地球型惑星の巨大衝突後の大気進化モデルに沿って、惑星年齢と中心星からの距離の関数として惑星放射スペクトルを予測し、マグマオーシャン保有惑星と水惑星の観測可能性を定量的に明らかにした。

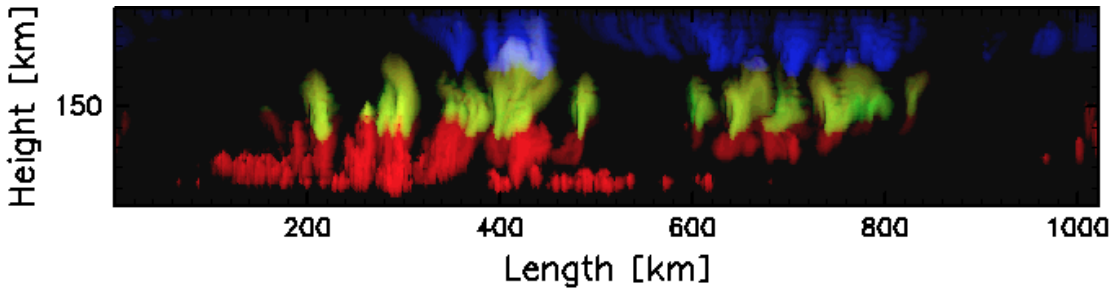

図：木星型惑星の大気循環シミュレーション凝結成分混合比が積乱雲発生間隔を決定。

木星型惑星の熱放射スペクトルや循環間欠性との調和。

Ⅲ.【計画研究 B01】

1．目標とその達成度

計画研究 B01 では、観測・理論・実験を結集し、原始惑星系円盤から地球型惑星形成へと至る過程の全貌解明を目指した。その実現のため、下記に示す 3 つの個別目標を設定した。全項目で当初の想定通り以上の進捗を得た。特に研究項目 B02 とは全項目で、研究項目 A01 とは(1)(2)で、それぞれ幅広い協同が展開され、想定を超える成果が多方面で挙がった。

① 多波長観測による円盤構造と進化の解明

ALMA により、中質量星 HD142527 に付随する円盤内で、星間空間に比べガスに対しダストが 30 倍以上濃集した領域の存在を明かした。これは、軸対称で動径方向にべき分布を円盤初期条件として仮定していた古典的な太陽系起源論とは、全く異なる状況である。また、赤外線データの統計解析により、円盤寿命の環境依存性（主星質量、金属量等）も明らかにした。これらは惑星系の多様な形成過程を示すもので、想定以上の成果である。一方高解像度観測に基づく研究では、すばるによるダスト散乱偏光撮像により、惑星存在を想起させる溝構造や渦巻構造を多数見出した。特に、密度波理論に基づく渦巻の形状解析は、惑星位置を推定する標準的手法となった。ALMA においても、おうし座 HL 星に対する公開画像で示された溝構造の形成機構について、惑星ギャップの場合とダスト成長・破壊による場合でそれぞれ、独自の解釈を提唱した。うみへび座 TW 星に対しても、一酸化炭素のスノーライン付近に数海王星質量の惑星で説明可能な溝構造を 1AU スケールの超高解像度観測により独自に発見した。観測結果自体はほぼ想定通りだったが、そこからは想定以上に多様な解釈を提示した。

② 円盤内固体物質の組成や成長の解明：ダストから微惑星へ

高空隙率氷ダストの付着成長により、微惑星が形成されうることを理論的に初めて示した。また、高空隙率ダスト存在の観測的実証に向け、観測と比較可能な高空隙率ダストの光学特性モデルを構築した。これらはこの後の研究発展の礎を築いた点も含め、想定を超える成果である。ダスト物性を基礎とした研究では、原始惑星系円盤や残骸円盤でみられる結晶化ダストの形成機構や、微惑星等からのダスト放出の解明で成果を得た。実験的手法では、天体衝突による残骸円盤へのダスト供給効率を明らかにするため、氷

微惑星の衝突破壊を模擬できる低温衝突実験設備を整備した。そして、複数回衝突を経た氷小天体の衝突破壊強度は積算エネルギー密度で決まることを明らかにするなど、十分な成果を得た。

③ 円盤内ガス物質の組成や化学進化の解明

円盤内での乱流拡散や重水素比まで考慮した化学反応ネットワークモデルを構築し、メタノールなどの大型有機分子の気相と固相での存在度比や、一酸化炭素分子の化学反応による減損を理論的に解明した。地球の海水に含まれる重水素の割合が宇宙元素存在度に比べて有意に高いことや近年原始星コアで地球の海水よりも高い重水素比をもつ水蒸気が検出されたことに関連して、星形成過程における重水素濃縮過程と、円盤での水分子の破壊・再生成過程をモデル計算に基づき明らかにした。さらに N_2H^+ など主要イオン分子の円盤内存在度の解析解を求め、ALMA の円盤観測に対する確固とした解釈を与えた。

２．研究成果

① 円盤構造と進化の解明

HD142527 に付随する原始惑星系円盤を ALMA で観測した結果、ダスト放射輝度の極めて高い領域を中心星から約 150 AU 離れた場所に見出した（図 1）。

ガス輝線データからダスト温度を推定し柱密度を見積る一方、一酸化炭素分子輝線の詳細なモデリングも行った。その結果、この領域が星間空間に比べガスに対しダストが 30 倍以上濃集していることを明らかにした。

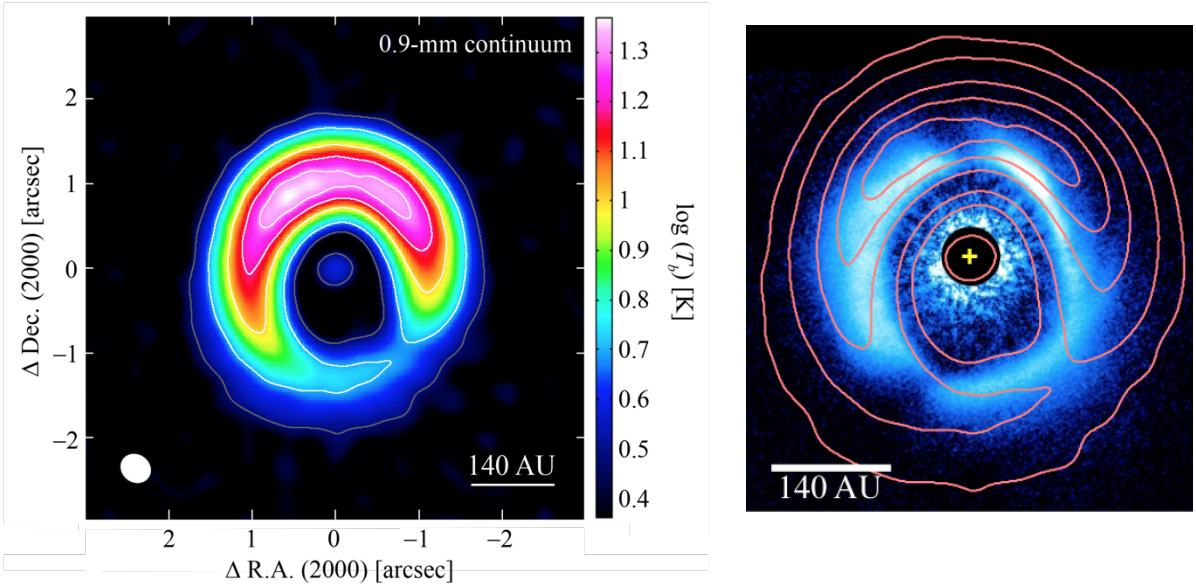

図：ALMA で観測した HD142527 の原始惑星系円盤の画像。右は電波強度の等高線図に重ねて、波長 1.6mm の散乱光の分布を示す。

また、おうし座 HL 星に対する 3AU 分解能の公開画像で示された溝構造の形成機構について、惑星ギャップの場合とダスト成長・破壊による場合でそれぞれ、独自の解釈を提唱した。惑星ギャップだとした場合、観測から求められる彫られた幅と深さから、土星から木星質量の惑星が３つ存在する可能性を示した。惑星がない場合でも、高空隙ダストが焼結によって脆くなる領域でダストが渋滞し、複数の明るいリング構造が形成されうることを示した。

うみへび座 TW 星では、一酸化炭素のスノーライン付近に数海王星質量の惑星で説

明可能な溝構造を 1AU スケールの超高解像度観測により発見した。また半径 22AU の場所にあるギャップ構造で、大きなダストが欠損している場合と整合するスペクトル指数の極大が見られた。これは、このギャップの中に海王星質量程度の惑星が存在している可能性を示唆している。

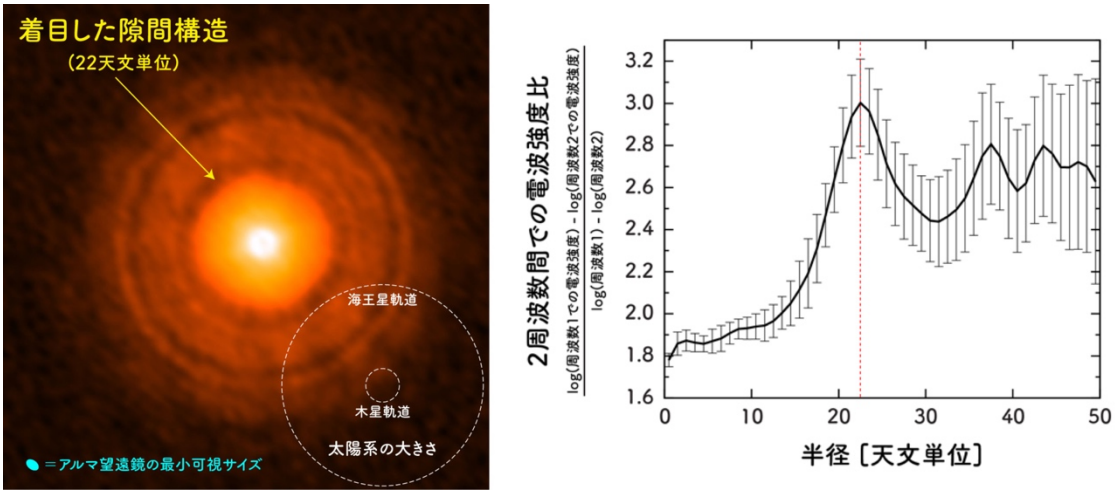

図：波長 1.7mm でのうみへび座 TW 星周囲の原始惑星系円盤の画像（左）と波長 1.3–2mm での連続波のスペクトル指数の動径分布（右）。半径 22AU のギャップで，大きなダストが欠損している場合と整合するスペクトル指数の極大が見られる。

一方、すばる望遠鏡 SEEDS プロジェクトでは 10 以上の原始惑星系円盤を観測し、太陽系サイズ程度の領域（30AU 以遠）で近赤外ダストからの散乱光の直接撮像に成功した。その結果、複数の円盤で，未検出の惑星に起因すると解釈できる溝状や非軸対称の構造を検出した。また、中質量前主系列星の中間赤外線撮像サーベイからは、フレアしている円盤内縁部にはギャップがあることを明らかにし、従来考えられていた進化シナリオを見直す必要があることを示した。さらに、赤外線データの統計解析により、円盤寿命の環境依存性（低金属量、星団環境下）も調べ、銀河系外縁部の低金属量の星団で、同年代の太陽近傍の星団に比して、円盤の存在確率が有意に低いことなどを明らかにした。

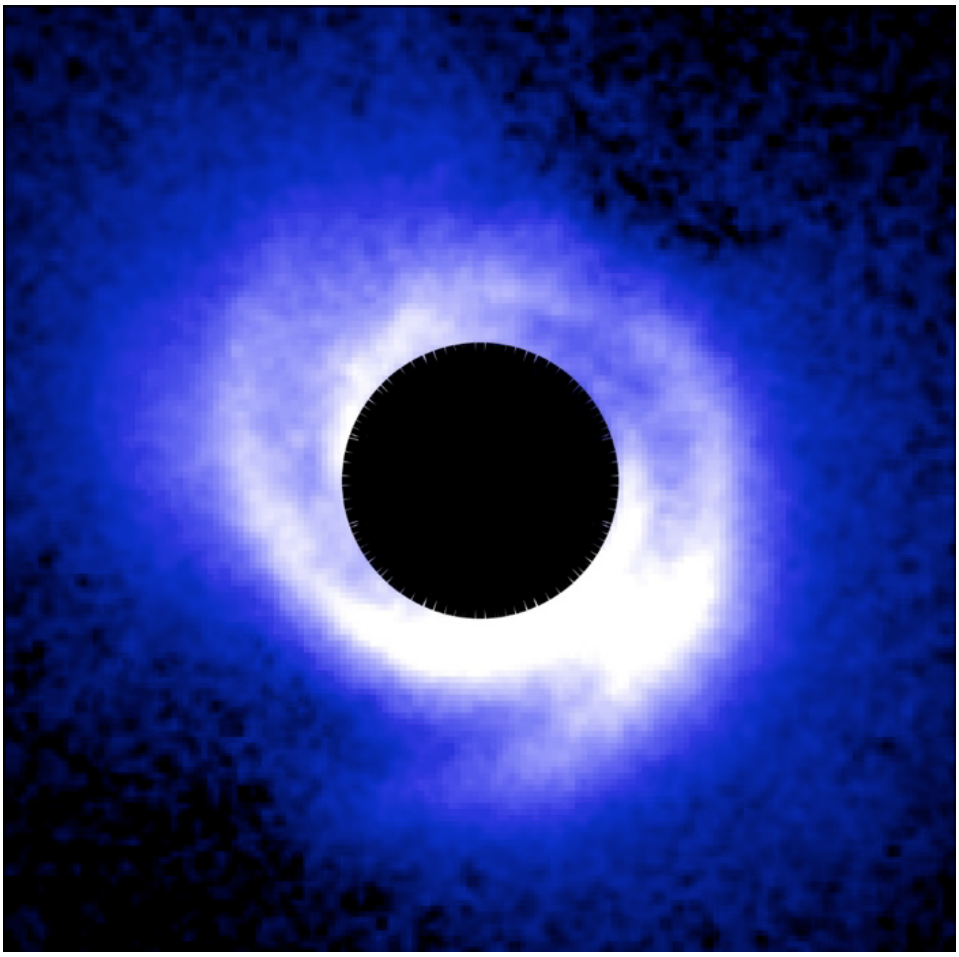

図：すばる望遠鏡 SEEDS プロジェクトで撮影した渦巻き状の原始惑星系円盤　SAO 206462

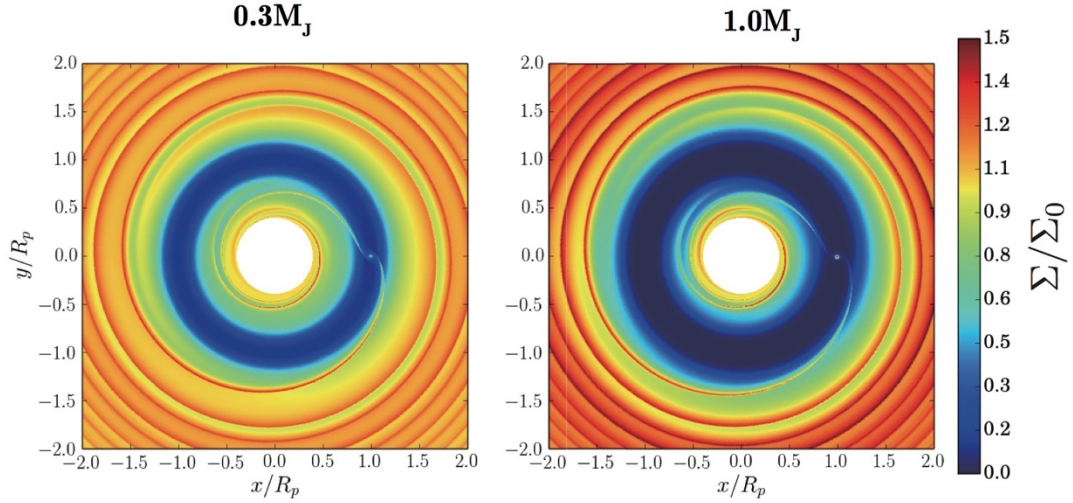

図：観測により測定可能な惑星ギャップの幅と深さから惑星質量を予言する理論式の基礎となった数値シミュレーションの結果例

② 円盤内固体物質の組成や成長の解明

ダスト成長に関する数値計算により、ダスト成長初期段階においては衝突圧縮が非効率的なため、まず形成されるのは高空隙率・低密度な氷天体であることを示した。さらにガス動圧や自己重力による圧縮効果を詳細に調べ、天体の大きさが 100m 程度以上になるとガス動圧の影響が、km サイズ以上では自己重力の影響がそれぞれ顕著となり、最終的に密度 0.1g cm^{-3} 以上にまで圧縮されうることを初めて明らかにした。

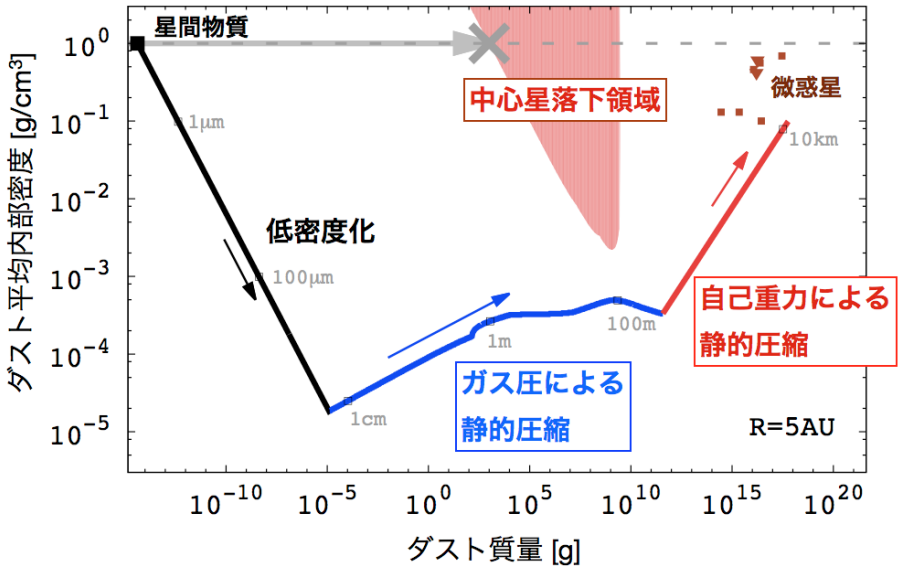

図：シミュレーションで初めて明らかとなった微惑星形成に至るパス

次に物性に基づく理論研究では、浮遊法を用いた融解粒子の室内実験結果を解析した結果、円盤ダストの結晶化は過冷却状態（融点よりも十分低温な条件下）で起ることを示し、あわせて結晶形態の冷却条件依存性を包括的に調べた。また、ダスト衝突付着条件や、微惑星等からのダスト放出についても詳しい再検討を行い、今後の原始惑星系円盤やデブリ円盤の高解像度観測での検証が期待される。一方、実験からは、多数回衝突で氷が破壊される場合の衝突破壊強度が、それを積算エネルギー密度で表したときに単発衝突破壊で得た値と一致することがわかった。さらに、石英粒子を用いたクレーター形成実験からイジェクタ速度分布を調べた結果、クレーターの掘削流に対する弾丸潜り込みの効果を定量的に明らかにした。これらと密接に関係する成果として、あかり衛星による中間赤外全天サーベイから抽出された残骸円盤の 1 つ(HD15407A)に対する追観測によってシリカの存在を確認し、惑星形成領域における巨大衝突に起因している可能性を指摘した。

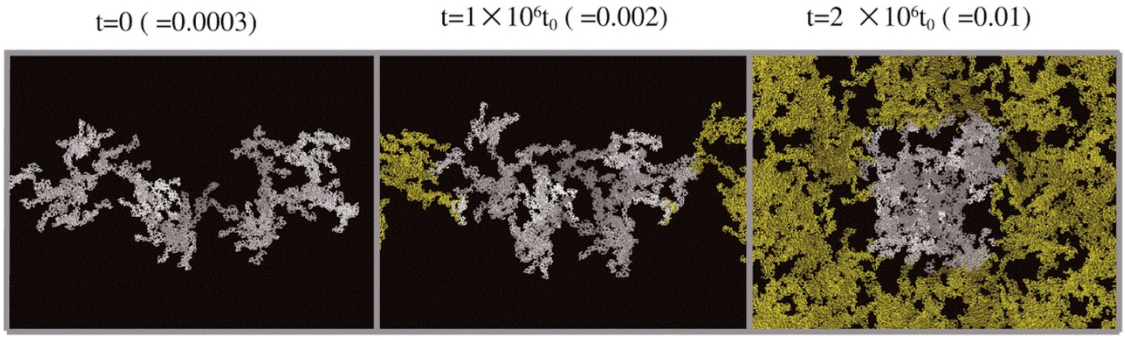

図：高空隙率ダストの衝突・圧縮の計算機シミュレーション結果の一例

③ 円盤ガス物質の組成や進化の解明

原始惑星系円盤の形成直前段階にあたる原始星について、その中心部（ファーストコア近傍）、及び外層部を対象にした分子ガス組成計算の結果をまとめ、論文発表した。また、地球の海水における HDO と H_2O の比（$\sim10^{-4}$）が太陽系近傍での D/H 値より一桁高い事実を説明するため、原始星外層部で観測されている極めて高い HDO/H_2O 比（$\sim10^{-2}$）をもつ水が原始惑星系円盤に取り込まれた後どのように破壊・再生成されるかをガス化学組成進化計算によって調べた。さらに、メタノールなどの大型有機分子の気相と固相での存在度比や、一酸化炭素分子（炭素の主要形態であり、円盤ガス観測の指標）の化学反応による減損を理論的に明らかにした。このうち、N_2H^+など円盤内の主要なイオン分子の存在度の解析解を求めた研究は、ALMA での観測結果の分析で用いられている。

Ⅳ.【計画研究 B02】

1．目標とその達成度

計画研究項目 B02 では、2011 年 7 月以来、すでに 160 編以上の論文を国際ジャーナルに発表し、10 編以上が印刷中である。十分な成果のもとに目標の大半を達成した。

観測との比較においては、円盤については ALMA の観測の急進展に伴って、研究項目 B01 との協同が大いに進み、当初の計画にはなかった、惑星形成の母体となる円盤構造形成について大きな成果が得られた。また短周期スーパーアースの大気の観測も進み、地球型惑星大気のモデリングも予定以上に進展した。このように、観測の進展により、当初予定していなかった分野の理論モデリングが大きく進んだ。当初からあった研究計画の各項目ついての達成度は以下のとおりである。

① 巨大ガス惑星の多様性

計画よりも根本に遡って、原始星および原始惑星系円盤の形成過程のシナリオの構築を行い、円盤ガスの磁気回転乱流の詳細を明らかにした。塵の空隙率進化に着目して、ガス抵抗による中心星落下を乗り越えて氷微惑星が形成されることを世界で初めて示した。また、新しい小石集積（ペブルアクリーション）モデルにも着目し、小石の形成を明らかにした。当初の計画以上に達成できた。

巨大ガス惑星の連鎖的形成も実際に数値計算で示し、木星・土星系の形成の新しいモデルを提案した。円盤の粘性散逸や光蒸発、円盤風による散逸に関しても詳細な解析を行った。目標は達成した。

巨大ガス惑星の軌道不安定の高精度軌道計算を行い、内側に飛ばされた惑星のうちの 30%は潮汐力により（逆行のものを含む）ホットジュピターとなり、中間領域には楕円軌道のものが残ることを示し、観測データを見事に説明した。研究項目 A01 の直接撮像法が目指す遠方領域の巨大ガス惑星の分布も予測した。予定以上の進展をした。

② スーパーアースの多様性

ケプラー宇宙望遠鏡などの観測結果は、短周期スーパーアース（大型地球型惑星）は普遍的に存在し、大多数は複数系であることを示す。それらの軌道分布は中心星と円盤ガスの磁気結合で決まるはずだが、観測の急速発展によりバルク密度（組成）に大きな

多様性があることがわかった。これは大気や揮発性成分の多様性を反映しているはずで、観測データを基礎にした惑星の組成や大気のモデリングを行い、さらに新たな観測も提案した。方向性を若干変えたが、十分な成果を得た。

原始惑星の巨大衝突の詳細な軌道計算により、中心星に近いスーパーアースの軌道分布を統計的に計算し、ケプラー宇宙望遠鏡のデータを定量的に説明した。十分な成果を得た。

③ ハビタブル惑星の存在確率

ハビタブル惑星の条件には、多数あるが、軌道安定性や衛星の存在の影響について一般的モデルの構築を行った。また、ハビタブルゾーンの地球型惑星に運ばれる H_2O 量が、陸と海が共存する範囲という新しい観点に注目し、小石での輸送のほか、巨大ガス惑星による氷微惑星の散乱についても徹底的に調べた。包括的なハビタブル惑星の存在確率の導出にまでは至らなかったが、ハビタブル惑星の重要な条件のいくつかを明らかにした。

２．研究成果

計画研究項目 B02 では、星・惑星形成プロセスの理論モデルの構築、観測と理論モデルの比較検討、系外地球型惑星の形成進化の理論において成果を出した。

① 星惑星形成過程の理論モデルの構築

原始星の形成およびその直後に始まる原始惑星系円盤の形成過程のシナリオを構築した。中心星が木星質量程度のときから円盤が形成され、ガス塊が円盤分裂によって多数形成されて中心星に落ちて行くという描像（下図）が得られ、これは惑星形成の初期条件の考え方を大きく変えた。

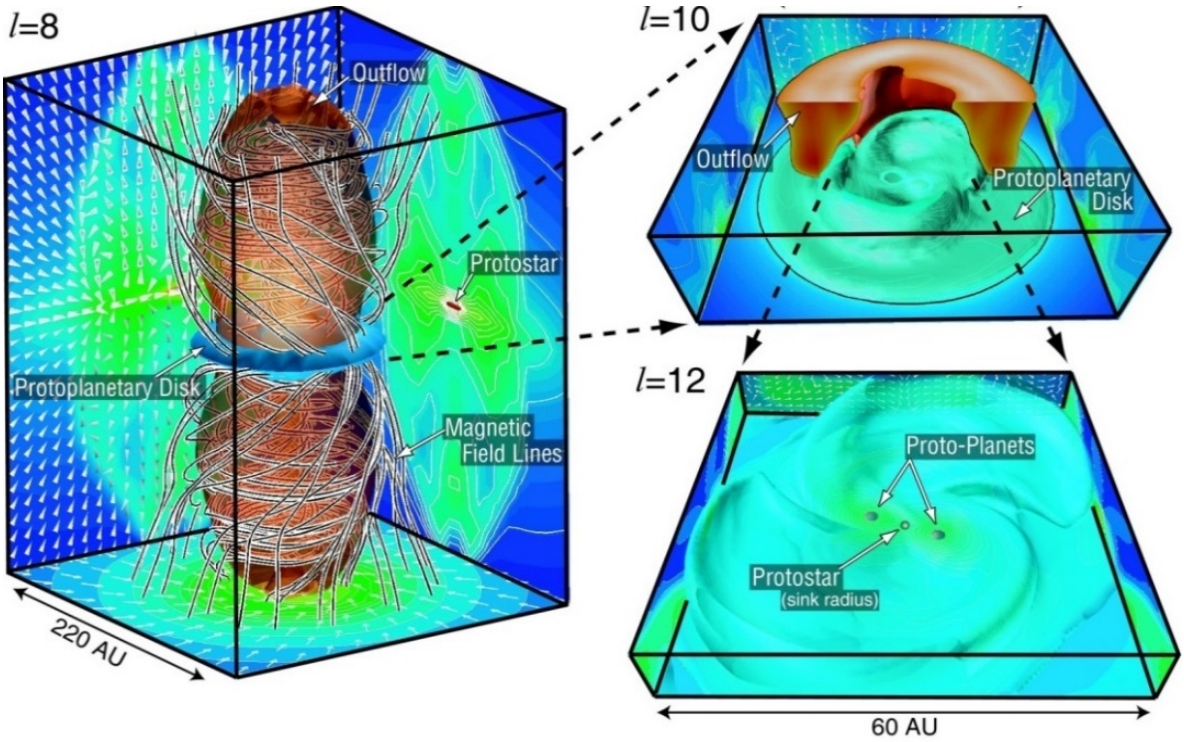

図：原始星及び原始惑星系円盤の形成過程の直接数値計算

円盤での磁気回転乱流の強度を支配する大局磁場の長時間進化を磁場輸送の平均場モデルを用いて詳細に調べ、乱流中でのプラズマの電場加熱を考慮した円盤電離モデルを世界に先駆けて完成させ、プラズマの加熱が円盤外側領域での磁気乱流を安定化させることを示した。

② 微惑星形成の理論シミュレーションの成功

円盤内のダストの合体成長・空隙率進化・軌道進化を整合的に考慮したダスト進化シミュレーションを実施し、高空隙率化に伴うダストのガス抵抗特性の変化が氷のダストの急速な合体成長を引き起こし、中心星に落下する前に、氷微惑星が形成されることを世界で初めて示した。これは研究項目B01との共同研究である。

また、新たな小石集積（ペブルアクリーション）モデルにも着目し、小石の形成を明らかにし、小石による地球型惑星へのH_2Oの輸送過程を明らかにした。

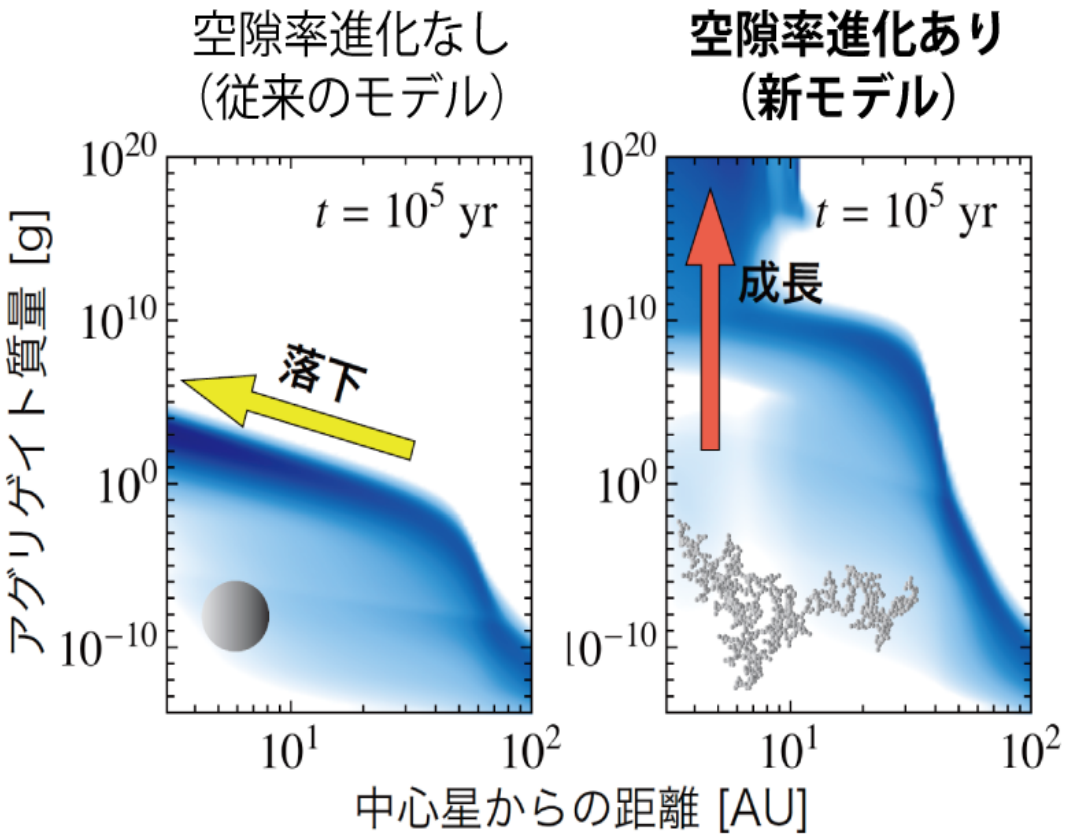

図：高空隙率ダストの集積により微惑星形成のシミュレーション

③ 系外惑星の観測と理論モデルの比較検討

巨大惑星の重力散乱についての N 体シミュレーションとモンテカルロ計算により、系外巨大惑星の軌道の楕円率の分布を見事に説明した。同時に、研究項目 A01 の観測が標的にする中心星から離れた巨大惑星の形成も、標準コア集積モデルで形成できることを示した。さらに、系外巨大惑星の重力散乱は、巨大惑星の軌道離心率を上げ、系外への放出も起こすが、それらのはるか内側領域に存在する地球型惑星のほとんども中心星に落とすことを示した。また、巨大惑星の重力散乱の過程で一定の割合で惑星同士が重力的に束縛されて連惑星となることを明らかにし、トランジット観測における検出可能性を議論した。

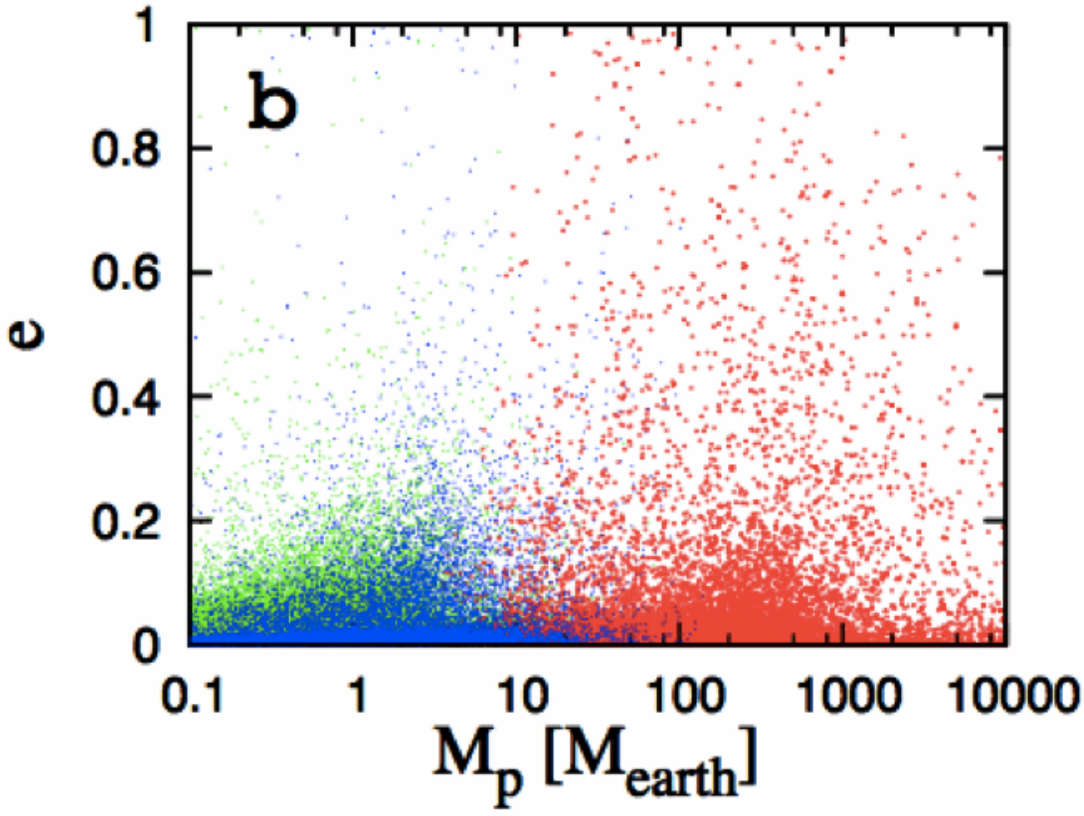

図：巨大惑星の重力散乱シミュレーション結果

原始惑星による円盤ガス獲得過程を系統的に調べ，それを木星型惑星の起源および短周期スーパーアースの大気の起源に応用した。微惑星の蒸発によって原始エンベロープが汚染されると、ガス捕獲可能な惑星質量が従来の値に比べて大幅に減少することを発見した。一方，中心星近くでスーパーアースが獲得できる大気量は，中心星からの距離

や円盤ガスの散逸時期によって様々であり，観測が示すスーパーアースのバルク密度の多様性を説明できることを示した。そうした形成理論の妥当性を検証するために，トランジット時の惑星大気透過スペクトルを理論的に予測し、観測提案もおこなった。

④ 原始惑星系円盤の観測と理論モデルの比較検討

ALMA によって撮像された、原始惑星系円盤のリング構造は非常に大きなインパクトを与えた。観測データはダストからの放射を観測しているので、リング構造は円盤ガス成分そのものの構造を表している可能性とダスト分布の構造を表している可能性の２つがある。われわれは研究項目 B01 との綿密な連携のもとに、原始惑星系円盤内のダストの成長・移動・焼結による破壊モデル、円盤永年重力不安定性、存在している惑星による円盤ガスの構造形成モデル(B01)など多方面から、その起源を探った。また、研究項目 B01 と共同して、ALMA に観測プロポーザルを出して採択され、他の円盤でも同様の円盤構造を発見した。

円盤の詳細な化学反応及び輻射輸送計算に基づき、円盤中の有機分子の生成過程と彗星内の有機分子との関連、また、その ALMA による観測可能性を調べた。これも研究項目 B01 との共同研究である。また、スノーラインの位置を ALMA や TMT、SPICA を用いた水輝線の観測により求める手法を提案し、実際の観測で氷微粒子（水の氷を多く含むダスト）の存在を確認した。

⑤ 系外地球型惑星の形成進化の理論モデルの構築

系外地球型惑星の軌道安定性の他にも、衛星の存在が惑星の気候や生命居住可能性にどのような影響を与えるのかに関する一般的モデルの構築を行った。地球型惑星形成過程の最終段階である巨大衝突によって形成される惑星系の軌道構造がどのように決まるかを多体シミュレーションを用いて調べ、形成される惑星系の軌道間隔と軌道離心率を予測し、生成される衝突破片を定量的に明らかにし、その観測可能性について議論した。ハビタブルゾーンに地球型惑星があっても、円盤でのその温度領域では H_2O は凝縮しないので、外側領域で凝縮した H_2O 氷をどのように惑星に運ぶのかが重要である。小石での輸送のほか、巨大ガス惑星による氷微惑星の散乱についても徹底的に調べた。

（２）公募研究

【公募研究】

将来地球型惑星の直接検出に有望なコロナグラフとして、ナル干渉型コロナグラフの実験で 3×10^{-7} のコントラストを達成した（村上）。惑星大気の理解に関する研究では、木星や土星に見られる低緯度のジェット気流などを理論的に再現することに成功した（竹広）。惑星系形成・原始惑星系円盤に関する研究では、微惑星が作る衝撃波によって氷微惑星が蒸発し、大量の微小ダスト粒子を原始惑星系円盤内に放出するという新たなメカニズムを提案し、これが原始惑星系円盤内で長いタイムスケールにわたって観測される赤外線スペクトルの超過を説明する可能性を示した（田中）。また、３次元高解像度数値流体シミュレーションの結果、原始惑星系円盤から周惑星円盤へのガス降着流は円盤中心面からはおこらず、円盤の上下方向から周惑星円盤表面に降着することが明らかとなった（谷川）。

（3）まとめ

1. これまでに直接撮像された6個の恒星周囲の惑星系のうち、本研究では新たに2個の恒星周囲の惑星系を撮像することに成功。（A01）

2. 直接検出された惑星では最小の質量をもつ「第二の木星」の撮像に成功。系外惑星の直接検出において大きなインパクトとなった。（A01）

3. CHARISが完成した。すばる望遠鏡の共同利用に供したことで、すべての日本の系外惑星研究者に系外惑星を分光観測する機会を与えた。（A01）

4. 地球型惑星大気は水惑星と灼熱惑星のふたつの型に別れることを発見。惑星のハビタビリティの研究を強く刺激し、発表後3年間で71回引用された。（A02）

5. SAO 206462やTW Hyaの原始惑星系円盤に渦巻や溝を検出し、これらが未検出の惑星によって作られている可能性を示唆。前者については発表後4年間で136回引用。（B01）

6. 原始惑星系円盤内に成長したダストが多量に集中している領域を発見。岩石微惑星の効率的な形成場所である可能性を示唆した。（B01）

7. 世界で初めてセルフ・コンシステントな氷微惑星形成シミュレーションに成功した。この論文は発表後4年間で81回引用された（B01/B02）

8. 最新の惑星形成理論をもとにした系外惑星の分布の理論推定。アルマ、ケプラーなど第一線の観測結果と頻繁に比較検討されている。（B02）

論文抜粋

The Astrophysical Journal, 804:143 (8pp), 2015 May 10 doi:10.1088/0004-637X/804/2/143

HIGH-RESOLUTION 25 μM IMAGING OF THE DISKS AROUND HERBIG AE/BE STARS*

M. Honda[1], K. Maaskant[2,3], Y. K. Okamoto[4], H. Kataza[5], T. Yamashita[6], T. Miyata[7], S. Sako[7], T. Fujiyoshi[8], I. Sakon[9], H. Fujiwara[8], T. Kamizuka[7], G. D. Mulders[10], E. Lopez-Rodriguez[11], C. Packham[11], and T. Onaka[9]
[1] Department of Mathematics and Physics, Kanagawa University, 2946 Tsuchiya, Hiratsuka, Kanagawa 259-1293, Japan
[2] Leiden Observatory, Leiden University, P.O. Box 9513, 2300 RA Leiden, The Netherlands
[3] Astronomical Institute Anton Pannekoek, University of Amsterdam, P.O. Box 94249, 1090 GE Amsterdam, The Netherlands
[4] Institute of Astrophysics and Planetary Sciences, Faculty of Science, Ibaraki University, 2-1-1 Bunkyo, Mito, Ibaraki 310-8512, Japan
[5] Department of Infrared Astrophysics, Institute of Space and Astronautical Science, Japan Aerospace Exploration Agency, 3-1-1 Yoshinodai, Sagamihara, Kanagawa 229-8510, Japan
[6] National Astronomical Observatory of Japan, 2-21-1 Osawa, Mitaka, Tokyo 181-8588, Japan
[7] Institute of Astronomy, School of Science, University of Tokyo, 2-21-1 Osawa, Mitaka, Tokyo 181-0015, Japan
[8] Subaru Telescope, National Astronomical Observatory of Japan, 650 North A'ohoku Place, Hilo, Hawaii 96720, USA
[9] Department of Astronomy, School of Science, University of Tokyo, Bunkyo-ku, Tokyo 113-0033, Japan
[10] Lunar and Planetary Laboratory, The University of Arizona, Tucson, AZ 85721, USA
[11] Department of Physics & Astronomy, University of Texas at San Antonio, One UTSA Circle, San Antonio, TX 78249, USA
Received 2014 September 21; accepted 2015 March 7; published 2015 May 12

ABSTRACT

We imaged circumstellar disks around 22 Herbig Ae/Be stars at 25 μm using Subaru/COMICS and Gemini/T-ReCS. Our sample consists of an equal number of objects from each of the two categories defined by Meeus et al.; 11 group I (flaring disk) and II (flat disk) sources. We find that group I sources tend to show more extended emission than group II sources. Previous studies have shown that the continuous disk is difficult to resolve with 8 m class telescopes in the Q band due to the strong emission from the unresolved innermost region of the disk. This indicates that the resolved Q-band sources require a hole or gap in the disk material distribution to suppress the contribution from the innermost region of the disk. As many group I sources are resolved at 25 μm, we suggest that many, but not all, group I Herbig Ae/Be disks have a hole or gap and are (pre-)transitional disks. On the other hand, the unresolved nature of many group II sources at 25 μm supports the idea that group II disks have a continuous flat disk geometry. It has been inferred that group I disks may evolve into group II through the settling of dust grains into the mid-plane of the protoplanetary disk. However, considering the growing evidence for the presence of a hole or gap in the disk of group I sources, such an evolutionary scenario is unlikely. The difference between groups I and II may reflect different evolutionary pathways of protoplanetary disks.

Key words: circumstellar matter – protoplanetary disks – stars: pre-main sequence

1. INTRODUCTION

Recent discoveries of numerous exoplanets have revealed the diversity of planetary systems (e.g., Marois et al. 2008). However, the origin of such variety is still uncertain. Planets should have formed in protoplanetary disks and it is essential to understand their evolution in order to resolve why such differences exist. In studies of lower-mass young stars such as T Tauri stars, transitional disks have received attention from the planet formation point of view. Transitional or pre-transitional disks are protoplanetary disks with an inner hole and/or gaps indicated by the weak near-infrared(NIR)/mid-infrared(MIR) excess in their spectral energy distribution (SED; Strom et al. 1989; Espaillat et al. 2007). Since a primordial protoplanetary disk must have a continuous distribution of dust/gas without gaps, and since the disk structure will be affected by planet formation, those disks with an inner hole and/or gaps must be in a transitional phase moving from a primordial to an evolved planetary-system stage.

Disks around nearby Herbig Ae/Be stars have also been studied extensively in the context of disk evolution and planet formation, but using a different classification approach. Based on an analysis of SEDs, Meeus et al. (2001) classified Herbig Ae/Be stars into two groups: group I sources, which show both power-law and blackbody components up to far-infrared (FIR) wavelengths in their SEDs, and group II sources, whose SEDs can be well modeled with only a single power law from MIR to FIR wavelengths. They suggested that group I has a flaring disk while the disk around group II is geometrically flat.

There have been several proposed scenarios for an evolutionary link between groups I and II sources. Dullemond & Dominik (2004) showed that SEDs of group I sources can be interpreted as hydrostatic disks with flaring geometry, while group II sources are an evolved version of group I sources that have undergone grain growth and grain settling onto the mid-plane of the disk. Such a settled disk would become a self-shadowed disk by a puffed-up inner rim that accounts for weak FIR emission (Dullemond & Dominik 2004). Mariñas et al. (2011) performed a MIR imaging survey of Herbig Ae/Be disks at 12 and 18 μm. They found that group I disks show more extended emission than those of group II and suggested that the trend can be naturally understood in terms of the difference in disk geometry.

Recent high spatial resolution observations at various wavelengths have revealed a more complex structure, including a hole or gaps in disks. In particular, there is growing evidence for the presence of a hole and/or gaps toward group I sources, such as AB Aur (Lin et al. 2006; Honda et al. 2010), HD 142527 (Fujiwara, et al. 2006; Fukagawa et al. 2006; Verhoeff et al. 2011), HD 135344 B (Brown et al. 2009; Grady, et al. 2009), HD 36112 (Isella et al. 2010), HD 169142 (Grady et al. 2007;

* Based on data collected at the Subaru Telescope, via the time exchange program between Subaru and the Gemini Observatory. The Subaru Telescope is operated by the National Astronomical Observatory of Japan.

Table 1
Summary of Subaru/COMICS and Gemini/T-ReCS Observations

Object	Subaru/COMICS Q24.5 Imaging			Subaru/COMICS Q18.8 Imaging			Gemini/T-ReCS Qb Imaging		
	Date	t^a	PSF	Date	t^a	PSF	Date	t^a	PSF
Elias3-1	2004 Jul 11, 12	399	βAnd	...	...	...	...	...	...
HD 100546	...	...	...	...	...	...	2011 Jun 27	638	γCru
HD135344B	...	...	...	...	...	...	2011 Jun 14	1361	αCen A
HD 139614	2004 Jul 11	101	δOph	...	...	...	2011 Jul 23	638	α Tra
HD 169142	...	...	...	...	...	...	2011 Jul 22	638	η Sgr
HD179218	2004 Jul 11	99	αHer	...	...	...	...	...	...
HD 36112	2005 Dec 14, 2011 Jan 26	3297	αTau	2011 Jan 26	438	αTau	...	...	...
HD97048	...	...	...	...	...	...	2011 Jun 28	638	γCru
RCrA	2004 Jul 11	100	δOph	2004 Jul 12	40	αHer	2011 Jun 28	203	η Sgr
TCrA	2004 Jul 11	312	αHer	2004 Jul 12	175	αHer	2011 Jul 21	638	η Sgr
51 Oph	2004 Jul 11	237	δOph	...	...	...	2011 Jul 21	638	η Sgr
AK Sco	...	...	...	...	...	...	2011 Jul 22	638	η Sgr
CQTau	2005 Dec 15	553	αTau	2005 Dec 15	541	αTau	...	...	...
HD142666	2004 Jul 11	148	δOph	...	...	...	2011 Jul 21	638	η Sgr
HD144432	2004 Jul 11	193	δOph	...	...	...	2011 Jul 24	638	δ Oph
HD150193	2004 Jul 12	168	αHer	...	...	...	2011 Jul 27	638	η Sgr
HD163296	2004 Jul 11, 12	557	δOph	...	...	...	2011 Jun 28	638	η Sgr
HD31648	2005 Dec 14	1510	αTau	2005 Dec 15	578	αTau	...	...	...
HD35187	2005 Dec 14, 16	1580	αTau	...	...	...	...	...	...
HR5999	...	...	...	...	...	...	2011 Jul 24	638	α Tra
KK Oph	...	...	...	...	...	...	2011 Jul 21	638	η Sgr

[a] Total integration time in seconds used in this study.

Honda et al. 2012), Oph IRS 48 (Geers et al. 2007), HD 100546 (Bouwman et al. 2003; Benisty et al. 2010), HD 139614 (Matter et al. 2014), and HD 97048 (Maaskant et al. 2013). Recently, Honda et al. (2012) and Maaskant et al. (2013) proposed that group I sources possess a disk with a strongly depleted inner region (i.e., a transitional disk). Such a discontinuous structure is different from that originally proposed for group I disks. As little or no evidence for a hole and/or gaps has been reported toward group II disks and they seem to have a radially continous structure, the previous interpretation of an evolutionary path from group I to group II needs to be reconsidered.

In this paper, we present the results of an imaging survey of nearby (roughly within 200 pc) Herbig Ae/Be stars at 24.5 μm using the 8.2 m Subaru Telescope and 8.1 m Gemini Telscope. At 24.5 μm, the point-spread function (PSF) is relatively stable compared to those at shorter wavelengths because of a larger Fried length, which enables us to discuss small extended structures with high reliability. In addition, it allows us to investigate the cooler outer part of the disk at a dust temperature $\sim$100 K. Early examples of our imaging survey have been published previously (Fujiwara, et al. 2006; Honda et al. 2010, 2012; Maaskant et al. 2013). This paper provides a summary of the survey.

2. OBSERVATIONS AND DATA REDUCTION

2.1. Subaru/COMICS Data

We performed imaging observations of Herbig Ae/Be stars using the Cooled MIR Camera and Spectrometer (COMICS; Kataza et al. 2000; Okamoto et al. 2003; Sako, et al. 2003) on the 8.2 m Subaru Telescope with the Q24.5 filter ($\lambda_c = 24.5$ μm, $\Delta\lambda = 0.8$ μm). We also observed a portion of the targets with the Q18.8 filter ($\lambda_c = 18.8$ μm, $\Delta\lambda = 0.8$ μm). The chopping throw was 10″ and the chopping frequency was 0.45 Hz. The pixel scale is 0.″130/pix. Immediately before and/or after observations of the target, we performed observations of PSF reference stars. A summary of the observations is provided in Table 1.

For data reduction, we employed a shift-and-add method to rectify the blurring caused by tracking and/or registration errors. The imaging data consist of 0.983 s on-source integration frames of coadded exposures at each beam position. First, the fluctuation of the thermal background and the dark current signals were removed through differentiation of the chopped pair frames. The object is bright enough to be recognized even in 0.983 s integration chop-subtracted frames. We estimated the peak position of the source without difficulty using a Gaussian fit. Then, we shifted the frames to align the peak position and summed the frames. We excluded those frames whose Gaussian FWHMs deviate by more than 1σ from the mean value.

2.2. Gemini/T-ReCS Data

Observations were performed using T-ReCS (Telesco et al. 1998) on the 8.1 m Gemini South telescope. T-ReCS uses a Raytheon 320 × 240 pixel Si:As IBC array with a pixel scale of $0.08633 \pm 0.''00013$ pixel^{-1}, providing a field of view (FOV) of 27.″6 × 20.″7. The Q_b ($\lambda_c = 24.56$ μm, $\Delta\lambda = 0.94$ μm, 50% cut-on/off) filter was used in the present observations. A summary of the observations is also shown in Table 1. Observations were performed using a standard chop-nod technique to remove time-variable sky background and telescope thermal emission, and to reduce the effect of 1/f noise from the array-electronics. In all of our observations, the chop-throw was 15″, the chop-angle was 45° E of N, and the telescope was nodded approximately every 40 s. Standard stars were observed immediately before and/or after each object observation using the same instrumental configuration (Cohen et al. 1999).

The data were reduced using the Gemini IRAF package. The difference for each chopped pair was calculated and a pair of

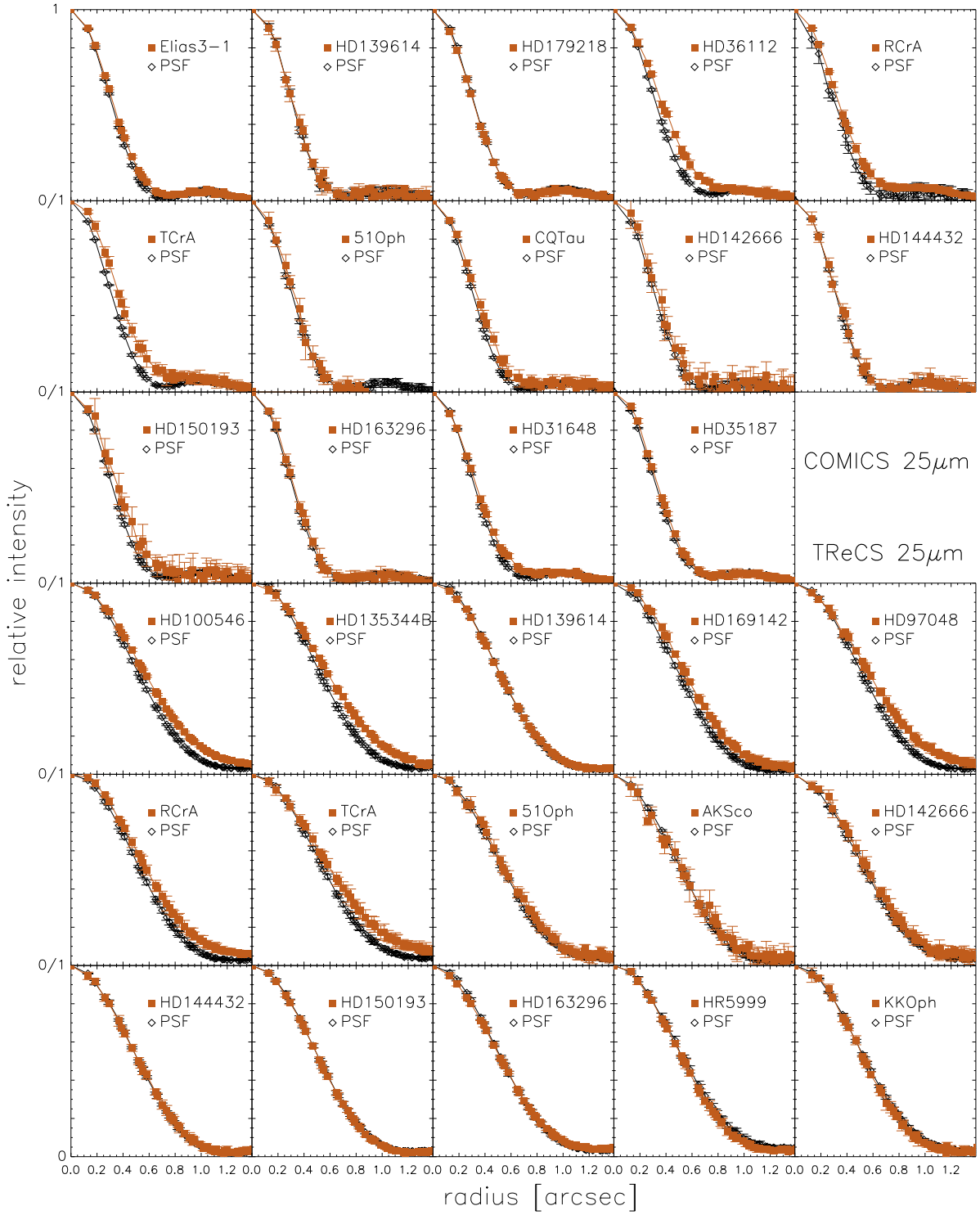

Figure 1. Peak-normalized azimuthally averaged radial profile plot of the targets and PSF stars at 25 μm. The panels of the upper three rows are from COMICS observations, while those of the lower three rows are from T-ReCS observations.

the nod sets were then differentiated and combined to create a single image. All of the nodding data were examined if they had high background due either to the presence of terrestrial clouds or temporarily high water vapor precipitation. No data were found to be severely affected by these problems.

Although there is slight differences in the characteristics of the filters used by COMICS and T-ReCS, we will refer to Q24.5 and Q_b as 25 μm throughout this paper.

3. RESULTS

Since the observed images show circularly symmetric shapes and the azimuthal variation is not significant, we focus on the radial profile of the targets and do not discuss their azimuthal structures in this study. First, we created azimuthally averaged radial profiles of the targets and relevant PSF stars at 25 μm as shown in Figure 1. We then measured their FWHMs from the

Table 2
FWHM Measurements of COMICS and T-ReCS Observations

Object	Subaru/COMICS Q24.5 Imaging			Subaru/COMICS Q18.8 Imaging			Gemini/T-ReCS Qb Imaging		
	$\Phi_{d,\mathrm{target}}(''$)	$\Phi_{d,\mathrm{PSF}}(''$)	?[a]	$\Phi_{d,\mathrm{target}}(''$)	$\Phi_{d,\mathrm{PSF}}(''$)	?[a]	$\Phi_{d,\mathrm{target}}(''$)	$\Phi_{d,\mathrm{PSF}}(''$)	?[a]
Elias3-1	0.672 ± 0.012	0.634 ± 0.003	Y	...	...	...	...	...	...
HD 100546	...	...	...	...	...	...	0.788 ± 0.006	0.716 ± 0.008	Y
HD135344B	...	...	...	...	...	...	0.804 ± 0.008	0.721 ± 0.004	Y
HD 139614	0.643 ± 0.031	0.633 ± 0.011	N	...	...	...	0.711 ± 0.005	0.710 ± 0.007	N
HD 169142	...	...	...	...	...	...	0.759 ± 0.014	0.692 ± 0.007	Y
HD179218	0.637 ± 0.009	0.645 ± 0.004	N	...	...	...	...	...	...
HD 36112	0.751 ± 0.009	0.649 ± 0.003	Y	0.559 ± 0.017	0.526 ± 0.027	N	...	...	...
HD97048	...	...	...	...	...	...	0.788 ± 0.014	0.714 ± 0.005	Y
RCrA	0.687 ± 0.016	0.629 ± 0.020	Y	0.547 ± 0.011	0.489 ± 0.008	Y	0.771 ± 0.028	0.704 ± 0.011	Y
TCrA	0.748 ± 0.013	0.634 ± 0.002	Y	0.586 ± 0.026	0.489 ± 0.004	Y	0.806 ± 0.023	0.732 ± 0.003	Y
51 Oph	0.663 ± 0.037	0.626 ± 0.006	N	...	...	...	0.730 ± 0.012	0.721 ± 0.007	N
AK Sco	...	...	...	...	...	...	0.695 ± 0.024	0.692 ± 0.005	N
CQTau	0.687 ± 0.023	0.627 ± 0.004	Y	0.519 ± 0.005	0.501 ± 0.011	Y?	...	...	...
HD142666	0.710 ± 0.063	0.637 ± 0.008	N	...	...	...	0.741 ± 0.008	0.714 ± 0.005	Y
HD144432	0.652 ± 0.031	0.639 ± 0.006	N	...	...	...	0.691 ± 0.014	0.690 ± 0.005	N
HD150193	0.728 ± 0.081	0.641 ± 0.002	N	...	...	...	0.696 ± 0.008	0.700 ± 0.007	N
HD163296	0.649 ± 0.011	0.632 ± 0.003	Y?	...	...	...	0.705 ± 0.008	0.711 ± 0.006	N
HD31648	0.677 ± 0.013	0.646 ± 0.006	Y	0.503 ± 0.007	0.493 ± 0.007	N	...	...	...
HD35187	0.689 ± 0.010	0.649 ± 0.002	Y	...	...	...	...	...	...
HR5999	...	...	...	...	...	...	0.709 ± 0.009	0.728 ± 0.012	N
KK Oph	...	...	...	...	...	...	0.721 ± 0.012	0.722 ± 0.007	N

[a] Resolved(Y) or not(N).

profiles directly; we call these "direct FWHMs" ($\Phi_{d,\mathrm{target}}$ and $\Phi_{d,\mathrm{PSF}}$ for the targets and PSFs, respectively). These FWHMs are the real extensions of the sources convolved with the instrumental FWHM. These measurements are summarized in Table 2, accompanied by those of the corresponding PSF stars.

The radial brightness profiles of most targets are comparable to or slightly wider compared to those of the PSF stars. As a quantitative measure of the intrinsic size of the MIR emission from the disk, we employ a quadrature-subtraction of the FWHM of the PSF star from that of the target following Mariñas et al. (2011). We refer to this as the "intrinsic FWHM" (Φ_i), which is derived from

$$\Phi_i = \sqrt{\Phi_{d,\mathrm{target}}^2 - \Phi_{d,\mathrm{PSF}}^2}\,.$$

Although this method provides a correct size only when the intrinsic radial profiles of both the target and the PSF star are given by a Gaussian, we adopt this method to semi-quantitatively discuss the extension of the sources with the same measure for the sake of simplicity. Eight sources are observed by both COMICS and T-ReCS, and the results were consistent with each other within the measurement errors. To be conservative, we adopt the smaller and more stringent value of the intrinsic FWHM in these cases. The derived values are summarized in Table 3.

4. DISCUSSION

4.1. Trends in Extended Emission

To investigate possible trends in the 25 μm extension of the Herbig Ae/Be stars with other parameters, we collected the distance, stellar luminosity, classification of the group proposed by Meeus et al. (2001), and the MIR spectral index given by the flux density ratio at 13.5 and 30 μm (Acke et al. 2004, 2010; Acke & van den Ancker 2006; Meeus et al. 2012). The flux densities at 13.5 and 30 μm reflect the underlying continuum shape and are chosen to avoid MIR dust features such as silicates and polycyclic aromatic hydrocarbons (PAHs). For those objects whose spectral index is not available, we calculated it ourselves using the *Infrared Space Observatory* or *Spitzer* archive spectra. We also converted the diameter in arcseconds to AU using the distance to the objects given in Table 3. We added AB Aur, which was part of our survey but with results published earlier in Honda et al. (2010), to Table 3.

We note that group I sources tend to show more extended MIR emission than group II sources. Nine out of 11 group I sources are resolved (i.e., 82%) with a signal-to-noise ratio larger than three, as are 4 out of 11 group II sources, which, however, is only 36%. This trend is similar to the results of the study by Mariñas et al. (2011) at 12 and 18 μm. The present results also confirm the trend at 25 μm.

In Figure 2, we plot the intrinsic FWHM (Φ_i) against the stellar luminosity (L_*). One may expect that luminous sources show more extended emission, however, we could not find a clear trend in the plot. Some sources in our sample are not resolved even though they are luminous ($L_* > 40 L_\odot$).

On the other hand, when we plot the intrinsic FWHM against the MIR spectral index (Figure 3), we find that significantly extended (FWHM > 40 AU) sources all belong to the "red" group I. Such objects exhibit MIR spectral indices [30/13.5] larger than 4.2, while moderately extended or unresolved sources all appear below that value, even among group I. It is also interesting to note that the MIR spectral indices of well-resolved MIR disk sources such as HD 142527 (Fujiwara, et al. 2006), Oph IRS48 (Geers et al. 2007), and HD141569 (Fisher et al. 2000; Marsh et al. 2002) are 5, 10.4, and 6.8, respectively, in agreement with the present finding. We therefore suggest that the redder Herbig Ae/Be stars with MIR spectral index larger than 4.2 exhibit more extended MIR emission. In general, group

Table 3
Summary of the Parameters of the Samples

Object	Distance(pc)	$L_*(L_\odot)$	Ref.	$\Phi_i(")$	Φ_i(AU)	Group	Ref.	[30/13.5]	Ref.
AB Aur	139.3	33.0	b	0.50 ± 0.05	70.2 ± 6.91	I	a	4.5	a
Elias3-1	160	0.7	d	0.22 ± 0.04	35.5 ± 6.1	I	c	2.3	e
HD 100546	96.9	22.7	b	0.33 ± 0.02	31.7 ± 2.3	I	a	3.5	a
HD135344B	142	8.1	b	0.36 ± 0.02	50.6 ± 2.7	I	a	10.9	a
HD 139614	140	7.6	b	0.04 ± 0.17	5.3 ± 24.0	I	a	4.2	a
HD 169142	145	9.4	b	0.31 ± 0.04	45.1 ± 5.4	I	a	7.8	a
HD179218	240	100.0	d	<0.12	<28.81	I	a	2.4	a
HD 36112	279.3	33.7	b	0.38 ± 0.02	105.6 ± 5.5	I	a	4.1	a
HD97048	158.5	30.7	b	0.33 ± 0.03	52.8 ± 5.5	I	a	5.9	a
RCrA	130	0.6	d	0.31 ± 0.07	40.9 ± 9.5	I	c	2.1	e
TCrA	130	0.7	d	0.34 ± 0.06	43.8 ± 7.2	I	a	5	a
51 Oph	124.4	285.0	b	0.11 ± 0.09	13.7 ± 11.4	II	a	0.59	a
AK Sco	150	8.9	d	0.06 ± 0.27	9.6 ± 40.1	II	a	3.3	a
CQTau	113	3.4	b	0.28 ± 0.06	31.5 ± 6.4	II	b	4.1	e
HD142666	145	13.5	b	0.20 ± 0.04	28.7 ± 5.3	II	a	1.53	a
HD144432	145	10.2	d	0.05 ± 0.23	6.6 ± 33.5	II	a	1.82	a
HD150193	216.5	48.7	b	<0.17	<37.3	II	a	1.42	a
HD163296	118.6	33.1	b	<0.16	<19.2	II	a	2	a
HD31648	137	13.7	b	0.20 ± 0.05	27.3 ± 6.3	II	a	1.19	a
HD35187	114.2	17.4	b	0.23 ± 0.03	26.5 ± 3.4	II	a	2.1	a
HR5999	210	87.1	d	<0.11	<23.6	II	a	0.96	a
KK Oph	260	13.7	b	<0.23	<58.9	II	a	1.04	a

References. (a) Acke et al. (2010), (b) Meeus et al. (2012), (c) Acke & van den Ancker (2006), (d) Acke et al. (2004), (e) derived from the archival spectra.

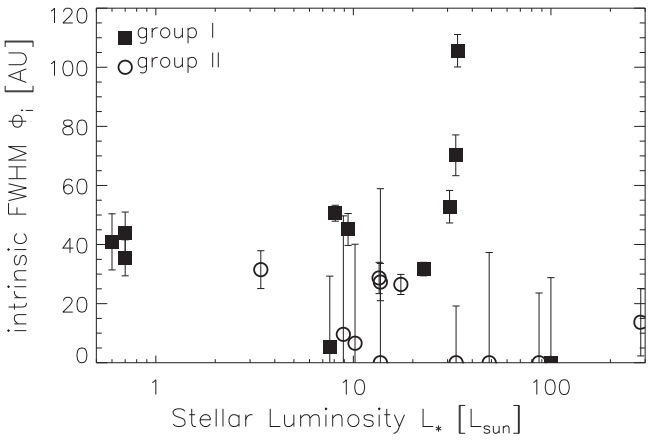

Figure 2. Intrinsic FWHM of extended emission at 25 μm against the stellar luminosity. The squares indicate group I sources, while the circles show group II sources. The points plotted with a FWHM value of zero are those of unresolved sources with 3σ upper limits.

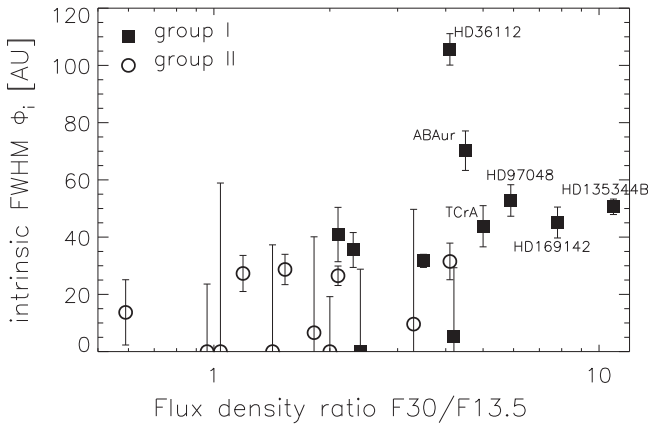

Figure 3. Intrinsic FWHM of extended emission at 25 μm against the MIR continuum flux ratio $F_{30}/F_{13.5}$. The symbols are the same as in Figure 2. Redder sources tend to show larger FWHM values.

I sources tend to show MIR continuum emission redder than for source in group II. Thus, the present findings are consistent with the trend wherein group I sources are likely to exhibit more extended emission than group II sources.

4.2. Origin of Extended Emission of MIR Red Source

The origin of the Q-band (16–25 μm) extended emission in group I Herbig Ae/Be stars or red MIR sources has been discussed previosuly by several groups. Honda et al. (2010, 2012) and Maaskant et al. (2013) demonstrated the difficulty in explaining the extended Q-band emission of group I sources with a continuous disk. The Q-band emission from a continuous disk mostly originates from dust grains located in the inner $\leqslant$ 10 AU, which corresponds to $\sim$0.″07, if located at a typical distance of $\sim$150 pc from our targets. Considering the PSF size ($\sim$0.″7) at 25 μm, this is too small to be resolved with 8 m class telescopes. This situation may apply to most of the unresolved targets in our sample. In contrast, we have definitely resolved many group I sources, indicating that the continuous disk interpretation is not valid for these objects.

The shape of the SEDs for group I sources can be interpreted as having an MIR dip because of the rising FIR emission. The dip indicates that hot/warm dust grains responsible for the MIR radiation are depleted in the inner region of the protoplanetary disk. An inner hole and/or gaps in the disk can naturally explain both the MIR dip in the SED and the extended emission in the Q band. The presence of an inner hole, for example, causes the inner edge of the disk to be directly illuminated by the central star. This edge, being relatively further away due to the inner hole, produces the red MIR index (i.e., a large [30/13.5] ratio)

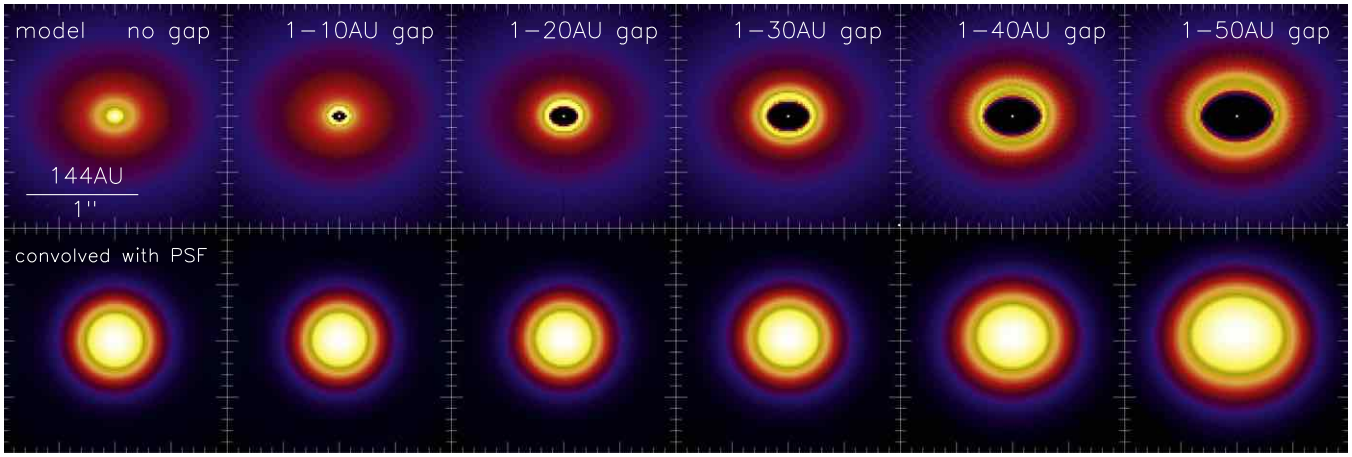

Figure 4. (Top) Model images of a Herbig Ae disk with typical parameters by changing gap outer radius at 25 μm. Images are shown in logarithmic scale to show faint outer disk emission. (Bottom) Model images convolved with the PSF, assumed to be an Airy function, with FWHM 0.″65. Images are shown in linear scale.

Table 4
Parameters Used in the Model

parameter	Values
Stellar paramters:	
Stellar effective temperature T_*	9280 K
Stellar mass M_*	2.4 $M_\odot$
Stellar luminosity L_*	40. $L_\odot$
Distance d	144. pc
Disk component:	
Dust composition	80% silicates + 20% carbon
Dust minimum size $a_{\rm min}$	0.1 μm
Dust minimum size $a_{\rm max}$	1. mm
Index of dust size power law	3.75
Dust mass	5×10^{-5} $M_\odot$
Disk inner radius $r_{\rm in}$	0.3 AU
Disk outer radius $r_{\rm out}$	400. AU
Disk inclination	35°
Halo component:	
Dust composition	100% carbon
Dust minimum size $a_{\rm min}$	0.1 μm
Dust minimum size $a_{\rm max}$	1. μm
Index of dust size power law	3.5
Dust mass	1.0×10^{-12} $M_\odot$
Halo inner radius $r_{\rm in}$	0.25 AU
Halo outer radius $r_{\rm out}$	0.35 AU

and the strong FIR radiation as reflected in the SED, as well as the extended Q-band emission. In fact, significantly extended sources (intrinsic FWHM > 40 AU) in our sample exhibit MIR spectral indices [30/13.5] larger than 4.2, indicating that the dust temperature of the inner edge of the outer disk is ~155 K assuming a blackbody. If the luminosity of the central star were 30 $L_\odot$ (a typical value for well-extended group I sources), then the distance to the 155 K blackbody would be about 18 AU, indicating an inner hole diameter of 36 AU, which corresponds to approximately 0.″24 if located at a typical distance of 150 pc. An emission region of this size, when convolved with the PSF of the telescope, can be (marginally) resolved with 8 m class telescopes in the Q band. We suggest that this applies to our resolved sample.

This interpretation is supported by an increasing number of detections of inner holes and gaps in group I protoplanetary disks by high-spatial resolution observations in the NIR and at radio wavelengths, as described in Section 1. On the other hand, little evidence has been reported for inner holes and/or gaps toward group II sources, which is also consistent with the present results of unresolved or limited extended emission. Continuous disks seem to be rather difficult to resolve in the Q band with 8 m class telescopes.

In general, group I sources tend to show redder MIR continuum emission than group II sources. In our sample, most group I sources show an MIR spectral index higher than 2, while most group II objects show an index below 2. This is consistent with a recent classification criterion put forward by S. Khalefinejad (2015, in preparation) that the MIR index [30/13.5] of group I sources is greater than 2.1. A blackbody at $T\sim$ 195 K would yeild an MIR index of 2. Thus, the dust temperature of the inner edge of the outer disk around group I objects must be below 195 K, which puts the inner edge at some distance from the central star, producing extended Q-band emission. Both the high MIR index and the extended Q-band emission can naturally be accounted for by the presence of the inner edge of the outer disk located at some distance.

As mentioned earlier, there is now growing evidence that an inner hole and/or gaps exist in the protoplanetary disk of group I sources. Our finding above (the general trend between the extended Q-band emission and the MIR color for group I objects) also appears to reconfirm this view.

4.3. Comparison with Models

To demonstrate the effect of a gap in the disk on Q-band image size, we constructed disk models and derived FWHM of the disk image at 25 μm for comparison with observations. We follow the model used in Maaskant et al. (2013), who employed the radiative transfer tool MCMax (Min et al. 2009). The parameters used in this model are summarized in Table 4. We focus on the model with these typical Herbig Ae parameters as an example only, and we are not going to construct models that best predict individual imaging results.

First, we constructed a continuous disk model (no gap) whose SED has a rising FIR flux density similar to the group I objects. The model image at 25 μm is displayed in the top panel

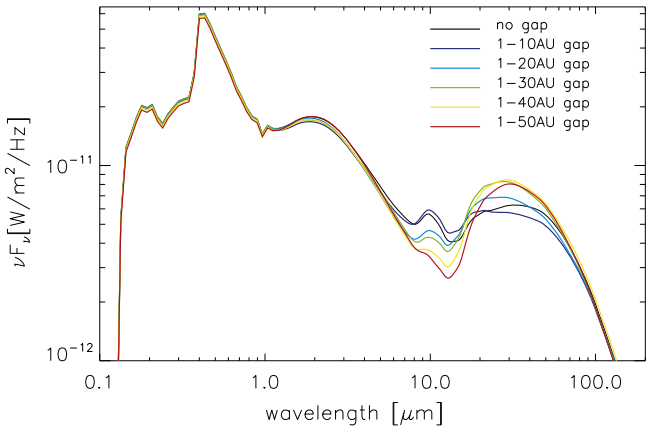

Figure 5. SEDs of each models shown in Figure 4.

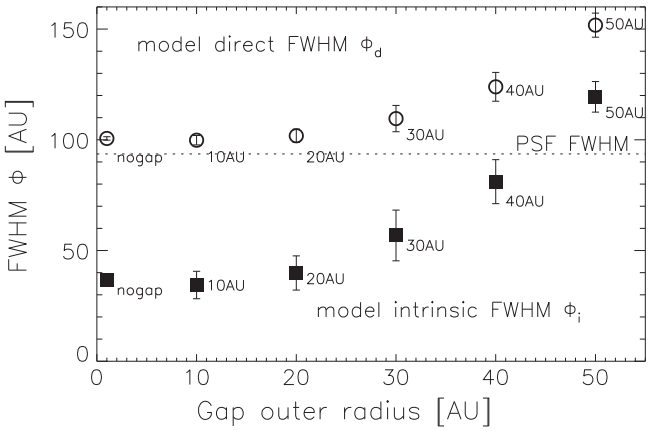

Figure 6. Direct FWHM Φ_d of the PSF convolved model image shown in Figure 4 plotted against the outer gap radius. A similar plot of instrinsic FWHM Φ_i derived via a quadratic subtraction method is also shown. Disks with a large gap (gap outer radius larger than 20 AU) show larger FWHM values than those with no gap or a small gap.

of Figure 4, and the SED is shown in Figure 5. Then, we introduced a radial gap into the model. The gap inner radius is fixed at 1 AU, and the gap outer radius increased from 10 to 50 AU in steps of 10 AU. Images and SEDs for these models are shown in Figures 4 and 5, respectively. The morphology of the gapped disk images is dominated by ring-like emission arising from the inner edge of the outer disk (see top panels of Figure 4). As the size of the gap is increased, more thermal radiation from the increasingly larger gapped area is removed from the SED, resulting in a weakened MIR emission and an enhanced FIR flux (see Figure 5). This, in turn, was reflected in an increasingly redder [30/13.5] color as the gap size widened. The disk images were subsequently convolved with an Airy pattern with FWHM = 0.″65 (assumed to represent the telescope beam; see the bottom panels of Figure 4). We measured Φ_d and derived Φ_i from these final images in the same manner as described in Section 3 (see Figure 6). As can be seen, the models with outer gap radii smaller than 20 AU are comparable with the "nogap" model (equivalent within uncertainties), implying that they would either be unresolved or only marginally resolved at best. On the other hand, when the outer gap radius $\gtrsim$30 AU, they would easily be resolved at 25 μm. Thus our 25 μm imaging survey is sensitive to the presence of a large ($\gtrsim$30 AU) gap. Figure 7 is the same as

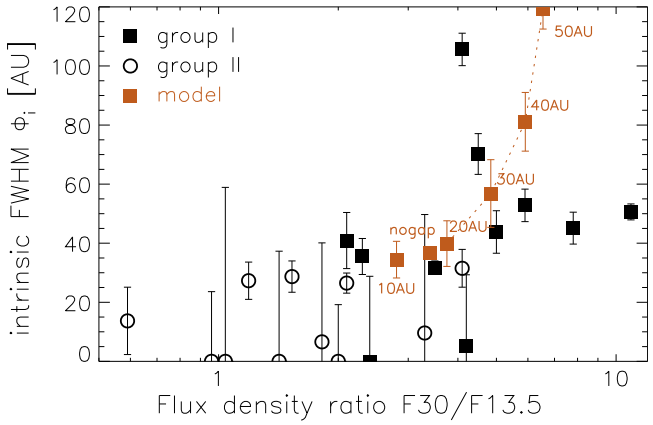

Figure 7. Plot of the instrinsic FWHM Φ_i of the model (red) against the MIR color overplotted in Figure 3. Again, disks with a large gap (gap outer radius larger than 20 AU) show a larger MIR index [30/13.5] than those with no gap or a small gap. In other words, redder sources show more extended emission.

Figure 3, except we added the models points. In our sample models, disks with [30/13.5] $\gtrsim$ 4.2 can be achieved when the gap outer radius becomes $\gtrsim$25 AU and such a disk can be well-resolved in our observations. This trend is almost consistent with our observational findings that the well-extended Herbig Ae/Be sources show MIR indexes larger than 4.2. Again, this demonstrates that our 25 μm imaging survey is sensitive to disks with large gaps.

4.4. Group I Sources as (Pre-)transitional Disks

Since the presence of an inner hole and/or gap has been shown to be a common characteristic for group I Herbig Ae/Be stars (e.g., Bouwman et al. 2003; Fujiwara, et al. 2006; Fukagawa et al. 2006; Lin et al. 2006; Geers et al. 2007; Grady et al. 2007; Brown et al. 2009; Grady, et al. 2009; Benisty et al. 2010; Honda et al. 2010, 2012; Isella et al. 2010; Verhoeff et al. 2011; Maaskant et al. 2013; Matter et al. 2014), Honda et al. (2012) and Maaskant et al. (2013) suggest that most group I sources can be classified as (pre-)transitional disks. Transitional or pre-transitional disks, which were originally suggested for low-mass young stars such as T Tauri stars, are protoplanetary disks with an inner hole and/or gaps indicated by weak NIR excess in the SED (Strom et al. 1989; Espaillat et al. 2007). Because the primordial disk is thought to have a continuous distribution of dust without gaps and because planet formation could produce a hole and/or gaps in the disk, those disks with a (large) inner hole and/or gaps must be in a transitional phase from a primordial to an evolved stage.

On the other hand, an evolutionary scenario for Herbig Ae/Be stars is still a matter of debate. Meeus et al. (2001) proposed that a group I disk is flared while that of group II is flat, based on the analysis of the SED. A possible evolutionary scenario was suggested in which a group I flaring disk evolves into a group II flat disk through grain growth and sedimentation/settling of grains onto the disk mid-plane. However, the present study indicates that the group I disk is a (pre-)transitional disk with an inner clear region and/or gaps, while the group II disk is a continuous disk. These observational pieces of information imply that evolution from group I to group II is unlikely. As Meeus et al. (2001) pointed out, there is no significant difference in age between groups I and II; therefore, it is more likely that both sources have evolved along different paths from

a primordial continuous flaring disk, a common ancester, as discussed in Maaskant et al. (2013). This scenario is quite similar to the T Tauri disk evolutionary scenario proposed by Currie (2010). He presented two main pathways for the evolution of T Tauri disks: those that form an inner hole/gap and others that deplete more homologously. The present study suggests a similarity between the evolutionary scenarios of T Tauri and Herbig Ae/Be disks.

We are grateful to all of the staff members of the Subaru Telescope.

We also thank Dr. Hitomi Kobayashi and Dr. Yuji Ikeda at Kyoto-Nijikoubou Co., Ltd.. This research was partially supported by KAKENHI (Grant-in-Aid for Young Scientists B: 21740141) by the Ministry of Education, Culture, Sports, Science and Technology (MEXT) of Japan.

REFERENCES

Acke, B., van den Ancker, M. E., Dullemond, C. P., van Boekel, R., & Waters, L. B. F. M. 2004, A&A, 422, 621
Acke, B., & van den Ancker, M. E. 2006, A&A, 457, 171
Acke, B., Bouwman, J., Juhász, A., et al. 2010, ApJ, 718, 558
Benisty, M., Tatulli, E., Ménard, F., & Swain, M. R. 2010, A&A, 511, A75
Bouwman, J., de Koter, A., Dominik, C., & Waters, L. B. F. M. 2003, A&A, 401, 577
Brown, J. M., Blake, G. A., Qi, C., et al. 2009, ApJ, 704, 496
Currie, T. 2010, arXiv:1002.1715
Cohen, M., Walker, R. G., Carter, B., et al. 1999, AJ, 117, 1864
Dullemond, C. P., & Dominik, C. 2004, A&A, 417, 159
Dullemond, C. P., & Dominik, C. 2004, A&A, 421, 1075
Espaillat, C., Calvet, N., D'Alessio, P., et al. 2007, ApJL, 670, L135
Fisher, R. S., Telesco, C. M., Piña, R. K., Knacke, R. F., & Wyatt, M. C. 2000, ApJL, 532, L141
Fujiwara, H., Honda, M., Kataza, H., et al. 2006, ApJL, 644, L133
Fukagawa, M., Tamura, M., Itoh, Y., et al. 2006, ApJL, 636, L153
Geers, V. C., Pontoppidan, K. M., van Dishoeck, E. F., et al. 2007, A&A, 469, L35
Grady, C. A., Schneider, G., Hamaguchi, K., et al. 2007, ApJ, 665, 1391
Grady, C. A., Schneider, G., Sitko, M. L., et al. 2009, ApJ, 699, 1822
Honda, M., Inoue, A. K., Okamoto, Y. K., et al. 2010, ApJL, 718, L199
Honda, M., Maaskant, K., Okamoto, Y. K., et al. 2012, ApJ, 752, 143
Isella, A., Natta, A., Wilner, D., Carpenter, J. M., & Testi, L. 2010, ApJ, 725, 1735
Kataza, H., Okamoto, Y., Takubo, S., et al. 2000, Proc. SPIE, 4008, 1144
Lin, S.-Y., Ohashi, N., Lim, J., et al. 2006, ApJ, 645, 1297
Mariñas, N., Telesco, C. M., Fisher, R. S., & Packham, C. 2011, ApJ, 737, 57
Marois, C., Macintosh, B., Barman, T., et al. 2008, Sci, 322, 1348
Marsh, K. A., Silverstonezz, M. D., Becklin, E. E., et al. 2002, ApJ, 573, 425
Maaskant, K. M., Honda, M., Waters, L. B. F. M., et al. 2013, A&A, 555, A64
Matter, A., Labadie, L., Kreplin, A., et al. 2014, A&A, 561, A26
Meeus, G., Montesinos, B., Mendigutía, I., et al. 2012, A&A, 544, A78
Meeus, G., Waters, L. B. F. M., Bouwman, J., et al. 2001, A&A, 365, 476
Min, M., Dullemond, C. P., Dominik, C., de Koter, A., & Hovenier, J. W. 2009, A&A, 497, 155
Okamoto, Y. K., Kataza, H., Yamashita, T., et al. 2003, Proc. SPIE, 4841, 169
Sako, S., Okamoto, Y. K., Kataza, H., et al. 2003, PASP, 115, 1407
Strom, K. M., Strom, S. E., Edwards, S., Cabrit, S., & Skrutskie, M. F. 1989, AJ, 97, 1451
Telesco, C. M., Pina, R. K., Hanna, K. T., et al. 1998, Proc. SPIE, 3354, 534
Verhoeff, A. P., Min, M., Pantin, E., et al. 2011, A&A, 528, A91

A&A 540, A78 (2012)
DOI: 10.1051/0004-6361/201015832

Astronomy & Astrophysics

A frozen super-Earth orbiting a star at the bottom of the main sequence⋆

D. Kubas[1,2], J. P. Beaulieu[1,3], D. P. Bennett[4], A. Cassan[1], A. Cole[5], J. Lunine[6,7], J. B. Marquette[1], S. Dong[8,9], A. Gould[10], T. Sumi[11], V. Batista[1,10], P. Fouqué[12], S. Brillant[2], S. Dieters[1,5], C. Coutures[1], J. Greenhill[5], I. Bond[13], T. Nagayama[14], A. Udalski[15], E. Pompei[2], D. E. A. Nürnberger[2], and J. B. Le Bouquin[2,16]

[1] Institut d'Astrophysique de Paris, UMR 7095 CNRS – Université Pierre & Marie Curie, 98 bis blv Arago, 75014 Paris, France
e-mail: dkubas@gmail.com
[2] European Southern Observatory, Casilla 19001, Vitacura 19, Santiago, Chile
[3] University College of London, Deparment of Physics and Astronomy, Gower Street, London, WC1E 6BT, UK
[4] University of Notre Dame, Department of Physics, 225 Nieuwland Science Hall Notre Dame, USA
[5] University of Tasmania, School of Mathematics and Physics, Private Bag 37, GPO Hobart, Tas 7001, Australia
[6] Dipartimento di Fisica, Università degli Studi di Roma "Tor Vergata", Rome, Italy
[7] Department of Astronomy, 610 Space Sciences Building, Cornell University, Ithaca, NY 14853, USA
[8] Sagan Fellow
[9] Institute for Advanced Study, Einstein Drive, Princeton, NJ 08540, USA
[10] Department of Astronomy, Ohio State University, 140 W. 18th Ave., Columbus, OH 43210, USA
[11] Department of Earth and Space Science, Osaka University, Osaka 560-0043, Japan
[12] Observatoire Midi-Pyrénées, UMR 5572, 14 avenue Edouard Belin, 31400 Toulouse, France
[13] Institute of Information and Mathematical Sciences, Massey University, Private Bag 102-904, North Shore Mail Centre, Auckland, New Zealand
[14] Department of Physics and Astrophysics, Faculty of Science, Nagoya University, Nagoya 464-8602, Japan
[15] Warsaw University Observatory. Al. Ujazdowskie 4, 00-478 Warszawa, Poland
[16] Laboratoire d'Astrophysique de Grenoble, UMR 5571 Université Joseph Fourier/CNRS, BP 53, 38051 Grenoble Cedex 9, France

Received 28 September 2010 / Accepted 7 February 2012

ABSTRACT

Context. Microlensing is a unique method to probe low mass exoplanets beyond the snow line. However, the scientific potential of the new microlensing planet discovery is often unfulfilled due to lack of knowledge of the properties of the lens and source stars. The discovery light curve of the super Earth MOA-2007-BLG-192Lb suffers from significant degeneracies that limit what can be inferred about its physical properties.

Aims. High resolution adaptive optics images allow us to solve this problem by resolving the microlensing target from all unrelated background stars, yielding the unique determination of magnified source and lens fluxes. This estimation permits the solution of our microlens model for the mass of the planet and its host and their physical projected separation.

Methods. We observed the microlensing event MOA-2007-BLG-192 at high angular resolution in *JHK*s with the NACO adaptive optics system on the VLT while the object was still amplified by a factor 1.23 and then at baseline 18 months later. We analyzed and calibrated the NACO photometry in the standard 2MASS system in order to accurately constrain the source and the lens star fluxes.

Results. We detect light from the host star of MOA-2007-BLG-192Lb, which significantly reduces the uncertainties in its characteristics as compared to earlier analyses. We find that MOA-2007-BLG-192L is most likely a very low mass late type M-dwarf ($0.084^{+0.015}_{-0.012}\ M_{\odot}$) at a distance of 660^{+100}_{-70} pc orbited by a $3.2^{+5.2}_{-1.8}\ M_{\oplus}$ super-Earth at $0.66^{+0.51}_{-0.22}$ AU. We then discuss the properties of this cold planetary system.

Key words. instrumentation: adaptive optics – stars: low-mass – planets and satellites: individual: MOA-2007-BLG-192Lb – gravitational lensing: micro

1. Introduction

Gravitational microlensing provides a unique window on extrasolar planetary systems with sensitivity to cool planets, particularly those of low mass (Bennett & Rhie 1996; Beaulieu et al. 2006; Gould et al. 2006; Bennett et al. 2008; Kubas et al. 2008; Sumi et al. 2010) that are currently well beyond the reach of other methods. Microlensing is also sensitive to planets orbiting very faint stars and hence spectral types not routinely examined with other techniques. In general it is a powerful tool to study the Galactic planetary population as a whole (Cassan et al. 2012).

Microlensing occurs when a foreground (lens) star passes close to the line of sight towards a background (source) star. The gravity of the foreground star acts as a magnifying lens, increasing the apparent brightness of the background star as it gets close to the line of sight. A planetary companion to the lens star will induce a perturbation to the microlensing light curve with a duration that scales with the square root of the planet mass,

⋆ Based on observations under ESO Prog.IDs: 279.C-5044(A) and 383-C.0495(A).

lasting typically a few hours for an Earth to a few days for a Jupiter (Gould & Loeb 1992; Mao & Paczynski 1991; Liebes 1964). Hence planets are now routinely discovered by dense photometric sampling of ongoing microlensing events. The inverse problem, finding the properties of the lensing system from an observed light curve, is a complex non-linear one within a wide parameter space. The planet/star mass ratio and projected star-planet separation can usually be measured with high precision. However in the absence of higher order effects such as parallax motion and/or extended source effects, in general there are no direct constraints on the physical masses and orbits of the planetary system. In the least information case, model distributions for the spatial mass density of the Milky Way, the velocity distribution of potential lens and source stars, and the mass function of the lens stars are used in a Bayesian analysis to derive probability distributions for the masses of the planet and the lens star and their distance, as well as the orbital radius and period of the planet.

With complementary high angular resolution observations, currently done either by HST or with adaptive optics, it is possible to get additional strong constraints on the system parameters and determine masses to about 10%. This can be done by directly measuring the light coming from the lens and measuring the lens and source relative proper motion (Bennett et al. 2006, 2007, 2010; Gaudi et al. 2008; Dong et al. 2009; Janczak et al. 2010)

An extrasolar planet with a best-fit mass ratio of $q \sim 2\times10^{-4}$ was discovered in the microlensing event MOA 2007-BLG-192 (Bennett et al. 2008) found by the MOA collaboration toward the Galactic bulge, (J2000: RA, Dec) = (18:08:03.8, −27:09:00). The best fit microlensing model shows both microlensing parallax and finite source effects. Combining these, we obtained the lens masses of $M_l = 0.06^{+0.028}_{-0.021}\ M_\odot$ for the primary and $3.3^{+4.9}_{-1.6}\ M_\oplus$ for the planet. The incomplete light curve coverage of the planetary anomaly led to a significant degeneracy in the lens models, and the lack of strong constraints on the source size to a poorly determined Einstein radius. Together this resulted in rather large uncertainties in the physical parameter estimates of the system.

Additional constraints are required to exclude competing microlens solutions and to refine our knowledge of the physical parameters of the system. It is possible to constrain masses and parameters of the system thanks to high angular resolution imaging. Most microlensing events only provide a single parameter, the Einstein ring crossing time t_E, that depends on the mass of the lens system M_L, its distance D_L, the source distance D_S and their relative velocity. However, when the relative lens-source proper motion μ_{rel} can be determined this yields the angular Einstein ring radius $\theta_E = \mu_{rel} t_E$. Moreover θ_E is linked to the lens system mass by

$$M_L = \frac{c^2}{4G}\theta_E^2 \frac{D_S D_L}{D_S - D_L}, \quad (1)$$

therefore, since the distance of the source D_S is known from its magnitude and colors, Eq. (1) is a mass-distance relation for the lens star. Another constraint is needed to obtain a complete solution to the microlensing event. This can be achieved by directly detecting light from the planetary host star (the lens). Combining this measurement with Eq. (1) and a mass luminosity relation will yield the mass of the lens. This has been done already for several microlensing events where the system is composed of a star and a gaseous planet (Bond et al. 2004; Bennett et al. 2006; Udalski et al. 2005; Dong et al. 2009; Gaudi et al. 2008; Janczak et al. 2010).

Table 1. Log of *JHK*s NACO data.

Band	$n \times$ Exp [s]	MJD	Airmass	FWHM [″]
		epoch 1		
J	6×60	54 350.00781250	1.005	0.14
H	20×25	54 350.02734375	1.023	0.19
Ks	10×25	54 349.98828125	1.002	0.09
		epoch 2		
J	23×60	55 036.08593750	1.015	0.34
H	22×30	55 036.06640625	1.034	0.29
Ks	24×30	55 015.10156250	1.088	0.10

Notes. According to the Paranal night logs the epoch 1 night was classified as photometric, whereas the epoch 2 observations were taken in clear sky condition. We give the exposure time, modified Julian date, airmass and measured full width at half max on the coadded frames.

We observed MOA-2007-BLG-192 in *JHK* using adaptive optics on the VLT while it was still amplified by a factor of 1.23 and again when the microlensing was over. Here, we combine the NACO *JHK* flux measurements at these 2 epochs with the color estimate of the source star (Gould et al. 2010) and the microlensing model (Bennett et al. 2008) to disentangle the flux coming from the source and from the lens star to refine estimates of the parameters of the system.

2. The data set

We obtained *JHK*s measurements using the NACO AO system (Lenzen et al. 2003; Rousset et al. 2003) mounted on Yepun during the night 6/7 Sept. 2007, while the source star was still magnified by a factor of 1.23. AO corrections were performed on a natural guide star[1] and observations with the S27 objective (27″ × 27″ FOV, pixelscale = 0.02715″) were conducted in jitter mode with multiple exposures at random offsets within 10″ of the target. In the absence of suitable "empty" sky patch close to the target, this strategy was chosen to ensure an accurate estimation of the sky background and to filter out bad pixels. The second epoch(s) were obtained with the same observing strategy more than 22 months later with the event being at baseline, i.e. when the source was not magnified anymore. An overview of the NACO data set is given in Table 1.

To perform absolute calibration of the NACO images we obtained 90 × 10 s dithered images in *JHK*s of the MOA-2007-BLG-192 field with the Sirius simultaneous 3-band camera (Nagayama et al. 2003) on the Japanese/South African IRSF 1.4 m telescope (Glass & Nagata 2000) at SAAO (non AO, ∼8′ × 8′ FOV, pixelscale = 0.45″) on 29th of Aug. 2008, i.e. at a time when the event was at baseline.

2.1. Reduction

Following a "lucky imaging" approach we visually inspect each of the NACO raw images and remove the ones for which the AO correction was obviously poor. The remaining raw frames are then dark-subtracted with darks of exposure times matching the science frames, flatfielded with skyflats, median co-added and sky-subtracted using recipes from the Jitter/Eclipse infrared data

[1] The LGSF, which in theory should have yielded better performance, was not available at that time. However the pro and contra of LGS vs. NGS for us have to be evaluated on a case by case base, since in the crowded field of microlensing targets one often finds suitable NGS references which may give even better corrections than the LGSF according to the ETC observation preparation software.

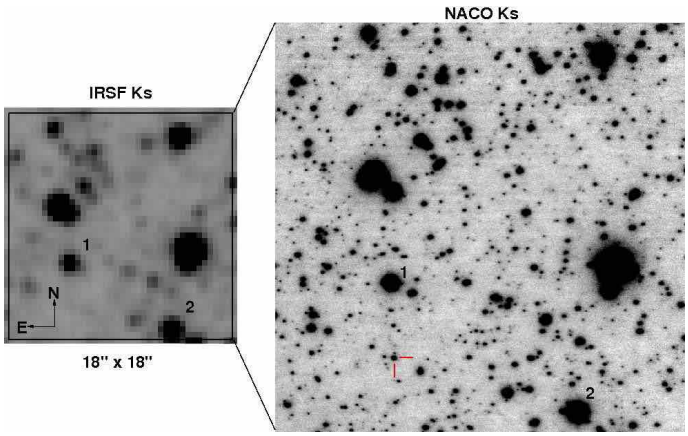

Fig. 1. *Left*: extract of IRSF Ks band image of MOA-2007-BLG-192 used to calibrate the NACO photometry of the 18″ × 18″ large intersection fov of the coadded NACO frames in *K*s band (*right*). MOA-2007-BLG-192 is marked with the half cross hair. The stars annotated with "1" and "2" serve as PSF-reference and photometric zeropoint calibrators. Furthermore these two stars are common to all bands and epochs. The bright stars north of the two references are either too crowded, in the non-linear regime or too far away from the target.

reduction package by Devillard (1997, 1999). To avoid border effects, we keep only the intersection of the different dither positions of the co-added frames for our photometric analysis.

The IRSF data, which was taken to gauge our NACO data, has been dark-subtracted, flat-fielded and sky subtracted using the on-the-mountain pipeline package for the SIRIUS camera (Nagayama et al. 2003).

3. Photometric analysis

As in our previous analysis of planetary microlensing event MOA-2008-BLG-310Lb (Janczak et al. 2010), we extract the photometry of NACO images using Starfinder (Diolaiti et al. 2000). This tool is tailor suited to perform photometry of AO images of crowded fields. It creates a numerical PSF template from chosen stars within the frame, which is then used for PSF-fitting of all stars in the field. To build our PSF reference we chose the star marked as "1" in Fig. 1 based on the following criteria. It is close to the target (within less than 4″), sufficiently bright but well within the linearity regime of the detector and common to all final reduced *JHK*s images of both epochs. Figure 6 shows the *JHK*s images centered on the target for the first epoch of NACO and the PSF subtracted residuals. The IRSF photometry catalog was created with DoPhot (Schechter et al. 1993).

3.1. Building a calibration ladder

In order to build the calibration ladder, we use three data sets: the 2MASS catalogue, photometry obtained at the IRSF telescope and then NACO data. It is necessary to use the intermediate step of IRSF observations because we have too few stars in common between 2MASS and NACO. Such ladder has been used already and described in the appendix of (Janczak et al. 2010). The three *JHK*s color systems are very close. For example, the color term for $J - K$s colors between 2MASS and IRSF is only 0.01. Accurate calibration between 2MASS and IRSF has been given in Kato et al. (2007). Janczak et al. (2010) did not detect color terms between NACO and IRSF filters. Therefore, our calibration ladder must only determine the zeropoint offsets.

Table 2. *JHK*s NACO photometry for MOA-2007-BLG-192, i.e. lens+source (no dereddening applied).

Band	J	H	K_s
NACO epoch 1			
calibrated against IRSF			
	19.209 ± 0.043	18.281 ± 0.042	17.948 ± 0.035
NACO epoch 2			
calibrated against IRSF			
	19.324 ± 0.073	18.548 ± 0.112	17.989 ± 0.038
Δ epochs	0.115 ± 0.085	0.267 ± 0.120	0.041 ± 0.052
aligned with respect to epoch 1			
	19.283 ± 0.071	18.498 ± 0.087	18.011 ± 0.042
Δ epochs	0.074 ± 0.083	0.217 ± 0.097	0.063 ± 0.055

Notes. The absolute photometry error budget is composed by adding in quadrature the errors on the zeropoint, the formal error reported by Starfinder and the background error as estimated from the scatter between epoch 1 and epoch 2 comparison stars. For epoch 1, J, and H bands, we adopt the background error estimate as derived from the K band, since the poor epoch 2 quality in J and H would overestimate the epoch 1 errors.

We first perform the astrometry of the IRSF images with respect to the online 2MASS catalog using GAIA/Skycat and WCSTools. Then, using only stars marked as AAA (highest 2MASS quality flag) in the *JHK*s bands we crossmatch the common stars to compute the photometric transformation between the two catalogs by sigma clipping, demanding an astrometric accuracy of the match of better than 0.6″. To minimize the effect of source confusion and blending contamination we cut off at magnitude 13 for the 2MASS reference stars and sum up the flux of close neighbors for the IRSF sources to account for the much coarser pixel scale of the 2MASS catalog.

The PSF reference star is contained in the IRSF catalog, as well as star "2" (Fig. 1). We examine their long term photometric stability in the OGLE database and find that over more than seven years both stars are stable (in the optical I-band) at levels of $\lesssim$1%, which makes them well suited as zeropoint calibrators of our NACO field. While we adopt star "1" as the primary photometric calibrator since star "2" is more crowded, we determine zeropoints from both stars as a consistency check. To account for the different plate scales between NACO and IRSF we sum up the flux of all the NACO sources which are contained within the IRSF PSF. We note that observing conditions (sky transparency and atmospheric coherence times) for the second epoch data set were inferior to the epoch 1 measurements and the uncertainties in the absolute zeropoints of epoch 2 are therefore larger. Since we are mainly interested however in the relative photometry of the two epochs we can align the epoch 2 photometry with respect to more accurately calibrated epoch 1. Table A.1 summarizes this way of determining the transformations to calibrate the NACO data with respect to the 2MASS system and Table 2 shows our derived photometry for MOA-2007-BLG-192.

4. Results

In Figs. 2 and 3 we present the color-magnitude diagrams for the combined IRSF and NACO (epoch 1) data. To estimate the interstellar extinction, we first determine the position of the red clump center by taking the median of the distributions in color and magnitude inside a window centered on a first guess estimated position. Then we fit the tip of the Red Giant Branch as given by the isochrones of Marigo et al. (2008) adopting the distance modulus dm = 14.38 ± 0.07 as found for the

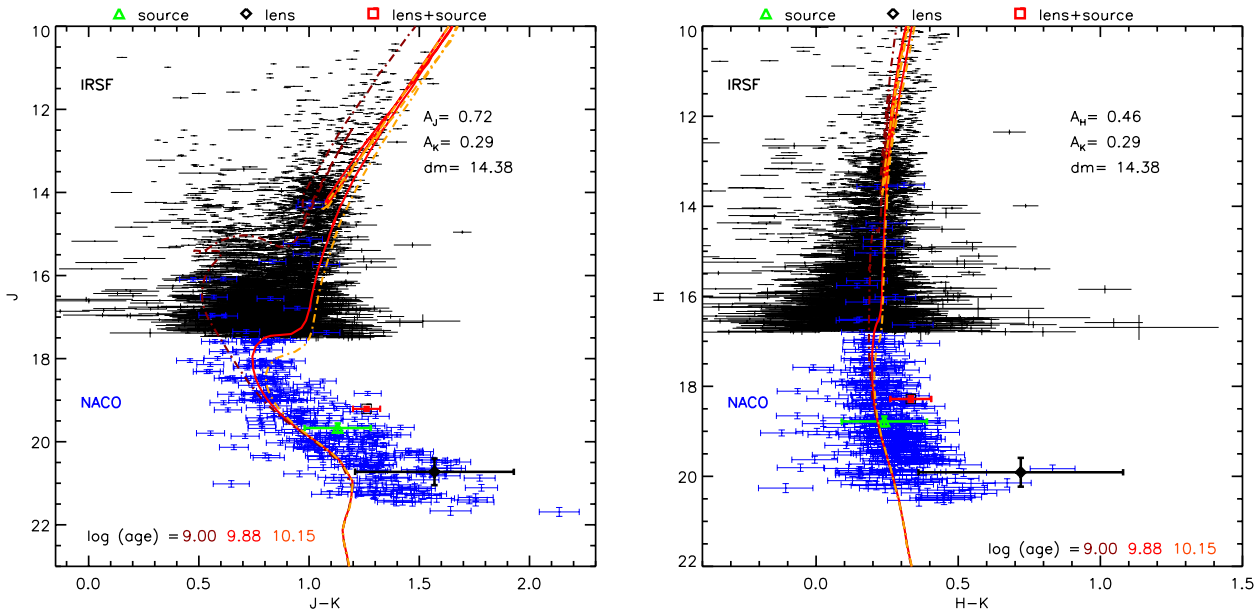

Fig. 2. *Left*: the $(J - Ks, J)$ CMD in the 2MASS system of the MOA-2007-BLG-192 field combining the data from the IRSF (within 3′ of target, black points) and NACO (within 18″, blue points). In red the photometry of the measured lens+source flux at magnification $A = 1.23$ is displayed together with the inferred decomposed fluxes of the source (green) and the lens (planetary host star, black). Overplotted are Marigo et al. (2008) solar metallicity isochrones of ages $\log(\mathrm{Gyr}) = 9.00, 9.88, 10.15$ at distance modulus of $\mathrm{dm} = 14.38$ and estimated extinction of $A_J = 0.72, A_{Ks} = 0.29$. *Right*: same as above but for $(H - Ks, H)$.

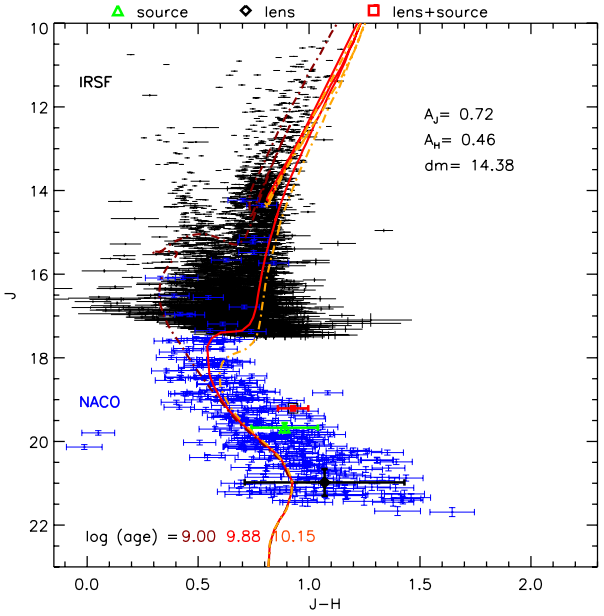

Fig. 3. Same as Fig. 2 but for $(J - H, J)$.

MOA-2007-BLG-192 field by Bennett et al. (2008). With a best fit age of $\log(\mathrm{Gr}) = 9.88$ we find for the extinction coefficients: $A_J = 0.72 \pm 0.10, A_H = 0.46 \pm 0.10, A_K = 0.29 \pm 0.10$, which for this line of sight is consistent with extinction maps from Schlegel et al. (1998) and Marshall et al. (2006).

4.1. The case for a luminous lens I: NACO-only

The standard general microlens light curve model is given as

$$F(t) = F_S A(t) + F_B, \quad (2)$$

where F is the measured flux at the telescope, F_S is the intrinsic unmagnified source flux, $A(t)$ the time dependent magnification given by the lens model and the blend flux $F_B = F_L + F_{\mathrm{Background}}$, which contains the lens flux F_L and $F_{\mathrm{Background}}$ the flux of any unrelated field stars within the aperture, $F_{\mathrm{Background}}$. While the source flux F_S can be determined with high precision from the light curve modeling of the non-AO data, given a large magnification gradient, the background term normally dominates over the lens term in seeing-limited photometry of typically crowded Galactic Bulge fields of microlensing. Hence the benefits of high spatial resolution imaging are obvious. Reducing or eliminating the contribution of contaminating background sources provides a better estimate of the lens flux and so finally of the physical characteristics of the lens system. In Janczak et al. (2010) the lens flux could be estimated by comparing a single NACO AO epoch with an excellent seeing-limited light curve in the same passband from which the source flux had been previously determined with good accuracy. For MOA-2007-BLG-192Lb we have no such light curve in the NACO passbands but a well determined measurement of the source flux in the I band (Cousins system), which we can transform into the expected source flux for $JHKs$ bands. Note that while in theory our two point NACO "light curve" can be used to solve Eq. (2) for the lens and source fluxes directly, the resulting uncertainties are very large (Dong et al. 2009) due to very small magnification "lever arm" for our event and so following the path of Janczak et al. (2010) is much more accurate.

First, however, the two epochs can be used as follows, without the knowledge of the source flux, to check whether there is an indication that light from the lens is detected. The expected magnification gradient between the two NACO epochs based on the best-fit model of Bennett et al. (2008) is $\Delta m = 0.230 \pm 0.015$ mag. Note that this gradient is basically the same for all competing planetary models, since the first epoch was taken close to the baseline of the event, where the single lens approximation describes the data very well. If the lens is dark and no unrelated source is contaminating our photometry (see Sect. 4.3) we then would expect to measure this difference in the

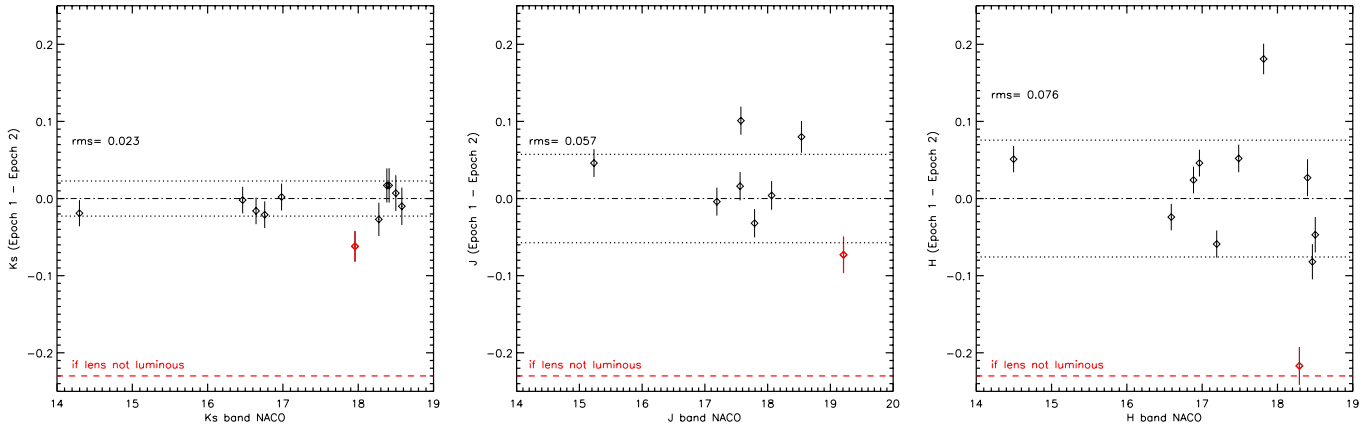

Fig. 4. Relative photometry of the NACO epochs for each band calibrated/aligned to epoch 1 based on stars within 4″ of MOA-2007-BLG-192. The black points are constant stars, so their scatter gives an estimate of the error. The red dashed line marks the expected magnitude difference of the target assuming no light from the lens is detected. The red diamonds show the flux changes of the target, which are inconsistent with such a scenario at a $3-\sigma$ level for J and even with higher significance for our best data set in K band. The poor quality of the epoch 2 H band data as evident by the large scatter does not provide any useful constraint. Table 2 gives the derived values for all bands and different choices of the field of comparison stars.

relative photometry of the two epochs in each band. Since the quality of epoch 1 is superior we choose epoch 1 as reference to which we align epoch 2. We compare the photometry between the two epochs for each band using 3 different alignment procedures. First we compare the derived absolute photometry (with respect to 2MASS using the calibration ladder described in Sect. 3.1).

Then we align epoch 2 with respect to (calibrated) epoch 1 using all common stars within 4″ (to minimize effect of PSF variations) of the target. The resulting magnitude differences for the target and the absolute photometry values are summarized in Table 2. The difference between the epochs is shown in Fig. 4. Regardless of the alignment method used, for all bands except H (the set with the poorest epoch 2 data quality), the measured difference is less than in the case of a dark lens, albeit with different levels of significance. For K band, the best data set, a dark lens is inconsistent with the measurement at 2σ for the absolute alignment and at 3σ for the relative alignment. The results for J band are also inconsistent with a dark lens, but in this case at slightly less than 2σ. This motivates a more careful examination of the evidence for a luminous lens.

4.2. The case for a luminous lens II: NACO+IRSF+optical

A more powerful test for the presence of "excess light" (in addition to that of the source) is possible by combining NACO, IRSF, and optical data. To maximize sensitivity, we will work entirely with *uncalibrated* data. This will eliminate any errors associated with calibration relations, extinction estimates, and color–color relations. The remaining errors, which are either measurement errors or intrinsic scatter, are both small and easy to measure.

We begin by constructing a color-+color diagram that combines optical V and I data from OGLE-II with K data from IRSF (see Fig. 5). The OGLE-II data are used because this is the system in which Gould et al. (2010) measured the color and magnitude of MOA-2007-BLG-192S,

$$(V-I)_{\rm s} = 2.36 \pm 0.03; \qquad I_{\rm s} = 21.45 \pm 0.05. \tag{3}$$

The OGLE-II data are in fact calibrated, but that is incidental: the important thing is that the optical color is measured in this

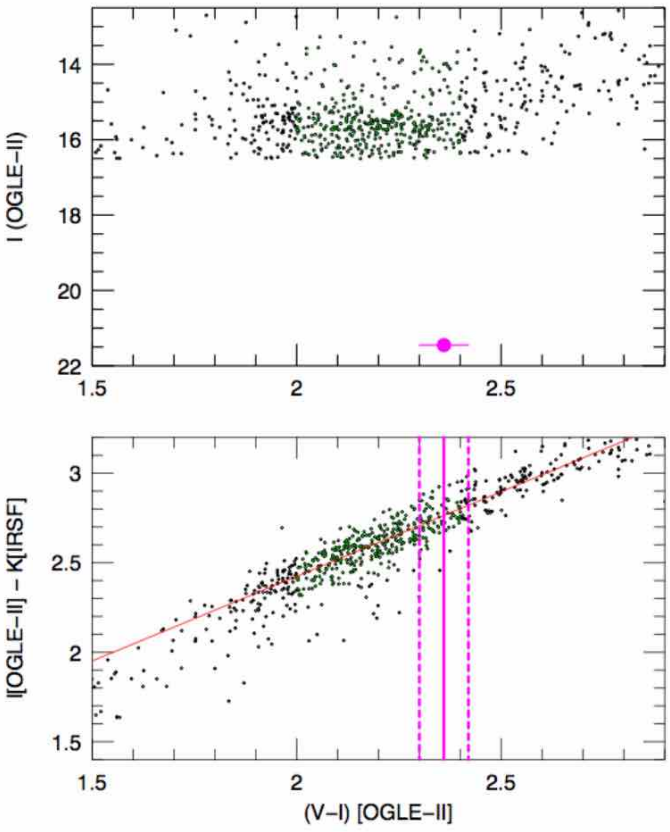

Fig. 5. Empirical VIK instrumental color–color relation. *Lower panel*: open black symbols show all astrometric matches (that survived a strict crowding criterion) between OGLE-II V/I data and instrumental IRSF K data. The green filled points show those used in the fit (red line), which are restricted to $2.0 < (V-I) < 2.4$ and exclude 3σ outliers. Vertical magenta lines show MOA-2007-BLG-192S $(V-I)$ color measurement by Gould et al. (2010). *Upper panel* shows the VI CMD positions of stars used to determine the VIK relation. They are all giants in or near the clump, whereas the source (magenta point) is a dwarf. Nevertheless, Bessell & Brett (1988) show that the VIK relations are essentially identical for giants and dwarfs in this color range (see text).

system. The K magnitudes are constructed directly from IRSF photometry fluxes $K = 22.155 - 2.5\log(\text{flux})$. The zero-point constant is chosen for convenience to be similar to the calibration constant, but this constant does not enter the calculation in any way. In particular, the data remain uncalibrated because there is no color term.

The open black circles are all the astrometric matches that meet a strict crowding criterion. A color–color relation (red) is derived by fitting the points in the range $2.0 < (V-I) < 2.4$ with 3σ rejection (green filled points). This choice of interval will be justified below. The relation is:

$$(I-K) = Z_1 + Z_2[(V-I) - 2.36];$$
$$Z_1 = 2.757 \pm 0.008; \quad Z_2 = 0.943 \pm 0.039 \qquad (4)$$

with a scatter of 0.080 mag.

The vertical lines represent the best fit and error bar of the Gould et al. (2010) optical-color measurement. From Eqs. (3) and (4), the best estimate of the source magnitude at the first epoch (when the source was magnified by $A = 1.23$) is therefore

$$K_s = [I_s - 2.5\log(A)] - Z_1 - Z_2[(V-I)_s - 2.36] = 18.468. \qquad (5)$$

We discuss all the errors in this estimate below.

We now compare this with the baseline flux as measured by NACO and transformed to the IRSF system:

$$K_{\text{base,IRSF}} = K_{\text{comp,IRSF}} + 2.5\log(F_{\text{comp,NACO}}/F_{\text{base,NACO}}) = 17.948 \qquad (6)$$

where $K_{\text{comp,IRSF}} = 14.261 \pm 0.016$ is the IRSF magnitude of the comparison star, and $F_{\text{comp,NACO}} = 88066 \pm 37$ and $F_{\text{base,NACO}} = 2952.2 \pm 12.1$ are the NACO fluxes of the comparison and baseline stars, respectively.

The baseline flux is clearly larger, $K_s - K_{\text{base}} = 0.520$, The question is, how large is the error in this difference? Equation (5) has 5 identifiable sources of error. First, the error in I_s is 0.05, but the error in $[I_s - 2.5\log(A)]$ is actually smaller than this by a factor 0.57 (see Eq. (10) of Janczak et al. 2010). Second, the error in Z_1 is 0.008. Third the error in the final term is Z_2 times the error in $(V-I)_s$, i.e., 0.056.

Fourth, we are using the VIK color–color relation of the field stars observed by IRSF as a proxy for the VIK color–color relation of the source. However, the source is a dwarf, while the field stars are all giants. Now, according to Fig. 1 of Bessell & Brett (1988) these VIK relations of giants and dwarfs are virtually identical for $(V-K)_0 < 3.0$ $[(V-I)_0 < 1.3]$, and diverge only very slowly at redder colors. The dereddened color of the source is $(V-I)_0 = 1.24 \pm 0.06$, so the entire 1σ error range lies within the "same relation" region. And again, the relations diverge only very slowly at redder colors. We note, however, from Fig. 2 of Bessell & Brett (1988), that the divergence is extremely rapid in $(J-K)$. This is the principal reason that we conduct this test in K rather than J.

Finally, the VIK relation in Fig. 5 exhibits a scatter of 0.08 mag. If this scatter is attributed to measurement errors, then the effect is very small. There is some reason to expect that this is the case because Fig. 1 of Bessell & Brett (1988) shows almost zero scatter. However, the bulge star population may be more diverse than the local one. For the moment we assume it is intrinsic, and that this scatter in the observed giant VIK relation also applies to dwarfs. Then, the error in $K_s(A = 1.23)$ is $[0.028^2 + 0.008^2 + 0.056^2 + 0.08^2]^{1/2} = 0.102$.

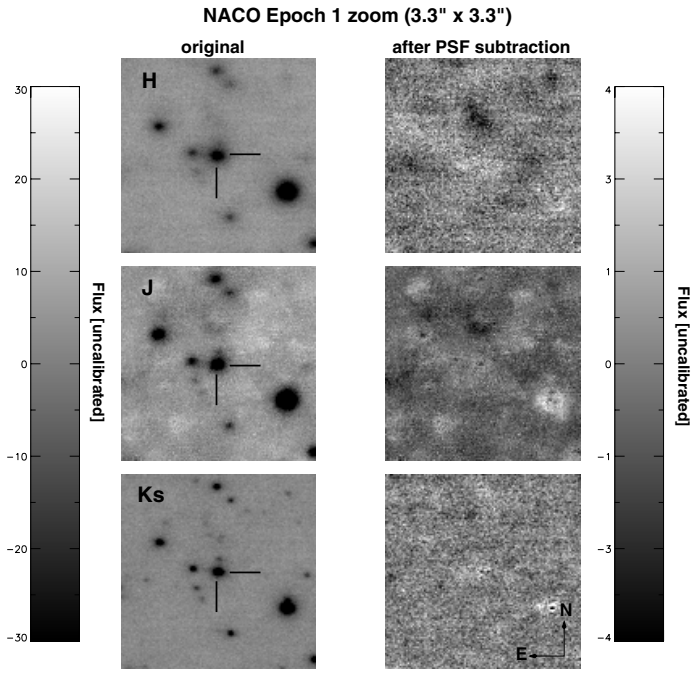

Fig. 6. *Left*: zoom ($3.3'' \times 3.3''$) of epoch 1 NACO images centered on the target in H (*top*), J (*middle*), and K (*bottom*). *Right*: images after PSF subtraction. The PSF subtraction does a good job of removing essentially all flux, particularly in K.

There are three errors contributing to K_{base}, which are listed below Eq. (6). Their sum in quadrature is 0.017. As seen in section 3 the *JHK*s bands from 2MASS, IRSF and NACO are very close, with negligible color terms in the transformations between the different systems. Next we note that photometry on AO images is notoriously difficult due to gradients in the PSF. This effect is hard to quantify. However, Fig. 6 shows that it must be quite small. The left (right) column shows the image before (after) PSF subtraction for the first epoch, for J, H, K, respectively. The K image in particular, looks extremely clean. We nevertheless conservatively estimate a 0.03 photometry error due to PSF gradient. This yields a total error on K_{base} of 0.034 mag.

Finally, we note that even if the scatter in Fig. 5 were due to measurement noise, rather than intrinsic scatter (and so should not have been included in the error in $K_s(A = 1.23)$, it would then contribute to the error in K_{base} through $K_{\text{comp,IRSF}}$. Hence, the impact on the final error would have been identical.

We therefore finally derive our estimate of the excess magnitude at baseline:

$$K_s - K_{\text{base}} = 0.520 \pm 0.108$$

which is a 4.8σ detection of additional light. It is either a blend aligned to better than 0.1 arcsec with the source star of the microlensing event or light coming from the lens star.

4.3. Is the blended light from the lens star?

The mean density of stars of comparable brightness and color ± 0.20 mag to the detected blend is less than 0.2 per arcsec^2 as derived from our best/sharpest data set, the Ks band of epoch 1. Given the image quality of $0.09''$ FWHM, this conservatively implies a probability of less than 2% for the blend being unrelated to the microlens event. Another possibility to consider is

that the blend stems from a companion to the source star. Close companions with periods $\lesssim$100 d can be ruled out by the xallarap signal limits in the light curve and very wide separation companions $\gtrsim$700 AU would be resolved in the *Ks* NACO data. This still leaves a large range of allowed separations but taking into account the color difference the possible fraction of low mass secondaries should not be larger then 8% according to Duquennoy & Mayor (1991). However only future AO or HST images, when the source and lens will have moved sufficiently far apart to be spatially resolved, will be able to securely rule out such a scenario.

4.4. Source star constraints

To compare the $(V-I)_0 = 1.24 \pm 0.06$ color found by Gould et al. (2010) to the NIR bands of this study we transform this $V-I$ color to $J-K$ in the 2MASS system using first the dwarf color table of Bessell & Brett (1988) to find $(J-K)_{0,s} = 0.73$ and then with the 2MASS-Bessell & Brett filter relation[2] we finally derive $(J-K)_{0,s} = 0.70 \pm 0.07$.

From our NACO "light curve" using Eq. (2) and our lens model , we find after dereddening $(J-K)_{0,s} = 0.66 \pm 0.51$. While the uncertainty derived from linear regression is large, this independent source color determination is very consistent with the colors found by Gould et al. (2010) as well as those of Bennett et al. (2008) and strengthens the case for the source being a K4-5 dwarf in the Bulge at 7.51 ± 0.25 kpc. However, given the better accuracy of the Gould et al. (2010) source color, we adopt their value in the following analysis.

4.5. Lens/planetary system constraints

From the MOA-2007-BLG-192 light curve the *I* band source flux is well determined to $I_s = 21.44 \pm 0.08$ (Bennett et al. 2008). Using the source color derived in the previous section and the extinction coefficients determined from the IRSF data, we can translate this *I* band estimate into the NACO passbands to derive $J_s = 19.67 \pm 0.12$, $H_s = 18.78 \pm 0.10$, $K_s = 18.54 \pm 0.10$ (2MASS system).

Using our best lens model and Eq. (2) we then derive the following estimates for the apparent lens flux: $J_l = 20.98 \pm 0.30$, $H_l = 19.91 \pm 0.30$, $K_l = 19.29 \pm 0.20$ from epoch 1 and $J_l = 20.59 \pm 0.40$, $H_l = 20.10 \pm 0.50$, $K_l = 19.04 \pm 0.20$ from epoch 2. Taking the weighted average we finally get as best estimate for the lens flux: $J_l = 20.73 \pm 0.32$, $H_l = 19.94 \pm 0.35$, $K_l = 19.16 \pm 0.20$.

We now can use mass luminosity relations to translate the photometry estimates of the apparent lens flux into estimates of the planetary host star mass. We adopt the relations of Delfosse et al. (2000) for M-dwarfs (with masses >0.10 $M_\odot$) and Chabrier et al. (2000) for L-dwarfs (masses <0.10 $M_\odot$), where the transition between the two relations at ~0.10 $M_\odot$ has been linearly interpolated. The best lens model gives an estimate for the distance and mass of the lens via the measurement of the parallax π_E using Eq. (1). In Fig. 7 the implied apparent lens brightness based on the mass-magnitude relations and our constraint on the parallax is plotted as a function of lens mass. All bands agree that the lens mass is in the range $0.07 < M_L/M_\odot < 0.10$ with a best estimate of $M_L/M_\odot = 0.087 \pm 0.010$, preferring a stellar over a sub-stellar host. This is consistent with the previous best estimate of $M_L/M_\odot = 0.06 \pm 0.04$ (Bennett et al. 2008), but

[2] http://www.astro.caltech.edu/~jmc/2mass/v3/transformations/

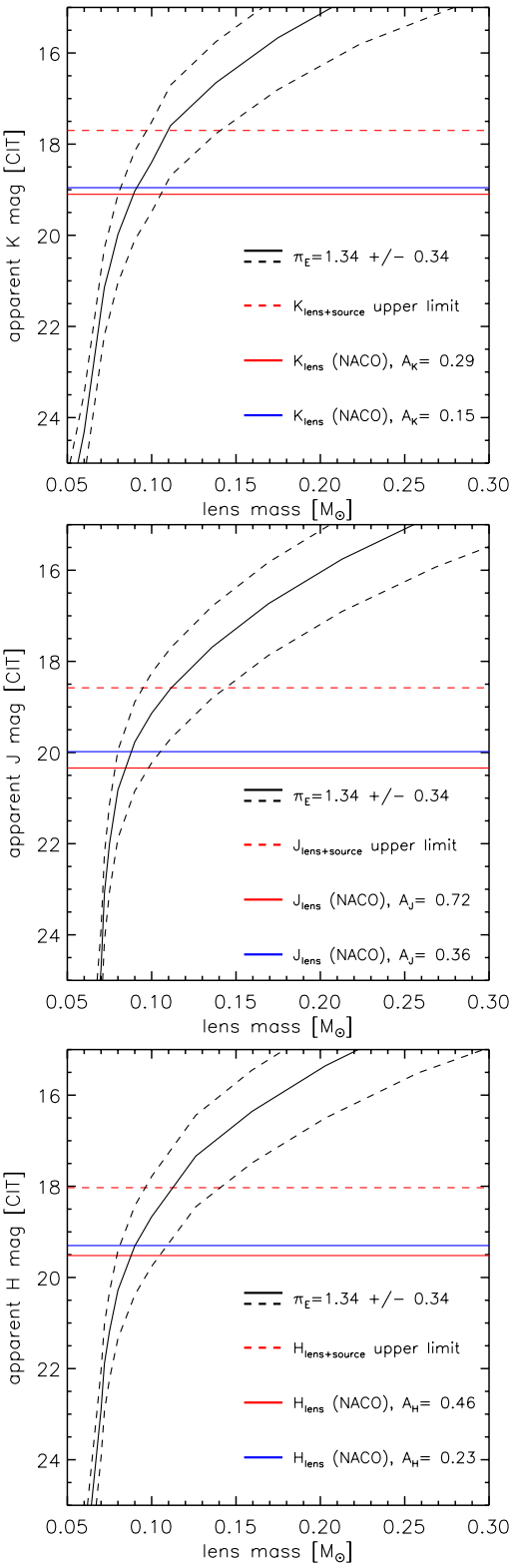

Fig. 7. Mass-Magnitude relations for *K* (*top*), *J* (*middle*) and *H* (*bottom*) bands [CIT system] derived from Delfosse et al. (2000) for M-dwarfs (with masses >0.10 $M_\odot$) and L-dwarfs (masses <0.10 $M_\odot$) from Chabrier et al. (2000). The transition between the two relations at ~0.10 $M_\odot$ has been linearly interpolated. The black curves show the most likely range of distances for the MOA-2007-BLG-192Lb system as found by Bennett et al. (2008) and the horizontal lines marks the estimate for the lens flux from the NACO data as well as the upper limit of the lens flux from measured lens+source flux for a range of possible interstellar extinctions.

which was not able to distinguish between the different host star possibilities. This new refined lens mass also affects the inferred planetary mass of MOA-2007-BLG-192Lb. This is due to a light curve degeneracy between the planetary mass ratio q, and the source star radius crossing time t_*. The detection of light from the lens star means that it must be massive enough to be above the hydrogen burning threshold, which constrains $t_* < 0.05$ days and rules out the cusp crossing models (models I-P of Table 1 in Bennett et al. 2008; the remaining surviving models consistent with the NACO data are listed here in the appendix in Table A.3). This constraint on t_* pushes the mass ratio, q, toward somewhat smaller values. As a result the range of allowed planetary masses is nearly unchanged.

The physical parameters of the star-planet system can be estimated by the same type of Markov chain Monte Carlo (MCMC) calculations used in Bennett et al. (2008) or Dong et al. (2009). But we now add constraints that the lens star must satisfy the *JHK* mass luminosity relations of Delfosse et al. (2000), under the assumption that 25% of the dust responsible for the extinction of the source star is also in the foreground of the lens star plus planet system. The uncertainty in the lens magnitude is taken to be 0.3 mag in each passband. This accounts for the uncertainty in the extinction as well as the uncertainty in the Delfosse et al. (2000) mass-luminosity relations, which become large at low masses because of the metallicity dependence of the minimum stellar mass. The parameter values resulting from this calculation are listed in Table A.2. The planet mass is now $3.2^{+5.2}_{-1.8}\ M_\oplus$, while the host star mass is $0.084^{+0.015}_{-0.012}\ M_\odot$ and the two dimensional star-planet separation during the event is $a = 0.66^{+0.51}_{-0.22}$ AU. The MCMC lens distance estimate is $D_L = 700^{+210}_{-120}$ pc which agrees with our more direct estimate of 660^{+100}_{-70} pc. This implies that the lens suffers less than half of the total extinction toward the source, and our derived lens colors are consistent with a late M spectral type (Leggett et al. 2010) of the planetary host.

4.6. Additional constraints from future high angular resolution observations

Another improvement can be achieved by measuring the amplitude and direction of the relative proper motion of source and lens in combination with the microlensing modeling of the parallax signal caused by the Earth's motion. Such physical measurements break a model degeneracy in the projected Einstein radius $\tilde{r}_E$ (Bennett et al. 2007, 2008). In the case of MOA-2007-BLG-192 the degeneracy is particularly acute because of a gap in event coverage, with different equally well-fitting models requiring widely different projections and hence directions for the relative proper motion, even though the models yield similar amplitudes: ~5 mas yr^{-1}. The measurement of both θ_E and $\tilde{r}_E$ yields the lens system mass $M_L = c^2/(4G)\ \theta_E \tilde{r}_E$. Ideally, the relative lens-source proper motion μ_{rel} is measured when detecting both the lens star and the source star as done by Alcock et al. (2001).

The two stars will not be fully resolved for many years. However, due to the unique stability of the HST point spread function (PSF) it is possible to measure source-lens separations (with position angles) much smaller than the width of the PSF. This is accomplished by measuring the elongation of the combined lens-source image due to the fact it is a combination of two point source images rather than one. The lens and source stars of MOA-2007-BLG-192 will already be about 25 mas apart in 2012.

Simulations by Bennett et. al. (2007) show that measurements of both the amplitude and orientation are possible for MOA-2007-BLG-192 already in 2012. These measurements combined with our modeling will improve the knowledge of system parameters (masses, orbital separation) to about 10%. The key point is that the direction of the elongation will give us a measurement of the direction of the relative lens-source proper motion μ_{rel} and therefore resolve the remaining parallax degeneracies (Ghosh et al. 2004; Bennett et al. 2007, 2008).

4.7. Properties of the planetary system

The effective temperature of the planet, for the parameters of the parent star and orbit separation given above, is 47^{+7}_{-8}K for an albedo of zero, and 40^{+6}_{-7}K for an albedo of 0.5. Based on observations of a tenuous atmosphere (20–60 microbars) of nitrogen on Pluto, the temperature of bright surfaces ices on Pluto at perihelion is estimated to be between 35–40 K (Stansberry & Yelle 1999). Thus, if nitrogen were available, the surface of this planet might look like that of Pluto on the basis of stellar heating alone. However, the large mass of the planet compared with that of Pluto necessitates examining the possible role of heat from the interior of the planet. The maximum temperature possible with zero albedo, 54 K, remains below the pure nitrogen melting point of 63 K, and well below the methane melting point of 91 K.

The present-day terrestrial heat flow (0.087 W/m^2) value is about 10 times less than the roughly 1 W/m^2 deposited by the lensing star on its planet at local noon. Thus the average heat flow coming from the planet itself will not raise the surface temperature significantly, even for a fully rocky body three times the mass of the Earth (Lunine 2010). Of course, we do not know the age of the star; were we to use the Hadean heat flow value for the Earth (Hopkins et al. 2008) for the 3.2 Earth mass body, the influx from geothermal heating could exceed the energy received from the star. The surface temperature could then be above the nitrogen melting point, leading to the possibility of liquid nitrogen lakes or seas if the atmospheric pressure were 0.1 bar or more. The lensing star-planet system is likely older than this, and hence the planet's heat flow correspondingly less.

Because the distribution of heat flow on a terrestrial planet can be strongly heterogeneous, one could imagine places on the surface with much higher heat flow than the average value for the planet, such that temperatures might exceed the melting point not just of nitrogen but of methane. Thus, if sufficient quantities of these molecules were present, the planet's surface might have zones resembling the hydrocarbon lakes and seas of Saturn's moon Titan. The possibility of liquid water cannot be discounted, but would most likely be below the surface or in very restricted, volcanically active, locales.

5. Conclusions

In this study we have presented the analysis of photometric data in the near infrared *JHK*s bands at two different epochs of planetary microlensing event MOA-2007-BLG-192, obtained with the AO system NACO mounted on UT4 at ESO. According to the best-fit lens models as given in Bennett et al. (2008) the difference in the magnification of the source is 0.230 ± 0.015 for the two epochs. If the lens is non-luminous this would be the expected photometric gradient in our data set in the absence any blended light contribution. Our *K*-band data, when combined with results from previous optical data, are inconsistent with

such a scenario at 4, 8σ. In fact the data imply that there is a significant amount of blended light at the location of MOA-2007-BLG-192. Assuming that this blend is the lens, the data favor a scenario in which the lens would be a closeby (660^{+100}_{-70} pc) late M-dwarf. This is consistent with the estimates for a stellar lens as based on constraints from extended source and parallax effects as discussed in Bennett et al. (2008). While the data available at the time of the discovery paper were consistent with a broad range of planetary host masses, the new NACO data presented here support the hypothesis of a stellar host for MOA-2007-BLG-192Lb. Of course it is conceivable that the detected blend stems not from the lens, but either from a stellar companion to the source, the lens or an unrelated background star. However the probabilities for such scenarios are low and using Ockham's razor the most likely explanation is that the lens is an M-dwarf, which implies a planetary mass of $3.2^{+5.2}_{-1.8}$ $M_{\oplus}$ for MOA-2007-BLG-192Lb, placing it among the front row of known least massive cool planets in orbit around one of the least massive host stars.

MOA-2007-BLG-192Lb is a landmark exoplanet discovery suggesting that planet formation occurs down to to the very low mass end of the stellar population. This is in agreement with the recent statistical results of Cassan et al. (2012) that on average, every star in the Milky Way hosts at least one planet. MOA-2007-BLG-192 is the first microlensing event for which multi epoch AO data has been obtained and demonstrates the usefulness of this technique for microlensing, by constraining the physical characteristics of microlensing planetary systems and providing important experiences to optimize future AO observations, which ideally should be carried out in ToO mode for the first epoch, to ensure the source is still significantly magnified.

Acknowledgements. We like to say thanks to the ESO Paranal and Garching teams for their high quality service and support in carrying out the NACO observations. Especially thanks to ESO staff C. Dumas, C. Lidman and P. Amico. Thanks also to the IRSF observatory staff. D.K. and A.C. especially thank ARI, where part of the work was done during a visit. Special thanks to the support from ANR via the HOLMES project grant. Special thanks to David Warren for supporting the work done at Canopus Observatory. D.P.B. was supported by grants NNX07AL71G & NNX10AI81G from NASA and AST-0708890 from the NSF. Work by S.D. was performed under contract with the California Institute of Technology (Caltech) funded by NASA through the Sagan Fellowship Program. A.G. was supported by NSF grant AST-0757888. J.L. work was financed within the scope of the program "Incentivazione alla mobilita' di studiosi straineri e italiani residenti all'estero". A.U. was supported from the European Research Council under the European Community's Seventh Framework Programme (FP7/2007-2013)/ERC grant agreement No. 246678. D.K. also likes to thank G. James for his graphic support.

References

Alcock, C., Allsman, R. A., Alves, D. R., et al. 2001, Nature, 414, 617
Beaulieu, J.-P., Bennett, D. P., Fouqué, P., et al. 2006, Nature, 439, 437
Bennett, D. P., & Rhie, S. H. 1996, ApJ, 472, 660
Bennett, D. P., Anderson, J., Bond, I. A., Udalski, A., & Gould, A. 2006, ApJ, 647, L171
Bennett, D. P., Anderson, J., & Gaudi, B. S. 2007, ApJ, 660, 781
Bennett, D. P., Bond, I. A., Udalski, A., et al. 2008, ApJ, 684, 663
Bennett, D. P., Rhie, S. H., Nikolaev, S., et al. 2010, ApJ, 713, 837
Bessell, M. S., & Brett, J. M. 1988, PASP, 100, 1134
Bond, I. A., Udalski, A., Jaroszyński, M., et al. 2004, ApJ, 606, L155
Cassan, A., Kubas, D., Beaulieu, J.-P., et al. 2012, Nature, 481, 167
Chabrier, G., Baraffe, I., Allard, F., & Hauschildt, P. 2000, ApJ, 542, 464
Delfosse, X., Forveille, T., Ségransan, D., et al. 2000, A&A, 364, 217
Devillard, N. 1997, The Messenger, 87, 19
Devillard, N. 1999, in Astronomical Data Analysis Software and Systems VIII, ed. D. M. Mehringer, R. L. Plante, & D. A. Roberts, ASP Conf. Ser., 172, 333
Diolaiti, E., Bendinelli, O., Bonaccini, D., et al. 2000, A&AS, 147, 335
Dong, S., Gould, A., Udalski, A., et al. 2009, ApJ, 695, 970
Duquennoy, A., & Mayor, M. 1991, A&A, 248, 485
Gaudi, B. S., Bennett, D. P., Udalski, A., et al. 2008, Science, 319, 927
Ghosh, H., DePoy, D. L., Gal-Yam, A., et al. 2004, ApJ, 615, 450
Glass, I. S., & Nagata, T. 2000, Monthly Notes of the Astronomical Society of South Africa, 59, 110
Gould, A., & Loeb, A. 1992, ApJ, 396, 104
Gould, A., Udalski, A., An, D., et al. 2006, ApJ, 644, L37
Gould, A., Dong, S., Bennett, D. P., et al. 2010, ApJ, 710, 1800
Hopkins, M., Harrison, T. M., & Manning, C. E. 2008, Nature, 456, 493
Janczak, J., Fukui, A., Dong, S., et al. 2010, ApJ, 711, 731
Kato, D., Nagashima, C., Nagayama, T., et al. 2007, PASJ, 59, 615
Kubas, D., Cassan, A., Dominik, M., et al. 2008, A&A, 483, 317
Leggett, S. K., Burningham, B., Saumon, D., et al. 2010, ApJ, 710, 1627
Lenzen, R., Hartung, M., Brandner, W., et al. 2003, in SPIE Conf. Ser. 4841, ed. M. Iye, & A. F. M. Moorwood, 944
Liebes, S. 1964, Phys. Rev., 133, 835
Lunine, J. 2010, in Through Time, A Workshop On Titan's Past, Present and Future, ed. V. Cottini, C. Nixon, & R. Lorenz, 75
Mao, S., & Paczynski, B. 1991, ApJ, 374, L37
Marigo, P., Girardi, L., Bressan, A., et al. 2008, A&A, 482, 883
Marshall, D. J., Robin, A. C., Reylé, C., Schultheis, M., & Picaud, S. 2006, A&A, 453, 635
Nagayama, T., Nagashima, C., Nakajima, Y., et al. 2003, in SPIE Conf. Ser. 4841, ed. M. Iye, & A. F. M. Moorwood, 459
Rousset, G., Lacombe, F., Puget, P., et al. 2003, in SPIE Conf. Ser. 4839, ed. P. L. Wizinowich, & D. Bonaccini, 140
Schechter, P. L., Mateo, M., & Saha, A. 1993, PASP, 105, 1342
Schlegel, D. J., Finkbeiner, D. P., & Davis, M. 1998, ApJ, 500, 525
Stansberry, J. A., & Yelle, R. V. 1999, Icarus, 141, 299
Sumi, T., Bennett, D. P., Bond, I. A., et al. 2010, ApJ, 710, 1641
Udalski, A., Jaroszyński, M., Paczyński, B., et al. 2005, ApJ, 628, L109

Appendix A: Zeropoints and uncertainties

Table A.1. Overview of applied calibrations and transformations between the photometric instrumental systems of IRSF and NACO into the 2MASS system.

Band	Photometric calibration	Number of stars used (after last clipping)
	IRSF single epoch	
J	$J_{\rm IRSF,2MASS} = 22.854 \pm 0.005 + J_{\rm IRSF,inst} - 0.046\ (J_{\rm IRSF,inst} - H_{\rm IRSF,inst}) + 0.015$	279
H	$H_{\rm IRSF,2MASS} = 22.919 \pm 0.003 + H_{\rm IRSF,inst} + 0.016\ (J_{\rm IRSF,inst} - H_{\rm IRSF,inst}) + 0.024$	451
Ks	$K_{\rm IRSF,2MASS} = 22.146 \pm 0.003 + K_{\rm IRSF,inst} + 0.010\ (J_{\rm IRSF,inst} - K_{\rm IRSF,inst}) + 0.014$	502
	NACO epoch 1	
Zeropoints calibrated against IRSF using star "1" (adopted)		*stars "1" + "2"*
J	$24.247 \pm 0.018 + J_{\rm NACO,inst}$	(24.254 ± 0.007)
H	$24.012 \pm 0.017 + H_{\rm NACO,inst}$	(23.987 ± 0.028)
Ks	$23.128 \pm 0.017 + K_{\rm NACO,inst}$	(23.105 ± 0.020)
	NACO epoch 2	
Zeropoints calibrated against IRSF using star "1" (adopted)		*stars "1" + "2"*
J	$24.315 \pm 0.018 + J_{\rm NACO,inst}$	(24.345 ± 0.030)
H	$24.024 \pm 0.017 + H_{\rm NACO,inst}$	(24.030 ± 0.060)
Ks	$23.067 \pm 0.017 + K_{\rm NACO,inst}$	(23.091 ± 0.023)
Zeropoints aligned with respect to epoch 1 [within 4″ of target]		
J	$24.289 \pm 0.019 + J_{\rm NACO,inst}$	8
H	$24.036 \pm 0.012 + H_{\rm NACO,inst}$	10
Ks	$23.116 \pm 0.008 + K_{\rm NACO,inst}$	10

Notes. The derived zeropoints for NACO are consistent with zeropoints from NACO based on regularly taken standard stars (after correction for atmospheric extinction) and that we do not find a color term between the NACO and 2MASS system.

Table A.2. Parameter values and MCMC uncertainties.

Parameter	Value	2-σ range
M	$0.084^{+0.015}_{-0.012}\,M_\odot$	0.062–0.120 $M_\odot$
m	$3.2^{+5.2}_{-1.8}\,M_\oplus$	0.8–14.8 $M_\oplus$
a	$0.66^{+0.51}_{-0.22}$ AU	0.35–3.17 AU
$D_{\rm L}$	$0.70^{+0.21}_{-0.12}$ kpc	0.5–1.4 kpc
$I_{\rm S}$	21.59 ± 0.07	21.46–21.64
q	$1.1^{+1.9}_{-0.6} \times 10^{-4}$	$0.3–5.2 \times 10^{-4}$

Table A.3. Fit parameters for the 8 distinct planetary models for MOA-2007-BLG-192 consistent with the NACO data.

Fit	χ^2	$t_{\rm E}$	t'_0	u_0	d	θ	q	t_*	$I_{\rm s}$	$\pi_{\rm E}$	$\phi_{\rm E}$
A	1121.12	82.5	5.442	0.00309	0.912	236.9°	3.7×10^{-5}	0.040	21.61	1.51	208.5°
B	1121.16	83.2	5.442	0.00306	1.120	236.8°	3.7×10^{-5}	0.041	21.62	1.49	208.7°
C	1121.66	82.9	5.456	–0.00349	0.807	105.5°	3.4×10^{-4}	0.041	21.60	1.47	209.2°
D	1122.08	83.5	5.448	–0.00296	1.113	121.9°	5.8×10^{-5}	0.041	21.62	1.44	209.8°
E	1125.41	83.2	5.454	0.00306	0.890	240.1°	7.6×10^{-5}	0.048	21.61	1.19	337.5°
F	1125.44	82.5	5.454	0.00309	1.118	239.9°	7.5×10^{-5}	0.049	21.60	1.16	332.3°
G	1125.48	81.8	5.450	–0.00313	0.897	120.3°	6.4×10^{-5}	0.049	21.60	1.13	336.5°
H	1125.50	80.8	5.450	–0.00309	1.110	120.6°	6.1×10^{-5}	0.048	21.61	1.19	337.8°

Notes. $t'_0 = t_0 - 4240$ days. t_0 and u_0 are the time and distance of the closest approach of the source to the lens center-of-mass. q and d are the planet: star mass ratio and separation, and θ is the angle between the source trajectory and the planet-star axis. $I_{\rm s}$ is the best-fit source magnitude, and $\pi_{\rm E}$ and $\phi_{\rm E}$ are the magnitude and angle of the microlensing parallax vector. The units for the Einstein radius crossing time, $t_{\rm E}$, the source radius crossing time, t_*, and t'_0 are days, and all other parameters are dimensionless.

The Astrophysical Journal, 794:159 (25pp), 2014 October 20 doi:10.1088/0004-637X/794/2/159

A STATISTICAL ANALYSIS OF SEEDS AND OTHER HIGH-CONTRAST EXOPLANET SURVEYS: MASSIVE PLANETS OR LOW-MASS BROWN DWARFS?*

Timothy D. Brandt[1], Michael W. McElwain[2], Edwin L. Turner[3,4], Kyle Mede[5], David S. Spiegel[1], Masayuki Kuzuhara[5,6,7], Joshua E. Schlieder[8], John P. Wisniewski[9], L. Abe[10], B. Biller[11], W. Brandner[8], J. Carson[12], T. Currie[13], S. Egner[14], M. Feldt[8], T. Golota[14], M. Goto[15], C. A. Grady[2], O. Guyon[14], J. Hashimoto[6], Y. Hayano[14], M. Hayashi[6], S. Hayashi[14], T. Henning[8], K. W. Hodapp[16], S. Inutsuka[17], M. Ishii[14], M. Iye[6], M. Janson[18], R. Kandori[6], G. R. Knapp[3], T. Kudo[6], N. Kusakabe[6], J. Kwon[6,19], T. Matsuo[6], S. Miyama[20], J.-I. Morino[6], A. Moro-Martín[21], T. Nishimura[14], T.-S. Pyo[14], E. Serabyn[22], H. Suto[6], R. Suzuki[6], M. Takami[23], N. Takato[14], H. Terada[14], C. Thalmann[24], D. Tomono[14], M. Watanabe[25], T. Yamada[26], H. Takami[14], T. Usuda[14], and M. Tamura[5,6]

[1] Institute for Advanced Study, Princeton, NJ, USA
[2] Exoplanets and Stellar Astrophysics Laboratory, Goddard Space Flight Center, Greenbelt, MD, USA
[3] Department of Astrophysical Sciences, Princeton University, Princeton, NJ, USA
[4] Kavli Institute for the Physics and Mathematics of the Universe (WPI), Todai Institutes for Advanced Study, University of Tokyo, Tokyo, Japan
[5] University of Tokyo, Tokyo, Japan
[6] National Astronomical Observatory of Japan, Tokyo, Japan
[7] Tokyo Institute of Technology, Tokyo, Japan
[8] Max Planck Institute for Astronomy, Heidelberg, Germany
[9] HL Dodge Department of Physics and Astronomy, University of Oklahoma, Norman, OK, USA
[10] Laboratoire Hippolyte Fizeau, Nice, France
[11] University of Edinburgh, Edinburgh, Scotland, UK
[12] College of Charleston, Charleston, SC, USA
[13] Department of Astronomy and Astrophysics, University of Toronto, Toronto, ON, Canada
[14] Subaru Telescope, Hilo, Hawai'i, USA
[15] Universitäts-Sternwarte München, Munich, Germany
[16] Institute for Astronomy, University of Hawai'i, Hilo, HI, USA
[17] Department of Physics, Nagoya University, Nagoya, Japan
[18] Queens University Belfast, Belfast, UK
[19] Department of Astronomical Science, Graduate University for Advanced Studies, Tokyo, Japan
[20] Hiroshima University, Higashi-Hiroshima, Japan
[21] Space Telescope Science Institute, Baltimore, MD, USA
[22] Jet Propulsion Laboratory, California Institute of Technology, Pasadena, CA, USA
[23] Institute of Astronomy and Astrophysics, Academia Sinica, Taipei, Taiwan
[24] Institute for Astronomy, ETH Zürich, Zürich, Switzerland
[25] Department of Cosmosciences, Hokkaido University, Sapporo, Japan
[26] Astronomical Institute, Tohoku University, Sendai, Japan
Received 2014 April 21; accepted 2014 August 29; published 2014 October 7

ABSTRACT

We conduct a statistical analysis of a combined sample of direct imaging data, totalling nearly 250 stars. The stars cover a wide range of ages and spectral types, and include five detections (κ And b, two $\sim$60 M_J brown dwarf companions in the Pleiades, PZ Tel B, and CD−35 2722B). For some analyses we add a currently unpublished set of SEEDS observations, including the detections GJ 504b and GJ 758B. We conduct a uniform, Bayesian analysis of all stellar ages using both membership in a kinematic moving group and activity/rotation age indicators. We then present a new statistical method for computing the likelihood of a substellar distribution function. By performing most of the integrals analytically, we achieve an enormous speedup over brute-force Monte Carlo. We use this method to place upper limits on the maximum semimajor axis of the distribution function derived from radial-velocity planets, finding model-dependent values of $\sim$30–100 AU. Finally, we model the entire substellar sample, from massive brown dwarfs to a theoretically motivated cutoff at $\sim$5 M_J, with a single power-law distribution. We find that $p(M, a) \propto M^{-0.65\pm0.60} a^{-0.85\pm0.39}$ (1σ errors) provides an adequate fit to our data, with 1.0%–3.1% (68% confidence) of stars hosting 5–70 M_J companions between 10 and 100 AU. This suggests that many of the directly imaged exoplanets known, including most (if not all) of the low-mass companions in our sample, formed by fragmentation in a cloud or disk, and represent the low-mass tail of the brown dwarfs.

Key words: brown dwarfs – methods: statistical – open clusters and associations: general – planetary systems – stars: activity – stars: imaging

Online-only material: color figures, machine-readable table

1. INTRODUCTION

Since the first exoplanet around a main-sequence star was discovered in 1995 (Mayor & Queloz 1995), large radial velocity (RV; e.g., Cumming et al. 2008; Bonfils et al. 2013) and transit surveys (Bakos et al. 2004; Pollacco et al. 2006; Batalha et al. 2013) have found many hundreds of worlds. Previous models of planet formation, extending back decades (e.g., Kuiper 1951; Hayashi 1981), were based heavily on the solar system. New discoveries have enabled a much fuller characterization of exoplanets within $\sim$3 AU of their host stars, around both main sequence (Cumming et al. 2008) and evolved (Johnson et al.

* Based on data collected at Subaru Telescope, which is operated by the National Astronomical Observatory of Japan.

2007b) systems. These distributions hold clues to the formation and subsequent dynamical evolution of planetary systems.

While constraints on the mass function of planets have only recently been determined, the initial mass function (IMF) of stars has been studied for many decades (Salpeter 1955), and is now well-constrained. The stellar IMF has also recently been extended to brown dwarfs (Kroupa 2001; Reid et al. 2002; Chabrier 2003), objects below the minimum mass ($\sim$80 M_J) necessary to sustain hydrogen fusion, but above the minimum mass for deuterium burning ($\sim$13 M_J). Large samples of substellar objects are difficult to assemble, both because brown dwarfs have a limited supply of internal energy, and because the IMF turns over near the hydrogen-burning boundary. Brown dwarfs are also uncommon as close companions to main-sequence stars, a phenomenon known as the "brown dwarf desert" (Marcy & Butler 2000; Grether & Lineweaver 2006). The companion mass function (CMF) rises from this "desert" both toward higher, stellar masses, and toward lower, planetary masses.

The CMF, well-established at small separations from RV surveys (Cumming et al. 2008), is much less clear at tens of AU. The conditions in a protoplanetary disk are very different far from the host star and may not support the formation mechanism responsible for the RV distribution (Dodson-Robinson et al. 2009), though such a conclusion is far from certain (Lambrechts & Johansen 2012; Kenyon & Bromley 2009). Companions near or below the deuterium-burning limit might form like stars in gravitational collapse or fragmentation (Boss 1997; Vorobyov 2013), by core-accretion in situ (Pollack et al. 1996; Alibert et al. 2005), or they might form in a location more conducive to planet formation and subsequently migrate or be scattered to their observed orbits. The distribution function of such objects could provide important clues to their formation mechanism, and connect them to either more massive brown dwarfs or to the planet populations observed at smaller separations. As a result, these massive exoplanets are being heavily targeted using large telescopes with adaptive optics.

The sensitivity to exoplanets with direct imaging has been rapidly improving, and recent discoveries have begun to fill the parameter space of substellar objects at separations of tens of AU. Companions near or below the deuterium burning limit have been discovered around the M-dwarfs 2MASS J01225093-2439505 (Bowler et al. 2013), 2MASS J01033563-5515561AB (Delorme et al. 2013), and ROXs 42B (Currie et al. 2014), the G-dwarf GJ 504 (Kuzuhara et al. 2013), the A stars HR 8799 (Marois et al. 2008, 2010), β Pictoris (Lagrange et al. 2009), and HD 95086 (Rameau et al. 2013), and the late B star κ And (Carson et al. 2013). These detections were made possible by recent technological advances in adaptive optics and the use of differential imaging techniques. In addition, recent work to identify nearby members of young moving groups (MGs; e.g., Torres et al. 2008; Zuckerman et al. 2011; Schlieder et al. 2012; Shkolnik et al. 2012; Malo et al. 2013; Moór et al. 2013; Rodriguez et al. 2013; Gagné et al. 2014) and stars that harbor debris disks (Rieke et al. 2005; Chen et al. 2006; Plavchan et al. 2009; Moór et al. 2011; Eiroa et al. 2011) has provided excellent targets for direct imaging searches. The stellar age is particularly important because substellar objects are unable to sustain hydrogen fusion in their cores, and quickly fade beneath the sensitivity limits of the best observing facilities on the ground and in space.

Over the last decade, numerous direct imaging surveys around nearby young stars have begun to constrain the distribution and frequency of substellar companions. These have mostly used non-detections to place upper limits on the planet fraction within a range of masses and semimajor axes, or upper limits beyond which the distribution function measured by RV surveys cannot extend. Lafrenière et al. (2007) used the Gemini Deep Planet Survey (GDPS) to place upper limits of $\sim$10% on the fraction of stars with 0.5–13 M_J companions in the range from 50 to 250 AU, assuming an RV-like mass distribution. Nielsen & Close (2010) used a sample of 118 targets, dominated by the GDPS, to find that the RV distribution of Cumming et al. (2008) cannot be extrapolated past a_{max} from $\sim$65–200 AU depending on the substellar cooling model and on the correlation between planet frequency and stellar mass. Chauvin et al. (2010) imaged 88 stars, around which they detected three substellar companions, including an $\sim$8 M_J companion to the brown dwarf 2M1207 and a $\sim$13 M_J companion to AB Pic. More recently, Vigan et al. (2012) placed a lower limit to the planet ($<$13 M_J) frequency around A stars of 6% based on the International Deep Planet Survey and the detections around HR 8799 and β Pictoris. Biller et al. (2013) placed a similar model-dependent upper limit of 6%–18% for companions from 1–20 M_J between 10 and 150 AU around later-type stars. Chauvin et al. (2014) observed 86 stars without detecting substellar companions, placing an upper limit of 10% on 5–10 M_J objects 50–500 AU from young solar-type stars. However, the distribution function for these companions remains uncertain, and statistical analyses often artificially truncate it at or near the deuterium burning threshold.

In this work, we provide a new framework for determining the distribution function of substellar companions to stars, and apply this framework to the published sub-sample of the Subaru SEEDS survey, combined with the publicly available GDPS (Lafrenière et al. 2007) and NICI MG sample (Biller et al. 2013). In Section 2, we discuss what is currently known about the stellar and substellar mass distributions. In Section 3, we present our combined data set, and in Section 4, we summarize our method for deriving their age probability distributions; in Section 5, we discuss our choice of substellar cooling models. We present our statistical framework and method for determining constraints on the substellar distribution function in Section 6, with additional details, derivations, and fitting functions in the Appendix. Section 7 presents and discusses our results, including our limits on an extrapolated RV-like distribution function, and the ability of a single distribution to include most or all wide-separation substellar objects. We conclude with Section 8.

2. A TAIL OF TWO DISTRIBUTIONS

In spite of their rarity, brown dwarf and very massive ($\gtrsim$10 M_J) giant planet companions are now being discovered at wide separations around nearby stars, both by dedicated high-contrast surveys and by mid-infrared space missions such as the *Wide-field Infrared Survey Explorer*. In contrast, less-massive exoplanets at wide separations remain extremely scarce: only two known companions to stellar primaries are likely to have masses less than 5 M_J: GJ 504b (Kuzuhara et al. 2013), and HD 95086b (Rameau et al. 2013). LkCa 15b (Kraus & Ireland 2012) and, especially, Fomalhaut b (Kalas et al. 2008; Janson et al. 2012; Currie et al. 2012) may also fall into this category, though their natures remain unclear. The paucity of known $\sim$3–5 M_J companions might indicate a lack of planets rather than simply our inability to detect them. High-contrast surveys have now observed $\sim$1000 nearby stars, often with sensitivities to objects significantly less massive than those detected around β Pictoris and HR 8799 at moderate to wide separations ($\gtrsim$1″).

The mass distribution function of short-period companions, as determined by RV surveys, is now well-determined. It decreases sharply from $\sim$1 M_J to $\sim$20 M_J, then increases toward stellar masses (Marcy & Butler 2000; Grether & Lineweaver 2006). Cumming et al. (2008), using eight years of RV data and assuming $dN/dM \propto M^{\beta}$, find $\beta_{pl} = -1.31 \pm 0.2$ for $M_{pl} > 0.3\,M_J$ and periods <2000 days. The relative lack of companions in the mass range from $\sim$10 M_J to $\sim$40 M_J is known as the brown dwarf desert. This "desert," however, is significantly less pronounced at wider separations (Gizis et al. 2001; Metchev & Hillenbrand 2009).

Recent discoveries have illuminated the brown dwarf mass function in the field, favoring a power law index $\beta_{BD} \sim 0$ for a mass distribution of the form $dN/dM \propto M^{\beta}$. The mass distribution is certainly not an extension of that of low-mass stars (Kroupa 2001; Reid et al. 2002; Chabrier 2003), and the best-fitting piecewise power law may be discontinuous (Thies & Kroupa 2007). Thies & Kroupa (2008) find a best fit $\beta_{BD} \sim -0.3$ using young clusters, while Kirkpatrick et al. (2012) find $0 \lesssim \beta_{BD} \lesssim 0.5$ in the very nearby field, and Sumi et al. (2011) report $\beta_{BD} = -0.49^{+0.27}_{-0.24}$ based on gravitational microlensing events. Sumi et al. (2011) hypothesized a distribution of low-mass "rogue planets" in the field to explain their shortest duration microlensing events, and found $\beta = -1.3^{+0.4}_{-0.3}$ for such a population, consistent with that found for RV companions. A value $\beta_{BD} = 0$ corresponds to equal numbers of objects at all brown dwarf masses, with most of the matter residing in massive objects.

The brown dwarf mass function in binaries is more controversial. Metchev & Hillenbrand (2009), in a high-contrast imaging survey of young stars, found their data to be consistent with a single power law CMF with $\beta \approx -0.4$ extending all the way from 1 $M_\odot$ down to the deuterium-burning limit of $\sim$13 M_J. This result is strongly inconsistent with the distribution of companion masses seen at small separations. In contrast, Zuckerman & Song (2009) derived the brown dwarf CMF from a survey of objects reported in the literature, and found a much steeper $\beta \sim -1.2$. However, hydrodynamical simulations disfavor such a strong peak at low masses, with Stamatellos & Whitworth (2009) finding a relatively flat distribution of cloud fragment masses over the brown dwarf regime.

As with the mass distribution, the semimajor axis distributions for stellar binaries and for close ($\lesssim$3 AU) exoplanets are both well-determined. Cumming et al. (2008) find $\alpha = -0.61 \pm 0.15$ for $dN/da \propto a^{\alpha}$ in the range from 0.03–3 AU, i.e., a distribution with planet incidence decreasing with separation, but still divergent if integrated to infinity. The semimajor axis distribution of companions to G-dwarfs is approximately log-normal, with a peak in the distribution at $\sim$30–50 AU for a star of 1 $M_\odot$ (Duquennoy & Mayor 1991; Raghavan et al. 2010). In the range $5 < a < 500$ AU, the space most relevant to high-contrast imaging, the observed distribution is very nearly flat in $\log a$ (varying by $\sim$30%).

The mass (and separation) ranges over which the planet and brown dwarf distributions apply are controversial. The IAU draft definition of a planet is simply any object which is both bound to a star and below the minimum mass for deuterium burning, currently calculated to be $\sim$13 M_J (Spiegel et al. 2011). However, this criterion holds no other physical significance and is independent of the object's formation mechanism. Brown dwarfs are thought to form like stars, and, though the minimum fragment mass is not known precisely, it is likely to fall at around 5 M_J (Low & Lynden-Bell 1976; Bate et al. 2003; Bate 2009). Some studies (Bate et al. 2003; Umbreit et al. 2005) suggest that brown dwarfs form when they are ejected from dynamically unstable systems, making it extremely difficult to form substellar companions to solar-type stars by cloud fragmentation. However, in the outer regions of a disk rather than in a molecular cloud, fragmentation may be more likely to produce substellar objects (Boss 1997), though the lower mass cutoff is still likely to be several M_J (Rafikov 2005; Whitworth & Stamatellos 2006).

Substellar objects near or below the deuterium burning limit of $\sim$13 M_J have been discovered at separations from $\sim$40 AU to $\sim$1000 AU around stars ranging in spectral type from late M to late B (e.g., Chauvin et al. 2005b; Marois et al. 2008; Lagrange et al. 2009; Bowler et al. 2013; Carson et al. 2013; Currie et al. 2014). Two recent discoveries, GJ 504b (Kuzuhara et al. 2013) and HD 95086b (Rameau et al. 2013), plus HR 8799b (Sudol & Haghighipour 2012), push the mass range of such companions down to $\sim$5 M_J. If these objects could form by core-accretion (Pollack et al. 1996; Alibert et al. 2005; Lambrechts & Johansen 2012), believed to be responsible for gas giants at smaller separations, they might be an extension of the RV distribution (nearly all planets of which, presumably, formed via core accretion). If, however, they form by fragmentation in a cloud or disk (e.g., Boss 1997; Vorobyov 2013), they should be considered together with low-mass brown dwarfs, and perhaps with the entire substellar distribution up to a mass of $\sim$0.1 $M_\odot$, where the IMF turns over and starts rising toward higher mass. It is also possible that more than one of these distributions overlap in parameter space, and that the sample of direct-imaging discoveries is a heterogeneous population with multiple modes of formation (Boley 2009).

Because many discoveries straddle the deuterium burning threshold (depending on the assumed age of the system and on the substellar cooling model), and because there is no theoretical motivation to separate objects at 13 M_J, we consider giant planets and low-mass brown dwarfs together. It is certainly possible that the most massive brown dwarfs ($\gtrsim$50 M_J) are drawn from a different distribution, but we see no reason to impose such a division a priori, particularly not at 13 M_J. The form of the distribution function and its limits in mass and semimajor axis should be powerful clues to the formation mechanism at work. We note, however, that we are still limited by our reliance on uncertain models of substellar cooling and by our parameterization of the distribution function with limited theoretical motivation.

3. HIGH-CONTRAST IMAGING DATA SET

We merge five samples to create our high-contrast data set: three published subgroups of the Strategic Exploration of Exoplanets and Disks with Subaru project (SEEDS; Tamura 2009), the GDPS (Lafrenière et al. 2007), and the MG targets from the NICI survey (Biller et al. 2013). We discuss each of these in turn. In total, our merged survey contains 248 unique stars with spectral types ranging from late B to mid M, at distances from $\sim$5 pc to $\sim$130 pc, with sensitivities down to $\sim$1 M_J around the nearest, youngest targets. We reduce most of the data, including that of GDPS targets but excepting the NICI stars, using ACORNS-ADI (Brandt et al. 2013); for GDPS stars, our results are very similar to those published in Lafrenière et al. (2007). For the NICI data, we use the published reductions as described by Wahhaj et al. (2013a).

After reviewing each of the five samples, we apply a uniform, Bayesian analysis to compute age probability distributions.

This analysis combines proposed MG membership, rotation and activity indicators, all of which are listed in Table 1. We provide a summary in Section 4, with the full procedure described in Brandt et al. (2014). The secondary age indicators of the SEEDS MG sample are listed in Brandt et al. (2014), while the indicators for the other samples are listed in Table 1. Our age analysis also requires us to estimate the probability of MG membership for each target. Most of our targets are either consensus members of a MG (listed as 95% + probability in Table 1) or consensus nonmembers, though a few are more uncertain. We briefly discuss each such case, including our adopted MG classification and membership probability, in Section 3.4.

In addition to the 248 stars in this sample, we consider two additional stars around which HiCIAO has detected substellar companions: GJ 758B (Thalmann et al. 2009; Janson et al. 2011), a $\sim$30 M_J brown dwarf around an old G star first imaged during HiCIAO commissioning, and GJ 504b (Kuzuhara et al. 2013; Janson et al. 2013a), a $\sim$3–8 M_J companion to an active field G star discovered during the full SEEDS survey. By using these discoveries in part of our statistical analysis, we assume that the stars and contrast curves of $\sim$200 as-yet-unpublished SEEDS targets are similar to those of the merged sample we discuss in this section. This is a fairly good approximation; in fact, the unpublished SEEDS targets are primarily a combination of relatively distant ($\sim$100 pc), very young ($\sim$5–10 Myr) pre-main-sequence stars, and very nearby stars ($\sim$5–50 pc) with a wide range of ages (tens of Myr to several Gyr) and spectral types (A through M).

3.1. SEEDS

SEEDS (Tamura 2009) is now mostly complete, having observed nearly 400 nearby stars with the high-contrast camera HiCIAO (Suzuki et al. 2010) behind the 188 actuator adaptive optics system AO188 (Hayano et al. 2008). For this study, we use the previously published data sets comprised of debris disk hosts (Janson et al. 2013b), proposed members of nearby MGs (Brandt et al. 2014), and Pleiades members (Yamamoto et al. 2013). The Pleiades targets are young, with ages that are better-constrained than those of typical field stars.

The SEEDS MG sample is described in detail in Brandt et al. (2014). That work includes stellar age indicators and Bayesian age estimates for all targets, both those that are reliable members of coeval MGs and those that are not. We adopt those indicators and ages throughout the rest of this work. There is much less controversy over membership in the Pleiades, a rich, young (125 ± 8 Myr; Stauffer et al. 1998) stellar cluster at a distance of $\sim$130 pc. There is, however, considerable controversy over the distance to the Pleiades, with *Hipparcos* parallaxes favoring a value of 120 pc (van Leeuwen 2009), against isochrone fitting and other techniques giving a value about 10% larger (An et al. 2007; Munari et al. 2004). These differences are of marginal significance to our work. We adopt a distance of 130 ± 10 pc for all imaged Pleiades targets, together with a slightly more conservative age of 125 ± 10 Myr.

The MG sample includes one substellar detection, κ And b (Carson et al. 2013). The object lies at a projected separation of 55 AU, and has a mass of $\sim$13 M_J assuming the primary, κ And, to be a member of the $\sim$30 Myr Columba MG. Recent papers have called its Columba membership into question due to the star's position on the color–magnitude diagram, which hints at an age of several hundred Myr and a mass of $\sim$50 M_J for the companion (Hinkley et al. 2013; Bonnefoy et al. 2014). The Pleiades targets include two substellar detections: H II 1348B (Geißler et al. 2012) and HD 23514B (Rodriguez et al. 2012). H II 1348B and HD 23514B lie at projected separations of 140 and 310 AU respectively, and each has a mass of $\sim$60 M_J. Neither discovery was published when the SEEDS observations were made.

The debris disk sample has its stellar properties listed in Table 4 of Janson et al. (2013b). For this work, we revisit the ages using the Bayesian techniques presented in Brandt et al. (2014) and summarized in Section 4.

3.2. GDPS

GDPS (Lafrenière et al. 2007) used the NIRI instrument on Gemini-North to take high-contrast near-infrared images of 85 nearby stars. The stars ranged from F to M dwarfs, and were selected to be young, as inferred from their membership in kinematic MGs or from fits to color–magnitude isochrones. As for our other data sets, we generally do not consider isochrone ages. These are typically unreliable for main-sequence stars that have completed $\lesssim$ one-third of their main-sequence lives (Soderblom 2010, and references therein), precisely those that we are most interested in dating. We do consider isochrones in some cases where a MG identification is in doubt (Brandt et al. 2014). GDPS did not detect any substellar companions to its targets, though the survey did find several new stellar binaries.

3.3. NICI

We also include the unique stars added by the southern sample observed by Biller et al. (2013) using the NICI instrument on Gemini-South. To enable a straightforward comparison to the data from the other surveys, we consider only those stars observed with angular differential imaging in the *H*-band, excluding those targets with spectral differential imaging. Biller et al. (2013) also report 95% completeness levels rather than 5σ (or 5.5 or 6σ) thresholds, where σ is the standard deviation of the background at a given separation. In order to convert these levels into a common framework with the values reported by other surveys, we assume the residuals to be Gaussian (a very good approximation for SEEDS and GDPS). A 95% completeness threshold, assuming a 5σ minimum for follow-up, corresponds to a source bright enough to be detected if it were located on 95% of the background fluctuations. Given that a Gaussian distribution with zero mean has 95% of its probability above -1.64σ, a 6.64σ source would be detected at 5σ or better 95% of the time. We therefore convert the 95% limits to 5σ sensitivity curves by adding

$$2.5 \log_{10} \frac{6.64}{5} \approx 0.31 \text{ mag}, \quad (1)$$

and proceed to include the modified sensitivity curves in the remainder of our analysis. The NICI sample includes two substellar detections: a $\sim$35 M_J brown dwarf around HIP 92680 (= PZ Tel; Biller et al. 2010), and a $\sim$30 M_J brown dwarf around TYC 7084-794-1 (= CD−35 2722; Wahhaj et al. 2011). HD 1160 was not in the NICI MG sample, so its brown dwarf companion (Nielsen et al. 2012) does not enter our analysis.

3.4. Targets with Uncertain MG Membership

Most of the stars in our combined sample are either very high probability members of a given MG (95% + in Table 1), or are unlikely to be members of any known MG. We generally consider a star to be an uncontroversial MG member if it has a 99% or higher membership probability as given by Malo

Table 1
Secondary Age Indicators

Name HIP/HD/GJ/Other	Moving Group	Prob. Member[a]	log R'_{HK}[b]	log R_X[c]	Li EW (mÅ)/ log A[d]	P_{rot} (days)	References[e]
SEEDS Debris Disk Targets							
HIP 682	...	...	−4.38	−4.15	150	...	T06
HIP 5944	...	...	−4.47	−4.68	[A] 2.73	5.67	Mi12, G00
HIP 6878	...	...	−4.43	−4.34	48	3.13	W07, W11
HIP 7345	...	...	...	<−5.89	...	...	...
HIP 7576	β Pic	95+	−4.49	−4.43	103	7.15	L06, S09
HIP 9141	Tuc-Hor	95+	−4.22	−3.97	190	3.02	T06, W11
HIP 11360	Columba	85	...	−4.86	...	...	...
HIP 11847	β Pic	50	...	<−4.69	...	...	...
HIP 13402	β Pic	20	−4.36[f]	−3.90	224	6.76	W07, W11
HIP 18859	AB Dor	95+	−4.40	−4.16	...	...	...
HD 281691	...	...	−3.97	−3.13[g]	345	2.65	W07, W11
HIP 22845	...	...	...	<−6.31	...	...	...
HIP 28103	...	...	...	−5.75	...	...	...
HIP 37170	...	...	−4.38	−4.26	107	...	W07
HIP 40693	...	...	−5.03	−5.90	2.5	...	T05
HD 70573	...	...	−4.16	−4.09	166	3.30	W07, S09
HIP 42333	...	...	−4.55	−4.78[g]	[A] 2.35	6.14	T05, G00
HIP 42430	...	...	−5.11	−6.03[g]	...	...	...
HIP 42438	UMa	60	−4.37[f]	−4.45	120	4.89	W07, G00
HIP 43726	...	...	−4.64[f]	−5.25	19	...	T05
HIP 49809	...	...	...	−6.22	...	...	...
HIP 51658	...	...	...	<−6.27	...	...	...
HIP 52462	...	...	−4.40	−4.37	138	13.5	T06, S09
HIP 57632	Argus	90	...	<−7.29	...	...	...
HIP 58876	...	...	−4.36	−4.36	122	...	W07
HIP 59774	UMa	95+	...	<−6.77	...	...	...
HIP 60074	...	...	−4.33	−4.33	123	7.13	W07, K02
HIP 61174	...	...	...	−5.59	...	...	...
HIP 61498	TW Hya	95+	...	−5.24	550[h]	...	D09
HIP 61960	...	...	...	<−6.22	...	...	...
HIP 63076	...	...	...	<−6.08	...	...	...
HIP 63584	...	...	...	−5.00[g]	...	...	...
HIP 69732	...	...	...	<−6.80	...	...	...
HIP 70952	...	...	...	−5.03	...	...	...
HIP 71284	...	...	...	−5.55	3	...	T05
HIP 71395	...	...	−4.52	−4.47	[A] −0.3	11.5	M08, W11
HIP 74702	...	...	−4.50	<−5.18	1.4	5.97	G09, G00
HIP 76267	UMa	95+	...	−6.64	...	...	...
HIP 76829	β Pic	84	...	−4.98	...	...	...
HIP 77542	...[i]	...	...	−4.45[g]	500[h]	...	F08
HIP 79977	USco	95+	...	<−4.27	66	...	C11
HIP 82587	...	...	...	−5.54	...	...	...
HIP 87108	...	...	...	<−6.61	...	...	...
HIP 87558	...	...	...	−5.33	...	...	...
HIP 92919	...	...	−4.23	−3.12	20	2.91	W07, P05
HIP 95793	...	...	...	<−5.80	...	...	...
HIP 99711	...	...	−4.64	−5.07	[A] −0.24	24.0	G10, S09
HIP 107649	...	...	−4.87	−5.61	38	...	T06
Non-SEEDS GDPS Targets							
HIP 919	...	...	−4.35	−4.19	122	6.05	W07, W11
HD 1405	AB Dor	95+	...	−2.90	267	1.76	D09, M10
HIP 4907	...	...	−4.48	−4.73	...	12.2	S09
HIP 7235	...	...	−4.63	−5.14	...	...	...
HIP 9291	Columba	75	...	−3.04	...	...	...
HIP 11072	...	...	−5.00	−4.51	50	...	T06
HIP 12530	...	...	−4.45	−4.54	...	...	...
HIP 12926	...	...	−4.93	<−5.08	...	...	...
HIP 13081	...	...	−4.57	−4.47	...	...	...
HIP 14150	...	...	−4.86	−6.03	3	...	T05
HIP 14954	...	...	−4.55	<−6.10	12	...	T05
HIP 15323	...	...	−4.47	−4.49	[A] 2.67	...	Go10
BD−19 660	...	...	...	<−3.53	...	...	...

Table 1
(Continued)

Name HIP/HD/GJ/Other	Moving Group	Prob. Member[a]	log R'_{HK}[b]	log R_X[c]	Li EW (mÅ)/ log A[d]	P_{rot} (days)	References[e]
HIP 16537	...	...	−4.52[f]	−4.68	1	11.68	T05, W11
HIP 17695	...	...	...	−3.07	0	3.87	D09, M10
HIP 21482	...	...	−4.06	−3.05	[A] 0.47	...	Mi12
HIP 22449	...	...	−4.71	−4.99	...	...	...
HIP 23200	β Pic	95+	−4.06	−3.20	270	1.86	T06, W11
HIP 30920	...	...	...	−3.30[g]	...	0.39	W11
HIP 37766	...	...	−3.62	−3.00	...	2.78	W11
HIP 43410	...	...	−4.50[f]	−4.35	...	...	...
HIP 44458	...	...	−4.30	−3.93[g]	170	2.86	W07, W11
HD 78141	...	...	...	−3.86	...	...	...
HIP 46816	...	...	−4.02	−3.01	245	1.70	W07, W11
HIP 51386	...	...	−4.46	−4.19	130	2.60	W07, W11
HIP 51931	...	...	−4.55	−4.92	...	...	...
HIP 52787	...	...	−4.46	−4.42	100	...	T06
HIP 54745	...	...	−4.42	−4.52	[A] 2.55	7.60	M08, W11
HIP 57370	...	...	−4.59	−5.12	[A] 0.46	12.3	G10, W11
HIP 57494	...	...	−4.92	<−4.35	...	...	...
HD 108767B	...	...	...	−4.47	...	...	...
BD+60 1417	...	...	...	−4.20	...	...	...
HIP 62523	...	...	−4.62	−5.08	[A] 1.5	15.8	M08, S09
HIP 63742	AB Dor	95+	−4.43	−4.26	142	6.47	D09, W11
HIP 65016	...	...	−4.91	<−4.47	...	...	...
HIP 65515	...	...	−4.47	−4.36	[A] 1.65	4.27	M08, S09
HIP 67092	...	...	...	<−4.11	...	...	...
HIP 69357	...	...	−4.60	−5.27	...	...	...
HD 234121	...	...	−4.28	−4.61	...	...	...
HIP 71631	...	...	−4.19[f]	−3.52	196	2.67	W07, W11
HIP 72146	...	...	−4.93	<−5.08	...	...	...
HIP 72339	...	...	−4.72	<−4.93	[A] 0.38	...	G10
HIP 72567	...	...	−4.46	−4.65	[A] 2.8	7.85	M08, S09
HIP 74045	...	...	−3.99	−2.92[g]	228	1.90	W07, W11
HIP 75829	...	...	−4.40	−3.80	145	...	W07
HIP 77408	...	...	−4.46	−4.41	[A] 0.50	14.05	M08, W11
HIP 79755	...	...	−4.92	−4.39	...	...	...
HIP 80824	...	...	−5.31	−5.11	...	...	...
HIP 81084	...	...	−4.53	−3.45	0	7.45	D09, M10
HIP 86346	AB Dor	95+	...	−3.02	40	1.84	D09, M10
HIP 87322	...	...	...	<−4.40	...	...	...
HIP 88848	...	...	−4.14	−2.98	179	...	W07
HIP 89005	...	...	...	−3.95	11	...	G09
HIP 97438	...	...	−3.77	−4.69	87	...	G09
HIP 101262	...	...	...	−4.99	...	...	...
HIP 104225	...	...	−4.97	<−5.24	...	...	...
HIP 105038	...	...	−4.56	−5.09	[A] −0.75	...	M08
HIP 106231	AB Dor	95+	...	−3.09	215	0.42	D09, M10
HIP 108156	...	...	−4.90	−5.23	[A] 0	4.51	M08, S09
V383 Lac	...	...	...	−3.06	270	2.47	W07, W11
HIP 112909	...	...	...	−3.06	...	1.64	N07
HIP 113020	...	...	...	<−4.16	...	...	...
HIP 115147	Columba	80	−4.16	−3.15	[A] 2.3	...	M08
HIP 116215	β Pic	20	−4.47	−4.51	0	...	T06
HIP 116384	...	...	...	−3.60	15	...	T06
HIP 117410	...	...	...	−3.47	0	...	T06
Non-SEEDS, non-GDPS NICI Moving Group ADI Targets							
HIP 560	β Pic	95+	...	−5.27	87	...	T06
HIP 1481	Tuc-Hor	95+	−4.37	−4.12	130	...	D09
HIP 2729	Tuc-Hor	95+	...	−3.23	360	0.37	D09, M10
HIP 5191	AB Dor	95+	...	−3.68	155	7.13	D09, M10
HIP 9685	Tuc-Hor	95+	...	−4.92	60	...	T06
HIP 12394	Tuc-Hor	95+	...	<−6.42	0	...	D09
TYC 8491-656-1	Tuc-Hor	95+	...	−2.99	298	1.28	D09, M10
AF Hor	Tuc-Hor	95+	...	−2.59	10	0.56	D09, K12
TYC 8497-995-1	Tuc-Hor	95+	...	−3.55	120	7.4	D09, M10
HIP 14684	AB Dor	95+	−4.38	<−4.27	191	5.5	D09, M10

Table 1
(Continued)

Name HIP/HD/GJ/Other	Moving Group	Prob. Member[a]	log R'_{HK}[b]	log R_X[c]	Li EW (mÅ)/ log A[d]	P_{rot} (days)	References[e]
TYC 5899-26-1	AB Dor	95+	...	−3.10	20	...	D09
TYC 8513-952-3	AB Dor	95+	...	−2.92	0	1.5	D09, M10
HIP 23309	β Pic	95+	...	−3.42	294	8.6	F08, M10
HIP 25283	AB Dor	95+	−4.32	−3.64	15	9.3	D09, M10
HIP 26373	AB Dor	95+	−4.21	−3.17	285	4.5	D09, M10
TYC 5361-1476-1	AB Dor	90	...	−3.50	230	5.6	D09, K12
TYC 7084-794-1	AB Dor	95+	...	−3.12	10	1.7	D09, M10
HIP 29964	β Pic	95+	−4.16	−2.83	357	2.7	F08, M10
HIP 30034	Car	95+	...	−3.16	320	3.9	D09, M10
HIP 30314	AB Dor	95+	−4.34	−4.14	150	0.48	D09, R12
GSC 08894-00426	AB Dor	95+	...	−2.84	0	1.0	D09, K12
GJ 9251 A	AB Dor	...	...	<−4.07	...	...	...
TWA 6	TW Hya	95+	...	−2.88	560	0.54	F08, M10
TWA 7	TW Hya	95+	...	−3.19	530	5.0	T06, M10
HIP 53911	TW Hya	95+	...	−2.12	426	2.8	F08, M10
TWA 14	TW Hya	95+	...	−2.89	600	0.63	F08, M10
TWA 13N	TW Hya	95+	...	−2.82	570	5.6	F08, M10
TWA 8A	TW Hya	95+	...	−2.92	530	4.7	F08, M10
TWA 9B	TW Hya	95+	...	−2.30	480	4.0	D09, M10
HIP 57589	TW Hya	95+	...	−2.88	470	5.0	F08, M10
TWA 25	TW Hya	95+	...	−3.05	494	5.1	F08, M10
TWA 20	TW Hya	95+	...	−3.37	160	0.65	F08, M11
TWA 10	TW Hya	95+	...	−3.02	460	8.4	F08, M10
TWA 11B	TW Hya	95+	...	−3.12	550	...	D09
TWA 11A	TW Hya	95+	...	−5.27	550	...	D09
HD 139084B	β Pic	95+	...	−1.58[g]	260	4.3	F08, M10
HD 155555C	β Pic	95+	...	−1.67[g]	250	1.7	D09, M10
TYC 8728-2262-1	β Pic	50	...	−3.08	360	1.8	D09, M10
HD 164249B	β Pic	95+	...	−3.01[g]	92	...	F08
HIP 92024	β Pic	95+	...	−5.64	490	0.35	T06, M10
TYC 9073-762-1	β Pic	80	...	−3.21	332	5.4	D09, M10
TYC 7408-54-1	β Pic	80	...	−3.04	492	1.1	D09, M10
HIP 92680	β Pic	95+	−3.82	−3.13	287	1.0	D09, M10
HIP 95261	β Pic	50	...	<−5.73	...	...	...
HIP 95270	β Pic	95+	...	<−4.39	120	...	D09
2MASS J19560294-3207186	β Pic	80	...	−2.85[g]	500	...	Mc12
TYC 7443-1102-1	β Pic	80	...	−3.00[g]	110	12	M11, Mc12
HIP 99273	β Pic	80	−4.59	−4.83	58	...	W07
HIP 104308	Tuc-Hor	80	...	<−5.34	...	...	...
HIP 107345	Tuc-Hor	95+	...	−3.22	55	4.5	D09, M10
TYC 9340-437-1	β Pic	95+	...	−2.90	440	4.5	D09, M10
HIP 112312	β Pic	95+	...	−2.68[g]	0	2.4	D09, M10
TX PsA	β Pic	95+	...	−2.31[g]	450	...	D09
TYC 5832-666-1	β Pic	95+	...	−3.05	185	5.7	D09, M10
HIP 118121	Tuc-Hor	95+	...	−5.79	...	...	...
Additional HiCIAO Detections							
HIP 64792 (GJ 504)	...	...	−4.45[f]	−4.42	83	3.3	T05, M03
HIP 95319 (GJ 758)	...	...	−5.08	<−5.04	2	...	T05

Notes.

[a] High-probability (95% +) members typically have a 99% + membership probability from Banyan (Malo et al. 2013), or a 95%+ probability from Banyan II (Gagné et al. 2014), plus an additional youth indicator. See Section 3.4 for details on other stars.

[b] From the catalog compiled by Pace (2013); see text for details. All targets bluer than $B - V = 0.45$ have been omitted.

[c] From the *ROSAT* satellite; see text for details.

[d] Logarithmic lithium abundances, A(H) = 12, are preceded by [A]. The other values are equivalent widths.

[e] References abbreviated as: C11 (Chen et al. 2011); D09 (da Silva et al. 2009); F08 (Fernández et al. 2008); G00 (Gaidos et al. 2000); G09 (Guillout et al. 2009); G10 (Gonzalez et al. 2010); (Ghezzi et al. 2010); K02 (Koen & Eyer 2002); K12 (Kiraga 2012); L06 (López-Santiago et al. 2006); M96 (Messina & Guinan 1996); M03 (Messina et al. 2003); M08 (Mishenina et al. 2008); M10 (Messina et al. 2010); M11 (Messina et al. 2011); Mi12 (Mishenina et al. 2012); Mc12 (McCarthy & White 2012); N07 (Norton et al. 2007); P05 (Pojmanski et al. 2005); S09 (Samus, & Durlevich 2009); T06 (Torres et al. 2006), T05 (Takeda & Kawanomoto 2005); W07 (White et al. 2007); W11 (Wright et al. 2011).

[f] R'_{HK} from multi-decade Mt. Wilson measurements (Baliunas et al. 1995; Radick et al. 1998; Lockwood et al. 2007).

[g] The star has a known binary companion that could contribute X-ray flux.

[h] Equivalent width in the secondary.

[i] Pre-main-sequence object with an age of 5 ± 1 Myr.

et al. (2013), or a 95% or higher membership probability according to Gagné et al. (2014; who updated Malo et al. to include non-uniform priors), together with at least one additional youth indicator. The Bayesian analyses of Malo et al. (2013) and Gagné et al. (2014) include position and proper motion and, where available, RV and parallax (giving a position in six-dimensional phase space). Not all of the high-probability members have RV and parallax measurements (e.g., most TW Hydrae stars were too faint for *Hipparcos*), but a Bayesian analysis accounts for this.

This section summarizes the information for those stars which fall short of our criteria for near-certain MG membership, but are still possible or likely members of a MG. All stars in the following summary have position, proper motion, parallax, and RV measurements unless otherwise noted.

3.4.1. SEEDS Debris Disk Targets

HIP 7345. Zuckerman & Song (2012) identify this early A star as a member of the Argus association, a classification definitively rejected by BANYAN II[27] at 99% probability. We decline to identify the star with any association.

HIP 7576. This mid-G star was classified in the Hercules–Lyra association, which we consider to be unreliable for dating (Brandt et al. 2014). It does show abundant youth indicators, and its kinematics and parallax also fit very nicely with the predictions for β Pic membership; BANYAN places it in β Pic with over 99% probability. We provisionally adopt the β Pic classification here, though the secondary age indicators are slightly more consistent with an age of several hundred Myr, rather than the ∼20 Myr of β Pic.

HIP 11360. This early F star is listed as a bona-fide member with ambiguous group membership (Malo et al. 2013). Torres et al. (2006) suggest membership in β Pic, while Malo et al. (2013) find a better fit with membership in Columba; the BANYAN II analysis (without a RV) also places a significant (∼15%) probability of field membership. We provisionally adopt the Columba classification, with its slightly older age, at 85% probability.

HIP 11847. The BANYAN web tool lists a 99% probability of β Pic membership for this early F star (with RV from Moór et al. 2011), though BANYAN II finds a probability of just ∼13%. Moór et al. (2011) also note a nearby star with similar space motions and strong youth indicators, supporting β Pic membership for both stars. HIP 11847 hosts a bright debris disk (Moór et al. 2011), and its isochrone-based age likelihood (see Brandt et al. 2014, for details) is consistent with an age from ∼20–200 Myr. For this work, we adopt a 50% probability of β Pic membership.

HIP 13402. BANYAN gives a ∼70% membership probability in β Pic for this early K star; BANYAN II gives 22%. It has abundant secondary age indicators, including vigorous X-ray and chromospheric activity, rapid rotation, and abundant lithium, all consistent with a very young age. We adopt the lower probability here.

HIP 57632. Zuckerman et al. (2011) classified this early A star as a member of the Argus association, which BANYAN II confirms, with a probability of just over 90%. We accept Argus membership with the latter's significance.

HIP 76829. This F4 star lacks any youth indicators apart from its kinematics, and has not been proposed as a bona fide member of any kinematic MG apart from the Hercules–Lyra association (López-Santiago et al. 2006), which we consider to be unreliable for dating (Brandt et al. 2014). The star is too massive to show strong magnetic activity. Its position on the color–magnitude diagram appears to be consistent with either an age of ∼20 Myr, consistent with β Pic, or several hundred Myr. For this analysis, we adopt BANYAN II's 84% membership probably in β Pic.

HIP 77542. This B9.5 star is a pre-main-sequence object with a relatively gas-rich disk (Merín et al. 2004), marking it as a very young object. We follow Merín et al. (2004) in adopting an age of 5 ± 1 Myr.

HIP 79977. This F2 star is a consensus member of the Upper Scorpuis OB association (de Zeeuw et al. 1999). We adopt an age of 11 ± 3 Myr for the association, consistent with two recent estimates (Pecaut et al. 2012; Song et al. 2012).

3.4.2. Non-SEEDS GDPS Targets

HIP 9291. BANYAN II places this mid-M star in Carina with ∼75% probability. It does show vigorous X-ray activity and is rapidly rotating, with $v \sin i \sim 15\,\mathrm{km\,s^{-1}}$ (Gnaciński 2005). Given these signs of youth, we provisionally accept the 75% probability estimate of Columba membership.

HIP 44458. This G0 star has very strong secondary youth indicators, including strong lithium absorption and rapid rotation. While BANYAN gives a 70% probability of membership in Columba, BANYAN II gives just 3%. We decline to identify the star with any MG, relying instead on its abundant secondary age indicators.

HIP 72339. BANYAN places this star in AB Dor with 96% probability based on its kinematics; BANYAN II gives a 24% probability of AB Dor membership. However, none of its youth indicators are consistent with such a young age; its lithium and activity levels are more consistent with an age of ∼1 Gyr. The isochrone-based likelihood shows two peaks, one around ∼50 Myr, and another around 1 Gyr. We therefore provisionally reject AB Dor membership.

HIP 105038. BANYAN places this K3 star in either Columba or β Pic with high probability based on its kinematics. However, its youth indicators favor a much older age, and BANYAN II places it in the field with over 90% probability. Similarly to HIP 72339, we provisionally reject Columba membership.

HIP 113020. This mid-M star, GJ 876, is known to host four planets discovered by RV (Delfosse et al. 1998; Marcy et al. 1998, 2001; Rivera et al. 2005, 2010). It has only a very weak upper limit on X-ray activity and a measurement of slow rotation (∼2 km s^{-1}, Gnaciński 2005) to corroborate BANYAN's 99.9% classification in β Pic (85% in BANYAN II). Marcy et al. (2001) estimate HIP 113020's age to be >1 Gyr due to its lack of activity, which would be exceptional in a ∼20 Myr old β Pic member. We decline to identify the star with any MG.

HIP 115147. This K1 star shows very strong chromospheric and X-ray activity, rapid rotation (∼16 km s^{-1}, Gnaciński 2005), and retains abundant lithium, all consistent with a young age. We therefore accept BANYAN's 80% probability in Columba membership.

HIP 116215. While BANYAN II places this mid-K star in β Pic with 77% probability, it lacks any detectable lithium, and shows only moderately vigorous chromospheric and coronal activity. We consider its membership to be doubtful, and provisionally assign a 20% membership probability in β Pic.

3.4.3. Non-SEEDS, Non-GDPS NICI MG ADI Targets

HIP 9685. This star is a high-probability (over 99% according to BANYAN II) member of Tuc-Hor neglecting a discrepant

[27] See http://www.astro.umontreal.ca/∼malo/banyan.php, http://www.astro.umontreal.ca/∼gagne/banyanII.php

RV. However, Biller et al. (2013) reported a $\sim$0.5 $M_{\odot}$ stellar companion at a projected separation of 0.″18 (9 AU), naturally explaining a 7–8 km s^{-1} shift in the RV. We therefore regard HIP 9685 as a reliable member of Tuc-Hor.

TYC 5899-26-1. With a measured RV (26.7 $\pm$ 1.5 km s^{-1} Schlieder et al. 2010) and parallax (61.4 $\pm$ 1.5 mas, Shkolnik et al. 2012), BANYAN II confirms AB Dor membership with 99.9% probability. This is consistent with the star's strong X-ray activity.

HIP 26373. BANYAN places this star in AB Dor with 100% probability, falling to 87% in BANYAN II. It shows a wide range of youth indicators consistent with an age of $\sim$100 Myr, including abundant lithium, rapid rotation, and saturated chromospheric and X-ray emission. We consider it to be a high-probability member of AB Dor.

TYC 5361-1476-1. da Silva et al. (2009) classified this star as a member of AB Dor, but BANYAN II places higher probability on its membership in β Pic (84% in β Pic; 3% in AB Dor, 13% in the field). The star does have strong youth indicators, including vigorous X-ray activity, rapid rotation, and abundant lithium, and is very likely to be young. Unfortunately, conclusive membership in a MG will require the measurement of a RV and a parallax. For now, we adopt a 90% membership probability in AB Dor, effectively being conservative about its identification with β Pic (and the younger age this would imply).

TYC 7084-794-1 (= CD−35 2722). While BANYAN II's membership probability of 85% is much lower than BANYAN's 99.9%, the star shows strong indicators of youth, and we consider it to be a reliable member of AB Dor. The star does have a measured radial velocity, but no parallax.

HIP 30034. Zuckerman & Song (2004) originally proposed this star to be a member of Tuc-Hor, though Torres et al. (2008) favor membership in Columba and Malo et al. (2013) favor membership in Carina. All of these associations are of similar age ($\sim$30 Myr), making the distinction not particularly meaningful for our analysis. HIP 30034 does show strong youth indicators and is highly likely to be young; BANYAN and BANYAN II both strongly disfavors membership in the field. We adopt a 95+% membership probability in Carina, with the understanding that this probability encompasses HIP 30034's possible membership in Columba (or, less likely, in Tuc-Hor).

GSC 08894-00426. This M dwarf lacks a RV or parallax, and is also almost fully depleted in lithium. BANYAN disfavors field membership, placing a 70% probability on β Pic membership, 12% in Argus, and 16% in AB Dor, while BANYAN II gives an 89% probability of β Pic membership and a 6% probability of AB Dor membership, with a 4% probability of membership in the field. Craig et al. (1997) list a spectral type of M5, which would make its lack of lithium somewhat surprising in the context of likely low-mass members of β Pic (Binks & Jeffries 2014); however, it is sufficiently close to the lithium depletion boundary to make a conclusive statement impossible. Unfortunately, a firm membership in any MG must await a RV and parallax measurement. We provisionally (and conservatively) assign it to AB Dor, the oldest MG of which GSC 08894-00426 is a plausible member.

GJ 9251 A. Listed as a member of AB Dor by Biller et al. (2013), this star is conclusively associated with the field by BANYAN (>99% probability). In addition, it has only an upper limit on X-ray luminosity, and lacks any detected rotation period or chromospheric emission; López-Santiago et al. (2010) measure $v \sin i < 1$ km s^{-1}. We therefore reject the proposed MG association.

TYC 8728-2262-1. This star presents an extreme disagreement between the results using BANYAN, which gives a 99% probability of β Pic membership, and BANYAN II, which gives the probability as just 4%. The star is certainly young: it shows saturated X-ray emission, rapid rotation, and abundant lithium. Lacking a parallax, we adopt a 50% probably of β Pic membership.

TYC 9073-762-1. This star is another case of a strong disagreement between BANYAN (99.9% in β Pic) and BANYAN II (67% in β Pic). As for TYC 8728-2262-1 above, the star shows abundant youth indicators but lacks a measured parallax. We adopt an 80% probability of β Pic membership.

TYC 7408-54-1. This star is similar to the two cases above, with nonuniform priors reducing BANYAN II's probability of β Pic membership from 99.9% to 60%. Due to its abundant youth indicators, we adopt an 80% membership probability. The measurement of a parallax will clear up each of these three cases.

HIP 95261. This A star is known to have a brown dwarf companion (Lowrance et al. 2000). Originally proposed as a member of TW Hya (Zuckerman & Webb 2000) but soon reclassified into β Pic (Zuckerman et al. 2001), BANYAN rejects membership in any MG due to a discrepant RV. Malo et al. (2013) suggest that the RV could be affected by the late-type companion, though a $\sim$0.2 $M_{\odot}$ companion 200 AU (4″ projected at 50 pc) from a $\sim$2 $M_{\odot}$ primary would induce a RV of just a few tenths of a km s^{-1}, far too little to explain a $\sim$15 km s^{-1} discrepancy. Malo et al. also suggest that, with such a rapid rotator ($v \sin i = 330$ km s^{-1}, da Silva et al. 2009), the RV could simply be in error. We acknowledge this as a possibility, but provisionally adopt a much lower β Pic membership probability of 50%.

2MASS J19560294-3207186 and TYC 7443-1102-1. These stars share a common proper motion, but lack a measured parallax. Kiss et al. (2011) have measured a radial velocity for TYC 7443-1102-1, resulting in a 99.8% membership probability in β Pic according to BANYAN, and 58% according to BANYAN II. They show clear signs of youth, and we adopt an 80% membership probability for the pair.

HIP 99273. This mid-F star, like the Tycho stars above, sees its membership probability in β Pic drop from 99.9% to $\sim$80% from BANYAN to BANYAN II. Given the (unsurprising for its temperature) lack of secondary age indicators to confirm its youth, we adopt the latter probability.

HIP 104308. This A star is a proposed member of TW Hya (Zuckerman & Song 2004). Malo et al. (2013) find a 99% probability of membership when neglecting RV data, which consist of a single uncertain measurement by Zuckerman & Song (2004). The addition of the RV, though at -10 ± 10 km s^{-1}, only 1σ away from the TW Hya distribution of -0.2 ± 3.5 km s^{-1}, reduces BANYAN's membership probability to zero (for comparison, HIP 95261 lies 5σ from its predicted RV). We decline to draw such a strong conclusion, adopting an 80% membership probability.

4. BAYESIAN AGES

We revisit the age estimates of all targets in our sample using the method detailed in Brandt et al. (2014), which we summarize here. Our method combines a possible identification with a MG of known age with secondary age indicators, including chromospheric and X-ray activity and stellar rotation. We use the MGs identified in that paper, to which we refer for discussion and references.

1. β Pictoris (21 ± 4 Myr)
2. AB Doradus (130 ± 20 Myr)
3. Columba (30^{+20}_{-10} Myr)
4. Tucana–Horologium (30^{+10}_{-20} Myr)
5. TW Hydrae (10 ± 5 Myr)
6. Ursa Major (500 ± 100 Myr)

We treat all age uncertainties as 2σ limits, and approximate the age probability distribution for each group as a Gaussian. Our sample also contains one star each from Upper Scorpius, Argus, and Carina. Upper Scorpius is a nearby very young (~10 Myr) star-forming region (de Zeeuw et al. 1999), while Argus and Carina have similar ages to Columba (~30 Myr, Torres et al. 2008).

We estimate the membership probability $p_{\rm MG}$ for each star as described in Section 3.4, basing our own probabilities primarily on the Banyan and Banyan II Bayesian analyses, and capping the membership probability at 95%. The probability distribution $\mathcal{P}(\tau)$ for the stellar age is then

$$\mathcal{P}(\tau) = p_{\rm MG}\mathcal{P}_{\rm MG}(\tau) + (1 - p_{\rm MG})\,\mathcal{P}(\tau|{\rm indic}), \quad (2)$$

where $\mathcal{P}_{\rm MG}$ is the probability distribution for the age of the MG and $\mathcal{P}(\tau|{\rm indic})$ is the probability distribution for the age given the observed activity and rotation indicators. We calculate this probability distribution as described in Brandt et al. (2014); we summarize the method here.

Main-sequence stars cooler than spectral type late-F have large convective zones in their outer regions. These regions support magnetic dynamos powered by the stellar differential rotation, which drive chromospheric and coronal activity and magnetized stellar winds. Over time, the stellar wind carries away angular momentum, and the star spins down. Stellar rotation, X-ray, and chromospheric activity in the Ca II HK line all therefore decline with time, and may be calibrated as crude clocks. These calibrations depend on the properties of the convective zone, generally parameterized using $B-V$ color for main-sequence stars. Young stars also spend a variable amount of time (longer for cooler stars) on a rapidly rotating C-sequence before approaching solid-body rotation and beginning to spin down.

Mamajek & Hillenbrand (2008) have calibrated each of these secondary indicators, $R_{\rm X}$ (the ratio of X-ray to bolometric power), $R'_{\rm HK}$ (the ratio of energy in Ca II HK emission to the underlying photospheric continuum), and rotation period, using a large sample of solar-type stars. We use each of these calibrations, with a correction for the time a star takes to settle on the slowly rotating I-sequence, as described in Brandt et al. (2014) and references therein. We do not assume the chromospheric and coronal activity measurements to be independent age indicators, but rather treat them both as proxies for the Rossby number (the ratio of the rotation period to the convective overturn timescale τ_C), which we convert to an age using a color-dependent estimate of τ_C and the period-age relations.

We then combine the activity age distribution with that inferred directly from the rotation period (if measured) and add an additional 15% (0.06 dex) to account for systematic uncertainties. We also add a 5% probability that the star is a pathological case, in the sense that its secondary age indicators do not correspond to its actual age and are useless for dating. Multiplying the resulting distribution by a prior uniform in time out to either 10 Gyr or the star's color-dependent main-sequence lifespan gives $\mathcal{P}(\tau|{\rm indic})$. Finally, we weight $\mathcal{P}(\tau|{\rm indic})$ by $1 - p_{\rm MG}$, the probability that the star is *not* a member of a well-defined MG, and use it in Equation (2).

When drawing ages for each star from these probability distributions, we account for the fact that the ages of each member of a MG should be the same. We first draw the ages for each of the MGs, then assign each suggested group member either to its group or to the field, and finally draw an age for each field star from its posterior age probability distribution. Given the large number of stars, the central limit theorem drives the predicted number of substellar companions to a relatively narrow Gaussian given a fixed substellar distribution function.

Table 2 lists the ages (in Myr) at 5%, 10%, 25%, 50%, 75%, 90%, and 95% of the cumulative posterior probability. The range of ages between the 25% and 75% levels thus contains half of the posterior probability, while the range from 5% to 95% contains nine-tenths of the posterior probability, and may be used as a 90% confidence age interval. We use the full posterior probability distributions summarized in Table 2 throughout the rest of our analysis. A few of these differ significantly from the distributions in Brandt et al. (2014); these targets had their Ca II HK and/or X-ray activity incorrectly input into the earlier paper's calculation.

5. SUBSTELLAR COOLING MODELS

Objects below ~80 $M_{\rm J}$ never attain the central densities and temperatures necessary to stabilize themselves by hydrogen fusion; instead, they simply cool and fade below the detectability limits of even the largest telescopes. Substellar cooling models simulate the structure and atmosphere of such an object as a function of its mass, age, and initial thermodynamic state, producing grids of spectra and luminosities. Many such models have been developed recently and are widely used (e.g., Chabrier et al. 2000; Allard et al. 2001; Baraffe et al. 2003; Marley et al. 2007; Allard et al. 2011; Spiegel & Burrows 2012). These models make a range of assumptions about dust settling, cloud structure, chemical composition, and initial thermodynamic state.

The formation mechanism of planetary mass objects is still debated, and can strongly impact their brightness at young ages. Direct gravitational collapse forms objects on a dynamical timescale (Boss 2000), giving them little time to radiate away their heat of formation. In contrast, an object formed by core-accretion accretes its gas over a viscous time, and is likely to radiate away much of its initial energy in an accretion shock (Hubickyj et al. 2005; Marley et al. 2007). However, the identification of a core-accretion formation scenario with a "cold start" is far from certain; a subcritical shock, for example, could prevent efficient cooling (Bromley & Kenyon 2011), while a very massive core could provide a substantial reservoir of heat (Mordasini 2013). Observational evidence also disfavors a very cold start for many imaged planets (Marleau & Cumming 2014). Massive brown dwarfs are generally accepted to form by direct gravitational collapse, either in a disk or a molecular cloud (Bate et al. 2002).

In this work, we explore whether the entire range of long-period substellar objects is compatible with a single distribution function. We therefore seek a single model applicable over this entire range, including the more massive brown dwarfs. Such a model would imply that all of these objects form by direct gravitational collapse, and therefore, form hot. We adopt the recent BT-Settl models (Allard et al. 2011), which incorporate clouds and dust settling in the appropriate physical regimes, and are intended to be valid all the way from ~1 $M_{\rm J}$ up to stellar

Table 2
Age Distributions of All Targets

Name	R.A. (J2000)	Decl. (J2000)	Age at Posterior CDF Value (Myr)						
HIP/HD/GJ/Other	(h m s)	(° ′ ″)	5%	10%	25%	50%	75%	90%	95%
HIP 544	00 06 36.8	+29 01 17	192	208	237	272	311	356	421
HIP 560	00 06 50.1	−23 06 27	17	18	19	21	22	24	27
HIP 682	00 08 25.7	+06 37 00	21	43	108	217	343	498	725
HIP 919	00 11 22.4	+30 26 58	205	221	251	287	326	372	436
HIP 1134	00 14 10.3	−07 11 57	21	23	26	30	37	45	56
HD 1405	00 18 20.9	+30 57 22	109	115	122	129	136	142	146
HIP 1481	00 18 26.1	−63 28 39	13	17	23	30	33	37	41
FK Psc	00 23 34.7	+20 14 29	19	20	194	300	389	455	510
HIP 2729	00 34 51.2	−61 54 58	13	17	23	30	33	37	40
HIP 3589	00 45 50.9	+54 58 40	111	115	122	129	137	143	148
HIP 4907	01 02 57.2	+69 13 37	686	732	812	912	1030	1160	1320
HIP 4979	01 03 49.0	+01 22 01	152	304	766	1530	2300	2760	2920
HIP 5191	01 06 26.2	−14 17 47	113	117	123	130	138	146	168
HIP 5944	01 16 29.3	+42 56 22	323	346	388	440	500	572	668
HIP 6869	01 28 24.4	+17 04 45	787	876	1040	1240	1510	1880	2500
HIP 6878	01 28 34.4	+42 16 04	226	255	304	367	458	660	2870
HIP 7235	01 33 15.8	−24 10 41	1340	1500	1810	2200	2680	3240	3740
HIP 7345	01 34 37.8	−15 40 35	62	124	313	625	938	1130	1200
HS Psc	01 37 23.2	+26 57 12	111	116	122	130	137	144	149
HIP 7576	01 37 35.5	−06 45 38	17	18	19	21	22	24	29
HIP 9141	01 57 49.0	−21 54 05	13	17	23	30	34	38	50
HIP 9291	01 59 23.5	+58 31 16	21	23	27	33	47	304	561
HIP 9685	02 04 35.1	−54 52 54	13	17	23	30	34	38	46
HIP 10679	02 17 24.7	+28 44 30	17	18	19	21	22	24	26
HIP 11072	02 22 32.5	−23 48 59	1820	2000	2340	2770	3280	3860	4330
HIP 11360	02 26 16.2	+06 17 33	22	24	27	32	41	1610	3220
BD+30 397B	02 27 28.0	+30 58 41	17	18	19	21	22	24	26
HIP 11437	02 27 29.3	+30 58 25	17	18	19	21	22	24	29
HIP 11847	02 32 55.8	+37 20 01	18	19	20	25	2120	3400	3820
HIP 12394	02 39 35.4	−68 16 01	13	17	23	30	33	37	43
HIP 12530	02 41 14.0	−00 41 44	188	267	421	1310	3730	5180	5670
HIP 12545	02 41 25.9	+05 59 18	17	18	19	21	22	24	25
TYC 8491-656-1	02 41 46.8	−52 59 52	13	17	23	30	33	37	40
AF Hor	02 41 47.3	−52 59 31	13	17	23	30	33	37	41
HIP 12638	02 42 21.3	+38 37 07	113	117	123	130	138	146	169
TYC 8497-995-1	02 42 33.0	−57 39 37	13	17	23	30	34	38	51
HIP 12925	02 46 14.6	+05 35 33	13	17	23	30	33	37	42
HIP 12926	02 46 15.2	+25 39 00	4260	4760	5560	6570	7770	8950	9470
HIP 13081	02 48 09.1	+27 04 07	810	937	1170	1480	1860	2320	2780
HIP 13402	02 52 32.1	−12 46 11	19	20	218	284	333	380	425
HIP 14150	03 02 26.0	+26 36 33	2920	3230	3760	4420	5200	6040	6670
HIP 14684	03 09 42.3	−09 34 47	113	117	123	130	138	146	161
HIP 14954	03 12 46.4	−01 11 46	371	433	550	708	905	1160	1440
HIP 15323	03 17 40.0	+31 07 37	179	233	314	416	544	708	928
BD−19 660	03 20 50.7	−19 16 09	820	1310	2770	5180	7590	9040	9510
HIP 16537	03 32 55.8	−09 27 30	619	659	728	812	909	1020	1160
HIP 17248	03 41 37.3	+55 13 07	21	23	26	30	37	45	54
HD 23061	03 42 55.1	+24 29 35	116	118	121	124	128	131	133
TYC 1803-1406-1	03 43 27.1	+25 23 15	116	118	121	124	128	131	133
HD 23247	03 44 23.5	+24 07 58	116	118	121	124	128	131	133
BD+23 514	03 45 41.9	+24 25 53	116	118	121	124	128	131	133
V1171 Tau	03 46 28.4	+24 26 02	116	118	121	124	128	131	133
HD 23514	03 46 38.4	+22 55 11	116	118	121	124	128	131	133
HD 282954	03 46 38.8	+24 57 35	116	118	121	124	128	131	133
H II 1348	03 47 18.1	+24 23 27	116	118	121	124	128	131	133
HIP 17695	03 47 23.3	−01 58 20	67	84	132	211	291	339	365
HD 23863	03 49 12.2	+23 53 12	116	118	121	124	128	131	133
H II 2311	03 49 28.7	+23 42 44	116	118	121	124	128	131	133
HD 23912	03 49 32.7	+23 22 49	116	118	121	124	128	131	133
H II 2366	03 49 36.5	+24 17 46	116	118	121	124	128	131	133
H II 2462	03 49 50.4	+23 42 20	116	118	121	124	128	131	133
BD+22 574	03 49 56.5	+23 13 07	116	118	121	124	128	131	133
V1174 Tau	03 50 34.6	+24 30 28	116	118	121	124	128	131	133
HIP 18050	03 51 27.2	+24 31 07	116	118	121	124	128	131	133

Table 2
(Continued)

Name	R.A. (J2000)	Decl. (J2000)	Age at Posterior CDF Value (Myr)						
HIP/HD/GJ/Other	(h m s)	(° ′ ″)	5%	10%	25%	50%	75%	90%	95%
V1054 Tau	03 51 39.3	+24 32 56	116	118	121	124	128	131	133
V885 Tau	03 53 45.3	+25 55 34	116	118	121	124	128	131	133
HIP 18859	04 02 36.7	−00 16 08	112	116	123	130	137	144	150
HD 281691	04 09 09.7	+29 01 30	52	61	80	107	134	159	225
HIP 21482	04 36 48.2	+27 07 56	22	46	116	234	358	477	662
HIP 22449	04 49 50.4	+06 57 41	315	630	1400	2770	4340	5280	5600
TYC 5899-26-1	04 52 24.4	−16 49 22	112	116	123	130	137	145	152
TYC 8513-952-3	04 53 31.2	−55 51 37	110	115	122	129	136	143	148
HIP 22845	04 54 53.7	+10 09 03	67	136	339	679	1020	1220	1300
HIP 23200	04 59 34.8	+01 47 01	17	18	19	21	22	24	26
HIP 23309	05 00 47.1	−57 15 25	17	18	19	21	22	24	29
HIP 23362	05 01 25.6	−20 03 07	21	23	26	30	37	45	55
HIP 25283	05 24 30.2	−38 58 11	113	117	123	130	138	146	169
HIP 25486	05 27 04.8	−11 54 03	17	18	19	21	22	24	25
HD 36869	05 34 09.2	−15 17 03	21	23	26	30	37	45	51
HIP 26373	05 36 56.9	−47 57 53	113	117	123	130	137	145	152
HIP 28103	05 56 24.3	−14 10 04	197	400	1000	2010	3010	3610	3820
TYC 5361-1476-1	06 02 21.9	−13 55 33	113	117	124	131	139	152	232
HIP 29067	06 07 55.3	+67 58 37	96	193	439	673	941	1280	1690
TYC 7084-794-1	06 09 19.2	−35 49 31	110	115	122	129	137	143	148
HIP 29964	06 18 28.2	−72 02 41	17	18	19	21	22	24	28
HIP 30030	06 19 08.1	−03 26 20	21	23	26	30	37	45	51
HIP 30034	06 19 12.9	−58 03 16	30	32	36	40	44	49	62
HIP 30314	06 22 30.9	−60 13 07	102	114	122	129	136	142	146
GSC 08894-00426	06 25 56.1	−60 03 27	110	115	122	129	136	143	147
HIP 30920	06 29 23.4	−02 48 50	8	18	50	112	195	277	339
HIP 32104	06 42 24.3	+17 38 43	21	23	26	30	37	46	58
V429 Gem	07 23 43.6	+20 24 59	111	116	122	130	137	143	148
HIP 37170	07 38 16.4	+47 44 55	24	50	127	255	393	562	806
HIP 37288	07 39 23.0	+02 11 01	1580	1780	2150	2620	3180	3830	4390
HIP 37766	07 44 40.2	+03 33 09	45	61	106	181	256	300	331
GJ 9251A	08 07 09.1	+07 23 00	840	1340	2800	5190	7600	9030	9520
FP Cnc	08 08 56.4	+32 49 11	23	25	29	50	169	243	267
HIP 40693	08 18 23.9	−12 37 56	4360	4840	5630	6620	7840	9020	9510
HIP 40774	08 19 19.1	+01 20 20	181	355	584	840	1160	1570	2030
HD 70573	08 22 50.0	+01 51 34	107	118	140	168	197	226	266
HIP 42333	08 37 50.3	−06 48 25	332	355	399	451	512	585	684
HIP 42430	08 39 07.9	−22 39 43	4520	5020	5850	6900	8190	9260	9640
HIP 42438	08 39 11.7	+65 01 15	238	261	315	457	514	554	580
HIP 43410	08 50 32.2	+33 17 06	267	299	359	437	532	654	833
HIP 43726	08 54 17.9	−05 26 04	1220	1340	1560	1840	2170	2570	2960
HIP 44458	09 03 27.1	+37 50 28	100	111	132	160	188	215	250
HIP 44526	09 04 20.7	−15 54 51	282	305	346	395	448	508	589
HD 78141	09 07 18.1	+22 52 22	26	54	139	279	448	810	1370
HIP 45383	09 14 53.7	+04 26 34	41	83	207	409	620	872	1210
HIP 46816	09 32 25.6	−11 11 05	25	32	52	84	117	137	148
HIP 46843	09 32 43.8	+26 59 19	164	178	204	236	270	308	362
HIP 49809	10 10 05.9	−12 48 57	207	418	1050	2100	3150	3780	4000
HIP 50156	10 14 19.2	+21 04 30	22	24	27	33	45	341	405
TWA 6	10 18 28.7	−31 50 03	5	6	8	10	11	13	16
GJ 388	10 19 36.3	+19 52 12	41	56	104	182	261	308	327
HIP 50660	10 20 45.9	+32 23 54	1170	1350	1680	2110	2640	3260	3830
HIP 51317	10 28 55.6	+00 50 28	113	117	123	130	138	146	169
HIP 51386	10 29 42.2	+01 29 28	100	112	135	164	195	228	277
HIP 51658	10 33 13.9	+40 25 32	126	253	636	1270	1910	2290	2430
HIP 51931	10 36 30.8	−13 50 36	948	1090	1340	1680	2090	2580	3060
TWA 7	10 42 30.1	−33 40 17	5	6	8	10	12	14	21
HIP 52462	10 43 28.3	−29 03 51	612	653	725	813	915	1040	1180
HIP 52787	10 47 31.2	−22 20 53	285	441	619	840	1120	1460	1860
HIP 53020	10 50 52.0	+06 48 29	4600	5160	6140	7500	8820	9550	9780
HIP 53486	10 56 30.8	+07 23 19	501	535	595	669	755	856	984
HD 95174	10 59 38.3	+25 26 15	20	23	358	3790	6890	8760	9380
HIP 53911	11 01 51.9	−34 42 17	5	6	8	10	12	14	20
HIP 54155	11 04 41.5	−04 13 16	24	49	125	251	392	576	870

Table 2
(Continued)

Name	R.A. (J2000)	Decl. (J2000)	Age at Posterior CDF Value (Myr)						
HIP/HD/GJ/Other	(h m s)	(° ′ ″)	5%	10%	25%	50%	75%	90%	95%
HIP 54745	11 12 32.4	+35 48 51	412	440	491	553	624	709	820
TWA 14	11 13 26.2	−45 23 43	5	6	8	10	11	13	16
TYC 3825-716-1	11 20 50.5	+54 10 09	28	57	145	292	471	777	1320
TWA 13N	11 21 17.2	−34 46 46	5	6	8	10	12	14	21
TWA 8A	11 32 41.3	−26 51 56	5	6	8	10	12	14	21
HIP 57370	11 45 42.3	+02 49 17	741	790	876	983	1110	1260	1430
HIP 57494	11 47 03.8	−11 49 27	3870	4310	5040	5940	7040	8290	9050
TWA 9B	11 48 23.7	−37 28 49	5	6	8	10	12	14	21
HIP 57589	11 48 24.2	−37 28 49	5	6	8	10	12	14	21
HIP 57632	11 49 03.6	+14 34 19	30	33	37	42	50	1090	1510
HIP 58876	12 04 33.7	+66 20 12	19	39	97	194	304	437	635
G 123-7	12 09 37.3	+40 15 07	1530	1720	2060	2500	3020	3640	4170
TYC 4943-192-1	12 15 18.4	−02 37 28	109	115	123	131	141	304	484
HIP 59774	12 15 25.6	+57 01 57	411	433	465	501	537	572	601
TWA 25	12 15 30.7	−39 48 43	5	6	8	10	12	14	21
HIP 60074	12 19 06.5	+16 32 54	349	373	417	470	532	606	704
HIP 60661	12 25 58.6	+08 03 44	2880	3210	3780	4500	5330	6240	6900
HD 108767B	12 29 50.9	−16 31 15	77	158	401	761	1240	1860	2520
TWA 20	12 31 38.1	−45 58 59	5	6	8	10	11	13	16
HIP 61174	12 32 04.2	−16 11 46	220	441	1100	2200	3310	3970	4190
TWA 10	12 35 04.3	−41 36 39	5	6	8	10	12	14	21
TWA 11B	12 36 00.6	−39 52 16	5	6	8	10	12	14	17
HIP 61498	12 36 01.0	−39 52 10	5	6	8	10	12	14	17
TWA 11A	12 36 01.0	−39 52 10	5	6	8	10	12	14	17
HIP 61960	12 41 53.1	+10 14 08	64	129	323	647	969	1160	1240
BD+60 1417	12 43 33.3	+60 00 53	35	72	184	376	694	1180	1780
HIP 62523	12 48 47.0	+24 50 25	1210	1290	1430	1590	1780	2000	2230
HIP 63076	12 55 28.5	+65 26 19	173	347	871	1740	2610	3140	3320
HIP 63317	12 58 32.0	+38 16 44	20	42	107	216	330	442	638
HIP 63584	13 01 46.9	+63 36 37	253	510	1280	2560	3850	4620	4880
HIP 63742	13 03 49.7	−05 09 43	113	117	123	130	138	146	164
HIP 64792	13 16 46.5	+09 25 27	166	180	205	236	268	303	352
HIP 65016	13 19 40.1	+33 20 48	3680	4080	4770	5620	6630	7810	8650
HIP 65515	13 25 45.5	+56 58 14	110	121	142	171	199	227	266
FH CVn	13 27 12.1	+45 58 26	41	60	111	130	154	209	228
HIP 66252	13 34 43.2	−08 20 31	75	88	120	173	226	259	287
HIP 67092	13 45 05.3	−04 37 13	880	1380	2820	5210	7600	9040	9520
HIP 67412	13 48 58.2	−01 35 35	1280	1440	1740	2130	2600	3150	3660
HIP 69357	14 11 46.2	−12 36 42	1390	1570	1890	2310	2810	3400	3920
HD 234121	14 16 12.2	+51 22 35	16	34	87	177	279	413	623
HIP 69732	14 16 23.0	+46 05 18	67	136	343	689	1030	1240	1320
HIP 70952	14 30 46.1	+63 11 09	258	518	1300	2590	3890	4670	4930
HIP 71284	14 34 40.8	+29 44 42	211	427	1070	2140	3210	3850	4070
HIP 71395	14 36 00.6	+09 44 47	501	536	598	673	760	862	992
HIP 71631	14 39 00.2	+64 17 30	76	85	104	131	157	180	209
HIP 72146	14 45 24.2	+13 50 47	4270	4760	5580	6580	7770	8940	9470
HIP 72339	14 47 32.7	−00 16 53	2060	2320	2790	3380	4090	4880	5500
HIP 72567	14 50 15.8	+23 54 43	481	514	572	643	726	824	945
HIP 73996	15 07 18.1	+24 52 09	296	461	884	2360	3840	4720	5020
HIP 74045	15 07 56.3	+76 12 03	29	36	59	95	132	154	166
HIP 74702	15 15 59.2	+00 47 47	187	203	232	269	309	359	434
HIP 75829	15 29 23.6	+80 27 01	33	67	173	354	554	799	1130
HIP 76267	15 34 41.3	+26 42 53	407	430	464	500	535	569	593
HD 139084B	15 38 56.8	−57 42 19	17	18	19	21	22	24	29
HIP 76829	15 41 11.4	−44 39 40	35	72	182	368	564	716	789
HIP 77408	15 48 09.5	+01 34 18	769	819	908	1020	1150	1300	1470
HIP 77542	15 49 57.7	−03 55 16	4	4	4	5	5	5	5
HIP 78557	16 02 22.4	+03 39 07	11	24	62	128	210	434	3360
HIP 79762	16 16 45.3	+67 15 23	2510	2770	3230	3800	4470	5210	5780
HIP 79977	16 19 29.2	−21 24 13	6	7	8	10	11	13	16
HIP 80824	16 30 18.1	−12 39 45	3610	3980	4610	5370	6240	7190	7860
HIP 81084	16 33 41.6	−09 33 12	162	189	255	358	460	531	655
HIP 82587	16 52 58.1	+31 42 06	185	371	923	1840	2770	3320	3510
HIP 82688	16 54 08.1	−04 20 25	111	116	122	130	137	143	148

Table 2
(Continued)

Name	R.A. (J2000)	Decl. (J2000)	Age at Posterior CDF Value (Myr)						
HIP/HD/GJ/Other	(h m s)	(° ′ ″)	5%	10%	25%	50%	75%	90%	95%
HIP 83494	17 03 53.6	+34 47 25	127	255	637	1270	1900	2280	2420
HD 155555C	17 17 31.3	−66 57 05	17	18	19	21	22	24	25
TYC 8728-2262-1	17 29 55.1	−54 15 49	18	19	20	24	82	118	130
HIP 86346	17 38 39.6	+61 14 16	111	116	122	129	137	143	148
HIP 87108	17 47 53.6	+02 42 26	53	108	274	550	825	993	1060
HIP 87322	17 50 34.0	−06 03 01	1130	1650	3070	5390	7690	9080	9540
HIP 87558	17 53 14.2	+06 06 05	268	538	1350	2710	4070	4880	5160
HIP 87579	17 53 29.9	+21 19 31	359	489	664	891	1170	1520	1920
HIP 87768	17 55 44.9	+18 30 01	29	59	151	305	484	706	1010
HD 164249B	18 03 04.1	−51 38 56	17	18	19	21	22	24	26
HIP 88848	18 08 16.0	+29 41 28	18	38	97	196	301	405	586
HIP 89005	18 09 55.5	+69 40 50	26	54	138	280	449	804	1360
HIP 91043	18 34 20.1	+18 41 24	30	36	52	78	104	120	133
HIP 92024	18 45 26.9	−64 52 17	17	18	19	21	22	24	27
TYC 9073-762-1	18 46 52.6	−62 10 36	17	18	20	21	24	253	331
TYC 7408-54-1	18 50 44.5	−31 47 47	17	18	19	21	23	88	153
HIP 92680	18 53 05.9	−50 10 50	17	18	19	21	22	23	25
HIP 92919	18 55 53.2	+23 33 24	55	63	85	121	156	179	200
HIP 93580	19 03 32.3	+01 49 08	113	117	124	132	144	1120	1680
HIP 95261	19 22 51.2	−54 25 26	18	19	20	24	451	722	815
HIP 95270	19 22 58.9	−54 32 17	17	18	19	21	22	24	27
HIP 95319	19 23 34.0	+33 13 19	5020	5660	6720	8040	9140	9690	9860
HIP 95793	19 29 01.0	+01 57 02	68	139	353	709	1070	1280	1360
HIP 97438	19 48 15.4	+59 25 22	14	29	74	152	242	355	532
2MASS J19560294-3207186	19 56 02.9	−32 07 19	17	18	19	21	23	301	511
TYC 7443-1102-1	19 56 04.4	−32 07 38	17	18	20	21	24	485	562
HIP 99273	20 09 05.2	−26 13 27	17	18	20	21	24	2760	4130
HIP 99711	20 13 59.8	−00 52 01	1670	1780	1960	2190	2440	2720	2990
HIP 101262	20 31 32.1	+33 46 33	696	898	1290	1810	2480	3270	3980
BD+05 4576	20 39 54.6	+06 20 12	47	95	124	141	334	560	854
HIP 102409	20 45 09.5	−31 20 27	17	18	19	21	22	24	29
HIP 104225	21 06 56.4	+69 40 29	4460	4980	5880	7060	8470	9420	9730
HIP 104308	21 07 51.2	−54 12 59	14	18	25	31	37	1420	2130
HD 201919	21 13 05.3	−17 29 13	113	117	123	130	137	145	152
HIP 105038	21 16 32.5	+09 23 38	1050	1190	1450	1790	2200	2690	3170
HIP 106231	21 31 01.7	+23 20 07	105	114	122	129	136	142	146
HIP 107345	21 44 30.1	−60 58 39	13	17	23	30	34	38	50
HIP 107350	21 44 31.3	+14 46 19	236	254	285	324	367	417	487
HIP 107649	21 48 15.8	−47 18 13	1680	1850	2170	2560	3030	3580	4020
HIP 108156	21 54 45.0	+32 19 43	3270	3620	4220	4960	5810	6720	7350
TYC 2211-1309-1	22 00 41.6	+27 15 14	14	18	20	23	85	166	211
V383 Lac	22 20 07.0	+49 30 12	46	53	70	98	126	145	162
HIP 111449	22 34 41.6	−20 42 30	265	537	1350	2710	4060	4880	5150
TYC 9340-437-1	22 42 48.9	−71 42 21	17	18	19	21	22	24	29
HIP 112312	22 44 58.0	−33 15 02	17	18	19	21	22	24	27
TX PsA	22 45 00.1	−33 15 26	17	18	19	21	22	24	26
HIP 112909	22 51 53.5	+31 45 15	12	21	47	96	155	202	223
HIP 113020	22 53 16.7	−14 15 49	940	1440	2870	5250	7630	9050	9520
HIP 114066	23 06 04.8	+63 55 34	113	117	123	130	137	145	151
HIP 115147	23 19 26.6	+79 00 13	21	23	27	32	43	232	356
HIP 115162	23 19 39.6	+42 15 10	112	116	123	130	137	144	150
TYC 5832-666-1	23 32 30.9	−12 15 51	17	18	19	21	22	24	29
HIP 116215	23 32 49.4	−16 50 44	19	20	436	789	1080	1400	1710
HIP 116384	23 35 00.3	+01 36 19	29	59	147	289	459	756	1260
HIP 116805	23 40 24.5	+44 20 02	21	25	34	130	293	393	430
HIP 117410	23 48 25.7	−12 59 15	26	54	138	278	445	751	1260
HIP 118121	23 57 35.1	−64 17 54	13	17	23	30	34	38	44

(This table is also available in a machine-readable form in the online journal.)

masses. BT-Settl reproduces the earlier COND/DUSTY hot-start models of Baraffe et al. (2003) and Chabrier et al. (2000) in the applicable limits.

We also explore the effects of the formation model on our results restricted to the planetary mass regime, below the deuterium-burning limit of $\sim 13\,M_{\rm J}$. In this case, we

parameterize our ignorance using the "warm-start" models of Spiegel & Burrows (2012), henceforth SB12. These model grids include an additional parameter—initial entropy—at each age, mass, and atmospheric composition. We restrict our analysis to a fiducial model with clouds and three times solar metallicity.

Under any formation scenario, the initial entropy is likely to be a function of mass. More massive objects can attain a higher entropy while still permitting hydrostatic equilibrium, resulting in hotter starts. However, they can also radiate more effectively (and for much longer) under a core-accretion scenario, producing an initially colder object. We parameterize the range of initial thermodynamic states using a single "warmth parameter," η, to fill the space between the high- and low-entropy envelopes given by SB12:

$$S_{\rm init}(M) = \eta S_{\rm init,\,max}(M) + (1-\eta) S_{\rm init,\,min}(M), \quad (3)$$

with $\eta \in [0,\ 1]$.

Much uncertainty remains throughout the modeling process, and we make no claim that our use of the BT-Settl and SB12 models here exhausts parameter space. We adopt the BT-Settl models in an attempt to include the entire range of substellar masses in a consistent manner, while we use the SB12 models to smoothly explore the effect of the initial thermodynamic conditions. Substellar luminosities depend strongly on both mass and age, limiting (at least somewhat) the impact of systematic errors in predicted luminosity on the expected distribution of objects detected by high-contrast imaging.

6. STATISTICAL FRAMEWORK

High-contrast imaging data provide a detection limit (or a detected companion) everywhere on the field of view; we want to compare these data to predictions made by models of exoplanet formation and evolution. The probability of a planet existing at any individual location around a particular star is tiny. Hence, in the absence of any other information about the star, the planet's existence is a Poisson process. If we denote by λ_i the expected number of substellar companions that exist and are detectable at a given position and luminosity i, given some detection limits and model of planet properties, then the probability of such a companion existing is $\lambda_i e^{-\lambda_i}$ ($\approx\lambda_i$), while the probability of its not existing (either because there is no companion or because it is too faint) is $e^{-\lambda_i}$ ($\approx 1-\lambda_i$). Here, i runs over both position and substellar luminosity, and the λ_i are functions of the substellar companion distribution function, cooling models, and survey contrast.

The approximation of planet occurrence as an independent Poisson process at every point around every star surveyed breaks down with multiple systems or when other information, such as stellar binarity, makes some positions more dynamically favorable than others. The famous four (or more) planet system HR 8799 illustrates this empirically. Various studies have found that few stars (typically no more than 5%–10%) host massive ($\gtrsim 5\,M_{\rm J}$), long-period exoplanets (e.g., Lafrenière et al. 2007; Vigan et al. 2012; Nielsen et al. 2013; Chauvin et al. 2014). If planet occurrence is independent at different locations, the number of single planet systems should exceed the number of four-planet systems by at least a factor of 10^3–10^4, while the number of two-planet systems should be larger than HR8799-like systems by a factor of at least 10^2–10^3. The fact that we have not found a single system with two $\sim$5–10 $M_{\rm J}$ companions argues powerfully against independent occurrence probabilities, even before considering theoretical arguments.

As high-contrast surveys improve in sensitivity and target hundreds of new stars, the number of known multiple systems will almost certainly rise. However, the data sets we consider here lack any detected multiple planet systems, freeing us (for now) from the statistical and theoretical problems they present. With the caveat that our statistical framework must be abandoned or at least modified if systems like HR 8799 are to be included, we therefore proceed by assuming planet occurrence to be an independent Poisson process. The likelihood function $\mathcal{L}$, the probability density of the given data set (detected companions plus sensitivity limits) given a model of planet frequency and properties, is then the product of the planet-occurrence probabilities over all elements of the fields of view of all stars, and over all substellar luminosities:

$$\mathcal{L} = \prod_i e^{-\lambda_i} \times \prod_{{\rm obj}\,j} \lambda_j e^{-\lambda_j}. \quad (4)$$

The index i runs over all locations around all stars and over all planet luminosities, apart from those positions and luminosities at which a companion was seen. The index j only runs over the pixels and luminosities where substellar companions were discovered. The latter term is the likelihood of finding all of the detected companions at their actual positions with their observed luminosities. The exponential term in the product over j combines with the identical term in the product over i to give a product over all pixels around all stars and over all planet luminosities, including those where companions were discovered. The likelihood is more conveniently written logarithmically, and reduces to

$$\ln\mathcal{L} = -\sum_i \lambda_i + \sum_{{\rm obj}\,j} \ln\lambda_j = -\langle N_{\rm obj}\rangle + \sum_{{\rm obj}\,j} \ln\lambda_j, \quad (5)$$

where now i runs over all pixels around all stars and over all companion luminosities. The first term, λ_i summed over all planet positions and luminosities, is simply the expected number of detectable companions, $\langle N_{\rm obj}\rangle$, given the substellar distribution function.

The substellar distribution function, from which the λ_i and λ_j are computed, can depend arbitrarily on parameters like the host stellar type, companion mass, separation, host metallicity, etc., as we discuss in the next section. Regardless of its functional form, the distribution function may be multiplied by a constant A, which multiplies all probabilities λ_i and λ_j (and, by extension, $\langle N_{\rm obj}\rangle$) by the same factor. This normalization constant is generally not known a priori and must be fit by our analysis; it gives, e.g., the total number of companions per star. Such a constant enters the likelihood calculation, Equation (5), in a particularly simple way. Multiplying the distribution function, and by extension, all λ_i and λ_j, by a constant A, the likelihood function becomes

$$\ln\mathcal{L} = -A\langle N_{\rm obj}\rangle + N_{\rm obs}\ln A + \ln\lambda_j, \quad (6)$$

where $N_{\rm obs}$ is the number of companions actually observed. If we hold all other parameters of the distribution fixed while determining the normalization, λ_j, $\langle N_{\rm obj}\rangle$, and $N_{\rm obs}$ are all constant, and Equation (6) is a gamma distribution. The maximum likelihood value of A is, as expected, $N_{\rm obs}/\langle N_{\rm obj}\rangle$. In other words, the maximum likelihood value of A is the one that makes the predicted number of detections $\langle N_{\rm obj}$ equal to $N_{\rm obs}$, the actual number of substellar companions seen in the survey.

Setting A equal to its maximum likelihood value, the likelihood function now reads

$$\mathcal{L} = \exp\left(-N_{\rm obs}\right) \prod_{{\rm obj}\,j} \frac{\lambda_j}{\langle N_{\rm obj}\rangle}. \quad (7)$$

As a result, all we need to calculate from the substellar distribution function, cooling model, and sensitivity curves are the probabilities of detecting companions at their observed positions with their observed properties, and the total number of expected detections. In the next section, we discuss the computation of λ_j and $\langle N_{\rm obj}\rangle$ in the case of a power-law companion distribution function.

6.1. The Exoplanet Distribution Function

Neglecting multiplicity, the exoplanet distribution function extends over three parameters of interest: mass M, semimajor axis a, and eccentricity e. Other orbital or orientation parameters are randomly distributed, with those distributions determined by geometry (assuming the systems to be randomly oriented). The distribution function is usually assumed to be separable, i.e.,

$$p(M, a, e) = p(M)p(a)p(e). \quad (8)$$

While this is unlikely to be true in reality, and may not even be a particularly good approximation, we adopt it for lack of a specific and well-motivated alternative.

When we observe a companion, the only measurements we can usually make are of its projected separation and its luminosity at various wavelengths. It is therefore the distribution of projected separation, a function of both the semimajor axis and eccentricity distributions, that is relevant to imaging surveys. The choice of eccentricity distribution turns out to be of secondary importance to this distribution. Indeed, in the special case that the semimajor axis is a power law truncated well outside the separations being probed, the eccentricity distribution drops out altogether–$p(M, a)$ is independent of $p(e)$ (see the Appendix for details).

We derive the distribution of projected separation based on an eccentricity distribution uniform in the range from 0 to 0.8 (Cumming et al. 2008); the result is nearly identical to that obtained using a Rayleigh distribution in eccentricity with $\sigma = 0.3$ (Jurić & Tremaine 2008). For completeness, we also include a distribution based on $p(e) = 2e$, the theoretical distribution expected if the phase space density of companions is a function of energy only (Ambartsumian 1937). Full details and piecewise analytic fitting functions are provided in the Appendix.

We take the exoplanet mass distribution to be a power law $p(M) \propto M^{\beta}$, and use cooling models of substellar objects to convert mass and age to a luminosity L in a given bandpass. The azimuthal variance in the detection limit is dominated by subtraction residuals from the stellar point-spread function (PSF) and by read noise—photon noise from the companion itself is nearly always negligible. These noise distributions are typically very nearly Gaussian. With a detection threshold of N_σ (usually 5–6), the probability of detecting a companion is therefore

$$\begin{aligned} p({\rm detect}|L) &= p(L + x > N_\sigma \cdot \sigma) \\ &= \frac{1}{2} + \frac{1}{2}{\rm erf}\left(\frac{(L/L_{\rm lim} - 1)N_\sigma}{\sqrt{2}}\right), \end{aligned} \quad (9)$$

where x, a Gaussian random variable with variance σ^2, represents the noise, $L_{\rm lim}$ is the formal $N_\sigma\sigma$ detection threshold, and $\sigma^2 = \sigma^2(D)$ is the annular variance in the final ADI-processed image. The total differential number of sources expected at angular separation D is

$$dN(D) = p(D)\,dD \int_0^\infty \frac{dN}{dM}\frac{dM}{dL}\,p({\rm detect}|L)\,dL. \quad (10)$$

The substellar-cooling models consist of grids in age and mass, which we interpolate using piecewise power laws. We, therefore, evaluate Equation (10) for the special case of a power law dM/dL; it reduces to a function of a single parameter with variable limits of integration. We tabulate these values, enabling us to evaluate Equation (10) to a typical accuracy of much better than 0.1% with no more than a few array lookups, $\lesssim$20 floating point operations, and at most one call to a special function like the error function. The full derivation is given in the Appendix.

Finally, we integrate Equation (10) over projected separations D to obtain the total number of expected detections around an object, giving us $\langle N_{\rm obj}\rangle$ in Equation (7). We perform the integral using the trapezoidal rule in logarithmic separation, interpolating from the input contrast curves using cubic splines. Our use of cubic splines virtually guarantees the lack of a finite second derivative, irrespective of any intrinsic features of the contrast curves themselves, and makes the trapezoidal rule first order. We therefore use Richardson extrapolation with a fit linear in step size, and accept the result of the extrapolation when it agrees with the previous extrapolated result (using half as many function evaluations) within a factor of 3×10^{-3}. This tolerance allows relatively few function evaluations, while preventing the integration from dominating our error budget. It generally requires using ~30–100 points in angular separation, at a cost of ~0.05–0.1 ms per star on a single 3.3 GHz thread. Processing an entire large survey of 200 stars with a single set of test parameters thus requires about 10–20 ms, an enormous improvement over Monte Carlo methods that generate millions of planets around each star.

After evaluating $\langle N_{\rm obj}\rangle$ by integrating Equation (10) and summing over stars, we need to evaluate the probabilities λ_j of detectable companions existing at their observed positions D_j and luminosities L_j. Substellar companions are inevitably followed up many times, making the uncertainties on their luminosities very small. The photometric uncertainties are often dominated by scatter in the host star's photometry and variation in the AO performance across the field, bearing little relation to the annular standard deviation in the discovery image. The probabilities λ_j, taking the L_j as known, become

$$\lambda_j = p({\rm detect}|D_j, L_j)\left(\frac{dN}{d\ln L\,dD}d\ln L\,dD\right)\Big|_{D_j, L_j}. \quad (11)$$

This is equivalent to using Monte Carlo to find the number of companions in a small interval Δmag. The detection probability is a function only of L_j (which is observed). Because it is independent of the substellar distribution function, the detection probability contributes to an overall scaling of the likelihood function and has no effect on our analysis.

In practice, it is problematic to use Equation (11) as written because the derivative can be discontinuous or even, near the deuterium-burning limit, singular. We therefore integrate it over a small interval in $\ln L$:

$$\lambda_j \propto \int_{x_1}^{x_2} \frac{dN}{d\ln L\,dD}d\ln L. \quad (12)$$

We adopt 0.1 magnitudes (∼10% in luminosity) as our fiducial half-width $(x_2 - x_1)/2$, which is comparable to the photometric errors on well-characterized companions like GJ 504b (Kuzuhara et al. 2013) and β Pictoris b (Bonnefoy et al. 2013). Though this width is somewhat arbitrary, we note that half-widths from 0.01 to 0.2 mag give indistinguishable best-fit parameters and confidence intervals in our final analysis. Constant factors, like a variable increment in dD, do not affect our result; they merely add a constant to the log likelihood (equivalently, they multiply the likelihood by a constant).

All of the approximations and tabulations described above introduce errors of $\lesssim$1% (and substantially less for most parameter values of interest), which are smaller than those introduced by interpolating substellar cooling models in mass and age. The tabulated cooling models (Section 5) and stellar ages (Section 4) dominate the errors in our analysis.

6.2. Model Constraints

Our model for the exoplanet distribution function,

$$N(M, a) = AM^{\beta}a^{\alpha}, \tag{13}$$

with

$$a_{\rm min} < a < a_{\rm max} \quad \text{and} \quad M_{\rm min} < M < M_{\rm max}, \tag{14}$$

has seven free parameters, not counting the substellar cooling model.

1. The normalization of the distribution function, or, equivalently, the fraction of stars hosting substellar companions with a given range of properties;
2. α, the slope of the semimajor axis distribution function;
3. β, the slope of the mass distribution function;
4. $M_{\rm min}$, the minimum mass of the population;
5. $M_{\rm max}$, the maximum mass of the population;
6. $a_{\rm min}$, the inner edge of the semimajor axis distribution; and
7. $a_{\rm max}$, the outer edge of the semimajor axis distribution.

The normalization could also be a function of the host stellar mass, while $a_{\rm min}$ and $a_{\rm max}$ are both likely to scale with stellar mass (as might $M_{\rm min}$ and $M_{\rm max}$), which could add even more parameters.

Unfortunately, our sample contains far too few detections—κ And b, plus two brown dwarf companions in the Pleiades and two companions to NICI targets—to provide meaningful constraints on the full companion distribution function. Instead, we ask two much simpler questions.

1. Out to what semimajor axis could the exoplanet distribution function measured by RV surveys extend?
2. Can we use a single power law to describe the full population of objects from ∼5 $M_{\rm J}$ to massive brown dwarfs?

In this way, we attempt to address the question of whether the planets now being discovered by direct imaging represent a new population, distinct from both an extrapolation of the RV sample and of the more massive brown dwarfs.

Even addressing these more limited questions poses considerable difficulties. The distribution function of RV planets around solar-type FGK stars has been reasonably well-measured (Cumming et al. 2008); however, it depends both on stellar mass and on metallicity (Johnson et al. 2007a; Fischer & Valenti 2005). We lack metallicity data on many of our stars, and the sample, being largely young, spans a relatively narrow range in metallicity. We therefore make no attempt to take stellar enrichment into account. We do, however, attempt to at least qualitatively correct for host stellar mass, by assuming the planet-hosting probability to be directly proportional to the stellar mass in units of $M_{\odot}$ (a crude fit to the histogram presented in Johnson et al. 2007a). This fits with the observed correlation of disk mass with stellar mass (Andrews et al. 2013), though a correlation between stellar and companion *mass* may be a more natural choice. The latter is equivalent to using an upper limit of the mass distribution that depends on host stellar mass, and emphasizes the artificial nature of using a power law truncated at the deuterium burning limit.

The substellar cooling model appropriate to the RV population is hotly debated (see the discussion in Section 5). Objects formed by direct gravitational collapse do not have time to radiate away their heat of formation, while objects formed by core-accretion could lose much of their initial entropy in an accretion shock. We parameterize our ignorance using the SB12 warm-start models, using a variable warmth parameter $\eta \in [0, 1]$ to interpolate between the warmest and coldest starts for each mass. We also include the BT-Settl hot-start models (Allard et al. 2011), which apply over the entire range of masses from ∼1 $M_{\rm J}$ to the hydrogen burning limit.

For our fits to a brown-dwarf-like distribution, we set the limits on the semimajor axis distribution to be 1–1000 AU, well outside the regions typically probed around our targets, and set the lower mass cutoff to be 5 $M_{\rm J}$, consistent with the minimum mass predicted by models of disk instability at wide separations (Rafikov 2005) and fragmentation in molecular clouds (Low & Lynden-Bell 1976; Bate et al. 2003). Unfortunately, the upper mass limit of this distribution is uncertain: the upper mass cutoff for disk fragmentation could differ from that for cloud fragmentation. However, our data lack the power to determine this cutoff, which we provisionally set at 70 $M_{\rm J}$. A brown-dwarf like distribution is generally accepted to form by direct gravitational collapse. The hot-start BT-Settl models thus provide an appropriate benchmark to constrain the properties of this distribution.

Finally, we adopt uniform priors on α and β and reinterpret the likelihood function as an unnormalized posterior probability distribution. Using Monte Carlo to compute the normalization, we may then place constraints on α and β.

7. RESULTS AND DISCUSSION

Figure 1 shows the completeness of our data set given our age estimates and assuming either the hot-start BT-Settl cooling models (Allard et al. 2011), or a warm-start model (SB12) with an initial entropy halfway between the coldest and hottest starts ($\eta = 0.5$). At separations of 50–100 AU, we are sensitive to ∼60% of objects near the deuterium burning limit. This value is higher around stars closer to Earth, which tend to be of lower mass, and around stars reliably identified with a young MG.

In this section, we use the detection limits to determine the limits we can place on an extrapolation of the distribution function measured by radial velocities. We then proceed to model the entire substellar distribution function using a single power law, and determine its parameters and their confidence intervals.

7.1. Limits on an RV Distribution Function

The distribution function as measured by Cumming et al. (2008) follows $M^{-1.3}a^{-0.6}$ from 0.5 to 10 $M_{\rm J}$ and from 0.03 to

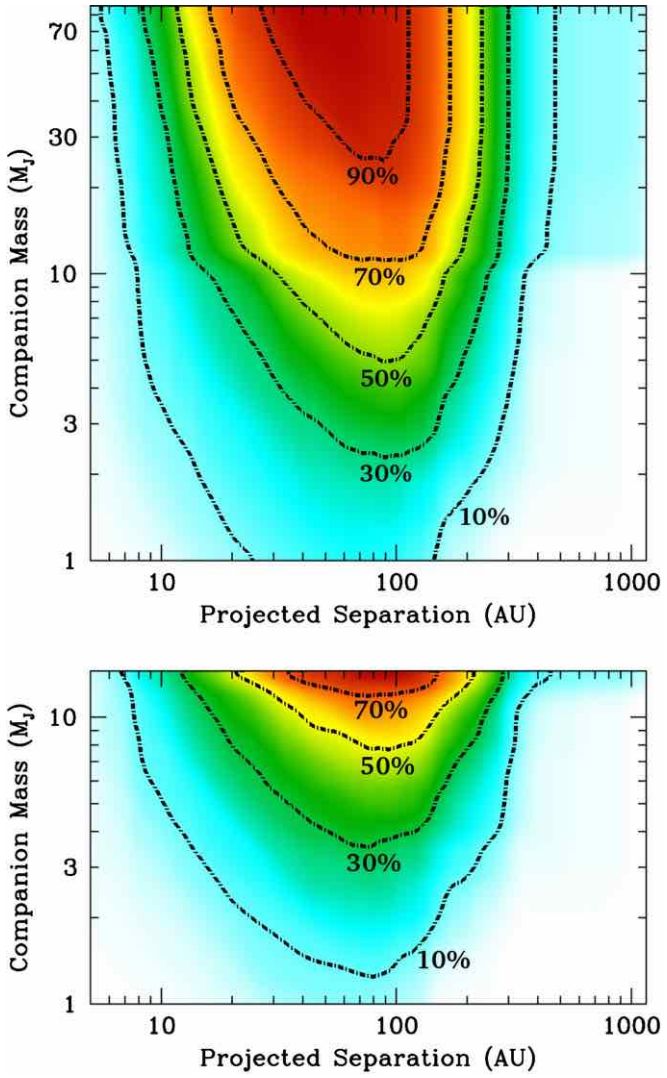

Figure 1. Completeness of our combined survey, calculated using the BT-Settl hot-start models (top panel) and a warm start model (initial entropy halfway between the hottest and coldest starts), and weighting all stars equally. At separations of 50–100 AU, we are about 70% complete at the deuterium burning threshold of ~13 M_J under both models.

(A color version of this figure is available in the online journal.)

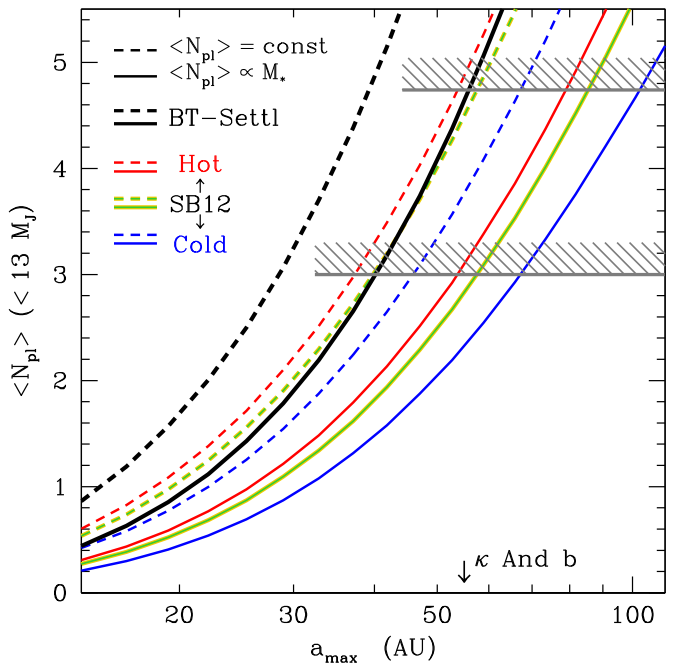

Figure 2. Expected number of planetary-mass detections as a function of semimajor axis cutoff and cooling model, computed by extrapolating the measured distribution function for RV planets (Cumming et al. 2008). The solid lines assume the number of companions to be proportional to host stellar mass, while the dashed lines assume no proportionality. The gray hatched regions are excluded at 2σ assuming κ And b to be drawn from this distribution (top, $\langle N_{pl} \rangle \approx 4.7$), or to belong to a separate distribution (bottom, $\langle N_{pl} \rangle \approx 3$).

(A color version of this figure is available in the online journal.)

3 AU. We extrapolate this up to the deuterium burning limit of ~13 M_J and out to a semimajor axis of a_{max}, which we seek to constrain. The normalization of the Cumming et al. distribution function is not free: 10.5% of 1 $M_\odot$ stars have a planet with a mass between 0.3 and 10 M_J and a semimajor axis between 0.03 and 3 AU. With the normalization fixed, we integrate Equation (10) over separations and sum over stars to get the expected number of detections, $\langle N_{obj} \rangle$. We then compare $\langle N_{obj} \rangle$ to the actual number of planet candidates in our sample using the Poisson distribution.

If an extrapolated RV planet distribution is to explain recent discoveries like GJ 504b, HR 8799b, κ And b, and HD 95086b, a_{max} must be $\gtrsim$50 AU, where these companions have been found. The sample we present here, depending on whether κ And b is hypothesized to arise from an RV-like distribution, has at most one detection in total, and zero around FGKM stars. If κ And b is more than ~15 M_J, as would be the case if, as suggested by Hinkley et al. (2013) and Bonnefoy et al. (2014), it is older than the ~30 Myr implied by membership in the Columba MG (Carson et al. 2013), we can exclude models that predict more than 3 detections with 95% confidence. If κ And b is considered to be a candidate member of an extrapolated RV distribution, the 2σ threshold rises to 4.7 predicted detections. We truncate the distribution at the deuterium burning threshold of 13 M_J for comparison to previous results and to facilitate the use of the SB12 models, which are only calculated for masses up to 15 M_J.

Figure 2 shows the predicted number of detections as a function of a_{max} for the BT-Settl model and for SB12 warm-start models spanning the range from hot to cold starts. For the BT-Settl hot start models, the 2σ upper limit on a_{max} varies from 30 to 50 AU, depending on whether we scale the companion frequency with stellar mass and whether we consider κ And b to arise from this distribution. If we adopt the SB12 models, the equivalent 2σ upper limits vary from 40 to 70 AU as long as we do not consider the very coldest start models (those with $\eta \lesssim 0.1$). If we do adopt these cold-start models, the upper limit on a_{max} rises to as much as ~150 AU. We note that cold-start models would predict a mass for κ And b well in excess of the deuterium burning limit (Carson et al. 2013) and would justify that object's classification as a nonmember of this distribution, regardless of its membership in Columba.

Our finding that the RV distribution function of Cumming et al. (2008) cannot be extrapolated past a semimajor axis of ~30–70 AU for most assumptions about the substellar cooling model is similar to the earlier results of Nielsen & Close (2010) and Chauvin et al. (2010). Nielsen & Close (2010) used a smaller sample of 118 targets dominated by the GDPS, finding limits on a_{max} from ~65–200 AU depending on the substellar cooling model and on the correlation between planet frequency and stellar mass. Chauvin et al. (2010) used 88 young stars to constrain this outer limit to be ~80 AU, again depending on

the cooling model and the details of the distribution function. These results are in mild tension with the discovery of objects like HR 8799b, GJ 504b. and HD 95086b. which all lie at separations of $\gtrsim$50 AU. There may be even more tension with the form of the mass distribution, which in RV surveys, is a power law increasing sharply toward low masses. Wahhaj et al. (2013b) found a positive power law index for the distribution in planet mass (more massive objects are more common), in sharp disagreement from the RV findings. This result, however, was driven by their inclusion of the four HR 8799 planets as independent detections and their lack of any detected companions $\lesssim$5 M_J. Excluding HR 8799 from the Wahhaj et al. (2013b) analysis weakens this finding considerably.

7.2. A Single Substellar Distribution Function

The preceding analysis artificially separates objects below and above the deuterium burning threshold, making the classification of substellar companions like κ And b problematic. It also does not consider the properties of the detected companions. We now consider a distribution function extending across the deuterium-burning threshold, up to the hydrogen burning limit of ~70 M_J. The predicted probability density of detections may be projected onto substellar mass and semimajor axis, and compared with our sample. For this exercise, and for the statistical analysis that follows, we add two additional substellar companions discovered by HiCIAO: GJ 758B (Thalmann et al. 2009; Janson et al. 2011), a ~30 M_J brown dwarf around an old G star first imaged during HiCIAO commissioning, and GJ 504b (Kuzuhara et al. 2013; Janson et al. 2013a), a ~3–8 M_J companion to an active field G star discovered during the full SEEDS survey. By doing this, we assume that the contrasts, distances, and ages of the as-yet-unpublished HiCIAO data are similar to those presented in Section 3. In reality, the unpublished stars represent a combination of very young members of star-forming regions and nearby stars with a wide range of ages, a heterogeneity to that of our combined sample.

We first show the predictions of two published distribution functions: $dN/dMda \propto M^{-0.4}a^{-1}$, derived for both stellar and substellar companions from ~30–1500 AU (Metchev & Hillenbrand 2009), and $dN/dMda \propto M^{-1.3}a^{-0.6}$, derived for ~1–10 M_J RV-detected companions from ~0.03–3 AU (Cumming et al. 2008). In the former case, we extend the distribution down to 1 M_J and out to 1000 AU, well outside the field of view around nearly all of our targets. In the latter case, we extrapolate the distribution function up to the hydrogen burning limit of ~70 M_J and out to 100 AU, roughly the outermost semimajor axis consistent with our analysis in Section 7.1, and scale companion frequency with stellar mass. Figure 3 shows the predicted probability densities, $dp/d\log M/d\log D$, for both of these distributions, together with contours of constant $dp/d\log M/d\log D$ enclosing 68% and 95% of the predicted detections. The five HiCIAO detections, including GJ 504b and GJ 758B, are in red, while the two NICI detections are shown in green.

The Metchev & Hillenbrand (2009) distribution, the top panel in Figure 3, appears to provide a reasonably good fit to our sample, though it has some difficulty accounting for objects like GJ 504b (depending on its age). The inclusion of intermediate separation low-mass companions from other surveys, like HD 95086b (which was discovered in a survey that did not detect any massive brown dwarfs), or of β Pic b and HR 8799bcde, would add to this tension. The RV-inspired distribution, bottom panel of Figure 3, terminates at 100 AU and is unable to account for

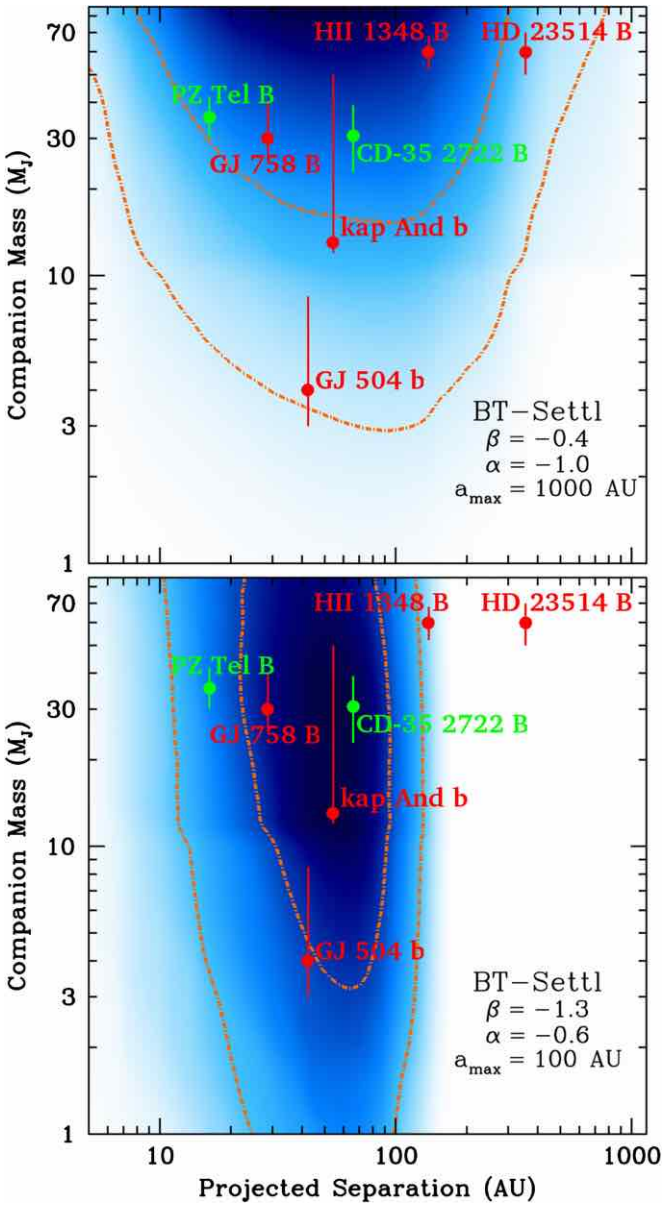

Figure 3. Probability distributions, $dp/d\log M/d\log D$, under two different substellar distribution functions, $p(M,a) \propto a^{\alpha}M^{\beta}$. NICI discoveries are shown in green; companions imaged by HiCIAO are shown in red. The distribution with $\beta = -0.4$, (top panel, taken from Metchev & Hillenbrand 2009), predicts a large number of massive brown dwarfs at separations of ~50–100 AU. The bottom distribution is that published in Cumming et al. (2008), with $\alpha = -0.6$ and $\beta = -1.3$, extrapolated out to higher masses and semimajor axes, and assuming planet frequency to scale with host stellar mass. The massive Pleiades brown dwarfs, H II 1348B and HD 23514B. would force the outer limit to extend to ~300 AU, which is excluded by our sample (Figure 2). They cannot arise from an extrapolation of the RV distribution function.

(A color version of this figure is available in the online journal.)

the massive (~60 M_J), long-period brown dwarfs discovered in the Pleiades. We note that the distribution advocated by Zuckerman & Song (2009), with $p(M,a) \propto M^{-1.2}a^{-1}$ (not shown), has a nearly identical mass dependence but extends to larger semimajor axes. This distribution can accommodate all of the detections, though only if we extend it well below the ~12 M_J limit suggested by Zuckerman & Song in order to match GJ 504b.

We now return to our sample, using our detections and contrast curves to constrain the substellar distribution function. Given an assumed form of the distribution function,

including the power-law indices and mass and semimajor axis limits, we may then use the likelihood function (in the form of Equation (7)) to compare the distribution to our actual detections. We assume uniform priors on the power law indices α and β, integrate the likelihood function, and treat it as a posterior probability distribution. The additional effect of including GJ 504b and GJ 758B in a full analysis may be crudely estimated by scaling up our sample size to qualitatively account for the as-yet-unpublished non-detections. Such a scaling would simply multiply $\langle N_{\rm obj} \rangle$ in Equation (7) by a constant, dropping out when constraining α and β. This implicitly assumes that the ages, distances, and masses probed by the as-yet-unpublished non-detections are similar to those of the sample presented here. Given the heterogeneity of both our combined sample and the unpublished SEEDS data, this is not a bad approximation. We set $a_{\rm min} = 1$ AU and $a_{\rm max} = 1000$ AU, well outside the regions of interest, and use a lower mass cutoff of $5\,M_{\rm J}$, appropriate to a gravitational collapse scenario.

Including all of the detections in our merged sample, and adding GJ 504b and GJ 758B. we obtain a best-fit distribution function $p(M, a) \propto M^{-0.65\pm0.60} a^{-0.85\pm0.39}$ (1σ errors). Abandoning the lower limit on companion mass favors a distribution function with somewhat more high-mass objects, with the mass exponent becoming -0.4 ± 0.5 (1σ errors). However, as discussed in Section 2, there are theoretical reasons to impose such a lower mass limit for gravitational collapse, and a cutoff is also suggested by the dearth of companions $<5\,M_{\rm J}$ in other high-contrast surveys.

The normalization of the distribution function is given by a gamma distribution at fixed α and β; its maximum likelihood value produces five detections (the observed number) in our sample of 248 stars. With $(\alpha, \beta) = (-0.85, -0.65)$, the maximum likelihood normalization constant gives 1.7% of stars with substellar companions between 5 and $70\,M_{\rm J}$ and between 10 and 100 AU. The gamma distribution is asymmetric; the 68% and 95% confidence intervals are 1.2%–2.8% and 0.74%–3.9%, respectively, of stars with companions in the given mass and semimajor axis range. If we also include uncertainty in α and β by integrating the likelihood function and treating it as a posterior distribution, the uncertainty in the normalization constant increases somewhat. For companions between 5 and $70\,M_{\rm J}$ and between 10 and 100 AU, the 68% and 95% confidence intervals become 1.0%–3.1% and 0.52%–4.9% of stars, respectively.

We also extrapolate our distribution out to $a = 1600$ AU to facilitate comparison with Metchev & Hillenbrand (2009), again using both the gamma distribution and uncertainties in α and β to derive the full probability distribution of the fraction of stars hosting companions. We find that, at 68% confidence, 1.8%–6.2% of stars host brown dwarfs between 12 and $72\,M_{\rm J}$ and between 28 and 1600 AU (0.92%–11% at 95% confidence). These results agree very well with the Metchev & Hillenbrand value of $3.2^{+3.1}_{-2.7}$% (2σ limits). The latter analysis fixed $\alpha = -1$ and assumed a continuous mass function extending to stellar companions, making the agreement particularly gratifying. Omitting the uncertainty in α and β, our results imply that 1.4%–7.2% of stars host 12–$72\,M_{\rm J}$ with semimajor axes from 28–1600 AU at 95% confidence.

The results from many other surveys in the H and K bands would fit nicely on Figure 4, and further suggest a smooth distribution across the deuterium burning threshold. Chauvin et al. (2010) reported the detection of three substellar objects in their survey, of which two, GSC-08047-00232B (Chauvin et al. 2005a), and AB Pic b (Chauvin et al. 2005b), are

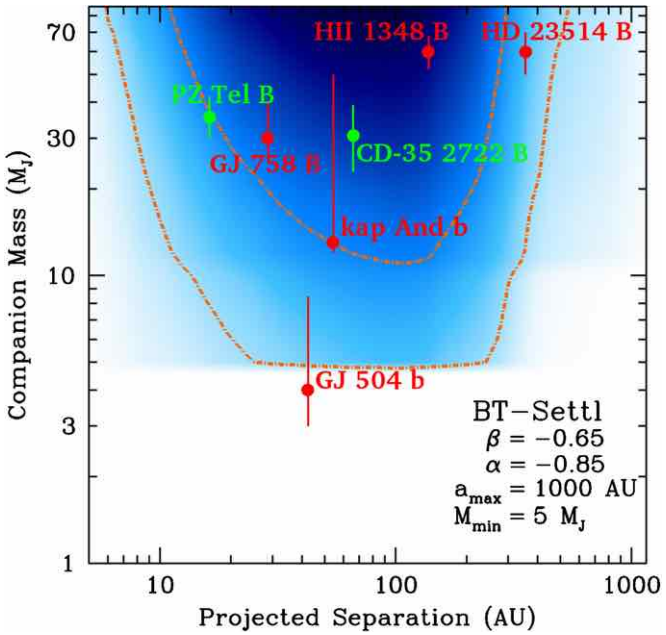

Figure 4. Probability distribution, $dp/d\log M/d\log D$, for the maximum likelihood power law distribution including all seven detections shown: $p(M, a) \propto M^{-0.65\pm0.60} a^{-0.85\pm0.39}$ (1σ errors). NICI discoveries are in green, while companions imaged by HiCIAO are in red. This result should be interpreted with caution, but is compatible with the distributions published in both Metchev & Hillenbrand (2009) and Zuckerman & Song (2009) within 1σ. It suggests that we cannot reject a single substellar distribution function extending from massive brown dwarfs to massive exoplanets based solely on the sample presented here.
(A color version of this figure is available in the online journal.)

$\sim$20 and $\sim 15\,M_{\rm J}$ brown dwarf companions 250–300 AU from their host stars. These data suggest that a smooth distribution extending all the way from massive brown dwarfs down to a theoretically motivated cutoff at $\sim 5\,M_{\rm J}$ is capable of explaining the vast majority of wide-separation companions below or near the deuterium-burning limit nominally separating planets from brown dwarfs.

7.3. Limitations

Our statistical analysis makes several assumptions that are not true in detail. For example, we do not distinguish between single stars and binaries (which make up a relatively small fraction of our sample, $\sim$10%). Some orbits are unstable around binaries (Holman & Wiegert 1999); however, simply excluding these regions of parameter space and considering the rest other orbits to be as probable as around a single star is not a well-motivated solution. Low-mass companions could be scattered to distant orbits by a close stellar binary, possibly making binaries better systems to find substellar objects. In most cases, the orbital elements of the stellar binary are unknown anyway. We therefore accept that our neglect of binarity might introduce a modest bias, but we lack a good solution other than excluding binaries altogether.

Our analysis also neglects sample biases, which can appear in many ways. Stars hosting debris disks may be more likely to harbor planets. Treating them identically to stars without infrared excesses, as we do here, could artificially depress the derived planet frequency. SEEDS also avoided including known planet hosts and attempted to avoid observing stars targeted by other high-contrast instruments. A tendency to avoid observing the same targets as other surveys, but to repeat some targets around which nothing was found, would likewise bias us against finding planets.

The choice of substellar cooling model introduces another opportunity for bias, as we discuss in Section 5. This is somewhat mitigated for our sample by the wide range of ages we probe, and by the fact that the luminosity of a brown dwarf or exoplanet depends so strongly on its mass and age. Particularly for objects formed by direct gravitational collapse, there is little doubt about the initial thermodynamic state, though systematic errors could still arise from, e.g., a poor treatment of cloud formation.

Possibly the most serious limitation of our analysis comes from our ignorance of the formation mechanism of substellar objects, and our resulting assumption of separable power law distribution functions. Substellar objects do not form in isolation; many have been imaged around stellar binaries. These objects would interact dynamically with other stars or brown dwarfs, with lighter companions being preferentially scattered outward, and more massive companions scattered inward. As a result, the initial and final companion mass distributions may be very different from one another. Models of brown dwarf formation (e.g., Stamatellos & Whitworth 2009; Bate 2009) are beginning to predict distribution functions, but have difficulty producing low-mass brown dwarfs at moderate separations. As a result, we have little choice but to proceed with simplistic models based only loosely on theoretical considerations.

In addition to these limitations, there are several objects not included in our sample that may be difficult to incorporate into a single substellar distribution like the one suggested in Section 7.2, and that may represent the high-mass, wide-separation tail of a core-accretion population. These objects, including HR 8799bcde, β Pic b, and HD 95086b. tend to occur around relatively massive A-type stars. A stars rotate very rapidly and are therefore poor targets for RV searches, making the application of a distribution function like that measured by Cumming et al. (2008; used in Section 7.1) an extrapolation in both separation and host stellar mass. The masses of β Pic b and at least some of the HR 8799 planets have been dynamically constrained to be $\lesssim 10\,M_{\rm J}$ (Lagrange et al. 2012; Dawson et al. 2011; Sudol & Haghighipour 2012). Such low-mass companions at ~10–40 AU are difficult to form in-situ by direct gravitational collapse (Rafikov 2005; Kratter et al. 2010), while some recent studies have found that core-accretion may be viable out to a few tens of AU (Lambrechts & Johansen 2012; Kenyon & Bromley 2009). Planet–planet scattering and migration do add some uncertainty to this picture.

As more low-mass companions are discovered, they may reveal a clear bimodal distribution in planet/star mass ratio, hints of which were shown by Currie et al. (2011). Such a clear separation would be strong evidence of different formation mechanisms. Even stronger evidence would be planetary chemical compositions differing strongly from those of their host stars. Konopacky et al. (2013) found signs of an enhanced C/O ratio in HR 8799c, though these results depend on chemical modeling of the atmosphere and were at modest significance. A bimodal distribution of metal and/or carbon enhancements, with a strong correlation between composition, separation, and mass ratio, would probably be conclusive. New and upcoming instruments like GPI (Macintosh et al. 2008), SPHERE (Beuzit et al. 2008), and CHARIS (Peters et al. 2012) may be able to provide these data over the next few years.

8. CONCLUSIONS

In this work, we present an analysis of high-contrast imaging of nearly 250 stars. The targets span a wide range of spectral types and ages, and are composed of three published subsets of the SEEDS survey on the Subaru telescope, combined with the GDPS and the NICI MG sample. We perform a uniform, Bayesian analysis of the ages of all of our targets, with determinations that are often more conservative than those adopted in previous papers. Our sample includes five detected substellar companions. Two of these are $\sim 60\,M_{\rm J}$ brown dwarfs around stars in the Pleiades; the others are a $\sim$13–50 $M_{\rm J}$ companion to the late B star κ And, a $\sim 35\,M_{\rm J}$ companion to the late G star PZ Tel, and a $\sim 30\,M_{\rm J}$ companion to the early M star CD−35 2722.

Our analysis includes a new method for calculating the likelihood function of a substellar distribution function by performing integrals analytically or evaluating them from tables whenever possible. This represents a large improvement in efficiency over using Monte Carlo to evaluate completeness, and allows us to efficiently compute the likelihood of a wide range of models. We use these techniques to compute the limits beyond which the distribution function measured for RV planets cannot be extended, finding a model-dependent maximum semimajor axis limit of ~30–100 AU, similar to previous results. However, we argue that the division of substellar objects at the deuterium burning limit is arbitrary, particularly in light of new discoveries that straddle that boundary, and we seek to model the entire substellar population using a single distribution function.

Finally, we use Monte Carlo to compute the likelihood function of a unified substellar distribution function, including the five companions detected in our sample, plus an additional two objects, GJ 758B. and GJ 504b. discovered by HiCIAO, for a total of seven. The inclusion of these objects does not bias the results as long as the distributions of target stars and contrast curves presented here are good matches to those of the unpublished non-detections from which GJ 758 and GJ 504 were culled. Given the wide range of stellar properties and ages in both samples, this is a fairly good assumption. With this caveat, we find that a single, separable power law, $p(M, a) \propto M^{-0.65\pm0.60} a^{-0.85\pm0.39}$ (1σ errors), truncated at a theoretically motivated minimum mass of $\sim 5\,M_{\rm J}$, can account for the entire range of substellar companions detected in SEEDS. The normalization of this distribution implies that, at 68% confidence, 1.0%–3.1% of stars have substellar companions between 5 and 70 $M_{\rm J}$ and between 10 and 100 AU (0.52%–4.9% at 95% confidence). Extrapolating to larger separations, 1.8%–6.2% of stars (at 68% confidence) have companions between 12 and 72 $M_{\rm J}$ and between 28 and 1600 AU (the limits used by Metchev & Hillenbrand 2009); or 0.92%–11% at 95% confidence. Our normalization is in excellent agreement with the Metchev & Hillenbrand (2009) result, that $3.2^{+3.1}_{-2.7}$% (2σ limits) of stars have brown dwarf companions within these limits.

Our results suggest that many, perhaps most, of the substellar companions currently being discovered near and somewhat below the deuterium burning limit may share a common origin with more massive brown dwarfs. Such objects would almost certainly form by gravitational collapse, either in a disk or in a fragmenting cloud. There is currently little reason to consider the substellar companions, at least in our combined sample, to be the high-mass, long-period tail of the RV planet distribution.

Upcoming surveys using instruments like GPI (Macintosh et al. 2008), SPHERE (Beuzit et al. 2008), and CHARIS (Peters et al. 2012) will dramatically improve our sensitivity to low-mass companions, a region of parameter space that should be richly populated if current detections are described by an

RV-like distribution function. The discovery of many such objects, below the mass limits at which clouds and disks are expected to fragment, could point to an alternative formation scenario, like core-accretion followed by dynamical evolution. If, however, such objects turn out to be exceptionally rare, the current population of directly imaged exoplanets likely represents the low-mass tail of the brown dwarfs.

This research is based on data collected at the Subaru Telescope, which is operated by the National Astronomical Observatories of Japan. T.D.B. gratefully acknowledges support from the Corning Glass Works Foundation through a fellowship at the Institute for Advanced Study. This research has been supported in part by the World Premier International Research Center Initiative, MEXT, Japan. M.K. acknowledges support from a JSPS Research Fellowship for Young Scientists (grant no. 25-8826). J.C. was supported by the U.S. National Science Foundation under award no. 1009203. This research has made use of the SIMBAD database and Vizier service, operated at CDS, Strasbourg, France. The authors wish to recognize and acknowledge the very significant cultural role and reverence that the summit of Mauna Kea has always had within the indigenous Hawaiian community. We are most fortunate to have the opportunity to conduct observations from this mountain.

APPENDIX

A.1. PROJECTED SEPARATION DISTRIBUTION FUNCTION

Denoting the projected separation (in physical units) as D, and the ratio of the projected distance to the semimajor axis by $s \in [0,\ 2]$, the probability distribution of D is

$$p(D) = \int_{s_1}^{s_2} ds\ p(s)\ p\left(a = \frac{D}{s}\right) \frac{1}{s}, \tag{A1}$$

where the last factor $1/s$ accounts for the volume element. If $p(a)$ is a power law a^α, truncated at $a_{\rm min}$ and $a_{\rm max}$, we have $s_1 = \min(2,\ D/a_{\rm max})$ and $s_2 = \min(2,\ D/a_{\rm min})$. In the special case that the power law is truncated well outside the separations of interest, $s_1 \approx 0$ and $s_2 \approx 2$, and the dependence of $p(D)$ on the eccentricity distribution drops out altogether.

We can empirically derive $p(s)$ from $p(e)$ using the method described in the appendix of Brandeker et al. (2006). This method assumes only that companions are observed at random times in their orbits and that their orbits are randomly oriented as seen from Earth. Brandeker et al. suggest an eccentricity distribution $p(e) = 2e$, the theoretical distribution expected if the phase space density of companions is a function of energy only (Ambartsumian 1937). However, planet–planet scattering disfavors eccentricities close to 1, producing distributions closer to the Rayleigh distribution with $\sigma \sim 0.3$ (Jurić & Tremaine 2008). Other authors (Cumming et al. 2008) have suggested a uniform distribution in eccentricity out to $e_{\rm max} \sim 0.8$. We adopt the latter distribution, noting, however, that a Rayleigh distribution with $\sigma = 0.3$ produces nearly indistinguishable results.

The top panel of Figure 5 shows all three distributions in s. The uniform distribution up to an eccentricity of 0.8 is well-fit by a piecewise linear function:

$$p(s) \approx \begin{cases} 1.3s & 0 \leqslant s \leqslant 1 \\ -\frac{35}{32}\left(s - \frac{9}{5}\right) & 1 < s < 1.8. \end{cases} \tag{A2}$$

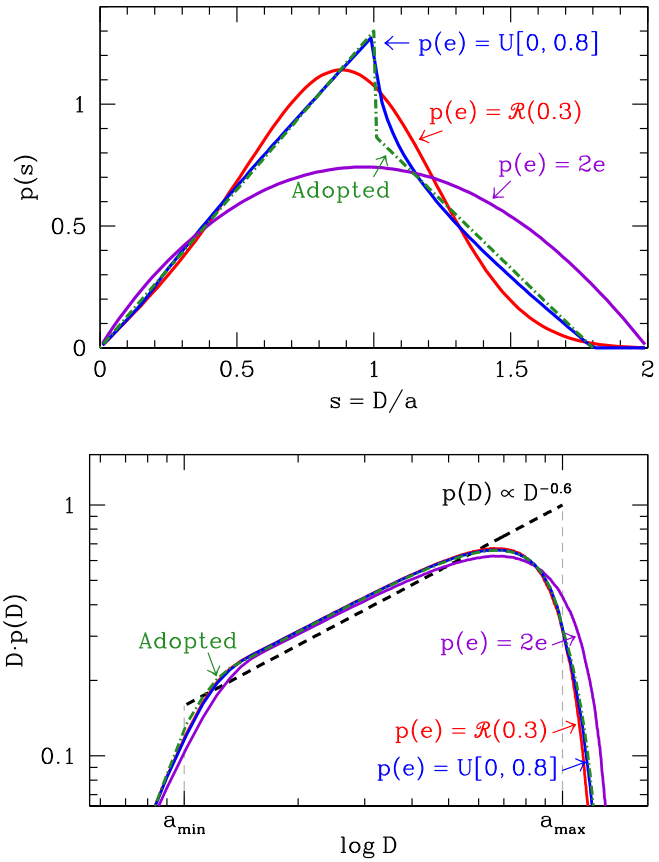

Figure 5. Top panel: the distribution of $s = D/a$ assuming the eccentricity to be uniformly distributed between 0 and 0.8 (blue curve), Rayleigh distributed with $\sigma = 0.3$ (red curve), or with $p(e) = 2e$ (violet curve). We adopt the piecewise linear approximation represented by the green curve. Bottom panel: the distributions of projected separation produced by a truncated power law distribution in semimajor axis (black curve) for each distribution in s from the top panel. We use the piecewise analytic green dot–dashed curve, which is nearly identical to the results from the Rayleigh and uniform distributions; we also provide an expression that is nearly indistinguishable from the violet curve.
(A color version of this figure is available in the online journal.)

Assuming $p(a) = a^\alpha$ for $a_{\rm min} \leqslant a \leqslant a_{\rm max}$, we then perform the integral

$$p(D) = \int_{s_1}^{s_2} ds\ p(s)\ p\left(a = \frac{D}{s}\right) \frac{1}{s}, \tag{A3}$$

with $s_1 = \min(D/a_{\rm max},\ 1.8)$ and $s_2 = \min(D/a_{\rm min},\ 1.8)$. We have, after a bit of algebra,

$$p(D) = \begin{cases} D\left[\frac{1.3}{1-\alpha}\left(a_{\rm min}^{\alpha-1} - a_{\rm max}^{\alpha-1}\right)\right] & D < a_{\rm min} \\ D^\alpha\left[\frac{315+68\alpha}{160\alpha(1-\alpha)}\right] & \\ \quad -D\left[\frac{1.3}{1-\alpha}a_{\rm max}^{\alpha-1} + \frac{35}{32(1-\alpha)}a_{\rm min}^{\alpha-1}\right] & \\ \quad -\frac{63}{32\alpha}a_{\rm min}^{\alpha} & a_{\rm min} \leqslant D < 1.8a_{\rm min} \\ D^\alpha\left[\frac{68\alpha+315(1-1.8^{-\alpha})}{160\alpha(1-\alpha)}\right] - D\left[\frac{1.3}{1-\alpha}a_{\rm max}^{\alpha-1}\right] & 1.8a_{\rm min} \leqslant D < a_{\rm max} \\ D^\alpha\left[-\frac{35}{32}\frac{1.8^{1-\alpha}}{\alpha(1-\alpha)}\right] + D\left[\frac{35}{32}\frac{a_{\rm max}^{\alpha-1}}{1-\alpha}\right] + \frac{63}{32\alpha}a_{\rm max}^{\alpha} & a_{\rm max} \leqslant D \leqslant 1.8a_{\rm max}. \end{cases} \tag{A4}$$

Given $a_{\rm min}$, $a_{\rm max}$, and α, Equation (A4) is a sum of piecewise power laws, and is trivial to integrate analytically. The bottom panel of Figure 5 shows the final distributions $p(D)$ for each of the eccentricity distributions we consider, together with the piecewise analytic approximation given by Equation (A4). The blue and green curves, representing the exact result and our

approximation, are nearly indistinguishable from one another and from the Rayleigh distribution (red curve).

For completeness, we also work out the case of an eccentricity distribution with

$$p(e) = 2e, \tag{A5}$$

the result obtained assuming the phase space density to be a function only of orbital energy. In this case, we can very closely approximate $p(s)$ by

$$p(s) \approx \frac{3}{4}(2s - s^2). \tag{A6}$$

In their paper, Brandeker et al. (2006) used a sine curve, which provides a slightly worse fit and is much more difficult to handle analytically. With our approximation, the distribution $p(D)$ becomes

$$p(D) = D^{\alpha}\left[\frac{3}{2(1-\alpha)}\left(s_2^{1-\alpha} - s_1^{1-\alpha}\right) - \frac{3}{4(2-\alpha)}\left(s_2^{2-\alpha} - s_1^{2-\alpha}\right)\right], \tag{A7}$$

with $s_1 = \min(D/a_{\max}, 2)$ and $s_2 = \min(D/a_{\min}, 2)$.

A.2. DETECTIONS AT A GIVEN SEPARATION

Suppose that the noise at angular separation D is σ_D, and the formal detection threshold is $L_{\lim} = N_{\sigma}\sigma_D$. The probability of detecting a companion of luminosity L, assuming Gaussian errors, is then

$$p(\text{detect}|L) = \frac{1}{2} + \frac{1}{2}\text{erf}\left(\frac{N_{\sigma}(L - L_{\lim})}{L_{\lim}\sqrt{2}}\right), \tag{A8}$$

where erf is the error function. The total number of detected companions at angular separation D is then

$$N(D) = \int_0^{\infty} \frac{dN}{dL} p(\text{detect}|L)\, dL = \int_0^{\infty} \frac{dN}{dM}\frac{dM}{dL} p(\text{detect}|L)\, dL. \tag{A9}$$

Substellar cooling models are generally presented as grids in mass-luminosity space, which we interpolate using piecewise power laws, with

$$\frac{L}{L_i} = \left(\frac{M}{M_i}\right)^{\gamma_i} \tag{A10}$$

for $M_{i,0} \leqslant M < M_{i,1}$ or, equivalently, for $L_{i,0} \leqslant L < L_{i,1}$. Defining

$$x \equiv \frac{L}{L_{\lim}} \quad \text{and} \quad \Gamma_i \equiv (\beta + 1 - \gamma_i)/\gamma_i, \tag{A11}$$

and assuming the distribution function of mass to be

$$p_M(M) \propto M^{\beta}, \tag{A12}$$

we have, after some algebra,

$$N(D) = \sum_i M_i\, p_M(M_i) \int_{x_{i,0}}^{x_{i,1}} \frac{1}{\gamma_i} x^{\Gamma_i} \times \left[\frac{1}{2} + \frac{1}{2}\text{erf}\left(\frac{(x-1)N_{\sigma}}{\sqrt{2}}\right)\right] dx. \tag{A13}$$

The integral in Equation (A13) is a function only of the limits of integration and of the quantity $\Gamma_i = (\beta + 1 - \gamma_i)/\gamma_i$. We approximate the integral in different regimes depending on the values of $x_{i,0}$, $x_{i,1}$, and γ_i. For $5 \leqslant N_{\sigma} \leqslant 6$, $x = 0.4$ corresponds to 3–4σ below the formal detection limit, while $x = 1.6$ is 3–4σ above the formal detection limit. We adopt the following approximations.

1. $x_{i,1} < 0.4$: The integral is nearly zero.
2. $x_{i,1} > 0.4$ and $\Gamma \notin [-6, 10]$: For $\beta \in [-3, 2]$ (ranging from exceptionally bottom heavy to exceptionally top-heavy; $\beta \sim -1$ from RV studies), this would imply $\gamma < 1/3$, i.e., the dependence of luminosity of mass is exceptionally weak. We approximate the error function as a constant, obtaining
$$\frac{1}{\beta+1}(M_{i,1}\, p_M(M_{i,1}) - M_{i,0}\, p_M(M_{i,0})) \times \left[\frac{1}{2} + \frac{1}{2}\text{erf}\left(\frac{(L_i/L_{\lim} - 1)\, N_{\sigma}}{\sqrt{2}}\right)\right]. \tag{A14}$$
3. $0.4 < x_{i,1} < 1.6$ and $-6 \leqslant \Gamma \leqslant 10$: We evaluate the integral from tabulated quadratic fits. We set the lower limit of integration to $\min(0.4,\ x_{i,0})$.
4. $x_{i,1} > 1.6$ and $-6 \leqslant \Gamma \leqslant 10$: We evaluate the integral from tabulated quadratic fits, setting the lower limit of integration to $\min(0.4,\ x_{i,0})$ and the upper limit to 1.6. We then integrate the entire rest of the mass distribution (assuming a nearly monotonic mass-luminosity relation), obtaining
$$\frac{1}{\beta+1}\left[M_{\max}\, p_M(M_{\max}) - M_i\, p_M(M_i)\left(\frac{1.6 L_{\lim}}{L_i}\right)^{(\beta+1)/\gamma_i}\right]. \tag{A15}$$

Assuming we pre-compute p_M at the tabulated masses, each of these approximations requires at most one call to a special function (power or erf), a handful of array lookups, and ~20 floating point operations. Our tabulated fits to the integrals are always accurate to better than 0.1% of the integral evaluated between $x = 0.4$ and 1.6; these approximations therefore introduce less error than the (inevitable) interpolations over the grid of models.

REFERENCES

Alibert, Y., Mordasini, C., Benz, W., & Winisdoerffer, C. 2005, A&A, 434, 343
Allard, F., Hauschildt, P. H., Alexander, D. R., Tamanai, A., & Schweitzer, A. 2001, ApJ, 556, 357
Allard, F., Homeier, D., & Freytag, B. 2011, in ASP Conf. Ser. 448, 16th Cambridge Workshop on Cool Stars, Stellar Systems, and the Sun, ed. C. Johns-Krull, M. K. Browning, & A. A. West (San Francisco, CA: ASP), 91
Ambartsumian, V. A. 1937, AZh, 14, 207
An, D., Terndrup, D. M., Pinsonneault, M. H., et al. 2007, ApJ, 655, 233
Andrews, S. M., Rosenfeld, K. A., Kraus, A. L., & Wilner, D. J. 2013, ApJ, 771, 129
Bakos, G., Noyes, R. W., Kovács, G., et al. 2004, PASP, 116, 266
Baliunas, S. L., Donahue, R. A., Soon, W. H., et al. 1995, ApJ, 438, 269
Baraffe, I., Chabrier, G., Barman, T. S., Allard, F., & Hauschildt, P. H. 2003, A&A, 402, 701
Batalha, N. M., Rowe, J. F., Bryson, S. T., et al. 2013, ApJS, 204, 24
Bate, M. R. 2009, MNRAS, 392, 590
Bate, M. R., Bonnell, I. A., & Bromm, V. 2002, MNRAS, 332, L65
Bate, M. R., Bonnell, I. A., & Bromm, V. 2003, MNRAS, 339, 577
Beuzit, J.-L., Feldt, M., Dohlen, K., et al. 2008, Proc. SPIE, 7014, 701418

Biller, B. A., Liu, M. C., Wahhaj, Z., et al. 2010, ApJL, 720, L82
Biller, B. A., Liu, M. C., Wahhaj, Z., et al. 2013, ApJ, 777, 160
Binks, A. S., & Jeffries, R. D. 2014, MNRAS, 438, L11
Boley, A. C. 2009, ApJL, 695, L53
Bonfils, X., Delfosse, X., Udry, S., et al. 2013, A&A, 549, A109
Bonnefoy, M., Boccaletti, A., Lagrange, A.-M., et al. 2013, A&A, 555, A107
Bonnefoy, M., Currie, T., Marleau, G.-D., et al. 2014, A&A, 562, A111
Boss, A. P. 1997, Sci, 276, 1836
Boss, A. P. 2000, ApJL, 536, L101
Bowler, B. P., Liu, M. C., Shkolnik, E. L., & Dupuy, T. J. 2013, ApJ, 774, 55
Brandeker, A., Jayawardhana, R., Khavari, P., Haisch, K. E., Jr., & Mardones, D. 2006, ApJ, 652, 1572
Brandt, T. D., Kuzuhara, M., McElwain, M. W., et al. 2014, ApJ, 786, 1
Brandt, T. D., McElwain, M. W., Turner, E. L., et al. 2013, ApJ, 764, 183
Bromley, B. C., & Kenyon, S. J. 2011, ApJ, 731, 101
Carson, J., Thalmann, C., Janson, M., et al. 2013, ApJL, 763, L32
Chabrier, G. 2003, PASP, 115, 763
Chabrier, G., Baraffe, I., Allard, F., & Hauschildt, P. 2000, ApJ, 542, 464
Chauvin, G., Lagrange, A.-M., Bonavita, M., et al. 2010, A&A, 509, A52
Chauvin, G., Lagrange, A.-M., Lacombe, F., et al. 2005a, A&A, 430, 1027
Chauvin, G., Lagrange, A.-M., Zuckerman, B., et al. 2005b, A&A, 438, L29
Chauvin, G., Vigan, A., Bonnefoy, M., et al. 2014, arXiv:1405.1560
Chen, C. H., Mamajek, E. E., Bitner, M. A., et al. 2011, ApJ, 738, 122
Chen, C. H., Sargent, B. A., Bohac, C., et al. 2006, ApJS, 166, 351
Craig, N., Christian, D. J., Dupuis, J., & Roberts, B. A. 1997, AJ, 114, 244
Cumming, A., Butler, R. P., Marcy, G. W., et al. 2008, PASP, 120, 531
Currie, T., Burrows, A., Itoh, Y., et al. 2011, ApJ, 729, 128
Currie, T., Daemgen, S., Debes, J., et al. 2014, ApJL, 780, L30
Currie, T., Debes, J., Rodigas, T. J., et al. 2012, ApJL, 760, L32
da Silva, L., Torres, C. A. O., de La Reza, R., et al. 2009, A&A, 508, 833
Dawson, R. I., Murray-Clay, R. A., & Fabrycky, D. C. 2011, ApJL, 743, L17
Delfosse, X., Forveille, T., Mayor, M., et al. 1998, A&A, 338, L67
Delorme, P., Gagné, J., Girard, J. H., et al. 2013, A&A, 553, L5
de Zeeuw, P. T., Hoogerwerf, R., de Bruijne, J. H. J., Brown, A. G. A., & Blaauw, A. 1999, AJ, 117, 354
Dodson-Robinson, S. E., Veras, D., Ford, E. B., & Beichman, C. A. 2009, ApJ, 707, 79
Duquennoy, A., & Mayor, M. 1991, A&A, 248, 485
Eiroa, C., Marshall, J. P., Mora, A., et al. 2011, A&A, 536, L4
Fernández, D., Figueras, F., & Torra, J. 2008, A&A, 480, 735
Fischer, D. A., & Valenti, J. 2005, ApJ, 622, 1102
Gagné, J., Lafrenière, D., Doyon, R., Malo, L., & Artigau, É. 2014, ApJ, 783, 121
Gaidos, E. J., Henry, G. W., & Henry, S. M. 2000, AJ, 120, 1006
Geißler, K., Metchev, S. A., Pham, A., et al. 2012, ApJ, 746, 44
Ghezzi, L., Cunha, K., Smith, V. V., et al. 2010, ApJ, 720, 1290
Gizis, J. E., Kirkpatrick, J. D., Burgasser, A., et al. 2001, ApJL, 551, L163
Głębocki, R., & Gnaciński, P. 2005, in 13th Cambridge Workshop on Cool Stars, Stellar Systems and the Sun, ed. F. Favata, G. A. J. Hussain, & B. Battrick (ESA Special Publication, Vol. 560; Noordwijk: ESA), 571
Gonzalez, G., Carlson, M. K., & Tobin, R. W. 2010, MNRAS, 403, 1368
Grether, D., & Lineweaver, C. H. 2006, ApJ, 640, 1051
Guillout, P., Klutsch, A., Frasca, A., et al. 2009, A&A, 504, 829
Hayano, Y., Takami, H., Guyon, O., et al. 2008, Proc. SPIE, 7015, 701510
Hayashi, C. 1981, PThPS, 70, 35
Hinkley, S., Pueyo, L., Faherty, J. K., et al. 2013, ApJ, 779, 153
Holman, M. J., & Wiegert, P. A. 1999, AJ, 117, 621
Hubickyj, O., Bodenheimer, P., & Lissauer, J. J. 2005, Icar, 179, 415
Janson, M., Brandt, T. D., Kuzuhara, M., et al. 2013a, ApJL, 778, L4
Janson, M., Brandt, T. D., Moro-Martin, A., et al. 2013b, ApJ, 773, 73
Janson, M., Carson, J., Thalmann, C., et al. 2011, ApJ, 728, 85
Janson, M., Carson, J. C., Lafrenière, D., et al. 2012, ApJ, 747, 116
Johnson, J. A., Butler, R. P., Marcy, G. W., et al. 2007a, ApJ, 670, 833
Johnson, J. A., Fischer, D. A., Marcy, G. W., et al. 2007b, ApJ, 665, 785
Jurić, M., & Tremaine, S. 2008, ApJ, 686, 603
Kalas, P., Graham, J. R., Chiang, E., et al. 2008, Sci, 322, 1345
Kenyon, S. J., & Bromley, B. C. 2009, ApJL, 690, L140
Kiraga, M. 2012, AcA, 62, 67
Kirkpatrick, J. D., Gelino, C. R., Cushing, M. C., et al. 2012, ApJ, 753, 156
Kiss, L. L., Moór, A., Szalai, T., et al. 2011, MNRAS, 411, 117
Koen, C., & Eyer, L. 2002, MNRAS, 331, 45
Konopacky, Q. M., Barman, T. S., Macintosh, B. A., & Marois, C. 2013, Sci, 339, 1398
Kratter, K. M., Murray-Clay, R. A., & Youdin, A. N. 2010, ApJ, 710, 1375
Kraus, A. L., & Ireland, M. J. 2012, ApJ, 745, 5
Kroupa, P. 2001, MNRAS, 322, 231
Kuiper, G. P. 1951, PNAS, 37, 1
Kuzuhara, M., Tamura, M., Kudo, T., et al. 2013, ApJ, 774, 11
Lafrenière, D., Doyon, R., Marois, C., et al. 2007, ApJ, 670, 1367
Lagrange, A.-M., De Bondt, K., Meunier, N., et al. 2012, A&A, 542, A18
Lagrange, A.-M., Gratadour, D., Chauvin, G., et al. 2009, A&A, 493, L21
Lambrechts, M., & Johansen, A. 2012, A&A, 544, A32
Lockwood, G. W., Skiff, B. A., Henry, G. W., et al. 2007, ApJS, 171, 260
López-Santiago, J., Montes, D., Crespo-Chacón, I., & Fernández-Figueroa, M. J. 2006, ApJ, 643, 1160
López-Santiago, J., Montes, D., Gálvez-Ortiz, M. C., et al. 2010, A&A, 514, A97
Low, C., & Lynden-Bell, D. 1976, MNRAS, 176, 367
Lowrance, P. J., Schneider, G., Kirkpatrick, J. D., et al. 2000, ApJ, 541, 390
Macintosh, B. A., Graham, J. R., Palmer, D. W., et al. 2008, Proc. SPIE, 7015, 701518
Malo, L., Doyon, R., Lafrenière, D., et al. 2013, ApJ, 762, 88
Mamajek, E. E., & Hillenbrand, L. A. 2008, ApJ, 687, 1264
Marcy, G. W., & Butler, R. P. 2000, PASP, 112, 137
Marcy, G. W., Butler, R. P., Fischer, D., et al. 2001, ApJ, 556, 296
Marcy, G. W., Butler, R. P., Vogt, S. S., Fischer, D., & Lissauer, J. J. 1998, ApJL, 505, L147
Marleau, G.-D., & Cumming, A. 2014, MNRAS, 437, 1378
Marley, M. S., Fortney, J. J., Hubickyj, O., Bodenheimer, P., & Lissauer, J. J. 2007, ApJ, 655, 541
Marois, C., Macintosh, B., Barman, T., et al. 2008, Sci, 322, 1348
Marois, C., Zuckerman, B., Konopacky, Q. M., Macintosh, B., & Barman, T. 2010, Natur, 468, 1080
Mayor, M., & Queloz, D. 1995, Natur, 378, 355
McCarthy, K., & White, R. J. 2012, AJ, 143, 134
Merín, B., Montesinos, B., Eiroa, C., et al. 2004, A&A, 419, 301
Messina, S., Desidera, S., Lanzafame, A. C., Turatto, M., & Guinan, E. F. 2011, A&A, 532, A10
Messina, S., Desidera, S., Turatto, M., Lanzafame, A. C., & Guinan, E. F. 2010, A&A, 520, A15
Messina, S., & Guinan, E. F. 1996, IBVS, 4286, 1
Messina, S., Pizzolato, N., Guinan, E. F., & Rodonò, M. 2003, A&A, 410, 671
Metchev, S. A., & Hillenbrand, L. A. 2009, ApJS, 181, 62
Mishenina, T. V., Soubiran, C., Bienaymé, O., et al. 2008, A&A, 489, 923
Mishenina, T. V., Soubiran, C., Kovtyukh, V. V., Katsova, M. M., & Livshits, M. A. 2012, A&A, 547, A106
Moór, A., Pascucci, I., Kóspál, Á., et al. 2011, ApJS, 193, 4
Moór, A., Szabó, G. M., Kiss, L. L., et al. 2013, MNRAS, 435, 1376
Mordasini, C. 2013, A&A, 558, A113
Munari, U., Dallaporta, S., Siviero, A., et al. 2004, A&A, 418, L31
Nielsen, E. L., & Close, L. M. 2010, ApJ, 717, 878
Nielsen, E. L., Liu, M. C., Wahhaj, Z., et al. 2012, ApJ, 750, 53
Nielsen, E. L., Liu, M. C., Wahhaj, Z., et al. 2013, ApJ, 776, 4
Norton, A. J., Wheatley, P. J., West, R. G., et al. 2007, A&A, 467, 785
Pace, G. 2013, A&A, 551, L8
Pecaut, M. J., Mamajek, E. E., & Bubar, E. J. 2012, ApJ, 746, 154
Peters, M. A., Groff, T., Kasdin, N. J., et al. 2012, Proc. SPIE, 8446, 84467U
Plavchan, P., Werner, M. W., Chen, C. H., et al. 2009, ApJ, 698, 1068
Pojmanski, G., Pilecki, B., & Szczygiel, D. 2005, AcA, 55, 275
Pollacco, D. L., Skillen, I., Collier Cameron, A., et al. 2006, PASP, 118, 1407
Pollack, J. B., Hubickyj, O., Bodenheimer, P., et al. 1996, Icar, 124, 62
Radick, R. R., Lockwood, G. W., Skiff, B. A., & Baliunas, S. L. 1998, ApJS, 118, 239
Rafikov, R. R. 2005, ApJL, 621, L69
Raghavan, D., McAlister, H. A., Henry, T. J., et al. 2010, ApJS, 190, 1
Rameau, J., Chauvin, G., Lagrange, A.-M., et al. 2013, ApJL, 772, L15
Reid, I. N., Gizis, J. E., & Hawley, S. L. 2002, AJ, 124, 2721
Rieke, G. H., Su, K. Y. L., Stansberry, J. A., et al. 2005, ApJ, 620, 1010
Rivera, E. J., Laughlin, G., Butler, R. P., et al. 2010, ApJ, 719, 890
Rivera, E. J., Lissauer, J. J., Butler, R. P., et al. 2005, ApJ, 634, 625
Rodriguez, D. R., Marois, C., Zuckerman, B., Macintosh, B., & Melis, C. 2012, ApJ, 748, 30
Rodriguez, D. R., Zuckerman, B., Kastner, J. H., et al. 2013, ApJ, 774, 101
Salpeter, E. E. 1955, ApJ, 121, 161
Samus, N. N., & Durlevich, O. V. 2009, yCat, 1, 2025
Schlieder, J. E., Lépine, S., & Simon, M. 2010, AJ, 140, 119
Schlieder, J. E., Lépine, S., & Simon, M. 2012, AJ, 143, 80
Shkolnik, E. L., Anglada-Escudé, G., Liu, M. C., et al. 2012, ApJ, 758, 56
Soderblom, D. R. 2010, ARA&A, 48, 581
Song, I., Zuckerman, B., & Bessell, M. S. 2012, AJ, 144, 8
Spiegel, D. S., & Burrows, A. 2012, ApJ, 745, 174
Spiegel, D. S., Burrows, A., & Milsom, J. A. 2011, ApJ, 727, 57
Stamatellos, D., & Whitworth, A. P. 2009, MNRAS, 392, 413

Stauffer, J. R., Schultz, G., & Kirkpatrick, J. D. 1998, ApJL, 499, L199
Sudol, J. J., & Haghighipour, N. 2012, ApJ, 755, 38
Sumi, T., Kamiya, K., Bennett, D. P., et al. 2011, Natur, 473, 349
Suzuki, R., Kudo, T., Hashimoto, J., et al. 2010, Proc. SPIE, 7735, 773530
Takeda, Y., & Kawanomoto, S. 2005, PASJ, 57, 45
Tamura, M. 2009, in AIP Conf. Ser. 1158, Exoplanets and Disks: Their Formation and Diversity, ed. T. Usuda, M. Tamura, & M. Ishii (Melville, NY: AIP), 11
Thalmann, C., Carson, J., Janson, M., et al. 2009, ApJL, 707, L123
Thies, I., & Kroupa, P. 2007, ApJ, 671, 767
Thies, I., & Kroupa, P. 2008, MNRAS, 390, 1200
Torres, C. A. O., Quast, G. R., da Silva, L., et al. 2006, A&A, 460, 695
Torres, C. A. O., Quast, G. R., Melo, C. H. F., & Sterzik, M. F. 2008, in Young Nearby Loose Associations, ed. B. Reipurth (San Francisco, CA: ASP), 757
Umbreit, S., Burkert, A., Henning, T., Mikkola, S., & Spurzem, R. 2005, ApJ, 623, 940
van Leeuwen, F. 2009, A&A, 497, 209
Vigan, A., Patience, J., Marois, C., et al. 2012, A&A, 544, A9
Vorobyov, E. I. 2013, A&A, 552, A129
Wahhaj, Z., Liu, M. C., Biller, B. A., et al. 2011, ApJ, 729, 139
Wahhaj, Z., Liu, M. C., Biller, B. A., et al. 2013a, ApJ, 779, 80
Wahhaj, Z., Liu, M. C., Nielsen, E. L., et al. 2013b, ApJ, 773, 179
White, R. J., Gabor, J. M., & Hillenbrand, L. A. 2007, AJ, 133, 2524
Whitworth, A. P., & Stamatellos, D. 2006, A&A, 458, 817
Wright, N. J., Drake, J. J., Mamajek, E. E., & Henry, G. W. 2011, ApJ, 743, 48
Yamamoto, K., Matsuo, T., Shibai, H., et al. 2013, PASJ, 65, 90
Zuckerman, B., Rhee, J. H., Song, I., & Bessell, M. S. 2011, ApJ, 732, 61
Zuckerman, B., & Song, I. 2004, ARA&A, 42, 685
Zuckerman, B., & Song, I. 2009, A&A, 493, 1149
Zuckerman, B., & Song, I. 2012, ApJ, 758, 77
Zuckerman, B., Song, I., Bessell, M. S., & Webb, R. A. 2001, ApJL, 562, L87
Zuckerman, B., & Webb, R. A. 2000, ApJ, 535, 959

The Astrophysical Journal, 774:11 (18pp), 2013 September 1 doi:10.1088/0004-637X/774/1/11

DIRECT IMAGING OF A COLD JOVIAN EXOPLANET IN ORBIT AROUND THE SUN-LIKE STAR GJ 504

M. Kuzuhara[1,2,3], M. Tamura[2,4,5], T. Kudo[6], M. Janson[7], R. Kandori[2], T. D. Brandt[7], C. Thalmann[8], D. Spiegel[7,9], B. Biller[10], J. Carson[11], Y. Hori[2], R. Suzuki[2], A. Burrows[7], T. Henning[10], E. L. Turner[7,12], M. W. McElwain[13], A. Moro-Martín[7,14], T. Suenaga[2,4], Y. H. Takahashi[2,5], J. Kwon[2,4], P. Lucas[15], L. Abe[16], W. Brandner[10], S. Egner[6], M. Feldt[10], H. Fujiwara[6], M. Goto[17], C. A. Grady[18,13], O. Guyon[6], J. Hashimoto[19], Y. Hayano[6], M. Hayashi[2], S. S. Hayashi[6], K. W. Hodapp[20], M. Ishii[6], M. Iye[2], G. R. Knapp[7], T. Matsuo[21], S. Mayama[22], S. Miyama[23], J.-I. Morino[2], J. Nishikawa[2,4], T. Nishimura[6], T. Kotani[2], N. Kusakabe[2], T.-S. Pyo[6], E. Serabyn[24], H. Suto[2], M. Takami[25], N. Takato[6], H. Terada[6], D. Tomono[6], M. Watanabe[26], J. P. Wisniewski[19], T. Yamada[27], H. Takami[2], and T. Usuda[2]

[1] Department of Earth and Planetary Science, The University of Tokyo, 7-3-1 Hongo, Bunkyo-ku, Tokyo 113-0033, Japan
[2] National Astronomical Observatory of Japan, 2-21-1 Osawa, Mitaka, Tokyo 181-8588, Japan; m.kuzuhara@nao.ac.jp
[3] Department of Earth and Planetary Sciences, Tokyo Institute of Technology, 2-12-1 Ookayama, Meguro-ku, Tokyo 152-8551, Japan
[4] Department of Astronomical Science, The Graduate University for Advanced Studies, 2-21-1 Osawa, Mitaka, Tokyo 181-8588, Japan
[5] Department of Astronomy, The University of Tokyo, 7-3-1 Hongo, Bunkyo-ku, Tokyo 113-0033, Japan
[6] Subaru Telescope, National Astronomical Observatory of Japan, 650 North A'ohoku Place, Hilo, HI 96720, USA
[7] Department of Astrophysical Sciences, Princeton University, Peyton Hall, Ivy Lane, Princeton, NJ 08544, USA
[8] Astronomical Institute "Anton Pannekoek," University of Amsterdam, Postbus 94249, 1090 GE, Amsterdam, The Netherlands
[9] Institute for Advanced Study, Princeton, NJ 08540, USA
[10] Max Planck Institute for Astronomy, Königstuhl 17, D-69117 Heidelberg, Germany
[11] Department of Physics and Astronomy, College of Charleston, 58 Coming Street, Charleston, SC 29424, USA
[12] Kavli Institute for Physics and Mathematics of the Universe, The University of Tokyo, 5-1-5 Kashiwanoha, Kashiwa, Chiba 277-8568, Japan
[13] Exoplanets and Stellar Astrophysics Laboratory, Code 667, Goddard Space Flight Center, Greenbelt, MD 20771, USA
[14] Department of Astrophysics, CAB-CSIC/INTA, E-28850 Torrejón de Ardoz, Madrid, Spain
[15] Centre for Astrophysics, University of Hertfordshire, College Lane, Hatfield AL10 9AB, UK
[16] Laboratoire Lagrange (UMR 7293), Université de Nice-Sophia Antipolis, CNRS, Observatoire de la Côte d'Azur, 28 Avenue Valrose, F-06108 Nice Cedex 2, France
[17] Universitäts-Sternwarte München, Ludwig-Maximilians-Universität, Scheinerstr. 1, D-81679 München, Germany
[18] Eureka Scientific, 2452 Delmer, Suite 100, Oakland, CA 96002, USA
[19] H. L. Dodge Department of Physics and Astronomy, University of Oklahoma, 440 West Brooks St Norman, OK 73019, USA
[20] Institute for Astronomy, University of Hawaii, 640 North A'ohoku Place, Hilo, HI 96720, USA
[21] Department of Astronomy, Kyoto University, Kitashirakawa-Oiwake-cho, Sakyo-ku, Kyoto, Kyoto 606-8502, Japan
[22] The Graduate University for Advanced Studies, Shonan International Village, Hayama, Miura, Kanagawa 240-0193, Japan
[23] Hiroshima University, 1-3-2, Kagamiyama, Higashihiroshima, Hiroshima 739-8511, Japan
[24] Jet Propulsion Laboratory, California Institute of Technology, Pasadena, CA 91109, USA
[25] Institute of Astronomy and Astrophysics, Academia Sinica, P.O. Box 23-141, Taipei 10617, Taiwan
[26] Department of Cosmosciences, Hokkaido University, Kita-ku, Sapporo, Hokkaido 060-0810, Japan
[27] Astronomical Institute, Tohoku University, Aoba-ku, Sendai, Miyagi 980-8578, Japan
Received 2013 February 8; accepted 2013 July 8; published 2013 August 8

ABSTRACT

Several exoplanets have recently been imaged at wide separations of >10 AU from their parent stars. These span a limited range of ages (<50 Myr) and atmospheric properties, with temperatures of 800–1800 K and very red colors ($J - H > 0.5$ mag), implying thick cloud covers. Furthermore, substantial model uncertainties exist at these young ages due to the unknown initial conditions at formation, which can lead to an order of magnitude of uncertainty in the modeled planet mass. Here, we report the direct-imaging discovery of a Jovian exoplanet around the Sun-like star GJ 504, detected as part of the SEEDS survey. The system is older than all other known directly imaged planets; as a result, its estimated mass remains in the planetary regime independent of uncertainties related to choices of initial conditions in the exoplanet modeling. Using the most common exoplanet cooling model, and given the system age of 160^{+350}_{-60} Myr, GJ 504b has an estimated mass of $4^{+4.5}_{-1.0}$ Jupiter masses, among the lowest of directly imaged planets. Its projected separation of 43.5 AU exceeds the typical outer boundary of ∼30 AU predicted for the core accretion mechanism. GJ 504b is also significantly cooler (510^{+30}_{-20} K) and has a bluer color ($J - H = -0.23$ mag) than previously imaged exoplanets, suggesting a largely cloud-free atmosphere accessible to spectroscopic characterization. Thus, it has the potential of providing novel insights into the origins of giant planets as well as their atmospheric properties.

Key words: planetary systems – stars: formation – stars: individual (GJ 504)

1. INTRODUCTION

More than 890 extrasolar planets (or exoplanets) have been discovered by now (Schneider et al. 2011), and NASA's *Kepler* mission alone has recently added more than 2000 exoplanet candidates (Batalha et al. 2013). The vast majority of exoplanets have been discovered using indirect detection techniques that infer the presence of the exoplanet by monitoring the host star, such as planetary transits or radial-velocity variations. The techniques require observations over at least one orbital period, making them impractical for detecting long-period exoplanets at large separations. Meanwhile, in spite of the technical challenges, 8 m class telescopes equipped with adaptive-optics (AO) systems and/or coronagraphs have

recently reached the high-contrast performance necessary to image massive planets at large orbital separations (Marois et al. 2008, 2010; Lagrange et al. 2010). Direct-imaging surveys using such instruments provide measurements of an exoplanet's position and luminosity, which can be used to estimate its mass using the age of its host star and models of luminosity evolution for planetary-mass objects.

Because massive exoplanets cool and fade with time, direct-imaging searches have been most successful around young stars. Mass estimates for young planets depend strongly on the assumed system age, planetary atmosphere models, and initial thermodynamic state, leading to large uncertainties in the inferred mass. Planetary-mass estimates conventionally assume a "hot start," in which the planet is initially in a high-temperature, high-entropy (and hence, luminous) state (Baraffe et al. 2003; Burrows et al. 1997). However, recent theoretical models suggest that giant planets produced according to standard formation theories could initially be much colder (Marley et al. 2007; Fortney et al. 2008; Spiegel & Burrows 2012). The difference between the mass–luminosity relations of the "hot-start" and "cold-start" models decreases with exoplanet age; the models converge after ∼100 Myr for a 5 $M_{\rm Jup}$ planet, and ∼1 Gyr for a 10 $M_{\rm Jup}$ planet (Marley et al. 2007; Fortney et al. 2008; Spiegel & Burrows 2012).

Previously imaged exoplanets are all younger than 50 Myr (Marois et al. 2008; Lagrange et al. 2010; Carson et al. 2013). The hot-start models imply planetary masses (Marois et al. 2008, 2010; Lagrange et al. 2010), while cold-start models cannot reproduce the high observed luminosities (Marley et al. 2007; Spiegel & Burrows 2012). Therefore, their planetary status would be negated if the cold-start models apply at such young ages. Nevertheless, independent constraints, such as dynamical stability analysis in the case of the HR 8799 system (e.g., Fabrycky & Murray-Clay 2010; Marois et al. 2010; Sudol & Haghighipour 2012), in some cases can be used to exclude the coldest range of initial conditions and confine their masses to the planetary-mass regime. In addition, we note that neither hot-start nor cold-start models have been calibrated against dynamical mass estimates. These arguments suggest that no fully established model for estimating the masses of directly imaged planets exists as of yet. However, direct imaging of an older system with a well-determined age could remove much of the model uncertainty related to the unknown initial conditions.

A common feature of the previously imaged planets is large effective temperatures (>800 K; Marois et al. 2008) and very red colors implying the presence of thick clouds in their atmospheres. Furthermore, they have generally been discovered as companions to massive (>1.5 $M_{\rm Sun}$) stars (e.g., Baines et al. 2012; Lagrange et al. 2010; Carson et al. 2013), and hence they populate a limited range in atmospheric conditions and host star properties. Widening this range would greatly enhance our understanding of the population of exoplanets in wide orbits.

Here, we report the detection of an exoplanet around the nearby Sun-like star GJ 504 using high-contrast near-infrared imaging on the Subaru Telescope. The projected separation of the planet (GJ 504b) is measured to be 43.5 AU from the star, and the mass of planet (GJ 504b) is estimated to be a few $M_{\rm Jup}$; because the system has an age of 160^{+350}_{-60} Myr, its mass estimate is only weakly dependent on the uncertainty of initial conditions in the cooling models of giant planets. In Section 2, we describe the properties of GJ 504. In Section 3, the observations and data reductions are detailed. Section 4 presents a derivation of the mass of GJ 504b and other interesting properties of this planet.

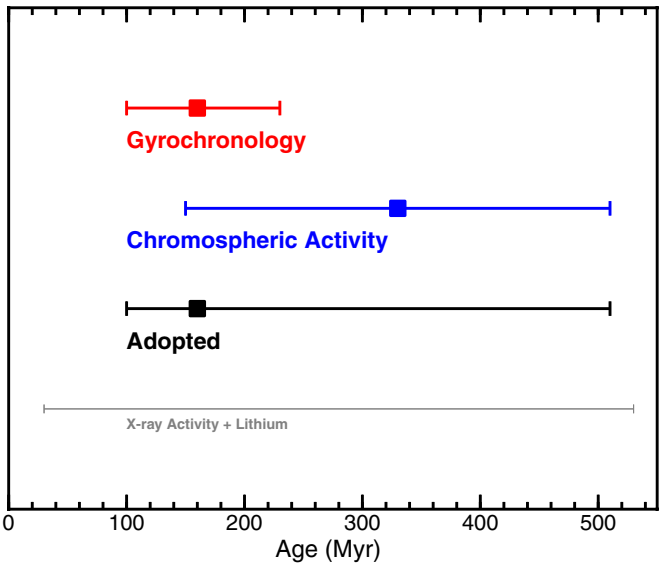

Figure 1. GJ 504's ages independently inferred from gyrochronology, chromospheric, and X-ray coronal activity, or lithium technique are summarized together with our adopted age for the system. The squares indicate the optimum estimates based on each technique, and the horizontal bars correspond to their error ranges. Because the gyrochronology and chromospheric activity could be the most reliable age indicators for isolated G-type stars with evolution stages near ZAMS, we use those as the fiducial age estimators. The best estimate in our adopted age for GJ 504 is the gyrochronology technique, which directly traces the stellar rotation than the activity. The estimates from lithium or X-ray activity are not adopted but are consistent with those from others.

Section 5 investigates the atmospheric properties and possible origin of GJ 504b. Our results are summarized in Section 6.

2. GJ 504 STELLAR PROPERTIES

GJ 504 is an isolated G0-type main-sequence star. It has a mass of 1.2 $M_{\rm Sun}$ and an age of 160^{+350}_{-60} Myr. In the following sections, we will describe the stellar properties in more detail, including its age estimate. Table 1 summarizes the properties of GJ 504.

2.1. Age of GJ 504

For an isolated main-sequence star like GJ 504, several methods of age estimation can be imagined, including gyrochronology, chromospheric, or coronal activity, lithium abundance, kinematics, or isochrones. Among them, two particularly relevant age indicators for GJ 504 are gyrochronology based on stellar rotation, and chromospheric activity as traced by Ca II H and K emission, and this study thus uses these indicators as the fiducial age estimators. Both stellar rotation and activity decline as a Sun-like star ages and sheds angular momentum in its stellar wind, and both age indicators have been accurately calibrated using stars in open clusters (Mamajek & Hillenbrand 2008, hereafter MH08). Chromospheric activity is powered by the stellar magnetic dynamo, which is closely related to the stellar rotation rate. Gyrochronology, which directly measures this rate, is therefore the most direct, and may be the most reliable, of our age estimators (MH08), and allows us to obtain a best estimate of 160^{+70}_{-60} Myr for the age of GJ 504. However, adopting the age as given by the star's chromospheric activity in addition to that from gyrochronology, we conservatively adopt 160^{+350}_{-60} Myr as the age estimate of GJ 504 system (see Figure 1 for summary). We describe these age estimations in

Table 1
Properties of GJ 504 System

Property	Primary	Planet
Spectral type	G0V[a]	late T–early Y
Distance (pc)	17.56 ± 0.08[b]	
Proper motion (mas yr^{-1}); μ_α, μ_β	-338.83 ± 0.25, 190.24 ± 0.21[b]	
Effective temperature; $T_{\rm eff}$ (K)	6234 ± 25[c]	510^{+30}_{-20} d
Surface gravity; log g	4.60 ± 0.02[c]	$3.9^{+0.4}_{-0.2}$ d
Luminosity; log $(L/L_\odot)$	0.332 ± 0.032[c]	$-6.09^{+0.06}_{-0.08}$ d
Metallicity; [Fe/H]	0.28 ± 0.03[c]	...
Adopted age (Myr)	160^{+350}_{-60}	
Age by gyrochronology (Myr)	160^{+70}_{-60}	
Age by chromospheric activity (Myr)	330 ± 180	
Mass	$1.22 \pm 0.08\ M_\odot$	$4.0^{+4.5}_{-1.0}\ M_{\rm Jup}$[d]
J-band mass	...	$3.5^{+3.5}_{-1.0}\ M_{\rm Jup}$
H-band mass	...	$3.0^{+4.0}_{-0.5}\ M_{\rm Jup}$
K_s-band mass	...	$6.5^{+5.0}_{-1.5}\ M_{\rm Jup}$
L'-band mass	...	$3.5^{+4.0}_{-1.5}\ M_{\rm Jup}$
NIR brightness[e] (mag) (J; $\sim$1.2 μm)	4.106	19.91 ± 0.15
(H; $\sim$1.6 μm)	3.860	20.14 ± 0.14[f]
(K_s; $\sim$2.2 μm)	3.808	19.19 ± 0.28
(L'; $\sim$3.8 μm)	3.94	16.84 ± 0.19

Notes.
[a] Valdes et al. (2004) and Takeda et al. (2005).
[b] van Leeuwen (2007).
[c] Valenti & Fischer (2005).
[d] GJ 504b's effective temperature, surface gravity, bolometric luminosity, and mass are estimated by comparing its age (160^{+350}_{-60} Myr) and JHK_sL'-band magnitude with the most commonly used cooling model (Baraffe et al. 2003). For quantifying best estimates and lower/upper limits for all of these quantities, we apply the same calculation as described in Section 4.2.
[e] The provided errors of the stellar JHK photometry are less than 0.01 mag (Kidger & Martín-Luis 2003), while L' photometry was obtained in this work with an error of 0.09 mag (see Section 3.5).
[f] The H-band photometric magnitude is based on the weighted mean of the March and May values.

detail below, along with several other age indicators that are less well suited for the purpose.

2.1.1. Gyrochronological Age

The rotation of a star slows as the star ages and the stellar wind carries away angular momentum. Gyrochronology, which estimates a star's age from its rotation rate and $B-V$ color (i.e., mass), is generally considered to be the most direct, and possibly the most accurate, method for inferring stellar age (MH08). Chromospheric and X-ray activity are powered by the stellar dynamo, which is closely related to the star's rotation rate. Indeed, chromospheric age estimators often use stellar activity to infer the rotation period, which is then used to infer an age (MH08). The rotation period of GJ 504 has been directly measured to be 3.328 days (Messina et al. 2003) and 3.33 days (Donahue et al. 1996). We adopt the average of these measurements, 3.329 days, as the star's rotation period. The possible error range of <0.01 days is small enough not to affect the uncertainty of the age estimate.

The gyrochronology can be applied to I-sequence stars whose dynamo mechanism is presumed to originate at the interface between the convective and radiative zones in the stellar interior (Barnes 2007). In contrast, this method cannot be applied to C-sequence stars that are fully convective and may thus have a different dynamo mechanism that prevents efficient spin-down. We can judge that GJ 504 is an I-sequence star using two different sets of criteria specified in the literature (Barnes 2007; Dupuy et al. 2009): one in which we relate the age-normalized rotation of GJ 504 to other stars of similar $B-V$ colors, and the other in which the X-ray luminosity and Rossby number are compared to other chromospherically active stars. Both of these methods confirm that GJ 504 is consistent with an I-sequence star. This conclusion agrees with the previous classification (Barnes 2007) of GJ 504 as an I-sequence star.

To rigorously establish the age of GJ 504, we use three gyrochronology relations independently proposed (MH08; Barnes 2007; Meibom et al. 2009). All the relations determine a stellar age as a function of rotation period and $B-V$ color. Using the rotation period (3.329 days) and $B-V$ color (0.585 ± 0.007) of GJ 504, we derive ages of 140–180 (MH08), 100–140 (Barnes 2007), and 110–230 Myr (Meibom et al. 2009), respectively. The error ranges for the age estimates were derived based on all the possible sources of error: the observed scatter in the period–age relation (0.05 dex; MH08) or errors of coefficients in the period–age function (Barnes 2007; Meibom et al. 2009), and the error of the $B-V$ color. Conservatively adopting all these ranges,[28] we estimate the age of GJ 504 to be 160^{+70}_{-60} Myr.

[28] For the optimal value of the gyrochronological age estimation, we adopt 160 Myr, which was calculated by MH08, because MH08 have updated the gyrochronological relation of Barnes (2007). Both relations of MH08 and Barnes (2007) have been derived by utilizing several stellar clusters, while Meibom et al. (2009) used only a single cluster.

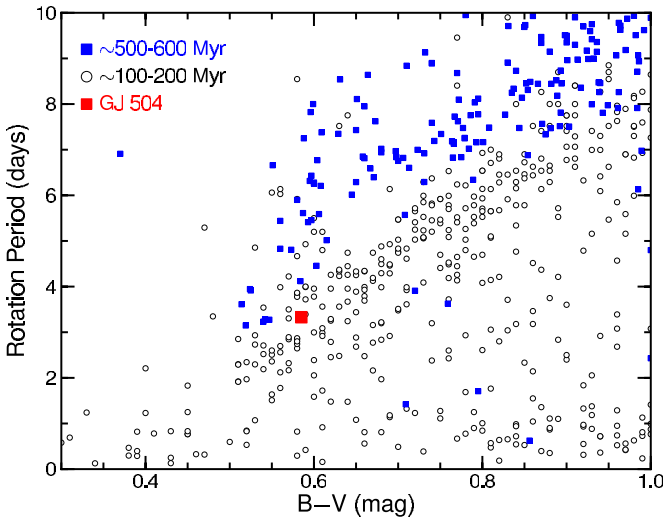

Figure 2. Stellar rotation of GJ 504, and of stars with $B - V < 1.0$ in various clusters. The horizontal axis shows the $B - V$ colors of the stellar samples, while the vertical axis denotes their rotations. The data of stars in ∼100–200 Myr old clusters (Pleiades, M35, M34, and M11) are plotted as open circles, and those of ∼500–600 Myr old clusters (M37, Hyades, and Praesepe) are plotted as blue squares. See the main text for the references of these data. The uncertainties in stellar rotation periods should be smaller than ∼10% in general (cf. Donahue et al. 1996; Barnes 2007; Hartman et al. 2009). The squares with $B - V$ colors bluer than 0.55 mag are M37 stars, with uncertainties of ∼0.01 mag. Thus, GJ 504 does not overlap with stars in 500–600 Myr clusters.

In order to verify the adequacy of GK 504's age assessed from the empirical relations of gyrochronology (see above), we directly compare the rotation period and $B - V$ color of GJ 504 to those of stars in young clusters (see Figure 2). The rotation data for stellar members in Pleiades (130 Myr; Hartman et al. 2010), M35 (150 Myr; Meibom et al. 2009), M34 (220 Myr; Meibom et al. 2011), M11 (230 Myr; Messina et al. 2010), M37 (550 Myr; Hartman et al. 2009), Hyades (630 Myr; Radick et al. 1987, 1995; Delorme et al. 2011), and Praesepe (600 Myr; Delorme et al. 2011) can be used for this purpose. As shown in Figure 2, the stars with similar $B - V$ colors to GJ 504 in 130–230 Myr old clusters have periods that are the most consistent with that of GJ 504, and the rotation periods in the older 500–600 Myr cluster are significantly longer,[29] thus verifying the age range of GJ 504 derived above. Additionally, combining the rotation data of stars in M11 with those in M34, Messina et al. (2010) derive a median rotation period of G-type stars in these clusters of 4.8 days, again supporting the age estimate of 160^{+70}_{-60} Myr for the G-type star GJ 504 (3.329 day period).

Since gyrochronology is a largely empirical method, there could in principle be uncertainties involved in the methodology that are not accounted for in the calibrations. For instance, if we hypothesize that the calibration could be metallicity-dependent, this would lead to systematic errors for targets with significantly different metallicity from the calibration clusters. For the case of GJ 504, it has a non-extreme value in this regard, and hence it is unlikely to be subject to such uncertainties. Another possible systematic uncertainty in gyrochronology involves the fact that rotation is easier to detect in rapidly rotating systems, which could result in a bias in the empirical gyrochronology relation. If this were a significant effect, it would cause the apparent mean rotation in a cluster of a given age to appear more rapid than it is in reality. Hence, age estimates for individual stars based on a relation calibrated against such clusters would result in an overestimation (i.e., an individual star would appear older than it really is). Given that no other age indicators imply a significantly younger age for GJ 504 this is also unlikely to be a real issue, but nonetheless, such uncertainties are important to keep in mind in the age analysis.

2.1.2. Chromospheric Activity Age

Stellar chromospheric activity, as traced by Ca II H and K emission, is a good indicator of stellar age. The strength of Ca II H and K emission is parameterized by $R'_{\rm HK}$, roughly the power in the H and K lines normalized to that in the underlying photospheric continuum. A relation between $R'_{\rm HK}$, $B - V$ color, and age has recently been derived for solar-type stars (MH08). For GJ 504, we adopt the value of $\log R'_{\rm HK} = -4.45$ measured at Mt. Wilson Observatory with a temporal baseline of 30 yr (Radick et al. 1998), the longest such baseline in the literature. In order to minimize the uncertainty in $R'_{\rm HK}$, the value for which the star has been monitored for the longest possible time should be adopted (see MH08), which also protects against accidentally adopting an outlier in the activity variation.

This activity level may be used to infer a Rossby number, the ratio of the stellar rotation period to the timescale of convective overturn, of 0.60 ± 0.10 following MH08.[30] We use this result,[31] together with a $B - V$ color of 0.585 ± 0.007 (van Leeuwen 2007), to estimate an age of 330 ± 100 Myr. We further add a 0.2 dex scatter in this relation, estimated from clusters[32] (MH08). We assume this scatter to be uncorrelated with other sources of error. As a result, we obtain a chromospheric age estimate of 330 ± 180 Myr.

Other studies using data from Mt. Wilson Observatory have measured $R'_{\rm HK}$ values of −4.443 (Baliunas et al. 1996) and −4.486 (Lockwood et al. 2007), which differ slightly from our adopted value of −4.45. The chromospheric activity level was also measured to be $R'_{\rm HK} = -4.44$ using 14 yr of observations at Fairborn and Lowell Observatories (Hall et al. 2009). Many of these studies' observational baselines overlap with the source of our adopted $R'_{\rm HK}$ value (Radick et al. 1998). Adopting the mean of these measurements would have little effect on our chromospheric age of 330 ± 180 Myr.

A primary uncertainty in age determination from chromospheric activity is long-term activity cycles, which may easily exceed the timescales over which the activity is measured, and thus may potentially provide a systematic error if the activity is measured at an extreme but is taken to represent the mean activity for the star. In addition, as in the case of gyrochronology, the stellar activity also depends on the metallicity, possibly contributing to the uncertainty. Since activity as an age estimator is thought to be closely related to gyrochronology through

[29] In addition to I-sequence stars, Figure 2 includes rotation data of C-sequence stars, which are widely scattered in the plot. However, the scatter is much smaller for the older clusters. GJ 504 is best represented by I-sequence stars, and young I-sequence stars such as provided in M35 or M34 (Meibom et al. 2009, 2011) are indeed in good agreement with GJ 504.

[30] MH08 have constructed an empirical function to convert a measurement of $R'_{\rm HK}$ to the Rossby number. The error in the inferred Rossby number was measured to be 0.10 for the multi-decade Mount Wilson data (see Section 4.1.2 and summary of MH08).

[31] The Rossby number is converted into a rotation period, which is used in the gyrochronology relation (i.e., activity–rotation–age relation) to estimate the stellar age. This scheme improves the accuracy of age estimation from chromospheric activity (see MH08).

[32] MH08 infer the uncertainty of their activity–rotation–age relation by calculating the rms of residuals between the ages of clusters and those of their stellar members, which were estimated by applying the activity–rotation–age relation to the members.

the stellar dynamo, the possibility of measuring both rotation (which is robust against activity cycles) and activity in the same star as for the case of GJ 504 can alleviate this uncertainty.

2.1.3. X-Ray Activity

Young solar-type stars are active X-ray emitters. As for Ca II H and K, a relation has been derived (MH08) between stellar age, color, and X-ray luminosity. The best estimate of the X-ray luminosity of GJ 504 comes from the *ROSAT* all-sky survey of nearby stars (Hünsch et al. 1999), which has provided a ratio of X-ray to bolometric power $\log L_X/L_{bol} = -4.42$ (Messina et al. 2003). This X-ray activity may be used to infer a Rossby number of 0.54 ± 0.25 (MH08) and lead to the age estimate of 90–530 Myr for GJ 504. Because the temporal baseline for the X-ray measurement is much shorter than for the multi-decade measurements of R'_{HK}, the inferred Rossby number is much more uncertain. Therefore, we do not adopt this estimate based on the X-ray emission, although it is consistent with the estimate from other methods.

2.1.4. Lithium Absorption

The strength of lithium absorption lines declines as a star burns its primordial supply of lithium, providing another indicator of stellar youth (Soderblom 2010). However, many effects, such as variations in the primordial supply of lithium, the extreme sensitivity of early lithium burning to the stellar accretion history (Baraffe & Chabrier 2010), and the importance of non-local thermodynamic equilibrium abundance corrections (Takeda & Kawanomoto 2005), make it difficult to obtain a reliable age estimate from lithium abundances. Therefore, we do not employ lithium as an indicator to date GJ 504, but it can provide a clue to the age of GJ 504 as discussed below. The equivalent width of Li in GJ 504 has been measured to be 0.08 Å, implying a lithium abundance of $\log n(\mathrm{Li}) = \log(N(\mathrm{Li})/N(\mathrm{H})) + 12 = 2.9$ (Takeda & Kawanomoto 2005). Extensive observations of well-dated open clusters (Sestito & Randich 2005) enable a lithium age estimate for GJ 504. At the effective temperature of a G0 star (∼6000 K), these cluster estimates can be used to infer an age range of approximately 30–500 Myr, fully consistent with our gyrochronological and chromospheric age estimates.

2.1.5. Kinematics

GJ 504 is not currently identified as a member of any clusters or moving groups (MGs), making it impossible to use population-based age estimators. The kinematic velocity of GJ 504 ($U = -38.6$, $V = 1.5$, $W = -18.0$; Mishenina et al. 2004) is consistent with thin disk stars, thus providing no tight constraint on the age, but remaining consistent with the young age provided by gyrochronology and chromospheric activity.

2.1.6. Isochrones

Since stars evolve along mass tracks in an H-R diagram with age, a common age determination method is based on isochronal analysis. This method can provide reasonable estimates for old stars that have evolved significantly off the main sequence and very young stars that are still undergoing rapid contraction. However, it is generally not useful for stars near the zero-age main sequence (ZAMS), around which stellar evolution proceeds slowly (e.g., Soderblom 2010). Indeed, generic isochronal estimates in the literature are known to give erroneous ages for young stars by up to two orders of magnitudes.

As illustrative examples, we consider the cases of HD 152555, HIP 10679, and HD 206860. These are all early G-type (G0–G2) stars which are members of young MGs; hence they are similar types of stars to GJ 504 with well-determined young ages, and thus can be used for comparison to isochronal ages of e.g., Valenti & Fischer (2005). HD 152555 is a member of the AB Dor MG (e.g., Torres et al. 2008) with an age of 50–100 Myr, whereas Valenti & Fischer (2005) give an age of 4.0 Gyr. HIP 10679 is a member of the β Pic MG (e.g., Torres et al. 2008) with an age of ∼10 Myr, whereas Valenti & Fischer (2005) give an age of 3.0 Gyr. Finally, HD 206860 is a member of the Her-Lya MG (e.g., López-Santiago et al. 2006) with an age of ∼200 Myr, whereas Valenti & Fischer (2005) give an age of 3.1 Gyr.

In light of these large discrepancies, it is unsurprising that literature estimates for the isochronal age of GJ 504 vary strongly from hundreds of Myrs to several Gyrs (e.g., Valenti & Fischer 2005; Takeda et al. 2007; Holmberg et al. 2009; da Silva et al. 2012). This implies that isochronal analysis should simply be disregarded for a star such as GJ 504, compared to the more reliable age estimators listed above. Nonetheless, since some of the isochronal literature estimates provide Gyr-range ages that are seemingly inconsistent with the younger age range we have adopted for GJ 504, we discuss their application to this star in more detail below.

An important limiting factor in isochrone analysis for age determination of an isolated main-sequence star such as GJ 504 is the sensitivity to uncertainties in input stellar parameters. This is in particular true for properties such as effective temperature and surface gravity, where the uncertainties are model-dependent and often tend to be underestimated in the literature. As an illustration, we consider the isochronal analysis in da Silva et al. (2012) based on the Yonsei–Yale isochrones (Yi et al. 2001), which gives an age of ∼3 Gyr, and appears to be inconsistent with ages of ⩽500 Myr within their quoted error bars. We have reproduced the analysis of da Silva et al. (2012) and confirmed these results with the same methodology and input observables. This is plotted in Figure 3. Also plotted in the same figure is the exact same analysis, but using the temperature estimates of GJ 504 from Valenti & Fischer (2005) instead; note that all other values are kept as in da Silva et al. (2012). This comparison immediately illuminates one of the considerable uncertainties related to isochronal analysis, which is uncertainties in the temperature scaling. The two temperature estimates in Valenti & Fischer (2005) and da Silva et al. (2012) are inconsistent within their quoted error bars, implying that neither error estimate should be trusted when translating this into an error on the age from the isochronal comparison. Moreover, we find that while the temperature estimate of da Silva et al. (2012) gives the aforementioned age of ∼3 Gyr and is inconsistent with ⩽500 Myr ages, the temperature estimate of Valenti & Fischer (2005) is fully consistent with these younger ages, and inconsistent with the ∼3 Gyr age.

It is also important to note that due to pre-main-sequence evolution, there is some overlap between the isochrones of stars arriving at the main sequence, and those leaving it. For instance, the 100 Myr isochrone overlaps with the 1 Gyr isochrone in the relevant temperature range. Hence, while the age is quoted as ∼1.4 Gyr in Valenti & Fischer (2005) which is reproduced in Figure 3, it can be equally well interpreted as being consistent with our adopted age range, and in fact preferentially supporting the youngest ages.

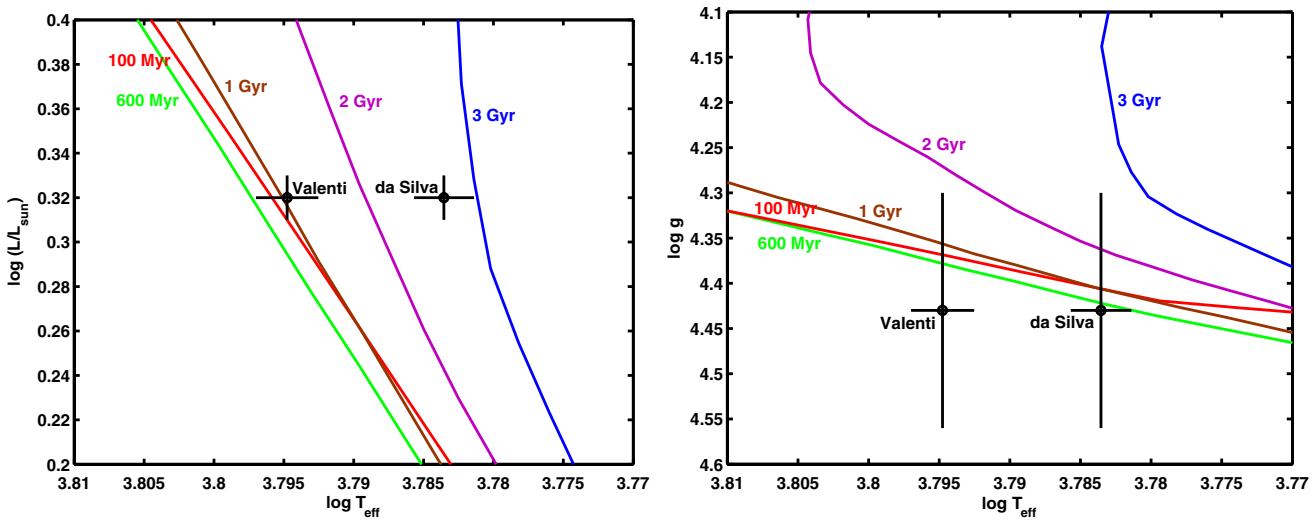

Figure 3. Isochronal analysis of GJ 504. Left: reproduction of the da Silva et al. (2012) result. Also plotted is another data point where all values are kept equal, except for the temperature which has been replaced with the one in Valenti & Fischer (2005), illustrating the real uncertainty in temperature. With the Valenti & Fischer (2005) temperature, the data are fully consistent with the ages derived from gyrochronology and activity. Right: the same analysis, again with all quantities except for temperature fixed to the da Silva et al. (2012) values, but replacing luminosity with surface gravity. In this framework, >3 Gyr ages are disfavored regardless of which temperature is chosen.

Furthermore, while the temperature and luminosity in da Silva et al. (2012) gives a certain age from comparison with the Yonsei–Yale isochrones, this does not account for the relatively high surface gravity they quote. We can see this in the second panel of Figure 3, where again we perform an isochronal analysis, but in surface gravity versus temperature as opposed to luminosity versus temperature. Here, regardless of which temperature value is used, the data are consistent with a $\leqslant$500 Myr age, but inconsistent with a $\sim$3 Gyr age.

It is instructive to think of these discrepancies in terms of the radius of the star. If we adopt the da Silva et al. (2012) temperature, then the luminosity is high for its mass, implying a large radius. On the other hand, the surface gravity is also high for its mass, implying a small radius. Hence, there is a tension in the radius between the luminosity and surface gravity if the da Silva et al. (2012) temperature is adopted, such that no self-consistent picture can be reached by either increasing or decreasing the stellar radius. By contrast, if we adopt the Valenti & Fischer (2005) temperature, then this tension disappears, and a self-consistent picture can be reached between the temperature, luminosity, and surface gravity—and simultaneously, we obtain a predicted age which is consistent with the estimates given by the age estimates in the previous sections. This could therefore be interpreted as supporting the higher temperature of Valenti & Fischer (2005) and thus a younger age.

Hence, we note that the isochronal age is readily consistent with gyrochronology and activity, using values for temperature, luminosity, and surface gravity published in the literature. This is also consistent with the arguably most detailed Bayesian isochronal analysis of Takeda et al. (2007), which was a study meant to improve on the analysis of Valenti & Fischer (2005) using the same input data, and which gives an age limit of <760 Myr. Nonetheless, the above discussions imply that it is not feasible to provide age constraints from isochronal dating that are as meaningful nor as stringent as those of gyrochronology and chromospheric activity. Thus, we do not include it in our adopted age range, but merely conclude that it is broadly consistent with such an age.

Finally, it can be noted that the existence of a star with such a short rotation period as GJ 504 ($\sim$3 days) would be unprecedented at the Gyr scale ages predicted by some isochrone analyses, such as da Silva et al. (2012). Indeed, although Reiners & Giampapa (2009) found an unusually rapid rotator in the $\sim$4 Gyr old M67 cluster, it has a rotation of approximately half the solar rotation rate ($P_\odot \sim 30$ days), which is significantly slower than the rotation of GJ 504. Aside from known close spectroscopic binaries, it is the largest known outlier at such an age. No indications of chromospheric activity corresponding to such rapid rotation have been found among 60 stars in the M67 cluster (Giampapa et al. 2006), which supports the notion that rapid rotators like GJ 504 must be exceedingly rare at ages of a few Gyr.

2.1.7. Summary of Age Estimate for GJ 504

As discussed above, we adopt the age estimated with gyrochronology as the most likely age (160^{+70}_{-60} Myr) for GJ 504. However, we conservatively adopt an age of 160^{+350}_{-60} Myr, with chromospheric activity providing the upper bound and gyrochronology providing the lower bound. Age indicators based on the lithium abundance, X-ray luminosity, kinematics, and isochrone technique are less precise than gyrochronology and chromospheric activity: in addition, for the Li-age estimate it is more difficult to quantify the uncertainty. We therefore do not attempt to combine those with the age range estimated from the gyrochronological and chromospheric activity techniques, although their estimates are consistent with our adopted age of GJ 504. Future asteroseismology studies, or detailed kinematic studies identifying GJ 504 as a member of an MG, may be able to refine our age estimate. The estimated ages are summarized in Table 1 and Figure 1.

2.2. Other Information

GJ 504 was previously reported to have a stellar companion at a projected separation of about 650 AU (Poveda et al. 1994), but subsequent observations showed that it does not share a common proper motion; the GJ 504 proper motions are -333.83 ± 0.25 mas yr^{-1} and 190.24 ± 0.17 mas yr^{-1} in right ascension and declination (van Leeuwen 2007), respectively, while those of the stellar companion candidates are 22.9 ± 11.2 mas yr^{-1}

Table 2
Observation Log and Astrometric Measurements of GJ 504b

Obs. Date (UT)	Inst.	Band	Total DIT (min)	Mode	FRA (°)	Proj. Sep. (arcsec)	P.A. (°)
2011 Mar 26	HiCIAO	H	12	ADI	52.7	2.479 ± 0.016	327.94 ± 0.39
2011 May 22	HiCIAO	H	21	ADI	56.9	2.483 ± 0.008	327.45 ± 0.19
2011 Aug 12	IRCS	L'	7	DI	...	2.481 ± 0.033	326.84 ± 0.94
2011 Aug 15	IRCS	L'	19	DI	...	2.448 ± 0.024	325.82 ± 0.66
2012 Feb 28	HiCIAO	K_s	38	ADI	42.5	2.483 ± 0.015	326.46 ± 0.36
2012 Apr 12	HiCIAO	J	40	ADI	66.1	2.487 ± 0.008	326.54 ± 0.18
2012 May 25	IRCS	L'	68	ADI	129.0	2.499 ± 0.026	326.14 ± 0.61

Notes. The dates, used instruments, observation bands, total detector integration times (DIT), observation modes, and field rotation angles (FRA) are summarized for each observation run. The measured projected separations and position angles (P.A.s) are also described.

and -51.7 ± 11.2 mas yr^{-1} in each direction (Roeser et al. 2010). Hence, we identify the stellar companion candidate as an unrelated background star.

The effective temperature, surface gravity, and metallicity [Fe/H] of GJ 504 were inferred by directly fitting the observed spectrum to the synthetic spectrum (Valenti & Fischer 2005). Interestingly, GJ 504 has a super-solar metallicity [Fe/H] = 0.28 (Valenti & Fischer 2005). In order to estimate the mass of the central star, we use an empirical relation of Torres et al. (2010), which is a function of the surface gravity, effective temperature, and metallicity of GJ 504 (Valenti & Fischer 2005). The error of the estimate was provided by including uncertainties in the spectroscopically determined input parameters, the reported intrinsic scatter in the relation, and correlations of the best-fit coefficients (Fleming et al. 2010). As a result, the mass of GJ 504 is estimated to be 1.22 ± 0.08 solar masses. The mass of GJ 504 can also be derived based on matching its spectroscopically determined surface parameters with theoretical stellar evolution models (Takeda et al. 2007; Valenti & Fischer 2005). The theoretical models infer the mass of GJ 504 to be $1.29^{+0.05}_{-0.04}$ (Takeda et al. 2007) or $1.28 \pm 0.03\,M_{\rm Sun}$ (Valenti & Fischer 2005), overlapping with the empirical estimate. For our analyses, we employ the mass estimate based on the empirical function for GJ 504.

Broadband observations of the infrared excess above the photosphere at 24 μm and 70 μm place constraints on the distribution of dust in the inner (<10 AU) and outer disks. A recent *Spitzer* survey showed that 4% of Sun-like stars have 24 μm excess, while 16% of Sun-like stars have 70 μm excess (Trilling et al. 2008). GJ 504 was shown to not have excesses at either of these band passes ($L_{\rm dust}/L_{\rm star} < 2.1 \times 10^{-6}$), and therefore does not seem to harbor a significant debris disk (Bryden et al. 2006).

3. OBSERVATIONS AND DATA REDUCTION

GJ 504 was observed as part of the Strategic Exploration of Exoplanets and Disks with Subaru (SEEDS) survey (Tamura 2009), which aims to detect and characterize giant planets and circumstellar disks using the 8.2 m Subaru Telescope. In 2011 and 2012, we obtained J- (~1.2 μm), H- (~1.6 μm), and K_s- (~2.1 μm) band images using the High Contrast Instrument for the Subaru Next Generation Adaptive Optics (HiCIAO; Suzuki et al. 2010) with AO188, a 188 actuator AO system (Hayano et al. 2008). Furthermore, we obtained follow-up L'-band (~3.8 μm) images using InfraRed Camera and Spectrograph (IRCS; Kobayashi et al. 2000) and AO188. See Table 2 for the summary of GJ 504 observations.

3.1. HiCIAO Observations

We discovered GJ 504b in H-band observations using HiCIAO on 2011 March 26 with AO188. We used GJ 504, its host, as the natural guide star, and used an atmospheric dispersion corrector (ADC) to prevent it from drifting on the detector due to differential refraction in the visible and near-infrared. We used a circular occulting mask 0.″4 in diameter and angular differential imaging (ADI; Marois et al. 2006) to remove the starlight and the stellar speckles. ADI keeps the telescope pupil fixed relative to the camera, while the field of view (FoV) rotates as the target moves across the sky. As a result, diffraction and speckle patterns in the stellar point-spread function (PSF), caused by the major part of telescope optics, remain fixed on the detector while real on-sky sources, such as a planet, rotate about the natural guide star. This allows ADI data processing to distinguish between stellar speckles and real objects, and to remove the starlight while preserving potential planets.

We conducted several follow-up observations in 2011 and 2012 using the same instrument and configuration. H-band follow-up observations were performed on 2011 May 22. The new H-band observations had both a longer total exposure time and better AO performance than the March observations, giving a higher signal-to-noise ratio (S/N) in the final images. We obtained the K_s- and J-band data in 2012 February and April. The seeing in the J-band observation was among the best ever measured during SEEDS observations, and the AO worked very well, but those in K_s-band observations were worse than J- and H-band observations.

To correct the optical distortions of HiCIAO (and IRCS), we observed the globular cluster M5 using both instruments and compared the results to distortion-corrected images taken using the Advanced Camera for Surveys (ACS) on the *Hubble Space Telescope*; the accuracy and calibration for plate scale, orientation angle, and distortion of ACS/WFC camera, whose data were used for our calibration, have been previously reported (van der Marel et al. 2007). The distortion-corrected plate scale was 9.500 ± 0.005 mas pixel^{-1} for HiCIAO, and its north orientation was $0.^{\circ}35 \pm 0.^{\circ}02$. Uncertainties in the distortion correction are less than 4 mas for HiCIAO within the central $10'' \times 10''$ of the FoV. We have included all of these uncertainties in our positional measurements for the planet detected in both HiCIAO and IRCS images, though they have little effect on our results. Photometric calibrations were performed by observing the central star itself with neutral density (ND) filters with transmissions of 0.590, 0.0628, and 1.14% for J, H, and K_s bands, respectively.

3.2. IRCS Observations

To obtain data at a longer wavelength, we observed GJ 504 in the L'-band using IRCS on 2011 August 12 and 15. We did not use either ADI or an occulting mask during these long-wavelength observations. In addition, we obtained each frame by dithering the target within the FoV, which allowed us to better subtract the high thermal background (see below). In order to confirm whether we can obtain advantages for L'-band observational results by employing ADI, we performed additional L'-band observations in 2012 May 25. The longer total exposure time, compared to the 2011 observations, as well as the usage of ADI, led to a higher S/N.

As in the case of HiCIAO, we observed M5 to obtain the calibration data for correcting the distortion of IRCS. After the distortion-correction, IRCS has the plate scale of 20.54 ± 0.03 mas pixel^{-1}, and its north orientation was tilted by $0\overset{\circ}{.}28 \pm 0\overset{\circ}{.}09$. Uncertainties in the distortion correction are less than 8 mas for IRCS within the central $10'' \times 10''$ of the FoV. Because the L'-band magnitude of GJ 504 has not been measured, we calibrated it using a standard star observed right before GJ 504 observations. As with HiCIAO observations, we then measured the flux of GJ 504 with an ND filter with a transmission of 0.67%.

3.3. High-contrast Data Reduction

3.3.1. HiCIAO Data Reduction

For the HiCIAO data reduction, we first removed stripe patterns (see Suzuki et al. 2010) emerged on each data frame, and subsequently performed the flat-fielding. After correcting the image distortion, we registered each data set to the centroid of GJ 504 A. For the HiCIAO observations, which used an opaque $0\overset{''}{.}4$ diameter occulting mask, we estimated the relative frame centers by calculating cross-correlations of the frames as a function of positional offset. The AO188 and ADC kept the PSF extremely stable and well centered. For confirmation, we fit linear and quadratic functions to the frame-to-frame positional offsets and estimated the positional drifts that remained after AO/ADC correction. The systematic drifts were less than 10 mas for all observations except K_s band (17 mas), with residual rms scatters of ~2–10 mas. These random positional jitters can be attributed to our registration inaccuracies.

We calibrated the absolute centers using a sequence of unsaturated, unmasked exposures taken with an ND filter. For the H-band data, the positional reference was acquired right after the end of the masked sequence. In the cases of the J- and K_s-band observations, we obtained the positional calibration data in a similar way as for the H-band observations, but with the calibration observations interspersed through the science sequence. The positional errors for the unsaturated data ranged from ~2 to ~5 mas, where the lower quality PSFs for the H-band data obtained in 2011 March observations or the K_s-band data in 2012 February caused the largest errors. The unsaturated data used a combination of ND filters and field lens that were different from the main science data, possibly introducing a small systematic offset in position. To measure offsets introduced by the insertion of ND filters, we obtained images of a pinhole mask at the focal plane of HiCIAO, with and without ND filters, and measured the offsets. To determine offsets introduced by the use of a different field lens, we examined stars in images of the M5 globular cluster, observed both with and without the mask field lens. We measured these offsets to be small, $<\sim$3 mas. The values of the offsets introduced by the mask field lens were confirmed with three binaries in the SEEDS samples. We did not attempt to remove the offsets, but we have instead considered both of the offsets in the measurements of positions by adding systematic errors of 3 mas to the image registration uncertainties. In total, for H-band observations, image registration conservatively contributed ~12 mas to our reported positional uncertainties for GJ 504b in March and ~6 mas in May. Those uncertainties are ~10 and ~6 mas in 2012 February (K_s) and April (J), respectively.

We used the Locally Optimized Combination of Images (LOCI) algorithm (Lafrenière et al. 2007) to reduce the HiCIAO data. LOCI constructs a model PSF for each frame using the other frames in that data set as references. The resulting PSF is locally a linear combination of the reference images, with the coefficients determined using a least-squares minimization. To avoid subtracting astrophysical sources, LOCI only uses reference frames with a minimum level of field rotation. For our reductions of GJ 504, we required at least 1.2 ($=N_\sigma$) $\times$ FWHM/R ($\times$ 180/π deg) of field rotation, where the FWHM of PSFs on HiCIAO images are ~50–60 mas and R is the radial distance from GJ 504. As a result, any physical source was displaced by at least 1.2 FWHM between the working frame and the reference frames. We investigated if the S/N was improved by applying $N_\sigma = 1.5$ to the reductions but the S/Ns remained almost the same or were slightly reduced compared with the cases for $N_\sigma = 1.2$, and we thus carry out all analyses based on the images reduced with $N_\sigma = 1.2$.

For the H-band observations, our analysis of the data from March 26 detected a faint companion at an S/N of 5, where we calculated the noise as the standard deviation of the intensity in concentric annuli about GJ 504. Because of the longer integration time and better observing conditions for the observations in 2011 May, we detected GJ 504b with S/N = 9.0. We detected no other companion candidates (S/N $\leqslant$ 5) in either observation. GJ 504b is clearly confirmed with S/N of 18.4 at J-band, while the S/N of the K_s-band observations is 4.6.

The J, H, and K_s-band images for GJ 504b are shown in Figure 4. Also, the high-contrast two-color composite images is shown in Figure 5, in which GJ 504b is clearly visible $2\overset{''}{.}48$ northwest of GJ 504.

3.3.2. IRCS Data Reduction

For the IRCS data, we first corrected flat-fielding. Subsequently, we subtracted the thermal background and then used an algorithm (Galicher et al. 2011) similar to LOCI in order to further reduce the background. We estimated the background value at each pixel and in each frame by dithering the images and using a linear combination of the frames in which the central source, GJ 504, is sufficiently displaced. As in LOCI, we computed the coefficients for this linear combination using a least-squares fit. Eventually, we subtracted the resulting estimate of the local background whose variation is a function of time. As in HiCIAO reductions, we subsequently corrected the distortion of IRCS images.

The IRCS L'-band data were taken without a mask, and were saturated out to a radius of about 3–4 pixels (~60–80 mas, 0.6–0.8 FWHM, where FWHM is the full width at half-maximum of the PSF). We first performed relative registration by cross-correlating these saturated images with one another. We then centroided a set of unsaturated reference images, and cross-correlated the mean of these unsaturated PSFs with each saturated frame to measure the positional offset. Finally,

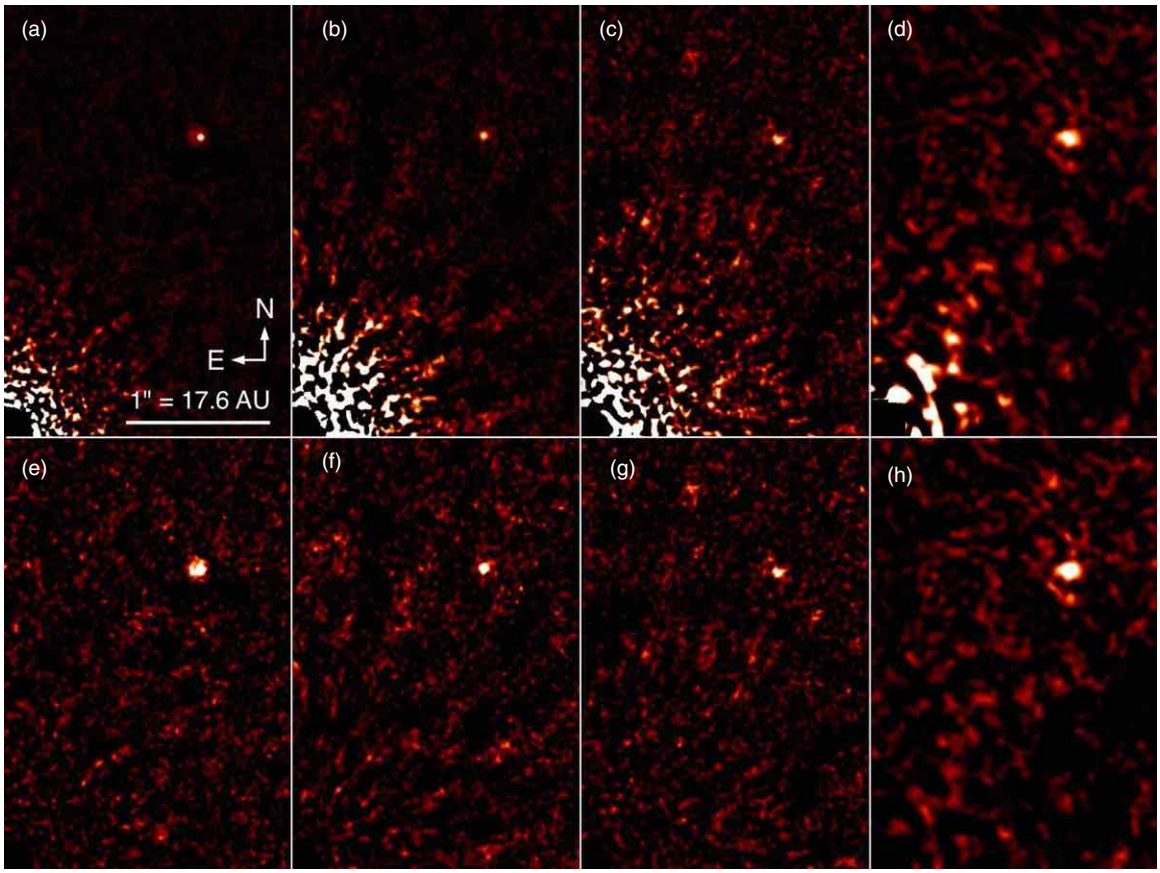

Figure 4. J- ($\sim$1.2 μm), H- ($\sim$1.6 μm), K_s- ($\sim$2.2 μm), and L'-band ($\sim$ 3.8 μm) images of the newly discovered exoplanet, GJ 504b. The four top panels show images reduced with the LOCI pipeline ((a) J, (b) H, (c) K_s, and (d) L'). The corresponding signal-to-noise maps are shown on the four bottom panels ((e) J, (f) H, (g) K_s, and (h) L'), in which the planet is detected with signal-to-noise ratios of 18.4, 9.0, 4.6, and 8.0, respectively. All signal-to-noise maps are shown at a stretch of [–5, 5]. In all panels, the star is located approximately in the lower left corner. North is up and east is left.

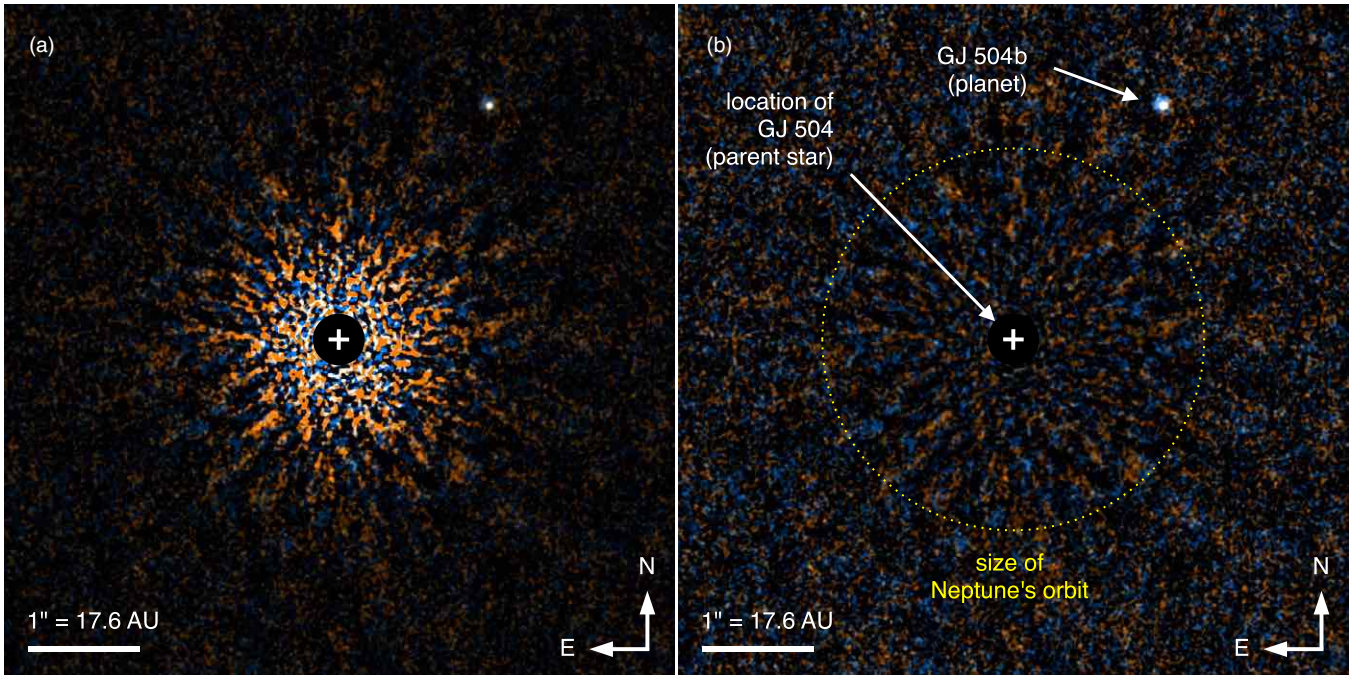

Figure 5. Discovery images of the exoplanet GJ 504b. The central $6'' \times 6''$ of two different high-contrast images were overlaid for this false color-composite image: orange represents H band ($\sim$1.6 μm; Subaru/HiCIAO; 2011 May 22), and blue represents J band ($\sim$1.2 μm; Subaru/HiCIAO; 2012 April 12). The J-band image was rotated by 0.°9 to compensate for the planet's observed orbital motion (cf. Figure 7). Panel (a) shows the intensity after suppressing flux from the central star. Panel (b) shows the associated signal-to-noise ratio ($\sim$9 in H; $\sim$18 in J). The orbital radius of Neptune ($\sim$30 AU) is shown for comparison with our own solar system. The planet GJ 504b is clearly visible as a white spot at a projected distance of 43.5 AU from the star GJ 504. The white color implies that the planet signal is persistent in both observations, setting it apart from the uncorrelated residual noise in each of the constituent images.

we applied this average offset to each of the saturated frames. The rms scatter of the offsets was ∼6 mas for both observations in 2011 August, and ∼4 mas for 2012 May. We adopt these scatters as the registration uncertainties in L'-band data.

We then combined these registered frames. We detected GJ 504b with an S/N of 3 and 4.3 in the August 12 and August 15 data, respectively. Because the data for 2012 May 25 were obtained with ADI, we could use LOCI for the PSF subtraction before stacking the registered data: the LOCI reduction parameters were set to be the same as the case of HiCIAO. In the resulting image, the companion was clearly detected with an S/N of 8.0 (see Figure 4).

3.4. Positional Measurements of GJ 504b

We measured the position of GJ 504b by fitting two-dimensional elliptical Gaussian functions to the final reduced data. Uncertainties in these Gaussian centroids range from 2 to 44 mas, and dominate the total uncertainties in the position of GJ 504b. Sometimes, LOCI introduces artificial shifts of the companion positions (Soummer et al. 2011). Measuring positions of artificial companions, which have the similar brightness and locations with the GJ 504b, we have investigated how large offsets are added to the positions of GJ 504b. Because our adaptation for LOCI parameters is not aggressive and the planet's separation is sufficiently large from the star ($r = 2''.48$), the astrometric biases are not large.[33] The positional measurements are converted to the projected separations and position angles (P.A.s) relative to the central star, and all of those are summarized in Table 2. Then, the uncertainties of measured separations and P.A.s were calculated by including the possible individual error sources of the image registration, distortion correction, plate scale, and orientation angle of each camera, and PSF-fit for GJ 504b.

3.5. Photometry

We performed aperture photometry on all of our observations of GJ 504b. For HiCIAO observations of the star GJ 504, we adopted magnitudes of 4.11, 3.86, and 3.81 for its J-, H-, and K_s-band brightness (Kidger & Martín-Luis 2003). The L'-band brightness of GJ 504 was calibrated with a standard star, so that we obtained $L' = 3.94 \pm 0.09$ mag for GJ 504. For all photometries of both the primary and the planet, we set the aperture radius to be 1.0 PSF FWHM, which ranged from 47 mas in J to 100 mas in L'.

By subtracting a (local) linear combination of frames from each image, LOCI can artificially reduce the flux of a point source (Lafrenière et al. 2007). We limit this effect by choosing a relatively large N_σ and estimate its magnitude using artificial point sources. We inject point sources in the HiCIAO data with projected separations and fluxes similar to those of GJ 504b, measuring their magnitudes before and after applying LOCI. We measured flux losses ranging from 13% to 23% for all LOCI reductions, where the typical scatter for the measurements of flux losses was 5%. We added this value to the final photometric errors. To verify this result, we re-reduced the HiCIAO data by subtracting a median PSF (Marois et al. 2006), but not applying LOCI. The resulting fluxes for GJ 504b had larger errors, but were consistent with their values in the final, LOCI-processed data. We estimated all of our photometric errors for the companion by calculating the rms scatter of aperture fluxes in blank-sky regions at the separation of GJ 504b. For the H-band data, these photometric errors were larger than the flux difference between the two sets of observations. For H-band observations, the unsaturated frames used to calibrate the companion fluxes were obtained before and after the main science sequences with the mask, while the unsaturated integrations for J, K_s, and L' bands were conducted in intervals among the main sequences as well. The total number of unsaturated frames that were used for photometric calibration was more than 31 for each epoch observation, except in 2011 March. We measured standard deviations of photometry of the primary using the unsaturated data; the worst value for the standard deviation was 22% in 2011 March, while these values were less than 12% in all other observations. We include these variations in the final photometric uncertainties, in addition to the errors of photometry for companion and self-subtraction estimates. For L'-photometry, we had three sets of images, but did not combine the result of 2012 with those derived from the data obtained in 2011, because the S/Ns of the L' images in 2011 were significantly worse than for the 2012 images; in the former case, no ADI was used and the observing conditions were very poor, with airmasses as high as 3.5 at maximum. Therefore, our adopted value for the L' photometry is based exclusively on the data obtained in 2012. The photometric measurements of GJ 504b at each band are summarized in Table 1, with the H-band flux computed using the weighted mean of the March and May values. Furthermore, the detection limits estimated from the reduced data are shown in Figure 6.

4. RESULTS

4.1. Astrometry

To confirm that GJ 504b is gravitationally bound to the host star, we tracked its proper motion over the course of more than a year, from 2011 March through 2012 May (Figure 7). Figure 7 allows to clearly visually distinguish the measured positions from the track expected for a background object. However, we also carried out a χ^2 test to derive a statistical confidence that the source is a background star. This yielded a value of $\chi^2 = 1340$ (12 dof). Therefore, the χ^2 test on the astrometry decisively excludes GJ 504b as an unrelated background source. On the other hand, if we assume GJ 504b to be an interloping foreground object, its color ($H - L' = 3.3$ mag) would rule out a star anyway, leaving only the possibility of a cool brown dwarf ($T < 600$ K) within a distance of ∼30 pc. Even under optimistic assumptions about the brown dwarf mass function (Kirkpatrick et al. 2011), less than one such object exists per 10 deg^2, and the probability of a chance alignment within $3''$ of GJ 504 is no more than 10^{-7}.

Furthermore, in order to demonstrate that the measured motion of GJ 504b relative to its parent star GJ 504 is indeed consistent with the expected orbital motion of a gravitationally bound planet, we have fitted a Keplerian curve to its measured positions relative to the star, and constrained its orbit (see the Appendix). Here we assumed that the star has 1.22 $M_\odot$. We show the best-fit curve in Figure 7. The best-fit χ^2 was derived to be 11.7 (8 dof), which confirms that the measured positions relative to the central star are consistent with dynamical orbital

[33] Typically, averages of amplitudes for offsets are smaller than 3 mas for all epochs of data, and the rms scatters are also sufficiently small compared to our assigned total positional errors. We do not add the possible systematic errors due to LOCI processing to our astrometric total errors since our measurements for the systematic offsets are degenerate to other error sources such as speckles or photon noise. However, if we include those in final astrometric errors, they have no impact on our conclusions.

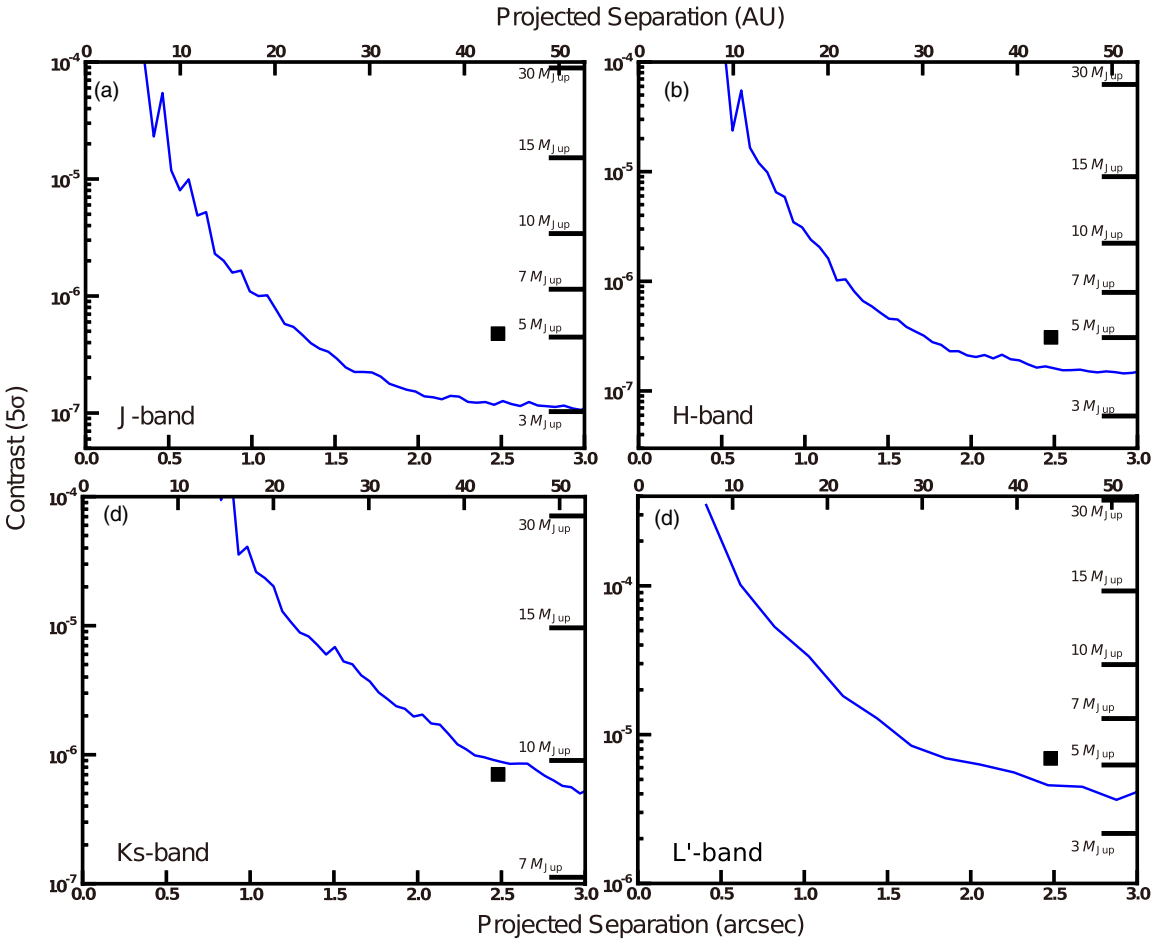

Figure 6. Detection limits for J, H, K_s, and L' bands. Each panel shows 5σ detection limits (blue curves) estimated with reduced J-, H-, K_s-, and L'-band data. The left vertical axes indicate measured contrasts relative to the primary at each separation. The corresponding detectable mass limits, at the system age of 300 Myr using COND models (Baraffe et al. 2003), are shown along the right axes. The bottom horizontal axes show angular separations projected from the primary in arcseconds. The top axis gives separations in AU. The contrasts for GJ 504b are indicated by black squares in each panel. (a) J-band detection under exceptionally good weather and seeing conditions, (b) H band, (c) K_s band, and (d) L' band.

motion around the star.[34] These analyses robustly prove that GJ 504 and GJ 504b comprise a physically associated system.

4.2. Mass Estimate

Using the luminosity and age of GJ 504b, we thus proceed to estimate its mass based on the hot-start model Baraffe et al. (2003, see Figure 8). We then calculate a mass by comparing the luminosity of GJ 504b at each band to the models, and eventually average the mass estimates at J, H, K_s, and L' bands, which provides a mass of the planet, and its error range, which includes the errors from age and photometry. Any bias in the mass estimate caused by focusing on the photometry in a particular band should be mitigated when taking the average of the photometry of all bands. For the upper bound, we estimate the mass of GJ 504b from the 1σ bright end of the photometry at each band, using hot-start models for an age of 510 Myr. The collective upper limit is then acquired by averaging the estimates at each band. The lower limit is calculated in an equivalent way, using the 1σ faint end photometry and an age of 100 Myr. Likewise, the best estimate uses the mean photometry in each band and an age of 160 Myr. As a result of this procedure, a mass estimate of $4^{+4.5}_{-1.0}$ $M_{\rm Jup}$ is derived. The age uncertainty dominates the errors. If we adopt the gyrochronological age of 160^{+70}_{-60} Myr, the most direct of our age indicators, the mass of GJ 504b is constrained to lie between 3 and 5.5 $M_{\rm Jup}$. This is well below 13.6 $M_{\rm Jup}$, the deuterium-burning threshold commonly used to divide planets and brown dwarfs (Marois et al. 2008; Burrows et al. 1997) and among the lowest masses for exoplanets discovered by direct imaging.

Adopting the K_s-band luminosity may result in a bias in the mass estimation, since this wavelength range is particularly sensitive to atmospheric parameters such as surface gravity and metallicity (Fortney et al. 2008; Spiegel & Burrows 2012; Janson et al. 2011). Indeed, Fortney et al. (2008) predict that raising the metallicity to five times solar metallicity results in a K_s-band brightening of a factor of two to six for a planet with temperature and surface gravity values in the range of what is expected for GJ 504b. Since the star GJ 504 has a metallicity above the solar value, it is very likely that the planet's metallicity is also enhanced. For reference, if we neglect the K_s-band photometry, the best-fit mass of GJ 504b becomes 3.5 $M_{\rm Jup}$, and is confined to be less than 8 $M_{\rm Jup}$ based on the adopted age range.

The robustness of mass estimates for directly imaged exoplanets is usually limited by theoretical models used to derive age–luminosity relations. One uncertainty in these relations is the choice of initial conditions, which influences the estimation

[34] The position measured in 2011 August 15 deviates from the best-fit orbit, which increases the χ^2. That measurement was obtained without ADI at high airmass.

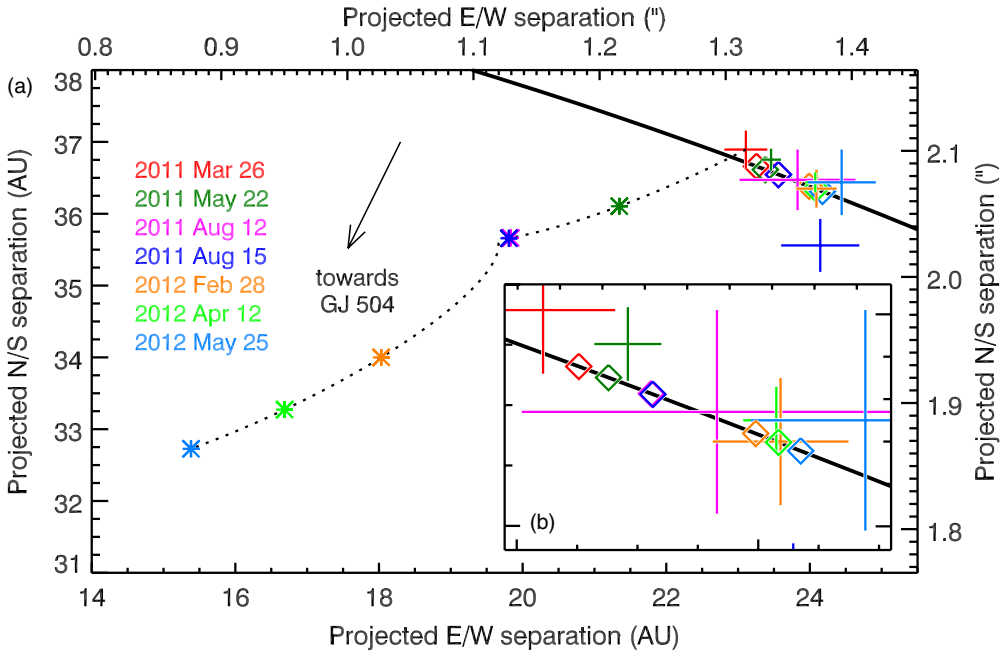

Figure 7. Astrometric analysis of GJ 504b. The measured positions of the planet relative to its parent star at the seven epochs of observation are shown as plus signs (size corresponds to error bars). A background star would follow the dotted trajectory, with star symbols marking the position at the epochs of observation. More information on the orbital simulation can be found in the Appendix. Diamond symbols mark the position of the planet along the most likely orbit at the epochs of observation. Plus, star, and diamond symbols are color-coded for epoch. (a) View of the planet's motion compared with the track expected if GJ 504b were a background star and (b) zoomed-in view of the observed positions of GJ 504b.

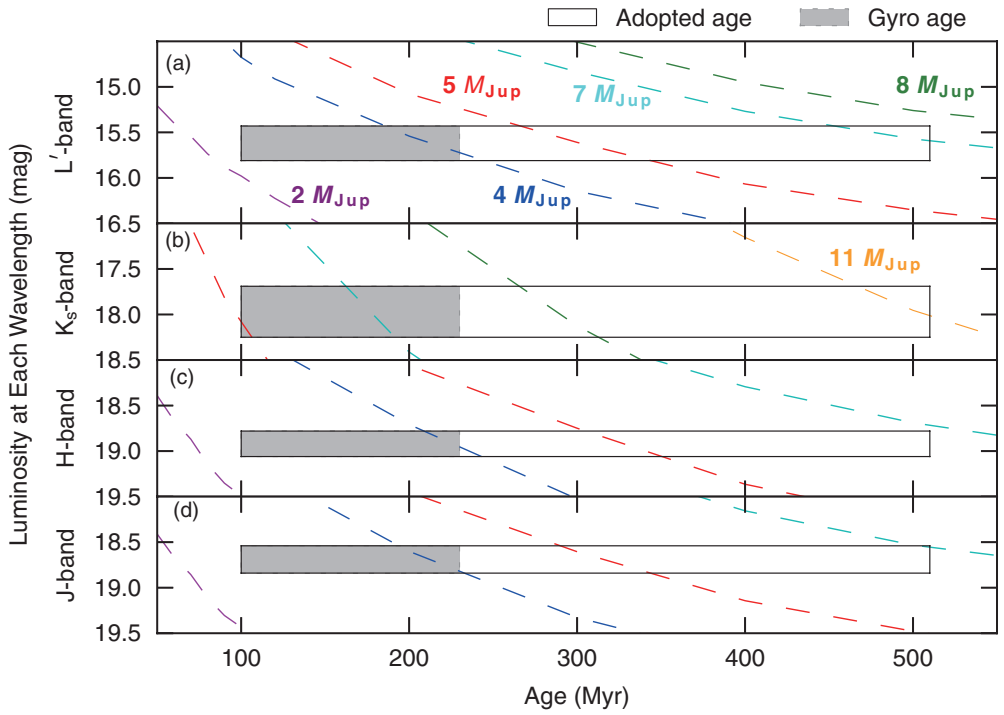

Figure 8. Mass of GJ 504b as derived from the theoretical relation between the planetary age and luminosities for various wavelengths. Estimated age (Myr) and near-infrared luminosities (absolute magnitudes) for GJ 504b are plotted over cooling curves for planets of various masses calculated from the hot-start model (Baraffe et al. 2003): (a) L'-band (∼3.8 μm) luminosity, (b) K_s band (∼2.1 μm), (c) H band (∼1.6 μm), and (d) J band (∼1.2 μm). The vertical size of each box shows the estimated luminosity range (∼ 1σ) in each band. The gyrochronological age (indicated by the gray box) is the most direct age estimate among all age indicators available for GJ 504; it implies a planet mass of $4^{+1.5}_{-1.0}$ $M_{\rm Jup}$. The open box with the solid black line boundary indicates the wider age range encompassing all of the adopted age estimates, and implies a mass of $4^{+4.5}_{-1.0}$ $M_{\rm Jup}$.

of a planetary mass. Since GJ 504 is older than 100 Myr, its inferred mass is less sensitive to the uncertainty in initial conditions for the employed model (Marley et al. 2007; Spiegel & Burrows 2012) than the previously imaged planets which have younger ages than GJ 504b. To test the sensitivity of the GJ 504b mass to uncertainties in the hot-start model, we compare the near-infrared luminosities of GJ 504b with a suite of models with ages between 100 and 510 Myr, initial thermal states

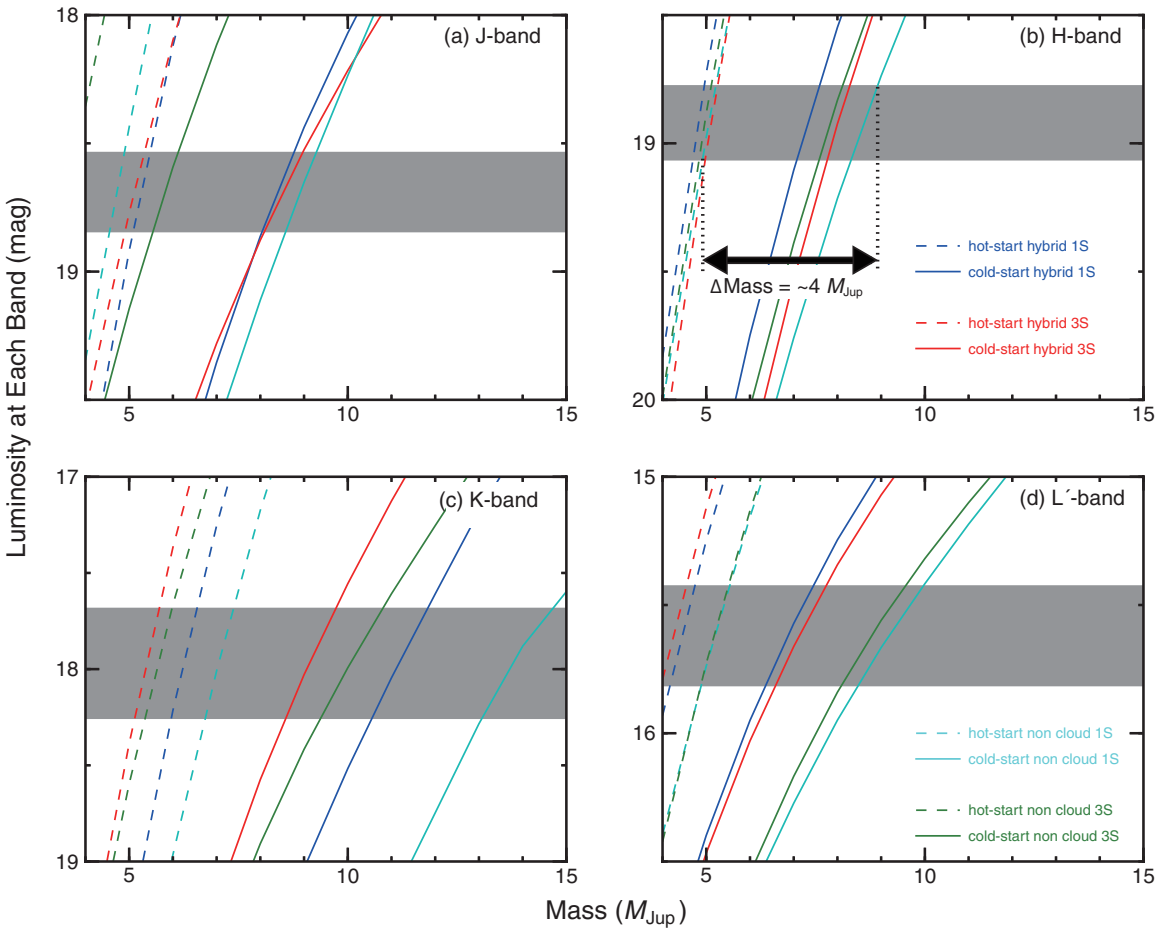

Figure 9. Differences between mass estimates from cold-start models and hot-start models for 100 Myr old planets. The mass–luminosity relations modeled in Spiegel & Burrows (2012) are illustrated with dashed and solid lines for hot-start (entropy = 13 k_B baryon^{-1}) and cold-start (8 k_B baryon^{-1}) initial conditions, respectively. We show the relations for four atmosphere types on each panel ((a) J, (b) H, (c) K_s, and (d) L'): "hybrid" means patchy cloud model and 1 or 3 S means one or three times solar-abundance model. The gray regions correspond to the absolute magnitudes of GJ 504b in each band and their error ranges ($\pm 1\sigma$). The lower age limit (100 Myr) of GJ 504 is chosen in this illustration since that is the stage at which the largest differences occur between hot-start and cold-start conditions. As an example, the arrow in panel (b) indicates the difference in mass arising from different initial conditions when the 1S cloud-free model atmosphere is adopted. The difference is ~4 M_{Jup}, which is also the median result for the full set of atmospheres and photometric bands.

ranging from hot to extremely cold (initial specific entropies from 8.0 to 12–13 k_B baryon^{-1}), masses between 1 and 20 M_{Jup}, varying cloud properties, and metallicities between one and three times the solar value (Spiegel & Burrows 2012). Even when adopting an age of 100 Myr, for which the largest differences arise between the hottest- and coldest-start models, the difference in the mass estimates between the two cases is typically ~4 M_{Jup}, which is calculated as the median of all estimates for each different model atmosphere and each band (see Figure 9). At older ages, the difference decreases even further. By contrast, if we use HR 8799b (20–50 Myr; Marois et al. 2008, 2010) as an example of planets younger than 50 Myr, the corresponding difference is higher than 10 M_{Jup}, which is significantly larger than the case of GJ 504b. Thus, in quantitative terms, the dependency on initial conditions for GJ 504b is indeed rather week. This also allows to confine the mass of GJ 504b to within the planetary-mass regime, essentially regardless of initial conditions (see Figure 10). The mass inferred from each of the J, H, and L' bands individually is practically always below the deuterium burning limit of ~14 M_{Jup}, apart from the most extreme cases in which both the coldest initial conditions and ages near the oldest end of the age range are adopted simultaneously. Note that these extreme cold-start models may be unrealistic for giant planets (Spiegel & Burrows 2012).

5. DISCUSSION

Here, we discuss the unique properties of GJ 504b through comparison with other imaged planets. Furthermore, the possible origin of GJ 504 is discussed.

5.1. Previously Imaged Planet Candidates

Some of the previously imaged exoplanets were discovered around young (10–50 Myr), relatively massive stars like HR 8799 (1.5 M_{Sun}; 20–50 Myr; Marois et al. 2008, 2010) and β Pictoris (1.75 M_{Sun}; 10–20 Myr; Lagrange et al. 2010), with masses estimated at 5–9 M_{Jup}, assuming hot-start conditions. Recently, SEEDS detected a ~13 M_{Jup} companion around the B9-type star Kappa And (2.5 M_{Sun}; 20–50 Myr; Carson et al. 2013). An exoplanet candidate around another massive star, Fomalhaut (2.0 M_{Sun}; ~200 Myr; Kalas et al. 2008), has been detected at optical wavelengths. The images were reanalyzed by Galicher et al. (2013) and Currie et al. (2012), who recovered the point source at an additional wavelength. In addition, new optical images were recently presented with a report of an eccentric orbit (Kalas et al. 2013). Very recently, another imaged planet candidate has been reported around the young star HD 95086 (10–17 Myr; ~1.6 M_{Sun}), but a robust second epoch confirmation still needs to be acquired (Rameau et al. 2013).

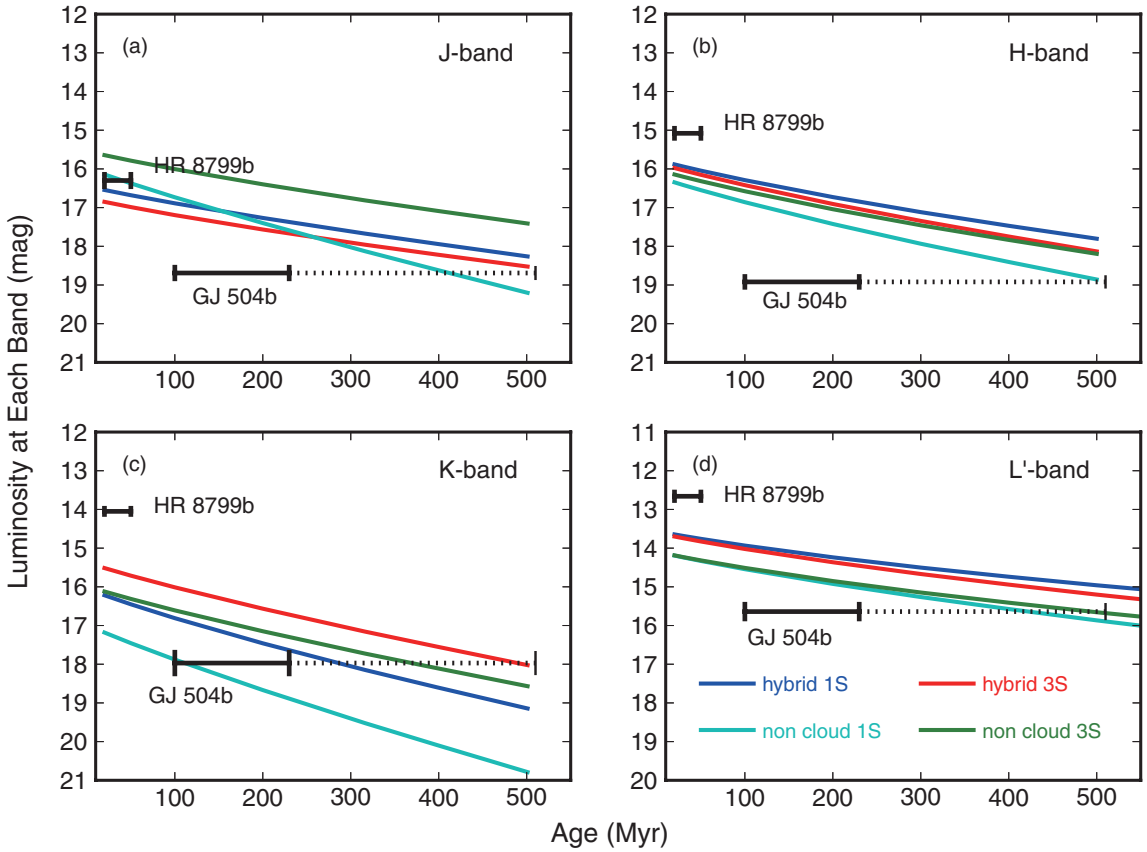

Figure 10. Comparison of multiple wavelength magnitudes of GJ 504b with cold-start model (Spiegel & Burrows 2012) predictions at the planet/brown dwarf boundary. In each panel, the cooling tracks predicted by the coldest-start models for a 14 $M_{\rm Jup}$ planet are plotted in the age range of 20–500 Myr. Different panels correspond to the different bands ((a) J, (b) H, (c) $K_{\rm s}$, and (d) L'). In addition, we show the cooling curves for four atmosphere types, where "hybrid" means patchy cloud model and 1 or 3 S means one or three times solar-abundance model (Spiegel & Burrows 2012). The age range of GJ 504b is indicated by solid and dotted lines. The solid lines and dotted lines correspond to the age range inferred with gyrochronology (160^{+70}_{-60} Myr) or chromospheric activity (330 ± 180 Myr), respectively. For comparison, we plot the brightness and age of HR 8799b (30^{+20}_{-10} Myr) (Marois et al. 2008; Metchev et al. 2009) in each panel.

Other giant planet candidates have also been imaged at wide separations around very young (<10 Myr) stars (see, e.g., Kuzuhara et al. 2011). Among these, 1RXS J1609b (Lafrenière et al. 2008) orbits a pre-main-sequence solar-mass star at a wide separation of 330 AU.

For all the aforementioned companions, their masses have been inferred from comparisons of their infrared luminosity with hot-start models. However, due to the youth of those systems, they are highly affected by hot- versus cold-start conditions. The cold-start models imply that even HR 8799b, which may have the lowest masses among them, would be more massive than ∼14 $M_{\rm Jup}$ (see Figure 10): its mass is estimated to be ∼20 $M_{\rm Jup}$ or higher (except at J band). Therefore, under cold-start assumptions, all the exoplanets around these young stars have much higher masses than currently inferred, and are pushed into the brown dwarf mass regime (>∼14 $M_{\rm Jup}$). One special case is the candidate around Fomalhaut, for which a mass below 3 $M_{\rm Jup}$ has been reported, but deep infrared non-detections indicate that the detected light from the candidate cannot arise from a planetary surface (Janson et al. 2012); hence, its physical nature remains unclear. Regardless of the caution for the hot-start models, a few independent constraints, such as dynamical stability analysis in the case of the HR 8799 system (e.g., Fabrycky & Murray-Clay 2010; Marois et al. 2010; Sudol & Haghighipour 2012), suggest that the hot-start models may be realistic.

As discussed above, the mass estimates for directly imaged planets suffer from uncertainties of cooling models for giant planets until future calibrations may be obtained by comparing model-dependent masses with improved dynamical mass estimates. However, due to its old age, GJ 504b is less dependent on the models' uncertainty related to the hot versus cold conditions, compared with previously imaged planets.

5.2. Color of GJ 504b

We can compare the magnitudes and colors of GJ 504b to similar objects in the literature in order to get a sense of the physical properties of this planet. For this purpose, it has been placed on color–magnitude diagrams (Figure 11) along with LT-type field brown dwarfs (Leggett et al. 2010) and HR 8799 bcde (Marois et al. 2010; Metchev et al. 2009; Skemer et al. 2012), Kappa And b (Carson et al. 2013), 1RXS J1609b (Lafrenière et al. 2008), 2M 1207b (Chauvin et al. 2004; Mohanty et al. 2007; Skemer et al. 2011), and GJ 758B (Thalmann et al. 2009; Janson et al. 2011).

Given the location of GJ 504b in the color–magnitude diagrams, it is clear that it is much colder than previous planet detections. Indeed, an application of $JHK_{\rm s}L'$ luminosities of GJ 504b to those predicted by the cooling models of Baraffe et al. (2003) implies an effective temperature of 510^{+30}_{-20} K for the planet, where we estimated the best estimate and

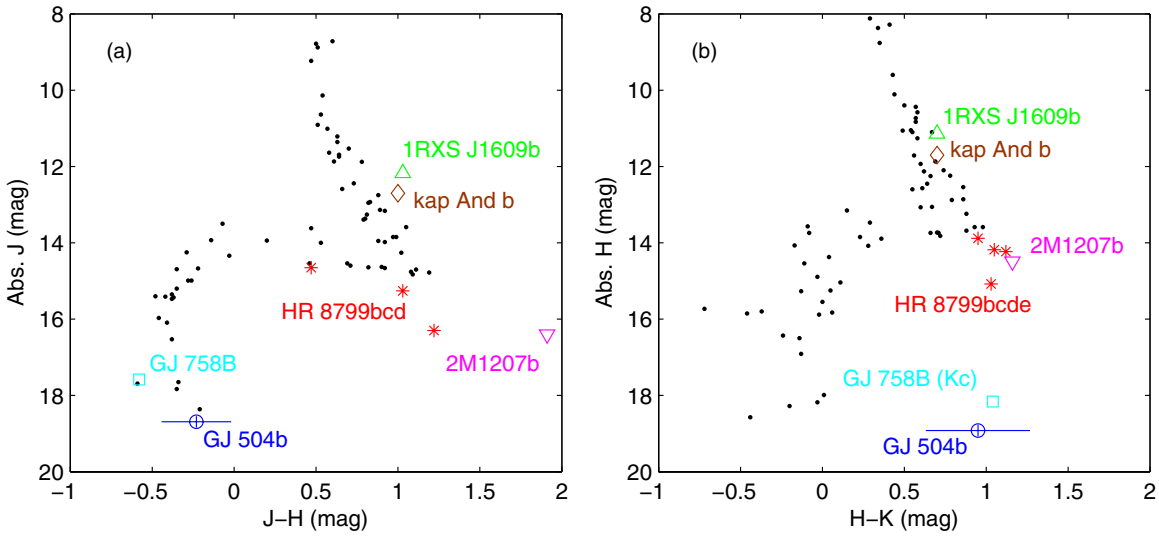

Figure 11. Color–magnitude diagrams for GJ 504b. Shown for comparison are LT-type field brown dwarfs as black dots (Leggett et al. 2010), and a sample of planet and brown dwarf companions from the literature. Panel (a) shows J-band luminosity (J-band absolute magnitude) vs. $J-H$ and panel (b) shows H-band luminosity vs. $H-K_s$ ($H-K_c$ for GJ 758B). Directly imaged planets are each labeled.

lower/upper limits in the same way as for the mass estimate of GJ 504b (see Section 4.2). The inferred effective temperature is significantly colder than the values of 800–1800 K inferred for previously imaged planets (Marois et al. 2008; Chauvin et al. 2004; Bonnefoy et al. 2011). The extrasolar giant planets other than GJ 504 are primarily located around the so-called LT transition, which corresponds to the transition from cloudy (L-type) to clear (T-type) atmospheres. GJ 504b is consistent with having a largely clear atmosphere analogous to the bottom of the T-type sequence, or the top of the yet colder Y-type sequence. It deviates from this sequence in $H-K_s$, due to overluminosity in K_s band, which is probably due to a low surface gravity or enrichment in heavy elements, both of which can reproduce such an effect (Burrows et al. 2006). These factors have been shown to possibly explain the same trend seen in GJ 758B (Janson et al. 2011), which is an older and more massive companion to a Sun-like star. We note that GJ 504b was observed with the K_s-band filter and GJ 758B with the K_c-band filter, which prevents a one-to-one comparison. However, models incorporating heavy element enrichment appear to be a promising option for reproducing the full set of magnitudes of GJ 504b.

It has been proposed that planetary candidates with hot atmospheres ($T_{\rm eff} \sim 1000$ K) around HR 8799 or 2M 1207 may have thick clouds (Barman et al. 2011a; Madhusudhan et al. 2011; Skemer et al. 2011; Marley et al. 2012) although their cloud properties are under discussion (Barman et al. 2011a, 2011b). By contrast, the relatively blue $J-H$ ($=-0.23$) color of GJ 504b is consistent with T-type brown dwarfs in the same temperature range (Leggett et al. 2010), which are representative of less cloudy atmospheres that could occur naturally in this temperature range (Allard et al. 2001). In addition, models examining cloud clearing as a function of temperature and surface gravity in Marley et al. (2012) do predict that a temperature of ~500 K and $\log g$ of ~4, as expected for GJ 504b (see Table 1), should lead to a clear atmosphere, while the properties of previously imaged planets place them in a cloudy regime. The cold and perhaps less cloudy atmosphere of GJ 504b thus places it in a physically distinct state from the hotter and cloudier atmospheres of previously imaged planets, and should be highly interesting for further atmospheric studies in the future. These properties imply that GJ 504b will become a benchmark object for the study of exoplanet atmospheres.

5.3. Implications for the Origin of GJ 504b

GJ 504b is a giant planet that lies at a projected separation of 43.5 AU. Two major scenarios could explain its formation: the core-accretion (CA) model (Pollack et al. 1996) and the gravitational instability (GI) model (Durisen et al. 2007). Here, we discuss whether the CA or GI can account for the origin of GJ 504b.

5.3.1. Core Accretion

In the CA model, the core of a giant planet accretes planetesimals and grows to a critical mass (~10 Earth masses), at which point the core begins to rapidly accrete gas directly from the protoplanetary disk. It is difficult for the CA model to explain the formation of giant planets in situ beyond 30 AU. A recent study (Dodson-Robinson et al. 2009) suggested that even a locally stable (but globally unstable) disk with an order of magnitude higher mass than the minimum mass solar nebula (Hayashi 1981) around a G-type star like GJ 504 was unable, in simulations, to form giant planets beyond 30 AU within the lifetime of the protoplanetary disk (Dodson-Robinson et al. 2009). Therefore, the presence of GJ 504b, as well as other directly imaged planets such as HR 8799 bcde, remains a particular challenge for the conventional CA theory. In this implication, we should note such numerical investigations as conduced by Dodson-Robinson et al. (2009) have typically neglected some theoretical processes that may enable the cores of giant planets to grow in the shorter timescale: effective damping of small planetesimal's eccentricity due to gas drag (Rafikov 2004) or efficient capture of planetesimals due to atmospheric drag (Inaba & Ikoma 2003) may accelerate the accumulations of planetesimals in such the outer region, so that the in situ formation of GJ 504b may become possible (Rafikov 2011). However, even the models incorporating these processes may not necessarily be promising for producing a planet more massive than the critical mass beyond 30 AU at least for disks that are not particularly massive, as demonstrated by the simulations of Kobayashi et al. (2011).

Even if the in situ formation of a giant planet is difficult in such outer regions, models incorporating planet scattering can account for the origin of GJ 504b. If multiple planets are formed by CA in the inner regions, one or more of them could be scattered outward due to dynamical interactions among the planets (Nagasawa et al. 2008) or between the planets and the protoplanetary disk (Paardekooper et al. 2010; Crida et al. 2009). GJ 504b may have been pushed outward by as-yet undiscovered companions. Multiple giant planets may be common in metal-rich protoplanetary disks (Fischer & Valenti 2005), because the high metallicity may enhance solid materials and planetesimals in their protoplanetary disks, resulting in rapid growth of planetary cores. Eventually, outward migration may frequently occur in the metal-rich systems. Hence, the relatively high metallicity of GJ 504 system (see Table. 1) may be a preferential property to explain the origin of GJ 504b under the outward migration hypothesis.

5.3.2. Gravitational Instability

In contrast to CA, the GI model can form massive planets in situ at large radii. In this model, a massive protoplanetary disk becomes gravitationally unstable in its outer regions ($>\sim$50 AU) as the cooling time becomes short relative to the local dynamical timescale (Durisen et al. 2007). The outer disk then fragments, collapsing directly into one or more giant planets. The instability can also occur between 20 and 50 AU, with continuous inflows of gas into the magnetically inactive region inducing fragmentation on a timescale of $\sim 10^3$ yr (Machida et al. 2011). However, the planet would have to escape the very rapid inward migration expected in a turbulent disk (Baruteau et al. 2011). In addition, if multiple massive planets are formed in the GI disk, they would still be scattered and eventually ejected from the systems, as in the case of CA. Therefore, GJ 504b would be a planet surviving against falling onto the central star or ejections form the system, if it was formed through the GI process. We should note that fragmentation could also be suppressed in a metal-rich disk like that expected for GJ 504; such a disk would cool less efficiently due to the higher opacities (Cai et al. 2006). Also, the significant gas accretion onto a clump formed according to the GI process may prevent the planet from remaining less massive (Zhu et al. 2012; Boley et al. 2010), disallowing the occurrence of a low-mass planet like GJ 504b.

5.3.3. Summary for Discussions of the Origin of GJ 504b and Future Prospect

Based on the available data, we cannot conclusively determine which process led to the formation of GJ 504b. However, it is interesting to note that GJ 504b is the first wide-orbit giant planet detected around a demonstrably metal-rich star. As discussed above, the high metallicity may enhance massive planetary cores, while preventing the effective cooling of a protoplanetary disk, and thus be more hospitable for CA formation than GI formation. Thus, given these measurable properties, planets such as GJ 504b may provide important clues for understanding the formation and evolution of giant planets.

For clarifying the origin of GJ 504b, the further observations may be crucial. Intriguingly, the CA model suggests the presence of unseen massive planets at smaller angular separations (Nagasawa et al. 2008; Chatterjee et al. 2008), making GJ 504 an outstanding candidate for follow-up observations by current and future instruments. *N*-body simulations for the dynamically unstable gas-free planetary system predict that such inner companions should orbit at a few AU from the host[35] and have masses equal or greater than the corresponding outer planets (Nagasawa et al. 2008; Chatterjee et al. 2008). Therefore, the inner counterpart for GJ 504b would have to be more massive than $\sim$4 $M_{\rm Jup}$ if it exists, although we note that radial-velocity observations have found few planets in this mass range at semi-major axes of a few AU (Mayor et al. 2011) and the remaining gasses in the disk may affect the scattering of planets, changing the configurations of planets predicted by the simulations for the gas-free cases (Moeckel & Armitage 2012).

Also, further monitoring of the orbit may be important, since scattered planets preferentially have high eccentricities (Chatterjee et al. 2008). Furthermore, modeling the atmosphere of GJ 504b may provide another piece of evidence to test whether it was produced by the CA process. The enhancement of heavy elements in the planetary atmosphere is a natural outcome of the CA process (Chabrier et al. 2007). It is possible to examine the abundances of such elements in the spectral energy distribution of GJ 504b through the use of atmospheric models. For this purpose, multiple wavelength photometric observations as well as the spectroscopy can play an important role.

Further observations of the GJ 504 system will constrain the origin of GJ 504b and may lead to a better understanding of the origin of planetary systems, including our solar system. Future instruments with direct (e.g., GPI, SPHERE, SCExAO) or indirect (e.g., IRD; Tamura et al. 2012) techniques that can explore more inner region may be able to find a promising evidence to clarify the origin of GJ 504b.

6. CONCLUSION

As part of the SEEDS direct-imaging survey, we have detected a giant planet around the Sun-like star GJ 504. The star has a spectral type of G0 and an approximate mass of 1.2 $M_{\rm Sun}$. Its age has been conservatively estimated as 160^{+350}_{-60} Myr based on a combination of gyrochronology and chromospheric activity. Gyrochronology alone, which is the most direct and likely the most reliable age estimator, places the age at the lower end of this range, at 160^{+70}_{-60} Myr. Observations over one year baseline provided confirmation that the detected planet is orbiting the star. Compared with previously imaged exoplanets, GJ 504b has a number of interesting features.

1. The age of this planet is the oldest among all directly imaged planets.
2. Its mass is estimated to be $4^{+4.5}_{-1.0}$ $M_{\rm Jup}$. This is among the least massive of imaged exoplanets. Because of its old age, the mass estimate is less dependent, compared to other imaged exoplanets, on the uncertainties of initial conditions in models used to convert its infrared luminosity into a mass.
3. GJ 504b is the first imaged giant planet on a wide orbit ($>$5 AU) around a G-type main-sequence star with a mass near the solar mass.
4. The planet's projected separation from the primary is about 43.5 AU, which is comparable to the widest-orbit planets around massive stars such as HR 8799.
5. The effective temperature of the planet (510^{+30}_{-20} K) is the coldest among all previously detected giant planets.
6. The blue $J-H$ color of -0.23 suggests that it has a less cloudy atmosphere than other imaged exoplanets. The cold temperature and color place the planet in a novel parameter space of atmospheres for exoplanets.

[35] The current detection limit cannot explore giant planets in such the inner regions (see Figure 6).

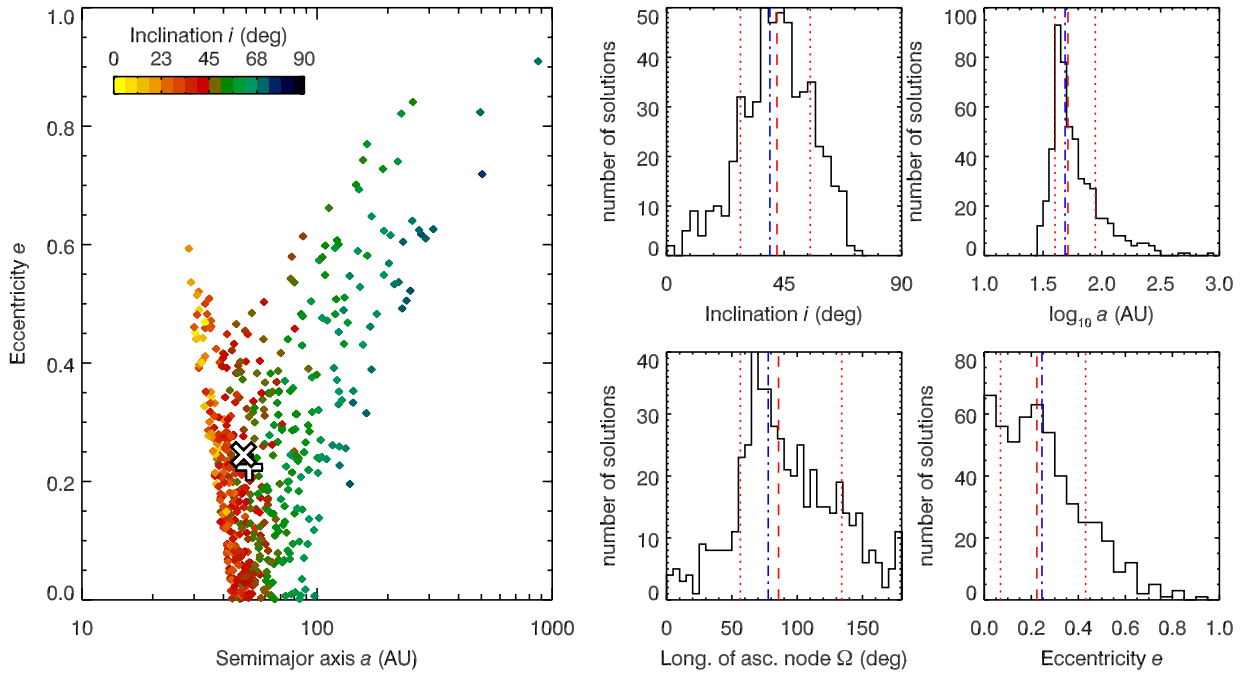

Figure 12. Well-fitting family ($\chi^2 < \chi^2_{\rm min} + 1$) of simulated orbits for GJ 504b. In the a/e scatter plot, a plus sign marks the location of the weighted median, whereas a cross sign marks the most likely orbit. In the histograms, red lines mark the weighted median (dashed) and the weighted 68% interval (dotted), whereas a blue dash-dotted line marks the most likely orbit.

7. GJ 504b is the first giant planet on a wide orbit discovered around a demonstrably metal-rich star.

The performed observations alone cannot conclusively uncover the origin of GJ 504b. Further observations of this system will enable more direct comparisons with our own solar system, and will help unveil the formation history of giant planets in the outer disk.

The authors thank Dr. I. N. Reid for discussions about age estimations of main-sequence stars. In addition, the authors have benefited from useful discussions with Drs. M. Ikoma, H. Nagahara, Y. Abe, S. Sugita, and B. Sato. Furthermore, the authors thank David Lafrenière for generously providing the source code for the LOCI algorithm. Our referee's careful reading of the manuscript and excellent suggestions have improved the quality of this paper. The help from Subaru Telescope staff is greatly appreciated. This work is partly supported by KAKENHI 22000005 (M.T.), KAKENHI 23103002 (M.H.), WPI Initiative, MEXT, Japan (E.L.T), NSF AST 1008440 (C.A.G), and NSF AST 1009203 (J.C.), and NSF AST 1009314 (J.P.W.). Also, M.K. is partly supported by the Global COE program "From the Earth to Earths." M.K., Y.H., Y.T., and J.K. are financially supported by the JSPS through the JSPS Research Fellowship for Young Scientists. Part of this work was carried out at the Jet Propulsion Laboratory, California Institute of Technology, under contract with NASA. Finally, the authors recognize and acknowledge the very significant cultural role and reverence that the summit of Mauna Kea has always had within the indigenous Hawaiian community. We are most fortunate to have the opportunity to conduct observations from this mountain.

Facility: Subaru (HiCIAO, IRCS)

APPENDIX

MONTE CARLO ORBITAL ANALYSIS

To demonstrate that the measured motion of GJ 504b relative to its parent star GJ 504 is indeed consistent with the expected orbital motion of a gravitationally bound planet, we have run a Monte Carlo simulation following Janson et al. (2011). A large number of physically plausible orbits is randomly generated and compared to the astrometric data points. The maximum of the χ^2 function is typically ill defined for an astrometric data set covering only a small fraction of an orbit: an entire family of orbits spanning a large range of semimajor axes match the data equally well. Thus, rather than ascribing an undue amount of significance to the simulated orbit with the smallest χ^2 value, we consider the entire well-fitting family of orbits with $\chi^2 < \chi^2_{\rm min} + 1$. The plots in Figure 12 summarize the properties of this well-fitting orbit family.

To characterize this distribution numerically, we determine the weighted median and the weighted 68% range for each parameter of the orbital simulation (semimajor axis a, eccentricity e, inclination i, longitude of ascending node Ω, and argument of periastron ω). We calculate the statistical weight W of each orbit as the mean orbital velocity divided by the local orbital velocity at the epoch of observation. This represents the fact that an eccentric planet orbits slower, spends more time, and is therefore more likely to be observed at apastron than at periastron.

However, some of the histograms are heavily skewed (e.g., $\log a$) or even periodic (e.g., Ω); as a result, the median badly represents the true behavior of the entire well-fitting orbit family. For this reason, we further define the most likely orbit (MLO).

For each simulated orbit n, we calculate as a measure of likelihood $L_{\rm n}$ the product of the histogram values of the $\log a$, e, i, Ω, ω histograms in the bin into which the orbit falls, as well as the statistical weight W:

$$L_n = {\rm hist}_{\log a}(\log a_n) \cdot {\rm hist}_e(e_n) \cdot {\rm hist}_i(i_n) \cdot {\rm hist}_\Omega(\Omega_n) \cdot {\rm hist}_\omega(\omega_n) \cdot W. \quad \text{(A1)}$$

The MLO can then be defined as the orbit with the highest measure of likelihood, $L_{\rm MLO} = \max_n L_n$.

REFERENCES

Allard, F., Hauschildt, P. H., Alexander, D. R., Tamanai, A., & Schweitzer, A. 2001, ApJ, 556, 357
Baines, E. K., White, R. J., Huber, D., et al. 2012, ApJ, 761, 57
Baliunas, S., Sokoloff, D., & Soon, W. 1996, ApJL, 457, L99
Baraffe, I., & Chabrier, G. 2010, A&A, 521, A44
Baraffe, I., Chabrier, G., Barman, T. S., Allard, F., & Hauschildt, P. H. 2003, A&A, 402, 701
Barman, T. S., Macintosh, B., Konopacky, Q. M., & Marois, C. 2011a, ApJ, 733, 65
Barman, T. S., Macintosh, B., Konopacky, Q. M., & Marois, C. 2011b, ApJL, 735, L39
Barnes, S. A. 2007, ApJ, 669, 1167
Baruteau, C., Meru, F., & Paardekooper, S.-J. 2011, MNRAS, 416, 1971
Batalha, N. M., Rowe, J. F., Bryson, S. T., et al. 2013, ApJS, 204, 24
Boley, A. C., Hayfield, T., Mayer, L., & Durisen, R. H. 2010, Icar, 207, 509
Bonnefoy, M., Lagrange, A.-M., Boccaletti, A., et al. 2011, A&A, 528, L15
Bryden, G., Beichman, C. A., Trilling, D. E., et al. 2006, ApJ, 636, 1098
Burrows, A., Marley, M., Hubbard, W. B., et al. 1997, ApJ, 491, 856
Burrows, A., Sudarsky, D., & Hubeny, I. 2006, ApJ, 640, 1063
Cai, K., Durisen, R. H., Michael, S., et al. 2006, ApJL, 636, L149
Carson, J., Thalmann, C., Janson, M., et al. 2013, ApJL, 763, L32
Chabrier, G., Baraffe, I., Selsis, F., et al. 2007, in Protostars and Planets V, ed. B. Reipurth, D. Jewitt, & K. Keil (Tucson, AZ: Univ. Arizona Press), 623
Chatterjee, S., Ford, E. B., Matsumura, S., & Rasio, F. A. 2008, ApJ, 686, 580
Chauvin, G., Lagrange, A.-M., Dumas, C., et al. 2004, A&A, 425, L29
Crida, A., Masset, F., & Morbidelli, A. 2009, ApJL, 705, L148
Currie, T., Debes, J., Rodigas, T. J., et al. 2012, ApJL, 760, L32
da Silva, R., Porto de Mello, G. F., Milone, A. C., et al. 2012, A&A, 542, A84
Delorme, P., Collier Cameron, A., Hebb, L., et al. 2011, MNRAS, 413, 2218
Dodson-Robinson, S. E., Veras, D., Ford, E. B., & Beichman, C. A. 2009, ApJ, 707, 79
Donahue, R. A., Saar, S. H., & Baliunas, S. L. 1996, ApJ, 466, 384
Dupuy, T. J., Liu, M. C., & Ireland, M. J. 2009, ApJ, 692, 729
Durisen, R. H., Boss, A. P., Mayer, L., et al. 2007, in Protostars and Planets V, ed. B. Reipurth, D. Jewitt, & K. Keil (Tucson, AZ: Univ. Arizona Press), 607
Fabrycky, D. C., & Murray-Clay, R. A. 2010, ApJ, 710, 1408
Fischer, D. A., & Valenti, J. 2005, ApJ, 622, 1102
Fleming, S. W., Ge, J., Mahadevan, S., et al. 2010, ApJ, 718, 1186
Fortney, J. J., Marley, M. S., Saumon, D., & Lodders, K. 2008, ApJ, 683, 1104
Galicher, R., Marois, C., Macintosh, B., Barman, T., & Konopacky, Q. 2011, ApJL, 739, L41
Galicher, R., Marois, C., Zuckerman, B., & Macintosh, B. 2013, ApJ, 769, 42
Giampapa, M. S., Hall, J. C., Radick, R. R., & Baliunas, S. L. 2006, ApJ, 651, 444
Hall, J. C., Henry, G. W., Lockwood, G. W., Skiff, B. A., & Saar, S. H. 2009, AJ, 138, 312
Hartman, J. D., Bakos, G. Á., Kovács, G., & Noyes, R. W. 2010, MNRAS, 408, 475
Hartman, J. D., Gaudi, B. S., Pinsonneault, M. H., et al. 2009, ApJ, 691, 342
Hayano, Y., Takami, H., Guyon, O., et al. 2008, Proc. SPIE, 7015, 701510
Hayashi, C. 1981, PThPS, 70, 35
Holmberg, J., Nordström, B., & Andersen, J. 2009, A&A, 501, 941
Hünsch, M., Schmitt, J. H. M. M., Sterzik, M. F., & Voges, W. 1999, A&AS, 135, 319
Inaba, S., & Ikoma, M. 2003, A&A, 410, 711
Janson, M., Carson, J. C., Lafrenière, D., et al. 2012, ApJ, 747, 116
Janson, M., Carson, J., Thalmann, C., et al. 2011, ApJ, 728, 85
Kalas, P., Graham, J. R., Chiang, E., et al. 2008, Sci, 322, 1345
Kalas, P., Graham, J. R., Fitzgerald, M. P., & Clampin, M. 2013,arXiv:1305.2222
Kidger, M. R., & Martín-Luis, F. 2003, AJ, 125, 3311
Kirkpatrick, J. D., Cushing, M. C., Gelino, C. R., et al. 2011, ApJS, 197, 19
Kobayashi, H., Tanaka, H., & Krivov, A. V. 2011, ApJ, 738, 35
Kobayashi, N., Tokunaga, A. T., Terada, H., et al. 2000, Proc. SPIE, 4008, 1056
Kuzuhara, M., Tamura, M., Ishii, M., et al. 2011, AJ, 141, 119
Lafrenière, D., Jayawardhana, R., & van Kerkwijk, M. H. 2008, ApJL, 689, L153
Lafrenière, D., Marois, C., Doyon, R., Nadeau, D., & Artigau, É. 2007, ApJ, 660, 770
Lagrange, A.-M., Bonnefoy, M., Chauvin, G., et al. 2010, Sci, 329, 57
Leggett, S. K., Burningham, B., Saumon, D., et al. 2010, ApJ, 710, 1627
Lockwood, G. W., Skiff, B. A., Henry, G. W., et al. 2007, ApJS, 171, 260
López-Santiago, J., Montes, D., Crespo-Chacón, I., & Fernández-Figueroa, M. J. 2006, ApJ, 643, 1160
Machida, M. N., Inutsuka, S.-i., & Matsumoto, T. 2011, ApJ, 729, 42
Madhusudhan, N., Burrows, A., & Currie, T. 2011, ApJ, 737, 34
Mamajek, E. E., & Hillenbrand, L. A. 2008, ApJ, 687, 1264
Marley, M. S., Fortney, J. J., Hubickyj, O., Bodenheimer, P., & Lissauer, J. J. 2007, ApJ, 655, 541
Marley, M. S., Saumon, D., Cushing, M., et al. 2012, ApJ, 754, 135
Marois, C., Lafrenière, D., Doyon, R., Macintosh, B., & Nadeau, D. 2006, ApJ, 641, 556
Marois, C., Macintosh, B., Barman, T., et al. 2008, Sci, 322, 1348
Marois, C., Zuckerman, B., Konopacky, Q. M., Macintosh, B., & Barman, T. 2010, Natur, 468, 1080
Mayor, M., Marmier, M., Lovis, C., et al. 2011, arXiv:1109.2497
Meibom, S., Mathieu, R. D., & Stassun, K. G. 2009, ApJ, 695, 679
Meibom, S., Mathieu, R. D., Stassun, K. G., Liebesny, P., & Saar, S. H. 2011, ApJ, 733, 115
Messina, S., Parihar, P., Koo, J.-R., et al. 2010, A&A, 513, A29
Messina, S., Pizzolato, N., Guinan, E. F., & Rodonò, M. 2003, A&A, 410, 671
Metchev, S., Marois, C., & Zuckerman, B. 2009, ApJL, 705, L204
Mishenina, T. V., Soubiran, C., Kovtyukh, V. V., & Korotin, S. A. 2004, A&A, 418, 551
Moeckel, N., & Armitage, P. J. 2012, MNRAS, 419, 366
Mohanty, S., Jayawardhana, R., Huélamo, N., & Mamajek, E. 2007, ApJ, 657, 1064
Nagasawa, M., Ida, S., & Bessho, T. 2008, ApJ, 678, 498
Paardekooper, S.-J., Baruteau, C., Crida, A., & Kley, W. 2010, MNRAS, 401, 1950
Pollack, J. B., Hubickyj, O., Bodenheimer, P., et al. 1996, Icar, 124, 62
Poveda, A., Herrera, M. A., Allen, C., Cordero, G., & Lavalley, C. 1994, RMxAA, 28, 43
Radick, R. R., Lockwood, G. W., Skiff, B. A., & Baliunas, S. L. 1998, ApJS, 118, 239
Radick, R. R., Lockwood, G. W., Skiff, B. A., & Thompson, D. T. 1995, ApJ, 452, 332
Radick, R. R., Thompson, D. T., Lockwood, G. W., Duncan, D. K., & Baggett, W. E. 1987, ApJ, 321, 459
Rafikov, R. R. 2004, AJ, 128, 1348
Rafikov, R. R. 2011, ApJ, 727, 86
Rameau, J., Chauvin, G., Lagrange, A.-M., et al. 2013, ApJL, 773, L15
Reiners, A., & Giampapa, M. S. 2009, ApJ, 707, 852
Roeser, S., Demleitner, M., & Schilbach, E. 2010, AJ, 139, 2440
Schneider, J., Dedieu, C., Le Sidaner, P., Savalle, R., & Zolotukhin, I. 2011, A&A, 532, A79
Sestito, P., & Randich, S. 2005, A&A, 442, 615
Skemer, A. J., Close, L. M., Szűcs, L., et al. 2011, ApJ, 732, 107
Skemer, A. J., Hinz, P. M., Esposito, S., et al. 2012, ApJ, 753, 14
Soderblom, D. R. 2010, ARA&A, 48, 581
Soummer, R., Brendan Hagan, J., Pueyo, L., et al. 2011, ApJ, 741, 55
Spiegel, D. S., & Burrows, A. 2012, ApJ, 745, 174
Sudol, J. J., & Haghighipour, N. 2012, ApJ, 755, 38
Suzuki, R., Kudo, T., Hashimoto, J., et al. 2010, Proc. SPIE, 7735, 773530
Takeda, G., Ford, E. B., Sills, A., et al. 2007, ApJS, 168, 297
Takeda, Y., & Kawanomoto, S. 2005, PASJ, 57, 45
Takeda, Y., Ohkubo, M., Sato, B., Kambe, E., & Sadakane, K. 2005, PASJ, 57, 27
Tamura, M. 2009, in AIP Conf. Ser. 1158, Exoplanets and Disks: Their Formation and Diversity, ed. T. Usuda, M. Tamura, & M. Ishii (Melville, NY: AIP), 11
Tamura, M., Suto, H., Nishikawa, J., et al. 2012, Proc. SPIE, 8446, 84461T
Thalmann, C., Carson, J., Janson, M., et al. 2009, ApJL, 707, L123
Torres, C. A. O., Quast, G. R., Melo, C. H. F., & Sterzik, M. F. 2008, in Handbook of Star Forming Regions, Vol. II: The Southern Sky, ed. B. Reipurth (ASP Monograph Publications, Vol. 5; San Francisco, CA: ASP), 757
Torres, G., Andersen, J., & Giménez, A. 2010, A&ARv, 18, 67
Trilling, D. E., Bryden, G., Beichman, C. A., et al. 2008, ApJ, 674, 1086
Valdes, F., Gupta, R., Rose, J. A., Singh, H. P., & Bell, D. J. 2004, ApJS, 152, 251
Valenti, J. A., & Fischer, D. A. 2005, ApJS, 159, 141
van Leeuwen, F. 2007, A&A, 474, 653
van der Marel, R. P., Anderson, J., Cox, C., et al. 2007, Calibration of ACS/WFC Absolute Scale and Rotation for Use in creation of a *JWST* Astrometric Reference Field, Technical Report
Yi, S., Demarque, P., Kim, Y.-C., et al. 2001, ApJS, 136, 417
Zhu, Z., Hartmann, L., Nelson, R. P., & Gammie, C. F. 2012, ApJ, 746, 110

The Astrophysical Journal, 786:1 (25pp), 2014 May 1 doi:10.1088/0004-637X/786/1/1

THE MOVING GROUP TARGETS OF THE SEEDS HIGH-CONTRAST IMAGING SURVEY OF EXOPLANETS AND DISKS: RESULTS AND OBSERVATIONS FROM THE FIRST THREE YEARS

Timothy D. Brandt[1], Masayuki Kuzuhara[2], Michael W. McElwain[3], Joshua E. Schlieder[4], John P. Wisniewski[5], Edwin L. Turner[1,6], J. Carson[4,7], T. Matsuo[8], B. Biller[4], M. Bonnefoy[4], C. Dressing[9], M. Janson[1], G. R. Knapp[1], A. Moro-Martín[10], C. Thalmann[11], T. Kudo[12], N. Kusakabe[13], J. Hashimoto[5,13], L. Abe[14], W. Brandner[4], T. Currie[15], S. Egner[12], M. Feldt[4], T. Golota[12], M. Goto[16], C. A. Grady[3,17], O. Guyon[12], Y. Hayano[12], M. Hayashi[18], S. Hayashi[12], T. Henning[4], K. W. Hodapp[19], M. Ishii[12], M. Iye[13], R. Kandori[13], J. Kwon[13,20], K. Mede[18], S. Miyama[21], J.-I. Morino[13], T. Nishimura[12], T.-S. Pyo[12], E. Serabyn[22], T. Suenaga[20], H. Suto[13], R. Suzuki[13], M. Takami[23], Y. Takahashi[18], N. Takato[12], H. Terada[12], D. Tomono[12], M. Watanabe[24], T. Yamada[25], H. Takami[12], T. Usuda[12], and M. Tamura[13,18]
[1] Department of Astrophysical Sciences, Princeton University, Princeton, NJ, USA
[2] Tokyo Institute of Technology, Tokyo, Japan
[3] Exoplanets and Stellar Astrophysics Laboratory, NASA Goddard Space Flight Center, Greenbelt, MD, USA
[4] Max Planck Institute for Astronomy, Heidelberg, Germany
[5] HL Dodge Department of Physics and Astronomy, University of Oklahoma, Norman, OK, USA
[6] Kavli Institute for the Physics and Mathematics of the Universe (WPI), Todai Institutes for Advanced Study, University of Tokyo, Japan
[7] College of Charleston, Charleston, SC, USA
[8] Department of Astronomy, Kyoto University, Kyoto, Japan
[9] Harvard-Smithsonian Center for Astrophysics, Cambridge, MA, USA
[10] Department of Astrophysics, CAB-CSIC/INTA, Madrid, Spain
[11] Astronomical Institute Anton Pannekoek, University of Amsterdam, Amsterdam, The Netherlands
[12] Subaru Telescope, Hilo, HI, USA
[13] National Astronomical Observatory of Japan, Tokyo, Japan
[14] Laboratoire Hippolyte Fizeau, Nice, France
[15] University of Toronto, Toronto, Canada
[16] Universitäts-Sternwarte München, Munich, Germany
[17] Eureka Scientific, Oakland, CA, USA
[18] University of Tokyo, Tokyo, Japan
[19] Institute for Astronomy, University of Hawaii, Hilo, HI, USA
[20] Department of Astronomical Science, Graduate University for Advanced Studies, Tokyo, Japan
[21] Hiroshima University, Higashi-Hiroshima, Japan
[22] Jet Propulsion Laboratory, California Institute of Technology, Pasadena, CA, USA
[23] Institute of Astronomy and Astrophysics, Academia Sinica, Taipei, Taiwan
[24] Department of Cosmosciences, Hokkaido University, Sapporo, Japan
[25] Astronomical Institute, Tohoku University, Sendai, Japan
Received 2013 May 30; accepted 2014 February 15; published 2014 April 8

ABSTRACT

We present results from the first three years of observations of moving group (MG) targets in the Strategic Exploration of Exoplanets and Disks with Subaru (SEEDS) high-contrast imaging survey of exoplanets and disks using the Subaru telescope. We achieve typical contrasts of $\sim 10^5$ at $1''$ and $\sim 10^6$ beyond $2''$ around 63 proposed members of nearby kinematic MGs. We review each of the kinematic associations to which our targets belong, concluding that five, β Pictoris ($\sim$20 Myr), AB Doradus ($\sim$100 Myr), Columba ($\sim$30 Myr), Tucana–Horogium ($\sim$30 Myr), and TW Hydrae ($\sim$10 Myr), are sufficiently well-defined to constrain the ages of individual targets. Somewhat less than half of our targets are high-probability members of one of these MGs. For all of our targets, we combine proposed MG membership with other age indicators where available, including Ca II HK emission, X-ray activity, and rotation period, to produce a posterior probability distribution of age. SEEDS observations discovered a substellar companion to one of our targets, κ And, a late B star. We do not detect any other substellar companions, but do find seven new close binary systems, of which one still needs to be confirmed. A detailed analysis of the statistics of this sample, and of the companion mass constraints given our age probability distributions and exoplanet cooling models, will be presented in a forthcoming paper.

Key words: binaries: close – brown dwarfs – open clusters and associations: general – stars: activity – stars: imaging – stars: low-mass – stars: planetary systems

Online-only material: color figures

1. INTRODUCTION

More than 850 exoplanets are now known to orbit other stars. Most were identified with indirect detection techniques, but exoplanets have now been imaged around several young, nearby stars. Direct imaging (DI) is the primary technique used to probe the frequency of giant exoplanets at separations similar to the outer solar system ($\sim$4–40 AU). DI is already providing important constraints on planetary formation mechanisms, complementing the well-characterized distribution and frequency of planets at separations similar to the inner solar system (e.g., Cumming et al. 2008; Howard et al. 2010). By measuring its emission spectrum, DI constrains an exoplanetary atmosphere's temperature, composition, and dynamics. DI of exoplanets of known age can also break the mass-age-luminosity degeneracy in exoplanet cooling models.

Several surveys have set out to directly image exoplanets around nearby stars. The DI of exoplanets is challenging observationally, due to their high contrast ($\gtrsim 10^4$) and small separations from the host star ($\lesssim 1''$). These observational requirements are mitigated by targeting young, nearby systems (see Oppenheimer & Hinkley 2009). Young exoplanets cool rapidly as they radiate away their residual heat of formation, quickly falling below the detectability limits of even the largest ground-based telescopes equipped with high-contrast instrumentation. This sub-stellar evolution is similar to that of brown dwarfs, but is distinct from stellar evolution (e.g., Burrows et al. 1997; Chabrier et al. 2000). Nearby stars are important because the angular resolution is set by Earth's atmosphere and the optical system; nearer stars can therefore probe smaller physical separations. Unfortunately, the vast majority of observations remain null detections: massive exoplanets and brown dwarfs at large separations appear to be rare (cf. McCarthy & Zuckerman 2004; Masciadri et al. 2005; Carson et al. 2006; Lafrenière et al. 2007a; Biller et al. 2007; Metchev & Hillenbrand 2009; Janson et al. 2011a; Vigan et al. 2012). In order to properly interpret these results, however, uncertainties in stellar ages must be taken into account.

We report the strategy and results from the first three years of the "moving groups" (MGs) subcategory of the Strategic Exploration of Exoplanets and Disks with Subaru (SEEDS) survey (Tamura 2009). An MG is a collection of stars that share a common age, metallicity, and space motion due to formation in the same event. Nearby MG stars are particularly promising targets for DI planet searches due to their proximity and well defined youthful ages. The SEEDS survey itself is briefly described in Section 2. The architecture and target selection strategy of the SEEDS MGs sub-category is discussed in Section 3. This section also includes a review of each of the MGs that were drawn upon for the target sample, as well as the age indicators used for the targets. In Section 4, individual stellar age indicators are described in the context of how they were implemented to constrain the ages of the target sample. Section 5 describes the Bayesian approach to assign statistically significant stellar ages for the target sample. The observations and details regarding individual stars are discussed in Section 7. The data reduction details are summarized in Section 6, and a discussion of the MG sample sensitivity is presented in Section 8. The concluding remarks are presented in Section 9.

2. THE SEEDS SURVEY

The SEEDS survey is the most ambitious high-contrast imaging survey to date. This survey is being carried out with a suite of high-contrast instrumentation at the Subaru telescope, including a second generation adaptive optics (AO) system with 188 actuators (AO188; Hayano et al. 2008) and a dedicated differential imaging instrument called HiCIAO (Suzuki et al. 2010). SEEDS is now $\sim$2/3 complete, and will ultimately observe $\sim$500 stars to search for exoplanets and disks with DI.

The SEEDS survey is organized into two separate classes: planets and disks. Each of SEEDS' target classes, planets and disks, is further subdivided into categories, including nearby stars, MGs (this work), debris disks (Janson et al. 2013), young stellar objects (containing the protoplanetary and transitional disks), and open clusters (Yamamoto et al. 2013). The nearby stars category is further separated into sub-categories that include high mass stars (J. Carson et al. 2013, in preparation), M dwarfs, white dwarfs, chromospherically active stars, stars with kinematic properties suggestive of youth, and stars with known radial velocity planets (e.g., Narita et al. 2010, 2012).

HiCIAO offers several observing modes, including polarized differential imaging (PDI), simultaneous imaging at different wavelengths (spectral differential imaging, or SDI), and simple DI (or angular differential imaging (ADI) when used with the image rotator off and the pupil rotation angle fixed on the detector). Young disks, with plentiful scattering by small grains, are typically observed in polarized light (PDI mode). PDI obtains simultaneous measurements of perpendicular polarization states; the two images are later subtracted to remove unpolarized light (Kuhn et al. 2001). SEEDS implements the double difference technique that subtracts a similar polarization scene modulated by 90°, effectively removing the non common path errors between the channels (e.g., Hinkley et al. 2009). Older debris disks have much weaker polarized scattering; only their total scattered intensity is typically observed. All stars without disks predicted from infrared excesses are observed only in total intensity (DI), and the data are processed using ADI.

Early survey highlights include three directly detected sub-stellar companions, GJ 758 B (Thalmann et al. 2009; Janson et al. 2011b), κ Andromedae b (Carson et al. 2013), and GJ 504 b (Kuzuhara et al. 2013; Janson et al. 2013). In addition, there has been a plethora of papers that investigate circumstellar disk properties in the protoplanetary (Hashimoto et al. 2011; Kusakabe et al. 2012), transitional (Thalmann et al. 2010; Muto et al. 2012; Hashimoto et al. 2012; Dong et al. 2012; Mayama et al. 2012; Tanii et al. 2012; Grady et al. 2013; Follette et al. 2013), and debris (Thalmann et al. 2011, 2013) phases of evolution. These include some of the first near-IR images of protoplanetary and transitional disks, including hints of substellar companions from disk structure, and characterizations of debris disks believed to be generated by the destruction of planetesimals.

The goal of the SEEDS survey is to provide observational constraints on all stages of exoplanet formation and evolution, from protoplanetary and transitional disks to older, disk-free systems. The survey therefore targets a wide range of host stars. Unfortunately, many of the SEEDS targets, while they do show indicators of youth, lack well-determined ages. This leads to large uncertainties when converting exoplanet luminosities into masses using theoretical cooling models (e.g., Burrows et al. 1997; Baraffe et al. 2003; Marley et al. 2007; Spiegel & Burrows 2012). The MG category is designed to overcome this problem by observing nearby stars reliably associated with kinematic MGs $\sim$ 10–500 Myr old.

Because of their distances and ages, the SEEDS MG sample includes some of the most promising targets in the sky for the direct detection of exoplanets. Many of these targets have been observed by other previous and ongoing surveys, and we make use of the publicly available data in our analysis, primarily as a means of identifying background stars in the field of view by confirming they do not share common proper motion with the target star (see Section 7).

3. SEEDS MOVING GROUPS

Many of the youngest stars near the Sun are members of MGs, loose associations of stars defined by their common Galactic kinematics and ages (see reviews by Zuckerman & Song 2004; Torres et al. 2008). Some MGs have been kinematically and chemically associated with nearby clusters, linking them to recent episodes of star formation near the Sun (Mamajek & Feigelson 2001; Ortega et al. 2002; Fernández

et al. 2008; Barenfeld et al. 2013; De Silva et al. 2013). MGs have members within the solar neighborhood ($\lesssim$100 pc) and ages ∼10–500 Myr. If a proposed MG is real, and not a dynamical stream (see the following subsections), the true members are coeval. Group ages are determined using many methods based on both individual proposed members and the group as an aggregate. These include: H-R diagrams, isochrone fitting, lithium depletion, chromospheric and coronal emission, rotation, and the kinematic trace back of the group members to the most compact volume in space where they were formed coevally. The likelihood that a star is a true MG member depends on both its kinematics and youth indicators. The targets for the SEEDS MGs category are proposed members of the nearby, young kinematic MGs AB Doradus, β Pictoris, Castor, Columba, Hercules–Lyra, the IC 2391 supercluster, the Local Association, Tucana–Horologium, TW Hydrae, and Ursa Major/Sirius. We briefly summarize each of these associations in the following subsections.

3.1. The AB Doradus Moving Group

Torres et al. (2003) and Zuckerman et al. (2004) independently proposed the AB Doradus MG via searches for stars with common kinematics and ages in publicly available catalogs. AB Dor has one of the largest proposed membership samples of any MG—Torres et al. (2008) list 89 members identified in their SACY survey. Newly proposed members push the total number to more than 100 stars (Schlieder et al. 2010, 2012a; Zuckerman et al. 2011; Shkolnik et al. 2012; Bowler et al. 2012). The AB Dor group also covers the entire celestial sphere, with many proposed members in the north.

The age of AB Dor has been revisited and revised many times in the literature. Ages between 50 and 150 Myr have been derived using H-R diagram studies, lithium depletion, activity, and detailed observations of the AB Doradus quadruple system (Zuckerman et al. 2004; Torres et al. 2008; Mentuch et al. 2008; Janson et al. 2007; Close et al. 2007). Several studies argue for a common origin of the AB Dor group and Pleiades open cluster (Luhman et al. 2005; Ortega et al. 2007).

Barenfeld et al. (2013) performed a chemical and kinematic analysis of proposed members and found strong evidence for a kinematic nucleus and associated stream. They caution, however, that their traceback studies and observed chemical inhomogeneity of the proposed members suggest a significant fraction of impostors. Barenfeld et al. also place a lower limit of 110 Myr on the group's age by using pre-main-sequence contraction times of reliable K-type members. We combine this well constrained age limit with the previous results showing similarities to the Pleiades to adopt the Pleiades age of 130 $\pm$ 20 Myr (Barrado y Navascués et al. 2004) for the AB Doradus MG.

3.2. The β Pictoris Moving Group

Barrado y Navascués et al. (1999) identified two young M dwarfs having proper motions consistent with the prototypical debris disk, and now-known planet host, β Pictoris (Lagrange et al. 2009, 2010); they estimated a system age of 20 $\pm$ 10 Myr via comparisons to theoretical isochrones. This led to a search for more stars with similar age and kinematics near β Pic by Zuckerman et al. (2001a). They identified 18 systems and coined the name the β Pictoris MG. Torres et al. (2006, 2008) proposed many β Pic members in their SACY survey, while other searches have since proposed the first isolated brown-dwarf member and several additional low-mass members (Lépine & Simon 2009; Rice et al. 2010; Schlieder et al. 2010, 2012a, 2012b; Kiss et al. 2011; Malo et al. 2013).

Torres et al. (2008) list 48 high probability members of β Pic; newer additions bring the total to more than 60 stars. β Pic members are spread over the sky with the majority at southern declinations. The galactic kinematics and age of the group are similar to those of the TW Hydrae association (see Section 3.9), and both groups may be related to star formation in Sco-Cen OB association subgroups (Mamajek & Feigelson 2001; Ortega et al. 2002).

The age of the β Pic group has been estimated at 10–20 Myr from H-R diagrams, comparison to evolution models, lithium depletion, and kinematics (Barrado y Navascués et al. 1999; Zuckerman et al. 2001a; Ortega et al. 2002; Mentuch et al. 2008). Two more recent evaluations of the group age include a study of the lithium depletion boundary by Binks & Jeffries (2014) and a reanalysis of the kinematic age in Soderblom et al. (2014). Binks & Jeffries constrain the age to 21 $\pm$ 4 Myr by comparing the minimum luminosity (i.e., minimum mass) of M-dwarf members that have fully burned their primordial lithium to predictions from evolutionary models. Soderblom et al. provide a new analysis of proposed member kinematics using revised *Hipparcos* astrometry and find that the group was not appreciably smaller any time in the past, excluding traceback as a useful dating method in this case. A detailed analysis by Jenkins et al. (2012) also provides an age of ∼20 Myr for the substellar host (Biller et al. 2010) and β Pic member, PZ Tel. We thus adopt the lithium depletion boundary age of 21 $\pm$ 4 Myr for our analyses.

3.3. The Castor Moving Group

The Castor MG was originally proposed by Anosova & Orlov (1991) in their study of the dynamical evolution of several multiple systems in the solar neighborhood. They searched the Catalog of Nearby Stars (Gliese 1969) for all systems inside a velocity cube 6 km s^{-1} on a side, centered on the Castor sextuple system. They found 13 additional stars in 9 systems, and proposed that these stars, together with the Castor system, constitute an MG.

Barrado y Navascues (1998) revisited the proposed members of the Castor MG and performed a more rigorous analysis using new kinematic measurements and age indicators. They began with a sample of 26 candidate members and found that only 16 met their kinematic and age criteria, which were based on isochrones, activity, and lithium depletion. Barrado y Navascues assigned an age of 200 $\pm$ 100 Myr to the group using the age of proposed member Fomalhaut and its companion TW PsA. The work of Montes et al. (2001b) led to the identification of eight possible late-type members of Castor, while Caballero (2010) and Shkolnik et al. (2012) present additional candidates.

The ages of several original Castor members have been recently reassessed using modern techniques. Yoon et al. (2010) redetermined the age of Vega to be 455 $\pm$ 13 Myr using spectroscopic, photometric, and interferometric data together with isochrones. A full interferometric analysis by Monnier et al. (2012) increased this age to ∼700 Myr. Mamajek (2012) revisited the age of Fomalhaut and its wide stellar companion and used modern isochrones, lithium depletion measurements, and age/rotation/activity diagnostics to assign them an age of 440 $\pm$ 40 Myr. These new results are incompatible with the proposed age of the Castor MG, and cast doubt on its physical reality as a coeval association.

In phase space, the Castor MG lacks a discernible core or tight nucleus of members (velocity dispersion $\sim$1 km s^{-1}). Although this may be due to its older age, it may also indicate that the Castor MG is really a complex of kinematically similar stars with a spread of ages. Zuckerman et al. (2013) and Mamajek et al. (2013) reach the latter conclusion and reject a common age for Castor. Thus, we do not assign the proposed group age to the candidate members in the SEEDS sample, relying instead on single-star age indicators such as activity and lithium depletion.

3.4. The Columba Association

Torres et al. (2008) discovered the Columba association in their SACY survey. Its kinematics and age are very similar to the Tucana–Horologium association (see Section 3.8), but it is considered to be kinematically distinct due to its significantly different W velocity. Torres et al. proposed 53 members of this association, including some stars originally proposed as members of Tucana–Horologium.

An additional 14 Columba members were proposed by Zuckerman et al. (2011). Their list included many high-mass stars including HR 8799 and κ Andromedae, two stars hosting substellar companions (Marois et al. 2008, 2010; Carson et al. 2013). Malo et al. (2013) performed a Bayesian analysis on the full sample of proposed candidates, finding 21 high-probability members on the basis of complete kinematic data.

The Columba association received some scrutiny in a kinematic study, which questioned HR 8799's membership due to its distance from the bulk of the association throughout an epicyclic orbit simulation (Hinz et al. 2010). Hinz et al. also suggest that since the proposed members of Columba cover such a large volume of space (>100 pc; Torres et al. 2008), it is more likely to be a complex of young stars with a range of ages. Torres et al. also noted the Columba association's large spatial extent, as a result of which membership probabilities for this group were significantly lower than for the more compact Tucana–Horologium association.

While the physical reality of the association may not yet be well-established, the stars proposed as members are still excellent targets for DI due to their relative proximity and young ages. We carefully investigate the age of each target member to verify that it is comparable to the 30^{+20}_{-10} Myr age (Marois et al. 2010) of the group.

3.5. The Hercules–Lyra Association

The first indication of this young kinematic group was found by Gaidos (1998) in their study of young solar analogs. Gaidos identified five nearly comoving young stars with a radiant in the constellation Hercules, calling them the Hercules Association.

Fuhrmann (2004) studied nearby stars of the galactic disk and halo to identify more stars with kinematics and ages similar to those identified by Gaidos. The resulting updated sample of 15 stars had a radiant point at the border between the constellations Hercules and Lyra, and the Hercules association was renamed the Hercules–Lyra association. The stars in the Fuhrmann (2004) sample exhibit rotations, activities, and lithium depletions that suggest generally young ages. Some stars appeared to be coeval with proposed Ursa Majoris MG members ($\sim$200 Myr, at the time), while others appeared younger or older, suggesting that the Hercules–Lyra association may not be coeval.

López-Santiago et al. (2006) revisited the proposed Hercules–Lyra association, searching their list of late-type members of kinematic groups (Montes et al. 2001b) for new candidates. They required Galactic UV velocities within 6 km s^{-1} of the mean values from Fuhrmann (2004) but imposed no restriction on the W component of the velocity. From their initial sample of 27 candidates, López-Santiago et al. found only 10 meeting their kinematic, lithium, and photometric criteria. They assigned an age of 150–300 Myr to the association due to consistent results from both lithium abundances and color–magnitude diagrams. Shkolnik et al. (2012) proposed an additional low-mass candidate.

Eisenbeiss et al. (2013) revisit the membership, age, and multiplicity of the previously proposed members and find only seven systems that meet all of their membership criteria. These stars exhibit Galactic velocity dispersions >3.5 km s^{-1} and have ages of $\sim$260 $\pm$ 50 Myr estimated from gyrochronology. As for the Castor MG (see Section 3.3), the small number and large velocity dispersion of reliably proposed members cast doubt on Hercules–Lyra as a true young stellar association. We therefore rely on youth indicators such as lithium and chromospheric activity to derive ages for each individual star.

3.6. The IC 2391 Supercluster

Eggen (1991) noted that more than 60 field stars and members of the IC 2391 open cluster all have motions directed toward a single convergent point. Color–magnitude diagrams and comparisons to available isochrones suggested a bimodal age distribution, with one subgroup at $\sim$80 Myr and the other at $\sim$250 Myr. Further comments on this kinematic group can be found in Eggen (1992, 1995).

Montes et al. (2001b) reassessed previously proposed members of the IC 2391 supercluster and searched for new late-type candidates using updated astrometry, photometry, and spectroscopy. After adopting a cluster age of 35–55 Myr from Eggen (1995), only 15 stars met their kinematic criteria. Maldonado et al. (2010) used similar techniques to search for new members of several proposed kinematic groups, including the IC 2391 supercluster. In addition to compiling literature data, they performed follow-up spectroscopy to measure radial velocities and stellar age indicators. They found that when strict kinematic and age criteria were employed, only 5 of 19 candidates remained as probable members. Furthermore, they caution that the supercluster may have two subgroups mixed in the UV velocity plane, one with an age of $\sim$200–300 Myr, and an older, $\sim$700 Myr component (López-Santiago et al. 2010).

Unfortunately, much of the existing literature disputes the physical reality of a coeval IC 2391 supercluster. Strict kinematic and age requirements give a sample with as few as five members, while the proposed ages for members vary by up to a factor of $\sim$20. We therefore consider claimed IC 2391 supercluster membership as a poor determinant of age and defer to each individual star's age indicators.

3.7. The Local Association

Eggen first noticed that several open clusters had galactic kinematics similar to the Pleiades (the Pleiades group). Eggen later identified more stars with similar kinematics, and proposed the Local Association (Eggen 1975, 1983a, 1983b). This kinematic stream included classical clusters such as the Pleiades, α Persei, and Scorpius-Centaurus, along with more than 100 other stars in a large volume of space around the Sun. The age of the stream was not well-defined, and subsequently spanned the estimated age ranges of its constituent clusters ($\sim$20 to $\sim$150 Myr).

Jeffries & Jewell (1993) studied the kinematics of X-ray and EUV selected late-type stars within 25 pc to identify more than

10 candidate members of the Local Association. A follow-up survey measured lithium abundances and rotational velocities (Jeffries 1995). Seventeen of their late-type candidates had age indicators and kinematics consistent with the Local Association. Montes et al. (2001a, 2001b) used similar techniques to search for new members, identifying seven stars with spectroscopic youth indicators out of 45 previously proposed candidates.

Although the proposed members of the Local Association do have similar galactic motions, the dispersion in *UVW* velocities is quite large ($\sim$20 km s^{-1}), the ages of constituent stars vary by $\sim$100 Myr, and the members are spread out over $\sim$150 pc. These features disfavor a common origin of the association, and in fact, many of the younger (and much better-defined) MGs have ages and kinematics placing them within the bounds of the Local Association. We therefore do not use Local Association membership to infer a star's age, relying instead on individual members' other age indicators.

3.8. The Tucana–Horologium Association

Zuckerman & Webb (2000) searched the *Hipparcos* catalog in the neighborhoods of a few dozen stars with 60 μm *IRAS* excesses, selecting targets with distances and proper motions similar to those of the infrared sample. Follow-up spectroscopy of these candidates led to the discovery of the Tucanae association, a well-defined kinematic group of stars $\sim$45 pc from the Sun with an age of about 40 Myr. Nearly simultaneously, Torres et al. (2000) searched for kinematically similar, X-ray bright stars near the active star EP Eri. Spectroscopic follow-up of active candidates revealed about 10 stars with very similar kinematics and spectroscopic youth indicators. These stars, comprising the Horologium association, had an isochronal age of $\sim$30 Myr and distances of $\sim$60 pc. Since the Tucanae and Horologium associations have similar kinematics and the same estimated age, they were later merged to form the Tucana–Horologium association (Zuckerman et al. 2001).

Zuckerman & Song (2004) listed 31 proposed members of Tucana–Horologium. Torres et al. (2008) identified 13 additional members in their SACY survey, bringing the total to 44. In the same review, Torres et al. associated Tucana–Horologium with two more recently discovered associations of similar age—Columba (see Section 3.4) and Carina—and suggested that these three groups together form a large complex of young stars (the Great Austral Young Association). Zuckerman et al. (2011) proposed several new members, including the first at northern declinations. Malo et al. (2013) have also presented a list of high-probability, low-mass candidate members. The value of these new candidates is exemplified by the recent imaging discovery of a very novel triple system comprised of two late M-dwarf Tucana–Horologium candidates and a 12–14 M_J substellar companion (Delorme et al. 2013).

The Tucana–Horologium association is one of the best-studied nearby young groups. Most of its proposed members are spatially and kinematically well-defined with little scatter in velocity space. An age of $\sim$30 Myr is consistently derived for its members; we adopt 30^{+10}_{-20} Myr (Zuckerman et al. 2001) as the age of the group.

3.9. The TW Hydrae Association

The TW Hydrae association, proposed by Kastner et al. (1997), was the first very young MG to be discovered. Early work by Rucinski & Krautter (1983) demonstrated that the nearby star TW Hya exhibited classical T-Tauri properties. The release of the *IRAS* point source catalog (Helou & Walker 1988) led to spectroscopic surveys of field stars with mid-IR excesses (de la Reza et al. 1989; Gregorio-Hetem et al. 1992). These surveys identified four additional T-Tauri stars near TW Hya, and suggested that they may be members of a nearby T-Tauri association. Kastner et al. (1997) later confirmed the five stars' common age by their strong X-ray emission and lithium absorption.

Webb et al. (1999) surveyed X-ray bright targets near TW Hydrae to identify additional members of the group. Subsequent surveys and analyses have since brought the number of proposed members to about 30 (Zuckerman et al. 2001b; Gizis 2002; Reid 2003; Torres et al. 2003, 2008; Zuckerman & Song 2004; Mamajek 2005; Barrado y Navascués 2006). One notable member is 2M1207, a young brown dwarf with a directly imaged planetary mass companion (Chauvin et al. 2004). The age of the association has been determined using many different methods, including H-R diagram placement, Hα diagnostics, lithium depletion, and kinematics; the most commonly cited age is $\sim$8 Myr.

More recent work on the TW Hydrae association has focused on identifying new, low-mass members. Looper et al. (2007, 2010a, 2010b) identified three late M type members, two of which host accretion disks. Rodriguez et al. (2011) and Shkolnik et al. (2011) used UV excesses as observed by the *GALEX* satellite to select low-mass candidate members, while Schneider et al. (2012) used IR excesses measured by the *WISE* satellite. Parallaxes for many proposed members were measured by Weinberger et al. (2013), who found that the association resembles an extended filament with an average member distance of 56 pc. These distance measurements enable precise H-R diagram placement and comparison to model isochrones. A Gaussian fit to the isochrone-based age distribution provides a mean age of 9.5 $\pm$ 5.7 Myr.

Despite the extensive study of the classical young association, TW Hydrae's evolution and membership are still being refined. Searches for new members continue (e.g., Malo et al. 2013), and may eventually lead to a complete census of this youngest and closest association. For our analyses, we adopt an age of 10 $\pm$ 5 Myr for the group.

3.10. The Ursa Major or Sirius Supercluster

The literature is rich with references to a kinematic association of stars related to the constellation Ursa Major, first introduced in the 19th century by Proctor (1869). A complete history of these stars is beyond the scope of this paper; however, we do mention prominent studies and refer the reader to references found therein for a complete review. We aim to establish in this subsection a distinction between the coeval Ursa Majoris MG and a dynamical stream of stars with generally consistent kinematics but heterogeneous ages known as the Ursa Major or Sirius supercluster.

The most modern and comprehensive study of the Ursa Majoris MG is King et al. (2003), which reevaluated previously proposed members using new astrometry, photometry, and spectroscopy. From an input list of $\sim$220 proposed Ursa Majoris candidates compiled from various sources, King et al. identified 57 probable and possible members that are well defined in kinematic and color–magnitude space. Comparison of evolution models to the color–magnitude diagram of their refined membership list suggests an age of 500 $\pm$ 100 Myr for the group. Shkolnik et al. (2012) later identified four additional candidate M-dwarf members. Since the Ursa Majoris MG

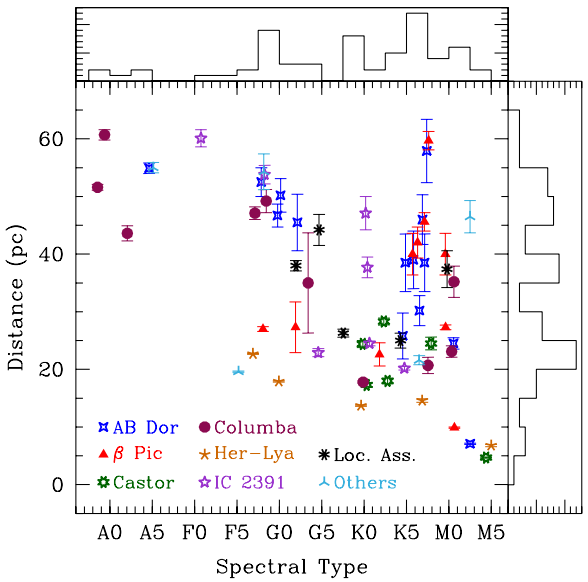

Figure 1. Distances, spectral types, and host moving group for our target sample. One star, HIP 78557 (spectral type G0), has a trigonometric distance of 82 ± 10 pc, placing it outside of the plot. Fifty-one of our 63 targets are within 50 pc, and all but 3 are within 60 pc, while their spectral types range from late B to early M.

(A color version of this figure is available in the online journal.)

contains a well defined nucleus with small velocity dispersions and is well characterized in a color–magnitude diagram, the estimated age of the group can be reliably applied to stars that meet membership criteria.

The Sirius supercluster was originally proposed as a remnant kinematic stream associated with the Ursa Majoris MG nucleus by Eggen (1958). Further members were proposed by Palous & Hauck (1986), who estimated an isochronal age of ∼490 Myr and proposed that the stars are chemically homogeneous. Famaey et al. (2005, 2008) present modern analyses of the proposed Sirius supercluster and other superclusters associated to well defined, coeval associations (Hyades, Pleiades) using new *Hipparcos* and *Tycho*-2 astrometry and radial velocity data from the CORAVEL spectrometer. Their analyses find that kinematically consistent members of the proposed superclusters do not have consistent isochronal ages. They propose that these structures in kinematic space are stellar streams likely generated by dynamical perturbations and are comprised of stars with heterogeneous ages that were not products of the same star formation event. Thus, kinematic membership to the Ursa Major or Sirius supercluster, in contrast to the well defined Ursa Majoris MG, is not useful as a stellar age indicator. We therefore do not assign the proposed supercluster age to the possible member we observed (HIP 73996) but rather rely on an individually assigned age from our own and literature measurements.

3.11. Target List and Selection Criteria

Table 1 lists the SEEDS MGs targets in order of right ascension. Figure 1 shows the targets' distances and spectral types. Fifty-one out of 63 targets are within 50 pc, and all but 3 are within 60 pc. The spectral types of the main MG sample vary from late F to early M, equivalent to a range of roughly 0.4–1.3 $M_{\odot}$. We also list five stars, HIP 23362, HIP 32104, HIP 83494, HIP 93580, and HIP 116805 (= κ And), which are more massive A and early B stars selected for the high-mass star sample, but which have been suggested to belong to young MGs.

The main SEEDS MG targets were selected according to the following criteria, in order of priority:

1. identification with a young MG ($\lesssim$500 Myr, with younger targets preferred),
2. proximity to Earth,
3. mass (∼1 $M_{\odot}$ preferred),
4. lack of a close binary companion,
5. lack of archival high-contrast observations,
6. R-magnitude <12 (for AO performance),
7. declination > −25°,
8. field rotation in one hour of observing time,
9. H-magnitude $\gtrsim$5 (to limit saturation),
10. high Galactic latitude (to limit chance alignments).

Targets were proposed before each observing run and observed as permitted by conditions and priorities for other SEEDS categories.

4. OTHER AGE INDICATORS

The most reliable age dating methods rely on coeval associations of stars, such as kinematic MGs or globular clusters. The members of such a coeval association may be placed on a color–magnitude diagram where isochrones of single stellar populations offer extremely reliable age estimates. Unfortunately, many stars in our sample (and a much larger fraction of other high-contrast imaging surveys) are not reliable members of a coeval association. For the sample presented here, we consider AB Dor, β Pic, Columba, Tuc–Hor, TW Hydrae, and Ursa Majoris as coeval associations (see Section 3). We rely on the age indicators described below to assign ages to the stars in Castor, Hercules–Lyra, IC 2391, and the Local Association.

All of these single star age indicators rely to some degree on stellar convection and rotation. Late F-type and later stars have large convective zones, where stellar dynamos generate substantial magnetic fields from differential rotation (Parker 1955; Glatzmaier 1985) and power vigorous chromospheric and coronal activity. As a star ages, its magnetized wind carries away angular momentum, and the stellar rotation and magnetically powered activity gradually decrease. Convection also carries material from the stellar surface down into the hotter interior, where fragile elements and isotopes like ^{7}Li are destroyed.

We discuss five individual age indicators in the following sections: chromospheric activity traced by Ca II HK emission, coronal activity traced by X-rays, stellar rotation, photospheric lithium abundance, and isochrone fitting. These indicators have been studied extensively and calibrated using coeval stellar clusters and associations.

4.1. Chromospheric Activity

The stellar chromosphere is a low-density region above the photosphere containing a strong temperature inversion. Magnetic reconnection is believed to be responsible for heating the chromosphere, which is visible as an emission line spectrum superimposed on the photosphere's continuum and absorption lines (Wilson 1963). The chromospheric emission lines are much narrower and fainter than the corresponding photospheric absorption lines. Two of the stronger lines are Ca II H and K at 3968 Å and 3934 Å, with the chromospheric emission line strengths often parameterized by $R'_{\rm HK}$, which is the ratio of

Table 1
The SEEDS Moving Group Target List: Basic Stellar Properties

Designations			Other	α (J2000)[a]	δ (J2000)[a]	Distance[a]	Spectral	V[c]	H[d]	Moving
HIP	HD	GJ		(h m s)	(° ′ ″)	(pc)	Type[b]	(mag)	(mag)	Group
544	166	5	V439 And	00 06 36.8	+29 01 17	13.7 ± 0.1	G8V (1)	6.06	4.63	Her Lya
1134	984	...	...	00 14 10.3	−07 11 57	47.1 ± 1.1	F7V (2)	7.32	6.17	Columba
...	...	...	FK Psc	00 23 34.7	+20 14 29	59.7 ± 1.6[e]	K7.5V (3)	10.84	7.50	β Pic
3589	4277	...	BD+54 144	00 45 50.9	+54 58 40	52.5 ± 2.5	F8V[f]	7.81	6.40	AB Dor
4979	6288A	...	26 Cet	01 03 49.0	+01 22 01	60.1 ± 1.5	A8IV (2)	6.07	5.51	IC 2391
6869	8941	...	...	01 28 24.4	+17 04 45	53.8 ± 1.6	F8IV-V (4)	6.60	5.40	IC 2391
...	...	...	HS Psc	01 37 23.2	+26 57 12	38.5[e]	K5Ve (5)	10.72	7.78	AB Dor
10679	14082B	...	BD+28 382B	02 17 24.7	+28 44 30	27.3 ± 4.4	G2V[f]	7.76	6.36	β Pic
...	...	...	BD+30 397B	02 27 28.0	+30 58 41	40.0 ± 3.6	M0 (6)	12.44	8.14	β Pic
11437	...	...	AG Tri	02 27 29.3	+30 58 25	40.0 ± 3.6	K7V (7)	10.08	7.24	β Pic
12545	...	...	BD+05 378	02 41 25.9	+05 59 18	42.0 ± 2.7	K6Ve (8)	10.20	7.23	β Pic
12638	16760	...	...	02 42 21.3	+38 37 07	45.5 ± 4.9	G2[f]	8.77	7.10	AB Dor
12925	17250	...	BD+04 439	02 46 14.6	+05 35 33	54.3 ± 3.1	F8[f]	7.88	6.63	Tuc–Hor
17248	...	...	...	03 41 37.3	+55 13 07	35.2 ± 2.7	M0.5 (9)	11.20	7.65	Columba
23362	32309	...	HR 1621	05 01 25.6	−20 03 07	60.7 ± 0.9	B9V (10)	4.88	5.02	Columba
25486	35850	...	AF Lep	05 27 04.8	−11 54 03	27.0 ± 0.4	F8V (11)	6.30	5.09	β Pic
...	36869	...	AH Lep	05 34 09.2	−15 17 03	35.0 ± 8.7[g]	G2V (10)	8.45	6.98	Columba
29067	...	9198	...	06 07 55.3	+67 58 37	24.5 ± 1.1	K6V (1)	9.74	6.81	Castor
30030	43989	...	V1358 Ori	06 19 08.1	−03 26 20	49.2 ± 2.0	G0V (2)	7.95	6.59	Columba
32104	48097	...	26 Gem	06 42 24.3	+17 38 43	43.6 ± 1.3	A2V (12)	5.22	5.07	Columba
...	...	...	V429 Gem	07 23 43.6	+20 24 59	25.8 ± 4.0[h]	K5V (13)	10.03	7.03	AB Dor
37288	...	281	...	07 39 23.0	+02 11 01	14.6 ± 0.3	K7 (14)	9.66	6.09	Her Lya
39896	...	1108A	FP Cnc	08 08 56.4	+32 49 11	20.7 ± 1.4	K7 (14)	9.99	6.58	Columba
40774	...	...	V397 Hya	08 19 19.1	+01 20 20	22.9 ± 0.7	G5V[f]	8.35	6.22	IC 2391
44526	77825	...	V405 Hya	09 04 20.7	−15 54 51	28.3 ± 0.6	K3V (11)	8.78	6.54	Castor
45383	79555	339	...	09 14 53.7	+04 26 34	18.0 ± 0.5	K3V (1)	7.96	5.40	Castor
46843	82443	354.1	DX Leo	09 32 43.8	+26 59 19	17.8 ± 0.2	K1V (11)	7.06	5.24	Columba
50156	...	2079	DK Leo	10 14 19.2	+21 04 30	23.1 ± 1.0	M0.7V (15)	10.13	6.45	Columba
...	...	388	AD Leo	10 19 36.3	+19 52 12	4.7 ± 0.1	M3 (14)	9.46	4.84	Castor
50660	...	...	NLTT 24062	10 20 45.9	+32 23 54	47.1 ± 2.9	K0V[f]	9.18	7.38	IC 2391
51317	...	393	LHS 2272	10 28 55.6	+00 50 28	7.1 ± 0.1	M2.5V (16)	9.59	5.61	AB Dor
53020	...	402	EE Leo	10 50 52.0	+06 48 29	6.8 ± 0.2	M5.0V (16)	11.68	6.71	Her Lya
53486	94765	3633	GY Leo	10 56 30.8	+07 23 19	17.3 ± 0.3	K2.5V (1)	7.37	5.35	Castor
...	95174	...	...	10 59 38.3	+25 26 15	22.6 ± 2.0[e]	K2 (17)	8.46	5.96	β Pic
54155	96064	...	HH Leo	11 04 41.5	−04 13 16	26.3 ± 0.7	G8V (1)	7.60	5.90	Loc. Ass.
...	...	...	TWA 2	11 09 13.8	−30 01 40	46.5 ± 2.8[i]	M2Ve (8)	11.12	6.93	TW Hya
...	...	...	TYC 3825-716-1	11 20 50.5	+54 10 09	57.9 ± 5.5[e]	K7 (18)	12.14	8.69	AB Dor
59280	105631	3706	G 123-7	12 09 37.3	+40 15 07	24.5 ± 0.4	G9V (1)	7.46	5.70	IC 2391
...	...	...	TYC 4943-192-1	12 15 18.4	−02 37 28	30.2 ± 2.6[h]	M0Ve (5)	11.34	8.00	AB Dor
60661	...	466	...	12 25 58.6	+08 03 44	37.4 ± 3.2	M0V (19)	10.29	7.31	Loc. Ass.
63317	112733	...	...	12 58 32.0	+38 16 44	44.2 ± 2.7	K0V (19)	8.64	6.95	Loc. Ass.
...	...	...	FH CVn	13 27 12.1	+45 58 26	46.0 ± 4.3[e]	K7 (18)	11.16	8.20	AB Dor
66252	118100	517	EQ Vir	13 34 43.2	−08 20 31	20.2 ± 0.3	K4.5V (1)	9.25	6.31	IC 2391
67412	120352	...	...	13 48 58.2	−01 35 35	37.7 ± 1.8	G8V (2)	8.51	6.89	IC 2391
73996	134083	578	c Boo	15 07 18.1	+24 52 09	19.6 ± 0.1	F5V (1)	4.93	4.01	UMa
78557	143809	...	BD+04 3100	16 02 22.4	+03 39 07	82 ± 10	G0V (2)	8.77	7.52	Loc. Ass.
82688	152555	...	...	16 54 08.1	−04 20 25	46.7 ± 2.0	F8/G0V (2)	7.82	6.48	AB Dor
83494	154431	...	HR 6351	17 03 53.6	+34 47 25	55.0 ± 0.9	A5V (12)	6.08	5.68	Tuc–Hor
87579	...	697	...	17 53 29.9	+21 19 31	24.4 ± 0.6	K2.5V (1)	8.50	6.30	Castor
87768	...	698	...	17 55 44.9	+18 30 01	25.0 ± 1.3	K5V (1)	9.24	6.42	Loc. Ass.
91043	171488	...	V889 Her	18 34 20.1	+18 41 24	38.0 ± 0.9	G0V (4)	7.40	5.90	Loc. Ass.
93580	177178	...	HR 7214	19 03 32.3	+01 49 08	54.9 ± 0.9	A4IV/V (2)	5.82	5.36	AB Dor
...	...	...	BD+05 4576	20 39 54.6	+06 20 12	38.5[e]	K7Ve (5)	10.52	7.35	AB Dor
102409	197481	803	AU Mic	20 45 09.5	−31 20 27	9.9 ± 0.1	M1Ve (8)	8.76	4.83	β Pic
...	201919	...	...	21 13 05.3	−17 29 13	39[e]	K6Ve (8)	10.43	7.75	AB Dor
107350	206860	9751	HN Peg	21 44 31.3	+14 46 19	17.9 ± 0.1	G0V (11)	5.95	4.60	Her Lya
...	...	...	TYC 2211-1309-1	22 00 41.6	+27 15 14	45.6 ± 1.6[e]	M0Ve (3)	11.37	7.95	β Pic
111449	213845	863.2	LTT 9081	22 34 41.6	−20 42 30	22.7 ± 0.1	F5V (11)	5.21	4.27	Her Lya
114066	...	9809	...	23 06 04.8	+63 55 34	24.5 ± 1.0	M0.3V (15)	10.92	7.17	AB Dor
115162	...	...	BD+41 4749	23 19 39.6	+42 15 10	50.2 ± 2.9	G8V (20)[j]	8.93	7.28	AB Dor
...	...	...	BD−13 6424	23 32 30.9	−12 15 51	27.3 ± 0.4[e]	M0Ve (8)	10.69	6.77	β Pic
116805	222439	...	κ And	23 40 24.5	+44 20 02	51.6 ± 0.5	B9IVn (21)	4.13	4.60	Columba

Table 1
(Continued)

Notes.
[a] Position and parallax from the *Hipparcos* catalog (van Leeuwen 2007) unless otherwise noted.
[b] References: (1) Gray et al. 2003; (2) Houk & Swift 1999; (3) Lépine & Simon 2009; (4) White et al. 2007; (5) Schlieder et al. 2010; (6) Zuckerman & Song 2004; (7) Torres et al. 2008; (8) Torres et al. 2006; (9) Zuckerman et al. 2011; (10) Houk & Smith-Moore 1988; (11) Gray et al. 2006; (12) Abt & Morrell 1995; (13) Reid et al. 2004; (14) Reid et al. 1995, Hawley et al. 1996; (15) Shkolnik et al. 2009; (16) Jenkins et al. 2009; (17) Scholz et al. 2005; (18) Schlieder et al. 2012b; (19) López-Santiago et al. 2010; (20) Ofek 2008; (21) Wu et al. 2011.
[c] Values taken from the Tycho-2 catalog (Høg et al. 2000) and converted to Johnson *V*, with the following exceptions: BD + 30 397B (Weis 1993); HIP 53020 (Landolt 1992).
[d] Values taken from the 2MASS catalog (Cutri et al. 2003).
[e] Kinematic distance assuming group membership. References: FK Psc, TYC 2211-1309-1, BD−13 6424 (Lépine & Simon 2009); HS Psc, BD+05 4576 (Schlieder et al. 2010); HD 95174, TYC 3825-716-1, FH CVn (Schlieder et al. 2012b); HD 201919 (Torres et al. 2008).
[f] Spectral type listed (but unsourced, or sourced as SIMBAD) in the *Hipparcos* catalog.
[g] This *Tycho* parallax (Høg et al. 2000) is far below the distance inferred from spectroscopy (59 pc, Zuckerman et al. 2011), and may be unreliable.
[h] Spectroscopic parallax. References: V429 Gem (Reid et al. 2004); TYC 4943-192-1 (Agüeros et al. 2009).
[i] Trigonometric parallax from Weinberger et al. (2013).
[j] Spectral type also discussed in this work.

the flux in the emission line cores to that in the underlying photospheric continuum (Noyes et al. 1984).

Chromospheric activity has long been known to correlate with stellar age on the main sequence; it is dramatically stronger in young clusters than in the Sun and local field stars (Wilson 1963). Multi-decade observations (Baliunas et al. 1996) have provided activity measurements for hundreds of stars in well-dated young clusters and (presumably coeval) binaries, enabling the calibration of $R'_{\rm HK}$ as an age indicator for young stars. Mamajek & Hillenbrand (2008), hereafter MH08, have recently re-calibrated $R'_{\rm HK}$ as an age indicator. They find the tightest correlation by first using chromospheric activity to estimate the Rossby number Ro, the ratio of the rotational period to the convective overturn timescale, and then using the Rossby number and $B-V$ color to infer an age. Practically, this means that the estimated age is a function of both activity and color (i.e., mass). Omitting uncertainties in the fitted parameters and combining Equations (4) and (12)– (14) from MH08, we have

$$\frac{\tau}{\rm Myr} \approx \left(\frac{\tau_C [0.808 - 2.966(\log R'_{\rm HK} + 4.52)]}{0.407(B-V-0.495)^{0.325}} \right)^{1.767}, \quad (1)$$

where τ_C is the convective overturn timescale, and is related to $B-V$ color by Equation (4) in Noyes et al. (1984):

$$\log \tau_C = 1.362 - 0.166x + 0.025x^2 - 5.323x^3, \quad (2)$$

with $x \equiv 1-(B-V)$ and $x > 0$ (spectral type mid K or earlier). For $x < 0$ (late K and M stars), the fit is

$$\log \tau_C = 1.362 - 0.14x. \quad (3)$$

Equation (1) applies to "active" stars with $-5.0 < \log R'_{\rm HK} < -4.3$. While nearly every star in the SEEDS MG sample with archival $R'_{\rm HK}$ data satisfies this minimum activity level, many are too active for Equation (1) to provide an accurate age estimate. Further, this relation requires $B-V \geqslant 0.5$ (spectral type late F or later), and is poorly calibrated for $B-V \gtrsim 1$. For some SEEDS targets, chromospheric activity provides only an upper limit on the age, while for others that do not satisfy the color criterion, chromospheric activity is of little value as an age indicator.

MH08 estimate the scatter about Equation (1) using both field binaries and well-dated clusters with ages ranging from 5 Myr to 4 Gyr. For stars in the "active" regime with multi-decade $R'_{\rm HK}$ data, they estimate a scatter of 0.10 in Rossby number Ro, while for single-epoch chromospheric measurements, they estimate a scatter of 0.16. We use multi-epoch data wherever possible. While only one of our targets (HIP 107350) has multi-decade Mt. Wilson data, many have several epochs from Isaacson & Fischer (2010). For targets with more than one single-epoch HK value (but no multi-epoch data), we take the median of the literature values. In two cases, We expect our precision to be somewhat better than is reflected in a scatter of 0.16 in Ro; however, we provisionally adopt an uncertainty of 0.16 for all but the Mt. Wilson data. Very active stars with $R'_{\rm HK} > -4.3$ have much larger uncertainties. We assign these targets only upper limits on age, using a uniform probability distribution between 0 and the minimum age accessible to chromospheric activity measurements.

We compile chromospheric activity measurements from a wide variety of sources, using the relations given in Noyes et al. (1984) to transform all onto the Mt. Wilson system. For two stars, HIP 40774 and HIP 50660, the original reference (Strassmeier et al. 2000) used different units, which were recently calibrated and transformed onto the Mt. Wilson system (Pace 2013). All of our literature $R'_{\rm HK}$ values are listed in Table 2.

4.2. X-Ray Activity

X-ray activity presents a similar measure of magnetic activity, though this emission comes from the high-temperature stellar corona. While the coronal heating mechanism remains uncertain and presents formidable modeling challenges (Klimchuk 2006), it almost certainly involves the deposition of magnetic energy, either from reconnection events (e.g., Parker 1988; Masuda et al. 1994) or the dissipation of magento-acoustic and/or Alfvén waves (e.g., Heyvaerts & Priest 1983; Davila 1987). As with chromospheric activity, X-ray activity declines as a star ages and loses angular momentum (Hempelmann et al. 1995).

X-ray activity is typically measured as the ratio of a star's X-ray flux (within the 0.1–2.4 keV *ROSAT* bandpass; Voges et al. 1999, with a hardness correction) to its bolometric flux. We use the formula given in Schmitt et al. (1995):

$$F_{\rm X} = (5.30{\rm HR} + 8.31)\,{\rm CR} \times 10^{-12}\ {\rm erg\ cm^{-2}\ s^{-1}}, \quad (4)$$

where the CR is the count rate and HR is the ratio of the difference in CR between the hard (0.52–2.1 keV) and soft

Table 2
The SEEDS Moving Group Target List: Age Indicators

Name	Moving Group	Group References[a]	$\log R'_{HK}$[b]	$\log R_X$[c]	Li EW (mÅ)		P_{rot} (days)	Activity/Rotation References[a]
					Lit	APO		
HIP 544	Her Lya	1, 2	−4.38	−4.22	75	92	6.23	13, 15, 16
HIP 1134	Columba	3	−4.42	−4.18	99	128	...	3, 15, 17, 18
FK Psc	...[d]	4/5	...	−3.35	...	...	7.7	19
HIP 3589	AB Dor	6	...	−3.87	199	...	...	11
HIP 4979	IC 2391	7	...	−5.46	...	...	...	...
HIP 6869	IC 2391	7	−4.76	−4.89	5	18	...	17, 18
HS Psc	AB Dor	8	...	−3.08	90	...	1.09	20, 21
HIP 10679	β Pic	6	−4.37	−3.84[B]	160	168	...	11, 17
BD+30 397B	β Pic	9	...	−2.55[B]	110	...	...	11
HIP 11437	β Pic	6	...	−2.98[B]	220	252	13.7	11, 21
HIP 12545	β Pic	6	...	−2.98[B]	450	436	1.25	11, 19
HIP 12638	AB Dor	6	−4.92	−3.90	158	...	...	11, 15
HIP 12925	Tuc–Hor	3	...	−4.26	145	144	...	3
HIP 17248	Columba	3	...	−3.36	...	...	...	3
HIP 23362	Columba	3	...	<−6.28	...	...	...	...
HIP 25486	β Pic	6, 9	−4.27	−3.46	191	154	...	11, 15
HD 36869	Columba	3, 5	...	−3.47	204	210	1.31	3, 22
HIP 29067	Castor	7, 10	−4.43	<−4.48	38	...	...	10, 15, 23, 24, 25
HIP 30030	...[d]	5/9/11	−4.18	−3.61	170	164	1.15	11, 15, 22
HIP 32104	Columba	3	...	−5.57	...	...	...	...
V429 Gem	AB Dor	6	−4.2	−3.37	105	122	2.80	11, 19, 26
HIP 37288	Her Lya	2	−4.67	<−4.74	43	...	...	10, 23
HIP 39896	Columba	5/7	−4.05	−3.13	...	25	3.37	13, 27
HIP 40774	IC 2391	7	−4.45	<−4.55	...	17	...	28
HIP 44526	Castor	7	−4.36	−4.02	...	58	8.64	29, 30
HIP 45383	Castor	10	−4.41	−3.97	9	...	...	10, 17, 23, 24, 25
HIP 46843	Columba[d]	5/7	−4.21	−3.84	176	188	5.38	10, 13, 31, 32
HIP 50156	Columba[d]	5/12	−3.96	−3.39	...	...	7.98	13, 33
GJ 388	Castor	13	−4.17	−3.10	...	...	2.23	15, 34, 35
HIP 50660	IC 2391	7	−4.60	<−4.35	...	...	...	28
HIP 51317	AB Dor	3, 5	−5.01	−5.18	...	...	...	15
HIP 53020	Her Lya	2	−5.29	<−4.36	...	...	...	15
HIP 53486	Castor	7	−4.48	−4.50	...	19	11.43	15, 30
HD 95174	β Pic	14	...	<−4.54[B]	...	3	...	...
HIP 54155	Loc. Ass.	7	−4.35	−3.63	104	114	...	10, 24, 25, 36
TWA 2	TW Hya	6	...	−3.26[B]	535	...	4.86	11, 19
TYC 3825-716-1	AB Dor	14	...	−3.28	...	36	...	...
HIP 59280	IC 2391	7, 10	−4.65	−5.13	26	18	...	10, 15, 17
TYC 4943-192-1	AB Dor	8	...	−3.45	...	...	...	8
HIP 60661	Loc. Ass.	7	−4.82	<−4.33	...	...	...	13
HIP 63317	Loc. Ass.	13	−4.19	−3.56	94	106	...	2, 13
FH CVn	AB Dor	14	...	−3.15	...	...	2.17	14, 27
HIP 66252	IC 2391	7, 10	−3.89	−3.12	65	47	3.9	25, 33
HIP 67412	IC 2391	7	−4.64	−5.00	...	15	...	37
HIP 73996	UMa[d]	7/10	−4.38	−5.33	...	20	...	15
HIP 78557	Loc. Ass.	13	−4.20	−4.60	103	...	...	13
HIP 82688	AB Dor	5, 6	−4.29	−4.18	133	137	...	11, 15
HIP 83494	Tuc–Hor[d]	3/5	...	<−6.01	...	...	...	...
HIP 87579	Castor	13	−4.44	−4.70	...	...	...	13, 17, 24, 25, 38
HIP 87768	Loc. Ass.	7	−4.27	−4.72	7	...	...	13, 24, 39
HIP 91043	Loc. Ass.	7	−4.21	−3.30	208	...	1.34	13, 18, 40
HIP 93580	AB Dor	3, 5	...	−5.21	...	...	...	...
BD+05 4576	AB Dor	8	...	−3.94	...	...	...	...
HIP 102409	β Pic	9	−4.11	−2.86	80	...	4.85	11, 15, 19
HD 201919	AB Dor	6	...	−3.49	20	...	4.92	11, 19
HIP 107350	Her Lya	1, 2	−4.42[MW]	−4.39	115	102	4.74	13, 31, 41
TYC 2211-1309-1	β Pic	4	...	−3.11	<40	...	0.476	19, 20
HIP 111449	Her Lya	2	−4.53	−5.03	...	...	...	36, 42
HIP 114066	AB Dor	6	...	−3.03	30	...	4.50	43, 44
HIP 115162	AB Dor	6	−4.22	−4.22	160	161	...	25, 43
BD−13 6424	β Pic	6	...	−3.05	185	184	5.68	11, 19
HIP 116805	Columba	3	...	<−6.59	...	...	...	...

Table 2
(Continued)

Notes.
[a] References: (1) Fuhrmann 2004; (2) López-Santiago et al. 2006; (3) Zuckerman et al. 2011; (4) Lépine & Simon 2009; (5) Malo et al. 2013; (6) Torres et al. 2008; (7) Montes et al. 2001b; (8) Schlieder et al. 2010; (9) Zuckerman & Song 2004; (10) Maldonado et al. 2010; (11) da Silva et al. 2009; (12) Schlieder et al. 2012a; (13) López-Santiago et al. 2010; (14) Schlieder et al. 2012b; (15) Isaacson & Fischer 2010; (16) Gaidos et al. 2000; (17) Wright et al. 2004; (18) White et al. 2007; (19) Messina et al. 2010; (20) McCarthy & White 2012; (21) Norton et al. 2007; (22) Messina et al. 2001; (23) Duncan et al. 1991; (24) Gray et al. 2003; (25) Martínez-Arnáiz et al. 2010; (26) Hernán-Obispo et al. 2010; (27) Hartman et al. 2011; (28) Pace 2013; (29) Arriagada 2011; (30) Strassmeier et al. 2000; (31) Baliunas et al. 1996; (32) Messina et al. 1999; (33) Torres et al. 1983; (34) Cincunegui et al. 2007; (35) Hunt-Walker et al. 2012; (36) Schröder et al. 2009; (37) Jenkins et al. 2011; (38) Soderblom 1985; (39) Favata et al. 1993; (40) Henry et al. 1995; (41) Frasca et al. 2000; (42) Gray et al. 2006; (43) Zuckerman et al. 2004; (44) Koen & Eyer 2002.
[b] Values marked with "MW" are from multi-decade Mt. Wilson measurements.
[c] Values or approximate upper limits from the *ROSAT* All Sky Survey (Voges et al. 1999, 2000; Hünsch et al. 1999). See Section 4.2 for details.
[d] References disagree on membership. See section on individual stars for details.

(0.1–0.41 keV) channels to the total CR. For targets not detected by *ROSAT*, we estimate upper limits on their X-ray fluxes using the exposure time of the nearest detected source (usually $\sim$0.5) in the faint source catalog (Voges et al. 2000), requiring no more than nine expected photons, and assuming a hardness ratio of 0 (roughly the mean of our sample). A source with nine expected photons would have a $\sim$90% probability of producing at least six detected photons, the minimum required for inclusion in the *ROSAT* catalog. Combined with a small correction for background subtraction and some uncertainty in the hardness ratio, these F_X values should be considered approximate upper limits.

The indicator R_X is F_X normalized to a star's bolometric flux. For G and earlier stars, we convert the V magnitudes in Table 1 to bolometric fluxes using the relations derived in Flower (1996)—these were originally misprinted and have been corrected in, e.g., Torres (2010). These bolometric corrections are not valid for M stars; we therefore adopt the bolometric correction of Kenyon & Hartmann (1995), which uses V, J, and K-band magnitudes, for K and M dwarfs, adjusting the zero-point of the correction scale accordingly (Torres 2010).

As for chromospheric activity, MH08 have calibrated an X-ray/color/age relation, equivalent to

$$\frac{\tau}{\mathrm{Myr}} \approx \left(\frac{\tau_C [0.86 - 0.79(\log R_X + 4.83)]}{0.407\,(B-V-0.495)^{0.325}} \right)^{1.767}, \quad (5)$$

where τ_C is the convective overturn timescale as approximated by Equations (2) and (3). MH08 report that this relation holds, with a scatter of 0.25 in Rossby number, for X-ray activity levels $-7 < \log R_X < -4$. At higher levels of X-ray activity, there appears to be little correlation between X-ray activity and stellar rotation, and hence age (e.g., Pizzolato et al. 2003). As for chromospheric activity, this relation requires $B-V > 0.5$, and is poorly calibrated for $B - V \gtrsim 1$. X-ray activity measurements thus provide only upper limits to the ages of many SEEDS MG targets. For these extremely active targets, we assign a uniform probability distribution in age up to the maximum age (dependent upon spectral type) accessible to these age indicators.

4.3. Gyrochronology

As F-type and later stars age, their rotation periods grow (Kraft 1967; Skumanich 1972). This is believed to be due to their convective zones, which generate stellar magnetic fields, extending to the surface and coupling to the stellar wind (Mestel 1968; Pinsonneault et al. 1989). Stars more massive than mid-F spectral type have radiative envelopes and weak stellar winds; they hardly spin down at all (Barnes 2003). Later-type stars with accurate cluster ages generally show one of two rotation patterns. At young ages, a large fraction of stars (especially low-mass stars) are extremely fast rotators, forming the so-called C-sequence (Barnes 2003). These fast rotators are believed to have their outer convective envelopes only weakly coupled to their inner radiative regions, resulting in inefficient angular momentum loss. Older clusters lack these rapid rotators, which are believed to have transitioned onto the I-sequence, in which the star approaches solid-body rotation (Barnes 2003).

Young stars spend a variable amount of time on the rapidly rotating C-sequence before transitioning to the I-sequence, the duration of rapid rotation decreasing with increasing stellar mass. This timescale varies from $\sim$300 Myr for early M stars to 0 for F stars (Barnes 2003). Some stars appear to be on the I-sequence even at substantially younger ages, indicating that these timescales include substantial scatter. We treat them as the youngest ages accessible to gyrochronology, lower bounds on our age constraints using these secondary criteria. For simplicity, we use a parameterization linear in $B-V$ color, from 300 Myr at $B - V = 1.5$ (early M) to 0 at $B - V = 0.5$ (late F).

For older stars on the I-sequence, color-dependent gyrochronology relations have been derived by Barnes (2007) and re-calibrated by MH08. The relation is identical to Equation (1), except that the rotation period is measured directly rather than inferred from chromospheric activity. The gyrochronological age estimate becomes

$$\frac{\tau}{\mathrm{Myr}} \approx \left(\frac{\tau_{\mathrm{rot}}}{0.407\,(B-V-0.495)^{0.325}} \right)^{1.767}. \quad (6)$$

The scatter about this relation is very large at young ages ($\sim$1 dex; Mamajek & Hillenbrand 2008); in addition, it only applies to stars on the rotational I-sequence. Barnes (2007) only applies such a result to stars rotating more slowly than the 100 Myr "gyrochrone." We adopt a similar criterion by setting a floor on the gyrochronological age of 0–300 Myr depending on color, as described above, together with an overall floor of 100 Myr. A star with a younger age according to Equation (6) will be assigned a uniform probability distribution of ages up to the floor appropriate to its color.

MH08 have measured a scatter about Equation (6) of 0.05 dex for stars on the I-sequence, and recommend adding an additional $\sim$15% ($\sim$0.06 dex) to account for systematic uncertainties in

the cluster ages used for calibration. We therefore adopt 0.8 dex as the age uncertainty for slow rotators.

4.4. Lithium Abundance

The strength of lithium absorption lines declines as a star ages and burns its initial supply of the fragile element. Stars with convective zones approaching the surface carry lithium down into the hotter interior where it is subsequently destroyed. Unfortunately, other mixing processes complicate this picture, and the details of convection depend strongly on stellar mass.

Lithium can be a problematic age indicator (Zuckerman & Song 2004), as its abundance is extremely sensitive to the stellar accretion history (Baraffe & Chabrier 2010), but abundant lithium is a reliable indicator of stellar youth (Bildsten et al. 1997). Extensive observations of open clusters do enable crude lithium age estimates for some stars (Sestito & Randich 2005), though for much of the SEEDS MG sample, lithium provides only upper limits. There is a considerable scatter between coeval stars and a strong color dependence, and therefore, lithium is considered more reliable for dating young clusters (Soderblom 2010).

In general, lithium abundance is significantly more problematic as an age indicator for single stars than the activity and rotation measurements described above (Soderblom 2010). In the notes for each individual star, we comment briefly on the consistency of lithium abundances with these other indicators (Section 7).

4.5. Isochrone Dating

Isochrones in color–magnitude space are among the most reliable methods for dating coeval clusters and associations of stars (Song et al. 2003). Unfortunately, they are much less reliable for individual stars. Isochrone dating fails to produce a robust peak in the probability distribution in a large fraction of field stars, and typically has uncertainties of $\gtrsim$1 Gyr even for those stars on which it is successful (Takeda et al. 2007). In order for isochrone placement to have any value as an age indicator, a main-sequence star must have completed at least $\sim$1/3 of its life (Soderblom 2010). This excludes most of the SEEDS MG sample. In addition, any isochrone-based age analysis should marginalize over uncertainties in convection, composition, rotation, and atmospheric modeling, among other numerical and theoretical considerations. We therefore do not attempt a full isochrone age analysis in this work. However, isochrone ages can still provide an important check on ages estimated from other methods, and in particular, on the likelihood of a star's membership in a young MG. We therefore use the PARSEC stellar models (Bressan et al. 2012) as a consistency check on the median ages we obtain by our full analysis (Section 5).

A model of stellar structure, combined with a model atmosphere, predicts absolute magnitudes M_i in a variety of bandpasses i. Given observed (apparent) magnitudes m_i in each band, we can write down the logarithmic likelihood of a model, together with a parallax ϖ (in milliarcseconds), as

$$-2\ln\mathcal{L}(\mathrm{mod},\varpi) = \sum_{\mathrm{bands}i}\frac{(M_i + 5\log_{10}100/\varpi - m_{\mathrm{obs},i})^2}{\sigma_i^2} + \frac{(\varpi-\varpi_{\mathrm{Hip}})^2}{\sigma_\varpi^2}. \quad (7)$$

We multiply Equation (7) by a prior in parallax prior equivalent to a uniform prior in space, $\varpi^{-4}d\varpi$, and marginalize over ϖ. We adopt a Gaussian prior on [Fe/H] centered on the solar value, with a standard deviation of 0.15 (40% in metallicity). This is nearly the same prior as that used by Nielsen et al. (2013), taken from the distribution of young FG dwarfs observed by Casagrande et al. (2011). While this metallicity distribution should be appropriate for young stars, it is likely to systematically overestimate the metallicity (and photospheric opacity) of older stars. Since stars brighten during their main-sequence lives, an overestimated metallicity would require an older age to compensate, and could produce large uncertainties in age determinations of several Gyr.

In an effort to be as uniform across the sample as possible, we restrict ourselves to the magnitudes measured by *Tycho* (Høg et al. 2000) and by Two Micron All Sky Survey (2MASS; Cutri et al. 2003). We do not attempt to marginalize over stellar mass and evolutionary rate in the color–magnitude diagram, both of which would be necessary for a full isochrone-based age analysis. Stellar rotation, which can have a significant effect on evolutionary tracks and produce colors and luminosities that vary with viewing angle (Ekström et al. 2012), becomes another major uncertainty for more massive stars.

Nordström et al. (2004) found that, for age probability distributions normalized over stellar mass, metallicity, and evolutionary rate in the color–magnitude diagram, 1σ confidence intervals corresponded roughly to a 60% of the marginalized peak likelihood. In our analysis, we adopt a more conservative threshold of $\Delta\ln\mathcal{L} = 1$, a ratio of $\sim$0.37. Table 2 includes the likelihood ratios; we comment on the stars with large discrepancies when we discuss the individual targets in Section 7. In two cases, the isochrone checks lead us to reduce our estimated probability of MG membership.

5. BAYESIAN STELLAR AGES

The SEEDS MG sample comes from many different associations; some of these are well-defined, while others are considered far less reliable. Likewise, the confidence with which each target is identified as an MG member varies considerably. Most of the targets also have other age indicators, described in the previous section, which should be combined with the age inferred from MG identification to produce the most reliable age estimate.

We adopt a Bayesian approach to stellar ages, using as our prior a flat age distribution out to 10 Gyr (appropriate to the local disk) or to the star's main sequence lifetime, and derive posterior probability distributions using age indicators and MG memberships. A slightly different star formation history, like the enhancement by a factor of 1.5 from 1 and 4 Gyr before the present (Girardi et al. 2005), would have little effect on our results. The resulting posterior probability distributions on age are suitable inputs to a statistical analysis of exoplanet frequencies and properties.

The likelihood function $\mathcal{L}$ is difficult to write down. If MG membership and the stellar age indicators were all independent of one another, then $\mathcal{L}$ would simply be the product of the probability of group membership and the probability distribution inferred for each indicator. However, MG membership is often assigned, at least partially, on the basis of stellar activity. Furthermore, indicators of stellar youth physically arise from the interplay of rotation and convection: chromospheric activity, rotation period, and coronal activity are not independent.

Many authors have performed detailed analyses of MGs, assigning membership probabilities to each proposed member. We generally defer to these probabilities and adopt the MG age

distribution $\mathcal{L}_{\rm MG}(\tau)$ weighted by the membership probability $P_{\rm MG}$. We approximate the MG age likelihood function as a Gaussian with the confidence intervals described in Section 3 representing its median age $\pm 2\sigma$. The other age indicators, described in Section 4 and listed in Table 2, complement the group age for stars with uncertain membership or which belong to less well-defined associations. We denote the likelihood function based solely on these single star indicators by $\mathcal{L}(\tau|{\rm indic})$; the total likelihood function is simply

$$\mathcal{L}(\tau) = P_{\rm MG}\mathcal{L}_{\rm MG}(\tau) + (1 - P_{\rm MG})\,\mathcal{L}(\tau|{\rm indic}). \quad (8)$$

Equation (8) assumes the age derived from secondary indicators and proposed MG membership to be independent, which could be problematic. In this analysis, it is not a major problem, as most of our stars are either reliably associated with an MG or have no kinematic age that we trust.

As described in the previous section, MH08 find the best results for the activity–age by first using chromospheric and coronal activity to estimate the Rossby number, and then using gyrochronology to estimate stellar age. We therefore treat coronal and chromospheric activity as independent measurements of Rossby number Ro. In practice, the scatter in Ro as estimated by X-ray activity is ∼1.5 times as large as that estimated by $R'_{\rm HK}$ (MH08) over the applicable activity regimes, so this approximation has little practical effect. The situation is dramatically better for the (one) object with multi-decade Mt. Wilson chromospheric data.

It is more difficult to estimate the covariance between stellar age as estimated from activity via the Rossby number and that inferred directly from a rotation period. The latter estimator, being more direct, has a smaller scatter reported in MH08 (∼0.05 dex) than the activity-rotation age (∼0.1 dex from binaries, ∼0.2 dex from clusters) for stars on the *I* rotational sequence. As the SEEDS sample painfully illustrates, however, this does not include all variation in rotation at a common age. Our slowest rotator, HIP 11437, has a gyrochronological age of ∼500 Myr, but is reliably identified with the β Pic MG. The star might still be contracting onto the main sequence, or it could simply be an outlier. MH08 also omitted two anomalously slow rotators in the Pleiades from their analysis.

With the above caveat, we note that assuming the age indicators to be independent makes little difference; the scatter in the period-age relation is much smaller than in the activity–age relations. We therefore simply set 0.05 dex as the floor in the uncertainty and add 0.06 dex to the error estimated from activity and rotation to account for systematic uncertainties in the cluster ages used to calibrate the relations (MH08). MH08 only used the slow, *I*-sequence rotators to derive their gyrochronological ages; we therefore add the range of time spent on the rapidly rotating *C*-sequence, ∼100–300 Myr, to the age distributions (see Section 4.3).

All of the activity/period/age relations have a strong color dependency, with later spectral types spinning down more rapidly after reaching the *I*-sequence. Spectral types earlier than late F, with $B-V$ colors $\lesssim$0.5, never reach the *I*-sequence. They never achieve the deep convective zone and strong dynamo necessary to drive a magnetized wind, and rotate rapidly throughout their main sequence lifetimes. For such stars in the SEEDS MG sample, we have little choice but to use a flat probability distribution out to the star's main sequence lifetime. We also note that the relations derived in MH08 were only tested for FGK stars, with $0.5 \lesssim B-V \lesssim 0.9$. Many of our targets are late K and M stars with colors as red as $B-V \sim 1.5$. The basic rotation/activity/age relation should continue to hold for these stars, albeit with larger uncertainties. We therefore continue to apply the relationships, noting that the ∼300 Myr timescale to reach the *I*-sequence adds a large spread to the derived ages.

Many of our targets are relatively faint and, as such, have poor *Tycho* measurements of $B-V$. We therefore combine the *Tycho* colors with a $B-V$ color estimated from $V-K$, with V measured from *Tycho* (transformed to Johnson) and K measured from 2MASS, using Table 5 of Pecaut & Mamajek (2013). We find that, in order to reproduce the scatter of *Tycho* colors using converted $V-K$ magnitudes, we need to add an empirical error of ∼0.03 mag to the interpolated result. We then combine the two estimates of $B-V$. This gives a median final uncertainty $\sigma_{B-V} = 0.018$ mag, and $\sigma_{B-V} < 0.05$ mag for all but one star.

The very old and very young tails of the probability distribution are important (and extremely difficult) to model properly. Several stars in our sample make this all too evident, with disturbingly discrepant kinematic and activity–ages. This will become much more of a problem as high-contrast surveys begin to report larger numbers of detections, and the properties of individual exoplanet host stars are subjected to higher scrutiny. For now, we note that authors estimating ages from clusters routinely throw out a few percent of their stars as pathological cases (e.g., Mamajek & Hillenbrand 2008). We therefore account for these long tails, at least qualitatively, by giving each target not definitively associated with an MG a 5% probability of being pathological, with utterly uninformative age indicators. More work on large samples of young stars should help to constrain the intrinsic scatter in activity and rotation at a common age.

Table 3 summarizes the posterior probability distributions on age for all of the SEEDS MG targets. The third column lists the adopted membership probability in the indicated MG (see Section 7 for details on individual stars), with "..." for those groups that we do not consider to be sufficiently well-defined to provide secure age estimates. The fourth and fifth columns list the 5% and 95% edges of the age probability distribution exclusively on the secondary age indicators, while the final three columns list the final 5%, 50%, and 95% ages based on all available information. For those stars without any age constraints beyond their finite main sequence lifetimes, we list "..." in Columns 4–8.

Figure 2 demonstrates our age determination method for HIP 107350. This star lacks a secure MG age, but has an exceptional array of secondary age indicators, including a measured rotation period and multi-decade Mt. Wilson chromospheric activity measurements. As a G0 star, HIP 107350 represents the best possible case for the use of secondary age indicators.

6. OBSERVATIONS AND DATA REDUCTION

Table 4 lists all of the SEEDS MGs targets and observations through May of 2013. All observations were made using the HiCIAO instrument (Suzuki et al. 2010) and AO188 (Hayano et al. 2008) on the Subaru telescope, and nearly all were made in the *H* band. As with many other high-contrast imaging surveys (e.g., Lafrenière et al. 2007a; Vigan et al. 2012), the *H* band was chosen due to both the AO performance and the relative brightness of the expected companions. A typical observation sequence consisted of target acquisition, AO tuning, and acquisition of photometric reference frames, followed by the main, saturated science data taken in pupil-tracking ADI mode. Including all overheads, ∼1–1.5 hr of telescope time were spent on a typical object.

Table 3
The SEEDS Targets' Ages

Name	Moving Group	Membership Prob. (%)[a]	No Group Data (Myr)[b] 5%	No Group Data (Myr)[b] 95%	All Data (Myr) 5%	All Data (Myr) 50%	All Data (Myr) 95%	$\Delta \ln \mathcal{L}$
HIP 544	Her Lya	...	190	370	190	270	370	0.1
HIP 1134	Columba	95+	24	940	20	30	54	0.38
FK Psc	β Pic	20	190	460	18	290	450	...
HIP 3589	AB Dor	95+	11	480	110	130	150	8.3
HIP 4979	IC 2391	...	...	...	...	...	...	6.4
HIP 6869	IC 2391	...	790	3300	790	1400	3300	...
HS Psc	AB Dor	95+	5	180	110	130	150	...
HIP 10679	β Pic	95+	620	8300	16	21	28	0.085
BD+30 397B	β Pic	95+	820	9200	16	21	28	...
HIP 11437	β Pic	95+	520	1100	16	21	29	...
HIP 12545	β Pic	95+	5	3900	16	21	24	...
HIP 12638	AB Dor	95+	1800	4500	110	130	170	0.27
HIP 12925	Tuc–Hor	95+	16	750	16	180	750	0.3
HIP 17248	Columba	95+	27	1100	20	30	54	...
HIP 23362	Columba	95+	...	...	20	30	54	1
HIP 25486	β Pic	95+	8	250	16	21	24	2.2
HD 36869	Columba	95+	26	120	20	30	50	0.17
HIP 29067	Castor	...	1100	9200	1100	5100	9200	...
HIP 30030	Columba	95+	27	120	20	30	50	0.072
HIP 32104	Columba	95+	...	...	20	30	57	0.023
V429 Gem	AB Dor	95+	45	240	110	130	150	...
HIP 37288	Her Lya	...	1500	9300	1500	5300	9300	...
HIP 39896	Columba	50	57	290	22	49	280	...
HIP 40774	IC 2391	...	1200	9300	1200	5100	9300	...
HIP 44526	Castor	...	310	570	310	430	570	...
HIP 45383	Castor	...	460	2000	460	970	2000	...
HIP 46843	Columba	...	160	310	160	240	310	0.61
HIP 50156	Columba	80	200	480	21	33	410	...
GJ 388	Castor	...	40	330	40	190	330	...
HIP 50660	IC 2391	...	980	9200	980	4900	9200	0.83
HIP 51317	AB Dor	95+	1800	9300	110	130	170	...
HIP 53020	Her Lya	...	1100	9200	1100	5000	9200	...
HIP 53486	Castor	...	540	990	540	720	990	...
HD 95174	β Pic	10	1200	9200	20	4600	9200	...
HIP 54155	Loc. Ass	...	28	990	28	300	990	0.4
TWA 2	TW Hya	95+	810	9200	5	10	19	...
TYC 3825-716-1	AB Dor	...	27	1100	27	280	1100	...
HIP 59280	IC 2391	...	670	2500	670	1300	2500	0.48
TYC 4943-192-1	AB Dor	80	27	1100	110	130	450	...
HIP 60661	Loc. Ass	...	980	9200	980	5000	9200	...
HIP 63317	Loc. Ass	...	25	870	25	260	870	0.0075
FH CVn	AB Dor	40	32	230	40	130	220	...
HIP 66252	IC 2391	...	73	270	73	170	270	...
HIP 67412	IC 2391	...	970	3100	970	1700	3100	0.46
HIP 73996	UMa	...	...	...	280	2700	5100	2.6
HIP 78557	Loc. Ass	...	57	1400	57	400	1400	0.2
HIP 82688	AB Dor	95+	16	530	110	130	150	0.41
HIP 83494	Tuc–Hor	...	...	...	...	...	...	4.3
HIP 87579	Castor	...	240	3200	240	1200	3200	...
HIP 87768	Loc. Ass	...	270	3100	270	1200	3100	...
HIP 91043	Loc. Ass	...	12	330	12	130	330	11
HIP 93580	AB Dor	80	...	...	110	130	1800	2.8
BD+05 4576	AB Dor	40	27	1100	46	140	800	...
HIP 102409	β Pic	95+	92	360	16	21	28	...
HD 201919	AB Dor	95+	110	290	110	130	150	...
HIP 107350	Her Lya	...	250	440	250	340	440	0.49
TYC 2211-1309-1	β Pic	50	6	220	13	22	190	...
HIP 111449	Her Lya	...	...	...	...	...	...	0.9
HIP 114066	AB Dor	95+	84	340	110	130	150	...
HIP 115162	AB Dor	95+	26	1400	110	130	150	0.078
BD−13 6424	β Pic	95+	120	390	16	21	28	...
HIP 116805	Columba	30	...	...	21	130	440	1.6

Notes.
[a] High-confidence classifications from, e.g., Torres et al. (2008) and Malo et al. (2013), including the corresponding web tool BANYAN. See notes on individual objects for more doubtful classifications.
[b] An entry of "..." indicates that the star is too blue for the activity/rotation/age relations to apply, and that its age probability distribution is therefore uniform out to 10 Gyr or its main sequence lifespan.

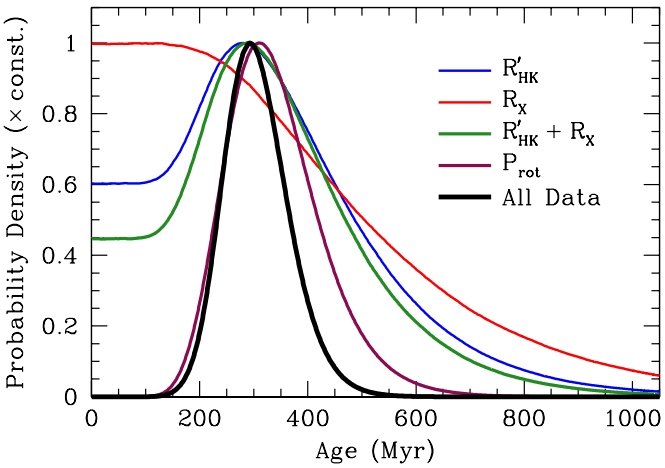

Figure 2. Calculation of an age probability distribution for a target, HIP 107350, without a reliable moving group age. HIP 107350 has an exceptional array of secondary age indicators, which enable a good constraint on its age. Most other stars without kinematic ages have much broader posterior probability distributions.

(A color version of this figure is available in the online journal.)

All of our data were taken in ADI mode and reduced using the ACORNS-ADI software package. The software and data reduction process are described in detail in Brandt et al. (2013); we therefore give only a brief summary here. The source code is freely available for download at http://www.github.com/t-brandt/acorns-adi.

For each sequence of images, we calibrate the data, register the frames, subtract the stellar point-spread function (PSF) using the LOCI algorithm (Lafrenière et al. 2007b), and combine the image sequence using an adaptive trimmed mean. Calibration consists of the usual flat-fielding and bad pixel masking, together with an algorithm to suppress correlated read noise in HiCIAO's H2RG detector. We then correct for field distortion by comparing observations of globular clusters made with HiCIAO and with the *Hubble Space Telescope* (*HST*). We register the frames in each ADI sequence using templates of saturated PSFs built from thousands of images of dozens of stars. This registration technique is accurate to ∼0.3 HiCIAO pixels, or 3 mas, under good observing conditions. We then set the absolute centroid of an image sequence by visual inspection.

ACORNS-ADI includes several algorithms to model and subtract the stellar PSF. In this work, we exclusively use the LOCI algorithm (Lafrenière et al. 2007b) due to its speed, simplicity, and Gaussian residuals. As our fiducial LOCI parameters, we use an angular protection zone of 0.7 times the PSF full width at half maximum (FWHM), and optimization zones 200 PSF footprints in area. Our subtraction regions vary in size from a few PSF footprints at small separations to a few tens of footprints several arcseconds from the central star. HiCIAO data is oversampled in the *H* band, with a typical FWHM of 6 pixels. We limit the number of LOCI comparison frames to avoid solving an under-constrained system and suppressing more companion flux than necessary—in the limit of an equal number of pixels and comparison frames, flux (and noise) suppression would be perfect. The final contrast of an ADI reduction with LOCI is a concave function of the number of comparison frames used for PSF modeling and subtraction, with a broad peak at ∼80 frames. We therefore treat large data sets as a number of smaller data sets (with every *n*th frame), reduce each of these small data sets separately using ACORNS-ADI, and then average the results to produce a map of residual intensity.

We calibrate the partial subtraction in LOCI using the procedure described in Brandt et al. (2013). We also include the much smaller effects of field rotation during each individual exposure and uncertainties in image registration, and approximate degradation in the AO performance with separation from the guide star by

$$\mathrm{SR} \propto \exp\left[-\left(\frac{\Delta\theta}{\theta_0}\right)^{5/3}\right], \quad (9)$$

where SR is the Strehl ratio, proportional to a point source's peak intensity, and we use an isoplanatic angle $\theta_0 = 30''$ (Minowa et al. 2010). These are all small corrections for our data, generally a few percent within ∼5″ of the central star. Finally, we convolve the map of residual intensity with a circular aperture, normalize by the azimuthal standard deviation in residual intensity, and search for 5.5σ outliers. We perform photometric calibrations using unsaturated reference frames taken before, after, and sometimes during an ADI sequence, and normalize to the central star's *H*-band magnitude in the 2MASS catalog (Cutri et al. 2003). ACORNS-ADI produces two-dimensional contrast maps. We azimuthally average these maps to obtain the contrasts reported in Table 5.

We follow up companion candidates (5.5σ detections), typically after ∼1 yr, to test for physical association. The SEEDS MGs targets are almost all within 50 pc, with proper motions of up to $1'' \mathrm{yr}^{-1}$. A physically unrelated background object will thus move by an easily detectable amount, while a bound companion will remain in nearly the same position relative to its parent star. None of our faint, substellar companion candidates thus far have passed the "common proper motion test," though we have detected several low-mass stellar companions, and a few substellar candidates remain to be followed up. Table 6 summarizes the new stellar companions to the MG targets, one of which does not yet have a second epoch to confirm common proper motion (though very close chance alignments of such bright stars at the targets' Galactic coordinates are unlikely). Unsurprisingly, the frequency of background objects increases sharply toward the Galactic plane.

7. NOTES ON INDIVIDUAL STARS

In this section, where appropriate, we provide details on each individual target. This includes both stellar properties (particularly age indicators) and noteworthy aspects of the SEEDS observations. We order the objects by right ascension.

HIP 544 (= HD 166 = GJ 5). This K0 star is a proposed member of the Hercules–Lyra association. It does have extensive secondary indicators, enabling a reasonable age estimate. SEEDS images do not detect any companion candidates within 8.″5 (∼110 AU projected).

HIP 1134 (= HD 984). This late F star is considered to be a reliable member of the Columba MG, and its abundant lithium and strong activity are consistent with a young age. SEEDS images detect no companion candidates within 7.″5 (∼350 AU projected).

FK Psc (= TYC 1186-706-1). The MG membership of this K7 star is disputed. Lépine & Simon (2009) propose membership in β Pic, while Malo et al. (2013) find it to be a field star with ∼55% confidence. SEEDS observations have resolved it as a binary with a separation of 1.″7 and a flux ratio of ∼2 in *H*. These results make the MG analyses much more difficult to interpret,

Table 4
The SEEDS Moving Group Observing Log

Name	α (J2000) (h m s)	δ (J2000) (° ′ ″)	N_{exp}	t_{tot} (min)	Rot (°)	Mean Airmass	Date (y m d)
HIP 544	00 06 36.8	+29 01 17	325	16.3	76	1.02	2010 Dec 1
HIP 1134	00 14 10.3	−07 11 57	151	37.8	29	1.14	2011 Aug 2
FK Psc	00 23 34.7	+20 14 29	98	24.5	172	1.00	2011 Sep 3
HIP 3589	00 45 50.9	+54 58 40	120	30.0	22	1.24	2011 Dec 30
–	00 45 50.9	+54 58 40	138	46.0	25	1.25	2012 Sep 12
HIP 4979	01 03 49.0	+01 22 01	47	22.9	23	1.06	2009 Nov 2
–	01 03 49.0	+01 22 01	80	13.3	13	1.06	2012 Sep 13
HIP 6869	01 28 24.4	+17 04 45	59	13.7	103	1.00	2009 Nov 2
HS Psc	01 37 23.2	+26 57 12	258	43.0	87	1.01	2012 Sep 14
HIP 10679	02 17 24.7	+28 44 30	111	27.8	67	1.01	2011 Dec 24
BD+30 397B	02 27 28.0	+30 58 41	116	38.7	68	1.02	2011 Dec 31
HIP 11437	02 27 29.3	+30 58 25	116	38.7	68	1.02	2011 Dec 30
–	02 27 29.3	+30 58 25	129	32.3	60	1.03	2011 Dec 31
HIP 12545	02 41 25.9	+05 59 18	135	31.3	39	1.05	2009 Dec 24
HIP 12638	02 42 21.3	+38 37 07	120	40.0	30	1.10	2011 Sep 6
HIP 12925	02 46 14.6	+05 35 33	120	30.0	48	1.03	2012 Jan 1
HIP 17248	03 41 37.3	+55 13 07	81	40.5	24	1.25	2012 Nov 7
HIP 23362	05 01 25.6	−20 03 07	55	27.5	13	1.33	2012 Nov 7
HIP 25486	05 27 04.8	−11 54 03	120	11.1	12	1.18	2010 Jan 24
HD 36869	05 34 09.2	−15 17 03	81	40.5	26	1.24	2012 Nov 6
HIP 29067	06 07 55.2	+67 58 37	162	40.5	20	1.75	2012 Apr 11
HIP 30030	06 19 08.1	−03 26 20	87	29.0	15	1.18	2011 Mar 25
HIP 32104	06 42 24.3	+17 38 43	135	11.3	39	1.00	2011 Dec 25
V429 Gem	07 23 43.6	+20 24 59	117	27.2	168	1.00	2010 Jan 23
HIP 37288	07 39 23.0	+02 11 01	124	31.0	40	1.06	2011 Jan 30
HIP 39896	08 08 56.4	+32 49 11	95	23.8	48	1.04	2011 Dec 25
HIP 40774	08 19 19.1	+01 20 20	121	28.1	27	1.08	2009 Dec 25
–	08 19 19.1	+01 20 20	87	21.8	43	1.06	2011 Jan 28
HIP 44526	09 04 20.7	−15 54 51	37	12.3	7	1.35	2011 Jan 30
–	09 04 20.7	−15 54 51	92	30.7	19	1.27	2012 Jan 1
HIP 45383	09 14 53.7	+04 26 34	90	30.0	47	1.04	2011 Mar 26
HIP 46843	09 32 43.8	+26 59 19	106	35.3	99	1.01	2011 Jan 28
HIP 50156	10 14 19.2	+21 04 30	137	34.3	166	1.00	2011 Dec 24
GJ 388	10 19 36.3	+19 52 12	105	26.3	2	1.06	2012 May 16
HIP 50660	10 20 45.9	+32 23 54	104	24.1	48	1.03	2009 Dec 23
HIP 51317	10 28 55.6	+00 50 28	118	19.7	29	1.08	2011 Jan 28
HIP 53020	10 50 52.0	+06 48 29	155	51.7	32	1.08	2011 Jan 29
–	10 50 52.0	+06 48 29	95	23.8	36	1.03	2011 May 25
HIP 53486	10 56 30.8	+07 23 19	223	20.7	53	1.03	2010 Jan 25
HD 95174	10 59 38.3	+25 26 15	112	28.0	66	1.01	2012 May 11
HIP 54155	11 04 41.5	−04 13 16	136	34.0	25	1.13	2011 May 26
TYC 3825-716-1	11 20 50.5	+54 10 09	101	33.7	22	1.22	2012 Feb 27
–	11 20 50.5	+54 10 09	171	42.8	33	1.24	2011 Dec 26
HIP 59280	12 09 37.3	+40 15 07	208	33.8	43	1.08	2009 Dec 23
TYC 4943-192-1	12 15 18.4	−02 37 28	51	25.5	14	1.13	2011 Feb 1
HIP 60661	12 25 58.6	+08 03 44	66	15.3	29	1.02	2010 Jan 23
–	12 25 58.6	+08 03 44	71	23.7	30	1.03	2011 May 21
HIP 63317	12 58 32.0	+38 16 44	131	32.8	42	1.07	2012 May 14
FH CVn	13 27 12.1	+45 58 26	115	38.3	31	1.12	2012 Feb 26
HIP 66252	13 34 43.2	−08 20 31	112	37.3	26	1.14	2011 May 26
–	13 34 43.2	−08 20 31	95	31.7	24	1.14	2012 May 12
HIP 67412	13 48 58.2	−01 35 35	157	36.4	38	1.08	2010 Jan 24
HIP 73996	15 07 18.1	+24 52 09	174	14.5	103	1.01	2011 Mar 26
–	15 07 18.1	+24 52 09	300	25.0	106	1.01	2013 Feb 26
–	15 07 18.1	+24 52 09	233	38.8	106	1.01	2013 Feb 27
HIP 78557	16 02 22.4	+03 39 07	213	35.5	41	1.05	2012 Jul 8
–	16 02 22.4	+03 39 07	30	5.0	4	1.19	2013 May 20
HIP 82688	16 54 08.1	−04 20 25	140	35.0	33	1.10	2011 May 24
–	16 54 08.1	−04 20 25	161	53.7	39	1.14	2012 Apr 11
HIP 83494	17 03 53.6	+34 47 25	36	18.0	15	1.10	2012 Feb 26
HIP 87579	17 53 29.9	+21 19 31	142	35.5	139	1.01	2011 May 22
–	17 53 29.9	+21 19 31	210	52.5	166	1.01	2012 May 13
HIP 87768	17 55 44.9	+18 30 01	192	32.0	38	1.01	2012 Jul 7

Table 4
(Continued)

Name	α (J2000) (h m s)	δ (J2000) (° ′ ″)	N_{exp}	t_{tot} (min)	Rot (°)	Mean Airmass	Date (y m d)
HIP 91043	18 34 20.1	+18 41 24	180	30.0	132	1.01	2012 Jul 10
–	18 34 20.1	+18 41 24	108	21.6	59	1.01	2013 May 18
HIP 93580	19 03 32.3	+01 49 08	150	25.0	22	1.06	2012 Jul 11
BD+05 4576	20 39 54.6	+06 20 12	102	34.0	32	1.05	2011 May 23
–	20 39 54.6	+06 20 12	24	6.0	15	1.04	2012 Sep 12
HIP 102409	20 45 09.5	−31 20 27	53	25.8	12	1.67	2009 Nov 1
HD 201919	21 13 05.3	−17 29 13	94	47.0	26	1.29	2012 Nov 7
HIP 107350	21 44 31.3	+14 46 19	137	17.1	72	1.01	2011 Aug 3
TYC 2211-1309-1	22 00 41.6	+27 15 14	138	34.5	82	1.01	2011 Sep 4
HIP 111449	22 34 41.6	−20 42 30	620	25.8	26	1.33	2012 Nov 6
HIP 114066	23 06 04.8	+63 55 34	105	52.5	22	1.40	2012 Nov 5
HIP 115162	23 19 39.6	+42 15 10	150	50.0	37	1.08	2012 Sep 13
BD−13 6424	23 32 30.9	−12 15 51	123	41.0	24	1.21	2011 Aug 3
HIP 116805	23 40 24.5	+44 20 02	246	20.5	14	1.18	2012 Jan 1
–	23 40 24.5	+44 20 02	201	26.8	26	1.10	2012 Jul 8

and we do not consider FK Psc to be reliably associated with any of the groups discussed in this paper. We follow Malo et al. (2013) in placing a ∼20% probability on β Pic membership. We also consider the kinematic distance given in Table 1 to be unreliable, making it difficult to interpret sensitivity limits. SEEDS observed FK Psc under poor conditions; due to this and its extremely uncertain age, FK Psc should probably be excluded from statistical analyses.

HIP 3589 (= HD 4277). This late F star has been classified as a member of AB Dor with high confidence by, e.g., Torres et al. (2008). The star does show a strong discrepancy between the MG age and the isochrone likelihood, with the isochrone analysis showing strong peaks at ∼20 Myr and ∼5 Gyr. The old age, however, is extremely inconsistent with HIP 3589's youth indicators. HIP 3589 has a neighbor at a separation of 3.″0 with an H-band flux ∼10% that of the primary; however, SEEDS observations indicate that this star is not bound to HIP 3589. SEEDS images did not detect any other companion candidates within 7.″5, ∼400 AU projected.

HIP 4979 (= HD 6288A). This early F star has been proposed to be a member of the IC 2391 supercluster. Unfortunately, its early spectral type renders secondary age indicators of little value, and the star is extremely difficult to date reliably. Our adopted age probability distribution is uniform out to HIP 4979's main sequence lifetime of ∼5 Gyr. SEEDS images detect no companion candidates, apart from a marginal, 5.7σ source at a separation (E, N) = (−3.″94, 6.″65), a projected distance of just under 500 AU. Follow-up observations with somewhat less integration time detected nothing at this position, but did detect an even more marginal source (∼4σ) near the candidate's expected background position.

HIP 6869 (= HD 8941). This F8 star has been proposed to be a member of the IC 2391 supercluster. Like HIP 4979, it is too blue to apply the age relations described in this paper, and we adopt a uniform probability distribution in age. HIP 6869 is a close binary, with an angular separation of 0.″44 and an H-band contrast of ∼100. At HIP 6869's distance, its companion has an absolute H-band magnitude of ∼7, consistent with a mid-M spectral type. No other companion candidates were detected in high-contrast imaging. We have not yet followed up the star to confirm its companion's common proper motion, though a close chance alignment of such a bright star at (l, b) = (135°, −45°) is unlikely.

HS Psc. This mid-K star was first proposed as a candidate member of AB Dor by Schlieder et al. (2010). Malo et al. (2013) confirmed this categorization, placing it in AB Dor with 98% confidence. SEEDS imaging detected a 5.9σ point source at a separation of (E, N) = (2.″85, 4.″04), a projected distance of just under 200 AU assuming the kinematic distance Schlieder et al. (2010) derived assuming membership in AB Dor. Follow-up images failed to detect any point source, making it a likely statistical fluctuation.

HIP 10679 (= BD 14082B). This early G star is in a binary system with the early F star HIP 10680, separated from its companion by 14″. It is considered to be a well-established member of the β Pic MG (e.g., Torres et al. 2008; Malo et al. 2013). SEEDS did not detect any companion candidates within a projected separation of 7.″5 (≈210 AU).

BD+30 397B. This M0 star is the binary companion of the K7 star HIP 11437; both are reliably identified with the β Pic MG. SEEDS images detected no companion candidates within 8.″5 (∼425 AU projected).

HIP 11437. Together with its companion BD+30 397B, this K6 star is reliably identified with the β Pic MG. It also represents a pathological case of exceptionally slow rotation (as measured from SuperWASP periodicity): HIP11437's gyrochronological age is ∼500 Myr. Its 14 day period is the longest in the SEEDS MG sample. SEEDS did not detect any companion candidates within 7.″5 (∼300 AU projected).

HIP 12545. This K6 star is considered a well-established member of the β Pic MG. Malo et al. (2013) found its photometry and radial velocity to be slightly more consistent with Columba, but due in large part to its exceptionally fast rotation and vigorous activity, they did not dispute the traditional association with β Pic (Zuckerman & Song 2004; Torres et al. 2008). SEEDS images do not detect any companion candidates within 8.″5 (∼350 AU projected).

HIP 12638 (= HD 16760). This G2 star is a well-established member of the AB Dor MG, and is known to host a companion, which was reported as a substellar object ($M \sin i \sim 14\ M_J$) on a 1.3 yr orbit (Bouchy et al. 2009; Sato et al. 2009). This companion was directly imaged on an almost face-on orbit, probably indicating that the companion has a stellar mass (Evans et al. 2012). Despite its very modest contrast, the companion has an angular separation of just ∼0.″026, less than the width of the H-band Subaru PSF; it was imaged using aperture-masking

Table 5
SEEDS Moving Group 5.5σ Contrast Limits

Name	H	5.5σ Contrast (mag)							
	(mag)	0.″25	0.″5	0.″75	1″	1.″5	2″	3″	5″
HIP 544	3.95 ± 0.02	...	9.1	11.2	12.6	14.1	14.6	14.8	14.8
HIP 1134	2.80 ± 0.05	...	10.1	12.1	13.4	14.8	15.3	15.5	15.6
FK Psc	3.62 ± 0.06	5.9	7.8	9.0	9.8	8.7	10.1	11.7	12.0
HIP 3589	2.80 ± 0.10	...	9.0	11.1	12.5	13.5	12.8	14.1	14.7
HIP 4979	1.62 ± 0.05	...	10.3	11.8	13.7	14.9	15.5	15.8	15.8
HIP 6869	1.75 ± 0.06	...	8.2	11.7	13.2	14.5	14.8	14.8	14.5
HS Psc	4.85	7.0	9.0	10.6	11.6	12.4	12.6	12.7	12.6
HIP 10679	4.18 ± 0.35	...	8.8	10.6	11.9	13.2	13.7	13.9	13.8
BD+30 397B	5.13 ± 0.20	7.7	9.6	11.5	12.5	13.2	13.4	13.4	13.3
HIP 11437	4.23 ± 0.20	7.5	9.6	11.6	12.7	13.7	13.9	13.9	13.9
HIP 12545	4.11 ± 0.14	7.8	10.0	11.8	13.0	13.7	14.0	14.1	14.1
HIP 12638	3.81 ± 0.23	...	9.4	11.4	12.6	13.7	14.1	14.3	14.5
HIP 12925	2.96 ± 0.12	6.2	8.2	10.2	11.4	11.5	10.8	13.5	13.7
HIP 17248	4.92 ± 0.17	...	9.8	11.5	12.8	13.6	13.8	13.9	13.9
HIP 23362	1.10 ± 0.03	...	8.8	10.5	12.3	14.2	15.3	15.9	16.1
HIP 25486	2.93 ± 0.03	...	9.1	10.8	12.5	13.9	14.4	14.6	14.7
HD 36869	4.26 ± 0.54	...	8.8	10.5	12.0	13.4	13.9	14.1	14.2
HIP 29067	4.86 ± 0.10	...	9.1	11.2	12.6	13.9	14.2	14.4	14.5
HIP 30030	3.13 ± 0.09	...	7.8	9.6	11.2	12.7	13.3	13.5	13.7
HIP 32104	1.87 ± 0.06	...	7.0	8.2	9.6	11.1	12.0	12.5	12.7
V429 Gem	4.97 ± 0.34	7.0	9.8	11.4	12.5	13.2	13.4	13.5	13.2
HIP 37288	5.27 ± 0.04	...	9.0	10.7	12.2	13.8	14.7	15.0	15.1
HIP 39896	5.00 ± 0.15	4.2	8.0	9.6	10.9	12.0	12.5	12.6	12.6
HIP 40774	4.42 ± 0.07	...	9.9	11.9	13.4	14.6	15.1	15.2	15.2
HIP 44526	4.28 ± 0.05	...	8.1	10.2	11.7	13.2	13.9	14.2	14.3
HIP 45383	4.12 ± 0.06	...	6.7	6.7	9.6	13.3	14.6	15.3	15.4
HIP 46843	3.99 ± 0.02	...	10.3	12.3	13.9	15.3	15.8	16.0	16.0
HIP 50156	4.63 ± 0.09	...	9.3	10.9	12.1	13.5	13.9	14.1	13.9
GJ 388	6.48 ± 0.05	...	...	...	...	10.9	12.4	14.0	15.1
HIP 50660	4.01 ± 0.13	...	9.7	11.6	12.9	13.6	13.8	13.8	13.7
HIP 51317	6.35 ± 0.03	...	8.7	10.7	12.6	14.0	14.6	14.9	14.9
HIP 53020	7.55 ± 0.06	...	10.6	12.1	13.6	14.6	14.9	15.1	15.1
HIP 53486	4.16 ± 0.04	...	9.6	11.6	13.1	14.4	15.0	15.2	15.2
HD 95174	4.19 ± 0.19	...	9.8	11.7	13.1	14.2	14.6	14.5	11.7
HIP 54155	3.80 ± 0.06	...	8.6	10.3	11.7	13.4	14.1	14.4	14.6
TYC 3825-716-1	4.88 ± 0.21	...	9.1	10.6	11.5	12.1	12.1	12.2	12.2
HIP 59280	3.75 ± 0.04	...	9.8	11.8	13.3	14.6	15.0	15.2	15.3
TYC 4943-192-1	5.60 ± 0.19	...	8.7	10.3	11.3	12.2	12.6	12.7	12.7
HIP 60661	4.45 ± 0.19	...	9.0	10.4	11.3	10.5	9.5	12.2	12.2
HIP 63317	3.72 ± 0.13	7.1	9.4	11.4	12.6	13.6	14.0	14.2	14.2
FH CVn	4.89 ± 0.20	...	9.7	11.1	12.2	12.8	13.0	13.1	13.1
HIP 66252	4.78 ± 0.03	...	9.7	11.4	12.8	14.1	14.7	15.1	15.2
HIP 67412	4.01 ± 0.10	7.7	10.5	12.3	13.4	14.1	14.4	14.4	14.4
HIP 73996	2.55 ± 0.01	...	9.8	11.6	12.9	14.4	15.3	15.8	16.0
HIP 78557	2.95 ± 0.26	6.8	8.4	10.5	11.6	12.5	12.9	12.8	12.9
HIP 82688	3.13 ± 0.09	...	11.1	12.6	13.9	14.9	15.2	15.0	15.3
HIP 83494	1.98 ± 0.04	...	8.4	10.8	12.1	13.7	14.6	15.1	15.2
HIP 87579	4.36 ± 0.05	...	10.5	12.1	13.5	14.5	14.9	15.0	15.1
HIP 87768	4.43 ± 0.11	6.3	8.0	9.8	11.1	12.5	13.3	13.7	14.0
HIP 91043	3.00 ± 0.05	...	9.1	10.7	12.0	13.5	14.0	14.0	15.1
HIP 93580	1.66 ± 0.04	...	9.2	11.0	12.4	13.7	14.4	14.5	14.6
BD+05 4576	4.42	...	10.0	11.5	12.8	13.8	14.0	14.2	14.2
HIP 102409	4.85 ± 0.02	...	7.8	10.3	11.8	13.4	14.0	14.7	...
HD 201919	4.79	...	9.1	11.0	12.3	13.2	13.5	13.7	13.7
HIP 107350	3.34 ± 0.01	...	10.0	11.9	13.5	14.8	15.4	15.5	15.5
TYC 2211-1309-1	4.66 ± 0.08	6.3	8.2	9.4	10.6	11.1	11.3	11.3	11.1
HIP 111449	2.49 ± 0.01	...	8.9	10.8	12.3	14.2	15.0	15.6	15.7
HIP 114066	5.22 ± 0.09	...	9.8	11.6	12.9	14.0	14.4	14.6	14.6
HIP 115162	3.78 ± 0.13	7.1	9.1	10.9	12.0	13.1	13.6	13.8	13.9
BD−13 6424	4.59 ± 0.03	...	9.3	10.9	12.5	13.8	14.3	14.6	14.7
HIP 116805	1.04 ± 0.02	...	9.4	10.8	12.2	14.1	15.1	15.8	15.9

Table 6
Newly Discovered Stellar Companions

Star	MJD +55,000	Separation (arcsec)	P.A. (deg)	*H*-band Contrast
HIP 6869[a]	137	0.444 ± 0.005	269.1 ± 0.6	100
HIP 12925	927	1.893 ± 0.005	252.9 ± 0.2	13
HIP 39896	920	0.252 ± 0.005	81 ± 1	6.4
HIP 45383	646	0.741 ± 0.005	45.9 ± 0.4	4.1
HIP 60661	219	1.92 ± 0.01	107.5 ± 0.3	5.7
HIP 78557	1116	0.565 ± 0.005	180.7 ± 0.5	190
HIP 82688	705	3.811 ± 0.005	58.3 ± 0.1	41

Note. [a] Common proper motion to be confirmed.

interferometry. SEEDS images detect no companion candidates within 7″ (∼320 AU projected).

HIP 12925 (= HD 17250). This F8 star has been reliably classified in the Tuc–Hor association (Zuckerman et al. 2011; Malo et al. 2013). SEEDS imaging detects a companion candidate with an *H*-band flux ratio of ∼13 and a separation of 1.″9 (∼100 AU projected); there are no other companion candidates within 7.″5 (∼400 AU projected). Archival images from Keck/NIRC2 confirm this candidate to be HIP 12925's stellar companion.

HIP 17248. This M0 star is considered to be a reliable member of the Columba MG (Zuckerman et al. 2011; Malo et al. 2013). SEEDS images detected five candidate companions within 7″, with *H*-band contrasts ranging from $\sim 10^4$ to $\sim 2 \times 10^5$, and separations ranging from ∼3″ to ∼6.″5. The star is less than a degree from the Galactic plane, making the density of background objects high. Indeed, all but one of our companion candidates are clearly visible as background objects in *HST*/NICMOS imaging from 2005. The final candidate, at a separation (E, N) = (−2.″85, 0.″72) in our images from 2012 November, also appears to be in its expected background position in the archival *HST*/NICMOS data, albeit at a modest signal-to-noise ratio.

HIP 23362 (= HD 32309). This late B star is a secure member of the Columba MG. At an age of 30 Myr for the group, the isochrone fit is modestly discrepant; however, the isochrone analysis produces a very broad peak in the likelihood centered at ∼60 Myr. Primarily part of the SEEDS high-mass sample, we include it here for completeness. SEEDS images detect two companion candidates which are currently awaiting follow-up observations.

HIP 25486 (= HD 35850). This F8 star is a well-established member of β Pic; its high activity and abundant lithium confirm its youth. The large discrepancy with the isochrone likelihood at 20 Myr is simply because the likelihood increases very sharply toward ∼25–30 Myr, and does not call the β Pic identification into question. SEEDS images do not detect any companion candidates within 7.″5 (∼200 AU projected).

HD 36869. This G3 star is a likely member of the Columba MG, but lacks a *Hipparcos* parallax. Though it is absent from the large Bayesian analysis of Malo et al. (2013), BANYAN gives a membership probability of more than 95%. HD 36869's *Tycho* parallax (Høg et al. 2000) is far below the distance inferred from its magnitude and spectral type (59 pc; Zuckerman et al. 2011); we consider the spectroscopic parallax to be more reliable. HD 36869 does feature extremely high levels of activity, abundant lithium, and rapid rotation consistent with the young (∼30 Myr) age of Columba. SEEDS does not detect any companion candidates within 7.″5, ∼400 AU projected.

HIP 29067 (= GJ 9198). This K8 star is associated with the Castor MG. HIP 29067 shows modest Ca II HK activity, but was not detected in the *ROSAT* all-sky survey and has little lithium. HS Psc, a ∼100 Myr-old mid-K star in our sample, shows much stronger activity and lithium absorption. HIP 29067 is likely a much older star than its proposed Castor membership would imply. SEEDS imaging does not detect any companion candidates within 7.″5 (∼180 AU projected).

HIP 30030 (= HD 43989). This F9 star has been classified both as a member of TW Hydrae (Zuckerman & Song 2004) and Columba (Malo et al. 2013). We adopt the newer classification, which favors membership in Columba due to HIP 30030's Galactic position. Both associations are young (∼8 Myr for TW Hydrae, ∼30 Myr for Columba), and HIP 30030 has strong youth indicators. SEEDS detects one highly significant companion candidate at a separation of 2.″57; however, archival images from NICMOS reveal it as a background star.

HIP 32104 (= HD 48097). This A2 star is a reliable member of the Columba MG. Primarily part of the SEEDS high-mass sample, it is included here for completeness. SEEDS images do not detect any companions.

V429 Gem. This K5 star is a reliable member of the AB Dor MG, and shows strong youth indicators. Radial velocity surveys have detected a 6.5 M_J companion on a 7.8 day orbit (Hernán-Obispo et al. 2010). However, V429 Gem's strong activity makes radial velocity measurements difficult, and other authors have disputed the existence of a companion (Figueira et al. 2010). SEEDS images reveal a bright background star at a separation of 6.″97 and a considerably fainter candidate at (E, N) = (−1.″92, 3.″19). Follow-up observations revealed that this candidate is also a background object. No other candidates were detected within 7″ (∼180 AU projected).

HIP 37288 (= GJ 281). This K7 star was originally proposed to be a member of the Local Association (Montes et al. 2001b), but was later reclassified in the Her-Lya association (López-Santiago et al. 2006). HIP 37288 shows only weak chromospheric activity and was not detected in the *ROSAT* all-sky survey; its lithium absorption lines are also weaker than the mid-K stars in our sample reliably associated with young, coeval MGs. SEEDS images reveal a companion candidate at (E, N) = (−3.″95, −1.″64); however, archival images from Gemini/NIRI reveal it to be an unrelated background star.

HIP 39896 (= GJ 1108 A). This K7 star was originally proposed to be a member of the Local Association. However, BANYAN indicates a possible membership in Columba, with ∼70% probability neglecting *I* and *J* photometry. HIP 39896 also has abundant youth indicators, including very rapid rotation and high chromospheric and coronal activity. We consider it a possible Columba member and provisionally assign a 50% membership probability. SEEDS has revealed, for the first time, a close binary companion, with a separation of 0.″25. With an *H*-band contrast of only a factor of ∼6.4, the companion is likely to be an early M dwarf. HIP 39896 is also bound to a spectroscopic M2.8+M3.3 binary (GJ 1108 B) at a separation of 14″ (Lépine & Bongiorno 2007; Shkolnik et al. 2010), ∼300 AU projected, making HIP 39896 part of a hierarchical quadruple system.

HIP 40774. This G5 star was proposed as a member of the IC 2391 supercluster. Archival data in the literature, including a non-detection by *ROSAT*, and weak photospheric lithium absorption, cast further doubt on the star's youth. Mishenina et al. (2008) report a lithium abundance $\log n(\mathrm{Li}) = 1.6$ on the scale with $H = 12$, which would be consistent with the values reported by Sestito & Randich (2005) for stars of similar

$T_{\rm eff}$ in clusters of several Gyr age. Taken together, these data suggest an age for HIP 40774 of $\gtrsim$1 Gyr. SEEDS images detect a companion candidate at a separation of (E, N) = ($-0\farcs10$, $-4\farcs48$); follow-up observations showed it to be an unrelated background object.

HIP 44526 (= HD 77825). This K2 star has been classified as a member of the Castor MG. It shows only modest levels of activity and lithium absorption, but does have a well-measured period. SEEDS images show two bright companion candidates at a separation of $\sim7\farcs5$; follow-up imaging concluded showed that both were unrelated background stars.

HIP 45383 (= HD 79555 = GJ 339). This K3 star has been classified as a member of the Castor MG. It does, however, have chromospheric measurements and X-ray activity consistent with a reasonably young age. SEEDS images reveal the system to be a binary with an angular separation of $0\farcs74$ and an *H*-band flux ratio of ∼4.1: a K-dwarf and an M dwarf with a projected separation of 13 AU. SEEDS images detected a more distant companion candidate at a separation of $7''$; however, follow-up observations revealed it to be an unrelated background star.

HIP 46843 (= HD 82443 = GJ 354.1). This K0 star was originally classified in the Local Association. However, BANYAN indicates that it is a likely member of Columba, estimating a membership probability of just over 95%. HIP 46843 also has an extraordinary suite of secondary age indicators, including a rotation period. The star's abundant lithium, rapid rotation, and high level of activity confirm its youth, and we estimate a 90% probability of bona fide membership in Columba. SEEDS images detect a companion candidate with a separation of $4''$; however, archival images from Gemini/NIRI confirm its status as an unrelated background object.

HIP 50156 (= GJ 2079). This M0 star was recently proposed as a member of β Pic (Schlieder et al. 2012a); however, the recent Bayesian analysis of Malo et al. (2013) finds a better match to the Columba MG. While the identity of its parent group remains ambiguous, the star is very active and unlikely to be a member of the field. Malo et al. (2013) mention a surprisingly large scatter in the radial velocity measurements necessary to clarify membership and suggest that HIP 50156 may be a spectroscopic binary. However, deep SEEDS images show no evidence for a stellar companion outside $\sim0\farcs02$, ∼0.5 AU. Assuming that HIP 50156 is a spectroscopic binary, its two components must be very close, potentially accounting for the strong observed activity (and large scatter in reported $R'_{\rm HK}$ values), and the system may be tidally locked. We tentatively consider it to be a member of Columba, although the similar ages of Columba and β Pic make the distinction somewhat minor for our purposes. SEEDS images detect no companion candidates within $7\farcs5$, ∼170 AU projected.

GJ 388. This M4 star has been classified in Castor. It shows significant activity and rapid rotation, but as an M star, these are difficult to use as indicators of youth. SEEDS images do not reveal any companion candidates. However, unfortunately, this data set features an exceptionally small amount of field rotation 2°. The target passed almost directly overhead but was not successfully tracked until after it had passed zenith.

HIP 50660. This K0 star has been proposed as a member of the IC 2391 supercluster. HIP 50660 was not detected by *ROSAT* and has few other measurements in the literature. SEEDS images detected a companion candidate with 5.9σ significance at a separation of $4\farcs2$. However, slightly deeper follow-up did not recover the point source, making it a likely statistical fluctuation.

HIP 51317 (= GJ 393). This M2 star is a reliable member of AB Dor. SEEDS images detect no companion candidates within $7\farcs5$ (∼50 AU projected).

HIP 53020 (= GJ 402). This nearby M5 star has been classified in Her Lya. There is little additional data on the star, and its late spectral type makes any sort of dating extremely difficult. SEEDS images detect no companion candidates within $8\farcs5$ (∼60 AU projected).

HIP 53486 (= HD 94765 = GJ 3633). This K0 star has been classified as a member of the Castor MG. Secondary age indicators show moderate levels of chromospheric and coronal activity together with a modest rotation period, and probably indicate an older age. SEEDS images detect no companion candidates within $7\farcs5$ (∼130 AU projected).

HD 95174. This K2 star, together with its K5 binary companion, has recently been proposed as a member of β Pic. It was not detected by *ROSAT*, but was instead selected as a candidate member based on its strong UV emission, and confirmed as a likely member based on its Galactic motion (Schlieder et al. 2012b). New spectroscopy, however, indicates an almost complete depletion of photospheric lithium, which is not expected for such a young K-dwarf. Chromospheric activity measurements are too uncertain to strongly constrain the system's youth. Further, as shown in Figure 1 of Schlieder et al. (2012b), its *UVW* velocity would place it right at the edge of the β Pic search area in all three velocity components, and it lies about 30 pc above the bulk of the bona fide β Pic members. With further age constraints from our spectroscopic follow-up, we consider HD 95174's classification in β Pic to be highly doubtful. SEEDS images reveal no companion candidates other than the known K5 secondary at a separation of $5''$.

HIP 54155 (= HD 96064). This G8 star is a proposed member of the Local Association. Though we do not infer an age from this, HIP 54155's secondary age indicators show high levels of activity and relatively abundant lithium. SEEDS images show a bright background star also detected in archival Gemini/NIRI images, together with a marginal, 5.5σ source at (E, N) = ($-3\farcs28$, $-3\farcs23$), $1''$ from the background star. In spite of their comparable sensitivity, the Gemini/NIRI images do not show this fainter source at either the same relative position or at the expected background position; it is almost certainly a statistical fluctuation.

TWA 2. This M2 star is a young T Tauri object in the TW Hydrae MG. It is a binary, with its two components of similar brightness and separated by $0\farcs4$. SEEDS observations were conducted in poor conditions, especially since the object's declination of $-30°$ makes it relatively inaccessible from Subaru. Less than 1 minute of integration time was obtained before the observation was abandoned. We have therefore omitted TWA 2 from our contrast tables.

TYC 3825-716-1. This K7 star was recently proposed as a member of the AB Dor MG. It is detected by *ROSAT* and shows strong UV emission consistent with youth (Schlieder et al. 2012b). TYC 3825-716-1 lies on the outskirts of the AB Dor MG in *UVW* velocity space, and ∼30 pc above most of the stars in Galactic Z distance. As a result, BANYAN gives a negligible probability for AB Dor membership. Our spectroscopy detects modest lithium absorption, but shows a chromospherically inactive star. Lacking a parallax or more compelling secondary age indicators, we decline to assign the star any probability of membership in AB Dor. SEEDS images do not detect any companions within $8''$ (∼460 AU projected

assuming the star's distance as inferred from kinematics and assuming AB Dor membership).

HIP 59280 (= HD 105631 = GJ 3706). This K0 star has been classified in the IC 2391 supercluster. Its secondary age indicators show only modest chromospheric and coronal activity and lithium absorption, measurements consistent with an age closer to 1 Gyr. SEEDS images detect no companion candidates within 7.″5 (∼190 AU projected).

TYC 4943-192-1. This M0 star was recently proposed to be a member of the AB Dor MG (Schlieder et al. 2010). Malo et al. (2013) confirmed it as an excellent candidate, but without a trigonometric parallax and with few secondary age indicators, a conclusive association is not yet possible. We consider TYC 4943-192-1 to be a likely member of AB Dor, provisionally adopting the ∼80% membership probability suggested by Malo et al. (2013). SEEDS images do not detect any companion candidates within 8.″5 (∼250 AU projected, assuming the distance inferred from kinematics and AB Dor membership).

HIP 60661 (= GJ 466). This M0 star is a proposed member of the Local Association (Montes et al. 2001a). López-Santiago et al. (2006) suggest membership in AB Dor, though HIP 60661 has the largest discrepancy in V and W with AB Dor's average kinematics of all of their proposed members. López-Santiago et al. (2010) note a significantly discrepant radial velocity in their measurements of HIP 60661 and suggest that it may be a binary. It has few secondary age indicators, and its weak chromospheric activity may indicate a much older age than that inferred for a young MG. We do not consider the star to be a likely member of AB Dor. SEEDS images confirm HIP 60661's binary status, with a companion separated by 1.″9 and an *H*-band contrast of ∼5.7 (∼70 AU projected). The companion detected by SEEDS is too far away, however, to account for the observed variation in radial velocity of several km s^{-1} over a period of a few years. There may be another, as-yet-undetected, companion lurking much closer to HIP 60661. SEEDS images do not detect any other companion candidates within 7.″5 (∼280 AU projected).

HIP 63317 (= HD 112733). This G5 star is a proposed member of the Local Association. HIP 63317 does show strong coronal and chromospheric activity and significant lithium, which provide some constraint on its age. SEEDS images detect no companion candidates within 7.″5 (∼330 AU projected).

FH CVn. This K7 star was recently proposed as a member of the AB Dor MG (Schlieder et al. 2012b). Its Galactic velocity is in excellent agreement with the bona fide members of the group, though FH CVn lies somewhat above the Galactic plane compared with the more established members. The star also shows very strong X-ray activity and rapid rotation. However, our spectroscopy indicates weak chromospheric activity and little photospheric lithium, giving some tension between different age indicators. FH CVn does lie at the lithium depletion boundary at an age of ∼130 Myr (Mentuch et al. 2008), making the weakness of photospheric lithium absorption somewhat expected. We provisionally consider it to be a moderately likely member of AB Dor, though additional follow-up is needed to clarify FH CVn's status. Using only the available kinematic data, BANYAN estimates a 40% probability of AB Dor membership, which we adopt for our analysis. SEEDS images do not detect any companions within 7.″5 (∼350 AU assuming the distance inferred from MG membership).

HIP 66252 (= HD 118100 = GJ 517). This K5 star has been classified in the IC 2391 supercluster. It has an extraordinary range of secondary age indicators, including vigorous activity, rapid rotation, and relatively abundant lithium, all of which point to youth. SEEDS imaging detects no companion candidates within 75″, ∼150 AU projected.

HIP 67412 (= HD 120352). This K0 star has been classified in the IC 2391 supercluster. Its secondary age indicators show only modest chromospheric and coronal activity, while our spectroscopy reveals little photospheric lithium. SEEDS images reveal no companion candidates within 7.″5, ∼280 AU projected.

HIP 73996 (= HD 134083 = GJ 578). This F5 star was classified as a member of the UMa supercluster by Montes et al. (2001a). However, more recent work disputes this classification. Maldonado et al. (2010) list HIP 73996 as a probable nonmember, while their Table 8 claims that López-Santiago et al. (2010) list it as a probable member (the latter paper does not include the star at all). The star is not especially active either chromospherically or coronally. Our spectroscopy shows little photospheric lithium. Regardless of its membership in the UMa supercluster, HIP 73996 is almost certainly not a member of the coeval UMa MG. SEEDS images revealed a 7σ companion candidate at (E, N) = (2.″76, −0.″33) with an *H*-band contrast of 2×10^6. However, this candidate was near an image artifact and was not detected in follow-up observations. No other candidates were detected within 7.″5 (∼280 AU projected).

HIP 78557 (= HD 143809). This G0 star is a proposed member of the Local Association. At 80 pc, it is also the most distant target in our sample. HIP 78577 has modest chromospheric, coronal activity, and reasonably abundant lithium. However, its relatively early spectral type makes these age indicators somewhat less useful. SEEDS detects a binary companion with a separation of 0.″57 (∼45 AU projected) and an *H*-band contrast of ∼190, which would make it a late M dwarf.

HIP 82688 (= HD 152555). This late F/early G star is considered a reliable member of AB Dor, and its secondary age indicators confirm its youth. SEEDS images detect two bright stars, one of which is HIP 82688's binary companion. The companion has a separation of 3.″8 (∼85 AU projected) and an *H*-band contrast of ∼41, making it likely a mid-M dwarf. SEEDS also detects a faint candidate at (E, N) = (−1.″62, 1.″82); however, follow-up observations revealed it to be a background star.

HIP 83494 (= 154431). This A5 star was proposed as a member of Tuc–Hor by Zuckerman et al. (2011). While it shows evidence of a debris disk, and is likely young, Malo et al. (2013) find a very poor match to Tuc–Hor, and classify HIP 83494 as a field star (nonmember of any of their studied associations) with high confidence. We decline to place a nonzero probability on Tuc–Hor membership. HIP 83494 is a member of the SEEDS high-mass sample, and is included here for completeness. The secondary age indicators that we use for our other targets are of little use for such a high-mass star. SEEDS images detected no companions.

HIP 87579 (= GJ 697). This K0 star is a proposed member of the Castor MG. Secondary age indicators show only modest coronal and chromospheric activity. SEEDS images detect many companion candidates within 8″ (∼200 AU projected); however, follow-up observations reveal them all to be background stars.

HIP 87768 (= GJ 698). This K5 star is a proposed member of the Local Association. SEEDS observations do not detect any companion candidates within 7.″5 (∼190 AU projected).

HIP 91043 (= HD 171488). This G2 star is a proposed member of the Local Association. Its secondary age indicators show an exceptionally active star with abundant lithium and rapid rotation. The isochrone analysis shows a strong discrepancy at

first glance, due to two strong peaks in the likelihood function, at ∼20 Myr and ∼10 Gyr. The latter age is certainly incompatible with the secondary age indicators. The isochrones may therefore indicate that our age estimates are overly conservative. SEEDS observations reveal many companion candidates; however, this is expected for a source at low Galactic latitude, with $(l, b) = (48^\circ, 12^\circ)$. Follow-up observations confirmed these sources to be background objects; several brighter sources were seen in Keck imaging and listed in Metchev & Hillenbrand (2009).

HIP 93580 (= HD 177178). This A4 star was proposed as a member of AB Dor by Zuckerman et al. (2011). It is part of the SEEDS high-mass sample, and included here for completeness. Malo et al. (2013) also favor membership in AB Dor, but with a somewhat low probability of 80% neglecting photometry, due to a discrepant *U* velocity. The isochrone analysis further calls this MG assignment into question. The likelihood function shows two peaks: one from ∼5 to 20 Myr, and a second, broad peak centered at ∼500 Myr. We provisionally adopt a lower probability of 30% for group membership. Due to HIP 93580's high mass, it never develops a large outer convective zone, and secondary age indicators are of little value. HIP 93580 lies just 2° from the Galactic plane and has many companion candidates awaiting follow-up observations.

BD+05 4576. This K7 star has recently been proposed as a member of AB Dor (Schlieder et al. 2010) on the basis of kinematics and its X-ray flux as measured by *ROSAT*. However, there is no trigonometric parallax, and our spectroscopy finds little photospheric lithium. The latter is not too surprising, as the star's spectral type places it right at the lithium depletion boundary for an age of ∼130 Myr. Given the paucity of data, we adopt the 80% membership probability as estimated by BANYAN based only on the available kinematics. SEEDS images do not detect any companion candidates within 8″ (∼300 AU assuming the distance inferred from kinematics and group membership).

HIP 102409 (= HD 197481 = GJ 803 = AU Mic). This M1 star hosts a well-known debris disk, and is reliably identified with the β Pic MG. The debris disk appears nearly edge-on and extends out to 200 AU in radius (Kalas et al. 2004), making AU Mic an excellent target for high-contrast observations. However, its declination of −31° makes it difficult to observe from Subaru; it is the most southerly target in the entire MG sample. SEEDS images do not detect any companions within 3.″2, ∼30 AU projected.

HD 201919. This K6 star is a likely member of the AB Dor MG, and its secondary age indicators confirm its youth. SEEDS images detect only a bright companion candidate just over 7″ away, a projected separation of nearly 300 AU at HD 201919's distance inferred from its kinematics assuming MG membership.

HIP 107350 (= HD 206860 = GJ 9751). This G0 star is a proposed member of the Her-Lya association. HIP 107350 does, however, have an exceptional set of measurements in the literature, including a rotation period and multi-decade Mt. Wilson chromospheric data. These secondary age indicators point to a relatively young system. SEEDS observations detect a single companion candidate around HIP 107350, but archival images from Gemini/NIRI reveal it to be an unrelated background star.

TYC 2211-1309-1. This K7 star was recently proposed as a likely member of β Pic based on its kinematics and strong secondary youth indicators. Indeed, this star is the fastest known rotator in our sample, with a period less than 0.5 day independently measured by Norton et al. (2007) and Messina et al. (2010). However, our new spectroscopic measurements introduce some tension with the strong X-ray activity and rapid rotation, finding little evidence of photospheric lithium. This may point to an unusual accretion history or recent merger responsible for both the high angular momentum and relative lack of lithium; TYC 2211-1309-1 certainly deserves more study. We consider it to be a likely, albeit far from certain, member of β Pic, and provisionally assign a 50% membership probability. SEEDS images were taken under very poor observing conditions and were made in the *K* band to enable even a basic AO correction. The only companion candidate detected was also visible in archival NACO images, which showed it to be an unrelated background star.

HIP 111449 (= HD 213845 = GJ 863.2). This F7 star is a proposed member of the Her-Lya association. It has limited activity measurements from the literature, is relatively inactive in X-rays, and lacks significant photospheric lithium. SEEDS detects a stellar companion at a separation of 6.″1 (∼140 AU projected); this object was previously reported in Lafrenière et al. (2007a).

HIP 114066 (= GJ 9809). This M0 star is a reliable member of the AB Dor MG, and shows relatively rapid rotation and vigorous X-ray activity. HIP 114066 lies nearly in the Galactic plane; as a result, it has an extremely high density of spurious background stars. Using archival Gemini/NIRI data, we have confirmed that all of these candidates are unrelated background stars.

HIP 115162. This star is a reliable member of the AB Dor MG. Its secondary age indicators show strong signs of youth, including abundant photospheric lithium and relative strong chromospheric and coronal activity. HIP 115162 has had some controversy over its spectral type, with Schlieder et al. (2010) listing it as G0V, while Zuckerman & Song (2004) list G4, and Ofek (2008) fit G8V to a spectral energy distribution template. We used the known spectral-class/temperature dependent line ratio of Fe II 6432.65 Å/Fe I 6430.85 Å (Strassmeier & Fekel 1990; Montes & Martin 1998) to better constrain the spectral classification of HIP 115162. The observed line ratio for HIP 115162, ∼0.22, was more consistent with that observed in K0V stars (∼0.2; Montes & Martin 1998) than in G0V (∼0.5; Montes & Martin 1998) or G5V (∼0.4; Montes & Martin 1998) stars. This supports a late G spectral type for HIP 115162, and we adopt the Ofek (2008) G8V classification. SEEDS images detect no companion candidates within 7″, or 350 AU projected.

BD−13 6424. This M0 star is a reliable member of the β Pic MG. Its secondary age indicators show rapid rotation, abundant lithium, and strong X-ray activity. SEEDS images detect no companion candidates within 7.″5, or ∼200 AU projected.

HIP 116805 (= HD 222439 = κ And). BANYAN gives a very high probability, 95%, of Columba membership, as was asserted in its companion's discovery paper (Carson et al. 2013). However, our isochrone analysis casts doubt on this classification, with a strong peak in the likelihood function at ∼200 Myr. Other authors have recently re-analyzed HIP 116805 and also find evidence for an older age and possible non-membership in Columba (Bonnefoy et al. 2014; Hinkley et al. 2013). We note however, that the rapid rotation and unknown inclination angle of the star may make isochronal age determination unreliable; if the star is viewed close to pole on, it could be as young as Columba. In this work, we provisionally assign the star a 30% probability of Columba membership. HIP 116805 is primarily part of the SEEDS high-mass sample, and is

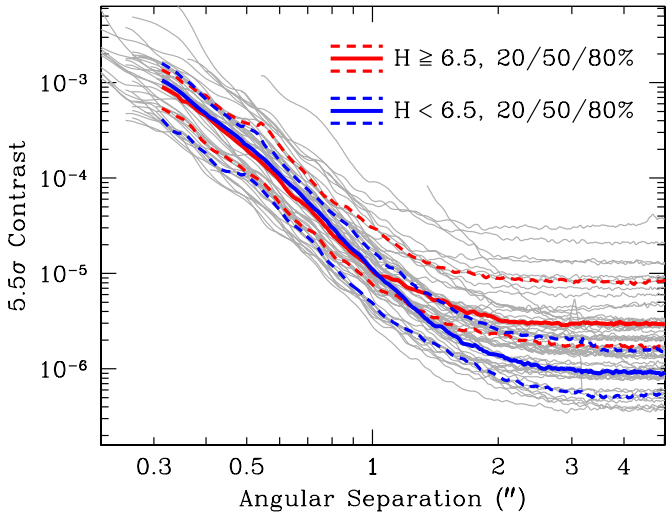

Figure 3. Contrast curves for the SEEDS MGs sample; FK Psc, HIP 3589, HIP 6869, HIP 12925, HIP 45383, HD 95174, HIP 60661, HIP 82688, and HIP 91043 show strong artifacts from bright neighbors and have been omitted. At separations of $\lesssim 1''$, the contrast limits depend on field rotation and observing conditions. Several arcseconds from the star, SEEDS observations are read noise limited, and the magnitude limits depend on AO performance, total integration time, and integration per frame. Fainter targets have less contrast, but fainter limiting magnitudes, at separations $\gtrsim 2''$.

(A color version of this figure is available in the online journal.)

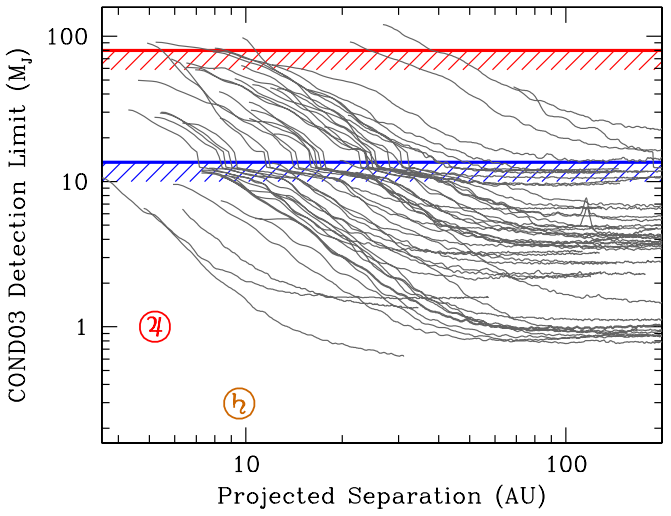

Figure 4. Mass sensitivity of the SEEDS MGs sample at the median age of the posterior probability distribution (Section 5, Table 3); FK Psc, HIP 3589, HIP 6869, HIP 12925, HIP 45383, HD 95174, HIP 60661, HIP 82688, and HIP 91043 show strong artifacts from bright neighbors and have been omitted. The COND03 models (Baraffe et al. 2003) have been used to convert from mass to luminosity. The red line marks the approximate stellar/brown dwarf boundary, while the blue line marks the brown dwarf/planet transition. Jupiter and Saturn are indicated near the lower-left corner. A thorough treatment of the statistics of the sample and its sensitivities as a function of mass will be presented in a forthcoming paper.

(A color version of this figure is available in the online journal.)

included here for completeness. HIP 116805 hosts a substellar companion, κ And b, recently discovered by SEEDS (Carson et al. 2013). κ And b has a mass of $\sim$13–50 M_J, depending on the assumed system age (Carson et al. 2013; Bonnefoy et al. 2014; Hinkley et al. 2013), and lies at a separation of $1''.06$, or 55 AU projected, from its host star.

8. DISCUSSION

Table 5 shows the 5.5σ detection limits for the SEEDS MG targets; Figure 3 plots these limits, together with 20%, 50%, and 80% curves, omitting stars with contrast artifacts from nearby bright stars. At small angular separations ($\lesssim 1''$), the limiting contrast depends mostly on observing conditions, AO performance, and field rotation, with only a weak dependence on stellar brightness. Far from the central star, SEEDS observations are read noise limited. In this regime, limiting magnitude is a more appropriate measure than limiting contrast. Sensitivity at these separations ($\gtrsim 2''$) depends almost exclusively on AO performance, total integration time, and integration time per frame.

The typical limiting contrast of a SEEDS observation varies from $\sim 10^3$ at $0''.3$, to $\sim 10^5$ at $1''$, to nearly 10^6 at separations $\gtrsim 2''$. The limiting masses are far more variable, due to the spread in ages (and often enormous uncertainties in age) of the targets observed. As a very crude guide to the mass sensitivity of our sample, Figure 4 plots the mass detection limit as a function of projected separation around each target, assuming the median age of the posterior probability distribution (Section 5, Table 3). These sensitivities assume the COND03 exoplanet cooling models (Baraffe et al. 2003) and neglect uncertainties in stellar age and exoplanet modeling. We defer a full analysis of our sensitivity as a function of exoplanet mass, together with a statistical analysis of the sample and its constraints on exoplanet frequency and properties, to a forthcoming paper (T. D. Brandt et al. 2013, in preparation).

Our sensitivity limits are competitive with other high-contrast instrumentation at other observatories, but should improve dramatically with the new extreme AO system, SCExAO, currently being commissioned at Subaru (Guyon et al. 2011). We are also exploring more minor upgrades to HiCIAO that may offer significant performance improvements. In the Southern hemisphere, Gemini Planet Imager (GPI; Macintosh et al. 2008) and SPHERE (Beuzit et al. 2008) will combine integral-field spectroscopy with high-performance AO to offer exceptional sensitivity at small angular separations. CHARIS, an integral-field spectrograph being developed and built for the Subaru telescope, will offer similar capabilities in the Northern hemisphere (McElwain et al. 2012; Peters et al. 2012).

9. CONCLUSIONS

We have presented high-contrast observations of 63 nearby stars in the SEEDS MG sample. All of the stars have been suggested to be members of coeval stellar associations. We have reviewed each proposed association, and conclude that five associations, β Pictoris, AB Doradus, Tucana–Horologium, Columba, and TW Hydrae, are sufficiently well-defined to provide conclusive age estimates for bona-fide members. Somewhat under half of our target sample have firm ages derived from MG membership.

For all stars, and in particular for those without a firm MG age, we use empirical age indicators including stellar rotation, chromospheric and coronal activity, and photospheric lithium abundance to estimate an age. Some of these data are new observations we have acquired at the Apache Point Observatory. The heterogeneity of our targets and their age indicators result in a wide range of constraints, with some of our targets having very precise ages and others being almost completely unconstrained. This picture should improve as transit surveys

measure photometric periods for an increasing fraction of field stars.

We have reduced all of our observations uniformly with the recently published software ACORNS-ADI (Brandt et al. 2013) and published contrast curves for our target stars. The contrast varies from $\sim 10^3$ at $0\farcs3$ to $\sim 10^5$ at $1''$ to $\sim 10^6$ at $2''$; it is limited by field rotation, PSF fluctuations, and AO performance at small separations, and by AO performance and exposure time at separations $\gtrsim 2''$. A full analysis of our sensitivity as a function of exoplanet mass, and the constraints on exoplanet frequency and properties, is beyond the scope of this paper. We will provide this analysis of the SEEDS MG sample, the debris disk sample, and archival data from other surveys in a forthcoming paper.

The authors thank an anonymous referee for many helpful suggestions that substantially improved the age analysis presented in this paper. This research is based on data collected at the Subaru telescope, which is operated by the National Astronomical Observatories of Japan. This material is based on work supported by the National Science Foundation Graduate Research Fellowship under grant No. DGE-0646086. Part of this research was carried out at the Jet Propulsion Laboratory, California Institute of Technology, under a contract with the National Aeronautics and Space Administration. The authors wish to recognize and acknowledge the very significant cultural role and reverence that the summit of Mauna Kea has always had within the indigenous Hawaiian community. We are most fortunate to have the opportunity to conduct observations from this mountain. This research has made use of the SIMBAD database, operated at CDS, Strasbourg, France.

REFERENCES

Abt, H. A., & Morrell, N. I. 1995, ApJS, 99, 135
Agüeros, M. A., Anderson, S. F., Covey, K. R., et al. 2009, ApJS, 181, 444
Anosova, J. P., & Orlov, V. V. 1991, A&A, 252, 123
Arriagada, P. 2011, ApJ, 734, 70
Baliunas, S., Sokoloff, D., & Soon, W. 1996, ApJL, 457, L99
Baraffe, I., & Chabrier, G. 2010, A&A, 521, A44
Baraffe, I., Chabrier, G., Barman, T. S., Allard, F., & Hauschildt, P. H. 2003, A&A, 402, 701
Barenfeld, S. A., Bubar, E. J., Mamajek, E. E., & Young, P. A. 2013, ApJ, 766, 6
Barnes, S. A. 2003, ApJ, 586, 464
Barnes, S. A. 2007, ApJ, 669, 1167
Barrado y Navascues, D. 1998, A&A, 339, 831
Barrado y Navascués, D. 2006, A&A, 459, 511
Barrado y Navascués, D., Stauffer, J. R., & Jayawardhana, R. 2004, ApJ, 614, 386
Barrado y Navascués, D., Stauffer, J. R., Song, I., & Caillault, J.-P. 1999, ApJL, 520, L123
Beuzit, J.-L., Feldt, M., Dohlen, K., et al. 2008, Proc. SPIE, 7014, 701418
Bildsten, L., Brown, E. F., Matzner, C. D., & Ushomirsky, G. 1997, ApJ, 482, 442
Biller, B. A., Close, L. M., Masciadri, E., et al. 2007, ApJS, 173, 143
Biller, B. A., Liu, M. C., Wahhaj, Z., et al. 2010, ApJL, 720, L82
Binks, A. S., & Jeffries, R. D. 2014, MNRAS, 438, 11
Bonnefoy, M., Currie, T., Marleau, G.-D., et al. 2014, A&A, 562, A111
Bouchy, F., Hébrard, G., Udry, S., et al. 2009, A&A, 505, 853
Bowler, B. P., Liu, M. C., Shkolnik, E. L., et al. 2012, ApJ, 753, 142
Brandt, T. D., McElwain, M. W., Turner, E. L., et al. 2013, ApJ, 764, 183
Bressan, A., Marigo, P., Girardi, L., et al. 2012, MNRAS, 427, 127
Burrows, A., Marley, M., Hubbard, W. B., et al. 1997, ApJ, 491, 856
Caballero, J. A. 2010, A&A, 514, A98
Carson, J., Thalmann, C., Janson, M., et al. 2013, ApJL, 763, L32
Carson, J. C., Eikenberry, S. S., Smith, J. J., & Cordes, J. M. 2006, AJ, 132, 1146
Casagrande, L., Schönrich, R., Asplund, M., et al. 2011, A&A, 530, A138
Chabrier, G., Baraffe, I., Allard, F., & Hauschildt, P. 2000, ApJ, 542, 464
Chauvin, G., Lagrange, A.-M., Dumas, C., et al. 2004, A&A, 425, L29
Cincunegui, C., Díaz, R. F., & Mauas, P. J. D. 2007, A&A, 469, 309
Close, L. M., Thatte, N., Nielsen, E. L., et al. 2007, ApJ, 665, 736
Cumming, A., Butler, R. P., Marcy, G. W., et al. 2008, PASP, 120, 531
Cutri, R. M., Skrutskie, M. F., van Dyk, S., et al. 2003, yCat, 2246, 0
da Silva, L., Torres, C. A. O., de La Reza, R., et al. 2009, A&A, 508, 833
Davila, J. M. 1987, ApJ, 317, 514
de la Reza, R., Torres, C. A. O., Quast, G., Castilho, B. V., & Vieira, G. L. 1989, ApJL, 343, L61
De Silva, G. M., D'Orazi, V., Melo, C., et al. 2013, MNRAS, 431, 1005
Delorme, P., Gagné, J., Girard, J. H., et al. 2013, A&A, 553, L5
Dong, R., Hashimoto, J., Rafikov, R., et al. 2012, ApJ, 760, 111
Duncan, D. K., Vaughan, A. H., Wilson, O. C., et al. 1991, ApJS, 76, 383
Eggen, O. J. 1958, MNRAS, 118, 65
Eggen, O. J. 1961, RGOB, 41, 245
Eggen, O. J. 1975, PASP, 87, 37
Eggen, O. J. 1983a, MNRAS, 204, 391
Eggen, O. J. 1983b, MNRAS, 204, 377
Eggen, O. J. 1991, AJ, 102, 2028
Eggen, O. J. 1992, AJ, 104, 2141
Eggen, O. J. 1995, AJ, 110, 2862
Eisenbeiss, T., Ammler-von Eiff, M., Roell, T., et al. 2013, A&A, 556, A53
Ekström, S., Georgy, C., Eggenberger, P., et al. 2012, A&A, 537, A146
Evans, T. M., Ireland, M. J., Kraus, A. L., et al. 2012, ApJ, 744, 120
Famaey, B., Jorissen, A., Luri, X., et al. 2005, A&A, 430, 165
Famaey, B., Siebert, A., & Jorissen, A. 2008, A&A, 483, 453
Favata, F., Barbera, M., Micela, G., & Sciortino, S. 1993, A&A, 277, 428
Fernández, D., Figueras, F., & Torra, J. 2008, A&A, 480, 735
Figueira, P., Marmier, M., Bonfils, X., et al. 2010, A&A, 513, L8
Flower, P. J. 1996, ApJ, 469, 355
Follette, K. B., Tamura, M., Hashimoto, J., et al. 2013, ApJ, 767, 10
Frasca, A., Freire Ferrero, R., Marilli, E., & Catalano, S. 2000, A&A, 364, 179
Fuhrmann, K. 2004, AN, 325, 3
Gaidos, E. J. 1998, PASP, 110, 1259
Gaidos, E. J., Henry, G. W., & Henry, S. M. 2000, AJ, 120, 1006
Girardi, L., Groenewegen, M. A. T., Hatziminaoglou, E., & da Costa, L. 2005, A&A, 436, 895
Gizis, J. E. 2002, ApJ, 575, 484
Glatzmaier, G. A. 1985, ApJ, 291, 300
Gliese, W. 1969, VeARI, 22, 1
Grady, C. A., Muto, T., Hashimoto, J., et al. 2013, ApJ, 762, 48
Gray, R. O., Corbally, C. J., Garrison, R. F., et al. 2006, AJ, 132, 161
Gray, R. O., Corbally, C. J., Garrison, R. F., McFadden, M. T., & Robinson, P. E. 2003, AJ, 126, 2048
Gregorio-Hetem, J., Lepine, J. R. D., Quast, G. R., Torres, C. A. O., & de La Reza, R. 1992, AJ, 103, 549
Guyon, O., Martinache, F., Clergeon, C., et al. 2011, Proc. SPIE, 8149, 814908
Hartman, J. D., Bakos, G. Á., Noyes, R. W., et al. 2011, AJ, 141, 166
Hashimoto, J., Dong, R., Kudo, T., et al. 2012, ApJL, 758, L19
Hashimoto, J., Tamura, M., Muto, T., et al. 2011, ApJL, 729, L17
Hawley, S. L., Gizis, J. E., & Reid, I. N. 1996, AJ, 112, 2799
Hayano, Y., Takami, H., Guyon, O., et al. 2008, Proc. SPIE, 7015, 701510
Helou, G., & Walker, D. W. (ed.) 1988, Infrared Astronomical Satellite (IRAS) Catalogs and Atlases. Volume 7: The Small Scale Structure Catalog (Hanover, MD: NASA STI)
Hempelmann, A., Schmitt, J. H. M. M., Schultz, M., Ruediger, G., & Stepien, K. 1995, A&A, 294, 515
Henry, G. W., Fekel, F. C., & Hall, D. S. 1995, AJ, 110, 2926
Hernán-Obispo, M., Gálvez-Ortiz, M. C., Anglada-Escudé, G., et al. 2010, A&A, 512, A45
Heyvaerts, J., & Priest, E. R. 1983, A&A, 117, 220
Hinkley, S., Oppenheimer, B. R., Soummer, R., et al. 2009, ApJ, 701, 804
Hinkley, S., Pueyo, L., Faherty, J. K., et al. 2013, ApJ, 779, 153
Hinz, P. M., Rodigas, T. J., Kenworthy, M. A., et al. 2010, ApJ, 716, 417
Høg, E., Fabricius, C., Makarov, V. V., et al. 2000, A&A, 355, L27
Houk, N., & Smith-Moore, M. 1988, Michigan Catalogue of Two-dimensional Spectral Types for the HD Stars, Vol. 4, Declinations $-26\fdg0$ to $-12\fdg0$ (Ann Arbor, MI: Department of Astronomy, Univ. Michigan)
Houk, N., & Swift, C. 1999, Michigan Catalogue of Two-dimensional Spectral Types for the HD Stars, Vol. 5 (Ann Arbor, MI: Department of Astronomy, Univ. Michigan)
Howard, A. W., Marcy, G. W., Johnson, J. A., et al. 2010, Sci, 330, 653
Hünsch, M., Schmitt, J. H. M. M., Sterzik, M. F., & Voges, W. 1999, A&AS, 135, 319
Hunt-Walker, N. M., Hilton, E. J., Kowalski, A. F., Hawley, S. L., & Matthews, J. M. 2012, PASP, 124, 545
Isaacson, H., & Fischer, D. 2010, ApJ, 725, 875
Janson, M., Bonavita, M., Klahr, H., et al. 2011a, ApJ, 736, 89

Janson, M., Brandner, W., Lenzen, R., et al. 2007, A&A, 462, 615
Janson, M., Brandt, T. D., Kuzuhara, M., et al. 2013, ApJL, 778, L4
Janson, M., Carson, J., Thalmann, C., et al. 2011b, ApJ, 728, 85
Jeffries, R. D. 1995, MNRAS, 273, 559
Jeffries, R. D., & Jewell, S. J. 1993, MNRAS, 264, 106
Jenkins, J. S., Murgas, F., Rojo, P., et al. 2011, A&A, 531, A8
Jenkins, J. S., Pavlenko, Y. V., Ivanyuk, O., et al. 2012, MNRAS, 420, 3587
Jenkins, J. S., Ramsey, L. W., Jones, H. R. A., et al. 2009, ApJ, 704, 975
Kalas, P., Liu, M. C., & Matthews, B. C. 2004, Sci, 303, 1990
Kastner, J. H., Zuckerman, B., Weintraub, D. A., & Forveille, T. 1997, Sci, 277, 67
Kenyon, S. J., & Hartmann, L. 1995, ApJS, 101, 117
King, J. R., Villarreal, A. R., Soderblom, D. R., Gulliver, A. F., & Adelman, S. J. 2003, AJ, 125, 1980
Kiss, L. L., Moór, A., Szalai, T., et al. 2011, MNRAS, 411, 117
Klimchuk, J. A. 2006, SoPh, 234, 41
Koen, C., & Eyer, L. 2002, MNRAS, 331, 45
Kraft, R. P. 1967, ApJ, 150, 551
Kuhn, J. R., Potter, D., & Parise, B. 2001, ApJL, 553, L189
Kusakabe, N., Grady, C. A., Sitko, M. L., et al. 2012, ApJ, 753, 153
Kuzuhara, M., Tamura, M., Kudo, T., et al. 2013, ApJ, 774, 11
Lafrenière, D., Doyon, R., Marois, C., et al. 2007a, ApJ, 670, 1367
Lafrenière, D., Marois, C., Doyon, R., Nadeau, D., & Artigau, É. 2007b, ApJ, 660, 770
Lagrange, A.-M., Bonnefoy, M., Chauvin, G., et al. 2010, Sci, 329, 57
Lagrange, A.-M., Gratadour, D., Chauvin, G., et al. 2009, A&A, 493, L21
Landolt, A. U. 1992, AJ, 104, 340
Lépine, S., & Bongiorno, B. 2007, AJ, 133, 889
Lépine, S., & Simon, M. 2009, AJ, 137, 3632
Looper, D. L., Bochanski, J. J., Burgasser, A. J., et al. 2010a, AJ, 140, 1486
Looper, D. L., Burgasser, A. J., Kirkpatrick, J. D., & Swift, B. J. 2007, ApJL, 669, L97
Looper, D. L., Mohanty, S., Bochanski, J. J., et al. 2010b, ApJ, 714, 45
López-Santiago, J., Montes, D., Crespo-Chacón, I., & Fernández-Figueroa, M. J. 2006, ApJ, 643, 1160
López-Santiago, J., Montes, D., Gálvez-Ortiz, M. C., et al. 2010, A&A, 514, A97
Luhman, K. L., Stauffer, J. R., & Mamajek, E. E. 2005, ApJL, 628, L69
Macintosh, B. A., Graham, J. R., Palmer, D. W., et al. 2008, Proc. SPIE, 7015, 701518
Maldonado, J., Martínez-Arnáiz, R. M., Eiroa, C., Montes, D., & Montesinos, B. 2010, A&A, 521, A12
Malo, L., Doyon, R., Lafrenière, D., et al. 2013, ApJ, 762, 88
Mamajek, E. E. 2005, ApJ, 634, 1385
Mamajek, E. E. 2012, ApJL, 754, L20
Mamajek, E. E., Bartlett, J. L., Seifahrt, A., et al. 2013, AJ, 146, 154
Mamajek, E. E., & Feigelson, E. D. 2001, in ASP Conf. Ser. 244, Young Stars Near Earth: Progress and Prospects, ed. R. Jayawardhana & T. Greene (San Francisco, CA: ASP), 104
Mamajek, E. E., & Hillenbrand, L. A. 2008, ApJ, 687, 1264
Marley, M. S., Fortney, J. J., Hubickyj, O., Bodenheimer, P., & Lissauer, J. J. 2007, ApJ, 655, 541
Marois, C., Macintosh, B., Barman, T., et al. 2008, Sci, 322, 1348
Marois, C., Zuckerman, B., Konopacky, Q. M., Macintosh, B., & Barman, T. 2010, Natur, 468, 1080
Martínez-Arnáiz, R., Maldonado, J., Montes, D., Eiroa, C., & Montesinos, B. 2010, A&A, 520, A79
Masciadri, E., Mundt, R., Henning, T., Alvarez, C., & Barrado y Navascués, D. 2005, ApJ, 625, 1004
Masuda, S., Kosugi, T., Hara, H., Tsuneta, S., & Ogawara, Y. 1994, Natur, 371, 495
Mayama, S., Hashimoto, J., Muto, T., et al. 2012, ApJL, 760, L26
McCarthy, C., & Zuckerman, B. 2004, AJ, 127, 2871
McCarthy, K., & White, R. J. 2012, AJ, 143, 134
McElwain, M. W., Brandt, T. D., Janson, M., et al. 2012, Proc. SPIE, 8446, 84469C
Mentuch, E., Brandeker, A., van Kerkwijk, M. H., Jayawardhana, R., & Hauschildt, P. H. 2008, ApJ, 689, 1127
Messina, S., Desidera, S., Tutatto, M., Lanzafame, A. C., & Guinan, E. F. 2010, A&A, 520, 15
Messina, S., Guinan, E. F., Lanza, A. F., & Ambruster, C. 1999, A&A, 347, 249
Messina, S., Rodonò, M., & Guinan, E. F. 2001, A&A, 366, 215
Mestel, L. 1968, MNRAS, 138, 359
Metchev, S. A., & Hillenbrand, L. A. 2009, ApJS, 181, 62
Minowa, Y., Hayano, Y., Oya, S., et al. 2010, Proc. SPIE, 7736, 77363N
Mishenina, T. V., Soubiran, C., Bienaymé, O., et al. 2008, A&A, 489, 923
Monnier, J. D., Che, X., Ming, Z., et al. 2012, ApJL, 761, L3
Montes, D., López-Santiago, J., Fernández-Figueroa, M. J., & Gálvez, M. C. 2001a, A&A, 379, 976
Montes, D., López-Santiago, J., Gálvez, M. C., et al. 2001b, MNRAS, 328, 45
Montes, D., & Martin, E. L. 1998, A&AS, 128, 485
Muto, T., Grady, C. A., Hashimoto, J., et al. 2012, ApJL, 748, L22
Narita, N., Kudo, T., Bergfors, C., et al. 2010, PASJ, 62, 779
Narita, N., Takahashi, Y. H., Kuzuhara, M., et al. 2012, PASJ, 64, L7
Nielsen, E. L., Liu, M. C., Wahhaj, Z., et al. 2013, ApJ, 776, 4
Nordström, B., Mayor, M., Andersen, J., et al. 2004, A&A, 418, 989
Norton, A. J., Wheatley, P. J., West, R. G., et al. 2007, A&A, 467, 785
Noyes, R. W., Hartmann, L. W., Baliunas, S. L., Duncan, D. K., & Vaughan, A. H. 1984, ApJ, 279, 763
Ofek, E. O. 2008, PASP, 120, 1128
Oppenheimer, B. R., & Hinkley, S. 2009, ARA&A, 47, 253
Ortega, V. G., de la Reza, R., Jilinski, E., & Bazzanella, B. 2002, ApJL, 575, L75
Ortega, V. G., Jilinski, E., de La Reza, R., & Bazzanella, B. 2007, MNRAS, 377, 441
Pace, G. 2013, A&A, 551, L8
Palous, J., & Hauck, B. 1986, A&A, 162, 54
Parker, E. N. 1955, ApJ, 122, 293
Parker, E. N. 1988, ApJ, 330, 474
Pecaut, M. J., & Mamajek, E. E. 2013, ApJS, 208, 9
Peters, M. A., Groff, T., Kasdin, N. J., et al. 2012, Proc. SPIE, 8446, 84467U
Pinsonneault, M. H., Kawaler, S. D., Sofia, S., & Demarque, P. 1989, ApJ, 338, 424
Pizzolato, N., Maggio, A., Micela, G., Sciortino, S., & Ventura, P. 2003, A&A, 397, 147
Proctor, R. A. 1869, RSPS, 18, 169
Reid, I. N., Cruz, K. L., Allen, P., et al. 2004, AJ, 128, 463
Reid, I. N., Hawley, S. L., & Gizis, J. E. 1995, AJ, 110, 1838
Reid, N. 2003, MNRAS, 342, 837
Rice, E. L., Faherty, J. K., & Cruz, K. L. 2010, ApJL, 715, L165
Rodriguez, D. R., Bessell, M. S., Zuckerman, B., & Kastner, J. H. 2011, ApJ, 727, 62
Rucinski, S. M., & Krautter, J. 1983, A&A, 121, 217
Sato, B., Fischer, D. A., Ida, S., et al. 2009, ApJ, 703, 671
Schlieder, J. E., Lépine, S., & Simon, M. 2010, AJ, 140, 119
Schlieder, J. E., Lépine, S., & Simon, M. 2012a, AJ, 143, 80
Schlieder, J. E., Lépine, S., & Simon, M. 2012b, AJ, 144, 109
Schmitt, J. H. M. M., Fleming, T. A., & Giampapa, M. S. 1995, ApJ, 450, 392
Schneider, A., Song, I., Melis, C., Zuckerman, B., & Bessell, M. 2012, ApJ, 757, 163
Scholz, R.-D., Meusinger, H., & Jahreiß, H. 2005, A&A, 442, 211
Schröder, C., Reiners, A., & Schmitt, J. H. M. M. 2009, A&A, 493, 1099
Sestito, P., & Randich, S. 2005, A&A, 442, 615
Shkolnik, E., Liu, M. C., & Reid, I. N. 2009, ApJ, 699, 649
Shkolnik, E. L., Anglada-Escudé, G., Liu, M. C., et al. 2012, ApJ, 758, 56
Shkolnik, E. L., Hebb, L., Liu, M. C., Reid, I. N., & Collier Cameron, A. 2010, ApJ, 716, 1522
Shkolnik, E. L., Liu, M. C., Reid, I. N., Dupuy, T., & Weinberger, A. J. 2011, ApJ, 727, 6
Skumanich, A. 1972, ApJ, 171, 565
Soderblom, D. R. 1985, AJ, 90, 2103
Soderblom, D. R. 2010, ARA&A, 48, 581
Soderblom, D. R., Hillenbrand, L. A., Jeffries, R. D., Mamajek, E. E., & Naylor, T. 2014, Protostars and Planets VI, ed. H. Beuther, R. Klessen, C. Dullemond, & Th. Henning (Tuscon, AZ: Univ. of Arizona Press)
Song, I., Zuckerman, B., & Bessell, M. S. 2003, ApJ, 599, 342
Spiegel, D. S., & Burrows, A. 2012, ApJ, 745, 174
Strassmeier, K., Washuettl, A., Granzer, T., Scheck, M., & Weber, M. 2000, A&AS, 142, 275
Strassmeier, K. G., & Fekel, F. C. 1990, A&A, 230, 389
Suzuki, R., Kudo, T., Hashimoto, J., et al. 2010, Proc. SPIE, 7735, 773530
Takeda, G., Ford, E. B., Sills, A., et al. 2007, ApJS, 168, 297
Tamura, M. 2009, in AIP Conf. Ser. 1158, Exoplanets and Disks: Their Formation and Diversity, ed. T. Usuda, M. Tamura, & M. Ishii (Melville, NY: AIP), 11
Tanii, R., Itoh, Y., Kudo, T., et al. 2012, PASJ, 64, 124
Thalmann, C., Carson, J., Janson, M., et al. 2009, ApJL, 707, L123
Thalmann, C., Grady, C. A., Goto, M., et al. 2010, ApJL, 718, L87
Thalmann, C., Janson, M., Buenzli, E., et al. 2013, ApJL, 763, L29
Thalmann, C., Janson, M., Buenzli, E., et al. 2011, ApJL, 743, L6
Torres, C. A. O., Busko, I. C., & Quast, G. R. 1983, in IAUC, Vol. 71, Activity in Red-dwarf Stars, ed. P. B. Byrne & M. Rodonò (Dordrecht: Reidel), 175

Torres, C. A. O., da Silva, L., Quast, G. R., de la Reza, R., & Jilinski, E. 2000, AJ, 120, 1410
Torres, C. A. O., Quast, G. R., da Silva, L., et al. 2006, A&A, 460, 695
Torres, C. A. O., Quast, G. R., de La Reza, R., et al. 2003, in Astrophysics and Space Science Library, Vol. 299, Open Issues in Local Star Formation, ed. J. Lépine & J. Gregorio-Hetem (Dordrecht: Kluwer), 83
Torres, C. A. O., Quast, G. R., Melo, C. H. F., & Sterzik, M. F. 2008, in Young Nearby Loose Associations, ed. B. Reipurth (San Francisco, CA: ASP), 757
Torres, G. 2010, AJ, 140, 1158
van Leeuwen, F. 2007, A&A, 474, 653
Vigan, A., Patience, J., Marois, C., et al. 2012, A&A, 544, A9
Voges, W., Aschenbach, B., Boller, T., et al. 1999, A&A, 349, 389
Voges, W., Aschenbach, B., Boller, T., et al. 2000, yCat, 9029, 0
Webb, R. A., Zuckerman, B., Platais, I., et al. 1999, ApJL, 512, L63
Weinberger, A. J., Anglada-Escudé, G., & Boss, A. P. 2013, ApJ, 762, 118
Weis, E. W. 1993, AJ, 105, 1962
White, R. J., Gabor, J. M., & Hillenbrand, L. A. 2007, AJ, 133, 2524
Wilson, O. C. 1963, ApJ, 138, 832
Wright, J. T., Marcy, G. W., Butler, R. P., & Vogt, S. S. 2004, ApJS, 152, 261
Wu, Y., Singh, H. P., Prugniel, P., Gupta, R., & Koleva, M. 2011, A&A, 525, A71
Yamamoto, K., Matsuo, T., Shibai, H., et al. 2013, PASJ, 65, 90
Yoon, J., Peterson, D. M., Kurucz, R. L., & Zagarello, R. J. 2010, ApJ, 708, 71
Zuckerman, B., Rhee, J. H., Song, I., & Bessell, M. S. 2011, ApJ, 732, 61
Zuckerman, B., & Song, I. 2004, ARA&A, 42, 685
Zuckerman, B., Song, I., & Bessell, M. S. 2004, ApJL, 613, L65
Zuckerman, B., Song, I., Bessell, M. S., & Webb, R. A. 2001a, ApJL, 562, L87
Zuckerman, B., Song, I., & Webb, R. A. 2001, ApJ, 559, 388
Zuckerman, B., Vican, L., Song, I., & Schneider, A. 2013, ApJ, 778, 5
Zuckerman, B., & Webb, R. A. 2000, ApJ, 535, 959
Zuckerman, B., Webb, R. A., Schwartz, M., & Becklin, E. E. 2001b, ApJL, 549, L233

The Astrophysical Journal, 767:11 (14pp), 2013 April 10 doi:10.1088/0004-637X/767/1/11

SIMULTANEOUS EXOPLANET CHARACTERIZATION AND DEEP WIDE-FIELD IMAGING WITH A DIFFRACTIVE PUPIL TELESCOPE

Olivier Guyon[1,2], Josh A. Eisner[1], Roger Angel[1], Neville J. Woolf[1], Eduardo A. Bendek[3], Thomas D. Milster[3], S. Mark Ammons[4], Michael Shao[5], Stuart Shaklan[5], Marie Levine[5], Bijan Nemati[5], Frantz Martinache[2], Joe Pitman[6], Robert A. Woodruff[7], and Ruslan Belikov[8]
[1] Steward Observatory, University of Arizona, Tucson, AZ 85721, USA; guyon@naoj.org
[2] National Astronomical Observatory of Japan, Subaru Telescope, Hilo, HI 96720, USA
[3] College of Optical Sciences, University of Arizona, Tucson, AZ 85721, USA
[4] Lawrence Livermore National Laboratory, Physics Division L-210, 7000 East Avenue, Livermore, CA 94550, USA
[5] Jet Propulsion Laboratory, 4800 Oak Grove Drive, Pasadena, CA 91109, USA
[6] Exploration Sciences, P.O. Box 24, Pine, CO 80470, USA
[7] Lockheed Martin, 2081 Evergreen Avenue, Boulder, CO 80304, USA
[8] NASA Ames Research Center, Moffett Field, CA 94035, USA
Received 2012 February 11; accepted 2012 August 25; published 2013 March 20

ABSTRACT

High-precision astrometry can identify exoplanets and measure their orbits and masses while coronagraphic imaging enables detailed characterization of their physical properties and atmospheric compositions through spectroscopy. In a previous paper, we showed that a diffractive pupil telescope (DPT) in space can enable sub-μas accuracy astrometric measurements from wide-field images by creating faint but sharp diffraction spikes around the bright target star. The DPT allows simultaneous astrometric measurement and coronagraphic imaging, and we discuss and quantify in this paper the scientific benefits of this combination for exoplanet science investigations: identification of exoplanets with increased sensitivity and robustness, and ability to measure planetary masses to high accuracy. We show how using both measurements to identify planets and measure their masses offers greater sensitivity and provides more reliable measurements than possible with separate missions, and therefore results in a large gain in mission efficiency. The combined measurements reliably identify potentially habitable planets in multiple systems with a few observations, while astrometry or imaging alone would require many measurements over a long time baseline. In addition, the combined measurement allows direct determination of stellar masses to percent-level accuracy, using planets as test particles. We also show that the DPT maintains the full sensitivity of the telescope for deep wide-field imaging, and is therefore compatible with simultaneous scientific observations unrelated to exoplanets. We conclude that astrometry, coronagraphy, and deep wide-field imaging can be performed simultaneously on a single telescope without significant negative impact on the performance of any of the three techniques.

Key words: astrometry – planets and satellites: detection – techniques: high angular resolution – telescopes

Online-only material: color figures

1. INTRODUCTION

Among the existing techniques for identifying exoplanets, astrometry and direct imaging are particularly well suited for identification and characterization of nearby habitable planets. Either technique can provide a full census of habitable planets around nearby (approximately $d < 10$ pc) F, G, and K main-sequence stars, provided that it achieves the required sensitivity (sub-μas single measurement precision for astrometry; 10^{-9} raw contrast at $\approx$100 mas for coronagraphy). Extensive characterization of the exoplanet does, however, require both techniques, which provide complementary information.

1. Direct imaging with a high-contrast instrument is required to acquire spectra allowing characterization of the planet's atmosphere. Direct imaging also reveals the exoplanet's environment (other planets in the system, structure of the exozodiacal cloud), and allows measurement of the planet's rotation period and weather variability through time-series photometry.
2. Astrometry[9] is a promising technique for measuring the mass of nearby exoplanets down to a fraction of an Earth mass, and this measurement is required to gain a physical understanding of the planet's surface and atmosphere. Although radial velocity (RV) measurements can also measure planet masses, their ability to reach Earth-mass planets around Sun-like stars is limited by stellar jitter (we note, however, that an Earth-mass planet in the habitable zone of a low-mass star can produce a signal that exceeds stellar jitter).

A planet's ability to retain an atmosphere and the composition of this atmosphere depend strongly on its mass. For low-mass planets, light observed by direct imaging may, for example, originate from the planet's surface, while planets with masses larger than a few Earth masses will likely retain a dense and opaque atmosphere hiding it. Meaningful interpretation of a planet's photometry and color/spectrum will therefore require prior knowledge of its mass, as colors alone can be ambiguous (see, for example, Cahoy et al. 2010).

Several astrometry (Unwin 2005; Shao et al. 2009; Malbet et al. 2011) and direct imaging concepts (Levine et al. 2009; Guyon et al. 2009; Trauger et al. 2010; Shao & Levine 2010; Clampin et al. 2006) have been proposed and studied

[9] In this paper, absolute astrometry (measurement of the absolute position of a star on the sky) is referred to as the *astrometry* measurement, while relative astrometry (measurement of the relative offset between an exoplanet and its host star, usually from a coronagraphic image) is referred to as the *coronagraphic* measurement.

for identification and characterization of nearby exoplanets, demonstrating the technical feasibility of either measurement approach. While the scientific value of both astrometry and direct imaging for characterization of exoplanets is widely recognized, either path requires a dedicated mission with its own technological challenges. Until recently, obtaining both astrometric and direct imaging measurements was assumed to require two separate missions, and simultaneous development, construction, and operation of both missions would likely be beyond available resources.

Guyon et al. (2012) recently proposed using a diffractive pupil telescope (DPT) to obtain both types of measurements simultaneously. The astrometric concept relies on simultaneous imaging of numerous background stars and diffraction spikes from the brighter target star on the same focal plane detector array. The diffraction spikes are created by a regular grid of dark spots on the telescope primary mirror. The submillimeter diameter dots cover a few percent of the primary mirror area, and in monochromatic light their regular arrangement in the pupil plane creates a regular grid of diffraction-limited spots in the focal plane. In broadband light, the spots are stretched into long thin spikes radiating from the central bright star (the target). Astrometric distortions in the imaging system (including the detector) are accurately measured by tracking the position of the spikes on the detector array, enabling high-precision astrometric calibration without requiring picometer-level stability of the telescope optics or focal plane detector array. The astrometric measurement is performed by differential position measurements of the diffraction spikes originating from the bright central star targeted for planet search, relative to field stars. Because the spikes are generated by the primary mirror, such measurements are largely immune from astrometric distortions, as they equally affect the spikes and the field stars. The unique feature of DPT is that it allows simultaneous coronagraphic imaging within a narrow-field instrument along with astrometry and general astrophysics imaging with a wide-field camera. An optical design for the DPT is shown in Figure 1 for a 1.4 m diameter telescope. This baseline configuration, adopted by Guyon et al. (2012), offers a 0.2 μas single-axis single measurement astrometric precision for a 0.3 deg^2 field of view. This precision is a steep function of the telescope diameter, and improves, to a lesser extent, with the camera's field of view.

While our first paper (Guyon et al. 2012) was focused on the technical aspects of the DPT concept and its expected astrometric precision and accuracy, in this paper we discuss and quantify its ability to identify and characterize exoplanets and perform deep wide-field observations that may not be related to exoplanet science. In Section 2, we quantify the required astrometric measurement precision for mass determination of exoplanets detectable by a coronagraph, and illustrate the scientific benefits of simultaneous coronagraphic imaging and astrometric measurement. We discuss in Section 3 the observation of planetary systems, which may consist of several planets. Finally we show in Section 4 that the DPT concept allows deep wide-field imaging at the full sensitivity offered by the telescope, and that the impact of the added diffraction spikes on wide-field imaging sensitivity is negligible, even when the telescope is pointed at a bright star during exoplanet science observations, suggesting that the telescope could also be valuable for general astrophysics purposes. Detection and mass measurement of exoplanets with astrometry alone, as was previously considered for astrometry mission concepts, is briefly discussed in the Appendix and referred to when discussing the scientific merit of the proposed technique.

2. EXOPLANET ORBITAL PARAMETERS AND MASS MEASUREMENT—SINGLE-PLANET CASE

2.1. Science Goal and Representative Example

The science goals of the astrometric measurement explored in this paper are twofold.

1. Assist the coronagraph in detecting exoplanets. At minimum, the astrometric measurement should confirm detections performed by the coronagraph and help constrain the orbital parameters of all planets identified by coronagraphic imaging. It may also uncover planets that are too close to the coronagraph's performance limits (especially the inner working angle, IWA) to be firmly identified from coronagraph images alone, even if the planet appears in at least one of the coronagraph observations.
2. Measure the mass of all planets imaged by the coronagraph in the habitable zone of nearby stars.

In this section, we quantify the astrometric measurement precision required to meet these goals. We note that the second goal is more challenging than the first one, and that the performance required can therefore be derived from the second goal (mass measurement) alone.

We assume that a 1.4 m telescope is used with a coronagraph offering a 2 λ/D IWA, following the baseline design adopted by Guyon et al. (2012), and inspired from the Pupil mapping Exoplanet Coronagraph Observer mission concept (Guyon et al. 2010). We consider that the number and duration of observations is driven by the coronagraph instrument's goal to identify and acquire spectra of potentially habitable planets around a few high-priority targets: each observation is 48 hr long, and each high-priority target is observed approximately every two months. The expected astrometric precision of this system has been described in Guyon et al. (2012), and was found to be 0.2 μas per axis per measurement for a 0.3 deg^2 field of view camera. We note that the astrometric precision is independent of the coronagraph instrument design and performance, as it is achieved with an optical path which is separate from the coronagraph instrument.

The relative mass estimation precision achieved for a fixed instrument design is a function of the planet type, stellar brightness (bright stars are easier, as their spikes are brighter in the astrometric camera), and star distance (the astrometric signal is smaller for more distant stars). We choose to adopt a Sun analog at 6 pc from Earth as a representative example of a challenging target for detection of an Earth-like planet with the coronagraph. The star apparent magnitude is $m_V = 3.7$. We choose to place an Earth-mass planet at 1.2 AU around this star with a 1.3 rad inclination, therefore avoiding complications associated with the 1 yr period blind spot in the astrometric measurement. We use this example, for which the planetary system characteristics are listed in the top part of Table 1, to quantify the relationship between astrometric measurement precision and mass estimation precision.

2.2. Planet Mass Measurement

In this section, we describe a simple model of simultaneous observation of the system by the coronagraph and the

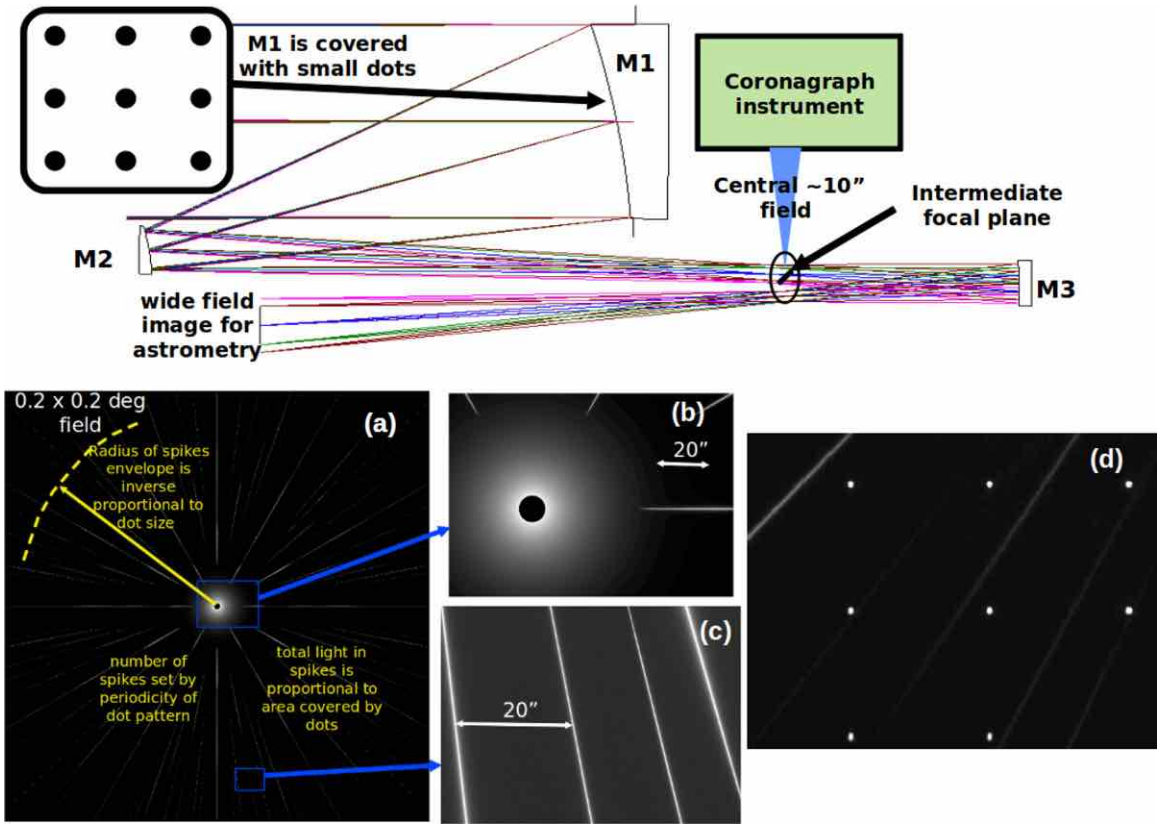

Figure 1. Conceptual optical design for the diffractive pupil telescope (DTP) proposed by Guyon et al. (2012). The top part of this figure shows how light is shared between two instruments. The central field containing the bright star and its immediate surroundings is extracted at the telescope's intermediate focus and fed to a coronagraph instrument for high-contrast imaging. The wide well-corrected outer field is imaged onto a large focal plane detector array. Panels (a)–(d) show details of the wide-field image acquired in the final focal plane. (a) The wide-field image shows the diffraction spikes introduced by the dots on the primary mirror. (b) The central part of the target image, containing most of the flux, is missing from the wide-field image as it has been directed to the coronagraph instrument. (c) Faint diffraction spikes pave the rest of the field. (d) Faint background stars are imaged simultaneously with the diffraction spikes. While images (a)–(c) are simulated, image (d) was acquired in a laboratory demonstration of the technique (Bendek et al. 2011).

(A color version of this figure is available in the online journal.)

Table 1
Observation Model

Parameter	Value
Planetary system characteristics	
Star	Sun analog
Distance	6 pc
Location	Ecliptic pole
Orbit semimajor axis	1.2 AU
Orbital period	1.3 yr
Planet mass	1 Earth mass
Orbit inclination	1.3 rad
Orbit eccentricity	0.2
Astrometric signal amplitude	0.5 μas
Orbit apparent semimajor axis	200 mas
Measurements	
Number of observations	32 (regularly spaced every 57 days)
Coronagraphic image: planet position precision	2.5 mas per axis (=3.6 mas in 2D)[a]
Coronagraphic image: inner working angle (IWA)	130 mas
Astrometry: single measurement precision	Variable (driven by science requirement)

Notes. [a] Corresponds to an S/N = 10 detection with $\lambda/D = 80$ mas (single-axis astrometric precision is theoretically equal to $(\lambda/D)/(\pi\sqrt{N_{\rm ph}})$). For a photon-noise-limited measurement with no background, this would be achieved with $N_{\rm ph} = 100$ photons at 550 nm for a 1.4 m telescope.

astrometric camera. We then use the model to estimate the astrometric precision required to achieve the science goals outlined in the previous section.

Measured quantities. The planet orbit and mass are measured by combining the simulated astrometric and coronagraphic data. Coronagraphic and astrometric observations are assumed to be simultaneous. For N epochs, the total set of measurements consists of $4N$ values: $2N$ absolute astrometric measurements and $2N$ relative planet to star astrometric measurements derived from the coronagraphic images. Unless otherwise noted, simulations for this paper use a total number of 32 epochs, regularly spaced every 57 days to span a total of 5 yr. With each observation assumed to be 2 days long, 28 targets could be observed at this cadence.

Planet image position measurements from coronagraphic images. We assume that each coronagraph observation yields the apparent position of the planet relative to the star with a 2.5 mas 1σ precision per axis, provided that the planet is outside the inner working of the coronagraph (assumed to be 130 mas). The assumed 2.5 mas 1σ precision per axis is equal to $1/30$ λ/D at $\lambda = 500$ nm, and would be achieved with a signal-to-noise ratio (S/N)=10 detection, or, in the photon-noise limit without background, with approximately 100 photons. While in a 2 day exposure, the number of photons collected from the planet is larger than 100, other sources of error will limit the measurement accuracy, such as centering error of the star on the coronagraph mask, and effect of uncorrected stellar speckles on the planet photocenter estimation. We have somewhat arbitrarily adopted $1/30$ λ/D as the single-axis measurement precision in this study, noting that a more detailed evaluation would be required to establish this measurement precision with high confidence. We note that centering errors in the coronagraph can be calibrated by introducing faint ghosts of the central star, as proposed by Sivaramakrishnan & Oppenheimer (2006) and Marois et al. (2006), and such a scheme is likely to be required to reach the $1/30$ λ/D accuracy assumed here. If the planet is within the coronagraph mask, the position measurement error is increased to the size of the focal plane mask, essentially removing the contribution of this measurement from the overall solution. The apparent position of the planet on the sky is shown in Figure 2 for each of the 32 observations. The planet can only be seen by the coronagraph for 17 out of the 32 observations, as it is located within the coronagraph's IWA for 15 of the observations.

Known variables. The following three parameters are assumed to be known.

1. *Star apparent location on the sky (two variables).* The parallax motion is therefore perfectly known if the star distance is known, and the aberration of light is therefore assumed to be perfectly known as it is only a function of source position on the sky
2. *Average radial velocity.* The perspective acceleration effect produced by the relative radial motion of the star is therefore assumed to be known, and is not included in our simulations. For a star at 6 pc with a 20 km s^{-1} velocity, the perspective acceleration ranges from 0 to 0.2 mas yr^{-2} depending on the perspective angle (angle between three-dimensional velocity motion of the target and observer), and is maximum for a 45° perspective angle. If unknown, perspective acceleration will only affect the detection of planets with periods longer than the observation time span, for which there is a degeneracy between the perspective acceleration and the exoplanet astrometric signature. For planets with orbital periods comparable to or less than the observation time span, the constant astrometric acceleration term is not strongly coupled with the planet signal, and can be included as a free parameter to the astrometric data fit with little impact on planet detection and characterization performance. The degeneracy described above may be solved with RV measurements of the host star to directly measure the three-dimensional velocity and thus calibrate the perspective acceleration. With a 1 m s^{-1} RV measurement accuracy and proper motion measurement obtained by astrometry with a 0.02 μas yr^{-2} accuracy as shown in Table 2, analytical derivations show that the error on the perspective acceleration is 0.02 μas yr^{-2} (this error is maximum when the perspective angle is close to 90°, corresponding to a near zero RV). Over a 5 yr mission duration, the cumulative error around the mid-point observation reaches 0.06 μas at the beginning and end points of the observation series, and is therefore comparable to the astrometric accuracy assumed in this paper. An RV estimate with poorer accuracy is not very useful, as the perspective acceleration is then better constrained by astrometry measurements alone. In this work, we do not take perspective acceleration into account in the global fit, implicitly assuming that (1) stellar RV is known to within 1 m s^{-1} or (2) the observation time span is comparable to or larger than the planet orbital period. Astrometric recovery of long-period planets (which is not the focus of this paper) would require a more careful treatment of perspective acceleration, and may be challenging as these planets are unlikely to be visible in coronagraphic images (reflected light decreases rapidly with orbital radius).

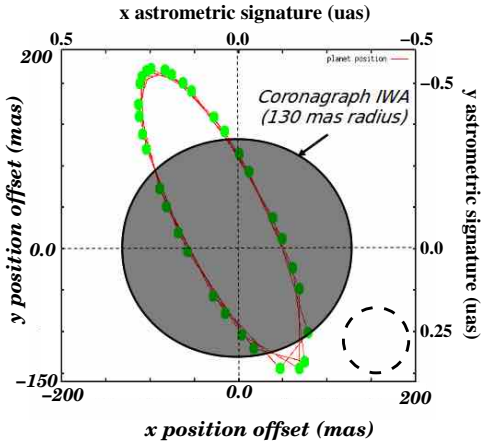

Figure 2. Coronagraphic (relative astrometric position of the planet referenced to the star) and astrometric (position of the star referenced to the sky) signatures are opposite in sign and of very different amplitude. The scale for the coronagraphic measurement is shown in the bottom and left while the scale for the astrometric measurement is shown at the top and right. The dark shaded disk shows the zone within which the planet cannot be seen by the coronagraph. The dashed circle diameter is the one-dimensional standard deviation of a single astrometric measurement (0.2 μas). The standard deviation of the coronagraph measurement (2.5 mas) is about half the size of the small green dots showing the planet position along its orbit.

(A color version of this figure is available in the online journal.)

In addition, it is assumed that observing epochs and standard deviation of all measurements (for both astrometry and coronagraphy) are known.

Stellar mass. We assume that stellar mass is known to a 5% 1σ accuracy prior to the observations, but we also treat it as a

Table 2
Uncertainties in the Combined (Astrometry and Coronagraphy) and Separate (Astrometry or Coronagraphy) Solutions[a]

Parameter	1σ uncertainty		
	Astrometry Only	Astrometry +Coronagraphy	Coronagraphy Only[b]
Parallax	0.037 μas	0.035 μas	2.949 μas
x proper motion	0.017 μas yr^{-1}	0.012 μas yr^{-1}	1.304 μas yr^{-1}
y proper motion	0.020 μas yr^{-1}	0.013 μas yr^{-1}	1.288 μas yr^{-1}
Planet mass	0.132 $M_{\rm Earth}$	0.098 $M_{\rm Earth}$	5.355 $M_{\rm Earth}$
Semimajor axis (SMA)	0.0228 AU	0.0052 AU	0.0047 AU
Orbital phase	0.653 rad	0.039 rad	0.039 rad
Orbit inclination	0.0968 rad	0.0065 rad	0.0060 rad
Position angle of SMA on sky	0.111 rad	0.0040 rad	0.0039 rad
Orbit ellipticity	0.098	0.0035	0.0034
Position angle of perihelion	0.648 rad	0.0034 rad	0.0033 rad
Stellar mass[c]	0.05 $M_{\rm Sun}$	0.013 $M_{\rm Sun}$	0.012 $M_{\rm Sun}$

Notes.
[a] Assumed measurement precisions: 0.2 μas per axis per measurement for absolute astrometry; 2.5 mas per axis per measurement for relative astrometry derived from coronagraphic images.
[b] Assumes that astrometry is available at the 20 μas per axis per observation from another mission to constrain parallax. Astrometric measurement at this precision level ($\gg \mu$as) only affects estimates of parallax and proper motion, and has no significant effect on other measured parameters.
[c] Assumed to be known to 5% accuracy independently of astrometry and coronagraphy measurements

parameter to be solved for. This is done in our model by treating stellar mass as a free parameter and adding, separately from astrometric and coronagraphic measurement, a single simulated stellar mass measurement with a 5% 1σ accuracy.

Correlation between measurements, systematic errors. We assume that all measurement errors are uncorrelated and all measurements are free of systematic errors. The validity of this assumption for the astrometric measurements is discussed in our previous publication on the DPT concept (Guyon et al. 2012), and based on the fact that the astrometric measurement is inherently differential. Existing performance estimates reflect our current assessment that dominant error sources in this system will be random, and that concurrent errors occurring in the different astrometric and coronagraphic fields of view will be primarily uncorrelated. However, we have begun to expand this assessment using detailed modeling and simulation, supported by lab testing, to characterize key error sources and quantify allocations of those errors in a comprehensive system error budget. We are particularly careful to identify any systemic error sources affecting the entire observational system, as well as the degree of correlation possible between errors both within our coronagraph and between our two concurrent observations.

Free parameters to be solved for. A planetary model is constructed and linked to the observed quantities. The model is defined by 11 free parameters: central star distance (one variable), proper motion (two variables), and mass (one variable), planet mass (one variable), and orbital parameters (six variables). The values of the 11 free parameters are derived from the maximum likelihood solution given the noisy measurements listed above.

Uncertainties for all 11 free parameters are determined using a Monte Carlo (MC) approach. For the single-planet case explored here, a total of 1000 simulations was used. Each data set is generated assuming a normal distribution, centered on the perfect solution, with standard deviation equal to the respective uncertainties of coronagraphy and astrometry.

2.3. Single-observation Astrometric Precision Required to Meet Science Goals

To estimate the astrometric measurement precision required to meet science requirements, simultaneous coronagraphic and astrometric measurements were simulated and fitted according to the scheme described in Section 2.2. For each simulation, the single astrometric measurement precision was chosen in the range between 0 (perfect astrometry) and 0.8 μas while the coronagraphic performance (both IWA and precision of the planet image position measurement) were kept constant. Figure 3 shows how the planet mass estimate changes as a function of the level of astrometric error per measurement, and shows that a 10% relative precision in the estimate of the Earth-mass planet requires a 0.2 μas precision per astrometric measurement.

The figure also shows that the mass estimate derived from the combined astrometry and coronagraphy measurements is more accurate than can be obtained from the astrometric measurements only. The difference between astrometry alone and astrometry + coronagraphy is especially significant when a high-precision mass measurement is to be obtained (left part of Figure 3), as inferring the planet's mass from astrometry alone is then constrained by uncertainties in the stellar mass, assumed to be at the 5% level in this example. In this regime, improving the astrometric precision below 0.1 μas does not significantly improve the planet mass measurement. With both astrometry and coronagraphy, the stellar mass is also measured, and high-precision planet mass measurement is possible. When the astrometric precision is relatively poor (right part of the figure) the astrometry+coronagraphy measurements yield a planet mass estimate standard deviation that is approximately half as large as would be obtained with astrometry alone. For example, with a 0.8 μas precision per measurement, the planet mass is still constrained $\pm 0.35\, M_{\rm Earth}$ with the combined measurements, while astrometry-only measurements would not be sufficient to unambiguously detect the planet and estimate its mass. The astrometry-only points in the figure are consistent with the findings of the double blind study summarized in the Appendix: for the 0.8 μas precision per astrometric measurement, the mission astrometric S/N is ≈ 4.5, insufficient (mission S/N $<$ 6) to unambiguously detect the Earth-like planet. This difference in mass measurement precision, due to the propagation of orbital parameter errors of the mass estimate, is described in the next section. Interestingly, the relative difference in planet mass error between the two scenarios is the smallest when the single-measurement astrometric precision is around 0.2 μas, which is the case considered in this paper for numerical evaluations.

Figure 4 shows how the precision on the planet mass and semimajor axis (SMA) varies as a function of both the relative and absolute astrometry measurement precisions. While the precision of the planet mass estimation (left) is mostly a function of absolute astrometry measurement precision, the precision of the planet's SMA estimate is mainly a function of relative astrometric precision. In both cases, however, both measurements participate in the parameter estimation. This figure illustrates the complementarity between the two measurements.

2.4. How Coronagraphic Imaging Helps Astrometry to Measure Planet Mass

While coronagraphic images (providing relative astrometry between the star and the plan) alone do not constrain planet

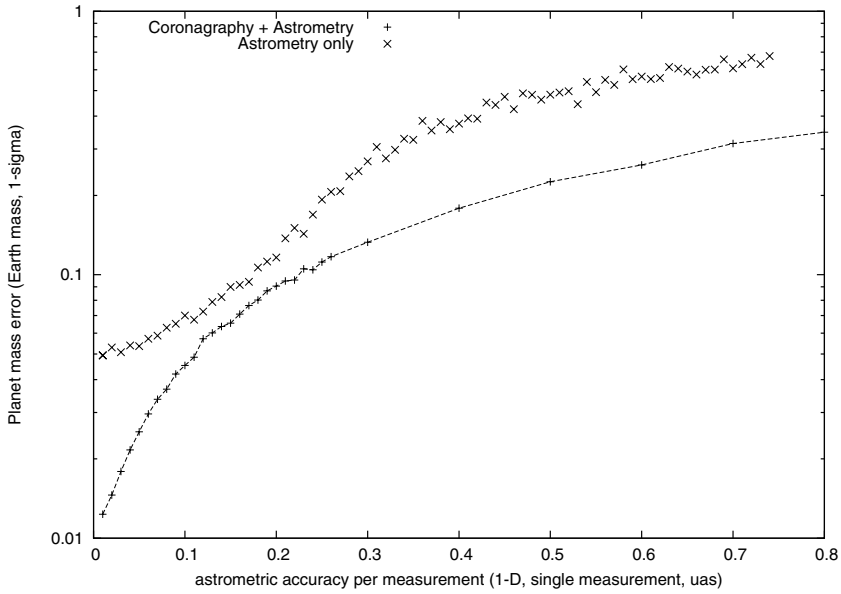

Figure 3. Error on planet mass measurement as a function of single-measurement astrometric precision. The lower curve and points show the planet mass measurement precision when both coronagraphic and astrometric data are used to constrain the solution. When only astrometric data are used, the mass measurement is less accurate. Each point in this figure shows the standard deviation of a set of 1000 solutions, each computed from an independent set of simulated data.

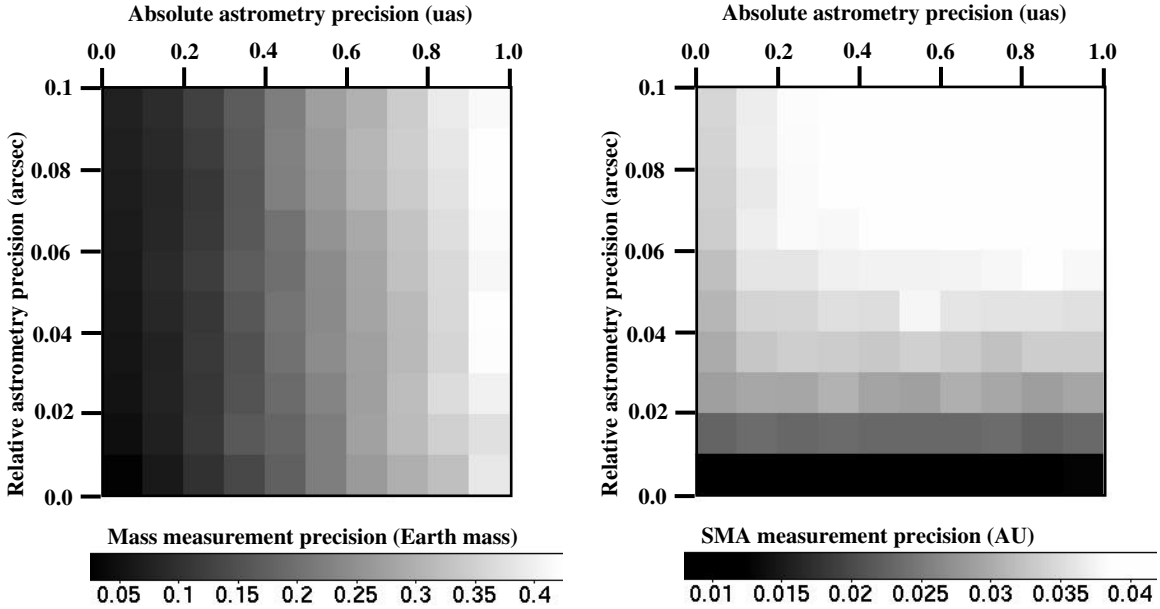

Figure 4. Error on planet mass measurement (left) and planet orbit semimajor axis (right) as a function of single-measurement relative (vertical axis) and absolute (horizontal axis) astrometric precision. The maps contain white noise due to the finite number of simulated measurements used to produce the figure.

mass, they constrain the values for the orbital parameters much more precisely than possible with absolute astrometric measurements alone. The relative astrometric signal given by the direct image has a large S/N advantage over absolute astrometry: for a 1 $M_{\rm Earth}$ planet on a 200 mas radius orbit, the assumed 2.5 mas uncertainty corresponds to 1/80th of the orbit radius. Constraining the orbital separation to the same level with astrometry alone would require a 0.006 μas astrometric precision (1/80th of the matching astrometric amplitude).

Solving for planet mass using the combined astrometry and coronagraphy measurements is therefore very powerful, and allows more accurate mass determination than would be possible with astrometry alone.

1. The coronagraphic images constrain the orbital parameters and reduce error propagation from orbital parameter to mass estimate. For instance, Torres (1999) demonstrates how even a single direct image (providing an instant measurement of the projected orbital separation) dramatically improves the constraint on the companion mass in binary systems for which only partial astrometric measurements are available.
2. With both coronagraphic imaging and astrometry, both the stellar and planet masses are directly measured. Relative astrometry provides the total mass, while the absolute astrometric signal is driven by the mass ratio: both are required for accurate measurement of the planet's mass.

The 1σ uncertainty for all parameters of the fit is shown in Table 2, for three cases: astrometric measurement only, combined astrometric and coronagraphic measurements, and coronagraphic measurement alone (assuming a lower precision

astrometric measurement is available to constrain the parallax). Adding coronagraphic images to the astrometric data reduces the standard deviation on orbital parameters by approximately a factor 10. The stellar mass is also directly measured, while with astrometry only, it is assumed to be known with a 5% standard deviation. The planet mass is estimated with a standard deviation below 0.1 $M_{\rm Earth}$ with the combined data, while it would be 35% larger with astrometry only. Table 2 shows that the uncertainties in planet orbit geometry and stellar mass are identical (to the numerical accuracy of our test) in the astrometry+coronagraphy and coronagraphy only cases, illustrating that these parameters are mostly constrained by the coronagraphic imaging data.

2.5. Improving Mass Measurement Precision for Planets with a Nearly 1 yr Period

The astrometric signature of a planet in a 1 yr period orbit can be partially absorbed in the parallax fitting of the astrometry measurements. With astrometric measurements only, the mass estimate error therefore grows as the planet's period becomes closer to 1 yr for particular orbit geometries. The problem is fundamentally that with finite S/N, the two signatures (parallax motion and planet orbital motion) cannot be separated if their frequencies are close. The width of this blind spot is thus reduced as the astrometric measurements span a longer period, corresponding to a better resolution in the frequency domain. For a 5 yr mission duration, the astrometric blind spot covers approximately 5% of the habitable zone, so the detection rate is still good (approximately 95%) but is not 100%. The relative astrometry obtained from the coronagraphic images is not affected by parallax motion, and therefore yields an estimate of the orbital parameters that does not have any ambiguity with parallax motion. With coronagraphic and astrometric data, the blind spot is therefore greatly reduced in size (although still not completely eliminated, as planet mass is still ambiguous if the planet orbit and phase matches the parallax motion exactly), especially for a short-duration mission. This benefit is critical for a combined astrometry + coronagraphy mission as confirmation that a planet is of sufficiently low mass to be potentially habitable needs to occur sufficiently early to allow allocation of significant coronagraphic follow-up time (for spectroscopy and time monitoring).

To illustrate how coronagraphic images mitigate the astrometric blind spot problem, we consider an Earth-mass planet at 1.01 AU from a Sun-mass star (period = 1.015 yr) at the ecliptic pole, orbiting a star at 6 pc. We assume circular orbits for both the Earth and the target planet, and a planet orbit phase equal to Earth orbit phase plus 1 rad, with a face-on orbit. This particularly unfavorable configuration is used as an example to illustrate the blind spot mitigation thanks to coronagraphy, but is not a representative case of a habitable planet. The system is observed 32 times over 5 yr with observations regularly spaced in time. To demonstrate the robustness of the combined solution, we assume here measurement precisions that are poorer than in the previous section: standard deviation of 0.3 μas and 5 mas per measurement per axis for respectively astrometry and coronagraphy (instead of 0.2 μm and 2.5 mas, respectively). With only the astrometry measurements, the model described above yields a mass estimate with a standard deviation of 4.17 $M_{\rm Earth}$: the planet is not detected. With both the astrometric and coronagraphic imaging, the planet mass is estimated with a standard deviation of 0.16 $M_{\rm Earth}$.

2.6. Discussion

We have so far evaluated the scientific value of combining astrometry and coronagraphy by considering a single example (5 yr observation of an Earth-like planet around a Sun-like star), and we now briefly discuss the applicability of the results presented in this section to other observation scenarios. While the orbit geometry (viewing angle, orbit eccentricity) are not expected to significantly impact detection sensitivity, the planet location (semimajor axis), planet and stellar masses, system distance and observation time span must be considered to generalize the findings presented so far.

The astrometric measurement is most sensitive to outer planets (the signal grows linearly with planet separation and planet mass) provided that the observation time span is not significantly shorter than the orbital period. The coronagraphic observations are most sensitive to inner planets (reflected light signal proportional to the inverse square of planet separation) provided that the separation is larger than the coronagraph's IWA, and the measurement sensitivity is only weakly function of planet mass (the reflected light is proportional to the planet's squared radius, which goes as the one-third power of mass for low-mass planets, and increases less rapidly with mass for larger planets). The example considered in this section shows that combined astrometric + coronagraphic measurement can identify inner planets near the coronagraph's IWA and measure their mass to approximately 0.1 Earth-mass accuracy. As the planet is moved outward, the astrometric sensitivity increases, allowing mass estimation to a $\approx$0.12/SMA Earth mass, where SMA is the orbit semimajor axis in AU. At a few AUs separation at most, however, the planet becomes too faint to be imaged, regardless of its mass. The optimal mission duration is therefore close to the period of the outermost planets that can be imaged with the coronagraph, and there is little benefit in extending the mission duration further.

Both astrometry and coronagraphy are more sensitive to potentially habitable planets as the stellar mass is reduced (stronger astrometric signal, shorter period, and more favorable reflected light contrast). The reduced planet's angular separation, however, becomes challenging for the coronagraph, and the performance of the combined measurement scheme becomes driven by the coronagraph's IWA.

As the system's distance to Earth is increased, both the astrometry and coronagraphic imaging signals become weaker, but this effect is much steeper for the coronagraphic imaging than for the astrometric measurement. The relative astrometric position derived from images suffers from the combined effects of smaller flux (planet flux scales as the inverse square of distance) and the angular resolution in absolute unit (scales linearly with distance). The planet is also more likely to fall within the coronagraph's IWA, and the relative contribution of zodiacal and exozodiacal backgrounds increases

3. BENEFIT OF COMBINING ASTROMETRY AND DIRECT IMAGING FOR CHARACTERIZATION OF PLANETARY SYSTEMS

3.1. Enhancement of Spectral Characterization Efficiency with Astrometry

The benefits of astrometry for an exoplanet characterization mission have been previously studied under the assumption that an astrometric measurement would occur prior to a direct

imaging mission (Shao et al. 2010; Davidson 2011; Savransky et al. 2009), and are twofold.

1. First, astrometric measurements would reveal the existence of planets and measure their masses, and therefore identify scientifically valuable targets for a future direct imaging mission aimed at acquiring spectra.
2. Second, the orbital parameters derived from the astrometric observations could allow optimal timing of the direct imaging observations when the planet is near maximum elongation. Telescope time can therefore be used more efficiently, as an imaging-only mission can be relatively inefficient at finding planets, as quantified by Brown (2005).

Shao et al. (2010) show that an astrometric precursor mission can reduce the coronagraphic observation time by a factor of 2–5 thanks to these two advantages. The last advantage (ability to optimally time direct imaging observations) is largely lost, however, if several years separate the two missions, as the propagation of orbital parameter errors over a long time span does not allow reliable prediction of the planet's apparent position.

The first advantage (identification of scientifically interesting targets) is immune to error propagation of orbital parameters, and would allow considerable time saving, as the direct imaging mission would spend less time searching for planets and more time characterizing them. A direct imaging mission alone is not efficient for identifying planets that spend a small fraction of their time outside the coronagraph's IWA, and the planet yield may be relatively small in that case. This is an unfortunate situation, as for most habitable planets the angular separation will statistically be close to the coronagraph's IWA. An imaging-only mission aimed at characterizing potentially habitable planets may also devote a significant fraction of time to acquiring spectra of planets outside the mass range suitable for habitability, as apparent brightness is a poor proxy for mass. With prior astrometric measurements, these risks are mitigated, and only a few direct imaging observations are required to recover the phase of the planet. Reconnecting the astrometric measurements with the direct imaging detection then allows accurate derivation of the orbital parameters if the time span between the measurements is large.

In this paper, we propose performing the astrometric and direct imaging measurement simultaneously, so we must reconsider the benefit of astrometry for improving the mission efficiency. Assuming a fixed mission duration, identification of high-priority targets must be performed rapidly in order to allow sufficient time in the second part of the mission for extended characterization. An optimal observing strategy for a multi-year mission would be to first perform high-cadence, short-duration observations to identify potentially habitable planets, followed by several years of follow-up in order to characterize the planet(s) through at least one full orbital period. Rapid identification of planets is especially challenging in multiple planet systems due to confusion between the astrometric signatures. In the following subsection, we use simulated observations of a multiple planet system to test how rapidly high-priority targets could be identified.

3.2. Multiple Planets

We have simulated observations of a planetary system consisting of three planets around a Sun-like star at 6 pc. The mass, SMA, and orbital period for each of the planets are given in Table 3.

Table 3
Multiple Planet System Characteristics

Planet	Mass ($M_{\rm Earth}$)	SMA (AU)	Period (yr)	Inclination (sin(i))
Planet 1	1.0	1.2	1.31	0.25
Planet 2	4.0	1.8	2.41	0.25
Planet 3	16.0	2.4	3.72	0.25

Telescope and instrument design are identical to what was used in the previous simulations. Following the precision requirement defined in Section 2, we assume a 0.2 μas uncertainty per astrometric measurement per axis.

The goal of this section is to evaluate the combined measurement's scientific value when observing a realistic planetary system. We therefore include several planets (three planets). While the astrometric precision is independent of the planetary system complexity, the relative astrometric measurement derived from coronagraphic images will be affected by confusion issues (such as the potential inability to link planets to their images for widely separated observations, relative astrometric error due to an unknown planet affecting the planet image photocenter measurement, and spatial structure in the exozodiacal cloud). For simplicity, we have chosen to not include these effects in our model, but to arbitrarily account for them by adopting a poorer relative astrometry precision. The relative astrometry measurement precision is thus assumed to be 0.0088 arcsec (one-tenth of the diffraction limit at λ = 550 nm) per axis per measurement for each of the three planets, provided that the planet image is outside the coronagraph's IWA.

To illustrate the complementarity of astrometric and coronagraphic measurements, and the value of performing both measurements, we have simulated two different mission scenarios.

1. *Astrometric mission*. One observation is performed every month, with a 0.2 μas precision per axis.
2. *Astrometry + coronagraphy mission*. Every two months, an astrometric measurement at the 0.2 μas precision per axis is performed simultaneously with a coronagraphic observation. The planet positions are measured to 0.0088 arcsec precision per axis only when outside the coronagraph's IWA.

A number of simplifications to the observing model have been used for the simulations.

1. The orbits are assumed to be circular and coplanar. This leaves a total of 12 free parameters: mass, SMA, and orbital phase for each of the three planets, in addition to the stellar mass, its distance, and the common orbital plane inclination.
2. The planets are assumed to be recognizable in the coronagraphic images: provided that a planet is seen outside the coronagraph's IWA, it is assumed that it cannot be confused with other planets (this would be the case if each planet had recognizable colors).
3. The planets are detected in the coronagraphic images if and only if they are outside the coronagraph's IWA, and the precision of the planet's measured image position is independent of its location in the image or phase. In reality, the measured planet position would gradually become more uncertain as it is closer to the coronagraph's IWA, and contrast/sensitivity limits would prevent its detection in coronagraphic images when the illumination fraction is

small. This assumption leads to an underestimate of the required number of observation epochs.

We use again an MC approach to determine how each mission scenario would perform on the simulated three-planet system. A total of 200 MC simulations were conducted in each case, using a normal distribution to produce each noisy data set. For each of the 200 MC simulations, a random initial solution is chosen with three planets as a starting point for a χ^2 minima search, with initial masses randomly chosen in the $0.5\,M_i$–$1.5\,M_i$ range, where M_i is the true mass of planet i, and with initial SMA randomly chosen in the $0.5\,SMA_i$–$2.5\,SMA_i$ range, where SMA_i is the true SMA for planet i. Similarly, the initial orbital phase is randomly chosen within 1 rad of the true orbital phase. The sine of the planetary system inclination $\sin incl$ is randomly chosen with uniform probability distribution between 0 and 1. This choice of initial conditions ensures that the search for the optimal solution is allowed to find minima outside the true solution of they exist. A simulated annealing is used to find the solution with the smallest χ^2, with 5e6 iterations. The estimated values for the 12 free parameters are derived from this maximum likelihood solution.

Results of this simulation are shown in Figures 5 and 6 for the astrometry-only and astrometry+coronagraphy mission scenarios. Measurements and solutions are shown for variable mission durations, and solutions are shown in the two-dimensional SMA versus planet mass space.

3.3. Results

Figure 5 shows how well the planetary system characteristics are estimated for the astrometric mission, assuming a total mission duration ranging from 1 yr (top) to 4 yr (bottom). With a 1 yr mission, none of the planets is unambiguously detected, and the measurements only show the existence of at least one planet with an orbital period exceeding the mission duration. With a 2 yr mission duration, the astrometric data can exclude the presence of massive planets at small angular separation: no solution places a planet of more than 10 Earth masses within the central 1.5 AU. With a 4 yr long mission, the three planets are identified, but their masses and SMAs are poorly constrained (relative errors are approximately 10% for the SMA and 30% for the mass). There is some confusion between planets 1 and 2, and a correlated error between the mass and SMA for each of the planets. These results show that identification of the potentially habitable inner planet in this case requires about 4 yr.

Figure 6 shows how well the planets' masses and SMAs are constrained for combined coronagraphy + astrometry missions with 1 yr, 2 yr, and 4 yr durations. After only 1 yr, the three planets are clearly identified, even if for the two inner planets, there is no strictly positive lower limit to the planet mass (detection is then confirmed by the coronagraphic images). The inner planet is unambiguously identified as a low-mass ($< 5\,M_{\rm Earth}$) planet in the star's habitable zone. The simulation therefore demonstrates that a 1 yr mission duration (with measurements at only six epochs) is sufficient to identify high-priority targets for follow-up. If only astrometric measurements were used, it would take approximately 4 yr to reach the same conclusion. This figure also shows that the outer planet's mass is relatively well constrained even though it has only covered about one quarter of its orbit. With a 2 yr mission duration, the relative errors in the masses and SMA estimates are better than what is obtained in the astrometry only mission in 4 yr.

3.4. Discussion

Results shown in Figure 6 demonstrate that a combined astrometry + coronagraphy mission can be deployed with no a priori knowledge of the target locations, and quickly (in 1–2 yr) identify potentially habitable planets. This is a significant advantage over the astrometry only case for which, as described in the Appendix, proper identification of planets requires that all planets of the system are either identified by RV or cover >80% of their orbit during the measurement span. This fast identification would allow the first phase of the an imaging mission + astrometry mission to perform high-cadence observations of a large number of targets, while the second phase of the mission could focus on acquiring high-quality spectra and astrometry of the low-mass planets identified in the habitable zone of the sample stars.

Figure 6 illustrates that a key advantage of the combined measurement, beyond the improvement in mass and orbital parameters estimations, is the very low probability of obtaining a false solution when solving for the orbital elements and masses of multiple planets. With astrometry alone (Figure 5) or combined RV and astrometry measurements (see the Appendix), the probability of obtaining false solutions is non-negligible and rapidly increases as the measurement S/N or number of measurements decrease. The combined astrometry and coronagraphy measurement is very robust against such errors even for low astrometry S/N. This good performance in determining the masses and orbits of planets in multiple systems is particularly relevant in light of recent *Kepler Space Telescope* results. Lissauer et al. (2011) find that 408 of the 1200 recently released *Kepler* candidate planets are in multiple transiting systems. Given that the orbits of planets in these systems must be co-aligned to $\approx 1^\circ$ to be detected by *Kepler*, this suggests that all or nearly all planets may be in multiple systems if the orbital inclinations of planets are aligned to only $\approx 10^\circ$ in each system.

While the planets chosen for this example are expected to have similar reflected light contrasts (the increased planet mass as a function of angular separation results in roughly constant surface area divided by squared SMA), the astrometric signal is dominated by the outer planet (32 times stronger signal than the inner planet). The results presented in this section thus indicate that the relatively small astrometric signature of a habitable planet can be reliably separated from the much stronger signal of outer planets. The ability to identify and measure the mass of planets as a function of planet mass and separation is expected to follow the trends discussed in Section 2.6: at the small separations, the coronagraph's IWA limits sensitivity, while the coronagraph contrast, and possibly mission duration, limit sensitivity for outer planets. With multiple planets, confusion between planets may also become an issue, and could be especially serious for a system viewed edge-on, for which the number of independent measurements is essentially halved. Planet colors and brightness as a function of illumination phase (ignored in this paper) would then need to be taken into account to help identify individual planets. We note that the proposed astrometry + coronagraphy measurement scheme is, however, well suited to this challenging configuration, compared to a much more degenerate astrometry only measurement scheme.

We note that our simulations do not assume availability of RV measurements, which have been shown to greatly mitigate confusion issues for an astrometry-only mission (see the Appendix). RV measurements are also expected to be valuable for an astrometry + coronagraphy mission, as massive

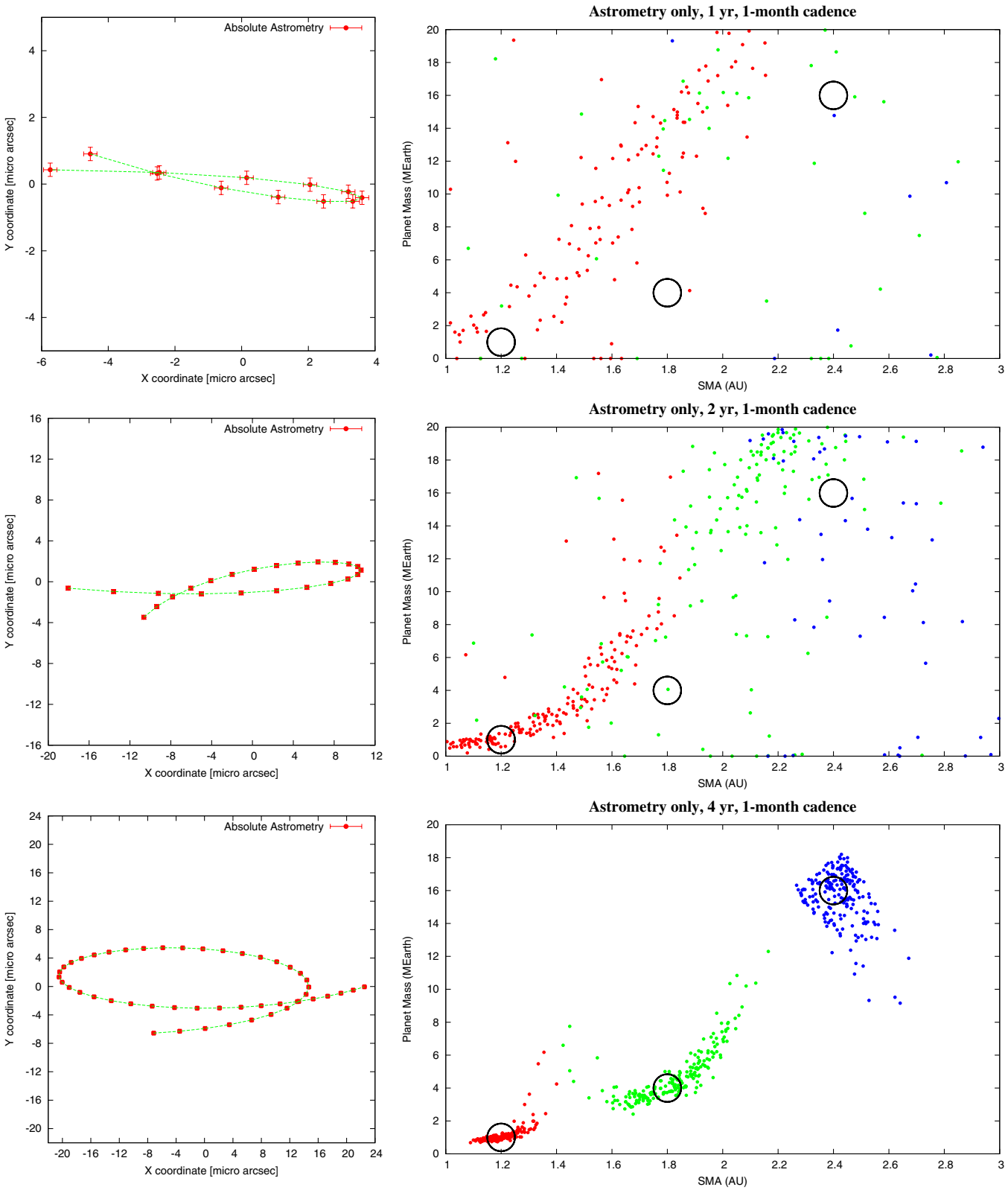

Figure 5. Result of the astrometry mission scenario, observing a three-planet system around a Sun-like star at 6 pc. Values to be measured are shown on the left with measurement error bars (1σ). Two hundred realizations of the observations are simulated, and the best three-planet solution is shown on the right for each simulation in the semimajor axis–mass plane. Total mission duration is increased from top to bottom, from 1 yr to 4 yr. The three dark circles indicate the actual configuration for the three-planet system. The initial starting point is the same for all scenarios: the first six absolute astrometry values are identical in all cases. However, the astrometric values shown in the left panel are corrected for uniform drift (proper motion) during the measurement period, resulting in different shapes and amplitude for the part of the astrometry trajectory curves common to all scenarios (first year).

(A color version of this figure is available in the online journal.)

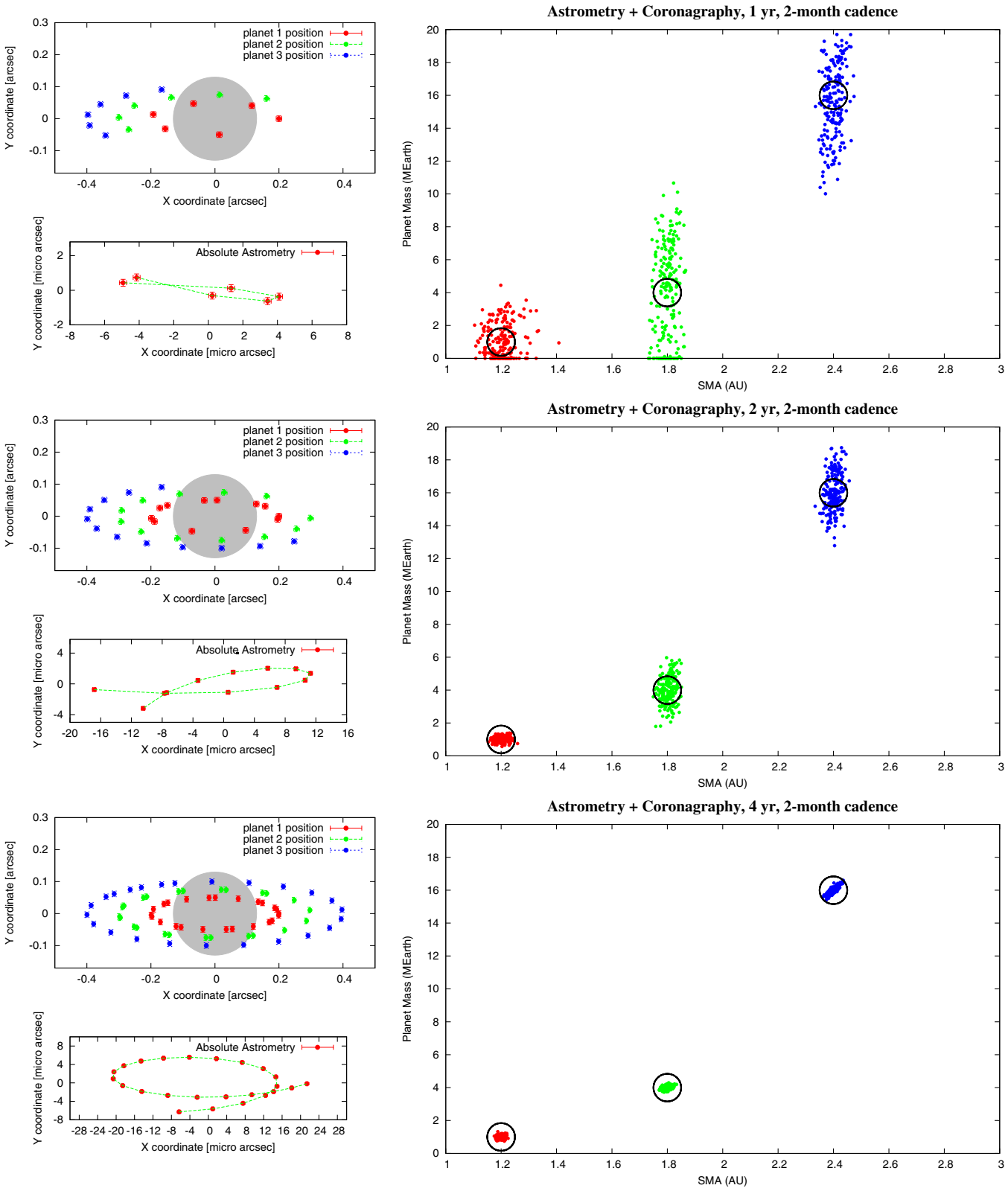

Figure 6. Result of the astrometry + coronagraphy mission scenario, observing a three-planet system around a Sun-like star at 6 pc. Values to be measured are shown on the left with measurement error bars (1σ). Two hundred realizations of the observations are simulated, and the best three-planet solution is shown on the right for each simulation in the semimajor axis (x-axis)–mass (y-axis) plane. Total mission duration is increased from top to bottom, from 1 yr (top) to 4 yr (bottom). The gray disk indicates the blind area (within coronagraph inner working angle) for the planet-to-star relative astrometry measurements. The three dark circles indicate the actual configuration for the three-planet system.

(A color version of this figure is available in the online journal.)

distant planets would not be visible in reflected light in the coronagraphic images, but would produce large-amplitude long-period astrometric signals. Unknown planets within the coronagraph IWA will produce astrometric noise for the combined astrometry + coronagraphy approach described in this paper. These planets will have shorter periods, and, at constant mass, a smaller astrometric signature than planets outside the IWA. They can therefore only compromise the solution if they are significantly more massive than the planets for which the mass is to be measured. This problem can be mitigated by a larger number of measurements, especially at high cadence, to (1) identify the inner planet(s) from astrometry alone and (2) average down the astrometric noise from unknown short-period planet(s). RV measurements, if available, would be very well suited to help identify such planets.

4. DEEP WIDE-FIELD IMAGING SENSITIVITY WITH A DIFFRACTIVE PUPIL TELESCOPE

The effect of the dots on the telescope primary mirror on general-purpose wide-field imaging is evaluated in this section. The baseline design described in Guyon et al. (2012) is adopted in this paper: a 1.4 m telescope with dots covering 1% of the primary mirror area, with a 0.29 deg^2 field of view camera with 44 mas pixels observing in visible light. We assume in this section that this system is observing a Sun-like star at 6 pc ($m_V = 3.7$).

4.1. Light Lost to the Dots

The light lost due to the dots is the sum of the light directly absorbed by the dots and the light they diffract out of the PSF core into a wide halo of spikes. This second component is diffracted out to large distances, and is considered lost for science. Both quantities are equal to the fractional area of the pupil occupied by the dots. In the baseline design chosen, the total photometric loss is therefore 1%+1% = 2%. We note that this loss is small compared to the sensitivity gain offered by adopting an unobstructed pupil, as the photometric sensitivity loss due to spiders and central obstruction in an on-axis telescope design would be larger than 2%.

4.2. Additional Background Due to Light of the Central Star Diffracted by the Dots

The central star's diffraction spikes extend over most of the wide-field image. Although their contrast relative to the central star is faint (approximately 1×10^{-8} along the spikes), the central star is much brighter than other sources in the field.

Over 50% of the field, the additional diffracted light is less than 2.8 photons per day per pixel. Table 4 shows how, for a $m_V = 3.7$ central star, the light from the central star compares with the zodiacal light background. The 50 percentile line shows that the median diffracted light surface brightness is 0.03% of the zodiacal light brightness. Over 95% of the field, the additional light introduced by the dots on the primary mirror is less than 1% of the zodiacal background. If the telescope were pointed on Sirius, 95% of the field sensitivity would be photon-limited from zodiacal light, while over 5% of the field, the photon noise from the spikes would limit sensitivity. The zodiacal light photon-noise-limited point source detection limit for the 1.4 m diameter telescope is $m_V \approx 32$ for a 2 day unfiltered exposure, and would be $m_V \approx 34$ for a full set of 32 observations, each 2 day long.

Table 4
Scattered Light Due to Primary Mirror Dots

Field Percentile[a]	Flux (photons s^{-1} pixel^{-1})[b]	Flux/Flux$_{zodi}$[c]
1%	8.28×10^{-6}	7.66×10^{-5}
5%	1.08×10^{-5}	9.96×10^{-5}
10%	1.28×10^{-5}	1.19×10^{-4}
20%	1.68×10^{-5}	1.55×10^{-4}
50%	3.23×10^{-5}	2.99×10^{-4}
80%	9.27×10^{-5}	8.56×10^{-4}
90%	3.06×10^{-4}	2.82×10^{-3}
95%	1.19×10^{-3}	1.10×10^{-2}
99%	4.35×10^{-2}	4.02×10^{-1}

Notes.
[a] All fluxes are measured in a 3 × 3 arcmin box centered 6 arcmin from the optical axis. Scattered light becomes smaller at larger separations due to the Airy pattern contribution and the diffraction envelope of the spikes (equal to the diffraction pattern of a single dot).
[b] All values in this table assume an unfiltered exposure (zero point = 5.5e10 photons s^{-1}) and an $m_V = 3.7$ central star.
[c] Assuming $m_V = 22.5$ mag arcsec^{-2} zodiacal light background level.

The diffraction spikes can also be numerically removed from the wide-field image to a high accuracy, as they are, to first order, static on the detector. Since the observation mode has the telescope slowly rolling during the observation, background sources are rotating on the detector while the spikes are static. A median of the images acquired during the roll contains only the spikes (and the zodiacal light background), and can then be subtracted to each individual frame prior to de-rotation and co-addition.

5. CONCLUSIONS

The DPT design allows simultaneous deep wide-field imaging, coronagraphic imaging, and astrometric mass determination of exoplanets around nearby stars. We have shown and quantified in both this paper and our previous publication that the different measurements can be performed without impacting each other's performance: the coronagraphic and deep wide-field observations are not significantly affected by the presence of dots on the primary mirror. The potential cost and complexity saving offered by combining three separate missions into one observatory could be significant, and we are thus currently evaluating the feasibility and performance of this concept through both simulations and laboratory demonstrations.

We note that the benefits of performing the three observations simultaneously extend beyond the quantifiable metrics (planet mass and orbital parameter uncertainties) discussed in this paper. Together, astrometric measurements and coronagraphic images are a powerful way to avoid confusion problems in complex planetary systems where a large number of planets, comets, and dust clouds may be present. Astrometric measurements may also allow recovery of planets that are at the limit of detection in the coronagraphic images, for example, because of residual structure in the scattered light halo: the astrometric measurements could confirm or eliminate features that could be either a planet or a speckle. This is particularly beneficial if the astrometric S/N is high but the contrast of the planet makes its identification in coronagraphic images ambiguous—images acquired at different epochs can then be co-added following the planet location to reach deeper contrast (by the square root of the

number of measurements) than otherwise possible. This scheme becomes especially valuable for planets at the outer edge of the habitable zone, which are fainter but have stronger astrometric signatures than planets closer in.

We note that these benefits do not require strict simultaneity of the astrometric and coronagraphic measurements as long as the two types of measurements can be connected together. Separate astrometry and direct imaging missions, if operating within a few years, would thus offer the same advantages, provided that the astrometry measurements are not performed after the direct imaging measurements (this would not allow prioritization of targets for follow-up spectroscopy of potentially habitable Earth-mass planets with the direct imaging mission).

Acquiring deep wide-field images around nearby stars may also reveal extended debris disks (analogous to the Kuiper Belt, scattered disk, or Oort Cloud in the solar system), and therefore advancing our understanding of the planetary system architecture and history. Finally, we note that the image of the spikes in the wide-field camera are a low-resolution spectrum of the central star, which, when acquired simultaneously with the coronagraphic and astrometric measurements, may allow additional calibration.

Our study also shows that coronagraphic imaging and astrometry enable stellar mass measurements to percent-level precision for any star around which planets can be identified, allowing calibration of the stellar mass–luminosity relationship.

A laboratory effort is under way to validate the concept and demonstrate that sub-μas level astrometric precision is attainable with a wide-field imaging telescope. A separate effort is aimed at laboratory demonstration that the DTP concept is compatible with high-contrast coronagraphic imaging. Results from these experiments will be reported in future publications.

This work is funded by the NASA Astronomy and Physics Research and Analysis (APRA) program and the State of Arizona Technology Research Initiative Fund (TRIF). Support for this work was also provided by NASA through Hubble Fellowship grant HST-HF-51250.01-A awarded to S. Mark Ammons by the Space Telescope Science Institute, which is operated by the Association of Universities for Research in Astronomy, Inc., for NASA, under contract NAS 5-26555.

APPENDIX

FINDING PLANETS FROM ASTROMETRY ONLY

In this Appendix, we briefly review what can be detected by astrometry alone, a scenario that has been studied as part of the Space Interferometry Mission (SIM) project. In addition to astrometry, it is assumed here that all the nearby stars will have been monitored by RV measurements. While RV cannot detect 1 $M_{\rm earth}$ mass planets in a 1 yr orbit, due to stellar RV noise, because of its long time baseline, RV will have found larger planets such as Jupiters and Neptunes with long orbital periods. A detailed study of what is possible when 5 yr of precision astrometric data plus ≈15 yr of 1 m s^{-1} RV data was conducted during a "double blind" simulation of a 5 yr SIM. We briefly summarize in this section the lessons learned during this double blind study. A more detailed description of the double blind study is provided in Traub et al. (2010) and Traub (2010).

The first conclusion is that astrometric detection of exo-Earths requires a mission S/N = 6. Here S/N is defined as signal-to-noise where signal is the SMA of the astrometric orbit and noise is the 1σ rms error of the whole 5 yr data set. If there were 100 measurements during the mission and 12 parameters are solved for (5 stellar parameters: position, proper motion, and parallax; 6 orbital parameters and the mass of the planet), the 1σ 5 yr mission noise is the single epoch noise divided by $\sqrt{100-12}$. With an S/N > 6, the false alarm probability (FAP) is <1%. FAP of 1% means that if there were no planets, and 100 stars are searched, noise will mistakenly be identified as a planet once. Second, at S/N = 6, the mass of a 1 $M_{\rm earth}$ planet would have a ≈25% 1σ error. The orbital phase in radians has an error that is ≈0.5 of the mass. The period is measured more accurately for short-period planets; a planet with a 2× shorter period has its period measured twice as accurately. Last of all, the ability to find a planet and measure its mass was independent of the planet's period as long as the period was less than ≈80% of the mission length. The sensitivity degraded with longer periods, by about 2× when the planet period equaled the mission length.

The main purpose of the double blind test was to examine the astrometric detection of multiple planets. In general the presence of multiple planets does not present a problem for astrometric detection if the planet's orbital frequencies are separated more than 1/mission length. The double blind test used a large variety of multiple planet systems and in general confusion in the frequency domain was not an issue except for planets whose periods were longer than the mission length. The parallax effect has a 1 yr period and planets whose orbital periods were between 0.9 and 1.1 yr would have part of their motion absorbed into the parallax solution. Again out of a randomly selected 100 planetary systems only one had an Earth-like planet close enough to 1.0 yr to present a problem but by chance its orbital plane was almost orthogonal to the parallax signature and its mass was properly measured. If a multiple planet system had one large outer planet, such as Jupiter in a 12 yr orbit, it was still possible to "fit" for the 12 yr planet and after that find all the planets with shorter periods whose S/N was > 6. The problem arose when there were two outer planets, for example with 12 and 20 yr periods. In this situation fitting a single long-period planet to the data when there were actually two long-period planets could result in significant residuals. The fitting error in general is an "arc" of motion over the 5 yr data period. But because proper motion is also fitted at the same time, the arc becomes a closed curve, mimicking a planet with a period slightly less than the mission lifetime. With experience, the teams participating in the double blind study were able to recognize this about 70% of the time and were then able to recover both long-period planets and shorter period planets. When discussing the ability of astrometry to detect a planet in a multiplanet system, there are two statistical metrics. The metric measures completeness what fraction of the planets whose S/N > 6 and had periods less than 5 yr were actually found and the confidence metric measures what fraction of "claimed" discoveries were actual planets. The result of the double blind test was very encouraging in that both completeness and confidence were above 90%.

REFERENCES

Bendek, E. A., Ammons, S. M., Shankar, H., & Guyon, O. 2011, Proc. SPIE, 8151, 81510U
Brown, R. A. 2005, ApJ, 624, 1010
Cahoy, K. L., Marley, M. S., & Fortney, J. J. 2010, ApJ, 724, 189
Clampin, M., Melnick, G., Lyon, R., et al. 2006, Proc. SPIE, 6265, 62651B
Davidson, J. M. 2011, PASP, 123, 923
Guyon, O., Ammons, S. M., Bendek, E. A., et al. 2012, ApJS, 200, 11
Guyon, O., Angel, J. R. P., Belikov, R., et al. 2009, Proc. SPIE, 7440, 74400F
Guyon, O., Shaklan, S., Levine, M., et al. 2010, Proc. SPIE, 7731, 773129

Levine, M., Lisman, D., Shaklan, S., et al. 2009, arXiv:0911.3200
Lissauer, J. J., Ragozzine, D., Fabrycky, D. C., et al. 2011, ApJS, 197, 8
Malbet, F., Léger, A., Shao, M., et al. 2011, Exp. Astron., 87, 534
Marois, C., Lafrenière, D., Macintosh, B., & Doyon, R. 2006, ApJ, 647, 612
Savransky, D., Kasdin, N. J. D., & Belson, B. A. 2009, Proc. SPIE, 7440, 74400B
Shao, M., Catanzarite, J., & Pan, X. 2010, ApJ, 720, 357
Shao, M., & Levine, B. M. 2010, in ASP Conf. Ser. 430, Pathways Towards Habitable Planets, ed. V. Coudé Du Foresto, D. M. Gelino, & I. Ribas (San Francisco, CA: ASP), 368
Shao, M., Marcy, G., Catanzarite, J. H., et al. 2009, in astro2010: The Astronomy and Astrophysics Decadal Survey, 271
Sivaramakrishnan, A., & Oppenheimer, B. R. 2006, ApJ, 647, 620
Torres, G. 1999, PASP, 111, 169
Traub, W. A. 2010, in ASP Conf. Ser. 430, Pathways Towards Habitable Planets, ed. V. Coudé Du Foresto, D. M. Gelino, & I. Ribas (San Francisco, CA: ASP), 249
Traub, W. A., Beichman, C., Boden, A. F., et al. 2010, in EAS Publications Series, Vol. 42, Extrasolar Planets in Multi-body Systems: Theory and Observations, ed. K. Gożdziewski, A. Niedzielski, & J. Schneider (Cambridge: Cambridge Univ. Press), 191
Trauger, J., Stapelfeldt, K., Traub, W. A., et al. 2010, in ASP Conf. Ser. 430, Pathways Towards Habitable Planets, ed. V. Coudé Du Foresto, D. M. Gelino, & I. Ribas (San Francisco, CA: ASP), 375
Unwin, S. C. 2005, in ASP Conf. Ser. 338, Astrometry in the Age of the Next Generation of Large Telescopes, ed. P. K. Seidelmann & A. K. B. Monet (San Francisco, CA: ASP), 37

The Astrophysical Journal Letters, 763:L32 (6pp), 2013 February 1 doi:10.1088/2041-8205/763/2/L32

DIRECT IMAGING DISCOVERY OF A "SUPER-JUPITER" AROUND THE LATE B-TYPE STAR κ And*

J. Carson[1,2], C. Thalmann[2,3], M. Janson[4], T. Kozakis[1], M. Bonnefoy[2], B. Biller[2], J. Schlieder[2], T. Currie[5], M. McElwain[5], M. Goto[6], T. Henning[2], W. Brandner[2], M. Feldt[2], R. Kandori[7], M. Kuzuhara[7,8], L. Stevens[1], P. Wong[1], K. Gainey[1], M. Fukagawa[9], Y. Kuwada[9], T. Brandt[4], J. Kwon[7], L. Abe[10], S. Egner[11], C. Grady[5], O. Guyon[11], J. Hashimoto[7], Y. Hayano[11], M. Hayashi[7], S. Hayashi[11], K. Hodapp[12], M. Ishii[11], M. Iye[7], G. Knapp[4], T. Kudo[11], N. Kusakabe[7], T. Matsuo[13], S. Miyama[14], J. Morino[7], A. Moro-Martin[15], T. Nishimura[11], T. Pyo[11], E. Serabyn[16], H. Suto[7], R. Suzuki[7], M. Takami[17], N. Takato[11], H. Terada[11], D. Tomono[11], E. Turner[4,18], M. Watanabe[19], J. Wisniewski[20], T. Yamada[21], H. Takami[7], T. Usuda[11], and M. Tamura[7]

[1] Department of Physics & Astronomy, College of Charleston, 58 Coming Street, Charleston, SC 29424, USA
[2] Max-Planck-Institut für Astronomie, Königstuhl 17, D-69117 Heidelberg, Germany
[3] Astronomical Institute "Anton Pannekoek," University of Amsterdam, Science Park 904, 1098-XH Amsterdam, The Netherlands
[4] Department of Astrophysical Sciences, Princeton University, NJ 08544, USA
[5] ExoPlanets and Stellar Astrophysics Laboratory, Code 667, Goddard Space Flight Center, Greenbelt, MD 20771, USA
[6] Young Stars and Star Formation Universitäts-Sternwarte München, Ludwig-Maximilians-Universität, D-81679 München, Germany
[7] National Astronomical Observatory of Japan, 2-21-1 Osawa, Mitaka, Tokyo 181-8588, Japan
[8] Department of Earth and Planetary Science, The University of Tokyo, 7-3-1, Hongo, Bunkyo-ku, Tokyo 113-0033, Japan
[9] Department of Earth and Space Science, Graduate School of Science, Osaka University, 1-1 Machikaneyama, Toyonaka, Osaka 560-0043, Japan
[10] Laboratoire Lagrange (UMR 7293), Universite de Nice-Sophia Antipolis, CNRS, Observatoire de la Cote dAzur, 28 avenue Valrose, F-06108 Nice Cedex 2, France
[11] Subaru Telescope, 650 North Aohoku Place, Hilo, HI 96720, USA
[12] Institute for Astronomy, University of Hawaii, 640 N. Aohoku Place, Hilo, HI 96720, USA
[13] Department of Astronomy, Kyoto University, Kitashirakawa-Oiwake-cho, Sakyo-ku, Kyoto 606-8502, Japan
[14] Hiroshima University, 1-3-2, Kagamiyama, Higashihiroshima, Hiroshima 739-8511, Japan
[15] Departamento de Astrofísica, CAB (INTA-CSIC), Instituto Nacional Técnica Aeroespacial, Torrejón de Ardoz, E-28850 Madrid, Spain
[16] Jet Propulsion Laboratory, California Institute of Technology, Pasadena, CA 171-113, USA
[17] Institute of Astronomy and Astrophysics, Academia Sinica, P.O. Box 23-141, Taipei 10617, Taiwan
[18] Kavli Institute for Physics and Mathematics of the Universe, The University of Tokyo, 5-1-5, Kashiwanoha, Kashiwa, Chiba 277-8568, Japan
[19] Department of Cosmosciences, Hokkaido University, Kita-ku, Sapporo, Hokkaido 060-0810, Japan
[20] HL Dodge Department of Physics & Astronomy, University of Oklahoma, 440 W Brooks St, Norman, OK 73019, USA
[21] Astronomical Institute, Tohoku University, Aoba-ku, Sendai, Miyagi 980-8578, Japan
Received 2012 October 21; accepted 2012 November 7; published 2013 January 16

ABSTRACT

We present the direct imaging discovery of an extrasolar planet, or possible low-mass brown dwarf, at a projected separation of 55 ± 2 AU (1.″058 ± 0.″007) from the B9-type star κ And. The planet was detected with Subaru/HiCIAO during the SEEDS survey and confirmed as a bound companion via common proper motion measurements. Observed near-infrared magnitudes of $J = 16.3 \pm 0.3$, $H = 15.2 \pm 0.2$, $K_s = 14.6 \pm 0.4$, and $L' = 13.12 \pm 0.09$ indicate a temperature of ∼1700 K. The galactic kinematics of the host star are consistent with membership in the Columba Association, implying a corresponding age of 30^{+20}_{-10} Myr. The system's age, combined with the companion photometry, points to a model-dependent companion mass ∼12.8 $M_{\rm Jup}$. The host star's estimated mass of 2.4–2.5 $M_\odot$ places it among the most massive stars ever known to harbor an extrasolar planet or low-mass brown dwarf. While the mass of the companion is close to the deuterium burning limit, its mass ratio, orbital separation, and likely planet-like formation scenario imply that it may be best defined as a "super-Jupiter" with properties similar to other recently discovered companions to massive stars.

Key words: brown dwarfs – planets and satellites: detection – stars: massive

Online-only material: color figures

1. INTRODUCTION

Stellar mass is emerging as one of the most important parameters in determining the properties of planetary systems, along with stellar metallicity. Radial velocity surveys have indicated that the frequency of giant planets increases with the mass of the stellar host (Johnson et al. 2010), and many of the roughly dozen exoplanets that have been directly imaged thus far have had A-type stellar hosts (e.g., Marois et al. 2008; Lagrange et al. 2009) despite such large stars being in the small minority of surveyed targets. These results have motivated targeted imaging surveys of planets around massive stars (e.g., Janson et al. 2011a). The increase in planet frequency with host star mass can be readily explained theoretically, through the consideration that more massive stars are likely to have more massive disks (Mordasini et al. 2012). On the other hand, massive stars also feature an increased intensity of high-energy radiation, which may significantly shorten the disk's lifetime due to photoevaporation; and thus, decrease the time window in which giant planets are allowed to form. This raises the question of whether there is a maximum stellar mass above which giant planets are unable to form.

In this Letter, we report the discovery of a ∼12.8 $M_{\rm Jup}$ companion to the ∼2.5 $M_\odot$ star κ And, the most massive star to host a directly detected companion below or near the planetary mass limit. In the following, we describe the acquisition, reduction,

* Based on data collected at Subaru Telescope, which is operated by the National Astronomical Observatory of Japan.

Table 1
Properties of the κ And System

Property	Primary	Companion
Mass	2.4–2.5 $M_{\odot}$ [a]	$12.8^{+2.0}_{-1.0}$ $M_{\rm Jup}$ [b]
$T_{\rm eff}$	11400 ± 100 K [c]	1680^{+30}_{-20} K [b]
	10700 ± 300 K [d]	...
Spectral type	B9 IV [d]	L2–L8 [e]
Age (Myr)	30^{+20}_{-10} [f]	...
Parallax (mas)	19.2 ± 0.7 [g]	...
Fe/H	-0.36 ± 0.09 [c]	...
	-0.32 ± 0.15 [d]	...
log g	4.10 ± 0.03 [c]	...
	3.87 ± 0.13 [d]	...
J (mag)	4.6 ± 0.3 [h]	16.3 ± 0.3
H (mag)	4.6 ± 0.2 [h]	15.2 ± 0.2
$K_{\rm s}$ (mag)	4.6 ± 0.4 [h]	14.6 ± 0.4
L' (mag)	...	13.12 ± 0.09
ΔJ (mag)	...	11.6 ± 0.2
ΔH (mag)	...	10.64 ± 0.12
$\Delta K_{\rm s}$ (mag)	...	10.0 ± 0.08
M_J (mag)	1.0 ± 0.3 [i]	12.7 ± 0.3
M_H (mag)	1.0 ± 0.2 [i]	11.7 ± 0.2
$M_{K_{\rm s}}$ (mag)	1.0 ± 0.4 [i]	11.0 ± 0.4
$M_{L'}$ (mag)	...	9.54 ± 0.09
Astrometry on 2012 January 1 (H band):		
— Proj. sep. ($''$)	...	1.070 ± 0.010
— Proj. sep. (AU)	...	56 ± 2 [j]
— Position angle ($^{\circ}$)	...	55.7 ± 0.6
Astrometry on 2012 July 8 (H band):		
— Proj. sep. ($''$)	...	1.058 ± 0.007
— Proj. sep. (AU)	...	55 ± 2 [j]
— Position angle ($^{\circ}$)	...	56.0 ± 0.4

Notes. Photometric values represent Subaru 2012 July measurements, unless noted otherwise.
[a] Calculated using the published temperature from Wu et al. (2011) and the evolutionary tracks from Ekström et al. (2012).
[b] Calculated using the H-band magnitude, estimated κ And age, and evolutionary models from Chabrier et al. (2000).
[c] Fitzpatrick & Massa (2005).
[d] Wu et al. (2011).
[e] Based on measured colors and Cruz et al. (2009) spectral identifications.
[f] Zuckerman et al. (2011) and Marois et al. (2010).
[g] *Hipparcos*; Perryman et al. (1997).
[h] 2MASS; Skrutskie et al. (2006).
[i] Calculated by the authors, using 2MASS photometry and the *Hipparcos* parallax.
[j] Uncertainty is dominated by the host star parallax measurement.

and analysis of the data used for detection, confirmation, and basic characterization of the companion, κ And b.

2. OBSERVATIONS AND DATA REDUCTION

Observations of the κ And system extended over a period of seven months (2012 January–July) and were carried out on the Subaru Telescope. *JHK* images were collected with AO188 (Hayano et al. 2010) coupled with HiCIAO (Hodapp et al. 2008). L' measurements were carried out with AO188 coupled with the Infrared Camera and Spectrograph (IRCS; Tokunaga et al. 1998). Figure 1 displays the multi-wavelength images of the newly discovered companion. Table 1 provides a summary of the experimental measurements, as well as the relevant values from the literature. Figure 2 shows the observed astrometric positions of κ And b, as compared to the expected motion of an unrelated background star. The subsections below describe the observations in greater detail.

2.1. Subaru HiCIAO/AO188 JHK Imaging

We first detected κ And b using AO188 coupled with HiCIAO on the Subaru Telescope on 2012 January 1, as part of the SEEDS survey (Tamura 2009). The observations used a $20'' \times 20''$ field of view, 9.5 mas pixels, and an opaque $0''.6$ diameter coronagraphic mask, which helped to keep the saturation radius $<0''.5$. The images were taken in the near-infrared (H band, 1.6 μm), where young substellar objects are expected to be bright with thermal radiation (Baraffe et al. 2003). Pupil tracking was used to enable angular differential imaging (ADI; Marois et al. 2006).

Data reduction of the 46 exposures of 5 s revealed, at 23σ confidence, a point-like source at $1''.07$ separation. Follow-up observations in J (1.3 μm; 177 exposures of 10 s), H (1.6 μm; 171 exposures of 8 s), and $K_{\rm s}$ (2.2 μm; 135 exposures of 10 s), collected on 2012 July 8–9, using the same observing setup, re-detected the source at 6, 28, and 49σ confidence levels, respectively. Unsaturated images of the primary, taken immediately before and after each filter's observing sequence, and using a neutral density filter (0.866% for H, 1.113% for $K_{\rm s}$, and 0.590% for J) provided photometric calibration.

To optimize the ADI technique, we first reduced the data using a locally optimized combination of images algorithm (LOCI; Lafrenière et al. 2007). HiCIAO observations of M5, combined with distortion-corrected images obtained with the Advanced Camera for Surveys (ACS) on the *Hubble Space Telescope*, enabled accurate pixel-scale calibration to within 0.2%; the ACS astrometric calibration was based on van der Marel et al. (2007). Figure 1 (left and middle panels) presents a *JHK* false-color image and corresponding signal-to-noise ratio (S/N) map after the ADI/LOCI data reduction.

Given the relatively high S/N ratios and the known difficulties in quantifying the impact of LOCI on planet photometry and astrometry, we also performed a classical ADI reduction (Marois et al. 2006) with `mean`-based point-spread function (PSF) estimation and frame co-adding. Unsharp masking on the spatial scale of 35 pixels ($\approx$ 7 FWHM) was applied to the final image to flatten the residual background. The planet signal was recovered with S/N ratios comparable (within 10%) to the LOCI reduction for all the July data sets. For the somewhat lower-quality January data, the measured S/N reduced from about 23σ to 7σ.

To achieve unbiased photometry and astrometry, we extracted the combined κ And PSF (S/N $>$ 1000) from the neutral density images, and placed it on an empty image frame at the location of κ And b. Applying the same unsharp masking and ADI reduction to this data as we did for the science data, we simulated the parallactic angle evolution, as recorded in the science frames. The resulting processed PSF acted as the photometric and astrometric reference for κ And b. The only nonlinear step in this process was the `median`-based unsharp masking, but the large spatial scale ($\approx$ 7 FWHM) ensured that the subtraction effects were minimal.

We calibrated the astrometry by cross-correlating the κ And b signal with the processed calibration PSF. We estimated the uncertainty in the κ And b center to be FWHM/(S/N), following Cameron et al. (2008). The uncertainties in the final relative astrometry were dominated by our ability to determine the host star center, which was carried out through Moffat fitting of each individual exposure. We conservatively estimated the uncertainty of the Moffat fit at 0.75 pixels (7 mas). For confirmation, we applied Moffat fitting and peak fitting to

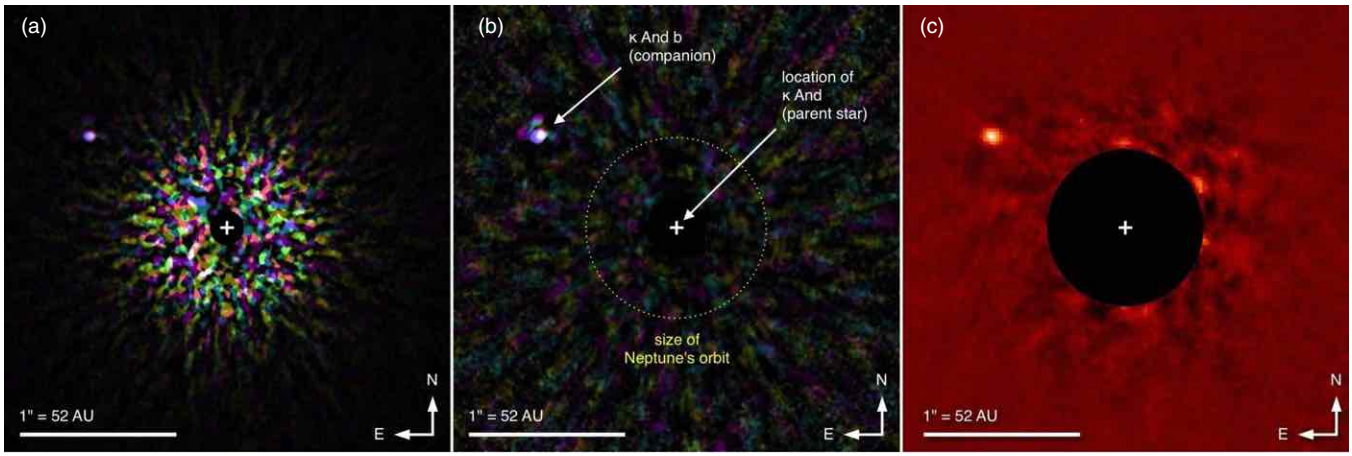

Figure 1. Left: *JHK* false-color image of κ And b after LOCI/ADI data reduction, for the 2012 July observations. Center: a corresponding S/N map created from the left frame. The S/N is calculated in concentric annuli around the star. The white plus sign in each panel marks the location of the host star κ And; the black disks designate the regions where field rotation is insufficient for ADI. The white features indicate where the signal is roughly equally strong in all wavelengths; the colored features indicate where the signal is mismatched between wavelengths and are often indicative of residual noise. The lobes around κ And b result from the Airy pattern produced by the Subaru AO188 system. Right: L'-band image of κ And b from the 2012 July observations.

(A color version of this figure is available in the online journal.)

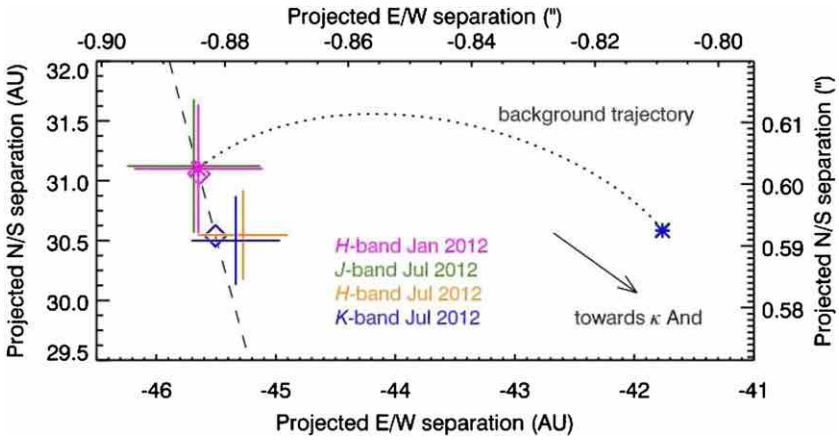

Figure 2. Proper-motion analysis of κ And b. The dotted curve designates the predicted parallactic and proper motion between epochs, if the detected January source was a background star. The dashed line indicates an example bound, orbital path of κ And b consistent with the observational data. The diamond symbols represent the predicted January and July astrometric measurements for κ And b, if it follows the dashed orbital path. κ And b is clearly inconsistent with the background behavior and instead demonstrates common proper motion with the host star.

(A color version of this figure is available in the online journal.)

unsaturated data of κ And and found that the methods agreed at the 0.5σ level. The photometric uncertainties were calculated as a combination of (1) representative noise in an annulus, centered on the host star, with a radius equal to the companion, (2) photometric variability in the neutral density calibration images, which yielded effective accuracies of 7%–11% for the combined data sets, and (3) uncertainties in the *JHK* magnitudes of κ And.

2.2. Subaru IRCS/AO188 L' Imaging

On 2012 July 28, we followed the *JHK* observations with L'-band observations (3.8 μm; 50 exposures of 30 s) using AO188 coupled with the IRCS on the Subaru Telescope. We employed a 10.″5 × 10.″5 field of view, 20.6 mas pixel scale, and no coronagraph. The host star saturated out to ∼0.″1. The dithered observations, carried out in ADI mode, were divided into two identical sequences bracketing observations of the star HR 8799, which provided the photometric calibration (Marois et al. 2008). Observations of a third star, S810-A, were collected before the science observations as a secondary calibration check (Leggett et al. 2003).

We sky-subtracted each image using a median combination of frames taken at the other dither positions. To help maximize the high-contrast sensitivity, we processed the data using an "adaptive" LOCI process (A-LOCI; Currie et al. 2012). We also employed a moving pixel mask, where the LOCI algorithm is prevented from using, in PSF construction, pixels lying within the subtraction zone (see Lafrenière et al. 2007 for details). Figure 1 (right) shows the final image.

To quantify the κ And b throughput, we used fake point sources added to the image and processed with the same algorithm settings. As an additional check on our flux calibration, we determined the relative brightness between the HR 8799 bcd planets (all detected at S/N > 7–10) using identical procedures, and confirmed its agreement with published values (Currie et al. 2011). The independent calibrations all yielded self-consistent results, ensuring confidence in the 22σ detection of κ And b in L'. As a final check, we re-processed the L'-band data using a more classical ADI method, similar to that described for the

JHK data set, and achieved consistent results. While the July L' astrometry was consistent with the July *JHK* results, we refrained from including it in our proper-motion analysis, due to our possession of poorer-quality astrometric calibration.

3. HOST STAR PROPERTIES

κ And is a B9 IV star (Wu et al. 2011) located at a distance of 52.0 pc (Perryman et al. 1997). Fitzpatrick & Massa (2005) report a temperature of 11,400 ± 100 K with a subsolar metallicity of [Fe/H] = −0.36 ± 0.09, while independent measurements by Wu et al. (2011) report values of 10,700 ± 300 K and −0.32 ± 0.15. Given the star's spectral classification, the measured low metallicity is likely due to the details of the star's accretion and atmospheric physics, as opposed to a true, initial, low metallicity (Gray & Corbally 2002). We estimate a mass of 2.4–2.5 $M_{\odot}$ using the published temperature and evolutionary tracks from Ekström et al. (2012). Table 1 summarizes the host star properties.

Zuckerman et al. (2011) proposed κ And to be a member of the ∼30 Myr old Columba Association. To further investigate κ And's likely membership in Columba, we (1) independently calculated its Galactic kinematics from astrometry available in the literature (Perryman et al. 1997; Zuckerman et al. 2011) and compared these to the young local associations reported in Torres et al. (2008), and (2) calculated its membership probability in these associations using the Bayesian methods of Malo et al. (2012). Our analyses showed that the star's kinematics imply a >95% probability of the star being part of the Columba Association.

As an additional check, we compared the κ And $B-V$ color and absolute V magnitude (Perryman et al. 1997; van Leeuwen 2009) with members of clusters and associations with ages ranging from ∼15 to 700 Myr. These include Lower Centaurus Crux, α Per, Pleiades, Coma Ber, Hyades, Praesepe, and young local associations (Torres et al. 2008; van Leeuwen 2009). The color–magnitude analysis showed that κ And is consistent with other early-type stars having ages ∼20–120 Myr. The results of our analyses are consistent with the conclusions reported in Zuckerman et al. (2011); κ And's age range and kinematics suggest that it is a member in the Columba association. We therefore adopt a system age of 30^{+20}_{-10} Myr (following Marois et al. 2010) for all subsequent analyses.

4. RESULTS

4.1. Proper-motion Analysis

Located 52.0 pc from the Sun, κ And exhibits a proper motion of 83.5 mas yr^{-1} (Perryman et al. 1997), enabling an effective test to distinguish bound companions from unrelated background stars. κ And's proper and parallactic motion translates to 76 mas (∼8 HiCIAO pixels) of net movement over the six-month period between epochs. As shown in Figure 2, the companion exhibits common proper motion with the host star, and deviates from the expected background star motion by 7σ. In addition to this 7σ deviation in the magnitude of the motion, the observed direction of the motion and scatter in astrometry are completely inconsistent with that of a background star.

4.2. Physical Properties of κ And b

Figure 3 shows that the κ And b colors are most consistent with cloudy L dwarfs and that they overlap with several other benchmark exoplanets and low-mass companions, including

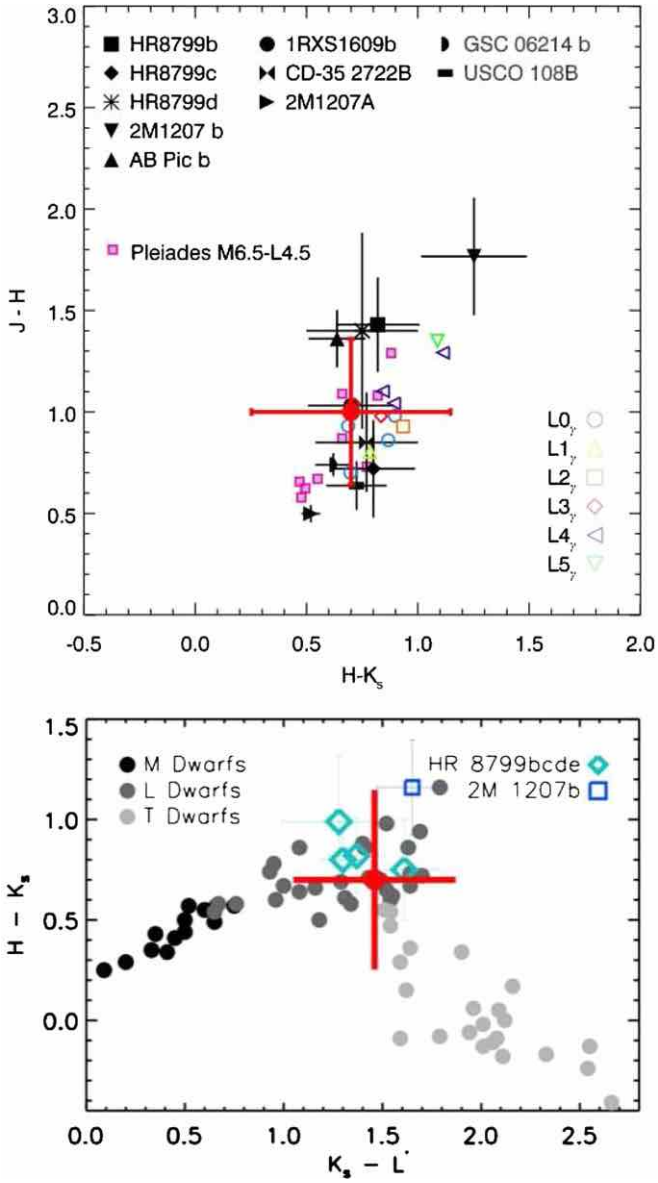

Figure 3. Position of κ And b colors (red points) with respect to reference objects. The top plot includes benchmark substellar companions: HR 8799 bcd (Marois et al. 2008), 2M1207 Ab (Chauvin et al. 2004), AB Pic b (Chauvin et al. 2005), 1RXS1609 b (Lafrenière et al. 2008), CD-35 2722 B (Wahhaj et al. 2011), GSC 06214 b (Ireland et al. 2011), and USCO 108 AB (Béjar et al. 2008). It also contains L dwarfs with spectral features indicative of reduced surface gravity (Cruz et al. 2009; Faherty et al. 2012), and Pleiades M-L dwarfs (Bihain et al. 2010). The bottom plot includes M, L, and T field dwarfs (Leggett et al. 2002), HR 8799 bcde (Currie et al. 2011; Skemer et al. 2012), and 2M1207 b (Chauvin et al. 2004).

(A color version of this figure is available in the online journal.)

HR 8799 bcd, AB Pic b, and 1RXS1609 b. Figure 4 compares κ And b colors and absolute magnitudes with DUSTY and COND evolutionary tracks (Baraffe et al. 2003; Chabrier et al. 2000), as well as low-mass companions around HR 8799 and AB Pic. The plots show κ And b to be well situated between HR 8799 cde and AB Pic b. Its infrared colors are slightly bluer than those of typical field L dwarfs, possibly indicating a low surface gravity (Cruz et al. 2009). However, improved photometry is required to confirm whether or not this color deviation is real.

The estimated temperature of κ And b suggests that its atmospheric properties should align more closely with those

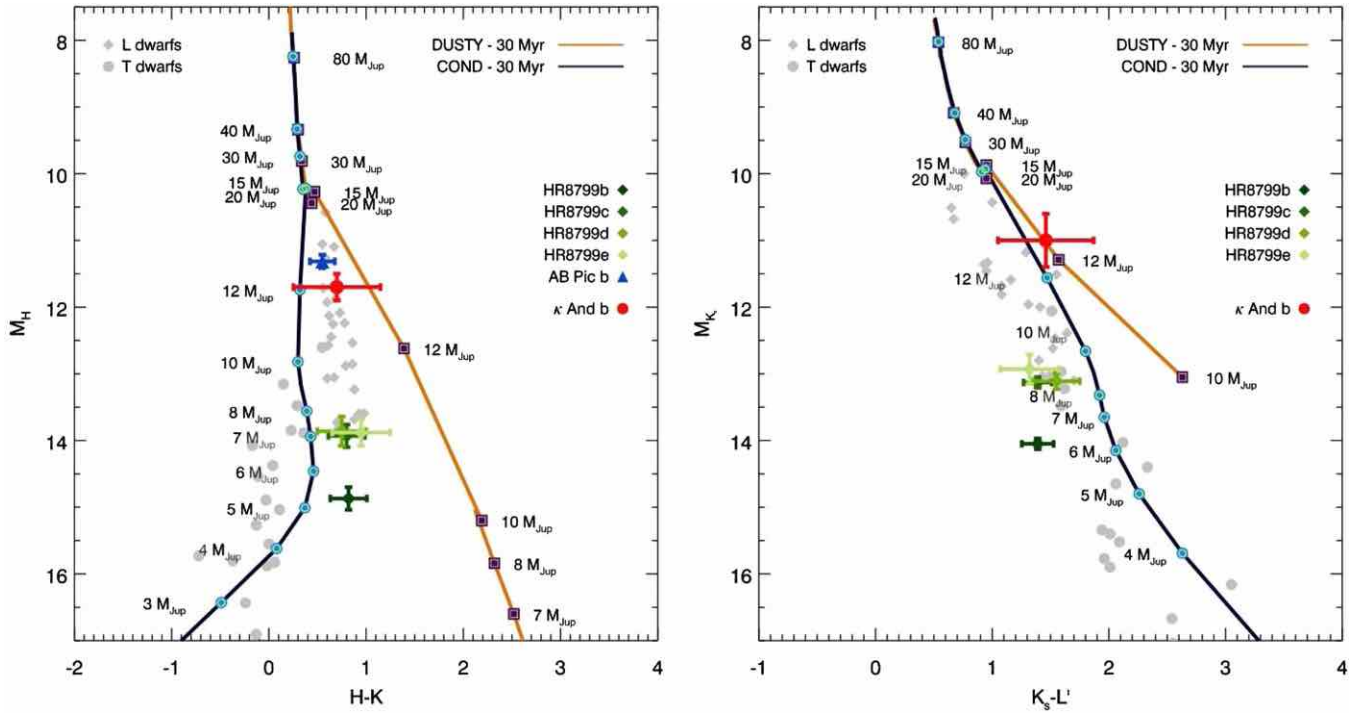

Figure 4. κ And b colors and absolute magnitudes (red points) compared with DUSTY and COND evolutionary tracks (Baraffe et al. 2003; Chabrier et al. 2000). (A color version of this figure is available in the online journal.)

of the DUSTY models (see discussions in Chabrier et al. 2000). In deriving a mass estimate from this track, we rely on the July H-band magnitude because (1) alternative J-band and January H-band measurements have higher uncertainties, (2) K_s-band mass estimates are more sensitive to atmospheric composition (see, e.g., Janson et al. 2011b), and (3) L'-band mass estimates have been less thoroughly tested with experimental data, and are more sensitive to age uncertainties for this age and magnitude range (see Chabrier et al. 2000).

Based on the July H-band magnitude of 15.2 ± 0.2, the estimated age of 30^{+20}_{-10} Myr, a parallax of 19.2 ± 0.7 (Perryman et al. 1997), and the DUSTY evolutionary models, we calculate a mass of $12.8^{+2.0}_{-1.0}$ $M_{\rm Jup}$ and a temperature of 1680^{+30}_{-20} K. As a consistency check, we calculate the predicted JK_sL' magnitudes based on the estimated 1680 K temperature, the 20–50 Myr system age, and the DUSTY evolutionary models. This yields $J = 16.5$–16.8, $K_s = 14.2$–14.4, and $L' = 13.1$–13.2 mag, all of which are in agreement with our measured multiband photometry. Additionally, the two epochs of H-band photometry are in agreement with one another. Table 1 summarizes the complete properties of κ And b.

While the DUSTY models are likely the more relevant, we estimate a possible alternative mass using the COND evolutionary tracks. In this scenario, we determine a mass of $11.5^{+2.4}_{-1.2}$ $M_{\rm Jup}$ and a temperature of 1640^{+40}_{-20} K. More recent evolutionary models by Spiegel & Burrows (2012) offer alternative "Warm Start" scenarios that consider formation with lower levels of initial entropy. While these models do not consider combinations of mass and temperature similar to that of κ And b, they do predict generally higher masses than that of the DUSTY and COND models. In the case of κ And b, such models place the most probable mass at a value above the typical deuterium burning limit. While we currently adopt a nominal mass estimate of $12.8^{+2.0}_{-1.0}$ $M_{\rm Jup}$ for the analyses in this discovery Letter (based on the DUSTY models), we defer a deeper investigation of the companion mass for a follow-up paper, where we will focus on a more thorough comparison of multiband photometry with synthetic spectra.

4.3. Orbital Properties of κ And b

We estimate the semimajor axis of κ And b from its observed separation. Assuming a uniform eccentricity distribution of $0 < e < 1$, and random viewing angles, Dupuy et al. (2010) compute a median correction factor between projected separation and semimajor axis of $1.1^{+0.91}_{-0.36}$. Using this relation, we derive a semimajor axis of 61^{+50}_{-20} AU based on its projected separation of 55.2 AU (1.″07) in 2012 January.

4.4. Possible Secondary Companions

The H-band sensitivity levels (see Section 2.1) allow us to rule out secondary companions with temperatures similar to or warmer than that of κ And b, for separations greater than 0.″9 (46 projected AU). For the κ And b separation (1.″1) and beyond, we may rule out secondary companions with masses $\geqslant 11.7$ $M_{\rm Jup}$, assuming a 30 Myr system age and the DUSTY evolutionary models.

5. DISCUSSION

κ And is the most massive star to host a directly imaged planet or brown dwarf near the deuterium burning boundary. The mass ratio between κ And b and its host is $\sim$0.5%, similar to the $\sim$0.4% ratios of the β Pic and HR 8799 planets (Lagrange et al. 2009; Marois et al. 2008). In comparison, this value is noticeably smaller than those of the reported directly imaged planets around 1RXS 1609 (Lafrenière et al. 2008) and 2M 1207 (Chauvin et al. 2004). The projected separation of κ And b is also intermediate between the two outer planets in HR 8799. The similarities between κ And b, β Pic, and HR 8799 could imply a similar formation mechanism, which may be distinct from recently

discovered brown dwarf companions of approximately an order of magnitude larger mass ratios (e.g., GJ 758 B; Thalmann et al. 2009) or semimajor axes (e.g., HIP 78530 B; Lafrenière et al. 2011). Strengthening the possibility of a planet-like formation for κ And b, theoretical models (e.g., Rafikov 2011) show that, for a minimum-mass solar nebula, the region of the primordial disk where core accretion formation of giant planets can occur overlaps with the separation range of κ And b. Furthermore, this formation mechanism may be significantly enhanced for a star as massive as κ And, and, assuming that it had a correspondingly more massive protoplanetary disk. Further studies will be needed to more stringently constrain the population properties of planets and brown dwarfs on intermediate and wide orbits.

The best-fit mass of κ And b lies just below the deuterium burning limit according to conventional evolutionary models, but may be above this limit if the initial entropy at formation is lower than such models assume (Spiegel & Burrows 2012). This leads to an ambiguity in whether or not the companion can be classified as an "exoplanet" using the present standard definition. Such a classification scheme can however be misleading, given that κ And b may well have formed in the same way as previously imaged planets, regardless of whether its mass falls just below or above this limit. Indeed, radial velocity studies have shown that massive stars tend to have massive planets, sometimes with companions having masses above the deuterium burning limit (e.g., Lovis & Mayor 2007), and which apparently form a high-mass tail of a lower-mass planetary population (e.g., Hekker et al. 2008). On the other hand, formation history can be difficult to assess in individual cases. In order to avoid these uncertainties, we simply classify κ And b as a "super-Jupiter," which we take to mean a group of objects that includes the previously imaged planets around HR 8799 and β Pic as well as the most massive radial velocity planets, and which one might suspect to have formed in a similar way to lower-mass exoplanets, but for which this has not necessarily been unambiguously demonstrated. This suggested class includes substellar objects with masses at or moderately above the deuterium burning limit, but excludes objects with orbital separations well beyond a typical disk truncation radius, or systems with mass ratios more indicative of a binary-like formation.

The authors thank David Lafrenière for providing the source code for his LOCI algorithm, the anonymous referee for useful comments, and Subaru Telescope staff for their assistance. The authors thank David Barrado and the Calar Alto Observatory staff for their efforts at carrying out supplementary observations of the host star. This work is partly supported by a Grant-in-Aid for Science Research in a Priority Area from MEXT, Japan, and the U.S. National Science Foundation under Award No. 1009203 (J.C., T.K., P.W., K.G.), 1008440 (C.G.), and 1009314 (J.W.). The authors recognize and acknowledge the significant cultural role and reverence that the summit of Mauna Kea has always had within the indigenous Hawaiian community. We are most fortunate to have the opportunity to conduct observations from this mountain.

Facility: Subaru (HiCIAO, IRCS, AO188)

REFERENCES

Baraffe, I., Chabrier, G., Barman, T. S., Allard, F., & Hauschildt, P. H. 2003, A&A, 402, 701
Béjar, V. J. S., Zapatero Osorio, M. R., Pérez-Garrido, A., et al. 2008, ApJL, 673, 185
Bihain, G., Rebolo, R., Zapatero Osorio, M. R., Béjar, V. J. S., & Caballero, J. A. 2010, A&A, 519, A93
Cameron, P. B., Britton, M. C., & Kulkarni, S. R. 2008, Proc. SPIE, 7015, 4
Chabrier, G., Baraffe, I., Allard, F., & Hauschildt, P. 2000, ApJ, 542, 464
Chauvin, G., Lagrange, A.-M., Dumas, C., et al. 2004, A&A, 425, L29
Chauvin, G., Lagrange, A.-M., Zuckerman, B., et al. 2005, A&A, 438, L29
Cruz, K. L., Kirkpatrick, J. D., & Burgasser, A. J. 2009, AJ, 137, 3345
Currie, T., Burrows, A., Itoh, Y., et al. 2011, ApJ, 729, 128
Currie, T., Debes, J., Rodigas, T. J., et al. 2012, ApJL, 760, 32
Dupuy, T. J., Liu, M. C., Bowler, B. P., et al. 2010, ApJ, 721, 1725
Ekström, S., Georgy, C., Eggenberger, P., et al. 2012, A&A, 537, A146
Faherty, J. K., Rice, E. L., Cruz, K. L., Mamajek, E. E., & Núñez, A. 2012, AJ, 145, 2
Fitzpatrick, E. L., & Massa, D. 2005, AJ, 129, 1642
Gray, R. O., & Corbally, C. J. 2002, AJ, 124, 989
Hayano, Y., Takami, H., Oya, S., et al. 2010, Proc. SPIE, 7736, 21
Hekker, S., Snellen, I. A. G., Aerts, C., et al. 2008, A&A, 480, 215
Hodapp, K. W., Suzuki, R., Tamura, M., et al. 2008, Proc. SPIE, 7014, 42
Ireland, M. J., Kraus, A., Martinache, F., Law, N., & Hillenbrand, L. A. 2011, ApJ, 726, 113
Janson, M., Bonavita, M., Klahr, H., et al. 2011a, ApJ, 736, 89
Janson, M., Carson, J., Thalmann, C., et al. 2011b, ApJ, 728, 85
Johnson, J. A., Aller, K. M., Howard, A. W., & Crepp, J. R. 2010, PASP, 122, 905
Lafrenière, D., Jayawardhana, R., Janson, M., et al. 2011, ApJ, 730, 42
Lafrenière, D., Jayawardhana, R., & van Kerkwijk, M. H. 2008, ApJL, 689, 153
Lafrenière, D., Marois, C., Doyon, R., Nadeau, D., & Artigau, É. 2007, ApJ, 660, 770
Lagrange, A.-M., Gratadour, D., Chauvin, G., et al. 2009, A&A, 493, L21
Leggett, S. K., Golimowski, D. A., Fan, X., et al. 2002, ApJ, 564, 452
Leggett, S. K., Hawarden, T. G., Currie, M. J., et al. 2003, MNRAS, 345, 144
Lovis, C., & Mayor, M. 2007, A&A, 472, 657
Malo, L., Doyon, R., Lafrenière, D., et al. 2012, ApJ, 762, 88
Marois, C., Lafrenière, D., Doyon, R., Macintosh, B., & Nadeau, D. 2006, ApJ, 641, 556
Marois, C., Macintosh, B., Barman, T., et al. 2008, Science, 322, 1348
Marois, C., Zuckerman, B., Konopacky, Q. M., Macintosh, B., & Barman, T. 2010, Natur, 468, 1080
Mordasini, C., Alibert, Y., Benz, W., Klahr, H., & Henning, T. 2012, A&A, 541, 97
Perryman, M. A. C., Lindegren, L., Kovalevsky, J., et al. 1997, A&A, 323, L49
Rafikov, R. 2011, ApJ, 727, 86
Skemer, A. J., Hinz, P. M., Esposito, S., et al. 2012, ApJ, 753, 14
Skrutskie, M. F., Cutri, R. M., Stiening, R., et al. 2006, AJ, 131, 1163
Spiegel, D. S., & Burrows, A. 2012, ApJ, 745, 174
Tamura, M. 2009, in AIP Conf. Proc. Exoplanets and Disks: Their Formation and Diversity, ed. T. Usuda, M. Tamura, & M. Ishii (Melville, NY: AIP), 1158, 11
Thalmann, C., Carson, J., Janson, M., et al. 2009, ApJL, 707, 123
Tokunaga, A. T., Kobayashi, N., Bell, J., et al. 1998, Proc. SPIE, 3354, 512
Torres, C. A. O., Quast, G. R., Melo, C. H. F., & Sterzik, M. F. 2008, Handbook of Star Forming Regions: Vol. II, The Southern Sky, ed. B. Reipurth (San Francisco, CA: ASP), 757
van der Marel, R. P., Anderson, J., Cox, C., et al. 2007, Instrument Science Report ACS 2007-07, 7
van Leeuwen, F. 2009, A&A, 497, 209
Wahhaj, Z., Liu, M. C., Biller, B. A., et al. 2011, ApJ, 729, 139
Wu, Y., Singh, H. P., Prugniel, P., Gupta, R., & Koleva, M. 2011, A&A, 525, A71
Zuckerman, B., Rhee, J. H., Song, I., & Bessell, M. S. 2011, ApJ, 732, 61

The Astrophysical Journal, 763:67 (13pp), 2013 January 20 doi:10.1088/0004-637X/763/1/67

MOA-2010-BLG-073L: AN M-DWARF WITH A SUBSTELLAR COMPANION AT THE PLANET/BROWN DWARF BOUNDARY

R. A. Street[1], J.-Y. Choi[2], Y. Tsapras[1,3], C. Han[2,65], K. Furusawa[4], M. Hundertmark[5], A. Gould[6], T. Sumi[7], I. A. Bond[8], D. Wouters[9], R. Zellem[10], A. Udalski[11]

and

(The RoboNet Collaboration)

C. Snodgrass[12], K. Horne[5], M. Dominik[5,66], P. Browne[5], N. Kains[13], D. M. Bramich[13], D. Bajek[5], I. A. Steele[14], S. Ipatov[15]

and

(The MOA Collaboration)

F. Abe[4], D. P. Bennett[16], C. S. Botzler[17], P. Chote[18], M. Freeman[17], A. Fukui[4], P. Harris[18], Y. Itow[4], C. H. Ling[8], K. Masuda[4], Y. Matsubara[4], N. Miyake[4], Y. Muraki[19], T. Nagayama[20], S. Nishimaya[21], K. Ohnishi[22], N. Rattenbury[17], To. Saito[23], D. J. Sullivan[18], D. Suzuki[7], W. L. Sweatman[8], P. J. Tristram[24], K. Wada[7], P. C. M. Yock[17]

and

(The OGLE Collaboration)

M. K. Szymański[11], M. Kubiak[11], G. Pietrzyński[11,25], I. Soszyński[11], R. Poleski[11], K. Ulaczyk[11], Ł. Wyrzykowski[11]

and

(The μFUN Collaboration)

J. Yee[6], S. Dong[26], I.-G. Shin[2], C.-U. Lee[27], J. Skowron[6], L. Andrade De Almeida[28], D. L. DePoy[29], B. S. Gaudi[6], L.-W. Hung[6], F. Jablonski[28], S. Kaspi[30], N. Klein[30], K.-H. Hwang[2], J.-R. Koo[27], D. Maoz[30], J. A. Muñoz[31], R. W. Pogge[6], D. Polishhook[30], A. Shporer[1,29], J. McCormick[32], G. Christie[33], T. Natusch[33], B. Allen[34], J. Drummond[35], D. Moorhouse[36], G. Thornley[36], M. Knowler[36], M. Bos[37], G. Bolt[38]

and

(The PLANET Collaboration)

J.-P. Beaulieu[9], M. D. Albrow[39], V. Batista[6], S. Brillant[40], J. A. R. Caldwell[41], A. Cassan[42], A. Cole[43], E. Corrales[42], Ch. Coutures[42], S. Dieters[43], D. Dominis Prester[44], J. Donatowicz[45], P. Fouqué[46,47], E. Bachelet[46,47], J. Greenhill[43], S. R. Kane[48], D. Kubas[47], J.-B. Marquette[42], R. Martin[49], J. Menzies[50], K. R. Pollard[17], K. C. Sahu[51], J. Wambsganss[52], A. Williams[49], M. Zub[52]

and

(MiNDSTEp)

K. A. Alsubai[15], V. Bozza[53], M. J. Burgdorf[54], S. Calchi Novati[55], P. Dodds[5], S. Dreizler[56], F. Finet[57], T. Gerner[52], S. Hardis[58], K. Harpsøe[59], F. Hessman[56], T. C. Hinse[27], U. G. Jørgensen[58], E. Kerins[60], C. Liebig[5], L. Mancini[53,55,61], M. Mathiasen[58], M. T. Penny[6,59], S. Proft[52], S. Rahvar[62], D. Ricci[57], G. Scarpetta[63], S. Schäfer[56], F. Schönebeck[52], J. Southworth[64], and J. Surdej[57]

[1] LCOGT, 6740 Cortona Drive, Suite 102, Goleta, CA 93117, USA; rstreet@lcogt.net
[2] Department of Physics, Institute for Astrophysics, Chungbuk National University, Cheongju 361-763, Republic of Korea
[3] School of Mathematical Sciences, Queen Mary, University of London, Mile End Road, London E1 4NS, UK
[4] Solar-Terrestrial Environment Laboratory, Nagoya University, Nagoya 464-8601, Japan
[5] SUPA/St Andrews, Department of Physics and Astronomy, North Haugh, St. Andrews, Fife KY16 9SS, UK
[6] Department of Astronomy, Ohio State University, McPherson Laboratory, 140 West 18th Avenue, Columbus, OH 43210-1173, USA
[7] Department of Earth and Space Science, Graduate School of Science, Osaka University, 1-1 Machikaneyama-cho, Toyonaka, Osaka 560-0043, Japan
[8] Institute of Information and Mathematical Sciences, Massey University, Private Bag 102-904, North Shore Mail Centre, Auckland, New Zealand
[9] UPMC-CNRS, UMR 7095, Institut d'Astrophysique de Paris, 98bis boulevard Arago, F-75014 Paris, France
[10] Lunar and Planetary Laboratory, Department of Planetary Sciences, University of Arizona, 1629 East University Boulevard, Tucson, AZ 85721-0092, USA
[11] Warsaw University Observatory, Al. Ujazdowskie 4, 00-478 Warszawa, Poland
[12] Max Planck Institute for Solar System Research, Max-Planck-Str. 2, D-37191 Katlenburg-Lindau, Germany
[13] European Southern Observatory, Karl-Schwarzschild-Straße 2, D-85748 Garching bei München, Germany
[14] Astrophysics Research Institute, Liverpool John Moores University, Twelve Quays House, Egerton Wharf, Birkenhead, Wirral CH41 1LD, UK
[15] Qatar Foundation, P.O. Box 5825, Doha, Qatar
[16] Department of Physics, University of Notre Dame, Notre Dame, IN 46556, USA
[17] Department of Physics, University of Auckland, Private Bag 92019, Auckland, New Zealand
[18] School of Chemical and Physical Sciences, Victoria University, Wellington, New Zealand
[19] Department of Physics, Konan University, Nishiokamoto 8-9-1, Kobe 658-8501, Japan
[20] Department of Physics and Astrophysics, Faculty of Science, Nagoya University, Nagoya 464-8602, Japan
[21] Extrasolar Planet Detection Project Office, National Astronomical Observatory of Japan (NAOJ), Osawa 2-12-1, Mitaka, Tokyo 181-8588, Japan
[22] Nagano National College of Technology, Nagano 381-8550, Japan
[23] Tokyo Metropolitan College of Industrial Technology, Tokyo 116-8523, Japan
[24] Mt. John Observatory, P.O. Box 56, Lake Tekapo 8770, New Zealand
[25] Universidad de Concepción, Departamento de Astronomia, Casilla 160-C, Concepción, Chile
[26] Institute for Advanced Study, Einstein Drive, Princeton, NJ 08540, USA
[27] Korea Astronomy & Space Science Institute, Daejeon 305-348, Republic of Korea
[28] Divisao de Astrofisica, Instituto Nacional de Pesquisas Espeaciais, Avenida dos Astronauntas, 1758 Sao José dos Campos, 12227-010 SP, Brazil
[29] Department of Physics and Astronomy, Texas A&M University College Station, TX 77843-4242, USA
[30] School of Physics and Astronomy and Wise Observatory, Tel-Aviv University, Tel-Aviv 69978, Israel

[31] Departamento de Astronomiá y Astrofísica, Universidad de Valencia, E-46100 Burjassot, Valencia, Spain
[32] Farm Cove Observatory, Farm Cove, Pakuranga, Auckland 2010, New Zealand
[33] Auckland Observatory, Auckland, New Zealand
[34] Vintage Lane Observatory, Blenheim, New Zealand
[35] Possum Observatory, Patutahi, New Zealand
[36] Kumeu Observatory, Kumeu, West Auckland, New Zealand
[37] Molehill Astronomical Observatory, North Shore City, New Zealand
[38] Craigie, Perth, Western Australia, Australia
[39] Department of Physics and Astronomy, University of Canterbury, Private Bag 4800, Christchurch 8020, New Zealand
[40] European Southern Observatory, Casilla 19001, Vitacura 19, Santiago, Chile
[41] McDonald Observatory, 16120 St Hwy Spur 78 #2, Fort Davis, TX 79734, USA
[42] Institut d'Astrophysique de Paris, UMR7095 CNRS-Université Pierre & Marie Curie, 98 bis Boulevard Arago, F-75014 Paris, France
[43] School of Math and Physics, University of Tasmania, Private Bag 37, GPO Hobart, Tasmania 7001, Australia
[44] Physics Department, Faculty of Arts and Sciences, University of Rijeka, Omladinska 14, 51000 Rijeka, Croatia
[45] Department of Computing, Technical University of Vienna, Wiedner Hauptstrasse 10, Vienna, Austria
[46] Institut de Recherche en Astrophysique et Planétologie (IRAP), Université de Toulouse, UPS-OMP, IRAP, BP 44346–31028 Toulouse cedex 04, Toulouse, France
[47] CNRS, IRAP, 14 Avenue Edouard Belin, F-31400 Toulouse, France
[48] NASA Exoplanet Science Institute, Caltech, MS 100-22, 770 South Wilson Avenue, Pasadena, CA 91125, USA
[49] Perth Observatory, Walnut Road, Bickley, Perth 6076, Australia
[50] South African Astronomical Observatory, P.O. Box 9, Observatory 7935, South Africa
[51] Space Telescope Science Institute, 3700 San Martin Drive, Baltimore, MD 21218, USA
[52] Astronomisches Rechen-Institut, Zentrum für Astronomie der Universität Heidelberg (ZAH), Mönchhofstr. 12-14, D-69120 Heidelberg, Germany
[53] Dipartimento di Fisica "E.R. Caianiello," Universitá degli Studi di Salerno, Via S. Allende, I-84081 Baronissi (SA), Italy
[54] SOFIA Science Center, NASA Ames Research Center, Mail Stop N211-3, Moffett Field, CA 94035, USA
[55] Istituto Internazionale per gli Alti Studi Scientifici (IIASS), I-84019 Vietri Sul Mare (SA), Italy
[56] Institut für Astrophysik, Georg-August-Universität, Friedrich-Hund-Platz1, D-37077 Göttingen, Germany
[57] Institut d'Astrophysique et de Géophysique, Allée du 6 Août 17, Sart Tilman, Bât. B5c, B-4000 Liége, Belgium
[58] Niels Bohr Institute, University of Copenhagen, Juliane Maries vej 30, DK-2100 Copenhagen, Denmark
[59] Centre for Star and Planet Formation, Geological Museum, Øster Voldgade 5, DK-1350 Copenhagen, Denmark
[60] Jodrell Bank Centre for Astrophysics, University of Manchester, Oxford Road, Manchester M13 9PL, UK
[61] Max Planck Institute for Astronomy, Königstuhl 17, D-619117 Heidelberg, Germany
[62] Department of Physics, Sharif University of Technology, P.O. Box 11155-9161, Tehran, Iran
[63] INFN, Gruppo Collegato di Salerno, Sezione di Napoli, Italy
[64] Astrophysics Group, Keele University, Staffordshire ST5 5BG, UK
Received 2012 September 12; accepted 2012 November 3; published 2013 January 8

ABSTRACT

We present an analysis of the anomalous microlensing event, MOA-2010-BLG-073, announced by the Microlensing Observations in Astrophysics survey on 2010 March 18. This event was remarkable because the source was previously known to be photometrically variable. Analyzing the pre-event source light curve, we demonstrate that it is an irregular variable over timescales >200 days. Its dereddened color, $(V - I)_{S,0}$, is 1.221 ± 0.051 mag, and from our lens model we derive a source radius of 14.7 ± 1.3 $R_\odot$, suggesting that it is a red giant star. We initially explored a number of purely microlensing models for the event but found a residual gradient in the data taken prior to and after the event. This is likely to be due to the variability of the source rather than part of the lensing event, so we incorporated a slope parameter in our model in order to derive the true parameters of the lensing system. We find that the lensing system has a mass ratio of $q = 0.0654 \pm 0.0006$. The Einstein crossing time of the event, $t_E = 44.3 \pm 0.1$ days, was sufficiently long that the light curve exhibited parallax effects. In addition, the source trajectory relative to the large caustic structure allowed the orbital motion of the lens system to be detected. Combining the parallax with the Einstein radius, we were able to derive the distance to the lens, $D_L = 2.8 \pm 0.4$ kpc, and the masses of the lensing objects. The primary of the lens is an M-dwarf with $M_{L,1} = 0.16 \pm 0.03\ M_\odot$, while the companion has $M_{L,2} = 11.0 \pm 2.0\ M_J$, putting it in the boundary zone between planets and brown dwarfs.

Key words: brown dwarfs – gravitational lensing: micro – planetary systems – planets and satellites: formation – planets and satellites: general – techniques: photometric

Online-only material: color figures

1. INTRODUCTION

The mass function of individual compact objects (brown dwarfs and planets) in the Galaxy remains poorly understood, particularly at the low-mass end. Brown dwarfs are commonly defined as objects with masses between the deuterium- and hydrogen-burning limits (DBL and HBL, respectively), but these can be hard to detect, being intrinsically faint and fading further as they cool over time. Below the DBL, the mass function for individual objects is even more poorly measured. Unbound, free-floating objects of planetary mass have been discovered via direct imaging of clusters (for example, in σ Orionis; Béjar et al. 2012) and in the field (e.g., the 6–25 M_J object reported by Kirkpatrick et al. 2006). Sumi et al. (2011) reported a population of planets that are either unbound or at very wide separations, discovered when their gravity caused short-timescale microlensing events.

At least partially as a result of these poor constraints, the origin of low-mass compact objects remains unclear. Although traditionally thought of as separate classes of objects, planets and brown dwarfs form a continuous scale of mass and are

[65] Corresponding author.
[66] Royal Society University Research Fellow.

best distinguished by the circumstances of their formation (Burrows et al. 2001; Chabrier et al. 2005, 2011; Sahlmann et al. 2010). Planets form in disks of material orbiting a protostellar object and may subsequently migrate to different period orbits. Brown dwarfs, on the other hand, are considered to be the extreme low-mass end of the star formation process by fragmentation of locally overdense cores caused by turbulence in a cloud (Chabrier et al. 2011), which can themselves form protoplanetary disks (Klein et al. 2003; Scholz et al. 2006). This mechanism may also produce objects of a few Jupiter masses. For a recent review, see Luhman (2012).

The mass function of free-floating low-mass objects is likely to be different from those bound to stars. Marcy & Butler (2000) identified a paucity of brown dwarfs orbiting close (<3 AU) to their host stars, a region where Jovian-mass planets are commonly found. This "brown dwarf desert" may represent the gap between the largest objects that can form in protoplanetary disks and the smallest objects that can concurrently collapse/condense next to a star.

Two different theories have been proposed to explain the formation of Jovian planets in disks (for a review, see Zhou et al. 2012). The core accretion model predicts that planets form from protoplanetary cores, growing up to tens of Jupiter masses (e.g., Mordasini et al. 2009; Baraffe et al. 2010), but predicts few giant planets around M-dwarfs. Higher mass stars are thought to have disks with enhanced surface densities that allow the cores to grow more rapidly (Laughlin et al. 2004), as do disks with a high fraction of dust, leading to enhanced planet formation around high-metallicity stars (Ida & Lin 2004). Alternatively, the model of planet formation via gravitational instabilities in the disk (e.g., Boss 2006) tends to favor the formation of more massive planets, in generally wider orbits.

A number of lines of evidence support the core accretion theory. There is a well-established correlation of increasing planet frequency with stellar metallicity (Santos et al. 2001; Fischer & Valenti 2005; Maldonado et al. 2012). The results of radial velocity surveys imply that there is a dearth of M-dwarf stars with massive, close-in planets. In part, this reflects an observational bias against these faint objects, but the sample is sufficiently large that a real statistical trend is emerging (Cumming et al. 2008; Johnson et al. 2010; Bonfils et al. 2011), for companions with $P < 2000$ days. Recent spectroscopic and *Kepler* results have confirmed the prediction of a rapid increase in frequency for planets with small radii (down to 2 $R_\oplus$) and $P < 50$ days for all spectral types and found that these small planets are several times more common around stars of late spectral type (Bonfils et al. 2011; Howard et al. 2012).

However, the core accretion model has difficulty forming massive planets at large orbital radii, and such systems have been discovered, for example, HR 8799 (Marois et al. 2008). Furthermore, a number of planets have been found orbiting M-dwarf hosts at larger orbital separations, for example, Dong et al. (2006), Forveille et al. (2011), and Batista et al. (2011). These systems may instead form through gravitational instability in the disk, which can account for companions up to several Jupiter masses around M-dwarfs (Boss 2006).

To better understand the formation mechanisms of heavy substellar companions in bound systems, we need to trace the distributions of the physical and orbital properties (such as mass ratio, orbital separation, occurrence frequency) of a significant number of systems. Yet relatively few bound brown dwarf companions have been reported, despite their being easy to detect at close orbital separations (the "brown dwarf desert").

Microlensing offers a complementary window onto brown dwarf and planet formation by probing for cooler companions of all masses in orbital radii between ~0.2 and 10 AU, separations that are difficult or time-consuming to explore by other methods (Shin et al. 2012b). It can probe the companion mass function down to M- and brown dwarf hosts and is sensitive to companions from nearly equal mass down to terrestrial masses.

Sixteen systems have been published to date,[67] and thanks to large-scale galactic lensing surveys and efficient follow-up, each season's bulge observing campaign is now producing a regular yield of new discoveries (e.g., Bachelet et al. 2012; Yee et al. 2012; Miyake et al. 2012). Of these 16 companions, 3 are giant planets orbiting M-dwarf stars: OGLE-2005-BLG-071Lb, a 3.8 M_J planet (Dong et al. 2009); MOA-2009-BLG-0387Lb, with an $M_P = 2.5$ M_J planet (Batista et al. 2011); and MOA-2011-BLG-293Lb, which hosts a 2.4 M_J companion (Yee et al. 2012).

Here we present the newly discovered system, MOA-2010-BLG-073L, an M-dwarf star with a companion whose mass is close to the DBL of ~12.6 M_J. The discovery and follow-up observations are described in Section 2, and we discuss the variability of the source star in Section 3. We describe our analysis in Section 4, from which we derive the physical properties of the lens in Section 5. Finally, we discuss our findings in Section 6.

2. OBSERVATIONS

The microlensing event, MOA-2010-BLG-073, was first announced by the Microlensing Observations in Astrophysics[68] (MOA; Bond et al. 2001 and Sumi et al. 2003 on the 1.8 m telescope at Mt. John Observatory, New Zealand) survey on 2010 March 18. A background source star in the Galactic bulge, $\alpha = 18{:}10{:}11.342$, $\delta = -26{:}31{:}22.544$ (J2000.0), previously having a mean baseline magnitude of $I \sim 16.5$ mag, was discovered to be rising smoothly in brightness consistent with a point-source, point-lens (PSPL) microlensing event. However, on 2010 May 3 the event was found to show an anomalous brightening of ~0.5 mag and an alert was issued (K. Furusawa 2010, private communication).

Microlensing follow-up teams worldwide—RoboNet-II[69] (Tsapras et al. 2009), μFUN[70] (Gould et al. 2006), PLANET[71] (Beaulieu et al. 2006), and MiNDSTEp[72] (Dominik et al. 2010)—responded to provide intensive coverage of the event for the duration of the anomaly (~2 days) and monitored the event as it returned to baseline, over the course of the next ~2 months.

In addition to the MOA data, taken with the wide-band "MOA-Red" filter (corresponding to *R*+*I* bandpasses), the event was observed from several other sites in New Zealand. The 0.41 m telescope at Auckland Observatory, the 0.35 m at Kumeu Observatory, and the 0.41 m Possum Observatory all used *R*-band filters while the 0.304 m Molehill Astronomical Observatory (MAO), the 0.35 m telescope at Farm Cove Observatory (FCO), and the 0.4 m telescope at Vintage Lane Observatory (VLO) all observed it unfiltered. The event was then picked up

[67] Listed on www.exoplanet.eu
[68] www.phys.canterbury.ac.nz/moa
[69] robonet.lcogt.net
[70] www.astronomy.ohio-state.edu/~microfun
[71] www.planet.iap.fr
[72] www.mindstep-science.org

Table 1
Summary of Observations

Telescope and Aperture (m)	Filter	u_λ[a]	Γ_λ[a]	N Frames Total	N Frames Used	a_0[a]	a_1[a] (mag)
MOA 1.8	R/I	0.7027	0.6118	1747	1726	1.305	0.005
OGLE 1.3[b]	I	0.6098	0.5103	47	42	2.188	0.005
Auckland 0.41	R	0.7027	0.6118	136	136	0.910	0.000
Canopus 1.0	I	0.6098	0.5103	162	159	1.310	0.005
CTIO 1.3	V	0.7817	0.7048	19	18	0.603	0.000
CTIO 1.3	I	0.6098	0.5103	162	162	1.010	0.003
CTIO 1.3	H	0.4145	0.3206	586	575	1.340	0.016
Danish 1.54	I	0.6098	0.5103	498	491	1.130	0.014
Farm Cove 0.4[c]	Unfiltered	...	0.5611	225	225	0.975	0.000
FTN 2.0	SDSS-i	0.6098	0.5103	159	158	1.055	0.011
FTS 2.0	SDSS-i	0.6098	0.5103	129	129	1.125	0.006
IRSF 1.4	J	0.4836	0.3844	4	4	1.000	0.000
IRSF 1.4	H	0.4145	0.3206	4	4	1.000	0.000
IRSF 1.4	K_S	0.3550	0.2684	4	4	1.000	0.000
Kumeu 0.35	R	0.7027	0.6118	272	272	0.772	0.000
Lemmon 1.0	I	0.6098	0.5103	116	105	1.290	0.020
LT 2.0	SDSS-i	0.6098	0.5103	167	167	1.155	0.006
MAO 0.304[c]	Unfiltered	...	0.5611	238	238	1.025	0.018
Perth 0.6	I	0.6098	0.5103	66	66	1.095	0.008
Possum	R	0.7027	0.6118	15	15	1.030	0.009
SAAO 1.0	I	0.6098	0.5103	30	30	1.050	0.011
Vintage Lane 0.4[c]	Unfiltered	...	0.5611	124	124	0.995	0.000

Notes.
[a] u_λ, Γ_λ are defined by Equations (3), (4), (5) and a_0, a_1 by Equation (6).
[b] Includes only OGLE-IV data taken during event MOA-2010-BLG-073.
[c] For unfiltered or very broadband observations we adopted a limb-darkening parameter value that was the average of that for R and I bands: $(\Gamma_R + \Gamma_I)/2$.

from three sites in Australia, first in I band by the 1 m Canopus telescope in Tasmania followed by the 2 m Faulkes Telescope South (FTS), where an SDSS-i filter was used. The 0.6 m telescope in Perth also observed in I band. Of the observing sites around longitude zero, the event was imaged from the 1 m telescope at the South African Astronomical Observatory (SAAO) using an I-band filter and in J, H, and K_S by the 1.4 m Infra Red Survey Facility (IRSF), also at SAAO. The 2 m Liverpool Telescope (LT) observed the event in SDSS-i from the Canary Islands.

As darkness fell in the Americas, a number of Chilean telescopes picked up the observing baton: the SMARTS 1.3 m at the Cerro Tololo Interamerican Observatory (CTIO) obtained data in V, I, and H bands with the ANDICAM camera, and the Danish 1.54 m used an I filter. Though in the midst of commissioning the new OGLE-IV camera at the time, the 1.3 m Warsaw telescope also covered the event in I band.[73] The 1 m Mt. Lemmon Telescope in Arizona imaged the event in the I band, and in the extreme west, the 2 m Faulkes Telescope North (FTN) in Hawaii used an SDSS-i filter to complete the 24 hr coverage of the event from the Pacific. Table 1 summarizes the data obtained, which are plotted in Figure 1.

The high density of Galactic bulge star fields and the consequent degree of overlap (or blending) in stellar point-spread functions (PSF) have long since made difference image analysis (DIA) the photometry method of choice among microlensing teams. Both MOA and OGLE make their photometry available to the community, automatically reducing their data with their custom pipelines described, respectively, in Bond et al. (2001) and Udalski et al. (2003). The RoboNet data (from FTN, FTS, and the LT) were reduced with the project's automated data reduction pipeline, which is based around the DanDIA package (Bramich 2008). This software was also later used to reduce data from Canopus, the Perth 0.6 m, the SAAO 1 m, and the H-band data from CTIO, while the DIAPL package was used to process the images from the Danish telescope. The PLANET team released their photometry (produced by the WISIS pipeline) in real time via their Web site, and the Pysis DIA pipeline (Albrow et al. 2009) was used for later re-reduction of these data sets.

[73] www.ogle.astrouw.edu.pl

3. VARIABILITY OF THE SOURCE STAR

MOA-2010-BLG-073 was present in the fields of the OGLE-II and OGLE-III surveys, so the source star's I-band photometric record extends from 1998 to 2006 (Figure 2). OGLE-IV was in the commissioning phase when this event took place. From this excellent baseline it was immediately clear that the source is variable over many-month timescales. This raised the possibility that shorter-term variability might obfuscate the microlensing signal, making it difficult to determine its properties.

To investigate this possibility, we performed a search for periodicities in the baseline OGLE-II and OGLE-III data, excluding the lensing event, using the ANOVA algorithm (Schwarzenberg-Czerny 1996). Due to the seasonal gaps in the baseline, we analyzed the OGLE-II data in yearly subsets as it is the best sampled, searching for periods between $P = 0.5$ and 200 days. As Figure 3 demonstrates, there are no significant or persistent periodicities, other than the expected integer multiples of the 1 day sampling alias.

We then combined the OGLE-II and III data sets in order to search for periods up to $P = 4000$ days. Figure 2 indicates a slight (~0.04 mag) magnitude offset between the OGLE-II and

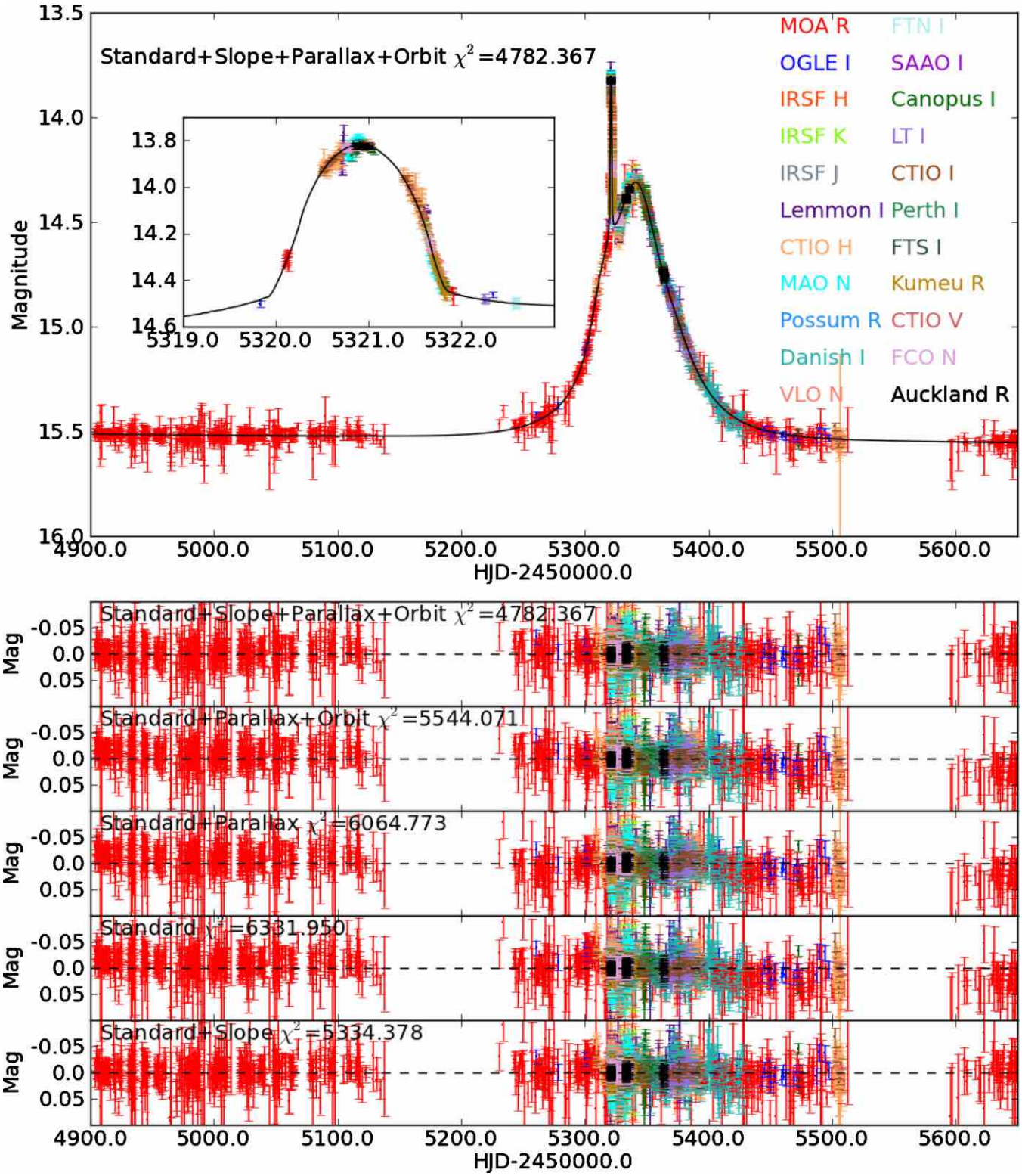

Figure 1. Top panel: the complete light curve of MOA-2010-BLG-073 with the data sets from the various observatories overlaid with our best-fitting model. The inset shows the anomaly in greater detail. Lower panels: the residuals of the fit for each of the best-fitting models of each class.

III data. This can occur as a residual of OGLE's photometric calibration between the two surveys, but it might also be the result of the intrinsic stellar variation. Therefore, we performed a search for periods between 0.5 and 4000 days based on the combined data both with and without this offset (estimated visually). In both cases, the periodogram was dominated by the window function; the only significant power was found in the peaks marking multiples of the 1 day alias, plus one peak at extreme low frequency corresponding to the finite length of the data set. We conclude that this star is an irregular, long-term variable, most likely as a result of pulsations.

However, there remained the possibility that the star could be irregularly variable on timescales comparable to that of the lensing event. To test this possibility, we binned the OGLE-II

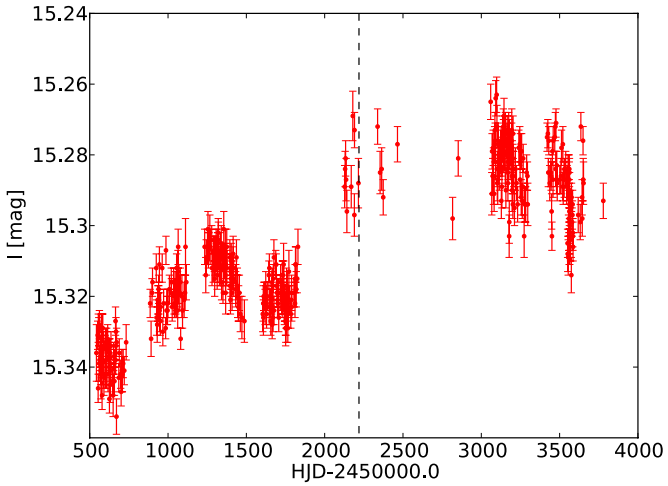

Figure 2. All available OGLE-II (1998–2001) and OGLE-III (2001 June to 2006) light-curve data for the source star of MOA-2010-BLG-073, taken prior to the event. The instrument upgrade to OGLE-III occurred around HJD = 2,452,000.0. The apparent offset in magnitude at this time may be due in part to the difficulties of accurately calibrating photometry between the two wide-field surveys.

(A color version of this figure is available in the online journal.)

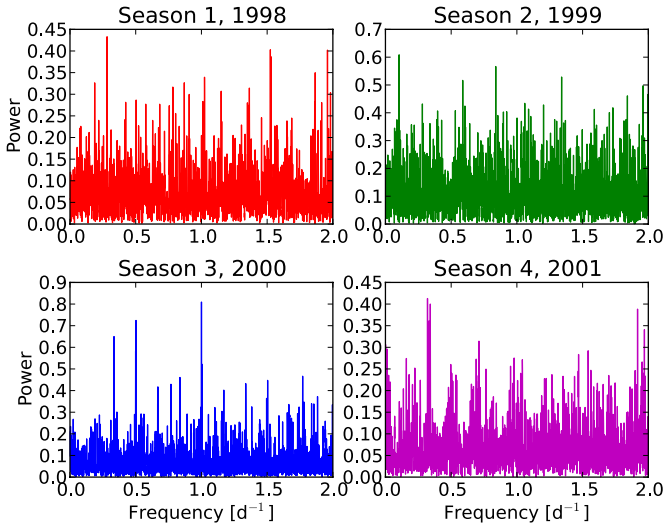

Figure 3. Periodograms of the OGLE-II (1998–2001) seasons of data, analyzed separately with the ANOVA algorithm. No significant periodicities were found in the range $P = 0.5$–200 days, aside from the expected aliases.

(A color version of this figure is available in the online journal.)

light curve on a range of timescales between 2 and 1200 days. To each bin we fitted two functions, one of constant brightness and one with a linear slope, and calculated the weighted rms photometric scatter around each function per bin. We plot the average and maximum rms (calculated over all bins in the light curve) against the width of the bins in time in Figure 4. On timescales shorter than 200 days the rms scatter in the binned light curve is reasonably constant, implying no significant short-term variability. The longer-term trend becomes clearly evident in the constant brightness curves for timescales longer than 400 days. We note that for bin widths between ~800 and 1200 days, this curve has an rms actually exceeding that of the whole light curve; this is because these bins were sufficiently wide that the first bin included the majority of the data and the most variable sections of the light curve. As the bin widths became longer, they included more data points from

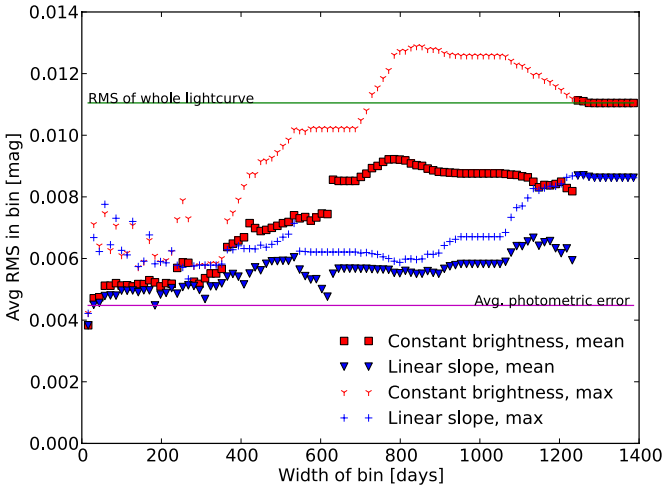

Figure 4. OGLE-II photometry was binned using a series of bins of varying width in time. The data in each bin were fitted with two functions, (1) constant brightness (2) with a linear slope, and the rms around these curves was averaged over all the bins in the light curve. The average and maximum rms for each binning is plotted here against the width of the bin, indicating variability over different timescales.

(A color version of this figure is available in the online journal.)

the relatively stable section toward the end of the OGLE-II data set, and the rms drops. The deviation of the OGLE light curve from a constant brightness exceeds 3σ for timescales longer than ~750 days. However, it deviates from a linear slope by $\leqslant 1.6\sigma$ for timescales less than 1000 days, so we represent this variation as a gradient in the light curve over the duration of the event.

The most intuitive way to account for the variation of the source was to measure the gradient of the light curve taken at baseline immediately before and after the event. Unfortunately, only one of the available data sets covered these periods. Fitting a straight-line model (via a nonlinear least-squares Marquardt–Levenberg algorithm) to the MOA 2009 and 2011 season data, we measured a slope of 0.018 mag yr^{-1}. However, the rms scatter in the residuals of this fit was 0.016 mag, making it difficult to properly determine the slope. Additionally, in order to remove this slope from the other data sets, it would be necessary to transform the fluxes measured by each telescope onto the same scale as the MOA data. We attempted this via a linear regression approach but found that significant residuals remained. These contributed to overall higher χ^2 values when the corrected data were fit with binary lensing models. We therefore adopted the alternative method of incorporating the slope as an additional parameter in our lensing model that we fit to the original, uncorrected data, and we describe this approach in the following sections.

4. ANALYSIS

In the analysis of this event, we used the established modeling software developed by S. Dong and C. Han (Dong et al. 2006; Shin et al. 2012a).

4.1. Initial Parameters

As a starting point for our analysis, we needed approximate values for the three parameters of the standard model for a PSPL event (not yet including the slope; this is discussed in Section 4.8): t_0, the time of peak magnification occurring at the closest projected separation between the lens and source, u_0,

and the Einstein radius crossing time, $t_{\rm E}$. Following standard convention, all distances are quoted in units of the angular Einstein radius, $\theta_{\rm E}$, of the lens.

To estimate these parameters, we combined all available data sets into a single light curve using the following scaling to take account of the varying degrees of PSF blending from different instruments:

$$f(t, k) = A(t) f_s(k) + f_b(k), \quad (1)$$

where $f(t, k)$ is the measured flux of the target at time t from data set k, $A(t)$ is the lensing magnification at that time, $f_s(k)$ is the flux of the source star, and $f_b(k)$ represents the flux of all stars blended with the source in the data set. A regression fit was used to measure f_s and f_b for each data set, producing an aligned light curve. Although the resulting parameter estimates are somewhat different from their "true" values due to the existence of the anomalous deviation on the light curve, they provided a starting point in parameter space.

We note that two additional parameters can contribute to a PSPL model. They are the lens parallax parameters $\pi_{{\rm E},N}$ and $\pi_{{\rm E},E}$ that account for the light-curve deviation caused by the motion of Earth in its orbit over the course of the event. The vector microlens parallax $\boldsymbol{\pi}_{\rm E} = {\rm AU}/\tilde{r}_{\rm E}$, where $\tilde{r}_{\rm E}$ is the Einstein radius projected onto the observer plane and

$$\boldsymbol{\pi}_{\rm E} \equiv (\pi_{{\rm E},N}, \pi_{{\rm E},E}) \equiv (\cos\phi_\pi, \sin\phi_\pi)\pi_{\rm E}, \quad (2)$$

where ϕ_π represents the direction of lens motion relative to the source as a counterclockwise angle, north through east. However, this is generally significant only for long-timescale (∼months) events and was included at a later stage (see Section 4.6).

4.2. Finite Source

The sharp spike feature in the light curve is indicative of the source closely approaching or crossing a caustic. In these circumstances, it cannot be approximated by a point light source and must be treated as a disk of finite angular radius, ρ, with wavelength-dependent limb darkening. This is addressed within our software using the ray-shooting approach (Kayser et al. 1986): the path of light rays is traced from the image plane back to the source, taking into account the bending of the trajectory according to the lens equation. If a ray is found to "land" within the radius of the source, its intensity is computed taking limb darkening into account. We derived this from the linear limb-darkening law:

$$I_\lambda(\cos\phi) = I_\lambda(1)\left[1 - u_\lambda(1 - \cos\phi)\right], \quad (3)$$

where I_λ is the intensity of the source at radius ϕ from the center, relative to the central intensity $I_\lambda(1)$ in the same wavelength, λ, scaled by the coefficient u_λ. While more accurate limb-darkening models are available, they are not commonly used in microlensing analyses due to the complexity introduced by combining data from many sources (Bachelet et al. 2012 discussed this in more detail). The values of u_λ for each passband were calculated from the Kurucz ATLAS9 stellar atmosphere models presented by Kurucz (1979) using the method of Heyrovský (2007). However, within the microlensing community and software, Equation (3) more commonly follows the formalism derived by Albrow et al. (1999):

$$I_\lambda = \frac{F_\lambda}{\pi\theta_*^2}\left[1 - \Gamma_\lambda\left(1 - \frac{3}{2}\cos\phi\right)\right], \quad (4)$$

where F_λ is the total flux from the source in a given passband and ϕ is the angle between the line of sight to the observer and the normal to the stellar surface. The limb-darkening coefficient, Γ_λ, is related to u_λ by

$$\Gamma_\lambda = \frac{2u_\lambda}{3 - u_\lambda}. \quad (5)$$

The values of u_λ and Γ_λ applied for each data set are presented in Table 1. The lensing magnification is then computed as the ratio of the number of rays reaching the source plane relative to the number in the image plane. This approach is only required while the source is close to the caustic. At larger separations, the software employs a semi-analytic hexadecapole approximation to the finite source calculation to improve computation speeds (Pejcha & Heyrovský 2009; Gould 2008).

4.3. Standard Binary Model Grid Search

To model the light curve of a binary lens event, we introduced three additional parameters: $q = M_{L,2}/M_{L,1}$, the ratio of the masses of the two bodies composing the lens, where $M_{L,1}$ is the more massive component; s_0, the projected separation of those masses; and α_0, the angle of the trajectory of the lensed source star, relative to the lens's binary axis. The frame of reference was defined to be at rest with respect to Earth at time $t_{0,\rm par}$, which we took to be the time of caustic crossing at HJD = 2,455,321.0, estimated from the easily identifiable feature in the light curve (following the notation of Skowron et al. 2011).

With seven variables in the model (t_0, u_0, $t_{\rm E}$, α_0, s_0, q, ρ), a number of different lens/source configurations may produce similar light curves, so it was necessary to thoroughly explore a large area of parameter space in order to ensure that all possible solutions are identified. We therefore constructed a grid of models, spanning set ranges in the values of the three variables upon which the overall χ^2 of the fit depended most sensitively, s_0, q, and α_0. Each node in this grid took fixed values of (s_0, q, α_0) and used a Markov Chain Monte Carlo (MCMC) approach (Dong et al. 2006) to find the best-fitting model by optimizing the other parameters. To improve efficiency, a magnification map is generated by ray shooting for each point in the grid from which the model light curves used to compute the χ^2 are drawn. The grid covered the following range: $\log(s_0) = -0.6{:}0.6$ in steps of 0.012, $\log(q) = -4.0{:}1.0$ in steps of 0.05, and $\alpha = 0.0{:}6.3$ in steps of 0.6.

Mapping out the χ^2 for each node in this grid, we found a number of local minima. Visual inspection of these models overlaid on the light curve demonstrated that some more closely followed the data than others. Our first pass analysis included substantial baseline photometry before and after the event. This was not well fit by the models due to the variability of the source, and hence the χ^2 map gave a distorted view of regions in parameter space that best match the event. For this reason, we proceeded by repeating the grid search using just data taken during 2010. This produced two clear minima in χ^2, of which one model stood out as by far the best match to the data. We then conducted a refined grid search over this restricted region of parameter space, taking smaller incremental steps.

4.4. Optimized Standard Binary Model

The refined grid search produced a reasonable model, fitting the majority of the data from all telescopes. This was used as a guide to identifying likely outlying data points, for which the quality of the reduction was then checked. A handful of data

Table 2
The χ^2 for the Best-fitting Model in Each Class, Comparing $u_0 > 0$ and $u_0 < 0$ Solutions

Model	χ^2	
	$u_0 > 0$	$u_0 < 0$
Standard	6331.950	6331.950
Standard+Parallax	6064.773	6099.487
Standard+Parallax+Orbital Motion	5544.071	5690.003
Standard+Parallax+Orbital Motion with Slope	4782.367	4802.606
Standard+Slope	5334.378	5334.378

points were removed at this stage. However, this model included only fixed values for s_0, q, and α_0. To properly determine the standard binary model for this event, our next step was to allow the seven parameters (t_0, u_0, t_E, α_0, s_0, q, ρ) to be optimized during the MCMC fitting process, which used the grid search results as its starting point. At this point we included the extended baseline data from MOA for seasons 2009 and 2011, as these fall within the period for which the source's variability can be approximated with a straight line; we address this in Section 4.8.

4.5. Normalization of Photometric Errors

When fitting microlensing events, the reduced χ^2 of the fit on a per data set basis, $\chi^2_{\rm red}$, typically produces a range of values both less than and exceeding the expected unity value. This can occur as different groups have slightly different ways of estimating photometric errors, but it can lead to over- or underemphasis being placed on particular data sets during the modeling process.

A common technique to address this issue is to arrive at a complete model for the event and then use this model to renormalize the original photometric errors of each data set, $e_{\rm orig}$, according to the expression

$$e_{\rm new} = a_0\sqrt{e^2_{\rm orig} + a_1^2}. \quad (6)$$

We first conducted the sequence of models described in the following sections in order to find the best model for the event. We then set the coefficients a_0, a_1 such that the $\chi^2_{\rm red}$ relative to that model equaled unity; the adopted values are given in Table 1. We then repeated our MCMC fitting process, starting with the standard binary model and systematically adding parameters in to determine the extent of improvement in the model χ^2 in each case. We compare models in Tables 2 and 3, and we plot the residuals (data − model) in Figure 1. In the following sections, the χ^2 values given are those post-renormalization.

4.6. Parallax

Given that the event's $t_E \sim 44$ days ~ 0.12 yr, it was necessary to include parallax in our model. Using the parameters of the standard binary model as a starting point, we allowed our fitting process to optimize for $\pi_{E,E}$ and $\pi_{E,N}$ also. We found that this significantly reduced the χ^2 of the overall fit to 6064.773. By default, this procedure explored models with positive projected separations at closest approach of the lens and source, that is, $u_0 > 0$, which we define as the source's trajectory passing the

Table 3
The Best-fitting Parameters

Parameter (Units)	Standard	Standard +Slope	Standard +Parallax	Standard+Parallax +Orbital Motion	Standard+Parallax +Orbital Motion+Slope
χ^2	6331.950	5334.378	6064.773	5544.071	4782.367
$\Delta\chi^2$[a]	1549.583	552.011	1282.406	761.704	0.0
t_0 (HJD′)[b]	5344.32	5344.38	5344.47	5344.83	5344.69
	±0.01	±0.01	±0.02	±0.03	±0.02
u_0	0.4089	0.403	0.403	0.381	0.386
	±0.0009	±0.001	±0.001	±0.001	±0.001
t_E (days)	43.82	44.84	43.49	43.4	44.3
	±0.08	±0.09	±0.09	±0.1	±0.1
s_0	0.7692	0.7725	0.7717	0.7792	0.7750
	±0.0005	±0.0005	±0.0006	±0.0007	±0.0007
q	0.0705	0.0677	0.0695	0.0683	0.0654
	±0.0005	±0.0005	±0.0006	±0.0006	±0.0006
α_0	0.180	0.171	0.198	0.297	0.221
	±0.003	±0.003	±0.003	±0.006	± 0.007
ρ	0.01963	0.01912	0.01931	0.0163	0.0165
	±0.00006	±0.00007	±0.00008	±0.0001	±0.0001
$\pi_{E,N}$			0.18	0.96	0.37
			±0.02	±0.04	±0.05
$\pi_{E,E}$			−0.124	0.09	0.01
			±0.007	±0.01	±0.01
ds/dt (yr^{-1})				0.53	0.49
				±0.02	±0.02
$d\alpha/dt$ (yr^{-1})				−1.21	−0.37
				±0.06	±0.08
Slope (mag yr^{-1})		−0.0160			−0.0153
		±0.0004			±0.0004

Notes.
[a] Improvement in χ^2 relative to that of the best-fitting model.
[b] All timestamps are abbreviated to HJD′ = HJD −2,450,000.0.

caustic at positive values of θ_y in the lens plane (see Figure 6). For the standard model case the symmetry with respect to the binary axis of the caustic means that the $u_0 < 0$ solutions are identical. However, once parallax was included, this was no longer the case, so we also explored $u_0 < 0$ solutions (this degeneracy is further discussed in Park et al. 2004). The parameters of the $u_0 > 0$ model were taken as a starting point for the fit, except that the sign of u_0 was reversed and the α_0 value became $2\pi - \alpha_0$. We found the best-fitting $u_0 < 0$ model to be slightly less favored, with $\chi^2 = 6099.487$.

4.7. Lens Orbital Motion

The mass ratio and projected separation determined from this model put this event close to the boundary between close and intermediate/resonant caustic structure. In this regime, small changes in the projected separation of the lensing bodies due to their orbital motion can effectively change the shape of the caustic (see Figure 6) while the event is underway, sometimes causing detectable deviations in the light curve. To explore this possibility, we included additional parameters in our model to describe the change in projected binary separation, ds/dt, and the rate of change of the angle of the projected binary axis, $d\alpha/dt$. Again we found that the $u_0 > 0$ model gave the best fit, with $\chi^2 = 5544.071$, compared with 5690.003 when $u_0 < 0$. This type of orbital motion is classified as "separational" in the schema put forward by Penny et al. (2010) and is detected in this event as the source happens to cross the cusp of the caustic in the position where the caustic changes most rapidly.

4.8. Sloping Baseline

While taking these second-order effects into account significantly improved the fit to the data, the overall χ^2 remained rather high. Visual inspection of the light curve still showed a gradient, especially in the 2010 baseline before, relative to after, the event. Based on our analysis in Section 3, this trend is likely to be part of the longer-term variability of the source and not associated with the microlens. In order to determine the true lens/source characteristics, though, this trend had to be taken into account.

The OGLE-II and III data demonstrate that the source variation over the ~150 day timescale of the event can be approximated by a straight line, rather than a higher-order function. We therefore introduced a "slope" parameter to our model, representing the linear rate of change in magnitude during the event. This further improved the χ^2, and the best-fitting model was once again the $u_0 > 0$ solution with $\chi^2 = 4782.367$.

We note that there exist degeneracies between the slope parameter and those for parallax and orbital motion as they can be used to fit similar residuals in the light curve. To test for possible degeneracies, we also fit a standard model plus the slope parameter alone and found that $\chi^2 = 5334.378$. The value for the slope from this model, -0.0160 ± 0.0004, was consistent with that derived from the model including parallax and orbital motion, -0.0153 ± 0.0004.

4.9. Second-order Effects

With the slope parameter included, we had accounted for all the physical effects that we expected to be present in the light curve. Having found that the residuals showed no further variation at a level detectable above the photometric noise, we did not attempt to include second-order effects such as xallarap, etc.

4.10. Final Model

All our models are compared in Table 2, and the parameters of the best-fitting models are presented in Table 3 and Figure 1. We plot the χ^2 for each link in the MCMC chain for all parameters against one another in the best-fitting model in Figure 5. This plot was used as a diagnostic throughout the fitting process, as any correlations between parameters display distinct trends as the chain moves toward the minimum. The caustic structure changed during the course of the event, so in Figure 6 we show the structure at two distinct times: the first at the time of the first caustic crossing during the anomaly, and the second at the time of closest approach.

5. PHYSICAL PARAMETERS

The purpose of this model is to ultimately arrive at the physical parameters of the lens and source, which can be achieved using the known relations between these and the lensing parameters obtained from the modeling.

Chiefly of interest is the mass of the lensing system, $M_{L,\mathrm{tot}}$, which can be determined explicitly for events where parallax is measurable provided that the angular extent of the Einstein radius, θ_E, is known from

$$M_{L,\mathrm{tot}} = \frac{c^2}{4G}\tilde{r}_\mathrm{E}\theta_\mathrm{E} = \frac{c^2 \mathrm{AU}}{4G}\frac{\theta_\mathrm{E}}{\pi_\mathrm{E}}, \quad (7)$$

where $\tilde{r}_\mathrm{E}$ is the Einstein radius projected from the source onto the observer's plane. The model parameter ρ represents the angular size of the source star θ_S in units of the angular Einstein radius θ_E. We derive this from the crossing time taken for the source to travel behind the lens, $t_* = \mu\theta_S$, where μ is the relative source–lens proper motion. ρ can then be written as

$$\rho = \frac{t_*}{t_\mathrm{E}} = \frac{\theta_S}{\theta_\mathrm{E}}. \quad (8)$$

These parameters also yield the distance to the lens,

$$\frac{\mathrm{AU}}{D_L} \equiv \pi_L = \theta_\mathrm{E}\pi_\mathrm{E} + \frac{\mathrm{AU}}{D_S}, \quad (9)$$

which in turn yields the projected separation between the lens components,

$$a_\perp = s_0 D_L \theta_\mathrm{E}, \quad (10)$$

and the relative proper motion between lens and source, when combined with t_E,

$$\mu = \frac{\theta_\mathrm{E}}{t_\mathrm{E}}. \quad (11)$$

The appreciable lens orbital motion during this event also allows us to test whether the companion object is bound to the primary lensing mass, via the ratio of its kinetic to potential energy:

$$\mathrm{KE/PE} = \frac{(s_0 R_\mathrm{E})^3 \gamma^2}{8\pi^2 M_L}, \quad (12)$$

where γ relates the two lens orbital parameters, $\gamma^2 = (ds/dt/s_0)^2 + (d\alpha/dt)^2$, and where the masses are in units of $M_\odot$, the distances in AU, and time measured in years.

However, these expressions include two key terms that are as yet unknown: θ_S, the angular source radius, and D_S, the distance to the source. In order to extract the physical characteristics of the lens, we therefore turned our attention to the characteristics of the source.

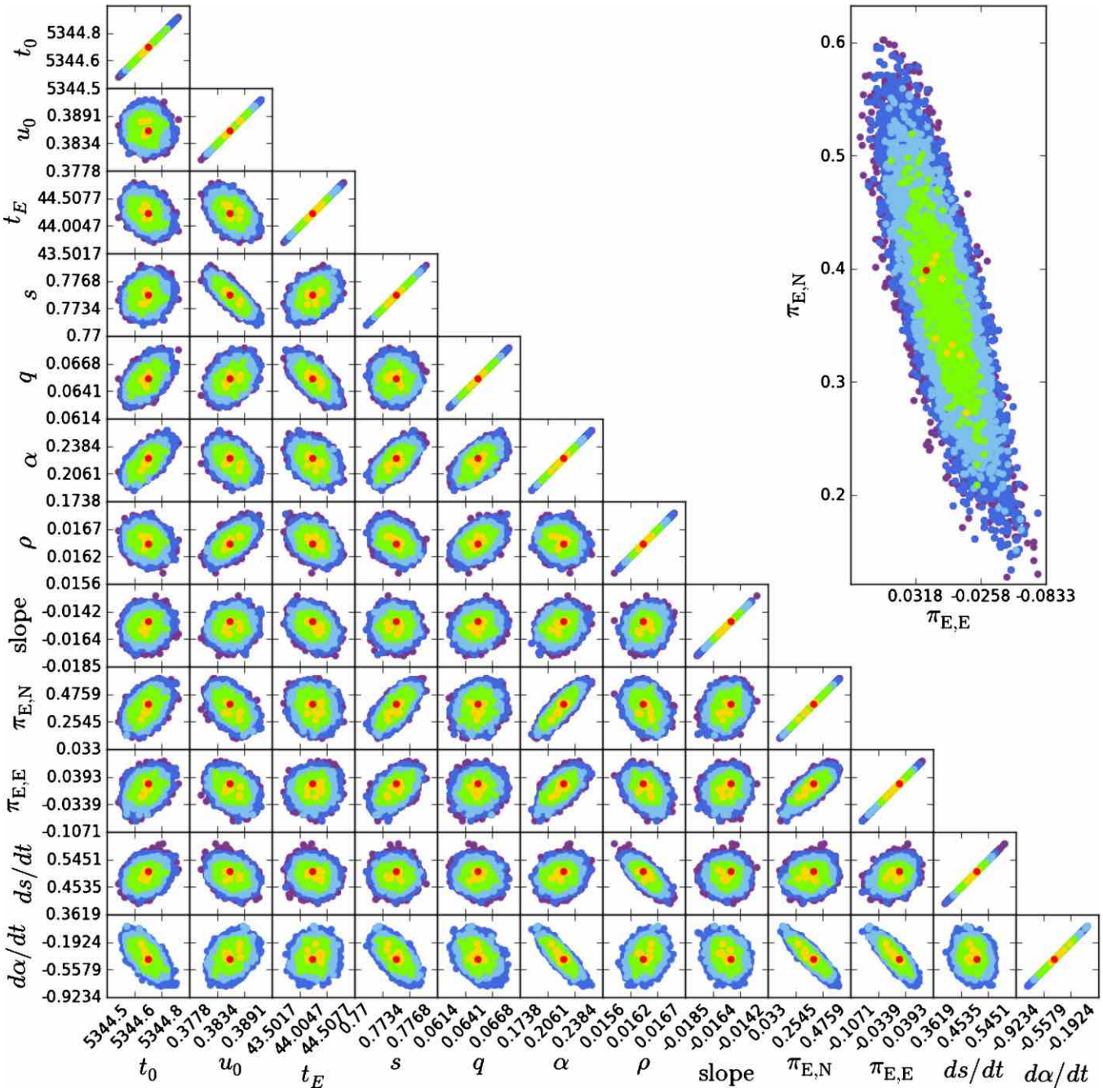

Figure 5. Chi-squared contours plotted as a function of the parameters fitted in the MCMC fit for the best model. The red, orange, green, light blue, dark blue, and purple colors indicate the regions with $\Delta\chi^2 < 1\sigma$–6σ (respectively) from the best-fit solution. Inset: close-up of the contours for the parallax parameters.

5.1. Source Star

Long-exposure V, I images were acquired by the CTIO 1.3 m at several epochs, which enabled us to plot the color–magnitude diagram for the field including the source star (Figure 7). By observing the event at different levels of lensing magnification, these data can be incorporated into the model that yields the source and blended light fluxes, f_s, f_b for those data, and hence the instrumental magnitudes and colors of the source and blend. But we note that these uncalibrated fluxes also suffer from the high degree of extinction along the line of sight to the Galactic bulge. To calculate the dereddened color, $(V-I)_{S,0}$, and magnitude, $I_{S,0}$, of the source, we needed to calibrate the instrumental fluxes f_s and f_b relative to a standard candle.

Figure 7 clearly shows a locus of stars centered at $I_{\rm RC,inst} = 15.821 \pm 0.05$ mag, $(V-I)_{\rm RC,inst} = -0.350 \pm 0.05$ mag. This consists of a clump of red giant stars, for which stellar theory predicts a stable absolute luminosity, varying only slightly with age and chemical composition. Their frequent occurrence makes these objects useful as standard candles. Stanek et al. (1998) established photometric calibrations for red clump magnitudes, which were later refined by Alves et al. (2002) using *Hipparcos* data. Most recently, Nataf et al. (2012) were able to measure

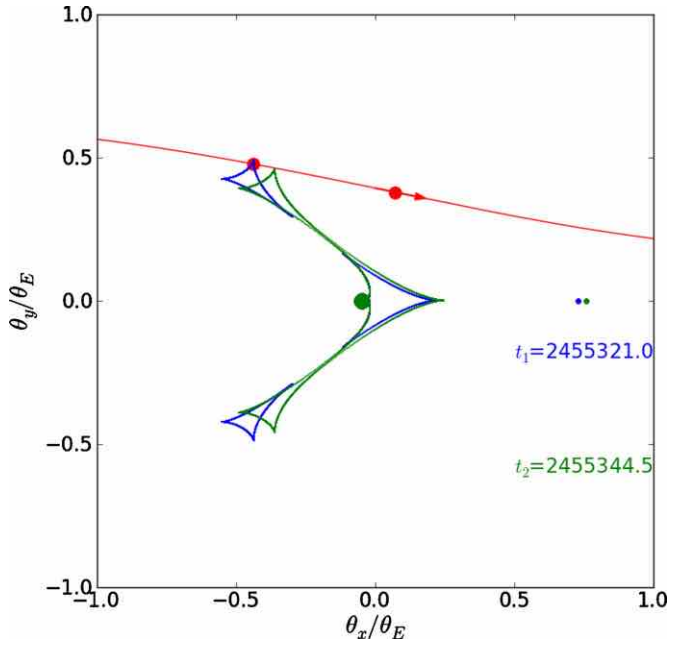

Figure 6. Maps of the caustic structure during the anomaly and at the time of closest approach. The red line and arrow indicate the trajectory of the source in a reference frame centered on the barycenter of the lensing system, while the red dots indicate the position of the source at these times. The green and blue dots indicate the positions of $M_{L,1}$ (largest) and $M_{L,2}$ at both times (radii of dots not to scale).

(A color version of this figure is available in the online journal.)

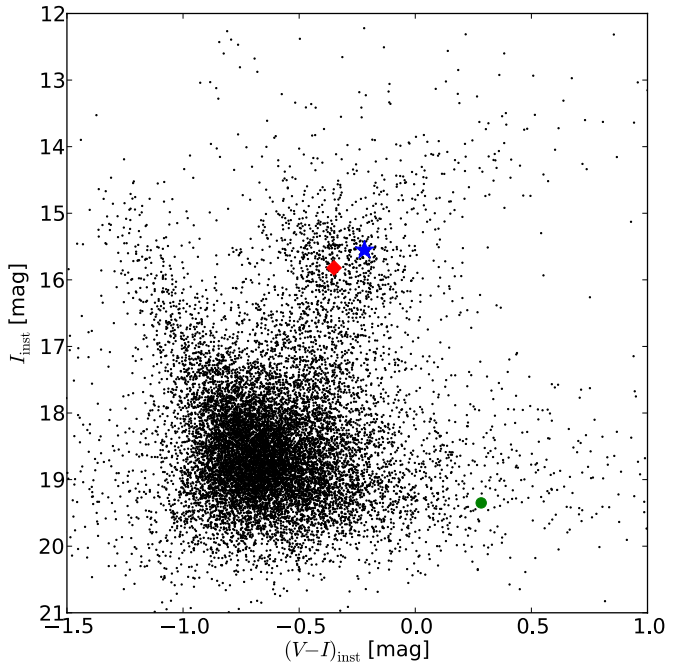

Figure 7. Instrumental color–magnitude diagram for the field of view including the lensing source star. The position of the source is marked with a blue star, relative to the center of the red giant clump highlighted with a red diamond. The green circle indicates the color and V magnitude of light blended in the CTIO photometry.

(A color version of this figure is available in the online journal.)

the dereddened apparent magnitude of the red clump stars at the Galactocentric distance, $I_{\rm RC,0} = 14.443$. By mapping the distances, $D_{\rm RC}$, to red clump stars in the Galactic bar as a function of Galactic longitude, l, they found an apparent viewing angle on the bar of $\phi_{\rm Bar} = 40^\circ$,

$$\frac{R_0}{D_{\rm RC}} = \frac{\sin\phi + l}{\phi} = \cos l + \sin l \cot\phi, \qquad (13)$$

where Nataf et al. (2012) measured R_0 to be 8.20 kpc. For the field of MOA-2010-BLG-073 (Galactic coordinates: $l = 4.^\circ81030$, $b = -3.^\circ50131$), we derive $D_{\rm RC} = 7.48$ kpc, and we assumed that the source star lies behind the same amount of dust as the red clump stars and at the same distance. Scaling the dereddened apparent magnitude of the red clump stars, $I_{\rm RC,0}$, appropriately for the slightly closer distance of the stars in this field, $I_{\rm RC,app} = I_{\rm RC,0} + \Delta I$, where

$$\Delta I = 5 \log_{10} R_0 / D_{\rm RC}. \qquad (14)$$

We found $\Delta I = 0.20$ mag, and so the distance modulus to the red clump and the source in this field is $I_{\rm RC,app} = 14.24$ mag. Bensby et al. (2011) determined the intrinsic $(V-I)_{\rm RC,0} = 1.09$ mag for red clump stars, so we were able to derive their absolute V magnitude of $M_{V,{\rm RC},O} = 0.97$ mag. Combining these results with the measured $\Delta(V-I)_{\rm inst}$ and $\Delta V_{\rm inst}$ between the source and red clump in the CTIO data, we then derived the dereddened color $(V-I)_{S,0}$ and magnitude $I_{S,0}$ of the source, summarized in Table 4.

Bessell & Brett (1988) provided a relationship between $(V-I)$ and $(V-K)$ color indices, and Kervella et al. (2004) related $(V-K)$ to angular radius for giant and dwarf stars. Having thus determined D_S and θ_S, we derived the physical parameters of the lensing system, which are also summarized in Table 4. The color and large source radius of $14.7 \pm 1.3\ R_\odot$ imply that this star is a K-type giant, which is consistent with the observed photometric variability. Jorissen et al. (1997) found that red giant stars with spectral types later than early-K are all variable, with amplitudes

Table 4
The Physical Parameters of the Lensing System and Source Star, Derived from the Model Including Slope, Parallax, and Orbital Motion, plus Color Information

Parameter	Units	Value
θ_S	μas	9.143 ± 0.792
$\theta_{\rm E}$	mas	0.557 ± 0.09
R_S	$R_\odot$	14.7 ± 1.3
$M_{L,1}$	$M_\odot$	0.16 ± 0.03
$M_{L,2}$	$M_{\rm J}$	11.0 ± 2.0
$M_{L,{\rm tot}}$	$M_\odot$	0.17 ± 0.03
D_L	kpc	2.8 ± 0.4
$a_\perp$	AU	1.21 ± 0.16
KE/PE		0.079
Proper motion	mas yr^{-1}	4.60 ± 0.4
$I_{S,{\rm inst}}$	mag	15.554 ± 0.007
$V_{S,{\rm inst}}$	mag	15.335 ± 0.007
$(V-I)_{S,{\rm inst}}$	mag	-0.22 ± 0.01
$I_{\rm RC,inst}$	mag	15.821 ± 0.05
$(V-I)_{\rm RC,inst}$	mag	-0.350 ± 0.05
$I_{\rm RC,0}$	mag	14.443
$(V-I)_{\rm RC,0}$	mag	1.09
$I_{S,0}$	mag	13.976
$V_{S,0}$	mag	15.197
$(V-I)_{S,0}$	mag	1.221 ± 0.051
$(V-K)_{S,0}$	mag	2.852
$K_{S,0}$	mag	12.345
J (2MASS)	mag	13.686 ± 0.053
H (2MASS)	mag	12.926 ± 0.057
K_S (2MASS)	mag	12.642 ± 0.054

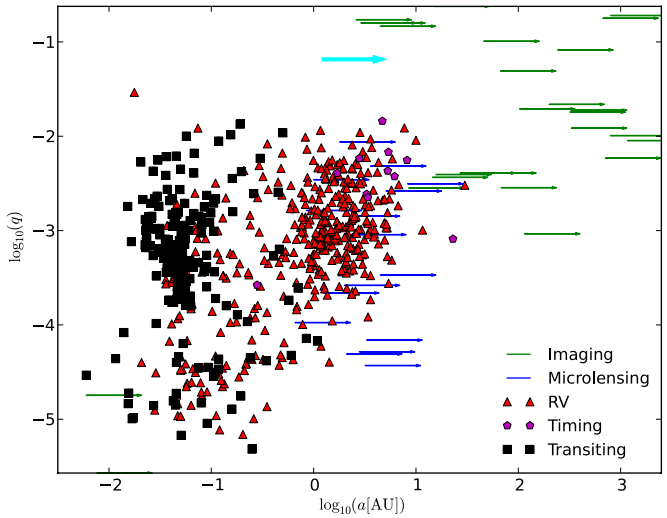

Figure 8. Ratio of planet mass to host star mass plotted against semimajor axis for all exoplanets for which these parameters are available (source: www.exoplanet.eu; Schneider et al. 2011). The true orbital semimajor axis is plotted where it has been measured; otherwise, the projected (minimum) separation has been indicated with an arrow, where the base of the arrow marks the measured value. Very few objects have been found between $\log_{10}(q) = -1$ and -2. This corresponds to the brown dwarf desert. The location of MOA-2010-BLG-073L, highlighted in cyan and bold, lies between the brown dwarf and planetary regimes.

increasing from microvariability to several magnitudes toward cooler temperatures and timescales from days to years. Kiss et al. (2006) note that irregular photometric variability may be caused by large convection cells, or may actually be the result of a number of simultaneous periodic pulsation modes, and many examples have been identified from time-domain surveys (e.g., Wray et al. 2004; Woźniak et al. 2004; Eyer & Blake 2005; Ciechanowska et al. 2006). We note that the star was detected by the Two Micron All Sky Survey (2MASS; Skrutskie et al. 2006) as source 2MASS J18101138−2631226 with colors $(J-H) = 0.76 \pm 0.078$ mag and $(H-K_S) = 0.284 \pm 0.079$ mag. Although the MASS field is crowded, the star's PSF is distinct and their photometry for it has the best-quality AAA flag. These colors are consistent with a giant star and with our derived value for $K_{S,0} = 12.345$ mag, when we take into account $AK_S = 0.24$ mag from the VVV survey (Gonzalez et al. 2012).

Nataf et al. (2012) explain that their value of our viewing angle of the Galactic bar is a "soft upper bound" because the distance along the plane to the greatest density of stars along the line of sight to a triaxial bar structure is less than the distance to the structure's major axis on the far side and greater on the near side. As the physical parameters derived for MOA-2012-BLG-073 are somewhat dependent on the value of our viewing angle of the Galactic bar and Nataf et al. (2012) quote consistent results with values as low as 25°, we explored the potential impact of this on our results. A reduced viewing angle would produce a smaller distance to the source, changing its dereddened magnitude and color. The resulting increase in source radius produces a corresponding reduction in the value of D_L and increases in the lens masses. However, we found that the physical parameter values do not change by more than the errors quoted in Table 4, implying that this is not the dominant source of uncertainty. Finally, we computed the physical parameters derived from the best-fitting $u_0 < 0$ model for comparison and found that the masses derived changed by $< 1\sigma$.

6. DISCUSSION

Earth's movement during this relatively long timescale ($t_E = 44.3$ days) microlensing event resulted in a gradual shift in our perspective on the lensing system, breaking the symmetry of the caustic. Meanwhile, the change in projected separation of the lensing objects modified the shape of the caustic just as the source's trajectory happened to pass close by. If not for these subtle variations, it can be seen from Figure 6 that a source trajectory $u_0 > 0$ would produce exactly the same light curve as a $u_0 < 0$ trajectory. As it is, for this event, the $u_0 > 0$ solution best explains our observations, though the difference in χ^2 relative to the corresponding $u_0 < 0$ solution is very small ($\Delta\chi^2 = 20.2$) compared with the χ^2 of both fits.

The measurable parallax signature enables us to determine the masses of the lensing bodies. The primary lensing object has $M_{L,1} = 0.16 \pm 0.03\ M_\odot$, making it an M-dwarf star. The companion's mass is $M_{L,2} = 11.0 \pm 2.0\ M_J$. This places it in the brown dwarf desert (see Figure 8), though we note that this traditionally refers to close-in companions, and since microlensing and direct imaging measure only the projected separation, we know only their *minimum* orbital semimajor radii. Regardless, it is clear that MOA-2010-BLG-073L b is close to the mass threshold for deuterium burning ($\sim 0.012\ M_\odot = 12.6\ M_J$) quoted as the nominal boundary between planets and brown dwarfs established by the IAU (Chabrier et al. 2005). So what kind of object is it?

No further orbital or metallicity information is available for this event, which might have shed light on its evolutionary history. Theoretical isochrones predict that a star of this low mass will not have lost a significant amount of material over its lifetime, so we can say that MOA-2010-BLG-073L b formed as a high mass ratio binary. Models of protoplanetary disks have the expectation that disk mass, M_D, will scale linearly with star mass M_* (Williams & Cieza 2011), $M_D/M_* \sim 1\%$ at young ages, but this would limit M_D—and hence $M_{P,\mathrm{max}}$—to $\sim$1–10 M_J in the case of MOA-2010-BLG-073L. So it seems questionable whether such a massive companion could have formed in a protostellar disk, via either core accretion or gravitational instability.

Bonnell et al. (2008) and Kroupa & Bouvier (2003) discuss a number of mechanisms that can produce an M-dwarf/brown dwarf binary following gravitational fragmentation in a molecular cloud.

1. *Embryo rejection model.* The nascent binary was ejected from a dynamically unstable multiple protostellar system, leading to the loss of its accretion envelope before the secondary component could acquire enough mass to become a star.
2. *Collision model.* The binary was prematurely ejected from a larger protostellar system by the close passage of another star.
3. *Photoevaporation model.* The accretion envelope around the binary was photoevaporated by the nearby presence of a massive star in the birth cluster before the secondary could accrete enough mass to become a star.
4. *"Star-like" model.* The object formed as a normal stellar binary with low-mass components.

The embryo rejection model predicts (Bate et al. 2002) that the maximum separation of binaries surviving this process is $a_{\mathrm{max}} \sim$ 10–20 AU. We cannot rule out this scenario as we only measure the projected separation of the lens, which is nevertheless below a_{max}. Since MOA-2010-BLG-073L is a field

object, we have no information regarding the proximity of other stars during its birth, so the collisional and photoevaporation models are equally plausible. However, we note that Whitworth & Stamatellos (2006) derived a minimum mass for primary fragmentation components of 0.004 $M_{\odot} \sim 4.2\ M_{\rm J}$. As this threshold is below the mass of MOA-2010-BLG-073L b, the simplest explanation is that the companion is an extremely low mass product of star formation. However, we note that the mass ratio of this system would match that of an object in the brown dwarf desert if the host were a more massive star. Recent surveys (e.g., Dieterich et al. 2012; Evans et al. 2012, though restricted to massive companions with $a > 10$ AU) hint that the brown dwarf desert may extend to M-dwarfs and beyond 3 AU, which would make MOA-2010-BLG-073L a rare example of its type.

R.A.S. is grateful to the Chungbuk University group and especially to C. Han and J.-Y. Choi for their advice and hospitality in Korea, where much of this work was completed. R.A.S. also expresses appreciation for Y. Tsapras, K. Horne, M. Hundertmark, S. Dong, and P. Fouqué for many useful discussions. K.A., D.M.B., M.D., K.H., M.H., C.L., C.S., R.A.S., and Y.T. thank the Qatar Foundation for support from QNRF grant NPRP-09-476-1-078. Work by C. Han was supported by the Creative Research Initiative Program (2009-0081561) of the National Research Foundation of Korea. C.S. received funding from the European Union Seventh Framework Programme (FP7/2007-2013) under grant agreement no. 268421. The OGLE project has received funding from the European Research Council under the European Community's Seventh Framework Programme (FP7/2007-2013)/ERC grant agreement no. 246678 to AU. This publication makes use of data products from the Exoplanet Encyclopeida and the Two Micron All Sky Survey, which is a joint project of the University of Massachusetts and the Infrared Processing and Analysis Center/California Institute of Technology, funded by the National Aeronautics and Space Administration and the National Science Foundation. M.O.A. acknowledges funding JSPS20340052, JSPS22403003, and JSPS19340058. T.C.H. gratefully acknowledges financial support from the Korea Research Council for Fundamental Science and Technology (KRCF) through the Young Research Scientist Fellowship Program. C.U.L. and T.C.H. acknowledge financial support from KASI (Korea Astronomy and Space Science Institute) grant number 2012-1-410-02. D.R. (boursier FRIA), F.F. (boursier ARC), and J. Surdej acknowledge support from the Communauté francaise de Belgique-Actions de recherche concertées-Académie universitaire Wallonie-Europe. A. Gould acknowledges support from NSF AST-1103471. B. S. Gaudi, A. Gould, and R. W. Pogge acknowledge support from NASA grant NNX12AB99G. Work by J. C. Yee is supported by a National Science Foundation Graduate Research Fellowship under grant No. 2009068160. S.D. is supported through a Ralph E. and Doris M. Hansmann Membership at the IAS and NSF grant AST-0807444.

Facilities: FTN, Liverpool:2m, CTIO:1.3m, MtCanopus:1m, Elizabeth, Danish 1.54m Telescope

REFERENCES

Albrow, M. D., Beaulieu, J.-P., Caldwell, J. A. R., et al. 1999, ApJ, 522, 1022
Albrow, M. D., Horne, K., Bramich, D. M., et al. 2009, MNRAS, 397, 2099
Alves, D. R., Rejkuba, M., Minniti, D., & Cook, K. H. 2002, ApJL, 573, 51
Bachelet, E., Shin, I.-G., Han, C., et al. 2012, ApJ, 754, 73
Baraffe, I., Chabrier, G., & Barman, T. 2010, RPPh, 73, 016901
Bate, M. R., Bonnell, I. A., & Bromm, V. 2002, MNRAS, 332, L65
Batista, V., Gould, A., Dieters, S., et al. 2011, A&A, 529, 102
Beaulieu, J.-P., Bennett, D. P., Fouqué, P., et al. 2006, Natur, 439, 437
Béjar, V. J. S., Zapatero Osorio, M. R., Rebolo, R., et al. 2012, ApJ, 743, 64
Bensby, T., Adén, D., Meléndez, J., et al. 2011, A&A, 533, 134
Bessell, M. S., & Brett, J. M. 1988, PASP, 100, 1134
Bond, I., Abe, F., Dodd, R. J., et al. 2001, MNRAS, 327, 868
Bonfils, X., Delfosse, X., Udry, S., et al. 2011, A&A, submitted (arXiv:1111.5019)
Bonnell, I. A., Clark, P., & Bate, M. R. 2008, MNRAS, 389, 1556
Boss, A. P. 2006, ApJ, 643, 501
Bramich, D. M. 2008, MNRAS, 386, L77
Burrows, A., Hubbard, J. I., Lunine, J. I., et al. 2001, RvMP, 73, 719
Chabrier, G., Baraffe, I., Allard, F., et al. 2005, in ASP Conf. Ser., Resolved Stellar Populations, ed. D. Valls-Gabaud & M. Chavez (San Francisco, CA: ASP)
Chabrier, G., Leconte, J., & Baraffe, I. 2011, in IAU Symp. 276, The Astrophysics of Planetary Systems: Formation, Structure, and Dynamical Evolution, ed. A. Sozzetti, M. G. Lattanzi, & A. P. Boss (Cambridge: Cambridge Univ. Press), 171
Ciechanowska, A., Pietrzynski, G., Wyrzykowski, L., et al. 2006, AcA, 56, 219
Cumming, A., Butler, R. P., Marcy, G. W., et al. 2008, PASP, 120, 531
Dieterich, S. B., Henry, T. J., Golimowski, D. A., et al. 2012, AJ, 144, 64
Dominik, M., Jørgensen, U. G., Rattenbury, N. J., et al. 2010, AN, 331, 671
Dong, S., DePoy, D. L., Gaudi, B. S., et al. 2006, ApJ, 642, 842
Dong, S., Gould, A., Udalski, A., et al. 2009, ApJ, 695, 970
Evans, T. M., Ireland, M. J., Kraus, A. L., et al. 2012, ApJ, 744, 120
Eyer, L., & Blake, C. 2005, MNRAS, 358, 30
Fischer, D. A., & Valenti, J. 2005, ApJ, 622, 1102
Forveille, T., Bonfils, X., Lo Curto, G., et al. 2011, A&A, 526, A141
Gonzalez, O. A., Rejkuba, M., & Zoccali, M. 2012, A&A, 543, A13
Gould, A. 2008, ApJ, 681, 1598
Gould, A., Udalski, A., An, D., et al. 2006, ApJL, 644, 37
Heyrovský, D. 2007, ApJ, 656, 483
Howard, A. W., Marcy, G. W., Bryson, S. T., et al. 2012, ApJS, 201, 15
Ida, S., & Lin, D. N. C. 2004, ApJ, 616, 567
Johnson, J. A., Aller, K. M., Howard, A. W., et al. 2010, PASP, 122, 905
Jorissen, A., Mowlavi, N., Sterken, C., & Manifroid, J. 1997, A&A, 324, 578
Kayser, R., Refsdal, S., & Stabell, R. 1986, A&A, 166, 36
Kervella, P., Bersier, D., Mourard, D., et al. 2004, A&A, 428, 587
Kirkpatrick, J. D., Barman, T. S., Burgasser, A., et al. 2006, ApJ, 639, 1120
Kiss, L. L., Szabó, Gy. M., & Bedding, T. R. 2006, MNRAS, 372, 1721
Klein, R., Apai, D., Pascucci, I., et al. 2003, ApJL, 593, 57
Kroupa, P., & Bouvier, J. 2003, MNRAS, 346, 369
Kurucz, R. L. 1979, ApJS, 40, 1
Laughlin, G., Bodenheimer, P., & Adams, F. C. 2004, ApJL, 612, 73
Luhman, K. L. 2012, ARA&A, 50, 65
Maldonado, J., Eiroa, C., Villaver, E., et al. 2012, A&A, 541, 40
Marcy, G. W., & Butler, R. P. 2000, PASP, 112, 137
Marois, C., MacIntosh, B., & Barman, T. 2008, Sci, 322, 1348
Miyake, N., Udalski, A., Sumi, T., et al. 2012, ApJ, 752, 82
Mordasini, C., Alibert, Y., & Benz, W. 2009, A&A, 501, 1139
Nataf, D. M., Gould, A., Fouqué, P., et al. 2012, ApJ, submitted (arXiv:1208.1263)
Park, B.-G., DePoy, D. L., Gaudi, B. S., et al. 2004, ApJ, 609, 166
Pejcha, O., & Heyrovský, D. 2009, ApJ, 690, 1772
Penny, M. T., Mao, S., & Kerins, E. 2010, MNRAS, 412, 607
Sahlmann, J., Ségransan, D., Queloz, D., et al. 2010, A&A, 525, A95
Santos, N. C., Israelian, G., & Mayor, M. 2001, A&A, 373, 1019
Schneider, J., Dedieu, C., Le Sidaner, P., et al. 2011, A&A, 532, A79
Scholz, A., Jayawardhana, R., & Wood, K. 2006, ApJ, 645, 1498
Schwarzenberg-Czerny, A. 1996, ApJL, 460, 107
Shin, I.-G., Han, C., Choi, J.-Y., et al. 2012a, ApJ, 746, 127
Shin, I.-G., Han, C., Gould, A., et al. 2012b, ApJ, 760, 116
Skowron, J., Udalski, A., Gould, A., et al. 2011, ApJ, 738, 87
Skrutskie, M. F., Cutri, R. M., Stiening, R., et al. 2006, AJ, 131, 1163
Stanek, K. Z., & Garnavich, P. M. 1998, ApJ, 503, 131
Sumi, T., Bond, I. A., & Dodd, R. J. 2003, ApJ, 591, 204
Sumi, T., Kamiya, K., Bennett, D. P., et al. 2011, Natur, 473, 349
Tsapras, Y., Street, R., Horne, K., et al. 2009, AN, 330, 4
Udalski, A. 2003, AcA, 53, 291
Whitworth, A. P., & Stamatellos, D. 2006, A&A, 458, 817
Williams, J. P., & Cieza, L. A. 2011, ARA&A, 49, 67
Woźniak, P. R., Williams, S. J., Vestrand, W. T., & Gupta, V. 2004, AJ, 128, 2965
Wray, J. J., Eyer, L., & Paczyński, B. 2004, MNRAS, 349, 1059
Yee, J. C., Shvartzvald, Y., Gal-Yam, A., et al. 2012, ApJ, 755, 102
Zhou, J.-L., Xie, J-W., Liu, H-G., et al. 2012, RAA, 12, 1081

The Astrophysical Journal Letters, 760:L26 (5pp), 2012 December 1 doi:10.1088/2041-8205/760/2/L26

SUBARU IMAGING OF ASYMMETRIC FEATURES IN A TRANSITIONAL DISK IN UPPER SCORPIUS*

S. Mayama[1,2], J. Hashimoto[3], T. Muto[4], T. Tsukagoshi[5], N. Kusakabe[3], M. Kuzuhara[3,6], Y. Takahashi[3,7], T. Kudo[8], R. Dong[9], M. Fukagawa[10], M. Takami[11], M. Momose[5], J. P. Wisniewski[12], K. Follette[13], L. Abe[14], E. Akiyama[3], W. Brandner[15], T. Brandt[9], J. Carson[16], S. Egner[8], M. Feldt[15], M. Goto[17], C. A. Grady[18,19,20], O. Guyon[8], Y. Hayano[2,8], M. Hayashi[2,3], S. Hayashi[2,8], T. Henning[15], K. W. Hodapp[21], M. Ishii[8], M. Iye[2,3], M. Janson[9], R. Kandori[3], J. Kwon[2], G. R. Knapp[9], T. Matsuo[22], M. W. McElwain[20], S. Miyama[23], J.-I. Morino[3], A. Moro-Martin[9,24], T. Nishimura[8], T.-S. Pyo[8], E. Serabyn[25], H. Suto[3], R. Suzuki[3], N. Takato[2,8], H. Terada[8], C. Thalmann[26], D. Tomono[8], E. L. Turner[9,27], M. Watanabe[28], T. Yamada[29], H. Takami[2,8], T. Usuda[2,8], and M. Tamura[2,3]

[1] The Center for the Promotion of Integrated Sciences, The Graduate University for Advanced Studies (SOKENDAI), Shonan International Village, Hayama-cho, Miura-gun, Kanagawa 240-0193, Japan; mayama_satoshi@soken. ac.jp
[2] Department of Astronomical Science, The Graduate University for Advanced Studies (SOKENDAI), 2-21-1 Osawa, Mitaka, Tokyo 181-8588, Japan
[3] National Astronomical Observatory of Japan, 2-21-1 Osawa, Mitaka, Tokyo 181-8588, Japan
[4] Division of Liberal Arts, Kogakuin University, 1-24-2, Nishi-Shinjuku, Shinjuku-ku, Tokyo 163-8677, Japan
[5] College of Science, Ibaraki University, 2-1-1 Bunkyo, Mito, Ibaraki 310-8512, Japan
[6] Department of Earth and Planetary Science, The University of Tokyo, Hongo 7-3-1, Bunkyo-ku, Tokyo 113-0033, Japan
[7] Department of Astronomy, The University of Tokyo, Hongo 7-3-1, Bunkyo-ku, Tokyo 113-0033, Japan
[8] Subaru Telescope, 650 North A'ohoku Place, Hilo, HI 96720, USA
[9] Department of Astrophysical Sciences, Princeton University, NJ 08544, USA
[10] Department of Earth and Space Science, Graduate School of Science, Osaka University, 1-1 Machikaneyama, Toyonaka, Osaka 560-0043, Japan
[11] Institute of Astronomy and Astrophysics, Academia Sinica, P.O. Box 23-141, Taipei 106, Taiwan
[12] H L Dodge Department of Physics and Astronomy, University of Oklahoma, 440 West Brooks St. Norman, OK 73019, USA
[13] Department of Astronomy and Steward Observatory, The University of Arizona, 933 North Cherry Avenue, Rm. N204, Tucson, AZ 85721-0065, USA
[14] Laboratoire Hippolyte Fizeau, UMR6525, Universite de Nice Sophia-Antipolis, 28, avenue Valrose, F-06108 Nice Cedex 02, France
[15] Max Planck Institute for Astronomy, Koenigstuhl 17, D-69117 Heidelberg, Germany
[16] Department of Physics and Astronomy, College of Charleston, 58 Coming Street, Charleston, SC 29424, USA
[17] Universitäts-Sternwarte München Scheinerstr. 1, D-81679, Munich, Germany
[18] Goddard Center for Astrobiology, NASA's Goddard Space Flight Center, Greenbelt, MD 20771, USA
[19] Eureka Scientific, 2452 Delmer, Suite 100, Oakland, CA 96002, USA
[20] ExoPlanets and Stellar Astrophysics Laboratory, Code 667, Goddard Space Flight Center, Greenbelt, MD 20771, USA
[21] Institute for Astronomy, University of Hawaii, 640 North A'ohoku Place, Hilo, HI 96720, USA
[22] Department of Astronomy, Kyoto University, Kitashirakawa-Oiwake-cho, Sakyo-ku, Kyoto 606-8502, Japan
[23] Office of the President, Hiroshima University, 1-3-2 Kagamiyama, Higashi-Hiroshima, Hiroshima 739-8511, Japan
[24] Departamento de Astrofisica, CAB (INTA-CSIC), Instituto Nacional de Técnica Aeroespacial, Torrejón de Ardoz, E-28850 Madrid, Spain
[25] Jet Propulsion Laboratory, California Institute of Technology, Pasadena, CA 91109, USA
[26] Astronomical Institute "Anton Pannekoek," University of Amsterdam, Science Park 904, 1098 XH Amsterdam, The Netherlands
[27] Institute for the Physics and Mathematics of the Universe, The University of Tokyo, Kashiwa 227-8568, Japan
[28] Department of Cosmosciences, Hokkaido University, Sapporo 060-0810, Japan
[29] Astronomical Institute, Tohoku University, Aoba, Sendai 980-8578, Japan

Received 2012 August 11; accepted 2012 October 1; published 2012 November 7

ABSTRACT

We report high-resolution (0.07 arcsec) near-infrared polarized intensity images of the circumstellar disk around the star 2MASS J16042165−2130284 obtained with HiCIAO mounted on the Subaru 8.2 m telescope. We present our *H*-band data, which clearly exhibit a resolved, face-on disk with a large inner hole for the first time at infrared wavelengths. We detect the centrosymmetric polarization pattern in the circumstellar material as has been observed in other disks. Elliptical fitting gives the semimajor axis, semiminor axis, and position angle (P.A.) of the disk as 63 AU, 62 AU, and −14°, respectively. The disk is asymmetric, with one dip located at P.A.s of ∼85°. Our observed disk size agrees well with a previous study of dust and CO emission at submillimeter wavelength with Submillimeter Array. Hence, the near-infrared light is interpreted as scattered light reflected from the inner edge of the disk. Our observations also detect an elongated arc (50 AU) extending over the disk inner hole. It emanates at the inner edge of the western side of the disk, extending inward first, then curving to the northeast. We discuss the possibility that the inner hole, the dip, and the arc that we have observed may be related to the existence of unseen bodies within the disk.

Key words: planetary systems – protoplanetary disks – stars: pre-main sequence – techniques: polarimetric

1. INTRODUCTION

Planets are believed to form in protoplanetary disks. To study the structures of protoplanetary disks, multi-wavelength observations have targeted such disks around young stellar objects located in nearby star-forming regions such as the Taurus, ρ Oph, and Upper Scorpius regions (e.g., Kenyon & Hartmann 1995; Preibisch & Zinnecker 1999; Furlan et al. 2006; Andrews et al. 2009; Dahm & Carpenter 2009; McClure 2009; Andrews et al. 2011; Mathews et al. 2012a). Among such nearby star-forming regions, Upper Scorpius, which is located at a distance of 145 pc (de Zeeuw et al. 1999), provides a unique environment, particularly in terms of its age. While the age is only ∼5–10 Myr (Pecaut et al. 2012; Song et al. 2012), the lack of dense molecular material and embedded young stellar objects

* Based on data collected at the Subaru Telescope, which is operated by the National Astronomical Observatory of Japan.

indicate that the star formation process in Upper Scorpius is over. The area is essentially free of dense gas and dust clouds, and the association members show only moderate extinctions ($A_V < 2$ mag). In fact, there are only two *K* and *M* stars (1.5%), including the star discussed here, in the Upper Scorpius region which exhibit a *K*-band excess, although about half of the stars in Taurus exhibit a *K*-band excess (Strom et al. 1989). This implies that there are very few stars still hosting protoplanetary disks in Upper Scorpius star-forming region.

Here, we introduce our target 2MASS J16042165−2130284 (hereafter J1604−2130) in Upper Scorpius. J1604−2130 was first identified as a member of the Upper Scorpius OB association in the spectroscopic survey of X-ray-selected sources of Preibisch & Zinnecker (1999), who found: stellar age 3.7 Myr, spectral type K2, stellar mass 1 $M_\odot$, $\log T_{\rm eff}[{\rm K}] = 3.658$, and $\log[L/L_\odot] = -0.118$. The spectral energy distribution (SED) of J1604−2130 has the features of a transitional disk (Dahm & Carpenter 2009), in which small dust grains have been partly cleared from the inner disk but are still abundant at larger radii. Recently, Mathews et al. (2012b) presented the Submillimeter Array (SMA) 880 μm images, which directly resolved a face-on protoplanetary disk around J1604−2130, and derived a dust mass of 0.1 $M_{\rm Jup}$. The availability of radio data was one advantage to selecting this target; however, other advantages abound and are as follows: (1) J1604−2130 is located in a nearby star-forming region, Upper Sco; (2) it hosts one of the largest inner holes in transitional disks discovered to date; (3) it hosts the most massive disk in Upper Scorpius; (4) the inclination $6^\circ \pm 1^\circ.5$ (Mathews et al. 2012b) is very close to face-on.

Infrared photometry and spectroscopy with *Spitzer* has shown that less than ∼10% of stars with disks show some degree of inner disk depletion yet still retain massive outer disks (e.g., Cieza et al. 2010; Muzerolle et al. 2010; Luhman et al. 2011). Although there have been several transitional disks detected with radio observations with SMA around single young solar mass sources (e.g., Piétu et al. 2006; Andrews et al. 2011), only a handful of transitional disks have been detected in the near-infrared (e.g., Fukagawa et al. 2006; Thalmann et al. 2010; Hashimoto et al. 2011). This is mainly because it is difficult to resolve structures with only a few 10 AU scale close to a bright central star. Furthermore, structures inside the hole of disks have rarely been directly imaged or resolved to date. To gain a better understanding of the morphological structures at radii where planets are expected to form, we conducted high-resolution near-infrared polarimetric observations of J1604−2130.

2. OBSERVATIONS AND DATA REDUCTION

We carried out polarimetry in *H* band (1.6 μm) toward J1604−2130 using the high-resolution imaging instrument HiCIAO (Tamura et al. 2006; Hodapp et al. 2006) with a dual-beam polarimeter at the Subaru 8.2 m Telescope on 2012 April 11. These observations are part of the ongoing high-contrast imaging survey (SEEDS; Tamura 2009). The polarimetric observation mode acquires *o*-rays and *e*-rays simultaneously, and images a field of view of $10'' \times 20''$ with a pixel scale of 9.53 mas pixel^{-1}. J1604−2130 was observed without an occulting mask in order to image the inner most region around the central star. The exposures were performed at four position angles (P.A.s) of the half-wave plate, with a sequence of P.A. = 0°, 45°, 22°.5, and 67°.5 to measure the Stokes parameters. The integration time per wave plate position was 15 s and we obtained 25 wave plate cycles. The adaptive optics system (AO188; Hayano et al. 2010) provides a diffraction limited and mostly stable stellar point spread function (PSF). The total integration time of the polarization intensity (hereafter PI) image was 750 s after removing low-quality images with large FWHMs by careful inspections of the stellar PSF.

Table 1
The Result of the Ellipse Fitting for the Disk of J1604−2130

Semimajor axis	63.4 ± 1.0 (AU)
Semiminor axis	62.4 ± 1.0 (AU)
Ellipse center (u, v)[a]	(−1.1 ± 1.1, 1.5 ± 1.1) (pixel)
Position angle	−14° ± 11°
Inclination	10°.2 ± 10°.1

Note. [a] Central position (0, 0) corresponds to the stellar position.

The Image Reduction and Analysis Facility (IRAF[30]) software was used for all data reduction. The polarimetric data reduction technique is described by Hashimoto et al. (2011) and Muto et al. (2012), using the standard approach for polarimetric differential imaging (Hinkley et al. 2009). By subtracting two images of extraordinary and ordinary rays at each wave plate position, we obtained $+Q$, $-Q$, $+U$, and $-U$ images, from which $2Q$ and $2U$ images were made by another subtraction to eliminate remaining aberration. The PI was then calculated using $PI = \sqrt{Q^2 + U^2}$. The instrumental polarization of HiCIAO at the Nasmyth platform was corrected for by following Joos et al. (2008).

3. RESULTS

The *H*-band PI image of J1604−2130 is presented in Figure 1(a). The emission arises from dust particles mixed with gas in the circumstellar structures, scattering the stellar light. Details of the near-infrared disk around J1604−2130 have for the first time emerged at 0″.07. The disk has a dip D, located around a P.A. ∼ 85°, making this transitional disk asymmetric. Inside the bright disk, we see a region where the surface brightness drops by a factor of ∼5 compared with the disk. We call this inner lower-brightness region the "hole" throughout the remainder of this paper. Figure 1(b) shows *H*-band polarization vectors. The disk with its centrosymmetric polarization pattern surrounds the central source J1604−2130 as previously observed in other disks using the technique of near-infrared imaging polarimetry (e.g., Hashimoto et al. 2011).

Elliptical fitting was performed to measure several disk parameters including the angular separations of the major and minor axes, the P.A., inclination, and the position of the ellipse center. We first measured disk radial profiles in 5° P. A. increments, and then extracted coordinates of the brightest peak area. Those coordinates were used to fit an ellipse. The nonlinear least-squares Levenburg–Marquardt algorithm with the above five free parameters was performed and its result is displayed in Table 1. Its shape is superimposed on Figure 1(a). The derived semimajor and semiminor axes are called "NIR peak radii" in this paper. The geometric center of the disk is consistent with the position of the star within errors. The disk P. A. has a relatively large error because the disk is close to circular.

Figure 2 shows the azimuthal surface brightness at $r = 33$, 63, 145 AU, which are illustrated in Figure 1(c), with the P. A. measured from north to east. The error bars shown in Figure 2 represent the calculated standard deviation. The left

[30] IRAF is distributed by National Optical Astronomy Observatory, which is operated by the Association of Universities for Research in Astronomy, Inc., under cooperative agreement with the National Science Foundation.

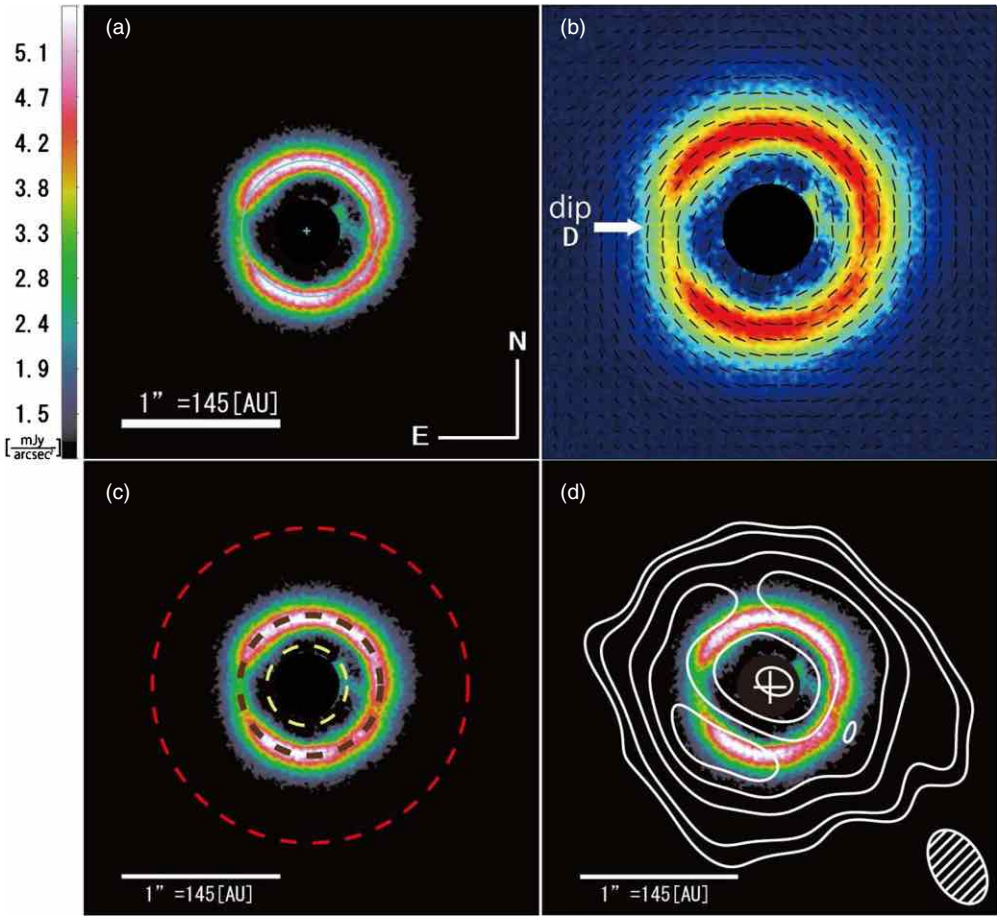

Figure 1. *H*-band HiCIAO images of J1604−2130. The saturated central area (radius = 0.″2) is masked in black. (a) The *PI* image of J1604−2130. The field of view (FOV) is 2.″9 × 2.″9. The unit of the color bar is mJy arcsec^{-2}. The light blue ellipse and plus sign are the best-fit result of our elliptical disk model and the ellipse center. (b) *H*-band polarization vectors superposed on the *PI* image. The vector directions indicate angles of polarization. The plotted vectors are based on 7 [pixel] × 7 [pixel] binning corresponding to the spatial resolution. The FOV is 2.″0 × 2.″0. The vector's lengths are arbitrary. (c) Red (r = 145 AU), brown (r = 63 AU), and yellow (r = 33 AU) circles, corresponding Figure 2, superimposed on the *PI* image. (d) SMA 880 μm continuum map (Mathews et al. 2012b) superimposed on the *PI* image. White color contours indicate 2σ, 3σ, 6σ, 9σ, and 12σ intensity (1σ = 1.3 mJy beam^{-1}). The ∼0.″5 × 0.″3 beam of SMA is shown in the bottom right.

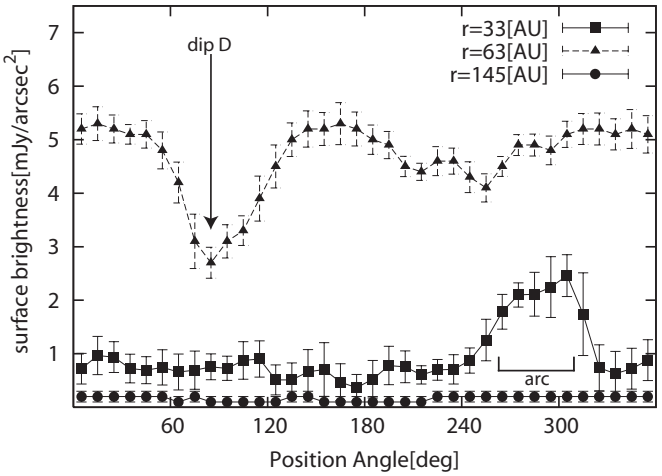

Figure 2. Azimuthal surface brightness profile at r = 33 AU (inner hole region), r = 63 AU (inner disk region), and r = 145 AU (outer region) with position angle measured from north to east. The radius 33 AU is measured as it is the brightest part of the arc.

panel of Figure 3 shows the radial surface brightness profile of J1604−2130 along the minor axis. The error bars shown in Figure 3 represent the calculated standard deviation. In the north, the surface brightness along the minor axis increases as $r^{3.6\pm0.2}$ from 40 to 62 AU, and decreases as $r^{-4.7\pm0.1}$ from 74 to 124 AU. In the south, the surface brightness along the minor axis increases as $r^{3.0\pm0.4}$ from 40 to 62 AU, and decreases as $r^{-4.7\pm0.2}$ from 74 to 124 AU. The right panel of Figure 3 shows the radial profile of the surface brightness along the major axis. In the east, the surface brightness along the major axis increases as $r^{2.6\pm0.2}$ from 40 to 62 AU, and decreases as $r^{-4.7\pm0.1}$ from 74 to 124 AU. In the west, the surface brightness along the major axis increases as $r^{1.9\pm0.2}$ from 40 to 62 AU, and decreases as $r^{-4.0\pm0.2}$ from 74 to 124 AU. The profiles along both the major and minor axes show a change of slope beyond 63 AU, thus reconfirming the NIR peak radius to be 63 AU. Along all four axes, the counts drop to half of the peak counts at around 50 AU from the central star. The width of the brightest region where counts exceeds half of the peak counts in the disk is around 30 AU.

A salient feature inside the hole is an elongated arc extending over the disk inner hole. It begins at the inner edge of the western side of the disk, extending inward first, then curving to the northeast. The whole arc extends at least 50 AU. This arc is equivalent in brightness to the inner edge of the disk and to the dip D region. This arc consists of a real feature and is not an artifact because in contrast to the inner hole errors (shown as squares in Figure 2), the surface brightness difference between the arc and the other regions in the inner hole has a 6σ significance, whereas the other directions show

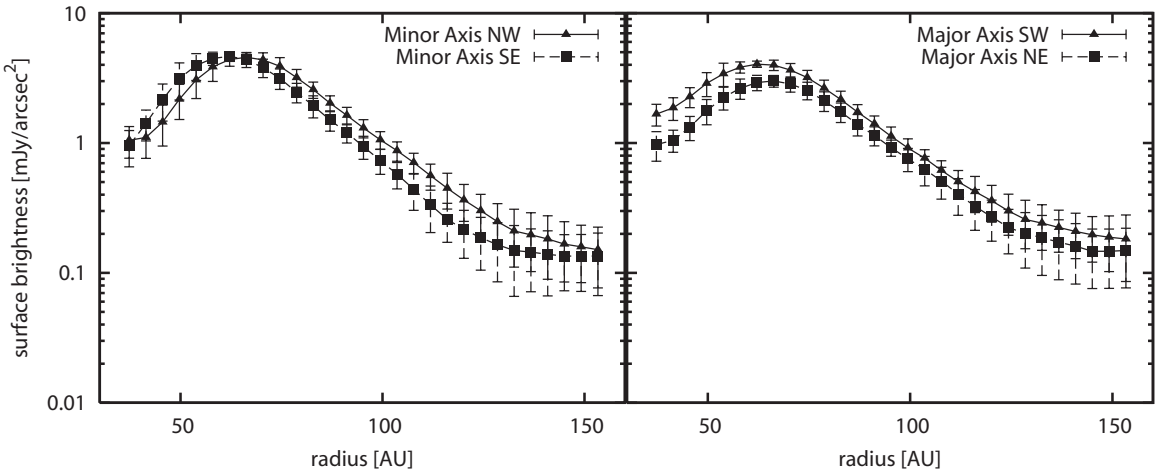

Figure 3. Left panel: radial profile along the minor axis. NW and SE radial profile are averaged over -25° < P.A. < 5° and 155° < P.A. < 185°, respectively. This is because the disk position angle derived from our near-infrared image and peak velocity of the sub-mm CO emission ($-5^\circ \pm 10^\circ$) are 9° different. Therefore, we centered our 30° wide radial profiles on the average of our near-infrared and sub-mm line emission. Right panel: radial profile along the major axis. In the same way, NE and SW radial profiles are averaged over 65° < P.A. < 95° and 245° < P.A. < 275°, respectively.

small fluctuations in emission. Furthermore, the polarization vectors in the region of the arc mostly face the central star as well as the region of the bright disk, indicating that the arc is also illuminated by central star and is physically connected to inner edge of the disk.

In the same way, the dip D is a real dip feature and is not an artifact because the difference in surface brightness between D and the rest of the disk is statistically significant and not within error bars. In addition, the polarization vectors in the region of the dip mostly face the central star.

There appears to be another dip located around a P. A. $\sim 255^\circ$, which is not azimuthally symmetric with D in terms of location and surface brightness. However, this another dip is not significant outside of the uncertainties of the observations, thus follow-up future observations are required to confirm its presence.

4. DISCUSSION

4.1. Comparison with the SMA Imaging

Mathews et al. (2012b) present SMA 880 μm continuum and CO (3–2) line observations of this source with a resolution of $0\farcs34$ and resolve the disk (Figure 1(d)). They determine the surface density distribution of the disk with inner cavity whose radius is 72 AU based on the model fitting to the visibility at 880 μm. They also suggest that sparse matter still remains inside the cavity (20–72 AU) because of the dust emission indicated by mid-infrared (Carpenter et al. 2009) excesses and their model fitting. The NIR peak disk radius of 63 AU derived from our *H*-band image roughly agrees or may be slightly smaller than their measurement and can be explained by scattered light reflected at the inner edge of the disk.

Based on their CO peak velocity map, Mathews et al. (2012b) derive the P.A.s of the major and minor axes to be $85^\circ \pm 10^\circ$ and $-5^\circ \pm 10^\circ$, respectively. Their derive disk parameters, including the P.A. and inclination, are in a good agreement with values derived from our near infrared observations.

Mathews et al. (2012b) point out that the relatively high mass of the gas-dust disk, its sharp inner edge, and the lack of gas accretion onto the star together point to a dynamical origin for the inner hole. No companions have been found down to brown dwarf masses (Kraus et al. 2008; Ireland et al. 2011). Based on their analysis, they suggest that the origin of the hole can be attributed to the unseen presence of one or several giant planets within about a 40 AU.

The width and depth of the hole depend on the planet mass, disk viscosity, and disk thickness (e.g., Takeuchi et al. 1996; Crida et al. 2006). As discussed by Dong et al. (2012a, 2012b), the radius of the inner hole is on the order of $\sim$60–70 AU. There have been extensive studies on the process of gap opening by a planet embedded in a disk (e.g., Lin & Papaloizou 1986; Takeuchi et al. 1996; Crida et al. 2006). A rough estimate of the upper limit of the size of the gap that one planet can make may be given by the location of the lowest order Lindblad resonances, which, in the case of the outer resonance (the outer edge of the gap), is at $\sim$1.6 times the orbital radius of the embedded planet (Takeuchi et al. 1996). If this is the case, the existence of the inner hole might indicate the existence of at least one planet at $\sim$40–50 AU from the central star (see also Crida et al. 2006), and the inner edge of the hole would be expected at $\sim$25–30 AU, which is inside of our saturation radius and is therefore unresolved in this study.

If multiple planets reside within the hole, the hole width can be wider and the inner disk may be much smaller than the single planet case (Zhu et al. 2011). To understand the properties of the whole of this object, it is important to give constraints on the inner disk structure using detailed SED modeling (see Dong et al. 2012a, 2012b) and/or high-resolution observations by ALMA. Our observations do not show a clear inner disk edge, suggesting that the inner disk radius must be inside of the saturation radius of our observations.

4.2. Non-axisymmetric Features

We list a few possibilities for origin of the two non-axisymmetric features, the dip and the arc since it is difficult to draw firm conclusions at this stage. According to Figure 6(c) in Mathews et al. (2012b), the only structures that are not reproduced by the axisymmetric disk model within 2σ error are the southeast component; the north dip is consistent with the axisymmetric disk model convolved with the elliptical beam. We, therefore, do not elaborate on the north dip on the submillimeter (sub-mm) disk in the following discussions. Mathews et al. (2012b) observe that the millimeter continuum emission has a peak at $0\farcs5$ southeast from the star in the 880 μm image.

A similar distribution is also seen in the total integrated intensity distribution of CO (3–2) emission. Our *H*-band image and Figure 3 show that the southeast of the disk is brighter than the east and the west, despite the fact that we observe the scattered light originating at the disk surface. This may be explained in a way that the more materials exist, the thicker the disk is, resulting in a higher grazing angle of the stellar light at the scattering surface (e.g., Muto 2011). In our near-infrared image, the north of the disk is also bright. The brightness of the disk in the north, together with sub-mm observations suggesting material accumulation in the south, infers that the northern portion of the disk is the near side. This assumes that forward scattering dominates. If this picture of the disk orientation is correct, the disk rotation is counterclockwise direction. This geometry might also explain the origins of the non-axisymmetric structures at **D**. **D** is at the interface between where the material accumulated (south) and where forward scattering is significant (north). However, it should be noted that since the disk is nearly face-on, significant forward scattering excess and precise prescriptions of the phase function should be required, and our discussion crucially depends on the details of the optical properties of the dust particles. It should also be noted that the material concentration in the south is within 2σ of the current sub-mm data (Mathews et al. 2012b). The detection of the non-axisymmetric structures at sub-mm wavelengths is needed to examine the details of the disk geometry.

Another possibility for the origin of the dip **D** is that there is a massive gravitating object at the disk's midplane. It could be a planet (which is not necessarily the same as the one discussed in the previous section as the origin of the inner hole), a clump formed by hydrodynamic instability (e.g., gravitational instability), or something else. Such objects can pull the materials from the surface toward the disk's midplane, thereby producing a shadow in the scattered light image (Jang-Condell 2009). This might produce features such as **D**. Such objects have sizes smaller than the SMA beam size, therefore cannot be resolved with the SMA.

For the arc structure in the west, the morphology is similar to spiral density waves in the disk. An arguably uniqueness is that this arc extends over the "disk inner hole" region. It also resembles to spiral density waves in terms of the pitch angle. Spiral waves can be produced by dynamical processes in the disk such as the turbulence or the planet–disk interaction (see, e.g., Papaloizou et al. 2007). If this feature is a spiral wave, its morphology indicates that the disk rotation is counterclockwise because spirals are in general trailing features. This rotation direction is consistent with the picture presented at the beginning of this section. Last, we note that the arc structure shows morphological similarity to the "planet shadows" discussed by Jang-Condell (2009). One possible way to distinguish the different scenarios is to observe the structures of the disk's midplane at longer wavelength. For instance, if a density enhancement is observed at the location of **D**, this might indicate the existence of a massive body there. If we see an arc structure in the sub-mm as well, then it is likely a density wave.

Another possible way to reveal the nature of the arc may be the contemporaneous SED and scattered light observations. Previous studies indicate that substantial variability has also been seen in MIR SED and has been linked to variable structures including arcs or rims of the disk (Dahm & Carpenter 2009; Wisniewski et al. 2008; Muzerolle et al. 2009; Espaillat et al. 2011; Flaherty et al. 2012). For the J1604−2130 case, the location of the arc and the rim of the disk wall is generally consistent with the radial location in the disk which possibly contributes to the SED variability.

We thank the telescope staff and operators at the Subaru Telescope for their assistance. We also thank our referee for the constructive comments that have helped to improve this manuscript. Part of this research was carried out at the JPL, under a contract with NASA. This work is partially supported by a Grant-in-Aid for Science Research in a Priority Area from MEXT 22000005 (M.T.), KAKENHI 23103004 (M.M. and M.F.), 24103504 (T.T.), 24840037 (T.M.), US NSF grant 1009314 (J.P.W.), and 1009203 (J.C.). This work was supported in part by the Center for the Promotion of Integrated Sciences (CPIS) of The Graduate University for Advanced Studies (SOKENDAI).

REFERENCES

Andrews, S. M., Wilner, D. J., Espaillat, C., et al. 2011, ApJ, 732, 42
Andrews, S. M., Wilner, D. J., Hughes, A. M., Qi, C., & Dullemond, C. P. 2009, ApJ, 700, 1502
Carpenter, J. M., Mamajek, E. E., Hillenbrand, L. A., & Meyer, M. R. 2009, ApJ, 705, 1646
Cieza, L. A., Schreiber, M. R., Romero, G. A., et al. 2010, ApJ, 712, 925
Crida, A., Morbidelli, A., & Masset, F. 2006, Icarus, 181, 587
Dahm, S. E., & Carpenter, J. M. 2009, AJ, 137, 4024
de Zeeuw, P. T., Hoogerwerf, R., de Bruijne, J. H. J., Brown, A. G. A., & Blaauw, A. 1999, AJ, 117, 354
Dong, R., Rafikov, R., Hashimoto, J., et al. 2012b, ApJ, submitted
Dong, R., Rafikov, R., Zhu, Z., et al. 2012a, ApJ, 750, 161
Espaillat, C., Furlan, E., D'Alessio, P., et al. 2011, ApJ, 728, 49
Flaherty, K. M., Muzerolle, J., Rieke, G., et al. 2012, ApJ, 748, 71
Fukagawa, M., Tamura, M., Itoh, Y., et al. 2006, ApJ, 636, L153
Furlan, E., Hartmann, L., Calvet, N., et al. 2006, ApJS, 165, 568
Hashimoto, J., Tamura, M., Muto, T., et al. 2011, ApJ, 729, L17
Hayano, Y., Takami, H., Oya, S., et al. 2010, Proc. SPIE, 7736, 21
Hinkley, S., Oppenheimer, B. R., Soummer, R., et al. 2009, ApJ, 701, 804
Hodapp, K. W., Tamura, M., Suzuki, R., et al. 2006, Proc. SPIE, 6269, 62693
Ireland, M. J., Kraus, A., Martinache, F., Law, N., & Hillenbrand, L. A. 2011, ApJ, 726, 113
Jang-Condell, H. 2009, ApJ, 700, 820
Joos, F., Buenzli, E., Schmid, H. M., & Thalmann, C. 2008, Proc. SPIE, 7016, 48
Kenyon, S. J., & Hartmann, L. 1995, ApJS, 101, 117
Kraus, A. L., Ireland, M. J., Martinache, F., & Lloyd, J. P. 2008, ApJ, 679, 762
Lin, D. N. C., & Papaloizou, J. 1986, ApJ, 307, 395
Luhman, K. L., Burgasser, A. J., & Bochanski, J. J. 2011, ApJ, 730, L9
Mathews, G. S., Williams, J. P., Ménard, F., et al. 2012a, ApJ, 745, 23
Mathews, G. S., Williams, J. P., & Ménard, F. 2012b, ApJ, 753, 59
McClure, M. 2009, ApJ, 693, L81
Muto, T. 2011, ApJ, 739, 10
Muto, T., Grady, C. A., Hashimoto, J., et al. 2012, ApJ, 748, L22
Muzerolle, J., Allen, L. E., Megeath, S. T., Hernández, J., & Gutermuth, R. A. 2010, ApJ, 708, 1107
Muzerolle, J., Flaherty, K., Balog, Z., et al. 2009, ApJ, 704, L15
Song, I., Zuckerman, B., & Bessell, M. S. 2012, AJ, 144, 8
Papaloizou, J. C. B., Nelson, R. P., Kley, W., Masset, F. S., & Artymowicz, P. 2007, in Protostars and Planets V, ed. B. Reipurth, D. Jewitt, & K. Keil (Tucson, AZ: Univ. Arizona Press), 655
Pecaut, M. J., Mamajek, E. E., & Bubar, E. J. 2012, ApJ, 746, 154
Piétu, V., Dutrey, A., Guilloteau, S., Chapillon, E., & Pety, J. 2006, A&A, 460, L43
Preibisch, T., & Zinnecker, H. 1999, AJ, 117, 2381
Strom, K. M., Strom, S. E., Edwards, S., Cabrit, S., & Skrutskie, M. F. 1989, AJ, 97, 1451
Takeuchi, T., Miyama, S. M., & Lin, D. N. C. 1996, ApJ, 460, 832
Tamura, M. 2009, in AIP Conf. Ser. 1158, Exoplanets and Disks: Their Formation and Diversity, ed. T. Usuda, M. Ishii, & M. Tamura (Melville, NY: AIP), 11
Tamura, M., Hodapp, K., Takami, H., et al. 2006, Proc. SPIE, 6269, 28
Thalmann, C., Grady, C. A., Goto, M., et al. 2010, ApJ, 718, L87
Wisniewski, J. P., Clampin, M., Grady, C. A., et al. 2008, ApJ, 682, 548
Zhu, Z., Nelson, R. P., Hartmann, L., Espaillat, C., & Calvet, N. 2011, ApJ, 729, 47

The Astrophysical Journal Letters, 748:L22 (7pp), 2012 April 1 doi:10.1088/2041-8205/748/2/L22

DISCOVERY OF SMALL-SCALE SPIRAL STRUCTURES IN THE DISK OF SAO 206462 (HD 135344B): IMPLICATIONS FOR THE PHYSICAL STATE OF THE DISK FROM SPIRAL DENSITY WAVE THEORY*

T. Muto[1,34,35], C. A. Grady[2,3,4], J. Hashimoto[5], M. Fukagawa[6], J. B. Hornbeck[7], M. Sitko[8,9,36], R. Russell[10,36], C. Werren[9,36], M. Curé[11], T. Currie[3], N. Ohashi[12,13], Y. Okamoto[14], M. Momose[14], M. Honda[15], S. Inutsuka[16], T. Takeuchi[1], R. Dong[17], L. Abe[18], W. Brandner[19], T. Brandt[17], J. Carson[20], S. Egner[13], M. Feldt[19], T. Fukue[5], M. Goto[19], O. Guyon[13], Y. Hayano[13], M. Hayashi[21,37], S. Hayashi[13], T. Henning[19], K. W. Hodapp[22], M. Ishii[13], M. Iye[5], M. Janson[17], R. Kandori[5], G. R. Knapp[17], T. Kudo[13], N. Kusakabe[5], M. Kuzuhara[5,23], T. Matsuo[24], S. Mayama[25], M. W. McElwain[3], S. Miyama[5], J.-I. Morino[5], A. Moro-Martin[17,26], T. Nishimura[13], T.-S. Pyo[13], E. Serabyn[27], H. Suto[5], R. Suzuki[28], M. Takami[12], N. Takato[13], H. Terada[13], C. Thalmann[29], D. Tomono[13], E. L. Turner[17,30], M. Watanabe[31], J. P. Wisniewski[32], T. Yamada[33], H. Takami[13], T. Usuda[13], and M. Tamura[5]

[1] Department of Earth and Planetary Sciences, Tokyo Institute of Technology, 2-12-1 Ookayama, Meguro, Tokyo 152-8551, Japan; muto@geo.titech.ac.jp
[2] Eureka Scientific, 2452 Delmer, Suite 100, Oakland CA 96002, USA
[3] ExoPlanets and Stellar Astrophysics Laboratory, Code 667, Goddard Space Flight Center, Greenbelt, MD 20771, USA
[4] Goddard Center for Astrobiology, Code 667, Goddard Space Flight Center, Greenbelt, MD 20771, USA
[5] National Astronomical Observatory of Japan, 2-21-1 Osawa, Mitaka, Tokyo 181-8588, Japan
[6] Department of Earth and Space Science, Graduate School of Science, Osaka University, 1-1, Machikaneyama, Toyonaka, Osaka 560-0043, Japan
[7] Department of Physics and Astronomy, University of Louisville, Louisville, KY 40292, USA
[8] Space Science Institute, 4750 Walnut St., Suite 205, Boulder, CO 80301, USA
[9] Department of Physics, University of Cincinnati, Cincinnati, OH 45221-0011, USA
[10] The Aerospace Corporation, Los Angeles, CA 90009, USA
[11] Departamento de Física y Astronomía, Universidad de Valparaíso, Avda. Gran Bretaña 1111, Casilla 5030, Valparaíso, Chile
[12] Institute of Astronomy and Astrophysics, Academia Sinica, P.O. Box 23-141, Taipei 106, Taiwan
[13] Subaru Telescope, 650 North A'ohoku Place, Hilo, HI 96720, USA
[14] College of Science, Ibaraki University, 2-1-1 Bunkyo, Mito, Ibaraki 310-8512, Japan
[15] Department of Information Science, Kanagawa University, 2946 Tsuchiya, Hiratsuka, Kanagawa 259-1293, Japan
[16] Department of Physics, Nagoya University, Furo-cho, Chikusa-ku, Nagoya, Aichi, 464-8602, Japan
[17] Department of Astrophysical Sciences, Princeton University, NJ08544, USA
[18] Laboratoire Lagrange, UMR7293, Université de Nice-Sophia Antipolis, CNRS, Observatoire de la Côte d'Azur, 06300 Nice, France
[19] Max Planck Institute for Astronomy, Heidelberg, Germany
[20] Department of Physics and Astronomy, College of Charleston, 58 Coming St., Charleston, SC 29424, USA
[21] Department of Astronomy, The University of Tokyo, Hongo 7-3-1, Bunkyo-ku, Tokyo 113-0033, Japan
[22] Institute for Astronomy, University of Hawaii, 640 North A'ohoku Place, Hilo, HI 96720, USA
[23] Department of Earth and Planetary Science, The University of Tokyo, Hongo, 7-3-1, Bunkyo-ku, Tokyo 113-0033, Japan
[24] Department of Astronomy, Kyoto University, Kitashirakawa-Oiwake-cho, Sakyo-ku, Kyoto, 606-8502, Japan
[25] The Graduate University for Advanced Studies(SOKENDAI), Shonan International Village, Hayama-cho, Miura-gun, Kanagawa 240-0193, Japan
[26] Departamento de Astrofísica, CAB (INTA-CSIC), Instituto Nacional de Técnica Aeroespacial, Torrejón de Ardoz, 28850, Madrid, Spain
[27] Jet Propulsion Laboratory, California Institute of Technology, Pasadena, CA 91109, USA
[28] TMT Observatory Corporation, 1111 South Arroyo Parkway, Pasadena, CA 91105, USA
[29] Astronomical Institute "Anton Pannekoek," University of Amsterdam, Science Park 904, 1098 XH Amsterdam, The Netherlands
[30] Kavli Institute for the Physics and Mathematics of the Universe, Todai Institutes for Advanced Study, The University of Tokyo, Kashiwa 227-8568, Japan (Kavli IPMU, WPI)
[31] Department of Cosmosciences, Hokkaido University, Sapporo 060-0810, Japan
[32] Department of Astronomy, University of Washington, Box 351580 Seattle, Washington 98195, USA
[33] Astronomical Institute, Tohoku University, Aoba, Sendai 980-8578, Japan
Received 2012 January 23; accepted 2012 February 27; published 2012 March 13

ABSTRACT

We present high-resolution, *H*-band imaging observations, collected with Subaru/HiCIAO, of the scattered light from the transitional disk around SAO 206462 (HD 135344B). Although previous sub-mm imagery suggested the existence of a dust-depleted cavity at $r \leqslant 46$ AU, our observations reveal the presence of scattered light components as close as 0.″2 (∼28 AU) from the star. Moreover, we have discovered two small-scale spiral structures lying within 0.″5 (∼70 AU). We present models for the spiral structures using the spiral density wave theory, and derive a disk aspect ratio of $h \sim 0.1$, which is consistent with previous sub-mm observations. This model can potentially give estimates of the temperature and rotation profiles of the disk based on dynamical processes, independently from sub-mm observations. It also predicts the evolution of the spiral structures, which can be observable on timescales of 10–20 years, providing conclusive tests of the model. While we cannot uniquely identify the origin of these spirals, planets embedded in the disk may be capable of exciting the observed morphology. Assuming that this is the case, we can make predictions on the locations and, possibly, the masses of the unseen planets. Such planets may be detected by future multi-wavelength observations.

Key words: circumstellar matter – instrumentation: high angular resolution – polarization – protoplanetary disks – stars: individual (SAO 206462, HD 135344B) – waves

* Based on data collected at the Subaru Telescope, which is operated by the National Astronomical Observatory of Japan.
[34] JSPS Research Fellow.
[35] Current address: Division of Liberal Arts, Kogakuin University, 1-24-2, Nishi-Shinjuku, Shinjuku-ku, Tokyo, 163-8677, Japan.
[36] Visiting Astronomer, NASA Infrared Telescope Facility, operated by the University of Hawaii under contract to NASA.
[37] Current address: National Astronomical Observatory of Japan.

1. INTRODUCTION

Dynamical processes in protoplanetary disks such as turbulence or disk–planet interaction are important in understanding physical condition and evolution of disks, and planet formation processes. High-resolution, direct imaging observations of circumstellar/protoplanetary disks can reveal non-axisymmetric structures, providing insight into such dynamical processes (e.g., Hashimoto et al. 2011).

Recent observations have identified a class of protoplanetary disks harboring tens of AU-scale holes/gaps at their centers: the so-called transitional disks. One well-studied system of that class is the rapidly rotating Herbig F star, SAO 206462 (HD 135344B, F4Ve, $d = 142 \pm 27$ pc, $M = 1.7^{+0.2}_{-0.1}\,M_{\odot}$, Müller et al. 2011). The observations of CO line profiles (Dent et al. 2005; Pontoppidan et al. 2008; Lyo et al. 2011) and stellar rotation (Müller et al. 2011) consistently indicate an almost face-on geometry ($i \sim 11^{\circ}$). The gap in the disk was predicted from the infrared (IR) spectral energy distribution (SED; Brown et al. 2007), and was subsequently imaged in sub-mm dust continuum at $\sim 0\farcs5 \times 0\farcs25$ resolution (Brown et al. 2009). Andrews et al. (2011) estimate the gap radius to be $\sim$46 AU and the surface density within the gap to be $10^{-5.2}$ times smaller than that extrapolated from the outer disk. The gas in Keplerian motion surrounding the gap region is also imaged by CO lines (Lyo et al. 2011). The CO rovibrational line observations (Pontoppidan et al. 2008) and [O I] spectral line observations (van der Plas et al. 2008) indicate the presence of a gas disk in the vicinity (several AU-scale) of the star. SED modeling (Grady et al. 2009) and NIR interferometry (Fedele et al. 2008) indicate the presence of an inner dust belt, which is temporally variable (Sitko et al. 2012) and not coplanar with the outer disk (M. Benisty 2011, private communication). New imaging with high spatial resolution and sensitivity is required to understand the inner structures of the disk. The outer portions of gaps can now be resolved using 8–10 m ground-based telescopes at near-infrared (NIR) wavelengths (e.g., Thalmann et al. 2010, for LkCa 15).

In this Letter, we present *H*-band polarized intensity (PI) observations of the disk of SAO 206462 down to $r \sim 0\farcs2$ ($\sim$28 AU) scale at $0\farcs06$ ($\sim$8.4 AU) resolution. Interior to the sub-mm resolved gap, we find spiral structures, indicative of dynamical processes. We use the spiral density wave theory to interpret the structure, and estimate disk's physical parameters.

2. OBSERVATIONS AND DATA REDUCTION

2.1. HiCIAO Observations

SAO 206462 was observed in the *H*-band (1.6 μm) using the high-contrast imaging instrument HiCIAO (Tamura et al. 2006; Hodapp et al. 2008; Suzuki et al. 2010) on the Subaru Telescope on 2011 May 20 UT as part of Strategic Explorations of Exoplanets and Disks with Subaru (SEEDS; Tamura 2009). The adaptive optics system (AO188; Hayano et al. 2004; Minowa et al. 2010) provided a stable stellar point-spread function (PSF; FWHM = $0\farcs06$). We used a combined angular differential imaging (ADI) and polarization differential imaging (PDI) mode with a field of view of $10'' \times 20''$ and a pixel scale of 9.5 mas pixel^{-1}. A $0\farcs3$ diameter circular occulting mask was used to suppress the bright stellar halo. The half-wave plates were placed at four angular positions from 0°, 45°, 22.5, and 67.5 in sequence with one 30 s exposure per wave plate position. The total integration time of the PI image was 780 s after removing low quality images with large FWHMs by careful inspections of the stellar PSF.

2.2. PDI Data Reduction

The raw images were corrected using IRAF[38] for dark current and flat-field following the standard reduction scheme. We applied a distortion correction using globular cluster M5 data taken within a few days, using IRAF packages GEOMAP and GEOTRAN. Stokes (Q, U) parameters and the PI image were obtained in the standard approach (e.g., Hinkley et al. 2009) as follows. By subtracting two images of extraordinary and ordinary rays at each wave plate position, we obtained $+Q$, $-Q$, $+U$, and $-U$ images, from which $2Q$ and $2U$ images were made by another subtraction to eliminate remaining aberration. PI was then given by PI $= \sqrt{Q^2 + U^2}$. Instrumental polarization of HiCIAO at the Nasmyth instrument was corrected by following Joos et al. (2008). From frame-by-frame deviations, the typical error of the surface brightness (SB) was estimated to be $\sim$5% at $r \sim 0\farcs5$ when averaged over 5×5 pixels ($\sim$PSF scale). Comparing different data reduction methods (frame selections and instrumental polarization estimates), we expect that the systematic uncertainty of the SB of PI to be $\sim$10%.

2.3. Contemporaneous Photometry

Since SAO 206462 shows variability in NIR wavelengths (Sitko et al. 2012), it is important to take photometry simultaneously with disk observations. *H*-band photometry was obtained just before and after the disk imaging without the coronagraphic spot with the adaptive optics, by sixteen 1.5 s exposures at four spatially dithered positions. An ND10 filter (9.8 ± 0.1% transmission) was used to avoid saturation. Using the MKO filter set, the *H*-band ($\lambda_{\rm eff} = 1.615\,\mu$m, FWHM $= 0.29\,\mu$m, Tokunaga et al. 2002) magnitude was 6.96 ± 0.07 mag.

Broadband *VRIJHK* photometry was obtained on 2011 May 23–26, starting within 48 hr of the HiCIAO observation, using the Rapid Eye Mount (REM) Telescope at La Silla, Chile (Covino et al. 2004). The REM *H*-band filter has $\lambda_{\rm eff} = 1.65\,\mu$m, FWHM $= 0.35\,\mu$m: broader and displaced to longer wavelengths than the MKO filter. The observed data were reduced differentially using SAO 206463 (A0V). The IR excess due to the inner disk (Figure 1) was average for the range observed in 2009–2011 (Sitko et al. 2012). No significant variation was observed during the 2011 May observations, except for the small long-term fading trend (δm $= 0.08 \pm 0.02$ mag) over the observation period.

Figure 1 also displays spectra obtained with the SpeX spectrograph (Rayner et al. 2009) on NASA's Infrared Telescope Facility (IRTF). The observations were obtained in the cross-dispersed (XD) echelle mode between 0.8 and 5.1 μm using a $0\farcs8$ slit ($R \sim 900$) and calibrated using HD 129685 (A0V) with SpeXtool (Vacca et al. 2003; Cushing et al. 2004). The absolute flux calibration, to correct for light loss at the spectrograph slits, was accomplished in two ways: using photometry and wide-slit spectroscopy (see Sitko et al. 2012). The March SpeX data were normalized using the REM photometry, obtained in the days immediately after the SpeX observations, and when the star was photometrically stable. In July, SAO 206462 and the calibration star were observed with the SpeX prism using a $3\farcs0$ slit, which, under good seeing and transparency

[38] IRAF is distributed by the National Optical Astronomy Observatory, which is operated by the Association of Universities for Research in Astronomy, Inc., under cooperative agreement with the National Science Foundation.

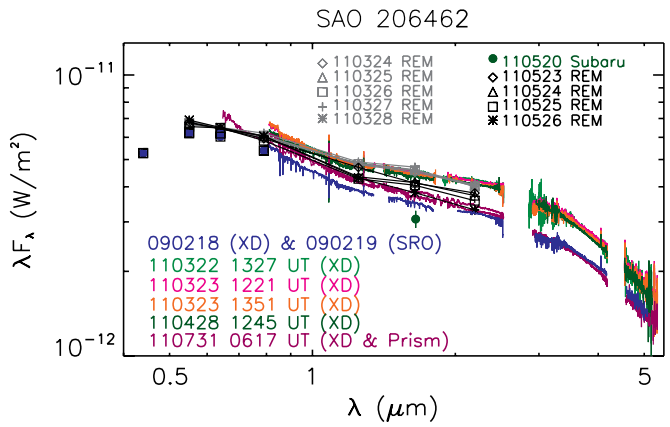

Figure 1. SED for SAO 206462 obtained by REM, adapted, in part, from Sitko et al. (2012). The REM observations consist of *VRIJHK* photometry. Also shown are spectra obtained with the SpeX spectrograph. See Section 2.3 for the data reduction techniques.

conditions, produces absolute flux to ∼5% accuracy. The REM photometry at the *H*-band in May is ∼0.25 mag brighter than the Subaru data. The Subaru photometry shows a low value even when considering the filter difference, suggesting that the outer disk is illuminated efficiently.

3. RESULTS

3.1. Spiral Structure

The SAO 206462 disk can be traced in PI from 0.″2 to ∼1.″0 (28–140 AU), similar to the range imaged with *HST*/NICMOS (Grady et al. 2009), but with a factor of ∼4 greater angular resolution. The total PI is 9.87 mJy ± 0.06% at $0.''2 < r < 1.''0$, which is 0.6% of the stellar intensity. The total PI at $0.''42 < r < 1.''0$ is 3.94 mJy ± 0.1% while the total intensity by *HST*/NICMOS F110W is 9.7 mJy (Grady et al. 2009). The average SB of PI at $r = 0.''46$ is ∼6 mJy asec^{-2}, whereas the total intensity by *HST*/NICMOS F160W is 30 mJy asec^{-2} (Grady et al. 2009). Given the NICMOS data uncertainties, the polarization fraction is ∼20%–40%, assuming no PSF halo in the HiCIAO data and no variable self-shadowing/illumination in the disk. Our measured polarization fraction is similar to that of HD 100546 ($14\%^{+19\%}_{-8\%}$, Quanz et al. 2011) and AB Aur (∼25%–45%, Perrin et al. 2009).

Figure 2 shows the PI image. The region interior to 0.″4 is not a void and we do not see clear structural evidence of the cavity wall in the Andrews et al. (2011) model ($R_{\rm cav} = 46$ AU ∼ 0.″33). We see spiral arcs S1 (east) and S2 (southwest). The PI at the location of the spirals is ∼30% larger than that extrapolated from the smooth outer profile (bottom of Figure 2). The brightest portions of the spirals roughly coincide with the bright thermal emission peaks at 12 μm (Mariñas et al. 2011) and lie inside the ring noted by Doucet et al. (2006). It is also noted that we see a dip in PI in the northwest, probably due to the depolarization in the minor axis direction (see below), and that we do not see a large-scale, localized shadow that might be cast by the inner dust belt if highly inclined relative to the outer disk.

3.2. Azimuthal and Radial Profiles

Here, we summarize the overall disk structure exterior to the spirals. Figure 3 (top panels) shows the azimuthal SB profiles at $r = 0.''5$ and $r = 0.''7$. At $r \gtrsim 0.''5$, SB has maxima around position angle (PA) ∼ 50°–60° and 230°–240°. Since the polarization is maximized at ∼90° scattering (e.g., Graham et al. 2007), it is implied that the disk major axis is at PA ∼ 50°–60°, comparable to estimates by CO observations: PA = 56° ± 2° by Pontoppidan et al. (2008) and 64° ± 2° by Lyo et al. (2011). We adopt PA = 55° for the major axis and $i = 11°$ for the inclination (see Section 1). Our spiral model fitting results (the next section) are little affected even if we assume a face-on geometry.

From CO observations, it is known that the southwest side is receding (e.g., Lyo et al. 2011). Therefore, either the northwest or southeast side is the near side. We do not see an obvious forward scattering excess in the NIR image. However, since the spirals are typically trailing, it is inferred that the southeast is the near side.

Figure 3 also shows the radial PI profiles along the major axis, which is roughly consistent with r^{-3} in the outer part, indicating a flat (not highly flared) disk (Whitney & Hartmann 1992). The radial slopes vary as PA from ∼−2 to ∼−4.5 (fitting at $0.''6 < r < 1.''0$) or from ∼−2.5 to ∼−5 (fitting at $0.''3 < r < 0.''9$), with shallower slopes typically appearing in the minor axis directions. However, r^{-3} is representative on average. This slope is observed in several other HAeBe disks (e.g., Fukagawa et al. 2010, for total intensity data), although HD 97048 disk exhibits a shallower slope (Quanz et al. 2012).

4. SPIRAL STRUCTURE MODELING

Among several features in the image, the most interesting one is the non-axisymmetric spirals. In order to understand them, we propose a model based on the spiral density wave theory (e.g., Lin & Shu 1964; Goldreich & Tremaine 1978, 1979; Ogilvie & Lubow 2002), assuming that NIR emission traces the disk surface density structure. With such a model, the spiral structures can be used to infer the disk temperature, independently of, for example, CO line observations.

The shape of the spiral density wave is determined by the location of the launching point (corotation radius $r_{\rm c}$) and disk's thermal and rotation profiles. When the disk rotation angular frequency is $\Omega(r) \propto r^{-\alpha}$ and the sound speed is $c(r) \propto r^{-\beta}$, the shape of the wave far from $r_{\rm c}$ is given by

$$\theta(r) = \theta_0 - \frac{{\rm sgn}(r - r_{\rm c})}{h_{\rm c}} \times \left[\left(\frac{r}{r_{\rm c}}\right)^{1+\beta} \left\{ \frac{1}{1+\beta} - \frac{1}{1-\alpha+\beta} \left(\frac{r}{r_{\rm c}}\right)^{-\alpha} \right\} - \left(\frac{1}{1+\beta} - \frac{1}{1-\alpha+\beta} \right) \right] \quad (1)$$

in the polar coordinate (r, θ), where $h_{\rm c} = c(r_{\rm c})/r_{\rm c}\Omega(r_{\rm c})$ denotes the disk aspect ratio at $r = r_{\rm c}$ and θ_0 gives the phase. Equation (1) approximates well the shape of the density wave given by the WKB theory (Rafikov 2002; Muto et al. 2011). When the spiral is excited by a planet in a circular orbit, its location is $\sim(r_{\rm c}, \theta_0)$. Equation (1) has five parameters, $(r_{\rm c}, \theta_0, h_{\rm c}, \alpha, \beta)$.

Two non-axisymmetric features, S1 and S2, (Figure 4) are identified as follows. First, local maxima in the radial SB profiles normalized by r^2 (to take into account the dilution of the stellar flux) are traced at every 1° step with data at 170° < PA < 360° (S1) and at 50° < PA < 190° (S2). The points near the minor axis (PA ∼ 325°) are excluded because the structure there may be affected by depolarization. The points at PA > 200° (S1) and PA > 114° (S2) may be a part of axisymmetric rings since they

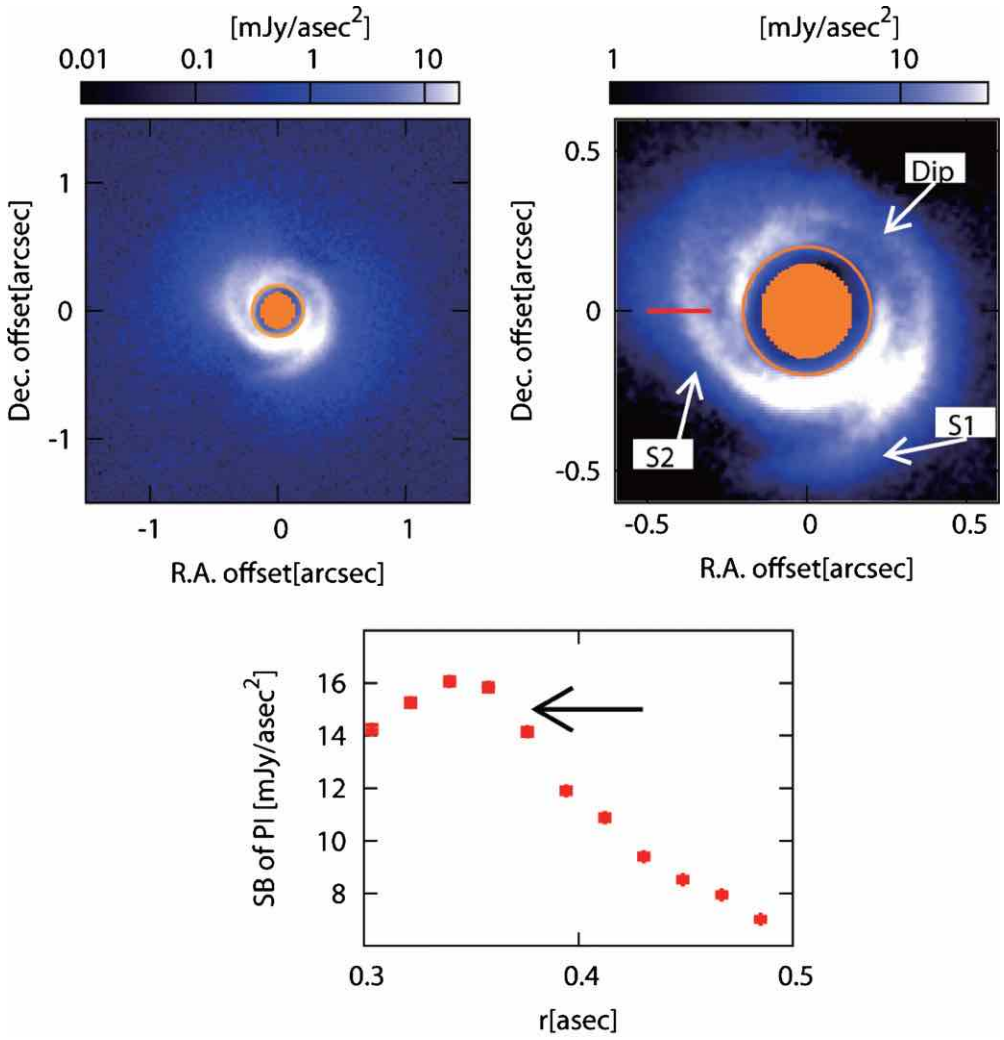

Figure 2. Top: PI image of SAO 206462 in the north-up configuration with log-stretch color scales. The filled orange circles at the center indicate the mask size ($r = 0\farcs15$). The circles have $r = 0\farcs2$, exterior to which the features are considered to be real. The right panel is central region's close-up. Different color scales are used to enhance the spirals labeled as "S1" and "S2." The "Dip" may be due to depolarization. Bottom: PI profile along the red line in the top right panel. The arrow indicates the location of S2. The position errors are not shown for visibility.

are found to have constant radii. After removing these points, we have 27 (S1) and 56 (S2) points as representing samples of non-axisymmetric spirals, with the opening angle of $\sim 15^\circ$ for both S1 and S2. We estimate that the uncertainty of the location of the maxima is given by the FWHM of the PSF.

In order to fit the non-axisymmetric structures by Equation (1), we fix α and β at 1.5 (Kepler rotation) and 0.4, respectively, as in Lyo et al. (2011), while other parameters are varied as ($0\farcs1 < r_c < 0\farcs9, 0 < \theta_0 < 2\pi, 0.05 < h_c < 0.25$). Note that different values of β yield similar results. Since it is difficult to fit S1 and S2 simultaneously, they are fitted independently.

The "best-fit" parameters are $(r_c, \theta_0, h_c) = (0\farcs39, 204^\circ, 0.08)$ for S1 (reduced $\chi^2 = 0.52$) and $(r_c, \theta_0, h_c) = (0\farcs9, 353^\circ, 0.24)$ for S2 (reduced $\chi^2 = 0.31$). The spiral shapes with these parameters are shown in Figure 4. However, the parameter degeneracy is significant. Figure 5 shows the parameter space of (r_c, θ_0) with 63.8% confidence level for $h_c = 0.1$ and $h_c = 0.2$. Note that in Figure 5, the "best-fit" of (r_c, θ_0) is outside the domain of confidence in some cases because h_c is not the same as the best-fit. Despite the parameter degeneracy, the values of the aspect ratio which fit the shape of the spiral ($h_c \sim 0.1$) are consistent with those obtained from the sub-mm map of the disk (e.g., $h = 0.096(r/100\ \mathrm{AU})^{0.15}$; Andrews et al. 2011).

The spiral density wave theory predicts that the pattern speed deviates from the local Kepler speed;

$$\Omega_{\mathrm{pattern}} = 0.8 \left(\frac{r_c}{70\ \mathrm{AU}}\right)^{-3/2} \left(\frac{M_*}{1.7\ M_\odot}\right)^{1/2} (\mathrm{deg\ yr^{-1}}) \quad (2)$$

is not necessarily equal to $\Omega(r)$. When $r_c = 0\farcs5 (\sim 70$ AU), the spiral will move $\sim 10^\circ$ in a decade, corresponding to a movement of $0\farcs1$. Considering the PSF scale of our observations and the locations of the spirals, such deviations can be detectable over a couple of decades. Moreover, if the two spirals have distinct corotation radii, their relative locations change in time due to the pattern speed difference. Such measurements will confirm that the observed feature is really the density wave, providing indisputable evidence of dynamical activity.

Note that it would be difficult to detect spirals in colder disks (smaller h_c), where spirals are more tightly wound, due to the blurring by the PSF. The lower detectable limit of h_c is typically $h_c \sim 0.01$–0.03 for our set of parameters. The combination of high angular resolution and warm temperatures allows the spiral

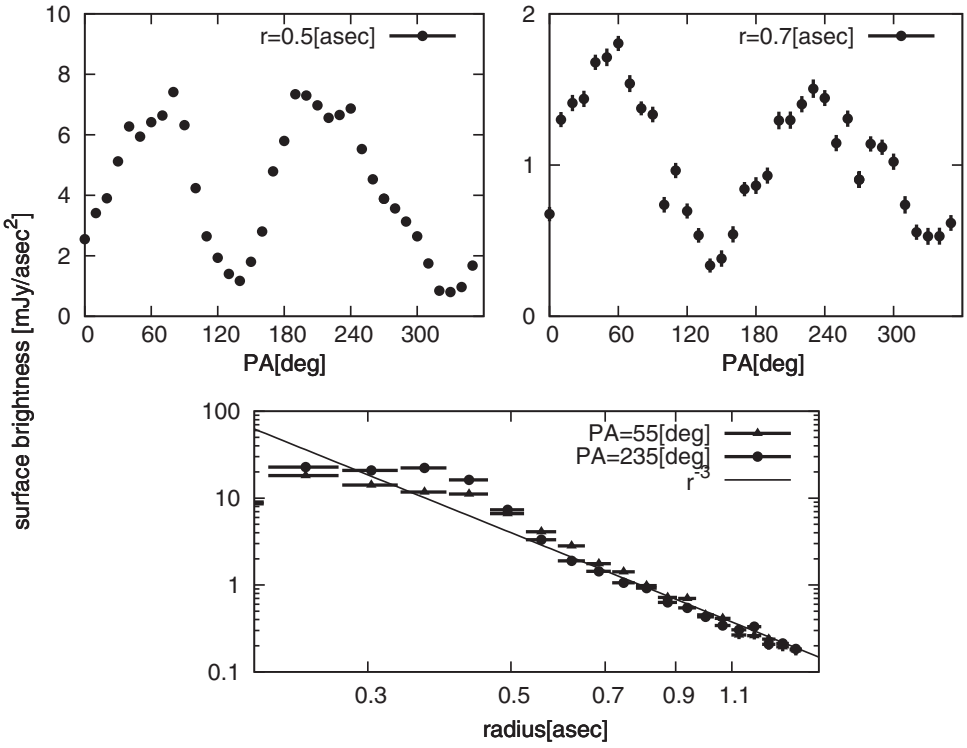

Figure 3. Top: azimuthal SB profile at $r = 0\farcs5$ (left) and $r = 0\farcs7$ (right) with PA measured from north to east. Bottom: radial profile along the major axis. Position errors indicate the FWHM of the PSF. SB errors are estimated using frame-by-frame deviations.

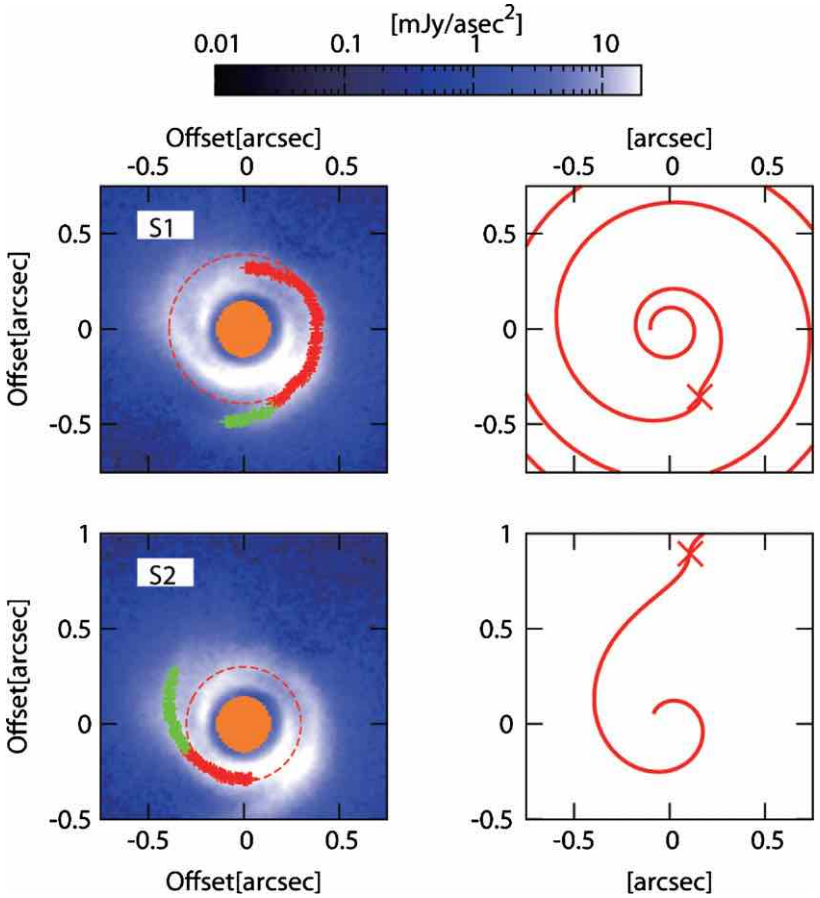

Figure 4. Left: red and green points indicate the locations of the maxima of radial profiles for S1 (top) and S2 (bottom). The green ones are used for the fitting by Equation (1) (Section 4). Dashed lines indicate circles with $r = 0\farcs39$ (top) and $r = 0\farcs3$ (bottom). Right: the spiral shape given by Equation (1) with the best-fit parameters of S1 (top) and S2 (bottom). Crosses show the locations of (r_c, θ_0).

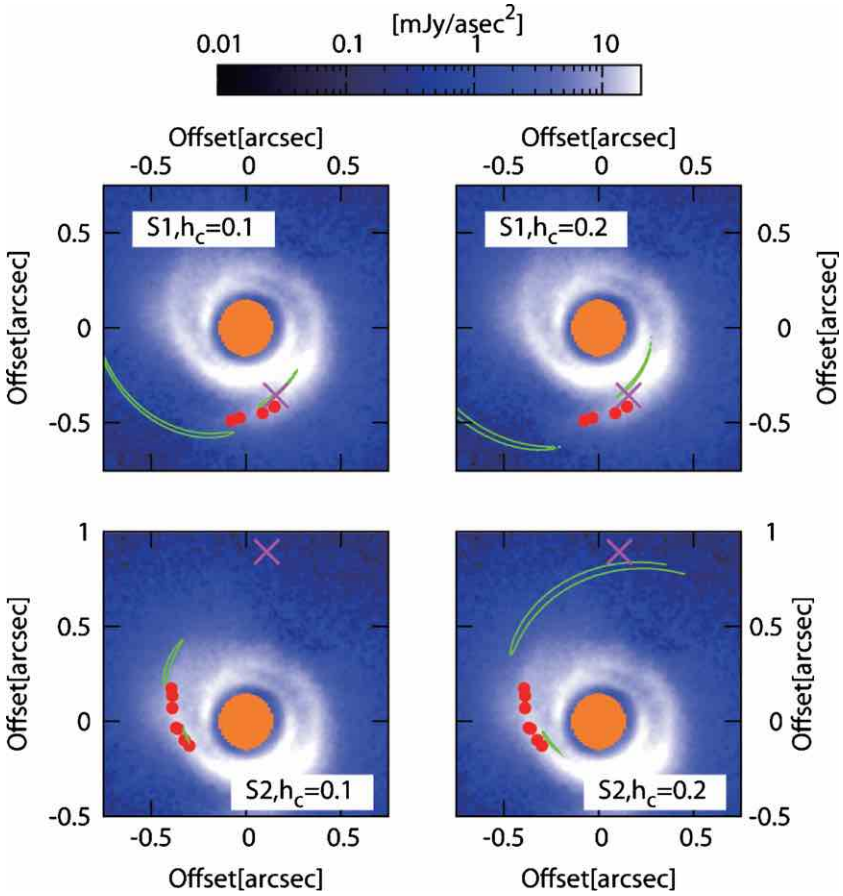

Figure 5. Parameter degeneracy of the fitting for S1 (top) and S2 (bottom) with $h_c = 0.1$ (left) and $h_c = 0.2$ (right). The red points show a part of the data fitted. The green curves indicate the 63.8% confidence level for the locations of (r_c, θ_0). The magenta crosses are (r_c, θ_0) for the best-fit parameters. Note that the best-fit values of h_c are different from those shown in the figure.

structure in the SAO 206462 disk to be resolved. Further spirals might be detectable in similarly warm disks.

5. SUMMARY AND DISCUSSION

In this Letter, we present a high-resolution image of the SAO 206462 transitional disk using Subaru/HiCIAO, with an inner working angle of 0.″2. We discover non-axisymmetric spiral features, which can be explained by the spiral density wave theory with a reasonable value of the disk aspect ratio ($h_c \sim 0.1$). The model is robust in a sense that it does not assume the origin of such structure explicitly.

The detection of scattered light within the sub-mm cavity itself is interesting, since Andrews et al. (2011) predicts that the sub-mm cavity is heavily depleted. Our data in tandem with the millimeter data may suggest that the depletion of grains at different sizes is not uniform. Dong et al. (2012) discuss such discrepancies between sub-mm dust continuum images and NIR scattered light images in terms of differing spatial distributions as a function of grain size from a general theoretical perspective.

Our major assumption is that PI at the *H*-band, tracing the scattered light at the disk surface, actually traces the surface density variations. This assumption is valid when the disk is in vertical, isothermal hydrostatic equilibrium without rapid radial surface density variations (e.g., Muto 2011). Structures near the midplane are, however, preferentially observed at longer wavelengths with high spatial resolution: Atacama Large Millimeter/Submillimeter Array (ALMA) can be an ideal instrument.

Among several possible causes for the spiral structures (see also Hashimoto et al. 2011), one interesting idea is that planets excite them. In this case, the domain of possible locations of the planets is given by the green curves in Figure 5. If the two spirals have distinct corotation radii, there may be two (unseen) planets embedded in the disk. The amplitude of the surface density perturbation scales with the planet mass as $\delta\Sigma/\Sigma \sim GM_p\Omega/c^3$ for non-gap-opening low-mass planets ($GM_p\Omega/c^3 \lesssim 1$, e.g., Tanaka et al. 2002). In our data, the amplitude of the spiral wave is typically ∼30% (Figure 2), implying $M_p \sim 0.5\,M_J$.

The typical error of PI in our image is ∼5%. If this is typical of HiCIAO, it is capable of detecting the indirect signatures of planets down to $M_p \sim 0.05\,M_J$. ADI is promising in finding a point source; however, small field rotation (∼13°) due to the southerly declination (−39°) of SAO 206462 makes obtaining the total intensity difficult in our data. Future *L*-band observations may reveal thermal emission from a planet, if it exists, or its surrounding (accreting) gas.

The authors thank Roman Rafikov for comments, the support staff members of the IRTF and REM telescopes for assistance in obtaining the SED data, and the IR&D program at The Aerospace Corporation. REM data in this study were obtained under Chilean National TAC programs CN2011A-050 and CN2011B-31. This work is partially supported by KAKENHI

22000005 (M.T.), 23103002 (M.H. and M.H.), 23103004 (M.M. and M.F.), 23103005, 23244027, 18540238 (S.I.), and 22·2942 (T.M.), WPI Initiative, MEXT, Japan (E.L.T.), NSF AST 1008440 (C.A.G.), 1009203 (J.C.), and 1009314 (J.P.W.), and NASA NNH06CC28C (M.L.S.) and NNX09AC73G (C.A.G. and M.L.S.). Part of this research was carried out at JPL.

REFERENCES

Andrews, S. M., Wilner, D. J., Espaillat, C., et al. 2011, ApJ, 732, 42
Brown, J. M., Blake, G. A., Dullemond, C. P., et al. 2007, ApJ, 664, L107
Brown, J. M., Blake, G. A., Qi, C., et al. 2008, ApJ, 704, 496
Covino, S., Stefanon, M., Sciuto, G., et al. 2004, Proc. SPIE, 5492, 1613
Cushing, M. C., Vacca, W. D., & Rayner, J. T. 2004, PASP, 116, 362
Dent, W. R. F., Greaves, J. S., & Coulson, I. M. 2005, MNRAS, 359, 663
Dong, R., et al. 2012, ApJ, in press (arXiv:1203.1612)
Doucet, C., Pantin, E., Lagage, P. O., & Dullemond, C. P. 2006, A&A, 460, 117
Fedele, D., van den Ancker, M. E, Acke, B., et al. 2008, A&A, 491, 809
Fukagawa, M., Tamura, M., Itoh, Y., et al. 2010, PASJ, 62, 347
Goldreich, P., & Tremaine, S. 1978, ApJ, 222, 850
Goldreich, P., & Tremaine, S. 1979, ApJ, 233, 857
Grady, C. A., Schneider, G., Sitko, M. L., et al. 2009, ApJ, 699, 1822
Graham, J. R., Kalas, P. G., & Matthews, B. C. 2007, ApJ, 654, 595
Hashimoto, J., Tamura, M., Muto, T., et al. 2011, ApJ, 729, L17
Hayano, Y., Saito, Y., Saito, N., et al. 2004, Proc. SPIE, 5490, 1088
Hinkley, S., Oppenheimer, B. R., Soummer, R., et al. 2009, ApJ, 701, 804
Hodapp, K. W., Suzuki, R., Tamura, M., et al. 2008, Proc. SPIE, 7014, 701419
Joos, F., Buenzli, E., Schmid, H. M., & Thalmann, C. 2008, Proc. SPIE, 7016, 48
Lin, C. C., & Shu, F. H. 1964, ApJ, 140, 646
Lyo, A.-R., Ohashi, N., Qi, C., Wilner, D. J., & Su, Y.-N. 2011, AJ, 142, 151
Mariñas, N., Telesco, C. M., Fischer, R. S., & Packham, C. 2011, ApJ, 737, 57
Minowa, Y., Hayano, Y., Oya, S., et al. 2010, Proc. SPIE, 7736, 77363N
Müller, A., van den Ancker, M. E., Launhardt, R., et al. 2011, A&A, 530, 85
Muto, T. 2011, ApJ, 739, 10
Muto, T., Suzuki, T. K., & Inutsuka, S. 2010, ApJ, 724, 448
Ogilvie, G. I., & Lubow, S. H. 2002, MNRAS, 330, 950
Perrin, M. D., Schneider, G., Duchene, G., et al. 2009, ApJ, 707, L132
Pontoppidan, K. M., Blake, G. A., van Dishoeck, E. F., et al. 2008, ApJ, 684, 1323
Quanz, S. P., Birkmann, S. M., Apai, D., Wolf, S., & Henning, T. 2012, A&A, 538, A92
Quanz, S. P., Schmid, H. M., Geissler, K., et al. 2011, ApJ, 738, 23
Rafikov, R. R. 2002, ApJ, 569, 997
Rayner, J. T., Cushing, M. C., & Vacca, W. D. 2009, ApJS, 185, 289
Sitko, M. L., Day, A. N., Kimes, R. L., et al. 2012, ApJ, 745, 29
Suzuki, R., Kudo, T., Hashimoto, J., et al. 2010, Proc. SPIE, 7735, 773530
Tamura, M. 2009, in AIP Conf. Proc. 1158, Proc. of the Intl. Conf., ed. T. Usuda, M. Ishii, & M. Tamura (Melville, NY: AIP), 11
Tamura, M., Hodapp, K., Takami, H., et al. 2006, Proc. SPIE, 6269, 28
Tanaka, H., Takeuchi, T., & Ward, W. R. 2002, ApJ, 565, 1257
Thalmann, C., Grady, C. A., Goto, M., et al. 2010, ApJ, 718, L87
Tokunaga, A. T., Simons, D. A., & Vacca, W. D. 2002, PASP, 114, 180
Vacca, W. D., Cushing, M. C., & Rayner, J. T. 2003, PASP, 115, 389
van der Plas, G., van der Ancker, M. E., Fedele, D., et al. 2008, A&A, 485, 487
Whitney, B. A., & Hartmann, L. 1992, ApJ, 395, 529

LETTER

doi:10.1038/nature12163

Emergence of two types of terrestrial planet on solidification of magma ocean

Keiko Hamano[1], Yutaka Abe[1] & Hidenori Genda[1,2]

Understanding the origins of the diversity in terrestrial planets is a fundamental goal in Earth and planetary sciences. In the Solar System, Venus has a similar size and bulk composition to those of Earth, but it lacks water[1–3]. Because a richer variety of exoplanets is expected to be discovered, prediction of their atmospheres and surface environments requires a general framework for planetary evolution. Here we show that terrestrial planets can be divided into two distinct types on the basis of their evolutionary history during solidification from the initially hot molten state expected from the standard formation model[4,5]. Even if, apart from their orbits, they were identical just after formation, the solidified planets can have different characteristics. A type I planet, which is formed beyond a certain critical distance from the host star, solidifies within several million years. If the planet acquires water during formation, most of this water is retained and forms the earliest oceans. In contrast, on a type II planet, which is formed inside the critical distance, a magma ocean can be sustained for longer, even with a larger initial amount of water. Its duration could be as long as 100 million years if the planet is formed together with a mass of water comparable to the total inventory of the modern Earth. Hydrodynamic escape desiccates type II planets during the slow solidification process. Although Earth is categorized as type I, it is not clear which type Venus is because its orbital distance is close to the critical distance. However, because the dryness of the surface and mantle predicted for type II planets is consistent with the characteristics of Venus, it may be representative of type II planets. Also, future observations may have a chance to detect not only terrestrial exoplanets covered with water ocean but also those covered with magma ocean around a young star.

Theoretical studies on planet formation suggest that Earth-sized planets (Earth and Venus) should form as a result of giant impacts between protoplanets[4], and probably all start their lives in a globally molten state[5]. The earliest phase of planetary evolution is thus solidification of a magma ocean, which provides the initial conditions for mantle differentiation and distribution of volatiles between the interior and the surface[6]. The timing of the end of this phase also determines the starting point for subsequent events such as water ocean formation, and possibly the onset of plate tectonics and the development of life.

The thermal evolution of a magma ocean is closely linked to the formation of a steam atmosphere[6–8]. A massive steam atmosphere decreases outgoing radiation from the planet through its strong greenhouse effects, and thus delays the solidification process. Degassing from a solidifying magma ocean can in turn greatly increase the amount of the steam atmosphere[6]. Therefore, evaluating the outgoing radiation during atmospheric evolution is the key to understanding the earliest thermal history of the planet.

Particularly for a hot steam atmosphere above a magma ocean, previous studies have shown that the outgoing radiation has a lower limit (about 300 W m^{-2}) owing to saturation of the upper troposphere with water vapour[9–11]. This is because its thermal structure is uniquely determined by the saturated-vapour-pressure curve of water (see ref. 11 for a further explanation). Because the net incoming stellar radiation in the zone of formation of terrestrial planets can be smaller or larger than this radiation limit, it can be speculated from heat balance that the presence of such a limit would produce an evolutionary dichotomy between terrestrial planets. The effect of the radiation limit, however, was neglected in a previously proposed coupled model for a deep magma ocean and steam atmosphere[6]. In addition, the greenhouse effect of water vapour has not been fully considered.

Here we perform radiative–convective equilibrium calculations to enable our model to be used to calculate the radiation limit for a saturated steam atmosphere. In addition we take into account the water loss associated with hydrodynamic escape[12], which is expected to occur in parallel with magma-ocean solidification. Competition between degassing and water loss determines whether the steam atmosphere grows or escapes. This would affect not only the thermal evolution of planets but also the planetary water inventory at the time of complete solidification.

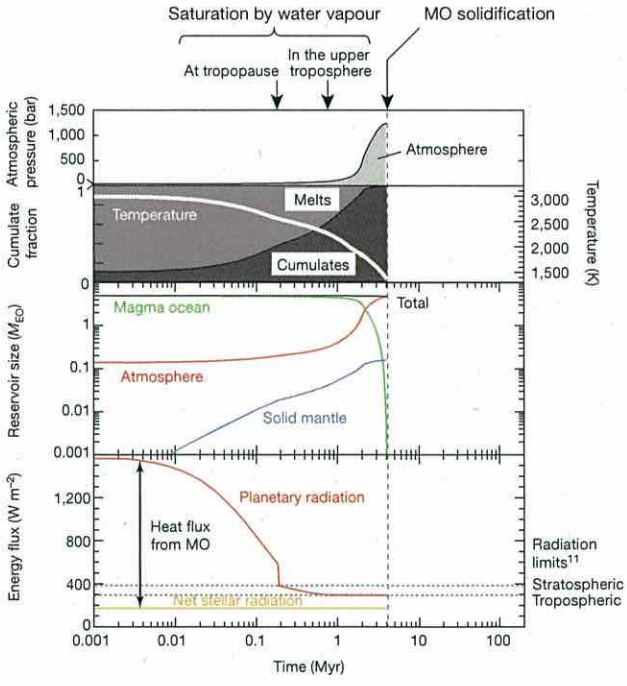

Figure 1 | Typical evolution of a type I planet. Evolution of a planet located at 1 AU, with an initial water mass of five times the current ocean mass on Earth (M_{EO}, 1.4×10^{21} kg). The grey dotted lines in the bottom panel indicate the radiation limits[11]. At ~0.7 Myr, the planetary radiation reaches the tropospheric radiation limit. After that, the heat flux from the magma ocean (MO) becomes constant. This results in rapid solidification at ~4 Myr. The solidification time and final water partitioning are comparable to those reported in ref. 6 for a MO 2,000 km deep on Earth and a total water mass of ~$10M_{EO}$.

[1]Department of Earth and Planetary Science, The University of Tokyo, 7-3-1 Hongo, Bunkyo-ku, Tokyo 113-0033, Japan. [2]Earth-Life Science Institute, Tokyo Institute of Technology, 2-12-1 Ookayama, Meguro-ku, Tokyo 152-8551, Japan.

Figure 1 shows the typical evolution of an Earth-sized planet located at a distance of 1 AU from its parent star. Because of the high solubility of water in silicate melts, a sizeable fraction of the water dissolves in the initial deep magma ocean. As the magma solidifies, degassing of water from the interior leads to an increase in the atmospheric mass. At about 0.2 million years (Myr), because of the growth of the atmosphere combined with the decrease in temperature, the atmosphere starts to be saturated with water vapour at the tropopause. As the saturation front moves deeper into the troposphere, the planetary radiation decreases until it finally becomes equal to the tropospheric radiation limit at about 0.7 Myr. The outgoing radiation flux then remains constant throughout the subsequent solidification period.

The overall solidification time is about 4 Myr in this case, and is mainly determined by the minimum net heat flux; this is defined as the difference between the radiation limit and the net incident stellar radiation. The existence of a minimum heat flux after saturation gives rise to rapid solidification because further atmospheric growth has no effect on the cooling rate of the planet. Hydrodynamic escape makes little contribution to the water inventory during the short magma-ocean period. We refer to this type of planet as type I.

This mechanism does not apply to the evolution of a planet at 0.7 AU (Fig. 2), in which the net incident stellar radiation exceeds the tropospheric radiation limit. In the earlier stages up to ~0.2 Myr, its evolution is similar to that of a type I planet. However, at ~1 Myr the outgoing radiation almost balances the net incident stellar radiation before a sufficiently deep part of the troposphere becomes saturated. This results in an extremely low heat flux so that the magma ocean is sustained for about 100 Myr, much longer than the value of 4 Myr at 1 AU, for an initial water amount of five times the current ocean mass on Earth ($5M_{EO}$). During this period there is a large decrease in the total water inventory of the planet.

The solidification rate is mainly governed by the water loss rate due to hydrodynamic escape. Because the outgoing radiation must exceed the incident stellar radiation for cooling, the steam atmosphere must be optically thinner for lower surface temperatures (Fig. 2), so that a net loss of the steam atmosphere is required. We refer to this type of planet as type II.

These two types of planet also have a different partitioning of water between the atmosphere and the interior (Fig. 3). For the type I planet at 1 AU, the total water inventory becomes less susceptible to loss for larger initial water masses. The primary water reservoir is the steam atmosphere, whereas the deep interior accounts for only a small percentage of the planetary water inventory. In contrast, the type II planet at 0.7 AU becomes desiccated during the longer magma-ocean period. The final total water inventory is less than $0.1M_{EO}$ even for an initial value of $10M_{EO}$. In addition, as the initial water inventory increases, the interior reservoir becomes larger than that of the atmosphere.

Figure 4 shows the solidification time and final total water inventory for Earth-sized planets within the terrestrial planet formation zone. The solidification time (see Supplementary Information for analytical expressions) is seen to peak at about 0.8 AU. Planets located beyond this range are classified as type I, whereas those inside it are classified as type II. Type I planets have maximum solidification times typically as short as several million years owing to the minimum heat flux. Because only a limited amount of hydrodynamic escape can occur within such a short period, it has a reduced impact on the thermal history and water budget of the planet. Soon after solidification, water oceans would probably form on the surface.

For a type I planet, the initial total water inventory simply affects the volume of the earliest oceans, whereas it has a strong influence on the solidification time for a type II planet. As seen in Fig. 4, the duration of the magma-ocean phase agrees well with the time required for total loss of the primordial water. This reflects the fact that the type II planet must lose water to cool down, and consequently a larger water endowment results in a longer magma-ocean period. The final total water inventory of type II planets never exceeds 0.1 M_{EO}, irrespective of the initial value.

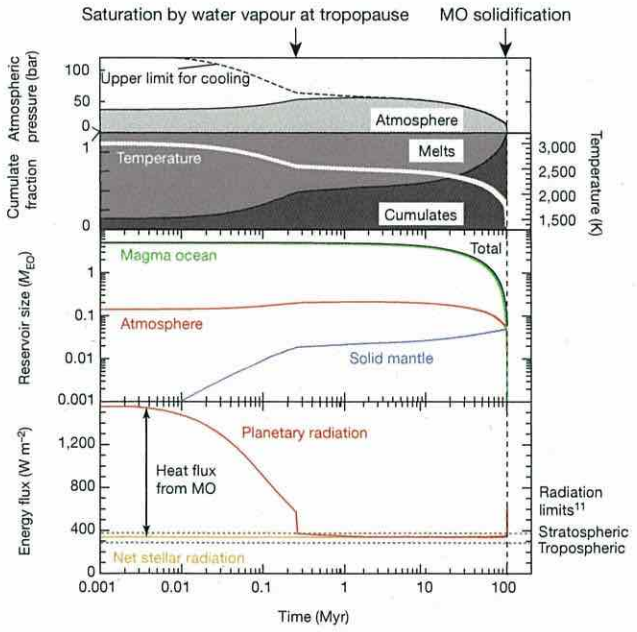

Figure 2 | Typical evolution of a type II planet. As in Fig. 1, but for an orbital distance of 0.7 AU. The net incident stellar radiation is larger than the tropospheric radiation limit. At ~1 Myr, planetary radiation almost balances the net stellar radiation. The subsequent heat flux from the MO is controlled by the rate of water loss. The dashed black line in the top panel represents the upper limit of atmospheric pressure for cooling, for which the planetary radiation is equal to the net stellar flux. The MO period is ~100 Myr, much longer than that for a type I planet.

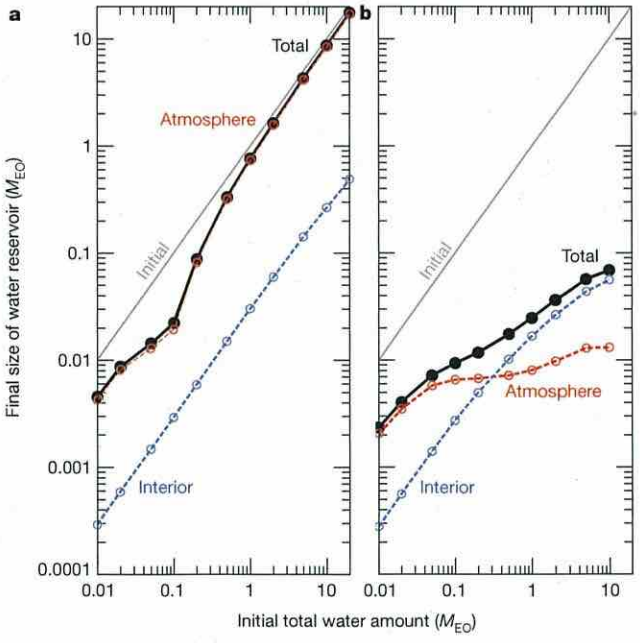

Figure 3 | Water partitioning between steam atmosphere and planetary interior. The amount of water depends on the rate of loss and the duration of the MO period. **a**, Planet at 1 AU (type I). Most of the primordial water remains and contributes to the steam atmosphere at the time of complete solidification. **b**, Planet at 0.7 AU (type II). The final total mass of water is less than $0.1M_{EO}$. The planetary interior may become the dominant reservoir if water is incorporated before the silicate melts become desiccated. The effect of a surface thermal boundary layer is discussed in Supplementary Information.

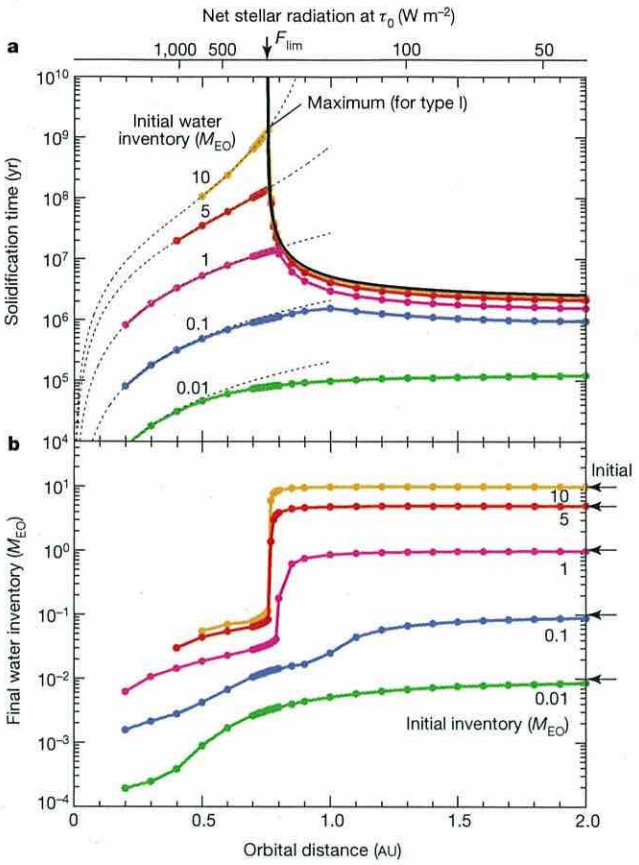

Figure 4 | Two distinct types of terrestrial planet. The upper x axis shows the corresponding initial net stellar radiation. The arrow indicates the tropospheric radiation limit. The critical orbital distance a_{cr} of ~0.76 AU separates the orbital regimes of the two types of planet. **a**, Solidification time. The dotted lines show the time required for complete loss of primordial water. This provides a good approximation of the solidification time of type II planets. The maximum solidification time for type I planets is also shown (see Supplementary Information). **b**, Total water inventory at the time of complete solidification. A strong transition is exhibited at about a_{cr}.

The different mechanisms determining the solidification rate thus also lead to a sharp transition in the planetary water budget.

Whether a type I or a type II planet is formed around a star depends on the critical orbital distance a_{cr}, which is defined as the distance at which the net stellar flux that the planet receives equals the tropospheric radiation limit F_{lim} of the steam atmosphere,

$$a_{cr} \approx 0.76 \left(\frac{F_{lim}}{294\ \mathrm{W\ m^{-2}}} \right)^{-1/2} \left(\frac{S_{stl}(\tau_0)}{0.7 S_\odot} \right)^{1/2} \left(\frac{1-\alpha}{1-0.3} \right)^{1/2} \mathrm{AU} \quad (1)$$

where $S_{stl}(\tau_0)$ is the stellar constant at a stellar age τ_0 when solidification starts. $S_\odot$ is the current solar constant and α is the planetary albedo. a_{cr}, which is about 0.76 in our model, can range from about 0.6 to 0.8 AU, as a result of parameter uncertainties and the atmospheric model used.

Earth is located at a distance of 1 AU from the Sun, which is sufficiently far for it to be a type I planet. Its deep interior would probably have solidified within about 5 Myr, even if it had acquired as much or more water than the current total inventory (~1.25–5M_{EO})[13]. This would support the rapid solidification and ocean formation condition suggested from geochemical data[14,15]. The overall water budget would have been only slightly affected by hydrodynamic escape, but this modest loss might still have contributed to oxidization of the interior through selective escape of hydrogen over oxygen. If a simple assumption is made that all of the dissociated oxygen atoms were consumed by oxidation of ferrous iron, the bulk Fe_2O_3 content in the early mantle would have increased by up to about 0.07wt% during the first several million years of Earth's history. This value is comparable to the current Fe_2O_3 content in the upper mantle (>0.2wt%)[16] and is consistent with the idea of an oxidized mantle possibly as early as 4.4 Gyr ago (ref. 17).

Because Venus's orbital distance of about 0.72 AU places it on the border zone, it is not exactly clear which planetary type it should be classified as. However, the significant water loss for a type II planet during the magma-ocean period might explain its dry interior and the fate of the remnant oxygen. The absence of water on its surface[1] and interior[2,3] is conventionally explained in terms of an inherently dry origin[18] or hydrodynamic escape after ocean evaporation[19]. The latter situation corresponds to the case in which Venus is a type I planet in our classification. In this case, the dryness of its interior depends on degassing efficiency during the subsequent evolution. Alternatively, if Venus belongs to type II, the occurrence of planetary desiccation during solidification can explain the dryness of its current mantle[2,3], even if it accreted with a certain amount of water. The presence of a dry mantle during the earliest stages might also have led to a subsequent tectonic evolution different from that of Earth[20,21] and possibly to the absence of a magnetic field[22].

One problem associated with the hydrodynamic escape of water is the accumulation of dissociated oxygen in the atmosphere as a result of the preferential escape of hydrogen[23], which would possibly lead to a shutdown of the hydrogen escape process itself. However, if Venus belongs to type II, the remnant oxygen issue can be avoided, regardless of the initial amount of water, because the abundant surface magma can act as a massive oxygen sink. Although the effects of other gaseous species such as carbon dioxide will need to be addressed in future work, the slight difference in the orbital distances of Earth and Venus might have been the critical factor making these planets totally different after solidification.

Although we have so far discussed only Earth-sized planets orbiting a Sun-like star, the conclusions can be qualitatively extended to all terrestrial planets that experienced global melting through giant impact. More than 750 exoplanets have already been confirmed[24], and 2,300 candidates[25] have been identified. Future space missions such as the Terrestrial Planet Finder and Darwin will provide us with a catalogue of atmospheres and surface environments for terrestrial planets of various ages. The present results indicate that for habitable planets, rapid ocean formation would have occurred within several million years of planet formation. In addition, the prediction that type II planets undergo a long-lived (~100 Myr) magma-ocean stage suggests that, apart from permanently molten planets very close to the host star, there may be a chance of detecting still-molten terrestrial planets as a consequence of planetary formation, especially around young stars. Although the molten surface would be hard to detect through the thick atmosphere, it can in principle be identified by detecting gaseous species such as NaOH and KOH that are indicative of hot atmospheres[26].

METHODS SUMMARY

Water reservoirs and budgets. Partition of water between planetary reservoirs was treated in basically the same way as in ref. 6. We used water solubility in basaltic-composition melts calculated from a solubility model in ref. 27. Water partition coefficient into cumulates and mass fraction of interstitially trapped melts were fixed at 10^{-4} and 0.01, respectively.

The water-loss rate was calculated from energy-limited escape rate of hydrogen[12] with a heating efficiency of 0.1 by assuming that all the dissociated oxygen would have been absorbed into the magma ocean. For the effects of the higher heating efficiency, see the online-only Methods and Supplementary Information section 4. We adopted an observational compilation of Sun-like stars for time-dependent extreme ultraviolet radiation[28].

Thermal evolution model. Assuming that the atmosphere has a negligible heat capacity, the thermal evolution model was formulated on the basis of heat balance:

$$C_{p,pl}(T_m)\frac{dT_m}{dt} = -4\pi R^2(F_{pl} - F_{stl}) \quad (2)$$

where $C_{p,pl}(T_m)$ is the heat capacity of the planet at potential temperature T_m of the interior, and R is the planetary radius. F_{pl} and F_{stl} are the outgoing planetary radiation and the incoming net stellar radiation, respectively. Calculation starts from temperature of 3,000 K, which corresponds to a mostly molten state of the mantle, and stops when it reaches the solidus temperature at the surface (~1,370 K). We assumed that the whole silicate portion could transfer heat by convection and therefore contribute to the heat capacity. We obtained the heat capacity, including latent heat of fusion, as a function of potential temperature, from its adiabatic temperature profile calculated according to ref. 29.

The planetary radiation was calculated with a modified radiative–convective equilibrium model of grey atmosphere[11]. We also performed non-grey calculations (Supplementary Information). We adopted a solar standard model for luminosity enhancement with stellar age[30]. A planetary albedo of 0.3 was assumed for the net stellar radiation.

Full Methods and any associated references are available in the online version of the paper.

Received 7 October 2012; accepted 5 April 2013.

1. Lewis, J. S. & Grinspoon, D. H. Vertical distribution of water in the atmosphere of Venus: a simple thermochemical explanation. *Science* **249,** 1273–1275 (1990).
2. Nimmo, F. & McKenzie, D. Volcanism and tectonics on Venus. *Annu. Rev. Earth Planet. Sci.* **26,** 23–51 (1998).
3. Kiefer, W. S., Richards, M. A., Hager, B. H. & Bills, B. G. A dynamic model of Venus's gravity field. *Geophys. Res. Lett.* **13,** 14–17 (1986).
4. Chambers, J. E. & Wetherill, G. W. Making the terrestrial planets: *N*-body integrations of planetary embryos in three dimensions. *Icarus* **136,** 304–327 (1998).
5. Canup, R. M. Dynamics of lunar formation. *Annu. Rev. Astron. Astrophys.* **42,** 441–475 (2004).
6. Elkins-Tanton, L. T. Linked magma ocean solidification and atmospheric growth for Earth and Mars. *Earth Planet. Sci. Lett.* **271,** 181–191 (2008).
7. Matsui, T. & Abe, Y. Evolution of an impact-induced atmosphere and magma ocean on the accreting Earth. *Nature* **319,** 303–305 (1986).
8. Zahnle, K. J., Kasting, J. F. & Pollack, J. B. Evolution of a steam atmosphere during Earth's accretion. *Icarus* **74,** 62–97 (1988).
9. Abe, Y. & Matsui, T. Evolution of an impact-generated H_2O–CO_2 atmosphere and formation of a hot proto-ocean on Earth. *J. Atmos. Sci.* **45,** 3081–3101 (1988).
10. Kasting, J. F. Runaway and moist greenhouse atmospheres and the evolution of Earth and Venus. *Icarus* **74,** 472–494 (1988).
11. Nakajima, S., Hayashi, Y. & Abe, Y. A study on the 'runaway greenhouse effect' with a one-dimensional radiative–convective equilibrium model. *J. Atmos. Sci.* **49,** 2256–2266 (1992).
12. Watson, A. J., Donahue, T. M. & Walker, J. C. G. The dynamics of a rapidly escaping atmosphere: applications to the evolution of Earth and Venus. *Icarus* **48,** 150–166 (1981).
13. Hirschmann, M. M. Water, melting, and the deep Earth H_2O cycle. *Annu. Rev. Earth Planet. Sci.* **34,** 629–653 (2006).
14. Caro, G. Early silicate Earth differentiation. *Annu. Rev. Earth Planet. Sci.* **39,** 31–58 (2011).
15. Cavosie, A. J., Valley, J. W., Wilde, S. A. & Edinburgh Ion Microprobe Facility. Magmatic $\delta^{18}O$ in 4400–3900 Ma detrital zircons: a record of the alteration and recycling of crust in the Early Archean. *Earth Planet. Sci. Lett.* **235,** 663–681 (2005).
16. Canil, D. & O'Neill, H. St C. Distribution of ferric iron in some upper-mantle assemblages. *J. Petrol.* **37,** 609–635 (1996).
17. Trail, D., Watson, E. B. & Tailby, N. D. The oxidation state of Hadean magmas and implications for early Earth's atmosphere. *Nature* **480,** 79–82 (2011).
18. Lewis, J. S. Venus: atmospheric and lithospheric composition. *Earth Planet. Sci. Lett.* **10,** 73–80 (1970).
19. Kasting, J. F. & Pollack, J. B. Loss of water from Venus. I. Hydrodynamic escape of hydrogen. *Icarus* **53,** 479–508 (1983).
20. Mackwell, S. J., Zimmerman, M. E. & Kohlstedt, D. L. High-temperature deformation of dry diabase with applications to tectonics on Venus. *J. Geophys. Res.* **103,** 975–984 (1998).
21. Moresi, L. & Solomatov, V. Mantle convection with a brittle lithosphere: thoughts on the global tectonic styles of the Earth and Venus. *Geophys. J. Int.* **133,** 669–682 (1998).
22. Nimmo, F. Why does Venus lack a magnetic field? *Geology* **30,** 987–990 (2002).
23. Chassefière, E. Hydrodynamic escape of oxygen from primitive atmospheres: applications to the cases of Venus and Mars. *Icarus* **124,** 537–552 (1996).
24. The Extrasolar Planets Encyclopedia. <http://exoplanet.eu/> (2012).
25. Batalha, N. M. *et al.* Planetary candidates observed by *Kepler*. III. Analysis of the first 16 months of data. *Astrophys. J. Suppl. S.* **204,** 24, http://dx.doi.org/10.1088/0067-0049/204/2/24 (2013).
26. Schaefer, L., Lodders, K. & Fegley B. Vaporization of the Earth: application to exoplanet atmospheres. *Astrophys. J.* **755,** 41, http://dx.doi.org/10.1088/0004-637X/755/1/41 (2012).
27. Papale, P. Modeling of the solubility of a one-component H_2O or CO_2 fluid in silicate liquids. *Contrib. Mineral. Petrol.* **126,** 237–251 (1997).
28. Ribas, I., Guinan, E. F., Güdel, M. & Audard, M. Evolution of the solar activity over time and effects on planetary atmospheres. I. High-energy irradiances (1–1700 Å). *Astrophys. J.* **622,** 680–694 (2005).
29. Abe, Y. Thermal and chemical evolution of the terrestrial magma ocean. *Phys. Earth Planet. Inter.* **100,** 27–39 (1997).
30. Gough, D. O. Solar interior structure and luminosity variations. *Sol. Phys.* **74,** 21–34 (1981).

Supplementary Information is available in the online version of the paper.

Acknowledgements We thank J.F. Kasting for constructive comments on the manuscript. We appreciate proofreading and editing assistance from the GCOE programme. This work was supported by Grants-in-Aid for Scientific Research (KAKENHI) from the Ministry of Education, Culture, Sports, Science and Technology (23103003) and from Japan Society for the Promotion of Science (23340168 and 22740291). This study is a part of the PhD thesis of K.H. submitted to the University of Tokyo.

Author Contributions K.H. and Y.A. conceived the initial idea. K.H. constructed the coupled model and performed the calculations. Y.A. contributed to the modelling as well. H.G. provided suggestions on exoplanetary science. All authors discussed the results and implications and commented on the manuscript.

Author Information Reprints and permissions information is available at www.nature.com/reprints. The authors declare no competing financial interests. Readers are welcome to comment on the online version of the paper. Correspondence and requests for materials should be addressed to K.H. (keiko@eps.s.u-tokyo.ac.jp).

METHODS

Water reservoirs and water budget. The partitioning of the total water inventory between planetary reservoirs was treated in basically the same way as in ref. 6. Three water reservoirs were considered: atmosphere, magma ocean (a wholly or partly molten region) and solid mantle. The partial pressure of water was calculated at each time step by assuming a solution equilibrium between the atmosphere and the silicate melts at the surface. The water solubility values used were for basaltic melts taken from ref. 31 and were calculated by using the model reported in ref. 27 for a temperature of 2,000 K (see Supplementary Information for the effect of this degassing assumption).

For the incorporation of water into solidifying silicates, two processes were considered: interstitial trapping of water-enriched melts and water partitioning between silicate melts and cumulates. The mass fraction of interstitially trapped melts was assumed to be 1%, as in ref. 6. Although the actual value for a solidifying magma ocean is highly uncertain, a value of 1% is likely to be an overestimate, taking into account the degree of melting estimated for abyssal peridotites when melt separation begins[32]. Few experimental results have been reported on the partition coefficient of water for minerals such as perovskites that make up the deep mantle. We adopted a water partition coefficient of 10^{-4} in our calculations. However, it should be noted that increasing this to 10^{-2} increases the amount of water in the interior at the time of complete solidification by only a factor of 2. This is because interstitial trapping of water-enriched melts dominates.

Because all surface water is in the vapour phase on a solidifying planet, intense hydrodynamic escape of hydrogen is expected to occur during the magma ocean period. We also considered a reduction in the total amount of water due to hydrodynamic escape. The water loss rate was calculated from the energy-limited escape rate for hydrogen[12] by assuming that all of the oxygen produced by dissociation of water vapour would be lost from the atmosphere by oxidation of the magma ocean. Extreme ultraviolet radiation levels for the host star were based on compiled observational data for Sun-like stars, taken from ref. 28, in which the decay with time is expressed as a power-law function of stellar age. A heating efficiency of 0.1 was used throughout all the calculations. Using the higher heating efficiency has less effect on the evolution of type I planets, whereas the solidification time of type II planets becomes shorter in inverse proportion to the heating efficiency (see Supplementary Information).

Thermal evolution model. A high degree of melting implies an extremely turbulent magma ocean with a viscosity probably as low as 0.1 Pa (ref. 33). This suggests that the magma ocean is effective in transporting internal heat to the surface. Planetary radiation into space would therefore be the main factor limiting the heat flux from the deep magma ocean. We assumed that the heat flux is given by the difference between the outgoing planetary radiation $F_{\rm pl}$ and incoming net stellar radiation $F_{\rm stl}$. On the assumption that the atmosphere has a negligible heat capacity, a thermal evolution model can be formulated on the basis of the heat balance for a planet,

$$C_{\rm p,pl}(T_{\rm m})\frac{{\rm d}T_{\rm m}}{{\rm d}t} = -4\pi R^2(F_{\rm pl} - F_{\rm stl}) \quad (2)$$

where $C_{\rm p,pl}(T_{\rm m})$ is the heat capacity of a planet with an interior potential temperature $T_{\rm m}$, and R is the planetary radius. Heat flux from the core and heat production by radiogenic elements are neglected. The simple assumption is made that the potential temperature matches the surface temperature $T_{\rm s}$—that is, $T_{\rm m} = T_{\rm s}$—during the solidification period of the magma ocean. The calculation starts with potential and surface temperatures of 3,000 K, implying a mostly molten mantle, and stops when the solidus temperature at the surface (~1,370 K) is reached.

We calculated the planetary heat capacity, including the latent heat of fusion, as a function of the potential temperature by assuming that the entire silicate portion can transfer heat by convection, and not only the molten part as considered in ref. 6. The heat capacity calculated in this way corresponds to the maximum value, thus providing a conservative estimate of the maximum solidification time for a type I planet. However, both assumptions about the interior temperature profile result in an almost identical solidification time for a type II planet, because the solidification rate is mainly determined not by the heat capacity but by the water loss rate. The adiabatic thermal structure in the interior was calculated according to ref. 29 by using the parameters therein, except for recent experimental data for the solidus and liquidus temperatures at great depth (see Supplementary Information). Differentiation of the mantle and its mineralogy on solidification were not considered in the calculations of the temperature profile, because these would be expected to make a smaller contribution to the overall heat capacity of the planet. See the next section for calculations of planetary radiation and net stellar radiation.

Atmospheric model. Planetary radiation was calculated by using a modified version of the radiative–convective equilibrium model in ref. 11, which was originally designed for a steam atmosphere saturated with water vapour and for moderate surface temperatures. However, in the present study the surface temperatures considered are extremely high, exceeding the critical temperature of water. In addition, the relative humidity of the atmosphere can vary because the partial pressure of water is determined by solution equilibrium at the surface. We have extended the grey atmosphere model in ref. 11 to be applicable to the conditions considered herein. The critical point of water was simply treated as the temperature above which no water condensation would occur. For atmospheric layers that were unsaturated by water vapour or for which the temperature was above the critical point, the temperature lapse rate in the troposphere was assumed to be a dry adiabatic temperature gradient, whereas for saturated parcels the lapse rate was assumed to be a pseudo-moist adiabatic temperature gradient, as in ref. 11. The atmosphere is considered to consist of 1 bar of N_2 in addition to water vapour, the amount of which is determined by the water budget. See Supplementary Information for results calculated with a non-grey atmospheric model in ref. 9, instead of our simple grey model.

For calculations of the net stellar radiation, the solar standard model[30] was adopted to describe the change in stellar luminosity with time. The planetary albedo was fixed at 0.3 in all calculations. The actual value of planetary albedo is highly uncertain, especially because of the unpredictability of cloud coverage with a one-dimensional atmospheric model. In the previous studies (refs 9, 10) a planetary albedo for a thick steam atmosphere was estimated as large as 0.4–0.5, whereas a recent study[34] with a non-grey atmospheric model using the HITEMP database has shown that including weak H_2O lines significantly lowers the planetary albedo.

31. Presnall, D. C. & Hoover, J. D. in *Magmatic Processes: Physicochemical Principles* (ed. Mysen, B. O.) vol. 1, 75–89 (Geochemical Society Special Publication, 1984).
32. Johnson, K. T. M. & Dick, H. J. B. Open system melting and temporal and spatial variation of peridotite and basalt at the Atlantis II fracture zone. *J. Geophys. Res.* **97,** 9219–9241 (1992).
33. Solomatov, V. in *Evolution of the Earth* (ed. Stevenson, D.) 91–119 (Treatise on Geophysics 9, Elsevier, 2007).
34. Kopparapu, R. K. *et al.* Habitable zones around main-sequence stars: new estimates. *Astrophys. J.* **765,** 131, http://dx.doi.org/10.1088/0004-637X/765/2/131 (2013).

The Astrophysical Journal, 806:216 (17pp), 2015 June 20 doi:10.1088/0004-637X/806/2/216

LIFETIME AND SPECTRAL EVOLUTION OF A MAGMA OCEAN WITH A STEAM ATMOSPHERE: ITS DETECTABILITY BY FUTURE DIRECT IMAGING

Keiko Hamano[1], Hajime Kawahara[1], Yutaka Abe[1], Masanori Onishi[2], and George L. Hashimoto[3]
[1] Department of Earth and Planetary Science, The University of Tokyo, 7-3-1 Hongo, Bunkyo-ku, Tokyo 113-0033, Japan; keiko@eps.s.u-tokyo.ac.jp
[2] Department of Earth and Planetary Sciences, Kobe University, 1-1 Rokkodai-cho, Nada, Kobe 657-8501, Japan
[3] Department of Earth Sciences, Okayama University, 3-1-1 Tsushima-Naka, Kita, Okayama, 700-8530, Japan
Received 2015 February 16; accepted 2015 May 8; published 2015 June 18

ABSTRACT

We present the thermal evolution and emergent spectra of solidifying terrestrial planets along with the formation of steam atmospheres. The lifetime of a magma ocean and its spectra through a steam atmosphere depends on the orbital distance of the planet from the host star. For a Type I planet, which is formed beyond a certain critical distance from the host star, the thermal emission declines on a timescale shorter than approximately 10^6 years. Therefore, young stars should be targets when searching for molten planets in this orbital region. In contrast, a Type II planet, which is formed inside the critical distance, will emit significant thermal radiation from near-infrared atmospheric windows during the entire lifetime of the magma ocean. The K_s and L bands will be favorable for future direct imaging because the planet-to-star contrasts of these bands are higher than approximately 10^{-7}–10^{-8}. Our model predicts that, in the Type II orbital region, molten planets would be present over the main sequence of the G-type host star if the initial bulk content of water exceeds approximately 1 wt%. In visible atmospheric windows, the contrasts of the thermal emission drop below 10^{-10} in less than 10^5 years, whereas those of the reflected light remain 10^{-10} for both types of planets. Since the contrast level is comparable to those of reflected light from Earth-sized planets in the habitable zone, the visible reflected light from molten planets also provides a promising target for direct imaging with future ground- and space-based telescopes.

Key words: infrared: planetary systems – planets and satellites: terrestrial planets – radiative transfer

1. INTRODUCTION

Theoretical studies predict that the final stage of terrestrial planet formation involves a series of giant impacts between protoplanets. This stage is triggered by the dispersal of nebula gas, and probably lasts approximately 10–100 Myr (e.g., Agnor et al. 1999; Chambers 2001). In the aftermath of the last impact, the planets probably begin in a molten state (e.g., Canup 2004). Detecting molten terrestrial planets in extrasolar systems is of great significance in testing the widely accepted view of their hot origins.

The rocky planets can acquire water throughout formation by various processes, such as the local accretion of hydrated and icy planetesimals (Muralidharan et al. 2008; King et al. 2010; Machida & Abe 2010), chemical reactions between nebula gas and silicate melts (Sasaki et al. 1990; Ikoma & Genda 2006), and delivery via ice-bearing bodies from the outer orbital region (Morbidelli et al. 2000; Raymond et al. 2007; Walsh et al. 2011). A substantial amount of water would be delivered during planetary formation. Water acquired through the lattermost process alone would exceed Earth's current ocean mass by more than ten times. Since giant impacts do not blow off the entire water inventory (Genda & Abe 2005), early molten planets are likely to be covered by a steam-rich atmosphere.

Emergent spectra of hot molten planets have been investigated for several atmospheric compositions, including water-rich atmospheres. Miller-Ricci et al. (2009) first presented thermal emission spectra for the hot surface conditions, considering various possible atmospheric compositions: solar and enhanced metallicity atmospheres, H_2O–CO_2 atmospheres, and Venus' composition atmospheres. Since the solidus temperature of peridotite rocks is approximately 1400 K at the planetary surface (e.g., Takahashi 1986), the molten surface emits strong radiation not only in the infrared (IR), but also in the visible and near-infrared (near-IR). They showed that, although the steam-rich atmosphere obscures the hot surface, intense thermal emission from the surface would leak through near-IR atmospheric windows, which are relatively transparent. Lupu et al. (2014) further explored emergent high-resolution spectra for atmospheric compositions in equilibrium with magmas with compositions of Earth's continental crust and the bulk silicate Earth, taking into account atmospheric chemistry and structure self-consistently. They found out that the atmospheres are dominated by H_2O and CO_2, considering quenching effects. Additional opacity sources, such as CH_4 and NH_3, could reduce the brightness temperature by a factor of two to three, but the emergent spectra still reveal features similar to those without these additional opacity sources. Lupu et al. (2014) concluded that the most favorable wavelength range for direct imaging with future telescopes will be 1–4 μm.

These previous studies revealed that the mass of the steam atmosphere is a determining factor for spectral detectability of hot molten planets. However, the mass of the steam atmosphere does not remain constant during the solidification process. The atmosphere would grow by degassing from the planetary interior or would escape into space (Elkins-Tanton 2011; Hamano et al. 2013; Lebrun et al. 2013). Atmospheric evolution would significantly affect the emergent spectra during solidification of the magma ocean.

In addition, atmospheric evolution is also crucial to the thermal evolution of magma oceans (Matsui & Abe 1986a, 1986b; Zahnle et al. 1988; Elkins-Tanton 2008, 2011; Hamano et al. 2013; Lebrun et al. 2013). Since the strong greenhouse effect of water vapor prevents heat from escaping, a magma ocean is sustained longer under a more massive atmosphere. Although a growing atmosphere keeps the planet in a molten

state for a longer period of time, its spectral signatures become fainter as a result of increasing surface obscuration. Conversely, if the atmosphere escapes with time, the planet becomes brighter, but the magma ocean quickly solidifies over a shorter timescale. Thus, a trade-off relationship is expected between the spectral intensity and occurrence rate of the magma-covered planets, as suggested by Miller-Ricci et al. (2009).

Variations in water inventory would also affect the planetary spectra and their time evolution. The water in Earth's current ocean amounts to approximately 0.023 wt% in bulk content, and its total, including the water stored in the crust and mantle, is probably at most 0.23 wt% (e.g., Ohtani 2005; Hirschmann 2006). Extrasolar terrestrial planets could exhibit large variations in water amount just after formation as a result of a combination of water supply and loss processes. Recent calculations have indicated that the lifetime of magma oceans depends on the initial water inventory and the orbital distance from the host star (Hamano et al. 2013). Therefore, the occurrence rate of hot molten planets as a function of orbital distance would be related to the expected variety in initial water endowment on terrestrial planets.

As described above, spectral calculations of hot molten planets have been presented for various atmospheric compositions by several authors (Miller-Ricci et al. 2009; Lupu et al. 2014). They have concluded that the detectability in terms of spectral intensities depends primarily on the mass of the atmosphere. On the other hand, recent evolutionary calculations have shown that the mass of the steam atmosphere overlying a magma ocean greatly varies with time by degassing and escape processes (Hamano et al. 2013). They also indicated that the evolutionary history of the steam atmosphere and its cooling time strongly depend on the orbital distance from the star. Although they suggested that the occurrence rate of molten planets depends on the planetary orbit as well, their evolutionary model is not able to predict the variations of thermal emission spectra along with the evolution of the steam atmosphere because of the assumption of a gray gas in their radiative transfer model.

In the present paper, we incorporate a newly developed non-gray radiative transfer model into the evolutionary model by Hamano et al. (2013) to describe the spectral evolution of hot molten planets along with the evolution of steam atmospheres during the solidification of a magma ocean. This enables us to self-consistently examine the brightness variations of solidifying planets and the duration of the molten state. We also investigate the dependence of the brightness of solidifying planets on orbital distance and obtain a consistent relationship between planet-to-star contrast and orbital separation. In this paper, we consider Earth-sized terrestrial planets around a Sun-like star.

In Section 2, we summarize our proposed model and its parameters. We describe the spectral features of thermal emission and the albedo of molten planets with a steam atmosphere. In Section 3, we describe the time evolution of surface temperature, atmospheric pressure, and thermal emission spectra. In Section 4, we present diagrams of planet-to-star contrast and orbital distance for near-IR atmospheric windows and discuss future prospects for direct imaging. We also address the possibility of putting constraints on water inventory originating from the formation stages of terrestrial planets from the predicted occurrence rate. Color variations of the solidifying planets are presented as well. In Section 5, we compare our model spectra with those obtained by previous models and discuss parameter uncertainties. In Section 6, we summarize our main findings and present our conclusions.

2. MODEL DESCRIPTION AND SPECTRAL FEATURES

2.1. Radiative Transfer Calculations

The evolutionary model used in the present study is that described in Hamano et al. (2013), except for the calculations of radiative transfer. In the present study, we replace a gray radiative transfer code used in Hamano et al. (2013) with a newly developed, non-gray code to calculate thermal emission and reflection spectra from the planet. In the non-gray code, a two-stream formulation is used to calculate the radiative transfer in a plane-parallel atmosphere. We calculate planetary and stellar radiation separately in a wavenumber range from 0 to 30,000 cm^{-1} with a spectral resolution of 0.01 cm^{-1}. The albedo of the planetary surface is fixed at 0.2. See the Appendix for details on the radiative transfer model and its validity.

A steam atmosphere is divided into 100 layers, which are equally spaced on a logarithmic scale of pressure. The pressure at the top of the atmosphere is fixed at 1 Pa in all calculations. The temperature structure is prescribed such that it follows an adiabatic lapse rate in all atmospheric layers, based on results of Abe & Matsui (1988). For atmospheric layers in which the temperature is above the critical temperature of water or the relative humidity is less than 1, the lapse rate is assumed to be a dry adiabat. For the other layers, the lapse rate is given by a pseudo-moist adiabat under the assumption that condensates are removed immediately as they form. For simplicity, the effects of clouds are ignored in the present study. Since we consider a pure steam atmosphere, the pseudo-moist adiabat overlaps the saturation curve of water in the present study. We apply a liquid–vapor saturation curve at temperatures above 273.16 K and an ice–vapor curve at temperatures below 273.16 K. The dry adiabat is calculated using the Peng–Robinson equation of state in a manner similar to Abe & Matsui (1988), but the heat capacity of water vapor in the ideal gas state is taken from Wagner & Pruß (2002) as a function of temperature in order to make the heat capacity applicable to higher-temperature conditions.

We use HITEMP 2010 (Rothman et al. 2010) as a spectral database to calculate the absorption coefficients for lines of water vapor. For all calculations, a Voigt line profile is used to consider the combined effect of Doppler and pressure broadening, using a computational code by Humlíček (1982). Although no reliable model for water continuum is available for the high-temperature, high-pressure conditions considered herein, we adopt a MT_CKD 2.5 (Mlawer et al. 2012) model for its continuum together with a wavenumber truncation of 25 cm^{-1}, which is similar to a procedure used in recent studies on radiative transfer calculations of hot and thick steam atmospheres (Goldblatt et al. 2013; Kopparapu et al. 2013). As the number of line transitions in the HITEMP 2010 exceeds 10^8, we generate a grid of absorption coefficients of water vapor and calculate the optical depth of each layer by interpolating the absorption coefficients.

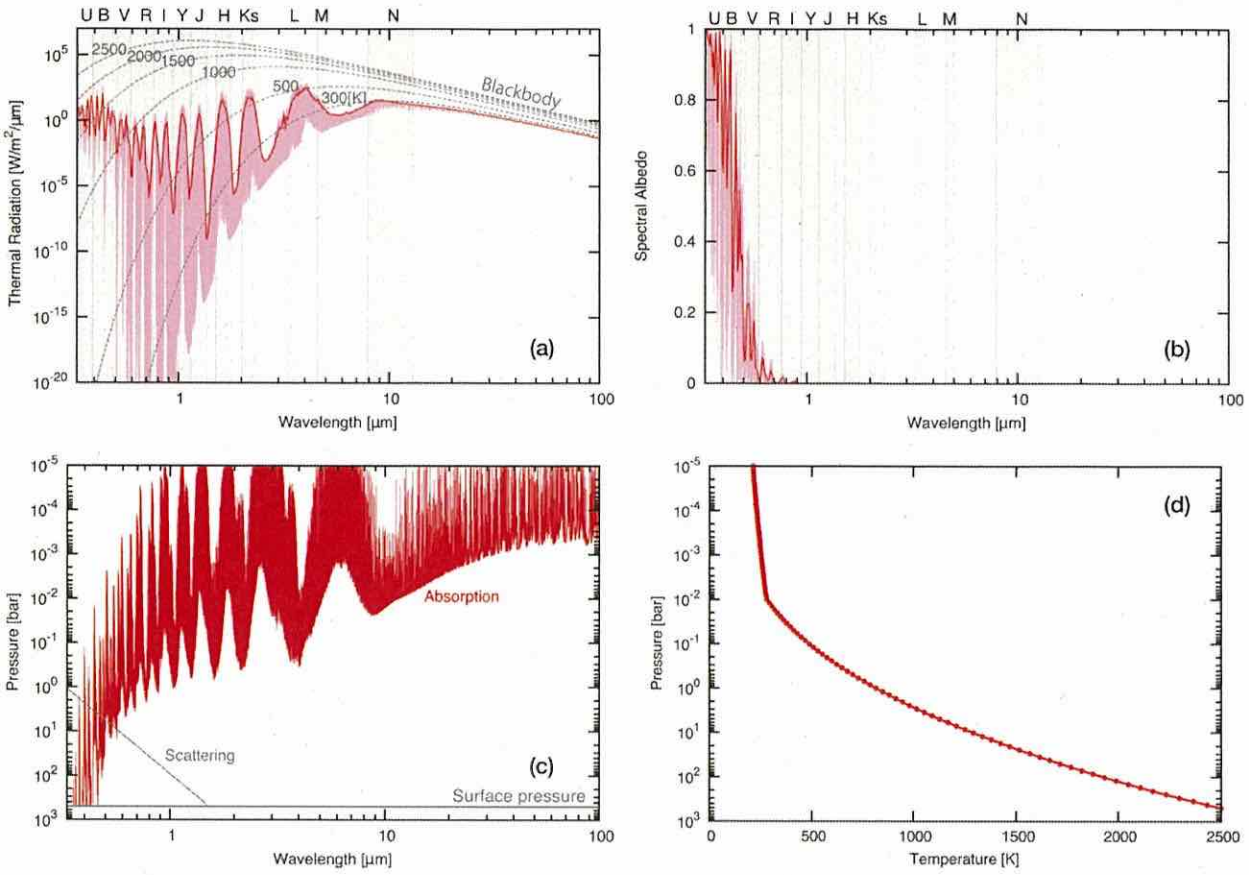

Figure 1. (a) Thermal emission spectrum through a steam atmosphere of 50 bar with a surface temperature of 2500 K. The light-pink line indicates a high-resolution spectrum with a wavenumber resolution of 0.01 cm^{-1}, corresponding to a resolving power R_λ of approximately 1,000,000 at 1 μm. The red line indicates the average thermal radiation such that R_λ becomes 100. Gray bands represent atmospheric windows, which are defined in Table 1. (b) High-resolution (pink) and average (red) spectral albedo for a stellar zenith angle $\theta_\star$ of $\cos^{-1}(1/\sqrt{3})$. (c) Pressure level at which the optical depth is unity for absorption (red line) and for scattering (dotted gray line). (d) Atmospheric structure.

We consider Rayleigh scattering by water vapor with a scattering cross-section per molecule of

$$\sigma_{sc} = \frac{32\pi^3}{3}\frac{1}{N_A^2}\left(\frac{m_0 - 1}{n_0}\right)^2 W_n^4, \quad (1)$$

assuming that the polarizability volume of water vapor does not depend on temperature or pressure. In the above equation, W_n is the wavenumber, N_A is the Avogadro constant, and n_0 and m_0 are the molar volume and the refractive index in the reference state, respectively. We adopt a refractive index of 1.000254 from Allen (1973) for D lines of Na at the standard temperature and pressure (0 °C, 1 atm).

2.2. Thermal Emission

Figure 1(a) shows the thermal emission spectrum from 0.33 to 100 μm with a surface pressure of 50 bar and a surface temperature of 2500 K. At this surface temperature, the peak wavelengths of the Planck function B_λ and λB_λ are approximately 1.2 and 2 μm, respectively. The planetary surface emits strong radiation in the visible and near-IR. Although the hot planetary surface emits significant radiation, the outgoing thermal emission from the top of the atmosphere is greatly attenuated by absorption and scattering by the steam atmosphere. The stronger thermal radiation passes through the wavelength regions corresponding to the atmospheric windows (Table 1), at which the absorption of water vapor is relatively weak.

Table 1
The Band Parameters used in the Present Study

Band	λ_c (μm)	$\Delta\lambda$ (μm)
U	0.365	0.068
B	0.44	0.098
V	0.55	0.089
R	0.70	0.22
I	0.85	0.18
Y	1.04	0.20
J	1.26	0.24
H	1.65	0.29
K_s	2.16	0.32
L	3.55	0.57
M	4.77	0.45
N	10.47	5.19

Note. The band parameters for *I*, *Y*, and *J* are defined by authors, and the other band parameters are taken from Traub & Oppenheimer (2010).

Figure 1(c) shows the atmospheric pressures at which the optical depth is unity for absorption and scattering, respectively. In the far-IR and absorption bands of water vapor, the upper layers, in which the pressure is typically less than 10^{-3} bar, are responsible for the thermal emission spectrum, whereas the atmospheric windows reveal the deeper and hotter layers. At wavelengths longward of approximately 0.6 μm, the pressure level at which the optical depth of absorption is unity is much lower than that of scattering. In the near-IR wavelength region, therefore, the brightness temperature provides a good estimate of the atmospheric temperature at an optical depth of unity.

At the visible wavelength, the scattering process has a dominant role in attenuating the thermal emission. At shorter wavelengths, the deepest layer could contribute to the emergent spectrum because of the absence of strong absorption lines. The actual probed depths, however, depend on the atmospheric amount and continuum absorption of water vapor, the physics of which remain poorly understood. If the atmosphere is thin enough to allow the thermal radiation emitted from the surface to pass through the atmosphere, a Rayleigh scattering slope appears in the planetary spectrum at sufficiently optically thin wavelengths. Measuring the scattering slope can, in principle, provide information about the atmospheric column mass, the surface temperature and the surface albedo.

2.3. Spectral Albedo

Figure 1(b) shows the spectral albedo for a stellar zenith angle $\theta_\star$ of $\cos^{-1}\left(1/\sqrt{3}\right)$. The spectral albedo is defined as the ratio of the upward diffusive radiation to the downward direct radiation at the top of the atmosphere. The bond albedo of the planet is obtained as a weighted mean of the spectral albedo by the Planck function with an effective stellar temperature.

In addition to the thermal radiation, the spectral albedo is higher within the atmospheric windows. Moreover, the spectral albedo varies greatly at the visible wavelengths, from approximately 1 at 0.4 μm to less than 0.1 beyond 0.9 μm. Therefore, in the near-IR, the reflected stellar light is expected to have a smaller contribution to the emergent spectrum. Although the spectral and resulting Bond albedos increase with stellar zenith angle, the difference is less than 0.2 throughout the visible wavelengths between $\theta_\star$ of 0° and 80°. In the present study, we use the spectral and Bond albedos with $\theta_\star$ of $\cos^{-1}\left(1/\sqrt{3}\right)$ degrees as a representative value. Spectra composed of both reflections and emissions are presented later herein under conditions that are consistent with the atmospheric evolution in the course of solidification of the magma ocean.

2.4. Evolutionary Model

Energy and water budgets during planetary solidification are treated in the same manner as Hamano et al. (2013). Here, we briefly summarize our proposed model, focusing especially on the major changes made in the present study. For additional details, see Hamano et al. (2013). We assume an adiabatic temperature profile in the planetary interior to obtain the heat capacity of the whole silicate portion. The heat flux from the magma ocean is calculated as the difference between the outgoing planetary radiation and the net incoming stellar radiation. In order to reduce the computing time for the evolution calculations, the planetary radiation and albedo are precalculated on 882 surface-temperature–pressure grid points, from 1350 to 3000 K and from 5×10^{-4} to 5000 bar, respectively. In order to follow the evolution of planet-to-star contrast, the thermal radiation from each band is also tabulated after averaging the high-resolution spectra with a resolving power of 100, which is a typical value for future direct imaging. We consider a Sun-like host star, the bolometric luminosity and XUV radiation of which evolve in a manner similar to solar analogs. We adopt a solar standard model by Gough (1981) for luminosity enhancement with stellar age and linearly extrapolate it after a stellar age of 4.567 Gyr. The stellar spectrum is assumed to be a blackbody spectrum with an effective stellar temperature of 5800 K.

Water is assumed to be partitioned between the atmosphere and the magma ocean according to its solubility into basaltic melts. The incorporation of water into cumulates is also considered according to the partition coefficients of water between melts and solids and by assuming 1% of trapped interstitial melts. The mass loss rate of water is calculated from an energy-limited escape flux of hydrogen $\Gamma_{\rm H}$ (Watson et al. 1981) with a heating efficiency η of 0.1, as follows:

$$\Gamma_{\rm H} = 4\pi R_{\rm pl}^2 \frac{R_{\rm pl}}{GM_{\rm pl}} \frac{\eta S_\star^{\rm XUV}}{4} \left(\frac{a}{1\ {\rm AU}}\right)^{-2}, \quad (2)$$

where $R_{\rm pl}$ and $M_{\rm pl}$ are the planetary radius and mass, respectively, a is the orbital distance from the host star in AU, and G the gravitational constant. Here, $S_\star^{\rm XUV}$ is the XUV flux from the host star at 1 AU. The stellar XUV flux decreases rapidly with time, whereas the ratio of the X-ray luminosity to the bolometric luminosity remains nearly constant at $\sim 10^{-3}$ for young active stars (Vilhu & Walter 1987; Stauffer et al. 1994; Pizzolato et al. 2003). Based on a power-law relation derived from observational data by Ribas et al. (2005) and Ribas (2009), we adopt the following expression for the evolution of $S_\star^{\rm XUV}$ as a function of stellar age τ in Gyr:

$$S_\star^{\rm XUV} = \begin{cases} S_\odot^{\rm XUV} \left(\dfrac{\tau_{\rm sat}}{\tau_\odot}\right)^{-1.23} & \text{for } \tau < \tau_{\rm sat} \\ S_\odot^{\rm XUV} \left(\dfrac{\tau}{\tau_\odot}\right)^{-1.23} & \text{for } \tau > \tau_{\rm sat} \end{cases} \quad (3)$$

and

$$\tau_{\rm sat} \equiv 1.66 \times 10^{20} L_{\rm bol}^{-0.64}, \quad (4)$$

where $L_{\rm bol}$ is the bolometric luminosity of the host star in erg s^{-1}, and $\tau_\odot$ and $S_\odot^{\rm XUV}$, which are the age and XUV flux at 1 AU of the current Sun, are fixed to 4.567 Gyr and 4.59×10^{-3} J s^{-1} m^{-2}, respectively. The value of $\tau_{\rm sat}$ is approximately 0.066 Gyr for the solar standard model by Gough (1981). The mass loss rate of water is nine times as large as the mass loss rate of hydrogen under the assumption that all the dissociated oxygen atoms are consumed to oxidize the abundant surface magma (Gillmann et al. 2009; Hamano et al. 2013).

We consider terrestrial planets with the same mass and bulk composition as Earth. We start the evolution calculations from a very hot state with a surface temperature of 3000 K and stop the calculations when the surface temperature reaches the solidus temperature at the surface (approximately 1370 K) or

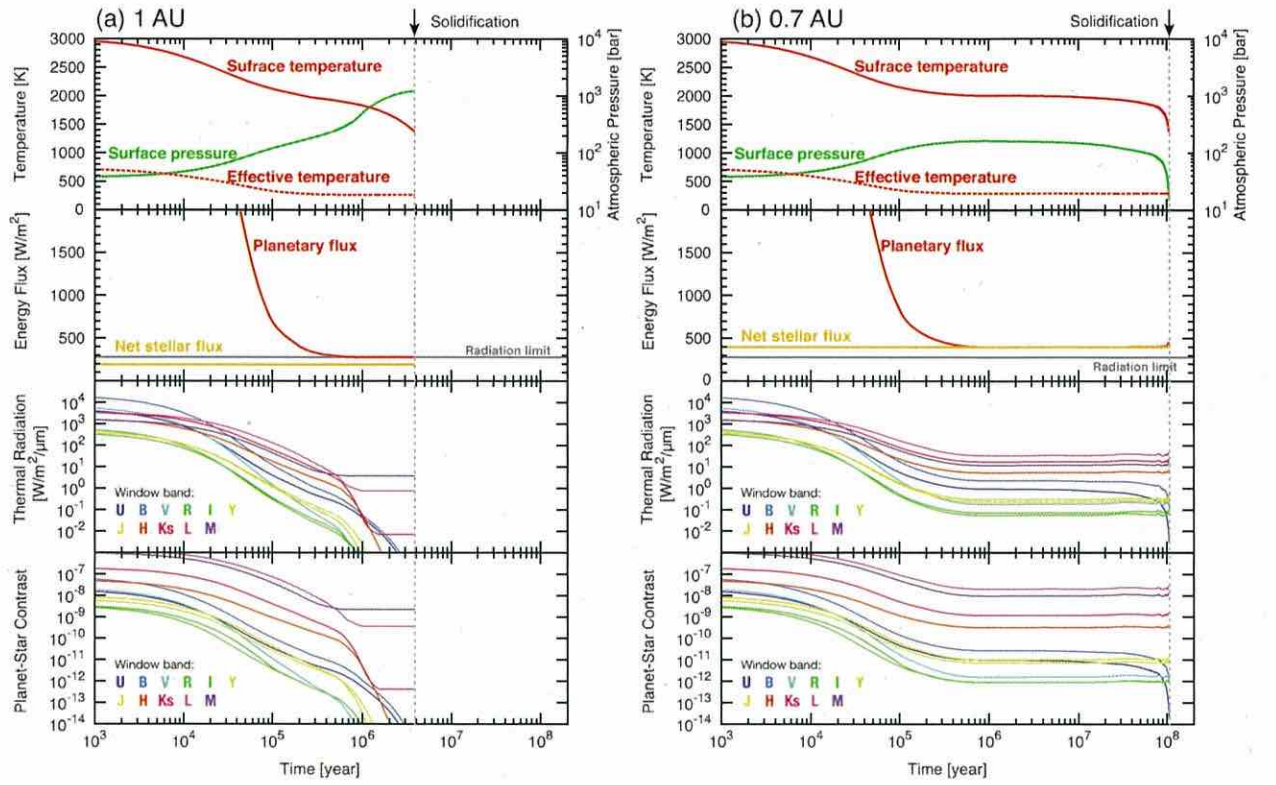

Figure 2. Evolution of a planet at (a) 1 AU (Type I) and (b) 0.7 AU (Type II) with an initial water mass of 5 $M_{\rm EO}$. The third and bottom panels, respectively, show the thermal radiation and the maximum value of the planet-to-star contrast within each atmospheric window. The dotted vertical line in each figure indicates the time at which the magma ocean has solidified, which is approximately 3.9 Myr for the Type I planet and 100 Myr for the Type II planet.

the stellar age reaches 10 Gyr, which is comparable to the main sequence lifetime of the host star. The solidification is assumed to start at a stellar age of 0.05 Gyr (τ_0). We consider the initial total inventory of water ranging from 0.01 to 50 times the current ocean mass of Earth $M_{\rm EO}$ of 1.4×10^{21} kg. This corresponds to a range in bulk water content from 2.3×10^{-4} to 1.2 wt%. Furthermore, we consider the orbital distance from the star of between 0.4 and 1.5 AU.

3. SPECTRUM EVOLUTION DURING SOLIDIFICATION

A hot planet cools and solidifies as it emits large outgoing radiation. Spectral variations during planetary solidification reflect the evolution of surface temperature and atmospheric pressure. At early stages of evolution, the highest fraction of water is expected to dissolve in a deep magma ocean because of the high solubility of water into silicate melts (Zahnle et al. 2010). The steam atmosphere therefore accounts for a modest fraction of its total inventory. As the solidification proceeds, the silicate magma becomes enriched in water and degases at a rate that depends on the solidification rate of the magma ocean (e.g., Elkins-Tanton 2008). Whether the steam atmosphere grows with time depends on the net balance of the degassing rate of water from the interior and its loss rate by hydrodynamic escape (Hamano et al. 2013).

Considering a magma ocean covered with a steam atmosphere, Hamano et al. (2013) proposed that terrestrial planets have a distinct early evolution that depends on whether the orbital distance from the host star exceeds a critical distance. The critical distance $a_{\rm cr}$ [4] is defined as the distance at which the net stellar heating flux is equal to the radiation limit $F_{\rm lim}$ of steam atmospheres:

$$a_{\rm cr} \approx 0.83 \left(\frac{F_{\rm lim}}{280\ {\rm Wm^{-2}}} \right)^{-1/2} \left(\frac{S_{\star}^{\rm bol}(\tau_0)}{0.7\ S_{\odot}^{\rm bol}} \right)^{1/2} \left(\frac{1-\alpha_{\rm pl}}{1-0.2} \right)^{1/2} {\rm AU} \quad (5)$$

where $\alpha_{\rm pl}$ is the Bond albedo of the planet, and $S_{\star}^{\rm bol}$ and $S_{\odot}^{\rm bol}$ are the bolometric fluxes at 1 AU of the host star and the current Sun, respectively.

When the troposphere is saturated by water vapor to a sufficiently deep level, the outgoing planetary flux becomes constant. This constant value is referred to as the radiation limit and corresponds to the lower limit of the planetary radiation for the hot surface conditions considered in the present study. The radiation limit of the steam atmospheres has been extensively investigated, and its value is approximately 280–310 W m^{-2} (Abe & Matsui 1988; Kasting 1988; Nakajima et al. 1992; Goldblatt et al. 2013; Kopparapu et al. 2013). Our model yields a radiation limit of 280 W m^{-2}. Hamano et al. (2013) also classified terrestrial planets into two types according to their orbital distance: Type I for planets beyond $a_{\rm cr}$ and Type II for planets inside $a_{\rm cr}$. These two types of planets will solidify over vastly different timescales, and their atmospheres also evolve

[4] We rescaled the expression for $a_{\rm cr}$ in Hamano et al. (2013) using the typical values in the present study.

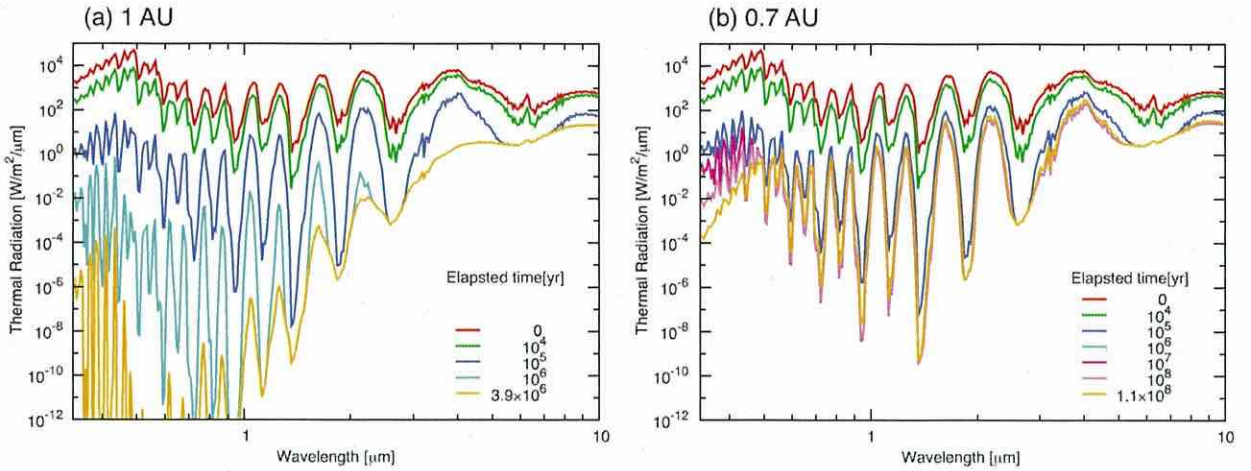

Figure 3. Spectral evolution in the visible and near-IR during the course of solidification of the planet at (a) 1 AU (type I) and (b) at 0.7 AU (type II) with an initial water mass of 5 $M_{\rm EO}$. The color of the thermal emission spectra represents the elapsed time after solidification starts. The orange line indicates the thermal spectrum at the time at which the planet has solidified.

differently, due to different cooling mechanisms. In the following subsections, we describe the spectral changes over the solidification of Type I and Type II planets with an initial water inventory of 5 $M_{\rm EO}$ as a nominal case.

3.1. Type I: Planets Beyond a_{cr}

The Type I planet is characterized by a sufficiently far distance from the host star, where the net incident stellar radiation is smaller than the radiation limit. Since the outgoing planetary radiation never falls below the radiation limit, the Type I planet is self-luminous over its solidification period. The minimum heat flux, which is given by the difference between the radiation limit and the net incident stellar flux, determines the overall solidification timescale, which is approximately 4 Myr in this nominal case (Figure 2(a)). The rapid solidification results in the monotonic growth of the steam atmosphere toward the end of the magma ocean period by keeping the degassing rate of water higher than its loss rate.

Although the surface temperature during the magma ocean period is extremely high, the bolometric luminosity is not so large compared to that from the hot surface. Here, we define an effective emission temperature $T_{\rm eff}$, using the planetary radiation $F_{\rm pl}$, as follows:

$$T_{\rm eff} = \sqrt[4]{F_{\rm pl}/\sigma}\,. \tag{6}$$

The effective emission temperature never exceeds 800 K in this nominal case and is typically as low as 300 K over the solidification period. The thick steam atmosphere thus sustains the magma ocean longer, whereas the planet itself looks as faint as a planet with a cool or moderate surface temperature.

The most recognizable diagnostic sign of a hot surface is emission at the visible and near-IR wavelengths. Although the massive steam atmosphere strongly absorbs the thermal emission from hotter and deeper layers, thermal emission can leak through atmospheric windows. The third panel of Figure 2(a) shows the time variations of thermal radiation from atmospheric windows. In the early stages (less than 10^4 years), the thermal radiation from all bands exceeds 10^2 W m^{-2} μm^{-1}. These high fluxes, however, do not last long. At most of the atmospheric windows, the thermal fluxes rapidly decrease with time and fall below 10^{-2} W m^{-2} μm^{-1} due to the decrease in the surface temperature and the growth of the steam atmosphere. The thermal radiation of the M, L, and K_s bands initially decreases with time as well, but eventually levels off.

Figure 3(a) shows the spectral evolution in the visible and near-IR. The planetary thermal radiation declines with time, and then, at wavelengths longer than approximately 2 μm, the thermal radiation becomes constant. This is a result of the same mechanism as the occurrence of the radiation limit of the steam atmospheres and indicates that, for the wavelengths at which water vapor has strong absorption, the emission level becomes as high as that at which the thermal structure is uniquely determined by the saturation curve of water. Since the thermal structure around the emission level remains the same, the thermal radiation from the M, L, and K_s bands becomes constant, as shown in Figure 2(a).

3.2. Type II: Planets Inside a_{cr}

In contrast to the Type I planet, the Type II planet receives a net stellar radiation that is larger than the radiation limit because of its proximity to the host star. The planet therefore would reach a radiative energy balance during the course of solidification. Early in its solidification, the outgoing planetary flux far exceeds the net stellar flux, and the planet is highly self-luminous, as in the case of the Type I planet (Figure 2(b)). In the case of the Type II planet, however, the planetary flux decreases with time and eventually balances the net stellar flux at approximately 0.6 Myr. If no water loss occurs, the radiative balance is perfectly achieved, and the magma ocean does not solidify. Actually, as the steam atmosphere becomes thinner with time due to the hydrodynamic escape, the planet emits slightly larger radiation than the net stellar radiation. The Type II planet thus slowly cools and solidifies, losing its atmosphere.

The solidification rate of the magma ocean is regulated by the loss rate of water such that a sufficient net loss of the steam atmosphere occurs so that the net outgoing flux becomes positive. The resulting solidification time is approximately 100 Myr in this nominal case, which is much longer than that

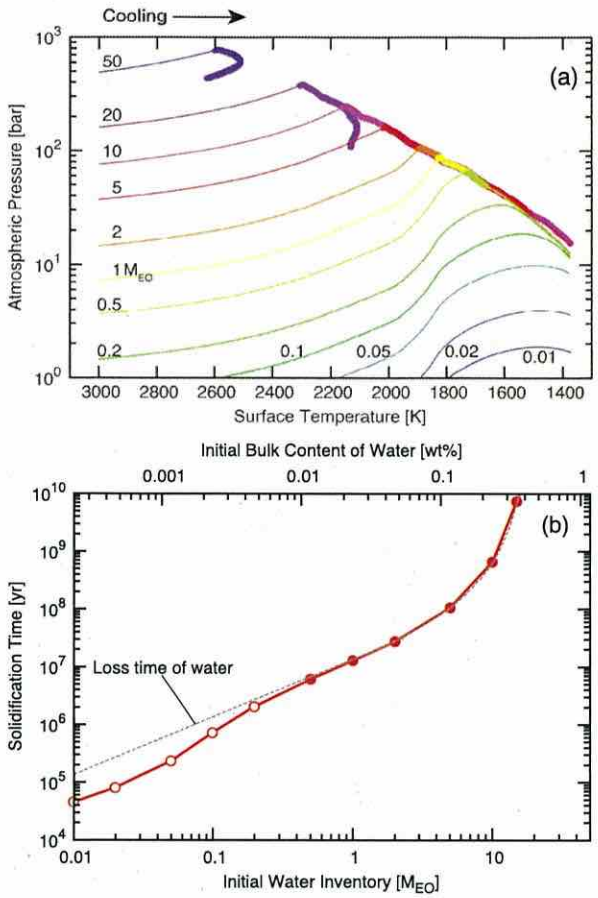

Figure 4. (a) $p_s - T_s$ evolutionary paths of the planet at 0.7 AU. The number on each curve indicates the initial inventory of water in Earth's current ocean mass M_{EO} of 1.4×10^{21} kg. The thick parts indicate that the planet is in quasi-energy balance. Here, the "quasi-energy balance state" is defined as the state in which the relative difference between the planetary and net stellar radiation is less than 5%. The hooks of the $p_s - T_s$ curves with an initial water inventory of 20 and 50 M_{EO} result from the enhancement of the stellar luminosity. (b) Solidification time of the planet at 0.7 AU as a function of initial water inventory. The filled circles represent the cases in which the quasi-energy balance state has been attained at some point during solidification, and the open circles indicate the cases in which the quasi-energy balance state has not been attained at some point during solidification. The gray dashed line is the time required for complete loss of water.

of the Type I planet. The most striking feature is that the higher band fluxes continue over this long solidification period (third panel in Figure 2(b)). The thermal radiation from the atmospheric windows ceases to decrease at ~0.6 Myr, at which radiative energy balance has been roughly achieved. The subsequent spectra do not vary with time at the opaque IR wavelengths or the atmospheric windows, which are relatively transparent (Figure 3(b)).

The long-lived and constant thermal emission in the window regions occurs by attaining quasi-energy balance on the Type II planet. In the quasi-energy balance state, the outgoing planetary radiation roughly balances the incoming net stellar radiation. In order to satisfy this requirement, the amount of atmosphere must be regulated during the course of solidification. As the surface temperature decreases with time, the amount of atmosphere must decrease such that the planet maintains a planetary radiation that is nearly equal to, or, strictly speaking, slightly larger than, the net stellar flux (Figure 2(b)). Consequently, the resulting spectra do not change during a quasi-energy balance state, except at the shorter wavelengths, at which the opacity of the atmosphere is thin enough for the outgoing thermal emission to be sensitive to surface temperature (Figure 3(b)).

The above requirement for planetary radiation generally applies to planets in (quasi-)energy balance, irrespective of the atmospheric amounts and composition. Although additional opacity sources would increase the opacities at some wavelengths and would change the overall spectra, the planet in quasi-energy balance is still expected to emit high thermal radiation from the relatively transparent wavelengths.

Figure 4(a) shows the evolutionary paths of surface temperature and pressure (the $p_s - T_s$ path) during solidification for various initial inventories of water. The atmospheric pressure increases at early stages due to the high degassing rate. For an initial water inventory larger than 0.2–0.5 M_{EO}, the quasi-energy balance is attained at some particular surface temperature. The $p_s - T_s$ paths in the quasi-energy balance states are approximately independent of the initial water endowment, as long as the planets solidify during the main sequence of the host star.

For a larger initial inventory of water, the planet reaches quasi-energy balance at a higher surface temperature and solidification requires a longer period of time. In particular, for the case in which the quasi-energy balance has been achieved during the course of solidification, the lifetime of the magma ocean is well approximated by the time required for total loss of the initial water inventory (Figure 4(b)). If the planet is endowed with water equivalent to more than 16 M_{EO}, the molten state would exist for over 10 Gyr, which is comparable to the lifetime of the G-type host star. In this case, the surface temperature gradually increases with time in accordance with the luminosity enhancement of the star.

4. DETECTABILITY OF MAGMA-COVERED PLANETS WITH A STEAM ATMOSPHERE

Dedicated space coronagraphic missions, such as the Terrestrial Planet Finder C (Levine et al. 2009), Occulting Ozone Observatory (Savransky et al. 2010), WFIRST-AFTA (Spergel et al. 2015), and Exo-C and Exo-S,[5] have been conducted over long periods of time. The primary goal of such missions is to detect reflected light in visible bands from Earth-sized or super-Earth-sized planets around solar-type stars. These missions will be capable of detecting the reflected light from an Earth-sized planet that is typically 10^{10} times fainter than the light of the host star. Moreover, recent progress in extreme adaptive optics has improved the limiting contrast of direct imaging using ground-based telescopes, such as Gemini Planet Imager (Macintosh et al. 2014), SPHERE (Zurlo et al. 2014), Palomar Project 1640 (Oppenheimer et al. 2012), and SCExAO (Jovanovic et al. 2013). These ground-based high-contrast instruments have the advantage of a small inner working angle on the future 30–40 m class telescope. These missions will open the possibility of detecting molten exoplanets. In this section, we discuss the feasibility of the direct detection of molten planets based on the capabilities of these future missions. We also discuss characterization via

[5] Exo-C and Exo-S Final Reports in 2015, http://exep.jpl.nasa.gov/stdt/.

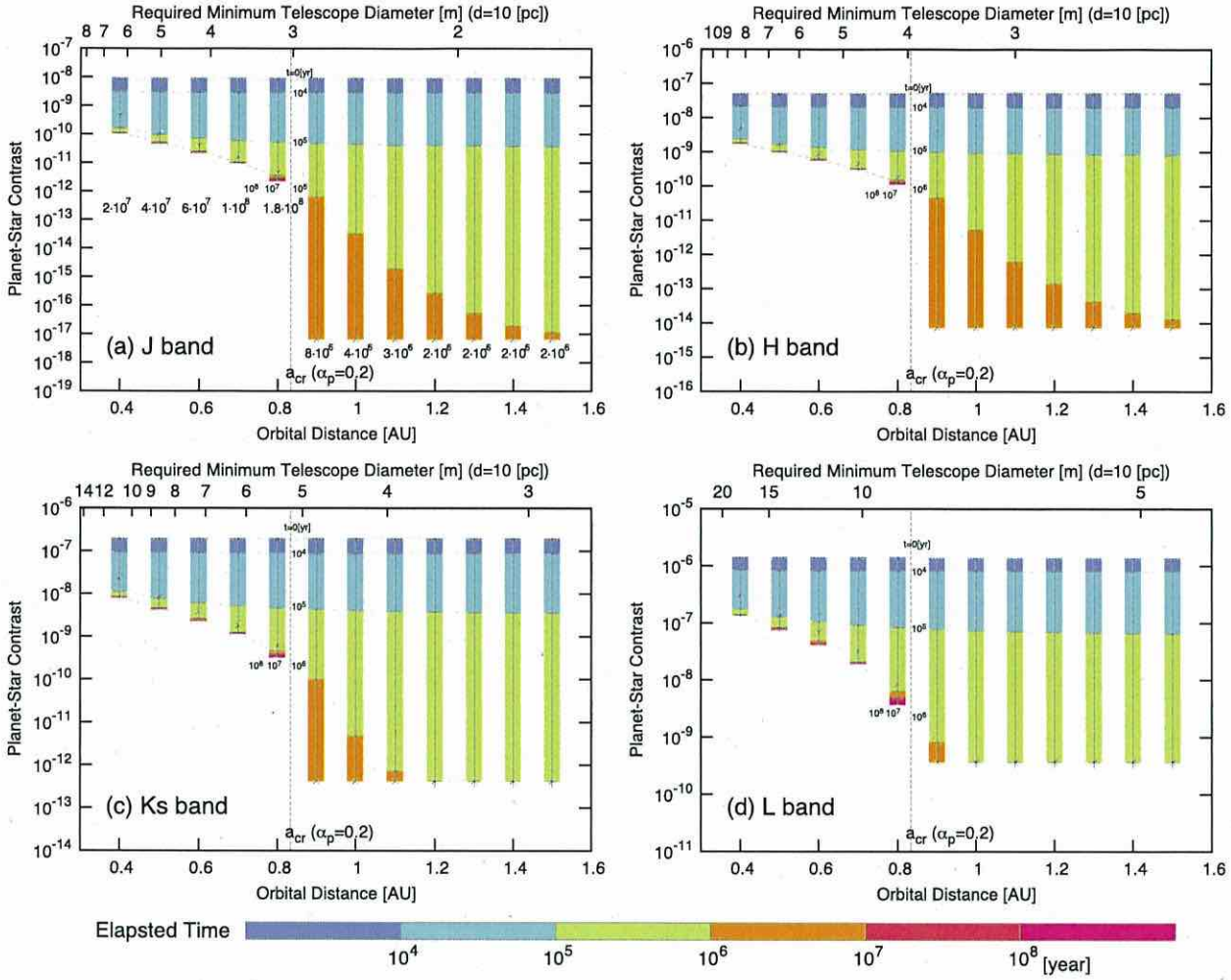

Figure 5. Contrast ranges of the thermal emission during the magma-ocean period at each orbital distance with an initial inventory of water of 5 M_{EO}: (a) J, (b) H, (c) K_s, and (d) L bands. Each color bar indicates a contrast range during solidification, with the tick marks indicating the elapsed time for each order of magnitude. The cross symbols indicate the contrasts at which the magma ocean has completely solidified. The numerical value under each color bar in Figure 5(a) is the overall solidification time. At orbital distance smaller than 0.8 AU, the planet-to-star contrast increases with time at the very last stage of solidification because of the low degassing rate. The increase in the contrast at the very last stage is neglected in this figure due to its short duration relative to the total solidification time. The upper horizontal axis shows the telescope diameter D_{tel} at which the angular separation is equal to the diffraction limit, $\theta_{dl} \sim 0.01 \times (\lambda_c/0.5\ \mu\text{m}) \times (D_{tel}/10\ \text{m})^{-1}$, for the case in which the distance to the system d is 10 pc.

direct imaging, which would provide evidence of the hot origins of molten planets as well as the basis for more extensive spectroscopic studies for the purpose of characterization of these planets.

We consider two important quantities that characterize the ease of detection of a planet against stellar speckles. One is planet-to-star contrast, which is defined by the ratio of the planet flux to the stellar flux, and the other is the planet–star angular separation on the celestial sphere. The latter can be converted to the semimajor axis a for a given distance assuming an observer-star-planet angle (phase angle) of 90°. For future space coronagraphic missions, we regard a contrast of 10^{-10} at 0.1 arcsec of angular separation, which corresponds to an Earth-twin at 10 pc, as a benchmark for detectability. For future ground-based high-contrast instruments, although it is difficult to set a benchmark, we fiducially regard 10^{-7}–10^{-8} of the contrast at 0.01–0.03 arcsec (corresponding to the diffraction limit of the J–L bands for a 30 m telescope), as a benchmark because one of the main goals of these missions is to detect Earth- or super-Earth-sized planets in the habitable zone around late-type stars (see e.g., Macintosh et al. 2006; Matsuo & Tamura 2010; Guyon et al. 2012; Kawahara et al. 2012; Crossfield 2013; Males et al. 2014).

4.1. Flux Contrast and Orbital Separation

Direct detection requires that the planets have a sufficiently high planet-to-star contrast. As described in the previous section, the time evolution of the thermal emission spectra is closely related to the atmospheric evolution during solidification, which strongly depends on the orbital distance from the star. Figure 5 shows the contrast evolution of the thermal radiation in near-IR windows for various orbital distances in the case of an initial water inventory of 5 M_{EO}. Although the total contrast consists of the thermal radiation and the

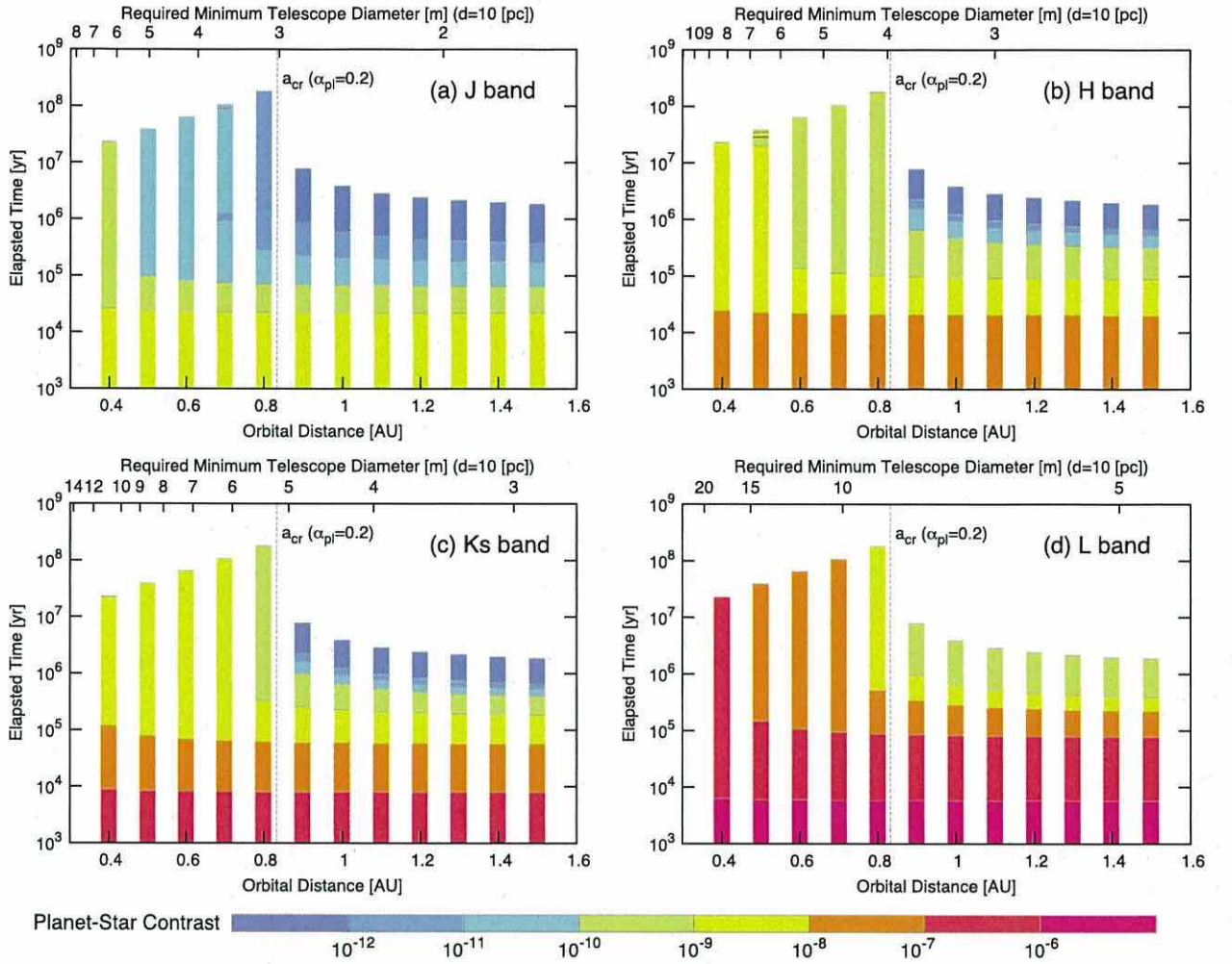

Figure 6. Contrast evolution of the thermal emission at each orbital distance with an initial inventory of water of 5 M_{EO}: (a) *J*, (b) *H*, (c) *Ks*, and (d) *L* bands. Color shows a planet–star contrast during solidification. The upper horizontal axis in each panel is the same as Figure 5.

reflected stellar light, in most cases, the thermal radiation is dominant in the near-IR band, especially for Type II planets (Section 4.3).

The contrast evolution of Type I planets is different from that of Type II planets. For Type I planets, which are located beyond a_{cr}, the range of the planet-to-star contrast is approximately independent of the semimajor axis. The planet-to-star contrast is initially as high as 10^{-8}–10^{-6}, and then decreases on a common timescale of less than $\sim 10^6$ years (Figure 6). This is because the magma-ocean lifetime of Type I planets is determined by the minimum heat flux, which is approximately independent of the orbital distance. In the case of a smaller inventory of water, the planet-to-star contrast would increase as the atmosphere becomes thinner, whereas the timescale for decreasing planet-to-star contrast becomes shorter. In the case of a larger inventory of water, the thermal radiation reaches the radiation limit earlier. This prolongs the duration of the magma ocean by a factor of at most 2.

The contrasts of Type II planets first decrease with time as well, but then cease to decrease during the course of solidification (Figure 5). The minimum value of the contrast of Type II planets is higher than that of Type I planets. Since the planets are in quasi-radiative energy balance, they spend most of the solidification period at the minimum contrast level in this nominal case (Figure 6). The minimum contrast level is insensitive to the initial water inventory. As long as the planet solidifies on a shorter timescale than the main sequence lifetime of the host star, the minimum contrast level has the highest likelihood of detection. For the case in which the magma ocean is sustained for as long as the main sequence of the star, the planet-to-star contrast gradually increases with time from the minimum contrast level, because the planet must emit a larger planetary radiation from the near-IR band in order to maintain quasi-energy balance in accordance with the luminosity enhancement.

The minimum contrast increases for the planet closest to the star, because this planet receives a larger net stellar flux and so must emit larger planetary radiation. Consequently, planets closer to a star are more favorable for direct imaging in terms of spectral contrast. On the other hand, the planet closest to the

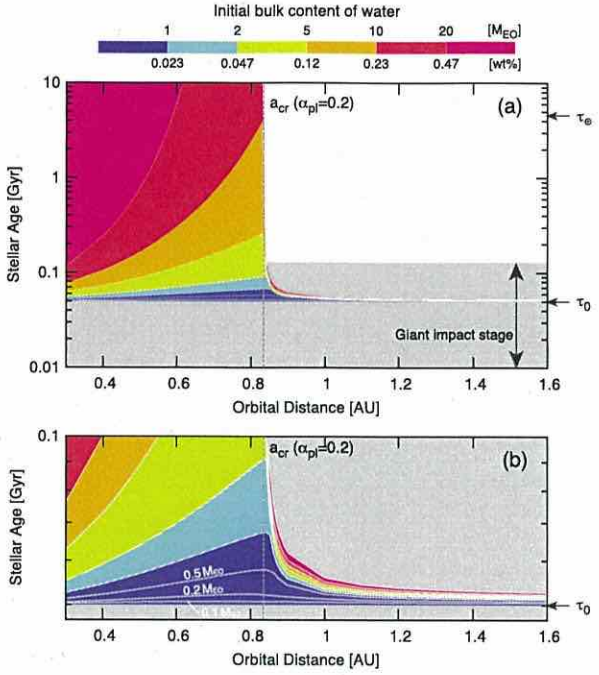

Figure 7. Orbital region where molten planets potentially exist as a function of stellar age in a range from 0.01 to 10 Gyr (a), with the assumption that the solidification starts at a stellar age τ_0 of 0.05 Gyr. The panel (b) is a zoom-in of the panel (a) for a stellar age younger than 0.1 Gyr. Each color represents the initial bulk content of water required for a molten state to be sustained for a given stellar age and orbital distance. As well as τ_0, the age of the Sun $\tau_\odot$, 4.567 Gyr, is indicated by an arrow on the right side. The critical distance with planetary albedo $\alpha_{\rm pl}$ of 0.2 is also shown in each panel.

star also receives a stronger stellar XUV flux, which fuels hydrodynamic escape. Since the solidification time of Type II planets is approximately equal to the loss time of water, the occurrence rate of molten terrestrial planets is expected to be higher at orbital distances closer to $a_{\rm cr}$.

As shown in Figures 2, 5 and 6, the Type II molten planets maintain relatively high contrasts in the near-IR band. The Type II planets with $a < 0.5$ AU are favorable targets for future ground-based direct imaging, because the contrasts of the K_s and L bands are above the levels of $\sim 10^{-8}$ and $\sim 10^{-7}$, respectively, for the entire life of the molten state. The duration with the contrast $>10^{-8}$ is approximated with the overall solidification time, which becomes longer with the initial water inventory, as shown in Section 4.2. Although these planets have smaller angular distances, in the near future, a 30–40 m ground-based telescope will resolve them within tens of parsecs. On the other hand, the near-IR contrast of the Type I planets declines below $\sim 10^{-8}$ and $\sim 10^{-7}$ on a short timescale of $\sim 10^5$ years for the K_s and L bands, respectively. Young stars should be targeted when searching for Type I planets.

The thermal radiation in the near-IR band overwhelms the reflected stellar radiation for Type II planets. The contrast of the emission in the visible bands rapidly decreases to the 10^{-10} level by a few 10^4 and $\sim 10^5$ years for the Type I and Type II planets, respectively (see Figure 2). Therefore, with respect to the visible band, the reflected light should be considered in order to discuss the total contrast of the planets. These issues are discussed in Section 4.3.

4.2. Relation between Predicted Occurrence Rate and Water Endowment

For the Type II planets, the lifetime of the magma ocean strongly depends on how much water is acquired during planet formation. This suggests the possibility of placing constraints on the initial water inventory based on the observed occurrence rate of hot molten planets. Figure 7 shows an orbital region where molten Earth-sized planets potentially exist as a function of stellar age. The predicted lifetime of the magma-covered planets shows a sharp transition around $a_{\rm cr}$. The Type I planets during the magma ocean period have less probability of being detected, whereas the probability of detecting molten Type II planets is greatly enhanced with initial water inventory.

The calculated lifetimes of Type I and Type II planets allow us to estimate an expected number of G-type stars which host Earth-sized molten planets. For G-type stars whose distance from the solar system is less than the distance d, the expected number of G-type stars with molten planets $N_{\rm D}(d)$ can be estimated as follows,

$$N_{\rm D}(d) \sim N_{\rm G}(d) \cdot P_{\rm EG} \cdot \frac{\Delta t_{\rm mol}^{\rm tot}}{\bar{\tau}_{\rm G}(d)}, \quad (7)$$

where $N_{\rm G}(d)$ and $\bar{\tau}_{\rm G}(d)$ are, respectively, the number and average age of G-type stars within the distance d from the solar system, $P_{\rm EG}$ is the fraction of G-type stars with terrestrial planets in a range of planetary orbital distances considered, $\Delta t_{\rm mol}^{\rm tot}$ is the total duration during which terrestrial planets are in a molten state. Let us consider the case when d is 10 pc. The total number of G-type stars is then around 30. The average age of G-type stars is assumed to be 5 Gyr. Using *Kepler* data, Petigura et al. (2013) reported that the fraction of GK-type stars which host Earth-sized planets is ~0.12 for orbital distances of 0.05–0.42 AU, and ~0.086 in the habitable zone. Here, we adopt $P_{\rm EG}$ of 0.1 for both Type I and Type II planets.

Type-I planets solidify on a timescale of the order of 10^6 years, which shorter than typical time intervals of giant impacts at a late stage of formation. In this case, the total duration would be expressed as a product of an average number of giant impacts $n_{\rm GI}$ and the duration of a molten state after one collision $\Delta t_{\rm mol}$. According to N-body simulations, Earth-like planets would experience 10–20 giant impacts during formation (Kokubo & Genda 2010; Stewart & Leinhardt 2012). We adopt $n_{\rm GI}$ of 10. Using a typical duration of a magma ocean of 2×10^6 years, we obtain ~0.01 for $N_{\rm D}(d = 10\ {\rm pc})$ in the Type I orbital region. This value is common for Type I planets which formed with initial water inventory comparable to or exceeding the total amount of water of the modern Earth. The potentially favorable target for molten Type I planets would be young and other spectral type stars such as Fomalhaut. On the other hand, Type II planets have a wide range of solidification time after single impact, which strongly depends on the initial amount of water. In the extreme case that the solidification time exceeds the period of giant impact phase, which probably lasts until the stellar age of 0.1 Gyr, the total duration of a molten state is given by the duration of a molten state after single collision. In the Type II orbital region, the initial amount of water thus greatly affects the probability of detecting molten planets. Given that $\Delta t_{\rm mol}^{\rm tot}$ does not exceed 10 Gyr, $N_{\rm D}(d = 10\ {\rm pc})$ ranges from ~0.01 to 6 in the case of Type II planets, considering the initial inventory of water of from one-tenth to several tens of times the Earth's ocean mass.

Here, we address the uncertainties in parameters which affect the loss time of water, the timing of the last giant impact, the heating efficiency and the EUV flux from the G-type host star. The giant impact phase is triggered by the dispersal of nebula gas and lasts until a stellar age of approximately 0.1 Gyr. Therefore, the last giant impact would occur between the stellar ages of 0.01 and 0.1 Gyr. The heating efficiency η in Equation (2) depends on the structure and details of the energy budget in the upper atmosphere and remains poorly constrained. The estimated values have a large spread and typically range from 0.1 to 0.5 (e.g., Watson et al. 1981; Chassefière 1996; Kulikov et al. 2007; Shematovich et al. 2014). The saturation level of XUV flux and its ending time $\tau_{\rm sat}$ remain quite uncertain. If we simply assume that the XUV-to-bolometric-luminosity ratio scales as the X-ray-to-bolometric-luminosity ratio, which is observationally estimated to be $10^{-3.2\pm0.3}$ during the saturation phase for one solar-mass star (Pizzolato et al. 2003), the variation of the XUV saturation level is nothing more than a factor of 3 and $\tau_{\rm sat}$ ranges from 0.06 to 0.13 Gyr. Although the XUV flux could exhibit greater fluctuation for pre-main sequence stars, its effects might not be so significant because of its short duration relative to the subsequent evolution. Although no observational data are available at wavelengths between 360 and 921 Å due to strong absorption by the interstellar medium, the total XUV flux would not have profound uncertainty compared with that of the other parameters, because the estimated energy flux in this wavelength range is at most 10% to 20% (Ribas et al. 2005).

Although our model cannot predict the exact inventory of primordial water due to the numerous uncertainties described above, estimating the order of magnitude of the exact inventory of primordial water would be still useful. Our model suggests that, if the initial bulk content of water exceeds approximately 1 wt%, molten planets would be present over the main sequence of the host G-type star (Figure 7). Since the critical distance, which separates the Type I and Type II planets, originates from the presence of the radiation limit of steam atmospheres, detection of a critical distance would offer a diagnostic test to determine whether water is generally one of the major volatile species of extrasolar terrestrial planets. In the orbital region of Type II planets, the detection of hot signatures in the planetary spectrum will provide a lower limit for initial water inventory, which is sufficient to sustain the molten state for a given stellar age, whereas no detection will constrain its upper limit, so that the planet will lose most of its water and become solidified.

4.3. Reflected Light and Color Variations of Solidifying Planets

The actual spectrum from the planet is obtained as the superposition of its thermal emission and reflected stellar light. The thermal radiation generally overwhelms the reflected stellar radiation during the highly self-luminous stage. Figure 8 shows the planet-to-star contrast of the superimposed spectra of the planet in quasi-energy balance. According to the Lambert assumption, the planet–star contrast $C_{\rm ps}^{\rm ref}(\lambda)$ of the reflected light is given as follows:

$$C_{\rm ps}^{\rm ref}(\lambda) = \frac{2\phi(\beta)}{3}\alpha(\lambda)\left(\frac{R_{\rm pl}}{a}\right)^2 \quad (8)$$

$$\phi(\beta) = \frac{[\sin\beta + (\pi-\beta)\cos\beta]}{\pi}, \quad (9)$$

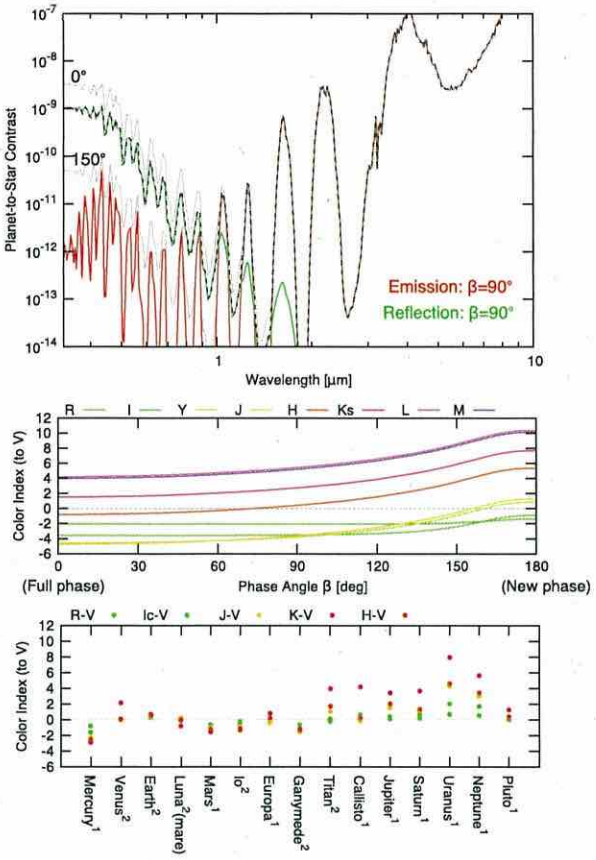

Figure 8. Superimposed spectra and band color of a planet at 0.6 AU with an atmospheric pressure of 100 bar and a surface temperature of 2000 K. Under this condition, the planet is in quasi-energy balance. The thin black lines in the top panel indicate the planet-to-star contrast of superimposed spectra. The spectrum components are indicated by the red line for the thermal emission and the green line for the reflected light, respectively, for a phase angle of 90°. The middle panel shows the color index of each band to the V band relative to the host star. As a reference, color indexes relative to the Sun are plotted in the bottom panel for all planets (Lundock et al. 2009). The superscript attached to the planet's name denotes the observational period of the data used: 1 for 2008 May and 2 for 2008 November.

where α is the spectral Bond albedo, and $\phi(\beta)$ is the Lambert phase function with respect to the phase angle $\beta = \angle(\text{star} - \text{planet} - \text{observer})$. The overall superposed spectrum in the quasi-energy balance state is V-shaped with a bottom around 1 μm, except for the phase angle very close to the new phase (Figure 8). The dominant component is thermal emission at wavelengths longer than $\sim$1 μm and is reflected stellar light at the shorter wavelengths. This originates from the difference in the peak wavelength of the Planck function between the surface temperature and the stellar effective temperature. The peak wavelengths are approximately 1.4 μm for 2000 K and 500 nm for 5800 K.

For $\beta = 90°$, the contrast of the reflection can be estimated as follows:

$$C_{\rm ps}^{\rm ref} \approx 3\times10^{-10}\left(\frac{\alpha(\lambda)}{1}\right)\left(\frac{R_{\rm pl}}{R_\oplus}\right)^2\left(\frac{a}{1\ \rm AU}\right)^{-2}, \quad (10)$$

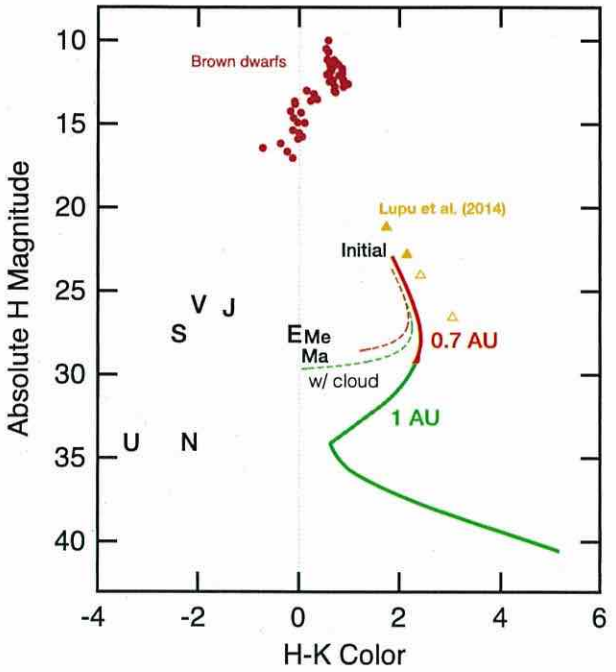

Figure 9. Color–magnitude relation of the thermal emission from the solidifying planets with a steam atmosphere at 1 AU (green) and 0.7 AU (red) with an initial water inventory of 5 M_{EO}. The dashed lines indicate data for the cases in which the stellar light reflected by clouds is taken into account with a phase angle of 90°. Here, we assume that the clouds are uniformly distributed and the coverage and albedo are 0.5. We adopt the $H - K$ color of the Sun (0.05) as that of the host star. The brown circles are observed brown dwarfs (Leggett et al. 2002; Knapp et al. 2004). The letters represent the planets in the solar system (Lundock et al. 2009). The results reported by Lupu et al. (2014) are also shown for total surface pressures of 10 bar (filled triangles) and 100 bar (open triangles) for surface temperatures of 2200 and 1600 K for the case in which the atmospheric composition is in equilibrium with magma having the composition of the Earth's continental crust.

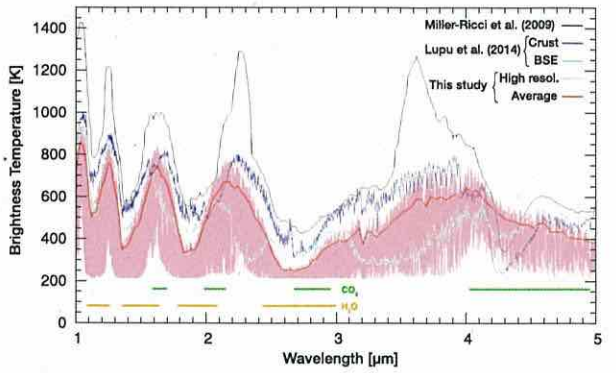

Figure 10. Brightness temperatures obtained by the different models. The total atmospheric pressure is 10 bar in all models, whereas the surface temperature is 1500 K for Miller-Ricci et al. (2009) and 1600 K for Lupu et al. (2014) and our model. We consider a pure steam atmosphere. The model atmosphere consists of 90% H_2O and 10% CO_2 for Miller-Ricci et al. (2009). Lupu et al. (2014) considered atmospheres in equilibrium with the hot surface having the composition of the Earth's continental crust and bulk silicate Earth (BSE). Although these model atmospheres are composed by various gaseous species, they consist primarily of H_2O and CO_2. Lupu et al. (2014) stated that, by taking into account quenching effects, the spectra for BSE composition magmas become similar to that of the Earth's continental crust.

where $R_\oplus$ is the Earth radius. Because the albedo in the U–B band is ~1, as shown in Figure 1(b) and the reflection dominates in this band, we roughly expect contrasts of $\sim 10^{-10}$ and $\sim 10^{-9}$ for the Type I and Type II planets, respectively. These contrasts are within the scope of the future space direct imaging survey. The contrasts decline steeply from the visible wavelengths to the near-IR wavelengths, which reflects the deep atmosphere of the planets.

The reflected light is bluer than that of the host star, whereas the thermal emission in the near-IR is redder than that of the host star. The middle panel in Figure 8 shows the color index of each band to the V band relative to the host star as a function of phase angle. As the phase angle increases, the color becomes redder for all bands because the contribution of the thermal emission increases. The color indexes of the I and R bands remain bluer than that of the host star, whereas the color indexes of the other spectral bands becomes redder than that of the host star. The color indexes could vary by approximately 6 for the J, H, K_s, and L bands during a complete cycle of orbital motion. These color changes are comparable to the color differences between rocky planets, such as Earth and Mars, and gaseous planets such as Uranus and Neptune.

Following Lupu et al. (2014), we consider the color–magnitude diagram of the molten planets. Figure 9 shows the evolutionary paths of the thermal emission in the $H - K$ color and absolute H magnitude diagram. The molten planets are as faint as the planets in the solar system, but are distinctly redder in color. This is because the thermal emission, which is much redder than the stellar light, dominates the planetary spectrum for molten planets, whereas the color of the planets in the solar system mostly reflects the reflected light. We also estimate the effects of stellar light reflected by clouds on the $H - K$ color by assuming that the cloud coverage is 0.5. In this case, as the thermal emission becomes fainter, the reflected light becomes more dominant in the near-IR spectrum. The reflected light could determine the color at the later stage for the planet at 1 AU, whereas the color is still much redder than that of the star during solidification of the planet at 0.7 AU, including the quasi-energy balance state. A self-consistent evolutionary calculation, including cloud formation, will be the subject of future research to examine actual color variations that occur during the course of solidification.

5. DISCUSSIONS

We compare the brightness temperatures of our model with those reported by Miller-Ricci et al. (2009) and Lupu et al. (2014) for wavelengths ranging from 1 to 5 μm (Figure 10). Although the atmospheric compositions differ among these models, our model spectrum is more similar to that in Lupu et al. (2014), especially for the atmospheric composition in a chemical equilibrium with silicate melts having the composition of the Earth's continental crust. The brightness temperature, i.e., the thermal radiation, of the our model tends to be lower than that of Lupu et al. (2014) for continental-crust-composition magmas, probably because of the H_2O-rich composition and the lower temperature in the upper atmosphere of our model.

Although we have thus far discussed only pure steam atmospheres, the inclusion of other gaseous species would not

substantially alter our conclusions. Adding other opacity sources would reduce the planet-to-star contrasts in atmospheric windows for Type I and -II planets in a self-luminous state, whereas doing so would only affect the relative contrast of atmospheric windows for the Type II planets in quasi-energy balance. If the thermal radiation decreases at certain wavelengths during the quasi-energy balance state, the planet must emit larger thermal radiation at other wavelengths in order to maintain the energy balance while reducing the amount of the steam atmosphere.

The same would be said of the effects of clouds. At very early stage, a molten planet would have no cloud cover because of the hot temperature. As the temperature drops and the atmosphere grows, however, clouds would start to form by condensation of water vapor in the atmosphere. Clouds would increase the planetary albedo, which makes the critical distance smaller by reducing the net incident stellar radiation. Clouds also would enhance a greenhouse effect, which makes the critical distance larger. The presence of clouds therefore would affect the actual position of the critical distance through a balance of the opposing effects of cloud albedo and a greenhouse effect. However, as long as a planet is type II, it would emit strong thermal radiation through the atmospheric windows even with some cloud cover, to maintain energy balance for the same reason as the case with additional gaseous opacity described above.

To a first order approximation, we have assumed that the planetary interior has an adiabatic temperature profile in our evolutionary model. Although horizontal inhomogeneity would exist in the convective magma ocean, especially around boundary layers, the planet would have a nearly uniform surface temperature under a thick and massive steam atmosphere considered in the present study, because the timescale of heat transfer by atmospheric circulation is generally much shorter than the timescale of radiative cooling and of heat transfer by convection of the magma ocean.

In the evolutionary model, we have also assumed that the magma ocean effectively transports internal heat to the surface and that the atmosphere is in solution equilibrium with the magma ocean for calculations of a degassing rate. Since the assumption of the solution equilibrium leads to a maximum estimate of the atmospheric growth rate, the thermal radiation predicted in the present study would be a minimum estimate, whereas the decline timescale of the emergent spectra would be overestimated.

Heat flux and a degassing rate from a magma ocean strongly depends on the magma viscosity. Thermal structure and heat transfer of a magma ocean has been extensively reviewed by Solomatov (2007). Viscosity of ultramafic silicate melt near liquidus is as low as 0.1 Pa s at low pressures (e.g., Shaw 1972). The similar value can be assumed for the magma viscosity under the mantle conditions because of small temperature and pressure effects for a low-viscosity and completely depolymerized melt (see discussions by Solomatov 2007). As the Rayleigh numbers are typically in the range of 10^{20}–10^{30} with the low viscosity (Solomatov 2007; Elkins-Tanton 2008), the magma ocean at early stage is expected to be highly turbulent and in a state of vigorous convection. The highly turbulent magma ocean is considered to be homogeneous and its thermal structure is to be nearly adiabatic.

Along with cooling, the magma ocean starts to solidify at great depth, because the slopes of liquidus and solidus of Earth's mantle are steeper than those of adiabats in the magma ocean (Andrault et al. 2011). On the other hand, when a solid crust starts to form depends on the energy balance at the surface. The energy balance between heat flux from the magma ocean and radiative heat flux from the surface determines the surface temperature. A steam atmosphere has a strong blanketing and greenhouse effect. Even with a surface atmospheric pressure of 10 bar, its total opacity exceeds 10^5 in the 10 μm atmospheric window. Therefore, the insulating atmosphere maintains the surface in a molten state if the heat flux from the magma ocean is sufficiently high.

The most important parameter for heat transport of the magma ocean is the magma viscosity, which varies dramatically depending on the melt fraction in the magma. Experimental studies have shown that viscosity of partial melts abruptly increases from a liquid-like low value to a solid-like high value (rheological transition), when its melt fraction falls below a critical value, approximately 40% (e.g., van der Molen & Paterson 1979). As long as the surface temperature is high enough to keep the melt fraction larger than the critical value, the magma ocean can transport the internal heat to the surface efficiently by vigorous convection, and also keep a high renewal rate of the surface. As the surface temperature decreases, the melt fraction decreases and reaches the critical value, and then solid-state convection takes over. The heat flux from the magma ocean is no longer high enough to keep the surface molten. The surface temperature rapidly drops and a conductive lid crust starts to develop at the surface (Solomatov 2007; Lebrun et al. 2013).

As the solidification proceeds, the depth of the magma ocean becomes shallow and the total mass of the magma decreases. The magma ocean becomes enriched in water, which is incompatible to silicate cumulates. The solution equilibrium of water between the atmosphere and the magma ocean is assumed in our model, whereas actually a certain degree of supersaturation of water might be required for degassing by bubbling and H_2O diffusion processes. Hamano et al. (2013) discussed the effects by the simple treatment for the degassing processes on the overall solidification time of the magma ocean. For degassing involving the bubble formation, bubbles are required to grow fast and detach from the magma flows. Although the supersaturation required for the efficient bubble detachment remains uncertain, even using 50-fold water solubility shortens the solidification time by a factor of at most 4, based on the results by Hamano et al. (2013). They also estimated the supersaturation required for the replenishment of the atmosphere against its loss by the molecular diffusion process only, using a molecular diffusion coefficient in basaltic melt by Zhang et al. (2007). They showed that a modest degree of supersaturation is enough for the replenishment, as long as the magma viscosity is a liquid-like low value. Eddy diffusion process would significantly lower the required supersaturation. However, at a very late stage after the melt fraction reaches the critical value, both the resurfacing rate and the efficiency of bubble detachment from the magma flows would be greatly reduced due to the solid-like high viscosity. Redefining the solidification time as the time required for the surface temperature to drop to 1700 K, around which the melt fraction is estimated to reach the critical fraction for the rheological transition, shortens the lifetime of the magma ocean on Type I planets by a factor of less than 5 in the parameter range considered herein. This estimate is consistent with the

typical duration of the magma ocean phase of 1 Myr reported by Lebrun et al. (2013). For Type II planets, the redefinition of the solidification time has less effect on the lifetime of the magma ocean, as long as the water endowment is sufficiently large so that the quasi-energy balance is attained at a surface temperature above 1700 K. These uncertainties would be smaller compared to the parameter uncertainties associated with the energy-limited escape rate, as discussed above.

Although we have examined only Earth-sized planets in the present study, the orbital-dependent dichotomy in lifetime and spectral evolution would exist for different planetary masses as well. Kopparapu et al. (2014) reported that the radiation limit increases by approximately 20% for a rocky planet with five times the Earth's mass. The critical distance therefore would become closer to the host star for larger planetary masses, compared to that for Earth-sized planets. Although the larger radiation limit would also have a role in making the cooling of a Type I planet faster, the overall duration of a molten state may be roughly proportional to the planetary mass because of the larger heat capacity of the planet (Elkins-Tanton 2011). On the other hand, for a massive Type II planet, the lifetime of a magma ocean would become extremely longer, with the assumption that the bulk content of water is the same. This is because the total amount of water is proportional to the planetary mass, whereas the total escape rate of hydrogen is independent on the planetary mass itself, as long as the energy-limited escape rate is considered. In terms of spectral detectability, more massive planets are expected to be brighter and therefore easier to detect because of their larger surface area (Miller-Ricci et al. 2009). Future studies will expand this line of research by taking into account planetary mass, different types of stars and an expected variety of atmospheric compositions.

6. CONCLUSIONS

We have examined the lifetime of the magma ocean and its spectral evolution for Earth-sized terrestrial planets along with the evolution of the steam atmosphere. Due to the presence of the radiation limit of steam atmospheres, the thermal and spectral evolution of the magma ocean strongly depends on the planetary orbital distance from the host star. Planets beyond the critical distance $a_{\rm cr}$ (type I) are self-luminous throughout solidification. The thermal radiation from atmospheric windows decreases on a timescale shorter than $\sim 10^6$ years. The lifetime of the magma ocean is less sensitive to the semimajor axis in the Type I orbital region. Consequently, young stars should be targets in searching for molten planets in this orbital region.

In the case of a planet formed inside $a_{\rm cr}$ (type II), the outgoing planetary radiation can balance the net incoming stellar radiation after a short self-luminous phase. The emergent spectra during the quasi-energy balance state are approximately independent of the surface temperature and pressure. The Type II planet maintains high thermal radiation from near-IR atmospheric windows throughout the lifetime of the magma ocean. The lifetime of the magma ocean increases for a larger initial inventory of water.

Type-II planets are brighter at smaller orbital distance so as to balance the larger stellar radiation, whereas these planets solidify on a shorter timescale because of the higher loss rate of water they experience. The sensitivity of the magma-ocean lifetime to the water amount and the orbital distance increases the possibility of placing constraints on the water endowment of terrestrial planets based on the occurrence rate of molten planets for a given stellar age. Our model predicts that terrestrial planets remain molten over the main sequence of the host star in the Type II orbital region if the initial bulk content of water exceeds approximately 1 wt%.

The composite spectrum is dominated by reflected light at the visible wavelengths and by thermal emission at the near-IR wavelengths for Type II planets in the quasi-energy balance state. The atmospheric windows in the near-IR are favorable for detecting thermal emission, as pointed out by Lupu et al. (2014). The $H-K$ color of the thermal emission is strikingly redder than that of the host star and the reflected light, whereas the solidifying Type I and Type II planets are typically as faint as planets having moderate surface temperature. Therefore, Type I and Type II planets could form a group distinct from the observed brown dwarfs and the planets in the solar system in the color–magnitude diagram. Evolution calculations including cloud formation will be required in order to make more detailed predictions regarding color and appearance.

The K and L bands will be favorable for future direct imaging because the planet-to-star contrast of the Type II planets is approximately $10^{-7}-10^{-8}$. In particular, the search around $a_{\rm cr}$, which is close to the inner edge of the habitable zone, will have a higher detection probability in terms of the duration of the molten state. For both the Type I and Type II planets, in visible atmospheric windows, the contrast of the thermal emission drops below 10^{-10} in less than 10^5 years, whereas that of the reflected stellar light remains 10^{-10}. Thus, the visible reflected light from molten planets will also be a promising target for direct imaging with ground-based high-contrast instruments and for second-Earths survey by space-based telescopes.

We are grateful to Colin Goldblatt for allowing us to use his spectral data for model comparison. We thank two anonymous reviewers for their careful reading and constructive comments. This work is supported by Grant-in-Aid for Scientific Research on Innovative Areas from the Ministry of Education, Culture, Sports, Science and Technology (MEXT) (No. 23103003). This work is also supported by Grant-in-Aid for Young Scientists (B) from Japan Society for the Promotion of Science (JSPS), No. 26800242 to K.H., No. 25800106 to H.K., and No. 25800264 to M.O. H.K. acknowledges support from Research Center for the Early universe (RESCEU).

APPENDIX
RADIATIVE TRANSFER

We use two-stream approximation to solve radiative transfer equation in a plane-parallel atmosphere, with diffusivity factor $r_{\rm df}$ of $\sqrt{3}$,

$$r_{\rm df}\frac{dF_\nu^\uparrow}{d\tau} = F_\nu^\uparrow - J_\nu(\tau)$$
$$-r_{\rm df}\frac{dF_\nu^\downarrow}{d\tau} = F_\nu^\downarrow - J_\nu(\tau). \quad (11)$$

Hereafter, the wavenumber subscript ν is suppressed to simplify the notation. We assume that scattering is isotropic, and treat stellar and planetary radiation separately. For the

planetary flux ($F^{\uparrow}_{\rm pl}$ and $F^{\downarrow}_{\rm pl}$) ,

$$J(\tau) = J_{\rm pl}(\tau) = \frac{\omega_0}{2}\left(F^{\uparrow}_{\rm pl} + F^{\downarrow}_{\rm pl}\right) + \left(1 - \omega_0\right)\pi B(T(\tau)), \tag{12}$$

where ω_0 is the single scattering albedo, and $B(T(\tau))$ is the Planck function with temperature at τ. Boundary conditions at the top and bottom of the atmosphere are given by

$$F^{\downarrow}_{\rm pl,t} = 0 \quad \text{and} \quad F^{\uparrow}_{\rm pl,b} = \left(1 - A_{\rm g}\right)\pi B\left(T_{\rm s}\right) + A_{\rm g}F^{\downarrow}_{\rm pl,b}, \tag{13}$$

where $A_{\rm g}$ is the ground albedo and $T_{\rm s}$ is the surface temperature. The subscripts t and b denote the top and the bottom of the atmosphere, respectively.

For the stellar diffusive flux ($F^{\uparrow}_{\rm sl}$ and $F^{\downarrow}_{\rm sl}$),

$$J(\tau) = J_{\rm sl}(\tau) = \frac{\omega_0}{2}\left(F^{\uparrow}_{\rm sl} + F^{\downarrow}_{\rm sl}\right) + \frac{r_{\rm df}\omega_0}{2}D_{\odot}e^{\tau/\mu_0}, \tag{14}$$

where $D_{\odot}$ is the stellar flux incident to the top atmospheric layer at optical depth of $\tau_{\rm t}$ with zenith angle θ_0 ($\mu_0 = \cos\theta_0$). The direct downward stellar flux is given by

$$D^{\downarrow}_{\rm sl}(\tau) = \left|\mu_0\right| D_{\odot}\, e^{\tau/\mu_0}. \tag{15}$$

We assume that the stellar spectrum profile incident to the top of the atmosphere is given by that of a blackbody radiation with an effective stellar temperature $T_{\star}$. It gives the boundary condition as follows,

$$F^{\downarrow}_{\rm sl,t} = 0, \quad D_{\odot} = F_{\odot}\frac{\pi B\left(T_{\star}\right)}{\sigma T^4_{\star}}, \quad \text{and}$$
$$F^{\uparrow}_{\rm sl,b} = A_{\rm g}\left(F^{\downarrow}_{\rm sl,b} + D^{\downarrow}_{\rm sl,b}\right), \tag{16}$$

where $F_{\odot}$ is the total stellar energy flux that the planet receives at its orbital position.

Wavenumber region is separated into two parts to calculate the radiative transfer equation efficiently and accurately. In the wavenumber region less than a certain wavenumber ν_a, we assume that the scattering process by gaseous molecules can be neglected. The net upward planetary and stellar fluxes are calculated using the integrated form of Equation (11), using Equations (12), (14) and (15), and the boundary conditions (13) and (16),

$$F^{\uparrow}_{\rm pl}(\tau) = \pi B(T(\tau)) + \pi\int_{\tau}^{\tau_{\rm b}}\frac{dB(T(t))}{dt}e^{-r_{\rm df}|t-\tau|}dt + \left\{F^{\uparrow}_{\rm pl,b} - \pi B\left(T(\tau_b)\right)\right\}e^{-r_{\rm df}(\tau_{\rm b}-\tau)}$$
$$F^{\downarrow}_{\rm pl}(\tau) = \pi B(T(\tau)) - \pi\int_{0}^{\tau}\frac{dB(T(t))}{dt}e^{-r_{\rm df}|t-\tau|}dt - \pi B(T(0))e^{-r_{\rm df}\tau} \tag{17}$$

and

$$F^{\uparrow}_{\rm sl}(\tau) = F^{\uparrow}_{\rm sl,b}e^{-(\tau_{\rm b}-\tau)} = A_{\rm g}e^{\tau_{\rm b}/\mu_0}e^{-(\tau_{\rm b}-\tau)}$$
$$F^{\downarrow}_{\rm sl}(\tau) = 0, \tag{18}$$

given the fact that the diffusive downward stellar flux is equal to 0 in a non-scattering atmosphere. We evaluate the integrals in Equation (17) by considering the contributions from the region where the optical distance from the midpoint of each layer is smaller than 10.

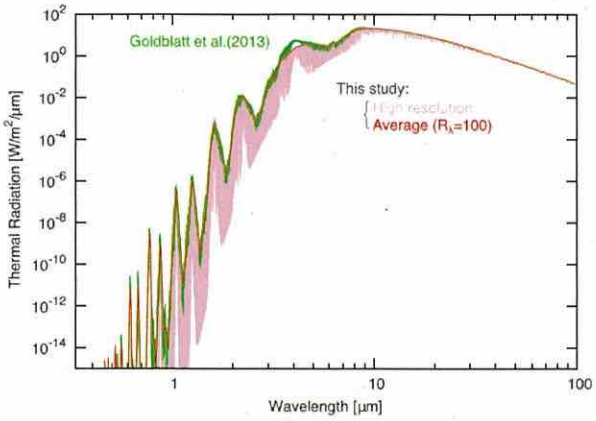

Figure 11. Spectrum of the thermal emission from the top of the steam atmosphere obtained using our model and that reported by Goldblatt et al. (2013) for a surface pressure of 123 bar and a surface temperature of 600 K.

At sufficiently large wavenumber, both the absorption and scattering processes are taken into account. The radiative flux in each layer is calculated using a formal solution of the radiative transfer Equation (11) similarly to Toon et al. (1989), but is solved iteratively by repeating upward and downward integrations to satisfy the boundary conditions at the top and the surface.

In this paper, we calculate the radiative transfer equations for both the planetary and stellar radiation in a wavenumber range from 0 to 30,000 cm^{-1}. The wavenumber ν_a, at which the way to calculate the radiative transfer equation is switched from one to another, is set to 5000 cm^{-1}. Beyond 30,000 cm^{-1}, only the scattering process is considered using the Rayleigh scattering cross-section at 30,000 cm^{-1}. This leads to underestimate the attenuations by the absorption and scattering processes, and overestimate the Bond albedo (see Figure 12). We define a spectral albedo α for the incident stellar radiation as the ratio of the diffusive upward radiation to the direct downward radiation at the top of the atmosphere, i.e., $F^{\uparrow}_{\rm sl}(\tau_{\rm t})/D^{\downarrow}_{\rm sl,t}$. The Bond albedo for stellar radiation with an effective temperature of $T_{\star}$ is obtained as a weighted mean of the spectral albedo as follows,

$$\alpha_{\rm p} = \frac{\int\alpha B\left(T_{\star}\right)d\nu}{\sigma T^4_{\star}}. \tag{19}$$

We compare the thermal emission spectra of our model with that reported by Goldblatt et al. (2013) (Figure 11). Our model spectra accord closely with that by Goldblatt et al. (2013). The thermal radiation calculated with our model is lower than that by Goldblatt et al. (2013) at the wavelengths between 3 and 5 μm, due to the difference in the continuum absorption models of water vapor (see below).

We also compare the planetary radiation and Bond albedos calculated with our radiative transfer model with those by previous studies to check the validity of our model (Figure 12). The radiation limit of our model is 280 Wm^{-2}, and is in close agreement with the value of 282 Wm^{-2} obtained by Goldblatt et al. (2013) with line-by-line calculations, with a difference of less than 1%. As the surface temperature increases, the planetary radiation starts to rise for all the three models due to the temperature increase in the upper atmosphere. In this phase, our results agree well with those by Kopparapu et al.

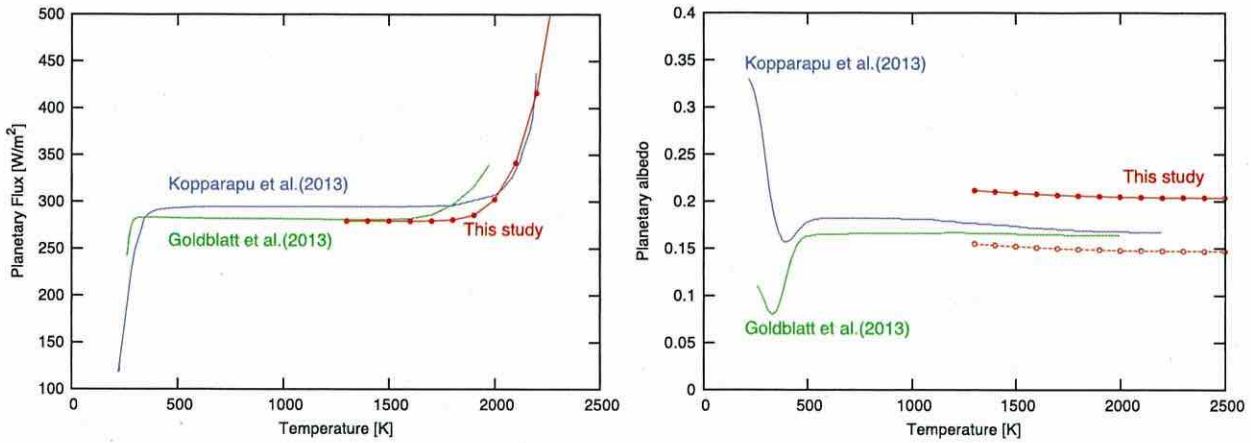

Figure 12. Planetary radiation and Bond albedos for a steam atmosphere with a surface pressure of 260 bar. Kopparapu et al. (2013) and Goldblatt et al. (2013) obtained the Bond albedos by averaging the stellar flux over six zenith angles, whereas we calculated the Bond albedos using a stellar zenith angle of $\cos^{-1}(1/\sqrt{3})$ (red closed circles and solid line). The open circles and dotted line represent the Bond albedos obtained by assuming that the stellar radiation is perfectly absorbed at wavenumbers beyond 30,000 cm^{-1}.

(2013), rather than by Goldblatt et al. (2013), probably because of the differences in the treatment of the continuum absorption of water vapor. Paynter & Ramaswamy (2011) indicated that the self continuum absorption of water vapor is underestimated in a MT_CKD 2.4 model, which was used by Goldblatt et al. (2013), especially in a wavenumber range from 2000 to 3000 cm^{-1}, compared with the MT_CKD 2.5 model used in our model and a BPS formalism used by Kopparapu et al. (2013). This likely explains why the planetary radiation starts to increase at the lower surface temperature in Goldblatt et al. (2013). The Bond albedos with our model are larger than those with the previous studies by about 0.05. This is probably because we underestimate the absorption and scattering processes at the wavenumbers larger than 30,000 cm^{-1}.

REFERENCES

Abe, Y., & Matsui, T. 1988, JAtS, 45, 3081
Agnor, C. B., Canup, R. M., & Levinson, H. F. 1999, Icar, 142, 219
Allen, C. W. 1973, Astrophysical Quantities (3rd ed.; London: Athlone)
Andrault, D., Bolfan-Casanova, N., Lo Nigro, G., et al. 2011, E&PSL, 304, 251
Canup, R. M. 2004, Icar, 168, 433
Chambers, J. E. 2001, Icar, 152, 205
Chassefière, E. 1996, JGR, 101, 26039
Crossfield, I. J. M. 2013, A&A, 551, A99
Elkins-Tanton, L. 2008, E&PSL, 271, 181
Elkins-Tanton, L. 2011, Ap&SS, 332, 359
Genda, H., & Abe, Y. 2005, Natur, 433, 842
Gillmann, C., Chassefière, E., & Lognonné, P. 2009, E&PSL, 286, 503
Goldblatt, C., Robinson, T. D., Zahnle, K. J., & Crisp, D. 2013, NatGe, 6, 661
Gough, D. O. 1981, SoPh, 74, 21
Guyon, O., Martinache, F., Cady, E. J., et al. 2012, Proc. SPIE, 8447, 84471X
Hamano, K., Abe, Y., & Genda, H. 2013, Natur, 497, 607
Hirschmann, M. M. 2006, AREPS, 34, 629
Humlíček, J. 1982, JQSRT, 27, 437
Ikoma, M., & Genda, H. 2006, ApJ, 648, 696
Jovanovic, N., Guyon, O., Martinache, F., et al. 2013, in Proc. of AO4ELTs 3, SCExAO as a Precursor to an ELT Exoplanet Direct Imaging Instrument, paper 13396
Kasting, J. F. 1988, Icar, 74, 472
Kawahara, H., Matsuo, T., Takami, M., et al. 2012, ApJ, 758, 13
King, H. E., Stimpfl, M., Deymier, P., et al. 2010, E&PSL, 300, 11
Knapp, G. R., Leggett, S. K., Fan, X., et al. 2004, ApJ, 127, 3553
Kokubo, E., & Genda, H. 2010, ApJL, 714, L21
Kopparapu, R. K., Ramirez, R., Kasting, J. F., et al. 2013, ApJ, 765, 16
Kopparapu, R. K., Ramirez, R. M., Kotte, J. S., et al. 2014, ApJL, 787, L29
Kulikov, Y. N., Lammer, H., Lichtenegger, H. I. M., et al. 2007, SSRv, 129, 207
Lundock, R., Ichikawa, R., Okita, H., et al. 2009, A&A, 507, 1649
Levine, M., Lisman, M., Shaklan, D., et al. 2009, arXiv:0911.3200L
Lebrun, T., Massol, H., Chassefière, E., et al. 2013, JGRE, 118, 1155
Leggett, S. K., Golimowsky, D. A., Fan, X., et al. 2002, ApJ, 564, 452
Lupu, R. E., Zahnle, K., Marley, M., et al. 2014, ApJ, 784, 27
Machida, R., & Abe, Y. 2010, ApJ, 716, 1252
Macintosh, B., Graham, J. R., Ingraham, P., et al. 2014, PNAS, 111, 12661
Macintosh, B., Graham, J., Palmer, D., et al. 2006, Proc. SPIE, 6272, 62720L
Males, J. R., Close, L. M., Guyon, O., et al. 2014, arXiv:1407.5099
Matsui, T., & Abe, Y. 1986a, Natur, 319, 303
Matsui, T., & Abe, Y. 1986b, Natur, 322, 526
Matsuo, T., & Tamura, M. 2010, Proc. SPIE, 7735, 773584
Miller-Ricci, E., Meyer, M. R., Seager, S., & Elkins-Tanton, L. 2009, ApJ, 704, 770
Morbidelli, A., Chambers, J., Lunine, J. I., et al. 2000, M&PS, 35, 1309
Mlawer, E. J., Payne, V. H., Moncet, J.-L., et al. 2012, RSPTA, 370, 2520
Muralidharan, K., Deymier, P., Stimpfl, M., et al. 2008, Icar, 198, 400
Nakajima, S., Hayashi, Y., & Abe, Y. 1992, JAtS, 49, 2256
Ohtani, E. 2005, Elements, 1, 25
Oppenheimer, B. R., Hinkley, S., Vasisht, et al. 2012, Proc. SPIE, 8447, 844720
Paynter, D. J., & Ramaswamy, V. 2011, JGR, 116, D20302
Petigura, E. A., Howard, A. W., & Marcy, G. W. 2013, PNAS, 110, 19273
Pizzolato, N., Maggio, A., Micela, G., et al. 2003, A&A, 397, 147
Raymond, S. N., Quinn, T., & Lunine, J. I. 2007, AsBio, 7, 66
Ribas, I., Guinan, E. F., Güdel, E. F., & Audard, M. 2005, ApJ, 622, 680
Ribas, I. 2009, in IAU Symp. 264, Solar and Stellar Variability: Impact on Earth and Planets, ed. A. G. Kosovichev, A. H. Andrei & J.-P. Rozelot (Cambridge: Cambridge University Press), p 3
Rothman, L. S., Gordon, I. E., Barber, R. J., et al. 2010, JQSRT, 111, 2139
Sasaki, S. 1990, in Origin of the Earth, ed. H. E. Newsom & J. H. Jones (Oxford: Oxford Univ. Press), p 195
Savransky, D., Spergel, D. N., Kasdin, N. J., et al. 2010, Proc. SPIE, 7731, 2
Shaw, H. R. 1972, AmJS, 272, 870
Shematovich, V. I., Ionov, D. E., & Lammer, H. 2014, A&A, 571, A94
Solomatov, V. 2007, in Treatise on Geophysics, ed. D. Stevenson (Amsterdam: Elsevier), p 9
Spergel, D., Gehrels, N., Baltay, C., et al. 2015, arXiv:1503.03757
Stauffer, J. R., Caillault, J.-P., Gagnè, M., et al. 1994, ApJS, 91, 625
Stewart, S. T., & Leinhardt, Z. M. 2012, ApJ, 751, 32
Takahashi, E. 1986, JGR, 91, 9367
Toon, O. B., Mckay, C. P., & Ackerman, T. P. 1989, JGR, 94, 287
Traub, W. A., & Oppenheimer, B. R. 2010, in Exoplanets, ed. S. Seager (Tucson, AZ: Univ. Arizona Press), p 111

van der Molen, I., & Paterson, M. S. 1979, CoMP, 70, 299
Vilhu, O., & Walter, F. M. 1987, ApJ, 321, 958
Wagner, W., & Pruß, A. 2002, JPCRD, 31, 387
Walsh, K. J., Morbidelli, A., Raymond, S. N., et al. 2011, Natur, 475, 206
Watson, A. J., Donahue, T. M., & Walker, J. C. G. 1981, Icar, 48, 150
Zahnle, K. J., Kasting, J. F., & Pollack, J. B. 1988, Icar, 74, 62
Zahnle, K., Schaefer, L., & Fegley, B. 2010, Cold Spring Harb. Perspect. Biol., 2, a004895
Zhang, Y., Xu, Z., Zhu, M., & Wang, H. 2007, RvGeo, 45, RG4004
Zurlo, A., Vigan, A., Mesa, D., et al. 2014, A&A, 572, A85

Earth and Planetary Science Letters 375 (2013) 312–318

Contents lists available at ScienceDirect

Earth and Planetary Science Letters

journal homepage: www.elsevier.com/locate/epsl

Effective hydrodynamic hydrogen escape from an early Earth atmosphere inferred from high-accuracy numerical simulation

Kiyoshi Kuramoto [a,b,*], Takafumi Umemoto [a,c], Masaki Ishiwatari [a,b]

[a] Department of Cosmosciences, Hokkaido University, Sapporo 060-0810, Japan
[b] Center for Planetary Sciences, Kobe 650-4407, Japan
[c] Nihon Unisys, Tokyo 650-4407, Japan

ARTICLE INFO

Article history:
Received 16 November 2012
Received in revised form
27 May 2013
Accepted 29 May 2013
Editor: B. Marty
Available online 21 June 2013

Keywords:
early Earth
hydrodynamic escape
hydrogen
atmospheric composition
solar radiation

ABSTRACT

Hydrodynamic escape of hydrogen driven by solar extreme ultraviolet (EUV) radiation heating is numerically simulated by using the constrained interpolation profile scheme, a high-accuracy scheme for solving the one-dimensional advection equation. For a wide range of hydrogen number densities at the lower boundary and solar EUV fluxes, more than half of EUV heating energy is converted to mechanical energy of the escaping hydrogen. Less energy is lost by downward thermal conduction even giving low temperature for the atmospheric base. This result differs from a previous numerical simulation study that yielded much lower escape rates by employing another scheme in which relatively strong numerical diffusion is implemented. Because the solar EUV heating effectively induces hydrogen escape, the hydrogen mixing ratio was likely to have remained lower than 1 vol% in the anoxic Earth atmosphere during the Archean era.

1. Introduction

The hydrodynamic escape of hydrogen driven by solar extreme ultraviolet (EUV) flux is a key process for controlling the evolution of the early Earth atmosphere and surface environment. For an atmosphere having a hydrogen-dominated upper layer, it was suggested that EUV heating energy is effectively transferred to mechanical energy of the outflow gas (e.g., Sekiya et al., 1980; Watson et al., 1981). Such effective escape, the rate of which can be limited by the diffusive separation rate of hydrogen across the homopause depending on the existing hydrogen mixing ratio (e.g., Walker, 1977), implies the rapid loss of hydrogen from early Earth and even possibly loss of entire water from Venus (e.g., Kasting and Pollack, 1983) under the enhanced EUV radiation emitted from the young Sun.

Early analytical studies of EUV-driven hydrodynamic escape investigated steady outflow solutions by solving simultaneous ordinary differential equations in the radial coordinate considering time derivatives to be zero in the conservation equations of mass, momentum, and energy with spherical symmetry. This approach sometimes faces difficulty in finding transonic solutions to avoid mathematical singularity. Numerical time integration of conservation equations is a possible approach to resolve this problem.

By performing this calculation, Tian et al. (2005a) reported escape rates significantly lower than those estimated by earlier studies. Their calculation was performed at a temperature as low as 250 K at the base of hydrogen-dominated region, which is presumably possible by effective cooling from a radiatively active secondary species. The obtained low escape rates would be attributed to the conductive loss of EUV heating energy toward the cold atmospheric base. Equating an estimate of the volcanic hydrogen degassing rate with the calculated escape rates, it was proposed that the early Earth atmosphere would be hydrogen rich with an H_2 mixing ratio as high as nearly 30%, even at 2.5 Ga. This significantly differs from the earlier estimates predicting an H_2 mixing ratio less than ~0.1 vol% during the Archean era (e.g., Walker, 1978).

Tian et al.'s numerical model, however, requires further testing for accuracy. In another paper (Tian et al., 2005b) they mentioned that their model scheme may have a difficulty in satisfying the radial uniformity of mass flux integral (taken over a sphere concentric with Earth) in steadily expanding isothermal solutions. This violation of the law of conservation of mass especially emerges at low altitudes in simulations with low atmospheric temperatures.

To avoid numerical instability, Tian et al. (2005a, 2005b) used the Lax–Friedrichs (LF) scheme, which introduces an artificial numerical diffusion (LeVeque, 1992; de Sterck et al., 2001). At low altitudes, the atmospheric density profile approximately

* Corresponding author at: Department of Cosmosciences, Hokkaido University, Kita 10 Nishi 8, Kita-ku, Sapporo 060-0810, Japan. Tel.: +81 11 706 3827; fax: +81 11 706 2760.
E-mail address: keikei@ep.sci.hokudai.ac.jp (K. Kuramoto).

0012-821X/$ - see front matter © 2013 Elsevier B.V. All rights reserved.
http://dx.doi.org/10.1016/j.epsl.2013.05.050

follows hydrostatic equilibrium. At low atmospheric temperature, the density contrast between altitudes in the lower atmosphere becomes significant owing to the decrease in atmospheric scale height. If the LF scheme is applied to such a system, the artificial numerical diffusive flux, approximately equivalent to that by a diffusion process with diffusivity given by the sound speed times the grid interval, may sometimes overwhelm the true mass flux, particularly at low atmospheric altitudes. This calculation would thus cause a violation of the law of conservation of mass. On the other hand, calculated mass fluxes at the upper boundary are in good agreement with the analytical solution by Parker (1963), which is the main reason for using the LF scheme by Tian et al. (2005a, 2005b).

It is still unclear whether the LF scheme adequately reproduces the escape rate even for non-isothermal atmosphere. At least, the problem with mass conservation in the lower altitudes implies significant errors in estimating energy balance in the outflow gas. Therefore, this study will simulate the EUV-driven hydrodynamic escape of hydrogen by using a more reliable numerical scheme.

We have developed a new numerical model that adopts the constrained interpolation profile (CIP) scheme (Yabe and Aoki, 1991; Yabe et al., 2001b), a high-accuracy method for solving advection equations. The advantage of the CIP scheme is that it causes few numerical dispersion errors by predicting the advection of both numerical values and their gradients at each grid point. Because of this nature and numerical stability, the CIP scheme is considered to be an adequate method to simulate atmospheric outflow.

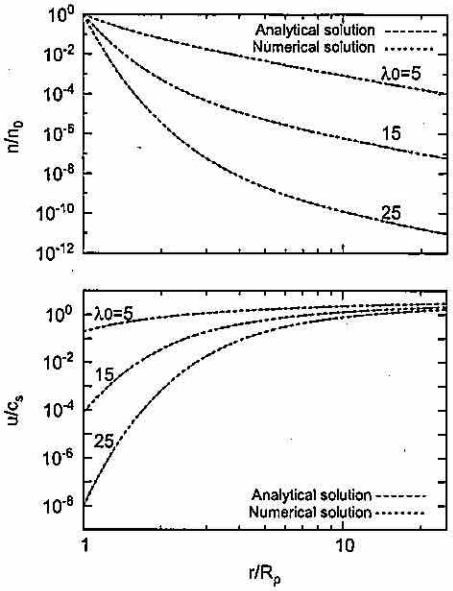

Fig. 1. Comparison of analytical solutions and numerical ones for the isothermal steady expansion of the atmosphere. Radial density (top panel) and velocity profiles (lower panel) are scaled by the basal density and sound velocity, respectively. Independent of the escape parameter over this range (taken at 5, 15, and 25), the numerical solutions are indistinguishable from the analytical ones.

2. Model

Following Tian et al. (2005a), the hydrodynamic flow of an ideal gas atmosphere composed of pure H_2 with radial symmetry is described by the inviscid Eulerian equations

$$\frac{\partial(\rho r^2)}{\partial t}+\frac{\partial(\rho u r^2)}{\partial r}=0, \tag{1}$$

$$\frac{\partial(\rho u r^2)}{\partial t}+\frac{\partial(\rho u^2 r^2+p r^2)}{\partial r}=-\rho GM+2pr, \tag{2}$$

$$\frac{\partial}{\partial t}\left[\left(\frac{\rho u^2}{2}+\frac{p}{\gamma-1}\right)r^2\right]+\frac{\partial}{\partial r}\left[\left(\frac{\rho u^2}{2}+\frac{\gamma p}{\gamma-1}\right)ur^2\right] =-\rho uGM+qr^2+\frac{\partial}{\partial r}\left(\kappa r^2\frac{\partial T}{\partial r}\right), \tag{3}$$

where r is the distance from the center, u is the radial velocity; ρ, p, T are the gas density, pressure, and temperature, respectively. γ is the ratio of specific heats considered as 7/5, G is the gravitational constant, M is the mass of the Earth, κ is the thermal conductivity, and q is the heating rate. The equation of state is given by that of the ideal gas composed of pure H_2. The thermal conductivity is given by

$$\kappa=\kappa_0\left(\frac{T}{T_0}\right)^s, \tag{4}$$

where T_0 is the reference temperature, κ_0 is the thermal conductivity at $T=T_0$ and s is the constant power index. We set $T_0=250$ K, $\kappa_0=1.62\times10^{-1}$ J/m s K, and $s=0.7$ (Hanley et al., 1970).

The heating rate q is calculated by the same method used by Tian et al. (2005a, 2005b), which numerically solves the 2D radiative transfer of solar EUV flux incident from the solar direction into the spherically expanded atmosphere, and then laterally averages the energy absorption to obtain the radial heating profile at each time step. The EUV spectrum and the absorption cross section are provided by Woods and Rottman (2002) and Avakyan et al. (1998), respectively, for wavelengths shorter than 105 nm. To express the early solar EUV flux, the present-day time-averaged EUV spectrum is multiplied by enhancement factors neglecting the possible change in the spectrum profile. Furthermore, the heating efficiency of absorbed energy is considered as 0.15 (Watson et al., 1981). The temperature at the lower boundary is fixed at 250 K. Each of these settings is basically the same as those used by Tian et al. (2005a).

Eqs. (1)–(3) are solved by explicit integration about time until the physical quantities settle into steady profiles. To perform time integration, we employ CIP schemes that are known to perform stable numerical integration of advection terms with a high degree of accuracy using reasonable computational resources. We adopted the CIP-CSL2 scheme (Yabe et al., 2001a) to solve the mass conservation equation because this method is optimized to guarantee the conservation of mass. To save computational resources, the original CIP scheme (Yabe and Aoki, 1991) is adopted for the advection terms of the momentum equation and the energy equation. The diffusion term in the energy equation is expressed by the centered difference formula. The upper and lower boundaries are set at $r=25$ Earth radius (6.36×10^3 km) and $r=6.46\times10^3$ km (the Earth radius + 100 km), respectively. The interval was divided into 1000 numerical grids with the grid-to-grid intervals exponentially increasing with r.

In each simulation run, the atmospheric density and temperature at the lower boundary are fixed as a parameter as well as the EUV enhancement factor. The other physical quantities in the lower and upper boundaries are estimated by linear extrapolations from the calculated domain. The initial density profile is given by the isothermal hydrostatic structure for the lower layer and is proportional to r^{-2} in the upper layer beyond an arbitrary radius. A constant velocity of 10^{-5} m/s is set as the initial velocity profile.

3. Results

3.1. Testing isothermal calculation

To test the performance of our model, we simulated the steady expansion of the isothermal atmosphere into the vacuum and

compared it with the analytical solution. This outflow is characterized by the escape parameter (Parker, 1963) defined as $\lambda_0 = GMm/kTr_0$ where m is the mass of an atmospheric molecule, k is the Boltzmann constant, and r_0 is the distance between the planetary center and the lower boundary of the atmosphere. Fig. 1 shows the comparison between the analytical solutions and the numerical ones with various escape parameters. The solutions appear to match quite well.

We also carried out isothermal simulations with different total grid numbers. As shown in Fig. 2, the calculated mass flux integrals approach the analytical ones with errors less than 2% as the total grid number increases up to 1000.

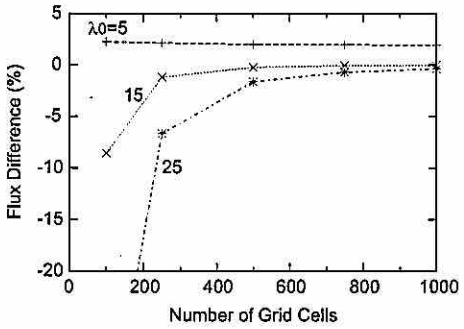

Fig. 2. Relative differences between mass fluxes obtained from numerical calculations and analytical solutions for the isothermal steady expansion of the atmosphere. When we increase grid numbers to 1000, the difference becomes less than 2% for escape parameters 5, 15, and 25.

3.2. Full simulation results

Typical steady state solutions obtained by our full simulation, i.e., the numerical integration of the conservation equations of mass, momentum, and energy, are shown in Fig. 3. For the solutions shown in Fig. 3a–c, we set the enhancement factor of solar EUV at unity and set several values of the gas density at the lower boundary. In each solution, the flow is radially accelerated from near zero velocity to supersonic, with the temperature profile peaking in the subsonic region.

In contrast to the results of Tian et al. (2005a), we obtained temperature profiles that did not approach constant temperature but continued to decrease at large distances from the center. This is due to the adiabatic cooling of expanding gas, which was also reproduced in earlier analytical studies (Sekiya et al., 1980; Watson et al., 1981). The approach to the isothermal profile observed by Tian et al. (2005a) may be caused by the lower gas density at great radial distances accompanied by a low outflow rate. In such a thin atmosphere, the thermal conduction may become very efficient to smooth out the temperature gradient.

Steady state solutions set at higher enhancement factors of solar EUV are shown in Fig. 3d–f, where the gas density at the lower boundary is maintained at 5×10^{18} m^{-3} for comparison. As the enhancement factor increases, the flow more strongly accelerates along with an increase in the temperature of the outflow gas. The temperature peak shifts upward with an enhanced EUV flux because the zone where EUV absorption occurs is pushed outward in the hotter, expanded atmosphere.

To confirm the reproducibility of energy conservation in our model, we compared the net energy outflow rate E_{out} with the net

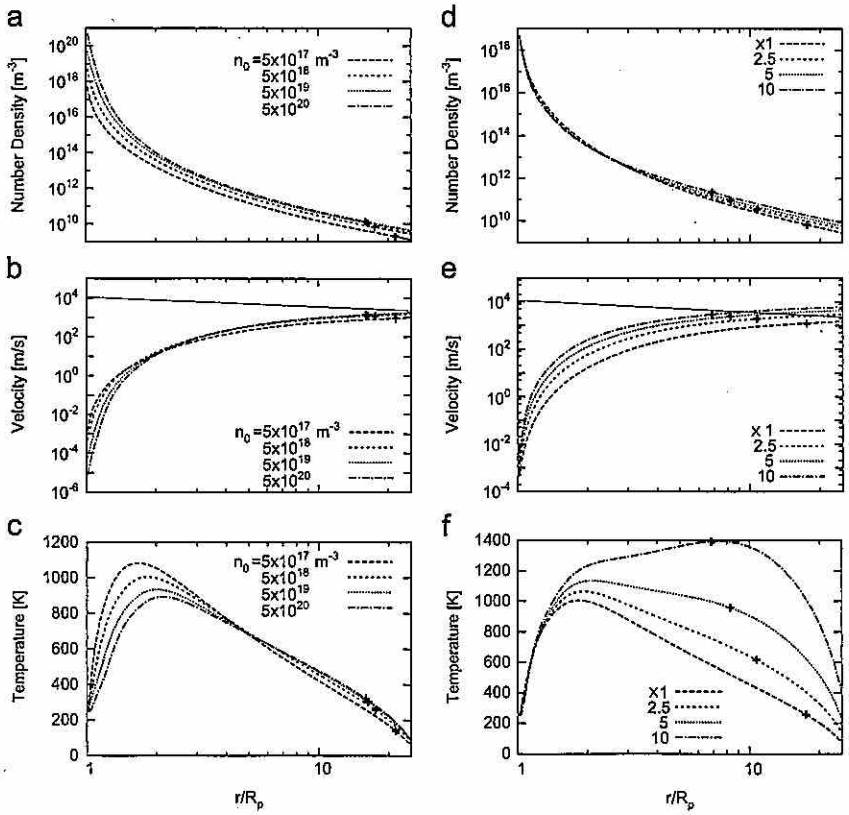

Fig. 3. Steady state solutions obtained by full numerical simulations. The left and right columns show dependence on the hydrogen density at the lower boundary and on the EUV flux, respectively. For each profile, the plus mark represents the sonic point. In the panels of the velocity profile, the escape velocity is also shown.

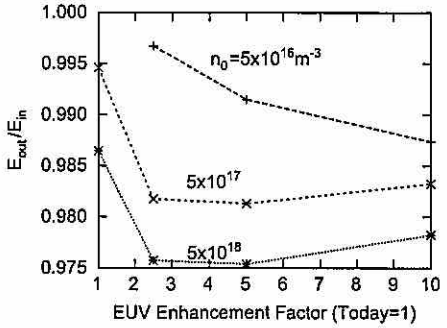

Fig. 4. Ratios of the net energy outflow rate and net heating rate for the steady numerical solutions.

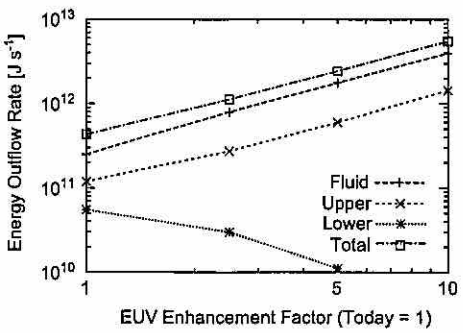

Fig. 5. Analysis of the energy outgoing rate. The total (square) is divided into the term of the flow flux of fluid energy (plus) and the heat flow terms due to the thermal conduction at the upper boundary (cross) and lower one (star). In this calculation, the hydrogen number density is considered to be 5×10^{18} m^{-3} at the lower boundary.

EUV heating rate E_{in} as follows:

$$E_{out} = 4\pi\rho_{top} r_{top}^2 u_{top}(H_{top} - H_0) - 4\pi\left(\kappa r^2 \frac{\partial T}{\partial r}\right)_{top} + 4\pi\left(\kappa r^2 \frac{\partial T}{\partial r}\right)_0 \quad (5)$$

$$E_{in} = 4\pi \int_{r_0}^{r_{top}} q r^2 \, dr \quad (6)$$

where the suffixes indicate the quantities estimated at the lower boundary (0) and the upper one (top), respectively, and H is the specific total energy of fluid given by the sum of the mechanical energy and enthalpy per unit mass given by

$$H = \frac{1}{2}u^2 + \frac{\gamma}{\gamma - 1}\frac{P}{\rho} - \frac{GM}{r}. \quad (7)$$

In Fig. 4, the ratios of E_{out}/E_{in} are shown for steady state numerical solutions. If the law of conservation of energy is satisfied, this ratio should be unity. For a given range of the EUV enhancement factor and the density at the lower boundary, the obtained E_{out}/E_{in} ratios are almost equal to unity with a relative error less than 3%. This indicates that our complete simulation preserves the law of conservation of energy very well.

In most of the steady numerical solutions, EUV heating energy is effectively transferred to mechanical energy. When we analyze the net energy outflow rate, the term of the flow flux of fluid energy predominates compared to the terms of thermal conduction across the upper and lower boundaries, irrespective of the EUV enhancement factor, as shown in Fig. 5. Furthermore, the specific energy of fluid is dominated by mechanical energy rather than internal energy since the gas temperature is not high at the upper boundary. Therefore, more than half of EUV heating energy is transferred to the acceleration of escaping fluid, at least for the settings in Fig. 5, implying that the solar EUV heating induces the effective escape of hydrogen.

4. Discussion

4.1. Escape rate of hydrogen

Our numerical results suggest that there is an effective loss of hydrogen from the early Earth atmosphere. In Fig. 6, the hydrogen escape rate is shown as a function of the homopause hydrogen mixing ratio, which is converted from the lower boundary gas density. The conversion is carried out by considering the diffusive separation of gas species in the layer above the homopause (see Appendix for details). Compared with the solutions obtained by Tian et al. (2005a), our numerical solutions yielded escape rates greater than several to several tens of factors, at the same hydrogen mixing ratios and EUV enhancement factors.

At a fixed EUV enhancement factor, we obtained escape rates that increase with the homopause hydrogen mixing ratio. When the mixing ratio, or the basal hydrogen density, is sufficiently high, the solar EUV is mostly absorbed in the atmospheric zone sufficiently far above the lower boundary. In such cases, the escape rate may gradually increase along with the basal hydrogen density. This is due to the expansion of the effective cross section of the whole Earth for the solar EUV radiation associated with the thickening of the atmosphere. However, when the basal hydrogen density is low, EUV may penetrate below the lower boundary. This suppresses the amount of EUV absorption heating in the calculated domain, resulting in a drop in the escape rate at low homopause hydrogen mixing ratios.

Our obtained escape rate is almost consistent with an order estimate, indicating that heating due to the solar EUV radiation accepted by the cross section of the solid Earth is fully transferred to the potential energy of the escaping gas, stated as follows:

$$\phi = \frac{\epsilon F_{EUV}}{4GM\mu/R_0} = 3.9 \times 10^{15}\left(\frac{\epsilon}{0.15}\right)\left(\frac{F_{EUV}}{F_{EUV,0}}\right) \text{molecules m}^2/\text{s} \quad (8)$$

where F_{EUV} is the solar EUV flux integrated about wavelength, $F_{EUV,0}$ is its present mean value 6.9×10^{-3} W/m, and ϵ is the heating efficiency of the absorbed EUV set at 0.15 in our simulations. This crude estimate closely follows the escape rates obtained at high basal hydrogen densities (Fig. 6). The difference of a factor can be explained by the partitioning of heating energy to kinetic energy of the escaping gas and less significantly to the conductive loss.

The relationship between the homopause mixing hydrogen ratio and escape rate asymptotically approaches the diffusion-limited flux as the EUV flux increases, as shown in Fig. 6. This is reasonable behavior because the upward transport is regulated by the diffusion process across a layer that lies under the region where outflow acceleration begins. Note that the diffusion-limited flux defines the envelope of the maximum rate of diffusive separation of hydrogen molecules through the background stationary gas, which is composed of heavy species.

The realistic temperature of the upper atmosphere on early Earth remains under debate (e.g., Catling, 2006; Tian et al., 2006). If a higher temperature, as suggested from recent modeling studies (e.g., Lammer et al., 2009, and references therein), is considered at the lower boundary, the escape rate increases expectedly. When the lower boundary density is fixed, the lower boundary pressure increases with temperature. This is equivalent to the increase in the column density of hydrogen, resulting in efficient EUV absorption above the lower boundary.

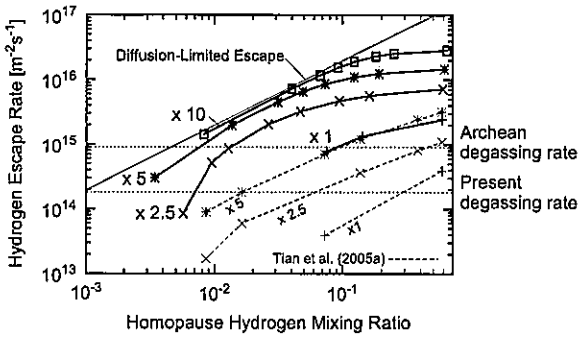

Fig. 6. Hydrogen escape rate as a function of the homopause hydrogen mixing ratio. Numerical solutions at EUV enhancement factors 1, 2.5, 5, and 10 are shown in each solid curve, which shows escape rates significantly larger than those obtained by the previous study (dashed curves Tian et al., 2005a). Volcanic outgassing rates of hydrogen estimated for the modern Earth mantle 1.8×10^{14} H_2 molecules/m^2 (Holland, 2002) and the Archean one (five times the present, Turcotte, 1980) are also shown by the horizontal lines. A comparison of the diffusion-limited escape flux is also shown here.

4.2. Level of hydrogen in early Earth atmosphere

From the Earth's atmosphere today, hydrogen escapes at a rate of approximately $1–1.5 \times 10^{12}$ H_2 molecules/m^2 s (Hunten and Donahue, 1976). For convenience, we use a value equivalent to the H_2 flux because hydrogen takes various chemical forms during its upward transport. A recent estimate of the current volcanic outgassing rate of hydrogen is $1.8 \pm 1.3 \times 10^{14}$ H_2 molecules/m^2 s (Holland, 2002; Martin et al., 2007), although much lower estimates on the order of 10^{12} H_2 molecules/m^2 s are also found in earlier literature (e.g., Walker, 1977; Kasting and Donahue, 1981). An uncertainty in these estimates is the volcanic outgassing rate of water vapor, from which the hydrogen outgassing rate is deduced that provides a typical H_2/H_2O ratio of volcanic gas. If a recent estimate is adopted, there should be some sink of H_2 on Earth because the outgassing rate is greater than the escape rate. In the oxidized Earth atmosphere of today, the oxidation of hydrogen through the photochemical reaction is most likely to be the major removal mechanism of free hydrogen (e.g., Walker, 1978).

During the Archean era (2.5–4.0 Ga), the atmospheric hydrogen level might have been substantially determined by the balance between the outgassing rate and the rate of escape because of the low oxygen level in the atmosphere. On the basis of the compilation of sedimentary rock records that indicate a constraint to the oxidation state of the surface environment, it is widely accepted that the Earth's atmosphere was anoxic before 2.45 Ga (e.g., Canfield, 2005; Holland, 2006). In such an anoxic atmosphere, the rate of the removal of H_2 by photochemical oxidation would be negligible. Therefore, we assume that the atmospheric hydrogen level was regulated by the balance between the rates of outgassing and escape during the Archean era. It should, however, be considered that other chemical pathways to consume hydrogen, including the reduction of the oxidized outgas component such as SO_2 and biological fixation, would also have played an important role on early Earth (e.g., Holland, 2002; Rosing et al., 2010). If these processes work, they should lower the hydrogen level below that achieved by the balance between outgassing and escape.

At the end of the Archean era, the solar EUV radiation was likely 2.5 times higher than the present flux (Ribas et al., 2005). At the same time, the volcanic H_2 outgassing flux may have been five times higher on the basis of thermal history model by Turcotte (1980), implying an outgassing flux 9×10^{14} H_2 molecules/m^2 s (Tian et al., 2005a). Setting these parameters, the balance of our obtained escape flux with the outgassing flux predicts a H_2 mixing ratio about 1.3 vol % at the homopause (Fig. 6). This is smaller than the previous estimate (Tian et al., 2005a) by a factor of nearly 25, although still slightly higher than the estimate derived from the balance using the diffusion-limited flux. Fig. 6 indicates that this value is weakly dependent on estimates of the outgassing rate of hydrogen but strongly dependent on the EUV enhancement factor.

As noted previously, the thermal state of the upper atmosphere of early Earth remains poorly constrained at 250 K, which we assume is a lower estimate for the base of the hydrogen-dominated layer. If a higher temperature is used at the base, the balancing H_2 mixing ratio should decrease because of more efficient escape. We therefore suggest that the H_2 mixing ratio at the homopause was likely below ~1 vol% in the early Earth atmosphere during the Archean era.

Rosing et al. (2010) proposed that the oxidation state of shallow marine Fe-bearing sediments may be used to constrain H_2 levels in the early Earth atmosphere. Assuming thermodynamic equilibrium, the widespread existence of Fe_3O_4 in Archean sediments implies that the corresponding H_2 level was $\sim 2 \times 10^{-2}$ atm at maximum, although the authors speculate that the actual H_2 level might have been much lower than this value because of hydrogen consumption by methanogen biological activity. Rosing et al.'s mineralogical estimate seems fairly consistent with ours, whereas the assumption of thermodynamic equilibrium between the atmosphere and sedimentary minerals needs to be further verified (e.g., Reinhard and Planavsky, 2011).

The low H_2 level might also be consistent with mass independent fractionation (MIF) of sulfur isotopes found in Archean sedimentary rocks (Farquhar et al., 2000). The sulfur MIF records have been accepted as strong evidence for an anoxic Earth atmosphere (e.g., Pavlov and Kasting, 2002) on the basis of geochemical modeling. Currently, the models explaining sulfur MIF implicitly assume that the hydrogen content is kept low by diffusion-limited escape. Because MIF of sulfur was probably caused by photolysis of atmospheric SO_2 (Farquhar et al., 2000, 2001), the Archean atmosphere likely had oxidation states opening the reaction path of SO_2 photolysis. If the atmosphere was abundant in H_2, outgassed SO_2 would have been easily reduced to H_2S or other species leaving few MIF anomalies (Kasting and Howard, 2006). Therefore, the existence of a sulfur MIF signature might constrain the upper limit for the atmospheric hydrogen level. At present, sulfur chemistry in a H_2-rich atmosphere remains an open issue, and its further examination would be worthwhile to constrain the hydrogen content in the early Earth atmosphere.

It is to be noted that the H_2 level at the homopause does not necessarily represent the hydrogen level in the lowermost atmosphere. It may instead represent an approximate net abundance of hydrogen-bearing chemical species at the cold trap, such as H_2O and CH_4, because these species release hydrogen by UV photolysis in the stratosphere unless UV is effectively shielded by other component(s). Therefore, our results imply that the Earth's atmosphere might have contained less than ~1 vol% of equivalent H_2 as a hydrogen-bearing species during the Archean era. According to the recent calculation of the greenhouse effect in the early Earth's atmosphere (Haqq-Misra et al., 2008), atmospheric methane, an expected major species hosting hydrogen in the early atmosphere, may have helped to warm the Earth by ~10 K in the mixing ratio from 10^{-3} to 10^{-2}. This may have helped to prevent global freezing of the early Earth under the faint Sun, but there is a need for other warming agent(s) to explain the high global temperature suggested by geological records (Haqq-Misra et al., 2008).

5. Conclusions

We have carried out numerical simulations of the hydrodynamic escape of hydrogen by adopting a high-accuracy scheme for

solving the one-dimensional advection equation. According to our results, EUV heating energy is effectively converted to mechanical energy of the outflow gas in contrast to an earlier study that employed another numerical scheme. The obtained numerical solutions more adequately reproduce the escape flow because they satisfy the laws of conservation of mass and energy with a small error. Our result suggests that the homopause mixing ratio of hydrogen in the early Earth atmosphere was likely maintained lower than ~1 vol% during Archean even when the higher volcanic degassing rate of hydrogen was considered. This appears consistent with geological evidence implying low hydrogen content in the early Earth atmosphere.

Acknowledgements

We thank Ko-ichiro Sugiyama and EPnetFaN members for providing us computation environment and technical advice. We also thank anonymous reviewers for constructive comments. The physics of diffusive separation of gas species is significantly improved by the suggestion from a reviewer. This work was supported by MEXT KAKENHI Grant number 23103003.

Appendix A. Estimation of homopause hydrogen mixing ratio

The homopause hydrogen mixing ratio is estimated for a two-component atmosphere with the following assumptions: (1) The homopause is located below the altitude of the lower boundary of outflow calculation. (2) Between the homopause and the lower boundary, the atmosphere is isothermal (at 250 K), and the diffusive separation of H_2 through background heavy gas occurs. (3) The heavy species has no vertical flux. (4) At the lower boundary, H_2 is dominant: the volume mixing ratio of H_2:heavy species is 10:1. (5) The homopause density is maintained at a characteristic constant value independent of the hydrogen flow. These assumptions follow those of Tian et al. (2005a) except in the detail of assumption (2), in which the effects of the H_2 diffusive flux on the gas density profile are not considered. These effects were considered in our study.

Subscripts 1 and 2 denote the physical quantities of light species and heavy ones, respectively. Following Hunten (1973) and given the above assumptions, the diffusion equations for both species having a vertical velocity w_i are

$$w_1 - w_2 = -\frac{b_{12}}{n_2}\left(\frac{1}{n_1}\frac{dn_1}{dz} + \frac{m_1 g}{kT}\right) \tag{A.1}$$

$$w_2 - w_1 = -\frac{b_{12}}{n_1}\left(\frac{1}{n_2}\frac{dn_2}{dz} + \frac{m_2 g}{kT}\right) \tag{A.2}$$

where g is the gravity, b_{12} is the binary diffusion coefficient, n_i is the number density, and z is the altitude.

When the heavy species remains stationary, i.e., $w_2 = 0$, Eq. (A.1) may be modified by using the upward flux of light species, $\phi_1 = n_1 w_1$

$$\phi_1 = -b_{12} f_1 \left(\frac{1}{f_1}\frac{df_1}{dz} + \frac{1}{n_2}\frac{dn_2}{dz} + \frac{m_1 g}{kT}\right) \tag{A.3}$$

where $f_1 = n_1/n_2$. From Eq. (A.2), the distribution of n_2 is expressed by

$$\frac{1}{n_2}\frac{dn_2}{dz} = -\frac{1}{H_2} \tag{A.4}$$

where

$$H_2 = \left(\frac{m_2 g}{kT} - \frac{\phi_1}{b_{12}}\right)^{-1}. \tag{A.5}$$

This formula indicates that the upward flux of light species has an effect of stretching the scale height, H_2, of heavy species. Substituting Eq. (A.4) in (A.3), the distribution of light species relative to the heavy one is expressed as

$$\frac{df_1}{dz} = -\frac{\phi_1(1+f_1) + \frac{(m_1 - m_2)g b_{12} f_1}{kT}}{b_{12}}. \tag{A.6}$$

Then

$$f_1(z) = c + (f_1(z_0) - c)\exp\left\{\frac{z - z_0}{H_{12}}\right\} \tag{A.7}$$

where z_0 is the reference altitude and

$$H_{12} = \left(\frac{(m_2 - m_1)g}{kT} - \frac{\phi_1}{b_{12}}\right)^{-1}, \quad c = \frac{\phi_1 H_{12}}{b_{12}}. \tag{A.8}$$

From Eq. (A.4)

$$n_2(z) = n_2(z_0)\exp\left\{-\frac{z - z_0}{H_2}\right\}. \tag{A.9}$$

Considering species 1 and 2 to be H_2 and N_2, respectively, the homopause hydrogen mixing ratio is estimated by the following procedure. First, z_0 is set to be the altitude of the lower boundary of outflow calculation, then we substitute the lower boundary hydrogen density to $n_1(z_0)$, $f_1(z_0) = 10$, and the hydrogen outflow rate to ϕ_1 in Eqs. (A7) and (A9). Here $b_{12} = 1.71 \times 10^{21}\,\mathrm{m^{-1}\,s^{-1}}$ at T=250 K (Hunten, 1973) and g=9.5 m/s^2 considering the layer to be ~100 km above the Earth's surface. Second, the homopause altitude $z = z_h$ (in practice, the difference $z_h - z_0$) is numerically obtained so as to satisfy $n_1(z_h) + n_2(z_h) = (f_1(z_h) + 1)n_2(z_h) = n_{homo}$, where the homopause gas density n_{homo} is considered to be $10^{19}\,\mathrm{m^{-3}}$ (Tian et al., 2005a). The homopause hydrogen mixing ratio, x_1, is then obtained as $x_1 = f_1(z_h)/(1 + f_1(z_h))$.

Note that Tian et al. (2005a) neglected the effects of the upward flux of hydrogen. This approximation may not be a serious error when the hydrogen flux is as small as they have estimated, but it is inappropriate to apply to our simulation runs. Because we found that the upward hydrogen flux has an effect of stretching the scale height of the heavy species, the homopause hydrogen mixing ratio becomes larger when this effect is considered.

By taking $df_1/dz \to 0$ from Eq. (A.6), the diffusion-limited escape flux of light species is acquired as

$$\phi_{1,lim} = \frac{(m_2 - m_1)g b_{12} x_1}{kT}. \tag{A.10}$$

This implies that the limiting flux is achieved when vertical fractionation between gas species is minimal. In Fig. 6, our obtained flux is always lower than the limiting flux for each homopause mixing ratio. This is consistent with our assumption that the hydrogen upward transport obeys the diffusion process before reaching the high altitude region where hydrodynamic acceleration occurs.

References

Avakyan, S.V., Il'in, R.N., Lavrov, V.M., Ogurtsov, G.N., 1998. Collision Processes and Excitation of UV Emission from Planetary Atmospheric Gases: A Handbook of Cross Sections. Gordon and Breach Science Publishers, Amsterdam.

Canfield, D.E., 2005. The early history of atmospheric oxygen: homage to Robert M. Garrels. Annu. Rev. Earth Planet. Sci. 33, 1–36.

Catling, D.C., 2006. Comment on "a hydrogen-rich early Earth atmosphere". Science 311, 38.

de Sterck, H., Abeele, D.V., Poedts, S., Deconinck, H., et al., 2001. Stationary two-dimensional magnetohydrodynamic flows with shocks: characteristic analysis and grid convergence study. J. Comput. Phys. 166, 28–62.

Farquhar, J., Bao, H., Thiemens, M.H., 2000. Atmospheric influence of Earth's earliest sulfur cycle. Science 289 (5480), 756–758.

Farquhar, J., Savarino, J., Airieau, S., Thiemens, M.H., 2001. Observation of wavelength-sensitive mass-independent sulfur isotope effects during SO_2

photolysis: implications for the early atmosphere. J. Geophys. Res. 106, 32829–32832.
Hanley, H.J.M., Intemann, H., McCarty, R.D., 1970. The viscosity and thermal conductivity of dilute gaseous hydrogen from 15 to 5000 K. J. Res. Nat. Bur. Stand., Sect. A 74, 331–353.
Haqq-Misra, J.D., Domagal-Goldman, S.D., Kasting, P.J., Kasting, J.F., 2008. A revised, hazy methane greenhouse for the Archean Earth. Astrobiology 8, 1127–1137.
Holland, H.D., 2002. Volcanic gases, black smokers, and the great oxidation event. Geochim. Cosmochim. Acta 66, 3811–3826.
Holland, H.D., 2006. The oxygenation of the atmosphere and oceans. Philos. Trans. R. Soc. B: Biol. Sci. 361, 903–915.
Hunten, D.M., 1973. The escape of light gases from planetary atmospheres. J. Atmos. Sci. 30, 1481–1494.
Hunten, D.M., Donahue, T.M., 1976. Hydrogen loss from the terrestrial planets. Annu. Rev. Earth Planet. Sci. 4, 265–292.
Kasting, J.F., Donahue, T.M., 1981. Evolution of oxygen and ozone in Earths atmosphere. In: Life in the Universe, Proceedings of the Conference, Moffett Field, CA, June 19, 20, 1979, Cambridge, MA, MIT Press, John Billingham (ed.), vol. 1, pp. 149–162.
Kasting, J.F., Howard, M.T., 2006. Atmospheric composition and climate on the early Earth. Philos. Trans. R. Soc. B: Biol. Sci. 361 (1474), 1733–1742.
Kasting, J.F., Pollack, J.B., 1983. Loss of water from Venus. I. Hydrodynamic escape of hydrogen. Icarus 53, 479–508.
Lammer, H., Kasting, J.F., Chassefière, E., Johnson, R.E., Kulikov, Y.N., Tian, F., 2009. Atmospheric escape and evolution of terrestrial planets and satellites. Space Sci. Rev. 139, 399–436.
LeVeque, R.J., 1992. Numerical Methods for Conservation Laws. Birkhäuser, Berlin.
Martin, R.S., Mather, T.A., Pyle, D.M., 2007. Volcanic emissions and the early Earth atmosphere. Geochim. Cosmochim. Acta 71, 3673–3685.
Parker, E.N., 1963. Interplanetary Dynamical Processes. Interscience Publishers, New York.
Pavlov, A.A., Kasting, J.F., 2002. Mass-independent fractionation of sulfur isotopes in archean sediments: strong evidence for an anoxic archean atmosphere. Astrobiology 2 (1), 27–41.
Reinhard, C.T., Planavsky, N.J., 2011. Mineralogical constraints on precambrian pCO_2. Nature 474, E1–E2.
Ribas, I., Guinan, E.F., Güdel, M., Audard, M., 2005. Evolution of the solar activity over time and effects on planetary atmospheres. I. High-energy irradiances 1–1700 Å. Astrophys. J. 622, 680–694.
Rosing, M.T., Bird, D.K., Sleep, N.H., Bjerrum, C.J., 2010. No climate paradox under the faint early Sun. Nature 464, 744–747.
Sekiya, M., Nakazawa, K., Hayashi, C., 1980. Dissipation of the primordial terrestrial atmosphere due to irradiation of the solar EUV. Prog. Theor. Phys. 64, 1968–1985.
Tian, F., Toon, O.B., Pavlov, A.A., 2006. Response to comment on "a hydrogen-rich early Earth atmosphere". Science 311, 38.
Tian, F., Toon, O.B., Pavlov, A.A., de Sterck, H., 2005a. A hydrogen-rich early Earth atmosphere. Science 308, 1014–1017.
Tian, F., Toon, O.B., Pavlov, A.A., de Sterck, H., 2005b. Transonic hydrodynamic escape of hydrogen from extrasolar planetary atmospheres. Astrophys. J. 621, 1049–1060.
Turcotte, D.L., 1980. On the thermal evolution of the Earth. Earth Planet. Sci. Lett. 48, 53–58.
Walker, J.C.G., 1977. Evolution of the Atmosphere. Macmillan and Collier Macmillan, New York and London.
Walker, J.C.G., 1978. Oxygen and hydrogen in the primitive atmosphere. Pure Appl. Geophys. 116, 222–231.
Watson, A.J., Donahue, T.M., Walker, J.C.G., 1981. The dynamics of a rapidly escaping atmosphere: applications to the evolution of Earth and Venus. Icarus 48, 150–166.
Woods, T.N., Rottman, G.J., 2002. Solar ultraviolet variability over time periods of aeronomic interest. In: Geophysical Monograph 130. American Geophysical Union, Washington, D.C, M. Mendillo, A. Nagy, and J. H. White (Eds.) pp. 221–234.
Yabe, T., Aoki, T., 1991. A universal solver for hyperbolic equations by cubic-polynomial interpolation. I. One-dimensional solver. Comput. Phys. Commun. 66, 219–232.
Yabe, T., Tanaka, R., Nakamura, T., Xiao, F., 2001a. An exactly conservative semi-Lagrangian scheme (CIP-CSL) in one dimension. Mon. Weather Rev. 129, 332–344.
Yabe, T., Xiao, F., Utsumi, T., 2001b. The constrained interpolation profile method for multiphase analysis. J. Comput. Phys. 169, 556–593.

The Astrophysical Journal, 812:165 (11pp), 2015 October 20 doi:10.1088/0004-637X/812/2/165

RAPID WATER LOSS CAN EXTEND THE LIFETIME OF PLANETARY HABITABILITY

Takanori Kodama[1], Hidenori Genda[2], Yutaka Abe[1], and Kevin J. Zahnle[3]
[1] Department of Earth and Planetary Science, The University of Tokyo, Tokyo 113-0033, Japan; koda@eps.s.u-tokyo.ac.jp
[2] Earth-Life Science Institute, Tokyo Institute of Technology, Tokyo 152-8550, Japan
[3] Space Science and Astrobiology Division, NASA Ames Research Center, California 94035, USA
Received 2015 July 31; accepted 2015 September 11; published 2015 October 20

ABSTRACT

Two habitable planetary states are proposed: an aqua planet like the Earth and a land planet that has a small amount of water. Land planets keep liquid water under larger solar radiation compared to aqua planets. Water loss may change an aqua planet into a land planet, and the planet can remain habitable for a longer time than if it had remained an aqua planet. We calculate planetary evolution with hydrogen escape for different initial water inventories and different distances from the central star. We find that there are two conditions necessary to evolve an aqua planet into a land planet: the critical amount of water on the surface ($M_{\rm ml}$) consistent with a planet being a land planet, and the critical amount of water vapor in the atmosphere ($M_{\rm cv}$) that defines the onset of the runaway greenhouse state. We find that Earth-sized aqua planets with initial oceans <10% of the Earth's can evolve into land planets if $M_{\rm cv} = 3$ m in precipitable water and $M_{\rm ml} = 5\%$ of the Earth's ocean mass. Such planets can keep liquid water on their surface for another 2 Gyr. The initial amount of water and $M_{\rm cv}$ are shown to be important dividing parameters of the planetary evolution path. Our results indicate that massive hydrogen escape could give a fresh start as another kind of habitable planet rather than the end of its habitability.

Key words: planets and satellites: atmospheres – planets and satellites: oceans – planets and satellites: terrestrial planets

1. INTRODUCTION

The advancement of observation technologies has facilitated an increase in the number of extrasolar planets detected. Some of these planets are considered to be terrestrial or rocky planets based on the relationship between their mass and radius (e.g., Batalha et al. 2013). Although it is not clear how much water exists on these planets, the marked variations in their bulk densities imply that considerable variation exists in the amount of water on these extrasolar terrestrial planets. The habitability of extrasolar planets has been actively discussed (e.g., Borucki et al. 2013). In particular, the stability of liquid water on the planetary surface has been extensively examined as liquid water is considered to be essential for the origin and evolution of life.

It is typical to assume that habitable planets, like the Earth, have liquid water oceans. Discussions of planetary habitability and the duration of planetary habitability (known as continuous habitability) have focused on the stability and evolution of such oceans. If the insolation that a planet covered with an ocean receives from a central star is not too high, then the upper atmosphere of such a planet would have a very low mixing ratio of water vapor due to the presence of a cold trap. Under these conditions, hydrogen escape is rather slow and partly dependent on the presence of other gases containing hydrogen (e.g., methane). As the luminosity of the central star increases with time, the planet gets warmer and the mixing ratio of water vapor in the upper atmosphere increases. When the central star gets bright enough, the cold trap disappears and the mixing ratio of water vapor in the upper atmosphere becomes high enough to cause rapid water loss. This planetary state is called the moist greenhouse state (Kasting et al. 1993). Somewhat later, the star becomes bright enough to trigger the runaway greenhouse effect: because water vapor is a strong greenhouse gas, a positive feedback works until all liquid water evaporates in the runaway greenhouse state (e.g., Abe & Matsui 1988; Kasting 1988; Zahnle et al. 1988; Nakajima et al. 1992).

The habitable zone (HZ) has been defined as the region around the central star where liquid water is stable on the planetary surface (e.g., Kasting et al. 1993; Kopparapu et al. 2013). The HZs for various planetary masses around central stars with various spectral types are also investigated (e.g., Kopparapu et al. 2014). Two concepts have been proposed to describe the inner edge of the HZ. One is to define it as the inner edge of the instantaneous HZ; that is, it does not matter how long the planet remains habitable. The other defines it as the inner edge of the continuously habitable zone (CHZ), by which it is meant that a given planet has been in the HZ from the time it was formed until present. The onset of the runaway greenhouse effect determines the instantaneous HZ. When considering the long-term stability of liquid water on the planetary surface, the water loss from the planet is an important consideration. Under the moist greenhouse state, hydrogen escapes rapidly. If the escape of hydrogen occurs rapidly enough, then the inner edge of the CHZ may be characterized by the onset of the moist greenhouse state (e.g., Kasting et al. 1993; Kopparapu et al. 2013).

It has recently been shown that the climates of planets with small or large amounts of water will differ markedly from each other (Abe et al. 2005, 2011). Using a general circulation model, Abe et al. (2011) examined the HZs of land planets. They found that the local balance between the precipitation and evaporation of water is controlled by the distribution of liquid water on the planetary surface. Liquid water typically accumulates in the cooler regions of a planet; that is, high-latitude regions and low-latitude regions typically become dry. Given that there is no upper limit on planetary radiation in dry areas (e.g., Nakajima et al. 1992), a land planet can maintain liquid water on its surface at a much larger incident of stellar radiation than is possible on aqua planets. In addition, the

mixing ratio of water vapor in the upper atmosphere is very low on land planets, which means that the hydrogen escape flux should also be very low. However, the liquid water on a land planet will evaporate if the incident stellar radiation is high enough. This radiation is called the threshold of the runaway greenhouse for a land planet. According to Abe et al. (2011), this is 415 W m^{-2}. The inner edge of the HZ for a land planet is determined by this threshold, which corresponds to 0.77 AU in our solar system. For aqua planets, the onset of the runaway greenhouse effect is about 375 W m^{-2} (Leconte et al. 2013). Therefore, the inner edge of the HZ for a land planet is much closer to the central star than that for an aqua planet.

The only difference between a land planet and an aqua planet is the amount of water that the planets have. If an aqua planet evolves into a land planet by rapid water loss before all of the water on its surface evaporates, then the lifetime of liquid water on its surface can be extended because land planets are highly resistant to both water loss and complete evaporation. In this way, rapid water loss might lead to maintaining, rather than ending, the habitable world.

When Abe et al. (2011) discussed the evolution from an aqua planet to a land planet, they assumed that the aqua planet can evolve to the land planet when the planetary surface becomes almost completely dry before the onset of the runaway greenhouse made the planet uninhabitable. They estimated how much water could escape from a planet in Earth's orbit using models that assumed both constant (0.3) and variable albedos. For the constant albedo scenario, an aqua planet with the Earth's ocean mass did not lose all of its water before the onset of the runaway greenhouse, because the duration of the moist greenhouse state was too short. Such planets lapsed into the runaway greenhouse state and became uninhabitable. Conversely, in the variable albedo scenario, the increase of the albedo due to Rayleigh scattering prolonged the duration of the moist greenhouse state. In this case, an aqua planet with the Earth's ocean mass lost almost all of its surface water before the onset of the runaway greenhouse state, and then evolved into a land planet. Here, we investigate the evolution from the aqua planet mode to the land planet mode invoking more realistic transition conditions for the amount of water vapor in the atmosphere and the amount of water on the planetary surface.

In the evolution from an aqua planet to a land planet, there is a race between rapid water loss and the increase in the luminosity from the central star that triggers the runaway greenhouse effect. Whether or not an aqua planet safely negotiates the evolutionary path from the aqua planet mode to the land planet mode is determined by the outcome of this race. Abe et al. (2011) only considered the evolution from aqua planet mode to the land planet mode for planets that have one Earth ocean mass in either the Earth's orbit or Venus's orbit. However, discoveries of many extrasolar planets have revealed the existence of a great diversity of planet types, and we consider that the amount of water that planets have should reflect this diversity.

We therefore systematically investigated evolutionary scenarios in which aqua planets can evolve into land planets under conditions with different initial amounts of water and distances from the central star. We discuss the evolution from aqua planet mode to land planet mode and re-evaluate the inner edge of the HZ. In addition, we investigate the effect of varying the transition conditions that determine whether an aqua planet can evolve into a land planet.

2. EVOLUTION MODEL

In this paper, we consider three planetary states (a water - planet state, a steam planet state, and a dry planet state), and two modes for a water planet state (an aqua planet mode and a land planet mode). Here, we describe the main characteristics of these states and modes in advance.

In a water planet state, liquid water is stably present on the planetary surface. In most previous studies, planets in the aqua planet mode are considered to be potentially habitable (e.g., Kasting et al. 1993; Kopparapu et al. 2013). In these studies, it has been implicitly assumed that planets have a large amount of water (e.g., the present Earth's oceans). On the other hand, if planets have a small amount of water, then they are considered to be in land planet mode (Abe et al. 2011).

Planets in a steam planet state have water vapor in their atmosphere but no liquid water on their surface. If planets with liquid water receive radiation exceeding the threshold for the runaway greenhouse effect, then all of the liquid water on their surface will evaporate and these planets will evolve into a steam planet state.

In a dry planet state, planets have no liquid water on their surface and no water vapor in their atmosphere. Dry planets are not the same as land planets, as the latter have a small amount of liquid water on their surface. If water vapor escapes from a steam planet, then it becomes a dry planet and both steam planets and dry planets are considered to be uninhabitable.

Here we simulate the changes of the amount of water on the planetary surface and in the atmosphere using a numerical model. In Section 2.1, we describe the basic processes that cause changes in the amount of atmospheric and surface water. The transition conditions from aqua planet mode to land planet mode are described in Section 2.2. In Section 2.3, we describe the hydrodynamic escape of hydrogen as a rapid water loss. The escape flux of hydrogen molecules depends on the mixing ratio of hydrogen molecules in the upper atmosphere and the evolution of the luminosity and extreme ultraviolet radiation (EUV) flux of the central star, which are described in Sections 2.4 and 2.5, respectively.

2.1. The Processes that Change the Amount of Water

The initial amount of water on terrestrial planets just after their formation is not known. We treat the initial amount of water as a parameter, i.e., we consider planets with various initial amounts of water. The amount of water on the surface of a planet would change through interaction with the planetary interior through processes such as subduction of hydrous minerals, outgassing of water at mid-ocean ridges and arcs, and so on. For the present Earth, the ingassing flux of water is estimated to be 5×10^{22}–1.1×10^{23} mol Gyr^{-1} (Rea & Ruff 1996; Javoy 1998), and the degassing flux of water is estimated to be 2.2×10^{22}–1.1×10^{23} mol Gyr^{-1} (Bounama et al. 2001; Hilton et al. 2002). Ingassing and outgassing fluxes in water appear to be in equilibrium on the present Earth. The difference between the ingassing and outgassing water fluxes is on the order of 10^{22} mol Gyr^{-1}. By comparison, once the rapid escape of water into space starts as the central star evolves, the escape flux of water vapor exceeds 10^{23} mol Gyr^{-1} (see Sections 3.1 and 3.2). For simplicity, we assume that the

change in the total amount of water on a planet is attributed solely to the loss of water into space.

We assume that the amount of water decreases via the hydrodynamic escape of hydrogen molecules. The change in the amount of water is given by

$$\frac{dM_{H_2O}}{dt} = -\phi_{esc} \quad (1)$$

where M_{H_2O} is the total amount of water and ϕ_{esc} is the escape flux of molecular hydrogen. The escape process of hydrogen is described in Section 2.3.

The amount of water vapor in the atmosphere depends on the atmosphere model used. For the aqua planet and land planet modes, the amount of water vapor is estimated by using the one-dimensional (1D), cloud-free, radiative-convective atmospheric model developed by Abe & Matsui (1988) and using the results obtained by Abe et al. (2011), respectively. The amount of water on the surface can then be estimated by subtracting the amount of water in the atmosphere from the total amount of water on the planet. An aqua planet is considered to evolve into a land planet if the amounts of water in both reservoirs meet specific transition conditions, described in detail in Section 2.2.

Planetary albedo, which plays an important role in climate, depends on the properties of the planetary surface and atmosphere. In our numerical simulation, we fixed the albedo of the planetary surface at 0.3, which is typical of deserts. When the amount of water vapor increases due to warming caused by an increase in the luminosity of the central star, the atmosphere gets denser and light from the central star is scattered more efficiently. Therefore, we also consider the scattering albedo for an aqua planet. Since the scattering albedo is negligible for a land planet (if the effect of dust is not considered), we consider that the planetary albedo for a land planet to be 0.3.

Here, we assume that the planets have zero obliquity and eccentricity, with a mass and a radius equivalent to those of the Earth. In the planetary atmosphere, 1 bar of the present Earth's atmosphere is considered as the background atmosphere. Except for water vapor, no changes in atmospheric components were considered in this study. It is possible that the carbon cycle exists on Earth-like planets. The carbon cycle in the presence of liquid water provides a negative feedback on surface temperature that maintains a stable climate (Walker et al. 1981). However, in the case of a central star with high luminosity, the feedback breaks down because there is too little CO_2 in the atmosphere to affect changes in surface temperatures owing to efficient chemical erosion (rapid fixing of CO_2 as carbonate rock). Therefore, the evolution of the atmosphere is driven almost entirely by changes in the amount of water in the planetary atmosphere.

2.2. Transition Conditions

Abe et al. (2011) assumed that an aqua planet with the present Earth's ocean mass could evolve to land planet mode just before all of its water is lost, and before there was a rapid increase in surface temperatures due to the runaway greenhouse effect. Under such transition conditions, it is possible that a planet with a large amount of water in its atmosphere can evolve from an aqua planet to a land planet. However, if the planet has a large amount of water vapor in its atmosphere before the loss of water, then it may maintain a heated state during atmospheric escape. Under these conditions, such a planet may not evolve into a land planet, even if it loses most of the water on the surface. It is therefore necessary to consider the amount of water vapor in the planetary atmosphere. We therefore imposed several conditions on the amounts of water on the planetary surface and the amounts of water vapor in its atmosphere for the transition from an aqua planet to land planet mode.

However, one problem is that we do not know the amount of water vapor in an aqua planet's atmosphere just before the threshold for the runaway greenhouse effect is reached. In order to evolve into land planet mode, there should be an upper limit to the amount of water in the atmosphere; we treat this upper limit to the amount of water as a parameter, which we denote as M_{cv} and refer to as "the critical amount of vapor for the runaway greenhouse effect." From previous studies (Abe & Matsui 1988; Kasting 1988; Goldblatt et al. 2013; Kopparapu et al. 2013), it appears that when M_{cv} is expressed as a column it is equivalent to 1–10 m of precipitable water. In this paper, to illustrate typical results, an M_{cv} of 3 m was used for our standard model.

Another important parameter is the maximum amount of water that a land planet can have and still behave as a land planet. We consider the distribution of surface water from the results of Abe et al. (2011). Surface water on a land planet is typically located at latitudes above 60°, which corresponds to 10% of the entire planetary surface. According to percolation theory, for any given area, only half of that area is required to form a connected area. The maximum unconnected oceanic area is thus half of the area above 60° latitude, which corresponds to 5% of the entire planetary surface. If planetary topography is ignored, then the typical amount of water on a land planet is 5% of the present Earth's ocean mass. If a planet has more water, that water will extend equatorward of 60° latitude. Therefore, we assume that 5% of the present Earth's ocean mass on the planetary surface approximates the transition conditions that are required for the maximum amount of water required for an aqua planet to evolve into a land planet. We refer to this condition "the maximum liquid water mass for a land planet mode," which we denote as M_{ml}. If the amounts of water on the planetary surface and in the atmosphere meet these conditions, then the aqua planet can evolve into a land planet. We treat $M_{ml} = 0.05\,M_{oc}$ as our standard case, but we also treat M_{ml} as a parameter that varies from 0.01 to 0.1 M_{oc}, where M_{oc} is the amount of the present Earth's ocean (8.4×10^{22} moles). In Section 4.1, we discuss the evolution of an aqua planet under several transition conditions.

2.3. Water Loss

Escape is an important process in atmospheric evolution. In this study, we consider the hydrodynamic escape of hydrogen molecules because it is the fastest process of hydrogen escape and has the most potential to decrease the water reservoir of a planet. We will address two major bottlenecks to hydrogen molecular escape from the planetary atmosphere. The first is the energy source required to drive the escape of hydrogen molecules. The main source of energy for escape is EUV, usually defined by $\lambda < 100$ nm from the central star, which is directly absorbed by hydrogen molecules and atoms. When the escape flux is controlled by the EUV flux, the escape is said to be "energy-limited." The other major bottleneck is the diffusion of hydrogen-containing molecules through the background

atmosphere to reach the altitudes where escape occurs. When escape is controlled by the diffusion of molecules through the upper atmosphere, then the escape is referred to as "diffusion-limited." We calculate escape fluxes in both modes and adopted the smaller one as the actual escape flux. Other possible bottlenecks, such as the photon-limited photochemistry that converts H_2O to H_2, magnetospheric drag, and radiative cooling by ions (e.g., H_3^+) and molecules embedded in the outflowing wind, are less well established and will be neglected here.

The escape flux of the diffusion-limited escape mode depends on the total mixing ratio of hydrogen-containing species in the upper atmosphere (Walker 1977, p. 164). The diffusion-limited escape flux (ϕ_d) of hydrogen molecules is given by

$$\phi_d = f_T(H_2)\frac{b(m_a - m_i)g}{kT_{str}} \quad (2)$$

where f_T (H_2) is the total mixing ratio of hydrogen molecules in all forms at homopause (f_T (H_2) = $f(H_2O) + f(H_2) + 2f$ (CH_4) + ⋯), T_{str} is the temperature in the stratosphere (T_{str} = 200 K), b is the binary diffusion coefficient between the background atmosphere and H_2 ($b = 1.9 \times 10^{19}$ (T_{str}/300 K)$^{0.75}$ cm^{-1} s^{-1} for H_2 in air), g is the acceleration due to gravity, k is Boltzmanns constant, and m_a and m_i are the average molecular masses of the background atmosphere and the molecular mass of hydrogen, respectively. We assumed that the major carrier of hydrogen is water vapor. Therefore, we adopt f_T (H_2) = $f(H_2O)$, where $f(H_2O)$ is the mixing ratio of water vapor in the upper atmosphere.

An escape flux is limited by EUV flux if the planetary upper atmosphere is hydrogen-rich atmosphere. The energy-limited escape flux (ϕ_e) is given by Watson et al. (1981) as

$$\phi_e = \frac{\epsilon S_{EUV} r_p}{m_i G M_p} \quad (3)$$

where ϵ is the escape efficiency, S_{EUV} is the EUV radiation flux, G is the gravitational constant, r_p is the radius of the planet, and M_p is the planetary mass. According to Watson et al. (1981), the escape efficiency ranges from 0.15 to 0.3; we adopted 0.15 as the escape efficiency. Since we used Earth-sized planets in this study, we used the Earth's radius and mass for r_p and M_p, respectively.

Atmospheric H_2O molecules are dissociated by UV radiation from the central star (via $H_2O + h\nu \rightarrow H + OH$) (e.g., Brinkmann 1969). Hydrogen molecules are transported to the upper atmosphere, where EUV radiation reaches, and are heated by such radiation. The resultant hydrogen molecules escape to space (e.g., Kasting et al. 1984). When hydrogen escapes, the oxygen left behind can build up in the planetary atmosphere. Because we assume diffusion-limited escape, oxygen does not escape. If an amount of water equivalent to the Earth's ocean mass escapes, approximately 240 bars of O_2 will remain (Kasting 1997). In this study, we assume that all of this oxygen is absorbed by the crust of the planet.

2.4. The Mixing Ratio of Water Vapor in the Upper Atmosphere

In order to estimate the escape flux of hydrogen molecules in the diffusion-limited escape mode, we need the mixing ratio of water vapor in the upper atmosphere. For the aqua planet mode, we estimate the mixing ratio of water vapor in the upper atmosphere as described by Abe & Matsui (1988). Figure 1 shows the mixing ratio of water vapor in the upper atmosphere as a function of the incident stellar radiation. It is very low until the cold trap region disappears. The escape flux of hydrogen molecules in the diffusion-limited escape mode is thus expected to be very low due to the very low mixing ratio of water vapor under these conditions. If an aqua planet receives incident solar flux from the central star that is sufficiently strong to eliminate the cold trap, the upper atmosphere will become humid and the escape of hydrogen molecules will be rapid.

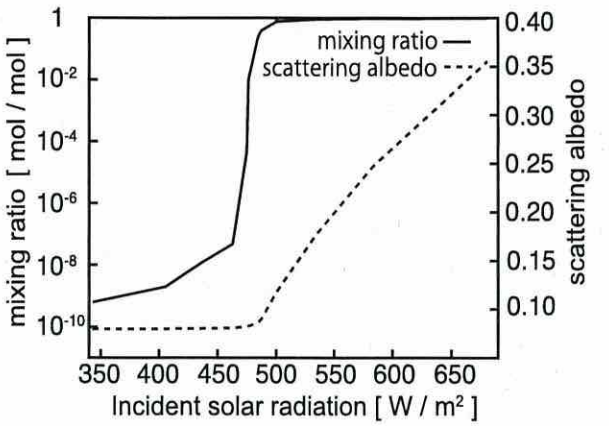

Figure 1. Mixing ratio of water vapor in the upper atmosphere and scattering albedo by water vapor for an aqua planet as a function of the incident solar radiation. The mixing ratio of water vapor increases rapidly at around 470 W m^{-2}. In our model, we assume a constant albedo for the planetary surface (0.3) and the scattering albedo by water vapor, which varies with the amount of water vapor in the atmosphere.

For the land planet mode, we estimate the mixing ratio of water vapor in the upper atmosphere using the results of Abe et al. (2011). The mixing ratio for a land planet also increases with the increasing luminosity of the central star. In a case where the insolation from the central star is above the threshold for the runaway greenhouse effect for a land planet, the upper atmosphere becomes humid and the escape of hydrogen is rapid (Figure 2).

2.5. Stellar Evolution

We consider the evolution of total luminosity and the EUV flux of a star because the escape flux of hydrogen molecules depends strongly on both. The total luminosity of a star increases over time. We treated the central star as a solar-type star. For the luminosity for a G-type star, we use the following expression given by Gough (1981):

$$S(t) = \left[1 + \frac{2}{5}\left(1 - \frac{t}{t_\odot}\right)\right]^{-1} S_\odot \quad (4)$$

where $S(t)$ is the incident stellar flux for a G-type star at 1 AU as a function of time, t is the time in Gyr,$t_\odot$ is the age of the Sun ($t_\odot$ = 4.5 Gyr), and $S_\odot$ is the solar constant ($S_\odot$ = 1366 W m^{-2}).

Since the EUV flux for young stars is stronger than that for old stars, we employed the following expression of Lammer

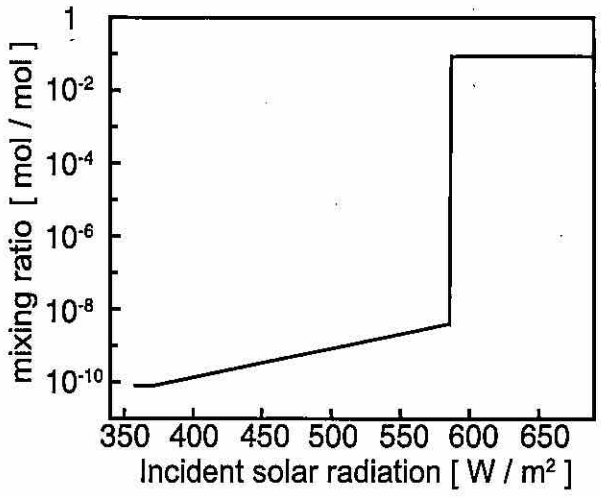

Figure 2. Mixing ratio of water vapor in the atmosphere for a land planet as a function of the incident solar radiation. If a land planet receives the incident solar radiation exceeding the threshold of the runaway greenhouse (585 W m^{-2}) for a land planet, then the mixing ratio of water vapor is high. In our model, we consider the constant albedo (0.3) throughout a period of time of a land planet because there is little water vapor before the threshold of the runaway greenhouse for a land planet.

et al. (2009) for a G-type star:

$$L_{\rm EUV} = \begin{cases} 0.375 L_0 t^{-0.425} & (t \leqslant 0.6\ {\rm Gyr}) \\ 0.19 L_0 t^{-1.69} & (t > 0.6\ {\rm Gyr}) \end{cases} \quad (5)$$

where $L_{\rm EUV}$ is the luminosity of EUV in $\rm W\,s^{-1}$, and $L_0 = 10^{22.35}$ W. The relation between the luminosity and the flux is given by $S_{\rm EUV} = L_{\rm EUV}/4\pi a^2$, where a is a distance from the central star to the planet in meters.

3. RESULTS

3.1. Effect of the Initial Amount of Water

In this section, we examine typical results obtained by our numerical simulations describing the planetary evolution. Figure 3 shows the evolution of a planet with the present Earth's ocean at the beginning ($M_{\rm ini} = 1.0\,M_{\rm oc}$) at $a = 0.80$ AU, where $M_{\rm ini}$ is the initial amount of water.

As long as the luminosity of the central star is low (<3 Gyr), the mixing ratio of water vapor in the upper atmosphere remains low (Figure 3(a)). Consequently, the escape flux of water vapor in the diffusion-limited escape mode also remains extremely low (Figure 3(b)) and the amount of water on the surface hardly changes during this period (Figure 3(c)). The atmosphere gets wetter as the luminosity of the central star increases over time, and after 3 Gyr, the mixing ratio of water vapor in the upper atmosphere increases rapidly. The increase in the mixing ratio in the upper atmosphere enhances the escape flux of water vapor in the diffusion-limited escape mode and decreases the amount of water on the planet (Figure 3(c)). In this calculation, this planet does not satisfy the transition conditions from aqua planet mode to land planet mode because the amount of surface water exceeds the maximum water mass for land planet mode ($0.05\,M_{\rm oc}$) when the average column mass of atmospheric water vapor reaches $M_{\rm cv}$ (i.e., a depth of 3 m), which is the critical amount for the runaway greenhouse effect. Therefore, the planet remains in aqua planet mode until the onset of the runaway greenhouse effect, eventually evolving into the uninhabitable steam planet state. Over a period of approximately 0.1 Gyr, all of the water escapes into space and the planet finally evolves into a dry planet state.

Figure 4 shows the evolution of a planet with $M_{\rm ini} = 0.1\,M_{\rm oc}$ and $a = 0.8$ AU. The difference between the cases shown in Figures 3 and 4 is the initial amount of water. The overall evolution of water is very similar to that shown in Figure 3 before $t = 3.19$ Gyr. However, when the amount of surface water decreases to $M_{\rm ml} = 0.05\,M_{\rm oc}$ (i.e., the maximum water mass for the land planet mode), the average column mass of the atmospheric water vapor is less than the 3 m threshold for the runaway greenhouse effect in Figure 4(d). This planet therefore satisfies the requirements for a transition from aqua planet mode to land planet mode and can evolve into land planet mode. Once in land planet mode, the planet's atmosphere becomes dry (Figure 4(a)) and escape shuts off (Figure 4(b)). This planet can keep liquid water on its surface until the central star has become sufficiently bright enough to exceed the runaway threshold of a land planet (Figure 4(c)). When the planet receives insolation above this limit, the planet evolves into the steam planet state and then the dry planet state once it has lost its remaining water into space over about 0.17 Gyr.

Whether or not an aqua planet can evolve into a land planet thus depends on the initial amount of water. Qualitatively, planets with small initial amounts of water can more easily evolve from the aqua planet mode to the land planet mode.

3.2. Effect of the Distance from the Central Star

Here we examine the effect of the distance from the central star on planetary evolution. Figure 5 shows the evolution of a planet with $M_{\rm ini} = 0.1\,M_{\rm oc}$ and $a = 1.0$ AU. In Figure 5(d), the amount of surface water remaining on the planet exceeds $M_{\rm ml}$ and the planet experiences the runaway greenhouse effect. This planet evolves into the steam planet state without passing through a land planet state. On the other hand, we have seen that a planet with the same initial amount of water at 0.8 AU can evolve from aqua planet mode to land planet mode (Figure 4). This evolution occurs because the planet closer to the central star evolves through the moist greenhouse stage when the star is younger, and the EUV flux and hydrogen escape flux are higher. Any planet near the central star will lose more water during the period of rapid escape of water vapor.

The timing of the onset and duration of rapid escape of water vapor are the two key events that determine whether or not an aqua planet will evolve into a land planet. In the case of a planet that is located far away from its central star, the onset of rapid escape of water vapor occurs later when the star is older and its EUV flux is lower. It therefore takes more time for a more distant planet to lose its surface water; phrased another way, the more distant planet loses less water between the onset of the moist greenhouse effect and the onset of the runaway greenhouse effect for an aqua planet. Moreover, because the rate of stellar luminosity increases with time (see Equation (4)), more distant planets have less time to shed excess water before the onset of runaway greenhouse effect. As a result, it is more difficult for a distant planet to evolve

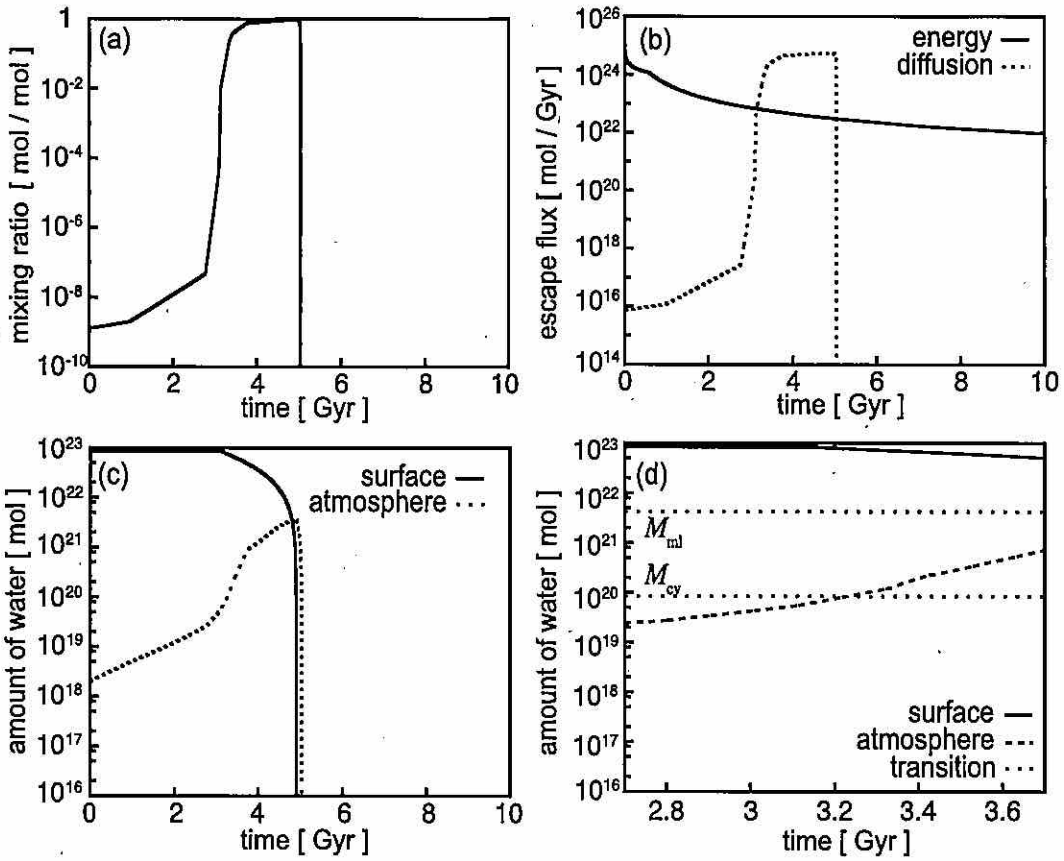

Figure 3. Evolution of a planet with $M_{ini} = 1.0\ M_{oc}$ at $a = 0.80$ AU. (a) The mixing ratio of water vapor in the upper atmosphere; (b) escape flux of hydrogen; ((c) and (d)) change in the amount of water in the atmosphere and on the surface are shown as a function of time. Figure (d) shows the change in the amount of water around 3.2 Gyr with two transition conditions (the critical amount of vapor for the runaway greenhouse effect, M_{cv}, and the maximum liquid water mass for a land planet, M_{ml}) from an aqua planet to a land planet. Here, M_{cv} are set at 3 m in global average for the precipitable water and M_{ml} is set to $0.05\ M_{oc}$. In this case, the aqua planet evolves directly to a steam planet and then a dry planet; it is never a land planet.

into a land planet, and easier to evolve directly into a steam planet.

3.3. Limit of the Initial Amount of Water to Evolve to a Land Planet

In the previous section, we showed several typical numerical results obtained for planetary evolution. We found that the initial amount of water (M_{ini}) and the distance from the central star (a) are important in determining whether or not an aqua planet can evolve into a land planet.

Figure 6 shows the maximum initial amount of water that is required for the transition from aqua planet mode to land planet mode as a function of the distance from the central star. In this figure, planets below the curve can evolve from aqua planet mode to land planet mode. Aqua planets close to a central star with small initial amounts of water can evolve into land planets, but aqua planets that are too far from a central star, or that are born with large amounts of water, evolve into steam planets without passing through the land planet stage.

Planets with less than the maximum liquid water mass for land planets ($M_{ini} < M_{ml}$) remain in land planet mode from the beginning. In cases of planets with small orbits ($a < 0.72$ AU), all of the water evaporates and such planets are in the steam planet state from the beginning.

3.4. Inner Edge of the HZ

Here we discuss the inner edge of the HZ of solar-type stars based on our results. Figure 7 shows the evolution of planets with $M_{ini} = 1.0\ M_{oc}$ at various distances from the central star under the same transition conditions. For planets with $M_{ini} = 1.0\ M_{oc}$, rapid escape of water occurs, but such planets cannot evolve into the land planet mode because they cannot lose enough water—they cannot get from $1.0\ M_{oc}$ to M_{ml}—before encountering the runaway greenhouse threshold for aqua planets. Therefore, the boundary between the aqua planet mode and the steam planet state corresponds to the inner edge of the classical instantaneous HZ, proposed in Kasting et al. (1993; Figure 7).

As in Figure 7, Figure 8 shows the time evolution of planets with $M_{ini} = 0.1\ M_{oc}$. When located between 0.72 and 0.82 AU, such planets can evolve from the aqua planet mode to the land planet mode. Planets in the land planet mode remain habitable for an additional 2 Gyr before evolving into the steam planet state and then to the dry planet state due to increased luminosity of the central star.

In both Figures 7 and 8, aqua planets closer than about 0.7 AU from the central star are in the steam planet state from the beginning. Such planets lose all of their water rapidly (over a few tens of million years) because the EUV flux at that time is

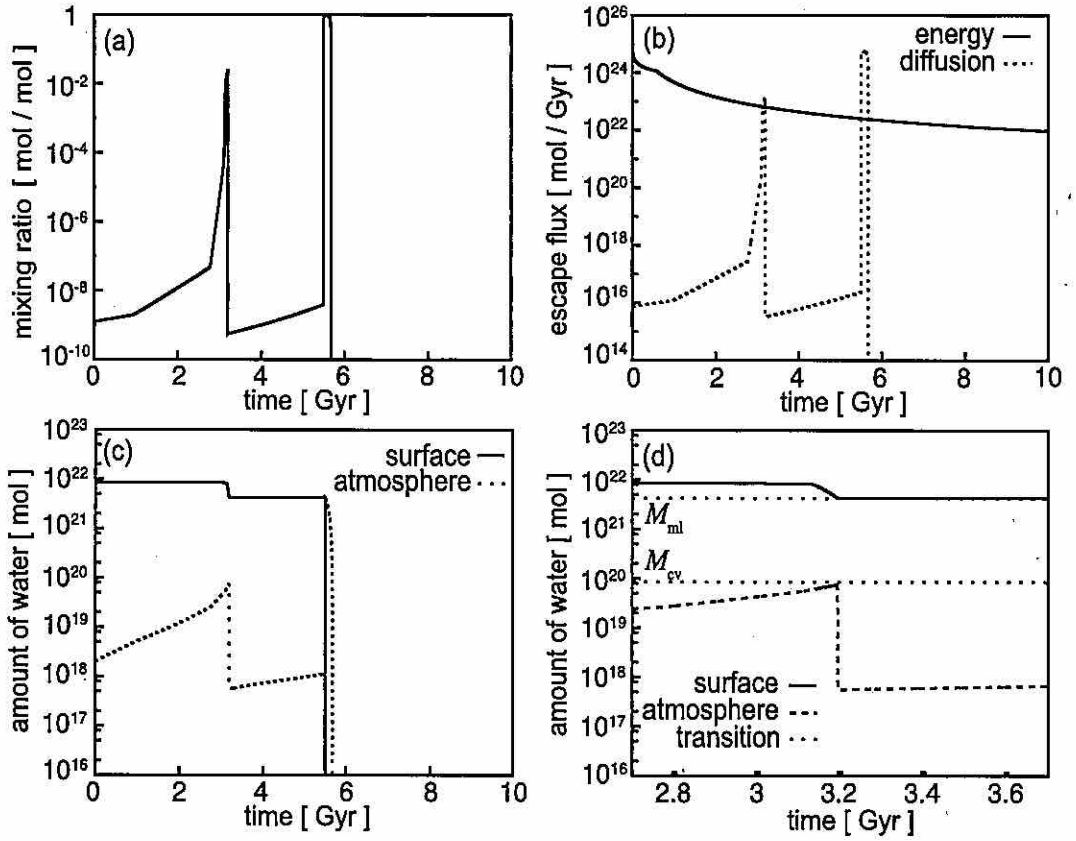

Figure 4. Like Figure 3, except that the planet has less initial water, $M_{ini} = 0.1\,M_{oc}$ at $a = 0.80$ AU. In this case, the aqua planet can evolve into a land planet and maintains liquid water on its surface for an additional 2 Gyr.

very strong; such planets are called Type II terrestrial planets (Hamano et al. 2013).

Figure 9 shows the inner edge of the CHZ, which is defined here as the region where a planet has liquid water on its surface for more than 4.6 Gyr. We divided the CHZ into two types according to the initial amount of water. One type of CHZ refers to those regions on aqua planets that maintain water on their surface for more than 4.6 Gyr; this type corresponds to the CHZ proposed in Kasting et al. (1993) and is referred to here as a type I CHZ. The other type of CHZ refers to regions on land planets that maintain water on their surface for a total of more than 4.6 Gyr; this is referred to as a type II CHZ.

In our model, planets with $M_{ini} > 0.22\,M_{oc}$ cannot evolve into land planets: such planets have a type I CHZ. On the other hand, planets with $M_{ini} < 0.22\,M_{oc}$ can evolve into land planets. However, planets with $0.19\,M_{oc} < M_{ini} < 0.22\,M_{oc}$ cannot maintain liquid water on their surface for 4.6 Gyr because the insolation on such planets exceeds the threshold of the runaway greenhouse effect. Planets with $M_{ini} \leqslant 0.19\,M_{oc}$ have a type II CHZ.

Figure 9 shows that planets that begin with $0.09\,M_{oc} < M_{ini} \leqslant 0.19\,M_{oc}$ have both type I and type II CHZs, but these two CHZs are not contiguous. However, planets with $0.05\,M_{oc} < M_{ini} \leqslant 0.09\,M_{oc}$ also have both CHZs and they are contiguous. Planets with an initial water mass less than the maximum water mass for a land planet ($M_{ml} = 0.05\,M_{oc}$) on their surface are in land planet mode from the beginning.

4. DISCUSSION

4.1. Effect on the Transition Condition

In previous sections, we showed results when M_{cv}, the critical water vapor amount for the runaway greenhouse, was taken as a global average of 3 m water depth equivalent and M_{ml}, the maximum liquid water mass for a land planet mode, was taken to be $0.05\,M_{oc}$. In this section, we investigate how the evolution from aqua planet mode to land planet mode changes when the transition conditions are altered.

Figure 10 shows the maximum M_{ini} required for a planet to evolve into a land planet for different values of M_{cv}. In these calculations, M_{ml} is fixed at $0.05\,M_{oc}$. If M_{cv} exceeds 3 m, then the maximum M_{ini} increases because the onset of the runaway greenhouse effect is delayed. For planets closer to the central star, the maximum M_{ini} is larger because the escape flux of water is larger before the onset of runaway greenhouse effect. However, if planets are too close to the central star, the maximum M_{ini} decreases and has a peak (see Figure 10). The amount of water that escapes is determined by the duration of the period of a rapid escape until the onset of the runaway greenhouse effect and the escape flux of water during this period. For planets that are very close to the central star, the runaway greenhouse effect occurs early and the duration of the period of rapid escape is short. Although the escape flux in the energy-limited escape mode is large, the rapid escape of water occurs in the diffusion-limited escape mode for these planets. Therefore, the total amount of escaped water hits a peak, which

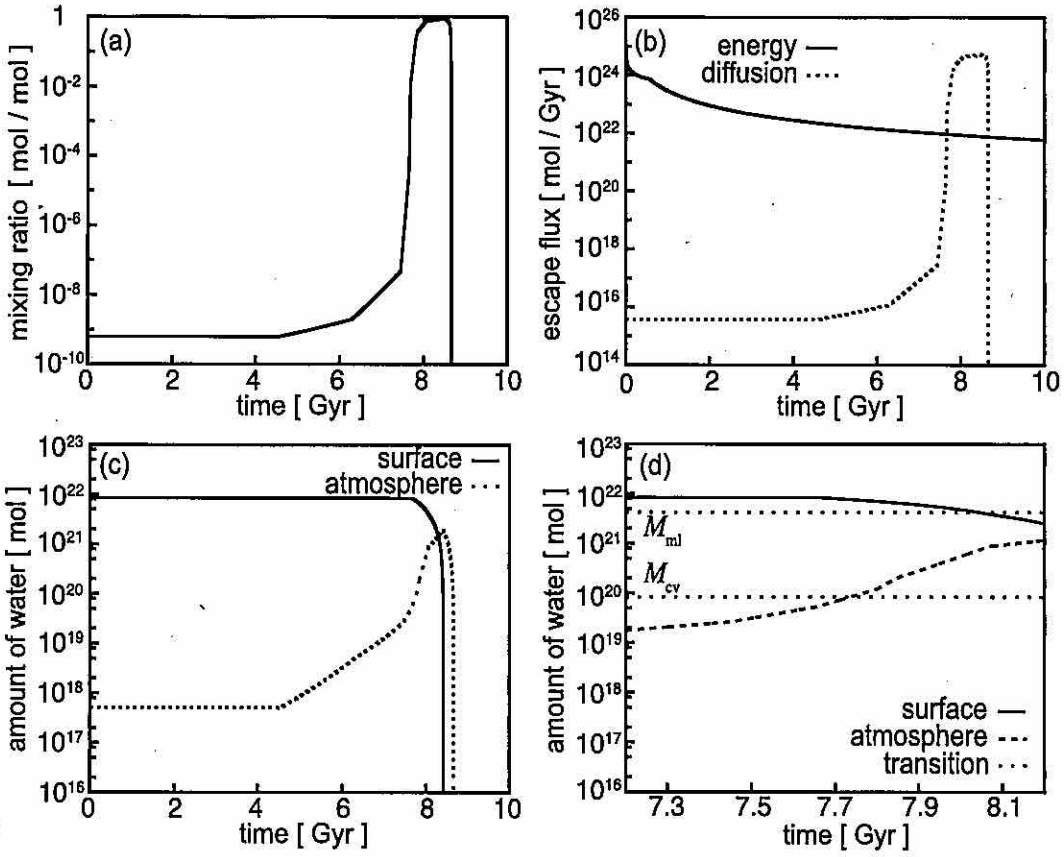

Figure 5. Like Figure 4, but for a planet a little farther from the central star, with $M_{ini} = 0.1\ M_{oc}$ at $a = 1.0$ AU. Panel (d) shows the change in the amount of water at approximately 7.7 Gyr. This aqua planet does not pass through a stage as a land planet, but instead evolves directly into a steam planet and then a dry planet.

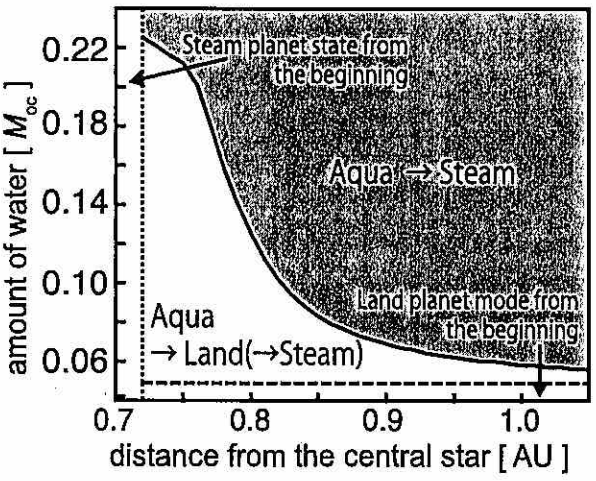

Figure 6. Initial planetary conditions required for the evolution of a land planet with a central star like the Sun. Planets at $a < 0.72$ AU are Type II planets (Hamano et al. 2013), which are in the steam planet state in the beginning and lose their water before cool down. Thus, they never have liquid water on their surface. On the other hand, planets at $a > 0.72$ AU and with $M_{ini} < 0.05\ M_{oc}$ may be land planets from the beginning.

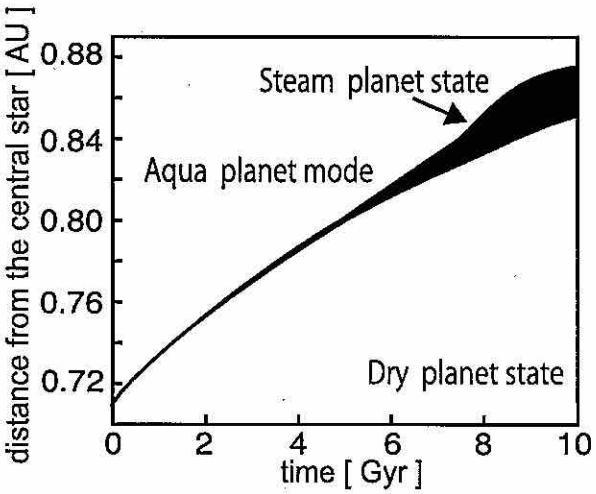

Figure 7. Evolution of planets with $M_{ini} = 1.0\ M_{oc}$ for central stars like the Sun. None of these planets become land planets. They have too much water initially. Note that some of the planets that orbit older stars spend considerable time as steam planets.

is shown by the maximum M_{ini} value in Figure 10. An aqua planet cannot evolve into a land planet when M_{cv} is 1 m (global average). In our model, the mixing ratio of water vapor in the upper atmosphere reached 10^{-3} when the column of water in the atmosphere is 1.9 m (global average). If M_{cv} is less than 1.9 m, then a planet in the aqua planet mode cannot lose enough water and it passes directly into the steam planet state.

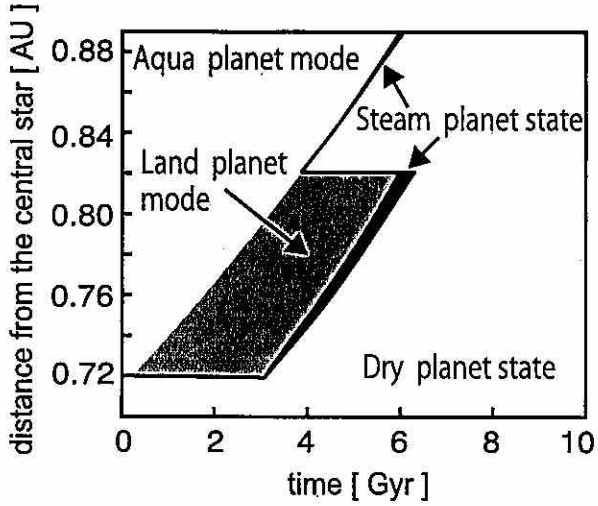

Figure 8. Like Figure 7 for initially drier planets with $M_{\rm ini} = 0.1\,M_{\rm oc}$. Aqua planets between 0.72 and 0.82 AU can transform into land planets, and as land planets they maintain liquid water on their surfaces for an additional 2 Gyr. Thereafter, such planets receive the solar radiation of the threshold of the runaway greenhouse for a land planet and become steam planets.

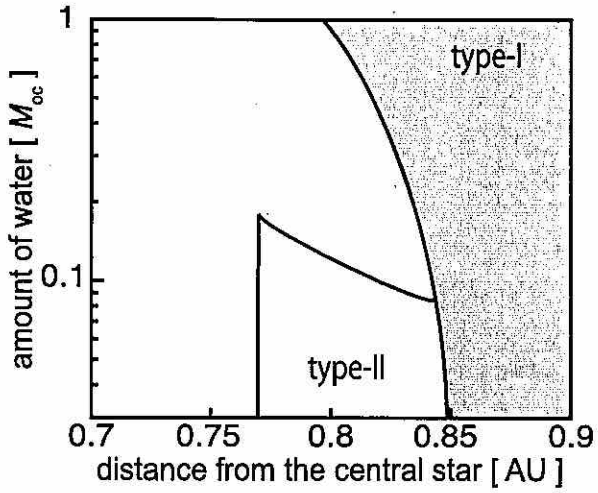

Figure 9. Inner edge of the CHZ, defined as the planet being in the HZ for at least 4.6 Gyr, considering the evolution from an aqua planet to a land planet. The region of the type I CHZ corresponds to the traditional CHZ for an aqua planet, while the region of the type II CHZ is a region where planets that are initially aqua planets become land planets.

Our standard case takes $M_{\rm ml} = 0.05\,M_{\rm oc}$. This value of $M_{\rm ml}$ is dependent upon the planetary topography. Figure 11 shows the dependence of the maximum $M_{\rm ini}$ on $M_{\rm ml}$ for a planet evolving into a land planet. In this calculation, the value of $M_{\rm cv}$ is fixed at our standard value of 3 m. A smaller value for $M_{\rm ml}$ results in smaller maximum $M_{\rm ini}$, but it is possible for aqua planets to evolve into land planets even if $M_{\rm ml} = 0.01\,M_{\rm oc}$. However, an aqua planet cannot evolve into a land planet when $M_{\rm cv}$ is less than 1 m (see Figure 10). Therefore, the parameter $M_{\rm cv}$ has a greater impact on the evolution path to land planets than the parameter $M_{\rm ml}$.

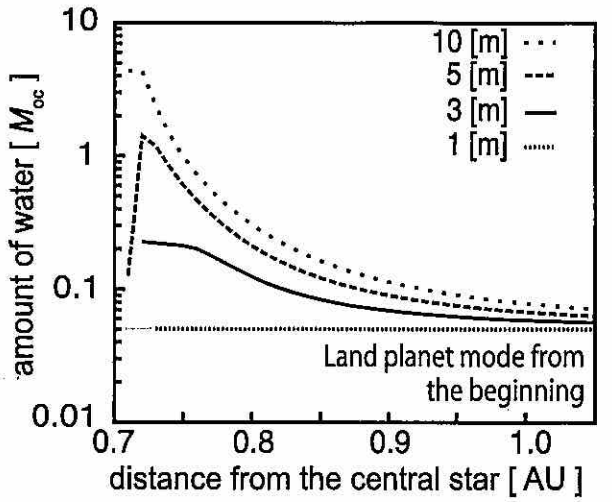

Figure 10. Effect of the critical vapor amount for the runaway greenhouse $M_{\rm cv}$ on the maximum initial amount of water, $M_{\rm ini}$ to evolve from the aqua planet mode into the land planet mode. The maximum water mass for a land planet, which is the other transition condition, is fixed at $M_{\rm ml} = 0.05\,M_{\rm oc}$. The result for (solid curve) the case where $M_{\rm cv}$ is equivalent to a column of 3 m of precipitable water is the same as that shown in Figure 6. Larger critical amount of vapor facilitates the evolution to land planets. However, if $M_{\rm cv}$ is less than 1 m, it is very difficult for an aqua planet to evolve into a land planet.

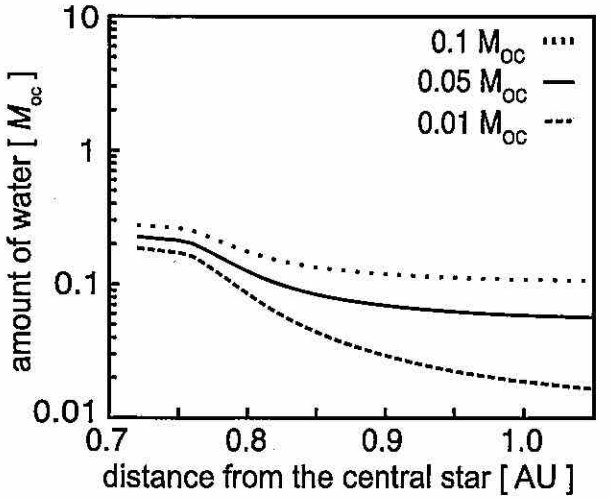

Figure 11. Effect of the maximum water mass for a land planet, $M_{\rm ml}$, on the maximum initial amount of water, $M_{\rm ini}$ to evolve from the aqua planet mode to the land planet mode. Here $M_{\rm cv}$, the other transition condition, is fixed to 3 m depth in global average. The result for the case of $M_{\rm ml} = 0.05\,M_{\rm oc}$ was shown in Figure 6. Changing $M_{\rm ml}$ has a smaller effect on the upper limit of the initial water mass to evolve from an aqua planet to a land planet than changing $M_{\rm cv}$. The amount of water for a land planet from the beginning corresponds with the maximum water amount for a land planet.

4.2. Atmospheric Models

We investigated the evolutionary paths of planets using a 1D, cloud-free, radiative–convective atmospheric model developed in the 1980s (Abe & Matsui 1988). The 1D atmospheric models have been improved by using more accurate opacity estimates for water vapor (Goldblatt et al. 2013; Kopparapu et al. 2013, 2014). The inner edge of the CHZ (defined by moist greenhouse effect) in Kopparapu et al. (2013) is 0.99 AU.

In our model, the onset of the moist greenhouse effect is $1.39\,S_{\odot}$. Since the onset of the runaway greenhouse effect is dependent on the value of M_{cv}, when M_{cv} is set to 3 m, the onset of the runaway greenhouse effect is $1.40\,S_{\odot}$. In Kopparapu et al. (2013), the onsets of the moist and runaway greenhouse effects are 1.015 and $1.06\,S_{\odot}$, respectively. The timing of the onset of rapid water loss and the amount of water that escaped should therefore be different between our atmospheric model and their model. In order to investigate the evolution from an aqua planet into a land planet, we need the relationship between the incident solar flux and the amount of water vapor in the atmosphere, but it was not shown in previous papers. We therefore qualitatively compared our results to those of Kopparapu et al. (2013).

We estimated how much water escapes during the period from the onset of the moist greenhouse effect to the onset of the runaway greenhouse effect using the results from Kopparapu et al. (2013). To estimate the escaped water amount by Kopparapu et al. (2013), we presume that the mixing ratio of water vapor is 10^{-3}, so that the escaped water amount during this period in the diffusion-limited escape mode is approximately 3×10^{21} moles (ca. $0.04\,M_{oc}$). The amount of escaped water under energy-limited escape mode conditions in the same period was estimated to be 10^{23} moles (ca. $1.19\,M_{oc}$). The actual amount of escaped water falls between these estimates (i.e., between 3×10^{21} and 1×10^{23} moles). In our model, planets that can evolve into land planets typically lose about $0.1\,M_{oc}$ of water (see Section 3.3), which is comparable to, or less than, the estimates of Kopparapu et al. (2013). Kopparapu et al. (2013) indicate that planets at $a < 0.84$ AU are in the steam planet state. Thus, the region where aqua planets can evolve into land planets moves outward (about 0.1 AU) when the model of Kopparapu et al. (2013) is applied. The type II CHZ (see Figure 9), in which aqua planets evolve to land planets, also moves outward.

4.3. Intensity of EUV Flux

We assessed the effect of EUV flux on our results. The uncertainty associated with the EUV flux from the central star is large (e.g., Zahnle & Walker 1982; Lammer et al. 2009). Just before an aqua planet evolves into a land planet, water escapes rapidly in the energy-limited escape mode (see Figure 4(b)). If the EUV flux is larger than that used in our model, then the escape flux increases. However, since the escape flux is limited by the diffusion process, a larger EUV flux does not markedly affect our results. On the other hand, if the EUV flux is smaller than that used in our model, then the escape flux decreases. This makes it harder for aqua planets to evolve into land planets.

4.4. Amount of Atmospheric CO_2

An important complication could be the evolution of the amount of CO_2 in the atmosphere. Since the carbon cycle on a land planet has not yet been investigated, we speculate possible effects of carbon cycle on a land planet climate in the following.

The amount of CO_2 in the atmosphere is governed by the balance between the degassing flux of CO_2 and the removal flux of CO_2 through chemical weathering. We expect the degassing flux of CO_2 to be smaller on a land planet than on an aqua planet because plate tectonics is likely to be less efficient on a water-poor mantle. Chemical weathering may be also less efficient on a land planet, because it occurs mainly in wet regions. If the former effect exceeds the latter, then the amount of CO_2 in the atmosphere should be smaller on a land planet than on an aqua planet. However, any decrease in the degassing flux would be difficult to estimate.

Therefore, it is not clear whether there would be more or less CO_2 on a land planet compared to an aqua planet. If the amount of CO_2 is balanced at a high value, then the period of habitability may be shorter than that estimated in our study because the greenhouse effect attributed to CO_2 may trigger the runaway greenhouse effect. On the other hand, if the CO_2 amount is balanced at a low value, the environment is cooler than our estimate. However, such an effect is likely minor, because the insolation is high enough to keep from the global freezing without CO_2 greenhouse effect. It should also be noted that a land planet is relatively resistant to global freezing (Abe et al. 2011). Even if ice caps appear, their size is regulated by the carbon cycle, because CO_2 removal through chemical weathering would be negligible in the ice-covered area. Under such a scenario, the lifetime of a habitable environment would likely be similar to that estimated in our study.

4.5. The Geologic H_2O Cycle

We have neglected the geologic water cycle by presuming that the fluxes of water into and out of the mantle are roughly in balance. This rough balance is likely to break down after an aqua planet has become a land planet, because the mantle may still be wet and outgassing may still be considerable, but the subduction of hydrous minerals is probably restricted to locations near the poles. Thus, water outgassing would be a potential hazard to the future habitability of the land planet over long timescales. However, while the aqua planet is losing its hydrogen in the moist greenhouse state, it is possible that the imbalance goes in the other direction, as the generally warm, wet climate of the moist greenhouse would likely promote weathering reactions and possibly promote the subduction of hydrous minerals. Thus, we believe it probable that the geologic water cycle would aid rather than subvert the transition of a suitable planet from aqua to land modes.

4.6. Other Stars

Stars of different spectral types evolve differently from the Sun. In particular, the luminosity evolution of stars of later spectral type (late G dwarfs, K dwarfs, and M dwarfs) is slower than in the Sun. These stars are fainter than the Sun and hence the HZ is closer to these stars than to the Sun. The ratio of EUV radiation to luminosity is about the same for K stars as for G stars, and the ratio is higher for most M stars (Lammer et al. 2009). Hence, these stars are at least as effective at driving hydrogen escape as a Sun-like star, and so we would expect similar or faster rates of hydrogen escape for an HZ planet around these other stars. The slower rate of luminosity evolution means that there is more time available for escape to take place before the moist greenhouse becomes a runaway greenhouse, and therefore we expect that late-type stars are more favorable to a planet making a continuously habitable transition from aqua state to land state. We will quantitatively investigate the evolution path from the aqua planet mode to the land planet mode for stars of different spectral types in a subsequent paper.

5. CONCLUSION

Planets can evolve from aqua planet mode to land planet mode and, in so doing, maintain liquid water on their surface for a longer time. Here we assess the various requirements of such a transition. We argue that the transition from an aqua planet into a land planet can occur if the amount of water on the surface is reduced rapidly by hydrogen escape via the photodissociation of H_2O vapor, while the amount of water vapor in the atmosphere remains sufficiently low to prevent the onset of runaway greenhouse effect—i.e., the planet must lose most of its water while in the moist greenhouse state. We considered two factors as being central to the evolution of a land planet from an aqua planet: the critical vapor amount for the runaway greenhouse, $M_{\rm cv}$, and the maximum liquid water mass for a land planet mode, $M_{\rm ml}$. We assumed that the star in our simulation was similar to the Sun. We examined temporal changes in the amount of water on a planet under conditions of different initial amounts of water and orbital distance. We illustrated the conditions for the evolution of an aqua planet to a land planet and applied this information to re-evaluate the inner edge of the HZ.

The evolutionary paths of aqua planets are mostly determined by the initial amount of water, $M_{\rm ini}$. Planets with large $M_{\rm ini}$ evolve into the runaway greenhouse state before entering the land planet mode, while planets with small $M_{\rm ini}$ can evolve into land planets. Planets closer to the central star can lose water more quickly because these events take place when the star is younger and thus a stronger source of the EUV radiation that drives hydrogen escape. These findings imply that it is generally easier for a land planet to form when it is closer to its star than when it is far from its star.

If $M_{\rm cv}$ is equivalent to 3 m of precipitable water, then an aqua planet with $M_{\rm ini} = 0.1\,M_{\rm oc}$ at 0.8 AU can evolve into a land planet. In addition, such a planet can retain liquid water on its surface for an additional 2 Gyr as a land planet. On the other hand, if $M_{\rm cv}$ is less than about 1 m, it is very difficult for any aqua planet to evolve into a land planet. This value for $M_{\rm cv}$ corresponds to the amount of water vapor in the atmosphere that causes the rapid water loss of a substantial fraction of the Earth's ocean mass. By contrast, the dependence of the evolutionary path on $M_{\rm ml}$ (the upper bound on the amount of water that defines a land planet) is not very large, implying that the value of $M_{\rm cv}$ is more important as a transition condition from an aqua planet to a land planet.

We describe a new type of CHZ where aqua planets can evolve into land planets and maintain liquid water on their surface for more than 4.6 Gyr (type II CHZ in Figure 9). Rapid escape of water is not necessarily the end of a planet's habitability; rather, such water loss can bring about a new and different kind of habitability.

This work was supported by Grant-in-Aid for Scientific Research on Innovative Areas from the Ministry of Education, Culture, Sports, Science and Technology (MEXT; No. 23103003). This work was also partly supported by GCOE program "From Earth to Earths" (MEXT) and research Grant 2015 of Kurita Water and Environment Foundation. We thank the anonymous referee for the constructive review and helpful comments that improved our manuscript.

REFERENCES

Abe, Y., Abe-Ouchi, A., Sleep, N. H., & Zahnle, K. J. 2011, AsBio, 11, 443
Abe, Y., & Matsui, T. 1988, JAtS, 45, 3081
Abe, Y., Numaguchi, A., Komatsu, G., & Kobayashi, Y. 2005, Icar, 178, 27
Batalha, N. M., Rowe, J. F., Bryson, S. T., et al. 2013, ApJS, 204, 24
Borucki, W. J., Agol, E., Fressin, F., et al. 2013, Sci, 240, 587
Bounama, C., Franck, S., & Von Bloh, W. 2001, HESS, 5, 569
Brinkmann, R. T. 1969, JGR, 74, 5355
Goldblatt, C., Robinson, T. D., Zahnle, K. J., & Crisp, D. 2013, NatGe, 6, 661
Gough, D. O. 1981, SoPh, 74, 21
Hamano, K., Abe, Y., & Genda, H. 2013, Natur, 497, 607
Hilton, D. R., Fischer, T. P., & Marty, B. 2002, Rev. Mineralogy Geochem., 47, 319
Javoy, M. 1998, ChGeo, 147, 11
Kasting, J. F. 1988, Icar, 74, 472
Kasting, J. F. 1997, OLEB, 27, 291
Kasting, J. F., Pollack, J. B., & Ackerman, T. P. 1984, Icar, 57, 335
Kasting, J. F., Whitmire, D. P., & Reynolds, R. T. 1993, Icar, 101, 108
Kopparapu, R. K., Ramirez, R., Kasting, J. F., et al. 2013, ApJ, 765, 131
Kopparapu, R. K., Ramirez, R., Kotte, J. S., et al. 2014, ApJL, 787, L29
Lammer, H., Odert, P., Leitzinger, M., et al. 2009, A&A, 506, 399
Leconte, J., Forget, F., Charnay, B., et al. 2013, Natur, 504, 268
Nakajima, S., Hayashi, Y.-Y., & Abe, Y. 1992, JAtS, 49, 2256
Rea, D. K., & Ruff, L. J. 1996, E&PSL, 140, 1
Walker, J. C. G. 1977, Evolution of the Atmosphere (New York: MacMillan)
Walker, J. C. G., Hays, P. B., & Kasting, J. F. 1981, JGR, 86, 9776
Watson, A. J., Donahus, T. M., & Walker, J. C. G. 1981, Icar, 48, 150
Zahnle, J. K., & Walker, J. C. G. 1982, RvGSP, 20, 280
Zahnle, K., Kasting, J. F., & Pollack, J. B. 1988, Icar, 74, 6297

Geosci. Model Dev., 5, 449–455, 2012
www.geosci-model-dev.net/5/449/2012/
doi:10.5194/gmd-5-449-2012

Geoscientific Model Development

"Gtool5": a Fortran90 library of input/output interfaces for self-descriptive multi-dimensional numerical data

M. Ishiwatari[1], E. Toyoda[2], Y. Morikawa[3], S. Takehiro[4], Y. Sasaki[5], S. Nishizawa[6], M. Odaka[1], N. Otobe[7], Y. O. Takahashi[6], K. Nakajima[8], T. Horinouchi[9], M. Shiotani[10], Y.-Y. Hayashi[6], and Gtool development group[11]

[1]Hokkaido University, Graduate school of Science, Sapporo, Japan
[2]Japan Meteorological Agency, Tokyo, Japan
[3]Parmy, Inc., Japan
[4]Kyoto University, Research Institute for Mathematical Sciences, Kyoto, Japan
[5]Kyoto University, Department of Mathematics, Kyoto, Japan
[6]Kobe University, Graduate school of Sciences, Kobe, Japan
[7]Fukuoka University, Faculty of Science, Fukuoka, Japan
[8]Kyushu University, Faculty of Science, Fukuoka, Japan
[9]Hokkaido University, Graduate school of Environmental Earth Science, Sapporo, Japan
[10]Kyoto University, Research Institute for Sustainable Humanosphere, Kyoto, Japan
[11]GFD Dennou Club, Japan

Correspondence to: S. Takehiro (takepiro@gfd-dennou.org)

Received: 4 November 2011 – Published in Geosci. Model Dev. Discuss.: 19 December 2011
Revised: 19 March 2012 – Accepted: 19 March 2012 – Published: 3 April 2012

Abstract. A Fortran90 input/output library, "gtool5", is developed for use with numerical simulation models in the fields of Earth and planetary sciences. The use of this library will simplify implementation of input/output operations into program code in a consolidated form independent of the size and complexity of the software and data. The library also enables simple specification of the metadata needed for post-processing and visualization of the data. These aspects improve the readability of simulation code, which facilitates the simultaneous performance of multiple numerical experiments with different software and efficiency in examining and comparing the numerical results. The library is expected to provide a common software platform to reinforce research on, for instance, the atmosphere and ocean, where a close combination of multiple simulation models with a wide variety of complexity of physics implementations from massive climate models to simple geophysical fluid dynamics models is required.

1 Introduction

General circulation models of the atmosphere and ocean (GCMs) are commonly utilized for research on the surface environment of the Earth and other planets. However, as described in the next section, research with GCMs requires not only high-end complex GCMs but also simplified models and/or process study models with a wide variety of complexity. In order to perform numerical experiments efficiently using a variety of simulation models with different complexities, numerical data should be self-descriptive and input/output of such data must be handled in a consolidated manner among the models. NetCDF is a data format commonly used in the Earth and planetary sciences and its manipulation library can handle metadata contained in netCDF data. However, netCDF operations are relatively low-level, so that many small steps are needed for data manipulation. This leads to a diversity of ways to implement input and output in models. These are considered to be obstacles for researchers who are developing and/or using numerical models in these fields. With these issues in mind, we have developed an input/output Fortran90 library, called "gtool5", which can be used commonly among numerical simulation

Published by Copernicus Publications on behalf of the European Geosciences Union.

models, and whose interfaces are improved so as to minimize the operational steps required in handling numerical data. The gtool5 library is distributed on our web page: http://www.gfd-dennou.org/library/gtool/gtool5.htm.en.

In the following paper, Sect. 2 will explain, using research with atmosphere and ocean models as an example, technical issues of concern in simulation research in the Earth and planetary sciences that have led us to the development of gtool5. In Sect. 3, the data format of the gtool5 library will be presented, and the sophisticated input/output interfaces of the library are described. Section 4 will introduce examples of implementation of the gtool5 library interfaces to numerical models. We will also demonstrate some tools for post-processing/visualization of output data. Concluding remarks are made in Sect. 5.

2 Current issues in research with atmosphere/ocean models

2.1 Necessity of hierarchical models

GCMs are numerical simulation models that calculate fluid motion of the atmosphere, oceans, and ice sheets, and incorporate various kinds of elemental physical processes such as radiation, turbulence, cloud formation and precipitation, and ground surface processes. Computation of each elemental physical process in GCMs is not based on the first principles of physics, but instead is carried out by implementing a model system derived as a certain approximation of the elemental process. This method of implementation is often referred to as "parameterization". Validity of the numerical results of GCMs that contain many parameterization processes is not guaranteed a priori, and should be checked independently. Comparison with observational data is the most direct validation method. However, acquiring observational data is a significant undertaking in itself and observable physical properties are limited.

In order to compensate for the limitation of observations, process study models that more precisely describe elementary processes or simplified conceptual models that enable us to understand possible behaviors of the system concerned have been developed and utilized. Some of the parameterizations implemented in GCMs have been validated by comparing the numerical results with those of corresponding process study models. Examples of simplified conceptual models used to capture the rough behavior of GCMs are energy balance models where hydrodynamic calculations are neglected, and geophysical fluid dynamics models that do not calculate radiation processes. In recent years, however, it has become increasingly difficult to check the validity of GCMs using these procedures, since GCMs have become so complicated that it is not easy for a researcher to understand the program as a whole in order to recognize the effect of a certain elementary physical process, or to reduce the system in order to build up a conceptual model. This has been recognized as a "model-gap" problem (Held, 2005). In order to fill the gap between high-end complex models (GCMs) and process studies or simplified conceptual models, it is necessary to prepare a software environment that enables the preparation of an arbitrary set of models in a hierarchical fashion with various levels of complexity ranging from GCMs to simplified conceptual models or process study models. Subsequently, we need to compare the results of multiple simultaneous numerical experiments with these hierarchical models.

2.2 Requirements for hierarchical models

In order to build up various numerical models with different complexities and carry out numerical experiments efficiently, readability of the program code is an important factor. Readability is a critical issue not only for model maintainers but also for model users. The model users, who are not necessarily professionals in software technology, should be able to understand how the source code of the numerical models realize the original physical systems, i.e. the corresponding set of mathematical equations. This is the most peculiar requirement for the software utilized in the research of these fields.

In addition to the readability of the program code, the content and structure of the output data also affect the efficiency of the research process, since the typical size of the output data produced by these models tends to be quite large. In order to perform post-processing and visualization operations on these massive datasets, they must be self-descriptive; the data of the dependent variables and coordinate variables are needed. In addition, for management of many massive datasets, we need to record the parameters of the experimental conditions in each dataset. However, if the input/output interfaces for such self-descriptive datasets differ in the program code, readability of the code from one program to another is reduced; and we may not be able to manipulate multiple simulation models hierarchically.

In these circumstances, we need an input/output interface in a consolidated form that is independent of the model complexities. Moreover, the output interface for recording metadata should not be complicated; it should be adequately simplified so as not to reduce the readability of the program code. Most GCMs and related models in atmosphere and ocean sciences have been developed as Fortran programs. In order to satisfy these requirements, we have designed and implemented "gtool5", as described in the following section.

3 Gtool5: a Fortran90 library for data input/output interfaces

3.1 Gtool5 data format

Gtool5 handles time series of multi-dimensional (mainly from one to three dimensional) grid data. For these data,

we adopted a self-descriptive data format netCDF that can contain the supplementary information needed for post-processing and parameter values used in numerical experiments together with numerical data. NetCDF has been developed by Unidata, part of the University Corporation for Atmospheric Research (UCAR). NetCDF files can store arrays of arbitrary size and attach an arbitrary number of metadata, which are called "attributes", to the file and variables.

In order to use netCDF metadata in post-processing/visualization tools, output data must contain attributes describing the title, variable names, variable units, and so on. Naming rules of attribute names and the format of attribute values should be standardized, since the usage of attributes are not prescribed in the framework of netCDF itself. Therefore, we firstly designed conventions which provide naming rules and usages of attributes of netCDF data suitable for research with GCMs and associated hierarchical models, i. e. gtool4 NetCDF Conventions. Gtool4 netCDF conventions started to be developed and have been maintained since 2001, when CF conventions (Eaton et al., 2003), used in meteorology and oceanography widely nowadays, were not present. In 2006, since CF conventions (ver.1.0) became popular, we reviewed our conventions and concluded that: gtool4 NetCDF Conventions were compatible enough to CF conventions in pragmatic sense of the time; some features missing in CF conventions were useful or deserved future testing, and hence it is too early to decide on migration into CF conventions. The two conventions have little difference so that most data can circulate only with changing "Conventions". The most notable extension to CF conventions (and its predecessors) is meaning of "positive" attribute. We generalized it to specify system behavior instead of description of coordinates represented by the variable. The attribute can be attached to any coordinate variables to specify "default direction of rendering". The default value positive = "up" stands for bottom-to-top or left-to-right direction of coordinate, and "down" for the opposite. Other extensions are attributes for visualization hints such as default values of contour intervals and ranges.

3.2 Gtool5 data input/output interfaces

3.2.1 Design policy of gtool5 interfaces

The gtool5 library provides input/output interfaces that resolve the problem of the gap of granularity between the standard netCDF application programming interface (API) and model data object. The standard netCDF API corresponds to a basic data structure such as an array or string, while "a unit of dataset" is usually considered as a number of associations of arrays and text attributes for researchers using GCMs. Many operation steps are needed for the original netCDF API to be used for self-descriptive data output of several variables, since preparative operations for the output must be called for each variable in the program source code. However, for the variables used in the GCMs and associated hierarchical models, there are many common preparative operations, such as settings of coordinate variables. Therefore, by hiding such common preparative operations into the input/output library, we reduce the number of operation steps in the program code of the models.

The input/output interfaces are designed not to degrade the readability of the program source code as described in Sect. 2. In order to retain traceability of source code for calculation of fluid motion and elemental physical processes, the library tries to encapsulate details of data input/output inside the library. Model users do not have to concern themselves with computational science concepts such as file handles (unit numbers in Fortran), filenames, or division of grids in parallel processing once they are configured in the initialization subroutine. The library provides two kinds of interfaces suitable for small and massive models. The interfaces have been constructed to be as similar as possible to minimize the cost of learning.

3.2.2 Data input/output interface for small models

A sample interface is shown in Table 1. This interface is for small models in which data are output at regular time intervals and multiple variables are output into a single file. Major subroutines of this interface are HistoryCreate, HistoryAddVariable, HistoryPut, HistoryAddAttr, and HistoryClose. The functions and major arguments of these five subroutines are summarized in Table 1.

The subroutine HistoryCreate initializes an output file with configurations for names, sizes, and units of coordinate (independent) variables, the title of the dataset, and data source information (such as a data provider or a model name). The supplementary information supplied is designed to meet the minimum requirements for post-processing.

One of the characteristics of the gtool5 library is that all variables in the output are referenced by their names, specified in initializer routines such as HistoryCreate, unlike its lower layer netCDF library where variables are referred to by the numbers of handles returned from NF_OPEN. All netCDF handles for files, dimensions, and variables are intentionally hidden and managed in the library. Otherwise, the readability of the simulation code would be significantly compromised. By hiding handles used in the netCDF library, we can easily implement data input/output operations to model programs.

3.2.3 Program example

Figure 1 shows an example of a typical program source code of a numerical model using the gtool5 library. Lines 45 and 46 describe the model equation (finite difference form of the diffusion equation), and calculate grid values of the variable "temp" at each time step. Lines 37–39 in Fig. 1 configure the metadata: the arguments "longname" and "units"

Table 1. Data input/output interface for small models in which multiple variables are output into a single file. Only major subroutines and some optional arguments (represented by parentheses) are shown. The item with an italic font does not exist in the interface shown in Table 2.

Operation	Subroutine name	Major arguments
Initialization	`HistoryCreate`	*File name*, title, source (the method of production of the data), institution (specifies where the data was produced), names of dimensions, sizes of dimensions, descriptive names of dimensions, units of dimensions, [interval of output].
Variable definitions	`HistoryAddVariable`	Name of variable, dimensions on which variable depends, descriptive name of variable, units of variable.
Attribute settings	`HistoryAddAttr`	Name of variable, name of attribute, value of attribute.
Output of data	`HistoryPut`	Name of variable, names of dimensions, numerical data.
Finalization	`HistoryClose`	(No Argument)

Table 2. Data input/output interface for massive models, where output data are separately stored into multiple files so that each file contains an output variable. Only major subroutines are shown. The items with an italic font do not exist in the interface shown in Table 1.

Operation	Subroutine name	Major arguments
Initialization	`HistoryAutoCreate`	Title, source (the method of production of the data), institution (specifies where the data was produced), names of dimensions, sizes of dimensions, descriptive names of dimensions, units of dimensions.
Output of dimension variable	*HistoryAutoPutAxis*	Name of dimension, data
Variable definitions	`HistoryAutoAddVariable`	Name of variable, dimensions on which variable depends, descriptive name of variable, units of variable.
Attribute settings	`HistoryAutoAddAttr`	Name of variable, name of attribute, value of attribute.
Output of data	`HistoryAutoPut`	*Time*, name of variable, data.
Finalization	`HistoryAutoClose`	(No Argument)

of subroutines HistoryAddVariable specify the variable name and unit of the variable, respectively. These metadata are contained in the output data as attributes, and are used in the post-processing/visualization tools described in Sect. 4. In the program shown in Fig. 1, there are only six subroutine calls for data output, and an additional variable, such as a handle for netCDF API, is not required. In contrast, when the same operations are implemented with standard netCDF API, the number of subroutine calls for data output becomes two or three times that of Fig. 1, and several handle variables are required.

3.2.4 Data input/output interface for massive models

An alternative interface is shown in Table 2. This is intended for massive simulation code with larger size and/or number of output variables, where it is unrealistic to combine all output into a single file. With this interface, output data are stored separately in multiple files so that each file contains an output variable. Also, output data can be recorded at unequal time intervals.

Major subroutines of this interface are HistoryAutoCreate, HistoryAutoPutAxis, HistoryAutoAddVariable,

```
1   != Sample program for gtool_history/gtool5
2   !
3   ! Solving diffusion equation
4   ! \[
5   !     du/dt = \kappa d^2 u/dx^2
6   ! \]
7   ! for giving values of $u$ at $x=[0,1]$.
8   !
9   program diffusion
10
11    use gtool_history                              ! specification of necessary module
12
13    integer, parameter     :: nx=30                  ! grid number
14    integer, parameter     :: nt=200                 ! number of time steps
15    integer, parameter     :: ndisp=10               ! output interval
16    real(8), parameter     :: dx=1.0/(nx-1)          ! grid spacing
17    real(8), parameter     :: dt=0.0005              ! time step
18    real(8), dimension(nx) :: x=(/(dx*(i-1),i=1,nx)/) ! coordinate variable
19    real(8), dimension(nx) :: temp                   ! temperature
20    real(8), parameter     :: kappa=1.0              ! diffusion coefficient of heat
21
22    tinit = 0.0                                     ! initial time
23
24    temp = exp(-((x-0.5)/0.1)**2)                   ! initial value
25
26    call HistoryCreate( &                          ! Initialization
27      & file='diffusion_1.nc', title='Diffusion equation', &
28      & source='Sample program of gtool_history/gtool5',   &
29      & institution='GFD_Dennou Club davis project',       &
30      & dims=(/'x','t'/), dimsizes=(/nx,0/),               &
31      & longnames=(/'X-coordinate','time      '/),         &
32      & units=(/'m','s'/),                                 &
33      & origin=real(tinit), interval=real(ndisp*dt) )
34
35    call HistoryPut('x',x)                         ! output of coordinate variable
36
37    call HistoryAddVariable( &                     ! definition of dependent variable
38      & varname='temp', dims=(/'x','t'/), &
39      & longname='temperature', units='K', xtype='double')
40
41    call HistoryPut('temp',temp)                   ! output of dependent variable
42
43    do it=1,nt
44
45      temp(2:nx-1) = temp(2:nx-1) &                 ! TIME INTEGRATION
46        & + kappa*(temp(3:nx)-2*temp(2:nx-1)+temp(1:nx-2))/dx**2*dt
47
48      if ( mod(it,ndisp) == 0 ) then
49        call HistoryPut('temp',temp)               ! output of dependent variable
50      endif
51    enddo
52
53    call HistoryClose
54    stop
55  end program diffusion
```

Fig. 1. An example of program source code of a numerical model using the gtool5 library. Numbers on the left-hand side indicate line numbers.

HistoryAutoPut, and HistoryAutoClose. As shown in Tables 1 and 2, the arguments of the two interfaces are almost identical, which contributes to the readability of program source code and reduces the maintenance cost of the library. The filenames of output data are automatically generated with this interface, whereas only a single filename is explicitly given in the simpler interface. Coordinate variables, called dimension or axis, are specified in the distinct subroutine, HistoryAutoPutAxis, while in the former interface, HistoryPut can deal with both data (dependent) and coordinate (independent) variables. This asymmetry is chosen to simplify the implementation with parallel processing in mind.

3.2.5 Data input with gtool5 library

The gtool5 library also hides netCDF handles when reading data, and users can specify a variable by its name. For a case of input of a variable specified by "U" contained in netCDF file inputfile.nc, the subroutine HistoryGet should be called as follows:

```
real(8) :: xyz_U(10,20,30)
...
call HistoryGet('inputfile.nc', 'U', xyz_U).
```

HistoryGet does not read metadata. The subroutine HistoryGetAttr is used for input of metadata, if necessary. By

specifying optional arguments, a portion of variable data can be extracted as follows:

```
real(8) :: y_V(20)
...
call HistoryGet('inputfile.nc', 'V', y_V,
range='x=180.0,y=-10.0:10.0,t=3.5').
```

The above example shows a case where a part of a variable specified by "V" is extracted in the range of $x = 180, -10 \leq y \leq 10, t = 3.5$ and is stored in an numerical array. The extracted range is specified with an optional argument in the form of "range = ⋯".

4 Software related to the gtool5 library

Based on the gtool5 library, we are now developing a series of hierarchical numerical models for research on the surface environment of the Earth and other planets (GFD Dennou Club dcmodel project). Our aims are to validate the results obtained by high-end models such as GCMs and to understand the circulation structures of the atmosphere and ocean by performing numerical experiments by using associated hierarchical models. Our high-end models are a three-dimensional general circulation model of the atmosphere, "DCPAM", and a three-dimensional non-hydrostatic convection model, "deepconv" . At the same time, we have been developing a series of simplified models illustrating standard problems of geophysical fluid dynamics, "SPMODEL" (Takehiro et al., 2006). The input/output parts of these models with different complexity are arranged in a consolidated form without reducing readability, thanks to the interface routines of gtool5.

We have been constructing a series of software based on the script language "ruby" for post-processing/visualization of data produced by the gtool5 library (GFD Dennou Club Davis project). As for the main end-user tools, there is a class library for analysis and visualization of multi-dimensional gridded physical quantities, "GPhys", and web-based data and knowledge server software, "Gfdnavi" (Horinouchi et al., 2010; Nishizawa et al., 2010) (Fig. 2). With Gfdnavi, we are aiming to construct a system for archiving and sharing of documentation, image data, and supplementary information for visualization. Using these tools, we can analyze output data of models of different sizes and complexities.

5 Conclusions

In this paper, we present a Fortran90 input/output library, "gtool5", for hierarchical models ranging from high-end models to simplified models. The input/output interfaces of the library can be implemented in model programs in a consolidated form independent of the complexity of the models. The interfaces are sufficiently simplified in spite of the concurrent output of supplementary information, which contributes to the readability of the program code.

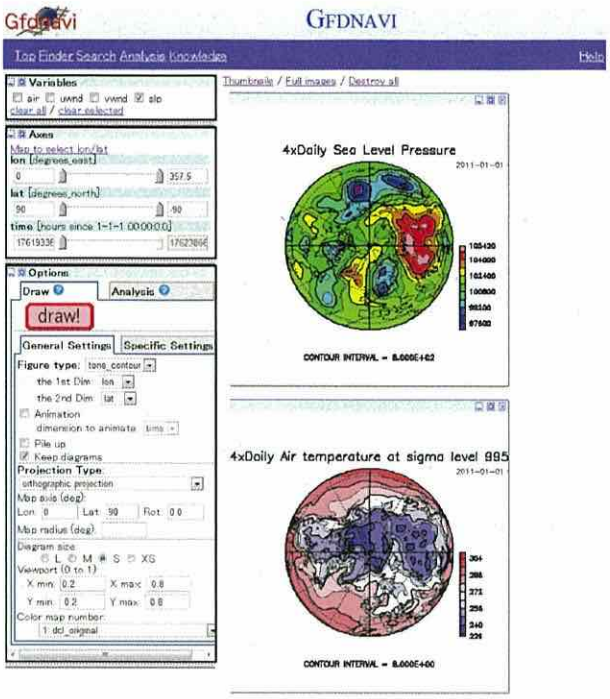

Fig. 2. A screenshot of web-based data and knowledge server software, Gfdnavi.

Moreover, use of gtool5 gives us possibility of adding to its capabilities in the future without changing existing interfaces used in current models. Relinking with a new version of the library would automatically provide the new functionality. For example, the present version of the gtool5 library can read compressed files by linking with netCDF-4 library, whereas it cannot output compressed data. However, it is expected to realize compression of model output by using newly implemented netCDF-4 functions, such as "nf90_def_var_deflate" and "nf90_def_var_chunking", instead of the old functions of netCDF-3 without changing the programs of present models. Another example is the parallel support. MPI-1 is originally implemented in the present version of gtool5 library so that, in parallel computations, you can realize separate input/output from each processor or bulk output by collecting data into a single processor even when you use netCDF-3 library without parallel functionality. We are now improving the gtool5 library to use parallel API of netCDF-4. Since the API of gtool5 would not be changed, present models can achieve better parallel functionality only by relinking the new version of the libraries.

Performance of data input/output using the present version of gtool5 is not so good. It takes about 50 % longer computational time for output of data with 8 GB size ($100\,000 \times 1000$ two-dimensional array with double precision) using gtool5 API than that with raw netCDF API. Moreover, data input takes about twice the time. Nevertheless, the computational

cost of data IO is sufficiently small in actual numerical computations of our models with gtool5 API, and benefits of the library, such as simplification of programming and improvement of readability, are provided satisfactory. However, there is potential possibility that data IO with gtool5 library may become a bottleneck in model calculations on a massive scale. We are now starting to improve performance of data IO of gtool5 library.

The gtool5 library proposed in this paper is not novel from the viewpoint of information technology; the data format mainly owes its design to the netCDF library used in the lower level of gtool5 library. The main achievement of the gtool5 library is to provide convenient interfaces for researchers working on numerical models for the Earth and planetary sciences. As is emphasized in Sect. 2, a particular requirement for the software utilized in the research of these fields is that the source code must be readable even by users. Hence, one of the issues for numerical research in these fields is the growing difficulty in tracing model source code because of the enlargement of the system. Expanded source code causes an "information explosion" for model developers and users. Construction of the gtool5 library and development of hierarchical models using gtool5 represent one approach to overcoming such difficulties.

Acknowledgements. Some of the authors were supported by a Grant-in-Aid for Scientific Research on Priority Areas "IT Infrastructures for Info-plosion" (subject number A01-14).

Edited by: P. Jöckel

References

Eaton, B., Gregory, J., Drach, B., Taylor, K., and Hankin, S.: NetCDF Climate and Forecast (CF) Metadata Conventions, Version 1.0., available at: http://cf-pcmdi.llnl.gov/documents/cf-conventions/1.0/cf-conventions.html (last access: 2 April 2012), 2003.

GFD Dennou Club Davis project: available at: http://www.gfd-dennou.org/library/davis/, last access: 2 April 2012.

GFD Dennou Club dcmodel project, available at: http://www.gfd-dennou.org/library/dcmodel/, last access: 2 April 2012.

Gfdnavi: available at: http://www.gfd-dennou.org/library/davis/gfdnavi/, last access: 2 April 2012.

GPhys: multi-purpose class to handle Gridded Physical quantities, available at: http://www.gfd-dennou.org/library/ruby/products/gphys/, last access: 2 April 2012.

gtool4 NetCDF Conventions: available at: http://www.gfd-dennou.org/library/gtool/gt4ncconv.htm.en, last access: 2 April 2012.

Held, I. M.: The gap between simulation and uderstandign in climate modeling, B. Am. Meteorol. Soc., 86, 1609–1614, 2005.

Horinouchi, T., Nishizawa, S., Watanabe, C., Tomobayashi, A., Otsuka, S., Koshiro, T., Hayashi, Y.-Y., and GFD Dennou Club: Gfdnavi, Web-based Data and Knowledge Server Software for Geophysical Fluid Sciences, Part I: rationales, stand-alone features, and supporting knowledge documentation linked to data, in: Database Systems for Advanced Apllications, Springer-Verlag, LNCS, 6193, 93–104, 2010.

Morikawa, Y., Takahashi, O. Y., Sasaki, Y., Nishizawa, S., Otobe, N., Ishiwatari, M., Odaka, M., Takehiro, S., Horinouchi, T., Hayashi, Y.-Y., Toyoda, E., and Gtool Devlopment Group: The gtool5 library, available at: http://www.gfd-dennou.org/library/gtool/ (last access: 2 April 2012), 2010.

NetCDF: available at: http://www.unidata.ucar.edu/software/netcdf/, last access: 2 April 2012.

Nishizawa, S., Horinouchi, T., Watanabe, C., Isamoto, Y., Tomobayashi, A., Otsuka, S., and GFD Dennou Club: Gfdnavi, web-based data and knowledge server software for geophysical fluid sciences, Part II: RESTful web services and object-oriented programming interface, in: Database Systems for Advanced Apllications, Springer-Verlag, LNCS, 6193, 105–116, 2010.

Ruby: available at: http://www.ruby-lang.org/en/, last access: 2 April 2012.

Sugiyama, K., Odaka, M., Yamashita, T., Nakajima, K., Hayashi, Y.-Y., and deepconv Development Group: Non-hydrostatic model deepconv, available at: http://www.gfd-dennou.org/library/deepconv/ (last access: 2 April 2012), 2010.

Takahashi, Y. O., Ishiwatari, M., Noda, S., Odaka, M., Horinouchi, T., Morikawa, Y., Hayashi, Y.-Y., and DCPAM Devlopment Group: DCPAM: planetary atmosphere model, available at: http://www.gfd-dennou.org/library/dcpam/ (last access: 2 April 2012), 2010.

Takehiro, S., Odaka, M., Ishioka, K., Ishiwatari, M., Hayashi, Y.-Y., and SPMODEL Development Group: SPMODEL: A series of hierarchical spectral models for geophyiscal fluid dynamics, Nagare Multimedia, available at: http://www2.nagare.or.jp/mm/2006/spmodel/index.htm (last access: 2 April 2012), 2006.

Icarus 229 (2014) 71–91

Contents lists available at ScienceDirect

Icarus

journal homepage: www.elsevier.com/locate/icarus

Numerical simulations of Jupiter's moist convection layer: Structure and dynamics in statistically steady states

K. Sugiyama [a,e,*], K. Nakajima [b], M. Odaka [c], K. Kuramoto [c,e], Y.-Y. Hayashi [d,e]

[a] Institute of Low Temperature Science, Hokkaido University, Sapporo 060-0819, Japan
[b] Department of Earth and Planetary Sciences, Kyushu University, Fukuoka 812-8581, Japan
[c] Department of Cosmosciences, Hokkaido University, Sapporo 060-0810, Japan
[d] Department of Earth and Planetary Sciences, Kobe University, Kobe 657-8501, Japan
[e] Center for Planetary Science, Kobe University, Kobe 650-0047, Japan

ARTICLE INFO

Article history:
Received 21 March 2013
Revised 16 September 2013
Accepted 12 October 2013
Available online 24 October 2013

Keywords:
Jovian planets
Jupiter, atmosphere
Atmospheres, dynamics
Atmospheres, structure

ABSTRACT

A series of long-term numerical simulations of moist convection in Jupiter's atmosphere is performed in order to investigate the idealized characteristics of the vertical structure of multi-composition clouds and the convective motions associated with them, varying the deep abundances of condensable gases and the autoconversion time scale, the latter being one of the most questionable parameters in cloud microphysical parameterization. The simulations are conducted using a two-dimensional cloud resolving model that explicitly represents the convective motion and microphysics of the three cloud components, H_2O, NH_3, and NH_4SH imposing a body cooling that substitutes the net radiative cooling. The results are qualitatively similar to those reported in Sugiyama et al. (Sugiyama, K. et al. [2011]. Intermittent cumulonimbus activity breaking the three-layer cloud structure of Jupiter. Geophys. Res. Lett. 38, L13201. doi:10.1029/2011GL047878): stable layers associated with condensation and chemical reaction act as effective dynamical and compositional boundaries, intense cumulonimbus clouds develop with distinct temporal intermittency, and the active transport associated with these clouds results in the establishment of mean vertical profiles of condensates and condensable gases that are distinctly different from the hitherto accepted three-layered structure (e.g., Atreya, S.K., Romani, P.N. [1985]. Photochemistry and clouds of Jupiter, Saturn and Uranus. In: Recent Advances in Planetary Meteorology. Cambridge Univ. Press, London, pp. 17–68). Our results also demonstrate that the period of intermittent cloud activity is roughly proportional to the deep abundance of H_2O gas. The autoconversion time scale does not strongly affect the results, except for the vertical profiles of the condensates. Changing the autoconversion time scale by a factor of 100 changes the intermittency period by a factor of less than two, although it causes a dramatic increase in the amount of condensates in the upper troposphere.

The moist convection layer becomes potentially unstable with respect to an air parcel rising from below the H_2O lifting condensation level (LCL) well before the development of cumulonimbus clouds. The instability accumulates until an appropriate trigger is provided by the H_2O condensate that falls down through the H_2O LCL; the H_2O condensate drives a downward flow below the H_2O LCL as a result of the latent cooling associated with the re-evaporation of the condensate, and the returning updrafts carry moist air from below to the moist convection layer. Active cloud development is terminated when the instability is completely exhausted. The period of intermittency is roughly equal to the time obtained by dividing the mean temperature increase, which is caused by active cumulonimbus development, by the body cooling rate.

1. Introduction

It is now an established fact that convective clouds are common entities in Jupiter's atmosphere (Vasavada and Showman, 2005). For example, Galileo and Cassini observed a number of small (~500–2000 km) convective clouds near the locations of lightning strikes (Little et al., 1999; Gierasch et al., 2000; Dyudina et al., 2004). Convective clouds are considered to play an important role

* Corresponding author. Present address: Institute of Space and Astronautical Science, JAXA, Sagamihara 252-5210, Japan.
E-mail address: sugiyama@gfd-dennou.org (K. Sugiyama).

0019-1035
http://dx.doi.org/10.1016/j.icarus.2013.10.016

in transferring heat from the interior of the planet to the upper troposphere (Gierasch et al., 2000). In due course, the mean vertical structure in the moist convection layer of Jupiter's atmosphere is thought to be maintained by the statistical contribution of a large number of clouds driven by internal and radiative heating/cooling over multiple cloud life cycles.

The mean vertical structure, i.e., the mean vertical profiles of temperature, condensates, and condensable gases, in the moist convection layer has been estimated using one-dimensional equilibrium cloud condensation models (ECCMs), where the profiles are derived from the thermodynamic equilibrium values of an adiabatically ascending air parcel from the deep atmosphere (Weidenschilling and Lewis, 1973; Atreya and Romani, 1985; Sugiyama et al., 2006). However, the results obtained by ECCMs should not be accepted without caution because they have neglected the effects of fluid dynamical and cloud microphysical processes associated with various atmospheric disturbances including convective clouds.

Although numerous attempts have been made to determine the vertical structure of Jupiter's atmosphere, many of the important properties of convective clouds are far from being constrained (reviewed by, e.g., West et al., 1986; Atreya et al., 1999; Vasavada and Showman, 2005), since the thick cloud deck prevents the vertical structure of the moist convection layer from being observed by remote sensing. Examples are the mean profiles of condensates and condensable gases; the Galileo probe is the first, and so far the only, spacecraft that carried out an in situ observation of the vertical structure of Jupiter's atmosphere from the level of visible clouds to approximately 20 bars. The results show an unexpectedly small amount of water vapor (Wong et al., 2004). However, the representativeness of the observed vertical structure is considered poor since the Galileo probe's entry site was one of the 5-μm hot spots which are atypical cloud-free regions in Jupiter's atmosphere. The mean atmospheric structure and its relationship to moist convection still remain unclear.

In order to investigate the possible structure and dynamics of the moist convection layer maintained by the statistical contribution of a large number of clouds over multiple cloud life cycles, numerical simulations using a cloud resolving model with long-term integration periods are indispensable. Such attempts have been rather rare, since most studies using cloud resolving models have focused on the evolution of a single cloud, in which the onset and initial expanding phase of a single cloud are considered under simplified and arbitrary initial conditions with short-term integration periods (e.g., Yair et al., 1992, 1995; Hueso and Sanchez-Lavega, 2001).

The purpose of our studies (Nakajima et al., 2000; Sugiyama et al., 2009, 2011) has been to investigate idealized mean profiles of condensable gases and condensates, which were formerly investigated by the use of ECCMs, and the temporal-spatial characteristics of convective motions that produce such profiles. For this purpose, we have been developing a two-dimensional cloud resolving model and performing long-term numerical simulations. The atmospheric structure obtained by Nakajima et al. (2000) is characterized by a thin but strong stable layer near the H_2O lifting condensation level that acts as a barrier for vertical convective motions, which is caused mainly by the change of mean molecular weight of atmospheric gases. This study suffered from two major limitations in that it considered only H_2O as a condensable component and employed unrealistically intense body cooling as a substitute for radiative cooling. Sugiyama et al. (2009) included, in addition to the condensation of H_2O, the condensation of NH_3 and the production reaction of NH_4SH, and Sugiyama et al. (2011) investigated the possible structure and dynamics of the moist convection layer using a body cooling whose cooling rate was of the order of that expected in Jupiter's atmosphere. The results suggested that the activity of moist convection is not steady but experiences a prominent quasi-periodic variation with a period of several tens of days. Around the levels where NH_3 condensation and NH_4SH chemical reaction occur, weak but definite stable layers develop and act as dynamical and compositional boundaries during the period of weak convective activity.

Although Sugiyama et al. (2011) succeeded in obtaining an insightful image of the structure and dynamics of the moist convection layer in Jupiter's atmosphere, the dependence of the structure and dynamics on parameters that are poorly constrained by observations remains to be examined. One of the most important parameters to be considered is the deep abundances of condensable gases. Not only the altitudes at which condensation and chemical reaction occur but also dynamical properties should be affected by this parameter, since the vertical profile of static stability is governed by the deep abundances of condensable gases (Sugiyama et al., 2006). The deep abundance of H_2O gas is the most ambiguous. The Galileo probe could not provide a confident estimate (Wong et al., 2004), and indirect evidence suggests that the deep abundance of H_2O gas is higher than the solar abundance (Atreya et al., 1999). We therefore perform a parameter experiment on the deep abundances of condensable gases.

Also poorly constrained are details of cloud microphysical processes. There have been some attempts (e.g., Rossow, 1978; Carlson et al., 1988) to estimate the time scales involved in such processes. Gibbard et al. (1994) and Yair et al. (1998) also considered cloud microphysical processes in order to investigate lightning in Jupiter's convective clouds observed by spacecraft, and succeeded in demonstrating its existence. However, there have been no quantitative measurements of the amount, size, type, and composition of cloud particles, to which the representation of cloud microphysics in numerical models can be compared. Thus, we hesitate to use a highly sophisticated bulk microphysical parameterization scheme such as that implemented in the EPIC model (Palotai and Dowling, 2008). Instead, we implement a simple bulk parameterization scheme, as will be fully described in Section 2, and perform a parameter experiment on the autoconversion time scale. The reason we chose the autoconversion time scale as the parameter to be varied is that it is the most ambiguous parameter of all those controlling the rate of condensate removal from an air parcel. For instance, at least for the case of Earth-like conditions, Nakajima and Matsuno (1988) showed by the use of long-term numerical calculations that switching off the autoconversion process destroys the asymmetry between narrow, strong, cloudy updrafts and wide, weak, dry downdrafts, which is a distinct characteristic of the troposphere of Earth, and produces a troposphere completely filled with condensate. Switching on/off other processes such as evaporation of precipitating condensate and negative buoyancy of condensate does not result in such an extreme change.

In this study, a number of long-term numerical simulations are performed in order to examine the dependence of the idealized structure and dynamics of the moist convection layer in statistically steady states on the autoconversion time scale and on the deep abundances of condensable gases. We also examine the mechanism of the most significant characteristic, the intermittent emergence of vigorous cumulonimbus clouds, obtained in most of our calculations. In Section 2, we present a brief description of our cloud resolving model and the settings for the parameter experiments. In Section 3, we summarize the characteristics of the structure and dynamics of the moist convection layer obtained by a control experiment in which the settings are identical to those of Sugiyama et al. (2011). In Sections 4 and 5, we demonstrate the dependences of the structure and dynamics of the moist convection layer on the autoconversion time scale and on the deep abundances of condensable gases, respectively. We discuss the

mechanism that causes intermittent cloud activity in Section 6, and provide concluding remarks in Section 7.

2. Numerical model and settings of parameter experiments

The framework of our numerical model and the experimental settings we adopt are chosen as simple ones that can mimic Jupiter's atmosphere, which is maintained by the balance among the upwelling heat flux from the deep interior, the upward heat transport by moist convection, and net radiative cooling caused by solar and long-wave radiation. The effect of the heat supply from the deep interior is realized by keeping the values of the potential temperature and mixing ratios constant at the lower boundary. By doing so, we assume the region below the lower boundary to be a huge reservoir, in which heat and condensable gases are transported upward and well mixed by convection in the deep atmosphere. The net radiative cooling is simply represented as horizontally and temporally uniform body cooling at the upper troposphere, instead of being calculated by the use of a radiative transfer model. We suppose that the assumption of temporally and horizontally uniform cooling is acceptable at least as the first step of consideration of statistically steady states.

Numerical experiments are conducted for periods much longer than the lifetime of individual cumulonimbus clouds, because the purpose of the experiments is to realize the possible structure and dynamics of the moist convection layer established as statistically steady states by the interaction among the internal heating from the deep interior, the moist convection, and net radiative cooling. During the course of long-term integration of the numerical model, the initially given vertical profiles of temperature and mixing ratios of the condensable gases are forgotten, and the mean atmospheric profiles gradually evolve to be those governed by the internal processes in the model, which are the states of the atmosphere with which we are concerned in this study. In this respect, the numerical experiments in the present study are distinctly different from those for the simulation of a single cloud (e.g., Yair et al., 1992, 1995; Hueso and Sanchez-Lavega, 2001), where the profiles of temperature and mixing ratios are important control parameters. In contrast, these profiles are not control parameters but part of the results of our calculations.

2.1. Numerical model

Here we briefly describe the cloud resolving model utilized in this study. A more complete description can be found in Sugiyama et al. (2009). Our model is available at http://www.gfd-dennou.org/library/deepconv/.

The dynamical framework of our model is two-dimensional in the horizontal and vertical directions, and is based on the quasi-compressible system (Klemp and Wilhelmson, 1978). In this framework, the variables are divided into a horizontally uniform basic state in hydrostatic equilibrium and residual perturbation, and prognostic equations of residual perturbations are solved.

Derivation of the momentum and pressure equations require use of an equation of state that includes the effects of condensable species.

$$\rho = \frac{p}{R_d T_v} = \frac{p}{R_d T}\left(\frac{1/M_d}{1/M_d + \sum q_v/M_v}\right)\left(1 + \sum q_v + \sum q_c\right), \tag{1}$$

where ρ is the density of moist air, p is the pressure, R_d is the gas constant for dry air per unit mass, T is the temperature, T_v is the virtual temperature, and M_d and M_v are the molecular weight of the non-condensable and condensable components, respectively. q_v is the mixing ratio of each condensable gas, q_c is the mixing ratio of each condensate, and $\sum$ indicates the summation regarding condensable gases or condensates. By using Eq. (1), the Exner function (non-dimensional pressure), π, is written in the form

$$\pi \equiv \left(\frac{p}{p^*}\right)^{R_d/c_{p_d}} = \left(\frac{R_d}{p^*}\rho\theta_v\right)^{R_d/c_{p_d}}, \tag{2}$$

where p^* is the reference pressure, c_{p_d} is the specific heat of dry air at constant pressure, and θ_v is the virtual potential temperature defined by

$$\theta_v \equiv \frac{\theta}{\left(\frac{1/M_d}{1/M_d + \sum q_v/M_v}\right)(1 + \sum q_v + \sum q_c)} \tag{3}$$

and the potential temperature θ is $\theta = T/\pi$. This dynamical framework ignores the dependence of the mean specific heat on the temperature and composition, since the potential temperature is utilized. However, the value of the static stability N^2, which governs the overall structure of the moist convection layer, is almost the same as that obtained when the dependences ignored above are taken into consideration (Sugiyama et al., 2009).

The momentum equations are expressed in the following forms,

$$\frac{\partial u}{\partial t} = -\left(u\frac{\partial u}{\partial x} + w\frac{\partial u}{\partial z}\right) - c_{p_d}\theta_{v0}\frac{\partial \pi'}{\partial x} + Turb.u, \tag{4}$$

$$\frac{\partial w}{\partial t} = -\left(u\frac{\partial w}{\partial x} + w\frac{\partial w}{\partial z}\right) - c_{p_d}\theta_{v0}\frac{\partial \pi'}{\partial z} + \left(\frac{\theta'_v}{\theta_{v0}}\right)g + Turb.w, \tag{5}$$

where u is the velocity in the x direction, w is the velocity in the z direction, g is the acceleration due to gravity, and $Turb.u$ and $Turb.w$ refer to subgrid scale turbulent momentum mixing. The variables denoted by "0" and "′" represent a horizontally uniform basic state and residual perturbation, respectively, which satisfy the relation, e.g., $\theta = \theta' + \theta_0$ ($\theta' \ll \theta_0$). The buoyancy term in Eq. (5) can be rewritten as

$$\left(\frac{\theta'_v}{\theta_{v0}}\right)g = \left(\frac{\theta'}{\theta_0} + \frac{\sum(q'_v + q_{v0})/M_v}{1/M_d + \sum q_{v0}/M_v} - \frac{\sum(q'_v + q_{v0}) + \sum q'_c}{1 + \sum q_{v0}}\right)g. \tag{6}$$

Note that the mixing ratio of each condensate in the basic state is set to zero. The pressure equation is derived by using Eqs. (1)–(3), the compressible continuity equation

$$\frac{\partial \rho}{\partial t} + \frac{\partial}{\partial x_j}(\rho u_j) = 0,$$

and the thermodynamic equation (Eq. (8)), which will be described later,

$$\frac{\partial \pi'}{\partial t} = -\frac{{C_{s0}}^2}{c_{p_d}\rho_0\theta_{v0}^2}\frac{\partial}{\partial x_j}(\rho_0\theta_{v0}u_j), \tag{7}$$

where C_{s0} is the phase velocity of sound given by ${C_{s0}}^2 = c_{p_d}R_d\pi_0\theta_{v0}/c_{v_d}$, and c_{v_d} is the specific heat at constant volume. The terms that correspond to pressure variation caused by diabatic heating are neglected following Klemp and Wilhelmson (1978). The thermodynamic equation can be written as

$$\frac{\partial \theta'}{\partial t} = -\left(u\frac{\partial \theta'}{\partial x} + w\frac{\partial \theta'}{\partial z}\right) - w\frac{\partial \theta_0}{\partial x} + \frac{1}{\pi_0}(Q_{cnd} - Q_{rad} + Q_{dis}) + Turb.\theta, \tag{8}$$

where Q_{cnd} refers to heating by condensation and chemical reaction, Q_{rad} represents body cooling, and Q_{dis} and $Turb.\theta$ refer to dissipative heating and subgrid scale turbulent mixing of potential temperature, respectively. The conservation equation for each condensable gas or condensate can be written in the form

$$\frac{\partial q'}{\partial t} = -\left(u\frac{\partial q'}{\partial x} + w\frac{\partial q'}{\partial z}\right) - w\frac{\partial q_0}{\partial x} + Src.q + Turb.q, \quad (9)$$

where *Src.q* refers to source terms associated with the cloud microphysical parameterization and *Turb.q* refers to the subgrid scale turbulent mixing terms. Eq. (9) represents nine equations, i.e., the conservation equations for three condensable gases, three non-precipitating condensates, and three precipitating condensates, because we consider three condensable components in Jupiter's atmosphere and employ the bulk parameterization scheme of Kessler (1969) as mentioned below.

As a minimal model that can represent the most essential processes of cloud microphysics, we use a bulk parameterization scheme based on Kessler (1969), which has been used in modeling studies on terrestrial moist convection. In the scheme, each condensate is simply divided into two categories, "non-precipitating condensate" and "precipitating condensate." Although it is unclear how well the scheme represents the actual cloud microphysical processes in Jupiter's atmosphere, Yair et al. (1992) uses the scheme as the first step in considering moist convection, and Hueso and Sanchez-Lavega (2001) uses a very similar scheme. As mentioned in Sugiyama et al. (2009), some of the parameters in Kessler's parameterization used in our model are modified from the original ones for Earth's atmosphere following Nakajima et al. (2000). The growth rate of precipitating condensates by collecting non-precipitating condensates and the terminal velocity for precipitating condensates are increased by a factor of 3, considering the terminal velocity of condensate particles calculated by Yair et al. (1995). In addition, autoconversion from non-precipitating to precipitating condensates is accelerated by 10 times considering the results of Rossow (1978) and Carlson et al. (1988), in which precipitation-size particles are expected to form rapidly in Jupiter's atmosphere.

We do not try to implement possible categories of condensates. In the case of Earth's clouds, highly sophisticated bulk microphysical parameterization schemes have been developed. Some of them treat liquid and solid phases separately, distinguish several categories of icy particles, i.e., ice crystals, snowflakes, graupel, and hail, and estimate the interactions among them (Straka, 2009). Naturally, we cannot use those schemes because their performance in Jupiter's atmosphere is not at all guaranteed. Not only the interaction among the categories but also the specifications of the categories themselves strongly depend on observational and experimental facts collected exclusively for Earth's clouds. Furthermore, the microphysical behavior of NH_3 and NH_4SH particles is completely unknown. Considering the currently available knowledge about the microphysics of Jupiter's clouds, we think that the use of the Kessler type scheme with minimal complexity is reasonable for the time being. Improvement of the microphysical scheme is important, but is a future issue.

We simplify the radiative process, instead of calculating it by the use of a radiative transfer model. The model atmosphere is subject to an externally given body cooling that is a substitute for radiative cooling, as mentioned in the first paragraph of Section 2. The subgrid scale turbulence parameterization scheme of 1.5-order closure (Klemp and Wilhelmson, 1978) is implemented, where turbulent mixing coefficients are diagnosed from turbulent kinetic energy that is predicted by a prognostic equation.

2.2. Experimental settings

The experimental settings are schematically shown in Fig. 1. The computational domain covers the region of 300 km in the vertical direction (from 30 bar to 0.001 bar) and 1024 km in the horizontal direction. The spatial resolution is 2 km in both the horizontal and the vertical directions. The cyclic boundary condition is applied in the horizontal direction. The conditions of free-slip and vanishing vertical velocity are applied at the upper and lower boundaries. Hereafter, as shown in Fig. 1, "dry convection layer," "moist convection layer," and "tropopause" are defined as the region from the lower boundary to the H_2O lifting condensation level, the region from the H_2O lifting condensation level to $p = 0.1$ bar, and the level at $p = 0.1$ bar, respectively.

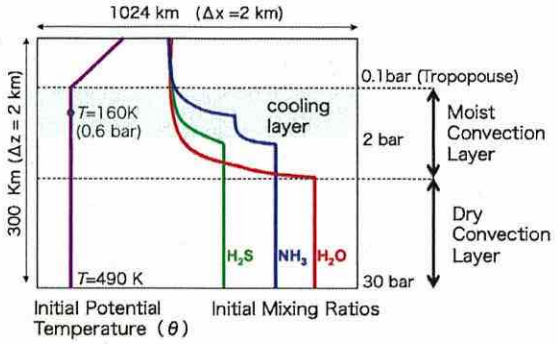

Fig. 1. Schematic view of experimental settings.

The model atmosphere consists of H_2, He, H_2O, NH_3, and H_2S. H_2 and He are treated as dry (non-condensable) components while H_2O, NH_3, and H_2S are treated as condensable components. Solid H_2O, solid NH_3, and solid NH_4SH are treated as condensates. The acceleration of gravity is set to 23.1 m/s. The values of potential temperature and mixing ratios of the condensable gases at the lower boundary are kept constant in order to represent the effect of convection in the deeper planetary interior implicitly, as mentioned in the first paragraph of Section 2.

The initial mixing ratio of each condensable gas is equal to that given at the lower boundary below the pressure level where condensation or chemical reaction of NH_4SH formation occurs. Above these levels, all mixing ratios are set to be slightly below their saturated values. The initial temperature profile from the lower boundary to $p = 0.1$ bar level is dry adiabatic, i.e., constant potential temperature, that passes through 490 K at the lower boundary and 160 K at 0.6 bar, and is isothermal above 0.1 bar. At the initial time, the model atmosphere is motionless. In order to seed a convective motion, a small random potential temperature perturbation is added to the grid points near the H_2O lifting condensation level.

2.3. Experimental parameters

The experimental parameters in our calculations are listed in Table 1. The autoconversion time scale, τ_{auto}, is varied. The conversion

Table 1
Experimental parameters.

Run	Body cooling rate (K/day)	Abundances at the lower boundary (solar)	Autoconversion time scale (s)
CTRL[a]	0.01	1.0	100
C10	0.01	1.0	1000
C100	0.01	1.0	10,000
R10S01	0.1	0.1	100
R10	0.1	1.0	100
R10S3	0.1	3.0	100
R10S10	0.1	10.0	100
R3[b]	0.3	1.0	100
R100[c,b]	1.0	1.0	100

[a] The settings for CTRL are identical to those of Sugiyama et al. (2011).
[b] The results are only shown in Appendix A.
[c] The settings for R100 are identical to those of Sugiyama et al. (2009), except for a change in the horizontal domain from 512 km to 1024 km.

rate from non-precipitating to precipitating condensate due to the autoconversion process, CN, is expressed as

$$CN = (q'_{c1} - q^0)/\tau_{auto},$$

where q'_{c1} and q^0 are the mixing ratio of each non-precipitating condensate and the threshold mixing ratio of each condensate, respectively. In the control experiment, the value of τ_{auto} is set to 100 s, which is an order of magnitude shorter than the standard value used for Earth's atmosphere as is noted in Section 2.1, and the value of q^0 is set to zero. The reason for adopting $q^0 = 0$ is that we have simply no clue as to choice of its value. We perform additional numerical calculations with larger values of τ_{auto}. The longest time scale employed, 10,000 s, is selected in order to satisfy the condition that the value of τ_{auto} is longer than the time scale of vertical advection in the moist convection layer.

The abundance of each condensable gas at the lower boundary is varied from 0.1 to 10 times solar. As for the solar abundance, mixing ratios of H_2O, NH_3, and H_2S are 6.1×10^{-3}, 7.6×10^{-4}, and 3.5×10^{-4} kg/kg, respectively (Grevesse et al., 2007).

The body cooling rate is also varied. The cooling rate for the control experiment is 0.01 K per terrestrial day, which is reasonably compatible with the cooling rate determined by the Galileo probe (Sromovsky et al., 1998), and the total energy loss $\sim$11.4 W/m^2 by cooling is also compatible with the globally averaged thermal emission (Hanel et al., 1981). However, it should be noted that, in the parameter experiment on the deep abundances of condensable gases, the specified body cooling rate is set to 0.1 K rather than 0.01 K per terrestrial day in order to reduce the CPU time required to achieve a statistical steady state in the model atmosphere. The dependence of the structure and dynamics of the moist convection layer on the body cooling rate is summarized in Appendix A. The structure and dynamics of the moist convection layer obtained in a calculation using a large amount of body cooling share several qualitative features with those in the control experiment, as will be shown later.

3. The structure and dynamics of the moist convection layer obtained in the control experiment

The CTRL listed in Table 1, whose settings are identical to those of Sugiyama et al. (2011), is chosen as the control experiment in our study. In this section, we describe key aspects of CTRL referring to the figures showing the thermal and the vertical velocity structures, which are not presented in detail in Sugiyama et al. (2011). In the following, the lifting condensation level (LCL) of each condensable gas is defined as the condensation or chemical reaction level obtained by an ECCM using the thermodynamic subroutine in the cloud resolving model, in which a thermally equilibrium air parcel adiabatically ascends from the lower boundary. The LCLs of H_2O, NH_4SH, and NH_3 are about 4.0 bar, 1.7 bar, and 0.5 bar, respectively.

3.1. Temporal variation of the structure and dynamics of the moist convection layer

The results of CTRL are characterized by a quasi-periodic emergence of vigorous deep clouds rising from the H_2O LCL to the tropopause. Hereafter, the vigorous deep clouds are referred to as "cumulonimbus clouds," and the periods of strong cumulonimbus activity are referred to as "active periods," whereas the periods between consecutive active periods are referred to as "quiet periods."

Fig. 2(a) shows a typical cycle of the horizontal-mean mixing ratios of the condensates. The durations of the active periods, marked as "A," are only 1–2 days, while that for the quiet period, marked as "Q," is considerably longer. At the beginning of the quiet period, only NH_3 clouds develop. Then, NH_4SH clouds appear, followed by H_2O clouds. The base of H_2O cloud gradually descends with time. Eventually, the quiet period ends with the explosive development of cumulonimbus clouds. The quasi-periodicity of this active-quiet cycle was exemplified in Fig. 1 and Animation 1 of Sugiyama et al. (2011) and will be shown later in Fig. 6(a1). The mean period

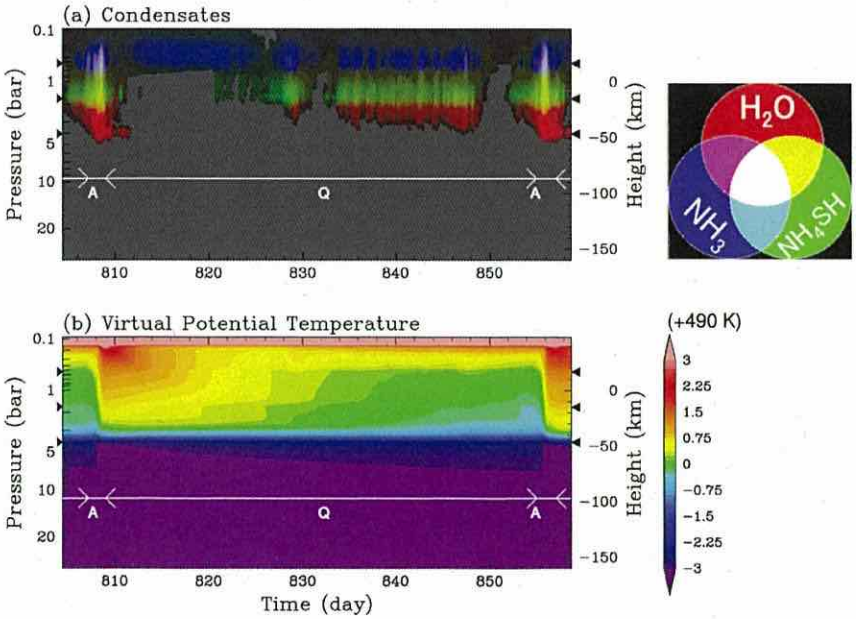

Fig. 2. Temporal variation of (a) horizontal mean mixing ratios of condensates and (b) horizontal mean virtual potential temperature obtained in CTRL. In (a), H_2O condensate, NH_4SH condensate, and NH_3 condensate are indicated by red, green, and blue color tones, respectively. Tone intensity represents mixing ratio (kg/kg) on a logarithmic scale ranging from 1.0×10^{-8} to 1.0×10^{-4} kg/kg. Multiple composition clouds are represented by a mixture of the three colors. Black triangles on the left and the right edges of each panel indicate the NH_3, NH_4SH, and H_2O LCLs from top to bottom. Active periods and quiet periods are marked as "A" and "Q," respectively. Altitude is measured from the level of 1 bar. (For interpretation of the references to color in this figure legend, the reader is referred to the web version of this article.)

of intermittency averaged over the last 4 active-quiet cycles is about 41 days.

Fig. 2(b) shows a typical cycle of virtual potential temperature, θ_v, in the same time span shown in Fig. 2(a). The definition of θ_v is as given in Eq. (3). In Fig. 2(b), a variation of θ_v synchronized with the intermittent cloud activity is clearly seen in the moist convection layer; the value of θ_v rapidly increases during the active periods, and decreases steadily with time during the quiet period. The variation of θ_v arises, since condensation heating in the moist convection layer is concentrated almost exclusively during the active periods. The temporal variation of θ_v at a pressure level is sawtooth-like, as will be shown later in Fig. 6(a2).

Fig. 3(a–c) shows snapshots of a selected set of variables during the quiet period shown in Fig. 2. At the beginning of this quiet period (Fig. 3(a)), moist convection associated with NH_3 condensation occurs and the NH_3 clouds are distributed horizontally. Vertical motion is present not only above the NH_3 LCL but also below this LCL, since evaporation of precipitating NH_3 condensate drives downdrafts below the NH_3 LCL. The peak velocities of the updrafts and downdrafts found near the tropopause are about 3 m/s and −3 m/s, respectively. The vertical motion below the H_2O LCL is the remnant of convective motion driven during the previous active period. As time progresses, NH_4SH clouds develop (Fig. 3(b)). Below each of the updrafts associated with NH_4SH condensation, a downdraft is driven by the evaporation of precipitating NH_4SH condensate. Following the onset of NH_4SH clouds, H_2O clouds begin to form locally (Fig. 3(c)) in the updrafts that develop as the returning flows associated with downward plumes driven by the evaporation of precipitating NH_4SH condensate. Mixing of different condensable gases and condensates across the NH_3 LCL or NH_4SH LCL is weak, but occurs occasionally due to the upward or downward penetration of convective plumes. The peak velocities of the updrafts and downdrafts in the moist convection layer are about 10 m/s and −10 m/s, respectively.

Fig. 3(d) shows snapshots of the active period that occurs after the quiet period shown in Fig. 3(a–c). The vertical motion in the moist convection layer is characterized by narrow, strong, cloudy updrafts and wide, weak, dry downdrafts. The maximum mixing ratio of H_2O condensate is about 4.0×10^{-3} kg/kg. The peak velocities of the updrafts and the downdrafts in the moist convection layer are about 50 m/s and −10 m/s, respectively. The updrafts during the active period are about five times as strong as those in the quiet period (Fig. 3(b) and (c)). In the dry convection layer, strong downdrafts (~ -50 m/s) are found just beneath cumulonimbus clouds, which are driven by the latent cooling caused by the re-evaporation of H_2O condensate. Fig. 3(d) also shows that the vigorous vertical transport associated with the convective circulation during the active periods strongly modifies the distributions of condensable gases and condensates from those expected by the ECCM. Considerable amounts of H_2O and NH_4SH condensates are transported upward from their respective LCLs to the tropopause as indicated by the white color region in Fig. 3(d1). The distribution of each condensable gas mixing ratio is highly inhomogeneous in the horizontal direction (Fig. 3(d2)). Even below the H_2O LCL, a slight inhomogeneity of mixing ratios of condensable gases associated with the downdrafts is found.

During the quiet period in Fig. 3(b6) and (c6), the vertical profiles of the intensity of vertical motion as represented by root mean square of the vertical velocity, $\sqrt{\overline{w^2}}$, have either a local minimum or inflection points at the NH_3 and the NH_4SH LCLs. Corresponding to these vertical profiles, a staircase-like structure of the horizontal mean mixing ratio of NH_3 gas develops (Fig. 3(b5) and (c5)); its vertical gradient is intensified at the NH_4SH LCL and the NH_3 LCL, whereas the mean mixing ratio becomes more uniform between the two LCLs resulting from the mixing caused by the vertical motions. These features could be regarded as the manifestation of a dynamical and compositional boundary resulting from the enhancement of static stability at the LCLs (e.g., Sugiyama et al., 2006).

During the active period, the NH_3 and NH_4SH LCLs act neither as dynamical nor compositional boundaries; not only the intense updrafts in the vigorous cumulonimbus clouds but also the dry downdrafts penetrate these two LCLs (Fig. 3(d3)). However, the H_2O LCL continues to act as a significant dynamical and compositional boundary implied by both $w \sim 0$ and the local minimum of $\sqrt{\overline{w^2}}$ at the H_2O LCL (Fig. 3(d3) and (d6)).

Fig. 4(a) shows the temporal variations of vertically integrated heating due to condensation, advection, body cooling, subgrid turbulence, and the heat flux at the lower boundary in the moist convection layer and dry convection layer during the quiet periods. Fig. 4(b) is the same as Fig. 4(a) but for the active periods. In the moist convection layer, the condensation heating associated with the cumulonimbus clouds is dominant during the active period, while the body cooling is dominant during the quiet period. The maximum rate of condensation heating in the active period is about 100 times larger than that of the body cooling. The intense condensation heating during the active period is caused by the successive formation of vigorous cumulonimbus clouds in a short time, as shown in Figs. 2 and 3(d).

In the dry convection layer, significant heating occurs only during the active period (Fig. 4(a) and (b)). During the active period, latent cooling due to the evaporation of precipitating H_2O condensate from cumulonimbus clouds drives vertical motion. The downward advected cold air parcels cool the region near the lower boundary. The cooling near the lower boundary is balanced by the heat flux from the lower boundary, where the potential temperature is kept constant.

3.2. Time and horizontal mean structure of the moist convection layer

Fig. 5(a) shows the horizontal mean profiles of the mixing ratios of the condensates averaged over the last 4 active-quiet cycles. The vertical profiles averaged only over the active periods and those only over the quiet periods are also shown by broken and dashed lines, respectively. Two distinct features can be observed in the mean vertical profiles. First, all of the condensates are advected upward to significant heights; H_2O and NH_4SH particles are advected up to altitudes above the NH_3 LCL. Second, the maximum values for mixing ratios of all of the condensates are fairly close to each other; they are approximately $1.0 - 2.0 \times 10^{-6}$ kg/kg. The mean mixing ratio of a condensate, $\bar{q}_c'$, can be estimated using that averaged only over the active periods, $\bar{q}_c'^a$, typical length of the active period, Δt^a, and the mean period of intermittency, Δt, as $\bar{q}_c' = \bar{q}_c'^a \Delta t^a / \Delta t$, since the contributions during the quiet periods are negligible.

Fig. 5(b) shows the vertical profiles of horizontal mean mixing ratios of condensable gases averaged over the last 4 active-quiet cycles. Also shown are the corresponding vertical profiles obtained by the ECCM. The profiles of the condensable gases in the cloud resolving model exhibit quite different characteristics from those obtained by the ECCM. In the cloud resolving model, each condensable gas is significantly undersaturated in the moist convection layer and mixing ratios of NH_3 and H_2S gases begin to decrease with height not at their respective LCLs, but at the H_2O LCL. These features are one of the manifestations of vigorous vertical mixing of dry and condensable gases caused by the intense convective circulation during the active periods.

Fig. 5(c) shows the horizontal mean vertical profiles of static stability N^2 (the square of buoyancy frequency, N). There is a distinct maximum of N^2 at the H_2O LCL, which explains the reason that the level acts as a both dynamical and compositional boundary even during the active periods shown in Fig. 3(d). Weaker peaks are also present at the NH_3 and NH_4SH LCLs. The reason

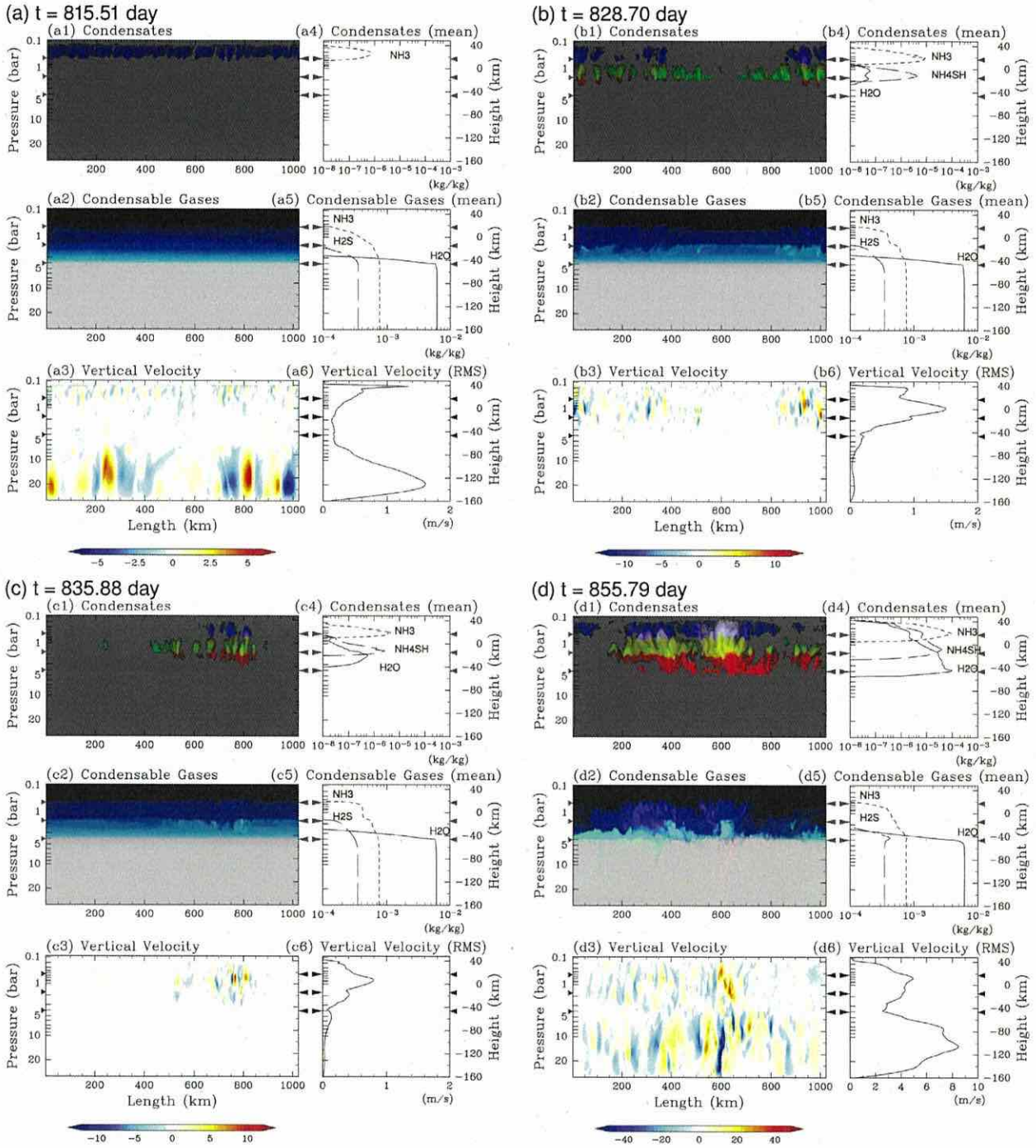

Fig. 3. Temporal evolution of convection obtained in CTRL. (a) Snapshots at $t = 815.51$ day in a quiet period. (a1) Mixing ratios of condensates plotted in the same manner as in Fig. 2 but with a different logarithmic scale ranging from 1.0×10^{-8} to 1.0×10^{-3} kg/kg for each condensate. (a2) Mixing ratios of condensable gases plotted indicating H_2O, H_2S, and NH_3 gases by red, green, and blue color tones, respectively. Tone intensity represents mixing ratio (kg/kg) on a linear scale normalized by the corresponding initial value. (a3) Vertical velocity. (a4) Horizontal mean mixing ratios of condensates. Solid, broken, and dashed lines indicate H_2O, NH_4SH, and NH_3 condensates, respectively. (a5) Horizontal mean mixing ratios of condensable gases. Solid, broken, and dashed lines indicate H_2O, H_2S, and NH_3 gases, respectively. (a6) Root mean square (RMS) of the vertical velocity. (b) Same as (a) but for $t = 828.70$ day. (c) Same as (a) but for $t = 835.88$ day. (d) Same as (a) but for $t = 855.79$ day in a active period. Black triangles on the left and the right edges of each panel indicate the NH_3, NH_4SH, and H_2O LCLs from top to bottom. (For interpretation of the references to color in this figure legend, the reader is referred to the web version of this article.)

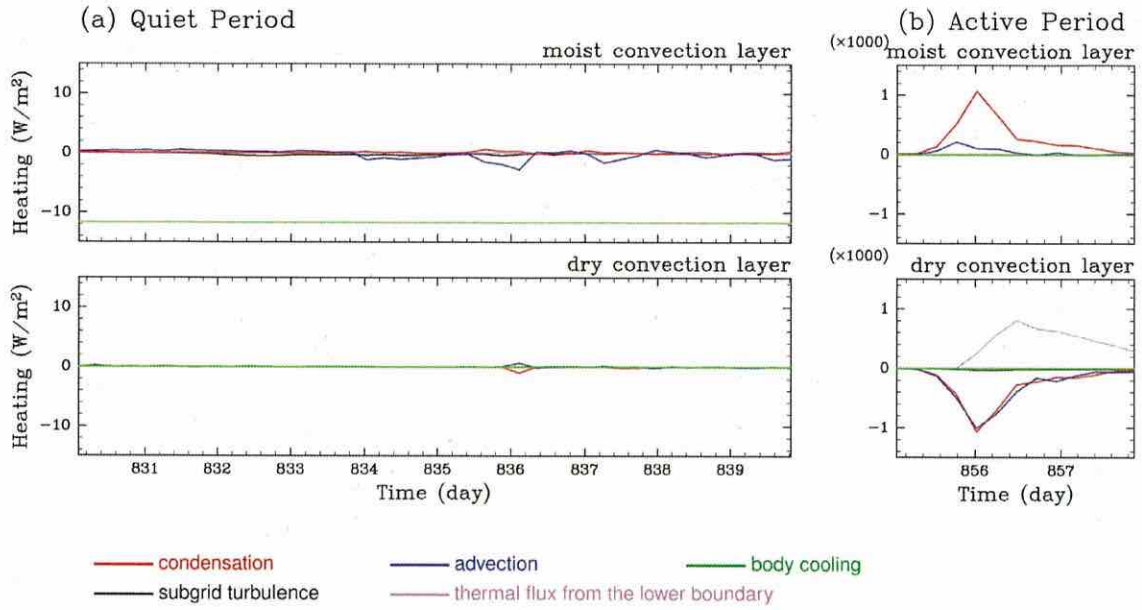

Fig. 4. Temporal variation of vertically integrated heating for (a) a quiet periods and (b) an active periods. Heating due to condensation, advection, body cooling, subgrid turbulence, and thermal flux from the lower boundary are indicated by red, blue, green, black, and violet lines, respectively. (For interpretation of the references to color in this figure legend, the reader is referred to the web version of this article.)

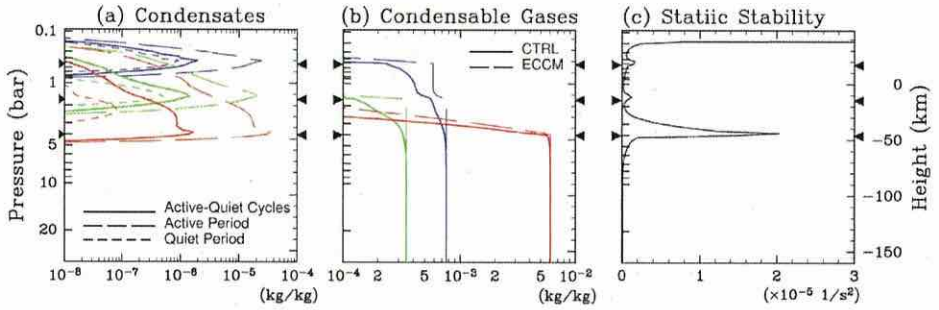

Fig. 5. (a) Vertical profiles of horizontal mean mixing ratios of condensates averaged over the last 4 active-quiet cycles. Blue, green, and red lines indicate NH_3, NH_4SH, and H_2O,respectively. Solid, broken, and dashed lines indicate the profiles averaged over the periods of the entire active-quiet cycles, those only over the active period, and those only over the quiet period, respectively. (b) Vertical profiles of horizontal mean mixing ratios of condensable gases. Blue, green, and red lines indicate NH_3, H_2S, and H_2O, respectively. Thin broken lines represent profiles obtained by the ECCM. (c) Static stability N^2. Black triangles on the left and the right edges of each panel indicate the NH_3, NH_4SH, and H_2O LCLs from top to bottom. (For interpretation of the references to color in this figure legend, the reader is referred to the web version of this article.)

for the formation of such stable layers is that condensation of these condensable gases not only releases latent heat energy but also reduces the mean molecular weight, since those gases are heavier than hydrogen, the dominant "dry" component of Jupiter. The H_2O LCL remains stable at all times, since the active periods begin before the atmosphere at the H_2O LCL becomes neutral or unstable due to the triggering effect caused by precipitating H_2O condensate as will be described in Section 6.

4. Dependence on the autoconversion time scale

In this section, the dependence of the structure and dynamics of the moist convection layer on the autoconversion time scale, τ_{auto}, is examined. The left panels of Fig. 6 show the temporal variations of the horizontal mean mixing ratios of the condensates and virtual potential temperature at $p = 2$ bar for CTRL, C10, and C100 listed in Table 1, where the values of τ_{auto} are 100 s, 1000 s, 10,000 s, respectively. The overall features of temporal variations of cloud activity and virtual potential temperature, namely the existence of the intermittency and sawtooth-like variation, do not seem to change greatly with the increase of τ_{auto}. However, there are modest quantitative differences among the three cases. For example, compared to the results of CTRL, the amplitude of temporal variation of virtual potential temperature is larger and the period of the intermittency observed is longer in C10 and C100. The mean periods of the intermittency in C10 and C100 averaged over the last 4 active-quiet cycles are about 54 and 61 days, 1.3 and 1.5 times that of CTRL, respectively.

The mean vertical profiles of the condensates, on the other hand, vary considerably with different values of τ_{auto} as is shown in the right panels of Fig. 6 for both the active and the quiet periods. There is a notable difference in the amount of condensates among these cases. Especially, considerable amounts of the NH_4SH and the H_2O condensates exist near the tropopause during the quiet periods in C100. Fig. 7(a–c) compares the vertical profiles of the horizontal mean mixing ratios of the condensates averaged over the last 4 active-quiet cycles. The mean vertical profiles observed in C100 are also very different to those observed in the

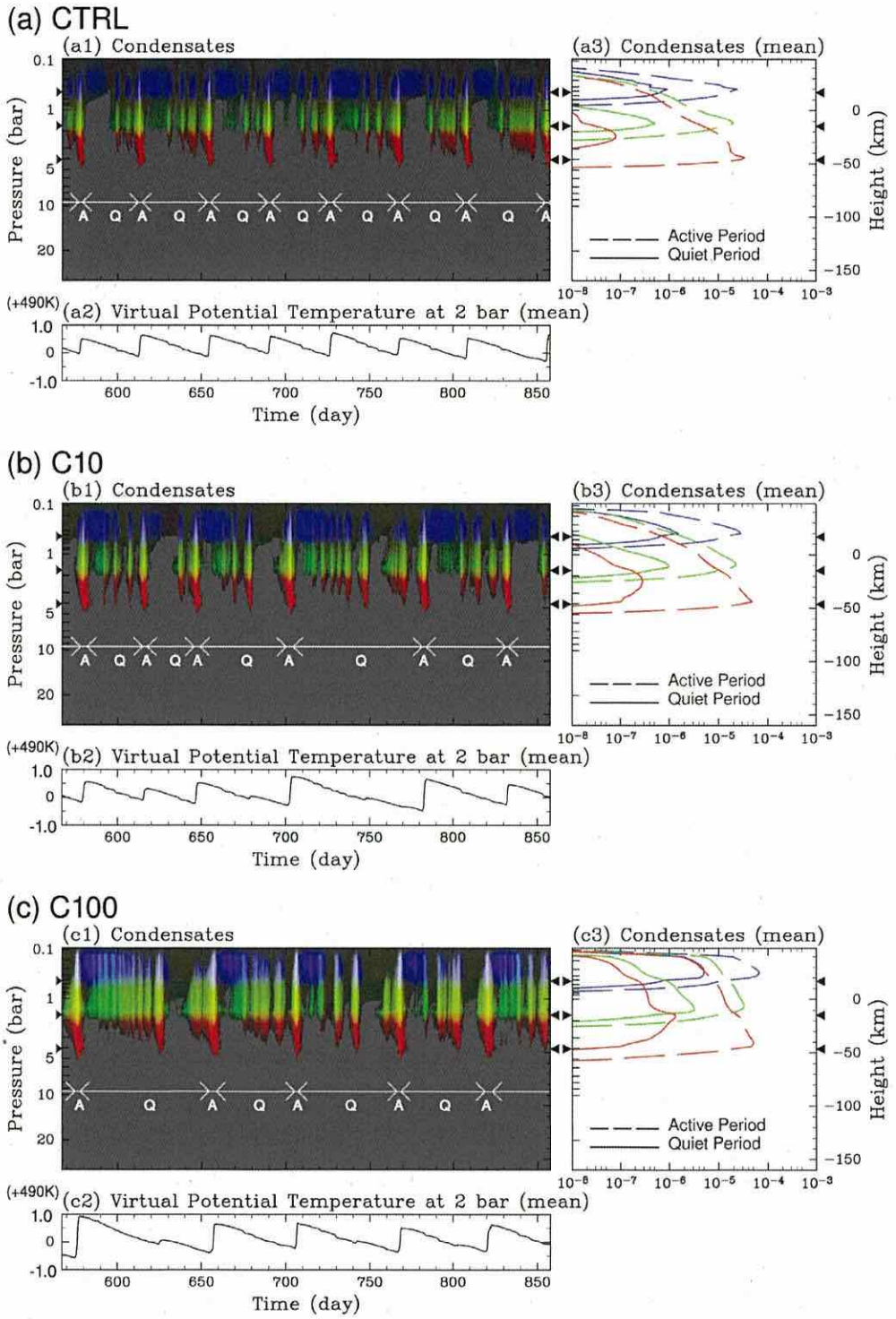

Fig. 6. (a) Temporal variations of mean mixing ratios of condensates and virtual potential temperature for CTRL. (a1) Temporal variations of horizontal mean mixing ratios of condensates plotted in the same manner as Fig. 2(a). (a2) Temporal variations of horizontal mean virtual potential temperature at $p = 2$ bar. (a3) The vertical profile of horizontal mean mixing ratios of condensates averaged only over the quiet periods and those only over the active periods. The solid and broken lines indicate profiles of quiet and active periods, respectively. (b) Same as (a) but for C10. (C) Same as (a) but for C100. Black triangles on the left and the right edges of each panel indicate the NH_3, NH_4SH, and H_2O LCLs from top to bottom for each simulation. (For interpretation of the references to color in this figure legend, the reader is referred to the web version of this article.)

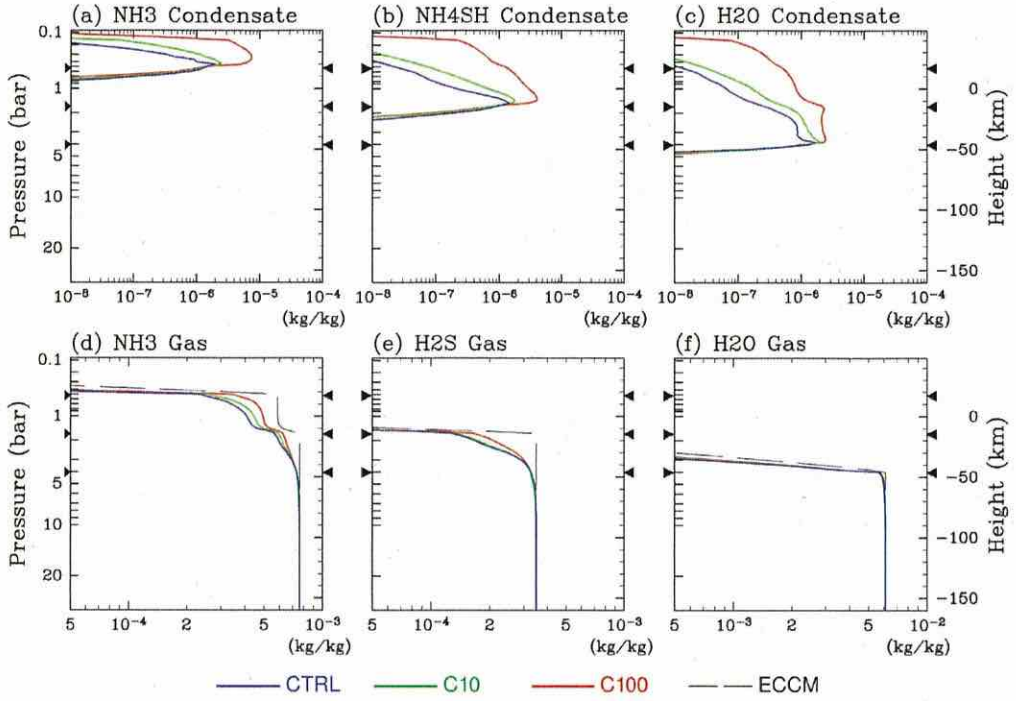

Fig. 7. Comparison of vertical profiles of horizontal mean mixing ratios of (a) NH_3, (b) NH_4SH, and (c) H_2O condensates and (d) NH_3, (e) H_2S, and (f) H_2O gases averaged over the last 4 active-quiet cycles. Blue, green, and red lines represent profiles for CTRL, C10, and C100, respectively. Thin broken lines in (d–f) represent the profiles obtained by the ECCM. Black triangles on the left and the right edges of each panel indicate the NH_3, NH_4SH, and H_2O LCLs from top to bottom. (For interpretation of the references to color in this figure legend, the reader is referred to the web version of this article.)

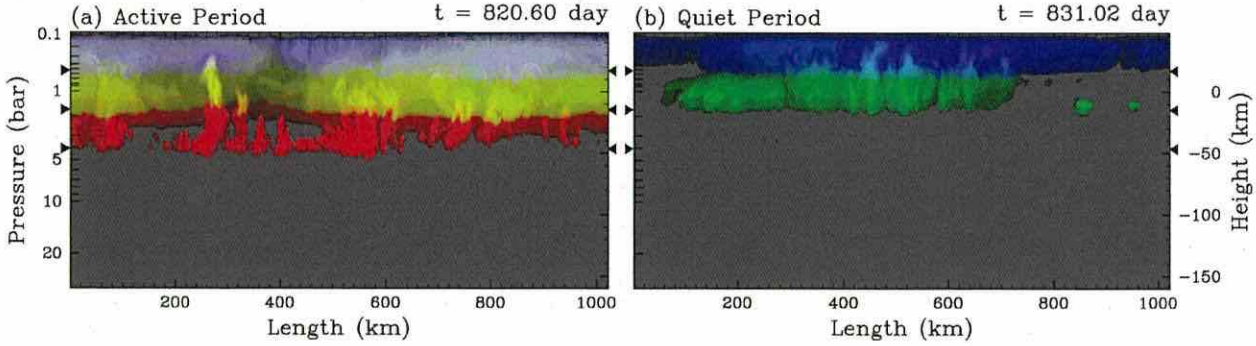

Fig. 8. Snapshots of mixing ratios of condensates obtained in C100 during (a) an active period at $t = 820.60$ day and (b) a quiet period at $t = 831.02$ day. Multiple composition condensates are represented in the same manner as in Fig. 3. Black triangles on the left and the right edges of each panel indicate the NH_3, NH_4SH, and H_2O LCLs from top to bottom.

other two cases. The values of mixing ratios in C100 are at least ten times larger than those obtained in CTRL near the tropopause. Fig. 8 shows representative snapshots of condensates in the active and quiet periods in C100. Fig. 8 indicates that the region above the NH_3 LCL is covered with condensates during the active and quiet periods.

From a comparison between τ_{auto} and the time scale of vertical advection, τ_{adv}, we can understand the reason why the amounts of condensates in C100 are much larger than those in the other two cases. According to our numerical results, a typical time scale of advection from the H_2O LCL to the tropopause, whose length scale $\Delta z \approx 8.0 \times 10^4$ m, during the active periods is $\tau^a_{adv} = \Delta z/w \approx 8.0 \times 10^4/50 = 1600$ s using the maximum vertical velocity in typical cumulonimbus clouds like that shown in Fig. 3(d3). Since the magnitude of the vertical velocity does not change greatly with τ_{auto}, we can adopt the same value of τ^a_{adv} for all cases. A typical time scale of advection from the NH_4SH LCL to the NH_3 LCL, whose length scale $\Delta z \approx 4.0 \times 10^4$ m, during the quiet periods is $\tau^q_{adv} = \Delta z/w \approx 4.0 \times 10^4/10 = 4000$ s by using the maximum vertical velocity in typical clouds like those shown in Fig. 3(b3) and (c3). We can adopt the same value of τ^q_{adv} for all cases, since the magnitude of vertical velocity also does not change greatly for the quiet periods. Now it is obvious that the values of τ^a_{adv} and τ^q_{adv} are larger than the values of τ_{auto} used in CTRL and C10, but are shorter than the value of τ_{auto} used in C100. This means, only in C100, that condensates can be advected up to the NH_3 LCL before being converted from non-precipitating to precipitating condensates, so the region above the NH_3 LCL, including downdrafts region, is covered with condensates. In CTRL and C10, even though $\tau_{auto} < \tau^a_{adv}$, the upward region can be covered with

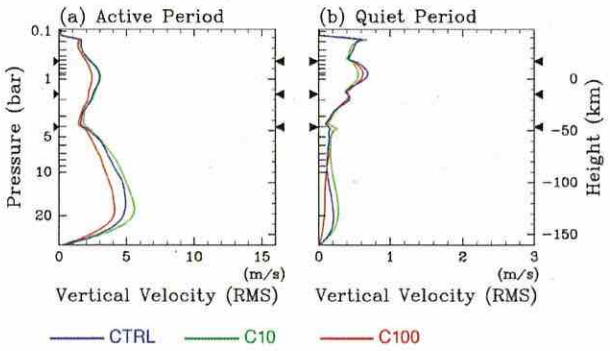

Fig. 9. Comparison of horizontal mean vertical profiles of root mean square (RMS) of vertical velocity, $\sqrt{\overline{w^2}}$, averaged (a) only over the active periods and (b) only over the quiet periods. Blue, green, red lines represent profiles of CTRL, C10, and C100, respectively. Black triangles on the left and the right edges of each panel indicate the NH_3, NH_4SH, and H_2O LCLs from top to bottom. (For interpretation of the references to color in this figure legend, the reader is referred to the web version of this article.)

condensates. This is because the terminal velocities of all precipitating condensates, which is at most 20 m/s, are smaller than the velocity of upward flow, which is typically 50 m/s.

Fig. 7(d–f) compares the horizontal mean mixing ratios of condensable gases averaged over the last 4 active-quiet cycles. The significant characteristic of the condensable gas profiles obtained by our numerical model, i.e., the mean mixing ratios of NH_3 and H_2S gases begin to decrease with height not at their respective LCLs but at the H_2O LCL, does not vary with τ_{auto}. But, the mixing ratios of NH_3 and NH_4SH gases in the moist convection layer increase with τ_{auto}. This tendency is quite obvious during the quiet periods in C100, where these gases are equilibrated with NH_3 and NH_4SH condensates that exist almost always in the moist convection layer (Fig. 6(c)).

The structure of the convective motion is, as is already mentioned above in the evaluation of time scales, qualitatively unchanged by the variation of τ_{auto}. Fig. 9(a) and (b) compare the vertical profiles of the root mean square of vertical velocity, $\sqrt{\overline{w^2}}$, averaged only over the active periods and those only over the quiet periods, respectively. The vertical profiles of $\sqrt{\overline{w^2}}$ in C10 and C100 are similar to that in CTRL for both of the periods.

5. Dependence on the deep abundances of condensable gases

In this section, the dependence of the structure and dynamics of the moist convection layer on the abundances of condensable gases at the lower boundary is examined. As is mentioned in Section 2.3, the body cooling rate used in this parameter experiment is set to be 10 times larger than that of CTRL in order to save the CPU time required to achieve statistically steady states of the model atmosphere. If we use the same cooling rate as that of CTRL for 10 times solar abundance calculation, about 10,000 h of CPU time would be required, which is beyond the computer resources available to us. This is because, as described later in this section, the period of intermittent cloud activity increases with the increasing deep abundances of condensable gases. The cloud convection obtained in R10 shares several principal features with those in CTRL except for a shorter period of intermittent cloud activity, as will be shown below. The detailed results of the parameter experiment in which the body cooling rate is varied but with the same condensable gas abundances as CTRL are described in Appendix A.

The abundances of condensable gases at the lower boundary used in this parameter experiment are summarized in Table 1. The deep abundances for R10 is the same as that for CTRL, i.e., given as the solar abundances. R10S10, R10S3, R10S01 are calculations with abundances of 10 times, 3 times, and 0.1 times solar, respectively. The heights of the LCLs depend on the deep abundances of condensable gases. For the solar composition case, as already mentioned, the LCLs of H_2O, NH_4SH, and NH_3 are about 4.0 bar, 1.7 bar, and 0.5 bar, respectively. For the 0.1 times solar case, they move toward the higher altitudes of about 2.8 bar, 1.2 bar, and 0.4 bar, respectively. For the 3 times solar case, they move toward the lower altitudes of about 4.9 bar, 1.9 bar, and 0.6 bar; and for the 10 times solar case, they go down to about 6.0 bar, 2.4 bar, and 0.7 bar, respectively.

The left panels of Fig. 10 show the temporal variations of the horizontal mean mixing ratios of condensates and virtual potential temperature at $p = 2$ bar for R10S01, R10, R10S3, R10S10, respectively. In most cases, intermittent cloud activity similar to that in CTRL is found. In R10, R10S3 and R10S10, distinct quasi-periodic cycles of cloud activity and sawtooth-like temperature variations are obtained (left panels of Fig. 10(b–d)). The exception is R10S01, where obvious quasi-periodic temporal cycle of cloud activity can not be found (left panels of Fig. 10(a)).

It should be noted that the mean period of the intermittent cycle of cloud activity is roughly proportional to the deep abundances of condensable gases. The mean periods of intermittency averaged over the last 4 active-quiet cycles are about 9, 19, and 139 days for R10, R10S3, and R10S10, respectively; their ratio is 1, 2.1, and 16, and is fairly close to the ratio for the deep abundances of 1, 3, and 10. The amplitudes of the mean virtual potential temperature variation at $p = 2$ bar during the active-quiet cycles also depend on the deep abundances of condensable gases. The amplitudes are about 0.9, 2.6, and 11 K for R10, R10S3, and R10S10, respectively; the ratio is 1, 2.9, and 12, and is also fairly close to the ratio for the deep abundances. The relationship of the period of the intermittency and the amplitude of temperature variation to the deep abundances of condensable gases will be discussed in Section 6.3.

The right panels of Fig. 10 compare the horizontal mean mixing ratios of condensates averaged only over the active periods and those only over the quiet periods. During the active periods, the peak values of the mean mixing ratios of all of the condensates have a dependence on the deep abundances of condensable gases. For example, the maximum values of mixing ratios of H_2O condensate are about 6×10^{-5}, 1.3×10^{-4}, and 5×10^{-4} kg/kg for R10, R10S3 and R10S10, respectively; the ratio is 1, 2.2, and 8.3, which again coincides with the ratio for the deep abundances of condensable gases. During the quiet period, the mean mixing ratio of H_2O condensate decreases as the deep abundances of condensable gases increase. On the other hand, the mean mixing ratios of NH_3 and NH_4SH condensates do not change much. The difference may be explained by differences in the temporal variation of condensates (see Fig. 10(b1), (c1), and (d1)); H_2O cloud activity during the quiet period is less frequent and the duration of the quiet period becomes longer as the deep abundances of condensable gases increase. The activity of NH_3 and NH_4SH clouds tends to persist even in the quiet periods, so that the change of the duration of the quiet periods matters only modestly.

Fig. 11(a–c) compares the vertical profiles of the horizontal mean mixing ratios of condensates averaged over the last 4 active-quiet cycles. The maximum value of the mean mixing ratio of each condensate is obviously insensitive to the deep abundances of condensable gases. This insensitivity can be understood from the following equation mentioned in Section 3.2, $\bar{q}_c' = \bar{q}_c'^a \Delta t^a / \Delta t$, where $\bar{q}_c'$ and $\bar{q}_c'^a$ are the mean mixing ratio of a condensate averaged over the entire active-quiet cycles and active periods, respectively, Δt is the period of the intermittency, and Δt^a is the duration of active periods. In our results, the values of Δt and $\bar{q}_c'^a$ are roughly proportional to the deep abundances of condensable gases, as is discussed above. The remaining difference can be explained by the

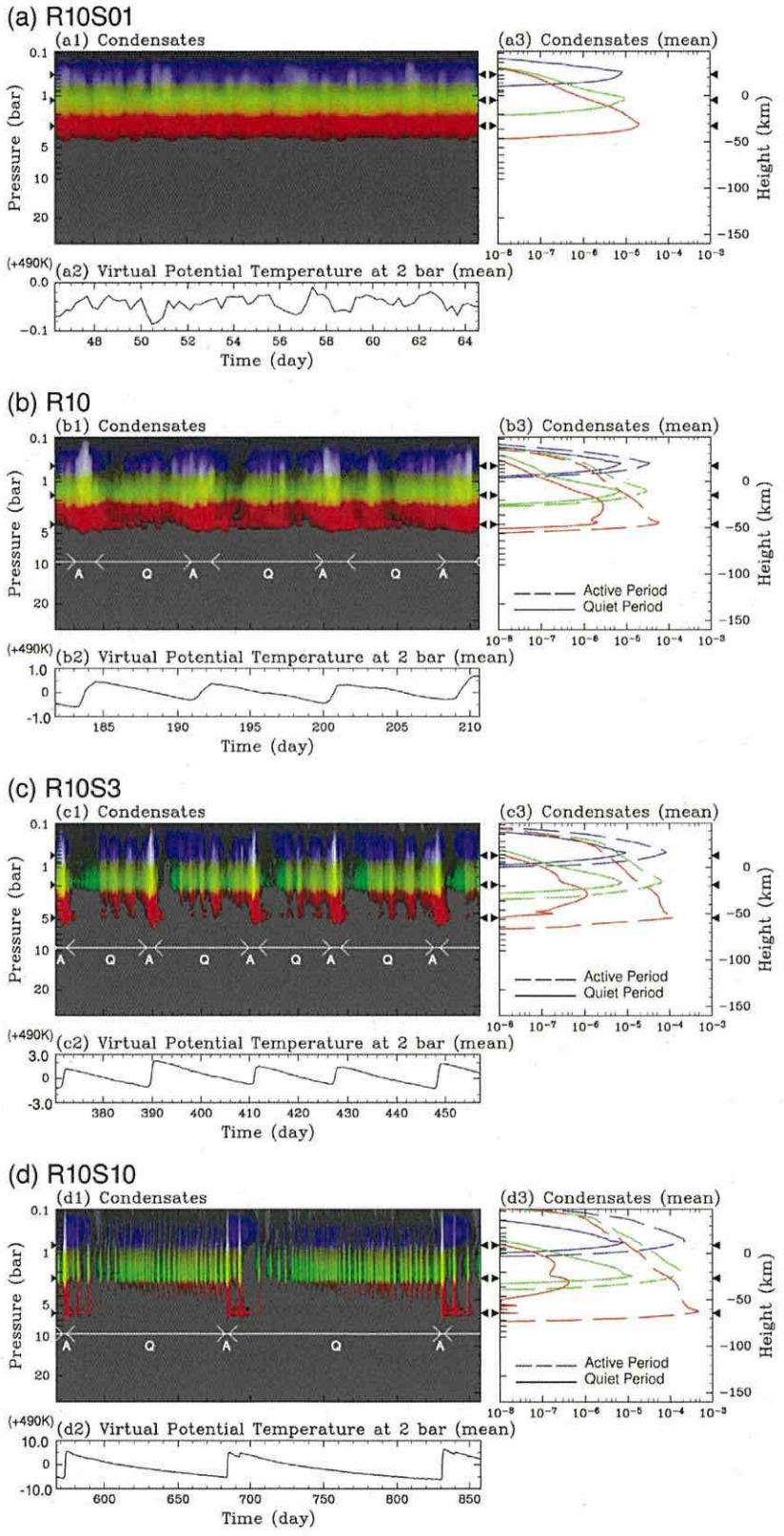

Fig. 10. Same as Fig. 6, but for (a) R10S01, (b) R10, (c) R10S3, and (d) R10S10.

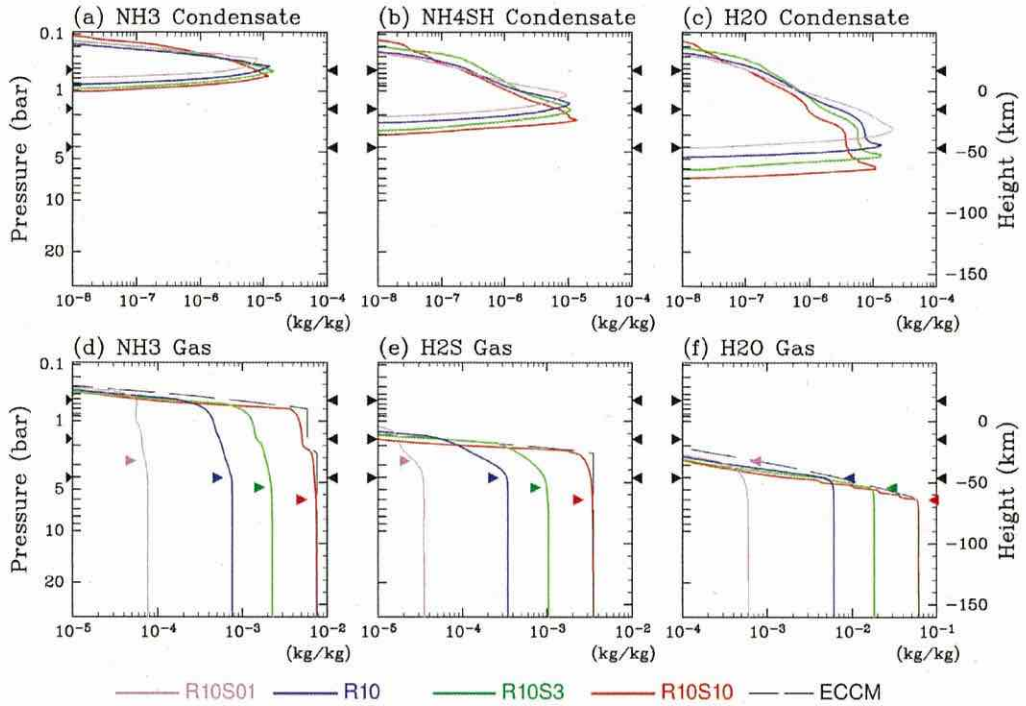

Fig. 11. Same as Fig. 7, but for R10S01, R10, R10S3, and R10S10, represented by violet, blue, green, and red lines, respectively. Thin broken lines in (d–f) represent the profiles obtained by the ECCM using the settings of R10S10. The violet, blue, green, and red triangles in (d–f) indicate the H_2O LCL for R10S01, R10, R10S3, and R10S10, respectively. (For interpretation of the references to color in this figure legend, the reader is referred to the web version of this article.)

dependence of the duration of active period on the deep abundances; the value of Δt^a is 1–2 days for CTRL and 4–5 days for R10S10 (not clearly shown here).

Fig. 11(d–f) compares the horizontal mean mixing ratios of condensable gases averaged over the last 4 active-quiet cycles. In most cases, the vertical profiles of the mean mixing ratios are similar to those in CTRL; the mixing ratio of each condensable gas begins to decrease with height from the H_2O LCL. The exception is R10S01. In R10S01, the altitude at which the mean mixing ratio of each condensable gas begins to decrease is approximately 4 bar, which is well below the H_2O LCL. This modest difference of the vertical profiles of condensable gases results from the change in vertical motion. Fig. 12 compares representative snapshots of R10 and R10S01. In R10, the vertical motion in the moist convection layer is characterized by the contrast between the narrow, strong, cloudy updrafts and the broad, weak, dry downdrafts, which resemble those in CTRL. On the other hand, in R10S01, the contrast is less definite. The widths and the intensities of the upward and downward flows are similar to each other and the convective motion resembles that of dry convection. The distributions of condensable gases of R10S01 are inhomogeneous just under the H_2O LCL. These features of the vertical motion and distribution of condensable gases observed in R10S01 imply that only the H_2O LCL acts as a weak dynamical and compositional boundary.

The convective motion characteristics in R10, R10S3 and R10S10 are fairly similar to those in CTRL. Fig. 13(a) and (b) compare the mean vertical profiles of the root mean square of vertical velocity, $\sqrt{\bar{w}^2}$, averaged only over the active periods and those only over the quiet periods, respectively. During the active periods, the vertical profiles of $\sqrt{\bar{w}^2}$ have a local minimum at the H_2O LCL in all three cases. The value of $\sqrt{\bar{w}^2}$ in the moist convection layer increases as the deep abundances of the condensable gases increase. During the quiet periods, on the other hand, the vertical profiles of $\sqrt{\bar{w}^2}$ have local minimums or inflection points at the NH_3 and NH_4SH LCLs in all of the three cases. As the deep abundances of condensable gases increase, the value of $\sqrt{\bar{w}^2}$ in the moist convection layer generally decreases, presumably because the stable layers at the LCLs strengthen. Note that the apparent sensitivity of $\sqrt{\bar{w}^2}$ in the dry convection layer results from the "contamination" of the strong circulation that occurs during the active periods, and this sensitivity should disappear if a more realistic and weaker body cooling is applied.

6. Dynamics of the quasi-periodic cloud activity

As has been examined in earlier sections, the principal feature of cloud convection in this paper is the intermittent emergence of vigorous cumulonimbus clouds. In this section, an explanation of the mechanism of the intermittency is given by considering the following three points of moist convection: (i) the trigger that causes the development of cumulonimbus clouds at the beginning of active periods; (ii) the mechanism that terminates active periods; and (iii) the factors that govern the period of the intermittent cloud activity.

6.1. Detailed temporal development at the beginning and the end of active periods

A notable characteristic of the moist convection layer observed near the end of a quiet period is rapid descent of the H_2O cloud base, which can be identified by close examination of Fig. 2(a). Fig. 14(a) shows typical snapshots of the distributions of condensates, virtual potential temperature, and wind vectors around the H_2O LCL superposed on relative humidity near the end of a quiet period. As indicated by the nearly homogeneous virtual potential temperature (Fig. 14(a3)), the atmosphere is neutral to dry convection from the NH_4SH LCL down to the altitudes just above the H_2O LCL. The downward plumes produced by the evaporation of H_2O condensate can easily go down to the altitudes near the H_2O LCL

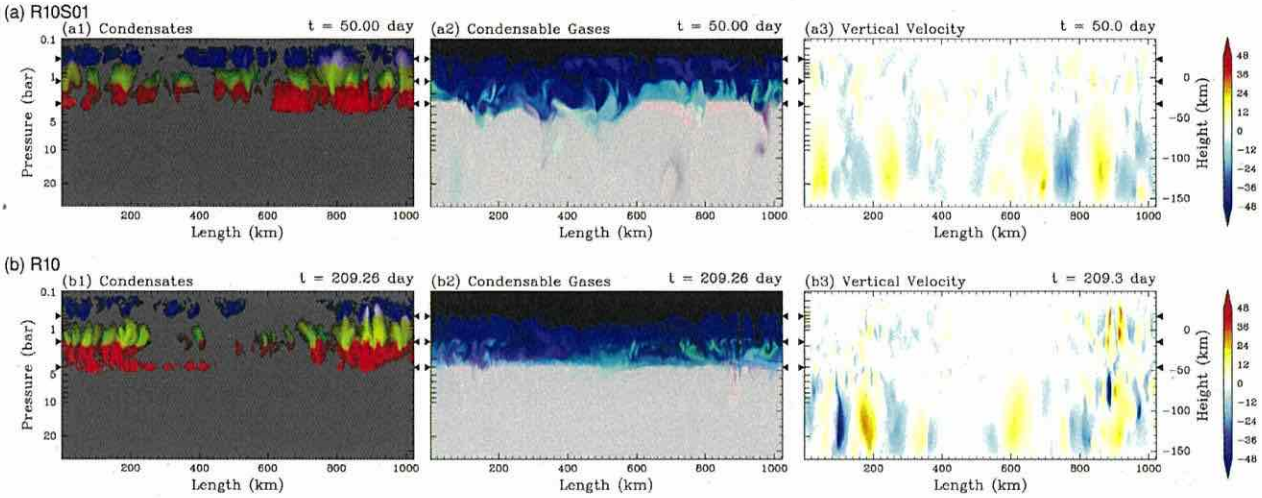

Fig. 12. (a) Snapshots in R10S01. (a1) Mixing ratios of condensates plotted in the same manner as in Fig. 3. (a2) Mixing ratios of condensable gases plotted in the same manner as in Fig. 3. (a3) Vertical velocity. (b) Same as (a) but for an active period in R10. Black triangles on the left and the right edges of each panel indicate the NH_3, NH_4SH, and H_2O LCLs for each simulation.

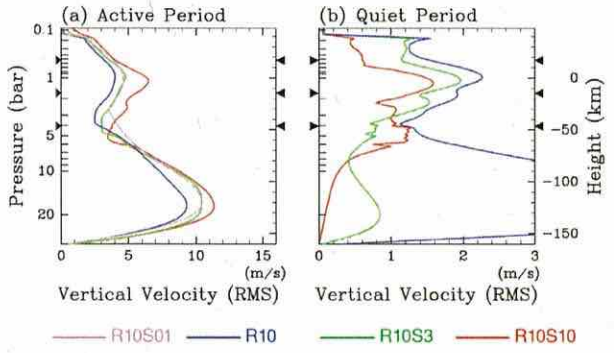

Fig. 13. Same as Fig. 9 but for R10S01, R10, R10S3, and R10S10, represented by violet, blue, green, and red lines, respectively. Note that R10S01 is regarded to consist only of active period. (For interpretation of the references to color in this figure legend, the reader is referred to the web version of this article.)

and cool the region below the NH_4SH LCL. Moist air in the vicinity of these downward plumes rises with the returning upward motions due to mass continuity, and forms H_2O clouds, resulting in the successive formation of H_2O clouds indicated by the tilted H_2O cloud bases in Fig. 14(a1). At this stage, vertical motion near the H_2O LCL is weak and the region near the LCL is unsaturated (Fig. 14(a2)).

Characteristic snapshots at the transition from the quiet period to the active period are shown in Fig. 14(b). A noteworthy feature is that precipitating H_2O condensate begins to fall below the H_2O LCL ($x \sim 300$ km of Fig. 14(b1)). At this stage, the vertical motion near the H_2O LCL is still weak and the region near the LCL is still unsaturated (Fig. 14(b2)).

An outbreak of vigorous cumulonimbus clouds at the beginning of the active period is shown in Fig. 14(c). H_2O condensate falls down below the H_2O LCL. There are upward and downward flows penetrating through the H_2O LCL, which can be observed under the base of the vigorous cumulonimbus clouds (arrows in Fig. 14(c2)). Relative humidity near the H_2O LCL is highly inhomogeneous (tone in Fig. 14(c2)). Virtual potential temperature in a cumulonimbus cloud ($x \sim 250$ km of Fig. 14(c3)) is higher than that of the surrounding region, implying that the cumulonimbus cloud is significantly buoyant. Fig. 14(d) shows snapshots at the peak of the active period. Two or three intense cumulonimbus towers develop simultaneously. The overall features of the structure and dynamics of the moist convection layer do not significantly change from those at the beginning of the active period shown in Fig. 14(c), except the overall rise of virtual potential temperature in the upper half of the moist convection layer (Fig. 14(d3)) due to the release of the latent heat of condensation in the vigorous cumulonimbus clouds.

Approaching the end of the active period (Fig. 14(e)), overall virtual potential temperature increases even in the lower half of the moist convection layer (Fig. 14(e3)). Virtual potential temperature observed in the cumulonimbus clouds base ($x \sim 600$ km of Fig. 14(e3)) is obviously lower than that of the surrounding regions, although that is still higher in the upper half of the moist convection layer. This negative anomaly of the virtual potential temperature mainly results from the large amount of condensable gases and condensates observed in the cumulonimbus cloud. Finally at the end of the active period (Fig. 14(f)), a further rise in the virtual potential temperature of the moist convection layer almost completely eliminates the buoyancy in clouds (Fig. 14(f3)); a developing cloud at around $x = 950$ km of Fig. 14 (f1) is no longer able to reach to the tropopause.

6.2. The conditions at the beginning and the end of active periods

The rapid development and large buoyancy of the cumulonimbus clouds at the beginning of the active period described above suggests that an ample amount of instability is accumulated before the beginning of the active period. Tapped by a certain triggering mechanism, the instability is abruptly released and vigorous cumulonimbus clouds develop. On the other hand, the end of active periods seems to result from the decrease of the instability, and the instability is completely exhausted at the transition to the quiet period which follows.

In order to analyze the conditions at the beginning and the end of active periods further, a quantitative definition of the instability is necessary. We can define an integral measure of convective instability considering that development of cumulonimbus clouds requires the existence of a negative pressure anomaly at the foot of the updraft, which accelerates horizontally converging wind near the cloud base. Indeed, Fig. 15(a) indicates that there is a negative pressure anomaly near the cumulonimbus clouds base at around $x = 600$ km at the time shown in Fig. 14(e1). Fig. 15(b) indicates

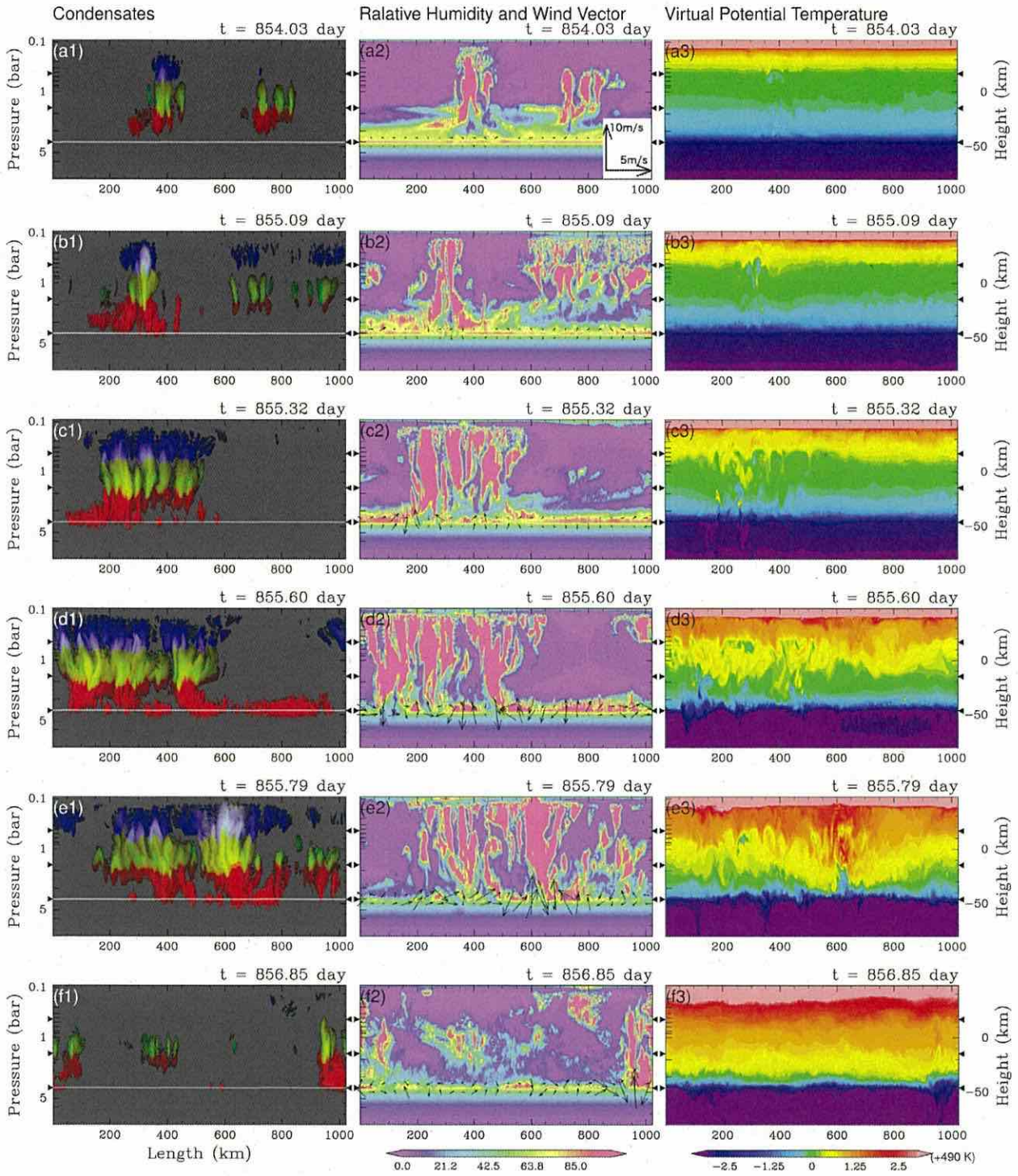

Fig. 14. Snapshots of (∗1) mixing ratios of condensates, (∗2) wind vector near the H_2O LCL superposed on relative humidity, and (∗3) virtual potential temperature obtained in CTRL. Each line of panels cover from (a) just before the start to (f) the end of an active period. Multiple compositions of condensates are represented in the same manner as in Fig. 3. Black triangles on the left and the right edges of each panel indicate the NH_3, NH_4SH, and H_2O LCLs, and white thin lines in (∗1) also indicate the H_2O LCL.

that the cloud at the end of the active period, located at around $x = 950$ km (see Fig. 14(f1)), is also associated with a negative pressure anomaly, but the anomaly is weak and the center of the anomaly is deviated from the cloud.

We vertically integrate Eq. (5) neglecting time-dependent terms and subgrid turbulence term, the difference between the values of the Exner function at the tropopause and the H_2O LCL can be expressed as

$$\int_{\pi_{H_2O}}^{\pi_{top}} d\pi' = \int_{z_{H_2O}}^{z_{top}} \frac{1}{c_{pd}\theta_{v0}} \left(\frac{\theta'_v}{\theta_{v0}}\right) g\, dz, \tag{10}$$

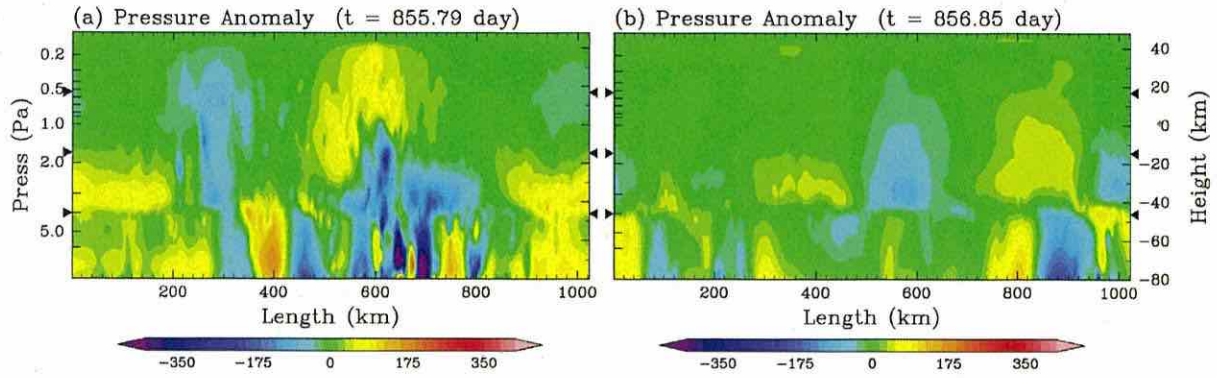

Fig. 15. The distributions of pressure anomaly, defined as the deviation from the horizontal average, at the time shown in Fig. 14(e) and (f).

where π_{top} and π_{H_2O} are the values of the Exner function at the tropopause and the H_2O LCL, respectively, and z_{H_2O} and z_{top} are the altitudes at the tropopause and the H_2O LCL, respectively. By applying Eq. (10) to an active updraft and surrounding environment and taking the difference, assuming the pressure difference at the tropopause to be zero, we obtain a reasonable maximum intensity of the pressure anomaly at the H_2O LCL as

$$(\pi'^{*}_{H_2O} - \pi'^{\dagger}_{H_2O}) = \int_{z_{H_2O}}^{z_{top}} \frac{g}{c_{p_d}\theta_{v0}} \left(\frac{\theta'^{*}_{v} - \theta'^{\dagger}_{v}}{\theta_{v0}} \right) dz, \tag{11}$$

where the variables denoted by an asterisk and a dagger represent a rising air parcel in an active updraft and surrounding air, respectively. By rewriting Eq. (11) in terms of pressure and virtual temperature, we define the integral measure of convective instability, A, as

$$A \equiv (p'^{*}_{H_2O} - p'^{\dagger}_{H_2O}) = \int_{z_{H_2O}}^{z_{top}} \rho_0 g \left(\frac{T'^{*}_{v} - T'^{\dagger}_{v}}{T_{v0}} \right) dz. \tag{12}$$

Fig. 16 shows the temporal variations of A in CTRL, C10, C100, R10, R10S3, and R10S10. In order to estimate the value of T^{*}_{v} and $T^{\dagger}_{v}$ in Eq. (12), we have to assume the vertical profiles of temperature, condensable gases, and condensates. As for the rising air parcel, the profiles of temperature and condensable gases are assumed to follow the moist adiabat of the rising air parcel from just below the H_2O LCL, and the temporal variation of the vertical profiles of condensates are given by those of peak values observed in our simulations. As for the surrounding air, the temporal variations of all of the profiles are given by horizontal mean profiles observed in our simulations; the resulting temporal variation of $T^{\dagger}_{v}$ shows sawtooth-like variation similar to that observed in horizontal-mean virtual potential temperature (Fig. 6(a2), (b2), and (c2); Fig. 10(b2), (c2), and (d2)). In each case, A shows a sawtooth-like temporal variation, which is similar to the variation of horizontal-mean virtual potential temperature in the moist convection layer upside down. This suggests that a considerable portion of the variation of A results from the variation of virtual temperature of the surrounding air.

An important feature commonly found in all cases is that the values of A become almost zero at the end of the active periods (Fig. 16). This proves that exhaustion of the convective instability is indeed the criterion for the end of the active periods. Re-examination of the distribution of virtual potential temperature just before the end of the active period (Fig. 14(e3)) indicates that the condition $A = 0$ is not realized as $\theta'^{*}_{v} - \theta'^{\dagger}_{v} = 0$ at every altitude in the moist convection layer, but is realized as a cancellation of the positive buoyancy, $(\theta'^{*}_{v} - \theta'^{\dagger}_{v})g/\theta_{v0} > 0$, in the upper levels and the negative buoyancy, $(\theta'^{*}_{v} - \theta'^{\dagger}_{v})g/\theta_{v0} < 0$, in the lower levels. The negative buoyancy in the lower levels results from the large mixing ratios of condensates and condensable gases, whose molecular weight is larger than that of the dry air of Jupiter's atmosphere.

It should be noted that, in all cases, a considerable amount of positive A is accumulated before the beginning of the active periods (Fig. 16). It is also notable that the value of A returns to positive more or less quickly after the end of the active periods, at which the value of A is zero. These features clearly indicate that the accumulation of instability is not a sufficient but a necessary condition for the onset of the active period. As was discussed in Section 6.1, the trigger is H_2O condensate that falls down through the stable layer at the H_2O LCL by gravitational settling (see Fig. 14). H_2O condensate evaporates and cools the surrounding air below the H_2O LCL by the negative latent heat and drives downward plumes. These downward plumes induce compensating updrafts that carry air parcels containing large amounts of condensable gases from below the H_2O LCL. The ascending air parcels form the outbreak of the vigorous cumulonimbus clouds. The gravitational settling of H_2O condensate is indispensable to the trigger because, without this process, evaporation cooling below the H_2O LCL, which drives the ascent of moist parcels crossing the stable layer at the H_2O LCL, would be impossible.

Of course, in order for an appreciable amount of precipitating H_2O condensate to travel down to below the H_2O LCL before being evaporated out, clouds have to develop from a low enough level. This is realized by successive formation of H_2O clouds with the help of downward plumes as shown in Fig. 14(a1) and (b1). The descent of plumes requires a nearly neutral environment. Thus, the final "sufficient" condition for the trigger to work is the decrease of the stability just above the H_2O LCL as is indeed realized in Fig. 14(a3) and (b3).

6.3. Period of intermittency

The period of intermittency Δt, which is approximately the duration of the quiet period, can be roughly estimated using both the magnitude of the temperature change during the quiet period, ΔT, and the body cooling rate, Q_{rad}, which is the primary thermal forcing during the quiet periods (Fig. 4). The following expression is then satisfied:

$$\int_{p_{H_2O}}^{p_{top}} \frac{c_{p_d}}{g} \Delta T \, dp = \int_{p_{rad}}^{p_{top}} \frac{c_{p_d}}{g} Q_{rad} \Delta t \, dp, \tag{13}$$

where p_{rad} is the pressure level of the bottom of the radiative region. Because c_{p_d} and Q_{rad} are constant in our model and the values of p_{H_2O} and p_{rad} are much larger than that of p_{top} (e.g., $p_{H_2O} = 4$ bar for CTRL, $p_{rad} = 2$ bar, and $p_{top} = 0.1$ bar), Eq. (13) can be approximated as,

$$\Delta t \approx \frac{\overline{\Delta T}}{Q_{rad}} \frac{p_{H_2O}}{p_{rad}}, \tag{14}$$

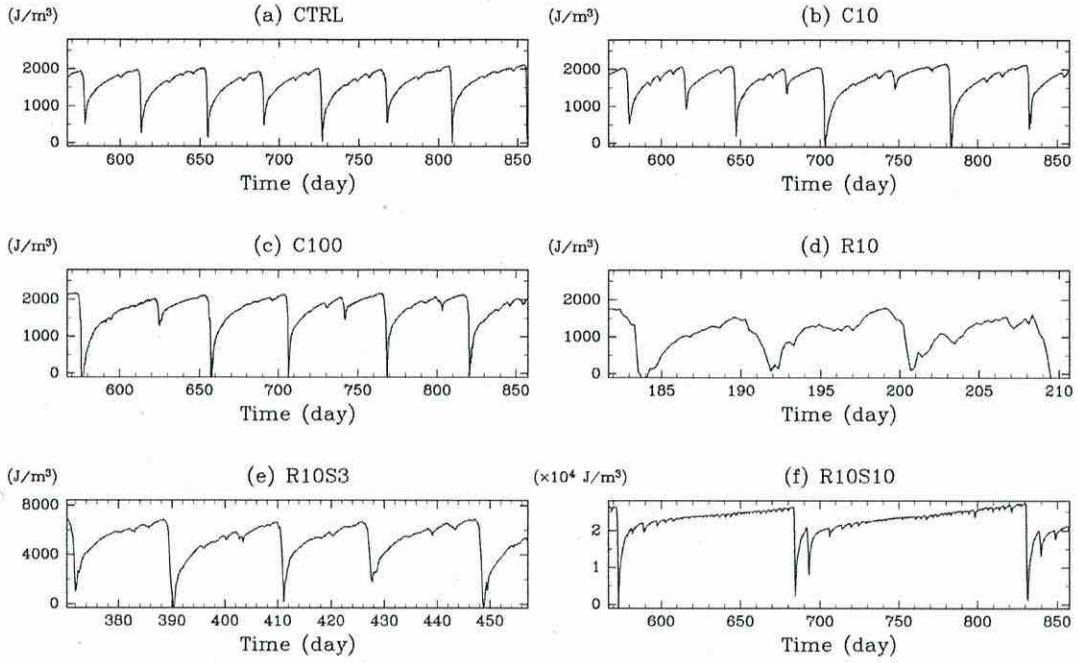

Fig. 16. Temporal variation of the integral measure of convective instability given by Eq. (12) in (a) CTRL, (b) C10, (c) C100, (d) R10, (e) R10S3, and (f) R10S10.

Table 2
Summary of intermittent cloud activity.

Run	Mean period (results)	Values of each terms included in Eq. (14)		
		p_{H_2O}	$\overline{\Delta T}$	Δt
CTRL	41	4.0	0.29	58
C10	54	4.0	0.33	65
C100	61	4.0	0.42	84
R3	17	4.0	0.3	20
R10	9	4.0	0.44	8.9
R10S3	19	4.9	0.94	23
R10S10	139	6.0	3.9	116

where

$$\overline{\Delta T} = \frac{1}{p_{H_2O}} \int_{p_{H_2O}}^{p_{top}} \Delta T \, dp.$$

Eq. (14) gives an estimate of the period of intermittency. The periods of intermittency realized in the numerical experiments are summarized and their estimates based on Eq. (14) are provided in Table 2. The values of $\overline{\Delta T}$ are also evaluated from the results of the numerical simulations. The estimated period for each case explains the result of each numerical calculation reasonably well.

Table 2 indicates that the period of intermittency is roughly proportional to the deep abundances of condensable gases, since $\overline{\Delta T}$ is also roughly proportional to the deep abundances of condensable gases. The dependence is actually stronger than what the proportionality predicts. The remaining tendency can be explained by the dependency of p_{H_2O} on the deep abundances. The value of p_{H_2O} observed in R10S10 is 1.5 times larger than that in CTRL. Additionally, the results of a parameter experiment with different intensities of body cooling, which are presented in the Appendix A, show that the period of intermittency is roughly inversely proportional to the intensity of body cooling, although an error factor of 2 remains resulting from the moderate dependence of $\overline{\Delta T}$ on the cooling rate. As for the value of $\overline{\Delta T}$, we have not succeeded in deriving its analytic expression yet. At the moment, no further pursuit is being undertaken to relate analytically $\overline{\Delta T}$ to the deep abundances of condensable gases and the body cooling rate. If we tentatively accept the dependence of the period of intermittency on the deep abundances and the cooling rate, we can very roughly estimate the periods of intermittency as around 200 days for 3 times solar and around 1000 days for 10 times solar in the case of using the same body cooling rate for CTRL.

Finally, it is worth considering the dependence of the period of intermittency on the autoconversion time scale. The difference in $\overline{\Delta T}$ for CTRL, C10, and C100 (Table 2) results mainly from the difference of virtual potential temperatures at the beginning of the active period (see Fig. 6); virtual potential temperatures at the end of the active periods are almost the same. The sensitivity of virtual potential temperature at the beginning of the active period to the autoconversion time scale can be understood as described below. As was shown in Fig. 14, the beginning of the active period is characterized by the development of cumulonimbus clouds triggered by the precipitating H_2O condensate falling down below the H_2O LCL. In order for this to happen, an appreciable amount of precipitating H_2O condensate must be produced at heights suitable for it to fall below the H_2O LCL before evaporation. Apparently, this condition is more easily satisfied with a shorter autoconversion time scale. In other words, in the case of a longer autoconversion time scale, a lower temperature of the moist convection layer, which leads to a further decrease of the stability just above the H_2O LCL, is required to have an appreciable amount of H_2O condensate at a suitable level for precipitation down to below the H_2O LCL.

7. Concluding remarks

In this paper, we have examined the idealized structure and dynamics of Jupiter's moist convection layer by using a two-dimensional numerical model, as well as their dependences on the autoconversion time scale and the deep abundances of condensable gases. Although the model used in the present study explicitly solves dynamical processes and includes thermodynamical and microphysical processes for all three important condensates in Jupiter's atmosphere, it contains several assumptions and simplifications that are not necessarily supported by physical prin-

ciples or observations. Thus, in this section, we try to make only qualitative comparisons and discussion about some observations. Of course, future studies will be indispensable to determine whether these comparisons are really appropriate or not. Observation of the physical properties of clouds below the visible cloud deck, in particular, is critically demanded.

In all of the cases described in this paper, vigorous cumulonimbus clouds develop from the H_2O LCL to above the NH_3 LCL. The existence of vigorous cumulonimbus clouds is supported by several recent observational studies (Gierasch et al., 2000; Simon-Miller et al., 2000; Sromovsky and Fry, 2010). The possibility of the cumulonimbus clouds development has been discussed in the previous theoretical and numerical studies on convection of a single cloud (Stoker, 1986; Yair et al., 1992, 1995; Hueso and Sanchez-Lavega, 2001). We emphasize here that vigorous cumulonimbus clouds are ubiquitous entities in a statistically steady state of our simulations that is free from any arbitrary choice of the initial conditions. The present study has firmly established that vigorous cumulonimbus clouds are "ordinary" entities in Jupiter's atmosphere.

A notable feature of the cumulonimbus convection realized in this study is that they develop successively as a "mesoscale convective system" with a lifetime of 1–2 day for CTRL and 4–5 days for R10S10. This feature is also supported by several recent observational studies. Based on cloud imaging (Li et al., 2004) and observations of lightning (Dyudina et al., 2004), it is known that cumulonimbus clouds in Jupiter's atmosphere develop with a lifetime of about 3.5 days, which is significantly longer than the lifetime of individual convective cells, about 3 h, simulated in the numerical simulations in the past (e.g., Yair et al., 1995; Hueso and Sanchez-Lavega, 2001). Gierasch et al. (2000) illustrates a schematic view of cloud system of Jupiter's atmosphere based on observations by Galileo, which consists of various developing convective cells. A closer comparison with the observational studies would require numerical calculations using three-dimensional numerical models, so this is a subject for future research.

Another observational fact which the present study may explain is the global average vertical distribution of NH_3. It is known but has remained difficult to explain that the abundance of NH_3 is globally subsaturated around the NH_3 cloud top ($0.4\ \text{bar} < p < 0.6\ \text{bar}$) and is subsolar by a factor of 2 below the NH_3 cloud base ($0.6\ \text{bar} < p < 2\ \text{bar}$) (de Pater et al., 2001; Gibson et al., 2005; Showman and de Pater, 2005). Interestingly, the mean vertical profiles of NH_3 gas obtained in the present study coincide fairly well in all cases. Our calculations suggest that the observed low NH_3 abundance is the result of the compensating downward motion associated with the intense cumulonimbus clouds that carries very dry air near the tropopause down to the H_2O LCL.

On the other hand, the present results do not reproduce the observation made by the Galileo probe that all condensable gases are depleted below the H_2O LCL (Wong et al., 2004). In all cases other than R10S01, dry air parcels can rarely penetrate below the H_2O LCL, since the H_2O LCL acts as a strong dynamical and compositional boundary, so the region below this level is kept homogeneously wet. In R10S01, since the H_2O LCL acts as a weak dynamical and compositional boundary, dry air parcels can reach to below the H_2O LCL, but the region below 4 bar level is also kept homogeneously wet (Fig. 12). Explanation of the Galileo probe observation would require some large-scale processes such as large-scale vortical wave disturbances (Showman and Dowling, 2000; Friedson, 2005) or meridional circulations, which are not considered in this study.

The intermittent cloud activity obtained in our experiments may be relevant to the observed "fading/revival" cycle in some of the major belts on Jupiter (Rogers, 1995; Sanchez-Lavega et al., 2008; Fletcher et al., 2011), which are associated with significant temporal variations of cloud activity. The temperature variation in the troposphere ($p > 0.3$ bar) observed by Fletcher et al. (2011), warm in the period with cumulonimbus clouds and cool in the period without cumulonimbus clouds, seems to be consistent with the present results. The episodic emergence of giant convective storms of Saturn (Fischer et al., 2011) may also be understood as an analog of the intermittent cloud activity in the present model. However, the intermittency found in this study and the observed fading/revival cycle of Jupiter's atmosphere differ at least in the following respects. First, the typical period of convective activity in the present study, e.g., the mean period of about 41 days in CTRL, differs considerably from that of the fading/revival cycle of Jupiter's belts, 3–10 years. Using the dependences on the deep abundances of condensable gases and the body cooling rate, which are discussed in Section 6.3, the observed time scale of the fading/revival phenomena could be reproduced by assuming a value about 10–30 times solar for the deep abundance of H_2O gas; if extrapolating the rough proportionality between the periods of the intermittent cloud activity and the deep abundances of condensable gases, the estimated abundance would be about 20–30 times solar based upon the result of CTRL. In addition, if scaling the period observed in R10S10 to the realistic body cooling rate, the estimated abundance would be about 10–15 times solar. These large enhancements are within the range predicted by the "clathrate hydrate scenario" for the formation of Jupiter (Gautier et al., 2001; Hersant et al., 2004)[1], and are somewhat close to the value deduced by Ingersoll and Kanamori (1995) (see [1]) from the propagation property of atmospheric waves excited by the collisions of Comet Shoemaker-Levy 9 in 1994. The JUNO mission is expected to find clues for assessing the deep abundances. Second, the cloud activity in the intermittency in the present model and that of the observed revival/fading cycle in South Equatorial Belt evolve differently; in the former, short outbreaks occur separated by long quiet periods, but in the latter, more or less steady convective activity continues in the "normal" period, followed by an interval of quiescence ("fading") that is then abruptly shifted to a short, very intense activity ("disturbance"), which returns to the "normal" state of moderate activity. The evolution of convective activity in the North Temperate Zone (Sanchez-Lavega et al., 2008) is more similar to that in the present study. The variety above may arise from the interaction between the convection and the large-scale motions in the real Jupiter's atmosphere such as possible meridional circulation associated with belt-zone structure or the large scale eddies. Exploration of this issue is left for a future three-dimensional numerical study.

The existence of lightning flashes also may provide a hint to the abundance of H_2O in the deep atmosphere because active charge separation is possible only in strong cumulonimbus clouds with large amount of condensates, whose development requires a large mixing ratio of H_2O gas (Gibbard et al., 1994; Yair et al., 1995, 1998). Gibbard et al. (1994) argues that a density of at least $1–2 \times 10^{-3}\ \text{kg/m}^{-3}$ of H_2O condensate is necessary for the development of a thunderstorm. In CTRL, the maximum mixing ratio of H_2O condensate in the cumulonimbus clouds developed in the active periods is nearly equal to this threshold, but the maximum mixing ratio in the quiet period is obviously smaller. During the active period, since the maximum mixing ratio of H_2O condensate is about 4×10^{-3} kg/kg (see Section 3.1) and the air density at the H_2O LCL is about 0.4 kg/m^3, the maximum density of H_2O condensate is about 1.6×10^{-3} kg/m^3. Thus, the present result implies that one time solar value of H_2O is the threshold for lightning, being also consistent with the results of Yair et al. (1998)[1]. Of

[1] Note that the solar abundance considered in previous studies is that reported by Anders and Grevesse (1989); the abundance of oxygen reported by Grevesse et al. (2007) used in our calculations is about twice as small as that reported by Anders and Grevesse (1989).

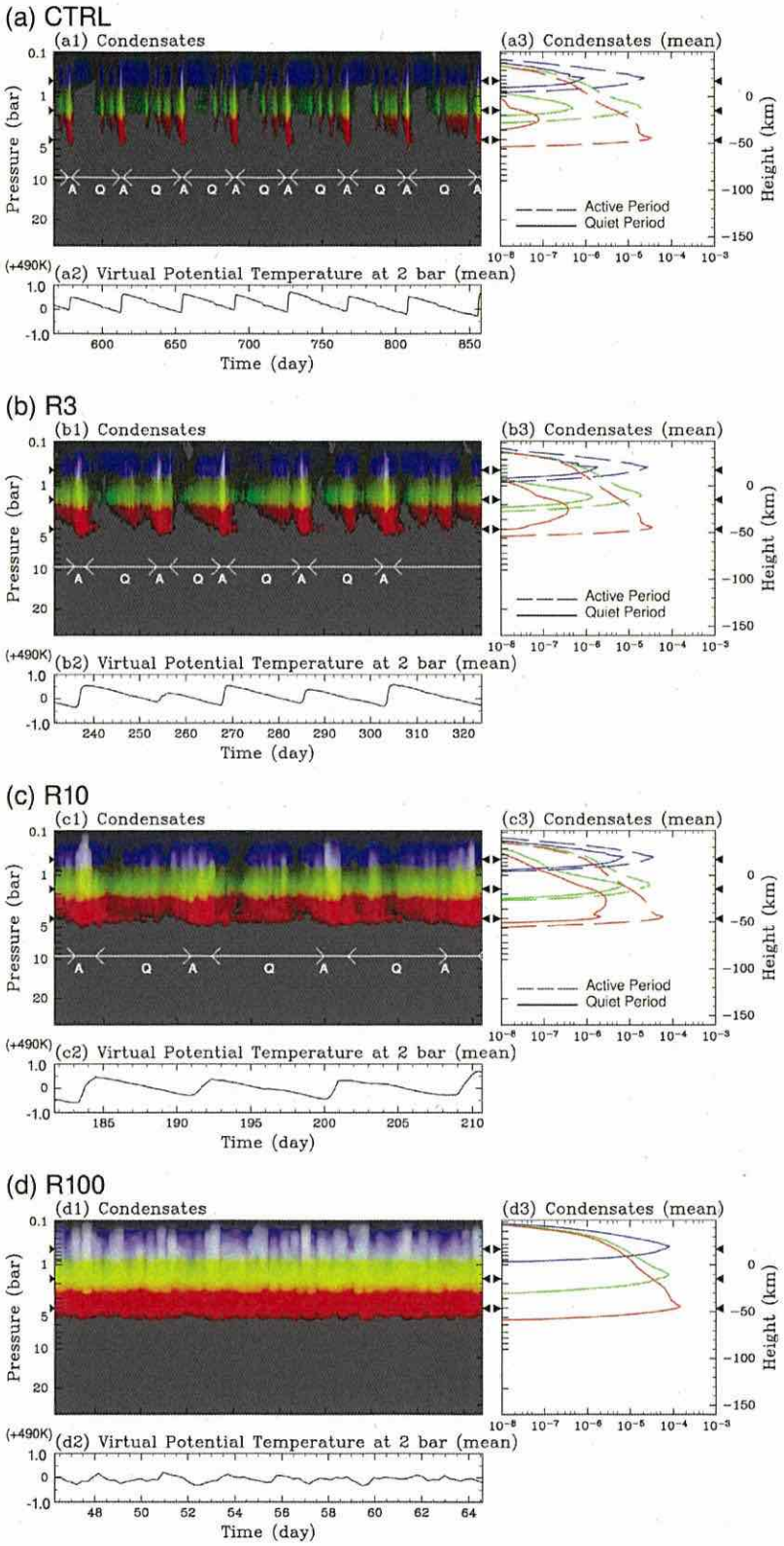

Fig. 17. Same as Fig. 6 but for (a) CTRL, (b) R3, (c) R10, and (d) R100.

course, the discussion above remains very crude, and more quantitative investigation requires implementation of charge generation models such as used in Yair et al. (1998).

One way which the present model is distinctly different from observational data is that the upper troposphere is almost always clear in most cases (e.g., Fig. 3 for CTRL) as opposed to the real

atmosphere of Jupiter, which is covered globally with a visible cloud deck. This may result partly from the value of the threshold mixing ratio for the autoconversion process being set to zero (see Section 2.3). If using a non-zero value of the threshold for NH_3 condensate, the upper troposphere would be completely cloudy. In order to explain the presence of the widespread cloud deck in the upper troposphere, an improvement of the bulk parameterization scheme to include possible categories of icy particles, i.e., cloud, ice crystals, snowflakes, graupel, and hail, for all of the three condensates, and interaction among different condensates would be necessary, but this is one of the issues for the future, when in situ observations and realistic laboratory experiments of Jupiter's clouds will be possible.

Acknowledgments

Numerical computations were carried out on Cray XT4 at Center for Computational Astrophysics, National Astronomical Observatory of Japan. The authors would like to thank Dr. Manabu Yamada for his suggestions concerning visualization and Dr. Yoshiyuki O. Takahashi, Dr. Seiya Nishizawa, Dr. Masaki Ishiwatari, and Dr. Shin-ichi Takehiro for useful comments. Products of GFD Dennou Club (http://www.gfd-dennou.org/), including Dennou Club Library (DCL), Dennou Ruby Project tools, and the gtool5 library, are used in this study. This work was supported by grants-in-aid (24740316 and 23103003) from the Ministry of Education, Culture, Sports, Science and Technology in Japan.

Appendix A. Dependence on the body cooling rate

In this appendix, the dependence of the structure and dynamics of the moist convection layer on the externally-given body cooling rate, Q_{rad}, which is a substitute for radiative cooling, is investigated. This additional investigation is necessary, as an large value of Q_{rad} is used in the parameter study examining the dependence on the deep abundances of condensable gases in Section 5. This section may also be useful for extending the applicability of this study to the atmospheres of a class of extra solar planets, "Hot Jupiter." We have performed two extra runs, R3 and R100. The values of the parameters for numerical simulations are also listed in Table 1.

The left panels of Fig. 17 show the temporal variations of the horizontal mean mixing ratios of condensates and virtual potential temperature at $p = 2$ bar for CTRL, R3, R10, and R100, where the values of Q_{rad} are 0.01, 0.03, 0.1, and 1.0 K/day, respectively. The intermittent cloud activity develops in all cases except for R100. The results in R100 (Fig. 17(d)) are consistent with those of Sugiyama et al. (2009), where the same value of cooling rate is employed and no obvious quasi-periodic temporal cycle appears. As for the temporal variations for R3 and R10, there appear intermittent vigorous cumulonimbus clouds marked as "A" in Fig. 17(b1) and (c1), and a sawtooth-like variation of potential temperature synchronizing with the intermittent cloud activity (Fig. 17(b2) and (c2)). The periods of intermittency averaged over the last 4 active-quiet cycles observed in CTRL, R3, and R10 are about 41, 17, and 9 days, respectively.

The most remarkable difference between R10 and CTRL is the vertical distribution of condensates during the quiet periods. The right panels of Fig. 17 show the vertical profiles of the condensates averaged only over the active periods and those only over the quiet periods. Although the vertical profiles for the active periods in R10 and in CTRL are similar, the peak values during the quiet periods in R10 are considerably larger than those in CTRL, and in R10, a small amount of H_2O and NH_4SH cloud particles continue to exist even above the NH_3 LCL during the quiet period. Clouds of all kinds of condensates continue to form throughout the time integration in R10 (Fig. 17(c1)), whereas there are intervals in which no H_2O or NH_4SH clouds are present in CTRL (Fig. 17(a1)).

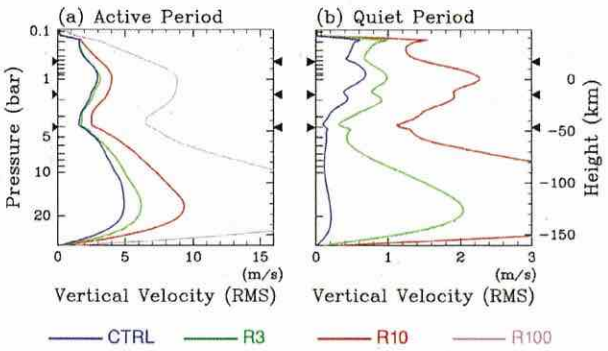

Fig. 18. Same as Fig. 9 but for CTRL, R3, R10, and R100, represented by blue, green, red and violet lines, respectively. Note that R100 is regarded to consist only of active period. (For interpretation of the references to color in this figure legend, the reader is referred to the web version of this article.)

The overall characteristics of convective motions are also similar among CTRL, R3, and R10. Fig. 18(a) and (b) show the vertical profiles of the root mean square of vertical velocity, $\sqrt{\overline{w^2}}$, averaged only over the active periods and those only over the quiet periods, respectively. The altitudes of the local minimum of $\sqrt{\overline{w^2}}$ generally coincide in all cases for both active and quiet periods. The larger value of $\sqrt{\overline{w^2}}$ during the quiet periods for the case with the stronger cooling indicates that the contrast between the active and the quiet periods becomes less distinct as the increase of body cooling rate.

The period of intermittency is expected to be inversely proportional to the cooling rate if factors other than Q_{rad} in Eq. (14) do not vary. The observed dependence is generally consistent with the expectation above, within a relative error of factor 2, as summarized in Table 2. One reason for the imperfection is that the duration of the active periods becomes non-negligible, since the duration of the quiet periods decreases as Q_{rad} increases. When the length of the active periods, which is typically 1–2 days, is considered, the correspondence between the periods estimated by Eq. (14) and those observed in the model slightly improves, especially in the cases of strong body cooling. Another reason is that the amplitude of the sawtooth-like temperature variation, $\overline{\Delta T}$, moderately depends on the intensity of body cooling; the amplitudes in R3 and R10 is about 1.03 times and 1.5 times as large as that in CTRL, respectively.

References

Anders, E., Grevesse, N., 1989. Abundances of the elements: Meteoritic and solar. Geochim. Cosmochim. Acta 53, 197–214.

Atreya, S.K., Romani, P.N., 1985. Photochemistry and clouds of Jupiter, Saturn and Uranus. Recent Advances in Planetary Meteorology, vol. 17–68. Cambridge Univ. Press, London.

Atreya, S.K., Wong, M.H., Owen, T.C., Mahaffy, P.R., Neimann, H.B., de Pater, I., Drossart, P., Encrenaz, T., 1999. A comparison of the atmosphere of Jupiter and Saturn: Deep atmospheric composition, cloud structure, vertical mixing and origin. Planet. Space Sci. 47, 1243–1262.

Carlson, B.E., Rossow, W.B., Orton, G.S., 1988. Cloud microphysics of the giant planets. J. Atmos. Sci. 45, 2066–2081.

Dyudina, U.A., Del Genio, A.D., Ingersoll, A.P., Porco, C.C., West, R.A., Vasavada, A.R., Barbara, J.M., 2004. Lightning on Jupiter observed in the H-alpha line by the Cassini imaging science subsystem. Icarus 172, 24–36.

de Pater, I., Dunn, D., Romani, P., Zahnle, K., 2001. Reconciling Galileo probe data and ground-based radio observations of ammonia on Jupiter. Icarus 149, 66–78.

Fischer, G. et al., 2011. A giant thunderstorm on Saturn. Nature 475, 75–77.

Fletcher, L.N., Orton, G.S., Rogers, J.H., Simon-Miller, A.A., de Pater, I., Wong, M.H., Mousis, O., Irwin, P.G.J., Jacquesson, M., Yanamandra-Fisher, P.A., 2011. Jovian temperature and cloud variability during the 2009–2010 fade of the South Equatorial Belt. Icarus 213, 564–580.

Friedson, A.J., 2005. Water, ammonia, and H_2S mixing ratios in Jupiter's five-micron hot spots: A dynamical model. Icarus 177, 1–17.
Gautier, D., Hersant, F., Mousis, O., Lunine, J.I., 2001. Enrichments in volatiles in Jupiter new interpretation of the Galileo measurements. Astrophys. J. 550, L227.
Gibbard, S., Lavy, E.H., Lunine, J.I., 1994. Generation of lightning in Jupiter's water cloud. Nature 378, 592–595.
Gierasch, P.J. et al., 2000. Observation of moist convection in Jupiter's atmosphere. Nature 403, 628–630.
Grevesse, N., Asplund, M., Sauval, A.J., 2007. The solar chemical composition. Space Sci. Rev. 130, 105–114.
Gibson, J., Welch, W.J., de Pater, I., 2005. Accurate jovian radio flux density measurements show ammonia to be subsaturated in the upper troposphere. Icarus 173, 439–446.
Hanel, R.A., Conrath, B.J., Herath, L.W., Kunde, V.G., Pirraglia, J.A., 1981. Albedo, internal heat, and energy balance of Jupiter: Preliminary results of the Voyager infrared investigation. J. Geophys. Res. 86, 8705–8712.
Hersant, F., Gautier, D., Lunine, J.I., 2004. Enrichment in volatiles in the giant planets of the Solar System. Planet. Space Sci. 52, 623–641.
Hueso, R., Sanchez-Lavega, A., 2001. A three-dimensional model of moist convection for the giant planets: The Jupiter case. Icarus 151, 257–274.
Ingersoll, A.P., Kanamori, H., 1995. Waves from the collisions of Comet Shoemaker-Levy 9 with Jupiter. Nature 374, 706–708.
Kessler, E., 1969. On the Distribution and Continuity of Water Substance in Atmospheric Circulation, Meteor. Monogr., 10. American Meteorological Society, Boston.
Klemp, J.B., Wilhelmson, R.B., 1978. The simulation of three-dimensional convective storm dynamics. J. Atmos. Sci. 35, 1070–1096.
Li, L., Ingersoll, A.P., Vasavada, A.R., Porco, C.C., DelGenio, A.D., Ewald, S.P., 2004. Life cycles of spots on Jupiter from Cassini images. Icarus 172, 9–23.
Little, B., Anger, C.D., Ingersoll, A.P., Vasavada, A.R., Senske, D.A., Breneman, H.H., Borucki, W.J., the Galileo SSI Team, 1999. Galileo images of lightning on Jupiter. Icarus 142, 302–323.
Nakajima, K., Matsuno, T., 1988. Numerical experiments concerning the origin of cloud clusters in the tropical atmosphere. J. Meteor. Soc. Japan 66, 309–329.
Nakajima, K., Takehiro, S., Ishiwatari, M., Hayashi, Y.-Y., 2000. Numerical modeling of Jupiter's moist convection layer. Geophys. Res. Lett. 27, 3129–3133.
Palotai, C., Dowling, T.E., 2008. Addition of water and ammonia cloud microphysics to the EPIC model. Icarus 194, 303–326.
Rogers, J.H., 1995. The Giant Planet Jupiter. Cambridge Univ. Press, London.
Rossow, W.B., 1978. Cloud microphysics: Analysis of the clouds of Earth, Venus, Mars, and Jupiter. Icarus 36, 1–50.
Sanchez-Lavega, A. et al., 2008. Depth of a strong jovian jet farm a planetary-scale disturbance driven by storms. Nature 451, 437–440.
Showman, A.P., Dowling, T.E., 2000. Nonlinear simulations of Jupiter's 5-micron hot spots. Science 289, 1737–1740.
Showman, A.P., de Pater, I., 2005. Dynamical implication of Jupiter's tropospheric ammonia abundance. Icarus 174, 192–204.
Simon-Miller, A.A., Conrath, B., Gierasch, P.J., Beebe, R.F., 2000. A detection of water ice on Jupiter with Voyager IRIS. Icarus 145, 454–461.
Sromovsky, L.A. et al., 1998. Galileo probe measurements of thermal and solar radiation fluxes in the jovian atmosphere. J. Geophys. Res. 103, 22929–22978.
Sromovsky, L.A., Fry, P.M., 2010. The source of 3-μm absorption in Jupiter's clouds: Reanalysis of ISO observations using new NH_3 absorption models. Icarus 210, 211–229.
Straka, J.M., 2009. Cloud and Precipitation Microphysics. Cambridge Univ. Press, New York, pp. 392.
Stoker, C.R., 1986. Moist convection: A mechanism for producing the vertical structure of the jovian equatorial plumes. Icarus 67, 106–125.
Sugiyama, K., Odaka, M., Kuramoto, K., Hayashi, Y.-Y., 2006. Static stability of the jovian atmospheres estimated from moist adiabatic profiles. Geophys. Res. Lett. 33, L03201. http://dx.doi.org/10.1029/2005GL024554.
Sugiyama, K., Odaka, M., Nakajima, K., Hayashi, Y.-Y., 2009. Development of a cloud convection model to investigate the Jupiter's atmosphere. Nagare Multimedia (J. Japan Soc. Fluid Mech.). <http://www2.nagare.or.jp/mm/2009/sugiyama/>.
Sugiyama, K. et al., 2011. Intermittent cumulonimbus activity breaking the three-layer cloud structure of Jupiter. Geophys. Res. Lett. 38, L13201. http://dx.doi.org/10.1029/2011GL047878.
Vasavada, A.R., Showman, A.P., 2005. Jovian atmospheric dynamics: An update after Galileo and Cassini. Rep. Prog. Phys. 68, 1935–1996.
Weidenschilling, S.J., Lewis, J.S., 1973. Atmospheric and cloud structure of the jovian planet. Icarus 20, 465–476.
West, R.A., Strobel, D.F., Tomasko, M.G., 1986. Clouds, aerosols, and photochemistry in the jovian atmosphere. Icarus 65, 161–217.
Wong, M.H., Mahaffy, P.R., Atreya, S.K., Niemann, H.B., Owen, T.C., 2004. Updated Galileo probe mass spectrometer measurements of carbon, oxygen, nitrogen, and sulfur on Jupiter. Icarus 171, 153–170.
Yair, Y., Levin, Z., Tzivion, S., 1992. Water-cumulus in Jupiter's atmosphere: Numerical experiments with and axisymmetric cloud model. Icarus 98, 72–81.
Yair, Y., Levin, Z., Tzivion, S., 1995. Microphysical processes and dynamics of a jovian thundercloud. Icarus 114, 278–299.
Yair, Y., Levin, Z., Tzivion, S., 1998. Model interpretation of jovian lightning activity and Galileos probe result. J. Geophys. Res. 103, 14,157–14,166.

Icarus 282 (2017) 1–18

Contents lists available at ScienceDirect

Icarus

journal homepage: www.elsevier.com/locate/icarus

The circulation pattern and day-night heat transport in the atmosphere of a synchronously rotating aquaplanet: Dependence on planetary rotation rate

S. Noda[a,1,*], M. Ishiwatari[b,c], K. Nakajima[d], Y.O. Takahashi[a,c], S. Takehiro[e], M. Onishi[a,2], G.L. Hashimoto[f], K. Kuramoto[b,c], Y.-Y. Hayashi[a,c]

[a] Department of Planetology, Kobe University, Kobe 657-8501, Japan
[b] Division of Earth and Planetary Sciences, Hokkaido University, Sapporo 060-0810, Japan
[c] Center for Planetary Science, Kobe University, Kobe 650-0047, Japan
[d] Department of Earth and Planetary Sciences, Kyushu University, Fukuoka 819-0395, Japan
[e] Research Institute for Mathematical Sciences, Kyoto University, Kyoto 606-8502, Japan
[f] Department of Earth Sciences, Okayama University, Okayama 700-8530, Japan

ARTICLE INFO

Article history:
Received 29 September 2015
Revised 21 August 2016
Accepted 6 September 2016
Available online 1 October 2016

Keywords:
Astrobiology
Atmospheres, dynamics
Atmospheres structure
Extra-solar, planets
Meteorology

ABSTRACT

In order to investigate a possible variety of atmospheric states realized on a synchronously rotating aquaplanet, an experiment studying the impact of planetary rotation rate is performed using an atmospheric general circulation model (GCM) with simplified hydrological and radiative processes. The entire planetary surface is covered with a swamp ocean. The value of planetary rotation rate is varied from zero to the Earth's, while other parameters such as planetary radius, mean molecular weight and total mass of atmospheric dry components, and solar constant are set to the present Earth's values. The integration results show that the atmosphere reaches statistically equilibrium states for all runs; none of the calculated cases exemplifies the runaway greenhouse state. The circulation patterns obtained are classified into four types: Type-I characterized by the dominance of a day-night thermally direct circulation, Type-II characterized by a zonal wave number one resonant Rossby wave over a meridionally broad westerly jet on the equator, Type-III characterized by a long time scale north-south asymmetric variation, and Type-IV characterized by a pair of mid-latitude westerly jets. With the increase of planetary rotation rate, the circulation evolves from Type-I to Type-II and then to Type-III gradually and smoothly, whereas the change from Type-III to Type-IV is abrupt and discontinuous. Over a finite range of planetary rotation rate, both Types-III and -IV emerge as statistically steady states, constituting multiple equilibria. In spite of the substantial changes in circulation, the net energy transport from the day side to the night side remains almost insensitive to planetary rotation rate, although the partition into dry static energy and latent heat energy transports changes. The reason for this notable insensitivity is that the outgoing longwave radiation over the broad area of the day side is constrained by the radiation limit of a moist atmosphere, so that the transport to the night side, which is determined as the difference between the incoming solar radiation and the radiation limit, cannot change greatly.

1. Introduction

A number of recent systematic surveys have discovered many earth-sized exoplanets (e.g., Torres et al., 2015). Many of those planets exist inside the tidal lock radius of their central stars, and are thought to be synchronously rotating (e.g., Von Bloh et al., 2007). Even when the global mean incoming heat flux from the central star is comparable to that of the present Earth's, the incident flux on the perpetual day side of a synchronously rotating planet can easily exceed the radiation limit of a moist atmosphere, which is the upper limit of outgoing longwave (infrared) radiation at the top of the atmosphere (OLR) defined by a one-dimensional radiative–convective equilibrium model of an atmosphere with a sufficient amount of liquid water on its bottom surface (Nakajima et al., 1992). So, a synchronously rotating planet may

* Corresponding author. Fax: +81 75 753 3715.
E-mail address: noda@gfd-dennou.org (S. Noda).
[1] Present address: Division of Earth and Planetary Sciences, Kyoto University, Kyoto 606-8502, Japan
[2] Present address: Department of Earth Sciences, Okayama University, Okayama 700-8530, Japan

http://dx.doi.org/10.1016/j.icarus.2016.09.004

easily enter the runaway greenhouse state if the day side to night side (hereafter, day-night) energy transport is insufficient.

However, in previous studies on atmospheres of synchronously rotating planets using general circulation models (GCMs), the runaway greenhouse state does not emerge for several different values of planetary rotation rate with the present value of the Earth's solar constant (e.g., Joshi, 2003; Merlis and Schneider, 2010; Edson et al., 2011). Even with the a solar constant 1.9 times that of the Earth, Yang et al. (2013) obtains statistically equilibrium states in an aquaplanet GCM experiment, in which high cloud albedo in the regions around the subsolar point presumably prevents a runaway greenhouse state. These results suggest that the mechanism that determines the amount of day-night energy transport still remains to be understood and its dependence on planetary rotation rate to be revealed. These issues may be crucial in considering the habitability of synchronously rotating exoplanets.

The atmospheric circulation structure, which should be related to day-night energy transport, has been shown to depend on the planetary rotation rate (e.g., Showman et al., 2013), which is, in this paper, represented by Ω^*, the value divided by that of the present Earth: 7.272×10^{-5} s^{-1}. Using a GCM with a slab ocean, Merlis and Schneider (2010) obtains a day-night thermally direct circulation in the case with $\Omega^* = 1/365$, whereas high-latitude westerlies emerge in the case with $\Omega^* = 1$. The latter circulation pattern is similar to that obtained earlier by Joshi (2003) with $\Omega^* = 1$. Merlis and Schneider (2010) names the two circulation regimes the "slowly rotating regime" and the "rapidly rotating regime", respectively. However, there is little information on the transition between these two regimes. Edson et al. (2011) explores the Ω^* dependence of the atmospheric circulation structures of both dry and moist planets, and shows that, in addition to the two regimes similar to those identified by Merlis and Schneider (2010), a regime with a strong westerly zonal wind in low latitudes appears with intermediate values of Ω^*. It is also shown that, for the dry planet condition, an abrupt change of zonal wind velocity occurs and multiple equilibria with hysteretic behavior exist between $\Omega^* = 0.109$ and $\Omega^* = 0.25$. However, corresponding multiple equilibria for the aquaplanet have not been described clearly.

As for day-night energy transport, Merlis and Schneider (2010) shows that the amounts of moist static energy transport are almost the same for the two cases with $\Omega^* = 1/365$ and $\Omega^* = 1$, but there is no information about energy transport for intermediate values of Ω^*. Edson et al. (2011) describes Ω^* dependences of minimum, maximum, and globally averaged mean surface temperature, but does not present that of energy transport. The dependence of day-night energy transport on Ω^*, together with possible constraints on it, remain to be explored.

Recently, GCM experiments have also been performed in order to examine possible climates on synchronously rotating terrestrial exoplanets with particular parameter setups estimated from observations (e.g., Heng and Vogt, 2011; Wordsworth et al., 2011). Naturally, detailed parameter dependence is not examined in these works, since they focus on exploration of climates for the parameters of particular exoplanets.

In this paper, a series of GCM runs with Ω^* incremented by small steps is performed under a simple setup considering a moist planet that rotates synchronously. We will attempt to confirm that, for the same value of incoming solar flux as that of the present Earth's, statistically equilibrium states are obtained and the runaway greenhouse state does not occur for various values of Ω^* including those that are not closely examined in the previous studies. We also examine how Ω^* affects the atmospheric circulation structure and day-night energy transport, and consider what determines the amount of day-night energy transport. The same simple model configuration as used in Ishiwatari et al. (2002) and Ishiwatari et al. (2007) is adopted, namely cloud-free conditions, gray radiation, swamp ocean and so on. This choice allows us to compare the results of the experiment directly with our previous studies showing that the three-dimensional moist atmosphere evolves into the runaway greenhouse state when the global mean insolation exceeds the radiation limit. Using the swamp condition allows the system to reach a statistically equilibrium state in a shorter time than with a slab ocean, and is convenient for execution of a large number of runs with various Ω^* and initial conditions. Varying these initial conditions is necessary to search for possible multiple equilibrium solutions.

The specification of the GCM and the experimental setups are described in Section 2. The realization of statistically equilibrium states is confirmed, and an overview of the dependence of the structure of the atmospheric circulation on Ω^* are given in Section 3. Four typical cases with different values of Ω^* are chosen and their associated structures of atmospheric circulation are described in Section 4. The dependence of day-night energy transport on Ω^* is analyzed, and it is argued that day-night energy transport is constrained by the radiation limit of a moist atmosphere in Section 5. Discussions and conclusions are given in Section 6.

2. Model and experimental setup

The GCM utilized in this study is DCPAM5 (the Dennou-Club Planetary Atmospheric Model, http://www.gfd-dennou.org/library/dcpam/index.htm.en), which is reconstructed from GFD-Dennou-Club AGCM5 used in Ishiwatari et al. (2002) and Ishiwatari et al. (2007) with a design convenient for numerical experiments on various planetary atmospheres. With DCPAM5, it is confirmed that the runaway greenhouse state emerges under the same conditions as those of Ishiwatari et al. (2002). Here we use the same model configuration as that of Ishiwatari et al. (2002). The governing equations for dynamical processes are the primitive equations. Simple parameterization schemes are adopted for physical processes. The atmosphere consists of water vapor and dry air. Both dry air and water vapor are transparent to shortwave radiation, and only water vapor absorbs longwave radiation with constant absorption coefficient (0.01 m^2 kg^{-1}). The moist convective adjustment scheme (Manabe et al., 1965) is used as a cumulus parameterization. Condensed water is immediately removed from the atmosphere as rain. There is no cloud; absorption and scattering of radiation by clouds are not incorporated. The surface of the planet is entirely covered with the swamp ocean, an ocean with zero heat capacity. It is assumed that the ocean does not transport heat horizontally and does not freeze. The surface albedo is set to zero. A bulk formula (Louis et al., 1982) is used for surface flux calculation.

In order to draw on existing knowledge of the present Earth's atmosphere, the values of parameters used in our experiment are basically those of the Earth except for planetary rotation rate and obliquity. The values of molecular weight and specific heat of dry air are set to 28.964×10^{-3} kg mol^{-1} and 1004.6 J K^{-1} kg^{-1}, respectively. The values of molecular weight and specific heat of water vapor are set to 18.0×10^{-3} kg mol^{-1} and 1810.0 J K^{-1} kg^{-1}, respectively. The planetary radius R_p is set to 6.371×10^3 km. The acceleration of gravity is 9.80665 m s^{-2}, and global mean surface pressure is 10^5 Pa. The synchronously rotating planet is configured with the obliquity set to zero, and the distribution of solar incident flux fixed to the planetary surface (Fig. 1) according to

$$S_{\mathrm{solar}} = S_0 \max[0, \cos\phi \cos(\lambda - \lambda_0)], \quad (1)$$

where ϕ is latitude and λ is longitude, with subsolar longitude $\lambda_0 = 90^\circ$ and solar constant $S_0 = 1380$ W m^{-2}, which is about 88% of the threshold value ($S_0 = 1570$ W m^{-2}) to enter the runaway greenhouse state obtained by the non-synchronously rotating aquaplanet experiment by Ishiwatari et al. (2002). We use 16 values of Ω^*: $\Omega^* = 0$, 0.05, 0.1, 0.15, 0.2, 0.25, 0.33, 0.5, 0.6,

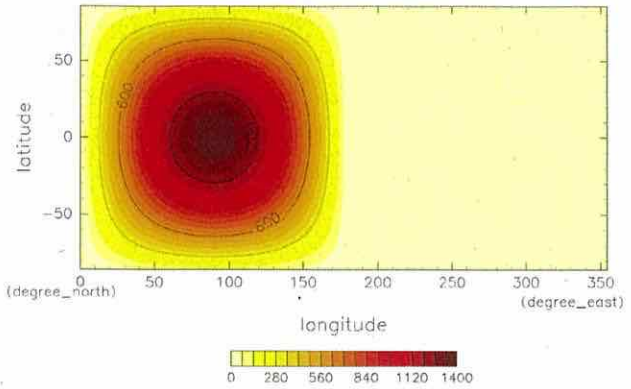

Fig. 1. Horizontal distribution of the incident solar flux [W m^{-2}] given by Eq. (1). Contour interval is 300 W m^{-2}.

0.67, 0.7, 0.75, 0.8, 0.85, 0.9, and 1. Hereafter each case will be referred to as character Ω followed by the value of Ω^*. For example, Ω0.05 is the case with orbital period of 20 Earth days. Note that changing Ω^* with fixed solar constant means changing the luminosity of the central star. Although no planet with $\Omega^* = 0$ exists in reality, we examine the circulation structure of this idealized non-rotating planet as the limiting case of small Ω^*.

For the horizontal discretization, we use the spherical spectral transform method with triangular truncation at total wavenumber 21 (T21), giving 64 grid-points for the longitudinal axis and 32 grid-points for the latitudinal axis. As the vertical coordinate, $\sigma \equiv p/p_s$ is adopted, where p_s is surface pressure. The number of vertical levels is set to 16. The model top level is set to $\sigma = 0.02$. We performed test runs for several values of Ω^* employing 32 vertical levels with the top level of $\sigma = 9.2 \times 10^{-5}$. The results show no qualitative change in either the atmospheric circulation characteristics or the energy budget compared with those with 16 vertical levels; the change in day side averaged OLR is at most 10 W m^{-2} (figures not shown), which is negligibly small compared to the value of OLR itself. We also conducted a high resolution test experiment up to T341 with $\Omega^* = 1$. and confirmed that the large scale circulation and the surface temperature patterns are mostly unchanged. These sensitivity tests show that the vertical and horizontal resolutions are adequate for the present purpose. Some aspects of the resolution dependence are demonstrated later in Appendix A .

For each Ω^*, we perform 10 runs. As will be discussed in the following sections, we have recognized that initial condition dependence appears for certain values of Ω^*; different types of circulation patterns result from slightly different initial conditions. The initial condition for each run is an isothermal (280K) resting atmosphere with a small temperature perturbation in the form of random noise with amplitude of 0.1 K added to all grid-points; we prepare ten different perturbation fields for the ten runs. Each run is integrated for 2000 Earth days, and the data from the last 1000 days are used for analysis.

3. Dependence of atmospheric circulation characteristics on planetary rotation rate

In all runs the atmosphere reaches a statistically equilibrium state; the runaway greenhouse state does not emerge. Fig. 2 shows temporal changes of the global mean values of surface temperature and OLR obtained in four typical runs with different values of Ω^*. In every case, the atmosphere settles down after about 300 days to a statistically equilibrium state in which both global mean surface temperature and OLR fluctuate around their equilibrium values. The temporal mean values of global mean surface temperature and the magnitudes of temperature fluctuation differ among runs.

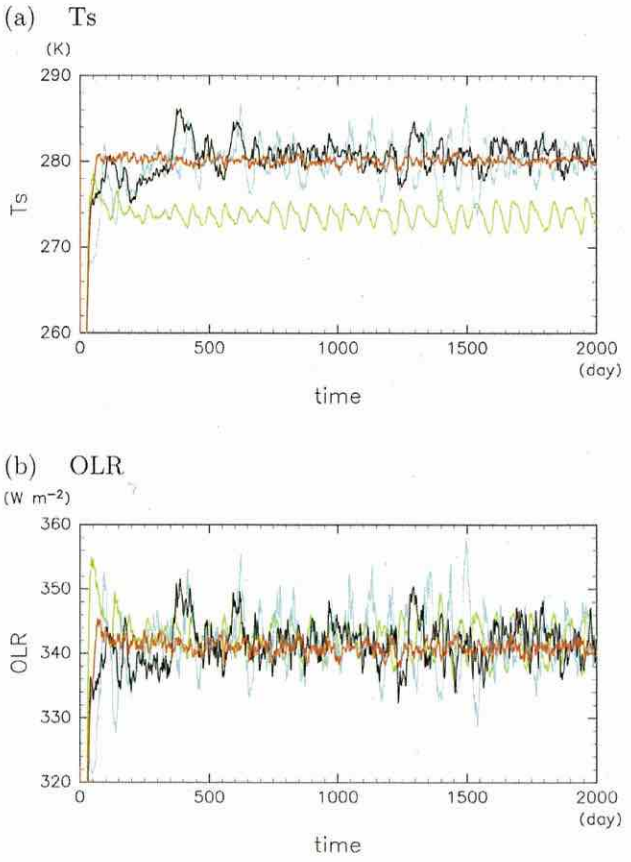

Fig. 2. Time series of global mean quantities. (a) Surface temperature [K] and (b) OLR [W m^{-2}]. Green, light-blue, black, and red lines indicate Ω0.0, Ω0.15, Ω0.75, and Ω1.0, respectively. (For interpretation of the references to colour in this figure legend, the reader is referred to the web version of this article.)

The structure of the atmospheric circulation varies with Ω^*. Fig. 3 summarizes the variety of global distributions of time mean surface temperature for various values of Ω^*. For each value of Ω^*, the result of a single run arbitrarily chosen from the ten runs is plotted. In Fig. 3, we can identify at least three features that characterize the variety of surface temperature. First, an equatorial warm belt in the night hemisphere is present in Ω0.05 – Ω0.8 (Fig. 3b–m), while it is absent in the other cases. Second, the equatorial region is generally warmer in Ω0.0 – Ω0.8 (Fig. 3a–m), while the mid-latitude regions are warmer in the other cases. These two features above reflect the meridional structures of zonal mean zonal wind, as will be shown later. Third, a north-south asymmetry is evident in Ω0.6 – Ω0.8 (Fig. 3i–m), while it is absent or weak in the other cases. This last feature reflects the presence of north-south asymmetric variability with long time scales, as will be described in Section 4.3.

For a more quantitative description of the general dependence of the atmospheric circulation structure on Ω^*, bearing in mind the three features of the surface temperature fields identified above, we examine the Ω^*-dependences of four quantities. These are the surface temperatures at the subsolar and antisolar points, the upper tropospheric zonal mean zonal wind at the equator, and a measure of north-south asymmetry in the surface temperature

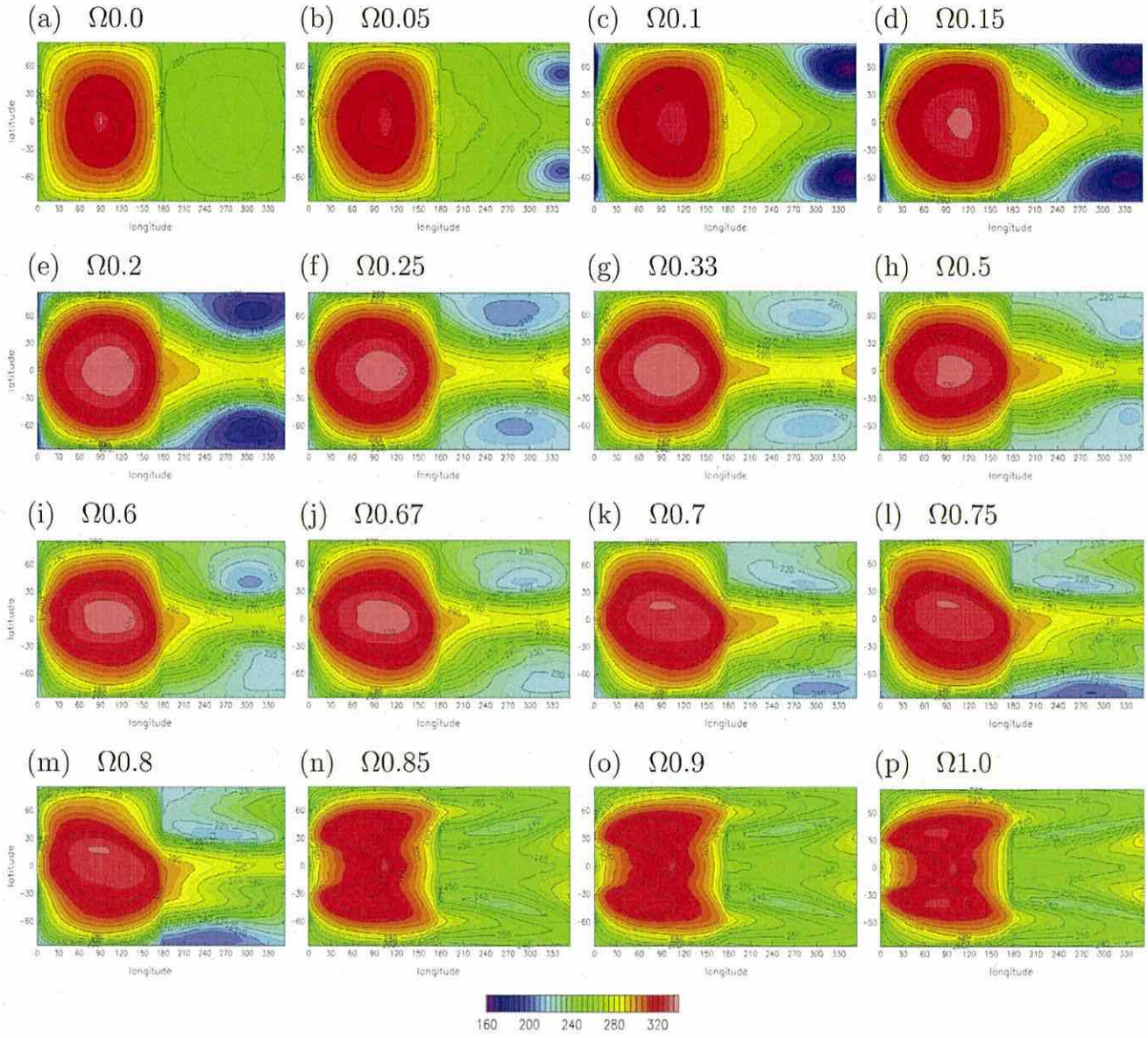

Fig. 3. Horizontal distributions of 1000-day mean surface temperature for all of the computed values of Ω^*. Contour interval is 5 K.

with short time scale transients filtered out defined by

$$\Delta_{NS}[T_s] \equiv \frac{1}{2\pi}\int_0^{\pi/2}\int_0^{2\pi} \overline{\left|\tilde{T}_s(\lambda,\phi) - \tilde{T}_s(\lambda,-\phi)\right|} d\lambda \cos\phi d\phi, \quad (2)$$

where $\tilde{T}_s$ is the 50 day running average of surface temperature, and the overbar means the temporal average over 1000 days. Fig. 4 shows the Ω^* dependences of these four quantities. Note that the ten runs for each value of Ω^* are plotted separately. Now we can identify two separate branches of atmospheric states: one extending from $\Omega^* = 0$ to $\Omega^* = 0.8$ (hereafter, the small-Ω branch), and the other from $\Omega^* = 0.7$ to $\Omega^* = 1$ (hereafter, the large-Ω branch). Between $\Omega^* = 0.7$ and $\Omega^* = 0.8$, these two branches coexist, giving multiple equilibria. The preference between the two branches in the range of the multiple equilibria seems to depend on the value of Ω^*; the ratio of runs on the large-Ω branch increases from 10% for $\Omega^* = 0.7$ to 80% for $\Omega^* = 0.8$. The branch taken by a particular run depends on small differences in the initial conditions. It is determined in the first ~500 days of the model integration, and there is no switching to the other branch after that. Note that those shown in Fig. 3k–m belong to the small-Ω branch by chance; there are also runs belonging to the large-Ω branch for this range of Ω^*, with surface temperature structure similar to those shown in Fig. 3n–p.

In Fig. 4 we observe that the atmospheric circulation characteristics change continuously but markedly on the small-Ω branch. When $\Omega^* = 0$, both zonal mean zonal wind and north-south asymmetry are negligible. As Ω^* increases, the westerly wind intensifies rapidly, and the night side surface temperature rises rapidly, both of which are tied to the appearance of the equatorial warm belt identified in Fig. 3b–m. The temperature at the subsolar point falls at first, then rises. The north-south asymmetry remains small. Around $\Omega^* = 0.5$, the north-south asymmetry increases, and continues to increases with increase of Ω^*. The asymmetry has been identified in Fig. 3i–m, but is not evident in cases Ω0.2–Ω0.5 (Fig. 3e–h), where, as will be shown later, the temporal scale of the variability is short compared with the averaging period of

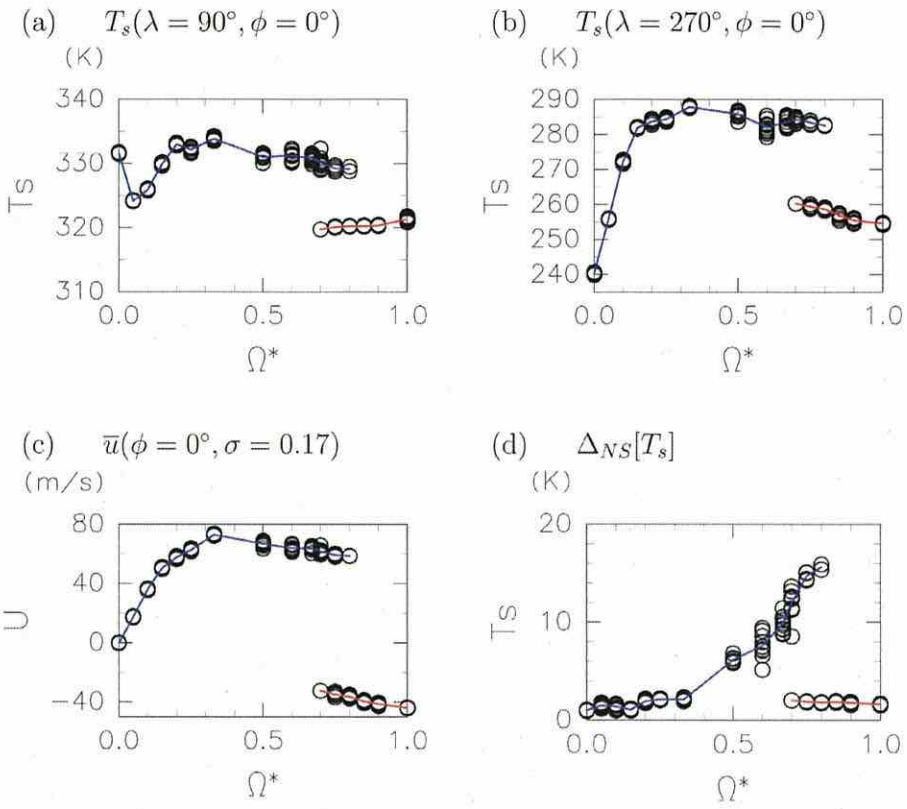

Fig. 4. Ω^* dependences of (a) surface temperature [K] at the subsolar point, (b) surface temperature [K] at the antisolar point, (c) zonal mean equatorial zonal wind [m s^{-1}] at $\sigma = 0.17$, and (d) degree of north-south asymmetry of surface temperature defined by Eq. 2 in the text [K]. The values are temporal averages between day 1000 and day 2000. All 10 runs for each Ω^* case are plotted. Red and blue lines are ensemble averages for the small-Ω and the large-Ω branches, respectively. (For interpretation of the references to colour in this figure legend, the reader is referred to the web version of this article.)

1000-days. Until the end of the small-Ω branch at Ω^*=0.8, the values of temperature at the subsolar and antisolar points remain high, and the zonal mean wind at the equator maintains its strength. On the large-Ω branch, the upper tropospheric zonal mean wind is easterly. The temperature is lower than that of the small-Ω branch at both the subsolar and antisolar points, and north-south asymmetry is weak. Changes in the four circulation characteristics are rather small over the entire range ($0.7 \lesssim \Omega^* \lesssim 1$) of the large-Ω branch.

4. Typical atmospheric circulation structures

In order to understand the atmospheric circulation and its dependence on Ω^* on the synchronously rotating planet, we examine here the spatial structures and temporal variation of the solutions in detail. Although the circulation structure changes more or less continuously as Ω^* changes on the small-Ω branch as implied in Figs. 3 and 4, we can classify the circulation structures into three types according to the zonal wind structure and the temporal variability. They are, in order of the planetary rotation rate where they appear, Type-I, characterized by day-night convection, Type-II, characterized by a broad equatorial westerly jet and a north-south symmetric stationary wave-like pattern that turns out to be a stationary Rossby wave, and Type-III, characterized by long time scale north-south asymmetric variability. In the large-Ω branch we can classify the circulation structure as Type-IV, characterized by a pair of mid-latitude deep westerly jets. For each of the four types, we choose one case and examine it in detail below.

4.1. Type-I: day-night convection (case Ω0.0)

The Type-I circulation appears in cases with very small values of Ω^*, and is characterized by day-night convection; it is similar to those obtained with small Ω^* in earlier studies (Edson et al., 2011; Merlis and Schneider, 2010). We examine case Ω0.0 as a representative case of Type-I.

The time mean structure of the atmospheric circulation in case Ω0.0 is shown in Fig. 5. Upper tropospheric horizontal flow diverges toward the night side (Fig. 5b) from the concentrated upward motion at the subsolar point, where intense precipitation develops (Fig. 5e). The outflow is strong not only in the upper troposphere ($\sigma \sim 0.23$) but also at the middle levels around $\sigma \sim 0.55$ (Fig. 5c). In the middle troposphere, the entire planet except at the subsolar point is covered with a widespread, weak, and almost homogeneous downward flow (Fig. 5c). In the lower troposphere ($\sigma \sim 0.9$), the air flow diverges from the antisolar point and returns to the day side, connected to the flow converging toward the subsolar point.

The surface temperature distribution (Fig. 5h) closely follows the incident solar flux distribution (Fig. 1). The night side surface temperature is almost homogeneous; its variation is as small as 10 K, being by far the smallest among all the experiments. The surface pressure distribution (Fig. 5a) can be interpreted as a direct response to the surface temperature distribution; a notable feature is the heat low in the lower troposphere of the day side (Fig. 5a and c). Temperature on the night side is generally highest in the middle levels ($\sigma \sim 0.6$) and lower nearer the surface (Fig. 5c). In contrast, temperature in the heat low around the subsolar point ($20° \leq \lambda \leq 160°$), increases with decreasing altitude.

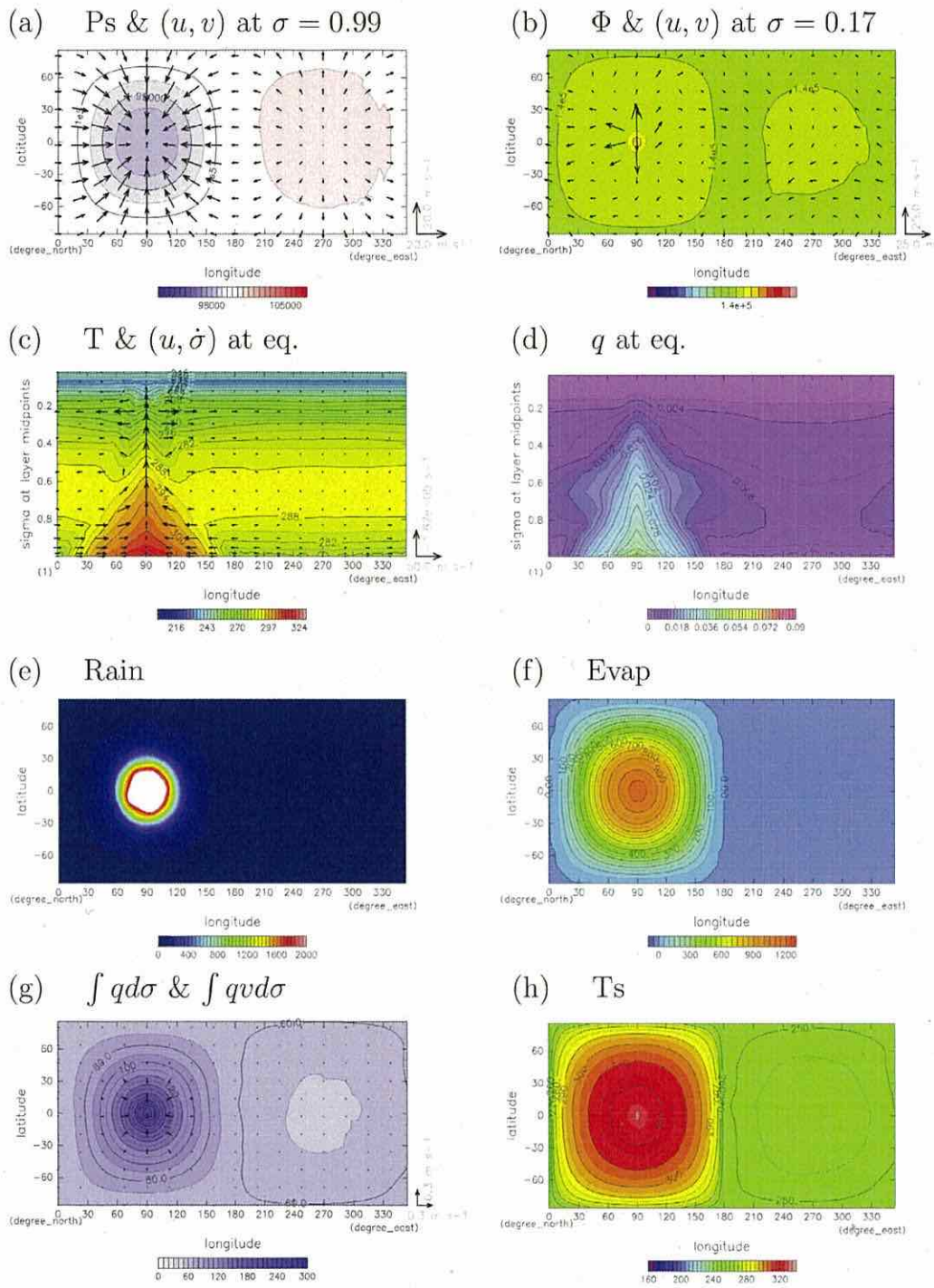

Fig. 5. Day 1000 to day 2000 temporal mean fields for case Ω0.0. (a) Surface pressure (color shading) [Pa] and horizontal wind vectors [m s^{-1}] at the lowest level. Contour interval of surface pressure is 5 × 10^2 Pa, and the unit vectors of zonal and meridional wind are 20 m s^{-1}. (b) Horizontal wind vector [m s^{-1}] and geopotential [J kg^{-1}] at $\sigma = 0.17$. Unit vector indicates 25 m s^{-1}. Contour interval of geopotential is 500 J kg^{-1}. (c) Vertical wind $-\dot{\sigma}$ [s^{-1}] and zonal wind [m s^{-1}] (vector), and temperature [K] (color) in the equatorial vertical section. Unit vectors of vertical wind and zonal wind are 1.67 × 10^{-5} s^{-1} and 50 m s^{-1}, respectively. Contour interval of temperature is 5 K. (d) Specific humidity at the equator. Contour interval is 2 × 10^{-3}. (e) Condensation heating [W m^{-2}]. Color interval is 50 W m^{-2}. White area represents heating over 2000 W m^{-2}. (f) Horizontal distribution of surface evaporation [W m^{-2}]. Color interval is 50 W m^{-2}. (g) Vertically integrated water vapor flux [m s^{-1}] and vertically integrated water vapor mass [kg m^{-2}]. Unit vector is 0.3 m s^{-1}. Contour interval is 10 kg m^{-2}. (h) Surface temperature [K]. Contour interval is 5 K. (For interpretation of the references to colour in this figure legend, the reader is referred to the web version of this article.)

The hydrological cycle is governed by the direct day-night circulation. Surface evaporation has its maximum at the subsolar point, and is very small over the whole night side (Fig. 5f). Rainfall occurs almost exclusively around the subsolar point (Fig. 5e). The middle level outflow from the subsolar point (Fig. 5c) advects moist air into the night side, producing relatively moist tongues ($0.45 \leq \sigma \leq 0.65$, $\lambda < 210°$ and $\lambda > 320°$) (Fig. 5d). However, the magnitude of the vertically integrated water vapor flux (Fig. 5g) is fairly small compared to those for the other circulation types.

4.2. Type-II: stationary Rossby wave on broad equatorial westerly jet (case Ω0.15)

The Type-II atmospheric circulation structure appears for $0.05 \lesssim \Omega^* \lesssim 0.2$ and is characterized by a warm region on the night side (Fig. 3b–d) below an intense broad equatorial westerly wind as shown in Fig. 4c, and large amplitude wavenumber one stationary waves in the higher latitudes. These features are also seen in the circulations obtained in an intermediate range of Ω^* by Edson et al. (2011). We examine case Ω0.15 as a representative case of Type-II.

The time mean structure of the atmospheric circulation in case Ω0.15 is shown in Fig. 6. The most notable feature is the emergence of a broad and deep westerly wind that covers almost the whole depth of the troposphere (Fig. 6c) of the low-latitudinal region (Fig. 6b). In the bottom layer near the surface, a trace signature of day-night circulation can still be noted (Fig. 6a). The location of maximum rainfall and the associated deep updraft are shifted eastward from the subsolar point by about 20° (Fig. 6c and e), possibly due to moisture advection by the deep westerly wind. The surface temperature peak is also shifted eastward from the subsolar point by 25° (Fig. 6h). A similar eastward shift emerges also in the other cases on the small Ω branch, explaining the drop in subsolar point surface temperature at $\Omega^* \sim 0$ (Fig. 4a). The peak of evaporation remains at the subsolar point (Fig. 6f). In fact, the latent heat flux around the equator on the day side changes little over the range of Ω^* examined in this study. The insensitivity to Ω^* results from the employment of the swamp surface condition and cloud free condition; the incoming shortwave radiation reaching the ground surface has fixed geographical distribution, and must be approximately balanced by the energy loss by latent heat of evaporation. The surface pressure minima are located at $(\lambda, \phi) \sim (120°, \pm 15°)$; these are not only to the east of the subsolar point, but also off the equator (Fig. 6a). The higher-latitude regions are characterized by intense wavenumber one stationary waves manifested as the ridge around $\lambda \sim 150°$ and the cyclones around $(\lambda, \phi) \sim (330°, \pm 60°)$ (Fig. 6b). The pressure signatures are generally geostrophic, and have an equivalent barotropic vertical structure suggested by the low surface pressure signatures below the upper level low pressure area (Fig. 6a).

The deep, broad equatorial westerly wind transports a large amount of sensible and latent heat to the night side, which is manifested as the warm and moist tongue in the lower to the middle troposphere extending eastward crossing the terminator at $\lambda = 180°$ (Fig. 6c and d). A considerable portion (about one fourth) of the water vapor transported to the night side at $\lambda = 180°$ returns to the day side at $\lambda = 360°$ (figure not shown). At $\lambda = 180°$, water vapor transport to the night side is more intense in the high-latitudinal regions than in the equatorial region, resulting from the meandering of the eastward wind associated with the intense wavenumber one stationary waves and near surface westward wind near the equator. Rainfall is no longer focused at the subsolar point, as it is associated with the moisture transport, and some amount of rainfall occurs even in the night hemisphere (Fig. 6e) despite the negligibly small amount of surface evaporation. Also due to the enhanced water vapor transport, the column integrated moisture content around the antisolar point reaches about three times that in case Ω0.0 (Fig. 6g). Actually, column integrated moisture content increases considerably also on the day side; the peak value near the subsolar point in case Ω0.15 is about 1.5 times the value of that in case Ω0.0, and its associated greenhouse effect results in the rise of surface temperature following the drop near $\Omega^* \sim 0$ (Fig. 4a).

It is notable that the horizontal distribution of surface temperature closely follows that of column moisture content on the night side (Fig. 6g and h); in an extensive region of high column water vapor content in the low latitudes, surface temperature is high, whereas it is very low in the dry regions located around the low pressure centers of wavenumber one structure at higher latitudes. The energy budget at the ground surface explains this close relationship; because incident solar flux is absent and both latent (~ 2 W m^{-2}) and sensible (~ -4 W m^{-2}) heat fluxes are negligibly small on the night side, the upward thermal radiation flux (~ 230 W m^{-2}) at the surface almost balances the downward longwave radiation from the atmosphere that is exclusively emitted by water vapor, the only radiatively active component in this model.

When all Type-II cases are compared, the broad equatorial jet is stronger for the cases with larger value of Ω^* as indicated in Fig. 7, where the values of mass weighted global mean zonal wind velocity in Type-II are shown. Moreover, for $\Omega^* \gtrsim 0.2$, the wind speed is close to the absolute values of the intrinsic phase speed of the normal mode Rossby wave of Longuet-Higgins (1968). The thin line in Fig. 7 shows the intrinsic phase speed of the meridionally gravest normal mode Rossby wave with wave number one, which we calculate with the spectral method of Kasahara (1976). Considering the vertical structure of the waves appearing in Type-II, we assume an equivalent depth of 10000 m, which is the value for the barotropic mode in an isothermal atmosphere of 245 K. The rough coincidence of the speed of the broad eastward equatorial jet and that of the intrinsically westward propagating normal mode Rossby wave for each Ω^* suggests that the wavenumber one planetary scale stationary wave in Type-II is resonantly excited on the broad westerly jet. Other evidence for the resonant excitation is the Ω^*-dependence of the amplitude and phase of the stationary wavenumber one waves. The cyclonic regions associated with the waves are expressed as the north-south symmetric cold regions in the night side mid to high latitudes (Fig. 3). For Ω^* from 0.05 to 0.2, the amplitude of the cyclonic regions is generally large. The longitudinal phase difference between the precipitation maximum and the cyclonic centers is about 270° for $\Omega^* = 0.05$. This is the largest eastward phase shift of the upper Rossby wave response to a wavenumber one thermal forcing in a westerly flow faster than the resonant speed. As Ω^* increases, the phase difference decreases, dropping below 180° for $\Omega^* = 0.25$ and 0.33. Possible mechanisms for the acceleration of the broad westerly wind and its resonant relation to the normal mode Rossby waves will be discussed in more detail in Section 6.3, referring to earlier studies.

For $\Omega^* \gtrsim 0.25$, the westerly wind does not reach the normal mode Rossby wave speed. Our preliminary analysis reveals that, in these cases, mid-latitude transient disturbances, which may originate from baroclinic instability given the development of meridional temperature gradient (not shown), transport westerly momentum poleward and decelerate the broad westerly jet. Detailed analysis on the nature of the transient disturbances and their possible role as the "governor" of the equatorial jet remains to be performed.

4.3. Type-III: long time scale north-south asymmetric variability (case Ω0.75)

The Type-III atmospheric circulation structure appears on the small-Ω branch for $0.5 \lesssim \Omega^* \lesssim 0.8$. The temporally averaged

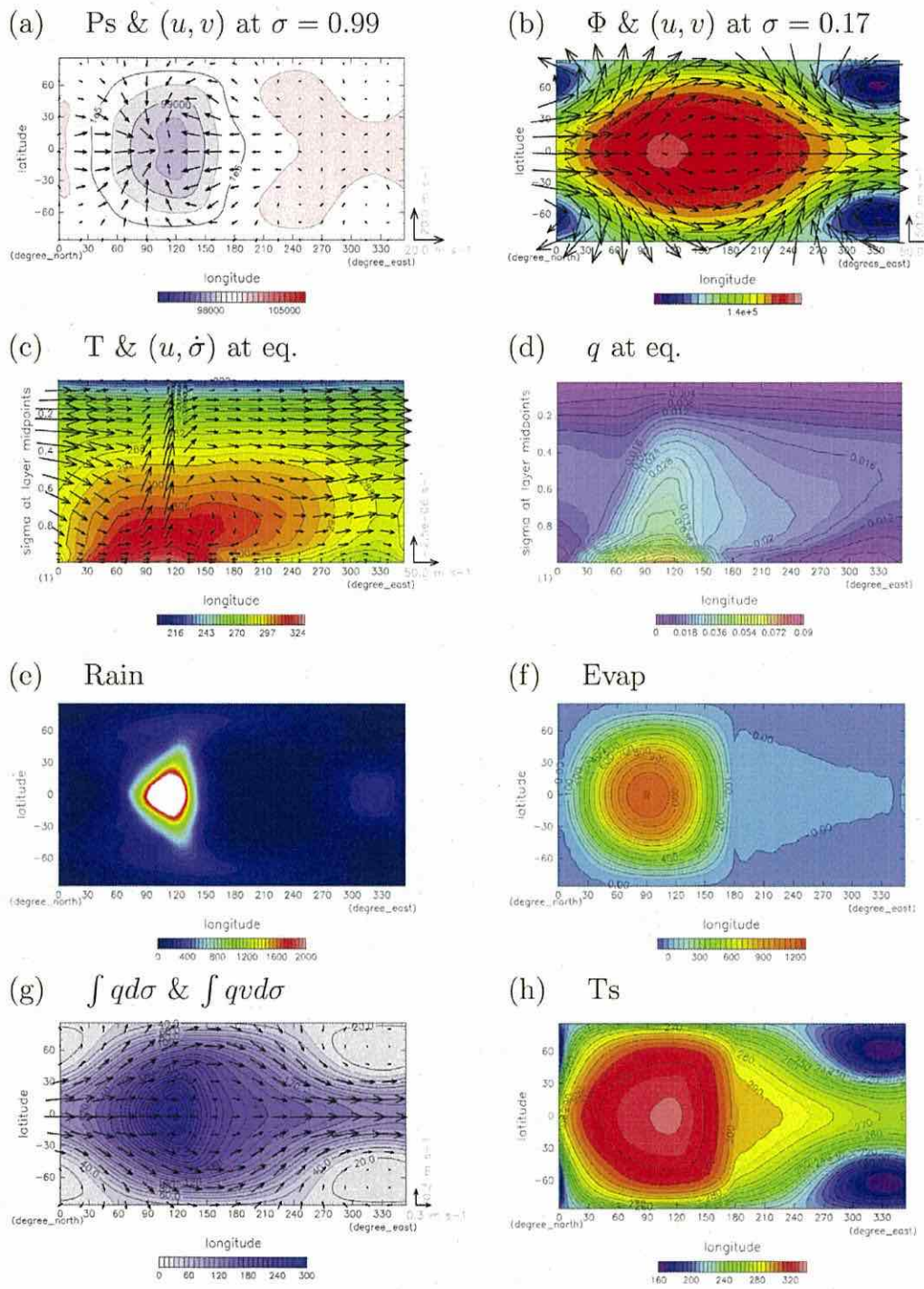

Fig. 6. Same as Fig. 5 but for case Ω0.15, except that the unit vector in (b) is 50 m s^{-1} and the unit vector of vertical wind in (c) is 2.5×10^{-6} s^{-1}.

characteristics of Type-III are similar to those of Type-II in terms of the strong eastward equatorial jet, but, as shown in Fig. 4d, differ in the presence of significant north-south asymmetric long time scale variability.

Before considering the Type-III circulation structure in detail, we summarize the Ω^* dependences of the amplitude and the typical oscillation period of the north-south asymmetric variability. Fig. 8 compares the time series of zonal mean surface pressure in four cases with different values of Ω^*. In case Ω0.2, where Type-II structure develops, a quasi periodic oscillation with amplitude of ~20 hPa and a temporal scale of ~10 days is notable. In case Ω0.5, in addition to an oscillation with ~20 day period, a slower, north-south asymmetric variability is evident; its period and amplitude are ~40–100 days and ~45 hPa, respectively. In cases with larger Ω^*, the slow, north-south asymmetric variability is more intense and its characteristic period is longer; in case Ω0.67, the

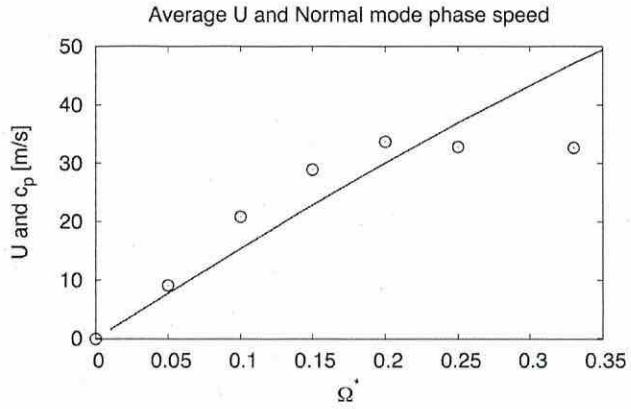

Fig. 7. Mass weighted global mean zonal wind velocity for cases with Ω^* from 0.0 to 0.33 (circles). Absolute value of westward phase velocity of the zonal wavenumber one gravest Rossby normal mode is indicated by the thin line for comparison.

amplitude is ~80 hPa, and the period is ~1000 days. In case Ω0.75, the amplitude is as large as ~160 hPa, and, looks almost permanent in Fig. 8d. However, by conducting several extended experiments, we have confirmed that the asymmetry does change its sign over a long time; the pressure deviation reverses at around t = 25000 days for the run shown in Fig. 8d. Furthermore, the sign of the asymmetry is determined by chance; in the ten runs conducted for Ω0.75, Type-III structure appears in four runs (not shown), and, during the period shown in Fig. 8d, two of them have a positive pressure anomaly in the northern high latitudes, and the remaining two are negative. We conclude that, despite the development of the distinct long time scale north-south asymmetric variation, the structure of the atmospheric circulation is, in a statistical sense, north-south symmetric, consistent with the symmetry of the applied solar flux.

Considering the characteristics of the north-south variation, we examine case Ω0.75 as representative of Type-III, where the north-south asymmetry appears as a quasi stationary structure that persists throughout the 1000 days of the temporal average. As shown in Fig. 8d, northern (southern) high latitudes are occupied by high (low) pressure throughout the averaging period. The north-south asymmetric features discussed below are naturally reversed in the time period when the surface pressure in the northern (southern) hemisphere is low (high). We also note that the north-south asymmetric atmospheric circulation features develop also in GCM experiments with higher horizontal resolution (T42 and T85), although they appear in slightly different ranges of Ω^* (see Appendix A), so we believe their emergence itself is insensitive to model resolution.

The time mean structure of the atmospheric circulation in case Ω0.75 is shown in Fig. 9. The deep westerly flow along the equator (Fig. 9b and c), and the associated eastward advection of water vapor (Fig. 9d and g) resulting in a warm belt along the equator in the night hemisphere (Fig. 9h), are features similar to those in Type-II (Fig. 6). However, except for the distribution of evaporation, which is strongly constrained by insolation as was discussed for Type-II, most of the off-equatorial features exhibit north-south asymmetry in contrast to the north-south symmetry in Type-II. Northern (southern) high latitudes are covered with surface high (low) pressure (Fig. 9a). The low pressure area in the day hemisphere also exhibits north-south asymmetry; the low pressure center in the southern hemisphere is much more intense than its counterpart in the northern hemisphere. Being in geostrophic balance with the pressure gradient around the polar pressure anomalies, north-easterly (north-westerly) wind prevails at the surface in northern (southern) mid latitude (arrows in Fig. 9a). This brings dry (moist) air into the mid latitudes of the day (night) hemisphere (Fig. 9g) crossing the day-night boundary at $\lambda = 180^\circ$. inducing the

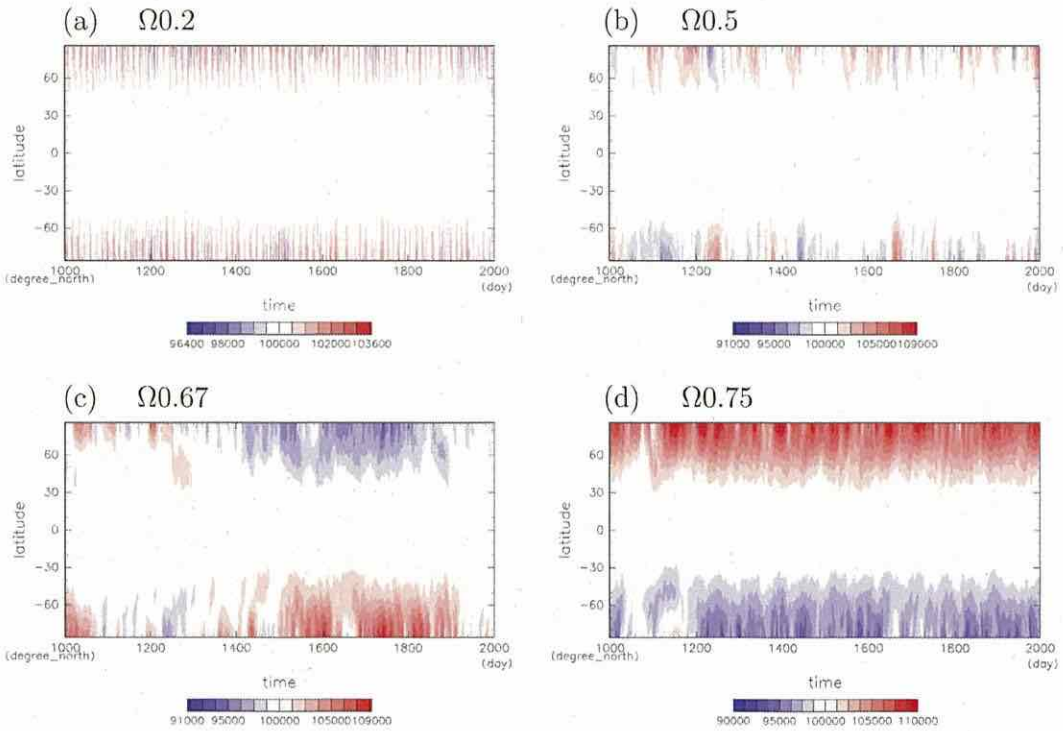

Fig. 8. Latitude–time distribution of zonal mean surface pressure [Pa] for (a) Ω0.2, (b) Ω0.5, (c) Ω0.67, and (d) Ω0.75.

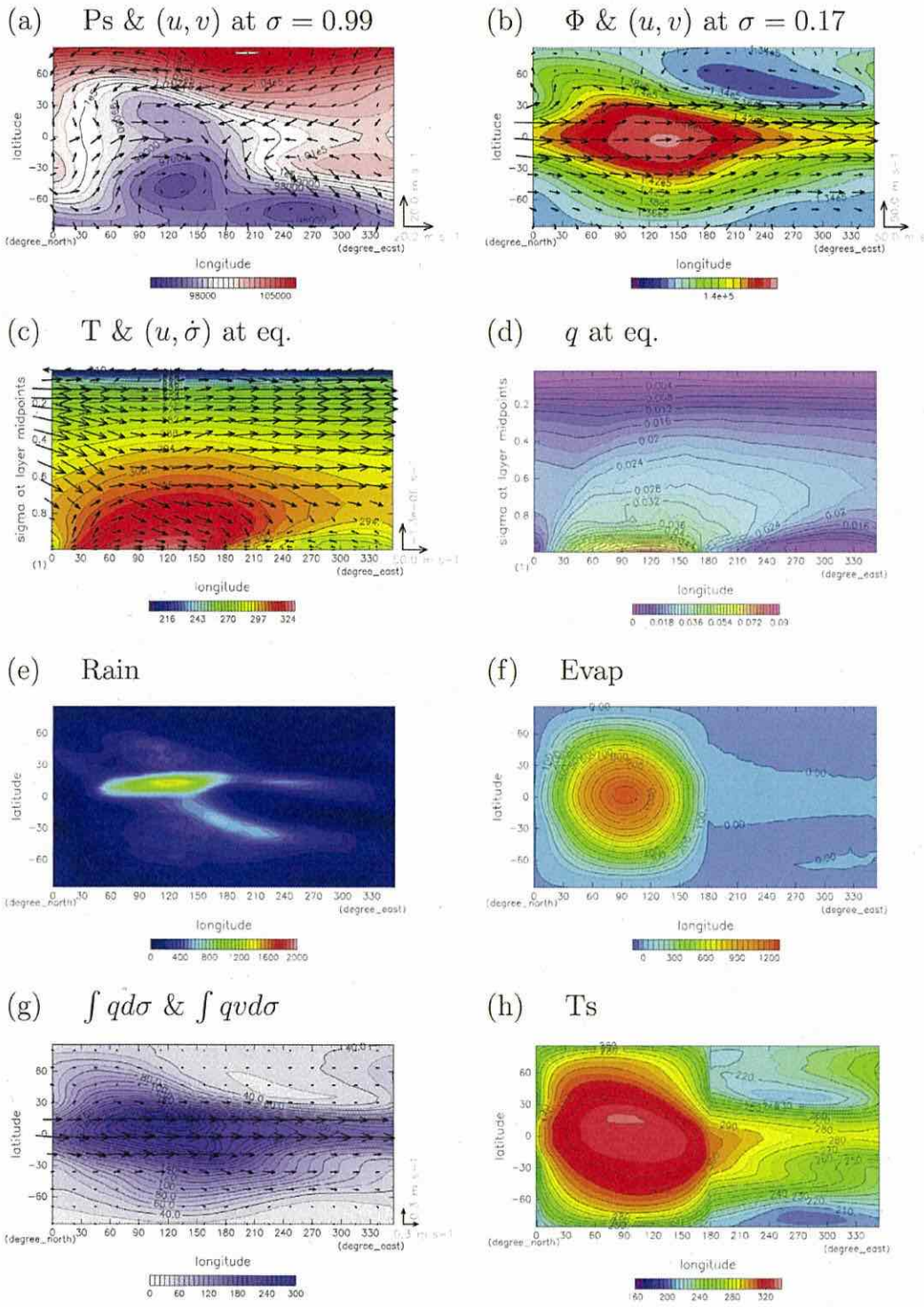

Fig. 9. Same as Fig. 6 but for case Ω0.75, except that the unit vector of vertical wind in (c) is 1.3×10^{-6} s^{-1}.

north-westward (south-eastward) development of the mid-latitude precipitation zone (Fig. 9e) and the north-south asymmetry of surface temperature in both the day and night hemispheres (Fig. 9h) through the anomaly in downward thermal radiation.

Two additional features characterize the north-south asymmetry. First, the westerly region extends farther poleward in the southern hemisphere than in the northern hemisphere (Fig. 10a), where intense baroclinic disturbances develop (not shown here), presumably transporting westerly momentum downward. Second, there is a baroclinic zonal wavenumber one feature (Fig. 9ab) which has markedly north-south asymmetric meridional phase tilt (Fig. 10b); the phase lines tilt from northwest to southeast in

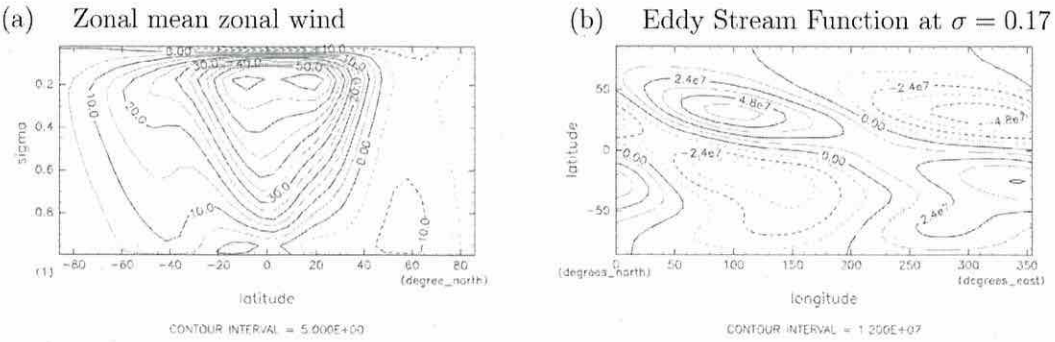

Fig. 10. Structure of the atmosphere averaged from day 1000 to day 2000 for case Ω0.75: (a) zonal mean zonal wind, and (b) eddy stream function at $\sigma = 0.17$.

a wide latitudinal zone from the northern high latitudes ($\phi \sim +70^\circ$) to southern mid latitudes ($\phi \sim -40^\circ$), crossing the equator. The phase tilt of the zonal wavenumber one feature, which implies southward transport of westerly momentum from northern to southern hemispheres, presumably contributes to driving the mid-latitude westerly jet in the southern hemisphere noted above (Fig. 10a).

According to our preliminary analysis (not shown here) of the vorticity sources following the formulation of Sardeshmukh and Hoskins (1988), the meridionally tilted wavenumber one feature seems to be forced jointly by tropical and extratropical precipitation (Fig. 9e); the heating near the subsolar point, which is distributed mainly in the northern tropics around $(\lambda, \phi) = (120^\circ, +12^\circ)$, can be regarded as an excitation source of a Rossby wave that contributes the northern half of the wavenumber one structure. Meanwhile the latent heating associated with the precipitation band in southern mid latitudes distributed around $(\lambda, \phi) = (180^\circ, -30^\circ)$, can be regarded as an excitation source of a Rossby wave that contributes the southern half. Upward cascade of baroclinic eddies developing in the westerly jet could also contribute to the southern half. The distribution of mid-latitude precipitation seems to be, in turn, induced by the north-south asymmetry of moisture flux associated with surface pressure as described in the previous paragraph. Combining these features, the north-south asymmetry may possibly be maintained through a positive feedback loop, so that the asymmetry tends to have long life time. Quantitative examination of the dynamics of this possible feedback loop remains for future studies.

4.4. Type-IV : mid-latitude westerly jets (case Ω1.0)

The Type-IV atmospheric circulation structure is found over the entire large-Ω branch for $\Omega^* \gtrsim 0.7$, and is characterized by somewhat Earth-like mid- to high- latitudes westerly jets. This is similar to the structures obtained by Merlis and Schneider (2010) and Edson et al. (2011) with $\Omega^* = 1$, although several points of difference can be noted (See Section 6.1). We examine case Ω1.0 as a representative case of Type-IV.

The time mean structure of the atmospheric circulation in case Ω1.0 is shown in Fig. 11. The mid latitudes are occupied by westerly winds through the whole depth of the troposphere (Fig. 11a and b). The low latitudes are occupied by easterly wind, but only in the upper troposphere. The lower tropospheric circulation along the equator (Fig. 11c) is more strongly controlled by the day-night contrast; zonal wind near the surface converges to form the upward motion at the subsolar point, and diverges around the antisolar point compensated by the broad downward motion. In the off-equatorial latitudes, latitudinal tilting of zonal wavenumber one wave features are notable, but these have generally baroclinic vertical structure, in contrast to the barotropic Rossby wave in Type-II. Polar regions are covered with deep low pressure areas.

The precipitation and water vapor distributions are more complicated than those on the small-Ω branch. Precipitation (Fig. 11e) is most intense in a zonally aligned V-shaped region extending from the equatorial point $(\lambda, \phi) \sim (110^\circ, 0^\circ)$ to $(\lambda, \phi) \sim (30^\circ, \pm 25^\circ)$, loosely overlapping the low pressure area in the western part of the day hemisphere (contours in Fig. 11a). The wings of the V-shaped precipitation region intrude into the night side from the regions around $\phi = \pm 25^\circ$ at $\lambda = 360^\circ$. There is also a pair of zonally elongated precipitation zone in the higher latitudes, which start at $(\lambda, \phi) \sim (45^\circ, \pm 45^\circ)$ and extend to $(\lambda, \phi) \sim (330^\circ, \pm 80^\circ)$ on the night side. The distribution of column integrated water vapor content roughly follows that of precipitation (Fig. 11g), but the areas of greatest moisture content are located far from the equator, poleward of the high-latitude parts of the equatorial V-shaped strong precipitation area at $(\lambda, \phi) \sim (50^\circ, \pm 30^\circ)$.

The distribution of night side surface temperature (Fig. 11h) closely follows that of the atmospheric water vapor content (Fig. 11g) as in the cases on the small-Ω branch. However, reflecting the complex structure of humidity, temperature varies longitudinally; it is warmer to the east along $\phi \sim \pm 30^\circ$, whereas it is warmer to the west along $\phi \sim \pm 50^\circ$. Also the distribution of surface temperature on the day side is affected by the distribution of water vapor content; the highest surface temperature appears at $(\lambda, \phi) \sim (80^\circ, \pm 40^\circ)$, the locations that are quite far from the subsolar point and below the belts of large water content (deep blue colors of Fig. 11g). The values of surface temperature at the subsolar and antisolar points are lower than the respective values in Types -II or -III (Fig. 4a and b), resulting from the reduction of atmospheric water content compared to those cases.

5. Day-night energy transport

5.1. Dependence on Ω*

In this section, we examine how day-night energy transport changes with Ω*, responding to the considerable variation of the atmospheric circulation structure described in the previous section. We analyze OLR on the night side, F_{OLR}, day-night dry static energy transport, $\mathcal{T}_{sens}$, and day-night latent energy transport, $\mathcal{T}_{lat}$, which, in equilibrium states, satisfy the energy balance of the night side:

$$\mathcal{T}_{sens} + \mathcal{T}_{lat} - 2\pi R_p^2 F_{OLR} = 0. \tag{3}$$

$\mathcal{T}_{sens}$ and $\mathcal{T}_{lat}$ are calculated assuming the approximate balances of heat and moisture budgets in the night side atmosphere, which are

$$2\pi R_p^2 (F_{SLR} + F_{sens} - F_{OLR} + LP) + \mathcal{T}_{sens} = 0, \tag{4}$$

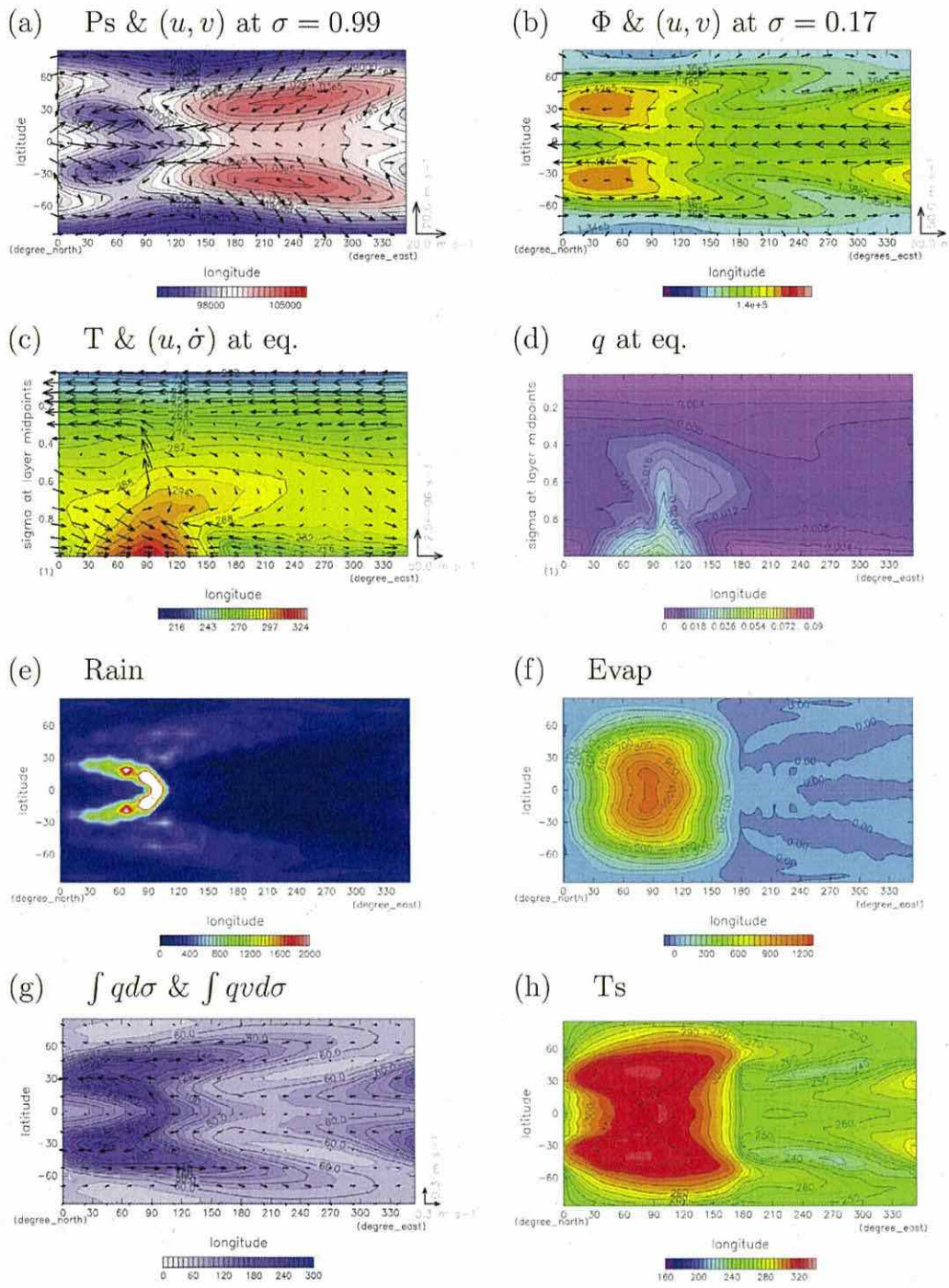

Fig. 11. Same as Fig. 9 but for case Ω1.0 except that unit vector of the vertical wind in (c) is 2.5×10^{-6} s^{-1}.

$$2\pi R_p^2(F_{evap} - P) + \mathcal{T}_{lat}/L = 0, \tag{5}$$

where F_{evap} is surface evaporation flux, F_{SLR} is net upward longwave radiation flux at the surface, F_{sens} is surface sensible heat flux, P is precipitation, and L is latent heat of water vapor. All of the terms are 1000-day mean values spatially averaged over the night side.

Fig. 12a shows Ω* dependences of F_{OLR}, $\mathcal{T}_{sens}/(2\pi R_p^2)$, and $\mathcal{T}_{lat}/(2\pi R_p^2)$. All 10 runs are plotted for each value of Ω*. The most remarkable feature is that total energy transport is almost unchanged regardless of the branch of the solution and the value of Ω*, while the partition into $\mathcal{T}_{sens}$ and $\mathcal{T}_{lat}$ changes. For $\Omega^* \sim 0$, where the Type-I structure appears, $\mathcal{T}_{lat}$ is negligible, as atmospheric water vapor content is very small (Fig. 5g). As Ω* increases and the Type-II structure appears, $\mathcal{T}_{lat}$ rapidly increases, but $\mathcal{T}_{sens}$ decreases correspondingly, keeping the sum of the two (F_{OLR}) almost unchanged. The increase of $\mathcal{T}_{lat}$ results from the development of the deep broad westerly wind (Fig. 6b and c) together with the increase of moisture in the day hemisphere (Fig. 6d). Further

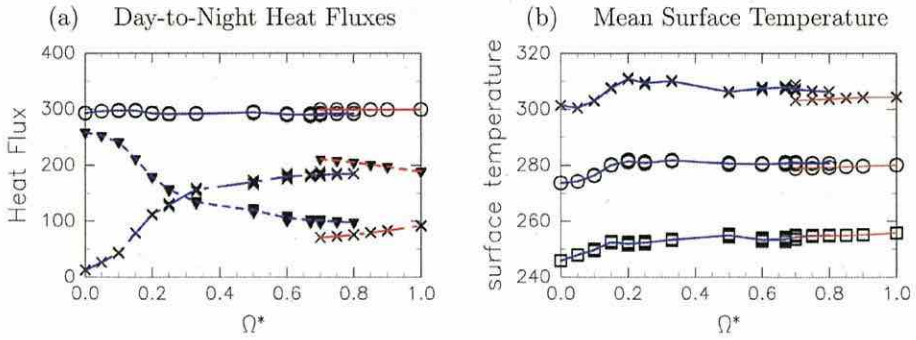

Fig. 12. (a) Ω^* dependences of outgoing longwave radiation on the night side, F_{OLR} (○), day-night dry static energy transport per unit area, $\mathcal{T}_{sens}/(2\pi R^2)$ (▼), and day-night latent energy transport per unit area, $\mathcal{T}_{lat}/(2\pi R^2)$ (×). Units are [W m^{-2}]. All 10 runs for each Ω^* case are plotted. Blue and red lines represent ensemble averages for the small-Ω and the large-Ω branches, respectively. (b) Same as (a) but for global mean (○), day side mean (×), and night side mean (□) of surface temperature [K]. (For interpretation of the references to colour in this figure legend, the reader is referred to the web version of this article.)

increase of $\mathcal{T}_{lat}$ and decrease of $\mathcal{T}_{sens}$ continue for larger Ω^* as the Type-III with north-south asymmetric variability appears. $\mathcal{T}_{lat}$ exceeds $\mathcal{T}_{sens}$ at $\Omega^* = 0.33$ and $\mathcal{T}_{lat}$ reaches about twice $\mathcal{T}_{sens}$ at the large-Ω end of the small-Ω branch ($\Omega^* = 0.8$). Still, the sum of the two (F_{OLR}) is kept almost constant. At the transition from the small-Ω branch to the large-Ω branch around $\Omega^* \sim 0.75$, $\mathcal{T}_{lat}$ suddenly reduces by about half. Nevertheless, an equally abrupt increase of $\mathcal{T}_{sens}$ means that total heat transport changes only a little. The decline of $\mathcal{T}_{lat}$ at the transition results from the associated disappearance of the broad westerly wind at low latitudes. The type-IV structure has a pair of deep mid-latitude westerly jets blowing through the day and night sides (Fig. 11b), but they cannot transport as much water vapor as the broad equatorial westerly wind in the Type-II or Type-III cases, because the water vapor mixing ratio in the mid latitudes is smaller than in the lower latitudes. The variation of total day-night energy transport is less than 2% over the wide range of Ω^*, while the atmospheric circulation structure varies considerably. Day-night total energy transport scarcely depends on the atmospheric circulation structure.

We have already seen in Fig. 4b that surface temperature at the antisolar point changes greatly with the change of Ω^*. This seems perplexing, since day-night total energy transport is almost constant. However, if we examine the hemispherically averaged temperature, the change is only modest. Fig. 12b shows Ω^* dependences of surface temperature averaged over the night side, the day side, and the whole globe. The range of the variation of night side average temperature is around 10 K, which is much smaller than the variation at the antisolar point of almost 50 K (Fig. 4b). This results from the compensation between the temperature variations in the lower and higher latitudes; in Type-II and Type-III, surface temperature in the low latitudes including the antisolar point is high, while regions of low surface temperature appear in the higher latitudes associated with the large amplitude Rossby waves (Fig. 3b–m). The remaining modest changes of averaged temperatures can be explained mainly by the change of mean column water vapor content.

5.2. Moist atmosphere radiation limit constraint

As described in the previous subsection, the total amount of day-night energy transport is found to be insensitive to the change of Ω^* and to the associated change of atmospheric circulation structure. The invariance of day-night total energy transport is equivalent to the invariance of day side OLR, because the day-night total energy transport is equal to the difference between the day side OLR and the incident solar flux; the latter is constant in the present study. It has been recognized that, in the framework of a

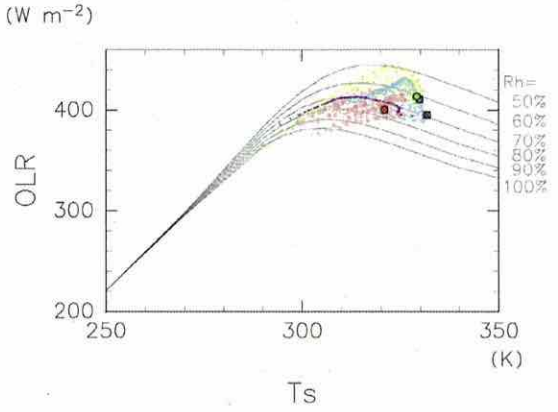

Fig. 13. Relationships between surface temperature and OLR obtained by the GCM and by the one-dimensional (vertical) radiative-convective equilibrium model. The GCM results are shown as colored dots: purple, light blue, green, and pink dots indicate runs Ω0.0, 0.15, 0.75, and 1.0, respectively. Data are from the grid points in the 120° × 120° rectangular region centered on the subsolar point. Crosses in black circles indicate the values at the subsolar point. Black lines are the one-dimensional model results with tropospheric relative humidity of (in order from the top) 50, 60, 70, 80, 90, and 100%, respectively. (For interpretation of the references to colour in this figure legend, the reader is referred to the web version of this article.)

one-dimensional radiative convective equilibrium model, the value of OLR from the atmosphere on a water covered planet can not exceed the radiation limit. In the following, we attempt to understand the invariance of day-night energy transport in relation to the constraint on the day side OLR from the radiation limit of a moist atmosphere.

Fig. 13 shows the relationship between surface temperature and OLR on the day side obtained by the present GCM calculations superposed on the relations obtained by the one-dimensional radiative convective equilibrium model described in Section 4 of Ishiwatari et al. (2002) with several specified values of tropospheric relative humidity. The relationship between surface temperature and OLR is sampled at the grid points within the 120° × 120° rectangular region centered on the subsolar point from the run for each Ω^* described in the previous section.

In all the GCM runs, the maximum values of OLR are between 400 and 430 W m^{-2}, and lie under the values of the radiation limits in the one-dimensional calculation, given that the values of relative humidity averaged over the troposphere on the day side of the GCM runs are within the range 60–80%. Moreover, in each of the GCM results, the relationship between surface temperature and OLR roughly follows those obtained in the one-dimensional calculations. These results imply that the day side OLR in the

present GCM calculations is constrained by the radiation limit of a moist atmosphere on a water covered planet. Now recalling that the system is in a statistically equilibrium state, the amount of day-night total energy transport should be equal to the difference between the incident solar flux and the radiation limit of a moist atmosphere. The results of our GCM calculations indicate that the change in atmospheric circulation structure associated with the change of Ω^* does not modify drastically the mean value of atmospheric humidity, and hence does not affect the value of the radiation limit. This explains the general insensitivity of day-night energy transport to Ω^* obtained in the present GCM calculations.

6. Concluding remarks

6.1. Summary of results and comparison with previous studies

Numerical experiments are performed using a cloud-free, swamp aquaplanet GCM with a gray absorption coefficient for longwave radiation and with the Earth's solar constant. The value of planetary rotation rate normalized by the Earth's value, Ω^*, is varied from 0 to 1. For all Ω^* cases, statistically equilibrium states are obtained; the runaway greenhouse state does not emerge. The circulation structures obtained are classified into four types: Type-I characterized by day-night convection, Type-II characterized by a broad equatorial westerly jet and a stationary Rossby wave, Type-III characterized by a long time scale north-south asymmetric variability, and Type-IV characterized by a pair of mid-latitudinal westerly jets. Types-I, II, and III evolve continuously from one to another as Ω^* increases, constituting one branch of the solution referred to as the small-Ω branch, whereas Type-IV belongs to a different branch referred to as the large-Ω branch (Fig. 4). For $0.7 \lesssim \Omega^* \lesssim 0.8$, multiple equilibrium states emerge; both Type-III and Type-IV are allowed. The dependence of the amount of day-night energy transport on Ω^* is analyzed. It is confirmed that the amount is large enough to prevent the day side atmosphere from entering a runaway greenhouse state. Moreover, the amount is found to be almost insensitive to Ω^* despite the drastic change in the structure of the atmospheric circulation, although the partition into latent and sensible energy transports varies. Day side OLR in the experiments is analyzed and compared with the values obtained with a one-dimensional radiative convective model. The results strongly suggest that day side OLR is constrained by the radiation limit of a moist atmosphere; the details of the circulation structure do not greatly change atmospheric humidity, so the value of the radiation limit is unchanged. This explains the invariance of day-night energy transport, as it is equal to the difference between incoming solar flux and day side OLR. The former is a constant prescribed amount in this study, and the latter is constrained by the radiation limit.

It should be useful to re-examine the circulation characteristics obtained in previous studies from the present viewpoint, since this study has performed a more complete investigation on their sensitivity to Ω^* than previous studies. The "slowly rotating regime" and the "rapidly rotating regime" identified by Merlis and Schneider (2010) presumably correspond to the small-Ω branch and the large-Ω branch in the present study, respectively. However, the correspondence is not certain because they present the horizontal distributions of atmospheric variables for only two values of Ω^*. Circulation structures similar to those of Type-I and Type-IV are obtained for those two values of Ω^*, but it remains unclear whether they obtained atmospheric structures similar to Type-II and Type-III. The dependence of the circulation structure on Ω^* obtained by Edson et al. (2011) can be compared with the results of the present study with more confidence. They observed two separate branches of solutions with multiple equilibria, and solutions with planetary waves of zonal wavenumber one superposed on broad westerly wind in the low latitudes for intermediate values of Ω^*. These features are similar to those obtained in the present study.

However, more careful comparison suggests a few differences. One is the difference of the directions of the zonal mean equatorial upper tropospheric wind obtained on the large-Ω branch. It is easterly in the present study, whereas it is westerly in Edson et al. (2011), at least in their "dry" experiment; the structure of the low to mid-latitude Rossby response in the upper troposphere implies that it is also westerly in their "aquaplanet" case, although its intensity and structure is unclear.[1] This difference may originate from the difference in the distribution of precipitation: the maximum of rainfall seems to be located at the equator in the case of $\Omega^* = 1$ of Edson et al. (2011), judging from the figures showing the distribution of cloud cover and the meridionally averaged latent heat flux convergence, whereas it is located in the subtropics in the present study, driving equatorward flow in the upper troposphere (not shown). The difference in precipitation distribution may arise from the differences in the GCM setups used by Edson et al. (2011) and the present study, namely the treatment of oceanic heat transport: they include linear oceanic heat transport, whereas we do not. The fact that Merlis and Schneider (2010), where oceanic heat transport is not included, obtains subtropical maxima of day side precipitation and easterly upper tropospheric zonal mean wind similar to ours supports the speculation. Another difference is in the ranges of planetary rotation rates allowing the multiple equilibria; it is around $\Omega^* = 0.2$ in Edson et al. (2011), but around $\Omega^* = 0.75$ in the present study. Part of the difference originates from our use of rather low horizontal resolution, T21; with T42 and T85, the range shifts to smaller value of Ω (Fig. A.1). Such a difference could be an important issue when considering whether the multiple equilibrium solutions are possible in the habitable zones around M type red dwarf stars, for which $\Omega^* \lesssim 0.5$. The possible sensitivity of the realizability of multiple equilibria to model physics, such as the treatment of cloud, surface albedo, or oceans, will be a focus of future studies.

One of the most novel features in the present experiments may be the global-scale north-south asymmetric variability (Type-III) appearing for a fairly wide range of Ω^*, and its origin remains to be examined in detail. Both Merlis and Schneider (2010) and Edson et al. (2011) do not mention such north-south asymmetric oscillating structures, which suggests that the occurrence of the oscillation may depend on the physical configurations of the experimental design. Both Merlis and Schneider (2010) and Edson et al. (2011) employ a slab ocean with finite heat storage as the surface condition, whereas the swamp condition with zero heat storage is used in the present study. However, oceanic heat storage does not seems to be a critical factor; we repeated several runs of Ω0.75 employing a slab ocean, and still obtained north-south asymmetric variation essentially similar to that described in Section 4.3. Oceanic heat transport, which Edson et al. (2011) considered, could be more important. Clarification of the conditions for the emergence of the global-scale north-south asymmetric variability, including the possible importance of ocean discussed above, is left for future studies, together with more detailed understanding of the nature and dynamics of the north-south asymmetric variability.

Provided that the north-south asymmetric variability of Type-III in the present study is theoretically permitted, an interesting question would be whether or not such a variability is observationally detectable on exoplanets. In fact, around M9 type red dwarf stars, synchronously rotating habitable planets should have

[1] Edson et al. (2011) presents the maximum values of zonal wind in each of the aquaplanet experiments in Table 3, but does not mention whether it occurs at the equator or not.

$\Omega^* \sim 0.5$ (Kaltenegger and Weslsy, 2009), which is in the range for Type-III structure. Typical differences between the northern and southern hemispherically averaged OLRs obtained in our GCM calculations reach about 30 W m^{-2}, which is about 10% of the OLR averaged over the entire day side. Since this difference in OLR is the same order of magnitude as the error in the observation of secondary eclipses of hot-Neptune (e.g., Deming et al., 2009), it might be detectable if the observational accuracy improves by another order of magnitude.

6.2. Mechanics of the broad equatorial jet in type-II

The latitudinally broad equatorial eastward jet in Type-II is similar to those of the synchronously rotating terrestrial planets (Joshi et al., 1997; Edson et al., 2011) and those of the hot Jupiters (Showman and Guillot, 2002; Dobbs-Dixon and Agol, 2013, and others). This universal appearance of equatorial prograde jets in synchronously rotating planetary atmospheres implies the existence of a common underlying mechanism. Showman and Polvani (2010, 2011) argues that the equatorward eddy transport of westerly momentum arising from the superposition of equatorial Kelvin and Rossby waves excited by the day-night contrast of heating is responsible to the appearance of equatorial jets. Preliminary analysis of the present experiments also indicates the importance of the equatorward westerly momentum transport due to stationary eddies, which can be interpreted as generated by Rossby and Kelvin responses to the equatorial thermal forcing as described by Showman and Polvani (2011).

A novel observation in the present study is that the broad equatorial eastward jet is accelerated for a relatively wide range of Ω^* up to or exceeding the speed of the wavenumber one normal mode Rossby wave (Fig. 7). The appearance of the large amplitude normal mode Rossby wave as a near resonance with the zonal mean wind is also noted by Edson et al. (2011) for the case with $\Omega^* \sim 0.2$ in a dry atmosphere of a synchronously rotating planet. Our novel point is that resonant-like behavior is established over much wider range of Ω^*, starting from very small values of Ω^*.

Using a three-dimensional atmospheric model with Earth-like parameters forced by a planetary scale wave-like tropical heat source, Arnold et al. (2012) obtains an abrupt transition of equatorial zonal wind to a westerly speed exceeding that of the propagation of the Rossby wave. Tsai et al. (2014) describes the equatorial acceleration due to a combination of the equatorial Kelvin and Rossby wave responses to thermal forcing, and demonstrates that the longitudinal phase of the Rossby wave is shifted eastward with increasing background westerly wind, and eventually the direction of the westerly momentum flux caused by the combined effect with the Kelvin response is reversed when the background westerly exceeds the resonant speed. The shift of the Rossby response phase is also observed as the difference in circulation pattern between the spin-up and mature periods of the broad equatorial jet formation in the simulation of hot Jupiters by Showman and Polvani (2011). A notable difference between the results of the present study and those for the hot Jupiters of previous studies is that the excited wave here is vertically barotropic rather than vertically propagating. The excitation of the barotropic wave by latent heating can be understood by considering the vertical shear of the broad equatorial westerly jet (e.g., Wang and Xie, 1996) and also the presence of the rigid lower boundary.

It should be kept in mind, however, that the equatorial Kelvin and Rossby responses can only re-distribute westerly momentum within the radius of deformation, and, cannot explain on their own the development of the broad equatorial westerly jet. As the equatorial radius of deformation associated with the barotropic mode concerned is comparable to or larger than the planetary radius, the dominant excitation of barotropic waves is favorable to driving a meridionally broad equatorial jet. However, there still has to be some other mechanisms to cancel the easterly acceleration at high latitudes, which should compensate for the westerly acceleration around the equator, so as to produce the Type-II wind structure in the present study, whose zonal mean zonal wind is westerly almost everywhere in the middle and upper troposphere (not shown). Downward motion at high latitudes associated with Hadley circulation may contribute to removing the easterly momentum. Detailed investigation of the driving mechanism of the broad equatorial jet, including the effects of various types of transient disturbance, is left for future studies.

6.3. Implications and remaining issues

The lack of sensitivity of the day-night energy transport to the variety of circulation structures demonstrated in the present study has an important implication when considering the habitability of a synchronously rotating planet. Since it ensures that a certain amount of energy is transported from the day side to the night side, relatively warm regions will be maintained at some locations on the night side regardless of Ω^*. In fact, regions with surface temperature warmer than freezing point of water appear on the night side in the present calculation. The location of warm regions on the night side changes with Ω^*; a warm region appears in the equatorial region to the east of the trailing terminator for the cases on the small-Ω branch, whereas it appears in the mid latitudes to the west of the leading terminator for cases on the large-Ω branch. Based on the location of possible habitable zone for a planetary system discussed by Kaltenegger and Weslsy (2009), Ω^* should be generally less than and not very close to one for synchronously rotating habitable exoplanets, which means that the cases on the small-Ω^* branch are more relevant.

It should be emphasized, however, that the insensitivity of day-night energy transport to Ω^* found in the present study is subject to several conditions. We list a few cases below as examples where the insensitivity could be broken. First, when the incident solar flux is small and the day side temperature is not warm enough to raise OLR to the radiation limit of a moist atmosphere, the value of the day side OLR, and therefore day-night energy transport, shall not be constrained by the radiation limit. Second, in contrast, when the incident solar flux is so large that the anticipated amount of day-night energy transport exceeds the amount that can escape from the night hemisphere to space at the radiation limit of a moist atmosphere, the day-night energy transport will differ from that determined by the values of incident solar flux and OLR constrained by the radiation limit on the day side. In this situation, a runaway greenhouse state is expected to occur, where day-night energy transport is also regulated by the radiation limit, but an increase of atmospheric temperature must be considered. Third, when the amount of water on the planetary surface is so small that it is difficult to establish the radiation limit of a moist atmosphere, energy transport may depend considerably on Ω^*. In such situation, i.e., "a land planet", the change of circulation pattern may even influence whether a statistically equilibrium state is possible (Abe et al., 2010).

Clouds, which are not considered in the present study, may well modify the thermal and dynamical aspects of the present results. Yang et al. (2013) performs a GCM experiment with cloud effects on synchronously rotating planets with increased solar constant. They show that equilibrium states can be obtained with values of the solar constant larger than those for the non-tidally locked case. However, they do not investigate the possible relationship between the emergence of the runaway greenhouse effect and the radiation limit. We have been investigating the latter point in a numerical study, and will report the results in the near future.

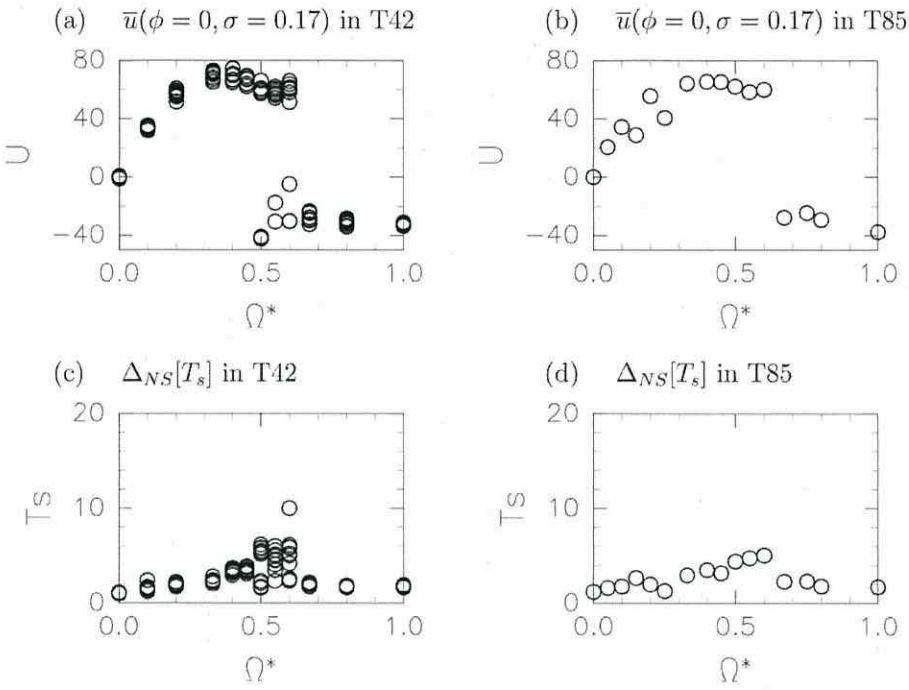

Fig. A.1. (a), (b) Same as Fig. 4c but for the T42 model (a) and T85 model (b), and (c), (d) same as Fig. 4d but for the T42 model (c) and T85 model (d).

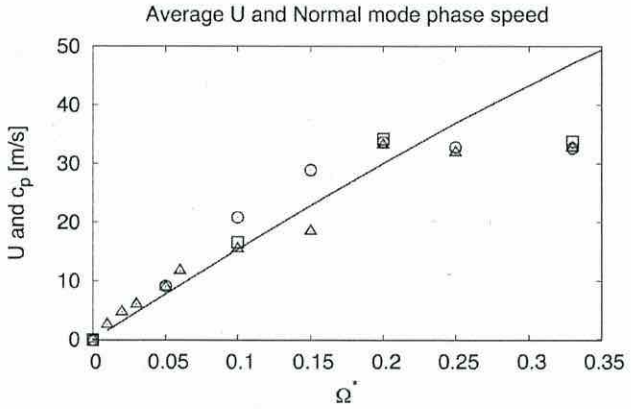

Fig. A.2. Same as Fig. 7, but showing values for horizontal resolutions of T42 (squares) and T85 (triangles) in addition to those for T21 (circles).

Finally, the dynamics of the ocean is undoubtedly an important element to be examined when considering the habitability of synchronously rotating exoplanets. Hu and Yang (2014) performs a series of climate simulation using a coupled atmosphere-ocean model with parameters following Gliese 581g. They find that the ocean can contribute greatly to the day-night hemisphere energy transport and that the partition of the heat transport into the atmospheric and oceanic transports varies considerably depending on the atmospheric CO_2 concentration and the incident short wave flux from the central star. The inclusion of a dynamically active ocean may possibly affect the insensitivity of day-night energy transport to Ω^*. This issue remains as a focus of future studies.

Acknowledgments

Two anonymous reviewers are sincerely acknowledged for carefully reading the original manuscript and providing many helpful comments. This study was supported by MEXT KAKENHI Grant Number JP23103003 of Ministry of Education, Culture, Sports, Science and Technology, Japan, and JSPS KAKENHI Grant Numbers JP20540223, JP24340016, JP25400219, JP25800264 and global COE program "Foundation of International Center for Planetary Science" of the Japan Society for the Promotion of Science. A part of calculations were performed by the SX8R of the Institute of Space and Astronautical Science supercomputer system, Japan Aerospace Exploration Agency. Resolution tests of numerical integrations used the SX series of Center for Global Environmental Research, National Institute of Environmental Studies, Japan. We used the software developed by Dennou Ruby Project (http://www.gfd-dennou.org/library/ruby/) for simulations, analyses, and drawings.

Appendix A. Dependence on resolution

Because of the large number of experiments required to examine the Ω^* dependence of circulation structures, including the possibility of multiple equilibrium solutions, the horizontal resolution of the GCM used in this study is limited to T21. In this appendix, we check the resolution dependence of the results, by briefly describing the results obtained in models with higher resolution, T42 and T85, focusing on some of the features that may be resolution sensitive. For T42, we have performed 10 runs for each of several selected values of Ω^*. For T85, only one run was performed for each values of Ω^*. In a qualitative sense the main results, namely the existence of the four types of solutions, are not sensitive to the model's resolution, as shown below. Figs. A.1a and A.1b show the upper tropospheric zonal mean zonal wind at the equator for various values of Ω^* in the T42 and T85 models, respectively; for T42, all runs for each Ω^* are plotted. These figures share the main features seen with T21 resolution (Fig. 4c): there are two branches of solutions, and the equatorial zonal wind velocity for each Ω^* is insensitive to the resolution. And, at least in the T42 model, the two branches coexist over a range of Ω^* giving multiple equilibria, although the values of Ω^* with multiple equilibria are about 0.1 smaller than in the T21 model. In the case of

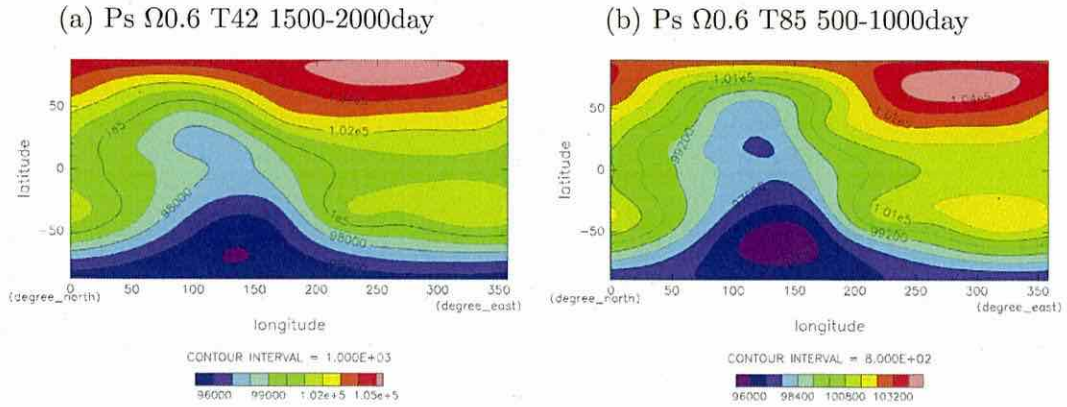

Fig. A.3. Mean surface pressure distributions for Ω0.6 in the T42 model (a) and T85 model (b) for 500 days during which high (low) pressure occupies the north (south) pole.

the T85 model, as we can only perform one run for each Ω^*, the existence of multiple equilibria cannot be confirmed. However, the overall behavior is not inconsistent with that in T42; the value of Ω^* for the upper end of the small Ω branch is the same.

Fig. A.2 shows the values of mass weighted zonal mean wind speed for different values of Ω^* obtained in the runs with T21, T42 and T85 resolutions, compared with the intrinsic phase speed of the Rossby wave normal mode. In a qualitative sense, we can confirm the main features described in Section 4.2; i.e., the mass weighted zonal mean wind speed closely follows or slightly exceeds the Rossby wave phase speed for $0.0 \lesssim \Omega^* \lesssim 0.2$, and levels off for larger Ω^*. The only slight exception is Ω0.15 in T85, where the zonal mean wind is decelerated by transient disturbance whose nature is unclear.

Figs. A.1c and A.1d show the measure of the north-south asymmetry of surface temperature defined by Eq. 2 for various values of Ω^* in the T42 and T85 models, respectively; for T42, all runs for each Ω^* are plotted. Compared to the corresponding figure for T21 resolution (Fig. 4d), the degree of north-south asymmetry seems to be weaker in higher resolution models. Still, we can identify features largely free from resolution dependence: the monotonic increase of the degree of north-south asymmetry on the small-Ω branch, and the smaller degree of north-south asymmetry on the large-Ω branch. The temporal scales of the north-south asymmetric variability are of the same order of magnitude for all model resolutions (not shown). The spatial structure of the north-south asymmetric variability in Type III, i.e., toward the large-Ω^* end of the small-Ω branch, is also common to all model resolutions. Fig. A.3 shows the horizontal structures of surface pressure in the T42 and T85 models for $\Omega^* = 0.6$ averaged for 500 days during which high (low) pressure occupies the north (south) pole. A comparison with Fig. 9a showing the structure of the variability for $\Omega^* = 0.75$ in the T21 model confirms that all resolutions share the same major features, such as the longitudes of the low pressure area in the southern day hemisphere and the high pressure area in the southern night hemisphere.

References

Abe, Y., Abe-Ouchi, A., Sleep, N.H., Zahnle, K., 2010. Habitable zone limits for dry planets. Astrobiol. 11, 443–460. doi:10.1089/ast.2010.0545.

Arnold, N.P., Tziperman, E., Farrell, B., 2012. Abrupt transition to strong superrotation driven by equatorial wave resonance in an idealized GCM. J. Atmos. Sci. 69, 626–640.

Deming, D., Seager, S., Miller-Ricci, E., Clampin, M., Lindler, D., Greene, T., Charbonneau, D., Laughlin, G., Ricker, G., Latham, D., Ennico, K., 2009. Discovery and characterization of transiting super earths using an all-sky transit survey and follow-up by the james webb space telescope. Publ. Astron. Soc. Pacific 121, 952–967. doi:10.1086/605913.

Dobbs-Dixon, I., Agol, E., 2013. Three-dimensional radiative hydrodynamical simulation of the highly irradiated short-period exoplanet HD 189733b. Mon. Not. R. Astron. Soc. 435, 3159–3168. doi:10.1093/mnras/stt1509.

Edson, A., Lee, S., Bannon, P., Kasting, J.F., Pollard, D., 2011. Atmospheric circulations of terrestrial planets orbiting low-mass stars. Icarus 212, 1–13. doi:10.1016/j.icarus.2010.11.023.

Heng, K., Vogt, S.S., 2011. Gliese 581g as a scaled-up version of earth: atmospheric circulation simulations. Mon. Not. R. Astron. Soc. 415, 2145–2157. doi:10.1111/j.1365-2966.2011.18853.x.

Hu, Y., Yang, J., 2014. Role of ocean heat transport in climates of tidally locked exoplanets around m dwarf stars. Proc. Natl. Acad. Sci. USA 111, 629–634. doi:10.1073/pnas.1315215111.

Ishiwatari, M., Nakajima, K., Takehiro, S.I., Hayashi, Y.-Y., 2007. Dependence of climate states of gray atmosphere on solar constant: From the runaway greenhouse to the snowball states. J. Geophys. Res. 112, D13. doi:10.1029/2006JD007368.

Ishiwatari, M., Takehiro, S., Nakajima, K., Hayashi, Y.-Y., 2002. A numerical study on appearance of the runaway greenhouse state of a three-dimensional atmosphere. J. Atmos. Sci. 59, 3223–3238. doi:10.1175/1520-0469(2002).059<3223:ANSOAO> 2.0.CO;2

Joshi, M.M., 2003. Climate model studies of synchronously rotating planets. Astrobiol. 3, 415–427. doi:10.1089/153110703769016488.

Joshi, M.M., Haberle, R.M., Reynolds, R.T., 1997. Simulations of the atmospheres of synchronously rotating terrestrial planets orbiting m dwarfs: Conditions for atmospheric collapse and the implications for habitability. ICARUS 129, 450–465. doi:10.1006/icar.1997.5793.

Kaltenegger, L., Weslsy, T.A., 2009. Transits of earth-like planets. Astrophys. J. 698, 519–527. doi:10.1088/0004-637X/698/1/519.

Kasahara, A., 1976. Normal modes of ultralong waves in the atmosphere. Mon. Wea. Rev. 104, 669–690. doi:10.1175/1520-0493(1976). 104< 0669:NMOUWI> 2.0.CO;2

Longuet-Higgins, M.S., 1968. The eigenfunctions of laplace's tidal equations over a sphere. Phil. Trans. Royal Soc. London A: Math. Phys. Eng. Sci. 262, 511–607. doi:10.1098/rsta.1968.0003.

Louis, J.-F., Tiedtke, M., Geleyn, J.-F., 1982. A short history of the PBL parameterization at ECMWF. Workshop on Planetary Boundary Layer Parameterization. 59–80, ECMWF, Reading, U.K.

Manabe, S., Smagorinsky, J., Strickler, R.F., 1965. Simulated climatology of a general circulation model with a hydrologic cycle. Mon. Wea. Rev. 93, 769–798. doi:10.1175/1520-0493(1965). 093< 0769:SCOAGC> 2.3.CO;2

Merlis, T.M., Schneider, T., 2010. Atmospheric dynamics of earth-like tidally locked aquaplanets. J. Adv. Model. Earth Syst. 2 (Art. #13), 17. doi:10.1029JAMES.2010.2.13

Nakajima, S., Hayashi, Y.-Y., Abe, Y., 1992. A study on the "runaway greenhouse effect" with a one dimensional radiative convective equilibrium model. J. Atmos. Sci. 49, 2256–2266. doi:10.1175/1520-0469(1992). 049< 2256:ASOTGE> 2.0.CO;2

Sardeshmukh, P.D., Hoskins, B.J., 1988. The generation of global rotational flow by steady idealized tropical divervence. J. Atmos. Sci. 45, 1228–1251. doi:10.1175/JAS-D-14-0235.1.

Showman, A.P., Guillot, T., 2002. Evolution of "51 pegasus b-like" planets. Astron. Astrophys. 385, 156–165.

Showman, A.P., Polvani, L.M., 2010. The matsuno-gill model and equatorial superrotation. Geophys. Res. Lett. 37. doi:10.1029/2010GL044343.

Showman, A.P., Polvani, L.M., 2011. Equatorial superrotation on tidally locked exoplanets. Astrophys. J. 738, 71. doi:10.1088/0004-637X/738/1/71.

Showman, A.P., Wordsworth, R.D., Merlis, T.M., Kaspi, Y., 2013. Atmospheric circulation of terrestrial planets. Comp. Climatol. Terr. Planets 1, 277–326.

Torres, G., Kipping, D.M., Fressin, F., Caldwell, D.A., Twicken, J.D., Ballard, S., Batalha, N.M., Bryson, S.T., Ciardi, D.R., Henze, C.E., Howell, S.B., Isaacson, H.T., Jenkins, J.M., Muirhead, P.S., Newton, E.R., Petigura, E.A., Barclay, T., Borucki, W.J., Crepp, J.R., Everett, M.E., Horch, E.P., Howard, A.W., Kolbl, R., Marcy, G.W., McCauliff, S., Quintana, E.V., 2015. Validation of 12 small kepler transiting planets in the habitable zone. Astrophys. J. 800 (99), 24. doi:10.1088/0004-637X/800/2/99.

Tsai, S.-M., Dobbs-Dixon, I., Gu, P.-G., 2014. Three-dimensional structures of equatorial waves and the resulting super-rotation in the atmosphere of a tidally locked hot jupiter. Astrophys. J. 793, 141. doi:10.1088/0004-637X/793/2/141.

Von Bloh, W., Bounama, C., Cuntz, M., Franck, S., 2007. The habitability of super-earth in gliese 581.. Astron. Astrophys. 476 (3), 1365–1371. doi:10.1051/0004-6361:20077939.

Wang, B., Xie, X., 1996. Low-frequency equatorial waves in vertically sheared zonal flow. part i: Stable waves. J. Atmos. Sci. 53, 449–467.

Wordsworth, R.D., Forget, F., Selsis, F., Millour, E., Charnay, B., Madeleine, J.-B., 2011. Gliese 581d is the first discovered terrestrial-mass exoplanet in the habitable zone. Astrophys. J. Lett. 733, L48. doi:10.1088/2041-8205/733/2/L48.

Yang, J., Cowan, N.B., Abbot, D.S., 2013. Stabilizing cloud feedback dramatically expands the habitable zone of tidally locked planets. Astrophys. J. Lett. 771, L45. doi:10.1088/2041-8205/771/2/L45.

Orig Life Evol Biosph (2013) 43:221–245
DOI 10.1007/s11084-013-9339-0

PREBIOTIC CHEMISTRY

Hydrogen Cyanide Production due to Mid-Size Impacts in a Redox-Neutral N_2-Rich Atmosphere

Kosuke Kurosawa · Seiji Sugita · Ko Ishibashi · Sunao Hasegawa · Yasuhito Sekine · Nanako O. Ogawa · Toshihiko Kadono · Sohsuke Ohno · Naohiko Ohkouchi · Yoichi Nagaoka · Takafumi Matsui

Received: 22 August 2012 / Accepted: 16 June 2013 /
Published online: 23 July 2013

Abstract Cyanide compounds are amongst the most important molecules of the origin of life. Here, we demonstrate the importance of mid-size (0.1–1 km in diameter) hence frequent meteoritic impacts to the cyanide inventory on the early Earth. Subsequent aerodynamic ablation and chemical reactions with the ambient atmosphere after oblique impacts were investigated by both impact and laser experiments. A polycarbonate projectile and graphite were used as laboratory analogs of meteoritic

K. Kurosawa · K. Ishibashi · S. Ohno · Y. Nagaoka · T. Matsui
Planetary Exploration Research Center, Chiba Institute of Technology, 2-17-1, Tsudanuma, Narashino, Chiba 275-0016, Japan

K. Ishibashi
e-mail: ko.ishibashi@perc.it-chiba.ac.jp

S. Ohno
e-mail: ohno@perc.it-chiba.ac.jp

Y. Nagaoka
e-mail: yoichi.nagaoka@perc.it-chiba.ac.jp

T. Matsui
e-mail: matsui@perc.it-chiba.ac.jp

S. Sugita · Y. Sekine
Department of Complexity Science and Engineering, The University of Tokyo, 5-1-5, Kashiwanoha, Kashiwa, Chiba 277-8561, Japan

S. Sugita
e-mail: sugita@k.u-tokyo.ac.jp

Y. Sekine
e-mail: sekine@k.u-tokyo.ac.jp

S. Hasegawa
Institute of Space and Astronautical Science, Japan Aerospace Exploration Agency, 3-1-1, Yoshinodai, Chuo-ku, Sagamihara, Kanagawa 252-5210, Japan
e-mail: hasehase@isas.jaxa.jp

organic matter. Spectroscopic observations of impact-generated ablation vapors show that laser irradiation to graphite within an N_2-rich gas can produce a thermodynamic environment similar to that produced by oblique impacts. Thus, laser ablation was used to investigate the final chemical products after this aerodynamic process. We found that a significant fraction (>0.1 mol%) of the vaporized carbon is converted to HCN and cyanide condensates, even when the ambient gas contains as much as a few hundred mbar of CO_2. As such, the column density of cyanides after carbon-rich meteoritic impacts with diameters of 600 m would reach ~10 mol/m^2 over ~10^2 km^2 under early Earth conditions. Such a temporally and spatially concentrated supply of cyanides may have played an important role in the origin of life.

Keywords Hydrogen cyanide · Redox-neutral atmosphere · Hypervelocity impacts · Aerodynamic ablation · Mass spectrometry · Emission spectroscopy

Introduction

The geologic record on the Moon investigated by the Apollo Project showed that the impact flux on Earth at >3.8 Ga during the heavy bombardment period was at least ~10^3 times more than that on the present Earth (e.g., BVSP 1981; Ryder 1990; Chyba 1991). During the heavy bombardment period, the influx of both material and energy into the Earth may have been the largest during its history. Such intense bombardment may have controlled the evolution of surface environments on the early Earth. Geologic evidence suggests that the emergence of life occurred ~3.8 Ga (Schidlowski 1988; Rosing 1999), at the termination of the heavy bombardment period.

Cyanides are considered as being amongst the most important and necessary compounds in the chemical evolution phase of the origin of life (e.g., Ferris and Hagan 1984). For example, concentrated solutions of HCN (0.1–0.01 mol/L) can produce nucleic acid bases (e.g., Chang et al. 1983; Ferris and Hagan 1984; Miyakawa et al. 2002a, b). Moreover, mixtures of HCN, NH_3, aldehyde compounds, and nitrile compounds can produce amino acids (e.g., Chang et al. 1983; Ferris and Hagan 1984; Miyakawa et al. 2002a, b). Thus, a number of cyanide production processes on the early Earth have been proposed, including lightning (e.g., Miller 1953; Chameides and Walker 1981; Miller and Schlesinger 1983;

N. O. Ogawa · N. Ohkouchi
Institute of Biogeosciences, Japan Agency for Marine-Earth Science and Technology, 2-15 Natsushima-cho, Yokosuka 237-0061, Japan

N. O. Ogawa
e-mail: nanaogawa@jamstec.go.jp

N. Ohkouchi
e-mail: nohkouchi@jamstec.go.jp

T. Kadono
School of Medicine, University of Occupational and Environmental Health, 1-1 Iseigaoka, Yahata, Kitakyusyu 807-8555, Japan
e-mail: kadono@med.uoeh-u.ac.jp

K. Kurosawa (✉)
421, 4th building, 2-17-1, Tsudanuma, Narashino, Chiba 275-0016, Japan
e-mail: kosuke.kurosawa@perc.it-chiba.ac.jp

Stribring and Miller 1986), photochemistry driven by ultraviolet (UV) light from the Sun (Zahnle 1986; Sekine et al. 2003), and meteoritic impacts (Fegley et al. 1986; Mukhin et al. 1989). Lightning and photochemistry form HCN constantly. However, after HCN is produced it is also destroyed continuously; efficient accumulation would not have occurred in the redox-neutral early Earth atmosphere. In contrast, meteoritic impacts would cause episodic production and concentration of cyanides. Furthermore, the continuous existence of life may have begun 3.8 Ga at about the time of the termination of the heavy bombardment period as mentioned above (e.g., Tera et al. 1974; Schidlowski 1988; Rosing 1999). Thus, meteoritic impacts might have played a key role in the origin of life.

Chyba and Sagan (1992) classified organic supply mechanisms by meteoritic impacts into three categories: (1) atmospheric heating due to fast-expanding vapor plumes, (2) post-impact recombination, and (3) delivery of intact extraterrestrial organic matter in impactors. The first category was proposed by Fegley et al. (1986), whose thermo chemical calculations clearly showed the importance of meteoritic impacts to the cyanide inventory on the early Earth. A reducing atmosphere (C/O molar ratio >1) is, however, required for efficient HCN production because the production efficiency of HCN in a redox-neutral atmosphere (C/O molar ratio <1) is rather low (Chameides and Walker 1981; Miller and Schlesinger 1983; Fegley et al. 1986). Although the exact chemical composition of the early planetary atmosphere is still a matter of controversy (e.g., Kasting 1990, 1993; Sagan and Chyba 1997; Hashimoto et al. 2007; Schaefer and Fegley 2010; Zahnle et al. 2011), recent theories for planetary formation suggest that a highly reducing atmosphere may not occur with the presence of a deep magma ocean (e.g., Hirschmann 2012), which likely form during the final stage of planetary accretion through giant impacts (e.g., Canup 2004). Subsequently, the early atmosphere will be oxidized due to the hydrodynamic escape of hydrogen driven by intense UV radiation from the young Sun (e.g., Kulikov et al. 2007). Furthermore, volcanic gases on the early Earth should have been redox-neutral (N_2–CO_2–H_2O) given the oxidation state of Hadean mantle at 4.35 Ga is similar to the present-day mantle (Trail et al. 2011). Thus, atmospheric heating due to meteoritic impacts was not likely to have been the dominant process in cyanide production on the early Earth. The second process was experimentally studied by Gerasimov et al. (1998) and Mukhin et al. (1989). These authors used laser pulse heating techniques to simulate the post-impact chemistry in vapor plumes. An unexpectedly large amount of oxidized gases, such as CO and CO_2, were detected along with a small amount of HCN using a gas chromatograph mass spectrometer (GCMS). Gerasimov et al. (1998) and Mukhin et al. (1989) concluded that oxygen released from thermally decomposed silicates efficiently oxidized carbon species to CO and CO_2. In this process, the amount of HCN produced is limited by the nitrogen content of the impactors. Nitrogen in chondritic material is highly depleted compared with microbial biomass (e.g., Wasson and Kallemeyn 1988; Chapin et al. 2008; Sugita and Schultz 2009). The final process was studied by hydrocode calculations (e.g., Pierazzo and Melosh 2000) and shock recovery experiments (Blank et al. 2001). Given that carbonaceous chondrites contain complex organic molecules (e.g., Hayatsu and Anders 1981; Cronin et al. 1988; Cooper et al. 2001; Pizzarello 2012), these materials may have delivered organic compounds to the early Earth if they survived the impact shocks. Hypervelocity oblique impact experiments (Schultz and Gault 1990) and the hydrocode calculations (Pierazzo and Melosh 2000) indicate that a large fraction of the impactor does not experience an extremely high shock pressure at low-angle oblique impacts. However, subsequent aerodynamic heating after oblique impacts must be considered to determine the fate of organic matter in meteorites. When hypervelocity oblique impacts occur, a large fraction of the impactor does not undergo vaporization but retains a downrange motion at velocities comparable to the initial impact velocity (Schultz and Gault 1990; Schultz and Sugita 1996), and this downrange-moving material suffers intense heating due to aerodynamic ablation (Sugita and Schultz 2003a). Hence, the vast majority

of the organic molecules in impacting carbonaceous chondrites are expected to have thermally decomposed, even if they survived the impact shock (Sugita and Schultz 2009), although a small but considerable fraction of organic matter at a small translational velocity to the ground may have been supplied to the surface of the early Earth (e.g., Blank et al. 2001).

In this study, we focus on the fate of the destroyed organic matter, which is most of the meteoritic organic molecules delivered to the Earth and planets with an atmosphere, due to aerodynamic heating after oblique impacts. Previous impact experiments showed that CN radicals were produced around fast moving, fine-grained projectile fragments from carbon in the impactor and nitrogen in the ambient gas (Sugita and Schultz 2009). This implies that impact-induced aerodynamic interactions are likely to produce a local and transient chemical environment that favors efficient cyanide production (Sugita and Schultz 2009). Hence, it is possible that destroyed organic matter from meteorites due to aerodynamic ablation is converted to cyanides via subsequent chemical reactions in the ablation vapor and its wake. However, the chemical composition and abundances of the final chemical products have not been well studied as the emission spectroscopy used in Sugita and Schultz (2009) is unable to quantify the chemical composition at a quenching temperature. The CN radicals may react with water vapor in an ambient atmosphere and generate HCN and nitrile compounds, but they may also be converted to CO and NO through oxidation by CO_2 in the ambient atmosphere. Thus, quantitative measurements of the conversion ratio from vaporized carbon to HCN in a redox-neutral atmosphere are necessary to assess the role of mid-size impacts to cyanide inventory. It should be noted that a large impactor (>10 km) does not interact with an ambient atmosphere efficiently because its size is larger than the scale height of the atmosphere (~8 km). As such, we studied relatively small-scale impact phenomena where the size of the impactor is 0.1–1 km.

In this study, to evaluate cyanide production processes in early Earth's atmospheres due to mid-size impactors (0.1–1 km in diameter), we have investigated impact-driven aerodynamic ablation by hypervelocity impacts and laser ablation. A series of laser ablation experiments were conducted to investigate the chemical compositions of the final products in the gas-and condensed-phase after laser ablation. The effects of oxidation by CO_2 on the amount of HCN in the final chemical products were investigated over a wide range of CO_2 mixing ratios. Also, we conducted hypervelocity oblique impact experiments to confirm that laser ablation can simulate CN production processes due to aerodynamic ablation after oblique impacts based on diatomic molecular emission.

First, we describe the impact and laser experiments in detail (Section 2) and the results are presented (Section 3). Then, in Sections 4.1 and 4.2, we show that laser ablation of a graphite target in a N_2-rich gas can simulate impact-induced aerodynamic ablation. The advantage of impact-induced aerodynamic ablation on the HCN production compared with the other impact-driven processes is discussed in Section 4.3. Based on the experimental results, the implications of our results for the cyanide inventory on the early Earth (the column density of HCN on the surface of the early Earth after a mid-size oblique impact) are discussed in Sections 4.4 and 4.5. Finally, the conclusions are presented in Section 5.

Impact and Laser Experiments

We conducted two types of experiments; hypervelocity impacts and laser ablation. In the two-stage gas-gun experiments, chemical analyses of the final chemical products are difficult to make due to chemical contamination from the acceleration gas and gun debris. Although Kurosawa et al. (2012) developed an experimental procedure to measure inorganic

gas-phase products after an impact in an open system using a two-stage light gas gun, analysis of minor organic compounds of ppm level is still technically challenging because they used a plastic diaphragm to minimize the intrusion of the acceleration gas into an experimental chamber. Thus, a Nd: YAG laser was used to investigate the fate of impact-generated CN radicals in this study. High-temperature CN radicals can be produced by laser irradiation of a graphite target in a N_2-rich gas via fluid instability near the boundary between the carbon vapor plume and the ambient gas (e.g., Vivien et al. 1998; Sharma and Thareja 2005; Kurosawa et al. 2009). Given that the laser pulse penetrates through a glass view port, experiments can be conducted in a closed vacuum chamber. The final chemical products can then be measured to high accuracy with little risk of chemical contamination (e.g., Mukhin et al. 1989; McKay and Borucki 1997; Gerasimov et al. 1998; Ohno et al. 2004; Ishibashi et al. 2006, 2013). The differences between the thermodynamic state of impact-and laser-generated CN radicals, however, has not been well studied. Chemical reactions are strongly dependent on the thermodynamic path and, as such, differences should be examined by conducting impact experiments prior to applying the results of laser experiments to real impact phenomena. Given this, the fate of hot CN radicals was investigated in detail using laser ablation.

Hypervelocity Oblique Impact Experiments

The two-stage light gas gun with 7 mm bore diameter (Physics Applications Inc.) in the Space Plasma Laboratory in Institute of Space and Astronautical Science (ISAS) of the Japan Aerospace and Exploration Agency (JAXA) was used for hypervelocity oblique impact experiments. We carried out high-resolution spectroscopic observations to determine both the vibrational structure and translational–rotational temperature of impact-generated CN radicals.

Experimental Setup

Our experimental system consists of four components; a two-stage light gas gun, a vacuum chamber, a gas cylinder of N_2, and a high-speed optical spectrometer using a intensified charge-coupled device (ICCD) camera (Acton, SpectraPro 2750 and Roper Scientific, PI-MAX). Figure 1a is a schematic diagram of the experimental system. The focal length of the spectrometer is 750 mm. We used two gratings with different groove densities. Wavelength resolutions and coverage are about 0.6 nm and 0.03 nm (full width at half maximum; FWHM) and 200 nm and 10 nm for the gratings with groove densities of 150 and 2,400 grooves/mm, respectively. Calibration experiments for both wavelength and irradiance were carried out with a mercury lamp (Electro-Technic Inc., MODEL SP 200) and a NIST-traceable tungsten halogen quartz lamp (ORIEL corporation, Model 63355), respectively. A photomultiplier tube was used to detect muzzle flash and to provide a trigger for the measurement system.

Experimental Conditions

Polycarbonate sphere (7 mm in diameter) and copper block (50 mm×100 mm×20 mm) were used as the projectile and target, respectively. Nitrogen was used as the ambient gas in the chamber. The total pressure in the chamber was fixed at 30 mbar. The impact angle was fixed at 30° from the horizontal and the impact velocity was ~7 km/s. The diameter of the field of view (FOV) of spectroscopic observations was fixed at ~3 cm, and the exposure time of ICCD camera was fixed at 30 μs after impact.

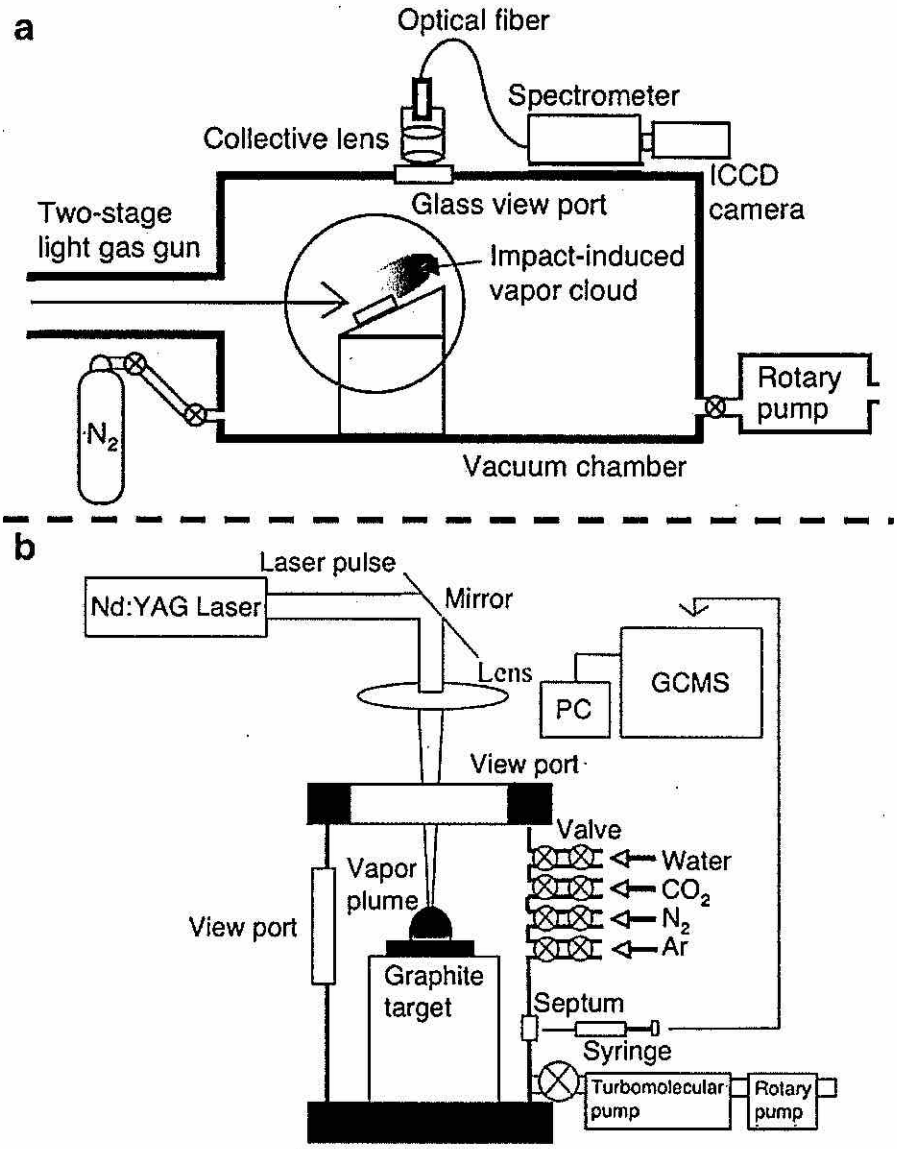

Fig. 1 A schematic diagram of the experimental system for impact (a) and laser experiments (b). Note that the glass view port at the side of the chamber for the laser experiments was used for spectroscopic observations in the study by Kurosawa et al. (2009)

Experimental Procedures

After a copper target was placed on the stage, the vacuum chamber was evacuated to a residual pressure of 8×10^{-2} mbar before each shot. N_2 gas was then introduced into the chamber before shooting a projectile into the target. An emission spectrum of self-luminous impact-induced vapor was recorded by the ICCD camera.

Laser Experiments

A Nd: YAG laser at the University of Tokyo was used to investigate the final chemical products. Two types of chemical analyses were conducted; mass spectrometry of the gas-phase products, and elemental analysis and infrared (IR) spectroscopy of the condensed-phase products deposited on a substrate. For the gas-phase products, we quantitatively

measured the amount of HCN per laser shot as a function of the partial pressure of CO_2 (hereafter referred to as P_{CO2}). The relative amounts of the other gas-phase products were measured based on the integrated peak area of the monitored ion current. For condensed-phase products, the mass contents of total nitrogen and carbon (hereafter referred to as *TN* and *TC*, respectively) were measured with an elemental analyzer. In addition, the effects of the partial pressure of N_2 (hereafter referred to as P_{N2}) on the chemical structure of the condensed products, such as the absorption depth of the C=N and C≡N bonds, were also investigated using a Fourier transform infrared spectrometer (FT-IR).

Experimental Setup

The system for laser experiments consists of a Nd: YAG laser, a vacuum chamber, gas cylinders, and a GCMS (Shimadzu Corporation, QP2010). A small tank filled with pure water was connected to the chamber to introduce water vapor up to a saturated vapor pressure of ~30 mbar. A gas chromatograph column suitable for inorganic and light organic gas analysis (Agilent Technologies, GS-Q) was used. The laser experimental system is shown schematically in Fig. 1b.

In order to collect the condensed products from the laser-generated ablation vapor, we placed a CaF_2 disk (2 mm thick, 25 mm diameter; IR Systems) at ~6 cm beside the laser spot on the target. To examine the effect of distance between the laser spot and the condensation disk, we conducted the same experiment with a disk placed at a different distance ~11 cm from the laser spot. Elemental analysis was performed with an online system comprising a Finnigan Delta Plus XP isotope ratio mass spectrometer coupled to a Flash EA1112 elemental analyzer (EA/IRMS system) at the Japan Agency for Marine-Earth Science and Technology (Ohkouchi et al. 2005). Infrared absorption spectroscopy was carried out with a FT-IR (Perkin Elmer, Spectrum 2000) at the University of Tokyo.

Experimental Conditions

A sintered graphite pellet (C=99.999 wt%; Kojundo Kagaku) was used as the target. The laser wavelength was 1,064 nm and the laser pulse width was ~13 ns. The energy of the laser pulse was fixed at ~380 mJ/pulse. The diameter of the laser beam on the target surface was ~2 mm, resulting in a laser intensity of 0.9 GW/cm^2, which was sufficient to evaporate graphite. The irradiation frequency of the laser pulse was fixed at 2 Hz. All laser experiments were conducted in a vacuum chamber with a volume of 890 mL. The vacuum chamber had four gas inlets in order to introduce a variety of gases individually. A manometer was used to adjust the partial pressure of each gas.

The experimental conditions for gas-phase chemical analysis are as follows. The total pressure in the chamber was fixed at 1,060 mbar. Two series of experiments were conducted. Firstly, four gas mixtures (Ar [N- and H-free], H_2O–Ar [N-free], N_2–Ar [H-free], N_2–H_2O–Ar) were used to examine the effects of the presence of H_2O and N_2 on HCN production. The partial pressures of N_2 and H_2O were fixed at 930 mbar and 30 mbar, respectively. Secondly, the effects of oxidation by CO_2 on the amount of HCN and the other products were investigated using N_2–CO_2–H_2O–Ar gas mixtures with different CO_2 mixing ratios. In order to examine the effects of P_{N2} on HCN yield, we used two values of P_{N2} (920 mbar and 500 mbar). P_{CO2} was varied from 0 mbar to 110 mbar and 0 mbar to 530 mbar, respectively. Argon gas was used to adjust the total pressure in the chamber to a constant value of 1,060 mbar. During the experiments, the temperature of the wall of the vacuum chamber was kept at 350 K to prevent water condensation.

The experimental conditions for condensate analysis are as follows. Water vapor was not used in condensate analysis to enhance the condensation of chemical products. The objective of the condensed-phase analysis was to examine whether fixation of CN bonds into the condensate occurred. Mass flow controllers and a vacuum pump were used to minimize changes in the chemical composition of the ambient gases. Flow-system experiments were necessary for the condensed-phase analyses because a large number of laser shots were necessary to collect a sufficient amount of condensed products for solid-phase chemical analyses. Necessary laser shots for condensed phase analyses is more than five times those for gas-phase analysis. We used N_2–CO_2–Ar gas mixtures with a variety of P_{CO2} and P_{N2} values. The equilibrium total pressure in the chamber was fixed at 13 mbar using Ar gas to adjust the total pressure in the chamber in the same way as the gas-phase analysis.

Experimental Procedures

A graphite target was placed on the stage in the chamber, and the position and the diameter of the laser beam on the target were adjusted. The vacuum chamber was then evacuated to ~10^{-6} mbar and the chamber wall heated to 350 K. The gas mixtures were then introduced into the vacuum chamber and laser irradiation started. As no clear signal could be detected after a single laser shot during chemical analyses, 300 and 1900 laser shots were accumulated for gas-and condensed-phase analysis, respectively. If the same point on the target was irradiated with the laser beam repeatedly for a long time, it gradually forms a pit, which would affect the condition of the carbon vapor and CN radicals. Thus, the position of the laser focus point on the target was changed continuously. After laser irradiation, 1 mL of the final gas-phase products was sampled using a syringe and analyzed with the GCMS. For condensed-phase analysis, the CaF_2 substrate was removed from the chamber and analyzed by FT-IR in order to measure the absorption depth due to nitrogen-bearing chemical bonds, such as C=N and C≡N, in the products. Following this, 1–10 mg of the condensed products were transferred into pre-cleaned capsules and introduced into the EA/IRMS system. The amounts of N_2 and CO_2 produced in the EA/IRMS system yielded the *TN* and *TC* in the condensed products, respectively.

Experimental Results

The main result of our study is the quantification of the conversion ratio from vaporized carbon to gaseous HCN as a function of P_{CO2}. Our spectroscopic results support the applicability of the conversion ratio obtained by laser ablation to real impact phenomena.

Spectroscopic Comparison Between Impact-and Laser-Induced Vapor Clouds

We obtained emission spectra from impact-generated ablation vapors produced at ~7 km/s under 30 mbar of N_2. Figure 2 shows high-speed photographs during impacts. A fast downrange-moving, self-luminous component was observed. Figure 3 is a comparison of the spectral outlines between impact-and laser-generated ablation vapors. The main emission source in both experiments is molecular emission from CN and C_2. The observed spectrum produced by impacts results in a strong continuum emission. The radiation source of the continuum emission is expected to be impact-generated fine-grained fragments, including melt droplets (Sugita and Schultz 2003b). Although strong continuum emission was not observed in laser experiments, the observed spectrum produced by impacts is similar to that

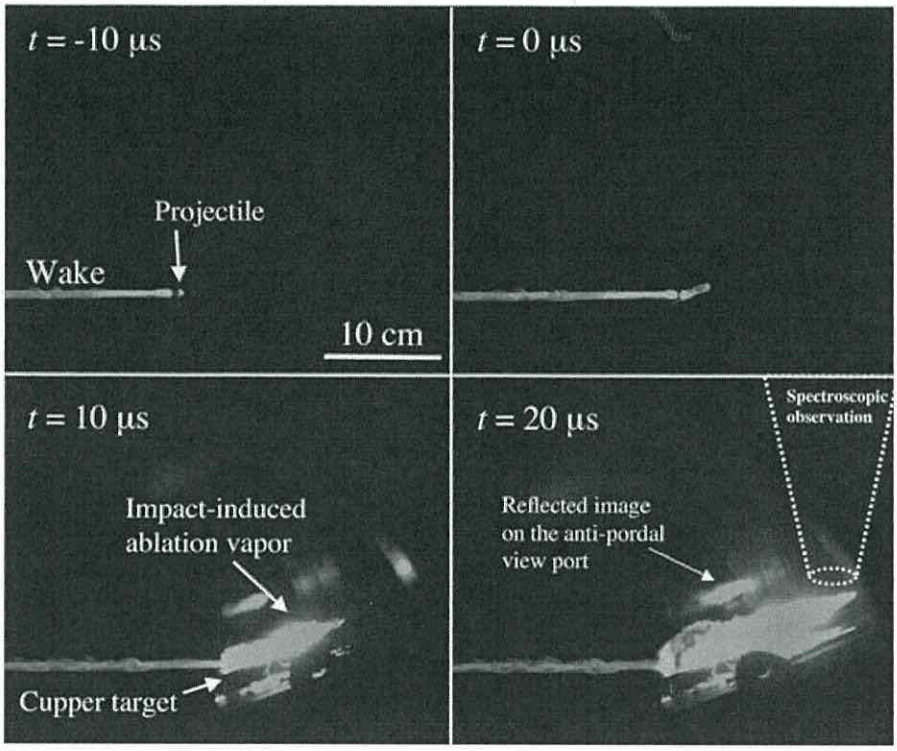

Fig. 2 High-speed photographs of a polycarbonate impact into a Cu target within 30 mbar of N_2 gas. The distance between the impact point and the field of view of the spectroscopic observation is 12 cm (the projectile is 0.7 cm in diameter)

produced by laser ablation. The blackbody temperature was estimated by Planck function fitting to the continuum spectra.

We then compared the vibrational state of CN in both types of vapor clouds. Figure 4 shows high-resolution spectra from impact (Fig. 4a) and laser ablation (Fig. 4b) experiments. For comparison, a theoretical synthetic spectrum in thermal equilibrium (7,000 K) is also shown in Fig. 4c. The computer software package SPRADIAN (structured package for radiation analysis) (Fujita and Abe 1997) was used to calculate the theoretical synthetic spectrum. This comparison clearly shows that the impact-generated CN radicals were not in vibrational equilibrium in the same way as the laser-generated one reported by the previous study (Kurosawa et al. 2009), because the ratio of intensities of different band heads deviates strongly from a Boltzmann distribution. The characteristic time scale of CN band emission due to transition from the upper quantum state to the lower one is ~60 ns (Hertzberg 1950), which is much shorter than the relaxation time scale for the vibrational state of ~1 μs (Slack 1976). Thus, the observed non-equilibrium CN is evidence for fast CN production via vaporized carbon and nitrogen from the ambient atmosphere in both the impact-and laser-generated ablation vapors.

Finally, we quantitatively compared the translational–rotational temperature of CN and C_2 in both vapors. The band-tail fitting method (Kurosawa et al. 2009) was used to measure the translational–rotational temperature for CN and C_2 as this method can be applied to molecular spectra from matter in vibrational non-equilibrium. The results of band-tail fitting for CN and C_2 in the impact vapor are shown in Fig. 5. The band-tails of the observed spectra and best-fit synthetics are in good agreement. Table 1 shows the summary of the obtained translational–rotational temperatures for CN and C_2 and blackbody temperatures. The translational–rotational temperatures of C_2 are nearly equal to the blackbody temperatures. This coincidence between C_2 translational-rotational and blackbody temperatures is consistent with the previous impact

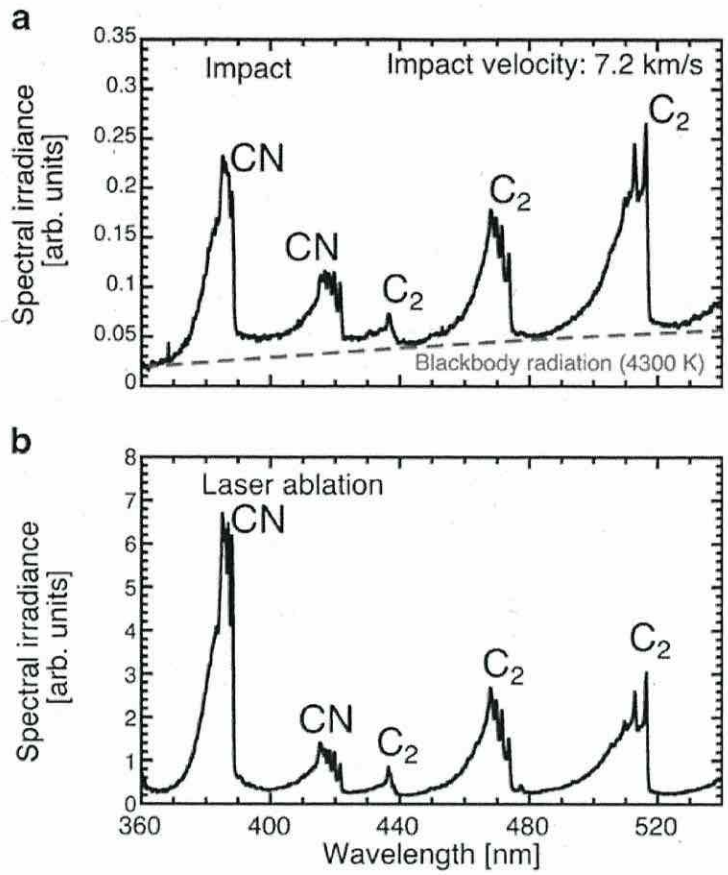

Fig. 3 A spectral comparison between impact-(**a**) and laser-induced (**b**) ablation vapors. The identified molecular emissions are shown on the figure. The emission spectrum from the laser-generated ablation vapor is taken from Kurosawa et al. (2009). The best-fit Planck function is also shown in (**a**)

experiments by Sugita and Schultz (2003a). The initial translational–rotational temperatures (2–4 μs) of CN and C_2 produced by laser ablation at 0.9 GW/cm^2 are also shown in Table 1. The translational–rotational temperatures of both CN and C_2 produced by impacts at ~7 km/s are similar to those produced by laser ablation. In both experiments, the translational–rotational temperature of CN is ~2,000 K higher than that of C_2. This difference is caused by the conversion of kinetic energy from the ablation vapor into the internal energy of CN due to aerodynamic deceleration. This phenomena is widely known as "collisional heating" in laser ablation studies (e.g., Wee and Park 1999).

The above spectroscopic results that both non-equilibrium CN and coincidence between translational-rotational temperature of impact-and laser-generated ablation vapor strongly suggest that very similar physical and chemical conditions occur in the two different types of experiments. This will allow us to use laser experiments to examine the chemical consequences of impact-generated high-temperature CN radicals observed by Sugita and Schultz (2009). The validity of using a simulation of aerodynamic interaction after oblique impacts by laser ablation is also discussed in Sections 4.1 and 4.2.

Cyanide Production due to Laser Ablation in a Redox-Neutral Gas Mixture

The Effects of the Composition of the Ambient Gas Mixture on HCN Production

Four gas mixtures were used to investigate the effects of the composition of the gas mixture on HCN production. We found that HCN formation by chemical reactions between laser-induced hot CN radicals and N_2 and H_2O in an ambient atmosphere occurs as follows. Figure 6 shows chromatograms, which are the total ion currents as a function of retention time, obtained with

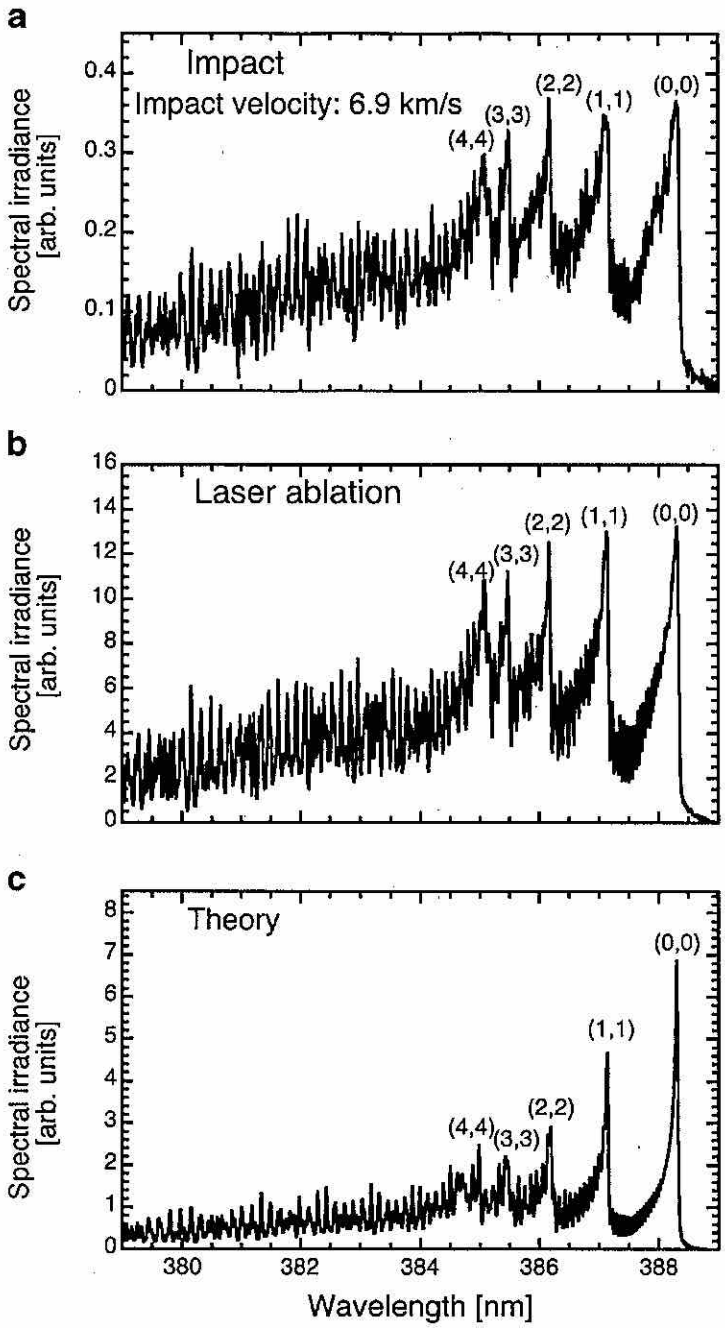

Fig. 4 High-resolution emission spectra of the CN Violet band system. The emission spectrum from the laser-induced ablation vapor is taken from Kurosawa et al. (2009). The vibrational quantum numbers for each band head are shown in the figure

four gas mixtures after 300 laser shots. The experimental results are also given in Table 2. These results clearly indicate that the chemical composition of the gas-phase products strongly depends on the composition of the ambient gas mixture. If a gas mixture included H_2O, hydrocarbons were formed. If a gas mixture included N_2, cyanide compounds were formed. In an Ar gas, HCN was not formed, and only a small peak of C_2H_2 was detected. C_2H_2 is likely to have formed by chemical reactions between the laser-induced carbon vapor and a contaminant gas (e.g., water vapor and/or hydrocarbons) in the chamber. In a H_2O–Ar gas mixture, some hydrocarbons were detected, such as C_2H_4, C_2H_2, and C_4H_2, but HCN was not detected. In a N_2–Ar gas mixture, a large peak of C_2N_2 and a small peak of HCN was detected. The detected HCN was possibly formed by chemical reactions between hot CN and contaminant gases in the chamber. In a N_2–H_2O–Ar gas mixture, a large peak of HCN, C_2H_2, and C_2N_2, and

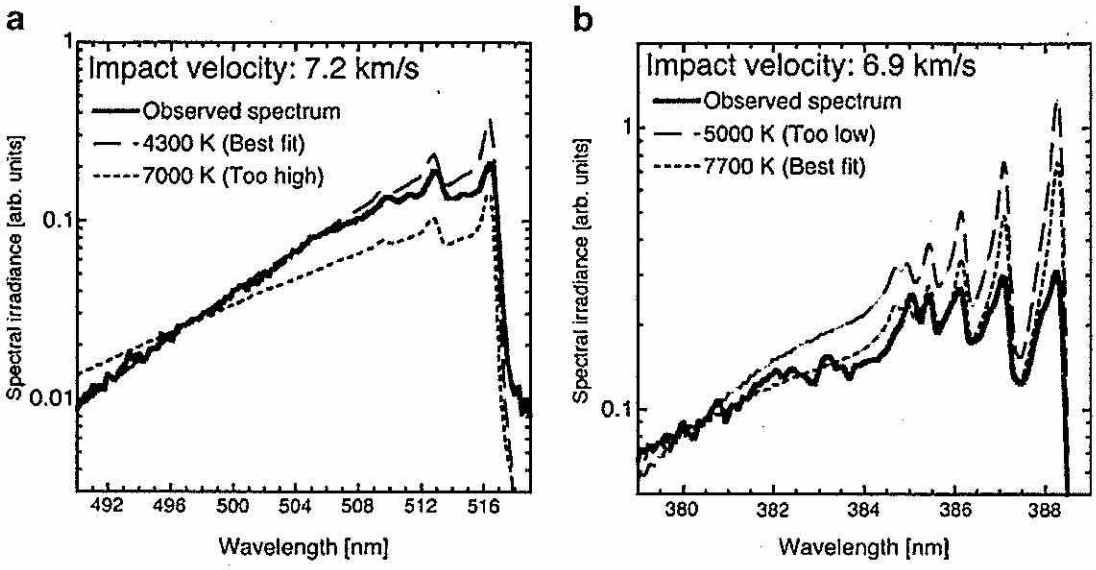

Fig. 5 The results of band-tail fitting for impact-induced C_2 (b) and CN (b). Note that the observed spectrum in (b) is smoothed by Gaussian convolution to reduce the effective spectral resolution. The smoothing is necessary because it is difficult to reproduce the fine structure of the band system, such as the exact wavelength of each rotational line in synthetic calculations

a small peak of nitrile compounds, such as C_2H_3N, C_3H_3N, and C_3H_5N, along with some hydrocarbons, such as C_2H_4, C_2H_6, and C_4H_2 were detected. It was possible to monitor the ion current for selected mass numbers (*M/Z*) using the GCMS and calculate the integrated peak area for HCN (*M/Z*=27). Hereafter, the ion current for a specific mass number is referred to as the monitored ion current (MIC). The integrated peak area of HCN in the N_2–H_2O–Ar gas mixture is about 7 times greater than in the N_2–Ar gas mixture. These results clearly indicate that whether or not the ambient atmosphere contains N_2 and H_2O controls the HCN yield, strongly suggesting that HCN is produced via chemical reactions between laser-generated carbon vapor and the ambient gas mixture, not contaminant gases in the chamber.

The Effects of Oxidation by CO_2 on HCN Yield

The results of gas-phase chemical analysis in N_2–H_2O–CO_2–Ar gas mixtures over a range of CO_2 mixing ratios were described in this section. We present the empirical conversion ratio

Table 1 Summary of the impact experiment results

Shot number	Grating [grooves/mm]	Impact velocity [km/s]	Temperature [K]		
			CN	C_2	Blackbody
205	150	7.17	–	4,800±250	4,300
207	2,400	6.9	7,700±190	–	–
		Laser intensity [GW/cm^2]			
Laser	150	0.9	–	4,600±300[a]	–
Laser	2,400	0.9	7,500±300[a]	–	–

[a] Data taken from Kurosawa et al. (2009). The time window for spectroscopic observations was 2–4 μs after laser irradiation

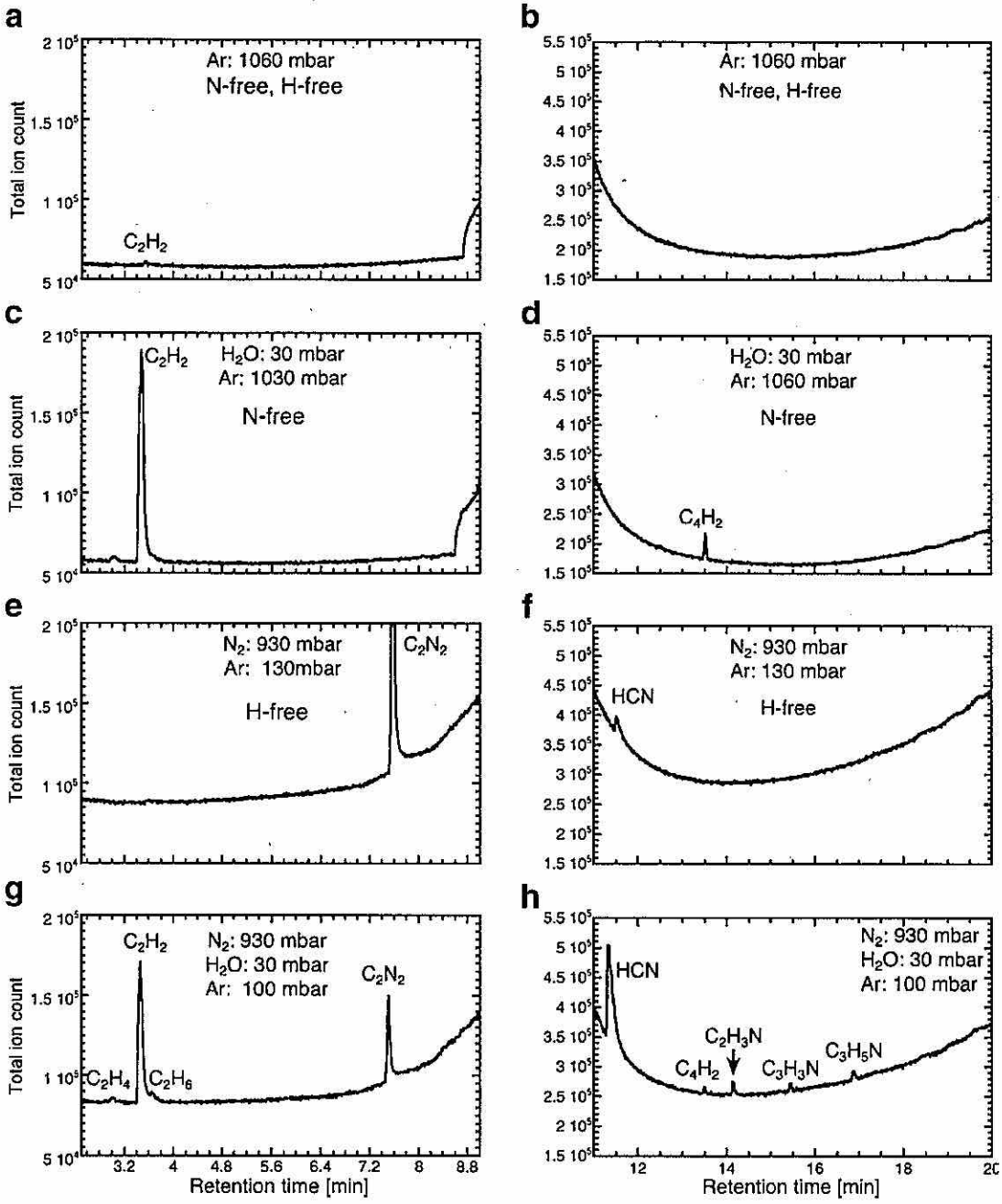

Fig. 6 Chromatograms with four types of gas mixtures. The compositions of the ambient gas mixtures are shown on the figure. The retention time for HCN is 11–12 min under these conditions. The chromatogram between 9 and 11 min is not shown because of a large peak of H_2O that appears at this time

from C to HCN as a function of P_{CO2}. Figure 7a shows the MIC for HCN with a range of P_{CO2} from 0 mbar to 530 mbar. The integrated peak area for HCN strongly depends on P_{CO2}. To convert from the integrated peak area to the molar mixing ratio of HCN in the produced gases, a sensitivity calibration for the GCMS was conducted with standard gases with a variety of HCN mixing ratios (Fig. 7b). Note that the calibration curve is non-linear under our experimental condition because HCN has a strong polarity. The accuracy of the calibration is about 6 % from 15 ppm to 87 ppm HCN. The detection limit of HCN is approximately 4 ppm under the experimental conditions used in our study. The HCN

Table 2 The results of GCMS measurements with four different gas mixtures

Gas mixture	Ethylene C_2H_4	Acetylene C_2H_2	Ethane C_2H_6	Butadiyne C_4H_2	Acetonitrile C_2H_3N	Propenitrile C_3H_3N	Propanenitrile C_3H_5N	Cyanogen C_2N_2	Hydrogen cyanide HCN	N_{HCN} [nmol/pulse]	ϕ mol%
Ar	N. D.	9.6E+03	N. D.	N. D.	N. D.	N. D.	N. D.	N. D.	N. D.	<0.4	<0.08
H_2O-Ar	N. D.	5.5E+05	8.0E+03	7.5E+04	N. D.	N. D.	N. D.	N. D.	N. D.	<0.4	<0.08
N_2-Ar	N. D.	N. D.	2.2E+03	N. D.	2.7E+03	N. D.	N. D.	8.0E+05	1.8E+05	5.3	1.1
N_2-H_2O-Ar	8.1E+03	3.5E+05	1.0E+04	1.7E+04	4.4E+04	1.2E+04	3.0E+04	1.6E+05	1.3E+06	14	2.8

The integrated peak area of the monitored ion current for each species, HCN production per laser pulse, and the conversion ratio ϕ from C to HCN are shown. "N. D." denotes not detected

production per laser pulse (N_{HCN}) can be calculated based on the molar mixing ratio, chamber volume, number of laser shots, and the ideal gas equation of state. We assumed that the temperature of the produced gases is equal to the temperature of the chamber wall (350 K) in this calculation. Figure 7a shows N_{HCN} as a function of P_{CO2} and P_{N2}. N_{HCN} decreases systematically as P_{CO2} increases, and a higher P_{N2} leads to larger N_{HCN}. HCN production could not be detected under P_{CO2} values of 530 mbar (i.e., N_2/CO_2 molar ratio <1). In order to apply the experimental results to real impact phenomena, the conversion ratio (ϕ) of vaporized carbon to gaseous HCN is determined as follows. To estimate the total amount of vaporized carbon N_c, we assumed that the shape of the vaporized region produced by laser ablation is cylindrical and the depth is equal to the wavelength of the laser pulse (~1 μm), which is a characteristic scale of energy deposition of laser irradiation. As a result, the amount of vaporized carbon (N_C) is estimated to be ~500 nmol/pulse. The conversion ratio is given by $\phi=N_{HCN}/N_C$. Figure 8b shows ϕ as a function of P_{CO2}. The conversion ratio varies from 0.1 mol% to 2 mol% over P_{CO2}=0–390 mbar. Although ϕ systematically decreases as P_{CO2} increases, a significant fraction (0.1–1 mol%) of vaporized carbon is converted to HCN in redox-neutral gas mixtures containing as much as a few hundred mbar of CO_2. It is noted that the HCN energy yield obtained in our experiments is 10^{15}–10^{16} molecules/J, which is ~4 orders of magnitude greater than that in simple gas-phase calculations due to Chameides and Walker (1981) for a redox-neutral atmosphere (i.e., C/O molar ratio <1). This suggests that the composition of vapor plumes generated by ablation stay reduced throughout their evolution despite their mixing with ambient atmospheric gas. The integrated peak area for each identified species, HCN production, and ϕ are given in Table 3. Hydrocarbons, cyanogen, and nitrile compounds were also produced within the redox-neutral gas mixtures, although the integrated peak area for these species decreases as P_{CO2} increases. Quantification of the amount of these species is a potential avenue for future research.

Chemical Analyses of the Condensates

The conversion ratio from vaporized carbon to gaseous HCN is only 0.1–2 mol% as shown in the previous section. The fate of other carbon, including spectroscopically detected CN radicals,

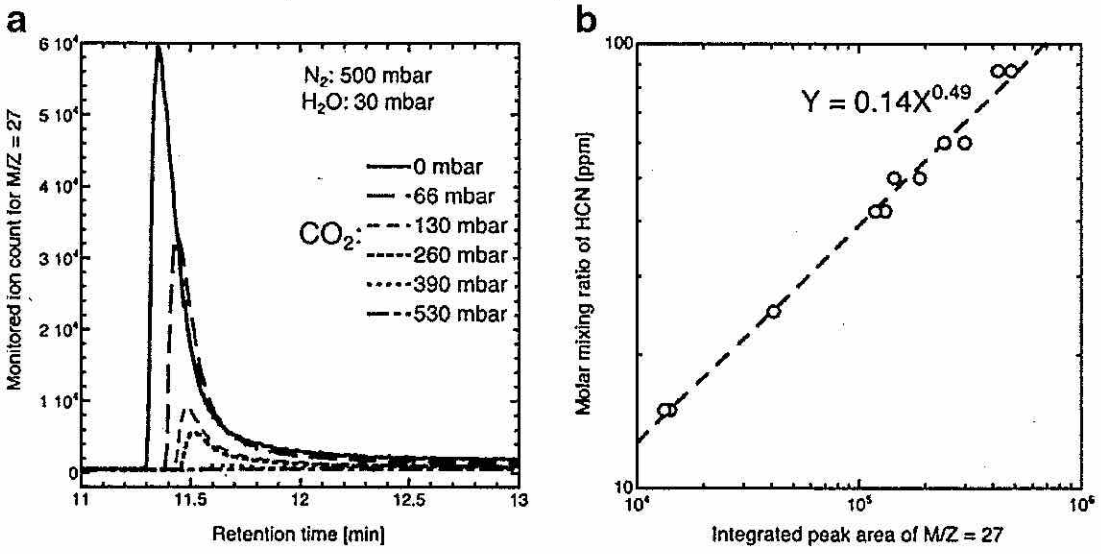

Fig. 7 **a** Monitored ion current for HCN (M/Z=27) as a function of the partial pressure of CO_2. **b** The results of the sensitivity calibration for the GCMS

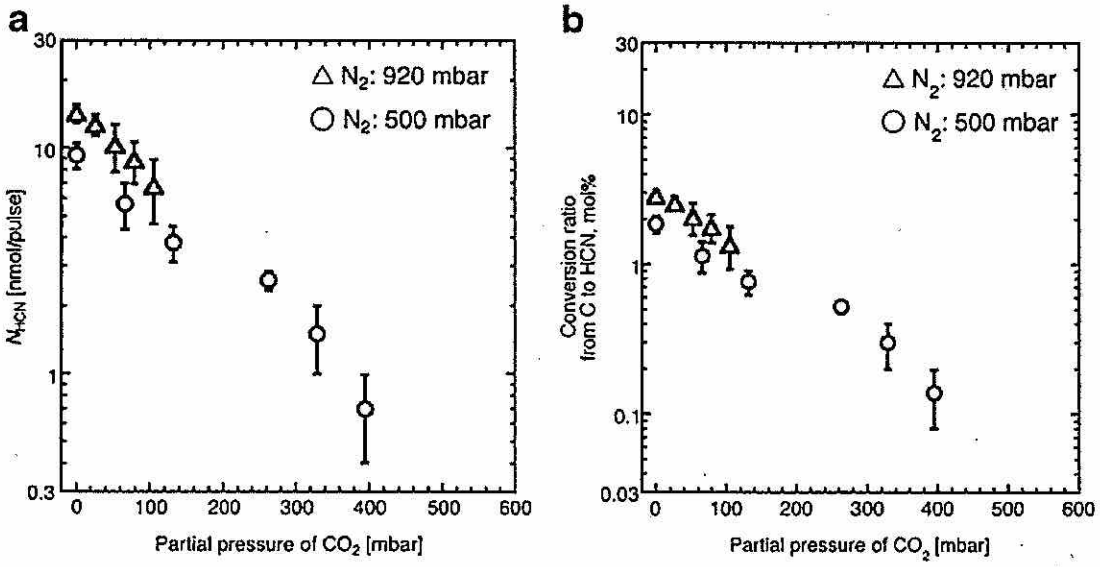

Fig. 8 The amount of HCN produced per laser shot as a function of the partial pressure of CO_2 (**a**) and the conversion ratio ϕ of vaporized carbon to gaseous HCN (**b**). Squares and circles indicate the data obtained under P_{N2}=920 mbar and 500 mbar, respectively. The arrows indicate the detection limit under the experimental conditions

in the ablation vapor is still uncertain. In this section, we examine whether the vaporized carbon is fixed into a condensed phase by forming CN bond or not. The main result of the chemical analyses of the condensed phase is identification of the dependence of both *TN* and the absorption depth of the CN bond of the condensed products on P_{N2}. We found that nitrogen in the gas phase was efficiently fixed into the solid products condensed from the laser-induced ablation vapor. The absorption depth of the CN bond also increases as P_{N2} increases.

The elemental analysis results of the condensed products are shown in Fig. 9. These results show that the chemical composition strongly depends on that of the ambient gas. The condensed products were not observed in the laser irradiation experiments onto a graphite target in CO_2 gas, suggesting that most of the carbon in the laser-generated ablation vapor is oxidized to CO gas by reactions with ambient CO_2 gas. When N_2 was used as the ambient gas, *TN* reaches up to ~10 wt% in the condensed products. This suggests that nitrogen in the gas phase is incorporated into the condensed phase (*TN* ~10 wt%) via chemical reactions with the laser-induced ablation vapor.

Infrared spectroscopy measurements of the condensed products also support the hypothesis that N_2 in the gas phase is incorporated into the condensed products by reacting with C in the laser-generated ablation vapor. Figure 10a shows IR absorption spectra of the condensed products formed by laser irradiation of graphite under various gas mixtures. This figure shows that the depth of the absorption bands around 2,200 cm^{-1} increase with the P_{N2}. This band corresponds to C≡N and −N=C=N bonds (e.g., Rao 1963), and also often seen in Titan tholin simulants synthesized in laboratory experiments under N_2-rich atmospheric conditions (e.g., Imanaka et al. 2004). The depth of the absorption bands around 1,600 cm^{-1} in the IR absorption spectra, which correspond to C=N bonds, also increase with P_{N2}. Figure 10b shows that the effects of the distance between the laser spot and the CaF_2 disk on IR spectra. This result clearly shows the distance does not affect the spectral shape qualitatively. Both absorption bands around 2,200 and 1,600 cm^{-1} contain contributions from the presence of C≡C and C=C bonds, respectively, in the condensed products. Therefore, the increase in the absorption depths may not only be due to the formation of C≡N and C=N bonds. Nevertheless, the observed systematic

Table 3 Results of GCMS measurements with N_2–H_2O–CO_2–Ar gas mixtures over a range of CO_2 mixing ratios

P_{CO2} [mbar]	P_{N2} [mbar]	Ethylene C_2H_4	Acetylene C_2H_2	Ethane C_2H_6	Butadiyne C_4H_2	Acetonitrile C_2H_3N	Propenitrile C_3H_5N	Cyanogen	C_2N_2	Hydrogen cyanide HCN	N_{HCN} [nmol/pulse]	ϕ mol%
0	920	8.1E+03	3.5E+05	1.3E+04	1.7E+04	4.4E+04	1.2E+04	3.0E+04	1.6E+05	1.3E+06	14	2.8
0	920	4.9E+03	2.4E+05	9.2E+03	7.8E+03	4.6E+04	1.2E+04	3.6+04	2.1E+05	1.1E+06	13	2.6
26	920	6.1E+03	3.1E+05	1.2E+04	1.1E+04	2.4E+04	7.5E+03	1.8E+04	6.2E+04	9.1E+05	12	2.4
26	920	7.3E+03	3.5E+05	1.1E+04	1.0E+04	2.7E+04	7.5E+03	2.1E+04	4.5E+04	1.0E+06	12	2.4
53	920	6.1E+02	2.3E+05	9.7E+03	1.1E+04	1.5E+04	4.2E+03	1.2E+04	1.3E+04	4.3E+05	8.2	1.64
53	920	7.0E+03	3.0E+05	9.0E+03	1.1E+04	2.0E+04	6.0E+03	2.0E+04	2.4E+04	7.9E+05	11	2.2
79	920	6.5E+03	3.0E+05	8.4E+03	1.3E+04	1.7E+04	4.8E+03	1.0E+04	7.2E+03	5.3E+05	9.1	1.82
79	920	3.1E+03	2.1E+05	2.2E+03	7.8E+03	1.3E+04	4.0E+03	5.0E+03	1.2E+04	3.5E+05	9.1	1.82
110	920	5.8E+03	1.7E+05	2.3E+03	1.1E+04	1.4E+04	4.3E+03	7.7E+03	8.5E+03	3.0E+05	6.8	1.36
110	920	4.9E+03	1.8E+05	3.7E+03	1.0E+04	1.6E+04	4.0E+03	1.0E+04	8.9E+03	3.4E+05	7.3	1.46
0	500	N. D.	1.9E+05	7.4E+03	1.4E+03	3.4E+04	5.7E+03	3.4E+04	1.1E+05	7.3E+05	11	2.2
0	500	N. D.	1.3E+05	N. D.	N. D.	2.8E+04	2.2E+03	2.6E+04	9.6E+04	5.8E+05	9.5	1.9
66	500	7.3E+03	1.3E+05	9.4E+03	4.9E+03	1.4E+04	2.3E+03	3.4E+04	1.1E+05	7.3E+05	11	2.2
66	500	N. D.	1.3E+05	5.9E+03	5.3E+03	7.5E+03	1.5E+03	6.1E+03	6.2E+03	1.9E+05	5.4	1.08
130	500	N. D.	6.9E+04	N. D.	4.0E+03	8.4E+03	1.5E+03	N. D.	5.7E+03	7.7E+04	3.5	0.7
130	500	N. D.	7.6E+04	N. D.	4.3E+03	9.1E+03	2.3E+03	N. D.	8.7E+03	1.3E+05	4.6	0.92
260	500	N. D.	7.6E+04	N. D.	4.3E+03	9.1E+03	2.3E+03	N. D.	2.4E+03	5.7E+04	3	0.6
260	500	N. D.	6.4E+04	N. D.	6.8E+03	8.3E+03	1.3E+03	N. D.	2.4E+03	4.4E+04	2.7	0.54
330	500	N. D.	4.4E+04	N. D.	5.2E+03	4.9E+03	1.2E+03	N. D.	1.6E+03	1.3E+04	1.5	0.3
330	500	N. D.	6.2E+04	N. D.	8.5E+03	6.8E+03	2.0E+03	N. D.	N. D.	4.2E+04	2.6	0.52
400	500	N. D.	4.6E+04	N. D.	7.8E+03	4.9E+03	N. D.	N. D.	N. D.	1.2E+04	1.4	0.28
400	500	N. D.	4.6E+04	N. D.	8.1E+03	4.6E+03	N. D.	N. D.	N. D.	3.5E+03	0.78	0.156
530	500	3.1E+03	3.6E+04	N. D.	8.9E+03	3.3E+03	N. D.	N. D.	N. D.	N. D.	<0.4	<0.08

The partial pressure of H_2O was fixed at 30 mbar in this series of experiments. In the same way as Table 2, the integrated peak area of the monitored ion current for each species, HCN production per laser pulse, and the conversion ratio ϕ from C to HCN are shown. "N. D." denotes not detected

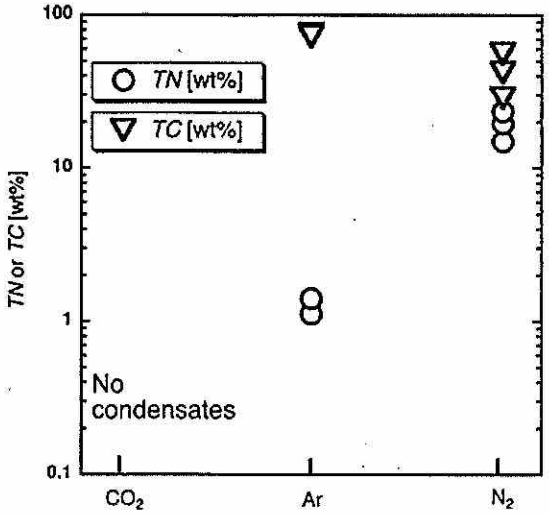

Fig. 9 The results of elemental analysis for condensed phase products. The mass contents of total nitrogen and carbon are abbreviated as *TN* and *TC*

changes in the depth of these absorption bands with P_{N2} strongly support the presence of C≡N, C=N, and −N=C=N bonds in the condensed products formed by laser irradiation under N_2-containing gas mixtures.

Discussion

In this section, we discuss whether laser ablation can simulate aerodynamic ablation processes due to mid-size impacts, based on the results of impact experiments in Section 4.1, the effect of the scale difference outlined in Section 4.2, the comparison with other impact-driven processes

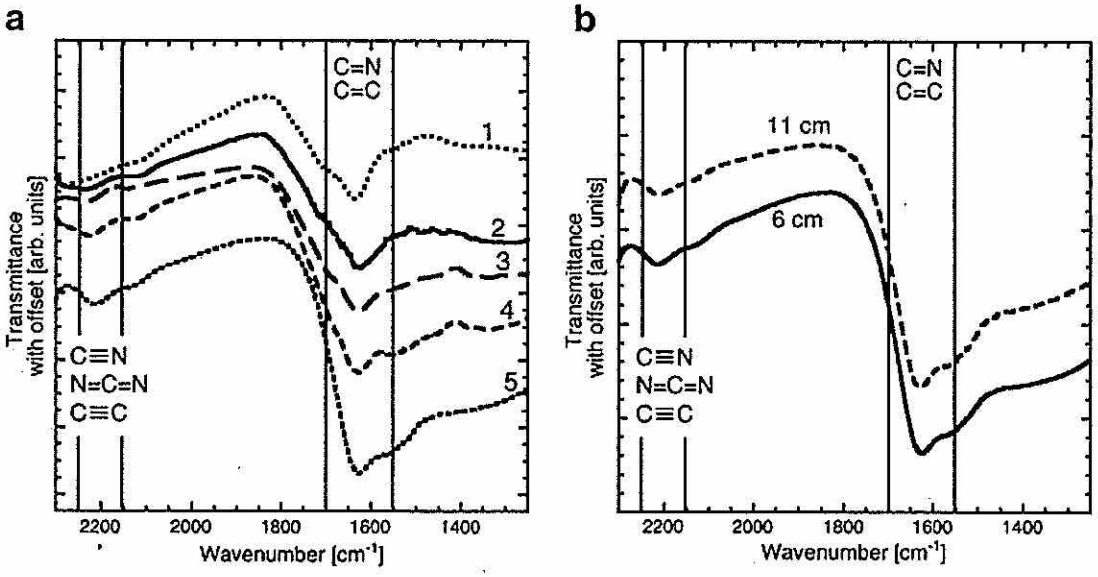

Fig. 10 The results of infrared spectroscopy for condensates: The effects of the composition of ambient gases (a) and the distance between the laser spot and the CaF_2 substrate. The positions of the absorption bands of C≡N, −N=C=N, and C=N are shown. In (a), the numbers indicate the difference in the composition of the ambient gas flow: (1) Ar=13 mbar, (2) N_2=3 mbar, CO_2=3 mbar, and Ar=7 mbar, (3) N_2=6 mbar, CO_2=3 mbar, and Ar=5 mbar, (4) N_2=10 mbar and CO_2=3 mbar, (5) N_2=13 mbar. In experiments (b), we chose 13 mbar of N2 as the ambient gas flow. The distances between the laser spots and the substrate of each experiments are shown in the figure

in Section 4.3, and the dominant impactor type during the heavy bombardment period in Section 4.4. Finally, we consider the implications of our study for the early Earth in Section 4.5.

The Thermodynamic State of the Impact-and Laser-Generated Ablation Vapor

The impact experiment results show that laser-and impact-generated ablation vapors qualitatively exhibit two similarities in terms of spectral shapes and the nature of vibrational non-equilibrium, and quantitatively are in accordance with translational–rotational temperatures.

Here, we discuss the location of CN formation and the pressure of impact-and laser-generated ablation vapors. The equilibration time scale of the translational temperature is very short (~20 ns for N_2 at 10^5 Pa) (Fujita 2007). Thus, the observed CN and C_2 in impact experiments are likely to be spatially separated as the translational temperature of CN is much higher (~2,000 K) than that of C_2. This situation is similar to laser-generated CN and C_2 (e.g., Thareja et al. 2002). We then consider the pressures of both vapors. Although we did not measure the pressure of the impact-generated ablation vapors, it should be controlled by aerodynamic ram pressure ($\sim\rho_a v^2$, where ρ_a and v are the atmospheric density and translational velocity of the vapor, respectively) from the colliding atmospheres. The translational velocities of both vapors are ~10 km/s (e.g., Schultz and Gault 1990; Kadono et al. 2002) and so the pressures of both vapors are expected to be similar. It is noteworthy that the typical peak shock pressure at impacts >100 GPa is much higher than the aerodynamic ram pressure (~0.1 GPa) at a translational velocity of 10 km/s and an atmospheric density of 1 kg/m^3. The possible production and subsequent chemical reaction processes of hot CN radicals due to both impacts and laser ablation are as follows. Gaseous carbon is produced by impact/laser ablation, followed by CN radical production near the material boundary due to mixing between N_2 and C_2, and then hot CN radicals react further with the ambient atmosphere in the wake. Both vapors may follow a similar chemical evolution because they follow similar pressure–temperature paths.

In this study, the absolute CN yield in either experiments is given. The absolute CN yield, however, is not necessary for obtaining the HCN yield from aerodynamic ablation investigated in this study because CN is a transient product via chemical reactions under high temperature conditions. The HCN yield can be estimated from mass spectrometric measurements without knowing the amount of CN radicals. In this study, CN radicals were used as a tracer to assess the impact-and laser-induced chemical reaction fields because CN is the evidence of chemical interaction between the N-free direct vaporization products and the C-free ambient gas. The observed non-equilibrium nature of the vibrational state of CN radicals in both experiments indicates that the rate of CN formation by laser ablation is as fast as that by hypervelocity impacts in terms of the breakdown of vibrational equilibrium in emission spectra. Furthermore, the series of mass spectrometry using a variety of ambient gases as presented in Section 3.2.1 clearly show that the detected HCN in the laser experiments is resulted from such chemical reactions between direct vaporization products and the ambient gases. These experimental results support the validity of the laser experiments to investigate the conversion ratio from vaporized carbon to HCN because similar chemical reaction fields and reaction paths should lead to similar final products after the chemically quenching.

Scaling Effects of Vapor Clouds on Cyanide Production

The size of laser-generated ablation vapor clouds in the laboratory is much smaller than the impactor size colliding with the early Earth. Precise assessment for scaling effects would require extensive effort and beyond the scope of this study. Nevertheless, the size of hot vapor possibly affects the mixing efficiency between the ablation vapor and the ambient

atmosphere and the cooling rate, which controls quenching temperature. Thus, the potential scaling effects on cyanide production should be discussed. Sugita and Schultz (2009) pointed out that CN production processes after oblique impacts is controlled by the physical strength of impactor fragments and their impact velocity, and not by the size of impactor. Thus, the mixing efficiency between generated carbon vapor and the ambient atmosphere is not expected to decrease even at planetary scale impacts. An impact-comminuted projectile is further broken up by high aerodynamic ram pressure after oblique impacts (i.e., ~10^8 Pa at the translational velocity of 10 km/s mentioned in Section 4.1). The strength of stony meteorites and silicate melt droplets are 1–5×10^7 Pa (e.g., Hills and Goda 1993) and 3–5×10^6 Pa (Murase and McBirney 1973; Kadono et al. 2008), respectively, which are both much smaller than the ram pressure. Therefore, the size of each ablation vapor around impact fragments may approach that of laser-generated ablation vapors. Thus, laser ablation may produce similar chemical reaction field, including pressure, temperature, and chemical composition, as impact-induced aerodynamic interactions because laser-and impact-induced ablation vapors are likely to allow similar thermodynamic tracks.

Assessment for cooling time scale is more difficult. Based on spectroscopic observations, the temperature difference between CN and C_2 discussed in Section 3.1 indicate that fast thermal equilibration in a bulk vapor cloud does not occur. Thus, the cooling rate of the ablation vapor may be controlled by gas dynamics around each small fragment, including adiabatic expansion, radiation, and collision with cold ambient atmospheric gases, not impactor size. Then, the cooling rate will be fast; comparable to the cooling time scale of small laser plumes generated in the laboratory in this study. Then the conversion ratio from carbon to HCN obtained from the laser experiments in this study will be applicable rather directly. However, we could not rule out the possibility that individual small ablation vapor plumes coalesce into a large vapor plume and cool slowly at this stage. The situation would be more complicated. Thermodynamic calculations indicate that HCN yield does not depend on quenching temperature (i.e., cooling time scale) when the C/O ratio in a vapor plume is higher than unity (Chameides and Walker 1981). Then, HCN yield obtained in our laser experiments is applicable. If the C/O ratio is lower than unity, however, the HCN yield would decrease by a factor of about hundred as quenching temperature decreases (i.e., slower cooling) from 5,000 K to 1,500 K. Nevertheless, because the composition of ablation vapor is likely to stay reduced throughout its expansion and mixing with the ambient atmosphere as discussed above in the section 3.2.2, the dependence of HCN yield on scale would be rather weak. Thus, the carbon conversion ratio to HCN obtained in our laboratory experiments may serve as a good estimate for mid-size impact events on the early Earth.

Advantages of Impact-Induced Aerodynamic Ablation Compared in Cyanide Production

Chemical reactions during a dynamic event are very complicated. Understanding all the impact-driven processes at different time scales and location, however, is extremely difficult. Thus, we did not discuss exact chemical pathways from meteoritic carbon and atmospheric nitrogen to HCN in detail in this study. Nevertheless, we considered multiple candidate processes for HCN production associated with impact-induced vapor plume evolution within an atmosphere and assessed which physical process is the most efficient for HCN production in actual planetary-scale impacts based on chemical equilibrium. More specifically, three candidates for HCN production via impact-induced gas-phase chemical reactions are considered: (1) air heating within a bow shock induced by high-speed downrange-moving impactor fragments emerging from the impact point, (2) pure vaporization of projectile material, and (3) the aerodynamic ablation of impactor material investigated in this study. First and second processes, however, are

likely to be inefficient on the early Earth because of the following reasons. The HCN production efficiency by first process strongly depends on the redox state in an ambient atmosphere, not the physical consequence in air heating. Thus, the HCN yield by first process is expected to be low in the case of oblique impacts because the early Earth's atmosphere may be redox-neutral as discussed in the Section 1. The HCN production due to second process is limited by the nitrogen content in the impactor. In general, chondritic materials are highly depleted in nitrogen compared with biomolecules on the Earth as discussed in Section 1. Thus, first and second processes are essentially unfavorable for an efficient HCN production on the early Earth in terms of chemical composition. The HCN production efficiency is likely to be rather low independently of the size of vapor plumes. Therefore, third process, aerodynamic ablation around downrange-moving impactor fragments, is the most plausible process for investigating the HCN yield because the spectroscopically detected CN radicals clearly shows that the ablation vapor contains both C-rich impactor materials and an N-rich ambient atmosphere due to mixing. This process has a great advantage on HCN production because meteoritic material is highly depleted in nitrogen. Such an efficient mixing process does not occur in the case of nearly vertical impacts. Furthermore, the ablation vapor has a high temperature due to energy conversion from the kinetic energy of impactor to the internal energy of the ablation vapor, resulting in efficient dissociation of the triple bond of atmospheric nitrogen (N_2).

Impactors During the Heavy Bombardment Period

Another important consideration is the type of impactors, as carbon-rich impactors are required for efficient cyanide production. There are two populations of asteroids, which are the near Earth asteroids (NEA) and the main belt asteroids (MBA). Most of the recent meteorite falls to Earth are ordinary chondrites that come from NEA. The dominant type of NEA is S-type, which is considered to originate from the parent bodies of ordinary chondrites (Binzel et al. 2004). The size distribution of MBA is similar to the impactor size distribution during the heavy bombardment period (Strom et al. 2005), and the dominant type of MBA is C-type, which is considered to be the source of carbonaceous chondrites (Bus and Binzel 2002). Thus, carbonaceous chondrites are expected to have been the most frequent impactors during the heavy bombardment period, and hence the HCN generation mechanism investigated in this study may have been prominent during the heavy bombardment period.

The Column Density of Cyanides After Impacts on the Early Earth

We have shown above that the production efficiency of HCN obtained by laser ablation experiments is expected to be applicable to real impact processes. We now estimate the resulting column density of cyanides after oblique impacts by considering the macroscopic motion of impactors after oblique impacts, based on the conversion ratio obtained in Section 3.2.2 and a simple physical model. A downrange moving projectile with lateral dispersal motion is referred to as a "debris cloud". The equation of motion of debris clouds is given, for example, by Hills and Goda (1993):

$$m\,\dot{v} = -C_D\,\rho_a\,S\,v^2,$$
$$S = \pi\left(\frac{D_p}{2} + v_{disp}\Delta t\right)^2,$$
$$v_{disp} = \beta\, v_{impact}.$$

where m, v, C_D=0.5, ρ_a=1 kg/m^3, S, D_P=600 m, v_{disp}, Δt, β=0.5, and v_{impact}=17 km/s are the mass of the debris cloud, translational velocity, drag coefficient, cross section of the debris

cloud, density of the ambient atmosphere, projectile diameter, lateral dispersal velocity of the debris cloud, time after the impact, a coefficient estimated by the impact experiments, and typical impact velocity (e.g., Ito and Malhotra 2006), respectively. We neglected deceleration of the dispersion velocity and the atmospheric structure for these first-order calculations. The deposition area is estimated to be ~10^2 km^2. The carbon content of a carbonaceous body (CI-like) 600 m in diameter is ~8×10^{11} mol (Wasson and Kallemeyn 1988). Using a conversion ratio of 0.1 mol% for converting vaporized carbon to HCN, the column density of HCN after impacts is ~10 mol/m^2 over ~10^2 km^2 of surface area. This column density is equivalent to 500–10,000 years of accumulated HCN production by lightning within a strongly reducing (i.e., highly fertile) atmosphere (e.g., Stribring and Miller 1986). Cyanides condensates are also produced over this area.

If all produced HCN injected on a lake or shallow marsh 1 m in depth via rain out, resulting HCN concentration reaches a possible range for adenine synthesis, 0.01 mol/L [e.g., Chang et al. 1983; Ferris and Hagan 1984; Miyakawa et al. 2002a, b]. Actual chemical conversion rate from simple cyanide compounds, such as HCN, to more complex biologically important more complex molecules, such as adenine, depends on many factors, such as temperature and pH of water (e.g., Miyakawa et al. 2002a). Nevertheless, a large surface area (~10^2 km^2) covered by fallout from a mid-size impactor, may contain a variety of surface conditions. Furthermore, the relatively small projectile size considered in this study would hit the Earth extremely frequently; a projectile 1 km in diameter or larger every ~1 month during the heavy bombardment period (e.g., Bottke et al. 2010). Then a very large surface area on Earth would have received a high-column density of cyanide many times. Then, if a temperature and pH conditions suitable for subsequent chemical evolution occurred near the surface, such sites are very likely to have received thick CN-loaded deposit. Because of the high concentration of cyanide, such localities may have led to high abundance of adenine and/or perhaps amino acid.

Note that impactors with <300 m in diameter are burned out during atmospheric passage under the current Earth's atmospheric condition [e.g., Melosh 1989]. The HCN production due to aerodynamic ablation around small high-speed fragments investigated in this study, however, would occur in a very similar way as discussed in Sections 4.1 and 4.2 even when the impactor is burned out in the atmosphere. This is because the "burn out" of such small impactors are estimated to be caused by mechanical disruption by aerodynamic ram pressure [e.g., Melosh 1989; Schultz 1992; Hills and Goda 1993; Artemieva and Shuvalov 2001]. Then, a cloud of high-speed fragments will form and aerodynamic ablation will occur, which will lead to intense chemical reaction between impactor-derived material and atmospheric gas.

Conclusions

We have conducted hypervelocity impact and laser ablation experiments within simulated early Earth's atmospheres to investigate cyanide production processes due to mid-size impactors (0.1–1 km in diameter). In situ spectroscopic observation of hypervelocity oblique impacts provides information on the thermodynamic state of the impact-induced ablation vapor. We obtained two qualitative similarities (i.e., spectral outline and vibrational non-equilibrium), and a quantitative agreement (i.e., translational-rotational temperature), between impact-and laser-induced ablation vapors, demonstrating that laser ablation can simulate CN production processes due to aerodynamic ablation after oblique impacts, including vibrational non-equilibrium. A series of laser ablation experiments showed that a part of the destroyed organic matter in the projectile is converted into cyanide compounds via subsequent chemical

reactions with the ambient gases, even though the ambient gases contains as much as ~400 mbar CO_2. We found that the conversion ratio of vaporized carbon to gaseous HCN is 0.1–2 mol% under partial pressures of CO_2 from 0 mbar to 390 mbar. The condensed-phase analyses show that nitrogen in an ambient atmosphere is incorporated into the condensed products by forming C≡N, −N=C=N, and C=N bonds. These experimental results suggest that the aerodynamic ablation of carbon-containing impactors in a N_2-rich atmosphere could have ultimately produced complex organic molecules containing cyanides on the early Earth. A simple model for the fragment dispersal dynamics of impacted bodies shows that the resulting column density is equivalent to ~1×10^4 year of HCN production by lightning in a strongly reducing atmosphere. Such a concentrated supply of cyanides due to small impacts may have played an important role in the origin of life on Earth.

Acknowledgments Hypervelocity impact experiments performed in this study were supported by the Institute of Space and Astronautical Science of the Japan Aerospace Exploration Agency, as a collaborative program of the Space Plasma Experiment. The authors appreciate M. Tabata for his help in the hypervelocity impact experiment. The authors thank R. Ishimaru, T. Sasaki, K. Fujita, K. Suzuki, M. Okada, and Y. Takase for their insightful comments. The authors also thank an anonymous referee for his critical reviews which helped improve the manuscript greatly and A. Schwartz for helpful comments as an editor. K. K. also thanks the members of the Graduate School of Environmental Studies of Nagoya University, S. Watanabe, M. Furumoto, and Y. Shimaki, for their support during writing of this manuscript. This study was supported in part by a Grant-in-Aid from the Japan Society for the Promotion Science.

References

Artemieva NA, Shuvalov VV (2001) Motion of a fragmented meteoroid through the planetary atmosphere. J Geophys Res 106:3297–3309

Binzel RP, Rivkin AS, Stuart JS et al (2004) Observed spectral properties of near-earth objects: Results for population distribution, source regions, and space weathering processes. Icarus 170:259–294

Blank JG, Miller GH, Ahrens MJ, Winans RE (2001) Experimental shock chemistry of aqueous amino acid solutions and the cometary delivery of prebiotic compounds. Orig Life Evol Biosph 31:15–51. doi:10.1023/A:1006758803255

Bottke WF, Walker RJ, Day JMD et al (2010) Stochastic late accretion to earth, the moon, and mars. Science 330:1527–1530

Bus SJ, Binzel RP (2002) Phase II of the small main-belt asteroid spectroscopic survey a feature-based taxonomy. Icarus 158:146–177

BVSP (1981) Basaltic volcanism on the terrestrial planets. Pergamon, New York

Canup RM (2004) Simulations of a late lunar-forming impact. Icarus 168:433–456

Chameides WL, Walker JCG (1981) Rates of fixation by lightning of carbon and nitrogen in possible primitive atmosphere. Orig Life Evol Biosph 11:291–302

Chang S, Des Marais D, Mack R et al. (1983) Prebiotic organic synthesis and the origin of life. In Schopf JW (ed) Earth's Earliest Biosphere: Its Origin and Evolution. Princeton University Press, pp 53–92

Chapin FS, Matson PA III, Mooney HA (2008) Principles of terrestrial ecosystem ecology. Springer, New York

Chyba CF (1991) Terrestrial mantle siderophiles and the lunar impact record. Icarus 92:217–233

Chyba CF, Sagan C (1992) Endogeneous production, exogeneous delivery and impact-shock synthesis of organic molecules: An inventory for the origins of life. Nature 355:125–132

Cooper G, Kimmich N, Belisle W et al (2001) Carbonaceous meteorites as a source of sugar-related organic compounds for the early Earth. Nature 414:879–883

Cronin JR, Pizzarello S, Cruikshank DP (1988) Organic matter in carbonaceous chondrites, planetary satellites, asteroids and comets. In Meteorites and the Early Solar System. University of Arizona Press, pp 819–857

Fegley B, Prinn RG, Hartman H, Watkins H (1986) Chemical effects of large impacts on the Earth's primitive atmosphere. Nature 319:305–308

Ferris JP, Hagan WJ (1984) HCN and chemical evolution: The possible role of cyano compounds in prebiotic synthesis. Tetrahedron 40:1093–1120

Fujita K (2007) Assessment of molecular internal relaxation and dissociation by DSMC-QCT analysis. 39th AIAA Thermophysics Conference, Miami
Fujita K, Abe T (1997) SPRADIAN, structured package for radiation analysis: Theory and application. ISAS report 669:1–47
Gerasimov MV, Ivanov BA, Yakovlev OI, Dikov YP (1998) Physics and chemistry of impacts. Earth Moon Planet 80:209–259. doi:10.1023/A:1006322032494
Hashimoto GL, Abe Y, Sugita S (2007) The chemical composition of the early terrestrial atmosphere: Formation of a reducing atmosphere from CI-like material. J Geophys Res 112, E05010. doi:10.1029/2006JE002844
Hayatsu R, Anders E (1981) Organic compounds in meteorites and their origins. Top Curr Chem 99:1c–37
Hertzberg G (1950) Molecular spectra and molecular structure, I, diatomic molecules, 2nd edn. Van Nostrand, Princeton
Hills JG, Goda MP (1993) The fragmentation of small asteroids in the atmosphere. Astron J 105:1114–1144
Hirschmann MM (2012) Magma ocean influence on early atmosphere mass and composition. Earth and Planetary Sci Lett 341–344:48–57
Imanaka H, Khare BN, Elsila JE, Bakes ELO, McKay CP, Cruikshank DP, Sugita S, Matsui T, Zare RN (2004) Laboratory experiments of Titan tholin formed in cold plasma at various pressures: implications for nitrogen-containing polycyclic aromatic compounds in Titan haze. Icarus 168:344–366
Ishibashi K, Ohno S, Sugita S et al (2006) Oxidation carbon compounds by SiO_2-derived oxygen within laser-induced vapor clouds. Lunar Planet Sci Conf XXXVII:1721
Ishibashi K, Ohno S, Sugita S et al. (2013) Oxidation carbon compounds by silica-derived oxygen within impact-induced vapor clouds. *Earth, Planet, Space*, in press
Ito T, Malhotra R (2006) Dynamical transport of asteroid fragments from υ6 resonance. Adv Space Res 38:817–825
Kadono T, Sugita S, Mitani NK et al. (2002) Vapor clouds generated by laser ablation and hypervelocity impact. Geophys Res Lett 29. doi: 10.1029/2002GL015694
Kadono T, Arakawa M, Kouchi A (2008) Size distributions of chondrules and dispersed droplets caused by liquid breakup: an application to shock wave conditions in the solar nebula. Icarus 197:621–626
Kasting JF (1990) Bolide impacts and the oxidation state of carbon in the Earth's early atmosphere. Orig Life Evol Biosph 20:199–231
Kasting JF (1993) Earth's Early atmosphere. Science 259:920–926
Kulikov YN, Lammer H, Lichtenegger HIM et al (2007) A comparative study of the atmospheres of earth, venus, and mars. Space Sci Rev 129:207–243
Kurosawa K, Sugita S, Fujita K et al (2009) Rotational-temperature measurements of chemically reacting CN using band-tail spectra. J Thermophys Heat Transfer 23:463–472
Kurosawa K, Ohno S, Sugita S et al (2012) The nature of shock-induced calcite ($CaCO_3$) devolatilization in an open system investigated using a two-stage light gas gun. Earth Planet Sci Lett 337–339:68–76
McKay CP, Borucki WJ (1997) Organic synthesis in experimental impact shocks. Science 276:390–392
Melosh HJ (1989) Impact cratering: A geologic process. 210 pp. Oxford University Press
Miller SL (1953) A production of amino acids under possible primitive Earth conditions. Science 117:528–529
Miller SL, Schlesinger G (1983) The atmosphere of the primitive Earth and the prebiotic synthesis of organic compounds. Adv Space Res 3:47–53
Miyakawa S, Cleaves FJ, Miller SL (2002a) The cold origin of life: A. Implications based on the hydrolytic stabilities of hydrogen cyanide and formamide. Orig Life Evol Biosph 32:195–208
Miyakawa S, Cleaves FJ, Miller SL (2002b) The cold origin of life: B. Implications based on pyrimidines and purines produced from frozen ammonium cyanide solutions. Orig Life Evol Biosph 32:209–218
Mukhin LM, Gerasimov MV, Safonova EN (1989) Origin of precursors of organic molecules during evaporation of meteorites and mafic terrestrial rocks. Nature 340:46–49
Murase T, McBirney AR (1973) Properties of some common igneous rocks and their melts at high temperatures. Geol Soc Am Bull 84:3563–3592
Ohkouchi N, Nakajima Y, Okada H et al (2005) Biogeochemical processes in a meromictic Lake Kaiike: Implications from carbon and nitrogen isotopic compositions of photosynthetic pigments. Environ Microbiol 7:1009–1016
Ohno S, Sugita S, Kadono T et al (2004) Sulfur chemistry in laser-simulated impact vapor clouds: Implications for the K/T impact event. Earth Planet Sci Lett 218:347–361
Pierazzo E, Melosh HJ (2000) Hydrocode modeling of oblique impacts: The fate of the projectile. Meteor Planet Sci 35:117–130
Pizzarello S (2012) Hydrogen cyanide in the Murchison meteorite, *The Astrophysical Journal Letters*, **754**, doi:10.1088/2041-8205/754/2/L27
Rao CNR (1963) Chemical applications of infrared spectroscopy. Academic, New York

Rosing MT (1999) C-13-depleted carbon microparticles in >3700-Ma sea-floor sedimentary rocks from west Greenland. Science 283:674–676
Ryder G (1990) Lunar samples, lunar accretion and the early bombardment of the Moon. EOS Trans AGU 71:322–395
Sagan C, Chyba C (1997) The early faint sun paradox: Organic shielding of ultraviolet-labile greenhouse gases. Science 276:1217–1221
Schaefer L, Fegley B Jr (2010) Chemistry of atmospheres formed during accretion of the Earth and other terrestrial planets. Icarus 208:438–448
Schidlowski M (1988) A 3,800-million-year isotopic record of life from carbon in sedimentary rocks. Nature 333:313–318
Schultz PH (1992) Atmospheric effects on ejecta emplacement and crater formation on Venus from Magellan. J Geophys Res 97:16183–16248
Schultz PH, Gault DE (1990) Prolonged global catastrophes from oblique impacts. Geol Soc Am Special Paper 247:239–261
Schultz PH, Sugita S (1996) Fate of the Chicxulub impactor (abstract). Lunar Planet Sci Conf 28:1261–1262
Sekine Y, Sugita S, Kadono T, Matsui T (2003) Methane production by large iron meteorite impacts on early Earth. J Geophys Res 108(E7):5070. doi:10.1029/2002JE002034
Sharma AK, Thareja RK (2005) Plume dynamics of laser-produced aluminum plasma in ambient nitrogen. Appl Surf Sci 243:68–75
Slack MW (1976) Kinetics and thermodynamics of the CN molecule. III. Shock tube measurement of CN dissociation dates. J Chem Phys 64:228–236
Stribring R, Miller SL (1986) Energy yields for hydrogen cyanide and formaldehyde syntheses: The HCN and amino acid concentrations in the primitive ocean. Orig Life Evol Biosph 17:261–273
Strom RG, Manuhotra R, Ito T, Yoshida F, Kring DA (2005) The origin of planetary impactors in the inner solar system. Science 309:1847–1850
Sugita S, Schultz PH (2003a) Interactions between impact-induced vapor clouds and the ambient atmosphere: 1. Spectroscopic observations using diatomic molecular emission. J Geophys Res 108(E6):5051. doi:10.1029/2002JE001959
Sugita S, Schultz PH (2003b) Interactions between impact-induced vapor clouds and the ambient atmosphere: 2. Theoretical modeling. J Geophys Res 108(E6):5052. doi:10.1029/2002JE001960
Sugita S, Schultz PH (2009) Efficient cyanide formation due to impacts of carbonaceous bodies on a planet with a nitrogen-rich atmosphere. Geophys Res Lett 36, L20204. doi:10.1029/2009GL040252
Tera F, Papanastassiou DA, Wasserburg GJ (1974) Isotopic evidence for a terminal lunar cataclysm. Earth Planet Sci Lett 22:1–21
Thareja RK, Dwivedi RK, Ebihara K (2002) Interactions of ambient nitrogen gas and laser ablated carbon plume: Formation of CN. Nucl Instrum Meth Phys Res B 192:301–310
Trail D, Watson EB, Tailby ND (2011) The oxidation state of Hadean magmas and implications for early Earth's atmosphere. Nature 480:79–82
Vivien C, Hermann J, Perrone A et al (1998) A study of molecule formation during laser ablation of graphite in low-pressure nitrogen. J Phys D: Appl Phys 31:1263–1272
Wasson JT, Kallemeyn WK (1988) Composition of chondrites. Phil Trans R Soc Lond A 325:535–544
Wee S, Park SM (1999) Reactive laser ablation of graphite in a nitrogen atmosphere: Optical emission studies. Opt Comm 165:199–205
Zahnle KJ (1986) Photochemistry of methane and the formation of hydrocyanic acid (HCN) in the Earth's early atmosphere. J Geophys Res 91:2819–2834
Zahnle KJ, Schaefer L, Fegley B Jr (2011) Earth's earliest atmosphere. CSH Persp Biol 2:a004895. doi:10.1101/cshperspect.a004895

Icarus 243 (2014) 39–47

Contents lists available at ScienceDirect

Icarus

journal homepage: www.elsevier.com/locate/icarus

Impact chemistry of methanol: Implications for volatile evolution on icy satellites and dwarf planets, and cometary delivery to the Moon

Yasuhito Sekine [a,*], Hidenori Genda [b], Yuta Muto [a], Seiji Sugita [a], Toshihiko Kadono [c], Takafumi Matsui [d]

[a] Department of Complexity Science & Engineering, University of Tokyo, Kashiwanoha, Kashiwa 277-8561, Japan
[b] Earth-Life Science Institute, Tokyo Institute of Technology, Ookayama, Meguro 152-8550, Japan
[c] School of Medicine, University of Occupational and Environmental Health, Iseigaoka, Kitakyusyu 807-8555, Japan
[d] Planetary Exploration Research Center, Chiba Institute of Technology, Tsudanuma, Narashino 275-0016, Japan

ARTICLE INFO

Article history:
Received 8 July 2014
Revised 15 August 2014
Accepted 19 August 2014
Available online 27 August 2014

Keywords:
Impact processes
Satellites, formation
Satellites, atmospheres
Moon, surface

ABSTRACT

Methanol (CH_3OH) is one of the primordial volatiles contained within icy solids in the outer solar nebula. This paper investigates the impact chemistry of CH_3OH ice through a series of impact experiments. We discuss its fate during the accretion and evolution stages of large icy bodies, and assess the possibility of intact delivery of cometary volatiles to the lunar surface. Our experimental results show that the peak shock pressures for initial and complete dissociation of CH_3OH ice are approximately 9 and 28 GPa, respectively. We also found that CO is more abundant than CH_4 in the gas-phase products of impact-induced CH_3OH dissociation. Our results further show that primordial CH_3OH within icy planetesimals could have survived low-velocity impacts during accretion of icy satellites and dwarf planets. These results suggest that CH_3OH may have been a source of soluble reducing carbon and that it may have acted as antifreeze in liquid interior oceans of large icy bodies. In contrast, CH_3OH acquired by accretion on icy satellites and Ceres would have been dissociated efficiently by subsequent impacts, perhaps during the heavy bombardment period, owing to the expected high impact velocities. For example, if Callisto originally contained CH_3OH, cometary impacts during the late heavy bombardment period would have resulted in the formation of a substantial atmosphere (ca. $\geqslant 10^{-4}$ bar) composed of CO, H_2, and CH_4. To account for the current CO levels in Titan's atmosphere, the CH_3OH content in its crust may have been much lower than that typical of comets. Our numerical simulations also indicate that intact delivery of cometary CH_3OH to the lunar surface would not have occurred, which suggests that CH_3OH found in a persistently-shadowed lunar region probably formed through low-temperature surface chemistry on regolith.

1. Introduction

Methanol (CH_3OH) is one of the major primordial volatiles in the outer Solar System and is commonly found in comets and around young stellar objects (Dartois et al., 1999; Ehrenfreund and Charnley, 2000; Irvine et al., 2000; Bockelée-Morvan et al., 2004). Methanol may have been formed in interstellar molecular clouds through surface chemistry on dust grains (e.g., Hiraoka et al., 1994; Watanabe and Kouchi, 2002; Hama and Watanabe, 2013), which in turn would have become the precursors of solids in the solar nebula. Compared with other volatiles, the condensation temperature of CH_3OH is high under nebula conditions (CO: ca. 30 K; CH_4: ca. 50 K; CO_2: ca. 70 K; NH_3: ca. 80 K; CH_3OH: ca. 100 K: Mousis et al., 2009, 2011; Johnson et al., 2012). This suggests that CH_3OH would have been widely incorporated into icy planetesimals in the solar nebula beyond the H_2O snowline.

The gas-starved model of a (gas giant) circumplanetary subnebula implies that regular icy satellites were formed from satellitesimals, which originated from largely unprocessed solar-nebula materials at the location where the gas giant formed (e.g., Canup and Ward, 2006; Alibert and Mousis, 2007). This suggests that primordial CH_3OH would have been contained in icy satellitesimals in the circumplanetary subnebula. In fact, CH_3OH has been found in Enceladus' plumes, although its abundance (0.01% relative to H_2O) is significantly less than that typically contained in comets (ca. 1% relative to H_2O: Waite et al., 2009). Given the proposed temperatures in the Ganymede–Callisto formation region in the

* Corresponding author. Mailing address: Department of Complexity Science & Engineering, University of Tokyo, Kiban Bldg., 5-1-5 Kashiwanoha, Kashiwa 277-8561, Chiba, Japan. Fax: +81 4 7136 3954.
E-mail address: sekine@k.u-tokyo.ac.jp (Y. Sekine).

http://dx.doi.org/10.1016/j.icarus.2014.08.034
0019-1035/

jovian subnebula (ca. 50–100 K; Canup and Ward, 2009), CH_3OH may also have been trapped in the icy satellitesimals in outer regions of the jovian subnebula. In fact, the presence of CO_2 ice in a fresh crater on Callisto suggests that its building materials would have contained primordial CO_2 (Hibbitts et al., 2002), supporting the notion that the nebular temperature in Callisto's formation region would have been low enough to trap CH_3OH in ice.

If primordial CH_3OH in icy planetesimals and satellitesimals survived the impact processes during accretion, it would have played an important part in the geological and chemical evolution of large icy bodies. First, CH_3OH would act as antifreeze, facilitating the existence of liquid water below the freezing point of H_2O (e.g., Shin et al., 2013). In particular, the presence of antifreeze may be important for maintaining interior liquid oceans and cryovolcanism for long periods on icy bodies that are not effectively heated by tidal processes, such as Callisto, Titan, Pluto, and Ceres (e.g., Fortes and Choukroun, 2010; Shin et al., 2013). Second, CH_3OH is an important source of soluble reducing carbon in interior oceans. Through subsequent geological processes, CH_3OH could have been converted into complex organic matter (e.g., Nna-Mvondo et al., 2008; Furukawa et al., 2008; Martins et al., 2013). Methanol would also provide chemical energy to biological processes as a reductant on potentially habitable icy satellites, such as Europa and Enceladus (Hand et al., 2007).

In addition to its importance on icy bodies, the presence of CH_3OH has been suggested as a possible indicator of volatile delivery from the outer to the inner Solar System. The persistently shadowed regions near the lunar poles could possess an abundance of volatile deposits, which have presumably accumulated from cometary and asteroid impacts (e.g., Watson et al., 1961; Heldmann et al., 2012). Remote sensing observations with the Lunar Crater Observation and Sensing Satellite (LCROSS) spacecraft have detected the presence of H_2O vapor, together with gaseous CH_3OH and NH_3, in the ejecta plume formed by an artificial impact onto a persistently shadowed region of the Moon (e.g., Colaprete et al., 2010; Paige et al., 2010). Given the presence of CH_3OH and NH_3 in comets (e.g., Bockelée-Morvan et al., 2004), the LCROSS observations might suggest the intact delivery of volatiles through cometary impacts onto the lunar surface (Colaprete et al., 2010). Alternatively, CH_3OH could also be produced from CO and H through surface chemistry at extremely low temperatures on regolith in a persistently shadowed region of the Moon (Crider and Vondrak, 2002). Based on chemical equilibrium calculations, Berezhnoy et al. (2012) suggest that CH_3OH would be thermochemically unstable in a high-temperature vapor cloud formed by a cometary impact on the Moon. However, the efficiency of impact-induced CH_3OH dissociation would be determined by the kinetics of the reactions, which, thus far, has been poorly investigated based on laboratory experiments.

Despite the importance of CH_3OH to many areas of research in planetary science, a lack of systematic investigations into the impact chemistry of CH_3OH leaves large uncertainties in the quantitative assessment of both its role in the evolution of large icy bodies and the origin of volatiles on the Moon. In the present study, we investigate impact-induced dissociation of CH_3OH through a series of impact experiments based on a CH_3OH–H_2O-ice target and using a chemically clean laser-gun system, which enabled us to investigate the chemical composition of gas species formed by impacts (e.g., Sekine et al., 2011). First, we determine the efficiency of impact-induced CH_3OH dissociation and the chemical composition of the degassing species (Section 3). Next, we discuss the survivability and fate of primordial CH_3OH on large icy bodies (Section 4). The origin of volatiles on the Moon observed by the LCROSS spacecraft is also considered using a combination of experimental results and hydrodynamic simulations of cometary impacts (Section 4). Finally, we present our summary (Section 5).

2. Methods

Fig. 1 shows the configuration of our experimental system, which consisted of a high-energy laser (a Nd:YAG oscillator and glass amplifiers), a stainless-steel vacuum chamber, and a quadrupole mass spectrometer (QMS: BGM-202 Qulee, ULVAC). In Section 2.1, we first explain the acceleration mechanism and our use of the laser gun. The impact conditions achieved in our experiments are also described in Section 2.1. Then, in Section 2.2, we explain the preparation of a CH_3OH–H_2O-ice target and the assumptions adopted to calculate the efficiency of impact-induced CH_3OH dissociation. More detailed descriptions of the laser-gun system and ice-target preparation in our experiments may be found in Ohno et al. (2008), Kawaragi et al. (2009), Fukuzaki et al. (2010) and Sekine et al. (2011).

2.1. Laser gun

Fig. 2 shows a schematic of the acceleration mechanism of our laser gun. We used a gold (Au) metallic foil, with thicknesses of 2.5, 5 and 10 μm (Nilaco Corporation, 99.95% purity), as impactor. The Au foil in the vacuum chamber was irradiated with a pulse laser, and the front surface of the Au foil (ca. 1 μm) was vaporized to form a plasma vapor (Fig. 2). Subsequently, the reaction of the expanding plasma vapor accelerated the other side of the foil (Fig. 2). The impactor was a thin disk with an approximate thickness of 1.5, 4, and 9 μm because the thickness of the original Au foil was reduced by approximately 1 μm by the laser irradiation. The diameter of the impactor was approximately 800 μm, corresponding to the spot diameter of the pulse laser (Fig. 2). Finally, the impactor collided with a CH_3OH–H_2O-ice target, and shock-induced degassing occurred. Using this method, we were able to significantly reduce chemical contamination by gun debris and combustion gases compared with the previous methods that used propellant guns or two-stage light-gas guns (e.g., Lange and Ahrens, 1987; Kato et al., 1995; Burchell et al., 1996; Stewart and Ahrens, 2005). Previous studies used direct laser irradiation to simulate hypervelocity impacts (e.g., Nna-Mvondo et al., 2008). However, the pressure and temperature conditions of vapor clouds formed by direct laser irradiation may be different to those achieved through actual impacts (Kadono et al., 2002). The laser-gun method enabled us to investigate gas species formed by actual hypervelocity impacts.

Table 1 summarizes the experimental conditions pertaining to the laser energy, the original thicknesses of the Au foil, the estimated impact velocities, and the peak shock pressures achieved

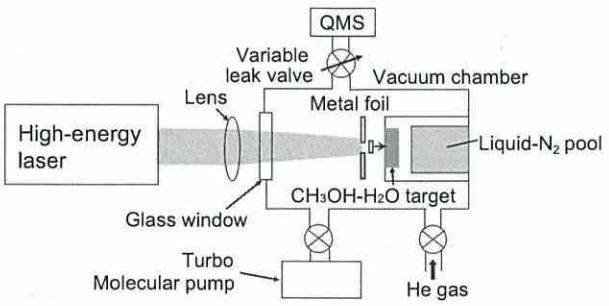

Fig. 1. Schematic diagram of the experimental setup of the laser-gun system. The laser system consists of a high-energy laser (an Nd:YAG oscillator and glass amplifiers), a stainless steel vacuum chamber, a quadrupole mass spectrometer (QMS), and a turbo molecular pump. A stainless-steel target holder containing CH_3OH–H_2O ice was placed in the vacuum chamber. The CH_3OH–H_2O ice was cooled with liquid N_2. Laser irradiation accelerates a gold (Au) metallic foil towards the CH_3OH–H_2O-ice target.

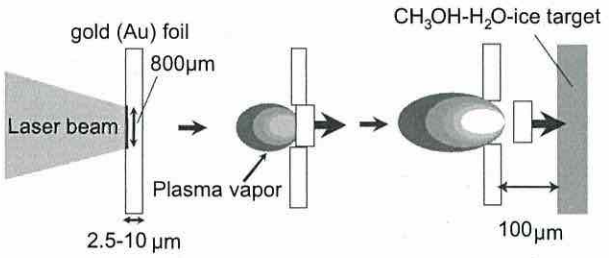

Fig. 2. Acceleration mechanism of the laser gun. See text for detailed explanation.

by the impacts. In the experiments, we varied both the laser energy and the thickness of the foils to achieve a wide range of impact velocities and peak shock pressures (Table 1). The impact velocities were calculated using the empirical equations that express the relationship between the laser energy, the density and thickness of the metal foils, and the impact velocities (Fukuzaki et al., 2010). We calculated the peak shock pressures achieved by the impacts using a one-dimensional impedance-matching solution assuming the planar-impact approximation (e.g., Melosh, 1989). As the Hugoniot parameters of CH_3OH ice have not been reported, we obtained the peak shock pressures using the Hugoniot parameters of H_2O ice for the CH_3OH–H_2O-ice target. We used the Hugoniot parameters and densities of both Au and H_2O reported previously (Zhernokletov et al., 1997; Trunin, 2001). The uncertainties associated with the impact velocities in Table 1 represent one standard deviation of the impact velocities obtained in our previous study (Ohno et al., 2008). In Ohno et al. (2008), the empirical relationship among the impact velocity, laser energy, and impactor's density and thickness was obtained from the results of 42 shots using various impactors (Al foils with thicknesses of 10, 12, 25, 50, and 100 μm; Cu foils with thicknesses of 5 and 10 μm; and Au foils with thicknesses of 2.5 and 10 μm). The errors in the impact velocity mainly results in errors in the resulting peak shock pressures.

In our experiments, the temperature of the impactor was increased by laser irradiation, possibly leading to thermal dissociation of CH_3OH in the target. However, the kinetic energy of the impactor (ca. 10^{-1}–1 J for a velocity of 3 km/s) was estimated to be much higher than the internal energy stored in the impactor (ca. $<10^{-3}$ to 10^{-2} J; Sekine et al., 2011). In addition, scattered laser or thermal irradiation from plasma vapor might have evaporated ice targets in the experiments. Nevertheless, using the same laser gun system with a high-speed camera set in the downstream of impactor's trajectory, Ohno et al. (2008) demonstrated that no significant light was reached to the target materials prior impacts. These results suggest that the effects of evaporation of targets by scattered laser or thermal irradiation from plasma vapor are negligible. Thus, in our experiments, degassing of the target is considered to occur mainly through shock heating associated with the hypervelocity impact.

2.2. Target material and gas analysis

We applied the isotopic labeling technique to the CH_3OH–H_2O-ice target (namely, $^{13}CH_3OH$–H_2O ice, $^{13}C > 99\%$; Isotec Stable Isotopes, Aldrich Chemistry). This was because CO production is expected to occur not only by CH_3OH dissociation, but also through thermal dissociation of CO_2 adsorbed on the wall of the vacuum chamber, owing to the laser irradiation (Kawaragi et al., 2009; Fukuzaki et al., 2010; Sekine et al., 2011). The isotopic labeling technique enables us to distinguish the impact-induced ^{13}CO ($m/z = 29$) from contamination by ^{12}CO ($m/z = 28$), based on mass spectrometry. We also performed control experiments using pure-H_2O ice targets (hereafter, we call these "blank experiments") to evaluate the impact-induced gas production from $^{13}CH_3OH$–H_2O-ice targets. The amounts of impact-induced gas species (in moles) were obtained by calibrating the QMS signals at $m/z = 29$ (^{13}CO) and $m/z = 17$ ($^{13}CH_4$) using an internal helium (He) standard gas of 10 Pa, which was introduced in the vacuum chamber prior to laser irradiation.

During a hypervelocity impact, the peak shock pressure in a target becomes almost uniform in the region near the impact point, referred to as the isobaric core, and the shock decays abruptly with propagation distance away from this point (Melosh, 1989). In the present study, the efficiency of impact-induced CH_3OH dissociation was obtained by normalizing the total amount of impact-induced ^{13}CO and $^{13}CH_4$ by the amount of $^{13}CH_3OH$ initially contained in the isobaric core (Sekine et al., 2011). As the previous models show that the mass of an isobaric core is approximately the same as that of the impactor (e.g., Melosh, 1989), we assumed that the mass ratio of the impactor to the target's isobaric core was unity. These assumptions may result in an uncertainty of up to 50% in the efficiency of impact-induced CH_3OH dissociation (Sekine et al., 2011). However, as discussed in Section 4, this does not significantly affect our conclusions. In the present study, we estimated the impactor mass from the density of Au and the impactor's volume, i.e., a disk-like shape with a diameter of 800 μm and a thickness of 1 μm thinner than the original thickness of the foil (see Section 2.1).

The method used to prepare the ice target followed that of our previous work (Sekine et al., 2011). First, we introduced approximately 0.1 ml of liquid $^{13}CH_3OH$–H_2O ($^{13}CH_3OH$:H_2O = 1:3, in volume) into the dent (with a diameter of 10 mm and a depth of 2 mm) of a copper loading cell and then sealed the dent with Au foil (Fig. 3a). Next, the liquid $^{13}CH_3OH$–H_2O was cooled for about 20 min with liquid N_2, poured into a liquid-N_2 pool in the target holder (Fig. 3b). After freezing the liquid $^{13}CH_3OH$–H_2O, we

Table 1
Experimental conditions. "Me-OH-W. ice" denotes CH_3OH–H_2O ice.

	Target	Impactor original thickness (μm)	Laser energy (J)	Impact velocity (km/s)	Peak shock pressure (GPa)
Shot 1	H_2O ice	2.5	32.1	3.92 ± 0.59	23.5 ± 5.6
Shot 2	Me-OH-W. ice	2.5	34.0	4.04 ± 0.62	24.7 ± 6.0
Shot 3	Me-OH-W. ice	2.5	30.9	3.85 ± 0.58	22.8 ± 5.4
Shot 4	Me-OH-W. ice	5	39.8	3.07 ± 0.40	16.1 ± 3.3
Shot 5	Me-OH-W. ice	5	33.5	2.81 ± 0.35	14.1 ± 2.7
Shot 6	Me-OH-W. ice	10	22.6	1.62 ± 0.13	6.33 ± 0.7
Shot 7	Me-OH-W. ice	10	51.7	2.46 ± 0.28	11.6 ± 2.0
Shot 8	Me-OH-W. ice	2.5	31.6	3.89 ± 0.59	23.2 ± 5.6
Shot 9	Me-OH-W. ice	5	48.1	3.38 ± 0.47	18.7 ± 4.1
Shot 10	H_2O ice	10	48.3	2.38 ± 0.27	11.0 ± 1.8
Shot 11	Me-OH-W. ice	2.5	27.4	3.61 ± 0.52	20.7 ± 4.7

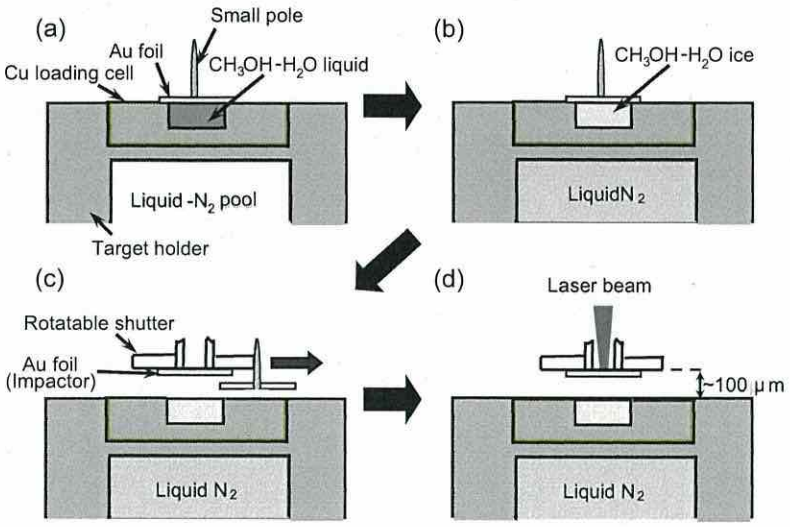

Fig. 3. Schematic illustrations of the preparation of the CH_3OH–H_2O-ice target in the vacuum chamber. See text for detailed explanation.

evacuated the vacuum chamber with a turbo pump to about 10^{-6} mbar for one hour (Fig. 1). Then, the Au foil covering the ice target was removed with a rotatable shutter and the fresh ice surface appeared in the vacuum chamber (Fig. 3c). After exposure of the fresh surface, we placed another Au foil (i.e., the impactor) in front of the ice surface in the vacuum chamber at a distance of approximately 100 μm and closed a valve to the turbo pump (Fig. 3c). Finally, we introduced an internal He standard gas into the vacuum chamber and irradiated a high-energy laser onto the foil (Fig. 3d). Given the sublimation rate of ice of $\sim 10^{12}$ moles/cm^2/s at 135 K (Sack and Baragiola, 1993), the thickness of the ice target sublimated prior to impact would be approximately 10 nm. The target temperature would be practically less than 135 K; accordingly, the above value would be an upper limit of the amount of sublimated ice. This value is negligible compared with the thickness of impactor (i.e., 1.5–9 μm) or the ice volume undergone shock-induced dissociation (see below). We obtained mass spectra of the gas in the vacuum chamber in the range of m/z = 1–50 with a resolution of 0.05 amu prior to, and after, the impact using the QMS, which was connected to the vacuum chamber via a variable leak valve (Fig. 1). The variable leak valve was adjusted to keep the total gas pressure in the vacuum chamber almost constant during the measurements. Due to the evacuation through the variable leak valve during the measurements, the total pressures in the vacuum chamber were reduced 1–3% from the values immediately after the impacts.

3. Results

3.1. Composition of impact-induced gas from CH_3OH–H_2O ice

Fig. 4 shows typical mass spectra of gas in the vacuum chamber after impacts onto (a) a $^{13}CH_3OH$–H_2O-ice target and (b) a pure-H_2O ice target (i.e., the blank experiment) (the mass spectra for all shots are shown in Supplementary Material). The QMS signal at m/z = 29 ice is remarkable for the shot onto $^{13}CH_3OH$–H_2O ice compared with that of the blank experiment (Fig. 4), although the pattern of the other peaks observed in the mass spectra (e.g., H_2, He, H_2O, and ^{12}CO) are similar. In the experiments, CO is produced by laser-induced dissociation of CO_2 adsorbed on the wall of the vacuum chamber. However, given the natural isotopic ratio of $^{13}C/^{12}C$ of about 0.0108, the intense QMS signal at m/z = 29 for the shot onto $^{13}CH_3OH$–H_2O ice cannot be explained by CO decomposed from adsorbed CO_2. These results indicate the formation of ^{13}CO through impact-induced dissociation of $^{13}CH_3OH$–H_2O ice.

Fig. 4c shows a comparison of the normalized QMS intensities around m/z = 17–18 for the shot onto $^{13}CH_3OH$–H_2O ice and the blank experiment. This figure indicates that the normalized QMS intensity at m/z = 17 for the shot onto $^{13}CH_3OH$–H_2O ice is higher than that of the blank experiment. In the blank experiment, the QMS signal at m/z = 17 is mainly contributed by OH formed by fragmentation of H_2O due to ionization in the mass spectrometer. On the other hand, in the shot onto $^{13}CH_3OH$–H_2O, both $^{13}CH_4$ and OH contribute to the QMS signal at m/z = 17. The fragmentation pattern of H_2O in the mass spectra is expected to remain unchanged for the same measurement conditions (the QMS signal ratio at m/z = 17–18 in the blank experiments is measured at 0.25 ± 0.05). Thus, the excess of the relative intensity at m/z = 17 in the shot onto $^{13}CH_3OH$–H_2O indicates impact-induced formation of $^{13}CH_4$ (Fig. 4c).

Fig. 5 shows the ratio of $^{13}CO/^{13}CH_4$ produced by impacts onto $^{13}CH_3OH$–H_2O ice as a function of peak shock pressure achieved by the impacts. These results indicate that the amount of ^{13}CO produced by impacts is $\geqslant$5 times that of $^{13}CH_4$ (Fig. 5), suggesting that impact-induced $^{13}CH_3OH$ dissociation proceeds mainly through the ^{13}CO-formation reaction (e.g., $CH_3OH \rightarrow CO + 2H_2$) rather than via the $^{13}CH_4$-formation reaction (e.g., $2CH_3OH \rightarrow CH_4 + CO_2 + 2H_2$ or $2CH_3OH \rightarrow CH_4 + CO + H_2O + H_2$). Fig. 5 also shows that the $^{13}CO/^{13}CH_4$ ratio seems to increase with peak shock pressure (i.e., with higher impact velocity). This may be because CO is thermochemically more stable than CH_4 at higher temperatures (McKay and Borucki, 1997; Kress and McKay, 2004).

3.2. Efficiency of impact-induced CH_3OH dissociation

Fig. 6 shows the relationship between the efficiency of impact-induced $^{13}CH_3OH$ dissociation and the peak shock pressure achieved by the impacts. Our results show that $^{13}CH_3OH$ dissociation begins around 9 GPa and that the efficiency increases almost linearly with peak shock pressure. Fig. 6 also shows that complete dissociation of $^{13}CH_3OH$ occurs at about 28 GPa. This trend of impact-induced CH_3OH dissociation shows good agreement with those of both NH_3 ice (Sekine et al., 2011) and ammonium sulfate (Fukuzaki et al., 2010). The peak shock pressures for initial and

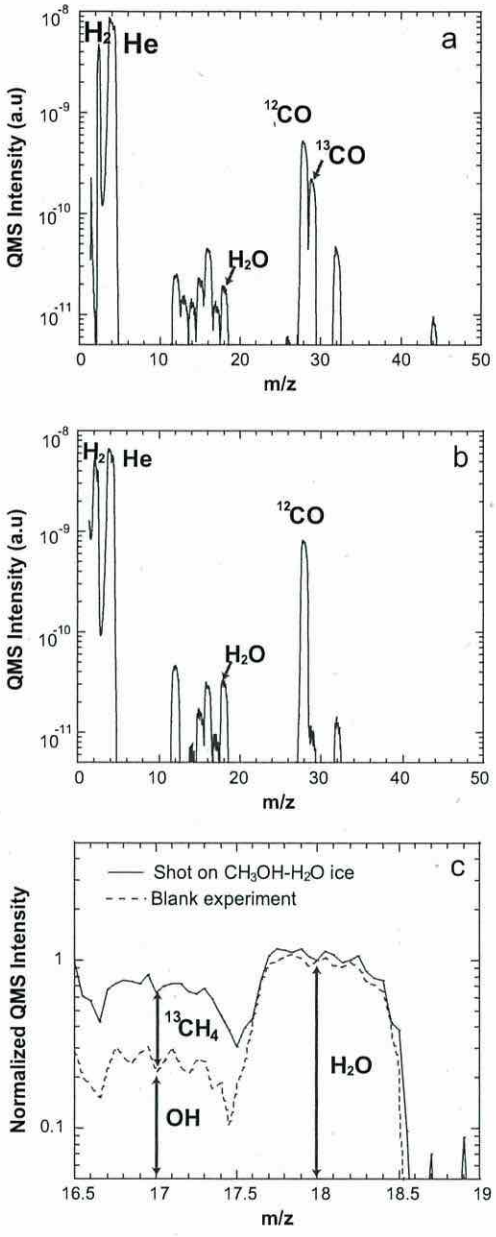

Fig. 4. Typical mass spectra (in arbitrary units: a.u.) of gas species in the vacuum chamber following impacts onto (a) $^{13}CH_3OH$–H_2O ice at about 3.9 km/s (Shot 8 in Table 1) and (b) pure-H_2O ice at about 3.9 km/s (blank experiment; Shot 1 in Table 1). A close-up view of the mass spectra at m/z = 17 and 18 is also shown in the panel (c). The solid and dashed lines in panel (c) show the results for impacts onto $^{13}CH_3OH$–H_2O ice and the blank experiment, respectively.

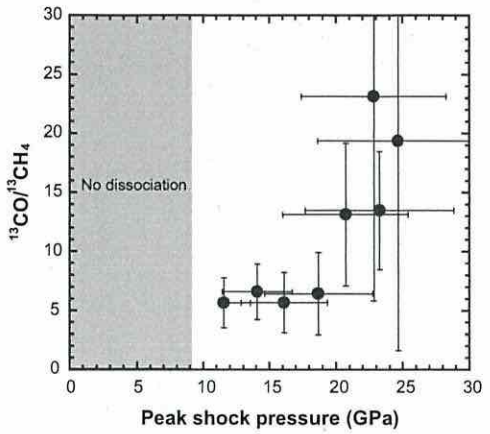

Fig. 5. $^{13}CO/^{13}CH_4$ ratio in the gas products formed by impact-induced $^{13}CH_3OH$–H_2O dissociation as a function of peak shock pressure obtained in our experiments. No $^{13}CH_3OH$ dissociation occurs at peak shock pressures below about 9 GPa (see Fig. 6).

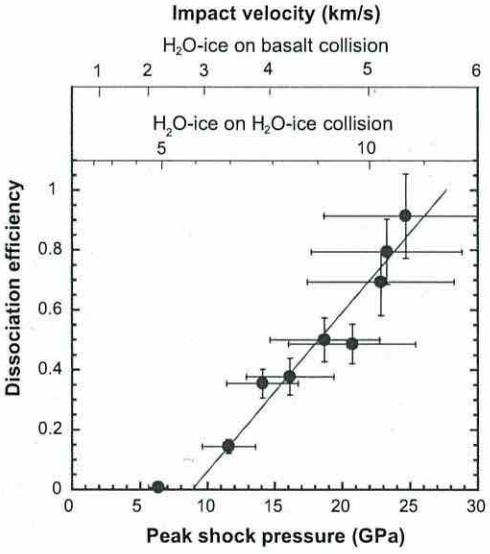

Fig. 6. Dissociation efficiency of $^{13}CH_3OH$ as a function of peak shock pressure obtained in our experiments. The top axis shows the impact velocity of H_2O-ice collision (and H_2O-ice and basalt collision) that generates the peak shock pressure shown along the bottom axis. The regression line for the data at >10 GPa shows that the peak shock pressures for initial and complete $^{13}CH_3OH$ dissociation are 9 and 28 GPa, respectively.

complete dissociation of CH_3OH are close to the equivalent values for NH_3 ice (i.e., ca. 8 and 23 GPa, respectively: Sekine et al., 2011). This may be because the binding energy of the C–H (or O–H) bond is close to that of the N–H bond (i.e., C–H: ca. 410 kJ/mol, O–H: ca. 460 kJ/mol; N–H: ca. 390 kJ/mol). Thus, the required shock energy for CH_3OH dissociation would be similar to that for NH_3.

The top axis of Fig. 6 shows the impact velocity of collisions between H_2O ices or between H_2O ice and basalt, which generate the peak shock pressures corresponding to the bottom axis. Here, we consider oblique impacts of an H_2O-ice impactor onto H_2O ice or a basaltic target at an angle of 45°, by assuming that the peak shock pressures achieved by the impacts are approximately the same as those of the normal impacts of the vertical component of the oblique impacts. The relationship between impact velocity and peak shock pressure was calculated based on one-dimensional impedance matching (Melosh, 1989). Fig. 6 shows that CH_3OH would be dissociated efficiently in impacts between icy materials at velocities in excess of about 5 km/s. In impacts between rocky and icy materials, effective CH_3OH dissociation would occur even at relatively low impact velocities, e.g., 2–5 km/s (Fig. 6).

For large icy satellites, the impact velocity of satellitesimals during accretion is suggested to be less than a few times the escape velocity (ca. 2–4 km/s for a Titan-sized satellite; e.g., McKay et al., 1988; Kuramoto and Matsui, 1994). Thus, our results strongly suggest that primordial CH_3OH in satellitesimals would not dissociate

during accretion. The impact velocity onto Pluto and Charon is also estimated to be too low to dissociate CH_3OH (ca. 2 km/s: Zahnle et al., 2003). These results suggest that primordial CH_3OH survived during the accretion events onto large icy satellites and dwarf planets. This, in turn, implies that CH_3OH, together with NH_3, acts as antifreeze in the deep interiors, which permits the presence of liquid water down to 176 K and affects the thermal evolution and interior structure (Fortes and Choukroun, 2010; Shin et al., 2013).

On the other hand, impact velocities of comets onto icy satellites after accretion become much higher than those of satellitesimals because of the gravity of the gas giants. For instance, the typical impact velocities of long-period comets become approximately 11 km/s for Titan, 15 km/s for Callisto, 20 km/s for Ganymede, and 25 km/s for Europa (Zahnle et al., 2003). In this case, near the impact point of icy satellites, CH_3OH would be dissociated effectively by these cometary impacts (Fig. 6). This, in turn, suggests that CO and CH_4 formed by impact-induced CH_3OH dissociation would have generated atmospheres surrounding large icy satellites. We will examine the amount of CH_4 and CO formed by CH_3OH dissociation on Titan and Callisto below, in Section 4.1.

Recent models suggest that some icy planetesimals in the outer Solar System may have migrated into the asteroid belt (Walsh et al., 2011), plausibly including Ceres. In the asteroid belt, Ceres would have experienced a number of impacts of rocky asteroids throughout its history. Given the relatively high impact velocity and density of asteroids (ca. 5 km/s; Bottke et al., 1994), the peak shock pressure achieved by asteroid impacts onto the icy surface of Ceres is estimated at 15–20 GPa, using the planer-impact approximation (Melosh, 1989) and Hugoniot parameters of the Murchison meteorite (Anderson and Ahrens, 1998). Thus, our results in Fig. 6 show that if Ceres originally contained CH_3OH in its interior, asteroid impacts would have provided CO and CH_4 on the surface, possibly forming a tenuous temporal exosphere. A fraction of the impact-induced CO and CH_4 may condense onto the low-temperature regions, such as polar regions, and possibly cause comet-like sublimation in response to the orbital motion. This could remove near-surface dust and expose fresh ice, leading to the ejection of water vapor, although the water activity detected by the Herschel space telescope seems to be not concentrated on the polar regions (Küppers et al., 2014).

Given the high velocity of cometary impacts on Earth's Moon (ca. 20 km/s: Chyba, 1991), CH_3OH contained in comets would also have been effectively dissociated by such impacts. During highly oblique impacts, however, the achieved peak shock pressures would be dramatically reduced, so that a fraction of the cometary volatiles could have survived the impacts. We will examine the survivability of cometary CH_3OH during impacts onto the Moon in Section 4.2 below.

4. Discussion

4.1. Formation of CO and CH_4 on a large icy satellite

In this section, we discuss the formation possibility of a CO–CH_4-containing atmosphere by impact-induced dissociation of CH_3OH on a large icy satellite, such as Callisto or Titan. We do not examine formation of CO and CH_4 on Ganymede, because it would not be able to retain a substantial atmosphere because of effective, impact-induced blow-off (Griffith and Zahnle, 1995). We focus on cometary impacts during the late heavy bombardment period (Sekine et al., 2011), which would have been caused by planetary migration (e.g., Gomes et al., 2005).

One of the largest uncertainties in the calculation is the initial abundance of CH_3OH on the primordial Callisto and Titan. The CH_3OH content in comets (typically 1% relative to H_2O; Bockelée-Morvan et al., 2004) would be an upper limit to the abundance of CH_3OH on these icy satellites. This is the case if primordial CH_3OH in the solar nebula was unprocessed in the jovian and saturnian subnebulae. A lower limit would be the CH_3OH content in Enceladus' plume (ca. 0.01% relative to H_2O; Waite et al., 2009). This assumes that loss of some CH_3OH proceeded in the saturnian subnebula, although it is unclear whether the loss occurred through aqueous/hydrothermal reactions or incorporation into clathrate hydrates in Enceladus.

We first calculate the total amounts of CO and CH_4 formed from CH_3OH by a cometary impact on the icy satellites based upon numerical simulations employing a smoothed particle hydrodynamic (SPH) method, discussed in our previous study (see Supplementary Fig. 5 of Sekine et al., 2011). The numerical simulations show that the volumes of the target- and impactor-experienced peak shock pressures for partial CH_3OH dissociation (i.e., 9–28 GPa) are approximately 4 and 0.6 times that of the impactor's, respectively (see Supplementary Fig. 5 of Sekine et al., 2011). The volumes of the target- and impactor-experienced complete CH_3OH dissociation (i.e., >28 GPa) are approximately 0.03 and 0.1 times that of the impactor's, respectively. We obtained the total amounts of CO and CH_4 production by integrating the amount of CH_3OH dissociation in the areas for complete and partial CH_3OH dissociation in both the target and the impactor.

We then calculated the evolution of the surface abundance of CO and CH_4 produced from CH_3OH during the late heavy bombardment period using a one-box model calculation (Sekine et al., 2011). The one-box model takes into account the supply and loss of the atmosphere by cometary impacts (Sekine et al., 2011). The loss of a pre-existing atmosphere by subsequent impacts is treated based on the results of the atmospheric-erosion model given by three-dimensional multi-material hydrocode calculations (Shuvalov, 2009). A detailed description of the one-box model is given by Sekine et al. (2011).

We varied the size of the impactor (15–30 km in radius; Barr and Canup, 2010) and the surface temperature of the satellites (70 K for Titan; Sekine et al., 2011, and 100 K for Callisto; Canup and Ward, 2009). The cumulative impactor mass during the late heavy bombardment era was given by Barr and Canup (2010) for Callisto and by Sekine et al. (2011) for Titan. We also assumed that the gas products formed by CH_3OH dissociation do not condense onto the surface. This assumption provides a lower limit to the total accumulation of CO and CH_4, because surface condensation prevents effective loss by subsequent impact-induced atmospheric erosion.

Fig. 7 shows the total amounts of CO and CH_4 on the surface of Callisto and Titan during the late heavy bombardment period. For Callisto and Titan, 0.01–1 bar of gaseous CO and CH_4 would have been produced during late heavy bombardment if the CH_3OH content in the crust is 1% relative to H_2O; these values must be reduced to $\sim 10^{-4}$ to 10^{-3} bar for 0.01% of the CH_3OH content (Fig. 7). Our results show that Titan tends to acquire greater amounts of CO and CH_4 than Callisto (Fig. 7). This is because impact velocity and surface temperature of Titan are lower than those of Callisto. Low surface temperatures result in a small scale atmospheric height, which leads to less effective loss of atmosphere by subsequent impacts. Impacts with lower velocities also cause less effective atmospheric losses.

Our experimental results show that CO is predominant in C-bearing gas species formed by shock-induced CH_3OH dissociation (Fig. 5). If these results are directly applicable to planetary-scale impacts, Titan might have possessed around 0.1 bar of CO during late heavy bombardment when the CH_3OH content in its crust was as high as that of comets (e.g., 1% relative to H_2O). Given the stability of CO against photochemical dissociation, this amount of CO would have been difficult to reduce to the present atmospheric

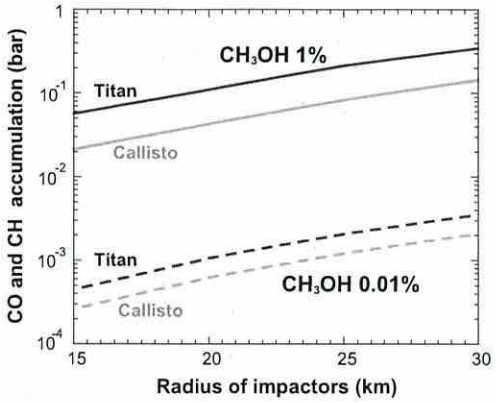

Fig. 7. Total amounts of CO and CH_4 produced by CH_3OH dissociation on Callisto and Titan during the late heavy bombardment period for 1% (solid) and 0.01% (dashed) of CH_3OH content in the target, surface temperatures of the satellites (70 K for Titan; black, and 100 K for Callisto; gray), and radius of the impactors (bottom axis).

level (mixing ratio of ca. 6×10^{-5}; Wong et al., 2002; Wilson and Atreya, 2004). On the other hand, if the CH_3OH content in the primordial Titan was as low as that in Enceladus' plume (e.g., ca. 0.01% relative to H_2O), the amount of CO immediately after the heavy bombardment period would be 10^{-4} to 10^{-3} bar (Fig. 7). These values are in good agreement with the proposed mixing ratio of CO in Titan's atmosphere at about 4 Gyr ago required to account for the present-day level based on photochemical modeling (Wong et al., 2002). In this case, the CH_3OH content in Enceladus' plume might reflect the primordial value contained in icy satellitesimals in the saturnian system. This further suggests that chemical alterations of primordial volatiles, at least regarding CH_3OH, may have occurred in the saturnian subnebula, contrary to the prediction from the simple gas-starved model (e.g., Canup and Ward, 2006).

Alternatively, even if the CH_3OH content on the primordial Titan was as high as that of comets, CO and H_2 formed through shock-induced dissociation of CH_3OH would have been converted into CH_4 and H_2O in an actual cometary impact on the icy satellites through gas–grain catalytic reactions (Kress and McKay, 2004; Sekine et al., 2006). In an impact vapor, catalytic reactions on the surface of Fe–Ni metals, which are derived from the impactor, could convert CO and H_2 into thermodynamically stable CH_4 and H_2O at 500–1000 K (the optimal temperature range for the catalytic reactions; Sekine et al., 2005). Our previous experimental study showed that the efficiency of the catalytic reactions strongly depends on pressure, suggesting that >1 bar of pressure would be necessary to sustain effective catalytic reactions in an impact vapor cloud (Sekine et al., 2006). In a cometary impact onto icy satellites, the vapor-cloud pressure at 500–1000 K would be high (>1 bar); i.e., sufficient to cause the catalytic reactions (Fig. 8). In future studies, it will be important to investigate whether a cometary impact can generate catalytically active metallic grains in order to understand not only the impact chemistry of volatile-rich materials, but also the chemical composition of icy satellitesimals in the outer Solar System.

Our results suggest the formation of a mildly reducing, CO–CH_4-containing atmosphere with a pressure of $\geqslant 10^{-4}$ bar on Callisto during late heavy bombardment. This would have been lost by ion sputtering and photochemical reactions over the course of its history (e.g., Griffith and Zahnle, 1995). Photo- and ion chemistry in such a CO–CH_4-containing atmosphere would have resulted in the formation of complex organic aerosols (Trainer et al., 2006; Hasenkopf et al., 2010), which would have precipitated onto the surface. As Griffith and Zahnle (1995) pointed out, we also speculate that organic materials on Callisto would contain photochemical products of complex organics, which may exhibit infrared absorption features that are distinct from those on C- and D-type asteroids. This could potentially be tested using detailed spectroscopic observations by future missions, including the JUICE mission (Grasset et al., 2013).

4.2. Survivability of CH_3OH in cometary impacts onto the Moon

In this section, we discuss the origin of CH_3OH found in a persistently shadowed region on the Moon by the LCROSS spacecraft (e.g., Colaprete et al., 2010; Paige et al., 2010). To examine the survivability of CH_3OH during impacts on the Moon, we performed numerical simulations of cometary impacts on the Moon using a SPH method (e.g., Monaghan, 1992; Bruesch and Asphaug, 2004; Canup, 2005). We used the Tillotson equation of state in the simulations (Tillotson, 1962). For simplicity, we consider collisions of an icy impactor with a diameter of 10 km onto rock ground at a velocity of 20 km/s and impact angles of 30°, 45°, 60°, and 90° from the horizontal surface. Parameter sets pertaining to ice and basalt (Benz and Asphaug, 1999) were used for the impactor and target, respectively. About 3.5 million and 30,000 SPH particles were used for the ground target and impactor, respectively. Material strength and gravity were not included. For a more detailed description of the SPH method used here, see Genda et al. (2012), Sekine and Genda (2012), and Fukuzaki et al. (2010).

Fig. 9 shows the normalized mass of an impactor that experiences a peak shock pressure that is less than a certain pressure, P. Although some fractions of SPH particles for the impactor experience a peak shock pressure of <28 GPa, all SPH particles escape from the Moon during impacts at $\geqslant 30°$ (Fig. 9). These results suggest that cometary materials supplied to the Moon experience peak shock pressures that are greater than that for complete CH_3OH dissociation, suggesting that CH_3OH cannot be directly supplied to the Moon in cometary impacts at angles $\geqslant 30°$. Given a peak shock pressure of about 23 GPa for complete dissociation of NH_3 (Sekine et al., 2011), our results show that intact delivery of cometary NH_3 to the Moon would not have occurred effectively either. On the other hand, the observations by the LCROSS spacecraft suggest the presence of 1–7% of CH_3OH and NH_3 relative to H_2O in the ejecta plume in an impact onto a persistently shadowed

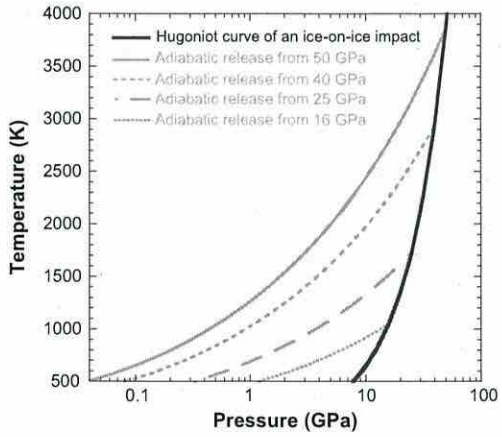

Fig. 8. Relationship between peak shock pressure and Hugoniot temperature achieved by H_2O-ice impacts (black curve). The peak shock temperatures (the Hugoniot temperatures) were calculated based on the relationship given by Stewart and Ahrens (2005), $T = 14.7 + 59.6P + 0.341P^2$, where T and P represent the Hugoniot temperature (K) and peak shock pressure (GPa), respectively. The gray curves are the pressure–temperature paths of adiabatic release from the respective points on the Hugoniot curve. The specific heat ratio assumed was 1.4.

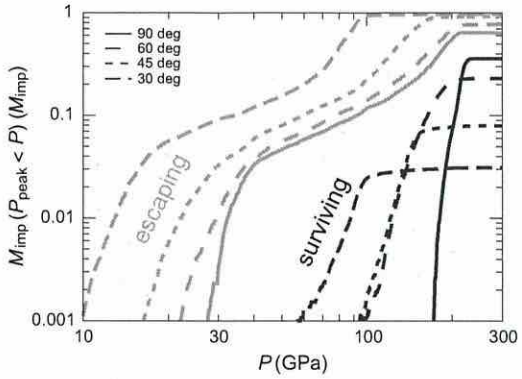

Fig. 9. Normalized mass of the impactor that experiences a peak shock pressure < P during cometary impacts (diameter = 10 km) on the Moon at a velocity of 20 km/s for various impact angles. We used the parameter set of the Tillotson equation of state for the basalt target and H_2O ice for the impactor (Tillotson, 1962). The black curves show the materials that are ejected at velocities less than the escape velocity of the Moon; the gray curves show those exceeding the escape velocity.

region (Colaprete et al., 2010). In highly oblique impacts at $\ll 30°$, CH_3OH and NH_3 could have been provided to the Moon; however, the fraction of such impactor materials should be very small (e.g., much less than 3% of the impactor mass; Fig. 9). Given that CH_3OH and NH_3 contents in comets range from 1% to 5% relative to H_2O (e.g., Bockelée-Morvan et al., 2004), our experiments and simulations lead to the conclusion that CH_3OH and NH_3 in a persistently shadowed region of the Moon could not be derived from intact supplies of cometary materials, supporting the suggestion given by the previous thermochemical equilibrium calculations (Berezhnoy et al., 2012). These results, in turn, support the alternative scenario that these molecules would have been produced through low-temperature surface reactions on the surface of the Moon from CO, N_2, H, and H_2 (Crider and Vondrak, 2002).

5. Summary

We performed impact experiments using a laser-gun system to investigate the impact chemistry of CH_3OH. We obtained the chemical compositions of gas species and the dissociation efficiency of CH_3OH–H_2O ice as a function of peak shock pressure. Despite uncertainties associated with the application of our experiments to planetary-scale impacts, we can draw the following conclusions based on the experimental results and numerical simulations.

1. Carbon monoxide and CH_4 were found in the gas-phase products formed by impact-induced dissociation of CH_3OH. Carbon monoxide is more abundant than CH_4 in the experiments ($CO/CH_4 \geqslant 5$).
2. The peak shock pressures for the initial and complete dissociation of CH_3OH are approximately 9 and 28 GPa, respectively. These values are close to those for NH_3 ice obtained in our previous study (Sekine et al., 2011). This is probably due to the similarities in the binding energies between C–H (O–H) and N–H bonds; accordingly, similar shock energies are required to dissociate these molecules.
3. Our results suggest that CH_3OH would not have been dissociated in impacts during accretion events onto large icy satellites and dwarf planets in the outer Solar System, including Callisto, Ganymede, Titan, Ceres, and Pluto. This implies that primordial CH_3OH would have acted as antifreeze for liquid subsurface oceans of large icy bodies. On geologically active icy satellites, such as Enceladus and Europa, CH_3OH would also have been an important reducing carbon source in interior liquid oceans.
4. Asteroid impacts onto Ceres would produce CO and CH_4 if the dwarf planet originally contained primordial CH_3OH. The CO and CH_4 could form a temporal exosphere and condense in the low-temperature polar regions.
5. In cometary impacts following accretion, CH_3OH dissociation proceeds efficiently on large icy satellites because of their higher impact velocities. On Callisto, CH_3OH dissociation would have resulted in the formation of a CO–CH_4 atmosphere of 10^{-4} to 10^{-2} bar on the surface during the late heavy bombardment period. Photochemical reactions in such a mildly reducing atmosphere may have produced complex organic molecules at the surface.
6. Titan may have acquired about 0.1 bar of CO during late heavy bombardment, if the CH_3OH content in icy satellitesimals in the saturnian system was as high as that of comets. A loss of this amount of CO may be difficult to achieve through photochemical processes, the present-day low CO concentrations in Titan's atmosphere would require that the abundance of CH_3OH in icy satellitesimals in the saturnian system was much lower than that of comets, in contrast to the prediction of the gas-starved model. Alternatively, efficient conversion of CO to CH_4 through catalytic reactions would have occurred in impact vapor clouds.
7. Our numerical simulations show that cometary materials supplied to the lunar surface by impacts at angles $\geqslant 30°$ should have experienced peak shock pressures $\gg 28$ GPa. Given the low probability of highly oblique impacts (e.g., $\ll 30°$), we conclude that CH_3OH and NH_3 abundances on a persistently shadowed region of the Moon are not of cometary origin. We support the formation of these molecules through low-temperature surface reactions in the persistently shadowed region.

Acknowledgments

This study was supported by Grant in Aid from Japan Society for the Promotion of Science, the Ministry of Education, Culture, Sports, Science, and Technology, and the Astrobiology Program of National Institutes of Natural Sciences (NINS). The authors thank two anonymous reviewers for their constructive suggestions and comments to our manuscript.

Appendix A. Supplementary material

Supplementary data associated with this article can be found, in the online version, at http://dx.doi.org/10.1016/j.icarus.2014.08.034.

References

Alibert, Y., Mousis, O., 2007. Formation of Titan in Saturn's subnebula: Constraints from Huygens probe measurements. Astron. Astrophys. 465, 1051–1060.
Anderson, W.W., Ahrens, T.J., 1998. Shock wave equations of state of chondritic meteorites. In: Schmidt, S.C., Dandekar, D.P., Forbes, J.W. (Eds.), Shock Compression of Condensed Matter-1997. The American Inst. Phys., pp. 115–118.
Barr, A.C., Canup, R.M., 2010. Origin of the Ganymede–Callisto dichotomy by impacts during the late heavy bombardment. Nat. Geosci. 3, 164–167.
Benz, W., Asphaug, E., 1999. Catastrophic disruptions revised. Icarus 142, 5–20.
Berezhnoy, A.A., Kozlova, E.A., Sinitsyn, M.P., Shangaraev, A.A., Shevchenko, V.V., 2012. Origin and stability of lunar polar volatiles. Adv. Space Res. 50, 1638–1646.
Bockelée-Morvan, D., Crovisier, D., Mumma, M.J., Weaver, H.A., 2004. The composition of cometary volatiles. In: Festou, M.C., Keller, H.U., Weaver, H.A. (Eds.), Comets II. Univ. Arizona Press, Tucson, pp. 391–423.
Bottke, W.F., Nolan, M.C., Greenberg, R., Kolvoord, R.A., 1994. Velocity distributions among colliding asteroids. Icarus 107, 255–268.
Bruesch, L.S., Asphaug, E., 2004. Modeling global impact effects on middle-sized icy bodies: Applications to Saturn's moons. Icarus 168, 457–466.

Burchell, M.J., Cole, M.J., Ratcliff, P.R., 1996. Light flash and ionization from hypervelocity impacts on ice. Int. J. Astrobiol. 8, 19–25.
Canup, R.M., 2005. A giant impact origin of Pluto-Charon. Science 307, 546–550.
Canup, R.M., Ward, W.R., 2006. A common mass scaling for satellite systems of gaseous planets. Nature 441, 834–839.
Canup, R.M., Ward, W.R., 2009. Origin of Europa and the Galilean satellites. In: Pappalardo, R.T., McKinnon, W.B., Khurana, K. (Eds.), Europa. Univ. Arizona Press, Tucson, pp. 59–83.
Chyba, C.F., 1991. Terrestrial mantle siderophiles and the lunar impact record. Icarus 92, 217–233.
Colaprete, A. et al., 2010. Detection of water in the LCROSS ejecta plume. Science 330, 463–468.
Crider, D.H., Vondrak, R.R., 2002. Hydrogen migration to the lunar poles by solar wind bombardment of the Moon. Adv. Space Res. 30, 1869–1874.
Dartois, E. et al., 1999. Methanol: The second most abundant ice species towards the high-mass protostars RAFGL7009S and W 33A. Astron. Astrophys. 342, L32–L35.
Ehrenfreund, P., Charnley, S.B., 2000. Organic molecules in the interstellar medium, comets, and meteorites: A voyage from dark clouds to the early Earth. Annu. Rev. Astron. Astrophys. 38, 427–483.
Fortes, A.D., Choukroun, M., 2010. Phase behavior of ices and hydrates. Space Sci. Rev. 153, 185–218.
Fukuzaki, S. et al., 2010. Impact-induced N_2 production from ammonium sulfate: Implications for the origin and evolution of N_2 in Titan's atmosphere. Icarus 209, 715–722.
Furukawa, Y., Sekine, T., Oba, M., Kakegawa, T., Nakazawa, H., 2008. Biomolecule formation by oceanic impacts on early Earth. Nat. Geosci. 2, 62–66.
Genda, H., Kokubo, E., Ida, S., 2012. Merging criteria for giant impacts of protoplanets. Astrophys. J. 144, 137 (8pp).
Gomes, R., Levison, H.F., Tsiganis, K., Morbidelli, A., 2005. Origin of the cataclysmic Late Heavy Bombardment period of the terrestrial planets. Nature 435, 466–469.
Grasset, O. et al., 2013. JUpiter ICy moons Explorer (JUICE): An ESA mission to orbit Ganymede and to characterise the Jupiter system. Planet. Space Sci. 78, 1–21.
Griffith, C.A., Zahnle, K., 1995. Influx of cometary volatiles to planetary moons: The atmospheres of 1000 possible Titans. J. Geophys. Res. 100, 16907–16922.
Hama, T., Watanabe, N., 2013. Surface processes on interstellar amorphous solid water: Adsorption, diffusion, tunneling reactions, and nuclear-spin conversion. Chem. Rev. 113, 8783–8839.
Hand, K.P., Carlson, R.W., Chyba, C.F., 2007. Energy, chemical, disequilibrium, and geological constraints on Europa. Astrobiology 7, 1006–1022.
Hasenkopf, C.A. et al., 2010. Optical properties of Titan and early Earth haze laboratory analogs in the mid-visible. Icarus 207, 903–913.
Heldmann, J.L. et al., 2012. LCROSS (Lunar Crater Observation and Sensing Satellite) observation campaign: Strategies, implementation, and lesions learned. Space Sci. Rev. 167, 93–140.
Hibbitts, C.A., Klemaszewski, J.E., McCord, T.B., Hansen, G.B., Greeley, R., 2002. CO_2-rich impact craters on Callisto. J. Geophys. Res. 107 (E10), 14-1–14-12.
Hiraoka, K. et al., 1994. Formation of formaldehyde and methanol from the reactions of H atoms with solid CO at 10–20 K. Chem. Phys. Lett. 229, 408–414.
Irvine, W.M., Schloerb, F.P., Crovisier, J., Fegley, B., Mumma, M.J., 2000. Comets: A link between interstellar and nebular chemistry. In: Manning, V., Boss, A.P., Russell, S.S. (Eds.), Protostars and Planets IV. Univ. Arizona Press, Tucson, pp. 1159–1200.
Johnson, T.V., Mousis, O., Lunine, J.I., Madhusudhan, N., 2012. Planetesimals compositions in exoplanet systems. Astrophys. J. 757, 192 (11pp).
Kadono, T. et al., 2002. Vapor clouds generated by laser ablation and hypervelocity impact. Geophys. Res. Lett. 29 (1979), 40-1–40-4.
Kato, M. et al., 1995. Ice-on-ice impact experiments. Icarus 113, 423–441.
Kawaragi, K. et al., 2009. Direct measurements of chemical composition of shock-induced gases from calcite: An intense global warming after the Chicxulub impact due to the indirect greenhouse effect of carbon monoxide. Earth Planet. Sci. Lett. 282, 56–64.
Kress, M.E., McKay, C.P., 2004. Formation of methane in comet impact: Implications for Earth, Mars, and Titan. Icarus 168, 475–483.
Küppers, M. et al., 2014. Localized sources of water vapour on the dwarf planet (1) Ceres. Nature 505, 525–527.
Kuramoto, K., Matsui, T., 1994. Formation of a hot proto-atmosphere on the accreting giant icy satellite: Implications for the origin and evolution of Titan, Ganymede, and Callisto. J. Geophys. Res. 99, 21183–21200.
Lange, M.A., Ahrens, T.J., 1987. Impact experiments in low-temperature ice. Icarus 69, 506–518.
Martins, Z. et al., 2013. Shock synthesis of amino acids from impacting cometary and icy planet surface analogues. Nat. Geosci. 6, 1045–1049.
McKay, C.P., Borucki, W.J., 1997. Organic synthesis in experimental impact shocks. Science 276, 390–392.
McKay, C.P., Scattergood, T.W., Pollack, J.B., Borucki, W.J., van Ghyseghem, H.T., 1988. High-temperature shock formation of N_2 and organics on primordial Titan. Nature 332, 520–522.
Melosh, H.J., 1989. Impact Cratering: A Geologic Process. Oxford Univ. Press, New York.
Monaghan, J.J., 1992. Smoothed particle hydrodynamics. Annu. Rev. Astron. Astrophys. 30, 543–574.
Mousis, O. et al., 2009. Formation conditions of Enceladus and origin of its methane reservoir. Astrophys. J. Lett. 701, L39–L42.
Mousis, O. et al., 2011. On the volatile enrichments and heavy element content in HD189733b. Astrophys. J. 727, 77 (7pp).
Nna-Mvondo, D., Khare, B., Ishihara, T., McKay, C.P., 2008. Experimental impact shock chemistry on planetary icy satellites. Icarus 194, 822–835.
Ohno, S. et al., 2008. Direct measurements of impact devolatilization of calcite using a laser gun. Geophys. Res. Lett. 35, L13202. http://dx.doi.org/10.1029/2008GL033796.
Paige, D.A. et al., 2010. Diviner lunar radiometer observations of cold traps in the Moon's south polar region. Science 330, 479–482.
Sack, N.J., Baragiola, R.A., 1993. Sublimation of vapor-deposited water ice below 170 K, and its dependence on growth conditions. Phys. Rev. B 48 (14), 9973–9978.
Sekine, Y., Genda, H., 2012. Giant impacts in the saturnian system: A possible origin of diversity in the inner mid-sized satellites. Planet. Space Sci. 63–64, 133–138.
Sekine, Y. et al., 2005. The role of Fischer–Tropsch catalysis in the origin of methane-rich Titan. Icarus 178, 154–164.
Sekine, Y. et al., 2006. An experimental study on Fischer–Tropsch catalysis: Implications for impact phenomena and nebular chemistry. Meteorit. Planet. Sci. 41, 715–729.
Sekine, Y. et al., 2011. Replacement and late formation of atmospheric N_2 on undifferentiated Titan by impacts. Nat. Geosci. 4, 359–362.
Shin, K. et al., 2013. Methanol incorporation in clathrate hydrates and the implications for oil and gas pipeline flow assurance and icy planetary bodies. Proc. Natl. Acad. Sci. 110, 8437–8442.
Shuvalov, V., 2009. Atmospheric erosion induced by oblique impacts. Meteorit. Planet. Sci. 44, 1095–1105.
Stewart, S., Ahrens, T.J., 2005. Shock properties of H_2O ice. J. Geophys. Res. 110, E03005. http://dx.doi.org/10.1029/2004JE002305.
Tillotson, J.H., 1962. Report No. GA-3216. General Atomic, San Diego, California.
Trainer, M.G. et al., 2006. Organic haze on Titan and the early Earth. Proc. Natl. Acad. Sci. 103, 18035–18042.
Trunin, R.F., 2001. Experimental data on shock compression and adiabatic expansion of condensed matter. RFNC-VNIEF. pp. 446. ISBN 5-85165-624-7.
Waite, J.H. et al., 2009. Liquid water on Enceladus from observations of ammonia and ^{40}Ar in the plume. Nature 460, 487–490.
Walsh, K.J., Morbidelli, A., Raymond, S.N., O'Brien, D.P., Mandell, A.M., 2011. A low mass for Mars from Jupiter's early gas-driven migration. Nature 475, 206–209.
Watanabe, N., Kouchi, A., 2002. Efficient formation of formaldehyde and methanol by the addition of hydrogen atoms to CO in H_2O–CO ice at 10 K. Astrophys. J. 571, L173–L176.
Watson, K., Murray, B.C., Brown, H., 1961. The behavior of volatiles on the lunar surface. J. Geophys. Res. 66, 3033–3045.
Wilson, E.H., Atreya, S.K., 2004. Current state of modeling the photochemistry of Titan's mutually dependent atmosphere and ionosphere. J. Geophys. Res. 109, E06002. http://dx.doi.org/10.1029/2003JE002181.
Wong, A.-S., Morgan, C.G., Yung, Y.L., Owen, T., 2002. Evolution of CO on Titan. Icarus 155, 382–392.
Zahnle, K., Schenk, P.M., Levison, H.F., 2003. Cratering rates in the outer Solar System. Icarus 163, 263–289.
Zhernokletov, M.V., Trunin, R.F., Gudarenko, L.F., Trushchin, V.D., Gushchina, O.N., 1997. Database for properties of materials studies in experiments using shock waves. American Physical Society, Shock Compression Meeting.

Space Sci Rev (2016) 205:153–211
DOI 10.1007/s11214-016-0280-1

Formation and Evolution of Protoatmospheres

H. Massol[1] · K. Hamano[2,3] · F. Tian[4] · M. Ikoma[2] · Y. Abe[2] · E. Chassefière[1] · A. Davaille[5] · H. Genda[6] · M. Güdel[7] · Y. Hori[8] · F. Leblanc[9] · E. Marcq[9] · P. Sarda[1] · V.I. Shematovich[10] · A. Stökl[7] · H. Lammer[11]

Received: 10 November 2015 / Accepted: 16 August 2016 / Published online: 27 September 2016

Abstract The origin and evolution of planetary protoatmospheres in relation to the protoplanetary disk is discussed. The initial atmospheres of planets can mainly be related via two formation scenarios. If a protoplanetary core accretes mass and grows inside the gas disk, it can capture H_2, He and other gases from the disk. When the gas of the disk evaporates, the core that is surrounded by the H_2/He gas envelope is exposed to the high X-ray and extreme ultraviolet flux and stellar wind of the young host star. This period can be considered as the onset of atmospheric escape. It is shown that lower mass bodies accrete less gas and

✉ H. Massol
helene.massol@u-psud.fr

K. Hamano
keiko@elsi.jp

F. Tian
tianfengco@mail.tsinghua.edu.cn

M. Ikoma
ikoma@eps.s.u-tokyo.ac.jp

Y. Abe
ayutaka@eps.s.u-tokyo.ac.jp

E. Chassefière
eric.chassefiere@u-psud.fr

A. Davaille
anne.davaille@u-psud.fr

H. Genda
genda@elsi.jp

M. Güdel
manuel.guedel@univie.ac.at

Y. Hori
yasunori.hori@nao.ac.jp

F. Leblanc
francois.leblanc@latmos.ipsl.fr

E. Marcq
emmanuel.marcq@latmos.ipsl.fr

depending on the host stars radiation environment can therefore lose the gaseous envelope after tens or hundreds of million years. Massive cores may never get rid of their captured hydrogen envelopes and remain as sub-Neptunes, Neptunes or gas giants for their whole life time. Terrestrial planets which may have lost the captured gas envelope by thermal atmospheric escape, or which accreted after the protoplanetary nebula vanished will produce catastrophically outgassed steam atmospheres during the magma ocean solidification process. These steam atmospheres consist mainly of water and CO_2 that was incorporated into the protoplanet during its accretion. Planets, which are formed in the habitable zone, solidify within several million years. In such cases the outgassed steam atmospheres cool fast, which leads to the condensation of water and the formation of liquid oceans. On the other hand, magma oceans are sustained for longer if planets form inside a critical distance, even if they outgassed a larger initial amount of water. In such cases the steam atmosphere could remain 100 million years or for even longer. Hydrodynamic atmospheric escape will then desiccate these planets during the slow solidification process.

1 Introduction

Stellar systems originate from the accumulations of gas and dust scattered in space. Such aggregations of matter form huge disks with the active young star in their center. The protoplanets grow from the dust to planetesimals and planetary embryos over timescales of several million to tens of million years. During the growth of the protoplanets in the primordial nebula, massive hydrogen/helium envelopes can be captured (e.g. Mizuno et al. 1978;

P. Sarda
philippe.sarda@u-psud.fr

V.I. Shematovich
shematov@inasan.ru

A. Stökl
alexander.stoekl@univie.ac.at

H. Lammer
helmut.lammer@oeaw.ac.at

1 GEOPS, Univ. Paris-Sud, CNRS, Université Paris-Saclay, Orsay, France

2 Department of Earth and Planetary Science, Graduate School of Science, The University of Tokyo, Tokyo, Japan

3 Present address: Earth-Life Science Institute, Tokyo Institute of Technology, Tokyo, Japan

4 National Astronomical Observatories, Chinese Academy of Sciences, Beijing, China

5 Lab. FAST, UMR 7608 CNRS-Université de Paris-Sud, Orsay, France

6 Earth-Life Science Institute, Tokyo Institute of Technology, Tokyo, Japan

7 Institute of Astronomy, University of Vienna, Vienna, Austria

8 National Astronomical Observatory of Japan/Astrobiology Center, National Institutes of Natural Sciences, Tokyo, Japan

9 Lab. LATMOS, UMR 9190 CNRS, Guyancourt, France

10 Department of Solar System Research, Institute of Astronomy of the Russian Academy of Sciences, Moscow, Russia

11 Austrian Academy of Sciences Space Research Institute, Graz, Austria

Wuchterl 1993; Ikoma et al. 2000; Rafikov 2006). The capturing and retaining portions of the local nebular gas depend on the conditions of the nebula and the evolution of the host star's stellar radiation and plasma environment. This process builds up the protoplanet's primordial atmosphere as long as solar wind and solar radiation have not depleted the disk's local matter resources. In the inner zones of an early stellar system, the removal of disk gas and matter may happen within three million years, while farther out, where dispersal most likely takes more time, planetary embryos have more time to collect matter and hence may become more massive.

In the above mentioned pioneering studies, it was shown that the capture of nebula gas can reach a stage where gas accretion exceeds the accretion of solid bodies (here called cores), so that the protoplanet evolves very quickly to a Jovian-like gas giant (e.g. Pollack 1985; Lissauer 1987; Wuchterl 1993, 2010). The results of these studies indicate that the onset of core instability occurs when the mass of the captured hydrogen/helium atmosphere around the core becomes comparable to the core mass (e.g. Mizuno et al. 1978, 1980; Hayashi et al. 1979; Stevenson 1982; Wuchterl 1993, 1994, 2010; Ikoma et al. 2000; Rafikov 2006).

However, the results and conclusions of the majority of these pioneering studies, that have been carried out decades ago, are based on very rough assumptions, because, no reliable observational data from discs and related nebula lifetimes, as well as no astrophysical observation of the radiation environment of very young solar-like stars have been available.

The recent discoveries of low mass exoplanets with known radii and masses by the Kepler and CoRoT satellites, combined with ground-based radial velocity follow-up and dynamical analyses of transit timing variations, indicate that there is a transition between small Earth-like rocky planets and Neptune-like planets, where many rocky planets may have kept their captured hydrogen envelopes during their lifetime (Marcy et al. 2014; Rogers 2015). Rogers (2015) found that the majority of so-called 'super-Earths' with radii of about 1.6 Earth-radius are too low in density to be composed of Fe and silicates alone. For discovered planets with larger radii, the constraints on their rocky fraction are even more strict. These findings agree with Lammer et al. (2014) who modeled the capture of nebula-based hydrogen envelopes and their escape from rocky protoplanetary cores of 'sub-' to 'super-Earths' within the mass range from Mars—like bodies up to cores with 5 Earth-masses. These authors found that protoplanets inside the habitable zone with core masses less than 1 Earth-mass, that are exposed to stellar soft X-ray and EUV fluxes (XUV) of an average young solar-like host star, can lose their captured hydrogen envelopes during the active stellar XUV saturation phase, but rocky cores within the so-called super-Earth domain most likely cannot get rid of their nebula captured hydrogen envelopes during their whole lifetime.

Planets that have too low masses during growth, when the nebula gas is not evaporated, but finish their accretion a few tens of million years later will produce catastrophically outgassed steam atmospheres during the solidification of their magma oceans (e.g. Elkins-Tanton 2008; Lebrun et al. 2013; Hamano et al. 2013). The same scenario can be expected for rocky planets that could lose their nebular captured hydrogen envelopes. The energy sufficient for melting the planet's mantle, thereby creating an ocean of liquid magma, originates from collisions with large planetesimals or planetary embryos or the decay of short lived radioactive isotopes. Over time, the planet's heat is continuously lost to space allowing the magma to cool down and eventually to solidify. The liquid magma contains large amounts of volatiles that were acquired during the accretion process. Since H_2O and CO_2 cannot be trapped in large amounts in the solid phase, these volatiles are outgassed during solidification together with minor amounts of other volatiles such as CH_4, N_2 and NH_3. All

these volatiles enter and thereby modify the pre-existing atmospheres (e.g., Lebrun et al. 2013; Hamano et al. 2013).

The major motivation of this work is to review the processes that affect and control timescales of atmospheric formation. Since atmospheres are an essential criterion for habitability and determine planetary evolution (e.g. towards super Earth or mini Neptune), it is important to investigate the capture and loss of nebula-based hydrogen envelopes, and magma ocean related outgassed steam atmospheres from protoplanets. In the first section, the origin of the captured hydrogen-dominated envelopes of nebular gas around accreting protoplanets is discussed. The second section presents the state of the art of thermal evolution processes taking place within magma oceans and surrounding degassed steam atmospheres at the end of accretion. These degassed atmospheres can be considered as the initial atmospheres of Earth-like terrestrial planets. In the third section, we discuss the atmospheric escape processes, including relevant processes such as the heating efficiency in upper atmospheres that are exposed to high XUV fluxes related to the young host stars. Finally, we conclude and address open questions that need some further investigations within the context of future missions and habitability on exo-planets.

2 Nebular Origin of Protoatmospheres

2.1 Introduction

Planets are born in protoplanetary disks composed predominantly of hydrogen and helium. The mass of Mars is large enough for a solid planet to attract hydrogen gas gravitationally, provided that the gas temperature is lower than 2000 K, since the gravitational-potential energy then dominates the thermal-motion energy of the gas. Thus, planetary atmospheres of disk origin should be an inevitable by-product of planet formation.

In our Solar System, the four giant planets have massive H + He envelopes, which must have come from the disk that surrounded the proto-sun (i.e., the solar nebula). The fractions of H + He differ from planet to planet: those of the two gas giants, Jupiter and Saturn, are more than about 85 % and 60 %, respectively, whereas those of the two ice giants, Uranus and Neptune, are both about 10 % (e.g., Fortney and Nettelmann 2010). In contrast, the four terrestrial planets, the Earth, Venus, Mars, and Mercury, retain no such atmospheres; instead they have thin hydrogen-poor atmospheres.

Beyond our Solar System, there are plenty of objects intermediate in size between the Earth and Uranus/Neptune, as revealed by observations with the Kepler space telescope (see Batalha 2014, for a recent review). Those objects are often called super-Earths or mini-Neptunes. Figure 1 shows the observed relationships between masses and radii of exoplanets of less than 20 $M_{\oplus}$, together with the theoretical relationships for rocky bodies with and without H/He atmospheres (see the caption for details). As seen from Fig. 1, many of the super-Earths are significantly larger in radius than they would be if they had an Earth-like core-mantle ratio (dashed line), indicating the possibility that they retain H/He atmospheres (solid lines) or have a smaller core-mantle ratio than the Earth. Furthermore, the radius differs largely among the planets of similar mass, which may mean that super-Earths are diverse in hydrogen content. What causes the diversity in hydrogen content of planets?

The gravitational capture of disk gas by protoplanets was first explored in the context of the formation of the solar-system giant planets. Pioneering studies were done by Perri and Cameron (1974) and Mizuno et al. (1978, 1980). They assumed that a growing solid

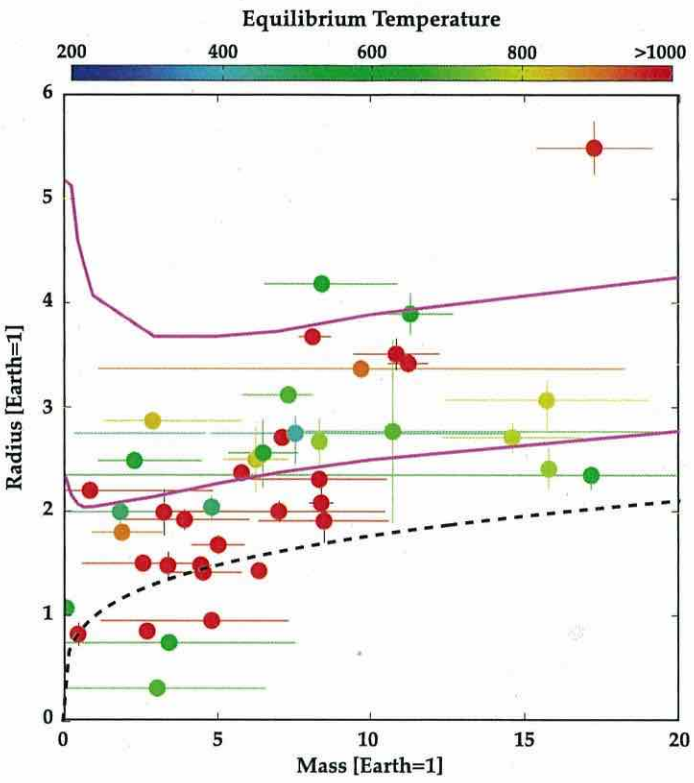

Fig. 1 The mass-radius relationships for exoplanets with mass less than 20 $M_{\oplus}$. The observational data are represented by *symbols*, which are *colored* according to the estimated zero-albedo equilibrium temperature. The *two solid lines* represent the theoretical relationships for rocky planets with 10 % (upper) and 1 % (lower) hydrogen contents (Lopez and Fortney 2014), while the *dashed line* is for rocky bodies with the terrestrial bulk composition. *Symbols with error bars* are from www.exoplanets.org. The *solid lines* were drawn based on Lopez and Fortney (2014)

protoplanet (or proto-core) was embedded in a protoplanetary disk and had a hydrostatic-equilibrium atmosphere (or proto-envelope) that connected smoothly to the ambient disk at the protoplanet's Hill radius (see below). They demonstrated that the proto-envelope mass increased with the proto-core mass and found a critical value of the proto-core mass beyond which no purely-hydrostatic solution was found. By performing not purely-hydrostatic but instead quasi-static simulations, Bodenheimer and Pollack (1986) demonstrated that run-away accretion of disk gas occurred after the core mass became comparable to the envelope mass (i.e., the crossover mass). As shown analytically (Stevenson 1982; Wuchterl 1993) and numerically (Ikoma et al. 2000), these two characteristic masses always have similar values. While the basic behavior of the critical core mass is well-studied, several issues remain unresolved such as the timescale and location of the formation of Jupiter and Saturn, the consistency of the inferred small core mass of Jupiter with formation theories, the difference between the solar-system giants and extrasolar gas giants with short orbital periods (i.e., hot Jupiters), and so on.

The hypothesis about the Earth's primordial atmosphere of nebular origin was developed by Hayashi, Nakazawa, and their colleagues. The primary aim was to explain the differentiated structure of the terrestrial planets, namely the presence of metallic cores surrounded by rocky mantles. As demonstrated by Hayashi et al. (1979), the blanketing effect of the primordial atmosphere is so strong that a large part of the interior of the proto-Earth is molten, making a global magma ocean, where molten iron can separate from silicate and settle down toward the planetary center. This hypothesis, however, yields several outcomes that seem to be inconsistent with geochemical facts such as the paucity of noble gases in the atmosphere and mantle. While the presence of a primordial atmosphere on the proto-Earth is controversial, this possibility should be revisited in the context of the diversity of exo-Earths.

In this section, we review our current understanding of the disk (nebular) origin of atmospheres of solar-system and extrasolar planets. First, we summarize the basic properties of

the atmospheres of protoplanets embedded in protoplanetary disks in Sect. 2.2. In Sect. 2.3, we discuss the relation between physics and observational constraints. Then, in Sect. 2.4, we review several important issues about low-density super-Earths (Sect. 2.4.1), exo-Earths (Sect. 2.4.2), and the primordial atmospheres of the Earth and Mars (Sect. 2.4.3).

2.2 Properties of the Protoatmosphere

Concerning the atmosphere of growing protoplanets embedded in protoplanetary disks, there are two characteristic radii, namely the Hill and Bondi radii, which are defined respectively as

$$R_{\rm H} = \left(\frac{M_p}{3M_*}\right)^{1/3} a \tag{1}$$

and

$$R_{\rm B} = \frac{\gamma - 1}{\gamma} \frac{GM_p \mu m_u}{kT}, \tag{2}$$

where M_p and M_* are the masses of the planet and its host star, respectively, a is the planet's orbital distance, μ, γ and T are the mean molecular weight, specific heat ratio and temperature of the disk gas, respectively, and G, m_u, and k are the gravitational constant, the atomic mass unit, and the Boltzmann constant, respectively. Outside the Hill radius, the stellar tidal force is greater than the protoplanet's gravity; outside the Bondi radius, the thermal motion of gas molecules dominates the protoplanet's gravity. Thus, only inside of both the Hill and Bondi radii can the atmosphere be in a gravitationally bound, hydrostatic equilibrium state. For the ranges of the protoplanet's bulk density and orbital distance of interest (i.e., $\bar{\rho} \gtrsim 0.1$ g/cm^3 and $a \gtrsim 0.01$ AU), the Hill radius is always larger than the protoplanet's radius; in contrast, the Bondi radius is smaller than the protoplanet's radius when the protoplanet's mass is smaller than a certain value. Thus, it sets a condition on the protoplanetary mass for the existence of a hydrogen atmosphere, which is:

$$M_p \gtrsim 1.1 \times 10^{23} \left(\frac{T}{300\ {\rm K}}\right)^{3/2} \left(\frac{\mu}{2}\right)^{-3/2} \left(\frac{\bar{\rho}}{5.5\ {\rm g/cm^3}}\right)^{-1/2} {\rm kg}, \tag{3}$$

where we have assumed $\gamma = 7/5$.

The embedded atmosphere is thus defined as the gas contained inside the smaller of the Bondi and Hill radii. The atmosphere is usually assumed to connect smoothly to the ambient disk, which means that the outer boundary conditions for the atmospheric structure are determined from the disk properties, namely,

$$P = P_d \quad \text{and} \quad T = T_d \quad \text{at } r = R_p, \tag{4}$$

where P is pressure, T is temperature and P_d and T_d are the pressure and temperature of the ambient disk gas, respectively, r is the radial distance from the protoplanet's center, R_p is the protoplanet's outer radius, which is defined by $R_p = \min(R_{\rm H}, R_{\rm B})$. This boundary condition (4) assumes that the planetary mass is sufficiently low for the radius of the embedded atmosphere to be smaller than the vertical thickness of the protoplanetary disk. Using $0.01a$ as a rough estimate for the latter, comparison with the Hill radius yields a mass limit of $M_p \leq 3 \times 10^{-6} M_*$ (i.e. $\lesssim 1\ M_\oplus$) for a solar mass star. This corresponds to the assumption that the gravitational perturbation to the disk structure by the planet's mass remains negligible and that the influx of disk gas into the planetary atmosphere does not exhaust the disk

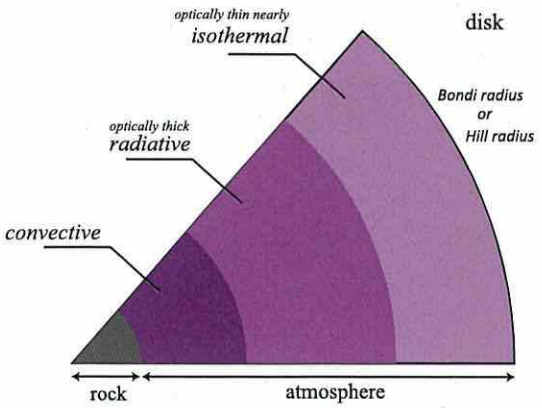

Fig. 2 Schematic illustration of the thermal structure of the protoatmosphere that connects to the ambient disk

gas reservoir or gas transport processes (viscous accretion) within the disk. For more massive planets, these assumptions eventually break down, at the latest when the atmospheric mass exceeds the critical crossover mass and the atmosphere undergoes runaway accretion that will quickly outstrip the gas reservoir of the disk leading to the opening of an annular gap in the disk.

The volume of the atmosphere is given by $4\pi(R_p^3 - R_s^3)/3$, R_s being the outer radius of the solid part of the protoplanet. It is a function of the mass and radius of the solid protoplanet and the properties of the ambient disk, provided the mass of the atmosphere is quite small relative to that of the solid protoplanet. The mass of the atmosphere depends on the structure of the atmosphere. In particular, the thermal structure is important, because it determines the atmospheric scale height. Due to the low mean molecular weight and high temperature, the pressure scale-height ($\propto T/\mu$) is large and usually comparable to the radius of the solid protoplanet, which is in clear contrast to the current atmospheres of the Earth and other terrestrial planets. Thus, as the lower atmosphere becomes hotter, the atmosphere becomes less massive due to enhanced escape.

When modeling embedded planetary atmospheres, it is usually assumed that the atmosphere is in dynamical and thermal equilibrium. Except for violent events such as the impact of a large planetesimal, the former is well justified as the typical sound crossing time, even for expanded atmospheres, is on the order of days at most. The assumption of thermal equilibrium is less well justified (Stökl et al. 2015), it is, however, probably still a good approximation during most phases of planetary evolution and therefore a frequently adopted simplification. Thermal equilibrium corresponds to the assumption of a constant luminosity throughout the atmosphere, namely at different atmospheric depths, which is, in the strict sense, incompatible with some of the atmospheric energy sources discussed in Sect. 2.3.1.

The atmosphere consists of three characteristic regions (see Fig. 2). The outer atmosphere is optically thin and nearly isothermal. Below the optically thin region, the thermal structure is governed by radiative transport and, in the stationary limit, can be described by (Kippenhahn and Weigert 1994):

$$\frac{dT}{dr} = -\frac{3\kappa\rho L}{64\pi\sigma r^2 T^3}, \tag{5}$$

where κ is the opacity, L is the energy flux passing through the sphere of radius r, ρ is the gas density, and σ is the Stefan-Boltzmann constant. In the deep atmosphere, the gas density is so high that convective transport dominates. The structure in that region is well

approximated to be iso-entropic and thus described by

$$\frac{dT}{dr} = \left(\frac{\partial T}{\partial P}\right)_{\rm ad} \frac{dP}{dr}, \tag{6}$$

where $(\partial T/\partial P)_{\rm ad}$ is the adiabatic temperature gradient. Note that the structure of the convective part of the atmosphere is independent of the planetary luminosity (as long as it is high enough for convective instability). This is one reason why thermal equilibrium is still a useful approximation, even if the luminosity is not constant in the deep atmosphere. Usually most of the atmospheric mass is contained in the convective region and of special importance is the entropy of the region, which is determined by the structure of the intermediate radiative region.

As seen from Eq. (5), the structure of the inner radiative region depends on the energy flux L and the opacity κ. The sources of the energy flux include the accretion energy of the solid protoplanet (i.e., the kinetic energy of incoming planetesimals), the accretion energy of the atmosphere, the radiogenic energy, and the stellar insolation. Below the critical core mass (see Introduction), the accretion energy of the solid protoplanet is much greater than the other three energy sources and is given approximately by

$$L = \frac{GM_s}{R_s}\dot{M}_s, \tag{7}$$

where M_s is the mass of the solid part of the protoplanet, $\dot{M}_s$ is the total mass of incoming planetesimals per unit time and G the gravitational constant. The sources of the opacity are absorption by gas molecules such as H_2O and scattering and absorption by dust grains floating in the atmosphere. For a given composition of gas, the gas opacity does not include any large uncertainty, whereas the grain opacity is quite uncertain, because we do not have enough knowledge of the amount and size distribution of the dust grains. The details of the sources of the energy flux and the grain opacity are discussed in Sect. 2.3.

Simple analytical argument helps us to know the basic properties of such an atmosphere. If the atmosphere is entirely radiative and $\kappa L/M_r$ and μ are radially constant (M_r being the mass inside a sphere of radius r), Eq. (5) combined with the equation of hydrostatic equilibrium (Eq. (1) from Ikoma and Genda 2006), can be integrated analytically with the ideal-gas equation of state (see Ikoma and Genda 2006). The pressure P_s at the bottom of the atmosphere is calculated to be

$$P_s \approx \frac{\pi\sigma G^5 m_u^4}{48k^4}\frac{M_s^5\mu^4}{R_s^4\kappa L} = 750\,{\rm MPa}\left(\frac{M_s}{M_\oplus}\right)^{11/3}\left(\frac{\kappa}{10^{-3}\ {\rm m^2/kg}}\right)^{-1}\left(\frac{L}{10^{17}\ {\rm W}}\right)^{-1}, \tag{8}$$

where we have assumed the solid protoplanet's bulk density $\bar{\rho}_s = 5500\ {\rm kg/m^3}$ and $\mu = 2$. Under the same assumptions, one can obtain the density as a function of radial distance from the protoplanet center. Then, integrating the density profile, the mass of the radiative atmosphere M_a, is given by:

$$M_a \approx \frac{\pi^2\sigma}{3\kappa L}\left(\frac{GM_s\mu m_u}{k}\right)^4 \ln\left(\frac{R_{\rm B}}{R_s}\right). \tag{9}$$

The atmospheric mass depends strongly on the mass of the solid protoplanet (i.e., $M_a \propto M_s^4$). Also, the atmospheric mass increases linearly with decreasing κ and L.

The temperature at the bottom of the radiative atmosphere (or the surface temperature) is given by

$$T_s \approx \frac{GM_s\mu m_u}{4kR_s} = 3700\ \mathrm{K}\left(\frac{M_s}{M_\oplus}\right)^{2/3}, \tag{10}$$

where we have assumed $\bar{\rho}_s = 5500\ \mathrm{kg/m^3}$ and $\mu = 2$ again. In the case of an Earth-mass protoplanet, the surface temperature is found to be higher than 3000 K. Note that Eq. (10) does not include radiative properties of the atmosphere such as κ and L. In reality, the opacity varies with radial distance, and the deep atmosphere is not radiative, but convective in most cases. Detailed numerical simulations (Ikoma and Genda 2006) show that T_s weakly depends on κ and L; nevertheless, the surface temperature is always above the liquidus temperature of basalt (~ 1500 K).

In the above discussion, we have implicitly assumed that the atmosphere is sufficiently bound; in other words, the surface pressure P_s and temperature T_s are sufficiently high relatively to the local pressure P_d and temperature T_d of the disk gas. The degree of gravitational binding can be measured by the escape parameter defined as

$$\lambda \equiv \frac{GM_s\mu m_u}{R_s k T_d} = 54\left(\frac{M_s}{M_\oplus}\right)^{2/3}\left(\frac{T_d}{280\ \mathrm{K}}\right)^{-1} \tag{11}$$

with $\mu = 2$ and $\bar{\rho}_s = 5500\ \mathrm{kg/m^3}$. Ikoma and Genda (2006) showed that the atmospheric structure and mass of the Earth-mass protoplanet ($\lambda = 56$) is insensitive to the outer boundary conditions, whereas those of the Mars-mass protoplanet ($\lambda = 12$) are quite sensitive to changes in the latter. Thus, the protoatmosphere of a Mars-mass protoplanet, if any, never survives the dispersal of the protoplanetary disk. The disk temperature may be estimated to be $T_d = 280(a/\mathrm{AU})^{-1/2}$ K around solar-type stars (Hayashi 1981), with which $\lambda = 17(M_s/M_\oplus)^{2/3}(a/0.1\ \mathrm{AU})^{1/2}$. This indicates that Earth-mass planets orbiting at 0.1 AU from solar-type stars are not massive enough to retain the protoatmospheres. The λ-values for super-Earths with short-orbital periods (~ 0.1 AU) are intermediate between those of Mars and Earth. This may cause the diversity in density of currently detected low-density super-Earths.

2.3 Constraints on Involved Processes

As described above, the structure and mass of the protoatmosphere depends on the mass of the solid protoplanet, the energy supply rate and opacity, the temperature and density of the ambient disk gas, and the composition (e.g., mean molecular weight) of the atmosphere. Of these, the most important factors are likely to be the energy supply rate and opacity. Below we describe our current understanding of these factors.

2.3.1 Energy Sources

Energy sources for maintaining the atmospheric pressure include accretion energy of solid, that of gas, radiogenic energy, and stellar insolation. The third and fourth sources are always negligible in the accretion era. For example, the radiogenic luminosity is estimated to be $\sim 10^{21}$ erg/s for the early Earth (O'Neill and Palme 1988), which corresponds to the solid accretion rate of $\sim 10^{-11}\ M_\oplus$/yr. Also, stellar light is unavailable for heating the atmosphere, since it is blocked by dust in the protoplanetary disk. Thus, the solid accretion energy is the

major source in the early stages of planet formation, namely, the runaway-growth (Wetherill and Stewart 1989; Kokubo and Ida 1996) and oligarchic-growth stages (Lissauer 1987; Kokubo and Ida 1998). The processes of solid accretion and its impact on the atmospheric accumulation are outlined briefly below.

The early runaway growth slows down relatively early, because of the enhanced velocity dispersion of planetesimals (Ida and Makino 1993). In the stage characterized by such a relatively slow accretion, the accretion rate is estimated to be approximately 2×10^{-6} $M_\oplus$/yr (or 2×10^{26} erg/s) at 1 AU and 1×10^{-7} $M_\oplus$/yr at 5 AU (or 1×10^{25} erg/s) for a 1 $M_\oplus$ protoplanet in the minimum-mass solar nebula (Tanaka and Ida 1999). Because of energy supply via solid accretion, the atmosphere is relatively less massive (see Eqs. (7) and (9)). For example, for the luminosity of 1×10^{26} erg/s, the atmospheric mass is calculated to be up to 3×10^{24} g (see Fig. 3a of Ikoma and Genda 2006), which corresponds to 0.05 % of the Earth mass.

N-body simulations, however, show that the runaway/oligarchic growth ends before protoplanets become massive enough, unless their feeding zones are replenished with planetesimals via gravitational perturbation by other protoplanets or sweeping during orbital migration. The protoplanets then become isolated. According to Kokubo and Ida (1998), in the minimum-mass solar nebula, the isolation mass $M_{\rm iso}$ is approximately as small as Mars' mass at 1 AU and ~ 2 $M_\oplus$ at 5 AU, which is well below the conventional critical core mass (e.g., 10 $M_\oplus$) (e.g. Mizuno et al. 1980 or Ikoma et al. 2000). This conventional critical core mass might be affected by the thermal state in the envelope of a planet. For instance, lower opacities in the envelope (e.g. Mizuno et al. 1980) and a lower rate of planetesimal accretion (e.g. Ikoma et al. 2000) result in a smaller critical core mass. Also, the density and temperature of an ambient disk gas (i.e., a distance from a central star) are thought to be key factors for determining a critical core mass especially in the case of fully-convective envelopes (Wuchterl 1993). Specifically, the higher density of a disk gas is and the lower temperature of a disk gas is, the smaller a critical core mass becomes (e.g. Ikoma et al. 2001).

Once a protoplanet becomes isolated, the major source is the energy supplied by the gravitational contraction of the atmosphere itself. In this stage, the atmospheric accumulation is dictated by cooling of the atmosphere; Namely, it proceeds on the Kelvin-Helmholtz timescale (Ikoma et al. 2000). The accumulation timescale $\tau_{\rm KH}$ is strongly dependent on the mass of the solid planet M_s and moderately dependent on the opacity $\bar{\kappa}$; $\tau_{\rm KH}$ decreases almost with the cube of M_s (the exact power being dependent on the opacity) and linearly with $\bar{\kappa}$. For 1 $M_\oplus$ planets, for example, $\tau_{\rm KH}$ is as long as more than 10 Myr except for the metal-free atmosphere (Hori and Ikoma 2010; Ikoma and Genda 2006).

Actual accretion processes including orbital migration are much more complicated. The details are delegated to Sect. 4.

2.3.2 *Opacity*

A planet radiates heat into space and continues to cool down until it reaches thermodynamic equilibrium. The heat transfer in a planetary atmosphere is controlled by conduction, radiation or convection. In the upper atmosphere, radiation carries energy away from it. The efficiency of energy transfer via radiation is regulated by the opacity of an ambient medium, as shown in Eq. (5). Dust grains are dominant absorbers for temperatures below the sublimation temperature ($\sim$ 1500 K), and for higher temperatures, gaseous species are the main sources of the opacity (Semenov et al. 2003). Optical properties of dust grains strongly depend on their particle sizes and structures, e.g., the shape of monomers and porosity of dust aggregates. Thus, a detailed prescription of the microphysical properties of dust grains in the atmosphere is essential to understanding the thermal evolution of a planet.

The growth of dust grains in a planetary atmosphere is mainly governed by six microscopic processes: the vertical transport via the eddy diffusion, collisions via the Brownian motion and sedimentation, electrostatic effects, condensation, and vaporization. The evolution of the size distribution of dust grains is described by a coagulation equation, the so-called Smoluchowski's equation (e.g. Wetherill 1990). Solving the coagulation equation that includes the microphysical effects mentioned above, Podolak (2003) computed the grain opacity in the atmospheres of proto-gas giants with cores of 11.5 $M_\oplus$ and 21.09 $M_\oplus$. He found that the size distribution of dust grains is significantly different from that of the interstellar medium (ISM), and concluded that the grain opacity in the planetary atmosphere is less than 0.1 $\mathrm{cm^2\,g^{-1}}$ because of the grain settling associated with the grain growth.

In the context of Jupiter formation, the grain opacity in the atmosphere is also found to be of the order of 0.01 $\mathrm{g\,cm^{-2}}$, which is much lower than the ISM value (Movshovitz and Podolak 2008; Movshovitz et al. 2010). Such a low grain opacity accelerates gas accretion onto protoplanets and reduces the formation timescale of giant planets (e.g. Ikoma et al. 2000; Hubickyj et al. 2005) because the gravitational contraction of the entire planet, i.e., the Kelvin-Helmholtz contraction, compensates for the energy loss via radiation. The conclusion of Movshovitz and Podolak (2008) was confirmed by two ensuing studies on the grain growth: analytical models of grain opacities Mordasini (2014) and grain growth models including effects of the mass deposition by incoming planetesimals and the porosity of dust grains (Ormel 2014). Although Podolak (2003) and Movshovitz and Podolak (2008) considered porous dust aggregates with a fractal dimension of 2.11, Ormel (2014)'s work adopted a detailed recipe for the porosity evolution of dust aggregates based on direct N-body collision simulations of collisions (see Sect. 2 in Okuzumi et al. 2012).

Recently, Mordasini (2014) introduced a constant reduction factor of ISM grain opacities (f), into their population synthesis model of planet formation; $\kappa = f\kappa_{\mathrm{grain}} + \kappa_{\mathrm{gas}}$, where κ is the opacity and the subscripts of "grain" and "gas" mean the ISM grain opacity and gas opacity, respectively. They concluded that an extremely-low grain opacity model with $f = 0.003$ is favorable in order to explain the observed population of exoplanets. This fact suggests that the atmosphere of a planet is close to being a grain-free environment, as discussed in Hori and Ikoma (2010).

2.4 Relevant Issues

2.4.1 Low-Density Super-Earths

As described in the introduction, many super-Earths larger in radius than their "naked" rocky counterparts have been found beyond the Solar System (see Fig. 1). Those large radii may be consistent with the presence of H/He atmospheres that constitute up to 10 wt% of the planetary total masses (see Lopez and Fortney 2014).

The in situ accretion of disk gas onto rocky super-Earths was examined by Ikoma and Hori (2012) in order to explain the origin of low-density, multiple super-Earths orbiting the star Kepler-11. They assume that disk gas dissipation triggers giant collisions of multiple protoplanets, followed by the cooling and accumulation of H/He atmospheres. They demonstrated that the accretion of disk gas occurring concurrently with disk dissipation results in an intermediate-mass atmospheres. One of their results is that atmospheric erosion occurs because of depressurization and cooling due to disk dissipation. Also, the thermal contribution of the rocky body to the atmospheric evolution was found to have a significant impact on the atmospheric erosion. As discussed in Sect. 2.2, the sensitivity to a change in disk gas

density is significant in relatively hot environments ($\gtrsim$ 500 K). They concluded that the in situ accumulation of super-Earths with intermediate-mass H/He atmospheres is in principle possible; however, the radius of Kepler-11e is too large to conclude that its H/He atmosphere was accreted in a hot environment, implying that the planet migrated from a cooler region. Recently, Lee et al. (2014) made a more extensive study on the in situ accretion of H/He atmospheres for different stellar metallicities, and confirmed that the suppression of gas accretion onto rocky cores in metal-rich environment leads to super-Earths with tiny H/He atmospheres (less than a few wt%), as well as grain-rich cases as suggested in Ikoma and Hori (2012).

Bodenheimer and Lissauer (2014) simulated the concurrent accretion of solid and gas that results in the formation of super-Earths of 2.2 to 2.5 $M_\oplus$ at 0.5, 1, 2, and 4 AU, adopting the numerical model developed by Pollack et al. (1996). They concluded that low-temperature environments are needed for such low-mass objects to have atmospheres with 2–7 wt% of planet total masses, and concluded that the in-situ accretion of Kepler-11f in a warm environment (i.e., 0.1 AU) cannot account for its large radius, which is also consistent with the conclusion of Ikoma and Hori (2012). This suggests that those super-Earths likely migrated from beyond the snowline.

The migration scenario has been examined via theoretical population synthesis. Mordasini et al. (2012a,b) presented their population synthesis models of planetary accretion, and compared the resultant relationships between the masses and radii of short-period super-Earths ($a \leq 0.1$ AU and $1R_\oplus \leq R_p \leq 2R_\oplus$). They found that super-Earths have proto-atmospheres of 0 to 20 wt% of their total masses at the end of migration. The theoretical radii are consistent with (but somewhat larger than) the observed radii of Kepler planets orbiting FGK host stars. Mordasini et al. (2012a,b) predict that the occurrence rate of planets decreases with planetary radius for $R_p < 2R_\oplus$, which, however, seems to be inconsistent with the Kepler results.

Formation of low-density super-Earths orbiting M stars (of 0.1 to 0.7 $M_\oplus$) was investigated recently via population synthesis modeling by Hori et al. (2016). They demonstrated that super-Earths of 1–10 $M_\oplus$ gain relatively massive atmospheres of 0.1–20 wt%, that more massive planets of more than 10 $M_\oplus$ obtain more massive atmospheres, and that sub-Earths (i.e., less than 1 $M_\oplus$) gain less massive atmospheres of less than 1 wt% of the planetary total masses.

Several effects that can modify the atmospheric mass and composition have been investigated, including heavy element enrichment due to planetesimal bombardment during migration (Fortney et al. 2013), which was followed by Dittkrist et al. (2014) who improved the migration model, the hydrodynamic escape of the atmosphere (Jin et al. 2014), reduction in opacity due to grain settling in the atmosphere (Mordasini 2014), and gravitational interaction among multiple planets (Alibert et al. 2013; Pfyffer et al. 2015). However, no detailed comparison with observation was provided.

While the above studies consider the 1D accretion of the atmosphere, Ormel et al. (2015a,b) examined the 2D and 3D effects of the accumulation of H/He atmospheres onto low-mass planets (i.e., the ratio of the Bondi radius to the disk scale height being 0.01), simulating the flow of the surrounding disk gas. They found the timescale for the disk gas to enter the Bondi radius is shorter than the Kelvin-Helmholtz timescale for the atmospheric contraction. Thus, super-Earths are unable to gain massive atmospheres from protoplanetary disks. This may be consistent with the fact that there are many super-Earths with moderate amounts of H/He gases.

2.4.2 *Exo-Earths in Habitable Zone*

The accumulation and evolution of a primordial, nebula-accreted planetary atmosphere has consequences for the habitability of a planet. Atmospheres are an essential criterion for habitability by moderating and steadying the surface conditions on a planet. A very massive and optically thick atmosphere, on the other hand, can also produce hot and inhospitable surface conditions as on present day Venus. Clearly, planetary habitability depends on various influences (see, e.g., Güdel et al. 2014).

There are good arguments to expect life on other planets also being based on a carbon based chemistry in a watery environment (Council 2007). The conventional limits of the habitable zone (Kasting et al. 1993) are therefore connected to the existence of liquid water on the planetary surface. This is certainly not a sufficient condition, but it allows an unambiguous definition of a circumstellar habitable zone, the radii of which depend on the type of host star and will change due to stellar evolution. The definition of the habitable zone fixes the position of a potentially habitable, embedded planet in the structure of the protoplanetary disk and thus allows a deduction of a range for the temperature (and to a lesser degree, also for the density) of the disk gas around the planet. Therefore, if a planetary core forms early enough to be embedded in the protoplanetary disk for a significant time, one can estimate, based on typical disk temperatures and densities for the habitable zone, that an Earth mass planetary core can accumulate $\sim 5 \times 10^{22}$–1.5×10^{26} g of steam atmosphere (Ikoma and Genda 2006; Lammer et al. 2014), corresponding to 0.3 to 1000 Earth oceans of water. As outlined above, the accumulation of a primordial atmosphere strongly depends on core mass; for planetary cores with Mars-mass, atmospheric masses between $\sim 3 \times 10^{19}$–6×10^{22} g can be captured from the nebula. For planetary cores more massive than 1 $M_{\oplus}$, correspondingly more gas is accreted from the disk, quickly reaching amounts of atmosphere that are unlikely to be lost in the later evolution. According to Lammer et al. (2014), planets with masses exceeding about 2 $M_{\oplus}$ will not lose their disk-accreted primordial atmospheres during the about 100 Myr phase of intensive extreme UV and soft X-ray irradiation in the early evolution of a sun-like star and retain a thick hydrogen envelope, eventually more resembling a "mini-Neptune" than an Earth-like planet.

2.4.3 *Primordial Earth and Mars*

Obviously, none of the terrestrial planets currently possess a massive hydrogen-dominated atmosphere that would be expected (see Sect. 2.4.2) around a planetary core of Mars to Earth mass embedded in the likely environment of the protoplanetary disk around the early sun (e.g. Hayashi 1981). Some insight into the formation and early history of the terrestrial planets can be gained from the abundance of the tungsten isotope ^{182}W. ^{182}W is produced from the decay of hafnium ^{182}Hf with a half-life of 8.9 Myr. During differentiation, the siderophile W sinks to the planetary core whereas the lithophile Hf remains in the mantle. The ratio of the abundance of ^{182}W in the mantle with respect to other W isotopes therefore allows some conclusions about the timescale of core-mantle differentiation. This and the similar, yet somewhat more complex, U-Pb systematics indicate that Earth's formation took about 30 Myr to 100 Myr to complete (Halliday 2004; Allègre et al. 2008; Kleine et al. 2009). This is consistent with numerical simulations of Earth's formation through the collision of planetesimals also predicting a typical formation time scale of up to 100 Myr (O'Brien et al. 2006; Raymond et al. 2006, 2014; Thommes et al. 2008; Morishima et al. 2010), though the formation time scale could have been shorter in the presence of a planetary nebula (Hayashi et al. 1985).

Confronted with the observed typical disk life time of a few Myr (Haisch et al. 2001; Hillenbrand 2005), these results indicate that Earth most likely formed only after the evaporation of the gas disk and therefore was unable to accumulate a primordial atmosphere from the disk.

For Mars, ^{182}W measurements from Martian meteorites indicate a faster accretion and core formation process lasting between 1 Myr and 10 Myr (Nimmo and Kleine 2007; Dauphas and Pourmand 2011; Brasser 2013). This suggests that Mars could be a leftover planetary embryo that escaped later collisions in the planetary growth process. Accordingly, Mars is a much more likely candidate for having had a primordial disk-accreted atmosphere. However, due to Mars' low gravity atmospheric escape driven by the intensive extreme UV and soft X-ray radiation of the young sun after the evaporation of the gas disk would have been very efficient, causing a complete loss of the primordial atmosphere after a few Myr, at the latest (Erkaev et al. 2014).

3 Magma Ocean Outgassed Atmospheres

3.1 Observational Constraints

It has been known for decades that the chemical compositions of the external gas layers surrounding the inner planets and the outer planets are completely different. Jupiter and Saturn's gas is essentially hydrogen with 10 % helium, and is therefore a sample of the protosolar nebula (e.g. Lewis and Prinn 1983). Envelopes of such gas around giant planets are thus called primary atmospheres. In contrast, the volatile envelopes around Venus and Mars are made of ~ 95 % CO_2 and 5 % N_2, excluding water, and this would be true for the Earth as well, if one considers that O_2 was produced by photosynthetic vegetal life along geologic times and that CO_2 is now stored in the carbonated rocks that we observe in sedimentary basins (Turekian and Clark 1975). Water is very variable, because it appears under various phases, and certainly had a more complex history. The atmospheres of the inner planets are thus called secondary atmospheres. That terrestrial air is very different from solar gas is recorded in a geochemical way by the drastically different abundances of the noble gases in both reservoirs, as observed by Brown (Brown et al. 1949) and Suess (Suess 1949). Such big differences again imply that the atmospheres of telluric planets have a different origin compared to primary atmospheres. Two main end-member possibilities then arise: either they come from the interior and this is planetary degassing, or they were brought in by a late bombardment with comets or meteorites. A combination of both is probable.

The idea that atmospheric volatiles (CO_2, N_2, H_2O) could originate from volcanic degassing was first conjectured in the XIXth century (e.g. Crawford 1997). W. Rubey (Rubey 1951) showed that alteration and erosion of surface rocks cannot account for the present atmospheric inventory of the various volatiles that make up the atmosphere. Degassing occurs at present mainly at mid-ocean ridges, as indicated by measuring the helium isotopic ratio, $^3He/^4He$ in sea water (e.g. Clarke et al. 1969; Jenkins et al. 1978; Craig and Lupton 1981) and in rocks collected on the seafloor (e.g. Kurz et al. 1982): the isotope ^3He indeed reveals gas that was never at the surface of the Earth. Degassing is recorded in the isotopic compositions of argon and xenon found in gas released by heating or crushing of mid-ocean ridge basalt glasses. Such volcanic rocks come directly from the convective upper mantle and enable the determination of the argon and xenon isotopic compositions of this reservoir because such heavy isotopes cannot easily fractionate. The data show enormous isotopic

anomalies compared to atmospheric values (e.g. Ozima and Kudo 1972; Fisher 1975; Staudacher and Allègre 1982; Sarda et al. 1985). These isotopic anomalies are a geochemical trace of degassing. Comparison of these isotopic compositions with those in the atmosphere indicate that degassing occurred extremely early in terrestrial history and that degassing was extremely strong, i.e. a volume comparable to the Earth's upper mantle, at least, was almost completely degassed (e.g. Hamano and Ozima 1978; Ozima 1975; Staudacher and Allègre 1982; Sarda et al. 1985; Allègre et al. 1987). Indeed, 90 % of primitive Argon was degassed within the first 100 Myr (Allègre et al. 1987). The measurement of noble gas isotopes in meteorites gives a consistent picture of atmosphere degassing on the Earth (see review by Moreira 2013). Even if neon possibly tells a more complex story, with hydrodynamic escape of part of the degassed atmosphere (Sarda et al. 1988), the geochemical picture given by neon, argon and xenon is robust and points to degassing to have been both very extensive and very early, sometimes called "early catastrophic degassing" (e.g. Fanale 1971). The exact way such early degassing occured was not clear. It was once envisioned that pressure increase upon impacts would devolatilize hydrous minerals, hence releasing water (Lange and Ahrens 1982; Abe and Matsui 1985). It was also realized that the energy of impacts is such that it should have led to melting of the silicate part of planetary embryos (e.g. Safronov 1978; Tonks and Melosh 1993). Consideration of noble gas diffusion also led to the conclusion that degassing should have demanded molten silicate, either through volcanism or during a magma ocean stage (Allègre et al. 1987).

Today, degassing at mid-ocean ridges occurs via melting of mantle peridotite, magma ascent, vesiculation during ascent, and vesicle bursting at eruption. But diffusion of volatiles through crystals and convective upwelling velocities in a solid-state mantle are far too slow to match the measured early degassing. The latter requires upwellings in a molten body. And so does iron cores segregation in planetesimals and planets (e.g. Fujii and Uyeda 1966; Yoshino et al. 2003; Wood et al. 2006; Li and Agee 1996; Righter and Drake 2000).

This is consistent with the early melting of planetesimals owing to radiogenic heating from short-lived radioisotopes such as ^{26}Al and ^{60}Fe (e.g. Urey 1955; Reynolds et al. 1966; MacDonald 1959; La Tourette and Wasserburg 1998; Monteux et al. 2007), and with the energetics of accretionary impacts, where conversion of kinetic energy to heat could induce the repeated formation of surface magma oceans on planets (e.g. Safronov 1978; Canup 2004b; Tonks and Melosh 1993; O'Brien et al. 2014; Monteux et al. 2007; Golabek et al. 2011). Moreover, a magma ocean would also be produced by gravitational energy released deep in the planet by core formation (Sasaki and Nakazawa 1986).

We define here "magma ocean" (hereafter "MO") to occur when at least 10 % of the silicate mantle is molten and when the magma behaves rheologically like a liquid, i.e. for a volume fraction of liquid above 40 % (e.g. Taylor and Norman 1992; Solomatov 2000). The evolution of primordial MOs, which involves cooling, solidification and degassing, is therefore of fundamental importance because it sets initial conditions for (1) the chemical stratification of a planet, (2) the composition of its degassed atmosphere, as well as (3) its subsequent tectonic regime. As such, it has been studied since the mid 60's, first to produce accurate thermal evolution models of the Earth capable of generating present-day heat flow measurements (Reynolds et al. 1966; MacDonald 1959), and then to determine the conditions for habitability—namely the existence of liquid water on a planet surface—(Abe 1997; Solomatov 2000; Elkins-Tanton 2008; Lebrun et al. 2013; Hamano et al. 2013). As will be shown below, all these studies concur that MO and atmosphere evolutions cannot be considered separately (Fig. 3).

Indeed, once an MO is formed, the atmospheric degassing rate depends on the degree of enrichment of volatile species in the magma. It is likely that gaseous species would be

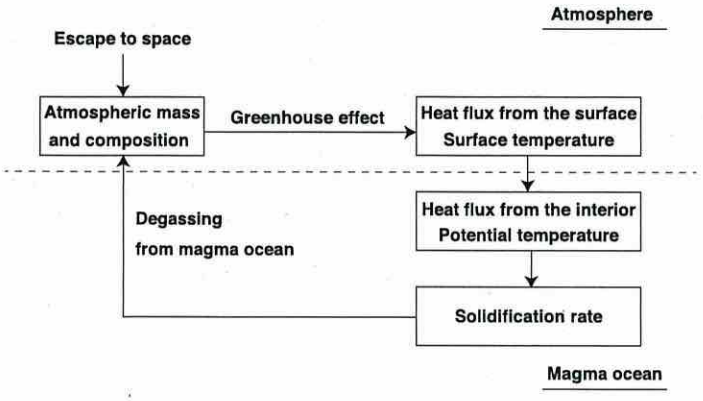

Fig. 3 Relationships between the magma ocean, the atmosphere and space

partitioned into a magma ocean according to their solubility into silicate melt at an early stage. As the solidification of the magma ocean proceeds, the residual magma is increasingly enriched in volatiles, which are usually incompatible with silicate cumulates. Volatiles in excess of the saturation limit are therefore exsolved and expelled out of the MO to form an outgassed atmosphere. In turn the rapid growth of the outgassed atmosphere slows down the MO cooling and solidification, due to enhancement of the thermal blanketing and greenhouse effects which prevent heat escape from the MOs. The final state of the planet will then be modulated by the atmospheric escape and by the sequence of accretion.

3.2 Heat and Mass Transfers in a Magma Ocean

Earlier and more complete reviews can be found in Solomatov (2007) and Elkins-Tanton (2012). Figure 4a presents the typical structure of an MO. Giant impacts should produce very deep and hot MO with an initial temperature distribution which is adiabatic and mostly above the liquidus (e.g. Lejeune and Richet 1995). Crystals grow as soon as the magma temperature is lower than the liquidus T_{liq}, and the liquid fraction at temperature T is usually taken as:

$$\phi = \frac{T - T_{sol}}{T_{liq} - T_{sol}}, \tag{12}$$

where T_{sol} is the solidus temperature. However, for liquid fractions lower than $\phi_c \sim 40$ %, the crystals are too closely-packed to move freely anymore and a solid skeleton starts to develop. A corresponding crystal volume fraction of 60 % therefore corresponds to a "rheological" front (e.g. Solomatov 2000). The end of the MO stage is usually defined as the time when the initially molten mantle has everywhere reached a liquid fraction lower than ϕ_c (e.g. Solomatov 2009, "soft magma ocean" of Abe in Abe 1993).

Given the pressure/depth-dependence of the adiabats, T_{sol} and T_{liq} (Fig. 4b), a solidification front (corresponding to temperature lower than T_{sol}) is expected to start from the MO bottom and to move up if the crystals density is greater than the residual liquid density. This is the most common case (e.g. Elkins-Tanton et al. 2003). However, as different mineral phases crystallize depending on temperature, pressure and magma composition, this situation depends on planetary radius and composition (see Elkins-Tanton 2012 for a review). For example, recent measurements on iron-partioning at pressures of the Earth's deep mantle seem to confirm that a liquid becomes denser than the coexisting solid at $\sim$ 1800 km-depth in the lower mantle (Nomura et al. 2011). If the Earth's mantle had initially been completely molten, that would imply that solidification started at a septum around 1800 km depth, soon separating an upper MO solidifying upwards from a bottom MO solidifying downwards

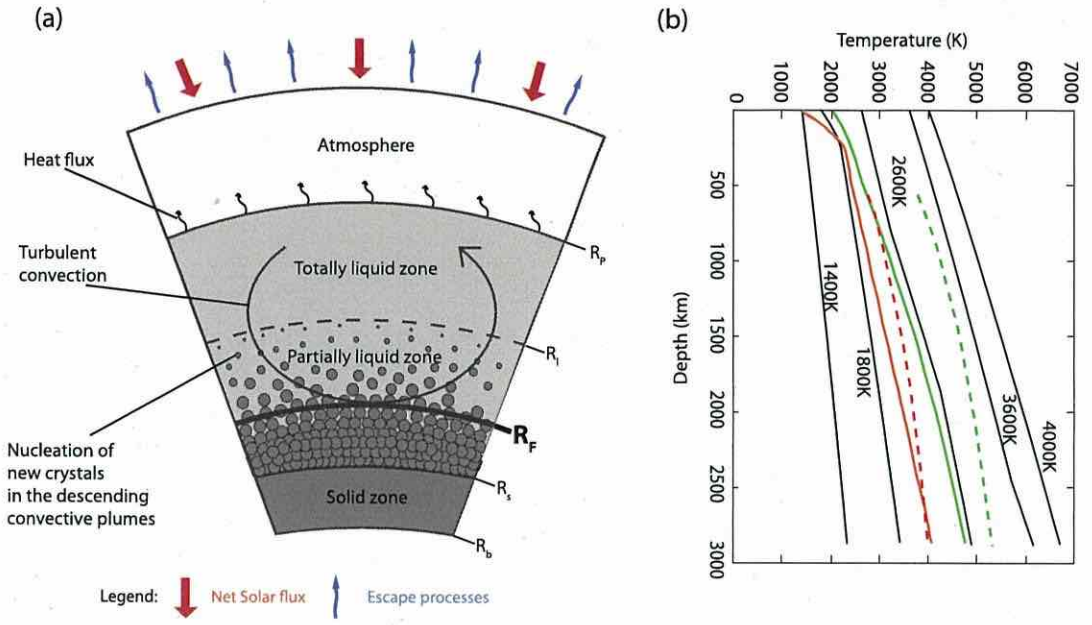

Fig. 4 (**a**) Schematics of magma ocean solidification adapted from Solomatov (2000). Radius R_b designates the base of the upper MO (see text), and R_F the position of the rheological front. (**b**) Selected adiabats (*solid black lines*), and the solidus (*red line*) and liquidus (*green line*) measured by Andrault et al. (2011) for a fertile peridotite and by Fiquet for a synthetic chondritic composition, Fiquet et al. (2010) (*dashed lines*) as a function of depth

(Labrosse et al. 2007). Early MO degassing therefore would only involve the upper MO. On the other hand, the anorthosites discovered on the lunar surface suggest that they formed by flotation of plagioclase crystals on top of the primordial lunar MO (Smith et al. 1970; Wood et al. 1970; Elkins-Tanton 2012). In that case, the late stages of the lunar MO cooling and degassing occurred in the presence of a solid lid at the surface.

3.2.1 MO Cooling

MO cooling is determined by the conservation of energy which can be written as (e.g. Abe 1997; Solomatov 2000; Lebrun et al. 2013):

$$\mathrm{SC} = \int_{R_b}^{R_p} \rho C_p \frac{dT_p}{dt} r^2 dr = R_P^2 Q_S + R_B^2 Q_B + H_{int} + H_{sol}. \tag{13}$$

SC represents the MO secular cooling, ρ is the melt + solid averaged density, C_p the specific heat, T_p designates the potential temperature, t is time and r radius. Q_S and Q_B are the heat flows getting out of the top and bottom surfaces, respectively. H_{int} is the internal heating due to radioactive elements, and H_{sol} is due to the latent heat release of solidification. H_{int} is usually negligible compared to Q_S, except for very small bodies (first planetesimals) cooling within ~ 3 Myr, i.e. when ^{26}Al and ^{60}Fe are still strongly active (Elkins-Tanton 2012, and references therein). Indeed the contribution of U, K and Th amounts at most to 140 mW/m^2 (e.g. Labrosse and Jaupart 2007) compared to the typical 10^2–10^6 W/m^2 going out of the MO (Fig. 5d; Abe and Matsui 1986; Elkins-Tanton 2008; Lebrun et al. 2013; Hamano et al. 2013; Zahnle et al. 1988). Similarly, the approximation $Q_B = 0$ is usually taken since heat transport in the solid bottom of the MO is much slower than convective transfer in the magma. The MO cools from above by losing its heat to outer space, either

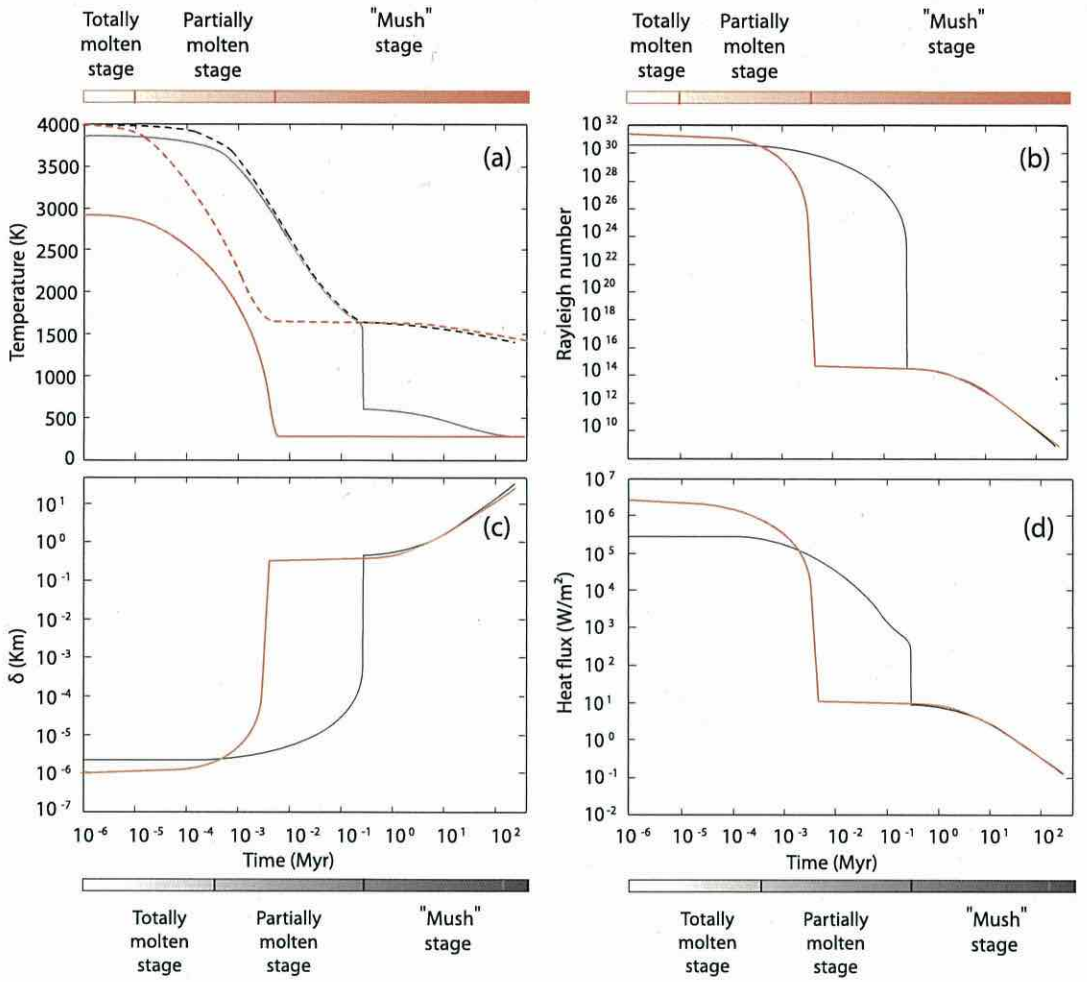

Fig. 5 Typical time evolution of (**a**) temperature (surface temperatures T_S are represented by the *solid lines*, and the potential temperatures T_p by the *dashed lines*), (**b**) Rayleigh number, (**c**) upper cold thermal boundary layer thickness given by $\delta = k(T_p - T_S)/Q_S$ and (**d**) surface heat flux, when the magma ocean is cooling directly through space (*red lines*) or through a grey atmosphere (*black lines*) (adapted from Lebrun et al. 2013)

directly or through an atmosphere. In the MO, heat transfer proceeds through thermal convection, with cold plumes sinking from the planet surface and a diffuse hot return flow. The convection intensity is characterized by the Rayleigh number:

$$Ra = \frac{\alpha g (T_p - T_S) D^3}{\kappa \nu} \tag{14}$$

where T_S is the surface temperature, α thermal expansion coefficient, g gravity acceleration, D the MO thickness (i.e. $R_p - R_F$), κ the heat conductivity, and ν the magma kinematic viscosity. Typical values of MO Ra range between 10^{20} and 10^{30} (Fig. 5b), similar to the values encountered in our present-day atmosphere (e.g. Priestley 1959). The surface heat flux out of the convective system then scales as:

$$Q_S = C_0 \frac{k(T_p - T_S)}{D} Ra^n \tag{15}$$

where k is the heat conductivity. Coefficients C_0 and n are constants which depend on the regime and pattern of convection (Malkus 1954; Siggia 1994; Grossmann and Lohse 2000; Solomatov 2007). These are still debated at very high Ra. An exponent $n = 1/3$ is usually taken which suggests that heat losses are governed solely by local instabilities of the upper thermal boundary layer and does not depend explicitly on the MO thickness (for a more complete discussion, see Solomatov 2007; Lebrun et al. 2013; Davaille and Limare 2015). Equations (14) and (15) show that the convective heat flux in the MO decreases when viscosity increases. Viscosity itself strongly increases when temperature or liquid fraction decrease. The low viscosity of basaltic magmas (as low as 0.01 Pa s, Shaw 1972) induces Q_S values as high as 10^6 W/m^2 (Fig. 5d) in the liquid MO stage. The value of Q_S however strongly decreases through time as crystallization proceeds (Fig. 5d). Besides, it could be strongly limited by the development of a high viscosity region ("lid") at the surface of the MO (like in the lunar case).

On the other hand, conservation of energy of the planet also requires that the MO convective heat flux Q_S be equal to the heat flux directly radiated through space (and given by a black body law) in absence of atmosphere, or to the heat flux transported through the atmosphere to space. The second limitation of the convective heat flux out of the MO is therefore the existence and dynamics of the atmosphere. Figure 5 shows that MO cooling is much faster in the first case than in the second case. The latter will be discussed in more details in Sect. 3.4.

3.2.2 *Crystallization and MO Segregation*

Crystallization influences MO cooling in two ways: through viscosity and therefore Q_S, and through the MO structure, and therefore SC, H_{sol}, and Q_S in Eq. (13). Of critical importance will especially be the development of a buoyant solid lid on top of the MO, which would drastically slow down MO cooling. There are two end-members: in batch solidification, liquid and solid remain in contact and in equilibrium throughout the whole MO, so that the final solid-state mantle composition will be homogeneous. In fractional solidification, segregation between solid and liquid occurs as the growing mineral grains settle; and therefore the residual liquid composition evolves with the removal of each package of solidified material. This leads to compositional stratification of the resulting solid, as is encountered in magma chambers. Hence, whether the MO can segregate, or on the contrary retain a well-mixed state while cooling, depends on the competition between crystal settling (due to gravity and the density difference $\Delta\rho$ between melt and crystals under mantle P and T conditions) and crystal entrainment due to the viscous stresses generated by the turbulent convective flow (Martin and Nokes 1988; Tonks and Melosh 1990; Solomatov and Stevenson 1993a,b). This simple balance gives an estimate of the critical crystal size above which settling occurs (Solomatov and Stevenson 1993a):

$$a_c = \frac{1}{\Delta\varrho g}\left(\frac{0.1\eta\alpha g Q_S}{C_p}\right)^{0.5}. \tag{16}$$

Typical density differences $\Delta\rho \sim$ 100–300 kg/m^3 and MO surface heat flux $Q_S \sim 10^2$–10^6 W/m^2 give critical sizes between a few μm and 1 mm. According to the 10^{-3}–1 cm-crystal size estimates (e.g. Solomatov and Stevenson 1993b), both settling and re-entrainment are therefore expected in an MO. This question of crystal settling in a turbulent magma flow is still not fully understood and is the subject of active research (e.g. Höink et al. 2005; Suckale et al. 2012).

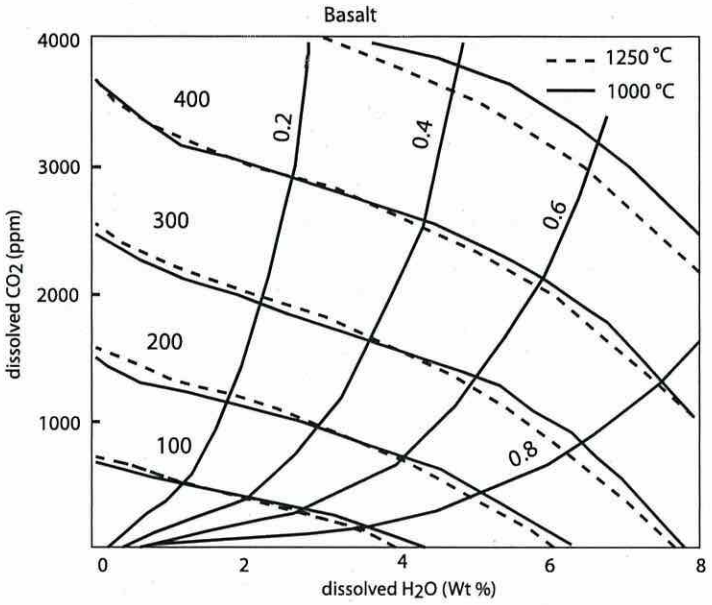

Fig. 6 Solubility curves redrawn from Berlo et al. (2011) and Papale (1999)

Meanwhile, assuming fractional crystallization leads to some interesting predictions for planetary mantle structures (for a review, see Elkins-Tanton 2012). In order to float, solid phases such as plagioclase on the lunar MO require the development of sufficiently iron-rich and dry, denser liquids, which can only form at the late stages of MO cooling, and for small planets (Elkins-Tanton 2012). On the other hand, larger and wetter planets like Mars or Earth are not expected to develop buoyant solid lids in the MO stage. Moreover, as fractional crystallization would render the solidifying liquids progressively denser, the inherited solid-state mantle stratification would be gravitationally unstable (with the top denser than the bottom). This would result in large-scale mantle overturn in the first Myr after the MO (Hess and Parmentier 1995; Elkins-Tanton et al. 2003, 2005; Elkins-Tanton 2008), before thermal mantle convection started. This scenario would be an efficient way to generate a denser reservoir at the bottom of the mantle, which could remain partially "hidden" from the surface for a long time, in agreement with geochemical mass balances and the presence of large seismic velocity heterogeneities at the base of the mantle (e.g. Brown and Lesher 2014). However, such an overturn could also establish too stable a layering to be overcome by thermal convection (e.g. Le Bars and Davaille 2004), as recent numerical simulations seem to suggest (Plesa et al. 2014; Tosi et al. 2013). Since plate tectonics on Earth, and volcanism on Mars both require solid-state mantle convection, this is an indication that fractional crystallization was not the only mode of MO solidification, but that batch solidification played also a significant role and that the onset of solid state convection, well before complete solidification, may have reduced strong mantle layering (Maurice et al. 2015; Solomatov 2015).

3.2.3 Volatiles and Degassing

A magma can contain dissolved volatiles only up to its saturation limit. The latter depends on the species (H_2O, CO_2, ...) considered, on temperature and pressure (Fig. 6), on the composition of the magma, and on the phase (liquid or solid). For example, in an Earth-scale MO with an initial whole-mantle bulk composition, saturation will be reached after 80 % and 40 % by volume of pure fractionation for an initial 500 ppm concentration in H_2O and CO_2, respectively (e.g. Elkins-Tanton 2012).

As the magma crystallizes, the volatiles go preferentially into the residual liquid, which becomes enriched in volatiles. Degassing can then occur by two processes: (i) exsolution of all volatiles in excess of the saturation limit in bubbles which burst at the MO surface, and (ii) diffusion of the volatiles through the liquid magma thermal boundary layer. This second process will dominate if the bubbles are small enough to be re-entrained in the MO by the vigorous convective motions, and the resulting diffusion-limited volatile flux constitutes a lower bound for degassing. Hamano et al. (2013) showed that even this lower bound is sufficient to generate a water atmosphere out of a solidifying MO.

More realistically, a number of authors (e.g. Zahnle et al. 1988; Elkins-Tanton 2008; Lebrun et al. 2013) consider that bubbles are indeed growing fast and will be able to escape from the MO to burst at the surface, so that the first mechanism is dominant. Indeed, by analogy to the fate of bubbles in terrestrial volcanism, small bubbles are likely to coalesce into larger gas pockets when upward melt flow rates decrease on approaching the surface. In low viscosity magmas (10 Pa s), ascent velocities of gas pockets given by the Stokes velocity range between 1 and 100 ms^{-1} for bubble diameters between 1 cm and 1 m. Compared to the typical MO convection velocity of 0.5 ms^{-1}, it is clear that such gas pockets will easily separate from the melt. Besides, with such convective velocities, the whole MO can circulate near to the surface in a few weeks: when a batch of melt travels upward, pressure decreases as well as volatile solubility, and a gas phase appears. All volatiles in excess of the saturation limit will be exsolved as bubbles, which, upon reaching the MO surface, will burst to the growing atmosphere (Zahnle et al. 1988; Elkins-Tanton 2008; Lebrun et al. 2013; Hamano et al. 2013). It is thus often assumed that the MO and the atmosphere are in equilibrium, and their volatiles partial pressures are given by (e.g. Carroll and Holloway 1994; Pan et al. 1991; Jendrzejewski et al. 1997):

$$pH_2O = \left(\frac{x_{H_2O}}{6.810^{-8}}\right)^{1/0.7}, \tag{17}$$

$$pCO_2 = \frac{x_{CO_2}}{4.410^{-12}}, \tag{18}$$

with x_{H_2O} and x_{CO_2} being respectively the mass fraction of water and CO_2 dissolved in the melt respectively expressed in wt% and ppm.

More recent solubility laws might also be used, such as in Liu et al. (2005), Witham et al. (2012), Burgisser et al. (2015) or Papale (1999) where a mixed CO_2-H_2O volatile phase is considered (see Fig. 6 in Berlo et al. 2011). Further, recent studies show that total pressure may be very important in changing completely the solubility law in the case of CO_2 at pressure higher than 1 GPa (e.g. Sarda and Guillot 2005; Guillot and Sarda 2006).

This avenue should be further pursued in the future generation of models.

3.3 Structure of Outgassed Atmospheres

3.3.1 History and Heritage of MO Atmospheric Models

The outgassed volatiles are able to form a secondary atmosphere, which will in turn impact the radiative cooling rate of the whole planet, and will be subject to the escape processes. All coupled magma-atmosphere models, even the most recent ones (Lebrun et al. 2013; Hamano et al. 2013) have used a global mean column (1D) atmospheres since the surface conditions for magma ocean planets are not thought to depend strongly on the location on the planet

(e.g. in latitude or local solar time). Moreover, the numerical solution of 1D models is much faster and therefore more convenient for further coupling.

Due to their common typical composition (usually including at least H_2O and most often CO_2 and/or N_2) and total inventory (from several tens to several hundred bars), these atmospheric models are inspired by similar models used to study the runaway greenhouse phenomenon (Ingersoll 1969) that some telluric planets experience at a later stage of their evolution. Thus, the atmospheric module of Lebrun et al. (2013), described in more detail by Marcq (2012), heavily draws on the runaway greenhouse model from Kasting (1988). Similarly, Hamano et al. (2013) have used a steam atmosphere model based on the runaway greenhouse studies from Nakajima et al. (1992).

There is nevertheless a major difference between these two kinds of models. Runaway atmospheres are in global radiative balance and are chiefly interested in the *greenhouse* effect: the absorbed stellar flux integrated over the whole planetary surface must be equal to the integrated outgoing radiative flux radiated by the planet back to space. This absorbed stellar flux can be described by the *equilibrium temperature* $T_{\rm eq}$ defined such as $\sigma T_{\rm eq} = \bar{F}_{\rm abs}$ where $\bar{F}_{\rm abs}$ is the spatially averaged absorbed stellar flux at shorter wavelengths. In a similar manner, the outgoing longwave radiation (OLR) can be described by the *effective temperature* $T_{\rm eff}$ defined such as $\sigma T_{\rm eff}^4 = \overline{OLR}$. The global radiative balance condition is then equivalent to $T_{\rm eff} = T_{\rm eq}$, and the temporal evolution of such runaway atmospheres is driven by the steady increase of $T_{\rm eq}$ caused by the aging of the main sequence star.

In contrast, atmospheres surrounding MO planets are out of global radiative balance, since they have to radiate not only the absorbed stellar flux, but also the internal heat flux originating from the magma ocean. Their main focus is therefore on the *blanketing effect* (Matsui and Abe 1986; Abe and Matsui 1988) of such atmospheres with respect to the internal heat loss.

The blanketing effect can be defined as the screening effect of a radiatively thick atmosphere on the magma ocean heat loss, and quantified using the difference between the magma ocean surface temperature $T_{\rm surf}$ and the effective temperature $T_{\rm eff}$: an hypothetical atmosphereless magma ocean planet would have $T_{\rm surf} = T_{\rm eff}$, whereas the blanketing effect implies that $T_{\rm surf} > T_{\rm eff}$. Nevertheless, the internal energy source ensures that $T_{\rm eff} > T_{\rm eq}$ in such atmospheres, since we have $F = \sigma(T_{\rm eff}^4 - T_{\rm eq}^4)$ where F stands for the internal heat flux (e.g. from the magma ocean). The secular cooling of the MO and the fact that $T_{\rm eq}$ remains quite constant during the early history of these telluric planets implies a secular decrease of $T_{\rm eff}$ towards a limit equal to $T_{\rm eq}$ when global radiative balance is finally reached. The temporal evolution of MO atmospheres therefore appears "reversed" compared to a runaway greenhouse. Depending on various parameters (chiefly the distance to parent star), the final stage can result in a permanent runaway greenhouse state (type II planets from Hamano et al. 2013) whose further evolution is ruled by atmospheric escape, or in a geologically fast exit of the runaway greenhouse state through an atmospheric water collapse. This results in the formation of a global water ocean (type I planets from Hamano et al. 2013), which mostly shelters H_2O from the atmospheric escape encountered by type II planets.

3.3.2 *Vertical Structure*

Due to the aforementioned heritage, the atmospheric models from Lebrun et al. (2013) and Hamano et al. (2013) both adopt a hydrostatic, three vertical regions, namely from bottom to top: (1) Dry (unsaturated) troposphere; (2) Moist (saturated) troposphere and (3) mesosphere (purely radiative). The first two layers may or may not exist, depending on criteria detailed below. Thus, the following vertical structures are possible: $(1 + 2 + 3)$, $(1 + 3)$ and $(2 + 3)$.

The dry troposphere is sometimes absent, provided the partial pressure of H_2O exceeds the saturation pressure of water (properly defined only below the critical point, e.g. for $P_S < P_c \approx 221$ bar and $T_S < T_c \approx 648$ K). This never occurs in the model of Hamano et al. (2013) since their simulations stop at a temperature of about 1370 K, but it sometimes does in the model of Lebrun et al. (2013). In such a case, $P_{\text{surf}}(H_2O)$ is set to the saturation pressure, and the extra water condenses into a water ocean that may coexist with an underlying magma ocean. Both are separated only by a thin, transient crust, that might break and recycles back in the MO at the beginning of its formation (Elkins-Tanton et al. 2005). This crust is supposed not to hamper heat transfers. Water clouds are included by Lebrun et al. (2013) but not by Hamano et al. (2013). They are supposed to extend throughout the moist tropospheric layer (provided it exists), with optical and microphysical properties similar to present day Earth's clouds. The radiative layer is isothermal in Lebrun et al. (2013) with a local radiative equilibrium condition in the longwave spectrum at the top of the atmosphere (null vertical divergence of spectrally integrated OLR at vanishing thermal opacities). On the other hand, Hamano et al. (2013), following Nakajima et al. (1992), adopt an analytic two-stream radiative temperature profile in their mesosphere $T(\tau)^4 = \frac{T_{\text{eff}}^4}{2}(1 + \frac{3}{2}\tau)$. This model is at radiative equilibrium in the mesosphere, but not spectrally resolved in the long wave range (grey model).

If the pressure and temperature profiles reach the top of atmosphere temperature without crossing the water saturation, then the moist tropospheric layer is absent, and clouds cannot exist. The atmospheric model from Marcq (2012) used by Lebrun et al. (2013) treated CO_2 as an ideal gas, but not H_2O whose thermodynamical properties were instead derived from thermodynamical steam tables like in Kasting (1988)'s model. The humidity profile is also constant in the dry troposphere as well as in the mesosphere, but decreases with increasing height in the moist troposphere. Atmospheres without water saturation therefore exhibit a vertically uniform humidity profile, without any vertical sequestration of water.

3.3.3 Radiative Transfer

The computation of OLR is performed only for the thermal radiation in the studies of Hamano et al. (2013) and Lebrun et al. (2013). The separation between stellar and planetary thermal radiation is justified in most situations, since thick outgassed atmospheres are optically thick enough so that radiating layers are usually below 700 K in most situations provided enough volatiles are available in the interior (Marcq 2012). Lebrun et al. (2013) use primarily a non-grey model, using a k-correlated code in 36 spectral bands in the longwave from 0 to 10^4 cm^{-1}, although they could revert to a grey model for easier comparison with previous works and accelerated computations. Conversely, Hamano et al. (2013) used primarily a grey radiative transfer model as Nakajima et al. (1992) did, although they discussed the effects of including water lines opacity in the visible and near IR based on the k-correlated model from Kopparapu et al. (2013). They could also use a non-grey, older, random band model from Abe and Matsui (1988) for further investigations; these did not undermine the main conclusions about the critical stellar distance separating type I from type II planets.

The non grey calculations from Kopparapu et al. (2013) also show that weak H_2O lines in the visible and near IR included in the HITEMP spectral database could significantly lower the planetary albedo below the usual value of 0.4–0.5 to about 0.3. Lebrun et al. (2013) prescribed different values for planetary albedos depending on the existence of a cloud cover (0.3 for a clear atmosphere and up to 0.7 for a cloudy atmosphere). In any case, precise determinations of globally averaged planetary albedos are out of reach of 1D models,

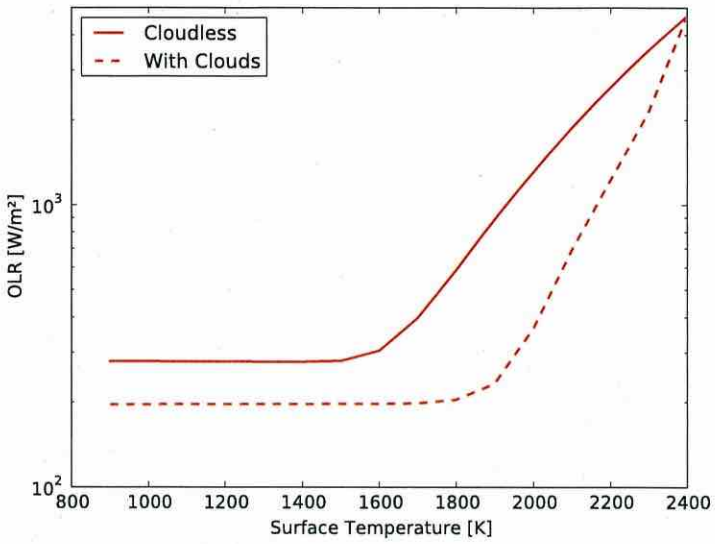

Fig. 7 OLR vs. T_{surf} for an Earth-like planet with an atmospheric inventory of 300 bar of H_2O and 100 bar of CO_2. Here, NL is reached for surface temperatures lower than 1500 to 1800 K (updated from Marcq 2012). Clouds are supposed to be present throughout the moist troposphere, and their optical properties follow Kasting (1988)

and would require the use of 3D General Circulation Model for further progress (see also Sect. 3.3.5): the cloud cover could not encompass the whole planet, and the planetary mean cannot simply be obtained with a mean 1D cloud opacity. In other words, the effect of cloud cover is highly non linear, and exact determinations of planetary albedos would require the horizontally-resolved determination of the stellar flux backscattered to space.

3.3.4 Atmospheric Regimes

The qualitative behavior of OLR vs. T_{surf} in both studies is very similar: for relatively high surface temperatures, the whole atmosphere is hot enough so that it radiates very effectively. In this high temperature regime, OLR increases rapidly with increasing surface temperature. Conversely, at relatively low surface temperatures, OLR is nearly independent of the surface temperature until values low enough for the steam to condense into a water ocean (see Fig. 7). This asymptotic OLR limit is already known from runaway greenhouse studies and is called *Nakajima's limit* (NL) following its discussion in Nakajima et al. (1992). NL for thermal opacities dominated by H_2O vapor (and neglecting clouds) has been estimated between 280 and 300 W/m^2 (equivalent to 265 K $< T_{eff} <$ 270 K) in a number of studies (Nakajima et al. 1992; Goldblatt et al. 2013; Leconte et al. 2013; Kopparapu et al. 2013). The atmospheric model from Marcq (2012) wrongly estimated a much lower NL value near 220 W/m^2, but has been corrected since. Depending on the cloud thickness and location within the moist troposphere, its radiative effect can be negligible, or could lower the NL value by about 30 %. Here also, 3D GCMs could lead to much better estimations of this Nakajima's limit, which is of uttermost importance for runaway greenhouse studies (Leconte et al. 2013). The threshold surface temperature value between these two regimes is primarily related to the atmospheric composition and inventory; it typically lies between 1500 and 2500 K for inventories comparable of H_2O, $\sim$ 100 bar of CO_2 and $\sim$ 1 bar of N_2.

High Temperature Regime This high-temperature regime can be labelled as *true runaway atmospheres*. It is defined by a high OLR, and characterized as follows (see Fig. 8): no water condensation within the atmosphere nor at the surface. The atmospheric humidity is vertically uniform, there is no moist troposphere, and temperatures are relatively warm

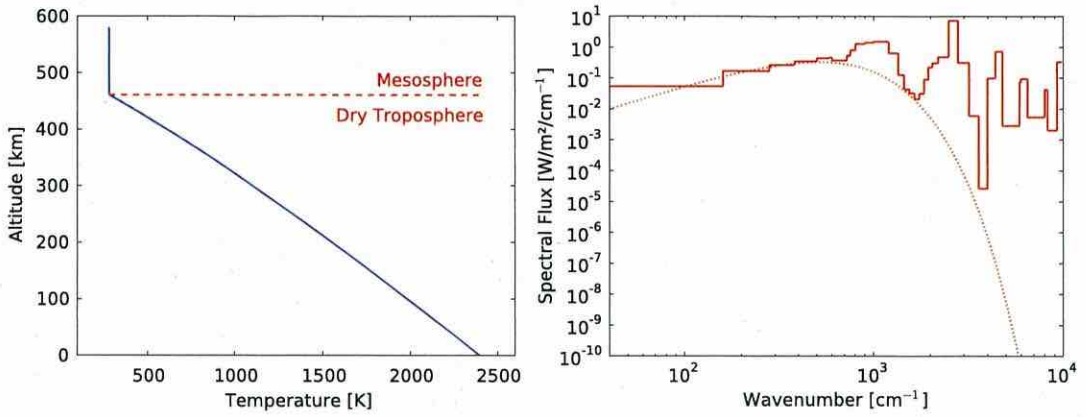

Fig. 8 *Left*: typical vertical $T(z)$ profile in a true runaway atmosphere (Planck curves corresponding to $T_{\rm surf} = 2400$ K) from updated Marcq (2012) model. *Right*: typical spectrum of the thermal emission in a runaway atmosphere according to updated Marcq (2012) model, for $T_{\rm surf} = 2400$ K

even in the radiative layers. These atmospheres are very thick due to their large hydrostatic scale heights and usually high surface pressures. This makes them particularly vulnerable to escape processes (see Sect. 4).

The spectrum of their thermal radiation is characterized by a several peaks in the near IR between 1 and 10 μm, where brightness temperatures can sometimes exceed 600 K. This would yield a good contrast with their host star in this spectral range, leading to good detectability prospects by future dedicated exoplanet observatories such as the ARIEL (Atmospheric Remote-Sensing Infrared Exoplanet Large-survey) ESA M4 mission candidate, based on the former EChO ESA M3 candidate (Tinetti et al. 2012).

The duration of this stage is highly variable depending on the planetary classification of Hamano et al. (2013). Type-II planets are characterized by a $T_{\rm eq} > 270$ K, so that they can reach global radiative balance during this stage. Cooling of the magma ocean becomes then extremely slow, and further atmospheric evolution is driven not by radiative cooling, but by escape processes that will slowly deplete the atmospheric inventory. This will progressively result in a cooler $T_{\rm surf}$ at a given OLR (now fixed by global radiative balance with the parent star) until the magma ocean can solidify. No water ocean is ever formed on this kind of planet, whose typical evolution is described in Hamano et al. (2013, their Fig. 2). For type-I planets, this stage is only transitory since they reach global radiative balance only for much lower OLR ($T_{\rm eq} < 270$ K), which lasts less than 1 Myr (Hamano et al. 2013, their Fig. 1).

Low Temperature Regime This (relatively) low-temperature regime can be labelled as *marginally runaway atmospheres*. They are defined by an OLR approximately equal to the NL value (±5 W/m^2 at most), and can be characterized as follows (see Fig. 9). Water condensation occurs in a moist troposphere located above a dry (unsaturated) troposhere. This would result in massive water clouds, whose detailed study would require a microphysical modeling effort beyond the scope of both Lebrun et al. (2013) and Hamano et al. (2013). The uppermost layers (top of the clouds, mesosphere) are relatively dry and cool, and comparable to the mesospheres of planets like Venus. The moist layer therefore acts as an efficient cold trap, making the water inventory of these planets much more stable with respect to escape processes. The fact that the OLR remains constant with surface temperature can be qualitatively explained following the discussion in Goldblatt et al. (2013): a hotter surface results in a thicker unsaturated troposphere, so that the moist layers lie further up in the atmosphere.

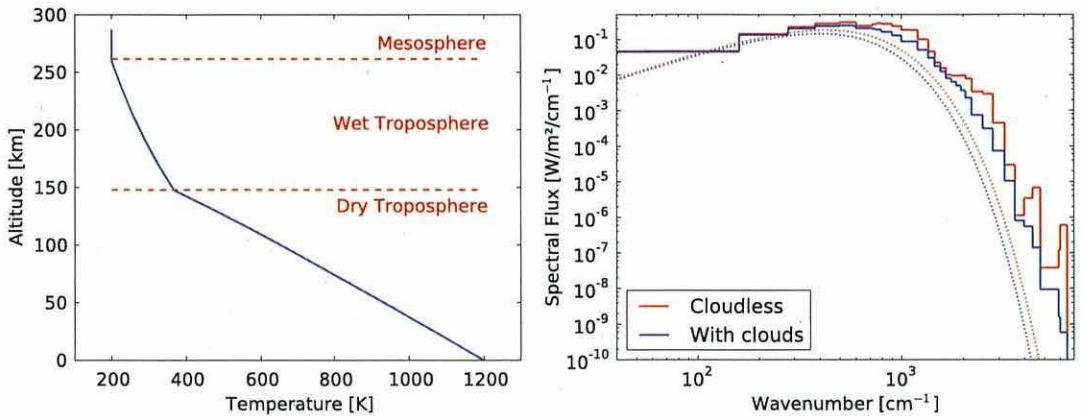

Fig. 9 *Left*: typical vertical $T(z)$ profile in a marginally runaway atmosphere ($T_{\rm surf} = 1200$ K) from updated Marcq (2012) model. *Right*: typical spectrum of the thermal emission in a marginally runaway atmosphere according to updated Marcq (2012) model. Clouds are supposed to be present throughout the moist troposphere, and their optical properties follow Kasting (1988)

But the temperature of these moist layers is unchanged, and since outgoing thermal radiation originated mostly from these layers, the spectrum and total radiated power exhibits very little dependence with respect to surface temperature in this regime. The lower end of possible surface temperatures in this regime results in thermal opacity windows reaching the ground level. This usually leads to the formation of a water ocean between the MO and the moist layer, provided enough water is present.

The spectrum of their thermal radiation is characterized by globally low brightness temperatures (around 200 K) except in a few narrow near-IR windows (provided the cloud layer is not too optically thick). This situation is very reminiscent of present-day near IR windows in Venus' thick CO_2 atmosphere (Kamp et al. 1988), which may have experienced a runaway greenhouse state, and is now in a dessicated state following the escape of H_2O evidenced by the very high D/H fractionation of remaining water vapor (Grinspoon 1993). The detectability prospect of exoplanets in this atmospheric regime is therefore much lower than for true runaway atmospheres, and virtually undistinguishable from more evolved planets like Venus.

As mentioned above, this stage (formation of a water ocean) is never reached by type-II planets. Type-I planets enter this stage after a short full runaway stage, and reach almost complete solidification after about 4 Myr according to Hamano et al. (2013): when most of the water has condensed into the oceans, the atmosphere becomes more and more transparent to the infrared radiation originating from the lowermost atmospheric layers or even the surface itself; this results again in a decreasing OLR with decreasing surface temperature. The atmosphere then leaves the marginally runaway state and enters a final stage similar to present day Earth provided enough water is present. Whether this stage is then reached depends on the incoming energy from the parent star ($T_{\rm eq} = T_{\rm eff}$). As a final note, we emphasize the fact that due to the independence of OLR versus surface temperature, a marginally runaway atmosphere is highly unstable: small increases in internal heat flux, impact energy or stellar radiation can force the atmosphere to reach a true runaway state with surface temperatures higher by several hundred Kelvins. Conversely, very small decreases in heat flux or stellar radiation can force the atmosphere to a partial collapse and an Earth-like state. This instability of surface temperature with respect to small variations in the internal or external heat fluxes may lead to chaotic alternations of condensed/vaporized water before stable oceans can form.

3.3.5 Limits and Desirable Improvements

Although the above atmospheric models include most of the relevant physical phenomena occurring during the evolution of MO planets, their limits of validity are often reached, and one must be careful when extrapolating their results out of their validity range. We already discussed one of these limits previously, namely the impossibility to predict with a good accuracy the planetary albedo with 1D models. Furthermore, a more sophisticated inclusion of stellar radiation would be desirable for other reasons: the presence of stellar light absorbers (whether gaseous or particulate) could significantly alter the temperature profile, including the possible formation of true stratospheres (defined as atmospheric layers where $dT/dz > 0$) that could act as effective seals with respect to the escape of condensible volatiles such as water vapor. Such modifications of the thermal profile of radiative layers could also in turn alter the thermal radiation of the upper layers, thus refining the determination of the various critical thresholds discussed by e.g. Hamano et al. (2013) and Lebrun et al. (2013).

There are other model limitations related to the earliest (and therefore hottest) stages of atmospheres surrounding MO's, especially for smaller, Mars-sized planets. Preliminary modeling using the Marcq (2012) model suggest that the 0.1 Pa mesopause level could be reached at altitudes reaching several thousands of kilometers in such cases. This evidently jeopardizes the plane-parallel assumption common to all 1D models discussed here, and even most 3D GCMs. The required adaptations would range from trivial (atmospheric mass calculations by integration on spherical shells, spherical instead of Cartesian divergence of the heat flux vector in the atmospheric layers) to very difficult problems (radiative transfer including multiple scattering in a curved atmosphere). Fortunately, these departures from plane-parallel geometry do not last long during the evolution of MO atmospheres, since the rapid initial cooling leaves much thinner atmospheres (mesopause below 1000 km) after about ten thousands years.

3.4 Coupled Evolution

The thermal evolution of an MO is closely linked to the formation of an outgassed atmosphere (Fig. 3). In the early stage of solidification, the cooling rate of an MO is limited by thermal blanketing and the greenhouse effect by the planetary atmosphere. It is because the heat transport in the vigorously convective MO is extremely efficient as long as the surface temperature is high enough for the liquid fraction in the magma to exceed the critical value for rheological transition.

Along with crystallization, an outgassed atmosphere would form by degassing from the interior. As water is highly soluble in silicate melt, a large fraction of water would be dissolved in the MO at an early stage. CO_2 has a moderate solubility, and would degas at an earlier stage of solidification, compared to H_2O, which is exsolved at a relatively later stage, when the magma becomes highly enriched in dissolved water (Elkins-Tanton 2008; Lebrun et al. 2013). Other gaseous species such as CO and N_2 are thought to be less soluble in silicate melt. The atmospheric amount of these gaseous components remains less affected by degassing from the interior, and therefore the coupling to the MO solidification is relatively weak.

Once the degassed atmosphere forms, it would slow the solidification process of the MO by preventing heat escaping from the planet. The gaseous species less soluble in silicate melt such as CO_2 and CO would be responsible for the thermal blanketing at an early stage when the largest fraction of water is dissolved in the MO.

As the magma volume decreases, the water vapor would degas and take CO_2 over as the main blanketing species. A rapidly solidifying MO becomes highly enriched in volatile components, leading to a large degassing rate. In turn, the rapid growth of the outgassed atmosphere makes solidification slower due to the enhancement of the thermal blanketing and greenhouse effects.

In parallel with the formation of an outgassed atmosphere, atmospheric escape would occur on early terrestrial planets. It is well known that young stars emit strong XUV radiation due to their high activities. After the nebula gas dissipates out, terrestrial proto-planets and planets would be exposed to extremely strong XUV radiation from the young host star. The stellar XUV radiation is strongly absorbed in the upper atmosphere, thus heating it up and dissociating atmospheric molecules and driving hydrodynamic escape (see Sect. 4 for more details). The outgassed atmosphere would then be partially lost from the planet. Hydrogen-bearing gaseous species such as H_2O are more susceptible to the hydrodynamic escape, because hydrogen is the lightest element. As long as the surface temperature is high enough, no condensation of water vapor occurs and atomic hydrogen is abundant in the thermosphere due to the high mixing ratio of water. The atmosphere can thus escape efficiently at a rate limited by the energy available to heat up the thermosphere. Based on the classification by Tian et al. (2008), the thermosphere is in a hydrodynamic regime in this case. As the surface temperature decreases, the temperature at the tropopause decreases as well so that water vapor starts to condense at the tropopause. Then, the tropopause starts to act as a cold trap, which limits the mixing ratio of water vapor entering the mesosphere and dehumidifies it. The escape rate of hydrogen then becomes diffusion-limited and starts to decrease. As the atmospheric escape rate decreases, the planetary thermosphere shifts from the hydrodynamic regime to a hydrostatic regime. The loss of water associated with the hydrodynamic escape of hydrogen plays a role in reducing the greenhouse effect by water vapor and accelerate the solidification of the magma ocean.

Recently, the MO thermal evolution of an Earth-sized planet along with the formation of a degassed atmosphere has been examined with simple coupled models for a H_2O-CO_2 atmosphere (Elkins-Tanton 2008; Lebrun et al. 2013) and a H_2O atmosphere (Hamano et al. 2013). Results with radiative-convective equilibrium calculations for a steam atmosphere indicate that two disparate types of planets can develop during solidification, depending on their orbital distance from the host star (Fig. 10): wet and potentially habitable planets like Earth (type I), and dried-out planets like Venus (type II) (Hamano et al. 2013). The orbital regions of the two distinct types of planets are limited by a critical distance from the host star (see below).

Type I planets are planets which formed further than a certain critical distance from the star. This type of planet monotonically cools and solidifies on a timescale of less than several million years. Condensation of water vapor starts to occur at the tropopause when the surface temperature becomes low and the amount of water vapor becomes large. Thereafter, the thermal radiation outgoing to space is fixed to 280–300 Wm^{-2}, which is called the radiation limit or runaway greenhouse limit of steam atmospheres (Kasting 1988; Abe and Matsui 1988; Kopparapu et al. 2013; Goldblatt et al. 2013). The fact that a radiation limit is present places an upper limit on the MO crystallization timescale.

In contrast, a type II planet, which formed closer to the star, reaches a radiative energy balance during the course of solidification and remains in a runaway greenhouse state by receiving a net stellar flux larger than the radiation limit. Indeed, the planet emits a slightly larger radiative flux than the net incoming stellar insolation by losing its water via hydrodynamic escape. In other words, the planet is desiccated by the hydrodynamic escape during solidification. The initial total water inventory determines the overall solidification time,

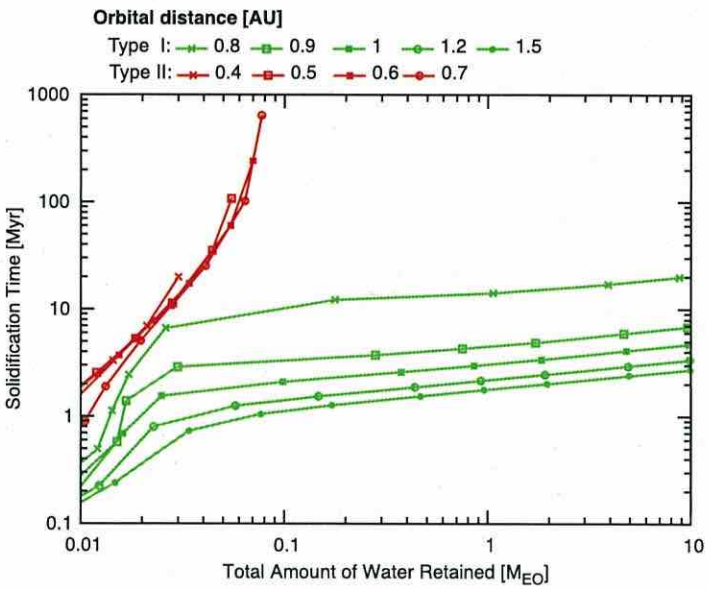

Fig. 10 Relation between final amount of water retained on the planet and its solidification time. The calculations are done with the evolutionary model by Hamano et al. (2013) in a range of initial water inventory from 0.01 to 10 times the Earth's ocean mass (M_{EO}). A critical distance is ~ 0.76 AU in their model

which could exceed 100 Myr for water endowment comparable to the total inventory of the current Earth. When a large amount of other gaseous species is added in the atmosphere, the diffusion-limited escape rate of hydrogen would become lower, due to the decrease of the mixing ratio of water vapor in the upper atmosphere. As a result, the loss rate of water would become lower so that the MO period would be prolonged.

A critical distance which separates the orbital region of the two distinct types of planets is defined as the distance at which the net stellar flux equals the radiation limit. The net stellar flux that a planet receives depends on the planetary albedo and the luminosity of the host star, as well as the planetary orbital distance. For a thick steam atmosphere, the clear-sky planetary albedo becomes small at lower effective stellar temperatures due to the shift of the stellar energy spectrum toward the longer wavelengths (Kopparapu et al. 2013). The stellar luminosity becomes small with decreasing stellar mass as well. For both reasons, smaller stars have a smaller critical distance. Although the stellar luminosity varies with time, the stellar age at which its influence is highest (time of giant impact) can be used to obtain a critical distance of low—and intermediate—mass stars such as the Sun. It is because the solidification timescale of type I planets is typically shorter than the timescale of the evolution of their central star. The critical distance can range from approximately 0.6 to 0.8 AU under solar system condition. This critical distance provides the innermost edge of the habitable zone in the sense that it determines whether water could remain and first form earliest oceans. On the other hand, the threshold orbital distance for ocean re-evaporation due to luminosity enhancement of the host star is larger than the critical distance and depends on various factors such as the distribution of surface water (Abe et al. 2011), the distribution of relative humidity in the atmosphere (Leconte et al. 2013), and the planetary rotation rate (Yang et al. 2014).

Earth is representative of type I planets. The time required for cooling to the sufficiently low surface temperature at which the liquid fraction at the surface reaches the critical value for the rheological transition would have been typically 1 Myr (Lebrun et al. 2013). The subsequent cooling history depends on the development time of a thermal boundary layer at the surface and solid-state convection of a 'hard magma ocean'. Even with a steam atmosphere equivalent to more than several times the Earth's ocean, the overall crystallization time of Earth would not have exceeded 5 Myr due to the presence of the radiation limit (Hamano

et al. 2013). The ocean formation after solidification can be estimated to occur roughly in the order of 1000 years for a 270-bar steam atmosphere. This short cooling time would have allowed Earth to maintain a certain amount of water until the ocean formation, whereas a modest loss could have partly oxidized the abundant surface magma.

Venus is on the borderline between the orbital regions of these two types of planets. If Venus is a type I planet, it would have once possessed water oceans, probably allowing formation of carbonate rocks. In accordance with the luminosity enhancement of the Sun, it would have lost its water in a moist greenhouse state, because of photodissociation of water vapor followed by escape of hydrogen (Kasting 1988). If the surface temperature becomes sufficiently high for carbonate decomposition, the carbonate rocks would have been decomposed and released CO_2 into the atmosphere. Although this type I scenario likely explains the dry and CO_2-rich atmosphere of the current Venus, an issue of leftover oxygen still remains. Selective escape of hydrogen could have left Venus with oxygen, which is a relatively heavy element compared to hydrogen. If Venus started with one Earth ocean of water, which is equivalent to the surface atmospheric pressure of ~ 270 bar, approximately 240-bar of oxygen would have been left on Venus. Although an energetic hydrogen wind would drag some of the oxygen to space, this could account for 60 bar of the oxygen at most (Chassefière 1996b), still leaving an oxygen-rich atmosphere on Venus. On the other hand, if Venus is a type II planet, this issue of leftover oxygen can be avoided, because abundant surface magma can serve as a massive oxygen sink. Venus would have lost most of the water during a long magma ocean period by escaping hydrogen to space and taking up oxygen in the interior. In this type II scenario, the final amount of water vapor which could have remained in the atmosphere would depend on the amount of the background gas. Under a 90-bar CO_2 background atmosphere, the hydrogen escape rate would have become extremely low, when the partial pressure of water vapor became lower than about 10 bar (Kasting et al. 1984). The evolution of the Venusian atmosphere based on both the type I and type II scenarios certainly deserves full investigation with detailed calculations of multi-component thermal and non-thermal escape processes.

The vast difference in solidification timescales between type I and type II planets suggests that occurrence rates of hot molten planets could show an orbital dependence reflecting the critical distance from the host star. According to spectral calculations on steam-bearing atmospheres, intense thermal emission from the hot surface could leak through near-infrared atmospheric windows and provide a diagnostic sign of its molten surface, depending on the atmospheric mass (Miller-Ricci et al. 2009; Lupu et al. 2014). Recent calculations predict that terrestrial planets remain molten over the main sequence of the G-type host star in the type-II orbital region if the initial bulk content of water exceeds ~ 1 wt% (Hamano et al. 2015). On the other hand, in the type-I orbital region, which is located further from the star than the critical distance, the lifetime of the magma ocean is typically less than several million years, irrespective of the initial amount of water. Detecting the critical distance could provide observational evidence that water is one of major volatile species on terrestrial planets in extrasolar planetary systems.

3.5 Effects of Multiple Impacts on Protoatmospheric Loss

When a giant impact occurs, there is a possibility that proto-atmospheres on protoplanets are lost through two processes: mechanical (or shock-induced) loss and thermal loss. In the mechanical loss process, a giant impact causes a strong shock wave traveling in the planetary interior, and then the globally expanding motion of the ground pushes out the proto-atmosphere. The thermal loss of the proto-atmosphere occurs after the mechanical

loss event. Protoplanets and protoatmospheres can achieve extremely high temperatures due to the energy release of a giant impact. Such a high-temperature proto-atmosphere would expand into space and would be lost through hydrodynamic escape. The fraction of the atmosphere lost by the mechanical process is sensitive to the protoplanet surface conditions. In particular, the existence of liquid water on the surface enhances the fraction lost. Genda and Abe (2003) considered giant impacts between solid protoplanets with various types of atmospheres but without an ocean, and calculated the relationship between atmospheric loss and global motion of the ground induced by a giant impact. They found that a significant loss of the atmosphere occurs only when the ground motion is close to the escape velocity. A typical impact velocity between protoplanets during terrestrial planet formation is approximately that of the two-body escape velocity of colliding protoplanets (Agnor et al. 1999), which is about 5 km/s and 10 km/s for Mars-sized and Earth-sized protoplanets, respectively. Therefore, the global motion of the ground should not exceed roughly half that of the escape velocity. Genda and Abe (2003) showed that such a global motion of the ground can blow off a maximum of about 30 % of the atmosphere by a single giant impact. Subsequently, Genda and Abe (2005) investigated the effect of a water ocean. They found that the presence of an ocean on the surface significantly enhances the atmospheric loss due to the following two effects. One is the vaporization of the ocean, which effectively pushes out the atmosphere. The other is lower shock impedance of the ocean compared to the ground, which causes an increase in the shock velocity at the interface between ocean and ground. Both effects accelerate the velocity at the ocean atmosphere interface close to the escape velocity. However, it should be noted that an entire ocean can survive a giant impact of a Mars-sized impactor.

The proto-atmosphere (including a steam atmosphere) that survives the mechanical loss would undergo thermal loss. The temperature of proto-planets becomes extremely high (5000–10000 K) just after a giant impact, according to the numerical simulations of giant impacts (e.g. Canup 2004a). A high-temperature proto-atmosphere would expand adiabatically, and would be lost through hydrodynamic escape.

The criterion for the onset of the hydrodynamic escape of the atmosphere is given by (e.g. Parker 1963)

$$\lambda_0 < \frac{\gamma}{\gamma - 1}, \tag{19}$$

where γ is the polytropic exponent of the atmosphere and λ_0 is the escape parameter defined by:

$$\lambda_0 = \frac{GMm}{kT_0 r_0}, \tag{20}$$

where G, M, m, k, T_0, and r_0 are the gravitational constant, the mass of the planet, the mass of the molecule of the atmosphere, the Boltzmann constant, the temperature at the planetary surface, and the planetary radius, respectively. In the case of adiabatic flow, the polytropic exponent is equal to the specific heat ratio. If we consider a pure hydrogen atmosphere, which is the lightest gas, the hydrodynamic escape occurs when $T_0 > 4200$ K. Here we assume hydrogen molecules with $\gamma = 1.4$ and an Earth-sized planet. Therefore, if the proto-atmosphere is composed of pure hydrogen just after a giant impact, the adiabatic expansion of the atmosphere results in rapid escape from the planetary surface. However, rock vapor should inevitably exist in very hot planetary atmosphere. Since rock vapor has typically a large molecular weight ($m = 30$ g/mol), the escape requires extremely high temperature ($T_0 > 21000$ K in the case of $\gamma = 1.1$). Moreover, the proto-atmosphere would be composed of various species with large molecular weight other than hydrogen, such as H_2O,

CO_2 and N_2. For example, H_2O with $m = 18$ g/mol and $\gamma = 1.33$ requires extremely high temperature ($T_0 > 30000$ K) for hydrodynamic escape. Therefore, it is impossible for the bulk of the proto-atmosphere to escape adiabatically.

The loss fraction of the atmosphere via mechanical loss is quite sensitive to the surface conditions of the protoplanet as discussed before. We consider four cases i.e. case 1: where the surface is covered by an MO, case 2: dry rock, case 3: an ocean and case 4: water ice.

Cases 2 and 3 were discussed by Genda and Abe (2003, 2005) as summarized above. In case 2, the lost fraction is insensitive to the atmospheric properties, and is approximately proportional to the ground motion velocity. A significant loss occurs only when the ground motion is close to the escape velocity. One third of original atmospheres are expected to survive the sequence of typical impacts among protoplanets (Genda and Abe 2005). In case 3, the atmosphere is efficiently blown away by the impact, while the water ocean survives (Genda and Abe 2005). Hence, giant impacts on such planets result in relative enrichment of water compared to other gases.

Though cases 1 and 4 have not been discussed yet, we can roughly estimate them based on cases 2 and 3. The efficiency of the atmosphere blow off in case 1 is expected to be similar to that of case 2, because the material behavior upon shock wave propagation is not much different between molten and solid silicate. However, the effect on the composition of volatile materials is likely different, because the atmospheric composition is affected by the solubility of gases in the MO. In particular, since the solubility of water vapor is large compared to other gases, such as CO_2, it is likely retained in the MO. Hence, the atmospheric blow off in case 1 likely causes relative enrichment of water vapor over other gases. The enrichment factor depends on the depth of the MO and the amount of atmosphere itself, because the solubility coefficient of water vapor in silicate melt is not constant but depends on the partial pressure of water vapor.

The efficiency of the atmosphere blow off in case 4 is expected to be intermediate between cases 2 and 3, because the mechanical material behavior upon shock wave propagation is not much different between ice and rock, although ice clearly vaporizes much more easily than rock. Therefore, the atmosphere is rather efficiently blown away but a fraction of the water may survive depending on the ice thickness at the time of impact and on impact conditions itself. Therefore, the atmosphere should be enriched in water compared to other gases. Thus, except for case 2, water is likely enriched over other gases, but the mechanism and efficiency of this enrichment are different.

The surface conditions of protoplanets depend on the time interval between giant impacts and on the distance from the central star. According to the terrestrial planet formation theory, several tens of Mars sized protoplanets are formed through the successive accretion of planetesimals in the terrestrial planet region on a timescale of 10^5 years (Kokubo and Ida 1998). After that, these protoplanets collide with each other to form terrestrial planets such as the Earth and Venus. The timescale for the Earth-sized planet to be fully grown is roughly 100 Myrs (Kokubo and Genda 2010; O'Brien et al. 2014). This timescale is consistent with the timing of the last giant impact that forms the Moon, which has been derived from Hf-W system of Earth's and lunar rocks (e.g. Touboul et al. 2007). Since the Earth and Venus experience giant impacts about 5 to 10 times during this stage (Kokubo and Genda 2010), the interval of giant impacts is roughly 10 Myrs in average. This time interval is longer than the typical cooling time of MO for type I planets (several Myr depending on their water content, see Fig. 10) reported by Lebrun et al. (2013) and Hamano et al. (2013). Another thing we have to take into account is the orbital change of protoplanets. We can expect giant impacts among protoplanets formed at various distances from the Sun. It means collisions among protoplanets with various volatile content. A protoplanet has either a solar-composition or

a mixed atmosphere. Since giant impacts are intrinsically related to the orbital change of protoplanets, the time scale of orbital change is basically the same as the interval between the giant impacts. It is much longer than the time scale of the atmosphere responses such as atmosphere cooling or ocean vaporization due to insolation change (Abe et al. 2000). Hence, the place of collision is more important than the original position of protoplanets (Abe 2011).

The average time interval between giant impacts is longer than the typical cooling time of type I planets, but it is much shorter than the typical cooling time of type II planets. Therefore, we can estimate the surface conditions of protoplanets at the time of giant impacts as a function of distance from the central star as follows:

(1) If the distance is smaller than the critical distance dividing type I and type II planets, the surface is covered by an MO. Thus, gases with high solubility in silicate melt, such as water vapor, are preferentially retained in the planets. It is hard to remove water molecules dissolved in silicate melt by giant impacts, while the atmosphere would be more or less removed. Therefore, water content will become relatively enriched through the sequence of giant impacts. If the depth of the MO just before a giant impact is deep (or shallow), large (or small) fraction of water molecules should be dissolved in MO. Therefore, the enrichment factor depends on the depth of the MO, which in turn depends on the time interval between giant impacts. A longer interval results in a smaller enrichment. However, after the giant impact stage, most water should be lost into space via hydrodynamic escape induced by the intensive irradiation of XUV from the Sun before the complete MO freezing, because such a planet is a type II terrestrial planet (Hamano et al. 2013).

(2) If the distance is larger than the critical distance for global freezing, the surface of planets is likely covered by water ice at the time of giant impacts. Thus, enrichment of water is expected. If the ice layer is thick, the atmospheric loss would be slightly suppressed. Therefore, the enrichment factor would be small for longer impact interval, because a longer interval results in a thicker ice layer.

(3) If the distance lies between the critical distances dividing type I and type II planets and the global freezing, the surface of planets is likely covered by water oceans at the time of giant impacts. Thus, the loss efficiency of gases other than water vapor is enhanced and water is relatively enriched.

It is very difficult to estimate the precise value of the loss efficiency of each gas component, because it depends on the interval of impacts, which varies stochastically. Generally speaking, however, we can expect the highest loss efficiency of gases other than H_2O molecules for the last case among the 3 cased discussed above, because H_2O exists in the liquid form as a water ocean and it survives a giant impact. This is expected between the Venusian and Martian orbits (Abe 1993). Thus, planets formed near Earth orbit are likely more enriched in water than those near Venus orbit or those which experienced no giant impact.

4 Escape from Protoatmospheres

4.1 Introduction

On all terrestrial planets, the dissipation timescales of protoatmospheres are short (Montmerle et al. 2006; Lammer et al. 2014). Observations of exoplanetary atmospheres under strong stellar radiation provide excellent opportunities to verify our theoretical understandings on this key process influencing planet evolution. Shortly after the observation of an extended hydrogen cloud around transiting hot Jupiter HD 209458b (Vidal-Madjar et al. 2003)

and the discovery that these planets experience most likely hydrodynamic atmospheric escape (Lammer et al. 2003), one dimensional hydrodynamic upper atmosphere models were independently developed by several research groups (e.g., Yelle 2004; García Muñoz 2007; Penz et al. 2008; Murray-Clay et al. 2009; Tian et al. 2005b) to understand this phenomenon. Despite the differences in model details (numerical solution methods, major atmosphere species, and complexity of chemistry networks, etc.), the orders of magnitude of calculated hydrogen escape rates from these models agree with each other. But unfortunately these studies did not thoroughly explore the long term evolution histories of close-in exoplanets, partially due to the perceived large uncertainties in factors influencing the model results (XUV energy flux, heating efficiency which converts absorbed photon energy into heat, geometric factors—where the stellar photons should be absorbed by the atmosphere gases, and how to treat heavier elements and molecules, etc.). More advanced models (Koskinen et al. 2010, 2013a,b; Guo 2011, 2013; Shaikhislamov et al. 2014) along this line have been developed.

On the other hand, other studies investigated the evolution of close-in exoplanets based on simple "energy-limited" escape formulae, first for hot Jupiters (Lammer et al. 2003; Baraffe et al. 2004; Lecavelier des Etangs et al. 2004), later for exoplanets with different masses, including the Neptune and super-Earth mass domain (e.g., Lecavelier des Etangs 2007; Davis and Wheatley 2009; Lammer et al. 2009; Sanz-Forcada et al. 2010; Lopez et al. 2012; Lanza 2013; Lopez and Fortney 2013; Kawahara et al. 2013; Kurosaki et al. 2014; Jin et al. 2014), the later works being successful at explaining some trends in the mass-size distribution of Kepler exoplanets. Triggered by the same Kepler observations, newer and more advanced hydrodynamic escape models (Owen et al. 2010; Owen and Wu 2013; Erkaev et al. 2013; Lammer et al. 2013, 2014) are also able to explain the Kepler data but provide somewhat different insights on the nature of physical processes controlling atmospheric escape from close-in exoplanets.

Readers familiar with works on atmospheric escape for solar system bodies such as Mars, in which the main focus is put on nonthermal escape processes, may be puzzled that very limited work regarding nonthermal escape processes is discussed in the exoplanet community. This is because the observed close-in exoplanets are under intense stellar XUV radiation and their upper atmospheres are necessarily hot, which makes hydrodynamic escape the most relevant when discussing escape from protoatmospheres.

All of these works contribute to improve our understanding of atmospheric escape. However, there are important differences among these recent works, mainly focusing on the following aspects: (1) what is the main driver of hydrodynamic escape from planetary atmospheres, the X-ray or EUV photons? (2) What is the proper heating efficiency in hydrodynamic escape from planetary atmospheres? (3) Is hydrodynamic escape from planetary atmospheres energy limited? It can be expected that future observations of exoplanets will present stronger constraints on and encourage improvements of atmospheric escape models, the applications of which will also lead to a better understanding of the paleoclimate and the evolution of solar system terrestrial planets.

In this section, we present a review on theories and observations relevant to escape from protoatmospheres. Although protoatmospheres are likely dominated by hydrogen, in this review we try to cover more general physics and thus sometimes discuss processes not limited to hydrogen atmospheres. We will first introduce basic concepts related to planetary upper atmospheres, followed by illustrations of different physical processes important to determine energy deposition and atmospheric escape processes, followed by some recent observations and theoretical results related to atmospheric escape from close-in exoplanets. After that we provide a brief discussion on the differences in recent atmospheric escape models, ending with a brief summary.

4.2 Basics Concepts

4.2.1 Planetary Upper Atmospheres

The term upper atmosphere can mean different things even to planetary atmospheric scientists. A planetary upper atmosphere can be defined as the region where the different atmospheric species begin to separate from each other due to the lack of mixing. In this definition the upper atmosphere is identical to the so called "heterosphere", in contrast to "homosphere" where atmospheric species are well mixed. An indicator of the mixing strength is the eddy diffusivity which is typically greater in the dense part of the atmosphere with a negative temperature gradient (troposphere and mesosphere in the Earth's atmosphere) and smaller in the atmosphere region with a positive temperature gradient (stratosphere of the Earth). In solar system planets, the number density of the lower boundary of the heterosphere is typically between 10^{12} and 10^{13} cm^{-3}.

Based on thermal structure one can define a planetary upper atmosphere as the region where a positive thermal gradient exists (we will soon find out that this definition is problematic). In this definition the upper atmosphere is identical to the so-called thermosphere. The thermosphere is heated by the absorption of solar or stellar soft X-ray (up to a few 100 Å) and EUV (up to 1000 Å) photons (hereafter called XUV). Since the energy of most XUV photons exceeds the ionization threshold of essentially all molecules and atoms, the absorption cross sections of gases for XUV photons are large, which in turn favors the absorption of XUV photons at low density and high altitude regions. The combination of sufficient energy deposition and a low local density makes the thermosphere hotter than the underlying atmosphere. Because of this internal link between the thermosphere density and temperature, the lower boundary of the heterosphere is normally located not far from that of the thermosphere. Thus in the following we do not distinguish between the two.

Note that atmospheric gases have smaller absorption cross sections for photons with wavelengths shorter than a few Å. These photons could penetrate deeper into the atmosphere below the upper atmosphere. Although these photons are energetic, the fluxes at these short wavelengths are orders of magnitude smaller than stellar UV radiation which forms the ozone layer in the Earth's atmosphere. In addition, the planetary atmosphere region where these energetic photons are absorbed is typically dominated by molecules, which have stronger radiative capabilities. Thus these photons do not necessarily cause significant heating of the middle atmosphere. Neither do they contribute to atmospheric escape.

Because XUV photons can ionize atmospheric species, the fraction of charged particles is higher in the thermosphere, which leads to the overlap of the ionosphere and the thermosphere. A quasi charge neutrality is reached in the thermosphere in which the total densities of ions and the density of electrons roughly balance each other at all altitudes in the thermosphere because the recombination reactions between (1) the ion species and the electrons provide a self-limiting control on the electron and ion densities; and (2) separation of charges will produce electric field which attracts opposite charges to each other.

The Earth's thermosphere temperature is ~ 900 K in solar minimum and ~ 1500 K in solar maximum with solar XUV energy flux changes by a factor of ~ 3 in a solar cycle. The most important radiative cooling agents in the Earth's thermosphere are CO_2 and NO in the lower thermosphere, and atomic oxygen in the upper part. In comparison the thermospheres of Venus and Mars are much colder, $200 \sim 300$ K respectively, and much more stable in response to variations of solar XUV radiation because CO_2 is the dominant gas in the atmospheres of these planets. On the other hand, the temperatures of hydrogen and helium dominated thermospheres of Jupiter and Saturn are on the order of 1000 K despite

their large distances from the Sun because of the relative weak radiative cooling capability of hydrogen and helium. Thus a general rule for the thermosphere temperature is that CO_2 atmospheres are cooler.

There are other sources of energy and ionization sources in addition to stellar photons. In the magnetic polar regions of the Earth, the magnetic field lines are either open to the solar wind or the Earth's magnetosphere where particles can be accelerated via various processes. Thus the thermosphere, in these polar regions, is subject to collisions of these energetic charged particles and can be heated by this so called energetic particle precipitation process. In addition, the ions and electrons in the ionosphere are accelerated by the magnetic field of the planet and thus have a differential velocity in comparison to the neutral species in the thermosphere. Collisions between ions/electrons and neutrals produce so called Joule heating which is more important than solar XUV heating in the polar regions of the Earth. Globally averaged, solar XUV heating dominates these other heating mechanisms (i.e. energetic particle precipitation, Joule heating, etc.) in the thermospheres of the Earth, Mars, Venus, Titan, and giant planets.

4.2.2 Physical Processes Related to Heating

Energy deposition in planetary upper atmospheres involves some complex and interesting fundamental processes. After an XUV photon is absorbed by atmospheric species, several results can occur. For photons absorbed by molecules, if the photon energy is lower than the dissociation energy threshold of the absorbing molecules, the energy would most likely be used to excite the molecule. If the photon energy is greater than the dissociation energy threshold, photo-dissociation could occur and the daughter particles produced could each carry some kinetic energy (heat) and some potential energy (forming excited atoms or molecules). Collisional de-excitation processes would convert the potential energy of the excited species into kinetic energy and heat the atmosphere. Alternatively the potential energy could be passed partially to other species through chemical reactions and heat is generated in the process.

For photons with even higher energy, ionization could occur in which a neutral is converted into a pair of ion and an electron. An ion can transfer its potential energy and charge to a neutral species through chemical reactions. The potential energy of the reactants needs to be greater than that of the products in order for the reaction to be exothermic (heat generated) and rapid. Charge transfer reactions, a good example of which are the $H^+ + O \longleftrightarrow H + O^+$, are rapid because the two reactants have similar potential energy.

Recombination reactions are the processes through which ion species return to neutrals. Because of the fundamental laws of energy and momentum conservation, radiative recombination reactions occur for atomic ions such as H^+. However, these processes are slower than dissociative recombination (DR) reactions such as $O_2^+ + e \rightarrow O + O$. Note that these DR reactions could produce neutrals in excited states and thus the kinetic energy of the products depends on which branch the neutrals are formed. For small planets such as Mars, the kinetic energy formed in DR reactions could be sufficient for the neutrals to escape—photochemical escape. In the Earth's thermosphere the molecular ion finally produced is NO^+ because it has a low potential energy out of all ions in the Earth's ionosphere. The recombination reaction of NO^+ forms an N and an O atoms which returns the upper atmosphere to its neutrality. Carefully accounting the energy stored in ions and neutrals and those released in chemical reactions is essential to calculate the energy deposition in planetary upper atmospheres.

The electron produced in a photo-ionization reaction is called a photo-electron, which could carry much more energy than the potential energy carried by the ion if the initial

photon has much greater energy than the ionization threshold of the species. In this case the photo-electron will have adequate energy to cause additional excitation, dissociation, and ionization. Electron impact cross sections are used to describe the occurrence probabilities of these events, which are measured in the laboratory and used to compute where and when the energy of photo-electrons deposit their energy. One energetic photo-electron can lead to the formation of another electron with less but still high energy, which can cause subsequent ionization. Thus one needs to trace these secondary electrons in order to correctly track the flow and deposition of energy. In the presence of a planetary magnetic field, the motion of photoelectrons and secondary electrons should be constrained, which further complicates the calculations of cascade electron transport and degradation. This is an area that multi-dimension numerical models for planetary upper atmospheres have not yet treated.

If the photon energy is exceedingly high, dissociative ionization, in which one neutral molecule is divided into one neutral and one ion, could occur. Similarly species except hydrogen can lose more than one electron when absorbing an energetic photon or when being hit by an energetic electron. A further complication is the possible multiple photon events which are unimportant in the upper atmospheres of Solar System terrestrial planets but could become non-negligible for planets under extreme strong stellar XUV radiation.

For pure hydrogen protoatmospheres, many of the above mentioned processes may not apply. However, even small amounts of other species such as CO_2, CO, H_2O, NH_3, CH_4, etc. may change the chemistry and energy network of planetary upper atmospheres. Thus it is useful to pay attention to what species and processes are involved in the deposition of photon energy in planetary upper atmospheres.

4.2.3 Escape Processes

The exobase is an altitude in the atmosphere beyond which few collisions between particles occur. Mathematically it can be defined as where the mean free path equals the atmospheric scale height. From a kinetic point of view, any particle at the exobase with outgoing velocity exceeding the escape velocity of a planet can escape. High particle velocity can be achieved in many processes. Those processes in which the high velocity is associated with the exobase temperature are called thermal escape.

Thermal Escape Although an exobase level can be defined, the collisional and collisionless regions near the exobase level cannot be divided by an arbitrary dimensionless boundary because the density distribution is a continuous function and thus a gradual transition exists between the two regions. When considering three dimensional geometry, the exobase may exist at different altitudes and pressures, because the probabilities of collisions only depend on number densities and temperature, at different longitudes and latitudes, which further complicates the problem.

In thermal escape, the percentage of escaping particles is governed by the local temperature. If the atmosphere near the exobase is in hydrostatic equilibrium, the local velocity distribution of particles follows the Maxwellian distribution and the escape is called Jeans escape (Chamberlain 1963; Opik and Singer 1961):

$$\Phi = \frac{n(z)V_0}{2\sqrt{\Pi}}\left(\frac{V_{esc}^2}{V_0^2}+1\right)\exp\left(-\frac{V_{esc}^2}{V_0^2}\right) \tag{21}$$

here Φ is the escape flux (number of escaping particles per unit area per unit time) at the exobase, $n(z)$ is the exobase number density, $V_0 = \sqrt{(2kT/m)}$ is the most probable velocity

with m the mass of the escaping particle, k the Boltzmannn constant, T the local temperature, $V_{esc} = \sqrt{(2GM/r)}$ with G the gravitational constant, M the mass of the planet, and r the distance from the center of planet. The ratio between the gravitational energy and the kinetic energy of particles near the exobase is often called the Jeans escape parameter,

$$\lambda = \frac{GMm}{kT} \tag{22}$$

When this parameter is close to unity, the gravity of the planet hardly binds its atmosphere and the upper planetary atmosphere deviates from hydrostatic equilibrium, in which case the local velocity distribution of particles can be described by a shifted Maxwellian distribution (Yelle 2004; Volkov et al. 2011a,b), with the outward velocity enhancing the escape probability of particles near the exobase. Traditionally this scenario is called the blowoff or hydrodynamic escape or planetary wind, an analog to the solar wind (Parker 1964; Watson et al. 1981).

Since it is the temperature of planetary upper atmosphere which drives atmospheric escape in both cases, both Jeans escape and hydrodynamic escape are special cases of thermal escape: in Jeans escape, the escape does not change the velocity distribution of particles (in another word the temperature) near the exobase or in the upper thermosphere; in hydrodynamic escape, the temperature and velocity distributions of particles in the upper thermosphere are influenced strongly by atmospheric escape. More discussions on hydrodynamic escape are in Sect. 2.4 because it is more relevant to the protoatmospheres.

Nonthermal Escape When the velocities of escaping particles are not determined by the exobase temperature, nonthermal escape processes occur (Lammer et al. 2013, and references therein). Most nonthermal escape processes are associated with the presence of ions and their behavior in the electric and magnetic field. Photochemical escape is a nonthermal escape process important for Mars (e.g., McElroy 1972; Ip 1988; Nagy and Cravens 1988; Lammer and Bauer 1991; Fox and Hać 2009; Krestyanikova and Shematovich 2006; Chassefière et al. 2007; Chaufray et al. 2007; Gröller et al. 2014) but is unlikely to be an efficient escape mechanism on Venus (Lichtenegger et al. 2009; Gröller et al. 2010), Earth or super Earths because the maximum kinetic energy an oxygen atom can obtain from dissociative recombination reaction of O_2^+ is fixed and lower than the escape energies of planets more massive than Mars. Neutral atoms and molecules in the atmosphere of the planet may be ionized through photoionization, impact ionization, or charge exchange with solar wind ions. Once formed around a nonmagnetized planet (or a weakly magnetized one), the ions can be accelerated by solar magnetic field and some could escape the planet (e.g., Lammer et al. 2013, and references therein). This ion pickup process is less efficient on a planet with a strong intrinsic magnetic field, such as Earth, because the solar or interplanetary electric and magnetic fields are kept at distances far from the planet. In this case, the ions can be trapped by the planet's magnetosphere and do not necessarily escape the planet. However various models for hydrodynamic escape from protoatmospheres shown that the upper atmosphere under strong stellar XUV radiation could be highly expanded, with the exobase beyond a few planetary radii. In combination with the fact that the magnetopause of a protoatmosphere could be suppressed to closer distances from the planet by stronger stellar wind from a young star, the protection from planetary magnetic fields could be inefficient for protoatmospheres. When energetic ions are trapped by the magnetic field of the planet, they can escape by transferring their charges to slowly moving atoms—charge exchange. They can also impact slowly moving atmospheric species and cause the latter to escape-sputtering (e.g., Luhmann et al. 1992; Jakosky et al. 1994).

Since electrons are much lighter than ions, in the regions with open magnetic field lines (magnetic poles), there is a deviation from exact neutrality. The separation of the outgoing electrons and the ions left behind attract each other and cause a net acceleration of the ions outward which can lead to atmospheric escape—the so called polar wind. The relative significance of thermal and nonthermal escape mechanisms on present day solar system terrestrial planets is summarized in a recent review paper (Tian 2013) and is not repeated here.

4.2.4 Escape from Protoatmospheres—The Hydrodynamic Regime

The section 'Thermal Escape' briefly discussed the differences between Jeans and hydrodynamic escape (or blow-off). The Direct Simulation Monte Carlo (DSMC) model of Volkov et al. (2011a,b) shows that the transition between hydrodynamic escape and Jeans escape occurs in a rather narrow range in terms of the escape parameter. This result was recently confirmed by Erkaev et al. (2015) who found also that when the Jeans escape parameter is fixed at values less or equal than 2.5, there is no transonic solution. This is the case for a fast explosive atmospheric expansion that results in extreme thermal atmospheric escape rates. It is important to note that the negative feedback between rapid escape and energy budget throughout the thermosphere is at work in this regime (Tian 2013) and the escape parameter could be regulated by this feedback: a low escape parameter induces a faster escape which in turn lowers the temperature and leads to a greater escape parameter and hence a slower escape; so that a smooth transition from the subsonic to supersonic hydrodynamic flow could occur (Erkaev et al. 2015). It will be interesting to model and observe an alternative scenario to the steady transition, which is an oscillating planetary upper atmosphere between a more stationary state with a larger escape parameter and an explosion state with an escape parameter less or equal than 2.5. It is likely that 3D models will be needed for this.

Tian et al. (2008) showed that if the energy associated with the outflow of the upper thermosphere, which is a result of enhanced Jeans escape at the exobase, is neglected, the temperature and exobase level can grow rapidly with increasing XUV leading to blow-off. However, when the cooling associated with the outflow is included in the energy budget, blow-off is prevented until much higher XUV radiation is imposed. Thus it is important to characterize planetary thermosphere based on the importance of atmospheric escape on the energy budget: a hydrodynamic regime in which the energy budget in the thermosphere provides an ultimate limit to atmospheric escape; a hydrostatic regime in which atmospheric escape does not affect the thermosphere temperature. Traditional hydrodynamic escape (blow-off) can be considered as an extreme case of the hydrodynamic regime. Tian et al. (2008) found that even when the escape parameter does not reach the low values required for traditional hydrodynamic escape to occur, the energy budget in the upper thermosphere could nevertheless already be strongly influenced by the escape. This finding is confirmed by Erkaev et al. (2015).

The other importance of the hydrodynamic regime classification is that atmospheric escape from a planet in the hydrodynamic regime is inherently limited by energy available to drive the escape through the whole thermosphere. Thus if the amount of heating in the thermosphere remains unchanged, no matter how efficiently atmospheric escape can be at the exobase level, total escape remains unchanged. Thus the calculations of atmospheric escape and the evolution history of planetary atmospheres under strong thermosphere heating can be simplified (Tian 2013). On the other hand, nonthermal escape processes would help the transition of planetary upper atmospheres from a hydrostatic regime to a hydrodynamic regime.

It is convenient to associate incoming stellar XUV energy and the escape rate from a planet with an escape efficiency. However to calculate such an escape efficiency is not simple. As discussed in previous sections, a careful accounting is necessary in order to not only trace all energy flowing through the chemistry network, but also to consider the energy carried from one place to another by photo—and secondary electrons. Thus, the calculations of heating efficiency, the ratio between energy released to the ambient upper atmosphere as heat and the absorbed photon energy, is complicated. Most up-to-date works estimate less than 20 % heating efficiency, the conversion factor from the energy in the absorbed XUV photons to heat in the upper atmosphere, for hydrogen-dominated upper atmospheres (Shematovich et al. 2014, more discussions in the following).

In addition, when a planetary upper atmosphere is heated up, the exobase moves to greater distances which enhances the probability for atmospheric escape, which in turn increases the fraction of energy associated with escape and decreases the fraction of energy being radiated into space. This further complicates the calculations of escape efficiency. However as we shall see in the following sections, it seems nature has prepared some interesting and easy-to-apply rules to govern escape from protoatmospheres.

4.2.5 Suprathermals and Heating Efficiency

The photolysis of hydrogen-dominated protoatmospheres of the close-in exoplanets, driven by the XUV radiation of the host star, leads to the formation of suprathermal particles (particles with an excess of kinetic energy, i.e., with kinetic energies above 5–10kT, where T is the temperature of an ambient atmospheric gas and k the Boltzmann constant). These particles can be primary photoelectrons from H_2/H/He ionization or hydrogen atoms from H_2 dissociation and dissociative ionization processes. Dissociative recombination, dissociation and ionization by ultraviolet photons and electrons, and exothermic chemical reactions are accompanied by the release of energy on the order of several eV; part of this energy can be stored as the internal excitation of the products (Wayne 1991; Marov et al. 1996; Johnson et al. 2008). Charge exchange and atmospheric sputtering induced by energetic plasma ions can result in much larger energy transfers, producing hot particles with energies up to several hundred eVs (Johnson et al. 2008). If the production rate of these particles, which are typically suprathermal, is faster than thermalization, then a stable fraction of them is formed. These particles with excess kinetic energies are an important source of thermal energy in the upper atmosphere of hydrogen-rich planets. Generally the kinetics of the suprathermals is not considered in the contemporary aeronomical models because fast local thermalization of the suprathermal hydrogen atoms by elastic collisions with the ambient gas is usually assumed in order to avoid the complicated numerics caused by the solution of the non-linear kinetic Boltzmann equation.

Heating Efficiency Only some fraction of the absorbed stellar XUV energy contributes to the heating of the upper atmosphere. Therefore, it is important to calculate this fraction, and to evaluate how deep in an atmosphere stellar XUV photons, continuously release part of their energy as heat.

To estimate the effect of the XUV emission from solar-type stars of different ages an accurate description of radiative transfer and photoelectron energy deposition is required. In the studies by Cecchi-Pestellini et al. (2009) it was shown that soft X-rays provide an important contribution to the heating of hydrogen-dominated planetary atmospheres of close-in exoplanets. The flux of stellar XUV emission photons incident upon a planetary atmosphere of hydrogen-dominated composition photoionize the gas so that a flux of high-energy

(suprathermal) photoelectrons can be produced, which again deposit their energy into the gas (described in Sect. 4.2.2). In a partially neutral gas, electrons ionize, excite, and dissociate atomic and molecular species, as well as heat the gas through Coulomb collisions. In determining these energy deposition, we must account for all the possible degradation histories of the energetic electrons. When the stopping medium is only partially neutral, electron-electron interactions contribute to the electron energy degradation, and a significant portion of the energetic electron energy is deposited into the stopping medium as heat. As the ionized fraction rises, more and more of the electron energy heats the gas, and the excitation and ionization yields decrease. The heating efficiency in the hydrogen-dominated upper atmosphere of the well studied "hot Jupiter" HD 209458b was calculated with the kinetic Monte Carlo model (Shematovich et al. 2014). The obtained results can also be used for any thermal escape study of hydrogen-rich protoatmospheres.

The XUV radiation of the star is absorbed by atmospheric gas and leads to the excitation, dissociation, and ionization of different components of the atmosphere. Photoionization could produce photoelectrons with energies sufficient for the subsequent ionization and excitation of atomic and molecular hydrogen (Ionov et al. 2014). The fresh electrons lose their excess kinetic energy in collisions with the ambient atmospheric particles. Their kinetics and transport is described by the kinetic Boltzmann equation (Shematovich et al. 2008) and the DSMC (Direct Simulation Monte Carlo) method is an efficient tool to solve atmospheric kinetic systems in the stochastic approximation (Marov et al. 1996; Shematovich 2010). In the numerical simulations, the evolution of the system of modeling particles due to collisional processes and particle transport is calculated from the initial to the steady state. The Monte Carlo model developed by Shematovich et al. (2008) and adapted for hydrogen atmospheres was used to calculate the collisional kinetics and the transport of photoelectrons in the atmosphere of HD 209458b (Shematovich 2010).

The heating efficiency by the stellar XUV radiation within a hydrogen-dominated atmosphere, such as that of the extrasolar gas giant HD 209458b, has been modeled (Shematovich et al. 2014). It is shown that one cannot neglect the effects caused by electron-impact processes together with the participation of suprathermal photoelectrons. By including these processes the results of the DSMC model indicate that the XUV heating efficiency $\lambda_{h\nu}$ in hydrogen-dominated planetary protoatmospheres do not exceed 20 % over most of the thermosphere. This result agrees well with the heating efficiency values assumed in the early studies by Kasting and Pollack (1983) and Chassefière (1996a). Therefore, one can conclude that atmospheric mass loss studies, that assumed $\lambda_{h\nu}$ values greater than 20 %, overestimate the hydrogen escape rates, while hydrogen escape studies that assumed $\lambda_{h\nu}$ values $\approx$ 10–15 % should likely yield accurate results.

Suprathermals in the Extended Atmospheres of Hot Jupiters Ballester et al. (2007) reported the results of observations of hot Jupiter HD 209458b with STIS (Space Telescope Imaging Spectrograph) onboard the Hubble Space Telescope (HST) in a broad UV-to-optical spectral range. They detected a new detail in the planetary atmosphere absorption spectrum at 356–390 nm that they interpreted as Balmer-continuum absorption by hot (suprathermal) neutral hydrogen atoms in the upper atmosphere of the planet. Such a fraction of suprathermal hydrogen was used (Ben-Jaffel and Hosseini 2010) to approach the observations (Vidal-Madjar et al. 2004).

As mentioned above the important sources of suprathermal hydrogen atoms in the upper atmosphere of HD 209458b are dissociation and ionization of molecular hydrogen by XUV radiation of the star that produces hydrogen atoms with an excess of kinetic energy. No detailed studies of suprathermal hydrogen atom kinetics and transfer have been performed

at the molecular level (Yelle et al. 2008), because this requires the solution of the non-linear kinetic Boltzmann equation (Marov et al. 1996; Johnson et al. 2008). Accordingly, it is necessary to consider the effect of molecular hydrogen dissociation by UV radiation and the subsequent flux of photoelectrons on the suprathermal atomic hydrogen production in the $H_2 \rightarrow H$ transition region and the formation of the corresponding outflow in the upper atmosphere of HD 209458b. Recently the stochastic planetary corona model (Shematovich 2004) was used to study the kinetics and transfer of the suprathermal hydrogen atoms in the extended hydrogen-dominated protoatmosphere and estimate of the atmospheric mass-loss rate were obtained (Shematovich 2010).

The thermal regime and escape rate in the atmospheres of hot Jupiters significantly depend on the chemical composition of the atmosphere. In contrast to the planets of the Solar System that have stable atmospheric compositions over geological timescales, the composition of giant exoplanets may change rapidly as a consequence of the influence of the intense radiation field of the host star. Moreover, the thermal regime and the composition of the atmosphere are tightly connected through heating and cooling (Yelle 2004; García Muñoz 2007). Aeronomical models such as that of Yelle (2004) generally assume that reaching temperatures of several thousand Kelvin at particle densities on the order of 10^{10} cm^{-3} leads to the thermal dissociation of molecular hydrogen, $H_2 + M \rightarrow H + H + M$, and the formation of the $H_2 \rightarrow H$ transition region in the inner thermosphere of the exoplanet. In the upper thermospheric layers, the photoionization of atomic hydrogen starts to play the dominant role. Correspondingly, the makeup of the upper atmosphere changes with altitude from H_2 to H to H^+, which is an additional factor forming the extended atmosphere, since such a change in the composition is accompanied by the growth of the characteristic scale height. The molecular-to-atomic transition occurs at altitudes of about (1–1.2) $\times$ R_p, where R_p is the planet radius, and the temperature of the gas attains values of about a few thousands of K. The temperature and density values in the transition region are consistent with the observations (Ballester et al. 2007). The model of the upper neutral atmosphere consisting primarily of H_2, H, and He (Yelle 2004) was used to trace the kinetic properties of suprathermal hydrogen atoms.

The dissociation processes such as photodissociation, collisional dissociation, dissociative ionization, etc., are the primary sources of thermal and suprathermal fragments of molecules in electronically excited states in the upper planetary atmospheres (Wayne 1991). Although a hydrogen molecule is relatively simple, the UV and/or electron collisional dissociation of H_2 may occur in several ways. If, as a result of the absorption of radiation, electrons are excited to unbound or antibound orbits and their excitation energy exceeds the binding energy of the molecule, the molecule may dissociate. This mechanism allows for the photodissociation of molecules excited either to a continuum bound state or immediately to an unbound (repulsive) state. The photo-dissociation cross sections for these processes are usually smooth functions dependent on the wavelength; therefore, low (0.05–0.1 nm) spectral resolution data on the incident flux and cross sections are sufficient to estimate the dissociation rate (Fox et al. 2008). Another important mechanism is a pre-dissociation, when an absorbed photon excites the molecule into a bound state of electron excitation, from which the subsequent non-radiative transition into an unbound state is possible. The dissociation rate depends on the absorption rates at the wavelengths of the selected line transitions and the pre-dissociation probabilities (Fox et al. 2008).

The excess kinetic energy ΔE_{dis} of the atoms formed through the photo-dissociation of the hydrogen molecule was calculated as the difference between the energy of the absorbed UV photon, the energy of electronically excited state, and the dissociation energy. In the case of the dissociation of H_2 by photoelectrons the distributions were calculated for several

electron beam energies and include the populations of relatively slow thermal energy (less than 1 eV) and fast high-energy (1–10 eV, with a main peak at about 4 eV) atoms. Since hydrogen atoms appear in the process of dissociation with an excess of kinetic energy, their distribution in the $H_2 \rightarrow H$ transition region of the upper atmosphere of HD 209458b is determined by the Boltzmann equation with a photochemical source function due to the dissociation.

The calculated formation rates and spectra were used as source functions in the kinetic Boltzmann equation for the suprathermal fraction of atomic hydrogen (Shematovich 2010). Simulations show that the distribution functions of hot H significantly deviate from the local equilibrium distributions. At heights of the maximal production of hydrogen atoms due to the dissociation of H_2, a significant fraction of hydrogen atoms with energies high enough to escape the planetary gravitational field (about 6.9 eV) is formed, in contrast to the local equilibrium distribution.

Using the numerical stochastic model created by Shematovich (2004) for a hot planetary corona the kinetics and transfer of suprathermal hydrogen atoms in the upper atmosphere and the emergent flux of atoms evaporating from the atmosphere were investigated. The latter is estimated as 5.8×10^{12} cm^{-2} s^{-1} for a moderate stellar activity level of XUV radiation, which leads to a protoatmosphere evaporation rate of 5.8×10^9 g/s due to the process of the dissociation of H_2. This estimate is approaching the observational value of $\sim 10^{10}$ g/s for the rate of atmospheric loss of HD 209458b.

These studies show that input of the suprathermals should be taken into account in the aeronomic models to estimate the escape of the hydrogen-dominated protoatmospheres.

4.3 Observations and Models of Hot Jupiters

HD 209458b is the first observed transiting exoplanet and presents the earliest evidence (transit depth of Lyman-α) of the existence of an extended hydrogen cloud surrounding hot Jupiters (Vidal-Madjar et al. 2004). Soon it was discovered that the extended cloud surrounding the planet includes not only hydrogen atoms but also other species: O and C^+ (Vidal-Madjar et al. 2004), Si^+ and Si^{2+} (Linsky et al. 2010), and Mg (Vidal-Madjar et al. 2013). These observations provide a unique opportunity to test upper atmosphere models.

Although many workers have theoretically studied the thermosphere of HD 209458b (Yelle 2004; Tian et al. 2005b; Erkaev et al. 2007; García Muñoz 2007; Schneiter et al. 2007; Penz et al. 2008; Holmstrom et al. 2008; Murray-Clay et al. 2009; Ekenback et al. 2010; Stone and Proga 2009; Guo 2011; Trammell et al. 2011; Shaikhislamov et al. 2014; Kislyakova et al. 2014b), Koskinen et al. (2013b) developed probably the most comprehensive model to date for the thermosphere of hot Jupiter HD 209458b. The model considered photochemistry of H, He, C, N, O, Si, and their ions, and computes the stellar heating rates based on previous estimates of photoelectron heating efficiencies (the fraction of photoelectron energy that heats the thermosphere, not the overall heating efficiency). The globally averaged mass loss rate for HD 209458b in Koskinen et al. (2013b) is close to those in Yelle (2004), Yelle et al. (2008), Tian et al. (2005b), and García Muñoz (2007), but is more than 6 times greater than the value in Murray-Clay et al. (2009), which could be due to the gray assumption and a factor of 4 lower total XUV energy used in the later. Koskinen et al. (2013b) showed that the velocity and temperature differences between different species in the thermosphere of HD 209458b are small—separation of species near the homopause level is not efficient in a hydrodynamic upper atmosphere and the single fluid approximation of the momentum and energy equations is valid. Koskinen et al. (2013b) also showed that (1) H and O remain neutral up to about $3R_p$ (planetary radii), explaining the—observed

transit depths in the H Lyman a and O lines (Vidal-Madjar et al. 2004, 2003); (2) C is ionized to C^+ at low altitude, explaining the observation of C^+ (Vidal-Madjar et al. 2004); (3) Si^+ is the dominant silicon species at heights less than $5R_p$ and Si^{2+} can be formed through charge exchange with H^+, explaining the observation of Si ions (Linsky et al. 2010).

Bourrier et al. have carried out a series of interesting observations and modeling of the highly extended upper atmospheres of HD 189733b and HD 209458b (Bourrier et al. 2013, 2014; Bourrier and Lecavelier des Etangs 2013). Most recently they concluded (Bourrier et al. 2015) that the Mg line at 2853 Å could provide observation opportunities to observe planets under severe mass change. Kislyakova et al. (2014a) adjusted their stellar wind upper atmosphere models in order to explain the Lyman-α transit observations of HD 209458b and found that the observations can be reproduced due to a complex interplay of the host star's radiation pressure, the hydrodynamically outward flowing upper atmosphere and the production of energetic hydrogen atoms via charge exchange around a magnetic obstacle that corresponds to a magnetic moment of the exoplanet that is about 10 % compared to that of Jupiter in the solar system.

Kislyakova et al. (2014b) applied a DSMC model on top of the upper atmosphere structures calculated in Erkaev et al. (2013) and Lammer et al. (2013) to calculate the hydrogen escape through stellar wind interaction from Kepler-11b-f. They found that the stellar wind erosion of the expanded hydrogen cloud around these super Earths enhances the total escape rates by only a few percent. However, the DSMC model suggests that high radiation pressure and frequent charge exchange between planetary wind and stellar wind result in highly asymmetric spatial distribution of the hydrogen cloud around these Kepler planets. Bisikalo et al. (2013a,b) studied the gas-dynamic interaction between the stellar wind and neutral planetary corona.

Usually the orbital velocities of hot Jupiters are supersonic relative to the stellar wind, resulting in the formation of a bow shock. Gas-dynamical modeling shows that the gaseous envelopes around hot Jupiters can belong to two classes, depending on the position of the collision point. If the collision point is inside the Roche lobe of the planet, the envelopes have almost the spherical shapes of classical atmospheres, slightly distorted by the influence of the star and interactions with the stellar-wind gas. Firstly, if the collision point is located outside the Roche lobe, outflows from the vicinity of the Lagrangian points L_1 and L_2 arise, and the envelope becomes substantially asymmetrical. The latter class of objects can also be divided into two types. If the dynamical pressure of the stellar-wind gas is high enough to stop the most powerful outflow from the vicinity of the inner Lagrangian point L_1, a closed quasi-spherical envelope with a complex shape forms in the system. Secondly, if the wind is unable to stop the outflow from L_1, an open non-spherical envelope forms. Using the typical hot Jupiter HD 209458b as an example, it was shown (Bisikalo et al. 2013a,b) that all three types of atmospheres could exist within the range of estimated parameters of this planet. Since different types of envelopes have different transit light curves, determining the type of envelope in HD 209458b could impose additional constraints on the parameters of this exoplanet.

Khodachenko et al. (2012) pointed out that hydrodynamic planetary atmospheres driven by stellar XUV radiation must necessarily lead to the formation of a plasmasphere much different from those around solar system planets. In this case, the expanding planetary plasma (planetary wind) interacts with the stellar winds and the intrinsic planetary magnetic fields, leading to the development of extended magnetodisks and the magnetic field produced by magnetodisk ring currents could dominate that of an intrinsic dipole magnetic field. As a result, the magnetospheres of planets with a hydrodynamic upper atmosphere could be more than 40 larger than those only considering a planetary dipole magnetic field. This point has important implications for estimating non-thermal escape due to erosion by the stellar wind.

Cohen and Glocer (2012) estimated that the polar wind effect, ions flowing out along open magnetic field lines, could increase the atmospheric escape rate from hot Jupiters by more than 10 times.

Tanaka et al. (2014) investigated mass loss driven by magnetohydrodynamic (MHD) waves in a 1D flux tube model and found mass loss rates similar to those inferred from observations. Valsecchi et al. (2014) studied how Roche lobe overflow could have reduced the mass of a hot Jupiter near the Roche limit of its orbit. Their model calculation results can produce small planets with masses ranging from that of the Earth to Neptune. Fortney et al. (2013) suggested that the atmospheres of sub-Neptune and Neptune-class exoplanets may experience dramatic increase in metallicity with time because of hydrogen escape.

Guo (2013) presented a two dimensional multi-fluid (H and H^+) hydrodynamic model with two-dimensional radiative transfer. They found that the planetary winds demonstrate significant horizontal movements and lower density and radial velocity are present near the polar regions. As a result, atmospheric escape is dominated by outflow from low-latitude regions. Guo (2013) also discussed the influence of two-dimensional radiative transfer on mass loss rates. They found that the 2D hydrodynamics together with the 2D radiative transfer model produced mass loss rates 7 times smaller than that of their 1D model due to a self-shielding effect (the night side upper atmosphere being shielded by the dayside and thus does not receive stellar XUV radiation). The Guo (2013) model also suggests the potential importance of multi-dimensionality in future planetary thermosphere modeling.

Volkov and Johnson (2013) studied the 1D single component hydrodynamic escape problem with a DSMC model. Since fluid models should not be used in collisionless regions, a combination of a fluid model, which requires collisions to be frequent enough, below the exobase level and a kinetic model, which does not assume frequent collisions, above this level is more physically consistent. Villarreal D'Angelo et al. (2014) investigated the dynamic response of close-in exoplanets to different stellar wind conditions and found that the mass loss rate from HD 209458b is not sensitive to the stellar wind conditions in comparison with the mass loss rates in the literature.

4.4 Evolution Models

Using a planet thermal evolution model, which studies how a giant planetary mass and radius evolve in time due to the loss of its internal heat, in combination with the energy limited formula discussed in Sect. 2 and a constant efficiency factor for atmospheric escape, Lopez et al. (2012) found that observed exoplanets could be characterized by a threshold with two controlling factors: (1) the product of planetary mass and mean density, and (2) the incident stellar bolometric flux at the top of the planetary atmosphere. They argue that planets above this threshold would not be able to maintain their hydrogen envelope because of efficient atmospheric escape driven by stellar XUV. The efficiency factor, as a free parameter in Lopez et al. (2012), is ~ 10 for all low mass low density exoplanets explored.

Lopez and Fortney (2013) further investigated the influence of the efficiency factor, total planet mass, and planet's core mass on atmospheric escape with similar methods as in Lopez et al. (2012) and suggested that the planet's core mass, not its total mass, and the efficiency factor are most important in controlling atmospheric escape of observed transiting exoplanets with masses less than 100 Earth mass. The Lopez and Fortney (2013) model can explain well the orders of density and size in multi-planet systems (Ciardi et al. 2013; Wu and Lithwick 2013). Furthermore Lopez and Fortney (2013) predicted that 1.8–4.0 Earth radii planets should be uncommon on orbits with period less than 10 days and proposed that there could be a narrow valley in the incident flux vs. planet size (between 1 and 4 Earth

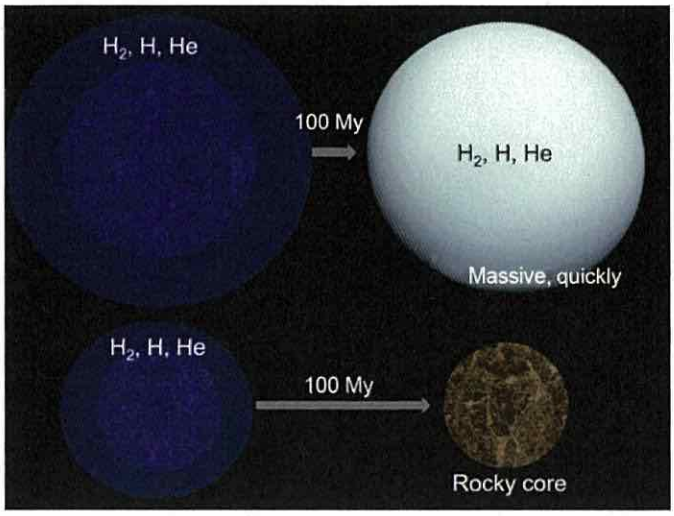

Fig. 11 *Upper panel*: a super-Earth mass core that accreted in the nebula and captured a dense H_2/He envelope may not completely lose its envelope after the nebula dissipated. As a result the planet evolves to a hydrogen-dominated mini-Neptune. *Lower panel*: a rocky core with lower mass may not accumulate enough gas envelope during the formation. Thus it may lose all of its captured H_2/He envelope and evolve to a "terrestrial" planet (Lammer et al. 2014; Luger et al. 2015)

radii) diagram where planet occurrence rate should be at a minimum. This is consistent with the physically intuitive concept that larger planets can better keep their hydrogen envelopes and smaller planets have stronger tendency to lose their hydrogen envelopes under certain stellar bolometric flux. Lopez and Fortney (2013) also proposed several uncertainty factors which could potentially smear the "occurrence valley".

Kurokawa and Nakamoto (2014) modeled the evolution of hot Jupiters around solar mass stars by considering atmospheric escape and thermal contraction. Under lower XUV conditions, they used the energy-limited escape formula of Lopez et al. (2012); under higher XUV conditions, a semianalytical model is applied following the analytical approach of Murray-Clay et al. (2009). They found that atmospheric escape leads to a dichotomy of populations: hot Jupiters keeping their envelopes and super Earths whose envelopes are completely lost, consistent with the findings of Lopez et al. (2012) and Lopez and Fortney (2013).

Kurosaki et al. (2014) studied the loss of water of hot super- and sub-Earths around solar mass stars by applying the energy limited escape formula and found that the threshold mass below which the planet has its water envelope stripped off in 1–10 Gyr is 10 times smaller than that for H and He envelope models by Lopez and Fortney (2013). In particular planets with masses less than 3 Earth masses orbiting at 0.03 AU could lose all of their oceans in 1–10 Gyrs; while water-rich planets with radii ~ 1.5 Earth radii should be common because they can keep their water envelopes against atmospheric escape.

Lammer et al. (2014) investigated how atmospheric escape influences the hydrogen envelopes of rocky planets from 0.1 to 5 Earth masses at 1 AU around solar mass stars. The model includes gravitational attraction and accumulation of nebula gas around a planet's core before the dissipation of the disk and the escape of these accumulated hydrogen-dominated protoatmospheres. A hydrodynamic upper atmosphere model is used to calculate the loss rates induced by stellar XUV radiation. As illustrated in Fig. 11, sub-Earths and Earth-mass planets can lose their captured hydrogen envelopes during the first 100 Myrs after the disc dissipated while more massive super-Earths are able to keep most of the captured hydrogen envelopes (Lammer et al. 2014). They concluded that habitable planets around solar mass stars should have core masses around 1 ± 0.5 Earth masses (corresponding to $0.8 \sim 1.15$ Earth radii). Recently, Luger et al. (2015) studied the atmospheric mass loss related transformation of hydrogen-dominated mini-Neptunes into super-Earth cores inside the habitable zone of M dwarfs and obtained similar results as Lammer et al. (2014) for similar bodies in the habitable zone of G stars. However, it is important to note that the

probability that rocky cores which experienced such transition to be able to maintain an Earth-like ocean is very small as shown by Tian and Ida (2015).

A most recent development on protoatmospheric escape concerns the effect of early luminosity evolution of M dwarfs. Since the stellar luminosity of M dwarfs decreases by more than one order of magnitude during their pre-main-sequence (PMS) phase, planets in the habitable zones of main sequence M dwarfs were much hotter during the PMS phase and thus could have become dehydrated (Ramirez and Kaltenegger 2014; Tian and Ida 2015; Luger et al. 2015). The result of this escape could lead to the formation of oxygen-rich atmospheres provided that the reaction between atmospheric oxygen and surface materials is slow (Luger et al. 2015). Tian (2015) showed that the same process could potentially lead to the loss of the dense O_2 atmospheres on low mass exoplanets. In addition the reactions between magma ocean and atmospheric oxygen could become efficient enough to remove dense O_2 atmospheres.

In comparison to the simple parameterized treatment of atmospheric escape (Lopez et al. 2012; Lopez and Fortney 2013; Kurokawa and Nakamoto 2014; Jin et al. 2014; Ramirez and Kaltenegger 2014; Tian and Ida 2015; Luger et al. 2015), Owen and Wu (2013) took a more sophisticated approach. They generated a table of atmospheric escape rates as functions of ionizing flux, planetary mass, and planetary radius based on calculations using the previously developed model of Owen and Jackson (2012), and considered atmospheric escape using the general purpose MESA (Modules FOR Experiments In Stellar Astrophysics) stellar evolution code to simulate planetary structure and evolution. Thus no direct assumption on escape or heating efficiency is made in Owen and Wu (2013).

However, the Owen and Jackson (2012) model uses a temperature-ionization parameter relationship taken from Owen et al. (2010), which was originally used in calculating the photo-evaporation of discs around solar-type stars, to compute the gas temperature from the local number density of planetary atmospheres and incident X-ray for the region where heating by X-rays is important. In the region where EUV heating is important, Owen and Jackson (2012) argues that the gas should thermostat to 10^4 K in radiative equilibrium and an isothermal equation of state is employed. The ionization parameter in Owen and Jackson (2012) model includes a parameterized metallicity scaling law also originally developed for protoplanetary disc. Owen and Jackson (2012) concluded that the main driving force of atmospheric escape in hydrogen dominated planetary upper atmosphere should be stellar X-ray, and suggested that stellar EUV radiation's contribution to atmospheric escape is less than 10 %. Note that Owen and Jackson (2012) derived an escape efficiency between 5 % and 20 %, which is the source of the 10 efficiency value used in the studies using simple parameterization.

The main conclusions of Owen and Wu (2013) are that atmospheres largely determine the observed size distribution of close-in Kepler planets. Similar to Owen and Jackson (2012) and Owen and Wu (2013), Erkaev et al. (2013) and Lammer et al. (2013) developed a hydrodynamic model to investigate atmospheric escape from hydrogen dominant planetary atmospheres. Their models use constant heating efficiencies, the conversion of absorbed stellar XUV photon energy to heat, of 15 % and 60 %, and employed a two dimensional radiative transfer scheme similar to that in Tian et al. (2005a,b). Lammer et al. (2013) applied this model to transiting super-Earths with inflated radii and known masses (Kepler-11b-f, GJ 1214b and 55 Cnc e) and found that all of them except Kepler-11c can reach the blow-off state because their thermospheres reach the Roche lobes. Note that the mass loss rates predicted in Lammer et al. (2013) are one to two orders of magnitude lower than that of hot Jupiters HD 209458b and XUV heating is the main driving force for atmospheric escape in Erkaev et al. (2013) and Lammer et al. (2013).

Regarding whether an energy limited formula can be used to estimate atmospheric escape rates from hydrodynamic planetary atmospheres, Erkaev et al. (2013) and Lammer et al. (2013) showed that, by comparing the escape rates obtained by the hydrodynamic upper atmosphere model with the energy-limited equation, the overestimation of escape rates can be as small as a factor of 2 for some Kepler super Earths, which is well within parametrical uncertainties. However, application of the energy-limited equation for cooler exoplanetary atmospheres can overestimate the escape rate by one or two orders of magnitude in comparison with the results of the hydrodynamical upper atmosphere model of Chadney et al. (2015). Moreover, the energy-limited formula may also overestimate the atmospheric loss rate if one assumes a hydrogen-dominated atmosphere but in reality heavier atoms or molecules are also present. Thus again caution is required when using the energy limited formula.

Despite the debate on what the correct escape efficiency should be for protoatmospheres, the suggestion that there is a threshold of stellar XUV irradiance beyond which hydrogen envelopes of low mass exoplanets are unstable should be robust for the current level of details of physics in the models.

4.5 Summary

Future modeling of protoatmospheres of rocky planets should include fully coupled photochemistry and radiative transfer. Two or three dimensional hydrodynamical models will be important not only to better calculate atmospheric escape rates, but also to be compared against observations. Since fluid models should not be used in collisionless regions, a combination of fluid models below the exobase level and kinetic models above this level is more physically self-consistent. In addition the effect of planetary magnetic field, the influences of stellar gravity and magnetic field are all important processes for close-in exoplanets.

With more exoplanet detection missions (TESS, CHEOPS, PLATO 2.0, etc.) and facilities (NGTS, etc.) planned and about to be put in action, hundreds if not thousands of low mass exoplanets will be available for future facilities to characterize. This will start a new age of study for protoatmospheric escape by providing unprecedented opportunities to compare numerical models with direct observations. The research field of atmospheric escape has already been invigorated by exoplanet discoveries. It can be expected that with the new wave of exoplanet discoveries, atmospheric escape research will soon enter an even more exciting period.

5 Conclusion and Perspectives

The formation and evolution of protoatmospheres depend on different factors that have been reviewed in this chapter. The first section concerns the initial conditions given by disk gas accretion, such as, the timing between dissipation and accretion of disk gas and thermodynamic conditions. The structure and mass of the protoatmosphere depend on the mass of the solid protoplanet, the energy supply rate and opacity, the temperature and density of the ambient disk gas, and the composition (e.g., mean molecular weight) of the atmosphere. Depending on the position within the disk and the timing of formation, a planet of the size of Earth is thought to be able to capture an atmosphere on the order of 0.3 to 1000 water oceans. Temperature at a given location in the disk gas depends on accretion energy and thus, should also be linked to the temperature conditions at the surface at an early stage in the planet's history. Since there is also an interplay between the surface and atmospheric

conditions at the end of accretion, and geodynamic regimes influencing heat flux from the planet's interior, the knowledge of surface conditions and volatile composition, is thus an important constraint to determine the future planetary evolution and this was the objective of the second section. Recent coupled atmospheric/interior models showed that two regimes exist depending on the distance from the star. For so called type II planets closer to the star than a critical distance, the surface might be covered by a magma ocean. For type I planets, farther from the star, the surface would either be covered by a water ocean or an ice layer. These first conclusions depend also on the modeling of the process of gas escape from protoatmospheres and multiple impacts during accretion will also change initial stage of the atmosphere and solid surface of a growing planets (see Sect. 4). Below, we summarize some current research directions and still open questions:

- What causes the diversity in the hydrogen content of planets?
- How much volatiles can be trapped in the planet interior?
- Required is to develop fully coupled models of photochemistry, radiative transfer and escape processes.

Aside from progressing in the knowledge of: thermal evolution of atmospheres, escape processes, convective models of planetary interiors, disk gas evolution and impact scenario, there is a need for more simple coupled models which take advantage of advances from all these fields. Applications of such models will be able to be tested in the forthcoming, promising period of further exoplanets discoveries.

Acknowledgements The authors greatly acknowledge both of the reviewers for their careful reading of our manuscript and valuable suggestions. H. Massol, P. Sarda, A. Davaille, E. Chassefière, E. Marcq and F. Leblanc are supported by the 2016 PNP program of INSU-CNRS. F. Tian is supported by the National Natural Science Foundation of China (41175039), the Startup Fund of the Ministry of Education of China, and the Tsinghua University Initiative Science Research Program (523001028). V. Shematovich acknowledges the support by the Russian Science Foundation Project No. 14-12-01048. H. Lammer acknowledges support by the FWF NFN project S11601-N16 'Pathways to Habitability: From Disks to Active Stars, Planets and Life', and the related FWF NFN subproject, S11607-N16 'Particle/Radiative Interactions with Upper Atmospheres of Planetary Bodies Under Extreme Stellar Conditions', as well as the FWF project P27256-N27 'Characterizing Stellar and Exoplanetary Environments via Modeling of Lyman-α Transit Observations of Hot Jupiters'. K. Hamano and Y. Abe are supported by a Grant-in-Aid for Scientific Research on Innovative Areas from the Ministry of Education, Culture, Sports, Science and Technology (MEXT) (No. 23103003) and K. Hamano by a Grant-in-Aid for Young Scientists (B) from Japan Society for the Promotion of Science (JSPS) (No. 26800242). Y. Hori is supported by Grant-in-Aid for Scientific Research on Innovative Areas (No. 26103711) from MEXT. M. Ikoma is supported by Grants-in-Aid for Scientific Research on Innovative Areas (No. 23103005) and Scientific Research (C) (No. 25400224) from the Ministry of Education, Culture, Sports, Science and Technology (MEXT) of Japan. Finally the authors thank the International Space Science Institute (ISSI) and ISSI-Beijing in Bern and Beijing.

References

Y. Abe, Physical state of the very early Earth. Lithos **30**(3), 223–235 (1993), the evolving Earth

Y. Abe, Thermal and chemical evolution of the terrestrial magma ocean. Phys. Earth Planet. Inter. **100**(1-4), 27–39 (1997)

Y. Abe, Protoatmospheres and surface environment of protoplanets. Earth Moon Planets **108**(1), 9–14 (2011)

Y. Abe, T. Matsui, The formation of an impact-generated H_2O atmosphere and its implications for the early thermal history of the Earth. J. Geophys. Res., Solid Earth **90**(S02), C545–C559 (1985)

Y. Abe, T. Matsui, Early evolution of the Earth: accretion, atmosphere formation, and thermal history. J. Geophys. Res., Solid Earth **91**(B13), E291–E302 (1986)

Y. Abe, T. Matsui, Evolution of an impact-generated H_2O-CO_2 atmosphere and formation of a hot protoocean on Earth. J. Atmos. Sci. **45**(21), 3081–3101 (1988)

Y. Abe, E. Ohtani, T. Okuchi, K. Righter, M. Drake, *Water in the Early Earth* (University of Arizona Press, Tucson, 2000), pp. 413–433
Y. Abe, A. Abe-Ouchi, N.H. Sleep, K.J. Zahnle, Habitable zone limits for dry planets. Astrobiology **11**, 443–460 (2011)
C.B. Agnor, R.M. Canup, H.F. Levison, On the character and consequences of large impacts in the late stage of terrestrial planet formation. Icarus **142**, 219–237 (1999)
Y. Alibert, F. Carron, A. Fortier, S. Pfyffer, W. Benz, C. Mordasini, D. Swoboda, Theoretical models of planetary system formation: mass vs. semi-major axis. Astron. Astrophys. **558**, A109 (2013)
C. Allègre, T. Staudacher, P. Sarda, Rare gas systematics: formation of the atmosphere, evolution and structure of the Earth's mantle. Earth Planet. Sci. Lett. **81**(2–3), 127–150 (1987)
C.J. Allègre, G. Manhès, C. Göpel, The major differentiation of the Earth at 4.45 Ga. Earth Planet. Sci. Lett. **267**, 386–398 (2008)
D. Andrault, N. Bolfan-Casanova, G.L. Nigro, M.A. Bouhifd, G. Garbarino, M. Mezouar, Solidus and liquidus profiles of chondritic mantle: implication for melting of the Earth across its history. Earth Planet. Sci. Lett. **304**(1–2), 251–259 (2011)
G.E. Ballester, D.K. Sing, F. Herbert, The signature of hot hydrogen in the atmosphere of the extrasolar planet HD 209458b. Nature **445**(7127), 511–514 (2007)
I. Baraffe, F. Selsis, G. Chabrier, T.S. Barman, F. Allard, P.H. Hauschildt, H. Lammer, The effect of evaporation on the evolution of close-in giant planets. Astron. Astrophys. **419**(2), L13–L16 (2004)
N.M. Batalha, Exploring exoplanet populations with NASA's Kepler mission. Proc. Natl. Acad. Sci. USA **111**, 12647–12654 (2014)
L. Ben-Jaffel, S. Hosseini, On the existence of energetic atoms in the upper atmosphere of exoplanet HD 209458b. Astrophys. J. **709**(2), 1284 (2010)
K. Berlo, J. Gardner, J. Blundy, Timescales of magma degassing, in *Timescales of Magmatic Processes: From Core to Atmosphere* (Wiley-Blackwell, Hoboken, 2011), Ch. 11
D.V. Bisikalo, P.V. Kaigorodov, D.E. Ionov, V.I. Shematovich, Types of gaseous envelopes of "hot Jupiter" exoplanets. Astron. Rep. **57**(10), 715–725 (2013a)
D. Bisikalo, P. Kaygorodov, D. Ionov, V. Shematovich, H. Lammer, L. Fossati, Three-dimensional gas dynamic simulation of the interaction between the exoplanet wasp-12b and its host star. Astrophys. J. **764**(1), 19 (2013b)
P. Bodenheimer, J.J. Lissauer, Accretion and evolution of ~2.5 $M_\oplus$ planets with voluminous H/He envelopes. Astrophys. J. **791**, 103 (2014)
P. Bodenheimer, J.B. Pollack, Calculations of the accretion and evolution of giant planets. The effects of solid cores. Icarus **67**, 391–408 (1986)
V. Bourrier, A. Lecavelier des Etangs, 3d model of hydrogen atmospheric escape from HD 209458b and HD 189733b: radiative blow-out and stellar wind interactions. Astron. Astrophys. **557**, A124 (2013)
V. Bourrier, A. Lecavelier des Etangs, H. Dupuy, D. Ehrenreich, A. Vidal-Madjar, G. Hébrard, G.E. Ballester, J.-M. Désert, R. Ferlet, D.K. Sing, P.J. Wheatley, Atmospheric escape from HD 189733b observed in hi Lyman α: detailed analysis of HST/STIS September 2011 observations. Astron. Astrophys. **551**, A63 (2013)
V. Bourrier, A. Lecavelier des Etangs, A. Vidal-Madjar, Modeling magnesium escape from HD 209458b atmosphere. Astron. Astrophys. **565**, A105 (2014)
V. Bourrier, A. Lecavelier des Etangs, A. Vidal-Madjar, The Mg i line: a new probe of the atmospheres of evaporating exoplanets. Astron. Astrophys. **573**, A11 (2015)
R. Brasser, The formation of Mars: building blocks and accretion time scale. Space Sci. Rev. **174**, 11–25 (2013)
E.L. Brown, C.E. Lesher, North Atlantic magmatism controlled by temperature, mantle composition and buoyancy. Nat. Geosci. **7**(11), 820–824 (2014)
H.P. Brown, A.J. Panshin, C.C. Forsaith, *Textbook of Wood Technology* (1949)
A. Burgisser, M. Alletti, B. Scaillet, Simulating the behavior of volatiles belonging to the C–O–H–S system in silicate melts under magmatic conditions with the software d-compress. Comput. Geosci. **79**, 1–14 (2015)
R.M. Canup, Dynamics of lunar formation. Annu. Rev. Astron. Astrophys. **42**, 441–475 (2004a)
R.M. Canup, Simulations of a late lunar-forming impact. Icarus **168**(2), 433–456 (2004b)
M.R. Carroll, J.R. Holloway, *Volatiles in Magmas*. Reviews in Mineralogy, vol. 30 (Mineralogical Society of America, Washington, 1994)
C. Cecchi-Pestellini, A. Ciaravella, G. Micela, T. Penz, The relative role of EUV radiation and x-rays in the heating of hydrogen-rich exoplanet atmospheres. Astron. Astrophys. **496**(3), 863–868 (2009)
J. Chadney, M. Galand, Y. Unruh, T.T. Koskinen, J. Sanz-Forcada, XUV-driven mass loss from extrasolar giant planets orbiting active stars. Icarus **250**, 357–367 (2015)
J.W. Chamberlain, Planetary coronae and atmospheric evaporation. Planet. Space Sci. **11**(8), 901–960 (1963)

E. Chassefière, Hydrodynamic escape of hydrogen from a hot water-rich atmosphere: the case of Venus. J. Geophys. Res., Planets **101**(E11), 26039–26056 (1996a)
E. Chassefière, Hydrodynamic escape of oxygen from primitive atmospheres: applications to the cases of Venus and Mars. Icarus **124**, 537–552 (1996b)
E. Chassefière, F. Leblanc, B. Langlais, The combined effects of escape and magnetic field histories at Mars. Planet. Space Sci. **55**(3), 343–357 (2007)
J.Y. Chaufray, R. Modolo, F. Leblanc, G. Chanteur, R.E. Johnson, J.G. Luhmann, Mars solar wind interaction: formation of the martian corona and atmospheric loss to space. J. Geophys. Res., Planets **112**(E9), E09009, e09009 (2007)
D.R. Ciardi, D.C. Fabrycky, E.B. Ford, T.N. Gautier III., S.B. Howell, J.J. Lissauer, D. Ragozzine, J.F. Rowe, On the relative sizes of planets within Kepler multiple-candidate systems. Astrophys. J. **763**(1), 41 (2013)
W. Clarke, M. Beg, H. Craig, Excess ^{3}He in the sea: evidence for terrestrial primodal helium. Earth Planet. Sci. Lett. **6**(3), 213–220 (1969)
O. Cohen, A. Glocer, Ambipolar electric field, photoelectrons, and their role in atmospheric escape from hot Jupiters. Astrophys. J. Lett. **753**(1), L4 (2012)
N.R. Council, *The Limits of Organic Life in Planetary Systems* (The National Academies Press, Washington, 2007)
H. Craig, J. Lupton, Helium 3 and mantle volatiles in the ocean and the oceanic crust, in *The Oceanic Lithosphere*, vol. 7 (Wiley, New York, 1981)
E. Crawford, Arrhenius' 1896 model of the greenhouse effect in context, in *Ambio*, Stockholm, vol. 26 (1997), pp. 6–11
N. Dauphas, A. Pourmand, Hf-W-Th evidence for rapid growth of Mars and its status as a planetary embryo. Nature **473**, 489–492 (2011)
A. Davaille, A. Limare, Laboratory studies of mantle convection, in *Treatise on Geophysics (Second Edition). Vol. "Mantle Dynamics"*, ed. by G. Schubert, D. Bercovici (Elsevier, Amsterdam, 2015), pp. 73–144
T.A. Davis, P.J. Wheatley, Evidence for a lost population of close-in exoplanets. Mon. Not. R. Astron. Soc. **396**(2), 1012–1017 (2009)
A. Lecavelier des Etangs, A diagram to determine the evaporation status of extrasolar planets. Astron. Astrophys. **461**(3), 1185–1193 (2007)
A. Lecavelier des Etangs, A. Vidal-Madjar, J.C. McConnell, G. Hébrard, Atmospheric escape from hot Jupiters. Astron. Astrophys. **418**(1), L1–L4 (2004)
K.-M. Dittkrist, C. Mordasini, H. Klahr, Y. Alibert, T. Henning, Impacts of planet migration models on planetary populations. Effects of saturation, cooling and stellar irradiation. Astron. Astrophys. **567**, A121 (2014)
A. Ekenback, M. Holmstrom, M. Wurz et al., Energetic neutral atoms around HD 209458b: estimations of magnetospheric properties. Astrophys. J. **709**, 670–679 (2010)
L.T. Elkins-Tanton, Linked magma ocean solidification and atmospheric growth for Earth and Mars. Earth Planet. Sci. Lett. **271**(1), 181–191 (2008)
L.T. Elkins-Tanton, Magma oceans in the inner solar system, in *Annual Review of Earth and Planetary Sciences*, ed. by R. Jeanloz. Annual Review of Earth and Planetary Sciences, vol. 40 (2012), pp. 113–139
L. Elkins-Tanton, E. Parmentier, P. Hess, Magma ocean fractional crystallization and cumulate overturn in terrestrial planets: implications for Mars. Meteorit. Planet. Sci. **38**(12), 1753–1771 (2003)
L. Elkins-Tanton, S. Zaranek, E. Parmentier, P. Hess, Early magnetic field and magmatic activity on Mars from magma ocean cumulate overturn. Earth Planet. Sci. Lett. **236**(1-2), 1–12 (2005)
N.V. Erkaev, Y.N. Kulikov, H. Lammer, F. Selsis, D. Langmayr, G.F. Jaritz, H.K. Biernat, Roche lobe effects on the atmospheric loss from "hot Jupiters". Astron. Astrophys. **472**(1), 329–334 (2007)
N.V. Erkaev, H. Lammer, P. Odert, Y.N. Kulikov, K.G. Kislyakova et al., XUV-exposed, non-hydrostatic hydrogen-rich upper atmospheres of terrestrial planets. Part i: Atmospheric expansion and thermal escape. Astrobiology **13**(11), 1011–1029 (2013)
N.V. Erkaev, H. Lammer, L.T. Elkins-Tanton, A. Stökl, P. Odert, E. Marcq, E.A. Dorfi, K.G. Kislyakova, Y.N. Kulikov, M. Leitzinger, M. Güdel, Escape of the martian protoatmosphere and initial water inventory. Planet. Space Sci. **98**, 106–119 (2014)
N.V. Erkaev, H. Lammer, P. Odert, Y.N. Kulikov, K.G. Kislyakova, Extreme hydrodynamic atmospheric loss near the critical thermal escape regime. Mon. Not. R. Astron. Soc. **448**(2), 1916–1921 (2015)
F.P. Fanale, A case for catastrophic early degassing of the Earth. Chem. Geol. **8**(2), 79–105 (1971)
G. Fiquet, A.L. Auzende, J. Siebert, A. Corgne, H. Bureau, H. Ozawa, G. Garbarino, Melting of peridotite to 140 gigapascals. Science **329**(5998), 1516–1518 (2010)
D. Fisher, Trapped helium and argon and the formation of the atmosphere by degassing. Nature **256**(5513), 113–114 (1975)

J.J. Fortney, N. Nettelmann, The interior structure, composition, and evolution of giant planets. Space Sci. Rev. **152**, 423–447 (2010)
J. Fortney, C. Mordasini, N. Nettelmann, E.M.-R. Kempton, T.P. Greene, K. Zahnle, A framework for characterizing the atmospheres of low-mass low-density transiting planets. Astrophys. J. **775**(1), 80 (2013)
J.L. Fox, A.B. Hać, Photochemical escape of oxygen from Mars: a comparison of the exobase approximation to a Monte Carlo method. Icarus **204**(2), 527–544 (2009)
J. Fox, M. Galand, R. Johnson, Energy deposition in planetary atmospheres by charged particles and solar photons. Space Sci. Rev. **139**(1–4), 3–62 (2008)
N. Fujii, S. Uyeda, Conditions for a once molten Earth to cool. J. Phys. Earth **14**(1), 15–26 (1966)
A. García Muñoz, Physical and chemical aeronomy of HD 209458b. Planet. Space Sci. **55**(10), 1426–1455 (2007)
H. Genda, Y. Abe, Survival of a proto-atmosphere through the stage of giant impacts: the mechanical aspects. Icarus **164**, 149–162 (2003)
H. Genda, Y. Abe, Enhanced atmospheric loss on protoplanets at the giant impact phase in the presence of oceans. Nature **433**, 842–844 (2005)
G.J. Golabek, T. Keller, T.V. Gerya, G. Zhu, P.J. Tackley, J.A.D. Connolly, Origin of the martian dichotomy and Tharsis from a giant impact causing massive magmatism. Icarus **215**(1), 346–357 (2011)
C. Goldblatt, T.D. Robinson, K.J. Zahnle, D. Crisp, Low simulated radiation limit for runaway greenhouse climates. Nat. Geosci. **6**, 661–667 (2013)
D. Grinspoon, Implications of the high D/H ratio for the sources of water in Venus' atmosphere. Nature **363**, 428–431 (1993)
H. Gröller, V.I. Shematovich, H.I.M. Lichtenegger, H. Lammer, M. Pfleger, Y.N. Kulikov, W. Macher, U.V. Amerstorfer, H.K. Biernat, Venus' atomic hot oxygen environment. J. Geophys. Res., Planets **115**(E12), e12017 (2010)
H. Gröller, H. Lichtenegger, H. Lammer, V.I. Shematovich, Hot oxygen and carbon escape from the martian atmosphere. Planet. Space Sci. **98**, 93–105 (2014)
S. Grossmann, D. Lohse, Scaling in thermal convection: a unifying theory. J. Fluid Mech. **407**, 27–56 (2000)
M. Güdel, R. Dvorak, N. Erkaev, J. Kasting, M. Khodachenko, H. Lammer, E. Pilat-Lohinger, H. Rauer, I. Ribas, B.E. Wood, Astrophysical conditions for planetary habitability, in *Protostars and Planets VI* (2014), pp. 883–906
B. Guillot, P. Sarda, The effect of compression on noble gas solubility in silicate melts and consequences for degassing at mid-ocean ridges. Geochim. Cosmochim. Acta **70**(5), 1215–1230 (2006)
J.H. Guo, Escaping particle fluxes in the atmospheres of close-in exoplanets. I. Model of hydrogen. Astrophys. J. **733**(2), 98 (2011)
J.H. Guo, Escaping particle fluxes in the atmospheres of close-in exoplanets. II. Reduced mass-loss rates and anisotropic winds. Astrophys. J. **766**(2), 102 (2013)
K.E. Haisch Jr., E.A. Lada, C.J. Lada, Disk frequencies and lifetimes in young clusters. Astrophys. J. **553**, L153–L156 (2001)
A.N. Halliday, Mixing, volatile loss and compositional change during impact-driven accretion of the Earth. Nature **427**, 505–509 (2004)
Y. Hamano, M. Ozima, Earth atmosphere evolution model based on Ar isotopic data, in *Terrestrial Rare Gases* (Japan Sci. Soc., Tokyo, 1978), pp. 155–171
K. Hamano, Y. Abe, H. Genda, Emergence of two types of terrestrial planet on solidification of magma ocean. Nature **497**(7451), 607–610 (2013)
K. Hamano, H. Kawahara, Y. Abe, M. Onishi, G. Hashimoto, Lifetime and spectral evolution of a magma ocean with a steam atmosphere: its detectability by future direct imaging. Astrophys. J. **806**(2), 216 (17 pp.) (2015)
C. Hayashi, Structure of the solar nebula, growth and decay of magnetic fields and effects of magnetic and turbulent viscosities on the nebula. Prog. Theor. Phys. Suppl. **70**, 35–53 (1981)
C. Hayashi, K. Nakazawa, H. Mizuno, Earth's melting due to the blanketing effect of the primordial dense atmosphere. Earth Planet. Sci. Lett. **43**, 22–28 (1979)
C. Hayashi, K. Nakazawa, Y. Nakagawa, Formation of the solar system, in *Protostars and Planets II*, ed. by D.C. Black, M.S. Matthews (1985), pp. 1100–1153
P. Hess, E. Parmentier, A model for the thermal and chemical evolution of the Moon's interior: implications for the onset of mare volcanism. Earth Planet. Sci. Lett. **134**(3-4), 501–514 (1995)
L.A. Hillenbrand, Observational constraints on dust disk lifetimes: implications for planet formation (2005). ArXiv Astrophysics e-prints
T. Höink, J. Schmalzl, U. Hansen, Formation of compositional structures by sedimentation in vigorous convection. Phys. Earth Planet. Inter. **153**, 1–3 (2005)
M. Holmstrom, A. Ekenback, F. Selsis, T. Penz, H. Lammer, P. Wurz, Energetic neutral atoms as the explanation for the high-velocity hydrogen around HD 209458b. Nature **451**(7181), 970–972 (2008)

Y. Hori, M. Ikoma, Critical core masses for gas giant formation with grain-free envelopes. Astrophys. J. **714**, 1343–1346 (2010)
Y. Hori, S. Ida, D.N.C. Lin, Characterization of sub/super-Earths orbiting cool stars: water content and hydrogen-rich atmospheres. Astrophysical Journal (2016, submitted)
O. Hubickyj, P. Bodenheimer, J.J. Lissauer, Accretion of the gaseous envelope of Jupiter around a 5–10 Earth-mass core. Icarus **179**, 415–431 (2005)
S. Ida, J. Makino, Scattering of planetesimals by a protoplanet—slowing down of runaway growth. Icarus **106**, 210 (1993)
M. Ikoma, H. Genda, Constraints on the mass of a habitable planet with water of nebular origin. Astrophys. J. **648**, 696–706 (2006)
M. Ikoma, H. Emori, K. Nakazawa, Formation of giant planets in dense nebulae: critical core mass revisited. Astrophys. J. **553**, 999–1005 (2001)
M. Ikoma, Y. Hori, In situ accretion of hydrogen-rich atmospheres on short-period super-Earths: implications for the Kepler-11 planets. Astrophys. J. **753**, 66 (2012)
M. Ikoma, K. Nakazawa, H. Emori, Formation of giant planets: dependences on core accretion rate and grain opacity. Astrophys. J. **537**, 1013–1025 (2000)
A.P. Ingersoll, The runaway greenhouse: a history of water on Venus. J. Atmos. Sci. **26**, 1191–1198 (1969)
D.E. Ionov, D.V. Bisikalo, V.I. Shematovich, B. Huber, Ionization fraction in the thermosphere of the exoplanet HD 209458b. Sol. Syst. Res. **48**(2), 105–112 (2014)
W.H. Ip, On a hot oxygen corona of Mars. Icarus **76**(1), 135–145 (1988)
B.M. Jakosky, R.O. Pepin, R.E. Johnson, J.L. Fox, Mars atmospheric loss and isotopic fractionation by solar-wind-induced sputtering and photochemical escape. Icarus **111**(2), 271–288 (1994)
N. Jendrzejewski, T. Trull, F. Pineau, M. Javoy, Carbon solubility in mid-ocean ridge basaltic melt at low pressures (250–1950 bar). Chem. Geol. **138**(1-2), 81–92 (1997)
W.J. Jenkins, J.M. Edmond, J.B. Corliss, Excess ^{3}He and ^{4}He in Galapagos submarine hydrothermal waters. Nature **272**(5649), 156–158 (1978)
S. Jin, C. Mordasini, V. Parmentier, R. van Boekel, T. Henning, J. Ji, Planetary population synthesis coupled with atmospheric escape: a statistical view of evaporation. Astrophys. J. **795**(1), 65 (2014)
R.E. Johnson, M.R. Combi, J.L. Fox, W.H. Ip, F. Leblanc, M.A. McGrath, V.I. Shematovich, D.F. Strobel, J.H. Waite, Exospheres and atmospheric escape. Space Sci. Rev. **139**(1–4), 355–397 (2008)
L. Kamp, F. Taylor, S. Calcutt, Structure of Venus's atmosphere from modelling of night-side infrared spectra. Nature **336**, 360–362 (1988)
J. Kasting, Runaway and moist greenhouse atmospheres and the evolution of Earth and Venus. Icarus **74**, 472–494 (1988)
J.F. Kasting, J.B. Pollack, Loss of water from Venus. I. Hydrodynamic escape of hydrogen. Icarus **53**(3), 479–508 (1983)
J.F. Kasting, J.B. Pollack, T.P. Ackerman, Response of Earth's atmosphere to increases in solar flux and implications for loss of water from Venus. Icarus **57**, 335–355 (1984). doi:10.1016/0019-1035(84)90122-2
J.F. Kasting, D.P. Whitmire, R.T. Reynolds, Habitable zones around main sequence stars. Icarus **101**, 108–128 (1993)
H. Kawahara, T. Hirano, K. Kurosaki, Y. Ito, M. Ikoma, Starspots-transit depth relation of the evaporating planet candidate KIC 12557548b. Astrophys. J. Lett. **776**(1), L6 (2013)
M.L. Khodachenko, I. Alexeev, E. Belenkaya, H. Lammer, J.-M. Grießmeier, M. Leitzinger, P. Odert, T. Zaqarashvili, H.O. Rucker, Magnetospheres of "hot Jupiters": the importance of magnetodisks in shaping a magnetospheric obstacle. Astrophys. J. **744**(1), 70 (2012)
R. Kippenhahn, A. Weigert, *Stellar Structure and Evolution* (Springer, Berlin, 1994)
K.G. Kislyakova, M. Holmström, H. Lammer, P. Odert, M.L. Khodachenko, Magnetic moment and plasma environment of HD 209458b as determined from Lyα observations. Science **346**(6212), 981–984 (2014a)
K.G. Kislyakova, C.P. Johnstone, P. Odert, N.V. Erkaev, H. Lammer, T. Lüftinger, M. Holmström, M.L. Khodachenko, M. Güdel, Stellar wind interaction and pick-up ion escape of the Kepler-11 "super-Earths". Astron. Astrophys. **562**, A116 (2014b)
T. Kleine, M. Touboul, B. Bourdon, F. Nimmo, K. Mezger, H. Palme, S.B. Jacobsen, Q.-Z. Yin, A.N. Halliday, Hf-W chronology of the accretion and early evolution of asteroids and terrestrial planets. Geochim. Cosmochim. Acta **73**, 5150–5188 (2009)
E. Kokubo, H. Genda, Formation of terrestrial planets from protoplanets under a realistic accretion condition. Astrophys. J. Lett. **714**, L21–L25 (2010)
E. Kokubo, S. Ida, On runaway growth of planetesimals. Icarus **123**, 180–191 (1996)
E. Kokubo, S. Ida, Oligarchic growth of protoplanets. Icarus **131**, 171–178 (1998)

R.K. Kopparapu, R. Ramirez, J.F. Kasting, V. Eymet, T.D. Robinson, S. Mahadevan, R.C. Terrien, S. Domagal-Goldman, V. Meadows, R. Deshpande, Habitable zones around main-sequence stars: new estimates. Astrophys. J. Lett. **765**, 131 (2013)
T.T. Koskinen, R.V. Yelle, P. Lavvas, N.K. Lewis, Characterizing the thermosphere of HD 209458b with UV transit observations. Astrophys. J. **723**(1), 116 (2010)
T. Koskinen, R. Yelle, M. Harris, P. Lavvas, The escape of heavy atoms from the ionosphere of HD 209458b. II. Interpretation of the observations. Icarus **226**(2), 1695–1708 (2013a)
T.T. Koskinen, M.J. Harris, R.V. Yelle, P. Lavvas, The escape of heavy atoms from the ionosphere of HD 209458b. I. A photochemical–dynamical model of the thermosphere. Icarus **226**(2), 1678–1694 (2013b)
M.A. Krestyanikova, V.I. Shematovich, Stochastic models of hot planetary and satellite coronas: a hot oxygen corona of Mars. Sol. Syst. Res. **40**(5), 384–392 (2006)
H. Kurokawa, T. Nakamoto, Mass-loss evolution of close-in exoplanets: evaporation of hot Jupiters and the effect on population. Astrophys. J. **783**(1), 54 (2014)
K. Kurosaki, M. Ikoma, Y. Hori, Impact of photo-evaporative mass loss on masses and radii of water-rich sub/super-Earths. Astron. Astrophys. **562**, A80 (2014)
M. Kurz, W. Jenkins, J. Schilling, S. Hart, Helium isotopic variations in the mantle beneath the central North Atlantic Ocean. Earth Planet. Sci. Lett. **58**(1), 1–14 (1982)
T. La Tourette, G.J. Wasserburg, Mg diffusion in anorthite: implications for the formation of early solar planetisimals. Earth Planet. Sci. Lett. **158**, 91–108 (1998)
S. Labrosse, C. Jaupart, Thermal evolution of the Earth: secular changes and fluctuations of plate characteristics. Earth Planet. Sci. Lett. **260**(3–4), 465–481 (2007)
S. Labrosse, J.W. Hernlund, N. Coltice, A crystallizing dense magma ocean at the base of the Earth's mantle. Nature **450**(7171), 866–869 (2007)
H. Lammer, S.J. Bauer, Nonthermal atmospheric escape from Mars and Titan. J. Geophys. Res. Space Phys. **96**(A2), 1819–1825 (1991)
H. Lammer, F. Selsis, I. Ribas, E.F. Guinan, S.J. Bauer, W.W. Weiss, Atmospheric loss of exoplanets resulting from stellar X-ray and extreme-ultraviolet heating. Astrophys. J. Lett. **598**(2), L121 (2003)
H. Lammer, P. Odert, M. Leitzinger, M.L. Khodachenko, M. Panchenko, Y.N. Kulikov, T.L. Zhang, H.I.M. Lichtenegger, N.V. Erkaev, G. Wuchterl, G. Micela, T. Penz, H.K. Biernat, J. Weingrill, M. Steller, H. Ottacher, J. Hasiba, A. Hanslmeier, Determining the mass loss limit for close-in exoplanets: what can we learn from transit observations? Astron. Astrophys. **506**(1), 399–410 (2009)
H. Lammer, N.V. Erkaev, P. Odert, K.G. Kislyakova, M. Leitzinger, M.L. Khodachenko, Probing the blow-off criteria of hydrogen-rich 'super-Earths'. Mon. Not. R. Astron. Soc. **430**(2), 1247–1256 (2013)
H. Lammer, A. Stökl, N.V. Erkaev, E.A. Dorfi, P. Odert, M. Güdel, Y.N. Kulikov, K.G. Kislyakova, M. Leitzinger, Origin and loss of nebula-captured hydrogen envelopes from 'sub'- to 'super-Earths' in the habitable zone of sun-like stars. Mon. Not. R. Astron. Soc. **439**(4), 3225–3238 (2014)
M.A. Lange, T.J. Ahrens, The evolution of an impact-generated atmosphere. Icarus **51**(1), 96–120 (1982)
A.F. Lanza, Star-planet magnetic interaction and evaporation of planetary atmospheres. Astron. Astrophys. **557**, A31 (2013)
M. Le Bars, A. Davaille, Whole layer convection in a heterogeneous planetary mantle. J. Geophys. Res., Solid Earth **109**, B03403 (2004)
T. Lebrun, H. Massol, E. Chassefiere, A. Davaille, E. Marcq, P. Sarda, F. Leblanc, G. Brandeis, Thermal evolution of an early magma ocean in interaction with the atmosphere. J. Geophys. Res., Planets **118**(6), 1155–1176 (2013)
J. Leconte, F. Forget, B. Charnay, R. Wordsworth, A. Pottier, Increased insolation threshold for runaway greenhouse processes on Earth-like planets. Nature **504**, 268–271 (2013)
E.J. Lee, E. Chiang, C.W. Ormel, Make super-Earths, not Jupiters: accreting nebular gas onto solid cores at 0.1 AU and beyond. Astrophys. J. **797**, 95 (2014)
A.M. Lejeune, P. Richet, Rheology of crystal-bearing silicate melts: an experimental study at high viscosities. J. Geophys. Res., Solid Earth **100**, 4215–4229 (1995)
J.S. Lewis, R.G. Prinn, *Planets and Their Atmospheres: Origin and Evolution*, vol. 33 (Elsevier, Amsterdam, 1983)
J. Li, C. Agee, Geochemistry of mantle-core differentiation at high pressure. Nature **381**(6584), 686–689 (1996)
H.I.M. Lichtenegger, H. Gröller, H. Lammer, Y.N. Kulikov, V.I. Shematovich, On the elusive hot oxygen corona of Venus. Geophys. Res. Lett. **36**(10), L10204 (2009)
J.L. Linsky, H. Yang, K. France, C.S. Froning, J.C. Green, J.T. Stocke, S.N. Osterman, Observations of mass loss from the transiting exoplanet HD 209458b. Astrophys. J. **717**(2), 1291 (2010)
J.J. Lissauer, Timescales for planetary accretion and the structure of the protoplanetary disk. Icarus **69**, 249–265 (1987)

Y. Liu, Y. Zhang, H. Behrens, Solubility of H_2O in rhyolitic melts at low pressures and a new empirical model for mixed H_2O-CO_2 solubility in rhyolitic melts. J. Volcanol. Geotherm. Res. **143**(1–3), 219–235 (2005)
E.D. Lopez, J. Fortney, The role of core mass in controlling evaporation: the Kepler radius distribution and the Kepler-36 density dichotomy. Astrophys. J. **776**(1), 2 (2013)
E.D. Lopez, J.J. Fortney, Understanding the mass-radius relation for sub-Neptunes: radius as a proxy for composition. Astrophys. J. **792**, 1 (2014)
E.D. Lopez, J. Fortney, N. Miller, How thermal evolution and mass-loss sculpt populations of super-Earths and sub-Neptunes: application to the Kepler-11 system and beyond. Astrophys. J. **761**(1), 59 (2012)
R. Luger, R. Barnes, E. Lopez, J. Fortney, B. Jackson, V. Meadows, Habitable evaporated cores: transforming mini-Neptunes into super-Earths in the habitable zones of M dwarfs. Astrobiology **15**(1), 57–88 (2015)
J.G. Luhmann, R.E. Johnson, M.H.G. Zhang, Evolutionary impact of sputtering of the martian atmosphere by O^+ pickup ions. Geophys. Res. Lett. **19**(21), 2151–2154 (1992)
R.E. Lupu, K. Zahnle, M.S. Marley, L. Schaefer, B. Fegley, C. Morley, K. Cahoy, R. Freedman, J.J. Fortney, The atmospheres of earthlike planets after giant impact events. Astrophys. J. **784**, 27 (2014)
G.J.F. MacDonald, Calculations on the thermal history of the Earth. J. Geophys. Res. **64**(11), 1967–2000 (1959)
W.V.R. Malkus, The heat transport and spectrum of thermal turbulence. Proc. R. Soc. A, Math. Phys. Eng. Sci. (1954). doi:10.1098/rspa.1954.0197
E. Marcq, A simple 1-D radiative-convective atmospheric model designed for integration into coupled models of magma ocean planets. J. Geophys. Res., Planets **117**, 1001 (2012)
G.W. Marcy, L. Weiss, E.A. Petigura, H. Isaacson, A.W. Howard, L.A. Buchhave, Occurrence and core-envelope structure of 1-4x Earth-size planets around sun-like stars. Proc. Natl. Acad. Sci. USA **111**(35), 12655–12660 (2014)
M. Marov, V. Shematovich, D. Bisikalo, Non equilibrium aeronomic processes. Space Sci. Rev. **76**(1–2), 1–204 (1996)
D. Martin, R. Nokes, Crystal settling in a vigorously convecting magma chamber. Nature **332**, 534–536 (1988)
T. Matsui, Y. Abe, Impact-induced atmospheres and oceans on Earth and Venus. Nature **322**(6079), 526–528 (1986)
M. Maurice, N. Tosi, A.C. Plesa, D. Breuer, Evolution and consequences of magma ocean solidification, in *Goldschmidt Abstracts. No. 2060* (2015)
M.B. McElroy, Mars: an evolving atmosphere. Science **175**(4020), 443–445 (1972)
E. Miller-Ricci, M.R. Meyer, S. Seager, L. Elkins-Tanton, On the emergent spectra of hot protoplanet collision afterglows. Astrophys. J. **704**, 770–780 (2009)
H. Mizuno, K. Nakazawa, C. Hayashi, Instability of a gaseous envelope surrounding a planetary core and formation of giant planets. Prog. Theor. Phys. **60**, 699–710 (1978)
H. Mizuno, K. Nakazawa, C. Hayashi, Dissolution of the primordial rare gases into the molten Earth's material. Earth Planet. Sci. Lett. **50**, 202–210 (1980)
J. Monteux, N. Coltice, F. Dubuffet, Y. Ricard, Thermo-mechanical adjustment after impacts during planetary growth. Geophys. Res. Lett. **34**, L24201 (2007)
T. Montmerle, J.-C. Augereau, M. Chaussidon, M. Gounelle, B. Marty, A. Morbidelli, Solar system formation and early evolution: the first 100 million years. Earth Moon Planets **98**(1–4), 39–95 (2006)
C. Mordasini, Grain opacity and the bulk composition of extrasolar planets. II. An analytical model for grain opacity in protoplanetary atmospheres. Astron. Astrophys. **572**, A118 (2014)
C. Mordasini, Y. Alibert, C. Georgy, K.-M. Dittkrist, H. Klahr, T. Henning, Characterization of exoplanets from their formation. II. The planetary mass-radius relationship. Astron. Astrophys. **547**, A112 (2012a)
C. Mordasini, Y. Alibert, H. Klahr, T. Henning, Characterization of exoplanets from their formation. I. Models of combined planet formation and evolution. Astron. Astrophys. **547**, A111 (2012b)
M. Moreira, Noble gas constraints on the origin and evolution of Earth's volatiles. Geochem. Perspect. **2**, 229–403 (2013)
R. Morishima, J. Stadel, B. Moore, From planetesimals to terrestrial planets: N-body simulations including the effects of nebular gas and giant planets. Icarus **207**, 517–535 (2010)
N. Movshovitz, M. Podolak, The opacity of grains in protoplanetary atmospheres. Icarus **194**, 368–378 (2008)
N. Movshovitz, P. Bodenheimer, M. Podolak, J.J. Lissauer, Formation of Jupiter using opacities based on detailed grain physics. Icarus **209**, 616–624 (2010)
R.A. Murray-Clay, E.I. Chiang, N. Murray, Atmospheric escape from hot Jupiters. Astrophys. J. **693**(1), 23 (2009)
A. Nagy, T. Cravens, Hot oxygen atoms in the upper atmosphere of Venus and Mars. Geophys. Res. Lett. **15**(5), 433–435 (1988)

S. Nakajima, Y.-Y. Hayashi, Y. Abe, A study on the 'runaway greenhouse effect' with a one-dimensional radiative-convective equilibrium model. J. Atmos. Sci. **49**, 2256–2266 (1992)
F. Nimmo, T. Kleine, How rapidly did Mars accrete? Uncertainties in the Hf W timing of core formation. Icarus **191**, 497–504 (2007)
R. Nomura, H. Ozawa, S. Tateno, K. Hirose, J. Hernlund, S. Muto, H. Ishii, N. Hiraoka, Spin crossover and iron-rich silicate melt in the Earth's deep mantle. Nature **473**(7346), 199–202 (2011)
D.P. O'Brien, A. Morbidelli, H.F. Levison, Terrestrial planet formation with strong dynamical friction. Icarus **184**, 39–58 (2006)
D.P. O'Brien, K.J. Walsh, A. Morbidelli, S.N. Raymond, A.M. Mandell, Water delivery and giant impacts in the 'Grand Tack' scenario. Icarus **239**, 74–84 (2014)
S. Okuzumi, H. Tanaka, H. Kobayashi, K. Wada, Rapid coagulation of porous dust aggregates outside the snow line: a pathway to successful icy planetesimal formation. Astrophys. J. **752**, 106 (2012)
H.C. O'Neill, H. Palme, Composition of the silicate Earth: implications for accretion of and core formation, in *The Earth's Mantle; Composition, Structure, and Evolution* (Cambridge University Press, Cambridge, 1988), pp. 3–126
E.J. Opik, S.F. Singer, Distribution of density in a planetary exosphere. II. Phys. Fluids **4**, 221–233 (1961)
C.W. Ormel, An atmospheric structure equation for grain growth. Astrophys. J. Lett. **789**, L18 (2014)
C.W. Ormel, R. Kuiper, J.-M. Shi, Hydrodynamics of embedded planets' first atmospheres—I. A centrifugal growth barrier for 2D flows. Mon. Not. R. Astron. Soc. **446**, 1026–1040 (2015a)
C.W. Ormel, J.-M. Shi, R. Kuiper, Hydrodynamics of embedded planets' first atmospheres—II. A rapid recycling of atmospheric gas. Mon. Not. R. Astron. Soc. **447**, 3512–3525 (2015b)
J.E. Owen, A. Jackson, Planetary evaporation by UV and X-ray radiation: basic hydrodynamics. Mon. Not. R. Astron. Soc. **425**(4), 2931–2947 (2012)
J.E. Owen, Y. Wu, Kepler planets: a tale of evaporation. Astrophys. J. **775**(2), 105 (2013)
J.E. Owen, B. Ercolano, C.J. Clarke, R.D. Alexander, Radiation-hydrodynamic models of X-ray and EUV photoevaporating protoplanetary discs. Mon. Not. R. Astron. Soc. **401**(3), 1415–1428 (2010)
M. Ozima, Ar isotopes and Earth-atmosphere evolution models. Geochim. Cosmochim. Acta **39**(8), 1127–1134 (1975)
M. Ozima, K. Kudo, Excess argon in submarine basalts and an Earth-atmosphere evolution model. Nature **239**(89), 23–24 (1972)
V. Pan, J.R. Holloway, R. Hervig, The pressure and temperature-dependence of carbon-dioxide solubility in tholeiitic basalt melts. Geochim. Cosmochim. Acta **55**(6), 1587–1595 (1991)
P. Papale, Modeling of the solubility of a two-component H_2O+CO_2 fluid in silicate liquids. Am. Mineral. **84**(4), 447–492 (1999)
E.N. Parker, *Interplanetary Dynamical Processes* (Interscience, New York, 1963)
E.N. Parker, Dynamical properties of stellar coronas and stellar winds. I. Integration of the momentum equation. Astrophys. J. **139**, 72–122 (1964)
T. Penz, N.V. Erkaev, Y.N. Kulikov, D. Langmayr, H. Lammer, G. Micela, C. Cecchi-Pestellini, H.K. Biernat, F. Selsis, P. Barge, M. Deleuil, A. Léger, Mass loss from "hot Jupiters"—implications for CoRoT discoveries, part ii: Long time thermal atmospheric evaporation modeling. Planet. Space Sci. **56**(9), 1260–1272 (2008)
F. Perri, A.G.W. Cameron, Hydrodynamic instability of the solar nebula in the presence of a planetary core. Icarus **22**, 416–425 (1974)
S. Pfyffer, Y. Alibert, W. Benz, D. Swoboda, Theoretical models of planetary system formation. II. Post-formation evolution (2015). ArXiv e-prints
A.C. Plesa, N. Tosi, D. Breuer, Can a fractionally crystallized magma ocean explain the thermo-chemical evolution of Mars? Earth Planet. Sci. Lett. **403**, 225–235 (2014)
M. Podolak, The contribution of small grains to the opacity of protoplanetary atmospheres. Icarus **165**, 428–437 (2003)
J.B. Pollack, Formation of giant planets and their satellite-ring systems, in *Protostars and Planets II* (University of Arizona Press, Tucson, 1985)
J.B. Pollack, O. Hubickyj, P. Bodenheimer, J.J. Lissauer, M. Podolak, Y. Greenzweig, Formation of the giant planets by concurrent accretion of solids and gas. Icarus **124**, 62–85 (1996)
C. Priestley, *Turbulent Transfer in the Lower Atmosphere* (University of Chicago Press, Chicago, 1959)
R. Rafikov, Microwave emission from spinning dust in circumstellar disks. Astrophys. J. **646**, 288–296 (2006)
R.M. Ramirez, L. Kaltenegger, The habitable zones of pre-main-sequence stars. Astrophys. J. Lett. **797**(2), L25–L33 (2014)
S.N. Raymond, T. Quinn, J.I. Lunine, High-resolution simulations of the final assembly of Earth-like planets I. Terrestrial accretion and dynamics. Icarus **183**, 265–282 (2006)

S.N. Raymond, E. Kokubo, A. Morbidelli, R. Morishima, K.J. Walsh, Terrestrial planet formation at home and abroad, in *Protostars and Planets VI* (2014), pp. 595–618
R.T. Reynolds, P.E. Fricker, A.L. Summers, Effects of melting upon thermal models of the Earth. J. Geophys. Res. **71**(2), 573–582 (1966)
K. Righter, M. Drake, Metal/silicate equilibrium in the early Earth—new constraints from the volatile moderately siderophile elements Ga, Cu, P, and Sn. Geochim. Cosmochim. Acta **64**(20), 3581–3597 (2000)
L. Rogers, Most 1.6 Earth-radius planets are not rocky. Astrophys. J. **801**(1), 41 (2015)
W.W. Rubey, Geologic history of sea water an attempt to state the problem. Geol. Soc. Am. Bull. **62**(9), 1111–1148 (1951)
V. Safronov, The heating of the Earth during its formation. Icarus **33**, 3–12 (1978)
J. Sanz-Forcada, I. Ribas, G. Micela, A.M.T. Pollock, D. García-Álvarez, E. Solano, C. Eiroa, A scenario of planet erosion by coronal radiation. Astron. Astrophys. **511**, L8 (2010)
P. Sarda, B. Guillot, Breaking of Henry's law for noble gas and CO_2 solubility in silicate melt under pressure. Nature **436**(7047), 95–98 (2005)
P. Sarda, T. Staudacher, C.J. Allègre, $^{40}Ar/^{36}Ar$ in MORB glasses: constraints on atmosphere and mantle evolution. Earth Planet. Sci. Lett. **72**(4), 357–375 (1985)
P. Sarda, T. Staudacher, C.J. Allègre, Neon isotopes in submarine basalts. Earth Planet. Sci. Lett. **91**(1–2), 73–88 (1988)
S. Sasaki, K. Nakazawa, Metal-silicate fractionation in the growing Earth: energy source for the terrestrial magma ocean. J. Geophys. Res., Solid Earth **91**(B9), 9231–9238 (1986)
E.M. Schneiter, P. Velázquez, A. Esquivel, A.C. Raga, X. Blanco-Cano, Three-dimensional hydrodynamical simulation of the exoplanet HD 209458b. Astrophys. J. Lett. **671**(1), L57 (2007)
D. Semenov, T. Henning, C. Helling, M. Ilgner, E. Sedlmayr, Rosseland and Planck mean opacities for protoplanetary discs. Astron. Astrophys. **410**, 611–621 (2003)
I.F. Shaikhislamov, M.L. Khodachenko, Y.L. Sasunov, H. Lammer, K.G. Kislyakova, N.V. Erkaev, Atmosphere expansion and mass loss of close-orbit giant exoplanets heated by stellar XUV. I. Modeling of hydrodynamic escape of upper atmospheric material. Astrophys. J. **795**(2), 132 (2014)
H.R. Shaw, Viscosities of magmatic silicate liquids: an empirical method of prediction. Am. J. Sci. **272**, 870–893 (1972)
V.I. Shematovich, Stochastic models of hot planetary and satellite coronas. Sol. Syst. Res. **38**(1), 28–38 (2004)
V.I. Shematovich, Suprathermal hydrogen produced by the dissociation of molecular hydrogen in the extended atmosphere of exoplanet HD 209458b. Sol. Syst. Res. **44**(2), 96–103 (2010)
V.I. Shematovich, D.V. Bisikalo, J.C. Gérard, C. Cox, S.W. Bougher, F. Leblanc, Monte Carlo model of electron transport for the calculation of Mars dayglow emissions. J. Geophys. Res., Planets **113**(E2), E02011 (2008)
V.I. Shematovich, D.E. Ionov, H. Lammer, Heating efficiency in hydrogen-dominated upper atmospheres. Astron. Astrophys. **571**, A94 (2014)
E.D. Siggia, High Rayleigh number convection. Annu. Rev. Fluid Mech. **26**(1), 137–168 (1994)
J. Smith, A.T. Anderson, R. Newton, E. Olsen et al., Petrologic history of the Moon inferred from petrography, mineralogy, and petrogenesis of Apollo 11 rocks, in *Proc. Apollo 11 Lunar Sci. Conf., vol. 1*, Houston, TX, Jan. 5–8 (Pergamon, New York, 1970), pp. 897–925
V.S. Solomatov, Fluid dynamics of a terrestrial magma ocean, in *Origin of the Earth and Moon* (2000), pp. 323–338
V. Solomatov, Magma oceans and primordial mantle differentiation, in *Treatise on Geophysics*, ed. by G. Schubert (Elsevier, Amsterdam, 2007), pp. 91–119
V. Solomatov, Magma oceans and primordial mantle differentiation, in *Treatise on Geophysics*, ed. by G. Schubert (Elsevier, Amsterdam, 2009), pp. 91–119
V. Solomatov, Magma oceans and primordial mantle differentiation—magma oceans and primordial mantle differentiation, in *Treatise on Geophysics*, ed. by G. Schubert (Elsevier, Amsterdam, 2015), 81–100
V.S. Solomatov, D.J. Stevenson, Suspension in convective layers and style of differentiation of a terrestrial magma ocean. J. Geophys. Res., Planets **98**(E3), 5375–5390 (1993a)
V.S. Solomatov, D.J. Stevenson, Kinetics of crystal growth in a terrestrial magma ocean. J. Geophys. Res., Planets **98**(E3), 5407–5418 (1993b)
T. Staudacher, C.J. Allègre, Terrestrial xenology. Earth Planet. Sci. Lett. **60**(3), 389–406 (1982)
D.J. Stevenson, Formation of the giant planets. Planet. Space Sci. **30**, 755–764 (1982)
A. Stökl, E. Dorfi, H. Lammer, Hydrodynamic simulations of captured protoatmospheres around Earth-like planets. Astron. Astrophys. **576**, A87 (2015)
J.M. Stone, D. Proga, Anisotropic winds from close-in extrasolar planets. Astrophys. J. **694**(1), 205 (2009)
J. Suckale, J.A. Sethian, J-d. Yu, L.T. Elkins-Tanton, Crystals stirred up: 1. Direct numerical simulations of crystal settling in nondilute magmatic suspensions. J. Geophys. Res., Planets **117**, E08004 (2012)

H.E. Suess, Die häufigkeit der edelgase auf der erde und im kosmos. J. Geol. **57**, 600–607 (1949)
H. Tanaka, S. Ida, Growth of a migrating protoplanet. Icarus **139**, 350–366 (1999)
Y.A. Tanaka, T.K. Suzuki, S. Inutsuka, Atmospheric escape by magnetically driven wind from gaseous planets. Astrophys. J. **792**(1), 18 (2014)
G. Taylor, M. Norman, *Evidence for Magma Oceans on Asteroids, the Moon, and Earth* (Lunar Planet. Inst., Houston, 1992), pp. 58–65
E. Thommes, M. Nagasawa, D.N.C. Lin, Dynamical shake-up of planetary systems. II. N-Body simulations of solar system terrestrial planet formation induced by secular resonance sweeping. Astrophys. J. **676**, 728–739 (2008)
F. Tian, Conservation of total escape from hydrodynamic planetary atmospheres. Earth Planet. Sci. Lett. **379**, 104–107 (2013)
F. Tian, History of water loss and atmospheric O_2 buildup on rocky exoplanets near M dwarfs. Earth Planet. Sci. Lett. **432**, 126–132 (2015)
F. Tian, S. Ida, Water contents of Earth-mass planets around M dwarfs. Nat. Geosci. **8**(3), 177–180 (2015)
F. Tian, O.B. Toon, A.A. Pavlov, H. De Sterck, A hydrogen-rich early Earth atmosphere. Science **308**(5724), 1014–1017 (2005a)
F. Tian, O.B. Toon, A.A. Pavlov, H. De Sterck, Transonic hydrodynamic escape of hydrogen from extrasolar planetary atmospheres. Astrophys. J. **621**(2), 1049 (2005b)
F. Tian, J.F. Kasting, H.-L. Liu, R.G. Roble, Hydrodynamic planetary thermosphere model: 1. Response of the Earth's thermosphere to extreme solar EUV conditions and the significance of adiabatic cooling. J. Geophys. Res., Planets **113**(E5), E05008 (2008)
G. Tinetti et al., EChO. Exoplanet characterisation observatory. Exp. Astron. **34**(2), 311–353 (2012)
W. Tonks, H. Melosh, The physics of crystal settling and suspension in a turbulent magma ocean, in *Origin of the Earth* (Oxford University Press, London, 1990), pp. 151–174
W.B. Tonks, H.J. Melosh, Magma ocean formation due to giant impacts. J. Geophys. Res., Planets **98**(E3), 5319–5333 (1993)
N. Tosi, A.C. Plesa, D. Breuer, Overturn and evolution of a crystallized magma ocean: a numerical parameter study for Mars. J. Geophys. Res., Planets **118**(7), 1512–1528 (2013)
M. Touboul, T. Kleine, B. Bourdon, H. Palme, R. Wieler, Late formation and prolonged differentiation of the Moon inferred from W isotopes in lunar metals. Nature **450**, 1206–1209 (2007)
G.B. Trammell, P. Arras, Z.-Y. Li, Hot Jupiter magnetospheres. Astrophys. J. **728**(2), 152 (2011)
K.K. Turekian, S.P. Clark Jr., The non-homogeneous accumulation model for terrestrial planet formation and the consequences for the atmosphere of Venus. J. Atmos. Sci. **32**(6), 1257–1261 (1975)
H. Urey, The cosmic abundances of potassium, uranium and thorium and the heat balances of the Earth, the Moon and Mars. Proc. Natl. Acad. Sci. USA **41**, 127–144 (1955)
F. Valsecchi, F.A. Rasio, J.H. Steffen, From hot Jupiters to super-Earths via Roche lobe overflow. Astrophys. J. Lett. **793**(1), L3 (2014)
A. Vidal-Madjar, A. Lecavelier des Etangs, J.M. Desert, G.E. Ballester, R. Ferlet, G. Hebrard, M. Mayor, An extended upper atmosphere around the extrasolar planet HD 209458b. Nature **422**(6928), 143–146 (2003)
A. Vidal-Madjar, J.M. Désert, A. Lecavelier des Etangs, G. Hébrard, G.E. Ballester, D. Ehrenreich, R. Ferlet, J.C. McConnell, M. Mayor, C.D. Parkinson, Detection of oxygen and carbon in the hydrodynamically escaping atmosphere of the extrasolar planet HD 209458b. Astrophys. J. Lett. **604**(1), L69 (2004)
A. Vidal-Madjar, C.M. Huitson, V. Bourrier, J.-M. Désert, G. Ballester, A. Lecavelier des Etangs, D.K. Sing, D. Ehrenreich, R. Ferlet, G. Hébrard, J.C. McConnell, Magnesium in the atmosphere of the planet HD 209458b: observations of the thermosphere-exosphere transition region. Astron. Astrophys. **560**, A54 (2013)
C. Villarreal D'Angelo, M. Schneiter, A. Costa, P. Velázquez, A. Raga, A. Esquivel, On the sensitivity of extrasolar mass-loss rate ranges: HD 209458b a case study. Mon. Not. R. Astron. Soc. **438**(2), 1654–1662 (2014)
A. Volkov, R.E. Johnson, Thermal escape in the hydrodynamic regime: reconsideration of Parker's isentropic theory based on results of kinetic simulations. Astrophys. J. **765**(2), 90 (2013)
A. Volkov, R.E. Johnson, O.J. Tucker, J.T. Erwin, Thermally driven atmospheric escape: transition from hydrodynamic to jeans escape. Astrophys. J. Lett. **729**(2), L24 (2011a)
A.N. Volkov, O.J. Tucker, J.T. Erwin, R.E. Johnson, Kinetic simulations of thermal escape from a single component atmosphere. Phys. Fluids **23**(6), 066601 (2011b)
A.J. Watson, T.M. Donahue, J.C. Walker, The dynamics of a rapidly escaping atmosphere: applications to the evolution of Earth and Venus. Icarus **48**(2), 150–166 (1981)
R. Wayne, *Chemistry of Atmospheres* (Oxford University Press, London, 1991) 312 pp.
G.W. Wetherill, Comparison of analytical and physical modeling of planetesimal accumulation. Icarus **88**, 336–354 (1990)

G.W. Wetherill, G.R. Stewart, Accumulation of a swarm of small planetesimals. Icarus **77**, 330–357 (1989)
F. Witham, J. Blundy, S.C. Kohn, P. Lesne, J. Dixon, S.V. Churakov, R. Botcharnikov, SolEx: a model for mixed COHSCl-volatile solubilities and exsolved gas compositions in basalt. Comput. Geosci. **45**, 87–97 (2012)
J. Wood, J.S. Dickey Jr., U.B. Marvin, B.N. Powell, Lunar anorthosites and a geophysical model of the Moon, in *Proceedings of the Apollo 11 Lunar Science Conference* (Pergamon, New York, 1970), pp. 965–988
B. Wood, M. Walter, J. Wade, Accretion of the Earth and segregation of its core. Nature **441**(7095), 825–833 (2006)
Y. Wu, Y. Lithwick, Density and eccentricity of Kepler planets. Astrophys. J. **772**(1), 74 (2013)
G. Wuchterl, The critical mass for protoplanets revisited—massive envelopes through convection. Icarus **106**, 323 (1993)
G. Wuchterl, Giant planet formation. Earth Moon Planets **67**(1–3), 51–65 (1994)
G. Wuchterl, Planet masses and radii from physical principles, in *Proceedings of the International Astronomical Union 6 (Symposium S276)* (2010), pp. 76–81
J. Yang, G. Boué, D.C. Fabrycky, D.S. Abbot, Strong dependence of the inner edge of the habitable zone on planetary rotation rate. Astrophys. J. Lett. **787**, L2 (2014)
R.V. Yelle, Aeronomy of extra-solar giant planets at small orbital distances. Icarus **170**(1), 167–179 (2004)
R. Yelle, H. Lammer, W.H. Ip, Aeronomy of extra-solar giant planets. Space Sci. Rev. **139**, 437–451 (2008)
T. Yoshino, M. Walter, T. Katsura, Core formation in planetesimals triggered by permeable flow. Nature **422**(6928), 154–157 (2003)
K. Zahnle, J. Kasting, J. Pollack, Evolution of a steam atmospheres during Earth's accretion. Icarus **74**(1), 62–97 (1988)

The Astrophysical Journal Letters, 829:L35 (6pp), 2016 October 1 doi:10.3847/2041-8205/829/2/L35

A GAP WITH A DEFICIT OF LARGE GRAINS IN THE PROTOPLANETARY DISK AROUND TW Hya

Takashi Tsukagoshi[1], Hideko Nomura[2], Takayuki Muto[3], Ryohei Kawabe[4,10,11], Daiki Ishimoto[2,5], Kazuhiro D. Kanagawa[6], Satoshi Okuzumi[2], Shigeru Ida[7], Catherine Walsh[8,12], and T. J. Millar[9]
[1] College of Science, Ibaraki University, Bunkyo 2-1-1, Mito, Ibaraki 310-8512, Japan; takashi.tsukagoshi.sci@vc.ibaraki.ac.jp
[2] Department of Earth and Planetary Sciences, Tokyo Institute of Technology, 2-12-1 Ookayama, Meguro, Tokyo 152-8551, Japan
[3] Division of Liberal Arts, Kogakuin University, 1-24-2 Nishi-Shinjuku, Shinjuku-ku, Tokyo 163-8677, Japan
[4] National Astronomical Observatory of Japan, 2-21-1 Osawa, Mitaka, Tokyo 181-8588, Japan
[5] Department of Astronomy, Graduate School of Science, Kyoto University, Kitashirakawa-Oiwake-cho, Sakyo, Kyoto 606-8502, Japan
[6] Institute of Physics and CASA*, Faculty of Mathematics and Physics, University of Szczecin, Wielkopolska 15, 70-451 Szczecin, Poland
[7] Earth-Life Science Institute, Tokyo Institute of Technology, 2-12-1 Ookayama, Meguro, Tokyo 152-8550, Japan
[8] Leiden Observatory, Leiden University, P.O. Box 9513, 2300 RA Leiden, The Netherlands
[9] Astrophysics Research Centre, School of Mathematics and Physics, Queen's University Belfast, University Road, Belfast BT7 1NN, UK
[10] SOKENDAI (The Graduate University for Advanced Studies), 2-21-1 Osawa, Mitaka, Tokyo 181-8588, Japan
[11] Department of Astronomy, School of Science, University of Tokyo, Bunkyo, Tokyo 113-0033, Japan
[12] School of Physics and Astronomy, University of Leeds, Leeds LS2 9JT, UK
Received 2016 April 29; revised 2016 August 25; accepted 2016 August 31; published 2016 September 30

ABSTRACT

We report ~3 au resolution imaging observations of the protoplanetary disk around TW Hya at 145 and 233 GHz with the Atacama Large Millimeter/submillimeter Array. Our observations revealed two deep gaps (~25%–50%) at 22 and 37 au and shallower gaps (a few percent) at 6, 28, and 44 au, as recently reported by Andrews et al. The central hole with a radius of ~3 au was also marginally resolved. The most remarkable finding is that the spectral index $\alpha(R)$ between bands 4 and 6 peaks at the 22 au gap. The derived power-law index of the dust opacity $\beta(R)$ is ~1.7 at the 22 au gap and decreases toward the disk center to ~0. The most prominent gap at 22 au could be caused by the gravitational interaction between the disk and an unseen planet with a mass of $\lesssim 1.5\ M_{\rm Neptune}$, although other origins may be possible. The planet-induced gap is supported by the fact that $\beta(R)$ is enhanced at the 22 au gap, indicating a deficit of ~millimeter-sized grains within the gap due to dust filtration by a planet.

Key words: protoplanetary disks – stars: individual (TW Hya)

1. INTRODUCTION

Protoplanetary disks are the birthplaces of planets. The complex structures of protoplanetary disks such as spiral arms, inner holes, and gap and ring, recently reported by high-resolution infrared observations (e.g., Espaillat et al. 2014 and references therein), are believed to be potential evidence of unseen planets in the disk. Most recently, high-resolution observations with Atacama Large Millimeter/submillimeter Array (ALMA) have found multiple gaps and rings in a disk even at submillimeter wavelengths (ALMA Partnership et al. 2015). Since submillimeter emission better traces the midplane density structures than infrared, the gaps and rings are thought to be direct evidence of the absence and enhancement of disk material, and therefore related to the planet formation process. The origin of multiple gaps and rings is still under debate: several theoretical studies predict a formation scenario due to material clearance by planets (Dipierro et al. 2015; Dong et al. 2015; Kanagawa et al. 2015, 2016; Tamayo et al. 2015; Jin et al. 2016), growth and destruction of icy dust aggregates near the snow lines of major volatiles (Zhang et al. 2015; Okuzumi et al. 2016), baroclinic instability triggered by dust settling (Lorén-Aguilar & Bate 2015), or secular gravitational instability (Youdin 2011; Takahashi & Inutsuka 2014).

TW Hya is a 0.8 $M_\odot$ T Tauri star surrounded by a disk at a distance of ~54 pc (e.g., Andrews et al. 2012). Since the disk is almost face-on with an inclination angle of 7° (Qi et al. 2004), TW Hya is one of the best astronomical laboratories to investigate the radial structure of protoplanetary disks. The disk mass has been measured to be $>0.05\ M_\odot$ from HD line observations by the *Herschel Space Observatory*, indicating that it is massive enough to form a planetary system (Bergin et al. 2013). Recently, a gap in the dust emission has been found at 20–30 au by submillimeter and near-infrared observations (Akiyama et al. 2015; Rapson et al. 2015; Debes et al. 2016; Nomura et al. 2016; Zhang et al. 2016), which is possibly associated with the CO snow line (Qi et al. 2013). Most recently, Andrews et al. (2016) reported the existence of multiple, axisymmetric gaps at 1, 22, 37, and 43 au at a spatial resolution of ~1 au. The depth and width of the submillimeter gap at 20–30 au are consistent with clearing by a super-Neptune-mass planet (Nomura et al. 2016). However, additional information on the dust size distribution with comparable spatial resolution is required to address the physical structure of the gap. In this Letter, we report multi-frequency observations of the disk around TW Hya with ALMA to probe the detailed disk structure and the change of dust spectral index across the dust gaps and rings at a spatial resolution of ~3 au.

2. OBSERVATIONS

High-resolution continuum observations at Bands 4 and 6 (145 and 233 GHz) with ALMA were carried out on 2015 December 1 and 2 (2015.A.00005.S). In the observation period, 36 of the 12 m antennas were operational and the antenna configuration was in transition from C36-7 to C36-1, resulting in maximum baselines of 6.5 and 10.4 km for Bands 4 and 6, respectively. We employed the Time Division Mode of the correlator, which is optimized for continuum observations. The correlator was configured to detect dual polarizations in four spectral windows with a bandwidth of 1.875 GHz each,

resulting in a total bandwidth of 7.5 GHz for each observed band. The amplitude and phase were calibrated by observations of J1103-3251, and J1037-2934 was used for absolute flux calibration. The observed passbands were calibrated by 5 minute observations of J1037-2934 and J1107-4449 for Bands 4 and 6, respectively.

The visibility data were reduced and calibrated using the Common Astronomical Software Application (CASA) package, version 4.5.0. After flagging bad data and applying the calibrations for bandpass, complex gain, and flux scaling, the corrected visibilities were imaged by the CLEAN algorithm. The visibilities at Band 6 with *uv* lengths >3000 kλ were flagged out because of significant phase noise. The *uv* sampling for baseline $\lesssim$400 m was particularly sparse along the north–south direction (i.e., *v*-axis of the *uv* coverage), which corresponds to $\lesssim$180 and $\lesssim$300 kλ for Bands 4 and 6, respectively. We have combined Band 6 archival data (2012.1.00422.S), in which the maximum baseline is ~500 kλ, with our Band 6 data after applying a phase shift to account for proper motion and different input phase centers. There were no available short-baseline data at Band 4; hence, only the long-baseline data were used for imaging.

To improve the image fidelity, we performed the iterative self-calibration imaging for each band data using the initial CLEAN image as a model image. The interval time to solve the complex gain was varied from 600 to 90 s for Band 4 and from 1200 to 240 s for Band 6. The resultant images after self-calibration were made by adopting briggs weighting of robust parameters 0.5 and 1.0 for Bands 4 and 6, respectively. We also employed the multiscale clean with scale parameters of [0, 100, 300] and [0, 50, 150] mas for Bands 4 and 6, respectively, for better reconstruction of extended emission. The spatial resolutions of the final images are 88.1 × 62.1 mas with a position angle (PA) of 57°.8 and 75.4 × 55.2 mas with a PA of 38°.0 for Bands 4 and 6, respectively. The noise levels of the Band 4 and 6 images are 12.4 and 28.7 μJy beam^{-1}, respectively.

To deduce the spectral index between the Bands 4 and 6 and to obtain a combined image around the center frequency (190 GHz), we also used the multi-frequency synthesis (MFS) method using all of the corrected visibilities after the iterative self-calibration imaging (*nterm* = 2 in CASA *CLEAN* task; see Rau & Cornwell 2011 for the MFS method). Briggs weighting with robust = 0.0 was employed for the deconvolution, and we also employed the multiscale option with scale parameters of 0, 60, and 180 mas. Using the MFS method, we obtain the combined image and the map of the spectral index at 190 GHz. The combined image achieves a better fidelity than the individual images since the observed data are combined to fill the gap in each other's *uv* coverage. The achieved spatial resolution of the combined image is 72.7 × 47.8 mas, with a PA of 52°.9, corresponding to 3.9 × 2.9 au. The noise level is 15.9 μJy beam^{-1}.

3. RESULTS

Figures 1(a) and (b) show the constructed continuum maps at Bands 4 and 6, respectively. Both images show circular multiple gaps and rings even though the resolution of the Band 4 image is ~1.3 times larger than that of Band 6. The total flux densities are 152.0 ± 0.3 and 558.3 ± 0.7 Jy for Bands 4 and 6, respectively.

Figure 1(c) shows the combined image of the Band 4 and 6 data with the MFS method (hereafter MFS image). The MFS image shows circular symmetric multiple gaps and rings. In addition, we have resolved an inner hole with radius ~3 au as predicted from an earlier analysis of the spectral energy distribution (SED; Calvet et al. 2002; Menu et al. 2014). This corresponds to the drop in the brightness temperature of dust continuum map recently found by Andrews et al. (2016). The total flux density integrated over the region with S/N > 10 is 360.3 ± 0.5 mJy at 190 GHz (S/N ~ 150), which agrees well with the previous estimation at submillimeter wavelengths (Qi et al. 2004; Andrews et al. 2012). There is no appreciable deviation from circular symmetry in the gaps, rings, and spectral index α. Ellipsoid fittings of gaps and rings show the deviation between major and minor axes is within the errors ($\lesssim$5%).

To confirm the gap structures, we plot the deprojected radial profile of the continuum emission in the top panel of Figure 2. The flux density is converted to the brightness temperature using the Planck function. There are two prominent gaps at 22 and 37 au, and relatively weak decrements are also seen at 6, 28, and 44 au. These observed features agree with those found by recent high-resolution (~1 au) observations at Band 7 (Andrews et al. 2016). The FWHM and the relative depth are roughly 7 au and 50% for the 22 au gap if the background with a power-law form is assumed, and 3 au and ~20% for the 37 au gap. The depths are deeper than that of the gaps at Band 7 (Andrews et al. 2016), while the widths are comparable. Both the emission at Bands 4 and 6 show comparable brightness temperature inside $R \sim 15$ au, the value of which is consistent with that of the Band 7 emission (Andrews et al. 2016). This result indicates that the disk is (at least moderately) optically thick in this region.

Figure 1(d) shows the spatial variation of the spectral index α (see Equation (2) for its definition). The distribution seems to be axisymmetric, and therefore we make the radial profile of α averaged over the full azimuth angle as shown in Figure 2. The spectral index α radially decreases approaching the disk center. There is a prominent peak around 22 au with $\alpha \sim 3.0$, which coincides well with the position of the gap. The enhancement in α is possible evidence of large grain deficit since α is related to the power-law index of the dust mass opacity if the emission is optically thin. The rapid decrease of α inside the 22 au peak is partly due to increase of optical depth and partly due to decrease of the power-law index of β, namely, the existence of larger dust grains near the central star (see the next section). There seems to be two weak (<10%) bumps at 37 and 44 au that are coincident with the locations of gaps in the intensity profile as for the 22 au gap, implying that there is a correlation between the surface brightness and α.

The error bars in Figure 2 are determined from the standard deviation determined by the azimuthal averaging. This is a conservative way of determining the error because it is the most dominant source of the deviation at >5 au. In fact, the uncertainty map for α produced by CASA shows an error is lower than the standard deviation. The uncertainty in the absolute flux density does not affect the shape of the α profile, but the absolute scale of α. If the accuracy of the absolute flux scale is assumed to be ~10%, the α scale would have an associated error of $\Delta\alpha \sim 0.4$. Therefore the weighted mean value is estimated to be $\langle\alpha\rangle = 2.42 \pm 0.42$, which agrees well

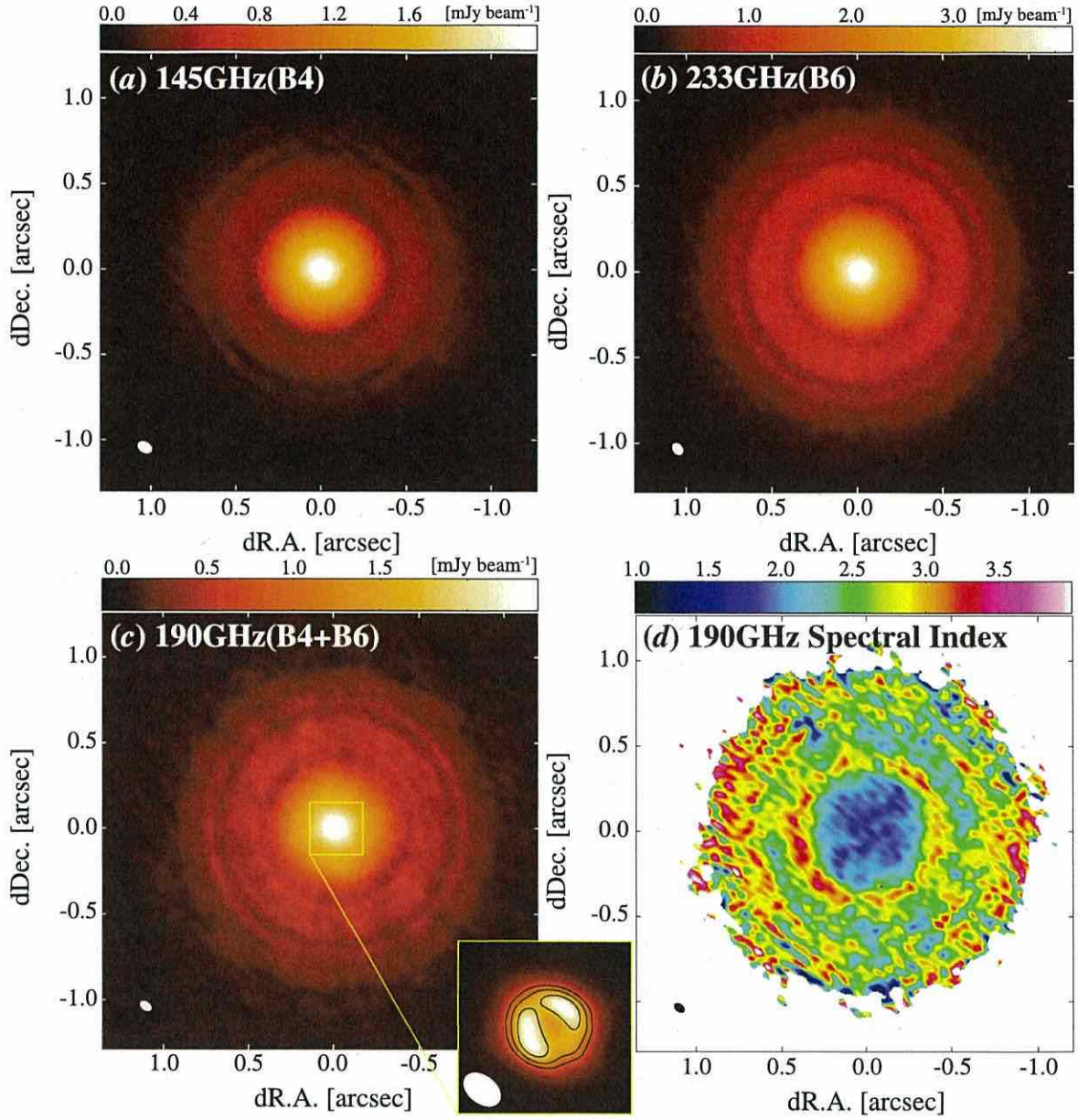

Figure 1. (a) and (b) ALMA continuum images at 145 GHz (Band 4) and 233 GHz (Band 6), respectively. The ellipse at the bottom left corner in each panel shows the synthesized beam. (c) Combined image of Bands 4 and 6 with the MFS method. The inset indicates a close-up view (0.″3 × 0.″3) for emphasis of the central structure. The contour indicates 130, 140, and 150σ. (d) Spectral index map derived from the MFS method.

with previous measurements for the entire disk (Menu et al. 2014; Pinilla et al. 2014).

4. DISCUSSION

4.1. Radial Profiles of Dust Optical Depth and Opacity β

The intensity $I_\nu(R)$ and the spectral index $\alpha(R)$ are related to the dust temperature $T_d(R)$, the optical depth $\tau_\nu(R)$, and the dust opacity index $\beta(R)$ by

$$I_\nu(R) = B_\nu(T_d(R))(1 - \exp[-\tau_\nu]) \quad (1)$$

and

$$\alpha(R) \equiv \frac{d\log(I_\nu)}{d\log\nu} = 3 - \frac{h\nu}{k_B T_d(R)} \frac{e^{h\nu/k_B T_d(R)}}{e^{h\nu/k_B T_d(R)} - 1} + \beta(R)\frac{\tau_\nu(R)}{e^{\tau_\nu(R)} - 1}. \quad (2)$$

Here, $B_\nu(T)$ is the Planck function, h is Planck's constant, c is the speed of light, and k_B is Boltzmann's constant. The optical depth is assumed to have the form $\tau_\nu(R) = \tau_{190\,\mathrm{GHz}}(R)(\nu/190\,\mathrm{GHz})^\beta$. There are three unknown variables in Equations (1) and (2), which are $T_d(R)$, $\tau_{190\,\mathrm{GHz}}(R)$,

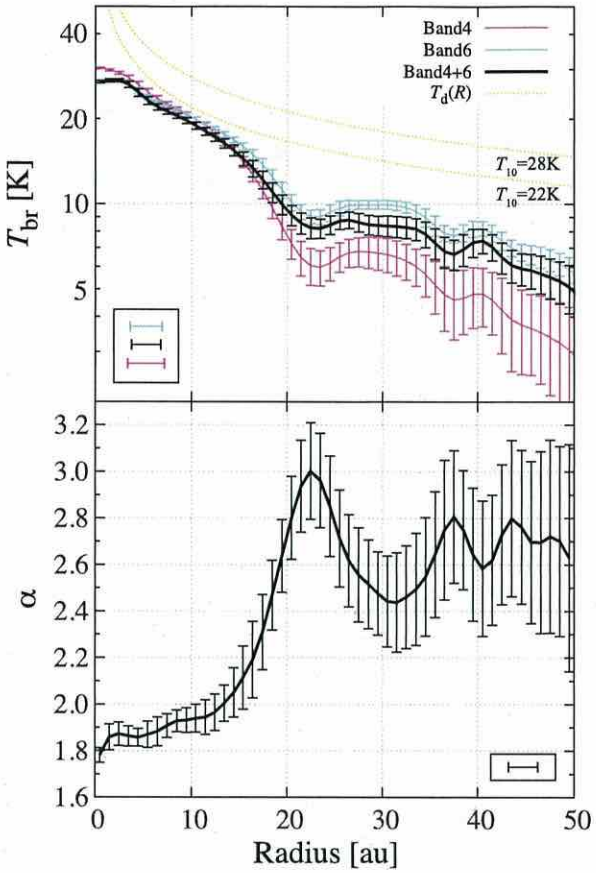

Figure 2. (Top) Radial profiles of the brightness temperature averaged over full azimuthal angle. The black line indicates the MFS combined image, and the lines in magenta and cyan show the Bands 4 and 6 data, respectively. The bars at the bottom left corner show the spatial resolutions. The error bar is determined from the standard deviation through the azimuthal averaging. The orange dashed lines indicate the assumed temperature profile of the dust disk when $T_{10} = 22$ and 28 K with $q = 0.4$. (Bottom) Radial profile of the spectral index α. The resolution is shown at the bottom right corner in the panel. The error bar follows the same manner as the top panel.

and $\beta(R)$. If we assume one of them, we are able to derive the rest of them by using the observation data of $I_\nu(R)$ and $\alpha(R)$. Here, we assume that $T_d(R)$ is given by $T_d(R) = T_{10}(R/10\ \mathrm{au})^{-q}$. We vary T_{10} from 22 to 30 K and q from 0.3 to 0.5 to see how the temperature affects the derived physical quantities. This assumption is based on our fitting to the temperature profile at the disk midplane in Andrews et al. (2012, 2016). The temperature profile models are chosen so that the observed brightness temperature does not exceed the kinetic temperature. The assumed temperature profiles, however, have no great impact on the following conclusions as shown in Figure 3.

Figure 3 shows the radial profiles of $\tau_{190\,\mathrm{GHz}}(R)$ and $\beta(R)$. The errors are estimated in a conservative way in which the combination between the maximum and minimum values of the error bars in the intensity and $\alpha(R)$ profiles is used for determining the maximum range of the error. The disk is optically thin at $R > 15$ au in all the cases and marginally optically thick at $R < 15$ au. This is in contrast with HL Tau (ALMA Partnership et al. 2015; Pinte et al. 2016), where an optically thick region extends out to $R \lesssim 40$ au. We see a prominent drop in the optical depth at $R < 5$ au, which likely corresponds to the inner hole derived from the SED (Calvet et al. 2002) and to the drop in the brightness temperature of the dust continuum map recently found by Andrews et al. (2016). The optical depth profiles have two dips at $R \sim 22$ au and ~37 au. Note that although β can not be determined where the optical thickness is considerably high, the β profile at <15 au is still accessible because τ is of order unity.

Overall, $\beta(R)$ increases from ~0 to ~1.7 with when moving from the disk center to ~20 au, where the disk is marginally optically thick. This implies that sufficient large dust grains ($\geqslant$ 10 mm) exist at 5–10 au. Radially increasing profiles of $\beta(R)$ are also seen in other T Tauri disks (e.g., Pérez et al. 2012), and compact distribution of the largest grains is suggested in the TW Hya disk, too (Menu et al. 2014).

One of the most remarkable features of the $\beta(R)$ profile is the peak at ~22 au, which corresponds to the location of the gap in the surface brightness profile. This indicates that large dust grains are less abundant within the gap compared to other locations in the disk. We also tentatively see the increase in $\beta(R)$ near the 37 au gap (and perhaps also near the 44 au gap), but further observations with better sensitivity is needed to confirm this.

At $R < 15$ au where $\tau(R) \sim 1$, $\beta(R)$ is derived to be ranging from 0.0 to 0.5, and according to the theoretical calculation of dust mass opacity (Draine 2006), small β value suggests that the power-law index of dust size distribution is very small and and the maximum dust size is large (>a few cm). Also, the result suggests that the column density would be at least an order of magnitude higher than that at the 22 au gap, giving us the column density with an power-law index of <-2. The steep profile is consistent with the previous measurement that large grains should be concentrated toward the inner disk region to reproduce the 9 mm emission (Menu et al. 2014).

The discussions of $\tau_{190\,\mathrm{GHz}}(R)$ and $\beta(R)$ presented here are based on the assumptions of smooth temperature profiles. Observations at additional bands (preferably at lower frequencies) may further constrain $T_d(R)$, $\tau_\nu(R)$ and $\beta(R)$ simultaneously. We note that our results are roughly consistent with the Band 7 observations by Andrews et al. (2016).

4.2. Origin of the Gaps

The enhancement of $\beta(R)$ indicates a deficit of large (millimeter-sized) grains at the gap position. These facts support the scenario that the gap is caused by planet–disk interaction because it is consistent with the picture of dust filtration and trapping due to a planet (Zhu et al. 2012). Using the relationship that connects the gap shape with the planet mass (Kanagawa et al. 2015, 2016), a planet with 1.5 M_{Neptune} may be responsible for the gap, assuming a viscosity parameter $\alpha = 10^{-3}$ and a disk aspect ratio of 0.05 (consistent with the assumption of $T_{10} = 22$ K). We note that similar values are derived from both gap width and depth. This planet mass should be considered as the upper limit since the formula by Kanagawa et al. (2015, 2016) is for the gas gap and the actual dust gap may be wider and deeper than the gas gap due to dust filtration (Zhu et al. 2012).

Alternatively, the multiple ring structures might be related to the snow lines of major volatiles (Zhang et al. 2015; Okuzumi et al. 2016). TW Hya is suggested to have a CO snow line at

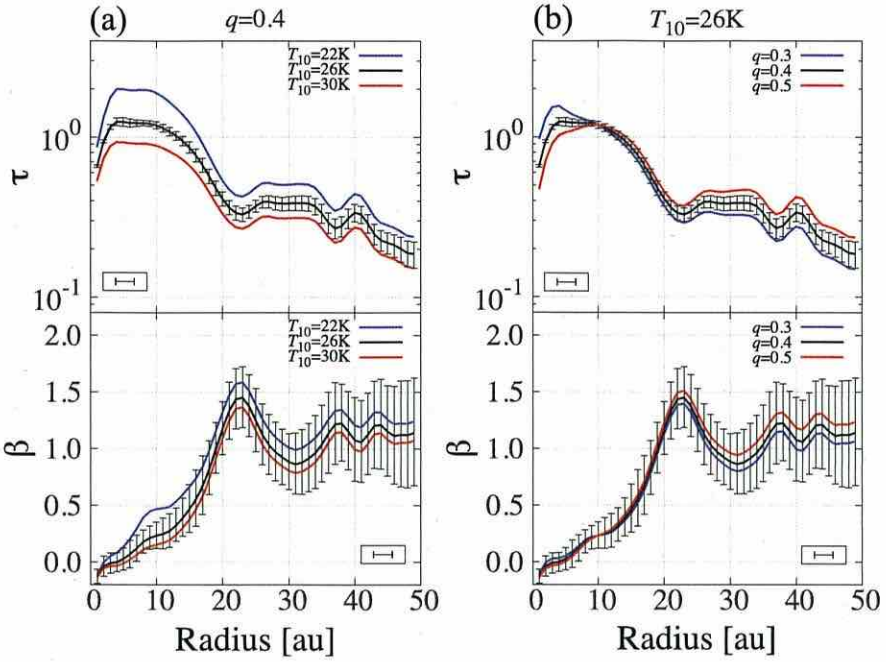

Figure 3. (a) Radial profile of the optical depth at 190 GHz (top) and β (bottom). The cases for T_{10} = 22, 26, and 30 K when q is fixed to 0.4 are shown in blue, black, and red lines, respectively. The error bar is shown for the case of T_{10} = 26 K representatively. The resolution is shown at the bottom left (top) or bottom right (bottom) corner in the panel. (b) Same as (a), but for checking the dependence on q from 0.3 to 0.5 when T_{10} is fixed to 26 K are shown in blue, black, and red lines, respectively. The error bar is shown for the q = 0.4 case representatively.

~30 au (Qi et al. 2013; Schwarz et al. 2016), and our observations identify a bright dust ring near this snow line. This is consistent with the dust ring formation scenario by Okuzumi et al. (2016), in which icy dust aggregates experience sintering, disrupt, and pileup near major snow lines. As noted by Andrews et al. (2016), the 40 au bright ring might correspond to the snow line of N_2, which has a sublimation temperature slightly lower than that of CO. However, the model of Okuzumi et al. (2016) does not predict a strong radial variation of $\beta(R)$, thus not explaining the enhancement of $\beta(R)$ we found near the 20 au dark ring.

The multiple gaps with intervals of 5–10 au beyond the 22 au gap (22, 28, 37, and 44 au) may be reminiscent of dynamical instabilities within the disk such as zonal flow patterns driven by MHD turbulence (Johansen et al. 2009), baroclinic instability driven by dust settling (Lorén-Aguilar & Bate 2015), and/or the secular gravitational instability (Youdin 2011; Takahashi & Inutsuka 2014). Different dynamical processes act under different physical conditions and therefore better constraints on the dust disk physical structure based on high-resolution observations at other bands (e.g., Andrews et al. 2016), and constraints of the density and temperature structures of gas component are essential in determining the origin of such structures.

We thank the referee for many useful comments and critiques which helped improve the contents of this paper. This paper makes use of the following ALMA data: ADS/JAO.ALMA#2015.A.00005.S and ADS/JAO.ALMA#2012.1.00422.S. ALMA is a partnership of ESO (representing its member states), NSF (USA) and NINS (Japan), together with NRC (Canada), NSC and ASIAA (Taiwan), and KASI (Republic of Korea), in cooperation with the Republic of Chile. The Joint ALMA Observatory is operated by ESO, AUI/NRAO and NAOJ. A part of data analysis was carried out on common use data analysis computer system at the Astronomy Data Center of NAOJ. This work is partially supported by JSPS KAKENHI grant numbers 24103504 and 23103004 (TT), 23103005 and 25400229 (HN), 26800106 and 15H02074 (TM), and 16K17661 (SO). K.D.K. was supported by Polish National Science Centre MAESTRO grant DEC- 2012/06/A/ST9/00276. Astrophysics at QUB is supported by a grant from the STFC.

REFERENCES

Akiyama, E., Muto, T., Kusakabe, N., et al. 2015, ApJL, 802, L17
ALMA Partnership, Brogan, C. L., Pérez, L. M., et al. 2015, ApJL, 808, L3
Andrews, S. M., Wilner, D. J., Hughes, A. M., et al. 2012, ApJ, 744, 162
Andrews, S. M., Wilner, D. J., Zhu, Z., et al. 2016, ApJL, 820, L40
Bergin, E. A., Cleeves, L. I., Gorti, U., et al. 2013, Natur, 493, 644
Calvet, N., D'Alessio, P., Hartmann, L., et al. 2002, ApJ, 568, 1008
Debes, J. H., Jang-Condell, H., & Schneider, G. 2016, ApJL, 819, L1
Dipierro, G., Price, D., Laibe, G., et al. 2015, MNRAS, 453, L73
Dong, R., Zhu, Z., Rafikov, R. R., & Stone, J. M. 2015, ApJL, 809, L5
Draine, B. T. 2006, ApJ, 636, 1114
Espaillat, C., Muzerolle, J., Najita, J., et al. 2014, in Protostars and Planets VI, ed. H. Beuther et al. (Tucson, AZ: Univ. Arizona Press), 497
Hogerheijde, M. R., Bekkers, D., Pinilla, P., et al. 2016, A&A, 586, A99
Jin, S., Li, S., Isella, A., Li, H., & Ji, J. 2016, ApJ, 818, 76
Johansen, A., Youdin, A., & Klahr, H. 2009, ApJ, 697, 1269
Kanagawa, K. D., Muto, T., Tanaka, H., et al. 2015, ApJL, 806, L15
Kanagawa, K. D., Muto, T., Tanaka, H., et al. 2016, PASJ, 68, 43
Lin, D. N. C., & Papaloizou, J. 1979, MNRAS, 186, 799
Lorén-Aguilar, P., & Bate, M. R. 2015, MNRAS, 453, L78
Menu, J., van Boekel, R., Henning, T., et al. 2014, A&A, 564, A93
Nomura, H., Tsukagoshi, T., Kawabe, R., et al. 2016, ApJL, 819, L7
Okuzumi, S., Momose, M., Sirono, S.-i., Kobayashi, H., & Tanaka, H. 2016, ApJ, 821, 82

Pérez, L. M., Carpenter, J. M., Chandler, C. J., et al. 2012, ApJL, 760, L17
Pinilla, P., Benisty, M., Birnstiel, T., et al. 2014, A&A, 564, A51
Pinte, C., Dent, W. R. F., Ménard, F., et al. 2016, ApJ, 816, 25
Qi, C., Ho, P. T. P., Wilner, D. J., et al. 2004, ApJL, 616, L11
Qi, C., Öberg, K. I., Wilner, D. J., et al. 2013, Sci, 341, 630
Rapson, V. A., Kastner, J. H., Millar-Blanchaer, M. A., & Dong, R. 2015, ApJL, 815, L26
Rau, U., & Cornwell, T. J. 2011, A&A, 532, A71
Schwarz, K. R., Bergin, E. A., Cleeves, L. I., et al. 2016, ApJ, 823, 91
Takahashi, S. Z., & Inutsuka, S.-i 2014, ApJ, 794, 55
Tamayo, D., Triaud, A. H. M. J., Menou, K., & Rein, H. 2015, ApJ, 805, 100
van Leeuwen, F. 2007, A&A, 474, 653
Youdin, A. 2011, ApJ, 731, 99
Zhang, K., Bergin, E. A., Blake, G. A., et al. 2016, ApJL, 818, L16
Zhang, K., Blake, G. A., & Bergin, E. A. 2015, ApJL, 806, L7
Zhu, Z., Nelson, R. P., Dong, R., Espaillat, C., & Hartmann, L. 2012, ApJ, 755, 6

Publ. Astron. Soc. Japan (2015) 67 (6), 122 (1–28)
doi: 10.1093/pasj/psv098
Advance Access Publication Date: 2015 November 3

Significant gas-to-dust ratio asymmetry and variation in the disk of HD 142527 and the indication of gas depletion

Takayuki Muto,[1] Takashi Tsukagoshi,[2] Munetake Momose,[2] Tomoyuki Hanawa,[3] Hideko Nomura,[4] Misato Fukagawa,[5] Kazuya Saigo,[6] Akimasa Kataoka,[5,7] Yoshimi Kitamura,[8] Sanemichi Z. Takahashi,[9] Shu-ichiro Inutsuka,[10] Taku Takeuchi,[4] Hiroshi Kobayashi,[10] Eiji Akiyama,[5] Mitsuhiko Honda,[11] Hideaki Fujiwara,[12] and Hiroshi Shibai[13]

[1]Division of Liberal Arts, Kogakuin University, 1-24-2 Nishi-Shinjuku, Shinjuku-ku, Tokyo 163-8677, Japan
[2]College of Science, Ibaraki University, 2-1-1 Bunkyo, Mito, Ibaraki 310-8512, Japan
[3]Center for Frontier Science, Chiba University, 1-33 Yayoi-cho, Inage-ku, Chiba 263-8522, Japan
[4]Department of Earth and Planetary Sciences, Tokyo Institute of Technology, 2-12-1 Ookayama, Meguro-ku, Tokyo 152-8551, Japan
[5]National Astronomical Observatory of Japan, 2-21-1 Osawa, Mitaka, Tokyo 181-8588, Japan
[6]Department of Physical Science, Graduate School of Science, Osaka Prefecture University, 1-1 Gakuen-cho, Naka-ku, Sakai, Osaka 599-8531, Japan
[7]Institute for Theoretical Astrophysics, Heidelberg University, Albert-Ueberle-Strasse 2, 69120, Heidelberg, Germany
[8]Institute of Space and Astronautical Science, Japan Aerospace Exploration Agency, 3-1-1 Yoshinodai, Chuo-ku, Sagamihara, Kanagawa 252-5210, Japan
[9]Astronomical Institute, Tohoku University, 6-3, Aramaki, Aoba-ku, Sendai, Miyagi 980-8587, Japan
[10]Department of Physics, Graduate School of Science, Nagoya University, Furo-cho, Chikusa-ku, Nagoya 464-8601, Japan
[11]Department of Mathematics and Physics, Kanagawa University, 2946 Tsuchiya, Hiratsuka, Kanagawa 259-1293, Japan
[12]Subaru Telescope, 650 North A'ohoku Place, Hilo, HI 96720, USA
[13]Graduate School of Science, Osaka University, 1-1 Machikaneyama, Toyonaka, Osaka 560-0043, Japan

*E-mail: muto@cc.kogakuin.ac.jp

Received 2015 January 28; Accepted 2015 September 12

Abstract

We investigate the dust and gas distribution in the disk around HD 142527 based on ALMA observations of dust continuum emissions, ^{13}CO $J = 3$–2 and C^{18}O $J = 3$–2. The disk shows strong azimuthal asymmetry in the dust continuum emission, while gas emission is more symmetric. In this paper, we investigate how gas and dust are distributed in the dust-bright northern part of the disk and in the dust-faint southern part. We construct two axisymmetric disk models. One reproduces the radial profiles of the continuum and the velocity moments 0 and 1 of CO lines in the north, and the other reproduces those in the south. We have found that the dust is concentrated in a narrow ring of $\sim$50 au width (in FWHM; $w_{\rm d} = 30$ au in our parameter definition), located at $\sim$170–200 au from

the central star. The dust particles are strongly concentrated in the north. We have found that the dust surface density contrast between the north and the south amounts to ∼70. Compared to the dust, the gas distribution is more extended in the radial direction. We find that the gas component extends at least from ∼100 au to ∼250 au from the central star, and there should also be tenuous gas remaining inside and outside of these radii. The azimuthal asymmetry of gas distribution is much smaller than dust. The gas surface density differs only by a factor of ∼3–10 between the north and south. Hence, the gas-to-dust ratio strongly depends on the location of the disk: ∼30 at the location of the peak of dust distribution in the south and ∼3 at the location of the peak of dust distribution in the north. Despite large uncertainties, we infer that the overall gas-to-dust ratio is ∼10–30, indicating that the gas depletion may already have been under way.

Key words: protoplanetary disks — radiative transfer — stars: individual (HD 142527) — stars: pre-main sequence — submillimeter: planetary systems

1 Introduction

Transitional disks are circumstellar disks having an inner hole of dust emission, and are considered to be in the evolutionary phase between gas-rich protoplanetary disks and gas-poor debris ones (Strom et al. 1999; Calvet et al. 2002; Andrews et al. 2011). The disk of this class has attracted much attention as a valuable sample to study disk evolution and planet formation processes. Among a number of transitional disk objects, HD 142527 is the subject of intense study. It is a Herbig Fe star (Waelkins et al. 1996) harboring a disk with a wide dust cavity with a radius of $\gtrsim$ 100 au (Fukagawa et al. 2006; Fujiwara et al. 2006; Verhoeff et al. 2011; Rameau et al. 2012; Casassus et al. 2012). Its stellar mass is $\sim 2.2\ M_\odot$ and its age is 5 Myr if we adopt $d = 140$ pc considering the association with Sco OB2 (Fukagawa et al. 2006; Verhoeff et al. 2011; Mendigutía et al. 2014). Recent observations have revealed the possible existence of a low-mass companion (∼0.1–0.4 $M_\odot$) at 13 au from the central star (Biller et al. 2012; Rodigas et al. 2014).

The disk moving around HD 142527 shows several interesting features. The near-infrared scattered light image of the disk shows extended emission up to $\gtrsim$ 300 au and large-scale spiral features are observed (Fukagawa et al. 2006; Casassus et al. 2012; Canovas et al. 2013; Rodigas et al. 2014), hinting that some dynamical activity is taking place in the disk (Casassus et al. 2012). ALMA observations of dust continuum emission show significant azimuthal asymmetry with a bright horseshoe-like emission in the northern part of the disk (Casassus et al. 2013; Fukagawa et al. 2013; Perez et al. 2015). It is indicated that large grains are concentrated in this northern region (Casassus et al. 2015). In the vicinity of the central star, a stream-like feature in $HCO^+ J =$ 4–3 emission (Casassus et al. 2013) and a point source of dust emission (Fukagawa et al. 2013) are observed. HCN $J = 4$–3 and CS $J = 7$–6 emissions are also spatially resolved with ALMA (van der Plas et al. 2014).

Fukagawa et al. (2013) presented the results of ALMA Band 7 observations of dust continuum and gas emission in ^{13}CO $J = 3$–2 and C^{18}O $J = 3$–2. On the basis of the very bright dust continuum emission ($\gtrsim$ 20 K) in the northern part, they discussed two possibilities for the disk gas distribution. One is that the gas-to-dust mass ratio is less than 100, at least in the northern part, and significant dust concentration occurs. The other is that the gas-to-dust mass ratio is the standard value of 100 and so the disk gas mass can be high enough for the onset of gravitational instability. In either case, the disk is likely to be in the process of ongoing planet formation.

It is important to pin down the amount of gas and dust by means of detailed modeling. In this paper, we derive the gas and dust distribution based on ALMA Cycle 0 Band 7 observations of HD 142527 using more detailed modeling of gas and dust emission than Fukagawa et al. (2013). We derive the dust distribution from the continuum emission and the gas distribution from the CO emission in order to obtain the gas-to-dust ratio in the northern and the southern part of the disk.

The paper is constructed as follows. In section 2, we summarize the results of observations. In section 3, we describe the method of modeling. In sections 4 and 5, we present the modeling results of dust and gas distribution, respectively. In section 6, we discuss the implications of our best-fitting model. Section 7 provides a summary.

2 Observation

2.1 Observation and data reduction

ALMA Band 7 Cycle 0 observations of HD 142527 (RA, Dec)$_{J2000.0}$ = ($15^h56^m41^s.9$, $-42°19'23''.3$) were

carried out in the extended array configuration with a maximum baseline of about 480 m. The observations consisted of six scheduling blocks during the period from 2012 June to August. The correlator was configured to store dual polarizations in four separate spectral windows with 469 MHz of bandwidth and 3840 channels each, and their central frequencies were 330.588, 329.331, 342.883 and 342.400 GHz, respectively, to target the molecular lines of ^{13}CO $J = 3$–2 and C^{18}O $J = 3$–2. The resultant channel spacing for the lines was 122 kHz, corresponding to 0.12 km s^{-1} in velocity at these frequencies, but the effective spectral resolution was lower by a factor of ∼2 (∼0.2 km s^{-1}) because of Hanning smoothing. The continuum data from all the spectral windows were aggregated and treated as a single data set of 336 GHz in central frequency and 1.8 GHz in bandwidth. The on-source integration after flagging aberrant data was 3.0 hr.

Calibration and reduction of the data were made with the Common Astronomy Software Applications (CASA) version 3.4, in almost the same way as in Fukagawa et al. (2013). Self-calibration was performed for the continuum to improve the sensitivity and image fidelity, and the final gain solution was also applied to ^{13}CO and C^{18}O data. The only difference between our reduction and Fukagawa et al. (2013)'s one was the visibility weighting applied in the final step of the imaging; we adopted in this study the Briggs weighting with a robust parameter of 0.5 to best recover the weak and extended components of the emission. The size in FWHM and the position angle (PA) for the major axis of each synthesized beam for the continuum at 336 GHz, ^{13}CO, and C^{18}O were 0.″47 × 0.″40 = 60 au × 56 au (PA = 59.°9), 0.″50 × 0.″42 = 70 au × 59 au (PA = 57.°4) and 0.″50 × 0.″42 = 70 au × 59 au (PA = 60.°6), respectively. Further details on bandpass and gain calibrations are described in Fukagawa et al. (2013). The rms noise is 0.13 mJy beam^{-1} for the continuum whereas it is 6.1 and 8.3 mJy beam^{-1} in the 0.12 km s^{-1} wide channels for the line emission of ^{13}CO and C^{18}O.

2.2 Results of dust continuum emission

Figure 1 shows the continuum map, which is quite similar to that presented by Fukagawa et al. (2013). An outer asymmetric ring as well as an inner unresolved component is detected, and these are separated by a radial gap. The position of the unresolved component coincides with the velocity centroid of ^{13}CO $J = 3$–2 (subsection 2.3), and it is regarded as the stellar position in the following. The radial profiles of surface brightness are well described by a Gaussian function, and the brightest and faintest of their peaks are located at $PA \approx 23°$ and $PA \approx 223°$, respectively (see also figure 4 of Fukagawa et al. 2013). The averaged surface

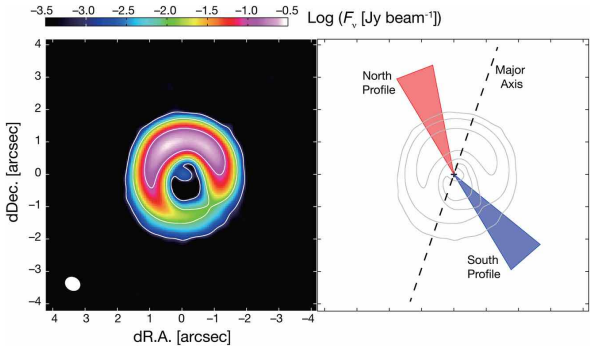

Fig. 1. Left: Map of the continuum emission at 336 GHz with the Briggs weighting with a robust parameter of 0.5. The synthesized beam, 0.″47 × 0.″40 with the major axis PA = 59.°9, is indicated by the white ellipse in the bottom left corner. The contours correspond to 1, 10, and 100 mJy beam^{-1}. The 1 σ level is 0.13 mJy beam^{-1}. Right: The position angle of the major axis is indicated by the dashed line. The regions where the azimuthal average is taken to obtain the north profiles (PA = 11°–31°) and the south profiles (PA = 211°–231°) are indicated by red and blue hatches, respectively. Contours are the same as the left panel. (Color online)

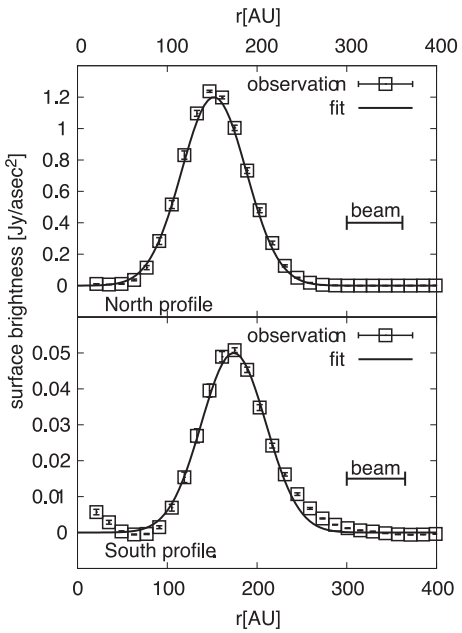

Fig. 2. Radial profiles of surface brightness of the continuum emission at 336 GHz for PA = 11°–31° (top panel, squares) and PA = 211°–231° (bottom panel, squares). Solid lines indicate the best-fitting Gaussian function (see table 1 for parameters). Error bars indicate the standard deviation after the averaging over 20° in PA.

brightness profiles $I(r)$ in PA = 11°–31° and 211°–231° are fitted by

$$I(r) = I_{\rm p} \exp\left[-\frac{(r - r_{0,\rm obs})^2}{w_{\rm obs}^2}\right], \quad (1)$$

where r is the angular distance from the star, $r_{0,\rm obs}$ is the peak position, and $w_{\rm obs}$ is the width of the Gaussian. The best-fitting profiles are shown in figure 2 and the best-fitting

Table 1. Best-fitting Gaussian parameters.*

PA	I_p [Jy arcsec^{-2}]	$r_{0,\,\mathrm{obs}}$ [au]	w_{obs} [au]
11°–31° (North profile)	1.2	152	51
211°–231° (South profile)	0.050	174	51

*Gaussian parameters [equation (1)] that are fitted to the radial profiles of dust continuum emission in the brightest and the faintest directions. The parameters r_0 and w are given in units of au, assuming that the distance to HD 142527 is 140 pc.

parameters are summarized in table 1. As shown in table 1, the contrast in I_p is 24 between these two position angles. In the following, we refer to the averaged profile in the section of $11^\circ < PA < 31^\circ$ as the "north profile" and that in $211^\circ < PA < 231^\circ$ as the "south profile" (see the right panel of figure 1).

2.3 Results of ^{13}CO and C^{18}O $J = 3$–2 emission

Figures 3 and 4 show the moment maps of the ^{13}CO $J = 3$–2 and C^{18}O $J = 3$–2 emissions, respectively. Moments 0, 1, and 2 correspond to the integrated intensity,

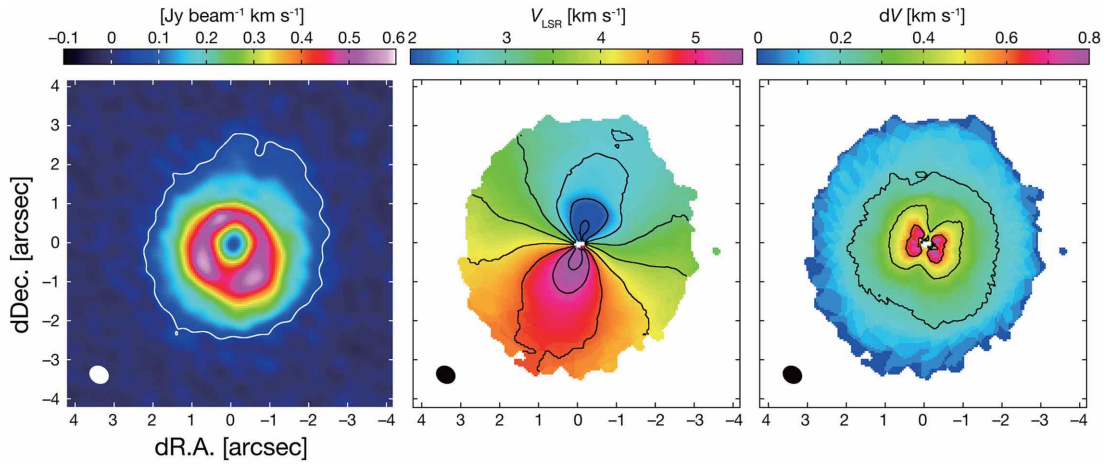

Fig. 3. Moment maps of the ^{13}CO $J = 3$–2 line. Left: Moment 0 map, integrated over the velocity range of $v_{\mathrm{LSR}} = (0.40$–$7.00)$ km s^{-1}. The white contour shows the 5 σ level (48 mJy beam^{-1} km s^{-1}). Middle: Moment 1 map, created by the emission above the 5 σ level in channel maps of 0.12 km s^{-1} resolution (figures 32–34 in appendix 1). The contours along $PA \approx 71^\circ$ are those of the systemic velocity ($v_{\mathrm{LSR}} = 3.7$ km s^{-1}), and the contour spacing is 0.5 km s^{-1}. Right: Moment 2 map, created by the emission above the 5 σ level in channel maps of 0.12 km s^{-1} resolution. The contour starts at 0.2 km s^{-1}, and its spacing is 0.2 km s^{-1}. The synthesized beam, 0.″50 × 0.″42 with the major axis $PA = 57.^\circ4$, is indicated by the ellipse in the bottom left corner of each panel. (Color online)

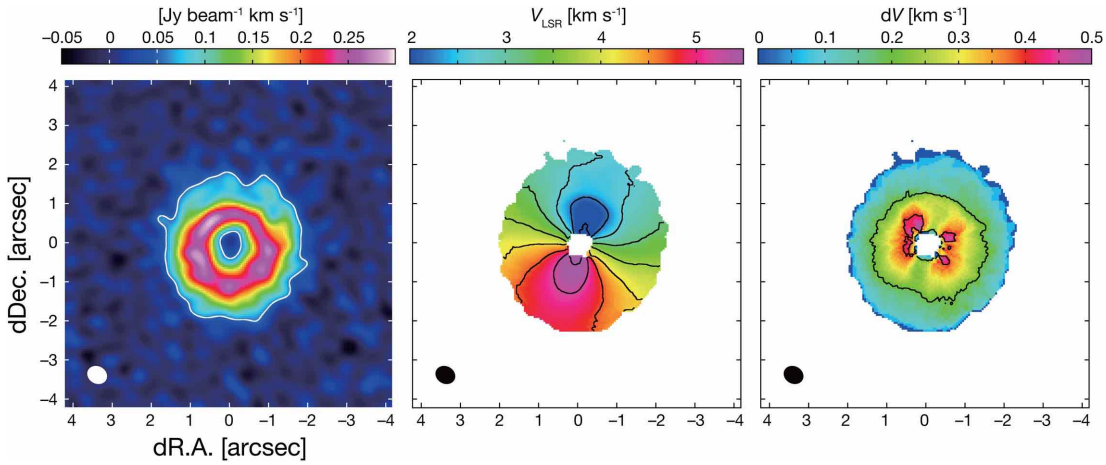

Fig. 4. Moment maps of the C^{18}O $J = 3$–2 line. Left: Moment 0 map, integrated over the velocity range of $v_{\mathrm{LSR}} = (1.0$–$6.40)$ km s^{-1}. The white contour shows the 5 σ level (55 mJy beam^{-1} km s^{-1}). Middle: Moment 1 map, created by the emission above the 5 σ level in channel maps of 0.12 km s^{-1} resolution (figures 35–36 in appendix 1). The contours along $PA \approx 71^\circ$ are those of the systemic velocity ($v_{\mathrm{LSR}} = 3.7$ km s^{-1}), and the contour spacing is 0.5 km s^{-1}. Right: Moment 2 map, created by the emission above the 5 σ level in channel maps of 0.12 km s^{-1} resolution. Contours at 0.2 and 0.4 km s^{-1} are shown. The synthesized beam, 0.″50 × 0.″42 with the major axis $PA = 60.6^\circ$, is indicated by the ellipse in the bottom left corner of each panel. (Color online)

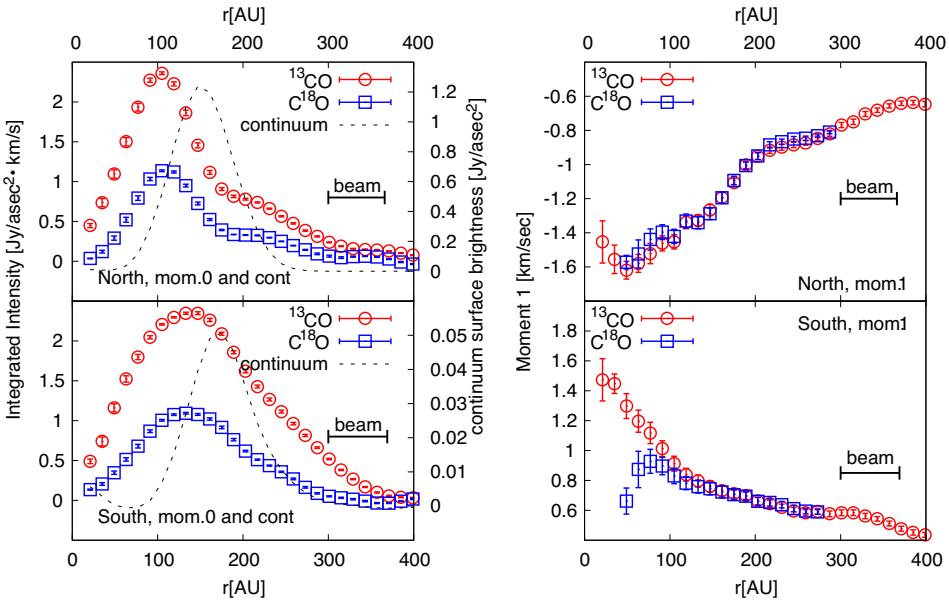

Fig. 5. The north (top row) and the south (bottom row) radial profiles of observed moment 0 (left panels) and moment 1 (right panels) of ^{13}CO (red circles) and C^{18}O (blue squares). The systemic velocity of 3.7 km s^{-1} is subtracted in calculating the moment 1 profiles. Error bars indicate the standard deviation after the averaging over 20° in *PA*. The radial profiles of the continuum emission are overplotted in the moment 0 radial profiles for comparison. (Color online)

intensity-weighted mean velocity, and velocity dispersion, respectively. As shown in appendix 1, the emission above the 5σ level is detected in $v_{\rm LSR} = (0.64$–$7.00)\,{\rm km\,s^{-1}}$ in ^{13}CO and $v_{\rm LSR} = (1.24$–$6.16)\,{\rm km\,s^{-1}}$ in C^{18}O. The azimuthal asymmetry is weak in the moment 0 map although the northern part tends to be slightly weaker, possibly due to higher continuum levels. Furthermore, the line emission (^{13}CO, in particular) is clearly detected in the inner regions down to $r \approx 20$ au (0.″15) as well as the outer regions up to $r \approx 400$ au (2.″8). The velocity distribution revealed in moments 1 and 2 is consistent with a disk in Keplerian rotation. A constant (systemic) velocity of 3.7 km s^{-1} is found along $PA = 71^\circ \pm 2^\circ$ in the moment 1 maps, and this is regarded as the direction of the minor axis of the system. The position–velocity (P–V) diagram along the major axis ($PA = -19^\circ$) is explained well by Keplerian rotation with a stellar mass of 2.2 $M_\odot$ and an inclination angle of 27°, as described in detail in appendix 1 (see also Fukagawa et al. 2013; Perez et al. 2015). We adopt these values for *PA* of the major axis and the inclination of the system throughout this paper.

Figure 5 shows the north and south profiles of moments 0 and 1, which is the main focus of the modeling described in later sections. It is clear that the moment 0 profiles of both ^{13}CO and C^{18}O are very different from those of dust continuum emission; these are more extended than the Gaussian-like dust emission profiles. The moment 1 profiles of these two lines agree with each other in 100 au $\leq r \leq$ 280 au, indicating that both these lines successfully reveal the Keplerian rotation in the regions where the emission is detected with a high signal-to-noise ratio (S/N). The moment 1 profile of ^{13}CO further reveals the gas motion down to $r \approx 20$ au and up to $r \approx 400$ au. As discussed in the following sections, this indicates the existence of tenuous gas components in these inner and outer regions. The ^{13}CO line has larger moments 0 and 2 in almost all the positions than the C^{18}O. This is because ^{13}CO has a larger optical depth at every velocity channel and hence has a broader line profile than C^{18}O (see also sub-subsection 6.2.2).

3 Method of modeling

Our goal is to find the density and temperature distribution of the disk moving around HD 142527 based on the continuum and CO line emission profiles described in the previous section. We construct axisymmetric models that can reproduce similar radial brightness profiles in the direction where dust emission is the brightest (north profile) and the faintest (south profile) since the model that fully accounts for the azimuthal asymmetry can be very complex. This approach is similar to that taken by Bruderer et al. (2014) in making the model for the disk around Oph IRS 48, which also exhibits strong azimuthal asymmetry.

3.1 Dust distribution models

We first derive density and temperature distributions of the continuum emission under the assumption that the disk is

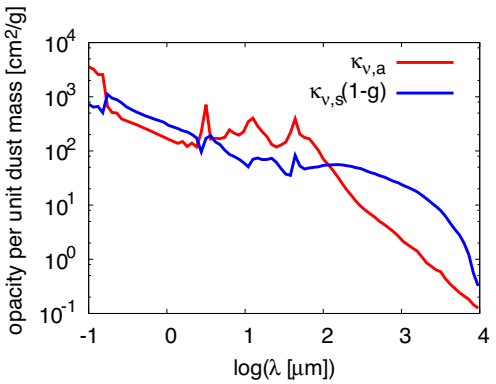

Fig. 6. The absorption (red) and the effective scattering (blue; see text for definition) coefficients for the dust model used in this paper. (Color online)

in thermal and hydrostatic equilibrium. For the sake of simplicity, the gas-to-dust ratio is assumed to be uniform in the vertical direction and the gas temperature is assumed to be the same as dust one. In other words, we have ignored dust sedimentation (e.g., Dubrulle et al. 1995) and temperature difference between gas and dust in the low-density upper layers (e.g., Kamp & Dullemond 2004; Nomura & Miller 2005). We note that the gas-to-dust ratio can vary in the radial direction, which is the main focus of the modeling of gas observations (see subsection 3.2 and section 5). The disk is assumed to be heated only by stellar irradiation, since viscous heating is less important in the region considered in this paper. The star is assumed to have an effective temperature of $T_{\rm eff} = 6250\,{\rm K}$ and a radius of $R = 3.8\,R_\odot$ (Verhoeff et al. 2011).[1] We solved the zeroth- and first-order moment equations of the radiative transfer (M1 method, see Kanno et al. 2013). We use 226 colors in the wavelength range of $0.1\mu{\rm m} \le \lambda \le 3.16\,{\rm mm}$, resulting in the spectral resolution of $\Delta\log\lambda = 0.02$ (i.e., $\lambda/\Delta\lambda = 21.7$). The computational box covers $30\,{\rm au} \le r \le 410\,{\rm au}$ and $|z| \le 120\,{\rm au}$ with a spatial resolution of 2 au in the cylindrical coordinates. The disk is assumed to be symmetric with respect to the midplane.

The dust is assumed to consist of silicate, carbonaceous grains, and water ice having mass fractional abundances of $\zeta_{\rm sil} = 0.0043$, $\zeta_{\rm carbon} = 0.0030$, and $\zeta_{\rm ice} = 0.0094$, respectively, which are consistent with solar elemental abundance (Anders & Grevesse 1989). The dust particles are assumed to have a power-law size distribution of $\propto a^{-3.5}$ with a maximum size of $a_{\rm max} = 1\,{\rm mm}$ (Nomura & Miller 2005). Figure 6 shows the absorption ($\kappa_{\nu,{\rm a}}$) and the effective scattering coefficients in units of cm^2 per unit gram of dust. Here, we define the effective scattering coefficient as $\kappa_{\nu,{\rm s}}(1-g)$, where $\kappa_{\nu,{\rm s}}$ is the scattering coefficient and $g = \langle\cos\theta\rangle$ is the scattering asymmetry factor.[2] The model with the maximum dust size of 1 mm gives a large value of opacity at sub-mm range (Aikawa & Nomura 2006). Consequently, the dust mass evaluated in this paper should be close to the lowest. Our opacity at 870 μm has values of $\kappa_{\rm a} = 2.9\,{\rm cm^2\,g^{-1}}$ with $\beta \sim 1.2$ at $0.3\,{\rm mm} \le \lambda \le 1\,{\rm cm}$ and $\kappa_{\rm s}(1-g) = 26\,{\rm cm^2\,g^{-1}}$ per unit dust mass. The absorption coefficient at 870 μm is 20% smaller than the value adopted by Beckwith et al. (1990), which is $\sim$3.5 cm^2 g^{-1} per unit dust mass. We also note that the effective scattering coefficient is large compared to the absorption coefficient in the sub-mm range since the maximum dust size is comparable with the wavelength.

The dust surface density is assumed to have the form

$$\Sigma_{\rm d}(r) = \Sigma_{\rm d,0}\exp\left[-\left(\frac{r-r_{\rm d}}{w_{\rm d}}\right)^2\right], \tag{2}$$

since the radial profile of the continuum emission is well approximated by a Gaussian function. For an assumed set of parameters ($\Sigma_{\rm d,0}$, $r_{\rm d}$, $w_{\rm d}$), we obtain the spatial distribution of dust density $\rho_{\rm d}(r, z)$, temperature $T(r, z)$, and the radiation energy density $J_\nu(r, z)$ for the 226 colors at each grid cell.

The expected observed surface brightness profiles of dust continuum emission are obtained by ray-tracing. The surface brightness I_ν at frequency ν is calculated by solving

$$\frac{dI_\nu}{ds} = -\rho_d\chi_\nu\left[I_\nu - S_\nu\right], \tag{3}$$

where s is the coordinate along the line of sight, and χ_ν is the extinction by absorption and (effective) scattering, $\chi_\nu = \kappa_{\nu,{\rm a}} + (1-g)\kappa_{\nu,{\rm s}}$. The source function, S_ν, is given by

$$S_\nu = (1-\omega_\nu)B_\nu(T) + \omega_\nu J_\nu, \tag{4}$$

where $\omega_\nu = (1-g)\kappa_{\nu,{\rm s}}/\chi_\nu$ is the (effective) albedo[3] and $B_\nu(T)$ is the Planck function. The second term in equation (4) represents the scattered light, and the scattering is assumed to be isotropic for simplicity. The optical depth τ_ν along the line of sight is given by

$$\frac{d\tau_\nu}{ds} = -\chi_\nu\rho_{\rm d}. \tag{5}$$

We compute the model image by using $(N_R, N_\Phi) = (128, 128)$ rays covering the $35\,{\rm au} < R < 400\,{\rm au}$ and $0 < \Phi < 2\pi$ region, where (R, Φ) are the polar coordinates on

[1] The stellar parameters are updated in Mendigutía et al. (2014), but the stellar luminosity is within the error for the parameters described here.

[2] We have left the term $(1-g)$ for consistency with the M1 method. See Mihalas and Mihalas (1984) and González, Audit, and Huynh (2007) for the appearance of the $(1-g)$ factor in the M1 method.

[3] With the dust model of $a_{\rm max} = 1\,{\rm mm}$, the value of $\bar{\omega}_\nu = \kappa_{\rm s}/(\kappa_{\rm a}+\kappa_{\rm s})$ and ω_ν given in the main text differ only by $\sim$5% at the wavelengths of interest.

the sky-plane with the central star at the origin. We use the inclination of 27°, as described in section 2.

Making a comparisons between the model and observations, we convolve the model images with the Gaussian function of the same beam size and orientation as the observations. We extract the radial surface brightness profiles from the convolved image and compare them with the observations. We iterate this procedure until the given set of parameters ($\Sigma_{\rm d,0}$, $r_{\rm d}$, $w_{\rm d}$) reproduces the observed profiles shown in figure 2 reasonably well.

3.2 Gas distribution models

We then derive the gas distribution that accounts for both moments 0 (integrated intensity) and 1 (intensity-weighted mean velocity) radial profiles in the northerly and southerly directions. We have chosen these moments of the line emission because they are least affected by beam dilution. It should also be noted that the observed moment 2 profiles contain the uncertainty coming from the choice of cutoff levels when producing the moment map from the data.

In later sections, we show that uniform gas-to-dust ratio models do not reproduce the observations. Therefore, we assume that the gas density $\rho_{\rm g}(r, z)$ is given by

$$\rho_{\rm g}(r, z) = \xi(r)\rho_{\rm d}(r, z), \tag{6}$$

where $\xi(r)$ represents the gas-to-dust ratio at each radius. The gas surface density $\Sigma_{\rm g}(r)$ is then given by

$$\Sigma_{\rm g}(r) = \xi(r)\Sigma_{\rm d}(r). \tag{7}$$

In later sections, we look for the forms of $\xi(r)$, or, equivalently, the form of $\Sigma_{\rm g}(r)$, that best reproduces the observed radial profiles of moments 0 and 1.

We assume that the gas rotation is Keplerian at the disk midplane,

$$v_{\rm rot}(r) = 3.13\left(\frac{r}{200\,{\rm au}}\right)^{-1/2}\ [{\rm km\,s^{-1}}], \tag{8}$$

where $3.13\,{\rm km\,s^{-1}}$ is the Keplerian velocity at 200 au moving around a 2.2 $M_\odot$ star. The rotation velocity can be slightly different from Keplerian owing to, for example, radial pressure gradient force, but the difference is at most of the order of the thermal velocity (∼10% of the Keplerian rotation velocity), which is hardly observed with the current velocity resolution. The gas temperature $T(r, z)$ is assumed to be the same as the dust temperature, as mentioned in subsection 3.1.

The expected brightness of line emission is calculated with ray-tracing methods by solving

$$\frac{dI_{\rm ul}}{ds} = -\chi_{\rm ul}\left(I_{\rm ul} - S_{\rm ul}\right), \tag{9}$$

where I_{ul} is the intensity of the line emission from the upper state u to the lower state l. The total extinction χ_{ul} comes from both dust and gas,

$$\chi_{\rm ul} = \rho_{\rm d}\chi_\nu + (n_{\rm l}B_{\rm lu} - n_{\rm u}B_{\rm ul})\,\phi_{\rm ul}\frac{h\nu_{\rm ul}}{4\pi}, \tag{10}$$

and the source function $S_{\rm ul}$ is given by spontaneous emission and dust emission S_ν given in equation (4),

$$S_{\rm ul} = \frac{1}{\chi_{\rm ul}}n_{\rm u}A_{\rm ul}\phi_{\rm ul}\frac{h\nu_{\rm ul}}{4\pi} + \frac{\rho_{\rm d}\chi_\nu}{\chi_{\rm ul}}S_\nu. \tag{11}$$

Here, $n_{\rm u}$ and $n_{\rm l}$ are level populations for the upper and lower state, respectively, $A_{\rm ul}$, $B_{\rm ul}$, and $B_{\rm lu}$ are Einstein coefficients, and $\phi_{\rm ul}$ is the line profile function. We note that the scattering of line emission by dust particles is not included in this work. Local thermal equilibrium is assumed to calculate the level population, which is a valid assumption for lower transition lines of CO in a protoplanetary disk where the typical density is much higher than the critical densities for these lines (Pavlyuchenkov et al. 2007). The fractional abundance of ^{13}CO and C^{18}O is assumed to be 9×10^{-7} and 1.35×10^{-7} (Qi et al. 2011). We have assumed that the line width is determined by thermal broadening.

We construct the model channel maps from $-4.5\,{\rm km\,s^{-1}}$ to $4.5\,{\rm km\,s^{-1}}$ with respect to the systemic velocity with a $0.06\,{\rm km\,s^{-1}}$ step, and each model channel map is convolved with the Gaussian beam. The model radial profiles of moments 0 and 1 are then extracted in the north and south directions for comparison with the observations. The continuum emission is subtracted on the image by using line-free channels, and the velocity channels showing emission only below the detection limit are excluded when calculating the moment maps from the model. To confirm the validity of continuum subtraction in the image plane, we have also made imaging simulations for several cases in a more rigorous way in which the visibilities for the baselines sampled in our observations are first generated from the disk model with the CASA simulator, and then continuum subtraction is made in the *uv*-plane. After imaging with the same procedure as described in subsection 2.1, we have confirmed that the resultant line profiles agree with those obtained with the image-based continuum subtraction within a few percent.

4 Results of dust distribution

We have searched for the parameters $\Sigma_{\rm d,0}$, $r_{\rm d}$, and $w_{\rm d}$ in equation (2) that can reproduce the observed north and south profiles. In the south profiles, the parameter search is straightforward since the dust emission is optically thin. In the north, on the other hand, it is necessary to carefully look at the dependence of surface brightness profiles

Table 2. Best-fit values for dust distribution.

	North	South
$\Sigma_{d,0}$ [g cm^{-2}]	0.6	8.45×10^{-3}
r_d [au]	173	196
w_d [au]	27	34

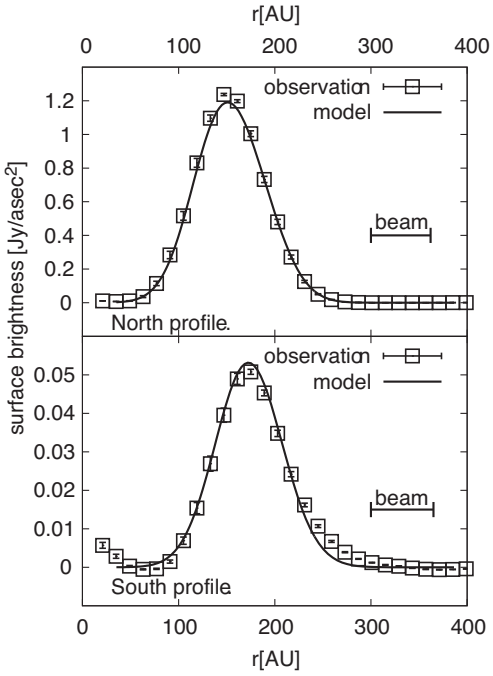

Fig. 7. Comparison of the continuum emission and the model surface brightness for the north (top) and south (bottom) profiles.

on dust distribution parameters since the dust emission is optically thick (see sub-subsection 6.2.1). The details of the parameter search for the north profiles are summarized in appendix 2. The best-fitting results are summarized in table 2, and figure 7 compares the radial profiles of the dust continuum emissions derived from the model and observations. The best-fitting models have the dust density and temperature distributions shown in figure 8. Our derived parameters for the dust disk (or ring) radius and width are consistent with the results of Verhoeff et al. (2011), who show that the massive outer disk radially extends from 130 au to 200 au based on their modeling of the spectral energy distribution (SED) and midinfrared images (and therefore dust emission).

The dust ring emission is only marginally resolved in ALMA Band 7 since the full width at half maximum (FWHM) of the radial Gaussian function of the model surface density is $\sim 2\sqrt{\ln 2} w_d \sim 50$ au (see table 2), which is slightly smaller than the beam size ($\sim$0.″45; $\sim$ 60 au at

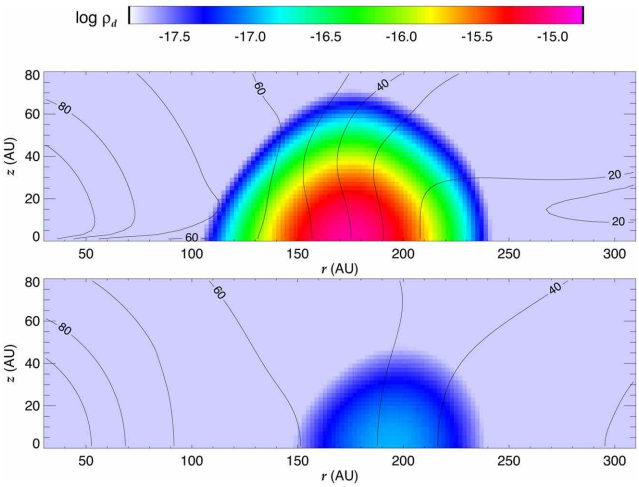

Fig. 8. Density and temperature distributions of dust for the best-fitting models of north (top) and south (bottom) profiles. Dust density is indicated by color in units of g cm^{-3} and the temperature is shown by contours. (Color online)

140 pc). As a result, the radial width of the observed surface brightness profile ($\sim 2\sqrt{\ln 2} w_{obs} = \sim$85 au in FWHM; see table 1) is larger than that of the model surface density. Perez et al. (2015) measured the radial width of the dust continuum emission at 230 GHz to be 0.″9, while at 345 GHz to be $\sim$0.″55. The difference in the width for different bands may be explained by the effect of the convolution by the beam. The radial width of the continuum emission is not well resolved. The ratio in the radial width of the continuum emission between 230 GHz and 345 GHz is $\sim$1.6, which is close to the frequency ratio (and thus the ratio of the beam size) between the two bands.

It is indicated that the amount of dust particles is $\sim$70 times more at the peak in north profiles than at the peak in south profile, although the surface brightness contrast of the dust emission between the north- and the south-peak locations is $\sim$24. The difference between the surface density contrast and the surface brightness one is largely due to the fact that the northern part of the disk is optically thick to dust emission. It should also be noted that the scattered light component in the dust continuum emission is not negligible in the north profile (see subsection 6.2 for discussion).

5 Results of gas distribution

We now turn our attention to gas distribution. We first show that the models with uniform gas-to-dust ratio of 100 do not reproduce the observed profiles in subsection 5.1. We then describe in detail how we construct the models for gas distribution step by step in subsequent subsections. Our final results are summarized in subsection 5.6.

5.1 Failure of uniform gas-to-dust ratio models

We first show that the models with uniform gas-to-dust ratio 100, i.e., $\xi(r) = 100$ in equation (6), fail to reproduce the observed radial profiles of moments 0 and 1. In this case, the radial gas surface density profile $\Sigma_g(r) = \xi(r)\Sigma_d(r)$ is given by a Gaussian function as the dust distribution is. Figure 9 shows the radial profiles of moments 0 and 1 for the north direction and figure 10 shows the same but for the south direction.

At inner radii ($r \lesssim 100$ au), the model profiles of moment 0 show too weak emission compared to observations, and those of moment 1 tend to be too slow compared

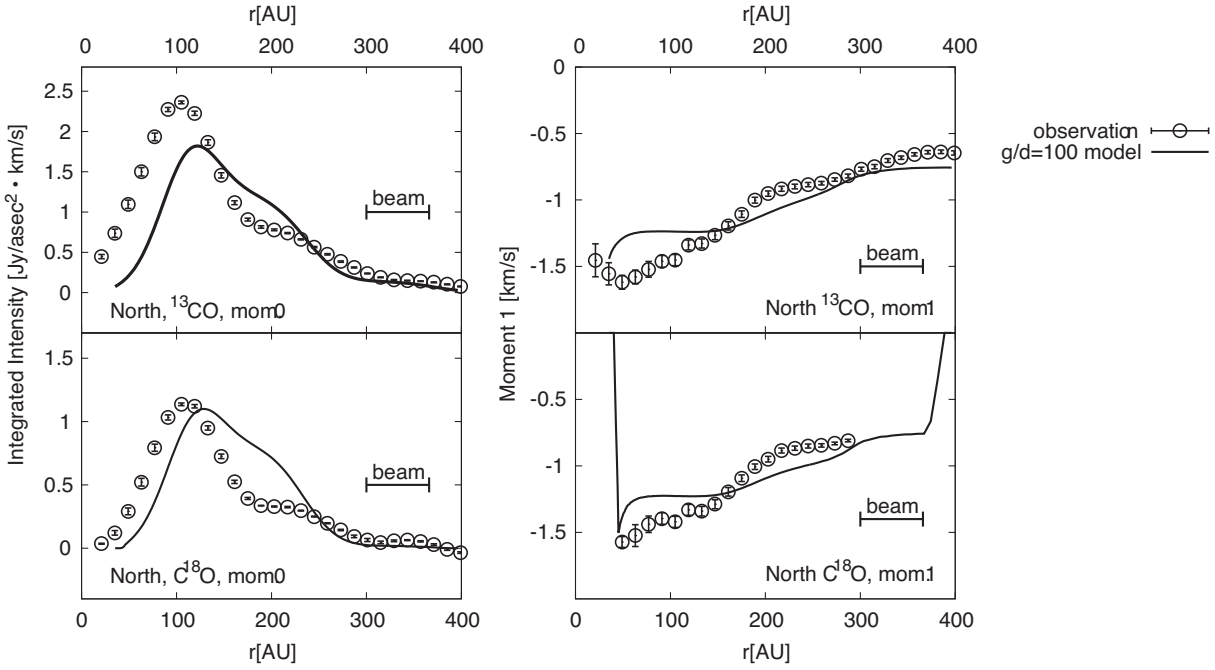

Fig. 9. The radial profiles of moment 0 (left panels) and moment 1 (right panels) for ^{13}CO (top row) and C^{18}O (bottom row) for the north profiles in the case where the gas-to-dust ratio is fixed to 100 everywhere in the disk.

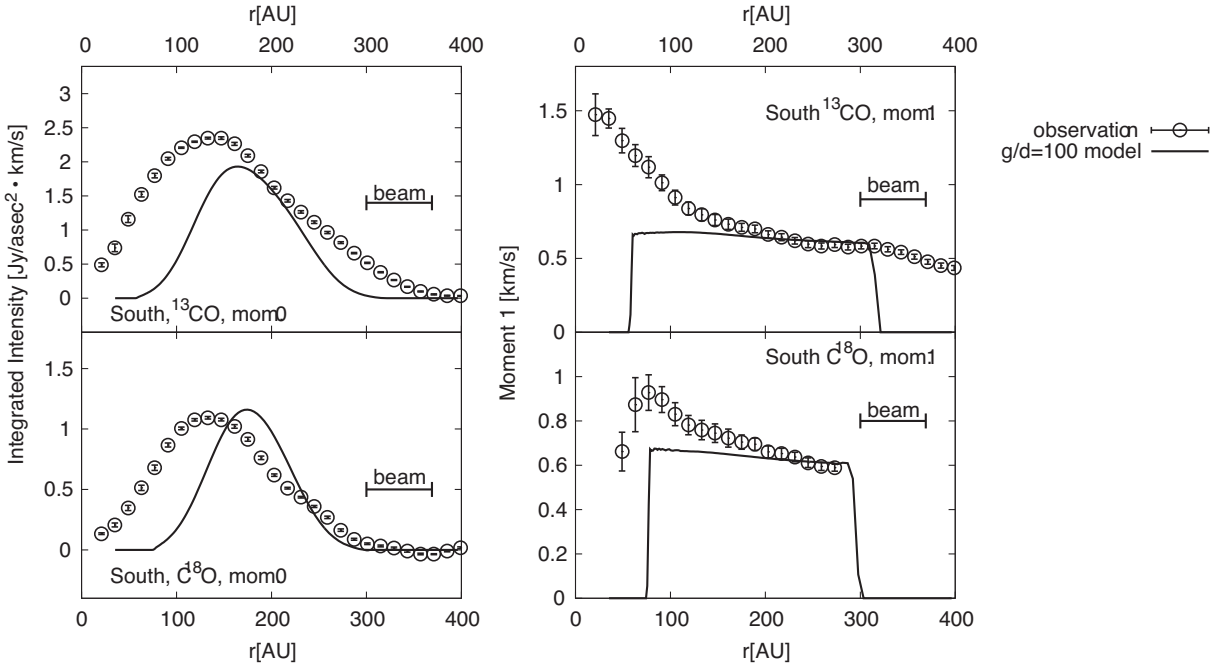

Fig. 10. Same as figure 9 except for the south profiles.

to the observations. These indicate that there has to be more gas within 100 au. On the other hand, around at the peak of the dust distribution ($r \sim 170$ au for north and $r \sim 200$ au for south), the model moment 0 is too bright compared to the observations, especially in the case of $C^{18}O$ profile. This suggests that the gas-to-dust ratio is smaller than 100 at the places where dust particles are concentrated. It is, however, impossible to decrease the amount of gas at ~200 au and to increase it at inner radii simultaneously under the assumption of uniform gas-to-dust ratio. The dust distribution was already determined in section 4. Therefore, we need to consider a completely different radial distribution of the gas from the dust by varying the gas-to-dust ratio $\xi(r)$ within the disk.

5.2 Power-law gas profiles

Having found that the uniform gas-to-dust ratio models do not reproduce the observed profile of gas emission, we now explore models of gas distribution that are not necessarily restricted to constant gas-to-dust ratio. To acquire results consistent with the dust distribution calculations described in subsection 3.1, we still assume that the gas-to-dust ratio is constant in the vertical direction *at each radius*, but it is not constant in the radial direction. With a trial function of gas surface density $\Sigma_g(r)$, it is possible to calculate the gas-to-dust ratio at each radius by calculating $\xi(r) = \Sigma_g(r)/\Sigma_d(r)$, which is then used to obtain the gas density at each grid cell from equation (6).

From the results presented in subsection 5.1, it is indicated that the gas distribution is more extended in the radial direction than the dust one. Therefore, we first try the model in which the gas surface density profile $\Sigma_g(r)$ is given by the r^{-1} power-law profile at $r_c < r < r_{out}$,

$$\Sigma_g(r) = \Sigma_0 \left(\frac{r}{200\,\mathrm{au}}\right)^{-1} \quad (r_c < r < r_{out}), \tag{12}$$

and zero otherwise. Here, r_c can be interpreted as the cavity radius. Since constant gas-to-dust ratio models fail to explain the observed profiles, it is necessary to make models with different gas distribution. The gas-to-dust ratio is not constant in such cases. We have first tried several models with Gaussian surface density profiles with different parameters, but we have found that these models fail to reproduce the observed profiles. This is primarily due to the fact that the gas emission extends to a large radius, but the Gaussian function falls off too rapidly. Therefore, we consider a power-law distribution of the gas surface density, which is more radially extended than Gaussian profiles. We choose the power-law distribution as a representative model of such radially extended gas profiles and fix the power-law exponent to -1 in order to reduce the number of free parameters. The choice of r^{-1} power is motivated by the models of the steady-state accretion disk, but we do not claim that this is the only possible solution. We aim to find one possible disk model that reasonably reproduces observations, and discuss its implications for the overall picture of how the dust and gas are distributed.

Table 3. Parameters explored for power-law gas distribution given by equation (12).

Σ_0 [g cm^{-2}]	0.0845, 0.2325, 0.845, 2.325
r_c [au]	90, 100, 110, 120
r_{out} [au]	200, 250, 300, 350

We explore the parameter space of (Σ_0, r_c, r_{out}) and look for values such as match the observed moments 0 and 1 profiles for the north and south profiles. Our strategy is to first find the values of Σ_0 that reasonably match with the observations in a range of 150 au $\lesssim r \lesssim$ 200 au, where dust emission is bright. Then we look for values of r_c by investigating the inner radii. Finally, we search for values of r_{out} by investigating the outer radii. We show the results one by one in the following subsections. The values of these three parameters explored in our set of calculations are summarized in table 3.

5.3 The overall gas distribution

We first find the values of Σ_0 that are reasonably matched to the observed profiles in the range of 150 au $\lesssim r \lesssim$ 250 au. For this purpose, we fix (r_c, r_{out}) = (100 au, 280 au) for both north and south profiles and change Σ_0 from 0.0845 g cm^{-2} to 2.325 g cm^{-2} in steps of factors of ~3 (see table 3 for specific parameters). The lowest value of Σ_0 is chosen in such a way that the gas-to-dust ratio at the peak of the dust distribution in the southerly direction is 10. Figures 11 and 12 show the results for the north and south profiles, respectively.

For the north profiles of $C^{18}O$ moment 0, the observations fall between the models with $\Sigma_0 = 0.845$ g cm^{-2} and $\Sigma_0 = 2.325$ g cm^{-2}. For ^{13}CO moment 0, the model with $\Sigma_0 = 2.325$ g cm^{-2} seems to show a better fit, but it is actually difficult to judge whether it is plausible when the existence of remaining gas inside the cavity is considered (see subsection 5.4). Note that all the models fail to explain the moment 0 profile within the cavity ($r < r_c =$ 100 au) as the model profiles fall off too rapidly toward inner radii. This is because there is no gas emission within a radius of 100 au in the model. We also point out that the model moment 1 profiles show too slow a velocity at inner radii. This is because moment 1 is calculated to be zero in such gas-free regions before we convolve the model with the beam. The apparent emission inside the cavity in

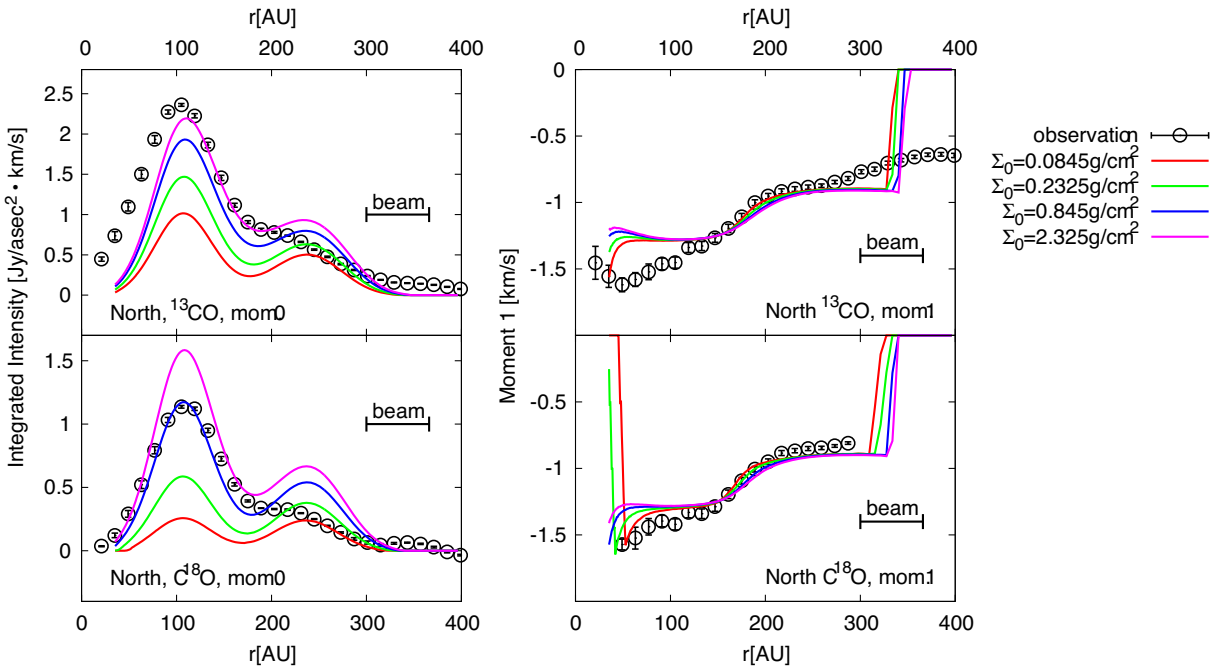

Fig. 11. The radial profiles of moment 0 (left panels) and moment 1 (right panels) for ^{13}CO (top row) and C^{18}O (bottom row) for the north profile when the parameter Σ_0 varies. (Color online)

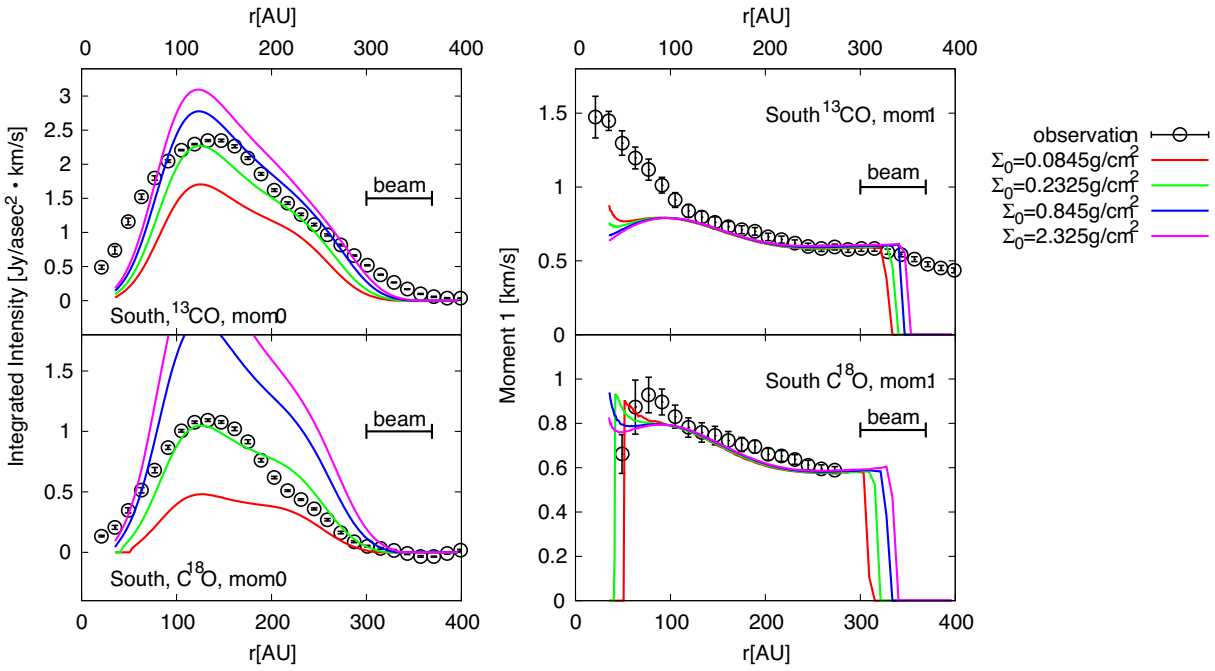

Fig. 12. Same as figure 11 except for the south profiles. (Color online)

the model is the result of beam dilution. A similar discrepancy between the model and observations can be found at the outer radii of $r \gtrsim 300$ au, while in this case the beam dilution is not as significant as for the inner radii.

One prominent feature of the model north profile is the two peaks of the surface brightness profiles at $r \sim 100$ au and $r \sim 250$ au, while the gas surface density profile is smooth. These peaks are primarily due to the existence of a large amount of dust in a relatively narrow radial range. The dust emission is optically thick and is very bright. The line emission is partially hidden by the optically thick dust. Therefore, the difference in brightness between

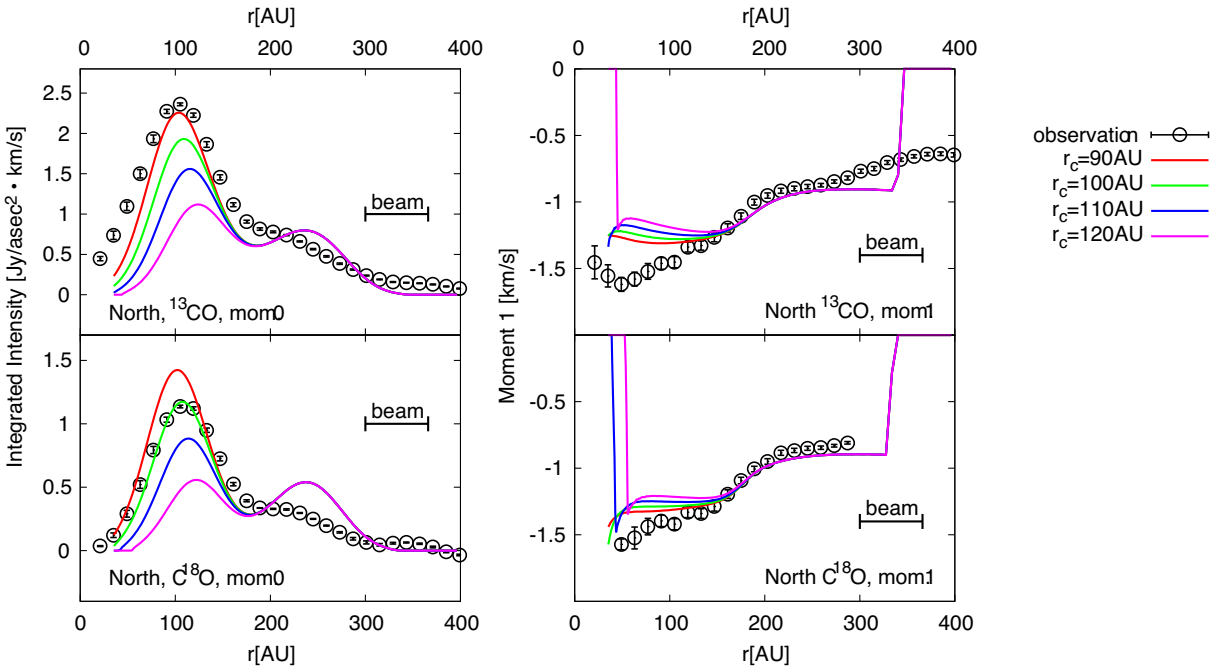

Fig. 13. The radial profiles of moment 0 (left panels) and moment 1 (right panels) for ^{13}CO (top row) and C^{18}O (bottom row) for the north direction when the parameter r_c is varied. (Color online)

continuum and line emissions is not very significant. The line emission at the peak of the dust emission is largely affected when the continuum emission is subtracted to calculate moment maps. The two "peaks" of gas emission should be considered as "one trough" caused by the subtraction of the bright continuum emission. Although not as prominent as the model profiles, it is possible to see this effect in the observed profiles, which show a slight dip of moment 0 at ∼170 au (see figures 5 and 11). We further discuss these apparent bump and/or trough structures in subsection 6.3.

For the south profiles, $\Sigma_0 = 0.2325\,\mathrm{g\,cm^{-2}}$ models show reasonable fit to both ^{13}CO and C^{18}O. However, the discrepancy between the model moment 1 profiles and the observations at inner and outer radii is present, as in the north profile case. This discrepancy is further studied in subsections 5.4 and 5.5. We note that the "trough" structure is not very significant in the south profile since the continuum emission is weak and the continuum level is sufficiently low. Comparing the values of Σ_0 derived for the south profile with those for the north, it can be seen that the azimuthal asymmetry of gas distribution is not as significant as dust distribution. The azimuthal contrast of gas surface density is only by a factor of ∼3–10 between the north and south profiles, while the peak dust surface density differs by a factor of ∼70.

5.4 Inner radius of the gas and remaining gas inside cavity

We now explore the parameter space for r_c, the cavity radius of the gas. We fix $(\Sigma_0, r_{out}) = (0.845\,\mathrm{g\,cm^{-2}}, 280\,\mathrm{au})$ and $(\Sigma_0, r_{out}) = (0.2325\,\mathrm{g\,cm^{-2}}, 280\,\mathrm{au})$ for the north and south profiles, respectively. We change r_c from 90 au to 120 au, and see whether we can match the observed profiles within $r \lesssim 150$ au. In particular, we look for values of r_c that match the peak locations of the moment 0 profiles residing at $r \sim 110$ au in the north profile and at $r \sim 140$ au in the south profile.

Figures 13 and 14 show the results for the north and south profiles, respectively. It is shown that $r_c \sim 100$–110 au can explain the location of the peak in the profiles of moment 0. However, all the models give slower velocity in the moment 1 profile than observations at $r \lesssim 100$ au. It should also be noted that the model profiles of moment 0 fall to zero quickly toward the inner radii while the observed profiles, especially the ^{13}CO south profiles, show a more gradual decrease.

The discrepancy between the model and observed profiles at inner radii can be explained if we assume that there is some remaining gas at $r < r_c$. The existence of gas inside the cavity is also indicated by the existence of ^{12}CO emission all the way to the central star (Casassus et al. 2013; Rosenfeld et al. 2014; Perez et al. 2015). To explore the

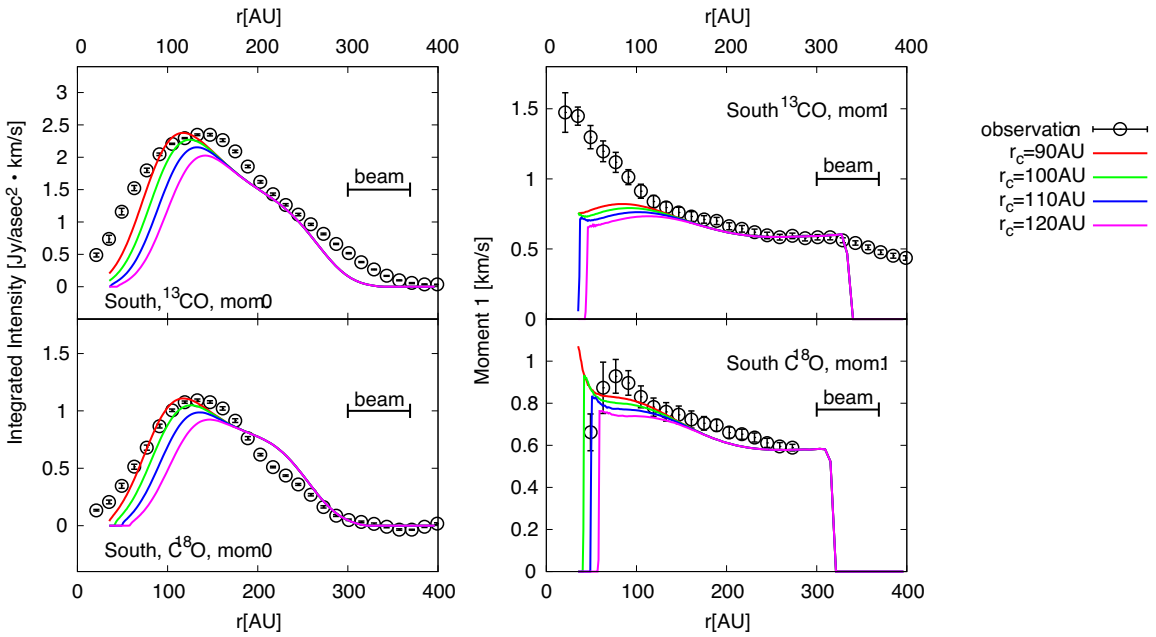

Fig. 14. Same as figure 13 except for the south profiles. (Color online)

Table 4. Parameters explored for remaining gas inside cavity.

Σ_0 [g cm^{-2}] (north)	0.845	Σ_0 [g cm^{-2}] (south)	0.2325
r_c [au] (north)	110	r_c [au] (south)	100
r_{out} [au]	280	r_{out} [au]	280
f_{in} (north)	0, 1/16, 1/8, 3/16	f_{in} (south)	0, 1/8, 1/4, 3/8

parameters, we assume that the gas surface density at $r < r_c$ is given by

$$\Sigma_g(r) = f_{in}\Sigma_g(r_c)\left(\frac{r}{r_c}\right) \quad (r < r_c), \tag{13}$$

while the gas at $r > r_c$ is kept the same as equation (12). The parameter f_{in} is changed from 0 (complete cavity) to 3/16 for the north models and from 0 to 3/8 for the south models (see table 4). Figures 15 and 16 show the results for the north and south profiles, respectively. It is clear that the match between the model and observations is better for the models with remaining inner gas. The values of f_{in} that give the best match between the model and observations seem to be ~1/8 for the south profile. For the north model, the best-fitting value lies somewhere between 1/16 and 1/8. To keep the parameter search simple, we allow an error factor of ~2 here, and use 1/8 as a representative value. An important indication of the modeling approach is that similar gas distribution models (within a factor of 2–3) can account for the observations both in the north and in the south regions of the disk, which is very different from the case of dust distribution.

We have assumed that the gas surface density increases linearly with radius within $r < r_c$. However, the functional form of the gas distribution does not affect the results. We have checked this by using a series of models with a constant gas surface density at $r < r_c$. This is partly because the beam size is relatively large and its dilution effect is significant, especially when we discuss the gas distribution at inner radii. We therefore robustly conclude that there should be some remaining gas within the cavity but there is an uncertainty in the details of how the gas is distributed. Indeed, Perez et al. (2015) have used a different functional form for the models of gas inside the cavity and obtained results consistent with observations. The amount of gas within the cavity in Perez et al. (2015)[4] is $\sim$ (1–2) $\times 10^{-3}$ $M_\odot$, while we have the gas mass inside the cavity being $\sim 5 \times 10^{-4}$ $M_\odot$ if we integrate the model with (Σ_0, r_c, f_{in}) = (0.845 g cm^{-2}, 110 au, 1/8), which is preferred for the north profile, from $r = 0$ to $r = r_c$. These results are consistent within an order of magnitude. We consider that the difference comes from the fact that they use lower temperature and smaller line width than our model in estimating the gas mass inside the cavity (see also sub-subsection 6.2.3).

[4] The cavity radius is 90 au in their model.

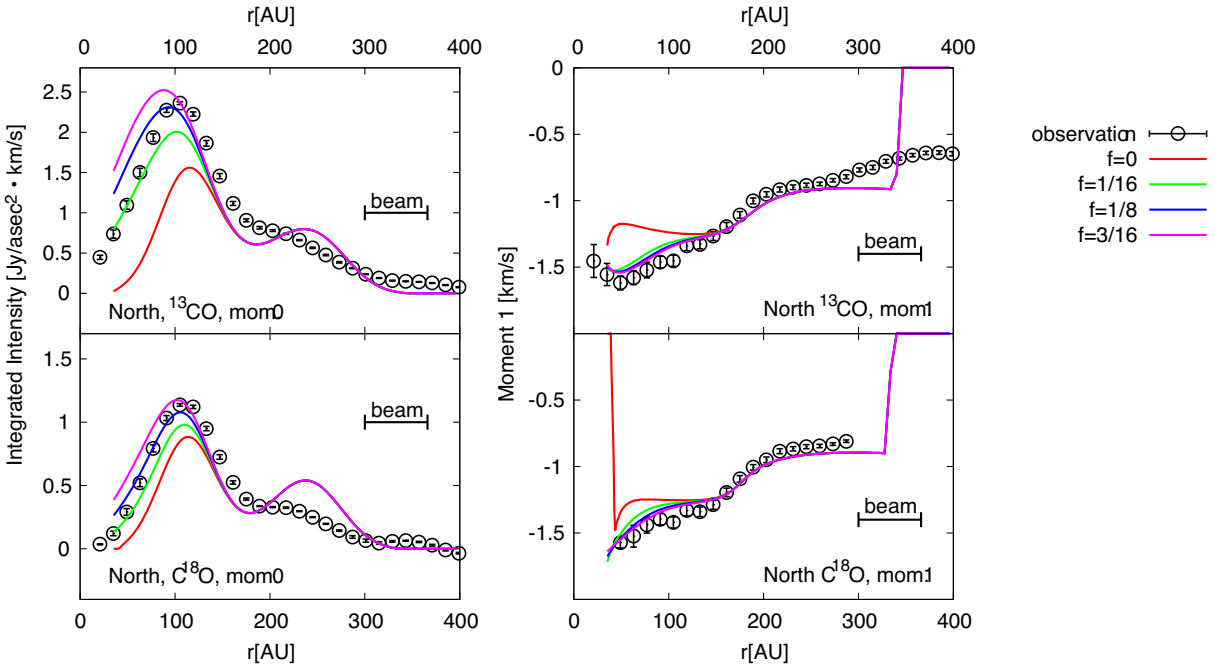

Fig. 15. The radial profiles of moment 0 (left panels) and moment 1 (right panels) for ^{13}CO (top row) and C^{18}O (bottom row) for the north direction when the parameter $f_{\rm in}$ varies. (Color online)

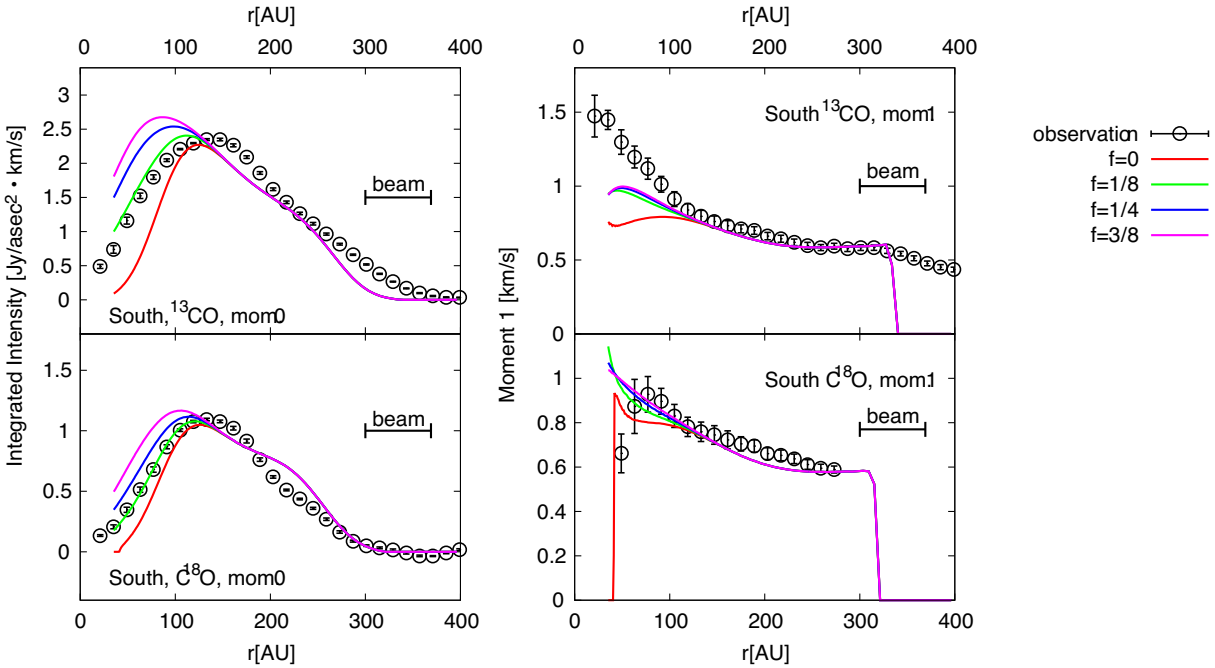

Fig. 16. Same as figure 15 except for the south profile. (Color online)

5.5 Outer radius of dense gas and remaining tenuous gas at large radii

We now turn our attention to the gas distribution at outer radii. In this series of models presented in subsections 5.3 and 5.4, the outer radius of the gas distribution is fixed at $r_{\rm out} = 280$ au. As indicated in figures 11–14, the moment 1 radial profiles of ^{13}CO cut off at $\sim$350 au while the observations indicate that there must be some gas at outer radii.

To explore the parameter space, we first vary $r_{\rm out}$ while keeping $(\Sigma_0, r_{\rm c}, f_{\rm in}) = (0.845\,{\rm g\,cm^{-2}}, 110\,{\rm au}, 0)$ and $(\Sigma_0, r_{\rm c}, f_{\rm in}) = (0.2325\,{\rm g\,cm^{-2}}, 100\,{\rm au}, 0)$ for the north and south models, respectively. We have checked that the details

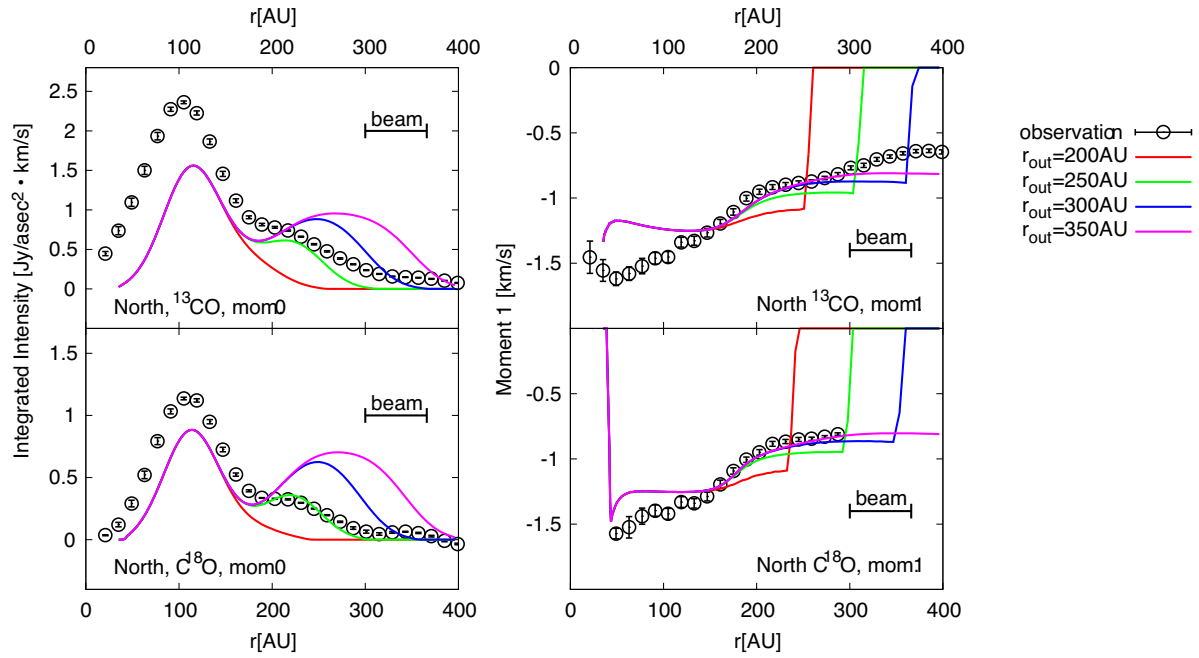

Fig. 17. The radial profiles of moment 0 (left panels) and moment 1 (right panels) for ^{13}CO (top row) and C^{18}O (bottom row) for the north profile when the parameter r_{out} varies. For this parameter search, we assume that there is no gas outside r_{out}. (Color online)

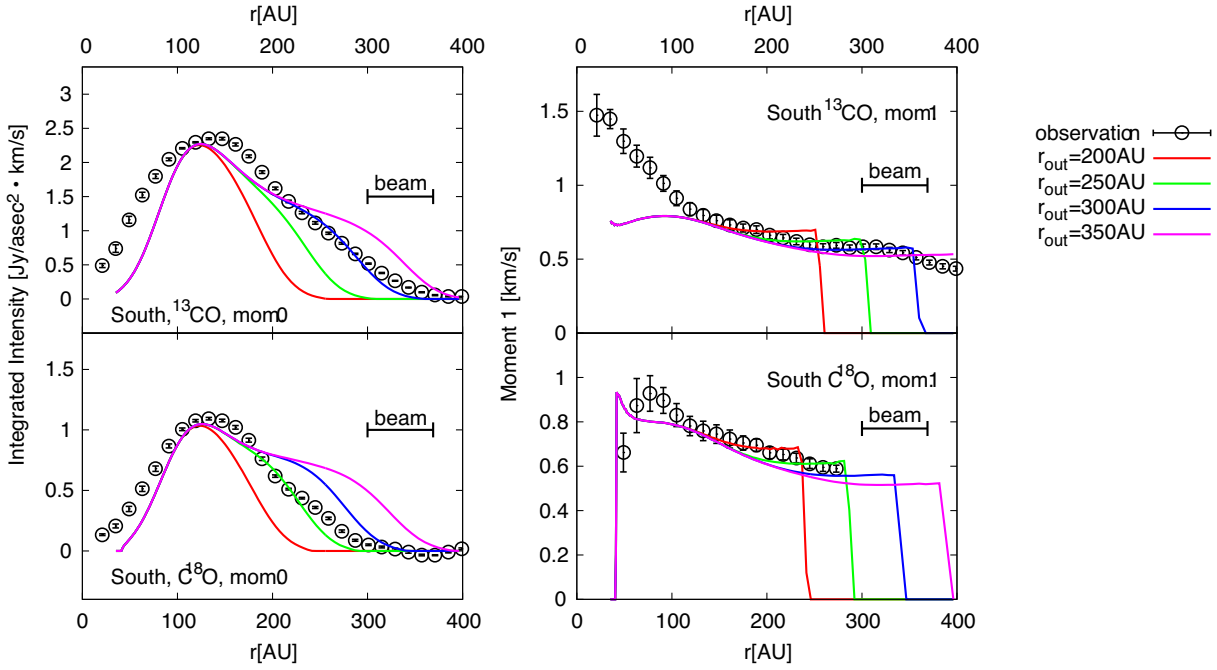

Fig. 18. Same as figure 17 except for the south profile. (Color online)

of the choice of r_c and f_{in} do not affect the brightness profiles at outer radii. Figures 17 and 18 show the results for the north and south profiles, respectively. It is shown that the moment 1 profiles indeed extend to larger radii as we increase r_{out}. However, if r_{out} exceeds 250 au, the models show much larger values of moment 0 than those observed at outer radii.

The discrepancy in moment 0 profile between the observations and models indicates that we need to decrease the amount of gas at outer radii from the currently assumed power-law profiles, especially at $r >$ 250 au. At the same time, there should still be some gas remaining at outer radii so that the moment 1 profiles do not cut off. As an alternative series of models,

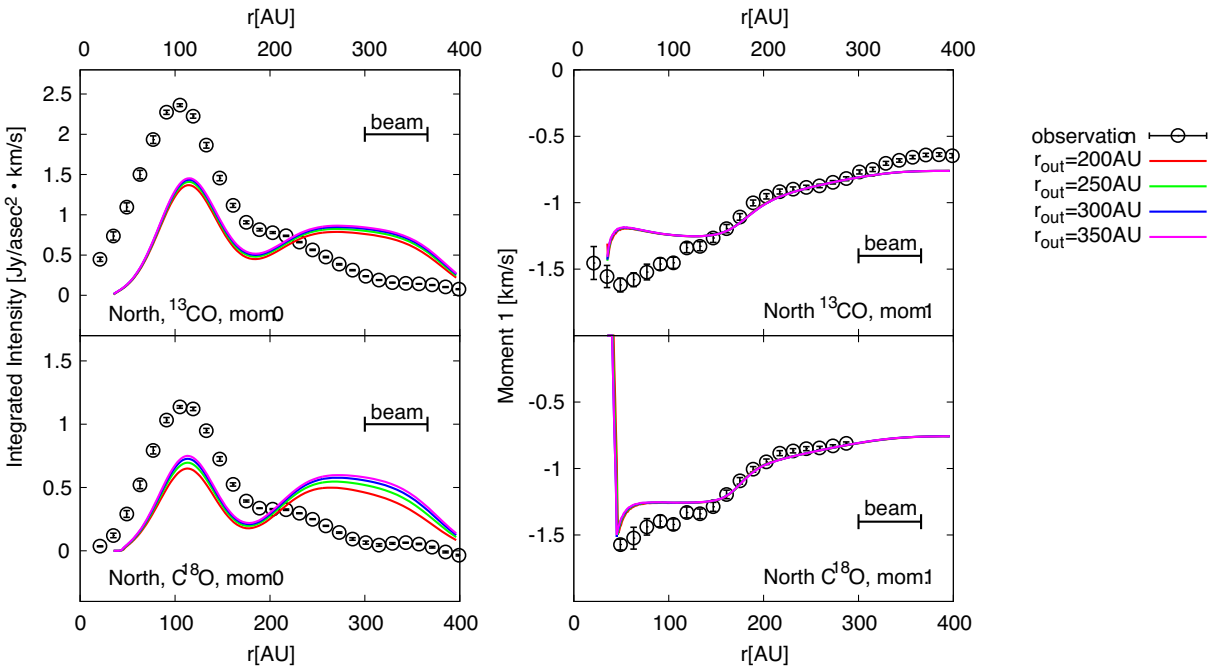

Fig. 19. The radial profiles of moment 0 (left panels) and moment 1 (right panels) for ^{13}CO (top row) and C^{18}O (bottom row) for the north profile when the parameter $r_{\rm out}$ varies. For this parameter search, we assume that the gas at outer radii exhibits exponential cutoff the same as in equation (14). (Color online)

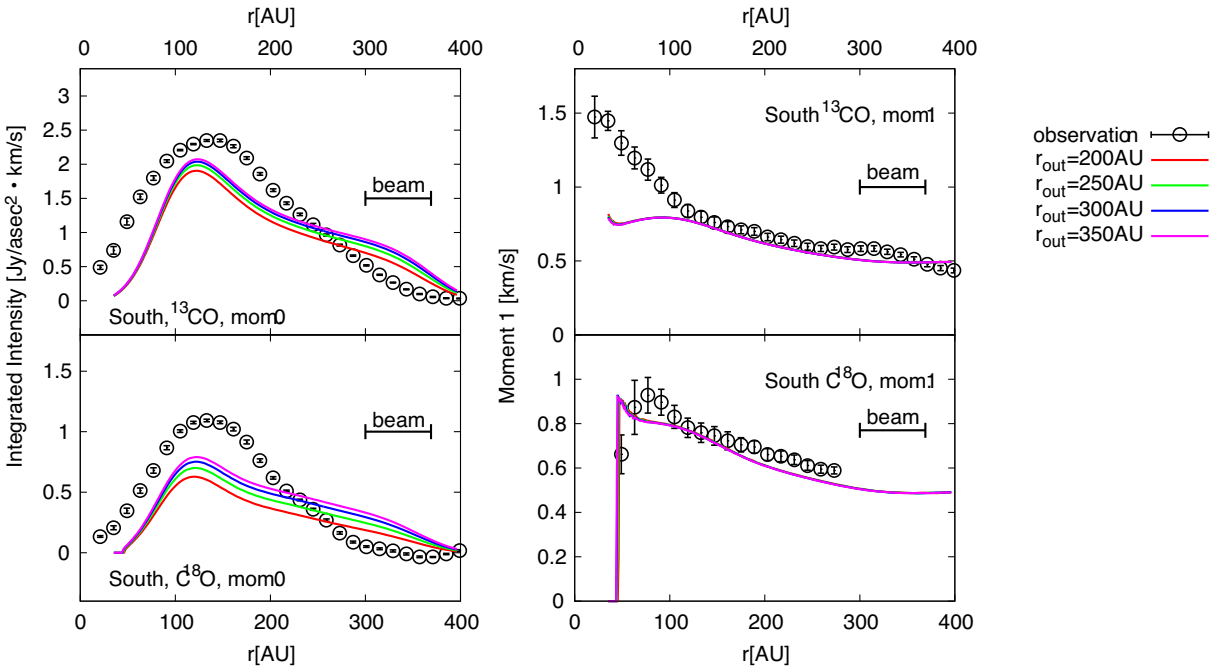

Fig. 20. Same as figure 19 except for the south profile. (Color online)

we now try the commonly used exponential taper model given by

$$\Sigma_{\rm g}(r) = \Sigma_0 \left(\frac{r}{200\ {\rm au}}\right)^{-1} \exp\left(-\frac{r}{r_{\rm out}}\right) \quad (r > r_{\rm c}). \tag{14}$$

The results shown in figures 19 and 20 are for the north and south profiles, respectively. Although the model moment 1 profiles match well with observations for both the north and the south profiles, the models still exhibit too-large values for the moment 0 profiles. This indicates that the gas

Table 5. Parameters explored for tenuous gas outside.

Σ_0 [g cm^{-2}] (north)	0.845	Σ_0 [g cm^{-2}] (south)	0.2325
r_c [au] (north)	110	r_c [au] (south)	100
r_{out} [au]	250	r_{out} [au]	250
f_{out}	1, 10^{-1}, 10^{-2}, 10^{-3}	f_{out}	1, 10^{-1}, 10^{-2}, 10^{-3}

surface density should decrease more rapidly than exponential profiles at outer radii.

To incorporate the rapid decrease of gas surface density at outer radii, we finally try a series of model gas surface density profiles that cut off at $r_{out} = 250$ au, but there is remaining, tenuous gas with a constant surface density at $r > r_{out}$ all the way to the outer edge of the computational domain. In this framework, the gas surface density at $r > r_{out}$ is given by

$$\Sigma_{g,out}(r) = f_{out}\Sigma_g(r_{out}) \quad (r > r_{out}), \tag{15}$$

where $\Sigma_g(r_{out})$ is the surface density at $r = r_{out}$ given by the power-law distribution in equation (12) and f_{out} controls the amount of remaining gas at outer radii. The parameters explored are given in table 5.

Figures 21 and 22 show the results for the north and south profiles, respectively. For the north profiles, the model profiles at $r \gtrsim 250$ au reasonably match with observations when $f_{out} \sim 10^{-2}$. For the south profiles, $f_{out} = 10^{-1}$ models agree with observations at $r \lesssim 300$ au while they show brighter emission than observations at the outermost radii. The moment 0 profiles of the model with $f_{out} = 10^{-2}$ are fainter than observations all the way in the outer radii. Therefore, the actual values of f_{out} may vary as a function of radius for the south profiles, but the overall value of f_{out} may be around $\sim 10^{-1}$ to $\sim 10^{-2}$. Finally, we briefly note that the appearance of the "trough" at $r \sim 170$ au in the north profile (see discussions in subsection 5.3) is different when we use different profiles at $r \gtrsim r_{out}$. This is because the change in gas surface density at outer radii (within the parameters explored in this section) mainly affects the moment 0 profiles at $r \gtrsim 200$ au. The strength of the second (apparent) bump at $r \sim 250$ au is therefore affected.

5.6 Summary of gas distribution

We have looked for the gas distribution model that reproduces the observed moment 0 and 1 profiles of ^{13}CO and C^{18}O. We have shown that the gas-to-dust ratio is not constant in the disk and that the gas distribution should be more extended in the radial direction than the dust

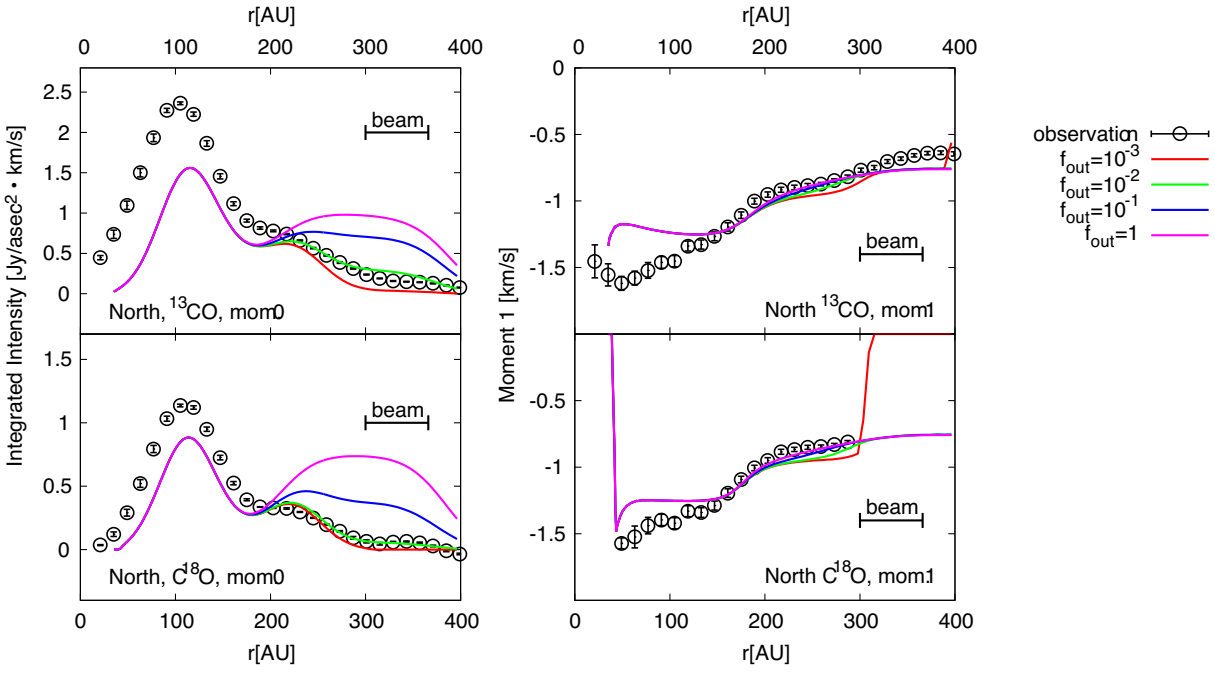

Fig. 21. The radial profiles of moment 0 (left panels) and moment 1 (right panels) for ^{13}CO (top row) and C^{18}O (bottom row) for the north profile when the parameter f_{out} varies. For this parameter search, we assume that the gas at outer radii exhibits a cutoff at 250 au, but there is still some remaining gas outside the cutoff radius, as in equation (15). (Color online)

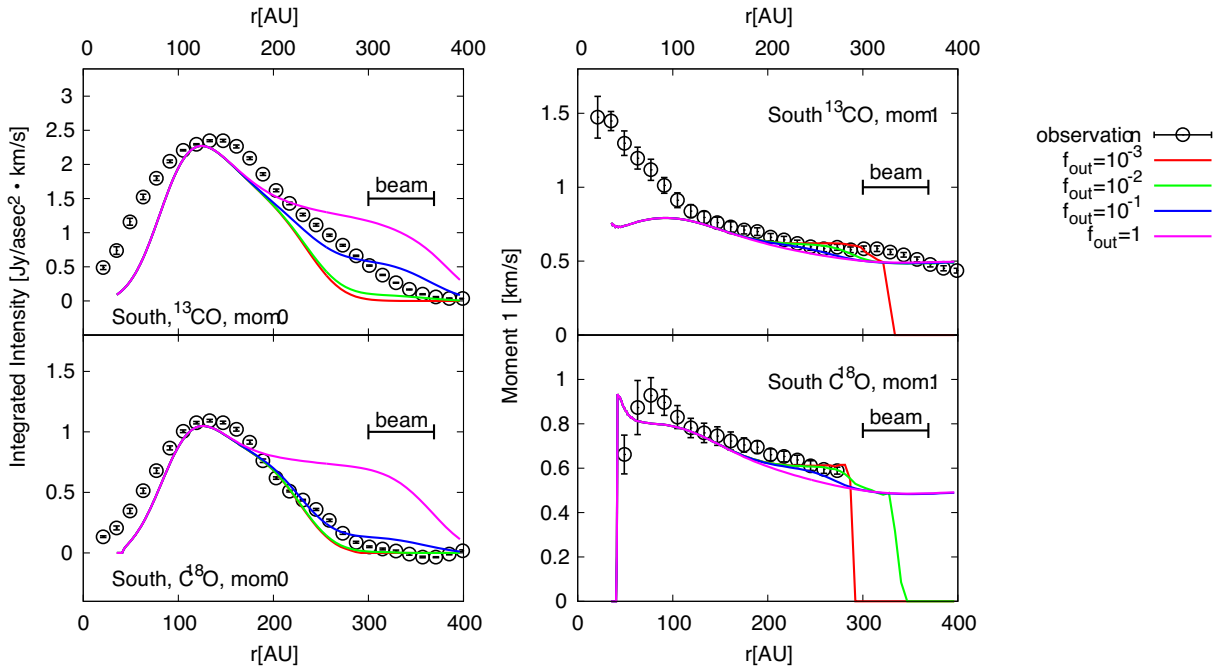

Fig. 22. Same as figure 21 except for the south profiles. (Color online)

distribution. We have seen that there should be some remaining gas inside ∼100 au and some tenuous gas at $r \gtrsim 250$ au.

To be more specific, we have assumed that the model surface density of gas is given by

$$\Sigma_g(r) = \begin{cases} f_{\rm in}\sigma(r_{\rm c})\left(\dfrac{r}{r_{\rm c}}\right) & (r < r_{\rm c}), \\ \sigma(r) & (r_{\rm c} < r < r_{\rm out}), \\ f_{\rm out}\sigma(r_{\rm out}) & (r > r_{\rm out}), \end{cases} \tag{16}$$

where $\sigma(r)$ is given by the power-law distribution,

$$\sigma(r) = \Sigma_0 \left(\frac{r}{200\ {\rm au}}\right)^{-1}. \tag{17}$$

There are five control parameters: Σ_0, which determines the overall amount of gas surface density; $r_{\rm c}$, which determines the inner cutoff (cavity) radius; $f_{\rm in}$, which determines the amount of gas within the cavity; $r_{\rm out}$, which determines the outer radius of the disk; and $f_{\rm out}$, which determines the amount of tenuous gas at large radii. The values of these parameters that give a reasonable fit to observations are given in table 6. Hereafter, we call these best-fitting models "reference models."

The comparisons in the radial profiles between the models and observations is given in figures 23 and 24 for the northerly and southerly directions, respectively. For these models, we show the comparison between the models and observations of the moment 2 radial profiles averaged over $11^\circ \le PA \le 33^\circ$ (north) and $211^\circ \le PA \le 233^\circ$ (south), as well as the moments 0 and 1 radial ones, which have been the main focus of the modeling. The radial profiles of all the moments show a reasonable match between observations and models. Finally, we show a comparison of P–V diagrams in the northerly and southerly directions for the reference models in figure 25. The models and observations show a reasonable match not only in the radial profiles of the moment maps but also in the P–V diagram.

Table 6. Parameters of the reference models for gas distribution.

	North	South
Σ_0 [g cm^{-2}]	0.845	0.2325
$f_{\rm in}$	1/8	1/8
$r_{\rm c}$ [au]	110	100
$r_{\rm out}$ [au]	250	250
$f_{\rm out}$	10^{-2}	10^{-1}

The radial profiles of the model moment 0 profiles exhibit some bumps and troughs, while observations show smoother profiles. This is the most prominent at around the ∼170–200 au region of the north profiles where the dust emission is very bright. These bumps are apparent structures due to the subtraction of bright continuum emission, and we discuss this further in subsection 6.3.

6 Discussions on the reference model

We have constructed models of dust and gas distribution in the protoplanetary disk around HD 142527. In this section,

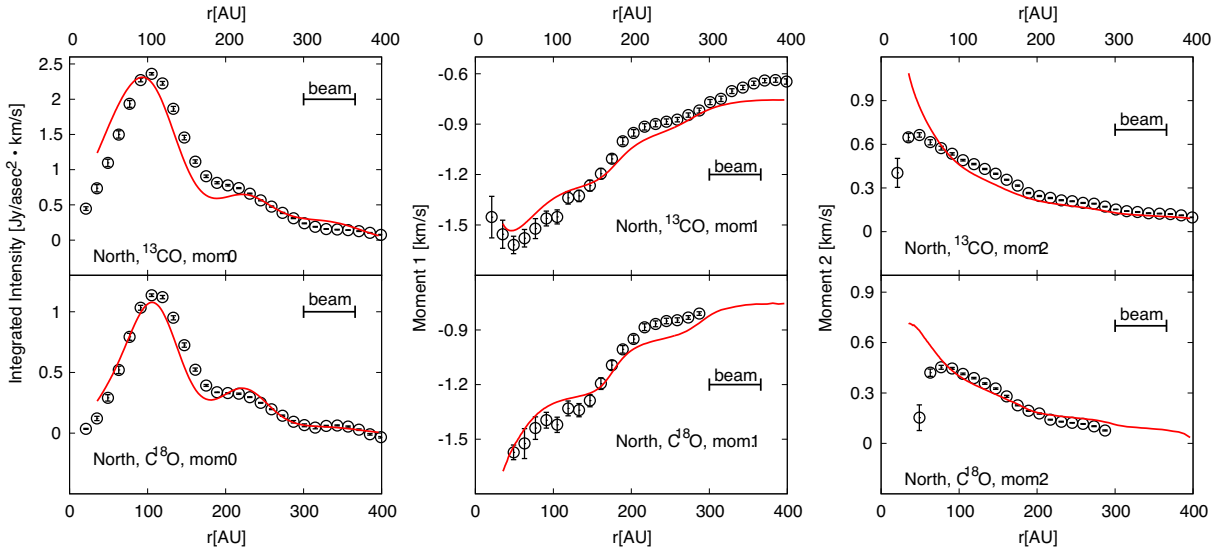

Fig. 23. North radial profiles of moment 0 (left), moment 1 (middle), and moment 2 (right) of ^{13}CO (top row) and C^{18}O (bottom row) for the reference model given by equation (16). The values of the model parameters are given in table 6. (Color online)

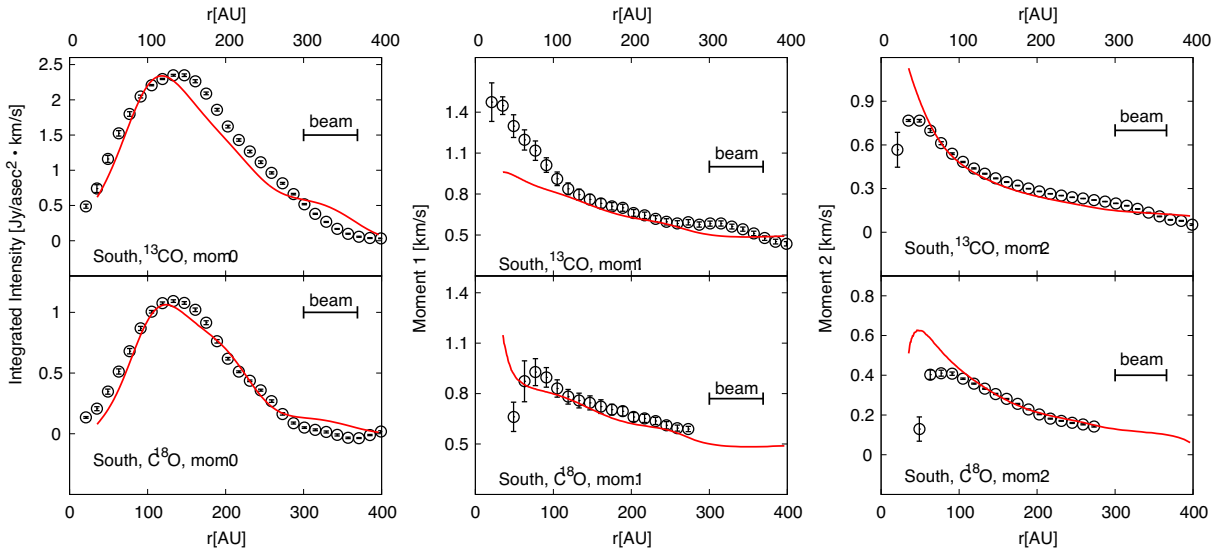

Fig. 24. Same as figure 23 except for the south profile. (Color online)

we look at our reference models of dust and gas distributions and discuss indications and caveats of our model.

6.1 Summary of gas and dust distributions

We have shown that the gas and dust are distributed very differently in the disk. Figure 26 shows the surface density profiles of gas and dust in the northern and the southern regions for the reference model. Dust distribution can be explained by the radial Gaussian ring like profile with a width of $w_d \sim 30$ au (50 au in FWHM) for both the northern and the southern regions. However, there is a difference in surface density between the two regions by a factor of $\sim$70 [see equation (2) and the parameters listed in table 2 for dust distribution]. Gas distribution is more or less axisymmetric and radially extended. The variation in surface density between the northern and southern part is a factor of $\sim$3 and the gas density cuts off at $r_c \sim 100$ au and $r_{out} \sim 250$ au, but both inner and outer regions are not completely devoid of gas [see equation (16) and the parameters listed in table 6 for gas distribution].

The gas-to-dust ratio is $\sim$30 at the peak of the dust emission in the southern part of the disk, while it reaches $\sim$3 in the northern peak. Since dust emission is optically thick in the northern part of the disk, the dust emission is not very sensitive to the amount of dust (see appendix 2),

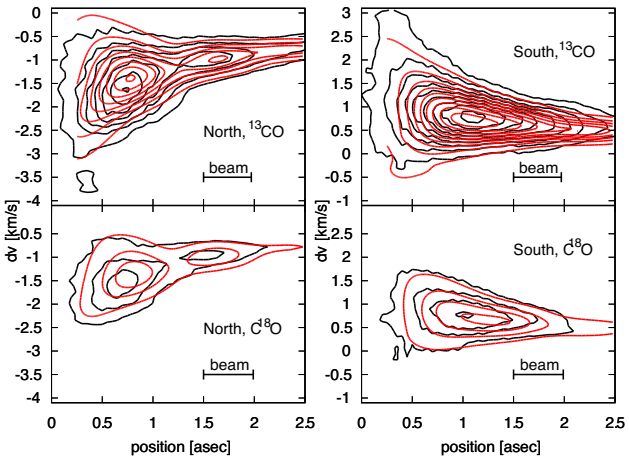

Fig. 25. Comparison of P–V diagram between observations (black contours) and the model (red contours) for the northerly and southerly directions. The left panels show the northerly direction and the right panels show the south direction, while the top row shows the results for ^{13}CO and the bottom row shows C^{18}O. Contours start from the 5 σ level (0.135 Jy arcsec^{-2} for ^{13}CO and 0.175 Jy arcsec^{-2} for C^{18}O, respectively) with a 10 σ step. (Color online)

and so the amount of dust in the northern part may be considered as a lower limit. Therefore, the gas-to-dust ratio may be even lower in the northern part of the disk. The gas-to-dust ratio significantly lower than the canonical value (100 in the ISM) in the northern part indicates that the disk surface density (dust+gas) is not high enough to collapse into a protoplanet by gravitational instability (Fukagawa et al. 2013).

The radial distributions of dust and gas are fixed to Gaussian and power-law (with modifications at inner and outer radii) functions, respectively, in our modeling. The parameters that give a reasonable fit to observations are sought manually. Our model is one of the solutions but is not unique, and we consider that the numbers listed in table 6 have at least a factor of ∼2 uncertainties, especially for Σ_0. It is difficult to constrain the radial distributions more definitely since the spatial resolution is limited. Still, we can argue that the gas distribution is more extended in the radial direction than dust and the gas-to-dust ratio is lower in the north than the south.

At a glance at figure 26, the gas distribution may be interpreted as a "radially extended bump" and the dust particles are strongly accumulated in this bump region. Although the locations of the peak of the continuum emission and gas moment 0 profiles are different in the observed profiles (see figure 5), our model indicates that the peak of dust surface density profiles is within the region of the gas surface density bump, which is between $r \sim 100$ au and $r \sim 250$ au. The peak of the gas emission at ∼100 au is partially due to the fact that the gas temperature is higher at inner radii. Interestingly, the bump in gas seems to be weaker in the south region than in the north. Such a distribution of dust and gas seems to be, at least qualitatively, consistent with the picture of dust particles trapped in a pressure bump, or large-scale vortex, in gas (Pinilla et al. 2012; Birnstiel et al. 2013; Lyra & Lin 2013). We also note that recent observations by ATCA at 34 GHz indicate that large grains are concentrated in the northern part of the disk (Casassus et al. 2015). Vortices should be confined within a narrow radial range of the scale comparable with the disk thickness in this case. It is hinted that there might exist small-scale structures close to the peak of dust distribution, as discussed at the end of subsection 5.6. Future higher resolution

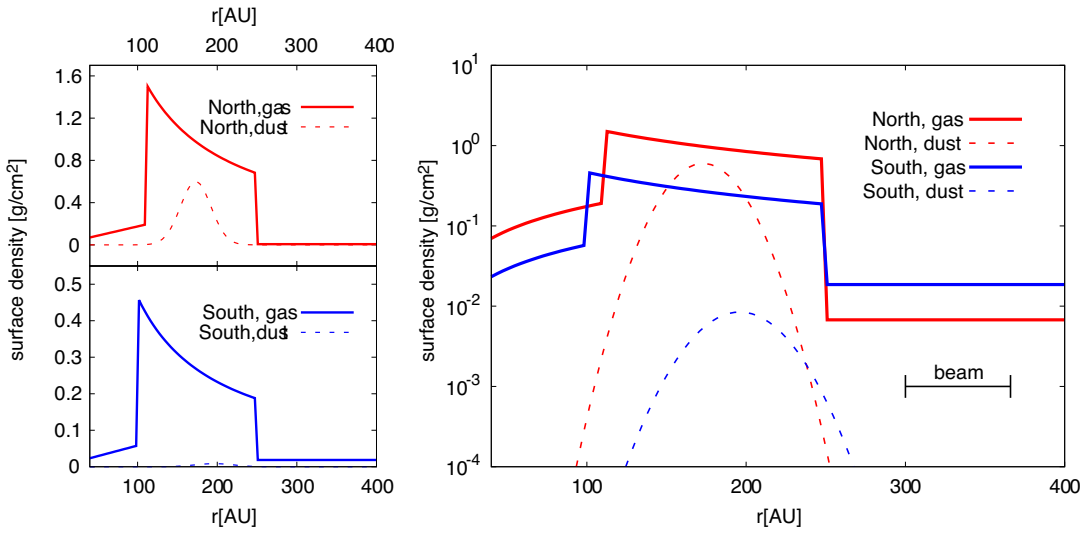

Fig. 26. Surface density distribution of gas (solid line) and dust (dashed line) in the northern (red) and southern (blue) parts of the disk. The left panels show surface density on a linear scale (top panel for the north and the bottom panel for the south model), while the right panel shows the surface density on a log scale. (Color online)

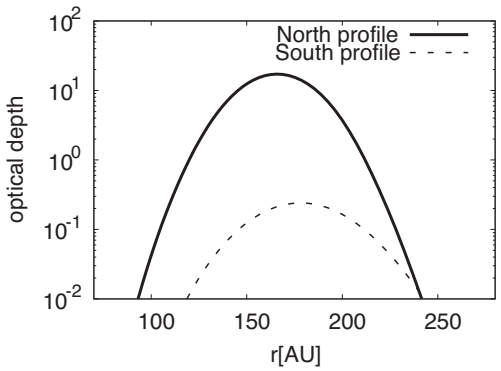

Fig. 27. Optical depth profiles for continuum emission. The solid line is for the north profile and the dashed line is for the south profile.

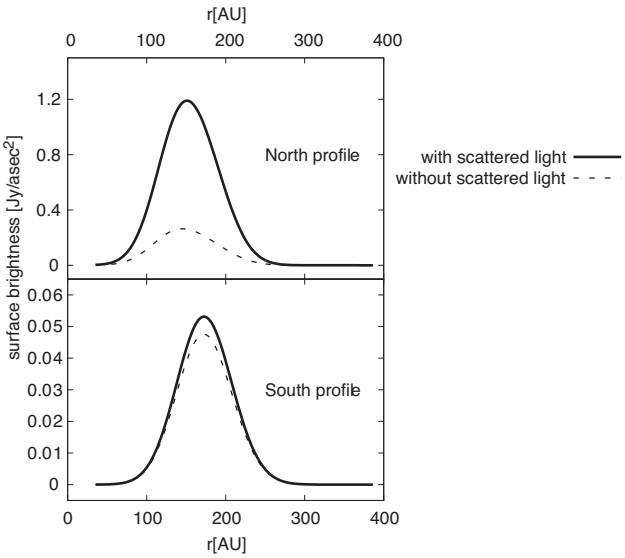

Fig. 28. Radial profiles of continuum emission calculated with (solid lines) and without (dashed lines) dust scattering. The left panel is for the north profile and the right panel is for the south profile.

observations may reveal the small-scale structures within the bright dust ring. Recently, Mittal and Chiang (2014) proposed that the global $m = 1$ mode might play an important role in producing radially extended lopsided structures. One interesting prediction of this model is that dust grains with different sizes accumulate at different locations within the disk. This may be addressed by higher resolution observations in multi-wavelengths and modeling effort including several dust species. Another interesting mechanism for the formation of dust-rich regions is the secular gravitational instability (Ward 2000; Youdin 2011; Michikoshi et al. 2012; Takahashi & Inutsuka 2014). Takahashi and Inutsuka (2014) have done two-fluid analysis of gas and dust and shown that (multiple) ring-like structure with low gas-to-dust mass ratio can be created in self-gravitationally stable disks. Since the initial gas mass should be relatively large in this case, significant gas dispersal should have occurred after the ring formation. This could be addressed, for example, by investigating the detailed kinematics of gas (e.g., Pontoppidan et al. 2011).

6.2 Optical depth and the total amount of dust and gas

6.2.1 Dust optical depth and dust properties

We have seen that the dust particles are strongly concentrated in the north region. The radial profiles of the optical depth at the observed frequency ($\sim$340 GHz) along the line of sight are shown in figure 27, and it is clear that, in the northern part, the optical depth of dust emission reaches $\gtrsim$10.

We have used the dust model with a maximum size of 1 mm. This is purely an assumption of this study, in order to estimate the minimum amount of dust grains needed to explain the bright thermal emission by using a dust model with maximum (or at least large within the models that are considered to be reasonable) opacity at sub-mm wavelengths. In the case of the dust model with $a_{\rm max} = 1$ mm, the dust continuum emission is dominated by a scattered light component if the disk is optically thick, which is the case for the northern part, because the dust scattering coefficient is much greater than the absorption coefficient (figure 6). Figure 28 compares the radial profiles of dust continuum emission between calculations with and without a scattered light component. We have artificially set the radiation energy density $J_\nu = 0$ in equation (4) in the calculations to omit the scattered light component. In the northern part of the disk, the contribution from the scattered light component is a factor of $\sim$5 larger than that from the thermal emission that has not experienced scattering. In the southern part, where the disk is optically thin, the contribution from the scattered light component is much smaller.

There may be a variety of dust models that are able to reproduce observations. For example, the SED of HD 142527 can be reproduced by using irregularly shaped micron-sized dust particles (Verhoeff et al. 2011). We have checked that the slope of the SED in the sub-mm range is consistent with observations in our model. Therefore, it is difficult to discriminate the dust size contributing most to sub-mm emission from current observations thus far. The scattering coefficient $\kappa_{\rm s}$ of micron-sized dust particles at sub-mm range is expected to be much smaller than that used in our work. If the scattered light component can be observed exclusively, it is possible to discriminate the dust size. The polarization of dust continuum emission, for example, can be a good tracer of the dust size (Kataoka et al. 2015).

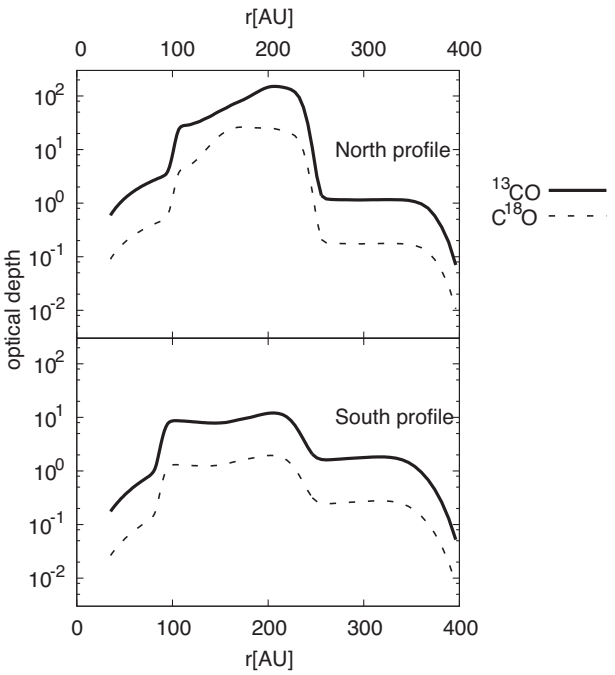

Fig. 29. The line-of-sight optical depth of ^{13}CO (solid line) and C^{18}O (dashed line). The top panel shows the optical depth of the northern part of the disk and the bottom panel shows that of the southern part.

6.2.2 Gas optical depth

We have used ^{13}CO $J = 3$–2 and C^{18}O $J = 3$–2 emission to determine the gas structure. Figure 29 shows the radial profiles of the maximum optical depth of these lines (gas+dust optical depth; see also figure 30) for the reference disk models. It is shown that the gas is optically thick at the peak of the lines. The maximum optical depth reaches an order of unity even for the south model of C^{18}O.

Despite the fact that the lines are mostly optically thick, we have seen that the integrated intensity of gas emission becomes brighter as we increase the gas surface density (figures 11 and 12). This is because gas emission is not entirely optically thick for all the velocity channels. When the amount of gas is increased, gas emissivity is increased, and therefore there are more velocity channels that contribute to the gas brightness at each given spatial location. Figure 30 shows the radial profiles of the optical depth of the line wings. We show the optical depth at the velocity channels that are different from those giving the maximum optical depth (line center) by 0.12 km s^{-1}, 0.24 km s^{-1}, and 0.36 km s^{-1}. For all of the calculations shown in figure 30, the optical depth of the continuum emission [which is derived using the first term of equation (10)] is subtracted from the gas+dust optical depth [which is derived using all the terms using the right-hand side of (10)] to show the gas-only optical depth.[5] The line emission becomes optically thin at 0.2–0.3 km s^{-1} away from the line center. Since the values of moment 2 shown in figures 23 and 24 are $\sim$0.3 km s^{-1} at $r \sim 150$ au, we consider that the line emission is optically thin when the velocity deviates from the line center by (only) half the width of the line, which is close to the value of moment 2. Therefore, line wings can be used to trace the gas surface density even in the case that the emission at the line center is optically thick. We therefore consider that we can reasonably constrain the amount of gas even when it is optically thick. However, we still see that ^{13}CO is more insensitive to the change of the amount of gas compared to C^{18}O, which is more optically thin. Overall, we expect that the amount of gas has an uncertainty of a factor of $\sim$2–3. For example, figure 11 indicates the models with $\Sigma_0 = 2.325\,\mathrm{g\,cm^{-2}}$ and $\Sigma_0 = 0.845\,\mathrm{g\,cm^{-2}}$ both explain the radial profiles of moment 0 in the north direction at $r = 150$–200 au region reasonably well. To better constrain the amount of gas, we may need observations of lines with lower optical depth by, for example, using rarer isotopologues or using lower transition lines. The values of isotope ratio and the dust opacity are also important in accurately determining the amount of gas. Since there is a fair amount of dust, the line emission is affected by the dust absorption, especially in the northern part of the disk. The scattering of gas lines by dust particles, which is not included in our model, can also be effective in determing the observed spatio-kinematic patterns.

6.2.3 Total amount of gas and dust

We now discuss the total amount of dust and gas indicated from our modeling. We have two surface density distribution models, namely the north and south model, for each dust and gas.

For dust mass, we obtain $M_{\rm dust} = 3.5 \times 10^{-3}\ M_\odot$ for the north profile and $M_{\rm dust} = 7 \times 10^{-5}\ M_\odot$ for the south profile when integrated over the entire disk. Verhoeff et al. (2011) obtained the dust mass of $1 \times 10^{-3}\ M_\odot$ from their SED modeling. Considering that the bright arc of dust emission extends about $\sim$1/3 of the whole azimuth, the value of dust mass we have obtained is similar to their results, despite the difference in grain properties. For gas mass, we obtain $M_{\rm gas} = 1.8 \times 10^{-2}\ M_\odot$ and $M_{\rm gas} = 5.7 \times 10^{-3}\ M_\odot$ for the reference north and south models, respectively, when integrated over the disk within 400 au.[6]

Although the total gas mass could have a factor of $\sim$2–3 uncertainty, as noted before, the overall gas-to-dust mass ratio may be $\lesssim$ 10–30, which is smaller than the interstellar value of 100. The derived gas-to-dust mass ratio is likely to be an upper limit. Since the north region is optically thick,

[5] In other words, gas-only optical depth is calculated by taking into account only the second term of the right-hand side of equation (10).

[6] Inside 400 au, the gas mass is dominated by the gas residing within $r \lesssim r_{\rm out}$, although we have assumed that constant surface density in the radial direction for outer tenuous gas.

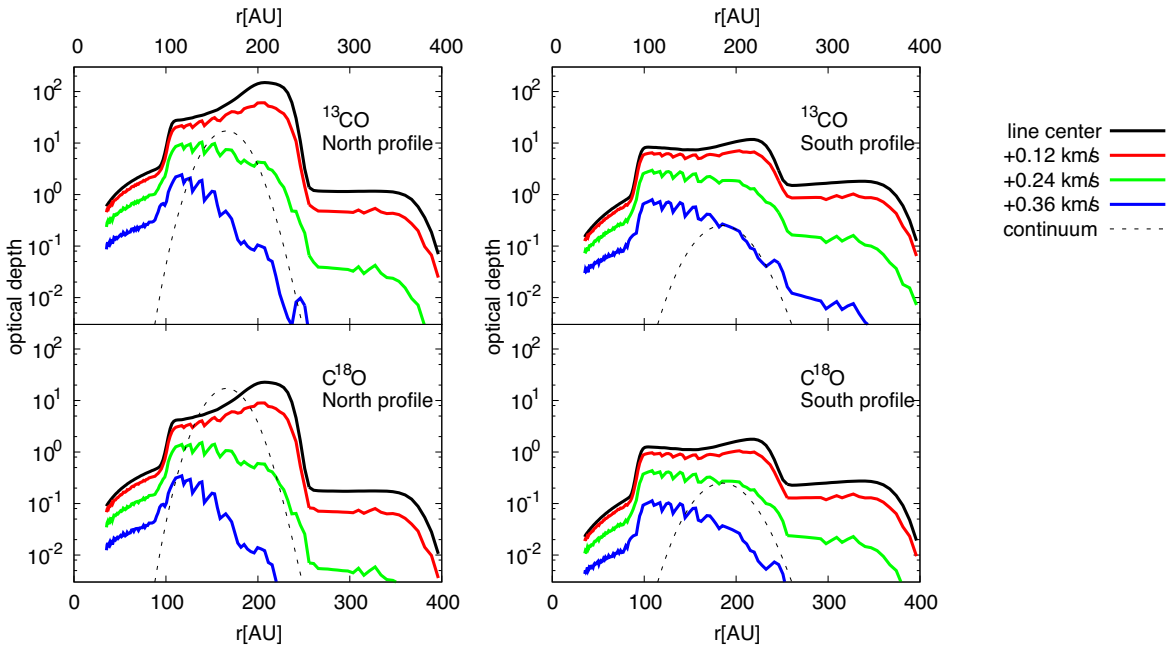

Fig. 30. The line-of-sight optical depth of the north profile (left) and south profile (right). The upper panels show the optical depth of ^{13}CO and the lower panels show that of C^{18}O. In each panel, the line-of-sight optical depth of the line center (the maximum optical depth of all the channels) is shown by black solid lines and those of the channels offset from the line center by 0.12 km s^{-1}, 0.24 km s^{-1}, 0.36 km s^{-1} are shown in red, green, and blue lines respectively. The optical depth of the continuum emission (black dashed lines) is subtracted for all of the gas optical depth. (Color online)

the dust emission is not very sensitive to the increase in the amount of dust (see appendix 2). We should also remember that the dust particles have relatively large opacity (and therefore emissivity) in the sub-mm range ($a_{\rm max} = 1$ mm). If smaller grains are more abundant, we expect that the disk midplane, where dust emission originates, is colder while the disk surface, where optically thick gas emission originates, is warmer (Inoue et al. 2009). Consequently, even if small grains are more abundant, we expect brighter emission in gas while fainter in dust, resulting in a smaller gas-to-dust ratio. We therefore propose that the dispersal of gas, or at least the depletion of CO gas, may already have taken place in the disk of HD 142527. However, it should be noted that detailed modeling with different dust grain properties is necessary to confirm this. Grain size and shape can strongly affect the observed emission properties (e.g., Min et al. 2003).

Perez et al. (2015) derived the total gas mass of 0.1 $M_\odot$ from their modeling effort. They used a model where the temperature is assumed to be 50 K at 50 au with $r^{-0.3}$ profile and the Doppler b parameter is assumed to be 50 m s^{-1}. Their radial temperature profile is flat and the temperature is smaller than our model by a factor of $\sim$1.7 at $r = 100$ au. We have calculated how the assumptions of the temperature and the line width affect the results by setting those parameters to be the same as Perez et al. (2015), but the density is given by our reference model [equation (16) and table 6]. The values of ^{13}CO $J = 3$–2 moment 0 are smaller by a factor of $\sim$2 at $r \sim 100$ au with this model. The impact of line width on the moment 0 profile comes from the fact that there are fewer velocity channels that contribute to the integrated intensity at each spatial position (see also the discussion in sub-subsection 6.2.2). To compensate for this by varying the amount of gas (parameter Σ_0 in our model), we need to increase the value of Σ_0 by a factor of $\sim$5–10, as seen in figure 11. Consequently, we consider that the difference in the total amount of gas comes from the different assumptions for the temperature and the line width. The temperature profile used by Perez et al. (2015) comes from ^{12}CO $J = 2$–1 observations, which may be smoothed by the relatively large beam. High resolution gas observations will play a decisive role in determining the distribution and total mass of the gas component more accurately.

6.3 Gas bump structures in the model

The north radial profiles of moment 0 of the reference model are bumpy at $r \sim 170$–200 au, where dust emission is the brightest. As discussed in subsection 5.3, these bumps and troughs in gas emission arise because the continuum emission is very bright and comes from a relatively narrow radial range. Since the line emission is partially hidden by dust, there is a significant effect on line emission when the dust continuum is subtracted.

There are at least two possible ways to obtain smoother moment 0 profiles. One possibility is to increase the amount of gas at the location of the peak of dust emission locally. In other words, there may be more detailed, small-scale (several tens of au scale) structures in the radial direction than we have considered. As seen in figure 11, a factor of ∼3 larger gas surface density locally at the peak of dust distribution may explain the observed values of moment 0 at this region. Since the dust emission is barely resolved in the radial direction, it may be difficult to see such small-scale variation of gas distribution. Higher angular resolution observations of gas are necessary to confirm this possibility.

The other possibility is to consider more optically thin dust particles. Since the dust scattering opacity is ∼10 times larger than the absorption opacity in our dust model, the total extinction coefficient of dust is dominated by the scattering opacity and is comparable with the gas opacity (figure 30). Therefore, if the dust scattering coefficient is much smaller than considered in this paper, the gas emission can be brighter so the effects of continuum subtraction is more insignificant. Smaller dust particles may be one solution, but in this case, it is necessary to have a larger amount of dust because the absorption coefficient (and therefore dust emissivity) is also small.

A large (effective) emissivity and small scattering coefficient may be obtained simultaneously if we consider dust sedimentation. In our framework, the gas-to-dust ratio is constant in the vertical direction, so large (∼mm in size) dust particles reside even in the upper layer of the disk. However, such large particles may be sedimented to the disk midplane. The surface of the CO emission resides in the upper layer of the disk, and therefore there may only be small dust particles having small scattering coefficient around the gas surface. The gas emission is not hidden by dust very much in this case and therefore the effects of the subtraction of the continuum emission are less significant. More sophisticated models that take into account the dust particle motion are necessary to verify this possibility. Also, the optical properties of the dust particles and their impact on observations should be carefully investigated. Detailed modeling in tandem with scattered light observations in near infrared (NIR; see also subsection 6.5), which is sensitive to the small dust particles in the upper layer of the disk, may be a key to verifying this possibility.

6.4 Discrepancy of moment 1 at inner radii

In the moment 1 profiles of the south gas models, we see that the reference model shows slower speed than observed at $r < 100$ au for ^{13}CO but faster at $r < 50$ au for C^{18}O, as shown in figure 24. We have checked that this discrepancy is also present when the surface density profiles for the remaining gas inside the cavity are taken to be constant so the details of the radial profile of gas surface density do not alter the results. C^{18}O data may be affected by the lower signal-to-noise ratio at high velocity channels, but the detection of ^{13}CO in the $r \sim 50$–100 au region is robust.

It is natural that the observed velocity should become smaller than Keplerian as one goes to inner radii, where the disk is barely spatially resolved in channel maps and the signal is weak. The gradient of line-of-sight velocity within the beam is large at inner radii and therefore emission at many velocity channels are averaged. The weak high velocity component may be discarded when the sensitivity is limited. These effects should properly be incorporated in our modeling since we convolve each channel map image by the Gaussian beam before calculating the model moment maps (see subsection 3.2). Therefore, the discrepancy between the observations and models might indicate that, in the southern region, the gas velocity is significantly faster than Kepler velocity at least for ^{13}CO at inner radii. Rosenfeld, Chiang, and Andrews (2014) discussed that there may be a fast radial flow in the inner region of the disk of HD 142527 based on ^{12}CO and HCO$^+$ data taken by ALMA Cycle 0. Marino, Perez, and Casassus (2015) suggested that the inner disk is significantly inclined relative to the outer disk based on the modeling of scattered light in the H-band. The discrepancy between the reference model and observations of ^{13}CO for the southern region may also indicate the existence of such a dramatic change of the inner disk structure. Observations with better spatial resolution are essential to clarify this point.

6.5 Outer tenuous gas and scattered light in near infrared

We have seen that there should be some amount of tenuous gas at $r > 250$ au. The surface density of the tenuous gas is estimated to be $\sim 7 \times 10^{-3}$–2×10^{-2} g cm^{-2}. It is known that the HD 142527 disk shows an extended (∼300 au scale) scattered light emission in NIR observations (Fukagawa et al. 2006; Casassus et al. 2012; Canovas et al. 2013; Rodigas et al. 2014). In particular, the large-scale spiral structure appears from the south of the disk and extends towards the west.

The extended scattered light emission in NIR may be connected to the existence of tenuous gas at outer radii. In NIR direct imaging observations, scattered light by small (typically, $\sim 1\,\mu$m in size) dust grains at the disk surface is observed. Since such particles are well coupled with gas, we expect that small grains are distributed as gas is. The amount of tenuous gas (∼0.02 g cm^{-2} at $r \sim 300$ au in the south model) is probably enough to make the disk optically

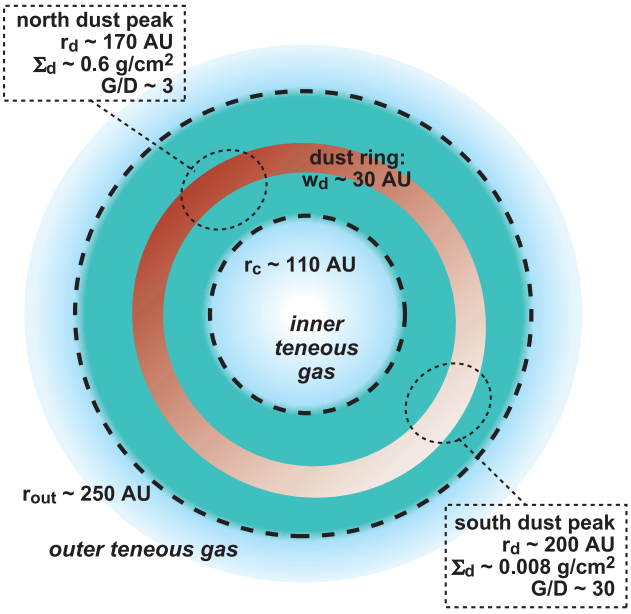

Fig. 31. Schematic picture of the disk around HD 142527. Green colors indicate gas distribution and brown indicate dust distribution. The dust ring with the width of $w_d \sim 30$ au is located at $r \sim 170$–200 au. The ring surface density differs by a factor of ~70 in the northern and the southern parts. The gas surface density is more radially extended. The gas distribution shows a bump-like structure from ~100 au to ~250 au but there is a remaining, tenuous gas component fir both inner and outer radii. (Color online)

thick in the NIR range, where dust opacity may be several tens of cm^2 per unit gram of gas in the case of $a_{\rm max} \sim 1\,\mu$m if the gas-to-dust ratio is 100 in the outer $r > 250$ au region (e.g., D'Alessio et al. 2001; Aikawa & Nomura 2006). Considering the detection limit of dust continuum, we expect that such (small) grains contained in the outer tenuous gas component are neither observable nor massive enough to contribute to the gas-to-dust ratio within 400 au (see subsubsection 6.2.3). To further investigate the distribution of small grains, we need simultaneous modeling of scattered light and mm-emission, which is beyond the scope of this paper.

7 Conclusion

We have presented models for gas and dust distribution for the disk around HD 142527 by using a series of axisymmetric models and by comparing the radial profiles of dust and gas emissions. A schematic picture of the gas and dust distributions is shown in figure 31. Below, we list the main conclusions of our work.

1. The dust particles are confined in a ring whose surface density profile is described by a Gaussian function in the radial directions with a width of $w_d \sim 30$ au for both the north and south regions. The location of the ring is slightly different between the north ($r_d \sim 170$ au) and south profiles ($r_d \sim 200$ au). To account for the strong azimuthal asymmetry of the continuum emission, the surface density of the dust ring is different by a factor of ~70 between the northern and southern parts of the ring. Note that these results are based on a dust model with a maximum size of 1 mm, where the opacity at sub-mm wavelengths is large, and therefore we expect that the dust mass derived in our work is close to the lower limit.
2. The gas distribution is azimuthally more symmetric than the dust distribution. The amount of gas in the northern region is indicated to be ~3 times as large as that in the southern region.
3. The gas radial surface density distribution is more radially extended than the dust. The radial profiles of the moment maps of ^{13}CO $J = 3$–2 and C^{18}O $J = 3$–2 emission can be described with a power-law profile between ~100 au and ~250 au, along with the remaining gas inside the cavity and with tenuous outer gas at $r >$ 250 au. Small-scale (~50 au-scale) variation in the radial directions of gas distribution with a factor of ~3 is also indicated around the peak of dust distribution.
4. The gas-to-dust ratio varies significantly within the disk. At the peak of the dust distribution, it is ~3 in the northern part of the disk while ~30 in the south. The gas-to-dust ratio over the whole disk is expected to be ~10–30 within 400 au, indicating that gas depletion has already occurred in this system.

We have used a series of axisymmetric disk models to do systematic parameter search while keeping the problem tractable. Since the CO isotopes used in this observation have turned out to be optically thick, observations of rarer isotopes or lower transitions are necessary to better constrain the amount of gas. More elaborate dust models will also be required to fully constrain the disk parameters and to account for observations at other wavelengths.

Acknowledgements

We thank Sebastian Perez for useful discussions. We also thank an anonymous referee for careful reading and useful suggestions to improve the paper. This paper makes use of the following ALMA data: ADS/JAO.ALMA#2011.0.00318.S. ALMA is a partnership of ESO (representing its member states), NSF (USA), and NINS (Japan), together with NRC (Canada) and NSC and ASIAA (Taiwan), in cooperation with the Republic of Chile. The Joint ALMA Observatory is operated by ESO, AUI/NRAO, and NAOJ. This work is partially supported by JSPS KAKENHI Grant Numbers 23103004, 26800106, and 26400224.

Appendix 1. Details of the ^{13}CO and C^{18}O results

Figures 32, 33, and 34 show the channel maps of ^{13}CO from which the moment maps shown in figure 3 are created.

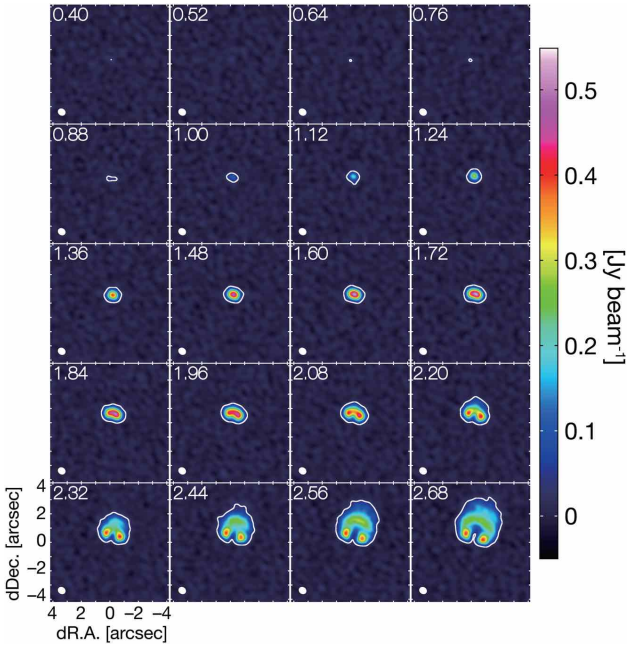

Fig. 32. Channel maps of ^{13}CO ($J = 3$–2). The LSR velocity is shown in the top left corner of each panel, and the synthesized beam, 0.″50 × 0.″42 with the major axis $PA = 57.°4$, is indicated by the ellipse in the bottom left corner of each panel. The white contours are the 5σ level, or 32 mJy beam^{-1}. (Color online)

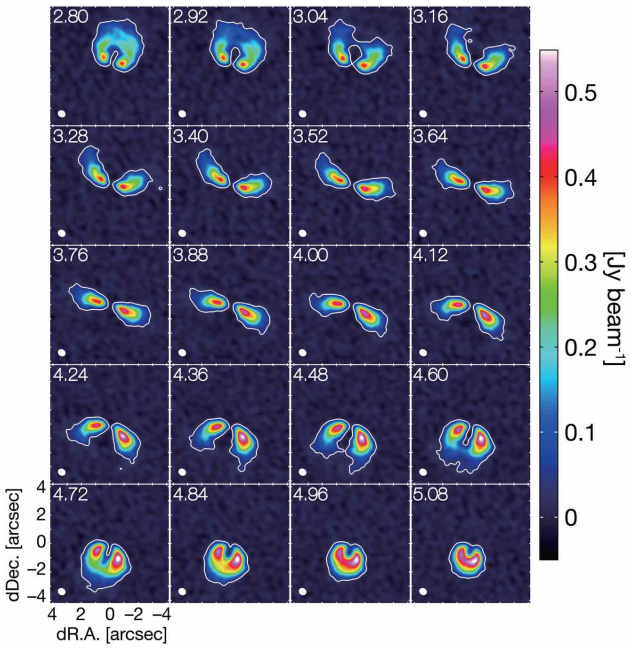

Fig. 33. Channel maps of ^{13}CO ($J = 3$–2), continued from figure 32. (Color online)

Figures 35 and 36 show the channel maps of C^{18}O from which the moment maps shown in figure 4 are created.

As described in subsection 2.3, a constant (systemic) velocity of 3.7 km s^{-1} is found along $PA = 71° \pm 2°$, which can be regarded as the direction of the minor axis of the system. The position–velocity diagram along the major axis ($PA = -19°$; figure 37) was fitted by circular Keplerian motion for the emission detected above 5σ (figure 37). The

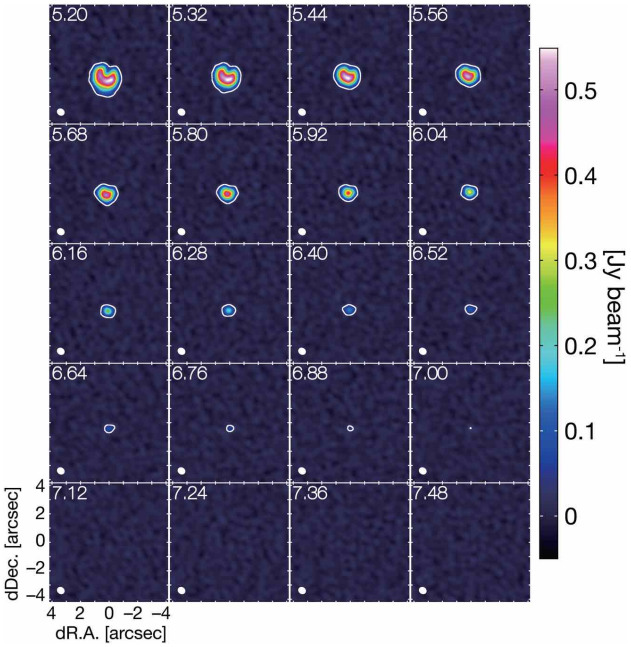

Fig. 34. Channel maps of ^{13}CO ($J = 3$–2), continued from figure 33. (Color online)

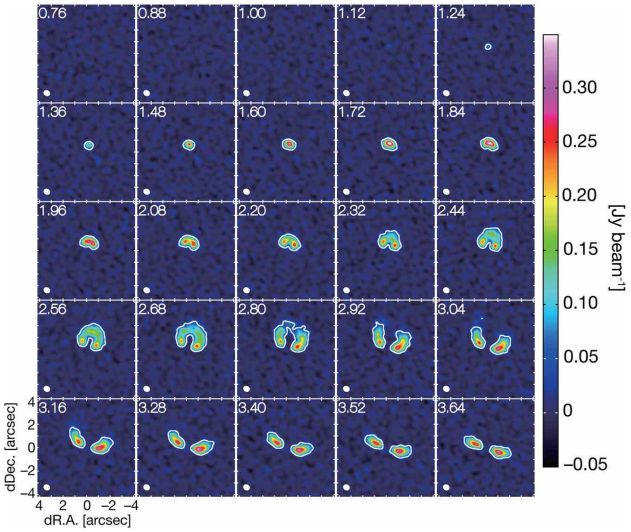

Fig. 35. Channel maps of C^{18}O ($J = 3$–2). The LSR velocity is shown in the top left corner of each panel, and the synthesized beam, 0.″50 × 0.″42 with the major axis $PA = 60.°6$, is indicated by the ellipse in the bottom left corner of each panel. The white contours are the 5σ level, or 41.5 mJy beam^{-1}. (Color online)

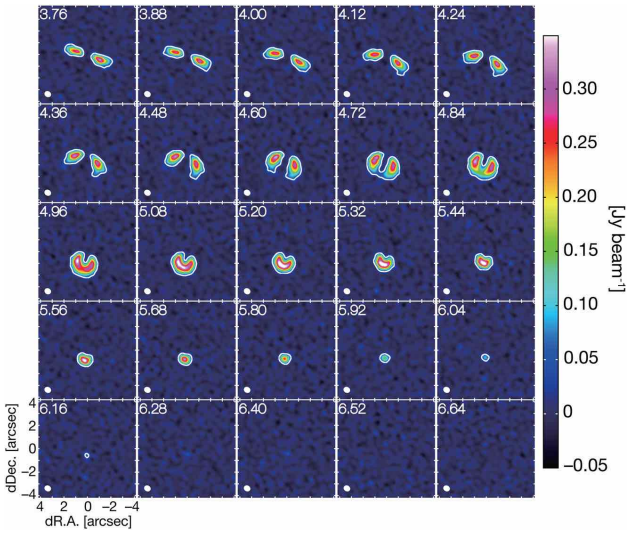

Fig. 36. Channel maps of $C^{18}O$ ($J = 3$–2), continued from figure 35. (Color online)

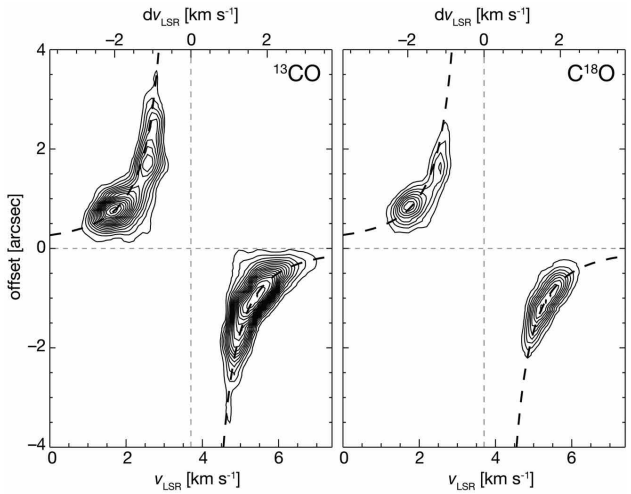

Fig. 37. P–V diagrams along the major axis ($PA = 341°$) for ^{13}CO and $C^{18}O$ ($J = 3$–2) lines. The contour spacing is 5σ, starting at the 5σ level. The dashed curves in each panel indicate the Keplerian rotation when $M = 2.2\,M_\odot$ and the inclination angle is $i = 27°$.

systemic velocity, position of the center of mass (the central star), and inclination relative to an observer are set as free parameters, whereas the central stellar mass is fixed in the range $2.2 \pm 0.3\,M_\odot$ (Verhoeff et al. 2011). The best-fit parameters obtained by χ^2 minimization are in good agreement between ^{13}CO and $C^{18}O$. Using ^{13}CO detected with a higher S/N, the system inclination angle is estimated as $i = 26.5^{+2.2}_{-1.7}$ degrees, where the uncertainty arises from the error in the stellar mass. Note that i is not large enough to yield reasonable constraints on both the stellar mass and the inclination (Simon et al. 2000). The systemic velocity is estimated to be $3.72 \pm 0.02\,\mathrm{km\,s^{-1}}$ in v_{LSR}, and the obtained location of the center of mass matches that of the compact component of the continuum emission, which most likely represents the inner disk. Figure 37 also shows the curves for the Keplerian rotation with the parameters adopted in the modeling, i.e., $i = 27°$, $M = 2.2\,M_\odot$, and the systemic velocity of $3.7\,\mathrm{km\,s^{-1}}$ in v_{LSR}. No significant deviation from the Keplerian motion was detected within the effective resolution of $0.2\,\mathrm{km\,s^{-1}}$ in our observations.

Appendix 2. Details of parameter search for dust distribution

In this section, we present the results of the parameter search for dust distribution models. We vary the parameters for dust distribution $\Sigma_{d,0}$, r_d, and w_d and look for a set of parameters that best reproduces the dust continuum observations. Here, we exclusively show the results of the north region where dust emission is optically thick. For the south region, the disk is optically thin and the parameter search is straightforward.

For each set of the parameters ($\Sigma_{d,0}$, r_d, w_d), we calculate the dust continuum emission and the model images. The model images are convolved with the Gaussian beam with the size of the observations. The convolved radial profiles of the surface brightness is fitted by the Gaussian function given in equation (1). The derived parameters (I_p, r_0, w) are compared with those derived from observations ($I_{p,obs}$, $r_{0,obs}$, w_{obs}). Tables 7, 8, and 9 show the results when $\Sigma_{d,0}$, r_d, and w_d are varied, respectively.

The peak brightness of dust emission depends weakly on the assumed peak surface density. It is 1.17 and

Table 7. Results of model dust continuum emission of the north profile with different $\Sigma_{d,0}$.*

Model parameters ($\Sigma_{d,0}$ [g cm^{-2}], r_d [au], w_d [au])	Model results (I_p [Jy arcsec^{-2}], r_0 [au], w [au])
(0.5, 173, 27)	(1.17, 152, 50)
(0.6, 173, 27)	(1.20, 153, 50)
(0.7, 173, 27)	(1.25, 150, 50)

*The observed parameters are ($I_{p,obs}$, $r_{0,obs}$ [au], w_{obs} [au]) = (1.2 Jy arcsec^{-2}, 152 au, 51 au).

Table 8. Results of model dust continuum emission of the north profile with different r_d.*

Model parameters ($\Sigma_{d,0}$ [g cm^{-2}], r_d [au], w_d [au])	Model results (I_p [Jy arcsec^{-2}], r_0 [au], w [au])
(0.6, 163, 27)	(1.24, 141, 51)
(0.6, 173, 27)	(1.20, 153, 50)
(0.6, 183, 27)	(1.19, 161, 51)

*The observed parameters are ($I_{p,obs}$, $r_{0,obs}$ [au], w_{obs} [au]) = (1.2 Jy arcsec^{-2}, 152 au, 51 au).

Table 9. Results of model dust continuum emission of the north profile with different w_d.*

Model parameters ($\Sigma_{d,0}$ [g cm^{-2}], r_d [au], w_d [au])	Model results (I_p [Jy arcsec^{-2}], r_0 [au], w [au])
(0.6, 173, 22)	(1.12, 154, 47)
(0.6, 173, 27)	(1.20, 153, 50)
(0.6, 173, 34)	(1.28, 146, 56)

*The observed parameters are ($I_{p,obs}$, $r_{0,obs}$ [au], w_{obs} [au]) = (1.2 Jy arcsec^{-2}, 152 au, 51 au).

1.25 Jy arcsec^{-2} for $\Sigma_{d,0} = 0.5$ and 0.7 g cm^{-2}, respectively, when the other parameters are fixed at $r_d = 173$ au and $w_d = 27$ au (the best-fit parameters; table 7). In other words, a factor of 1.4 increase in surface density results in only ~7% in the surface brightness. The peak brightness depends weakly on r_d and w_d as well. It is 1.24 and 1.19 Jy arcsec^{-2} for $r_d = 163$ and 183 au, respectively (table 8), meaning that a 12% change in r_d results in a 4% change in the peak brightness. In this case, r_0 also changes by ~20 au so r_0 is more affected by the change in r_d. When w_d is varied from 22 to 34 au, the peak brightness changes from 1.12 to 1.28 Jy arcsec^{-2} (table 9), meaning that ~50% change in the width of the dust distribution results in ~14% change in the peak brightness. In this case, the width of the surface brightness changes by ~20% so it is more affected than the peak brightness.

References

Aikawa, Y., & Nomura, M. 2006, ApJ, 642, 1152

Anders, E., & Grevesse, N. 1989, Geochem. Cosmochim. Acta, 53, 197

Andrews, S. M., Wilner, D. J., Espaillat, C., Hughes, A. M., Dullemond, C. P., McClure, M. K., Qi, C., & Brown, J. M. 2011, ApJ, 732, 42

Beckwith, S. V. W., Sargent, A. I., Chini, R. S., & Guesten, R. 1990, AJ, 99, 924

Biller, B., Lacour, S., & Juhász, A. 2012, ApJ, 753, L38

Birnstiel, T., Dullemond, C. P., & Pinilla, P. 2013, A&A, 550, L8

Bruderer, S., van der Marel, N., van Dishoeck, E. F., & van Kempen, T. A. 2014, A&A, 562, A26

Calvet, N., D'Alessio, P., Hartmann, L., Wilner, D., Walsh, A., & Sitko, M. 2002, ApJ, 568, 1008

Canovas, H., Ménard, F., Hales, A., Jordán, A., Schreiber, M. R., Casassus, S., Gledhill, T. M., & Pinte, C. 2013, A&A, 556, A123

Casassus, S., et al. 2013, Nature, 493, 191

Casassus, S., et al. 2015, ApJ, 812, 126

Casassus, S., Perez, M. S., Jordán, A., Ménard, F., Cuadre, J., Schreiber, M. R., Hales, A. S., & Ercolano, B. 2012, ApJ, 754, L31

D'Alessio, P., Calvet, N., & Hartmann, L. 2001, ApJ, 553, 321

Dubrulle, B., Morfill, G., & Sterzik., M. 1995, Icarus, 114, 237

Fujiwara, H., et al. 2006, ApJ, 644, L133

Fukagawa, M., et al. 2013, PASJ, 65, L14

Fukagawa, M., Tamura, M., Itoh, Y., Kudo, T., Imaeda, Y., Oasa, Y., Hayashi, S. S., & Hayashi, M. 2006, ApJ, 636, L153

González, M., Audit, E., & Huynh, P. 2007, A&A, 464, 429

Inoue, A. K., Oka, A., & Nakamoto, T. 2009, MNRAS, 393, 1377

Kamp, I., & Dullemond, C. P. 2004, ApJ, 615, 991

Kanno, Y., Harada, T., & Hanawa, T. 2013, PASJ, 65, No. 72

Kataoka, A., et al. 2015, ApJ, 809, 78

Lyra, W., & Lin, M.-K. 2013, ApJ, 775, 17

Marino, S., Perez, S., & Casassus, S. 2015, ApJ, 798, L44

Mendigutía, I., Fairlamb, J., Montesinos, B., Oudmeijer, R. D., Najita, J. R., Brittain, S. D., & van den Ancker, M. E. 2014, ApJ, 790, 21

Michikoshi, S., Kokubo, E., & Inutsuka, S. 2012, ApJ, 746, 35

Mihalas, D., & Mihalas, B. W. 1984, Foundations of Radiation Hydrodynamics, (New York: Oxford University Press)

Min, M., Hovenier, J.-W., & de Koter, A. 2003, A&A, 404, 35

Mittal, T., & Chiang, E. 2014, 2015, ApJ, L25

Nomura, M., & Millar, T. J. 2005, A&A, 438, 923

Pavlyuchenkov, Y., Semenov, D., Henning, T., Guilloteau, S., Piétu, V., Launhardt, R., & Dutrey, A. 2007, ApJ, 669, 1262

Perez, S., et al. 2015, ApJ, 798, 85

Pinilla, P., Birnstiel, T., Ricci, L., Dullemond, C. P., Uribe, A. L., & Natta, A. 2012, A&A, 538, A114

Pontoppidan, L. M., Blake, G. A., & Smette, A. 2011, ApJ, 733, 84

Qi, C., D'Alessio, P., Öberg, K. I., Wilner, D. J., Hughes, A. M., Andrews, S. M., & Ayala, S. 2011, ApJ, 740, 84

Rameau, J., Chauvin, G., Lagrange, A.-M., Thébault, P., Milli, J., Girard, J. H., & Bonnefoy, M. 2012, A&A, 546, A24

Rodigas, T. J., Follette, K. B., Weinberger, A., Close, L., & Hines, D. C. 2014, ApJ, 791, L37

Rosenfeld, K., Chiang, E., & Andrews, S. M. 2014, ApJ, 782, 9

Simon, M., Dutrey, A., & Guilloteau, S. 2000, ApJ, 545, 1034

Strom, K. M., Strom, S. E., Edwards, S., Cabrit, S., & Strutskie, M. F. 1999, AJ, 97, 1451

Takahashi, S. Z., & Inutsuka, S. 2014, ApJ, 794, 55

van der Plas, G., Casassus, S., Ménard, F., Perez, S., Thi, W. F., Pinte, C., & Christiaens, V. 2014, ApJ, 792, L25

Verhoeff, A. P., et al. 2011, A&A, 528, A91

Waelkins, C., Waters, L. B. F. M., & de Graauw, M. S. 1996, A&A, 315, L245

Ward, W. R. 2000, in Origin of the Earth and Moon, eds. R. M. Canup & K. Righter (Tucson, AZ: University of Arizona Press), 75

Youdin, A. N. 2011, ApJ, 731, 99

Publ. Astron. Soc. Japan (2015) 67 (6), 120 (1–9)
doi: 10.1093/pasj/psv094
Advance Access Publication Date: 2015 October 12

Impact of the initial disk mass function on the disk fraction

Ryou Ohsawa,[1,*] Takashi Onaka,[2] and Chikako Yasui[2]

[1]Institute of Astronomy, The University of Tokyo, 2-21-1 Osawa, Mitaka, Tokyo 181-0015, Japan
[2]Department of Astronomy, Graduate School of Science, The University of Tokyo, 7-3-1 Hongo, Bunkyo-ku, Tokyo 113-0033, Japan

*E-mail: ohsawa@ioa.s.u-tokyo.ac.jp

Received 2015 July 10; Accepted 2015 September 7

Abstract

The disk fraction, the percentage of stars with a disk in a young cluster, is widely used to investigate the lifetime of the protoplanetary disk, which can impose an important constraint on the planet formation mechanism. The relationship between the decay timescale of the disk fraction and the mass dissipation timescale of individual disks, however, remains unclear. Here we investigate the effect of the disk mass function (DMF) on the evolution of the disk fraction. We show that the time variation in the disk fraction depends on the spread of the DMF and the detection threshold of the disk. In general, the disk fraction decreases more slowly than the disk mass if a typical initial DMF and a detection threshold are assumed. We find that, if the disk mass decreases exponentially, the mass dissipation timescale of the disk can be as short as 1 Myr even when the disk fraction decreases with a time constant of $\sim$2.5 Myr. The decay timescale of the disk fraction can be a useful parameter to investigate the disk lifetime, but the difference between the mass dissipation of individual disks and the decrease in the disk fraction should be properly appreciated to estimate the timescale of the disk mass dissipation.

Key words: protoplanetary disks — stars: protostars — stars: statistics

1 Introduction

Protostars are surrounded by disks consisting of gas and dust (referred to as a protoplanetary disk), which have been investigated as sites of planet formation. Young stellar objects (YSOs) of low and intermediate masses, systems consisting of a protostar and a protoplanetary disk, are roughly categorized into three classes by their spectral energy distributions (SEDs): Class I objects are the youngest with infrared emission from dust dominating the SED; Class II objects have intermediate ages with the SEDs characterized by a combination of stellar and hot-dust emission; Class III objects are the oldest, consequently showing the weakest-dust emission (e.g., Williams & Cieza 2011; Bachiller 1996). The mass and surface density of protoplanetary disks decrease with time (Wyatt et al. 2007; Wyatt 2008), and this mechanism is still under debate. Although the dissipation involves a number of processes, photo-evaporation likely plays an important role, especially in low-mass stars (Armitage 2011). Planets are thought to form in the protoplanetary disk. The dust and gas surface densities of the protoplanetary disk are important parameters that determine the accretion rates to the cores and the final mass of gas giant planets (e.g., Ida & Lin 2004). It is therefore important to understand the evolution of the protoplanetary disk for the investigation of planet formation.

Different regions within a protoplanetary disk can be investigated with different wavelengths. Continuum emission in the near-infrared comes mostly from hot dust in the innermost part of the disk. Emission in the mid-infrared comes either from the surface of the disk or the mid-plane at the disk at a distance of several astronomical units. The far-infrared emission is dominated either by the mid-plane or the outermost part of the disk (Dullemond & Monnier 2010). Atomic and molecular emission lines trace gas components and accretion activities. The investigation of the planet-forming disk evolution requires observations in the near- or mid-infrared.

There are, however, difficulties in the observational investigation of the evolution of protoplanetary disks. First, the age of individual YSOs is difficult to estimate. It can be estimated from the loci in the Hertzsprung–Russell diagram (e.g., Strom et al. 1989; Kenyon & Hartmann 1995) or by near-infrared and X-ray photometry (Getman et al. 2014). However, these have inherent non-negligible uncertainties. The estimate based on the equivalent width of absorption lines has a better accuracy (Takagi et al. 2010, 2011), but it requires high-resolution spectroscopy, which is not always available. The mass of protoplanetary disks is also difficult to estimate from near- and mid-infrared observations since they are optically thick at these wavelengths.

The disk fraction, defined as the fraction of stars with a disk in a star cluster, is widely used to study the evolution of protoplanetary disks since it relies on the age of star clusters, which reduces the uncertainties in the ages of individual stars, and since the presence of a disk can be estimated directly from the loci in the color–color diagram of near- and mid-infrared photometry as excess emission, although it does not estimate the disk mass ($m_{\rm d}$). Haisch, Lada, and Lada (2001) show that the disk fraction estimated in the near-infrared decreases gradually with the cluster age, while Mamajek (2009) reports that the disk fraction decreases exponentially with a time constant of 2.5 Myr (decay timescale of the disk fraction, hereafter DTDF).

The DTDF may change with the stellar mass and metallicity of the cluster (e.g., Yasui et al. 2009). Hernández et al. (2005) derive the disk fraction of nearby OB associations using the *JHK*-bands and suggest that the disk fraction for intermediate-mass stars is lower than that for low-mass ($\lesssim 1\,M_{\odot}$) stars. The result indicates the fast dissipation of the inner-disk for intermediate-mass stars. A similar result is reported by Carpenter et al. (2006), based on the Spitzer observations of U Sco OB association. Kennedy and Kenyon (2009) investigate the disk fraction of nine clusters, using infrared excess estimated from Spitzer observations and Hα equivalent width, and show that the disk fraction decreases with increasing stellar mass. Hernández et al. (2008), using 2MASS and Spitzer data, find that the disk fraction of γ Vel cluster is smaller than other clusters at a similar age ($\simeq$5 Myr). They suggest that the small disk fraction may be attributed to the strong radiation field from massive stars in the cluster. For low-mass ($\lesssim 2\,M_{\odot}$) stars, we do not detect any appreciable difference between the disk fractions estimated at the near- and mid-infrared. On the other hand, Yasui et al. (2014) suggest that the disk disappears by $\sim$3 Myr faster at the near-infrared than at the mid-infrared for intermediate-mass (~ 1.5–$7\,M_{\odot}$) stars, being consistent with the lack of planets discovered in the vicinity of the intermediate-mass stars. Ribas et al. (2014) investigate the disk fraction of 22 young clusters using SED fitting from optical to mid-infrared. They show that the primordial disk detected at shorter (3.4–12 μm) wavelengths disappears faster than that at longer (22–24 μm) wavelengths, indicating that the disk closer to the star evolves more rapidly.

Although the evolution of the disk can be studied efficiently by the disk fraction, the DTDF is not equal to the mass dissipation timescale of individual disks (MDTID). The DTDF is a statistical measure and does not directly indicate the variation in the disk mass of individual objects. It is the timescale of the disk dissipation that governs the planet formation process. However, the reliability of the DTDF as an estimator of the MDTID has not been studied systematically. Thus it is of importance to understand the relation between the DTDF and the MDTID in a semi-quantitative manner.

How the disk fraction decreases with the cluster age depends on the statistical properties of the cluster. Owen, Ercolano, and Clarke (2011) investigate the photoevaporation mechanism of the protoplanetary disk by X-rays with radiation-hydrodynamic simulations. They demonstrate that the observed disk fraction at the near-infrared can be reproduced by the X-ray luminosity function of the cluster. Therefore, the behavior of the disk fraction must be investigated by taking account of the distribution of physical parameters of the cluster. Submillimeter observations indicate that the total dust mass in the disk is distributed over a wide range (e.g., Andrews & Williams 2005, 2007). Armitage, Clarke, and Palla (2003) show that the observed spread of the disk lifetime in the Taurus cloud is consistent with theoretical models of disk evolution if a dispersion in the initial disk mass is assumed. Thus the initial disk mass function (DMF) can affect the time variation of the disk fraction in a statistical way, but this effect has not been investigated in detail yet.

In this paper, we devise a simple model to estimate the effect of the initial DMF on the time variation of the disk fraction. The difference between DTDF and MDTID is calculated, by taking account of the broadness of the DMF. Details of the model are described in section 2. In section 3,

the variation in the calculated disk fraction is investigated and compared with the observed disk fraction. The results are summarized in section 4.

2 Model

The evolution of the disk fraction is investigated by taking into account the disk mass distribution. In the present model, we consider the observation of a young star cluster in the near- or mid-infrared, where the protoplanetary disk is optically thick. In observations, the target stars are selected by their spectral types, and thus the stellar mass is in a narrow range. In the following, we do not consider the distribution of the mass of the central star. Infrared excess ($f^{\rm ex}$) is assigned to each star. The star is recognized as being associated with a protoplanetary disk when $f^{\rm ex}$ is larger than a critical value ($f^{\rm th}$). All stars in the cluster are assumed to be born as a single star at the same time with different disk masses. The effect of the age dispersion within the cluster is discussed in subsection 3.3. The disk fraction is defined by the fraction of such stars with $f^{\rm ex} > f^{\rm th}$ in the cluster.

The DMF, the fractional number of the disk with the mass between $m_{\rm d}$ and $m_{\rm d} + dm_{\rm d}$, is defined by $\phi_0(m_{\rm d})dm$, and $\phi_0(m_{\rm d})$ is normalized as

$$\int \phi_0(m_{\rm d})dm_{\rm d} = 1. \tag{1}$$

Based on a survival analysis, Andrews and Williams (2005) show that the DMF of the Taurus–Auriga region is well approximated by a log-normal distribution. Similar results are also reported by Andrews and Williams (2007) and Mann and Williams (2010). According to their results, the initial DMF is approximated by

$$\phi_0(m_{\rm d})dm_{\rm d} = \frac{1}{m_{\rm d}\sqrt{2\pi}\sigma}\exp\left\{-\frac{1}{2}\left[\frac{\log(m_{\rm d}/\mu)}{\sigma}\right]^2\right\}dm_{\rm d}, \tag{2}$$

where μ and σ define the location and width of the distribution.

The disk dissipates with time. Luhman et al. (2010) suggest that the optically thick inner disk rapidly evolves into an optically thin phase because the number of transitional disks may be small. The evolution of the inner-disk mass is, however, not well understood. If the disk is regarded as an isolated system, the mass-loss rate of the disk should be determined by the parameters of the disk itself, such as the disk mass, the luminosity of the central star, and the angular momentum. To simplify the case, we assume that the dissipation of the disk mass is given by a unary function of the disk mass:

$$\frac{dm_{\rm d}}{{\rm d}t} = -\frac{1}{\zeta(m_{\rm d})}, \tag{3}$$

where $\zeta(m)$ is an arbitrary positive definite function to define the disk mass-loss rate. By integrating equation (3), the relationship between $m_{\rm d}(t)$ and t is obtained.

$$\int_{m_{\rm d}(0)}^{m_{\rm d}(t)} \zeta(m)dm = -t. \tag{4}$$

We define $\mathcal{Z}(m)$ as the integration of $\zeta(m)$.

$$\mathcal{Z}\left[m_{\rm d}(t)\right] - \mathcal{Z}\left[m_{\rm d}(0)\right] = -t. \tag{5}$$

Since $\zeta(m)$ is positive definite, the integrated function $\mathcal{Z}(m)$ is a monotonically increasing function, for which the inverse function $\mathcal{Z}^{-1}(m)$ is uniquely defined. Thus $m_{\rm d}(t)$ is solved as

$$m_{\rm d}(t) = \mathcal{M}\left[t, m_{\rm d}(0)\right] = \mathcal{Z}^{-1}\left\{-t + \mathcal{Z}\left[m_{\rm d}(0)\right]\right\}. \tag{6}$$

The inverse function $\mathcal{Z}^{-1}(m)$ is also a monotonically increasing function. $\mathcal{M}\left[t, m_{\rm d}(0)\right]$ monotonically decreases with t:

$$t > t' \iff \mathcal{M}\left[t, m_{\rm d}(0)\right] < \mathcal{M}\left[t', m_{\rm d}(0)\right]. \tag{7}$$

The MDTID is defined as a typical timescale of the decrease in $\mathcal{M}\left[t, m_{\rm d}(0)\right]$ as discussed in subsection 3.1. Instead, $\mathcal{M}\left[t, m_{\rm d}(0)\right]$ is an increasing function in terms of $m_{\rm d}(0)$:

$$m_{\rm d}(0) > m'_{\rm d}(0) \iff \mathcal{M}\left[t, m_{\rm d}(0)\right] > \mathcal{M}\left[t, m'_{\rm d}(0)\right]. \tag{8}$$

Equation (8) assures that the mass dissipation process does not change the order of the disk mass. Equation (5) can be solved in terms of $m_{\rm d}(0)$:

$$m_{\rm d}(0) = \mathcal{Z}^{-1}\left\{t + \mathcal{Z}\left[m_{\rm d}(t)\right]\right\} = \mathcal{M}\left[-t, m_{\rm d}(t)\right]. \tag{9}$$

The relationship between the initial DMF and the DMF at t is given by

$$\phi_t\left(m_{\rm d}\right)dm_{\rm d} = \phi_0\left[\mathcal{M}\left(-t, m_{\rm d}\right)\right]d\mathcal{M}\left(-t, m_{\rm d}\right). \tag{10}$$

The DMF changes in time depending on the time evolution of $\mathcal{M}(-t, m_{\rm d})$. Although we assume that the initial DMF is given by a log-normal distribution, the shape of the DMF at t can be different from a log-normal function. Here we discuss a general case of $\mathcal{M}(-t, m_{\rm d})$.

The near-infrared excess is directly related to the inner disk mass, not the total disk mass. The mass function of the inner disk is, however, not observationally constrained.

Here, we simply assume that the inner-disk mass is proportional to the total disk mass. The amount of the excess should depend on the disk inclination and the shape of the inner rim of the disk (Dullemond & Monnier 2010). The connection between $f^{\rm ex}$ and the disk mass has not yet been understood well. For the sake of simplicity, we assume that $f^{\rm ex}$ is given by a unary function of $m_{\rm d}$. The infrared excess $f^{\rm ex}(m_{\rm d})$ should be a nondecreasing function with $m_{\rm d}$. The threshold mass ($m_{\rm d}^{\rm th}$) is defined by $f^{\rm ex}(m_{\rm d}^{\rm th}) = f^{\rm th}$. The disk is detected in the infrared when $m_{\rm d} \geq m_{\rm d}^{\rm th}$, while infrared excess is not detectable when $m_{\rm d} < m_{\rm d}^{\rm th}$. In this formalism, we do not specify the relationship between $f^{\rm ex}$ and $m_{\rm d}$. The presence or absence of the disk is determined only by $m_{\rm d}$, *irrespective* of the functional form of $f^{\rm ex}(m_{\rm d})$. The infrared excess $f^{\rm ex}$ may depend on several parameters such as the disk inclination. Justification of this simple formulation is discussed in subsection 3.3.

The disk fraction at the age of t is calculated by

$$\mathcal{F}(t) = \int_{m_{\rm d}^{\rm th}}^{\infty} \phi_t(m) dm. \tag{11}$$

Then, by substituting equations (2), (3), and (10) for equation (11), the disk fraction $\mathcal{F}(t)$ becomes

$$\mathcal{F}\left(t, m_{\rm d}^{\rm th}, \mu, \sigma\right) = \frac{1}{2}{\rm erfc}\left[\frac{\log \mathcal{M}\left(-t, m_{\rm d}^{\rm th}\right) - \log \mu}{\sqrt{2}\sigma}\right], \tag{12}$$

where erfc(x) is the complementary error function. Since erfc(x) is a decreasing function on x, the disk fraction, $\mathcal{F}\left(t, m_{\rm d}^{\rm th}, \mu, \sigma\right)$, decreases as t increases. The DTDF is defined as a typical timescale of the decrease in equation (12).

3 Discussion

3.1 Behavior of disk fraction

Since the complementary error function erfc(x) is a monotonically decreasing function, the disk fraction will decrease with increasing $\mathcal{M}[-t, m_{\rm d}(0)]$, which increases monotonically with t. Equation (12) shows that the central locus of the DMF, μ, shifts the disk function along the axis of age. The width of the DMF, σ, normalizes the argument of the complementary error function in equation (12). As σ increases by a factor of x, the time variation of the disk fraction is decelerated by a factor of x. This suggests that the broadness of the DMF has a large impact on the evolution of the disk fraction.

To investigate a typical decreasing timescale of equation (6), we define the time $T(\xi)$ such that the disk with the initial mass of $\xi m_{\rm d}^{\rm th}$ loses its mass down to $m_{\rm d}^{\rm th}$ at $t = T(\xi)$:

$$\mathcal{M}\left[T(\xi), \xi m_{\rm d}^{\rm th}\right] = m_{\rm d}^{\rm th}. \tag{13}$$

The duration means an observational lifetime of the disk with the initial mass of $\xi m_{\rm d}^{\rm th}$. Equation (13) is equivalent to

$$\begin{aligned} -T(\xi) + \mathcal{Z}\left(\xi m_{\rm d}^{\rm th}\right) &= \mathcal{Z}\left(m_{\rm d}^{\rm th}\right) \\ \iff T(\xi) &= \mathcal{Z}\left(\xi m_{\rm d}^{\rm th}\right) - \mathcal{Z}\left(m_{\rm d}^{\rm th}\right). \end{aligned} \tag{14}$$

$T(\xi)$ increases with ξ since $\mathcal{Z}(m)$ is an increasing function. When ξ is unity, $T(\xi)$ is equal to zero. The time $T(\xi)$ is regarded as a typical timescale for the disk mass to decrease by a factor of ξ. By substituting equation (14), the following relationship is obtained:

$$\mathcal{M}\left[-T(\xi), m_{\rm d}^{\rm th}\right] = \mathcal{Z}^{-1}\left[T(\xi) + \mathcal{Z}(m_{\rm d}^{\rm th})\right] = \xi m_{\rm d}^{\rm th}. \tag{15}$$

The disk fraction at $T(\xi)$ is obtained as

$$\mathcal{F}\left[T(\xi); m_{\rm d}^{\rm th}, \mu, \sigma\right] = \frac{1}{2}{\rm erfc}\left[\frac{\log\left(\xi m_{\rm d}^{\rm th}/\mu\right)}{\sqrt{2}\sigma}\right]. \tag{16}$$

The disk fraction decreases with ξ as well as $T(\xi)$. Equation (16) does not include $T(\xi)$ explicitly, indicating that the relationship between the disk fraction and ξ does not depend on the functional form of $T(\xi)$. Thus, the evolution of the disk fraction can be described in a general manner in terms of ξ. Figure 1 shows the evolution of the disk fractions normalized at age zero against ξ. The DMF of the Taurus cloud is assumed to be a representative one, so that μ and σ are fixed at $1.0 \times 10^{-3}\,M_\odot$ and 1.31 dex, respectively (the "full" sample in Andrews & Williams 2005).[1] By comparing sub-mm and near-infrared observations, Andrews and Williams (2005) suggest that the near-infrared ($K_{\rm s} - L$) color excess method can detect the protoplanetary disk with a mass down to $\sim 10^{-4}\,M_\odot$. The disk fractions are plotted for $m_{\rm d}^{\rm th} = 0.5 \times 10^{-4}$, 1.0×10^{-4}, and $2.0 \times 10^{-4}\,M_\odot$. The gray dotted curve shows the reciprocal of ξ, representing the dissipation of the disk mass. If the disk fraction decreases on the same timescale as the disk mass, the curve should follow the dotted curve. When the disk fraction decreases slower than the disk mass, the curve will deviate upward, and vice versa. All the disk fractions deviate

[1] Although Andrews and Williams (2005) have reported that the median and the variance are $5 \times 10^{-3}\,M_\odot$ and 0.50 dex for the "detection" subsample, we adopt the values for the "full" sample because nondetected samples should be properly taken into account.

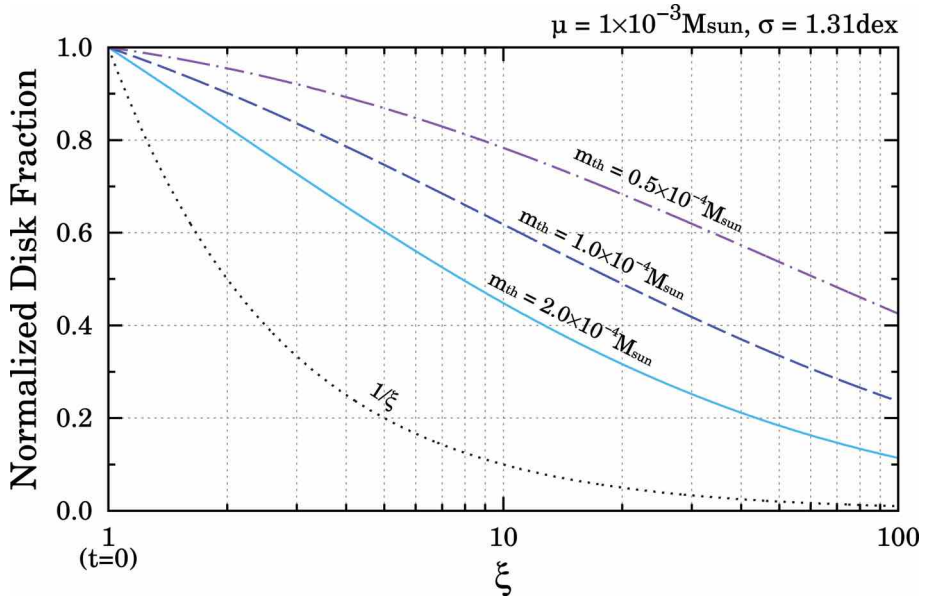

Fig. 1. Time evolution of the disk fraction against ξ. Note that the horizontal axis is ξ, not the time t, because the variation of the disk fraction can be described in terms of ξ in a more general manner than that of t (see text). The disk fractions normalized at age zero are plotted for $m_{\rm d}^{\rm th} = 2.0 \times 10^{-4}$, 1.0×10^{-4}, and $0.5 \times 10^{-4}\,M_\odot$ by the solid, dashed, and dot-dashed lines, respectively. The median and variance of the DMF are fixed at $10^{-3}\,M_\odot$ and 1.31 dex, respectively. The dotted curve shows the reciprocal of ξ, indicating the decrease in the individual disk masses (see text). (Color online)

upward in figure 1. An e-folding time of individual disk mass dissipation is estimated by T(e), which corresponds to the MDTID. On the other hand, the disk fraction for $m_{\rm d}^{\rm th} = 1.0 \times 10^{-4}$ does not decrease by a factor of e until ξ increases to about 40, suggesting that the DTDF is as long as $T(40)$. We found that the disk fraction decreases as fast as the disk mass only when $m_{\rm d}^{\rm th} \sim 2 \times 10^{-1}\ M_\odot$. Such an extreme case is excluded from observations. Figure 1 indicates that the disk fraction generally decreases slower than the disk mass when a typical initial DMF and a detection threshold are assumed.

3.2 Case study: exponential decay

To quantitatively compare the MDTID and DTDF, we consider a special case of $\zeta(m) = \tau/m$, which corresponds to an exponential decay. Equation (6) is reduced to

$$m_{\rm d}(t) = m_{\rm d}(0) e^{-t/\tau}. \tag{17}$$

Here τ is equivalent to $T(e)$. In this section, we define the MDTID by the e-folding time τ. Under the assumption of $\zeta(m) = \tau/m$, the DMF at t is given by

$$\phi_t\,(m_{\rm d})\,dm_{\rm d} = \frac{1}{m_{\rm d}\sqrt{2\pi}\sigma} \times \exp\left[-\frac{1}{2}\left(\frac{\log m_{\rm d} - \log \mu e^{-t/\tau}}{\sigma}\right)^2\right] dm_{\rm d}. \tag{18}$$

Here, the DMF remains a log-normal distribution. The median of the DMF at t is given by $\mu e^{-t/\tau}$, indicating that the location of the DMF shifts with the time constant of τ, while the scale parameter of the log-normal distribution, σ, is constant in time. By applying equation (17), the disk fraction is given by

$$\mathcal{F}\left(t, m_{\rm d}^{\rm th}, \mu, \sigma\right) = \frac{1}{2}{\rm erfc}\left[\frac{t/\tau + \log\left(m_{\rm d}^{\rm th}/\mu\right)}{\sqrt{2}\sigma}\right]. \tag{19}$$

Figure 2 shows the time variation of the disk fractions for different DMFs. The horizontal axis denotes the cluster age t measured by τ. The median mass of DMF is set to $1.0 \times 10^{-3}\,M_\odot$ (Andrews & Williams 2005). Figure 2a shows the results for different DMFs, $\sigma = 0.65$, 1.31, and 2.62 dex, where $m_{\rm d}^{\rm th}$ is fixed at $10^{-4}\,M_\odot$. The figure indicates that the disk fraction decreases slower as the DMF mass function becomes broader, because t is normalized by $\sigma\tau$ in equation (19). The disk fraction is not unity even at age zero, simply because some disks do not have a large amount of initial mass enough to be detected. Figure 2b shows the disk fractions for different detection thresholds, $m_{\rm d}^{\rm th} = 0.5 \times 10^{-4}$, 1.0×10^{-4}, and $2.0 \times 10^{-4}\,M_\odot$. The disk fraction shifts to the left with increasing $m_{\rm d}^{\rm th}$. The parameter $(m_{\rm d}^{\rm th}/\mu)$ affects the disk fraction at age zero, but does not change the slope of the disk fraction.

The red dotted line in figure 2b shows an exponential decay curve with the time constant of τ: $\exp(-t/\tau)$. All

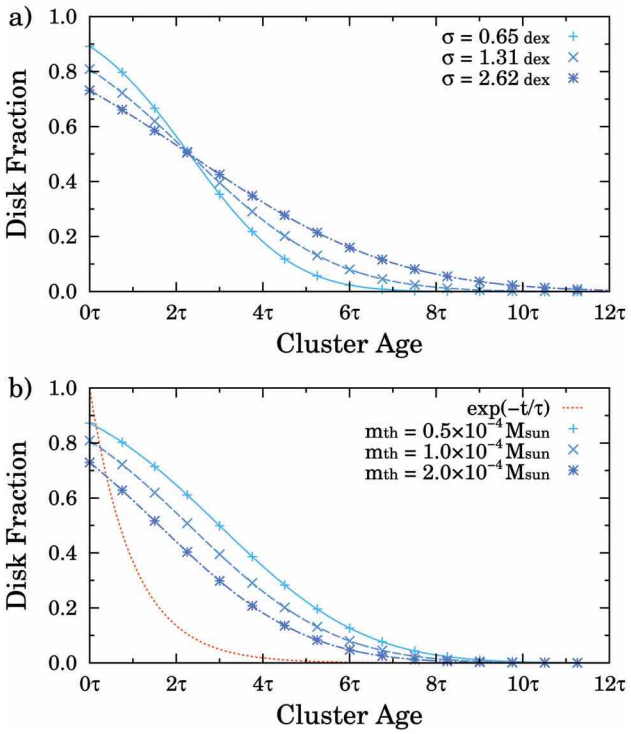

Fig. 2. (a) Disk fractions for different values of σ. (b) Disk fractions for different $m_{\rm d}^{\rm th}$ values. The horizontal axis is the cluster age t measured by τ. The red dotted line shows an exponential decay with a time constant of τ. (Color online)

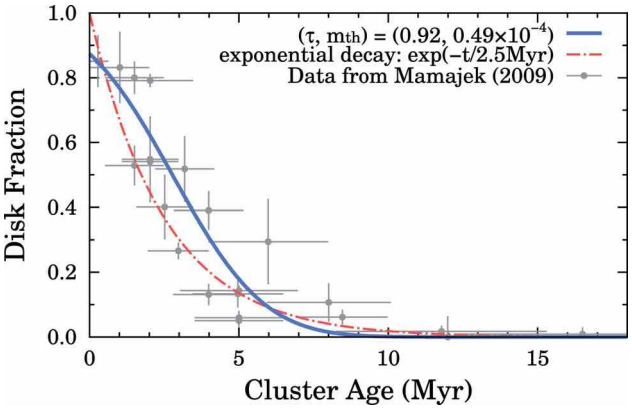

Fig. 3. Comparison with observed disk fractions. The gray filled circles with errors are observed disk fractions from Mamajek (2009). The blue solid line shows the disk fraction with the best-fitting parameters. The red dotted line shows an exponential decay with a time constant of 2.5 Myr. (Color online)

the disk fractions in figure 2b decrease more slowly than the exponential curve. The e-folding time of the disk fractions ranges between 2τ and 4τ, depending on $m_{\rm d}^{\rm th}$. This is consistent with the discussion in subsection 3.1; the disk fraction decreases generally more slowly than the disk dissipates. Figure 2 implies that the difference between the MDTID and DTDF is not negligible.

As a demonstration, we calculate the difference between DTDF and MDTID using a real data set. Since the present model is highly simplified, this practice is to demonstrate the degree of effect of the initial DMF on the estimate of the MDTID. We do not intend to derive an accurate estimate of the MDTID. Figure 3 shows that the observed disk fractions of a number of star clusters collected in Mamajek (2009) and references therein. In the current model, the disk fraction is given by equation (19). The location and width of the initial DMF, μ and σ, are fixed at $1.0 \times 10^{-3}\,M_\odot$ and 1.31 dex, respectively (Andrews & Williams 2005). The other two parameters, τ and $m_{\rm d}^{\rm th}$, are estimated by a maximum likelihood method. The likelihood function is defined as

$$\mathcal{L}(\tau, \gamma) \propto \prod_i \exp\left\{-\frac{1}{2}\left[\frac{f_i - \mathcal{F}\left(t_i; \tau, m_{\rm d}^{\rm th}\right)}{\Delta f_i}\right]^2\right\}, \qquad (20)$$

where f_i and Δf_i are the observed disk fraction and its uncertainty, and t_i is the cluster age. The parameters, τ and $m_{\rm d}^{\rm th}$, are estimated by maximizing equation (20). The errors in τ and $m_{\rm d}^{\rm th}$ are estimated by parametric bootstrapping. The best-fitting parameters are $\tau = 0.92^{+0.39}_{-0.28}$ Myr and $m_{\rm d}^{\rm th} = 0.48^{+0.71}_{-0.26} \times 10^{-4}\ M_\odot$. Even though the model is simple and ignores many effects, the detection threshold presented above is consistent with the value reported by Andrews and Williams (2005) ($\sim 10^{-4}\,M_\odot$). The blue line with the crosses in figure 3 shows the best-fitting curve. Mamajek (2009) suggests that the evolution of the observed disk fraction is well represented by an exponential decay with a time constant of 2.5 Myr, which is shown by the red dot-dashed line. The decrease in the disk fraction is well approximated by $\exp(-t/T)$, where $T = 2.5$ Myr, suggesting that DTDF is about 2.5 Myr. The present result, however, suggests that MDTID τ is as short as 0.9 Myr.

3.3 Justification of model

The discussion in subsection 3.1 is applied to an ordinary case, where various physical processes—such as binarity, variable X-ray flux, and photo-evaporation—can contribute to the dissipation. It assumes that the initial DMF is given by a log-normal function, but does not have a constraint on the DMF at a given time. Although the present model is rather robust in this sense, it is simplified and based on several assumptions. Effects of the simplification on the results are discussed.

In the present model, the stars in the cluster are assumed to be coeval. The star formation is, however, not instantaneous. Getman et al. (2014) investigate the age of individual YSOs in massive star forming regions and show that the spread of the stellar ages in a cluster is about 1–2 Myr,

comparable with the DTDF (∼2.5 Myr). The spread of age within a cluster should not be neglected in the discussion of the disk fraction. At a given epoch, YSOs formed earlier have lost more mass than those formed later, and vice versa. Thus, the apparent width of the DMF is broadened if the age distribution is taken into account in the present model. While the width of DMFs has been observationally measured (e.g., Andrews & Williams 2005), the intrinsic width of the DMF and the broadening effect due to the age spread are not distinguished. The observationally estimated width of the DMF should include the effect of the age distribution. Since we employ the observationally estimated width of the DMF (Andrews & Williams 2005) in our discussion, the present results indirectly take account of the effect of the age distribution.

The present model assumes that the mass of the inner disk is proportional to the total disk mass. This is not observationally confirmed, because the inner disk is optically thick in the infrared and the infrared excess does not reflect directly the amount of the inner-disk mass. The present results, however, mainly depend on the width of the initial DMFs. The results are expected to be valid as long as the distribution of the inner-disk mass is relatively as wide as the DMFs observed in the sub-mm wavelength.

The present model does not include any inclination effect on the infrared excess, although the infrared excess $f^{\rm ex}$ should be changed with inclinations. The relationship between $f^{\rm ex}$ and the inclination angle may be complicated. Since the near-infrared emission is mainly from the inner rim of the dusty disk (Dullemond et al. 2001; Natta et al. 2001; Muzerolle et al. 2003), the effect of the inclination angle can heavily depend on the shape of the inner rim (Dullemond & Monnier 2010). If the inner rim has a round shape (Isella & Natta 2005), the effect of the inclination on $f^{\rm ex}$ can be small. Observationally the infrared excess has no strong correlation with the inclination (Dullemond & Monnier 2010), suggesting that the inclination effect on the present result is not significant. Although the inclination significantly changes the infrared excess $f^{\rm ex}$, it is hard to distinguish the contributions from the inclination and the disk mass unless the inclination angle is determined. The effect of the inclination can be practically taken into account in the present model by broadening the initial DMF.

The relationship between the infrared excess $f^{\rm ex}$ and the disk mass, which is important for connecting the initial DMF with the disk fraction, remains to be understood. We assume that the infrared excess $f^{\rm ex}$ does not decrease as the disk mass increases. In the present model, the infrared excess $f^{\rm ex}$ is given by a unary function of the disk mass. The amount of the infrared excess is closely related to the shape of the inner rim (Dullemond & Monnier 2010; Isella & Natta 2005). The shape of the rim depends on the pressure scale height at the inner rim $H_{p,\,\rm rim}$, which is proportional to $1/\sqrt{M_\star}$, where $M_\star$ is the stellar mass (Isella & Natta 2005). Therefore, the neglect of the mass dependence can have a moderate effect on the result and should be taken into account in the next step. The effect on the present results due to this simplification is not expected to be severe as long as the mass range is sufficiently narrow.

In equation (3), we assume that the decrease in the disk mass is given by a unary function of $m_{\rm d}$. This assumption can be rephrased as "disks with the same disk mass have the same lifetime." The decreasing rate of the disk mass should depend on the radiation from the central star and neighborhood stars. The assumption can become invalid if the mass range is not sufficiently narrow or the radiation field significantly changes within the cluster. Consequently, the lifetime of the disk can be extended or shortened. The effects of the mass range and the radiation field of neighborhood stars can be qualitatively estimated by broadening the width of the initial DMF. As shown in equation (12), the disk fraction decreases more slowly than the disk mass as the initial DMF becomes wider. Although the present model does not correctly take account of the effects of the mass range and the radiation field from neighborhood stars, those effects should not change the conclusion of the present result qualitatively.

3.4 Implications of results

As shown in figure 2, the apparent evolution of the disk fraction depends on the shape of the initial DMF. The disk fractions of clusters with different initial DMFs should follow different curves. In most observational studies, the disk fractions are assumed to follow a single curve (e.g., Haisch et al. 2001; Yasui et al. 2009, 2014; Ribas et al. 2014). In other words, they assume that the initial DMFs are assumed to be the same. However, the DMF has so far been obtained for only a few clusters, e.g., in the Taurus, Ophiuchus, and Orion regions (e.g., Williams & Cieza 2011). Those observations suggest that the DMF can be approximated fairly well by a single log-normal function, while Mann et al. (2015) suggest that the DMF of NGC 2024 is possibly top-heavy in comparison with those of the Taurus cloud and Orion Nebula clusters. If the DMF is top-heavy in the sample clusters, the DTDF will become even longer than the present estimate. Only by investigating the evolution of the disk fraction, it is not possible to disentangle the variation in the MDTID and the variation in the initial DMFs. Further investigation on the variation in the initial DMF is needed.

Previous studies have compared the disk fractions of different clusters and discussed the DTDF (e.g., Haisch et al. 2001; Yasui et al. 2010). The present results suggest that

the apparent evolution of the disk fraction depends on the threshold mass. The disk detected in the near-infrared is expected to be fully optically thick. The amount of excess $f^{\rm ex}$ in the near-infrared is insensitive to the disk mass in the optically thick phase (Wood et al. 2002). The choice of the detection threshold ($f^{\rm th}$) does not matter. In general, the transition from a thick disk to a thin occurs in a small mass range at the near-infrared wavelength. The fraction of disks in the transition in a cluster is small (e.g., Skrutskie et al. 1990; Wolk & Walter 1996; Cieza et al. 2007). Thus, the dependence of the threshold mass $m_{\rm d}^{\rm th}$ is negligible. At wavelengths longer than 25 μm, the disk can be detected in the optically thin phase and the excess becomes sensitive to the disk mass (Wood et al. 2002). The difference in the detection threshold may have to be taken into account.

4 Conclusion

The disk fraction, which is the fraction of stars with a disk in a young cluster, is widely used to observationally investigate the lifetime of the protoplanetary disk. The time evolution of the disk fraction should depend on the disk mass function (DMF) at age zero. We discuss a simple model to analytically investigate the relationship between the mass dissipation timescale of individual disks (MDTID) and the decay timescale of the disk fraction (DTDF).

In the present model, the evolution of the disk fraction can be described by the detection threshold of the disk mass ($m_{\rm d}^{\rm th}$), and the locus (μ) and the dispersion (σ) of the initial DMF. The DMF of the Taurus cluster has $\mu \simeq 10^{-3}\,M_\odot$ and $\sigma \simeq 1.31$ dex (Andrews & Williams 2005). By using the near-infrared color excess method, a disk with a mass of $\sim 10^{-4}\,M_\odot$ can be detected (Andrews & Williams 2005). Under the assumption of these parameters, the present model indicates that the disk fraction generally decreases more slowly than the disk mass, suggesting that the DTDF is longer than the MDTID. Given that the disk mass dissipates exponentially, the difference between the DTDF and the MDTID is suggested not to be negligible. A comparison between the present results and the observational data (Mamajek 2009) suggests that the MDTID is as small as 1 Myr even if the disk fraction exponentially decreases with a time constant of 2.5 Myr, corresponding to the DTDF. Although the present model is simple and primitive, we are confident that the present results are qualitatively valid.

The present results suggest that the evolution of the disk fraction depends on the shape of the initial DMF. The variation in the DMF remains to be understood. Further observational investigation is needed. Although the apparent evolution of the disk fraction may depend on the detection threshold mass, the matching of the detection threshold does not matter unless the disk fraction is measured at a longer ($\gtrsim$25 μm) wavelength.

The study of the protoplanetary disk is being accelerated by the advent of Atacama Large Millimeter/submillimeter Array (ALMA), which can resolve the disk structure and precisely measure the mass of the disk. However, until the disk mass is accurately measured for a sufficiently large sample of disks in various environments, a statistical approach is still important for the study of the disk evolution. The disk fraction remains efficient and useful if the relationship between the DTDF and the MDTID is properly appreciated.

Acknowledgement

This research is supported in part by Grants-in-Aid for Scientific Research (25-8492, 23103004, 26247074, and 26800094) by Japan Society of the Promotion of Science.

References

Andrews, S. M., & Williams, J. P. 2005, ApJ, 631, 1134
Andrews, S. M., & Williams, J. P. 2007, ApJ, 671, 1800
Armitage, P. J. 2011, ARA&A, 49, 195
Armitage, P. J., Clarke, C. J., & Palla, F. 2003, MNRAS, 342, 1139
Bachiller, R. 1996, ARA&A, 34, 111
Carpenter, J. M., Mamajek, E. E., Hillenbrand, L. A., & Meyer, M. R. 2006, ApJ, 651, L49
Cieza, L., et al. 2007, ApJ, 667, 308
Dullemond, C. P., Dominik, C., & Natta, A. 2001, ApJ, 560, 957
Dullemond, C. P., & Monnier, J. D. 2010, ARA&A, 48, 205
Getman, K. V., et al. 2014, ApJ, 787, 108
Haisch, K. E., Lada, E. A., & Lada, C. J. 2001, ApJ, 553, L153
Hernández, J., Calvet, N., Hartmann, L., Briceño, C., Sicilia-Aguilar, A., & Berlind, P. 2005, AJ, 129, 856
Hernández, J., Hartmann, L., Calvet, N., Jeffries, R. D., Gutermuth, R., Muzerolle, J., & Stauffer, J. 2008, ApJ, 686, 1195
Ida, S., & Lin, D. N. C. 2004, ApJ, 604, 388
Isella, A., & Natta, A. 2005, A&A, 438, 899
Kennedy, G. M., & Kenyon, S. J. 2009, ApJ, 695, 1210
Kenyon, S. J., & Hartmann, L. 1995, ApJS, 101, 117
Luhman, K. L., Allen, P. R., Espaillat, C., Hartmann, L., & Calvet, N. 2010, ApJS, 186, 111
Mamajek, E. E. 2009, in AIP Conf. Proc., 1158, Exoplanets and disks: their formation and diversity (Melville, NY: AIP), 3
Mann, R. K., Andrews, S. M., Eisner, J. A., Williams, J. P., Meyer, M. R., Di Francesco, J., Carpenter, J. M., & Johnstone, D. 2015, ApJ, 802, 77
Mann, R. K., & Williams, J. P. 2010, ApJ, 725, 430
Muzerolle, J., Calvet, N., Hartmann, L., & D'Alessio, P. 2003, ApJ, 597, L149
Natta, A., Prusti, T., Neri, R., Wooden, D., Grinin, V. P., & Mannings, V. 2001, A&A, 371, 186

Owen, J. E., Ercolano, B., & Clarke, C. J. 2011, MNRAS, 412, 13
Ribas, Á., Merín, B., Bouy, H., & Maud, L. T. 2014, A&A, 561, 54
Skrutskie, M. F., Dutkevitch, D., Strom, S. E., Edwards, S., Strom, K. M., & Shure, M. A. 1990, AJ, 99, 1187
Strom, K. M., Strom, S. E., Edwards, S., Cabrit, S., & Skrutskie, M. F. 1989, AJ, 97, 1451
Takagi, Y., Itoh, Y., & Oasa, Y. 2010, PASJ, 62, 501
Takagi, Y., Itoh, Y., Oasa, Y., & Sugitani, K. 2011, PASJ, 63, 677
Williams, J. P., & Cieza, L. A. 2011, ARA&A, 49, 67
Wolk, S. J., & Walter, F. M. 1996, AJ, 111, 2066
Wood, K., Lada, C. J., Bjorkman, J. E., Kenyon, S. J., Whitney, B., & Wolff, M. J. 2002, ApJ, 567, 1183
Wyatt, M. C. 2008, ARA&A, 46, 339
Wyatt, M. C., Clarke, C. J., & Greaves, J. S. 2007, MNRAS, 380, 1737
Yasui, C., Kobayashi, N., Tokunaga, A. T., & Saito, M. 2014, MNRAS, 442, 2543
Yasui, C., Kobayashi, N., Tokunaga, A. T., Saito, M., & Tokoku, C. 2009, ApJ, 705, 54
Yasui, C., Kobayashi, N., Tokunaga, A. T., Saito, M., & Tokoku, C. 2010, ApJ, 723, L113

Publ. Astron. Soc. Japan (2015) 67 (5), 83 (1–16)
doi: 10.1093/pasj/psv051
Advance Access Publication Date: 2015 August 11

Detailed structure of the outer disk around HD 169142 with polarized light in *H*-band

Munetake Momose,[1,*] Ayaka Morita,[1] Misato Fukagawa,[2] Takayuki Muto,[3] Taku Takeuchi,[4] Jun Hashimoto,[5] Mitsuhiko Honda,[6] Tomoyuki Kudo,[7] Yoshiko K. Okamoto,[1] Kazuhiro D. Kanagawa,[8] Hidekazu Tanaka,[8] Carol A. Grady,[9,10,11] Michael L. Sitko,[12,13,†] Eiji Akiyama,[14] Thayne Currie,[7] Katherine B. Follette,[15] Satoshi Mayama,[16,17] Nobuhiko Kusakabe,[14] Lyu Abe,[18] Wolfgang Brandner,[19] Timothy D. Brandt,[20] Joseph C. Carson,[21] Sebastian Egner,[7] Markus Feldt,[19] Miwa Goto,[22] Olivier Guyon,[7] Yutaka Hayano,[7] Masahiko Hayashi,[14] Saeko S. Hayashi,[7] Thomas Henning,[19] Klaus W. Hodapp,[23] Miki Ishii,[14] Masanori Iye,[14] Markus Janson,[24] Ryo Kandori,[14] Gillian R. Knapp,[25] Masayuki Kuzuhara,[4] Jungmi Kwon,[26] Taro Matsuo,[27] Michael W. McElwain,[9] Shoken Miyama,[28] Jun-Ichi Morino,[14] Amaya Moro-Martin,[25,29] Tetsuo Nishimura,[7] Tae-Soo Pyo,[7] Eugene Serabyn,[30] Takuya Suenaga,[14,17] Hiroshi Suto,[14] Ryuji Suzuki,[14] Yasuhiro H. Takahashi,[14,26] Michihiro Takami,[31] Naruhisa Takato,[7] Hiroshi Terada,[7] Christian Thalmann,[32] Daigo Tomono,[7] Edwin L. Turner,[25,33] Makoto Watanabe,[34] John Wisniewski,[5] Toru Yamada,[35] Hideki Takami,[14] Tomonori Usuda,[14] and Motohide Tamura[14,26]

[1]College of Science, Ibaraki University, 2-1-1 Bunkyo, Mito, Ibaraki 310-8512, Japan
[2]Graduate School of Science, Osaka University, 1-1 Machikaneyama, Toyonaka, Osaka 560-0043, Japan
[3]Division of Liberal Arts, Kogakuin University, 1-24-2 Nishi-Shinjuku, Shinjuku-ku, Tokyo 163-8677, Japan
[4]Department of Earth and Planetary Sciences, Tokyo Institute of Technology, Meguro-ku, Tokyo 152-8551, Japan
[5]H. L. Dodge Department of Physics and Astronomy, University of Oklahoma, 440 W Brooks St Norman, OK 73019, USA
[6]Department of Mathematics and Physics, Kanagawa University, 2946 Tsuchiya, Hiratsuka, Kanagawa 259-1293, Japan
[7]Subaru Telescope, 650 North A'ohoku Place, Hilo, HI 96720, USA
[8]Institute of Low Temperature Science, Hokkaido University, Sapporo, Hokkaido 060-0819, Japan
[9]Exoplanets and Stellar Astrophysics Laboratory, Code 667, Goddard Space Flight Center, Greenbelt, MD 20771, USA
[10]Eureka Scientific, 2452 Delmer, Suite 100, Oakland, CA 96002, USA
[11]Goddard Center for Astrobiology, NASA/GSFC, Greenbelt, MD 20771, USA
[12]Space Science Institute, 4750 Walnut St., Suite 205, Boulder, CO 80301, USA
[13]Department of Physics, University of Cincinnati, Cincinnati, OH 45221-0011, USA
[14]National Astronomical Observatory of Japan, 2-21-1 Osawa, Mitaka, Tokyo 181-8588, Japan

[15]Steward Observatory, University of Arizona, 933 N Cherry Ave, Tucson, AZ 85721, USA
[16]The Center for the Promotion of Integrated Sciences, The Graduate University for Advanced Studies (SOKENDAI), Shonan International Village, Hayama-cho, Miura-gun, Kanagawa 240-0193, Japan
[17]Department of Astronomical Science, The Graduate University for Advanced Studies (SOKENDAI), 2-21-1 Osawa, Mitaka, Tokyo 181-8588, Japan
[18]Laboratoire Lagrange (UMR 7293), Université de Nice-Sophia Antipolis, CNRS, Observatoire de la Côte d'Azur, 28 avenue Valrose, 06108 Nice Cedex 2, France
[19]Max Planck Institute for Astronomy, Königstuhl 17, 69117 Heidelberg, Germany
[20]Astrophysics Department, Institute for Advanced Study, Princeton, NJ 08540, USA
[21]Department of Physics and Astronomy, College of Charleston, 66 George St., Charleston, SC 29424, USA
[22]Universitäts-Sternwarte München, Ludwig-Maximilians-Universität, Scheinerstr. 1, 81679 München, Germany
[23]Institute for Astronomy, University of Hawaii, 640 N. A'ohoku Place, Hilo, HI 96720, USA
[24]Department of Astronomy, Stockholm University, AlbaNova University Center, 106 91 Stockholm, Sweden
[25]Department of Astrophysical Science, Princeton University, Peyton Hall, Ivy Lane, Princeton, NJ 08544, USA
[26]Department of Astronomy, The University of Tokyo, 7-3-1 Hongo, Bunkyo-ku, Tokyo 113-0033, Japan
[27]Department of Astronomy, Kyoto University, Kitashirakawa-Oiwake-cho, Sakyo-ku, Kyoto, Kyoto 606-8502, Japan
[28]Hiroshima University, 1-3-2, Kagamiyama, Higashihiroshima, Hiroshima 739-8511, Japan
[29]Department of Astrophysics, CAB-CSIC/INTA, 28850 Torrejón de Ardoz, Madrid, Spain
[30]Jet Propulsion Laboratory, California Institute of Technology, 4800 Oak Grove Drive, Pasadena, CA 91109, USA
[31]Institute of Astronomy and Astrophysics, Academia Sinica, P.O. Box 23-141, Taipei 10617, Taiwan
[32]Astronomical Institute "Anton Pannekoek", University of Amsterdam, Postbus 94249, 1090 GE, Amsterdam, The Netherlands
[33]Kavli Institute for Physics and Mathematics of the Universe, The University of Tokyo, 5-1-5 Kashiwanoha, Kashiwa, Chiba 277-8568, Japan
[34]Department of Cosmosciences, Hokkaido University, Kita-ku, Sapporo, Hokkaido 060-0810, Japan
[35]Astronomical Institute, Tohoku University, Aoba-ku, Sendai, Miyagi 980-8578, Japan

*E-mail: momose@mx.ibaraki.ac.jp

[†]Visiting Astronomer at the Infrared Telescope Facility, which is operated by the University of Hawaii under Cooperative Agreement no. NNX-08AE38A with the National Aeronautics, and Space Administration, Science Mission Directorate, Planetary Astronomy Program.

Received 2014 October 20; Accepted 2015 May 19

Abstract

Coronagraphic imagery of the circumstellar disk around HD 169142 in *H*-band polarized intensity (PI) with Subaru/HiCIAO is presented. The emission scattered by dust particles at the disk surface in $0\farcs2 \leq r \leq 1\farcs2$, or $29 \leq r \leq 174$ au, is successfully detected. The azimuthally averaged radial profile of the PI shows a double power-law distribution, in which the PIs in $r = 29$–52 au and $r = 81.2$–145 au respectively show r^{-3} dependence. These two power-law regions are connected smoothly with a transition zone (TZ), exhibiting an apparent gap in $r = 40$–70 au. The PI in the inner power-law region shows a deep minimum whose location seems to coincide with the point source at $\lambda = 7$ mm. This can be regarded as another sign of a protoplanet in the TZ. The observed radial profile of the PI is reproduced by a minimally flaring disk with an irregular surface density distribution, an irregular temperature distribution, or with a combination of both. The depletion factor of surface density in the inner power-law region ($r < 50$ au) is derived to be ≥ 0.16 from a simple model calculation. The obtained PI image also shows small-scale asymmetries in the outer power-law region. Possible origins for these asymmetries include corrugation

of the scattering surface in the outer region, and a shadowing effect by a puffed-up structure in the inner power-law region.

Key words: infrared: planetary systems — planet–disk interactions — protoplanetary disks — stars: individual (HD 169142) — stars: pre-main-sequence

1 Introduction

Circumstellar disks around young stars are key targets in obtaining a better understanding of the formation of planetary systems (Dullemond & Monnier 2010; Williams & Cieza 2011). During the ongoing formation of a planet, the disk is expected to manifest observable signatures inside, such as an inner hole, a gap, spirals, and other asymmetric patterns. Recent progress in the technique of differential imaging at near-infrared wavelengths finally allows us to detect small-scale complex features in the disks (e.g., Hashimoto et al. 2011, 2012; Muto et al. 2012; Mayama et al. 2012; Grady et al. 2013; Follette et al. 2013). Most of these objects are classified as transitional disks, which show significant amounts of excess emission at wavelengths $\lambda \gtrsim 10\,\mu$m but little excess at shorter wavelengths, suggesting that dust in the inner regions has already been depleted (Strom et al. 1989; Skrutskie et al. 1990). Imaging surveys of transitional disks in dust thermal emission at submillimeter wavelengths clearly show that these disks do commonly possess inner holes (Brown et al. 2009; Andrews et al. 2011). Recently, even more complex distributions of dust emission on a smaller size scale are also revealed in some of these objects (e.g., Casassus et al. 2013; van der Marel et al. 2013; Fukagawa et al. 2013; Pèrez et al. 2014). These asymmetric features may be caused by trapping of dust particles in a vortex with a higher pressure, which can lead to efficient formation of rocky planetesimals (Regály et al. 2012; Birnstiel et al. 2013).

HD 169142 is a Herbig Ae star located at 145 pc from the Sun (Sylvester et al. 1996), and the spectral type of the star is classified as A5Ve (Dunkin et al. 1997) or A8Ve (Grady et al. 2007). The age is estimated to be 6^{+6}_{-3} Myr from the ages of two pre-main sequence stars located $9''.3$ to the southwest and are comoving with HD 169142 (Grady et al. 2007). The luminosity of $9.4\,L_\odot$ is used by Meeus et al. (2012), while Manoj et al. (2006) derive $18.2\,L_\odot$ with $A_V = 0.61$ (see also Osorio et al. 2014). Judging from the observed $B - V$ color 0.26, however, $A_V \approx 0.5$ was the case only if the stellar spectral type was as early as B8. Wagner et al. (2015), in fact, find a good fit to the spectral energy distribution (SED), including the UV data, for the spectral type of A7, the effective temperature of 7500 K, and the stellar radius of $1.7\,R_\odot$ (resulting in $8.7\,L_\odot$) with no foreground extinction. It exhibits significant amounts of excess emission at longer wavelengths and its SED is categorized as group I (Meeus et al. 2001). Interferometric observations of CO lines at millimeter wavelengths revealed a gas disk with a radius of $2''$ (≈ 300 au), and their velocity fields are consistent with Keplerian rotation of a central stellar mass of $2\,M_\odot$ and its inclination angle 13° (Raman et al. 2006; Panić et al. 2008). Scattered light at near-infrared wavelengths from the disk outer regions was also imaged with coronagraph instruments (Grady et al. 2007; Fukagawa et al. 2010).

More recently, the inner regions of the disk have been investigated by both the analysis on its broadband SED and higher-resolution imagery. It was claimed that there should be an inner cavity around HD 169142 to reproduce its SED, but its size was rather unclear solely from the SED analysis (Grady et al. 2007; Meeus et al. 2010). Honda et al. (2012) carried out imaging of the disk at $\lambda = 18.8$ and $24.5\,\mu$m with Subaru/COMICS, and by combining these data with a two-dimensional radiative transfer model for the SED, they determined the location of the inner wall of the disk to be 23 ± 3 au from the star. They also speculate that the SED classification as group I may correspond to the object accompanied by a (pre)transitional disk in which there is a large inner hole, and the inner wall of the disk just outside the hole can account for its characteristic large excess emission at mid-infrared wavelengths (see also Maaskant et al. 2013). Quanz et al. 2013 made observations of polarization intensity (PI) in H-band ($\lambda = 1.65\,\mu$m) with VLT/NACO. They found a bright ring of $r \approx 25$ au that agreed with the estimate from the SED analyses (Meeus et al. 2010; Honda et al. 2012), as well as an annular gap extending over $r = 40$–70 au. Furthermore, imaging of dust thermal radiation at $\lambda = 7$ mm with J-VLA also shows asymmetric ring-like emission at $r \approx 25$ au and a hint of an outer gap at 40–70 au, suggesting that the structure seen in the scattered light at near-infrared wavelengths may correspond to real variations in surface density (Osorio et al. 2014). Although these are not decisive evidence for the existence of protoplanet(s), such a gap is reminiscent of that induced by a planet in the disk (e.g., Lin & Papaloizou 1993; Crida et al. 2006). The latest observations in L'-band ($\lambda = 3.8\,\mu$m) with an annular groove phase mask (AGPM) vector-vortex coronagraph mounted on VLT detect a companion candidate inside the inner cavity ($0''.156$, or 23 au from the star), which might be the direct detection of radiation from a protoplanet (Biller et al. 2014; Reggiani et al. 2014).

This paper presents coronagraphic imagery of the circumstellar disk around HD 169142 in H-band polarized intensity (PI) with Subaru/HiCIAO. We describe the details of the observations in section 2 and present the results in section 3. Based on our results, as well as those obtained by previous studies, we discuss in section 4 the disk structure and estimate the nature of a possible protoplanet embedded in the disk from our results.

2 Observations and data reduction

2.1 Observations with Subaru/HiCIAO

HD 169142 was observed in H-band ($\lambda = 1.65\,\mu$m) with the high-contrast imaging instrument HiCIAO (Tamura et al. 2006; Hodapp et al. 2008; Suzuki et al. 2010) on the Subaru Telescope on 2011 May 23 UT as part of Strategic Explorations of Exoplanets and Disks with Subaru (SEEDS: Tamura 2009). The data were taken in a combined angular differential imaging (ADI) and polarization differential imaging (PDI) modes with a field of view of $10'' \times 20''$ and a pixel scale of 9.5 milli-arcsecond (mas). A circular occulting mask $0''.15$ in radius was used to suppress the bright stellar halo. The half-wave plates were periodically placed at four angular positions from 0°, 45°, $22^\circ.5$, and $67^\circ.5$ in sequence with 30 s exposure per wave plate position. The total integration time of the PI image was 1080 s after removing low-quality frames with large FWHMs by careful inspection of the stellar point-spread function (PSF). Data of the reference star HD 166903, whose apparent magnitude in H-band is 5.837 mag (SIMBAD), were also taken in the same observing mode. It was proved that a stable stellar PSF of FWHM $= 0''.06$ was achieved for the selected images of HD 169142 by the adaptive optics system AO188 (Hayano et al. 2004; Minowa et al. 2010).

2.2 Data reduction

The data reduction procedure was the same as that described by Muto et al. (2012). The raw images were first corrected with IRAF[1] for bias and dark current, and flat-fielding was performed after sky subtraction. We applied a distortion correction using globular cluster M5 data taken within a few days, with IRAF packages GEOMAP and GEOTRAN. The images of Stokes (Q, U) parameters were obtained in the standard way (e.g., Hinkley et al. 2009); by subtracting two images of extraordinary and ordinary rays at each wave plate position, we got $+Q$, $-Q$, $+U$, and $-U$ images, from which $2Q$ and $2U$ images were made by another subtraction to eliminate any remaining aberration. Instrumental polarization of HiCIAO was corrected as described by Joos et al. (2008).

We needed to fix the rotation center of the field of view by ADI in de-rotating the Q and U images. It was determined in the following way. A pair of I-frames that were taken more than 300 s apart from each other was picked up, and then the rotation center and rotation angle for the pair were derived so that the two background stars in the differential image between the two frames were best cancelled out. These values were collected for all the possible I-frame pairs, and their average position was regarded as the image rotation center in our observations. There were four background stars in each frame, but two of them were not used because their positions were so far from the image center that the distortion correction might be imperfect. It proved that the mask center position was shifted from the image rotation center by $(+1, -4)$ pixels in (α, δ), or $(+9.5\,\mathrm{mas}, -38\,\mathrm{mas})$. On the other hand, the stellar position was estimated from elliptical fitting to an iso-intensity contour of the periphery of the stellar halo in I-frames. The stellar location measured in this way was proved to be the same as the image rotation center. The Q and U images were de-rotated at this center, then averaged to increase the signal-to-noise. PI was then obtained by $\mathrm{PI} = \sqrt{Q^2 + U^2}$. The misalignment between the mask center and image rotation center made the resultant working angle $\geq 0''.2$ from the star, which is slightly larger than the actual mask size.

3 Results

Figure 1 shows the PI image of HD 169142 in H-band with Subaru/HiCIAO. The infrared emission scattered by dust particles at the disk surface is successfully detected. The typical PI value is $\approx 0.21\,\mathrm{mJy\,arcsec^{-2}}$ in $r > 3''$, well beyond the disk outer radius derived from the CO observations (Raman et al. 2006; Panić et al. 2008), and the scattered light of the disk should be negligible. This corresponds to a $1\,\sigma$ level of $0.168\,\mathrm{mJy\,arcsec^{-2}}$ if the values in the region of no polarized emission follow the Rayleigh distribution. In the following quantitative analyses, we will regard the PI emission of $> 0.5\,\mathrm{mJy\,arcsec^{-2}}$ ($= 3\,\sigma$ level) as a significant detection. The region of significant detection extends up to $r \approx 1''.2$ from the star, as presented in figure 1c. Figure 1d shows the polarization vectors derived from Stokes Q and U images. The polarization vectors align azimuthally, as expected for the stellar light scattered at the disk surface.

The overall structure of the PI is roughly consistent with that obtained by Quanz et al. (2013) with VLT/NACO. The obtained PI in figure 1a shows an axisymmetric distribution as follows: (i) the bright ring just outside the mask, (ii) a ring-like feature at $r \approx 0''.55$, or 80 au from the star,

[1] IRAF is distributed by the National Optical Astronomy Observatory, which is operated by the Association of Universities for Research in Astronomy, Inc., under cooperative agreement with the National Science Foundation.

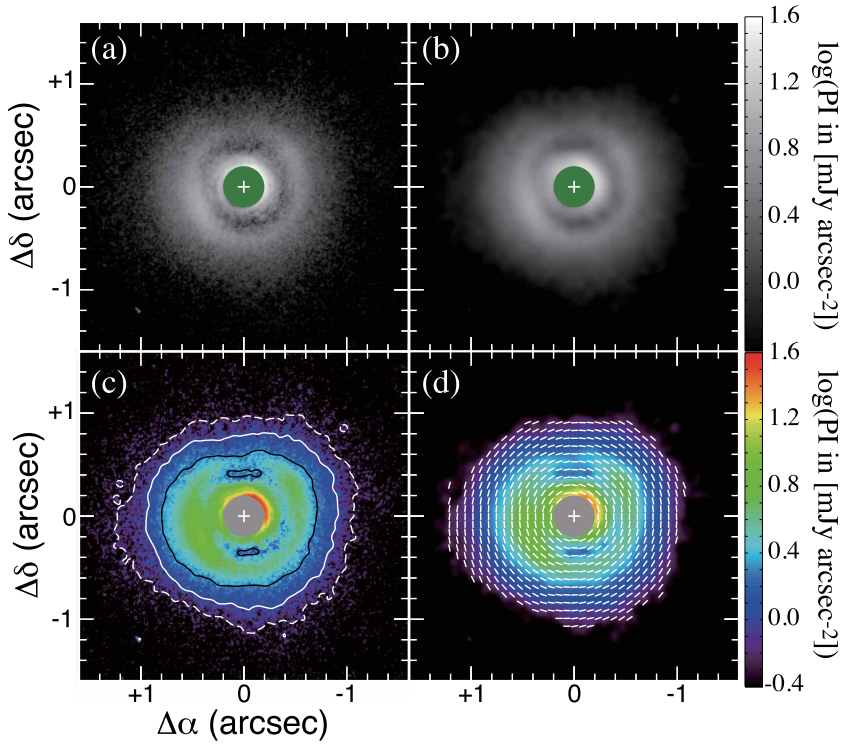

Fig. 1. (a) Coronagraphic image of the polarization intensity (PI) in *H*-band around HD 169142 obtained with Subaru/HiCIAO. The white cross is the stellar position, and the green circle shows the regions affected by the mask, or $<0''.2$ from the stellar position. (b) PI image convolved with a Gaussian function whose FWHM is 8 pixels, or $0''.072$. (c) Same as (a), but in different color code so that asymmetric features are easily identified. The white broken lines are the contours of 0.5 mJy arcsec^{-2}, corresponding to the 3σ level (see the text). The solid lines in white and black are the contours at 1.0 mJy arcsec^{-2}(6σ) and 1.5 mJy arcsec^{-2}(9σ) levels, respectively. The contours are generated in the convolved image shown in (b). (d) Same as (b), but in the color code as (c), superposed on the polarization vectors where the PI is detected above the 3σ level. The polarization vectors are drawn every 8 pixels.

(iii) the apparent gap between these two ring-like features, and (iv) the outermost part in which the PI gets gradually weaker at a larger radius. Note that the PI is significantly detected in the gap (iii) with at least 9σ. These axisymmetric features can be seen even more clearly in the smoothed image convolved with a Gaussian function (figure 1b). The inner bright rim at $r \approx 0''.2$ (Quanz et al. 2013) is only marginally confirmed because the inner working angle of our observation is slightly larger than that of VLT/NACO.

To describe the axisymmetric distribution of the PI more quantitatively, its azimuthally averaged radial profile is presented in figure 2; the projection on the sky is corrected under the assumptions that the disk inclination angle is 13° and the disk major axis is in PA = 5° (Raman et al. 2006). The radial profile shows a double power-law distribution, as expressed by

$$\mathrm{PI}(r) = 20.7 \left(\frac{r}{29\,\mathrm{au}}\right)^{-3.0025} [\mathrm{mJy\,arcsec^{-2}}] \quad (1)$$

in $29 \leq r \leq 52.2$ au and

$$\mathrm{PI}(r) = 96.2 \left(\frac{r}{29\,\mathrm{au}}\right)^{-3.0037} [\mathrm{mJy\,arcsec^{-2}}] \quad (2)$$

in $81.2 \leq r \leq 145$ au, respectively. The formal statistical uncertainties in the amplitudes are estimated to be $\lesssim 10\%$ for equation (1) and $\lesssim 1.3\%$ for equation (2), and those in the exponents are $\lesssim 0.1$ dex. These two power-law regions are connected smoothly with a "transition zone" (hereinafter denoted by TZ) extending over $r = 52$–81 au. The apparent gap located in $r \approx 40$–70 au (Quanz et al. 2013; Osorio et al. 2014) consists of the outer part of the inner power-law region and TZ, while the bright ring at $r \approx 0''.55$ in the PI image (figures 1a and 1b) corresponds to the inner boundary of the outer power-law region. It should be noted, however, that the surface brightness normalized by the r^{-3} power law (figure 2c) changes smoothly even in TZ. There is no break of the exponent at $r = 120$ au claimed by Quanz et al. (2013), though a subtle irregularity may be identified at $r \approx 100$ au. The r^{-3} dependence was also found in the total intensity distribution at 1.1 μm in $r \geq 80$ au with the coronagraphic imaging by HST/NICMOS (Grady et al. 2007). It is also consistent with the radial exponent in $116 \leq r \leq 174$ au derived from the imagery in *H*-band with Subaru/CIAO (-3.0 ± 0.2: Fukagawa et al. 2010), suggesting that there is no significant radial variation of polarization degree in these regions. The

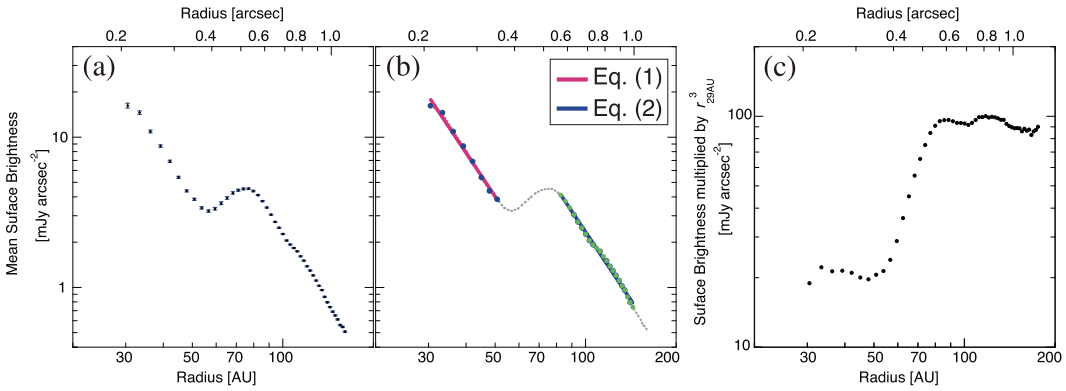

Fig. 2. (a) Averaged radial profile of the PI above the 3σ level (0.5 mJy arcsec^{-2}) between (29–159.5) au, or 0.″2–1.″1. Averages and their uncertainties are calculated in annuli of 2.9 au (=0.″02) width after the correction for the projection on the sky under the assumptions that the position angle of the disk major axis is 5° and the disk inclination angle is 13°. (b) Results of the fitting by a power-law function to the data points in 29–52.2 au (red) and in 81.2–145 au (blue); the data points used in the power-law fitting are shown in blue and green dots. The radial profile in (a) is shown by a gray dotted line. (c) Same as (a), but normalized by $r^{-3}_{29\,au}$, where $r_{29\,au}$ is a dimensionless radius normalized by 29 au.

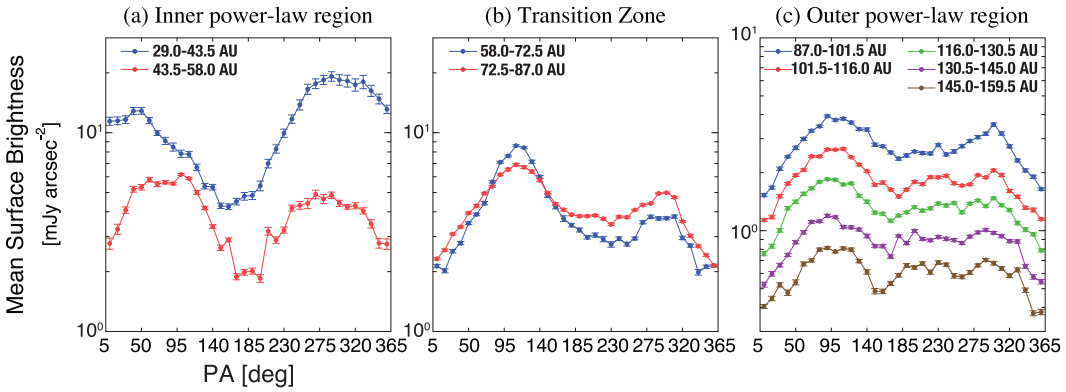

Fig. 3. Azimuthal distributions of the PI in annuli of 14.5 au (or 0.″1) width. The projection on the sky is corrected under the same assumptions as those described in the caption of figure 2. The abscissa starts from PA = 5°, corresponding to the major axis of the disk. (a) The inner power-law region, (b) the transition zone (TZ), and (c) the outer power-law region.

polarization degree estimated from the comparisons between the PI in figure 1 and the total intensity by Fukagawa et al. (2010) is ∼65% in 0.″8 ≤ r ≤ 1.″1. This is higher than that obtained in the H-band PI imaging of the disk around HD 142527 (Avenhaus et al. 2014). It may be due to the nearly pole-on configuration of HD 169142; the scattering angle at the disk surface should be ∼90°, at which the polarization degree is ∼100% when the particle size is much smaller than the wavelength (Bohren & Huffman 1983). Alternatively, it might be due to an underestimate of total scattered-light intensity caused by a systematic error during PSF subtraction by Fukagawa et al. (2010). The rest of the discussion in this paper will not be affected by any uncertainties in polarization degree.

The PI image also manifests asymmetric features, which are easily identified in figure 1c. To see the asymmetry at each radius, azimuthal distributions of the PI in annuli of 14.5 au width are presented in figure 3. In the innermost annulus (29.0 ≤ r ≤ 43.5 au), the northwestern part (260° ≲ PA ≲ 340°) is quite bright. This may be a part of the inner rim distorted outwardly (Quanz et al. 2013). Except for this innermost annulus, all the azimuthal distributions have their maxima at PA ≈ 110°, close to the disk minor axis east of the star. This may imply that the eastern part is the near side of the disk and is brighter than the western side because of the forward scattering. In the outer power-law region, the PI near the major axis (PA = 5° and 185°) is dimmer than those near the minor axis (PA = 95° and 275°), which is also found in figure 4. As a consequence, the lowest contour of the significant detection in figure 1c is slightly elongated in the east–west direction. This situation is completely different from other disks in scattered light detected with Subaru/HiCIAO, in which the PI is brighter along the major axis (e.g., Muto et al. 2012; Kusakabe et al. 2012). The variation in each annulus is systematically larger at inner radii; in the inner power-law region and TZ, the amount of variation in each annulus is

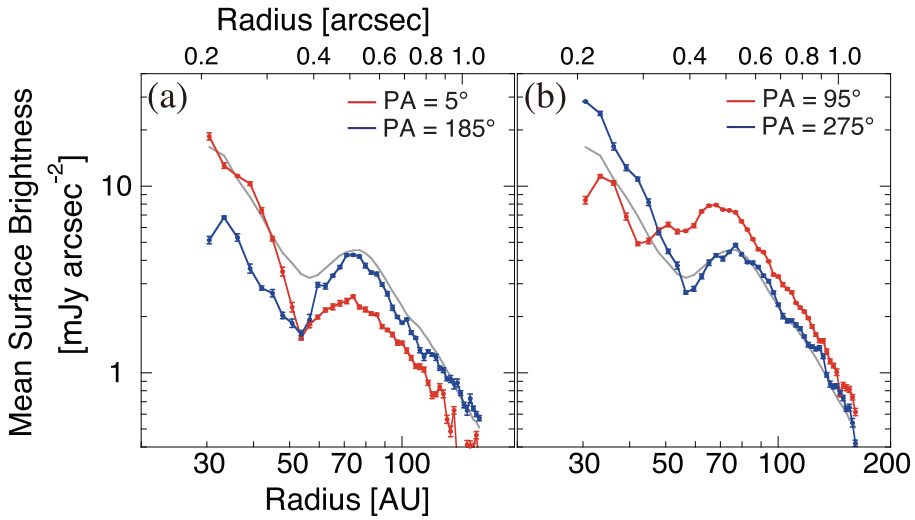

Fig. 4. (a) Radial profiles of the PI along the major axis of the disk: PA $= 5° \pm 5°$ in red and PA $= 185° \pm 5°$ in blue. (b) Radial profiles of the PI along the minor axis of the disk: PA $= 95° \pm 5°$ in red and PA $= 275° \pm 5°$ in blue. The radial profile averaged over the whole direction (shown in figure 2) is indicated by a gray line in each panel.

4.5–3.3, but those of annuli in the outer power-law region is less than 2.6.

To clearly identify these asymmetric features in the image, figure 5 shows the map of "modulated PI," the PI normalized by $r_{29\,\mathrm{au}}^{-3}$, where $r_{29\,\mathrm{au}}$ is a dimensionless radius normalized by 29 au. Two distinct power-law regions, divided by TZ where the contours are crowded, can be recognized. As indicated by the normalized intensities in equations (1) and (2), the average of modulated PI in the inner and outer power-law regions should be $\approx 21\,\mathrm{mJy\,arcsec^{-2}}$ and $\approx 96\,\mathrm{mJy\,arcsec^{-2}}$ (see also figure 2c). However, the variation of modulated PI in the inner power-law region is quite remarkable, ranging from 10 to 40 $\mathrm{mJy\,arcsec^{-2}}$. This is significant compared to the uncertainties estimated from the original PI map ($3\sigma = 0.5\,\mathrm{mJy\,arcsec^{-2}}$ in the original PI corresponds to $\approx 7.8\,\mathrm{mJy\,arcsec^{-2}}$ in modulated PI at $r = 0\farcs5$). These asymmetries in the inner power-law region could be related to the perturbation by a protoplanet inside the inner ring (Biller et al. 2014; Reggiani et al. 2014). Another intriguing feature is that the location of deep minimum in the southern part of the inner power-law region seems to coincide with the point source at $\lambda = 7$ mm revealed with J-VLA, as indicated in figure 5b′. Osorio et al. (2014) speculate that it might originate from the circumplanetary disk associated with a protoplanet inside the gap, which is also identified in thermal emission at $\lambda = 7$ mm. The relation between these features and the possible protoplanet in TZ will be discussed further in subsection 4.2.

To quantitatively describe the shape of the TZ, an elliptical fit is made to the contours of 40 and 80 $\mathrm{mJy\,arcsec^{-2}}$ in modulated PI; the results are presented in table 1. These ellipses delineate well the edges of the TZ in the original PI map, as shown in figure 5c. The major axes of the ellipses nearly agree with the disk major axis (PA $=5°$), and the ratio of minor to major axes is ≈ 0.8, which is smaller than the case when an infinitesimally thin disk is observed from the inclination angle of 13°. These are consequences of the asymmetry that the PI near the minor axis of the disk is brighter than near the major axis (see also figures 1 and 3). The centers of the ellipses agree with each other but are shifted $\approx 0\farcs047$ northwest from the stellar position, caused by the east–west asymmetry along the minor axis in the outer power-law region.

4 Discussion

In the following subsections, we discuss observed features of the disk from larger to smaller size scales in order; a double power-law distribution seen in the radial profile of PI is discussed in subsection 4.1, the possible presence of a protoplanet in the TZ is examined in subsection 4.2, and asymmetries on smaller azimuthal scales are mentioned in subsection 4.3. It is impossible to derive the realistic internal structure of the disk solely from the PI image in *H*-band. The existence of a gap between 40–70 au in radius has been inferred by recent J-VLA observations (Osorio et al. 2014), which provided us with important information about the disk internal structure. The emission at $\lambda = 7$ mm, however, is mainly arising from dust grains with a larger size, and we cannot make any combined analysis of these two images unless we make further assumptions on dust size distribution as well as on the size dependence of the dust spatial distribution. We therefore decide in this paper to interpret

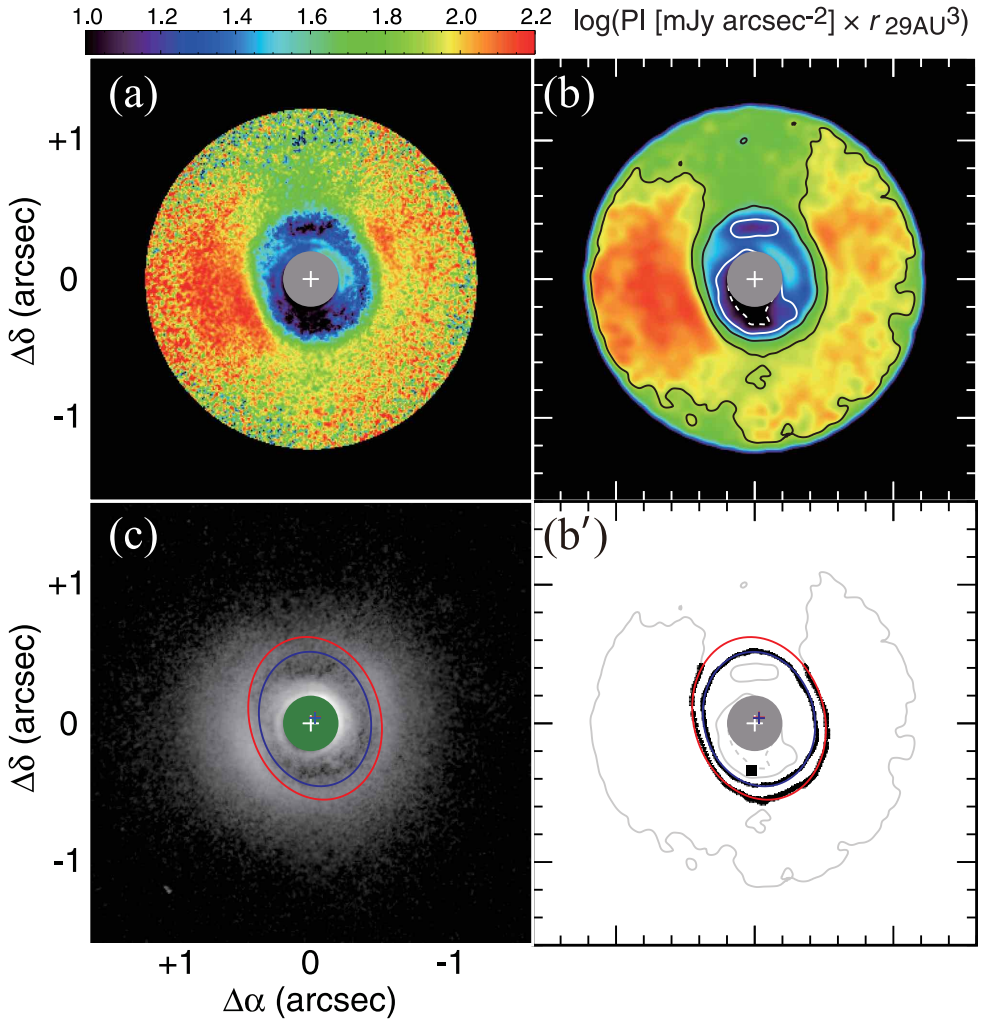

Fig. 5. (a) The image in $r \leq 1\farcs1$ of "modulated PI," which is the PI multiplied by the dimensionless parameter $r^3_{29\,\mathrm{au}}$, where $r_{29\,\mathrm{au}}$ is the radius normalized by 29 au. The white cross and gray circle show the stellar position and the regions affected by the mask, respectively. (b) The image of PI multiplied by $r^3_{29\,\mathrm{au}}$ after the convolution with a Gaussian function whose FWHM is 8 pixels, $0\farcs072$. The contours of 10 and 20 mJy arcsec^{-2} are shown in white broken lines and white solid lines, and the levels of 40 and 80 mJy arcsec^{-2} are shown in black solid lines. (b′) The results of elliptical fits to the contours of 40 mJy arcsec^{-2} (blue) and 80 mJy arcsec^{-2} except $-45^\circ \leq \mathrm{PA} \leq 40^\circ$ (red). The centers of the ellipses are indicated by blue and red crosses, though the latter is hard to see because they almost perfectly agree with each other (see table 1). The pixels used in the fit are shown in black crosses. (c) The PI image, as in figure 1a, superposed on the results of the elliptical fits.

Table 1. Results of elliptical fit in figure 5.

Contour (mJy arcsec^{-2})	Major axis ($''$)	Minor axis ($''$)	$\Delta\alpha$* ($''$)	$\Delta\delta$* ($''$)	PA ($^\circ$)
40	0.490	0.399	−0.030	+0.033	14.2
80†	0.596	0.471	−0.031	+0.038	16.8

*Offset from the stellar position.
†Only in $40^\circ \leq \mathrm{PA} \leq 315^\circ$.

the *H*-band image with a simple disk model whose surface density and temperature distributions (Σ and T) have a power law and the vertical density distribution is determined by hydrostatic equilibrium (appendix 1). Although our disk model is simple, it is useful for analyzing the location of the scattering surface, the key to interpreting the PI image in *H*-band. As explained in appendix 1, Σ essentially parameterizes the volume emissivity of disk material while T parameterizes the vertical distribution of disk material. Further analysis on disk structure based on a more realistic model should be made after sensitive observations of dust emission at millimeter/submillimeter wavelengths are made with ALMA in angular resolutions similar to this study.

4.1 Disk structure that reproduces a double power-law distribution of PI's radial profile

An azimuthally averaged radial profile of the PI in *H*-band shows a double power-law distribution, and the exponents

in both power-law regions are -3 (figure 2). The same exponent was also obtained in total intensity at $\lambda = 1.1\,\mu$m and $1.6\,\mu$m (Grady et al. 2007; Fukagawa et al. 2010). A geometrically thin but optically thick disk model (e.g., Whitney & Hartmann 1992) has been frequently referred to as an analytical explanation for an r^{-3} distribution (e.g., Wisniewski et al. 2008), but this is not the only explanation for such radial dependence. Grady et al. (2007) showed that a model disk with a pressure scale height of $H(r) \propto r^{+1.065}$ can reproduce the r^{-3} distribution of surface brightness at $\lambda = 1.1\,\mu$m by using three-dimensional Monte Carlo radiative transfer code (Whitney et al. 2003a, 2003b, 2004). It was also reported that such a minimally flaring disk (i.e., the aspect ratio $H(r)/r$ is independent of r)[2] with surface density $\Sigma(r) \propto r^{-1}$ can explain not only the radial distribution of scattered light but also the visibility amplitudes at $\lambda = 1.3$ mm (Panić et al. 2008) and the SED at longer wavelengths (Meeus et al. 2010; Honda et al. 2012).

In fact, r^{-3} dependence of the disk emission may be a natural consequence of the combination of $\Sigma(r) \propto r^{-1}$ and $H(r) \propto r$. The scattering surface of a disk corresponds to the positions where the optical depth measured radially from the star is ≈ 1, while the energy flux of incident stellar radiation can be scaled by β/r^2, where β is the grazing angle at the scattering surface. It can be derived analytically that β is nearly proportional to r^{-1} for an axisymmetric disk when $\Sigma(r) \propto r^{-1}$ and $H(r) \propto r$, accounting for the r^{-3} brightness distribution (appendix 2). This means that the double power-law distribution (figures 2 and 5) is realized if β is proportional to r^{-1} in each power-law region but its value in the inner region is significantly smaller than that in the outer region. It can happen when the height of the scattering surface normalized by the radius in the inner region is smaller than that in the outer region.

A simple example for such a case is that the surface density distribution of dust particles responsible for the scattering in near infrared, $\Sigma_{\rm d}(r)$, is not a smooth power law but has an irregularity. To roughly estimate the amount of irregularity in $\Sigma_{\rm d}(r)$, we compare the observed PI distribution with a simple model calculation whose details are described in appendix 1. As discussed later, Wagner et al. (2015) also carry out more elaborate modeling, but our simple model is helpful for analyzing the location of the scattering surface. $\Sigma_{\rm d}(r)$ of the model disk is expressed by

$$\Sigma_{\rm d}(r) = f_{\rm d}(r)\Sigma_{\rm out}\left(\frac{r}{r_{\rm out}}\right)^{-1}, \tag{3}$$

where

$$f_{\rm d}(r) = \begin{cases} f_{\rm in}^{\Sigma} & (r \le r_{\rm in}), \\ f_{\rm TZ}(r) & (r_{\rm in} < r < r_{\rm out}), \\ 1 & (r_{\rm out} \le r). \end{cases} \tag{4}$$

Here, $f_{\rm in}^{\Sigma}$ ($0 \le f_{\rm in}^{\Sigma} \le 1$) is a depletion factor for the surface density in the inner power-law region, ($r_{\rm in}$, $r_{\rm out}$) are the inner and outer boundaries of the TZ and are set to be (50 au, 85 au) based on the fitting results expressed by equations (1) and (2), and $\Sigma_{\rm out}$ is the surface density at $r_{\rm out}$. The surface brightness distribution normalized by $r_{29\,{\rm au}}^{-3}$ does not show any gap but a smooth rise in the TZ (figure 2c), and this cannot be reproduced by a model disk with a dust-devoid zone. To smoothly connect $\Sigma_{\rm d}(r)$ in the TZ as well as at its boundaries, $f_{\rm TZ}(r)$ in equation (4) is defined as a third-order polynomial that simultaneously satisfies the following equations:

$$\begin{aligned} & f_{\rm TZ}(r_{\rm in}) = f_{\rm in}^{\Sigma}, \\ & f_{\rm TZ}(r_{\rm out}) = 1, \\ & \frac{d}{dr} f_{\rm TZ}(r_{\rm in}) = 0, \\ & \frac{d}{dr} f_{\rm TZ}(r_{\rm out}) = 0. \end{aligned} \tag{5}$$

We also assume that $T(r) \propto r^{-1}$ to set the pressure scale height $H(r) \propto r^{+1}$ (appendix 1; see also Chiang & Goldreich 1997), and that the disk is isothermal and in hydrostatic equilibrium along the vertical axis. The multiple scattering effect is ignored in the radiative transfer calculation for simplicity. Figure 6a shows the results of the model calculations. The r^{-3} dependence is reproduced in both $r < 50$ au and $r > 85$ au regions, but a larger proportionality constant for $\Sigma_{\rm d}(r)$ in the outer region makes the location of the scattering surface higher from the midplane, resulting in larger β and brighter PI. Judging from figure 6a, $f_{\rm in}^{\Sigma} = 10^{-0.8}$ (≈ 0.16) seems to give the best fit to the observed contrast between the two power-law regions. $\Sigma_{\rm d}(r)$ given by equations (4) and (5) with $f_{\rm in}^{\Sigma} = 10^{-0.8}$ is presented in figure 6b. There seems to be a gap in $r \approx 40$–70 au with the minimum at $r \approx 55$ au, as suggested by previous studies (Quanz et al. 2013; Osorio et al. 2014), though the profile shape is qualitatively different from a planetary gap having a characteristic size scale of the width (e.g., Zhu et al. 2011). Despite many simplifications, the estimate by our model is roughly consistent with the results obtained by Wagner et al. (2015): $f_{\rm in}^{\Sigma} \approx 0.3$ in the model disk with $H(r) \propto r^{+1.3}$.

However, the above depletion factor for the inner power-law region should be regarded as the lower limit, i.e., $f_{\rm in}^{\Sigma}$

[2] Such a case has been referred to as a "flat disk" in some studies (e.g., Chiang & Goldreich 1997).

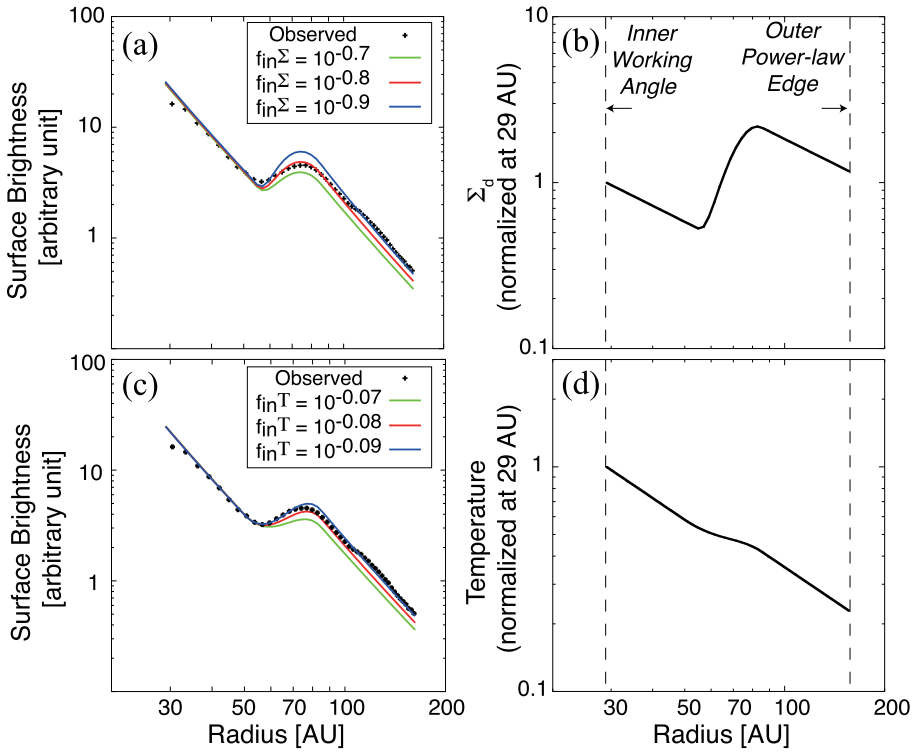

Fig. 6. Model calculations that reproduce the averaged radial profile (black crosses) shown in figure 2. The surface density distribution $\Sigma_d(r)$ and scale height of the model disk $H(r)$ are proportional to r^{-1} and r^{+1}, respectively, in $r = 29$–50 au and $r = 85$–160 au. Σ_{out} and T_{out} at $r_{out} = 85$ au are set to be 9 g m^{-2} and 53 K, but these choices are not important in the estimate for f_{in}^{Σ} or f_{in}^{T} (see appendix 1 for more detail). (a) The proportionality constant for $\Sigma_d(r)$ is changed, as described in equation (3). The lines in green, red, and blue represent the results of model calculations for $f_{in}^{\Sigma} = 10^{-0.7}$, $10^{-0.8}$, and $10^{-0.9}$, respectively. (b) $\Sigma_d(r)$ given by equations (3) and (4) when $f_{in}^{\Sigma} = 10^{-0.8}$, normalized by the surface density at $r = 29$ au. (c) The proportionality constant for $T(r)$ is changed, as described in the equations (3) and (4), but replace each Σ with T. The lines in green, red, and blue represent the results of model calculations for $f_{in}^{T} = 10^{-0.07}$, $10^{-0.08}$, and $10^{-0.09}$, respectively. (d) $T(r)$ when $f_{in}^{T} = 10^{-0.09}$, normalized by the temperature at $r = 29$ au.

should be ≥ 0.16. This is because irregularity in radial temperature distribution can also produce the observed double power-law distribution of PI, even without any irregularity in $\Sigma_d(r)$ like equations (4) and (5); if the temperature proportionality constant is slightly higher in the outer power-law region, it makes the disk aspect ratio $h \equiv H(r)/r$ and β in this region also larger. Our simple model similar to the above one but with each Σ in equations (3)–(5) replaced by T reproduces the observed PI profile when $f_{in}^{T} = 10^{-0.09}$–$10^{-0.08}$ (≈ 0.81–0.83), corresponding to a change in h by a factor of 0.90–0.91 (see appendix 2 for further details). This is again consistent with the model calculations by Wagner et al. (2015) who show that a scale height change of 0.86 in the inner power-law region can reproduce the observed PI image in H-band.[3] There is a degeneracy between f_{in}^{Σ} and f_{in}^{T} in models that reproduce the PI image, as pointed out by Wagner et al. (2015). The radial intensity profile at $\lambda = 7$ mm is reproduced by a disk model in which there is no significant discrepancy in dust surface density between $r = 30$–40 au and $r > 70$ au (Osorio et al. 2014), which might favor a larger f_{in}^{Σ}. Further imaging studies, especially at millimeter and submillimeter wavelengths, will still be necessary to clearly disentangle this degeneracy.

[3] Another important conclusion obtained by Wagner et al. (2015) is that the apparent gap in PI at $40 \leq r \leq 70$ au cannot be reproduced solely by changing the scale height of the inner wall at $r \approx 25$ au.

4.2 Possible presence of a protoplanet in the transition zone

The change of β described in subsection 4.1 may be caused by interaction between a protoplanet and the disk. Jang-Condell and Turner (2012), for example, examine the detail disk structure under the influence of a forming planet and simulate the images at various wavelengths. They obtain a radial distribution of near-infrared scattered light qualitatively similar to our observed results. Such a double power-law distribution is produced because the protoplanet creates a gap in the disk initially having a flared surface, resulting in larger β on the scattering surface at outer radii. Furthermore, cooling within the trough and heating on the far wall alter the vertical density profile of the gap region in

such a way that the difference in β is enhanced even more. In their simulations, the brightness contrast between the inside and outside of the gap is much larger (a factor of $\sim 10^2$ in normalized intensity even in the lowest contrast case) than our observational results, suggesting that the mass of a protoplanet in the TZ is so low that it only creates a shallower gap than the cases of Jang-Condell and Turner (2012); they deal with the cases of planet masses much higher than the critical mass for a gap opening proposed by Crida, Morbidelli, and Masset (2006).

More recently, Osorio et al. (2014) obtain the image of dust thermal emission at $\lambda = 7$ mm with J-VLA. They detect a ring-like emission delineating the bright rim at $r \approx 0''.2$ revealed by the *H*-band PI image with VLT/NACO (Quanz et al. 2013). The azimuthally averaged radial intensity profile at $\lambda = 7$ mm gives a hint that there is an annular gap in $r = 40$–70 au from the star that coincides with the gap seen in the *H*-band PI images. Based on these results, Osorio et al. 2014 carry out disk modeling in which there is a dust-devoid zone in $r = 40$–70 au, and they successfully reproduce the radial intensity profile at $\lambda = 7$ mm. Meanwhile, the scattered light in *H*-band is detected even in the gap (figures 1 and 2), indicating that there is some amount of small dust particles in this zone. These two observational results are compatible if larger dust particles responsible for thermal emission at millimeter wavelengths are more deficient in the gap region. In fact, previous studies on the motion of dust particles in a gas disk under the influence of a planet show that particles with a modest size (i.e., millimeter and centimeter in size) tend to be removed more quickly compared to the smaller particles during the formation of a planetary gap near the orbit (Paardekooper & Mellema 2006; Lyra et al. 2009; Muto & Inutsuka 2009).

The J-VLA image at $\lambda = 7$ mm also reveals a faint point source, $0''.34$ at PA $= 175°$ from the central star. Osorio et al. (2014) discuss the possibility that it arises from thermal dust radiation of a circumplanetary disk associated with the protoplanet sculpting the gap. In the image of modulated PI in *H*-band, on the other hand, there is a deep minimum in the inner power-law region whose location seems to coincide with the point source at $\lambda = 7$ mm (figure 5b′; see also figure 3a). This can be regarded as another sign of the protoplanet, because the disk scattering surface can be lowered by the protoplanet's gravity, making an observable dip in near-infrared scattered light (Jang-Condell 2009).

To constrain the planet mass, it is important to precisely measure the depth and width of the gap and to compare them with the latest theoretical model of gap structure (e.g., Duffell & MacFadyen 2013; Kanagawa et al. 2015a). An analytic formula combining the gap depth, planet mass, disk aspect ratio, and viscosity is presented in a separate paper (Kanagawa et al. 2015b), in which the formula is applied to the gap depth inferred from J-VLA observations of HD 169142 by Osorio et al. (2014). Imaging studies of both dust and gas emission with ALMA will also be important in the near future.

4.3 Asymmetric features in the outer power-law regions

As mentioned above, there are remarkable asymmetries both in the inner and outer power-law regions. Significant asymmetric variation in the inner power-law region (figures 3 and 5) could be due to perturbation by a protoplanet inside the inner ring (Biller et al. 2014; Reggiani et al. 2014). The deep minimum of PI in *H*-band in the inner power-law region coincides with the point source at $\lambda = 7$ mm, which can be regarded as another sign of a protoplanet surrounding the circumplanetary disk. The azimuthal distributions at the outer radii tend to have maxima at PA $\approx 110°$, along the disk minor axis east of the star.

Besides these features, there are small-scale asymmetries in the outer power-law region (see figure 5), though the amount of variation is smaller than in the inner power-law region. There are two possibilities for the origin of these small-scale asymmetries. One is corrugation of the scattering surface in the outer region, causing a small-scale variation in grazing angle (β). Such corrugation may be due to local fluctuations in disk surface density that may affect the self-gravity of the disk and hydrostatic balance in its vertical direction (Muto 2011). The other possibility is a shadowing effect of the structure in the inner power-law regions. As described in subsection 4.1, the radial intensity profile of near-infrared scattered light as well as the broadband SED are basically explained by a minimally flaring disk (see also Grady et al. 2007; Panić et al. 2008; Meeus et al. 2010; Honda et al. 2012; Wagner et al. 2015). If a part of the inner structure of such a disk is slightly puffed up, it may cast a shadow on the outer region observable in the near-infrared image. Radial profiles along the major and minor axes (figure 4) actually show that the surface brightness in the inner ($r \leq 50$ au) and the outer ($r \geq 80$ au) regions are anti-correlated with each other. A similar tendency is also seen in all the pairs of radial profile 180° apart in PA from each other (figure 7). These two possibilities may be disentangled by searching for time variation on a shorter timescale in scattered-light images; if the asymmetries in the outer disk are caused by shadowing of the inner region, asymmetric patterns in the outer disk may vary on a short timescale that synchronizes with the change of disk structure in the inner power-law region (see also Wagner et al. 2015 for discussion on the relationship between the

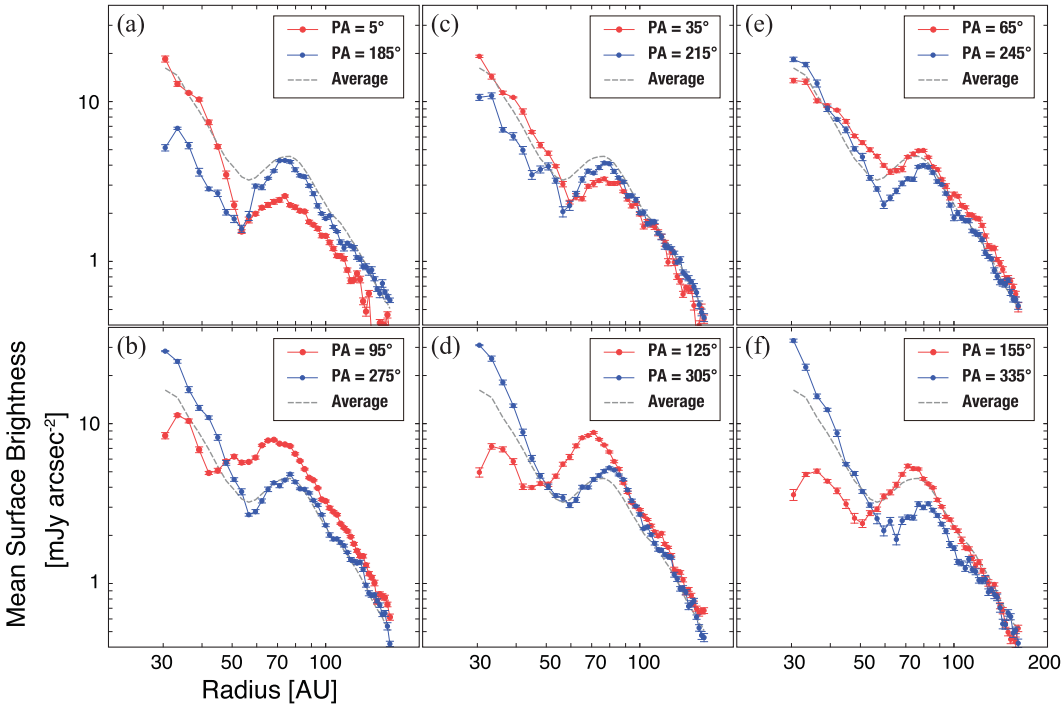

Fig. 7. Radial profiles of the PI along the pairs separated by 180° in PA. (a) PA = 5° ± 5° in red and PA = 185° ± 5° in blue. Same as figure 4a. (b) PA = 95° ± 5° in red and PA = 275° ± 5° in blue. Same as figure 4b. (c) PA = 35° ± 5° in red and PA = 215° ± 5° in blue. (d) PA = 65° ± 5° in red and PA = 245° ± 5° in blue. (e) PA = 125° ± 5° in red and PA = 305° ± 5° in blue. (f) PA = 155° ± 5° in red and PA = 335° ± 5° in blue. Radial profile averaged over the whole direction (shown in figure 2) is indicated by a gray broken line in each panel.

time variation seen in SED and structural change at inner radii as small as $r \sim 0\farcs3$).

The PI in the outer region tends to be higher along the minor axis than the major axis (figure 4). This is completely opposite to other disks showing brighter PI along the minor axis (Muto et al. 2012; Kusakabe et al. 2012), which is naturally explained by the highest polarization degree in 90° scattering. The observed features of the disk around HD 169142 are rather difficult to interpret in terms of simple Rayleigh scattering by an axisymmetric disk in nearly face-on geometry. It is more likely that most of these asymmetric features reflect real disk structure on smaller scales, as discussed above.

5 Conclusions

We carried out coronagraphic observations of the circumstellar disk around HD 169142 in *H*-band polarized intensity (PI) with Subaru/HiCIAO. The emission scattered by dust particles at the disk surface in $0\farcs2 \leq r \leq 1\farcs2$, corresponding to $29 \leq r \leq 174$ au at the distance to HD 169142, was successfully detected. Our conclusions are summarized as follows:

1. The overall structure of the PI is nearly axisymmetric. The azimuthally averaged radial profile of the PI shows a double power-law distribution, in which the PIs in $r = 29$–52 au and $r = 81.2$–145 au respectively show r^{-3} dependence. These two power-law regions are connected smoothly with a transition zone (TZ). The apparent gap in $r = 40$–70 au, previously reported by Quanz et al. (2013) and Osorio et al. (2014), corresponds to the outer part of the inner power-law region and TZ.
2. The PI image also contains asymmetric features. The variation along the azimuthal direction in each annulus is systematically larger at inner radii, and the amount of variation in the inner power-law region is greater than 4. This could be due to perturbation by a protoplanet inside the inner ring (Biller et al. 2014; Reggiani et al. 2014). The azimuthal distributions at the outer radii tend to have maxima at PA $\approx 110°$, implying that the eastern part is the near side of the disk and is brighter than the western part because of the forward scattering.
3. The radial profile of r^{-3} dependence is realized by the combination of surface density $\Sigma(r) \propto r^{-1}$ and the pressure scale height $H(r) \propto r$. The observed double power-law distribution of the PI can be reproduced when the proportionality constant of surface density in the inner power-law region is smaller than that in the outer power-law region. Simple model calculation shows that the observed PI profile matches the case of $f_{\rm in}^{\Sigma} = 0.16$, where $f_{\rm in}^{\Sigma}$ is the depletion factor for the proportionality constant

of surface density in the inner power-law region. However, this should be regarded as a lower limit because irregularity in temperature can also produce a double power-law distribution. Even with no irregularity in surface density, the observed PI profile is reproduced when $f_{\rm in}^{T} = 0.81$–0.83, where $f_{\rm in}^{T}$ is the proportionality constant of temperature in the inner power-law region relative to the outer region. These results are consistent with more elaborate modeling by Wagner et al. (2015). The degeneracy between $f_{\rm in}^{\Sigma}$ and $f_{\rm in}^{T}$ in models that reproduce the PI image should be disentangled by further imaging studies, especially at millimeter and submillimeter wavelengths.

4. The modeling based on the image at $\lambda = 7$ mm (Osorio et al. 2014) requires a dust-devoid zone between $r = 40$–70 au, while the scattered light in H-band is significantly detected even in this gap. These observations suggest that larger dust particles responsible for thermal emission at millimeter wavelengths may be more deficient in the gap, as predicted by previous theoretical studies.
5. The PI in the inner power-law region shows a deep minimum whose location seems to coincide with the point source at $\lambda = 7$ mm. This can be regarded as another sign of a protoplanet, because the scattering surface of the disk can be lowered by the protoplanet's gravity, making an observable dip in near-infrared scattered light (Jang-Condell 2009).
6. The obtained PI image also shows small-scale asymmetries in the outer power-law region. Possible origins for these asymmetries include corrugation of the scattering surface in the outer region, and the shadowing effect of a puffed-up structure in the inner power-law region. These two may be disentangled by a search for time variation on a shorter timescale in the scattered-light image.

Acknowledgments

We are grateful to the referee for valuable comments that improved our manuscript. This work is supported by MEXT KAKENHI Nos. 23103004 and 23103005, and by the U.S. National Science Foundation under Award No. 1009203. This research has made use of the SIMBAD database, operated at CDS, Strasbourg, France. Part of this research was carried out during the workshop "Recent Development in Studies of Protoplanetary Disks with ALMA", hosted by the Institute of Low Temperature Science, Hokkaido University.

Appendix 1. Description of the model calculations

The model is based on a disk where the surface density and temperature distributions are given by power-law forms:

$$\Sigma = \Sigma_{\rm out}\left(\frac{r}{r_{\rm out}}\right)^{-p}, \tag{A1}$$

$$T = T_{\rm out}\left(\frac{r}{r_{\rm out}}\right)^{-q}, \tag{A2}$$

where $\Sigma_{\rm out}$ and $T_{\rm out}$ are the surface density and temperature at $r_{\rm out}$. In the model, the sound speed $c_{\rm s}$ is approximated by

$$c_{\rm s} = 10^{5}\left(\frac{T}{300\,{\rm K}}\right)^{1/2}\ {\rm cm\,s^{-2}} \tag{A3}$$

for simplicity.

The disk is assumed to be vertically isothermal and in hydrostatic balance with the gravity of the central star. The density profile is then expressed by

$$\rho(r, z) = \rho_{\rm c}(r)\exp\left(-\frac{z^2}{2H^2}\right), \tag{A4}$$

where $\rho_{\rm c}(r)$ is the mid-plane density and $H = c_{\rm s}/\Omega$ is the pressure scale height. Assuming Keplerian rotation, it is easy to see that $H \propto r^{(3-q)/2}$ is realized from equations (A2) and (A3). Using equation (A3), the disk aspect ratio $h = H/r$ scales with

$$h = 0.1\left(\frac{r}{100\,{\rm au}}\right)^{(1-q)/2}\left(\frac{M_*}{M_\odot}\right)^{-1/2}. \tag{A5}$$

The mid-plane density, on the other hand, is related to the surface density as

$$\rho_{\rm c} = \frac{\Sigma}{\sqrt{2\pi}H} \propto r^{-(2p-q+3)/2}. \tag{A6}$$

Since our goal in this study is to assess the location of the scattering surface in a simple setup, we do not care about consistency between the temperature and density profile in terms of the energy balance.

In the radiative transfer calculation, we assume a single and isotropic scattering.[4] The equation to be solved is

$$\frac{dI}{dZ} = -\sigma\, W(r, z)\, B(T_*)\exp\left[-\tau_{\rm rad}(Z) - \tau(Z)\right], \tag{A7}$$

where σ is the scattering coefficient, Z is the coordinate along the line of sight, $W(r, z) = 1/4(r^2 + z^2)$ is the geometric dilution factor, $\tau_{\rm rad}$ is the optical depth between the central star and the location of the disk, and $\tau(Z)$ is the optical depth along the line of sight. In integrating equation (A7), we first calculate $\tau_{\rm rad}$ at all the locations of the disk in the grid and then integrate over line of sight from the observer position to the disk.

To compare with the observed radial profile of the PI, we modify the surface density or temperature distribution as described in section 4. The averaged PI is assumed to be

[4] Thermal emission is included in the code as well, but it is not significant as long as we consider the intensity in near infrared beyond 10 au.

proportional to the averaged total intensity, which seems reasonable because the total intensity has a similar radial profile to PI (Grady et al. 2007; Fukagawa et al. 2010). We treat the unit of calculated intensities as an arbitrary one partly because of the uncertainty in polarization efficiency, and we fit the shape of the PI radial profile to estimate $f_{\rm in}^{\Sigma}$ or $f_{\rm in}^{T}$.

In this paper, we only deal with the cases of $p = 1$ and $q = 1$ and look at how the observed radial profile can be reproduced. The $q = 1$ case corresponds to the disk whose aspect ratio h is independent of r as shown in equation (A5) (Grady et al. 2007; Panić et al. 2008) and successfully reproduces the r^{-3} dependence of the PI profile. The r^{-3} dependence can also be derived analytically in the $p = 1$ and $q = 1$ cases, as shown in appendix 2. Figure 6 shows the cases of $\Sigma_{\rm out} = 9\,{\rm g\,cm^{-2}}$, $T_{\rm out} = 53\,{\rm K}$ at $r_{\rm out} = 85\,{\rm au}$ taken from the equilibrium temperature for blackbodies directly exposed to stellar radiation with 9.4 $L_{\odot}$ (Meeus et al. 2012). Although the fiducial grain temperatures are set to the local blackbody temperature, the grains are assumed to be highly reflective, with scattering albedo of $\omega = 0.9$, and their total extinction coefficient is set to be $\chi = 100\,{\rm cm^2\,g^{-1}}$ ($\sigma = \chi\omega$). The change of $\Sigma_{\rm out}$ or $T_{\rm out}$, however, almost scales the overall profile unless the disk gets optically thin, and it does not significantly affect the estimate for $f_{\rm in}^{\Sigma}$ or $f_{\rm in}^{T}$.

The position of the scattering surface depends on two factors: (i) the volume emissivity of disk material determined by its density and emissivity, and (ii) the vertical distribution of disk material. The model described here essentially parameterizes (i) with Σ and (ii) with T. The change of Σ can be interpreted not only by the change of material density but also by the spatial variation of optical properties of the dust particles. The change of T, on the other hand, can be related not only to the temperature, or the pressure scale height $H = c_s/\Omega$, but also to the degree of dust settlement toward the disk mid-plane. Since it is impossible to disentangle all these factors solely from the PI image in H-band, we do not examine the detailed disk structure based on a realistic disk model in this study. Further detailed analysis on disk structure should be made after sensitive observations of dust emission at millimeter/submillimeter wavelengths are carried out with ALMA at a similar angular resolution.

Appendix 2. Analytic consideration for the cases of $p = 1$ and $q = 1$

The results of the model calculation show that the cases of $p = 1$ and $q = 1$ successfully reproduce the r^{-3} dependence of surface brightness. In fact, it is possible to predict the radial profile of the surface brightness analytically in these cases as follows.

The approximate solution to equation (A7) is given by

$$I \propto \beta/r^2, \tag{A8}$$

where β is the grazing angle of the stellar light at the disk surface. Here, the disk scattering surface is determined by the height $z_{\rm s}$ at which the optical depth from the central star becomes unity. The optical depth $\tau_{\rm rad}$ can be calculated by

$$\tau_{\rm rad}(r, z) = \int_{r_{\rm in}}^{r} \chi\rho(r', z)\frac{dr'}{\cos\theta}, \tag{A9}$$

where θ is given by

$$\tan\theta = \frac{z}{r}. \tag{A10}$$

Substituting the density profile given by equation (A4), we have

$$\int_{r_{\rm in}}^{r} \chi\rho(r', z)\frac{dr'}{\cos\theta} = \int_{r_{\rm in}}^{r} \chi\rho_{\rm c}(r')\exp\left[-\frac{\tan^2\theta}{2h(r')^2}\right]\frac{dr'}{\cos\theta}. \tag{A11}$$

Here, we have assumed that the central star is at the origin and used the fact that $z' = r'\tan\theta$ along the line connecting the location of the disk considered and the stellar position. If we assume a disk with constant h, the exponential term is constant in the integration and therefore

$$\tau_{\rm rad}(r, z) = \chi\exp\left[-\frac{1}{2h^2}\left(\frac{z}{r}\right)^2\right]\sqrt{1+\left(\frac{z}{r}\right)^2}\int_{r_{\rm in}}^{r}\rho_{\rm c}(r')dr'. \tag{A12}$$

Finally, if the mid-plane density profile is given by

$$\rho_{\rm c}(r) = \rho_{\rm c0}\left(\frac{r}{r_{\rm in}}\right)^{-2}, \tag{A13}$$

its integration can be calculated as

$$\int_{r_{\rm in}}^{r}\rho_{\rm c}(r')dr' = \rho_{\rm c0}r_{\rm in}\left[1-\left(\frac{r}{r_{\rm in}}\right)^{-1}\right]. \tag{A14}$$

Note that $\tau_{\rm rad}(r, z)$ has the form

$$\tau_{\rm rad}(r, z) = f(r)g(z/r) \equiv f(r)g(u), \tag{A15}$$

where

$$f(r) = \rho_{\rm c0}r_{\rm in}\left[1-\left(\frac{r}{r_{\rm in}}\right)^{-1}\right] \tag{A16}$$

and

$$g(u) = \chi \exp\left[-\frac{u^2}{2h^2}\right]\sqrt{1+u^2}. \quad \text{(A17)}$$

We can define the disk scattering surface $z_s(r)$ by

$$\tau_{\rm rad}(r, z_s) = \tau_0, \quad \text{(A18)}$$

where τ_0 is the value of the order unity. Then, the location of the scattering surface is given by

$$\frac{z_s}{r} \sim h\sqrt{\log C^2 - 2\left(\frac{r_{\rm in}}{r}\right)}, \quad \text{(A19)}$$

where we have used $h \ll 1$ and

$$C = \frac{\chi \rho_{c0} r_{\rm in}}{\tau_0}. \quad \text{(A20)}$$

In the regions of $r \gg r_{\rm in}$, z_s/r in equation (A19) only weakly depends on the radius, and the scattering surface always resides a few times higher than the disk scale height. Unlike a flared disk (e.g., Chiang & Goldreich 1997), the aspect ratio of the scattering surface, z_s/r, is almost constant [i.e., the scattering surface is nearly parallel to the radial direction from the star; see equation (A19) in appendix 2] when $p = 1$ and $q = 1$. In such a case, the surface brightness of the resultant scattering light is changed rather sensitively by the change of Σ.

The grazing angle can be calculated by

$$\beta = \frac{dz_s}{dr} - \frac{z_s}{r}. \quad \text{(A21)}$$

Since

$$\frac{dz_s}{dr} = -\frac{\partial \tau_{\rm rad}/\partial r}{\partial \tau_{\rm rad}/\partial z}, \quad \text{(A22)}$$

we have

$$\beta = -\frac{r f'(r) g(z_s/r)}{f(r) g'(z_s/r)}, \quad \text{(A23)}$$

where $'$ denotes the derivative with respect to the argument. Substituting the expressions for the f and g functions and using $h \ll 1$, we obtain

$$\beta \sim \frac{h^2 r_{\rm in}}{r}\left[\frac{z_s}{r}\left(1 - \frac{r_{\rm in}}{r}\right)\right]^{-1}. \quad \text{(A24)}$$

In $r \gg r_{\rm in}$, the last part in the bracket is a weak function of r. We therefore conclude that the grazing angle scales with

$$\beta \propto r^{-1}, \quad \text{(A25)}$$

and combining this with equation (A8), the radial profile of the scattered light is given by

$$I \propto r^{-3}. \quad \text{(A26)}$$

Equation (A24) indicates that β is nearly proportional to h when Σ distributes smoothly, while h is proportional to c_s, or $T^{1/2}$. The difference in the observed proportionality constant of PI(r) between $r < 50$ au and $r > 85$ au is 0.22, as shown in equations (1) and (2). This difference corresponded to 0.47 in temperature if the aspect ratio h remained constant at all radii. In our model, however, h in $r < 50$ au is smaller than that in $r > 85$ au, and the stellar radiation incident at the scattering surface at $r > 85$ au is brighter than the case of $h =$ constant at all radii. This is why the models with $f_{\rm in}^T$ closer to unity (= 0.81–0.83) in subsection 4.1 reproduce the observed radial profile.

References

Andrews, S. M., Wilner, D. J., Espaillat, C., Hughes, A. M., Dullemond, C. P., McClure, M. K., Qi, C., & Brown, J. M. 2011, ApJ, 732, 42

Avenhaus, H., Quanz, S. P., Schmid, H. M., Meyer, M. R., Garufi, A., Wolf, S., & Dominik, C. 2014, ApJ, 781, 87

Biller, B. A., et al. 2014, ApJ, 792, L22

Birnstiel, T., Dullemond, C. P., & Pinilla, P. 2013, A&A, 550, L8

Bohren, C. F., & Huffman, D. R. 1983, Absorption and Scattering of Light by Small Particles (New York: Wiley)

Brown, J. M., Blake, G. A., Qi, C., Dullemond, C. P., Wilner, D. J., & Williams, J. P. 2009, ApJ, 704, 496

Casassus, S., et al. 2013, Nature, 493, 191

Chiang, E. I., & Goldreich, P. 1997, ApJ, 490, 368

Crida, A., Morbidelli, A., & Masset, F. 2006, Icarus, 181, 587

Dong, R., et al. 2012, ApJ, 750, 161

Duffell, P. C., & MacFadyen, A. I. 2013, ApJ, 769, 41

Dullemond, C. P., & Monnier, J. D. 2010, ARA&A, 48, 205

Dunkin, S. K., Barlow, M. J., & Ryan, S. G. 1997, MNRAS, 286, 604

Fukagawa, M., et al. 2010, PASJ, 62, 347

Fukagawa, M., et al. 2013, PASJ, 65, L14

Follette, K. B., et al. 2013, ApJ, 767, 10

Grady, C. A., et al. 2007, ApJ, 665, 1391

Grady, C. A., et al. 2013, ApJ, 762, 48

Hashimoto, J., et al. 2011, ApJ, 729, L17

Hashimoto, J., et al. 2012, ApJ, 758, L19

Hayano, Y., et al. 2004, Proc. SPIE, 5490, 1088

Hinkley, S., et al. 2009, ApJ, 701, 804

Hodapp, K. W., et al. 2008, Proc. SPIE, 7014, 701419

Honda, M., et al. 2012, ApJ, 752, 143

Inoue, A. K., Honda, M., Nakamoto, T., & Oka, A. 2008, PASJ, 60, 557

Jang-Condell, H. 2009, ApJ, 700, 820

Jang-Condell, H., & Turner, N. J. 2012, ApJ, 749, 153

Joos, F., Buenzli, E., Schmid, H. M., & Thalmann, C. 2008, Proc. SPIE, 7016, 48
Kanagawa, K. D., Muto, T., Tanaka, H., Tanigawa, T., Takeuchi, T., Tsukagoshi, T., & Momose, M. 2015b, ApJ, 806, L15
Kanagawa, K. D., Tanaka, H., Muto, T., Tanigawa, T., & Takeuchi, T. 2015a, MNRAS, 448, 994
Kusakabe, N., et al. 2012, ApJ, 753, 153
Lin, D. N. C., & Papaloizou, J. C. B. 1993, in Protostarsand Planets III, ed. E. H. Levy & J. I. Lunine (Tucson: University of Arizona Press), 749
Lyra, W., Johansen, A., Klahr, H., & Piskunov, N. 2009, A&A, 493, 1125
Maaskant, K. M., et al. 2013, A&A, 555, A64
Manoj, P., Bhatt, H. C., Maheswar, G., & Muneer, S. 2006, ApJ, 653, 657
Mayama, S., et al. 2012, ApJ, 760, L26
Meeus, G., et al. 2010, A&A, 518, L124
Meeus, G., et al. 2012, A&A, 544, A78
Meeus, G., Waters, L. B. F. M., Bouwman, J., van den Ancker, M. E., Waelkens, C., & Malfait, K. 2001, A&A, 365, 476
Minowa, Y., et al. 2010, Proc. SPIE, 7736, 77363N
Muto, T. 2011, ApJ, 739, 10
Muto, T., et al. 2012, ApJ, 748, L22
Muto, T., & Inutsuka, S.-I. 2009, ApJ, 695, 1132
Osorio, M., et al. 2014, ApJ, 791, L36
Paardekooper, S.-J., & Mellema, G. 2006, A&A, 453, 1129
Panić, O., Hogerheijde, M. R., Wilner, D., & Qi, C. 2008, A&A, 491, 219
Pérez, L. M., Isella, A., Carpenter, J. M., & Chandler, C. J. 2014, ApJ, 783, L13
Quanz, S. P., Avenhaus, H., Buenzli, E., Garufi, A., Schmid, H. M., & Wolf, S. 2013, ApJ, 766, L2
Raman, A., Lisanti, M., Wilner, D. J., Qi, C., & Hogerheijde, M. 2006, AJ, 131, 2290
Regály, Z., Juhász, A., Sándor, Z., & Dullemond, C. P. 2012, MNRAS, 419, 1701
Reggiani, M., et al. 2014, ApJ, 792, L23
Skrutskie, M. F., Dutkevitch, D., Strom, S. E., Edwards, S., Strom, K. M., & Shure, M. A. 1990, AJ, 99, 1187
Strom, K. M., Strom, S. E., Edwards, S., Cabrit, S., & Skrutskie, M. F. 1989, AJ, 97, 1451
Suzuki, R., et al. 2010, Proc. SPIE, 7735, 773530
Sylvester, R. J., Skinner, C. J., Barlow, M. J., & Mannings, V. 1996, MNRAS, 279, 915
Tamura, M. 2009, in AIP Conf. Proc. 1158, Proc. of the Intl. Conf., ed. T. Usuda et al. (Melville, NY: AIP), 11
Tamura, M., et al. 2006, Proc. SPIE, 6269, 28
van den Ancker, M. E., The, P. S., Tjin A Djie, H. R. E., Catala, C., de Winter, D., Blondel, P. F. C., & Waters, L. B. F. M. 1997, A&A, 324, L33
van der Marel, N., et al. 2013, Science, 340, 1199
Wagner, K. R., et al. 2015, ApJ, 798, 94
Whitney, B. A., & Hartmann, L. 1992, ApJ, 395, 529
Whitney, B. A., Indebetouw, R., Bjorkman, J. E., & Wood, K. 2004, ApJ, 617, 1177
Whitney, B. A., Wood, K., Bjorkman, J. E., & Cohen, M. 2003a, ApJ, 598, 1079
Whitney, B. A., Wood, K., Bjorkman, J. E., & Wolff, M. J. 2003b, ApJ, 591, 1049
Williams, J. P., & Cieza, L. A. 2011, ARA&A, 49, 67
Wisniewski, J. P., Clampin, M., Grady, C. A., Ardila, D. R., Holland, C. F., Golimowski, D. A., Illingworth, G. D., & Krist, J. E. 2008, ApJ, 682, 548
Zhu, Z., Nelson, R. P., Hartmann, L., Espaillat, C., & Calvet, N. 2011, ApJ, 729, 47

The Astrophysical Journal, 807:120 (19pp), 2015 July 10 doi:10.1088/0004-637X/807/2/120

ANALYTICAL FORMULAE OF MOLECULAR ION ABUNDANCES AND THE N_2H^+ RING IN PROTOPLANETARY DISKS

Yuri Aikawa[1], Kenji Furuya[2], Hideko Nomura[3], and Chunhua Qi[4]
[1] Center for Computational Sciences, University of Tsukuba, 1-1-1 Tennoudai, Tsukuba 305-8577, Japan; aikawa@ccs.tsukuba.ac.jp
[2] Leiden Observatory, Leiden University, P.O. Box 9513, 2300 RA Leiden, The Netherlands
[3] Department of Earth and Planetary Science, Tokyo Institute of Technology, 2-12-1 Ookayama, Meguro-ku, 152-8551 Tokyo, Japan
[4] Harvard-Smithsonian Center for Astrophysics, Cambridge, MA 02138, USA
Received 2014 November 14; accepted 2015 May 21; published 2015 July 7

ABSTRACT

We investigate the chemistry of ion molecules in protoplanetary disks, motivated by the detection of the N_2H^+ ring around TW Hya. While the ring inner radius coincides with the CO snow line, it is not apparent why N_2H^+ is abundant outside the CO snow line in spite of the similar sublimation temperatures of CO and N_2. Using the full gas-grain network model, we reproduced the N_2H^+ ring in a disk model with millimeter grains. The chemical conversion of CO and N_2 to less volatile species (sink effect hereinafter) is found to affect the N_2H^+ distribution. Since the efficiency of the sink depends on various parameters such as activation barriers of grain-surface reactions, which are not well constrained, we also constructed the no-sink model; the total (gas and ice) CO and N_2 abundances are set constant, and their gaseous abundances are given by the balance between adsorption and desorption. Abundances of molecular ions in the no-sink model are calculated by analytical formulae, which are derived by analyzing the full-network model. The N_2H^+ ring is reproduced by the no-sink model, as well. The 2D (R-Z) distribution of N_2H^+, however, is different among the full-network model and no-sink model. The column density of N_2H^+ in the no-sink model depends sensitively on the desorption rate of CO and N_2 and the cosmic-ray flux. We also found that N_2H^+ abundance can peak at the temperature slightly below the CO sublimation, even if the desorption energies of CO and N_2 are the same.

Key words: astrochemistry – protoplanetary disks

1. INTRODUCTION

A ring of N_2H^+ emission was found in the disk around TW Hya using the Atacama Large Millimeter/submillimeter Array (Qi et al. 2013b). N_2H^+ is considered to be a useful probe of the CO snow line, because it is destroyed by the proton transfer to CO,

$$N_2H^+ + CO \rightarrow HCO^+ + N_2. \quad (1)$$

The inner radius of the N_2H^+ ring is indeed consistent with the CO snow line predicted from a disk model of TW Hya. The anticorrelation of N_2H^+ and CO emission is also often observed in prestellar cores (e.g., Tafalla et al. 2004), which strengthen the above statement.

The bright emission of N_2H^+ outside the CO snow line is, however, puzzling. Laboratory experiments show that the sublimation temperatures of CO and N_2 are similar (Collings et al. 2004; Öberg et al. 2005). Since N_2H^+ is formed by protonation of N_2, N_2H^+ should also be depleted outside the CO snow line. In the case of prestellar cores, there are two possible explanations for the survival of N_2H^+ in the CO depleted region. First, destruction of N_2H^+ is temporally suppressed by the freeze-out of its major reactant, CO. Second, the slow formation of N_2 from N atoms in molecular clouds aids the temporal survival of N_2 (Aikawa et al. 2001; Maret et al. 2006; Bergin & Tafalla 2007). The first mechanism could work in the disk as well, in a narrow range of temperatures where the positive effect of depletion on N_2H^+ abundance (i.e., decrease of CO) wins against the negative effect (i.e., depletion of N_2). The second mechanism, on the other hand, seems irrelevant for disks. In protoplanetary disks, in which the gas density is much higher than molecular clouds, it is not likely that N atoms are more abundant than N_2, except for the photodissociation layer at the disk surface.

In chemistry models of disks, it is often found that CO is depleted even in regions warmer than its sublimation temperature (~20 K) via conversion to less volatile species (Aikawa et al. 1997; Bergin et al. 2014; Furuya & Aikawa 2014). Since the conversion works as a sink in the chemical reaction network of gaseous species, we call it the sink effect in the present work. Favre et al. (2013) showed, for the first time, observational evidences for such CO depletion toward TW Hya. Furuya & Aikawa (2014) showed that N_2 is also subject to the sink effect; it is converted to NH_3 via the gas-phase reactions of

$$N_2 + H_3^+ \rightarrow N_2H^+ + H_2, \quad (2)$$

$$N_2H^+ + e \rightarrow NH + N, \quad (3)$$

and subsequent hydrogenations of NH on grain surfaces. It should be noted that this conversion is not efficient when CO is abundant, because N_2H^+ mainly reacts with CO to reform N_2. The longer timescale required for N_2 depletion could explain the N_2H^+ ring. But then the lifetime of the ring should be similar to the difference in the depletion timescales of CO and N_2, which is rather short, $\lesssim 10^5$ yr, if the ionization rate is $\sim 5 \times 10^{-17}\,s^{-1}$ (Furuya & Aikawa 2014). Since N_2 is considered to be a major nitrogen carrier in protoplanetary disks, but cannot be directly observed, it is important to constrain its distribution based on N_2H^+ observation. The formation mechanism of the N_2H^+ ring is thus worth investigating via theoretical calculations.

The abundance of N_2H^+ could also be a probe of ionization degree in the regions of CO depletion. The ionization degree

depends on the gas density and ionization rate, which is an important parameter for both chemical and physical evolutions of the disk. Since ionizations trigger the chemical reactions, as in molecular clouds, the timescale of chemical evolution depends on the ionization rate (Aikawa et al. 1997). The ionization degree determines the coupling with magnetic fields, e.g., which disk region is subject to magnetorotational instability (Baulbus & Hawley 1991). The major ionization sources are X-rays from the central star, cosmic rays, and decay of radioactive nuclei (Umebayashi & Nakano 1988; Glassgold et al. 1997; Cleeves et al. 2013). The ionization rate thus depends on the flux and hardness of X-ray radiation and the abundances of radioactive nuclei. In addition, the stellar winds and/or magnetic fields of the star-disk system could prevent the penetration of the cosmic ray to the disk. Since these parameters are unknown and could vary among objects, the ionization degree should be probed via observations. The observation of ionization degree is principally possible using major ion molecules. But a quantitative estimate of the ionization degree from the observational data is not straightforward, because the gas density, major ion molecules, and their abundances change spatially within the disk (e.g., Aikawa et al. 2002; Qi et al. 2008; Cleeves et al. 2014).

In this work, we investigate the spatial distribution of N_2H^+ and other major molecular ions in protoplanetary disks. First, we calculate the full chemical network model, which includes gas-phase and grain-surface reactions. The radial distribution of N_2H^+ column density has a peak around the radius of CO sublimation temperature, i.e., the N_2H^+ ring is reproduced. We found that the sink effect on CO significantly affects the distribution of N_2H^+. By analyzing the full chemical network, we also found that the abundances of major molecular ions, H_3^+, HCO^+, and N_2H^+, can be described by analytical functions of gas density, temperature, ionization rate, and abundances of CO and N_2. Such formulae are useful in deriving the ionization degree from the observations of molecular ions, combined with the dust continuum and CO observations, to constrain the gas density and CO abundance.

While the sink effect plays an important role in determining the N_2H^+ distribution in the full-network model, the efficiency of the sink depends on various parameters that are not well constrained yet. For example, the conversion timescale of CO and N_2 to less volatile species depends on ionization rate and activation barriers of the reactions. The sink effect could be less significant, if the disk is turbulent and the diffusion timescale is shorter than the conversion timescale. Since there are various chemical paths for the conversion, it is difficult to directly control the efficiency of sink in the full-network model. In order to investigate the abundances of N_2H^+ and other molecular ions in the limit of no sink, we construct the "no-sink" model; we assume that the total (gas and ice) abundances of CO and N_2 are constant, and that their gas-phase abundances are given by the balance between adsorption and desorption. The abundances of molecular ions are calculated using the analytical formulae.

The plan of this paper is as follows. In Section 2, we describe our disk model and chemical model. The molecular distributions in the full-network model are presented in Section 3. In Section 4, we derive analytical formulae for abundances of electrons, H_3^+, HCO^+, and N_2H^+. The formulae are used to calculate their abundances in the disk model, which are compared with the results of the full-network calculation. Section 5 presents the results of the no-sink model. Since the no-sink model is analytical, we can easily investigate the dependence of N_2H^+ column density on desorption rate (i.e., sublimation temperature) of CO and N_2. We also investigate how much the N_2H^+ column density is reduced, if the penetration of cosmic rays to the disk is hampered by the stellar wind and/or magnetic fields. We summarize our results and conclusions in Section 6.

2. MODELS

We adopt the same disk model as in Furuya & Aikawa (2014). In addition to the disk model with small grains, which is assumed in Furuya & Aikawa (2014), we also investigate a disk model in which the dust grains have grown up to a radius of 1 mm. The turbulent mixing is not explicitly included in the present work. The model of the full chemical network is also the same as in Furuya & Aikawa (2014), but includes some updates. The models are briefly described in the following.

2.1. Disk Model

Since we aim to understand the mechanism for forming the N_2H^+ ring, rather than investigating the disk structure of a specific object (i.e., TW Hya) we adopt a steady, axisymmetric Keplerian disk around a T Tauri star. The stellar mass, radius, and effective temperature are $M_* = 0.5M_\odot$, $R_* = 2R_\odot$, and $T_* = 4000$ K, respectively. The disk structure is given by solving the radiation transfer, thermal balance of gas and dust, and hydrostatic equilibrium in the vertical direction in the disk. Basic equations and calculation procedures are described in Nomura et al. (2007). We assume a stellar UV and X-ray luminosity of 10^{31} and 10^{30} erg s^{-1}, respectively. The cosmic-ray ionization rate of H_2 is set to be 5×10^{-17} s^{-1} (Dalgarno 2006), while the ionization rate by the decay of radioactive nuclei is set to be 1×10^{-18} s^{-1} (Umebayashi & Nakano 2009). The dust-to-gas mass ratio is 0.01. We consider two disk models: one with the dark cloud dust and the other with millimeter-sized grains (Aikawa & Nomura 2006). The former assumes the dust properties of Weingartner & Draine (2001) ($R_v = 5.5$, $b_c = 3 \times 10^{-5}$, case B); while the silicate grains have a rather steep size distribution with a maximum radius of $\sim$0.2 μm, the carbonaceous grains have polycyclic-aromatic-hydrocarbon-like properties in the small-size limit and graphite-like properties at larger sizes. The maximum size of carbonaceous grains is $\sim$10 μm. In the latter model, we assume the power-law size distribution of dust grains $dn(a)/da \propto a^{-3.5}$, where a is the grain radius, referring to the ISM dust model of Mathis et al. (1977), but the minimum and maximum sizes are set to be 0.01 μm and 1 mm, respectively. It would be more appropriate for T Tauri disks than the dark cloud dust model, since the grain growth is indicated by the disk observations (e.g., Williams & Cieza 2011). The dust opacities for the two models are calculated using the Mie theory. The gas temperature, dust temperature, and density distributions in the disk are calculated self-consistently, by considering various heating and cooling mechanisms. Figure 1 shows the distribution of gas density, gas temperature, dust temperature, and ionization rate by X-ray in our models. Cosmic-ray ionization dominates in the midplane, where the X-ray ionization rate is $\lesssim 5 \times 10^{-17}$ s^{-1}. The temperature in the model with millimeter grains is lower than that in the dark

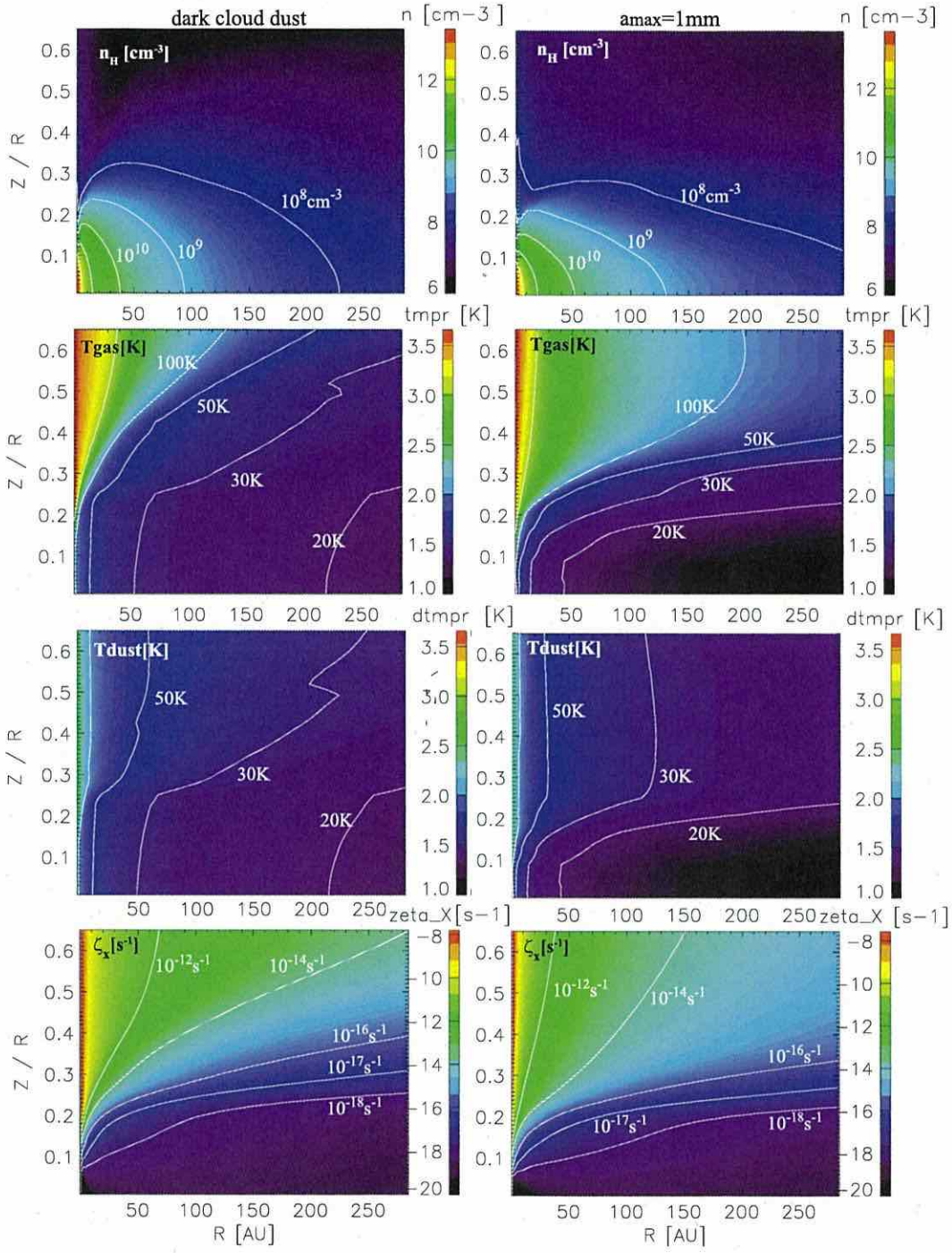

Figure 1. Distribution of the density of hydrogen nuclei n_H(top), gas temperature, dust temperature, and ionization rate by X-rays ζ_X (bottom) in the disk model with dark cloud dust (left panels) and millimeter grains (right panels).

cloud dust model owing to the lower dust opacity at a given disk height (Z) to receive the radiation from the central star. Column density in these disk models is determined by assuming a steady-state disk structure with constant viscosity and accretion rate (although we consider turbulent diffusion and/or radial accretion only implicitly in the chemical model), so that the masses of the two disks are slightly different: $1 \times 10^{-2} M_\odot$ for the dark cloud dust model and $1.7 \times 10^{-2} M_\odot$ for the millimeter grain model.

2.2. Chemical Model: Full Network

Our chemical network is based on Garrod & Herbst (2006). We added photoionization, photodissociation, and

photodesorption by UV radiation from the central star; self-shielding of H_2, CO, and N_2 (Furuya et al. 2013; Li et al. 2013); X-ray chemistry; and charge balance of dust grains. Although our model includes deuteration and ortho/para (o/p) states of several species, such as H_2 and H_3^+ (K. Furuya et al. 2015, in preparation, U. Hincelin et al. 2014, in preparation), we present only the molecular abundances, i.e., the sum of isotopomers and o/p states. The D/H ratio and o/p ratios will be presented in forthcoming papers. Our model consists of two phases, gas phase and ice mantle, i.e., we do not discriminate layers of ice mantles, unless otherwise stated. Desorption energies ($E_{\rm des}$) of assorted species are listed in Table 1 in Furuya & Aikawa (2014). Desorption energies of atomic hydrogen, CO, and N_2 are set to be 600, 1150, and 1000 K, respectively; they are the values on water-ice substrates (Garrod & Herbst 2006; Al-Halabi & van Dishoeck 2007). The sublimation temperatures of CO and N_2 are then ~23 and ~19 K, respectively, when the gas density is 10^6 cm^{-3}. We investigate the dependence of N_2H^+ abundance on the desorption energies of CO and N_2 in Sections 3 and 5.

Adsorbed species on grains migrate via thermal hopping and react with each other when they meet. We adopt the modified rate of Caselli et al. (1998, 2002) for grain-surface reactions of H atoms. The adsorption rate of gaseous species onto grain surfaces and grain-surface reaction rates (e.g., if the rate is limited by the accretion of gaseous particles) depend on the size distribution of grains. Ideally, the grain size distribution should be taken into account (Acharyya et al. 2011). Most chemical models of disks and molecular clouds, however, assume a single size of 0.1 μm, for simplicity, which we follow in the present work. The rate coefficients of gas-dust interactions (e.g., adsorption) are basically proportional to the total grain-surface area. The assumption of a single grain size in the chemical model is thus a reasonable approximation, as long as the total surface area of grains is consistent with that in the physical disk model. The total surface area of the 0.1 μm dust model agrees with that of our dark cloud dust model within a factor of a few. In the chemical model for the disk model with millimeter grains, we adopt the same uniform grain size (0.1 μm) but decrease the dust-gas ratio by one order of magnitude; according to the power-law size distribution, the number of small grains, which dominate in the grain-surface area, is decreased compared with the dark cloud dust model by an order of magnitude (Aikawa & Nomura 2006). One caveat for this single-size approximation is that we may underestimate the rate of grain-surface recombination. In the dense regions, such as disk midplane at small radii, recombinations are more efficient on grain surfaces than in the gas phase. Owing to the Coulomb focusing, the cross-section of grain-surface recombination is much larger than the geometrical cross-section of dust grains. The rate of grain-surface recombination thus cannot be scaled by the total grain-surface area.

The photodissociation rates are calculated by convolving the attenuated stellar and interstellar UV spectrum and wavelength-dependent photodissociation cross-sections at each position in the disk (van Zadelhoff et al. 2003; van Dishoeck et al. 2006). UV radiation induced by X-ray and cosmic ray (Gredel et al. 1989) is also taken into account. For ice-mantle species, we assume that only the uppermost layers can be dissociated; i.e., while the UV radiation can penetrate into deeper layers of the ice mantle, we assume that the photo products in deeper layers recombine immediately. The effective rate of photodissociation is thus reduced. Considering the fluffiness and pores on the grain surfaces, we let the uppermost two layers, rather than one, be dissociated.

Table 1
Elemental Abundance and Initial Abundances of Assorted Molecules

Element	Abundance[a]	Element	Abundance
H	1.0	He	9.75(−2)
N	2.47(−5)	O	1.80(−4)
C	7.86(−5)	S	9.14(−8)
Si	9.74(−9)	Fe	2.74(−9)
Fe	2.74(−9)	Na	2.25(−9)
Mg	1.09(−8)	...	...
Species	Abundance	Species	Abundance
H_2O	1.15(−4)	CO	3.57(−5)
CO_2	3.52(−6)	CH_4	1.50(−5)
H_2CO	1.20(−5)	CH_3OH	6.50(−6)
N_2	4.47(−6)	NH_3	1.44(−5)

Note.
[a] $A(-B)$ means $A \times 10^{-B}$.

We take into account three non-thermal desorption processes: photodesorption, stochastic heating by cosmic rays, and reactive desorption. We adopt the photodesorption yields per incident far-UV photon derived from the laboratory experiment for H_2O, CO_2, CO, O_2, and N_2 (Öberg et al. 2009a, 2009b; Fayolle et al. 2011, 2013). A yield is set to 10^{-3} for other species.

Initial molecular abundance in the disk is given by calculating the molecular evolution in the star-forming core model of Masunaga & Inutsuka (2000) (see also Masunaga et al. 1998; Aikawa et al. 2008). The initial abundances of assorted molecules and the elemental abundances in our model are listed in Table 1. Major carriers of oxygen and carbon are H_2O and CO, while the major N-bearing species are NH_3 and N_2. We adopt a low metal abundance, i.e., the abundances of metals such as Mg and Si are about two orders of magnitude lower than observed in diffuse clouds.

We calculate the chemical reaction network (i.e., rate equations) as an initial value problem at each position in the disk. As we will see in Section 3, the abundances of electrons, HCO^+, N_2H^+, and H_3^+ reach the steady state, which are determined by the ionization rate, gas density, temperature, and the abundances of CO and N_2, in a short timescale. On the other hand, CO and N_2 decrease slowly with time mainly as a result of the sink effect. Vertical diffusion and radial accretion, which are not explicitly included in the present work, could suppress or slow down the sink effect (Furuya et al. 2013; Furuya & Aikawa 2014). Therefore, we present molecular abundances at an early time of 1×10^5 yr, as well as at the typical timescale of T Tauri stars, $\sim 10^6$ yr.

2.3. Chemical Model: No-sink Model

In the full-network model, we will see that the distribution of N_2H^+ is significantly affected by the CO depletion via the sink effect. The efficiency of the sink effect, however, depends on various parameters, such as CO_2 formation (CO + OH) rate on dust grains, initial CO abundance, ionization rate, and turbulent mixing (Bergin et al. 2014; Furuya & Aikawa 2014). A strong

vertical turbulence, for example, tends to smooth out the molecular abundances, so that the local CO abundance minima due to the sink could be less significant. Although the observation of TW Hya indicates the CO depletion via the sink effect (Favre et al. 2013), the spatial distribution of CO abundance is not well constrained yet. It is therefore useful to calculate the distribution of N_2H^+ in a model without the sink effect.

In the no-sink model, we assume that the sum of gas-phase and ice-mantle abundances of CO are equal to its canonical abundance, i.e., 1×10^{-4} relative to the hydrogen nuclei. The gas-phase abundance of CO is given by a simple balance between adsorption and desorption:

$$\frac{n_{\rm COgas}}{n_{\rm COice}} = \frac{\nu \exp\left(-\frac{E_{\rm des}({\rm CO})}{kT}\right) + \nu_{\rm CR} C_{\rm Fe} \exp\left(-\frac{E_{\rm des}({\rm CO})}{kT_{\rm max}}\right)}{S\pi a^2 n_{\rm dust} v_{\rm th}} \quad (4)$$

$$n_{\rm COgas} + n_{\rm COice} = 10^{-4} n_{\rm H}, \quad (5)$$

where $n_{\rm COgas}$ and $n_{\rm COice}$ are number densities of CO in the gas phase and ice mantle, respectively. While the first term in the numerator represents the thermal desorption, the second term represents the non-thermal desorption. Although our full-network model includes various mechanisms of non-thermal desorption, here we consider only the stochastic heating by cosmic rays for simplicity. It is the effective desorption mechanism in the cold midplane for species with relatively low desorption energies (Hasegawa & Herbst 1993). The frequency of CO oscillation on grain surface ν is set to be 10^{12} s^{-1}. When a cosmic-ray particle hits a dust grain, the grain is heated temporally for $\tau_{\rm CR} \sim 10^{-5}$ s. The peak temperature of the temporal heating is set to be $T_{\rm max} = 70$ K. The rate for a grain to encounter an Fe ion particle, which is the most efficient in dust heating among cosmic-ray particles, is $C_{\rm Fe} = 3 \times 10^{-14}$ s^{-1}. The denominator represents the sticking rate of gaseous CO onto grain surfaces. The sticking probability on collision is set to be $S = 1.0$. The grain size a is 0.1 μm (see Section 2.2), and $v_{\rm th}$ is the thermal velocity of CO particles. The abundance of gaseous N_2 is formulated similarly, with the total N_2 abundance set to be 4.5×10^{-6}. It should be noted that this desorption rate by the cosmic-ray heating is a rough estimate. In reality and in our physical disk models, the grains actually have a size distribution, and parameters such as $\tau_{\rm CR}$ and $T_{\rm max}$ depend on the grain size. Léger et al. (1985), however, showed that the desorption rate via cosmic-ray heating does not sensitively depend on the grain size as long as the grains are small, $\lesssim$0.2 μm. Since the small grains contribute most to the total surface area of grains, the desorption rate obtained here would be reasonable.

In Section 4, we analyze the results of the full-network model to find out whether the abundances of electrons, H_3^+, HCO^+, and N_2H^+ can be well described by analytical formulae, which are the functions of density, temperature, ionization rate, and abundances of CO and N_2. We use these analytical formulae to obtain the molecular ion abundances in the no-sink model. A combination of the analytical formulae of molecular ions and equilibrium abundances of gaseous CO and N_2 (Equations (4) and (5)) makes it very easy to investigate the dependence of N_2H^+ abundance on various parameters, such as desorption energies of CO and N_2 and ionization rate in the disk.

3. RESULTS: FULL NETWORK

3.1. Disk with Dark Cloud Dust

Figure 2 shows the distributions of CO, HCO^+, N_2, N_2H^+, H_3^+, and electron abundances at the time of 1×10^5 yr and 9.3×10^5 yr in the model with dark cloud dust. N_2H^+ exists mostly in the upper layers of the disk. H_3^+ is more abundant than HCO^+ in the disk surface owing to a relatively high abundance ratio of electrons to CO (see Section 4.4). N_2H^+ is thus kept abundant there, via $N_2 + H_3^+$, in spite of the destruction via reaction (1).

The dashed lines in the panels of CO and N_2 depict the position where the gas-phase abundance and ice abundance become equal in the adsorption–desorption equilibrium:

$$\frac{n_{\rm gas}}{n_{\rm ice}} = \frac{\nu \exp\left(-\frac{E_{\rm des}}{kT}\right) + \nu_{\rm CR} C_{\rm Fe} \exp\left(-\frac{E_{\rm des}}{kT_{\rm max}}\right)}{S\pi a^2 n_{\rm dust} v_{\rm th}} = 1, \quad (6)$$

where $n_{\rm gas}$ and $n_{\rm ice}$ are number densities of CO (or N_2) in the gas phase and ice mantle, respectively. It defines the "snow surface" of volatile species in the disk. We define the CO and N_2 "snow line" as the radius at which Equation (6) is satisfied in the midplane.

In Figure 2, we can see that both CO and N_2 are depleted in the midplane even inside their snow lines, especially at the later stage, $t = 9.3 \times 10^5$ yr; CO is converted to CO_2 ice, CH_3OH ice, and hydrocarbons such as CH_4 ice and C_2H_6 ice, while N_2 is converted to NH_3 ice. N_2H^+ is not abundant in the CO-depleted region, since its mother molecule, N_2, is depleted there as well. At $t = 1 \times 10^5$ yr, the sink effect is still moderate, and N_2H^+ abundance in the midplane has a local peak at ~200 AU. N_2 is depleted in the outer radius, while N_2H^+ is destroyed by CO in the inner radius.

3.2. Disk with Millimeter Grains

Figure 3 shows the distributions of CO, HCO^+, N_2, N_2H^+, H_3^+, and electron abundances in the disk model with millimeter grains. The midplane temperature is warmer than 20 and 30 K inside ~40 and ~10 AU, respectively. Although the sink effect is less significant owing to the smaller total surface area of dust grains than in the model with dark cloud dust, CO is converted to CO_2 ice via the grain-surface reaction of CO + OH and is depleted from the gas phase even in the intermediate ($Z/R \sim 0.2$) layers above the dashed line, where the dust temperature is higher than the sublimation temperature of CO. In the midplane region with $T \lesssim 20$ K, on the other hand, major carbon reservoirs are CO ice, CO_2 ice, and CH_3OH ice.

While the spatial distributions of CO and N_2 are similar in the dark cloud dust model, they are significantly different in the millimeter grain model; N_2 is abundant in a layer at $Z/R \sim 0.2$, where CO is depleted. In regions closer to the midplane, N_2 ice and NH_3 ice are the dominant N-bearing species. The conversion of N_2 to NH_3 ice proceeds via gas-phase reactions

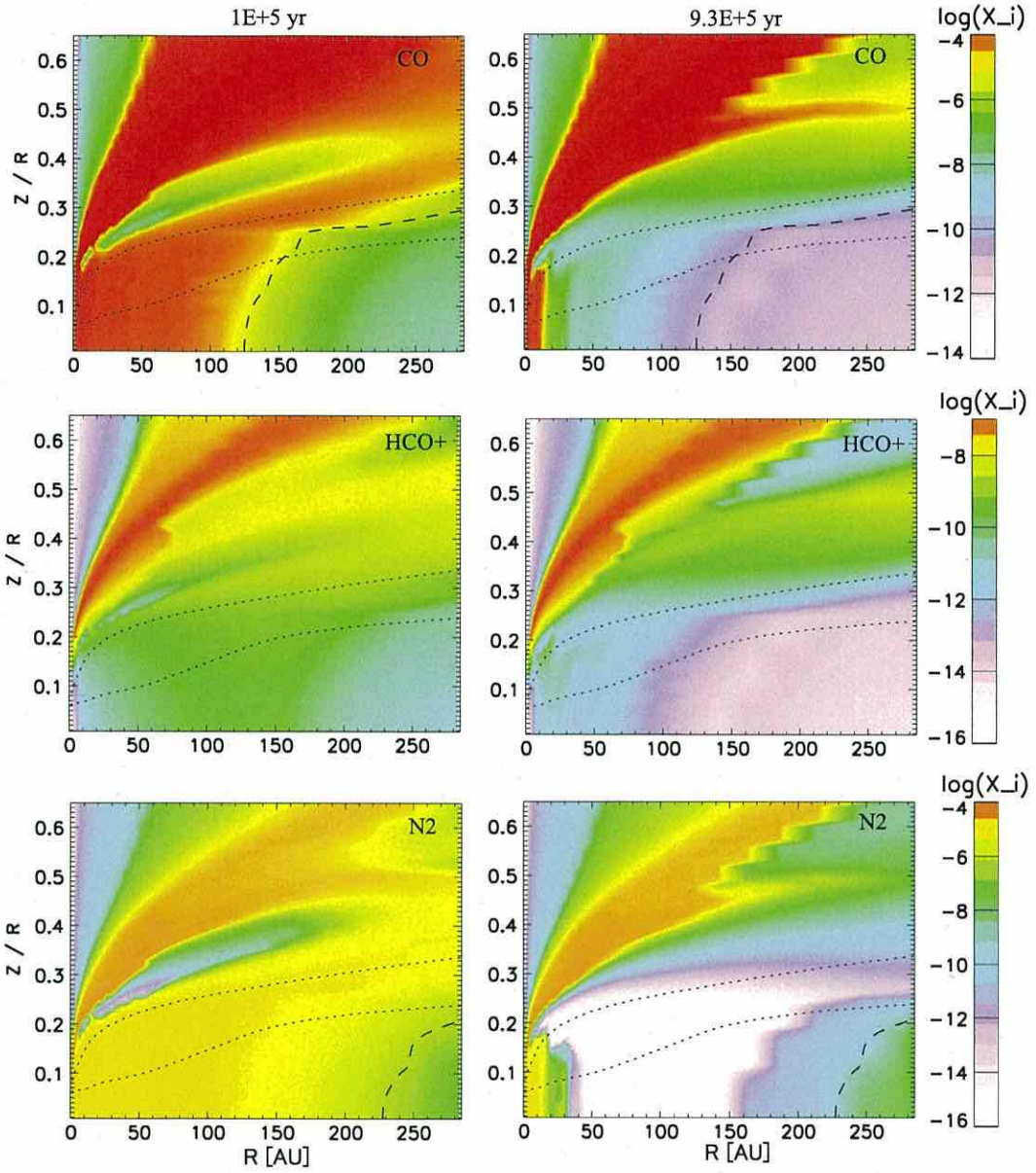

Figure 2. Distributions of CO, HCO^+, N_2, N_2H^+, H_3^+, and electrons in the gas phase at $t = 1 \times 10^5$ yr (left panels) and 9.3×10^5 yr (right panels) in the model with dark cloud dust. Dashed lines in the panels of CO and N_2 depict the position where the gas-phase and ice-mantle abundances become equal in the adsorption–desorption equilibrium (Equation (6)). The dotted lines depict the position where the X-ray ionization rate is equal to the cosmic-ray ionization rate (5×10^{-17} s^{-1}) and to the ionization rate by decay of radioactive nuclei (1×10^{-18} s^{-1}).

(2) and (3) and subsequent hydrogenation of NH on grain surfaces. At $Z/R \sim 0.2$, the photodissociation of NH (NH → N + H) is effective, which prevents the conversion of N_2 to NH_3 ice. The product of photodissociation, N atoms, is converted back to N_2 via the reaction of N + NO. In other words, a deeper penetration of UV radiation in the millimeter grain model is a key to suppressing the sink effect on N_2.

Another key difference between the models with dark cloud dust and millimeter grains is that H_3^+ is not the dominant ion in the disk surface in the latter model. Since the UV shielding via dust grains is less effective in the millimeter grain model, UV radiation ionizes atoms, such as C and S, to make electrons abundant. Dissociative recombination of a molecular ion with an electron is much more efficient than the radiative recombination of an atomic ion. Thus, the photoionization of atoms results in depletion of H_3^+ and N_2H^+ in the disk surface (e.g., $Z/R \gtrsim 0.3$). In lower layers, the distribution of N_2H^+ is basically similar to that of N_2, except for the midplane in the inner radius, where CO is abundant (i.e., $R <$ a few tens of AU at $t = 1 \times 10^5$ AU).

It should be noted that the layer with abundant N_2 and CO depletion (and thus abundant N_2H^+) at $Z/R \sim 0.2$ is formed

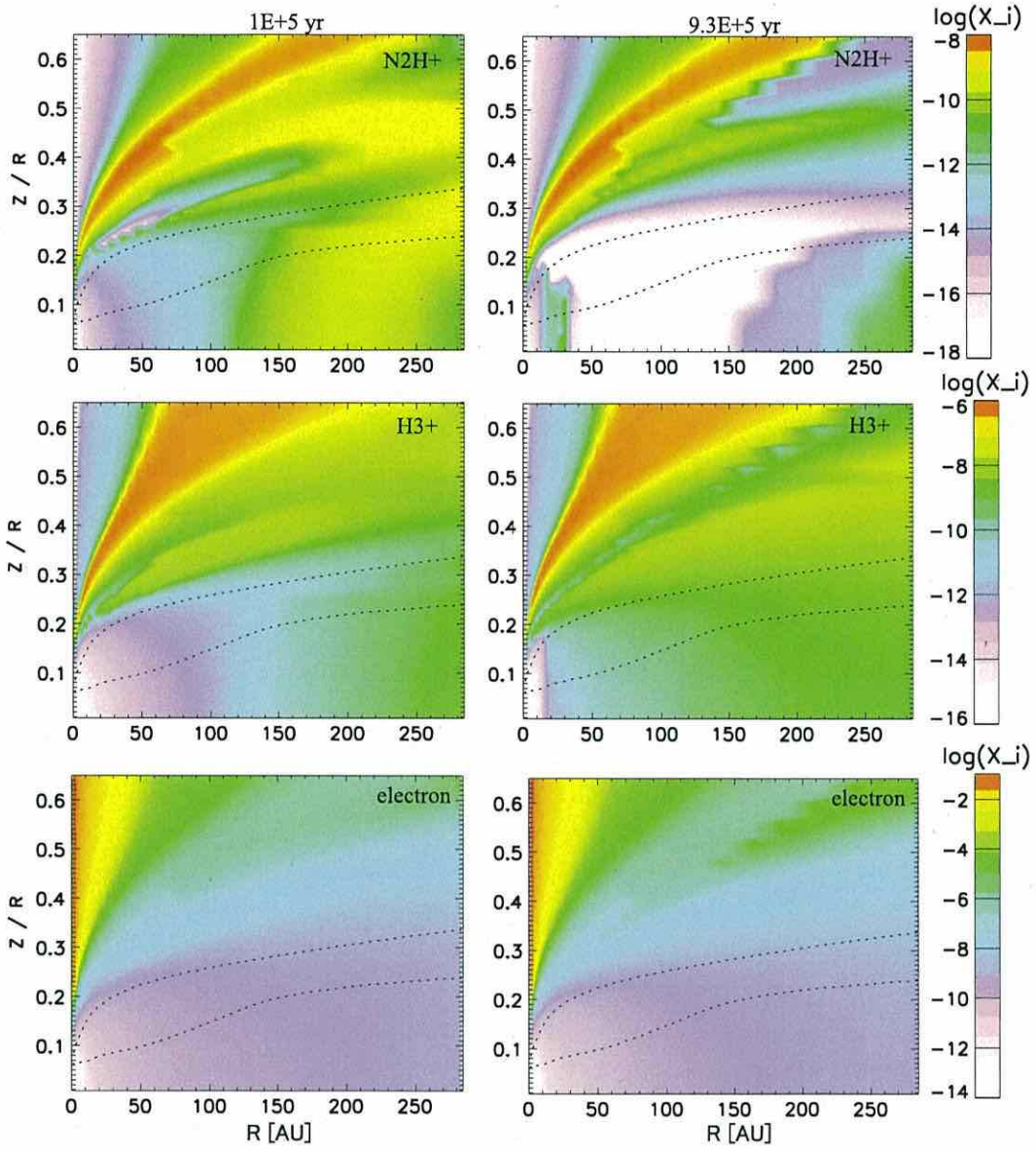

Figure 2. (Continued.)

via the combination of the sink effect on CO and photodissociation of NH, rather than via the difference in sublimation temperature of CO and N_2. We performed a calculation of the same disk model but setting the desorption energies of both CO and N_2 to be 1000 K. Distributions of CO, HCO^+, N_2, and N_2H^+ are shown in Figure 4. The resultant distribution of molecules is basically the same as in Figure 3.

3.3. Column Densities

Although we do not aim to construct a best-fit model for a specific object, it is useful to briefly compare our models with observations to see which model reproduces the N_2H^+ ring better. Since the radiative transfer calculation is out of the scope of the present work, we compare the column density of N_2H^+ in our full-network models with the estimated values in TW Hya.

In the N_2H^+ observation by Qi et al. (2013b), the 1σ detection limit corresponds to the N_2H^+ column density of $2 \times 10^{11}\,\mathrm{cm}^{-2}$. Qi et al. (2013b) constructed disk models to fit their observational data. In the models that can reasonably fit the observational data, the N_2H^+ column density at the inner edge of the ring ranges from 4×10^{12} to $2 \times 10^{15}\,\mathrm{cm}^{-2}$. They also found that the column density contrast at the inner edge of the N_2H^+ ring is at least 20 and could be larger.

We also calculated the optical depth of the N_2H^+ ($J = 4 - 3$) line for a slab of H_2 and N_2H^+ gas using the Radex code (van der Tak et al. 2007). Assuming an H_2

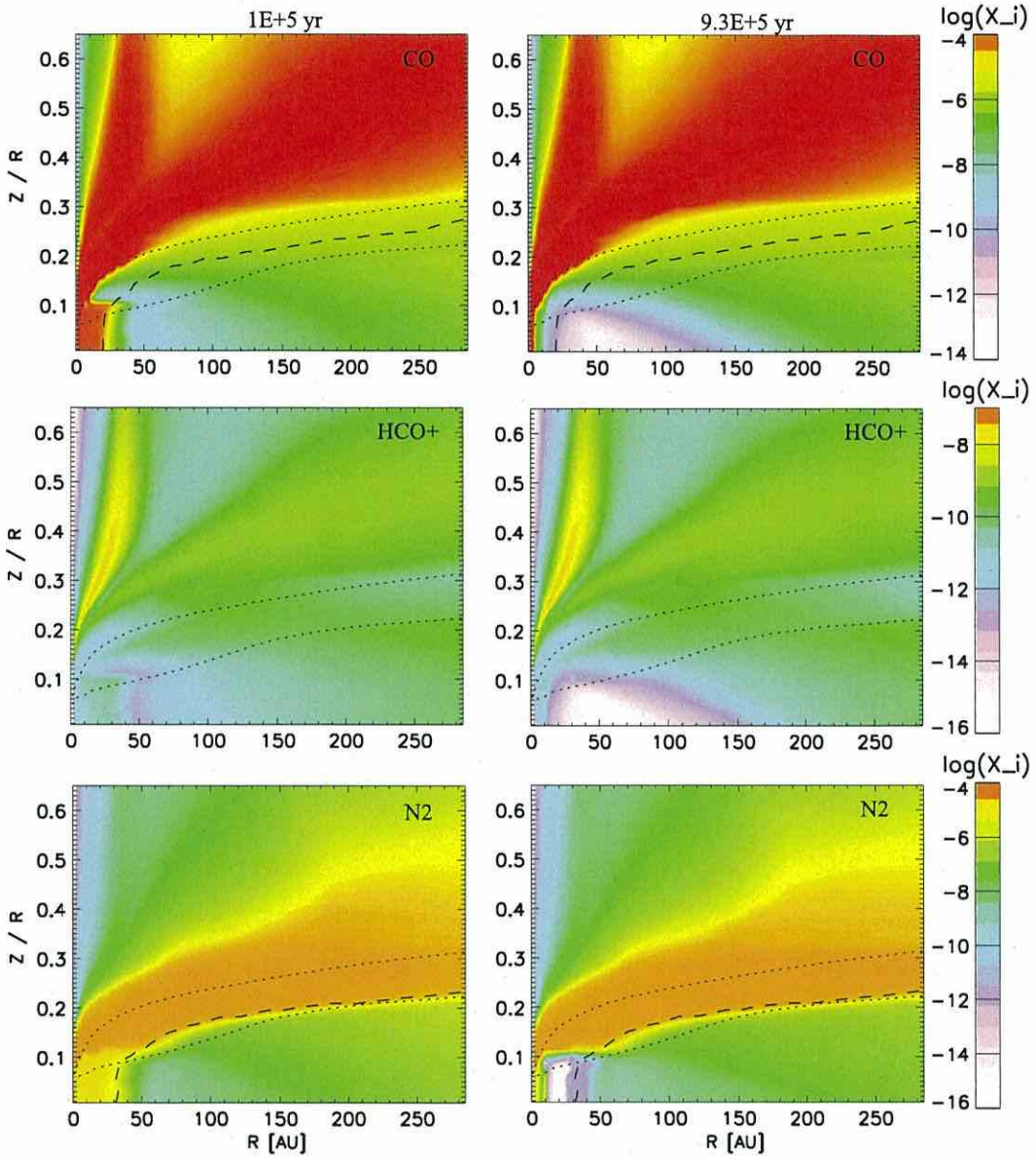

Figure 3. Distributions of CO, HCO^+, N_2, N_2H^+, H_3^+, and electrons as in Figure 2, but for the model with millimeter grains.

density of $10^8\,cm^{-3}$ and line width of $0.15\,km\,s^{-1}$, the N_2H^+ column density of $10^{12}\,cm^{-2}$ corresponds to an optical depth of $\tau = 0.60$ and 0.49 for a gas temperature of 17 and 30 K, respectively. In order to reproduce the N_2H^+ ring, the column density of N_2H^+ should be at least higher than $\sim 10^{12}\,cm^{-2}$, which is consistent with Qi et al. (2013b).

Radial distributions of column densities of CO, HCO^+, N_2, and N_2H^+ in the dark cloud dust model are plotted in Figures 5(a) and (c). The horizontal axis, R, is linear in (a), while it is logarithmic to highlight the inner radius in (c). The distribution of N_2H^+ column density is rather flat. At $t = 1 \times 10^5$ yr, the N_2H^+ abundance has a peak in the midplane at $R \sim 200$ AU, which is outside the CO snow line. But N_2H^+ column density does not sharply drop inward at the CO snow line (~125 AU), because N_2H^+ is abundant in the disk surface even in the inner radius. At 9.3×10^5 yr, the N_2H^+ is abundant only in the disk surface, and the N_2H^+ column density shows a peak at ~30 AU, which is inside the CO snow line.

The column densities of molecules in the millimeter grain model are shown in Figures 5(b) and (d). At $t = 1 \times 10^5$ yr, the N_2H^+ column density has a peak at a radius of ~40 AU and significantly decreases inward at ~20 AU, which corresponds to the CO snow line in the disk model with millimeter grains. This model is thus in better agreement with the observation of TW Hya than the dark cloud dust model. At $t = 9.3 \times 10^5$ yr, the radius of the N_2H^+ column density peak is shifted inward owing to the sink effect on CO and N_2.

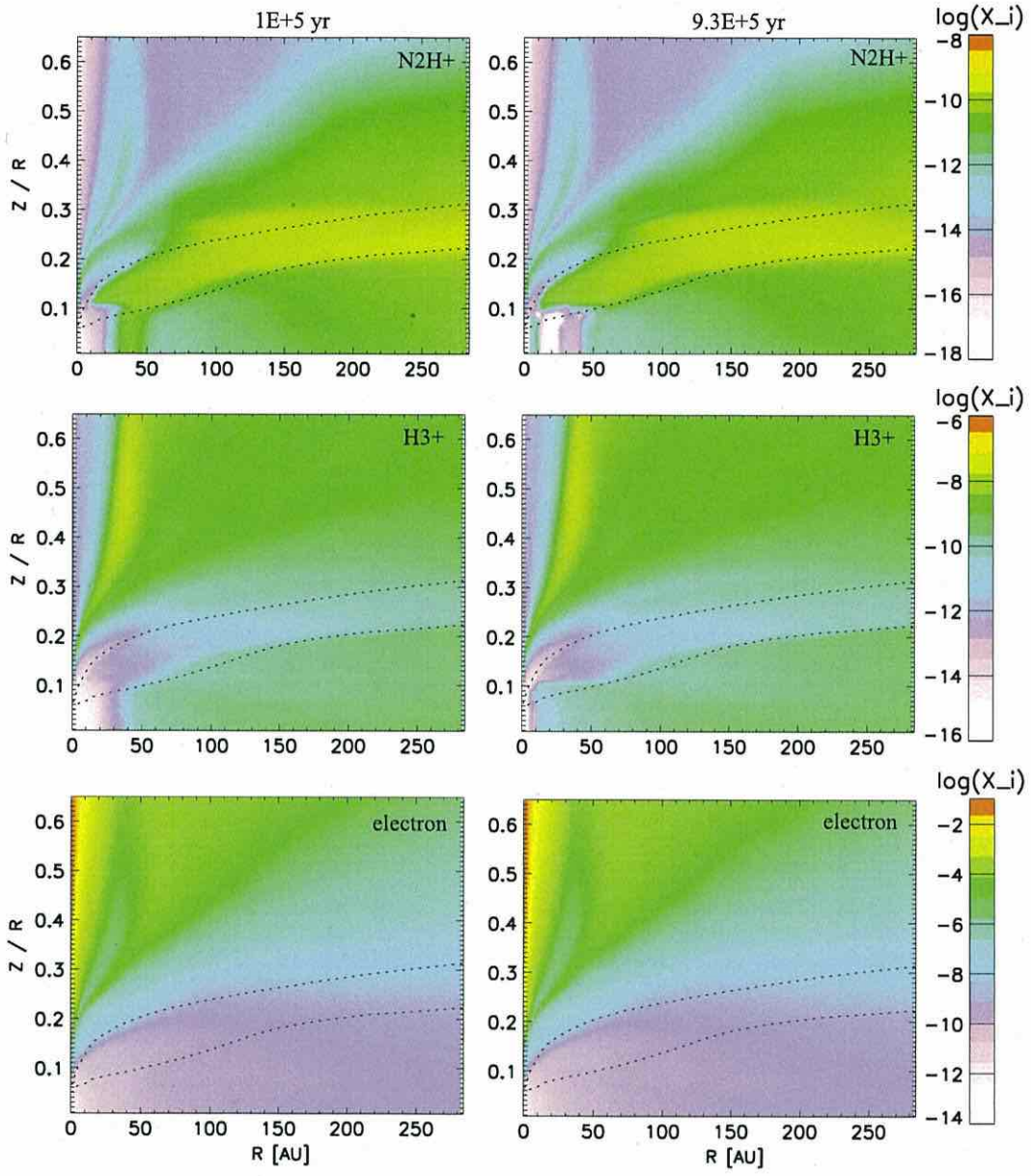

Figure 3. (Continued.)

4. ANALYTICAL SOLUTION FOR MOLECULAR ION ABUNDANCES

In the molecular layer, the major ions are HCO^+, H_3^+, and N_2H^+. In this section we derive analytical formulae for their abundances. The analysis helps us to better understand the spatial distributions of these species (Figures 2 and 3). We will show that we can calculate HCO^+ and N_2H^+ abundances in a disk model, if the distributions of gas density, temperature, ionization rate, and abundances of CO and N_2 are given. The formulae are useful in constraining the ionization rate from the observation of CO, HCO^+, and N_2H^+.

4.1. Electrons

Electron abundance, i.e., the ionization degree, is determined by the balance between ionization and recombination. Let us first assume that HCO^+ is the dominant ion in the disk, for simplicity. A sequence of reactions starts with the ionization of H_2 via cosmic ray, X-rays, or decay of radioactive nuclei:

$$H_2 \rightarrow H_2^+ + e \quad (7)$$

$$H_2^+ + H_2 \rightarrow H_3^+ + H \quad (8)$$

$$H_3^+ + CO \rightarrow HCO^+ + H_2 \quad (9)$$

$$HCO^+ + e \rightarrow H + CO. \quad (10)$$

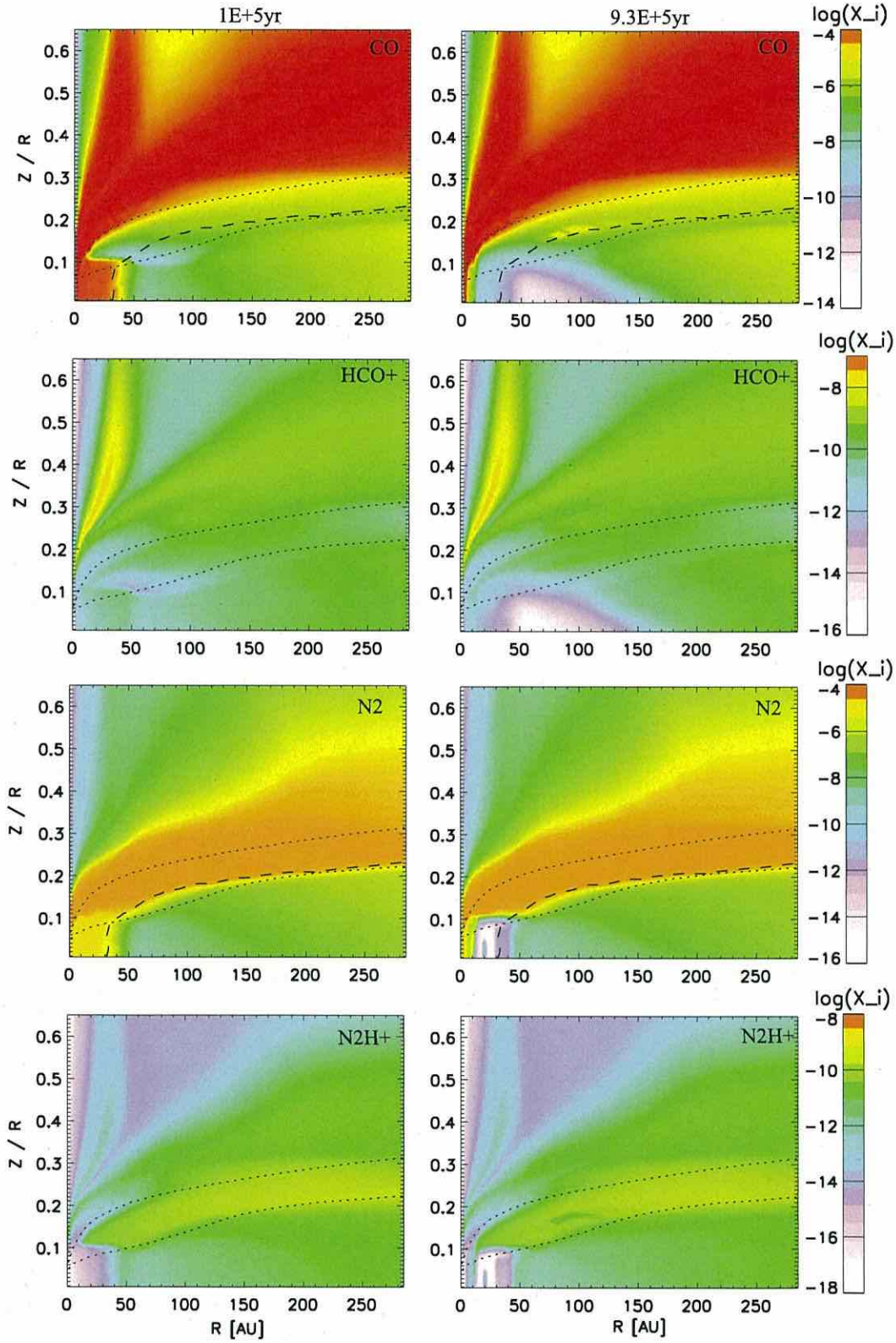

Figure 4. Distributions of CO, HCO^+, N_2, and N_2H^+ in the model with millimeter grains, as in Figure 3. The desorption energies of CO and N_2 are set to be equal (1000 K).

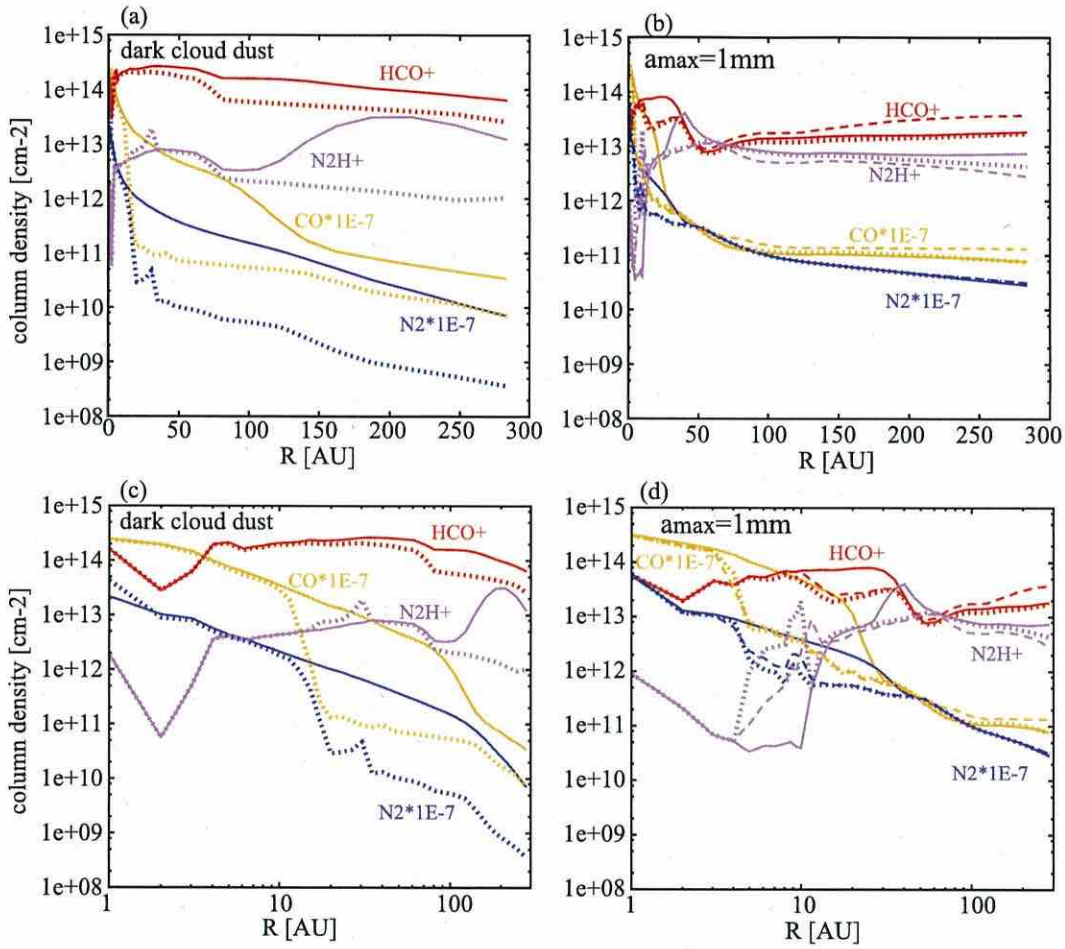

Figure 5. Radial distributions of column densities of CO, HCO^+, N_2, and N_2H^+ in the gas phase at $t = 1 \times 10^5$ yr (solid lines) and 9.3×10^5 yr (dotted lines) in the model with (a and c) dark cloud dust and (b and d) millimeter grains. The column densities of CO and N_2 are multiplied by a factor of 10^{-7} to fit in the figure. The horizontal axis, R, is linear in (a) and (b), while it is logarithmic to highlight the inner radius in (c) and (d). The dashed lines in the right panel depict the column densities of molecules in the model with $E_{\rm des}({\rm CO}) = E_{\rm des}({\rm N_2}) = 1000$ K at 9.3×10^5 yr.

We define the ionization degree $x(\mathrm{e})$ as $n(\mathrm{e})/n_{\rm H}$ rather than $n(\mathrm{e})/n(\mathrm{H_2})$; while the latter is the usual definition, molecular abundances are relative to hydrogen nuclei in our numerical calculation. Considering the neutrality, the ionization degree in molecular gas is given by

$$x(\mathrm{e}) = \frac{n(\mathrm{e})}{n_{\rm H}} = \frac{n(\mathrm{e})}{2n(\mathrm{H_2})} = \sqrt{\frac{\zeta}{2k_{10}n_{\rm H}}}. \quad (11)$$

The ionization rate ζ is a sum of the rates by cosmic rays, X-rays (Figure 1), and decay of radioactive nuclei. The rate coefficients k of relevant reactions are listed in Table 2 in Appendix A.

Now, it should be noted that the dominant ion varies within the disk. Although the rate coefficients of the dissociative recombination of molecular ions are mostly of the same order ($\sim 10^{-7}\,\mathrm{cm^3\,s^{-1}}$), the values vary slightly among molecular ions. We thus adopt an iteration to evaluate the ionization degree. Initially, we assume that reaction (10) dominates in the recombination of electrons in the gas phase, and we calculate the ionization degree, which is used to evaluate the abundances of molecular ions (see the following sections). Then we recalculate Equation (11) by replacing k_{10} with the average of the recombination rate coefficients of molecular ions weighted by their abundances.

In the midplane at $R \lesssim$ a few times 10 AU, the gas density is so high that the grain-surface recombination becomes more effective than the gas-phase recombination:

$$\mathrm{HCO^+ + G(-) \rightarrow H + CO + G(0)}, \quad (12)$$

where G(−) and G(0) represent a negatively charged grain and a neutral grain, respectively. Then the ionization balance is described as

$$\begin{aligned}\zeta n(\mathrm{H_2}) &= k_{10} n(\mathrm{HCO^+}) n(\mathrm{e}) + k_{\rm G} n(\mathrm{G-}) n(\mathrm{HCO^+}) \\ &= k_{10} n^2(\mathrm{e}) + k_{\rm G} n(\mathrm{G-}) n(\mathrm{e}), \end{aligned} \quad (13)$$

where $k_{\rm G}$ is the rate coefficient of the grain-surface recombination of HCO^+ (see, e.g., Umebayashi 1983). Assuming that most grains are negatively charged, which is valid when $n_{\rm H}/\zeta \lesssim 10^{30}\,\mathrm{cm^{-3}\,s}$ (Umebayashi 1983), the electron abundance is calculated by solving this quadratic function. It should be noted that Equation (13) is equivalent to Equation (11),

when the gas-phase recombination is more effective than the grain-surface recombination. Thus, we use Equation (13) rather than Equation (11) in the calculation of ionization degree in the whole disk, and k_{10} is replaced by the weighted mean of the recombination rate coefficients in the iteration.

In deriving Equations (11) and (13), we have assumed that the molecular ions are the dominant charge carrier. In the disk surface, however, atomic ions such as C^+ and S^+ are produced via photoionization and dominate over molecular ions (Section 3.2). In the transition layer from such an atomic-ion-dominated (AID) layer to the molecular layer, many reactions contribute to the ionization balance, and the major reactions vary over the transition layer. It is thus difficult to derive analytical formulae of electron abundances there. In the present work, we compare the electron abundance obtained by Equation (13) with the calculation of the full reaction network at each position in the disk. We adopt the latter, when it is twice as large as the former. As we have seen in the previous section, the position of the transition region depends sensitively on the grain-size distribution in the disk model, as well as on the assumed UV flux from the central star and the interstellar radiation fields. Readers are advised to use the photon-dominated region (PDR) codes to calculate the electron abundance in the AID layer and the transition region for a specific disk model. The PDR codes or their analogs are commonly used to calculate the vertical distributions of gas density and temperatures in disk models (e.g., Kamp & Dullemond 2004; Nomura & Millar 2005; Gorti & Hollenbach 2008).

4.2. H_3^+

H_3^+ is produced by reaction (8). The major destruction paths of H_3^+ are recombination and proton transfer to CO and N_2. In the midplane at $R \lesssim$ a few times 10 AU, the grain-surface recombination also becomes effective:

$$H_3^+ + e \rightarrow H_2 + H \text{ or } H + H + H \quad (14)$$

$$H_3^+ + G(-) \rightarrow H_2 + H + G(0) \text{ or } H + H + H + G(0) \quad (15)$$

$$H_3^+ + CO \rightarrow HCO^+ + H_2, \quad (16)$$

$$H_3^+ + N_2 \rightarrow N_2H^+ + H_2. \quad (17)$$

Considering the balance between the formation and destruction, H_3^+ abundance is given by

$$x\left(H_3^+\right) = \frac{1}{2}\frac{\zeta/n_H}{k_{14}x(e) + k_{15}x(G-) + k_{16}x(CO) + k_{17}x\left(N_2\right)}. \quad (18)$$

4.3. N_2H^+

N_2H^+ is formed by reaction (17) and is destroyed by the proton transfer to CO (reaction (1)) and recombination in the gas phase and on negatively charged grains:

$$N_2H^+ + e \rightarrow NH + N \text{ or } N_2 + H \quad (19)$$

$$N_2H^+ + G(-) \rightarrow NH + N + G(0) \text{ or } N_2 + H + G(0). \quad (20)$$

Then its abundance is given by

$$x\left(N_2H^+\right) = \frac{k_{17}x\left(H_3^+\right)x\left(N_2\right)}{k_{19}x(e) + k_1x(CO) + k_{20}x(G-)}. \quad (21)$$

4.4. HCO^+

HCO^+ is formed by reactions (1) and (16) and destroyed by the recombination in the gas phase (10) and on grain surfaces (12). Once the dust temperature exceeds ~100 K, molecules with a higher proton affinity than CO, such as NH_3, are desorbed to the gas phase to destroy HCO^+. In this section, we neglect such a high-temperature region, which is rather limited in our disk model. It is straightforward to derive

$$\frac{n\left(HCO^+\right)}{n(CO)} = \frac{k_{16}n\left(H_3^+\right) + k_1n\left(N_2H^+\right)}{k_{10}n(e) + k_{12}n(G-)}. \quad (22)$$

At the disk-surface region, where the grain-surface recombination is not effective and H_3^+ dominates over N_2H^+, the equation is modified to

$$\frac{n\left(HCO^+\right)}{n\left(H_3^+\right)} = \frac{k_{16}n(CO)}{k_{10}n(e)}. \quad (23)$$

It shows that HCO^+ is less abundant than H_3^+, if the abundance ratio of CO to electrons is lower than $\frac{k_{10}}{k_{16}} = 1.5 \times 10^2(T/300\text{ K})^{-0.69}$ (see Section 3.1).

4.5. Comparison with Numerical Results

We now check how the analytical formulae compare with the full-network calculation. We adopt the physical parameters (density, temperature, and ionization rate) and abundances of CO and N_2 from the full-network model at $t = 1 \times 10^5$ yr and calculate the abundances of electrons, H_3^+, N_2H^+, and HCO^+ using the analytical formulae at each position in the disk models with dark cloud dust and millimeter grains. As described in Section 4.1, our analytical solution applies to a layer in which the major ions are molecular ions. When the electron abundance obtained in the full-network calculation is twice as large as given by the analytical formula (i.e., AID layer), we adopt the electron abundance from the former. It should be noted, however, that the analytical formulae for H_3^+, N_2H^+, and HCO^+ are appropriate even in the AID layer, if the electron abundance is adopted from the full network.

Figure 6 shows the 2D distributions of electrons, H_3^+, N_2H^+, and HCO^+ abundances calculated using the analytical formulae in the disk models with dark cloud dust (left panel) and millimeter grains (right panel). The distributions of molecular ions are to be compared with those in the left columns of Figures 2 and 3. The dashed lines indicate the height (Z) above which we adopt the electron abundance of the full-network calculation. For a more quantitative comparison, Figure 7 shows the molecular distribution in the Z-direction at $R = 53.4$ AU in the disk models with dark cloud dust and millimeter grains. The solid lines depict the abundances calculated by the full reaction network, while the dotted lines depict the analytical solution.

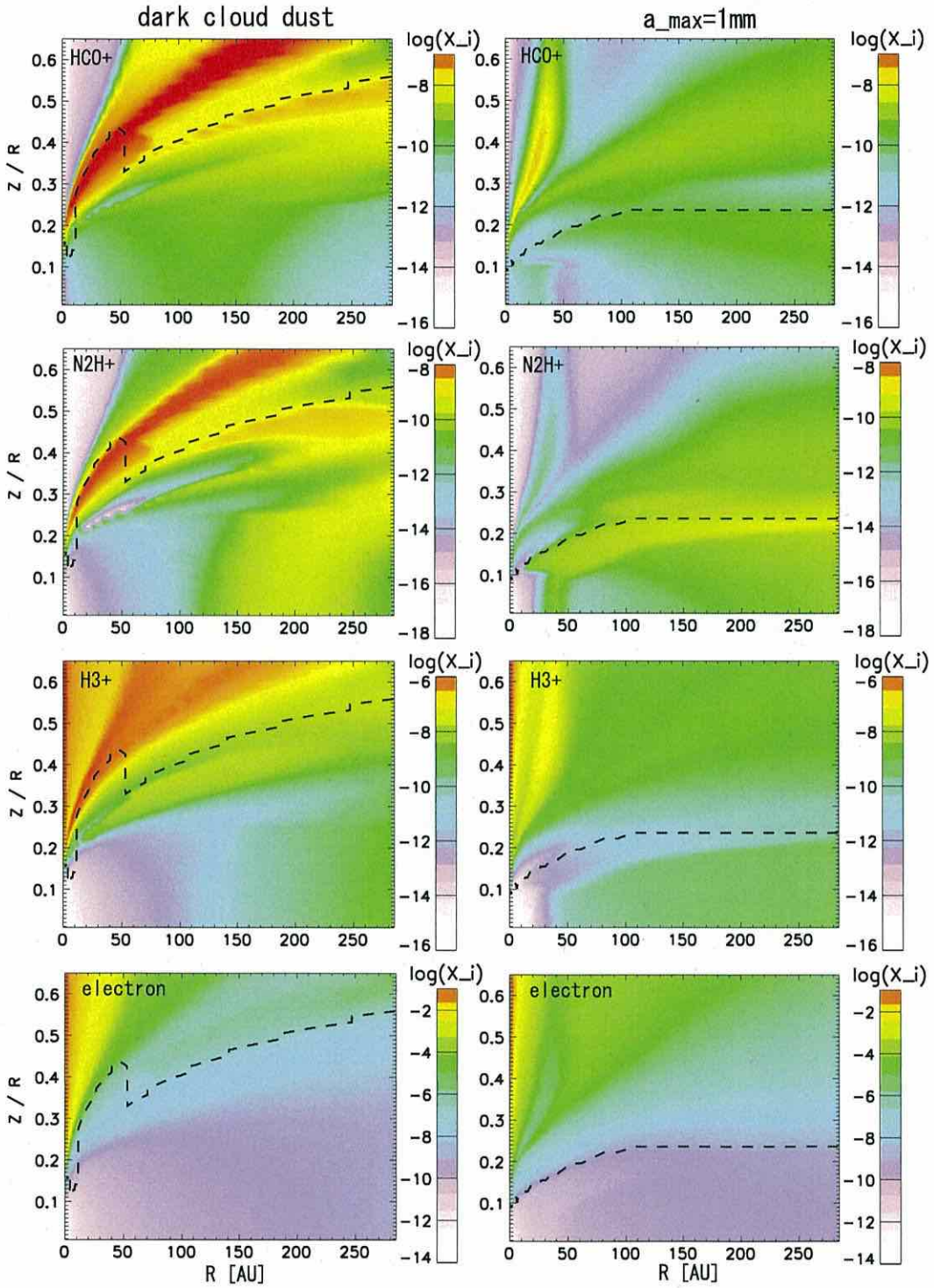

Figure 6. 2D distributions of HCO^+, N_2H^+, H_3^+, and electrons calculated using the analytical formulae in the disk models with dark cloud dust (left panel) and millimeter grains (right panels). CO and N_2 abundances are adopted from the full-network model at $t = 1 \times 10^5$ yr. The dashed line depicts the layer above which the electron abundance is adopted from the full-network model.

We can see that the analytical formulae are in reasonable agreement with the results of the full-network calculation in both models. At high Z (e.g., $Z \gtrsim 0.4$ at $R \sim 30$ AU), H_3^+ is overestimated; while analytical formula (18) assumes that the hydrogen is all in H_2, it is photodissociated in the full-network model in such unshielded low-density regions. In molecular layers at lower Z, on the other hand, the analytic formulae tend to slightly overestimate the molecular ion abundances, partly

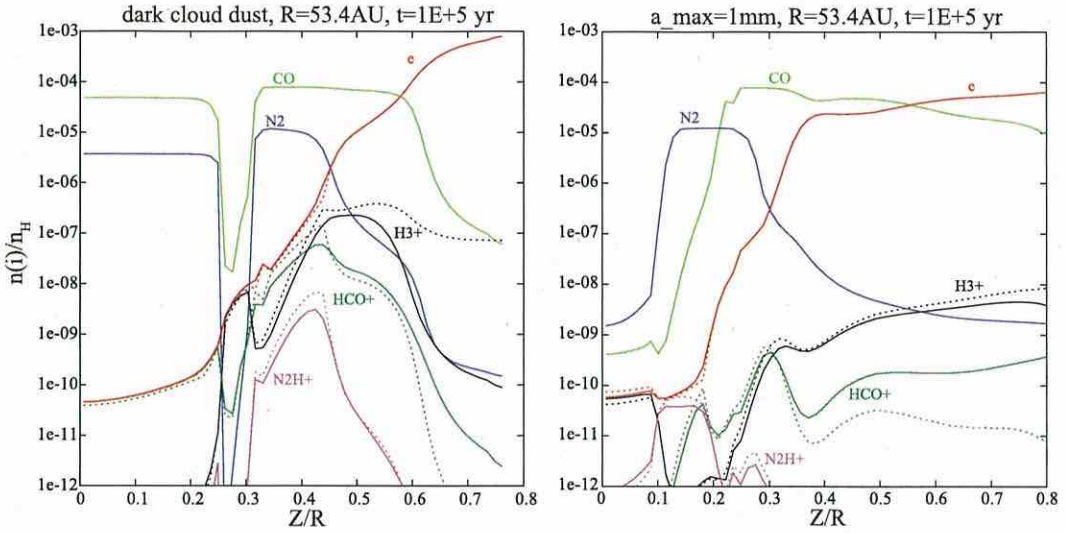

Figure 7. Molecular abundances as a function of height from the midplane (Z/R) at $R = 53.4$ AU in the disk models with dark cloud dust (left panel) and millimeter grains (right panel) at $t = 1 \times 10^5$ yr. The solid lines depict the results of the full-network model, while the dotted lines depict the abundances obtained by the analytical formulae.

because the analytical formulae neglect the neutral species other than CO and N_2. In the full-network model, there are minor neutral species, such as OH, which have a larger proton affinity than N_2 and CO. In the upper layers of the millimeter grain model, the analytical formula underestimates the HCO^+ abundance; another formation path, $CO^+ + H_2$, becomes effective in this region.

Figure 8 shows the column densities of HCO^+ and N_2H^+ obtained by the full-network calculation in the millimeter grain model at $t = 1 \times 10^5$ yr (solid lines) and the analytical formulae (dotted lines). The column densities of the analytical model agree with the full-network model within a factor of 2. Although the analytical formula underestimates the HCO^+ abundance at the disk surface, the surface region does not contribute much to the HCO^+ column density.

In summary, we have demonstrated that the analytical formulae of molecular ion abundances agree well with the full-network results. The analytical formulae give reasonable spatial distributions of molecular ions, taking into account the spatial variation of gas density and ionization rate. They can thus be used to compare a disk model with molecular line observations without performing the full chemical network calculations. The input parameters of the formulae are density, temperature, ionization rate, and abundances of CO and N_2. The distributions of density and temperature should be prepared for a specific object. Then the ionization rate can be calculated by X-ray radiation transfer and by assuming a cosmic-ray penetration depth and abundances of radioactive nuclei (e.g., Cleeves et al. 2014). The electron abundance in the disk surface is also needed and can be obtained by the PDR calculation. An alternative option is to simply assume a height from the midplane below which molecular ions are more abundant than atomic ions. Finally, we need spatial distributions of CO and N_2. While the full-network calculations show that they are subject to the sink effect and thus could decrease with time even in the region warmer than their sublimation temperature, the simplest assumption would be the equilibrium abundance between adsorption and desorption, as we will see in the next section.

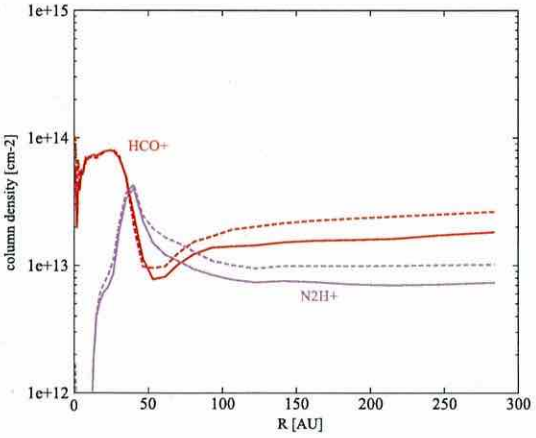

Figure 8. Radial distributions of column densities of HCO^+ and N_2H^+ in the full-network model with millimeter grains at $t = 10^5$ yr (solid lines). The column densities obtained by the analytical formulae are depicted by the dotted lines.

5. RESULTS: NO-SINK MODEL

In our full-network calculations, the N_2H^+ ring is reproduced in a millimeter grain model with a significant CO depletion due to the sink effect. Efficiency of the sink effect, however, depends on various parameters. It is therefore useful to calculate the distribution of N_2H^+ in a model without the sink effect. As described in Section 2.3, here we assume that the total (gas and ice) abundances of CO and N_2 are constant, and that their gas/ice ratios are determined by the equilibrium between the adsorption onto and desorption from the grain surfaces (Equations (4) and (5)).

A combination of the analytical formulae of molecular ions and equilibrium abundances of CO and N_2 make it very easy to

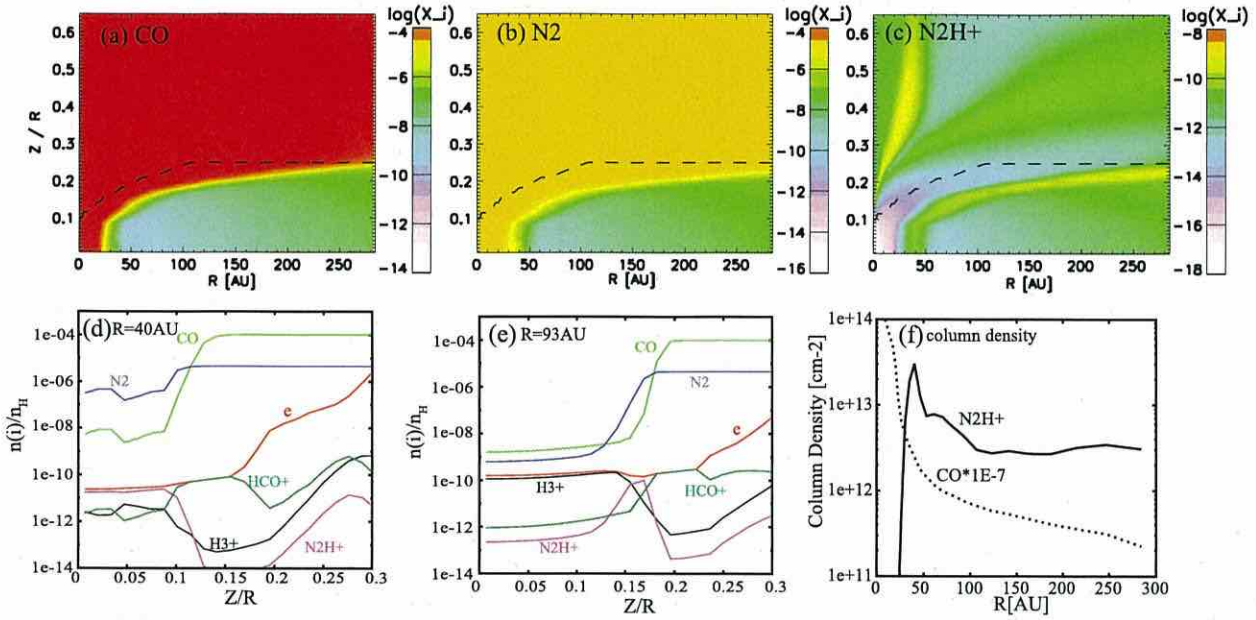

Figure 9. (a)–(c): Distributions of abundances of CO, N_2, and N_2H^+ in the no-sink model. The desorption energies are set to be $E_{des}(CO) = 1150$ K and $E_{des}(N_2) = 1000$ K. The dashed lines depict the layer above which the electron abundance is adopted from the full-network model. (d)–(e): Vertical distributions of molecules at $R = 40$ and 93 AU. (f) Column densities of N_2H^+ and CO. The column density of CO is multiplied by a factor of 10^{-7} to fit in the figure.

investigate the dependence of N_2H^+ abundance on various disk parameters. Here we demonstrate this merit of the analytical formulae by investigating the dependence of N_2H^+ abundance on desorption energies of CO and N_2 and on ionization rate in the disk model with millimeter grains. We could apply the no-sink model to the disk model with dark cloud dust, as well, but the relatively high abundance of N_2H^+ in the disk surface makes the radial distribution of N_2H^+ column density flatter than observed (Section 3.1).

5.1. N_2H^+ in Disk Models without the Sink Effect

Figures 9(a)–(c) show the distributions of CO, N_2, and N_2H^+ in the no-sink model in the disk model with millimeter grains. The desorption energies of CO and N_2 are assumed to be 1150 and 1000 K, respectively. The dashed line depicts the height above which the electron abundance is adopted from the full-network model. Figures 9(d)–(e) show the verticaldistributions of molecules at radii of 40 and 93 AU. At $R = 40$ AU, the temperature is close to the sublimation temperatures of CO and N_2 even in the midplane. The gas-phase abundances of CO and N_2 are thus mostly determined by the thermal desorption. In the midplane at $R = 93$ AU, on the other hand, the non-thermal desorption by cosmic rays dominates over the thermal desorption. The abundance of N_2H^+ is determined by Equation (21). As expected, N_2H^+ abundance is high in layers where N_2 is more abundant than CO. We note, however, that N_2H^+ abundance is determined not only by the abundance ratio of N_2/CO. For example, in Figures 9(d)–(e), the N_2H^+ abundance varies among the three positions where the abundances of CO and N_2 are equal. The absolute values of CO and N_2 abundances matter, since they control the abundance of H_3^+ (Equation (18)), from which N_2H^+ is formed. Note that N_2H^+ abundance in the very surface region of the disk (e.g., $Z \gtrsim 0.3$ at $R \sim 50$ AU) could be overestimated; its mother molecule, N_2, is photodissociated in the disk surface in the full-network model.

The radial distribution of N_2H^+ column density is shown in Figure 9(f). The dotted line depicts the CO column density multiplied by a factor of 10^{-7}. In order to avoid the photodissociation region at the disk surface, N_2H^+ column density is calculated by the integration at $|Z| \leqslant 0.3$ ($R > 50$ AU), $|Z| \leqslant 0.15$ ($10 < R \leqslant 50$ AU), and $|Z| \leqslant 0.1$ ($R \leqslant 10$ AU), while the CO column density is obtained by the integration along the whole disk height. We can see that N_2H^+ column density indicates a ring structure, as in the full-network model. The spatial distribution of N_2H^+ is, however, different from that in the full-network model. First, the N_2H^+ ring is sharp and exists right outside the CO snow line in the no-sink model, simply reflecting the lower desorption energy of N_2 than that of CO, while it is broader in the full-network model, especially in the late stage ($t = 9.3 \times 10^5$ yr). The peak N_2H^+ column density at $R \sim 50$ AU and $t > 10^5$ yr is lower in the full-network model, because N_2 is depleted via the sink effect in the midplane. Second, N_2H^+ is confined to a thin layer colder than the CO sublimation temperature in the no-sink model, while it is abundant also in the upper warmer layers in the full-network model. The two models can thus be distinguished by constraining the vertical distributions of N_2H^+ from observations.

In the case of TW Hya, N_2H^+ lines of $J = 3 - 2$ and $J = 4 - 3$ are observed (Qi et al. 2013a, 2013b). Assuming that the lines are optically thin under LTE conditions, the excitation temperature is derived to be 35 ± 10 K. The relatively high excitation temperature of N_2H^+, together with the low CO abundance indicated by $C^{18}O$ and HD observations (Favre et al. 2013), might be better explained by the full-network model. We postpone the discussion on TW Hya to a future work, in which we will apply our network model and analytical formulae to a disk model specified for TW Hya and

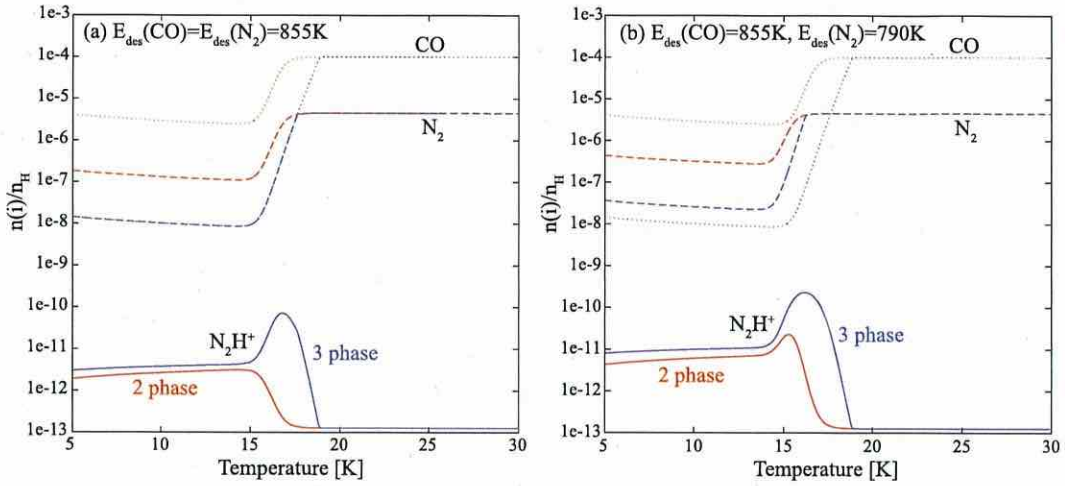

Figure 10. Abundances of CO (dotted lines), N_2 (dashed lines), and N_2H^+ (solid lines) as a function of temperature. The total (gas and ice) abundances of CO and N_2 are assumed to be 1×10^{-4} and 4.5×10^{-6}, respectively. The gas density is set to be 1×10^8 cm^{-3}, and ionization rate is 5×10^{-17} s^{-1}. As for the desorption rate, the two-phase model (Equation (4)) is assumed for the red lines, while the three-phase model (Equation (24)) is assumed for the blue lines. The desorption energies of CO and N_2 are 855 K in panel (a), while $E_{\rm des}$ (CO) is 855 K and $E_{\rm des}$ (N_2) is 790 K in panel (b).

simulate molecular emission with non-LTE radiative transfer calculations for more quantitative comparisons with the observational data.

5.2. Dependence on Desorption Rates

So far we have set the desorption energies of CO and N_2 to be 1150 and 1000 K, respectively. It is well known, however, that the desorption energies of molecules depend on the chemical compositions and physical structure (e.g., crystal or amorphous) of the ice mantle. While the values we adopted from Garrod & Herbst (2006) are desorption energies on water-dominated ice surfaces derived from the temperature-programmed desorption experiments (Collings et al. 2004), the desorption energies of pure ices of CO and N_2 are $E_{\rm des}$(CO) $= 855 \pm 25$ K and $E_{\rm des}(N_2) = 790 \pm 25$ K (Öberg et al. 2005). In Section 3.2, we have shown that in the full-network model the N_2H^+ distribution does not sensitively depend on the desorption energies of CO and N_2, because the layer of CO depletion, where N_2H^+ is abundant, is determined by the sink effect rather than thermal desorption. If the CO sink is not effective, on the other hand, the abundance of N_2H^+ could be more sensitive to their desorption energies.

We also note that Equation (4) assumes the first-order desorption, i.e., the desorption rate is proportional to the abundance of the species in the ice mantle, $n_{\rm COice}$. In the following, we call this model "two phase," since this equation is usually used in the two-phase gas-grain chemical models, which do not discriminate the layers of the ice mantle. In reality, the migration (and thus desorption) of molecules deeply embedded in the ice mantle could be inefficient, at least at low temperatures (e.g., Collings et al. 2004). We therefore consider another model, i.e., the "three-phase" model, in which only the surface monolayer is subject to desorption:

$$S\pi a^2 v_{\rm th} n_{\rm COgas} n_{\rm dust} = \min\left[4\pi a^2 n_{\rm dust} N_{\rm site},\, n_{\rm COice}\right] \times \left\{\nu \exp\left(-\frac{E_{\rm des}^{\rm CO}}{kT}\right) + \nu\tau_{\rm CR} C_{\rm Fe} \exp\left(-\frac{E_{\rm des}^{\rm CO}}{kT_{\rm max}}\right)\right\}, \quad (24)$$

where $N_{\rm site} = 1.5 \times 10^{15}$ cm^{-2} is the number density of the adsorbing site on a grain surface. The desorption is zeroth order, as long as the ice is abundant enough to occupy more than a monolayer in the ice mantle, i.e., $n_{\rm COice} > 4\pi a^2 n_{\rm dust} N_{\rm site}$. Then the gaseous abundance is independent of the total abundance. In the two-phase model, on the other hand, the gaseous CO (N_2) abundance is proportional to the assumed total abundance of CO (N_2).

Before showing the N_2H^+ abundance in the disk model with various desorption rates, it is instructive to apply the analytical formulae to a simpler model, where the gas density and ionization rate are constant, 10^8 cm^{-3} and 5×10^{-17} s^{-1}, respectively. Figure 10 shows the gaseous abundances of CO, N_2, and N_2H^+ as a function of temperature. The gas and dust temperatures are set to be equal. The total (gas and ice) abundances of CO and N_2 are 1×10^{-4} and 4.5×10^{-6}, respectively. The desorption energies are set to be $E_{\rm des}$(CO) $= E_{\rm des}$ (N_2) $= 855$ K in Figure 10(a) and $E_{\rm des}$(CO) $= 855$ K and $E_{\rm des}(N_2) = 790$ K in Figure 10(b). The desorption rate of the two-phase model (Equation (4)) is assumed for the red lines, while the three-phase model is assumed for the blue lines. The abundances change drastically at the sublimation temperature ~20 K. At $T \lesssim 15$ K, the gaseous abundances of CO and N_2 slightly increase with decreasing temperature; desorption rate is kept constant owing to the non-thermal desorption, while the adsorption rate is proportional to $T^{1/2}$. By comparing the red and blue lines, we can see that the sublimation temperature and gaseous abundances of CO and N_2 at low temperatures are significantly different between the two-phase and three-phase models; the three-phase model gives a much smaller desorption rate than the two-phase model, when the ice mantle is thick. In the three-phase model with the same $E_{\rm des}$ for CO and N_2 (blue lines in panel (a)), the gaseous abundances of CO and N_2 are the same below the sublimation temperature. It is interesting that the N_2H^+ abundance shows a sharp peak slightly below the sublimation temperature. It clearly shows that the N_2H^+ abundance depends not only on the abundance ratio of CO/N_2 but also on the absolute values of their abundances.

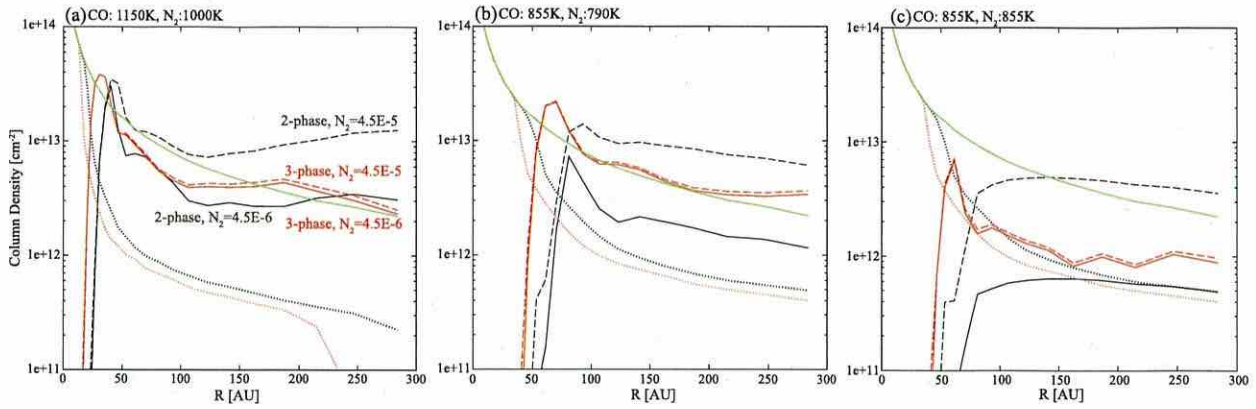

Figure 11. Column density of N_2H^+ in the no-sink models; the total (gas and ice) N_2 abundance is set to be 4.5×10^{-6} for the solid lines, while it is 4.5×10^{-5} for the dashed lines. Black and red lines represent the two-phase and three-phase models, respectively. The dotted lines depict the column density of CO, which is multiplied by a factor of 10^{-7} to fit in the figure. The green lines depict the column density of hydrogen nuclei multiplied by a factor of 10^{-11}. N_2H^+ column density is calculated by the integration at $Z \leqslant 0.3$ ($R < 50$ AU), $Z \leqslant 0.15$ ($10 < R \leqslant 50$ AU), and $Z \leqslant 0.1$ ($R \leqslant 10$ AU) to avoid the photodissociation region at the disk surface, while CO and hydrogen column densities are obtained by integrating over the whole disk height.

Specifically, the N_2H^+ abundance reaches the maximum value when the abundance ratio of CO to electron is $\sim k_{19}/k_1$, which is about 3.3×10^3 at $T = 17$ K (see Appendix B). In the models of Figure 10, the electron abundance is about several $\times 10^{-10}$ and varies slightly with temperature and desorption model. At warm temperatures where the abundance ratio of CO to electrons is higher than this critical value, HCO^+ is the dominant ion, while H_3^+ dominates at lower temperatures. In the case of the two-phase model with the same $E_{\rm des}$ for CO and N_2(red lines), on the other hand, N_2H^+ abundance does not show such a sharp peak around the CO sublimation temperature, because the abundance ratio of CO to electrons is always higher than the critical value mentioned above. In the case of $E_{\rm des}$ (N_2) < $E_{\rm des}$ (CO) (Figure 10(b)), there is a narrow temperature range in which N_2 is relatively abundant but CO is not, so that N_2H^+ abundance has the maximum value, even in the two-phase model.

Figure 11 shows the radial distributions of N_2H^+ (solid lines) and CO (dotted lines) column densities in the disk model with millimeter grains as in Figure 9(f), but for three sets of desorption energies of CO and N_2: $E_{\rm des}$(CO) = 1150 K and $E_{\rm des}$(CO) = 1000 K in panel (a), $E_{\rm des}$(CO) = 855 K and $E_{\rm des}$ (CO) = 790 K in panel (b), and $E_{\rm des}$(CO) = 855 K and $E_{\rm des}$ (CO) = 855 K in panel (c). The column density of hydrogen nuclei is multiplied by a factor of 10^{-11} and is shown by the green line. The black and red lines depict the two-phase and three-phase models, respectively. The total (gas and ice) abundance of N_2 is 4.5×10^{-6} relative to hydrogen for the solid lines. In order to investigate the dependence of N_2H^+ abundance on the total N_2 abundance, it is set to be 10 times higher for the dashed lines. We can see that all the models show a ring-like structure of N_2H^+. The N_2H^+ column density and its radial gradient, however, depend significantly on the desorption energies and the model of desorption. The CO snow line and the inner edge of N_2H^+ ring are at smaller radii in the model with higher $E_{\rm des}$(CO). They are also at smaller radii in the three-phase model than in the two-phase model, because of the lower desorption rate in the three-phase model. While the N_2H^+ column density significantly depends on the total N_2 abundance in the two-phase model, the dependence is weak in the three-phase model. Dependence of the N_2H^+ column density on the desorption energies of CO and N_2 is complex, as expected from Figure 10. In the models with $E_{\rm des}$(CO) > $E_{\rm des}$ (N_2), there is a region where N_2 is thermally desorbed but CO is not, which results in a peak of N_2H^+ column density with a width of a few times 10 AU. In the models with $E_{\rm des}$(CO) = $E_{\rm des}$ (N_2) = 855 K, the N_2H^+ column density shows a sharp peak in the three-phase model, but not in the two-phase model, as expected from Figure 10.

5.3. Dependence on Ionization Rate

Although we have assumed that the attenuation length of the cosmic-ray ionization is 96 g cm^{-2}(Umebayashi & Nakano 1981), the stellar winds and/or magnetic fields could hamper the penetration of cosmic rays to the disk. Then X-rays would be the major ionization source (Glassgold et al. 1997; Cleeves et al. 2013). The dotted lines in Figure 3 depict the height from the midplane below which the X-ray ionization rate is lower than 10^{-17} and 10^{-18} s^{-1}, respectively. The layers with abundant N_2H^+ are around or below these lines in both the full-network model (i.e., with CO sink) and the no-sink model. Here we investigate how the N_2H^+ column density changes, if the cosmic ray does not reach the disk.

Figure 12 shows the radial distribution of N_2H^+ column density without the cosmic-ray ionization. X-rays are the only ionization source for the dashed lines, while the decay of radioactive nuclei is considered for the solid lines. It should be noted that cosmic rays also cause non-thermal desorption in our models; the non-thermal desorption by cosmic rays is neglected for the solid lines and dashed lines. For a comparison, the dotted lines depict the model in which the non-thermal desorption is included but the ionization source is X-rays and radioactive nuclei; although such a model is not self-consistent, we can see the importance of the non-thermal desorption by comparing the solid lines with dotted lines. The blue and green lines depict the model in which CO and N_2 abundances in the gas phase are given by the three-phase model; labels in the figure depict the assumed desorption energies of CO and N_2. For the red lines, we refer to the CO and N_2 abundances in our full-network model at 1×10^5 yr, i.e., the model with sink. Note that there is thus no red dotted line. Compared with the models with cosmic-ray ionization

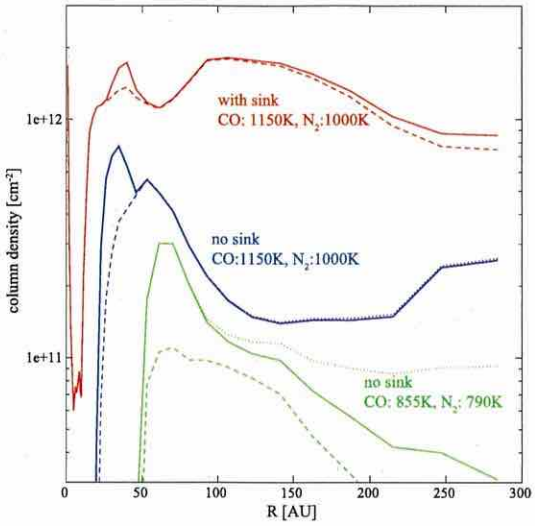

Figure 12. Column density of N_2H^+ in the models without cosmic-ray ionization. X-rays are the only ionization source for the dashed lines, while the decay of radioactive nuclei is considered for the solid lines and the dotted lines. The non-thermal desorption by cosmic rays is neglected for the solid lines, while it is included for the dotted lines. For the blue and green lines, gaseous CO and N_2 abundances are given by the three-phase model with the desorption energies labeled in the figure. For the red lines, CO and N_2 abundances are adopted from the full-network model at 1×10^5 yr, in which the sink effect on CO is at work.

(Figures 8 and 11), the N_2H^+ column density is reduced significantly. The reduction factor, the ratio of the peak column density in the model with cosmic rays to that in the model without cosmic rays, is the highest (~70) in the no-sink model with low CO and N_2 desorption energies, while it is the lowest (factor of ~20) for the model with sink. In the latter model, N_2H^+ is relatively abundant even in the layer with the X-ray ionization rate $\gtrsim 10^{-18}$ s^{-1} (i.e., $Z/R \gtrsim 0.2$). In the no-sink models, on the other hand, N_2H^+ is depleted at $0.2 \lesssim Z \lesssim 0.3$. In the model with lower desorption energy of CO, the CO freeze-out region, where the N_2H^+ is abundant, is confined to the layer closer to the midplane with low X-ray ionization rate.

6. SUMMARY

In this work we calculated the molecular abundances in disk models to investigate the origin of the N_2H^+ ring recently found at the CO snow line in the disk of TW Hya (Qi et al. 2013b). We adopt two disk models with different dust properties; dust grains are similar to dark cloud dust in one model, while they have grown to millimeter size in the other model. We first calculated a full network of gas-grain chemical reactions. Our findings in the full-network model are as follows.

1. In the model with dark cloud dust, N_2H^+ is abundant in the disk surface. Although N_2H^+ abundance near the midplane has a local maximum outside the radius of the CO snow line, N_2H^+ column density is rather high even inside the CO snow line because N_2H^+ in the disk surface contributes significantly to the column density.
2. In the model with millimeter grains, the column density of N_2H^+ shows a local peak around the CO snow line. N_2H^+ is abundant in the warm intermediate layer where CO is depleted via the sink effect, while N_2H^+ is destroyed by the proton transfer to CO inside the CO snow line. Penetration of UV radiation (i.e., lower extinction than the dark cloud dust model) plays two important roles. First, UV radiation makes the atomic ions dominant in the disk surface, so that N_2H^+ is not abundant there. In the intermediate layer where CO is depleted via the sink effect, the conversion of N_2 to NH_3 (i.e., the sink effect on N_2) is prevented by the photodissociation of NH, so that N_2H^+ is abundant.
3. In the model with millimeter grains, the distributions of N_2H^+ and its column density do not change significantly when the desorption energies of CO and N_2 are varied. The N_2H^+ column density shows a local peak at the radius of the CO snow line, even if the desorption energies of CO and N_2 are equal, because in the region with abundant N_2H^+, CO is depleted via the sink effect rather than the adsorption of CO itself onto grain surfaces.
4. By analyzing the results of the full-network model, we derived analytical formulae of electron, H_3^+, N_2H^+, and HCO^+ abundances as functions of gas density, temperature, ionization rate, and abundances of CO and N_2. The analytical formulae would be useful for radio observers to derive the abundances of these molecular ions from the observational data using a reasonable physical model for a well-observed disk such as TW Hya.

While the sink effect on CO plays an important role in determining the N_2H^+ abundance in the full-network model, the efficiency of the sink depends on various parameters such as turbulence in the disk and the rates of chemical conversion of CO to less volatile species. We thus constructed the no-sink model, in which the total (gas and ice) abundances of CO and N_2 are set constant, and their gas-phase abundances are determined by the balance between the adsorption and desorption. The abundances of molecular ions are calculated using the analytical formulae. The results of the no-sink models are as follows.

1. The column density of N_2H^+ shows a ring-like structure in the no-sink model with millimeter dust grains. Since the abundance of N_2H^+ is given by a non-linear function of CO and N_2 abundances, it can reach a moderate value even in the cold N_2 freeze-out region, depending on the abundances of CO and N_2.
2. Even if the desorption energies of CO and N_2 are the same, N_2H^+ abundance peaks at the temperature slightly below the CO (and N_2) sublimation temperature, where the abundance ratio of CO to electrons is $\sim k_{19}/k_1 \sim 10^3$.
3. Although the N_2H^+ ring is produced both in the full-network model and in the no-sink model, the detailed distributions of N_2H^+ are different between the two models. In the no-sink model, the N_2H^+ abundant layer is confined to a layer colder than the sublimation temperature of CO, while in the full-network model (i.e., with CO sink), the N_2H^+ abundant layer extends to warmer layers. These models can thus be discriminated in observations if we can determine the vertical distribution of N_2H^+ in disks, specifically starting with constraining the excitation temperature of N_2H^+ emission.
4. The column density of N_2H^+ in the no-sink model sensitively depends on the desorption rates of CO and N_2.
5. If the cosmic ray does not reach the disk, the N_2H^+ column density is reduced by a factor of 20 in the model with CO sink and by a factor of 70 in the no-sink model.

Table 2
Reaction Rate Coefficients Relevant to the Analytical Formulae[a]

Reaction	α	β
$H_3^+ + CO \rightarrow HCO^+ + H_2$	1.61(−9)[b]	0.0
$H_3^+ + N_2 \rightarrow N_2H^+ + H_2$	1.7(−9)	0.0
$H_3^+ + e \rightarrow H_2 + H$	2.59(−8)	−0.5
$H_3^+ + e \rightarrow H + H + H$	4.61(−8)	−0.5
$HCO^+ + e \rightarrow H + CO$	2.40(−7)	−0.69
$N_2H^+ + CO \rightarrow HCO^+ + N_2$	8.8(−10)	0.0
$N_2H^+ + e \rightarrow NH + H$	1.30(−8)	−0.84
$N_2H^+ + e \rightarrow N_2 + H$	2.47(−7)	−0.84

Notes.
[a] Rate coefficients are given in the format $k = \alpha \times (T/300.0)^{\beta}$ cm^3 s^{-1}.
[b] $A(B)$ stands for $A \times 10^B$.

The reduction is more significant in the model with lower desorption energy of CO, because N_2H^+ (i.e., CO freeze-out) is confined to a layer closer to the midplane, where the X-ray ionization rate is lower.

We thank Karin Öberg and Catherine Walsh for helpful discussions. We thank the anonymous referee for his/her constructive comments. This work was supported by JSPS KAKENHI Grant Numbers 23103004, 23103005, 23540266, and 25400229. Numerical calculation was partly conducted using SR16000 at YITP in Kyoto University for numerical calculations. K.F. is supported by the Research Fellowship from the Japan Society for the Promotion of Science (JSPS).

APPENDIX A
REACTION RATE COEFFICIENTS

We list the rate coefficients of the reactions relevant to the analytical formulae of molecular ions in Table 2. In the full-network model, the spin state (ortho and para) of H_3^+ is discriminated, and the reaction rates actually vary with the spin state. For those reactions, we use the rate coefficients from Garrod & Herbst (2006) in the analytical formulae, for simplicity.

APPENDIX B
DEPENDENCE OF N_2H^+ ABUNDANCE ON TEMPERATURE

Figure 10 shows that N_2H^+ abundance reaches the maximum value at $T \sim 17$ K in the three-phase model, even if we assume the same desorption energy for CO and N_2. Here we analyze the model to show that N_2H^+ abundance is maximized when the abundance ratio of CO to electrons is $\sim 10^3$.

At the density of $n_H = 10^8$ cm^{-3}, gas-phase recombination is more effective than the grain-surface recombination. Then the analytic formula of the N_2H^+ abundance (Equation (21)) becomes

$$x(N_2H^+) = \frac{k_{17}x(H_3^+)x(N_2)}{k_{19}x(e) + k_1x(CO)}. \quad (25)$$

When the abundance ratio of CO to electrons is higher than k_{19}/k_1, which is about 3.3×10^3 at $T = 17$ K, the denominator is dominated by the second term. Substituting the analytical formula of H_3^+ abundance (Equations (18)–(25)), it is straightforward to show that N_2H^+ abundance is proportional to $x(N_2)/x^2(CO)$ and thus increases with decreasing CO abundance at $T \sim 17-20$ K. If the first term dominates in the denominator, on the other hand, N_2H^+ abundance is proportional to N_2 abundance. The N_2H^+ abundance decreases with decreasing temperature at $T \sim 15-17$ K.

REFERENCES

Acharyya, K., Hassel, G. E., & Herbst, E. 2011, ApJ, 732, 73
Aikawa, Y., & Nomura, H. 2006, ApJ, 642, 1152
Aikawa, Y., Ohashi, N., Inutsuka, S., Herbst, E., & Takakuwa, S. 2001, ApJ, 552, 639
Aikawa, Y., Umebayashi, T., Nakano, T., & Miyama, S. M. 1997, ApJL, 486, L51
Aikawa, Y., van Zadelhoff, G. J., van Dishoeck, E. F., & Herbst, E. 2002, A&A, 386, 622
Aikawa, Y., Wakelam, V., Garrod, R. T., & Herbst, E. 2008, ApJ, 674, 993
Al-Halabi, A., & van Dishoeck, E. F. 2007, MNRAS, 382, 1648
Baulbus, S. A., & Hawley, J. F. 1991, ApJ, 376, 214
Bergin, E. A., Cleeves, L. I., Crockett, N., & Blake, G. A. 2014, FaDi, 168, 61
Bergin, E. A., & Tafalla, M. 2007, ARA&A, 45, 339
Caselli, P., Stantcheva, T., Shalabiea, O., Shematovich, V. I., & Herbst, E. 2002, P&SS, 50, 1257
Caselli, P., Walmsley, C. M., Terzieva, R., & Herbst, E. 1998, ApJ, 499, 234
Cleeves, L. I., Adams, F. C., & Bergion, E. A. 2013, ApJ, 772, 5
Cleeves, L. I., Bergin, E. A., & Adams, F. C. 2014, ApJ, 794, 123
Collings, M. P., Anderson, M. A., Rui, C., et al. 2004, MNRAS, 354, 1133
Dalgarno, A. 2006, PNAS, 103, 12269
Favre, C., Cleeves, L. I., Bergin, E. A., Qi, C., & Blake, G. A. 2013, ApJL, 776, L38
Fayolle, E. C., Bertin, M., Romanzin, C., et al. 2011, ApJL, 739, L36
Fayolle, E. C., Bertin, M., Romanzin, C., et al. 2013, A&A, 556, 122
Furuya, K., & Aikawa, Y. 2014, ApJ, 790, 97
Furuya, K., Aikawa, Y., Nomura, H., Hersant, F., & Wakelam, V. 2013, ApJ, 779, 11
Furuya, K., Aikawa, Y., Tomida, K., et al. 2012, ApJ, 758, 86
Garrod, R. T., & Herbst, E. 2006, A&A, 457, 927
Glassgold, A. E., Najita, J., & Igea, J. 1997, ApJ, 480, 344
Gorti, U., & Hollenbach, D. 2008, ApJ, 683, 287
Gredel, R., Lepp, S., Dalgrano, A., & Herbst, E. 1989, ApJ, 347, 289
Hasegawa, T. I., & Herbst, E. 1993, MNRAS, 261, 83
Kamp, I., & Dullemond, C. P. 2004, ApJ, 615, 991
Léger, A., Jura, M., & Omont, A. 1985, A&A, 144, 147
Li, X., Heays, A. N., Visser, R., et al. 2013, A&A, 555, 14
Maret, S., Bergin, E. A., & Lada, C. 2006, Natur, 442, 425
Masunaga, H., & Inutsuka, S. 2000, ApJ, 531, 350
Masunaga, H., Miyama, S. M., & Inutsuka, S. 1998, ApJ, 495, 346
Mathis, J. S., Rumpl, W., & Nordsieck, K. H. 1977, ApJ, 217, 425
Nomura, H., Aikawa, Y., Tsujimoto, M., Nakagawa, Y., & Millar, T. J. 2007, ApJ, 661, 334
Nomura, H., & Millar, T. J. 2005, A&A, 438, 923
Öberg, K. I., Linnartz, H., Visser, R., & van Dishoeck, E. F. 2009a, ApJ, 693, 1209
Öberg, K. I., van Broekhuizen, F., Fraser, H. J., et al. 2005, ApJL, 621, L33
Öberg, K. I., van Dishoeck, E. F., & Linnartz, H. 2009b, A&A, 496, 281
Okuzumi, S. 2009, ApJ, 698, 1122
Qi, C., Öberg, K. I., & Wilner, D. J. 2013a, ApJ, 765, 34
Qi, C., Öberg, K. I., Wilner, D. J., et al. 2013b, Sci, 341, 6146
Qi, C., Wilner, D. J., Aikawa, Y., Blake, G. A., & Hogerheijde, M. R. 2008, ApJ, 681, 1396
Tafalla, M., Myers, P. C., Caselli, P., & Walmsley, C. M. 2004, A&A, 416, 191
Umebayashi, T. 1983, PThPh, 69, 480
Umebayashi, T., & Nakano, T. 1981, PASJ, 33, 617
Umebayashi, T., & Nakano, T. 1988, PThPS, 96, 151
Umebayashi, T., & Nakano, T. 2009, ApJ, 690, 69
van der Tak, F. F. S., Black, J. H., Schöier, F. L., Jansen, D. J., & van Dishoeck, E. F. 2007, A&A, 468, 627
van Dishoeck, E. F., Jonkheid, B., & van Hemert, M. C. 2006, FaDi, 133, 231
van Zadelhoff, G.-H., Aikawa, Y., Hogerheijde, M. R., & van Dishoeck, E. F. 2003, A&A, 397, 789
Weingartner, J. C., & Draine, B. T. 2001, ApJ, 548, 296
Williams, J. P., & Cieza, L. A. 2011, ARA&A, 49, 67

Monthly Notices
of the
ROYAL ASTRONOMICAL SOCIETY

MNRAS **448,** 994–1006 (2015) doi:10.1093/mnras/stv025

Formation of a disc gap induced by a planet: effect of the deviation from Keplerian disc rotation

K. D. Kanagawa,[1]★ H. Tanaka,[1] T. Muto,[2] T. Tanigawa[3] and T. Takeuchi[4]

[1]*Institute of Low Temperature Science, Hokkaido University, Sapporo 060-0819, Japan*
[2]*Division of Liberal Arts, Kogakuin University, 1-24-2, Nishi-Shinjuku, Shinjuku-ku, Tokyo 163-8677, Japan*
[3]*School of Medicine, University of Occupational and Environmental Health, Yahatanishi-ku, Kitakyushu, Fukuoka 807-8555, Japan*
[4]*Department of Earth and Planetary Sciences, Tokyo Institute of Technology, Meguro-ku, Tokyo 152-8551, Japan*

Accepted 2015 January 6. Received 2015 January 6; in original form 2014 June 2

ABSTRACT

The gap formation induced by a giant planet is important in the evolution of the planet and the protoplanetary disc. We examine the gap formation by a planet with a new formulation of one-dimensional viscous discs which takes into account the deviation from Keplerian disc rotation due to the steep gradient of the surface density. This formulation enables us to naturally include the Rayleigh stable condition for the disc rotation. It is found that the derivation from Keplerian disc rotation promotes the radial angular momentum transfer and makes the gap shallower than in the Keplerian case. For deep gaps, this shallowing effect becomes significant due to the Rayleigh condition. In our model, we also take into account the propagation of the density waves excited by the planet, which widens the range of the angular momentum deposition to the disc. The effect of the wave propagation makes the gap wider and shallower than the case with instantaneous wave damping. With these shallowing effects, our one-dimensional gap model is consistent with the recent hydrodynamic simulations.

Key words: accretion, accretion discs – planets and satellites: formation – protoplanetary discs.

1 INTRODUCTION

A planet in a protoplanetary disc gravitationally interacts with the disc and exerts a torque on it. The torque exerted by the planet dispels the surrounding gas and forms a disc gap along the orbit of the planet (Lin & Papaloizou 1979; Goldreich & Tremaine 1980). However, a gas flow into the gap is also caused by viscous diffusion and hence the gap depth is determined by the balance between the planetary torque and the viscous diffusion. Accordingly, only a large planet can create a deep gap (Lin & Papaloizou 1993; Takeuchi, Miyama & Lin 1996; Ward 1997; Rafikov 2002; Crida, Morbidelli & Masset 2006).

The gap formation strongly influences the evolution of both the planet and the protoplanetary disc in various ways. For example, a deep gap prevents disc gas from accreting on to the planet and slows down the planet growth (D'Angelo, Henning & Kley 2002; Bate et al. 2003; Tanigawa & Ikoma 2007), and also changes the planetary migration from the type I to the slower type II (Lin & Papaloizou 1986; Ward 1997). Furthermore, a sufficiently deep gap inhibits gas flow across the gap (Artymowicz & Lubow 1996; Kley 1999; Lubow, Seibert & Artymowicz 1999), which is a possible mechanism for forming an inner hole in the disc (Dodson-Robinson & Salyk 2011; Zhu et al. 2011).

Because of their importance, disc gaps induced by planets have been studied by many authors, using simple one-dimensional disc models (e.g. Takeuchi et al. 1996; Ward 1997; Crida et al. 2006; Lubow & D'Angelo 2006) and numerical hydrodynamic simulations (Artymowicz & Lubow 1994; Kley 1999; Varnière, Quillen & Frank 2004; Duffell & MacFadyen 2013; Fung, Shi & Chiang 2014). One-dimensional disc models predict an exponential dependence of the gap depth. That is, the minimum surface density at the gap bottom is proportional to $\exp[-A(M_{\rm p}/M_*)^2]$, where $M_{\rm p}$ and M_* are the masses of the planet and the central star, and A is a non-dimensional parameter (see also equation 38). On the other hand, recent high-resolution hydrodynamic simulations done by Duffell & MacFadyen (2013, hereafter DM13) show that the gap is much shallower for a massive planet than the prediction of one-dimensional models. According to their results, the minimum surface density at the gap is proportional to $(M_{\rm p}/M_*)^{-2}$. Varnière et al. (2004) and Fung et al. (2014) obtained similar results from their hydrodynamic simulations. Its origin has not yet been clarified by the one-dimensional disc model. Fung et al. (2014) also estimated the gap depth with a 'zero-dimensional' analytic model, by simply assuming that the planetary gravitational torque is produced only at the gap bottom. Their simple model succeeds in explaining

★ E-mail: kanagawa@lowtem.hokudai.ac.jp

the dependence of the minimum surface density of $\propto (M_{\rm p}/M_*)^{-2}$. However, the zero-dimensional model does not give the radial profile of the surface density (or the width of the gap). It is not well understood what kind of profile accepts their assumption on the planetary torque. Further development of the one-dimensional gap model is required in order to clarify both the gap depth and width. Such a model enables us to connect the gaps observed in protoplanetary discs with the embedded planets.

One of the problems of the one-dimensional disc model is the assumption of the Keplerian rotational speed. The disc rotation deviates from the Keplerian speed due to a radial pressure gradient (Adachi, Hayashi & Nakazawa 1976). When a planet creates a deep gap, the steep surface density gradient increases the deviation of the disc rotation significantly, which affects the angular momentum transfer at the gap (see Sections 2.1 and 2.2). Furthermore, a large deviation of the disc rotation can also violate the Rayleigh stable condition for rotating discs (Chandrasekhar 1939). A violation of the Rayleigh condition promotes the angular momentum transfer and makes the surface density gradient shallower so that the Rayleigh condition is only marginally satisfied (Tanigawa & Ikoma 2007; Yang & Menou 2010). To examine such feedback on the surface density gradient, we should naturally include the deviation from the Keplerian disc rotation in the one-dimensional disc model.

Another simplification is in the wave propagation at the disc–planet interaction. The density waves excited by planets radially propagate in the disc and the angular momenta of the waves are deposited on the disc by damping. This angular momentum deposition is the direct cause of the gap formation. Most previous studies simply assume instantaneous damping of the density waves after their excitation (e.g. Ward 1997; Crida et al. 2006). If the wave propagation is taken into account, the angular momentum is deposited in a wider region of the disc, which increases the width of the gap (Takeuchi et al. 1996; Rafikov 2002). In a wide gap, the disc–planet interaction would be weak because the disc gas around the planet decreases over a wide region. Hence, we cannot neglect the effect of wave propagation on the gap formation.

In this paper, we re-examine the gap formation by a planet with the one-dimensional disc model, taking into account the deviation from Keplerian rotation and the effect of wave propagation. To include the deviation from Keplerian disc rotation, we modify the basic equations for one-dimensional accretion discs, detailed in the next section. The effect of the wave propagation is included using a simple model. In Section 3, we obtain estimates of gap depths for two simple cases. One estimate for a wide gap corresponds to the zero-dimensional model proposed by Fung et al. (2014). In Sections 4 and 5, we present numerical solutions of the gap without and with wave propagation, respectively. We find that the gap becomes shallow due to the effects of the deviation from Keplerian rotation, the violation of the Rayleigh condition and the wave propagation. With these shallowing effects, our results are consistent with the recent hydrodynamic simulations. In Section 6, we summarize and discuss our results.

2 MODEL AND BASIC EQUATIONS

We examine an axisymmetric gap in the disc surface density around a planet by using the one-dimensional model of viscous accretion discs. Although the Keplerian angular velocity is assumed in most previous studies, we take into account a deviation from Keplerian disc rotation in our one-dimensional model. The deviation cannot be neglected for a deep gap, as will be shown below. We also assume non-self-gravitating and geometrical thin discs. For simplicity, the planet is assumed to be in a circular orbit. We also adopt simple models for density wave excitation and damping to describe the gap formation.

2.1 Angular velocity of a protoplanetary disc with a gap

The angular velocity, Ω, of a gaseous disc around a central star with mass M_* is determined by the balance of radial forces:

$$\Omega^2 R - \frac{GM_*}{R^2} - \frac{1}{\Sigma}\frac{\partial P_{\rm 2D}}{\partial R} = 0, \tag{1}$$

where R is the radial distance from the central star, Σ is the surface density of the disc and $P_{\rm 2D}$ denotes the vertically averaged pressure. On the left-hand side of equation (1), the first term represents the centrifugal force on a unit mass of the disc. The second and third terms are the gravitational force by the central star and the force of the radial pressure gradient, respectively. For $P_{\rm 2D}$, we adopt the simple equation of state $P_{\rm 2D} = c^2\Sigma$, where c is the isothermal sound speed. Using this equation of state, equation (1) can be rewritten as

$$\Omega^2 = \Omega_{\rm K}^2 (1 - 2\eta), \tag{2}$$

with

$$\eta = -\frac{h^2}{2R}\left(\frac{\partial \ln \Sigma}{\partial R} + \frac{\partial \ln c^2}{\partial R}\right), \tag{3}$$

where $\Omega_{\rm K} = \sqrt{GM_*/R^3}$ is the Keplerian angular velocity, and $h = c/\Omega_{\rm K}$

For a disc with no gap, the order of magnitude of the non-dimensional parameter η is $\mathrm{O}(h^2/R^2)$ (Adachi et al. 1976), because the term in parentheses in equation (3) is comparable to $\sim 1/R$. On the other hand, if a planet opens a deep gap with a width of $\sim h$, the steep gradient of the surface density increases η to $\mathrm{O}(h/R)$. Hence, it also enhances the deviation of the disc rotation from the Kepler rotation in the deep gap. We neglect the term $\partial c/\partial R$ in equation (3) because the temperature gradient would be small. Neglecting the smaller terms of $\mathrm{O}(h/R)$, we approximately obtain $\partial\Omega/\partial R$ as

$$\frac{\partial \Omega}{\partial R} = -\frac{3\Omega_{\rm K}}{2R}\left[1 - \frac{h^2}{3}\frac{\partial^2 \ln \Sigma}{\partial R^2}\right]. \tag{4}$$

Note that the second term in the parentheses is of order unity since $\mathrm{d}^2 \ln \Sigma/\mathrm{d}x^2 \sim 1/h^2$ in a deep gap. Therefore, it is found that $\partial\Omega/\partial R$ is significantly altered from the Keplerian value due to the steep gradient of the surface density, though the deviation of Ω is small ($\sim h/R$). As shown later, this deviation promotes radial viscous transfer of angular momentum and makes a gap shallower.

2.2 Basic equations describing a disc gap around a planet

The equations for conservation of mass and angular momentum are given by

$$\frac{\partial \Sigma}{\partial t} + \frac{1}{2\pi R}\frac{\partial F_{\rm M}}{\partial R} = S_{\rm M}, \tag{5}$$

and

$$\frac{\partial}{\partial t}(\Sigma j) + \frac{1}{2\pi R}\frac{\partial F_{\rm J}}{\partial R} = j S_{\rm M} + \frac{1}{2\pi R}\Lambda_{\rm d}, \tag{6}$$

where $F_{\rm M}$ and $F_{\rm J}$ are the radial fluxes of mass and angular momentum, and $j(= R^2\Omega)$ is the specific angular momentum. In equation (5), the source term $S_{\rm M}$ represents the mass accretion rate

on to a unit surface area of the disc. The accretion of disc gas on to the planet can be included in S_M as a negative term. In equation (6), $\Lambda_d(R)$ represents the deposition rate of the angular momentum from the planet on the ring region with radius R.

To describe the deposition rate Λ_d, we consider the angular momentum transfer from the planet to the disc. This transfer process can be divided into two steps. First, the planet excites a density wave by the gravitational interaction with the disc (e.g. Goldreich & Tremaine 1980). Secondly, the density waves are gradually damped due to the disc viscosity or a non-linear effect (Takeuchi et al. 1996; Goodman & Rafikov 2001). As a result of the wave damping, the angular momenta of the waves are deposited on the disc. If instantaneous wave damping is assumed, the deposition rate Λ_d is determined only by the wave excitation. In Section 2.4.1, we will describe the deposition rate for the case with instantaneous wave damping. In Section 2.4.2, we will give a simple model of Λ_d for the case of gradual wave damping.

The radial angular momentum flux F_J is given by (e.g. Lynden-Bell & Pringle 1974)

$$F_J = jF_M - 2\pi R^3 \nu\Sigma\frac{\partial\Omega}{\partial R}. \tag{7}$$

The first term is the advection transport by the disc radial mass flow, F_M, and the second term represents the viscous transport. For the kinetic viscosity, we adopt the α prescription, i.e. $\nu = \alpha ch$ (Shakura & Sunyaev 1973). Note that F_J does not include the angular momentum transport by the density waves in our formulation.

Equations (5)–(7) describe the time evolution of the three variables Σ, F_M and F_J with the given mass source term S_M, the angular momentum deposition rate from a planet Λ_d and the disc angular velocity Ω. Note that Ω depends on $\partial\Sigma/\partial R$, as in equations (2) and (3).

Next, we consider the disc gap in a steady state ($\partial/\partial t = 0$). The time-scale for the formation of a steady gap is approximately equal to the diffusion time within the gap width, $t_{\rm diff} = h^2/\nu$. For a nominal value of α ($\sim 10^{-3}$), the diffusion time is roughly given by 10^3 Keplerian periods, which is shorter than the growth time of planets (10^{5-7} yr; Kokubo & Ida 2000, 2002) or the lifetime of protoplanetary discs (10^{6-7} yr; Haisch, Lada & Lada 2001). Hence, the assumption of a steady gap would be valid. In addition, we assume $S_M = 0$ for simplicity. Although gas accretion on to the planet occurs for $M_p \gtrsim 10\,M_\oplus$ (Mizuno 1980; Kanagawa & Fujimoto 2013), the assumption of $S_M = 0$ would be valid if the accretion rate on to the planet is smaller than the radial disc accretion rate, F_M.

Under these assumptions, equation (5) shows that F_M is constant. Equation (6) yields

$$F_J = F_J(\infty) - \int_R^\infty \Lambda_d dR', \tag{8}$$

where $F_J(\infty)$ is the angular momentum flux without the planet. From equations (7) and (8), we obtain

$$jF_M - 2\pi R^3\Sigma\nu\frac{d\Omega}{dR} = F_J(\infty) - \int_R^\infty \Lambda_d dR'. \tag{9}$$

Equation (9) with a constant mass accretion rate describes a steady disc gap around a planet for a given Λ_d. Since $d\Omega/dR$ is given by equation (4), equation (9) is the second-order differential–integral equation. Note that equation (9) is derived from equation (6) and indicates the angular momentum conservation.

By differentiating equation (9), we obtain a rather familiar expression for the mass flux:

$$F_M = \left(\frac{dj}{dR}\right)^{-1}\left[\frac{d}{dR}\left(2\pi R_p^3\nu\Sigma\frac{d\Omega}{dR}\right) + \Lambda_d\right]. \tag{10}$$

Note that this expression is valid only for the steady state. In a time-dependent case, equation (10) should include the term $-2\pi R\Sigma(\partial j/\partial t)$ in the parentheses. As a boundary condition, the disc surface density should approach its unperturbed values at both sides of the gap far from the planet.

Here, we also consider the unperturbed surface density. In the unperturbed state, Ω can be replaced by Ω_K, by neglecting the smaller term $O(h^2/R^2)$ (see equations 2 and 3). Furthermore, setting $\Lambda_d = 0$ in equation (9), we obtain the unperturbed surface density Σ_0 as

$$3\pi R^2\nu\Omega_K\Sigma_0(R) = -R^2\Omega_K F_M + F_J(\infty). \tag{11}$$

Thus, Σ_0 is given by

$$\Sigma_0 = -\frac{F_M}{3\pi\nu}\left(1 - \frac{F_J(\infty)}{R^2\Omega_K F_M}\right). \tag{12}$$

This agrees with the well-known solution for steady viscous accretion discs (e.g. Lynden-Bell & Pringle 1974).

2.3 Rayleigh condition

For a deep gap around a large planet, the derivative of the angular velocity deviates significantly from the Keplerian velocity, as shown in Section 2.1. A sufficiently large deviation in Ω violates the so-called Rayleigh stable condition of $dj/dR \geq 0$ (see Chandrasekhar 1961). Such a steep gap is dynamically unstable, which would cause a strong angular momentum transfer, lessening the steepness of the gap. This would make the unstable region marginally stable (i.e. $dj/dR = 0$).

Using equation (4), we give dj/dR as

$$\frac{dj}{dR} = \frac{1}{2}R_p\Omega_{Kp}\left(1 + h_p^2\frac{d^2\ln\Sigma}{dR^2}\right), \tag{13}$$

where the suffix p indicates the value at $R = R_p$; this suffix is also used for other quantities. Hence, using the second-derivative of the surface density, the marginally stable condition $dj/dR = 0$ can be rewritten as (Tanigawa & Ikoma 2007).

$$h_p^2\frac{d^2\ln\Sigma}{dR^2} = -1. \tag{14}$$

Actually, around a sufficiently large planet, equation (9) gives $h_p^2 d^2\ln\Sigma/dR^2 < -1$ in some radial regions. In such unstable regions, we have to use equation (14) instead of equation (9).

The breakdown of equation (9) indicates that the flux F_J of equation (7) cannot transport all of the angular momentum deposited by the planet. In a real system, however, the instability would enhance the angular momentum flux, which keeps the gap marginally stable. The enhancement of F_J can be considered to be due to an effective viscosity $\nu_{\rm eff}$ enhanced by the instability. Since such an effective viscosity restores equation (9), $\nu_{\rm eff}$ in the unstable region is given by

$$\nu_{\rm eff} = \frac{-jF_M + F_J(\infty) - \int_R^\infty \Lambda_d dR'}{4\pi R^2\Sigma\Omega}, \tag{15}$$

where we use the relation $d\Omega/dR = -2\Omega/R$ obtained from the marginally stable condition. Furthermore, by using $\nu_{\rm eff}$ instead of

ν, equation (7) gives the enhanced angular momentum flux in the unstable region.

The Rossby wave instability may be important for the gap formation (e.g. Richard, Barge & Le Dizès 2013; Zhu, Stone & Rafikov 2013; Lin 2014). As well as the Rayleigh condition, the Rossby wave instability relates to the disc rotation (Li et al. 2000). Because it can occur before the Rayleigh condition is violated, however, the Rossby wave instability may suppress the surface density gradient more than the Rayleigh condition. For simplicity, we include only the Rayleigh condition in the present study. A further detail treatment including the Rossby wave instability should be done in future works.

2.4 Angular momentum deposition from a planet

In the disc–planet interaction, a planet excites density waves and the angular momenta of the waves are deposited on the disc through their damping. The angular momentum deposition rate $\Lambda_{\rm d}$ is determined by the later process. First, we will consider the deposition rate $\Lambda_{\rm d}$ in the case with instantaneous wave damping. In this case, the deposition rate is governed only by the wave excitation. Next, taking into account the wave propagation before damping, we will model the deposition rate in a simple form.

2.4.1 Case with instantaneous wave damping

Under the assumption of instantaneous wave damping, the angular momentum deposition rate $\Lambda_{\rm d}(R)$ is equal to the excitation torque density $\Lambda_{\rm ex}(R)$, which is the rate at which a planet adds angular momenta to density waves per unit radial distance at R. That is,

$$\Lambda_{\rm d} = \Lambda_{\rm ex}. \tag{16}$$

At a position far from the planet, the excitation torque density is given by the WKB formula (e.g. Ward 1986) as

$$\Lambda_{\rm ex}^{\rm WKB} = \pm C\pi R_{\rm p}^2 \Sigma \left(\frac{M_{\rm p}}{M_*}\right)^2 \left(R_{\rm p}\Omega_{\rm Kp}\right)^2 \left(\frac{R_{\rm p}}{R-R_{\rm p}}\right)^4, \tag{17}$$

where $C = (2^5/3^4)[2K_0(2/3) + K_1(2/3)]^2/\pi \simeq 0.798$ and K_i denote the modified Bessel functions. The sign of equation (17) is positive for $R > R_{\rm p}$ or negative for $R \leq R_{\rm p}$. In the close vicinity of the planet, $|R - R_{\rm p}| \lesssim h_{\rm p}$, on the other hand, the WKB formula is overestimated. Thus, we model the excitation torque density $\Lambda_{\rm ex}$ with a simple cutoff as

$$\Lambda_{\rm ex} = \begin{cases} \Lambda_{\rm ex}^{\rm WKB} & \text{for } |R-R_{\rm p}| > h_{\rm p}\Delta, \\ 0 & \text{for } |R-R_{\rm p}| \leq h_{\rm p}\Delta. \end{cases} \tag{18}$$

The cutoff length $h_{\rm p}\Delta$ is determined so that the one-sided torque T $(= \int_{R_{\rm p}}^{\infty} \Lambda_{\rm ex} {\rm d}R)$ agrees with the result of the linear theory for realistic discs (Takeuchi & Miyama 1998; Tanaka, Takeuchi & Ward 2002; Muto & Inutsuka 2009). Then, we obtain $\Delta = 1.3$.

Note that the WKB formula is derived for discs with no gap. Petrovich & Rafikov (2012) reported that the torque density is altered by the steep gradient of the surface density because of the shift of the Lindblad resonances. For simplicity, however, we ignore this effect in this paper. Hence, in our model, the excitation torque density $\Lambda_{\rm ex}$ is simply proportional to the disc surface density at R, $\Sigma(R)$, and is independent of the surface density gradient even for deep gaps. For a large planet with a mass of $M_{\rm p}/M_* \gtrsim (h_{\rm p}/R_{\rm p})^3$; furthermore, the non-linear effect would not be negligible for wave excitation (Ward 1997; Miyoshi et al. 1999). This non-linear effect is also neglected in our simple model.

2.4.2 Case with wave propagation

When wave propagation is included, the angular momentum deposition occurs at a different site from the wave excitation and equation (18) is not valid. In this case, the angular momentum deposition is also governed by the damping of the waves. Although the wave damping has been examined in previous studies (e.g. Korycansky & Papaloizou 1996; Takeuchi et al. 1996; Goodman & Rafikov 2001), it is not clear yet how the density waves are damped in a disc with deep gaps. In the present study, therefore, we adopt a simple model of angular momentum deposition, described below.

Since the waves are eventually damped in the disc, the one-sided torque (i.e. the total angular momentum of the waves excited at the outer disc in unit time) is equal to the total deposition rate in the steady state. That is,

$$T = \int_{R_{\rm p}}^{\infty} \Lambda_{\rm ex} {\rm d}R' = \int_{R_{\rm p}}^{\infty} \Lambda_{\rm d} {\rm d}R'. \tag{19}$$

Using the one-sided torque, the angular momentum deposition rate can be expressed by

$$\Lambda_{\rm d} = \pm T f(R), \tag{20}$$

where the distribution function $f(R)$ satisfies $\int_{R_{\rm p}}^{\infty} f(R){\rm d}R = 1$, and the sign is the same as in equation (17). As a simple model, we assume a distribution function $f(R)$ given by

$$f(R) = \begin{cases} \dfrac{1}{w_{\rm d}} & \text{for } x_{\rm d}h_{\rm p} - \dfrac{w_{\rm d}}{2} < |R-R_{\rm p}| < x_{\rm d}h_{\rm p} + \dfrac{w_{\rm d}}{2}, \\ 0 & \text{otherwise.} \end{cases} \tag{21}$$

In this simple model, the non-dimensional parameter $x_{\rm d}$ determines the position of the angular momentum deposition and the parameter $w_{\rm d}$ represents the radial width of the deposition site. The waves propagate from the excitation site to the deposition site around $|x| = x_{\rm d}$. Since the density waves propagate away from the planet, the deposition site is farther from the planet than the excitation site. The parameter $x_{\rm d}$ should be consistent with this condition.

In the case with wave propagation, we use equations (20) and (21) to obtain the gap structure with equation (9). It should be noted that T in equation (20) depends on the surface density distribution through the definition of equation (19), because $\Lambda_{\rm ex}$ is proportional to Σ. These coupled equations are solved as follows. First, we obtain the surface density distribution with equation (9) for a given T. Next, we determine the corresponding mass of the planet from equation (19), using the obtained surface density.

2.5 Local approximation and non-dimensional equations

The typical width of a disc gap is comparable to the disc scaleheight and much smaller than the orbital radius of the planet. Thus, it is convenient to use the local coordinate defined by

$$x = \frac{R - R_{\rm p}}{h_{\rm p}}. \tag{22}$$

Note that the suffix p indicates the value at $R = R_{\rm p}$.

We adopt a local approximation in which terms proportional to $h_{\rm p}/R_{\rm p}$ and higher order terms are neglected. From equations (2) and (3), the deviation in Ω from $\Omega_{\rm K}$ is given by

$$\Omega - \Omega_{\rm K} = \frac{h_{\rm p}\Omega_{\rm Kp}}{2R_{\rm p}} \frac{{\rm d}\ln\Sigma}{{\rm d}x}, \tag{23}$$

and is proportional to h_p/R_p. Thus, the disc angular velocity Ω is replaced by the angular velocity of the planet Ω_{Kp} under the local approximation, and the specific angular momentum j also is given by $R_p^2\Omega_{Kp}$. As for the derivative $d\Omega/dR$, we cannot neglect the deviation from the Keplerian value. Equation (4) yields

$$\frac{d\Omega}{dR} = -\frac{3\Omega_{Kp}}{2R_p}\left(1 - \frac{1}{3}\frac{d^2 \ln \Sigma}{dx^2}\right). \tag{24}$$

Equation (9) can be rewritten in the local approximation as

$$R^2\Omega_{Kp}F_M + 3\pi R_p^2 \nu_p \Sigma \Omega_{Kp}\left(1 - \frac{1}{3}\frac{d^2 \ln \Sigma}{dx^2}\right) = F_J(\infty) - \int_x^\infty \Lambda_d h_p dx'. \tag{25}$$

Because of the local approximation, equation (25) cannot be applied for the wide gap formation. If the half width of gap is narrower than about $1/3R_p$, equation (25) would be valid.

Here, we introduce the non-dimensional surface density, s, defined by

$$s = \frac{\Sigma}{\Sigma_0(R_p)}, \tag{26}$$

where $\Sigma_0(R_p)$ is the unperturbed surface density at $R = R_p$ given by equation (12). Dividing equation (25) by $3\pi R_p^2 \nu_p \Sigma_0(R_p)\Omega_{Kp}$ and using equation (11), we obtain a non-dimensional form:

$$\left(1 - \frac{1}{3}\frac{d^2 \ln s}{dx^2}\right)s = 1 - \frac{1}{3}\int_x^\infty \lambda_d dx', \tag{27}$$

where λ_d is the non-dimensional angular momentum deposition rate defined by

$$\lambda_d = \frac{\Lambda_d h_p}{\pi R_p^2 \nu_p \Sigma_0(R_p)\Omega_{Kp}}. \tag{28}$$

The marginally stable condition can be rewritten as

$$\frac{d^2 \ln s}{dx^2} = -1. \tag{29}$$

This equation is used instead of equation (27) in the Rayleigh unstable region.

The non-dimensional excitation torque density, λ_{ex}, is defined by

$$\lambda_{ex} = \frac{\Lambda_{ex} h_p}{\pi R_p^2 \nu_p \Sigma_0(R_p)\Omega_{Kp}} = \begin{cases} \pm K \dfrac{C}{x^4} s(x) & \text{for } |x| > \Delta, \\ 0 & \text{for } |x| \le \Delta, \end{cases} \tag{30}$$

where the non-dimensional parameter K is given by

$$K = \left(\frac{M_p}{M_*}\right)^2 \left(\frac{R_p}{h_p}\right)^5 \alpha^{-1}. \tag{31}$$

In the above, we use $\nu_p = \alpha h_p^2 \Omega_{Kp}$. In our model, the parameter K is the only parameter that determines the gap structure for the instantaneous damping case.

In the case with instantaneous wave damping, the angular momentum deposition rate is given by $\lambda_d = \lambda_{ex}$ (equation 16). In the case with wave propagation, equation (20) gives

$$\lambda_d(x) = \tilde{T} h_p f(R_p + h_p x), \tag{32}$$

where the non-dimensional one-sided torque, $\tilde{T}$, is given by

$$\tilde{T} = K \int_\Delta^\infty \frac{C}{x^4} s(x) dx. \tag{33}$$

Note that the deposition rate λ_d includes two parameters x_d and w_d, in addition to K. In this case, we solve equation (27) for a given value of $\tilde{T}$. Then, we can obtain K by substituting the solution $s(x)$ into equation (33), as mentioned at the end of the last subsection. In order to obtain the solution for a certain K, we need an iteration of the above procedure with trial values of $\tilde{T}$.

The boundary conditions of equations (27) and (29) are

$$s = 1, \quad \text{at } x = \pm\infty. \tag{34}$$

Under the local approximation, the surface density has a symmetry of $s(x) = s(-x)$, since both the above basic equations and the deposition rate are symmetric.

3 ESTIMATES OF GAP DEPTHS FOR SIMPLE SITUATIONS

3.1 Case of the Keplerian discs

Before deriving the gap solution in our model described in Section 2, we examine the gaps for two simple situations. First, we consider a disc with Keplerian rotation, as assumed in previous studies. Neglecting the deviation in $d\Omega/dR$ from the Keplerian (i.e. the term of $d^2 \ln s/dx^2$) in equation (27), we have

$$s = 1 - \frac{1}{3}\int_x^\infty \lambda_d dx'. \tag{35}$$

Here, we also assume instantaneous wave damping and adopt $\lambda_d = \lambda_{ex}$ (equation 30). Differentiating equation (35), we obtain

$$\frac{d \ln s}{dx} = \begin{cases} \pm \dfrac{C}{3x^4} K & \text{for } |x| > \Delta, \\ 0 & \text{for } |x| \le \Delta. \end{cases} \tag{36}$$

Hence, we obtain the surface density in the Keplerian discs with the instantaneous wave damping as

$$s(x) = \begin{cases} \exp\left(-\dfrac{C}{9|x|^3} K\right) & \text{for } |x| > \Delta, \\ \exp\left(-\dfrac{C}{9\Delta^3} K\right) & \text{for } |x| \le \Delta. \end{cases} \tag{37}$$

Using equation (31), $C = 0.798$ and $\Delta = 1.3$, the minimum surface density, s_{min}, is

$$s_{min} = \exp\left[-0.040\alpha^{-1}\left(\frac{R_p}{h_p}\right)^5 \left(\frac{M_p}{M_*}\right)^2\right]. \tag{38}$$

This solution is almost the same as that in the previous one-dimensional gap model (e.g. Lubow & D'Angelo 2006).

For a very large K, the Rayleigh condition is violated and equations (37) and (38) are invalid. Tanigawa & Ikoma (2007) obtained the gap structure in Keplerian discs, including the Rayleigh condition. Their solution is described in Appendix A. In Appendix B, we also derive gap solutions in Keplerian discs, taking into account the wave propagation with the simple model of equations (20) and (21).

3.2 Case of the wide-limit gap

Next, we consider a situation implied by the zero-dimensional analysis done by Fung et al. (2014), which assumes that the wave excitation occurs only the gap bottom. This assumption would be valid if the gap bottom region is wide enough. Hence, we call this situation 'wide-limit gap' case. Since the density waves are excited

at the gap bottom with $s \simeq s_{\rm min}$, the one-sided torque of equation (33) is simply given by

$$\tilde{T} = \frac{C}{3\Delta^3} K s_{\rm min} \simeq 0.121 K s_{\rm min}. \tag{39}$$

Using equation (27), we can estimate $s_{\rm min}$ of the wide-limit gap. The right-hand side of equation (27) can be rewritten as $1 - \tilde{T}/3$ at $x = 0$. In the left-hand side of equation (27), moreover, we can neglect the term $\mathrm{d}^2 \ln s/\mathrm{d}x^2$ when a flat-bottom gap is assumed. Then, the relation between $s_{\rm min}$ and $\tilde{T}$ is obtained as

$$s_{\rm min} = 1 - \frac{\tilde{T}}{3}. \tag{40}$$

Equations (39) and (40) yield

$$s_{\rm min} = \frac{1}{1 + 0.040K}. \tag{41}$$

For a large K, $s_{\rm min}$ given by equation (41) is proportional to $1/K$. This result agrees with the zero-dimensional model by Fung et al. (2014).[1] In the zero-dimensional model, the minimum surface density is estimated from a balance between the planetary torque and the viscous angular momentum flux outside the gap. Such a balance is also seen from equation (40) (and equation 27). The first and second terms in the right-hand side of equation (40) correspond to the viscous angular momentum flux outside the gap and the planetary torque and the left-hand side is negligibly small for a large K.

With their hydrodynamic simulations for $K \lesssim 10^4$, DM13 derived a similar result,[2]

$$s_{\rm min} = \frac{29}{29 + K} = \frac{1}{1 + 0.034K}. \tag{42}$$

It is found that equations (41) and (42) are consistent with each other. Note that these minimum surface densities are much larger than that of the Keplerian disc (equation 38) for a large K because equation (39) is not accepted in the Keplerian solution. The wide-limit gaps assume that all the waves are excited in the bottom region with $s \simeq s_{\rm min}$, i.e. equation (39). In Sections 4 and 5, we will check whether or not this assumption is valid, by comparing it with our one-dimensional solutions.

4 GAP STRUCTURE IN THE CASE WITH INSTANTANEOUS WAVE DAMPING

4.1 Linear solutions for shallow gaps

Here, we present the numerical solution of the gap in the case with instantaneous wave damping (i.e. $\lambda_{\rm d} = \lambda_{\rm ex}$).

First, we consider the case with a small K in equation (27), in which $\lambda_{\rm d}$ is proportional to K. This case corresponds to a shallow gap around a small planet. Since $|s - 1|$ is small, it is useful to express the solution as

$$s = \exp(Ky), \tag{43}$$

or $s = 1 + Ky$. As seen in the next subsection, the former expression is better for an intermediate K ($\sim$10). Substituting equation (43) into equation (27) with equation (16), we can expand it into a power series of Ky. The first-order terms give the linear equation of y:

$$\frac{\mathrm{d}^2 y}{\mathrm{d}x^2} - 3y = \mp \begin{cases} \dfrac{C}{3|x|^3} & \text{for} \quad |x| > \Delta, \\ \dfrac{C}{3\Delta^3} & \text{otherwise}, \end{cases} \tag{44}$$

where the sign in the right-hand side is negative for $x > 0$ and positive for $x \le 0$. Equation (44) is an inhomogeneous linear differential equation, and can be integrated with the boundary conditions of equation (34). We do not need to take care of the Rayleigh condition in the shallow gaps. A detailed derivation of the linear solution is described in Appendix C.

Fig. 1(a) shows y, which can be converted into the surface density s by equation (43). In these shallow gaps, the gap depth is almost the same as for the Keplerian case, though our model gives a smooth surface density distribution.

Fig. 1(b) shows the derivative of y which is related to $\Delta\Omega$, as

$$\Delta\Omega = \Omega - \Omega_{\rm K} = K \frac{h_{\rm p}\Omega_{\rm Kp}}{2R_{\rm p}} \frac{\mathrm{d}y}{\mathrm{d}x}, \tag{45}$$

using equations (23) and (43). The absolute value of $\Delta\Omega$ attains a maximum at $|x| \simeq 1.5$. The second-order derivative of y gives the shear, $\mathrm{d}\Omega/\mathrm{d}x$, as

$$\frac{\mathrm{d}\Omega}{\mathrm{d}x} = \frac{\mathrm{d}\Omega_{\rm K}}{\mathrm{d}x} \left(1 - \frac{K}{3} \frac{\mathrm{d}^2 y}{\mathrm{d}x^2} \right), \tag{46}$$

as seen from equation (24). At $|x| > 1.5$, the shear motion is enhanced compared to the Keplerian case, because $\mathrm{d}^2 y/\mathrm{d}x^2 < 0$. Since the shear motion causes viscous angular momentum transfer, this enhancement makes the surface density gradient less steep compared with the Keplerian case, as shown in Fig. 1(a).

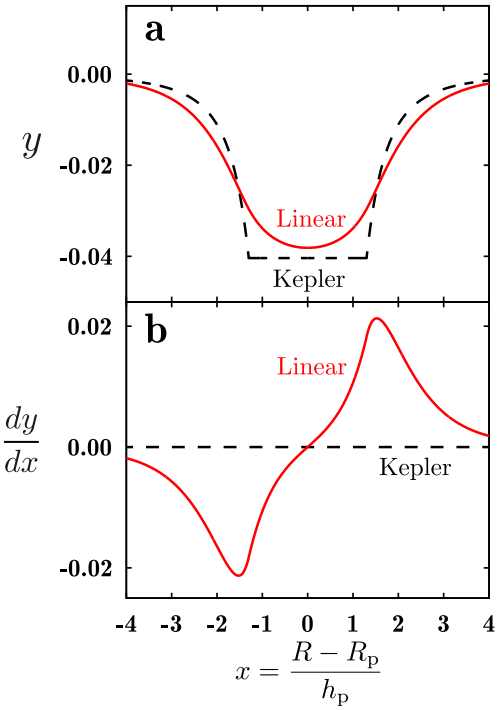

Figure 1. Linear solution for y (a) and $\mathrm{d}y/\mathrm{d}x$ (b). The surface density and angular velocity are given by y and $\mathrm{d}y/\mathrm{d}x$ with equations (43) and (45), respectively. The dashed line is the solution for the Keplerian disc.

[1] In the notation of Fung et al. (2014), K is given by $q^2/(\alpha[h/r]^5)$.
[2] In the notation of DM13, K is given by $\mathcal{M}^{-1}(M_{\rm sh}/M_{\rm p})^2\alpha^{-1}$.

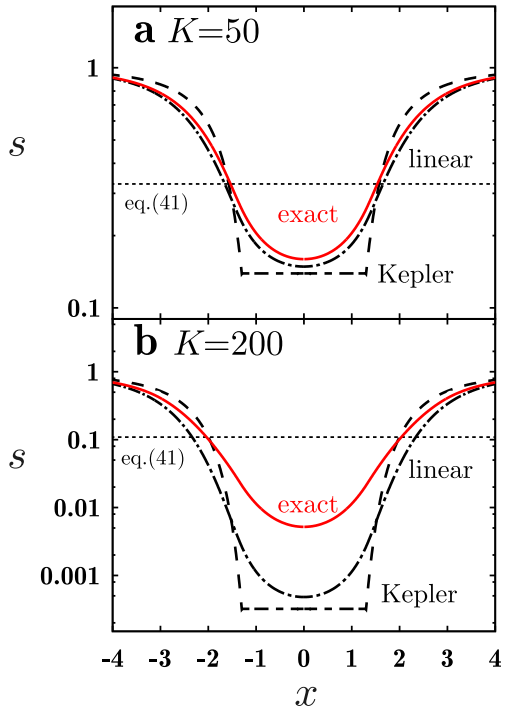

Figure 2. Surface density distributions for $K = 50$ (a) and 200 (b). The red line is the exact solution (see text). The chain line is the linear solution given by equation (43) and the dashed line is the solution for the Keplerian case (equation 37). The dotted line represents the minimum surface densities for the wide-limit gap given by equation (41).

4.2 Non-linear solutions for deep gaps

Next, we consider deep gaps around relatively large planets. In this case, we numerically solve the non-linear equation (27) with the Rayleigh condition. We call the obtained non-linear solution the 'exact' solution.

At regions far from the planet, the surface density perturbation is rather small and the linear approximation is valid. Thus, we adopt a linear solution at $|x| > 10$. Note that this linear solution has different coefficients for the homogeneous terms from those in Section 4.1 (see Appendix C). The coefficients of the homogeneous solution are given to satisfy the boundary conditions of equation (34). At $|x| \leq 10$, we integrate equation (27) with the fourth-order Runge–Kutta integrator. In the Rayleigh unstable region, the surface density is governed by the marginally stable condition (equation 29), instead of equation (27). Fig. 2 shows the surface density distributions of the exact solutions for $K = 50$ (a) and 200 (b). If we assume a disc with $h_p/R_p = 0.05$ and $\alpha = 10^{-3}$, these cases correspond to $M_p = 1/8M_J$ and $1/4M_J$, respectively, where M_J is the mass of Jupiter. For comparisons, the Keplerian solution (equation 37) and the linear solution with equation (43) are also plotted. For $K = 50$, the linear solution almost agrees with the exact solution, while it is much deeper than the exact solution for $K = 200$. For $K = 200$, the Keplerian solution has a much smaller $s_{\rm min}$ than the exact solution. Fig. 3 illustrates the angular velocities (a) and specific angular momenta (b) for the exact solutions for $K = 50$ and 200. Similar to the linear solution in Fig. 1, the shear motion is enhanced at $|x| \gtrsim 1.4$. This enhancement of the shear motion is also seen in Fig. 4. The enhancement promotes the angular momentum transfer and makes the surface density gradient less steep. For $K = 200$, the Rayleigh condition is violated. In the unstable region, the marginally stable condition further reduces the surface density gradient. This

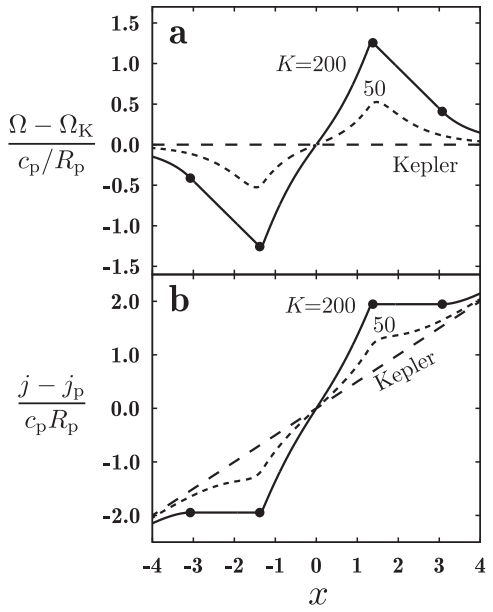

Figure 3. (a) Deviation from Keplerian disc rotation and (b) specific angular momentum, for $K = 50$ (dashed) and 200 (solid). The filled circles indicate the edge of the marginally stable region for the Rayleigh condition.

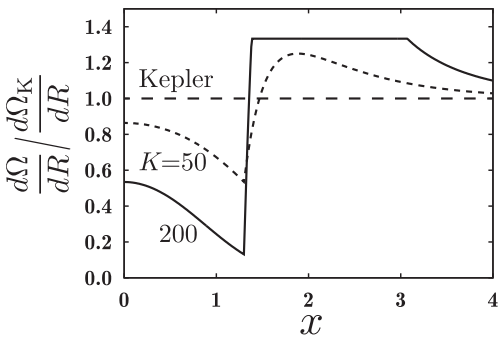

Figure 4. Shear of exact solutions for $K = 50$ (dashed) and 200 (solid).

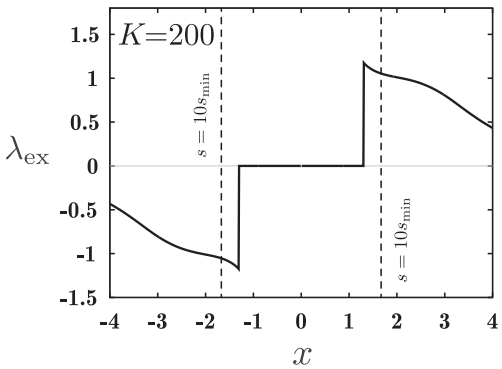

Figure 5. Excitation torque density given by equation (30) for $K = 200$. The two vertical lines indicate the positions with $s = 10s_{\rm min}$.

makes the gap much shallower than for the Keplerian solution, as seen in Fig. 2(b). We also plot the minimum surface densities, $s_{\rm min}$, of the wide-limit gap (equation 41) in Fig. 2. The wide-limit gap gives a much larger $s_{\rm min}$ than the exact solution for $K = 200$. In the wide-limit gap, it is assumed that the density waves are excited only at the gap bottom with $s \simeq s_{\rm min}$. Fig. 5 shows the excitation

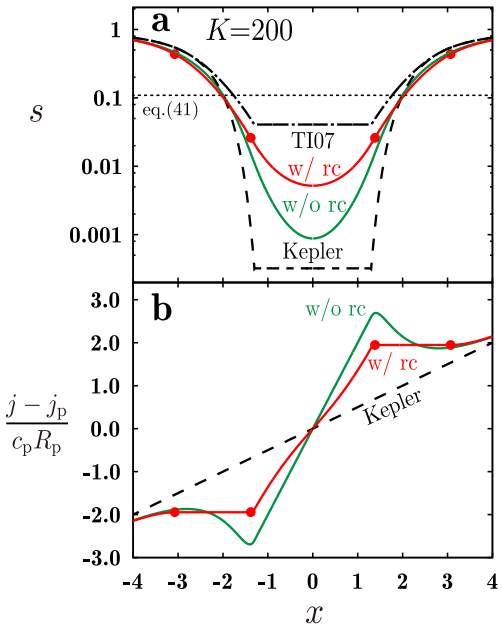

Figure 6. (a) Surface density distribution and (b) specific angular momentum distribution, for $K = 200$. The red line indicates the exact solution. The green line is the solution without the Rayleigh condition (see text). The chain line in (a) denotes the surface density distribution given by the model of TI07(equation A3).

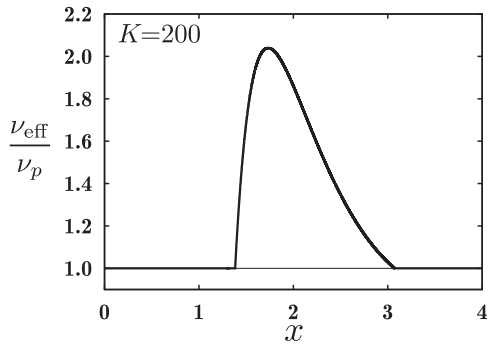

Figure 7. Effective viscosity $\nu_{\rm eff}$ of the exact solution with $K = 200$.

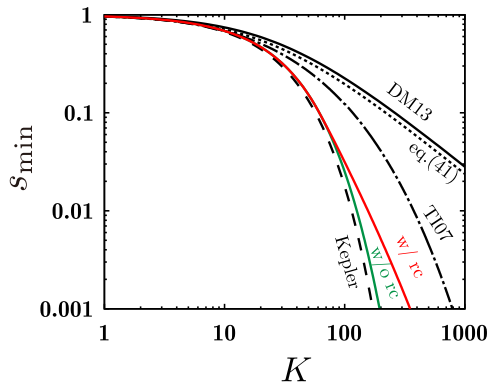

Figure 8. Minimum surface densities, $s_{\rm min}$, for the exact solution (red line) and the solution without the Rayleigh condition (green line). The dashed line is $s_{\rm min}$ in the Keplerian case. The chain, dotted and solid lines denote $s_{\rm min}$ given by the model of TI07, the wide-limit gap (equation 41) and the empirical relation of DM13 (equation 42), respectively.

torque density given by equation (18) for the exact solution with $K = 200$. This torque density indicates that the waves are excited mainly in the region with $s > 10 s_{\rm min}$. Thus, the assumption of wave excitation at the gap bottom is not valid in this case. Since wave excitation with a larger s increases the one-sided torque, this can explain why the gap of the exact solution is much deeper than the wide-limit gap in Fig. 2. Note that this result for the wave excitation is obtained in the case of instantaneous wave damping. The effect of the wave propagation can change the gap width and the mode of wave excitation, as seen in the next section.

4.3 Effect of the Rayleigh condition

We further examine the effect of the Rayleigh condition on the gap structure. Fig. 6 shows the surface densities (a) and specific angular momenta (b) for the exact solution and the solution without the Rayleigh condition. The solution without the Rayleigh condition has unstable regions with $\mathrm{d}j/\mathrm{d}x < 0$ (i.e. $1.4 < |x| < 3.1$). This comparison between these two solutions directly shows how the Rayleigh condition changes the gap structure. The Rayleigh condition increases $s_{\rm min}$ by a factor of 6 for $K = 200$. This is because the marginal condition of $\mathrm{d}^2 \ln s/\mathrm{d}x^2 \geq -1$ keeps the surface density gradient less steep and makes the gap shallow.

It can be considered that the marginally stable state is maintained by $\nu_{\rm eff}$ of equation (15). The non-dimensional form of equation (15) is given by

$$\frac{\nu_{\rm eff}}{\nu} = \frac{3 - \int_x^\infty \lambda_{\rm d} \mathrm{d}x'}{4s}. \tag{47}$$

Fig. 7 shows $\nu_{\rm eff}$ in the unstable region for $K = 200$. The effective viscosity is twice as large as the original value at $x = 1.8$. This enhancement of the effective viscosity causes the shallowing effect in Fig. 6(a).

In Fig. 6(a), we also plot the surface density distribution given by Tanigawa & Ikoma (2007, hereafter TI07), in which the Rayleigh condition is taken into account (for details, see Appendix A). Their model gives a shallower gap than our exact solution. This is because a very steep surface density gradient in the Keplerian solution is suppressed by the Rayleigh condition to a greater extent than in our model.

We also show that the Keplerian solution by TI07 does not satisfy the angular momentum conservation. The Keplerian solution without the Rayleigh condition (equation 37) is derived just from equation (35) (or equation 27), which is originated from equation (9). In this solution, thus, the angular momentum conservation is satisfied. However, when the Rayleigh condition is violated, the marginal stable condition (equation 29) is used instead of equation (37). Because of this, the surface density at the flat-bottom of TI07's solution does not satisfy equation (35) or the angular momentum conservation, either. This violation is resolved in our formulation because our exact solution always satisfies equation (27) outside the Rayleigh unstable region.[3]

4.4 Gap depth

Fig. 8 shows the minimum surface densities, $s_{\rm min}$, as a function of K for the exact solutions. For comparison, we also plot $s_{\rm min}$

[3] By introducing the effective viscosity of equation (47) and multiplying the LHS of equation (27) by $\nu_{\rm eff}/\nu_0$, equation (27) is recovered in the Rayleigh unstable region.

for the solutions without the Rayleigh condition and the Keplerian solutions. These solutions give deeper gaps than the exact solution, similar to the result of Section 4.2. It is found that the shallowing effect due to the Rayleigh condition becomes significant with an increase in K. This is because the Rayleigh condition is violated more strongly for large K.

In Fig. 8, on the other hand, the exact solution is much deeper than DM13's results and the wide-limit gap, though the latter two cases agree well with each other. The model of TI07 also gives much deeper gaps than DM13. These comparisons indicate that in the case with instantaneous wave damping, our exact solution cannot reproduce the hydrodynamic simulations of DM13. This difference in the gap depth from DM13 is likely to be due to the fact that the assumption of the wide-limit gap is not satisfied in the case with instantaneous wave damping (see Fig. 5). In the next section, we will see that the effect of wave propagation widens the gap and makes the assumption of the wide-limit gap valid.

5 EFFECT OF DENSITY WAVE PROPAGATION

In this section, we consider the effect of wave propagation. Wave propagation changes the radial distribution of the angular momentum deposition. A simple model of angular momentum deposition rate altered by wave propagation is described in Section 2.4.2. Using this simple model, we solve equation (27) with the Rayleigh condition in the similar way to the previous section. At the region far from the planet (i.e. $|x| > 10$), we use the linear solution to equation (C1) with $g(x) = 0$ in this case.

5.1 Gap structure for $K = 200$

Fig. 9 illustrates the surface densities (a) and the excitation torque densities (b) of the exact solutions in the case with wave propagation. The angular momenta of the excited waves are deposited around $|x| = x_{\rm d}$ in our model. A large $x_{\rm d}$ indicates a long propagation length between the excitation and the damping. The parameter K is set to 200. For an increasing $x_{\rm d}$, the gap becomes wider and shallower. The gap width is directly governed by the position of the angular momentum deposition. For $x_{\rm d} = 3$ and 4, the gap depths are consistent with the wide-limit gap (and also DM13). For $x_{\rm d} = 4$, the density waves are excited mainly at the bottom region with $s \simeq s_{\rm min}$, as seen in Fig. 9(b). Moreover, for $x_{\rm d} = 3$, a major part of the wave excitation occurs at the bottom. That is, the assumption of the wide-limit gap is almost satisfied for the solutions with $x_{\rm d} = 3$ and 4. This explains why the gap depths are consistent with the wide-limit gap for these large $x_{\rm d}$.

It is also valuable to compare the gap width with hydrodynamic simulations. DM13 performed a simulation for the case of $M_{\rm p} = 1/4M_{\rm J}$ ($2M_{\rm sh}$ in their notation), $\alpha = 10^{-3}$ and $h_{\rm p}/R_{\rm p} = 0.05$. This case corresponds to $K = 200$. In this simulation, they found that the gap width is about $6h_{\rm p}$, assuming that these gap edges are located at the position with $\Sigma = (1/3)\Sigma_0(R_{\rm p})$ (i.e. $s = 1/3$). If we adopt the same definition of the gap edge, the gap widths of our exact solutions with $x_{\rm d} = 3$ and 4 are $6.1h_{\rm p}$ and $7.7h_{\rm p}$, respectively. Hence, if we take into account the wave propagation and adopt $x_{\rm d} = 3$–4, our exact solution can almost reproduce both of the gap width and depth of the hydrodynamic simulations by DM13, for $K = 200$.

It should be also noted that, for $x_{\rm d} = 2$, the wave excitation mainly occurs at $|x| > x_{\rm d}$ (80 per cent of the excitation torques come from this region). However, the deposition site should be farther from the planet than the excitation site because the density waves propagate away from the planet. Thus, the case with $x_{\rm d} = 2$ does not represent a realistic wave propagation. From now on, we judge that our simple model for the wave propagation is valid if more than half of the one-sided torque arises from the excitation at $|x| < x_{\rm d}$. In the case with $x_{\rm d} = 3$ or 4, the excitation at $|x| < x_{\rm d}$ contributes 55 per cent or 78 per cent of the one-sided torque, respectively. In Fig. 10, we check the effect of the width of the deposition site, $w_{\rm d}$, for $x_{\rm d} = 3$ and $K = 200$. It is found that the width $w_{\rm d}$ has only a small influence on the gap structure. We show that the deviation from the Keplerian rotation is also important in the case with wave

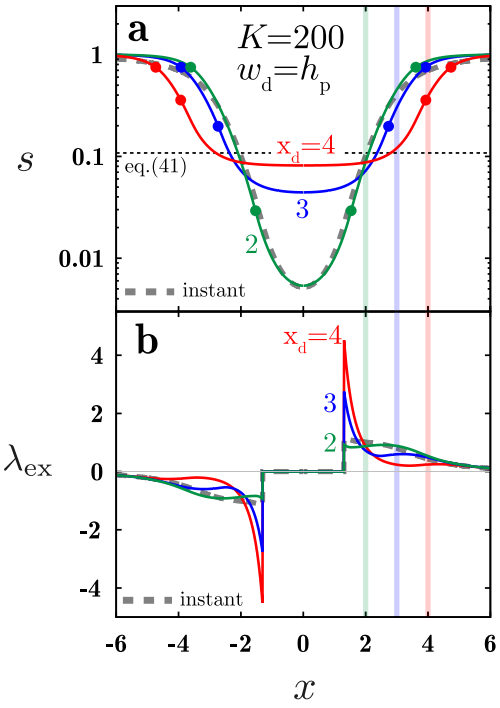

Figure 9. Surface densities (a) and excitation torque densities (b) in the case with the wave propagation for $K = 200$. The green, blue and red lines denote the solutions with $x_{\rm d} = 2$, 3 and 4, respectively. The parameter $w_{\rm d}$ is set to $h_{\rm p}$. The grey dashed line is the surface density in the case with instantaneous wave damping. The dotted line in (a) represents the minimum surface density for the wide-limit gap given by equation (41), i.e. $s_{\rm min} = 0.109$.

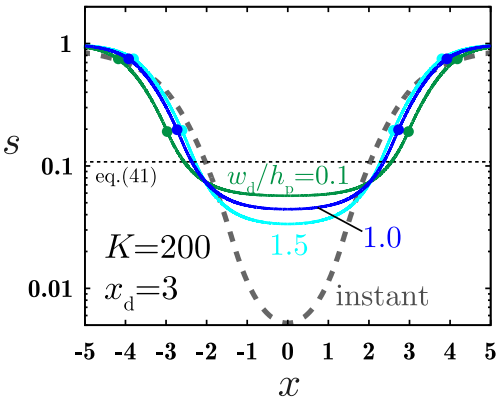

Figure 10. Gap structures for $w_{\rm d} = 0.1h_{\rm p}$ (green), $h_{\rm p}$ (blue) and $1.5h_{\rm p}$ (light-blue). The parameters K and $x_{\rm d}$ are set to 200 and 3, respectively. The grey dashed line indicates the solution in the instantaneous damping case and the dotted line is the minimum surface density of the wide-limit gap (equation 41).

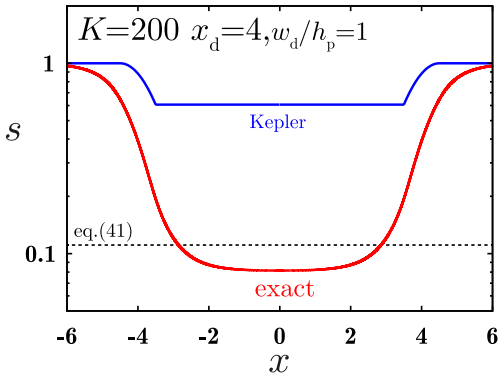

Figure 11. The Keplerian solution in the case of wave propagation for $K = 200$, $x_d = 4$ and $w_d = h_p$ (bule line). For comparison, the exact solution (red line) is also plotted.

propagation. In Fig. 11, we plot the solution with the Keplerian rotation and our exact solution. The Keplerian solution is derived from equation (35) with the angular momentum deposition model (equations 20 and 21). When the Rayleigh condition is violated, the marginal stable condition (equation 29) is used. A detail derivation of this solution is described in Appendix B. In the Keplerian solution of Fig. 11, the Rayleigh condition is violated over the whole region of the angular momentum deposition. Then, the minimum surface density is given by equation (B3), which is much larger than our solution and equation (41). Because equation (B3) does not satisfy equation (35), the Keplerian solution does not satisfy the angular momentum conservation, as pointed out in Section 4.3. On the other hand, in the zero-dimensional analysis by Fung et al. (2014, or in equation 41), s_{min} is estimated from a balance between the planetary torque and the viscous angular momentum flux (i.e. from the angular momentum conservation). Because of this difference, the Keplerian solution gives a much shallower gap than the estimation in equation (41). Note that because our exact solutions are given by equation (27), the balance between the planetary torque and the viscous angular momentum flux is always satisfied in our solutions. Hence, our solutions always satisfy the angular momentum conservation and gives a similar s_{min} to equation (41) for a sufficiently wide gap.

5.2 Dependences of the gap depth and width on *K*

Fig. 12 shows the minimum surface densities s_{min} as a function of the parameter K similar to Fig. 8 but the effect of the wave propagation is included in this figure. In this figure, we also show the dependence on the parameter x_d while w_d is fixed at h_p since w_d does not change the surface density distribution much (see Fig. 10). At $K = 200$, as also seen in Fig. 9, our exact solutions reproduce the gap depth of DM13 (or the wide-limit gap) for $x_d \geq 3$. At $K = 1000$, on the other hand, a larger x_d (≥ 6) is required for agreement with DM13. That is, with an increase of K, a large x_d is necessary for the values of the depth of the hydrodynamic simulations to agree. Note that the dashed lines in Fig. 12 represent the cases of unrealistic wave propagation, in which more than half of the one-sided torque is due to the excitation at $|x| > x_d$, as for the case of $x_d = 2$ in Fig. 9. At large K, a large x_d is also required for realistic wave propagation.

We also show the Keplerian solution with the wave propagation of $x_d = 6$ (see Appendix B). For $K > 30$, s_{min} is given by equation (B3) and independent of K because of the Rayleigh condition, as seen in Fig. 9. This unrealistic result in the Keplerian solution is related with the violation of the angular momentum conservation, as pointed out in Section 4.3 (and see also Appendix B). To check which x_d is preferable, we also compare the gap width with the hydrodynamic simulations. Fig. 13 shows the gap width of the exact solutions as a function of K. Similar to DM13, the gap edge is defined by the position with $s = 1/3$. In this definition, the gap width is roughly given by twice $x_d h$ for our exact solutions with $K > 50$. Note that this definition is useless for $K < 50$ because of shallow gaps with $s_{min} > 1/3$. The dashed lines represent the cases of unrealistic wave propagation, similar to Fig. 12. The results of DM13 and Varnière et al. (2004) are also plotted in fig. 13. Varnière et al. (2004) also performed hydrodynamic simulations of gap formation for $M_p/M_* = 10^4$–2×10^3, $\alpha = 6 \times 10^{-2}$–$6 \times 10^{-5}$ and $h_p/R_p = 0.04$ (i.e. $K = 600$–6×10^5). Their gap depths almost agree with DM13's relation. For $K < 300$, our exact solutions with $x_d = 3$ and 4 agree with the results of DM13 and Varnière et al. (2004), respectively. For $K > 300$, on the other hand, the widths obtained by Varnière et al. (2004) are wider than those given by DM13. Our exact solution with $x_d = 6$ agrees with the widths of Varnière et al. (2004), while widths of DM13 correspond to our

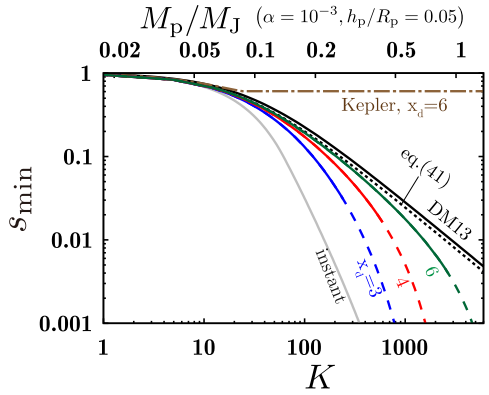

Figure 12. Minimum surface densities, s_{min}, of the exact solutions in the case with the wave propagation for $x_d = 3$ (blue), 4 (red) and 6 (green). The parameter w_d is h_p. We also plot results by DM13 (equation 42, solid line) and the wide-limit gap (equation 41, dotted line) and the exact solution with instantaneous damping (grey line). The dashed lines indicate exact solutions with unrealistic wave propagation.

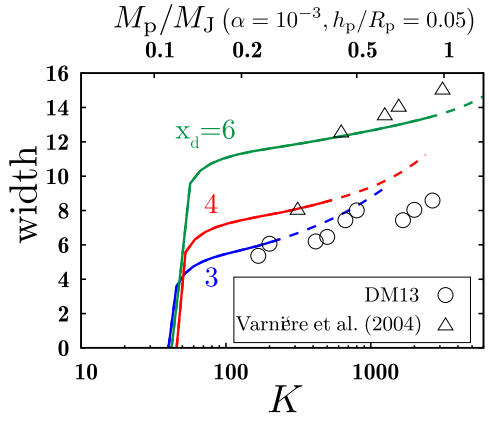

Figure 13. Gap widths of our solutions for $x_d = 3$ (blue), 4 (red) and 6 (green). The edge of the gap is defined by the position with $s = 1/3$, in the same way as defined by DM13. The parameter w_d is set to h_p. The dashed lines represent solutions with unrealistic wave propagation, similar to Fig. 12. The circles indicate the gap widths obtained by DM13 (fig. 6 of their paper), and the triangles show the gap widths by Varnière et al. (2004, twice Δ_{1000} in table 1 of Varnière et al.).

solutions of unrealistic wave propagation. The preferable x_d cannot be determined only by this comparison, and we still have a large uncertainty in the preferable value of x_d.

The difference of widths between DM13 and Varnière et al. (2004) would be caused by different parameters in their simulations (e.g. the disc viscosity, spatial resolution and width of a computation domain). However, the origin of the difference is still unclear. Note that the results of Kley & Dirksen (2006) and Fung et al. (2014) may support the wide gap formation of Varnière et al. (2004). Kley & Dirksen (2006) also showed that the disc rotation has some eccentricity when the gap is extended to the 1:2 Lindblad resonance. The eccentric gaps are formed for a large K ($\gtrsim 10^4$) (e.g. Kley & Dirksen 2006; Fung et al. 2014). Such wide gaps by massive giant planets are beyond the scope of our one-dimensional disc model adopting the local approximation.

In the above, we found that a larger x_d is required for a larger K (i.e. a massive planet) in order to reproduce the minimum surface densities derived by DM13 and Varnière et al. (2004). It should be noted that the propagation distance is not proportional to the parameter x_d. The propagating distance of waves is defined by the distance from the wave excitation site to the angular momentum deposition site (i.e. x_d). Since the one-sided torque is radially distributed (see Fig 9b), the wave excitation site can be approximately given by the median of the distribution, i.e. the point within the half of the one-sided torque arises. Such an excitation site shifts away from the planet with an increase of K (see Fig. 12).[4] D'Angelo & Lubow (2010) also showed this tendency that the peak of the excitation torque density shifts away from the planet as a deep gap is formed (fig. 15 in that paper), using hydrodynamic simulations. Hence, because of this shift of the excitation site, the propagating distance does not increase much as x_d with K. Goodman & Rafikov (2001) showed that the propagating distance of waves decreases with an increase of the planet mass due to the non-linear wave damping. Hence, further studies are needed in order to confirm whether this results given by Goodman & Rafikov (2001) conflicts with ours because of the shift of the excitation site. Furthermore, the non-linear wave damping would be weakened by the steep surface density gradient at the gap edge, as pointed out by Petrovich & Rafikov (2012). In order to fix the parameter x_d, such a wave damping effect in the gap should be taken into account in future work.

6 SUMMARY AND DISCUSSION

We re-examined the gap formation in viscous one-dimensional discs with a new formulation. In our formulation, we took into account the deviation from Keplerian disc rotation and included the Rayleigh stable condition, consistently. We also examined the effect of wave propagation. Our results are summarized as follows.

(i) The deviation from the Keplerian disc rotation makes the gap shallow. This is because of the enhancement of the shear motion and the viscous angular momentum transfer at the gap edges (see Fig. 4).

(ii) For deep gaps, the deviation from the Keplerian disc rotation is so large that the Rayleigh stable condition is violated. An enhanced viscosity dissolves such unstable rotation and makes it marginally stable (see Fig. 7). This effect also makes the gap shallower (see Fig. 6).

(iii) To include the effect of wave propagation, we adopted a simple model where the position of the angular momentum deposition is parametrized by x_d. A large x_d indicates a long propagation length. The effect of wave propagation makes the gap wider and shallower (Fig. 9). In a wide gap, the waves are mainly excited at the flat bottom, which reduces the one-sided torque and the gap depth. For a sufficiently large x_d, the gap depth of our exact solution agrees well with the wide-limit gap and with the results of hydrodynamic simulations. At $K = 1000$, our model requires $x_d \geq 6$ for the agreement (Fig. 12). In the case of instantaneous wave damping, on the other hand, our exact solution gives much deeper gaps than those of hydrostatic simulations.

(iv) To check the validity of the large x_d, the gap width of our exact solution is compared with results of hydrodynamic simulations. For $K = 1000$, our exact solution with $x_d \geq 6$ has a gap width of $12h_p$, which is larger than those of DM13 ($\sim 8h_p$). The gap widths of Varnière et al. (2004), on the other hand, are almost consistent with our exact solutions. Because of this uncertainty in the gap width of hydrodynamic simulations, it is difficult to fix the preferable x_d by this comparison.

(v) When the Rayleigh condition is taken into account, the deviation from the Keplerian rotation should also be included in order to keep the angular momentum conservation. The Keplerian solutions with the Rayleigh condition give much shallower gaps, as shown in Figs 8 and 12.

In future works, we need to determine the preferable value of x_d. Previous studies (e.g. Korycansky & Papaloizou 1996; Takeuchi, Miyama & Lin 1996; Goodman & Rafikov 2001; Dong, Rafikov & Stone 2011) have investigated the wave propagation with no gap. As pointed out by Petrovich & Rafikov (2012), however, the gap structure can affect the wave damping. Since our result shows that the wave damping significantly affects both the gap depth and width, the wave damping should be treated accurately in both one-dimensional models and hydrodynamic simulations for gap formation.

Our simple model does not include the effect of the deviation from Keplerian disc rotation on the wave excitation. Petrovich & Rafikov (2012) showed that a steep surface density gradient modifies the excitation torque. Such an effect on the wave excitation should be included in future studies on the gap formation. Nevertheless, it is also considered that when the waves are mainly excited at the flat-bottom, such as for the wide-limit gap, the deviation of the disc rotation would not affect the wave excitation significantly.

We also neglect the non-linearity of wave excitation, whereas the non-linearity cannot be neglected for large planets as $M_p/M_* \gtrsim (h_p/R_p)^3$. According to Miyoshi et al. (1999), the non-linearity makes the excitation torque small compared to the value for linear theory. This possibly leads to an additional shallowing effect. However, this effect would not significantly influence the gap depth since s_{min} is scaled by only K in DM13's relation (equation 42).

The Rossby wave instability may be essential for the gap formation. In the present study, we included only the Rayleigh condition. A more detail investigation including both the Rayleigh condition and the Rossby wave instability should be done in future works.

ACKNOWLEDGEMENTS

We are grateful to Aurélien Crida, and Alessandro Morbidelli for their valuable comments. We also thank the anonymous referee for useful comments on the manuscript. KDK is supported by Grants-in-Aid for Scientific Research (26103701) from the MEXT

[4] In Fig. 12, the exact solution have transition points from the realistic wave propagation (solid lines) to the unrealistic one (dashed lines) for each x_d. At the transition point of K, the excitation site defined by the median is equation to x_d. Fig. 12 shows that the excitation site moves away from the planet with an increasing K since the transition point of K increases with x_d.

of Japan. TT (Takayuki Tanigawa) is supported by Grants-in-Aid for Scientific Research (23740326 and 24103503) from the MEXT of Japan.

REFERENCES

Abramowitz M., Stegun I. A., 1965, Handbook of Mathematical Functions with Formulas, Graphs, and Mathematical Tables. Dover Press, New York
Adachi I., Hayashi C., Nakazawa K., 1976, Prog. Theor. Phys., 56, 1756
Artymowicz P., Lubow S. H., 1994, ApJ, 421, 651
Artymowicz P., Lubow S. H., 1996, ApJ, 467, L77
Bate M. R., Lubow S. H., Ogilvie G. I., Miller K. A., 2003, MNRAS, 341, 213
Chandrasekhar S., 1939, Ciel Terre, 55, 412
Chandrasekhar S., 1961, Hydrodynamic and Hydromagnetic Stability. Oxford Univ. Press, Oxford
Crida A., Morbidelli A., Masset F., 2006, Icarus, 181, 587
D'Angelo G., Lubow S. H., 2010, ApJ, 724, 730
D'Angelo G., Henning T., Kley W., 2002, A&A, 385, 647
Dodson-Robinson S. E., Salyk C., 2011, ApJ, 738, 131
Dong R., Rafikov R. R., Stone J. M., 2011, ApJ, 741, 57
Duffell P. C., MacFadyen A. I., 2013, ApJ, 769, 41 (DM13)
Fung J., Shi J.-M., Chiang E., 2014, ApJ, 782, 88
Goldreich P., Tremaine S., 1980, ApJ, 241, 425
Goodman J., Rafikov R. R., 2001, ApJ, 552, 793
Haisch K. E., Jr, Lada E. A., Lada C. J., 2001, ApJ, 553, L153
Kanagawa K. D., Fujimoto M. Y., 2013, ApJ, 765, 33
Kley W., 1999, MNRAS, 303, 696
Kley W., Dirksen G., 2006, A&A, 447, 369
Kokubo E., Ida S., 2000, Icarus, 143, 15
Kokubo E., Ida S., 2002, ApJ, 581, 666
Korycansky D. G., Papaloizou J. C. B., 1996, ApJS, 105, 181
Li H., Finn J. M., Lovelace R. V. E., Colgate S. A., 2000, ApJ, 533, 1023
Lin D. N. C., Papaloizou J., 1979, MNRAS, 186, 799
Lin D. N. C., Papaloizou J., 1986, ApJ, 309, 846
Lin D. N. C., Papaloizou J. C. B., 1993, in Levy E. H., Lunine J. I., eds, Protostars and Planets III. Univ. Arizona Press, Tucson, AZ, p. 749
Lin M.-K., 2014, MNRAS, 437, 575
Lubow S. H., D'Angelo G., 2006, ApJ, 641, 526
Lubow S. H., Seibert M., Artymowicz P., 1999, ApJ, 526, 1001
Lynden-Bell D., Pringle J. E., 1974, MNRAS, 168, 603
Miyoshi K., Takeuchi T., Tanaka H., Ida S., 1999, ApJ, 516, 451
Mizuno H., 1980, Prog. Theor. Phys., 64, 544
Muto T., Inutsuka S.-i. 2009, ApJ, 701, 18
Petrovich C., Rafikov R. R., 2012, ApJ, 758, 33
Rafikov R. R., 2002, ApJ, 572, 566
Richard S., Barge P., Le Dizès S., 2013, A&A, 559, A30
Shakura N. I., Sunyaev R. A., 1973, A&A, 24, 337
Takeuchi T., Miyama S. M., 1998, PASJ, 50, 141
Takeuchi T., Miyama S. M., Lin D. N. C., 1996, ApJ, 460, 832
Tanaka H., Takeuchi T., Ward W. R., 2002, ApJ, 565, 1257
Tanigawa T., Ikoma M., 2007, ApJ, 667, 557 (TI07)
Varnière P., Quillen A. C., Frank A., 2004, ApJ, 612, 1152
Ward W. R., 1986, Icarus, 67, 164
Ward W. R., 1997, Icarus, 126, 261
Yang C.-C., Menou K., 2010, MNRAS, 402, 2436
Zhu Z., Nelson R. P., Hartmann L., Espaillat C., Calvet N., 2011, ApJ, 729, 47
Zhu Z., Stone J. M., Rafikov R. R., 2013, ApJ, 768, 143

APPENDIX A: GAP MODEL BY TI07

Following TI07, we describe surface density structures of gap in a disc with the Keplerian rotation. In this section, we consider the gap structure in the case of instantaneous wave damping. The gap structure in the case with wave propagation is discussed in Appendix B. In the case of instantaneous wave damping, the angular momentum deposition rate is given by $\lambda_{\rm ex}$ given by equation (30). At far from a planet, the Rayleigh condition is always satisfied because the planetary gravity is weak. Hence, the gradient of surface density is given by equation (36) and the second derivative of surface density is given by

$$\frac{{\rm d}^2 \ln s}{{\rm d}x^2} = \mp \frac{4KC}{3x^5}. \tag{A1}$$

The stability of the Rayleigh condition is checked by equation (A1). Namely, when ${\rm d}^2 \ln s/{\rm d}x^2 < -1$ in equation (A1), the surface density is described by the marginal Rayleigh stable state, instead of equation (37). We should point out that the second derivative given by equation (A1) is used to determine the stability of the Rayleigh condition and does not affect the surface density distribution. Because of this, the surface density gradient is steeper and the shallowing effect of the Rayleigh condition is much higher than in our model. Using equation (30), we obtain the outer edge of the marginal Rayleigh stable region, $x = x_{\rm m}$, as

$$x_{\rm m} = \left(\frac{4}{3}CK\right)^{1/5}. \tag{A2}$$

In consideration of the continuity of the surface density distribution, the surface density in the marginal Rayleigh stable region ($x < x_{\rm m}$) is given by

$$\ln s = -\frac{5}{6}x_{\rm m}^2 + \frac{5}{4}x_{\rm m}|x| - \frac{1}{2}x^2, \tag{A3}$$

$$= -0.854K^{2/5} + 1.266K^{1/5}|x| - 0.5x^2, \tag{A4}$$

and the surface density for $x > x_{\rm m}$ is given by equation (37). Since there is no torque density for $x > 1.3$ in this case, the minimum surface density $s_{\rm min}$ is given by $s(x = 1.3)$. Thus, we give $s_{\rm min}$ as

$$s_{\rm min} = \exp\left(-0.854K^{2/5} + 1.645K^{1/5} - 0.845\right). \tag{A5}$$

Note that if $x_{\rm m} < 1.3$, the whole region of the gap is the Keplerian rotating part and $s_{\rm min}$ is given by equation (37) with $x = 1.3$. It should be also noticed that the angular momentum conservation is not satisfied at the flat-bottom region with $s = s_{\rm min}$ of equation (A5), as explained in the subsection 4.3 (and see also, Appendix B).

APPENDIX B: GAP MODEL IN A KEPLERIAN ROTATING DISC WITH WAVE PROPAGATION

Here, by assuming the Keplerian disc rotation, we derive gap solutions in the case with wave propagation. Following TI07, we consider the marginal condition when the Rayleigh condition is violated. The angular momentum deposition rate is given by equation (32). Ignoring deviation in ${\rm d}\Omega/{\rm d}R$ form the Keplerian and differentiating, we give

$$\frac{{\rm d}s}{{\rm d}x} = \begin{cases} \dfrac{\bar{T}}{3}\dfrac{h_{\rm p}}{w_{\rm d}} & \text{for } x_{\rm d} - \dfrac{w_{\rm d}}{2h_{\rm p}} < |x| < x_{\rm d} + \dfrac{w_{\rm d}}{2h_{\rm p}}, \\ 0 & \text{otherwise.} \end{cases} \tag{B1}$$

Integrating equation (B1), we obtain the surface density without the Rayleigh condition as

$$s = \begin{cases} 1 & \text{for } |x| > x_{\rm d} + \frac{w_{\rm d}}{2h_{\rm p}}, \\ 1 - \frac{\bar{T}h_{\rm p}}{3w_{\rm d}}\left[\left(x_{\rm d} + \frac{w_{\rm d}}{2h_{\rm p}}\right) - x\right] & \text{for } x_{\rm d} - \frac{w_{\rm d}}{2h_{\rm p}} < |x| < x_{\rm d} + \frac{w_{\rm d}}{2h_{\rm p}}, \\ 1 - \frac{\bar{T}}{3} & \text{for } |x| < x_{\rm d} - \frac{w_{\rm d}}{2h_{\rm p}}. \end{cases} \tag{B2}$$

Equation (B2) does not satisfy the Rayleigh condition, especially for a large K (or a large $\tilde{T}$). First, the Rayleigh condition is violated near $|x| = x_{\rm d} + w_{\rm d}/2h_{\rm p}$ because ${\rm d}s/{\rm d}x$ of equation (B1) is not continuous there. In order to make ${\rm d}s/{\rm d}x$ continuous, the marginally stable condition (equation 29) is used instead of equation (B1) in the region where $x_{\rm d} + w_{\rm d} - (\tilde{T}h_{\rm p})/(3w_{\rm d}) < |x| < x_{\rm d} + w_{\rm d}/2h_{\rm p}$. In addition, the marginally stable condition should also be used near $|x| = x_{\rm d} - w_{\rm d}/2h_{\rm p}$ for a large $\tilde{T}$. From equation (B1), we find that the Rayleigh condition is violated from $|x| = x_{\rm d} - w_{\rm d}/2h_{\rm p}$ to $x_{\rm d} + (w_{\rm d}/2h_{\rm p})(1 - 6/\tilde{T}) + 1$. These two Rayleigh unstable regions are merged for $\tilde{T} > 3(w_{\rm d}/h_{\rm p})$. In such large-$K$ cases, since the marginally stable condition is used in the whole region of the angular momentum deposition, the minimum surface density is given by

$$s_{\rm min} = \exp\left[-\left(\frac{1}{2} + \frac{h_{\rm p}}{w_{\rm d}}\right)\right] \tag{B3}$$

which is independent of K. This unrealistic minimum surface density does not satisfy equation (35) which is originated by the angular momentum conservation. As indicated by Fung et al. (2014), the planetary torque should balance with the viscous angular momentum flux outside the gap for the angular momentum conservation. In our formulation, two terms in the right-hand side of equation (27) balance with each other in the bottom region (the left-hand side is negligibly small). However, the minimum surface density given by equation (B3) independent of K breaks down such a balance. Hence, equation (B3) also violates the angular momentum conservation.

For a small K, equation (B2) is approximately valid because the Rayleigh unstable region near $|x| = x_{\rm d} + w_{\rm d}/2h_{\rm p}$ does not significantly affect $s_{\rm min}$. Substituting equation (B2) into equation (33), we give $\tilde{T}$ as

$$\tilde{T} = 3\left[\frac{9\Delta^3}{KC}\left(1 - \frac{KCx_{\rm d}}{9\left[x_{\rm d}^2 - (w_{\rm d}/2h_{\rm p})^2\right]^2}\right) + 1\right]^{-1}. \tag{B4}$$

Substituting equation (B2) into equation (B4), we obtain $s_{\rm min}$ for a small K as

$$s_{\rm min} = \left[\frac{CK}{9\Delta^3}\left(1 - \frac{KCx_{\rm d}}{9\left[x_{\rm d}^2 - (w_{\rm d}/2h_{\rm p})^2\right]^2}\right)^{-1} + 1\right]^{-1}. \tag{B5}$$

APPENDIX C: SOLUTIONS FOR THE LINEARIZED EQUATION OF GAPS

Here, we consider solutions to the following differential equation:

$$\frac{{\rm d}^2 y}{{\rm d}x^2} - 3y = g(x), \tag{C1}$$

where $g(x)$ is an arbitrary odd function of x. A general solution of this equation is given by a combination of homogeneous solutions, $e^{\pm\sqrt{3}x}$, and a particular solution. We seek a solution which satisfies the boundary conditions of $y = 0$ at $x = \pm\infty$. Since $g(x)$ is odd in this case, the solution is an even function of x. For simplicity, we consider the solution for $x > 0$. Because of the symmetry of the equation, the solution of $x < 0$ can be obtained by inverting the sign of x in the solution for $x > 0$.

A particular solution $y_{\rm p}(x)$ of equation (C1) can be given by

$$y_{\rm p}(x) = \frac{1}{2\sqrt{3}}\left[e^{\sqrt{3}x}\int_x^\infty g(x')e^{-\sqrt{3}x'}{\rm d}x' - e^{-\sqrt{3}x}\int_x^\infty g(x')e^{\sqrt{3}x'}{\rm d}x'\right]. \tag{C2}$$

In the case with instantaneous wave damping (see equation 44), $g(x)$ is given by

$$g(x) = -\begin{cases} \dfrac{C}{3|x|^3} & \text{for } |x| > \Delta, \\ \dfrac{C}{3\Delta^3} & \text{otherwise.} \end{cases} \tag{C3}$$

Substituting equation (C3) into equation (C2), the particular solution for $x > \Delta$ is obtained as

$$y_{\rm p}(x) = \frac{\sqrt{3}C}{18}\left[-\frac{\sqrt{3}}{x} + \frac{3}{2}\left\{e^{-\sqrt{3}x}Ei(\sqrt{3}x) - e^{\sqrt{3}x}Ei(-\sqrt{3}x)\right\}\right], \tag{C4}$$

where $Ei(ax)$ denotes the exponential integral function (e.g. Abramowitz & Stegun 1965). For $x \leq \Delta$, the particular solution is given by

$$y_{\rm p}(x) = a_+ e^{\sqrt{3}x} + a_- e^{-\sqrt{3}x} + \frac{C}{9\Delta^3}, \tag{C5}$$

where a_+ and a_- are defined by

$$a_\pm = \frac{C}{6}\left[\mp Ei(\mp\sqrt{3}\Delta) - \frac{1}{\Delta}\left(\frac{1}{3\Delta^2} + \frac{1}{2}\right)e^{\mp\sqrt{3}\Delta}\right]. \tag{C6}$$

Using this particular solution given by equations (C4) and (C5), we can obtain the general solution of equation (44). Since this particular solution vanishes at $x \to \infty$, the coefficient of the homogeneous solution $e^{\sqrt{3}x}$ is zero. The coefficient of $e^{-\sqrt{3}x}$, B, is obtained as

$$B = \frac{1}{\sqrt{3}}\left.\frac{{\rm d}y_{\rm p}}{{\rm d}x}\right|_{x=0}. \tag{C7}$$

This paper has been typeset from a TEX/LATEX file prepared by the author.

Monthly Notices
of the
ROYAL ASTRONOMICAL SOCIETY

MNRAS **442,** 2543–2559 (2014) doi:10.1093/mnras/stu1013

Rapid evolution of the innermost dust disc of protoplanetary discs surrounding intermediate-mass stars

Chikako Yasui,[1]★ Naoto Kobayashi,[2] Alan T. Tokunaga[3] and Masao Saito[4,5]

[1]*Department of Astronomy, Graduate School of Science, University of Tokyo, Hongo 7-3-1, Bunkyo-ku, 113-0033 Tokyo, Japan*
[2]*Institute of Astronomy, School of Science, University of Tokyo, 2-21-1 Osawa, Mitaka, Tokyo 181-0015, Japan*
[3]*Institute for Astronomy, University of Hawaii, 2680 Woodlawn Drive, Honolulu, HI 96822, USA*
[4]*National Astronomical Observatory of Japan 2-21-1 Osawa, Mitaka, Tokyo 181-8588, Japan*
[5]*Joint ALMA Observatory (JAO), Alonso de Cordova 3107, Vitacura, Santiago 763-0355, Chile*

Accepted 2014 May 20. Received 2014 May 19; in original form 2013 September 26

ABSTRACT

We derived the intermediate-mass ($\simeq$1.5–7 $M_\odot$) disc fraction (IMDF) in the near-infrared *JHK* photometric bands as well as in the mid-infrared (MIR) bands for young clusters in the age range of 0 to ∼10 Myr. From the *JHK* IMDF, the lifetime of the innermost dust disc (∼0.3 au; hereafter the *K* disc) is estimated to be ∼3 Myr, suggesting a stellar mass (M_*) dependence of *K*-disc lifetime $\propto M_*^{-0.7}$. However, from the MIR IMDF, the lifetime of the inner disc (∼5 au; hereafter the MIR disc) is estimated to be ∼6.5 Myr, suggesting a very weak stellar mass dependence ($\propto M_*^{-0.2}$). The much shorter *K*-disc lifetime compared to the MIR-disc lifetime for intermediate-mass (IM) stars suggests that IM stars with *transition discs*, which have only MIR excess emission but no *K*-band excess emission, are more common than classical Herbig Ae/Be stars, which exhibit both. We suggest that this prominent early disappearance of the *K* disc for IM stars is due to dust settling/growth in the protoplanetary disc, and it could be one of the major reasons for the paucity of close-in planets around IM stars.

Key words: planets and satellites: formation – protoplanetary discs – circumstellar matter – stars: pre main-sequence – stars: variables: T Tauri, Herbig Ae/Be – infrared: stars.

1 INTRODUCTION

Understanding protoplanetary discs is not only essential for understanding the star formation process, but it is also critical for understanding planet formation (e.g. Lada & Lada 2003). The lifetime of protoplanetary discs is one of the most fundamental parameters of a protoplanetary disc because it directly restricts the time for planet formation (e.g. Williams & Cieza 2011). Many studies that derive the lifetime of protoplanetary discs are now available. In a pioneering work, Strom et al. (1989) studied the frequency of disc-harbouring stars with known ages in the Taurus molecular cloud that have a *K*-band excess and suggested that the disc lifetime is in the range from ≪3 Myr to ∼10 Myr. Subsequently, a more direct method using the 'disc fraction', which is the frequency of near-infrared (NIR) or mid-infrared (MIR) excess stars within a young cluster *with an assumed age*, has been widely adopted to study the disc lifetime following the work by Lada (1999) and Haisch, Lada & Lada (2001b). Using the disc fraction that monotonically decreases as a function of cluster age, the disc lifetime is estimated at about 5–10 Myr in the solar neighbourhood (Lada 1999; Haisch et al. 2001b; Hernández et al. 2008; see also Yasui et al. 2010). Mamajek (2009) compiled disc fractions for about 20 clusters and derived the characteristic disc decay time-scale (τ) of 2.5 Myr, assuming the disc fraction[per cent] $\propto \exp(-t[\mathrm{Myr}]/\tau)$.

These estimated disc lifetimes were mainly derived from the disc fraction with all detected cluster members and thus the estimated lifetime has been primarily for low-mass (LM) stars (<2 $M_\odot$), considering the characteristic mass of the initial mass function(IMF, ∼0.3 $M_\odot$; Elmegreen 2009) and the typical stellar mass detection limit (∼0.1 $M_\odot$). However, a number of assessments of the effect of the stellar mass dependence of the disc lifetime have recently suggested a shorter disc lifetime for the higher mass stars (e.g. Hernández et al. 2005; Carpenter et al. 2006; Kennedy & Kenyon 2009). Although the existence of discs of high-mass stars ($\gtrsim$8 $M_\odot$) is still under debate (e.g. Fuente et al. 2002; Mann & Williams 2009), the discs of intermediate-mass (IM) stars have been extensively studied and are well characterized (Hernández et al. 2005, 2007a, 2008). IM stars with optically thick discs are known as Herbig Ae/Be (HAeBe) stars. They were originally discovered with strong emission lines by Herbig (1960). After Hernández et al. (2004) established the method for selecting HAeBe stars using the spectral energy distribution (SED) slope from the *V* band to the *IRAS* 12 μm band, Hernández et al. (2005) derived the HAeBe-star disc fraction for six clusters in the age range of 3–10 Myr. They showed that

★ E-mail: ck.yasui@astron.s.u-tokyo.ac.jp

the disc fraction is lower compared to the previously derived disc fraction for LM stars, in particular by a factor of ∼10 lower at ∼3 Myr.

Recently, the disc fraction studies have shifted to longer wavelengths (MIR or submm) mainly because of the interest in tracing the outer disc, where most of the disc mass resides (Williams & Cieza 2011). However, the disc fractions can also be estimated using only *JHK* data, in particular, for the IM stars. Originally, the disc lifetime was estimated with disc fractions derived by using the colour–colour diagram based on imaging in the *JHK* and *JHKL* photometric bands (e.g. Lada 1999; Haisch et al. 2001b). After the advent of the *Spitzer Space Telescope*, the SED slope ($\alpha = \mathrm{d}\ln\lambda F_\lambda/\mathrm{d}\ln\lambda$) in the MIR wavelength range (3.6, 4.5, 5.8, and 8.0 μm) is used for selecting disc-harbouring stars (e.g. $\alpha \geq -2.0$; Lada et al. 2006). However, the derived disc fractions and disc lifetime with *Spitzer* data were found to be almost the same as those with *JHKL* data (see Sicilia-Aguilar et al. 2006; Hernández et al. 2008), and even with *JHK* data (Lada 1999; Yasui et al. 2010). Although the NIR disc fractions are known to show values systematically smaller and with a larger uncertainty due to contamination of the non-disc-harbouring stars on the colour–colour diagram (Haisch, Lada & Lada 2001a; Yasui et al. 2010), Hernández et al. (2005) showed that the *JHK* colour–colour diagram can clearly distinguish disc-harbouring IM stars from non-disc IM stars. The *JHK*-disc fraction value is robust both because of the large infrared excess and the higher stellar effective temperature of the IM stars, compared to LM stars.

In this paper, we derived the *JHK* intermediate-mass disc fraction (IMDF) using the Two Micron All Sky Survey (2MASS) Point Source Catalog of a large number (∼20) of well-established nearby ($D \lesssim 1.5$ kpc) young clusters with an age span of 0 to ∼10 Myr in order to quantitatively and comprehensively study the lifetime of protoplanetary discs surrounding IM stars (≃1.5–7 $\mathrm{M}_\odot$). In particular, we included as many clusters as possible with ages <5 Myr. To securely identify IM cluster members, we made use of the spectral types of each cluster member from the literature, assuming a single age for each cluster. With the derived *JHK* IMDFs for a large number of younger clusters (<5 Myr), we estimated the disc lifetime of the IM stars. We then estimated the stellar mass dependence of the disc lifetime by comparing the lifetime of IM stars to that of LM stars. We also derived the MIR IMDFs with *Spitzer* data in the literature to compare them to the *JHK* IMDFs. We found that the derived *JHK* IMDFs are significantly lower than the MIR IMDFs, in particular at younger ages (<3 Myr), which results in shorter lifetime of the *K* disc than the MIR disc. This suggests a potentially larger fraction of 'transition discs' for IM stars compared to those for LM stars. We discuss the implications of these results for dust growth and planet formation.

Because the sample clusters and the selection of the IM stars are critical for this paper, we discuss these in detail in Section 2. The definition and derivation of the *JHK* IMDF and the MIR IMDF are described in Sections 3 and 4, respectively. Before interpreting the results of the IMDFs, the definition of the disc lifetime is discussed in Section 5. Section 6 then discusses the results for *JHK* IMDFs. The MIR-disc fraction is discussed in Section 7. Subsequently, Section 8 discusses the large difference between *JHK* and MIR IMDFs found in this study and potential disc evolution consequences for IM stars. Finally, Section 9 discusses the possible physical mechanisms of this rapid evolution of the *K* disc. At the end, in Section 10, we briefly discuss possible implications for planet formation. Section 11 summarizes this paper.

2 TARGET CLUSTERS AND SELECTION OF IM-STAR SAMPLES

2.1 Target clusters

We selected our target clusters from previous studies of the disc fraction/disc evolution (Haisch et al. 2001b; Hernández et al. 2005, 2008; Gáspár et al. 2009; Kennedy & Kenyon 2009; Mamajek 2009; Fedele et al. 2010; Roccatagliata et al. 2011). For estimating the disc lifetime with acceptable accuracy, it is necessary to derive the IMDFs for as many as young clusters as possible, ideally more than 10. We thus selected our target young clusters from the above papers, but with the following criteria: (1) cluster ages are spaced from 0 to ∼10 Myr, to cover the time period of disc dispersal. (2) The cluster membership is well defined from a variety of observations (astrometry, radial velocity, variability, Hα, X-ray, NIR excess, MIR excess, optical spectroscopy, NIR spectroscopy, etc.). This criterion naturally leads to clusters in the solar neighbourhood (distance <1.5 kpc). (3) The spectral types of a large number of cluster members are available by spectroscopy. (4) Well-defined NIR and MIR photometry of the cluster members with $M_{\mathrm{limit}} \sim 1\,\mathrm{M}_\odot$ is published in a widely available catalogue, such as 2MASS. (5) At least three IM stars are available per cluster for IMDF derivation.

The resultant 19 target clusters are summarized in Table 1 along with the age, distance, and references for the disc fraction study. Almost all young (<5 Myr) clusters in the references (Table 1) are included, though three young clusters (MBM 12, NGC 6231, and NGC 7129) are excluded. This is because it appears that no IM stars are present in MBM 12 (Luhman 2001), and the spectral types of stars in NGC 6231 and NGC 7129 are limited only to brightest members (OB, A stars), and are not adequate to cover the entire IM-star mass range down to 1.5 $\mathrm{M}_\odot$. Some older clusters (>5 Myr), mostly those from Fedele et al. (2010), are excluded because they do not satisfy the above criterion. For several well-known clusters within the target clusters (Trapezium, Ori OB1a, Ori OB1bc, Per OB2), we could derive only *JHK*-disc fractions because we could not find published *Spitzer* MIR data for the IM stars, probably because of saturation. As a result, we obtained the *JHK* IMDF for 19 clusters and the MIR IMDF for 13 clusters.

2.2 Selection of IM stars

Although the original definition of mass for HAeBe is ∼2–10 $\mathrm{M}_\odot$ with spectral types of B and A (and in a few cases F; Herbig 1960), the presence of discs around stars earlier than B5 (≃6–7 $\mathrm{M}_\odot$ in the main-sequence phase) is not well established since the disc lifetime of high-mass stars is very rapid, e.g. ∼1 Myr (Fuente et al. 2002; Zinnecker & Yorke 2007). Also, the number of high-mass stars (>6–7 $\mathrm{M}_\odot$) is very small because of the IMF, and the number stochastically fluctuates from cluster to cluster. Therefore, we set the upper mass limit as 7 $\mathrm{M}_\odot$ in this paper. This is also a good match with the mass range of the isochrone model by Siess, Dufour & Forestini (2000, $M_{\mathrm{max}} = 7\,\mathrm{M}_\odot$), which is used throughout this paper. As for the lower mass limit, we employed 1.5 $\mathrm{M}_\odot$, which corresponds to spectral type 'F1' for main sequences, following past comprehensive works of discs for IM stars by Hernández et al. (2005) and Kennedy & Kenyon (2009). The latter defined a mass range bin of 1.5–7 $\mathrm{M}_\odot$, which can be directly compared to our results.

The IM-star selection is a critical item for this study. Ideally, stellar mass and the age of each cluster member are determined from the

Table 1. Summary of target clusters.

	Cluster	Age[a] (Myr)	Distance[b] (pc)	References for the disc fraction study[c]
1	NGC 1333	1 ± 1 (He08)	318 (LL03)	He08, Ma09, Ro11
2	Trapezium	1 ± 1 (Mu02)	450 (LL03)	Ha01, He08, Ma09
3	ρ Oph	1 ± 1 (Fe10)	125 (LL03)	Fe10
4	Taurus	1.5 ± 1.5 (He08)	140 (El78)	Ha01, He08, Ke09, Ma09, Fe10, Ro11
5	Cha I	2 ± 1 (Ro11)	170 (Lu08)	Ha01, He08, Ke09, Ma09, Fe10, Ro11
6	NGC 2068/71	2 ± 1.5 (Ro11)	400 (LL03)	He08, Ma09, Ro11
7	IC 348	2.5 ± 0.5 (He08)	320 (Ha01a)	Ha01, He08, Ke09, Ma09, Fe10, Ro11
8	σ Ori	3 ± 1 (Ro11)	440 (He07a)	He08, Ma09, Fe10, Ro11
9	NGC 2264	3 ± 1 (He08)	760 (Da08a)	Ha01, He08, Ma09
10	Tr 37	4 ± 1 (He08)	900 (Si05)	He08, Ke09, Ma09, Ro11
11	Ori OB1bc	4 ± 3 (He05)	443 (He05)	He05, He08, Ke09, Ma09, Ga09
12	Upper Sco	5 ± 1 (Pr02)	144 (He05)	He05, He08, Ke09, Ma09, Ga09, Fe10, Ro11
13	NGC 2362	5 ± 1 (He08)	1500 (Da08b)	Ha01, He08, Ke09, Ma09, Fe10, Ro11
14	γ Vel	5 ± 1.5 (He08)	350 (He08)	He08, Ma09, Ro11
15	λ Ori	5 ± 1 (He08)	450 (He09)	He08, Ma09
16	Per OB2	6 ± 2 (He05)	320 (He05)	He05
17	η Cham	7 ± 1 (He08)	100 (Ma99)	He08,Ma09, Ga09, Fe10, Ro11
18	Ori OB1a	8.5 ± 1.5 (Br05)	330 (He05)	He05, He08, Ke09, Ma09, Ga09
19	NGC 7160	11 ± 1 (He08)	900 (Si05)	He08, Ke09, Ma09, Ro11

[a]Adopted age with reference in parentheses.
[b]Distance with reference in parentheses.
[c]Literatures for disc fraction study in the past. Note that some references show different cluster names (e.g. 25 Ori, which is named as Ori OB1a in our list).
References: Br05: Briceño et al. (2005); Da08a: Dahm (2008a); Da08b: Dahm (2008b); El78: Elias (1978); Fe10: Fedele et al. (2010); Ga09: Gáspár et al. (2009); Ha01a: Haisch et al. (2001b); Ha01b: Haisch et al. (2001a); He05: Hernández et al. (2005); He07a: Hernández et al. (2007a); He08: Hernández et al. (2008); He09: Hernández et al. (2009); Ke09: Kennedy & Kenyon (2009); LL03: Lada & Lada (2003); Lu08: Luhman (2008); Ma09: Mamajek (2009); Ma99: Mamajek, Lawson & Feigelson (1999); Mu02: Muench et al. (2002); Pr02: Preibisch et al. (2002); Ro11: Roccatagliata et al. (2011); Si05: Sicilia-Aguilar et al. (2005).

HR diagram with the extinction-corrected luminosity and spectroscopically determined effective temperature through an isochrone model. However, this requires a time-consuming observational programme, and thus the number of target clusters is limited as in the previous studies. Even if we had the complete observational data, the value of mass and age depends on the isochrone model, and could strongly depend on the extinction correction with different R_V (e.g. Hernández et al. 2004, 2005). Another approach is to use a limited number of parameters, such as only the spectral type, to pick up cluster members in a broad mass range, such as IM or LM stars, and to use a larger number of clusters. Although sacrificing the accuracy of the mass estimate, a study including a larger number of clusters is possible. Although some past studies, in fact, focus on targets of certain spectral types (e.g. earlier than F1) to pick up IM stars (Hernández et al. 2005; Uzpen, Kobulnicky & Kinemuchi 2009), the true mass for a star of a certain spectral type varies with the age of the star, and such spectral-type-limited samples should be viewed with caution (Kennedy & Kenyon 2009). We assume that the cluster age is the age of the members in the selection of the IM stars.

The choice of the isochrone model is critical for the mass estimate. Although a number of recent isochrone models are available (e.g. such as Yi, Kim & Demarque 2003; Tognelli, Prada Moroni & Degl'Innocenti 2011), we choose Siess et al. (2000) because it is the most used isochrone track in the target mass range with the reliability through various tests and application to many observational data. Using dynamically and kinematically determined stellar masses, Hillenbrand & White (2004) confirmed that virtually any isochrone model provides similar mass estimate for masses more than 1.2 $M_\odot$. Hillenbrand & White (2004) also noted that the introduction of new isochrone models tends to bring new systematic uncertainty and should be used with caution. For this study, using Siess's isochrone is also critical for comparison with the previous studies which used Siess's isochrone in most cases (e.g. Kennedy & Kenyon 2009).

We take particular note of the fact that the age spread of young clusters in the solar neighbourhood is in many cases small enough so that a single age can be assumed for each cluster (see Table 1). Therefore, the boundary masses of the IM stars (7 and 1.5 $M_\odot$) theoretically correspond to a unique spectral type for each cluster, which enables IM-star selection only with the spectral type of the members without considering differential extinction. This method should be effective, in particular, for IM stars because most of the time they evolve along the Henyey track, which is roughly horizontal on the HR diagram, and even when the IM stars are on the Hayashi track before switching to the Henyey track, the spectral type does not change because the track is almost vertical on the HR diagram. Table 2 shows the unique spectral types corresponding to the boundary masses for each cluster age based on the isochrone model by Siess et al. (2000).

However, there are several points to take note for using the above method in selecting the IM stars. First, each spectral type, in particular the later spectral type (G7–K5), corresponds to a slightly broader mass range as shown in the third column of Table 2. For example, the boundary spectral type K5 corresponds to 1.2–1.5 $M_\odot$ for the age of 2 Myr. Therefore, the sampling by spectral type naturally leads to the inclusion of stars with a mass of slightly lower than the nominal 1.5 $M_\odot$. Next, note that the age spread of each

Table 2. Adopted spectral type for the boundary masses of IM stars.

t^a		SpType^b	Boundary mass with Δt^c	
(Myr)	7 $M_\odot$	1.5 $M_\odot$	7 $M_\odot$ ($\Delta t = \pm 2$ Myr)	1.5 $M_\odot$ ($\Delta t = \pm 2$ Myr)
1	B2.5	K5 (1.5–1.6 $M_\odot$)	$\gtrsim$7 $M_\odot$	1.2–1.5 $M_\odot$
1.5	B3	K5 (1.2–1.5)	$\gtrsim$7 $M_\odot$	1.2–<2.2 $M_\odot$
2	B3	K5 (1.2–1.5)	7	1.2–<2.2 $M_\odot$
2.5	B3	K5 (1.2–1.5)	6–7	1.2–1.8 $M_\odot$
3	B3	K4 (1.5–1.6)	>6–7	1.2–1.6 $M_\odot$
4	B3	K4	7	1.4–1.8 $M_\odot$
5	B3	K4 (1.4–1.5)	7	>1.4–1.6 $M_\odot$
6	B3	K3	7	1.4–1.6 $M_\odot$
7	B3	K2	7	1.4–1.7 $M_\odot$
8.5	B3	K1	7	1.4–1.7 $M_\odot$
10	B2	K2	~7	1.3–1.5 $M_\odot$
11	B3	G7	7	>1.3–<1.7 $M_\odot$

[a] Age of cluster.
[b] Spectral type for the boundary mass (7 and 1.5 $M_\odot$) based on the isochrone model by Siess et al. (2000). The range of stellar mass corresponding to the spectral type is shown in the parentheses when the range covers more than $\Delta M \geq 0.1\,M_\odot$.
[c] The possible shift of boundary mass for the age spread of ± 2 Myr based on the isochrone model by Siess et al. (2000).

cluster may cause contamination of lower mass stars in our IM-star samples in the case where the age of the star is older than the cluster age. Table 2 also shows the possible mass range for an age spread of $\Delta t = 2$ Myr, which is the maximum possible age spread in most cases (typically $\Delta t = 1$ Myr: see Table 1). Although the ages of most stars are within the age spread of 2 Myr, there are ~15 per cent stars at most which are older than the age spread and are actually lower mass stars (see figs 1–5 in Palla & Stahler 2000). Lastly, the distance uncertainties of target clusters may also influence the selection of the IM stars. The typical uncertainties of distance are about 10 per cent for the clusters in the solar neighbourhood (Reipurth 2008a,b). For the clusters studied by Hernández et al. (2005), the uncertainties are even smaller (less than 5 per cent) with *Hipparcos* data. For deriving the mass and age of a star on the HR diagram, the effective temperature is independent of the distance because it is derived from spectroscopy, while luminosity is directly affected. However, the luminosity can differ by only 0.2 mag with the assumed distance uncertainties, which then cause a mass difference of $\lesssim 0.1\,M_\odot$ around the lower mass limit of this study, 1.5 $M_\odot$,[1] from the isochrone models by Siess et al. (2000) in the target age range of this paper ($\leq$11 Myr). Because this mass uncertainty is very small, the distance uncertainties for the selection of IM stars do not affect our results. The above three points (or any other unconsidered uncertainties) might mask the possible lifetime difference between IM and LM stars. However, if we find any significant difference, it is likely to be real and should be clearly seen with better selected IM-star samples in the future. Note that contamination of higher mass stars can occur, but that should not affect the lifetime differences between the discs of IM and LM stars. We discuss the effect of IM-star selection on the derived IMDF in Section 8.1.2.

[1] Note that the age differences are $\leq$1 Myr for stars $\leq$3 Myr and $\lesssim$2 Myr for older stars. These differences are within the age spread (2 Myr) we are considering.

2.3 Selected samples

We searched the literature to gather all of the available spectral type information for the stars in the sample clusters. We then made a list of all the IM stars by selecting cluster members by spectral type earlier than that of the lower mass boundary and also later than that of the higher mass boundary. The clusters chosen are shown in column 1 and the references to the papers from which the IM stars were selected are shown in column 2 of Table 3. Following the fifth criterion in Section 2.1, we removed any target clusters for which less than three IM stars can be identified. Also, because IMDFs for clusters with age of >5 Myr are found to be $\simeq$0 per cent as discussed in the following sections, we obtained IMDFs for only about 10 clusters. Disc fractions for clusters with age of $\leq$5 Myr are the most useful for studying stellar mass dependence of disc dispersal (cf. Kennedy & Kenyon 2009).

As a result, the total number of stars used for deriving *JHK* and MIR IMDF becomes 799 and 365, respectively. In Appendix , the IM-star samples for all clusters are summarized in tables as well as in colour–colour diagrams. For the following five clusters, the spectral type information for lower mass stars in the literature is incomplete, and we could not reach to the mass limit of 1.5 $M_\odot$: γ Vel (F5: 2 $M_\odot$), λ Ori (G0: 2 $M_\odot$), Per OB2 (G8:1.8 $M_\odot$), OB1bc (G3: 2.2 $M_\odot$), and OB1a (G6:1.7 $M_\odot$). Although it is desirable to set exactly the same mass limit, such as 2 $M_\odot$, we used 1.5 $M_\odot$ as the lowest mass for the other clusters in order to obtain as many IM stars as possible.[2]

3 *JHK* IMDF

The optical–NIR SED difference between stars with and without discs is more prominent for IM stars than LM stars (Lada & Adams 1992; Carpenter et al. 2006). This is mainly because the stellar SED

[2] We checked how much the IMDF changes with a mass limit of 2 $M_\odot$ and confirmed that the resultant IMDFs do not change within the uncertainty.

Table 3. IM-star selection and *JHK*/MIR IMDF of target clusters.

Cluster	Membership ref[a]	Age (Myr)	SpT[b]	SpT ref[c]	*JHK* IMDF[d] (%)	MIR Ref[e]	MIR IMDF[f] (%)
NGC 1333	St76, As97, Wi04	1 ± 1	B2.5–K5	Win10, Co10, SB	17 ± 17 (1/6)	Gu09	100 ± 50 (4/4)
Trapezium	Hi97	1 ± 1	B2.5–K5	Hi97	9 ± 3 (8/89)	–	–[g]
ρ Oph	Wi08	1 ± 1	B2.5–K5	Wi08	0 ± 5 (0/20)	Wi08	80 ± 20 (4/5)
Taurus	Fu06, Fu11	1.5 ± 1.5	B3–K5	Fu06, Fu11	31 ± 10 (9/29)	Fu06, Lu06	72 ± 16 (21/29)
Cha I	Lu04	2 ± 1	B3–K5	Lu04	29 ± 13 (5/17)	Lu08	60 ± 35 (3/5)
NGC 2068/71	Fl08	2 ± 1.5	B3–K5	Fl08	15 ± 11 (2/13)	Fl08	69 ± 23 (9/13)
IC 348	Lu03	2.5 ± 0.5	B3–K5	Lu03	0 ± 3 (0/34)	La06	21 ± 8 (7/34)
σ Ori	He07a	3 ± 1	B3–K4	Ca10, Re09, SB	0 ± 4 (0/23)	He07a	17 ± 9 (4/23)
NGC 2264	Re02	3 ± 1	B3–K4	Re02	0 ± 2 (0/55)	–	–[g]
Tr 37	Si05	4 ± 1	B3–K4	Si05, SB	3 ± 2 (2/69)	Si05, Si06	22 ± 10 (5/23)
Ori OB1bc	He05	4 ± 3	B3–K4†	He05	4 ± 2 (4/94)	–	–[g]
Upper Sco	Ca06	5 ± 1	B3–K4	Ca06	0 ± 1 (0/94)	Ca06	2 ± 2 (2/94)[h]
NGC 2362	Da07	5 ± 1	B3–K4	Da07	0 ± 5 (0/19)	Da07	0 ± 5 (0/19)
γ Vel	He08	5 ± 1.5	B3–K4†	Ho78, SB	0 ± 6 (0/17)	He08	0 ± 6 (0/17)
λ Ori	He09	5 ± 1	B3–K4†	He09	8 ± 8 (1/13)	He09	4 ± 4 (1/27)
Per OB2	He05	6 ± 2	B3–K3†	He05	0 ± 3 (0/31)	–	–[g]
η Cham	Me05	7 ± 1	B3–K2	Me05	0 ± 33 (0/3)	Me05	–[i]
Ori OB1a	He05	8.5 ± 1.5	B2–K1†	He05	2 ± 1 (2/98)	–	–[g]
NGC 7160	Si05	11 ± 1	B3–G7	Si05	0 ± 1 (0/82)	Si06	3 ± 2 (2/78)

[a]References from which the members of the clusters were picked up. The IM stars that were used for deriving the *JHK* IMDF were obtained from these references. For the Trapezium Cluster, members are selected from Hi97, but only those whose stated membership probability is more than 50 per cent were used.

[b]The range of spectral type for the target mass range ($1.57\,M_{\odot}$) for the cluster age listed in the third column. † shows cluster for which the observed spectral types of cluster members do not completely reach to the boundary spectral type for the lowest mass (see the main text).

[c]References from which the spectral types in the clusters were obtained. For some clusters for which the spectral type listing in the published papers is incomplete, we supplemented the spectral type information with those listed in the SIMBAD data base at http://simbad.u-strasbg.fr/simbad/ (denoted as SB).

[d]Derived *JHK* IMDF and uncertainties based on Poisson errors. Numbers in parentheses show the number of disc-harbouring members over total number of members. For the treatment of Poisson errors for zero detection, see the main text.

[e]References for the MIR photometric data.

[f]Derived MIR IMDF and uncertainties based on Poisson errors. Numbers in the parentheses show the number of disc-harbouring members over total number of members. For the treatment of Poisson errors for zero disc-harbouring members, see the main text.

[g]The clusters for which *Spitzer* MIR data are unavailable.

[h]For MIR-disc classification of this cluster, we use the slope between [4.5] and [8] rather than [3.6] and [8] because Carpenter et al. (2006) do not list photometry data in [3.6]. However, Kennedy & Kenyon (2009) confirm that use of [4.5] instead of [3.6] does not change the classification.

[i]MIR IMDF was not derived because of the small number of sample IM stars (<3).

References:

As97: Aspin & Sandell (1997); Ca06: Carpenter et al. (2006); Ca10: Caballero, Albacete-Colombo & López-Santiago (2010); Co10: Connelley & Greene (2010); Da07: Dahm & Hillenbrand (2007); Fl08: Flaherty & Muzerolle (2008); Fu06: Furlan et al. (2006); Gu09: Gutermuth et al. (2009) He05: Hernández et al. (2005); He07a: Hernández et al. (2007a); He08: Hernández et al. (2008); He09: Hernández et al. (2009); Hi97: Hillenbrand (1997); Ho78: Houk (1978); La06: Lada et al. (2006); Lu03: Luhman et al. (2003); Lu04: Luhman (2004); Lu06: Luhman et al. (2006); Lu08: Luhman et al. (2008); Me05: Megeath et al. (2005). Re02: Rebull et al. (2002); Re09: Renson & Manfroid (2009); Si05: Sicilia-Aguilar et al. (2005); Si06: Sicilia-Aguilar et al. (2006); St76: Strom, Vrba & Strom (1976); Wi04: Wilking et al. (2004); Wi08: Wilking, Gagné & Allen (2008); Win10: Winston et al. (2010).

for stars with higher masses peaks at the shorter wavelength side of the *U* and *B* bands (e.g. ∼0.3 μm for A0V stars, with mass of $\sim 3\,M_{\odot}$ and $T_{\rm eff}$ of 9790 K; Cox 2000) compared to the disc SED that peaks near the *K* band ($\gtrsim$2 μm). HAeBe stars also have a large infrared excess from the optically thick disc 'wall', which arises from the inner edge of the discs and where dust disc is so hot as to evaporate (Dullemond, Dominik & Natta 2001; Natta et al. 2001). Therefore, even in the case of using only *JHK* photometry, IM stars with discs can be much more easily and more accurately selected than LM stars with discs. Indeed, Hernández et al. (2005) found an intrinsic region for HAeBe stars on a *JHK* colour–colour diagram (see their fig. 2). Also, the photometric uncertainties for IM stars in nearby clusters are very small, typically $\lesssim$0.02 mag for all *JHK* bands. We make use of these characteristics to derive the *JHK* IMDF for each target cluster with the selected sample of IM stars.

3.1 Identification of IM stars in the colour–colour diagram

On the *JHK* colour–colour diagram, the stars with discs are known to be lying in the infrared excess region that is separated from the region of stars without discs (e.g. Lada & Adams 1992). For LM stars, disc fractions of various young clusters have been derived using the *JHK* colour–colour diagram (Lada 1999; Yasui et al. 2010; see also Hillenbrand 2005). For IM stars, Lada & Adams (1992) showed that HAeBe stars occupy completely separated regions even from those for classical Be (CBe) stars based on the modelling of disc emission. CBe stars show NIR excess from gaseous free–free emission and are often confused with HAeBe stars, but the disc excess from HAeBe stars is much larger. After Hernández et al. (2005) defined the locus of HAeBe stars on the intrinsic *JHK* colour–colour diagram, Wolff, Strom & Rebull (2011) identified HAeBe stars of IC 1805 using their definition. Comerón et al. (2008a)

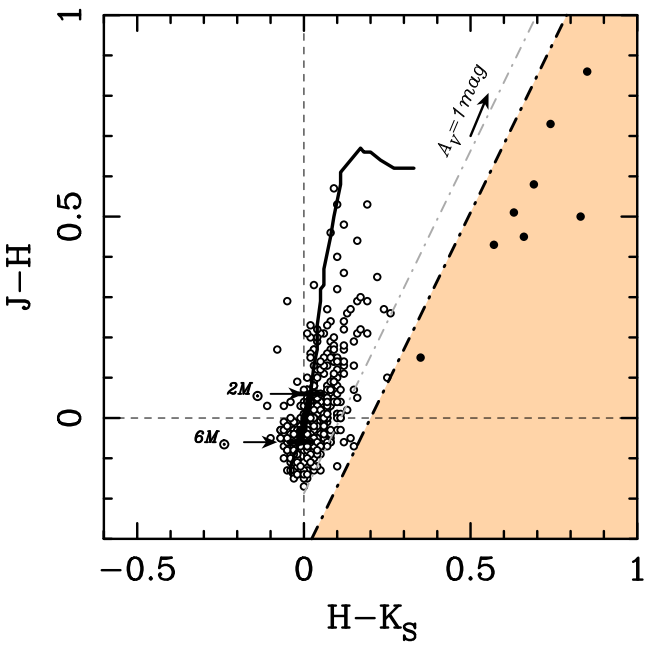

Figure 1. *JHK* colour–colour diagram for IM stars. The observed colours of HAeBe stars (filled circles) and CBe stars (open circles) in nearby clusters from Hernández et al. (2005, Upper Scorpius, Per OB2, Lac OB1, Ori OB1a, and Ori OB1bc) are shown with the dwarf track (Bessell & Brett 1988, black line). The estimated border line, which is parallel to the reddening vector and distinguishes HAeBe stars from other objects, is shown with a dot–dashed line: the grey dot–dashed line shows the definition by Comerón et al. (2008a) while the black dot–dashed line shows our definition. The region to the right of the border line (orange colour) is defined as the 'IM-disc excess region'.

defined the disc excess region for HAeBe stars on the *JHK* colour–colour diagram (non-intrinsic) by using a line that passes through $(H-K, J-H) = (0.11, 0)$ and is parallel to the reddening vector as a border line between the HAeBe stars and CBe stars.

In Fig. 1, we plot the *observed* colours of the HAeBe stars (filled circles) and the CBe stars (open circles) for all the samples in Hernández et al. (2005, Upper Sco, Lac OB1, Ori OB 1a, Ori OB 1bc, and Tr 37) on the *JHK* colour–colour diagram. This shows that the HAeBe stars are spatially separated from the main-sequence track (Bessell & Brett 1988, black line in the colour–colour diagram). Note that the data points shown are not corrected for reddening. There is a clear division between HAeBe stars and other objects, and a border line can be set as the dot–dashed line, which passes through the point of $(H-K_S, J-H) = (0.2, 0)$ and is parallel to the reddening vector (black arrow). This border line is slightly shifted to the right compared to Comerón et al.'s border line (Fig. 1) to completely avoid contamination from CBe stars. Hereafter, we call the right-hand side region of the border line the 'IM disc excess region' (orange shaded region). This border line is more precise for dividing HAeBe stars and CBe stars than that of Comerón et al. (2008a, grey dot–dashed line in Fig. 1) because some CBe stars are included in the IM disc excess region when using Comeron's border line. Therefore, we use the line passing through $(H-K_S, J-H) = (0.2, 0)$ as the border line, and the *JHK* IMDF is defined to be the ratio of the stars located in the IM disc excess region to the total number of stars in a cluster that are selected with the criteria in Section 2.2.

Note that there is a well-known classification for HAeBe stars by Meeus et al. (2001): Group I for younger flared disc phase and Group II for older flat disc phase. We confirmed that all stars in Groups I and II, except for one star (HD 135344 in Group I) out of 14 stars, are recognized as HAeBe stars in our method.

3.2 Determination of the IMDF

We used the 2MASS Point Source Catalog[3] (Skrutskie et al. 2006) to obtain the *JHK* magnitudes of all the sample IM stars. We rejected all IM stars that do not have an 'A' photometric quality flag (signal-to-noise ≥10 for all *JHK* bands) in the 2MASS catalogue. We then obtained the IMDF of the IM stars from the *JHK* colour–colour diagrams of each target cluster.

From previous studies of the disc fractions for LM stars, the systematic errors of the disc fraction are known to be less than the statistical errors when using data with small photometric uncertainties (Liu, Najita & Tokunaga 2003; Yasui et al. 2009). The present data should be in the same situation in view of the small uncertainties in *JHK* photometry of the IM-star samples. For estimating the statistical errors of the disc fraction, we assumed that the errors are dominated by Poisson errors ($\sqrt{N_{\rm disc}}$), and we used $\sqrt{N_{\rm disc}}/N_{\rm all}$ for the 1σ uncertainty of the disc fraction, where $N_{\rm disc}$ is the number of stars with optically thick discs (= HAeBe stars) and $N_{\rm all}$ is the number of all cluster members, respectively. However, if the number of HAeBe stars is zero, the statistical error was calculated assuming one HAeBe star in the examined target cluster to give a 1σ uncertainty of $1/N_{\rm all}$ (e.g. Hernández et al. 2005). Table 3 summarizes the derived *JHK* IMDFs for all the target clusters.

4 MIR IMDF

In the previous studies utilizing the data from the *Spitzer Space Telescope*, the SED slope ($\alpha = {\rm d}\ln\lambda F_\lambda/{\rm d}\ln\lambda$; Adams, Lada & Shu 1987) in the MIR wavelength range (3.6, 4.5, 5.8, and 8.0 μm) is used for selecting disc-harbouring stars (e.g. $\alpha \geq -2.0$; Lada et al. 2006; Hernández et al. 2007b). The number of such IM stars should be precisely determined with this method since discs show a large flux excess compared to the central star continuum in the MIR. For the derivation of the MIR IMDF, we made use of the published *Spitzer* photometric results in the literature because of the signal-to-noise and uniformity across target clusters.

For the definition of the MIR-disc fraction, we followed the procedure by Kennedy & Kenyon (2009), who derived α using the SED slope of *Spitzer*'s Infrared Array Camera (IRAC) [3.6] to [8] and regarded those with $\alpha > -2.2$ as cluster members with MIR dust discs. We estimated α of the IM stars only in the cases where reliable photometry in all four IRAC bands is available. However, for the derivation of α, we used only [3.6] and [8.0] because those two bands determine α for almost all cases. For several clusters (e.g. IC 348, which shows moderate extinction), we cross-checked our α values with those in the literature (Hernández et al. 2008) and confirmed that they are almost the same. Following Kennedy & Kenyon (2009), we set the boundary at $\alpha = -2.2$ to separate all the IM stars into the categories of 'with disc' and 'without disc'.

For the target clusters with published *Spitzer* data (13 clusters out of 19 target clusters; see Table 3), we estimated α for the IM stars. Unfortunately, the MIR *Spitzer* photometry of some IM stars in the nearby star-forming regions could not be obtained because they are too bright for *Spitzer*. Therefore, the number of IM stars for the MIR IMDF is, in most cases, less than those for the *JHK* IMDF (e.g. Tr 37). In some cases, we have more sample stars for

[3] http://www.ipac.caltech.edu/2mass/releases/allsky/doc/sec6_2.html

the MIR than those for *JHK* (e.g. λ Ori) because some of the MIR stars do not have good *JHK* photometry with 2MASS. In this case, we calculated the MIR IMDF by rationing the number of stars with discs by the total number of stars in each MIR sample. The results are summarized in Table 3. The treatment of uncertainty is similar to that for the *JHK* IMDF, as described in Section 3.

5 DEFINITION OF THE DISC LIFETIME

Different terms have been used for the disc dispersal time-scale: e.g. disc lifetime (Lada 1999; Haisch et al. 2001b; Hernández et al. 2008), disc decay time-scale (Mamajek 2009), and disc dissipation time-scale (Fedele et al. 2010). These terms are based on the observed cluster age–disc fraction plot with age on the horizontal axis and disc fractions on the vertical axis. However, these terms are not consistently used. Moreover, the value of disc fraction at zero age has not been considered with care because these studies are performed mainly for LM stars and all LM stars are thought to initially have discs in the standard picture of LM star formation (Shu, Adams & Lizano 1987). Since this may not be the case for IM stars, we define these terms explicitly in this section.

To fit with a single function to the disc fraction evolution curve, an exponential function is appropriate. The *'disc decay time-scale'* (τ) is defined as DF[per cent] $\propto \exp(-t[\mathrm{Myr}]/\tau)$ (e.g. Mamajek 2009). The decay time-scale is proportional to the slope of the curve on a semilog plot, log (IMDF)–age plot (Fig. 2). On the other hand, the most often used term *'disc lifetime'* (t^{life}) is originally defined as the x-intercept of the cluster age–disc fraction plotted as a linear function. However, fitting with a linear function does not appear appropriate to describe the shape of disc fraction evolution, which appears to decrease and level out at about 5–10 per cent (Hernández et al. 2008). Therefore, we define the disc lifetime to be the time when the disc fraction is 5 per cent (t^{life}) and use this for the discussion throughout this paper.

We define the *'initial disc fraction'* (DF_0) as the disc fraction at $t = 0$. Fig. 2 shows two possible cases: $\mathrm{DF}_0 = 100$ per cent and $\mathrm{DF}_0 < 100$ per cent for the same t^{life}. The value of $\mathrm{DF}_0 = 100$ per cent (the dark grey line in Fig. 2) means that all stars initially have discs, while that of $\mathrm{DF}_0 < 100$ per cent (the light grey line in Fig. 2) means that all stars do not necessarily have discs from the beginning or that some discs disappear quickly within a very short time-scale that is not recognized within the accuracy of the age determination. Note that if DF_0 is constant, then the disc lifetime is proportional to the disc decay time-scale.

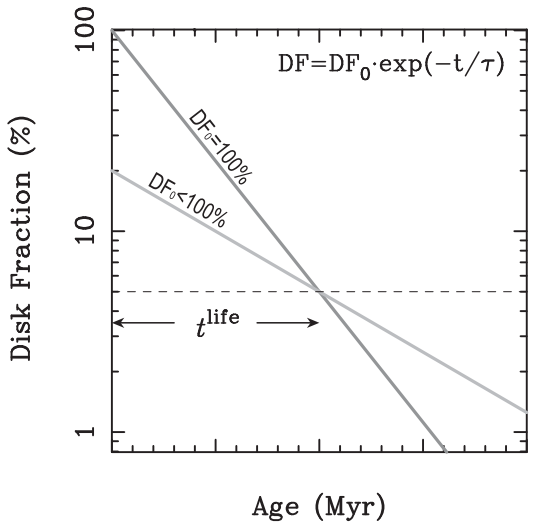

Figure 2. Definitions of disc decay time-scale (τ), disc lifetime (t^{life}), and initial disc fraction (DF_0).

6 EVOLUTION OF THE *K* DISC

The stellocentric distance of the *K* disc (r_K) for HAeBe stars has a wide range, ∼0.1–1.0 au for HAe stars to ∼1–10 au for HBe stars (Millan-Gabet et al. 2007). However, because a large part of the IM stars in this paper are HAe stars, r_K of ∼0.3 au is taken to be the nominal radius in this paper. The *JHK* IMDF derived in this paper is the fraction of the HAeBe stars whose discs at a stellocentric distance (r_K) of ∼0.3 au are optically thick with a temperature of ∼1500 K (see e.g. fig. 2 in Millan-Gabet et al. 2007).

In this section, we discuss the evolution of the *K* disc of IM stars traced by *K*-band excess emission and on the *JHK* IMDF change with cluster age.

6.1 Disc lifetime

By making use of the method described in Section 3, the *JHK* IMDFs of ∼20 clusters are derived for the first time, in particular for clusters at ages <3 Myr. Fig. 3 shows the derived IMDF as a function of ages (black filled circles). The *JHK* IMDF is found to show an exponentially decreasing trend with increasing cluster age as seen in previous studies. There is a large scatter with many upper limits at 1–3 Myr. In view of the upper limit points, we used the astronomical survival analysis methods (Isobe, Feigelson & Nelson

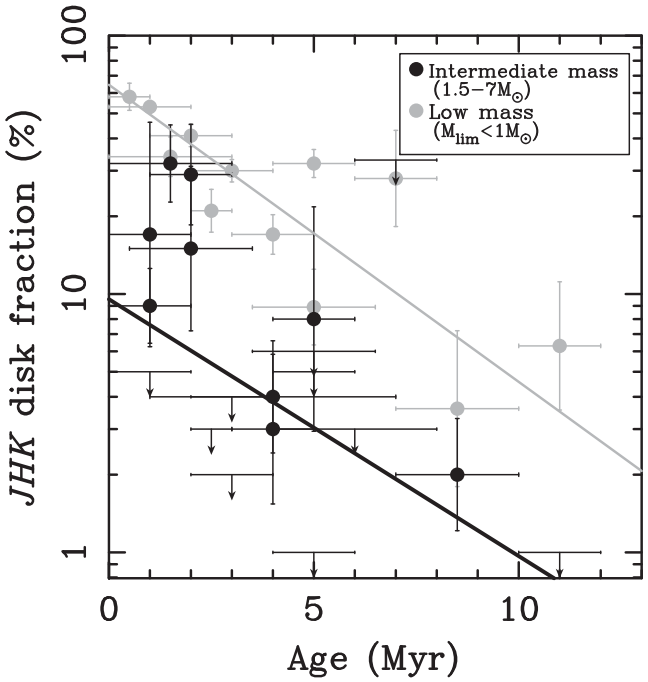

Figure 3. *JHK* IMDF (black) and *JHK* LMDF (grey) of young clusters in the solar neighbourhood as a function of cluster age. For the IMDF, the data for clusters in Table 3 are shown with black filled circles, while upper limits are shown with downward arrows. The fitted curve with the survival analysis for all the clusters, including the upper limits, is shown with the black line. For comparison, the LMDF from Yasui et al. (2009, 2010) is shown with the grey line.

1986; Lavalley, Isobe & Feigelson 1992) as a primary analysis tool. We used the `schmidttbin` task in the IRAF/STSDAS package. The resultant disc decay time-scale is $\tau = 4.4 \pm 2.2$ Myr with $DF_0 = 10 \pm 4$ per cent. The resulting disc lifetime is $t^{life}_{IM,JHK} = 2.8 \pm 2.4$ Myr. The fitted curve is shown in Fig. 3 as a thick black line. We refer to this fitting as 'survival fitting'.

The IMDF data points at ages <3 Myr show a rather large scatter with upper limit points. The clusters with zero disc fraction (ρ Oph, IC 348, σ Ori, NGC 2264) do not appear to have obvious common features. As for the initial disc fraction (DF_0), the fitting results show a low value of <20 per cent. Although some non-zero data points at 1–2 Myr are apparently above the fitted line, all of them show relatively low values that are not more than ∼40 per cent. Whether all high-mass stars initially have discs or not is still under debate (e.g. Zinnecker & Yorke 2007). On the other hand, all LM stars are thought to initially have discs in the standard picture of LM star formation (Shu et al. 1987). Our results suggest a possible low initial disc fraction for IM stars, and further study of the IMDF is important, in particular, those of the younger clusters.

6.2 Comparison with LM stars

In Fig. 3, we show the *JHK* LMDF for comparison. The LMDF data points are for 12 clusters in the solar neighbourhood from Yasui et al. (2009, 2010). The fitting result of LMDFs is shown with a grey line (Fig. 3), which has $\tau_{LM,JHK} = 3.8 \pm 0.4$ Myr and $LMDF_{0,JHK} = 64 \pm 6$ per cent, leading to a disc lifetime of $t^{life}_{LM,JHK} = 9.7 \pm 1.1$ Myr. Fig. 3 clearly shows the difference in the disc fraction value, as well as the disc lifetime difference, between the IM and LM stars. The IMDFs for older clusters (age > 3 Myr) show systematically lower values compared to the LMDF, as Hernández et al. (2005) initially found for five clusters (Tr 37, Ori OB1bc, Upper Sco, Per OB2, and Ori OB1a). We increased the number of target clusters of age >3 Myr to 10 and confirmed this tendency. However, while fig. 10 in Hernández et al. (2005) shows an IMDF curve with only a single zero disc fraction point (Per OB2), our results in Table 3 show about half of the target clusters with a zero disc fraction (Fig. 3). Because the number of IM stars for each cluster is typically more than 20, a simple stochastic effect due to a small number of stars is not likely to be the reason for the many zero disc fraction points.

As a result of the fitting, the lifetime for the IM stars is found to be significantly shorter than that for the LM stars. The above results are summarized in Table 4. In the case of fitting, including the upper limits (survival fitting), the estimated lifetime ($t^{life}_{IM,JHK} = 2.8 \pm 2.4$ Myr) is much shorter than that of the LM stars ($t^{life}_{LMJHK} = 9.7 \pm 1.1$ Myr) by about 7 Myr. These results clearly show the existence of a stellar mass dependence for the lifetime of the innermost disc.

6.3 Stellar mass dependence of the disc lifetime

The stellar mass dependence of the disc lifetime can be a strong constraint on the disc dispersal mechanism and the theory of planet formation, as discussed by Kennedy & Kenyon (2009). They compared the disc fraction for different mass bins, ∼1 $M_\odot$ (0.6–1.5 $M_\odot$) and ∼3 $M_\odot$ (1.5–7 $M_\odot$), in seven clusters and suggested that their data are more consistent with $\tau_{KK09} \propto M_*^{-1/2}$ than with $\propto M_*^{-1/4}$. τ_{KK09} is the disc decay time-scale defined by their model, in which the discs are dispersed when the accretion rate drops below the wind-loss rate. However, only four clusters appear to be the main contributors to the resultant mass dependence (see fig. 9 in Kennedy & Kenyon 2009) – the Hα disc fraction for three clusters and the MIR-disc fraction for one cluster. Although Hernández et al. (2005) and Carpenter et al. (2006) found similar stellar mass dependence for clusters with ages >3 Myr, the dependence is uncertain because of an insufficient number of clusters, in particular those with ages ≤3 Myr. Obviously, it is necessary to increase the number of data points to clarify the mass dependence. Also, the large uncertainty in previous studies might be the result of differences in the evolution of the *K* and MIR discs. Thus, studying of only the *JHK* disc (or only the MIR disc) might show a clearer mass dependence.

The stellar mass dependence of the disc lifetime can be quantitatively estimated by combining the time-scales for the two mass ranges. For the IMDF, stars with mass of 1.5–7 $M_\odot$ are used in this paper. Considering the larger number of lower mass stars with the typical universal IMF (e.g. Kroupa 2002), the characteristic mass is set as 2–3 or 2.5 $M_\odot$. We estimated the stellar mass dependence with a characteristic mass from 2–3 $M_\odot$, but no significant difference was found within the uncertainties. The characteristic mass of 0.5 ± 0.5 $M_\odot$ (0.1–1 $M_\odot$) for the LMDF is set by considering the IMF and mass detection limit (∼0.1 $M_\odot$) for clusters used to derive disc fractions. Assuming the stellar mass dependence of the disc lifetime as a power-law function of stellar mass, we find $t^{life}_{JHK} \propto M_*^{-0.8\pm0.7}$ using the survival fitting. These results are tabulated in Table 4. Our result is consistent with the results by Kennedy & Kenyon (2009), who found that τ_{KK09} is proportional to about $M^{-0.5}$. However, note again that our results are derived only from the *K*-disc data, while Kennedy & Kenyon (2009) used mostly data from the MIR disc or the Hα gas disc. We discuss the difference of disc lifetimes of the *K* disc, MIR disc, and gas accretion disc in Section 8.

7 EVOLUTION OF THE MIR DISC

In this section, we discuss the evolution of the inner disc of IM stars traced by the MIR excess emission and using the results on the MIR IMDF derived in Section 4.

Table 4. Summary of disc lifetime.

	$\langle M_* \rangle^a$	t^{life}_{JHK} (Myr)			t^{life}_{MIR} (Myr)		
		Yasui et al. (2010)	Survival	Binning[b]	Yasui et al. (2010)	Survival	Binning[b]
Intermediate-mass	2.5 $M_\odot$	–	2.8 ± 2.4	3.3 ± 0.9	–	6.1 ± 4.2	6.7 ± 1.1
Low-mass	0.5 $M_\odot$	9.7 ± 1.1	–	–	8.6 ± 0.7	–	–
Mass dependence			$M_*^{-0.8\pm0.7}$	$M_*^{-0.7\pm0.3}$		$M_*^{-0.2\pm0.3}$	$M_*^{-0.2\pm0.1}$

[a]Characteristic mass for the mass range (see details in the main text).
[b]See Section 8.1 for the definition of this fitting.

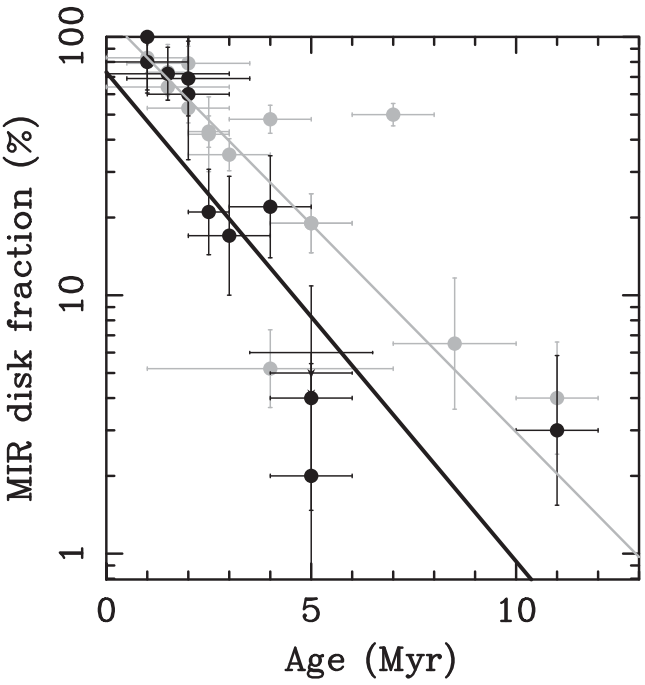

Figure 4. MIR IMDF (black) and MIR LMDF (grey) of young clusters in the solar neighbourhood as a function of cluster age. For the IMDF, the data for clusters in Table 3 are shown with black filled circles, while upper limits are shown with downward arrows (only two clusters at 5 Myr, NGC 2362 and γ Vel). The fitted curve using survival analysis for all the data including the upper limits is shown with the thick black line. The fitting for the LMDF is shown with the grey line.

7.1 Disc lifetime

In Fig. 4, we plot the MIR IMDFs, showing a relatively clear exponential decay curve from cluster age zero to ∼10 Myr. We performed fitting in the same way as for the *K* discs (Section 6). By including the upper limits (two clusters: NGC 2362 and γ Vel), a survival analysis was performed to obtain $\tau = 2.3 \pm 1.4$ Myr and $\mathrm{DF}_{0(\mathrm{MIR})}$ of 73 ± 57 per cent, which leads to a disc lifetime of $t^{\mathrm{life}}_{\mathrm{IM,MIR}} = 6.1 \pm 4.2$ Myr. The resultant fitted line is shown with the black line in Fig. 4. The fitted results are consistent with a 100 per cent initial disc fraction for the MIR IMDF.

7.2 Comparison with LM stars

We also plot the MIR LMDF for comparison in Fig. 4. The data points for MIR LMDFs are for 18 clusters from *Spitzer* observations: 16 clusters in Roccatagliata et al. (2011)[4] and Orion OB1bc and Orion OB1a/25 Ori in Kennedy & Kenyon (2009). We performed fitting in the same way as in Section 6 to obtain $t^{\mathrm{life}}_{\mathrm{LM,MIR}} = 8.6 \pm 0.7$ Myr and $\mathrm{DF}_{0(\mathrm{MIR})} = 120 \pm 12$ per cent with a reduced χ^2 value of 1.0 with a degree of freedom of 16. This result is consistent with 100 per cent initial disc fraction for the MIR LMDF. There is no significant difference in the disc fraction lifetime between the IMDF and LMDF disc, unlike for the *K* disc in the previous section.

[4] For the LMDF, we excluded two clusters from their 18 target clusters. First, NGC 2244 is excluded because the detection limit is not given. Secondly, γ Vel is excluded because the completeness limit for this cluster does not reach the LM (<1 $\mathrm{M}_{\odot}$) limit.

7.3 Stellar mass dependence of the disc lifetime

The results of the lifetimes for the MIR discs of both IM and LM stars are summarized in Table 4. We derived the stellar mass dependence of the MIR-disc lifetime as $t^{\mathrm{life}} \propto M_*^{-0.2\pm0.3}$, assuming a power-law function and using the characteristic masses for the two mass ranges as for the *JHK*-disc lifetime (Section 6.2) and the results for the survival fitting. These results are tabulated in Table 4.

Our results show no significant stellar mass dependence of the disc lifetime, which is apparently inconsistent with Kennedy & Kenyon (2009), who derived a steeper stellar mass dependence of $\tau_{\mathrm{KK09}} \propto M_*^{-0.5}$. However, note that their results are based on the lifetime of both dust and gas discs. The strong dependence appears to be mainly contributed from the inclusion of Hα gas disc. They suggested an $M_*^{-0.5}$ dependence rather than $M_*^{-0.25}$ dependence mostly based on the data for three clusters [Taurus (Hα), Tr 37 (Hα and MIR), and OB1bc (Hα); see their fig. 9], but the existence of the discs is based mostly on the Hα gas disc for those three clusters. Using their data, we attempted to estimate the mass dependence and confirmed that $\tau \propto M_*^{-0.5}$ is obtained in the case of using only the Hα disc fraction for the eight clusters in their list except for OB1a/25Ori, while $\tau \propto M_*^{-0.2}$ is obtained in the case of using only the MIR-disc fraction for the same eight clusters. Therefore, we conclude that there is no mass dependence of the lifetime of an MIR disc within the uncertainties.

8 DIFFERENCE IN THE EVOLUTION OF *K* AND MIR DISCS

In the previous sections, we discussed the disc lifetime of the *K* disc, which traces the innermost dust disc, and the MIR disc, which traces the inner disc outside of the *K* disc. In this section, we compare the *K* and MIR-disc fractions and discuss the evolution of the *K* disc and the MIR disc. We also discuss the relation of the MIR disc to the inner *gas* disc, which is traced by accretion signatures, such as the Hα emission line.

8.1 Comparison of the *K* disc and the MIR disc

8.1.1 LM stars

Before discussing the case for the IM stars, we take a look at the case for the LM stars as a reference. Fig. 5 (right) shows the comparison of the *JHK* LMDF (red) and the MIR LMDF (blue). The derived lifetime for the *K* disc (9.7 ± 1.1 Myr) and that for the MIR disc (8.6 ± 0.7 Myr) are identical within the uncertainties (see Table 4), which suggests that the *K* disc and the MIR disc disperse almost simultaneously in the discs of LM stars. This is consistent with the recent view of disc dispersal that the *entire* disc disperses almost simultaneously for LM stars ($\Delta t \lesssim 0.5$ Myr; Andrews & Williams 2005).

8.1.2 IM stars

We compared *JHK* and the MIR IMDFs in Fig. 5 (left). The filled circles showing IMDFs and the arrows showing upper limits are labelled with the cluster numbers in Table 1. This figure immediately suggests that the MIR IMDFs are systematically larger than the *JHK* IMDFs. The MIR IMDF appears to be almost as high as 100 per cent at $t \sim 0$ and exponentially declines, while the *JHK* IMDF is less than 50 per cent at the beginning and keeps smaller values than the MIR IMDF throughout the age span. Because this offset might be

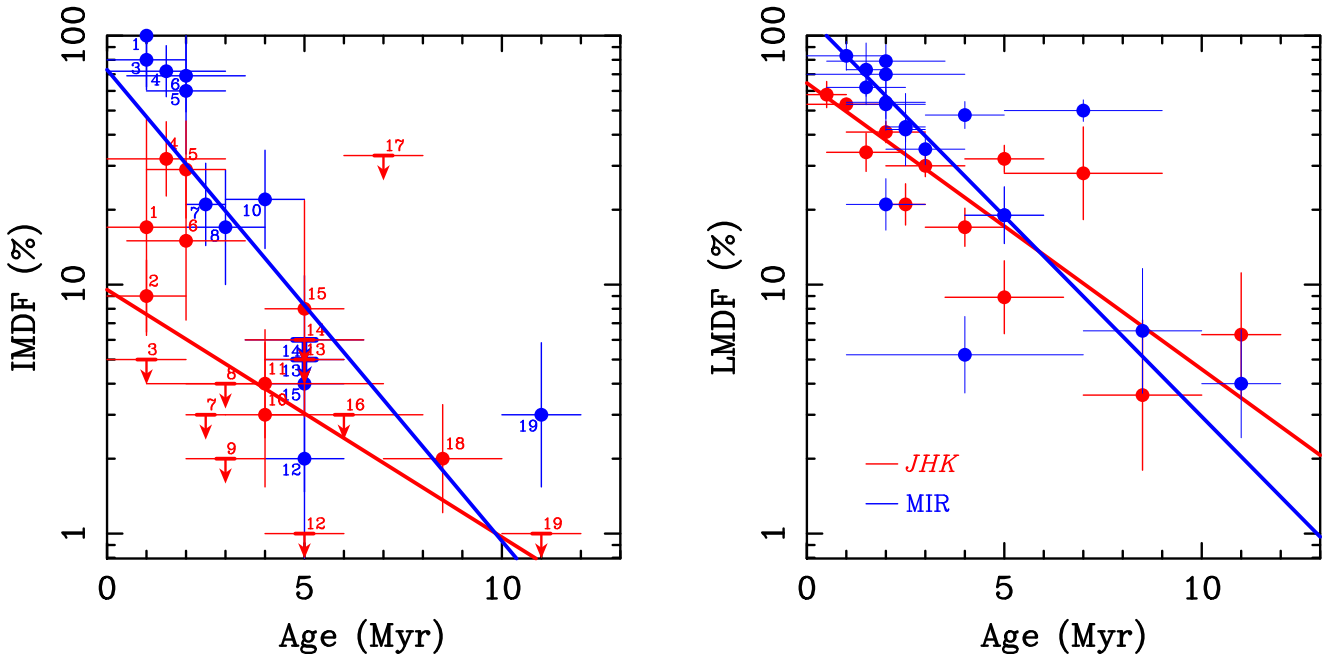

Figure 5. Comparison of *JHK*-disc fraction (red) to MIR-disc fraction (blue) as a function of cluster age. The left figure is for intermediate-mass stars (IMDF), while the right figure is for low-mass stars (LMDF). For the IMDF, the red filled circles show the *JHK* IMDF from Section 6 (Table 3), while the blue filled circles show the MIR IMDFs from the same table. The arrows show the upper limits. Both circles and arrows are labelled with the cluster numbers in Table 1. The lines show the fits with survival analysis including the upper limits. For the LMDF, red filled circles are from Yasui et al. (2009, 2010), while blue filled circles are mainly from Roccatagliata et al. (2011, see the text for the details).

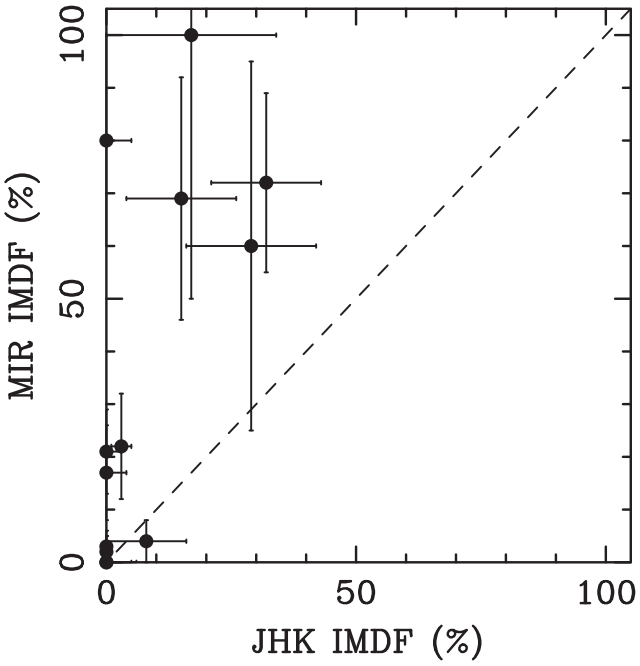

Figure 6. Comparison of *JHK* IMDF to MIR IMDF for 13 target clusters for which both *JHK* and MIR IMDFs are available (see Table 3).

due to an incomplete cluster sampling that favours only the higher MIR or the lower *JHK* IMDFs, we directly compared the MIR and *JHK* IMDFs for the clusters that have both fractions estimated. The results (see Fig. 6) show that the MIR IMDFs are systematically larger than the *JHK* IMDFs for all the 13 clusters that have both. We thus conclude that the large offset of the IMDFs is real, and that the smaller *JHK* IMDF is a unique property of the IM-star disc lifetimes compared to those of the LM stars. The significantly lower disc fraction of the *K* discs means they disappear much *earlier* than the MIR discs. The lifetime difference is about 3 Myr ($6.1 - 2.8 = 3.3$ Myr; see Table 4).

As suggested in Section 2.2, possible contamination of LM stars in selecting IM stars may affect the above discussion. Therefore, it is safer to set the lower limit mass for IM stars as $2\,M_{\odot}$, which is slightly larger than the nominal mass limit in this paper ($1.5\,M_{\odot}$). With this lower limit mass, we derived the *JHK*/MIR IMDFs in the same way as in Sections 2–4. As a result, the derived IMDFs do not largely differ, and the estimated lifetimes of *K* and MIR discs are 2.7 ± 3.6 and 6.0 ± 6.1 Myr, respectively, which are very close to the results for the lower mass limit of $1.5\,M_{\odot}$ although the uncertainties for both disc fractions and disc lifetimes become larger. Therefore, we conclude that the effect of possible contamination of LM stars on our IM-star samples is very small, and that it does not change the conclusion.

An alternative approach was tried to confirm these results. To increase the statistical significance, we binned all of the disc-harbouring stars and cluster members in the cluster age range from 1 to 5 Myr with 1 Myr bins and 1 Myr steps and computed both the *JHK* and MIR IMDFs. To have enough clusters, all the members of the four clusters in the 6–11 Myr range are accumulated to estimate a binned IMDF at 8.5 ± 2.5 Myr for the *JHK* IMDF. Because we have only one data point at $t = 11$ Myr for the MIR IMDF, we simply used it without binning. This 'binning' process effectively reduces the number of upper limit points, and the disc fraction curve becomes clearer with less scatter.

The results are plotted in Fig. 7, which suggests the disc fraction offset between the *JHK* and the MIR IMDFs as well as the lifetime difference. The fitting results for the *JHK* IMDFs are as follows: disc lifetime ($t^{\rm life}_{{\rm IM},JHK}$) of 3.3 ± 0.9 Myr with $DF_{0(JHK)}$ of 35 ± 13 per cent

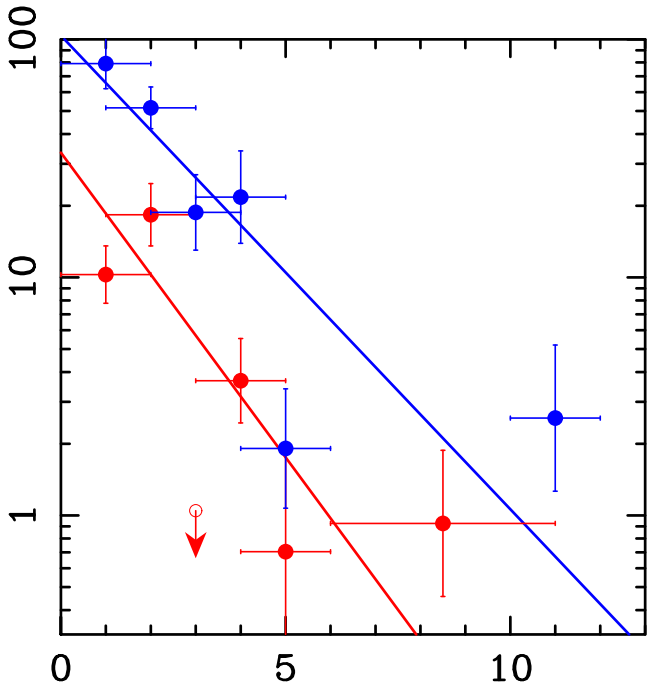

Figure 7. Comparison of the *JHK* IMDF (red) to the MIR IMDF (blue) as a function of age. Same as the left figure of Fig. 5, but the data are binned in the age axis direction (see Section 8.1 for details). The straight lines show the fits to the data points with the upper limit at 3 Myr excluded from the fitting of *JHK* IMDF.

with χ^2_ν of 1.0 with degree of freedom of 3. The derived lifetime is, in fact, very close to the results without binning (2.8 Myr). Note that the data point at $t = 3$ Myr was not used because it remains an upper limit due to many upper limits in this age bin. As for MIR IMDF, a disc lifetime ($t^{\rm life}_{\rm IM,MIR}$) of 6.7 ± 1.1 Myr with $\rm DF_{0(MIR)}$ of 104 ± 26 per cent with χ^2_ν of 2.2 with degree of freedom of 4 was obtained. In summary, these 'binning' fitting results (see Table 4) confirm the survival analysis results without binning although there are very few data points in the binning fitting and we should be cautious of any unknown biases. The stellar mass dependence for this binning analysis is also listed in Table 4 and is consistent with previous results. Therefore, we conclude that there is a lifetime difference of ∼3–4 Myr between *K* and MIR discs.

8.2 Comparison with the submm disc

To investigate further the dependence on stellocentric distance, we also compared the disc fraction and lifetime of the *K* and MIR discs with that of the outer cold (∼10 K) dust disc traced by the submm and mm continuum. There are a number studies of submm observations of IM stars in Taurus (1.5 Myr), ρ Oph (2 Myr), and Upper Sco (5 Myr) (Andrews & Williams 2005, 2007; Mathews et al. 2012). We confirmed that the MIR disc is well correlated with the submm disc for the IM stars. Out of the observed 20 B-, A-, F, and G-type stars in the above papers, 19 stars are detected with MIR and submm discs, and only one star, HIP 76310 in Upper Sco, lacks an MIR disc but has a submm disc. The strong correlation clearly suggests that the MIR inner disc and submm outer disc disperse almost simultaneously for the IM stars. This behaviour is similar to that for LM stars (Andrews & Williams 2005, 2007; Mathews et al. 2012). Thus, the early disappearance of the innermost *K* disc again appears to be the only unique property of the IM stars compared to the LM stars.

8.3 Comparison with the Hα gas disc

Another question we investigated is how the dust disc evolution is synchronized with the *gas*-disc evolution. We compared the disc fraction and lifetime of the *K* and MIR discs with those of the innermost gas disc traced by the Hα emission as has been comprehensively studied by Fedele et al. (2010). They used spectroscopy of the Hα emission for the clusters in the solar neighbourhood. Because the Hα emission was not observed for many IM stars, we used the Hα disc fractions from Kennedy & Kenyon (2009, their 1.5–7 $\rm M_\odot$ samples for IMDF and all mass range samples for LMDF) and directly compared them with those of *K* and MIR discs. This is shown in Fig. 8. The left-hand panel includes eight clusters (Taurus, Cha I, IC 348, Tr 37, Ori OB1bc, Upper Sco, NGC 2362, and NGC 7160), and the right-hand panel includes an additional cluster (OB1a/25Ori).

In the right-hand panel of Fig. 8, the Hα LMDF closely traces *JHK* and MIR LMDFs, and this shows the co-evolution of the dust and gas discs for LM stars. This is consistent with the results of Fedele et al. (2010), who found that the time-scale of Hα mass accretion is almost the same as that of the dust disc. In the left figure, however, the Hα IMDF shows a different cluster age dependence compared to the IMDF of the dust disc. We note that (1) it overlaps the MIR IMDF at younger ages (<5 Myr), and (2) it is systematically larger than the *JHK* IMDF at younger ages with a longer lifetime than the *K* disc. While the first point suggests the co-evolution of the gas and dust disc, which is suggested by Fedele et al. (2010), the second point has not been noted before. Only the *K* disc appears to have a unique cluster age dependence among the different disc components of the IM stars.

8.4 Long transition disc phase for IM stars

In summary, for the IM stars there appears to be the following lifetime sequence for the various stellocentric radii: $t^{\rm life}_K < t^{\rm life}_{\rm H\alpha} \lesssim t^{\rm life}_{\rm MIR} \sim t^{\rm life}_{\rm submm}$. On the other hand, all these time-scales are nearly the same for the LM stars (Andrews & Williams 2005, 2007; Mathews et al. 2012). The above result suggests that for the IM stars the *K* disc has a shorter time-scale and an evolutionary history that is different from that of the LM stars. The observed longer lifetime with larger stellocentric distance is qualitatively consistent with the recent view of the disc dispersal sequence for protoplanetary discs of LM stars (Williams & Cieza 2011). However, the lifetime difference between the *K* and MIR discs for the IM stars (∼3–4 Myr) is significantly longer than that suggested previously for LM stars ($\Delta t \lesssim 0.5$ Myr; e.g. Williams & Cieza 2011).

That a time lag is clearly seen *only for the IM stars* gives us a clue to the mechanism of disc evolution. The time-lag between *K*- and MIR-disc lifetimes can be interpreted as a *transition disc phase*, in which the innermost *K* disc disappears while the outer MIR disc remains. Discs with no *JHK* excess emission and with MIR excess are called 'classical' transition discs (Muzerolle et al. 2010), while the original definition of 'transition disc' is a disc that has no or little excess emission at $\lambda < 10\,\mu$m and a significant excess at $\lambda \geq 10\,\mu$m (Strom et al. 1989; Wolk & Walter 1996). The two significant processes, disc dispersal (e.g. Muzerolle et al. 2010) and planet formation (e.g. Calvet et al. 2002), are thought to happen during this phase. Therefore, our finding suggests that such critical evolutionary events can be clearly recognized in the transition disc

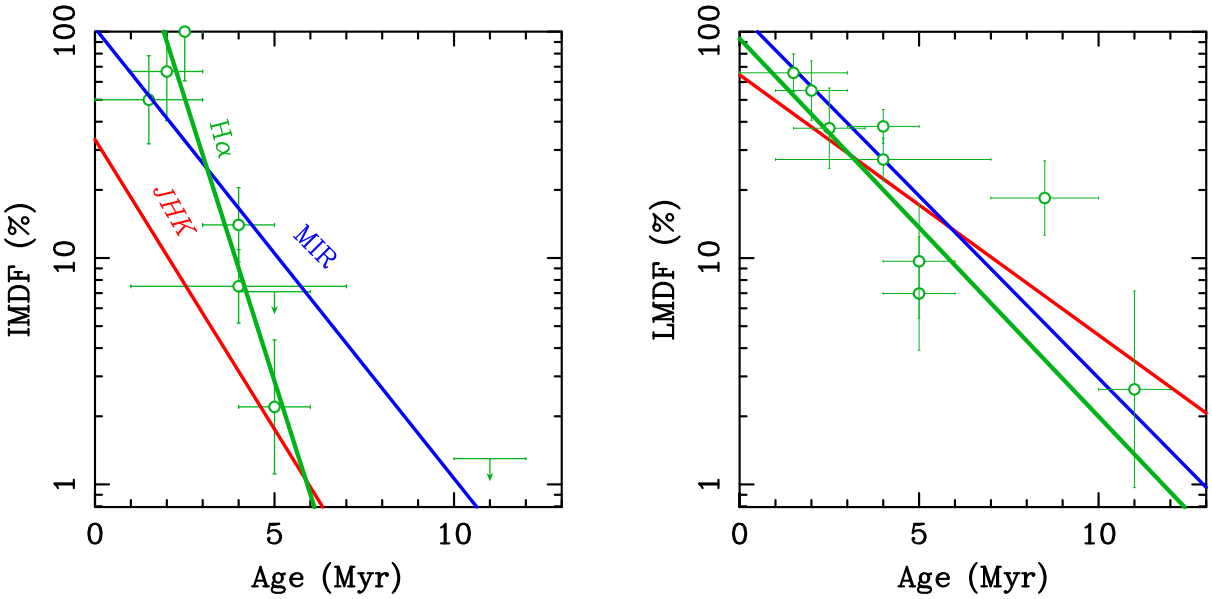

Figure 8. Comparison of disc fraction curves of the *K* disc (red line), MIR disc (blue line), and Hα disc (green line). For the *JHK* and the MIR IMDFs, the binned fitting results are shown (see Section 8.1.2). The Hα disc fraction from Kennedy & Kenyon (2009) is plotted with open circles. The left figure is for the IMDF, while the right figure is for the LMDF.

phase for IM stars as a time lag between the dispersal of the *K* disc and the dispersal of the MIR disc, while both events happen nearly simultaneously for the LM stars ($\Delta t \lesssim 0.5$ Myr).

9 PHYSICAL MECHANISM OF THE DISC EVOLUTION OF IM STARS

In this section, we discuss the implications of the observed timescales of the gas/dust discs on the mechanism of disc evolution of the IM stars. Although there are many detailed processes related to disc evolution, we focus on discussing the following two categories, which are not intended to be comprehensive but broadly cover basic processes related to disc evolution: (1) the disc dispersal processes, such as mass accretion and dissipation by photoevaporation, and (2) the dust settling to the disc mid-plane and dust growth, which could be connected to planetesimal formation and planet formation. We suggest that the latter process is more likely for the early disappearance of the *K* discs.

Before discussing the detailed evolution mechanisms, we first remark on the radial configuration of the dust disc in the steady state. If we consider an optically thick disc for discs with IR excess, the radius (R) with a temperature (T) is given by $R = (L_*/4\pi T^4\sigma)^{1/2}$, where L_* is the stellar luminosity and σ is the Stefan–Boltzmann constant. The dust temperature is about 1500 K for the *K* disc and ∼500 K for the MIR disc as inferred from the peak wavelength of the blackbody emission. From those typical temperatures, the stellocentric distances to those disc regions are estimated to be $r_K \sim 0.3$ au, $r_{\rm MIR} \simeq 5$ au for IM stars (with the characteristic mass $M_* \sim 2.5\,{\rm M}_\odot$) and $r_K \simeq 0.1$ au, $r_{\rm MIR} \simeq 1$ au for LM stars (with the characteristic mass $M_* \sim 0.5\,{\rm M}_\odot$) (see Fig. 9), considering the effective temperatures of the central star (see Millan-Gabet et al. 2007). Because the radius R of an optically thick disc with IR excess is expressed with $R = (L_*/4\pi T^4\sigma)^{1/2}$, R is proportional to M_*^2 with the mass–luminosity relation of $L_* \propto M_*^4$ (Siess et al. 2000). Therefore, r_K and $r_{\rm MIR}$ should be roughly proportional to M_*^2.

9.1 Disc dispersal?

The disc dispersal process consists of two kinds of processes: *mass accretion* on to the central star and *dissipation* into interstellar space (Hollenbach, Yorke & Johnstone 2000). The combination of mass accretion and dissipation due to photoevaporation (e.g. the so-called UV-switch model; Alexander 2008) is thought to be one of the major mechanisms of overall disc dispersal (Williams & Cieza 2011), because this can explain the almost simultaneous dispersal of the entire disc ($\Delta t \lesssim 0.5$ Myr), and thus the short transition disc phase as implied in Fig. 8 (right). Although there are a number of other proposed dispersal mechanisms (e.g. stellar encounter, disc wind), our discussion here focuses on the dispersal due to photoevaporation.

9.1.1 *Accretion on to the central star?*

The first possible mechanism for the short *K*-disc lifetime of the IM stars is the faster mass accretion on to the central star for higher mass stars. Mendigutía et al. (2011) suggested a very strong mass dependence of the mass accretion rate from observations of UV Balmer excess. However, our results suggest that the gas accretion disc has a longer lifetime than the *K* disc (Fig. 8, left), about equal to that of the MIR disc. Therefore, more rapid accretion and the resultant deficiency of material are not likely to be the cause of the faster destruction of the *K* disc.

9.1.2 *Photoevaporation?*

Photoevaporation is another strong candidate for the dispersal mechanism that may cause the short *K*-disc lifetime. Photoevaporation is known to be effective for outside of the gravitational radius, $r_{\rm g}$, where the thermal energy balances the gravitational potential. This radius scales with the stellar mass as $r_{\rm g} \sim GM_*/c^2$ (Alexander 2008), and $r_{\rm g}$ for IM stars (2.5 $\rm M_\odot$) and LM stars (0.5 $\rm M_\odot$) are ∼25 and ∼5 au, respectively. The corresponding *K*-disc radii (r_K) for IM and LM stars are only ∼0.3 and ∼0.1 au, respectively, which are less than 1/50 of $r_{\rm g}$. Similarly, the corresponding MIR-disc radii

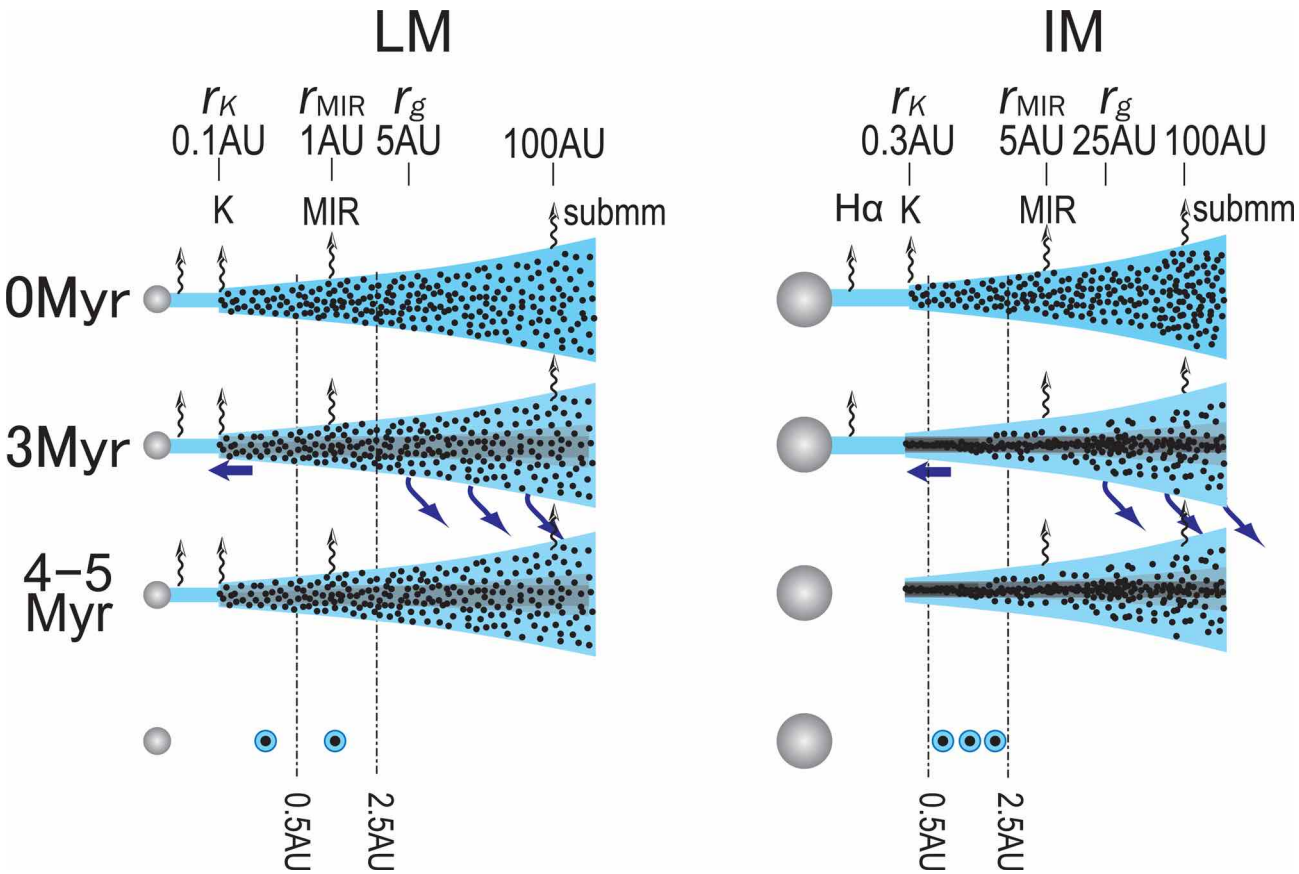

Figure 9. Proposed disc evolution sequences for LM stars (left) and IM stars (right) as discussed in Section 9. The radius in the horizontal direction is roughly shown with a logarithmic scale. r_K, r_{MIR}, and r_g denote the *K*-disc radii, MIR-disc radii, and photoevaporation radii, respectively. Blue arrows show the dispersal of gas/dust. Black dots and the cyan region show the dust and gas distribution, respectively, while Jupiter-mass planets are shown by circles with cyan and black. *K*, MIR, submm, and Hα emissions are shown by arrows with wavy lines. After 4–5 Myr, the entire gas/dust disc disperses before the dust settling is completed for LM stars (left), while the entire gas/dust disc disperses after dust settling is completed in the *K* disc for IM stars (right). After the dispersal, the Jupiter-mass planets are left (bottom). It is known that a larger number of Jupiter-mass planets are distributed at <2.5 au for IM stars than for LM stars. The thin vertical lines at $r = 0.5$ au show the inner region where close-in planets are rarely found for IM stars (see Section 9.3). Note that this is intended to describe the typical case and is not applicable to all stars.

are $\sim$5 and $\sim$1 au, respectively. Although all these radii change with the stellar mass (from 1.5 to 7 $M_\odot$ for IM stars), the relative magnitude of the radii, $r_K < r_{MIR} < r_g$, should not change for both IM and LM star mass ranges, even considering the scaling with the stellar mass mentioned above. Therefore, photoevaporation is not likely the main cause of the fast *K*-disc dispersal for IM stars.

9.2 Dust settling, dust growth, and planet formation

The transition disc phase is now interpreted as the most important phase in the standard planet-formation scenario, and now much observational effort has been put into characterizing this phase (Williams & Cieza 2011). In this interpretation, the early disappearance of the innermost dust disc compared to other portions of disc is due to dust settling to disc mid-plane (Kenyon & Hartmann 1987; Dullemond & Dominik 2005) and/or dust growth (Weidenschilling 1997; Dullemond & Dominik 2004). We discuss those possibilities in the following section with a schematic picture shown in Fig. 9.

9.2.1 Dust settling and growth

From the basic equations of protoplanetary discs in equilibrium, the radial dependence of the dust settling time can be analytically shown to be proportional to the *Kepler* rotation period, which is proportional to $r^{3/2} M_*^{-1/2}$ (Nakagawa, Nakazawa & Hayashi 1981). Although there are many new simulations incorporating more physical processes to show the dust settling time with a different r or M_* dependence (e.g. Tanaka, Himeno & Ida 2005), we compare our results with this base relationship by Nakagawa et al. (1981) as an initial consistency check.

First, as for the radius r dependence, the shorter *K*-disc lifetime than that of MIR disc for the IM stars (Fig. 9, right, Table 4) is qualitatively consistent with the base relationship in that the dust settling/growth is occurring more effectively in the inner disc. Although the observed results ($t^{life} \sim 3$ Myr at $r_K \sim 0.3$ au and $t^{life} \sim 6$–7 Myr at $r_{MIR} \sim 5$ au) do not quantitatively follow the base $r^{3/2}$ relation and instead show a much weaker r dependence, this can be interpreted as that the turbulent process or some other processes that prevent the dust settling/growth have the opposite r dependence to reduce the r dependence of dust settling/growth (e.g. Dullemond & Dominik 2005). For the LM stars, on the other hand, the lifetimes of the inner *K*, MIR, and the outer submm discs do not show any significant difference (see discussions in Sections 8.1.1 and 8.2). This is even more inconsistent with the base $r^{3/2}$ relation than the IM stars. Most likely this means that the disc disperses before dust is totally settled in the entire disc, although dust settling/growth is

reported for some LM stars (e.g. Pinte et al. 2008). In this case, the dust in the upper disc layer is dissipated in the process of mass accretion and photoevaporation (Fig. 9, left), and the disc lifetime (∼9–10 Myr) sets the lower limit of the dust setting/growth time-scale for most of the LM stars. However, it should be noted that the above discussion is intended to describe the typical case and is not applicable to all stars. The time-scale of transition disc is still under debate, short (∼0.2 Myr; e.g. Luhman et al. 2010) or long (∼ a few Myr; e.g. Currie & Sicilia-Aguilar 2011), although the discrepancies among these studies are largely due to differing definitions of the transition disc and how to estimate the total disc lifetime (Espaillat et al. 2014).

Next, as for the stellar mass M_* dependence, the much shorter K-disc lifetime of the IM stars than that of the LM stars ($t^{\rm life}_{{\rm IM},JHK} \sim 3$ Myr, while $t^{\rm life}_{{\rm LM},JHK} \sim 9$–10 Myr; see Table 4; Fig. 5, left) is apparently consistent with the base relation in that dust settling/growth occurring effectively for higher mass stars. However, if we also consider the r dependence, the characteristic IM stars ($M_* = 2.5\,{\rm M}_\odot$, $r_K = 0.3$ au) are expected to have longer settling time-scale (about twice) than the characteristic LM stars ($M_* = 0.5\,{\rm M}_\odot$, $r_K = 0.1$ au) which shows the opposite tendency compared to the observed time-scales. This might suggest that turbulence of the innermost disc is much weaker for the IM stars than for the LM stars so that the dust growth/settling occurs quickly. Although the larger disc mass (surface density) for stars with higher mass (Andrews & Williams 2005) might cause such a situation, the physical process is unknown.

9.2.2 *Planet formation*

Planetesimal and planet formation results from the dust settling/growth processes according to the standard core-accretion model (Lissauer & Stevenson 2007). For IM stars, the quick dust settling/growth processes *in the presence of gas* may cause effective planetesimal formation (Hubickyj, Bodenheimer & Lissauer 2005). This results in effective Jupiter-mass planet formation (e.g. Ida & Lin 2004a; Laughlin, Bodenheimer & Adams 2004; Robinson et al. 2006), which could accelerate the disappearance of the innermost disc with clearing by migration (Lin, Bodenheimer & Richardson 1996; Trilling et al. 1998; Trilling, Lunine & Benz 2002). Such a scenario is consistent with the trend of a higher probability of Jupiter-mass planets with a larger stellar mass for stars in the mass range of 0.2–1.9 $\rm M_\odot$ for semimajor axes of <2.5 au (Johnson et al. 2010). However, the mass range for IM stars (1.5–7 $\rm M_\odot$) has only a small overlap with this trend. This trend is generally interpreted as a result of larger disc mass (high surface density) for larger stellar mass, which enables the rapid formation of Jupiter-mass planets (e.g. within 1 Myr; Ida & Lin 2004b).

9.2.3 *Summary*

In summary, dust settling/growth (and some planet formation) can generally explain the shorter K-disc lifetime of IM stars, although the specific physical processes are not known. This interpretation is summarized in the schematic pictures shown in Fig. 9 (right): (1) The K disc ($r_K \sim 0.3$ au): dust settling/growth works very efficiently from the beginning of disc evolution (cluster age = 0) and is almost completed in ∼3 Myr. Because there is no leftover IR-emitting grains even in the upper disc layer, no NIR continuum is emitted, (2) The MIR disc ($r \sim 5$ au): a significant amount of dust grains is in the upper disc layer due to the turbulence and gives rise to the MIR continuum emission. After ∼4–5 Myr, dust settling has occurred, or dust in the upper layer of the MIR disc is dissipated, resulting in no emission of MIR–thermal continuum emission. If this picture is correct, the lifetime difference of *JHK* and MIR IMDFs constrains the time-scale of this settling process in the K disc to about ∼4 Myr (Section 8.1.2) (Table 4). The low initial value of the *JHK* IMDF (∼50 per cent) might also be naturally explained with the effective settling in the inner disc. Future MIR spectroscopy of the silicate emission lines and the SED slope (Furlan et al. 2006) of those IM stars with and without the K disc will test the idea that the disappearance of the K disc is due to dust settling/growth.

10 IMPLICATIONS FOR PLANET FORMATION AROUND IM STARS

Two remarkable trends are known for the Jupiter-mass planets around IM stars: (1) the lack of close-in planets with semimajor axes of $\lesssim$0.5 au orbiting stars with masses $M > 1.5\,{\rm M}_\odot$ (such planets are common for stars with $M_* < 1.2\,{\rm M}_\odot$), and (2) the higher probability of having planets with semimajor axes of <2.5 au compared to LM stars. In this section, we discuss these trends in the context of our disc fraction lifetime results.

10.1 Implications for the lack of close-in planets

There appears to be a lack of close-in planets with semimajor axes of $\lesssim$0.5 au orbiting stars with masses of 1.5–3 $\rm M_\odot$ in planet-search surveys, while close-in planets are more frequent for lower mass stars (Wright et al. 2009). Because planets are thought to form *in situ* or migrate inwards in the formation phase (e.g. Lin et al. 1996), our suggestion of rapid planet formation in the K disc appears to be inconsistent with the paucity of close-in planets. However, considering the possible radial range of 'K disc' (from ∼0.3 to 1 au, depending on the mass of the central star, disc mass, etc.), the higher planet occurrence for higher mass stars (Johnson et al. 2010) may reflect the rapid planet formation at $r \gtrsim 0.5$ au. The planets that formed at $r \lesssim 0.5$ au may have dropped into the central stars due to migration (Papaloizou et al. 2007) because the gas disc traced by Hα still remains for about 2 Myr after the disappearance of the K disc. Or, they may have disappeared due to collisional destruction that may have effectively occurred along with grain growth (Johansen et al. 2008). In any case, more studies are necessary to understand the precise relation between disc lifetime and planet formation.

Regarding the lack of close-in planets for IM stars, two major scenarios have been proposed. The first scenario is planet engulfment caused by the stellar evolution of primary stars in the RGB phase (Villaver & Livio 2009). Another scenario is that the observed differences in orbital distribution are primordial, and they are a consequence of the planet-formation mechanism around the more massive stars (Currie 2009). In this section, we focus on the latter scenario because our results are relevant to the early stages of star formation. Currie (2009) suggests that planets around IM stars cannot migrate to inner orbits because of the shorter gas-disc lifetime for IM stars. In addition, Kretke et al. (2009) suggest that the inner edge of the dead zone in protoplanetary disc, where the dead zone is the region of the disc without magnetorotational instability (Gammie 1996), effectively determines the semimajor axes of giant planets because the dead zone traps inwardly migrating solid bodies. Thus, they suggested that the larger radius of the inner edge for higher mass stars explains the lack of close-in planets.

Our results are qualitatively consistent with Currie's scenario in that shorter disc lifetimes are expected for higher mass stars.

We estimated that the stellar mass dependence of gas-disc lifetime $t_{\rm H\alpha}^{\rm life}$ is about $M_*^{-0.5}$ ($t_{\rm IM,H\alpha}^{\rm life} \sim 5$ Myr and $t_{\rm LM,H\alpha}^{\rm life} \sim 10$ Myr in Fig. 8). However, this dependence is not as steep as assumed in Currie (2009), $t_{\rm gas}^{\rm life} \propto M_*^{-\beta}$ with $\beta = 0.75$–1.5. In any case, migration alone may not be able to explain the observed sharp outward step in giant planet orbits as pointed out in Kennedy & Kenyon (2009).

Our results that the innermost discs of IM stars disappear at a very early time also seem to be consistent with Kretke's dead zone model. Kretke et al. (2009) assumed a smooth stellar mass dependence of the inner edge radius of the dead zone (proportional to M_*) from the theoretical relationship between the radius and the mass accretion, and they compared this to the mass accretion rate derived from observations. Our results, showing the early disappearance of the innermost *K* disc, suggest that the radius becomes even larger because of low opacity, which makes the formation of dead zone difficult. If the critical stellar mass where the time lag between the *K*- and the MIR-disc dispersal is observationally determined, then this dead zone idea may be able to explain the lack of close-in planets even for the sharp cut-off at 0.5 au in the planet semimajor axes in the distribution of Jupiter-mass planets.

In addition, the difference in the planet-formation site in discs of IM stars and LM stars may explain the lack of close-in planets for the IM stars. Planets are thought to form outwards of the snow line, ∼3 au for LM stars and ∼10 au for IM stars (Kennedy & Kenyon 2008). This difference might explain the observed difference in planet location even after the smearing out by the migration processes, although this idea does not explain the sharp step in planet semimajor axes.

10.2 Implications for higher planet-formation probability

The probability of IM stars having Jupiter-mass planets is found to be proportional to $M_*^{1.0}$ for semimajor axes $<2.5\,{\rm M}_\odot$ (Johnson et al. 2010). This observed frequency is likely to be determined by two competing effects: the tendency of shorter disc lifetimes for more massive stars reduces the likelihood of giant planets forming (Butler et al. 2006), and the tendency of higher disc masses for more massive stars increases the probability of gas-giant planet formation (Wyatt, Clarke & Greaves 2007). In Kennedy & Kenyon (2009), the stellar mass dependence of disc lifetime is estimated using the Hα disc and MIR-disc fractions as $\tau_{\rm KK09} \propto M_*^{-1/2}$, where $\tau_{\rm KK09}$ is the disc decay time-scale defined by their model. However, from our results, the disc lifetime at $r \gtrsim r_{\rm g}$ for IM and LM stars is not significantly different, and the stellar mass dependence of disc lifetime ($t_{\rm MIR}^{\rm life}$) is as small as $M_*^{-0.2}$. The disc mass is known from submm observations to be roughly proportional to the stellar mass (Andrews & Williams 2005). The stellar mass dependence of the disc lifetime is negative, while the stellar mass dependence of the disc mass is positive. Therefore, the higher probability of IM stars having planets compared to LM stars seems to be due to the difference in disc mass instead of the difference in disc lifetime.

11 CONCLUSION

We derived and compiled protoplanetary disc fractions of IM stars (1.5–7 ${\rm M}_\odot$) for a large number of nearby young clusters (within 3 kpc and $\lesssim$5 Myr old) with the available *JHK* photometric data in the literature. From the results and by comparing them with those for other wavelengths (Hα, MIR, and submm), we found the following results.

(i) The *K*-disc lifetime of IM stars ($t_{JHK}^{\rm life}$), which is defined as the time-scale of disc fraction to bottom out at 5 per cent, is estimated to be 3.3 ± 0.9 Myr.

(ii) The *K*-disc lifetime for the IM stars, $t_{JHK}^{\rm life}$, is about one-third of that for the LM stars. Assuming a power-law dependence, the stellar mass dependence of the *K*-disc lifetime is found to be proportional to $M_*^{-0.7\pm0.3}$.

(iii) By comparing the *K*-disc ($r \sim 0.3$ au) evolution to that of the MIR disc ($r \sim 5$ au) for IM stars, we find that the *K* disc seems to disperse earlier than the MIR disc by ∼3–4 Myr.
Because the *K* disc and the MIR disc disperse almost simultaneously in LM stars ($\Delta t \lesssim 0.5$ Myr), the long time lag may be a characteristic of IM stars, suggesting that the transition disc is the common phase in IM stars.

(iv) Because the disc time-scale at $r \gtrsim r_{\rm MIR}$ for the IM stars does not seem to be significantly different from that of LM stars, the most likely cause for the time lag seems to be early dust growth/settling and/or Jupiter-mass planet formation in the innermost disc (*K* disc) in IM stars.

(v) Our results for the *K* disc of the IM stars suggest the possible reasons for the paucity of close-in planets around IM stars, but they are not conclusive. Our results also suggest that the disc mass is a more important factor for the stellar mass dependence of planet occurrence than the disc lifetime.

ACKNOWLEDGEMENTS

We thank the anonymous referee for careful reading and thoughtful suggestions that improved this paper. This work was supported by JSPS KAKENHI Grant Number 24103509, 26800094. We also thank Taku Takeuchi, Hideko Nomura, and Masanobu Kunitomo for helpful discussions on theoretical issues.

REFERENCES

Adams F. C., Lada C. J., Shu F. H., 1987, ApJ, 312, 788
Alexander R., 2008, New Astron. Rev., 52, 60
Andrews S. M., Williams J. P., 2005, ApJ, 631, 1134
Andrews S. M., Williams J. P., 2007, ApJ, 671, 1800
Aspin C., Sandell G., 1997, MNRAS, 289, 1
Bessell M. S., Brett J. M., 1988, PASP, 100, 1134
Briceño C., Calvet N., Hernández J., Vivas A. K., Hartmann L., Downes J. J., Berlind P., 2005, AJ, 129, 907
Butler R. P., Johnson J. A., Marcy G. W., Wright J. T., Vogt S. S., Fischer D. A., 2006, PASP, 118, 1685
Caballero J. A., Albacete-Colombo J. F., López-Santiago J., 2010, A&A, 521, A45
Calvet N., D'Alessio P., Hartmann L., Wilner D., Walsh A., Sitko M., 2002, ApJ, 568, 1008
Carpenter J. M., Mamajek E. E., Hillenbrand L. A., Meyer M. R., 2006, ApJ, 651, L49
Comerón F., Pasquali A., Figueras F., Torra J., 2008, A&A, 486, 453
Connelley M. S., Greene T. P., 2010, AJ, 140, 1214
Cox A. N., 2000, Allen's Astrophysical Quantities. Am. Inst. Phys., New York
Currie T., 2009, ApJ, 694, L171
Currie T., Sicilia-Aguilar A., 2011, ApJ, 732, 24
Dahm S. E., 2008a, in Reipurth B., ed., Handbook of Star Forming Regions, Volume I. Astron. Soc. Pac., San Francisco, p. 966
Dahm S. E., 2008b, in Reipurth B., ed., Handbook of Star Forming Regions, Volume II. Astron. Soc. Pac., San Francisco, p. 26
Dahm S. E., Hillenbrand L. A., 2007, AJ, 133, 2072
Dullemond C. P., Dominik C., 2004, A&A, 417, 159
Dullemond C. P., Dominik C., 2005, A&A, 434, 971

Dullemond C. P., Dominik C., Natta A., 2001, ApJ, 560, 957
Elias J. H., 1978, ApJ, 224, 857
Elmegreen B. G., 2009, in Sheth K., Noriega-Crespo A., Ingalls J., Paladini R., eds, Proc. The Fourth Spitzer Science Center Conf., The Evolving ISM in the Milky Way and Nearby Galaxies. Pasadena, CA
Espaillat C. et al., 2014, preprint (arXiv:1402.7103)
Fedele D., van den Ancker M. E., Henning T., Jayawardhana R., Oliveira J. M., 2010, A&A, 510, A72
Flaherty K. M., Muzerolle J., 2008, AJ, 135, 966
Fuente A., Martın-Pintado J., Bachiller R., Rodrıguez-Franco A., Palla F., 2002, A&A, 387, 977
Furlan E. et al., 2006, ApJS, 165, 568
Furlan E. et al., 2011, ApJS, 195, 3
Gammie C. F., 1996, ApJ, 457, 355
Gáspár A., Rieke G. H., Su K. Y. L., Balog Z., Trilling D., Muzzerole J., Apai D., Kelly B. C., 2009, ApJ, 697, 1578
Gutermuth R. A., Megeath S. T., Myers P. C., Allen L. E., Pipher J. L., Fazio G. G., 2009, ApJS, 184, 18
Haisch K. E., Jr, Lada E. A., Lada C. J., 2001a, AJ, 121, 2065
Haisch K. E., Jr, Lada E. A., Lada C. J., 2001b, ApJ, 553, L153
Herbig G. H., 1960, ApJS, 4, 337
Hernández J., Calvet N., Briceño C., Hartmann L., Berlind P., 2004, AJ, 127, 1682
Hernández J., Calvet N., Hartmann L., Briceño C., Sicilia-Aguilar A., Berlind P., 2005, AJ, 129, 856
Hernández J. et al., 2007a, ApJ, 662, 1067
Hernández J. et al., 2007b, ApJ, 671, 1784
Hernández J., Hartmann L., Calvet N., Jeffries R. D., Gutermuth R., Muzerolle J., Stauffer J., 2008, ApJ, 686, 1195
Hernández J., Calvet N., Hartmann L., Muzerolle J., Gutermuth R., Stauffer J., 2009, ApJ, 707, 705
Hillenbrand L. A., 1997, AJ, 113, 1733
Hillenbrand L. A., 2008, in Livio M., Sahu K., Valenti J., eds, Proc. STScI Symp. 19, A Decade of Extrasolar Planets around Normal Stars. Space Telescope Science Institute, Baltimore, MD, p. 84
Hillenbrand L. A., White R. J., 2004, ApJ, 604, 741
Hollenbach D. J., Yorke H. W., Johnstone D., 2000, in Mannings V., Boss A., Russell S. S., eds, Protostars and Planets IV. Univ. Arizona Press, Tucson, AZ, p. 401
Houk N., 1978, Michigan Catalogue of Two-Dimensional Spectral Types for the HD Stars. Univ. Michigan, Ann Arbor
Hubickyj O., Bodenheimer P., Lissauer J. J., 2005, Icarus, 179, 415
Ida S., Lin D. N. C., 2004a, ApJ, 604, 388
Ida S., Lin D. N. C., 2004b, ApJ, 616, 567
Isobe T., Feigelson E. D., Nelson P. I., 1986, ApJ, 306, 490
Johansen A., Brauer F., Dullemond C., Klahr H., Henning T., 2008, A&A, 486, 597
Johnson J. A., Aller K. M., Howard A. W., Crepp J. R., 2010, PASP, 122, 905
Kennedy G. M., Kenyon S. J., 2008, ApJ, 673, 502
Kennedy G. M., Kenyon S. J., 2009, ApJ, 695, 1210
Kenyon S. J., Hartmann L., 1987, ApJ, 323, 714
Kretke K. A., Lin D. N. C., Garaud P., Turner N. J., 2009, ApJ, 690, 407
Kroupa P., 2002, Science 295, 82
Lada E. A., 1999, in Lada C. J., Kylafis N. D., eds, The Origin of Stars and Planetary Systems. Kluwer, Dordrecht, p. 441
Lada C. J., Adams F. C., 1992, ApJ, 393, 278
Lada C. J., Lada E. A., 2003, ARA&A, 41, 57
Lada C. J. et al., 2006, AJ, 131, 1574
Laughlin G., Bodenheimer P., Adams F. C., 2004, ApJ, 612, L73
Lavalley M., Isobe T., Feigelson E., 1992, in Worrall D. M., Biemesderfer C., Barnes J., eds, ASP Conf. Ser. Vol. 25, Astronomical Data Analysis Software and Systems I. Astron. Soc. Pac., San Francisco, p. 245
Lin D. N. C., Bodenheimer P., Richardson D. C., 1996, Nature, 380, 606
Lissauer J. J., Stevenson D. J., 2007, in Reipurth B., Jewitt D., Keil K., eds, Protostars and Planets V. Univ. Arizona Press, Tucson, AZ, p. 591
Liu M. C., Najita J., Tokunaga A. T., 2003, ApJ, 585, 372
Luhman K. L., 2001, ApJ, 560, 287
Luhman K. L., 2004, ApJ, 602, 816
Luhman K. L., 2008, in Reipurth B., ed., Handbook of Star Forming Regions, Volume II. Astron. Soc. Pac., San Francisco, p. 169
Luhman K. L., Allen P. R., Espaillat C., Hartmann L., Calvet N., 2010, ApJS, 186, 111
Luhman K. L., Stauffer J. R., Muench A. A., Rieke G. H., Lada E. A., Bouvier J., Lada C. J., 2003, ApJ, 593, 1093
Luhman K. L., Whitney B. A., Meade M. R., Babler B. L., Indebetouw R., Bracker S., Churchwell E. B., 2006, ApJ, 647, 1180
Luhman K. L. et al., 2008, ApJ, 675, 1375
Mamajek E. E., 2009, in Usuda T., Ishii M., Tamura M., eds, AIP Conf. Proc. Vol. 1158, Exoplanets and Disks: Their Formation and Diversity. Am. Inst. Phys., New York, p. 3
Mamajek E. E., Lawson W. A., Feigelson E. D., 1999, ApJ, 516, L77
Mann R. K., Williams J. P., 2009, ApJ, 694, L36
Mathews G. S., Williams J. P., Ménard F., Phillips N., Duchêne G., Pinte C., 2012, ApJ, 745, 23
Meeus G., Waters L. B. F. M., Bouwman J., van den Ancker M. E., Waelkens C., Malfait K., 2001, A&A, 365, 476
Megeath S. T., Hartmann L., Luhman K. L., Fazio G. G., 2005, ApJ, 634, L113
Mendigutía I., Calvet N., Montesinos B., Mora A., Muzerolle J., Eiroa C., Oudmaijer R. D., Merín B., 2011, A&A, 535, A99
Millan-Gabet R., Malbet F., Akeson R., Leinert C., Monnier J., Waters R., 2007, in Reipurth B., Jewitt D., Keil K., eds, Protostars and Planets V. Univ. Arizona Press, Tucson, AZ, p. 539
Muench A. A., Lada E. A., Lada C. J., Alves J., 2002, ApJ, 573, 366
Muzerolle J., Allen L. E., Megeath S. T., Hernández J., Gutermuth R. A., 2010, ApJ, 708, 1107
Nakagawa Y., Nakazawa K., Hayashi C., 1981, Icarus, 45, 517
Natta A., Prusti T., Neri R., Wooden D., Grinin V. P., Mannings V., 2001, A&A, 371, 186
Palla F., Stahler S. W., 2000, ApJ, 540, 255
Papaloizou J. C. B., Nelson R. P., Kley W., Masset F. S., Artymowicz P., 2007, in Reipurth B., Jewitt D., Keil K., eds, Protostars and Planets V. Univ. Arizona Press, Tucson, AZ, p. 655
Pinte C. et al., 2008, A&A, 489, 633
Preibisch T., Brown A. G. A., Bridges T., Guenther E., Zinnecker H., 2002, AJ, 124, 404
Rebull L. M. et al., 2002, AJ, 123, 1528
Reipurth B., 2008a, in Reipurth B., Handbook of Star Forming Regions, Volume I: The Northern Sky ASP Monograph Publications. Vol. 4
Reipurth B., 2008b, in Reipurth B., Handbook of Star Forming Regions, Volume II: The Southern Sky ASP Monograph Publications. Vol. 5.
Renson P., Manfroid J., 2009, A&A, 498, 961
Robinson S. E., Laughlin G., Bodenheimer P., Fischer D., 2006, ApJ, 643, 484
Roccatagliata V., Bouwman J., Henning T., Gennaro M., Feigelson E., Kim J. S., Sicilia-Aguilar A., Lawson W. A., 2011, ApJ, 733, 113
Schaefer G. H., Simon M., Beck T. L., Nelan E., Prato L., 2006, AJ, 132, 2618
Shu F. H., Adams F. C., Lizano S., 1987, ARA&A, 25, 23
Sicilia-Aguilar A., Hartmann L. W., Hernández J., Briceño C., Calvet N., 2005, AJ, 130, 188
Sicilia-Aguilar A. et al., 2006, ApJ, 638, 897
Siess L., Dufour E., Forestini M., 2000, A&A, 358, 593
Simon M., Dutrey A., Guilloteau S., 2000, ApJ, 545, 1034
Skrutskie M. F. et al., 2006, AJ, 131, 1163
Strom S. E., Vrba F. J., Strom K. M., 1976, AJ, 81, 314
Strom K. M., Strom S. E., Edwards S., Cabrit S., Skrutskie M. F., 1989, AJ, 97, 1451
Tanaka H., Himeno Y., Ida S., 2005, ApJ, 625, 414
Tognelli E., Prada Moroni P. G., Degl'Innocenti S., 2011, A&A, 533, A109
Trilling D. E., Benz W., Guillot T., Lunine J. I., Hubbard W. B., Burrows A., 1998, ApJ, 500, 428

Trilling D. E., Lunine J. I., Benz W., 2002, A&A, 394, 241
Uzpen B., Kobulnicky H. A., Kinemuchi K., 2009, AJ, 137, 3329
Villaver E., Livio M., 2009, ApJ, 705, L81
Weidenschilling S. J., 1997, Icarus, 127, 290
Wilking B. A., Meyer M. R., Greene T. P., Mikhail A., Carlson G., 2004, AJ, 127, 1131
Wilking B. A., Gagné M., Allen L. E., 2008, in Reipurth B., ed., Handbook of Star Forming Regions, Volume II. Astron. Soc. Pac., San Francisco, p. 351
Williams J. P., Cieza L. A., 2011, ARA&A, 49, 67
Winston E. et al., 2010, AJ, 140, 266
Wolff S. C., Strom S. E., Rebull L. M., 2011, ApJ, 726, 19
Wolk S. J., Walter F. M., 1996, AJ, 111, 2066
Wright J. T., Upadhyay S., Marcy G. W., Fischer D. A., Ford E. B., Johnson J. A., 2009, ApJ, 693, 1084
Wyatt M. C., Clarke C. J., Greaves J. S., 2007, MNRAS, 380, 1737
Yasui C., Kobayashi N., Tokunaga A. T., Saito M., Tokoku C., 2009, ApJ, 705, 54
Yasui C., Kobayashi N., Tokunaga A. T., Saito M., Tokoku C., 2010, ApJ, 723, L113
Yi S. K., Kim Y.-C., Demarque P., 2003, ApJS, 144, 259
Zinnecker H., Yorke H. W., 2007, ARA&A, 45, 481

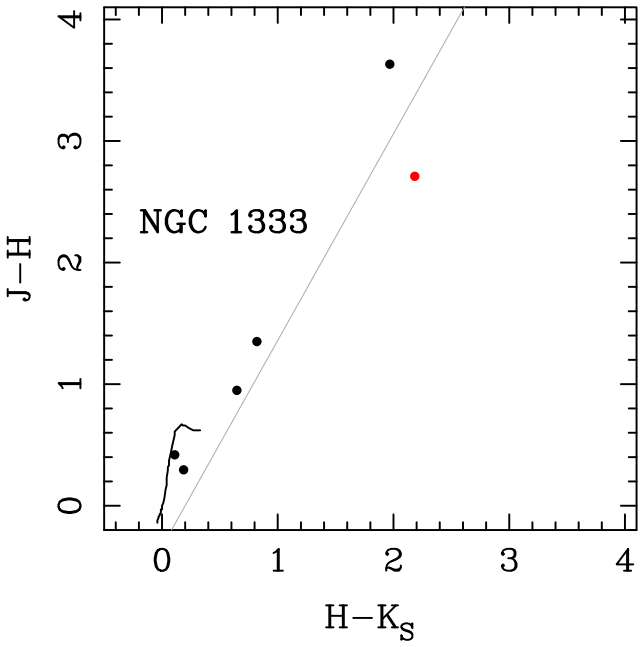

Figure A1. NGC 1333.

Table A1. NGC 1333. The α values for MIR disc are directly referred from Gutermuth et al. (2009). Though extinction is not corrected for α values in this reference, it should not affect the disc judgement because the α value is much larger than −2. The spectral type with ⋆ mark is from the SIMBAD data base.

Name	RA J2000 (h:m:s)	Dec. J2000 (d:m:s)	SpT	*K* disc	MIR disc
2MASS J03291977+3124572	03 29 19.77605	+31 24 57.0474	B8*	X	–
2MASS J03285720+3114189	03 28 57.2107	+31 14 19.056	B*	X	–
2MASS J03290575+3116396	03 29 05.754	+31 16 39.69	A3	X	o (−0.28)
2MASS J03291037+3121591 (LZK 12)	03 29 10.379	+31 21 59.16	F4–G0	o	o (−0.40)
2MASS J03285930+3115485	03 28 59.306	+31 15 48.52	K2	X	o (−0.25)
2MASS J03292187+3115363 (LkHA 271)	03 29 21.873	+31 15 36.30	K4.0	X	o (−1.49)

APPENDIX A: LIST OF SAMPLE IM STARS IN TARGET CLUSTERS

In this appendix, the IM-star samples for all 19 clusters listed in Table 3 are summarized in Tables A1– A19 as well as in colour–colour diagrams (Figs A1–A19). The complete tables and figures are available in the online version of the article.

In the tables, only RA, Dec. coordinates (in J2000) are shown in case object names are not available in the references. 'SpT' shows the spectral types in the literatures. The '*K* disc' and 'MIR disc' columns show objects with a disc (o) and without a disc (X). The numbers in the parentheses in MIR disc column is α as defined in Section 1. The stars with *K*-disc emission are judged from the colour–colour diagram, in which the red and black circles show those with a *K* disc and without a *K* disc, respectively.

SUPPORTING INFORMATION

Additional Supporting Information may be found in the online version of this article:

Appendix A. List of sample IM stars in target clusters (http://mnras.oxfordjournals.org/lookup/suppl/doi:10.1093/mnras/stu1013/-/DC1).

Please note: Oxford University Press is not responsible for the content or functionality of any supporting materials supplied by the authors. Any queries (other than missing material) should be directed to the corresponding author for the paper.

This paper has been typeset from a TEX/LATEX file prepared by the author.

Icarus 233 (2014) 293–305

Contents lists available at ScienceDirect

Icarus

journal homepage: www.elsevier.com/locate/icarus

Impact strength of small icy bodies that experienced multiple collisions

Minami Yasui [a,*], Ryo Hayama [b], Masahiko Arakawa [b]

[a] Organization of Advanced Science and Technology, Kobe University, 1-1, Rokkodai-cho, Nada-ku, Kobe 657-8501, Japan
[b] Graduate School of Science, Kobe University, 1-1, Rokkodai-cho, Nada-ku, Kobe 657-8501, Japan

ARTICLE INFO

Article history:
Received 6 November 2013
Revised 2 February 2014
Accepted 4 February 2014
Available online 20 February 2014

Keywords:
Impact processes
Ices
Cratering
Kuiper belt
Satellites, surfaces

ABSTRACT

Frequent collisions are common for small bodies in the Solar System, and the cumulative damage to these bodies is thought to significantly affect their evolution. It is important to study the effects of multiple impacts such as the number of impacts on the impact strength and the ejection velocity of impact fragments. Here we conducted multiple-impact experiments using a polycrystalline water ice target, varying the number of impacts from 1 to 10 times. An ice cylindrical projectile was impacted at 84–502 m s^{-1} by using a single-stage gas gun in a cold room between −10 and −15 °C. The impact strength of the ice target that experienced a single impact and multiple impacts is expressed by the total energy density applied to the same target, ΣQ, and this value was observed to be 77.6 J kg^{-1}. The number of fine impact fragments at a fragment mass normalized by an initial target mass, $m/M_{t0} \sim 10^{-6}$, n_m, had a good correlation with the single energy density at each shot, Q_j, and the relationship was shown to be $n_m = 10^{1.02\pm0.22} \cdot Q_j^{1.31\pm0.12}$. We also estimated the cumulative damage of icy bodies as a total energy density accumulated by past impacts, according to the crater scaling laws proposed by Housen et al. (Housen, K.R., Schmidt, R.M., Holsapple, K.A. [1983]. J. Geophys. Res. 88, 2485–2499) of ice and the crater size distributions observed on Phoebe, a saturnian icy satellite. We found that the cumulative damage of Phoebe depended significantly on the impact speed of the impactor that formed the craters on Phoebe; and the cumulative damage was about one-third of the impact strength ΣQ^* at 500 m s^{-1} whereas it was almost zero at 3.2 km s^{-1}.

1. Introduction

In the evolution of Solar System bodies, collisional disruption has played an important role. For example, the proto-planets were formed by collisional disruption and the re-accumulation of planetesimals, and asteroids are believed to be survivors of planetesimals that experienced collisional disruption. In order to study the formation processes of Solar System bodies, the impact condition of catastrophic disruption for solid materials simulating various Solar System bodies should be clarified.

The impact condition for catastrophic disruption is called the impact strength, Q^*, and Q^* is one of the most important properties of Solar System bodies related to mutual impact. Q^* is defined by the energy density Q when the largest fragment mass is equal to one-half of the original target mass (Davis and Ryan, 1990), and the energy density Q is defined by the kinetic energy of the impactor (or projectile) divided by the original target mass. Over the past 30 years, many studies have been conducted to discern the impact strength of various solid materials simulating Solar System bodies, such as laboratory impact experiments using basalt and ice (e.g., Fujiwara et al., 1977; Kawakami et al., 1983; Takagi et al., 1984; Davis and Ryan, 1990; Kato et al., 1995).

As spacecraft explorations and ground-based observations have advanced, more and more details of Solar System bodies have been revealed. For example, some asteroids and small icy satellites have low bulk density, i.e., large porosity (Consolmagno and Britt, 1998; Britt et al., 2002; Porco et al., 2007), and they are composed of a mixture of several components such as ices and silicates. Intensive studies to elucidate the effects of the porosity and the mixture on the impact strength have been conducted using various porous materials and mixtures (e.g., Arakawa and Tomizuka, 2004; Shimaki and Arakawa, 2012). These studies clarified that the porosity and the multiple components significantly affected the impact strength, increasing or decreasing them. We propose that it is very important to study the impact strength of various materials simulating Solar System bodies with a wider range of physical and chemical properties.

One of the most important and most interesting physical properties is "multiple impacts". The term "multiple impacts" refers to when a Solar System body has experienced many impacts with other bodies. In this study, we focused on Solar System bodies that have experienced multiple impacts. These bodies experienced

* Corresponding author. Fax: +81 78 803 6684.
E-mail address: minami.yasui@pearl.kobe-u.ac.jp (M. Yasui).

http://dx.doi.org/10.1016/j.icarus.2014.02.008
0019-1035/

multiple impacts are called as "pre-impacted bodies". Laboratory experiments, exploratory observations, and numerical simulations have obtained some potential evidence of multiple impacts for small bodies such as asteroids, comets, and icy satellites. The many craters found on the small bodies are expected to be accompanied by many fractures under and around the craters, because laboratory impact cratering experiments in water ice and gypsum demonstrated that the impact craters were always surrounded by many cracks (Kato et al., 1995; Yasui et al., 2012). Veverka et al. (2000) found a large impact crater together with many grooves on the surface of Eros, and they suggested that the grooves may extend toward the interior as fractures. They speculated that the grooves might be formed simultaneously by the impact forming the crater. Michel et al. (2003) did numerical simulations of collisions of parent bodies to explore the properties of the Karin family (one of the large asteroid families), and the outcomes of the simulations showed that the Karin family members must be the products of collisions of a parent body that experienced impacts previously. In order to study the collisional evolutions of Solar System bodies, the impact strength of the bodies that experienced multiple impacts should be also clarified, because the pre-impacted bodies could have many fractures inside, so that their impact strength could be smaller than that of an intact body. It is thus important to know how the impact strength decreases with the number of impacts compared with the intact body.

Several experimental studies have investigated the effects of multiple impacts on the impact strength of small bodies by using target materials of glass and basalt simulating a tektite and an asteroid. Gault and Wedekind (1969) conducted impact experiments using spherical glass targets simulating a tektite at the impact velocity of 7.55 km s^{-1}, for 1, 4, 7, and 19 impacts on different impact surfaces. They examined the relationship between the largest fragment mass normalized by the original target mass, m_l/M_t, and the total energy density, ΣQ, where ΣQ was the sum of each projectile kinetic energy applied to the same target divided by the initial target mass. They found that the relationship was very similar to that obtained for single-impact experiments, irrespective of the number of impacts. Housen (2009) conducted impact experiments on cylindrical basalt targets at the impact velocity of 0.73–1.97 km s^{-1} and he studied a single impact and two impacts on the same and different impact surfaces. He reported almost the same result as that obtained by Gault and Wedekind (1969). Nakamura et al. (1994) also conducted impact experiments on a spherical basalt target at impact velocities of 2.8–3.2 km s^{-1} for a single impact and two impacts. We found that the result reported by Nakamura et al. was very different from that obtained by Housen (2009): the relationships between m_l/M_t and ΣQ in the two impacts was not consistent with that obtained by Housen (2009), whereas the relationship between m_l/M_t and the single energy density in the two impacts was almost similar to that obtained in single-impact experiments (Fujiwara and Tsukamoto, 1980; Takagi et al., 1984).

This difference could be caused by one or more target physical conditions such as the crack number density or distribution. Nakamura et al. (1994) used a barrel-shaped core fragment for the second shot, which was derived from an original target at the first shot. It was shown by a numerical simulation that the core fragment is not fractured so severely (Benz and Asphaug, 1993), and the pre-existing cracks inside the target given by the previous impacts in the target were fewer than that used by Housen (2009) in the second shot. Thus, in order to determine the precise effects of multiple impacts on the impact strength, the target physical conditions should be controlled. The crack number density and the distribution, in particular, should be systematically controlled.

In this study, we conducted multiple-impact experiments to study the effects of multiple impacts on the impact strength. We used a polycrystalline water ice target because there are no experimental results for multiple impacts using an ice target, and water ice is a transparent material that is suitable for recognizing cracks in the target. In order to control the crack number density and the distribution in the targets, we systematically selected the number of impacts, the energy density at each impact shot (the single energy density: Q_j), and the total energy density (ΣQ). We also measured the ejecta velocity and the size distribution of impact fragments to characterize the degree of the impact disruption. Lastly, we attempted to apply our laboratory results for the estimation of the internal damage of a saturnian icy satellite, Phoebe, by using the crater scaling law proposed by Housen et al. (1983) and the cumulative size distributions of impact craters observed on the satellite.

2. Experimental methods

2.1. Samples

We used polycrystalline water ice as a projectile and as a target simulating icy bodies such as icy satellites and comets. The projectile was cylindrical (15-mm dia., height of 9–11 mm), with the mass, m_p, of 1.40–1.66 g. It was made by putting tap water put into a mold, and then freezing the water in a cold room (−10 °C) for a few tens of minutes. The projectile looked cloudy because tiny bubbles were incorporated in it, and thus the projectile had a small amount of porosity (less than a few percent); however, the porosity did not affect the impact outcomes (Kato et al., 1995; Arakawa et al., 2002).

The target had a cubic shape with the initial mass ranging from 0.60 to 2.69 kg and the size from 8.7 to 14.0 cm. It was prepared by cutting a large commercial ice block. The density of the ice target was 917 kg m^{-3}, and the target was so-called "columnar ice" with large ice crystals elongated toward one direction with the size of several cm (Kato et al., 1995). There were no bubbles in it, so it looked completely transparent.

2.2. Impact experiments

We conducted impact experiments by using a one-stage light-gas gun installed in a cold room at the Institute of Low Temperature Science, Hokkaido University. A schematic illustration of the experimental setup is shown in Fig. 1. The impact velocity, V_i, ranged from 84 to 502 m s^{-1}. The room temperature was set between −10 and −15 °C.

In the present study, an ice projectile was impacted on the same target from 1 to 10 times (=the number of impacts), and each impact was conducted on different target surfaces: the projectile was impacted on the intact surface up to four times, after that the surface that experienced the impact before was impacted again. A second shot was given to the opposing surface of the first shot, a third shot was given to the surface perpendicular to those of the first and second shots, and a fourth shot was given to the opposing surface of the third shot, and so on. We used these four surfaces to give the impact on the target, and then these surfaces were impacted two to three times repeatedly in one series of experiment for fifth to tenth shots. The other two intact surfaces were used for a window to observe the generated cracks inside the target.

In the present study, we describe the target mass according to the number of impacts: (1) the target mass before the first impact, M_{t0} (initial target mass), and (2) the target mass before the jth impact (j = 2–10), M_{t_j}. We describe the impact condition by using two parameters: (1) the energy density at each shot or a single energy density, Q_j, where the subscript j is the number of impacts, and (2) the total energy density, ΣQ, which corresponds to the sum of each energy density applied to the same target, that is,

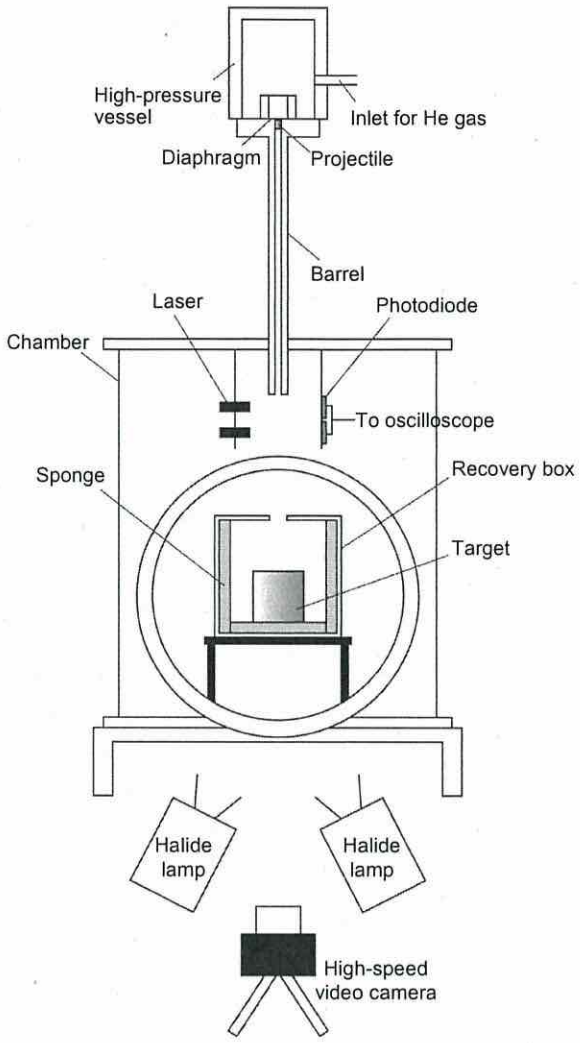

Fig. 1. Schematic of the experimental apparatus of the single-stage gas gun.

the ΣQ is equal to $\sum_{j=1}^{n} Q_j$ (j = 1–10). The single energy density Q_j is written as $Q_j = \frac{1}{2} m_p V_i^2 / (m_p + M_{t\_j})$ where M_{t_j} is the target mass before the jth impact. At j = 1, Q_1 is written as $Q_1 = \frac{1}{2} m_p V_i^2 / (m_p + M_{t0})$.

As illustrated in Fig. 1, the target was placed at the bottom of a recovery box so that we could collect the impact fragments after the shot, and the box was covered with sponge plates on the bottom and three sides to prevent these fragments from secondary collisions against the walls of the box. The uncovered side was used for the window to observe the impact phenomena, from which we measured the ejecta velocity, particularly that ejected from the corner points on the impact surface. The recovery box was set in a sample chamber, and the impact experiment was conducted under air pressure during the shots at impact velocities lower than 340 m s^{-1}. At impact velocities higher than 340 m s^{-1}, the chamber was evacuated below 10^4 Pa to avoid loud noise generation in air. After the shot, we measured the mass of each recovered fragment one by one with an electric mass balance for the fragments larger than 0.01 g. The residual fragments smaller than 0.01 g were sieved into seven groups of size range, and we measured the total mass of fragments at each size range.

We observed the collisional disruption of the target using a high-speed digital video camera to measure the ejecta velocity. The frame rate was set from 4.0×10^3 to 1.0×10^4 frames s^{-1}, and the shutter speed was set from 10 to 50 μs. We observed the collisional disruption process by illuminating the target using two metal halide lamps from the front of the target.

The fluctuation of the room temperature did not affect the experimental results in this study. This temperature range is higher than the average temperature of the outer Solar System where icy satellites exist (below 100 K). Kato et al. (1992) did impact experiments using polycrystalline water ice at 77 and 255 K, and they found that the energy density, Q, required to disrupt the 77-K ice target to about 1/20 of the original target mass was five times larger than that required for the 255-K ice target. We therefore felt that the effect of multiple impacts on the impact strength of polycrystalline water ice at lower temperatures should be examined, and we are planning to conduct such a study.

3. Results

The experimental condition of each shot is summarized in Table 1. In this study, we made a series of multiple-impact experiments with 32 targets, and then 92 shots in total were conducted. We changed both the energy density for each shot, Q_j, and the total energy density, ΣQ, and the series was classified into three groups. The first group was the series with an equal energy density for every shot on the same target. The second group was the series with a final energy density, Q_f, larger than the impact strength of polycrystalline ice, $Q^*_{ice} = 71.5$ J kg^{-1} (Kato et al., 1995). The third group was the series of different energy densities for every shot on the same target, but not satisfying the condition of the second group, that is, $Q_f < Q^*_{ice}$. This classification is shown in Table 1 as $Q_j \sim$ const, $Q_f > Q^*_{ice}$, and $Q_j \neq$ const, respectively.

3.1. Observation of collisional disruption

Fig. 2a–c are snapshots taken by the high-speed video camera during the disruption. All figures were taken for the shot at the same total energy densities, ΣQ, approx. 100 J kg^{-1}, however, the total numbers of impacts are different. The energy densities for one target given at every shot were almost the same; i.e., Q_j is a constant ($Q_j \sim$ const). Fig. 2a shows the snapshots of the catastrophic disruption by a single impact, and the impact velocity was 387 m s^{-1}. The movie recorded during the collisional disruption is shown as Supplementary video S1 as Supplementary online material. The projectile impacted on the center of the top surface (the first image in Fig. 2a). After the projectile was impacted, many cracks were generated around the upper half region of the target (second image from the top), and then many small fragments were ejected outward from the impact points (third image from the top). After 30 ms, the target was largely deformed and looked to be disrupted catastrophically, and many fragments were scattered in the recovery box in the bottom image.

Fig. 2b and c are snapshots of the target damaged by multiple impacts; a double impact for Fig. 2b and a four-times impact for Fig. 2c. The final shots with the impact velocity of 235 m s^{-1} and 181 m s^{-1}, respectively are shown in Fig. 2b and c. The movies recorded during the collisional disruption for the double impact and the four-times impact are provided as Supplementary videos S2 and S3, respectively. In both cases, a few small impact fragments were observed to be ejected from their impact points at 10 ms (second images from the top of Fig. 2b and c). The targets were then split vertically and divided into two separate parts, and the V-shaped vertical gap is shown in the third images from the top of Fig. 2b and c.

Most of the fragments looked to be generated according to the pre-existing cracks which were formed by the previous shots: the pre-existing cracks were slightly disconnected from each other,

Table 1
Impact conditions and results of all shots.

Number of impacts	Run number	Shot number	V_i (m s^{-1})	m_p (g)	M_{t0} or M_{t_f} (g)	Q_f (J kg^{-1})	ΣQ (J kg^{-1})	m_l (g)	V_{c-g} (m s^{-1})		Q_f series
									Left	Right	
1	20121123-4	1	253	1.60	1089.0	47.06	47.06	1064.6	–	–	–
	20121123-5	1	254	1.60	1020.0	50.44	50.44	761.3	–	1.81 (1.39 × 10^{-1})	–
	20120221-5	1	256	1.50	764.9	64.26	64.26	559.8	–	–	–
	20110930-6*	1	387	1.60	1160.9	103.21	103.21	168.6	2.89 (9.37 × 10^{-2})	–	–
	20130911-1	1	395	1.58	803.4	153.62	153.62	85.5	4.06 (9.14 × 10^{-2})	4.44 (1.06 × 10^{-1})	–
	20110707-1	1	482	1.54	1014.4	176.35	176.35	60.4	8.28 (3.14 × 10^{-1})	7.97 (1.71 × 10^{-1})	–
	20130911-2	1	448	1.59	793.4	200.89	200.89	38.6	7.34 (9.54 × 10^{-2})	8.10 (1.14 × 10^{-1})	–
	20130914-3	1	502	1.57	595.5	332.00	332.00	30.4	13.39 (5.80 × 10^{-1})	11.13 (1.11 × 10^{-1})	–
2	20120221-1	1	266	1.40	1395.0	35.51	35.51	1383.4	–	–	$Q_f \sim$ const
	20120225-2	2	215	1.61	1380.7	26.95	62.46	1371.3	–	–	
	20130914-1	1	244	1.59	1030.6	45.97	45.97	1018.0	–	–	$Q_f \sim$ const
	20130914-2	2	237	1.58	1018.0	43.67	89.64	554.6	–	–	
	20130912-9	1	236	1.56	808.9	53.92	53.92	759.4	–	–	$Q_f \sim$ const
	20130912-10*	2	235	1.57	759.4	56.93	110.85	135.4	0.95 (3.78 × 10^{-2})	1.44 (6.47 × 10^{-2})	
	20130912-1	1	285	1.60	1051.6	61.57	61.57	835.4	1.78 (5.47 × 10^{-2})	2.47 (1.36 × 10^{-1})	$Q_f \sim$ const
	20130912-2	2	280	1.57	835.4	73.87	135.44	80.9	2.37 (6.72 × 10^{-2})	2.65 (6.08 × 10^{-2})	
	20120222-6	1	263	1.60	747.4	74.03	74.03	625.5	–	–	$Q_f \sim$ const
	20120222-7	2	256	1.61	625.5	84.35	158.38	39.9	–	–	
	20130913-5	1	234	1.57	596.1	71.90	71.90	513.2	–	–	$Q_f \sim$ const
	20130913-6	2	236	1.60	513.2	86.81	158.71	55.7	2.39 (7.13 × 10^{-2})	2.98 (5.36 × 10^{-2})	
	20110929-5	1	180	1.58	996.1	25.70	25.70	994.6	–	–	$Q_f \neq$ const
	20111001-1	2	246	1.58	994.6	48.07	73.76	559.9	–	–	
	20110929-4	1	184	1.58	1270.3	21.06	21.06	1269.6	–	–	$Q_f > Q^*_{ice}$
	20110930-5	2	383	1.59	1269.6	91.85	112.91	68.6	6.99 (1.15 × 10^{-1})	–	
	20120220-1	1	140	1.57	1330.8	11.56	11.56	1329.6	–	–	$Q_f > Q^*_{ice}$
	20120225-3	2	408	1.57	1324.2	98.68	110.24	109.2	5.91 (2.81 × 10^{-2})	–	
	20110929-1	1	254	1.60	1014.9	50.85	50.85	994.2	–	–	$Q_f > Q^*_{ice}$
	20110930-1	2	385	1.58	994.2	117.78	168.64	43.6	2.95 (1.23 × 10^{-1})	5.16 (1.73 × 10^{-1})	
3	20130912-6	1	231	1.63	1535.3	28.43	28.43	1530.6	–	–	$Q_f \sim$ const
	20130912-7	2	227	1.58	1530.6	26.71	55.14	1525.1	–	–	
	20130912-8	3	231	1.56	1525.1	27.33	82.47	1084.0	–	–	
	20121122-1	1	188	1.60	1005.6	28.09	28.09	1002.7	–	–	$Q_f \sim$ const
	20121122-2	2	188	1.60	1002.2	28.06	56.15	1000.2	–	–	
	20121122-3	3	193	1.60	999.1	29.83	85.98	590.7	0.47 (2.90 × 10^{-2})	0.80 (1.62 × 10^{-1})	
	20121121-1	1	189	1.60	989.7	28.87	28.87	986.8	–	–	$Q_f \sim$ const
	20121121-2	2	185	1.60	985.6	27.78	56.65	981.2	–	–	
	20121121-3	3	192	1.60	980.6	30.07	86.73	971.0	–	–	
	20130912-3	1	198	1.56	801.7	38.03	38.03	800.4	–	–	$Q_f \sim$ const
	20130912-4	2	197	1.62	800.4	39.39	77.41	796.5	–	–	
	20130912-5	3	200	1.66	796.5	41.65	119.06	485.6	1.37 (1.05 × 10^{-1})	1.75 (1.27 × 10^{-1})	
	20110709-1	1	259	1.60	999.3	53.71	53.71	986.6	–	–	$Q_f > Q^*_{ice}$
	20110709-2	2	252	1.60	986.1	51.52	105.22	257.0	–	–	
	20110709-3	3	250	1.60	241.6	206.96	312.19	12.7	4.86 (1.59 × 10^{-1})	3.61 (1.14 × 10^{-1})	
4	20130913-1	1	171	1.59	1254.4	18.48	18.48	1251.6	–	–	$Q_f \sim$ const
	20130913-2	2	192	1.56	1251.6	23.07	41.55	1249.8	–	–	
	20130913-3	3	197	1.57	1249.8	24.35	65.90	1242.6	–	–	
	20130913-4	4	196	1.57	1242.6	24.25	90.15	462.7	–	–	
	20110708-2	1	186	1.60	1007.9	27.46	27.46	1006.1	–	–	$Q_f \sim$ const
	20110708-3	2	186	1.60	1006.3	27.50	54.96	1004.9	–	–	
	20110708-4	3	184	1.60	1003.6	26.99	81.95	967.1	–	–	
	20110708-5*	4	181	1.60	967.1	27.10	109.05	120.8	0.66 (6.52 × 10^{-2})	0.70 (3.31 × 10^{-2})	
	20110929-6	1	185	1.58	1173.1	23.05	23.05	1160.6	–	–	$Q_f \neq$ const

	20111001-5	2	132	1.60	1160.6	12.01	35.06	1162.3	–	–	
	20111001-6	3	137	1.62	1162.7	13.08	48.14	1159.9	–	–	
	20111001-7	4	186	1.58	1159.9	23.56	71.70	1062.5	1.21 (2.69 × 10^{-2})	–	
	20110929-2	1	254	1.60	1143.2	45.15	45.15	1151.6	–	–	$Q_j \neq$ const
	20110930-2	2	160	1.60	1151.6	17.78	62.93	1150.3	–	–	
	20110930-3	3	186	1.58	1150.3	23.76	86.69	1143.0	–	–	
	20110930-4	4	186	1.60	1143.0	24.21	110.91	521.6	0.60 (3.26 × 10^{-2})	–	
	20110929-3	1	247	1.60	1170.3	41.70	41.70	1162.0	–	–	$Q_j \neq$ const
	20111001-2	2	140	1.60	1162.0	13.49	55.20	1161.3	–	–	
	20111001-3	3	138	1.57	1161.3	12.87	68.07	1159.3	–	–	
	20111001-4	4	194	1.60	1159.3	25.97	94.04	928.5	1.61 (5.90 × 10^{-2})	1.99 (2.94 × 10^{-2})	
	20120224-4	1	142	1.56	985.5	15.96	15.96	983.9	–	–	$Q_f > Q^*_{ice}$
	20120224-5	2	147	1.60	983.9	17.57	33.53	983.4	–	–	
	20120224-6	3	138	1.62	983.4	15.69	49.22	983.5	–	–	
	20120224-7	4	464	1.64	983.5	179.50	228.72	36.3	5.95 (2.09 × 10^{-2})	–	
7	20120221-2	1	141	1.60	1447.6	10.99	10.99	1437.5	–	–	$Q_j \sim$ const
	20120221-3	2	140	1.59	1437.5	10.84	21.83	1432.9	–	–	
	20120221-4	3	124	1.60	1432.9	8.58	30.41	1432.0	–	–	
	20120225-1	4	143	1.57	1427.0	11.25	41.66	1425.1	–	–	
	20120225-4	5	141	1.60	1424.2	11.17	52.83	1420.6	–	–	
	20120225-5	6	146	1.59	1420.6	11.93	64.76	1410.5	–	–	
	20120225-6	7	142	1.58	1410.5	11.29	76.05	738.2	–	–	
8	20130913-7	1	132	1.58	800.1	17.22	17.22	799.6	–	–	$Q_j \neq$ const
	20130913-8	2	112	1.58	799.6	12.34	29.56	799.5	–	–	
	20130913-9	3	128	1.59	799.5	16.32	45.88	798.2	–	–	
	20130913-10	4	111	1.59	798.2	12.30	58.19	796.0	–	–	
	20130913-11	5	115	1.58	796.0	13.09	71.27	681.1	–	–	
	20130913-12	6	84	1.57	681.1	8.12	79.40	679.3	–	–	
	20130913-13	7	148	1.58	679.3	25.33	104.72	588.7	–	0.57 (2.83 × 10^{-2})	
	20130913-14	8	126	1.56	588.7	20.93	125.65	182.9	–	0.66 (1.85 × 10^{-2})	
10	20120223-1	1	143	1.61	2689.0	6.12	6.12	2689.0	–	–	$Q_j \sim$ const
	20120223-2	2	123	1.58	2688.1	4.45	10.57	2686.8	–	–	
	20120223-3	3	140	1.62	2686.8	5.91	16.48	2684.8	–	–	
	20120223-4	4	124	1.59	2682.2	4.56	21.03	2681.1	–	–	
	20120223-5	5	143	1.57	2679.2	5.99	27.03	2676.5	–	–	
	20120223-6	6	140	1.58	2676.3	5.79	32.81	2672.3	–	–	
	20120223-7	7	145	1.65	2671.3	6.49	39.30	2669.5	–	–	
	20120224-1	8	103	1.57	2637.4	3.16	42.46	2636.5	–	–	
	20120224-2	9	149	1.61	2635.1	6.78	49.24	2632.9	–	–	
	20120224-3	10	144	1.60	2632.9	6.30	55.55	977.5	–	–	

Number of impacts: The total numbers of projectiles impacted on the same target.
Run number: Asterisk (*) indicates the results shown in Figs. 2, 4 and 5.
Shot number: The jth impact for a series of impact experiments on the same target.
V_i: Impact velocity.
m_p: Projectile mass.
M_{t0} or M_{t_j}: M_{t0} is the initial target mass, and M_{t_j} is the target mass before the jth impact (j = 2–10).
Q_j: Energy density at the jth impact.
ΣQ: Total energy density, which is the sum of each energy density applied to the same target obtained from first to jth shots.
m_l: Largest impact fragment mass at the jth impact.
V_{e-g}: The fragment velocities at two corners on the impact surface. The "left" is the velocity at the left corner of the target, and the "right" is the velocity at the right corner. The numbers in parentheses indicate the error.
Q_j series: The classification of energy density obtained at each shot on the same target for a series of impact experiments. It is described in detail in the beginning of Section 3.

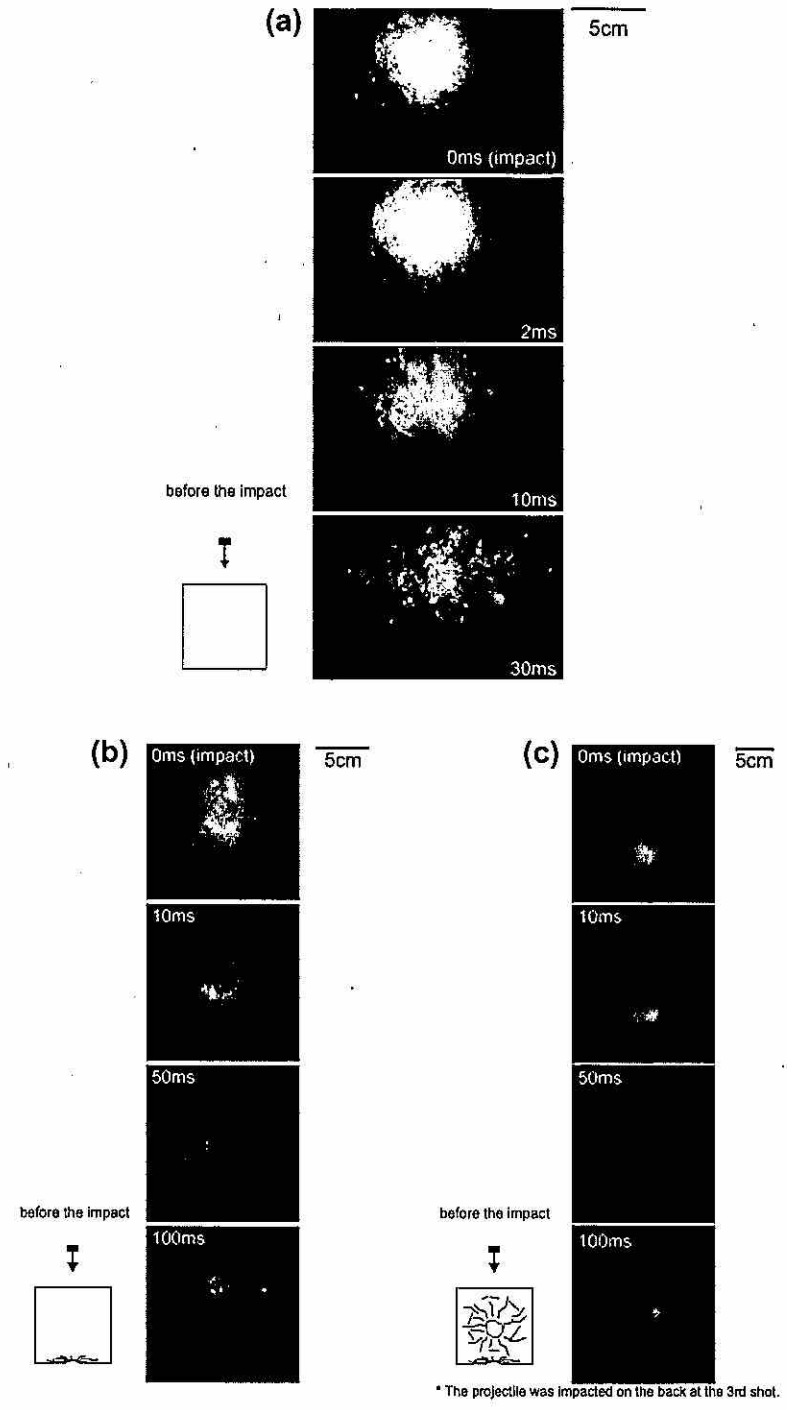

Fig. 2. Snapshots taken by the high-speed digital video camera. The number in each shot represents the elapsed time after the impact in ms. An elapsed time of 0 ms means the moment of impact. The scale is shown in each panel. The run numbers and the number of impacts were (a) 20110930-6, a single impact, (b) 20130912-10, a double impact, and (c) 20110708-5, a four-times impact. All panels show the Q_f series of $Q_f \sim$ const, and they used the same total energy density ΣQ of approx. 100 J kg^{-1}. The schematic illustration on each panel at the bottom left shows the appearance of the projectile and target before the impact. The frame rates were 4000 fps in panel (a) and 5000 fps in panels (b) and (c).

and these cracks might be activated to grow slightly and connect to each other to form new fragments on the final shots. As shown in Fig. 2b and c, several large fragments at these corners were detached and had fallen over on the base of the recovery box from the initial positions shown in the bottom images of Fig. 2b and c. Thus, we observed that these fragments were ejected slowly compared to those of the single-impact experiments shown in Fig. 2a.

3.2. Fragment velocities

We measured the fragment velocities at two corners on the impact surface because these fragment velocities could be recognized as a representative of high-velocity fragments generated in a moderate disruption (Housen, 2009; Yasui and Arakawa, 2011). Fig. 3 shows the relationship between the V_{e-g} and the energy density

at each shot, Q_j, where V_{e-g} is the fragment velocity ejected from two corners on the impact surface in the center of the mass system. The velocity of the center of the mass system, V_g, is calculated by $V_g = m_p V_i/(m_p + M_{t\_j}$ or $m_p + M_{t0})$. The detailed method to derive V_{e-g} is described in Yasui and Arakawa (2011).

We were able to measure two values of V_{e-g} on one target, so the average value for each target is plotted in Fig. 3, and the error bar indicates the range of the two V_{e-g} values at the left and right corners. We could measure the V_{e-g} at only one corner for some targets because of the haze covering the optical window. The V_{e-g} increased with the increase of energy density Q_j, irrespective of the number of impacts and the impact history for each target. All of the data can be fitted by one empirical equation as follows:

$$V_{e-g} = 10^{-1.53\pm0.18} \cdot Q_j^{1.03\pm0.09}, \quad (1)$$

for ice-on-ice impacts at the impact velocity V_i smaller than 500 m s^{-1} and the ratio of projectile to initial target, m_p/M_{t0}, from 1.3×10^{-3} to 2.7×10^{-3}.

3.3. Size distribution of recovered fragments

Fig. 4a–c are photographs of the recovered fragments from the different series of impact experiments with the same total energy density of 100 J kg^{-1}, but with different numbers of impacts: a single impact for Fig. 4a, a double impact for Fig. 4b, and a four-times impact for Fig. 4c. They are the same runs as those shown in Fig. 2. We found that the mass of the largest fragment in these figures was almost the same, irrespective of the number of impacts. On the other hand, the amount of fine fragments depended on the number of impacts: it was smaller for the multiple-impact experiments. Fig. 5 shows the size distribution of the recovered fragments in Fig. 4: the relationships between the cumulative number of fragments and the fragment mass normalized by the initial target mass, m_l/M_{t0}, are shown, so that the largest fragment mass corresponds to that at the cumulative number of unity. We were able to recover the impact fragments of >95% of the initial target for all shots. These distributions are almost similar until the normalized fragment mass was greater than approx. 3.0×10^{-4}, but they are clearly different at the normalized fragment mass smaller than approx. 3.0×10^{-4}: the cumulative number of fine fragments is smaller for the multiple impacts even if the total energy density is the same.

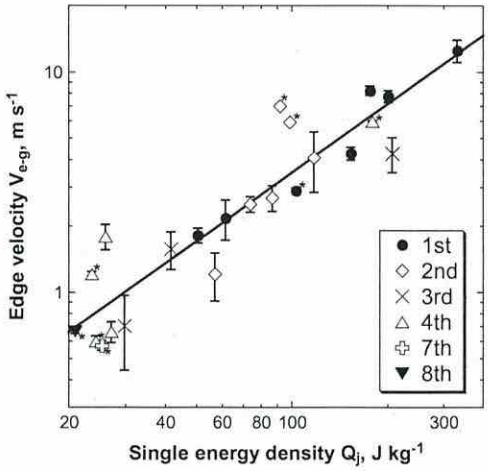

Fig. 3. The relationship between the fragment velocity at two corners on the impact surface in the center of the mass system, V_{e-g}, and the single energy density Q_j. The average values of the V_{e-g} measured at the left corner and at the right corner for each target are shown as a symbol. Error bar: the range of two V_{e-g} values. The solid line represents the fitting line determined using the power law function of Eq. (1). The asterisk * at the upper or lower right corners of the symbol means the V_{e-g} at only one side corner on the target because of a fuzzy image.

In the following sections we describe the characteristics of the largest fragment mass and the fine fragments separately, because the effects of total energy density ΣQ and the single energy density Q_j on the catastrophic disruption are thought to be different: the ΣQ is an important parameter to determine the largest fragment mass, and the Q_j is related to the amount of fine fragments. We therefore discuss the effects of ΣQ on these fragments in the conditions classified based on the Q_j as follows: $Q_j \sim$ const, $Q_f > Q^*_{ice}$, and $Q_j \neq$ const. It is well known that the largest fragment mass represents the degree of impact fragmentation, and it is usually used to determine the impact strength. Thus we first attempted to determine the impact strength of pre-impacted targets according to the largest fragment mass.

3.3.1. Impact condition for the onset of collisional fragmentation and impact strength

We showed in Fig. 5 that the largest fragment mass normalized by the initial target mass was almost the same when the total energy density, ΣQ, was close. We therefore studied the impact condition for the onset of collisional fragmentation, and we determine the impact strength of pre-impacted targets, which was usually derived from the relationship between the energy density and the largest fragment mass.

Fig. 6 shows the relationship between the ΣQ and the kinetic energy of the projectile for each shot. In this figure, the impact outcomes are divided into two groups: one group shows the normalized largest fragment mass larger than 0.95 and the other group shows that smaller than 0.95. The former group is classified as crater formation, and the latter group is classified as impact fragmentation. As shown in Fig. 6, the boundary between the area of crater formation and that of impact fragmentation was determined by a constant ΣQ value. This value was independent on the number of impacts and the series of impacts, although the boundary had a range of some width to show that both types appear at the ΣQ from 50.4 J kg^{-1} to 86.7 J kg^{-1}. It is very reasonable that the pre-impacted target was easily fractured by a small single energy density because of the pre-existing cracks inside the target given by the previous impacts. However, our results revealed an essential property of the pre-impacted target, that is, the onset of impact fragmentation for the pre-impacted target is always described by only one parameter of the constant total energy density, ΣQ_{onset}, irrespective of the impact history of each target. This means that a pre-impacted target that already received ΣQ_j by j-times impact will be disrupted by giving a single energy density Q_{j+1} at $j+1$ times impact, which is equal to $\Sigma Q_{onset} - \Sigma Q_j$. The ΣQ_{onset} corresponding to this boundary was found to be 68.6 ± 18.2 J kg^{-1}.

Fig. 7 shows the relationship between the single energy density Q_j and the largest fragment mass normalized by the initial target mass, m_l/M_{t0}, that is, when the same target was impacted at j times. The m_l/M_{t0} for each shot from the first to the jth shot was plotted in this figure. Each symbol indicates the turn of each impact. We found that the m_l/M_{t0} decreased with the increase of the number of impacts at the constant single energy density Q_j. Our single-impact (1st) data agreed well with those of the polycrystalline ice obtained in the single-impact experiments by Kato et al. (1995).

The impact strength Q^* is defined as the Q_j when the largest fragment mass is one-half of the original target mass, and thus we obtained the Q^* for each number of impacts from the single impact (1st) to the four-times impact (4th), respectively. We used the following equation to fit the data:

$$m_l/M_{t0} = 10^A \cdot Q_j^{-B}, \quad (2)$$

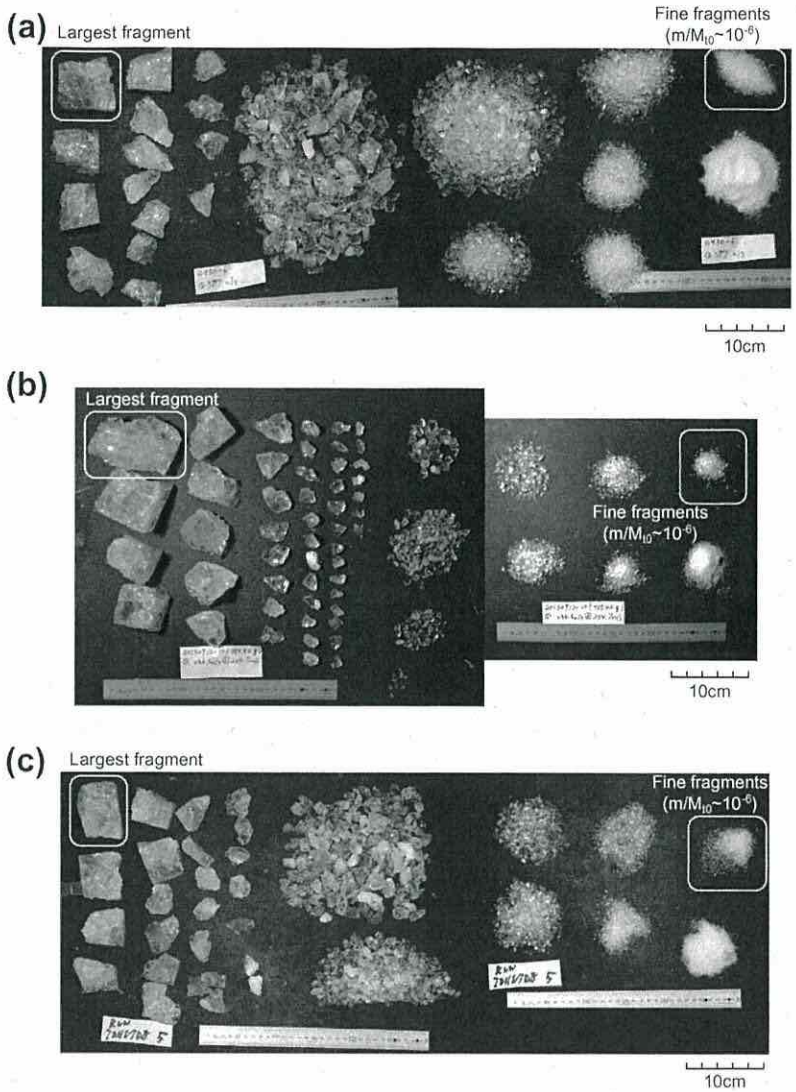

Fig. 4. Photographs of the recovered samples for the same targets as those shown in Fig. 2. (a) 20110930-6, a single impact, (b) 20130912-10, a double impact, and (c) 20110708-5, a four-times impact.

where A and p are constants, depending on the number of impacts. The parameters of A and p, and the impact strength Q^* for jth impacts (j = 1–4) are shown in Table 2, and the relationship between the number of impacts and the Q^* are shown in Fig. 8. The data for the three-times impact (3rd) and the four-times impact (4th) were not enough to obtain the constants of Eq. (2). Thus, we assumed that the p for the three-times impact (3rd) and the four-times impact (4th) was the same as that for the double impact (2nd).

From Table 2, it can be seen that the parameters of our data and those of Kato et al. (1995) for single impacts are almost consistent with each other in the error range. We found that the impact strength Q^* decreased with the number of impacts j, and the empirical equation fitted by a power law equation could be obtained as $Q^* = 10^{1.86\pm0.04} j^{-0.66\pm0.09}$. Then, we consider the relationship between the m_l/M_{t0} and the total energy density, ΣQ, in the next paragraph.

Fig. 9 shows the relationship between the ΣQ and the m_l/M_{t0} for each series of impact experiments. The data were slightly scattered but they were almost all well approximated by one line. These results agreed very well with the results of the single-impact experiments conducted by Kato et al. (1995). Thus, we can conclude that the m_l/M_{t0} was determined by the ΣQ, irrespective of the impact history for each target and the magnitude of each single energy density given to the same target. We can determine the empirical equation representing the relationship between the m_l/M_{t0} and the ΣQ for our results (not including the results of Kato et al. (1995)) at the m_l/M_{t0} smaller than 0.95 as follows:

$$\frac{m_l}{M_{t0}} = 10^{4.05\pm0.46} \cdot \Sigma Q^{-2.30\pm0.22}. \quad (3)$$

Compared with the A and the p of Eq. (2) for the results of Kato et al. (1995), it is clear that our results of Eq. (3) agree well with those of Kato et al. (1995) in the error range. Here, according to the definition of impact strength Q^* as mentioned above, we expanded the definition of the impact strength to the multiple impacts, ΣQ^*, which can be obtained from the relationship between m_l/M_{t0} and ΣQ for m_l/M_{t0} = 0.5. Then, the ΣQ^* is determined as 77.6 J kg^{-1}, irrespective of the number of impacts.

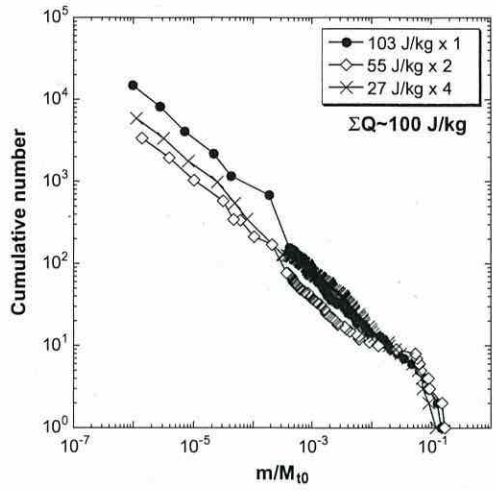

Fig. 5. Cumulative number of recovered impact fragments for the same targets as those shown in Fig. 4. The number in the J kg^{-1} before the "×" in the legend indicates the impact energy at each shot, and the number after the "×" in the legend indicates the number of impacts.

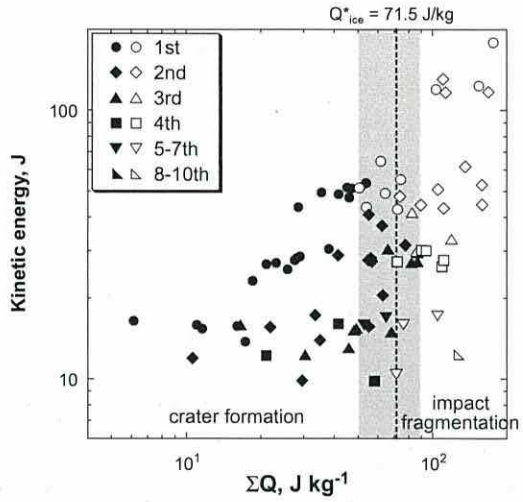

Fig. 6. The relationship between the kinetic energy of the projectile and the total energy density ΣQ with different number of impacts. The solid symbols show the largest impact fragment mass normalized by the initial target mass, m_l/M_{t0}, larger than 0.95 (crater formation), and the open symbols show those smaller than 0.95 (impact fragmentation). The dotted line shows the impact strength of polycrystalline ice for the single-impact experiments at the energy density smaller than 400 J kg^{-1} obtained by Kato et al. (1995). The gray zone shows the boundary area between the crater formation and the impact fragmentation.

From the results shown in Figs. 7 and 9, we found that the relationship between the normalized impact fragment mass m_l/M_{t0} and the single energy density Q_j depended on the number of impacts, whereas the relationship between m_l/M_{t0} and the total energy density ΣQ did not depend on the number of impacts. We speculate that the damage generated at every shot accumulates in the interior of the same target, which could explain our findings. However, further studies to clarify the elementary processes in pre-impacted targets are necessary to address this issue.

3.3.2. The size distributions of impact fragments

As explained in Section 3.3.1, the relationship between m_l/M_{t0} and ΣQ obtained by multiple impacts is similar to the relationship

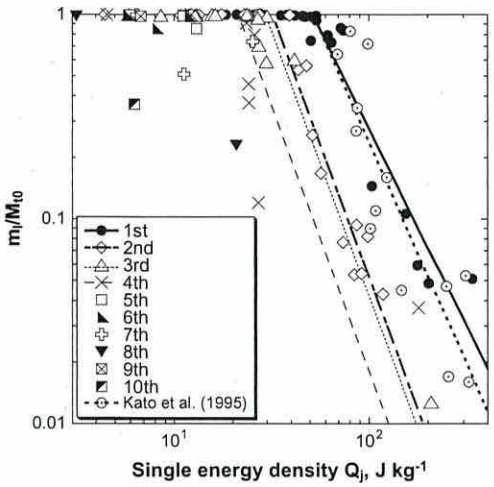

Fig. 7. The relationship between the largest fragment mass normalized by the initial target mass, m_l/M_{t0}, and the single energy density at the jth impact, Q_j.

Table 2
Parameters A and p of Eq. (2), and the impact strength Q^*.

	A [(J kg^{-1})^p]	p	Impact strength Q^* (J kg^{-1})
Number of impacts j (our study)			
1	3.34 (0.45)	1.95 (0.22)	74.0
2	3.93 (0.65)	2.60 (0.35)	42.1
3	3.83 (0.14)	2.60 (assumed)	38.7
4	3.46 (0.23)	2.60 (assumed)	28.0
Kato et al. (1995) (j = 1)	3.76 (0.79)	2.19 (0.37)	71.5

The numbers in parentheses indicate the error.

obtained by a single impact, irrespective of the number of impacts. However, the size distribution of impact fragments in a fine range is quite different with the number of impacts even if the ΣQ is almost the same, as shown in Fig. 5. We therefore examined how the cumulative number of fine impact fragments depends on Q_j or ΣQ. To study the amount of fine fragments, we compared the number of fine fragments at $m/M_{t0} \sim 10^{-6}$, n_m, which corresponds to the smallest fragment that we measured in this study. Fig. 10a and b shows the n_m as a function of total energy density ΣQ and single energy density Q_j, respectively. We chose these distributions for the m_l/M_{t0} smaller than 0.95, the group of impact fragmentation described in Section 3.3.1 and shown in Fig. 6. The data in Fig. 10a show that the n_m increases with the decrease of number of impacts. Notably, the n_m for the single impact was an order of magnitude larger than that for the seven-times impact and the ten-times impact at the same total energy densities, ~100 J kg^{-1} and ~55 J kg^{-1}. On the other hand, the n_m shown in Fig. 10b has a good correlation with Q_j, and it increased with the increase of Q_j even when the number of impacts was different. This means that the number of smallest fragments was determined by the single energy density Q_j rather than ΣQ. The relationship between n_m and Q_j could be fitted by a power law equation and is described by the following equation:

$$n_m = 10^{1.02\pm0.22} \cdot Q_j^{1.31\pm0.12}. \quad (4)$$

The cumulative number of impact fragments with the mass larger than m, N (>m), is described by the following equation (Takagi et al., 1984):

$$N(>m) = B \cdot (m/M_{t0})^{-q}, \quad (5)$$

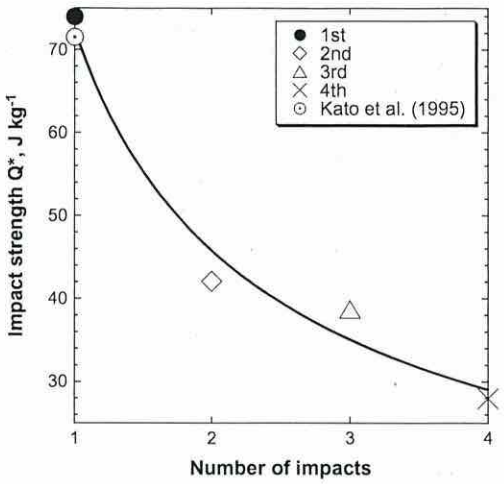

Fig. 8. The relationship between the impact strength, Q^*, and the number of impacts.

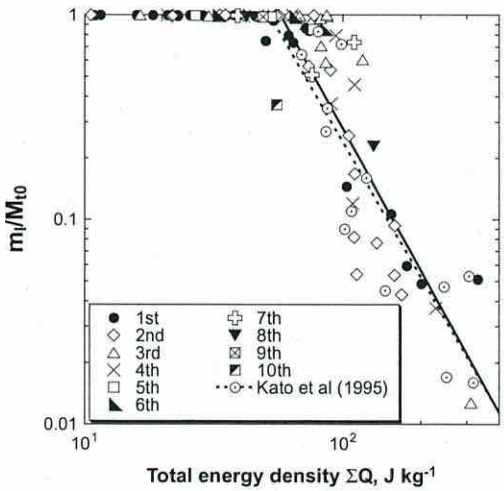

Fig. 9. The relationship between the largest fragment mass normalized by the initial target mass, m_l/M_{t0}, and the total energy density from the first to the jth impact, ΣQ. The open circles represent the results of polycrystalline ice in the single-impact experiments at the energy density smaller than 400 J kg^{-1} conducted by Kato et al. (1995). The solid line represents the fitting line determined using the power law function of Eq. (3) at the normalized largest fragment mass smaller than 0.95.

where B and q are constants. The size distribution written by the cumulative numbers of fragments are believed to be divisible into three regimes according to the size of impact fragments. Regime 1 covers the size range of fragment mass normalized by the target mass from 10^{-2} to 10^{-3}. Regime 3 covers that from 10^{-3} to 10^{-5}, and regime 2 is the intermediate regime (Takagi et al., 1984), and thus the constants B and q are expected to change in each regime. We examined the B and q for all regimes in the normalized fragment mass larger than 10^{-2} in regime 1, in that smaller than 10^{-4} in regime 3, and in that between 10^{-2} and 10^{-4} in regime 2.

The B for each regime is as follows: from 7.19×10^{-3} to 1.19 in regime 1, from 4.30×10^{-3} to 2.50 in regime 2, and from 7.24×10^{-3} to 28.81 in regime 3. In regime 1, the B increased with the decrease of the number of impacts at the constant single energy density Q_j. This means that the normalized largest fragment mass m_l/M_{t0} is larger as the number of impacts is smaller, and this

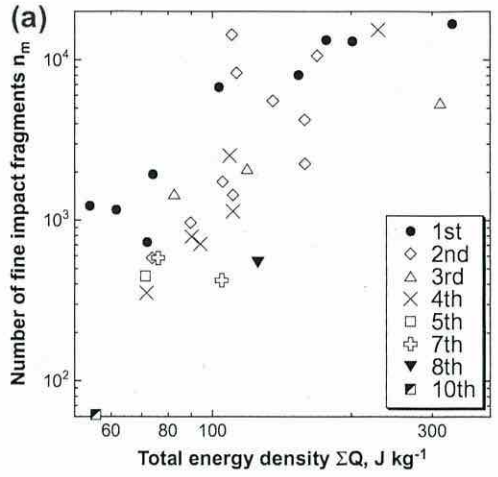

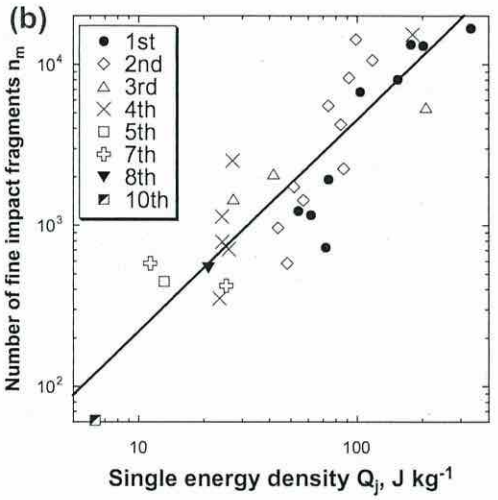

Fig. 10. The relationship between the number of fine impact fragments and (a) the total energy density, ΣQ, or (b) the single energy density, Q_j, respectively. The solid line in panel (b) represents the fitting line determined using the power law function of Eq. (4).

result is consistent with the results shown in Fig. 7. Similar results, in which B increased with the decrease of the number of impacts were observed in the other regimes.

The power law index q was 0.16–1.81 in regime 1 and 0.28–1.26 in regime 2. The q is independent on the number of impacts. In regime 2, the q increased with the decrease of the Q_j, whereas in regime 1 it was also independent on the Q_j within the error range. Several research groups have studied the q for regime 3 in impact experiments. Our q for regime 3 was found to be 0.66 ± 0.19. This value is close to that of polycrystalline cubic ices impacted by a nylon projectile with impact velocities from 2.3 to 4.7 km s^{-1} in single-impact experiments conducted by Arakawa (1999), 0.64 ± 0.06, whereas it is larger than that of rectangular parallelepiped ices impacted by a stainless steel ball with impact velocities up to 5 km s^{-1} in experiments performed by Miljkvic et al. (2011), 0.49 ± 0.05.

4. Discussion

We would like to estimate the cumulative damage in small icy satellites generated by past impacts using the crater size

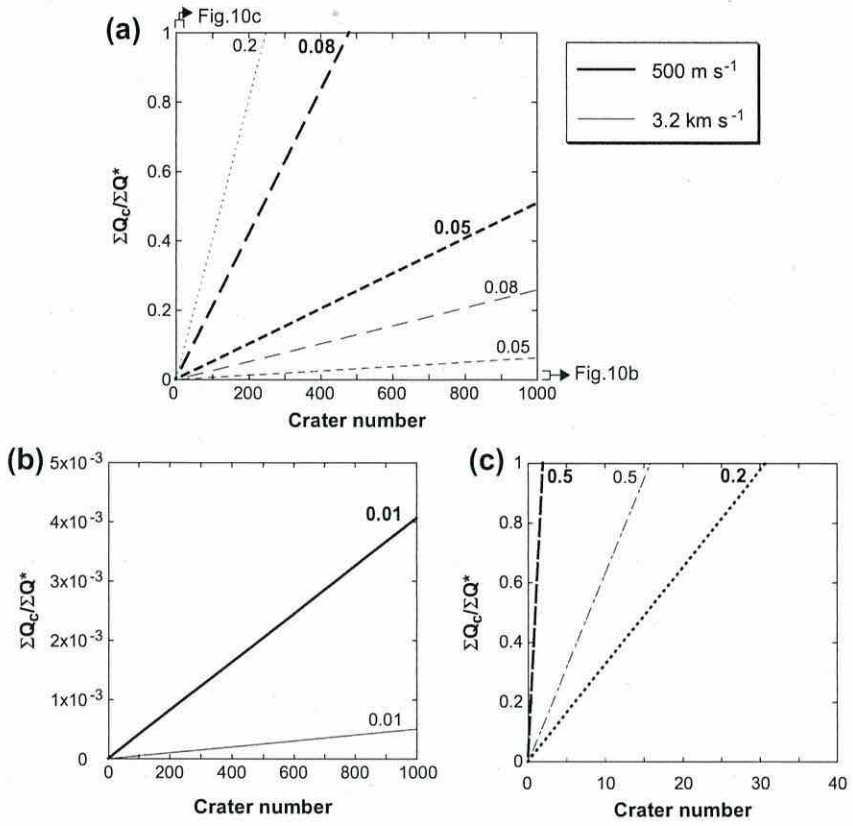

Fig. 11. The relationship between the cumulative damage of a theoretical icy body normalized by the impact strength of polycrystalline ice in the present multiple-impact experiments obtained in this study, $\Sigma Q_c/\Sigma Q^*$, and the crater number. Each line shows the difference of the ratio of the crater diameter to the target body diameter, D_{cr}/D_t, and the number near each line shows the value of D_{cr}/D_t. The thick line shows the results calculated at the impact speed of the impactor, 500 m s^{-1}, and the thin line shows that at 3.2 km s^{-1}. The enlarged part of the vertical axis ranging from 0 to 5×10^{-3} and the horizontal axis ranging from 0 to 40 are presented as panels (b) and (c), respectively.

distributions of actual small icy satellites, and here we discuss the degree of internal damage by comparing the estimated values with the impact strength. In this model, we calculate the energy density Q_c necessary for the formation of a crater having a certain diameter, and we estimate the total energy density ΣQ_c by accumulating the calculated energy densities Q_c from the crater sizes on these satellites. In order to estimate the individual Q_c corresponding to the crater, we must determine the impactor size and the impact velocity. In this discussion, we simply assume the crater formation mechanism in the strength regime because the small icy satellites have gravity that is rather weaker than that of the Earth, as weak as $<\sim 10^{-3}$ G. We then estimate the impactor size by using the cratering scaling law in the strength regime proposed by Housen et al. (1983).

The cratering scaling law used in this calculation is as follows:

$$\frac{R_{cr}}{r_p} = K\left(\frac{Y}{\rho_t V_i^2}\right)^{\alpha}, \tag{6}$$

where R_{cr} is the crater radius, r_p is the impactor radius, ρ_t is the density of the target body, V_i is the impact velocity, Y is the material strength, and K and α are the constants, depending on the material properties. The non-dimensional parameters of R_{cr}/r_p and $Y/\rho_t V_i^2$ can be expressed as π_R and π_Y, respectively, where we assume that the impactor and the target are the same materials in this model. We also assume the simple case that an impactor and a target body consist of polycrystalline ice without any inclusions, although it is well known that the mean densities of small icy satellites range from 300 to 2600 kg m^{-3}, and they are thought to be a mixture of ice that includes non-water ice such as CO_2, rocky materials, and pores. Therefore, we ignore the density ratio of an impactor to a target body in Eq. (6) of this model, so that we use the crater scaling law of Eq. (6) for ice–ice impacts obtained by Iijima et al. (1995), written as $\pi_R = 1.90\pi_Y^{0.52}$. We used the dynamical tensile strength of ice, 17 MPa, obtained by Stewart and Ahrens (1999), as the material strength, Y. We chose the impact velocities of V_i, 500 m s^{-1}, which corresponds to a probable collisional speed of the Kuiper belt objects estimated by the numerical simulation for collisions with minor bodies in the Kuiper belt by Dell'Oro et al. (2001), and 3.2 km s^{-1}, which corresponds to a typical collisional speed of present outer icy satellites such as Phoebe orbiting Saturn, estimated by using the numerical simulations of collisions of icy satellites with comets in the outer Solar System by Zahnle et al. (2003).

First, we calculate the Q_c of hypothetical icy satellites with craters with a single crater size. That is, the ΣQ_c is described as $\Sigma Q_c = -nQ_c$, where n is the crater number. In this calculation, the crater diameter normalized by the target diameter, D_{cr}/D_t, was changed from 0.01 to 0.5.

Fig. 11 shows the relationship between the crater number and the cumulative damage ΣQ_c normalized by the impact strength ΣQ^* obtained by this impact experiment, 77.6 J kg^{-1}, so that the unity of $\Sigma Q_c/\Sigma Q^*$ means that the target body would disrupt catastrophically. At the constant impact velocity, the cumulative damage ΣQ_c increases with the increase of the ratio of the crater diameter to the target body diameter. For example, in the case of $V_i = 500$ m s^{-1}, the ΣQ_c is almost zero at the diameter ratio of 0.01; that is, the target body is hardly damaged, whereas at the diameter ratio of 0.5, the ΣQ_c increases abruptly and then the

target body disrupts catastrophically after the two impacts of the small body.

At the constant diameter ratio, the ΣQ_c decreases with the increase of the impact velocity; the number of colliding small bodies necessary for the catastrophic disruption of the target body ($\Sigma Q_c/\Sigma Q^* = 1$) at $V_i = 3.2$ km s^{-1} is about eight times larger than that at $V_i = 500$ m s^{-1}. In the same manner, we were able to easily calculate the cumulative damage of actual small bodies by using their crater size distributions on the surface.

Lastly, we estimate the cumulative damage of a saturnian icy satellite, Phoebe, by using the method described above. The mean density, ρ_t, is 1630 kg m^{-3} (Porco et al., 2005). As the impact velocity, V_i, we chose to be 500 m s^{-1} and 3.2 km s^{-1}. We used the database of impact craters of Phoebe provided by the WGPSN (Working Group for Planetary System Nomenclature) at IAU for the crater diameters larger than 10 km, and we used the cumulative crater size distribution obtained by Kirchoff and Schenk (2009a,b) for the crater diameters smaller than 10 km.

The cumulative damage in the target body can be calculated by using Eq. (6), the scaling parameters obtained by Iijima et al. (1995), and the crater size distribution as follows:

$$\Sigma Q_c = \frac{(3.07 \times 10^{-1})\rho_p Y^{1.56}}{M_t \rho_t^{1.56} V_i^{1.12}} \Sigma(R_{cr}^3), \quad (7)$$

where ρ_p is the density of the impactor (in this case, $\rho_p = 917$ kg m^{-3}) and M_t is the mass of the target body (in this case, the mass of Phoebe). As a result, the cumulative damage for Phoebe is 22.1 J kg^{-1} or 6.72×10^{-2} J kg^{-1} at the impact velocity of 500 m s^{-1} or 3.2 km s^{-1}, respectively, by using only the data for the crater diameters >10 km. Even if we consider the data for the crater diameters <10 km, this damage is not changed much: 22.3 J kg^{-1} and 6.78×10^{-2} J kg^{-1}. Phoebe also has a crater with a diameter larger than 100 km, Jason crater. We found that the energy density necessary for the formation of this crater was one-third of the total energy density, ΣQ_c.

We know that the impact strength of polycrystalline ice for multiple impacts ΣQ^* is 77.6 J kg^{-1}, irrespective of the number of impacts, so we can say that the cumulative damage in Phoebe is as large as approx. 30% of the intact body if the impact speed of the impactor is 500 m s^{-1}. On the other hand, the cumulative damage is almost zero if the impact speed of the impactor is 3.2 km s^{-1}. Thus, we notice that the cumulative damage is significantly dependent on the impact speed of the impactor. However, the generated fractures in the target body have been sintered after the formation of these craters by the impact, although the sintering duration might be very long to heal these fractures.

From these results, we speculate that the interior of Phoebe is as follows. In the case of the impacts at 3.2 km s^{-1}, the impact energy necessary to form each crater on Phoebe is much smaller than the ΣQ^*, and thus we suspect that the impactors excavated just under the impact surface, and the re-accumulated ejecta layer, the so-called "regolith layer", was formed on the surface of Phoebe. On the other hand, in the case of impacts at 500 m s^{-1}, the energy necessary to form some larger craters is larger (>1 J kg^{-1}) than that at 3.2 km s^{-1}, and thus some large cracks might exist under these craters. However, the energies necessary to form other craters are not so large, and thus the regolith was also formed on the surface, as in the case of the impacts at 3.2 km s^{-1}.

It has been speculated that the crater formation occurs in the gravity regime on middle-to-large icy satellites, at the radius of a few tens of km, depending on the model (e.g., Benz and Asphang, 1999; Stewart and Leinhardt, 2009). Thus, we calculated the ΣQ_c of Phoebe based on the scaling law of the gravity regime. However, there are no experimental data for ice–ice impacts in the gravity regime, so we used the cratering scaling law of dry sand in the gravity regime summarized in Housen and Holsapple (2011). As a result, the ΣQ_c is more than 2500 J kg^{-1} at both impactor speeds, and thus the catastrophic disruption should occur, and this is not realistic. It is advisable to revise the crater scaling laws in the gravity regime suitable for Phoebe. We plan to study the crater scaling law in the gravity regime for porous ice–silicate mixtures (which are applicable to Phoebe) in the future.

5. Summary

We conducted multiple-impact experiments for polycrystalline ice targets at impact velocities from 84 to 502 m s^{-1} and using the number of impacts from 1 to 10 times, and we studied the effects of multiple impacts on the impact strength, the size distribution of impact fragments, and the ejecta velocity. Our results are summarized as follows:

1. The fragment velocities at two corners on the impact surface in the center of the mass system, V_{e-g}, had a good correlation with the single energy density Q_j, and they increased with the increase of Q_j irrespective of the number of impacts for each target. The relationship between the V_{e-g} and the Q_j was obtained as $V_{e-g} = 10^{-1.53\pm0.18} \cdot Q_j^{1.03\pm0.09}$.
2. The onset of impact fragmentation and the largest fragment mass could be described by the total energy density, ΣQ. The onset of impact fragmentation for the pre-impacted ice, ΣQ_{onset}, was 68.6 ± 18.2 J kg^{-1}. The impact strength ΣQ^*, which was defined as the ΣQ when the m_l/M_{t0} was one-half of the initial target mass, was 77.6 J kg^{-1}, which is very close to be the impact strength of polycrystalline ice in single-impact experiments conducted by Kato et al. (1995).
3. The number of fine fragments at $m/M_{t0} \sim 10^{-6}$, n_m, was well correlated with the single energy density Q_j, and the relationship was written as $n_m = 10^{1.02\pm0.22} \cdot Q_j^{1.31\pm0.12}$. The cumulative number of impact fragments N ($>m$) was described as $N(>m) = B \cdot (m/M_{t0})^{-q}$, and the power law index q, in the normalized fragment mass smaller than 10^{-4}, was obtained as 0.66 ± 0.19. This value is close to that of polycrystalline ice in the single-impact experiments performed by Arakawa (1999).
4. We estimated the internal cumulative damage of small icy satellites caused by past impacts according to the crater scaling law proposed by Housen et al. (1983) and the cumulative size distributions of impact craters on these satellites. In the case of hypothetical icy bodies with constant-size craters on these surfaces, the cumulative damage ΣQ_c increases with the increase of the ratio of the crater diameter to the target body diameter and decreased with the increase of the impact velocity of the impactor. We estimated the ΣQ_c for the saturnian satellite Phoebe by using the database of impact craters provided by WGPSN at IAU and the cumulative crater size distribution obtained by Kirchoff and Schenk (2009a,b), and we observed the ΣQ_c of 22.3 J kg^{-1} at the impact velocity 500 m s^{-1}, which was about one-third of the impact strength ΣQ^*, and 6.78×10^{-2} J kg^{-1} at impact velocity 3.2 km s^{-1}, which was close to zero, so that the damage was hardly accumulated in the interior of the target body.

Acknowledgments

We thank Mr. S. Nakatsubo of the Contribution Division of the Institute of Low Temperature Science, Hokkaido University, for his technical help. We also appreciate the help with the experiments provided by Dr. Yuri Shimaki of the Institute for the Study of the Earth's Interior, Okayama University. This work was

supported in part by Grants-in-Aid for Scientific Research (22244056, 23103004, and 25870419) from the Japan Ministry of Education, Culture, Sports, Science and Technology, and by a grant for a Joint Research Program from the Institute of Low Temperature Science, Hokkaido University.

Appendix A. Supplementary material

Supplementary data associated with this article can be found, in the online version, at http://dx.doi.org/10.1016/j.icarus.2014.02.008.

References

Arakawa, M., 1999. Collisional disruption of ice by high-velocity impact. Icarus 142, 34–45.
Arakawa, M., Tomizuka, D., 2004. Ice–silicate fractionation among icy bodies due to the difference of impact strength between ice and ice–silicate mixture. Icarus 170, 193–201.
Arakawa, M., Leliwa-Kopystynski, J., Maeno, N., 2002. Impact experiments on porous icy-silicate cylindrical blocks and the implication for disruption and accumulation of small icy bodies. Icarus 158, 516–531.
Benz, W., Asphang, E., 1999. Catastrophic disruption revisited. Icarus 142, 5–20.
Benz, W., Asphaug, E., 1993. Impact simulations with fracture. I. Method and tests. Icarus 107, 98–116.
Britt, D.T., Yeoman, D., Housen, K., Consolmagno, G., 2002. Asteroid density, porosity, and structure. In: Bottke, W.F., Cellino, A., Paolicchi, P., Binzel, R. (Eds.), Asteroids III. Univ. Arizona Press, Tucson, AZ, pp. 485–500.
Consolmagno, G.J., Britt, D.T., 1998. The density and porosity of meteorites from the Vatican collection. Meteorit. Planet. Sci. 33, 1231–1240.
Davis, D.R., Ryan, E.V., 1990. On collisional disruption: Experimental results and scaling law. Icarus 83, 156–182.
Dell'Oro, A., Marzari, F., Paolicchi, P., Vanzani, V., 2001. Updated collisional probabilities of minor body populations. Astron. Astrophys. 366, 1053–1060.
Fujiwara, A., Tsukamoto, A., 1980. Experimental study on the velocity of fragments in collisional breakup. Icarus 44, 142–153.
Fujiwara, A., Kamimoto, G., Tsukamoto, A., 1977. Destruction of basaltic bodies by high-velocity impact. Icarus 31, 277–288.
Gault, D.E., Wedekind, J.A., 1969. The destruction of tektites by micrometeoroid impact. J. Geophys. Res. 74, 6780–6794.
Housen, K., 2009. Cumulative damage in strength-dominated collisions of rocky asteroids: Rubble piles and brick piles. Planet. Space Sci. 57, 142–153.
Housen, K., Holsapple, K.A., 2011. Ejecta from impact craters. Icarus 211, 856–875.
Housen, K.R., Schmidt, R.M., Holsapple, K.A., 1983. Crater ejecta scaling laws: Fundamental forms based on dimensional analysis. J. Geophys. Res. 88, 2485–2499.
Iijima, Y., Kato, M., Arakawa, M., Maeno, N., Fujiwara, A., Mizutani, H., 1995. Cratering experiments on ice: Dependence of crater formation on projectile materials and scaling parameter. Geophys. Res. Lett. 22, 2005–2008.
Kato, M. et al., 1992. Impact experiments on low temperature H_2O ice. In: Maeno, N., Hondoh, T. (Eds.), Physics and Chemistry of Ice. Hokkaido Univ. Press, Japan, pp. 237–244.
Kato, M., Iijima, Y., Arakawa, M., Okimura, Y., Fujiwara, A., Maeno, N., Mizutani, H., 1995. Ice-on-ice impact experiments. Icarus 113, 423–441.
Kawakami, S., Mizutani, H., Takagi, Y., Kato, M., Kumazawa, M., 1983. Impact experiments on ice. J. Geophys. Res. 88, 5806–5814.
Kirchoff, M.R., Schenk, P., 2009a. Crater modification and geologic activity in Enceladus' heavily cratered plains: Evidence from the impact crater distribution. Icarus 202, 656–668.
Kirchoff, M.R., Schenk, P., 2009b. Impact cratering records of the mid-sized, icy saturnian satellites. Icarus 206, 485–497.
Michel, P., Benz, W., Richardson, D.C., 2003. Disruption of fragmented parent bodies as the origin of asteroid families. Nature 421, 608–611.
Miljkvic, K., Mason, N.J., Zarnecki, J.C., 2011. Ejecta fragmentation in impacts into gypsum and water ice. Icarus 214, 739–747.
Nakamura, A.M., Fujiwara, A., Kadono, T., Shirono, S., 1994. Fragmentation of intact and pre-impacted basalt target. In: Kozai, Y., Binzel, R.P., Hirayama T. (Eds.), Seventy-Five Years of Hirayama Asteroid Families, ASP Conference Series 63, pp. 237–242.
Porco, C.C. et al., 2005. Cassini imaging science: Initial results on Phoebe and Iapetus. Science 307, 1237–1242.
Porco, C.C., Thomas, P.C., Weiss, J.W., Richardson, D.C., 2007. Saturn's small inner satellites: Clues to their origins. Science 318, 1602–1607.
Shimaki, Y., Arakawa, M., 2012. Experimental study on collisional disruption of highly porous icy bodies. Icarus 218, 737–750.
Stewart, S.T., Ahrens, T.J., 1999. Correction to the dynamic tensile strength of ice and ice–silicate mixtures (Lange -&- Ahrens 1983). Lunar Planet. Sci. 30, 2037.
Stewart, S.T., Leinhardt, Z.M., 2009. Velocity-dependent catastrophic disruption criteria for planetesimals. Astrophys. J. 691, L133–L137.
Takagi, Y., Mizutani, H., Kawakami, S., 1984. Impact fragmentation experiments of basalts and pyrophyllites. Icarus 59, 462–477.
Veverka, J. et al., 2000. NEAR at Eros: Imaging and spectral results. Science 289, 2088–2097.
Yasui, M., Arakawa, M., 2011. Impact experiments of porous gypsum-glass bead mixtures simulating parent bodies of ordinary chondrites: Implications for re-accumulation processes related to rubble-pile formation. Icarus 214, 754–765.
Yasui, M., Arakawa, M., Hasegawa, S., Fujita, Y., Kadono, T., 2012. In situ flash X-ray observation of projectile penetration processes and crater cavity growth in porous gypsum target analogous to low-density asteroids. Icarus 221, 646–657.
Zahnle, K., Schenk, P., Levison, H., Dones, L., 2003. Cratering rates in the outer Solar System. Icarus 163, 263–289.

The Astrophysical Journal Letters, 783:L36 (4pp), 2014 March 10 doi:10.1088/2041-8205/783/2/L36

AN EXAMINATION OF COLLISIONAL GROWTH OF SILICATE DUST IN PROTOPLANETARY DISKS

Tetsuo Yamamoto[1], Toshihiko Kadono[2], and Koji Wada[3]
[1] Center for Planetary Science, Integrated Research Center of Kobe University, Minatojima, Chuo-ku, Kobe 650-0047, Japan; ty@cps-jp.org
[2] School of Medicine, University of Occupational and Environmental Health, Yahatanishi-ku, Kitakyushu, Fukuoka 807-8555, Japan
[3] Planetary Exploration Research Center, Chiba Institute of Technology, Tsudanuma 2-17-1, Chiba 275-0016, Japan
Received 2014 January 1; accepted 2014 February 12; published 2014 February 26

ABSTRACT

N-body simulations of collisions of dust aggregates in protoplanetary disks performed so far have revealed that silicate aggregates suffer from catastrophic disruption if the collision velocities are higher than about $10\,\mathrm{m\,s^{-1}}$, which is much lower than those expected in the disks. This is mainly due to the low surface energy of the quartz used in the simulations. We find a simple relation between the surface energy and melting temperature for various materials including those of astrophysical interest, and show that the surface energy of the quartz used in the previous simulations is much lower than the present estimate. This result may provide a way out of the difficulty of growing silicate dust inside the snowline in disks. We show that silicate dust can evade catastrophic disruption and grow even at high-velocity collisions expected in the disks if one takes the present estimate of the surface energy into account.

Key words: dust, extinction – planets and satellites: formation – protoplanetary disks

1. INTRODUCTION

One of the key processes in the formation of planetary systems is the growth of dust into planetesimals. A pioneering work by Dominik & Tielens (1997) considered dust as aggregates composed of small ($0.1\,\mu$m) monomers and formulated monomer interaction based on the Johnson–Kendall–Roberts (JKR) theory (Johnson et al. 1971; Johnson 1987), which deals with monomer displacements in the elastic regime (see also Derjaguin et al. 1975). They performed numerical simulations and proposed conditions for various outcomes of aggregate collisions, although their simulations were limited to two-dimensional aggregates of one kind of structure composed of 40 monomers. After that, intensive *N*-body simulations of collisions of large three-dimensional aggregates have been carried out covering wide ranges of conditions with varying mass ratios of aggregates and impact parameters to reveal the dependence of the outcomes of the collisions on the collision velocity (Wada et al. 2007, 2008; Suyama et al. 2008; Paszun & Dominik 2009; Wada et al. 2009, 2011, 2013; Seizinger & Kley 2013). Recent simulations introduce energy dissipation through viscoelasticity in addition to the elastic treatment (Seizinger et al. 2013).

N-body simulations revealed that silicate aggregates represented by quartz suffer from catastrophic disruption if the collision velocities are higher than $8\,\mathrm{m\,s^{-1}}$, which is much lower than those expected in the disks. The viscoelastic theory is one of the approaches to resolve the difficulty in the silicate growth. If the displacements of the monomers at the collisions are beyond the elastic limit, one must take into account viscoelasticity and other energy dissipative processes; these will be important in high velocity collisions. Another approach is an examination of the parameter values, in particular the surface energies, used in the simulations based on the JKR theory. We must emphasize that both approaches are never the opposed ones; energy dissipation must in any case be taken into account in a future comprehensive theory of collisions. The present Letter limits itself to the displacements in the elastic regime and examines the values of the surface energies. This will also be helpful to provide the viscoelastic theories with sound grounds.

Summarizing their simulations, Wada et al. (2013) postulated a criterion for the net growth of the dust of a BPCA structure (ballistic particle–cluster aggregation), which is a probable structure caused by collisional compression (Wada et al. 2008; Suyama et al. 2008) or by static compression by the disk gas (Kataoka et al. 2013a, 2013b), to be

$$v_{\mathrm{cr}} = k\sqrt{E_{\mathrm{br}}/m} \tag{1}$$

averaged over the impact parameters, where m is the monomer mass and k is a numerical factor. Its values are $k \simeq 20$ for collisions of different-sized aggregates and $k \simeq 15$ for those of equal-sized ones. We use $k = 20$ hereafter because collisions of the former type is more ubiquitous. E_{br} is the energy needed to separate a pair of monomers in contact from the equilibrium position and is given (Wada et al. 2013) by

$$E_{\mathrm{br}} \simeq 23[\gamma^5 r^4(1-\nu^2)^2/\mathcal{E}^2]^{1/3} \tag{2}$$

for a pair of identical monomers of mass m, radius r, Young's modulus $\mathcal{E}$, and Poisson's ratio ν. We set $m = 4\pi\rho r^3/3$, where ρ is the density of the monomer material.

The simulations done so far adopt SiO_2 (quartz, Qz) as representative of silicates and H_2O ice as a typical volatile; for both of them γ and $\mathcal{E}$ data are available. The results of the simulations showed that aggregates composed of H_2O ice can grow by collisions with velocities comparable to turbulent velocities $80\,\mathrm{m\,s^{-1}}$ expected in protoplanetary disks (Cuzzi et al. 2001; Dominik et al. 2007), whereas Qz aggregates suffer from catastrophic disruption if their collision velocities are higher than $8\,\mathrm{m\,s^{-1}}$ (e.g., Wada et al. 2013), which is much lower than the collision velocities expected in models of the disks at various evolutionary stages (Adachi et al. 1976; Kusaka et al. 1970; Weidenschilling & Cuzzi 1993; Chiang & Golreich 1997; Chiang et al. 2001; Cuzzi et al. 2001; Tanaka et al. 2005; Dominik et al. 2007; Blum & Wurm 2008; Suyama et al. 2008). Okuzumi et al. (2012) considered the porosity

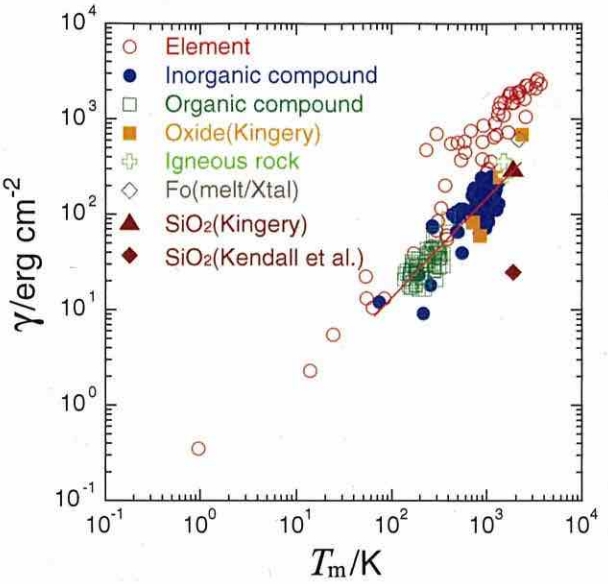

Figure 1. Correlation between surface energy γ and melting temperature T_m. The red line indicates the fitting formula given by Equation (3).

evolution of icy aggregates outside the snow line and showed that icy planetesimals can form via direct collisional growth of icy aggregates overcoming the rapid orbital drift (see also Kataoka et al. 2013b). However, the problem of growth of silicate aggregates, a major dust component inside the snowline, still remains open.

Many of the simulations are based on the JKR theory, in which the surface energy γ and Young's modulus $\mathcal{E}$ of the monomers composing the aggregates are the key physical quantities, i.e., the adhesion of two monomers is expressed by γ and the hardness by $\mathcal{E}$. Therefore, to evaluate Equation (2) and to apply the results to dust growth in the disks, we must know the γ and $\mathcal{E}$ of materials of astrophysical interest. In general, however, it is rather difficult to obtain these values, in particular, the surface energies of materials of astrophysical interest. In this Letter, we propose a new method of evaluating surface energies of a variety of materials and show a way to resolve the problem of silicate growth in protoplanetary disks.

2. A METHOD OF ESTIMATING SURFACE ENERGY AND NEW CRITICAL VELOCITY

We note that both surface energy and melting temperature are relevant to the energy needed for the rearrangement of atoms in a condensed matter. Namely, the surface energy is the energy needed to move atoms to the surface layer from the layer below it to fill the vacancy created in the surface layer by its extension. The melting temperature is relevant to the energy needed to move atoms vibrating near their lattice points in a solid to the places far from those points. Figure 1 plots the surface energies γ of melts (liquids) versus the melting temperatures T_m for about 200 materials of various kinds, including elements (Weast 1983), inorganic and organic compounds (Janz 1979, 1980, 1983; Weast 1983), oxides (Kingery 1959; Weast 1983), and igneous rocks (Murase & McBirney 1973). The red circles in the region $\gamma \gtrsim 10^3\,\mathrm{erg\,cm^{-2}}$ are those for metals. The points in the region $\gamma \lesssim 200\,\mathrm{erg\,cm^{-2}}$ are those for materials of astrophysical ice candidates; the blue filled circle in the region around $\gamma \simeq 200\,\mathrm{erg\,cm^{-2}}$ is the plot for CO_2, and the red circles in $\gamma \lesssim 100\,\mathrm{erg\,cm^{-2}}$ include other volatile materials such as nitrogen and oxygen (the one plotted at the lowest γ and T_m is for liquid helium).

Figure 1 indicates that γ is nearly proportional to T_m for a wide range of T_m. Elements of high T_m (red circles in the top-right region) and compounds have different absolute values of γ but both γ are nearly proportional to T_m. We fit the γ of inorganic and organic compounds, oxides, and igneous rocks to a power law of T_m and obtain an empirical relation expressed by

$$\gamma = (0.1244 \pm 0.0278)\, T_m^{1.015\pm0.037}, \quad (3)$$

where γ is in units of $\mathrm{erg\,cm^{-2}}$ and T_m is in kelvin. The fitting line given by Equation (3) is shown by a red line in Figure 1.

There are few appropriate measurements or calculations of γ for silicates such as forsterite (Fo) and enstatite (En) to our knowledge, but, if the relation (3) holds in the range of melting temperatures of silicates, we can estimate their γ once T_m is known. For example, the γ of Fo is estimated to be $305 \pm 155\,\mathrm{erg\,cm^{-2}}$ for $T_m = 2183$ K (Poirier 1991) from Equation (3). For comparison, Nakajima (1994) estimated $\gamma = 520\,\mathrm{erg\,cm^{-2}}$ for Fo by applying an empirical interpolation formula used in metallurgy to a mixture of 2MgO + SiO_2 (corresponding to Mg_2SiO_4). Tanaka et al. (2008) derived $\gamma = 610\,\mathrm{erg\,cm^{-2}}$ (green diamond in Figure 1) for the melt–crystalline interfacial energy from an analysis of the experiment of crystallization of melt droplets of forsterite composition under levitation. Our estimate agrees with these values within a factor <2. On the other hand, theoretical calculations of the γ of crystalline Fo yielded $\gamma = (2\text{–}3) \times 10^3\,\mathrm{erg\,cm^{-2}}$ depending on the crystalline surfaces (de Leeuw et al. 2000). This high value implies that solids have higher surface energies than melts in general as is inferred from the origin of the surface energy. For En, we obtain $\gamma = 255 \pm 128\,\mathrm{erg\,cm^{-2}}$ for $T_m = 1834$ K (Richet & Bottinga 1986) from Equation (3), whereas Nakajima's interpolation yielded $\gamma = 430\,\mathrm{erg\,cm^{-2}}$.

The critical velocity v_{cr} given by Equation (1) is plotted in Figure 2 as a function of surface energy γ for Young's modulus in the range of $1 < \mathcal{E} < 10^3$ GPa. Also plotted are the v_{cr} for possible dust materials present in protoplanetary disks. We set $\nu = 0$ for simplicity because the critical velocity v_{cr} is insensitive to ν. The material data used are summarized in Table 1. The γ values of MgO, Fo, and En are estimated from Equation (3), and those of Qz, corundum, iron, and H_2O are the results of direct measurements of these melts. Figure 2 indicates that the v_{cr} of the materials including silicates are around several tens of $\mathrm{m\,s^{-1}}$. It is interesting to note that v_{cr} does not much depend on the dust materials in view of the uncertainties in γ as seen in Figure 1. The critical velocities v_{cr} are 30–40 $\mathrm{m\,s^{-1}}$ for silicate aggregates ($36 \pm 15\,\mathrm{m\,s^{-1}}$ for Fo and $32 \pm 13\,\mathrm{m\,s^{-1}}$ for En), and $v_{cr} = 55\,\mathrm{m\,s^{-1}}$ for Qz. These velocities are comparable to the collision velocities expected in protoplanetary disks (see Wada et al. (2013) and references therein), although the v_{cr} values for Fo and En have large uncertainties stemming from those in their surface energies.

3. CONCLUSION AND DISCUSSION

The results obtained above indicate that aggregates composed of silicates (Fo, En) and quartz (Qz) may elude catastrophic disruption and can grow as H_2O ice even at high-velocity collisions expected in protoplanetary disks. Iron aggregates can grow even at collisions with velocity $\sim 100\,\mathrm{m\,s^{-1}}$. It should

Table 1
Surface Energy γ, Young's Modulus $\mathcal{E}$, Density ρ, and the Critical Velocity v_{cr} for Aggregates Composed of Monomers of Radius 0.1 μm

Material	γ (erg cm^{-2})	$\mathcal{E}$[a] (erg cm^{-3})	ρ (g cm^{-3})	v_{cr} (m s^{-1})	Reference
Forsterite (Mg_2SiO_4)	305[b]	2.0×10^{12}	3.2	36	1
Enstatite ($MgSiO_3$)	255[b]	1.8×10^{12}	3.2	32	1, 2
Quartz (SiO_2)	307	0.72×10^{12}	2.7	55	3, 4
MgO	439[b]	3.1×10^{12}	3.6	40	1
Corundum (Al_2O_3)	690	4.0×10^{12}	4.0	50	1, 4
Iron (Fe)	1880	2.1×10^{12}	7.9	102	1, 3
H_2O	73	0.94×10^{11}	0.92	56	3, 5

Notes.
[a] In the case where Young's modulus $\mathcal{E}$ is not available but bulk modulus K and shear modulus μ are available, $\mathcal{E}$ is calculated from $1/\mathcal{E} = (1/3)(1/3K + 1/\mu)$.
[b] Estimated from Equation (3).
References. (1) Poirier 1991; (2) Richet & Bottinga 1986; (3) Weast 1983; (4) Kingery 1959; (5) Fletcher 1970.

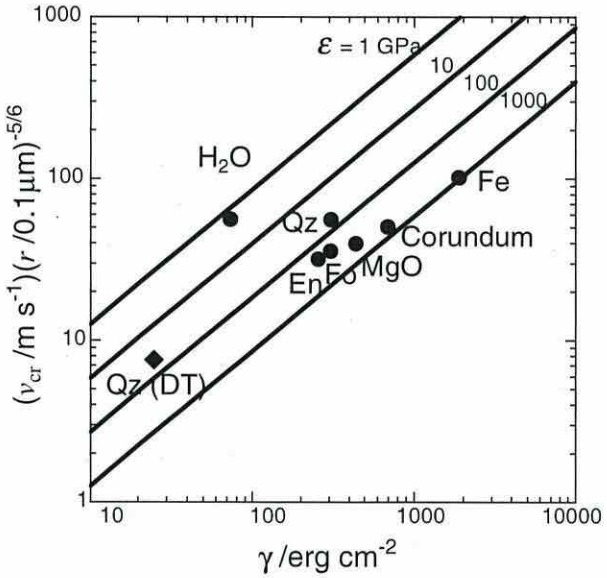

Figure 2. Critical velocity v_{cr} as a function of surface energy γ and Young's modulus $\mathcal{E}$, where v_{cr} is calculated by assuming the density of $\rho = 3\,\mathrm{g\,cm^{-3}}$; the v_{cr} lines should be moved vertically by a factor of $(3\,\mathrm{g\,cm^{-3}}/\rho)^{1/2}$ for materials of density ρ. Critical velocities of materials of astrophysical interest are also plotted. The v_{cr} for quartz of surface energy $\gamma = 25\,\mathrm{erg\,cm^{-2}}$ used in the previous simulations is marked by a diamond labeled Qz(DT).

be pointed out that the critical velocities v_{cr} estimated in the present study should be regarded as underestimates because we used the surface energies of melts; v_{cr} would be higher if one uses the γ of solids because solids have larger γ than melts in general. Furthermore, the present estimate of v_{cr} is based on the JKR theory, which is applicable to the displacement within the elastic limit. If one considers inelastic collisions (Krijt et al. 2013), the critical velocities will increase further.

Wurm and his colleagues report based on their experiments that Qz aggregates can grow even if the collision velocities are higher than $20\,\mathrm{m\,s^{-1}}$, when the mass ratio of colliding aggregates is large (Wurm et al. 2005; Teiser & Wurm 2009; Teiser et al. 2011; Paraskov et al. 2007). The critical velocity for Qz estimated here seems consistent with the results of their experiments, although their results might be due to the small impact parameters of the collisions in their experiments (Wada et al. 2013).

The large surface energy enables the aggregates to grow in the disks on the one hand, but makes their restructuring, such as compaction of aggregates of BCCA (ballistic cluster–cluster aggregation) structure (Suyama et al. 2008; Kataoka et al. 2013a, 2013b), difficult on the other hand because restructuring by rolling motion of the monomers becomes hard. In consequence, the density evolution of aggregates at the stage of the aggregates of BCCA structure will be modified.

It must be stated that there is large difference in the critical velocity for Qz between $v_{cr} = 8\,\mathrm{m\,s^{-1}}$ obtained in the previous simulations and $v_{cr} = 55\,\mathrm{m\,s^{-1}}$ in this study as seen in Figure 2. This is mainly because of the large difference in the value of the surface energy used. In the previous simulations, the surface energy was set to be $\gamma = 25\,\mathrm{erg\,cm^{-2}}$ determined by Kendall et al. (1987), which agrees within a factor of two with the results of measurement by means of atomic force microscopy by Heim et al. (1999, see also Blum & Wurm 2000, 2008). On the other hand, the surface energy $\gamma = 307\,\mathrm{erg\,cm^{-2}}$ of Qz melt measured by Kingery (1959) that we used is obviously higher than that by Kendall et al. (1987) and Heim et al. (1999) but is consistent with the data of the other materials having similar T_m as shown in Figure 1. The reason for the discrepancy is unclear at present and should be addressed in a future study.

We thank an anonymous reviewer for useful comments, which helped in improving the original manuscript. We thank T. Kondo, H. Terasaki, and H. Miura for letting us know about some literatures that provide material data. This study was supported by the Grant-in-Aid for Scientific Research from JSPS (23103004, 24540459).

REFERENCES

Adachi, I., Hayashi, C., & Nakazawa, K. 1976, PThPh, 56, 1756
Blum, J., & Wurm, G. 2000, Icar, 143, 138
Blum, J., & Wurm, G. 2008, ARA&A, 46, 21
Chiang, E. I., & Goldreich, P. 1997, ApJ, 490, 368
Chiang, E. I., Joung, M. K., & Creech-Eakman, N. J. 2001, ApJ, 547, 1077
Cuzzi, J. N., Hogan, R. C., Paque, J. M., & Dobrovolskis, A. R. 2001, ApJ, 546, 496
de Leeuw, N. H., Parker, S. C., Catlow, C. R. A., & Price, G. D. 2000, PCM, 27, 332
Derjaguin, B. V., Muller, V. M., & Toporov, Y. P. 1975, JCIS, 53, 314
Dominik, C., & Tielens, A. G. G. M. 2010, ApJ, 480, 647

Dominik, C., Blum, J., Cuzzi, J. N., & Wurm, G. 2007, in Protostars and Planets V, ed. B. Reipurth, D. Jewitt, & K. Kei (Tucson, AZ: Univ. Arizona Press), 783
Fletcher, N. H. 1970, The Chemical Physics of Ice (Cambridge: Cambridge Univ. Press)
Heim, L.-O., Blum, J., Preuss, M., & Butt, H.-J. 1999, PhRvL, 83, 3328
Janz, G. J. 1979, JPCRD, 8, 125
Janz, G. J. 1980, JPCRD, 9, 831
Janz, G. J. 1983, JPCRD, 12, 591
Johnson, K. L. 1987, Contact Mechanics (Cambridge: Cambridge Univ. Press)
Johnson, K. L., Kendall, K., & Roberts, A. D. 1971, RSPSA, 324, 301
Kataoka, A., Tanaka, H., Okuzumi, S., & Wada, K. 2013a, A&A, 554, A4
Kataoka, A., Tanaka, H., Okuzumi, S., & Wada, K. 2013b, A&A, 557, L4
Kendall, K., McN. Alford, N., & Birchall, J. D. 1987, Natur, 325, 794
Kingery, W. D. 1959, JACS, 42, 6
Krijt, S., Heißelmann, D., Dominik, C., & Tielens, A. G. G. M. 2013, JPhD, 46, 435303
Kusaka, T., Nakano, T., & Hayashi, C. 1970, PThPh, 44, 1580
Murase, T., & McBirney, A. R. 1973, GSAB, 84, 3563
Nakajima, K. 1994, Tetsu to Hagane (The Iron and Steel Institute of Japan), 80, 599
Okuzumi, S., Tanaka, H., Kobayashi, H., & Wada, K. 2012, ApJ, 752, 106
Paraskov, G. B., Wurm, G., & Krauss, O. 2007, Icar, 191, 779
Paszun, D., & Dominik, C. 2009, A&A, 507, 1023
Poirier, J.-P. 1991, Introduction to the Physics of the Earth's Interior (Cambridge: Cambridge Univ. Press)
Richet, P., & Bottinga, Y. 1986, RvGeo, 24, 1
Seizinger, A., & Kley, W. 2013, A&A, 561, A65
Seizinger, A., Krijt, S., & Kley, W. 2013, A&A, 560, A45
Suyama, T., Wada, K., & Tanaka, H. 2008, ApJ, 684, 1310
Tanaka, H., Himeno, Y., & Ida, S. 2005, ApJ, 625, 414
Tanaka, K. K., Yamamoto, T., Nagashima, K., & Tsukamoto, K. 2008, JCrGr, 310, 1281
Teiser, J., Küpper, M., & Wurm, G. 2011, Icar, 215, 596
Teiser, J., & Wurm, G. 2009, MNRAS, 393, 1584
Wada, L., Tanaka, H., Okuzumi, S., et al. 2013, A&A, 559, A62
Wada, K., Tanaka, H., Suyama, T., Kimura, H., & Yamamoto, T. 2007, ApJ, 661, 320
Wada, K., Tanaka, H., Suyama, T., Kimura, H., & Yamamoto, T. 2008, ApJ, 677, 1296
Wada, K., Tanaka, H., Suyama, T., Kimura, H., & Yamamoto, T. 2009, ApJ, 702, 1490
Wada, K., Tanaka, H., Suyama, T., Kimura, H., & Yamamoto, T. 2011, ApJ, 737, 36
Weast, R. C. (ed.) 1983, CRC Handbook of Chemistry and Physics (Boca Raton, FL: CRC Press)
Weidenschilling, S. J., & Cuzzi, J. N. 1993, in Protostars and Planets III, ed. E. H. Levy & J. I. Lunine (Tucson, AZ: Univ. Arizona Press), 1031
Wurm, G., Paraskov, G., & Krauss, O. 2005, Icar, 178, 253

PASJ: Publ. Astron. Soc. Japan **65**, L14, 2013 December 25

Local Enhancement of the Surface Density in the Protoplanetary Ring Surrounding HD 142527

Misato FUKAGAWA,[1] Takashi TSUKAGOSHI,[2] Munetake MOMOSE,[2] Kazuya SAIGO,[3] Nagayoshi OHASHI,[4] Yoshimi KITAMURA,[5] Shu-ichiro INUTSUKA,[6] Takayuki MUTO,[7] Hideko NOMURA,[8] Taku TAKEUCHI,[9] Hiroshi KOBAYASHI,[6] Tomoyuki HANAWA,[10] Eiji AKIYAMA,[3] Mitsuhiko HONDA,[11] Hideaki FUJIWARA,[4] Akimasa KATAOKA,[3,12] Sanemichi Z. TAKAHASHI,[6,8] and Hiroshi SHIBAI[1]

[1]*Graduate School of Science, Osaka University, 1-1 Machikaneyama, Toyonaka, Osaka 560-0043*
misato@iral.ess.sci.osaka-u.ac.jp
[2]*College of Science, Ibaraki University, 2-1-1 Bunkyo, Mito, Ibaraki 310-8512*
[3]*National Astronomical Observatory of Japan, 2-21-1 Osawa, Miaka, Tokyo 181-8588*
[4]*Subaru Telescope, 650 North A'ohoku Place, Hilo, HI 96720, USA*
[5]*Institute of Space and Astronautical Science Aerospace Exploration Agency, 3-1-1 Yoshinodai, Chuo-ku, Sagamihara 252-5210*
[6]*Department of Physics, Graduate School of Science, Nagoya University, Furo-cho, Chikusa-ku, Nagoya 464-8601*
[7]*Division of Liberal Arts, Kogakuin University, 1-24-2 Nishi-Shinjuku, Shinjuku-ku, Tokyo 163-8677*
[8]*Department of Astronomy, Graduate School of Science, Kyoto University, Kitashirakawa-Oiwake-cho, Sakyo-ku, Kyoto 606-8502*
[9]*Department of Earth and Planetary Sciences, Tokyo Institute of Technology, Meguro-ku, Tokyo 152-8551*
[10]*Center for Frontier Science, Chiba University, 1-33 Yayoi-cho, Inage-ku, Chiba 263-8522*
[11]*Department of Mathematics and Physics, Kanagawa University, 2946 Tsuchiya, Hiratsuka, Kanagawa 259-1293*
[12]*School of Physical Sciences, Graduate University for Advanced Studies (SOKENDAI), 2-21-1 Osawa, Mitaka, Tokyo 181-8588*

(Received 2013 July 18; accepted 2013 September 13)

Abstract

We report on ALMA observations of the dust continuum, and ^{13}CO $J = 3$–2 and C^{18}O $J = 3$–2 line emission toward a gapped protoplanetary disk around HD 142527. The outer horseshoe-shaped disk shows a strong azimuthal asymmetry in the dust continuum with a ratio of ~ 30 to 1 at 336 GHz between the northern peak and the south-western minimum. In addition, the maximum brightness temperature of 24 K at its northern area is exceptionally high at 160 au from a star. To evaluate the surface density in this region, the grain temperature needed constraining, and was estimated from the optically thick ^{13}CO $J = 3$–2 emission. The lower limit of the peak surface density was then calculated to be 28 g cm^{-2} by assuming a canonical gas-to-dust mass ratio of 100. This finding implies that the region is locally too massive to withstand self-gravity, since Toomre's $Q \lesssim 1$–2, and thus it may collapse into a gaseous protoplanet. Another possibility is that the gas mass is low enough to be gravitationally stable, and only dust grains are accumulated. In this case, a lower gas-to-dust ratio by at least 1 order of magnitude is required, implying the possible formation of a rocky planetary core.

Key words: instabilities — stars: individual (HD 142527) — stars: planetary systems: formation — stars: planetary systems: protoplanetary disk — submillimeter

1. Introduction

In order to find the way planets form, it is critical and most straightforward to observe the actual process of planet building at their birthplaces (Beckwith et al. 1990; Williams & Cieza 2011). The key approach is to determine the detailed structure of a protoplanetary disk, which can provide an indicator of planet-forming activity (Muto et al. 2012). Great attention has therefore been paid to transitional disks with holes or gaps in the materials (Strom et al. 1989; Andrews et al. 2011). Such structures are often interpreted as being a consequence of the occurrence of giant planets that can clear the disk along their orbits. From another perspective, the outer ringlike disk, itself, may serve as a clue to the cause of planet formation (Mathews et al. 2012; Mayama et al. 2012; Pinilla et al. 2012).

HD 142527 is a Herbig Fe star (Waelkens et al. 1996) surrounded by a disk exhibiting a wide gap with a radial width of approximately 100 au (Fukagawa et al. 2006; Fujiwara et al. 2006; Verhoeff et al. 2011, hereafter V11; Rameau et al. 2012; Casassus et al. 2012). The distance is assumed to be 140 pc in this paper, considering its association with Sco OB2. The stellar mass and age are $\sim 2\,M_\odot$ and 5 Myr, respectively, estimated by adopting 140–145 pc (Fukagawa et al. 2006; V11). Most recently, faint streamlike features were found in the HCO$^+$ and dust continuum at 345 GHz with ALMA; these were interpreted as being funnel flows into the inner disk through giant planets (Casassus et al. 2013). Here, we revisit the disk structure based on our ALMA data with higher sensitivity and angular resolution. We confirmed the presence of the inner disk, and particularly emphasize the surprisingly high surface density of dust at 160 au from the star in this letter.

2. Observations and Data Reduction

HD 142527 was observed with ALMA in Band 7 by using 20–26 12 m antennas in the Extended array configuration in

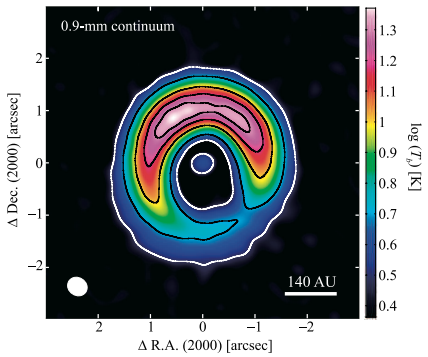

Fig. 1. Dust continuum map at 336 GHz (890 μm) for the disk of HD 142527. The color scale shows the brightness temperature on a logarithmic scale. The black contours denote T_b = 5, 10, 15, and 20 K, while the white one denotes the 5 σ level. The size of the synthesized beam is shown at the left corner of the image with a white ellipse of 0.″39 × 0.″34 (= 55 au × 48 au) with a major-axis PA of 57°.

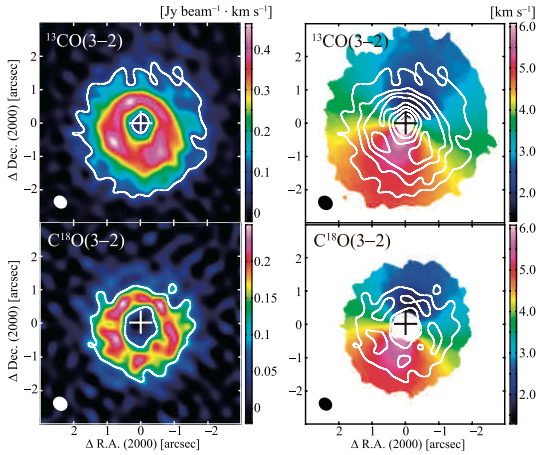

Fig. 2. Moment 0 (left) and 1 (right) maps in ^{13}CO (upper) and C^{18}O J = 3–2 (lower). The contours in the left panels show the 5 σ levels. In the right panels, the first moment maps are presented for the emission detected above 5 σ. The contours for the integrated intensity are overplotted, starting from 5 σ and increasing by 5 σ steps. The cross in each panel denotes the position of the central star. The synthesized beam size is displayed with a white ellipse in each panel, and is 0.″43 × 0.″37 with a PA of 50° for both ^{13}CO and C^{18}O.

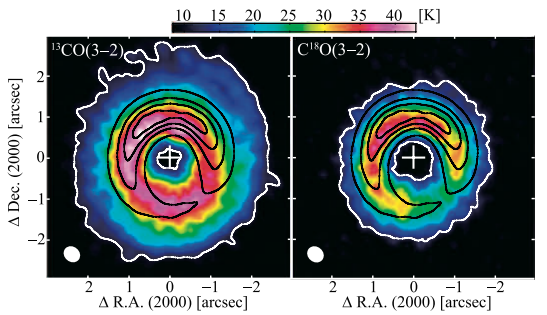

Fig. 3. Peak-intensity maps of ^{13}CO (left) and C^{18}O J = 3–2 (right). The peak intensity denoted by color includes the underlying continuum. The white contour shows the 5 σ level. T_b for the continuum is also plotted with black contours, indicating 5, 10, 15, and 20 K. The cross denotes the stellar position. The faint armlike feature is seen in the ^{13}CO map in the northwest at the disk outer edge, which corresponds to the arm detected in scattered light (Fukagawa et al. 2006).

Cycle 0. The maximum and minimum baselines were 380 m and 20 m, respectively, and the latter corresponded to the largest angular scale of the detectable component of 10″. The observations reported in this letter consisted of four scheduling blocks over the period from 2012 June to August. The correlator was configured to store dual polarizations in four separate spectral windows with a bandwidth of 469 MHz and with 3840 channels, providing a channel spacing of 0.122 MHz (0.11 km s^{-1}). Note that the effective spectral resolution is lower by a factor of ∼2 (∼0.2 km s^{-1}) because of Hanning smoothing. The central frequencies for these four windows are 330.588, 329.331, 342.883, and 342.400 GHz, respectively, allowing us to observe molecular lines of ^{13}CO J = 3–2, C^{18}O J = 3–2, and CS J = 7–6. The results of the CS observations will be reported elsewhere. The quasars 3C 279 and QSO J1924−2914 were targeted as bandpass calibrators, whereas the amplitude and phase were monitored through observations of the quasar QSO B1424−41. The absolute flux density was determined from observations of Titan and Neptune.

The data were calibrated and analyzed by using the Common Astronomy Software Applications package, version 3.4. After flagging the aberrant data and calibrating the bandpass, gain, and flux scaling, the corrected visibilities were imaged and deconvolved by using the CLEAN algorithm with Briggs weighting with a robust parameter of 0.5. In addition, to improve the sensitivity and image fidelity, the self-calibration was performed for the continuum the distinct structure of which was detected with a very high signal-to-noise ratio (S/N). We started with the CLEAN-ed image as an initial model of the source brightness distribution. The phase alone was first corrected via six iterative model refinements; then, the calibration was obtained for the phase-plus-amplitude without iteration. The solution for the continuum was applied to ^{13}CO and C^{18}O data. The final CLEANing was performed with Uniform weighting for both the continuum and emission lines. The self-calibration reduced the fluctuation in the continuum to a level that 2–3 times the brightness of the theoretical thermal origin can account for, resulting in clear detection of compact emission at the stellar position.

Uncertainty associated with the absolute flux density is 10%. The synthesized beam size for the continuum is 0.″39 × 0.″34 at a position angle (PA) of 57° for the major axis; those for ^{13}CO and C^{18}O are 0.″43 × 0.″37 at PA = 50°. The rms noise is 0.19 mJy beam^{-1} for the continuum, whereas they are 12 and 15 mJy beam^{-1} in the 0.11 km s^{-1} wide channels for the line emission of ^{13}CO and C^{18}O, respectively. Since the positional information was lost in the self-calibration, we determined that the stellar position is the brightness centroid of the compact continuum detected at around the stellar coordinates.

3. Results

3.1. *Continuum at 336 GHz*

3.1.1. *Outer disk*

Figure 1 shows the continuum emission at 336 GHz (890 μm). The outer disk was readily detected, and the total

flux density ($> 5\,\sigma$) was measured as being 2.7 Jy. It significantly departs from a uniform ring, and exhibits a horseshoe-like distribution, as reported on in previous studies (Ohashi 2008; Casassus et al. 2013). The northern region is brighter than the southwestern (SW) area, with an emission peak of 213 mJy beam^{-1} at a projected distance of 1.″0 (140 au) from the star, and at a PA of 30°. When the continuum is probed along the annular emission ridge, both ends of the horseshoe appear to connect at the brightness minimum of 7 mJy beam^{-1} at 1.″3 (180 au) and $PA = 220°$. The contrast in the flux density thus reaches to the ratio 30 : 1 between the northern peak and the SW minimum. The peak flux density is expressed by a brightness temperature ($T_{\rm b}$) of 24 K without the Rayleigh–Jeans approximation. This $T_{\rm b}$ is much higher than those beyond 100 au in other disks. Unless the emitting grains are significantly warmer than 24 K, the region should be optically thick to submillimeter radiation due to its high column density.

3.1.2. Inner disk and radial gap

At the position of the star, emission was detected with a significance of $16\,\sigma$ at the peak (figure 1). The χ^2-fitting of an elliptic Gaussian function resulted in a *FWHM* of $(0.''33 \pm 0.''02) \times (0.''29 \pm 0.''02)$ with a PA of $99° \pm 3°$ for the major axis. It was thus spatially unresolved, if given the beam size of $0.''39 \times 0.''34$. The integrated flux density over the Gaussian was 2.3 ± 0.2 mJy, substantially higher than the photospheric level of 0.02 mJy. This suggests that the emission comes from the inner disk, whose presence has been predicted from the near-infrared excess, and the mid-infrared imaging (V11; Fujiwara et al. 2006) where the inner disk was marginally resolved with an inferred size of $\sim$30–50 au in radius. The gaseous emission from the inner disk was also imaged and kinematically resolved (Casassus et al. 2013; Öberg et al. 2011; Pontoppidan et al. 2011). The mass of the inner disk ($M_{\rm in}$) can be crudely estimated, assuming that the majority of the mass resides in the outer, optically thin part, by using the equation $M_{\rm in} = F_\nu d^2/[\kappa_\nu B_\nu(T)]$, where F_ν is the observed flux density, d the distance to the star, κ_ν the opacity, and T the characteristic temperature of the disk. We adopted $T = 50$ K (Chiang & Goldreich 1997) and κ_{336} of 0.034 cm^2 g^{-1}, assuming a gas-to-dust mass ratio (hereafter, referred to as "g/d") of 100, on the basis of the conventional relation $\kappa_\nu = 0.1(\nu/10^{12}\,{\rm Hz})^\beta$ cm^{2}g^{-1} with $\beta = 1.0$ (Beckwith et al. 1990; V11); then, we calculated that the total (gas and dust) disk mass is $(4.3 \pm 0.4) \times 10^{-5}\,M_\odot$. Note that a considerable uncertainty exists in the assumption of optical thickness, and the mass derived here can give a lower limit. In the previous modeling of the spectral energy distribution, the dust (not including gas) mass of the inner disk was estimated to be $2.5 \times 10^{-9}\,M_\odot$, but the model was constrained primarily based on the near- and mid-infrared excess and the assumption of grains of size $\sim$1 micron (V11). The flux density at 890 μm obtained with ALMA seems to be by about one order of magnitude higher than that expected in their modeling. The detection of the submillimeter continuum in our imaging suggests that the bulk of the mass resides in grains of larger size.

In the radial gap, the surface brightness decreases to the background level. Dust streamers from the outer disk reported on in a previous study (Casassus et al. 2013) were not confirmed.

3.2. ^{13}CO J = 3–2 and $C^{18}O$ J = 3–2

3.2.1. Integrated intensity and gas kinematics

The left panels of figure 2 present integrated intensity (0th-moment) maps of the ^{13}CO J = 3–2 and C^{18}O J = 3–2 line emission. The brightness distributions do not show such a strong azimuthal asymmetry as that observed in the dust continuum, and fluctuate by a factor of less than 2. In the radial direction, the integrated intensity has peaks at a range of $r = 0.''7$–$1.''1$, depending on the position angle in ^{13}CO, and at $r = 0.''8$–$1.''2$ in C^{18}O. No emission was detected above $3\,\sigma$ around the stellar position in both lines ($1\,\sigma = 18.9$ and 19.6 mJy beam^{-1} km s^{-1} for ^{13}CO and C^{18}O, respectively).

The right panels of figure 2 show 1st-moment maps in ^{13}CO and C^{18}O. Despite the highly structured continuum, the velocity fields are consistent with a simple, circular Keplerian motion within a resolution of 0.2 km s^{-1}, which was confirmed as follows. The position–velocity relation was extracted along the major axis ($PA = -19° \pm 2°$), and the peak velocity was estimated by Gaussian fitting at each radius at the interval of 0.″03. Then, an S/N-weighted least-squares fitting of an analytic Kepler equation was performed to the measured peak velocity as a function of the radius. In the fitting, the systemic velocity, position of the center of mass (the star), and inclination relative to the observer were a set of free parameters, whereas the stellar mass was fixed at the range of $2.2 \pm 0.3\,M_\odot$ (V11). By using the ^{13}CO data with a higher S/N, the inclination was estimated to be $i = 26.°9^{+2.2}_{-1.8}$, where the uncertainty is dominated by the error in the adopted stellar mass. Note that i is not large enough to yield reasonable ($|\Delta i| < 10°$, $|\Delta M_*| < 50\%$) constraints on both the inclination and the stellar mass (Simon et al. 2000). We determined that the systemic velocity is 3.70 ± 0.02 km s^{-1}. The location of the velocity centroid matches with the compact component of the continuum emission within a range of 0.″04.

3.2.2. Temperature estimate

The line results mentioned above were obtained after subtracting the underlying continuum, by the same method that was adopted in earlier studies. However, the continuum from the outer disk of HD 142527 shows strong azimuthal asymmetry of $T_{\rm b}$ (sub-subsection 3.1.1). In fact, the peak-intensity maps of ^{13}CO and C^{18}O most evidently show a flux deficit in the north. When the $T_{\rm b}$ map of the continuum is added to that of the line peak intensity, after matching the beam size to each of the line data, the resultant distribution of $T_{\rm b}(^{13}{\rm CO})$ is ring-like and azimuthally uniform (figure 3). In the radial direction, the maximum $T_{\rm b}(^{13}{\rm CO})$ is 41 K at 40 au inside the peak of the continuum, when measured in the deprojected ($i = 27°$) profile averaged in a position angle range of from $-49°$ to 51° for the bright continuum. The $T_{\rm b}(^{13}{\rm CO})$ at the location of the continuum peak is 36 K, and it happens to coincide with the highest $T_{\rm b}({\rm C}^{18}{\rm O})$ inwardly located 28 au apart from the continuum peak.

The optical depth of ^{13}CO is greater than unity over the entire disk detected above $5\,\sigma$ in C^{18}O, judging from the continuum-subtracted ratio between the C^{18}O peak intensity and the ^{13}CO intensity at the same velocity as C^{18}O. Here, we assume the same excitation temperature ($T_{\rm ex}$) for both lines and an abundance ratio of X(C^{13}O)/X(C^{18}O) $\sim$ 7 (Qi

et al. 2011). In addition, except for the SW region, $T_{\rm b}(C^{18}O)$ is systematically lower by ~ 5 K than $T_{\rm b}(^{13}CO)$ in the outer region beyond the radial $T_{\rm b}$ peak; this relation can be naturally understood to mean that the line emission comes from optically thick surfaces in the upper layer for ^{13}CO and in the lower for $C^{18}O$. Moreover, the radial shifts of the highest $T_{\rm b}$ for the lines from that for the continuum can be attributed to the inner, warmer emitting surfaces for the gaseous component exposed to the central star. Therefore, the line intensity, at least for ^{13}CO, reflects the physical (kinetic) temperature and not the column density under local thermodynamic equilibrium (LTE). The emission can be approximated by the LTE conditions because the density that will be discussed below (see sub-subsection 4.1) is well above the critical densities for ^{13}CO and $C^{18}O$ $J = 3$–2 (Pavlyuchenkov et al. 2007). In order to estimate the temperature of the optically thick surface, the continuum needs adding, since it is non-negligible for this object.

4. Discussion

4.1. Constraint on the Surface Density

The bulk of grains is expected to be closer to the disk mid-plane, and it is unlikely that it is warmer than the emitting surfaces in ^{13}CO and $C^{18}O$ $J = 3$–2. Therefore, we conservatively regard 36 K, which is $T_{\rm b}(^{13}CO)$ at the radius of the continuum peak, as an upper limit for the grain temperature ($T_{\rm dust}$). The lower limit for the surface density can thus be estimated with $T_{\rm dust} = 36$ K. The optical depth (τ) of the dust was derived by comparing $T_{\rm dust}$ with the continuum $T_{\rm b}$. In the northern horseshoe peak, using $\tau = 0.9$ along with $\kappa_{336} = 0.034\,{\rm cm^2\,g^{-1}}$ for a g/d of 100 (sub-subsection 3.1.2), we calculated that the surface density is $\Sigma_{\rm peak} = 28.1\,{\rm g\,cm^{-2}}$. In the SW minimum, the same assumption of 36 K resulted in $\Sigma_{\rm min} = 0.7\,{\rm g\,cm^{-2}}$, showing a density ratio of 40 to 1. Integrating the surface density yielded the mass for the entire outer disk of 0.09 $M_\odot$, which turns out consistent with the previous estimate of 0.1 $M_\odot$ obtained through the conventional, optically thin prescription for 40 K (V11).

Because $T_{\rm b} \approx T_{\rm dust}\,\tau$, grains must be warmed in the dense region near to the mid-plane so as to account for the observed high $T_{\rm b}$. We investigated whether this condition can be realized by employing radiative transfer calculations in the disk vertical direction of the disk. We performed the 1+1D modeling (Nomura et al. 2009), assuming the surface density estimated above, the vertical hydrostatic equilibrium, and an incident stellar luminosity of 15 $L_\odot$, and considering the possible shadow of the inner disk (V11). The observed $T_{\rm b}$ was reproduced by using a plausible opacity of the grain in protoplanetary disks (Nomura & Millar 2005).

The optical depth of $C^{18}O$ may drop below unity in the SW region, given the lower $T_{\rm b}$ (figure 3). We thus attempted to estimate the surface density of gas using a one-zone approximation in the vertical direction. The optical depth was derived from the line ratio of $C^{18}O$ to ^{13}CO with the abundance ratio taken from Qi et al. (2011), and the temperature was provided by $T_{\rm b}(^{13}CO)$ (figure 3). The calculations indicated a g/d of 14 at $PA = 210°$–$230°$. However, they suggested that the optical depth is ~ 1.0. In addition, we cannot completely exclude the possibility that the $C^{18}O$ emission is more optically thick with a lower $T_{\rm ex}$. Thus, the derived g/d can provide a lower limit.

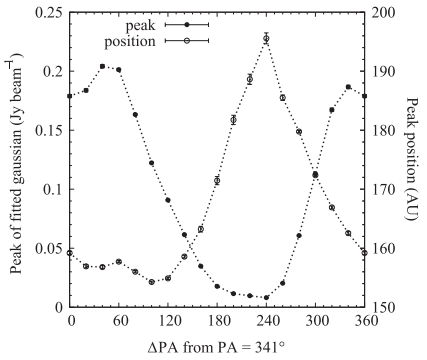

Fig. 4. Peak intensity and its location from the star obtained by the Gaussian fitting to the profile averaged over every 20° bin in PA. PA in this plot is measured from the major axis ($PA = -19°$).

4.2. Spatial Structure

The radial profile for the continuum emission is well described by a Gaussian function, rather than a power law, at all position angles. A Gaussian fitting to the deprojected, azimuthally averaged profile gave $I_{\rm average}({\rm Jy\,beam^{-1}}) = 9.95 \times 10^{-2}\,\exp\{-[(R - 161.1)/(48.2)]^2\}$, where R is the distance from the star in au. Assuming a g/d of 100 and a temperature of 36 K, the Gaussian fitted to the azimuthally averaged profile has a peak surface density, $\Sigma_{\rm average}$, of $11.3\,{\rm g\,cm^{-2}}$ at $R = 161$ au. The Gaussian fitting to the radial profile in each PA yielded one clear feature, which is anticorrelation between the peak intensity of the Gaussian and its deprojected distance from the star (figure 4). This anticorrelation excludes the possible explanation that the azimuthal asymmetry is due to eccentric orbits of the dust particles. If the orbits are eccentric, they concentrate near the apastron.

If the *density* profile is confirmed to be Gaussian after incorporating a realistic temperature gradient, it is natural to understand the disk as being a ring or torus. In a primordial disk, the radial distribution of the surface density can be expressed as a power law accompanied by an outer, exponential tapered edge (Hughes et al. 2008). An inner gap or hole can then be created by being carved by a planet(s), for instance, but the outer boundary should remain unaffected unless the gap stretches to nearly the outher edge of the disk or the source experiences stellar encounters. It would be worth noting that the formation of a ring can be explained by different mechanisms without the aid of planets, such as a secular process through viscous overstability (S. Z. Takahashi & S. Inutsuka in preparation; Schmit & Tscharnuter 1995).

On the other hand, the ^{13}CO emission was detected so far as $r \sim 350$ au on average at all position angles ($5\,\sigma$, figure 3), which is not reconciled with the Gaussian profile for the continuum. The ^{13}CO intensity at 350 au is by several orders of magnitude higher than that predicted by an extrapolation from the Gaussian for any excitation temperature, assuming LTE and a g/d of 100. This suggests an additional floor spreading outward. The nondetection of the dust continuum for this floor is not inconsistent with the assumption of a g/d of 100, considering the detection limit in our observations.

4.3. Stability against Self-Gravity

What can be expected from the local density enhancement in a Keplerian disk? To evaluate the gravitational stability, Toomre's Q parameter (Toomre 1964) was computed under the assumption of a g/d of 100. It was first estimated toward the averaged surface density to examine the global stability, resulting in $Q(R = 161\,\mathrm{au}) = 2.2$ using $\Sigma_{\mathrm{average}} = 11\,\mathrm{g\,cm^{-2}}$, the isothermal sound speed for 36 K, and a stellar mass of $2.2\,M_{\odot}$. Locally estimated at the horseshoe peak at $R = 156$ au, Q was found to be 0.9 for $\Sigma_{\mathrm{peak}} = 28\,\mathrm{g\,cm^{-2}}$. Note that Σ is at its lower limit, whereas the temperature (sound speed) is the upper limit; therefore, the obtained Q is considered to provide the upper limit. $Q \lesssim 1$–2 indicates that the disk is vulnerable to gravitational instability if g/d is $\sim$100. Crudely assuming that a resultant fragment acquires the mass within a local volume of the size of the disk scale height (16 au at 36 K), it gains ~ 3 Jupiter-masses. The dynamical clumping of the ring structure may be considered in such a way that filaments fragment into stars in molecular clouds (Inutsuka & Miyama 1992, 1997). Note that the disk fragmentation likely occurs on a dynamical timescale ($\sim 10^3$ yr), which is much shorter than the stellar age ($\sim 10^6$ yr), suggesting that we are observing HD 142527 in its transient phase.

The caveat in the above discussion is the assumption about g/d (e.g., Tilling et al. 2012). For instance, if g/d is at the lower end of that estimated in the SW region (~ 10, subsection 4.1), or even smaller, Toomre's Q becomes $\gg 1$, and the disk can be stable against its self-gravity. This situation is allowed since $C^{18}O$ emission is expected to stay optically thick at the horseshoe peak, even if g/d is as small as unity. Such a g/d, lower by more than a factor of ~ 10 than the ISM value, suggests grain accumulation. As a result, the process may lead to the efficient growth of a solid planetary core. This phenomenon is consistent with the scenario of particle trapping at pressure maxima that can be caused by several possible mechanisms, including a perturbation by an already formed planet (Regály et al. 2012; Birnstiel et al. 2013).

In either case, the pileup of disk material beyond 100 au is quite surprising in the classical scenario of planet formation. HD 142527 is indeed unique compared to other ringlike disks that have been spatially resolved. They show relatively smaller disk masses ($\sim 1\%$ of M_* for a g/d of 100), and their azimuthal brightness fluctuations in the continuum are lower by an order of magnitude (Andrews et al. 2011; Mathews et al. 2012; Isella et al. 2010; Tang et al. 2012). In terms of azimuthal asymmetry, the similarity can be found only in the recent discovery of the crescent-shaped disk with an azimuthal ratio in flux density of at least 130 to 1 at 680 GHz (van der Marel et al. 2013). Therefore, HD 142527 offers a rare opportunity for us to directly observe the critical moment of planet formation, and can provide a fresh insight into the origin of wide-orbit planetary bodies (Marois et al. 2008; Ireland et al. 2011)

We are grateful to the referee for valuable comments that improved our manuscript. We also thank Y. Aikawa for helpful discussion. This paper makes use of the following ALMA data: ADS/JAO.ALMA#2011.0.00318.S. ALMA is a partnership of ESO (representing its member states), NSF (USA), and NINS (Japan), together with NRC (Canada) and NSC and ASIAA (Taiwan), in cooperation with the Republic of Chile. The Joint ALMA Observatory is operated by ESO, AUI/NRAO and NAOJ. This work is supported by MEXT KAKENHI Nos. 23103004 and 23103005.

References

Andrews, S. M., Wilner, D. J., Espaillat, C., Hughes, A. M., Dullemond, C. P., McClure, M. K., Qi, C., & Brown, J. M. 2011, ApJ, 732, 42
Beckwith, S. V. W., Sargent, A. I., Chini, R. S., & Güsten, R. 1990, AJ, 99, 924
Birnstiel, T., Dullemond, C. P., & Pinilla, P. 2013, A&A, 550, L8
Casassus, S., et al. 2013, Nature, 493, 191
Casassus, S., Perez M., S., Jordán, A., Ménard, F., Cuadra, J., Schreiber, M. R., Hales, A. S., & Ercolano, B. 2012, ApJ, 754, L31
Chiang, E. I., & Goldreich, P. 1997, ApJ, 490, 368
Fujiwara, H., et al. 2006, ApJ, 644, L133
Fukagawa, M., Tamura, M., Itoh, Y., Kudo, T., Imaeda, Y., Oasa, Y., Hayashi, S. S., & Hayashi, M. 2006, ApJ, 636, L153
Hughes, A. M., Wilner, D. J., Qi, C., & Hogerheijde, M. R. 2008, ApJ, 678, 1119
Inutsuka, S., & Miyama, S. M. 1992, ApJ, 388, 392
Inutsuka, S., & Miyama, S. M. 1997, ApJ, 480, 681
Ireland, M. J., Kraus, A., Martinache, F., Law, N., & Hillenbrand, L. A. 2011, ApJ, 726, 113
Isella, A., Natta, A., Wilner, D., Carpenter, J. M., & Testi, L. 2010, ApJ, 725, 1735
Marois, C., Macintosh, B., Barman, T., Zuckerman, B., Song, I., Patience, J., Lafreniére, D., & Doyon, R. 2008, Science, 322, 1348
Mathews, G. S., Williams, J. P., & Ménard, F. 2012, ApJ, 753, 59
Mayama, S., et al. 2012, ApJ, 760, L26
Muto, T., et al. 2012, ApJ, 748, L22
Nomura, H., Aikawa, Y., Nakagawa, Y., & Millar, T. J. 2009, A&A, 495, 183
Nomura, H., & Millar, T. J. 2005, A&A, 438, 923
Öberg, K. I., et al. 2011, ApJ, 734, 98
Ohashi, N. 2008, Ap&SS, 313, 101
Pavlyuchenkov, Y., Semenov, D., Henning, T., Guilloteau, S., Piétu, V., Launhardt, R., & Dutrey, A. 2007, ApJ, 669, 1262
Pinilla, P., Benisty, M., & Birnstiel, T. 2012, A&A, 545, A81
Pontoppidan, K. M., Blake, G. A., & Smette, A. 2011, ApJ, 733, 84
Qi, C., D'Alessio, P., Öberg, K. I., Wilner, D. J., Hughes, A. M., Andrews, S. M., & Ayala, S. 2011, ApJ, 740, 84
Rameau, J., Chauvin, G., Lagrange, A.-M., Thébault, P., Milli, J., Girard, J. H., & Bonnefoy, M. 2012, A&A, 546, A24
Regály, Z., Juhász, A., Sándor, Z., & Dullemond, C. P. 2012, MNRAS, 419, 1701
Schmit, U., & Tscharnuter, W. M. 1995, Icarus, 115, 304
Simon, M., Dutrey, A., & Guilloteau, S. 2000, ApJ, 545, 1034
Strom, K. M., Strom, S. E., Edwards, S., Cabrit, S., & Skrutskie, M. F. 1989, AJ, 97, 1451
Tang, Y.-W., Guilloteau, S., Piétu, V., Dutrey, A., Ohashi, N., & Ho, P. T. P. 2012, A&A, 547, A84
Tilling, I., et al. 2012, A&A, 538, A20
Toomre, A. 1964, ApJ, 139, 1217
van der Marel, N., et al. 2013, Science, 340, 1199
Verhoeff, A. P., et al. 2011, A&A, 528, A91 (V11)
Waelkens, C., et al. 1996, A&A, 315, L245
Williams, J. P., & Cieza, L. A. 2011, ARA&A, 49, 67

A&A 554, A4 (2013)
DOI: 10.1051/0004-6361/201321325

Astronomy & Astrophysics

Static compression of porous dust aggregates

A. Kataoka[1,2], H. Tanaka[3], S. Okuzumi[4,5], and K. Wada[6]

[1] Department of Astronomical Science, School of Physical Sciences, Graduate University for Advanced Studies (SOKENDAI), Mitaka, 181-8588 Tokyo, Japan
e-mail: akimasa.kataoka@nao.ac.jp
[2] National Astronomical Observatory of Japan, Mitaka, 181-8588 Tokyo, Japan
[3] Institute of Low Temperature Science, Hokkaido University, Kita, 060-0819 Sapporo, Japan
[4] Department of Physics, Nagoya University, Nagoya, 464-8602 Aichi, Japan
[5] Department of Earth and Planetary Sciences, Tokyo Institute of Technology, Meguro, 152-8551 Tokyo, Japan
[6] Planetary Exploration Research Center, Chiba Institute of Technology, Narashino, 275-0016 Chiba, Japan

Received 20 February 2013 / Accepted 11 March 2013

ABSTRACT

Context. In protoplanetary disks, dust grains coagulate with each other and grow to form aggregates. While these aggregates are growing by coagulation, their filling factor ϕ decreases to $\phi \ll 1$; however, comets, the remnants of these early planetesimals, have $\phi \sim 0.1$. Thus, static compression of porous dust aggregates is important in planetesimal formation. However, the static compressive strength has only been investigated for relatively high-density aggregates ($\phi > 0.1$).
Aims. We investigate and find the compressive strength of highly porous aggregates ($\phi \ll 1$).
Methods. We performed three-dimensional N-body simulations of aggregate compression with a particle-particle interaction model. We introduced a new method of static compression: the periodic boundary condition was adopted, and the boundaries move with low speed to get closer. The dust aggregate is compressed uniformly and isotropically by themselves over the periodic boundaries.
Results. We empirically derive a formula of the compressive strength of highly porous aggregates ($\phi \ll 1$). We check the validity of the compressive strength formula for wide ranges of numerical parameters, such as the size of initial aggregates, the boundary speed, the normal damping force, and material. We also compare our results to the previous studies of static compression in the relatively high-density region ($\phi > 0.1$) and confirm that our results consistently connect to those in the high-density region. The compressive strength formula is also derived analytically.

Key words. planets and satellites: formation – methods: numerical – methods: analytical – protoplanetary disks

1. Introduction

Planetesimal formation is a key issue in the study of how planets form in protoplanetary disks (Hayashi et al. 1985; Weidenschilling & Cuzzi 1993). However, the collisional growth of the dust from submicron-sized dust to kilometer-sized planetesimals is still unknown.

In the growth process, one of the most important but unresolved problems is to determine the internal structural evolution of dust aggregates. The internal structure of dust is important in planetesimal formation because the dynamics of dust aggregates in protoplanetary disks are determined by coupling of gas and dust, in other words, the size and internal density of dust aggregates. In the early stage of dust coagulation in protoplanetary disks, the collision energy of the aggregates is too low to cause collisional compression (Blum 2004; Ormel et al. 2007; Zsom et al. 2010, 2011; Okuzumi et al. 2012). As a result, the internal mass density ρ decreases to $\rho < 1.0$ g cm^{-3}.

Both theoretical and experimental studies have shown that mutual collisions lead dust aggregates to have their fractal dimension $D \sim 2$, which is so-called ballistic cluster-cluster aggregation (BCCA; Smirnov 1990; Meakin 1991; Kempf et al. 1999; Blum & Wurm 2000; Krause & Blum 2004; Paszun & Dominik 2006). The dust aggregates would be gradually compacted or disrupted in coagulation because of the increase in impact energy. This compaction has been investigated with numerical N-body simulations that consider particle-particle interactions (Dominik & Tielens 1997; Wada et al. 2007, 2008, 2009; Suyama et al. 2008, 2012; Paszun & Dominik 2008, 2009; Seizinger et al. 2012).

In most previous studies investigating dust growth in protoplanetary disks, dust grains have been assumed to have constant internal mass density for simplicity (Nakagawa et al. 1981; Tanaka et al. 2005; Brauer et al. 2008; Birnstiel et al. 2010). However, dust porosity evolves during dust growth in real protoplanetary disks. In recent dust coagulation calculations, porosity evolution has been considered to be based on experimental and theoretical results (Ormel et al. 2007; Okuzumi et al. 2009, 2012; Zsom et al. 2011). These results also suggest that ρ decreases as $\rho \ll 0.1$ g cm^{-3}.

In the most recent work, the dominant coagulation mode has been shown to be similar-size collisions of dust aggregates though dust grains have size distribution (Okuzumi et al. 2012). As a result, their fractal dimension is approximately equal to two, and their internal mass density ρ has been shown to become 10^{-5} g cm^{-3} (equivalent to be the filling factor $\phi = 10^{-5}$ for ice particles with a density of 1.0 g cm^{-3}). Such fluffy dust aggregates are believed to become planetesimals. Since comets in our solar system, which would be remnants of planetesimals, have their internal mass density of ~0.1 g cm^{-3} (A'Hearn 2011), dust aggregates must be compressed from $\rho \ll 0.1$ g cm^{-3} to $\rho \sim 0.1$ g cm^{-3} in protoplanetary disks.

Table 1. Material parameters in our simulation.

Material	Ice	Silicate (same as Seizinger et al. 2012)
Monomer radius r_0 [μm]	0.1	0.6
Surface energy γ [mJ m^{-2}]	100	20
Young's modulus E [GPa]	7.0	2.65
Poisson's ratio ν	0.25	0.17
Material density ρ_0 [g cm^{-3}]	1.0	2.65
critical rolling displacement $\xi_{\rm crit}$ [Å]	8	20

Compression at dust aggregate collisions has been investigated in previous studies. When collisional impact energy exceeds the critical energy, dust aggregates are compacted by their collision (e.g., Dominik & Tielens 1997; Suyama et al. 2008; Wada et al. 2007, 2008, 2009). However, the collisional compression is not effective at compressing dust aggregates (Okuzumi et al. 2012).

One of the other compression mechanisms in protoplanetary disks is static compression by disk gas or self-gravity. The static compressive strength of dust aggregates has been investigated both experimentally and numerically (Paszun & Dominik 2008; Güttler et al. 2009; Seizinger et al. 2012). However, the compressive strength has examined only relatively compact aggregates with $\rho \gtrsim 0.1$ g cm^{-3} because their initial aggregates are ballistic particle-cluster aggregation (BPCA) clusters. Because ρ decreases to $\rho \ll 0.1$ g cm^{-3}, at least in the early stage of dust growth, we need to reveal the static compressive strength with $\rho \ll 0.1$ g cm^{-3}.

In this work, we investigate the static compression of highly porous aggregates with $\rho < 0.1$ g cm^{-3} by means of numerical simulations and an analytical approach. It is challenging to perform numerical simulations of the static and uniform compression of highly porous aggregates. Because such porous aggregates have low sound speed, we have to compress them at a much slower velocity than in the case of compact aggregates, as is shown in our simulations. Such a slow compression of the fluffy aggregates costs much computational time.

In previous numerical studies of static compression, a dust aggregate is compressed by a wall moving in one direction (Paszun & Dominik 2008; Seizinger et al. 2012). However, this method has disadvantages when reproducing uniform and isotropic compression. There are also side walls that do not move. These side walls also obstruct the tangential motion of monomers in contact with the walls, causing artificial stress on the aggregate, which restructures them. Moreover, since they measure the pressure with the force on the moving wall, the side walls may affect the pressure measurement. In the present work, we develop a new method reproducing static compression. Instead of the walls, we adopt periodic boundary conditions and the boundaries get closer to each other. With these slowly moving periodic boundaries, the aggregate is compressed uniformly and naturally. The periodic boundary condition also enables us to represent a much larger aggregate than inside the computational region. This saves on computational time remarkably.

This paper is organized as follows. We describe the model of our numerical simulations in Sect. 2. We show the results of our simulations and find the compressive strength in Sect. 3. We confirm the obtained compressive strength formula analytically in Sect. 4, and present our conclusion in Sect. 5.

2. Simulation setting

We performed three-dimensional numerical simulations of the compression of a dust aggregate consisting of a number of spherical monomers. As the initial aggregate, we adopted a BCCA cluster. In this method, we solved interactions between all monomers in contact in each time step. Interactions between monomers in contact are formulated by Dominik & Tielens (1997) and reformulated by using the potential energies by Wada et al. (2007). We used the interaction model proposed by Wada et al. (2007) in this work. We briefly summarize the particle interaction model and material constants (see Wada et al. 2007, for details). Moreover, we describe the additional damping force in normal direction and the simulation setting in this section. In our simulations, the aggregate is gradually compressed by its copies over the moving periodic boundaries. This is an appropriate method of simulating uniform and isotropic compression. We also describe the boundary condition in this section. Since we do not have walls to measure the pressure in the periodic boundary condition, we use a similar manner of pressure measurement in molecular dynamics simulations. We also introduce the method of pressure measurement below.

2.1. Interaction model

We calculate the direct interaction of each connection of particles, taking all mechanical interactions modeled by Dominik & Tielens (1997) and Wada et al. (2007) into account. The material parameters are the monomer radius r_0, surface energy γ, Young's modulus E, Poisson's ratio ν, and the material density ρ_0. Table 1 lists the values of the material parameters for ice and silicate.

We perform N-body simulations with ice particles except for one case with silicate particles. In protoplanetary disks, ice particles are the most dominant dust material beyond the snowline. Moreover, the computational time required for calculating ice particles is less than for silicate. Thus, we adopt ice particles in most simulations. We also treat a silicate case to compare with a previous study (Seizinger et al. 2012).

The critical displacement still shows a discrepancy between theoretical ($\xi_{\rm crit} = 2$ Å) and experimental ($\xi_{\rm crit} = 32$ Å) studies (Dominik & Tielens 1997; Heim et al. 1999). We adopt the same parameter as in Wada et al. (2011), $\xi_{\rm crit} = 8$ Å as a typical length for ice particles, and $\xi_{\rm crit} = 20$ Å for silicate particles to compare with Seizinger et al. (2012).

The parameter $\xi_{\rm crit}$ is related to strength of rolling motion. The rolling motion between monomers is crucial in compression. The rolling energy $E_{\rm roll}$ is the energy required to rotate a particle around a connecting point by 90°. The rolling energy can be written as

$$E_{\rm roll} = 6\pi^2 \gamma r_0 \xi_{\rm crit} \tag{1}$$

(see Wada et al. 2007, for details). In the case of ice monomers, for example, $E_{\rm roll} = 4.37 \times 10^{-9}$ erg for $\xi_{\rm crit} = 8$ Å.

We use a normalized unit of time in our simulations. For ice particles, the normalized unit of time is

$$t_0 = 0.95 \left(\frac{\rho_0^{1/2} r_0^{7/6}}{E^{1/3} \gamma^{1/6}} \right) = 1.93 \times 10^{-10} \text{ s}, \tag{2}$$

which is a characteristic time, and it approximately represents the oscillation time of particles in contact at the critical collision velocity (see Wada et al. 2007, for details).

2.2. Damping force in normal direction

The normal force between two monomers is repulsive when the monomers are close or attractive when they are stretched out. Thus, normal oscillations occur at each connection. For realistic particles, these oscillations would dissipate because of viscoelasticity or hysteresis in the normal force (e.g., Greenwood & Johnson 2006; Tanaka et al. 2012). For such damping of normal oscillation, we add an artificial normal damping force to the particle interaction model, following the previous studies (Suyama et al. 2008; Paszun & Dominik 2008; Seizinger et al. 2012).

Assuming that two particles in contact have their position vectors $\boldsymbol{x}_1$ and $\boldsymbol{x}_2$, respectively, the contact unit vector $\boldsymbol{n}_{\rm c}$ is defined as

$$\boldsymbol{n}_{\rm c} = \frac{\boldsymbol{x}_1 - \boldsymbol{x}_2}{|\boldsymbol{x}_1 - \boldsymbol{x}_2|} \tag{3}$$

(see Fig. 2 in Wada et al. 2007). We introduce a damping force between contact particles in normal direction, defined as

$$\boldsymbol{F}_{\rm damp} = -k_{\rm n} \frac{m_0}{t_0} \boldsymbol{n}_{\rm c} \cdot \boldsymbol{v}_{\rm r}, \tag{4}$$

where $k_{\rm n}$ is the damping coefficient in normal direction and m_0 the monomer mass. The adopted value of $k_{\rm n}$ is on the order of 0.01. To show that the result is independent of the normal oscillation damping, we perform N-body simulations with the damping factor $k_{\rm n}$ as a parameter.

The timescale of damping is

$$\tau_{\rm damp} \sim \frac{t_0}{k_{\rm n}} \sim 10^2 t_0, \tag{5}$$

for $k_{\rm n} = 0.01$, it is much shorter than the simulation timescale, which is typically $\sim 10^7 t_0$. We show that the obtained compressive strength is independent of the artificial normal damping force in our simulations (see Sect. 3.4).

2.3. Uniform compression by moving boundaries

We adopt the periodic boundary condition in our simulations. The aggregate in the computational region is surrounded by its copies, as shown in Fig. 1. Initially, we set a cubic box whose sides are periodic boundaries with a size of L larger than the aggregate. Thus, the initial BCCA cluster is detached from its

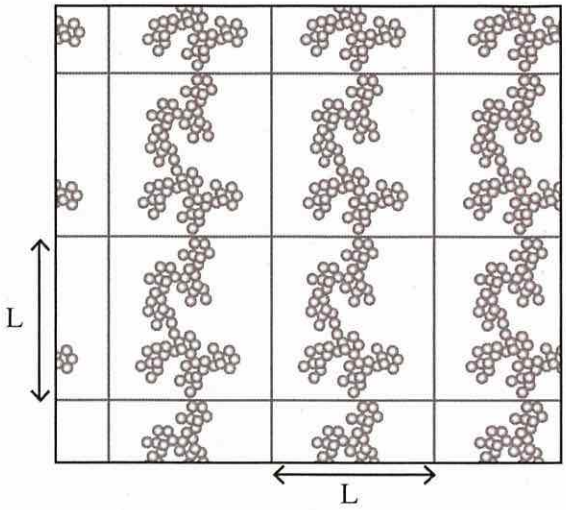

Fig. 1. Schematic drawing of the periodic boundary condition. Each box illustrates a boundary box with a side length L for all directions. When the boundary starts to get closer, the aggregate sticks to the neighboring aggregates over the boundary and is compressed by them. It should be noted that this picture is illustrated in the 2D direction, but our simulations are performed in 3D.

neighboring copies over the periodic boundaries. In our simulations, we gradually move the boundaries to the center of the aggregate to get closer to one another. As a result, the aggregate sticks to the neighboring copies and is compressed by them in a natural way. Therefore, the aggregate in the computational region corresponds to a small part of a whole large aggregate. In other words, although the number of particles in numerical simulations are limited because of computational cost, the periodic boundary condition enables us to investigate a large aggregate, such as a ~cm-sized dust aggregate in protoplanetary disks.

Another advantage of the periodic boundary condition is that we do not need to introduce the wall for compression. In the previous N-body simulations of static compression, dust aggregates are compressed by using the wall against the dust aggregate (Paszun & Dominik 2008; Seizinger et al. 2012). The wall itself may have some artificial effects on such experiments. For example, the wall moves in one direction and thus this may be different from isotropic compression. Besides, wall-particle interaction is different from particle-particle interaction, so it must be treated carefully. In contrast, the periodic boundary condition does not need walls for compression because a dust aggregate is compressed by the neighboring aggregate over the periodic boundary. In addition, the periodic boundaries in three directions make it possible to compress the aggregate isotropically. We calculate not only the interactions of particles in contact inside the computational region but also the interactions of the particles in contact across the periodic boundaries. Thus, no special treatment of interactions, which is wall-particle interactions in the case of simulations with walls in previous studies, is required when a particle crosses the periodic boundaries.

The computational cubic region has length L, and the coordinates in x, y, and z directions are set to be $-L/2 < x < L/2$, $-L/2 < y < L/2$, and $-L/2 < z < L/2$, respectively. We adopt periodic boundary conditions for all directions to reproduce a part of a large aggregate, where L decreases with time t, $L = L(t)$. The initial size of the box L_0 is adopted as the maximum size of the dust aggregate in x, y, and z directions.

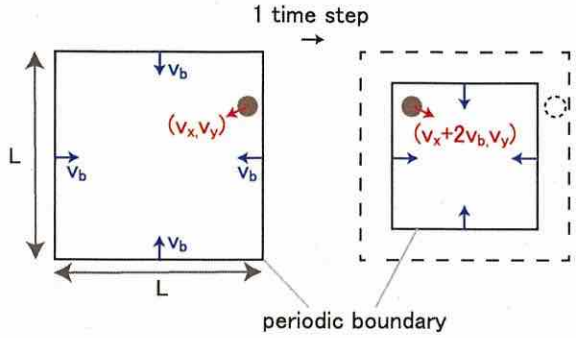

Fig. 2. Schematic drawing to illustrate how the particle velocity is calculated when a particle crosses a periodic boundary. For simplicity, we consider this situation in a 2D field, but we actually calculate this in a 3D situation. We consider that a dust particle is close to the boundary in the left figure. In the next time step, the particle crosses the boundary (dashed circle in the right figure). We put the particle on the other side of the boundary as expressed in Eqs. (8) and (10). The velocity component is converted as expressed in Eqs. (9) and (11). This treatment reproduces the isotropic compression in the velocity field well.

With the settings above, we move the boundaries of the computational region toward the center of the region. The velocity at the boundary is given by

$$v_b = -\frac{C_v}{t_0} L(t), \tag{6}$$

where C_v is a dimensionless parameter (we call C_v the strain rate parameter hereafter). Owing to this definition of the boundary speed, the aggregate is compressed at a constant strain rate independent of the region scale L.

The box size decreases with the constant rate C_v in three directions. This corresponds to isotropic compression. Since $\frac{dL}{dt} = 2v_b$, the box size is written as

$$L = L_0 \exp\left(-2C_v \frac{t}{t_0}\right). \tag{7}$$

Therefore, the whole time of compression is t_0/C_v. Typically we chose $C_v = 3 \times 10^{-7}$ so the compression time is $\sim 3 \times 10^6\, t_0 \sim 0.6$ ms.

When a particle crosses a periodic boundary, the velocity should be treated carefully to reproduce the quasi-static compression with periodic boundary condition. Figure 2 illustrates how to calculate the velocity of particles across the periodic boundary. When a particle goes out of the computational region across the boundary at $x = L/2$, we relocate the particle to the opposite side (i.e., from the boundary at $x = -L/2$). In that case, the position of the particle in x direction is converted as

$$x \longmapsto x - L \tag{8}$$

Since the two boundaries at $x = -L/2$ and $x = L/2$ have a relative velocity of $2v_b$, the x-component of the velocity v_x of the particle is also converted as

$$v_x \longmapsto v_x + 2v_b. \tag{9}$$

Owing to the conversion of v_x, the velocity of particle against the boundary that the particle crosses does not change before and after the crossing. For a particle across the boundary at $x = -L/2$, the position and the velocity are converted as

$$x \longmapsto x + L \tag{10}$$

$$v_x \longmapsto v_x - 2v_b. \tag{11}$$

We also have the same treatments for particles across the boundaries at $y = \pm L/2$ and $z = \pm L/2$.

We introduce the constant strain rate at the boundaries for scaleless discussion. However, the initial aggregate is not moving. As the simulation starts, if all the particles in the aggregate are not moving, only the particles close to the boundaries have initial velocity. This is not a constant strain rate. To reproduce the scaleless constant strain rate initially, therefore, we first give all monomers the velocity smoothly connected to the boundary speed. The initial velocity is expressed as

$$\boldsymbol{v}(\boldsymbol{r}) = v_b \times \frac{\boldsymbol{r}}{L_0/2}, \tag{12}$$

where $\boldsymbol{r}$ is the position vector of the monomers.

2.4. Pressure measurement

In previous studies, a dust aggregate is enclosed by walls, and the pressure is calculated by measuring the force exerted on the walls by the dust aggregate. In this work, a dust aggregate is compressed by themselves because of the periodic boundary condition. Therefore, we introduce another method of measuring the pressure on the aggregate. We calculate the pressure of the dust aggregate in the standard way in molecular dynamics simulations using the virial theorem as follows (e.g., Haile 1992).

We consider a virtual box that encloses the aggregate under consideration. We define the force acting from the walls of the virtual box on the particle i as $\boldsymbol{W}_i$, and the sum of the forces from other particles on the particle i as $\boldsymbol{F}_i$. The equation of motion of the particle i is given by

$$m\frac{d^2\boldsymbol{r}_i}{dt^2} = \boldsymbol{W}_i + \boldsymbol{F}_i. \tag{13}$$

We take a scalar product of both sides of the equation with $\boldsymbol{r}_i$ and take a long time average of both sides with time interval τ. The lefthand side becomes

$$m\frac{1}{\tau}\int_0^\tau \boldsymbol{r}_i \cdot \frac{d^2\boldsymbol{r}_i}{dt^2} = m\frac{1}{\tau}\left[\boldsymbol{r}_i \cdot \frac{d\boldsymbol{r}_i}{dt}\right]_0^\tau - m\frac{1}{\tau}\int_0^\tau \frac{d\boldsymbol{r}_i}{dt}\cdot\frac{d\boldsymbol{r}_i}{dt}dt. \tag{14}$$

The first term on the righthand side vanishes in the limit of $\tau \to \infty$. We define the taking-a-long-time average in t as $\langle\rangle_t$. Taking a summation of all particles and a long time average of Eq. (13), we obtain

$$\left\langle \sum_{i=1}^N \frac{1}{2} m \left(\frac{d\boldsymbol{r}_i}{dt}\right)^2 \right\rangle_t = -\frac{1}{2}\left\langle \sum_{i=1}^N \boldsymbol{r}_i \cdot (\boldsymbol{W}_i + \boldsymbol{F}_i) \right\rangle_t. \tag{15}$$

The first term on the righthand side is related to pressure P. The pressure is an average of all forces acting on the wall from all particles. Using the normal vector $\boldsymbol{n}$ of the wall surface directed outward, the force received by the wall that has an area dS is $P\boldsymbol{n}dS$. Therefore,

$$\left\langle \sum_i \boldsymbol{r}_i \cdot \boldsymbol{W}_i \right\rangle_t = -\int_S P\boldsymbol{n}\cdot\boldsymbol{r}dS = -3PV. \tag{16}$$

This equation is obtained by taking surface integral as

$$\int_S \boldsymbol{n}\cdot\boldsymbol{r}dS = \int_V \mathrm{div}\,\boldsymbol{r}dV = \int_V \left(\frac{\partial x}{\partial x} + \frac{\partial y}{\partial y} + \frac{\partial z}{\partial z}\right)dV = 3V. \tag{17}$$

The translational kinetic energy K, averaged over a long time, is given by

$$K = \left\langle \sum_{i=1}^N \frac{1}{2} m \left(\frac{d\boldsymbol{r}_i}{dt}\right)^2 \right\rangle_t. \tag{18}$$

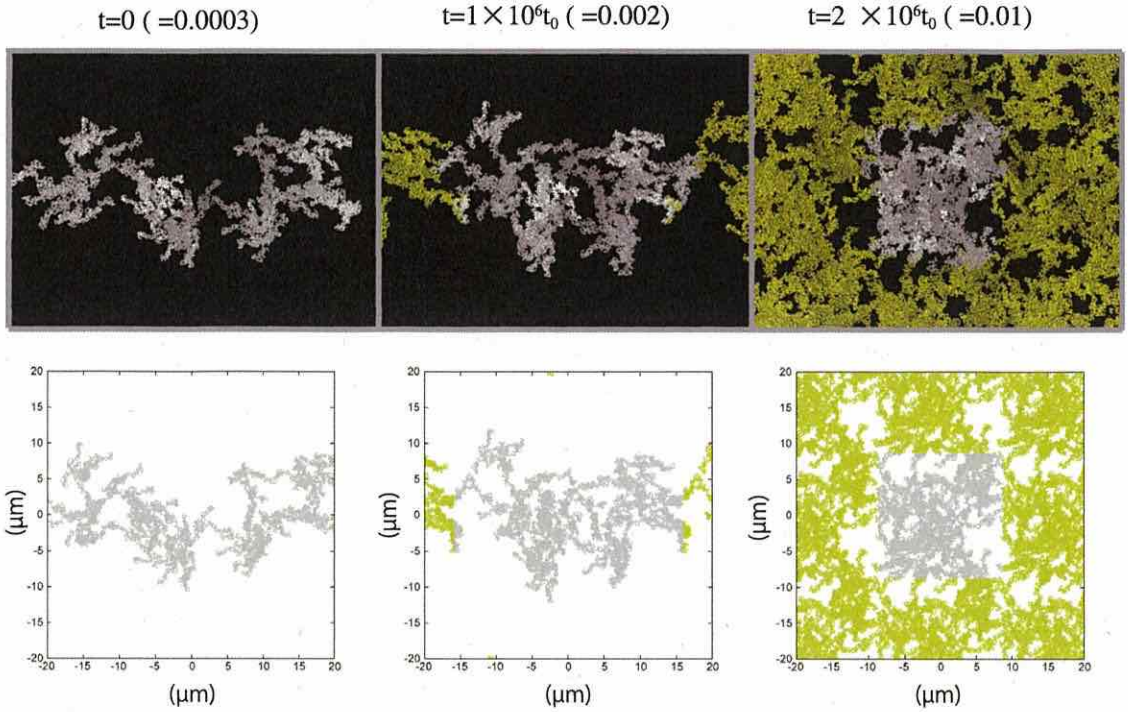

Fig. 3. Snapshots of the evolution of an aggregate under compression in the case of $N = 16\,384$. The *top three figures* are 3D visualizations. They have the same scale with different time epochs. The white particles are inside a box enclosed by the periodic boundaries. The yellow particles are in neighboring boxes to the box of white particles. For visualization, we do not draw the copies on the back and front sides of the boundaries but only 8 copies of the white particles across the boundaries. *Each bottom figure* represents projected positions onto 2D plane of all particles in each corresponding top figure. The gray points in the bottom figures correspond to the positions of the white particles in the top figures, and the yellow points correspond to those of the yellow particles in the top figures. Scales are in μm.

Using K and P, Eq. (15) gives an expression of P as

$$P = \frac{2}{3}K/V + \frac{1}{3}\left\langle \sum_i \boldsymbol{r}_i \cdot \boldsymbol{F}_i \right\rangle_t /V. \tag{19}$$

We define the force from particle j on particle i as $\boldsymbol{f}_{i,j}$. Force $\boldsymbol{F}_i$ can be written as a summation of the force from another particle as

$$\boldsymbol{F}_i = \sum_{j\neq i} \boldsymbol{f}_{i,j}. \tag{20}$$

Using $\boldsymbol{f}_{i,j} = -\boldsymbol{f}_{j,i}$, we finally obtain the pressure measuring formula as

$$P = \frac{2}{3}K/V + \frac{1}{3}\left\langle \sum_{i<j} (\boldsymbol{r}_i - \boldsymbol{r}_j) \cdot \boldsymbol{f}_{i,j} \right\rangle_t /V. \tag{21}$$

The first term on the righthand side of the equation represents the translational kinetic energy per unit volume, and the second term represents the summation of the force acting at all connections per unit volume. This expression is useful for measuring the pressure of a dust aggregate under compression. We do not need to put any artificial object, such as walls, in simulations because Eq. (21) is totally expressed in terms of the summation of the physical quantities of each particle, which are the mass, the position, the velocity, and the force acting on the particle. In our calculations, we take an average of pressure for every 10 000 time steps, corresponding to 1000 t_0 because we set 0.1 t_0 as one time step in our simulation.

As mentioned in Sect. 2.2, the adopted damping force corresponds to rapid damping of normal oscillations. Thus, the kinetic energy of random motion rapidly dissipates. This corresponds to the static compression, and thus the compressive strength is determined by the second term of Eq. (21).

3. Results

The top three panels of Fig. 3 show snapshots of the evolution of an aggregate under compression in the case where $N = 16\,384$, $C_v = 3 \times 10^{-7}$, $k_n = 0$, and $\xi_{crit} = 8$ Å. The top three panels have the same scale but different time epochs, which are $t = 0$, $1 \times 10^6 t_0$, and $2 \times 10^6 t_0$. The white particles are inside the computational region enclosed by the periodic boundaries, while the yellow particles are in the neighboring copy regions (for visualization, we do not draw particles on the front and backsides copy regions). The bottom three panels represent the projected positions onto the two-dimensional plane for the correspondent top three figures. We confirm that the dust aggregate is compressed by their copies from all directions. As the compression proceeds, the aggregate of white particles is compressed by the neighboring aggregate of yellow particles. We focus on how high pressure is generated by quasi-static compression in numerical simulations. Our numerical simulations have several parameters: the size of the initial BCCA cluster, the compression rate, the normal damping force, and the critical displacement (corresponds to the rolling energy). We investigate the dependence of the pressure on these parameters, by performing several runs with different parameter sets. Although we assume ice aggregates in most runs,

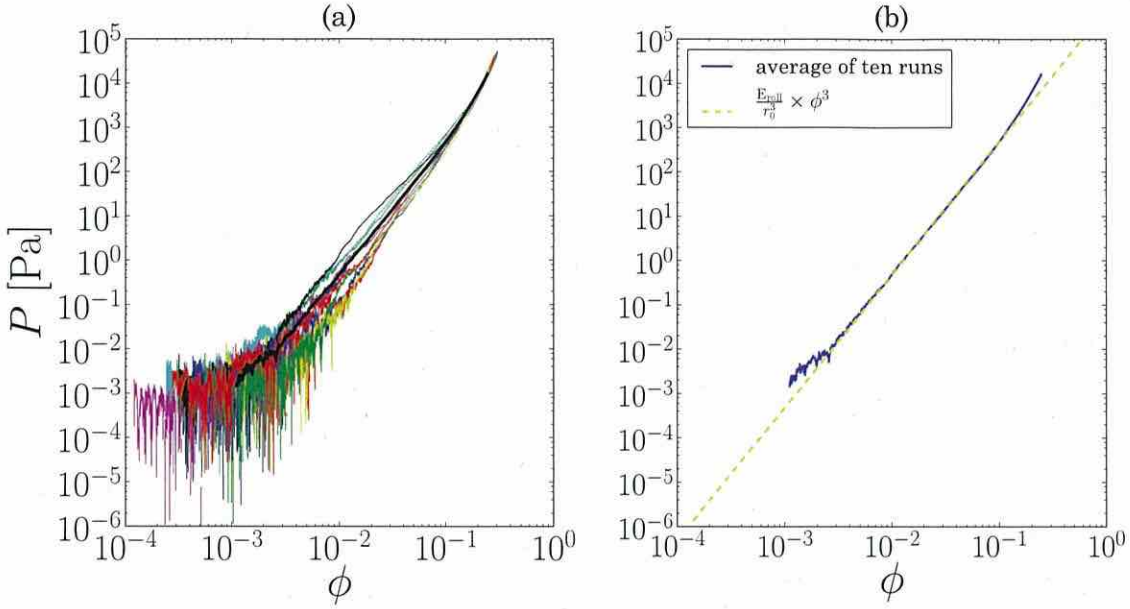

Fig. 4. a) Pressure P in [Pa] against filling factor ϕ. The ten thin solid lines show the results for the initial BCCA clusters with different initial random numbers and thick solid line shows the arithmetic average of the ten runs. **b)** Pressure P in [Pa] against filling factor ϕ. Same as the thick solid line in **a)** plotted with a dotted line of Eq. (25). The parameters are $N = 16\,384$, $C_v = 3 \times 10^{-7}$, $k_n = 0.01$, and $\xi_{crit} = 8$ Å.

we also investigate cases of silicate aggregates to compare them with previous studies.

3.1. Fiducial run: obtaining the compressive strength

We put a BCCA cluster as the initial aggregate. For each set of parameters, we randomly create ten BCCA clusters following Okuzumi et al. (2009) and take arithmetic averages of the ten simulations of the different initial clusters. The pressure is measured using Eq. (21) at each run. We define the filling factor of an aggregate as

$$\phi = \frac{V_0 N}{V}, \tag{22}$$

where V_0 is the monomer volume, N the number of monomers of the aggregate, and V the volume enclosed by the boundaries, which has a length of L. The filling factor also can be written as $\phi = \rho/\rho_0$. Figure 4 shows that the measured pressure as a function of the filling factor $\phi(t)$. The parameters of the simulations are $N = 16\,384$, $C_v = 3 \times 10^{-7}$, $k_n = 0.01$, and $\xi_{crit} = 8$ Å. The corresponding E_{roll} is 4.74×10^{-9} erg for $\xi_{crit} = 8$ Å. Each colored line in Fig. 4a shows each simulation with the different initial shape of the aggregate. Figure 4b shows the arithmetic average of the pressure measured in ten different runs. Each line shows in different ranges of ϕ. The lowest ϕ is determined with the largest size of the initial boundary boxes of the ten runs. We find that the compressive strength is reproduced well by

$$P = P_0 \phi^3, \tag{23}$$

where $P_0 = 4.74 \times 10^5$ Pa. We analytically discuss why the compressive strength is proportional to ϕ^3 in Sect. 4. In the high-density region ($\phi \gtrsim 10^{-1}$), the measured strength deviates from the line of $P = P_0\phi^3$. This is because the dissipation mechanism changes in the high-density region (see Sect. 3.4). The deviation in the low-density region ($\phi \lesssim 3 \times 10^{-3}$) is partly caused by a finite boundary speed (or compression rate) as discussed in the next section. Another reason for the deviation in the low-density region is related to the density of the initial BCCA cluster. The filling factor of BCCA ϕ_{BCCA} is estimated as

$$\phi_{BCCA} = \frac{V_0 N}{V_{BCCA}} = \left(\frac{3}{5}\right)^{3/2} N^{-1/2}, \tag{24}$$

where we use the radius and the volume of a BCCA cluster, $r_{BCCA} = \sqrt{5/3} N^{1/2} r_0$ and $V_{BCCA} = (4\pi/3) r_{BCCA}^3$, respectively (e.g., Suyama et al. 2008). For $N = 16\,384$, we obtain $\phi_{BCCA} \sim 3 \times 10^{-3}$. In the early stage of compression, ϕ is lower than ϕ_{BCCA} because the initial BCCA clusters are apart from each other. This space between BCCA clusters would also cause the deviation from the line of $P = P_0\phi^3$.

We now discuss the coefficient P_0 of the compressive strength. Wada et al. (2008) show that E_{roll} is important in the collisional compressive strength. Thus, E_{roll} is expected to also be important in the static compressive strength. Considering that the characteristic volume is the monomer's volume $\sim r_0^3$, we suppose $P_0 = E_{roll}/r_0^3$, based on dimension analysis. Therefore, the compressive strength can be written as

$$P = \frac{E_{roll}}{r_0^3} \phi^3. \tag{25}$$

We analytically discuss and confirm this equation in Sect. 4. We also plot this equation in Fig. 4b. This figure clearly shows that the result is well fit by Eq. (25).

We show that compressive strength is proportional to ξ_{crit}, which is proportional to the rolling energy E_{roll} in Sect. 3.5. We also confirm that Eq. (25) is applicable to the case of different r_0 in the silicate case.

3.2. Dependence on the boundary speed

To statically compress the aggregate, we should move the boundary at a low enough velocity not to create inhomogeneous structure. Figure 5 shows the dependency on the strain rate parameter.

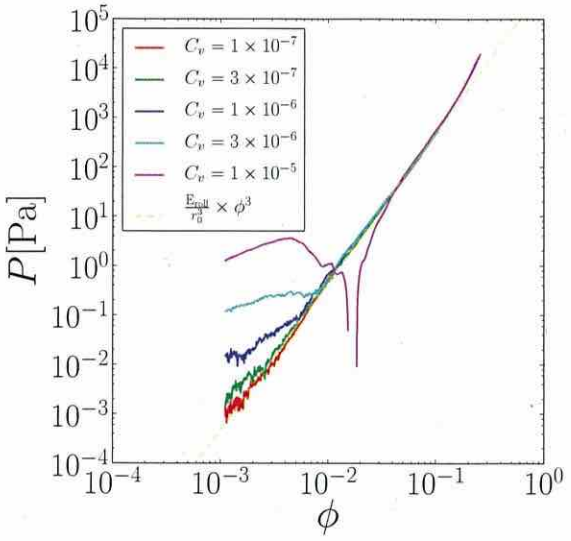

Fig. 5. Pressure P in [Pa] against filling factor ϕ with different strain rate parameter C_v. Each line shows the average of ten runs of the fixed strain rate: $C_v = 1 \times 10^{-7}$, 3×10^{-7}, 1×10^{-6}, 3×10^{-6}, 1×10^{-5}. The other parameters are the same for every ten runs: $N = 16\,384$, $k_n = 0.01$, and $\xi_{crit} = 8$ Å. The dashed line is Eq. (25).

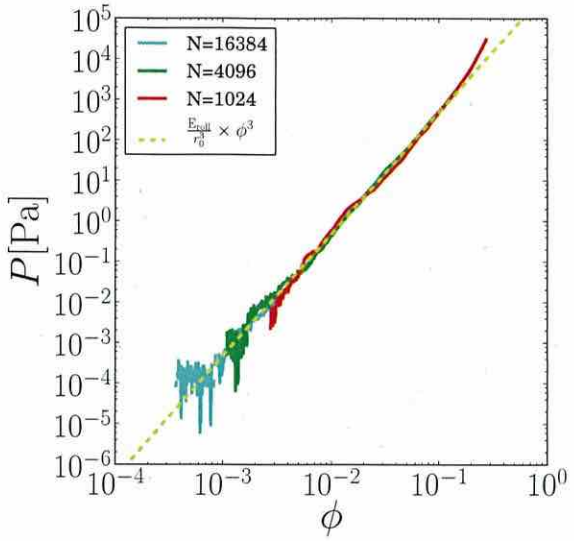

Fig. 6. Pressure P in [Pa] against filling factor ϕ with a different number of particles N. Each line shows the average of ten runs of the fixed number of particles: $N = 1024$, 4096, and 16 384. The other parameters are $C_v = 3 \times 10^{-7}$, $k_n = 0.01$, and $\xi_{crit} = 8$ Å in the case of $N = 1024$, 4096, and $C_v = 1 \times 10^{-7}$, $k_n = 0.01$, and $\xi_{crit} = 8$ Å in the case of $N = 16\,384$. The dashed line is Eq. (25).

Each line shows the average of ten runs. The fixed parameters are $N = 16\,384$, $k_n = 0.01$, and $\xi_{crit} = 8$ Å. The strain rate parameter C_v is equal to 1×10^{-7}, 3×10^{-7}, 1×10^{-6}, 3×10^{-6}, and 1×10^{-5}. The higher C_v, the higher pressure in the low-density region is required for compression. This is mainly caused by the ram pressure from the boundaries with high speed.

When the compression proceeds and the density becomes higher to reach the line of Eq. (25), the pressure follows the equation. From Fig. 5, $C_v = 3 \times 10^{-7}$ creates a sufficiently low boundary speed. The boundary speed can be calculated as a function of ϕ. Using Eq. (6) and $\phi = (4/3)\pi r_0^3 N/L^3$, the velocity difference between a boundary and the next boundary, v_d, can be written as

$$v_d = |2v_b| = 2\frac{C_v}{t_0}\left(\frac{\frac{4}{3}\pi r_0^3 N}{\phi}\right)^{1/3}. \quad (26)$$

In the case of $C_v = 3 \times 10^{-7}$, $v_d = 12.7$, 5.9, and 2.7 cm/s for $\phi = 10^{-3}$, 10^{-2}, and 10^{-1}, respectively.

Here, we discuss the velocity difference of boundaries, comparing with the effective sound speed of the aggregates. The effective sound speed can be estimated as

$$c_{s,eff} \sim \sqrt{\frac{P}{\rho}} \sim \sqrt{\frac{E_{roll}}{\rho_0 r_0^3}\frac{\rho}{\rho_0}} \sim \sqrt{\frac{E_{roll}}{m_0}\phi}. \quad (27)$$

where we use Eq. (25). Using the rolling energy of ice particles, $c_{s,eff}$ is given by

$$c_{s,eff} \sim 1.1 \times 10^3 \phi \text{ cm/s}. \quad (28)$$

Therefore, in the case of $C_v = 3 \times 10^{-7}$, v_d is not low enough in the beginning of the simulation, where the aggregate has a low filling factor. However, the boundary velocity difference reaches lower than the effective sound speed when $\phi \gtrsim 10^{-2}$.

3.3. Dependence on the size of the initial BCCA cluster

To confirm that Eq. (25) is valid in the lower density region, we perform the simulations with the different number of particles, which is equivalent to the different sizes of the initial dust aggregates. Figure 6 shows dependence on the number of particles of the initial BCCA cluster. The initial numbers of particles are 1024, 4096, and 16 384. The other parameters are $C_v = 3 \times 10^{-7}$, $k_n = 0.01$, and $\xi_{crit} = 8$ Å in the case of $N = 1024$ and $N = 4096$, and $C_v = 1 \times 10^{-7}$, $k_n = 0.01$, and $\xi_{crit} = 8$ Å in the case of $N = 16\,384$. We chose lower C_v in the case of $N = 16\,384$ to investigate the strength in lower ϕ region. Each line represents the average of ten runs for each simulation as in Figs. 4b and 5. We draw the averaged line from lower ϕ than in Fig. 5. In such a low ϕ region, we consider that the pressure is zero for some runs because the aggregate is isolated from the copies of the aggregate over the periodic boundaries. Except for the initial deviation in low ϕ, all lines show good agreement with Eq. (25) where $\phi \lesssim 0.1$. The result agrees in lower ϕ for runs with larger N. Therefore, we conclude that the formula Eq. (25) is valid for $\phi \lesssim 0.1$.

3.4. Dependence on the normal damping force

As described in Sect. 2.2, we adopt the normal damping force to reduce the normal oscillations in addition to Wada et al. (2007). To confirm that this damping factor does not affect the simulation results, we set the damping factor k_n as a parameter. Figure 7 shows dependence of pressure on the normal damping factor k_n. The fixed parameters are $N = 16\,384$ $C_v = 3 \times 10^{-7}$, and $\xi_{crit} = 8$ Å. Each line represents the result of one run for $k_n = 0$, 10^{-2}, and 10^{1}, respectively. This figure clearly shows that the normal damping force does not affect the simulation results.

As mentioned in Sect. 3.1, the compressive strength in the low-density region ($\phi \lesssim 0.1$) is expected to be determined by the rolling motion. To confirm this, we calculate the total energy

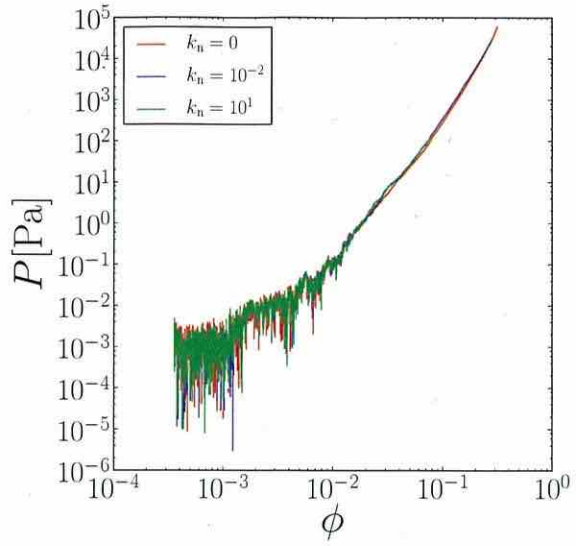

Fig. 7. Pressure P in [Pa] against filling factor ϕ with different normal damping force. We put the same ten initial conditions varying the normal damping force with $k_n = 0$, $k_n = 10^{-2}$, and $k_n = 10^{1}$. Each line shows the result of one run. The other parameters are $N = 16\,384$, $C_v = 3 \times 10^{-7}$, and $\xi_{crit} = 8$ Å.

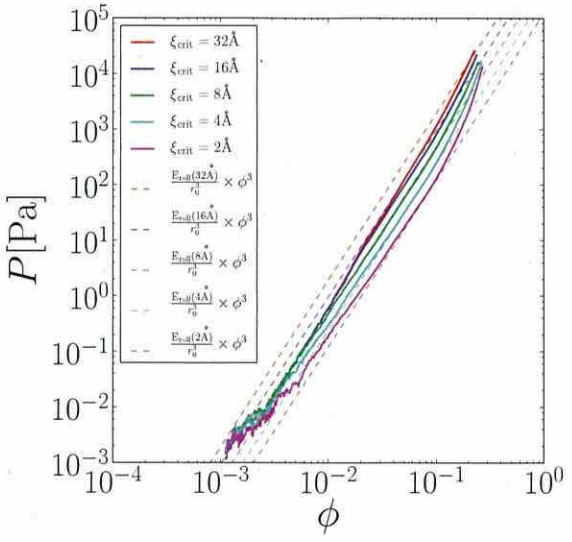

Fig. 9. Pressure P in [Pa] against filling factor ϕ with different critical displacement, ξ_{crit}. We put the same ten initial conditions varying ξ_{crit} with $\xi_{crit} = 32, 16, 8, 4$, and 2 Å, respectively. Each line shows the average of ten runs. The other parameters are $N = 16\,384$ $C_v = 3 \times 10^{-7}$, and $k_n = 10^{-2}$.

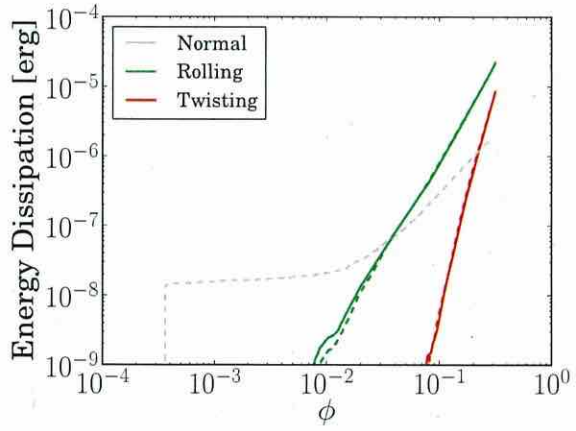

Fig. 8. Energy dissipation of each dissipation mechanism in [erg] against filling factor ϕ. The solid lines show the result in the case without the normal damping and the dashed lines in the case of $k_n = 0.01$ and The results in the case of $k_n = 10$ are not plotted because they are the same as those in the case of $k_n = 0.01$ and indistinguishable. The dissipation mechanisms are normal damping, rolling, sliding, and twisting. The dissipation energy by sliding motion is less than 10^{-9} erg.

dissipations of all motions, which are normal damping, rolling, sliding, and twisting. Figure 8 shows the dissipated energy for each mechanism, the dissipated energies in the case without the normal damping and those in the case of $k_n = 0.01$.

The dissipated energy in the case of $k_n = 10$ is indistinguishable from those in the case of $k_n = 0.01$, and thus we do not plot them. The dissipation energy of the sliding force is less than 10^{-9} erg, so it is not depicted in this figure. The dissipation by the rolling and twisting is almost the same in the cases with and without the normal damping. Thus, we confirm that the normal damping does not affect the compressive strength, although it dissipates the energy of the normal oscillations. Aside from the normal dissipation, the dominant dissipation mechanism is the rolling motion. This clearly shows that the static compression is determined by the rolling motion of each connection, as mentioned in Sect. 3.1. Where $\phi \gtrsim 0.1$, the energy dissipation by twisting motion occurs. This is why Eq. (25) is valid until the filling factor reaches 0.1 as mentioned in Sect. 3.1. In the high-density region, where $\phi \gtrsim 0.1$, another formulation is required but that is beyond the scope of this paper.

3.5. Dependence on the rolling energy

We also investigate the dependence of the compressive strength on ξ_{crit}. Since E_{roll} is proportional to ξ_{crit}, we investigate the dependence on the rolling energy in this section. Figure 9 shows the dependency on ξ_{crit}. We vary ξ_{crit} with 32, 16, 8, 4, and 2 Å. The fixed parameters are $N = 16\,384$, $C_v = 3 \times 10^{-7}$, and $k_n = 10^{-2}$. This result shows that the compressive strength is almost the same in the low-density region. This is because the periodic boundary creates the additional voids as discussed in Sect. 3.1, so we should not focus on the low-density region. The lines in the case of $\xi_{crit} = 2, 4$, and 8 Å are on the corresponding lines of Eq. (25) where $\phi \lesssim 0.1$. The line in the case of $\xi_{crit} = 16$ Å has a little deviation, and in the case of $\xi_{crit} = 32$ Å it has a deviation from their corresponding lines of Eq. (25). The reason the lines in the case of $\xi_{crit} = 16, 32$ Å deviate from the corresponding lines of Eq. (25) is that the dissipation energy is dominated not by rolling motion but by a twisting motion as indicated in Fig. 10. This figure shows that dissipated energy of each dissipation mechanism.

We show the results of the cases with $\xi_{crit} = 8$, 16, and 32 Å. The normal damping does not contribute to the compressive strength as discussed in Sect. 3.4, and thus we focus on the rolling and twisting motions.

When $\xi_{crit} \leq 8$ Å, the dissipation energy is dominated by rolling motion. For $\xi_{crit} = 32$ Å, on the other hand, the dissipation energy is dominated by a twisting motion. For $\xi_{crit} = 16$ Å, the dissipation energy of rolling and twisting motion is comparable, and making it the marginal case. Thus, the reason

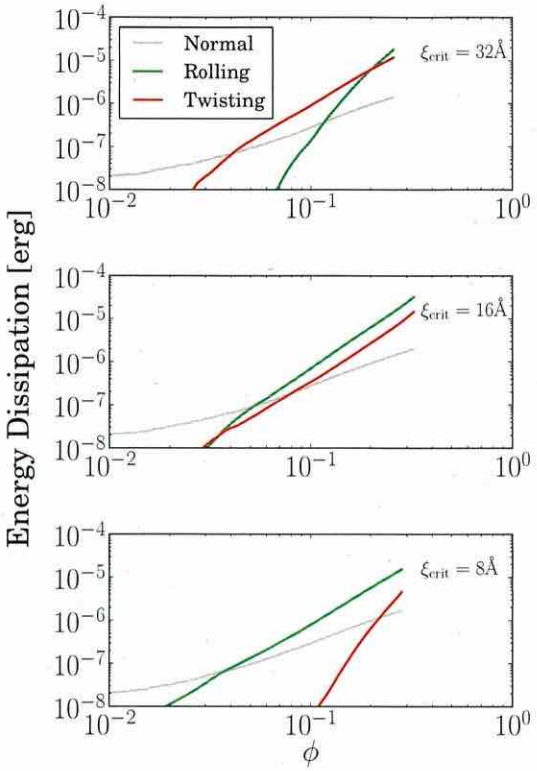

Fig. 10. Energy dissipation of each dissipation mechanism in [erg] against filling factor ϕ. Each panel represents the case of different $\xi_{\rm crit}$, which are 32, 16, and 8 Å, corresponding to Fig. 9.

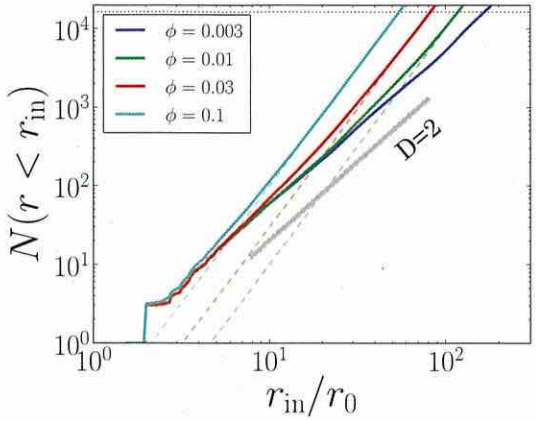

Fig. 11. Number of particles inside the radius $r_{\rm in}$ against normalized radius $r_{\rm in}/r_0$. This figure represents the fractal structure of the compressed aggregates in our simulation for various ϕ. We set a particle as an origin and count the number of particles inside $r < r_{\rm in}$, where r is the distance from the origin to each particle's center. Then we count the same correlation of all particles as an origin and take their average (similar figure of Fig. 7 in the paper of Wada et al. 2008). Each line shows the result at the different time steps. The solid thick lines represents the structure of fractal dimension $D = 2$, and dashed lines represent $D = 3$ for each corresponding ϕ. The dotted line shows the number of particles in calculation. The region below this line corresponds to inside the periodic boundaries.

Eq. (25) is not valid when $\xi_{\rm crit} \geq 16$ Å is that the twisting motion is the dominant mechanism for determining the compressive strength. Therefore, we conclude that Eq. (25) is valid when $\xi_{\rm crit} \leq 8$ Å.

3.6. Fractal structure

We also investigate how the fractal structure of the dust aggregate changes. Figure 11 shows how many particles are inside the distance $r_{\rm in}$ for four snapshots. We select one run from the case with $N = 16\,384$, $C_{\rm v} = 3\times10^{-7}$, $k_{\rm n} = 10^{-2}$, and $\xi_{\rm crit} = 8$ Å. Each snapshot is when $\phi = 0.003, 0.01, 0.03$ and 0.1, respectively. We take a particle as an origin and count the number of particles inside $r < r_{\rm in}$, where r is the length from the origin. Then we set the computational region as an origin for all the other particles inside and take an average of them. We obtain the same trend in several runs in the cases of different shapes of initial aggregates.

We also count particles beyond the periodic boundaries. In high $r_{\rm in}$, $N \propto r_{\rm in}^3$ because of copies over the periodic boundary distributed as a fractal dimension of three. Therefore, where $N(r < r_{\rm in}) \gtrsim 16\,384$, N must be $N \propto r_{\rm in}^3$. However, it is almost out of the range of Fig. 11. Figure 11 shows the number of particles in calculation, which is $N = 16\,384$. The results over this line are affected by the periodic boundary condition and those below this line are in computational region. Thus, the results below the line represent the fractal structure inside the computational region and are not the artificial effect of the periodic boundary condition.

Since the initial aggregate is a BCCA cluster, N is proportional to $r_{\rm in}^2$. In the case of $\phi = 0.003$, which is equivalent to ϕ of the initial BCCA cluster, $N \propto r_{\rm in}^2$ as shown in Fig. 11. When the fractal dimension is three, N can be written as

$$N(r < r_{\rm in}) = \frac{\phi V(r < r_{\rm in})}{V_0} = \phi\left(\frac{r_{\rm in}}{r_0}\right)^3, \tag{29}$$

where $V(r < r_{\rm in}) = (4/3)\pi r_{\rm in}^3$. We also plot this equation for each ϕ in Fig. 11, with good agreement on a large scale, while maintaining $N \propto r_{\rm in}^2$ on a small scale.

Therefore, the structure evolution in the static compression is as follows. Initially, $N \propto r_{\rm in}^2$ because the aggregate is a BCCA cluster. As compression proceeds, the fractal dimension D becomes three on a large scale, while it is two on a small scale. The transit scale from $D = 2$ to $D = 3$ becomes smaller as compression proceeds until $D = 3$ on any scale. This structure evolution means that the static compression reconstructs the aggregate first on a large scale when keeping the small-scale BCCA structure. This is the reason the rolling motion determines the compressive strength, as discussed in Sect. 4.

3.7. Silicate case: comparison with previous studies

The compressive strength has been investigated in the previous study (Seizinger et al. 2012). To investigate the connection of compressive strength from the low-density to the high-density regions, we perform simulations in the case of silicate with the same parameters of Seizinger et al. (2012). Figure 12 shows compression in the case of silicate whose monomer size is 0.6 μm. The parameters are $N = 16\,384$, $C_{\rm v} = 3\times10^{-7}$, and $k_{\rm n} = 0.01$. Figure 12a shows the results of ten runs with different initial aggregates and Fig. 12b shows their average. Using the rolling energy of silicate, which is $E_{\rm roll} = 1.42\times10^{-8}$ erg, we also plot the line of Eq. (25) in Fig. 12b. Since t_0 is given by 1.71×10^{-9} s for silicate aggregates, $v_{\rm d}$ becomes 4.01 cm/s for $\phi = 10^{-2}$ with $C_{\rm v} = 3\times10^{-7}$. This $v_{\rm d}$ is larger than $c_{\rm s,eff}$(=0.77 cm/s when $\phi = 0.01$) for silicate aggregates, allowing the numerical

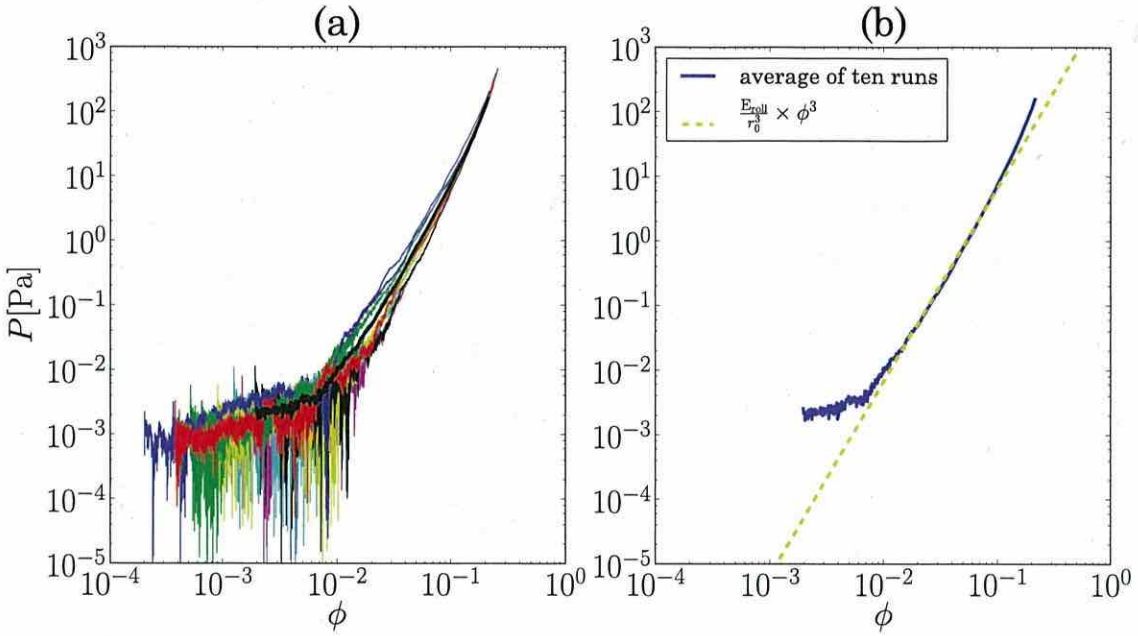

Fig. 12. Pressure P in [Pa] against filling factor ϕ. This figure is same as Fig. 4 but for the case of silicate particles ($r_0 = 0.6\,\mu$m).

results shown in Fig. 12 to deviate from the line of Eq. (25) in the low ϕ region. When $v_d = c_{s,eff}$, $\phi = 3.4 \times 10^{-2}$, the compressive strength should obey Eq. (25) when $\phi \gtrsim 3.4 \times 10^{-2}$. In the case of silicate, computational time is huge compared with ice particles. We take a relatively high value of the boundary speed to save on computational time. Therefore, the result deviates from Eq. (25) in the low-density region because of the high velocity. In other words, the compression is not static in the low density region. In the high-density region, on the other hand, the result is in good agreement with Eq. (25), suggesting that Eq. (25) is applicable to aggregates consisting of silicate particles with different r_0.

Figure 13 compares our simulation results and Eq. (25) in the low-density region ($\phi < 0.1$) with the results of Seizinger et al. (2012) and the fitting formula to experiments (Güttler et al. 2009). This figure corresponds to Fig. 4 in Seizinger et al. (2012). They performed similar N-body simulations to ours but using a BPCA aggregate composed of silicate particles as an initial condition. The compressive strength of our simulations shows good agreement with the same interaction model in Seizinger et al. (2012) with a little discrepancy: $\phi = 0.24$ at $P = 300$ Pa in our simulations and $\phi = 0.21$ at $P = 300$ Pa in Seizinger et al. (2012). The discrepancy, 13% in ϕ, may be caused by the difference in the initial aggregate or the pressure measurement method. The fitting formula of Güttler et al. (2009) suggests $\phi = 0.17$ at $P = 300$ in the experiments. The discrepancy from our simulations is 29% in ϕ. In applicable uses of the static compression formula, we focus on obtaining ϕ with a given P.

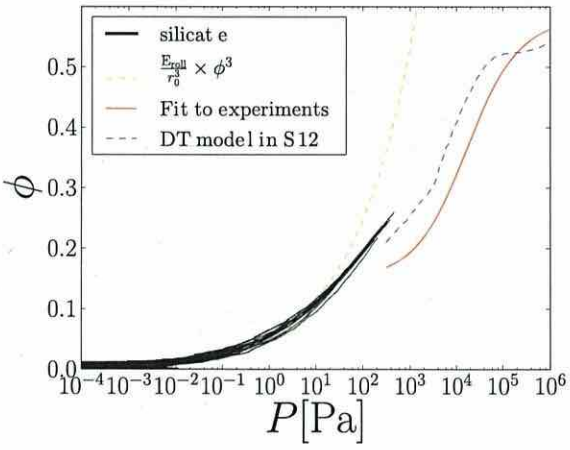

Fig. 13. The filling factor ϕ against pressure P in [Pa]. This figure is same as Fig. 12, but plotted with a linear scale of ϕ and reversal of xy axis to compare with previous studies (see Fig. 4 in Seizinger et al. 2012). The dotted line is the result of numerical simulations in the high-density region ($\phi \gtrsim 0.1$) in Seizinger et al. (2012) and the thin solid line is the fitting formula proposed by Güttler et al. (2009). Our results consistently connect to the previous simulations in the high-density region.

4. Understanding the compressive strength formula

In this section, we analytically derive the compressive strength and confirm Eq. (25). First, we consider the structure of a fluffy aggregate in static compression in our simulations. As described in Sect. 2.3, we adopt the periodic boundary condition and put a BCCA cluster as the initial condition. This corresponds to a large aggregate that filled up with BCCA clusters three dimensionally. As compression proceeds, the initial BCCA cluster is compressed but the aggregate keeps smaller BCCA structure as confirmed in Sect. 3.6. Therefore, the aggregate in static compression always consists of BCCA clusters on some scale and filled up with them. Figure 14 illustrates the aggregate in static compression. The enclosed lines depict BCCA clusters on a small scale.

Next, we consider why the compressive strength can be determined by the rolling energy. The internal mass density and the volume filling factor of the aggregate are equal to those of the BCCA clusters. Compression of the whole aggregate proceeds by compression of each cluster. Therefore, the compressive strength of the whole aggregate would be determined by

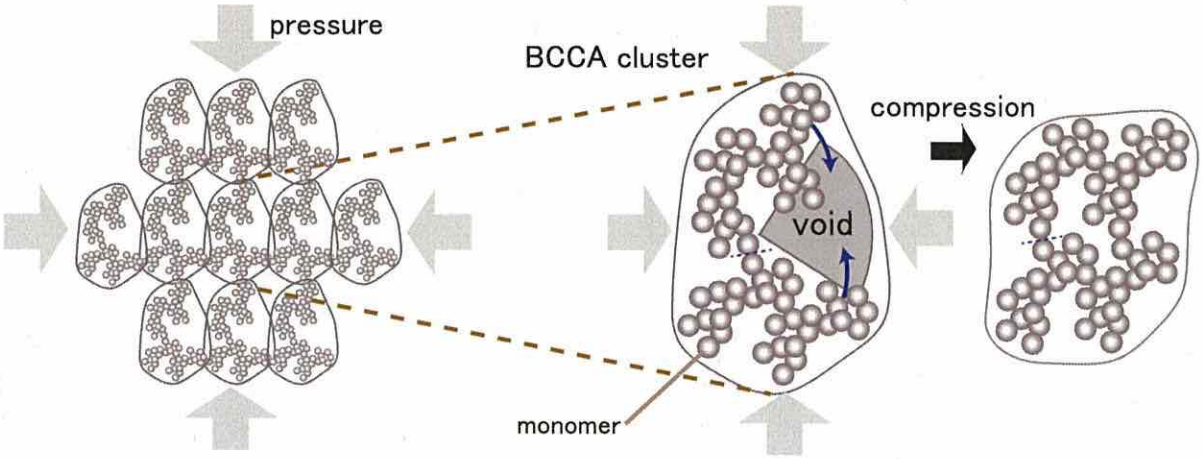

Fig. 14. Schematic drawing of compression of a dust aggregate consisting of a number of BCCA clusters. *The left figure* shows a dust aggregate consisting of many BCCA clusters and the BCCA clusters are distributed three dimensionally. Each enclosed line represents each region dominated by the BCCA clusters. *The central figure* is a BCCA cluster, receiving pressure from the next clusters. The BCCA cluster has a large void depicted in *the central figure*, and thus the void would be compressed, as expressed in *the right figure*. The required energy to compress the void is the energy to rotate the connection of monomers in contact. Therefore, the compression can be determined by the rolling motion of monomer connection on the connecting point of the subclusters.

BCCA clusters. The righthand panel of Fig. 14 illustrates compression of one of BCCA clusters. The pressure on the BCCA cluster is exerted by neighbor clusters, which causes the compression of the BCCA cluster. The BCCA cluster can be divided further into two smaller subclusters because BCCA clusters are created by cluster-cluster aggregation. A large void exists between the two smaller clusters, and they are connected with one connection of monomers in contact. The compression of the BCCA cluster occurs by crashing the large void, which only requires rolling the monomers at the connection.

We now estimate the compressive strength. In static compression, the aggregate is compressed by external pressure. Each BCCA cluster feels a similar pressure, P. Using the pressure, the force on the BCCA cluster is approximately given by

$$F \sim P \cdot r_{\rm BCCA}^2. \tag{30}$$

Since the crashing of the large void is accompanied by the rolling of a pair of monomers in contact, the work required for the crashing is given by so-called the rolling energy of monomers, $E_{\rm roll}$ (Dominik & Tielens (1997) or see Eq. (1) for its definition). Therefore, the required force to compress the aggregate satisfies

$$F \cdot r_{\rm BCCA} \sim E_{\rm roll}. \tag{31}$$

Substituting Eq. (30), we further obtain the required pressure to compress the aggregate as

$$P \sim \frac{E_{\rm roll}}{r_{\rm BCCA}^3}. \tag{32}$$

The radius of the BCCA clusters can be written by using the physical values of the whole aggregate. The internal density of the BCCA cluster is dependent on its radius. The BCCA cluster has the fractal dimension of two, and its radius is approximately given by $r_{\rm BCCA} = N^{1/2} r_0$, where N is the number of constituent monomers in the BCCA subcluster. The internal density of the BCCA cluster is evaluated as

$$\rho \sim \frac{N m_0}{r_{\rm BCCA}^3} \sim \left(\frac{r_{\rm BCCA}}{r_0}\right)^{-1} \rho_0. \tag{33}$$

Using Eqs. (32) and (33), we finally obtain the required pressure (or the compressive strength) as

$$P \sim \frac{E_{\rm roll}}{r_0^3} \left(\frac{\rho}{\rho_0}\right)^3. \tag{34}$$

This is the same as Eq. (25) obtained from our numerical simulations.

5. Summary

We investigated the static compressive strength of highly porous dust aggregates, whose filling factor ϕ is lower than 0.1. We performed numerical N-body simulations of static compression of highly porous dust aggregates. The initial dust aggregate is assumed to be a BCCA cluster. The particle-particle interaction model is based on Dominik & Tielens (1997) and Wada et al. (2007). We introduced a new method for compression and adopted the periodic boundary condition in order to compress the dust aggregate uniformly and naturally. Because of the periodic boundary condition, the dust aggregate in the computational region represents one part of a large aggregate, and thus we could investigate the compression of a large aggregate. The periodic boundaries move toward the center, and the distance between the boundaries becomes small. To measure the pressure of the aggregate, we adopted a similar manner to the one used in molecular-dynamics simulations. As a result of the numerical simulations, our main findings are as follows.

- The relation between the compression pressure P and the filling factor ϕ can be written as

$$P = \frac{E_{\rm roll}}{r_0^3} \phi^3, \tag{35}$$

where $E_{\rm roll}$ is the rolling energy of monomer particles and r_0 the monomer radius. We defined the filling factor as $\phi = \rho/\rho_0$, where ρ is the mass density of the whole aggregate,

and ρ_0 is the material mass density. Equation (35) is independent of the numerical parameters: the number of particles, the size of the initial BCCA cluster, the boundary speed, and the normal damping force. We confirmed that Eq. (35) is applicable in different $E_{\rm roll}$ and r_0. We also analytically confirmed Eq. (35).

- Equation (35) is valid where $\phi \lesssim 0.1$ in the high-density region. In the low-density region, we confirmed that Eq. (35) is valid for $\phi \gtrsim 10^{-3}$ in the case of $N = 16\,384$. From the results of different initial sizes of the aggregates, Eq. (35) is valid in the lower-density region in the case of the larger aggregates.
- The initial BCCA cluster has a fractal dimension of two in the radius of the cluster, although the whole aggregate has a fractal dimension of three because of the periodic boundary. As compression proceeds, the fractal dimension inside the radius of the initial BCCA cluster becomes three, while the fractal dimension on a smaller scale keeps being two. This means that the initial set up, which is that the fractal dimension on a large scale is three and that on a small scale is two, reproduce the structure of a dust aggregate well in static compression as a consequence. This also supports the compressive strength being determined by BCCA structure on a small scale as shown in the analytical approach.
- The static compression in the high-density region ($\phi \gtrsim 0.1$) has been investigated in the silicate case in previous studies (e.g., Seizinger et al. 2012). We also performed the numerical simulations in the silicate case and confirmed that our results are consistent with those of previous studies in the high-density region.

The compressive strength formula allowed us to study how static compression affects the porosity evolution of dust aggregates in protoplanetary disks. In applications to dust compression in protoplanetary disks, we use the compressive strength formula to obtain ϕ with a given P. Moreover, the obtained compressive strength would be applicable to SPH simulations of dust collisions (Geretshauser et al. 2010, 2011). This application of the static compression process is important future work. In this work, we did not study shear or tensile strengths, but they are also worth investigating in future work.

Acknowledgements. We thank Kohji Tomisaka and Hiroki Senshu for fruitful discussions. We appreciate the careful reading and fruitful comments by the anonymous referee and the editor, Tristan Guillot. A.K. is supported by the Research Fellowship from the Japan Society for the Promotion of Science (JSPS) for Young Scientists (24-2120). S.O. acknowledges support by Grants-in-Aid for JSPS Fellows (22-7006) from MEXT of Japan. K.W. acknowledges support by Grants-in- Aid for Scientific Research (24540459) from MEXT of Japan.

References

A'Hearn, M. F. 2011, ARA&A, 49, 281
Birnstiel, T., Dullemond, C. P., & Brauer, F. 2010, A&A, 513, A79
Blum, J. 2004, in Astrophysics of Dust, eds. A. N. Witt, G. C. Clayton, & B. T. Draine, ASP Conf. Ser., 369, 309
Blum, J., & Wurm, G. 2000, Icarus, 143, 138
Brauer, F., Dullemond, C. P., & Henning, T. 2008, A&A, 480, 859
Dominik, C., & Tielens, A. G. G. M. 1997, ApJ, 480, 647
Geretshauser, R. J., Speith, R., Güttler, C., Krause, M., & Blum, J. 2010, A&A, 513, A58
Geretshauser, R. J., Meru, F., Speith, R., & Kley, W. 2011, A&A, 531, A166
Greenwood, J., & Johnson, K. 2006, J. Colloid Interf. Sci., 296, 284
Güttler, C., Krause, M., Geretshauser, R. J., Speith, R., & Blum, J. 2009, ApJ, 701, 130
Haile, J. M. 1992, Molecular Dynamics Simulation: Elementary Methods, 1st edn. (New York, NY, USA: John Wiley & Sons, Inc.)
Hayashi, C., Nakazawa, K., & Nakagawa, Y. 1985, in Protostars and Planets II, eds. D. C. Black, & M. S. Matthews, 1100
Heim, L.-O., Blum, J., Preuss, M., & Butt, H.-J. 1999, Phys. Rev. Lett., 83, 3328
Kempf, S., Pfalzner, S., & Henning, T. K. 1999, Icarus, 141, 388
Krause, M., & Blum, J. 2004, Phys. Rev. Lett., 93, 1103
Meakin, P. 1991, Rev. Geophys., 29, 317
Nakagawa, Y., Nakazawa, K., & Hayashi, C. 1981, Icarus, 45, 517
Okuzumi, S., Tanaka, H., & Sakagami, M.-A. 2009, ApJ, 707, 1247
Okuzumi, S., Tanaka, H., Kobayashi, H., & Wada, K. 2012, ApJ, 752, 106
Ormel, C. W., Spaans, M., & Tielens, A. G. G. M. 2007, A&A, 461, 215
Paszun, D., & Dominik, C. 2006, Icarus, 182, 274
Paszun, D., & Dominik, C. 2008, A&A, 484, 859
Paszun, D., & Dominik, C. 2009, A&A, 507, 1023
Seizinger, A., Speith, R., & Kley, W. 2012, A&A, 541, A59
Smirnov, B. M. 1990, Phys. Rep., 188, 1
Suyama, T., Wada, K., & Tanaka, H. 2008, ApJ, 684, 1310
Suyama, T., Wada, K., Tanaka, H., & Okuzumi, S. 2012, ApJ, 753, 115
Tanaka, H., Himeno, Y., & Ida, S. 2005, ApJ, 625, 414
Tanaka, H., Wada, K., Suyama, T., & Okuzumi, S. 2012, Prog. Theor. Phys. Suppl., 195, 101
Wada, K., Tanaka, H., Suyama, T., Kimura, H., & Yamamoto, T. 2007, ApJ, 661, 320
Wada, K., Tanaka, H., Suyama, T., Kimura, H., & Yamamoto, T. 2008, ApJ, 677, 1296
Wada, K., Tanaka, H., Suyama, T., Kimura, H., & Yamamoto, T. 2009, ApJ, 702, 1490
Wada, K., Tanaka, H., Suyama, T., Kimura, H., & Yamamoto, T. 2011, ApJ, 737, 36
Weidenschilling, S. J., & Cuzzi, J. N. 1993, in Protostars and Planets III, eds. E. H. Levy, & J. I. Lunine, 1031
Zsom, A., Ormel, C. W., Güttler, C., Blum, J., & Dullemond, C. P. 2010, A&A, 513, A57
Zsom, A., Ormel, C. W., Dullemond, C. P., & Henning, T. 2011, A&A, 534, A73

The Astrophysical Journal Letters, 748:L22 (7pp), 2012 April 1 doi:10.1088/2041-8205/748/2/L22

DISCOVERY OF SMALL-SCALE SPIRAL STRUCTURES IN THE DISK OF SAO 206462 (HD 135344B): IMPLICATIONS FOR THE PHYSICAL STATE OF THE DISK FROM SPIRAL DENSITY WAVE THEORY*

T. Muto[1,34,35], C. A. Grady[2,3,4], J. Hashimoto[5], M. Fukagawa[6], J. B. Hornbeck[7], M. Sitko[8,9,36], R. Russell[10,36], C. Werren[9,36], M. Curé[11], T. Currie[3], N. Ohashi[12,13], Y. Okamoto[14], M. Momose[14], M. Honda[15], S. Inutsuka[16], T. Takeuchi[1], R. Dong[17], L. Abe[18], W. Brandner[19], T. Brandt[17], J. Carson[20], S. Egner[13], M. Feldt[19], T. Fukue[5], M. Goto[19], O. Guyon[13], Y. Hayano[13], M. Hayashi[21,37], S. Hayashi[13], T. Henning[19], K. W. Hodapp[22], M. Ishii[13], M. Iye[5], M. Janson[17], R. Kandori[5], G. R. Knapp[17], T. Kudo[13], N. Kusakabe[5], M. Kuzuhara[5,23], T. Matsuo[24], S. Mayama[25], M. W. McElwain[3], S. Miyama[5], J.-I. Morino[5], A. Moro-Martin[17,26], T. Nishimura[13], T.-S. Pyo[13], E. Serabyn[27], H. Suto[5], R. Suzuki[28], M. Takami[12], N. Takato[13], H. Terada[13], C. Thalmann[29], D. Tomono[13], E. L. Turner[17,30], M. Watanabe[31], J. P. Wisniewski[32], T. Yamada[33], H. Takami[13], T. Usuda[13], and M. Tamura[5]

[1] Department of Earth and Planetary Sciences, Tokyo Institute of Technology, 2-12-1 Ookayama, Meguro, Tokyo 152-8551, Japan; muto@geo.titech.ac.jp
[2] Eureka Scientific, 2452 Delmer, Suite 100, Oakland CA 96002, USA
[3] ExoPlanets and Stellar Astrophysics Laboratory, Code 667, Goddard Space Flight Center, Greenbelt, MD 20771, USA
[4] Goddard Center for Astrobiology, Code 667, Goddard Space Flight Center, Greenbelt, MD 20771, USA
[5] National Astronomical Observatory of Japan, 2-21-1 Osawa, Mitaka, Tokyo 181-8588, Japan
[6] Department of Earth and Space Science, Graduate School of Science, Osaka University, 1-1, Machikaneyama, Toyonaka, Osaka 560-0043, Japan
[7] Department of Physics and Astronomy, University of Louisville, Louisville, KY 40292, USA
[8] Space Science Institute, 4750 Walnut St., Suite 205, Boulder, CO 80301, USA
[9] Department of Physics, University of Cincinnati, Cincinnati, OH 45221-0011, USA
[10] The Aerospace Corporation, Los Angeles, CA 90009, USA
[11] Departamento de Física y Astronomía, Universidad de Valparaíso, Avda. Gran Bretaña 1111, Casilla 5030, Valparaíso, Chile
[12] Institute of Astronomy and Astrophysics, Academia Sinica, P.O. Box 23-141, Taipei 106, Taiwan
[13] Subaru Telescope, 650 North A'ohoku Place, Hilo, HI 96720, USA
[14] College of Science, Ibaraki University, 2-1-1 Bunkyo, Mito, Ibaraki 310-8512, Japan
[15] Department of Information Science, Kanagawa University, 2946 Tsuchiya, Hiratsuka, Kanagawa 259-1293, Japan
[16] Department of Physics, Nagoya University, Furo-cho, Chikusa-ku, Nagoya, Aichi, 464-8602, Japan
[17] Department of Astrophysical Sciences, Princeton University, NJ08544, USA
[18] Laboratoire Lagrange, UMR7293, Université de Nice-Sophia Antipolis, CNRS, Observatoire de la Côte d'Azur, 06300 Nice, France
[19] Max Planck Institute for Astronomy, Heidelberg, Germany
[20] Department of Physics and Astronomy, College of Charleston, 58 Coming St., Charleston, SC 29424, USA
[21] Department of Astronomy, The University of Tokyo, Hongo 7-3-1, Bunkyo-ku, Tokyo 113-0033, Japan
[22] Institute for Astronomy, University of Hawaii, 640 North A'ohoku Place, Hilo, HI 96720, USA
[23] Department of Earth and Planetary Science, The University of Tokyo, Hongo, 7-3-1, Bunkyo-ku, Tokyo 113-0033, Japan
[24] Department of Astronomy, Kyoto University, Kitashirakawa-Oiwake-cho, Sakyo-ku, Kyoto, 606-8502, Japan
[25] The Graduate University for Advanced Studies(SOKENDAI), Shonan International Village, Hayama-cho, Miura-gun, Kanagawa 240-0193, Japan
[26] Departamento de Astrofísica, CAB (INTA-CSIC), Instituto Nacional de Técnica Aeroespacial, Torrejón de Ardoz, 28850, Madrid, Spain
[27] Jet Propulsion Laboratory, California Institute of Technology, Pasadena, CA 91109, USA
[28] TMT Observatory Corporation, 1111 South Arroyo Parkway, Pasadena, CA 91105, USA
[29] Astronomical Institute "Anton Pannekoek," University of Amsterdam, Science Park 904, 1098 XH Amsterdam, The Netherlands
[30] Kavli Institute for the Physics and Mathematics of the Universe, Todai Institutes for Advanced Study, The University of Tokyo, Kashiwa 227-8568, Japan (Kavli IPMU, WPI)
[31] Department of Cosmosciences, Hokkaido University, Sapporo 060-0810, Japan
[32] Department of Astronomy, University of Washington, Box 351580 Seattle, Washington 98195, USA
[33] Astronomical Institute, Tohoku University, Aoba, Sendai 980-8578, Japan
Received 2012 January 23; accepted 2012 February 27; published 2012 March 13

ABSTRACT

We present high-resolution, *H*-band imaging observations, collected with Subaru/HiCIAO, of the scattered light from the transitional disk around SAO 206462 (HD 135344B). Although previous sub-mm imagery suggested the existence of a dust-depleted cavity at $r \leqslant 46$ AU, our observations reveal the presence of scattered light components as close as 0.″2 (~28 AU) from the star. Moreover, we have discovered two small-scale spiral structures lying within 0.″5 (~70 AU). We present models for the spiral structures using the spiral density wave theory, and derive a disk aspect ratio of $h \sim 0.1$, which is consistent with previous sub-mm observations. This model can potentially give estimates of the temperature and rotation profiles of the disk based on dynamical processes, independently from sub-mm observations. It also predicts the evolution of the spiral structures, which can be observable on timescales of 10–20 years, providing conclusive tests of the model. While we cannot uniquely identify the origin of these spirals, planets embedded in the disk may be capable of exciting the observed morphology. Assuming that this is the case, we can make predictions on the locations and, possibly, the masses of the unseen planets. Such planets may be detected by future multi-wavelength observations.

Key words: circumstellar matter – instrumentation: high angular resolution – polarization – protoplanetary disks – stars: individual (SAO 206462, HD 135344B) – waves

* Based on data collected at the Subaru Telescope, which is operated by the National Astronomical Observatory of Japan.
[34] JSPS Research Fellow.
[35] Current address: Division of Liberal Arts, Kogakuin University, 1-24-2, Nishi-Shinjuku, Shinjuku-ku, Tokyo, 163-8677, Japan.
[36] Visiting Astronomer, NASA Infrared Telescope Facility, operated by the University of Hawaii under contract to NASA.
[37] Current address: National Astronomical Observatory of Japan.

1. INTRODUCTION

Dynamical processes in protoplanetary disks such as turbulence or disk–planet interaction are important in understanding physical condition and evolution of disks, and planet formation processes. High-resolution, direct imaging observations of circumstellar/protoplanetary disks can reveal non-axisymmetric structures, providing insight into such dynamical processes (e.g., Hashimoto et al. 2011).

Recent observations have identified a class of protoplanetary disks harboring tens of AU-scale holes/gaps at their centers: the so-called transitional disks. One well-studied system of that class is the rapidly rotating Herbig F star, SAO 206462 (HD 135344B, F4Ve, $d = 142 \pm 27$ pc, $M = 1.7^{+0.2}_{-0.1}\ M_{\odot}$, Müller et al. 2011). The observations of CO line profiles (Dent et al. 2005; Pontoppidan et al. 2008; Lyo et al. 2011) and stellar rotation (Müller et al. 2011) consistently indicate an almost face-on geometry ($i \sim 11°$). The gap in the disk was predicted from the infrared (IR) spectral energy distribution (SED; Brown et al. 2007), and was subsequently imaged in sub-mm dust continuum at $\sim$0.″5 $\times$ 0.″25 resolution (Brown et al. 2009). Andrews et al. (2011) estimate the gap radius to be $\sim$46 AU and the surface density within the gap to be $10^{-5.2}$ times smaller than that extrapolated from the outer disk. The gas in Keplerian motion surrounding the gap region is also imaged by CO lines (Lyo et al. 2011). The CO rovibrational line observations (Pontoppidan et al. 2008) and [O I] spectral line observations (van der Plas et al. 2008) indicate the presence of a gas disk in the vicinity (several AU-scale) of the star. SED modeling (Grady et al. 2009) and NIR interferometry (Fedele et al. 2008) indicate the presence of an inner dust belt, which is temporally variable (Sitko et al. 2012) and not coplanar with the outer disk (M. Benisty 2011, private communication). New imaging with high spatial resolution and sensitivity is required to understand the inner structures of the disk. The outer portions of gaps can now be resolved using 8–10 m ground-based telescopes at near-infrared (NIR) wavelengths (e.g., Thalmann et al. 2010, for LkCa 15).

In this Letter, we present H-band polarized intensity (PI) observations of the disk of SAO 206462 down to $r \sim 0.''2$ ($\sim$28 AU) scale at 0.″06 ($\sim$8.4 AU) resolution. Interior to the sub-mm resolved gap, we find spiral structures, indicative of dynamical processes. We use the spiral density wave theory to interpret the structure, and estimate disk's physical parameters.

2. OBSERVATIONS AND DATA REDUCTION

2.1. HiCIAO Observations

SAO 206462 was observed in the H-band (1.6 μm) using the high-contrast imaging instrument HiCIAO (Tamura et al. 2006; Hodapp et al. 2008; Suzuki et al. 2010) on the Subaru Telescope on 2011 May 20 UT as part of Strategic Explorations of Exoplanets and Disks with Subaru (SEEDS; Tamura 2009). The adaptive optics system (AO188; Hayano et al. 2004; Minowa et al. 2010) provided a stable stellar point-spread function (PSF; FWHM = 0.″06). We used a combined angular differential imaging (ADI) and polarization differential imaging (PDI) mode with a field of view of $10'' \times 20''$ and a pixel scale of 9.5 mas pixel^{-1}. A 0.″3 diameter circular occulting mask was used to suppress the bright stellar halo. The half-wave plates were placed at four angular positions from 0°, 45°, 22.°5, and 67.°5 in sequence with one 30 s exposure per wave plate position. The total integration time of the PI image was 780 s after removing low quality images with large FWHMs by careful inspections of the stellar PSF.

2.2. PDI Data Reduction

The raw images were corrected using IRAF[38] for dark current and flat-field following the standard reduction scheme. We applied a distortion correction using globular cluster M5 data taken within a few days, using IRAF packages GEOMAP and GEOTRAN. Stokes (Q, U) parameters and the PI image were obtained in the standard approach (e.g., Hinkley et al. 2009) as follows. By subtracting two images of extraordinary and ordinary rays at each wave plate position, we obtained $+Q$, $-Q$, $+U$, and $-U$ images, from which $2Q$ and $2U$ images were made by another subtraction to eliminate remaining aberration. PI was then given by PI $= \sqrt{Q^2 + U^2}$. Instrumental polarization of HiCIAO at the Nasmyth instrument was corrected by following Joos et al. (2008). From frame-by-frame deviations, the typical error of the surface brightness (SB) was estimated to be $\sim$5% at $r \sim 0.''5$ when averaged over 5 $\times$ 5 pixels ($\sim$PSF scale). Comparing different data reduction methods (frame selections and instrumental polarization estimates), we expect that the systematic uncertainty of the SB of PI to be $\sim$10%.

2.3. Contemporaneous Photometry

Since SAO 206462 shows variability in NIR wavelengths (Sitko et al. 2012), it is important to take photometry simultaneously with disk observations. H-band photometry was obtained just before and after the disk imaging without the coronagraphic spot with the adaptive optics, by sixteen 1.5 s exposures at four spatially dithered positions. An ND10 filter (9.8 ± 0.1% transmission) was used to avoid saturation. Using the MKO filter set, the H-band ($\lambda_{\rm eff} = 1.615\ \mu$m, FWHM $= 0.29\ \mu$m, Tokunaga et al. 2002) magnitude was 6.96 ± 0.07 mag.

Broadband $VRIJHK$ photometry was obtained on 2011 May 23–26, starting within 48 hr of the HiCIAO observation, using the Rapid Eye Mount (REM) Telescope at La Silla, Chile (Covino et al. 2004). The REM H-band filter has $\lambda_{\rm eff} = 1.65\ \mu$m, FWHM $= 0.35\ \mu$m: broader and displaced to longer wavelengths than the MKO filter. The observed data were reduced differentially using SAO 206463 (A0V). The IR excess due to the inner disk (Figure 1) was average for the range observed in 2009–2011 (Sitko et al. 2012). No significant variation was observed during the 2011 May observations, except for the small long-term fading trend (δm $= 0.08 \pm 0.02$ mag) over the observation period.

Figure 1 also displays spectra obtained with the SpeX spectrograph (Rayner et al. 2009) on NASA's Infrared Telescope Facility (IRTF). The observations were obtained in the cross-dispersed (XD) echelle mode between 0.8 and 5.1 μm using a 0.″8 slit ($R \sim 900$) and calibrated using HD 129685 (A0V) with SpeXtool (Vacca et al. 2003; Cushing et al. 2004). The absolute flux calibration, to correct for light loss at the spectrograph slits, was accomplished in two ways: using photometry and wide-slit spectroscopy (see Sitko et al. 2012). The March SpeX data were normalized using the REM photometry, obtained in the days immediately after the SpeX observations, and when the star was photometrically stable. In July, SAO 206462 and the calibration star were observed with the SpeX prism using a 3.″0 slit, which, under good seeing and transparency

[38] IRAF is distributed by the National Optical Astronomy Observatory, which is operated by the Association of Universities for Research in Astronomy, Inc., under cooperative agreement with the National Science Foundation.

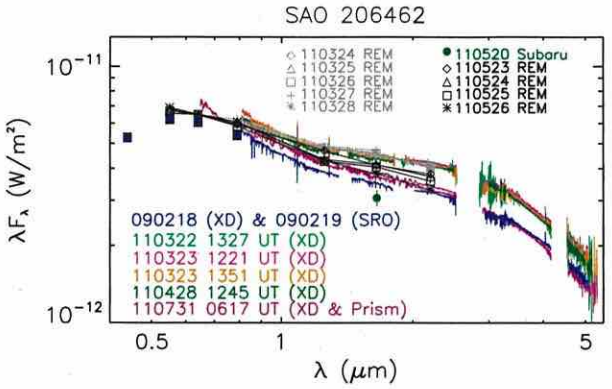

Figure 1. SED for SAO 206462 obtained by REM, adapted, in part, from Sitko et al. (2012). The REM observations consist of *VRIJHK* photometry. Also shown are spectra obtained with the SpeX spectrograph. See Section 2.3 for the data reduction techniques.

conditions, produces absolute flux to ∼5% accuracy. The REM photometry at the *H*-band in May is ∼0.25 mag brighter than the Subaru data. The Subaru photometry shows a low value even when considering the filter difference, suggesting that the outer disk is illuminated efficiently.

3. RESULTS

3.1. Spiral Structure

The SAO 206462 disk can be traced in PI from 0.″2 to ∼1.″0 (28–140 AU), similar to the range imaged with *HST*/NICMOS (Grady et al. 2009), but with a factor of ∼4 greater angular resolution. The total PI is 9.87 mJy ± 0.06% at $0.''2 < r < 1.''0$, which is 0.6% of the stellar intensity. The total PI at $0.''42 < r < 1.''0$ is 3.94 mJy ± 0.1% while the total intensity by *HST*/NICMOS F110W is 9.7 mJy (Grady et al. 2009). The average SB of PI at $r = 0.''46$ is ∼6 mJy asec^{-2}, whereas the total intensity by *HST*/NICMOS F160W is 30 mJy asec^{-2} (Grady et al. 2009). Given the NICMOS data uncertainties, the polarization fraction is ∼20%–40%, assuming no PSF halo in the HiCIAO data and no variable self-shadowing/illumination in the disk. Our measured polarization fraction is similar to that of HD 100546 ($14\%^{+19\%}_{-8\%}$, Quanz et al. 2011) and AB Aur (∼25%–45%, Perrin et al. 2009).

Figure 2 shows the PI image. The region interior to 0.″4 is not a void and we do not see clear structural evidence of the cavity wall in the Andrews et al. (2011) model ($R_{\rm cav} = 46$ AU ∼ 0.″33). We see spiral arcs S1 (east) and S2 (southwest). The PI at the location of the spirals is ∼30% larger than that extrapolated from the smooth outer profile (bottom of Figure 2). The brightest portions of the spirals roughly coincide with the bright thermal emission peaks at 12 μm (Mariñas et al. 2011) and lie inside the ring noted by Doucet et al. (2006). It is also noted that we see a dip in PI in the northwest, probably due to the depolarization in the minor axis direction (see below), and that we do not see a large-scale, localized shadow that might be cast by the inner dust belt if highly inclined relative to the outer disk.

3.2. Azimuthal and Radial Profiles

Here, we summarize the overall disk structure exterior to the spirals. Figure 3 (top panels) shows the azimuthal SB profiles at $r = 0.''5$ and $r = 0.''7$. At $r \gtrsim 0.''5$, SB has maxima around position angle (PA) ∼ 50°–60° and 230°–240°. Since the polarization is maximized at ∼90° scattering (e.g., Graham et al. 2007), it is implied that the disk major axis is at PA ∼ 50°–60°, comparable to estimates by CO observations: PA = 56° ± 2° by Pontoppidan et al. (2008) and 64° ± 2° by Lyo et al. (2011). We adopt PA = 55° for the major axis and $i = 11°$ for the inclination (see Section 1). Our spiral model fitting results (the next section) are little affected even if we assume a face-on geometry.

From CO observations, it is known that the southwest side is receding (e.g., Lyo et al. 2011). Therefore, either the northwest or southeast side is the near side. We do not see an obvious forward scattering excess in the NIR image. However, since the spirals are typically trailing, it is inferred that the southeast is the near side.

Figure 3 also shows the radial PI profiles along the major axis, which is roughly consistent with r^{-3} in the outer part, indicating a flat (not highly flared) disk (Whitney & Hartmann 1992). The radial slopes vary as PA from ∼−2 to ∼−4.5 (fitting at $0.''6 < r < 1.''0$) or from ∼−2.5 to ∼−5 (fitting at $0.''3 < r < 0.''9$), with shallower slopes typically appearing in the minor axis directions. However, r^{-3} is representative on average. This slope is observed in several other HAeBe disks (e.g., Fukagawa et al. 2010, for total intensity data), although HD 97048 disk exhibits a shallower slope (Quanz et al. 2012).

4. SPIRAL STRUCTURE MODELING

Among several features in the image, the most interesting one is the non-axisymmetric spirals. In order to understand them, we propose a model based on the spiral density wave theory (e.g., Lin & Shu 1964; Goldreich & Tremaine 1978, 1979; Ogilvie & Lubow 2002), assuming that NIR emission traces the disk surface density structure. With such a model, the spiral structures can be used to infer the disk temperature, independently of, for example, CO line observations.

The shape of the spiral density wave is determined by the location of the launching point (corotation radius $r_{\rm c}$) and disk's thermal and rotation profiles. When the disk rotation angular frequency is $\Omega(r) \propto r^{-\alpha}$ and the sound speed is $c(r) \propto r^{-\beta}$, the shape of the wave far from $r_{\rm c}$ is given by

$$\theta(r) = \theta_0 - \frac{{\rm sgn}(r - r_{\rm c})}{h_{\rm c}} \times \left[\left(\frac{r}{r_{\rm c}}\right)^{1+\beta} \left\{ \frac{1}{1+\beta} - \frac{1}{1-\alpha+\beta} \left(\frac{r}{r_{\rm c}}\right)^{-\alpha} \right\} - \left(\frac{1}{1+\beta} - \frac{1}{1-\alpha+\beta} \right) \right] \quad (1)$$

in the polar coordinate (r, θ), where $h_{\rm c} = c(r_{\rm c})/r_{\rm c}\Omega(r_{\rm c})$ denotes the disk aspect ratio at $r = r_{\rm c}$ and θ_0 gives the phase. Equation (1) approximates well the shape of the density wave given by the WKB theory (Rafikov 2002; Muto et al. 2011). When the spiral is excited by a planet in a circular orbit, its location is $\sim(r_{\rm c}, \theta_0)$. Equation (1) has five parameters, $(r_{\rm c}, \theta_0, h_{\rm c}, \alpha, \beta)$.

Two non-axisymmetric features, S1 and S2, (Figure 4) are identified as follows. First, local maxima in the radial SB profiles normalized by r^2 (to take into account the dilution of the stellar flux) are traced at every 1° step with data at 170° < PA < 360° (S1) and at 50° < PA < 190° (S2). The points near the minor axis (PA ∼ 325°) are excluded because the structure there may be affected by depolarization. The points at PA > 200° (S1) and PA > 114° (S2) may be a part of axisymmetric rings since they

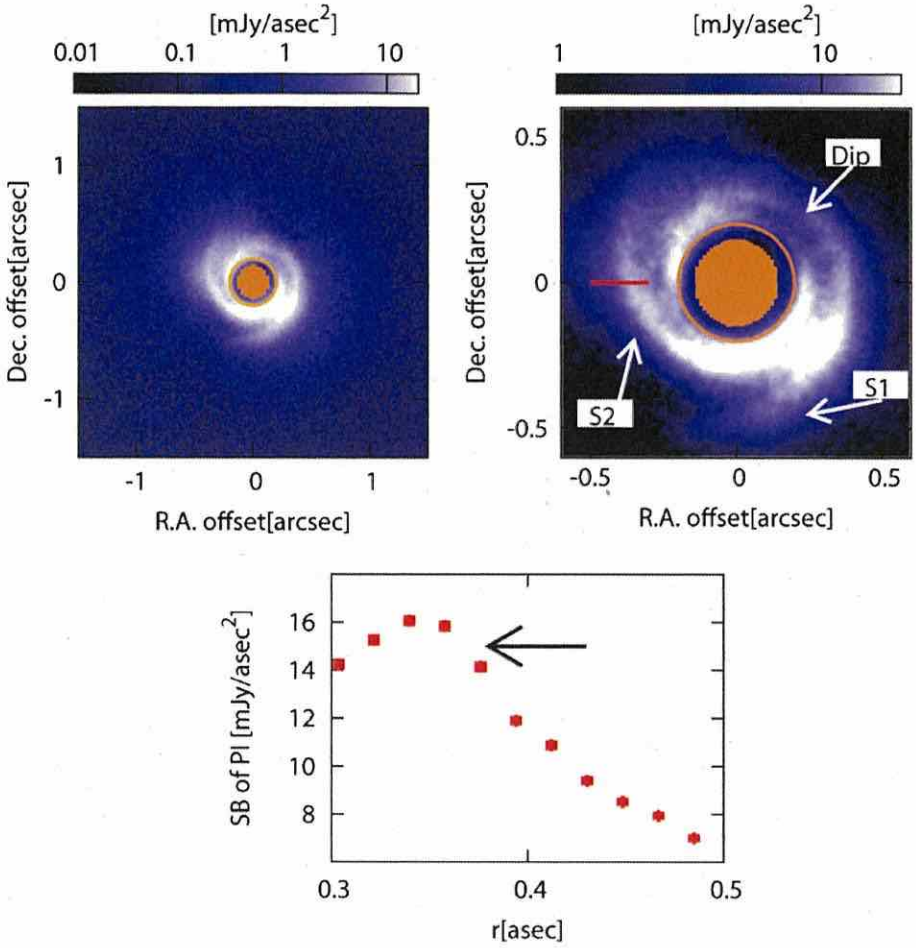

Figure 2. Top: PI image of SAO 206462 in the north-up configuration with log-stretch color scales. The filled orange circles at the center indicate the mask size ($r = 0\farcs15$). The circles have $r = 0\farcs2$, exterior to which the features are considered to be real. The right panel is central region's close-up. Different color scales are used to enhance the spirals labeled as "S1" and "S2." The "Dip" may be due to depolarization. Bottom: PI profile along the red line in the top right panel. The arrow indicates the location of S2. The position errors are not shown for visibility.

are found to have constant radii. After removing these points, we have 27 (S1) and 56 (S2) points as representing samples of non-axisymmetric spirals, with the opening angle of ~15° for both S1 and S2. We estimate that the uncertainty of the location of the maxima is given by the FWHM of the PSF.

In order to fit the non-axisymmetric structures by Equation (1), we fix α and β at 1.5 (Kepler rotation) and 0.4, respectively, as in Lyo et al. (2011), while other parameters are varied as ($0\farcs1 < r_c < 0\farcs9$, $0 < \theta_0 < 2\pi$, $0.05 < h_c < 0.25$). Note that different values of β yield similar results. Since it is difficult to fit S1 and S2 simultaneously, they are fitted independently.

The "best-fit" parameters are $(r_c, \theta_0, h_c) = (0\farcs39, 204°, 0.08)$ for S1 (reduced $\chi^2 = 0.52$) and $(r_c, \theta_0, h_c) = (0\farcs9, 353°, 0.24)$ for S2 (reduced $\chi^2 = 0.31$). The spiral shapes with these parameters are shown in Figure 4. However, the parameter degeneracy is significant. Figure 5 shows the parameter space of (r_c, θ_0) with 63.8% confidence level for $h_c = 0.1$ and $h_c = 0.2$. Note that in Figure 5, the "best-fit" of (r_c, θ_0) is outside the domain of confidence in some cases because h_c is not the same as the best-fit. Despite the parameter degeneracy, the values of the aspect ratio which fit the shape of the spiral ($h_c \sim 0.1$) are consistent with those obtained from the sub-mm map of the disk (e.g., $h = 0.096(r/100\ \mathrm{AU})^{0.15}$; Andrews et al. 2011).

The spiral density wave theory predicts that the pattern speed deviates from the local Kepler speed;

$$\Omega_{\mathrm{pattern}} = 0.8 \left(\frac{r_c}{70\ \mathrm{AU}}\right)^{-3/2} \left(\frac{M_*}{1.7\,M_\odot}\right)^{1/2} (\mathrm{deg\ yr^{-1}}) \quad (2)$$

is not necessarily equal to $\Omega(r)$. When $r_c = 0\farcs5 (\sim 70\ \mathrm{AU})$, the spiral will move ~10° in a decade, corresponding to a movement of $0\farcs1$. Considering the PSF scale of our observations and the locations of the spirals, such deviations can be detectable over a couple of decades. Moreover, if the two spirals have distinct corotation radii, their relative locations change in time due to the pattern speed difference. Such measurements will confirm that the observed feature is really the density wave, providing indisputable evidence of dynamical activity.

Note that it would be difficult to detect spirals in colder disks (smaller h_c), where spirals are more tightly wound, due to the blurring by the PSF. The lower detectable limit of h_c is typically $h_c \sim 0.01$–0.03 for our set of parameters. The combination of high angular resolution and warm temperatures allows the spiral

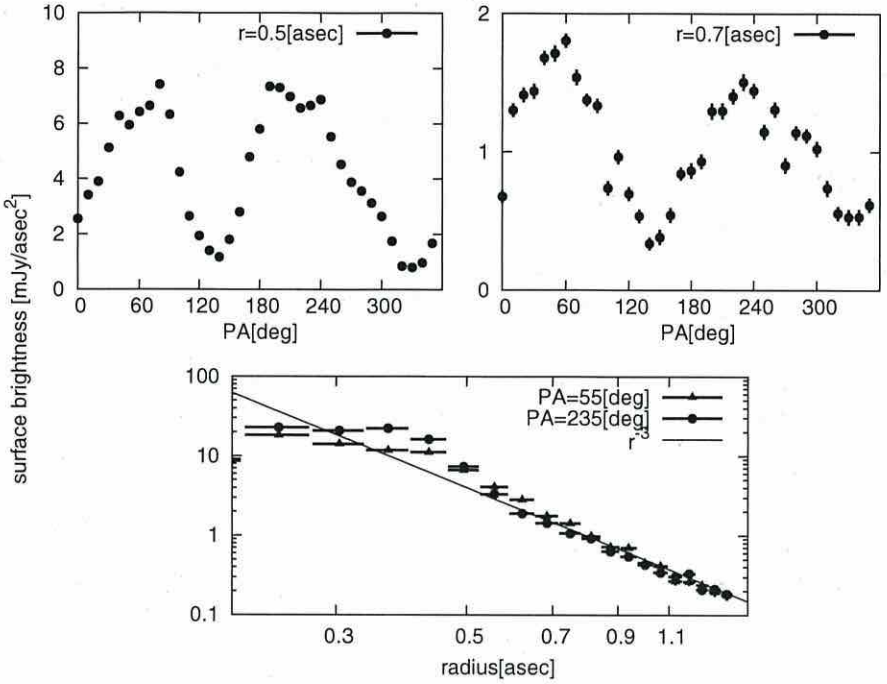

Figure 3. Top: azimuthal SB profile at $r = 0''.5$ (left) and $r = 0''.7$ (right) with PA measured from north to east. Bottom: radial profile along the major axis. Position errors indicate the FWHM of the PSF. SB errors are estimated using frame-by-frame deviations.

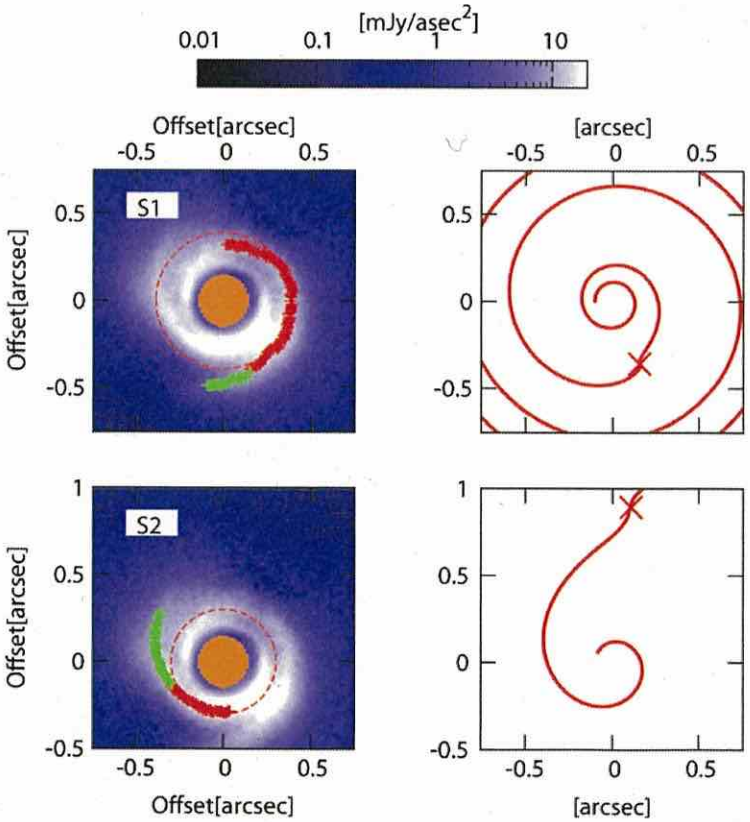

Figure 4. Left: red and green points indicate the locations of the maxima of radial profiles for S1 (top) and S2 (bottom). The green ones are used for the fitting by Equation (1) (Section 4). Dashed lines indicate circles with $r = 0''.39$ (top) and $r = 0''.3$ (bottom). Right: the spiral shape given by Equation (1) with the best-fit parameters of S1 (top) and S2 (bottom). Crosses show the locations of (r_c, θ_0).

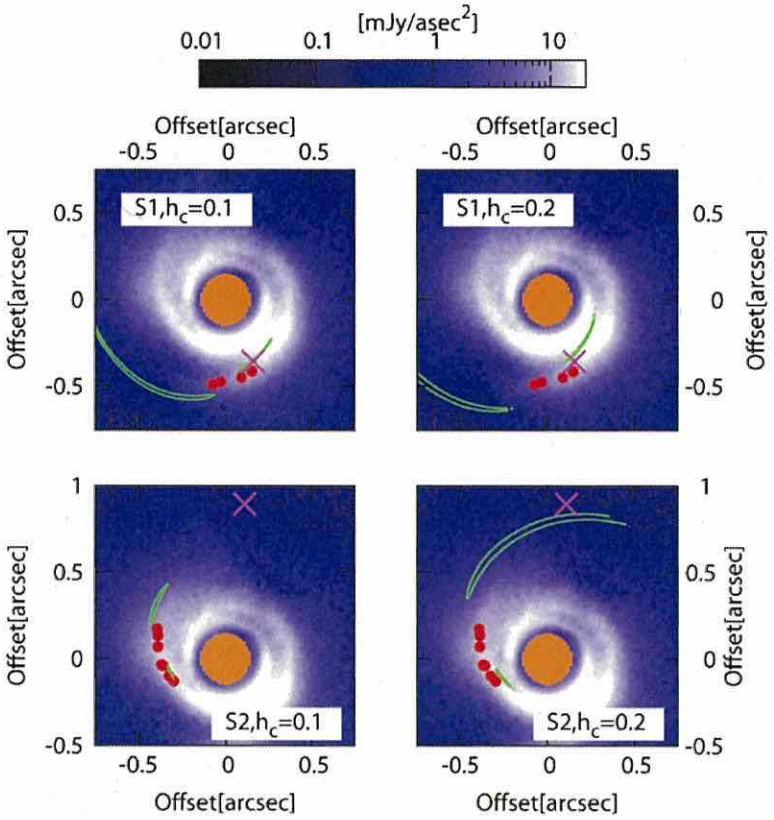

Figure 5. Parameter degeneracy of the fitting for S1 (top) and S2 (bottom) with $h_c = 0.1$ (left) and $h_c = 0.2$ (right). The red points show a part of the data fitted. The green curves indicate the 63.8% confidence level for the locations of (r_c, θ_0). The magenta crosses are (r_c, θ_0) for the best-fit parameters. Note that the best-fit values of h_c are different from those shown in the figure.

structure in the SAO 206462 disk to be resolved. Further spirals might be detectable in similarly warm disks.

5. SUMMARY AND DISCUSSION

In this Letter, we present a high-resolution image of the SAO 206462 transitional disk using Subaru/HiCIAO, with an inner working angle of 0.″2. We discover non-axisymmetric spiral features, which can be explained by the spiral density wave theory with a reasonable value of the disk aspect ratio ($h_c \sim 0.1$). The model is robust in a sense that it does not assume the origin of such structure explicitly.

The detection of scattered light within the sub-mm cavity itself is interesting, since Andrews et al. (2011) predicts that the sub-mm cavity is heavily depleted. Our data in tandem with the millimeter data may suggest that the depletion of grains at different sizes is not uniform. Dong et al. (2012) discuss such discrepancies between sub-mm dust continuum images and NIR scattered light images in terms of differing spatial distributions as a function of grain size from a general theoretical perspective.

Our major assumption is that PI at the H-band, tracing the scattered light at the disk surface, actually traces the surface density variations. This assumption is valid when the disk is in vertical, isothermal hydrostatic equilibrium without rapid radial surface density variations (e.g., Muto 2011). Structures near the midplane are, however, preferentially observed at longer wavelengths with high spatial resolution: Atacama Large Millimeter/Submillimeter Array (ALMA) can be an ideal instrument.

Among several possible causes for the spiral structures (see also Hashimoto et al. 2011), one interesting idea is that planets excite them. In this case, the domain of possible locations of the planets is given by the green curves in Figure 5. If the two spirals have distinct corotation radii, there may be two (unseen) planets embedded in the disk. The amplitude of the surface density perturbation scales with the planet mass as $\delta\Sigma/\Sigma \sim GM_p\Omega/c^3$ for non-gap-opening low-mass planets ($GM_p\Omega/c^3 \lesssim 1$, e.g., Tanaka et al. 2002). In our data, the amplitude of the spiral wave is typically ~30% (Figure 2), implying $M_p \sim 0.5\,M_J$.

The typical error of PI in our image is ~5%. If this is typical of HiCIAO, it is capable of detecting the indirect signatures of planets down to $M_p \sim 0.05\,M_J$. ADI is promising in finding a point source; however, small field rotation (~13°) due to the southerly declination (−39°) of SAO 206462 makes obtaining the total intensity difficult in our data. Future L-band observations may reveal thermal emission from a planet, if it exists, or its surrounding (accreting) gas.

The authors thank Roman Rafikov for comments, the support staff members of the IRTF and REM telescopes for assistance in obtaining the SED data, and the IR&D program at The Aerospace Corporation. REM data in this study were obtained under Chilean National TAC programs CN2011A-050 and CN2011B-31. This work is partially supported by KAKENHI

22000005 (M.T.), 23103002 (M.H. and M.H.), 23103004 (M.M. and M.F.), 23103005, 23244027, 18540238 (S.I.), and 22·2942 (T.M.), WPI Initiative, MEXT, Japan (E.L.T.), NSF AST 1008440 (C.A.G.), 1009203 (J.C.), and 1009314 (J.P.W.), and NASA NNH06CC28C (M.L.S.) and NNX09AC73G (C.A.G. and M.L.S.). Part of this research was carried out at JPL.

REFERENCES

Andrews, S. M., Wilner, D. J., Espaillat, C., et al. 2011, ApJ, 732, 42
Brown, J. M., Blake, G. A., Dullemond, C. P., et al. 2007, ApJ, 664, L107
Brown, J. M., Blake, G. A., Qi, C., et al. 2008, ApJ, 704, 496
Covino, S., Stefanon, M., Sciuto, G., et al. 2004, Proc. SPIE, 5492, 1613
Cushing, M. C., Vacca, W. D., & Rayner, J. T. 2004, PASP, 116, 362
Dent, W. R. F., Greaves, J. S., & Coulson, I. M. 2005, MNRAS, 359, 663
Dong, R., et al. 2012, ApJ, in press (arXiv:1203.1612)
Doucet, C., Pantin, E., Lagage, P. O., & Dullemond, C. P. 2006, A&A, 460, 117
Fedele, D., van den Ancker, M. E, Acke, B., et al. 2008, A&A, 491, 809
Fukagawa, M., Tamura, M., Itoh, Y., et al. 2010, PASJ, 62, 347
Goldreich, P., & Tremaine, S. 1978, ApJ, 222, 850
Goldreich, P., & Tremaine, S. 1979, ApJ, 233, 857
Grady, C. A., Schneider, G., Sitko, M. L., et al. 2009, ApJ, 699, 1822
Graham, J. R., Kalas, P. G., & Matthews, B. C. 2007, ApJ, 654, 595
Hashimoto, J., Tamura, M., Muto, T., et al. 2011, ApJ, 729, L17
Hayano, Y., Saito, Y., Saito, N., et al. 2004, Proc. SPIE, 5490, 1088
Hinkley, S., Oppenheimer, B. R., Soummer, R., et al. 2009, ApJ, 701, 804
Hodapp, K. W., Suzuki, R., Tamura, M., et al. 2008, Proc. SPIE, 7014, 701419
Joos, F., Buenzli, E., Schmid, H. M., & Thalmann, C. 2008, Proc. SPIE, 7016, 48
Lin, C. C., & Shu, F. H. 1964, ApJ, 140, 646
Lyo, A.-R., Ohashi, N., Qi, C., Wilner, D. J., & Su, Y.-N. 2011, AJ, 142, 151
Mariñas, N., Telesco, C. M., Fischer, R. S., & Packham, C. 2011, ApJ, 737, 57
Minowa, Y., Hayano, Y., Oya, S., et al. 2010, Proc. SPIE, 7736, 77363N
Müller, A., van den Ancker, M. E., Launhardt, R., et al. 2011, A&A, 530, 85
Muto, T. 2011, ApJ, 739, 10
Muto, T., Suzuki, T. K., & Inutsuka, S. 2010, ApJ, 724, 448
Ogilvie, G. I., & Lubow, S. H. 2002, MNRAS, 330, 950
Perrin, M. D., Schneider, G., Duchene, G., et al. 2009, ApJ, 707, L132
Pontoppidan, K. M., Blake, G. A., van Dishoeck, E. F., et al. 2008, ApJ, 684, 1323
Quanz, S. P., Birkmann, S. M., Apai, D., Wolf, S., & Henning, T. 2012, A&A, 538, A92
Quanz, S. P., Schmid, H. M., Geissler, K., et al. 2011, ApJ, 738, 23
Rafikov, R. R. 2002, ApJ, 569, 997
Rayner, J. T., Cushing, M. C., & Vacca, W. D. 2009, ApJS, 185, 289
Sitko, M. L., Day, A. N., Kimes, R. L., et al. 2012, ApJ, 745, 29
Suzuki, R., Kudo, T., Hashimoto, J., et al. 2010, Proc. SPIE, 7735, 773530
Tamura, M. 2009, in AIP Conf. Proc. 1158, Proc. of the Intl. Conf., ed. T. Usuda, M. Ishii, & M. Tamura (Melville, NY: AIP), 11
Tamura, M., Hodapp, K., Takami, H., et al. 2006, Proc. SPIE, 6269, 28
Tanaka, H., Takeuchi, T., & Ward, W. R. 2002, ApJ, 565, 1257
Thalmann, C., Grady, C. A., Goto, M., et al. 2010, ApJ, 718, L87
Tokunaga, A. T., Simons, D. A., & Vacca, W. D. 2002, PASP, 114, 180
Vacca, W. D., Cushing, M. C., & Rayner, J. T. 2003, PASP, 115, 389
van der Plas, G., van der Ancker, M. E., Fedele, D., et al. 2008, A&A, 485, 487
Whitney, B. A., & Hartmann, L. 1992, ApJ, 395, 529

The Astrophysical Journal Letters, 819:L7 (7pp), 2016 March 1 doi:10.3847/2041-8205/819/1/L7

ALMA OBSERVATIONS OF A GAP AND A RING IN THE PROTOPLANETARY DISK AROUND TW HYA

Hideko Nomura[1,13], Takashi Tsukagoshi[2,14], Ryohei Kawabe[3,4,5], Daiki Ishimoto[1,6], Satoshi Okuzumi[1], Takayuki Muto[7], Kazuhiro D. Kanagawa[8,9], Shigeru Ida[10], Catherine Walsh[11], T. J. Millar[12], and Xue-Ning Bai[13]
[1] Department of Earth and Planetary Sciences, Tokyo Institute of Technology, 2-12-1 Ookayama, Meguro, Tokyo, 152-8551, Japan; nomura@geo.titech.ac.jp
[2] College of Science, Ibaraki University, Mito, Ibaraki 310-8512, Japan
[3] National Astronomical Observatory of Japan, 2-21-1 Osawa, Mitaka, Tokyo 181-8588, Japan
[4] SOKENDAI (The Graduate University for Advanced Studies), 2-21-1 Osawa, Mitaka, Tokyo 181-8588, Japan
[5] Department of Astronomy, School of Science, University of Tokyo, Bunkyo, Tokyo 113-0033, Japan
[6] Department of Astronomy, Graduate School of Science, Kyoto University, Kitashirakawa-Oiwake-cho, Sakyo-ku, Kyoto 606-8502, Japan
[7] Division of Liberal Arts, Kogakuin University, 1-24-2 Nishi-Shinjuku, Shinjuku-ku, Tokyo, 163-8677, Japan
[8] Institute of Low Temperature Science, Hokkaido University, Sapporo 060-0819, Japan
[9] Institute of Physics and CASA*, Faculty of Mathematics and Physics, University of Szczecin, Wielkopolska 15, 70-451 Szczecin, Poland
[10] Earth-Life Science Institute, Tokyo Institute of Technology, 2-12-1 Ookayama, Meguro, Tokyo 152-8550, Japan
[11] Leiden Observatory, Leiden University, P.O. Box 9513, 2300 RA Leiden, The Netherlands
[12] Astrophysics Research Centre, School of Mathematics and Physics, Queen's University Belfast, University Road, Belfast BT7 1NN, UK
[13] Institute for Theory and Computation, Harvard-Smithsonian Center for Astrophysics, 60 Garden Street, MS-51, Cambridge, MA 02138, USA
Received 2015 December 16; accepted 2016 February 5; published 2016 February 24

ABSTRACT

We report the first detection of a gap and a ring in 336 GHz dust continuum emission from the protoplanetary disk around TW Hya, using the Atacama Large Millimeter/Submillimeter Array (ALMA). The gap and ring are located at around 25 and 41 au from the central star, respectively, and are associated with the CO snow line at ~30 au. The gap has a radial width of less than 15 au and a mass deficit of more than 23%, taking into account that the observations are limited to an angular resolution of ~15 au. In addition, the ^{13}CO and C^{18}O $J = 3 - 2$ lines show a decrement in CO line emission throughout the disk, down to ~10 au, indicating a freeze-out of gas-phase CO onto grain surfaces and possible subsequent surface reactions to form larger molecules. The observed gap could be caused by gravitational interaction between the disk gas and a planet with a mass less than super-Neptune ($2M_{\rm Neptune}$), or could be the result of the destruction of large dust aggregates due to the sintering of CO ice.

Key words: molecular processes – planet–disk interactions – protoplanetary disks – stars: individual (TW Hya) – submillimeter: planetary systems

1. INTRODUCTION

The physical structures and chemical compositions of gas, dust, and ice in protoplanetary disks control the formation processes of planets and the compositions of their cores and atmospheres. The Atacama Large Millimeter/Submillimeter Array (ALMA) long baseline campaign has detected gaps and rings in dust continuum emission from the circumstellar disk around a very young star (~0.1–1 Myr), HL Tau (ALMA Partnership et al. 2015). The origin of this complex disk structure in such a young object remains under debate.

In this Letter, we present ALMA observations of the relatively old (~3–10 Myr) gas-rich disk around the young Sun-like star, TW Hya (~$0.8M_{\odot}$), which show the presence of a gap and a ring associated with the CO snow line. TW Hya's proximity (54 ± 6 pc) makes it an ideal source for studying the formation environment of a planetary system (e.g., Andrews et al. 2012). The disk is old compared with other gas-rich protoplanetary disks, whose lifetimes are typically ~3 Myr (e.g., Hernández et al. 2007). Nevertheless, the disk gas mass is $>0.05M_{\odot}$, inferred through HD line observations with *Herschel* (Bergin et al. 2013). In exoplanetary systems giant planets have been discovered at/beyond Neptune orbits around Sun-like stars by direct imaging observations using Subaru/HiCIAO (Thalmann et al. 2009; Kuzuhara et al. 2013). Thus, planets are able to form even at large distances within disk lifetimes by, for example, scattering of planetary cores (Kikuchi et al. 2014). Given that planet–disk interaction is key for planet orbital evolution and planet population synthesis (e.g., Kley & Nelson 2012; Ida et al. 2013), understanding gap formation in protoplanetary disks helps us to gain insight into the early evolution of our own solar system, as well as the observed diversity of exoplanetary systems.

2. OBSERVATIONS AND DATA REDUCTION

TW Hya was observed with ALMA in Band 7 on 2015 May 20–21 with 40 antennas in Cycle 2 with a *uv*-coverage of 22–580 kλ (PI: D. Ishimoto). The spectral windows were centered at 329.295 GHz (SPW1), 330.552 GHz (SPW0), 340.211 GHz (SPW2), and 342.846 GHz (SPW3), covering C^{18}O $J = 3 - 2$, ^{13}CO $J = 3 - 2$, CN $N = 3 - 2$, and CS $J = 7 - 6$. The channel spacing was $\delta\nu = 30.52$ kHz and the bandwidth was 117.188 MHz, except for SPW2, in which a channel spacing of $\delta\nu = 15.26$ kHz and a bandwidth of 58.594 MHz were used. The quasar J1058+0133 was observed as a bandpass calibrator, while the nearby quasar J1037-2934 was used for phase and gain calibration. The mean flux density of J1037-2934 was 0.58 Jy during the observation period.

The visibility data were reduced and calibrated using CASA, versions 4.3.1 and 4.4.0. The visibility data were separately reduced for each SPW, and the continuum visibilities were extracted by averaging the line-free channels in all SPWs. The corrected visibilities were imaged using the CLEAN algorithm with Briggs weighting with a robust parameter of 0 after calibration of the bandpass, gain in amplitude and phase, and absolute flux scaling, and then flagging for aberrant data. In addition to the usual CLEAN imaging, we performed self-

[14] These authors contributed equally to this work.

calibration of the continuum emission to improve the sensitivity and image quality. The obtained solution table of the self-calibration for the continuum emission was applied to the visibilities of the lines. The self-calibration significantly improved the sensitivity of the continuum image by one order of magnitude from 2.6 to 0.23 mJy. In addition, the continuum visibility data with deprojected baselines longer than 200 kλ were extracted in order to enhance small-scale structure around the gap. The high spatial resolution data were analyzed in a similar way, but were imaged using the CLEAN algorithm with uniform weighting. Also, the ALMA archived data of the N_2H^+ $J = 4 - 3$ line at 372.672 GHz were reanalyzed in a similar way to compare with the data obtained by our observations. The reanalyzed data is consistent with that in Qi et al. (2013). For the N_2H^+ line data, the synthesized beam and the 1σ rms noise level in 0.1 km s^{-1} were $0\farcs44 \times 0\farcs41$ (P.A. = 12°.4) and 31.2 mJy beam^{-1}.

3. RESULTS

3.1. Dust Continuum Emission

The observed dust continuum emission maps at 336 GHz are plotted for both the full data (Figure 1(a)) and high spatial frequencies only (>200 kλ, Figure 1(b)). The synthesized beam and rms noise were $0\farcs37 \times 0\farcs31$ (~20 au, P.A. = 55°.7) and 0.23 mJy beam^{-1}. The total and peak flux density were 1.41 Jy and 0.15 Jy beam^{-1}, with signal-to-noise ratios (S/N) of 705 and 652, respectively. The results agree well with the previous SMA observations (Andrews et al. 2012) and ALMA observations (Hogerheijde et al. 2016) with lower spatial resolution and sensitivity. The synthesized beam and rms for the data at high spatial resolution data only were $0\farcs32 \times 0\farcs26$ (~15 au, P.A. = 54°.5) and 0.49 mJy beam^{-1}.

As shown by the black line in Figure 2(a), the dust continuum emission of the full data has a shallow dip in the radial profile of the surface brightness obtained by deprojecting the observed image data assuming an inclination angle of 7° and a position angle of −30° (Qi et al. 2008). By imaging the data at high spatial frequencies only (>200 kλ), we identify a gap and a ring at around 25 and 41 au, respectively (Figure 1(b) and gray line in Figure 2(a)). The *uv*-coverage of the full data set (from 22 to 580 kλ) is sufficiently high and indeed vital for this analysis. The continuum visibility profile as a function of the deprojected baseline length is plotted in Figure 3. Our result is consistent with the recent ALMA observations with higher spatial resolution and sensitivity (Zhang et al. 2016). Since the high spatial frequency data miss the flux of spatially extended structure, the total flux is lower than that of the full data by an order of magnitude. Artificial structure appears at $R > 70$ au in the high spatial frequency data, probably due to a failure to subtract the side lobe pattern of the synthesized beam. Its intensity is less than the 2σ noise level and the structure is masked in Figure 2(a). The location of the gap is similar to that of the axisymmetric depression in polarized intensity of near-infrared scattered light imaging of dust grains recently found by Subaru/HiCIAO and *Gemini*/GPI (Akiyama et al. 2015; Rapson et al. 2015).

3.2. Dust Surface Density and Gap Parameters

We extract the radial dust surface density distribution (Figure 2(b)), using the deprojected data of the dust continuum emission and the equation,

$$I_{d,\nu} = B_\nu(T_d)[1 - \exp(-\tau_{d,\nu})], \quad (1)$$

where $I_{d,\nu}$ is the observed intensity of the dust continuum emission at the frequency ν, and $B_\nu(T_d)$ is the Planck function at the dust temperature, T_d. The optical depth, $\tau_{d,\nu}$, is defined as $\tau_{d,\nu} = \kappa_\nu \Sigma_{\rm dust}$, where $\Sigma_{\rm dust}$ is the dust surface density and the dust opacity, κ_ν, is set as $\kappa_\nu = 3.4\,{\rm cm^2\,g^{-1}}$. We adopt $T_d = 22\,{\rm K}(R/10\,{\rm au})^{-0.3}$, where R is the disk radius, by fitting the model result in Andrews et al. (2012) and assume a uniform temperature distribution in the vertical direction. The derived dust optical depth is shown in Figure 2(c). We note that the derived dust surface density distribution is consistent with that derived from SMA observations of dust continuum emission and model calculations (Andrews et al. 2012). Also, the assumed dust temperature is consistent with the color temperature obtained from the spectral index of continuum emission across the observed four basebands between 329 and 343 GHz (Figure 2(d)) in the optically thick regions (⩽30 au, Figure 2(c)).

To estimate the gap width, $\Delta_{\rm gap}$, and depth, $(\Sigma_0 - \Sigma)/\Sigma_0$, where Σ_0 and Σ are the basic surface density and the surface density with the gap at the gap center, the intensity at the gap, $I_{\rm gap}$ (red crosses in Figure 2(a)), is derived by completing the missing flux of the high spatial frequency data, $I_{\rm gap}^{\rm high}$ (gray line in Figure 2(a)), with the full spatial frequency data, $I^{\rm full}$ (black line in Figure 2(a)). The intensity profile across the gap was obtained as follows: (i) fit the high-frequency data without the gap using a power-law profile of $I_0^{\rm high} = 1.1 \times 10^3 R_{\rm au}^{-1.5}$ mJy beam^{-1}, (ii) fit the gap region in the high-frequency data using a single Gaussian profile of $\Delta I_{\rm gap} = I_0^{\rm high} - I_{\rm gap}^{\rm high} = 7.7\exp(-(R_{\rm au} - 24.7\,{\rm au})^2/\{2(5.9\,{\rm au})^2\})$ mJy beam^{-1} (whose FWHM is 13.9 ± 1.0 au and depth is 7.7 ± 0.5 mJy) (green line in Figure 2(a)), and (iii) obtain the intensity at the gap as $I_{\rm gap} = I^{\rm full} - \Delta I_{\rm gap}$, where $I^{\rm full}$ is the intensity of the full data. In this fitting, we adopted the edges of the gap at R = 9–13 au (inner edge) and 39–43 au (outer edge) so that $\Delta I_{\rm gap}$ is overlaid to $I^{\rm full}$ smoothly. The optical depth at the gap is derived using $I_{\rm gap}$ and Equation (1), and then the dust surface density at the gap is derived using the same method mentioned above (red crosses in Figure 2(b)). The resulting gap width is $\Delta_{\rm gap} \sim 15$ au and the depth is $(\Sigma_0 - \Sigma)/\Sigma_0 \sim 0.23$. We note that our estimate of the gap width is limited by the angular resolution of the high spatial frequency data. The pattern of the gap and ring is also affected by residual artifacts due to the cutoff at 200 kλ, which introduces uncertainties in the location of the gap center, and the width and depth of the gap.

3.3. CO Isotopologue Line Emission

The observed ^{13}CO and C^{18}O $J = 3 - 2$ rotational line emission maps are plotted in Figures 1(c) and (d). The resulting synthesized beam and the 1σ rms noise level in the 0.03 km s^{-1} width-channels were $0\farcs41 \times 0\farcs33$ (P.A. = 53°.4), 12.0 mJy beam^{-1} (^{13}CO), and $0\farcs41 \times 0\farcs33$ (P.A. = 53°.8), 13.4 mJy beam^{-1} (C^{18}O). The integrated intensity maps were created by integrating from 1.18 to 4.30 km s^{-1} (^{13}CO) and from 1.48 to 4.15 km s^{-1} (C^{18}O). The resulting noise levels of the map were 8.4 mJy beam^{-1} km s^{-1} (^{13}CO) and 6.5 mJy beam^{-1} km s^{-1} (C^{18}O). The deprojected radial profiles

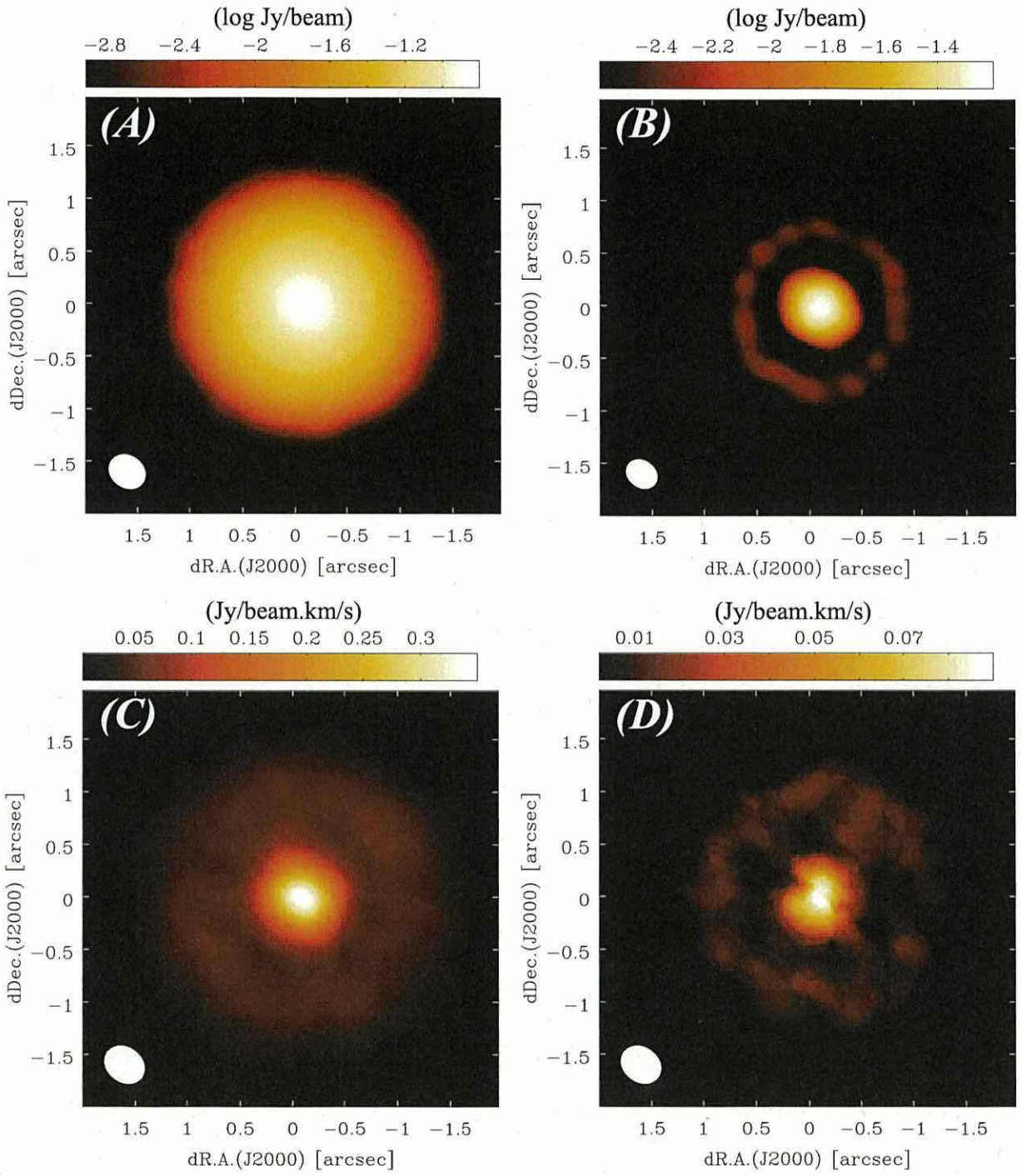

Figure 1. 336 GHz dust continuum map imaged using (A) all spatial frequency data, (B) only high spatial frequency (>200 kλ) data, and (C) ^{13}CO $J = 3 - 2$ and (D) C^{18}O $J = 3 - 2$ integrated line emission maps. Emission that was less than the 5σ noise level were masked. The synthesized beam sizes are shown in the bottom left corner of each panel.

of the integrated line emission of the ^{13}CO and C^{18}O following the subtraction of the dust continuum emission are plotted in Figure 4(a). The S/N is not sufficiently high enough to analyze the high spatial resolution data.

3.4. CO Column Density

We obtain the CO radial column density distribution, using the deprojected data of the ^{13}CO and C^{18}O line observations (Figure 4(d)). The CO column density, $N_{\rm CO}$, is derived from the

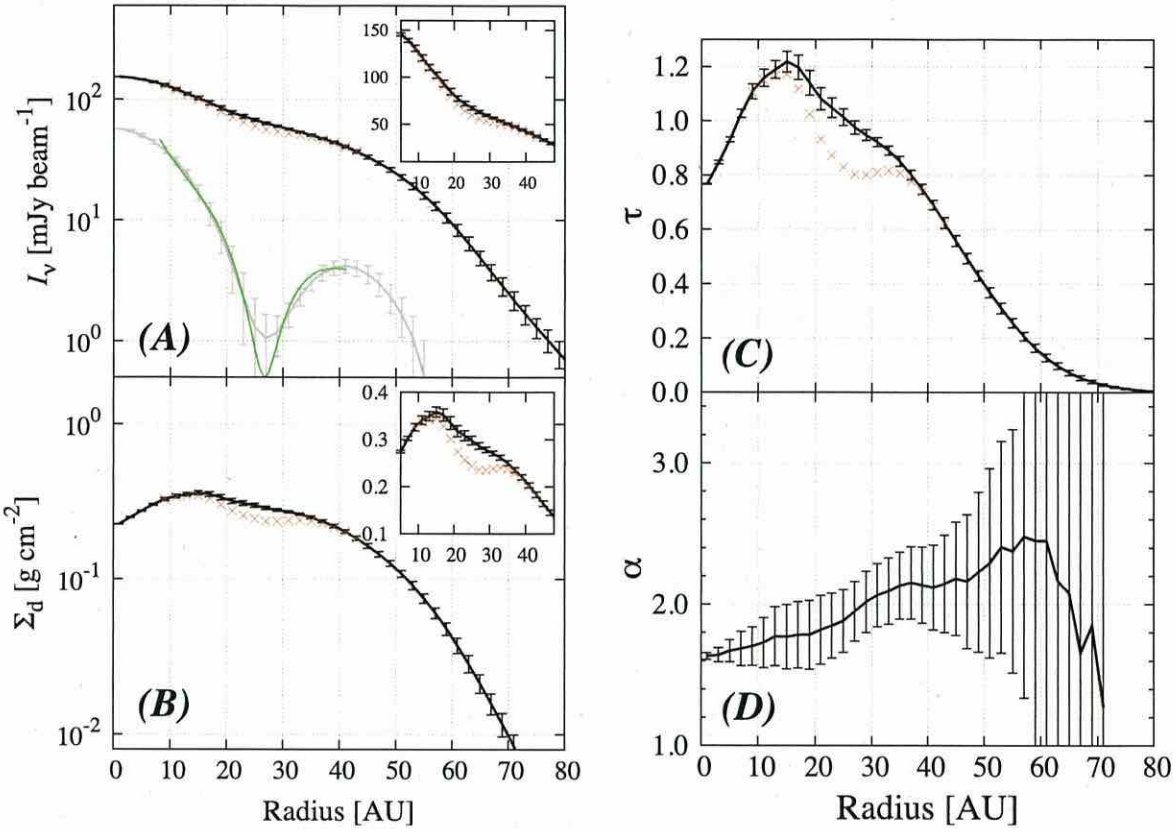

Figure 2. Radial distributions of (A) intensity of 336 GHz dust continuum emission, (B) dust surface density, (C) optical depth, and (D) spectral index between 329 and 343 GHz. The gray line in Figure (A) shows the data of only high spatial frequency with its Gaussian fit (green line). Red crosses in (A)–(C) are derived from high spatial frequency data recovered by the full spatial frequency data at the gap. The inserts show a close-up of the region around the gap.

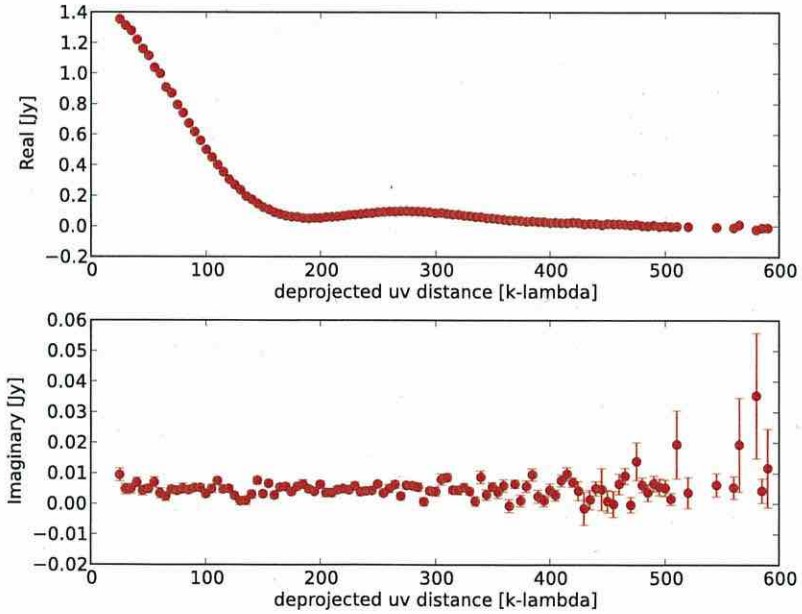

Figure 3. Real (top) and imaginary (bottom) parts of the azimuthally averaged continuum visibility profile as a function of the deprojected baseline length.

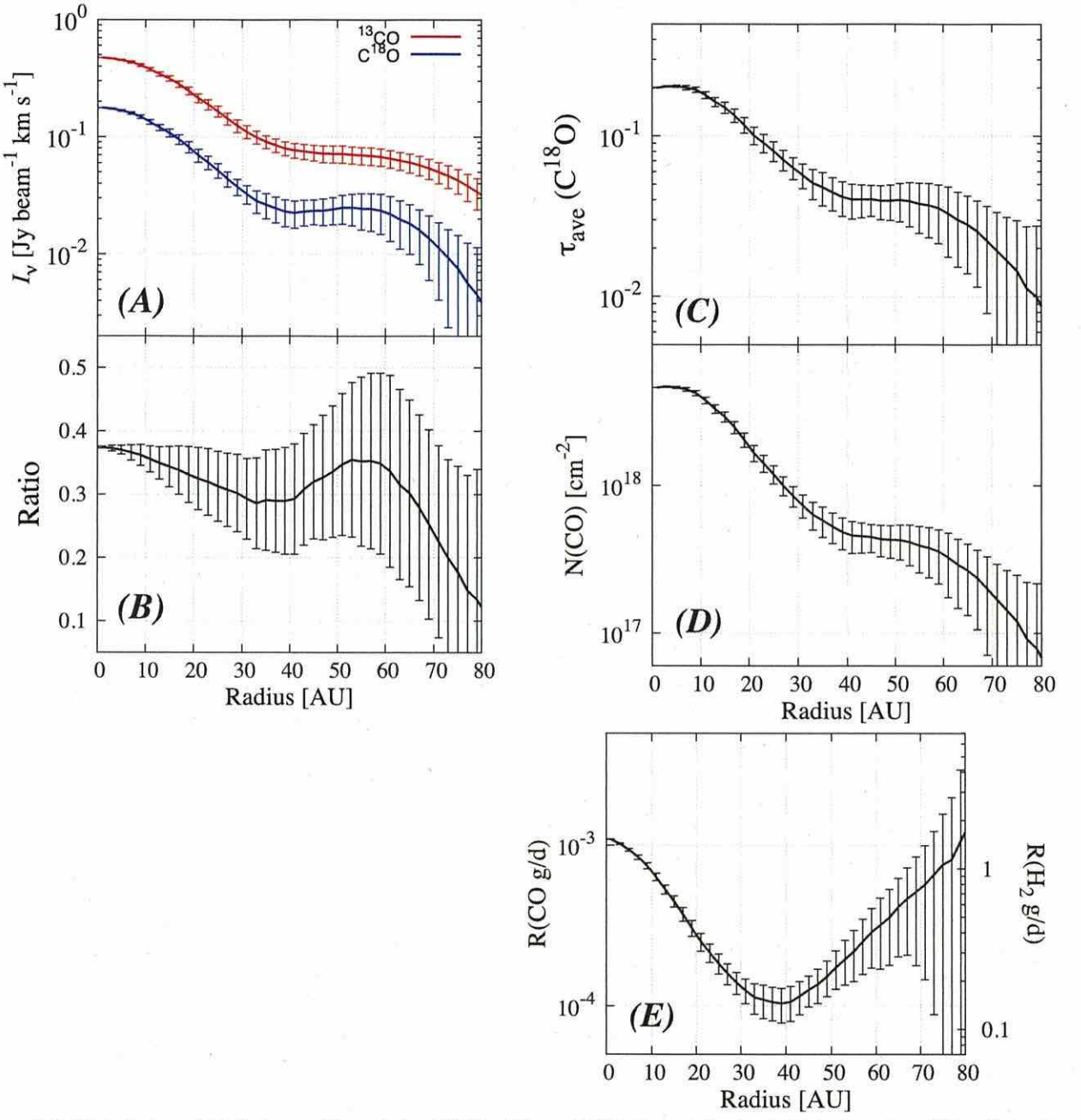

Figure 4. Radial distributions of (A) the integrated line emission of ^{13}CO (red line) and C^{18}O (blue line) $J = 3 - 2$, (B) the line ratio of C^{18}O to ^{13}CO, (C) the averaged optical depth of the C^{18}O line, (D) the CO column density, and (E) the CO gas-to-dust surface density ratio. The H_2 gas-to-dust ratio is also marked as a reference by simply assuming the abundance ratio of CO to H_2 to be 6×10^{-5}. All data are smoothed to a beam size of $0\farcs45 \times 0\farcs45$.

integrated line emission of C^{18}O $J = 3 - 2$ (Rybicki & Lightman 1979; Turner 1991), assuming abundance ratios of CO:^{13}CO = 67:1 and ^{13}CO:C^{18}O = 7:1 (Qi et al. 2011). The optical depth of the C^{18}O line emission, $\tau_{C^{18}O,\nu}$ (Figure 4(c)), is obtained from the observed line intensity as follows. We assume that the CO line-emitting region is mainly in the surface layer, while the dust continuum-emitting region is near the midplane. Thus, the deprojected intensity of the CO line emission plus dust continuum emission can be approximately derived from the following equation by simply assuming three zones in the vertical direction of the disk,

$$I_{C^{18}O+cont,\nu} = B_\nu(T_g)(1 - e^{-\tau_{C^{18}O,\nu}/2}) + B_\nu(T_d)(1 - e^{-\tau_{d,\nu}})e^{-\tau_{C^{18}O,\nu}/2} + B_\nu(T_g)(1 - e^{-\tau_{C^{18}O,\nu}/2})e^{-\tau_{d,\nu}-\tau_{C^{18}O,\nu}/2}, \quad (2)$$

where T_g is the gas temperature of the CO line-emitting region and T_d is the dust temperature near the midplane. The continuum-subtracted data, $I_{C^{18}O+cont,\nu} - I_{d,\nu}$, together with Equation (1) are used for the analysis. Since the observed line

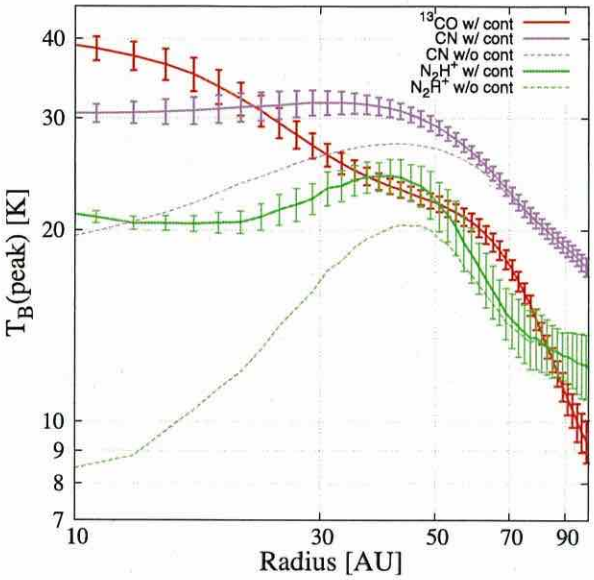

Figure 5. Radial distributions of the observed brightness temperature at the peak of ^{13}CO $J = 3 - 2$ (red) and N_2H^+ $J = 4 - 3$ (green) lines. The dust temperature at the midplane (dotted–dashed gray line) and the brightness temperature of the CN $N = 3 - 2$ (purple) line are also plotted for comparison. Dashed lines show the data subtracted by the dust continuum emission for N_2H^+ and CN. All data are smoothed to a beam size of $0\farcs45 \times 0\farcs45$.

ratio of $\int I_{C^{18}O,v}dv / \int I_{^{13}CO,v}dv$ is larger than 1/7 (Figure 4(b)), the ^{13}CO line is optically thick. Therefore, we adopt the brightness temperature at the peak of the ^{13}CO line (Figure 5) as the gas temperature, T_g. Also, we adopt a dust temperature of $T_d = 22\,\mathrm{K}(R/10\,\mathrm{au})^{-0.3}$ and the dust optical depth, $\tau_{d,\nu}$, is derived from the dust continuum observations (Figure 2(c)). We note that in the analysis we simply assume that the gas temperature is uniform in the vertical direction, and the gas temperature of the C^{18}O line-emitting region is the same as that of the ^{13}CO line-emitting region, although it could be lower in reality. In addition, C^{18}O could be depleted due to the effect of isotopologue-dependent photodissociation, and $N_{CO}/N_{C^{18}O}$ is possibly higher than 440 (Miotello et al. 2014). The CO column density will be underestimated due to these effects.

3.5. CO Gas-to-dust Surface Density Ratio

Using the obtained CO column density and dust surface density (Figures 4(d) and 2(b)), we derive the CO gas-to-dust surface density ratio (Figure 4(e)). If we convert it to the H_2 surface density, assuming an abundance ratio of CO to H_2 of 6×10^{-5} (Qi et al. 2011), the estimated H_2 gas mass is orders of magnitude lower than that predicted from the observations of the HD line emission by the *Herschel Space Observatory* (Bergin et al. 2013). The resulting H_2 gas-to-dust surface density ratio (~0.1–1) is about two orders of magnitude lower than the typical interstellar value of ~100, which suggests strong CO depletion throughout the disk down to ~10 au.

The CO gas-to-dust surface density ratio increases beyond a radius of ~40 au since the dust surface density drops dramatically in this region. It could be due to the drift of pebbles from the outer disk toward the central star (e.g., Takeuchi et al. 2005; Andrews et al. 2012; Walsh et al. 2014b).

4. DISCUSSIONS

4.1. Origin of the Gap and Ring in the Dust Continuum Emission

The gap and ring resemble those in the HL Tau system, recently found by the ALMA long baseline campaign (ALMA Partnership et al. 2015). Our result shows that gaps and rings in the (sub)millimeter dust continuum can exist, not only in relatively young disks (0.1–1 Myr) but also in relatively old disks (3–10 Myr). One possible mechanism for opening a gap is the gravitational interaction between a planet and the gas (e.g., Lin & Papaloizou 1979; Goldreich & Tremaine 1980; Fung et al. 2014). Such an interaction may also produce the spiral density waves recently found in optical and near-infrared scattered light imaging of dust grains in protoplanetary disks (e.g., Muto et al. 2012). According to recent theoretical analyses of gap structure around a planet (Kanagawa et al. 2015a, 2015b, 2016), the depth and width of the gap are controlled by the planetary mass, the turbulent viscosity, and the gas temperature. The shape of the gap is strongly influenced by angular momentum transfer via turbulent viscosity and/or instability caused by a steep pressure gradient at the edges of a gap. The observed gap has an apparent width and depth of $\Delta_{gap} \sim 15$ au and $(\Sigma_0 - \Sigma)/\Sigma_0 \sim 0.23$, respectively. This is too shallow and too wide compared with that predicted by theory. However, the observations are limited to an angular resolution of ~15 au, and the depth and width could be deeper and narrower in reality. For instance, if we assume that the gap depth times the gap width retains the value derived from the observations, it is possible for the gap to have a width and depth of $\Delta_{gap} \sim 6$ au and $(\Sigma_0 - \Sigma)/\Sigma_0 \sim 0.58$, which is similar to the GPI result (Rapson et al. 2015). Such a gap could be opened by a super-Neptune-mass planet, depending on the parameters of the disk, such as the turbulent viscosity (Kanagawa et al. 2015a, 2015b, 2016). If the gap in the larger dust grains is deeper than that in the gas, the planet could be lighter than super-Neptune mass. We note that a planet of even a few Earth masses, although it cannot open a gap in the gas, can open a gap in the dust distribution if a certain amount of pebble-sized particles, whose motions are not perfectly coupled to that of gas, are scattered by the planet and/or the spiral density waves excited by the planet (Paardekooper & Mellema 2006; Muto & Inutsuka 2009).

Another possible mechanism to form a gap and an associated ring in dust continuum emission is the microscopic process of sintering CO ice on dust aggregates (Sirono 2011; Okuzumi et al. 2016). The gaps and rings observed in the younger and more luminous HL Tau system could be explained by the sintering of various molecular ices in the disk at their distinct snow line locations (Okuzumi et al. 2016). Although our observations indicate that the CO-depleted region is located down to ~10 au in the TW Hya system, model calculations of the temperature in the disk suggest that the CO snow line is located at ~30 au. Sintering is a process that renders an aggregate less sticky (Sirono 2011). Just outside the CO snow line where sintering occurs, large aggregates are easily destroyed, becoming small fragments through collisions, and their radial drift motion by the above-mentioned mechanism slows down. Thus, dust grains are stuck just outside the CO

snow line, and a bright ring and a dark lane inside the ring is formed in the dust continuum emission. If another sintering region is formed inside the dark lane by, for example, CH_4 sintering, the region between the bright CO and CH_4 sintering regions would look like a gap. According to model calculations (Okuzumi et al. 2016), the CH_4 sintering region is located at ~10 au in the TW Hya disk.

4.2. CO Gas Depletion Inside the CO Snow Line

From the CO line observations, we find a very low column density of CO compared with dust throughout the disk, down to a radius of about 10 au. This CO depletion could indicate a general absence of H_2 gas compared with dust. However, the *Herschel* HD observations (Bergin et al. 2013) indicates that it is more likely that it is due to CO freeze-out on grains with the possibility that subsequent grain-surface reactions form larger molecules even inside the CO snow line (Favre et al. 2013; Williams & Best 2014). The CO column density derived from our observations, $N_{CO} \sim 10^{18}\,cm^{-2}$, can be explained by detailed model calculations using a chemical network that includes freeze-out of molecules on grains and grain-surface reactions (Aikawa et al. 2015). The model calculations show that the CO depletion will proceed inside the CO snow line due to the sink effect: conversion of CO to less volatile species on grain surfaces. In the case of TW Hya, it could occur on a timescale shorter than the disk lifetime, depending on the amount of small grains. See Aikawa et al. (2015) for more detailed discussions, including the effect on other species. The CO depletion spread over the disk is inconsistent with the prediction by the previous ALMA N_2H^+ observations that depletion would be localized beyond the CO snow line (Qi et al. 2013). This could be because the N_2H^+ line emission traces the disk surface and not the CO-depleted region.

Figure 5 shows the brightness temperature at the peak of the $^{13}CO\ J = 3 - 2$ line obtained by our observations and the $N_2H^+\ J = 4 - 3$ line at 372.672 GHz obtained by the ALMA archived data (2011.0.00340.S). Since the ^{13}CO line is optically thick, the brightness temperature at the peak of the line emission represents the gas temperature of the line-emitting region. If LTE is applicable, the N_2H^+ brightness temperature is higher than the gas temperature of the ^{13}CO line-emitting region at the disk radius of ~40 au, and higher than the dust temperature near the midplane down to ~15 au (Figure 5). If the N_2H^+ line is optically thin, the gas temperature of the line-emitting region is higher than the brightness temperature. Therefore, the N_2H^+ line should come from the surface layer of the disk. Model calculations also predict that N_2H^+ exists in the disk surface for the model with (sub)micron-sized grains, similar to radical species abundant in the disk surface, such as CN and C_2H (e.g., Walsh et al. 2010; Aikawa et al. 2015). Our results (Figure 5) and the SMA observations of C_2H (Kastner et al. 2015) show that the radial intensity profiles of these species are similar. They have peaks around the disk radius of 40 au, beyond which the dust surface density drops. The result suggests that in order to trace the CO-depleted region, the $C^{18}O$ line may be more robust than the N_2H^+ line.

In the CO-depleted region, complex organic molecules would be produced via grain-surface reactions because hydrogen attachment to CO is thought to produce methanol and more complex species (e.g., Watanabe & Kouchi 2008; Walsh et al. 2014a). Methyl cyanide, which has recently been detected from a protoplanetary disk for the first time by ALMA (Öberg et al. 2015), could be formed through such grain-surface reactions.

We would like to thank the referee for comments that improved our paper. We are also grateful to Sean Andrews and Joel Kastner for their fruitful comments. This paper makes use of the following ALMA data: ADS/JAO.ALMA#2013.1.01397.S and ADS/JAO.ALMA#2011.0.00340.S. ALMA is a partnership of ESO (representing its member states), NSF (USA), and NINS (Japan), together with NRC (Canada), NSC, ASIAA (Taiwan), and KASI (Republic of Korea), in cooperation with the Republic of Chile. The Joint ALMA Observatory is operated by ESO, AUI/NRAO, and NAOJ. This work is partially supported by Grants-in-Aid for Scientific Research 23103005, 25108004, 25400229, and 15H03646. T.T. was supported by JSPS KAKENHI grant No. 23103004. C.W. is supported by the Netherlands Organisation for Scientific Research (program number 639.041.335). Astrophysics at QUB is supported by a grant from the STFC.

Facility: ALMA.

REFERENCES

Aikawa, Y., Furuya, K., Nomura, H., & Qi, C. 2015, ApJ, 807, 120
Akiyama, E., Muto, T., Kusakabe, N., et al. 2015, ApJL, 802, L17
ALMA Partnership, Brogan, C. L., Pérez, L. M., et al. 2015, ApJL, 808, L3
Andrews, S. M., Wilner, D. J., Hughes, A. M., et al. 2012, ApJ, 744, 162
Bergin, E. A., Cleeves, L. I., Gorti, U., et al. 2013, Natur, 493, 644
Favre, C., Cleeves, L. I., Bergin, E. A., Qi, C., & Blake, G. A. 2013, ApJL, 776, L38
Fung, J., Shi, J.-M., & Chiang, E. 2014, ApJ, 782, 88
Goldreich, P., & Tremaine, S. 1980, ApJ, 241, 425
Hernández, J., Hartmann, L., Megeath, T., et al. 2007, ApJ, 662, 1067
Hogerheijde, M. R., Bekkers, D., Pinilla, P., et al. 2016, A&A, 589, A99
Ida, S., Lin, D. N. C., & Nagasawa, M. 2013, ApJ, 775, 42
Kanagawa, K. D., Muto, T., Tanaka, H., et al. 2015a, ApJL, 806, L15
Kanagawa, K. D., Muto, T., Tanaka, H., et al. 2016, PASJ, submitted
Kanagawa, K. D., Tanaka, H., Muto, T., Tanigawa, T., & Takeuchi, T. 2015b, MNRAS, 448, 994
Kastner, J. H., Qi, C., Gorti, U., et al. 2015, ApJ, 806, 75
Kikuchi, A., Higuchi, A., & Ida, S. 2014, ApJ, 797, 1
Kley, W., & Nelson, R. P. 2012, ARA&A, 50, 211
Kuzuhara, M., Tamura, M., Kudo, T., et al. 2013, ApJ, 774, 11
Lin, D. N. C., & Papaloizou, J. 1979, MNRAS, 186, 799
Miotello, A., Bruderer, S., & van Dishoeck, E. F. 2014, A&A, 572, A96
Muto, T., & Inutsuka, S.-i. 2009, ApJ, 695, 1132
Muto, T., Grady, C. A., Hashimoto, J., et al. 2012, ApJL, 748, L22
Öberg, K. I., Guzmán, V. V., Furuya, K., et al. 2015, Natur, 520, 198
Okuzumi, S., Momose, M., Sirono, S.-i., Kobayashi, H., & Tanaka, H. 2016, ApJ, in press (arXiv:1510.03556)
Paardekooper, S.-J., & Mellema, G. 2006, A&A, 453, 1129
Qi, C., D'Alessio, P., Öberg, K. I., et al. 2011, ApJ, 740, 84
Qi, C., Wilner, D. J., Aikawa, Y., Blake, G. A., & Hogerheijde, M. R. 2008, ApJ, 681, 1396
Qi, C., Öberg, K. I., Wilner, D. J., et al. 2013, Sci, 341, 630
Rapson, V. A., Kastner, J. H., Millar-Blanchaer, M. A., & Dong, R. 2015, ApJL, 815, L26
Rybicki, G. B., & Lightman, A. P. 1979, Radiative Processes in Astrophysics (New York: Wiley)
Sirono, S.-i. 2011, ApJ, 735, 131
Takeuchi, T., Clarke, C. J., & Lin, D. N. C. 2005, ApJ, 627, 286
Thalmann, C., Carson, J., Janson, M., et al. 2009, ApJL, 707, L123
Turner, B. E. 1991, ApJS, 76, 617
Watanabe, N., & Kouchi, A. 2008, PrSS, 83, 439
Walsh, C., Juhász, A., Pinilla, P., et al. 2014b, ApJL, 791, L6
Walsh, C., Millar, T. J., & Nomura, H. 2010, ApJ, 722, 1607
Walsh, C., Millar, T. J., Nomura, H., et al. 2014a, A&A, 563, A33
Williams, J. P., & Best, W. M. J. 2014, ApJ, 788, 59
Zhang, K., Bergin, E. A., Blake, G. A., et al. 2016, ApJL, 818, L16

A&A 589, A15 (2016)
DOI: 10.1051/0004-6361/201527069

Astronomy & Astrophysics

On the water delivery to terrestrial embryos by ice pebble accretion

Takao Sato, Satoshi Okuzumi, and Shigeru Ida

Department of Earth and Planetary Sciences, Tokyo Institute of Technology, Meguro, Tokyo, 152-8551, Japan
e-mail: okuzumi@geo.titech.ac.jp

Received 27 July 2015 / Accepted 18 December 2015

ABSTRACT

Standard accretion disk models suggest that the snow line in the solar nebula migrated interior to the Earth's orbit in a late stage of nebula evolution. In this late stage, a significant amount of ice could have been delivered to 1 AU from outer regions in the form of mm to dm-sized pebbles. This raises the question why the present Earth is so depleted of water (with the ocean mass being as small as 0.023% of the Earth mass). Here we quantify the amount of icy pebbles accreted by terrestrial embryos after the migration of the snow line assuming that no mechanism halts the pebble flow in outer disk regions. We use a simplified version of the coagulation equation to calculate the formation and radial inward drift of icy pebbles in a protoplanetary disk. The pebble accretion cross section of an embryo is calculated using analytic expressions presented by recent studies. We find that the final mass and water content of terrestrial embryos strongly depends on the radial extent of the gas disk, the strength of disk turbulence, and the time at which the snow lines arrives at 1 AU. The disk's radial extent sets the lifetime of the pebble flow, while turbulence determines the density of pebbles at the midplane where the embryos reside. We find that the final water content of the embryos falls below 0.023 wt% only if the disk is compact (<100 AU), turbulence is strong at 1 AU, and the snow line arrives at 1 AU later than 2–4 Myr after disk formation. If the solar nebula extended to 300 AU, initially rocky embryos would have evolved into icy planets of 1–10 Earth masses unless the snow-line migration was slow. If the proto-Earth contained water of ~1 wt% as might be suggested by the density deficit of the Earth's outer core, the formation of the proto-Earth was possible with weaker turbulence and with earlier (>0.5–2 Myr) snow-line migration.

Key words. Earth – planets and satellites: composition – planets and satellites: formation – protoplanetary disks

1. Introduction

Terrestrial planets in our solar system are characterized by their extremely low water content. The ocean of the Earth comprises only 0.023 wt% of the total mass of the planet. The water content of the present Earth's interior is uncertain, but the 10% density deficit of the Earth's outer core might suggest that that water of up to ~1 wt% existed in the proto-Earth and provided a large amount of hydrogen to the outer core (Okuchi 1997; Abe et al. 2000; see Nomura et al. 2014 for experiments supporting the large amount of hydrogen partitioning into the core). An initial water content much in excess of ~1 wt% seems unlikely because neither stellar irradiation at ~1 AU (Machida & Abe 2010) nor giant impacts (Genda & Abe 2005) are able to vaporize the majority of the water from the Earth's gravitational potential. Mars might possess, or might have possessed, subsurface water/ice of 0.01–0.1% of the total Mars mass (Kurokawa et al. 2014). Venus has a very dry atmosphere with the low-altitude H_2O mixing ratio of 10–100 ppm (Prinn & Fegley 1987; Donahue & Hodges 1992) and the high viscosity of Venus's mantle suggests that its interior is also dry (Nimmo & McKenzie 1998). The low water content of the terrestrial planets is in stark contrast to the high ice content of outer solar system bodies; in the extreme example of comets, the ice-to-rock mass ratio is generally thought to be close to unity (e.g., A'Hearn 2011).

The fact that the Earth was born dry might not be surprising at first sight given that the Earth's orbit is well inside the snow line of the current solar system. The snow line is defined by the orbit inside which water ice sublimates into vapor. Assuming that water ice sublimates at 170 K, the snow line of the present solar system lies at about 3 AU from the Sun. The snow line in the solar nebula, which is the protoplanetary disk that formed the solar system, would have been at the same location if the nebula was optically thin to direct stellar radiation (Hayashi 1981).

However, the solar nebula was presumably optically thick at least in its early evolutionary stage because of the presence of abundant small dust grains. In an optically thick protoplanetary disk, the snow line can be either inside or outside the Earth's orbit (1 AU) depending on how much accretion heating is effective. The disk is hottest in its earliest evolutionary stage where the central pre-main-sequence star is most luminous (e.g., Kusaka et al. 1970; Turner et al. 2012) and where the accretion rate is the highest (e.g., Hartmann et al. 1998). Standard viscous accretion disk models show that the snow line, or the location where the gas temperature is 150–170 K, around a solar-mass star lies at about 5 AU when the accretion rate of the disk $\dot{M}$ is $10^{-7}\ M_\odot\ \mathrm{yr}^{-1}$ (Davis 2005; Garaud & Lin 2007; Min et al. 2011; Oka et al. 2011; Bitsch et al. 2015; Baillié et al. 2015; Mulders et al. 2015). However, as the accretion rate decreases with time, the disk cools down and the snow line moves inward. Assuming standard viscous accretion, the snow line passes 1 AU at $\dot{M} \approx$ a few $\times 10^{-9}\ M_\odot\ \mathrm{yr}^{-1}$ if all dust in the disk is in the form of opacity-dominating micron-sized grains (Davis 2005; Garaud & Lin 2007; Oka et al. 2011; Bitsch et al. 2015), and at $\dot{M} \approx 1 \times 10^{-8}\ M_\odot\ \mathrm{yr}^{-1}$ if the grains are depleted by an order of magnitude (Bitsch et al. 2015). The migration of the snow line stops at ~0.7 AU (for the stellar luminosity of 1 $L_\odot$) when accretion heating ceases to be important around these orbits (Sasselov & Lecar 2000; Davis 2005; Garaud & Lin 2007; Oka et al. 2011). At this stage, the interior of the disk is much colder than that of an optically thin disk because the disk can only receive stellar radiation on its surface. The snow line moves out toward the final position ≈3 AU only after the interior of the disk becomes

optically thin to direct stellar radiation ($\dot{M} \lesssim 10^{-10}\ M_\odot\ \mathrm{yr}^{-1}$, Oka et al. 2011).

The above picture is based on standard accretion disk models in which turbulence is assumed to be spatially uniform. For example, accretion heating would be much less significant than anticipated by the uniformly turbulent models if the disk is only turbulent on its surface. This is the case in magnetically driven accretion models where the magnetorotational instability (Balbus & Hawley 1991), which is the driver of disk turbulence, is suppressed by magnetic diffusion near the midplane (Hirose & Turner 2011; Flock et al. 2013). On the other hand, the nonsteady accretion model of Martin & Livio (2012), which incorporates the gravitational instability and suppression of magnetic turbulence by magnetic diffusion, suggests that the gas temperature at 1 AU could be maintained high enough to sublimate ice even in the late stage of disk evolution. The snow line would not have reached the terrestrial region if X-ray-driven photoevaporation had cleared the gas in that region when $\dot{M} \approx 1 \times 10^{-8}\ M_\odot\ \mathrm{yr}^{-1}$ (Owen et al. 2010).

The inward migration of the snow line, if it really occurs in protoplanetary disks, gives two important constraints on the formation of terrestrial planets at ~1 AU like the Earth. Earth-sized terrestrial planets are generally believed to form through giant impacts of Mars-sized (~0.1 $M_\oplus$) solid bodies called planetary embryos (e.g., Wetherill & Stewart 1989; Kokubo & Ida 2002). Given the inefficiency of removing water from embryos through giant impacts (Genda & Abe 2005), water-devoid planets must form from water-devoid embryos. Such embryos can form at 1 AU only when intense accretion heating pushes the snow line to >1 AU; otherwise, like comets, they would have an ice-to-rock ratio of ≈1. In the standard viscous disk models, this constraint means that the terrestrial embryos can only form when $\dot{M} \lesssim$ a few to $10 \times 10^{-9}\ M_\odot\ \mathrm{yr}^{-1}$ with the exact value depending on how much of the small dust grains are depleted (see above). Assuming the correlation between the stellar age and mass accretion rate suggested by observations (Hartmann et al. 1998; Bitsch et al. 2015), this also means that terrestrial planet formation needs to have been completed within ~1–3 Myr after disk formation (there is, however, a large scatter in the $\dot{M}$-age correlation). The Hf-W dating of Martian meteorites indicates that Mars, a possible planetary embryo that survived giant impacts, formed during the first ~1–3 Myr of the solar system formation (Dauphas & Pourmand 2011). This Hf-W dating implies that the terrestrial embryo formation in the solar system barely satisfied this time constraint. One should keep in mind, however, that magnetically driven accretion models might predict very different time constraints as discussed above.

The second important constraint is that the rocky embryos must avoid accretion of a significant amount of ice that could occur after the inward migration of the snow line. It is known that solid particles in a gas disk drift toward the central star because the gas drag robs the particles of angular momentum (Adachi et al. 1976; Weidenschilling 1977). The angular momentum loss is most effective for millimeter- to meter-sized particles that are marginally decoupled from the gas disk. Models incorporating the drift and coagulation of solid particles predict that a significant amount of millimeter to decimeter-sized ice aggregates flow from outer disk regions toward the snow line (e.g., Garaud 2007; Brauer et al. 2008a; Birnstiel et al. 2010). Without any mechanisms preventing the pebble flow, the total amount of ice that is delivered to the inner orbits is comparable to the total amount of ice in the disk (~10–100 $M_\oplus$) because the majority of solids in a disk generally reside in outer regions. The problem here is that large solid bodies like planetary embryos are efficient at capturing pebble-sized particles because of the help of the disk's gas drag (Ormel & Klahr 2010; Lambrechts & Johansen 2012). Therefore, if the snow line in the solar nebula migrated inside 1 AU, rocky embryos at 1 AU could have accreted a non-negligible amount of ice. One might expect that this water delivery mechanism is potentially relevant to the origin of the Earth's ocean; however, the immediate problem with this interpretation is that the D/H ratio of icy pebbles from outer disk regions would presumably have been similar to those of comets, which are on average higher than the Earth ocean water value (e.g., Altwegg et al. 2015). If this is the case, the amount of water supplied by the icy pebbles must have been much smaller than that of ocean water, or at least smaller than the water capacity of the Earth's interior, in order to avoid an enhancement of the ocean D/H ratio.

The question of how much water is delivered to terrestrial embryos by icy pebbles is closely linked to the so-called pebble accretion scenario for giant planet formation recently proposed by (Lambrechts & Johansen 2012, 2014; see also Kretke & Levison 2014; Johansen et al. 2015; Morbidelli et al. 2016, 2015; Moriarty & Fischer 2015; Levison et al. 2015a,b). They showed that efficient icy pebble accretion enables embryos of 1000 km in size outside the snow line to grow to the critical core mass for runway gas accretion (~10 $M_\oplus$) within the lifetime of protoplanetary disks. Our study focuses on another aspect of the pebble accretion scenario: while the radial pebble flux feeds giant planet cores in outer disk regions, the same pebble flux could deliver an excessive amount of water to terrestrial embryos in inner disk regions.

While this paper was under revision, a paper that discusses the issue of the snow-line migration appeared in print (Morbidelli et al. 2016). The paper proposes the scenario that proto-Jupiter halted the pebble flow from outer disk regions by carving a pebble-trapping gap in the gas nebula. Although this is one plausible scenario (see also the discussions in our Sect. 4.3), it is also important to pursue the possibility that Earth-forming embryos avoided excessive water delivery even if no mechanism stopped the icy pebble flow. This is the subject of this paper.

In this study, we calculate the amount of ice accreted by an embryo at ~1 AU based on the assumption that the snow line migrates inward across 1 AU. We employ a simple model of global dust evolution in which the collisional growth (coagulation) and radial drift of icy dust particles in a disk are treated in a self-consistent way. We compute the amount of water delivered to a terrestrial embryo for a range of model parameters including the strength of turbulence, the time at which the snow line moves interior to 1 AU, and the radial extent of the gas disk. Our model is technically similar to the analytic model of Lambrechts & Johansen (2014) in that both treat the dominant particle size at each orbital radius instead of treating the full particle size distribution. An important difference from the previous study by Lambrechts & Johansen (2014) is that we apply the concept of pebble accretion to the problem of water delivery to terrestrial planets. In addition, our numerical model includes a more detailed calculation of the relative velocity between particles and also takes the finite radial extent of a protoplanetary disk into account, both of which affect the properties of the radial pebble flow. We also calibrate our model using the result of a detailed coagulation simulation that resolves the full particle size distribution (Okuzumi et al. 2012).

The structure of the paper is as follows. In Sect. 2, we introduce the models of the solar nebula, dust evolution, and pebble accretion, emphasizing how disk turbulence affects dust coagulation and pebble accretion quantitatively. In Sect. 3, we present the results of our model calculations and highlight how

the rate of pebble accretion by an embryo depends on the radial extent of the disk and on turbulence strength. We give some discussions in Sect. 4 and summarize in Sect. 5. Appendix A is devoted to the validation of the simplified dust evolution model employed in this work.

2. Model

2.1. Overview

We describe the model we use to quantify how much water is delivered to rocky embryos at 1 AU through icy pebble accretion (see Fig. 1 for a schematic of the model). We consider a solar-mass star and a protoplanetary disk of outer radius $r_{\rm out}$. We assume that the snow line is initially well beyond 1 AU and migrates in across 1 AU at time $t_{\rm start}$ after the beginning of dust evolution. We take $t_{\rm start}$ as a free parameter to avoid complications that would result from detailed modeling of the snow-line evolution. We assume that the solids in the disk are initially in the form of 0.1 μm-sized dust grains, and calculate the growth and radial inward drift of ice particles outside the snow line via a simplified dust coagulation model described in Sect. 2.3. The calculation gives us the mass flux (in the direction of the central star) and typical size of icy pebbles that arrive at 1 AU as a function of time t. The ice-to-rock mass ratio of the icy pebbles is assumed to be unity in accordance with the solar system composition compiled by Lodders (2003). Millimeter observations of protoplanetary disks suggest that $r_{\rm out}$ is typically within the range 100–300 AU (e.g., Andrews & Williams 2007). We consider the two values $r_{\rm out}$ = 100 AU and 300 AU.

We then place a rocky embryo of initial mass $M_{\rm e,0}$ at 1 AU and allow it to accrete ice particles at $t > t_{\rm start}$. We consider two cases, $M_{\rm e,0} = 10^{-1}\ M_\oplus$ and $10^{-2}\ M_\oplus$. The larger $M_{\rm e,0}$ is the typical mass of terrestrial embryos predicted from planetesimal accumulation without fragmentation (e.g., Wetherill & Stewart 1989; Kokubo & Ida 2002). The final water fraction of the embryo is compared with the minimum water fraction of the present Earth given by the ocean (0.023 wt%) and with the hypothetical water fraction of the proto-Earth inferred from the density deficit of the Earth's outer core (1 wt%).

The radial drift of ice particles considered in this study is due to their angular momentum in a sub-Keplerian rotating protoplanetary disk (Adachi et al. 1976; Weidenschilling 1977). In reality, solids in a disk have an additional inward velocity owing to the accretion of the background gas onto the central star. However, this latter velocity component is negligible compared to the former component whenever dust grows into pebble-sized particles (Brauer et al. 2008a; Birnstiel et al. 2012).

We neglect possible filtration by planetesimals, planetary embryos, or gas giants exterior to 1 AU. As already shown by previous studies (Lambrechts & Johansen 2014; Guillot et al. 2014; Morbidelli & Nesvorny 2012), a swarm of planetesimals or embryos filters only a minor fraction of the pebble flow (typically <50%) unless the size distribution of the bodies is narrowly peaked at 10^3–10^4 km in radius (see Guillot et al. 2014). By contrast, if massive planets already exist at $t \sim t_{\rm start}$, they can efficiently halt the flow of the pebbles by opening a gap in the gas disk (e.g., Paardekooper & Mellema 2006; Rice et al. 2006; Zhu et al. 2012; Pinilla et al. 2012; Morbidelli & Nesvorny 2012; Lambrechts et al. 2014). By neglecting this effect, we effectively assume that such gap-forming planets form only after the snow line migrates inside 1 AU. We discuss this point in more detail in Sect. 4.3. We also neglect the loss of the pebble flux due to the accretion by adjacent rocky embryos. Thus, the problem we are considering reduces to the problem of calculating the pebble accretion rate of each isolated rocky embryo.

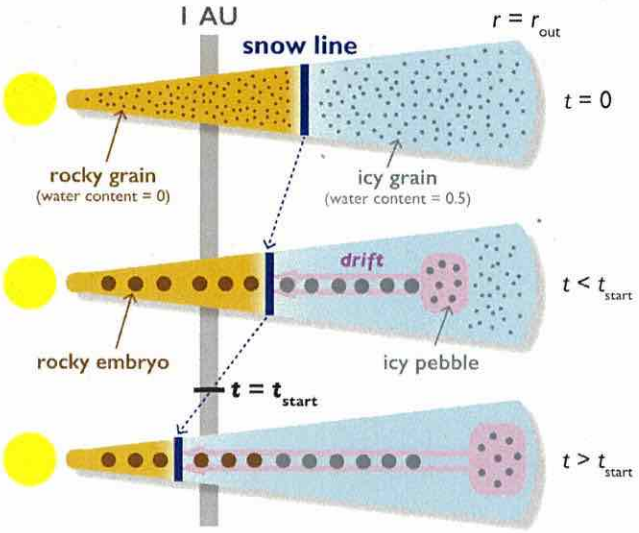

Fig. 1. Schematic illustration showing the radial inward drift of icy pebbles and the inward migration of the snow line in a protoplanetary disk. Rocky embryos at 1 AU accrete radially drifting icy pebbles when the snow line resides at <1 AU. Time $t = t_{\rm start}$, at which the snow line passes 1 AU, is taken as a free parameter.

In the following subsections, we describe our disk model in Sect. 2.2, the equations that determine the evolution of icy pebbles in Sects. 2.3 and 2.4, our pebble accretion model in Sect. 2.5, and our parameter choices in Sect. 2.6.

2.2. Disk model

The radial distribution of the gas surface density $\Sigma_{\rm g}$ is taken from the minimum mass solar nebula (MMSN) model of Hayashi (1981),

$$\Sigma_{\rm g} = 1700 \left(\frac{r}{1\ {\rm AU}}\right)^{-3/2}\ {\rm g\ cm^{-2}}, \tag{1}$$

where r is the distance from the central star. We cut off $\Sigma_{\rm g}$ at $r > r_{\rm out}$ and take the cutoff radius $r_{\rm out}$ as a free parameter (either 100 AU or 300 AU). The initial dust surface density $\Sigma_{\rm d,0}$ is taken to be 1% of $\Sigma_{\rm g}$. The total dust mass within the initial disk is

$$M_{\rm d} = 2\pi \int_{r_{\rm in}}^{r_{\rm out}} r\Sigma_{\rm d,0} {\rm d}r \approx 80\ M_\oplus \left(\frac{r_{\rm out}}{100\ {\rm AU}}\right)^{1/2}, \tag{2}$$

where we have used $r_{\rm in} \ll r_{\rm out}$. Since $M_{\rm d}$ is an increasing function of $r_{\rm out}$, the dominant part of the mass resides in the outermost region of the disk. We come back to this point in Sect. 3.1.

The gas disk is assumed to be isothermal and hydrostatic in the vertical direction. The gas density at the midplane is thus given by $\rho_{\rm g} = \Sigma_{\rm g}/(\sqrt{2\pi}h_{\rm g})$, where $h_{\rm g} = c_{\rm s}/\Omega$ is the gas scale height, $c_{\rm s} = \sqrt{k_{\rm B}T/m_{\rm g}}$ is the isothermal sound speed, $\Omega = \sqrt{GM_\odot/r^3} = 2.0 \times 10^{-7}(r/1\ {\rm AU})^{-3/2}\ {\rm s^{-1}}$ is the Keplerian frequency with $k_{\rm B}$, $m_{\rm g}$, G being the Boltzmann constant, mean molecular mass (taken to be 2.34 amu), and gravitational constant, respectively.

As stated earlier, we do not directly treat the evolution of the snow line and instead express the migration of the snow line

with $t_{\rm start}$. However, we do need a model of the gas temperature T when we calculate the density structure of the gas disk and the thermal and turbulent velocity of particles. For this purpose, we simply use a fixed power-law temperature profile

$$T = 170\left(\frac{r}{1\ \mathrm{AU}}\right)^{-1/2}\ \mathrm{K}, \tag{3}$$

where the slope has been taken from the optically thin disk model of Hayashi (1981). The value at 1 AU has been chosen so that the snow line lies at ~1 AU, which is motivated by our results that the water content of an embryo increases most rapidly just after the snow line passes the embryo ($t \approx t_{\rm start}$; see Sect. 3.4). This temperature profile gives $c_{\rm s} = 7.8\times10^4(r/1\ \mathrm{AU})^{-1/4}$ cm s^{-1}, $h_{\rm g} = 0.026(r/1\ \mathrm{AU})^{5/4}$ AU, and $\rho_{\rm g} = 1.7\times10^{-9}(r/1\ \mathrm{AU})^{-11/4}$ g cm^{-3}. In reality, in an optically thick disk, the radial temperature profile would be steeper than in Eq. (3) when accretion heating dominates (e.g., Lin & Papaloizou 1980), and would be shallower when stellar irradiation dominates (Kusaka et al. 1970; Lin & Papaloizou 1980). However, as we demonstrate in Sect. 4.1, the evolution and accretion of pebbles onto an embryo are fairly insensitive to the details of the temperature profile as long as an isolated single embryo is considered.

Our model takes the effects of disk turbulence on the growth and vertical diffusion of dust particles into account. Turbulent diffusion is particularly important in our model because it determines the efficiency of pebble accretion by an embryo lying at the midplane (Guillot et al. 2014; Johansen et al. 2015; Morbidelli et al. 2015; Moriarty & Fischer 2015). We parametrize the turbulent diffusion coefficient as $D = \alpha c_{\rm s} h_{\rm g}$, where α is a dimensionless free parameter. If D is equal to the turbulent viscosity (which is not used in this study), α corresponds to the viscosity parameter of Shakura & Sunyaev (1973). For simplicity, we take α to be constant both in time and space. The turnover time of the largest turbulent eddies, which is implicitly used in evaluating the turbulence-driven particle relative velocity, is taken to be Ω^{-1} in accordance with the typical correlation time of magnetorotational turbulence (e.g., Fromang & Papaloizou 2006). The role of disk turbulence as an effective viscosity is not taken into account in our model since we do not evolve $\Sigma_{\rm g}$ or T.

2.3. Dust growth and radial drift

We employ a simplified approach to calculate the mass flux of radially drifting pebbles. We assume that the mass distribution of dust particles at each orbit r is singly peaked at a mass $m_{\rm p}(r)$. We then follow the evolution of the dust surface density $\Sigma_{\rm d}$ and peak mass $m_{\rm p}$ due to coagulation and radial drift by assuming that particles with mass $\sim m_{\rm p}$ dominate the dust surface density at each r. Such a single-size approximation, also known as the two-moment bulk approximation in cloud modeling (Ferrier 1994), has been applied to modeling dust evolution in protoplanetary disks (Kornet et al. 2001; Garaud 2007; Birnstiel et al. 2012) as well as in protoplanetary atmospheres (Ormel 2014)[1]. This allows us to track the global evolution of dust particles that dominate the radial mass flux at a much less computational cost than solving the exact coagulation equation that resolves the full particle size distribution. In Appendix A, we give analytic and numerical justifications of this approach as well as the formal definition of the peak mass $m_{\rm p}$.

Following Brauer et al. (2008a), the vertical distribution of the particles is approximated by a Gaussian $\propto \exp(-z^2/2h_{\rm d}^2)$ and we determine the dust scale height $h_{\rm d}$ from the balance between sedimentation and diffusion (see Eq. (11) below). We neglect particle diffusion in the radial direction because its timescale (~10^4 yr for $\alpha = 10^{-2}$ at 1 AU) is typically longer than the drift timescale of pebble-sized particles (~10^3 yr at 1 AU).

We assume that ice aggregates are so sticky that no fragmentation or bouncing occurs upon collision. Numerical studies of aggregate collisions (Dominik & Tielens 1997; Wada et al. 2009, 2011, 2013) have shown that aggregates made of 0.1 μm-sized icy grains undergo catastrophic disruption only at collision velocities higher than 50–80 m s^{-1}. With this high sticking efficiency, pebble-sized aggregates do not experience disruption in protoplanetary disks (e.g., Brauer et al. 2008a). Krijt et al. (2015) have recently pointed out that erosion by small projectiles might limit the growth of icy aggregates outside the snow line. We do not consider this effect because the threshold velocity for erosion is still controversial (see the discussion in Sect. 2.3.2 of Krijt et al. 2015). We also neglect condensation growth and sintering of icy aggregates in the vicinity of the snow line. While condensation would facilitates pebble growth (Ros & Johansen 2013), sintering would induce destruction of pebble-sized aggregates (Sirono 2011a,b; Okuzumi et al. 2016). These processes could potentially change our results, but we ignore them as a first step toward a full understanding of the problem. The aggregate internal density is fixed to be $\rho_{\rm int} = 1.4$ g cm^{-3} for simplicity, but in reality the porosity of ice aggregates may evolve as they coagulate (Suyama et al. 2008; Okuzumi et al. 2012; Kataoka et al. 2013a). Influences of the porosity evolution will be discussed in future work.

Under the assumptions mentioned above, the equations governing the evolution of $\Sigma_{\rm d}$ and $m_{\rm p}$ are given by

$$\frac{\partial\Sigma_{\rm d}}{\partial t} + \frac{1}{r}\frac{\partial}{\partial r}(rv_{\rm r}\Sigma_{\rm d}) = 0, \tag{4}$$

$$\frac{\partial m_{\rm p}}{\partial t} + v_{\rm r}\frac{\partial m_{\rm p}}{\partial r} = \frac{2\sqrt{\pi}a^2\Delta v_{\rm pp}}{h_{\rm d}}\Sigma_{\rm d}, \tag{5}$$

where $a = (3m_{\rm p}/4\pi\rho_{\rm int})^{1/3}$ is the particle radius corresponding to $m_{\rm p}$, and $v_{\rm r}$ and $\Delta v_{\rm pp}$ are the radial and relative velocities of the particles at the midplane, respectively. Our Eqs. (4) and (5) are essentially equivalent to Eqs. (3) and (8) of Ormel (2014), although the deposition terms are not included here. The formal derivation of Eqs. (4) and (5) from the exact coagulation equation is cumbersome (see Appendix A.1), but their physical interpretation is clear. Equation (4) is merely the equation of continuity while Eq. (5) states that the growth rate of peak-mass particles along their trajectory, $\mathrm{d}m_{\rm p}/\mathrm{d}t \equiv \partial m_{\rm p}/\partial t + v_{\rm r}\partial m_{\rm p}/\partial r$, is proportional to the product of the particle–particle collision cross section $\pi(a+a)^2 = 4\pi a^2$, relative velocity $\Delta v_{\rm pp}$, and dust density at the midplane $\Sigma_{\rm d}/(\sqrt{2\pi}h_{\rm d})^2$.

2.4. Particle stopping time, scale height, and velocity

The velocity and scale height of a particle depends on its stopping time $t_{\rm s}$, which is the timescale of particle's momentum

[1] Recently, Krijt et al. (2016) proposed a single-size scheme based on the Lagrangian description.

[2] Precisely, the right-hand side of Eq. (5) is $1/\sqrt{2}$ times the product of $4\pi a^2$, $\Delta v_{\rm pp}$, and $\Sigma_{\rm d}/(\sqrt{2\pi}h_{\rm d})$.

relaxation due to the gas drag. We evaluate t_s with the piecewise formula

$$t_s = \begin{cases} \dfrac{\rho_{\rm int} a}{\rho_g v_{\rm th}}, & a < \dfrac{9}{4}\lambda_{\rm mfp}, \\ \dfrac{4\rho_{\rm int} a^2}{9\rho_g v_{\rm th}\lambda_{\rm mfp}}, & a > \dfrac{9}{4}\lambda_{\rm mfp}, \end{cases} \tag{6}$$

where $v_{\rm th} = \sqrt{8k_B T/\pi m_g}$ and $\lambda_{\rm mfp}$ are the thermal velocity and mean free path of gas particles, respectively. The mean free path is related to the gas density as $\lambda_{\rm mfp} = m_g/(\sigma_{\rm mol}\rho_g)$, where $\sigma_{\rm mol} = 2.0\times10^{-15}$ cm^2 is the molecular collision cross section. The first and second expressions of Eq. (6) are known as the Epstein and Stokes laws, respectively. In many cases, it is useful to express the stopping time in terms of the dimensionless Stokes number

$$\mathrm{St} \equiv \Omega t_s. \tag{7}$$

Using the relations between Σ_g, ρ_g, h_g, Ω, c_s, and $v_{\rm th}$, one can rewrite Eq. (6) in terms of St as

$$\mathrm{St} = \frac{\pi}{2}\frac{\rho_{\rm int} a}{\Sigma_g}\max\left(1, \frac{4a}{9\lambda_{\rm mfp}}\right). \tag{8}$$

The radial drift velocity of particles is given by (Adachi et al. 1976; Weidenschilling 1977)

$$v_r = -\frac{2\mathrm{St}}{1+\mathrm{St}^2}\eta v_K, \tag{9}$$

where

$$\eta = -\frac{1}{2}\left(\frac{c_s}{v_K}\right)^2 \frac{\mathrm{d}\ln(c_s^2\rho_g)}{\mathrm{d}\ln r} \tag{10}$$

is a dimensionless quantity characterizing the pressure gradient of the disk gas (which is the ultimate cause of the radial particle drift) and $v_K = r\Omega$ is the Kepler velocity. Our disk model gives $\eta = 1.1\times10^{-3}(r/1\mathrm{AU})^{1/2}$ and $\eta v_K = 33$ m s^{-1}. The value of η is smaller than that of the optically thin MMSN model (Hayashi 1981) by the factor 0.6, which reflects the lower gas temperature in our model.

The particle scale height is given by (Dubrulle et al. 1995; Youdin & Lithwick 2007; Okuzumi et al. 2012)

$$h_d = h_g\left(1 + \frac{\mathrm{St}}{\alpha}\frac{1+2\mathrm{St}}{1+\mathrm{St}}\right)^{-1/2}. \tag{11}$$

Equation (11) assumes that vertical settling of the particles balances with vertical turbulent diffusion.

The particle collision velocity $\Delta v_{\rm pp}$ is given by

$$\Delta v_{\rm pp} = \sqrt{(\Delta v_B)^2 + (\Delta v_r)^2 + (\Delta v_\phi)^2 + (\Delta v_z)^2 + (\Delta v_t)^2}, \tag{12}$$

where $\Delta v_B, \Delta v_r, \Delta v_\phi, \Delta v_z$ and Δv_t are the relative velocities induced by Brownian motion, radial drift, azimuthal drift, vertical settling, and turbulence, respectively. We evaluate these velocity components with the equations given in Sect 2.3.2 of Okuzumi et al. (2012), but with the assumption that the particle mass distribution is narrowly peaked at $m = m_p$. For example, the Brownian component is given by $\Delta v_B = \sqrt{8(m_1+m_2)k_B T/(\pi m_1 m_2)}$, where m_1 and m_2 are the masses of the colliding aggregates[3], and we evaluate this by setting $m_1 = m_2 = m_p$. The differential drift velocities Δv_r, Δv_ϕ, and Δv_z are functions of the Stokes numbers St_1 and St_2 of the colliding pair. Evaluation of these components within the single-size approximation is more tricky because they vanish for $\mathrm{St}_1 = \mathrm{St}_2$ but have a finite value for $\mathrm{St}_1 \sim \mathrm{St}_2$. Since the real size distribution has a finite width, the naive choice $\mathrm{St}_1 = \mathrm{St}_2 = \mathrm{St}(m_p)$ results in a significant underestimation of the particle velocities and, hence, of the particle growth rate s shown in Appendix A.2. We introduce a dimensionless control parameter $\epsilon(<1)$ and set $\mathrm{St}_1 = \mathrm{St}(m_p)$ and $\mathrm{St}_2 = \epsilon\mathrm{St}(m_p)$ whenever we evaluate the drift velocities to take the effect of the size dispersion into account. We show in Appendix A.2 that the choice $\epsilon = 0.5$ best reproduces the results of a coagulation simulation that treats the fill size distribution. We adopt this choice throughout the paper. The turbulence-induced relative velocity Δv_t is also a function of St_1 and St_2 (assuming that the turnover time of the largest turbulent eddies is Ω^{-1}), and we evaluate it using Eqs. (16)–(18) of Ormel & Cuzzi (2007). For $\mathrm{St}_1 \sim \mathrm{St}_2 \ll 1$, which is true for pebble-sized particles, Δv_t has approximate expressions (see Eqs. (27) and (28) of Ormel & Cuzzi 2007)

$$\Delta v_t \approx \begin{cases} \sqrt{\alpha} c_s \mathrm{Re}_t^{1/4}|\mathrm{St}_1 - \mathrm{St}_2|, & \mathrm{St}_1 \ll \mathrm{Re}_t^{-1/2}, \\ \sqrt{3\alpha} c_s \mathrm{St}_1^{1/2}, & \mathrm{St}_1 \gg \mathrm{Re}_t^{-1/2}, \end{cases} \tag{13}$$

where $\mathrm{Re}_t = D/\nu_{\rm mol}$ is the turbulent Reynolds number and $\nu_{\rm mol} = v_{\rm th}\lambda_{\rm mfp}/2$ is the molecular viscosity. We set $\mathrm{St}_1 = \mathrm{St}(m_p)$ and $\mathrm{St}_2 = \epsilon\mathrm{St}(m_p)$ when evaluating Δv_t since it vanishes for $\mathrm{St}_1 = \mathrm{St}_2$ in the case of $\mathrm{St}_1 \ll \mathrm{Re}_t^{-1/2}$.

Which component of $\Delta v_{\rm pp}$ dominates depends not only on the particle size but also on the turbulence strength. To illustrate this, in Fig. 2 we plot all components of $\Delta v_{\rm pp}$ at $r = 100$ AU as a function of a for different values of α. We assume $\epsilon = 0.5$ when evaluating the non-Brownian components. In general, the particle relative velocity has a maximum at $\mathrm{St} \approx 1$, which corresponds to $a \approx 1$ cm at this location. When $\alpha = 10^{-4}$, laminar components such as Δv_z and Δv_r are dominant for all a. The turbulent component Δv_t becomes more important when $\alpha = 10^{-3}$, and dominates over the laminar components for all a when $\alpha = 10^{-2}$.

Since Δv and h_d are already given, we are able to estimate the timescale of dust growth as a function of particle size. Here we define the particle growth timescale as

$$t_{\rm grow} \equiv \left(\frac{1}{a}\frac{\mathrm{d}a}{\mathrm{d}t}\right)^{-1} = 3\left(\frac{1}{m_p}\frac{\mathrm{d}m_p}{\mathrm{d}t}\right)^{-1} = \frac{3m_p h_d}{2\sqrt{\pi}a^2\Delta v_{\rm pp}\Sigma_d}, \tag{14}$$

where $(\mathrm{d}/\mathrm{d}t) \equiv (\partial/\partial t) + v_r(\partial/\partial r)$ is the Lagrangian time derivative, and we have used Eq. (5) in the final expression. Figure 3 shows $t_{\rm grow}$ at 100 AU and 1 AU as a function of a for three different values of α. Here, the dust-to-gas ratio is taken to be the initial value $\Sigma_{d,0}/\Sigma_g = 10^{-2}$. It can be seen that $t_{\rm grow} \sim 10^4$–10^5 yr at 100 AU and ~1–100 yr at 1 AU, indicating that $t_{\rm grow}$ scales approximately linearly with the orbital timescale $\propto\Omega^{-1} \propto r^{3/2}$. In fact, one can show that the simple relation

$$t_{\rm grow} \approx \frac{4}{\sqrt{3\pi}}\frac{\Sigma_g}{\Sigma_d}\Omega^{-1} \approx 2\times10^4\left(\frac{\Sigma_g/\Sigma_d}{100}\right)\left(\frac{r}{100\ \mathrm{AU}}\right)^{3/2}\ \mathrm{yr} \tag{15}$$

holds in the special case where the conditions $a \ll \lambda_{\rm mfp}$, $\Delta v_{\rm pp} \approx \Delta v_t$, and $\mathrm{St}_1 \gg \max(\mathrm{Re}_t^{-1/2}, \alpha)$ are met (see Takeuchi & Lin 2005 and Brauer et al. 2008a for the derivation). This expression, which is employed in the analytic pebble formation model of Lambrechts & Johansen (2014), is extremely useful as an order-of-magnitude estimate, since it only depends on the gas-to-dust ratio and orbital frequency. However, caution should be

[3] There is a typographical error in the expression for Δv_B in Okuzumi et al. (2012, their Eq. (17)).

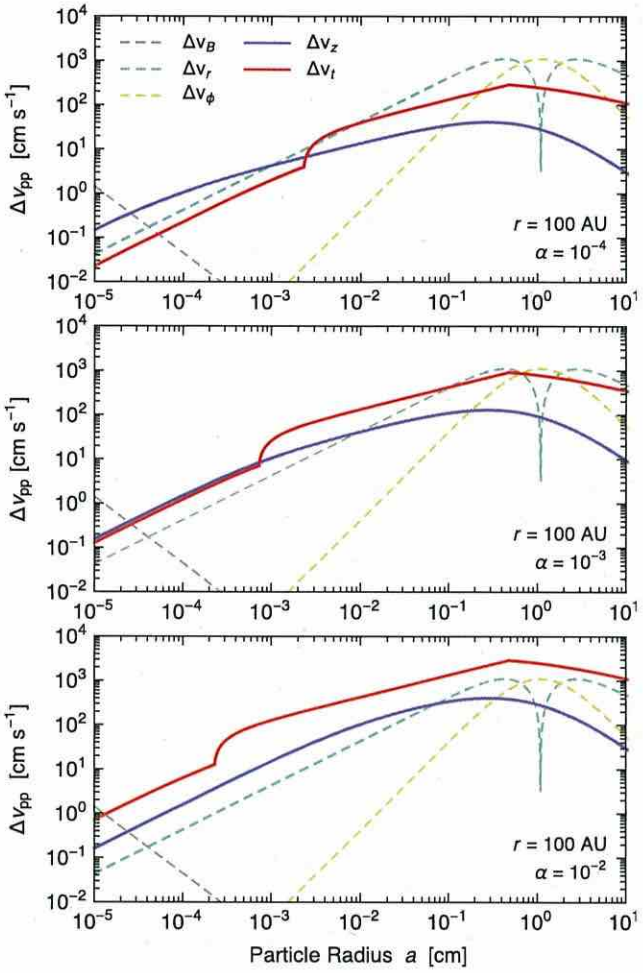

Fig. 2. Components of the particle relative velocity $\Delta v_{\rm pp}$ at 100 AU as a function of particle radius a for three values of the turbulence parameter $\alpha = 10^{-4}$ (*top panel*), 10^{-3} (*middle panel*), and 10^{-2} (*bottom panel*). The velocity components that depend on α are shown by the solid curves. The stopping time ratio of $\epsilon = 0.5$ is assumed for $\Delta v_{\rm r}$, Δv_ϕ, Δv_z, and $\Delta v_{\rm t}$.

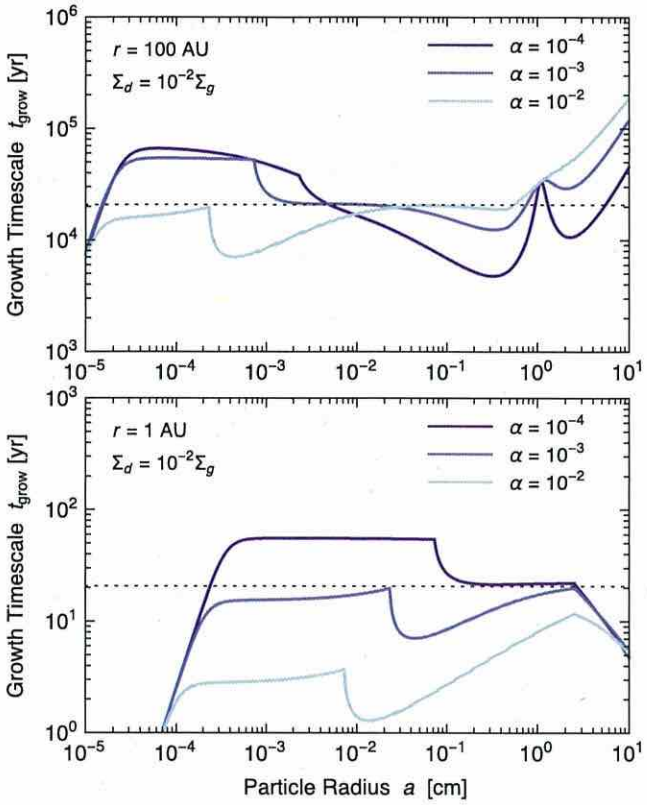

Fig. 3. Particle growth timescale $t_{\rm grow}$ (Eq. (14)) at 100 AU as a function of particle radius a for $\Sigma_{\rm d} = 10^{-2}\Sigma_{\rm g}$ with different values of the turbulence parameter α. The dotted line shows the simple estimate $t_{\rm grow} = (4/\sqrt{3\pi})(\Sigma_{\rm g}/\Sigma_{\rm d})\Omega^{-1}$ (Eq. (15)).

exercised when using Eq. (15) for more precise calculations because the expression is less accurate if one or more of the conditions mentioned above is not met. For example, we can see in Fig. 3 that Eq. (15) overestimates the actual growth timescale by a factor of several when $\alpha \le 10^{-3}$ and $a \lesssim 10^{-3}$ cm, for which $\Delta v_{\rm pp} \approx \Delta v_z$ (see Fig. 2) and St $\lesssim \alpha$. For this reason, the time required for micron-sized dust particles to grow into pebbles is longer when $\alpha \le 10^{-3}$ than when $\alpha = 10^{-2}$.

2.5. Pebble accretion

As mentioned at the beginning of Sect. 2, we place an rocky embryo at 1 AU in a protoplanetary disk and allow it to accrete icy pebbles at times $t > t_{\rm start}$. Following Guillot et al. (2014), we evaluate the rate of pebble accretion by an embryo, $\dot{M}_{\rm e}$, as

$$\dot{M}_{\rm e} = \min\left(2b_{\rm set}, \frac{\pi b_{\rm set}^2}{\sqrt{2\pi}h_{\rm d}}\right)\Delta v_{\rm set}\Sigma_{\rm d}, \tag{16}$$

where $b_{\rm set}$ is the effective pebble accretion radius of the embryo and

$$\Delta v_{\rm set} = \eta v_{\rm K} + \frac{3}{2}b_{\rm set}\Omega \tag{17}$$

is the (maximum) encounter velocity of the embryo and pebbles. In Eq. (16), the factor $\min(\cdots)$ accounts for the effect of the sedimentation of the pebbles onto the midplane: the accretion is two-dimensional ($\dot{M}_{\rm e} \approx 2b_{\rm set}\Delta v_{\rm set}\Sigma_{\rm d}$) for $b_{\rm set} \gg h_{\rm d}$ and three-dimensional ($\dot{M}_{\rm e} \approx \pi b_{\rm set}^2\Delta v_{\rm set}\rho_{\rm d}$, where $\rho_{\rm d} = \Sigma_{\rm d}/\sqrt{2\pi}h_{\rm d}$ is the midplane pebble density) for the opposite limit (see Sect. 3.2 of Guillot et al. 2014). In the 3D case, $\dot{M}_{\rm e}(\propto h_{\rm d}^{-1})$ decreases with increasing α, reflecting the fact that turbulence diffuses pebbles away from the midplane where the embryo resides. The first and second terms on the right-hand side of Eq. (17) represents the encounter velocity arising from the sub-Keplerian orbital velocity of the pebbles and from the Keplerian shear, respectively (see Sect. 5.1.3 of Ormel & Klahr 2010). Equation (17) neglects the turbulence-driven encounter velocity $\approx\sqrt{\alpha}c_{\rm s}$, but this does not affect our results significantly as long as $\alpha \lesssim 10^{-3}$ (for which $\sqrt{\alpha}c_{\rm s} \lesssim \eta v_{\rm K}$).

For the accretion radius $b_{\rm set}$, we use a simple empirical relation (Ormel & Kobayashi 2012)

$$b_{\rm set} = b_{\rm set,0}\exp\left[-({\rm St}/2)^{0.65}\right]. \tag{18}$$

Here, $b_{\rm set,0}$ is the solution to (Ormel & Klahr 2010)

$$3b_{\rm set,0}^3 + 2\eta r b_{\rm set,0}^2 - 24{\rm St}R_{\rm H}^3 = 0, \tag{19}$$

where

$$R_{\rm H} \equiv \left(\frac{M_{\rm e}}{3M_*}\right)^{1/3} r \tag{20}$$

is the Hill radius of the embryo. Equations (18) and (19) apply when the particles are coupled to the disk gas so strongly that they accrete onto the embryo at a terminal velocity. Ormel & Klahr (2010) called this regime the *settling regime*. Equation (19) originally comes from the consideration that an embryo accretes pebbles whose trajectories are greatly deflected by the embryo's gravity (Ormel & Klahr 2010; Lambrechts & Johansen 2012). The exponential cutoff appearing in Eq. (18) assumes that $R_{\rm H}$ is considerably smaller than the Bondi radius of the embryo defined with respect to the headwind $\eta v_{\rm K}$,

$$R_{\rm B} \equiv \frac{GM_{\rm e}}{(\eta v_{\rm K})^2}. \tag{21}$$

Since $(R_{\rm H}/R_{\rm B})^3 = (\eta^6/3)(M_{\rm e}/M_*)^{-2}$, the assumption $R_{\rm H} < R_{\rm B}$ holds when $M_{\rm e} > 0.58\eta^3 M_*$. At 1 AU, this condition is satisfied for $M_{\rm e} \gtrsim 10^{-3}\ M_\oplus$. The exponential cutoff accounts for the fact that efficient accretion through settling takes place only when $\mathrm{St} \ll 1$. The Bondi and Hill radii satisfy the relations $R_{\rm B}/(\eta r) = M_{\rm e}/(\eta^3 M_*)$ and $R_{\rm H}/(\eta r) = 0.58(R_{\rm B}/R_{\rm H})^{1/2}$. The latter relation implies that $R_{\rm H} \gg \eta r$ when $R_{\rm H} \ll R_{\rm B}$.

As pointed out by Lambrechts & Johansen (2012) and Guillot et al. (2014), the settling regime can be divided into two subregimes depending on which of the headwind $\eta v_{\rm K}$ and Keplerian shear $3b_{\rm set}\Omega/2$ dominates. When $\eta v_{\rm K} \gg 3b_{\rm set}\Omega/2$, or equivalently $b_{\rm set} \ll 2\eta r/3$, the first term in Eq. (19) is negligible compared to the second term, and hence $b_{\rm set}$ is approximately given by

$$b_{\rm set} \approx \sqrt{\frac{12\mathrm{St}R_{\rm H}^3}{\eta r}} = 2\sqrt{\frac{GM_{\rm e}t_{\rm s}}{\eta v_{\rm K}}}. \tag{22}$$

This regime was referred to as the drift accretion regime by Lambrechts & Johansen (2012, see their Eq. (27)) and the Bondi regime by Guillot et al. (2014, the third expression of their Eq. (C.3)). In the opposite limit, $b_{\rm set} \gg 2\eta r/3$, the second term in Eq. (19) is negligible, and we obtain

$$b_{\rm set} \approx 2\mathrm{St}^{1/3} R_{\rm H} \tag{23}$$

($b_{\rm set} < R_{\rm H}$ because $\mathrm{St} \ll 1$ in the settling regime). This corresponds to the Hill accretion regime of Lambrechts & Johansen (2012, see their Eq. (40)). This regime is also essentially equivalent to the Hill regime of Guillot et al. (2014), but the factor $2\mathrm{St}^{1/3}$ appearing in our Eq. (23) is neglected in their limiting expression for $b_{\rm set}$ (the fourth expression of their Eq. (C.3)). A comparison between Eqs. (22) and (23) shows that the Hill accretion applies (i.e., $\eta v_{\rm K} \gg b_{\rm set}\Omega$) when St satisfies

$$\mathrm{St} = \frac{\eta^3 M_*}{9M_{\rm e}} \approx 4\times 10^{-4}\left(\frac{\eta}{10^{-3}}\right)^3\left(\frac{M_{\rm e}}{10^{-1}\ M_\oplus}\right)^{-1}\left(\frac{M_*}{M_\odot}\right). \tag{24}$$

At 1 AU, this condition is equivalent to $a \gtrsim 3$ mm. As we see in Sect. 3.2, the pebbles drifting to 1 AU mostly satisfy this condition.

As an example, Fig. 4 shows $b_{\rm set}$ of an embryo located at 1 AU as a function of the pebble size a and of the pebble Stokes number St. For comparison, we also plot the embryo's geometric radius $R_{\rm geo} = (3M_{\rm e}/4\pi\rho_{\rm e})^{1/3}$ where the embryo's internal density $\rho_{\rm e}$ is set to 3 g cm^{-3}. For $M_{\rm e} \gtrsim 10^{-3} M_\oplus$, the accretion radius is considerably larger than $R_{\rm geo}$ as long as $a \gtrsim 0.1$ mm (see also Fig. 10 of Guillot et al. 2014). At $\mathrm{St} \sim 1$ ($a \sim 1$ m), the accretion radius reaches the Hill radius $R_{\rm H} = (4\pi\rho_{\rm e} r^3/9M_*)^{1/3} R_{\rm geo} \approx 200\, R_{\rm geo}$.

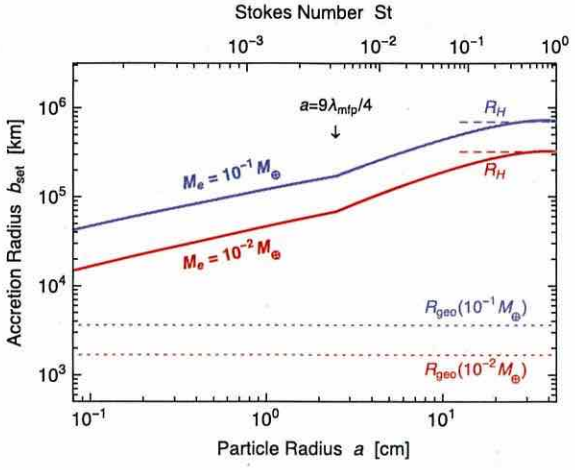

Fig. 4. Pebble accretion radius of an embryo $b_{\rm set}$ (Eq. (18); solid curve) as a function of the pebble radius a. The upper and lower solid curves show $b_{\rm set}$ for embryos of masses $M_{\rm e} = 10^{-1}\ M_\oplus$ and $10^{-2}\ M_\oplus$, respectively. The dashed and dotted lines indicate the Hill radii $R_{\rm H}$ (Eq. (20)) and geometric radii $R_{\rm geo} = (3\ M_{\rm e}/4\pi\rho_{\rm e})^{1/3}$ of the embryos, respectively, where we take $\rho_{\rm e} = 3$ g cm^{-3}.

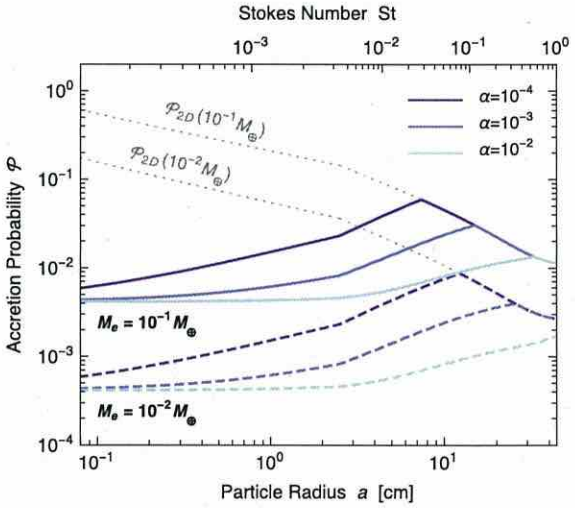

Fig. 5. Pebble accretion probability by a single embryo, $\mathcal{P}$ (Eq. (25)), as a function of the pebble radius a for different values of the turbulence parameter α. The solid and dashed curves are for embryos of masses $M_{\rm e} = 10^{-1}\ M_\oplus$ and $10^{-2}\ M_\oplus$, respectively. The dotted lines indicate the accretion probability in the two-dimensional limit, $\mathcal{P}_{\rm 2D} = 2b_{\rm set}\Delta v_{\rm set}/(2\pi r|v_{\rm r}|)$.

Figure 5 shows some examples of the pebble accretion rate as a function of a. We here express the accretion rate in terms of the accretion probability

$$\mathcal{P} \equiv \frac{\dot{M}_{\rm e}}{\dot{M}_{\rm r}} = \frac{\min\left(2b_{\rm set}, \frac{\pi b_{\rm set}^2}{\sqrt{2\pi}h_{\rm d}}\right)\Delta v_{\rm set}}{2\pi r|v_{\rm r}|}, \tag{25}$$

where

$$\dot{M}_{\rm r} \equiv 2\pi r|v_{\rm r}|\Sigma_{\rm d} \tag{26}$$

Table 1. Free parameters in this study.

Quantity	Description	Value
$r_{\rm out}$ (AU)	Disk size	100, 300
α	Turbulence parameter	10^{-2}, 10^{-3}, 10^{-4}
$M_{\rm e,0}$ ($M_\oplus$)	Embryo mass before pebble accretion	10^{-1}, 10^{-2}
$t_{\rm start}$ (Myr)	Initial time of pebble accretion	0.5, 1, 2, 3, 4, 5

is the radial inward mass flux of dust in the gas disk. By construction, $\mathcal{P}$ measures the fraction of radially drifting pebbles that are filtered by a single embryo. The accretion probability depends on the turbulence strength α via the pebble scale height $h_{\rm d}$. For comparison, the accretion probability in the two-dimensional limit, $\mathcal{P}_{\rm 2D} \equiv 2b_{\rm set}\Delta v_{\rm set}/(2\pi r|v_{\rm r}|)$, is also plotted. Since $h_{\rm d}$ decreases with increasing a, accretion of large particles (typically of sizes $a \gtrsim 10$ cm) takes place in a 2D manner. In this case, the accretion probability decreases with increasing a because larger particles have a higher drift speed $|v_{\rm r}|$ ($b_{\rm set}$ and $\Delta v_{\rm set}$ also increase with a, but more slowly than $|v_{\rm set}|$). Accretion of smaller particles ($a \lesssim 10$ cm) is limited by their large scale height $h_{\rm d}$ compared to the accretion radius $b_{\rm set}$. For these reasons, the accretion probability has a maximum at the pebble size corresponding to $h_{\rm d} \approx b_{\rm set}$. The maximum probability is $\sim 10^{-2}$–10^{-1} for $M_{\rm e} = 10^{-1}\ M_\oplus$ and $\sim 10^{-3}$–10^{-2} for $M_{\rm e} = 10^{-2}\ M_\oplus$.

2.6. Parameter choice

The free parameters of our model are the disk size $r_{\rm out}$, turbulence parameter α, embryos mass before icy pebble accretion $M_{\rm e,0}$, and the initial time $t_{\rm start}$ of icy pebble accretion by an embryo at 1 AU. Table 1 lists the parameter choices adopted in this study.

3. Results

We now present the results of our calculations step by step. In Sect. 3.1, we start by presenting the global evolution of icy particles to emphasize how the parameters $r_{\rm out}$ and α control the lifetime of the radial inflow of icy pebbles in a disk. Sect. 3.2 presents the properties of drifting pebbles at 1 AU in more detail. We then consider a rocky embryo forming at the Earth's orbit and calculate its pebble accretion rate in Sect. 3.3. The resulting evolution of the embryo's mass and water content is presented in Sect. 3.4.

3.1. Global picture of dust evolution

The top and middle panels of Fig. 6 show the global evolution of the dust surface density $\Sigma_{\rm d}$ and particle size a for $\alpha = 10^{-3}$. The left and right panels correspond to small and large disks with $r_{\rm out} = 100$ AU and 300 AU, respectively. The radial mass flux of the particles, $\dot{M}_{\rm d}$ (Eq. (26)), is shown in the bottom panels. The results for different values of α are presented in Fig. 7. One can see that dust particles grow significantly and are piled up at $r \approx 1$ AU in the very early stage of $t = 0.1$ Myr. This occurs because dust particles initially located at these inner orbits grow beyond the radial drift barrier owing to accelerated coagulation in the Stokes regime (Birnstiel et al. 2010; Okuzumi et al. 2012). However, this feature is immediately erased by the significant amount of pebbles flowing from outer disk regions. Furthermore, in this very early stage, the snow line would be in reality well outside 1 AU. If this is the case, dust particles near 1 AU would be made of silicates rather than water ice, and their collisional growth would be limited by fragmentation (Blum & Wurm 2008; Wada et al. 2009). Since we assume that pebble accretion starts only after $t = 0.5$ Myr, this early feature has no effect on the results of our pebble accretion calculations.

As demonstrated by many previous studies (e.g., Takeuchi & Lin 2005; Garaud 2007; Brauer et al. 2008a; Birnstiel et al. 2010, 2012; Okuzumi et al. 2012), global dust evolution can be understood from timescale arguments as presented in Sect. 2.4. In protoplanetary disks, dust growth commences from inside out because the growth timescale $t_{\rm grow}$ (Eq. (14)) is roughly proportional to the orbital period. At each orbital distance, dust particles initially grow without appreciable drift, conserving the dust surface density at that location. This local growth stage continues until the particles acquire a high drift velocity. Once the drift timescale becomes comparable to the growth timescale, the particles start drifting inward so that the two timescales balance each other. In this second stage, the dust surface density at each location is no longer locally conserved and is instead determined by the mass flow of particles drifting from further out. To an order of magnitude, the time required for initially micron-sized particles to grow into drifting pebbles is estimated as $\sim 10 t_{\rm grow}$, where the factor 10 accounts for the fact that the particles need to grow by several orders of magnitude in size to acquire a high drift velocity (Lambrechts & Johansen 2014). If we take $t_{\rm grow} \sim 100/\Omega$ (see Eq. (15)), we have $10t_{\rm grow} \sim 0.1$ Myr at $r = 60$ AU and $10t_{\rm grow} \sim 1$ Myr at $r = 300$ AU. This is consistent with the results shown in Fig. 6, where we can see that the radial dust flow originates at $\approx$60 AU and $\approx$300 AU for $t = 0.1$ Myr and 1 Myr, respectively. However, the growth timescale also depends on turbulence strength α as already noted in Sect. 2.4. For example, we can see in Fig. 7 that dust particles at 100 AU have already grown significantly even at 0.1 Myr in the case of $\alpha = 10^{-2}$. This is because of the short growth timescale at $a \lesssim 10^{-2}$ cm for this value of α (see Fig. 3).

A key parameter that controls the global dust evolution is the radial extent of the initial dust disk, $r_{\rm out}$. In a typical protoplanetary disk with a surface density gradient $\mathrm{d}\ln\Sigma_{\rm g}/\mathrm{d}\ln r > -2$, the dominant part of the disk mass resides in outer regions of the disk. The outer edge of a disk thus generally acts as a dust reservoir that produces inwardly drifting pebbles (Garaud 2007; Birnstiel et al. 2012; Lambrechts & Johansen 2014). For example, one can see in the top panels of Fig. 6 that the dust surface density $\Sigma_{\rm d}$ starts decreasing at all orbital distances as the outer edge of the disk gets depleted of dust. The pebble size a decreases at the same time, since the growth timescale becomes longer and longer as $\Sigma_{\rm d}$ declines (see Eq. (14)). The lifetime of this dust reservoir is essentially determined by the growth timescale of the dust at $r \sim r_{\rm out}$, and hence increases with $r_{\rm out}$. This explains why the pebble flow in the $r_{\rm out} = 100$ AU disk diminishes faster than in the $r_{\rm out} = 300$ AU disk. Our numerical simulations show that dust depletion starts at $t \approx 0.2$ Myr for $r_{\rm out} = 100$ AU and at $t \approx 1$ Myr for $r_{\rm out} = 300$ AU.

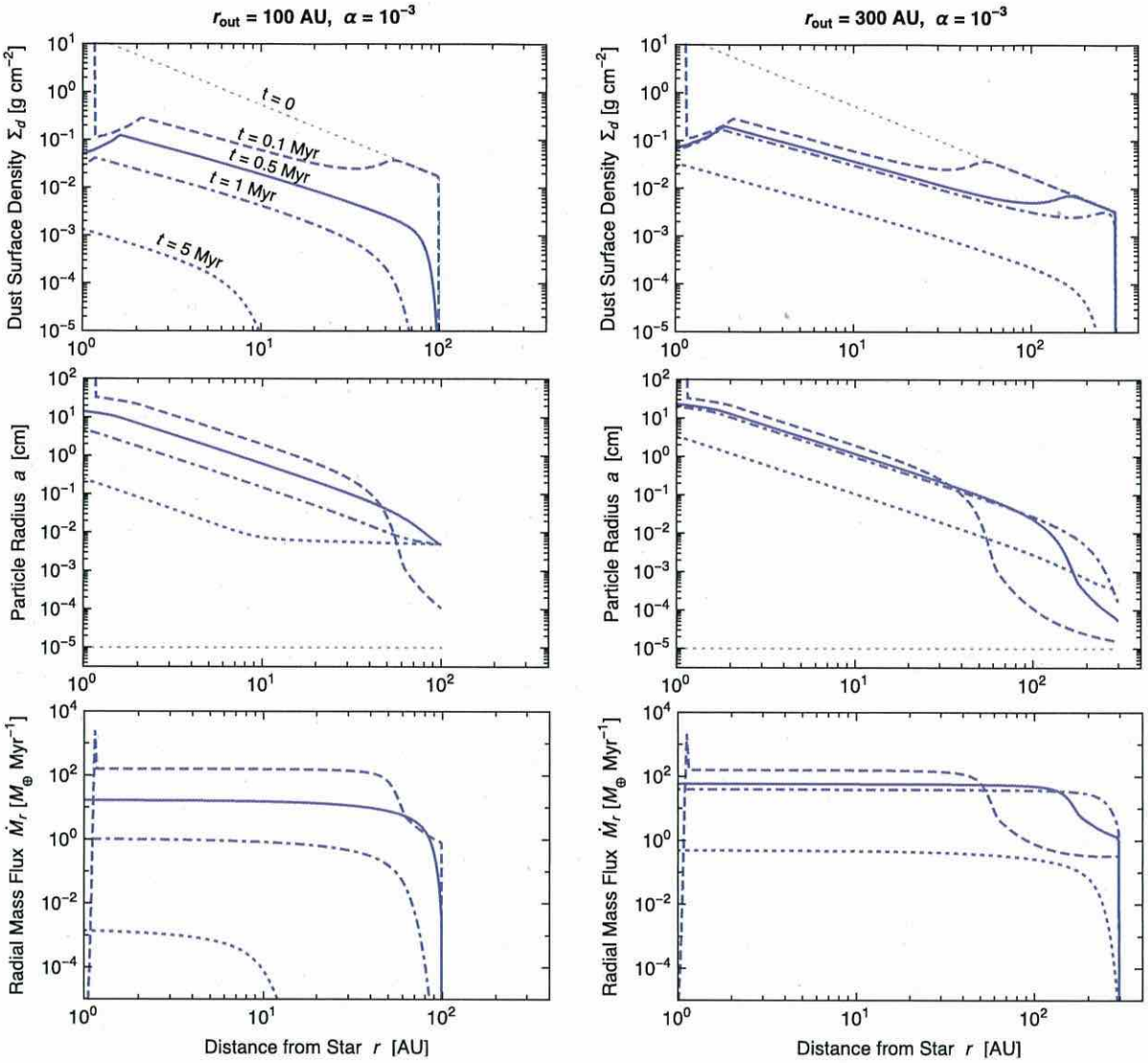

Fig. 6. Time evolution of the surface density Σ_d (*top panels*), radius a (*middle panels*), and radial mass flux $\dot{M}_r$ (*bottom panels*) of dust particles as a function of orbital radius r for models with $\alpha = 10^{-3}$ and with $r_{out} = 100$ AU (*left panels*) and 300 AU (*right panels*). The black dotted lines show the initial condition, while the blue dashed, solid, dash-dotted, and dotted lines are the snapshots at times $t = 0.1$, 0.5, 1, and 5 Myr, respectively. The jumps in Σ_d and a at $r \approx 1$ AU, $t = 0.1$ Myr are caused by rapid coagulation of particles initially located at these orbits (see text).

3.2. Size and mass flux of pebbles at 1 AU

In the context of pebble accretion, the quantities of interest are the size and radial mass flux of drifting particles at the embryo's orbit. Figure 8 shows these quantities at the Earth's orbit, $r = 1$ AU. As explained in the previous subsection, the size and surface density of the particles decrease as the outer region of the disk is depleted of dust. Before this depletion occurs, particles arriving at 1 AU have a nearly constant radius $a \approx 20$–30 cm and a nearly constant Stokes number St $\approx$ 0.2–0.5, which is consistent with the results of previous studies (Brauer et al. 2008a; Birnstiel et al. 2012; Okuzumi et al. 2012; Lambrechts & Johansen 2014). The radial mass flux at this early time is on the order of 10^2 $M_\oplus$ Myr^{-1}. This directly follows from fact that the dust in outer disk regions has a total mass of $\sim 10^2$ $M_\oplus$ (see Eq. (2)) and grows into drifting pebbles on a timescale of $\sim 10\, t_{grow}|_{r=r_{out}} \sim 1$ Myr (see Sect. 3.1).

Once the dust depletion at the outer edge begins, the particle size and radial flux decrease with time. The decrease of the particle size can be understood from the competition between coagulation and radial drift. In general, dust particles are allowed to grow as along as the growth timescale is shorter than the drift timescale $\sim r/|v_r| \propto |v_r|^{-1}$. As Σ_d decreases, the growth timescale increases (since $t_{grow} \propto \Sigma_d^{-1}$), and consequently balances with the drift timescale at smaller particle size (since $|v_r| \propto \mathrm{St} \propto a$).

3.3. Pebble accretion rate

Now we apply the results presented in Sect. 3.2 to pebble accretion by an embryo located at the Earth's orbit. To begin with, we calculate the pebble accretion rate $\dot{M}_e$ (Eq. (16)) of an embryo of *fixed* mass M_e. The evolution of M_e is discussed in Sect. 3.4.

In the upper panels of Fig. 9, we plot $\dot{M}_e$ of an embryo with $M_e = 10^{-1}$ $M_\oplus$ as a function of time t for different values of r_{out}.

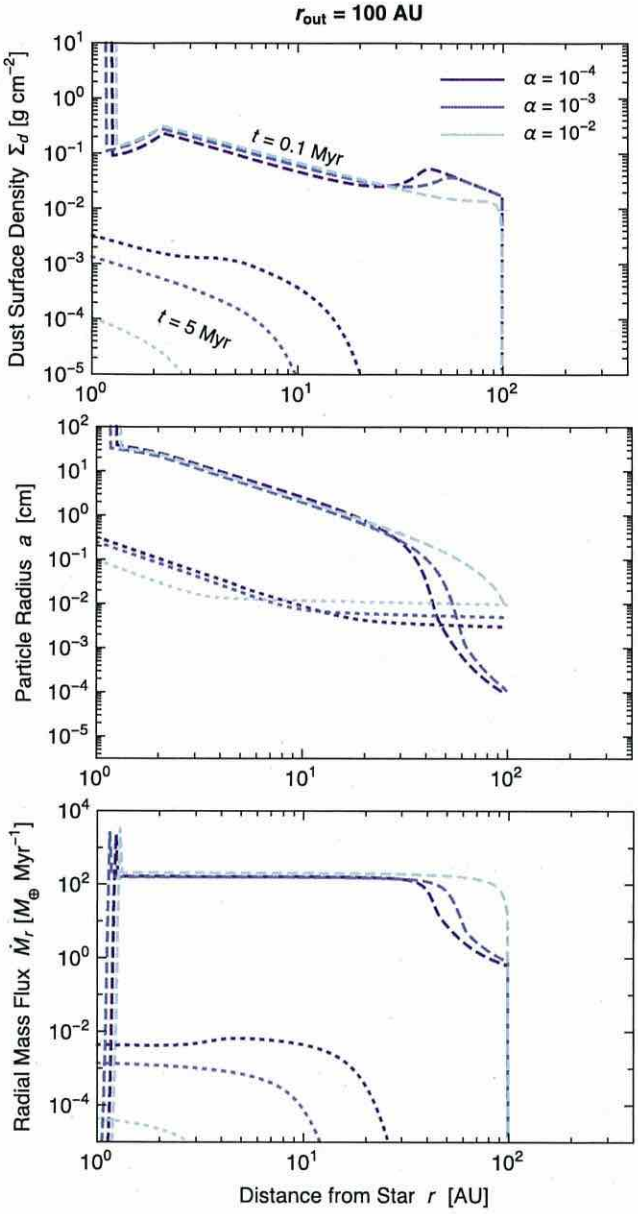

Fig. 7. Time evolution of the surface density Σ_d (*top panel*), radius a (*middle panel*), and radial mass flux $\dot{M}_r$ (*bottom panel*) of dust particles as a function of orbital radius r for models with r_{out} = 100 AU and with different values of α. The dashed and dotted lines are the snapshots at times t = 0.1 and 5 Myr, respectively.

Again, the result significantly depends on the value of r_{out} as it determines the lifetime of the dust reservoir at the disk outer edge. At early times when a substantial amount of dust remains at the outer edge ($t \lesssim 0.5$ Myr for r_{out} = 100 AU and $t \lesssim 1$ Myr for r_{out} = 300 AU), particles drifting to 1 AU are 20–30 cm in size (see the upper panels of Fig. 8) and, hence, are swept up by a single 10^{-1} $M_\oplus$ embryo at a probability of ≈1–2% (Fig. 5). Since the radial mass flux of these decimeter-sized particles is 10^2 $M_\oplus$ Myr^{-1} (the lower panels of Fig. 8), the accretion probability of about 1% results in an accretion rate of ≈1 $M_\oplus$ Myr^{-1} as shown in Fig. 9. This value is insensitive to the choice of α, as long as $\alpha \leq 10^{-2}$, because the particle accretion is nearly two-dimensional ($h_d \lesssim b_{set}$) at these particle sizes (see Fig. 5). As the dust in the outer disk is depleted, $\dot{M}_e$ decreases with decreasing $\dot{M}_r$. In this late stage, $\dot{M}_e$ becomes more sensitive to α with a higher α resulting in an even smaller $\dot{M}_e$. This is mainly because the smaller drifting particles in this stage accrete onto the embryo in a 3D manner (i.e., $h_d > b_{set}$), for which case a higher α results in a lower $\dot{M}_e$. We can see that $\dot{M}_e$ for $\alpha = 10^{-2}$ is approximately 10–100 times smaller than that for $\alpha = 10^{-4}$ in this stage.

The results for $M_e = 10^{-2} M_\oplus$ (the lower panels of Fig. 9) are qualitatively similar to those for $M_e = 10^{-1} M_\oplus$ except that the magnitude of $\dot{M}_e$ is decreased by a factor of 5–10. As we show below, this directly follows from the dependence of the pebble accretion radius b_{set} on M_e. Comparison between Eq. (24) and the Stokes number plotted in Fig. 8 shows that pebble accretion occurs in the Hill accretion regime for both values of M_e. Since $b_{set} \propto R_H \propto M_e^{1/3}$ and $v_{set} \propto b_{set} \propto M_e^{1/3}$ in this accretion regime (see Sect. 2.5), we obtain $\dot{M}_e \propto M_e^{2/3}$ in the 2D case ($b_{set} \lesssim h_d$) and $\dot{M}_e \propto M_e$ in the 3D case ($b_{set} \gtrsim h_d$). Therefore, decreasing M_e by the factor of 10 results in a decrease in $\dot{M}_e$ by a factor of $10^{2/3}$–$10 \approx 5$–10.

It is worth mentioning at this point that the timescale of embryo growth by pebble accretion, $M_e/\dot{M}_e$, is a weak function of the embryo mass: $M_e/\dot{M}_e \propto M_e^{1/3}$ in the 2D case and $M_e/\dot{M}_e \propto M_e^0$ in the 3D case. This implies that the rate at which the embryo's water mass fraction increases is insensitive to the choice of M_e. We confirm this expectation in the following subsection.

3.4. Evolution of embryo's mass and water fraction

We now let an embryo grow through icy pebble accretion to study how much water is delivered to the embryo from icy pebbles. We place a rocky embryo initially devoid of water at 1 AU and allow it to start accreting icy pebbles at $t = t_{start}$. We calculate the evolution of the embryo mass M_e at $t > t_{start}$ by integrating Eq. (16) taking the change in the accretion radius b_{set} with the change in M_e into account. The evolution of the embryo's water fraction, f_{H_2O}, is computed assuming that the water content of the accreted pebbles is 50 wt%, i.e.,

$$f_{H_2O}(t) \equiv \frac{\int_{t_{start}}^{t} 0.5\dot{M}_e(t')dt'}{M_{e,0} + \int_{t_{start}}^{t} \dot{M}_e(t')dt'} = \frac{M_e(t) - M_{e,0}}{2M_e(t)}, \quad (27)$$

where $M_{e,0}$ is the initial embryo mass and $M_e(t)$ is the embryo mass at time t ($>t_{start}$). We have assumed that $f_{H_2O} = 0$ in the initial state.

Table 2 lists the mass and water content in the final state (taken to be t = 6 Myr) for various sets of model parameters (see Table 1 for the parameter grid). We immediately find that the final water fraction is insensitive to $M_{e,0}$, which is because the scaled pebble accretion rate $\dot{M}_e/M_e$ is nearly independent of M_e as already noted in Sect. 3.3. In the following, we focus on the results for $M_e = 10^{-1}$ $M_\oplus$.

Figure 10 shows the evolution of M_e and f_{H_2O} in the r_{rout} = 100 AU disk model for various values of α and t_{strart}. The results for the larger disk model (r_{rout} = 300 AU) are shown in Fig. 11. In the plots of f_{H2O}, the dashed lines indicate the minimum water content of the present Earth given by the ocean mass, 0.023 wt%. The dotted lines indicate f_{H_2O} = 1 wt%, which corresponds to the hypothetical water content of the proto-Earth assuming that the density deficit of the outer core is due to hydrogen delivered in the form of water (Okuchi 1997; Abe et al. 2000). The

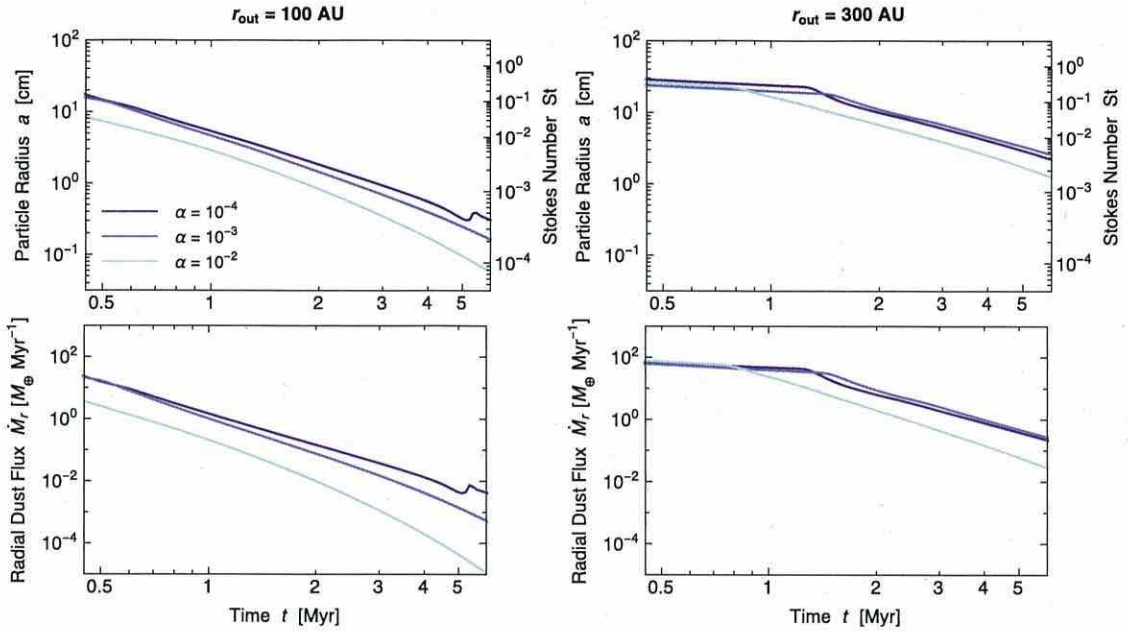

Fig. 8. Radius a (*upper panels*) and radial mass flux $\dot{M}_r$ (*lower panels*) of drifting particles observed at 1 AU as a function of time t. The *left and right panels* are for r_{out} = 100 AU and 300 AU, respectively.

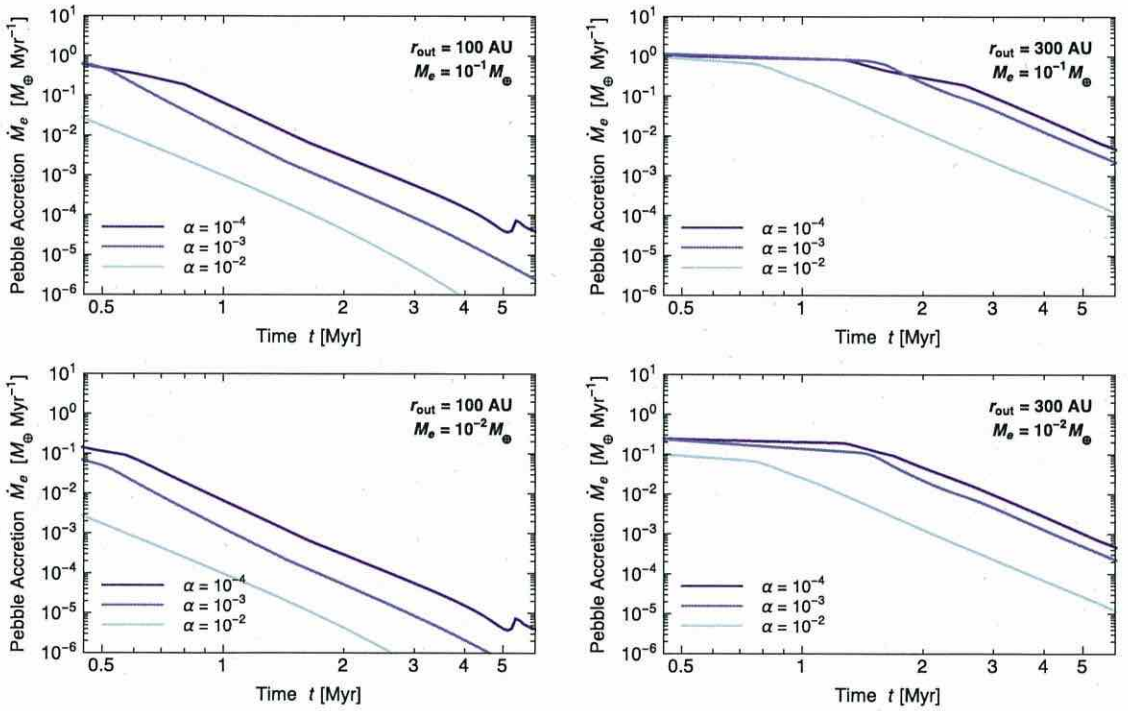

Fig. 9. Pebble accretion rate $\dot{M}_e$ of a single embryo (Eq. (16)) located at 1 AU as a function of time t for $M_e = 10^{-1}\ M_\oplus$ (*upper panels*) and $10^{-2}\ M_\oplus$ (*lower panels*). The *left and right panels* are for r_{out} = 100 AU and 300 AU, respectively.

water content of the proto-Earth much in excess of ~1% seems unlikely (Machida & Abe 2010).

In the case of r_{rout} = 100 AU, whether Earth-forming rocky embryos avoid excessive ice accretion depends on the values of α and t_{start}. For $\alpha = 10^{-4}$ (the left panels of Fig. 10), the embryo's final water content exceeds 0.023 wt% for all $t_{start} \lesssim$ 5 Myr. It even exceeds 1 wt% if t_{start} is as short as ≲2 Myr. In the extreme case of t_{start} = 0.5 Myr, the final embryo mass is four times larger than the initial mass, meaning that the rocky embryo has evolved into an icy embryo mostly composed of icy pebbles. The embryo acquires a smaller amount of water if the disk is more turbulent (α is higher). For $\alpha = 10^{-3}$ and 10^{-2} (the middle and right panels of Fig. 10), the final f_{H_2O} does not exceed 1% if t_{start} > 1 Myr and 0.5 Myr, respectively. A water fraction of ≲0.023 wt% is achieved if t_{start} > 4 Myr for $\alpha = 10^{-3}$ and if t_{start} > 2 Myr for $\alpha = 10^{-2}$. This reduction is due to the combination of the accelerated coagulation and 3D pebble accretion already discussed in Sect. 3.3.

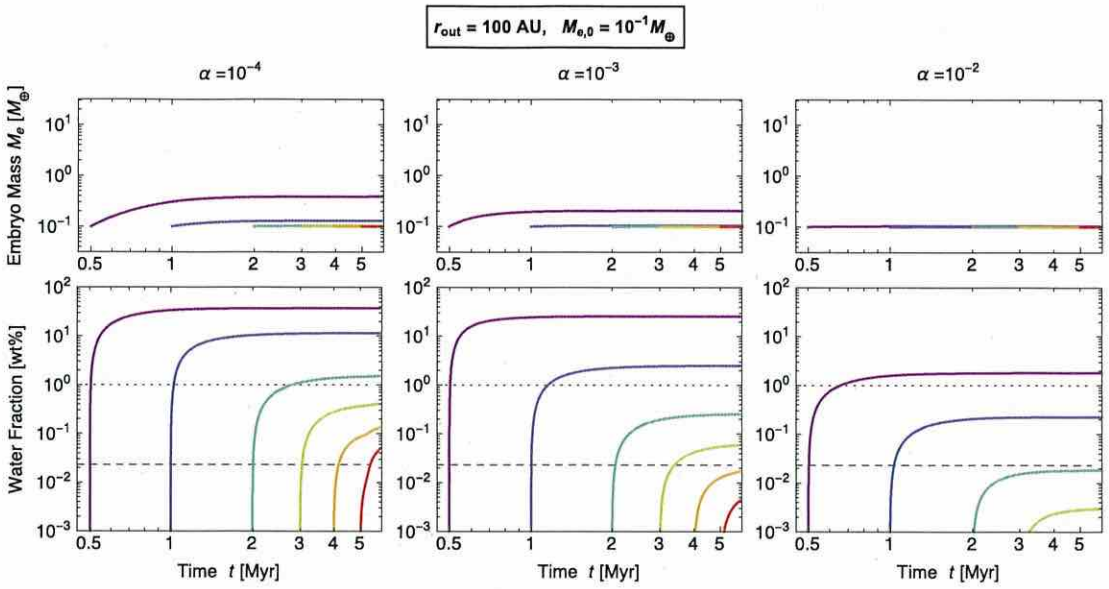

Fig. 10. Time evolution of the mass M_e and water fraction f_{H_2O} of an embryo placed at 1 AU with initial mass $M_{e,0} = 10^{-1}\ M_\oplus$ for the case of r_{out} = 100 AU. The different curves show results for different initial times of pebble accretion, t_{start} = 0.5, 1, 2, 3, 4, and 5 Myr (*from left to right*).

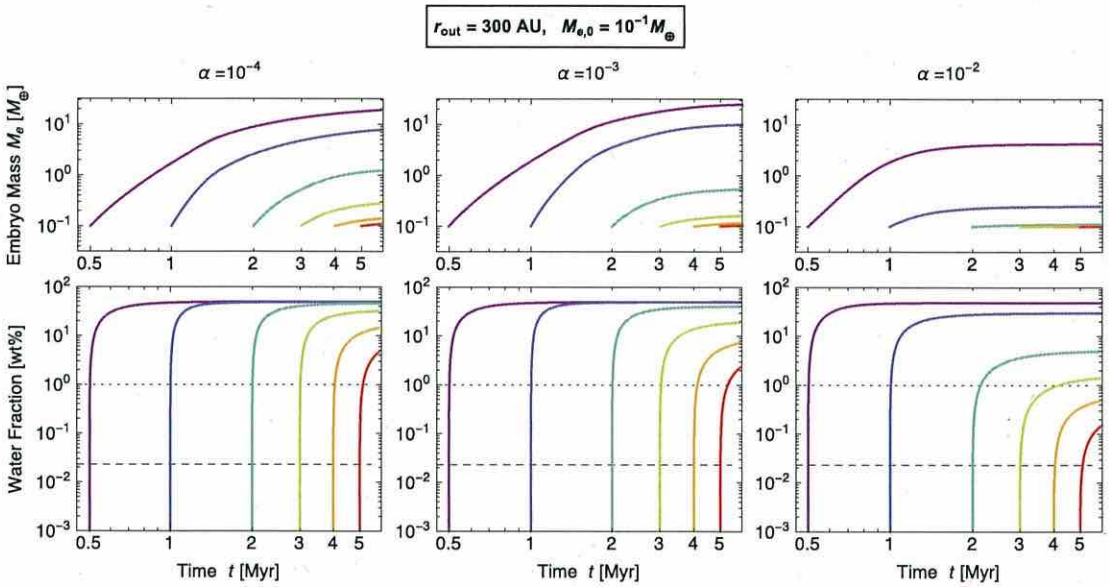

Fig. 11. Same as Fig. 10, except for r_{out} = 300 AU.

Preserving a rocky embryo from icy pebbles is much more difficult when the gas disk extends to 300 AU (Fig. 11). In this case, no parameter set is found to result in a final water content smaller than 0.023 wt%. Even a final water content of ≲1 wt% is realized only if $\alpha = 10^{-2}$ and $t_{start} \gtrsim 3$ Myr. Instead, we find that the initially rocky embryo evolves into a super-Earth to Neptune-mass icy planet if $t_{start} \lesssim 0.5$–2 Myr (the smaller and large values correspond to $\alpha = 10^{-2}$ and 10^{-4}, respectively). Our results for r_{out} = 300 AU and t_{start} = 0.5 Myr are similar to the results of Lambrechts & Johansen (2014) for giant planet core formation in outer disk regions. This is reasonable because the pebble flow of Lambrechts & Johansen (2014) is assumed to decay on the timescale of 3 Myr, while the pebble flow in our r_{out} = 300 AU calculations decays on a similar timescale.

In summary, we find that embryos orbiting at 1 AU can remain rocky at a level of $f_{H_2O} \lesssim 0.023$ wt% if the disk size is 100 AU or smaller, turbulence is stronger than $\alpha = 10^{-3}$, and the snow line passes 1 AU later than 2–4 Myr after disk formation. Keeping the water fraction at a level of $f_{H_2O} \lesssim 1$ wt% with a disk size of 100 AU is possible if the snow line migrates in after t = 0.5–2 Myr. If the disk is as large as 300 AU, a final water fraction of ≲0.024 wt% is very unlikely, and a final fraction of ≲1 wt% is possible only if turbulence is strong ($\alpha = 10^{-2}$) and if the snow line migrates later than 3 Myr.

4. Discussion

4.1. Dependence on the temperature profile

We have simplified the radial temperature profile $T(r)$ with a single power law for an optically thin disk (Eq. (3)). In an optically thick disk, the temperature profile is steeper in inner regions

Table 2. Mass M_e and water content f_{H_2O} of a rocky embryo at 1AU for various sets of model parameters.

r_{out} (AU)	α	$M_{e,0}$ ($M_\oplus$)	t_{start} (Myr)	$M_{e,6\ Myr}$ ($M_\oplus$)	$f_{H_2O,6\ Myr}$ (wt%)
100	10^{-4}	0.1	0.5	0.39	37
			1	0.13	12
			2	0.10	1.5
			4	0.10	0.14
100	10^{-4}	0.01	0.5	0.11	45
			1	0.014	15
			2	0.010	2.2
			4	0.010	0.21
100	10^{-3}	0.1	0.5	0.20	26
			1	0.11	2.5
			2	0.10	0.25
			4	0.10	0.017
100	10^{-3}	0.01	0.5	0.024	29
			1	0.011	3.4
			2	0.010	0.38
			4	0.010	0.028
100	10^{-2}	0.1	0.5	0.10	1.8
			1	0.10	0.23
			2	0.10	0.018
			4	0.10	0.00063
100	10^{-2}	0.01	0.5	0.010	2.3
			1	0.010	0.32
			2	0.010	0.028
			4	0.010	0.0011
300	10^{-4}	0.1	0.5	19.	50
			1	7.8	49
			2	1.2	46
			4	0.14	15
300	10^{-4}	0.01	0.5	15.	50
			1	5.5	50
			2	0.52	49
			4	0.016	19
300	10^{-3}	0.1	0.5	25.	50
			1	10.	49
			2	0.54	41
			4	0.12	7.5
300	10^{-3}	0.01	0.5	20.	50
			1	7.0	50
			2	0.073	43
			4	0.012	9.7
300	10^{-2}	0.1	0.5	4.2	49
			1	0.25	30
			2	0.11	5.0
			4	0.10	0.49
300	10^{-2}	0.01	0.5	0.76	49
			1	0.029	33
			2	0.011	6.4
			4	0.010	0.70

Notes. The values are measured at time $t = 6$ Myr after disk formation.

where viscous heating dominates and is shallower in outer regions where stellar irradiation dominates. Detailed modeling of the temperature profile is beyond the scope of this paper, but we show below that our results are fairly insensitive to the choice of the temperature profile.

We adopt the temperature profile of an optically thick disk around a Sun-like star presented by Oka et al. (2011). We select one of their models in which $\dot{M} = 10^{-8}\ M_\odot\ \mathrm{yr}^{-1}$ and $\alpha = 10^{-3}$ with a dust opacity mimicking that of Garaud & Lin (2007). We chose this model because the midplane temperature reaches 170 K at 1 AU as in our fiducial temperature profile. The radial profile of the midplane temperature for this model is shown in their Fig. 8 (black solid line). We find that this profile can be reasonably reproduced by a simple analytic fit

$$T(r) = \sqrt{[160(r/1\ \mathrm{AU})^{-1.15}]^2 + [70(r/1\ \mathrm{AU})^{-0.26}]^2}\ \mathrm{K}, \quad (28)$$

which is shown by the dashed curve in our Fig. 12. In this model, viscous heating is effective at $\lesssim 4$ AU and the temperature in that region rises toward the central star as steeply as $T \propto r^{-1.15}$. However, as far as the region 1 AU $\leq r \leq 300$ AU is concerned, the difference in the values of T between the two models is small with the maximum deviation of $\approx 60\%$. The surface density profile in this viscous disk model differs from the MMSN model (Eq. (1)). However, we keep using the MMSN density profile to isolate the effects of changing the temperature profile.

We fix $M_{e,0} = 10^{-1}\ M_\oplus$ and $\alpha = 10^{-3}$ and only vary the values of r_{out} and t_{start}. The results for the two different temperature models are compared in Fig. 13. Here, the solid curves show the evolution of the embryo water fraction f_{H_2O} for our temperature profile (Eq. (3)), which is already shown in the lower center panels of Figs. 10 and 11, while the dashed curves are for the viscous disk temperature profile given by Eq. (28). One can see that the predicted water fraction of the embryo is very insensitive to the choice of the temperature profile. A closer inspection shows that in the $r_{out} = 100$ AU case (the left panel of Fig. 12), the viscous temperature model leads to a slightly higher f_{H_2O}, in particular, at $t \gtrsim 2$ Myr at which the radial pebble flux has already decayed to 0.1 $M_\oplus\ \mathrm{Myr}^{-1}$ (see the lower left panel of Fig. 8). However, the final values of f_{H_2O} in the viscous model are only larger than those in our fiducial model by a factor of less than 2. We conclude that the details of the assumed temperature profile do not affect our conclusions.

4.2. Migration timescale of the snow line

We have shown in Sect. 3 that the fate of terrestrial embryos largely depends on the timing of inward snow-line migration, t_{start}. Rocky embryos are able to avoid excessive icy pebble accretion only if the snow line migrates in *after* the radial pebble flux in the disk is sufficiently depleted. This is already obvious from the estimate of the pebble accretion rate presented in Sect. 3.3. The pebble accretion rate of a 0.1 Earth mass embryo before dust depletion is $\sim 1\ M_\oplus\ \mathrm{Myr}^{-1}$, which roughly amounts to 0.1 Earth ocean mass ($\sim 10^{-5}\ M_\oplus$) in 10 years. If the Earth-forming embryos contained less water than on the ocean of the present Earth (water content $\lesssim 0.023$ wt%), the snow line must have migrated to 1 AU as late as 2–4 Myr after nebula formation (assuming that the nebula had a radial extent of ~ 100 AU; see Fig. 10). Even if the Earth formed from wetter embryos of water content 1 wt% (Machida & Abe 2010), the migration of the snow line must have occurred no earlier than 0.5–2 Myr.

The remaining question is then whether these conditions can be satisfied in a realistic protoplanetary disk. Addressing this questing with a detailed model of snow-line migration is beyond the scope of this paper. Here we attempt to estimate the timescale of snow-line migration assuming that (i) viscous heating dominates over stellar irradiation; and that (ii) the disk opacity is constant in time. In this simplest case, the timescale of snow-line

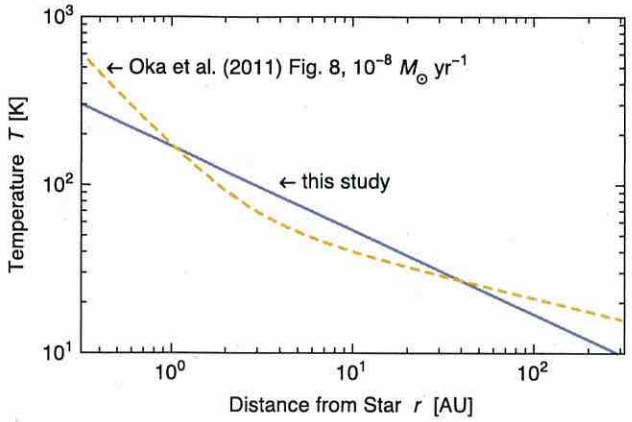

Fig. 12. Temperature profiles adopted in this study (Eq. (3); solid line) and from a viscous accretion model of Oka et al. (2011; Eq. (28); dashed curve).

evolution is essentially given by the viscous evolution timescale of the disk,

$$t_{\rm visc} \sim \frac{r_{\rm out}^2}{\nu|_{r=r_{\rm out}}} \sim 2\ {\rm Myr}\left(\frac{\alpha|_{r=r_{\rm out}}}{10^{-2}}\right)^{-1}\left(\frac{r_{\rm out}}{100\ {\rm AU}}\right), \quad (29)$$

where $\nu = \alpha c_{\rm s} h_{\rm g}$ is the turbulent viscosity and we have used Eq. (3) in the final expression. If we take $r_{\rm out} = 100$ AU and $\alpha|_{r=r_{\rm out}} = 10^{-2}$, we obtain $t_{\rm visc} \sim 2$ Myr, which is comparable to the time required for sufficient dust depletion. Therefore, snow-line migration after the decay of the radial pebble flow is a possible explanation for the origin of the dry Earth. However, Eq. (29) only serves as a rough estimate of $t_{\rm start}$, and a more precise assessment taking into account viscous evolution, stellar evolution, and the evolution of the disk opacity due to dust evolution is necessary. This will be addressed in future work.

We point out that $t_{\rm visc} \propto r_{\rm out}$ whereas $t_{\rm grow}|_{r=r_{\rm out}} \propto \Omega^{-1}|_{r=r_{\rm out}} \propto r_{\rm out}^{3/2}$. This implies that when $r_{\rm out}$ is small, the snow line tends to migrate more slowly than icy dust in the disk becomes depleted (whose timescale is $\propto t_{\rm grow}$ at $r = r_{\rm out}$). This argument also supports the idea that preservation of rocky embryos from ice pebbles favors a compact protoplanetary disk.

On the other hand, an extended disk is beneficial for forming the cores of gas giants at wider orbits through the pebble accretion mechanism (Lambrechts & Johansen 2014). As we discuss below, such fully grown cores could save the rocky embryos in the inner disk by halting the ice pebble flow.

4.3. Possible mechanisms for pebble filtration outside 1 AU

We have restricted ourselves to the simplest (and most pessimistic) case where all icy pebbles forming in outer disk regions are allowed to drift to 1 AU. In fact, there are some known mechanisms that might halt or filter the pebble flux before they reach rocky embryos. Ignoring such possibilities effectively means that we have assumed these mechanisms operate only after the snow line migrates to 1 AU. We here mention some import mechanisms and discuss whether they are likely to have operated in the solar nebula.

The most straightforward scenario would be that planetesimals or embryos outside the Earth's orbit filter out incoming pebbles just in the same way as what we considered for Earth-forming embryos. However, it turns out an efficient filtration is not expected with this mechanism in many cases. We have shown in Sect. 3.3 that each $0.1 M_\oplus$-mass embryo captures only ≈1–2% of the pebble flux in a disk. Assuming that the total mass of terrestrial embryos in the minimum-mass solar nebula is ≈2 $M_\oplus$ (Earth + Venus), the total number of the embryos is ≈20, and therefore they filter only ≈20–40% of the pebble flux in total. The low (<50%) efficiency of dust filtration by a small number of embryos are consistent with the results by Morbidelli & Nesvorny (2012), Lambrechts & Johansen (2014), and Morbidelli et al. (2015). A more systematic study on pebble filtration by planetesimal- or embryo-sized objects has been carried out by Guillot et al. (2014) using essentially the same pebble accretion formula as ours. They found that perfect filtration beyond 1 AU is possible only if most of the dust in the planet-forming region is converted into ~1000 km-sized embryos and if disk turbulence is $\alpha = 10^{-4}$ (see their Fig. 22). Moriarty & Fischer (2015) obtained qualitatively similar results; these authors considered the accretion of cm-sized drifting pebbles by initially 100 km-sized planetesimals in an $\alpha = 10^{-3}$ gas disk and showed that the inward flux of cm-sized pebbles is nearly constant down to 1 AU (see their Fig. 2). These suggest that a swarm of outer planetesimals and embryos is only able to fully filter the icy pebble flow in a particular range of parameter space. Whether such a situation was realized in the solar nebula over the lifetime of pebble flow (~0.5–2 Myr) is unclear.

A more promising mechanism for pebble filtration is particle trapping at pressure maxima in the gas disk. In general, the direction of particle radial drift is determined by the sign of the pressure gradient of the disk (Eq. (10)), and therefore particles tend to accumulate toward locations where the gas pressure is locally maximized (Whipple 1972). A pressure bump may be created by magnetorotational turbulence (e.g., Johansen et al. 2009; Uribe et al. 2011), by a steep gradient in the gas viscosity (e.g., Kretke & Lin 2007; Dzyurkevich et al. 2010; Flock et al. 2015), or by a massive planet or embryo that carves a gap in the gas disk (e.g., Paardekooper & Mellema 2006; Rice et al. 2006; Zhu et al. 2012; Morbidelli & Nesvorny 2012; Lambrechts et al. 2014).

Interestingly, the snow line has been regraded as a candidate that might naturally produce a pressure bump (Kretke & Lin 2007; Dzyurkevich et al. 2010; Brauer et al. 2008b; Drążkowska et al. 2013). This idea is based on the assumptions that (i) the dust surface density has a jump there and that (ii) the jump in the surface density leads to a jump in the magnetic turbulent viscosity large enough to build up a pressure bump via ionization chemistry. Although the first assumption is likely to be true qualitatively, the second assumption has not yet been validated with magnetohydrodynamic simulations incorporating a realistic ionization model.

By contrast, hydrodynamical simulations have demonstrated the viability of particle trapping at the edges of planetary gaps (Paardekooper & Mellema 2006; Zhu et al. 2012). Simulations by Paardekooper & Mellema (2006) and Lambrechts et al. (2014) show that a planet larger than ~20 $M_\oplus$ in mass carves a gap that can efficiently trap incoming pebbles. This suggests that excessive water delivery to terrestrial planetary embryos may be avoided if such a massive planet forms prior to the inward migration of the snow line. This possibility has also been pointed out in a recent paper by Morbidelli et al. (2016). Assuming that the snow line moves on a timescale of ~2 Myr as estimated in Sect. 4.2, the standard planet formation from planetesimals is too slow to satisfy this requirement unless the disk is massive and the collisional fragmentation of the bodies is negligible (Kokubo & Ida 2002; Kobayashi et al. 2010). By contrast, planet growth driven by pebble accretion can take place on this timescale as demonstrated by Lambrechts & Johansen (2014).

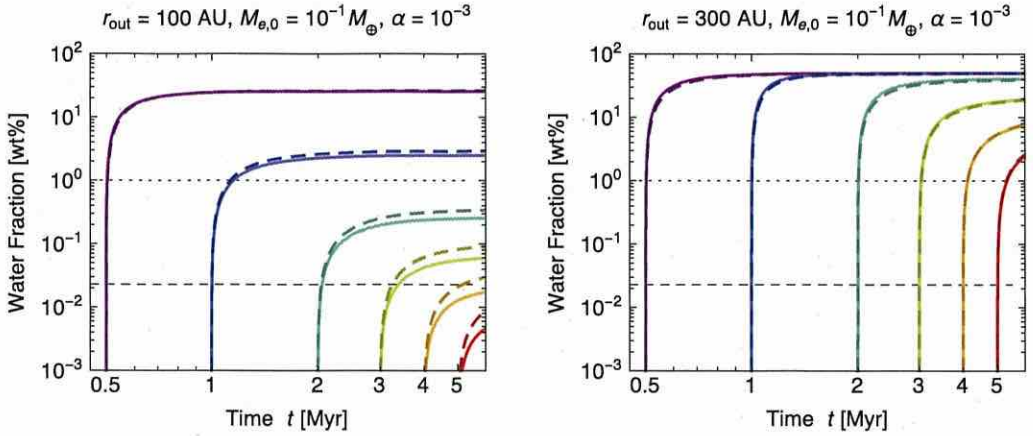

Fig. 13. Same as the *lower center panels* of Figs. 10 and 11, but here the results for the temperature profile from an optically thick viscous disk model (Eq. (28)) are overplotted (dashed curves).

To conclude, this study has shown that depletion of icy pebbles before the migration of the snow line is a possible explanation for the origin of water-devoid terrestrial planets, but pebble filtration by a gap-forming planet (in the solar system, Jupiter or Saturn) that forms before the snow-line migration might be an equally viable alternative. The scenario that is favored for the solar system is unclear and needs to be answered in future studies.

5. Conclusions

We have studied how icy pebbles drifting from outer regions of protoplanetary disks affect the water fraction of terrestrial embryos near the Earth's orbit. We numerically solved a simplified version of the coagulation equation to calculate the global evolution of the characteristic size and mass flux of drifting icy pebbles. In contrast to the previous study on pebble accretion by Lambrechts & Johansen (2014), our model explicitly takes the finite radial extent of a protoplanetary disk into account, and therefore automatically includes the effect that the radial pebble flux diminishes as the outermost region of the disk is depleted of icy dust. We calculated the rate of pebble accretion by a single embryo following the analytic expressions by Ormel & Klahr (2010) and Guillot et al. (2014). Our calculation accounts for the 3D nature of pebble accretion, i.e., the reduction of the accretion rate due to vertical pebble diffusion, in the presence of strong gas turbulence. We have predicted how the mass and water content of an initially rocky embryo increase with time after icy pebble accretion sets in. The predicted water fraction was compared with the minimum water fraction of the present Earth inferred from the ocean mass (0.023 wt%) and with the hypothetical water fraction of the proto-Earth inferred from the density deficit of the Earth's outer core (1 wt%).

Our key findings are summarized as follows:

1. The evolution of the icy pebble flow largely depends on the radial extent of the gas disk r_{out} (Sects. 3.1 and 3.2). In general, radially drifting pebbles form from inside out in protoplanetary disks because the timescale of pebble formation roughy scales with the orbital timescale. The radial extent of a disk therefore sets the lifetime of the pebble flow in the disk with smaller r_{out} corresponding to a shorter lifetime. Turbulence somewhat accelerates pebble formation in outermost regions, but its effect is relatively minor when compared to the effect of r_{out}. The radial pebble flux is $\sim 10^2\ M_\oplus\ \mathrm{Myr}^{-1}$ at early times, and starts decaying with time at $t \approx 0.2$ Myr for $r_{out} = 100$ AU and at $t \approx 1$ Myr for $r_{out} = 300$ AU. The pebble size observed at 1 AU is a few decimeters at early times, and decreases with the pebble flux because a lower particle density generally leads to slower particle growth.
2. The rate of pebble accretion onto an embryo also decreases with time, the details of which depend on r_{out} and on turbulence strength α (Sect. 3.3). The pebble accretion rate is initially $\sim 1\ M_\oplus\ \mathrm{Myr}^{-1}$, reflecting the fact that the radial mass flux is $\sim 10^2\ M_\oplus\ \mathrm{Myr}^{-1}$ and the accretion efficiency of dm-sized particles is $\sim 1\%$ (Fig. 5). The accretion rate roughly scales linearly with the embryo mass, and therefore the embryo's water fraction increases with time nearly independent of the embryo mass. Turbulence suppresses the accretion rate at late times by diffusing small pebbles away from the midplane. Combining this effect with the acceleration of pebble depletion mentioned above, strong turbulence of $\alpha = 10^{-2}$ reduces the pebble flux by 1–2 orders of magnitude from the cases with weaker turbulence ($\alpha = 10^{-3}$ and 10^{-4}).
3. Preserving water-devoid embryos at 1 AU generally requires that the snow line reaches that location after the radial pebble flux through the disk has already decayed to a sufficient extent (Sect. 3.4). In a disk of $r_{out} \lesssim 100$ AU and $\alpha \gtrsim 10^{-3}$, the fractional water content of the embryos is kept below the current Earth's water content based on the ocean mass (0.023 wt%) if the time t_{start} at which the snow lines passes 1 AU is longer than 2–4 Myr (smaller t_{start} corresponds to stronger turbulence). If $r_{out} \geq 300$ AU or $\alpha \leq 10^{-4}$, the water content greatly exceeds 0.023 wt% for all $t_{start} \lesssim 5$ Myr. Keeping the water fraction at a level of $\lesssim 1$ wt% is possible in a $r_{out} = 100$ AU disk if $t_{start} \gtrsim 0.5$–2 Myr. Keeping the water fraction at the same level is much more difficult in a $r_{out} = 300$ AU disk because of a prolonged pebble flow.

Our results provide strong constraints on the formation history and environment of Earth-forming embryos in the solar nebula within the assumption that no mechanism halted the ice pebble flow upstream. Overall, our results suggest that the solar nebula must have been relatively compact ($r_{out} = 100$ AU or smaller), so that the pebble flow had decayed at early times. The formation of terrestrial embryos as dry as the present Earth was possible if

moderately strong turbulence ($\alpha \gtrsim 10^{-3}$) was present at 1 AU. However, the latest magnetohydrodynamical disk models (e.g., Bai & Stone 2013; Lesur et al. 2014) suggest that turbulence is considerably weaker than this requirement in inner regions of protoplanetary disks[4] For $r_{\rm out} = 100$ AU and $\alpha = 10^{-4}$, embryos as dry as the present Earth would not have formed, but embryos containing $\lesssim$1 wt% water would have formed if the snow line migrated on a timescale of $\gtrsim$2 Myr. This is one plausible scenario that can explain the origin of our dry Earth because the snow line in the nebula could indeed have migrated on a similar timescale (Sect. 4.2).

Another possible scenario, which we have not tested in this study, is that a massive planet (a gas giant or its core) formed and created a pebble gap in the nebula before the snow line reached 1 AU (Sect. 4.3; see also Morbidelli et al. 2016). The scenario favored as the explanation for the dry Earth remains to be studied in future work.

One important caveat of this study is that our pebble evolution model greatly simplifies the collisional growth of ice aggregates. Future models should include the evolution of aggregate porosity (Ormel et al. 2007; Okuzumi et al. 2009; Kataoka et al. 2013b) since porous aggregates tend to collide more frequently than compact equivalents in protoplanetary disks (Okuzumi et al. 2012; Kataoka et al. 2013a). The global simulation of dust coagulation and porosity evolution by Okuzumi et al. (2012) shows that highly fluffy ice aggregates produced in inner ($\lesssim$10 AU) protoplanetary disks grow to planetesimal-mass objects with little appreciable drift. However, the simulation also shows that fluffy aggregates forming in the outer ($\gtrsim$10 AU) region drift in until they arrive at the snow line. The accretion rate of these fluffy aggregates onto inner embryos could be greatly different from that of compact aggregates. Bounding and fragmentation of aggregates are also potentially important, but might not be crucial given the sticky nature of ice aggregates (see Wada et al. 2009, 2011, 2013; Gundlach & Blum 2015).

Another important caveat is that it is still a matter of debate whether the snow line around a solar-mass star really migrates inward to 1 AU. The model of Martin & Livio (2012), which predicts that the snow line never reaches 1 AU in late evolutionary stages, relies on the idea that weak magnetic turbulence expected at ~1 AU (e.g., Gammie 1996; Sano et al. 2000) triggers gravitational instability that in turn heats up the disk gas at that location. On the other hand, recent magnetohydrodynamical simulations have shown that, even without magnetic turbulence, large-scale (non-turbulent) magnetic fields are still able to provide inner protoplanetary disks with high gas accretion rates (e.g., Turner & Sano 2008; Bai & Stone 2013; Lesur et al. 2014; Gressel et al. 2015). A model incorporating these important accretion mechanisms is needed to fully understand the evolution of the snow line.

The results of this study also have important implications for the water content of exoplanets lying inside the habitable zone. Mulders et al. (2015) recently predicted the water content distribution of habitable-zone terrestrial planets assuming that the planets acquire water by accreting water-bearing (water content =5%) embryos and planetesimals. However, our results suggest that a significantly higher amount of water could be delivered to habitable-zone planets in the form of icy pebbles from outer orbital radii. A significant amount of water does not necessarily make habitable-zone planets habitable because the presence of land might be required for the emergence of life (Dohm & Maruyama 2015). In any case, it would be interesting to predict the water content of habitable-zone exoplanets by taking ice pebble accretion into account.

[4] In addition, turbulence of $\alpha > 10^{-3}$ would inhibit the formation of rocky embryos via rocky pebble accretion within the lifetime of protoplanetary disks (Johansen et al. 2015; Morbidelli et al. 2015) for the same reason that it prevents excessive water delivery.

Acknowledgements. We would like to thank Takanori Sasaki for pointing out the importance of pebble accretion in the context of water delivery to the Earth. We also thank Chris Ormel for discussions on the modeling of pebble accretion; Taishi Nakamoto, Hidenori Genda, Masanobu Kunitomo, Tetsuo Taki, for helpful comments; and Sebastiaan Krijt for sharing with us an early version of his paper prior to publication. S.O. especially thanks Chris Ormel for his very insightful comments on the formulation of the single-size approach based on the moment method. Finally, we thank the referee, Michiel Lambrechts, for his prompt and constructive report which significantly improved the quality of this paper. This work is supported by Grants-in-Aid for Scientific Research (#23103005, 15H02065) from MEXT of Japan.

References

Abe, Y., Ohtani, E., Okuchi, T., Righter, K., & Drake, M. 2000, in Water in the Early Earth, Origin of the Earth and the Moon, eds. R. M. Canup, K. Righter, et al. (Tucson: University of Arizona Press), 413
Adachi, I., Hayashi, C., & Nakazawa, K. 1976, Prog. Theor. Phys., 56, 1756
A'Hearn, M. F. 2011, ARA&A, 49, 281
Altwegg, K., Balsiger, H., Bar-Nun, A., et al. 2015, Science, 347, 1261952
Andrews, S. M., & Williams, J. P. 2007, ApJ, 659, 705
Bai, X.-N., & Stone, J. M. 2013, ApJ, 769, 76
Baillié, K., Charnoz, S., & Pantin, E. 2015, A&A, 577, A65
Balbus, S. A., & Hawley, J. F. 1991, ApJ, 376, 214
Birnstiel, T., Dullemond, C. P., & Brauer, F. 2010, A&A, 513, A79
Birnstiel, T., Klahr, H., & Ercolano, B. 2012, A&A, 539, A148
Bitsch, B., Johansen, A., Lambrechts, M., & Morbidelli, A. 2015, A&A, 575, A28
Blum, J., & Wurm, G. 2008, ARA&A, 46, 21
Brauer, F., Dullemond, C. P., & Henning, T. 2008a, A&A, 480, 859
Brauer, F., Henning, T., & Dullemond, C. P. 2008b, A&A, 487, L1
Dauphas, N., & Pourmand, A. 2011, Nature, 473, 489
Davis, S. S. 2005, ApJ, 620, 994
Dohm, J. M., & Maruyama, S. 2015, Geoscience Frontiers, 6, 95
Dominik, C., & Tielens, A. G. G. M. 1997, ApJ, 480, 647
Donahue, T. M., & Hodges, Jr., R. R. 1992, J. Geophys. Res., 97, 6083
Drążkowska, J., Windmark, F., & Dullemond, C. P. 2013, A&A, 556, A37
Dubrulle, B., Morfill, G., & Sterzik, M. 1995, Icarus, 114, 237
Dzyurkevich, N., Flock, M., Turner, N. J., Klahr, H., & Henning, T. 2010, A&A, 515, A70
Estrada, P. R., & Cuzzi, J. N. 2008, ApJ, 682, 515
Ferrier, B. S. 1994, J. Atm. Sci., 51, 249
Flock, M., Fromang, S., González, M., & Commerçon, B. 2013, A&A, 560, A43
Flock, M., Ruge, J. P., Dzyurkevich, N., et al. 2015, A&A, 574, A68
Fromang, S., & Papaloizou, J. 2006, A&A, 452, 751
Gammie, C. F. 1996, ApJ, 457, 355
Garaud, P. 2007, ApJ, 671, 2091
Garaud, P., & Lin, D. N. C. 2007, ApJ, 654, 606
Genda, H., & Abe, Y. 2005, Nature, 433, 842
Gressel, O., Turner, N. J., Nelson, R. P., & McNally, C. P. 2015, ApJ, 801, 84
Guillot, T., Ida, S., & Ormel, C. W. 2014, A&A, 572, A72
Gundlach, B., & Blum, J. 2015, ApJ, 798, 34
Hartmann, L., Calvet, N., Gullbring, E., & D'Alessio, P. 1998, ApJ, 495, 385
Hayashi, C. 1981, Prog. Theor. Phys. Suppl., 70, 35
Hirose, S., & Turner, N. J. 2011, ApJ, 732, L30
Johansen, A., Youdin, A., & Klahr, H. 2009, ApJ, 697, 1269
Johansen, A., Mac Low, M.-M., Lacerda, P., & Bizzarro, M. 2015, Sci. Adv., 1, 15109
Kataoka, A., Tanaka, H., Okuzumi, S., & Wada, K. 2013a, A&A, 557, L4
Kataoka, A., Tanaka, H., Okuzumi, S., & Wada, K. 2013b, A&A, 554, A4
Kobayashi, H., Tanaka, H., Krivov, A. V., & Inaba, S. 2010, Icarus, 209, 836
Kokubo, E., & Ida, S. 2002, ApJ, 581, 666
Kornet, K., Stepinski, T. F., & Różyczka, M. 2001, A&A, 378, 180
Kretke, K. A., & Levison, H. F. 2014, AJ, 148, 109
Kretke, K. A., & Lin, D. N. C. 2007, ApJ, 664, L55
Krijt, S., Ormel, C. W., Dominik, C., & Tielens, A. G. G. M. 2015, A&A, 574, A83
Krijt, S., Ormel, C. W., Dominik, C., & Tielens, A. G. G. M. 2016, A&A, 586, A20
Kurokawa, H., Sato, M., Ushioda, M., et al. 2014, Earth and Planetary Science Letters, 394, 179

Kusaka, T., Nakano, T., & Hayashi, C. 1970, Prog. Theor. Phys., 44, 1580
Lambrechts, M., & Johansen, A. 2012, A&A, 544, A32
Lambrechts, M., & Johansen, A. 2014, A&A, 572, A107
Lambrechts, M., Johansen, A., & Morbidelli, A. 2014, A&A, 572, A35
Lesur, G., Kunz, M. W., & Fromang, S. 2014, A&A, 566, A56
Levison, H. F., Kretke, K. A., & Duncan, M. J. 2015a, Nature, 524, 322
Levison, H. F., Kretke, K. A., Walsh, K. J., & Bottke, W. F. 2015b, Proc. National Academy of Science, 112, 14180
Lin, D. N. C., & Papaloizou, J. 1980, MNRAS, 191, 37
Lodders, K. 2003, ApJ, 591, 1220
Machida, R., & Abe, Y. 2010, ApJ, 716, 1252
Martin, R. G., & Livio, M. 2012, MNRAS, 425, L6
Min, M., Dullemond, C. P., Kama, M., & Dominik, C. 2011, Icarus, 212, 416
Morbidelli, A., & Nesvorny, D. 2012, A&A, 546, A18
Morbidelli, A., Lambrechts, M., Jacobson, S., & Bitsch, B. 2015, Icarus, 258, 418
Morbidelli, A., Bitsch, B., Crida, A., et al. 2016, Icarus, 267, 368
Moriarty, J., & Fischer, D. 2015, ApJ, 809, 94
Mulders, G. D., Ciesla, F. J., Min, M., & Pascucci, I. 2015, ApJ, 807, 9
Nimmo, F., & McKenzie, D. 1998, Ann. Rev. Earth Planet. Sci., 26, 23
Nomura, R., Hirose, K., Uesugi, K., et al. 2014, Science, 343, 522
Oka, A., Nakamoto, T., & Ida, S. 2011, ApJ, 738, 141
Okuchi, T. 1997, Science, 278, 1781
Okuzumi, S., Tanaka, H., & Sakagami, M.-A. 2009, ApJ, 707, 1247
Okuzumi, S., Tanaka, H., Kobayashi, H., & Wada, K. 2012, ApJ, 752, 106
Okuzumi, S., Momose, M., Sirono, S.-i., Kobayashi, H., & Tanaka, H. 2016, ApJ, in press [arXiv:1510.03556]
Ormel, C. W. 2014, ApJ, 789, L18
Ormel, C. W., & Cuzzi, J. N. 2007, A&A, 466, 413
Ormel, C. W., & Klahr, H. H. 2010, A&A, 520, A43
Ormel, C. W., & Kobayashi, H. 2012, ApJ, 747, 115
Ormel, C. W., & Spaans, M. 2008, ApJ, 684, 1291
Ormel, C. W., Spaans, M., & Tielens, A. G. G. M. 2007, A&A, 461, 215
Owen, J. E., Ercolano, B., Clarke, C. J., & Alexander, R. D. 2010, MNRAS, 401, 1415
Paardekooper, S.-J., & Mellema, G. 2006, A&A, 453, 1129
Pinilla, P., Benisty, M., & Birnstiel, T. 2012, A&A, 545, A81
Prinn, R. G., & Fegley, B. 1987, Ann. Rev. Earth Planet. Sci., 15, 171
Rice, W. K. M., Armitage, P. J., Wood, K., & Lodato, G. 2006, MNRAS, 373, 1619
Ros, K., & Johansen, A. 2013, A&A, 552, A137
Sano, T., Miyama, S. M., Umebayashi, T., & Nakano, T. 2000, ApJ, 543, 486
Sasselov, D. D., & Lecar, M. 2000, ApJ, 528, 995
Shakura, N. I., & Sunyaev, R. A. 1973, A&A, 24, 337
Sirono, S.-I. 2011a, ApJ, 733, L41
Sirono, S.-I. 2011b, ApJ, 735, 131
Suyama, T., Wada, K., & Tanaka, H. 2008, ApJ, 684, 1310
Takeuchi, T., & Lin, D. N. C. 2005, ApJ, 623, 482
Turner, N. J., & Sano, T. 2008, ApJ, 679, L131
Turner, N. J., Choukroun, M., Castillo-Rogez, J., & Bryden, G. 2012, ApJ, 748, 92
Uribe, A. L., Klahr, H., Flock, M., & Henning, T. 2011, ApJ, 736, 85
Wada, K., Tanaka, H., Suyama, T., Kimura, H., & Yamamoto, T. 2009, ApJ, 702, 1490
Wada, K., Tanaka, H., Suyama, T., Kimura, H., & Yamamoto, T. 2011, ApJ, 737, 36
Wada, K., Tanaka, H., Okuzumi, S., et al. 2013, A&A, 559, A62
Weidenschilling, S. J. 1977, MNRAS, 180, 57
Wetherill, G. W., & Stewart, G. R. 1989, Icarus, 77, 330
Whipple, F. L. 1972, in From Plasma to Planet, Proc. of Symp., ed. A. Elvius, 211
Youdin, A. N., & Lithwick, Y. 2007, Icarus, 192, 588
Zhu, Z., Nelson, R. P., Dong, R., Espaillat, C., & Hartmann, L. 2012, ApJ, 755, 6

Appendix A: Derivation and justification of the single-size approach

A.1. Derivation of Eqs. (4) and (5) from the coagulation equation

In this subsection, we derive the single-size Eqs. (4) and (5) from the coagulation (Smoluchowski) equation. We define the size distribution function $n(r, z, m)$ as the particle number density per unit particle mass m at orbital radius r and distance from midplane z. Assuming the balance between vertical sedimentation and turbulent diffusion of the particles, the particle size distribution can be written as $n = (\mathcal{N}/\sqrt{2\pi}h_{\rm d})\exp(-z^2/2h_{\rm d}^2)$, where $\mathcal{N}(r, m)$ is the column number density of dust particles per unit m and $h_{\rm d}(m)$ is the dust scale height. The evolution of $\mathcal{N}$ is given by the vertically integrated coagulation equation with the drift term (Brauer et al. 2008a)

$$\frac{\partial \mathcal{N}(r,m)}{\partial t} = \frac{1}{2}\int_0^m K(r;m',m-m')\mathcal{N}(r,m')\mathcal{N}(r,m-m')\mathrm{d}m' - \mathcal{N}(r,m)\int_0^\infty K(r;m,m')\mathcal{N}(r,m')\mathrm{d}m' - \frac{1}{r}\frac{\partial}{\partial r}\left[rv_{\rm r}(r,m)\mathcal{N}(r,m)\right]. \quad (A.1)$$

Here, K is the vertically integrated collision rate coefficient given by

$$K(r;m_1,m_2) = \frac{\sigma_{\rm coll}}{2\pi h_{\rm d,1}h_{\rm d,2}}\int_{-\infty}^{\infty}\Delta v_{\rm pp} \times\exp\left[-\frac{z^2}{2}\left(\frac{1}{h_{\rm d,1}^2}+\frac{1}{h_{\rm d,2}^2}\right)\right]\mathrm{d}z, \quad (A.2)$$

where $h_{\rm d,1}$ and $h_{\rm d,2}$ are the scale heights of the two colliding particles. On the right-hand side of Eq. (A.1), the first term represents the gain of $\mathcal{N}(m)$ by coagulation of two particles of masses m' and $m - m'$, the second term the loss of $\mathcal{N}(m)$ by coagulation of a particle of mass m with a particle of mass m', and the third term the advection of $\mathcal{N}(m)$ due to radial drift. Because we assume perfect sticking upon collision, the collisional cross section is simply given by $\sigma_{\rm coll} = \pi(a_1 + a_2)^2$, where a_1 and a_2 are the particle radii.

Since we are interested in the mass flow of radially drifting dust particles, it is useful to introduce the surface *mass* density of dust per unit particle mass

$$\mathcal{S}(r,m) \equiv m\mathcal{N}(r,m). \quad (A.3)$$

Multiplying Eq. (A.1) by m, the equation for $\mathcal{S}$ is obtained as

$$\frac{\partial \mathcal{S}(m)}{\partial t} = \frac{m}{2}\int_0^m K'(m',m-m')\mathcal{S}(m')\mathcal{S}(m-m')\mathrm{d}m' - m\mathcal{S}(m)\int_0^\infty K'(m,m')\mathcal{S}(r,m')\mathrm{d}m' - \frac{1}{r}\frac{\partial}{\partial r}\left[rv_{\rm r}(m)\mathcal{S}(m)\right], \quad (A.4)$$

where $K'(m,m') \equiv K(m,m')/mm'$ and we have omitted the argument r from the expression for clarity.

One important quantity characterizing the mass distribution $\mathcal{S}$ is the so-called peak mass defined by (Ormel & Spaans 2008)

$$m_{\rm p} \equiv \frac{\int m\mathcal{S}\mathrm{d}m}{\int \mathcal{S}\mathrm{d}m}. \quad (A.5)$$

When $\mathcal{S}$ is a unimodal function of m, this quantity is approximately equal to the mass at the peak of $\mathcal{S}$ (see Ormel & Spaans 2008). Another important quantity is of course the total surface density defined by

$$\Sigma_{\rm d} \equiv \int_0^\infty \mathcal{S}(m)\mathrm{d}m. \quad (A.6)$$

We now derive the equations that determine the evolution of $\Sigma_{\rm d}$ and $m_{\rm p}$ from Eq. (A.4). We begin by introducing the ith moment of the surface mass density distribution $\mathcal{S}$,

$$\mathcal{M}_i \equiv \int_0^\infty m^i\mathcal{S}(m)\mathrm{d}m. \quad (A.7)$$

The quantity $\mathcal{M}_i$ is equal to the $(i+1)$-th moment of the surface number density distribution $\mathcal{N}$ since $\mathcal{S} = m\mathcal{N}$. It follows from Eqs. (A.5) and (A.6) that the total dust surface density $\Sigma_{\rm d}$ and peak mass $m_{\rm p}$ are related to $\mathcal{M}_i$ as

$$\Sigma_{\rm d} = \mathcal{M}_0, \quad (A.8)$$

$$m_{\rm p} = \frac{\mathcal{M}_1}{\mathcal{M}_0}, \quad (A.9)$$

respectively.

The equation that determines the evolution of $\mathcal{M}_i$ can be derived by multiplying Eq. (A.4) by m^i and integrating over m. After some algebra, the result can be simplified as (see, e.g., Estrada & Cuzzi 2008; Ormel & Spaans 2008, but note that they define the moment in terms of the number density)

$$\frac{\partial \mathcal{M}_i}{\partial t} = \frac{1}{2}\int_0^\infty \mathrm{d}m\,\mathrm{d}m'\,K'(m,m')\mathcal{S}(m)\mathcal{S}(m') \times\left[(m+m')^{i+1} - \left(m^{i+1}+m'^{i+1}\right)\right] - \frac{1}{r}\frac{\partial}{\partial r}\left(r\langle m^i v_{\rm r}\rangle\Sigma_{\rm d}\right), \quad (A.10)$$

where

$$\langle m^i v_{\rm r}\rangle \equiv \frac{1}{\Sigma_{\rm d}}\int_0^\infty m^i v_{\rm r}(m)\mathcal{S}(r,m)\mathrm{d}m. \quad (A.11)$$

For $i = 0$, Eq. (A.10) has the simple form

$$\frac{\partial \Sigma_{\rm d}}{\partial t} = \frac{1}{r}\frac{\partial}{\partial r}\left(r\langle v_{\rm r}\rangle\Sigma_{\rm d}\right). \quad (A.12)$$

The coagulation terms (the first and second terms) in Eq. (A.10) have canceled out, as it should be since $\Sigma_{\rm d}$ is a conserved quantity in the absence of advection and diffusion. Since $\mathcal{M}_1 = m_{\rm p}\Sigma_{\rm d}$, the equation for $i = 1$ can be written as

$$\frac{\partial (m_{\rm p}\Sigma_{\rm d})}{\partial t} = \int_0^\infty \mathrm{d}m\,\mathrm{d}m'\,K(m,m')\mathcal{S}(m)\mathcal{S}(m') - \frac{1}{r}\frac{\partial}{\partial r}\left(r\langle mv_{\rm r}\rangle\Sigma_{\rm d}\right). \quad (A.13)$$

The right-hand sides of Eqs. (A.12) and (A.13) are not closed with respect to $\Sigma_{\rm d}$ and $m_{\rm p}$ because of the presence of the $\langle m^i v_{\rm r}\rangle$ terms. To derive approximate but *closed* equations for $\Sigma_{\rm d}$ and $m_{\rm p}$, we assume that $\mathcal{S}$ is narrowly peaked at $m \approx m_{\rm p}$. Specifically, we assume

$$\mathcal{S}(m) \approx \Sigma_{\rm d}\delta(m - m_{\rm p}), \quad (A.14)$$

where the normalization is determined by Eq. (A.8). If we use Eq. (A.14), the term $\langle m^i v_{\rm r}\rangle$ can now be replaced by $m_{\rm p}^i v_{\rm r}(m_{\rm p})$,

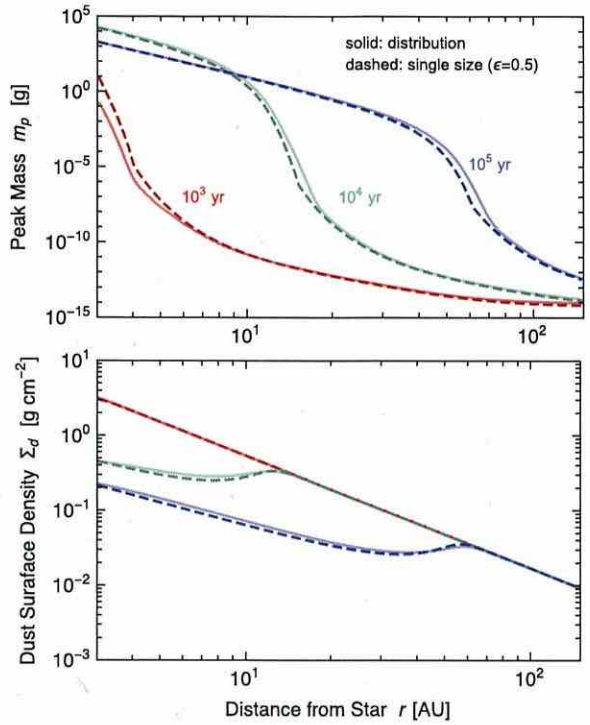

Fig. A.1. Comparison between single- and full-size coagulation calculations. The solid lines show the snapshots of the peak mass m_p (Eq. (A.9); *upper panel*) and total dust surface density Σ_d (Eq. (A.8); *lower panel*) at different times as a function of orbital radius r obtained from the full coagulation simulation for the compact aggregation model by Okuzumi et al. (2012, see also their Fig. 2). The dashed line shows our reproduction using the single-size approach (Eq. (4) for Σ_d and Eq. (5) for m_p) with $\epsilon = 0.5$ (see Sect. 2.4 for the definition of ϵ).

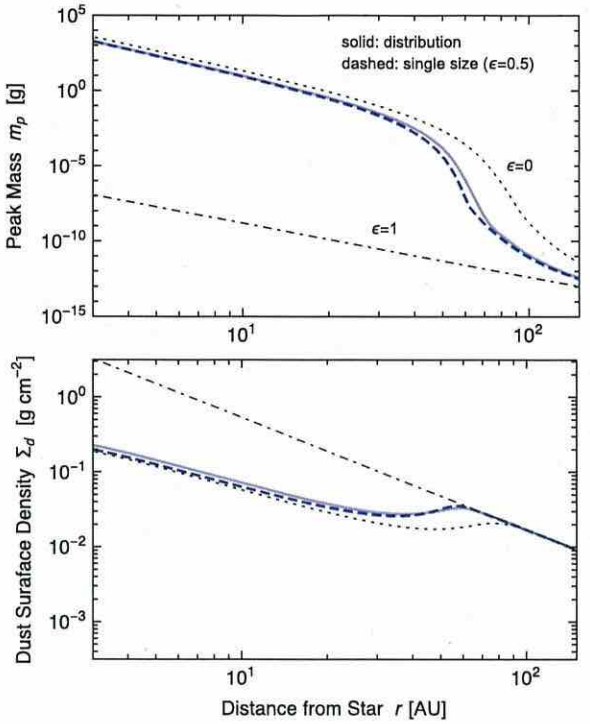

Fig. A.2. Comparison between the full-size simulation (Okuzumi et al. 2012) and single-size simulations using different values of ϵ. The solid lines show the snapshots of the peak mass m_p (Eq. (A.9); *upper panel*) and total dust surface density Σ_d (Eq. (A.8); *lower panel*) at 10^5 yr, while the dotted, dashed, and dash-dotted lines show the reproductions with $\epsilon = 0$, 0.5, and 1, respectively. The comparison shows that the single-size approach best reproduces the result of the full-size simulation when ϵ is chosen to be 0.5.

and hence Eq. (A.12) immediately reduces to Eq. (4) in the main text. Equation (A.13) reduces to

$$\frac{\partial(m_\mathrm{p}\Sigma_\mathrm{d})}{\partial t} \approx K_\mathrm{pp}\Sigma_\mathrm{d}^2 - \frac{1}{r}\frac{\partial}{\partial r}\left(r m_\mathrm{p} v_\mathrm{r}(m_\mathrm{p})\Sigma_\mathrm{d}\right), \tag{A.15}$$

where

$$K_\mathrm{pp} \equiv K(m_\mathrm{p}, m_\mathrm{p}) = \frac{2a^2}{h_\mathrm{d}(m_\mathrm{p})^2}\int_{-\infty}^{\infty}\Delta v \exp\left(-\frac{z^2}{h_\mathrm{d}(m_\mathrm{p})^2}\right)\mathrm{d}z \tag{A.16}$$

and a is the radius of peak-mass particles. If Δv can be taken outside the vertical integration, we have $K^* = 2\sqrt{\pi}a^2\Delta v/h_\mathrm{d}$. Substituting this expression into Eq. (A.15) and combining with Eq. (4), we obtain Eq. (5) in the main text.

A.2. Comparison with full-size calculations

To test the validity of the simple size approach, we attempt to reproduce the result of a full size calculation by Okuzumi et al. (2012). They calculated the evolution of the full size distribution with and without porosity evolution. We select the result of the compact aggregation model where the particle internal density is fixed to 1.4 g cm^{-3}. In accordance with Okuzumi et al. (2012), we assume the optically thin MMSN with temperature profile $T = 280(r/1\mathrm{AU})^{-1/2}$ K and compute dust evolution in the region 3 AU $< r <$ 150 AU. The particle collision velocity Δv_pp is given by Eq. (12) in Sect. 2.4. As we explained there, we introduce a free parameter ϵ to Δv_pp to account for the effect of a finite size dispersion. Below we consider three choices $\epsilon = 0$, 0.5, and 1.

Figure A.1 shows the radial distribution of the particle peak mass m_p and total dust surface density Σ_d at different times obtained from the full size calculation by Okuzumi et al. (2012, see their Fig. 2 for the corresponding snapshots of the size distribution). These are directly obtained from the data of the full size distribution together with the definitions of m_p and Σ_d, Eqs. (A.8) and (A.9). We find that the single-size calculation with $\epsilon = 0.5$ reproduces these results with reasonably good accuracy (see Fig. A.1). The agreement is particularly good for drifting pebbles (e.g., for $t = 10^5$ yr, particles at $\lesssim$60 AU) whose mass are determined by the balance between radial drift and local coagulation.

Figure A.2 demonstrates the importance of taking into account the effect of a finite size dispersion in evaluating Δv_pp. Here we compare the snapshots of the single-size calculations with different values of ϵ at $t = 10^5$ yr. We can see that the single-size calculation significantly underestimates the rate of particle evolution if the effect of size dispersion is ignored, i.e., $\epsilon = 1$. The reason is that equal-sized particles have vanishing non-Brownian relative velocities when they are so small (e.g., $a \lesssim 10^{-3}$ cm at 100 AU) that their stopping time is shorter than the turnover time of the smallest turbulent eddies (see, e.g., Ormel & Cuzzi 2007). We find that the opposite limit, $\epsilon = 0$, gives a much better agreement and the intermediate choice, $\epsilon = 0.5$, gives the best match to the full solution.

The Astrophysical Journal, 775:42 (25pp), 2013 September 20 doi:10.1088/0004-637X/775/1/42

TOWARD A DETERMINISTIC MODEL OF PLANETARY FORMATION. VII. ECCENTRICITY DISTRIBUTION OF GAS GIANTS

S. Ida[1], D. N. C. Lin[2,3], and M. Nagasawa[4]
[1] Earth-Life Science Institute, Tokyo Institute of Technology, Meguro-ku, Tokyo 152-8551, Japan; ida@geo.titech.ac.jp
[2] UCO/Lick Observatory, University of California, Santa Cruz, CA 95064, USA; lin@ucolick.org
[3] Kavli Institute for Astronomy and Astrophysics, Peking University, Beijing, China
[4] Department of Earth and Planetary Sciences, Tokyo Institute of Technology, Meguro-ku, Tokyo 152-8551, Japan; nagasawa.m.ad@m.titech.ac.jp
Received 2013 April 25; accepted 2013 July 24; published 2013 September 3

ABSTRACT

The ubiquity of planets and diversity of planetary systems reveal that planet formation encompasses many complex and competing processes. In this series of papers, we develop and upgrade a population synthesis model as a tool to identify the dominant physical effects and to calibrate the range of physical conditions. Recent planet searches have led to the discovery of many multiple-planet systems. Any theoretical models of their origins must take into account dynamical interactions between emerging protoplanets. Here, we introduce a prescription to approximate the close encounters between multiple planets. We apply this method to simulate the growth, migration, and dynamical interaction of planetary systems. Our models show that in relatively massive disks, several gas giants and rocky/icy planets emerge, migrate, and undergo dynamical instability. Secular perturbation between planets leads to orbital crossings, eccentricity excitation, and planetary ejection. In disks with modest masses, two or less gas giants form with multiple super-Earths. Orbital stability in these systems is generally maintained and they retain the kinematic structure after gas in their natal disks is depleted. These results reproduce the observed planetary mass–eccentricity and semimajor axis–eccentricity correlations. They also suggest that emerging gas giants can scatter residual cores to the outer disk regions. Subsequent in situ gas accretion onto these cores can lead to the formation of distant ($\gtrsim$30 AU) gas giants with nearly circular orbits.

Key words: planets and satellites: formation – planet–disk interactions – protoplanetary disks – stars: statistics

Online-only material: color figures

1. INTRODUCTION

The accelerating pace of observational discovery (with radial velocity, transit, microlensing, and direct imaging surveys) provide rich data sets on the statistical properties of extra solar planets and planetary systems. In order to extract from these data, useful information on the dominant physical processes and appropriate range of physical conditions associated with planetary formation and evolution, population synthesis models have been developed. In a series of papers (Ida & Lin 2004a, 2004b, 2005, 2008a, 2008b, referred to as Papers I–V), we and others (Mordasini et al. 2009a, 2009b; Alibert et al. 2011) have outlined prescriptions for various physical processes and described attempts to reproduce observational data with simulated models. Some of the relevant effects that have been taken into account so far include the coagulation of planetesimals into embryos, gas accretion onto sufficiently massive cores, and type I and II migration of individual protoplanets due to their interaction with their natal disks.

A recent transit search by the *Kepler* space telescope indicates that many, if not most, super-Earths have siblings, i.e., they are members of multiple-planet systems. In these systems, gravitational interaction between planets affects not only their formation, but also their evolution and destiny. There have been several attempts to describe the dynamical evolution of these systems with N-body simulations. Due to the time consuming nature of such approaches, only a limited range of initial parameters have been explored. It is not clear whether these models adequately represent the distribution of multiple-planet systems.

The population synthesis method is based on a statistical mechanics approach to evaluate the most likely outcome of dynamical interactions between planets. In order to describe the statistical outcome of gravitational interactions and collisions between rocky planetary embryos, we have upgraded our population synthesis method to generate a series of simulations. In Paper VI (Ida & Lin 2010), we described our analytic prescription for the collisions and close scatterings between modest-mass planets. We applied this method to show that super-Earths may be the in situ merger products of a population of embryos with Earth-mass or less which converged toward the proximity of their host stars through type I migration.

Radial velocity surveys show that modest to long-period (>7–10 days) gas giants also have significant eccentricity. These planets were most likely formed in their natal disks with nearly circular orbits as in the cases of Jupiter and Saturn (Pollack et al. 1996; Ida & Lin 2004a). Their eccentricity may have been excited by the gravitational perturbation of their planetary siblings (Rasio & Ford 1996; Zhou et al. 2007; Jurić & Tremaine 2008; Chatterjee et al. 2008). Indeed, many gas giant planets are members of known multiple-planet systems.

In order to simulate the outcome of dynamical interaction between gas giants and their siblings, including other gas giants as well as less massive protoplanetary embryos, we construct in this paper, a "multiple-planet-in-a-disk model." This approach is a natural continuation of the method presented in Paper VI. The main technical challenge is that the gravitational perturbations from gas giants significantly affect orbital configuration of the entire planetary system.

The method we have developed to approximate the evolution of systems of N gas giants is presented in Section 2. This prescription takes into account gravitational interactions between all of the planets around their common host stars. It reproduces the general results of direct N-body simulations with a

large reduction (by many orders of magnitude) in the computational cost. A detailed description of the method is given in the Appendix.

We incorporate this prescription into the latest version of the population synthesis models. In Section 3, we briefly recapitulate the methodology used in our population synthesis models including prescriptions for: (1) disk structure and evolution, (2) planetesimal growth and the planetary embryos' dynamical isolation, (3) migration due to tidal interaction between protoplanets and their natal disks, and (4) resonant interaction between protoplanets.

In Section 4, we apply these prescriptions to simulate sample multiple-planet systems. These results show that (1) the most favorable location for gas giant formation in the core-accretion scenario occurs at a few AUs, (2) the emergence of gas giants leads to the scattering of residual protoplanetary embryos, some of which may subsequently undergo gas accretion and form later-generation gas giants, (3) and that as a consequence of dynamical instability, some gas giants in multiple-planet systems may be scattered to attain the observed eccentricity distribution.

One advantage of the population synthesis model is its computational efficiency. With it, we are able to simulate, in Section 5, rich sets of planetary systems based on the observed range of disk properties. We compare the results obtained from the population synthesis models with the observational data. Our models reproduce the observed planetary mass–eccentricity and semimajor axis–eccentricity correlations. These comparisons are important not only to calibrate some uncertainties in the model parameters but also to highlight the dominant physical processes.

Finally, in Section 6, we summarize our results and discuss their implications.

2. MODELING OF ECCENTRICITY EXCITATION AND EJECTION OF GIANT PLANETS AS A RESULT OF GRAVITATIONAL INSTABILITY

The objective of this section is to introduce a simple-to-use and computationally efficient prescription to approximate the dynamical interaction between multiple planets around common host stars.

2.1. An Overview of Our Technical Approach

Before outlining the technical details of our prescription, we first qualitatively describe the principles of our analytic approximation for the gravitational interactions between several gas giants. This approach is guided by the results generated from various N-body simulations of the dynamical interaction between giant planets. Many such simulations have been carried out for the purpose of studying the statistical properties associated with close encounters between multiple planets, especially with regard to the origin of the eccentric as well as short-period Jupiter-mass planets (e.g., Rasio & Ford 1996; Weidenschilling & Marzari 1996; Ford et al. 2001; Zhou et al. 2007; Ford & Rasio 2008; Jurić & Tremaine 2008; Marzari & Weidenschilling 2002; Nagasawa et al. 2008; Chatterjee et al. 2008).

Most of the N-body experiments have been carried out with idealized initial conditions. They show that (1) the onset of dynamical instability is sensitively determined by the planets' initial normalized (in terms of their Hill's radius) separation and (2) dynamically unstable systems undergo orbit crossing and relaxation which generally lead to a Rayleigh distribution in the planets' asymptotic eccentricity (Ida & Makino 1992; Zhou et al. 2007). In order to check the validity of our prescription (to be presented below), we perform calculations with our analytic prescriptions for the same initial conditions as those adopted by the previous N-body simulations.

There are some analytic approximations for the stability of planetary systems. Two planets with masses m_1 and m_2 on initially circular orbits around a common host star with a mass M_* ($\gg m_1, m_2$) would immediately cross each other's path if the difference between their semimajor axes, Δa, is smaller than a critical value,

$$\Delta a_c \simeq 2\sqrt{3} r_H, \tag{1}$$

where a is the average of their semimajor axis and

$$r_H = ((m_1 + m_2)/3M_*)^{1/3} a \tag{2}$$

is there mutual Hill's radius. But, orbital crossings in such a system would not occur if, initially, Δa is slightly larger than Δa_c (Gladman 1993). In Section 2.2, we present a prescription to evaluate the asymptotic semimajor axis and eccentricity distributions of two-planet systems which undergo orbital crossings.

In systems with three or more gas giants, the orbit-crossing condition is significantly different. For a finite duration of time, systems with initial Δa larger than Δa_c may be maintained in a quasi-stable state with a limited variation in the amplitude of eccentricity. However, in due course, such systems may undergo a transition with a rapid eccentricity increase which is followed by orbital crossings (Chambers et al. 1996; Lin & Ida 1997; Marzari & Weidenschilling 2002; Zhou et al. 2007). The timescale, τ_{cross}, for the onset of this transition depends sensitively on the normalized initial orbital separation $\Delta a/r_H$, the planet-to-star mass ratio, and weakly on the number of planets.

In the population synthesis model (see Section 3), we consider the possibility that the giant planets and rocky/icy planetary embryos may form, coexist, and evolve contemporaneously in a gaseous environment. During advanced stages of their formation, gas giants grow through runaway gas accretion, i.e., the timescale τ_{KH} for them to double their mass M_p decreases with M_p. Their Hill's radius and the width of their feeding zone also increases with their M_p. The eccentricity of the nearby planetary siblings and residual embryos (with $\Delta a < \Delta a_c$) would be excited over their synodic periods τ_{syn} with respect to the orbits of the gas giants.

While multiple planets' eccentricity is excited by their secular interaction with each other, it is also damped by their tidal interaction with their natal disks (Artymowicz 1993; Ward 1993; Tanaka & Ward 2004). It is appropriate to take into account these competing effects (Iwasaki et al. 2002; see Section 3). Planet–disk interaction also leads to type I and II migration (for modest-mass embryos and high-mass gas giants, respectively). Idealized prescriptions for isolated planets' migration have already been incorporated into the early versions of population synthesis models (Papers I and V). In a subsequent paper, we will develop and apply a new prescription for embryos' type I migration (Paardekooper et al. 2011) and consider the feedback on the disk structure by multiple gas giants and their interference on each other's direction and speed of migration.

In this paper, we focus on the dynamical interaction between multiple gas giants. In two giant cases, the difference between their semimajor axis may be reduced during the course of their migration. The two gas giants would capture each other onto their mutual low-order mean-motion resonances, provided that

the convergent speed is slow. This effect has already been analyzed with our population synthesis models for interaction between rocky and icy embryos (Paper VI). In Section 2.2, we modify our prescription to take into the nonlinear interaction and determine the resonant capture condition between multiple gas giants. We also consider the critical converging speed above which the gas giants may overcome the resonances' barrier and intrude into each other's Hill's sphere and undergo close encounters (see Section 3.6).

The intensity of planet–disk interaction reduces with the depletion of the disk gas. Observational signatures of protostellar disks diminish on a timescale of 3–5 Myr. The accretion rate from the disk to the central stars (inferred from the UV veiling) also declines on a similar timescale (Hartmann et al. 1998). Our population synthesis models take into account disk evolution and adjust for the effects of gas accretion, eccentricity damping, and orbital migration accordingly. After the disk gas is severely depleted, both gas damping and accretion cease while secular interaction between the planets persists.

In Paper VI, we presented prescriptions for eccentricity excitations and merging events (giant impacts) among the rocky/icy planetary embryos. For these relatively low-mass objects, we construct an analytic approximation to determine the outcome of the dynamical interaction between planets based on celestial mechanics. This prescription quantitatively reproduces the results of N-body simulations. We applied this prescription to simulate the evolution of systems of 10–20 embryos with a total mass of a few $M_\oplus$. This initial condition corresponds to the advanced stage of oligarchic growth when the embryos become dynamically isolated. We showed that close encounters generally lead to a velocity dispersion, σ, which is a significant fraction of the embryos' surface escape speed (original argument was done by Safronov 1969). Within a few AUs, embryos are unlikely to be ejected because σ is smaller than the local Keplerian speed, v_K. After the gas depletion, repeated close encounters lead to mergers and the emergence of one or two Earth-mass planets with few residual embryos. Thereafter, the magnitude of $\tau_{\rm cross}$ increases beyond the main-sequence life span of solar-type stars (i.e., 10^9–10^{10} yr). We also used this prescription to show that some super-Earths may be the merger products of a population of embryos which migrated to the proximity of their host stars.

In Section 2.3 of this paper, we generalize our prescription to simulate the onset of dynamical instability and resultant orbital crossings among multiple gas giants in the outer regions of an evolving disk environment. The recoil motion excites the eccentricity of the retained planets to establish a Rayleigh's distribution similar to that observed among eccentric gas giants (Rasio & Ford 1996; Weidenschilling & Marzari 1996; Lin & Ida 1997; Marzari & Weidenschilling 2002). In contrast to the embryos close to their host stars, the surface escape speed of typical gas giants exceeds the Keplerian speed in the outer regions of their natal disks where they emerge. Close encounters with gas giants at a few AU from the host stars may lead to ejection rather than merger events.

The crossing timescale, $\tau_{\rm cross}$, increases with the semimajor axis separations and decreases with the orbital eccentricities. As the population of gas giants declines through merger and ejection events or migration and stellar consumption, their normalized semimajor axis separation, $(\Delta a/r_{\rm H})$, is enlarged. Energy dissipation during cohesive collisions also leads to eccentricity damping. These combined effects lengthen $\tau_{\rm cross}$ by several orders of magnitude after each merger or ejection event.

Recent numerical simulations show that there is a ~30% chance for orbital crossings to eventually excite one of the gas giants to attain nearly parabolic orbit by Kozai effect (Nagasawa et al. 2008).[5] The orbit of an inwardly scattered gas giant may be circularized if its pericenter distance is sufficiently close to the host star (Ivanov & Papaloizou 2004). This scenario has been suggested as one of the mechanisms for the origin of "hot Jupiters" (Rasio & Ford 1996; Nagasawa et al. 2008). We have not incorporated tidal circularization and secular perturbations, including the Kozai effect, into the current version of the population synthesis models, although the overall effects of secular eccentricity excitation is implicitly taken into account through the assumption that the orbital crossings start on timescale $\tau_{\rm cross}$.

2.2. Two Gas Giants Case

The above description qualitatively outlines the overall methodology of our population synthesis model. We now provide some technical details on its latest upgrade, i.e., the construction of an analytic plus Monte Carlo prescription.

We begin with the simplest case of dynamical interaction between two gas giants. As we have indicated above, in this case, orbit crossings are expected to occur between two planets with nearly circular coplanar orbits which are initially separated in semimajor axis by $\Delta a < \Delta a_c$. Extensive numerical simulations show that close encounters between these planets generally lead to the expansion of their semimajor axis separation and eccentricity excitation. We construct a method to compute the outcome of these close encounters. This prescription is calibrated with the statistical results generated from numerical simulations (Ford et al. 2001; Ford & Rasio 2008). Detailed prescriptions are described in Appendix A1.

The procedure of our model for two-planet encounters is structured in the following manner.

(A1) We first identify two interacting gas giants, with mass m_1 and m_2.

(A2) We compute the maximum relative eccentricity attainable during a close scattering in terms of the two-body surface escape velocity ($v_{\rm esc,12}$) scaled by the local Keplerian velocity (v_K), such that

$$e_{\rm esc,12} = \frac{v_{\rm esc,12}}{v_{\rm K}} \simeq 1.6\left(\frac{m_1+m_2}{M_{\rm J}}\right)^{1/3}\left(\frac{\rho}{1\,{\rm g\,cm^{-3}}}\right)^{1/6}\left(\frac{a}{1\,{\rm AU}}\right)^{1/2}. \quad (3)$$

A probable eccentricity is generated for individual bodies $j (j = 1, 2)$ with

$$e_j^{\rm max} = \left(\frac{m_k \mathcal{R}_j}{m_1+m_2}\right) e_{\rm esc,12}, \quad (4)$$

where $k \neq j$ refers to the perturbing companions and

$$\mathcal{R}_j(x,\sigma) = (x/\sigma^2)\exp(-x^2/2\sigma^2) \quad (5)$$

is a random number with a Rayleigh distribution of unit root mean square dispersion, σ.

[5] The frequency of close approaches to a host star during orbital crossings among planets found by Nagasawa et al. (2008) was confirmed by Beaugé & Nesvorný (2012). However, since Beaugé & Nesvorný (2012) used a formula of weaker tidal damping, they did not find as many circularized close-in giants as Nagasawa et al. (2008) found.

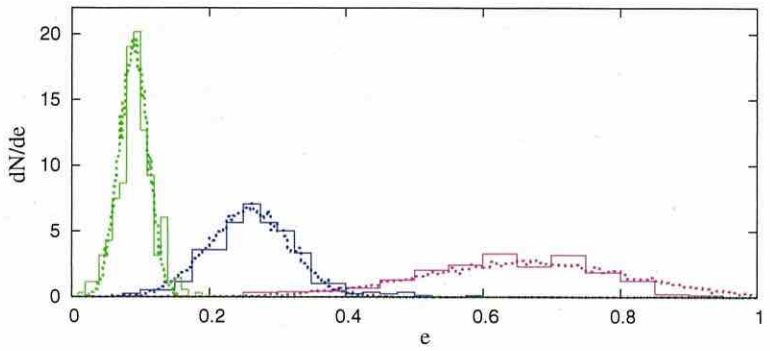

Figure 1. Dynamical instability and asymptotic properties of systems with two closely separated gas giant planets. All of the models start with two planets with a total mass $(m_1 + m_2)/M_* = 0.006$ around a common host star. Their initial orbits are nearly circular and coplanar with an unstable semimajor axis separation (i.e., $\Delta a < \Delta a_c$). In the absence of gas drag, one planet in each system is eventually ejected while the other is retained with a changed orbit. The eccentricity distributions of the retained planets are plotted for three sets of models (with $\beta = m_2/m_1 = 0.1$, 0.25, and 0.5 from left to right). The solid and dotted lines represent results obtained from our *N*-body simulations and our analytic plus Monte Carlo prescription.

(A color version of this figure is available in the online journal.)

(A3-a) If at least one of the trial eccentricities (given by Equation (4)) exceeds unity, the body with the larger eccentricity would be identified as the planet to be ejected. The remaining planet is assumed to be retained. For the remaining planet, a new eccentricity is generated (with Equations (6) and (7)) together with an associated semimajor axis (with Equation (A9)); see Section 2.2.1.

(A3-b) If the trial eccentricities of both planets are less than unity, they would be adopted as the expected values for the two planets after their close encounters with some damping (see step 3-b in Appendix A1). The associated semimajor axis changes are evaluated in accordance with the prescription in Section 2.2.2.

This procedure is applied throughout the disk evolution. Prior to severe gas depletion, the damping of eccentricity due to the planets' tidal interaction with their natal disks is taken into account. The combined effect of planet–planet scattering and planet–disk tidal interaction induce the two planets to enlarge their semimajor axis separation, Δa, until they become dynamically isolated with $\Delta a > \Delta a_c$. The efficiency of gas damping declines during gas depletion. In the absence of any significant amount of residual disk gas, two planets with $\Delta a > \Delta a_c$ would continue to scatter each other until they either merge with each other or one of them is ejected.

2.2.1. Planetary Escape after Close Encounters between Two Planets

We consider the possibility that one member of a planet pair may attain sufficient recoil velocity to escape from the gravitational potential of their host star. We compare the results generated with our analytic plus Monte Carlo prescription with those obtained from *N*-body simulations which were computed without taking into account of any eccentricity damping effect (due to either planet–disk interaction or dissipative collisions.).

Since both interacting planets were initially bound to their host stars, conservation of energy implies that at least one of them must be retained. We label the retained and ejected planets as body 1 and 2, respectively. In Appendix A1, we derived the differential distribution function of the post-scattering eccentricity of the retained body 1 as

$$f(e)de \propto \frac{1}{\sqrt{2\pi}(e^*/3)} \exp\left(-\frac{(e-e^*)^2}{2(e^*/3)^2}\right) de, \qquad (6)$$

where

$$e^* = 0.83\frac{m_2}{m_1} - 0.17\left(\frac{m_2}{m_1}\right)^2, \qquad (7)$$

and m_1 and m_2 are the masses of the retained and ejected planets, respectively. Since it takes less energy to eject the lighter body, we assume $m_1 > m_2$ which is also consistent with the results of *N*-body simulations.

In Equations (6) and (7), the eccentricity distribution function depends on the ratio rather than the individual values of m_1 and m_2. The results of numerical simulation of close encounters between two equal-mass planets (Ford & Rasio 2008) also show a negligible dependence of $\mu = m_1/M_* = m_2/M_*$ (in the range between 0.001–0.01). Note that from Equation (3), ejection cannot be produced from close encounters between planets with $\mu \ll 10^{-4}(\rho/1\,\mathrm{g\,cm^{-3}})^{-1/2}(a/1\,\mathrm{AU})^{-3/2}$.

In order to verify the validity of the analytic plus Monte Carlo prescription, we compare the results it generated and those obtained from a series of *N*-body simulations with a set of similar initial conditions as those presented by Ford & Rasio (2008). In all of these models, we consider the interaction between two planets with small initial eccentricities and inclinations. We set their initial semimajor axis to be $a_1 = 1$ and a_2 is randomly specified to be in the range of $[0.9(1 + \Delta a_c), (1 + \Delta a_c)]$ so that they generally undergo orbital crossings.

We consider three series with $\beta = m_1/m_2 = 0.1$, 0.25, and 0.5. In all cases, $(m_1 + m_2)/M_* = 0.006$. For each value of β, we carried out ~300 *N*-body simulations with different random number seeds for initial relative orbital phases between the two planets. In the absence of gas drag, one planet is eventually ejected. The differential eccentricity distribution function of the retained planet is represented by the solid lines in Figure 1. For the cases with $\beta = m_1/m_2 = 0.1$ and 0.25, the more massive planet 2 is generally retained. But, this mass preference is reduced for the $\beta = 0.5$ cases.

We also adopted the analytic plus Monte Carlo prescription to generated 10^4 models for the same sets of β values with the distribution in Equations (6) and (7). The results of the Monte Carlo calculations are represented by the dotted lines in Figure 1. They are in good agreement with those of the *N*-body simulations.

Depending on the difference between their semimajor axes, two planet systems either rapidly undergo orbital crossings (if

$\Delta a < \Delta a_c$) or completely avoid close encounters. Some systems may evolve into unstable states through disk migration (which leads to a reduction in Δa) or gas accretion (which widens Δa_c). In their natal disks, the eccentricities of gas giants are also damped. In our population synthesis simulations, we include the effect of eccentricity damping for the retained planet. The efficiency of this effect depends on the mass ratio between the planet and local disk (see Appendix A1).

Finally, the semimajor axis of the retained planet (a_1) is obtained from the conservation of energy, such that

$$\frac{m_1}{a_1} = \frac{m_1}{a_{1,0}} + \frac{m_2}{a_{2,0}}, \tag{8}$$

where $a_{j,0}$ is the semimajor axis before scattering. For computational simplicity, we neglect (1) the decrease in the semimajor axis change associated with the eccentricity damping of the retained planet and (2) the finite kinetic energy of the ejected planet.

2.2.2. Retention of both Gas Giants after Close Encounters between Them

If the trial eccentricities (generated at step 3) of both planets are less than unity, they would both be adopted as the asymptotic values. The effect of the eccentricity damping due to the post-encounter disk–planet interactions is applied to both planets with the same prescription as that described in the previous section (i.e., in Section 2.2.1). In Section 5.4, we also discuss the eccentricity damping due to disk gas accretion onto a planet.

Close encounters launch both planets into eccentric orbits from nearly circular initial orbits through changes in their energy and semimajor axis. We assume that a less massive body (represented by the subscript "2") is always scattered outward such that its semimajor axis prior to the close encounter, $a_{2,0}$, becomes its new periastron distance, such that

$$a_2 = \frac{a_{2,0}}{1 - e_2}. \tag{9}$$

The new semimajor axis of the inwardly scattered planet (a_1) is given by the energy conservation such that

$$\frac{m_1}{a_1} = \frac{m_1}{a_{1,0}} + \frac{m_2}{a_{2,0}} - \frac{m_2}{a_2}. \tag{10}$$

2.3. Three Gas Giants Case

In contrast to the stability criterion in Equation (1) for two planet systems, three planet systems may maintain relatively low-eccentricity states until gas in their natal disk is severely depleted and then undergo close encounters after a timescale, $\tau_{\rm cross}$. The magnitude of $\tau_{\rm cross}$ is a sensitive function of their initial separation in semimajor axis Δa.

In order to develop an easy-to-use and robust prescription for close encounters among three planets, we consider the situation that $\tau_{\rm cross}$ is smaller than the expected main-sequence lifespan of their host stars. In these systems, eccentricities of the planets are always excited during the close encounters. Since these events take place in the absence of residual gas drag, the planets' excited eccentricity can only be damped through (1) dissipative merger events, (2) tidal dissipation in the proximity of their host stars, or (3) dynamical friction by a residual population of planetesimals. In this paper, we neglect the effect of the tidal dissipation and residual planetesimals.

Following a similar procedure from the previous section, we construct an analytic plus Monte Carlo prescription for the outcomes of close encounters and compare it with the result generated from N-body simulations of three-giant-planet systems which undergo orbital crossings in a gas-free environment (Marzari & Weidenschilling 2002; Nagasawa et al. 2008; Chatterjee et al. 2008). In this case, two or more planets ensure repeated encounters with a range of impact parameters. Physical collisions occur when the impact parameter is less than the sum of the planets' radii. Such merger events reduce the number of residual planets bound to the host star and consequently, stabilize the remaining systems.

Slightly wider scatterings, with impact parameter marginally larger than the sum of the planets' radii, lead to recoil velocities comparable to their surface escape speed. At a distance of several AU from their solar-type host stars, such strong orbital deflection generally leads to the escape of one planet from the gravitational potential of the host star. The remaining two planets are retained with modest to high eccentricities and widely separated semimajor axes such that the residual systems are stabilized.

We present below our analytic plus Monte Carlo prescriptions for the outcomes of close encounters in three-planet systems. Based on N-body simulations, we assume that this intense interaction leads to (1) mostly the ejection of one planet and (2) a significant fractional (~30%) incidents of physical collisions and merger events. In both outcomes, the residual systems are left with two remaining planets. The main objective of our prescription is to evaluate the asymptotic eccentricities and semimajor axes of these two retained planets.

We justify the validity of our prescription based on the direct comparison of our results with those generated from the N-body simulations. The technical procedure essentially follows that constructed for the two-planet case in Section 2.2, with some modifications applied to the inwardly and outwardly scattered retained planets. Their detailed description and physical justification are given in Appendix A2. We outline the following basic steps.

(B1) We first set initial conditions of the three giants and assign the identity of the most massive planet to be $j = 1$.

(B2-a) We assign a probability (30%) that two planets physically collide and merge with each other (assumed to always occur after each collision). A merged planet is formed from a randomly selected pair of planets which are involved in the orbital crossings. Its resultant semimajor axis and eccentricity are calculated under the assumed conservation of total mass, orbital energy, and angular momentum.

(B2-b) We also assign a probability (70%) that one of the three planets is ejected while the other two residual planets are retained.

For the ejection events,

(B3) we compute the maximum eccentricity, $e_j^{\rm max}$, for all three ($j = 1, 2, 3$) planets, in accordance with the procedure described in step 2 in Appendix A2. The magnitude, $e_j^{\rm max}$, of the most massive body tends to be less than those of the other bodies.

(B4) We select the planet with the largest value of $e_j^{\rm max}$ to be the ejector.

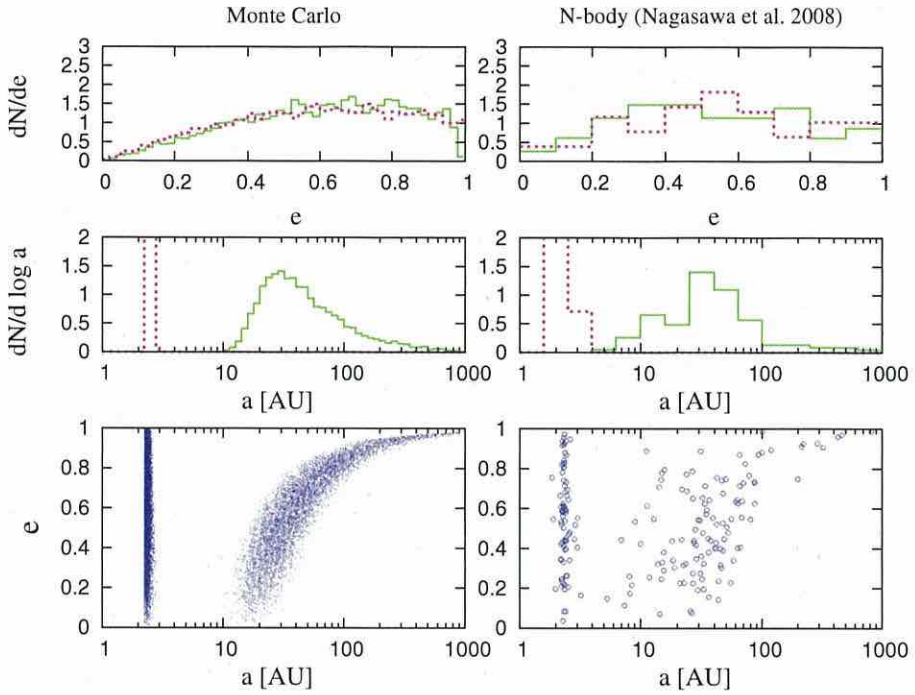

Figure 2. Eccentricity and semimajor axis distributions of surviving planets in the case of three Jupiter-mass planets with $a_1 = 5$ AU, $a_2 = 7.25$ AU, $a_3 = 9$ AU, and $e = 0$, initially. The dotted and solid lines represent the distributions of inner and outer planets in the top and middle panels. The left panels show the results of 10^4 models generated with our analytic plus Monte Carlo prescription and the right panels are the results of 75 models obtained from Nagasawa et al.'s (2008) *N*-body simulations.

(A color version of this figure is available in the online journal.)

(B5) We determine asymptotic eccentricities of the two retained planets to be

$$e_j = \begin{cases} \left(\frac{m_1+m_{\rm ejc}}{m_1+m_j}\right)^{1/2} \left(\frac{R_1+R_{\rm ejc}}{R_1+R_j}\right)^{1/2} \mathcal{R}_j & (\text{for } j \neq 1), \\ \left(\frac{m_2}{m_1}\right) \left(\frac{m_1+m_{\rm ejc}}{m_1+m_2}\right)^{1/2} \left(\frac{R_1+R_{\rm ejc}}{R_1+R_2}\right)^{1/2} \mathcal{R}_j & (\text{for } j = 1). \end{cases} \quad (11)$$

where R_j is the physical radius of planet j and $\mathcal{R}_j$ is a random number following a Rayleigh distribution of unit root mean square. The above expression is similar to that in Equation (4) with the consideration of incomplete stirring (see Appendix A2 for justification).

(B6) Among the two retained planets, we select the inwardly scattered body with a probability distribution function which is weighted by the square of their masses.

(B7) Based on the nature of close scattering, the new semimajor axis of the outwardly scattered body is prescribed to be

$$a_{\rm out}(1 - e_{\rm out}) = \sqrt{a_{\rm max} a_{\rm min}} + a_{\rm max} \mathcal{R}_j, \quad (12)$$

where $e_{\rm out}$ is the excited eccentricity of the outer planet, and $a_{\rm max}$ and $a_{\rm min}$ are the maximum and minimum semimajor axes of the three planets in their initial state prior to orbital crossings.

(B8) The semimajor axis of the inwardly scattered body is determined by

$$\frac{m_{\rm in}}{a_{\rm in}} = E - \frac{m_{\rm out}}{a_{\rm out}}, \quad (13)$$

where $m_{\rm in}$ is the mass of the inner planet and E is the total energy calculated from the initial semimajor axes of the three planets.

In order to compare the results of our prescription with those obtained from previous *N*-body simulations, we adopt a set of models with three planets in nearly circular and coplanar orbits as initial conditions in step B1. For these test cases, we consider the situation that orbital crossings have already been initiated after a timescale of $\sim \tau_{\rm cross}$ has elapsed, so that the initial orbital separations are arbitrarily set. In the actual population synthesis simulations, $\tau_{\rm cross}$ is calculated and compared with the system time at each timestep (see Appendix A3).

The comparison of our prescribed method and *N*-body simulations is shown in Figure 2 where we illustrate the eccentricity and semimajor axis distributions of the surviving planets for a test case with three Jupiter-mass planets ($m_1 = m_2 = m_3 = M_J$). We adopt a set of initial conditions with $a_1 = 5$ AU, $a_2 = 7.25$ AU, $a_3 = 9$ AU, and $e = 0$, in accordance with some existing *N*-body simulations by Marzari & Weidenschilling (2002) and Nagasawa et al. (2008; their set N without tidal damping).

The left panels show the results of 10^4 models generated with our analytic plus Monte Carlo prescription and the right panels illustrate the results of 75 models of Nagasawa et al.'s (2008) *N*-body simulations. The initial orbital phase distributions of planets are modified in each of the *N*-body simulations. In the analytic plus Monte Carlo simulations, the seed for random number ($\mathcal{R}$) generation to determine eccentricity is changed in each simulation.

The *N*-body simulations are carried out in three dimensions, i.e., the orbital inclinations of each planet are also calculated. In our analytic plus Monte Carlo simulations, although the planets'

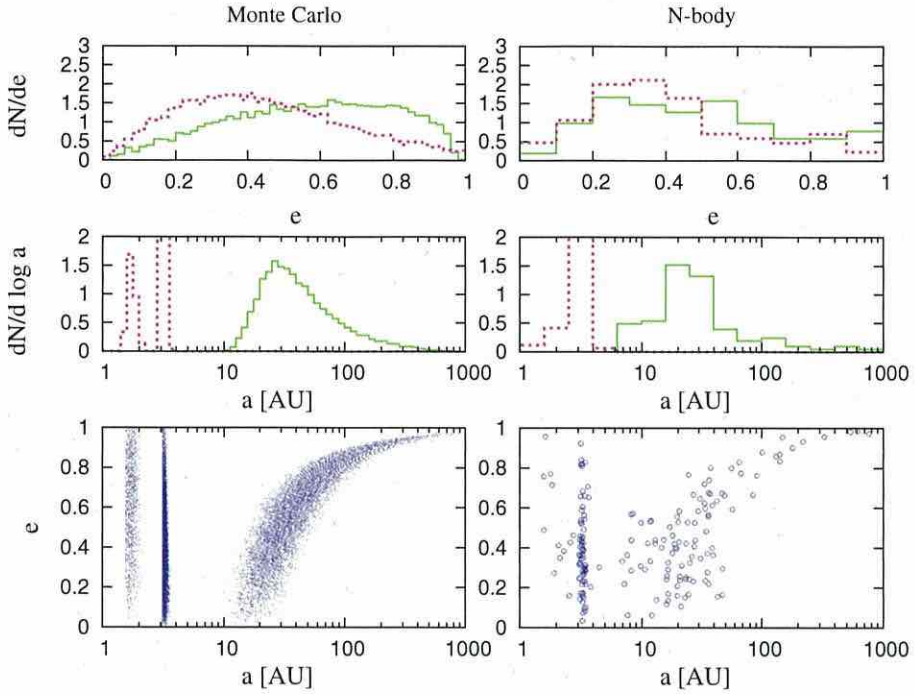

Figure 3. Eccentricity and semimajor axis distributions of the retained planets in the case of $m_1 = 2M_J$, $m_2 = m_3 = M_J$. All other initial conditions are the same as those in Figure 2.

(A color version of this figure is available in the online journal.)

inclinations are not explicitly computed, their distributions can be evaluated by i (in radian) $\sim e/2$ (Nagasawa et al. 2008).

In this equal-mass example, the top panel of Figure 2 shows that the analytic plus Monte Carlo prescription produces a broad differential eccentricity distribution which is similar for the inner and outer planets. We prescribed (in step B5) a Rayleigh's distribution through ($\mathcal{R}_j$) which has the form $f(e)de = 2e\exp(-e^2)de$ (see Equation (11)). The peak of this distribution function occurs at $1/\sqrt{2} \simeq 0.71$.

The middle panel of Figure 2 shows a bimodal semimajor axis distribution because inwardly scattered planets are generally well separated from outwardly scattered planets. The middle panel of Figure 2 shows a correlation between semimajor axis (a) and eccentricity (e) of the outwardly scattered planets. This correlation arises because we assume (in step B7) that these planets are scattered from the region near the initial locations and their periastron radii are close to their original semimajor axes, despite some outward diffusion before the scattering (see Appendix A2). These results are all consistent with the results obtained by the previous N-body simulations.

Marzari & Weidenschilling (2002) also carried out simulations with $m_1 = 2M_J$ and $m_2 = m_3 = M_J$. They found that in 54 of 64 runs (corresponds to ~84% probability), the more massive planet (with $m_1 = 2M_J$) is scattered inward and the inner retained planets have a broad eccentricity distribution peaked around $e \sim 0.3$. Here, we carry out a similar simulation with the analytic plus Monte Carlo prescription to generate 10^4 models. These results show that the massive planet is scattered inward in 8382 models (~83.8%) with a peak eccentricity of $1/2\sqrt{2} \simeq 0.36$ (in accordance with Equation (11)).

For comparison purposes, we also simulated 100 N-body models. For the massive planets' inward scattering probability and their average peak eccentricities, the results obtained with the analytic plus Monte Carlo prescription are almost consistent with those generated with the N-body simulation, which provides support for the validity of the mass-weighted probability function we have assumed. The middle panel in Figure 3 shows two sharp peaks in the semimajor axis distribution for the inwardly scattered planets. These peaks are also found in the N-body simulations. They are generated from the requirement for energy conservation such that

$$\frac{m_{\rm in}}{a_{\rm in}} \sim \frac{2M_J}{5\,{\rm AU}} + \frac{M_J}{7.25\,{\rm AU}} + \frac{M_J}{9\,{\rm AU}}. \quad (14)$$

If the inner planet has a mass $m_{\rm in} = M_J$, then $a_{\rm in} \simeq 1.54$ AU, whereas $a_{\rm in} \simeq 3.08$ AU if $m_{\rm in} = 2M_J$.

2.4. General Case

In the population synthesis simulations, multiple giant planets and rocky/icy planetary embryos coexist. Here, we describe a summary of the prescriptions for dynamical interactions in the general case.

During the early stages of their dynamical evolution, newly formed planets are embedded in and interact with their natal disks. In the presence of the disk gas, we only consider scattering between two planets when their orbital separation, Δa, becomes less than the critical value $\Delta a_c \simeq 2\sqrt{3}r_H$ with the prescription given in Section 2.2.

We calculate the planets' eccentricity damping timescale ($\tau_{\rm damp}$), due to their gravitational interaction with the residual disk, and the orbit-crossing timescale ($\tau_{\rm cross}$) for all pairs of existing planets in a gas-free environment. As the disk gas is depleted, $\tau_{\rm damp}$ eventually becomes larger than $\tau_{\rm cross}$ and the

planets' eccentricity grows due to secular excitation (Iwasaki et al. 2002). It then becomes possible for planets with initial separation greater than $\Delta a_c \simeq 2\sqrt{3} r_H$ to cross each other's orbits.

Orbital crossings and close encounters among gas giants strongly affect the asymptotic global structure of planetary systems. The gas giants' eccentricities are highly excited during their orbital crossings. The order of their semimajor axis is occasionally swapped. Their secular resonances may sweep across the entire system multiple times. Most of the residual small planets are either ejected or collide with their host stars (Matsumura et al. 2013).

For the evaluation on the outcome of planetary scattering after the severe disk-gas depletion, we apply the following prescription. The details are presented in Appendix A3. Note that the order of the prescription presented in this section is different from those in Appendix A3, for the purpose of easier understanding.

(C1) We identify the "giant planets" from a list of all the planets in the system with the criteria that they have (1) a mass $m > 30\,M_\oplus$ and (2) $e_{esc} > 1$ (Equation (A15)).

(C2-a) We apply the procedures for orbital crossings among the small planets (as outlined in Paper VI) if there is only one (or less) giant planet.

(C2-b) In systems with two (and only two) widely separated (with $\Delta a > \Delta a_c$) giant planets, they retain their initial kinematic properties (because they do not significantly perturb each other). Their dynamical influence on the less massive planets is computed independently, following the procedures in step C2.

(C2-c) In systems with two (and only two) closely separated (with $\Delta a < \Delta a_c$) giant planets, the outcome of their dynamical interaction is computed following steps A2–A3 in Section 2.2. We also remove all the small planets under the assumption that they are ejected by the gas giants' sweeping secular resonances.

(C2-d) In systems with 3 or more giant planets around the same host stars, we first evaluate τ_{cross} for all pairs. For this case,

(C3-a) if τ_{cross} for all giant planet pairs is longer than the system time (τ_{sys}), we would neglect any interaction between them and compute their influence on the low-mass planets following step C2-a.

(C3-b) If τ_{cross} for one or more pairs of giant planets is less than τ_{sys} but there are no triples (overlapping pairs) with $\tau_{cross} < \tau_{sys}$, we would determine the outcome of interaction between the giant planets following step C2-b or C2-c.

(C3-c) Any groups of three giant planets around the same host stars would be labeled as interacting triples if $\tau_{cross} < \tau_{sys}$ for at least two planet pairs. In this case, we follow steps B2–B8 for the triple giants interaction case (see Section 2.3). All of the small planets would be removed under the assumption that they are ejected by the triple giants' sweeping secular resonances.

(C4) After the kinematic properties of interacting triple systems are modified to a set of new configurations in the previous step, we re-calculate the τ_{cross} for each pair of giant planets. Steps C2–C3 are repeated until either (1) there are only two giant planets remaining around the host stars or (2) when $\tau_{sys} + \tau_{cross} > 10^9$ yr.

(C2-e) For systems with more than three giant planets, we follow the same procedure as C3-a and C4 and eject all of the small planets. But, we let only one giant planet be scattered inward and all other giant planets are assumed to be scattered outward.

3. PRESCRIPTIONS OF OTHER PHYSICAL PROCESSES IN THE POPULATION SYNTHESIS MODELS

We follow Paper VI for prescriptions of (1) planetesimals' growth through cohesive collisions, (2) the evolution of planetesimal surface density, (3) embryos' type I migration, and their stoppage at the disk inner edge. For the gas giants, (4) the onset, rate, and termination (through gap opening or and global depletion) of efficient gas accretion, and (5) their type II migration, we follow prescriptions in Paper IV, except for a slight modification on gas accretion termination due to global depletion. Here we present a brief summary.

3.1. Disk Models

We adopt the minimum mass solar nebula (MMSN) model (Hayashi 1981) as a fiducial set of initial conditions for planetesimal surface density (Σ_d) and introduce a multiplicative factor (f_d). For gas surface density Σ_g, although we adopt the r-dependence of steady accretion disk with constant α viscosity ($\Sigma_g \propto r^{-1}$), rather than that of the original MMSN model ($\Sigma_g \propto r^{-1.5}$), we scale Σ_g by that of the MMSN at 10 AU with a scaling factor (f_g). Following Paper IV, we set

$$\begin{cases} \Sigma_d = \Sigma_{d,10}\eta_{ice} f_d (r/10\,\mathrm{AU})^{-1.5}, \\ \Sigma_g = \Sigma_{g,10} f_g (r/10\,\mathrm{AU})^{-1}, \end{cases} \quad (15)$$

where normalization factors $\Sigma_{d,10} = 0.32$ g cm^{-2} and $\Sigma_{g,10} = 75$ g cm^{-2} correspond to 1.4 times of Σ_g and Σ_d at 10 AU of the MMSN model, and the step function $\eta_{ice} = 1$ inside the ice line at a_{ice} (Equation (17)) and 4.2 for $r > a_{ice}$ (the latter can be slightly smaller (~2–3); Pollack et al. 1994). We specify an inner disk boundary where Σ_g vanishes and planetesimals' type I migration is arrested (see Section 3.5).

Neglecting the detailed energy balance in the disk (Chiang & Goldreich 1997; Garaud & Lin 2007), we adopt the equilibrium temperature distribution of optically thin disks prescribed by Hayashi (1981) such that

$$T = 280 \left(\frac{r}{1\,\mathrm{AU}}\right)^{-1/2} \left(\frac{L_*}{L_\odot}\right)^{1/4} \mathrm{K}, \quad (16)$$

where L_* and $L_\odot$ are stellar and solar luminosity. We set the ice line to be that determined by an equilibrium temperature (Equation (16)) in optically thin disk regions,

$$a_{ice} = 2.7 (L_*/L_\odot)^{1/2}\,\mathrm{AU}. \quad (17)$$

The effects of evolution of the disk temperature and associated migration of the ice line adopting more realistic thermal disk structure (Garaud & Lin 2007; Oka et al. 2011; Min et al. 2011) will be studied in a subsequent paper.

Dependence of disk metallicity is attributed to the distribution of $f_{d,0} = f_{g,0} 10^{[Fe/H]_d}$, where $f_{d,0}$ and $f_{g,0}$ are initial values of f_d and f_g, respectively. Due to viscous diffusion and photoevaporation, f_g decreases with time. For simplicity, we adopt

$$f_g = f_{g,0} \exp(-t/\tau_{dep}), \quad (18)$$

where $\tau_{\rm dep}$ is disk lifetime (for detailed discussion, see Paper IV). The constant α self-similar solution obtained by Lynden-Bell & Pringle (1974) is expressed by $\Sigma_g \propto r^{-1}$ with an asymptotic exponential cut-off at radius $r_{\rm m}$ of the maximum viscous couple. In the region at $r < r_{\rm m}$, Σ_g decreases uniformly independent of r as the exponential decay does, although the time dependence is different. In the self-similar solution, Σ_g at $r < r_{\rm m}$ decays as $\Sigma_g \propto (t/\tau_{\rm dep}+1)^{-3/2}$. In the exponential decay model that we adopt, Σ_g decays more rapidly as $t/\tau_{\rm dep}$ becomes larger at $t > \tau_{\rm dep}$. If the effect of photoevaporation is taken into account, Σ_g decays rapidly after it is significantly depleted, so that the exponential decay partially mimics the effect of photoevaporation. However, the final planet distributions hardly depend on whether $\Sigma_g \propto (t/\tau_{\rm dep}+1)^{-3/2}$ or $\Sigma_g \propto \exp(-t/\tau_{\rm dep})$. The parameter values of $f_{g,0}$, $\tau_{\rm dep}$, and [Fe/H] are specified for each run.

3.2. From Oligarchic Growth to Isolation

On the basis of the oligarchic growth model (Kokubo & Ida 1998, 2002), the growth rate of embryos/cores at any location, a, and time, t, in the presence of disk gas, is described by $dM_{\rm c}/dt = M_{\rm c}/\tau_{\rm c,acc}$ where, after correcting some typos in Paper IV,

$$\tau_{\rm c,acc} = 3.5\times10^5 \eta_{\rm ice}^{-1} f_d^{-1} f_{\rm g}^{-2/5} \left(\frac{a}{1\,{\rm AU}}\right)^{5/2} \times \left(\frac{M_{\rm c}}{M_\oplus}\right)^{1/3} \left(\frac{M_*}{M_\odot}\right)^{-1/6} {\rm yr}, \quad (19)$$

where $M_{\rm c}$ is the mass of the embryo (core), and we set the mass of the typical field planetesimals to be $m = 10^{20}$ g.

If type I migration is not effective, embryos would form through oligarchic growth and attain a local isolation mass, $M_{\rm c,iso} = 2\pi r \Sigma_d \Delta a_{\rm c}$, where the full width of the feeding zone of an embryo with a mass $M_{\rm c}$ is given by (Kokubo & Ida 1998, 2002)

$$\Delta a_{\rm c} \simeq 10 r_{\rm H} = 10\left(\frac{2M_{\rm c}}{3M_*}\right)^{1/3} a, \quad (20)$$

and $r_{\rm H}$ is the Hill radius for two bodies with comparable masses. From Equations (15) and (20) we find

$$M_{\rm c,iso} \simeq 0.16 \eta_{\rm ice}^{3/2} f_d^{3/2} \left(\frac{a}{1\,{\rm AU}}\right)^{3/4} \left(\frac{M_*}{M_\odot}\right)^{-1/2} M_\oplus. \quad (21)$$

However, type I migration may induce embryos to migrate before they acquire all of the residual planetesimals within their feeding zone and acquire their isolation mass. Type I migration may also be stalled near some trapping radius. At these locations, the congregation of planetesimals may increase the magnitude of Σ_d and enlarge the magnitude of $M_{\rm c,iso}$.

We compute the evolution of Σ_d distribution due to accretion by all of the emerging embryos in a self-consistent manner. The growth and migration of many planets are integrated simultaneously with the evolution of the Σ_d-distribution. We set up linear grids for f_d across the disk with typical width of $\sim10^{-3}$ AU. We introduce a population of seed embryos, all with an initial mass of 10^{20} g (i.e., that of the residual planetesimals) and compute their mass accretion rate. In the inner disk region, we set their initial separation of the full feeding-zone width ($\Delta a_{\rm c} = 10 r_{\rm H}$) of embryos with local asymptotic isolation mass, $M_{\rm c,iso}$.

The planetesimals' growth timescale increases rapidly with their distance from the central stars, and embryos in the outer disk region of the disk are unlikely to attain a local isolation mass within the life span of their host stars. There, we place seed embryos which are separated by feeding-zone width of embryos with masses evaluated (using Equation (19)) for the local Σ_d after $t \sim 1$ Gyr. We follow the growth of the seed embryos due to planetesimal accretion in accordance with Equations (19) and (20). The planetesimals' mass accreted by the embryos is uniformly subtracted within the embryos' current feeding zone. We follow the evolution of Σ_d throughout the disk and use its values to evaluate embryos' local accretion rates. We also use $\Sigma_d(r,t)$ to estimate the strength of planetesimals' dynamical friction on the embryos.

During the early phase of evolution, embryos are embedded in their natal disks. Despite their mutual gravitational perturbation, the embryos preserve their circular orbits due to the gravitational drag from disk gas (Artymowicz 1993; Ward 1993) and dynamical friction from the residual planetesimals (e.g., Stewart & Ida 2000). However, after the disk gas is severely depleted, the efficiency of eccentricity damping mechanism is reduced. The embryos' eccentricity grow until they cross each others' orbits. We use the prescription in Paper VI and Appendix A3 to compute the occurrence and consequence of giant impacts between embryos.

3.3. Type I Migration

Type I migration of an embryo is caused by the sum of tidal torque from the disk regions both interior and exterior to the embryos. The rate and direction of embryos' migration are determined by the differential Lindblad and corotation torques. While a conventional formula of type I migration, assuming locally isothermal disks (e.g., Tanaka et al. 2002), shows that the migration is always inward, recent developments of type I migration of isolated embryos in non-isothermal disks (e.g., Paardekooper et al. 2011) show the magnitude and sign of the tidal torque, especially that due to corotation resonances is a sensitive function of the surface density and temperature distribution of the disk gas.

Since the properties of migration depend on detailed thermal/dynamical structure of disks and "saturation" degree of the corotation torque (e.g., Kretke & Lin 2012), substantial discussions are required for the effects of type I migration in non-isothermal disks. The pace of individual embryos' type I migration in dense multiple-planet systems remains uncertain because mutual perturbation between nearest neighbors may modify their Lindblad and especially corotation torque. On the other hand, as shown below, the eccentricity distributions that we are primarily interested in here are not sensitive to a change in the formula of type I migration. Thereby, in order to highlight the validity of our treatment of dynamical interaction between multiple planets in this paper, we postpone the detailed discussions on the non-isothermal type I migration to a subsequent paper. While we also show a result with a non-isothermal formula, in most of the results we present here, we use a conventional formula of type I migration in isothermal disks derived by Tanaka et al. (2002) with a scaling factor C_1:

$$\tau_{\rm mig1} = \frac{a}{\dot a} = \frac{1}{C_1}\frac{1}{3.81}\left(\frac{c_s}{a\Omega_{\rm K}}\right)^2 \frac{M_*}{M_p}\frac{M_*}{a^2\Sigma_g}\Omega_{\rm K}^{-1} \simeq 1.5\times10^5 \times \frac{1}{C_1 f_g}\left(\frac{M_{\rm c}}{M_\oplus}\right)^{-1}\left(\frac{a}{1\,{\rm AU}}\right)\left(\frac{M_*}{M_\odot}\right)^{3/2} {\rm yr}. \quad (22)$$

The expression of Tanaka et al. (2002) corresponds to $C_1 = 1$, and for slower migration, $C_1 < 1$. We study a dependence of the eccentricity distribution by changing a value of C_1, rather than using variations of non-isothermal formula.

We assume type I migration ceases inside the inner boundary of the disk, because f_g is locally zero there. For computational convenience, we set the disk inner boundary to be the edge of the magnetospheric cavity at ~0.04 AU.

3.4. Formation of Gas Giant Planets

Prescriptions for formation of gas giant planets are the same as those used in Paper IV, except for slight modification for reduction and termination of gas infall. Embryos are surrounded by gaseous envelopes when their surface escape velocity becomes larger than the sound speed of the surrounding disk gas. When their mass grow (through planetesimal bombardment) above a critical mass

$$M_{\rm c,hydro} \simeq 10 \left(\frac{\dot{M}_{\rm c}}{10^{-6}\, M_\oplus\ {\rm yr}^{-1}} \right)^{0.25} M_\oplus, \quad (23)$$

both the radiative and convective transport of heat become sufficiently efficient to allow their envelope to contract dynamically (Ikoma et al. 2000).

In the above equation, we neglected the dependence on the opacity in the envelope (see Paper I and Hori & Ikoma 2010). In regions where the cores have already acquired isolation mass, their planetesimal-accretion rate, $\dot{M}_{\rm c}$, would be much diminished (Ikoma et al. 2000; Zhou et al. 2007) and $M_{\rm c,hydro}$ can be comparable to an Earth-mass, $M_\oplus$. But, gas accretion also releases energy and its rate is still regulated by the efficiency of radiative transfer in the envelope such that

$$\frac{dM_p}{dt} \simeq \frac{M_p}{\tau_{\rm KH}}, \quad (24)$$

where $M_{\rm p}$ is the planet mass including gas envelope.

In Paper I, we approximated the Kelvin–Helmholtz contraction timescale, $\tau_{\rm KH}$, of the envelope with

$$\tau_{\rm KH} \simeq \tau_{\rm KH1} \left(\frac{M_p}{M_\oplus} \right)^{-k2}, \quad (25)$$

where $\tau_{\rm KH1}$ is the contraction timescale for $M_p = M_\oplus$. Since there are uncertainties associated with dust sedimentation and opacity in the envelope (Pollack et al. 1996; Helled et al. 2008; Hori & Ikoma 2011), we adopt a range of values, $\tau_{\rm KH1} = 10^8$–10^{10} yr and $k2 = 3$–4. Here we fix $k2 = 3$ and change $\tau_{\rm KH1}$ (in a nominal case, we use $\tau_{\rm KH1} = 10^9$ yr).

Equation (24) shows that $dM_{\rm p}/dt$ rapidly increases as M_p grows. But, it is limited by the global gas accretion rate throughout the disk and by the process of gap formation near the protoplanets' orbits. The disk accretion rate is

$$\dot{M}_{\rm disk} \simeq 3\pi \Sigma_g \nu \simeq 3 \times 10^{-9} f_g \left(\frac{\alpha}{10^{-3}} \right) \ [M_\odot\ {\rm yr}^{-1}], \quad (26)$$

where α is a parameter of alpha prescription for turbulent viscosity (Shakura & Sunyaev 1973). During the advanced stage of disk evolution, we assume both $\dot{M}_{\rm disk}$ and Σ_g evolve $\propto \exp(-t/\tau_{\rm dep})$, where $\tau_{\rm dep}$ is the gas depletion timescale. The rate of accretion onto the cores cannot exceed $\dot{M}_{\rm disk}$.

An (at least partial) gap is formed when the planets' tidal torque exceeds the disk's intrinsic viscous stress (Lin & Papaloizou 1985). This viscous condition for gap formation is satisfied for planets with

$$M_p > M_{\rm g,vis} \simeq 30 \left(\frac{\alpha}{10^{-3}} \right) \left(\frac{a}{1\ {\rm AU}} \right)^{1/2} \left(\frac{L_*}{L_\odot} \right)^{1/4} M_\oplus. \quad (27)$$

Then, type I migration is switched to type II migration. Fluid dynamical simulations (e.g., D'Angelo et al. 2003; D'Angelo & Lubow 2008) show that some faction of gas still flows into the gap. According to this, we allow a protoplanet to continue accreting the residual gas which flows past it, as shown below. These fluid dynamical simulations, however, also show that the accretion rate rapidly decreases with M_p after M_p exceeds a Jupiter mass. According to this result and the analysis by Dobbs-Dixon et al. (2007), we completely terminate gas accretion, when the planet's Hill radius ($r_{\rm H}$) becomes larger than two times the disk scale height (H), which corresponds to the (extended) thermal condition (Lin & Papaloizou 1985), that is,

$$M_p > M_{\rm g,th} \simeq 0.95 \times 10^3 \left(\frac{a}{1\ {\rm AU}} \right)^{3/4} \left(\frac{L_*}{L_\odot} \right)^{3/8} \left(\frac{M_*}{M_\odot} \right)^{-1/2} M_\oplus. \quad (28)$$

In general, our prescriptions for gas accretion rates onto the cores are

$$\frac{dM_p}{dt} = f_{\rm gap} \dot{M}_{p,\rm nogap}, \quad (29)$$

where $\dot{M}_{p,\rm nogap}$ is that in the absence of any feedback on the disk structure, i.e., that without the effect of gap opening,

$$\dot{M}_{p,\rm nogap} = \min \left(\frac{M_{\rm p}}{\tau_{\rm KH}}, \dot{M}_{\rm disk} \right), \quad (30)$$

and $f_{\rm gap}$ is a reduction factor due to gap opening,

$$f_{\rm gap} = \begin{cases} 1 & [\text{for } M_p < M_{\rm g,vis}] \\ \dfrac{\log M_p - \log M_{\rm g,vis}}{\log M_{\rm g,th} - \log M_{\rm g,vis}} & [\text{for } M_{\rm g,vis} < M_p < M_{\rm g,th}] \\ 0 & [\text{for } M_p > M_{\rm g,th}]. \end{cases} \quad (31)$$

The formula for $M_{\rm g,vis} < M_p < M_{\rm g,th}$ is constructed to avoid any abrupt truncation.

In Papers I–III, we incorporated the effect of the global depletion by setting a limiting value for the planet's mass to be $M_p < M_{\rm g,noiso} \sim \pi a^2 \Sigma_g$. This prescription was modified in Paper IV, in which we constrained $M_p < \int_0^{2a} 2\pi a \Sigma_g da$. These previous prescriptions do not take into account the viscous diffusion of gas from other disk regions. In order to consider the possibility that gas accretion may also occur in the inner disk regions where the local gas content is limited, we evaluate in this paper both $\dot{M}_{p,\rm nogap}$ and $\dot{M}_{\rm disk}$ using the instantaneous values of Σ_g ($\propto \exp(-t/\tau_{\rm dep})$). The quenching of gas accretion due to the disk's global depletion is taken into account without any additional specification. This modification enables us to compute the gas accretion rate onto cores with a relatively small semimajor axis.

3.5. Type II Migration

During the gap formation, embedded gas giants adjust their positions in the gap to establish a quasi equilibrium between the torque applied on them from the regions of the disk both interior and exterior to their orbits. Subsequently, as the disk

gas undergoes viscous diffusion, this interaction leads to type II migration.

We assume that planets undergo type II migration after they have accreted a sufficient mass to satisfy the viscous ($M_{\rm g,vis} < M_p$) condition for gap formation, as commented in Section 3.4.

While M_p increases, the disk mass declines due to stellar and planetary accretion and photoevaporation. While the disk mass exceeds M_p (during the disk-dominated region), planets' type II migration is locked with the viscous diffusion of the disk gas. During the advanced stages of the disk evolution when its mass become smaller than M_p (during the planet-dominated region), the embedded planets carry a major share of the total angular momentum content. A significant fraction of the total (viscous plus advective) angular momentum flux transported by the disk gas is absorbed by the planet in its orbital evolution (for detailed discussion, see Paper IV).

For the disk-dominated regime, the migration timescale is given by

$$\tau_{\rm mig2,disk} = \left|\frac{a}{\dot{a}}\right| = \frac{a}{(3/2)\nu/a} \simeq 0.7\times10^5\left(\frac{\alpha}{10^{-3}}\right)^{-1}\left(\frac{a}{1\,\rm AU}\right)\left(\frac{M_*}{M_\odot}\right)^{-1/2}\ \rm yr. \quad (32)$$

For the temperature distribution given by Equation (16), $\nu \propto r$ and $\tau_{\rm mig2,disk}$ reduces to

$$\tau_{\rm mig2,disk} = \frac{a}{r_{\rm m}}\frac{2r_{\rm m}^2}{3\nu(r_{\rm m})} \simeq \frac{a}{r_{\rm m}}\tau_{\rm dep}, \quad (33)$$

where $\tau_{\rm dep}$ is global disk viscous-evolution timescale and $r_{\rm m}$ is the disk radius where the viscous couple attains a maximum value. (The magnitude of $r_{\rm m}$ is approximately the characteristic disk size.) In general, $\tau_{\rm mig2,disk}$ is a fraction of the disk lifetime except for the planets which formed near $r_{\rm m}$.

Observationally, the inferred disk lifetime is 1–10 Myr. If this lifetime is comparable to the disk viscous-evolution timescale, $r_{\rm m} \sim$ (15–150) $\times$ ($\alpha/10^{-3}$) AU. In this limit, Equation (33) would imply that many gas giants formed just beyond the snow line migrate to the proximity of their host stars and become hot Jupiters unless they emerged during the advanced (planet-dominated) stage of disk evolution or the type II tidal torque is significantly reduced by the disk flow through the gap or by the mutual interaction between multiple planets and their natal disks.

In Paper IV, we showed that the type II migration timescale in the planet-dominated regime can be evaluated in terms of

$$\tau_{\rm mig2,pl} = \frac{1}{C_2}\frac{(1/2)M_p a^2\Omega_{\rm K}(a)}{\dot{M}_{\rm disk}r_m^2\Omega_{\rm K}(r_m)} = \frac{1}{2C_2}\left(\frac{a}{r_{\rm m}}\right)^{1/2}\frac{M_p}{\dot{M}_{\rm disk}} \simeq 5\times10^5 f_g^{-1}\left(\frac{C_2\alpha}{10^{-4}}\right)^{-1}\left(\frac{M_{\rm p}}{M_{\rm J}}\right)\left(\frac{a}{1\,\rm AU}\right)^{1/2} \times\left(\frac{r_{\rm m}}{10\,\rm AU}\right)^{-1/2}\left(\frac{M_*}{M_\odot}\right)^{-1/2}\ \rm yr, \quad (34)$$

where C_2 is an efficiency factor associated with the degree of asymmetry in the torques between the inner and outer disk regions. If the inner disk is severely depleted, $C_2 = 1$. But, in evolving disks with comparable surface density on either sides of multiple planets, the degree of torque asymmetry has large uncertainties in both the disk- and planet-dominated regimes. Although the reduction factors for the disk- and planet-dominated regimes may be independent from each other, we adopt the same reduction factor, C_2, for both regimes and treat the factor C_2 as a model parameter. In the results shown in this paper, we set $C_2 = 0.1$. The kinematic distribution of the planets are weakly affected by the choice of C_2, as long as $C_1 \gtrsim 0.03$. The eccentricity distribution of the emerging gas giant planets is not strongly affected by the magnitude of C_2.

3.6. Resonant Capture

The pace of both type I and II depends on both the disk structure and M_p. As different-mass planets migrate, the separation between their semimajor axes may either increase or decrease through divergent and convergent migration, respectively. Multiple planets may also converge near some special disk locations such as the edge of the magnetospheric cavity near the inner disk boundary. As the migration of first-born planets is stalled at these trapping radii, later-generation planets may continue to arrive.

The planets gradually converging orbits capture each other on their mutual mean-motion resonances, provided their migration timescale across the resonances' width is shorter than the resonances' libration timescales. After they enter into their mean-motion resonances, these planets have a tendency to migrate together while maintaining the ratio of their semimajor axes (McNeil et al. 2005; Ogihara & Ida 2009). In their simulations, Ogihara & Ida (2009) and Ogihara et al. (2010) found that outside of the disk inner boundary at ~0.1–0.3 AU, it is possible for a few dozen rocky planetary embryos to be trapped in adjacent embryos' mean-motion resonances. During and after the depletion of the disk gas, their orbits become unstable, and they undergo orbit crossing and cohesive collisions to merge into a few super-Earths.

In Paper VI, we implemented a prescription for resonant capture between rocky/icy planets into our sequential planet formation model. With this prescription, we constructed population synthesis models for multiple super-Earth systems. These simulations showed that a rich population of embryos accumulate near the inner disk boundary. Although differential migration leads to embryos' orbital convergence, stochastic secular perturbation between multiple embryos induces orbital diffusion. Instead of locking into the most widely separated 2:1 mean-motion resonances, the nearest neighbors are packed into low-order main-motion resonance with semimajor axis separations comparable to several $r_{\rm H}$. The Hill radius, $r_{\rm H}$, is defined to be $r_{\rm H} = ((m_i + m_j)/3M_*)^{1/3}a$ where m_i and m_j are the masses of the closest pairs, M_* is the host star's mass, and $a = \sqrt{a_i a_j}$ is the mean semimajor axis of the pair.

For computational simplicity, we adopted in Paper VI, a prescription that, as a consequence of converging migration, the closest embedded embryo pairs enter into and are locked in mean-motion resonances with a separation of $5r_{\rm H}$ between their semimajor axes. After capturing each other, the resonant embryos migrate in steps while maintaining their semimajor axis ratios and sharing angular momentum loss associated with the gravitational interactions between the disk and individual embryos.

In the present paper, we consider the possibility that the converging differential migration may proceed so rapidly that the neighboring embryos may not have time to capture each other into mean-motion resonances. We evaluate the condition for a dynamical equilibrium in which convergence timescale (due to

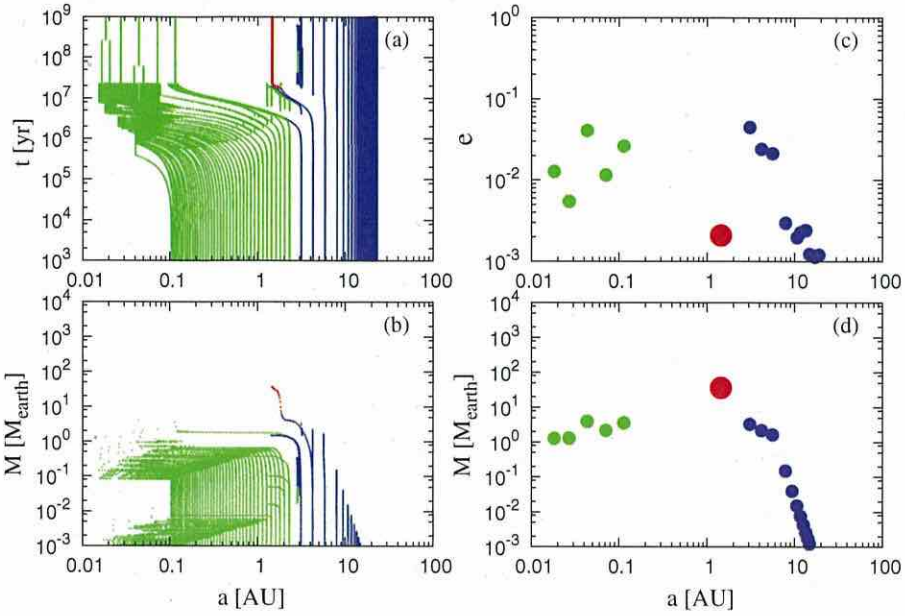

Figure 4. Growth and migration of planets in a system with $C_1 = 0.1$ and $f_{d,0} = 2.0$. In the color version, the green, blue, and red lines represent planets where the main component is rock, ice, and gas, respectively.
(A color version of this figure is available in the online journal.)

differential migration) matches with the mean-motion libration timescale (see Paper VI). If this equilibrium is established with an orbital separation which is less than $\Delta a_c \simeq 2\sqrt{3} r_H$, we assume the converging embryos will collide and coalesce (see Section 2.2).

We further extend the resonant capture condition for planet pairs including both super-Earths and gas giants. Based on the rate of orbital decay due to gas drag, Shiraishi & Ida (2008) derived a criterion for non-resonant planetesimals to enter the feeding zone of a growing gas giant. Here we adopt their criterion for the embryos, the migration of which is determined by their tidal interaction with the disk gas. We replace the migration rate due to gas drag with differential speed between type II migration of a giant and type I migration of rocky/icy embryos.

In the case that a planet (an embryo or another giant) enters a feeding zone of a gas giant, we apply the prescription in Section 2.1 to determine the outcome of their encounters. Although the treatment in Section 2.1 is constructed for scattering between two gas giants, the same prescriptions are also applicable for the case where an embryo is scattered by a giant. In this limit, the perturbations from the giant is so strong and dominant that these events tend to result in the ejection of the embryos or in widely separated orbits rather than cohesive collisions.

In Paper VI, we assumed that the disk inner edge is a rigid wall for type I migration of embryos. This assumption is based on a strong "eccentricity trapping" effect (Ogihara et al. 2010). The torque exerted onto the innermost embryo in an eccentric orbit is so strong that it can halt the type I migration and offset the angular momentum loss of several outer embryos. The magnitude of torque associated with embryo–planet interaction depends on the planet's mass. The condition for a single planet (with a mass m_1) to frustrate the inner migration of other embryos (with masses m_j ($j \geqslant 2$)) at the inner boundary (Ogihara et al. 2010) is

$$\sum_{j=1} m_j^2 < \frac{5}{C_1} m_1^2. \tag{35}$$

Leakage of the innermost embryo across the disk inner boundary would be imposed if the above condition is not satisfied. We also allow the leakage of embryos across the disk inner boundary if they lie in the path of an inwardly migrating gas giant planet.

4. SIMULATED INDIVIDUAL SYSTEMS

Before we enter into an comprehensive discussion on the statistical properties and population synthesis of multiple-planet systems, we first highlight the dynamical interaction among several bodies around common host stars with a few sample simulations of individual systems. Such studies have not been possible with the "one-planet-per-disk-model" prescription in which planet–planet interactions are neglected (e.g., Papers I–V and the models of Mordasini et al. 2009b).

For illustration purposes, we choose for Model 1, $C_1 = 0.1$, $f_{g,0} = f_{d,0} = 2.0$ ([Fe/H] = 0), $\tau_{KH1} = 10^9$ yr, $\tau_{dep} = 3 \times 10^6$ yr around a solar-mass star ($M_* = 1\ M_\odot$). Figures 4(a) and (b) show time and mass evolution of planets for Model 1. The green, blue, and red lines represent rocky, icy, and gas giant planets with their main component being rock, ice, and gas, respectively. Although rocky and icy planets are formed, respectively, interior and exterior to the snow line, their migration and dynamical interaction may lead to their spatial diffusion. The main composition of the planets may change through gas or planetesimal accretion or embryo–embryo collisions (giant impacts).

The results in panel (b) show that at 0.1–1 AU small embryos grow in situ until their masses reach $\sim 0.1\ M_\oplus$–$1\ M_\oplus$ and then undergo type I migration to accumulate near the inner boundary of their natal disks. We can determine the critical embryo mass

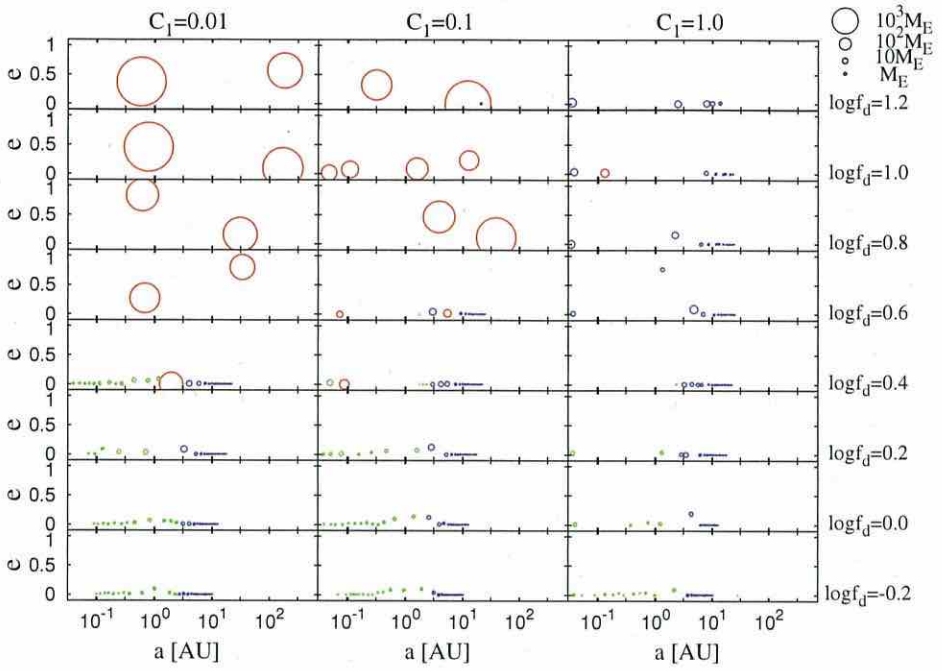

Figure 5. Planetary systems as functions of C_1 and $f_{d,0}$. The radii of circles are proportional to cubic root of planetary mass; legends are shown in upper right of the figure. In the color version, the green, blue, and red lines represent planets where the main component is rock, ice, and gas, respectively.
(A color version of this figure is available in the online journal.)

for transition from local mass growth to efficient type I migration by matching Equations (19) and (22) such that

$$M_{c,\max} \simeq 1.0 \left(\frac{C_1}{0.1}\right)^{-3/4} \left(\frac{f_g}{2}\right)^{3/10} \left(\frac{\eta_{\rm ice} f_d}{f_g}\right)^{3/4} \times \left(\frac{a}{1\,\mathrm{AU}}\right)^{-9/8} \left(\frac{M_*}{M_\odot}\right)^{5/4} M_\oplus. \quad (36)$$

A few small ($10^{-3}\,M_\oplus$–$10^{-2}\,M_\oplus$) embryos are also induced to undergo orbital decay. The orbital evolution of these low-mass embryos is induced by the perturbation from the migrating planets.

Many resonant embryos accumulate in the vicinity of the disk inner boundary which is set to be 0.04 AU (Figure 4(a)). These planets are preserved in the disk region, provided that the condition (35) is satisfied. But when the total mass of the trapped planets in the proximity of the inner disk edge exceeds the critical mass given by Equation (35), innermost planets are driven to cross the disk inner edge until the retention condition in Equation (35) is restored. In this model, more than half of the embryos that arrive in the inner disk region eventually cross its inner boundary. We assume that after planets migrate inside the central magnetospheric cavity in the disk, their tidal and magnetic interaction with their host stars provide an effective torque to induce them to undergo further orbital decay. Note that in the weak-field limit, the size of the magnetospheric cavity is much smaller and the disk inner boundary is adjacent to the stellar surface. In this limit, the innermost planets are unlikely to survive (Paper VI).

In the intermediate disk region, a migrating core attains $M_p \sim 5\,M_\oplus$ just outside of the ice line at $a \sim 3$ AU. This core starts its runaway gas accretion without any significant type I migration. When it evolves into a gas giant with a surrounding gap, it undergoes type II migration which is much slower than type I migration. The emerging gas giant scatters and ejects nearby embryos (they are represented by the lines which are discontinued at $t \sim 2 \times 10^7$ yr.)

In order to explore the dependence of various model parameters, we simulated a series of models with a range of different C_1 and $f_{d,0}$ values. We use the same values (as Model 1) for [Fe/H] = 0, $\tau_{\rm dep} = 3 \times 10^6$ yr, and $M_* = 1\,M_\odot$. The asymptotic distributions of mass, semimajor axis, and eccentricity of planets for these models are summarized in Figure 5.

For high values of $C_1 (= 1)$, type I migration is so efficient that gas giants are rarely formed. In runs with $\log f_{d,0} \gtrsim 0$, rocky/icy planets are not retained at $a \lesssim 1$ AU except in the vicinity of the disk edge at which type I migration is halted.

For models with $C_1 = 0.1$ and 0.01, the planet distributions are sensitively determined by the total planetesimal mass in the disk, i.e., the value of $\log f_{d,0}$. In our procedures, close scattering (see Section 2.2) depends on the choice of random number seeds. In order to test the robustness and dispersion of our models, two additional series of models are carried out for $C_1 = 0.1$ with different random number seeds for the scattering prescription (Figure 6).

All of these models show similar planetary systems' dependence on values of $f_{d,0}$. With relatively high values of $f_{d,0}$, the emerging planetary systems consist mostly of gas giants. In these massive disks, the amount of rocky/icy materials is sufficiently large to enable the formation of multiple cores of gas giants. Dynamical instability leads to giant planets to undergo close encounters which excite their eccentricity. Some giant planets may collide and coalesce into massive and eccentric merger products (Lin & Ida 1997). Other planets attain eccentric orbits including those which are ejected from the system or scattered

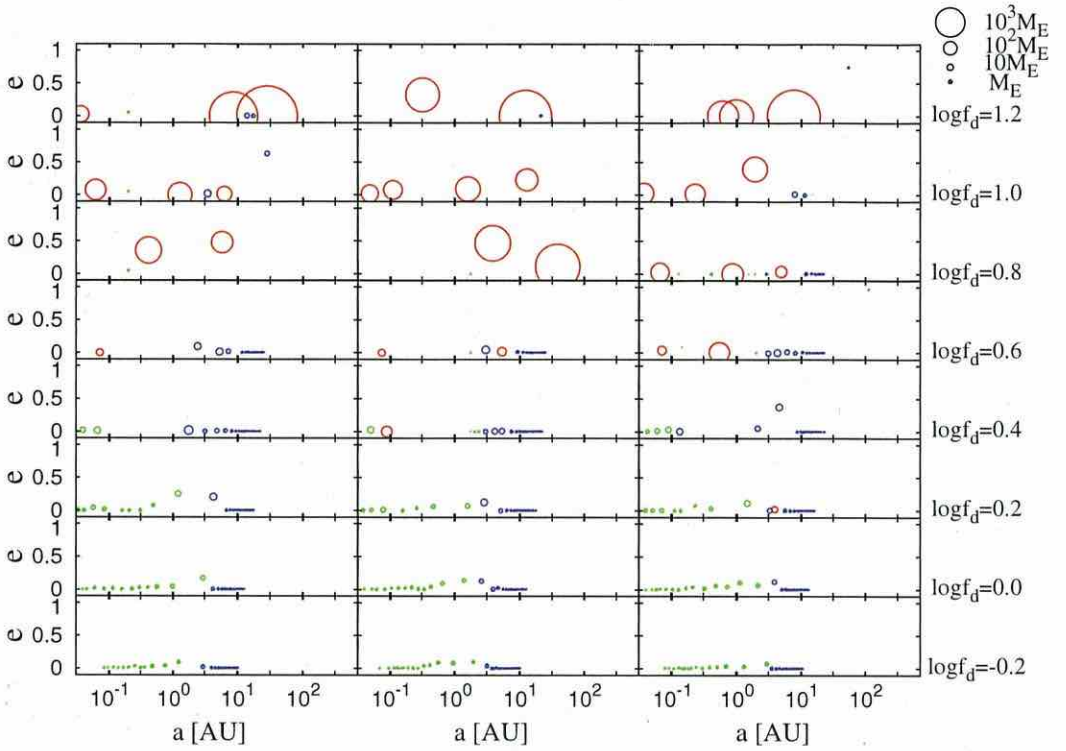

Figure 6. Planetary systems with $C_1 = 0.1$ as functions of $f_{d,0}$. In order to test the dispersion of the simulated results, we choose three random number seeds for the scattering prescription. Models in the middle column are identical to those in the middle column in Figure 5.
(A color version of this figure is available in the online journal.)

to endure close encounters with their host stars. During these violent dynamical relaxations, the orbits of rocky/icy planets are strongly perturbed by the giant planets and they are generally not retained.

In contrast, disks with moderate masses (or values of $f_{d,0}$) generally nurture fewer and more widely separated cores. Gas accretion leads to the emergence of either single or widely separated and sparsely populated giant planets. The mass of these planets is determined by the gap formation condition and is generally smaller than that of merger products. The mutual interaction between single gas giant planets and residual embryos, or between sparsely populated gas giant planets, is generally too weak for them to become dynamically unstable. They then retain relatively low eccentricities.

Comparison of Figures 5 and 6 indicates that relatively massive and eccentric gas giant planets are formed out of massive disks, whereas disks with modest masses generally produce gas giant planets with lower masses and eccentricities. Through the population synthesis models (next section), we show that this correlation can be used to infer an initial formation condition of mature planets long after their natal disks have been depleted.

5. POPULATION SYNTHESIS OF PLANETARY SYSTEMS

This set of prescriptions enables us to incorporate gravitational interactions among planets into our population synthesis models. The main objective of simulating "multi-planets-in-a-disk" models is to generate mass and eccentricity distributions of the emerging multiple-planet systems. These quantities can be directly compared with observational data.

5.1. Initial Conditions

We adopt a range of disk model parameters (see Section 3.1) and assign each their values with appropriate statistical weights to match the observed distribution of disk properties. We assume that $f_{g,0}$ and $\tau_{\rm dep}$ have log normal distributions in the ranges of 0.1–10 and 10^6–10^7 yr, respectively. We use a normal distribution of [Fe/H] in a range of -0.2 to 0.2 which corresponds to that of typical target stars in various on-going radial velocity surveys. Since the target stars of radial velocity surveys are mostly G dwarfs, we use a log normal distribution, in a range of 0.8–1.25 $M_\odot$, for the host stars' mass (M_*).

The initial distributions of seed planetesimals are described in Section 3.1 and their growth rate and migration timescales are specified in Sections 3.2–3.5. Prescriptions for dynamical interactions among multiple planets are presented in Sections 2.1–2.3 and 3.6.

5.2. Distributions of Mass, Semimajor Axis, and Eccentricities

The asymptotic e–a, e–M_p, and M_p–a distributions of a population of 10^4 multiple-planet systems are shown in Figure 7. Similar to previous figures, the green, blue, and red symbols represent rocky, icy, and gas giant planets, respectively.

Models with similar parameters have been simulated in Paper IV with the "one-planet-in-a-disk" prescription. In these previous models, the formation of gas giant planets require a substantial reduction in the pace of their cores' type I migration (with $C_1 = 0.01$–0.03). This result reflects the requirement for not only the formation but also retention of sufficiently massive cores (Section 3.6) to efficiently accrete gas. The present

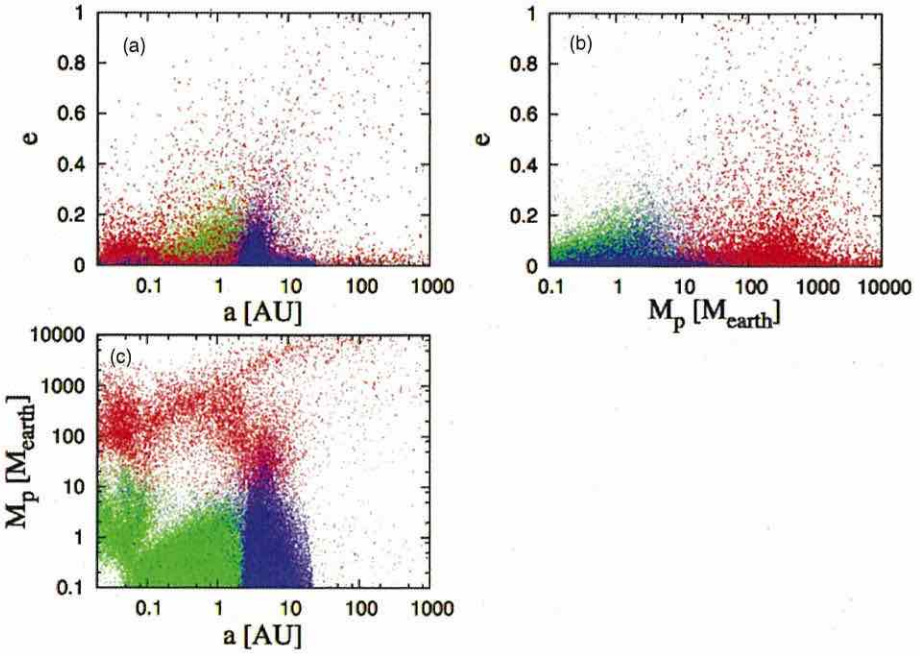

Figure 7. Asymptotic kinematic distributions of a simulated population of planets in multiple-planet systems. For these fiducial models, we adopt $\tau_{KH1} = 10^9$ yr, $k_2 = 3$, and $C_1 = 0.1$. The eccentricity e vs. semimajor axis a distribution is plotted in panel (a). The e–M_p distribution is plotted in panel (b). The M_p–a distribution is plotted in panel (c). The green, blue, and red symbols represent rocky, icy, and gas giant planets, respectively.

(A color version of this figure is available in the online journal.)

prescription bypasses this competition between type I migration and mass growth because it takes into consideration the possibility that multiple embryos may undergo convergent migration, dynamical instability, orbit crossing, and close encounters. Coalescence of two or more embryos (with relatively low masses and long type I migration timescales) promote sporadic, substantial mass increases. The merger products can impulsively acquire a critical mass for the onset of gas accretion before they undergo extensive migration.

A direct comparison between Figure 7(c) and Figure 5 in Paper IV show that, with $C_1 = 0.1$, the new prescription indeed leads to much more prolific production of gas giants. Some of these gas giant planets form during the advanced stages of disk evolution after 90% of the disk gas been depleted. In these low density environments, the eccentricity of embryos may be excited by their perturbation on each other but not effectively damped. Eventually they cross each other's orbit, merge into sufficiently massive cores to accrete residual disk gas and evolve into gas giant planets.

In contrast to the "one-planet-in-a-disk" models, we can determine, with the new prescription, planets' velocity dispersion from their mutual interaction in multiple-planet systems. From this kinematic information, we obtain the e–a and e–M_p distributions in Figures 7(a) and (c). The "V" shape centered at a few AU in the e–a distribution is a signature of strong scatterings by the most massive planets in the system which preferentially form near the snow line (at a few AUs). Less massive planets are either scattered inward, outward, or collide with the gas giant planets. The left/right branch of the "V" corresponds to the loci of planets which have been scattered inward/outward. These inwardly/outwardly scattered planets preserve their apo/periastrons to be orbital radii of the gas giant planets. Finally, the e–M_p distribution shows that eccentricity distribution is uniform or rather increases with M_p. If we consider only massive planets that are currently observable by radial velocity survey, eccentricity distribution clearly increases with M_p as shown below.

We compare our simulated population synthesis models with observational data. In Figure 8, we plot observed (a) e–M_p, (b) e–a, and (c) M_p–a distributions in the left, middle, and right columns, respectively. The observational data are displayed in the top row. These data include only those planets which were first discovered by radial velocity surveys. We excluded planetary candidates which were first discovered by transit surveys, regardless of whether or not they were confirmed by follow-up radial velocity observations. The main rationale for this selection is that the detection probability by transit surveys is highly biased to short-period planets.

The simulated population of 10^4 multiple-planet systems is plotted in the bottom row. Here, M refers to $M_p \sin i$ with a distribution of inclination angle i between the line of sight and the planets' orbital angular momentum axis that assumes random orientations of orbit normals of the planets. Some of these planets have low-mass and large semimajor axes. They are below the present-day detection capability. In order to take into account the limited radial velocity precision and data base line, we selected a subset of data in which the predicted reflective motion of the host stars is larger than 1 m s^{-1} and the planets' orbital period is shorter than 10 yr. These "detectable planets" are plotted in the middle row.

Comparison between the top and middle panels in Figures 8(a) and (b) shows that the theoretical models match well the observed kinematic distributions. Both observations and population synthesis models show that e increases with M_p and a. In the next subsection, we will show that these correlations are robustly reproduced, almost independent of model parameters.

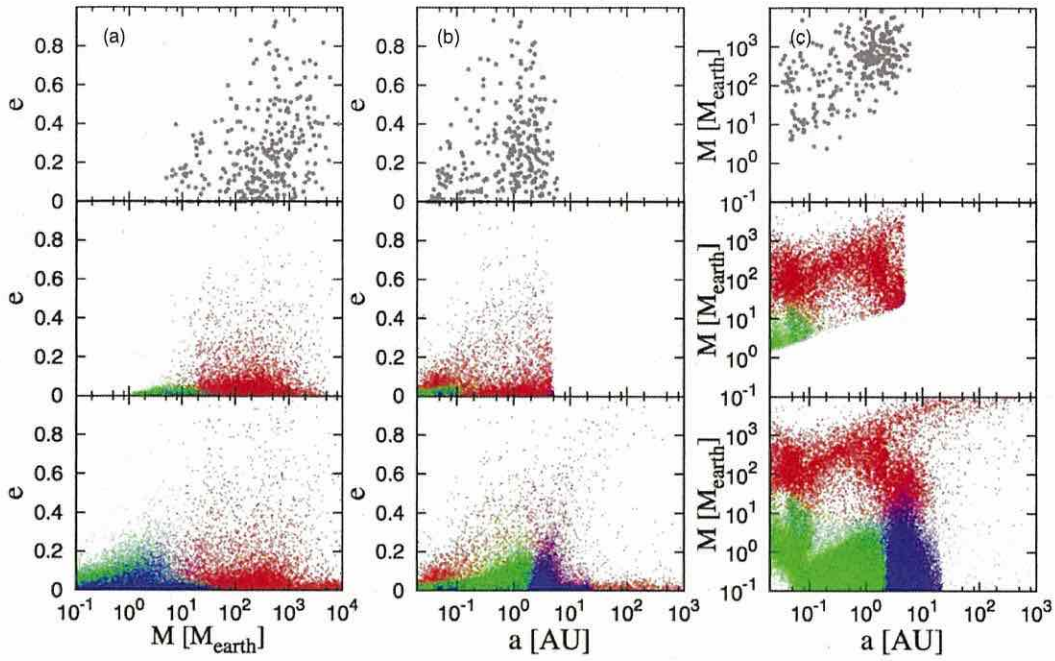

Figure 8. Comparison of theoretical results in a nominal case with observational data: (a) e–M_p, (b) e–a, and (c) M_p–a distributions. The top row are the data obtained from radial velocity surveys. The planets that were discovered in transit surveys and confirmed with follow-up radial velocity observation are excluded. The bottom row are the distributions of planets in 10^4 systems simulated with the updated population-synthesis prescription. Panels in the middle row represent only the simulated observable planets, i.e., those with radial velocities greater than 1 m s^{-1} and periods less than 10 yr.

(A color version of this figure is available in the online journal.)

Most gas giants have semimajor axes $a \gtrsim 0.5$ AU. Their eccentricities are not affected by the dissipation of tidal perturbation induced by the host stars on the planets. Detailed comparison of the top and mid row of the middle column indicate that the fraction of high-eccentricity ($e \gtrsim 0.2$) planets in the theoretical model is low (~10%) compared with that (~50%) in observed data. This discrepancy may be observational uncertainties which generally tend to introduce over-estimates for planets' eccentricities. It may also be due to the secular perturbations between gas giants which has not yet been incorporated in our prescription. In multiple-planet systems with significant angular momentum deficit, secular interaction can induce large-amplitude angular momentum exchange, eccentricity modulation, and long-term orbital instabilities. A treatment of secular perturbations will be constructed and presented elsewhere.

In this paper, we focus primarily on the planets' eccentricity distributions. Comparison between the top and middle panels in Figure 8(c) show that our prescription qualitatively reproduces the observed correlations in the M_p–a distribution. Whereas the observational data clearly show an over-density of gas giants at $a \gtrsim 0.7$ AU, their semimajor axes distribution in the simulated population synthesis models is relatively uniform on a log scale. The sensitive dependence of the M_p–a distribution on the parameters of population synthesis models will be discussed in detail in the next paper.

5.3. Correlations between Eccentricity and Mass or Semimajor Axis

The origin of the correlation of eccentricity and semimajor axis can be traced back through the procedures of our theoretical model. In the observed e–a distribution, e is apparently lower at $a \lesssim 0.1$ AU than at $a \sim 1$ AU (the top panel in Figure 8(b)). This correlation has been attributed to the dissipation of stellar tidal perturbation inside the planetary envelope which leads to the orbital circularization of close-in planets. The tidal effects have not yet been implemented in the population synthesis models. Yet, this e–a correlation is also very well established in the simulated results. In Equation (3), we showed that the maximum eccentricity excited by close scattering between gas giants is $\propto a^{1/2}$, because the two-body surface escape velocity ($v_{\mathrm{esc},jk}$) is independent of a whereas the Kepler velocity (v_K) is $\propto a^{-1/2}$. Consequently, in the deep potential near the host stars, it is difficult for close scattering to excite high eccentricities. Based on the above prescription, the maximum e we obtain at $a \sim 0.1$ AU is three times smaller than that at $a \sim 1$ AU in the simulated models (the middle panel in Figure 8(b)).

Multiple massive giants are preferentially formed in relatively massive disks (see discussions in Section 4). These dynamically packed systems are more prone to dynamical instabilities, orbit crossing, excitation of high eccentricities, and cohesive collisions. A correlation between high eccentricity and planetary mass is naturally expected. In order to verify this scenario, we plot in Figure 9, e and M_p of gas giants as a function of $f_{d,0}$ in the fiducial models (in which $\tau_{\mathrm{KH1}} = 10^9$ yr and $C_1 = 0.1$) of Figure 7. This figure clearly shows that, in the range of $f_{d,0} = 1$–10, both the mass of gas giants and the fraction of high e planets increase with $f_{d,0}$. Based on this inference, we can infer the distribution of disk masses from the observed e–M_p distribution. Raymond et al. (2010) performed N-body simulations of multiple giant planets with different masses and found a similar correlation between high eccentricity and planetary mass, although their initial conditions are artificial. Note that Figure 9 only includes gas giants at $a < 30$ AU. As

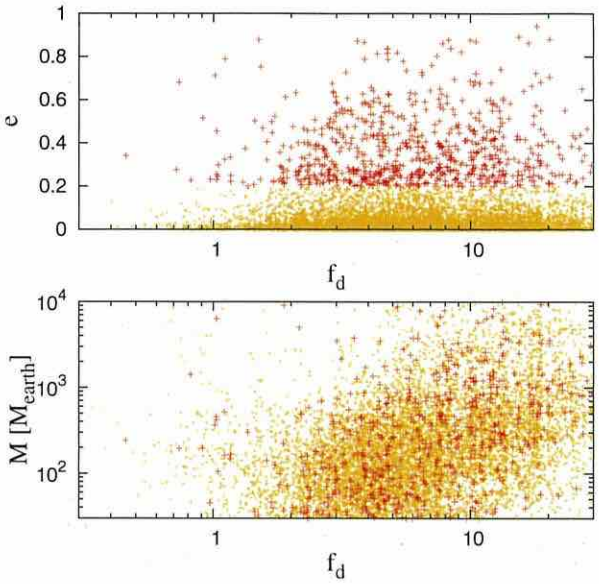

Figure 9. Distributions of e and M of gas giants with $a < 30$ AU as a function of $f_{d,0}$ in the fiducial models of Figure 7. The thick and thin symbols represent giants with $e > 0.2$ and $e < 0.2$, respectively (In the color version, red and orange symbols).

(A color version of this figure is available in the online journal.)

shown in Figures 7(a) and (c), the kinematic distribution of gas giants with $a \gtrsim 30$ AU have two (high e and low e) components. We discuss this issue in the next subsection.

The above discussion indicates that the e–a and e–M_p correlations are the natural outcome of close scatterings and the formation of gas giants. It also shows that these correlations are insensitive to other physical parameters such as the rate of type I migration (C_1) and the magnitude of the gas accretion timescale ($\tau_{\rm KH1}$). These independences are reflected in Figures 10 and 11 for simulated populations with different values of C_1 and $\tau_{\rm KH1}$. Although the number of gas giants per host star is lower among populations with relatively high C_1 and long $\tau_{\rm KH1}$, the trend that e is lower at $a \lesssim 0.1$ AU than at $a \sim 1$ AU persists.

This trend is less conspicuous in the limit of relatively small C_1 (0.03 in Figure 10) and gas accretion timescale $\tau_{\rm KH1}$ (10^8 yr in Figure 11). In these limits, the prolific formation of gas giants and the high frequency of their close scattering leads to a prominent "V" feature in the e–a distribution. This feature also affects the distribution of observable planets (displayed in the upper rows of these figures). The lack of any obvious evidence of this "V" feature in the observational data (Figure 8(a)), places a limit on the efficiency of gas giant formation and constraints on the magnitude of C_1 and $\tau_{\rm KH1}$. In the fiducial population synthesis model (with $C_1 = 0.1$ and $\tau_{\rm KH1} = 10^9$ yr), the fraction of solar-type stars that harbor gas giants with $a = 0.5$–5 AU and $M_p > 100\,M_\oplus$ (cool Jupiters) is 21%. This fraction for both the $C_1 = 0.03$ models (47%) and the $\tau_{\rm KH1} = 10^8$ yr models (42%) are both much higher than that inferred by radial velocity surveys.

Figures 12 and 13 show the dependence of the e–M_p distribution on C_1 and $\tau_{\rm KH1}$, respectively. Although more massive planets, in general, tend to have larger e, this trend is less conspicuous for models with $C_1 = 0.3$ and $\tau_{\rm KH1} = 10^{10}$ yr. In these limiting cases, the formation of gas giants is affected by the rapid migration of the cores and slow gas accretion. These restrictions are more severe for the formation of the relatively massive gas giants. Despite these extreme cases, the correlations in e–a and e–M_p distributions are well established in the population synthesis models for a wide range of parameters. The general reproduction of the observed correlations suggests that these properties are associated with close scattering among gas giants.

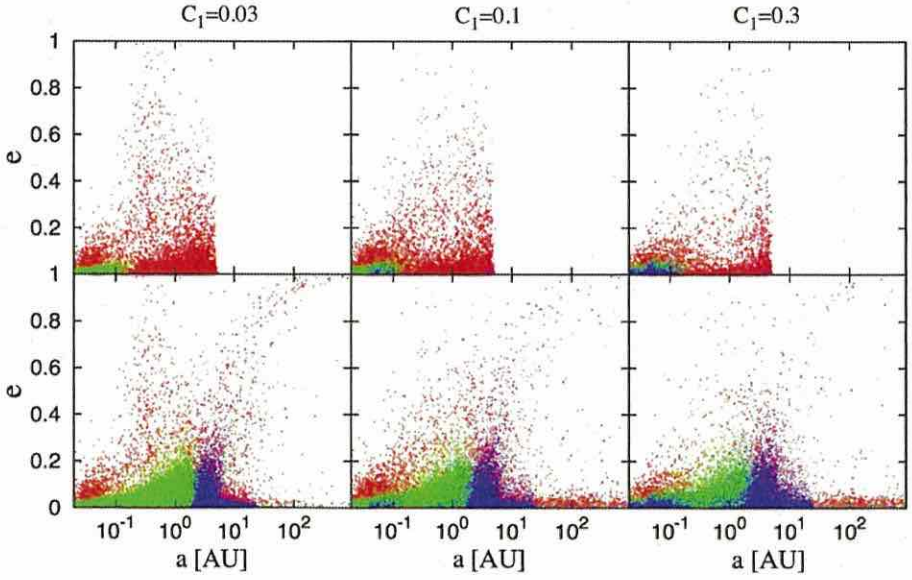

Figure 10. Dependence on C_1 of the simulated e–a distribution. The lower panels are distributions of 10^4 systems of planets generated with our Monte Carlo simulation. The upper panels contain only the observable (with radial velocities greater than 1 m s^{-1} and periods less than 10 yr) simulated planets. These observable criteria correspond to the technical limitation of current radial velocity surveys. The left, middle, and right panels display results for models with type I migration coefficient $C_1 = 0.03$, 0.1, and 0.3, respectively. The symbols are the same as those in Figure 8.

(A color version of this figure is available in the online journal.)

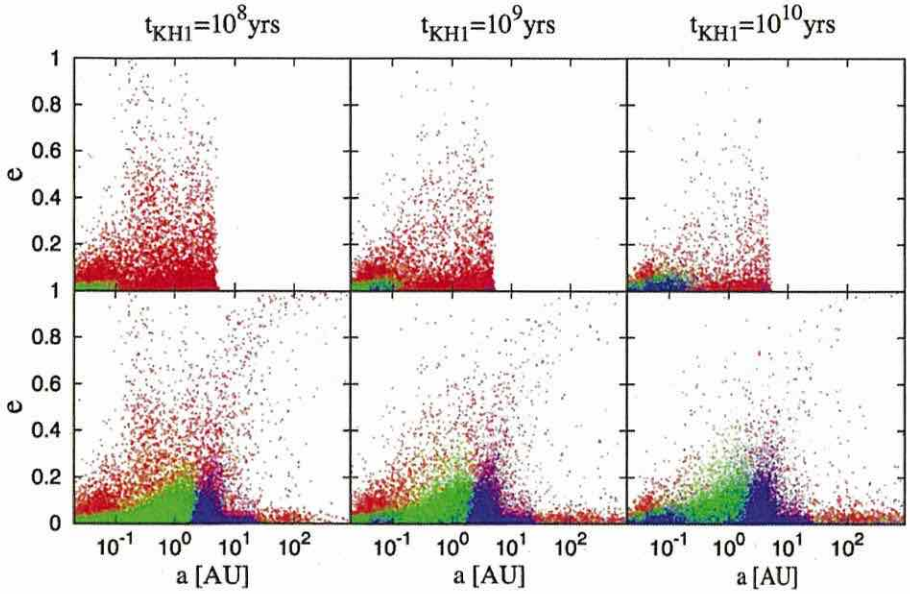

Figure 11. e–a distribution of simulated models with various values of τ_{KH1}. The left, middle, and right panels include results generated with the parameter for envelope contraction timescale (for $M_p = M_\oplus$) $\tau_{KH1} = 10^8$, 10^9, and 10^{10} yr, respectively. The meaning of upper and lower panels are the same as in Figure 10.
(A color version of this figure is available in the online journal.)

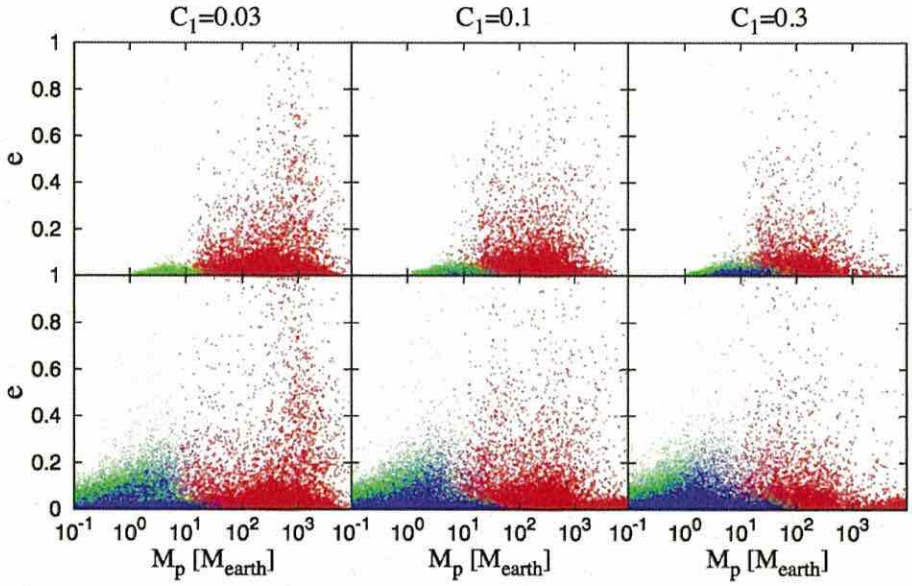

Figure 12. Dependence on C_1 of the predicted e–M_p distribution. The meaning of panels are the same as in Figure 10.
(A color version of this figure is available in the online journal.)

In Figures 14(a)–(c), we show the e–a, e–M_p, and M_p–a distributions with the non-isothermal type I migration formula. Because in inner (optically thick) disk regions, migration is outward for some range of M_p (Kretke & Lin 2012), many gas giants survive even without any reduction in amplitude of the migration velocity. While the M_p–a distribution is affected by the different migration formula, the e–a and e–M_p distributions are similar to those obtained by the isothermal migration formula and they are within a range of variations of the results with different values of C_1 and τ_{KH1} in Figures 10–13. Therefore, here we do not go into the details of the non-isothermal migration formula and focus on the eccentricity distributions obtained with the isothermal migration formula and a scaling factor C_1, as discussed in Section 3.3.

5.4. Formation of Distant Large Gas Giants in Circular Orbits

The population synthesis models also generate a population of massive ($M_p \gtrsim 10 M_J$) gas giants with large semimajor axes ($a \gtrsim 30$ AU) (Figure 7(c)). In principle, these planets can be observationally detected during their infancy with direct imaging searches. In the fiducial models, the fraction of host

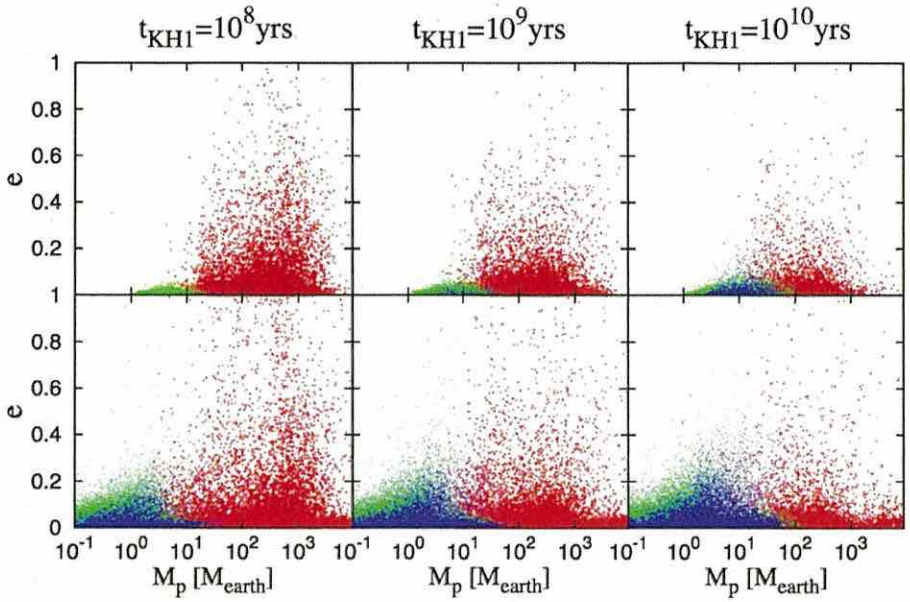

Figure 13. Dependence on τ_{KHI} of the predicted e–M_p distribution. The meaning of panels are the same as in Figure 11.
(A color version of this figure is available in the online journal.)

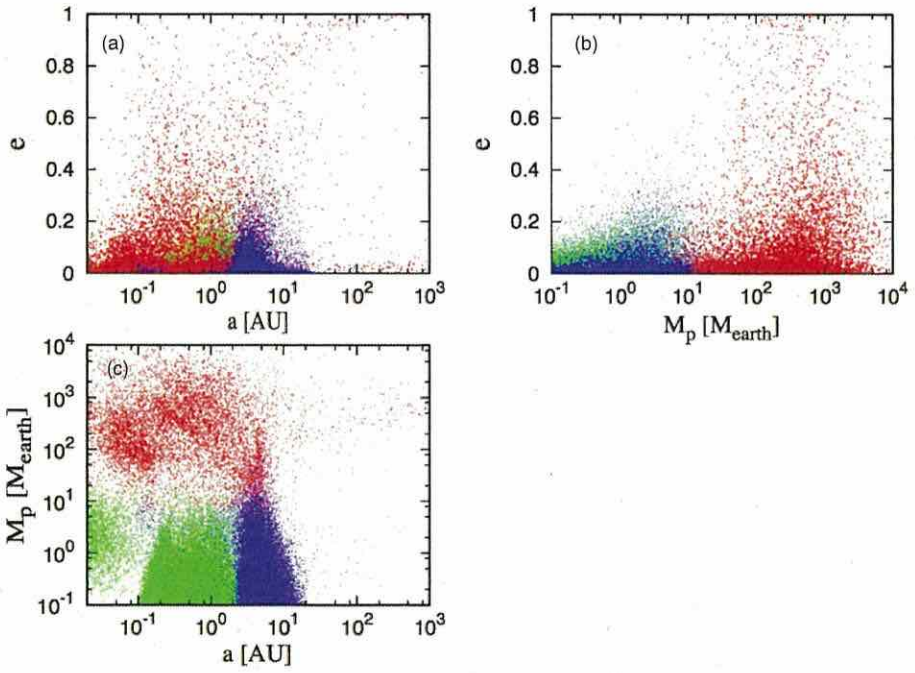

Figure 14. Same as Figure 7 except for use of non-isothermal type I migration formula instead of isothermal one with $C_1 = 0.1$.
(A color version of this figure is available in the online journal.)

stars that have these planets is ~3.7% and most of them have low-eccentricity ($e \lesssim 0.1$) orbits (Figure 7(a)). If these planets were grown to gas giants near the snow line and scattered to these large distances, they would preserve their periastron distance. For example, planets formed interior to 30 AU may be scattered to attain a semimajor axis $\gtrsim$100 AU with $e \gtrsim 0.7$. Although the effect of eccentricity damping is included in our prescription for disk–planet interaction, its efficiency is generally too low to account for the low eccentricity of distant, massive planets generated in these population synthesis models (step 3-a of Appendix A1).

A close inspection of our results yields an alternative path for the formation of distant gas giant planets. In systems which contain multiple gas giants, the rapid gas accretion of first generation gas giants destabilize the orbits of nearby residual embryos. Some embryos are scattered to large distances where the surface densities of both residual planetesimals and gas are relatively low. Because the scattered embryo

masses are usually well below the local disk mass, even the relatively low surface density gas damps the eccentricity of the scattered embryos to the level below 0.1 (also see the discussion below).

A reduction in the planetesimal-accretion rate at these distances also lowers the critical core mass for the onset of gas accretion (see Equation (23)). In extended protostellar disks, there is an adequate gas supply, even during the advanced stages of disk evolution to enable the circularized planets to acquire masses larger than that of Jupiter.

The ratio of planets' asymptotic mass to that of their host stars is a monotonically increasing function of their natal disks' aspect ratio which is also an increasing function of a (see Equations (27) and (28)). The simulated populations confirm that the masses of the long-period gas giants are robustly correlated with a in the fiducial (Figure 7(c)) and other models. If this trend is confirmed by observation, it provides evidence to support the scenario that long-period, low-eccentricity, massive gas giants are the byproducts of gas accretion onto outwardly scattered cores.

During the course of mass accretion, the planets also acquire angular momentum of the disk gas. Although the scattered embryos have high eccentricity initially, they gain angular momentum through planet–disk tidal interaction. Our prescription for the eccentricity damping may be less efficient than that, due to supersonic relative velocity between the core and disk gas (Ostriker 1999; Papaloizou & Larwood 2000; Muto et al. 2010), although it nonetheless may lead to the circularization of planets' orbits. In addition to the tidal torque, E. Thommes (2010, private communication) used a hybrid N-body and two-dimensional hydrodynamical (FARGO) scheme to demonstrate that during their eccentric excursion, scattered embryos take longer time to pass through their apoastrons and they tend to accrete gas from that region which has relatively large specific angular momentum. We anticipate that as the embryos evolve into gas giants, their specific angular momentum becomes comparable to that of the disk gas near their apoastron and their orbits become circularized with a radius close to their apoastron radius. The detailed calculation will be shown in a separate paper (A. Kikuchi et al., in preparation).

Through this process, multiple cores can be scattered outward to initiate gas accretion. We find that in the fiducial models, the fraction of systems with two, three, and four giants with low-eccentricity orbits (such as the solar system) is 0.4%, 0.07%, and 0.04%, respectively. The orbital configuration of systems of multiple gas giants with relatively large masses, low eccentricities, and long periods are consistent with the observed data obtained from the direct imaging initiatives.

We have not introduced an outer boundary for planets' natal disks. If most protostellar disks are truncated, either by photoevaporation or magnetic braking, the outwardly scattered cores would not have access to gas beyond the truncation radius. An abrupt decline in the observed semimajor axis distribution of gas giant planets could be used to place constraints on the structure and evolution of their natal disks.

In the models where $C_1 = 0.3$, the fraction of systems with massive, low-eccentricity, and long-period gas giants is similar to that of the fiducial models (with $C_1 = 0.1$). But this fraction is reduced to 0.04% in the models where $C_1 = 0.03$. This dichotomy suggests that type I migration of cores is a major cause for them to be scattered by a giant planet. In order to match the frequency of planets discovered through direct imaging observation, type I migration cannot be neglected.

6. SUMMARY AND DISCUSSIONS

Radial velocity and transit surveys indicate that multiple-planet systems are common around solar-type stars. We adopt a new paradigm that all planets are formed in families (as in the case of the solar system) and their asymptotic properties are determined by their dynamical interaction with each other, as well as with their natal disks.

In order to incorporate this scenario into our population synthesis models, we upgrade an existing numerical population synthesis scheme which was developed in Papers I–IV for idealized "one-planet-in-a-disk" models. The original prescriptions were constructed and applied to simulate the semimajor axis and mass distributions of extrasolar planets, calculating the growth and migration of each planet, independently of any other planets. Similar approaches have also been adopted by other authors (Mordasini et al. 2009a, 2009b; Alibert et al. 2011).

In Paper VI, we first introduced a modification to partly include the gravitational interactions and collisions between rocky planetary embryos. In this paper, we generalize an efficient and robust prescription to take into account close scattering between all planets. We calibrate our prescriptions for scattering among gas giants with the results of comprehensive N-body simulations. For example, in the aftermath of close scatterings between gas giants, ejection commonly occurs. Our prescriptions reproduce well the distributions of eccentricity and semimajor distributions of retained giants obtained from the N-body simulations.

With this upgraded tool, we can adopt a Monte Carlo approach to simulate a large sample of population synthesis models. In this paper, we mostly investigate the effects of scattering by giant planets on asymptotic architecture of planetary systems and their eccentricity distributions. We focus on the correlations between the eccentricity of gas giants with their mass and semimajor axis.

Observational data obtained through radial velocity surveys clearly shows that the mean eccentricity increases with planetary mass (at least for $M \lesssim 10 M_J$) and with semimajor axis (at least for $a \lesssim 1$ AU). Our new population synthesis models show that in relatively massive disks, several massive giants may form and intensely interact with each other. Dynamical instabilities lead to eccentricity excitation, orbit crossing, close encounters, collisions, and ejection. But in protostellar disks with moderate masses (comparable to the surface density distribution of the minimum mass nebula model), one or two relatively small-mass giants are formed. They commonly avoid dynamical instability and preserve their low initial eccentricities. The observationally inferred correlation between gas giants' eccentricity and mass is robustly reproduced by our models.

Both gas giants and rocky/icy planets form prolifically in massive disks. But the low-mass planets are mostly ejected or accreted by the gas giants. Moderate planetary systems in which rocky/icy planets preserve their modest eccentricity and coexist with one or two sibling gas giants are preferentially formed in disks with modest masses (analogous to the formation of the solar system in an MMSN). Multiple, short-period super-Earths, which are commonly found around solar-type stars, are also retained only in the systems formed from such modest-mass disks but not in the massive disks.

The observed correlation between eccentricity and semimajor axis is also reproduced by the population synthesis models. After the onset of dynamical instability and orbit crossing, planets' velocity dispersion is determined by close scatterings.

The maximum recoil speed is comparable to the surface escape velocity of the dominant perturber, which is independent of semimajor axis. Since mean eccentricity is given approximately by velocity dispersion scaled by the local Keplerian velocity, the mean eccentricity is proportional to the square root of the semimajor axis. Although we have not included the effect of tidal circularization, which preferentially damps the eccentricity of short-period planets, the correlation of eccentricity and semimajor axis can also be produced by close scatterings alone.

Recently, direct imaging surveys discovered several systems which contain massive ($M_p \gtrsim 10 M_J$) gas giants in distant ($a \gtrsim 100$ AU) orbits with small eccentricities ($e \lesssim 0.1$). Some of these planets are members of multiple-planets systems. We found analogous planets among a non-negligible fraction (a few percent) of systems in our population synthesis simulations. In our models, the cores of these gas giants were originally formed well interior to their present-day semimajor axis (with $a \lesssim 30$ AU). They were scattered outwardly by first generation gas giants to the outer regions of their natal disks. The surface density of field planetesimals and their collision frequency with the cores rapidly decreases with the disk radius. A reduction in the planetesimal bombardment rate also decreases the critical core mass needed for the onset of efficient gas accretion. In the outer regions of relatively massive disks, there is an adequate supply of gas to enable the cores to accrete gas even during the advanced stage of disk evolution. The high eccentricity of the scattered cores is damped by disk–planet interactions and accretion of gas in the outer disk where its specific angular momentum is relatively high.

The emergence of single massive giants can scatter multiple nearby cores; we also found systems with multiple massive gas giants in nearly circular distant orbits. Therefore, the core-accretion model can indeed produce the systems that are similar to those discovered by direct imaging surveys. This origin predicts a clear correlation that the mass increases with the semimajor axis for these giants by the following reasoning. The aspect ratio of the disks increases with their radius. At these large distances, gas giants continue to accrete gas until they acquire sufficient mass to open gaps in the disks near their orbits. Because the critical mass for gap opening is higher for larger orbital radius, the correlation is established. It is of interest to check if observed data also indeed exhibits such a trend.

This work is partially supported by NASA (NNX08AM84G), NSF (AST-0908807), JSPS (23103005) and a University of California Lab Fee grant.

APPENDIX

PRESCRIPTION FOR ECCENTRICITY EXCITATION AND EJECTION OF GIANT PLANETS AS A RESULT OF ORBITAL INSTABILITY

In our simulations, giant planets and rocky/icy planetary embryos coexist. We separate the treatment of planets' dynamical interactions into those between (1) giant planets, (2) embryos, and (3) a giant planet and an embryo.

We consider two-giants scatterings in a disk environment with residual gas. We adopt an assumption that three-giants scatterings mostly occur after the disk has been depleted in a gas-free environment (see Section 2). The prescriptions for scattering between two gas giants and three gas giants are described in Appendices A1 and A2, respectively. In Appendix A3, we present prescriptions for dynamical interactions in general cases in which giant planets and rocky/icy planetary embryos coexist.

A.1. Two Giants

The prescriptions for scattering of two giants with mass m_1 and m_2 are as follows.

(1) *Specify initial conditions.* We assume that orbital instability between two gas giants occurs when their orbital separation becomes smaller than $2\sqrt{3}r_H$, where $r_H = ((m_1+m_2)/3M_*)^{1/3}a$, $a = \sqrt{a_1 a_2}$, and m_j and a_j are the mass and semimajor axis of planets j with $(j = 1, 2)$. For comparison with N-body simulations, we consider nearly circular and coplanar orbits (see Section 2.1).

(2) *Compute trial eccentricities.* After close encounters, the maximum eccentricity of body j $(j = 1, 2)$ is given by

$$e_j^{\max} = \frac{m_k \mathcal{R}_j}{m_1 + m_2} e_{\rm esc,12}, \tag{A1}$$

where

$$e_{{\rm esc},jk} = \frac{v_{{\rm esc},jk}}{v_K} = \frac{\sqrt{2G(m_j+m_k)/(R_j+R_k)}}{\sqrt{GM_*/a}} \simeq 1.6 \left(\frac{m_j+m_k}{M_J}\right)^{1/3} \left(\frac{\rho}{1\,{\rm g\,cm^{-3}}}\right)^{1/6} \left(\frac{a}{1\,{\rm AU}}\right)^{1/2}, \tag{A2}$$

v_K is the Keplerian velocity, $v_{{\rm esc},jk}$ is the two-body surface escape velocity, and R_j is the physical radius of planet j. In Equation (A1), $\mathcal{R}_j$ is a random number chosen from a Rayleigh distribution with the root mean square of unity (Ida & Makino 1992). We use different seed random numbers for different bodies. This is the same expression as we constructed, in Paper VI, to simulate eccentricity excitations of embryos.

(3-a) *Execute a planet's ejection*

1. *Select the body to be ejected.* We specify that an ejection would occur if $e_j^{\max} > 1$ for at least one of the bodies. (Since the total energy of the system is conserved to its negative values prior to the close encounters, it would not be possible for both planets to escape from their host stars). We identify the ejected planet with a candidate that has a larger value of $e_j^{\max}$.
2. *Evaluate the asymptotic semimajor axis and eccentricity of the retained planet.* N-body simulations indicate that in two planet systems, ejection of a planet primarily occurs after a series of weak distant encounters between it and the retained planet. As it attains a parabolic orbit, the eccentricity of the escaping planet (with a subscript label $j = 2$) gradually increases slightly above unity.

We assume that the initial (denoted by "0") orbits of the two giants were circular. Angular momentum conservation during the close encounters would imply

$$m_1\sqrt{a_{1,0}} + m_2\sqrt{a_{2,0}} = m_1\sqrt{a_1(1+e_1)(1-e_1)} + m_2\sqrt{a_2(1-e_2)(1+e_2)} \tag{A3}$$

$$\simeq m_1\sqrt{a_{1,0}(1-e_1)} + m_2\sqrt{a_{2,0}\times 2}, \tag{A4}$$

where a_1 and e_1 are the asymptotic semimajor axis and eccentricity of the retained gas giant (with a subscript label $j = 1$). In the above approximation, we have assumed the post-encounter apoastron distance of the retained planet $a_1(1 + e_1) \sim a_{1,0}$ and periastron distance of the ejected planet $a_2(1 - e_2) \sim a_{2,0}$.
From this equation, we obtain

$$e_1 \simeq e_1^* \equiv 2(\sqrt{2} - 1)\frac{m_2}{m_1}\sqrt{\frac{a_{2,0}}{a_{1,0}}} - (\sqrt{2} - 1)^2 \left(\frac{m_2}{m_1}\right)^2 \frac{a_{2,0}}{a_{1,0}} \quad \text{(A5)}$$

$$\simeq 0.83\frac{m_2}{m_1} - 0.17\left(\frac{m_2}{m_1}\right)^2. \quad \text{(A6)}$$

In order to reproduce the results of N-body simulation, we assume that close encounters generate e_1 with a Gaussian distribution with a peak value around $\sim e_1^*$ and a dispersion $\sim (e_1^*/3)$:

$$f(e_1)de_1 = \frac{1}{\sqrt{2\pi}(e_1^*/3)} \exp\left(-\frac{(e_1 - e_1^*)^2}{2(e_1^*/3)^2}\right) de_1. \quad \text{(A7)}$$

Energy conservation implies that at least one of the two planets must remain gravitationally bound to the host star after the intense scattering. This requirement also implies that e_1 must be <1. We truncate the high value tail in the e_1 distribution and renormalize the numerical factor such that integral of the probability is unity.
After the scattering, disk–planet interactions tend to damp the eccentricity of the retained planet (i.e., $j = 1$). In relatively massive disks, the planets' eccentricity damping timescale may be shorter than disk depletion timescale while in disks with modest or low masses, planets may retain residual asymptotic eccentricity. We estimate the local disk mass to be

$$M_{\rm disk} \sim \int_{a/2}^{2a} 2\pi r \Sigma_g dr \sim 30 f_g \left(\frac{a}{1\,\rm AU}\right) M_\oplus, \quad \text{(A8)}$$

where Σ_g is disk gas surface density (the scaling factor f_g is defined by Equation (15) in Section 3.1) and a is the semimajor axis of the remaining planet. If the planet is beyond a truncation distance of the power-law disk, $M_{\rm disk}$ is further reduced. In order to reflect the possibility of incomplete damping, we compare the angular momentum decrease due to the eccentricity damping with the total angular momentum of the local disk and limit the damping of eccentricity by $\Delta e^2 = (M_{\rm disk}/m_1)^2$. In our prescription, we impose a lower limit to the asymptotic eccentricity to be $e_1' = \sqrt{e_1^2 - \Delta e^2}$ if $\Delta e < e_1$.
Since the energy carried by the ejected planet is negligibly small, the semimajor axis of the retained planet (a_1) is accurately obtained from the conservation of energy such that

$$\frac{m_1}{a_1} = \frac{m_1}{a_{1,0}} + \frac{m_2}{a_{2,0}}. \quad \text{(A9)}$$

(3-b) *The non-ejection case.* Both planets would be retained if both of their $e_j^{\rm max} < 1$ after their close encounters. In gas-free environments, such scatterings would recur until either one of the planets is ejected or they undergo direct collisions. We assume this relaxation occurs on such a sufficiently short timescale that the scattering events occur in the presence of disk gas. Close scattering generally results in expansion of semimajor axis separation in addition to eccentricity excitation. The excited eccentricity is eventually damped by disk–planet interactions, leading the scattered planets to attain dynamical isolation. The eccentricity damping is applied for both planets with the same prescription as that used in the ejection case.

A.2. Three Giants

In Section 2.2, we discuss the interaction between three or more gas giant planets. After the disk depletion, long-term secular perturbation between three or more gas giant planets leads to dynamical instability and scattering between them. In a gas-free environment, such scatterings recur until one or more planet is ejected or some planets collide with each other. We do not consider the possibility that after the onset of orbit crossing, all members of multiple-planet systems (with three or more gas giants) can be retained.
N-body simulations (Marzari & Weidenschilling 2002; Nagasawa et al. 2008; Chatterjee et al. 2008) showed that the most probable outcome of orbit crossing in systems of three gas giant planets is the retention of two widely separated, eccentric planets and the ejection of one planet. The asymptotic orbits of the two retained planets are stable within the main-sequence lifetime of their host stars.
N-body simulations show that direct collisions may also occur in relatively early stages before the eccentricities of all three planets are fully excited. We assume that ~30% of the systems undergo direct collisions. Although there are some uncertainties in the collisional frequency, we have found that the merger events do not significantly modify the planets' asymptotic distribution provided their probability is less than 50%.
The procedures to calculate the asymptotic eccentricities and semimajor axes of the retained planets are similar to those applied in the case of two giants except that we need to distinguish between the inwardly and outwardly scattered planet and evaluate their orbital elements independently. The prescriptions for determining the dynamical outcomes are as follows.

(1) *Specification of the initial conditions.* In the population synthesis simulations, the criterion for orbital crossing is that its evaluated timescale, $\tau_{\rm cross}$, is smaller than the system evolution timescale (see Appendix A3 below). For a test case, we consider systems of three planets with narrowly separated, nearly circular and coplanar initial orbits under the assumption that orbit crossing is initiated on a timescale of $\sim \tau_{\rm cross}$.
(2) *Determination of collision or scattering.* Based on the results of N-body simulations, we assume direct collisions occur in 30% of scattering events. A merged planet is formed from a randomly selected pair of planets which are involved in the orbital crossings. Its resultant semimajor axis and eccentricity are calculated under the assumed conservation of total mass, orbital energy (assuming that the energy dissipated during the collisions is equal to the binding energy of the colliding planets), and angular momentum. In the N-body simulations, physical collisions between pairs of planets usually occur shortly

after their orbits begin to cross, before their semimajor axis and eccentricity have evolved significantly from their original values. Therefore, we neglect the effect of eccentricity excitation induced by the orbital crossings. In the remaining 70% of cases, we assume one or more planets are ejected.

(3) *Computation of trial eccentricities.* First, we simulate the maximum eccentricities excited by the close encounters between multiple planets. We denote planets 1 and 2 to be the most massive and second most massive planets. The maximum eccentricities excited through repeated close scatterings are calculated with Equations (A1) and (A2) where $e_{\rm esc,12}$ is that of planet 1 and $e_{{\rm esc},j1}$ is that of the two less massive planets ($j = 2, 3$). Because all of the planets cross each other's orbits, the eccentricities of planets 2 and 3 (e_2 and e_3) are primarily by the perturbation of planet 1 to the expected values of

$$e_j^{\rm max} = \begin{cases} \frac{m_1 \mathcal{R}_j}{(m_1+m_j)} e_{\rm esc,1j} & (\text{for } j \neq 1), \\ \frac{m_2 \mathcal{R}_j}{(m_2+m_1)} e_{\rm esc,12} & (\text{for } j = 1), \end{cases} \quad \text{(A10)}$$

where $\mathcal{R}_j$ is a random number chosen from a Rayleigh distribution with the root mean square of unity (see Equation (A1)).

(4) *Identification of an ejected planet.* We identify the planet with the largest value of the maximum eccentricity. If its eccentricity exceeds unity, we would consider this planet as an ejected body.

(5) *Determination of the asymptotic eccentricities of retained planets.* In contrast to the two giants case, the orbital eccentricities of the two retained planets are not constrained by the amount of residual angular momentum because it is freely exchanged and distributed between them.
Following the same argument as step 3-a in Appendix A1, we assume that the escaping planet (j = ejc) is ejected with a parabolic orbit, i.e., it carries little total energy and its $e_{\rm ejc} \simeq 1$.
Assuming the same degree of incomplete excitation, we obtain from Equation (A10) (with $\mathcal{R}_j \simeq 1$) that

$$e_j \sim \frac{e_j^{\rm max}}{e_{\rm ejc}^{\rm max}} e_{\rm ejc} \sim \begin{cases} \left(\frac{m_1+m_{\rm ejc}}{m_1+m_j}\right)^{1/2} \left(\frac{R_1+R_{\rm ejc}}{R_1+R_j}\right)^{1/2} & (\text{for } j \neq 1), \\ \left(\frac{m_2}{m_1}\right) \left(\frac{m_1+m_{\rm ejc}}{m_1+m_2}\right)^{1/2} \left(\frac{R_1+R_{\rm ejc}}{R_1+R_2}\right)^{1/2} & (\text{for } j = 1). \end{cases} \quad \text{(A11)}$$

Adding new values of $\mathcal{R}_j$ from those in Equation (A10), we use

$$e_j = \begin{cases} \left(\frac{m_1+m_{\rm ejc}}{m_1+m_j}\right)^{1/2} \left(\frac{R_1+R_{\rm ejc}}{R_1+R_j}\right)^{1/2} \mathcal{R}_j & (\text{for } j \neq 1), \\ \left(\frac{m_2}{m_1}\right) \left(\frac{m_1+m_{\rm ejc}}{m_1+m_2}\right)^{1/2} \left(\frac{R_1+R_{\rm ejc}}{R_1+R_2}\right)^{1/2} \mathcal{R}_j & (\text{for } j = 1). \end{cases} \quad \text{(A12)}$$

(6) *Determination of an inwardly scattered planet.* The inwardly scattered planet is selected with a mass-square weighted probability. We adopt this statistical weight because the less massive member of the system tends to be scattered outward. The mass weight function was calibrated with the N-body simulations.

(7) *Determination of the semimajor axis of an outwardly scattered body.* Since the outwardly scattered planet carries a small fraction of the total energy, its asymptotic semimajor axis ($a_{\rm out}$) is not well constrained by the constraint of total energy conservation. The outer planet is scattered from the "vicinity" of the region in which planets initially reside and its asymptotic periastron is close to the region. We estimate the outer planet's periastron distance to be

$$a_{\rm out}(1 - e_{\rm out}) = \sqrt{a_{\rm max} a_{\rm min}} + a_{\rm max} \mathcal{R}, \quad \text{(A13)}$$

where $e_{\rm out}$ is its excited eccentricity of the outer planet, and $a_{\rm max}$ and $a_{\rm min}$ are the maximum and minimum semimajor axes of the planets in initial state prior to the orbit crossing. Energy diffusion and semimajor axis redistribution generally occur before an ejection. Due to the requirement of energy conservation, they generally lead to an expansion of the planetary system. Assuming that diffusion length is scaled by $a_{\rm max}$, we adopt a "typical" semimajor axis of the outwardly scattered planet to be the right hand side of Equation (A13). Since $e_{\rm out}$ is already determined in step 4, $a_{\rm out}$ is given by Equation (A13).

(8) *Determination of the semimajor axis of an inwardly scattered body.* The semimajor axis of the inner planet ($a_{\rm in}$) is obtained under the constraint of energy conservation,

$$\frac{m_{\rm in}}{a_{\rm in}} = E - \frac{m_{\rm out}}{a_{\rm out}}, \quad \text{(A14)}$$

where $m_{\rm in}$ is the mass of the inner planet and E is the total energy calculated by the initial semimajor axes of the three planets. Since the energy carried by the ejected body is very small, $a_{\rm in} \simeq m_{\rm in}/E$.

A.3. The General Case

In the population synthesis calculations, giant planets and rocky/icy planetary embryos form in common disk environments, coexist, and dynamically evolve during and after the gas depletion. During the early stages of their life span, i.e., while there is still substantial disk gas, we only consider scattering events between two planets involving a gas giant when their orbital separation becomes less than $\Delta a_{\rm c} \simeq 2\sqrt{3} r_{\rm H}$. Under this condition, we apply the prescription given in Section 2.1.

The prescriptions for scattering after disk gas depletion in a general case are as follows.

(1) We identify "giant planets" from a list of all the bodies in the system by the conditions that (i) the planetary mass $m > 30\,M_\oplus$ and (ii) $e_{\rm esc} > 1$, where

$$e_{\rm esc} = \frac{v_{\rm esc}}{v_{\rm K}} = \frac{\sqrt{2Gm/R}}{\sqrt{GM_*/a}} \simeq 1.6 \left(\frac{m}{M_J}\right)^{1/3} \left(\frac{\rho}{1\,{\rm g\,cm^{-3}}}\right)^{1/6} \left(\frac{a}{1\,{\rm AU}}\right)^{1/2}. \quad \text{(A15)}$$

We evaluate $\tau_{\rm cross}$ for all pairs of the giant planets, using the fitting formula obtained by Zhou et al. (2007) with some minor modifications:

$$\log\left(\frac{\tau_{\rm cross}}{T_{\rm K}}\right) = A + B \log\left(\frac{b}{2.3 r_{\rm H}}\right), \quad \text{(A16)}$$

where $T_{\rm K}$ is Keplerian time at the mean semimajor axis $a(= \sqrt{a_i a_j})$ of the pair, $b = |a_i - a_j|$, $r_{\rm H} = ((m_i +$

$m_j)/3M_*)^{1/3}\min(a_i, a_j)$ (which is slightly modified from Paper VI), and

$$A = -2 + e_0 - 0.27\log\mu,$$
$$B = 18.7 + 1.1\log\mu - (16.8 + 1.2\log\mu)e_0,$$
$$e_0 = \frac{1}{2}\frac{(e_i + e_j)a}{b}, \quad \text{(A17)}$$
$$\mu = \frac{(m_i + m_j)/2}{M_*}.$$

(2-a) We assume that the systems of only two giant planets are stable against mutual long-term secular perturbations such as that between Jupiter and Saturn. Nevertheless, systems of three or more gas giant planets with widely separated nearly circular orbits may retain their initial semimajor axes and eccentricities. But, if $\tau_{\rm cross}$ of some giant planet with two or more other giants is less than the age of the system ($\tau_{\rm sys}$), we would assume that orbit crossing of these planets has occurred at $t = \tau_{\rm sys} + \tau_{\rm cross}$. In our population synthesis models, if the expected t is less than the calculation termination time that is 10^9 yr, we would apply the following procedures to simulate the outcomes of orbital crossing among giant planets.

1. The pair of gas giant planets with the shortest orbital crossing time ($\tau^*_{\rm cross}$) is assumed to undergo close encounters before any other pairs. We select giant planets which participate in follow-up (secondary) orbit crossings using the conditions that radial excursions of their initial orbits overlap with the hypothetical orbits of the pair with $\tau^*_{\rm cross}$ predicted by the maximum eccentricities given by Equation (A10).
2. We follow steps 2–6 of the three giants case in Appendix A2. For systems with more than three gas giants, we assume only one gas giant planet is scattered inwardly while all of the other gas giant planets are scattered outwardly. This assumption is based on the results of N-body simulations which suggest this is the most common outcome.
3. We calculate $\tau_{\rm cross}$ from the new orbital configurations and go back to step 1 until $\tau_{\rm sys} + \tau^*_{\rm cross}$ exceeds 10^9 yr. When the number of remaining gas giant planets is reduced to two, we no longer apply this procedure.

Finally, we remove all of the planets other than the gas giant planets. This operation is based on the assumption that violent secular perturbations from the highly eccentric giants destabilize the other planets' orbits (Matsumura et al. 2013).

(2-b) In systems without any gas giant planets or systems with widely separated gas giants in which the orbit-crossing timescale is longer than the age of their host stars, we consider the possibility of orbit crossing and dynamical relaxation among the small planets. In these simulations, we assume negligible dynamical perturbation on the gas giant planets by the smaller super-Earths and terrestrial planets. The procedures for simulating the evolution of the smaller planets are extensively described in Paper VI, except for step 6 in which perturbations from a giant planet(s) are taken into account. Here we present a brief summary (for details, see Paper VI).

1. *Specification of the initial conditions.* We select non-giant planets that can undergo eccentricity excitations. We assume the amount of residual planetesimals is small enough that dynamical friction from the planetesimals does not inhibit the eccentricity excitations by mutual distant perturbations of the planets.
2. *Evaluation of* $\tau_{\rm cross}$. We evaluate $\tau_{\rm cross}$ of all of the low-mass planets, using Equation (A16). The pair of planets with the shortest orbit-crossing time ($\tau^*_{\rm cross}$) is assumed to undergo close encounters before any other pairs.
3. *Determination on the excited eccentricities and changes in semimajor axes of orbit-crossing planets.* We determine non-giant planets participating in the secondary orbit crossing and evaluate their excited eccentricities with Equation (A10). We determine changes in their semimajor axes due to radial diffusion by successive close encounters after adjustment to satisfy conservation of energy.
4. *Identification of collision pairs.* Close encounters can also lead to physical collisions. We assume all physical collisions are cohesive and they lead to merger events. Among the planets in the orbit-crossing group, a colliding pair is chosen with a weighted collisional probability which is proportional to a^{-3}.
5. *Creation of a merger.* A merged planet is created from the colliding pair. It acquires the total mass of the colliding pair. We determine orbital elements of the merged planet, using conservation of energy and Laplace–Runge–Lenz vector. We randomly select the relative angle between longitudes of periastrons of the colliding pair from its range that allows actual crossing of their unperturbed orbits.
6. *Imposition of perturbations from the giant planets.* If there is one or more gas giants in the system, the following procedure is applied. If the range of radial excursion of non-giant planets in the new orbital configuration overlaps with the strongly perturbed zone of any gas giant planets, we assume that the non-giant planets are scattered by the giant planet. The width of the strongly perturbed zone is assumed to be $\sim 3.5 r_{\rm H}$. Using Equation (A10), we evaluate eccentricities of the non-giant planets excited by the giant planets. If the perturbed e exceeds unity, we regard that the planet is ejected. If it is less than unity, we evaluate a new semimajor axis for the scattered planet by $a_{\rm new} = a_{\rm old}/(1 - e)$. This procedure is added to the prescriptions described in Paper VI.
7. *Update of the system.* We update $\tau_{\rm sys}$, adding $\tau_{\rm cross}$ and a collision timescale after onset of orbit crossing. We go back to step 2 until the updated $\tau_{\rm sys}$ exceeds $\sim 10^9$ yr.

REFERENCES

Alibert, Y., Mordasini, C., & Benz, W. 2011, A&A, 526, 63
Artymowicz, P. 1993, ApJ, 419, 166
Beaugé, C., & Nesvorný, D. 2012, ApJ, 751, 119
Chambers, J. E., Wetherill, G. W., & Boss, A. P. 1996, Icar, 119, 261
Chatterjee, S., Ford, E., Matsumura, S., & Rasio, F. A. 2008, ApJ, 686, 580
Chiang, E. I., & Goldreich, P. 1997, ApJ, 490, 368
D'Angelo, G., Kley, W., & Henning, T. 2003, ApJ, 586, 540
D'Angelo, G., & Lubow, S. H. 2008, ApJ, 685, 560
Dobbs-Dixon, I., Li, S.-L., & Lin, D. N. C. 2007, ApJ, 660, 791
Ford, B. E., Havlickova, M., & Rasio, F. A. 2001, Icar, 150, 303
Ford, B. E., & Rasio, F. A. 2008, ApJ, 686, 621
Garaud, P., & Lin, D. N. C. 2007, ApJ, 654, 606
Gladman, B. 1993, Icar, 106, 247
Hartmann, L., Calvet, N., Gullbring, E., & D'Alessio, P. 1998, ApJ, 495, 385
Hayashi, C. 1981, PThPS, 70, 35
Helled, R., Podolak, M., & Kovetz, A. 2008, Icar, 195, 863

Hori, Y., & Ikoma, M. 2010, ApJ, 714, 1343
Hori, Y., & Ikoma, M. 2011, MNRAS, 416, 1419
Ida, S., & Lin, D. N. C. 2004a, ApJ, 604, 388 (Paper I)
Ida, S., & Lin, D. N. C. 2004b, ApJ, 616, 567 (Paper II)
Ida, S., & Lin, D. N. C. 2005, ApJ, 626, 1045 (Paper III)
Ida, S., & Lin, D. N. C. 2008a, ApJ, 673, 487 (Paper IV)
Ida, S., & Lin, D. N. C. 2008b, ApJ, 685, 584 (Paper V)
Ida, S., & Lin, D. N. C. 2010, ApJ, 719, 810 (Paper VI)
Ida, S., & Makino, J. 1992, Icar, 96, 107
Ikoma, M., Nakazawa, K., & Emori, H. 2000, ApJ, 537, 1013
Ivanov, P. B., & Papaloizou, J. C. B. 2004, MNRAS, 347, 437
Iwasaki, K., Emori, H., Nakazawa, K., & Tanaka, H. 2002, PASJ, 54, 471
Jurić, M., & Tremaine, S. 2008, ApJ, 686, 603
Kokubo, E., & Ida, S. 1998, Icar, 131, 171
Kokubo, E., & Ida, S. 2002, ApJ, 581, 666
Kretke, K. A., & Lin, D. N. C. 2012, ApJ, 755, 74
Lin, D. N. C., & Ida, S. 1997, ApJ, 477, 781
Lin, D. N. C., & Papaloizou, J. C. B. 1985, in Protostars and Planets II, ed. D. C. Black & M. S. Matthew (Tucson, AZ: Univ. Arizona Press), 981
Lynden-Bell, D., & Pringle, J. E. 1974, MNRAS, 168, 603
Marzari, F., & Weidenschilling, S. J. 2002, Icar, 156, 570
Matsumura, S., Ida, S., & Nagasawa, M. 2013, ApJ, 767, 129
McNeil, D., Duncan, M., & Levison, H. 2005, AJ, 130, 2884
Min, M., Dullemond, C. P., Kama, M., & Dominik, C. 2011, Icar, 212, 416
Mordasini, C., Alibert, Y., & Benz, W. 2009a, A&A, 501, 1139
Mordasini, C., Alibert, Y., & Benz, W. 2009b, A&A, 501, 1161
Muto, T., Takeuchi, T., & Ida, S. 2010, ApJ, 737, 37
Nagasawa, M., Ida, S., & Bessho, T. 2008, ApJ, 678, 498
Ogihara, M., Duncan, M., & Ida, S. 2010, ApJ, 721, 1184
Ogihara, M., & Ida, S. 2009, ApJ, 699, 824
Oka, A., Nakamoto, T., & Ida, S. 2011, ApJ, 738, 141
Ostriker, E. C. 1999, ApJ, 513, 252
Paardekooper, S.-J., Baruteau, C., & Kley, W. 2011, MNRAS, 410, 293
Papaloizou, J. C. B., & Larwood, J. D. 2000, MNRAS, 315, 823
Pollack, J. B., Hollenbach, D., Beckwith, S., et al. 1994, ApJ, 421, 615
Pollack, J. B., Hubickyj, O., Bodenheimer, P., et al. 1996, Icar, 124, 62
Rasio, F. A., & Ford, B. E. 1996, Sci, 274, 954
Raymond, S. N., Armitage, P. J., & Gorelick, N. 2010, ApJ, 711, 772
Safronov, V. 1969, Evolution of the Protoplanetary Cloud and Formation of the Earth and Planets (Moscow: Nauka)
Shakura, N. I., & Sunyaev, R. A. 1973, A&A, 24, 337
Shiraishi, M., & Ida, S. 2008, ApJ, 684, 1416
Stewart, G. R., & Ida, S. 2000, Icar, 143, 28
Tanaka, H., Takeuchi, T., & Ward, W. 2002, ApJ, 565, 1257
Tanaka, H., & Ward, W. 2004, ApJ, 602, 388
Ward, W. 1993, Icar, 106, 274
Weidenschilling, S. J., & Marzari, F. 1996, Natur, 384, 619
Zhou, J., Lin, D. N. C., & Sun, Y. 2007, ApJ, 666, 423

The Astrophysical Journal, 821:82 (24pp), 2016 April 20 doi:10.3847/0004-637X/821/2/82

SINTERING-INDUCED DUST RING FORMATION IN PROTOPLANETARY DISKS: APPLICATION TO THE HL TAU DISK

Satoshi Okuzumi[1,2], Munetake Momose[3], Sin-iti Sirono[4], Hiroshi Kobayashi[5], and Hidekazu Tanaka[6]
[1] Department of Earth and Planetary Sciences, Tokyo Institute of Technology, Meguro, Tokyo, 152-8551, Japan; okuzumi@geo.titech.ac.jp
[2] Jet Propulsion Laboratory, California Institute of Technology, Pasadena, CA 91109, USA
[3] College of Science, Ibaraki University, Mito, Ibaraki 310-8512, Japan
[4] Department of Earth and Environmental Sciences, Nagoya University, Nagoya 464-8601, Japan
[5] Department of Physics, Nagoya University, Nagoya, Aichi 464-8602, Japan
[6] Institute of Low Temperature Science, Hokkaido University, Sapporo 060-0819, Japan
Received 2015 October 12; accepted 2016 February 3; published 2016 April 13

ABSTRACT

The latest observation of HL Tau by ALMA revealed spectacular concentric dust rings in its circumstellar disk. We attempt to explain the multiple ring structure as a consequence of aggregate sintering. Sintering is known to reduce the sticking efficiency of dust aggregates and occurs at temperatures slightly below the sublimation point of the constituent material. We present a dust growth model that incorporates sintering and use it to simulate global dust evolution due to sintering, coagulation, fragmentation, and radial inward drift in a modeled HL Tau disk. We show that aggregates consisting of multiple species of volatile ices experience sintering, collisionally disrupt, and pile up at multiple locations slightly outside the snow lines of the volatiles. At wavelengths of 0.87–1.3 mm, these sintering zones appear as bright, optically thick rings with a spectral slope of ≈ 2, whereas the non-sintering zones appear as darker, optically thinner rings of a spectral slope of ≈ 2.3–2.5. The observational features of the sintering and non-sintering zones are consistent with those of the major bright and dark rings found in the HL Tau disk, respectively. Radial pileup and vertical settling occur simultaneously if disk turbulence is weak and if monomers constituting the aggregates are ~ 1 μm in radius. For the radial gas temperature profile of $T = 310(r/1\ \mathrm{au})^{-0.57}$ K, our model perfectly reproduces the brightness temperatures of the optically thick bright rings and reproduces their orbital distances to an accuracy of $\lesssim 30\%$.

Key words: dust, extinction – planets and satellites: composition – protoplanetary disks – stars: individual (HL Tau) – submillimeter: planetary systems

1. INTRODUCTION

HL Tau is a flat spectrum T Tauri star with a circumstellar disk that is very luminous at millimeter wavelengths (Beckwith et al. 1990). Although the age of HL Tau has not been well constrained, its low bolometric temperature and high mass accretion rate (e.g., White & Hillenbrand 2004), as well as the presence of an optical jet (Mundt et al. 1988) and an infalling envelope (Hayashi et al. 1993), suggest that the stellar age is likely less than 1 Myr. For these reasons, HL Tau is considered to be an ideal observational target for studying the very initial stages of disk evolution and planet formation.

The recent Long Baseline Campaign of the Atacama Large Millimeter/submillimeter Array (ALMA) provided spectacular images of the HL Tau disk (ALMA Partnership et al. 2015). ALMA resolved the disk at three millimeter wavelengths with an unprecedented spatial resolution of ≈ 3.5 au at 0.87 mm. The observations revealed a pattern of multiple bright and dark rings that are remarkably symmetric with respect to the central star. The spectral index at 1 mm is ~ 2 in the central emission peak and some of the bright rings, and is ~ 2.3–3 in the dark rings (ALMA Partnership et al. 2015; Zhang et al. 2015). The fact that the millimeter spectral index is $\lesssim 3$ in the dark, presumably optically thin rings suggests that dust grains in the HL Tau disk have already grown into aggregates whose radius is larger than a few millimeters, assuming that the aggregates are compact (Draine 2006, see Kataoka et al. 2014 for how the aggregates' porosity alters this interpretation). The observed continuum emission is best reproduced by models assuming substantial dust settling (Kwon et al. 2011, 2015; Pinte et al. 2016), implying that the large aggregates are dominant in mass and that the turbulence in the gas disk is weak. Because dust growth and settling are key processes in planet formation, understanding the origin of this axisymmetric dust structure is greatly relevant to understanding how planets form in protoplanetary disks.

There are a variety of mechanisms that can produce axisymmetric dust rings and gaps in a protoplanetary disk. One of the most common mechanisms of creating a dust ring is dust trapping at local gas pressure maxima under the action of gas drag (Whipple 1972). In a protoplanetary disk, pressure bumps may be created by disk–planet interaction (Paardekooper & Mellema 2004, 2006; Fouchet et al. 2010; Gonzalez et al. 2012; Pinilla et al. 2012; Zhu et al. 2012; Dipierro et al. 2015; Dong et al. 2015), magnetorotational instability (Johansen et al. 2009; Uribe et al. 2011), and/or steep radial variation of the disk viscosity (Kretke & Lin 2007; Dzyurkevich et al. 2010; Flock et al. 2015). Axisymmetric dust rings may also be produced by secular gravitational instability (Youdin 2011; Takahashi & Inutsuka 2014), baroclinic instability arising due to dust settling (Lorén-Aguilar & Bate 2015), or a combined effect of dust coagulation and radial drift (Laibe 2014; Gonzalez et al. 2015). Planet-carved gaps may explain the observed features of the HL Tau disk even if dust trapping at the pressure maxima is ineffective (Kanagawa et al. 2015).

Another intriguing possibility is that the multiple ring patterns of the HL Tau disk are related to the snow lines of various solid materials. Recently, Zhang et al. (2015) used a temperature profile based on a previous study (Men'shchikov

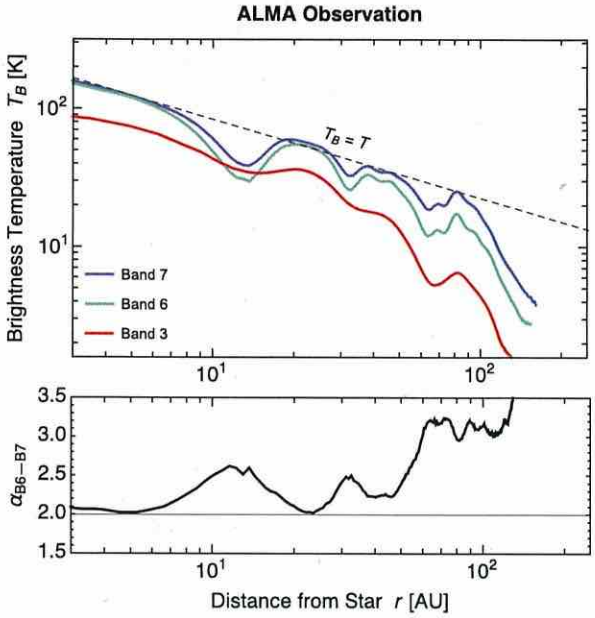

Figure 1. Upper panel: radial profiles of the brightness temperature T_B of the HL Tau disk retrieved from the ALMA data (ALMA Partnership et al. 2015; see text for details). The red, green, and blue curves are for ALMA Bands 3, 6, and 7, respectively. The dashed line shows the gas temperature profile $T(r)$ adopted in this study (Equation (1)). Lower panel: spectral index between Bands 6 and 7, α_{B6-B7}, vs. radial distance r.

et al. 1999) and showed that the major dark rings seen in the ALMA images lie close to the sublimation fronts of some main cometary volatiles, such as H_2O and NH_3. They interpreted this as being evidence of rapid particle growth by condensation, as recently predicted by Ros & Johansen (2013) for H_2O ice particles. However, it is unclear whether relatively minor volatiles such as NH_3 and clathrates indeed accelerate dust growth.

In this study, we focus on another important mechanism that can affect dust growth near volatile snow lines: sintering. Sintering is the process of fusing grains together at a temperature slightly below the sublimation point. Sintered aggregates are characterized by thick joints, called necks, that connect the constituent grains (e.g., see Figures 3 and 4 of Poppe 2003; Figure 1 of Blackford 2007). A familiar example of a sintered aggregate is a ceramic material (i.e., pottery), which is an agglomerate of micron-sized clay particles fused together by sintering. Sintered aggregates are less sticky than unsintered ones because the necks prevent collision energy from being dissipated through plastic deformation. For example, unsintered dust aggregates are known to absorb much collision energy through rolling friction among constituent grains (Dominik & Tielens 1997). However, sintered aggregates are unable to lose their collision energy in this way, and therefore their collision tends to end up with bouncing, fragmentation, or erosion rather than sticking (Sirono 1999; Sirono & Ueno 2014). Thus, sintering suppresses dust growth in regions slightly outside the snow lines.

The importance of sintering in the context of protoplanetary dust growth was first pointed out by Sirono (1999), and has been studied in more detail by Sirono (2011a, 2011b) and Sirono & Ueno (2014). Sirono (1999) simulated collisions of two-dimensional sintered and unsintered aggregates (both made of 0.1 μm sized icy grains) with a wall, taking into account the high mechanical strength of the sintered necks. At collision velocities lower than 10 m s^{-1}, the sintered aggregates were found to bounce off a wall, whereas the unsintered ones stuck to it. By using the same sintered neck model, Sirono & Ueno (2014) simulated collisions between two identical sintered aggregates, each of which consists of up to 10^4 icy grains (again of 0.1 μm radius) and has a porosity of 30%–80%. They found that the aggregates erode each other rather than stick if the collision velocity is above 20 m s^{-1}. This threshold is considerably lower than that for unsintered aggregates, which is around 50 m s^{-1} when the constituent grains are ice and 0.1 μm in radius (Dominik & Tielens 1997; Wada et al. 2009, 2013).

Another important fact about sintering is that it can occur at multiple locations in a protoplanetary disk, as noted by Sirono (1999, 2011b). In contrast to condensational growth as envisioned by Zhang et al. (2015), sintering requires only a small amount of volatiles because the volume of a neck is generally a small fraction of the grain volume. For example, the volume fraction is only 0.2% even if the neck radius is as large as 30% of the grain radius (Sirono 2011b). Therefore, the inclusion of NH_3 ice at a standard cometary abundance (~0.2%–1.4%; Mumma & Charnley 2011) is enough to sinter the grains near the NH_3 snow line.

In this study, we investigate how this "sintering barrier" against dust coagulation affects the global evolution of dust in a protoplanetary disk. We present a simple recipe to account for the change in the mechanical strength of dust aggregates due to sintering, and apply it to global simulations of dust evolution in a disk that take into account coagulation, fragmentation, and radial inward drift induced by gas drag (Adachi et al. 1976; Weidenschilling 1977). Our simulations for the first time show that sintering-induced fragmentation leads to a pile up of dust materials in the vicinity of each volatile snow line. We demonstrate that at millimeter wavelengths, these pileups can be seen as multiple bright dust rings, as observed in the HL Tau disk.

The structure of this paper is as follows. We begin by modeling the HL Tau gas disk in Section 2. Section 3 introduces our model for aggregate sintering and sublimation. Section 4 describes our simulation method, Section 5 presents the results from our fiducial simulation run, and Section 6 presents a parameter study. The validity and possible limitations of our model are discussed in Section 7. A summary is presented in Section 8.

2. DISK MODEL

We model the HL Tau protoplanetary disk as a static, axisymmetric, and vertically isothermal disk. The radial profiles of the temperature and gas density are presented in Sections 2.1 and 2.2, respectively.

2.1. Temperature Profile

We construct a radial temperature profile $T(r)$ of the HL Tau disk based on the data of the surface brightness profiles provided by ALMA Partnership et al. (2015). We deproject the intensity maps of the disk's dust continuum at ALMA Bands 3, 6, and 7 into circularly symmetric views, assuming the disk inclination angle of 46°.7 and the position angle of 138° (ALMA Partnership et al. 2015). We then obtain the radial

profiles of the intensities I_ν by azimuthally averaging the deprojected images. The upper panel of Figure 1 shows the derived radial emission profiles. Here, the intensities are expressed in terms of the Planck brightness temperature T_B. Shown in the lower panel is the spectral index between Bands 6 and 7, $\alpha_{B6-B7} \equiv \ln(I_{B7}/I_{B6})/\ln(\nu_{B7}/\nu_{B6})$, where $\nu_{B6} = 233.0$ GHz and $\nu_{B7} = 343.5$ GHz are the frequencies at Bands 6 and 7, respectively.

As noted by ALMA Partnership et al. (2015), the HL Tau disk has a pronounced central emission peak at $\lesssim$10 au and three major bright rings at ~20, 40, and 80 au. The central emission peak and two innermost bright rings have a spectral index of $\alpha_{B6-B7} \approx 2$. In general, this indicates that the emission at these wavelengths is either optically thick, or optically thin but from dust particles larger than millimeters. The brightness temperature is equal to the gas temperature in the former case and is lower in the latter case. While Zhang et al. (2015) adopted the latter interpretation, we now pursue the former interpretation. Specifically, we assume that the Band 7 emission is optically thick and hence $T(r) = T_B$ at the center, 20 au, and 40 au. The simplest profile satisfying this assumption is the single power law

$$T(r) = 310\left(\frac{r}{1\ \mathrm{au}}\right)^{-0.57}\ \mathrm{K}, \quad (1)$$

which is shown by the dashed line in the upper panel of Figure 1. We adopt this temperature profile in this study.

2.2. Density Structure

The density structure of the HL Tauri gas disk is unknown. Therefore, we simply assume that the gas surface density $\Sigma_d(r)$ obeys a power law with an exponential taper (Hartmann et al. 1998; Kitamura et al. 2002; Andrews et al. 2009),

$$\Sigma_g(r) = \frac{(2-\gamma)M_{\rm disk}}{2\pi r_c^2}\left(\frac{r}{r_c}\right)^{-\gamma}\exp\left[-\left(\frac{r}{r_c}\right)^{2-\gamma}\right], \quad (2)$$

where r_c and $M_{\rm disk}$ are a characteristic radius and the total mass of the gas disk, respectively, and γ ($0 < \gamma < 2$) is the negative slope of Σ_g at $r \ll r_c$. We take $\gamma = 1$ as the fiducial value but also consider $\gamma = 0.5$ and 1.5. The dependence of our simulation results on γ will be studied in Section 6.1. The values of $M_{\rm disk}$ and r_c are fixed to $0.2M_\odot$ and 150 au, respectively. The adopted disk mass is about twice the upper end of the previous mass estimates for the HL Tau disk (Guilloteau et al. 2011; Kwon et al. 2011, 2015). We assume such a massive disk because the dust mass in the disk decreases with time due to the radial drift of dust particles (see Section 5.1). Figure 2 shows the surface density profiles for $\gamma = 1$, 0.5, and 1.5.

Because the disk is assumed to be vertically isothermal, the vertical distribution of the gas density obeys a Gaussian with the midplane value $\rho_g = \Sigma_g/(\sqrt{2\pi}H_g)$, where $H_g = c_s/\Omega$ is the gas scale height, c_s is the sound speed, and Ω is the Keplerian frequency. The isothermal sound speed is given by $c_s = \sqrt{k_B T/m_\mu}$, where k_B is the Boltzmann constant and m_μ is the mean molecular mass of the disk gas assumed to be $m_\mu = 2.3$ amu. The Keplerian frequency is given by $\Omega = \sqrt{GM_*/r^3}$, where G is the gravitational constant and M_* is the stellar mass. We adopt $M_* = 1M_\odot$ so that the sum of the stellar and disk masses in the fiducial model, $M_* + M_{\rm disk} = 1.2M_\odot$, is within the range of the previous estimates for the HL Tau system (Beckwith et al. 1990; Sargent & Beckwith 1991; ALMA Partnership et al. 2015).

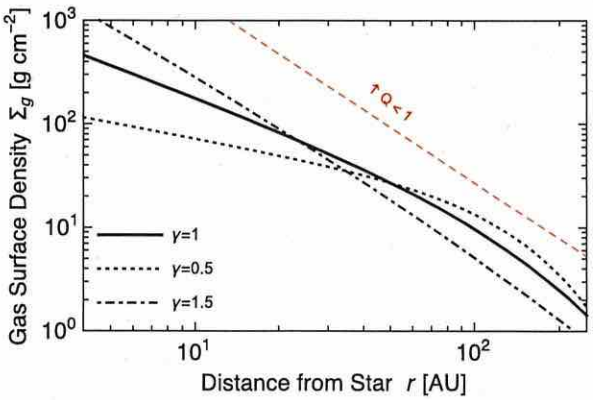

Figure 2. Radial profiles of the gas surface density Σ_g adopted in this study (Equation (2)). The solid, dotted, and dotted–dashed lines are for $\gamma = 1$ (fiducial), 0.5, and 1.5, respectively. The dashed line shows $Q \equiv c_s\Omega/\pi G\Sigma_g = 1$.

We note here that the assumed disk model is marginally gravitationally stable: the Toomre stability parameter $Q \equiv c_s\Omega/(\pi G\Sigma_g)$ satisfies $Q \gtrsim 1$ at all radii for all choices of γ. This can be seen in Figure 2, where the surface density corresponding to $Q = 1$ is shown by the dashed line.

3. SUBLIMATION AND SINTERING OF ICY DUST

We model dust in the HL Tau disk as aggregates of (sub) micron-sized grains. Each constituent grain, which we call a monomer, is assumed to be coated by an ice mantle composed of various volatile molecules (Section 3.1). The composition of the mantle at a given distance from the central star is determined using the equilibrium vapor pressure curves for the volatile species (Sections 3.2 and 3.3). The equilibrium vapor pressures also determine the rate at which the sintering of aggregates proceeds at each orbital distance (Section 3.4). The sintering rate will be used to determine the sticking efficiency of the aggregates in our dust coagulation simulations (see Section 4.4).

3.1. Volatile Composition

We assume that the volatile composition of the HL Tau disk is similar to that of comets in our solar system. We select six major cometary volatiles in addition to H_2O and take their abundances relative to H_2O to be consistent with cometary values (Mumma & Charnley 2011). The volatiles we select are ammonia (NH_3), carbon dioxide (CO_2), hydrogen sulfide (H_2S), ethane (C_2H_6), methane (CH_4), and carbon monoxide (CO). We neglect another equally abundant species, methanol (CH_3OH), because the snow line of CH_3OH is very close to that of more abundant H_2O (Sirono 2011b). Table 1 lists the abundances we adopt and the observed ranges of cometary abundances taken from Mumma & Charnley (2011).

3.2. Equilibrium Vapor Pressures

The equilibrium vapor pressures of volatiles determine the temperatures at which sublimation and sintering occurs. In this

Table 1
Abundances of Major Cometary Volatiles Relative to H_2O (in Percent)

Species	Cometary Value[a]	Adopted Value f_j
H_2O	100	100
NH_3	0.2–1.4	1
CO_2	2–30	10
H_2S	0.12–1.4	1
C_2H_6	0.1–2	1
CH_4	0.4–1.6	1
CO	0.4–30	10

Note.
[a] Mumma & Charnley (2011).

Table 2
Vapor Pressure Parameters

Species	L_j (K)	A_j	Ref.	$L_{j,\mathrm{tuned}}$ (K)
H_2O	6070	30.86	1	5463
NH_3	3754	30.21	2	3379
CO_2	3148	30.01	2	...
H_2S	2860	27.70	3	...
C_2H_6	2498	30.24	4	2248
CH_4	1190	24.81	2	...
CO	981.8	26.41	2	...

References. (1) Bauer et al. (1997), (2) Yamamoto et al. (1983), (3) Haynes (2014), (4) Moses et al. (1992).

study, we approximate the equilibrium vapor pressure for each volatile species j by the Arrhenius form

$$P_{\mathrm{ev},j} = \exp\left(-\frac{L_j}{T} + A_j\right) \mathrm{dyn\ cm^{-2}}, \quad (3)$$

where L_j is the heat of sublimation in Kelvin and A_j is a dimensionless constant. Table 2 summarizes the values of L_j and A_j for the seven volatile species considered in this study. For CO, CH_4, CO_2, and NH_3, we follow Sirono (2011b) and take the values from Table 2 of Yamamoto et al. (1983). The values for C_2H_6 are derived from the analytic expression of the vapor pressure by Moses et al. (1992, see their Table III; note that we here neglect the small offset of T in their original expression). For H_2S, we determined L_j and A_j by fitting Equation (3) to the vapor pressure data provided by (Haynes 2014, page 6–92). Figure 3 shows $P_{\mathrm{ev},j}$ of the seven volatile species as a function of r for the temperature distribution given by Equation (1).

Strictly speaking, the vapor pressure data given in Table 2 only apply to pure ices. In protoplanetary disks, volatiles may be trapped inside the H_2O mantle of dust grains instead of being present as pure ices. If this is the case, the volatiles would sublimate not only at the sublimation temperatures for pure ices but also at higher temperatures where monolayer desorption from the H_2O substrate, phase transition of H_2O ice, or codesorption with the H_2O ice takes place (Collings et al. 2003, 2004; Martín-Doménech et al. 2014). However, all these high-temperature desorption processes are irrelevant to neck formation (sintering) because the desorbed molecules are unable to recondense onto grain surfaces at such high temperatures. By using the vapor pressure data for pure ices, we effectively neglect all these desorption processes.

When estimating the locations of the snow lines, it is important to note that the vapor pressure data in the literature are subject to small but still non-negligible uncertainties. For example, the values of the sublimation energies we use for H_2O, NH_3, CO_2, and CO are 10%–20% higher than those derived from the very recent temperature programmed desorption experiments by Martín-Doménech et al. (2014, see their Table 4). Luna et al. (2014) compiled the sublimation energies of major cometary volatiles from different experimental methods, and showed that the published sublimation energies have a standard deviation of 14%, 8%, 11%, and 8% for NH_3, CO_2, CH_4, and CO, respectively (see their Table 2 and Figures 4 and 5). Such uncertainties might be present in the vapor pressure data for other volatiles species. As we demonstrate in Section 6.4, even a 10% uncertainty in L_j can lead to a 20%–30% uncertainty in the location of its snow line, and a better match between our simulation results and the ALMA observation can be achieved if the sublimation energies of H_2O, NH_3, and C_2H_6 are taken to be 10% lower than the fiducial values. We denote these tuned sublimation energies by $L_{j,\mathrm{tuned}}$ (see Table 2). For H_2O and NH_3, the tuned sublimation energies are more consistent with the results of Martín-Doménech et al. (2014).

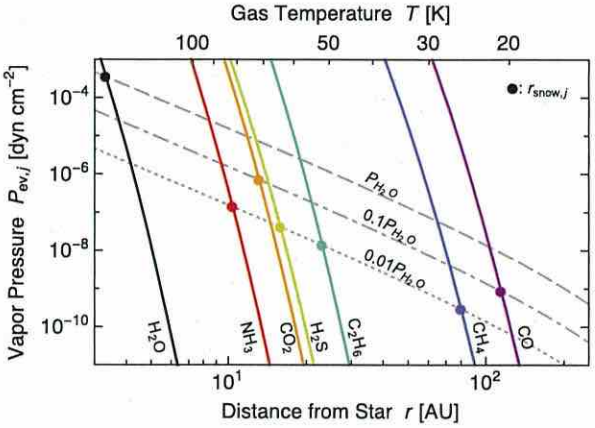

Figure 3. Equilibrium vapor pressures $P_{\mathrm{ev},j}$ (Equation (3)) of major cometary volatiles as a function of orbital distance r for the temperature profile given by Equation (1). From left to right: H_2O (black), NH_3 (red), CO_2 (orange), H_2S (yellow), C_2H_6 (green), CH_4 (blue), and CO (purple). The gray curves show the partial pressures of the volatiles (dashed curve for H_2O, dotted–dashed curve for CO and CO_2, dotted curve for the other species) for the gas density profile given by Equation (2) with $\gamma = 1$ and $\Sigma_{\mathrm{d}} = 0.01\Sigma_{\mathrm{g}}$. The filled circles indicate the locations of the snow lines, $r = r_{\mathrm{snow},j}$.

3.3. Snow Lines

For each volatile species j, we define the snow line as the orbit inside which the equilibrium pressure $P_{\mathrm{ev},j}$ exceeds the partial pressure P_j. Assuming that the disk gas is well mixed in the vertical direction, P_j is related to the surface number density of j-molecules in the gas phase, N_j, as

$$P_j = \frac{N_j k_{\mathrm{B}} T}{\sqrt{2\pi} H_{\mathrm{g}}}. \quad (4)$$

In this study, we do not directly treat the evolution of N_j, but instead estimate them by assuming that the ratio between N_j and the surface number density of H_2O molecules in the solid

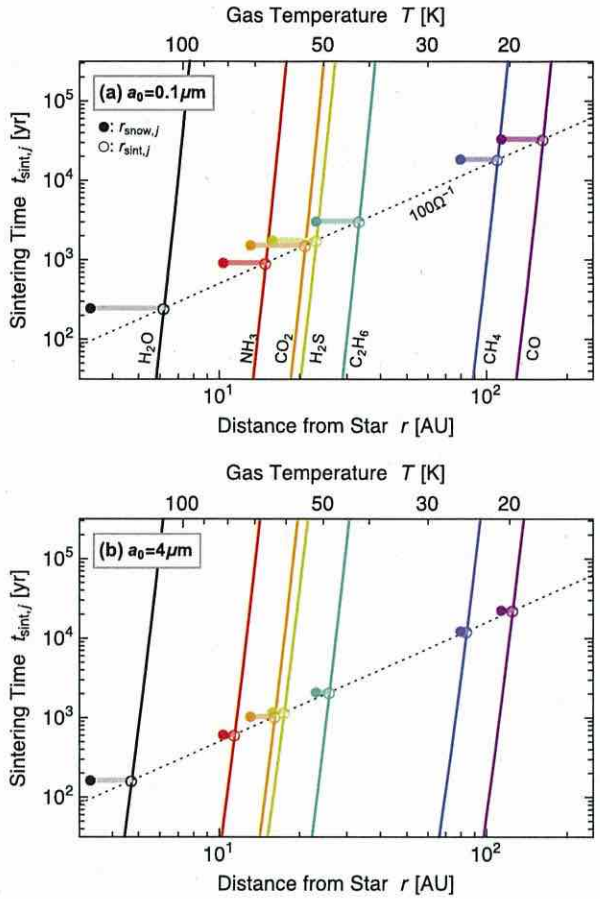

Figure 4. Sintering timescales $t_{\rm sint}$ (Equation (6)) for major cometary volatiles as a function of orbital distance r for our HL Tau disk model. From left to right: H_2O (black), NH_3 (red), CO_2 (orange), H_2S (yellow), C_2H_6 (green), CH_4 (blue), and CO (purple). Panels (a) and (b) are for monomer sizes $a_0 = 0.1$ μm and 4 μm, respectively. The dashed gray curve indicates $100\Omega^{-1}$, which is the typical timescale for particle collision in a disk (Takeuchi & Lin 2005; Brauer et al. 2008). The filled circles indicate the locations of the snow lines, $r = r_{{\rm snow},j}$ (see also Figure 3), whereas the open circles indicate the locations of the sintering lines, $r = r_{{\rm sint},j}$. Icy aggregates experience sintering in the sintering zones defined by $r_{{\rm snow},j} < r < r_{{\rm sint},j}$ (horizontal bars).

phase is equal to the cometary abundance f_j given in Table 1. We also assume that the mass fraction of H_2O ice inside the aggregates is 50%. Under these assumptions, N_j can be expressed as

$$N_j = \frac{0.5 f_j \Sigma_{\rm d}}{m_{{\rm mol},H_2O}}. \quad (5)$$

The adopted relative abundances give the relations $P_j = 0.1 P_{H_2O}$ for $j =$ CO and CO_2, and $P_j = 0.01 P_{H_2O}$ for $j = NH_3$, H_2S, C_2H_6, and CH_4. For the purpose of calculating the locations of the snow lines, the simplification made here is acceptable as a first-order approximation, because the locations of the snow lines are predominantly determined by the strong dependence of $P_{{\rm ev},j}$ on $T(r)$ and are much less sensitive to a change in P_j.

To see the approximate locations of the snow lines in our HL Tau disk model, we temporarily assume the standard dust-to-gas mass ratio of $\Sigma_{\rm d} = 0.01\Sigma_{\rm g}$ throughout the disk. The dashed, dotted–dashed, and dotted lines in Figure 3 show the partial pressure curves $P_j = \{1, 0.1, 0.01\} P_{H_2O}$ for the fiducial disk model ($\gamma = 1$). For each volatile species, the location of the snow line is given by the intersection of $P_{{\rm ev},j}$ and P_j, which is indicated by a filled circle in Figure 3. In this example, the H_2O snow line lies at a radial distance of 3.5 au, which is well interior to the innermost dark ring of the HL Tau disk lying at $\sim$ 13 au (see Figure 1). Zhang et al. (2015) suggested that the H_2O snow line lies on the 13 au dark ring, assuming a higher gas temperature than ours. The snow lines of NH_3, CO_2, H_2S, and C_2H_6 are narrowly distributed over the intermediate region of 10–30 au, and those of CH_4 and CO are located in the outermost region of 100–150 au.

3.4. Sintering Zones

Sintering is the process of neck growth, and its timescale is inversely proportional to the rate at which the neck radius increases (e.g., Swinkels & Ashby 1981). The timescale depends on the size of monomers, with larger monomers generally leading to slower sintering. In this study, we simply assume monodispersed monomers and treat their radius a_0 as a free parameter (see Section 6.3 for parameter study). We only consider $a_0 \leqslant 4$ μm because sintering is too slow to affect dust evolution in a protoplanetary disk beyond this size range (see below).

When neck growth is driven by vapor transport of volatile j, its timescale is given by (Sirono 2011b)

$$t_{{\rm sint},j} = 4.7 \times 10^{-3} \frac{a_0^2 (2\pi m_{{\rm mol},j})^{1/2} (k_{\rm B}T)^{3/2}}{P_{{\rm ev},j}(T) V_{{\rm mol},j}^2 \gamma_j}, \quad (6)$$

where $m_{{\rm mol},j}$, $V_{{\rm mol},j}$, and γ_j are the molecular mass, molecular volume, and surface energy of the species, respectively. The small prefactor 4.7×10^{-3} comes from the fact that the neck radius is much smaller than a_0. In general, $t_{{\rm sint},j}$ rapidly decreases with increasing T because $P_{{\rm ev},j}$ strongly depends on T. For species other than H_2S and C_2H_6, we use the same set of $V_{{\rm mol},j}$ and γ_j adopted by Sirono (2011b). The molecular volumes of H_2S and C_2H_6 are estimated as $V_{{\rm mol},H_2S} = 5.7 \times 10^{-23}$ cm^3 and $V_{{\rm mol},C_2H_6} = 7.1 \times 10^{-23}$ cm^3 assuming that the densities of H_2S and C_2H_6 solids are 1 g cm^{-3} and 0.7 g cm^{-3} (Moses et al. 1992), respectively. We assume that the surface energy of H_2S ice is equal to that of H_2S liquid: 30 erg cm^{-2} (Meyer 1977). For C_2H_6, we use $\gamma_{C_2H_6} = 40$ erg cm^{-2}, which is the value at $\sim$50 K (Moses et al. 1992). The locations of the sintering lines discussed below are insensitive to the values of $V_{{\rm mol},j}$ and γ_j because of the strong temperature dependence of $P_{{\rm ev},j}$.

The necks not only grow but also are destroyed by at least two processes.

1. The necks evaporate when the ambient gas temperature exceeds the sublimation temperature of the volatile j that constitutes the necks. This occurs at $r < r_{{\rm snow},j}$, where $r_{{\rm snow},j}$ is the orbital radius of the snow line of the volatile.
2. The necks break when the aggregate is plastically deformed by another aggregate upon collision. Unsintered aggregates are known to experience substantial plastic deformation even if the collision velocity is much

below the fragmentation threshold (Dominik & Tielens 1997; Wada et al. 2008). Therefore, fully sintered aggregates form only if they do not collide with each other until the sintering is completed, i.e., only if the sintering timescale is shorter than their collision timescale, which we will denote by $t_{\rm coll}$. Because $t_{{\rm sint},j}$ falls off rapidly toward the central star, there exists a location $r = r_{{\rm sint},j}$ inside which $t_{{\rm sint},j} < t_{\rm coll}$ for a given volatile species j. In this study, we call these locations the sintering lines.

Taken together, each volatile species j causes aggregate sintering only inside the annulus defined by $r_{{\rm snow},j} < r < r_{{\rm sint},j}$. We call such regions the sintering zones. Our sintering zones are essentially equivalent to the "sintering regions" of Sirono (2011b).

In order to find the location of the sintering zones, one needs to estimate $t_{\rm coll}$. In principle, the collision time can be calculated using the size, number density, and relative speed of aggregates, as we do in our simulations (see Equation (12)). In this subsection, we avoid such detailed calculations and instead use the formula $t_{\rm coll} = 100\Omega^{-1}$, which is an approximate expression for the collision timescale of macroscopic aggregates in a turbulent disk with the dust-to-gas mass ratio of 0.01 (Takeuchi & Lin 2005; Brauer et al. 2008). This is a rough estimate (see Sato et al. 2015), but still provides a reasonable estimate for $r_{{\rm sint},j}$ because $t_{{\rm sint},j}$ is a steep function of r.

In Figure 4, we plot the sintering timescales of the seven volatile species as a function of r for our HL Tau disk model with $\gamma = 1$. We also indicate $t_{\rm coll} = 100\Omega^{-1}$ by the dotted lines, the location of the sintering lines ($r_{{\rm sint},j}$) by the open circles, and the locations of the sintering zones ($r_{{\rm snow},j} < r < r_{{\rm sint},j}$) by the horizontal bars. We consider two different values of a_0—0.1 and 4 μm (panels (a) and (b), respectively)—to highlight the importance of this parameter in our sintering model. For $a_0 = 0.1$ μm, the width of each sintering zone is 30%–50% of $r_{{\rm sint},j}$, and the sintering zones of NH_3, CO_2, and H_2S significantly overlap with each other. A larger a_0 leads to longer sintering timescales and hence to narrower sintering zones. For $a_0 = 4$ μm, the sintering zones for species other than H_2O almost disappear. For this reason, we restrict ourselves to $a_0 \leqslant 4$ μm in the following sections.

4. SIMULATION METHOD

As introduced in Section 1, sintering is expected to reduce the sticking efficiency of dust aggregates. In protoplanetary disks, this can occur in the sintering zones defined in Section 3.4. To study how the presence of the sintering zones affects the radial distribution of dust in a disk, we conduct global simulations of dust evolution, including sintering-induced fragmentation. In our simulations, we calculate the evolution of the surface density and representative size of icy aggregates due to coagulation and radial drift using the single-size approach (Section 4.1). The radial drift is due to aerodynamical drag by the gas disk (Adachi et al. 1976; Weidenschilling 1977), and its velocity depends on the size of the aggregates and the gas surface density (Section 4.2). We also consider turbulence in the gas disk to compute the vertical scale height and collision velocity of the aggregates (Section 4.3). The sticking efficiency of the aggregates is given as a function of their sintering timescale (Section 4.4). Based on the work of Sirono (1999) and Sirono & Ueno (2014), we assume that sintered aggregates have a lower sticking efficiency than unsintered aggregates. We do not consider a spontaneous (noncollisional) breakup of icy aggregates due to sintering (Sirono 2011a) and sublimation (Saito & Sirono 2011) near the snow lines. These effects might be important in the vicinity of the H_2O snow line, where grains constituting the aggregates would lose a significant fraction of their volume (see Section 7.3). The aggregate internal density is fixed at 0.26 g cm^{-3}, assuming a material (monomer) density of 1.3 g cm^{-3} and a constant aggregate porosity of 80%. Possible effects of porosity evolution will be discussed in Section 7.4.

The output of the simulations is then used to generate the radial profiles of dust thermal emission (Sections 4.5 and 4.6), which we will compare with the ALMA observation of the HL Tau disk in Sections 5 and 6.

4.1. The Single-size Approach for Global Dust Evolution

We simulate the global evolution of particles in a gas disk using the single-size approximation. We assume that the total solid mass at each orbital radius r is dominated by particles with a mass $m = m_*(r)$. We then follow the evolution of the solid surface density $\Sigma_{\rm d}(r)$ and "representative" (mass-dominating) particle mass $m_*(r)$, taking into account aggregate collision and radial drift (see Equations (7) and (8) below). The single-size approach (or mathematically speaking, moment approach) has often been used in the modeling of particle growth in planetary atmospheres (e.g., Ferrier 1994; Ormel 2014) as well as in protoplanetary disks (e.g., Kornet et al. 2001; Garaud 2007; Birnstiel et al. 2012; Estrada et al. 2015; Krijt et al. 2016, see also Appendix of Sato et al. 2015 for the mathematical background of the single-size approximation and a comparison between single-size and full-size simulations). This approach allows us to track the evolution of the mass budget of dust in a disk without using the computationally expensive Smoluchowski's coagulation equation. A drawback of this approach is that one has to assume the aggregate size distribution at each orbit whenever it is needed. In this study, we assume a power-law size distribution when we predict dust emission from the disk (see Section 4.5).

Under the single-size approximation, the evolution of $\Sigma_{\rm d}$ and m_* is described by (Ormel 2014; Sato et al. 2015)

$$\frac{\partial \Sigma_{\rm d}}{\partial t} + \frac{1}{r}\frac{\partial}{\partial r}(r v_{\rm r} \Sigma_{\rm d}) = 0, \tag{7}$$

$$\frac{\partial m_*}{\partial t} + v_{\rm r}\frac{\partial m_*}{\partial r} = \frac{\Delta m_*}{t_{\rm coll}}, \tag{8}$$

where $v_{\rm r}$ and $t_{\rm coll}$ are the radial drift velocity and mean collision time of the representative particles, respectively, and Δm_* is the change of m_* upon a single aggregate collision. Equation (7) expresses the mass conservation for solids, while Equation (8) states that the growth rate of representative particles along their trajectory, $Dm_*/Dt \equiv \partial m_*/\partial t + v_{\rm r}\partial m_*/\partial r$, is equal to $\Delta m_*/t_{\rm coll}$. The mass change Δm_* is equal to m_* when the collision results in pure sticking, while $\Delta m_* < m_*$ when fragmentation or erosion occurs. Our Equations (7) and (8) correspond to Equations (3) and (8) of Ormel (2014), respectively, although Equation (8) of Ormel (2014) assumes $\Delta m_* = m_*$. The expressions for $v_{\rm r}$, $t_{\rm coll}$, and Δm_* will be given in Sections 4.2–4.4, respectively.

We solve Equations (7) and (8) by discretizing the radial direction into 300 logarithmically spaced binds spanning from $r_{\rm in} = 1$ au to $r_{\rm out} = 1000$ au. The parameter sets and initial conditions used in the simulations are described in Section 4.7.

4.2. Radial Drift

The motion of a particle in a gas disk is characterized by the dimensionless Stokes number $\mathrm{St} \equiv \Omega t_{\rm s}$, where Ω is the Keplerian frequency and $t_{\rm s}$ is the particle's stopping time. When the particle radius is much smaller than the mean free path of the gas molecules in the disk, as is true for the particles in our simulations, the stopping time is given by Epstein's drag law. The Stokes number of a representative aggregate at the midplane can then be written as (Birnstiel et al. 2010)

$$\mathrm{St} = \frac{\pi}{2}\frac{\rho_{\rm int} a_*}{\Sigma_{\rm g}}, \tag{9}$$

where $\rho_{\rm int} = 0.26\ \mathrm{g\ cm^{-3}}$ and $a_* \equiv (3m_*/4\pi\rho_{\rm int})^{1/3}$ are the internal density and radius of the aggregate, respectively. We use Equation (9) whenever we calculate St.

The drift velocity $v_{\rm r}$ is given by (Adachi et al. 1976; Weidenschilling 1977)

$$v_{\rm r} = -2\eta v_{\rm K}\frac{\mathrm{St}}{1+\mathrm{St}^2}, \tag{10}$$

where

$$\eta = -\frac{1}{2}\left(\frac{c_{\rm s}}{v_{\rm K}}\right)^2\frac{d\ln P_{\rm g}}{d\ln r} \tag{11}$$

is the parameter characterizing the sub-Keplerian motion of the gas disk, $v_{\rm K} = r\Omega$ is the Keplerian velocity, and $P_{\rm g} = \rho_{\rm g}c_{\rm s}^2$ is the midplane gas pressure. In our disk model, $dP_{\rm g}/dr < 0$ and therefore $v_{\rm r} < 0$ everywhere. At $r \ll r_{\rm c}$, we approximately have $\eta \approx 1.8\times10^{-3}(r/1\ \mathrm{au})^{0.43}$ and $\eta v_{\rm K} \approx 52(r/1\ \mathrm{au})^{-0.07}\ \mathrm{m\ s^{-1}}$.

4.3. Collision Time

We evaluate the collision term $\Delta m_*/t_{\rm coll}$ assuming that collisions between representative aggregates dominate the evolution of m_*. Under this assumption, the collision time is approximately given by

$$t_{\rm coll} = \frac{1}{4\pi a_*^2 n_* \Delta v}, \tag{12}$$

where $4\pi a_*^2$, n_*, and Δv are the collisional cross section, number density, and collision velocity of the representative aggregates, respectively. We use the midplane values for n_* and Δv. We do not consider the erosion of representative aggregates by a number of small grains (Seizinger et al. 2013; Krijt et al. 2015) because there remain uncertainties in the threshold velocity for erosive collisions as a function of the projectile mass (see Section 2.3.2 of Krijt et al. 2015).

To evaluate n_*, we consider disk turbulence and assume that vertical settling balances with turbulent diffusion for the representative aggregates. We parameterize the strength of disk turbulence with the dimensionless parameter $\alpha_{\rm t} = D/c_{\rm s}H_{\rm g}$, where D is the particle diffusion coefficient in the turbulence. For simplicity, $\alpha_{\rm t}$ is assumed to be independent of time and distance from the midplane, but we allow $\alpha_{\rm t}$ to depend on r (see Section 4.7). Under this assumption, n_* at the midplane can be written as

$$n_* = \frac{\Sigma_{\rm d}}{\sqrt{2\pi}H_{\rm d}m_*}, \tag{13}$$

where

$$H_{\rm d} = \left(1 + \frac{\mathrm{St}}{\alpha_{\rm t}}\frac{1+2\mathrm{St}}{1+\mathrm{St}}\right)^{-1/2}H_{\rm g}. \tag{14}$$

is the scale height of the representative aggregates (Dubrulle et al. 1995; Youdin & Lithwick 2007).

The collision velocity Δv is given by the root sum square of the contributions from Brownian motion, gas turbulence (Ormel & Cuzzi 2007), and size-dependent drift relative to the gas disk (Adachi et al. 1976; Weidenschilling 1977). The expressions for these contributions can be found in, for example, Section 2.3.2 of Okuzumi et al. (2012). The contributions from turbulence and drift motion are functions of the Stokes numbers of two colliding aggregates, St_1 and St_2. In this study, we set $\mathrm{St}_1 = \mathrm{St}$ and $\mathrm{St}_2 = 0.5\mathrm{St}$ because we consider collisions between aggregates similar in size. Sato et al. (2015) and Krijt et al. (2016) have recently shown that such a choice best reproduces the results of coagulation simulations that resolve the full size distribution of the aggregates. As long as $\mathrm{St} \ll 1$, the collision velocity is an increasing function of St.

For macroscopic aggregates satisfying $10^{-4} \lesssim \mathrm{St} \ll 1$, either turbulence or radial drift mostly dominates their collision velocity. For this range of St, the collision velocities driven by turbulence and radial drift are approximately given by $\Delta v_{\rm t} \approx \sqrt{2.3\alpha_{\rm t}\mathrm{St}}\,c_{\rm s}$ and $\Delta v_{\rm r} \approx 2\eta v_{\rm K}|\mathrm{St}_1 - \mathrm{St}_2| \approx \eta v_{\rm K}\mathrm{St}$, respectively, where we use $\mathrm{St}_1 = \mathrm{St}$ and $\mathrm{St}_2 = 0.5\mathrm{St}$ (for the expression of $\Delta v_{\rm t}$, see Equation (28) of Ormel & Cuzzi 2007).

4.4. Collisional Mass Gain/Loss

We denote the change in m_* due to a single collision between two mass-dominating aggregates by Δm_*. Following Okuzumi & Hirose (2012), we model Δm_* as

$$\Delta m_* = \min\left\{1, -\frac{\ln(\Delta v/\Delta v_{\rm frag})}{\ln 5}\right\}m_*, \tag{15}$$

where the fragmentation threshold $\Delta v_{\rm frag}$ characterizes the sticking efficiency of the colliding aggregates. The mass change is positive for $\Delta v < \Delta v_{\rm frag}$ and negative for $\Delta v > \Delta v_{\rm frag}$ as shown in Figure 5(a). Equation (15) is a fit to the data of the collision simulations for unsintered aggregates by Wada et al. (2009, their Figure 11). For sintered aggregates, Equation (15) overestimates the sticking efficiency at low collision velocities where the aggregates bounce rather than stick (Sirono 1999). However, we show in Section 7.1 that the bouncing hardly alters the evolution of m_* in the sintering zone. For simplicity, we use Equation (15) for both unsintered and sintered aggregates.

To account for the effect of sintering on the aggregate sticking efficiency, we model the fragmentation threshold

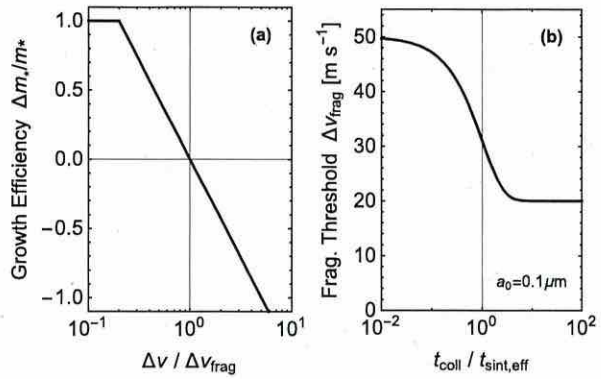

Figure 5. Panel (a): growth efficiency $\Delta m_*/m_*$ (Equation (15)) vs. the scaled collision velocity $\Delta v/\Delta v_{\rm frag}$. Panel (b): catastrophic fragmentation threshold $\Delta v_{\rm frag}$ (Equation (16)) vs. the ratio between the collision and effective sintering timescales $t_{\rm coll}/t_{\rm sint,eff}$ for $a_0 = 0.1$ μm.

$\Delta v_{\rm frag}$ as

$$\Delta v_{\rm frag} = \Delta v_{\rm frag,NS} \exp\left(-\frac{t_{\rm coll}}{t_{\rm sint,eff}}\right) + \Delta v_{\rm frag,S}\left[1 - \exp\left(-\frac{t_{\rm coll}}{t_{\rm sint,eff}}\right)\right], \quad (16)$$

where

$$t_{\rm sint,eff} \equiv \left(\sum_j t_{{\rm sint},j}^{-1}\right)^{-1} \quad (17)$$

is the effective sintering timescale (see Equation (6) for the definition of the individual sintering timescale $t_{{\rm sint},j}$) and $\Delta v_{\rm frag,NS}$ and $\Delta v_{\rm frag,S}(<\Delta v_{\rm frag,NS})$ are the thresholds for unsintered and sintered aggregates, respectively. In Equation (17), the summation is taken over all solid-phase volatiles (i.e., volatiles satisfying $r > r_{{\rm snow},j}$). As described in Section 3.3, the snow line location $r_{{\rm snow},j}$ for each species is calculated from the relation $P_{{\rm ev},j}(r_{{\rm snow},j}) = P_j(r_{{\rm snow},j})$ with Equations (4) and (5). At $r < r_{\rm snow,H_2O}$, where all volatile ices sublimate, we exceptionally set $\Delta v_{\rm frag} = \Delta v_{\rm frag,S}$ to mimic the low sticking efficiency of bare silicate grains compared to (unsintered) ice-coated grains (e.g., Chokshi et al. 1993).

Equation (16) is constructed so that $\Delta v_{\rm frag} \approx \Delta v_{\rm frag,NS}$ in the non-sintering zones ($t_{\rm coll} \ll t_{\rm sint,eff}$) and $\Delta v_{\rm frag} \approx \Delta v_{\rm frag,S}$ in the sintering zone ($t_{\rm coll} \gg t_{\rm sint,eff}$). Simulations of aggregate collisions suggest that $\Delta v_{\rm frag,NS} \sim 50$ m s^{-1} (Wada et al. 2009) and $\Delta v_{\rm frag,S} \sim 20$ m s^{-1} (Sirono & Ueno 2014) if the colliding aggregates are identical and made of 0.1 μm sized ice monomers. The theory of particle sticking (Johnson et al. 1971), on which the simulations by Wada et al. (2009) are based, indicates that $\Delta v_{\rm frag,NS}$ scales with the monomer size as $a_0^{-5/6}$ (Chokshi et al. 1993; Dominik & Tielens 1997). For $\Delta v_{\rm frag,S}$, the scaling is yet to be studied, so we simply assume the same scaling as for $\Delta v_{\rm frag,NS}$. We thus model $\Delta v_{\rm frag,NS}$ and $\Delta v_{\rm frag,S}$ as

$$\Delta v_{\rm frag,NS} = 50\left(\frac{a_0}{0.1\ \mu{\rm m}}\right)^{-5/6} {\rm m\ s^{-1}}, \quad (18)$$

$$\Delta v_{\rm frag,S} = 20\left(\frac{a_0}{0.1\ \mu{\rm m}}\right)^{-5/6} {\rm m\ s^{-1}}. \quad (19)$$

Figure 5(b) shows $\Delta v_{\rm frag}$ versus $t_{\rm coll}/t_{\rm sint,eff}$ for $a_0 = 0.1$ μm.

4.5. Aggregate Opacity

We calculate the absorption cross section of porous aggregates using the analytic expression by Kataoka et al. (2014, their Equation (18)), which is based on Mie calculations with effective medium theory. Monomers are treated as composite spherical grains made of astronomical silicates, carbonaceous materials, and water ice with the mass abundance ratio of 2.64:3.53:5.55 (Pollack et al. 1994). We calculate the effective refractive index of the monomers using the Bruggeman mixing rule. The optical constants of silicates, carbons, and water ice are taken from Draine (2003), Zubko et al. (1996, data for ACH2 samples), and Warren (1984, data for $T = -60$°C), respectively. We neglect the contribution of volatiles other than H_2O to the monomer optical properties. The effective refractive index of porous aggregates is computed using the Maxwell–Garnett rule in which the monomers are regarded as inclusions in vacuum.

Because we adopt the single-size approach, we only track the evolution of aggregates dominating the dust surface density. However, these aggregates do not necessarily dominate millimeter dust emission from a disk. While the mass-dominating aggregates are generally the largest aggregates in the population (e.g., Birnstiel et al. 2012; Okuzumi et al. 2012), smaller ones can dominate the millimeter opacity of the population when the largest aggregates are significantly larger than a millimeter in radius. In order to take into account this effect, we only assume a size distribution when we calculate dust opacities. Specifically, we assume a power-law distribution

$$N_{\rm d}'(a) = \begin{cases} Ca^{-3.5}, & a_{\rm min} < a < a_* \\ 0, & \text{otherwise}, \end{cases} \quad (20)$$

where $N_{\rm d}'(a)$ is the column number density of aggregates per unit aggregate radius a ($<a_*$), $a_{\rm min}$ is the minimum aggregate radius, and C is the normalization constant determined by the condition $\int_0^\infty mN_{\rm d}'(a)\,{\rm d}a = \Sigma_{\rm d}$. We fix $a_{\rm min}$ to be 0.1 μm with the understanding that millimeter opacities are insensitive to the choice of $a_{\rm min}$ as long as $a_{\rm min} \ll 1$ mm. The slope of -3.5 is based on the classical theory of fragmentation cascades (Dohnanyi 1969; Tanaka et al. 1996; see Birnstiel et al. 2011 for how the coagulation of the fragments modifies this value). Therefore, Equation (20) would overestimate the amount of fragments when the collisions between the largest aggregates (which are the source of the fragments) do not lead to their catastrophic disruption. Possible effects of this simplification are discussed in Section 7.2.

The upper panel of Figure 6 shows our dust opacities $\kappa_{{\rm d},\nu}$ at wavelengths $\lambda = 0.87$, 1.3, and 2.9 mm (corresponding to ALMA Bands 7, 6, and 3, respectively) as a function of a_*. Note that the opacities are expressed in units of cm^2 per gram of dust. In the lower panel of Figure 6, we plot the opacity slope measured at $\lambda = 0.87$–1.3 mm, $\beta_{0.87-1.3\,{\rm mm}} \equiv \ln(\kappa_{0.87\,{\rm mm}}/\kappa_{1.3\,{\rm mm}})/\ln(\nu_{0.87\,{\rm mm}}/\nu_{1.3\,{\rm mm}})$. Our model gives $\beta_{0.87-1.3\,{\rm mm}} \approx 1.7$ at $a_* \ll 1$ cm and $\beta_{0.87-1.3\,{\rm mm}} \approx 0.8$ in the opposite limit.

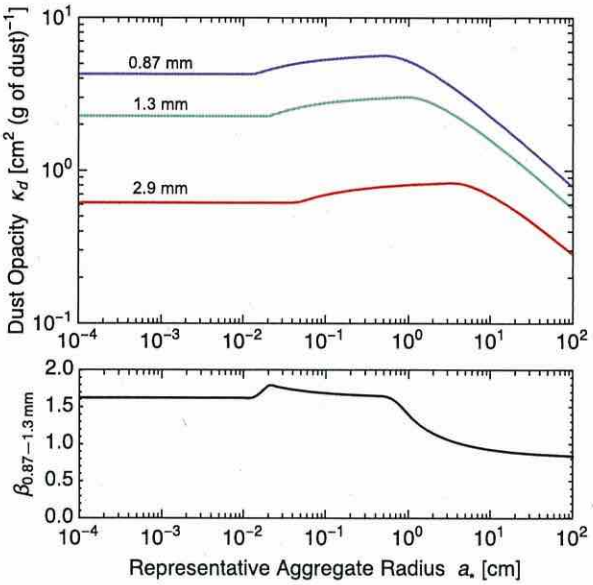

Figure 6. Upper panel: absorption opacities $\kappa_{d,\nu}$ (in units of cm^2 per gram of dust) of dust at wavelengths $\lambda = 0.87$, 1.3, and 2.9 mm as a function of the representative aggregate radius a. The opacities are calculated by assuming that the aggregate size distribution (not resolved in our simulation) obeys a power law $N_d'(a) \propto a^{-3.5}$ (Equation (20)). Lower panel: opacity slope at $\lambda = 0.87$–1.3 mm vs. a_*.

4.6. Dust Thermal Emission

We calculate the intensities I_ν of dust thermal emission at each orbital radius r as

$$I_\nu(r) = [1 - \exp(-\tau_\nu(r))]B_\nu(T(r)), \tag{21}$$

where $B_\nu(T)$ is the Planck function,

$$\tau_\nu(r) = \frac{\kappa_{d,\nu}(r)\Sigma_d(r)}{\cos i} \tag{22}$$

is the line of sight optical depth, and i is the disk inclination. We use $i = 46.^\circ7$ for the HL Tau disk (ALMA Partnership et al. 2015). The Planck brightness temperature T_B is computed by solving the equation $I_\nu = B_\nu(T_B)$ for T_B. Equation (22) assumes that the dust disk is geometrically thin (i.e., the radial distance over which $\kappa_{d,\nu}(r)$ and $\Sigma_d(r)$ vary is longer than the dust scale height). This assumption is, however, not always satisfied in our simulations, as we discuss in detail in Section 6.3.

We will also use the flux density

$$F_\nu = \frac{2\pi \cos i}{d^2}\int_{r_{in}}^{r_{out}} I_\nu(r) r dr, \tag{23}$$

where d is the distance to HL Tau, $r_{in} = 1$ au and $r_{out} = 1000$ au are the boundaries of our computational domain (see Section 4.1), and the factor $\cos i$ accounts for the ellipticity of the disk image. In accordance with ALMA Partnership et al. (2015), we set $d = 140$ pc, the standard mean distance to Taurus.

When comparing our simulation results with the ALMA observation, it is useful to smooth the simulated radial emission profiles at the spatial resolution of ALMA. In this study, we do this in two steps. First, we generate projected images of our simulation snapshots assuming the disk inclination of $46.^\circ7$. For simplicity, the geometrical thickness of the disks is neglected in this process. Second, we smooth the "raw" images along their major axis using a circular Gaussian with the FWHM angular resolutions of $\sqrt{85.3 \times 61.1}$, $\sqrt{35.1 \times 21.8}$, and $\sqrt{29.9 \times 19.0}$ mas for $\lambda = 2.9$, 1.3, and 0.87 mm, in accordance with the ALMA observation of HL Tau at Bands 3, 6, and 7, respectively (ALMA Partnership et al. 2015). Because we assume $d = 140$ pc, these angular resolutions translate into the spatial resolutions of $\approx$10, 3.9, and 3.3 au at Bands 3, 6, and 7, respectively.

4.7. Parameter Sets and Initial Conditions

We conduct 10 simulation runs with different sets of model parameters. Columns 1 through 4 of Table 3 list the run names and parameter choices (γ, a_0, α_t) for the simulation runs. Run Sa0 is our fiducial model and assumes $\gamma = 1$, $a_0 = 0.1$ μm, and $\alpha_t = 0.03(r/10\,\text{au})^{1/2}$. Model Sa0-NoSint is the same as model Sa0 but neglects sintering. Runs Sa0-Lgam and Sa0-Hgam are designed to study the dependence of the results on the gas surface density slope γ. Runs Sa0-Lalp and Sa0-Halp will be used to study how the sintering-induced ring formation scenario constrains the radial distribution of α_t in the HL Tau disk. Runs La0 and LLa0 assume more fragile aggregates (i.e., larger a_0) and weaker turbulence than in the fiducial run. As we will see, the set of a_0 and α_t controls the degree of dust sedimentation (i.e., the geometrical thickness of the dust disk). Runs Sa0-tuned and La0-tuned are the same as runs Sa0 and La0, respectively, except that they adopt slightly lower L_j for H_2O, NH_3, and C_2H_6 (see $L_{j,\text{tuned}}$ in Table 2). These runs will be used to quantify possible uncertainties of our results that might arise from the uncertainties in the vapor pressure data.

The initial conditions are given by $\Sigma_d(t = 0, r) = 0.01\Sigma_g(r)$ and $a_*(t = 0, r) = a_0$, where we have assumed that the dust-to-gas mass ratio of the initial disk is 0.01.

5. RESULTS FROM THE FIDUCIAL SIMULATION

We now present the results of our simulations in the following two sections. In this section, we particularly focus on the fiducial run Sa0 and analyze its results in detail. The dependence on model parameters will be discussed in Section 6.

5.1. Evolution of the Total Dust Mass and Flux Densities

In our simulations, the observational appearance of the disk changes with time because dust particles grow and drift inward. In particular, the millimeter emission of the disk diminishes as the particles drain onto the central star. For this reason, we select from each simulation run one snapshot that best reproduces the millimeter flux densities of the HL Tau disk reported by ALMA Partnership et al. (2015). Specifically, we calculate the relative errors between the simulated and observed flux densities at $\lambda = 0.87$, 1.3, and 2.9 mm as a function of time, and search for the time $t = t_{snap}$ at which the sum of the relative errors is minimized. For reference, the flux densities reported by the ALMA observation are 0.0743, 0.744, and 2.14 Jy at $\lambda = 0.87$, 1.3, and 2.9 mm (Bands 7, 6, and 3), respectively (ALMA Partnership et al. 2015).

Figure 7 illustrates such an analysis for our fiducial simulation run Sa0. This figure shows the simulated time evolution of the flux densities at the three wavelengths as well

Table 3
List of Simulation Runs

Run	γ	a_0 (μm)	α_t	t_{snap} (Myr)	F_ν (Jy) at $t = t_{snap}$			Section
					2.9 mm	1.3 mm	0.87 mm	
Sa0	1	0.1	$0.03(r/10\,\mathrm{au})^{1/2}$	0.26	0.070	0.79	2.2	5
Sa0-NoSint[a]	1	0.1	$0.03(r/10\,\mathrm{au})^{1/2}$	0.12	0.063	0.79	2.3	5.5
Sa0-Lgam	0.5	0.1	$0.03(r/10\,\mathrm{au})^{1/2}$	0.29	0.076	0.76	2.1	6.1
Sa0-Hgam	1.5	0.1	$0.03(r/10\,\mathrm{au})^{1/2}$	0.05	0.072	0.80	2.3	6.1
Sa0-Lalp	1	0.1	0.03	0.18	0.066	0.77	2.2	6.2
Sa0-Halp	1	0.1	0.1	0.29	0.075	0.75	2.1	6.2
La0	1	1	$10^{-3}(r/10\,\mathrm{au})^{1/2}$	0.41	0.064	0.78	2.3	6.3
LLa0	1	4	$10^{-4}(r/10\,\mathrm{au})^{1/2}$	0.45	0.062	0.80	2.4	6.3
Sa0-tuned[b]	1	0.1	$0.03(r/10\,\mathrm{au})^{1/2}$	0.27	0.068	0.77	2.2	6.4
La0-tuned[b]	1	1	$10^{-3}(r/10\,\mathrm{au})^{1/2}$	0.41	0.063	0.79	2.3	6.4

Notes.
[a] No sintering.
[b] Uses $L_{j,\mathrm{tuned}}$ instead of L_j for H_2O, NH_3, and C_2H_6 (see Table 2).

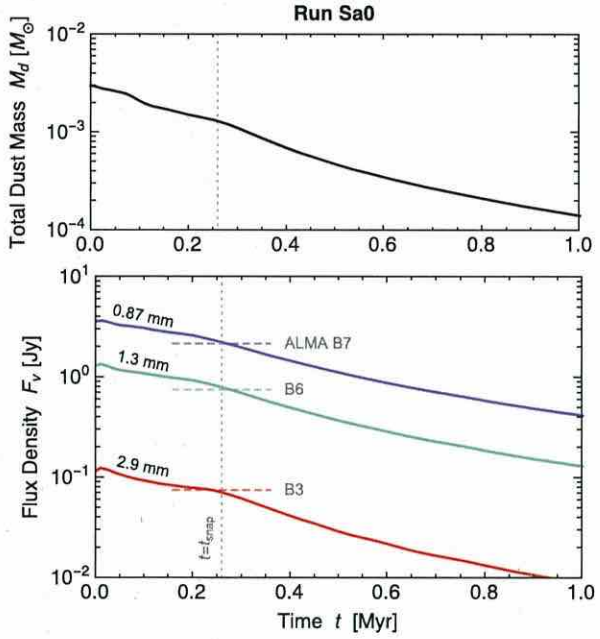

Figure 7. Simulated time evolution of the total dust mass M_d (upper panel) and flux densities F_ν (lower panel) of the HL Tau disk from simulation run Sa0. The blue, green, and red solid curves in the lower panel are F_ν at wavelengths $\lambda = 0.87$ mm, 1.3 mm, and 2.9 mm, respectively. The dashed horizontal line segments indicate the ALMA measurements of the flux densities at these wavelengths (Bands 7, 6, and 3, respectively). The vertical dotted line indicates the time $t = t_{snap}$ at which the simulated flux densities best reproduce the ALMA measurements ($t_{snap} = 0.26$ Myr for run Sa0; see Section 5.1).

as the evolution of the total dust mass M_d within the computational domain. The dust mass and flux densities decrease on a timescale of $\sim$1 Myr, which reflects the timescale on which the dust near the disk's outer edge (which dominates M_d) grows into rapidly drifting pebbles (see, e.g., Sato et al. 2015). Comparing the flux densities from the simulation with those from the ALMA observations (shown by the dashed horizontal line segments in the lower panel of Figure 7), we find that the sum of the relative errors in the flux densities is minimized when $t = 0.26$ Myr. At this time, the flux densities in the simulation are 0.070, 0.79, and 2.2 Jy at $\lambda = 2.9$, 1.3, and 0.87 mm, respectively, which is in agreement with the ALMA measurements to an accuracy of less than 6%.

Columns 5 through 8 of Table 3 list the values of t_{snap} and $F_\nu(t = t_{snap})$ for all simulation runs. We find that t_{snap} falls within the range 0.1–0.5 Myr. Since t_{snap} may be regarded as the time after disk formation, our results are consistent with the idea that HL Tau is younger than 1 Myr. In fact, the age predicted from our simulations depends on the disk mass M_{disk} assumed: a higher M_{disk} leads to a larger t_{snap} because it takes longer for dust emission to decay to the observed level when the initial dust mass is larger. However, a disk mass much in excess of 0.2 $M_\odot$ seems to be unrealistic because the disk would then be gravitationally unstable at outer radii (see Section 2.2).

5.2. Aggregate Size and Dust Surface Density

Below we fix t to be $t_{snap} = 0.26$ Myr and look at the radial distribution of dust in detail. Figures 8(a) and (b) show the radial distribution of the representative aggregate radius a_* and dust surface density Σ_d at this time. We also show in Figure 8(c) the Stokes number St of the representative aggregates, which is more directly related to their dynamics than a_*. In these figures, the vertical stripes indicate the locations of the sintering zones. Here, the sintering zone of each volatile j is defined by the locations where $r > r_{snow,j}$ and $r < r_{sint,j}$, with the latter being equivalent to $t_{coll} < t_{sint,j}$ (see Figure 8(e) for the radial distribution of t_{coll} and $t_{sint,eff}$). The sintering zones of NH_3, CO_2, and H_2S partially overlap with each other and form a single sintering zone. The exact locations of the sintering zones are 3–6 au (H_2O), 11–23 au (NH_3–CO_2–H_2S), 24–33 au (C_2H_6), 80–106 au (CH_4), and 116–160 au (CO). Strictly speaking, the locations of the sintering zones are time-dependent because the volatile partial pressures P_j and aggregate collision timescale t_{coll} evolve with Σ_d (see Equations (4), (5), and (12)). However, a comparison of Figures 4 and 8 shows that the sintering zones little migrate during this 0.26 Myr. This is because the locations of the sintering zones depend on the radial distribution of the gas temperature T (which is taken to be time-independent) much more strongly than on the distribution of Σ_g.

Figures 8(a) and (b) show that sintering produces a clear pattern in the radial distribution of the dust component. We see that dust aggregates in the sintering zones tend to have a high

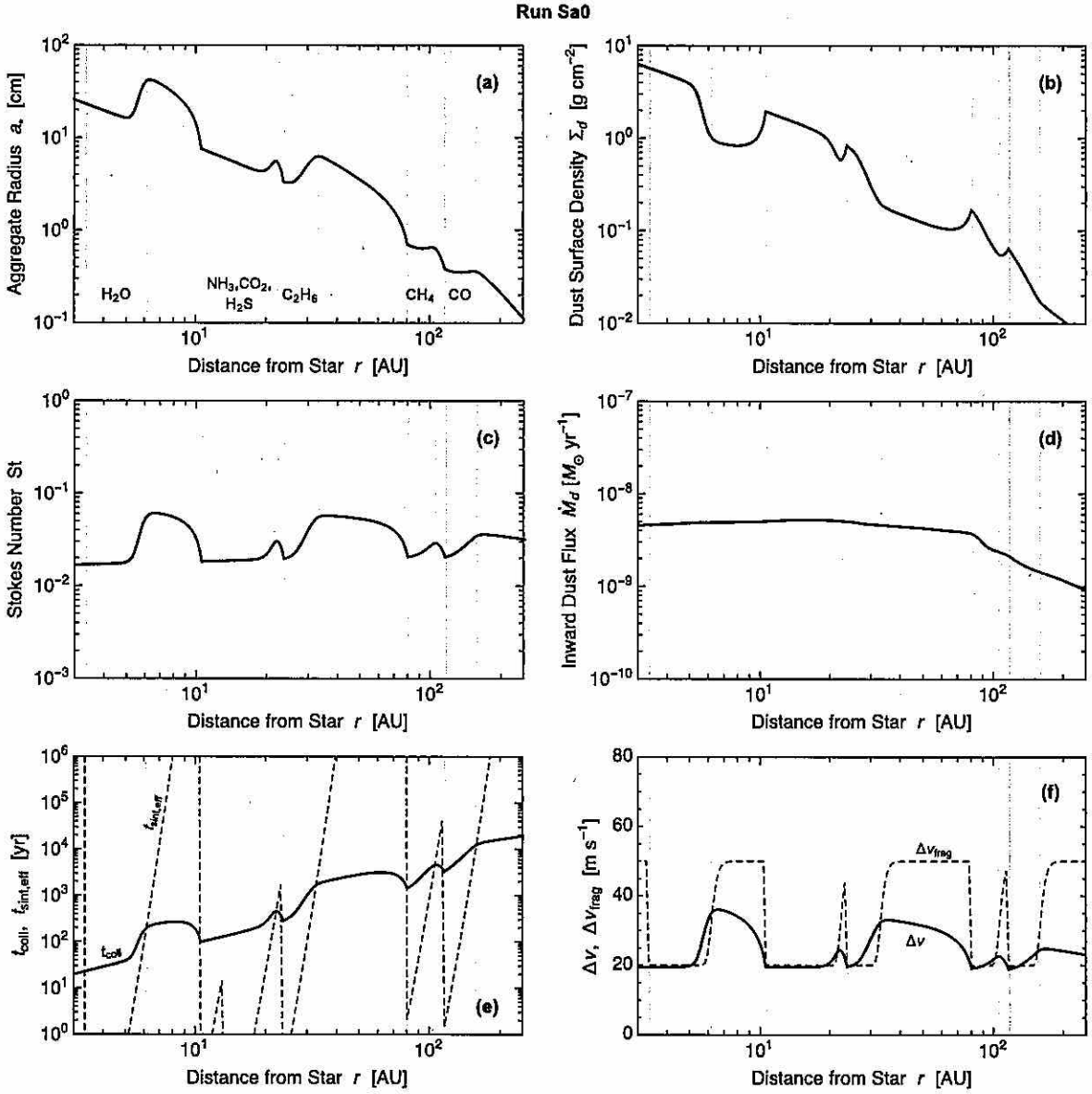

Figure 8. Radial distribution of the representative aggregate radius a_* (panel (a)), dust surface density Σ_d (panel (b)), aggregate Stokes number St (panel (c)), and radial inward dust flux $\dot{M}_d$ (panel (d)) at time $t = t_{snap} = 0.26$ Myr from the fiducial simulation. The shaded areas mark the sintering zones defined by $r_{subl,i} < r < r_{subl,i}$ (see Section 3.4 for details). Panel (e) shows the collision timescale t_{coll}' (Equation (12); solid line) and effective sintering timescale $t_{sint,eff}$ (Equation (17); dashed line), while panel (f) plots the collision velocity Δv (solid line) and fragmentation threshold Δv_{frag} (Equation (16); dashed line) for the representative aggregates.

surface density and a small radius compared to those in the adjacent non-sintering zones. The small aggregate size is a direct consequence of fragmentation induced by sintering. To see this, we plot in Figure 8(f) the collision velocity Δv and fragmentation threshold Δv_{frag} as a function of r. In the non-sintering zones, we find $\Delta v_{frag} \approx 50$ m s^{-1} and $\Delta v \approx$ 25–35 m s^{-1}, implying that no disruptive collisions occur for the unsintered aggregates (as we show below, the maximum size of the unsintered aggregates is determined by radial drift rather than fragmentation). In the sintering zones, Δv_{frag} is decreased to 20 m s^{-1} and Δv is suppressed down to the same value. Since Δv is an increasing function of a_* (as long as St $\ll$ 1), this indicates that the sintered aggregates disrupt each other so that Δv never exceeds Δv_{frag}. The disrupted aggregates pile up there because the inward drift speed $|v_r|$ decreases with decreasing a_*. These pileups provide the high surface densities in the sintering zones.

To understand the radial distribution of Σ_d and a_* more quantitatively, we look at the radial inward mass flux of drifting aggregates,

$$\dot{M}_d \equiv 2\pi r |v_r| \Sigma_d. \quad (24)$$

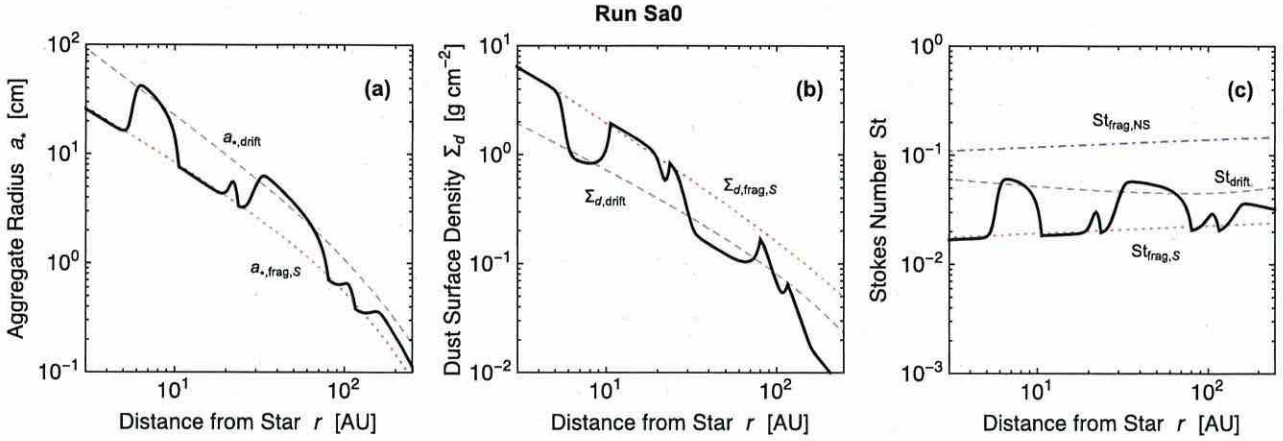

Figure 9. Same as panels (a)–(c) of Figure 8, but compared with the analytic estimates assuming a steady inward dust flow ($\dot{M}_{\rm d} = 5 \times 10^{-9}\,M_\odot\ {\rm yr}^{-1}$). The dashed curves show the drift-limited solution for unsintered aggregates (labeled by "NS"), while the dotted curves show the fragmentation-limited solution of sintered aggregates (labeled by "S").

The radial distribution of $\dot{M}_{\rm d}$ is shown in Figure 8(d). The mass flux is radially constant ($\approx 5 \times 10^{-9}\,M_\odot\ {\rm yr}^{-1}$) at $\lesssim$100 au, which indicates that the radial dust flow in this region can be approximated by a steady flow. Such a quasi-steady dust flow is commonly realized when some mechanism like radial drift or fragmentation limits dust growth (see, e.g., Birnstiel et al. 2012; Lambrechts & Johansen 2014). Substituting $|v_{\rm r}| \approx 2\eta v_{\rm K}\,{\rm St}$ (${\rm St} \ll 1$) into Equation (24), we obtain the relation between $\Sigma_{\rm d}$ and St,

$$\Sigma_{\rm d} = \frac{\dot{M}_{\rm d}}{2\pi r|v_{\rm r}|} \approx \frac{\dot{M}_{\rm d}}{4\pi\eta r v_{\rm K}\,{\rm St}}. \tag{25}$$

Because ${\rm St} \propto a_*$, we have $\Sigma_{\rm d} \propto 1/a_*$ for constant $\dot{M}_{\rm d}$.

Using Equation (25) with the assumption that either radial drift or fragmentation limits dust growth, one can analytically estimate the radial distribution of $\Sigma_{\rm d}$ and a_* in the non-sintering and sintering zones. When radial drift limits dust growth, the maximum aggregate size is determined by the condition (Okuzumi et al. 2012)

$$\frac{t_{\rm coll}}{t_{\rm drift}} \approx \frac{1}{30}, \tag{26}$$

where $t_{\rm coll}$ is the collision timescale given by Equation (12) and

$$t_{\rm drift} \equiv \frac{r}{|v_{\rm r}|} \approx \frac{1}{2\eta\Omega\,{\rm St}} \tag{27}$$

is the timescale of radial drift. Substituting $H_{\rm d} \approx (1 + {\rm St}/\alpha_{\rm t})^{-1/2} H_{\rm g}$ (${\rm St} \ll 1$) and $m_*/\pi a_*^2 = (4/3)\rho_{\rm int} a_* = (8/3\pi)\Sigma_{\rm g}\,{\rm St}$ into Equation (13), the collision timescale can be evaluated as

$$t_{\rm coll} \approx 0.53 \frac{\Sigma_{\rm g}}{\Sigma_{\rm d}} \frac{H_{\rm g}\,{\rm St}}{\Delta v\sqrt{1 + {\rm St}/\alpha_{\rm t}}}. \tag{28}$$

Furthermore, the collision velocity can be approximated as the root square sum of the turbulence-driven velocity $\Delta v_{\rm t}$ and differential radial drift velocity $\Delta v_{\rm r}$,

$$\Delta v \approx \sqrt{(\Delta v_{\rm t})^2 + (\Delta v_{\rm r})^2} \approx \sqrt{2.3\alpha_{\rm t} c_{\rm s}^2\,{\rm St} + (\eta v_{\rm K}\,{\rm St})^2}, \tag{29}$$

where we have used the approximate expressions for $\Delta v_{\rm t}$ and $\Delta v_{\rm r}$ given in Section 4.3. Substituting Equations (25) and (27)–(29) into Equation (26), we obtain the equation for the maximum Stokes number in the drift-limited growth,

$$\frac{{\rm St}_{\rm drift}^{5/2}}{\sqrt{(2.3\alpha_{\rm t} c_{\rm s}^2 + \eta^2 v_{\rm K}^2\,{\rm St}_{\rm drift})(1 + {\rm St}_{\rm drift}/\alpha_{\rm t})}} = \frac{0.0025\dot{M}_{\rm d}}{\eta^2 r v_{\rm K} c_{\rm s}\Sigma_{\rm g}}, \tag{30}$$

where we labeled St by the subscript "drift" to emphasize drift-limited growth. In Figure 9(c), we compare ${\rm St}_{\rm drift}$ to $\dot{M}_{\rm d} = 5 \times 10^{-9}\,M_\odot\ {\rm yr}^{-1}$ with the Stokes number directly obtained from run Sa0 at $t = t_{\rm snap}$. We find that ${\rm St}_{\rm drift}$ reproduces St in the non-sintering zones, implying that radial drift limits the growth of unsintered aggregates. We are also able to estimate a_* and $\Sigma_{\rm d}$ in the non-sintering zones by substituting ${\rm St} = {\rm St}_{\rm drift}$ into $a_* = (2/\pi)\Sigma_{\rm g}\,{\rm St}/\rho_{\rm int}$ and Equation (25), respectively. These are shown by the dashed lines in Figures 9(a) and (b).

If fragmentation limits dust growth, the maximum Stokes number is simply determined by the balance

$$\Delta v\,({\rm St}) = \Delta v_{\rm frag}. \tag{31}$$

We will denote the solution to this equation by ${\rm St}_{\rm frag}$. If we approximate Δv by Equation (29), Equation (31) can be rewritten as a quadratic equation for St, and its positive root gives

$${\rm St}_{\rm frag} = \frac{-2.3\alpha_{\rm t} c_{\rm s}^2 + \sqrt{(2.3\alpha_{\rm t} c_{\rm s}^2)^2 + 4(\eta v_{\rm K}\Delta v_{\rm frag})^2}}{2(\eta v_{\rm K})^2}. \tag{32}$$

The dotted–dashed and dotted lines in Figure 9(c) show ${\rm St}_{\rm frag}$ for $\Delta v_{\rm frag} = \Delta v_{\rm frag,NS}$ and $\Delta v_{\rm frag,S}$ (denoted by ${\rm St}_{\rm frag,NS}$ and ${\rm St}_{\rm frag,S}$), respectively. We can see that ${\rm St}_{\rm frag,S}$ reproduces St in the sintering zones, which confirms that fragmentation limits the growth of sintered aggregates. One can estimate the values of a_* and $\Sigma_{\rm d}$ in the sintering zones by substituting ${\rm St} = {\rm St}_{\rm frag,S}$ into $a_* = 2\Sigma_{\rm g}\,{\rm St}/(\pi\rho_{\rm int})$ and Equation (25). These estimates are in excellent agreement with the simulation results, as shown by the dotted lines of Figures 9(a) and (b).

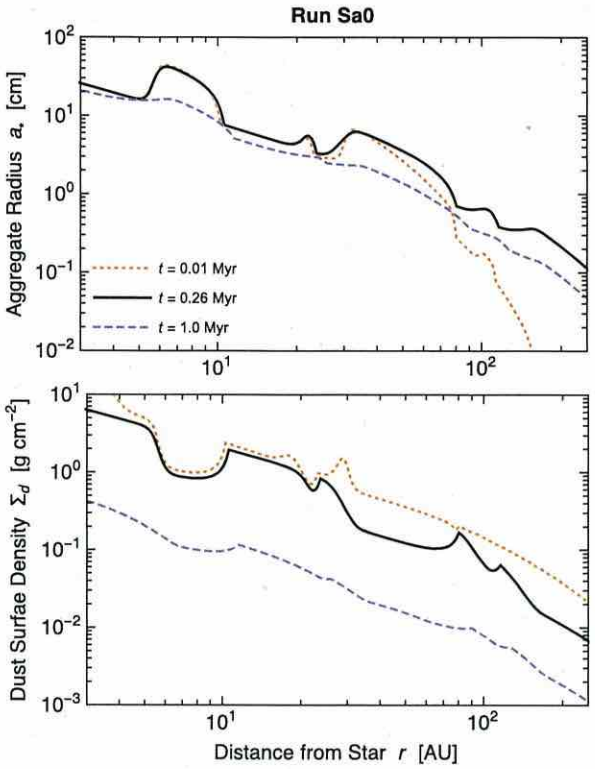

Figure 10. Radial distribution of the representative aggregate radius a (upper panel) and dust surface density Σ_d (lower panel) at $t = 0.01$ Myr (dotted lines), 0.26 Myr (solid lines), and 1 Myr (dashed line) from simulation run Sa0.

5.3. Lifetime of the Ring Patterns

It is worth mentioning at this point that the radial pattern of dust shown in Figure 8 fades out as the disk becomes depleted of dust. As the dust-to-gas mass ratio Σ_d/Σ_g decreases, the collision timescale t_{coll} of the aggregates increases, and consequently the maximum aggregate size set by radial drift (Equation (26)) decreases. The radial pattern disappears when the radial drift barrier dominates the fragmentation barrier at all r because sintering has no effect on radial drift. This is illustrated in Figure 10, where we plot the radial distribution of a_* and Σ_d for model Sa0 at different values of t. We find that the radial pattern present at $t = t_{snap} = 0.26$ Myr has disappeared by $t = 1$ Myr. In this particular example, St_{drift} falls below $St_{frag,S}$ at all r when $M_d < 10^{-11}\,M_\odot\ yr^{-1}$. In models La0 and LLa0, which assume weaker turbulence, dust evolution is slower than in model Sa0 owing to the lower turbulence-driven collision velocity (see t_{snap} in Table 3). However, even in these cases, the sintering-induced ring patterns are found to decay in 2 Myr. We note that the lifetime of the pattern would be longer for radially more extended ($r_c > 150$ au) disks, because the lifetime of dust flux in a disk generally scales with the orbital period at the disk's outer edge (Sato et al. 2015).

5.4. Optical Depths and Brightness Temperatures

We move on to the observational appearance of the sintering-induced dust rings at millimeter wavelengths. The upper left panel of Figure 11 shows the radial distribution of the line of sight optical depths τ_ν (Equation (22)) from the snapshot of run Sa0 at $t = t_{snap}$. We here present the optical depths at three wavelengths $\lambda = 0.87$, 1.3, and 2.9 mm, which correspond to ALMA Bands 7, 6, and 3, respectively.

Overall, the optical depths in the sintering zones are higher than in the non-sintering zones. This mainly reflects the higher dust surface density in the sintering zones (see Figure 8(b)). The radial variation of $\kappa_{d,\nu}$ represents only a minor contribution to the radial variation of τ_ν, in particular in outer regions where the representative aggregates are smaller than $\sim$1 cm in radius. At $\lambda = 0.87$ and 1.3 mm, the three inner sintering zones (of H_2O, NH_3–CO_2–H_2S, and C_2H_6) are optically thick, while the two outer sintering zones (of CH_4 and CO) are optically thin or marginally thick. The CO sintering zone is much darker than the other sintering zones because the disk surface density drops at $r > r_c = 150$ au. The non-sintering zones are optically thin or marginally thick at all three wavelengths. The opacity index at $\lambda = 0.87$–1.3 mm, $\beta_{0.87-1.3\,mm} \equiv \ln(\kappa_{0.87\,mm}/\kappa_{1.3\,mm})/\ln(\nu_{0.87\,mm}/\nu_{1.3\,mm})$ is shown in the lower left panel of Figure 11. We see that $\beta_{0.87-1.3\,mm} \sim 1$ at $\lesssim$70 au and approaches the interstellar value $\sim$1.7 beyond 80 au.

The upper right panel of Figure 11 shows the distribution of the brightness temperatures T_B for the same snapshot. For comparison, we also plot the gas temperature T of our disk model given by Equation (1). We find that the three innermost sintering zones are optically thick ($T_B \approx T$) at $\lambda = 0.87$ and 1.3 mm.

An interesting observational signature of the sintering-induced rings appears in the radial variation of the spectral slope. In the lower right panel of Figure 11, we plot the spectral index at 0.87–1.3 mm, $\alpha_{0.87-1.3\,mm} \equiv \ln(I_{0.87\,mm}/I_{1.3\,mm})/\ln(\nu_{0.87\,mm}/\nu_{1.3\,mm})$, as a function of r. In the three innermost sintering zones, we have $\alpha_{0.87-1.3\,mm} \approx 2$ because these zones are optically thick at these wavelengths. If these regions were optically thin, we would have $\alpha_{0.87-1.3\,mm} \approx 3$ because $\beta_{0.87-1.3\,mm} \approx 1$ (see the lower left panel of Figure 11). In the non-sintering zones lying at $\sim$6–11 au and $\sim$33–80 au, we obtain $\alpha_{0.87-1.3\,mm} \approx 2.3$–2.5, which is between the values in the optically thick and thin limits. This reflects the fact that the non-sintering zones are marginally thick at 0.87–1.3 mm.

5.5. Comparison with the ALMA Observation

Now we make more detailed comparisons between the simulation results and the ALMA observation of the HL Tau disk. We smooth the radial profiles of the intensities I_ν from run Sa0 ($t = t_{snap}$) at the ALMA resolutions as described in Section 4.6. In the center panels of Figure 12, the solid lines show the radial profiles of the brightness temperatures T_B and spectral slope α_{B6-B7} obtained from the smoothed I_ν. For comparison, T_B and α_{B6-B7} from the raw I_ν are shown by the dotted lines. The left panels show the profiles from the ALMA observations (same as Figure 1). We also show in the right panels the results from the non-sintering run Sa0-NoSint to clarify the features of the sintering-indued structures.

After smoothing, the innermost emission dip lying at 6–11 au has been partially smeared at 0.87 mm (Band 7) and 1.3 mm (Band 6). The emission dip in the smoothed images has a lower spectral slope than that in the raw images directly obtained from the simulation. This is a consequence of the frequency-dependent angular resolution: Because Band 6 has a coarser resolution than Band 7, the emission dip seen at Band 6 is more significantly buried than that seen at Band 7, resulting in a decrease in the spectral slope after smoothing. At 2.9 mm

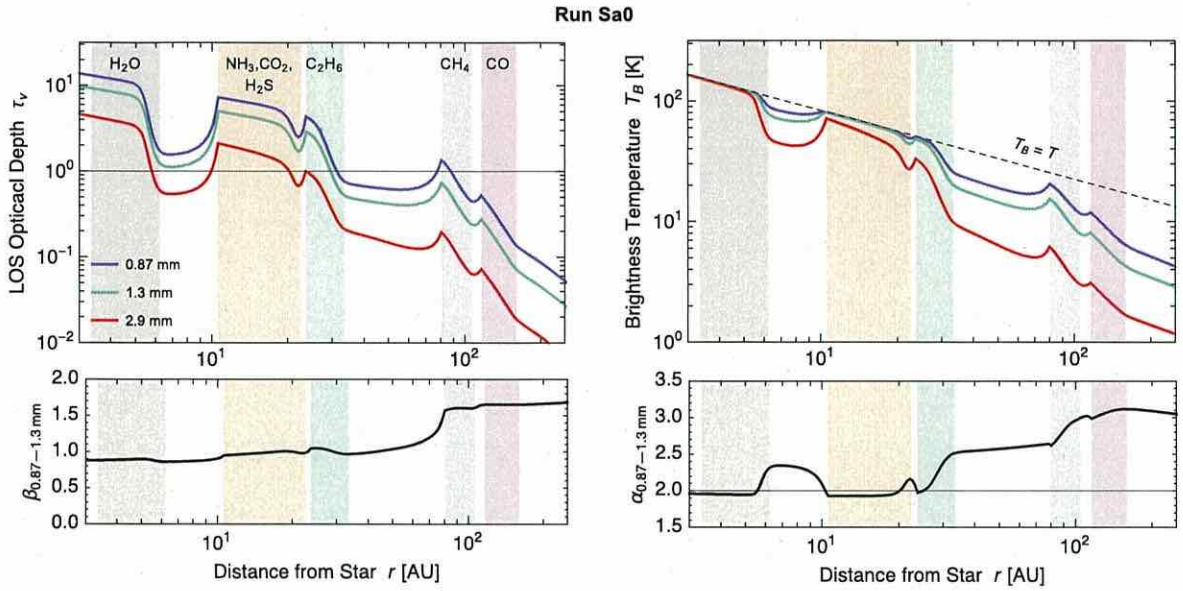

Figure 11. Radial distribution of the line of sight optical depths τ_ν (upper left panel), brightness temperatures T_B (upper right panel), opacity slope $\beta_{0.87-1.3\,\mathrm{mm}}$ (lower left panel), and spectral slope $\alpha_{0.87-1.3\,\mathrm{mm}}$ (lower right panel) at $t = t_{\mathrm{snap}} = 0.26$ Myr from run Sa0. The blue, green, and red curves in the upper panels correspond to wavelengths $\lambda = 0.87$, 1.3, and 2.9 mm (ALMA Bands 7, 6, and 3), respectively. The dashed line in the upper right panel shows the gas temperature profile T in our disk model (Equation (1)). The shaded areas mark the sintering zones.

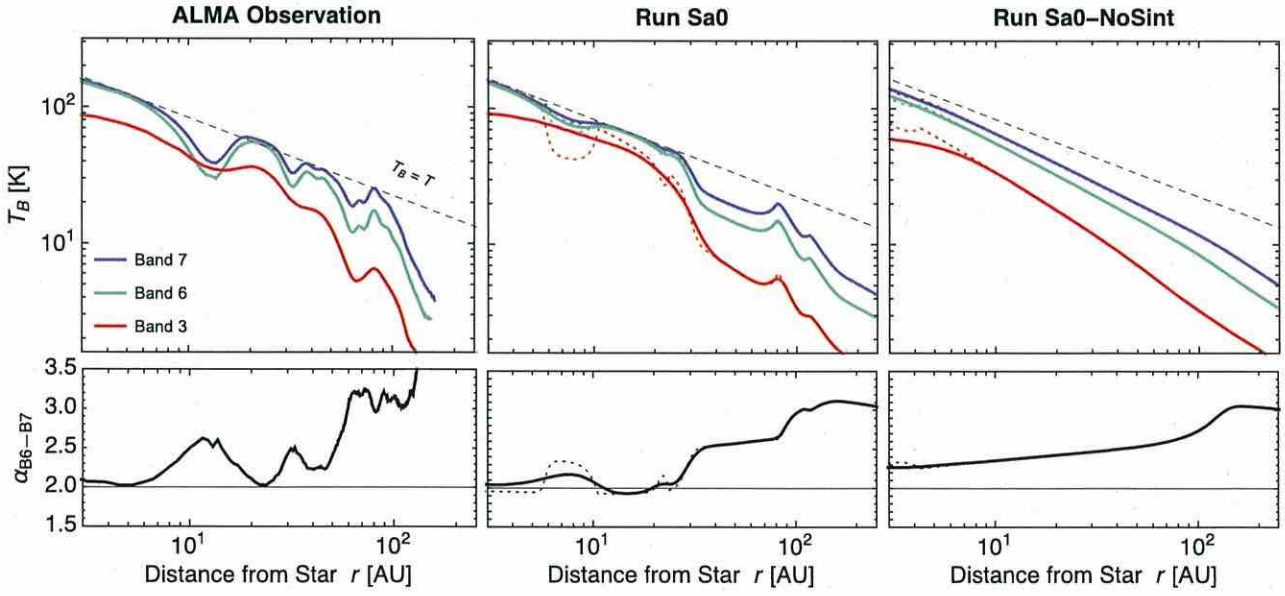

Figure 12. Comparison between the ALMA observation and our fiducial model calculation Sa0. The left panels show the radial profiles of T_B at Bands 3, 6, and 7 and α_{B6-B7} of the HL Tau disk obtained from the ALMA observation (same as Figure 1). The center and right panels are from simulation runs Sa0 and Sa0-NoSint. The simulated profiles are obtained by smoothing the raw simulation data (dotted curves) at the ALMA resolutions (see text for details). The dashed lines show $T_B = T$, where T is the gas temperature given by Equation (1).

(Band 3), the radial structure of T_B at $\lesssim$10 au has been significantly smoothed out.

We find that our simulation reproduces many observational features of the HL Tau disk. First, the simulation predicts a central emission peak that closely resembles the observed one. This central emission peak is associated with the H_2O sintering zone as shown in Figure 11. The radial extent of the simulated central peak is $\approx$6 au, which is comparable to $\approx$8 au of the observed peak. The simulation perfectly reproduces the emission features of the central region: the magnitudes and radial slopes of T_B at all three ALMA Bands, and the millimeter spectral slope of $\alpha_{B6-B7} \approx 2$. In our simulation, the spectral slope simply reflects the high optical thickness of the central region, and has nothing to do with the optical properties of the aggregates in the region. Sintering plays an essential role in the buildup of the optically thick region; without sintering, the disk would be entirely optically thin at these bands, as shown by run Sa0-NoSint (see the right panels of Figure 12). The fact that the

central emission peak has a lower intensity at Band 3 than at Bands 6 and 7 is explained as a consequence of the lower spatial resolution (≈10 au) at Band 3 (i.e., this compact emission is underresolved at this band).

The simulation also predicts two bright rings in the region of ∼10–30 au that might be identified with the two innermost bright rings of HL Tau observed at ∼20 and 40 au. In our simulation, the two emission rings are associated with the sintering zones of NH_3–CO_2–H_2S (11–23 au) and C_2H_6 (24–33 au). These rings are optically thick at Bands 6 and 7 (and therefore $\alpha_{B6-B7} \approx 2$) and are optically thin at Band 3. These features are consistent with those of the two innermost bright rings of HL Tau. However, the separation of the predicted rings is much smaller than in the observed rings, as we discuss below.

Farther out in the disk, the simulation predicts an optically thin emission peak at 80 au associated with CH_4 sintering. Its location coincides with the 80 au bright ring in the ALMA image of HL Tau, and its brightness temperatures agree with those of the observed ring at all three wavelengths to within a factor of two. The simulation also predicts a less pronounced peak at 120 au associated with CO sintering. As mentioned in Section 5.4, this 120 au peak is much less pronounced than other inner peaks because this location is close to the outer edge of our modeled gas disk. Interestingly, the observed HL Tau disk also has a minor emission peak exterior to the 80 au ring ($r \sim 97$ au; see ALMA Partnership et al. 2015).

The innermost dark ring seen at 6–11 au in the simulated image is optically marginally thick and has $\alpha_{B6-B7} > 2$, which is consistent with the observed innermost dark ring at ∼13 au. Our simulation also explains why this innermost emission dip is much shallower at Band 3 than at Bands 6 and 7: as mentioned, this is simply because the spatial resolution at Band 3 is no high enough to distinguish the dark ring from the central emission peak.

However, there are some discrepancies between the prediction from the fiducial model and the observation of the HL Tau disk. For example, the second innermost ring predicted by the model, which is associated with the C_2H_6 sintering zone, is about 10 au interior to that observed by ALMA. For this reason, the dark ring just inside the C_2H_6 sintering zone is much narrower than the second innermost dark ring of HL Tau extending from 30 to 40 au. In addition, as we explain in detail in Section 6.3, the fiducial model predicts that dust particles are vertically well mixed in the gas disk, which seems to be inconsistent with the observations of HL Tau, suggesting that large dust particles settle to the disk midplane (Kwon et al. 2011; Pinte et al. 2016). In the following section, we examine if these discrepancies can be removed or alleviated by tuning the parameters in our model.

6. PARAMETER STUDY

The previous section mainly focused on our fiducial simulation (run Sa0). We here study how the simulation results depend on the model parameters.

6.1. Gas Surface Density Slope

Because the gas density distribution of the HL Tau disk is unknown, it is important to quantify how strongly our results depend on the assumption about the gas density profile.

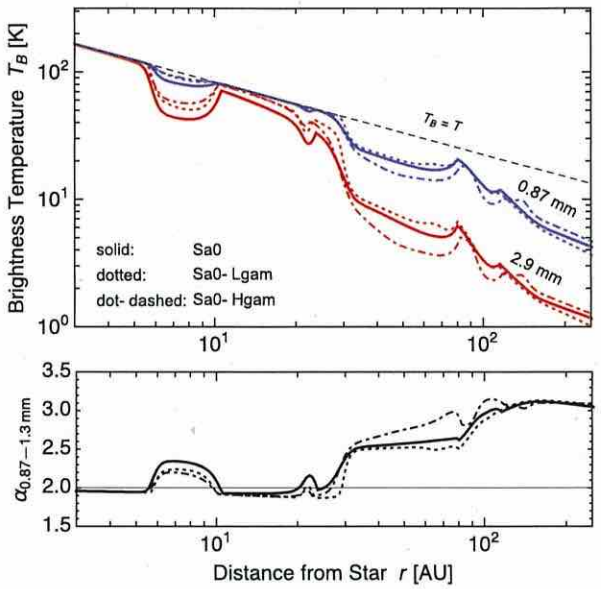

Figure 13. Comparison between runs Sa0 (solid curves), Sa0-Lgam (dotted curves), and Sa0-Hgam (dotted–dashed curves). The upper panel shows the brightness temperatures T_B as a function of orbital distance r at wavelengths 0.87 mm (blue curves) and 2.9 mm (red curves) at time $t = t_{snap}$. The gas temperature profile T (Equation (1)) is shown by the dashed line. The lower panel shows the opacity index at 0.87–1.3 mm.

We present the results of two simulation runs—Sa0-Lgam and Sa0-Hgam—in which we change γ in Equation (2) to 0.5 and 1.5, respectively. The other parameters are unchanged form the fiducial run.

Figure 13 compares the radial profiles of the brightness temperature and spectral slope at 0.87 and 2.9 mm from these runs with those from run Sa0. The three snapshots are taken at different times but still provide similar flux densities (see Table 3) because t_{snap} is defined as such. We find that the variation of γ within the range 0.5–1.5 little affects the emission properties of the disk, with the variation of T_B within a factor of 2 and the variation of $\alpha_{0.87-1.3\,mm}$ as small as $\lesssim 25\%$ at all r. This is mainly because the steady-state radial distribution of the dust surface density Σ_d is insensitive to γ. If we measure the aggregate size by St, the steady-state distribution of Σ_d is determined from Equation (25) with either $St = St_{drift}$ (Equation (30)) or $St = St_{frag}$ (Equation (32)). The γ dependence of the radial dust flux $\dot{M}_d$ is weak as long as we fix M_{disk} and r_c. St_{frag} depends on γ only through $\eta \propto \gamma + 1.8$ (for $T \propto r^{-0.57}$ and $r \ll r_c$), and its variation is small as long as we vary γ within the range 0.5–1.5. For St_{drift}, the dependence is less obvious from Equation (30), but it turns out that the weak γ dependences of $\eta^2\Sigma_d$ and $\dot{M}_d$ partly cancel out in this equation.

6.2. Radial Variation of Turbulence

The radial distribution of turbulence strength α_t is another important uncertainty in our simulations. Our fiducial model assumes $\alpha_t \propto \sqrt{r}$, which gives a turbulence-driven collision velocity nearly independent of r ($\Delta v_t \propto \sqrt{\alpha_t} c_s \propto \sqrt{\alpha_t T} \propto r^{-0.035}$). In fact, a radially constant collision velocity is required in our model to simultaneously reproduce

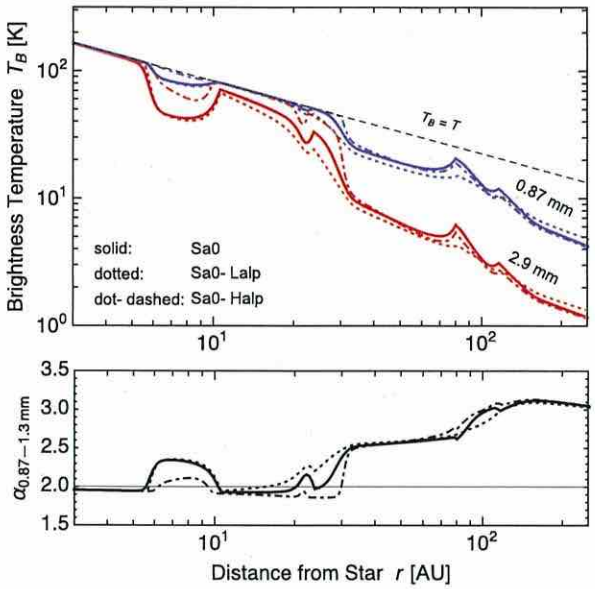

Figure 14. Comparison between runs Sa0 (solid curves), Sa0-Lalp (dotted curves), and Sa0-Halp (dotted–dashed curves). The upper panel shows the brightness temperatures T_B as a function of orbital distance r at wavelengths 0.87 mm (blue curves) and 2.9 mm (red curves) at time $t = t_{snap}$. The gas temperature profile T (Equation (1)) is shown by the dashed line. The lower panel shows the opacity index at 0.87–1.3 mm.

dark rings at small r and bright rings at large r.[7] To demonstrate this, we consider two models in which α_t is fixed to 0.03 and 0.1 at all r (models Sa0-Lalp and Sa0-Halp, respectively). These values correspond to the values of α_t in the fiducial Sa0 model at $r \approx 10$ au and 100 au, respectively.

Figure 14 compares the result of fiducial run Sa0 with those of runs Sa0-Lalp and Sa0-Halp. We find that model Sa0-Lalp fails to produce an emission peak at $\approx$80 au, because turbulence is too weak to cause fragmentation of sintered aggregates at that location. By contrast, model Sa0-Halp produces only shallow dips at $r \lesssim 30$ au. In this high-α_t model the maximum aggregate size at $r \lesssim 30$ au is limited by turbulent fragmentation, even in the non-sintering zones. The suppressed dust growth causes a slowdown of radial drift, which acts to fill the density dips in the non-sintering zones. Thus, a model assuming a high α_t in the outer regions and a low α_t in the inner regions best reproduces the observation of HL Tau.

Theoretically, a α_t that is lower at smaller r is expected for turbulence driven by the magnetorotational instability (MRI; Balbus & Hawley 1991). Because the origin of the MRI is the coupling between the gas disk and magnetic fields, MRI turbulence tends to be weaker at locations where the ionization degree is lower. In protoplanetary disks, a lower ionization degree corresponds to a higher gas density and hence to a smaller orbital radius, because ionizing cosmic-rays or X-rays are attenuated at large column densities and recombination is faster in denser gas (e.g., Sano et al. 2000; Bai 2011).

[7] In most of our simulation runs, the turbulence-driven velocity is the dominant component of the aggregate collision velocity. The only exception is run LLa0, in which the turbulence-driven velocity is only slightly larger than the drift-driven velocity. In this run, radial drift and turbulence nearly equally contribute to the aggregate fragmentation.

6.3. Monomer Size and Dust Settling

As mentioned in Section 4.6, our calculations of dust thermal emission neglect the geometrical thickness of the dust subdisk. In reality, if a dust disk has an inclination of $\sim$45° and a finite vertical extent H_d, then any radial structure of the disk emission is smeared out over this length scale in the direction of the minor axis of the disk image. Pinte et al. (2016) point out that the scale height of large dust particles in the HL Tau disk must be as small as $\sim$1 au at $r = 100$ au in order to be consistent with the well separated morphology of the bright rings observed by ALMA. Such a small dust scale height strongly indicates that dust settling has occurred in the gas disk; without settling, the dust scale height would be $\sim$10 au at 100 au.

However, in our fiducial model, the settling of representative aggregates is severely prevented by turbulent diffusion. According to Equation (14), significant settling of dust particles ($H_d \ll H_g$) requires $\mathrm{St} \gg \alpha_t$. This condition is not satisfied in fiducial run Sa0, because the value of St of the representative aggregates observed in the simulation is comparable to the value of α_t assumed (see Figure 8(c)). In this run, α_t is arranged to have a high value so that aggregates disrupt and pile up in the sintering zones. If turbulence were weak, sintered aggregates would not experience disruption as long as we maintain the assumption $\Delta v_{frag,S} = 20\ \mathrm{m\ s^{-1}}$.

One way to reconcile sintering-induced ring formation with dust settling in our model is to assume weaker turbulence *and* a lower fragmentation velocity. Within our dust model, a lower value of Δv_{frag} corresponds to a larger monomer size a_0 (see Equations (18) and (19)). However, aggregates made of larger monomers tend to be sintered less slowly, as demonstrated in Section 3.4. To examine if there is a range of a_0 where the aggregates can experience settling and sintering simultaneously, we performed two simulations (La0 and LLa0). In run La0, we increase a_0 to 1 μm while lowering α_t to $10^{-3}(r/10\ \mathrm{au})^{1/2}$. Run LLa0 is a more extreme case of $a_0 = 4\ \mu$m and $\alpha_t = 10^{-4}(r/10\ \mathrm{au})^{1/2}$. The other parameters are the same as in the fiducial run Sa0.

Figure 15 shows the raw radial profiles of T_B and the 0.87–1.3 mm spectral index at $t = t_{snap}$ obtained from runs La0 and LLa0. The profiles after smoothing at the ALMA resolutions are shown in Figure 16. Note that we neglect the geometric thickness of the dust disk when calculating T_B. Indeed, the dust disks in models La0 and LLa0 are geometrically thin, unlike in model Sa0 because turbulent diffusion is inefficient in these two models. We plot in Figure 17 the dust scale height H_d from Equation (14) as a function of r for the three models. At $r = 100$ au, we find $H_d \approx 3$ au for model La0 and $H_d \approx 1$ au for model LLa0. Models Sa0, La0, and LLa0 give similar results for the radial distribution of T_B, particularly in inner disk regions. However, model LLa0 fails to produce an emission peak at 80 au because the CH_4 sintering zone completely disappears for $a_0 = 4\ \mu$m.

In summary, we find that dust settling gives a strong constraint on the turbulence strength and monomer grain size in the HL Tau disk. Dust settling and pile up occur simultaneously only if $10^{-4} < \alpha_t \lesssim 10^{-3}$ and $1\ \mu\mathrm{m} \lesssim a_0 < 4\ \mu$m. If $a_0 \gtrsim 4\ \mu$m, sintering would be too slow to provide an appreciable emission peak at $\sim$80 au. If $a_0 \ll 1\ \mu$m, sintered aggregates would be disrupted only when $\alpha_t \gg 10^{-3}$, but such a strong turbulence would inhibit dust settling.

Interestingly, the above results suggest that the grains constituting the aggregates in the HL Tau disk are considerably

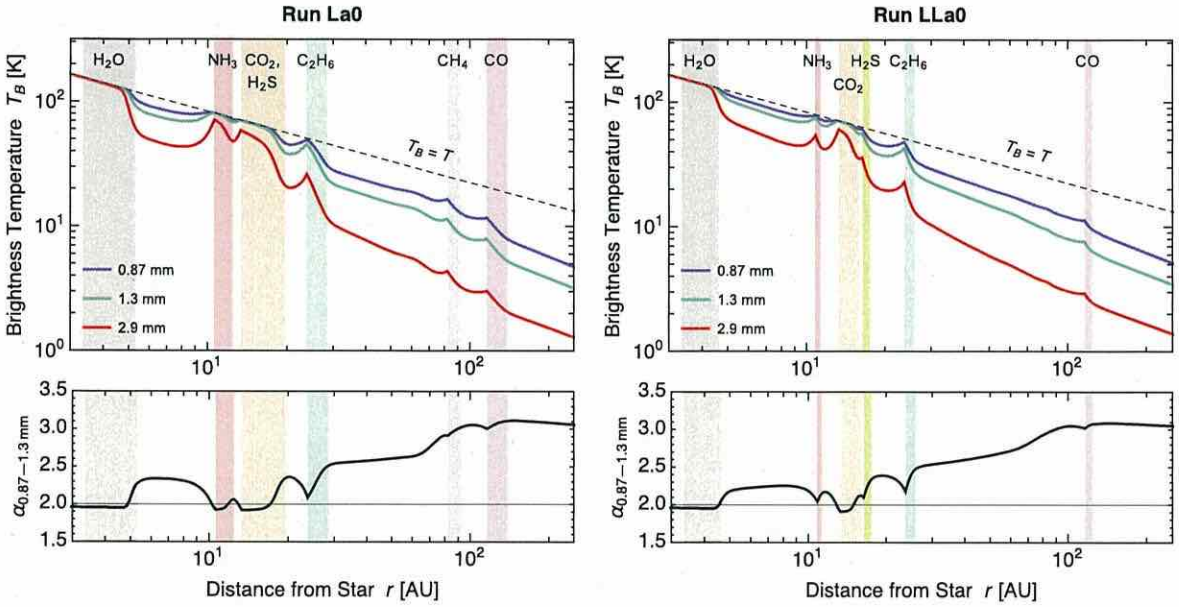

Figure 15. Same as the right panels of Figure 11, but for models La0 (left panels) and LLa0 (right panels).

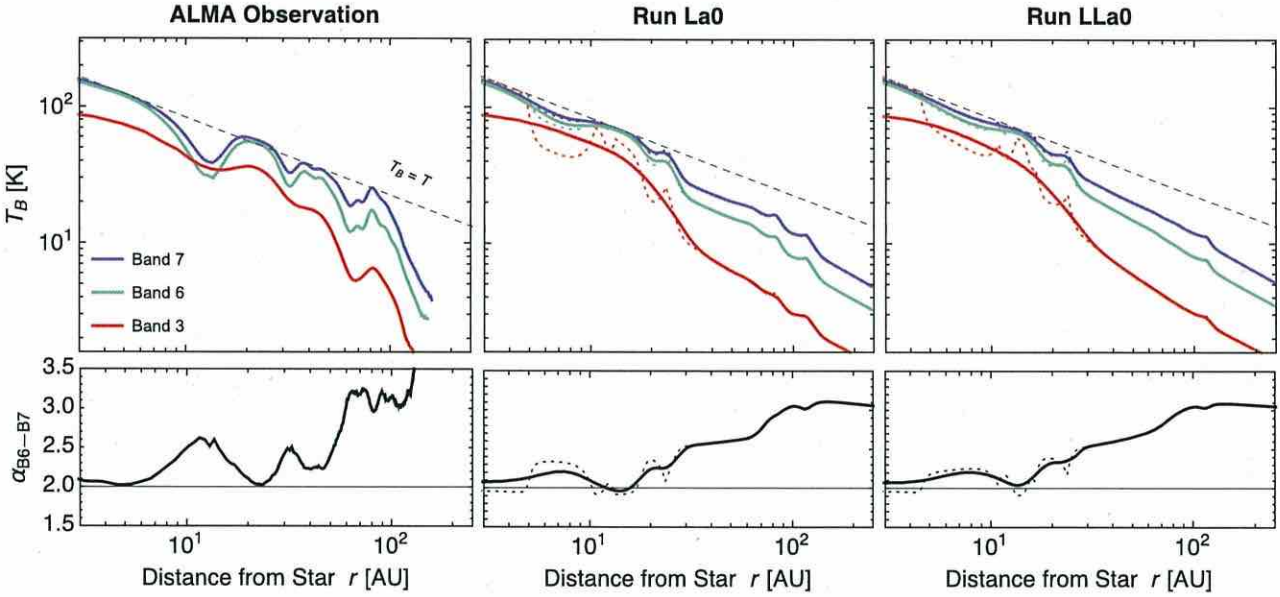

Figure 16. Same as Figure 12, but for models La0-tuned (center panels) and LLa0-tuned (right panels).

larger than the interstellar grains ($\lesssim$0.25 μm in radius; e.g., Mathis et al. 1977). They are also larger than the grains constituting interplanetary dust particles of presumably cometary origin (typically 0.1–0.5 μm in diameter; e.g., Rietmeijer 1993). However, such a large grain size is not excluded by previous observations of HL Tau. The near-infrared scattered light images of the envelope of HL Tau are best reproduced by models that assume the maximum particle size of more or less 1 μm (Lucas et al. 2004; Murakawa et al. 2008). Because the scattered light probes the envelope's surface layer where coagulation is inefficient, the observed micron-sized particles might be monomers rather than aggregates.

6.4. Sublimation Energies

As mentioned in Section 5.5, the fiducial model does not fully explain the exact locations and widths of all major HL Tau rings. For example, the innermost dark ring predicted by model Sa0 lies somewhat closer to the central star than the observed one. If we define the position of the innermost dark ring as the location where T_B/T at Band 6 is maximized, the radius of the predicted innermost dark ring (8 au) is $\approx$40% smaller than that of the observed one (13 au). Furthermore, the second innermost dark ring in model Sa0 is much narrower than that observed because the C_2H_6 snow line lies very close to the H_2S sintering line. Of course, a different temperature

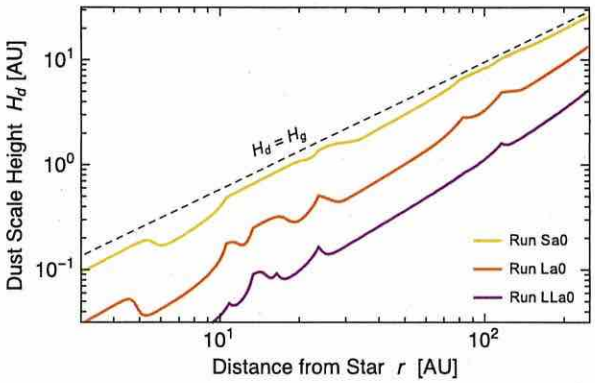

Figure 17. Dust scale height H_d vs. orbital radius r at time $t = t_{\rm snap}$ for runs Sa0 (black curve) and La0 (dashed curve). The dashed line shows the gas scale height H_g.

profile would provide a different configuration of the sintering zones. However, as long as $T(r)$ is assumed to obey a single power law, it is generally impossible to move some of the sintering zones while leaving the positions of the others unchanged. For example, a temperature profile that is slightly higher than Equation (1) would shift the C_2H_6 sintering zone to 40 au, but would also shift the CH_4 sintering zone to 100 au. Moreover, a different $T(r)$ would make our prediction for the brightness temperatures in the optically thick regions less good.

However, the locations of the sintering zones depend not only on the gas temperature profile but also on the sublimation energies L_j in $P_{{\rm ev},j}(T)$. As mentioned in Section 3.2, there is typically a 10% uncertainty in the published data of L_j. In general, a 10% uncertainty in the sublimation energy causes a $\sim$10% uncertainty in the sublimation temperature $T_{{\rm subl},j}$ because $P_{{\rm ev},j}$ is a function of the ratio L_j/T. Assuming the temperature profile given by Equation (1), we have $r_{{\rm snow},j} \propto T_{{\rm subl},j}^{-1.8}$ and hence $|\delta r_{{\rm snow},j}|/r_{{\rm snow},j} \approx 1.8|\delta T_{{\rm subl},j}|/T_{{\rm subl},j} \sim 2|\delta L_j|/L_j$, where δL_j, $\delta T_{{\rm subl},j}$, and $\delta r_{{\rm snow},j}$ denote the uncertainties of L_j, $T_{{\rm subl},j}$, and $r_{{\rm snow},j}$, respectively. Consequently, a 10% uncertainty in L_j leads to a $\sim$20% uncertainty in the snow line location. Such an uncertainty can be significant because the separation of the observed rings is only a fraction of their radii.

To demonstrate the potential importance of uncertainties in the sublimation energies, we performed two simulations (Sa0-tuned and La0-tuned). The parameters adopted in these simulations are the same as those in Sa0 and La0, respectively, except that the sublimation energies of H_2O, NH_3, and C_2H_6 are lowered by 10% from our baseline values (see column 5 of Table 2). According to the estimate shown previously, such modifications shift the sintering zones of these volatiles outward by $\sim$20%. The resulting radial profiles of $T_{\rm B}$ and $\alpha_{0.87-1.3\,{\rm mm}}$ before smoothing are shown in Figure 18. In model Sa0-tuned, the three innermost sintering zones are located at 4–8 au (H_2O), 13–23 au (NH_3–CO_2–H_2S), and 29–40 au (C_2H_6) instead of 3–6 au, 11–23 au, and 24–33 au as in model Sa0. Figure 19 shows the radial emission profiles after smoothing, which we compare with the ALMA observation. For the sake of comparison, we define the radii of the bright and dark rings by the orbital radii at which $T_{\rm B}/T$ at Band 6 is locally maximized and minimized, respectively. Then, the radii of four innermost bright/dark rings are found to be 13, 23, 32, and 38 au for the observation, 9, 16, 24, and 30 au for model Sa0-NoSint, and 9, 15, 24, and 29 au for model La0-NoSint. Thus, model Sa0-NoSint reproduces the ring radii in the observed image to an accuracy of $\lesssim$30%, which is about 10% better than model Sa0. Model La0-NoSint is slightly less accurate, with a maximum error of 35%, but it is still 10% better than the original model La0. Furthermore, the second innermost dark ring in these models is much wider than that in model Sa0. As a consequence, the radial distribution of $\alpha_{\rm B6-B7}$ now has a clear peak structure at the position of this ring, and the peak value $\approx$2.3 agrees with the observed value $\approx$2.5 to within a relative error of 10%.

Thus, assuming sublimation energies of H_2O, NH_3, and C_2H_6 that are only 10% lower than the baseline values significantly improves our predictions for the radial configuration of the dust rings. Interestingly, for H_2O and NH_3, the tuned values of the sublimation energies are more consistent with the results of recent experiments by Martín-Doménech et al. (2014; 5165 K for H_2O and 2965 K for NH_3) than our fiducial values. However, not all new data for sublimation energies improve our predictions. Martín-Doménech et al. (2014) also measured the sublimation energies of CO_2 and CO, and the measured values (2605 K for CO_2 and 890 K for CO) are also lower than ours by about 10%. A 10% change in the sublimation energy of CO_2 has little effect on the resulting ring patterns, because the CO_2 sintering zone partially overlaps with the sintering zones of NH_3 and H_2S. A 10% decrease in the sublimation energy of CO shifts the CO sintering zone to 143–197 au, which makes the correspondence between the CO sintering zone and the faint 97 au ring of HL Tau (see Section 5.5) less good.

7. DISCUSSION

7.1. Possible Effects of Bouncing

As mentioned in the introduction, sintered aggregates tend to bounce rather than stick when they collide at a velocity below the fragmentation threshold. For example, sintered aggregates made of 0.1 μm sized icy grains bounce at 1 m s^{-1} $\lesssim \Delta v \lesssim$ 20 m s^{-1} (Sirono 1999; S. Sirono 2016, in preparation). This effect was neglected in this study by simply applying Equation (15) to both sintered and unsintered aggregates. In principle, such a simplification causes an overestimate of the maximum size of aggregates in the sintering zones. However, this effect is expected to be minor because sintered aggregates grow only moderately even without the bouncing effect. To see this, we go back to the radial profile of the radius a_* of the representative aggregates from run Sa0 shown in Figure 8(a). Because the radial inward flow of the aggregates is nearly stationary (see Figure 8(d)), this figure shows how the size of individual representative aggregates evolve as they move inward. We find that a_* is radially constant in the CH_4 and CO sintering zones, meaning that the aggregates do not grow at all when they go through these zones. Appreciable growth of sintered aggregates occurs only in inner regions of the H_2O and NH_3–CO_2–H_2S sintering zones. However, even at these locations, the aggregate size increases only by a factor of less than two until they reach the inner edges of the sintering zones. Therefore, we can conclude that inclusion of bouncing collisions would little change the evolution of representative aggregates in the sintering zones.

7.2. Limitations of the Single Size Approach

Our single-size approach (Section 4.1) relies on the assumption that the mass budget of dust at each orbital radius

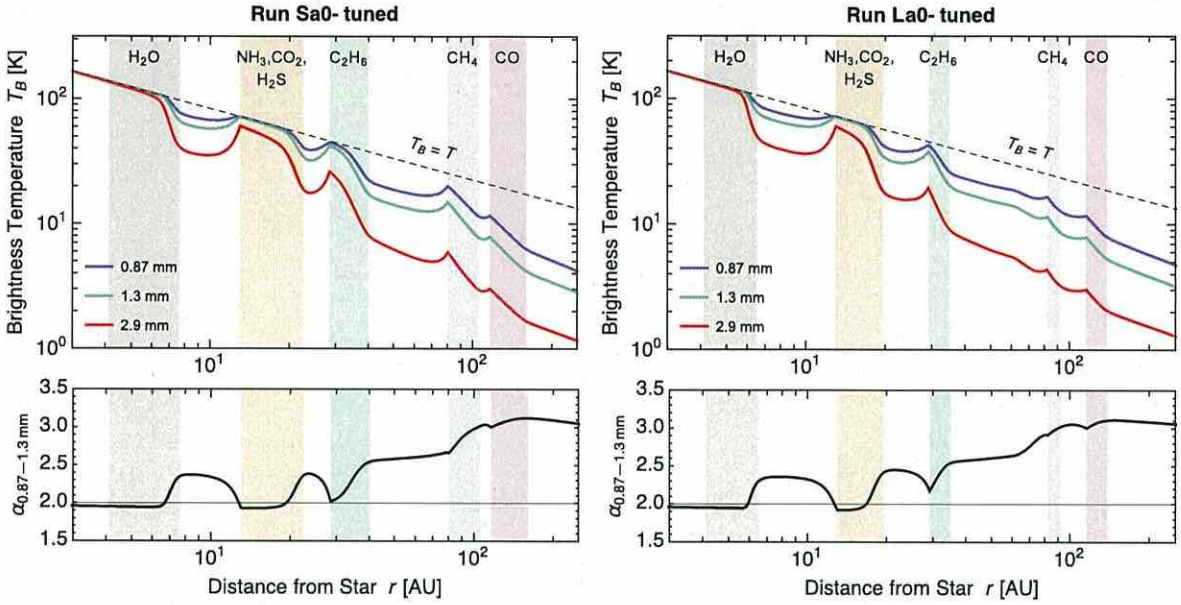

Figure 18. Same as the right panels of Figure 11, but for runs Sa0-tuned (left panels) and La0-tuned (right panels).

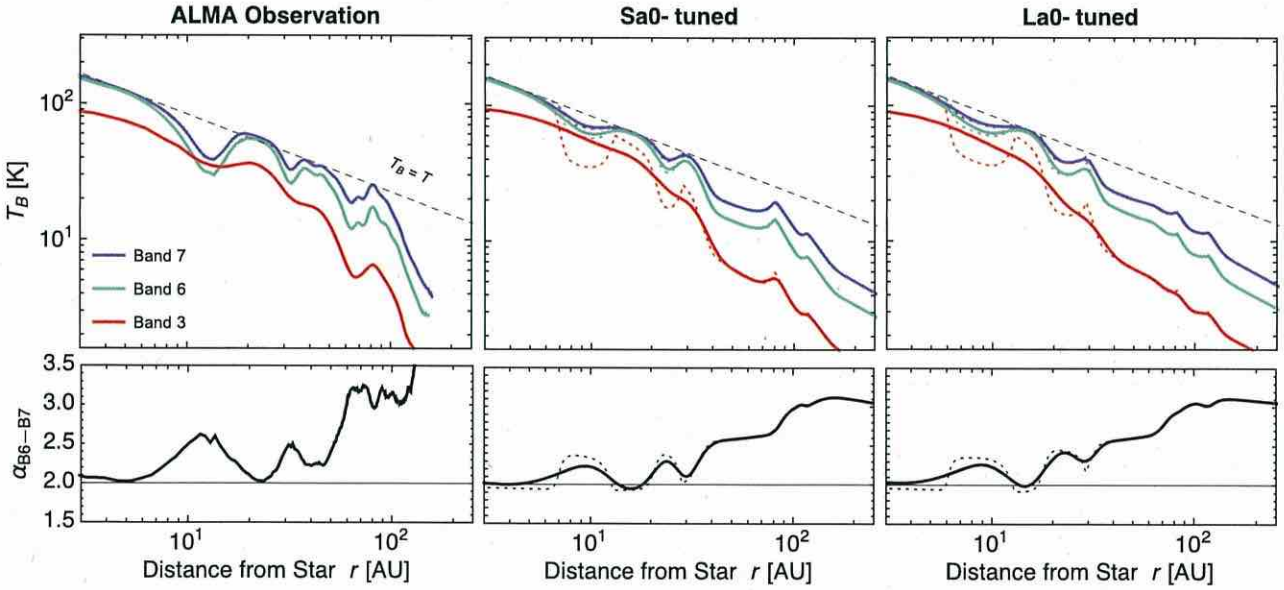

Figure 19. Same as Figure 12, but for models Sa0-tuned (center panels) and La0-tuned (right panels), which adopt optimized sublimation energies for H_2O, NH_3, and C_2H_6.

is dominated by a single population of aggregates having mass $m = m_*(r)$. This assumption might be inadequate at the boundaries of sintering and non-sintering zones, around which two populations of aggregates of different characteristic sizes (i.e., sintered and unsintered aggregates) can coexist. However, this effect would only be important in the close vicinity of the boundaries because the sintering timescale is a steep function of r and the aggregates in our simulations do not drift faster than they collide with each other.

A probably more critical limitation of the single-size approach is that one has to assume the size distribution of fragments produced by the collisions of the mass-dominating aggregates. In this study we avoided detailed modeling of the fragmentation process by assuming a simple power-law fragment size distribution (Equation (20)) independent of the collision velocity of the largest aggregates. The assumed power-law distribution would reasonably approximate the true fragment size distribution when the collisions of the mass-dominating aggregates are highly disruptive. In fact, however, unsintered aggregates in our simulations do not experience catastrophic disruption because their collision velocity is always below the catastrophic disruption threshold

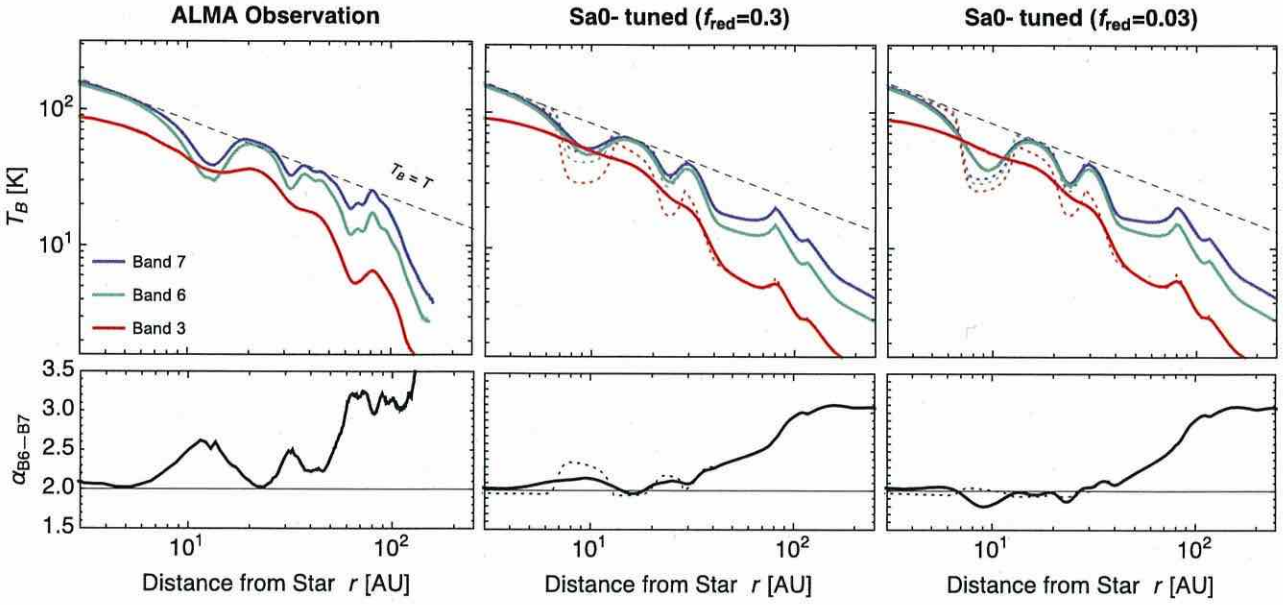

Figure 20. Same as Figure 12, but for model Sa0-tuned with the modified fragment size distribution given by Equation (33). The center and right panels are for fragment reduction factor $f_{\rm red} = 0.3$ (center panels) and 0.03 (right panels).

$\Delta v_{\rm frag}$. For example, our fiducial run Sa0 shows that $\Delta m_*/m_* \approx 0.2$–$0.4$ in the non-sintering zones, which implies that fragments would carry away only a few tens of percent of the total mass of two colliding mass-dominating aggregates in these zones. Equation (20) might also overestimate the amount of fragments from sintered aggregates because they actually bounce off, rather than fragment at low collision velocities (see Section 7.1). The preliminary results of our aggregate collision simulations (S. Sirono 2015, in preparation) show that fragments from two colliding sintered aggregates carry away only a few percent of their total mass even when $\Delta v \approx \Delta v_{\rm frag}$.

Therefore, it important to assess how the predictions from our models depend on the amount of fragments assumed. We consider a fragment size distribution that is similar to Equation (20), but assumes a reduced amount of fragments in the size range $a < a_*/10$,

$$N_{\rm d}'(a) = \begin{cases} Ca^{-3.5}, & a_*/10 < a < a_*, \\ f_{\rm red} Ca^{-3.5}, & a_{\rm min} < a < a_*/10, \\ 0, & \text{otherwise}, \end{cases} \quad (33)$$

where the factor $f_{\rm red}$ (<1) encapsulates the reduction of fragment production, and C is again determined by the condition $\int_0^\infty mN_{\rm d}'(a){\rm d}a = \Sigma_{\rm d}$. We consider two values—$f_{\rm red} = 0.3$ and 0.03—based on the estimates for unsintered and sintered aggregates mentioned above.

We now recalculate the radial profiles of $T_{\rm B}$ and $\alpha_{\rm B6-B7}$ for model Sa0-tuned using Equation (33) instead of Equation (20). The results are shown in the center and right panels of Figure 20. These, together with the result for $f_{\rm red} = 1$ (the center panels in Figure 19), show that both $T_{\rm B}$ and $\alpha_{\rm B6-B7}$ in the two innermost emission dips decrease as $f_{\rm red}$ is decreased. In these inner regions, the radius a_* of the largest (mass-dominating) aggregates is significantly larger than millimeters, and therefore the fragments smaller than millimeters have a non-negligible contribution to the millimeter dust opacity. In this case, the opacity index $\beta_{0.87-1.3\,\rm mm}$ decreases toward zero, which is the value in the geometric optics limit, as the amount of the fragments decreases (see, e.g., Draine 2006). This explains why a lower value of $f_{\rm red}$ leads to a lower value of the spectral slope in the optically thin inner dips where the relation $\alpha_{0.87-1.3\,\rm mm} \approx \beta_{0.87-1.3\,\rm mm} + 2$ applies. In the case of $f_{\rm red} = 0.03$, the spectral slope in the innermost emission dip falls below two, due to the effect of the frequency-dependent angular resolution already mentioned in Section 5.5. We find that the results for $f_{\rm red} = 0.3$ and 0.03 better reproduce the observed depths of the two innermost emission dips than the result for $f_{\rm red} = 1$. However, these low-$f_{\rm red}$ models yield poorer agreement with the observed value of $\alpha_{\rm B6-B7}$ in these emission dips. Varying the value of $f_{\rm red}$ within the range 0.03–1 has no effect on the predictions for $T_{\rm B}$ and $\alpha_{\rm B6-B7}$ outside the two innermost emission dips. Taken together, we cannot judge at this point which value of $f_{\rm red}$ best reproduces the observed appearance of HL Tau. In any case, the effects of assuming the lower values of $f_{\rm red}$ are not significant as long as $f_{\rm red}$ is higher than 0.3, which is the value we expect for unsintered aggregates in the dark rings.

7.3. Evolution of the Monomer Size Distribution and Possible Planetesimal Formation Near the H_2O Sintering Zone

We have assumed that vapor transport within an aggregate, which drives sintering, does not alter the size of monomer grains. In reality, this is not true because the growth of necks must be compensated by the shrinkage of the bodies of monomers. Furthermore, if the monomers within an aggregate are not uniform in size, a small number of large monomers may grow—the phenomenon known as Ostwald ripening (see, e.g., Lifshitz & Pitaevskii 1981)—while smaller ones may completely evaporate leaving silicate grains (Kuroiwa & Sirono

2011; Sirono 2011a).[8] The evolution of the monomer size distribution is negligible in the sintering zones of minor volatiles like NH_3 and CH_4 (as noted in the introduction, sintering can still occur because the neck volume is much smaller than the monomer volume). However, this is not the case for water ice because it constitutes more than half of the monomer volume.

As pointed out by Kuroiwa & Sirono (2011), the evolution of the monomer size distribution due to water vapor transport would result in a decrease in the sticking efficiency of the icy aggregates. Kuroiwa & Sirono (2011) showed that water vapor transport within an aggregate produces a small number of large ice-rich monomers and a large number of small bare silicate monomers. Aggregates made of the two populations of monomers would be fragile, like sintered aggregates made of equally ice-coated grains, because the total binding energy ($\propto$number of contacts) of the former would be determined by weak silicate–silicate contacts. These aggregates would experience catastrophic disruption and pile up near the H_2O snow line in a similar way to sintered aggregates.

In addition, the evaporation of small monomers could directly result in the fragmentation of icy aggregates. Sirono (2011a) demonstrated that an aggregate made of initially submicron-sized H_2O monomers breaks up into large detached monomers of radii $\sim$1–10 μm (see also Kuroiwa & Sirono 2011). This spontaneous breakup would also produce a pileup of dust near the H_2O snow line, but the surface density contrast provided by this effect could be much more significant than that by than sintering-induced fragmentation, because the micron-sized monomers are much more strongly coupled to the disk gas than aggregates. Sirono (2011a) notes that the dust surface density in the H_2O sintering zone can become high enough to trigger the formation of icy planetesimals via the gravitational instability (Goldreich & Ward 1973; Sekiya 1998; Youdin & Shu 2002).

Thus, the evolution of the monomer size distribution due to vapor transport would further promote the fragmentation and accumulation of aggregates in the H_2O sintering zone. This may not affect the observational appearance of the HL Tau disk because the H_2O sintering zone is already optically thick, even without the monomer size evolution. However, this could have a significant effect on planet(esimal) formation near the H_2O snow line.

7.4. Possible Effects of Porosity Evolution

We neglected the evolution of the porosity of icy aggregates by assuming the fixed aggregate internal density of 0.24 g cm^{-3}. In reality, the porosity of aggregates (much smaller than planetesimals) can vary greatly through collisions (e.g., Ormel et al. 2007; Suyama et al. 2008; Okuzumi et al. 2009), compression by gas drag (Kataoka et al. 2013a, 2013b), and condensation and sintering of H_2O ice (again, minor volatile ices occupy only a small fraction of grain volume and are therefore negligible here). In the absence of the compaction due to condensation and sintering, the internal density of icy aggregates in protoplanetary disks can decline to as low as 10^{-4}–10^{-3} g cm^{-3} (Okuzumi et al. 2012; Kataoka et al. 2013b).

The porosity evolution has two important effects on the evolution of icy aggregates. First, fluffy aggregates tend to grow to the size regime where the gas drag onto the aggregates is determined by Stokes' law. This particularly occurs in the inner regions of protoplanetary disks, where the mean free path of the disk gas molecules is short. In the Stokes drag regime, the growth limit given by Equation (30) no longer applies because that limit assumes Epstein's drag law. Okuzumi et al. (2012) found that fluffy aggregates that are subject to Stokes' drag law grow fast enough to overcome the radial drift barrier. In a massive protoplanetary disk as considered in this study, icy aggregates break through the drift barrier and form icy planetesimals at $r \lesssim 10$ au (see the bottom right panel of Kataoka et al. 2013a). Second, the millimeter absorption opacity of large porous aggregates is similar to that of small compact aggregates because $\kappa_{\mathrm{d},\nu}$ can be approximated as a function of the product $\rho_{\mathrm{int}} a$ (Kataoka et al. 2014).

In this study, these important effects have been neglected by fixing the aggregate porosity to a relatively low value. Rapid coagulation beyond the Epstein drag regime could strongly reduce the optical depth in the non-sintering zone lying at $r \sim 10$ au, where the radial drift barrier determines the maximum size of the relatively compact aggregates that we assumed in this study. This effect should be studied in detail in future work.

On the other hand, the above two effects are less important at $r \gtrsim 10$ au, where even the highly fluffy aggregates would grow within the Epstein drag regime. To show this, we first note that neither $\mathrm{St}_{\mathrm{drift}}$ (Equation (30)) nor $\mathrm{St}_{\mathrm{frag}}$ (Equation (32)) depends on ρ_{int} (note again that Epstein's law is used in the derivation of Equation (30)). This means that porosity evolution has no effect on the maximum attainable Stokes number at each r, and therefore does not change the radial distribution of Σ_{d} because the radial advection velocity v_r is a function of St (see Equation (10)). Porosity evolution does not change the dust absorption opacity $\kappa_{\mathrm{d},\nu}$ either, because the product $\rho_{\mathrm{int}} a_*$ is proportional to St in the Epstein regime (see Equation (9)). This is a natural consequence of the fact that both the stopping time in the Epstein regime and the absorption opacity are determined by the mass-to-area ratio $m/\pi a^2 (\sim \rho_{\mathrm{int}} a)$ of the aggregates. Taken together, the radial distribution of the absorption optical depth $\tau_\nu \propto \kappa_{\mathrm{d},\nu} \Sigma_{\mathrm{d}}$ is independent of the aggregate porosity, as long as the aggregates grow within the Epstein drag regime.

Nevertheless, porosity evolution might have some important observational consequence in the outer disk region. The millimeter continuum emission from the HL Tau disk is known to be polarized in the direction roughly perpendicular to the disk major axis at a level of 0.9% in the average degree of polarization (Stephens et al. 2014). Yang et al. (2015) and Kataoka et al. (2015b) point out that self-scattering of thermal emission by dust rings (Kataoka et al. 2015a) can explain the polarization observation. However, this mechanism produces a degree of polarization of $\approx$1% only when the size of the dust particles falls within a particular range. For example, if the particles are compact and their size distribution obeys our Equation (20), the self-scattering scenario is consistent with the observation only when the maximum particle size a_{max} ($=a_*$ in this study) is $\sim$0.1 mm (Kataoka et al. 2015b; Yang et al. 2015), which is considerably smaller than the size of mass-

[8] In general, vapor tends to be transported from solid surfaces of a high positive curvature (e.g., bumps) to surfaces of a high negative curvature (e.g., dips) so that the total energy of the solid associated with surface tension is minimized (see, e.g., Blackford 2007). Sintering (neck growth) is simply driven by the high negative curvature of the necks. Ostwald ripening is the phenomenon in which large monomers with a (positive) surface curvature lower than the average surface curvature within the aggregate grow at the expense of small monomers with a curvature higher than the average.

dominating aggregates predicted in this study. In the compact particle model, a particle size larger than a millimeter is ruled out because the scattered emission would be too weakly polarized (see also Kataoka et al. 2015a). By contrast, large but fluffy aggregates are known to produce highly polarized scattered light like constituent monomers do (Min et al. 2016), and therefore might be able to explain the polarization observation of HL Tau.

7.5. Possible Effects of Condensation Growth

We neglected the condensation growth of ice particles near the snow lines. In fact, a recent study by Ros & Johansen (2013) has shown that condensation growth can be effective at locations slightly outside the H_2O snow line. This effect might change our predictions for dust evolution near H_2O snow line because condensation dominantly takes place on the smallest particles (i.e., monomers). If condensation dominates over sintering-induced fragmentation and bouncing, the regions slightly outside the snow lines would be seen as *dark* rings at millimeter wavelengths, as noted by Zhang et al. (2015). However, it is unclear whether condensation growth becomes important for volatiles less abundant than H_2O, like CO and NH_3. To address this open question, we will incorporate condensation growth into our global dust evolution simulations in future work.

7.6. Sintering-induced Ring Formation in Other Objects?

Perhaps the strongest prediction from our model, as well as from the model of Zhang et al. (2015), is that the multiple dust rings may not be peculiar to the HL Tau disk. In principle, sintering-induced ring formation operates as long as the disk is not too depleted of dust (or not too old), the monomers are sufficiently small to cause rapid sintering, and turbulence is strong enough to cause the disruption of sintered aggregates. If these conditions are satisfied, axisymmetric dust rings emerge slightly outside the snow lines of relatively major volatiles. An intriguing object in this context is TW Hya. For this system, the CO snow line was indirectly detected at an orbital distance of ~30 au (Qi et al. 2013), and furthermore, near-infrared scattered light images of the disk suggest the presence of two axisymmetric dust gaps at ~80 au (Debes et al. 2013) and ~20 au (Akiyama et al. 2015; Rapson et al. 2015). A latest ALMA observation has shown that there is also a gap in millimeter dust emission in the vicinity of the 20 au scattered light gap (Nomura et al. 2015). The gaps at 80 au and 20 au could be associated with non-sintering zones exterior to and interior to the CO sintering zone, respectively. However, it is not obvious whether our ring formation mechanism directly applies to TW Hya because this object is known to be much older than HL Tau (at least 3 Myr; Vacca & Sandell 2011). This question should also be addressed in future work.

8. CONCLUSIONS

Motivated by the recent ALMA observations of the HL Tau disk, we explored the possibility that sintering of icy dust aggregates might lead to the formation of multiple dust rings in a protoplanetary disk. Sintering is a particle fusion process that occurs when the temperature is slightly below the melting point. Sintered aggregates are generally harder but less sticky than unsintered aggregates. Therefore, if dust aggregates in a protoplanetary disk consist of various materials, their growth can be suppressed at different orbits corresponding to the sublimation fronts of different materials. This possibility was originally pointed out by Sirono (1999, 2011b), and here we have for the first time studied its effects on the global evolution of dust in a protoplanetary disk.

Following Sirono (2011b), we regard aggregates as sintered if their sintering timescale is shorter than their collision timescale (Section 3.4). This criterion defines the "sintering zones" in which one of the volatile species included in the aggregates causes sintering. The temperature profile of the HL Tau disk has been modeled based on the millimeter intensity maps provided by the ALMA observations (ALMA Partnership et al. 2015), together with the assumption that the central emission peak and inner bright rings are optically thick at 1 mm (Section 2.1, Figure 1). Based on the aggregate collision simulations by Sirono & Ueno (2014), we assumed that sintered aggregates have a maximum sticking velocity that is 60% lower than that for unsintered aggregates (Equations (18) and (19); Figure 5(a)). For both sintered and unsintered aggregates, we regarded collisions at velocities higher than the threshold disruptive (Equation (15); Figure 5(b)).

Using the aggregate sintering model described above, we simulated the global evolution of dust in the HL Tau disk for various sets of model parameters. As a first step toward more comprehensive modeling, we focused on the evolution of the mass-dominating (largest) aggregates, and assumed a power-law size distribution for smaller aggregates when we convert the simulation data into radial profiles of millimeter dust emission. Key parameters in our model are the strength of turbulence (α_t), the size of monomers that constitute the aggregates (a_0), and the sublimation energies of the volatiles (L_j). The monomer size is relevant here because it controls the timescale of sintering (Equation (6)) and the fragmentation strength of dust aggregates (Equations (18) and (19)).

Our key findings are summarized as follows.

1. Because dust is gradually lost to the central star owing to radial drift, the total dust mass in the disk decreases with time (Section 5.1). For the total disk mass of 0.2 $M_\odot$ and the initial dust-to-gas mass ratio of 0.01, our HL Tau disk models best reproduce the millimeter flux densities from the ALMA observations when the disk age in the models is chosen to be 0.1–0.5 Myr. This is consistent with the general belief that HL Tau is a young ($\lesssim$1 Myr) protoplanetary disk.
2. Dust aggregates pile up in the sintering zones due to the combined effect of radial drift and sintering-induced fragmentation (Section 5.2). In general, aggregates grow locally until either rapid radial drift or fragmentation starts to halt their growth. After that, the aggregates start to drift toward the central star at a velocity proportional to the maximum size. Sintered aggregates have a lower maximum size and hence a lower inward drift velocity than unsintered aggregates simply because the former tend to disrupt more easily upon collision. For this reason, aggregates tend to pile up in the sintering zones.
3. At millimeter wavelengths, the sintering zones are seen as *bright* rings because the dust surface density in the sintering zones is higher than in the non-sintering zones (Section 5.4). In particular, at the wavelengths of 0.87 mm and 1.3 mm, the three innermost sintering zones (which correspond to H_2O, NH_3–CO_2–H_2S, and C_2H_6,

respectively) are optically thick, producing a millimeter spectral index of ≈2. The predicted spectral index and brightness temperatures are consistent with those of the central emission peak and the two innermost bright rings of the HL Tau disk (Section 5.5). Our model also predicts an optically thin emission peak at ≈80 au, which is associated with the CH_4 sintering zone, and two optically thin dark rings of a spectral slope of 2.3–2.5 at $\lesssim$40 au, which are associated with the two innermost non-sintering zones. These are all consistent with the ALMA observation.

4. The sintering-induced ring patterns diminish as the disk becomes depleted of dust (Section 5.3). As the dust-to-gas mass ratio decreases, aggregates collide with each other less frequently, making their maximum size more severely limited by radial drift rather than fragmentation. The sintering-induced rings disappear once radial drift dominates over fragmentation, even in the sintering zones. For a disk with a total mass of $0.2\,M_\odot$, the characteristic radius of 150 au, and the initial dust-to-gas mass ratio of 0.01, we find that the sintering-induced rings decay in 2 Myr. The ring patterns of HL Tau might be a sign of its youth.
5. Models that assume a lower turbulence parameter α_t toward the central star best reproduce the multiple ring structure of HL Tau (Section 6.2). If α_t were radially constant, turbulence-driven collision velocity $\propto\sqrt{\alpha_t T}$ would increase with decreasing radial distance r. In this case, either unsintered aggregates would fragment at small r or sintered aggregates would fragment at large r. The former case does not reproduce dark rings at small r, while the latter case does not reproduce bright rings at large r. The radial dependence of α_t suggested by our model is qualitatively consistent with the predictions from magnetohydrodynamical turbulence models.
6. The vertical extent of the observed dust rings places a strong constraint on the turbulence strength and monomer size assumed in our model (Section 6.3). When $a_0 \gg 1\ \mu$m, sintering would be too slow to induce dust ring formation. When $a_0 \ll 1\ \mu$m, disruption of sintered aggregates would require turbulence that is too strong to allow dust settling to the midplane. If the macroscopic dust particles in the HL Tau disk have already settled, as suggested by previous studies (Kwon et al. 2011; Pinte et al. 2016), disk turbulence must be moderately weak ($10^{-4} < \alpha_t \lesssim 10^{-3}$) *and* monomers must be micron-sized ($1\ \mu\text{m} \lesssim a_0 < 4\ \mu$m). The predicted monomer size might be consistent with the near-infrared observations of HL Tau, suggesting the presence of micron-sized grains on the surface of its circumstellar envelope (Lucas et al. 2004; Murakawa et al. 2008).
7. The exact locations and widths of the dust rings predicted by our model are subject to uncertainties in the vapor pressure data (Section 6.4). In general, a 10% uncertainty in the sublimation energy of a volatile species causes a ∼20% uncertainty in the predicted location of the volatile's sintering zone. We find that reducing the sublimation energies of H_2O, NH_3, and C_2H_6 by only 10% from our fiducial values significantly improves our predictions for the observational appearance of the ring structures in an inner region of the HL Tau disk. The models using the tuned sublimation energies reproduce the radial positions of the HL Tau's inner rings to an accuracy of $\lesssim$30%.

The authors thank Neal Turner for discussions on the temperature distribution of the HL Tau disk, and Akimasa Kataoka for useful comments on the modeling of aggregate porosity. We also thank Takashi Tsukagoshi, Tetsuya Hama, Misato Fukagawa, Hideko Nomura, and Mario Flock for comments and discussions, and the anonymous referee for prompt and constructive comments. This work is supported by Grants-in-Aid for Scientific Research (nos. 23103004, 23103005, 25400447, 26287101, 15H02065) from MEXT of Japan and by the Astrobiology Center Project of National Institutes of Natural Sciences (NINS) (grant no. AB271020). This paper makes use of the following ALMA data: ADS/JAO.ALMA#2011.0.00015.SV. ALMA is a partnership of ESO (representing its member states), NSF (USA) and NINS (Japan), together with NRC (Canada), NSC and ASIAA (Taiwan), and KASI (Republic of Korea), in cooperation with the Republic of Chile. The Joint ALMA Observatory is operated by ESO, AUI/NRAO, and NAOJ.

REFERENCES

Adachi, I., Hayashi, C., & Nakazawa, K. 1976, PThPh, 56, 1756
Akiyama, E., Muto, T., Kusakabe, N., et al. 2015, ApJL, 802, L17
ALMA Partnership, Brogan, C. L., Pérez, L. M., et al. 2015, ApJL, 808, L3
Andrews, S. M., Wilner, D. J., Hughes, A. M., Qi, C., & Dullemond, C. P. 2009, ApJ, 700, 1502
Bai, X.-N. 2011, ApJ, 739, 50
Balbus, S. A., & Hawley, J. F. 1991, ApJ, 376, 214
Bauer, I., Finocchi, F., Duschl, W. J., Gail, H.-P., & Schloeder, J. P. 1997, A&A, 317, 273
Beckwith, S. V. W., Sargent, A. I., Chini, R. S., & Guesten, R. 1990, AJ, 99, 924
Birnstiel, T., Dullemond, C. P., & Brauer, F. 2010, A&A, 513, A79
Birnstiel, T., Klahr, H., & Ercolano, B. 2012, A&A, 539, A148
Birnstiel, T., Ormel, C. W., & Dullemond, C. P. 2011, A&A, 525, A11
Blackford, J. R. 2007, JPhD, 40, 355
Brauer, F., Dullemond, C. P., & Henning, T. 2008, A&A, 480, 859
Chokshi, A., Tielens, A. G. G. M., & Hollenbach, D. 1993, ApJ, 407, 806
Collings, M. P., Anderson, M. A., Chen, R., et al. 2004, MNRAS, 354, 1133
Collings, M. P., Dever, J. W., Fraser, H. J., McCoustra, M. R. S., & Williams, D. A. 2003, ApJ, 583, 1058
Debes, J. H., Jang-Condell, H., Weinberger, A. J., Roberge, A., & Schneider, G. 2013, ApJ, 771, 45
Dipierro, G., Price, D., Laibe, G., et al. 2015, MNRAS, 453, L73
Dohnanyi, J. S. 1969, JGR, 74, 2531
Dominik, C., & Tielens, A. G. G. M. 1997, ApJ, 480, 647
Dong, R., Zhu, Z., & Whitney, B. 2015, ApJ, 809, 93
Draine, B. T. 2003, ApJ, 598, 1026
Draine, B. T. 2006, ApJ, 636, 1114
Dubrulle, B., Morfill, G., & Sterzik, M. 1995, Icar, 114, 237
Dzyurkevich, N., Flock, M., Turner, N. J., Klahr, H., & Henning, T. 2010, A&A, 515, A70
Estrada, P. R., Cuzzi, J. N., & Morgan, D. A. 2015, ApJ, in press (arXiv:1506.01420)
Ferrier, B. S. 1994, JAtS, 51, 249
Flock, M., Ruge, J. P., Dzyurkevich, N., et al. 2015, A&A, 574, A68
Fouchet, L., Gonzalez, J.-F., & Maddison, S. T. 2010, A&A, 518, A16
Garaud, P. 2007, ApJ, 671, 2091
Goldreich, P., & Ward, W. R. 1973, ApJ, 183, 1051
Gonzalez, J.-F., Laibe, G., Maddison, S. T., Pinte, C., & Ménard, F. 2015, MNRAS, 454, L36
Gonzalez, J.-F., Pinte, C., Maddison, S. T., Ménard, F., & Fouchet, L. 2012, A&A, 547, A58
Guilloteau, S., Dutrey, A., Piétu, V., & Boehler, Y. 2011, A&A, 529, A105
Hartmann, L., Calvet, N., Gullbring, E., & D'Alessio, P. 1998, ApJ, 495, 385
Hayashi, M., Ohashi, N., & Miyama, S. M. 1993, ApJL, 418, L71
Haynes, W. M. 2014, CRC Handbook of Chemistry and Physics (95th ed.; Boca Raton, FL: CRC Press)

Johansen, A., Youdin, A., & Klahr, H. 2009, ApJ, 697, 1269
Johnson, K. L., Kendall, K., & Roberts, A. D. 1971, RSPSA, 324, 301
Kanagawa, K. D., Muto, T., Tanaka, H., et al. 2015, ApJL, 806, L15
Kataoka, A., Muto, T., Momose, M., Tsukagoshi, T., & Dullemond, C. P. 2015a, arXiv:1507.08902
Kataoka, A., Muto, T., Momose, M., et al. 2015b, ApJ, 809, 78
Kataoka, A., Okuzumi, S., Tanaka, H., & Nomura, H. 2014, A&A, 568, A42
Kataoka, A., Tanaka, H., Okuzumi, S., & Wada, K. 2013a, A&A, 557, L4
Kataoka, A., Tanaka, H., Okuzumi, S., & Wada, K. 2013b, A&A, 554, A4
Kitamura, Y., Momose, M., Yokogawa, S., et al. 2002, ApJ, 581, 357
Kornet, K., Stepinski, T. F., & Różyczka, M. 2001, A&A, 378, 180
Kretke, K. A., & Lin, D. N. C. 2007, ApJL, 664, L55
Krijt, S., Ormel, C. W., Dominik, C., & Tielens, A. G. G. M. 2015, A&A, 574, A83
Krijt, S., Ormel, C. W., Dominik, C., & Tielens, A. G. G. M. 2016, A&A, 586, A20
Kuroiwa, T., & Sirono, S.-i. 2011, ApJ, 739, 18
Kwon, W., Looney, L. W., & Mundy, L. G. 2011, ApJ, 741, 3
Kwon, W., Looney, L. W., Mundy, L. G., & Welch, W. J. 2015, ApJ, 808, 102
Laibe, G. 2014, MNRAS, 437, 3037
Lambrechts, M., & Johansen, A. 2014, A&A, 572, A107
Lifshitz, E. M., & Pitaevskii, L. P. 1981, Physical Kinetics (Oxford: Pergamon)
Lorén-Aguilar, P., & Bate, M. R. 2015, MNRAS, 453, L78
Lucas, P. W., Fukagawa, M., Tamura, M., et al. 2004, MNRAS, 352, 1347
Luna, R., Satorre, M. Á, Santonja, C., & Domingo, M. 2014, A&A, 566, A27
Martín-Doménech, R., Muñoz Caro, G. M., Bueno, J., & Goesmann, F. 2014, A&A, 564, A8
Mathis, J. S., Rumpl, W., & Nordsieck, K. H. 1977, ApJ, 217, 425
Men'shchikov, A. B., Henning, T., & Fischer, O. 1999, ApJ, 519, 257
Meyer, B. 1977, Sulfur, Energy, and Environment (Amsterdam: Elsevier)
Min, M., Rab, C., Woitke, P., Dominik, C., & Ménard, F. 2016, A&A, 585, A13
Moses, J. I., Allen, M., & Yung, Y. L. 1992, Icar, 99, 318
Mumma, M. J., & Charnley, S. B. 2011, ARA&A, 49, 471
Mundt, R., Buehrke, T., & Ray, T. P. 1988, ApJL, 333, L69
Murakawa, K., Oya, S., Pyo, T.-S., & Ishii, M. 2008, A&A, 492, 731
Nomura, H., Tsukagoshi, T., Kawabe, R., et al. 2015, arXiv:1512.05440
Okuzumi, S., & Hirose, S. 2012, ApJL, 753, L8
Okuzumi, S., Tanaka, H., Kobayashi, H., & Wada, K. 2012, ApJ, 752, 106
Okuzumi, S., Tanaka, H., & Sakagami, M.-a. 2009, ApJ, 707, 1247
Ormel, C. W. 2014, ApJL, 789, L18
Ormel, C. W., & Cuzzi, J. N. 2007, A&A, 466, 413
Ormel, C. W., Spaans, M., & Tielens, A. G. G. M. 2007, A&A, 461, 215
Paardekooper, S.-J., & Mellema, G. 2004, A&A, 425, L9
Paardekooper, S.-J., & Mellema, G. 2006, A&A, 453, 1129
Pinilla, P., Benisty, M., & Birnstiel, T. 2012, A&A, 545, A81
Pinte, C., Dent, W. R. F., Ménard, F., et al. 2016, ApJ, 816, 25
Pollack, J. B., Hollenbach, D., Beckwith, S., et al. 1994, ApJ, 421, 615
Poppe, T. 2003, Icar, 164, 139
Qi, C., Öberg, K. I., Wilner, D. J., et al. 2013, Sci, 341, 630
Rapson, V. A., Kastner, J. H., Millar-Blanchaer, M. A., & Dong, R. 2015, ApJL, 815, L26
Rietmeijer, F. J. M. 1993, E&PSL, 117, 609
Ros, K., & Johansen, A. 2013, A&A, 552, A137
Saito, E., & Sirono, S.-i. 2011, ApJ, 728, 20
Sano, T., Miyama, S. M., Umebayashi, T., & Nakano, T. 2000, ApJ, 543, 486
Sargent, A. I., & Beckwith, S. V. W. 1991, ApJL, 382, L31
Sato, T., Okuzumi, S., & Ida, S. 2015, A&A, in press (arXiv:1512.02414)
Seizinger, A., Krijt, S., & Kley, W. 2013, A&A, 560, A45
Sekiya, M. 1998, Icar, 133, 298
Sirono, S. 1999, A&A, 347, 720
Sirono, S.-i. 2011a, ApJL, 733, L41
Sirono, S.-i. 2011b, ApJ, 735, 131
Sirono, S.-i., & Ueno, H. 2014, in COSPAR Meeting 40, 40th COSPAR Scientific Assembly, Abstract B0.5-2-14, 3110
Stephens, I. W., Looney, L. W., Kwon, W., et al. 2014, Natur, 514, 597
Suyama, T., Wada, K., & Tanaka, H. 2008, ApJ, 684, 1310
Swinkels, F., & Ashby, M. 1981, AcMet, 29, 259
Takahashi, S. Z., & Inutsuka, S.-i. 2014, ApJ, 794, 55
Takeuchi, T., & Lin, D. N. C. 2005, ApJ, 623, 482
Tanaka, H., Inaba, S., & Nakazawa, K. 1996, Icar, 123, 450
Uribe, A. L., Klahr, H., Flock, M., & Henning, T. 2011, ApJ, 736, 85
Vacca, W. D., & Sandell, G. 2011, ApJ, 732, 8
Wada, K., Tanaka, H., Okuzumi, S., et al. 2013, A&A, 559, A62
Wada, K., Tanaka, H., Suyama, T., Kimura, H., & Yamamoto, T. 2008, ApJ, 677, 1296
Wada, K., Tanaka, H., Suyama, T., Kimura, H., & Yamamoto, T. 2009, ApJ, 702, 1490
Warren, S. G. 1984, ApOpt, 23, 1206
Weidenschilling, S. J. 1977, MNRAS, 180, 57
Whipple, F. L. 1972, in From Plasma to Planet, ed. A. Elvius (New York: Wiley), 211
White, R. J., & Hillenbrand, L. A. 2004, ApJ, 616, 998
Yamamoto, T., Nakagawa, N., & Fukui, Y. 1983, A&A, 122, 171
Yang, H., Li, Z.-Y., Looney, L., & Stephens, I. 2016, MNRAS, 456, 2794
Youdin, A. N. 2011, ApJ, 731, 99
Youdin, A. N., & Lithwick, Y. 2007, Icar, 192, 588
Youdin, A. N., & Shu, F. H. 2002, ApJ, 580, 494
Zhang, K., Blake, G. A., & Bergin, E. A. 2015, ApJL, 806, L7
Zhu, Z., Nelson, R. P., Dong, R., Espaillat, C., & Hartmann, L. 2012, ApJ, 755, 6
Zubko, V. G., Mennella, V., Colangeli, L., & Bussoletti, E. 1996, MNRAS, 282, 1321

A&A 568, A42 (2014)
DOI: 10.1051/0004-6361/201323199

Astronomy & Astrophysics

Opacity of fluffy dust aggregates

Akimasa Kataoka[1,2], Satoshi Okuzumi[3], Hidekazu Tanaka[4], and Hideko Nomura[3]

[1] Department of Astronomical Science, School of Physical Sciences, Graduate University for Advanced Studies (Sokendai), Mitaka, 181-8588 Tokyo, Japan
e-mail: akimasa.kataoka@nao.ac.jp
[2] National Astronomical Observatory of Japan, Mitaka, 181-8588 Tokyo, Japan
[3] Department of Earth and Planetary Sciences, Tokyo Institute of Technology, Meguro, 152-8551 Tokyo, Japan
[4] Institute of Low Temperature Science, Hokkaido University, Kita, 060-0819 Sapporo, Japan

Received 5 December 2013 / Accepted 12 June 2014

ABSTRACT

Context. Dust grains coagulate to form dust aggregates in protoplanetary disks. Their porosity can be extremely high in the disks. Although disk emission may come from fluffy dust aggregates, the emission has been modeled with compact grains.
Aims. We aim to reveal the mass opacity of fluffy aggregates from infrared to millimeter wavelengths with the filling factor ranging from 1 down to 10^{-4}.
Methods. We use Mie calculations with an effective medium theory. The monomers are assumed to be 0.1 μm sized grains, which is much shorter than the wavelengths that we focus on.
Results. We find that the absorption mass opacity of fluffy aggregates is characterized by the product $a \times f$, where a is the dust radius and f is the filling factor, except for the interference structure. The scattering mass opacity is also characterized by af at short wavelengths while it is higher in more fluffy aggregates at long wavelengths. We also derive the analytic formula of the mass opacity and find that it reproduces the Mie calculations. We also calculate the expected difference of the emission between compact and fluffy aggregates in protoplanetary disks with a simple dust growth and drift model. We find that compact grains and fluffy aggregates can be distinguished by the radial distribution of the opacity index β. The previous observation of the radial distribution of β is consistent with the fluffy case, but more observations are required to distinguish between fluffy or compact. In addition, we find that the scattered light would be another way to distinguish between compact grains and fluffy aggregates.

Key words. planets and satellites: formation – protoplanetary disks

1. introduction

Optical properties of dust grains have been investigated by many authors to understand the emission from various kinds of astronomical objects. In protoplanetary disks, dust grains are important not only as the emitter of radiation, but also as the seeds of planets. The size of dust grains increases by coagulation from submicron size to millimeter size or larger. A number of radio observations suggest that dust grains have been grown to millimeter-sized grains in protoplanetary disks (Andrews & Williams 2005; Isella et al. 2009; Ricci et al. 2010b,a; Guilloteau et al. 2011; van der Marel et al. 2013).

The silicate feature at 10 μm is evidence of grain growth (e.g., van Boekel et al. 2005). The infrared observations suggest that the size of silicate dust grains is spreading from 0.1 μm to a few μm. The infrared emission is expected to come from the surface region of protoplanetary disks. Tiny grains are kinematically well coupled to the disk gas and thus stirred up to the disk surface. Thus, we cannot carry out information of dust grains larger than the micron size from infrared observations. In addition, infrared scattered light images of protoplanetary disks are less luminous than expected from other observations. This may infer the presence of large compact grains or porous aggregates at the disk surface (Mulders et al. 2013).

The opacity index at submillimeter wavelengths is used as another clue of grain growth (Beckwith et al. 1990; Beckwith & Sargent 1991; Miyake & Nakagawa 1993). The most striking evidence of dust growth is the opacity index β, where $\kappa_\nu \propto \nu^\beta$; β is estimated from observed flux slope α, where $F_\nu \propto \nu^\alpha$. If the dust emission is optically thin, the dust slope has a relation of $\beta = \alpha - 2$. The index β is typically from 1 to 0 in protoplanetary disks, which means grain growth in protoplanetary disks (Andrews & Williams 2005; Lommen et al. 2010; Pérez et al. 2012). The recent observations using radio interferometers have revealed the radial profile of β. Pérez et al. (2012) made a model fit of β and suggested that β is different between in the inner and outer part of the disk. Thus, the dust grains in the inner part of the disk are expected to grow to a larger size.

Although the protoplanetary disk emissions are usually modeled with compact dust grains, recent numerical simulations have shown that dust grains coagulate to form fluffy structure, especially in the case of icy dust aggregates. With low speed collisions, dust grains form fluffy aggregates. However, it has been shown that aggregate are not effective in compressing the fluffy dust aggregates. Wada et al. (2008) and Suyama et al. (2008, 2012) investigated collisional compression of icy dust aggregates, and Okuzumi et al. (2012) performed coagulation simulations including the collisional compression. They revealed that the initial fractal growth stops when the collisional energy exceeds the rolling energy. They derived that the achievable lowest filling factor is $\sim 10^{-5}(m_{\rm roll}/10^{-4}\ {\rm g})$, where $m_{\rm roll}$ is the aggregate mass when the impact energy is equal to the rolling energy. Moreover, Kataoka et al. (2013a,b) introduced the static compression of dust aggregates. They showed that the filling factor decreases to as low as 10^{-4} even when considering the effects of the static compression. However, the porosity evolution of icy

dust aggregates has not been confirmed by laboratory experiments yet.

The icy and fluffy aggregates are expected to overcome theoretical problems in planetesimal formation. Fluffy aggregates are expected to overcome the radial drift barrier (Okuzumi et al. 2012; Kataoka et al. 2013b) and the bouncing barrier (Wada et al. 2011). Moreover, if particles are composed of ice, the dust aggregates overcome the fragmentation barrier because they are sticky (Wada et al. 2009, 2013).

Dust coagulation has also been investigated in laboratory experiments. As an analog to silicate dust grains, which are expected to be inside the snowline in protoplanetary disks, silica particles have been used in laboratory experiments. Conditions for bouncing and fragmentation have been studied in laboratory experiments (Blum & Wurm 2008; Zsom et al. 2010) and some scenarios for planetesimal formation breaking through the bouncing barrier have been proposed (Windmark et al. 2012; Drążkowska et al. 2013). From the viewpoint of porosity evolution, silicate dust aggregates are expected to be less fluffy than icy dust aggregates because the surface energy of silicate is lower than ice. Microgravity experiments have confirmed the hit-and-stick process of forming fluffy dust aggregates (Kothe et al. 2013). However, further growth concerning compression is still uncertain in laboratory experiments. Zsom et al. (2011) performed numerical simulations of dust coagulation of silicate particles, using the hit-and-stick model proposed by Okuzumi et al. (2009). They showed that the filling factor of dust aggregates can reach 10^{-3} before the onset of compaction[1].

Observational constraints of porosity of dust aggregates in protoplanetary disks are important. However, studies of interpreting disk observations have assumed $f \geq 0.1$ (e.g., Birnstiel et al. 2010), which is relatively compact compared with the extremely porous aggregates, whose filling factor is 10^{-4}, as discussed above. In this paper, as a first step to constrain the porosity of dust aggregates in protoplanetary disks, we investigate optical properties of dust aggregates including the extremely porous aggregates.

Opacity of porous aggregates has been investigated by several theoretical methods. In the context of explaining cometary dust, scattering properties of BPCA and BCCA aggregates have been studied (Kimura et al. 2003, 2006; Kolokolova et al. 2007). The number of constituent particles was limited to ~60 000 (~10^{-10} g in mass if the particle size is 0.1 μm), and the opacity was only studied at infrared wavelengths. In the context of explaining the interstellar silicate feature, in addition, the effects of monomer shapes on optical properties at infrared wavelength have been also studied (Min et al. 2003, 2005, 2007). In this paper, we examine the absorption and scattering mass opacities of dust aggregates at wavelengths ranging from 1 μm to 10 cm. The aggregates have a size ranging from micron to kilometer and a filling factor ranging from 1 to 10^{-4}.

One of the popular methods for calculating the mass opacity of porous aggregates is the discrete dipole approximation (DDA; Draine & Flatau 1994; Min et al. 2006). This calculation takes a huge computational time for large aggregates. To investigate the opacities of highly porous aggregates for a wide size range, the method would not be suitable. In this paper, we aim to reveal the mass opacity of fluffy aggregates from infrared to millimeter wavelengths with the filling factor ranging from 1 down to 10^{-4}. Thus, we use the effective medium theory (EMT). This method is fast in calculation but inaccurate in some parameters. Kozasa et al. (1992) have shown that EMT reproduces the absorption opacity of BCCA and BPCA clusters, whose constituent monomers are up to 1024, within a error of a factor of two. The EMT is also known to be accurate for porous aggregates whose constituent particles are small compared with the wavelength of incident radiation (Voshchinnikov et al. 2005; Shen et al. 2008). Because the dust aggregates considered in this paper are highly porous aggregates consisting of submicron-sized monomers, EMT would be a good approximation for calculations in this paper. We note that the scattering opacity derived with EMT largely deviates from the actual value in some parameter space (Shen et al. 2009). The accuracy of EMT in a large parameter space should be tested in the future work.

This paper is organized as follows. We describe the composition of dust grains and the calculating method of mass opacities in Sect. 2. We show the results of the absorption and scattering mass opacities of highly porous aggregates by using Mie theory with EMT in Sect. 3. We derive analytic formulae to reproduce the results in Sect. 4. Then, we construct a simple dust growth and drift model in protoplanetary disks and propose a method to distinguish compact and fluffy aggregates in radio observations by using the slope at millimeter wavelengths, the so-called dust β, in Sect. 5. Finally, we summarize and discuss the previous observations with porous aggregates in Sect. 6.

2. Method

Here, we briefly summarize the definitions of optical properties following Bohren & Huffman (1983, hereafter BH83) and Miyake & Nakagawa (1993). We consider a particle or an aggregate with radius a and internal mass density ρ. The radius of an aggregate represents the characteristic radius, defined as $a = \sqrt{5/3}a_g$, where a_g is the gyration radius (Mukai et al. 1992). We define the size parameter x as

$$x = \frac{2\pi a}{\lambda}, \tag{1}$$

where λ is the wavelength. We also define the relative refractive index m as

$$m = n + ik, \tag{2}$$

where n and k are the real and imaginary parts of the refractive index, respectively.

2.1. Dust grains: monomers

We consider a dust aggregate, which consists of a number of monomers. The monomers are assumed to be composed of silicate, organics, and water ice without any void structure. The mass fractional abundance is set to be consistent with Pollack et al. (1994), where $\zeta_{\rm silicate} = 2.64 \times 10^{-3}$, $\zeta_{\rm organics} = 3.53 \times 10^{-3}$, and $\zeta_{\rm ice} = 5.55 \times 10^{-3}$. The internal densities of silicate, organics, and ice are taken to be 3.5 g cm^{-3}, 1.5 g cm^{-3}, and 0.92 g cm^{-3}, respectively. The mean internal density is therefore 1.68 g cm^{-3}. The resultant volume fractions are 8% of silicate, 26% of organics, and 66% of water ice. We use the refractive index of astronomical silicate from Weingartner & Draine (2001), organics from Pollack et al. (1994), and water ice from Warren (1984).

Here, we discuss the structure of a monomer composed of various materials. We assume that the monomer has a core-mantle structure, where silicate components are inside and ice

[1] Zsom et al. (2010) obtained less fluffy aggregates than Zsom et al. (2011) because Zsom et al. (2010) adopted the porosity model proposed by Ormel et al. (2007), which is not as accurate as the model of Okuzumi et al. (2009).

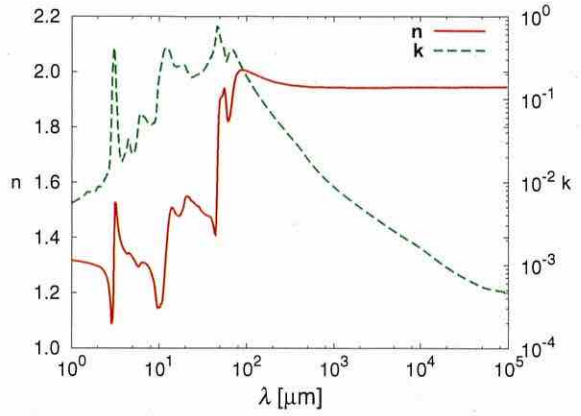

Fig. 1. Complex refractive index of the mixture of silicate, organics, and water ice.

and organics cover the silicate core. This assumption is reasonable because the condensation temperature of silicates is much higher than those of ices and organics[2]. The collisional and static compression and fragmentation velocity are determined by the surface material of monomers, which is expected to be ice or organics. Therefore, the structure and fluffiness of the aggregates are expected to be similar to icy aggregates (Okuzumi et al. 2012; Kataoka et al. 2013b).

The effective refractive index of the mixture can be derived from dielectric functions. By using Maxwell-Garnett rule without voids, the effective dielectric function is obtained as

$$\epsilon_{\rm mix} = \frac{\Sigma f_j \gamma_j \epsilon_j}{\Sigma f_j \gamma_j}, \tag{3}$$

where

$$\gamma_j = \frac{3}{\epsilon_j + 2}, \tag{4}$$

and f_j and ϵ_j represent the volume filling factor and the dielectric function of each species. The dielectric function is related to the refractive index as $\epsilon = m^2$.

Figure 1 shows the real and imaginary part of the effective refractive index of the mixture. We use this effective refractive index as the material refractive index in the following discussion.

The simplified fractional abundance based on Pollack et al. (1994) has been widely used in several papers (e.g., D'Alessio et al. 2001; Tanaka et al. 2005; Isella et al. 2009; Ricci et al. 2010b,a; Pérez et al. 2012). Some recent studies use the dielectric functions of carbonaceous material (Zubko et al. 1996) instead of organics (Pollack et al. 1994; Li & Greenberg 1997). In protoplanetary disks, the carbonaceous materials would interact with other species to produce organics. Thus, we use the dielectric function of organics based on Pollack et al. (1994) in this paper. However, the optical properties of organics in protoplanetary disks have large uncertainties because astronomical organics may be different from laboratory data.

2.2. Aggregates of monomers

To calculate the opacity of fluffy aggregates, we use the effective medium theory again. In the case of the mixture of monomers and voids, Maxwell-Garnett theory is applicable to obtain the effective dielectric function as

$$\epsilon_{\rm eff} = \frac{1 + 2fF}{1 - fF}, \tag{5}$$

where

$$F = \frac{\epsilon_{\rm mix} - 1}{\epsilon_{\rm mix} + 2}, \tag{6}$$

$\epsilon_{\rm mix}$ is the effective dielectric function of the mixture, and f is the volume filling factor of the aggregate.

We will investigate the mass opacity of dust aggregates for a wide range of the dust radius a and the filling factor f. We adopt the Mie calculation with the effective medium theory described above. Voshchinnikov et al. (2005) show that the EMT is a good approximation when the inclusions are smaller than the wavelengths of radiation. Here, the monomer size is 0.1 μm while the wavelengths are larger than 1 μm. Thus, the EMT would be a good approximation in the calculations in this paper. The filling factor is expected to decrease to $f \sim 10^{-4}$ and the dust radius grows from micron to kilometer (Kataoka et al. 2013b). Therefore, we will investigate the mass opacity in such parameter space.

We note that we do not choose a set of a and f where both a and f are too small. In the porosity evolution scenario proposed by Kataoka et al. (2013b), the dust aggregates grow as fractals in the very early stage of the coagulation. This stage corresponds to the lower limit of a and f. In this paper, we consider a set of a and f where $af \geq 0.1$ μm.

2.3. Mass opacity

We use the Mie calculation with the effective medium theory to calculate dimensionless absorption and scattering coefficients $Q_{\rm abs}$ and $Q_{\rm sca}$. Then, we obtain absorption and scattering mass opacities defined as

$$\kappa_{\rm abs} = \frac{\pi a^2}{m} Q_{\rm abs}, \tag{7}$$

$$\kappa_{\rm sca} = \frac{\pi a^2}{m} Q_{\rm sca}. \tag{8}$$

We note that the mass opacities are given per gram of dust. To obtain the mass opacities per gram of gas, one should divide the mass opacities by the dust-to-gas mass ratio.

3. Results

3.1. Absorption mass opacity

The absorption mass opacity of porous dust aggregates strongly depends on their size and filling factor. In protoplanetary disks, radio emission at millimeter wavelengths provide optically thin emission, in other words, directly reflects the opacity. Therefore, we aim to reveal what properties of dust aggregates determine the mass opacity.

Figure 2 shows the dependency of the mass opacities of dust aggregates on the dust radius a and the filling factor f. Figure 2b shows the mass opacity of different dust radius while the filling factor is fixed at unity (i.e., compact growth). The absorption mass opacity from optical to infrared wavelengths decreases as the aggregate size increases, and it has an enhancement because of the interference at the millimeter wavelengths depending on the aggregate size. This trend is well known as the grain-growth

[2] The material properties of organics, such as surface energy and Young's modulus, are still uncertain, but they are considered to be similar to those of ice (e.g., Kudo et al. 2002).

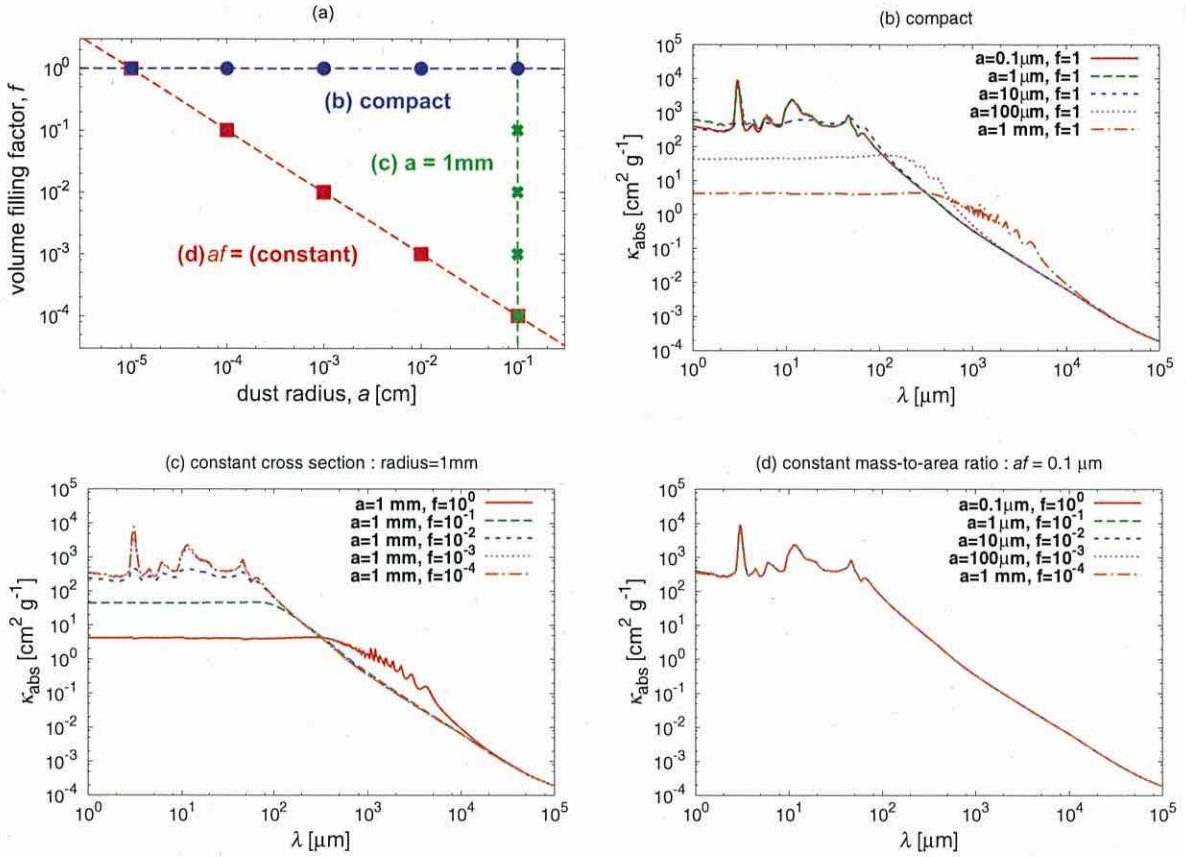

Fig. 2. Absorption mass opacities for each dust radius and filling factor. **a)** Parameter space in volume filling factor f against dust radius a to investigate mass opacity. The dotted lines correspond to **b)**–**d)**. **b)** Absorption mass opacity when dust radius a changes while $f = 1$. **c)** When the dust filling factor changes while $a = 1$ mm. **d)** When both a and f change while af keeps constant. The constant af corresponds to the same mass-to-area ratio of the dust aggregates.

effects on the dust opacity. Figure 2c shows the mass opacity of different filling factors while the dust radius is fixed at $a = 1$ mm. The mass opacity strongly depends on the filling factor but cannot be characterized by one parameter. Figure 2d shows that the mass opacity when both a and f change but af remains constant. The mass opacity is almost the same in this case. This result suggests that the optical properties of fluffy dust aggregates are characterized by af.

Here, we introduce a new parameter af, where a is the dust radius and f is the filling factor. Keeping af constant corresponds to the constant mass-to-area ratio of the dust aggregates because (mass-to-area ratio) $\sim(a^3 f)/(a^2) \sim af$. We already find that the mass opacity is characterized by af in the case of $af = 0.1\,\mu$m in Fig. 2d. Next, we investigate whether the mass opacity is characterized by one parameter af in the wide range of af.

Figure 3 shows the mass opacity where af is fixed for each panel: af has values of 1 μm, 10 μm, 100 μm, 1 mm, and 1 cm. This figure clearly shows that the absorption mass opacity is almost the same in the cases of the same af. For example, dust aggregates that have a size of 10 m and a filling factor of 10^{-4} are optically equivalent to 1 mm compact grains except for the interference structure. We will show the reason why the absorption mass opacity is characterized by af in Sect. 4.

That the absorption mass opacity is characterized by af is a very naive result for observations: the filling factor cannot be measured because it is degenerated with the dust radius. Therefore, to derive both the filling factor and the dust radius separately, we should find another clue rather than the general behavior of the absorption mass opacity. We find two differences which might be ways to distinguish between a and f: the interference structure of the absorption mass opacity and the scattering mass opacity at long wavelengths. We discuss the interference first and will discuss the scattering mass opacity later in this section.

The only difference in the absorption mass opacity between the compact and fluffy cases if af is the same is the interference structure, which appears when the size parameter x is close to unity. In the case of $af = 1$ mm, for example, the absorption mass opacity in the compact case is one order of magnitude higher than the fluffy cases. This is a way to distinguish between compact grains and fluffy aggregates in protoplanetary disks. We will discuss the reason why the interference structure is unique only in the compact case in Sect. 4, and also discuss the feature as a way to distinguish between compact and fluffy aggregates by using the dust opacity index β in Sect. 5.

3.2. Scattering mass opacity

We also calculate the scattering mass opacity by using Mie calculations. Figure 4 shows the scattering mass opacities in the case of $af = 0.1\,\mu$m, 1 μm, 100 μm, and 1 mm. This figure

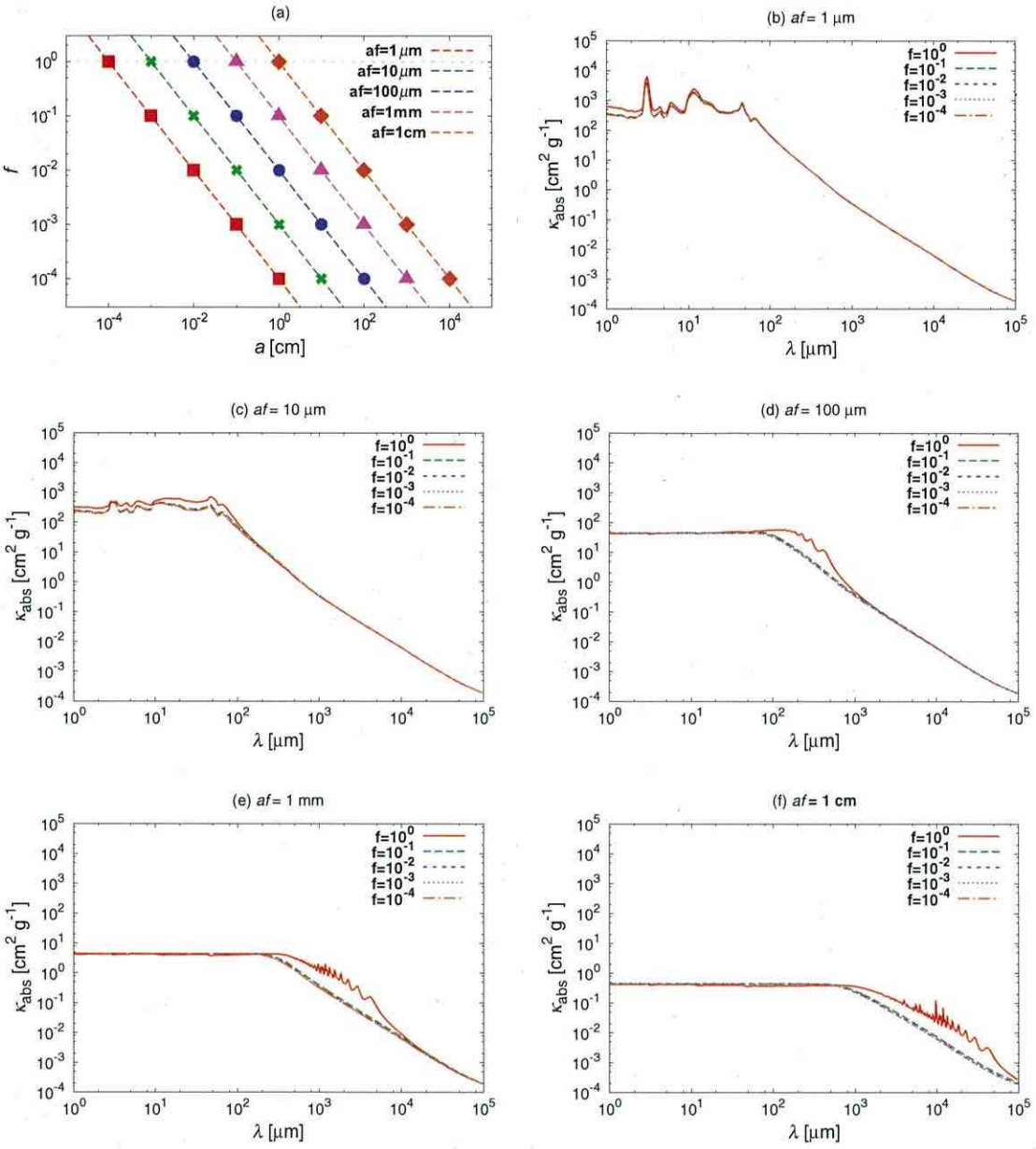

Fig. 3. Absorption mass opacity in cases of different af. **a)** Parameter space of f and a in the cases of **b)** to **f)**. The mass opacities are shown in the cases of **b)** $af = 1\,\mu$m, **c)** $af = 10\,\mu$m, **d)** $af = 100\,\mu$m, **e)** $af = 1$ mm, and **f)** $af = 10$ mm.

suggests that the scattering mass opacity is not characterized by af at the longer wavelengths. At the shorter wavelengths, the mass opacity corresponds to the geometric cross section. In the compact case, the mass opacity scales as λ^{-4} at the longer wavelengths. On the other hand, in the fluffy case, the mass opacity scales as λ^{-2} at the inter mediate wavelengths, then scales as λ^{-4} at the longer wavelengths. We will come back to this point with a physical explanation in Sect. 4.

As shown in Fig. 4, the scattering mass opacity of the fluffy aggregates is expected to be higher than the compact case at the longer wavelengths even when the absorption mass opacity is almost the same. Thus, we investigate the ratio of $\kappa_{\rm sca}$ against $\kappa_{\rm abs}$. Figure 5 shows the ratio in each case corresponding to Fig. 4. In the case of compact and $af = 0.1\,\mu$m, the scattering mass opacity is less than absorption. On the other hand, the scattering mass opacity dominates the absorption mass opacity in fluffy cases when $af = 0.1\,\mu$m. This greatly affects the infrared observations of dust grains. For example, Pagani et al. (2010) reported that dust grains in dense interstellar medium is composed of micron-sized grains (and not $0.1\,\mu$m) because of the high scattering efficiency observed by the *Spitzer* space telescope. Thus, they infer that the monomer size must be micron. However, Fig. 5 suggests that even if the monomers are $0.1\,\mu$m in size, the aggregates of $0.1\,\mu$m sized monomers represent the high albedo and thus might account for the observed high efficiency of scattering.

Figure 5c and d shows the scattering mass opacity in the case of $af = 100\,\mu$m and 1 mm. The scattering mass opacity at the millimeter wavelengths is ten times larger than the absorption mass opacity in the compact case, and it is tens of times larger

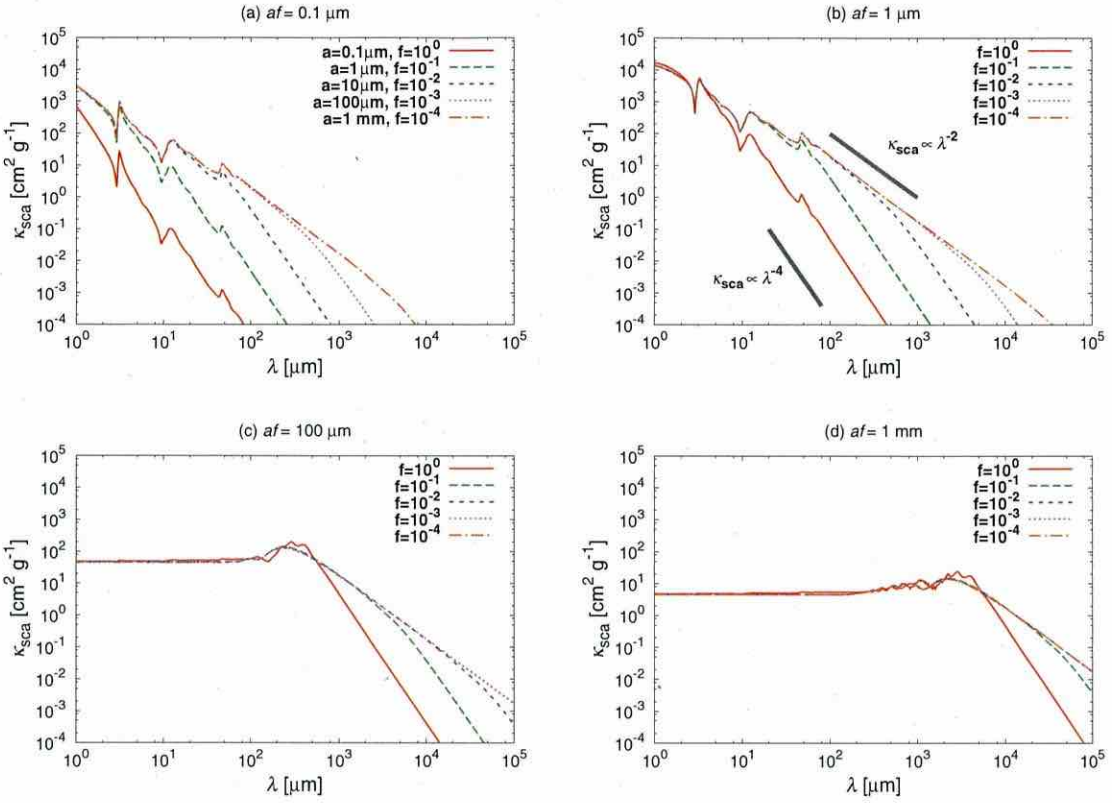

Fig. 4. Same as Fig. 3 but for scattering mass opacities.

in the fluffy cases. This suggests that the millimeter continuum emission is dominated not by direct thermal emission, but by scattered emission in transition disks if the dust aggregates are grown to have a millimeter size. Moreover, determining the ratio of the scattering mass opacity over the absorption mass opacity at the millimeter wavelengths is a way to characterizing the porosity of the dust aggregates.

4. Analytic formulae of the opacities

In the previous section, we used the Mie calculations to obtain the mass opacity. In this section, we derive the analytic formulae of the mass opacity and compare them to the results of Mie calculations. By deriving analytic formulae, we explain why the mass opacity can be characterized by af. In addition, the analytic formulae would be a computationally less expensive method to calculate the opacity of large aggregates.

4.1. Approximation of refractive index

When we consider fluffy aggregates, the filling factor satisfies $f \ll 1$. If $f \ll 1$, from Eq. (5) and $\epsilon = m^2$, we obtain

$$n \simeq 1 + \frac{3}{2} f \mathrm{Re}(F), \tag{9}$$

$$k \simeq \frac{3}{2} f \mathrm{Im}(F), \tag{10}$$

to the first order of f. From these equations, we obtain that $n - 1 \propto f$ and $k \propto f$ in the case of fluffy aggregates where $f \ll 1$. We check the validity of the relations in Appendix A.1.

We do not assume $f \ll 1$ when deriving the analytic formulae. After deriving the formulae, we assume $f \ll 1$ and use the relations of $n - 1 \propto f$ and $k \propto f$ to explain why the mass opacity is characterized by af.

4.2. Absorption mass opacity

We derive the approximated formulae of $Q_{\rm abs}$ in three limited cases, illustrated in Fig. 6: (1) $x \ll 1$; (2) $x \gg 1$ and optically thin ($kx \ll 3/8$) media; and (3) $x \gg 1$ and optically thick ($kx \gg 3/8$) media. We note that the absorption mass opacity is $Q_{\rm abs}$ divided by the mass-to-area ratio of the aggregates.

4.2.1. $x \ll 1$

When the dust radius a is much smaller than the wavelength λ, the opacity goes into Reyleigh regime. This corresponds to $x = 2\pi a/\lambda \ll 1$. In this case, $Q_{\rm abs}$ can be written as

$$Q_{\rm abs} \simeq 4x \, \mathrm{Im}\left(\frac{m^2 - 1}{m^2 + 2}\right) = \frac{24nkx}{(n^2 - k^2 + 2)^2 + (2nk)^2}. \tag{11}$$

(see Eq. (5.11) in BH83). The imaginary part k of the refractive index is much smaller than the real part n (see Figs. 1 and A.1). So, we can approximate $Q_{\rm abs}$ as

$$Q_{\rm abs} \simeq Q_{\rm abs,1} \equiv \frac{24nkx}{(n^2 + 2)^2}. \tag{12}$$

This equation explains the fact that the absorption mass opacity is characterized by mass-to-area ratio or af. At the longer wavelengths, n is almost unity while $k \propto f$. Using $f \propto m/a^3$,

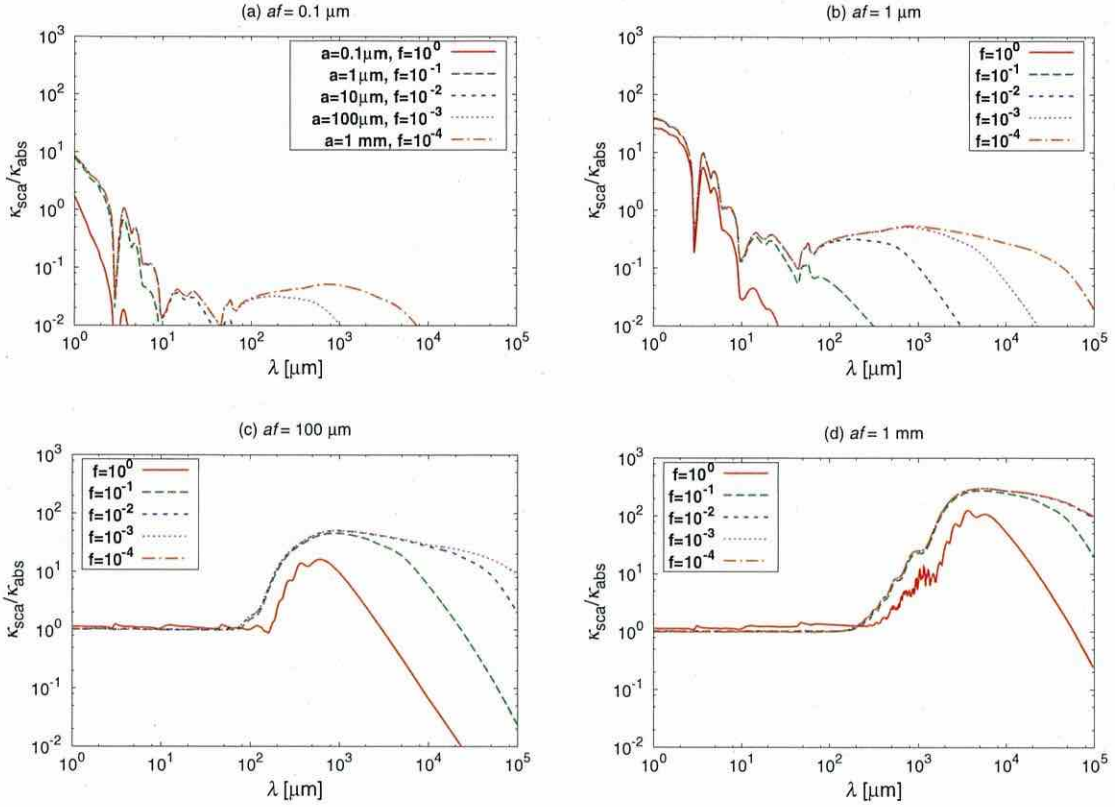

Fig. 5. Ratio of scattering mass opacity over absorption mass opacity $\kappa_{\rm sca}/\kappa_{\rm abs}$ in the cases of $af = 0.1$ μm, 1 μm, 100 μm, and 1 mm. Each panel shows the cases with the same af, but the filling factor ranges are in $f = 1, 10^{-1}, 10^{-2}, 10^{-3}$, and 10^{-4}.

we obtain that kx is proportional to m/a^2, which is mass-to-area ratio. Since $\kappa_{\rm abs}$ is $Q_{\rm abs}$ divided by mass-to-area ratio, $\kappa_{\rm abs}$ is independent of dust properties.

4.2.2. $x \gg 1$ and optically thin

When the dust radius a is much larger than the wavelength λ, the opacity goes into geometric optics regime. In this regime, the optical properties can be understood by tracing the ray inside the material. The fraction of energy that transmits the material is $1-\exp(-\alpha\xi)$ where $\alpha = 4\pi k/\lambda$, and ξ is the path of the ray inside the material. If $\alpha\xi < 1$, the incident light is weakly absorbed by the material because it is optically thin on the ray. We set the length $\xi = 2a$, the diameter of the sphere. Thus, the condition $\alpha\xi < 1$ corresponds to $kx < 1$.

In the limit of $a \gg \lambda$ (or equivalently $x \gg 1$) and optically thin, we obtain

$$Q_{\rm abs} \simeq Q_{\rm abs,2} \equiv \frac{8kx}{3n}\left(n^3 - (n^2-1)^{3/2}\right), \tag{13}$$

(see Eq. (7.2) in BH83).

We note that if $n = 1$, which is usually satisfied in the case of fluffy medium, $Q_{\rm abs}$ yields

$$Q_{\rm abs} = Q_{\rm abs,1} = Q_{\rm abs,2} = \frac{8kx}{3}. \tag{14}$$

This equation is also characterized by the mass-to-area ratio or af because $k \propto f$ and $x \propto a$. We also note that the analytic formula between optically thick and thin regimes should be changed when $Q_{\rm abs}$ is unity. Thus, we define optically thin as $kx \ll 3/8$.

4.2.3. $x \gg 1$ and optically thick

In the limit of $a \gg \lambda$ (equivalent to $x \gg 1$) and optically thick ($kx \gg 3/8$), on the other hand, the absorption coefficient is described as

$$Q_{\rm abs} \simeq Q_{\rm abs,3} \equiv \int_0^{\pi/2} (1 - R(\theta_i)) \sin 2\theta_i {\rm d}\theta_i, \tag{15}$$

where the reflectance $R(\theta)$ is written as

$$R(\theta_i) = \frac{1}{2}\left(\left|\frac{\cos\theta_t - m\cos\theta_i}{\cos\theta_t + m\cos\theta_i}\right|^2 + \left|\frac{\cos\theta_i - m\cos\theta_t}{\cos\theta_i + m\cos\theta_t}\right|^2\right), \tag{16}$$

and

$$\sin\theta_t = \frac{\sin\theta_i}{m} \tag{17}$$

(see Eqs. (2.71), (7.5), and (7.7) in BH83). This regime is valid at shorter wavelengths (see Appendix A.3 for the optical depth of the aggregate). As shown in Appendix A.2, $Q_{\rm abs,3} \sim 1 - 0.1 \times f$: $Q_{\rm abs,3} \sim 0.9$ for compact case and $Q_{\rm abs,3} \sim 0.99$ for $f = 0.1$. These values are regarded as unity in application to astronomical observations. Therefore, $Q_{\rm abs,3} \sim 1$ for most cases: the absorption cross section yields the geometric cross section. Because $Q_{\rm abs,3}$ has no dependency on f and a, $\kappa_{\rm abs}$ is characterized by af.

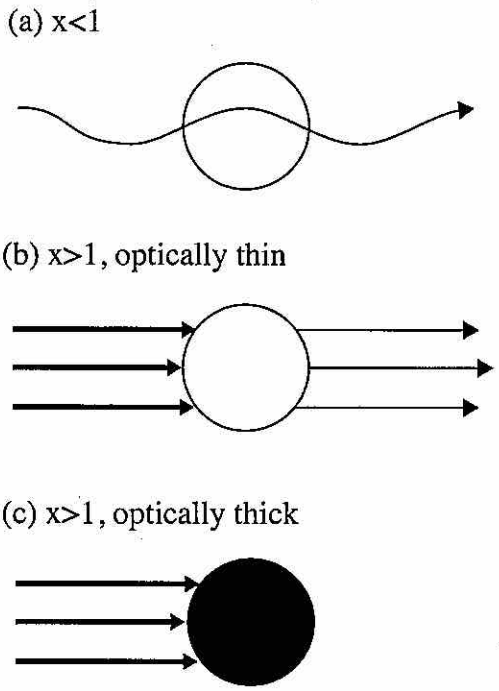

Fig. 6. Three limiting regimes. **a)** When $x \ll 1$, the opacity goes into the Rayleigh regimes. **b)** When $x \gg 1$ and is optically thin ($kx \ll 3/8$), the opacity goes into the optically thin geometric regime. **c)** When $x \gg 1$ and is optically thick ($kx \gg 3/8$), the opacity goes into the optically thick geometric regime.

4.2.4. Analytic formula of absorption mass opacity

Combining the three limiting regimes, we obtain the analytic formula of the absorption mass opacity of dust aggregates as

$$Q_{\rm abs} = \begin{cases} Q_{\rm abs,1} & (x < 1) \\ \min(Q_{\rm abs,2}, Q_{\rm abs,3}) & (x > 1). \end{cases} \quad (18)$$

Figure 7 shows the absorption mass opacities calculated with both the Mie calculation and the analytic formula. The absorption mass opacities of Fig. 7a and b are the same because $af = 0.1\,\mu$m but only the filling factor is different ($f = 1$ and $f = 0.01$), as shown in the previous sections (see Fig. 3). Figure 7a shows the case of $af = 0.1\,\mu$m and $f = 1$ (compact). The whole wavelengths in this panel satisfy $x < 1$, and thus $Q_{\rm abs} \simeq Q_{\rm abs,1}$. The analytic formula greatly reproduce the Mie calculations. Figure 7b shows the case of $af = 0.1\,\mu$m and $f = 0.01$ (fluffy). In this case, $a = 10\,\mu$m, and thus $x = 1$ at $\lambda = 2\pi a \simeq 63\,\mu$m. We use $Q_{\rm abs} = Q_{\rm abs,1}$ for $x > 1$ and $Q_{\rm abs} = Q_{\rm abs,2}$ for $x < 1$ and connect them at $x = 1$. This also reproduces the Mie calculation.

Figure 7c and d shows the case of $af = 1$ mm, but the filling factor is 1 and 0.01, respectively. The absorption mass opacities of Fig. 7c and d are almost the same except for the interference structure. The interference structure corresponds to where $x > 1$ and $kx < 3/8$, the optically-thin geometric optics regime. We note that the difference between the Mie calculation and the analytic formulae is the interference structure. In Fig. 7c, which is the compact case, the real part of the refractive index is greater than unity. Thus, $Q_{\rm abs}$ has an enhancement because of the interference. In Fig. 7d, which is the fluffy case, on the other hand, the real part of the refractive index is almost unity and thus no enhancement appears and smoothly connects to $x < 1$ region at the longer wavelengths. From the analytic formula, we conclude that the interference structure only appears in the compact cases because n is still larger than unity when $x > 1$ and $kx < 3/8$.

4.3. Scattering mass opacity

In the same manner of obtaining the analytic formula of the absorption mass opacity, we also derive the analytic formula of the scattering mass opacity. In addition, by using the analysis, we explain why the mass opacity can and cannot be characterized by af.

4.3.1. $x \ll 1$

When $x \ll 1$, in the Rayleigh regime, $Q_{\rm sca}$ can be written as

$$Q_{\rm sca} \simeq \frac{8}{3}x^4 \left|\frac{m^2-1}{m^2+2}\right|^2, \quad (19)$$

(see Eq. (5.8) in BH83). At the longer wavelengths, $n - 1 \ll 1$ and $k \ll 1$. Therefore, the equation can be approximated to

$$Q_{\rm sca} \simeq Q_{\rm sca,1} \equiv \frac{32}{27}x^4\left((n-1)^2 + k^2\right). \quad (20)$$

As shown in Appendix A.1, $(n-1) > k$ at the longer wavelengths. Therefore, $Q_{\rm sca,1} \propto x^4(n-1)^2$. By using $x \propto a$ and $(n-1) \propto f$, we obtain $Q_{\rm sca,1} \propto a^4 f^2$. This is *not characterized* by af. When we consider two aggregates whose af is the same, the aggregate that has the larger radius has the larger scattering mass opacity at the longer wavelengths although $Q_{\rm abs}$ is same. In other words, the scattering efficiency at the longer wavelengths is a way to determine the filling factor of fluffy aggregates.

4.3.2. $x \gg 1$ and optically thin

If $x \ll 1$, the scattering mass opacity of an aggregate is regarded as the sum of the scattering mass opacity of each monomer because the scattered waves from all the constituent monomers have approximately the same phase. If $x \gg 1$, by contrast, scattered waves with scattering angle $\theta > \theta_{\rm max} \sim 1/x$ cancel out because of the phase difference. Thus, the radiation within the solid angle of $\pi\theta_{\rm max}/4\pi$ is scattered. With the condition that $\theta_{\rm max} \sim 1/x$ and that $Q_{\rm sca,2}$ is smoothly connected to $Q_{\rm sca,1}$ at $x = 1$, we obtain

$$Q_{\rm sca} \simeq Q_{\rm sca,2} \equiv \frac{1}{x^2}Q_{\rm sca,1}. \quad (21)$$

Using the same discussion in the previous section, we obtain $Q_{\rm sca,2} \propto x^2(n-1)^2 \propto a^2 f^2$. This is again characterized by af. We note that the optical depth of the aggregate is unity when $Q_{\rm sca}$ is unity. Thus, the optical depth becomes unity where $x(n-1) \sim 1$ because $n - 1 > k$.

4.3.3. $x \gg 1$ and optically thick

When $x \gg 1$ and the medium is optically thick, $Q_{\rm sca} + Q_{\rm abs} = 2$. Therefore, in the same manner of the absorption mass opacity, we obtain

$$Q_{\rm sca} \simeq Q_{\rm sca,3} \equiv \int_0^{\pi/2} (1 + R(\theta_i)) \sin 2\theta_i \mathrm{d}\theta_i, \quad (22)$$

(see Eqs. (7.5) and (7.6) in BH83).

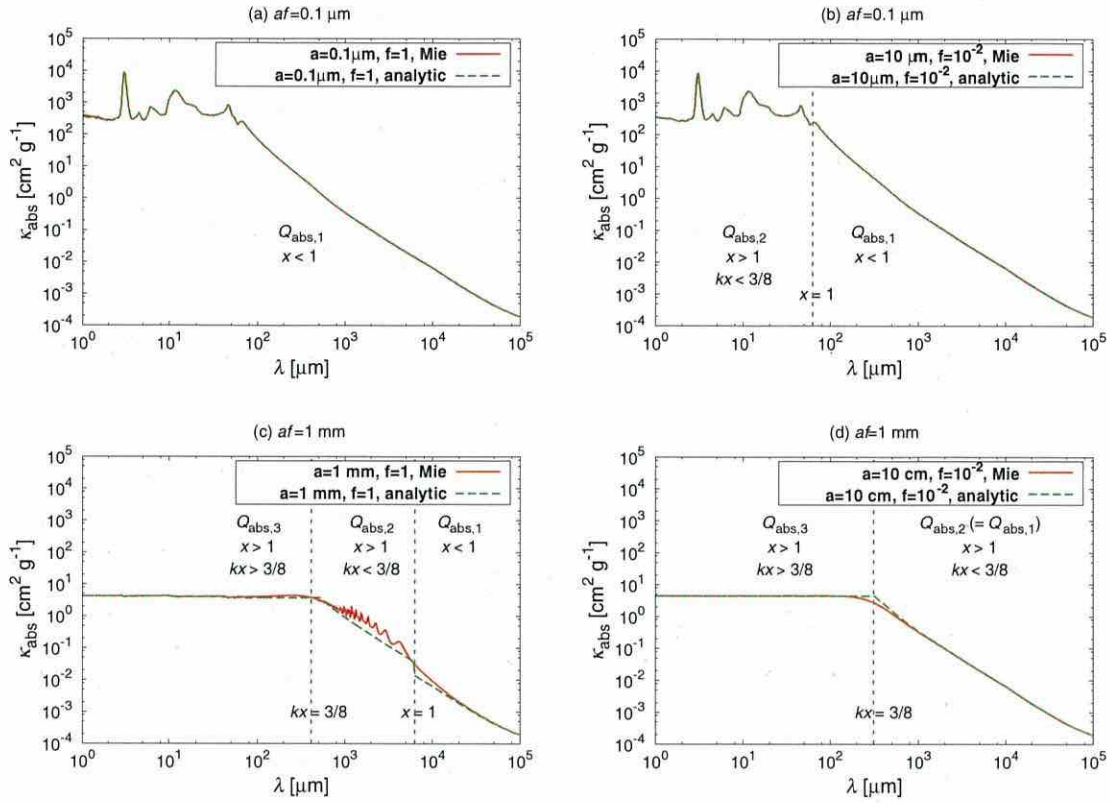

Fig. 7. Comparison of Mie calculations and the analytic formulae. The dotted lines show where $x = 1$ and $kx = 3/8$. **a)** Mass opacity in the case of $af = 0.1$ μm and $f = 1$; **b)** $af = 0.1$ μm and $f = 10^{-2}$; **c)** $af = 1$ mm and $f = 1$; **d)** $af = 1$ mm and $f = 10^{-2}$.

As discussed in Sect. 4.2.3, the integrated reflectance is $\sim 0.1 \times f$. Thus, $Q_{\rm sca,3} \sim 1 + 0.1 \times f$. This is regarded as $Q_{\rm sca,3} \sim 1$. Thus, the scattering mass opacity also goes to the geometric cross section at shorter wavelengths and is characterized by af.

4.3.4. Analytic formula of scattering mass opacity

Combining the three limiting regimes, we obtain the analytic formula of scattering mass opacity as

$$Q_{\rm sca} = \begin{cases} Q_{\rm sca,1} & (x < 1) \\ \min(Q_{\rm sca,2}, Q_{\rm sca,3}) & (x > 1). \end{cases} \quad (23)$$

Figure 8 shows the comparison of scattering mass opacity obtained with the Mie calculation and the analytic formula. Figure 8a and b shows the case of $af = 0.1$ μm, but the filling factor is $f = 1$ and $f = 0.01$, respectively. The analytic formula in both cases reproduces the Mie calculation. Figure 8c and d shows the case of $af = 1$ mm, but the filling factor is $f = 1$ and $f = 0.01$, respectively. In this case, the analytic formula reproduces the Mie calculation except for the interference structure because we assume that all the amplification by interference is damped when $x > 1$ and optically thin, which corresponds to $Q_{\rm sca} = Q_{\rm sca,2}$. However, the difference of the mass opacity between the analytic and Mie calculations is less than one order. Except for the interference structure, the analytic formula reproduces the Mie calculation even in the case of scattering mass opacity.

As already shown in Fig. 4, the scattering mass opacity is proportional to λ^{-2} at the intermediate wavelengths and λ^{-4} at the longer wavelengths in fluffy cases. This can be explained by $Q_{\rm sca,2}$. If $x = 2\pi a/\lambda$ is less than unity, which occurs at the longer wavelengths, $Q_{\rm sca} = Q_{\rm sca,1}$ and thus scales as λ^{-4} because $Q_{\rm sca,1} \propto x^4$. However, in the case of fluffy aggregates, we find the region where $x > 1$ and optically thin, and therefore $Q_{\rm sca} = Q_{\rm sca,2} = Q_{\rm sca,1}/x^2$. This is the reason why the scattering mass opacity at the intermediate wavelengths in fluffy cases scales as λ^{-2}.

5. Implications for opacity evolution in protoplanetary disks

The index of the dust opacity β has been widely used as an indicator of the dust growth. In this section, we will show how β changes as aggregates grow and drift both in compact and fluffy cases. Then, we propose a detection method of fluffy aggregates in protoplanetary disks by using the opacity index β.

5.1. Fluffy dust growth and opacity evolution

Before starting the discussion of β, we discuss the general mass opacity change as dust grains grow to fluffy aggregates in protoplanetary disks. We adopt a fluffy dust growth model proposed by Kataoka et al. (2013b). In this model, they reveal the overall porosity evolution from micron-sized grains to kilometer-sized planetesimals through direct sticking. In the coagulation, icy particles are sticky and thus they are not disrupted or bounced, but grow to a larger size (Wada et al. 2009, 2011, 2013). Moreover, the large radius of fluffy aggregates enables them to grow rapidly

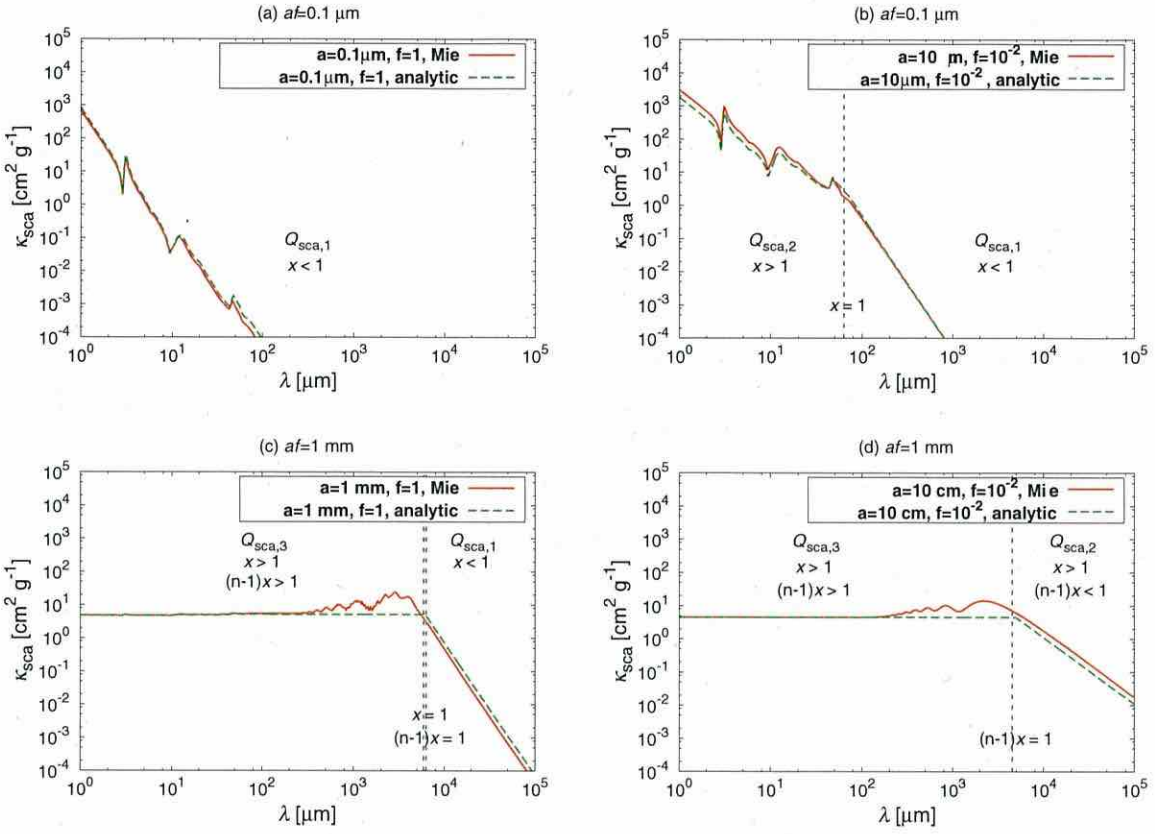

Fig. 8. Same as Fig. 7, but for scattering mass opacity.

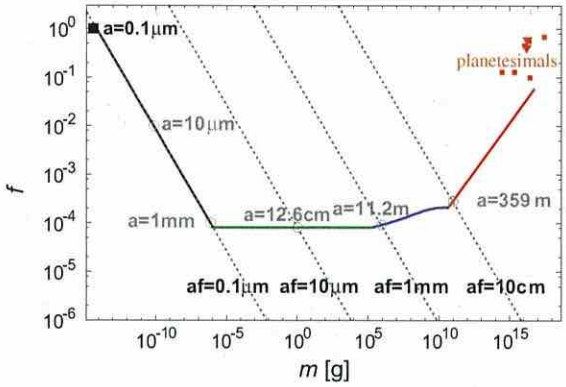

Fig. 9. Internal density evolution at $r = 30$ AU in the minimum mass solar nebula model (see Kataoka et al. 2013b, for more details). The solid line represents the evolution. The black, green, blue, and red lines are in the coagulation phase of hit-and-stick, collisional compression, gas compression, and self-gravitational compression, respectively. The dotted lines show the af = (constant) lines, where $af = 0.1$ μm, 10 μm, 1 mm, and 10 cm, respectively.

to avoid the radial drift barrier (Okuzumi et al. 2012; Kataoka et al. 2013b). Thus, the model is a complete scenario of growing path from dust grains to planetesimals by direct sticking.

Figure 9 shows the internal density evolution at 30 AU in orbital radius in a minimum mass solar nebula model, proposed by Kataoka et al. (2013b). We note that the figure shows the local porosity evolution, but dust aggregates start to drift inward once they grow to be decoupled from the gas. We discuss the radial drift later in this section. The turbulent parameter α_D is set to be 10^{-3} and the mean internal density is set to be 1.68 g cm^{-3}. The picture of the overall porosity evolution is as follows. As the dust grains first coagulate to form fluffy aggregates, the filling factor decreases to $f \sim 10^{-4}$. Once the collisional compression becomes effective, the density keeps constant. Then, the gas compression and the self-gravity compression make the dust aggregates compact.

The open circles represent the characteristic dust radius a, while the dotted lines show the lines of constant af. From this figure, the dust aggregates in the initial growth stage is optically the same. The initial growth is expected to be fractal. The dust aggregates coagulate with aggregates of similar sizes, and thus the fractal dimension is expected to be 2 (Okuzumi et al. 2012). Thus, the mass-to-area ratio of the aggregates keeps constant. In other words, af keeps the same value. Therefore, the initial growth is indistinguishable with no growth in the absorption mass opacity. After the initial growth, when the compression mechanisms become effective, the opacity is expected to change because the mass-to-area ratio changes.

Figure 10 shows the mass opacity change, corresponding to open circles in Fig. 9. The first three cases are degenerated in mass opacity because af is the same. Once the compression becomes effective, the mass opacity changes as expected in the dust growth. For example, when dust aggregates grow to have their radius of $a = 12.6$ cm, they have almost the same opacity as 10 μm compact grains. We note that the interference structure does not appear as aggregates grow because the filling factor is typically $f \sim 10^{-4}$ in this growth scenario.

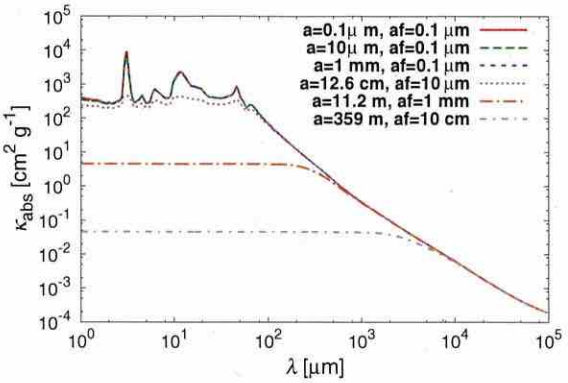

Fig. 10. Mass opacity change in the case of fluffy dust growth. Each line shows the mass opacity in the cases of different radii and filling factors, which correspond to open circles in Fig. 9. The dust properties of the lines are as follows: red: $a = 0.1\,\mu$m, and $af = 0.1\,\mu$m; green: $a = 10\,\mu$m, and $af = 0.1\,\mu$m; blue: $a = 1$ mm, and $af = 0.1\,\mu$m; magenta: $a = 12.6$ cm, and $af = 10\,\mu$m; brown: $a = 11.2$ m, and $af = 1$ mm; purple: $a = 359$ m, and $af = 10$ cm.

5.2. Dust opacity index beta

We define β as an opacity slope between 1 mm and 3 mm. Here, we use af again because optical properties are characterized by af. We note that $af = a$ in the case of compact grains ($f = 1$). We consider several cases for calculating dust β where the filling factor f is fixed in each case. Calculating β, we consider a grain size distribution with a power law as $n \propto (af)^{-2}$ between a minimum and a maximum size, $(af)_{\rm min}$ and $(af)_{\rm max}$, respectively; $(af)_{\rm min}$ is chosen to be 0.1 μm. Figure 11 shows how the absorption mass opacity $\kappa_{\rm abs}$ at 1 mm and β changes as the aggregate size increases. The compact case in this figure corresponds to Fig. 3 in Ricci et al. (2010b). The red line shows the compact case, while green and blue lines are fluffy cases. The lines in the cases of $f < 10^{-2}$ are indistinguishable from the line of $f = 10^{-2}$, and thus we do not plot them. The absorption mass opacity has a strong bump around $a_{0,\rm max} \sim 1$ mm. This bump corresponds to the interference structure where the size parameter $x \sim 1$. On the other hand, the fluffy cases does not show such a bump because there is no interference. The bump of the mass opacity results in a bump of β in the compact case. The dust β increases up to ~2.7 in the compact case, but there is no bump in fluffy cases. In other words, β is always equal to or less than $\beta_{\rm ISM} = 1.7$ in fluffy cases.

From this result, the difference in the absorption mass opacity between compact and fluffy dust appears in the intermediate size, which is between 0.1 mm and 1 mm.

5.3. Radial profile of β

The radial size distribution of dust aggregates is determined by both dust growth and drift. In protoplanetary disks, the dust growth timescale strongly depends on orbital radius. In the inner part of disks, dust grains coagulate faster than in the outer part because of the shorter Keplerian period. Thus, dust aggregates have a larger size at the inner part and smaller at the outer part when considering only dust growth. When dust aggregates grow to larger sizes, they start to drift inward. Thus, the size where the aggregates start to drift is the maximum size of the aggregates at each orbital radius. The maximum size also depends on an orbital radius: the maximum size is larger in the inner part and smaller in the outer part. Combining both effects of dust growth and drift, the radial profile of the size of dust aggregates is expected to be smaller in the outer part and larger in the inner part. Observationally, the radial profile of β have the information of the radial size distribution.

To obtain the radial profile of β, we adopt the following simple dust growth and drift model. We assume that there are initially 0.1 μm sized dust grains in the entire disk. We trace the growth and drift motion of each set of dust grains initially located at each orbital radius.

To calculate the time evolution of dust mass $M = M(t)$ and the orbital radius $r = r(t)$ at each orbital radius, we assume that dust grains have a monodisperse distribution at each orbital radius. Under this assumption, the dust growth and drift is described by (e.g., Okuzumi et al. 2012)

$$\frac{{\rm d}M(t)}{{\rm d}t} = \rho_{\rm d}\pi a^2 \Delta v \tag{24}$$

and

$$\frac{{\rm d}r(t)}{{\rm d}t} = -v_{\rm r}(M(t)), \tag{25}$$

where $\rho_{\rm d}$ is the spatial dust density, a the dust radius, Δv the relative velocity of dust grains or aggregates, and $v_{\rm r}(M(t))$ the drift velocity. We use the disk model of Kataoka et al. (2013b) (see also Okuzumi et al. 2012, for the definitions of the dust velocity and the disk model). Here, we briefly summarize the model. At a radial distance $r(t)$ from the central star, the gas-surface density profile is $1700(r/1{\rm AU})^{-p}$ g cm^{-2} where we use $p = 1$ in this paper. We note that the gas-surface density does not change with time to clarify the effects of dust growth and drift (e.g., Okuzumi et al. 2012). The initial dust-to-gas mass ratio is 0.01. The adopted temperature profile is $137(r/1{\rm AU})^{-3/7}$ K, which corresponds to midplane temperature (Chiang et al. 2001). This is cooler than optically thin disk models to focus on the dust coagulation in the midplane. The value of Δv is assumed be the root mean square of Brownian motion and turbulent motion (see Eq. (32) in Okuzumi et al. 2012). The diffusion coefficient $\alpha_{\rm D}$ is taken to be 10^{-3}. For the velocity induced by turbulence, we denote the velocity difference of dust and gas as dust-dust velocity for simplicity. We determine the dust scaleheight from the balance between sedimentation and turbulent diffusion (Brauer et al. 2008). The filling factor is fixed to be unity in the compact case and changes as a function of the orbital radius in the fluffy case following Kataoka et al. (2013b).

Figure 12 shows the dust growth and drift paths. The dashed lines show the paths of growing dust aggregates and the colored dotted and solid lines represent isochrones at $t = 10^5$ and $t = 10^6$ years. The isochrones represent the radial grain/aggregate-size distribution at the specific time. The size of dust aggregates increases with a decreasing orbital radius. This is caused by two effects: dust growth and drift. For example, on the line of the isochrone at 10^5 years in the compact case, shown in Fig. 12a, the dust growth determines the aggregate size beyond ~30 AU. At 30 AU or larger in orbital radius, dust growth is faster at the inner part of the disk than the outer part because the growth timescale is proportional to the Keplerian period (e.g., Okuzumi et al. 2012). At the orbital radius less than 30 AU, the maximum size is determined by the drift motion. The aggregates grow so large that they are decoupled from the gas, and drift inward. Therefore, the aggregate size at orbital radius less than 30 AU corresponds to the maximum size determined by the radial drift.

Figure 13 shows the radial β distribution for both compact and fluffy cases at the isochrones shown in Fig. 12. In the compact case, β increases to around $\beta \sim 2.7$ at 40 AU in the range

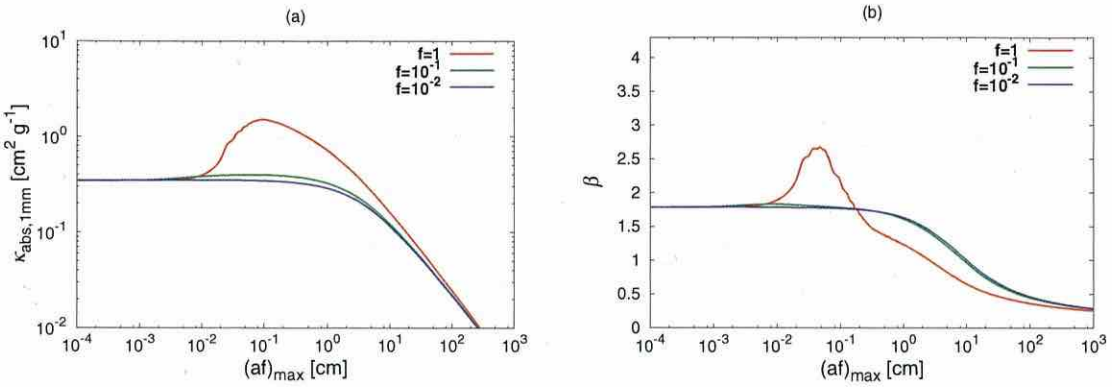

Fig. 11. **a)** Absorption mass opacity at $\lambda = 1$mm against $(af)_{\rm max}$. The red, green, and blue lines show the cases of $f = 1, 10^{-1}$, and 10^{-2}. The lines in the cases of $f < 10^{-2}$ are indistinguishable from the line of $f = 10^{-2}$. The aggregate size distribution is assumed to be $n \propto (af)^{-2}$ where f is fixed in each case. **b)** Opacity slope β between 1 mm and 3 mm, against $(af)_{\rm max}$.

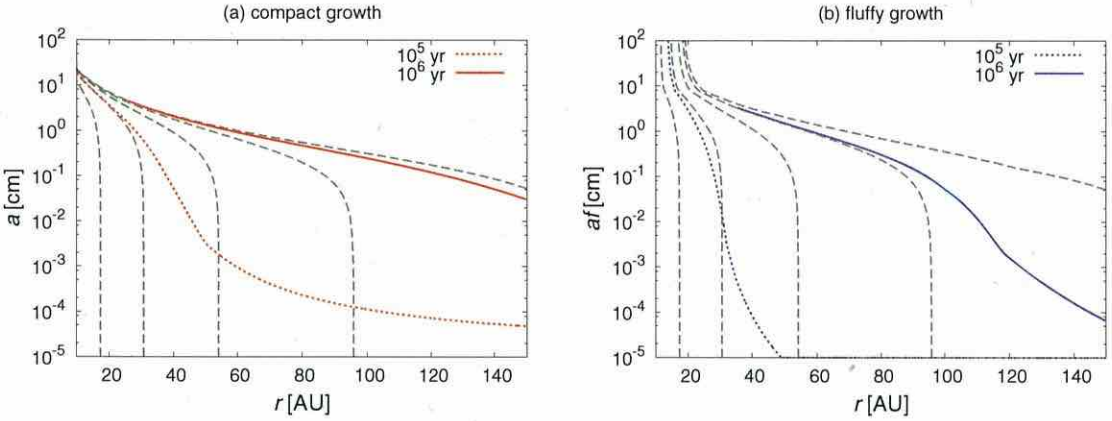

Fig. 12. Paths of the growth and drift of dust aggregates at each initial orbital radius (dashed gray lines). Radial size distribution of dust aggregates at the specific time (solid and dotted lines). **a)** Compact case, where the red dotted line shows the isochrone at $t = 10^5$ years and the solid red line shows at $t = 10^6$ years. **b)** Fluffy growth case, where the dotted blue line shows the isochrone at $t = 10^5$ years and the solid blue line at $t = 10^6$ years.

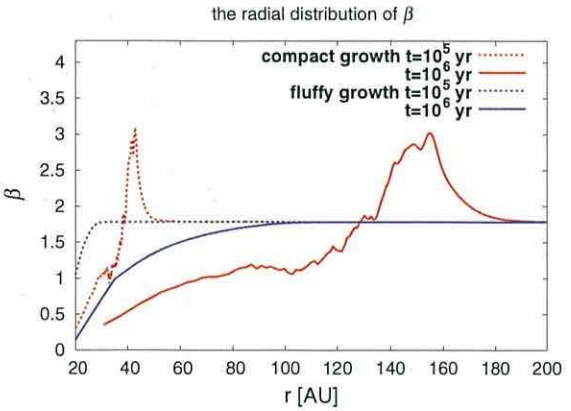

Fig. 13. Radial β distribution for compact and fluffy cases. Each line corresponds to the same line as in Fig. 12.

of 10 AU at $t = 10^5$ years and at 150 AU in the range of 20 AU at $t = 10^6$ years. This means that protoplanetary disks have a specific radius where β is greater than $\beta_{\rm ISM} = 1.7$ in the compact case. In the fluffy case, on the other hand, β is always equal to or less than $\beta_{\rm ISM} = 1.7$. Therefore, if the radial β distribution always has a value of $\beta_{\rm ISM} = 1.7$ or less, it means that the millimeter emission comes from fluffy aggregates.

5.4. Silicate feature

In the inner part of the disk, ice particles are expected to be sublimated and there are dust aggregates whose constituent particles are made of silicate. Micron-sized silicate grains show the broad feature at 10 μm. The feature is used as a signature of grain growth (e.g., van Boekel et al. 2005). To show how the porosity affects the silicate feature, we also calculate the silicate feature of fluffy aggregates. In this section, we change the material constant: we assume pure silicate monomers. The material density is taken to be $\rho_{\rm mat} = 3.5$ g cm^{-3} and the refractive index is taken from Weingartner & Draine (2001).

Figure 14 shows the absorption mass opacity in cases of silicate aggregates. Each panel shows the mass absorption opacities where af is constant. When $af = 0.1$ μm, the broad silicate feature is seen at around $\lambda = 10$ μm and does not significantly change as the aggregate size increases from 0.1 μm to 1 mm. In the cases of $af = 1$–10 μm, the silicate feature becomes weaker as af increases. The absorption mass opacity of porous

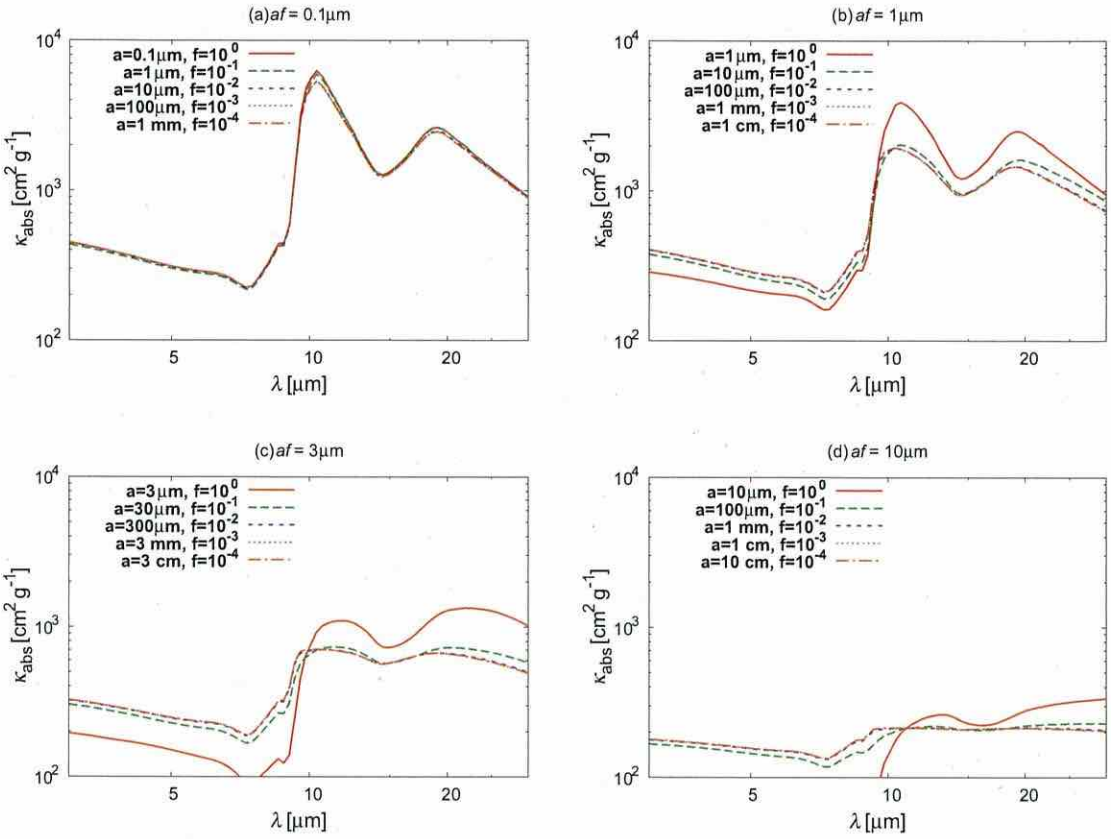

Fig. 14. Absorption mass opacity for silicate aggregates in cases of different af. The mass opacities are shown in the case of **a)** $af = 0.1\ \mu$m, **b)** $af = 1\ \mu$m, **c)** $af = 3\ \mu$m, and **d)** $af = 30\ \mu$m.

aggregates ($f \leq 0.1$) is independent of the aggregate size as long as af is constant, as is also shown in the case of icy aggregates. The small differences between the cases of $f = 1$ and $f \leq 0.1$ derive from the interference as well as the icy aggregates. Thus, except for the interference, the silicate feature disappears as af increases.

6. Summary and discussion

We calculated the mass opacity of fluffy dust aggregates expected to be in protoplanetary disks. The wavelengths are in the range of $1\ \mu\text{m} < \lambda < 1$ cm and the filling factor in the range of $10^{-4} < f < 1$. The assumed composition is the mixture of silicate, organics, and water ice (Pollack et al. 1994). We used the Mie calculation with the effective medium theory to calculate the mass opacity of fluffy aggregates. Our main findings are as follows.

- The absorption mass opacity of dust aggregates is characterized by af, where a is the dust radius and f is the filling factor. The absorption mass opacity is almost independent of the aggregate size when af is constant. This makes it difficult to distinguish between fluffy aggregates and compact grains in observations. The only difference of the absorption mass opacity between compact grains and fluffy aggregates where af is the same appears as the interference structure in the compact case at the size parameter $x \sim 1$.
- The scattering mass opacity at short wavelengths is also characterized by af, but not at long wavelengths. The scattering mass opacity at the long wavelengths is higher in more fluffy aggregates even if af is the same. The scattering mass opacity scales as λ^{-2} at intermediate wavelengths and scales as λ^{-4} at the longer wavelengths.
- We also derived the analytic formulae of the absorption and scattering mass opacities, connecting the three limiting cases, which are the Rayleigh regime, the optically-thin geometric regime, and the optically-thick geometric regime. The analytic formulae reproduce the results of the Mie calculations. The formulae are expected to greatly reduce the computational time to calculate the opacity of large fluffy aggregates. By using the analytic formulae, we analytically showed that the absorption mass opacity is characterized by one parameter af except for the interference structure. We also showed that the scattering mass opacity at the shorter wavelengths is also characterized by af, but not at the longer wavelengths. Thus, the fact that the mass opacity is characterized by af is valid even out of the range investigated in the Mie calculation in this paper and is also applicable to other materials.
- The opacity index β is a good way to distinguish between fluffy aggregates and compact grains at observations of protoplanetary disks. If we assume the compact grain growth, with increasing grain size, the opacity index β increases to ~2.7 and then decreases. If we assume fluffy aggregate growth, the index β monotonously decreases from its initial value $\beta_{\rm ISM} = 1.7$ (see Fig. 11). If dust grains are compact in protoplanetary disks, the radial distribution of the index β should have a peak of ~2.7 (see Fig. 13).

– We also calculated the absorption mass opacity of silicate aggregates at around $\lambda = 10\,\mu$m. The opacity of fluffy aggregates has the $10\,\mu$m feature as well as compact silicate grains. The silicate feature is also appropriately characterized by af.

In this paper, as a first step, we use the effective medium theory. Voshchinnikov et al. (2005) have shown that EMT is a good approximation when considering small inclusions. We considered 0.1 μm sized monomers and the wavelength ranges from 1 μm to 10 cm. Because the monomer size is less than the wavelengths, EMT would be a good approximation. However, the validity of EMT at infrared, especially at short wavelengths, is somewhat marginal because the wavelengths are close to the monomer size. Thus, the validity of the effective medium theory should be further tested by future work.

We proposed that the radial profile of β is a way to distinguish between compact grains and fluffy aggregates. Pérez et al. (2012) have put a constraint on the radial β distribution by observing a protoplanetary disk AS 209 with VLA, SMA, and CARMA. They found that β has a lower value inside the disk rather than the constant β in the whole disk. It is consistent with the model of Fig. 12, where the grain size is distributed because of the difference of growth time and the maximum grain size is limited by radial drift. The results of Pérez et al. (2012) also prefer the fluffy growth scenario to the compact because there is no signature that β is large as $\beta \sim 3$. However, the observation has little information about β in the outer part of the disk because of the sensitivity limitation at the longer wavelengths. Thus, to clearly determine whether the emission comes from compact grains or fluffy aggregates, we need higher sensitivity at the longer wavelengths. Moreover, to reject the possibility of $\beta > \beta_{\rm ISM}$, we need a high spatial resolution to resolve 20 AU bump in the compact case at $t = 10^6$ years. This observation is challenging, but would be a good target of ALMA.

The fact that the scattering mass opacity at the longer wavelengths cannot characterized by af is another way to distinguish between compact grains and fluffy aggregates. Here, we propose the polarization observation of the millimeter continuum emission. The scattered light is expected to be linearly polarized, and thus by comparing the intensity and the polarized intensity, the ratio of the scattering and absorption mass opacity can be directly observed. Although the polarized emission depends on the disk geometry and has many uncertainties, it would be a good target in the next phase of ALMA.

In addition, Mulders et al. (2013) proposed that to interpret the low effective albedo of protoplanetary disks, there are large particles at the outer disk surface and they should be porous structures to be stirred up to the surface. However, we showed that the infrared scattering opacity is determined by af. In addition, the coupling efficiency of aggregates to the disk gas is also determined by af. Thus, the optical and kinematical properties are degenerated. Therefore, the porous aggregates would not help to interpret the observations of the low effective albedo.

Acknowledgements. We acknowledge Masaomi Tanaka for fruitful discussions, Takaya Nozawa, Andrea Isella for their kind cooperation about opacity tables, Munetake Momose, Takashi Tsukagoshi for great discussions from an observational point of view. A.K. acknowledges Kohji Tomisaka's support for PhD life. A.K. is supported by the Research Fellowship from JSPS for Young Scientists (24·2120).

Appendix A: Refractive index of fluffy aggregates

In this section, we confirm the validity of the assumptions used to derive the analytic formula in Sect. 4.

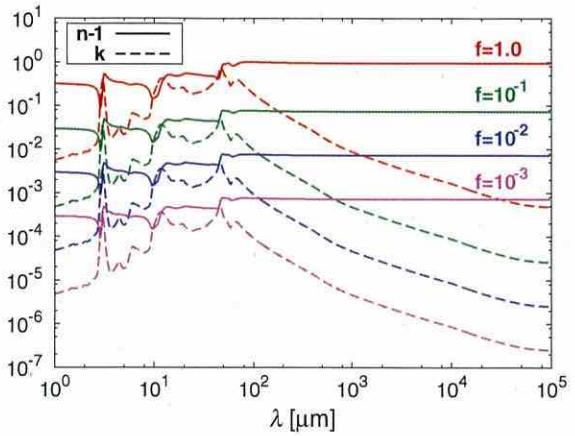

Fig. A.1. $n-1$ and k against the wavelengths when $f = 1, 10^{-1}, 10^{-2}$, and 10^{-3}.

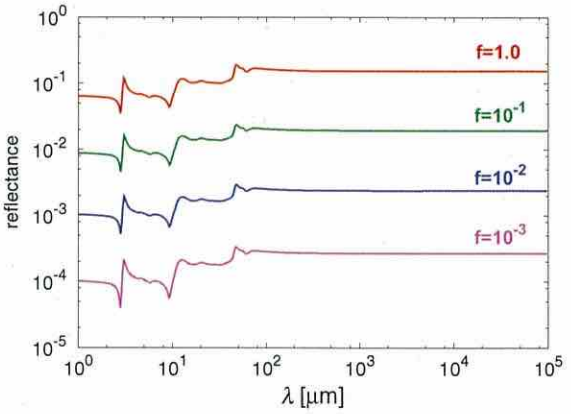

Fig. A.2. Integrated reflectance when $f = 1, 10^{-1}, 10^{-2}$, and 10^{-3}.

A.1. $(n-1) > k$ at the longer wavelengths

Figure A.1 shows the comparison of $n-1$ and k when $f = 1, 10^{-1}, 10^{-2}, 10^{-3}$, and 10^{-4}. We confirm that the refractive index always satisfies $n-1 > k$ at the longer wavelengths in any value of f. Moreover, we also confirm that $(n-1) \propto f$ and $k \propto f$ when $f < 1$.

A.2. Reflectance

We define the integrated reflectance as

$$R \equiv \int_0^{\pi/2} R(\theta_i) \sin 2\theta_i \mathrm{d}\theta_i. \tag{A.1}$$

When the medium satisfies $x \gg 1$ and is optically thick, $Q_{\rm abs}$ and $Q_{\rm sca}$ are written as $Q_{\rm abs} = Q_{\rm abs,3} = 1 - R$ and $Q_{\rm sca} = Q_{\rm sca,3} = 1 + R$. We assume that $R \ll 1$, and therefore $Q_{\rm abs}$ and $Q_{\rm sca}$ are unity in Sect. 4. Figure A.2 shows the integrated reflectance R. Roughly speaking, $R \sim 0.1 \times f$ and thus we can assume that $Q_{\rm abs}$ and $Q_{\rm sca}$ are unity in the regime.

A.3. Optical thickness inside the material

We discuss the optical thickness inside the medium by considering whether kx is greater than 3/8. Figure A.3 shows kx in the case of $af = 0.1\,\mu$m, $10\,\mu$m, and 1 mm. We confirm that if af is

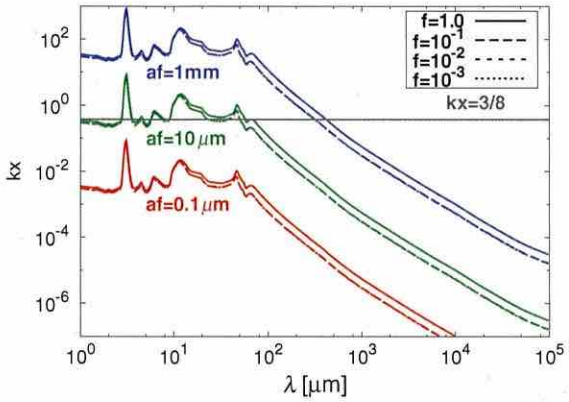

Fig. A.3. kx against wavelengths when $af = 0.1\ \mu$m, 10 μm, and 1 mm. The solid lines represent the compact cases and the dashed lines fluffy cases.

the same, kx is almost the same at all wavelengths. In the case of $af = 0.1\ \mu$m, the medium is totally optically thin. In the case of $af = 10\ \mu$m, the medium is optically thin at the longer wavelengths and marginally optically thick when $\lambda \lesssim 10^{-2}$ cm. In the case of $af = 1$ mm, the medium is optically thin at the longer wavelengths and optically thick when $\lambda \lesssim 6 \times 10^{-2}$ cm.

References

Andrews, S. M., & Williams, J. P. 2005, ApJ, 631, 1134
Beckwith, S. V. W., & Sargent, A. I. 1991, ApJ, 381, 250
Beckwith, S. V. W., Sargent, A. I., Chini, R. S., & Guesten, R. 1990, AJ, 99, 924
Birnstiel, T., Ricci, L., Trotta, F., et al. 2010, A&A, 516, L14
Blum, J., & Wurm, G. 2008, ARA&A, 46, 21
Bohren, C. F., & Huffman, D. R. 1983, Absorption and scattering of light by small particles (New York: Wiley)
Brauer, F., Dullemond, C. P., & Henning, T. 2008, A&A, 480, 859
Chiang, E. I., Joung, M. K., Creech-Eakman, M. J., et al. 2001, ApJ, 547, 1077
D'Alessio, P., Calvet, N., & Hartmann, L. 2001, ApJ, 553, 321
Draine, B. T., & Flatau, P. J. 1994, J. Opt. Soc. Am. A, 11, 1491
Drążkowska, J., Windmark, F., & Dullemond, C. P. 2013, A&A, 556, A37
Guilloteau, S., Dutrey, A., Piétu, V., & Boehler, Y. 2011, A&A, 529, A105
Isella, A., Carpenter, J. M., & Sargent, A. I. 2009, ApJ, 701, 260
Kataoka, A., Tanaka, H., Okuzumi, S., & Wada, K. 2013a, A&A, 554, A4
Kataoka, A., Tanaka, H., Okuzumi, S., & Wada, K. 2013b, A&A, 557, L4
Kimura, H., Kolokolova, L., & Mann, I. 2003, A&A, 407, L5
Kimura, H., Kolokolova, L., & Mann, I. 2006, A&A, 449, 1243
Kolokolova, L., Kimura, H., Kiselev, N., & Rosenbush, V. 2007, A&A, 463, 1189
Kothe, S., Blum, J., Weidling, R., & Güttler, C. 2013, Icarus, 225, 75
Kozasa, T., Blum, J., & Mukai, T. 1992, A&A, 263, 423
Kudo, T., Kouchi, A., Arakawa, M., & Nakano, H. 2002, Meteoritics, 37, 1975
Li, A., & Greenberg, J. M. 1997, A&A, 323, 566
Lommen, D. J. P., van Dishoeck, E. F., Wright, C. M., et al. 2010, A&A, 515, A77
Min, M., Hovenier, J. W., & de Koter, A. 2003, A&A, 404, 35
Min, M., Hovenier, J. W., & de Koter, A. 2005, A&A, 432, 909
Min, M., Dominik, C., Hovenier, J. W., de Koter, A., & Waters, L. B. F. M. 2006, A&A, 445, 1005
Min, M., Waters, L. B. F. M., de Koter, A., et al. 2007, A&A, 462, 667
Miyake, K., & Nakagawa, Y. 1993, Icarus, 106, 20
Mukai, T., Ishimoto, H., Kozasa, T., Blum, J., & Greenberg, J. M. 1992, A&A, 262, 315
Mulders, G. D., Min, M., Dominik, C., Debes, J. H., & Schneider, G. 2013, A&A, 549, A112
Okuzumi, S., Tanaka, H., & Sakagami, M.-A. 2009, ApJ, 707, 1247
Okuzumi, S., Tanaka, H., Kobayashi, H., & Wada, K. 2012, ApJ, 752, 106
Ormel, C. W., Spaans, M., & Tielens, A. G. G. M. 2007, A&A, 461, 215
Pagani, L., Steinacker, J., Bacmann, A., Stutz, A., & Henning, T. 2010, Science, 329, 1622
Pérez, L. M., Carpenter, J. M., Chandler, C. J., et al. 2012, ApJ, 760, L17
Pollack, J. B., Hollenbach, D., Beckwith, S., et al. 1994, ApJ, 421, 615
Ricci, L., Testi, L., Natta, A., & Brooks, K. J. 2010a, A&A, 521, A66
Ricci, L., Testi, L., Natta, A., et al. 2010b, A&A, 512, A15
Shen, Y., Draine, B. T., & Johnson, E. T. 2008, ApJ, 689, 260
Shen, Y., Draine, B. T., & Johnson, E. T. 2009, ApJ, 696, 2126
Suyama, T., Wada, K., & Tanaka, H. 2008, ApJ, 684, 1310
Suyama, T., Wada, K., Tanaka, H., & Okuzumi, S. 2012, ApJ, 753, 115
Tanaka, H., Himeno, Y., & Ida, S. 2005, ApJ, 625, 414
van Boekel, R., Min, M., Waters, L. B. F. M., et al. 2005, A&A, 437, 189
van der Marel, N., van Dishoeck, E. F., Bruderer, S., et al. 2013, Science, 340, 1199
Voshchinnikov, N. V., Il'in, V. B., & Henning, T. 2005, A&A, 429, 371
Wada, K., Tanaka, H., Suyama, T., Kimura, H., & Yamamoto, T. 2008, ApJ, 677, 1296
Wada, K., Tanaka, H., Suyama, T., Kimura, H., & Yamamoto, T. 2009, ApJ, 702, 1490
Wada, K., Tanaka, H., Suyama, T., Kimura, H., & Yamamoto, T. 2011, ApJ, 737, 36
Wada, K., Tanaka, H., Okuzumi, S., et al. 2013, A&A, 559, A62
Warren, S. G. 1984, Appl. Opt., 23, 1206
Weingartner, J. C., & Draine, B. T. 2001, ApJ, 548, 296
Windmark, F., Birnstiel, T., Güttler, C., et al. 2012, A&A, 540, A73
Zsom, A., Ormel, C. W., Güttler, C., Blum, J., & Dullemond, C. P. 2010, A&A, 513, A57
Zsom, A., Ormel, C. W., Dullemond, C. P., & Henning, T. 2011, A&A, 534, A73
Zubko, V. G., Mennella, V., Colangeli, L., & Bussoletti, E. 1996, MNRAS, 282, 1321

The Astrophysical Journal, 752:106 (18pp), 2012 June 20 doi:10.1088/0004-637X/752/2/106

RAPID COAGULATION OF POROUS DUST AGGREGATES OUTSIDE THE SNOW LINE: A PATHWAY TO SUCCESSFUL ICY PLANETESIMAL FORMATION

Satoshi Okuzumi[1], Hidekazu Tanaka[2], Hiroshi Kobayashi[1], and Koji Wada[3]
[1] Department of Physics, Nagoya University, Nagoya, Aichi 464-8602, Japan; okuzumi@nagoya-u.jp
[2] Institute of Low Temperature Science, Hokkaido University, Sapporo 060-0819, Japan
[3] Planetary Exploration Research Center, Chiba Institute of Technology, Narashino, Chiba 275-0016, Japan
Received 2012 January 26; accepted 2012 April 22; published 2012 June 4

ABSTRACT

Rapid orbital drift of macroscopic dust particles is one of the major obstacles to planetesimal formation in protoplanetary disks. We re-examine this problem by considering the porosity evolution of dust aggregates. We apply a porosity model based on recent *N*-body simulations of aggregate collisions, which allows us to study the porosity change upon collision for a wide range of impact energies. As a first step, we neglect collisional fragmentation and instead focus on dust evolution outside the snow line, where the fragmentation has been suggested to be less significant than inside the snow line because of the high sticking efficiency of icy particles. We show that dust particles can evolve into highly porous aggregates (with internal densities of much less than $0.1\,\mathrm{g\,cm^{-3}}$) even if collisional compression is taken into account. We also show that the high porosity triggers significant acceleration in collisional growth. This acceleration is a natural consequence of the particles' aerodynamical properties at low Knudsen numbers, i.e., at particle radii larger than the mean free path of the gas molecules. Thanks to this rapid growth, the highly porous aggregates are found to overcome the radial drift barrier at orbital radii less than 10 AU (assuming the minimum-mass solar nebula model). This suggests that, if collisional fragmentation is truly insignificant, formation of icy planetesimals is possible via direct collisional growth of submicron-sized icy particles.

Key words: dust, extinction – planets and satellites: formation – protoplanetary disks

Online-only material: color figures

1. INTRODUCTION

Growth of dust particles is a key process in protoplanetary disks. Current theories of planet formation assume kilometer-sized solid bodies called "planetesimals" to form from dust contained in protoplanetary disks. As the dominant component of disk opacity, dust also affects the temperature and observational appearance of the disks. Furthermore, dust particles are known to efficiently capture ionized gas particles in the gas disk, thereby controlling its magnetohydrodynamical behavior (Sano et al. 2000).

Theoretically, however, how the dust particles evolve into planetesimals is poorly understood. One of the most serious obstacles is the radial inward drift of macroscopic aggregates due to the gas drag (Whipple 1972; Adachi et al. 1976; Weidenschilling 1977). Because of the gas pressure support in addition to the centrifugal force, protoplanetary disks tend to rotate at sub-Keplerian velocities. By contrast, dust particles are free from the pressure support, and hence tend to rotate faster than the gas disk. The resulting headwind acting on the dust particles extracts their angular momentum and thus causes their drift motion toward the central star. In order to go beyond this "radial drift barrier," dust particles must decouple from the gas drag (i.e., grow large) faster than they drift inward. However, previous work by Brauer et al. (2008a) showed that dust particles finally fall onto the central star unless the initial dust-to-gas mass ratio is considerably higher than the canonical interstellar value.

Several mechanisms have so far been suggested to explain how dust particles overcome the radial drift barrier. A classical idea is that dust particles "jump" across the barrier by forming a gravitationally unstable thin dust layer at the midplane and directly collapsing into planetesimal-sized objects (Safronov 1969; Goldreich & Ward 1973; Hayashi et al. 1985). However, this classical scenario has been challenged by the fact that the dust layers are easily stirred up by disk turbulence (Weidenschilling & Cuzzi 1993; Turner et al. 2010). Moreover, the dust sublayer is known to induce the Kelvin–Helmholtz instability, which prevents further sedimentation of dust even without disk turbulence unless the dust-to-gas surface density ratio is considerably high (Sekiya 1998). Recently, a two-fluid instability of dust and gas was discovered (Youdin & Goodman 2005), which can lead to the fast formation of gravitationally bound dust clumps (e.g., Johansen & Youdin 2007; Johansen et al. 2007; Bai & Stone 2010a). However, this mechanism requires marginally decoupled dust particles, the formation of which is already questioned by the radial drift barrier itself. Other possibilities include the trapping of dust particles in vortices (e.g., Barge & Sommeria 1995; Klahr & Henning 1997) and at gas pressure maxima (e.g., Kretke & Lin 2007; Brauer et al. 2008b; Suzuki et al. 2010; Pinilla et al. 2012).

This study re-examines this problem by considering a new physical effect: the porosity evolution of dust aggregates. Most previous coagulation models (e.g., Nakagawa et al. 1981; Tanaka et al. 2005; Brauer et al. 2008a; Birnstiel et al. 2010) assumed that dust particles grow with a fixed internal density. In reality, however, the internal density of aggregates changes upon collision depending on the impact energy. The evolution of porosity directly affects the growth history of the aggregates since the porosity determines the coupling of the aggregates to the gas motion. For example, Ormel et al. (2007) and Zsom et al. (2011) simulated dust growth with porosity evolution at fixed disk orbital radii and found that porous evolution delays the settling of dust onto the disk midplane. However, how the porosity evolution affects the radial drift barrier has so far been unaddressed.

How the internal structure changes upon collision by laboratory (e.g., Blum & Wurm 2000; Weidling et al. 2009) and numerical (e.g., Dominik & Tielens 1997; Wada et al. 2008; Suyama et al. 2008, 2012) collision experiments has been studied over last two decades. One robust finding of these studies is that aggregates grow into low density, fractal objects if the impact energy is lower than a threshold $E_{\rm roll}$ determined by material properties (Blum & Wurm 2000; Suyama et al. 2008; Okuzumi et al. 2009). The fractal dimension d_f of the resulting aggregates depends weakly on the size ratio between targets and projectiles, and falls below two when the target and projectile have similar sizes (Mukai et al. 1992; Okuzumi et al. 2009). The fractal dimension of two is equivalent to an internal density decreasing inversely proportional to the aggregate radius. The density decrease occurs because each merger event involves the creation of "voids" whose volume is comparable to those of the aggregates before the merger (Okuzumi et al. 2009). Suyama et al. (2008) estimated the collision energy of aggregates in protoplanetary disks as a function of size and showed that aggregates composed of 0.1 μm sized particles undergo fractal growth in planet-forming regions until their size reaches centimeters. This means that the building blocks of planetesimals should once have evolved into very fluffy objects with mean internal densities many orders of magnitude lower than the solid material density.

More strikingly, recent N-body experiments suggest that the porosity of aggregates can be kept considerably high even after the collision energy exceeds the threshold $E_{\rm roll}$. Wada et al. (2008) numerically simulated head-on collisions between equal-sized fractal aggregates of $d_f \approx 2$ and found that the fractal dimension after the collision does not exceed 2.5 even at high collision energies. Suyama et al. (2008) confirmed this by repeating head-on collisions of the resulting aggregates at fixed collision velocities. Furthermore, compaction is even less efficient in offset collisions, where the collision energy is spent for stretching rather than compaction of the merged aggregate (Wada et al. 2007; Paszun & Dominik 2009). These results mean that the creation of voids upon merger is non-negligible even when the impact energy is large; in other words, the voids are only imperfectly crushed in collisional compaction. Because of technical difficulties, these theoretical predictions have not yet been well tested, either by laboratory or microgravity experiments. Nevertheless, it is worth investigating how aggregates grow and drift inward if they evolve into highly porous objects.

In this study, we simulate the temporal evolution of the radial size distribution of aggregates using the advection–coagulation model developed by Brauer et al. (2008a). Unlike the previous work, we allow the porosities of aggregates to change upon collision, depending on their impact energies. To do so, we adopt the "volume-averaging method" proposed by Okuzumi et al. (2009). In this method, aggregates of equal mass are regarded as having the same volume (or equivalently, the same internal density) at each orbital distance, and the advection–coagulation equation for the averaged volume is solved simultaneously with that for the radial size distribution. To determine the porosity change upon collisional sticking, we use an analytic recipe presented by Suyama et al. (2012) that well reproduces the collision outcomes of recent N-body simulations (Wada et al. 2008; Suyama et al. 2008) as a function of the impact energy. These theoretical tools allow us to study for the first time how the porosity evolution affects the growth and radial drift of dust aggregates in protoplanetary disks.

In order to clarify the role of porosity evolution, we ignore many other effects relevant to aggregate collision, including Coulomb interaction (Okuzumi 2009; Okuzumi et al. 2011a, 2011b; Matthews et al. 2012), bouncing (Zsom et al. 2010, 2011; Windmark et al. 2012), and collisional fragmentation (Brauer et al. 2008a, 2008b; Birnstiel et al. 2009, 2012). Coulomb repulsion due to negative charging can significantly slow down the initial fractal growth, but may be negligible once the collisional compaction becomes effective (Okuzumi et al. 2011b). Bouncing is often observed in laboratory experiments for relatively compact (filling factor $\gtrsim 0.1$) aggregates, but is less likely to occur when aggregates are highly porous as we consider in this study (Langkowski et al. 2008; Wada et al. 2011). Seemingly more problematic is fragmentation at high-speed collisions. This is particularly so when the aggregates are mainly composed of silicate particles for which catastrophic disruption begins at collision speeds as low as a few $\mathrm{m\,s^{-1}}$ (Blum & Wurm 2008; Wada et al. 2009; Güttler et al. 2010). By contrast, collisional fragmentation may be less problematic for aggregates made of icy particles for which a higher sticking threshold has been anticipated (Chokshi et al. 1993; Dominik & Tielens 1997; Gundlach et al. 2011). For instance, N-body collision experiments by Wada et al. (2009) suggest that aggregates made of 0.1 μm sized icy grains do not experience catastrophic disruption at collision velocities up to 35–70 $\mathrm{m\,s^{-1}}$. For this reason, instead of neglecting collisional fragmentation, we focus on dust evolution *outside the snow line* in protoplanetary disks. A more comprehensive model including the above-mentioned effects will be presented in future work.

We will show that dust particles evolve into highly porous aggregates even if collisional compaction is taken into account. Furthermore, we will show that the porosity evolution triggers significant acceleration in collisional growth at early stages, allowing the dust aggregates to grow across the radial drift barrier in inner regions of protoplanetary disks. Interestingly, this acceleration involves neither enhancement of the collision velocity nor suppression of the radial drift speed of marginally decoupled aggregates. As we will see, this acceleration is a natural consequence of the particles' aerodynamical property at low Knudsen numbers, i.e., at particle radii larger than the mean free path of the gas molecules, and the porosity evolution only allows the dust aggregates to reach that stage with small aggregate masses. Our model calculation shows that the breakthrough of the radial drift barrier can occur in "planet-forming" regions, i.e., at <10 AU from the central star. This result suggests that, if the fragmentation of icy aggregates is truly negligible, the formation of icy planetesimals is possible via direct collisional growth of dust particles even without an enhancement of the initial dust-to-gas mass ratio.

This paper is organized as follows. In Section 2, we describe the disk and collision models that we use in this study. Simulation results are presented in Section 3, which we interpret in terms of the timescales for collisional growth, and radial inward drift in Section 4. The validity and limitations of our model are discussed in Section 5, and our conclusions are presented in Section 6.

2. MODEL

2.1. Disk Model

We adopt the minimum-mass solar nebula (MMSN) model of Hayashi (1981) with a solar-mass central star. The radial profiles of the gas surface density Σ_g and disk temperature T are given

by $\Sigma_g = 152(r/5\,\mathrm{AU})^{-3/2}\,\mathrm{g\,cm^{-2}}$ and $T = 125(r/5\,\mathrm{AU})^{-1/2}\,\mathrm{K}$, respectively, where r is the distance from the central star. In this study, we focus on dust evolution outside the snow line, which is located at $r \approx 3\,\mathrm{AU}$ in the adopted disk model. The vertical structure is assumed to be in hydrostatic equilibrium, and hence the vertical structure of the gas density ρ_g is given by $\rho_g = (\Sigma_g/\sqrt{2\pi}h_g)\exp(-z^2/2h_g^2)$, where $h_g = c_s/\Omega$ is the gas scale height, c_s is the isothermal sound speed, and Ω is the Kepler frequency. The isothermal sound speed is given by $c_s = \sqrt{k_\mathrm{B}T/m_g}$, where k_B is the Boltzmann constant and m_g is the mean molecular mass. We assume the mean molecular weight of 2.34, which gives $m_g = 3.9\times10^{-24}\,\mathrm{g}$ and $c_s = 6.7\times10^4(r/5\,\mathrm{AU})^{-1/4}\,\mathrm{cm\,s^{-1}}$. The assumed stellar mass ($1\,M_\odot$) leads to $\Omega = \sqrt{GM_\odot/r^3} = 1.8\times10^{-8}(r/5\,\mathrm{AU})^{-3/2}\,\mathrm{rad\,s^{-1}}$ and $h_g/r = 0.05(r/5\,\mathrm{AU})^{1/4}$, where G is the gravitational constant.

In reality, protoplanetary disks can be heavier than the MMSN. The gravitational stability criterion (Toomre 1964) $\Sigma_g < \Omega c_s/\pi G \approx 5.6\times10^3(r/5\,\mathrm{AU})^{-7/4}\,\mathrm{g\,cm^{-2}}$ allows the surface density to be up to about 10 times higher than the MMSN value. The dependence of our result on the disk mass will be analytically discussed in Section 4.

Initial dust particles are modeled as compact spheres of equal size $a_0 = 0.1\,\mu\mathrm{m}$ and equal internal density $\rho_0 = 1.4\,\mathrm{g\,cm^{-3}}$, distributed in the disk with a constant dust-to-gas surface density ratio $\Sigma_d/\Sigma_g = 0.01$. The mass of each initial particle is $m_0 = (4\pi/3)\rho_0 a_0^3 = 5.9\times10^{-15}\,\mathrm{g}$. In the following, we will refer to the initial dust particles as "monomers." We define the radius of a porous aggregate as $a = [(5/6N)\sum_{i=1}^N\sum_{j=1}^N(\boldsymbol{x}_i-\boldsymbol{x}_j)^2]^{1/2}$, where N is the number of the constituent monomers and $\boldsymbol{x}_k (k = 1, 2, \ldots, N)$ is the position of the monomers (Mukai et al. 1992). This definition is in accordance with previous N-body experiments (Wada et al. 2008; Suyama et al. 2008; Okuzumi et al. 2009) on which our porosity model is based (see Section 2.3.1).

Disk turbulence affects the collision and sedimentation of dust particles. To include these effects, we consider gas turbulence in which the turnover time and the mean-squared random velocity of the largest turbulent eddies are given by $t_L = \Omega^{-1}$ and $\delta v_g^2 = \alpha_D c_s^2$, respectively, where α_D is the dimensionless parameter characterizing the strength of the turbulence. The assumption for t_L is based on theoretical anticipation for turbulence in Keplerian disks (Dubrulle & Valdettaro 1992; Fromang & Papaloizou 2006; Johansen et al. 2006). The diffusion coefficient for the gas is given by $D_g = \delta v_g^2 t_L = \alpha_D c_s^2/\Omega$. If the gas diffusion coefficient is of the same order as the turbulent viscosity, α_D is equivalent to the so-called alpha parameter of Shakura & Sunyaev (1973). However, for simplicity, we do not consider the viscous evolution of the gas disk. We adopt $\alpha_D = 10^{-3}$ in our numerical simulations. A higher value of α_D would cause catastrophic collisional fragmentation of aggregates, which is not considered in this study (see Section 5.3).

2.2. Evolutionary Equations

We solve the evolution of the radial size distribution of dust aggregates using the method developed by Brauer et al. (2008a). This method assumes the balance between sedimentation and turbulent diffusion of aggregates in the vertical direction. Thus, the vertical number density distribution of aggregates is given by a Gaussian $(\mathcal{N}/\sqrt{2\pi}h_d)\exp(-z^2/2h_d^2)$, where $\mathcal{N}(r, m)$ is the column number density of aggregates per unit mass and $h_d(r, m)$ is the scale height of aggregates at orbital radius r and with mass m (Dubrulle et al. 1995). This approach is valid if the coagulation timescale is longer than the settling/diffusion timescale, which is true except for very tiny particles with short collision times (Zsom et al. 2011).

The evolution of the radial size distribution $\mathcal{N}(r, m)$ is given by the vertically integrated advection–coagulation equation, which reads (Brauer et al. 2008a)

$$\frac{\partial\mathcal{N}(r,m)}{\partial t} = \frac{1}{2}\int_0^m K(r,m',m-m')\mathcal{N}(r,m')\mathcal{N}(r,m-m')dm' - \mathcal{N}(r,m)\int_0^\infty K(r,m,m')\mathcal{N}(r,m')dm' - \frac{1}{r}\frac{\partial}{\partial r}\left[rv_r(r,m)\mathcal{N}(r,m)\right], \quad (1)$$

where v_r is the radial drift velocity and K is the vertically integrated collision rate coefficient given by

$$K(r,m_1,m_2) = \frac{\sigma_\mathrm{coll}}{2\pi h_{d,1}h_{d,2}}\int_{-\infty}^{\infty}\Delta v\exp\left(-\frac{z^2}{2h_{d,12}^2}\right)dz. \quad (2)$$

Here, σ_coll is the collisional cross section, $h_{d,1}$ and $h_{d,2}$ are the scale heights of the colliding aggregates 1 and 2, Δv is the collision velocity, and $h_{d,12} = (h_{d,1}^{-2}+h_{d,2}^{-2})^{-1/2}$. As mentioned in Section 1, we neglect electrostatic and gravitational interactions between colliding aggregates and assume perfect sticking upon collision. Thus, the collisional cross section is simply given by $\sigma_\mathrm{coll} = \pi(a_1+a_2)^2$, where a_1 and a_2 are the radii of the colliding aggregates. The validity of neglecting fragmentation will be discussed in Section 5.3.

The dust scale height h_d in the sedimentation–diffusion equilibrium has been analytically obtained by Youdin & Lithwick (2007). For turbulence of $t_L = \Omega^{-1}$ and $D_g = \alpha_D c_s^2/\Omega$, it is given by

$$h_d = h_g\left(1+\frac{\Omega t_s}{\alpha_D}\frac{1+2\Omega t_s}{1+\Omega t_s}\right)^{-1/2}, \quad (3)$$

where t_s is the stopping time of the aggregates. We use this expression in this study.

For the stopping time, we use

$$t_s = \begin{cases} t_s^{(\mathrm{Ep})} \equiv \dfrac{3m}{4\rho_g v_\mathrm{th}A}, & a < \dfrac{9}{4}\lambda_\mathrm{mfp}, \\ t_s^{(\mathrm{St})} \equiv \dfrac{4a}{9\lambda_\mathrm{mfp}}t_s^{(\mathrm{Ep})}, & a > \dfrac{9}{4}\lambda_\mathrm{mfp}, \end{cases} \quad (4)$$

where $v_\mathrm{th} = \sqrt{8/\pi}c_s$ and λ_mfp are the thermal velocity and mean free path of gas particles, respectively, and A is the projected area of the aggregate. The mean free path is related to the gas density as

$$\lambda_\mathrm{mfp} = \frac{m_g}{\sigma_\mathrm{mol}\rho_g}, \quad (5)$$

where $\sigma_\mathrm{mol} = 2\times10^{-15}\,\mathrm{cm^2}$ is the collisional cross section of gas molecules. Our gas disk model gives $\lambda_\mathrm{mfp} = 120(r/5\,\mathrm{AU})^{11/4}\,\mathrm{cm}$ at the midplane. Equation (4) satisfies the requirement that the stopping time must obey Epstein's law $t_s = t_s^{(\mathrm{Ep})}$ at $a \ll \lambda_\mathrm{mfp}$ and Stokes' law $t_s = t_s^{(\mathrm{St})}$ at $a \gg \lambda_\mathrm{mfp}$, respectively. Since $t_s^{(\mathrm{St})} \propto at_s^{(\mathrm{Ep})}$, an aggregate growing in the Stokes regime decouples from the gas motion more quickly than

in the Epstein regime. In reality, Stokes' law breaks down when the particle Reynolds number (the Reynolds number of flow around the particle) is much greater than unity, but we neglect this in our simulations for simplicity. We will discuss this point further in Section 5.1.

The radial drift velocity is taken as

$$v_r = -\frac{2\Omega t_s}{1+(\Omega t_s)^2}\eta v_K, \tag{6}$$

where

$$2\eta \equiv -\left(\frac{c_s}{v_K}\right)^2 \frac{\partial \ln\left(\rho_g c_s^2\right)}{\partial \ln r} \tag{7}$$

is the ratio of the pressure gradient force to the stellar gravity in the radial direction and $v_K = r\Omega$ is the Kepler velocity (Adachi et al. 1976; Weidenschilling 1977; Nakagawa et al. 1986). The radial drift speed has a maximum ηv_K, which is realized when $\Omega t_s = 1$. In our disk model, η scales with r as $\eta = 4.0 \times 10^{-3}(r/5\,\mathrm{AU})^{1/2}$, and the maximum inward speed $\eta v_K = 54\,\mathrm{m\,s^{-1}}$ is independent of r. Since η is proportional to the gas temperature, the maximum drift speed would be somewhat lower in colder disk models (Kusaka et al. 1970; Hirose & Turner 2011). Equation (6) neglects the frictional backreaction from dust to gas assuming that the local dust-to-gas mass ratio is much lower than unity or the stopping time of aggregates dominating the dust mass is much longer than Ω^{-1}. We examine the validity of this assumption in Section 5.2.1.

In this paper, we also consider the collisional evolution of aggregate porosities. We treat the mean volume $V = (4\pi/3)a^3$ of aggregates with orbital radius r and mass m as a time-dependent quantity. The evolutionary equation for $V(r,m)$ is given by

$$\begin{aligned}\frac{\partial(V\mathcal{N})}{\partial t} = &\frac{1}{2}\int_0^m [V_{1+2}K](r,m',m-m')\\ &\times \mathcal{N}(r,m')\mathcal{N}(r,m-m')dm'\\ &- V(r,m)\mathcal{N}(r,m)\int_0^\infty K(r,m,m')\mathcal{N}(r,m')dm'\\ &- \frac{1}{r}\frac{\partial}{\partial r}[r v_r(r,m)V(r,m)\mathcal{N}(r,m)],\end{aligned} \tag{8}$$

where

$$\begin{aligned}[V_{1+2}K](r,m_1,m_2) = &\frac{\sigma_{\mathrm{coll}}}{2\pi h_{d,1}h_{d,2}}\int_{-\infty}^{\infty} V_{1+2}\Delta v\\ &\times \exp\left(-\frac{z^2}{2h_{d,12}^2}\right)dz\end{aligned} \tag{9}$$

with V_{1+2} being the volume of merged aggregates (described in Section 2.3.1). Equation (8) is identical to the original evolutionary equation for V derived by Okuzumi et al. (2009, their Equation (16)) except that here we take the vertical integration of the equation and take into account the radial advection of dust. In deriving Equation (8), we have assumed that the dispersion of the volume is sufficiently narrow at every r and m (see Okuzumi et al. 2009). This "volume-averaging" approximation allows us to follow the porosity evolution of aggregates without solving higher-order moment equations for the volume, and hence with small computational costs. This approximation is valid unless the porosity distribution at fixed r and m is significantly broadened by, e.g., collisional fragmentation cascades (Okuzumi et al. 2009).

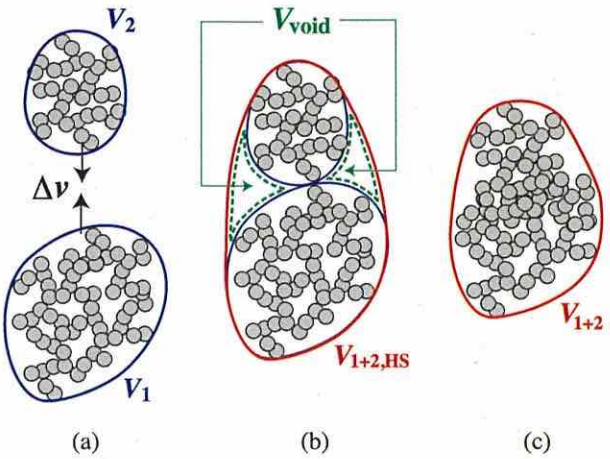

Figure 1. Schematic illustration of our porosity change model. Porous aggregates with volumes V_1 and V_2 (a) before contact, and (b) just after contact. At this moment, the volume of the new aggregate is given by $V_{1+2,\mathrm{HS}} = V_1 + V_2 + V_{\mathrm{void}}$, where $V_{\mathrm{void}} = V_{\mathrm{void}}(V_1, V_2)$ is the volume of newly formed voids (Equation (11)). If the collision energy E_{imp} is much smaller than the rolling energy E_{roll}, the final volume of the new aggregate is equal to $V_{1+2,\mathrm{HS}}$. (c) If $E_{\mathrm{imp}} \gtrsim E_{\mathrm{roll}}$, collisional compression occurs. In this case, the final volume $V_{1+2}(<V_{1+2,\mathrm{HS}})$ depends on E_{imp}.

(A color version of this figure is available in the online journal.)

2.3. Dust Model

2.3.1. Porosity Change Recipe

The functional form of V_{1+2} determines the evolution of aggregate porosities in our simulation. In this study, we give V_{1+2} as a function of the volumes of the colliding aggregates, $V_1 = V(r,m_1)$ and $V_2 = V(r,m_2)$, and the impact energy $E_{\mathrm{imp}} = m_1 m_2 \Delta v^2/[2(m_1+m_2)]$. Before introducing the final form of our porosity change recipe (Equation (15)), we briefly review recent N-body collision experiments on which our recipe is based.

Collisional compression depends on the ratio between E_{imp} and the "rolling energy" E_{roll} (Dominik & Tielens 1997; Blum & Wurm 2000; Wada et al. 2007). The rolling energy is defined as the energy needed for one monomer to roll over 90° on the surface of another monomer in contact (Dominik & Tielens 1997). When $E_{\mathrm{imp}} \ll E_{\mathrm{roll}}$, two aggregates stick without visible restructuring (the so-called hit-and-stick collision; see Figure 1(b)). In this case, the volume of the merged aggregate is determined in a geometric manner, i.e., independently of E_{imp}. When $E_{\mathrm{imp}} \gtrsim E_{\mathrm{roll}}$, internal restructuring occurs through inelastic rolling among constituent monomers (Dominik & Tielens 1997; see also Figure 1(c)). In this case, the final volume V_{1+2} depends on E_{imp} as well as on V_1 and V_2.

For hit-and-stick collisions ($E_{\mathrm{imp}}/E_{\mathrm{roll}} \to 0$), Okuzumi et al. (2009) obtained an empirical formula for V_{1+2},

$$V_{1+2} = V_{1+2,\mathrm{HS}} \equiv V_1 + V_2 + V_{\mathrm{void}}, \tag{10}$$

where V_1 and $V_2(\leqslant V_1)$ are the volumes of the two colliding aggregates, and

$$V_{\rm void} = \min\left\{0.99 - 1.03\ln\left(\frac{2}{V_1/V_2+1}\right), 6.94\right\} V_2 \quad (11)$$

is the volume of the voids created in the collision (see Figure 1(b)). For $V_1 \approx V_2$, the void volume is approximately equal to V_1, and hence the volume of the new aggregate is approximately given by $V_{1+2} \approx 3V_1$. This is equivalent to a fractal relation $V \propto m^{3/d_f}$, where $d_f \approx 2$ (see Section 4.2.1 of Okuzumi et al. 2009).

In the limit of $E_{\rm imp} \gg E_{\rm roll}$ and for a head-on collision of equal-sized aggregates ($V_1 = V_2$), Suyama et al. (2008) showed that V_{1+2} obeys the relation

$$E_{\rm imp} = -\int_{2^{6/5}V_1}^{V_{1+2}} P(V)dV. \quad (12)$$

Here, $P \equiv -dE_{\rm imp}/dV$ is the dynamic compression strength of the merged aggregate given by (Wada et al. 2008)

$$P(V) = 2\left(\frac{5}{3}\right)^6 \frac{bE_{\rm roll}}{V_0}\left(\frac{\rho_{\rm int}(V)}{\rho_0}\right)^{13/3} N_{1+2}^{2/3}, \quad (13)$$

where $b = 0.15$ is a dimensionless fitting parameter, $V_0 = m_0/\rho_0 = (4\pi/3)a_0^3$ is the monomer volume, $N_{1+2} = 2m_1/m_0$ is the number of monomers contained in the merged aggregate, and $\rho_{\rm int} = 2m_1/V$ is the internal density of the merged aggregate. If we substitute Equation (13) into Equation (12), we obtain the equation that explicitly gives V_{1+2} as a function of $E_{\rm roll}$ and V_1,

$$V_{1+2} = \left[\frac{(3/5)^5 E_{\rm imp}}{N_{1+2}^5 bE_{\rm roll}V_0^{10/3}} + \left(2V_1^{5/6}\right)^{-4}\right]^{-3/10}. \quad (14)$$

This equation basically expresses the energy balance in collisional compression, but some caution is needed in interpreting it. Firstly, the initial state for the compression is chosen to be $V = 2^{6/5}V_1$, although the volume just after contact is $V = 3V_1$ (see above). This is based on the fact that compaction from $V = 3V_1$ to $V = 2^{6/5}V_1$ occurs through partial compression of the new voids, which requires little energy (Suyama et al. 2008). Secondly, the dynamic compression strength P depends on mass N_{1+2} as well as on internal density $\rho_{\rm int}$, meaning that P is not an intensive variable. This is due to the fact that dynamically compressed parts in the merged aggregate have a fractal structure with a fractal dimension of 2.5 (Wada et al. 2008). In fact, Equations (12)–(14) are more naturally described in terms of variables in the 2.5-dimensional space, $V_f \propto a^{5/2}$, $\rho_f \propto N_{1+2}/V_f$, and $P_f = -dE_{\rm imp}/dV_f$ (see Wada et al. 2008; Suyama et al. 2008). An important point here is that aggregates become stronger and stronger against dynamic compression as they grow because of the $N_{1+2}^{2/3}$ factor in P.

Equations (10) and (14) express how the volume of the merged aggregate is determined in the limits of $E_{\rm imp} \ll E_{\rm roll}$ and $E_{\rm imp} \gg E_{\rm roll}$, respectively. To properly take into account the intermediate cases ($E_{\rm imp} \sim E_{\rm roll}$), we adopt an updated analytic formula given recently by Suyama et al. (2012). This reads

$$V_{1+2} = \begin{cases} \left[\left(1 - \dfrac{E_{\rm imp}}{3bE_{\rm roll}}\right)V_{1+2,\rm HS}^{5/6} + \dfrac{E_{\rm imp}}{3bE_{\rm roll}}\left(V_1^{5/6}+V_2^{5/6}\right)\right]^{6/5} \\ \quad \left(\text{if } V_{1+2,\rm HS}^{5/6} > V_1^{5/6}+V_2^{5/6} \text{ and } E_{\rm imp} < 3bE_{\rm roll}\right), \\ \left[\dfrac{(3/5)^5(E_{\rm imp}-3bE_{\rm roll})}{N_{1+2}^5 bE_{\rm roll}V_0^{10/3}} + \left(V_1^{5/6}+V_2^{5/6}\right)^{-4}\right]^{-3/10} \\ \quad \left(\text{if } V_{1+2,\rm HS}^{5/6} > V_1^{5/6}+V_2^{5/6} \text{ and } E_{\rm imp} > 3bE_{\rm roll}\right), \\ \left[\dfrac{(3/5)^5 E_{\rm imp}}{N_{1+2}^5 bE_{\rm roll}V_0^{10/3}} + V_{1+2,\rm HS}^{-10/3}\right]^{-3/10} \\ \quad \left(\text{if } V_{1+2,\rm HS}^{5/6} < V_1^{5/6}+V_2^{5/6}\right), \end{cases} \quad (15)$$

where N_{1+2} is now defined as $(m_1+m_2)/m_0$. Note that this equation reduces to Equation (10) when $E_{\rm imp} \ll E_{\rm roll}$, and to Equation (14) when $V_1 = V_2$ and $E_{\rm imp} \gg E_{\rm roll}$. Suyama et al. (2012) derived Equation (15) by taking into account small energy losses in the partial compression of the new voids. In addition, unlike Equation (14), Equation (15) takes into account the cases where colliding aggregates have different volumes and masses ($V_1 \neq V_2$, $m_1 \neq m_2$). Suyama et al. (2012) confirmed that Equation (15) reproduces the results of numerical collision experiments within an error of 20% as long as the mass ratio $m_2/m_1(\leqslant 1)$ between the colliding aggregates is larger than 1/16.

We comment on three important caveats regarding our porosity recipe. Firstly, Equation (15) is still untested for cases where colliding aggregates have very different sizes ($m_2/m_1 < 1/16$). Therefore, the validity of using Equation (15) is at present only guaranteed for the case where "similar-sized" ($m_2/m_1 \gtrsim 1/16$) collisions dominate the growth of aggregates. We will carefully check this validity in Section 3.2. Secondly, Equation (15) ignores offset collisions, in which a considerable fraction of the impact energy is spent for stretching rather than compaction (Wada et al. 2007; Paszun & Dominik 2009). For this reason, Equation (15) underestimates the porosity increase upon collision. Thirdly, we do not consider non-collisional compression (e.g., static compression due to gas drag forces), which could contribute to the compaction of very large aggregates. We will discuss the second and third points in more detail in Section 5.4.

In addition to V, we need to know the projected area A of aggregates to calculate the stopping time t_s. Unfortunately, a naive relation $A = \pi a^2$ breaks down when the fractal dimension of the aggregate is less than 2, since πa^2 increases faster than mass for this case while A does not. A projected area growing faster than mass means a coupling to the gas becoming stronger and stronger as the aggregate grows, which is clearly unrealistic. To avoid this, we use an empirical formula by Okuzumi et al. (2009) that well reproduces the mean projected area $\overline{A}$ of aggregates with monomer number $N = m/m_0$ and radius a for both fractal and compact aggregates. With this formula, all aggregates in our simulations are guaranteed to decouple from the gas as they grow. We remark that this treatment is only relevant for fractal aggregates with $d_f \lesssim 2$; for more compact aggregates, the empirical formula reduces to the usual relation $A \approx \pi a^2$.

The rolling energy $E_{\rm roll}$ has so far not been measured for submicron-sized icy particles, but can be estimated in the following way. It is anticipated by microscopic friction theory (Dominik & Tielens 1995) that the critical rolling

force $F_{\rm roll} \equiv E_{\rm roll}/(\pi a_0/2)$ is a material constant (i.e., $E_{\rm roll}$ is proportional to the monomer radius a_0). A rolling force of $F_{\rm roll} = (1.15 \pm 0.24) \times 10^{-3}$ dyn has recently been measured for micron-sized ice particles (Gundlach et al. 2011). Given that $F_{\rm roll}$ is independent of a_0, the measured force implies the rolling energy of $E_{\rm roll} = (\pi a_0/2) F_{\rm roll} \approx 1.8 \times 10^{-8}$ erg for $a_0 = 0.1\ \mu$m. We use this value in our simulations.

2.3.2. Collision Velocity

We consider Brownian motion, radial and azimuthal drift, vertical settling, and turbulence as sources of the collision velocity, and give the collision velocity Δv as the root sum square of these contributions,

$$\Delta v = \sqrt{(\Delta v_B)^2 + (\Delta v_r)^2 + (\Delta v_\phi)^2 + (\Delta v_z)^2 + (\Delta v_t)^2}, \quad (16)$$

where Δv_B, Δv_r, Δv_ϕ, Δv_z, and Δv_t are the relative velocities induced by Brownian motion, radial drift, azimuthal drift, vertical settling, and turbulence, respectively.

The Brownian-motion-induced velocity is given by

$$\Delta v_B = \sqrt{\frac{\pi m_1 m_2}{8(m_1+m_2) k_{\rm B} T}}, \quad (17)$$

where m_1 and m_2 are the masses of the two colliding aggregates.

The relative velocity due to radial drift is given by $\Delta v_r = |v_r(t_{s,1}) - v_r(t_{s,2})|$, where $t_{s,1}$ and $t_{s,2}$ are the stopping times of the colliding aggregates, and v_r is the radial velocity given by Equation (6). Similarly, the relative velocity due to differential azimuthal motion is given by $\Delta v_\phi = |v'_\phi(t_{s,1}) - v'_\phi(t_{s,2})|$, where

$$v'_\phi = -\frac{\eta v_K}{1 + (\Omega t_s)^2} \quad (18)$$

is the deviation of the azimuthal velocity from the local Kepler velocity (Adachi et al. 1976; Weidenschilling 1977; Nakagawa et al. 1986). Here, we have neglected the backreaction from dust to gas as we did for the radial velocity (see Sections 2.3.2 and 5.2.1).

For the differential settling velocity, we assume $\Delta v_z = |v_z(t_{s,1}) - v_z(t_{s,2})|$, where

$$v_z = -\frac{\Omega^2 t_s z}{1 + \Omega t_s}. \quad (19)$$

Equation (19) reduces to the terminal settling velocity $v_z = -\Omega^2 t_s z$ in the strong coupling limit $\Omega t_s \ll 1$, and to the amplitude of the vertical oscillation velocity at $\Omega t_s \gg 1$ (Brauer et al. 2008a).

For the turbulence-driven relative velocity, we use an analytic formula for Kolmogorov turbulence derived by Ormel & Cuzzi (2007, their Equation (16)). This analytic formula has three limiting expressions (Equations (27)–(29) of Ormel & Cuzzi 2007):

$$\Delta v_t \approx \begin{cases} \delta v_g {\rm Re}_t^{1/4} \Omega |t_{s,1} - t_{s,2}|, & t_{s,1} \ll t_\eta, \\ (1.4 \ldots 1.7) \times \delta v_g \sqrt{\Omega t_{s,1}}, & t_\eta \ll t_{s,1} \ll \Omega^{-1}, \\ \delta v_g \left(\dfrac{1}{1+\Omega t_{s,1}} + \dfrac{1}{1+\Omega t_{s,2}} \right)^{1/2}, & \Omega t_{s,1} \gg 1, \end{cases} \quad (20)$$

where ${\rm Re}_t$ is the turbulent Reynolds number, $t_\eta = {\rm Re}_t^{-1/2} t_L$ is the turnover time of the smallest eddies, and the numerical prefactor $(1.4 \ldots 1.7)$ in the second equality depends on the ratio between the stopping times, $t_{s,2}/t_{s,1}$. The turbulent Reynolds number is given by ${\rm Re}_t = D_g/\nu_{\rm mol}$, where $\nu_{\rm mol} = v_{\rm th} \lambda_{\rm mfp}/2$ is the molecular viscosity. For $t_{s,1} \sim t_{s,2}$, the maximum induced velocity is $\Delta v_t \approx \delta v_g$, which is reached when $\Omega t_{s,1} \approx 1$.

When two colliding aggregates belong to the Epstein regime and their stopping times are much shorter than $t_\eta (\ll \Omega^{-1})$, the relative velocity driven by sedimentation and turbulence is approximately proportional to the difference between the mass-to-area ratios m/A of two colliding aggregates. In this case, as pointed out by Okuzumi et al. (2011a), the dispersion of the mass-to-area ratio becomes important for fractal aggregates of $d_f \lesssim 2$, since the mean mass-to-area ratio of the aggregates approaches a constant, and hence the difference in $m/\overline{A}(m)$ vanishes. To take into account the dispersion effect, we evaluate the differential mass-to-area ratio as $|\Delta(m/A)|^2 = |m_1/\overline{A}_1 - m_2/\overline{A}_2|^2 + \epsilon^2[(m_1/\overline{A}_1)^2 + (m_2/\overline{A}_2)^2]$, where $\overline{A}_j = \overline{A}(m_j)$ $(j = 1, 2)$ are the mean projected area of aggregates with mass m_j (see Section 2.3.1) and ϵ is the standard deviation of the mass-to-area ratio divided by the mean (for the derivation, see the Appendix of Okuzumi et al. 2011a). We assume $\epsilon = 0.1$ in accordance with the numerical estimate by Okuzumi et al. (2011a).

2.4. Numerical Method

We solve Equations (1) and (8) numerically with an explicit time-integration scheme and a fixed-bin method. The radial domain is taken to be outside the snow line, $3\ {\rm AU} \leqslant r \leqslant 150\ {\rm AU}$, discretized into 100 rings with an equal logarithmic width $\Delta \ln(r[{\rm AU}]) = (\ln 150 - \ln 3)/100$. The advection terms are calculated by the spatially first-order upwind scheme. We impose the outflow and zero-flux boundary conditions at the innermost and outermost radii ($r = 3\ {\rm AU}$ and 150 AU), respectively; thus, the total dust mass inside the domain is a decreasing function of time. Our numerical results are unaffected by the choice of the boundary condition at the outermost radius, since dust growth at this location is too slow to cause appreciable radial drift within the calculated time. The coagulation terms are calculated by the method given by Okuzumi et al. (2009). Specifically, at the center of each radial ring we divide the mass coordinate into linearly spaced bins $m_k = k m_0 (k = 1, 2, \ldots, N_{\rm bd})$ for $m \leqslant N_{\rm bd} m_0$ and logarithmically spaced bins $m_k = m_{k-1} 10^{1/N_{\rm bd}} (k = N_{\rm bd}+1, \ldots)$ for $m > N_{\rm bd} m_0$, where $N_{\rm bd}$ is an integer. We adopt $N_{\rm bd} = 40$; as shown by Okuzumi et al. (2009), the calculation results converge well as long as $N_{\rm bd} \geqslant 40$. The time increment Δt is adjusted at every time step so that the fractional decreases in $\mathcal{N}$ and $V\mathcal{N}$ fall below 0.5 (i.e., $\Delta t < -0.5(\partial \ln \mathcal{N}/\partial t)^{-1}$ and $\Delta t < -0.5(\partial \ln V\mathcal{N}/\partial t)^{-1}$) at all bins.

3. RESULTS

3.1. Compact Aggregation

To begin with, we show the result of compact aggregation. In this simulation, we fixed the internal density $\rho_{\rm int} \equiv m/V$ of the aggregates to the material density $\rho_0 = 1.4\ {\rm g\ cm^{-3}}$, and solved only the evolutionary equation for the radial size distribution $\mathcal{N}(r, m)$ (Equation (1)), as in previous studies (e.g., Brauer et al. 2008a). Figure 2 shows the snapshots of the radial size distribution at different times. Here, the distribution is represented by the dust surface density per decade of aggregate mass, $\Delta\Sigma_d/\Delta \log m \equiv \ln(10) m^2 \mathcal{N}(r, m)$. At each orbital radius,

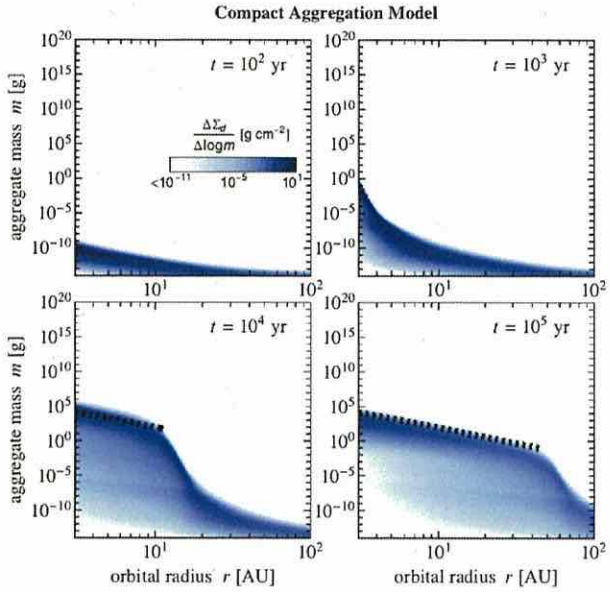

Figure 2. Aggregate size distribution $\Delta\Sigma_d/\Delta \log m$ at different times t for the compact aggregation model ($\rho_{\rm int} = 1.4\,{\rm g\,cm^{-3}}$) as a function of orbital radius r and aggregate mass m. The dotted lines mark the aggregate size at which Ωt_s exceeds 0.1.

(A color version of this figure is available in the online journal.)

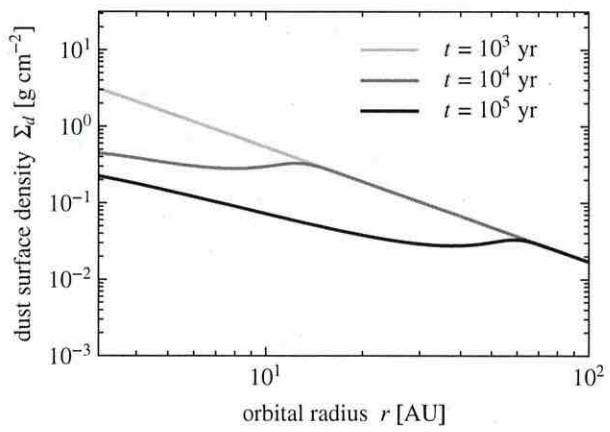

Figure 3. Radial profiles of the total dust surface density Σ_d at different times for the compact aggregation model ($\rho_{\rm int} = 1.4\,{\rm g\,cm^{-3}}$).

dust growth proceeds without significant radial drift until the stopping time of the aggregates reaches $\Omega t_s \sim 0.1$ (the dotted lines in Figure 2). However, as the aggregates grow, the radial drift becomes faster and faster, and further growth becomes limited only along the line $\Omega t_s \sim 0.1$ on the r–m plane. Figure 3 shows the evolution of the total dust surface density $\Sigma_d \equiv \int m\mathcal{N} dm = \int (\Delta\Sigma_d/\Delta \log m) d \log m$. We see that a significant amount of dust has been lost from the planet-forming region $r \lesssim 30$ AU within 10^5 yr. In this region, the dust surface density[4] scales as r^{-1}, and hence the dust-to-gas surface density ratio $\propto r^{-1}/\Sigma_g \propto r^{1/2}$ decreases toward the central star.

[4] It can be analytically shown (Birnstiel et al. 2012) that the dust surface density profile obeys a scaling $\Sigma_d \propto \sqrt{\Sigma_g/(r^2\Omega)}$ ($\propto r^{-1}$ for $\Sigma_g \propto r^{-3/2}$) when radial drift balances with turbulence-driven growth.

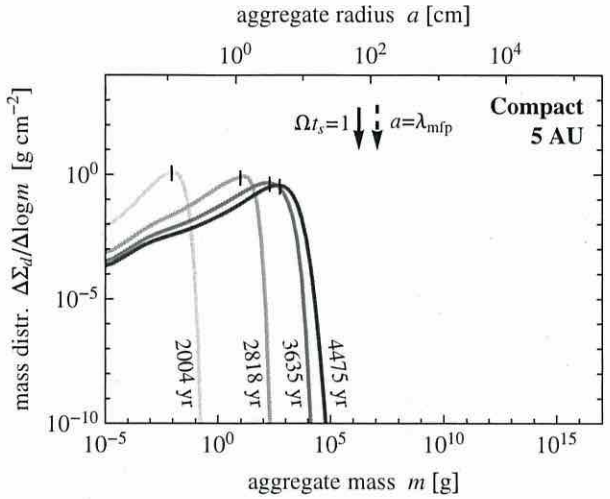

Figure 4. Aggregate size distribution $\Delta\Sigma_d/\Delta \log m$ at $r = 5$ AU and $t = 2000$–4470 yr for the compact aggregation model. The dashed and solid arrows indicate the aggregate sizes at which $a = \lambda_{\rm mfp}$ and $\Omega t_s = 1$, respectively. Shown at the top of the panel is the aggregate radius a. The vertical bars indicate the weighted average mass $\langle m \rangle_m$ (Equation (21)).

Figure 4 shows the evolution of the dust size distribution observed at $r = 5$ AU. Here, in order to characterize the typical aggregate size at each evolutionary stage, we introduce the weighted average mass $\langle m \rangle_m$ defined by

$$\langle m \rangle_m \equiv \frac{\int m^2 \mathcal{N} dm}{\int m \mathcal{N} dm} = \frac{1}{\Sigma_d} \int m \frac{\Delta\Sigma_d}{\Delta \log m} d \log m. \quad (21)$$

The weighted average mass approximately corresponds to the aggregate mass at the peak of $\Delta\Sigma_d/\Delta \log m$ (see, e.g., Ormel et al. 2007; Okuzumi et al. 2011a). In Figure 4, the weighted average mass at each time is indicated by the short vertical line. At $r = 5$ AU, the growth–drift equilibrium is reached at $t \approx 4000$ yr, and the typical size of the aggregates is $\langle m \rangle_m \approx 500$ g in mass ($\approx$4 cm in radius, $\approx 0.07\Omega^{-1}$ in stopping time). Note that the final aggregate radius is much smaller than the mean free path $\lambda_{\rm mfp}$ of gas molecules (the dashed arrow in Figure 4), which means that the gas drag onto the aggregates is determined by Epstein's law. As we will see in the following, porosity evolution allows aggregates to reach the Stokes drag regime at much smaller Ωt_s.

3.2. Porous Aggregation

Now we show how porosity evolution affects dust evolution. Here, we solve the evolutionary equation for $V(r, m)$ (Equation (8)) simultaneously with that for $\mathcal{N}(r, m)$ (Equation (1)). The result is shown in Figure 5, which displays the snapshots of the aggregate size distribution $\Delta\Sigma_d/\Delta \log m$ and internal density $\rho_{\rm int} = m/V$ at different times t as a function of r and m. The evolution of the total dust surface density Σ_d is shown in Figure 6.

The left four panels of Figure 5 show how the radial size distribution evolves in the porous aggregation. At $t < 10^3$ yr, the evolution is qualitatively similar to that in compact aggregation (Section 3.1). However, in later stages, the evolution is significantly different. We observe that aggregates in the inner region of the disk ($r < 10$ AU) undergo rapid growth and eventually overcome the radial drift barrier lying at $\Omega t_s \sim 1$

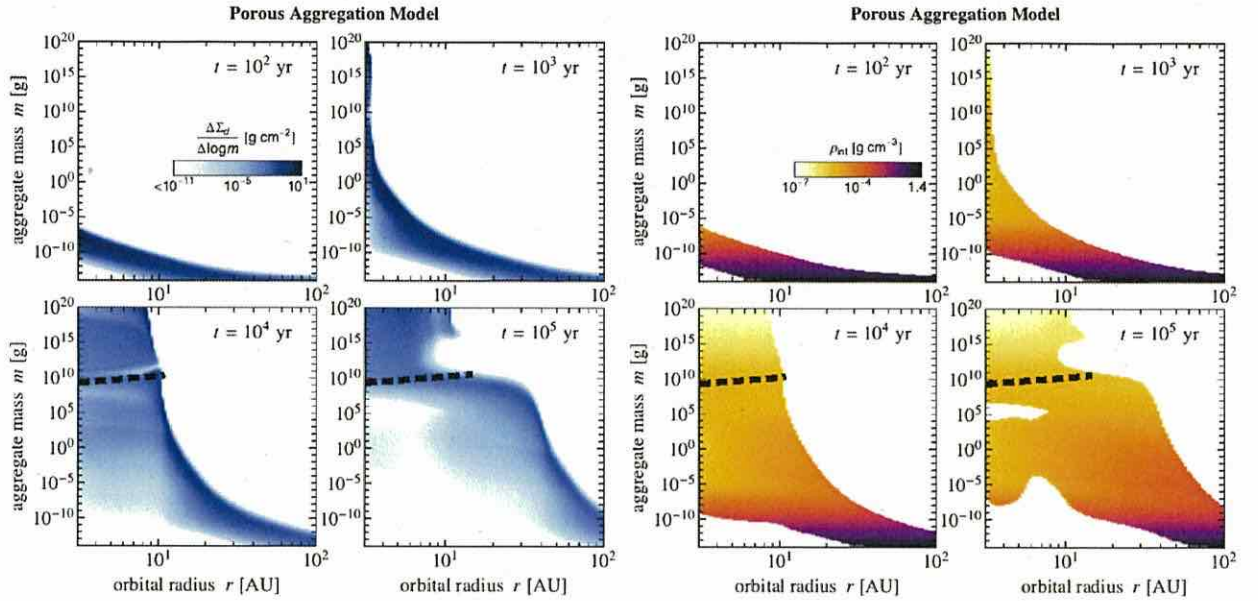

Figure 5. Aggregate size distribution $\Delta\Sigma_d/\Delta\log m$ (left four panels) and internal density $\rho_{\rm int} = m/V$ (right four panels) at different times t for the porous aggregation model as a function of orbital radius r and aggregate mass m. The dashed lines mark the aggregate size at which Ωt_s exceeds unity.
(A color version of this figure is available in the online journal.)

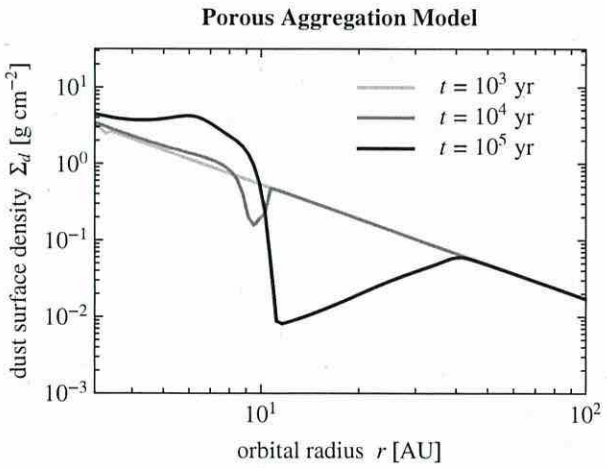

Figure 6. Radial profiles of the total dust surface density Σ_d at different times for the porous aggregation model.

(dashed lines in Figure 5) within $t \sim 10^4$ yr. At this stage, the radial profile of the total dust surface Σ_d is hardly changed from the initial profile, as seen in Figure 6. In the outer region ($r > 10$ AU), aggregates do drift inward before they reach $\Omega t_s \sim 1$ as in the compact aggregation model. However, unlike in the compact aggregation, the inward drift results in the pileup of dust materials in the inner region ($r \approx 4$–9 AU) rather than the loss of them from outside the snow line (see Figure 6). This occurs because most of the drifting aggregates are captured by aggregates that have already overcome the drift barrier. As a result, the dust-to-gas mass ratio in the inner regions is enhanced by a factor of several in 10^5 yr.

The right four panels of Figure 5 show the evolution of the internal density $\rho_{\rm int} = m/V$ as a function of r and m. The first thing to note is that the dust particles grow into low-density objects at every location until their internal density reaches $\rho_{\rm int} \sim 10^{-5}$–$10^{-3}$ g cm^{-3}. In this stage, the internal density decreases as $\rho_{\rm int} \approx (m/m_0)^{-1/2}\rho_0$, meaning that the dust particles grow into fractal aggregates with the fractal dimension $d_f \approx 2$ (Okuzumi et al. 2009). The fractal growth generally occurs in early growth stages where the impact energy is too low to cause collisional compression, i.e., $E_{\rm imp} \ll E_{\rm roll}$ (e.g., Blum 2004; Ormel et al. 2007; Zsom et al. 2010). At $m \sim 10^{-4}$–10^{-6} g, the fractal growth stage terminates, followed by the stage where collisional compression becomes effective ($E_{\rm imp} \gg E_{\rm roll}$). In this late stage, the internal density decreases more slowly or is kept at a constant value depending on the orbital radius. We will examine the density evolution in more detail in Section 3.2.2.

Figure 7 shows the evolution of the mass distribution function at $r = 5$ AU during $t \approx 1200$–2500 yr. The evolution of the weighted average mass $\langle m\rangle_m$ is shown in Figure 8. It is seen that the acceleration of the growth begins when the aggregate size a exceeds the mean free path of gas molecules, $\lambda_{\rm mfp}$ (the dashed arrow in Figure 7). This suggests that the acceleration is due to the change in the aerodynamical property of the aggregates. At $a \approx \lambda_{\rm mfp}$, the gas drag onto the aggregates begins to obey Stokes' law. In the Stokes regime, the stopping time t_s of aggregates increases rapidly with size (see Section 2.2). This causes the quick growth of the aggregates since the relative velocity between aggregates increases with t_s (as long as $\Omega t_s < 1$). As a result of the growth acceleration, the aggregates grow from $a \approx \lambda_{\rm mfp}$ to $\Omega t_s \approx 1$ within 300 yr, which is short enough for them to break through the radial drift barrier.

The decrease in the internal density plays an important role in the growth acceleration. More precisely, the low internal density allows the aggregates to reach $a \approx \lambda_{\rm mfp}$ at early growth stages, i.e., at small Ωt_s. In fact, the growth acceleration was not observed in the compact aggregation, since the aggregate size is smaller than the mean free path at *all* $\Omega t_s < 1$ (see Figure 4). A more rigorous explanation for this will be given in Section 4.

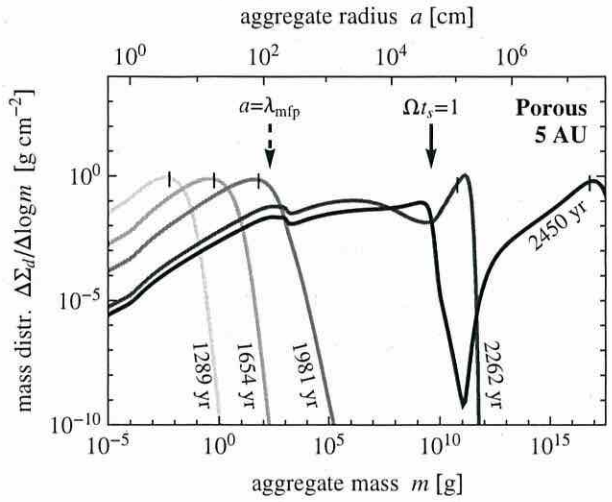

Figure 7. Aggregate mass distribution $\Delta\Sigma_d/\Delta\log m$ at $r = 5$ AU and $t = 1289$–2450 yr for the porous aggregation model. The dashed and solid arrows indicate the sizes at which $a = \lambda_{\rm mfp}$ and $\Omega t_s = 1$, respectively. Shown at the top of the panel is the aggregate radius a measured at $t = 2450$ yr. The vertical bars indicate the weighted average mass $\langle m\rangle_m$ (Equation (21)).

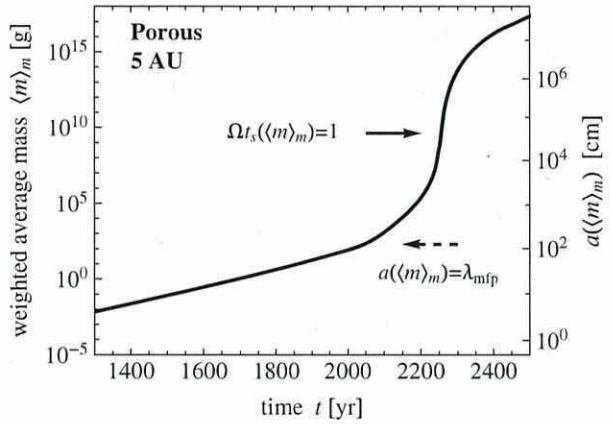

Figure 8. Weighted average mass $\langle m\rangle_m$ (Equation (21)) at $r = 5$ AU as a function of time t for the porous aggregation model. Shown at the right of the panel is the corresponding aggregate radius $a(\langle m\rangle_m)$. The dashed and solid arrows indicate the sizes at which $a(\langle m\rangle_m) = \lambda_{\rm mfp}$ and $\Omega t_s(\langle m\rangle_m) = 1$, respectively.

3.2.1. Projectile Mass Distribution

As noted in Section 2.3.1, our porosity change model has only been tested for collisions between similar-sized aggregates. To check the validity of using this model, we introduce the projectile mass distribution function (Okuzumi et al. 2009):

$$C_{m_t}(m_p) \equiv \frac{m_p K(m_p, m_t)\mathcal{N}(m_p)}{\int_0^{m_t} m'_p K(m'_p, m_t)\mathcal{N}(m'_p)dm'_p}, \quad m_p \leqslant m_t, \tag{22}$$

which is normalized so that $\int_0^{m_t} C_{m_t}(m_p)dm_p = 1$. The denominator of $C_{m_t}(m_p)$ is equal to the growth rate $t_{\rm grow}^{-1} \equiv d\ln m_t/dt$ of a target having mass m_t (see Okuzumi et al. 2009). Hence, the quantity $C_{m_t}(m_p)dm_p$ measures the contribution of projectiles within mass range $[m_p, m_p + dm_p]$ to the growth of the target.

Figure 9 shows the projectile mass distribution per unit $\ln m_p$, $m_p C_{m_t}(m_p)$, for targets with mass $m_t = \langle m\rangle_m$ at $r = 5$ AU and at different t. We see that the growth of

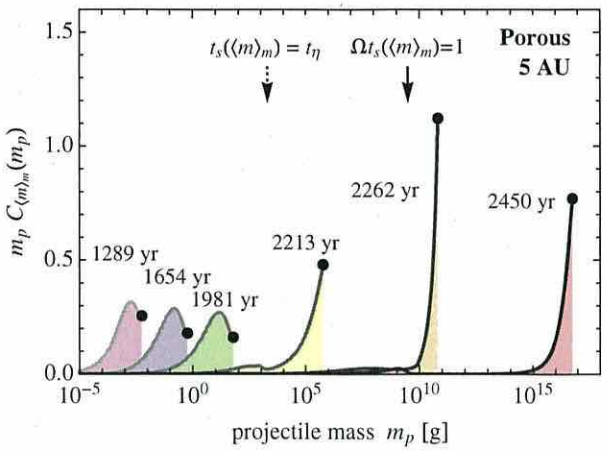

Figure 9. Normalized projectile mass distribution per unit logarithmic projectile mass, $m_p C_{m_t}(m_p)$, for a target with mass $m_t = \langle m\rangle_m$ at different times $t(=1289$–2450 yr) at $r = 5$ AU for the porous aggregation model (see Equation (22) for the definition of $C_{m_t}(m_p)$). The filled circles show the values for equal-sized collisions, $m_p = m_t(=\langle m\rangle_m)$. The dotted and solid arrows indicate the target mass at which $t_s = t_\eta$ and $\Omega t_s = 1$, respectively.

(A color version of this figure is available in the online journal.)

the $m_t = \langle m\rangle_m$ target is dominated by projectiles within a mass range $0.1m_t \lesssim m_p \leqslant m_t$. In fact, the projectile mass distribution integrated over $0.1m_t \leqslant m_p \leqslant m_t$ exceeds 50% for all the cases presented in Figure 9. This means that the growth of aggregates is indeed dominated by collisions with similar-sized ones as required by the limitation of our porosity model. This is basically a consequence of the fact that the aggregate mass distribution $\Delta\Sigma_d/\Delta\log m$ is peaked around the target mass $m \sim \langle m\rangle_m$ (see Figure 7). The mass ratio m_p/m_t at the peak of $m_p C_{m_t}(m_p)$ reflects the size dependence of the turbulence-driven relative velocity Δv_t, which is the main source of the collision velocity in our simulation. At $t \lesssim 2000$ yr ($\langle m\rangle_m \lesssim 10^3$ g), the dominant projectile mass is lower than $m_t(= \langle m\rangle_m)$, since both the target and projectiles are tightly coupled to turbulence (i.e., $t_s(m_t), t_s(m_p) < t_\eta$) and hence Δv_t vanishes at equal-sized collisions (see the first expression of Equation (20)). At $t \gtrsim 2000$ yr ($\langle m\rangle_m \gtrsim 10^3$ yr), the target decouples from small turbulent eddies ($t_s(m_t) > t_\eta$). This results in a shift of the dominant collision mode to $m_p \approx m_t$ because Δv_t no longer vanishes at equal-sized collisions (see the second expression of Equation (20)).

3.2.2. Density Evolution History

To see the density evolution history in detail, we plot in Figure 10 the temporal evolution of the weighted average mass $\langle m\rangle_m$ and the internal density of aggregates with mass $m = \langle m\rangle_m$ at orbital radii $r = 5$ AU and 20 AU.

As mentioned above, dust particles initially grow into fractal aggregates of $d_f \approx 2$ until the impact energy $E_{\rm imp}$ becomes comparable to the rolling energy $E_{\rm roll}$. With this information, one can analytically estimate the aggregate size at which the fractal growth terminates. Our simulation shows that the collision velocity between the fractal aggregates is approximately given by the turbulence-driven velocity in the strong-coupling limit (Equation (20) with $t_s \ll t_\eta$). Assuming that the collisions mainly occur between aggregates of similar sizes (see Section 3.2.1), the reduced mass and the collision velocity are roughly given by $m/2$ and $\delta v_g {\rm Re}_t^{1/4}\Omega t_s$, respectively. In

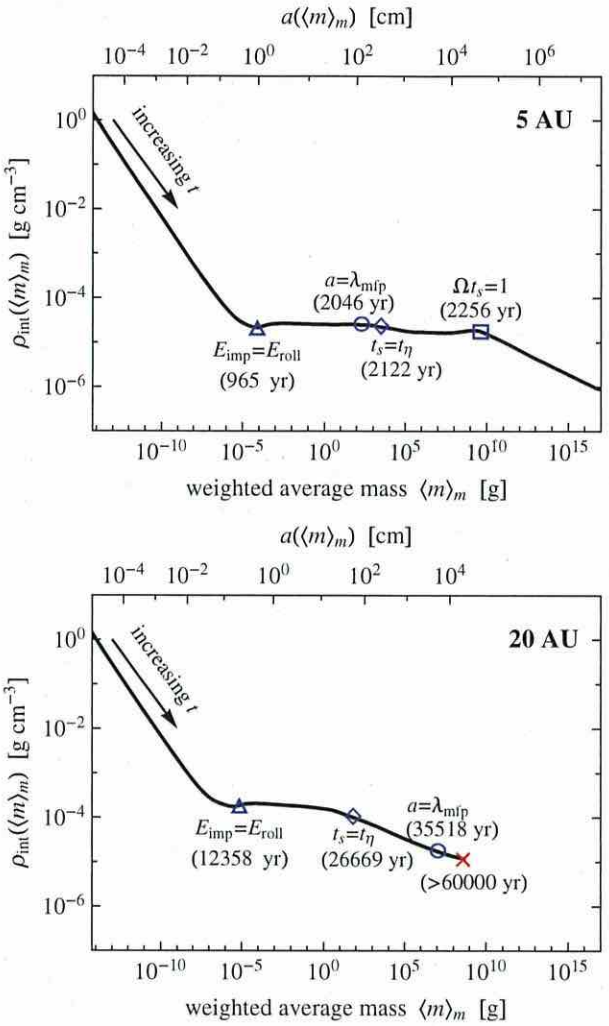

Figure 10. Temporal evolution of the weighted average mass $\langle m\rangle_m$ and the internal density $\rho_{\rm int}(\langle m\rangle_m)$ at orbital radii $r = 5$ AU (upper panel) and 20 AU (lower panel). Shown at the top of the panels is the aggregate radius $a(\langle m\rangle_m)$ at each orbital radius. The triangles, circles, diamonds, and square mark the sizes at which $E_{\rm imp} = E_{\rm roll}$, $a = \lambda_{\rm mfp}$, $t_s = t_\eta$, and $\Omega t_s = 1$, respectively. At $r = 20$ AU, dust growth stalls due to the radial drift barrier (cross symbol) before reaching $\Omega t_s = 1$.

(A color version of this figure is available in the online journal.)

addition, we use the fact that fractal aggregates with $d_f \approx 2$ have a mass-to-area ratio which is comparable to their constituent monomers. This means that the stopping time of the aggregates is as short as the monomers and is hence given by Epstein's law. Thus, the impact energy is approximated as

$$E_{\rm imp} \approx \frac{m}{4}\Delta v_t^2 \approx \frac{3}{8}m\left(\frac{\delta v_g {\rm Re}_t^{1/4}\Omega}{\rho_g v_{\rm th}}\right)^2\left(\frac{3m}{4A}\right)^2. \quad (23)$$

Furthermore, using the definitions for ρ_g, $v_{\rm th}$, and ${\rm Re}_t$, we have $\rho_g v_{\rm th} = (2/\pi)\Sigma_g\Omega$ and ${\rm Re}_t = \alpha_D\Sigma_g\sigma_{\rm mol}/(2m_g)$ for the midplane. Substituting them into Equation (23) and using $\delta v_g = \sqrt{\alpha_D}c_s$ and $m/A \approx m_0/(\pi a_0^2) = 4\rho_0 a_0/3$, we obtain

$$E_{\rm imp} \approx \frac{3\pi^2}{32\sqrt{2}}\alpha_D^{3/2}mc_s^2\left(\frac{\Sigma_g\sigma_{\rm mol}}{m_g}\right)^{1/2}\left(\frac{\rho_0 a_0}{\Sigma_g}\right)^2. \quad (24)$$

Thus, the impact energy is proportional to the mass. We define the rolling mass $m_{\rm roll}$ by the condition $E_{\rm imp} = E_{\rm roll}$. Using Equation (24), the rolling mass is evaluated as

$$m_{\rm roll} \approx \frac{32\sqrt{2}}{3\pi^2}\frac{E_{\rm roll}}{c_s^2\alpha_D^{3/2}}\left(\frac{m_g}{\Sigma_g\sigma_{\rm mol}}\right)^{1/2}\left(\frac{\Sigma_g}{\rho_0 a_0}\right)^2$$
$$\sim 10^{-4}\,{\rm g}\left(\frac{\alpha_D}{10^{-3}}\right)^{-3/2}\left(\frac{T}{100\,{\rm K}}\right)^{-1}\left(\frac{\Sigma_g}{100\,{\rm g\,cm^{-2}}}\right)^{3/2}$$
$$\times\left(\frac{F_{\rm roll}}{10^{-3}\,{\rm dyn}}\right)\left(\frac{\rho_0}{1\,{\rm g\,cm^{-3}}}\right)^{-2}\left(\frac{a_0}{0.1\,\mu{\rm m}}\right)^{-1}, \quad (25)$$

where we have used that $E_{\rm roll} = (\pi a_0/2)F_{\rm roll}$ (see Section 2.3.1). Using the relations $a \approx (m/m_0)^{1/2}a_0$ and $\rho_{\rm int} \approx (m/m_0)^{-1/2}\rho_0$ for $d_f \approx 2$ aggregates, the corresponding radius and internal density are found to be

$$a_{\rm roll} \sim 1\,{\rm cm}\left(\frac{m_{\rm roll}}{10^{-4}\,{\rm g}}\right)^{1/2}, \quad (26)$$

$$\rho_{\rm int,\,roll} \sim 10^{-5}\,{\rm g\,cm^{-3}}\left(\frac{m_{\rm roll}}{10^{-4}\,{\rm g}}\right)^{-1/2}. \quad (27)$$

The triangles in Figure 10 mark the rolling mass at $r = 5$ AU and 20 AU predicted by Equation (25). The analytic prediction well explains when the decrease in $\rho_{\rm int}$ terminates.

The density evolution is more complicated at $m > m_{\rm roll}$, where collisional compression is no longer negligible (i.e., $E_{\rm imp} > E_{\rm roll}$). At $r = 5$ AU, the internal density is approximately constant until the stopping time reaches $\Omega t_s = 1$, and then decreases as $\rho_{\rm int} \propto m^{-1/5}$. At $r = 20$ AU, by contrast, the density is kept nearly constant until $m \sim 10^2$ g ($a \sim 10^2$ cm), and then decreases as $\rho_{\rm int} \propto m^{-1/8}$.

As shown below, the density histories mentioned above can be directly derived from the porosity change recipe we adopted. Let us assume again that aggregates grow mainly through collisions with similar-sized ones ($m_1 \approx m_2$ and $V_1 \approx V_2$). In this case, the evolution of $\rho_{\rm int}$ at $E_{\rm imp} \gg E_{\rm roll}$ is approximately given by Equation (14). Furthermore, we neglect the term $(2V_1^{5/6})^{-4}$ in Equation (14) assuming that the impact energy is sufficiently large (which is true as long as $\Omega t_s < 1$; see below). Given these assumptions, the internal density of aggregates after collision, $\rho_{\rm int} = 2m_1/V_{1+2}$, is approximately given by

$$\rho_{\rm int} \approx \left(\frac{3}{5}\right)^{3/2}\left(\frac{E_{\rm imp}}{N_{1+2}bE_{\rm roll}}\right)^{3/10}N_{1+2}^{-1/5}\rho_0, \quad (28)$$

where $N_{1+2} = 2m_1/m_0$. Since the impact energy $E_{\rm imp} \approx m_1(\Delta v)^2/4$ is proportional to $N_{1+2}(\Delta v)^2$, Equation (28) implies that

$$\rho_{\rm int} \propto (\Delta v)^{3/5}m^{-1/5}, \quad (29)$$

where we have dropped the subscript for mass for clarity. Equation (29) gives the relation between $\rho_{\rm int}$ and m if we know how the impact velocity depends on them. Explicitly, if $\Delta v \propto m^\beta\rho_{\rm int}^\gamma$, Equation (29) leads to

$$\rho_{\rm int} \propto m^{(3\beta-1)/(5-3\gamma)}. \quad (30)$$

In our simulation, the main source of the relative velocity is turbulence. The turbulence-driven velocity depends on t_s as $\Delta v_t \propto t_s$ at $t_s \ll t_\eta$ and $\Delta v_t \propto \sqrt{t_s}$ at $t_\eta \ll t_s \ll t_L(=\Omega^{-1})$

(see Equation (20)). As found from Equation (4), the stopping time depends on $\rho_{\rm int}$ and m as $t_s \propto m/A \propto m/a^2 \propto m^{1/3}\rho_{\rm int}^{2/3}$ in the Epstein regime ($a \ll \lambda_{\rm mfp}$) and as $t_s \propto ma/A \propto m^{2/3}\rho_{\rm int}^{1/3}$ in the Stokes regime ($a \gg \lambda_{\rm mfp}$). Using these relations with Equation (30), we find four regimes for density evolution,

$$\rho_{\rm int} \propto \begin{cases} m^0, & a \ll \lambda_{\rm mfp} \quad \text{and } t_s \ll t_\eta, \\ m^{1/4}, & a \gg \lambda_{\rm mfp} \quad \text{and } t_s \ll t_\eta, \\ m^{-1/8}, & a \ll \lambda_{\rm mfp} \quad \text{and } t_\eta \ll t_s \ll t_L, \\ m^0, & a \gg \lambda_{\rm mfp} \quad \text{and } t_\eta \ll t_s \ll t_L. \end{cases} \tag{31}$$

The circles, diamonds, and square in Figure 10 mark the size at which $a = \lambda_{\rm mfp}$ (i.e., $t_s^{\rm (Ep)} \sim t_s^{\rm (St)}$), $t_s = t_\eta$, and $\Omega t_s = 1$, respectively. At $r = 5$ AU, the sizes at which $a = \lambda_{\rm mfp}$ and $t_s = t_\eta$ nearly overlap, and hence only two velocity regimes $t_s = t_s^{\rm (Ep)} \ll t_\eta$ and $t_\eta \ll t_s = t_s^{\rm (St)} \ll t_L$ are effectively relevant. For both cases, Equation (31) predicts flat density evolution. At $r = 20$ AU, there is a stage in which $t_s \gg t_\eta$ and $a \ll \lambda_{\rm mfp}$, for which Equation (31) predicts $\rho_{\rm int} \propto m^{-1/8}$. These predictions are in agreement with what we see in Figure 10.

Equation (28) does not apply to the density evolution at $\Omega t_s > 1$, where the collision velocity no longer increases and hence collisional compression becomes less and less efficient as the aggregates grow. However, if we go back to Equation (14) and assume that the impact energy $E_{\rm imp}$ is sufficiently small, we obtain $V_{1+2} \approx 2^{6/5}V_1$, or equivalently $V_{1+2}/m_{1+2}^{6/5} \approx V_1/m_1^{6/5}$, where $m_{1+2} = 2m_1$ is the aggregate mass after a collision. This implies that $V/m^{6/5}$ is kept constant during the growth, i.e., $V \propto m^{6/5}$, and hence we have $\rho_{\rm int} = m/V \propto m^{-1/5}$. This is consistent with the density evolution at $\Omega t_s > 1$ seen in the upper panel of Figure 10.

4. CONDITION FOR BREAKING THROUGH THE RADIAL DRIFT BARRIER

In this section, we explain why porous aggregates overcome the radial drift barrier in the inner region of the disk. We do this by comparing the timescale of aggregate growth and radial drift. We assume that dust aggregates grow mainly through collisions with similar-sized aggregates. As shown in Section 3.2.1, this is a good approximation for the growth of aggregates dominating the total mass of the system (i.e., aggregates with mass $m \sim \langle m \rangle_m$). The growth rate of the aggregate mass m at the midplane is then given by

$$\frac{dm}{dt} = \rho_d \sigma_{\rm coll} \Delta v = \frac{\Sigma_d}{\sqrt{2\pi} h_d} A \Delta v, \tag{32}$$

where $\rho_d = \Sigma_d/(\sqrt{2\pi}h_d)$ is the spatial dust density at the midplane, and we have approximated $\sigma_{\rm coll}$ as the projected area A. Equation (32) can be rewritten in terms of the growth timescale as

$$t_{\rm grow} \equiv \left(\frac{d\ln m}{dt}\right)^{-1} = \sqrt{2\pi}\frac{h_d}{\Delta v}\frac{m/A}{\Sigma_d} = \frac{4\sqrt{2\pi}}{3}\frac{h_d}{\Delta v}\frac{\rho_{\rm int} a}{\Sigma_d}, \tag{33}$$

where we have used that $m = (4\pi/3)\rho_{\rm int}a^3$ and $A = \pi a^2$. Here, we compare $t_{\rm grow}$ with the timescale for the radial drift given by

$$t_{\rm drift} \equiv \left|\frac{d\ln r}{dt}\right|^{-1} = \frac{r}{|v_r|}. \tag{34}$$

Now we focus on the stage at which the radial drift velocity reaches the maximum value, i.e., $\Omega t_s = 1$. At this stage, the dust scale height is given by $h_d \approx (2\alpha_D/3)^{1/2}h_g$ according to Equation (3). In addition, we set $\Delta v \approx \sqrt{\alpha_D}c_s$ since the collision velocity between $\Omega t_s = 1$ particles is dominated by the turbulence-driven velocity. Using these relations and $h_g = c_s/\Omega$, we can rewrite Equation (33) as

$$t_{\rm grow}|_{\Omega t_s=1} = \frac{4}{3}\sqrt{\frac{4\pi}{3}}\frac{(\rho_{\rm int}a)_{\Omega t_s=1}}{\Sigma_d \Omega} \approx 40\left(\frac{\Sigma_d/\Sigma_g}{0.01}\right)^{-1}\frac{(\rho_{\rm int}a)_{\Omega t_s=1}}{\Sigma_g} t_K, \tag{35}$$

where $t_K = 2\pi/\Omega$ is the Keplerian orbital period. Thus, the growth timescale is shorter when the mass-to-area ratio $m/A \propto \rho_{\rm int}a$ is smaller. Note that $t_{\rm grow}|_{\Omega t_s=1}$ is independent of α_D since both h_d and Δv scale with $\sqrt{\alpha_D}$. By contrast, the drift timescale for $\Omega t_s = 1$ particles is

$$t_{\rm drift}|_{\Omega t_s=1} = \frac{1}{\eta\Omega} \approx 40\left(\frac{\eta}{4\times 10^{-3}}\right)^{-1} t_K. \tag{36}$$

The ratio of the two timescales is

$$\left(\frac{t_{\rm grow}}{t_{\rm drift}}\right)_{\Omega t_s=1} = \frac{4}{3}\sqrt{\frac{4\pi}{3}}\eta\frac{(\rho_{\rm int}a)_{\Omega t_s=1}}{\Sigma_d} \approx 1\left(\frac{\eta}{4\times 10^{-3}}\right)\left(\frac{\Sigma_d/\Sigma_g}{0.01}\right)^{-1}\frac{(\rho_{\rm int}a)_{\Omega t_s=1}}{\Sigma_g}. \tag{37}$$

The ratio $(t_{\rm grow}/t_{\rm drift})_{\Omega t_s=1}$ determines the fate of dust growth at $\Omega t_s = 1$. If $(t_{\rm grow}/t_{\rm drift})_{\Omega t_s=1}$ is very small, dust particles grow beyond $\Omega t_s = 1$ without experiencing significant radial drift; otherwise, dust particles drift inward before they grow. We expect growth without significant drift to occur if

$$\left(\frac{t_{\rm grow}}{t_{\rm drift}}\right)_{\Omega t_s=1} \lesssim \frac{1}{30}, \tag{38}$$

where the threshold value 1/30 takes into account the fact that $t_{\rm grow}$ is the timescale for mass doubling while the particles experience the fastest radial drift over decades in mass. Below, we examine in what condition this requirement is satisfied.

The ratio $(\rho_{\rm int}a)_{\Omega t_s=1}/\Sigma_g$ depends on the drag regime at $\Omega t_s = 1$. We consider the Epstein regime first. Using $\rho_g = \Sigma_g/(\sqrt{2\pi}h_g)$ and $h_g = c_s/\Omega$, one can rewrite Epstein's law as $\Omega t_s = (\pi/2)\rho_{\rm int}a/\Sigma_g$. Thus, for $\Omega t_s = 1$, we have a surprisingly simple relation

$$\frac{(\rho_{\rm int}a)_{\Omega t_s=1}}{\Sigma_g} = \frac{2}{\pi}. \tag{39}$$

Inserting this relation into Equation (35), we obtain

$$t_{\rm grow}|_{\Omega t_s=1} \approx 30\left(\frac{\Sigma_d/\Sigma_g}{0.01}\right)^{-1} t_K. \tag{40}$$

Hence, the growth condition (Equation (38)) is not satisfied for the standard disk parameters $\eta \approx 10^{-3}$ and $\Sigma_d/\Sigma_g = 0.01$, in agreement with the results of our own and previous (Brauer et al. 2008a) simulations. Note that the right-hand side of Equation (40) is independent of $\rho_{\rm int}$. Thus, the porosity of aggregates has no effect on the radial drift barrier within the Epstein regime.

The situation differs in the Stokes drag regime. A similar calculation as above leads to

$$\frac{(\rho_{\rm int}a)_{\Omega t_s=1}}{\Sigma_g} = \frac{9}{2\pi}\frac{\lambda_{\rm mfp}}{a|_{\Omega t_s=1}} \tag{41}$$

and

$$t_{\rm grow}|_{\Omega t_s=1} \approx 60\left(\frac{\Sigma_d/\Sigma_g}{0.01}\right)^{-1}\frac{\lambda_{\rm mfp}}{a|_{\Omega t_s=1}}. \tag{42}$$

Note that the growth timescale is inversely proportional to the aggregate radius, in contrast to that in the Epstein regime (Equation (40)) being independent of aggregate properties. Substituting Equations (36) and (42) into the growth condition (Equation (38)), we find that the aggregates break through the radial drift barrier in the "deep" Stokes regime, $a|_{\Omega t_s=1}/\lambda_{\rm mfp} \gtrsim 45$. Unlike Equation (40), Equation (42) implicitly depends on $\rho_{\rm int}$ through $a_{\Omega t_s=1}/\lambda_{\rm mfp}$ (see below), so the porosity of aggregates does affect the growth timescale in this case. It is interesting to note that the speed-up of dust growth occurs even though the maximum collision velocity is the same. Indeed, the collision velocity depends only on Ωt_s and is thus independent of the drag regime. We remark that Stokes' law breaks down when a becomes so large that the particle Reynolds number becomes much larger than unity, as already mentioned in Section 2.2. We will show in Section 5.1 that this fact sets the minimum value of $t_{\rm grow}|_{\Omega t_s=1}$ to $\approx 0.3 t_K$; see Equation (47).

The internal density of aggregates controls the growth timescale through the aggregate size a at $\Omega t_s = 1$. For given $\rho_{\rm int}$, one can analytically calculate $a|_{\Omega t_s=1}$ from Equations (39) and (41). Explicitly,

$$a|_{\Omega t_s=1} = \frac{2\Sigma_g}{\pi\rho_{\rm int}} \tag{43}$$

for the Epstein regime, and

$$a|_{\Omega t_s=1} = \frac{3}{(2\pi)^{1/4}}\sqrt{\frac{m_g h_g}{\rho_{\rm int}\sigma_{\rm mol}}} \tag{44}$$

for the Stokes regime, where we have used $\lambda_{\rm mfp} = m_g/(\rho_g\sigma_{\rm mol})$ and $\rho_g = \Sigma_g/(\sqrt{2\pi}h_g)$. For fixed $\rho_{\rm int}$, $a|_{\Omega t_s=1}$ decreases with increasing r in the Epstein regime, but increases in the Stokes regime. The upper panel of Figure 11 plots $a|_{\Omega t_s=1}$ for three different values of the aggregate internal density $\rho_{\rm int}$. If dust particles grow into compact spheres ($\rho_{\rm int} \sim 1\,{\rm g\,cm^{-3}}$), Epstein's law governs the motion of $\Omega t_s = 1$ particles in almost the entire snow region ($r > 3$ AU). However, if dust particles grow into highly porous aggregates with $\rho_{\rm int} \sim 10^{-5}\,{\rm g\,cm^{-3}}$, the particles growing at $r \lesssim 60$ AU enter the Stokes regime before Ωt_s reaches unity. The lower panel of Figure 11 shows the two timescales $t_{\rm grow}|_{\Omega t_s=1}$ and $t_{\rm drift}|_{\Omega t_s=1}$ as calculated from Equations (35) and (36), respectively. We see that compact particles with $\rho_{\rm int} \sim 1\,{\rm g\,cm^{-3}}$ do not satisfy the growth condition (Equation (38)) outside the snow line, while porous aggregates with $\rho_{\rm int} \sim 10^{-5}\,{\rm g\,cm^{-3}}$ do in the region $r \lesssim 10$ AU. These explain our simulation results presented in Section 3.

Finally, we remark that a high disk mass (i.e., a high Σ_g with fixed Σ_d/Σ_g) favors the breakthrough of the radial drift barrier. Figure 12 shows the size a and the timescales $t_{\rm grow}$ and $t_{\rm drift}$ at $\Omega t_s = 1$ for a disk 10 times heavier than the MMSN. We see that the growth condition (Equation (38)) is now satisfied at $r \lesssim 25$ AU for $\rho_{\rm int} = 10^{-5}\,{\rm g\,cm^{-3}}$ and at

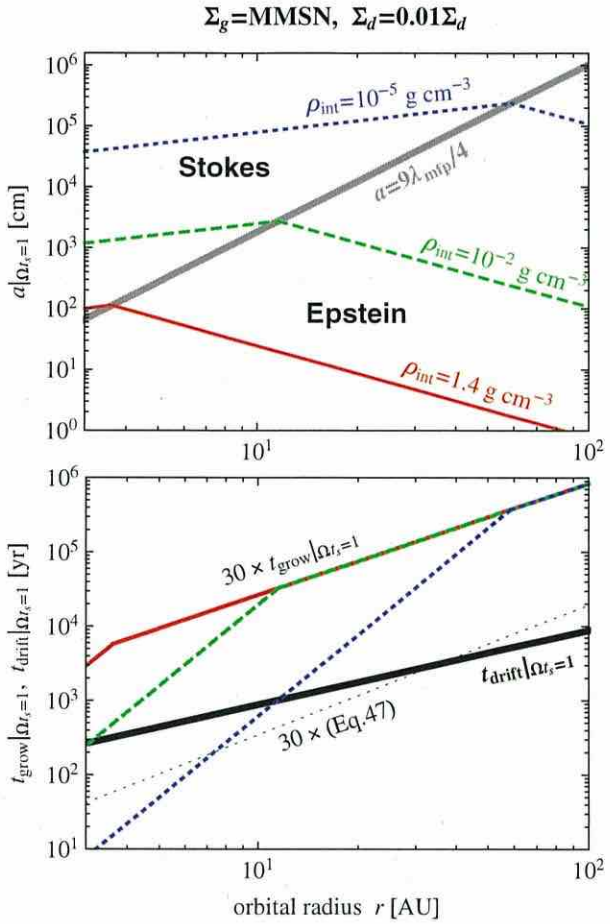

Figure 11. Size a (upper panel) and growth timescale $t_{\rm grow}$ (lower panel) of dust aggregates at $\Omega t_s = 1$ as a function of orbital radius r for internal densities $\rho_{\rm int} = 1.4\,{\rm g\,cm^{-3}}$ (solid line), $10^{-2}\,{\rm g\,cm^{-3}}$ (dashed line), and $10^{-5}\,{\rm g\,cm^{-3}}$ (dotted line). The MMSN with the dimensionless diffusion coefficient $\alpha_D = 10^{-3}$ is assumed for the disk model. The thick line in the upper panel indicates $a = 9\lambda_{\rm mfp}/4$, at which the drag law changes from the Epstein regime to the Stokes regime. The thick line in the lower panel shows the drift timescale $t_{\rm drift}$ at $\Omega t_s = 1$ (independent of $\rho_{\rm int}$). For $\rho_{\rm int} = 10^{-5}\,{\rm g\,cm^{-3}}$, $t_{\rm grow}|_{\Omega t_s=1}$ satisfies the growth criterion (Equation (38)) at $r \lesssim 10$ AU. In reality, $t_{\rm grow}|_{\Omega t_s=1}$ does not fall below the value given by Equation (47) (thin dotted line) because of the effect of the gas drag at high particle Reynolds numbers (see Section 5.1). However, this does not change the location where the growth condition is satisfied.

(A color version of this figure is available in the online journal.)

$r \lesssim 7$ AU even for $\rho_{\rm int} = 10^{-2}\,{\rm g\,cm^{-3}}$. This is because a higher Σ_g leads to a shorter $\lambda_{\rm mfp}$ and hence allows aggregates to reach the Stokes regime $a/\lambda_{\rm mfp} \gg 1$ at larger r or with higher $\rho_{\rm int}$ (note that the enhancement of Σ_g by a constant remains η and hence $t_{\rm drift}|_{\Omega t_s=1}$ unchanged). Interestingly, our porosity model predicts that $\rho_{\rm int}|_{\Omega t_s=1}$ is independent of Σ_g. In fact, substituting Equation (44) with $(\Delta v)_{\Omega t_s=1} \approx \sqrt{\alpha_D}c_s$ and $N_{1+2} \propto \rho_{\rm int}a^3$ into Equation (28), we obtain the equation for $\rho_{\rm int}|_{\Omega t_s=1}$ that does not involve Σ_g.

5. DISCUSSION

So far we have shown that the evolution of dust into highly porous aggregates is a key to overcome the radial drift barrier. However, in order to clarify the role of porosity evolution, we have ignored many other effects relevant to dust growth in

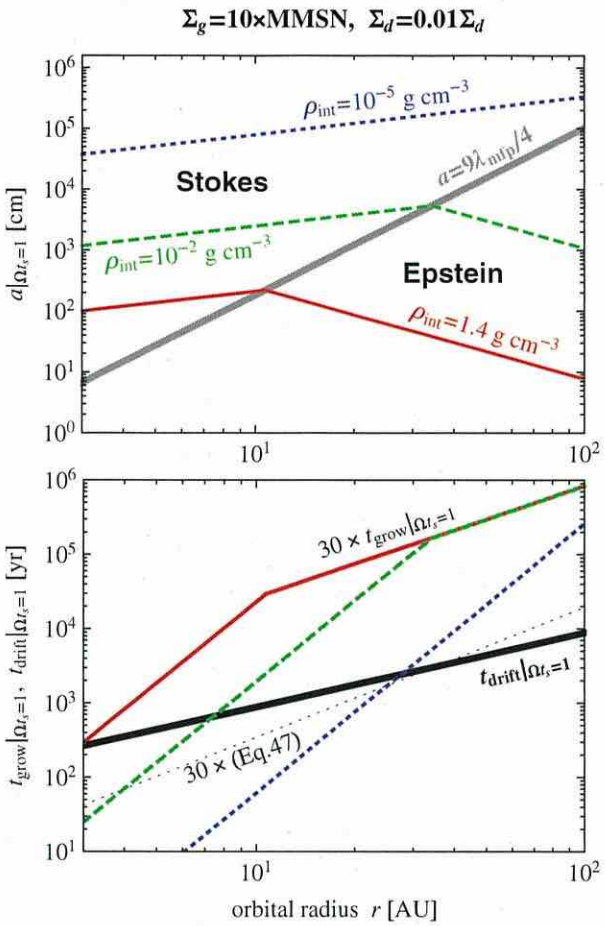

Figure 12. Same as Figure 11, but for a disk 10 times heavier than the MMSN. The growth criterion (Equation (38)) is satisfied at $r \lesssim 25$ AU for $\rho_{\rm int} = 10^{-5}$ g cm^{-3} and at $r \lesssim 7$ AU for $\rho_{\rm int} = 10^{-2}$ g cm^{-3}.
(A color version of this figure is available in the online journal.)

protoplanetary disks. In this section, we discuss how the ignored effects would affect dust evolution.

5.1. Effect of the Friction Law at High Particle Reynolds Numbers

In this study, we have assumed that the stopping time t_s obeys Stokes' law whenever $a \gtrsim \lambda_{\rm mfp}$. In reality, Stokes' law applies only when the particle Reynolds number (the Reynolds number of the gas flow around the particle) ${\rm Re}_p \equiv 2a|\boldsymbol{v}_d - \boldsymbol{v}_g|/\nu_{\rm mol}$ is less than unity, where $|\boldsymbol{v}_d - \boldsymbol{v}_g|$ is the gas–dust relative velocity. When ${\rm Re}_p \gtrsim 1$, i.e., when the particle becomes so large and/or the gas–dust relative velocity becomes so high, the stopping time becomes dependent on the particle velocity (see, e.g., Weidenschilling 1977). In this subsection, we discuss how this effect affects our conclusion.

In general, the stopping time at $a \gg \lambda_{\rm mfp}$ can be written as

$$t_s = \frac{2m}{C_D \rho_g |\boldsymbol{v}_d - \boldsymbol{v}_g| A}, \tag{45}$$

where C_D is a dimensionless coefficient that depends on ${\rm Re}_p$. Stokes' law, which applies when ${\rm Re}_p \ll 1$, is given by $C_D = 24/{\rm Re}_p$. In the opposite limit, ${\rm Re}_p \gg 1$, the drag coefficient C_D approaches a constant value (typically of order unity; e.g., $C_D \approx 0.5$ for a sphere with $10^3 \lesssim {\rm Re}_p \lesssim 10^5$), which is known as Newton's friction law. Thus, in the Newton regime, the stopping time depends on the particle velocity, unlike in the Stokes regime. In this case, one has to calculate the stopping time and particle velocity simultaneously since the particle velocity in turn depends on the stopping time.

In the previous sections, we have ignored the Newton regime to avoid the above-mentioned complexity. However, it is easy to calculate the growth timescale in the Newton regime for given Ωt_s, for which the gas–dust relative velocity can be known in advance. Below, we show that the Newton drag sets the *minimum* value of $t_{\rm grow}|_{\Omega t_s=1}$ (Equation (35)) for given orbital radius and internal density, which was not taken into account in Section 4. At the midplane, Equation (45) can be rewritten as $\Omega t_s = (2\sqrt{2\pi}/C_D)(c_s/|\boldsymbol{v}_d - \boldsymbol{v}_g|)m/(\Sigma_g A)$, where we have used that $\rho_g = \Sigma_g \Omega/(\sqrt{2\pi} c_s)$. When $\Omega t_s = 1$, the gas–dust relative velocity is dominated by the dust radial velocity $v_r = -\eta v_K$, so we can set $|\boldsymbol{v}_d - \boldsymbol{v}_g| \approx \eta v_K$. Thus, at the midplane, we obtain a relation

$$\frac{(\rho_{\rm int} a)_{\Omega t_s=1}}{\Sigma_g} \approx \frac{3C_D}{8\sqrt{2\pi}} \frac{\eta v_K}{c_s} \approx 0.07 \left(\frac{C_D}{0.5}\right) \frac{\eta v_K}{c_s}, \tag{46}$$

where we have used that $m/A = 4\rho_{\rm int} a/3$. If C_D reaches a constant, $(\rho_{\rm int} a)_{\Omega t_s=1}/\Sigma_g$ no longer depends on aggregate properties. Putting this equation into Equation (35), we have

$$t_{\rm grow}|_{\Omega t_s=1} \approx 0.3 \left(\frac{\Sigma_d/\Sigma_g}{0.01}\right)^{-1} \left(\frac{C_D}{0.5}\right) \left(\frac{\eta v_K/c_s}{0.08}\right) t_K. \tag{47}$$

When $C_D = 24/{\rm Re}_p$, Equation (47) reduces to the equation for the Stokes drag (Equation (42)), where $t_{\rm grow}|_{\Omega t_s=1}$ decreases with increasing aggregate size a. However, when ${\rm Re}_p$ becomes so large that C_D reaches a constant value, $t_{\rm grow}|_{\Omega t_s=1}$ no longer decreases with increasing a. Thus, we find that the Newton drag sets the minimum value of $t_{\rm grow}|_{\Omega t_s=1}$. For our disk model, in which $\Sigma_d/\Sigma_g = 0.01$ and $\eta v_K/c_s = 0.08(r/5\,{\rm AU})^{1/4}$, the minimum growth timescale is $\approx$0.2–0.3$(C_D/0.5)t_K$ at $r \approx$ 3–10 AU.

Since the Newton drag regime was ignored in our model, the growth rate of aggregates was overestimated at high ${\rm Re}_p$. As seen in the lower panel of Figure 11, the growth timescale $t_{\rm grow}|_{\Omega t_s=1}$ for the $\rho_{\rm int} = 10^{-5}$ g cm^{-3} aggregates falls below the minimum possible value given by Equation (47) at $r \lesssim 7$ AU. This implies that dust growth is somewhat artificially accelerated in our simulation presented in Section 3.2. However, this artifact is *not* the reason why porous aggregates grow across the radial drift barrier in the simulation. Indeed, the drift timescale $t_{\rm grow}|_{\Omega t_s=1}$ is $\approx 40 t_K$ at these orbital radii, and hence the minimum growth timescale still satisfies the condition for breaking through the drift barrier, Equation (38) (see Section 4). Thus, highly porous aggregates are still able to break through the radial drift barrier even if Newton's law at high particle Reynolds numbers is taken into account.

In summary, we have shown that Newton's friction law ($C_D \approx$ constant) at high particle Reynolds numbers sets a floor value for the growth timescale at $\Omega t_s = 1$. In the numerical simulation presented in Section 3.2, the neglect of the Newton drag regime causes artificial acceleration of the growth of $\Omega t_s \gtrsim 1$ aggregates. However, comparison with the drift timescale shows that the floor value of $t_{\rm grow}|_{\Omega t_s=1}$ is sufficiently small for dust to grow across $\Omega t_s = 1$. Therefore, the deviation

from Stokes' law at high particle Reynolds numbers has little effect on the successful breakthrough of the radial drift barrier observed in our simulation.

5.2. Effects of Frictional Backreaction

So far we have neglected the frictional backreaction from dust to gas when determining the velocities of dust aggregates (Equations (6) and (18)). Here, we discuss the validity of this assumption.

5.2.1. Effect on the Equilibrium Drift Velocity

Frictional backreaction generally modifies the equilibrium velocities of both gas and dust. The equilibrium velocities in the presence of the backreaction are derived by Tanaka et al. (2005) for arbitrary dust size distribution. The result shows that the radial and azimuthal velocities v_r and $v_\phi = v'_\phi + v_K$ of dust particles with stopping time t_s are given by

$$v_r = \frac{1}{1+(\Omega t_s)^2} v_{g,r} + \frac{2\Omega t_s}{1+(\Omega t_s)^2} v'_{g,\phi}, \tag{48}$$

$$v'_\phi = -\frac{\Omega t_s}{2[1+(\Omega t_s)^2]} v_{g,r} + \frac{1}{1+(\Omega t_s)^2} v'_{g,\phi}, \tag{49}$$

where

$$v_{g,r} = \frac{2Y}{(1+X)^2+Y^2}\eta v_K, \tag{50}$$

$$v'_{g,\phi} = -\frac{1+X}{(1+X)^2+Y^2}\eta v_K, \tag{51}$$

are the radial and azimuthal components of the gas velocity relative to the local circular Keplerian motion, respectively, and

$$X = \int \frac{\rho_d(m)}{\rho_g} \frac{1}{1+(\Omega t_s(m))^2} dm, \tag{52}$$

$$Y = \int \frac{\rho_d(m)}{\rho_g} \frac{\Omega t_s(m)}{1+(\Omega t_s(m))^2} dm, \tag{53}$$

with $\rho_d(m)$ being the spatial mass density of dust particles per unit aggregate mass.[5] In the limit of $X, Y \to 0$, the gas velocities approach $v_{g,r} \to 0$ and $v'_{g,\phi} \to -\eta v_K$, and hence Equations (48) and (49) reduce to Equations (6) and (18), respectively. Thus, the dimensionless quantities X and Y measure the significance of the frictional backreaction. As found from the integrands in Equations (6) and (18), the backreaction is non-negligible when the local dust-to-gas mass ratio exceeds unity and the aggregates dominating the dust mass couple tightly to the gas.

To test the effect of fractional backreaction, we have also simulated porous aggregation using Equations (48) and (49) instead of Equations (6) and (18) for the aggregate velocities. However, it is found that the effect of backreaction is so small that the resulting dust evolution is hardly distinguishable from that presented in Section 3. The upper panel of Figure 13 shows the temporal evolution of the gas velocities $v_{g,r}$ and $v'_{g,\phi}$ observed in this simulation as a function of the weighted average mass $\langle m\rangle_m$. We see that the observed gas velocities deviate at most only by $9\,\mathrm{m\,s^{-1}} \approx 0.17\eta v_K$ from the velocities when the backreaction is absent (dotted lines). As a result, the inward velocity $-v_r$ of aggregates with $m = \langle m\rangle_m$ is decreased only by 15% even when $\Omega t_s(\langle m\rangle_m) \approx 1$ (see the black solid curve in the lower panel of Figure 13). The above result can be understood in the following way. As found from the definitions of X and Y (Equations (52) and (53)), the effect of the backreaction is significant only when the density of dust coupled to the gas ($\Omega t_s \lesssim 1$) is comparable to or higher than the gas density. When $\Omega t_s(\langle m\rangle_m) \lesssim 1$, the density of the coupled dust at the midplane is $\lesssim \Sigma_d/h_d|_{\Omega t_s=1} \sim \Sigma_d/(h_g\sqrt{\alpha_D}) \sim (0.01/\sqrt{\alpha_D})\rho_{g,\mathrm{mid}} \sim 0.3\rho_{g,\mathrm{mid}} \lesssim \rho_{g,\mathrm{mid}}$, where $\rho_{g,\mathrm{mid}}$ is the midplane gas density and we have used that $h_d|_{\Omega t_s=1} \sim \sqrt{\alpha_D}h_g \sim 0.03h_g$ (Equation (3)) and $\Sigma_d/\Sigma_g \approx 0.01$ (the latter is true as long as $\Omega t_s(\langle m\rangle_m) \lesssim 1$). When $\Omega t_s(\langle m\rangle_m) \gtrsim 1$, the dust density does exceed the gas density at the midplane, but the most part of the dust mass is now carried by *decoupled* ($\Omega t_s > 1$) aggregates, which do not affect the gas motion.[6] Thus, the density of coupled dust is always lower than the gas density, and hence the backreaction effect is insignificant at all times.

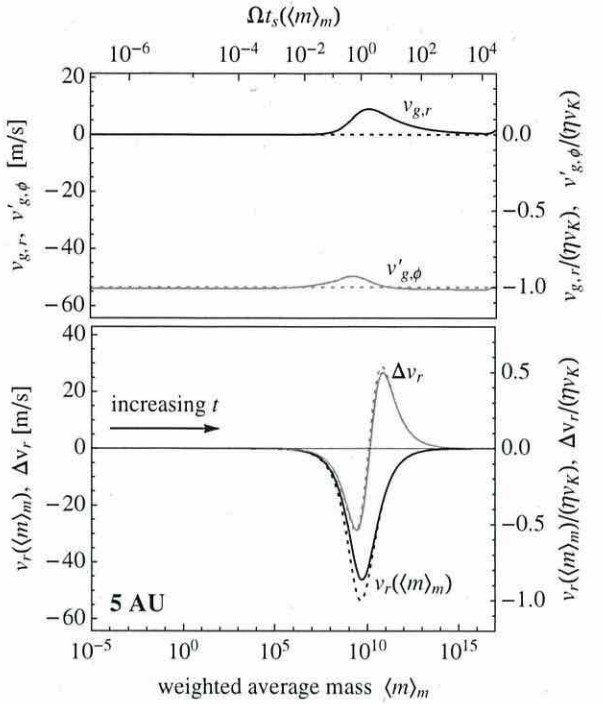

Figure 13. Radial and azimuthal velocities of gas (upper panel) and radial velocity of dust (lower panel) at $r = 5$ AU as a function of the weighted average mass $\langle m\rangle_m$. The solid black and gray curves in the upper panel show $v_{g,r}$ and $v'_{g,\phi} = v_{g,\phi} - v_K$, respectively, obtained from the simulation including porosity evolution of aggregates and fractional backreaction from dust to gas. The dotted curves are the velocities when the fractional backreaction is neglected.

Furthermore, the effect on the *differential* drift velocity is even less significant because the decreases in the inward velocities nearly cancel out. As an example, the gray solid and dotted curves in the lower panel of Figure 13 show the differential radial velocity Δv_r between aggregates of stopping times $t_s = t_s(\langle m\rangle_m)$ and $0.3t_s(\langle m\rangle_m)$ obtained from the simulations with and without the backreaction, respectively. We see that the maximum values of $|\Delta v_r|$, which are reached when $\Omega t_s(\langle m\rangle_m) \approx 0.7$, differ only by 5%. Therefore, the frictional backreaction from dust to gas

[5] Equations (48)–(53) are equivalent to the "multi-species NSH solution" of Bai & Stone (2010a, their Equations (A4) and (A5)).

[6] Indeed, X and Y are insensitive to $\Omega t_s \gg 1$ particles because the factors $1/[1+(\Omega t_s)^2] \approx t_s^{-2}$ and $\Omega t_s/[1+(\Omega t_s)^2] \approx t_s^{-1}$ decrease faster than the spatial dust density $\rho_d \propto \Sigma_d/h_d \propto t_s^{1/2}$ increases (see Equation (3)).

hardly affects the drift-induced collision velocity between dust aggregates.

5.2.2. Streaming Instability

The backreaction of dust on gas causes another phenomenon, the so-called streaming instability (Youdin & Goodman 2005). This means that the equilibrium gas–dust motion as described by Equations (6)–(18) is unstable against perturbation. One important consequence of this instability is rapid clumping of marginally decoupled ($\Omega t_s \sim 1$) dust particles (e.g., Johansen & Youdin 2007; Johansen et al. 2007; Bai & Stone 2010a). The clumping proceeds in a runaway manner (i.e., turbulent diffusion no longer limits the clumping) once the dust density exceeds the gas density at the midplane (e.g., Johansen & Youdin 2007; see also the analytic explanation of this by Johansen et al. 2009). The runaway clumps could eventually be gravitationally bound and form 100 km sized planetesimals (Johansen et al. 2007). For more tightly coupled ($\Omega t_s \ll 1$) particles, however, the clumping occurs only moderately unless the dust-to-gas surface density ratio is high and/or the radial drift speed is low (Johansen et al. 2009; Bai & Stone 2010b). This is also true for loosely coupled particles ($\Omega t_s \gg 1$) for which the interaction with the gas is weak.

As seen in Section 3.2, porous aggregates are able to reach $\Omega t_s \sim 1$ in inner regions of disks. These aggregates likely trigger the streaming instability and can even experience runaway collapse. However, it is not obvious whether the clumps really do experience the runaway collapse, since the growth timescale of the $\Omega t_s \sim 1$ aggregates can be as short as one orbital period (see Section 5.1), which is comparable to the growth time of the streaming instability at $\Omega t_s = 1$ (Youdin & Goodman 2005). If the aggregates cross $\Omega t_s \sim 1$ faster than the clumps develop, planetesimal formation will occur via direct collisional growth rather than gravitational instability. In order to address this issue, we will need to simulate coagulation and streaming instability simultaneously.

5.3. Fragmentation Barrier

In this study, we have assumed that all aggregate collisions lead to sticking. This assumption breaks down if the collisional velocity is so high that the collision involves fragmentation and erosion. If the mass loss due to fragmentation and erosion is significant, it acts as an obstacle to planetesimal formation (the so-called fragmentation barrier; e.g., Brauer et al. 2008a). Here, we discuss the validity and possible limitations of this assumption.

Recent N-body simulations predict that very fluffy aggregates made of 0.1 μm sized icy particles experience catastrophic disruption at collision velocities $\Delta v \gtrsim 35\,\mathrm{m\,s^{-1}}$ (Wada et al. 2009). If a large aggregate grows mainly through collisions with similar-sized ones (which is true in our simulations; see Figure 9), the collision velocity at $\Omega t_s \approx 1$ is dominated by the turbulence-driven velocity $\Delta v_t \approx \delta v_g \approx \sqrt{\alpha_D} c_s$ (Section 2.3.2). If the disk is optically thin and moderately turbulent ($\alpha_D = 10^{-3}$) as in our model, the collision velocity is $\approx 21\,\mathrm{m\,s^{-1}}$ at $r = 5$ AU, so catastrophic disruption is likely insignificant for such collisions. However, if turbulence is as strong as $\alpha_D = 10^{-2}$, the collision velocity at $r = 5$ AU and $\Omega t_s = 1$ goes up to $67\,\mathrm{m\,s^{-1}}$. In protoplanetary disks, strong turbulence with $\alpha_D \gtrsim 10^{-2}$ can be driven by magnetorotational instability (MRI; e.g., Balbus & Hawley 1998). If such strong turbulence exists, fragmentation becomes no more negligible even for icy aggregates. Besides, the collision velocity can become higher than the above estimate when a large aggregate collides with much smaller ones, since the collision velocity is then dominated by the radial drift motion. For example, the differential radial drift velocity between an $\Omega t_s = 1$ aggregate and a much smaller one is as high as $\approx \eta v_K \approx 56\,\mathrm{m\,s^{-1}}$ in optically thin disks. At such a high velocity, erosion by small aggregates can also slow down the growth of $\Omega t_s \approx 1$ aggregates, although net growth might be possible (see, e.g., Teiser & Wurm 2009; Teiser et al. 2011).

On the other hand, resupply of small dust particles by fragmentation/erosion has positive effects on dust growth. First, small dust particles stabilize MRI-driven turbulence because they efficiently capture ionized gas particles and thereby reduce the electric conductivity of the gas (e.g., Sano et al. 2000). This process generally leads to the reduction of the gas random velocity (and hence the reduction of turbulence-induced collision velocity), especially when the magnetic fields threading the disk are weak (Okuzumi & Hirose 2011). In addition, small fragments enhance the optical thickness of the disk, and thus reduce the temperature of the gas in the interior of the disk (given that turbulence is stabilized there). Since the radial drift velocity is proportional to the gas temperature, this leads to the reduction of the drift-induced collision velocity. In the limit of large optical depths, the gas temperature is reduced by a factor $\approx (h/r)^{1/4} \approx 0.5$ near the midplane (Kusaka et al. 1970), resulting in the reduction of the drift-induced collision velocity to $28\,\mathrm{m\,s^{-1}}$. These effects may help the growth of large aggregates beyond the fragmentation barrier.

The size of monomers is another key factor. Although we have assumed monodisperse monomers of $a_0 = 0.1\,\mu$m, the size of interstellar dust particles ranges from nanometers to microns. It is suggested both theoretically (Chokshi et al. 1993; Dominik & Tielens 1997) and experimentally (Blum & Wurm 2008) that the threshold velocity for sticking is roughly inversely proportional to a_0. Thus, inclusion of larger monomers generally leads to a decrease in the sticking efficiency. However, it is not obvious whether aggregates composed of multi-sized interstellar particles are mechanically weaker or stronger than aggregates considered in this study. For example, if the monomer size distribution dn_0/da_0 obeys that of interstellar dust particles, $dn_0/d\log a_0 \propto a_0^{-5/2}$ (Mathis et al. 1977), the total mass of the aggregates is dominated by the largest ones ($m_0 \propto a_0^3$ and hence $m_0 dn_0/d\log a_0 \propto a_0^{1/2}$). Nevertheless, the existence of smaller monomers can still be important, since the binding energy per contact E_{break} is proportional to $a_0^{4/3}$ (Chokshi et al. 1993; Dominik & Tielens 1997) and hence the total binding energy tends to be dominated by the smallest ones ($E_{\mathrm{break}} dn_0/d\log a_0 \propto a_0^{-7/6}$). The net effect of multi-sized monomers needs to be clarified by future numerical as well as laboratory experiments.

Another issue concerning the growth efficiency of icy aggregates arises from sintering. Sintering is the redistribution of ice molecules on solid surfaces due to vapor transport and other effects. In this process, ice molecules tend to fill dipped surfaces (i.e., surfaces with negative surface curvature) since the equilibrium vapor pressure decreases with decreasing surface curvature. In an aggregate composed of equal-sized icy monomers, this process leads to growth of the monomer contact areas (Sirono 2011b) and consequently to enhancement of the aggregate's mechanical strength such as F_{roll}. Significant growth of the contact areas could cause the reduction of the aggregate's sticking efficiency since the dissipation of the

collision energy through internal rolling/sliding motion could then be suppressed (Sirono 1999). Furthermore, if the monomers have different sizes, sintering leads to the evaporation of smaller monomers (having higher positive curvature), which may result in the breakup of the aggregate (Sirono 2011a). Therefore, sintering can prevent the growth of icy aggregates near the snow line where sintering proceeds rapidly. Sirono (2011b) shows that the timescale of H_2O sintering falls below 10^3 yr in the region between the snow line (3 AU) and 7 AU for the radial temperature adopted in our study, This is comparable to the timescale on which submicron-sized icy particles grow into macroscopic objects in this region (see Figure 7). However, if the disk is passive and optically thick (Kusaka et al. 1970), no icy materials (including H_2O and CO_2) undergo rapid sintering at $r \gtrsim 4$ AU (Sirono 2011b). Moreover, the required high optical depth can be provided by tiny fragments that would result from the sintering-induced fragmentation itself. Consistent treatment of the two competing effects is necessary to precisely know the location where sintering is really problematic.

To summarize, whether icy aggregates survive catastrophic fragmentation and erosion crucially depends on the environment of the protoplanetary disks as well as on the size distribution of the aggregates and constituent monomers. However, we emphasize that icy aggregates can survive within a realistic range of disk conditions as explained above. Indeed, the range is much wider than that for rocky aggregates for which catastrophic disruption occurs at collision velocities as low as a few $\mathrm{m\,s^{-1}}$ (Blum & Wurm 2008; Wada et al. 2009; Güttler et al. 2010). In order to precisely predict in what conditions icy aggregates overcome the fragmentation barrier, we need to take into account the mass loss due to fragmentation/erosion and the reduction of collision velocities due to the resupply of small particles in a self-consistent way. This will be done in our future work.

5.4. Validity and Limitations of the Porosity Model

Aggregates observed in our simulation have very low internal densities. This is a direct consequence of the porosity model we adopted (Equation (15)). Here, we discuss the validity and limitations of our porosity model.

As mentioned in Section 2.3.1, our porosity change recipe at $E_{\rm imp} \gtrsim E_{\rm roll}$ is based on head-on collision experiments of similar-sized aggregates. In our simulation, dust growth is indeed dominated by collisions with similar-sized aggregates (see Section 3.2.1), so our result is unlikely affected by the limitation of the porosity model regarding the size ratio. By contrast, the neglect of offset collisions may cause underestimation of the porosity increase, since the impact energy is spent for stretching rather than compaction at offset collisions (Wada et al. 2007; Paszun & Dominik 2009). If this is the case, then the breakthrough of the radial drift barrier can occur even outside 10 AU.

On the other hand, the formation of very low density dust aggregates is apparently inconsistent with the existence of massive and much less porous aggregates in our solar system. For example, comets, presumably the most primitive dust "aggregates" in the solar system, are expected to have mean internal densities of $\rho_{\rm int} \sim 0.1\,\mathrm{g\,cm^{-3}}$ (e.g., Greenberg & Hage 1990). Since our porosity model does not explain the formation of such large and less porous "aggregates," some compaction mechanisms have yet to be determined.

One possibility is *static* compression due to gas drag and self-gravity. Although static compression is ignored in our porosity model, it can contribute to the compaction of aggregates that are massive or decoupled from the gas motion. For relatively compact ($\rho_{\rm int} \sim 0.1\,\mathrm{g\,cm^{-3}}$) dust cakes made of micron-sized SiO_2 particles, static compaction is observed to occur at static pressure >100 Pa (Blum & Schräpler 2004; Güttler et al. 2009). By contrast, the static compression strength has not yet been measured so far for icy aggregates with very low internal densities ($\rho_{\rm int} \ll 0.1\,\mathrm{g\,cm^{-3}}$). However, for future reference, it will be useful to estimate here the static pressures due to gas drag and self-gravity.

The ram pressure, the gas drag force per unit area, is given by $P_{\rm ram} = C_D \rho_g |\boldsymbol{v}_d - \boldsymbol{v}_g|^2/2$, where C_D is the drag coefficient and $|\boldsymbol{v}_d - \boldsymbol{v}_g|$ is the gas–dust relative speed (see Section 5.1). At $\Omega t_s \gtrsim 1$, the gas–dust relative speed is approximately equal to ηv_K. Thus, assuming Newton's drag law $C_D \sim 1$ for $\Omega t_s \gtrsim 1$ aggregates (Section 5.1), the ram pressure at $\Omega t_s \gtrsim 1$ is estimated as

$$P_{\rm ram} \sim \rho_g (\eta v_K)^2 \sim 10^{-5} \left(\frac{\rho_g}{10^{-11}\,\mathrm{g\,cm^{-3}}}\right)\left(\frac{\eta v_K}{50\,\mathrm{m\,s^{-1}}}\right)^2 \mathrm{Pa} \tag{54}$$

independently of aggregate properties. Thus, if the static compression strength of our high porous aggregates is lower than 10^{-5} Pa, compression of the aggregates will occur at $\Omega t_s \gtrsim 1$ due to ram pressure.

The static pressure due to self-gravity is estimated from dimensional analysis as

$$P_{\rm grav} \sim \frac{Gm^2}{a^4} \sim 10^{-7} \left(\frac{m}{10^{10}\,\mathrm{g}}\right)^{2/3} \left(\frac{\rho_{\rm int}}{10^{-5}\,\mathrm{g\,cm^{-3}}}\right)^{4/3} \mathrm{Pa}. \tag{55}$$

For $m \sim 10^{10}$ g and $\rho_{\rm int} \sim 10^{-5}\,\mathrm{g\,cm^{-3}}$, which correspond to the $\Omega t_s = 1$ aggregates observed in our simulation (Figure 5), the gravitational pressure is much weaker than the ram pressure. However, since $P_{\rm grav} \propto m^{2/3}$, compression due to self-gravity becomes important for much heavier aggregates. For example, if $\rho_{\rm int} \sim 10^{-5}(m/10^{10}\,\mathrm{g})^{-1/5}\,\mathrm{g\,cm^{-3}}$ as is the case for the $\Omega t_s \gtrsim 1$ aggregates observed in our simulation, $P_{\rm grav}$ exceeds $P_{\rm ram}$ at $m \sim 10^{17}$ g, which is comparable to the mass of comet Halley. Moreover, since $P_{\rm grav} \propto \rho_{\rm int}^{4/3}$, gravitational compaction will proceed in a runaway manner unless the static compression strength increases more rapidly than $P_{\rm grav}$. Thus, static compression due to self-gravity may be a key to fill the gap between our high porous aggregates and more compact planetesimal-mass bodies in the solar system.

6. SUMMARY AND OUTLOOK

We have investigated how the porosity evolution of dust aggregates affects their collisional growth and radial inward drift. We have applied a porosity model based on *N*-body simulations of aggregate collisions (Suyama et al. 2008, 2012). This porosity model allows us to study the porosity change upon collision for a wide range of impact energies. As a first step, we have neglected the mass loss due to collisional fragmentation and instead focused on dust evolution outside the snow line, where aggregates are mainly composed of ice and hence catastrophic fragmentation may be insignificant (Wada et al. 2009). Our findings are summarized as follows.

1. Icy aggregates can become highly porous even if collisional compression is taken into account (Section 3.2). Our model calculation suggests that the internal density of icy aggregates at 5 AU falls off to $10^{-5}\,\mathrm{g\,cm^{-3}}$ by the end of the initial fractal growth stage and is then kept at this level until the aggregates decouple from the gas motion (Figure 10).

Stretching of merged aggregates at offset collisions, which is not taken into account in our porosity model, could further decrease the internal density (Wada et al. 2007; Paszun & Dominik 2009).

2. A high porosity triggers significant acceleration in collisional growth. This acceleration is a natural consequence of particles' aerodynamical property in the Stokes regime, i.e., at particle radii larger than the mean free path of the gas molecules (Section 4). The porosity (or internal density) of an aggregate determines whether the aggregate reaches the Stokes regime before the radial drift stalls its growth. Compact aggregates tend to drift inward before experiencing rapid growth, while highly porous aggregates are able to experience it over a wide range of the orbital radius (Figure 11).
3. The growth acceleration enables the aggregates to overcome the radial drift barrier in inner regions of the disks. Our model calculation shows that the breakthrough of the radial drift barrier can occur at orbital radii less than 10 AU in the MMSN (Figure 5). A higher disk mass allows this to occur at larger orbital radii or higher internal densities (Figure 12). The radial drift barrier has been commonly thought to be one of the most serious obstacles against planetesimal formation. Our result suggests that, if the fragmentation of icy aggregates is truly insignificant (see Section 5.3), formation of icy planetesimals is possible via direct collisional growth of submicron-sized icy particles, even without an enhancement of the initial dust-to-gas mass ratio.
4. Further out in the disk, the growth of porous icy aggregates is still limited by the radial drift barrier, but their inward drift results in enhancement of the dust surface density in the inner region (Figure 6). This enhancement may help the cores of giant planets to form within a disk lifetime (Kobayashi et al. 2010, 2011).

We remark that the quick growth in the Stokes regime was also observed in recent coagulation simulations by Birnstiel et al. (2010, see their Figure 11) and Zsom et al. (2011, see their Figure 3). Birnstiel et al. (2010) observed the breakthrough of the radial drift barrier only at small orbital radii ($r \lesssim 0.5$ AU) since they assumed compact aggregation. Zsom et al. (2011) found rapid growth of porous aggregates in the Stokes regime, but did not consider the loss of the dust surface density through radial drift. What we have clarified in this study is that porosity evolution indeed enables the breakthrough of the radial drift barrier at much larger orbital radii.

The porosity evolution can even influence the evolution of solid bodies after planetesimal formation. It is commonly believed that the formation of protoplanets begins with the runaway growth of a small number of planetesimals due to gravitational focusing (e.g., Wetherill & Stewart 1989). The runaway growth requires a sufficiently high gravitational escape velocity $v_{\rm esc} = \sqrt{2Gm/a}$ relative to the collision velocity. Since the escape velocity decreases with decreasing internal density ($v_{\rm esc} \propto m^{1/3}\rho_{\rm int}^{1/6}$), it is possible that high porosity delays the onset of the runaway growth and thereby affects its outcome. For example, a recent protoplanet growth model including collisional fragmentation/erosion (Kobayashi et al. 2010, 2011) suggests that planetesimals need to have grown to $>10^{21}$ g before the runaway growth begins in order to enable the formation of gas giant planets within the framework of the core accretion scenario (Mizuno 1980; Pollack et al. 1996). The size of the "initial" planetesimals can even determine the mass distribution of asteroids in the main belt (Morbidelli et al. 2009; Weidenschilling 2011). As we pointed out in Section 5.4, compaction of large and massive aggregates may occur through static compression due to gas drag or self-gravity. To precisely determine when it occurs is beyond the scope of this work, but it will thus be important to understand the later stages of planetary system formation. We will address this in future work.

The authors thank the anonymous referee for useful comments. We also thank Tilman Birnstiel, Frithjof Brauer, Cornelis Dullemond, Shu-ichiro Inutsuka, Chris Ormel, Taku Takeuchi, Takayuki Tanigawa, Fredrik Windmark, and Andras Zsom for fruitful discussions. S.O. acknowledges support by Grants-in-Aid for JSPS Fellows (22 · 7006) from MEXT of Japan.

REFERENCES

Adachi, I., Hayashi, C., & Nakazawa, K. 1976, Prog. Theor. Phys., 56, 1756
Bai, X.-N., & Stone, J. 2010a, ApJ, 722, 1437
Bai, X.-N., & Stone, J. 2010b, ApJ, 722, L220
Balbus, S. A., & Hawley, J. F. 1998, Rev. Mod. Phys., 70, 1
Barge, P., & Sommeria, J. 1995, A&A, 295, L1
Birnstiel, T., Dullemond, C. P., & Brauer, F. 2009, A&A, 503, L5
Birnstiel, T., Dullemond, C. P., & Brauer, F. 2010, A&A, 513, 79
Birnstiel, T., Klahr, H., & Ercolano, B. 2012, A&A, 539, A148
Blum, J. 2004, in ASP Conf. Ser. 309, Astrophysics of Dust, ed. A. N. Witt, G. C. Clayton, & B. T. Draine (San Francisco, CA: ASP), 369
Blum, J., & Schräpler, R. 2004, Phys. Rev. Lett., 93, 115503
Blum, J., & Wurm, G. 2000, Icarus, 143, 138
Blum, J., & Wurm, G. 2008, ARA&A, 46, 21
Brauer, F., Dullemond, C. P., & Henning, Th. 2008a, A&A, 480, 859
Brauer, F., Henning, Th., & Dullemond, C. P. 2008b, A&A, 487, L1
Chokshi, A., Tielens, A. G. G. M., & Hollenbach, D. 1993, ApJ, 407, 806
Dominik, C., & Tielens, A. G. G. M. 1995, Phil. Mag. A, 72, 783
Dominik, C., & Tielens, A. G. G. M. 1997, ApJ, 480, 647
Dubrulle, B., Morfill, G., & Sterzik, M. 1995, Icarus, 114, 237
Dubrulle, B., & Valdettaro, L. 1992, A&A, 263, 387
Fromang, S., & Papaloizou, J. 2006, A&A, 452, 751
Goldreich, P., & Ward, W. R. 1973, ApJ, 183, 1051
Greenberg, J. M., & Hage, J. I. 1990, ApJ, 361, 260
Gundlach, B., Kilias, S., Beitz, E., & Blum, J. 2011, Icarus, 214, 717
Güttler, C., Blum, J., Zsom, A., Ormel, C. W., & Dullemond, C. P. 2010, A&A, 513, A56
Güttler, C., Krause, M., Geretshauser, R. J., Speith, R., & Blum, J. 2009, ApJ, 701, 130
Hayashi, C. 1981, Prog. Theor. Phys. Suppl., 70, 35
Hayashi, C., Nakazawa, K., & Nakagawa, Y. 1985, in Protostars and Planets II, ed. D. C. Black & M. S. Matthews (Tucson, AZ: Univ. Arizona Press), 1100
Hirose, S., & Turner, N. J. 2011, ApJ, 732, L30
Johansen, A., Klahr, H., & Mee, A. J. 2006, MNRAS, 370, L71
Johansen, A., Oishi, J. S., Mac Low, M.-M., et al. 2007, Nature, 448, 1022
Johansen, A., & Youdin, A. 2007, ApJ, 662, 627
Johansen, A., Youdin, A., & Mac Low, M.-M. 2009, ApJ, 704, L75
Klahr, H. H., & Henning, T. 1997, Icarus, 128, 213
Kobayashi, H., Tanaka, H., & Krivov, A. V. 2011, ApJ, 738, 35
Kobayashi, H., Tanaka, H., Krivov, A. V., & Inaba, S. 2010, Icarus, 209, 836
Kretke, K. A., & Lin, D. N. C. 2007, ApJ, 664, L55
Kusaka, T., Nakano, T., & Hayashi, C. 1970, Prog. Theor. Phys., 44, 1580
Langkowski, D., Teiser, J., & Blum, J. 2008, ApJ, 675, 764
Mathis, J. S., Rumpl, W., & Nordsieck, K. H. 1977, ApJ, 217, 425
Matthews, L. S., Land, V., & Hyde, T. W. 2012, ApJ, 744, 8
Mizuno, H. 1980, Prog. Theor. Phys., 64, 544
Morbidelli, A., Bottke, W. F., Nesvorný, D., & Levison, H. F. 2009, Icarus, 204, 558
Mukai, T., Ishimoto, H., Kozasa, T., Blum, J., & Greenberg, J. M. 1992, A&A, 262, 315
Nakagawa, Y., Nakazawa, K., & Hayashi, C. 1981, Icarus, 45, 517
Nakagawa, Y., Sekiya, M., & Hayashi, C. 1986, Icarus, 67, 375
Okuzumi, S. 2009, ApJ, 698, 1122
Okuzumi, S., & Hirose, S. 2011, ApJ, 742, 65
Okuzumi, S., Tanaka, H., & Sakagami, M-a. 2009, ApJ, 707, 1247
Okuzumi, S., Tanaka, H., Takeuchi, T., & Sakagami, M-a. 2011a, ApJ, 731, 95
Okuzumi, S., Tanaka, H., Takeuchi, T., & Sakagami, M-a. 2011b, ApJ, 731, 96

Ormel, C. W., & Cuzzi, J. N. 2007, A&A, 466, 413
Ormel, C. W., Spaans, M., & Tielens, A. G. G. M. 2007, A&A, 461, 215
Paszun, D., & Dominik, C. 2009, A&A, 507, 1023
Pinilla, P., Birnstiel, T., Ricci, L., et al. 2012, A&A, 538, A114
Pollack, J. B., Hubickyj, O., Bodenheimer, P., et al. 1996, Icarus, 124, 62
Safronov, V. S. 1969, Evolution of the Protoplanetary Cloud and Formation of the Earth and the Planets (Moscow: Nauka)
Sano, T., Miyama, S. M., Umebayashi, T., & Nakano, T. 2000, ApJ, 543, 486
Sekiya, M. 1998, Icarus, 133, 298
Shakura, N. I., & Sunyaev, R. A. 1973, A&A, 24, 337
Sirono, S. 1999, A&A, 347, 720
Sirono, S. 2011a, ApJ, 733, L41
Sirono, S. 2011b, ApJ, 735, 131
Suyama, T., Wada, K., & Tanaka, H. 2008, ApJ, 684, 1310
Suyama, T., Wada, K., Tanaka, H., & Okuzumi, S. 2012, ApJ, in press (arXiv:1205.1894)
Suzuki, T. K., Muto, T., & Inutsuka, S. 2010, ApJ, 718, 1289
Tanaka, H., Himeno, Y., & Ida, S. 2005, ApJ, 625, 414
Teiser, J., Küpper, M., & Wurm, G. 2009, Icarus, 215, 596
Teiser, J., & Wurm, G. 2009, MNRAS, 393, 1584
Toomre, A. 1964, ApJ, 139, 1217
Turner, N. J., Carballido, A., & Sano, T. 2010, ApJ, 708, 188
Wada, K., Tanaka, H., Suyama, T., Kimura, H., & Yamamoto, T. 2007, ApJ, 661, 320
Wada, K., Tanaka, H., Suyama, T., Kimura, H., & Yamamoto, T. 2008, ApJ, 677, 1296
Wada, K., Tanaka, H., Suyama, T., Kimura, H., & Yamamoto, T. 2009, ApJ, 702, 1490
Wada, K., Tanaka, H., Suyama, T., Kimura, H., & Yamamoto, T. 2011, ApJ, 737, 36
Weidenschilling, S. J. 1977, MNRAS, 180, 57
Weidenschilling, S. J. 2011, Icarus, 214, 671
Weidenschilling, S. J., & Cuzzi, J. N. 1993, in Protostars and Planets III, ed. E. H. Levy & J. I. Lunine (Tucson, AZ: Univ. Arizona Press), 1031
Weidling, R., Güttler, C., Blum, J., & Brauer, F. 2009, ApJ, 696, 2036
Wetherill, G. W., & Stewart, G. R. 1989, Icarus, 77, 330
Whipple, F. L. 1972, in From Plasma to Planet, ed. A. Elvius (New York: Wiley), 211
Windmark, F., Birnstiel, T., Güttler, C., et al. 2012, A&A, 540, A73
Youdin, A. N., & Goodman, J. 2005, ApJ, 620, 459
Youdin, A. N., & Lithwick, Y. 2007, Icarus, 192, 588
Zsom, A., Ormel, C. W., Dullemond, C. P., & Henning, T. 2011, A&A, 534, A73
Zsom, A., Ormel, C. W., Güttler, C., Blum, J., & Dullemond, C. P. 2010, A&A, 513, A57

Monthly Notices
of the
ROYAL ASTRONOMICAL SOCIETY

MNRAS **452,** 278–288 (2015) doi:10.1093/mnras/stv1290

Effects of Ohmic and ambipolar diffusion on formation and evolution of first cores, protostars, and circumstellar discs

Y. Tsukamoto,[1,2]★ K. Iwasaki,[2,3] S. Okuzumi,[4] M. N. Machida[5] and S. Inutsuka[2]

[1]*Laboratory of Computational Astrophysics, RIKEN, Saitama, Japan*
[2]*Department of Physics, Nagoya University, Aichi, Japan*
[3]*Department of Environmental Systems Science, Faculty of Science and Engineering, Doshisha University, Kyoto, Japan*
[4]*Department of Earth and Planetary Sciences, Tokyo Institute of Technology, Tokyo, Japan*
[5]*Department of Earth and Planetary Sciences, Kyushu University, Fukuoka, Japan*

Accepted 2015 June 7. Received 2015 May 27; in original form 2015 March 16

ABSTRACT

We investigate the formation and evolution of a first core, protostar, and circumstellar disc with a three-dimensional non-ideal (including both Ohmic and ambipolar diffusion) radiation magnetohydrodynamics simulation. We found that the magnetic flux is largely removed by magnetic diffusion in the first-core phase and that the plasma β of the centre of the first core becomes large, $\beta > 10^4$. Thus, proper treatment of first-core phase is crucial in investigating the formation of protostar and disc. On the other hand, in an ideal simulation, $\beta \sim 10$ at the centre of the first core. The simulations with magnetic diffusion show that the circumstellar disc forms at almost the same time of protostar formation even with a relatively strong initial magnetic field (the value for the initial mass-to-flux ratio of the cloud core relative to the critical value is $\mu = 4$). The disc has a radius of $r \sim 1$ AU at the protostar formation epoch. We confirm that the disc is rotationally supported. We also show that the disc is massive ($Q \sim 1$) and that gravitational instability may play an important role in the subsequent disc evolution.

Key words: MHD – methods: numerical – protoplanetary discs – stars: formation.

1 INTRODUCTION

The molecular cloud core is the formation site of the star. Already almost half-a-century ago, Larson (1969) investigated the formation process of the protostar with one-dimensional radiation hydrodynamics simulation starting from a gravitationally unstable cloud core. An overview of the evolution obtained from that simulation is as follows. While the dust thermal emission effectively removes the thermal energy generated by the compressional heating caused by the gravitational collapse, the gas evolves almost isothermally. At $\rho \sim 10^{-13}\,\mathrm{g\,cm^{-3}}$, the compressional heating overtakes the radiative cooling and the gas begins to evolve adiabatically. In this adiabatic evolution phase, the temperature evolves as $T \propto \rho^{\gamma-1}$, where γ is the adiabatic index ($\gamma = 5/3$ for $T \lesssim 100$ K and $\gamma = 7/5$ for $100 \lesssim T \lesssim 2000$ K). Because this index is larger than the critical adiabatic index for spherical gravitational collapse, $\gamma_{\rm crit} = 4/3$, the gravitational collapse temporarily halts and a quasi-hydrostatic core forms, commonly known as the *first core*. When the central temperature of the first core reaches ∼2000 K, the hydrogen molecules begin to dissociate. This endothermic reaction changes the effective adiabatic index to $\gamma_{\rm eff} = 1.1$. Because this is smaller than $\gamma_{\rm crit}$, the gravitational collapse resumes, which is known as the *second collapse*. Finally, when the molecular hydrogen is completely dissociated, the gas evolves adiabatically again and the gravitational collapse finishes. The adiabatic core formed at the centre is the protostar (or the second core). This evolution process was later confirmed, more sophisticated one-dimensional simulations (Masunaga & Inutsuka 2000; Vaytet et al. 2012, 2013).

Although, the general picture of the formation process of the protostar was established by Larson (1969) with one-dimensional simulations, multidimensional simulations are necessary to investigate important phenomena such as the formation and evolution of the circumstellar disc. After the radiation hydrodynamics simulations done by Larson (1969), it took several decades to develop and perform three-dimensional radiation hydrodynamics simulations of gravitational collapse (Whitehouse & Bate 2006; Bate 2010, 2011; Tomida et al. 2013; Tsukamoto, Machida & Inutsuka 2013b; Tsukamoto et al. 2015). These studies revealed that the multidimensionality causes new and interesting phenomena. For example, Bate (2010) found that the bipolar outflow from the first core can be driven by radiative feedback from the protostar. Tsukamoto et al. (2015) investigated the evolution of the circumstellar discs in the unmagnetized cloud core and found that the temperature structure of the disc is determined by diffusive radiative transfer in the radial direction in its early evolution phase.

The magnetic field is another important ingredient in the star formation process. Observations suggest that the molecular cloud cores

★ E-mail: yusuke.tsukamoto@riken.jp

are magnetized (e.g. Heiles & Troland 2005; Troland & Crutcher 2008). Troland & Crutcher (2008) showed that the mean value of the mass-to-flux ratio relative to the critical value, μ, of the nearby dark cloud cores is $\mu \sim 2$–3 and suggested that the magnetic field of the typical cloud core is relatively strong. The magnetic field drives the outflow from both the first core and the protostar. The typical velocity of the outflow is determined by the rotational velocity at the launching point ($v \sim 2$ km s^{-1} from the first core and $v \sim 20$ km s^{-1} from the protostar; Tomisaka 2002; Machida, Inutsuka & Matsumoto 2008; Hennebelle & Fromang 2008; Price, Tricco & Bate 2012). Another important effect caused by the magnetic field is the removal of the gas angular momentum. This effect is known as *magnetic braking* (Mouschovias & Paleologou 1979). Until recently, it was believed that the disc formation is a natural consequence of the gravitational collapse of a rotating molecular cloud core. Actually, three-dimensional simulations, with a weak magnetic field or without it, show that a relatively large circumstellar disc (with a radius of several tens of AU) develops in the early phase of protostar formation (Bate 1998, 2011; Tsukamoto & Machida 2011, 2013; Tsukamoto et al. 2013b) However, previous works with ideal magnetohydrodynamics (MHD) simulations have shown that the relatively strong magnetic field ($\mu \sim 1$) completely suppresses the formation of a rotationally supported disc around the protostar at its formation epoch (Mellon & Li 2008; Hennebelle & Fromang 2008).

Ideal MHD is, however, not a good approximation for the simulations of the magnetized molecular cloud core. Because the ionization degree of the cloud core is quite low, it is expected that non-ideal magnetic effects such as Ohmic diffusion, Hall effect, and ambipolar diffusion play important roles during the formation and evolution of the circumstellar disc.

The influence of non-ideal magnetic effects on the disc formation is still controversial. Li, Krasnopolsky & Shang (2011) investigated the influences of the non-ideal magnetic effects. They pointed out that ambipolar diffusion is the dominant diffusion process of the magnetic field and concluded that neither Ohmic nor ambipolar diffusion weakens the magnetic braking and that the disc formation is still strongly suppressed even with the magnetic diffusion. On the other hand, Machida, Inutsuka & Matsumoto (2011) showed that a relatively large disc of about a few tens of AU in size forms in the early phase of the protostar formation although they considered only Ohmic diffusion.

The discrepancy could come from the difference in the initial conditions and the treatment of the inner boundary (or a sink at the centre) of the simulations. In the simulations of Mellon & Li (2008) and Li et al. (2011), the inner boundary or sink is set from the beginning of the simulations. In such a set-up, the simulations cannot follow the evolution of a first core which is mainly supported by gas pressure and not necessarily by rotation. Although the first core is a transient object, its density is high enough that the magnetic flux is efficiently removed from the first core during its evolution (Dapp, Basu & Kunz 2012). Furthermore, it is suggested that the greater part of the first core directly becomes the circumstellar disc (Machida & Matsumoto 2011) just after the protostar formation. Therefore, calculating the first-core phase correctly in the simulations is crucial to investigate the very early phase of disc evolution. On the other hand, Machida et al. (2011) used sink cells with 'threshold density'. In their simulations, the sink cell takes in the gas when its density becomes larger than the threshold density. In this case, the gas whose density is smaller than the threshold density can reside inside or around the sink cell regardless of whether the gas is rotationally supported or not. This treatment may also affect the disc evolution process. Machida, Inutsuka & Matsumoto (2014) showed that the sink treatment (its radius and the threshold density) significantly affects the formation and evolution of the circumstellar disc.

To reveal the realistic formation and evolution processes of the first core, the protostar, and the circumstellar disc, appropriate treatment of the radiation transfer in the simulation is crucial, because the magnetic diffusion coefficients are functions of temperature. The previous studies with MHD simulations mentioned above do not include radiation transfer and employ a simplified equation of state (EOS) which mimics the temperature evolution of the *centre* of the cloud core. We call this the barotropic approximation. The simulations with radiation transfer, however, have shown that the temperature structures in the first core or around the protostar are strikingly different from those expected from the barotropic approximation (Whitehouse & Bate 2006; Bate 2010; Tomida et al. 2013; Tsukamoto et al. 2015).

Three-dimensional simulations which include both the magnetic field and radiation transfer have not been successful until recently. Tomida et al. (2013) were the first to succeed with such a simulation with a grid code and found that the Ohmic diffusion alters the structure around the protostar significantly. With ideal radiation magnetohydrodynamics (RMHD) simulations using the smoothed particle hydrodynamics (SPH) method, Bate, Tricco & Price (2014) also investigated the formation and evolution of the protostar, especially the long-term evolution of the bipolar jets driven around the protostar. They showed that the jets heat up the gas in the envelope after they break up the remnant of the first core. Such a radiative heating process may affect the ionization degree of the gas and change the magnetic diffusion coefficients. However, Bate et al. (2014) did not consider magnetic diffusion processes.

As pointed out in previous studies (Li et al. 2011), it is expected that ambipolar diffusion will play a role during the formation process of the protostar and the disc around it. Very recently, Tomida, Okuzumi & Machida (2015) conducted a simulation with both Ohmic and ambipolar diffusion. However, they only calculated the evolution until the end of the first-core phase with ambipolar diffusion and the effect of the ambipolar diffusion is still unclear.

In this paper, we investigate the formation of the first core, protostar, and the circumstellar disc using a three-dimensional non-ideal RMHD simulation. We employ the SPH method and use it to produce the first results of the three-dimensional non-ideal RMHD simulations with SPH. Here, we focus on the effects of magnetic (Ohmic and ambipolar) diffusion, but do not include the Hall effect. To avoid the numerical artefact caused by the sink, we do not introduce it, but rather investigate the structure around the protostar to determine whether the formation of the circumstellar disc is possible at the very early phase of protostar formation. This paper is organized as follows. In Section 2, we briefly describe the non-ideal magnetohydrodynamic effects. In Section 3, we describe the numerical method and initial conditions for the simulations, the results of which are given in Section 4, and then summarized and discussed in Section 5.

2 NON-IDEAL MAGNETOHYDRODYNAMIC EFFECTS

The ionization degree in the molecular cloud core is quite low and the gas can be regarded as weakly ionized plasma. In weakly ionized plasma, the microscopic collisions between neutral, positively charged, and negatively charged particles produce finite

conductivity and non-ideal magnetohydrodynamic effects, or in short, non-ideal effects arise.

The non-ideal effects appear as the correction terms in the induction equation. They can be derived by calculating the drift velocity of the charged particles. Here, we derive the induction equation for the weakly ionized plasma according to Wardle & Ng (1999) and Wardle (2007).

We start with

$$\frac{\partial \boldsymbol{B}}{\partial t} = -c\nabla \times \boldsymbol{E}, \tag{1}$$

$$\boldsymbol{J} = \frac{c}{4\pi}\nabla \times \boldsymbol{B}. \tag{2}$$

where $\boldsymbol{B}$ is the magnetic field, $\boldsymbol{J}$ is the current density, $\boldsymbol{E}$ is the electric field, and c is the speed of light. By the Lorentz transformation to the rest frame of the fluid (that is essentially the rest frame of bulk of neutral particles), the electric field becomes

$$\boldsymbol{E}' = \boldsymbol{E} + \frac{\boldsymbol{v} \times \boldsymbol{B}}{c}. \tag{3}$$

Here, $\boldsymbol{v}$ and $\boldsymbol{E}'$ are the fluid velocity and the electric field in the rest frame of the fluid, respectively. The conductivity in the weakly ionized plasma can be calculated using the balance of the force that acts on the charged particles,

$$Z_j e\left(\boldsymbol{E}' + \frac{\boldsymbol{v}_j \times \boldsymbol{B}}{c}\right) - \gamma_j \rho m_j \boldsymbol{v}_j = 0. \tag{4}$$

Here, subscript j denotes the species of charged particles, $Z_j e$ is the charge, $\boldsymbol{v}_j$ is the relative velocity of charged particles in the fluid rest frame, $\gamma_j = \langle \sigma v \rangle_j/(m_j + m)$ where $\langle \sigma v \rangle_j$ is the rate coefficient for momentum transfer, m_j is the mass of charged particles, m is the mean mass of neutral particles, and ρ is the density of neutral particles. Note that, in the weakly ionized plasma, most of the particles are neutral and the inertia of the charged particles and the collisions with other charged particles are negligible. Note also that, under the MHD approximation, the difference between the magnetic field and the current density in computation frame and those in the rest frame is negligible. We assumed the local charge neutrality $\sum_j n_j Z_j = 0$. By inverting equation (4) for $\boldsymbol{v}_j$ and calculating the current density, $\boldsymbol{J} = \sum_j n_j Z_j e \boldsymbol{v}_j$, we obtain

$$\boldsymbol{J} = \sigma_{\rm O}\boldsymbol{E}' + \sigma_{\rm H}\hat{\boldsymbol{B}} \times \boldsymbol{E}' - (\sigma_{\rm P} - \sigma_{\rm O})\hat{\boldsymbol{B}} \times \hat{\boldsymbol{B}} \times \boldsymbol{E}', \tag{5}$$

where

$$\sigma_{\rm O} = \frac{ec}{B}\sum_j n_j Z_j \beta_j, \tag{6}$$

$$\sigma_{\rm H} = \frac{ec}{B}\sum_j \frac{n_j Z_j}{1+\beta_j^2}, \tag{7}$$

$$\sigma_{\rm P} = \frac{ec}{B}\sum_j \frac{n_j Z_j \beta_j}{1+\beta_j^2}, \tag{8}$$

are the Ohmic, Hall, and Pedersen conductivities, respectively. Here, $\beta_j = Z_j eB/(m_j c \gamma_j \rho)$ is the Hall parameter which is the product of the cyclotron frequency and stopping time. Finally, by inverting equation (5) for $\boldsymbol{E}'$ and using equations (1) and (3), we obtain

$$\frac{\partial \boldsymbol{B}}{\partial t} = \nabla \times (\boldsymbol{v} \times \boldsymbol{B}) - \nabla \times \left\{\eta_{\rm O}(\nabla \times \boldsymbol{B}) + \eta_{\rm H}(\nabla \times \boldsymbol{B}) \times \hat{\boldsymbol{B}} - \eta_{\rm A}((\nabla \times \boldsymbol{B}) \times \hat{\boldsymbol{B}}) \times \hat{\boldsymbol{B}}\right\}. \tag{9}$$

This is the induction equation with non-ideal effects. The second, third, and fourth terms on the right-hand side of equation (9) describe the Ohmic diffusion, Hall term, and ambipolar diffusion, respectively. Here,

$$\eta_{\rm O} = \frac{c^2}{4\pi\sigma_{\rm O}}, \tag{10}$$

$$\eta_{\rm H} = \frac{c^2\sigma_{\rm H}}{4\pi(\sigma_{\rm H}^2 + \sigma_{\rm P}^2)}, \tag{11}$$

$$\eta_{\rm A} = \frac{c^2\sigma_{\rm P}}{4\pi(\sigma_{\rm H}^2 + \sigma_{\rm P}^2)} - \eta_{\rm O}, \tag{12}$$

are the Ohmic, Hall, and ambipolar diffusion coefficients, respectively. In this paper, the Hall term is neglected owing to the numerical difficulty associated with it. The effect of the Hall term will be investigated in future works.

We constructed the data table of the diffusion coefficients by calculating a chemical reaction network of H_3^+, HCO^+, Mg^+, He^+, C^+, H^+, e^- in gas phase and the positively charged, neutral, and negatively charged dust grain of uniform size using the methods described in Nakano, Nishi & Umebayashi (2002) and Okuzumi (2009). We assumed that the dust to gas ratio is 10^{-2}. We also assumed that the dust grain size and density are $a = 3.5 \times 10^{-2}$ μm and $\rho_{\rm d} = 2\,{\rm g\,cm^{-3}}$, respectively. We considered non-thermal ionization by the cosmic rays and thermal ionization in our calculations. The cosmic ray ionization rate was fixed to be $\xi_{\rm CR} = 10^{-17}\,{\rm s^{-1}}$. When the temperature reaches $T \sim 1000$ K, thermal ionization is the dominant source of ionization. In this paper, we consider the effect of the thermal ionization by considering the thermal ionization of potassium. The coupling between the magnetic field and the gas quickly recovers around $T \sim 1000$ K because the thermal ionization provides a sufficient ionization degree.

In Fig. 1, we show the Ohmic and ambipolar diffusion coefficients under the typical evolution of the gas. To make Fig. 1, we assumed that the temperature and magnetic field change as,

$$B(\rho) = 100\left(\frac{\rho}{10^{-15}\,{\rm g\,cm^{-3}}}\right)^{2/3}\ \mu{\rm G},$$

$$T(\rho) = 10\left\{1 + \left(\frac{\rho}{10^{-13}\,{\rm g\,cm^{-3}}}\right)^{2/5}\right\}{\rm K}. \tag{13}$$

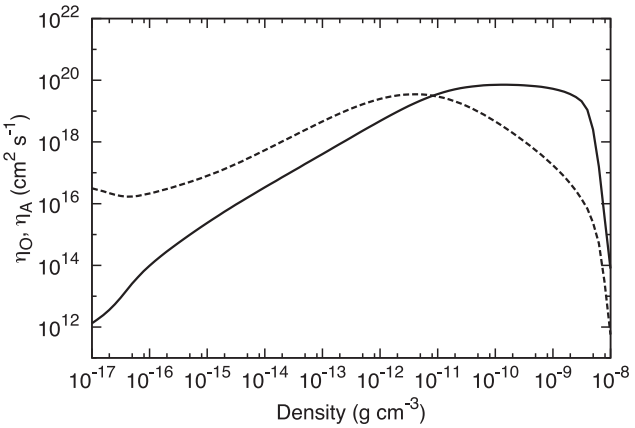

Figure 1. Diffusion coefficients, $\eta_{\rm O}$ (solid) and $\eta_{\rm A}$ (dotted) as a function of density. For this plot, we assumed that the temperature and magnetic field are functions of density (see equation 13).

The figure shows that the diffusion coefficients suddenly drop around $\rho = 5 \times 10^{-9}\,\mathrm{g\,cm^{-3}}$, where the temperature is about $T = 1000$ K and the ionization degree quickly increases owing to the thermal ionization of potassium.

3 NUMERICAL METHOD AND INITIAL CONDITIONS

In this study, we solve the non-ideal RMHD equations with self-gravity,

$$\frac{\mathrm{D}\boldsymbol{v}}{\mathrm{D}t} = -\frac{1}{\rho}\left\{\nabla\left(P + \frac{1}{2}B^2\right) - \nabla\cdot(\boldsymbol{B}\boldsymbol{B})\right\} - \nabla\Phi, \tag{14}$$

$$\frac{\mathrm{D}}{\mathrm{D}t}\left(\frac{\boldsymbol{B}}{\rho}\right) = \left(\frac{\boldsymbol{B}}{\rho}\cdot\nabla\right)\boldsymbol{v} - \frac{1}{\rho}\nabla\times\left\{\eta_{\mathrm{O}}(\nabla\times\boldsymbol{B}) - \eta_{\mathrm{A}}(\nabla\times\boldsymbol{B})\times\hat{\boldsymbol{B}}\times\hat{\boldsymbol{B}}\right\}, \tag{15}$$

$$\frac{\mathrm{D}}{\mathrm{D}t}\left(\frac{E_{\mathrm{r}}}{\rho}\right) = -\frac{\nabla\cdot\boldsymbol{F}_{\mathrm{r}}}{\rho} - \frac{\nabla\boldsymbol{v}:\boldsymbol{P}_{\mathrm{r}}}{\rho} + \kappa_{\mathrm{P}}c(a_{\mathrm{r}}T_{\mathrm{g}}^4 - E_{\mathrm{r}}), \tag{16}$$

$$\begin{aligned}\frac{\mathrm{D}}{\mathrm{D}t}\left(\frac{e}{\rho}\right) = &-\frac{1}{\rho}\nabla\cdot\left\{\left(P + \frac{1}{2}B^2\right)\boldsymbol{v} - \boldsymbol{B}(\boldsymbol{B}\cdot\boldsymbol{v})\right\} \\ &- \kappa_{\mathrm{P}}c(a_{\mathrm{r}}T_{\mathrm{g}}^4 - E_{\mathrm{r}}) - \boldsymbol{v}\cdot\nabla\Phi \\ &- \frac{1}{\rho}\nabla\cdot[\{(\eta_{\mathrm{O}}(\nabla\times\boldsymbol{B}) \\ &- \eta_{\mathrm{A}}(\nabla\times\boldsymbol{B})\times\hat{\boldsymbol{B}}\times\hat{\boldsymbol{B}}\}\times\boldsymbol{B}],\end{aligned} \tag{17}$$

$$\nabla^2\Phi = 4\pi G\rho. \tag{18}$$

Here, ρ is the gas density, $\boldsymbol{v}$ is the velocity, $\boldsymbol{B}$ is the magnetic field, $\hat{\boldsymbol{B}}$ is the unit directional vector of the magnetic field, P is the gas pressure, E_{r} is the radiation energy, $\boldsymbol{F}_{\mathrm{r}}$ is the radiation flux, $\boldsymbol{P}_{\mathrm{r}}$ is the radiation pressure, T_{g} is the gas temperature, κ_{P} is the Plank mean opacity, $e = \rho u + \frac{1}{2}(\rho\boldsymbol{v}^2 + \boldsymbol{B}^2)$ is the total energy with u specific internal energy, and Φ is the gravitational potential. Parameters, a_{r} and G are the radiation and gravitational constants, respectively. We adopt the grey approximation (frequency-integrated radiation transfer) and we assume local thermodynamic equilibrium. To close the equations for radiation transfer, we employ flux-limited diffusion (FLD) approximations,

$$\boldsymbol{F}_r = \frac{c\lambda}{\kappa_{\mathrm{R}}\rho}\nabla E_{\mathrm{r}}, \quad \lambda(R) = \frac{2+R}{6+2R+R^2},$$

$$R = \frac{|\nabla E_{\mathrm{r}}|}{\kappa_{\mathrm{R}}\rho E_{\mathrm{r}}}, \quad \boldsymbol{P}_{\mathrm{r}} = \mathbb{D}E_{\mathrm{r}},$$

$$\mathbb{D} = \frac{1-\chi}{2}\mathbb{I} + \frac{3\chi-1}{2}\boldsymbol{n}\otimes\boldsymbol{n}, \quad \chi = \lambda + \lambda^2R^2,$$

$$\boldsymbol{n} = \frac{\nabla E_{\mathrm{r}}}{|\nabla E_{\mathrm{r}}|}.$$

Here, κ_{R} is the Rosseland mean opacity. FLD is a diffusion scheme which is designed to maintain the causality of $|\boldsymbol{F}_{\mathrm{r}}| < cE_{\mathrm{r}}$. It is suitable for optically thick gas owing to its diffusive nature.

In this paper, we use the SPH method to investigate the formation of a protostar and disc. The SPH method can be easily implemented and is suitable for simulations which treat the large dynamic range because of its adaptive nature. The ideal MHD part was solved by adopting the Godunov smoothed particle magnetohydrodynamics (GSPMHD) method in which the Godunov method and the method of characteristics are used to calculate the interactions between the particles instead of artificial dissipation terms (Iwasaki & Inutsuka 2011). The divergence-free constraint on the magnetic field was maintained using the hyperbolic divergence cleaning method for GSPMHD (Iwasaki & Inutsuka 2013). The radiative transfer was treated by the FLD-SPH method (Whitehouse & Bate 2004; Whitehouse, Bate & Monaghan 2005). We treated Ohmic and ambipolar diffusion with the method described by Tsukamoto, Iwasaki & Inutsuka (2013a) and Wurster, Price & Ayliffe (2014), respectively. Both diffusion processes were accelerated by super-time-stepping method (Alexiades, Amiez & Gremaud 1996). To calculate the self-gravity, we adopted the Barnes–Hut tree algorithm with opening angle of $\theta = 0.5$ (Barnes & Hut 1986). We do not use the individual time-steps and the particles are updated simultaneously.

We adopted the tabulated EOS used in Tomida et al. (2013), in which the internal degrees of freedom and chemical reactions of seven species $\mathrm{H_2}, \mathrm{H}, \mathrm{H^+}, \mathrm{He}, \mathrm{He^+}, \mathrm{He^{++}}, e^-$ are included. We assumed that the hydrogen and helium mass fractions were $X = 0.7$ and $Y = 0.28$, respectively. The dust opacity table was obtained from Semenov et al. (2003) and the gas opacity table was obtained from Ferguson et al. (2005). The resistive model is described in Section 2.

We modelled the initial cloud core using an isothermal uniform gas sphere. The initial mass and temperature of the core were fixed at 1 $\mathrm{M_\odot}$ and 10 K, respectively, with an initial core radius of $R \sim 3.0 \times 10^3$ AU. The core is initially rigidly rotating with an angular velocity of $\Omega_0 = 2.2 \times 10^{-13}\,\mathrm{s^{-1}}$. The product of the angular velocity and the free-fall time is $t_{\mathrm{ff}}\Omega_0 = 0.19$. The initial magnetic field was uniform and parallel to the rotation (z-)axis with a strength of $B_0 = 1.7 \times 10^2\,\mu\mathrm{G}$. The corresponding initial mass-to-flux ratio relative to the critical value was $\mu = (M/\Phi)/(M/\Phi)_{\mathrm{crit}} = 4$ where $\Phi = \pi R^2 B_0$. We adopted a critical mass-to-flux ratio of $(M/\Phi)_{\mathrm{crit}} = (0.53/3\pi)(5/G)^{1/2}$ suggested by Mouschovias & Spitzer (1976). The initial cores were modelled with about 10^7 SPH particles. The boundary conditions of radiation transfer were introduced by fixing the gas temperature to be 10 K when the gas density was less than $2.0 \times 10^{-17}\,\mathrm{g\,cm^{-3}}$.

We performed three simulations with and without Ohmic and ambipolar diffusion. The model names and the diffusion processes included in each model are summarized in Table 1.

Table 1. The model names and the magnetic diffusion they include. 'Yes' means that the corresponding magnetic diffusion is included while a 'No' means that it is not.

Model	Ohmic diffusion	Ambipolar diffusion
1	No	No
2	Yes	No
3	Yes	Yes

4 SIMULATION RESULTS

4.1 Evolution at the centre of the cloud core

To investigate how the magnetic field evolves during the gravitational collapse, we show the evolution of the central magnetic

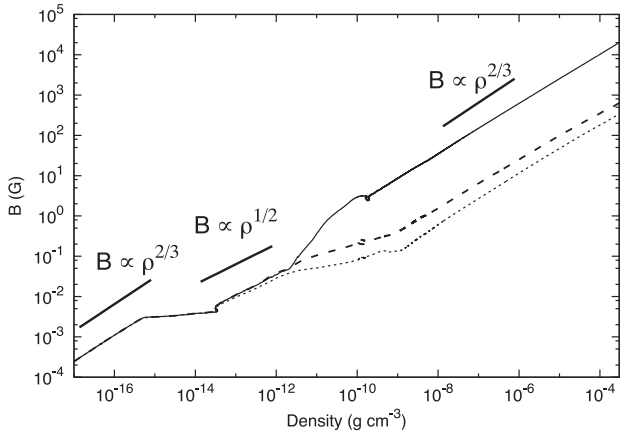

Figure 2. The evolution of the central magnetic field as a function of central density. The solid, dashed, and dotted lines show the results of model 1 (ideal), model 2 (with Ohmic diffusion), and model 3 (with Ohmic and ambipolar diffusion), respectively. Differences between the models can be seen when the central density exceeds $\rho_c > 10^{-12}\,\mathrm{g\,cm^{-3}}$ and magnetic diffusion becomes effective.

field as a function of the central density in Fig. 2. At first, the magnetic field evolves as $B_c \propto \rho_c^{2/3}$. This evolution is expected from a spherically symmetric collapse during which the central magnetic field evolves as $B_c \propto R^{-2}$ due to the conservation of the magnetic flux, where R is the radius of the cloud. On the other hand, the central density evolves as $\rho_c \propto R^{-3}$ or, equivalently, $R \propto \rho_c^{-1/3}$. Thus, $B_c \propto R^{-2} \propto \rho_c^{2/3}$. The increase in the magnetic field almost stops ($B_c \propto \rho_c^0$) at $10^{-15} \lesssim \rho_c \lesssim 10^{-14}\,\mathrm{g\,cm^{-3}}$ because the Lorentz force becomes comparable to the gravitational force and the gas moves almost parallel to the magnetic field. The z-component of the magnetic field still dominates other components and the gas moves almost vertically. As a result, a sheet-like structure (or pseudo-disc) forms. When the central density reaches $\rho_c \sim 10^{-13}\,\mathrm{g\,cm^{-3}}$, the central magnetic field evolves as $B_c \propto \rho_c^{1/2}$ which indicates that the collapse becomes sheet-like. In the gravitationally collapsing isothermal sheet (whose scaleheight is $H = c_s^2/(G\Sigma) = c_s/\sqrt{G\rho_c}$), the central magnetic field and density evolves as $B_c \propto R^{-2}$ and $\rho_c \propto R^{-2}H^{-1} \propto R^{-4}$ and hence $B_c \propto \rho_c^{1/2}$.

Once the central density exceeds $\rho \sim 10^{-12}\,\mathrm{g\,cm^{-3}}$, the magnetic diffusions becomes effective and the magnetic freezing is no longer valid for resistive models. The magnetic flux is removed from the central part and the difference between the ideal model and resistive models can be seen. The central magnetic field of model 1 (the ideal model) is about 60 times larger than that of model 3 (with Ohmic and ambipolar diffusion) when the central density reaches $\rho_c \sim 10^{-9}\,\mathrm{g\,cm^{-3}}$. Around the $\rho_c \sim 10^{-9}\,\mathrm{g\,cm^{-3}}$, the magnetic diffusion becomes ineffective again owing to the thermal ionization and the flux freezing recovers in the resistive models. This causes $B_c \propto \rho_c^{2/3}$ again.

4.2 Structure of the first core

When the central density reaches $\rho_c \sim 10^{-13}\,\mathrm{g\,cm^{-3}}$, the gas becomes opaque and the compressional heating due to the gravitational contraction cannot radiate away efficiently. As a result, the gas evolves adiabatically and a pressure-supported core, the first core, forms. The first-core phase lasts until the central temperature becomes $T_c \sim 2000$ K (or $\rho_c \sim 10^{-8}\,\mathrm{g\,cm^{-3}}$) at which point the dissociation of hydrogen molecules begins. The durations of the first-core phase are about 620 yr for model 1, 810 yr for model 2, and 940 yr for model 3. The first-core phase is defined as the phase in which the central density is $10^{-13}\,\mathrm{g\,cm^{-3}} < \rho_c < 10^{-8}\,\mathrm{g\,cm^{-3}}$. The difference in the duration is due to the rotation of the first core.

To investigate the structure in and around the first core, we show the cross-sections of the density, gas temperature, and plasma β around the first core in the $y = 0$ plane in Fig. 3 at the end of the first-core phase ($\rho_c \sim 3 \times 10^{-9}\,\mathrm{g\,cm^{-3}}$). The plasma β is defined as $\beta = P_{\rm gas}/P_{\rm mag}$ where $P_{\rm gas}$ and $P_{\rm mag}$ are the gas pressure and magnetic pressure, respectively. Note that the box size of the density cross-sections is four times that of the other cross-sections to compare the outflow structures of each model.

To obtain the cross-section and the profiles, the physical quantities are needed at grid points. In this paper, the physical quantities are calculated at grid points through,

$$f(\boldsymbol{x}_{\rm grid}) = \frac{\sum_j m_j \frac{f(\boldsymbol{x}_j)}{\rho_j} W(\boldsymbol{x}_{\rm grid} - \boldsymbol{x}_j, h_j)}{\sum_j m_j \frac{1}{\rho_j} W(\boldsymbol{x}_{\rm grid} - \boldsymbol{x}_j, h_j)}. \quad (19)$$

In the left-hand panels, we show the density cross-section. The thick black solid lines show the $v_z = 0$ contour and trace the outflow structure. The outflow formed in both models 1 and 2, but did not in model 3 at the epochs. Although the outflow did not form in model 3, we confirmed that the outflow does form in a simulation with both Ohmic and ambipolar diffusion when the initial rotation of the cloud core is slightly larger than in the model 3. Therefore, we conclude that the magnetic resistivity delays the formation of the outflow rather than suppressing it. In our results, both the magneto-centrifugal force and the magnetic pressure play a role in driving the outflow.

In the middle panels, we show the temperature cross-section around the first core. The high-temperature ($T \sim 1000$ K) regions with radius of $r \sim 5$ AU are formed at the centre due to the radiative transfer. The high-temperature region is extended compared to the case in which the barotropic EOS is adopted. Because the thermal ionization becomes effective at $T \sim 1000$ K, the coupling between the magnetic field and the gas recovers in the relatively large part of the first core when the radiative transfer is taken into account. This recoupling causes the amplification of the magnetic field inside the first core due to the rotation.

In the right-hand panels, we show the cross-section of the plasma β. Because of the magnetic diffusion, the magnetic flux is efficiently removed from the first core in the resistive models. Thus, in the resistive models, $\beta \gtrsim 10^3$ at the centre of the first core while in the ideal model, $\beta \sim 10$. After the removal of the magnetic flux, the coupling between the gas and the magnetic field recovers at the central region of the first core owing to the thermal ionization and the magnetic field in the first core is reamplified by the rotation. As a result, the plasma β around the centre slightly decreases in the resistive models. This amplification is clearly seen in the middle right panel.

Fig. 4 shows the profiles of the density, gas temperature, and plasma β at the same epoch of Fig. 3. In all models, the central density and the central temperature of the first core are $\rho_c \sim 3 \times 10^{-9}\,\mathrm{g\,cm^{-3}}$ and $T_c \sim 10^3$ K, respectively. The density and temperature profiles show that the first cores formed in each model have very similar structures. This is because the angular momenta of the first cores are not significantly different and the structural difference caused by rotation is negligible. The density on the x-axis is larger than that on the z-axis outside of the first

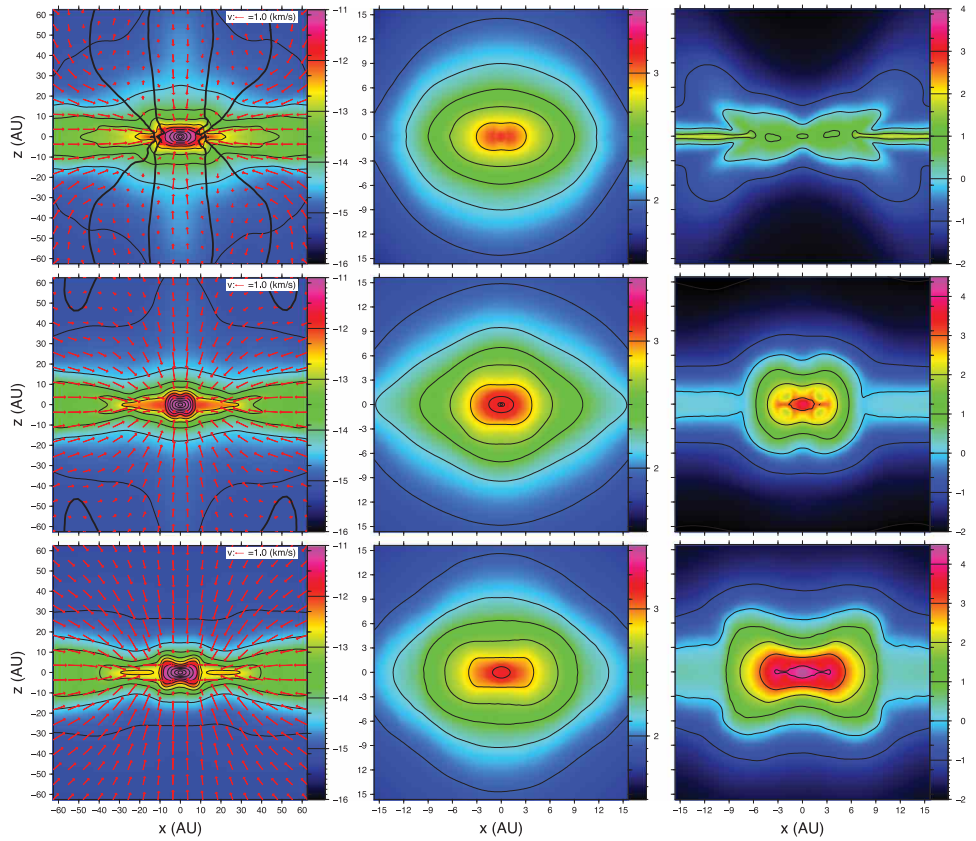

Figure 3. The cross-sections of the density, gas temperature, and plasma β (from left to right) around the first core in the $y = 0$ plane. The top row corresponds to model 1, the middle row to model 2, and the bottom row to model 3. The thin black lines show the contour of each quantity, while the thick black lines in the density cross-sections show the $|v_z| = 0$ contour. This traces the outflow regions. The red arrows in the density cross-sections show the velocity field. The box size of the density cross-sections is four times larger than the other cross-sections to show the outflow structures. The colour bars of the density, temperature, and plasma β show $\log(\rho\,(\mathrm{g\,cm^{-3}}))$, $\log(T\,(\mathrm{K}))$, and $\log(\beta)$, respectively.

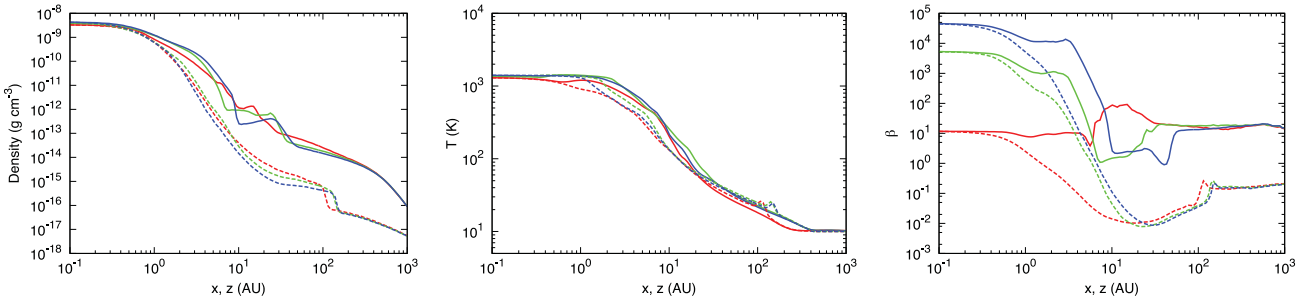

Figure 4. The density (left), gas temperature (middle), and plasma β (right) profiles. The epochs are the same as in Fig. 3. The solid and dashed lines show the profiles of the x- and z-directions, respectively. The red, green, and blue lines show the results of model 1 (ideal model), model 2 (with Ohmic diffusion), and model 3 (with Ohmic and ambipolar diffusion), respectively.

core because the pseudo-disc has formed in the x-direction. On the other hand, the temperature profiles along the x- and z-axis do not differ significantly and the temperature structure is hence almost spherically symmetric.

Due to the magnetic diffusions, the plasma β in the central region of the first core differs significantly between the ideal model and the resistive models. In model 1, the plasma β inside the first core is $\beta \sim 10$ and almost constant in the x-direction. In the model 2, the plasma β at the centre of the first core becomes $\beta \sim 6 \times 10^3$. This is hence about 3 orders magnitude greater than for the ideal model. The magnetic flux removed from the first core piles up around it and the plasma β on the x-axis becomes smaller than the ideal model at the perimeter of the first core ($x \sim 10$ AU). In model 3, the plasma β at the centre of the first core becomes $\beta \sim 6 \times 10^4$, which is much higher than for the model 2. In the z-direction, the plasma β quickly decreases in all models because of the large density gradient in this direction and the magnetic field amplification by the first-core rotation. Because the plasma β is larger than 10 inside the first core, the magnetic pressure does not affect the pressure support in the first core.

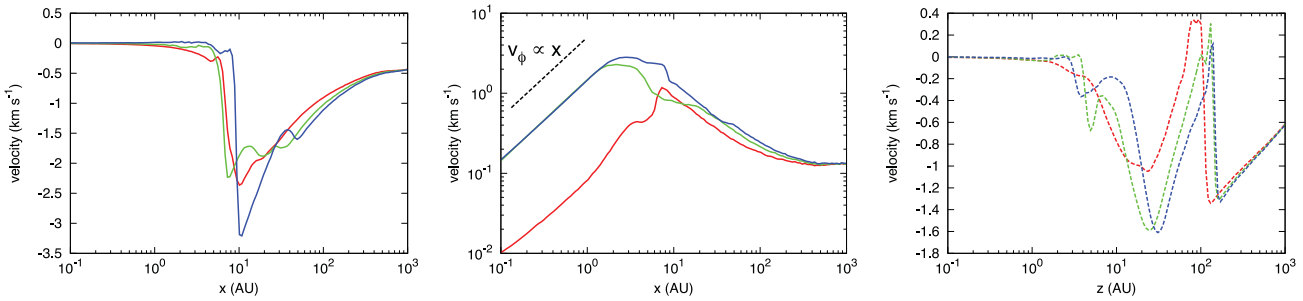

Figure 5. The profiles of the infall velocity (left) and rotation velocity (middle) in the x-direction and the infall velocity in the z-direction (right). The epochs are the same as in Fig. 3. The red, green, and blue lines show the results of model 1 (ideal model), model 2 (with Ohmic diffusion), and model 3 (with Ohmic and ambipolar diffusion), respectively.

A notable difference between models 2 and 3 is the plasma β in the x-direction *at the perimeter of* the first core. In the model 2, only Ohmic diffusion is considered. The Ohmic diffusion coefficient is an increasing function of density and does not depend on the magnetic field. Roughly speaking, the Ohmic diffusion does not play a role when $\rho \lesssim 10^{-13}\,\mathrm{g\,cm^{-3}}$ (Machida, Inutsuka & Matsumoto 2007). Because the density of the first core is $\rho \gtrsim 10^{-13}\,\mathrm{g\,cm^{-3}}$, the magnetic flux piles up outside the first core. By this pile-up, the plasma β beyond the first core in model 2 is $\beta \sim 1$ around $x = 10$ AU and becomes much smaller than for model 1 at larger x. In model 3, the ambipolar diffusion is included as well. The diffusion coefficient of the ambipolar diffusion is a function of the magnetic field and does not depend strongly on the density. Therefore, it is expected that the pile-up of the magnetic flux is smoothed by the ambipolar diffusion. Actually, the region of small plasma β ($\beta \sim 1$) in the x-direction broadens in the right-hand panel. This difference can also be seen in the right-hand panels of Fig. 4.

In Fig. 5, we show the infall and rotation velocities along the x-axis and the infall velocity along the z-axis. The infall velocity along the x-axis is larger than that along the z-axis and the density on the x-axis is also much higher than on the z-axis at the surface of the first core ($x, z \sim 10$ AU). Therefore, the mass accretion on to the first core is asymmetric and is maximal in the horizontal direction.

The rotation velocity v_ϕ reaches its maximum value at $x \sim 2$ AU in models 2 and 3. Inside this radius, the velocity profile obeys the rigid rotation relation, $v_\phi \propto x$. Note that a rigid rotation is expected when the density is constant because $v_\phi \propto \sqrt{M_r/r} \propto \sqrt{\rho_0 r^3/r} \propto r$, where M_r and ρ_0 are the mass inside r and the density, respectively. In model 2, v_ϕ sharply decreases at the $r \sim 4$ AU. This is caused by the strong magnetic braking by the piled-up magnetic field. As mentioned above, the magnetic flux piles up around the first core. Hence, the magnetic braking is locally enhanced at $r \sim 4$ AU and the rotation velocity is decreases. The profile of the model 1 also obeys the relation of $v_\phi \propto x$ for $x \lesssim 1$ AU. On the other hand, for 3 AU $\lesssim x \lesssim 10$ AU, the profile has a complex structure. This structure is also caused by the magnetic braking. Note that the plasma β inside the first core is still small in model 1.

In Fig. 6, we show the evolution of the angular momentum of the first core in relation to the central density. We define the first core as the region where $\rho > 10^{-13}\,\mathrm{g\,cm^{-3}}$. As we have seen above, the magnetic field in the first core becomes weak due to the magnetic diffusion which causes an inefficient angular momentum transfer by the magnetic braking. Thus, it is expected that the angular momentum of the first core becomes large in resistive models and it indeed becomes large when the magnetic diffusion is included. The difference in the angular momentum between model 1 and model 3 is a factor of 6 and hence, insignificant. Most of the initial angular momentum of the fluid element has already been removed during the isothermal collapse phase. With the parameters adopted in our simulations, a disc of $r \sim 100$ AU forms when the magnetic field is neglected (see e.g. Tsukamoto & Machida 2011; Tsukamoto et al. 2015). Therefore, we conclude that the angular momentum of the first core depends more strongly on the initial condition of the molecular cloud cores (see e.g. Joos, Hennebelle & Ciardi 2012).

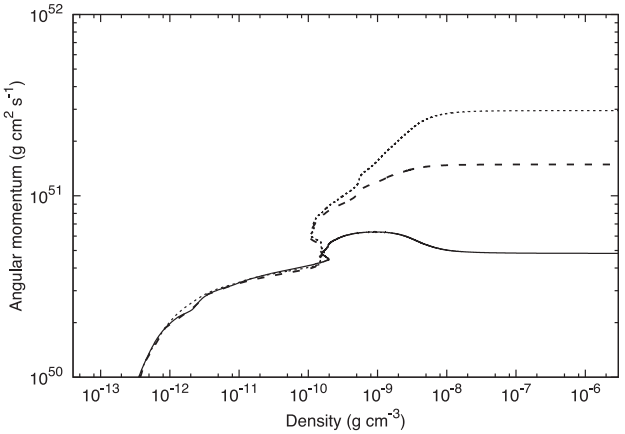

Figure 6. The evolution of the angular momentum of the first core in relation to the central density. The solid, dashed, and dotted lines show the results of models 1, 2, and 3, respectively.

4.3 Formation of the protostar

When the central density reaches $\rho_c \sim 10^{-3}\,\mathrm{g\,cm^{-3}}$ and the hydrogen molecules are completely dissociated, the gas evolves adiabatically and the protostar forms at the centre of the first core. In Fig. 7, we show the cross-sections of density, temperature, and plasma β around the protostar. The central density is $\rho_c \sim 10^{-3}\,\mathrm{g\,cm^{-3}}$ at this epoch and just after the protostar formation. Note that the x, y, and colour-bar scales differ between the ideal model and resistive models because the structure around the protostar in the ideal model is quantitatively different from the one in the other models. The density distributions of the resistive models (middle and bottom left panels) exhibit the dumbbell-like structures. These structures indicate that the rotation plays a role in the resistive models. On the other hand, in model 1 (the ideal model), the density structure is elliptical and there is no dumbbell-like structure even in vicinity of the protostar. As we will show below, the rotationally supported

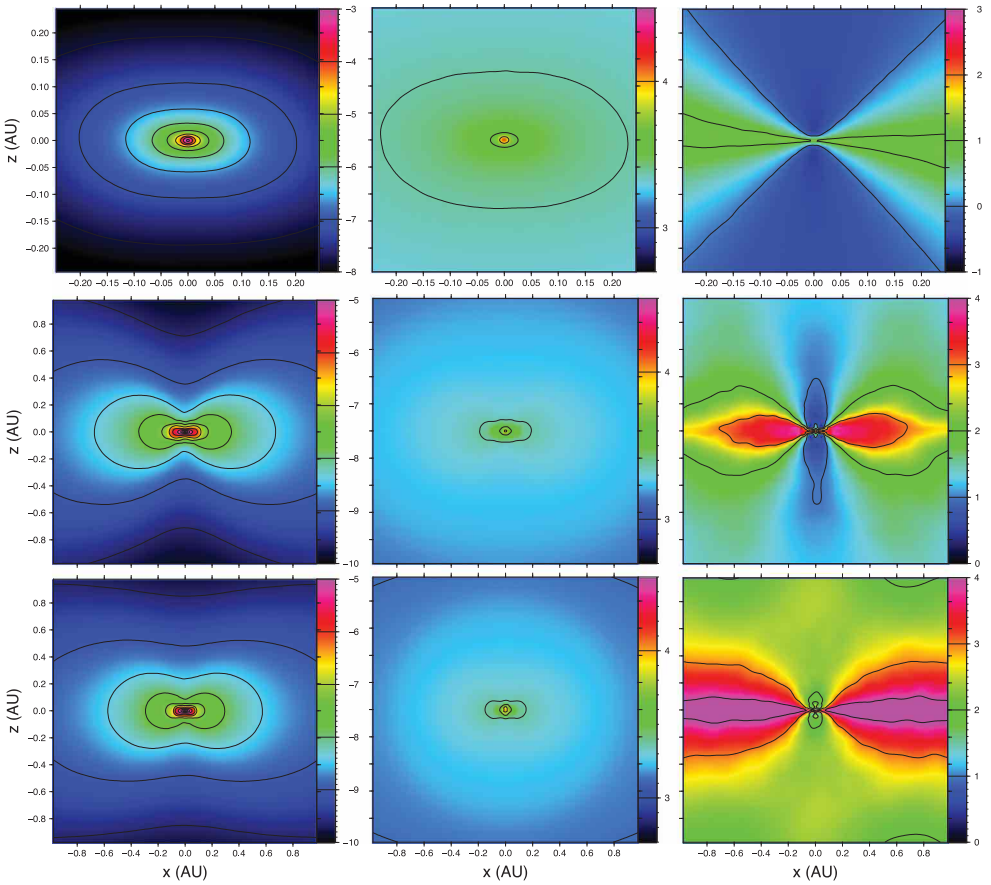

Figure 7. The cross-sections of the density, gas temperature, and plasma β (from left to right) around the protostar in the $y = 0$ plane. The top, middle, and bottom rows correspond to model 1, 2, and 3, respectively. The thin black lines show the contours of each quantity. The colour bars of the density, temperature, and plasma β are expressed as $\log(\rho\,(\mathrm{g\,cm^{-3}}))$, $\log(T\,(\mathrm{K}))$, and $\log(\beta)$, respectively. Note that the x, y, and colour-bar scales differ between the ideal model and the resistive models.

disc quickly forms during the subsequent evolution in the resistive models but does not form in the ideal model. The temperature distributions around the protostar are smooth and roughly spherically symmetric in all models. The temperature exceeds 1000 K and the magnetic diffusion is no longer effective in the entire region. In the model 2, the low β region forms in the vertical direction. This structure is created by the rotational amplification of the magnetic field. As a result, the plasma β becomes $\beta \sim 10^{-1}$. The magnetic field is also magnified in model 3. However, it is not a significant magnification and the plasma β in the vertical direction is still $\beta \sim 10^{2}$ at this epoch. We cannot find any signature of the rotational amplification in model 1. The low β region in the vertical direction is created by a dragging of the poloidal magnetic field. Fig. 7 shows that the structures around the protostar are significantly different even just after the protostar formation when the magnetic diffusion is considered.

After the protostar forms, it evolves via the mass accretion from the remnant of the first core. In Fig. 8, we show the density and gas temperature along the x-axis (solid lines) and z-axis (dashed lines) at the end of the simulations. The central densities and temperatures reach $\rho_{\mathrm{c}} \sim 10^{-2}$–$10^{-1}\,\mathrm{g\,cm^{-3}}$ and $T_{\mathrm{c}} \gtrsim 10^{4}$ K, respectively. From the decrease in the density and temperature of the red lines around $x, z \sim 10^{-2}$ AU, we can identify the radius of the protostar in the ideal model as $r \sim 10^{-2}$ AU. In the ideal model, the difference between the density in the horizontal and the vertical directions is not large and the density structure is almost spherically symmetric. On the other hand, the density profiles of the resistive models show a different structure around the protostar. After the formation of the protostar, the rotationally supported disc of size 1 AU quickly forms in resistive models in these epochs. Because of the disc formation, the boundary of the protostar becomes ambiguous in the density and temperature profiles in the horizontal direction. Weak shock wave structures can be seen at $x \sim 1$ AU in the green and blue solid lines of density. This is the boundary of the circumstellar discs.

In Fig. 9, we show the infall and rotation velocity along the x-axis. The left-hand panel shows the infall velocity. In the ideal model, the infall reaches $x \sim 10^{-2}$ AU, which shows that the first-core remnant accretes directly on to the central protostar. On the other hand, the infall stops at $x \sim 1$ AU in the resistive models. This radius corresponds to the shocks in the density profiles and thus to the edges of the discs. Note that there are the other shocks at $x \sim 10$ AU. These are the accretion shocks at the surface of the first core. The remnant of the first core still exists in these epochs.

We can see a clear transition of the rotation profile at $x \sim 10^{-2}$ AU in the resistive models (blue and green lines). In $x \lesssim 10^{-2}$ AU, the profile obeys $v_{\phi} \propto x$ and the gas rigidly rotates. This rigidly rotating region is the protostar and its radius in the resistive models is also $r \sim 10^{-2}$ AU. In $10^{-2} \lesssim x \lesssim 1$ AU, the profile follows $v_{\phi} \propto x^{-0.2}$.

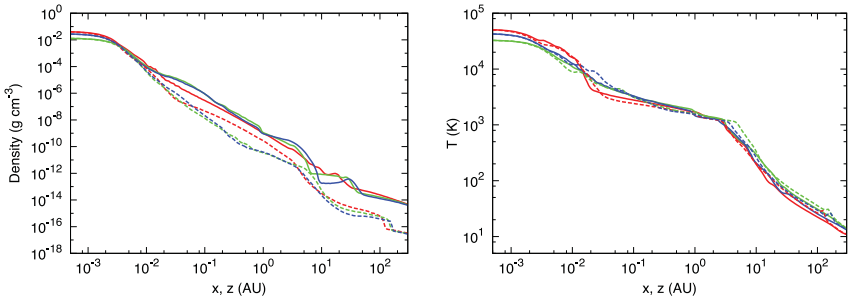

Figure 8. The profiles of the density (left) and gas temperature (right) at the end of the simulations. The solid and dashed lines show the profiles in the x- and z-directions, respectively. The red, green, and blue lines show the results of models 1, 2, and 3, respectively.

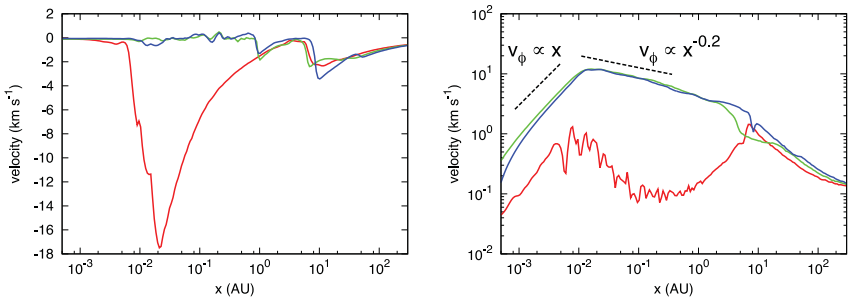

Figure 9. The profiles of the infall velocity (left) and rotation velocity (right) in the x-direction. The epochs are the same as in Fig. 8. The red, green, and blue lines are also defined as in Fig. 8.

This is the rotation profile of the disc around the protostar. The rotation profile of the disc is more shallow than for a Keplerian disc (or disc subjected to a gravitational potential created by a point mass) which obeys the profile of $v_\phi \propto x^{-0.5}$. This means that both the self-gravity of the disc and the gravity of the central protostar influence the rotation profile.

4.4 Rotationally supported disc around protostar

As we have seen above, there are several features of the density and velocity profiles which suggest the existence of a circumstellar disc. For example, the rotational velocity at the mid-plane of models 2 and 3 is considerably larger than the radial velocity in $10^{-2} \lesssim x \lesssim 1$ AU. In addition, shocks exist at $x \sim 1$ AU in the density and infall velocity profiles. However, it is not clear from the above analysis whether the disc is rotationally supported or not.

To confirm that the disc is really rotationally supported, the ratio of the sum of the centrifugal and the pressure gradient forces to the radial gravitational force,

$$q_1 = \left| \frac{v_\phi^2/r + \nabla_r p/\rho}{\nabla_r \Phi} \right|, \tag{20}$$

is plotted in Fig. 10 with the solid lines and the ratio of the centrifugal to the radial gravitational force,

$$q_2 = \left| \frac{v_\phi^2/r}{\nabla_r \Phi} \right|, \tag{21}$$

with the dashed lines. Here, p and Φ are the pressure and the gravitational potential, respectively. When $q_1 = 1$ and $q_2 \ll q_1$, the gas is supported by the pressure gradient force. On the other hand, when $q_1 = 1$ and $q_2 \sim q_1$, the gas is mainly supported by the centrifugal force.

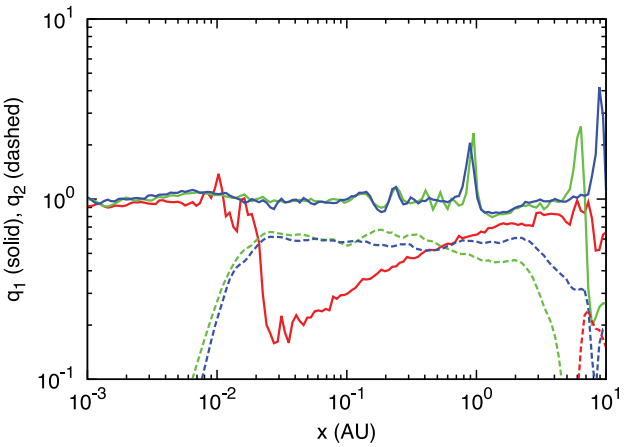

Figure 10. Solid lines show the ratio of the sum of the centrifugal force and the pressure gradient force to the radial gravitational force, $q_1 = |\frac{v_\phi^2/r + \nabla_r p/\rho}{\nabla_r \Phi}|$, as a function of the radius. Here, p and Φ are the pressure and the gravitational potential, respectively. The dashed lines show the ratio of the centrifugal force to the radial gravitational force, $q_2 = |\frac{v_\phi^2/r}{\nabla_r \Phi}|$. The red, green, and blue lines show the results of models 1, 2, and 3, respectively. The epochs are the same as in Fig. 8.

The red lines show that $q_1 \sim 1$ and $q_2 \ll q_1$ for $x \lesssim 10^{-2}$ AU. This means that a pressure-supported second core (the protostar), whose radius is $r \sim 10^{-2}$ AU exists at the centre. On the other hand, the radial gravitational force always dominates other forces for 10^{-2} AU $\lesssim x \lesssim 5$ AU. Therefore, neither the pressure gradient force nor the centrifugal force can cancel the gravitational collapse and no rotationally supported disc forms in the ideal model. On the other hand, the green and blue lines show that q_1 is almost unity for $x \lesssim 1$ AU and the gravitational force is cancelled in this region. For $x \lesssim 10^{-2}$ AU, the $q_1 \sim 1$ and $q_2 \ll q_1$, which shows the existence

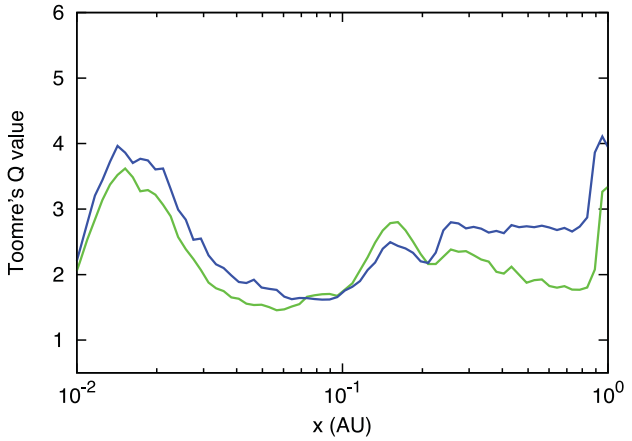

Figure 11. Toomre's Q value as a function of the radius in the x-direction. The green and blue lines show the results of models 2 and 3, respectively. The epochs are the same as in Fig. 8.

of a pressure-supported protostar. Meanwhile, q_2 is about 0.6 for $10^{-2}\,\mathrm{AU} \lesssim x \lesssim 1\,\mathrm{AU}$ and 60 per cent of the gravitational force is cancelled by the centrifugal force and the remaining 40 per cent is cancelled by the pressure gradient force in this region. Thus, the gas is supported mainly by the centrifugal force. From these results, we conclude that the rotationally supported disc forms naturally in the very early phase of the protostar formation when the magnetic resistivity is included and the first-core phase is considered correctly. Note that the dips of the green and blue solid lines at the edge of the disc are due to the large pressure gradient there. The ram pressure caused by the mass accretion should balance this.

The first core directly becomes the disc and its mass is much larger than that of the protostar during its formation epoch. Thus, it is expected that the self-gravity plays an important role in the early phase of the disc evolution (Inutsuka, Machida & Matsumoto 2010). In Fig. 11, we show Toomre's Q value of the disc $Q = \frac{c_s \Omega}{\pi G \Sigma}$, where we approximate the epicycle frequency κ as Ω. In the disc region $10^{-2}\,\mathrm{AU} \lesssim x \lesssim 1\,\mathrm{AU}$ Toomre's Q value is $Q \sim 2$–3. As pointed out in previous studies, the disc becomes unstable against non-axisymmetric perturbations when $Q \sim 1.5$ and the spiral arms develop (Laughlin, Korchagin & Adams 1998). The spiral arms invoke an angular momentum transfer. Although, the Q value is still slightly larger than 1.5, it is expected that the gravitational instability plays a very important role for the angular momentum transfer in the subsequent disc evolution because a large amount of the remnant of the first core is still accreting to the disc and the disc mass increases quickly.

5 SUMMARY AND DISCUSSIONS

In this paper, we investigated the formation and evolution of the first core, the protostar and the disc around the protostar by using three-dimensional simulations with radiation transfer, as well as Ohmic and ambipolar diffusions.

Our findings are summarized as follows.

(i) The magnetic flux is largely removed in the first-core phase. As a result, at the centre of the first core, plasma β becomes $\beta > 10^4$. On the other hand, the β at the centre of the first core in ideal simulation is $\beta \sim 10$.

(ii) Even though the plasma β inside the first core is significantly different in the resistive and the ideal models, the angular momentum of the first core is not (within an order of magnitude). This is because most of the angular momentum has been removed before the magnetic diffusion processes play a role. Actually, fig. 11 of Machida et al. (2007) suggests that most of the angular momentum is removed from the gas during the isothermal collapse phase. When the magnetic field is neglected, a disc with $r \sim 100$ AU forms in the cloud core for the parameters adopted in our simulations (see e.g. Tsukamoto & Machida 2011; Tsukamoto et al. 2015). This also suggests that most of the angular momentum is removed during the isothermal phase.

(iii) With magnetic diffusions, a circumstellar disc forms around the protostar just after protostar formation even with a relatively strong initial magnetic field (we employ a uniform density sphere and an initial mass-to-flux ratio relative to the critical value of $\mu = 4$). We confirmed that the disc is rotationally supported. The disc is massive enough to enable gravitational instability to develop in the subsequent disc evolution. Thus, the gravitational instability plays an important role in the early evolution of the circumstellar discs.

The reason why most of the angular momentum is removed from the gas in the isothermal collapse phase can be understood by comparing the magnetic braking time-scale $t_\mathrm{b} \sim \lambda_\mathrm{J}/v_\mathrm{A}$ to the free-fall time-scale t_ff, where λ_J and v_A are the Jeans length and Alfvén velocity, respectively. The magnetic braking time-scale is estimated as the time in which the inertia of the central region is equal to the inertia of the envelope where the Alfvén wave sweeps (Matsumoto & Tomisaka 2004). The ratio of the two time-scale $t_\mathrm{b}/t_\mathrm{ff}$ is given as $t_\mathrm{b}/t_\mathrm{ff} \sim \lambda_\mathrm{J}/(v_\mathrm{A} t_\mathrm{ff}) \sim \sqrt{\beta}$. In our simulations, the plasma β is $\beta = 1.7$ at the initial condition ($\rho = 5.5 \times 10^{-18}\,\mathrm{g\,cm^{-3}}$) and decreases during the early isothermal collapse phase as $\beta \propto c_\mathrm{s}^2/v_\mathrm{A}^2 \propto \rho^{-1/3}$, where we assume that c_s is constant and $B \propto \rho^{2/3}$ as shown in Fig. 2. When the central density reaches $\rho_\mathrm{c} = 10^{-15}\,\mathrm{g\,cm^{-3}}$, $t_\mathrm{b}/t_\mathrm{ff} = \sqrt{\beta} = 0.71$ and the magnetic braking time-scale becomes shorter than the free-fall time-scale. Therefore, $t_\mathrm{b}/t_\mathrm{ff} \lesssim 1$ and the angular momentum is largely removed during the isothermal collapse phase.

Our results about the disc formation are largely consistent with those of the previous studies which followed the protostar formation with sufficient resolution and considered the first-core phase (e.g. Machida & Matsumoto 2011; Tomida et al. 2013). We believe that the development of a disc at the very early phase of the star formation is a robust consequence. The previous research we mentioned above considered only Ohmic diffusion. On the other hand, we also included ambipolar diffusion. This does not change the overall formation process of the disc significantly. However, it is possible that the ambipolar diffusion plays a more important role in the subsequent evolution of the disc because it extends the density range in which the magnetic field and the gas are decoupled and allows the magnetic flux to escape from the disc.

The difference in disc formation between the ideal model and resistive models is due to the strength of the magnetic field and not the difference in the angular momentum of the first core. In our simulations, the circumstellar disc forms in the resistive models (models 2 and 3) and does not in the ideal model (model 1). As we have seen above, in resistive models, the plasma β of the envelope around the protostar is $\beta \gtrsim 10^1$ except for the vicinity of the protostar of model 2 (the middle and bottom right panels of Fig. 7) and the magnetic braking is ineffective. On the other hand, the magnetic field removes the angular momentum from the gas during the second collapse in the ideal model because the plasma β of envelope is $10^{-1} < \beta < 10^1$ (see the top right panel of Fig. 7) and the magnetic braking time-scale is comparable or less than the free-fall

time-scale ($t_b/t_{ff} \sim \sqrt{\beta}$). This is why the circumstellar disc does not form in the ideal model. The simulation with Ohmic diffusion in Tomida et al. (2015) showed that the circumstellar disc forms even in the slowly rotating first core ($J \sim 2 \times 10^{50}$ g cm^2 s^{-1} where J is the angular momentum). Thus, the several-fold difference in the angular momentum does not affect whether or not the disc forms.

Because the magnetic flux is largely removed in the first-core phase, the proper treatment of the first core is necessary to investigate the formation of the protostar and disc. In previous works that argue that the disc formation is strongly suppressed by the magnetic braking (e.g. Mellon & Li 2008; Li et al. 2011), the inner boundary was set from the beginning of the simulations. With this treatment, the previous works cannot follow the first-core phase properly that should be supported by gas pressure. The discrepancy between our results and those of these works should be due to the different treatments of the first-core phase (see also Dapp et al. 2012).

It is expected that the disc size becomes larger than the size obtained in our simulations ($r < 1$ AU) once the mass accretion from the remnant of the first core finishes because the massive remnant still exists and is accreting on to the disc, even at the end of the simulations. Unfortunately, it is almost impossible to investigate the further evolution of the disc without a sink. Although the sink may introduce numerical artefacts (especially in the few sink radius), it is an essential technique for investigating the long-term evolution of the disc. We will investigate the further evolution of the disc with the sink technique while remembering that this introduces numerical artefacts.

In this paper, we showed that the SPH method is capable of treating MHD and non-ideal processes in realistic astrophysical simulations. Our results are largely consistent with those of the recent non-ideal RMHD simulations with the static-mesh-refinement code (Tomida et al. 2015). Thus, our method is reliable and can be used for astrophysical simulations. Because the SPH method is relatively easily implemented and more flexible than static-mesh-refinement code, it can be used as an alternative method for many astrophysical problems in which the magnetic field play the important role.

In the simulations presented in this paper, several approximations were adopted. The influences of these simplifications should be investigated in future studies. For example, we used a fixed dust grain size of $a = 0.035$ μm and a fixed the cosmic ray ionization of $\xi_{CR} = 10^{-17}$ s^{-1}. The latter is not good approximation for the dense region, $\rho \sim 10^{-11}$ g cm^{-3}. We also used a simple rigidly rotating gas sphere as the initial condition. As Joos et al. (2012) and Machida et al. (2014) have pointed out, the initial density profile and the magnetic field configuration strongly affect the size of the circumstellar discs. In future, we will investigate how the differences in the initial configuration affect the disc evolution.

ACKNOWLEDGEMENTS

We thank Dr. K. Tomida, Dr. T. Matsumoto, and Dr. D. Stamatellos for their fruitful discussions. We also thank Dr. K. Tomida and Dr. Y. Hori to provide their EOS table to us. We also thank anonymous referee for helpful comments. The computations were performed on a parallel computer, XC30 system at CfCA of NAOJ. YT and KI are financially supported by Research Fellowships of JSPS for Young Scientists.

REFERENCES

Alexiades V., Amiez G., Gremaud P.-A., 1996, Com. Num. Meth. Eng, 12, 12
Barnes J., Hut P., 1986, Nature, 324, 446
Bate M. R., 1998, ApJ, 508, L95
Bate M. R., 2010, MNRAS, 404, L79
Bate M. R., 2011, MNRAS, 417, 2036
Bate M. R., Tricco T. S., Price D. J., 2014, MNRAS, 437, 77
Dapp W. B., Basu S., Kunz M. W., 2012, A&A, 541, A35
Ferguson J. W., Alexander D. R., Allard F., Barman T., Bodnarik J. G., Hauschildt P. H., Heffner-Wong A., Tamanai A., 2005, ApJ, 623, 585
Heiles C., Troland T. H., 2005, ApJ, 624, 773
Hennebelle P., Fromang S., 2008, A&A, 477, 9
Inutsuka S., Machida M. N., Matsumoto T., 2010, ApJ, 718, L58
Iwasaki K., Inutsuka S., 2011, MNRAS, 418, 1668
Iwasaki K., Inutsuka S.-I., 2013, in Pogorelov N. V., Audit E., Zank G. P., eds, ASP Conf. Ser. Vol. 474, Numerical Modelling of Space Plasma Flows (ASTRONUM2012). Astron. Soc. Pac., San Francisco, p. 239
Joos M., Hennebelle P., Ciardi A., 2012, A&A, 543, A128
Larson R. B., 1969, MNRAS, 145, 271
Laughlin G., Korchagin V., Adams F. C., 1998, ApJ, 504, 945
Li Z.-Y., Krasnopolsky R., Shang H., 2011, ApJ, 738, 180
Machida M. N., Matsumoto T., 2011, MNRAS, 413, 2767
Machida M. N., Inutsuka S., Matsumoto T., 2007, ApJ, 670, 1198
Machida M. N., Inutsuka S.-i., Matsumoto T., 2008, ApJ, 676, 1088
Machida M. N., Inutsuka S.-I., Matsumoto T., 2011, PASJ, 63, 555
Machida M. N., Inutsuka S.-i., Matsumoto T., 2014, MNRAS, 438, 2278
Masunaga H., Inutsuka S., 2000, ApJ, 531, 350
Matsumoto T., Tomisaka K., 2004, ApJ, 616, 266
Mellon R. R., Li Z.-Y., 2008, ApJ, 681, 1356
Mouschovias T. C., Paleologou E. V., 1979, ApJ, 230, 204
Mouschovias T. C., Spitzer L., Jr, 1976, ApJ, 210, 326
Nakano T., Nishi R., Umebayashi T., 2002, ApJ, 573, 199
Okuzumi S., 2009, ApJ, 698, 1122
Price D. J., Tricco T. S., Bate M. R., 2012, MNRAS, 423, L45
Semenov D., Henning T., Helling C., Ilgner M., Sedlmayr E., 2003, A&A, 410, 611
Tomida K., Tomisaka K., Matsumoto T., Hori Y., Okuzumi S., Machida M. N., Saigo K., 2013, ApJ, 763, 6
Tomida K., Okuzumi S., Machida M. N., 2015, ApJ, 801, 117
Tomisaka K., 2002, ApJ, 575, 306
Troland T. H., Crutcher R. M., 2008, ApJ, 680, 457
Tsukamoto Y., Machida M. N., 2011, MNRAS, 416, 591
Tsukamoto Y., Machida M. N., 2013, MNRAS, 428, 1321
Tsukamoto Y., Iwasaki K., Inutsuka S.-i., 2013a, MNRAS, 434, 2593
Tsukamoto Y., Machida M. N., Inutsuka S., 2013b, MNRAS, 436, 1667
Tsukamoto Y., Takahashi S. Z., Machida M. N., Inutsuka S., 2015, MNRAS, 446, 1175
Vaytet N., Audit E., Chabrier G., Commerçon B., Masson J., 2012, A&A, 543, A60
Vaytet N., Chabrier G., Audit E., Commerçon B., Masson J., Ferguson J., Delahaye F., 2013, A&A, 557, A90
Wardle M., 2007, Ap&SS, 311, 35
Wardle M., Ng C., 1999, MNRAS, 303, 239
Whitehouse S. C., Bate M. R., 2004, MNRAS, 353, 1078
Whitehouse S. C., Bate M. R., 2006, MNRAS, 367, 32
Whitehouse S. C., Bate M. R., Monaghan J. J., 2005, MNRAS, 364, 1367
Wurster J., Price D., Ayliffe B., 2014, MNRAS, 444, 1104

This paper has been typeset from a TEX/LATEX file prepared by the author.

A&A 579, A65 (2015)
DOI: 10.1051/0004-6361/201525636

Astronomy & Astrophysics

Formation of terrestrial planets in disks evolving via disk winds and implications for the origin of the solar system's terrestrial planets

Masahiro Ogihara[1], Hiroshi Kobayashi[2], Shu-ichiro Inutsuka[2], and Takeru K. Suzuki[2]

[1] Observatoire de la Côte d'Azur, Boulevard de l'Observatoire, 06304 Nice Cedex 4, France
e-mail: omasahiro@oca.eu
[2] Nagoya University, Furo-cho, Chikusa-ku, Nagoya, Aichi 464-8602, Japan

Received 9 January 2015 / Accepted 20 April 2015

ABSTRACT

Context. Recent three-dimensional magnetohydrodynamical simulations have identified a disk wind by which gas materials are lost from the surface of a protoplanetary disk, which can significantly alter the evolution of the inner disk and the formation of terrestrial planets. A simultaneous description of the realistic evolution of the gaseous and solid components in a disk may provide a clue for solving the problem of the mass concentration of the terrestrial planets in the solar system.
Aims. We simulate the formation of terrestrial planets from planetary embryos in a disk that evolves via magnetorotational instability and a disk wind. The aim is to examine the effects of a disk wind on the orbital evolution and final configuration of planetary systems.
Methods. We perform N-body simulations of sixty 0.1 Earth-mass embryos in an evolving disk. The evolution of the gas surface density of the disk is tracked by solving a one-dimensional diffusion equation with a sink term that accounts for the disk wind.
Results. We find that even in the case of a weak disk wind, the radial slope of the gas surface density of the inner disk becomes shallower, which slows or halts the Type I migration of embryos. If the effect of the disk wind is strong, the disk profile is significantly altered (e.g., positive surface density gradient, inside-out evacuation), leading to outward migration of embryos inside ∼1 AU.
Conclusions. Disk winds play an essential role in terrestrial planet formation inside a few AU by changing the disk profile. In addition, embryos can undergo convergent migration to ∼1 AU in certainly probable conditions. In such a case, the characteristic features of the solar system's terrestrial planets (e.g., mass concentration around 1 AU, late giant impact) may be reproduced.

Key words. planets and satellites: formation – protoplanetary disks – planet-disk interactions

1. Introduction

Planets with masses larger than approximately 0.1 $M_\oplus$ significantly excite density waves in a protoplanetary disk, which in turn exerts torque on the planets, and migrate toward the central star (Type I migration; e.g., Goldreich & Tremaine 1980; Ward 1986). It is known that the inward migration timescale for an Earth-mass planet at 1 AU is $\sim 10^5$ yr in a locally isothermal disk (e.g., Tanaka et al. 2002), which is shorter than the disk lifetime and thus can be a problem for terrestrial planet formation in the solar system. Recent studies have shown that in an adiabatic disk, fully unsaturated positive corotation torques can compensate for negative Lindblad torques, which can change the direction and rate of migration (e.g., Paardekooper et al. 2010). If this effect is significant, a convergence zone where migration is convergent can be created in a disk and gas giant cores can form at a few tens of AU (Horn et al. 2012).

Paardekooper et al. (2011) revised the torque formula by taking into account the effects of viscous and thermal diffusion on the corotation torque, which indicates that only planets with a limited range of masses can experience the non-linear corotation torque due to saturation effects. In fact, planets with masses smaller than a few Earth masses are not affected by the non-linear corotation torque (the horseshoe torque) and they migrate inward under the influence of the Lindblad torque (e.g., Kretke & Lin 2012; Hellary & Nelson 2012; Cossou et al. 2014), which means that the solar system's terrestrial planets still have the problem of inward migration. However, if the slope of the gas surface density becomes large enough, the positive linear corotation torque can reverse the migration.

During the evolution of protoplanetary disks, vertical winds as well as radial accretion play a significant role in the dispersal of the gas component. While photoevaporating winds by UV and X-rays from a central star have been widely discussed (e.g., Alexander et al. 2006; Ercolano et al. 2009), the importance of spontaneously-driven disk winds has also been pointed out (Suzuki & Inutsuka 2009; Suzuki et al. 2010); using magnetohydrodynamic (MHD) simulations they showed that MHD turbulence triggered by magnetorotational instability (MRI) in disks inevitably drives vertical outflows as well as the radial transport of angular momentum and consequent accretion. The detailed properties of such disk winds driven by turbulent Poynting flux have been studied (Bai & Stone 2013; Fromang et al. 2013; Lesur et al. 2013). An intriguing characteristic of the disk wind is that disk dispersal proceeds gradually in an inside-out manner because the dispersal timescale is approximately proportional to rotation time $\propto r^{3/2}$, where r is the radial distance from the star. As a result, the surface density gradient at $r \lesssim 1$ AU becomes much shallower than the typical values of −0.5 to −1.5, and could even be positive, which will drastically affect the migration of protoplanets.

As we are interested in seeing how planet formation proceeds in such a disk, we investigate the formation of terrestrial planets

using N-body simulations in a disk where the effect of a disk wind is considered. We calculate the disk evolution using a one-dimensional disk with viscous diffusion and a disk wind based on Suzuki et al. (2010). In this work, we focus on the late phase of planet formation when the effect of a disk wind is clearly visible, and calculate the accretion and orbital evolution of planets from planetary embryos with masses of 0.1 $M_\oplus$ for ∼100 Myr. The N-body code includes the effect of Type I migration that depends on the slope of gas surface density and the mass of the planets using the prescription described by Paardekooper et al. (2011). We also include the influence of eccentricity on the corotation torque.

Our primary aim is to clarify the effect of a disk wind on terrestrial planet formation. In addition, we also discuss the origin of the terrestrial planets in the solar system. A number of authors (e.g., Kominami & Ida 2002; Nagasawa et al. 2005; Ogihara et al. 2007; Raymond et al. 2009; Morishima et al. 2010) have studied the origin of these planets using N-body simulations; however, no single simulation has yet convincingly reproduced the observed constraints simultaneously (e.g., eccentricities, spatial concentration around 1 AU, late moon-forming giant impact). We will propose a possible model for the origin of the inner solar system.

The plan of the paper is as follows. In Sect. 2 we describe our model and the initial conditions of the simulations; in Sect. 3 we present the results of N-body simulations; in Sect. 4 we discuss the origin of the terrestrial planets in the solar system; in Sect. 5 we give our conclusions.

2. Model description

2.1. Disk model

We calculate the time evolution of the gas component of a protoplanetary disk by taking into account the radial mass flows by the transport of angular momentum through MHD turbulence and the mass loss due to the disk wind. Although there are uncertainties in the mass flux of the disk wind, we follow the simple framework of Suzuki et al. (2010). The evolution of gas surface density Σ_g can be expressed in the form of a diffusion equation,

$$\frac{\partial \Sigma_g}{\partial t} = \frac{3}{r}\frac{\partial}{\partial r}\left[r^{1/2}\frac{\partial}{\partial r}(\nu\Sigma_g r^{1/2})\right] - C_w\frac{\Sigma_g}{\sqrt{2\pi}}\Omega, \quad (1)$$

where Ω is the Keplerian frequency. The standard α viscosity prescription, $\nu = \alpha c_s h$, is used, where c_s indicates the sound velocity and h is the disk scale height. The second term on the right-hand side of Eq. (1) is the disk wind flux ρv_z, which can be expressed as $C_w\rho_0 c_s$ using the mid-plane density ρ_0, c_s, and a non-dimensional constant C_w (Suzuki et al. 2010). We note that the coefficient of the first term on the right-hand side of Eq. (1) is not exactly the same as that of Eq. (9) of Suzuki et al. (2010) owing to a different definition of ν, which gives a slightly different evolution of the disk surface density.

For the initial distribution of the gas disk, we assume

$$\Sigma_{g,ini} = 2400 f_g\left(\frac{r}{1\ \mathrm{AU}}\right)^{-3/2}\exp\left(-\frac{r}{r_{cut}}\right)\ \mathrm{g\,cm^{-2}}, \quad (2)$$

where f_g is a dimensionless parameter and $r_{cut} = 50$ AU is used as a cutoff radius. In our N-body code, we use the evolution of Σ_g to calculate the effect of the gas disk on planet evolution.

The temperature distribution is assumed to be that of an optically thin disk (Hayashi 1981),

$$T = 280\left(\frac{r}{1\ \mathrm{AU}}\right)^{-1/2}\ \mathrm{K}. \quad (3)$$

We note that although Type I migration is also dependent on the temperature profile, we fix the temperature distribution to clarify the effect of the disk wind via surface density distribution. Then the disk scale height h is given by

$$h/r = 0.047\left(\frac{r}{1\ \mathrm{AU}}\right)^{1/4}\left(\frac{L_*}{L_\odot}\right)^{1/8}\left(\frac{M_*}{M_\odot}\right)^{-1/2}, \quad (4)$$

where L_* and M_* are the luminosity and mass of the host star, respectively.

2.2. Type I migration and eccentricity damping

The orbits of planetary embryos with masses $M_1, M_2, ...$ and position vectors $\boldsymbol{r}_1, \boldsymbol{r}_2, ...$ relative to the host star are calculated by numerically integrating the equation of motion,

$$\frac{d^2\boldsymbol{r}_k}{dt^2} = -GM_*\frac{\boldsymbol{r}_k}{|\boldsymbol{r}_k|^3} - \sum_{j\neq k} GM_j\frac{\boldsymbol{r}_k-\boldsymbol{r}_j}{|\boldsymbol{r}_k-\boldsymbol{r}_j|^3} - \sum_j GM_j\frac{\boldsymbol{r}_j}{|\boldsymbol{r}_j|^3} + \boldsymbol{F}_{damp} + \boldsymbol{F}_{mig}, \quad (5)$$

where $\boldsymbol{F}_{damp}$ is a specific force for eccentricity and inclination damping and $\boldsymbol{F}_{mig}$ is a specific force for Type I migration (see Ogihara et al. 2014 for each formula). The timescale for damping of the eccentricity, t_e, is given by

$$t_e = \frac{1}{0.78}\left(\frac{M}{M_*}\right)^{-1}\left(\frac{\Sigma_g r^2}{M_*}\right)^{-1}\left(\frac{c_s}{v_K}\right)^4\Omega^{-1} \quad (6)$$

$$\simeq 3\times10^2 f_g^{-1}\left(\frac{r}{1\ \mathrm{AU}}\right)^2\left(\frac{M}{M_\oplus}\right)^{-1}\left(\frac{M_*}{M_\odot}\right)^{-1/2}\left(\frac{L_*}{L_\odot}\right)^{1/2}\ \mathrm{yr}, \quad (7)$$

where $\Sigma_g = 2400 f_g (r/1\ \mathrm{AU})^{-3/2}\ \mathrm{g\,cm^{-2}}$ is used in the second equality. Here the relative motion between gas and planets is assumed to be subsonic ($ev_K \lesssim c_s$). For planets with high eccentricities and inclinations, we include a correction factor according to Eqs. (11) and (12) of Cresswell & Nelson (2008).

The migration timescale, t_a, is given by

$$t_a = \frac{1}{\beta}\left(\frac{M}{M_*}\right)^{-1}\left(\frac{\Sigma_g r^2}{M_*}\right)^{-1}\left(\frac{c_s}{v_K}\right)^2\Omega^{-1} \quad (8)$$

$$\simeq 2\times10^5 f_g^{-1}\beta^{-1}\left(\frac{r}{1\ \mathrm{AU}}\right)^{3/2}\left(\frac{M}{M_\oplus}\right)^{-1}\left(\frac{M_*}{M_\odot}\right)^{1/2}\left(\frac{L_*}{L_\odot}\right)^{1/4}\ \mathrm{yr}, \quad (9)$$

where β is a coefficient that determines the direction and speed of Type I migration. According to Paardekooper et al. (2010), the Type I migration torque depends on the Lindblad torque, the barotropic part of the horseshoe drag (or the non-linear corotation torque), the entropy-related part of the horseshoe drag, the barotropic part of the linear corotation torque, and the entropy-related part of the linear corotation torque. Paardekooper et al. (2011) derived the total Type I migration torque including both saturation and the cutoff at high viscosity. Thus we write the migration coefficient in the form

$$\beta = \beta_L + \beta_{c,baro} + \beta_{c,ent}, \quad (10)$$

where β_L, $\beta_{c,baro}$, and $\beta_{c,ent}$ are related to the Lindblad torque, the barotropic part of the corotation torque, and the entropy-related part of the corotation torque, respectively. Each formula

is given as

$$\beta_{\rm L} = \frac{2}{\gamma}(-2.5 - 1.7q + 0.1p), \tag{11}$$

$$\beta_{\rm c,baro} = \frac{2}{\gamma}\Bigg(F(P_\nu)G(P_\nu)1.1\left[\frac{3}{2} - p\right] + [1 - K(P_\nu)]\,0.7\left[\frac{3}{2} - p\right]\Bigg), \tag{12}$$

$$\beta_{\rm c,ent} = \frac{2}{\gamma}\Bigg(F(P_\nu)F(P_\chi)\sqrt{G(P_\nu)G(P_\chi)}7.9\frac{\xi}{\gamma} + \sqrt{(1 - K(P_\nu))(1 - K(P_\chi))}\left[2.2 - \frac{1.4}{\gamma}\right]\xi\Bigg), \tag{13}$$

where $-p$ and $-q$ denote the local surface density gradient ($p(r) = -{\rm dln}\,\Sigma_{\rm g}/{\rm dln}\,r$) and the local temperature gradient ($q(r) = -{\rm dln}\,T/{\rm dln}\,r$), γ is the adiabatic index, and $-\xi$ is the local entropy gradient ($\xi = q - (\gamma - 1)p$). In this work, $\gamma = 1.4$ and $q = 0.5$. The function $F(P)$ is a decreasing function with the value of [0,1] that is related to saturation, and the functions $G(P)$ and $K(P)$ are increasing functions with the value of [0,1] related to cutoff. Paardekooper et al. (2011) introduced viscous and thermal parameters P_ν and P_χ, which are expressed by the ratio between the viscous/thermal diffusion timescales τ_ν/τ_χ and the horseshoe libration timescale $\tau_{\rm lib}$,

$$P_\nu = \frac{2}{3}\sqrt{\frac{\Omega r^2 x_{\rm s}^3}{2\pi\nu}}\left(= \sqrt{\frac{16}{27}\frac{\tau_\nu}{\tau_{\rm lib}}}\right), \tag{14}$$

$$P_\chi = \sqrt{\frac{\Omega r^2 x_{\rm s}^3}{2\pi\chi}}\left(= \sqrt{\frac{4}{3}\frac{\tau_\chi}{\tau_{\rm lib}}}\right), \tag{15}$$

where the dimensionless half-width of the horseshoe region is

$$x_{\rm s} = \frac{w_{\rm s}}{r} = \frac{1.1}{\gamma^{1/4}}\sqrt{\frac{M}{M_*}\frac{r}{h}}, \tag{16}$$

where $w_{\rm s}$ is the half-width of the horseshoe region. For prescriptions of $F(P)$, $G(P)$, and $K(P)$, we refer the readers to Eqs. (23), (30), and (31) in Paardekooper et al. (2011).

For the thermal diffusivity, we assume $\chi = \nu$ in this work for simplicity. The thermal diffusivity determines the saturation of the entropy-related part of the corotation torque. The thermal diffusivity is considered to be large when the disk surface density decreases and the disk is optically thin, and thus radiative cooling is efficient. In this case, the entropy-related corotation torque diminishes, and one might speculate that the orbital evolution of planets would change. However, we do not expect that this can change our results in this paper. In the terrestrial planet forming region, the disk opacity is about $1{-}10\,{\rm cm^2\,g^{-1}}$ (e.g., Bell & Lin 1994). This means that the disk is optically thin only when the disk is significantly dispersed ($\Sigma_{\rm g} \sim 0.1{-}1\,{\rm g\,cm^{-2}}$) and Type I migration is no longer effective. Therefore, our simplified model ($\chi = \nu$) may be justified. In addition, we observe that our qualitative results are not affected in test simulations in which the entropy-related torque is switched off from the beginning of the simulations.

Table 1. List of parameters of each model.

Model	α	$C_{\rm w}$	Comment
1	8×10^{-3}	0	without disk wind
2	8×10^{-3}	2×10^{-5}	weak magnetic field
3	Eq. (19)	Eq. (20)	strong magnetic field
4	2×10^{-5}	5×10^{-7}	described in Sect. 2.3

Notes. The variable α indicates the strength of turbulent viscosity while $C_{\rm w}$ is a scaling factor for the disk wind.

Recent studies (e.g., Bitsch & Kley 2010) suggest that the corotation torque decreases as the planet eccentricity increases; therefore, we also consider this effect using the formulae (Fendyke & Nelson 2014),

$$\beta_{\rm c,baro}(e) = \beta_{\rm c,baro}\exp\left(-\frac{e}{e_{\rm f}}\right), \tag{17}$$

$$\beta_{\rm c,ent}(e) = \beta_{\rm c,ent}\exp\left(-\frac{e}{e_{\rm f}}\right), \tag{18}$$

where $e_{\rm f} = 0.5h/r + 0.01$. We note that the Lindblad torque can also be reduced when planets have high eccentricities and inclinations (e.g., Papaloizou & Larwood 2000). In some runs of our simulations, we also add a reduction factor to Eq. (11), which is given by Eq. (13) of Cresswell & Nelson (2008). However, we found that even if this factor is ignored, the results do not change very much.

There are several works that take into account the effect of magnetic field on Type I migration (Terquem 2003; Fromang et al. 2005; Muto et al. 2008; Uribe et al. 2015; Bans et al. 2015). Among these works, Bans et al. (2015) consider the vertical transport of angular momentum by disk winds. In our paper, we assume the net vertical magnetic field is very weak and the disk wind is driven by the MRI triggered turbulent magnetic field, which is in contrast to the disk wind by relatively strong net magnetic field assumed in Bans et al. (2015). Therefore, the Type I migration formula based on pure hydrodynamics (which corresponds to the limit of weak magnetic field) by Paardekooper et al. (2011) is probably still reasonable in our setting.

2.3. Set of parameters and orbital integration

In our series of simulations, we mainly vary the following parameters: turbulent viscosity α, disk wind efficiency $C_{\rm w}$. Although the efficiency of the disk wind should be related to the turbulent viscosity, we vary α and $C_{\rm w}$ independently to explore parameter space. The list of parameters for each model is summarized in Table 1.

In model 1, the effect of the disk wind is not considered to clarify its effect on planet formation. The strength of the net vertical magnetic field is an important control parameter that determines α and $C_{\rm w}$ (Suzuki et al. 2010; Okuzumi & Hirose 2011). If the net vertical magnetic field is sufficiently weak, α and $C_{\rm w}$ stay more or less constant during the disk evolution. Model 2 corresponds to this weak regime; we adopt $\alpha = 8\times10^{-3}$ and $C_{\rm w} = 2\times10^{-5}$ according to the MHD simulations of Suzuki et al. (2010). If the net vertical magnetic field is relatively strong,

α and $C_{\rm w}$ increase with time as gas materials are dispersed (Suzuki et al. 2010). In model 3 we consider this strong regime, and we use

$$\alpha = 8 \times 10^{-3} \times \max\left(1, \frac{0.01\Sigma_{\rm g,ini}(r)}{\Sigma_{\rm g}(r)}\right), \quad (19)$$

$$C_{\rm w} = 2 \times 10^{-5} \times \max\left(1, \frac{0.01\Sigma_{\rm g,ini}(r)}{\Sigma_{\rm g}(r)}\right). \quad (20)$$

In addition, in model 4 we use $\alpha = 2 \times 10^{-5}$ and $C_{\rm w} = 5 \times 10^{-7}$.

The parameter set for model 4 may require some explanation. The slope of gas surface density basically depends on $\alpha/C_{\rm w}$. In other words, if the ratio of $\alpha/C_{\rm w}$ is the same, the distribution of gas surface density takes the same form while the evolution timescale depends on α and $C_{\rm w}$. In model 4 we consider the case of a more efficient disk wind ($\alpha/C_{\rm w} = 40$) than that of model 2 ($\alpha/C_{\rm w} = 400$). The value of α is also changed because we wish to discuss the origin of the solar system's terrestrial planets in this paper. As we show in Sects. 3 and 4, outward migration of 0.1 Earth-mass embryos is favorable for reproducing the observed properties of the solar system and $\alpha \sim 10^{-5}$ is required to avoid the saturation of the corotation torque for these bodies. Therefore, $\alpha = 2 \times 10^{-5}$ and $C_{\rm w} = \alpha/40 = 5 \times 10^{-7}$ are adopted. While the evolution of the surface density of model 4 is slower than models 2 and 3 because both α and $C_{\rm w}$ are smaller, the trend of the radial dependence of the surface density of this model represents a case more or less between model 2 and model 3. The initial amount of gas and the gas dispersal time are also changed in model 4. The scaling factor for the initial gas density $f_{\rm g}$ is increased by a factor of three. In the other models, $f_{\rm g}$ is set to unity. In addition, the disk would rapidly disperse (~0.1 Myr) after typical disk lifetimes of a few Myr, and additional effects are required to achieve this (e.g., photoevaporating winds; e.g., Alexander et al. 2014). In model 4, in order to mimic this disk evolution, α and $C_{\rm w}$ are increased by a factor of 100 after $t = 3$ Myr.

For the initial distribution of embryos, we put 60 protoplanets with mass $M = 0.1\ M_\oplus$ between $a = 0.1$–3 AU. Their orbital separation, Δ, measured in mutual Hill radii is set to 10. We perform three runs of simulations for each model with different initial locations of protoplanets.

For numerical integration, we use a fourth-order Hermite scheme (Makino & Aarseth 1992). When the physical radii of two bodies overlap, they are assumed to merge into one body, conserving total mass and momentum assuming perfect accretion. The physical radius of an embryo R is determined by $R = (3M/4\pi\rho)^{1/3}$, where we assume the internal density of $\rho = 3$ g cm^{-3}.

3. Results

3.1. Disk evolution

We first show the disk evolution and its contribution to Type I migration. The solid lines in Fig. 1 show the evolution of the disk surface density for models 2–4 while the dotted lines in each panel represent the surface density for model 1. Figure 2 shows the migration timescale (t_a) for model 2 and model 4, where the migration rate and direction are indicated by the color (see color bar). When the migration timescale is negative, the direction of migration is inward. As we saw in Sect. 2, Type I migration depends on the eccentricity of planets. We assume $e = 0.01$ in these plots.

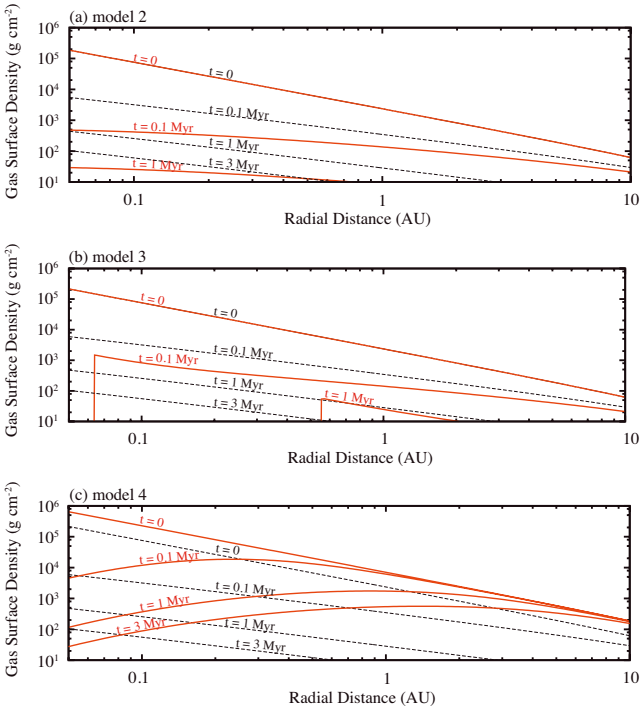

Fig. 1. Evolution of gas surface density profile for **a)** model 2; **b)** model 3; and **c)** model 4. Solid lines in each panel indicate the gas surface density at $t = 0, 0.1$ Myr, 1 Myr, and 3 Myr, respectively. Dotted lines show results for model 1. In panels **a)** and **b)**, the solid and dotted lines overlap for $t = 0$ because of the initial conditions.

Figure 1a clearly shows that the disk evolution of model 2 is altered by the disk wind in the following two aspects. First, the slope of the disk becomes shallow in the inner region. Second, the disk is depleted faster than the case without the disk wind. These two factors significantly reduce the inward migration of embryos. From the migration map of model 2 in Fig. 2a, we find that the inward migration timescale for sub-Earth mass planets is over 1 Myr at $t = 0.1$ Myr, which means they no longer undergo migration. We also observe no migration at $t = 1$ Myr and 3 Myr.

For the disk evolution of model 3 that has larger $C_{\rm w}$ and α shown in Fig. 1b, an inner cavity is created inside a certain radius at which 99% of the initial gas is dispersed according to Eqs. (19) and (20). As time passes, the inner cavity grows gradually and the disk inner edge moves outward. The inside-out evacuation of the disk can significantly affect the orbital evolution of planets, which will be shown in Sect. 3.2.

We also examine the disk evolution for model 4, in which the radial profile of the surface density in the inner region is approximately between model 2 and model 3. In Figs. 1 and 2 for model 2, we see the disk is depleted in the early stage of planet formation; therefore, a larger amount of initial gas disk is assumed ($f_{\rm g} = 3$). The evolution of the surface density in Fig. 1c shows that the slope becomes positive inside 1 AU. In order to get a positive surface density gradient inside 1 AU, we find that $\alpha/C_{\rm w} \lesssim 100$ is required. The disk lifetime is longer than model 2, which is more consistent with the observationally inferred disk lifetime. The migration map in Fig. 2b is more complicated. Because the effect of the disk wind is stronger in the inner region, the orbital region where planets can move outward is limited to $r \lesssim 1$ AU. The saturation of the corotation torque depends on the mass and the disk viscosity. If $\alpha = 2 \times 10^{-5}$ is assumed, the saturation effect is weakest for bodies with $M \simeq 0.1\ M_\oplus$. Therefore, only sub-Earth-mass

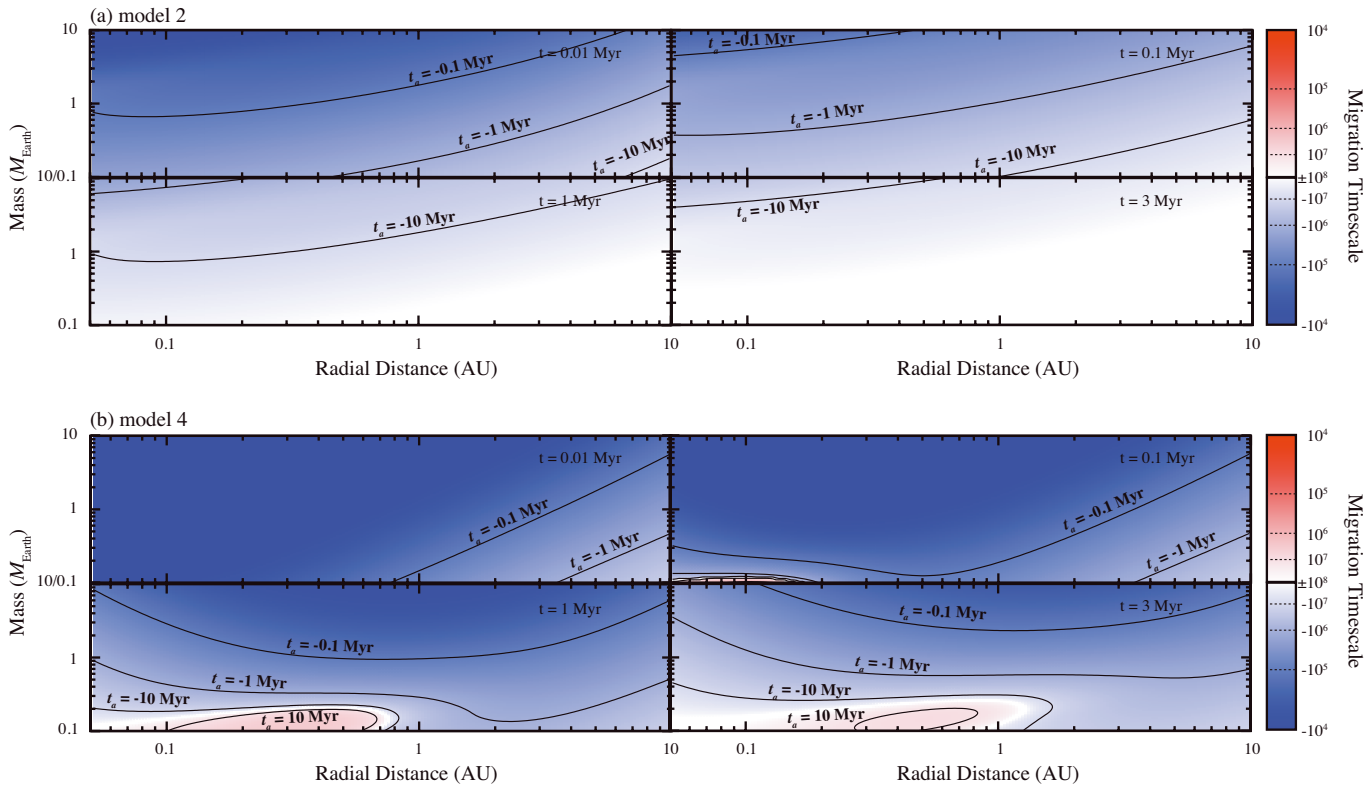

Fig. 2. Time evolution of migration rate and direction for bodies with $e = 0.01$ for **a)** model 2 and **b)** model 4. The color indicates the migration timescale. The contours show migration timescales of 0.1 Myr, 1 Myr, and 3 Myr.

planets can undergo outward migration. It is also worth noting that planetary orbits can evolve until a few Myr because the disk is almost completely depleted after 10 Myr.

Before proceeding to the next subsection, where the results of N-body simulations are shown, here we briefly discuss how the inner disk profile is determined by viscous diffusion and the disk wind. We note that the disk wind brings about the variety in the radial dependence of the surface density in the inner region ranging from a clear hole (model 3) to mild inside-out evacuation (model 2). We suppose that the inner hole seen in model 3 is an extreme case. In a realistic situation low-density gas should remain in the inner region and a low level of accretion would continue, rather than the formation of a clear inner hole, even at later times as seen in model 4, because the origin of the energy to drive the disk wind is the gravitational energy liberated by gas accretion (Suzuki et al. 2010); the infall of a certain amount of gas is required to launch vertical outflows. Suzuki et al. (2010) demonstrated the time evolution of a global disk by a simple model taking into account such energy-limited disk winds, which shows that the radial profile of the surface density is slightly modified at $\lesssim$1 AU.

3.2. Orbital evolution

We show the results of N-body simulations in disks that evolved via viscous diffusion and a disk wind. Figure 3 shows the orbital evolution of planets. The size of each filled circle represents the radii of bodies. The color of lines indicates the eccentricity of the planets. Each panel shows the results for model 1, model 2, model 3, and model 4. We performed three runs for each model, and typical runs are shown in the plots. Figure 4 shows the final orbital configurations in the semimajor axis-mass plane for all runs of model 2, model 3, and model 4 (the results for model 1 are not shown), where planets that formed through the same run are connected with the same line.

In Fig. 3a, the results for model 1 (in which the disk wind is not considered) is shown for comparison. Planetary embryos migrate inward and 12 bodies are lost by $t = 20$ Myr. The computational cost is huge for this run because the bodies do not collide with each other and the orbital period of the innermost planet is short; therefore, the computation was stopped at $t = 20$ Myr, which took over four months of CPU time. Orbit crossings are not observed before $t = 20$ Myr; however, the system is expected to be destabilized at $\sim$100 Myr according to previous studies on the stability of multi-planet systems (Chambers et al. 1996).

In the results for model 2, we find that planetary embryos do not migrate inward any more as expected from Figs. 1 and 2. In this model, as the disk dissipates, the eccentricity of the embryos is excited and they exhibit orbit crossings, leading to giant impacts between the bodies. At $t = 100$ Myr, the number of planets has decreased to 13 and their eccentricities are between about 0.01 and 0.1. The final orbital configurations are almost the same among the three different runs (see Fig. 4a). The averaged mass of the largest body in each run is $\simeq$0.9 $M_\oplus$. The typical orbital separation between the planets is $\simeq 10-40 r_H$.

For model 3, the orbital evolution is significantly different from that without a disk wind. As seen in Fig. 1b, the disk's inner edge moves outward. The migrating inner edge sweeps up embryos and almost all bodies migrate outward. As a result, no planets are left inside 0.4 AU and a large planet forms at 5 AU. The eccentricities of the planets are $\sim$0.04–0.3 (some bodies are still exhibiting orbit crossings). In the other two runs, the results are almost the same (see Fig. 4b). The mass of the largest body is $\simeq$3.8 $M_\oplus$, while the second largest planet is located at around 1 AU with a mass of $\simeq$ 0.5 $M_\oplus$.

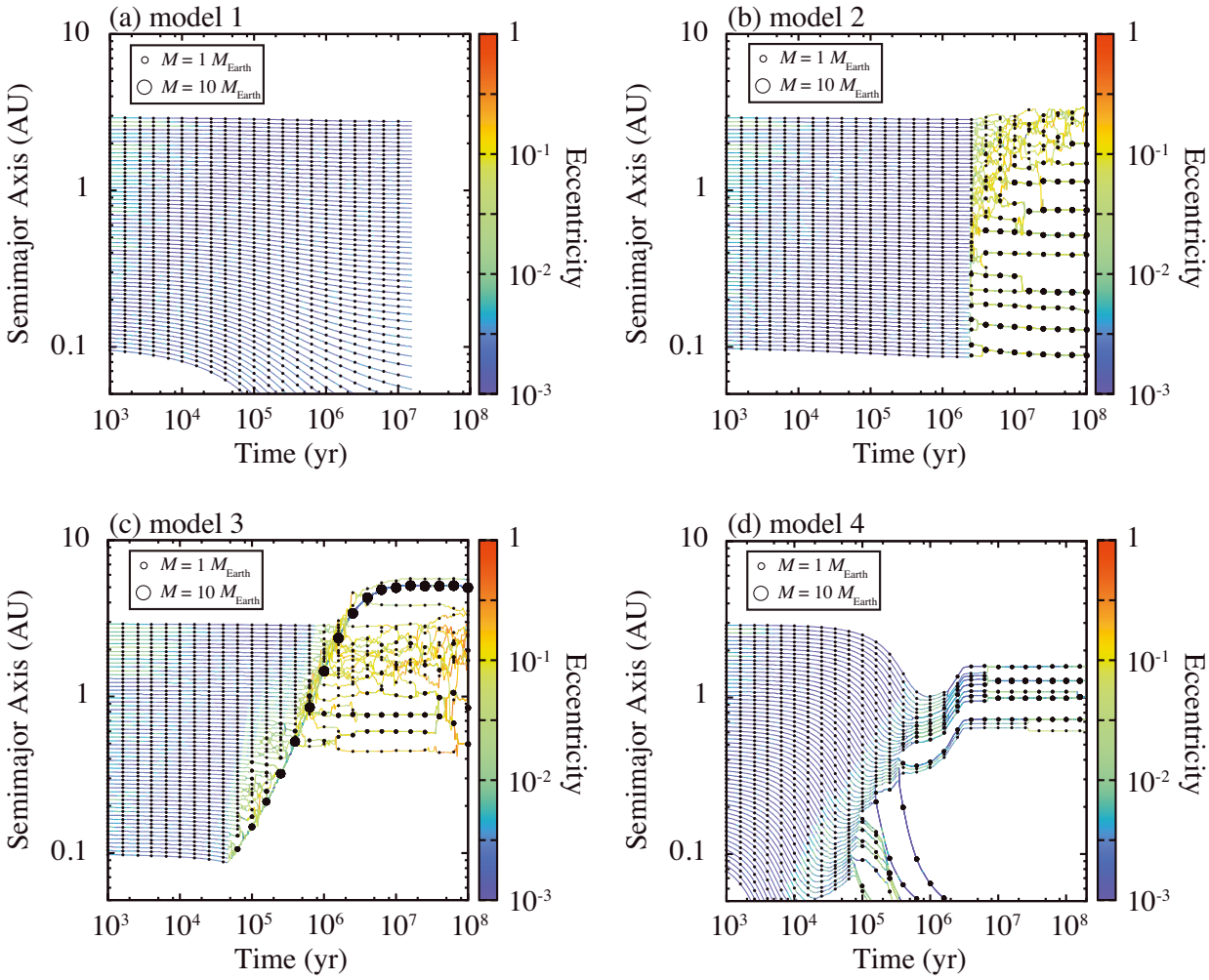

Fig. 3. Orbital evolution of planetary embryos for **a)** model 1; **b)** model 2; **c)** model 3; and **d)** model 4. The filled circles connected with lines represent each body. The color of lines indicates the eccentricity (see color bar). The size of circles is proportional to the radius of the body.

We observe an interesting orbital evolution in model 3 in which most protoplanets are swept up by the disk edge before $t \simeq 0.3$ Myr but afterward several bodies drift through the edge. We briefly discuss how bodies follow the migration of the disk edge or not. First, just as there are for torques on planets, there are two different positive torques, namely the Type I migration torque and the edge torque. As seen in Sect. 2, the former can become positive owing to the corotation torque, which depends on the slope of the gas surface density. The latter is a torque recently found by Ogihara et al. (2010). When a body with non-zero eccentricity straddles a sharp disk inner edge, the body gains a net positive torque from the disk depending on the sharpness of the edge and on the eccentricity. Whether planets can follow the movement of the disk edge depends on the migration speeds of the planets and the edge. If the outward migration rate of the planets due to the positive torque (which is the sum of the Type I migration torque and the edge torque) is smaller than the migration rate of the edge, the planets go through the disk edge and stay in place. Through a series of test calculations, we find that the positive torque exerted on the planets is usually large for this model and 0.1 Earth-mass planets can follow the disk edge. Therefore, there is another reason why some planets drift through the disk, which is that small embryos are scattered inside the disk edge by larger bodies. Larger bodies grow at the disk edge by sweeping up smaller embryos. At $t \simeq 1$ Myr, the planets at the edge already have masses of $\simeq 3.5\ M_\oplus$ and scatter embryos inside the edge.

The results for model 4 are also interesting. Before $t \simeq 0.02$ Myr, all bodies undergo inward migration, but afterward ~0.1 Earth-mass embryos in close-in orbits move outward while bodies in distant regions migrate inward, leading to a convergence of planets at around 1 AU. For $\alpha = 2 \times 10^{-5}$, the positive corotation torque can be saturated for bodies larger than $\simeq 0.3$ Earth masses; as a result, several planets that undergo collisional growth migrate inward and are lost to the central star. As the disk disperses after $t = 3$ Myr, all the bodies cease their migration. At $t = 100$ Myr, a system with six planets with a maximum mass of 0.7 $M_\oplus$ and $e \simeq 0.01$ had formed. The orbital separations between the planets are relatively small (down to $\lesssim 10 r_{\rm H}$), and giant impacts can occur after $t = 100$ Myr. Thus we continued simulation until $t = 200$ Myr for this run. The system underwent a giant impact at $t = 145$ Myr, which is discussed in Sect. 4. In the other two runs, although the mass distributions are slightly different from each other, the results are qualitatively the same (Fig. 4c).

4. Origin of the solar system's terrestrial planets

Here we discuss our results in terms of the origin of terrestrial planets in the solar system. The important characteristics are

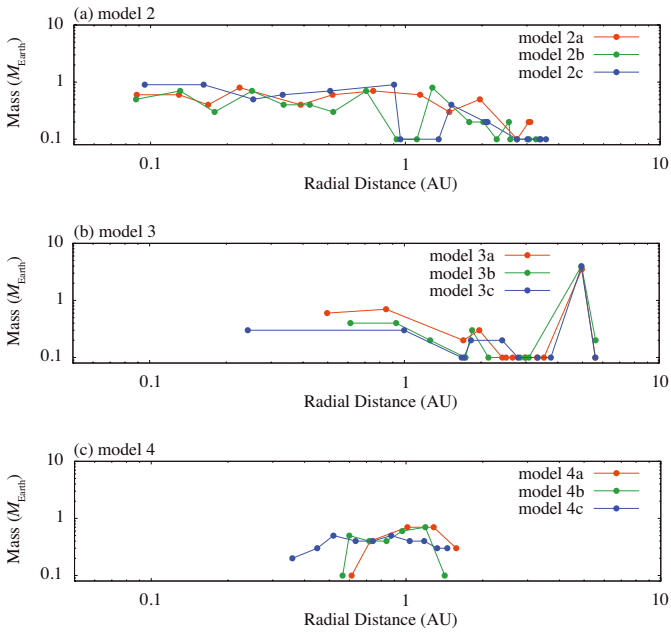

Fig. 4. Final orbital configurations for **a)** model 2; **b)** model 3; and **c)** model 4. Only for model 4a is the configuration at $t = 200$ Myr shown. Results of three different runs are plotted in each panel.

the radial mass concentration and small eccentricities of planets, which we characterize using two statistical measures, $S_{\rm c}$ and $S_{\rm d}$. The radial mass concentration statistic is (Chambers 2001)

$$S_{\rm c} = \max\left(\frac{\sum m_j}{\sum m_j [\log_{10}(a/a_j)]^2}\right), \tag{21}$$

where $j = 1, 2, ..., N$. The angular momentum deficit, which represents the deviation from circular and coplanar orbits, is (Laskar 1997)

$$S_{\rm d} = \frac{\sum m_j \sqrt{a_j}\left[1 - \cos(i_j)\sqrt{1-e_j^2}\right]}{\sum m_j \sqrt{a_j}}, \tag{22}$$

where i_j is the orbital inclination of the body j.

The radial mass concentration of the solar system's terrestrial planets is $S_{\rm c} = 89.9$, which indicates high radial mass concentration because the masses of Mercury and Mars are small and the orbital distance between Venus and the Earth is also relatively small. Previous studies have shown that it is difficult to reproduce such a high mass concentration (e.g., Raymond et al. 2009; Morishima et al. 2010); a way to account for this statistic in N-body simulations is to assume a mass distribution initially confined to a narrow annulus (Morishima et al. 2008; Hansen 2009), or in other words to assume an initially large $S_{\rm c}$. In the grand tack model (e.g., Walsh et al. 2011; Jacobson & Morbidelli 2014), Jupiter sweeps up to ~1.5 AU and embryos are eventually confined to a relatively compact region. However, they assumed an inner cutoff at ≃0.7 AU, which means that $S_{\rm c}$ is already relatively large in the initial state.

The angular momentum deficit for the terrestrial planets in the solar system is $S_{\rm d} = 0.0018$, which means that the eccentricities of the terrestrial planets in the solar system are relatively small ($e \simeq 0.01$–0.1). We note that Jupiter and Saturn increase $S_{\rm d}$ after their formation, which is ignored in this paper. Therefore, the necessary condition for our results to explain terrestrial planets in the solar system is that $S_{\rm d} \lesssim 0.0018$.

Table 2. Statistical measures for final planetary systems.

Run	$S_{\rm c}/89.9$	$S_{\rm d}/0.0018$	$t_{\rm imp,last}$ (Myr)
1a	0.042	0.0016	>20
1b	0.050	0.0016	>20
1c	0.050	0.0013	>20
2a	0.048	1.7	61
2b	0.052	1.5	30
2c	0.047	9.1	80
3a	0.086	3.7	99
3b	0.12	1.5	57
3c	0.098	0.87	72
4a	0.80	0.046	145
4b	0.81	0.0045	>100
4c	0.35	0.020	>100

Notes. $S_{\rm c}$ is a measure of the radial mass concentration. $S_{\rm d}$ measures how a system deviates from circular and coplanar orbits. The last column shows the timing of the last giant impact, although last impact events do not occur within the simulation time for model 1 and model 4 (except for 4a).

Table 2 shows the statistical measures for all runs. In the cases of model 1 (1a, 1b, 1c) and model 2 (2a, 2b, 2c), $S_{\rm c}$ is kept small from the beginning of the simulations because the planets do not undergo convergent migration. The initial value of $S_{\rm c,0}$ is 5.4. In the results of model 3 (3a, 3b, 3c), $S_{\rm c}$ is slightly increased to ≃9. The final system is more concentrated than the initial distribution, but the value is still not consistent with the value of the current solar system. In the results of model 4 (4a, 4b, 4c), $S_{\rm c}$ is as large as the value of the inner solar system ($S_{\rm c}$ is between 30 and 70). The mass concentration at around 1 AU is clearly seen in Fig. 3d.

Regarding the angular momentum deficit, $S_{\rm d}$ for model 1 is small because planets do not exhibit orbit crossings. In contrast, in model 2 and model 3, planets experience orbit crossings and the gas disk is depleted early, thus $S_{\rm d}$ is larger than that of model 1. We neglect the forced eccentricity by Jupiter and Saturn such that additional damping may be required for model 2 and model 3. In the results of model 4, $S_{\rm d}$ is sufficiently small ($\simeq 4 \times 10^{-5}$).

The timing of a moon-forming impact is also a key constraint on formation models of the solar system. According to recent work, the time of the last giant impact on Earth could have been significantly late (50–150 Myr after the formation of the first solids in the solar system; e.g., Touboul et al. 2007; Allégre et al. 2008; Jacobson et al. 2014). The timing of the latest impact for model 2 is $t \sim 50$ Myr, and that for model 3 is $t \simeq 50$–100 Myr, consistent with the timing of the last giant impact on Earth. Particularly interesting is that the timing of the last giant impacts is delayed after 100 Myr for model 4. In fact, we continue simulation for 4a until $t = 200$ Myr and find that the last giant impact occurs at $t = 145$ Myr.

In conclusion, we find that a disk wind can increase the radial mass concentration. In particular, $S_{\rm c}$ can be as large as that of the solar system even if we assume that the initial embryo distribution is extended to 0.1 AU. In the result of 4a, the orbital properties including the timing of the moon-forming impact are similar to those of the solar system. We have only performed simulations in a limited number of cases; however, we can identify a significantly large parameter space that may allow us to find a best-fit model for the observed properties of the solar system. To assess the possibility, we have to explore a broad range of parameter space to find a condition that can create a solar system analog.

We also discuss one other problem in the formation of the solar system. Recent numerical simulations on the evolution of the snow line in the solar system that solve the detailed radiative energy transfer have shown that the snow line moves in the disk and comes inside Earth's orbit to ≃0.5 AU (e.g., Oka et al. 2011; Davis 2005; Graud & Lin 2007) during a phase with a disk accretion rate of $\sim 10^{-10}\ M_\odot\ \mathrm{yr}^{-1}$. If planetesimals formed during this stage, the terrestrial planets in the solar system should have formed from icy planetesimals and contain significant amounts of water, which is not consistent with the current water content of the terrestrial planets. We can provide a pathway to avoid this problem. Protoplanets that formed from rocky planetesimals inside the snow line within ≲0.5 AU migrate outward in disks that are affected by a disk wind, resulting in water-poor planets at around 1 AU.

5. Conclusions

We performed N-body simulations that include the effects of a disk wind and found that the orbital evolution of terrestrial planets and their precursor protoplanets can significantly differ from the results of previous simulations. Because of the disk wind, the efficiency of which depends approximately on $r^{3/2}$, gas materials blow out from the surface of the disk from the inside out, leading to a shallower surface density profile in the inner region (≲1 AU). Planets with masses less than a few Earth masses would no longer migrate inward. The orbital evolution depends on the parameters (α, C_w), and in fact, 0.1 Earth-mass embryos inside 1 AU never undergo significant inward migration for all the parameters in our simulations. In an extreme case in which the vertical magnetic field is strong, we observed the inner edge of the disk move outward and sweep up embryos.

In a certain parameter range, we found that planetary embryos move outward. When α/C_w is less than ∼100, the surface density slope becomes positive in the inner region, which can induce convergent migration to around 1 AU. In order for outward migration to take place, the corotation torque should not be saturated, which depends on diffusion. For 0.1 Earth-mass embryos, the saturation is inhibited when α is $\simeq 10^{-5}$. Thus, we performed additional simulations with $\alpha = 2 \times 10^{-5}$ and $C_\mathrm{w} = 5 \times 10^{-7}$ and found that the resultant systems are radially concentrated at around 1 AU. This is an important result. In this case, the observed constraints of the inner solar system (e.g., eccentricity, radial mass concentration, late moon-forming impact) may be reproduced. This expectation requires that the turbulent viscosity be quite low ($\alpha \sim 10^{-5}$) in the terrestrial planet-forming region in the protosolar nebula. Although we focus on the properties of the terrestrial planets, other observed properties in the solar system (e.g., the dynamically excited asteroid belt) should be reproduced in future work. A combination of our model with the grand tack model (Walsh et al. 2011), which explains asteroid excitation, may be a possible scenario. In addition, a disk wind can play other important roles. For example, if the snow line had been located inside 1 AU, the Earth would have accreted a significant amount of icy planetesimals. However, this problem can be overcome if the Earth formed from rocky protoplanets that migrated outward owing to the effect of the disk wind.

The disk wind can also apply to exoplanet formation models. A large number of close-in low-mass planets have been discovered, and thus we can statistically compare observational results with theoretical models. To do so, we need to explore parameter space (α, C_W), which we leave for future work. If disk winds operate efficiently in exoplanet systems, super-Earths would tend to pile up at around 1 AU rather than 0.1 AU.

Acknowledgements. We thank the anonymous referee for helpful comments. M.O. thanks Shigeru Ida and Alessandro Morbidelli for helpful discussions. We also thank Jennifer M. Stone for valuable comments. Numerical computations were in part conducted on the general-purpose PC farm at the Center for Computational Astrophysics, CfCA, of the National Astronomical Observatory of Japan. H.K. gratefully acknowledges support from Grant-in-Aid for Scientific Research (B) (26287101). S.I. is supported by Grant-in-Aid for Scientific Research (23244027, 23103005).

References

Alexander, R. D., Clarke, C. J., & Pringle, J. E. 2006, MNRAS, 369, 229
Alexander, R. D., Pascucci, I., Andrews, S., Armitage, P., & Cieza, L. 2014, in Protostars and Planets VI, eds. H. Beuther, R. Klessen, C. Dullemond, & Th. Henning (Tucson: Univ. Arizona Press)
Allègre, C. J., Manhès, G., & Göpel, C. 2008, Earth Planet. Sci. Lett., 267, 386
Bai, X.-N., & Stone, J. M. 2013, ApJ, 767, 30
Bans, A., Königl, A., & Uribe, A. 2015, ApJ, 802, 55
Bell, K. R., & Lin, D. N. C. 1994, ApJ, 427, 987
Bitsch, B., & Kley, W. 2010, A&A, 523, A30
Chambers, J. E. 2001, Icarus, 152, 205
Chambers, J. E., Wetherill, Q. W., & Boss, A. P. 1996, Icarus, 119, 261
Cossou, C., Raymond, S. N., Hersant, F., & Pierens, A. 2014, A&A, 569, A56
Cresswell, P., & Nelson, R. P. 2008, A&A, 482, 677
Davis, S. S. 2005, ApJ, 620, 994
Ercolano, B., Clarke, C. J., & Drake, J. J. 2009, ApJ, 699, 1639
Fendyke, S. M., & Nelson, R. P. 2014, MNRAS, 437, 96
Fromang, S., Terquem, C., & Nelson, R. P. 2005, MNRAS, 363, 943
Fromang, S., Latter, H., Lesur, G., & Ogilvie, G. I. 2013, A&A, 552, A71
Garaud, P., & Lin, D. N. C. 2007, ApJ, 654, 606
Goldreich, P., & Tremaine, S. 1980, ApJ, 241, 425
Hansen, B. M. 2009, ApJ, 703, 1131
Hayashi, C. 1981, Prog. Theor. Phys. Suppl., 70, 35
Hellary, P., & Nelson, R. P. 2012, MNRAS, 419, 2737
Horn, B., Lyra, W., Mac Low, M. -M., & Sándor, Zsolt. 2012, ApJ, 750, 34
Jacobson, S. A., & Morbidelli, A. 2014, Phil. Trans. R. Soc. A, 372, 20130174
Jacobson, S. A., Morbidelli, A., Raymond, S. N., et al. 2014, Nature, 508, 84
Kominami, J., & Ida, S. 2002, Icarus, 157, 43
Kretke, K. A., & Lin, D. N. C. 2012, ApJ, 755, 74
Laskar, J. 1997, A&A, 317, L75
Lesur, G., Ferreira, J., & Ogilvie, G. I. 2013, A&A, 550, A61
Makino, J., & Aarseth, S. J. 1992, PASJ, 44, 141
Morishima, R., Schmidt, M. W., Stadel, J., & Moore, B. 2008, ApJ, 685, 1247
Morishima, R., Stadel, J., & Moore, B. 2010, Icarus, 207, 517
Muto, T., Machida, M. N., & Inutsuka, S. 2008, ApJ, 679, 813
Nagasawa, M., Lin, D. N. C., & Thommes, E. 2005, ApJ, 635, 578
Ogihara, M., Ida, S., & Morbidelli, A. 2007, Icarus, 188, 522
Ogihara, M., Duncan, M. J., & Ida, S. 2010, ApJ, 721, 1184
Ogihara, M., Kobayashi, H., & Inutsuka, S. 2014, ApJ, 787, 172
Oka, A., Nakamoto, T., & Ida, S. 2011, ApJ, 738, 1413
Okuzumi, S., & Hirose, S. 2011, ApJ, 742, 65
Paardekooper, S.-J., Baruteau, C., Crida, A., & Kley, W. 2010, MNRAS, 401, 1950
Paardekooper, S.-J., Baruteau, C., & Kley, W. 2011, MNRAS, 410, 293
Raymond, S. N., O'Brien, D. P., Morbidelli, A., & Kaib, N. A. 2009, Icarus, 203, 644
Suzuki, T. K., & Inutsuka, S. 2009, ApJ, 691, L49
Suzuki, T. K., Muto, T., & Inutsuka, S. 2010, ApJ, 718, 1289
Tanaka, H., Takeuchi, T., & Ward, W. R. 2002, ApJ, 565, 1257
Terquem, C. E. J. M. L. J. 2003, MNRAS, 341, 1157
Touboul, M., Kleine, T., Bourdon, B., Palme, H., & Wieler, R. 2007, Nature, 450, 1206
Uribe, A., Bans, A., & Königl, A. 2015, ApJ, 802, 54
Walsh, K. J., Morbidelli, A., Raymond, S. N., O'Brien D. P., & Mandell, A. M. 2011, Nature, 475, 206
Ward, W. R. 1986, Icarus, 67, 164

THE ASTROPHYSICAL JOURNAL, 753:66 (6pp), 2012 July 1 doi:10.1088/0004-637X/753/1/66

IN SITU ACCRETION OF HYDROGEN-RICH ATMOSPHERES ON SHORT-PERIOD SUPER-EARTHS: IMPLICATIONS FOR THE KEPLER-11 PLANETS

M. IKOMA (生駒大洋)[1,2] AND Y. HORI (堀安範)[3]
[1] Department of Earth and Planetary Science, The University of Tokyo, 7-3-1 Bunkyo-ku, Tokyo 113-0033, Japan; ikoma@eps.s.u-tokyo.ac.jp
[2] Department of Earth and Planetary Sciences, Tokyo Institute of Technology, 2-12-1 Ookayama, Meguro-ku, Tokyo 152-8551, Japan
[3] Division of Theoretical Astronomy, National Astronomical Observatory of Japan, 2-21-1 Osawa, Mitaka, Tokyo 181-8588, Japan; yasunori.hori@nao.ac.jp
Received 2012 January 30; accepted 2012 April 22; published 2012 June 14

ABSTRACT

Motivated by recent discoveries of low-density super-Earths with short orbital periods, we have investigated in situ accretion of H–He atmospheres on rocky bodies embedded in dissipating warm disks, by simulating quasi-static evolution of atmospheres that connect to the ambient disk. We have found that the atmospheric evolution has two distinctly different outcomes, depending on the rocky body's mass: while the atmospheres on massive rocky bodies undergo runaway disk-gas accretion, those on light rocky bodies undergo significant erosion during disk dispersal. In the atmospheric erosion, the heat content of the rocky body that was previously neglected plays an important role. We have also realized that the atmospheric mass is rather sensitive to disk temperature in the mass range of interest in this study. Our theory is applied to recently detected super-Earths orbiting Kepler-11 to examine the possibility that the planets are rock-dominated ones with relatively thick H–He atmospheres. The application suggests that the in situ formation of the relatively thick H–He atmospheres inferred by structure modeling is possible only under restricted conditions, namely, relatively slow disk dissipation and/or cool environments. This study demonstrates that low-density super-Earths provide important clues to understanding of planetary accretion and disk evolution.

Key word: planets and satellites: formation

Online-only material: color figure

1. INTRODUCTION

An increasing number of low-mass exoplanets with masses of less than about 20 $M_\oplus$, which are often called super-Earths (SEs),[4] have been detected recently, thanks to progresses in radial velocimetry and transit photometry including operation of two space telescopes, *Kepler* and *CoRoT*. The size measurement allows us to access the planetary interiors theoretically and thereby estimate the planetary bulk compositions. It has been revealed that there are many low-density SEs that are larger in size than rocky (i.e., iron-silicate) objects of the same masses. As for SEs, the variety of possible ingredients obscures the composition estimation, namely, causing degeneracy in composition (Valencia et al. 2007; Seager et al. 2007; Adams et al. 2008; Grasset et al. 2009; Rogers & Seager 2010). In particular, low-density SEs are subject to the degeneracy. Sometimes, the degeneracy has a crucial impact on understanding the origin of planets and planetary systems.

A typical example is degeneracy originating from the uncertainty of the presence and mass of H–He atmospheres. The mass–radius relationship for a planet alone is insufficient to distinguish whether the planet is rock-dominated or water-dominated because the H–He atmosphere makes up the difference in size between rocky and water bodies of the same mass. Since transiting SEs in general orbit close to their host stars (namely, well inside the snow line), whether they are rocky or water planets would affect considerably the understanding of the accretion and migration history of the planets. An example of that is recently detected SEs orbiting a Sun-like star named Kepler-11.

The Kepler-11 system is a multiple-planet system that contains at least five low-density SEs (Lissauer et al. 2011). Of them, the densities of Kepler-11d and 11e are as low as $0.9^{+0.5}_{-0.3}$ g cm^{-3} and $0.5^{+0.2}_{-0.2}$ g cm^{-3}, respectively, which are lower than those of pure-water planets. This suggests the presence of H–He atmospheres on the planets. Indeed, the structure modeling by Lissauer et al. (2011) suggests a possibility that those two SEs are rock-dominated planets with thick H–He atmospheres that account for 10%–20% of the planetary masses. If so, they are a new type of planet that we have never seen in the current solar system.

The H–He atmospheres, if primordial, came from the protoplanetary disk where the planets formed. In the framework of the core accretion model (Hayashi et al. 1985), solid planetary embryos first form, and then collect the ambient disk gas gravitationally to form H–He atmospheres. If this proceeds well before disk dispersal, the disk-gas accretion enters a runaway state at some critical point, which results in forming envelopes of gas giants (Mizuno 1980; Bodenheimer & Pollack 1986) which are much more massive than the predicted atmospheres of the Kepler-11 planets. The critical point is when the atmospheric mass is approximately one-fourth to one-third of the protoplanet's total mass (Stevenson 1982; Wuchterl 1993)—the fraction being similar to those of the atmospheres of interest. This means that the inferred masses of the H–He atmospheres of the Kepler-11 planets are close to critical, which motivates us to investigate the possible amounts of H–He gas that proto-SEs with short orbital periods gain from protoplanetary disks.

In this study, we explore the possibility of the in situ accretion of H–He atmospheres. As for the origin of H–He atmospheres of short-period SEs, possibilities of Neptune-like planets (i.e., water-dominated SEs) that form far out and migrate close to host stars (Rogers et al. 2011) and remnants of gas giants whose envelopes were stripped (Nayakshin 2011) were previously discussed. The in situ accretion of H–He atmospheres on rocky SEs from disks has not been explored by direct simulation of disk-gas accretion in the mass and orbital period regimes of

[4] While exoplanets with masses of 10–20 $M_\oplus$ are sometimes called exo-Neptunes instead of super-Earths, we simply call them super-Earths in this paper.

transiting SEs. The in situ accumulation of H–He atmospheres would be reasonable in the modern picture of planet formation. Short-period SEs are likely to have migrated to their current locations. The promising mechanism to move them inward is the type-I migration which occurs via planet–disk tidal interaction (Ward 1986). The protoplanets formed in this way are packed closely together due to resonance capture, according to recent N-body simulations (Terquem & Papaloizou 2007). After the migration, the disk dissipates. In many cases, the decline of disk-gas density triggers dynamical instability of a multiple-protoplanet system, resulting in orbital crossing and collisions of the protoplanets (e.g., Ogihara & Ida 2009). Subsequently, the protoplanets collect the surrounding disk gas to form atmospheres in the dissipating disk. Thus, the competition between the atmospheric accumulation and the disk dissipation may yield intermediate-mass atmospheres like the predicted atmospheres for the Kepler-11 planets.

This paper is organized as follows. In Section 2, we describe our theoretical model of the atmospheric accumulation with emphasis on effects that we newly incorporate in this study. Then, we show numerical results of the atmospheric growth and the sensitivities of the final atmospheric masses to parameters involved in the model. In Section 3, the masses of the accreted atmospheres that we calculate are compared with those of the atmospheres of Kepler-11 planets inferred by internal-structure modeling. Based on the comparison, we discuss the possibility of the in situ accretion of the atmospheres. Other possibilities are also discussed. Finally, we conclude this paper in Section 4.

2. ACCUMULATION OF ATMOSPHERE

2.1. Model

We simulate the radially one-dimensional structure and quasi-static evolution of the atmosphere of a protoplanet embedded in a protoplanetary disk. The atmosphere's contraction (or expansion) results in its mass gain (or loss). The detail of the model is described in Ikoma & Genda (2006). The numerical integration is done with the code that we developed and used in Hori & Ikoma (2010, 2011). Below is a brief summary of the model.

The planet consists of a compressive atmosphere with solar elementary abundance on top of an incompressive "rocky" body with density of 3.9 g cm^{-3}. Choice of value of the rocky density and incorporation of rocky small compressibility have tiny impacts on the structure and mass of the atmosphere. We integrate a usual set of four equations describing the spherically symmetric, quasi-hydrostatic structure of a self-gravitating atmosphere, which includes the equations of hydrostatic equilibrium, mass conservation, radiative/convective energy transfer, and energy conservation (i.e., time change in entropy). The equation of state for the atmospheric gas that we use in this study is from Saumon et al. (1995).

The atmosphere is assumed to be equilibrated with the disk at the smaller of the Bondi and Hill spheres (see Ikoma & Genda 2006); namely, the atmospheric density and temperature are equal to those of the ambient disk gas there. On the other hand, the bottom of the atmosphere corresponds to the interface between the atmosphere and the rocky body. The atmosphere is heated by the underlying rocky body at the bottom. In this study, the energy flux from the rocky body is given at the atmospheric bottom as an inner boundary condition, as described below.

In this paper, we consider grain-free atmospheres, unless otherwise noted, to investigate upper limits to the masses of the H–He atmospheres that the SEs gain via the in situ accretion. Thus, we assume that the atmospheric opacity includes only the gas opacity, which is taken from Freedman et al. (2008) in this study. We suppose that the protoplanet formed via giant impacts in a dissipating disk. Each simulation of the atmospheric growth starts with an arbitrarily hot state (i.e., a given high luminosity). The initial choices of the luminosity do not affect our results because the initial cooling of the atmosphere occurs fast relative to the disk dissipation. No continuous energy supply by planetesimal bombardment is assumed. This assumption also leads to finding upper limits of the atmospheric mass.

In this study, we include two effects newly: we assume that disk dissipation occurs concurrently with the atmospheric growth. Furthermore, we incorporate the effect of the heat capacity of the rocky body. While both effects were not included in previous studies, they have crucial impacts on atmospheric growth in the situations considered in this study, as shown below.

The disk-gas density, $\rho_d(a, t)$, is assumed to decrease in an exponential fashion, namely,

$$\rho_d(a, t) = \rho_d^0(a) \exp(-t/\tau_d), \tag{1}$$

where a is the semimajor axis, t is time, and τ_d is the dissipation time that is regarded as a parameter; the initial disk density, $\rho_d^0(a)$, is taken from Hayashi (1981) in this study. According to modern theories of disk evolution (see Calvet et al. 2000 for a review), the overall dissipation first occurs via viscous diffusion in $\sim 10^7$ yr. Once the gas density becomes so low in the inner disk that the stellar UV penetrates through the disk, photoevaporation occurs around the gravitational radius of several AU. From that time on, the inner disk is separated from the outer disk and evolves via viscous diffusion separately. Since this is equivalent to the fact that the disk size decreases by a factor of 10, the diffusion timescale (being proportional to the square of disk size) for the inner disk decreases by a factor of 100 to become $\sim 10^5$ yr. Based on a simple analytical argument, namely, solving the one-dimensional viscous-diffusion equation for surface gas density, Σ_d,

$$\frac{\partial \Sigma_d}{\partial t} = \frac{1}{a}\frac{\partial}{\partial a}\left[3a^{1/2}\frac{\partial}{\partial a}\left(\Sigma_d \nu a^{1/2}\right)\right] \tag{2}$$

with $\Sigma_d = 0$ at the inner and outer edges, one finds that the inner disk dissipates in such a way that $\rho_d \propto \exp(-\pi^2 t/10^5 \text{ yr})$, which corresponds to $\tau_d \sim 10^4$ yr. This is consistent with results from recent numerical simulations of disk evolution (e.g., Gorti et al. 2009).

Decrease in disk density results in cooling of the atmosphere (Ikoma & Genda 2006). The rocky body below the atmosphere also cools down. Detailed treatment of the rocky body's thermal evolution is beyond the scope of this paper. Instead, we evaluate its contribution by inputting the luminosity from the rocky body in the form of $L_{\rm rock} = -C_{\rm rock} M_{\rm rock} dT_b/dt + L_{\rm radio}$ as an inner boundary condition for the atmospheric structure, where $C_{\rm rock}$ is the specific heat of silicate ($= 1.2 \times 10^7$ erg K^{-1} g^{-1}), $M_{\rm rock}$ is the mass of the rocky body, T_b is the temperature at the atmospheric bottom, and $L_{\rm radio}$ is the luminosity due to the radioactive decay of chondrites, $2 \times 10^{20}(M_{\rm rock}/M_\oplus)$ erg s^{-1} (see Guillot et al. 1995). In the present case, since the decline of T_b is caused by that of ρ_d,

$$\frac{dT_b}{dt} = \frac{d\ln\rho_d}{dt}\frac{dT_b}{d\ln\rho_d} = -\frac{1}{\tau_d}\frac{dT_b}{d\ln\rho_d}. \tag{3}$$

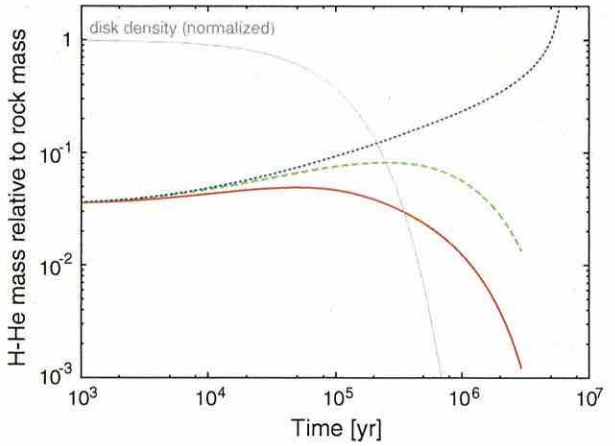

Figure 1. Evolution of the atmosphere on the 4 $M_\oplus$ rocky body for disk temperature $T_d = 550$ K. In the dotted-line (blue-line) case, the disk density, ρ_d, is assumed to be constant through the simulation. In the dashed-line (green-line) and solid-line (red-line) cases, the disk is assumed to dissipate as $\rho_d \propto \exp(-t/10^5\ \mathrm{yr})$, which is shown by a thin gray line. Also, the rocky heat capacity, $C_{\rm rock}$, is 1.2×10^7 erg K^{-1} g^{-1} in the solid-line (red-line) case, while $C_{\rm rock} = 0$ in the dashed-line (green-line) case. Note that the radioactive luminosity is also included, but has a negligible impact on the atmospheric evolution.

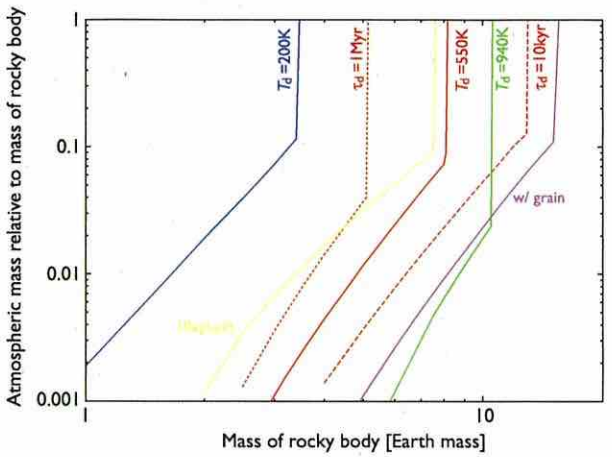

Figure 2. Final atmospheric mass as a function of the rocky body's mass. The red solid line represents a fiducial model where the disk temperature, T_d, is 550 K, the disk dissipation time, τ_d, is 100 kyr, and the initial disk density, ρ_d^0, is equal to that of the minimum-mass solar nebula, $\rho_{\rm MSN}$ (Hayashi 1981); the values of the three parameters are used below unless otherwise specified. The red dashed and dotted lines are for $\tau_d = 10$ kyr and 1 Myr, respectively. The green and blue lines are for $T_d = 940$ K and 200 K, respectively. In the yellow-line case, ρ_d^0 is 10 times as large as $\rho_{\rm MSN}$. While grain-free opacity is assumed in the other cases, the grain opacity for protoplanetary disks from Semenov et al. (2003) is used in the purple-line case.

Furthermore, from the analytical solution of the radiative atmosphere (Ikoma & Genda 2006), T_b is related to the disk temperature, T_d, as $dT_b/d\ln\rho_d = T_d/4$. Hence, we calculate $L_{\rm rock}$ as

$$L_{\rm rock} = \frac{M_{\rm rock} C_{\rm rock} T_d}{4\tau_d} + L_{\rm radio}. \quad (4)$$

2.2. Atmospheric Growth

Examples of atmospheric growth are shown in Figure 1. In the simulations, $M_{\rm rock}$ is assumed to be 4 $M_\oplus$. The dotted (blue) line shows the atmospheric growth when the disk gas density is constant through the simulation. In this case, after gradual growth, runaway gas accretion starts at $t \sim 3$ Myr, resulting in forming an atmosphere that is much more massive than the atmospheres of interest in this study.

The dashed (green) and solid (red) lines show the atmospheric mass evolution with concurrent disk dissipation with $\tau_d = 1 \times 10^5$ yr; the former and latter represent the cases with $C_{\rm rock} = 0$ (i.e., no contribution of the rocky body's cooling to heating the atmosphere) and $C_{\rm rock} = 1.2 \times 10^7$ erg K^{-1} g^{-1}, respectively. As shown by the two lines, the atmospheric growth levels off at some point in these cases because the disk is assumed to disperse before the runaway gas accretion would happen if it were not for disk dispersal. After the leveling-off, the atmosphere is found to be eroded. The simulations were stopped when the disk-gas density became low enough that the mean free path of the ambient gas molecules was longer than the planetary radius;

$$\rho_d = \frac{kT_d}{GM_{\rm rock}\sigma} = 1.4 \times 10^{-19} \left(\frac{M_{\rm rock}}{1\,M_\oplus}\right)^{-1} \times \left(\frac{T_d}{100\,\mathrm{K}}\right) \mathrm{g\ cm^{-3}} \quad (5)$$

$$= 10^{-10} \rho_d^0(a) \left(\frac{M_{\rm rock}}{1\,M_\oplus}\right)^{-1} \left(\frac{T_{\rm d}}{100\,\mathrm{K}}\right) \left(\frac{a}{1\,\mathrm{AU}}\right)^{11/4}, \quad (6)$$

where k is the Boltzmann constant, G is the gravitational constant, and σ is the collisional cross-section of the molecule ($=2.5 \times 10^{-16}$ cm^2).

The atmospheric erosion during disk dissipation has been newly found in this study. The erosion is due to atmospheric expansion. The expansion occurs because disk depressurization enhances the outward pressure gradient near the outer boundary, which pushes the atmosphere outward. Then, the atmospheric gas seeps out from the protoplanet's gravitational sphere, which continues until the atmosphere is equilibrated with the ambient, depressurized disk. The decrease in atmospheric mass due to this effect (the dashed, green line) is, however, small, relative to the decrease due to heatup by the cooling rocky body (the solid, red line). As described in Section 2.1, the disk dissipation cools the surface of the rocky body, resulting in heat supply to the atmosphere. This lifts up the atmosphere, which results in further atmospheric erosion. This is why the atmospheric erosion is more significant when the rocky heat capacity is incorporated.

2.3. Final Masses of the H–He Atmospheres

In Figure 2, the final mass of the H–He atmosphere, $M_{\rm H+He}$, which is divided by the rocky body's mass, $M_{\rm rock}$, is shown as a function of $M_{\rm rock}$ for different values of the disk's temperature, T_d, and dissipation time, τ_d. While those two parameters are focused on in this study because upper limits of $M_{\rm H+He}$ are of special interest, the sensitivity of $M_{\rm H+He}$ to the initial disk density, ρ_d^0, and the atmospheric opacity is briefly seen below.

First, for a given set of the parameters, $M_{\rm H+He}$ increases with $M_{\rm rock}$ in the small-$M_{\rm rock}$ regime. Also, it is found that there is a critical value of the rocky body's mass, $M_{\rm rock}^*$, beyond which the atmosphere becomes quite massive eventually. This is because the atmospheric accretion enters the runaway state before the disk is depleted significantly. Thus, the atmospheric growth has two distinctly different outcomes, depending on $M_{\rm rock}$. The

atmospheric growth beyond the critical point is discussed in Section 3.

The three red lines of different types show the sensitivity of $M_{\rm H+He}$ to τ_d. For a given $M_{\rm rock}$, larger τ_d results in larger $M_{\rm H+He}$. The sensitivity is not large; $M_{\rm H+He}$ increases by a factor of less than 10 for two-order-of-magnitude increase in τ_d. Also, $M^*_{\rm rock}$ increases, as τ_d decreases. This is because a short lifetime of the disk (i.e., small τ_d) allows only massive protoplanets to start runaway accretion. Difference in τ_d also makes only a small change in $M^*_{\rm rock}$ and also $M_{\rm H+He}$ at the critical point ($<0.1 M_{\rm rock}$). It is noted that while physically small, the sensitivities of $M_{\rm H+He}$ may suffice to validate observationally inferred masses of the atmospheres, as discussed in Section 3.

The results for different three disk temperatures are shown by the solid green ($T_d = 940$ K), red ($T_d = 550$ K), and blue ($T_d = 200$ K) with $\tau_d = 100$ kyr in Figure 2. It is found that T_d has a significant impact on $M_{\rm H+He}$ and $M^*_{\rm rock}$. Qualitatively, high T_d results in small $M_{\rm H+He}$ and, therefore, large $M^*_{\rm rock}$. This is basically because atmospheres made from warmer gas (more exactly, higher-entropy gas) are gravitationally less bound. However, the impact of the outer boundary conditions on the atmospheric mass is known to be negligibly small in the case of massive atmospheres embedded in cool disks like proto-envelopes of gas giants. This is because most of the atmospheric mass is concentrated in the deep region of the atmosphere whose structure is insensitive to the outer boundary conditions (Mizuno 1980; Stevenson 1982; Wuchterl 1993; Ikoma et al. 2001). In contrast, in the case of low-mass atmospheres embedded in warm disks which are appropriate to SEs with short orbital periods, our results in Figure 2 reveal that the impact is significantly large.

The initial disk density, ρ_d^0, has only a small impact on $M_{\rm H+He}$ and $M^*_{\rm rock}$. For example, the yellow line shows the result for the case of ρ_d^0 being 10 times larger than that used for the red solid line. Since high density corresponds to low entropy, the atmosphere embedded in denser disks tends to be more massive for the same reason described above. However, it is realized that the atmosphere before being eroded is massive enough that the structure in its deep part is insensitive to disk properties.

Finally, the values of $M_{\rm H+He}$ and $M^*_{\rm rock}$ that we have derived are upper and lower limits, respectively, for a given set of T_d and τ_d in the sense that no grain opacity and no additional energy input are assumed. In the case represented by the purple line, the effect of grain opacity is evaluated. To do so, we have adopted Semenov et al.'s (2003) protoplanetary-disk grain-opacity model. This would be an extreme case of large opacity, namely, a lower limit to $M_{\rm H+He}$ because large opacity slows down contraction of the atmosphere (Ikoma et al. 2000). Thus, the actual solutions are in between the lines of grain-free (red solid line) and grain-rich (purple line) atmospheres.

3. APPLICATION TO KEPLER-11 SUPER-EARTHS

3.1. Comparison with Atmospheric Masses Inferred by Modeling

The SEs orbiting Kepler-11 are thought to have relatively thick H–He atmospheres, as described in the Introduction. In this section, we apply our theory to the planets and, thereby, get some implications for their composition and origin. Specifically, we compare the atmospheric masses derived from modeling with those which we have calculated in this study.

The comparison is made in Figure 3: the x-axis is the planetary total mass, M_p (i.e., $M_{\rm rock} + M_{\rm H+He}$); the y-axis is the percentage

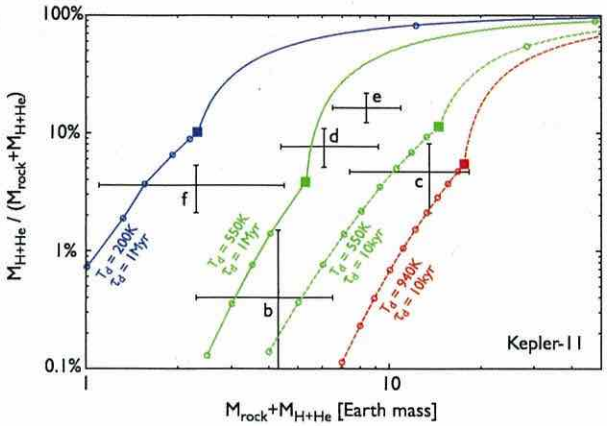

Figure 3. Application to the Kepler-11 planets. The black crosses represent the estimated atmospheric masses of Kepler-11b to 11f, the data of which were provided by Lopez et al. (2012). The red, green, and blue lines are for T_d = 940 K, 550 K, and 200 K, respectively. The solid and dashed lines are for τ_d = 1 Myr and 10 kyr, respectively. We have drawn the extrapolated lines beyond the critical points represented by filled squares, assuming that H–He gas accumulates on the rocky body with the critical mass. The points on the extrapolation lines are the results of simulations where the atmospheric accretion is limited by supply of gas from the disk that evolves via viscous diffusion; α-viscosity is adopted and the values of α are 1×10^{-4} for $\tau_d = 1$ Myr and 1×10^{-2} for $\tau_d = 10$ kyr.

of $M_{\rm H+He}$ relative to M_p. The black crosses represent $M_{\rm H+He}$ derived by the structure modeling of the planets, which account for the observed masses and radii. The data were kindly provided by Lopez et al. 2012 who calculated them using a modified version of the modeling method from Lissauer et al. (2011); the effect of the rocky heat capacity having been incorporated in the thermal evolution, which yielded a slight decrease in $M_{\rm H+He}$ (Lopez et al. 2012).

The curves show the results of our calculations in this study for four different cases. The temperatures 940 K and 550 K correspond to those at Kepler-11b's and 11f's semimajor axes ($a = 0.088$ and 0.25 AU), respectively, in an optically thin disk (Hayashi 1981). Points indicated by filled squares are the critical points (see Section 2.3). Beyond the critical points, we have also drawn extrapolated lines (hereafter called super-critical lines) by assuming that H–He atmospheres accrete on the non-growing rocky bodies with the critical masses; mathematically, the super-critical lines are expressed by $y = (1 - M^*_{\rm rock}/x) \times 100\%$, where $x = M_{\rm rock} + M_{\rm H+He}$ and $y = M_{\rm H+He}/(M_{\rm rock} + M_{\rm H+He})$. To check the validity of the super-critical lines, we have simulated the super-critical (i.e., runaway) accretion whose rate is not higher than supply limit of the disk gas due to viscous diffusion, $3\pi\Sigma_d\nu_d$, where Σ_d and ν_d are the surface density and viscosity of the disk gas, respectively. We have adopted the α-prescription for the disk viscosity; $\tau_d = 10$ kyr and 1 Myr correspond to $\alpha \simeq 10^{-2}$ and 10^{-4}, respectively. It is shown that the numerical solutions are certainly on the super-critical lines. In the case of $T_d = 550$ K and $\tau_d = 10$ kyr, for example, $M_{\rm rock} = 13.0\,M_\oplus$ at the point on the super-critical line, which is close to $M^*_{\rm rock} = 12.9\,M_\oplus$; nevertheless, $M_{\rm H+He}/M_p$ is larger by a factor of $\sim$5. This demonstrates that a slight difference in $M_{\rm rock}$ around $M^*_{\rm rock}$ results in a large difference in $M_{\rm H+He}$.

Recent N-body simulations of the formation of hot SEs (Terquem & Papaloizou 2007; Ogihara & Ida 2009) suggest that disk dissipation often causes collisions between embryos of SEs. The major accretion of atmospheres occurs after the

collisions. In the late stages of disk evolution, photoevaporation separates the inner disk from the outer disk; then, the inner disk dissipates on a timescale of as short as 10^4 yr (Gorti et al. 2009). The dashed lines in Figure 3 correspond to the cases of $\tau_d = 1 \times 10^4$ yr. Comparing the lines with the crosses, one finds that the values of $M_{\rm H+He}$ inferred from modeling are much larger than those derived in this study, except for Kepler-11b and 11c. Furthermore, because the atmospheres are assumed to contain no grains, the derived atmospheric masses are maximal. Thus, the predicted atmospheres of the Kepler-11 planets are not accounted for by the in situ accretion in such a quickly dissipating disk.

Slower disk dissipation may be preferable in this respect. The green solid line shows the case of $\tau_d = 1$ Myr and $T_d = 550$ K. While the corresponding line for $T_d = 940$ K is not drawn, the difference between the solid and dashed lines is similar to that for $T_d = 550$ K. In this case, as far as Kepler-11b to 11e are concerned, the values of $M_{\rm H+He}$ inferred from modeling seem to be consistent with those derived in this study. Kepler-11f lies above the line; only the high-mass end is close to the line. Furthermore, a cooler disk would be compatible with the $M_{\rm H+He}$ inferred for all the planets. As a reference, we show the result for $T_d = 200$ K by a blue solid line. However, it would be worth noting that Kepler-11d and 11e are near the critical points in the super-critical regime. As seen above, such cases are rare because slightly large cores result in much more massive $M_{\rm H+He}$.

3.2. Mass Loss

Before concluding this study, we discuss the loss of the atmospheres. The Kepler-11 planets are orbiting relatively close to their host star which is a G dwarf aged 8 ± 2 Gyr. Since the star is old, the current irradiation level of X-ray and EUV (XUV) is low. In the past, however, the planets should have been exposed to intense stellar XUV. Stellar-XUV irradiation results in loss of planetary atmospheres.

Here we estimate the mass of the H–He atmosphere that a planet with a given density loses via the energy-limited hydrodynamic escape (e.g., Watson et al. 1981). We integrate the equation

$$\dot{M}_{\rm loss} = \frac{3\epsilon F_{\rm XUV}}{4G\bar{\rho}K_{\rm tide}}, \quad (7)$$

where ϵ is the heating efficiency, $F_{\rm XUV}$ is the incident flux of stellar XUV, $\bar{\rho}$ is the planetary bulk density, and $K_{\rm tide}$ is a correction factor for the Roche lobe effect (Erkaev et al. 2007; Lecavelier des Etangs et al. 2004). We adopt $\epsilon = 0.4$ (see Valencia et al. 2010), the fitting formula of $F_{\rm XUV}$ from Ribas et al. (2005), and $K_{\rm tide} = 0.92$ appropriate for the Kepler-11 system.

Figure 4 shows the mass that the planet loses for 10 Gyr as a function of semimajor axis and planetary bulk density, together with the measured values of a and $\bar{\rho}$ for Kepler-11b to 11f. It is revealed that despite different distances to the host star, all the planets have lost similar amounts of atmospheric gas, which are of the order of 0.1 $M_\oplus$. Even for Kepler-11b ($M_p = 4.3^{+2.2}_{-2.0}\, M_\oplus$) and 11f ($M_p = 2.3 \pm 1.2\, M_\oplus$) which are the two lightest planets among them, the amounts of mass loss correspond to ~1%–10% of the planetary masses. (Although their early-stage inflated structure being neglected in this estimate, the results are similar to those from more detailed simulations by Lopez et al. 2012). Thus, the consideration of mass loss does not affect the implications obtained above for Kepler-11c to 11f. As for Kepler-11b, the condition becomes more severe.

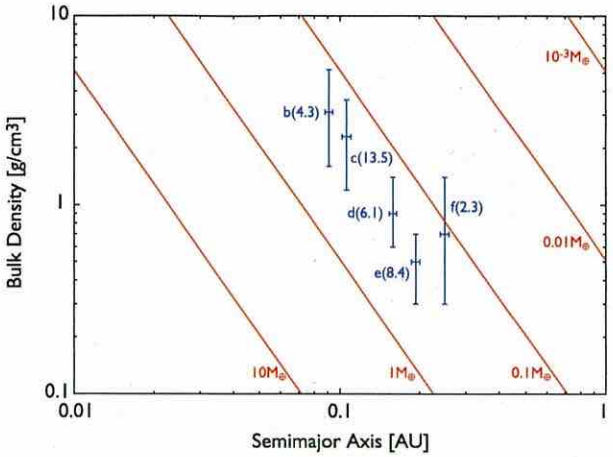

Figure 4. Mass of atmospheric gas that a planet loses for 10 Gyr (solid lines). The numbers attached to lines indicate the estimated values. The mass loss is assumed to occur via the energy-limited hydrodynamic escape driven by XUV from a G dwarf like Kepler-11. Stellar-XUV data have been taken from Ribas et al. (2005). Measured semimajor axes and bulk densities of Kepler-11b, 11c, 11d, 11e, and 11f (Lissauer et al. 2011) are shown by crosses. The numbers in parentheses are the likelihood values of the measured planetary masses.

(A color version of this figure is available in the online journal.)

3.3. Other Possibilities

3.3.1. Degassing

Hydrogen-rich atmospheres may also be formed on rocky SEs via degassing. Planetesimals contain metallic iron, which is oxidized by water to produce hydrogen (Abe et al. 2000). However, detailed calculations show that the resultant hydrogen-rich atmosphere accounts for, at most, several percents of the planetary mass (Elkins-Tanton & Seager 2008; Rogers et al. 2011). This suggests that degassing is insufficient to explain, at least, the inferred masses of the atmospheres of Kepler-11d and 11e.

3.3.2. Water-dominated Planets

Another possibility is that those planets are water-dominated and covered with relatively thin H–He atmospheres, namely, warm Neptunes, which would have formed beyond the snow line, followed by inward migration. The structure and formation of warm Neptunes were recently discussed by Rogers et al. (2011). Looking at results of their modeling, one finds that the atmosphere constituting <1% of the planetary mass is compatible with the observed radii of Kepler-11d and 11e. Such atmospheres are stable for the current level of stellar XUV, as mentioned above (see also Rogers et al. 2011). However, the origin is yet to be explored. Also, the resultant masses and radii of the planets formed in the simulations by Rogers et al. (2011) do not match those of the Kepler-11 planets, although they do not have a special focus on Kepler-11 in the paper. Since migration requires the persistence of the disk gas, further gas accretion should occur after arriving near the host star. Hence the origin of such atmospheres is also a challenging issue.

4. CONCLUSION

Motivated by recent discoveries of low-density SEs with short orbital periods, we have investigated the in situ accretion of H–He atmospheres on short-period SEs. Specifically, we have simulated the quasi-static evolution of the H–He atmospheres

embedded in dissipating, warm disks and, thereby, derived the atmospheric masses at the time when disk gas has disappeared. We have also applied our theory to recently detected short-period SEs orbiting Kepler-11, and examined the possibility that the planets are rocky with relatively thick H–He atmospheres. The application demonstrates that the in situ formation of relatively thick H–He atmospheres inferred by structure modeling is possible only under restricted conditions, namely, relatively slow disk dissipation and/or cool environments.

Through the application of our theory to detected low-density SEs, we have gotten some important suggestions for future improvement in the theory of the formation of H–He atmospheres of low-mass planets. (1) Atmospheric erosion occurs during disk dissipation. This suggests that not only when but also how protoplanetary disks dissipate are crucial factors for determining the atmospheric mass. (2) The thermal contribution of the rocky body to the atmospheric evolution has a significant impact on the atmospheric erosion. Thus, it is important to investigate in more detail the thermal evolution of the rocky body that concurrently occurs with the accretion of the surrounding atmosphere. (3) In relatively hot environments considered in this study, the atmospheric mass is rather sensitive to disk temperature, which means that the late-stage thermal evolution of disks should be also taken into account in simulating the formation of H–He atmospheres of disk origin.

Degeneracy in composition between rocky planets with thick hydrogen-rich atmospheres and water planets is a critical issue in planet formation theories. Findings from this study are applicable to any short-period SEs and would be helpful for removing the degeneracy. As demonstrated in this paper, the atmospheric mass inferred by structure modeling with observed mass and radius can be evaluated by comparison with that derived from the accretion theory. Also, low-density SEs provide important clues to understanding of planetary accretion and disk evolution. Planetary candidates observed by *Kepler* contain about thousand SE-size objects (Borucki et al. 2011). We expect that follow-up observations will identify them and determine their masses, which will lead to better understanding of the origins of low-mass planets.

We are grateful to T. Guillot and J. Fortney for fruitful discussions. We also thank E. Lopez for kindly providing us with the data of his modeling of the structure and thermal evolution of the Kepler-11 planets. We appreciate the anonymous referee's critical and constructive comments which helped us to improve this paper. M.I. is supported by the Challenging Research Award from the Tokyo Institute of Technology and Grant-in-Aid for Scientific Research on Innovative Areas (No. 23103005) from the Ministry of Education, Culture, Sports, Science and Technology (MEXT) of Japan. Y.H. is supported by the Grant-in-Aid for JSPS Fellows (No. 23003491) from MEXT, Japan.

REFERENCES

Abe, Y., Ohtani, E., Okuchi, T., Righter, K., & Drake, M. 2000, in Origin of the Earth and Moon, ed. R. M. Canup & K. Righter (Tucson, AZ: Univ. Arizona Press), 413
Adams, E. R., Seager, S., & Elkins-Tanton, L. 2008, ApJ, 673, 1160
Bodenheimer, P., & Pollack, J. B. 1986, Icarus, 67, 391
Borucki, W. J., Koch, D. G., Basri, G., et al. 2011, ApJ, 736, 19
Calvet, N., Hartmann, L., & Strom, S. E. 2000, in Protostars and Planets IV, ed. V. Mannings, A. P. Boss, & S. S. Russell (Tucson, AZ: Univ. Arizona Press), 377
Elkins-Tanton, L. T., & Seager, S. 2008, ApJ, 685, 1237
Erkaev, N. V., Kulikov, Y. N., Lammer, H., et al. 2007, A&A, 472, 329
Freedman, R. S., Marley, M. S., & Lodders, K. 2008, ApJS, 174, 504
Gorti, U., Dullemond, C. P., & Hollenbach, D. 2009, ApJ, 705, 1237
Grasset, O., Schneider, J., & Sotin, C. 2009, ApJ, 693, 722
Guillot, T., Chabrier, G., Gautier, D., & Morel, P. 1995, ApJ, 450, 463
Hayashi, C. 1981, Prog. Theor. Phys. Suppl., 70, 35
Hayashi, C., Nakazawa, K., & Nakagawa, Y. 1985, in Protostars and Planets II, ed. D. C. Black & S. Matthews (Tucson, AZ: Univ. Arizona Press), 1100
Hori, Y., & Ikoma, M. 2010, ApJ, 714, 1343
Hori, Y., & Ikoma, M. 2011, MNRAS, 416, 1419
Ikoma, M., Emori, H., & Nakazawa, K. 2001, ApJ, 553, 999
Ikoma, M., & Genda, H. 2006, ApJ, 648, 696
Ikoma, M., Nakazawa, K., & Emori, H. 2000, ApJ, 537, 1013
Lecavelier des Etangs, A., Vidal-Madjar, A., McConnell, J. C., & Hébrard, G. 2004, A&A, 418, L1
Lissauer, J. J., Fabrycky, D. C., Ford, E. B., et al. 2011, Nature, 470, 53
Lopez, E. D., Fortney, J. J., & Miller, N. K. 2012, arXiv:1205.0010
Mizuno, H. 1980, Prog. Theor. Phys., 64, 544
Nayakshin, S. 2011, MNRAS, 416, 2974
Ogihara, M., & Ida, S. 2009, ApJ, 699, 824
Ribas, I., Guinan, E. F., Güdel, M., & Audard, M. 2005, ApJ, 622, 680
Rogers, L. A., Bodenheimer, P., Lissauer, J. J., & Seager, S. 2011, ApJ, 738, 59
Rogers, L. A., & Seager, S. 2010, ApJ, 712, 974
Saumon, D., Chabrier, G., & van Horn, H. M. 1995, ApJS, 99, 713
Seager, S., Kuchner, M., Hier-Majumder, C. A., & Militzer, B. 2007, ApJ, 669, 1279
Semenov, D., Henning, T., Helling, C., Ilgner, M., & Sedlmayr, E. 2003, A&A, 410, 611
Stevenson, D. J. 1982, Planet. Space Sci., 30, 755
Terquem, C., & Papaloizou, J. C. B. 2007, ApJ, 654, 1110
Valencia, D., Ikoma, M., Guillot, T., & Nettelmann, N. 2010, A&A, 516, A20
Valencia, D., Sasselov, D. D., & O'Connell, R. J. 2007, ApJ, 665, 1413
Ward, W. R. 1986, Icarus, 67, 164
Watson, A. J., Donahue, T. M., & Walker, J. C. G. 1981, Icarus, 48, 150
Wuchterl, G. 1993, Icarus, 106, 323

The Astrophysical Journal, 744:137 (8pp), 2012 January 10 doi:10.1088/0004-637X/744/2/137

MERGING CRITERIA FOR GIANT IMPACTS OF PROTOPLANETS

H. Genda[1], E. Kokubo[2], and S. Ida[3]
[1] Department of Earth and Planetary Science, The University of Tokyo, Hongo, Bunkyo-ku, Tokyo 113-0033, Japan; genda@eps.s.u-tokyo.ac.jp
[2] Division of Theoretical Astronomy, National Astronomical Observatory of Japan, Osawa, Mitaka, Tokyo 181-8588, Japan
[3] Earth and Planetary Sciences, Tokyo Institute of Technology, Ookayama, Meguro-ku, Tokyo 152-8551, Japan
Received 2011 June 27; accepted 2011 September 16; published 2011 December 22

ABSTRACT

At the final stage of terrestrial planet formation, known as the giant impact stage, a few tens of Mars-sized protoplanets collide with one another to form terrestrial planets. Almost all previous studies on the orbital and accretional evolution of protoplanets in this stage have been based on the assumption of perfect accretion, where two colliding protoplanets always merge. However, recent impact simulations have shown that collisions among protoplanets are not always merging events, that is, two colliding protoplanets sometimes move apart after the collision (hit-and-run collision). As a first step toward studying the effects of such imperfect accretion of protoplanets on terrestrial planet formation, we investigated the merging criteria for collisions of rocky protoplanets. Using the smoothed particle hydrodynamic method, we performed more than 1000 simulations of giant impacts with various parameter sets, such as the mass ratio of protoplanets, γ, the total mass of two protoplanets, $M_{\rm T}$, the impact angle, θ, and the impact velocity, $v_{\rm imp}$. We investigated the critical impact velocity, $v_{\rm cr}$, at the transition between merging and hit-and-run collisions. We found that the normalized critical impact velocity, $v_{\rm cr}/v_{\rm esc}$, depends on γ and θ, but does not depend on $M_{\rm T}$, where $v_{\rm esc}$ is the two-body escape velocity. We derived a simple formula for $v_{\rm cr}/v_{\rm esc}$ as a function of γ and θ (Equation (16)), and applied it to the giant impact events obtained by N-body calculations in the previous studies. We found that 40% of these events should not be merging events.

Key words: accretion, accretion disks – hydrodynamics – planets and satellites: formation

Online-only material: color figures

1. INTRODUCTION

Planets are formed in a disk around a star called a protoplanetary disk, which is composed of gas and dust. Terrestrial planets are formed mainly from the dust component. Their formation process can be divided into three stages. The first stage is the formation of a large number of kilometer-sized bodies called planetesimals by accretion among dust particles (e.g., Goldreich & Ward 1973; Youdin & Shu 2002). In the second stage, these planetesimals collide to produce a few tens of Mars-sized objects called protoplanets (e.g., Wetherill 1985; Kokubo & Ida 1998). The final stage is the formation of terrestrial planets from protoplanets (e.g., Chambers & Wetherill 1998; Agnor et al. 1999). The collisions among protoplanets are referred to as giant impacts, and thus this final stage is known as the giant impact stage.

Giant impacts have a large influence on the various features such as the number of terrestrial planets formed, their mass, and spin state (e.g., Agnor et al. 1999; Kokubo et al. 2006). Giant impacts are highly energetic events and are responsible for the creation of large satellites, such as the Moon (e.g., Canup 2004a) and planets with extremely large cores such as Mercury (e.g., Benz et al. 2007). Moreover, giant impacts are closely related to the thermal state such as a magma ocean (e.g., Tonks & Melosh 1992), and the origins of the terrestrial planet atmospheres (Genda & Abe 2005).

A large number of simulations of giant impacts have been devoted to the specific giant impact events related to the origin of the Moon or Mercury. However, since it is recently believed that multiple giant impacts are common during the last stage of terrestrial planet formation, several studies (Agnor & Asphaug 2004a; Asphaug 2009; Marcus et al. 2009, 2010) have investigated the giant impact simulations under various impact parameters. Agnor & Asphaug (2004a) were the first to show that collisions of protoplanets during the giant impact stage are not always merging events; that is, two colliding protoplanets sometimes move apart after the collision. They called such a collision a hit-and-run collision. Except for Kokubo & Genda (2010), all the previous studies on the orbital and accretional evolution of protoplanets during the giant impact stage have been based on the assumption of perfect accretion, where two colliding protoplanets always merge. However, the hit-and-run collisions demonstrated by Agnor & Asphaug (2004a) may have an important influence on many of the physical characteristics of terrestrial planets.

In order to investigate the effects of such imperfect accretion of protoplanets on terrestrial planet formation, the merging criteria during protoplanet collisions must be clarified. Agnor & Asphaug (2004a) performed 48 simulations of the collisions between same-sized protoplanets with masses of $0.1\,M_\oplus$, where $M_\oplus$ is the Earth mass. They found that hit-and-run collisions occurred when $v_{\rm imp} \geqslant 1.5 v_{\rm esc}$ for $\theta = 30°$ and $v_{\rm imp} \geqslant 1.2 v_{\rm esc}$ for $\theta = 45°$ or $60°$, where $v_{\rm imp}$ is the impact velocity, $v_{\rm esc}$ is the two-body escape velocity (Equation (8)), and θ is the impact angle. Since they varied $v_{\rm imp}$ in steps of $0.1 v_{\rm esc}$ for low-velocity collisions, the transition between the merging and hit-and-run collisions was estimated to be $v_{\rm imp} = 1.4$–$1.5 v_{\rm esc}$ for $\theta = 30°$ and $v_{\rm imp} = 1.1$–$1.2 v_{\rm esc}$ for $\theta = 45°$ or $60°$.

Subsequently, Agnor & Asphaug (2004b) investigated collisions between different-sized protoplanets with mass ratios of 1:2 and 1:10. Their results were presented in Asphaug (2009). The transition was able to be estimated as follows. In the case of a 1:2 mass ratio, the transition occurs at $v_{\rm imp} = 1.4$–$1.5 v_{\rm esc}$ for $\theta = 30°$ and $v_{\rm imp} = 1.1$–$1.2 v_{\rm esc}$ for $\theta = 45°$ or $60°$, whereas in a case of 1:10 mass ratio, $v_{\rm imp} = 1.5$–$2.0 v_{\rm esc}$ for $\theta = 30°$, $v_{\rm imp} = 1.2$–$1.3 v_{\rm esc}$ for $\theta = 45°$, and $v_{\rm imp} = 1.0$–$1.1 v_{\rm esc}$ for $\theta = 60°$.

Marcus et al. (2009, 2010) investigated collisions of the rocky and icy super-Earths (up to 10 $M_\oplus$), respectively. They focused on the stripping of the rocky or icy mantle resulting from a high-velocity impact. Although they did not perform the various simulations with low-impact velocities, we were able to find that the transition occurs at roughly $v_{\rm imp} = 1.0$–$1.5 v_{\rm esc}$ from their figures.

As described above, the merging criteria has already been roughly determined for certain discrete values of the impact parameters. However, in order to carry out N-body orbital calculations with the merging criteria for the giant impact stage, a simple formula describing the dependence of the merging criteria on the impact parameters is required. To achieve this, it is necessary to determine the merging criteria over a wide range of impact parameters. In the present study, we performed more than 1000 simulations of giant impacts for various impact parameter sets using the smoothed particle hydrodynamic (SPH) method in order to formulate the merging criteria.

In Section 2, we present the SPH code and initial conditions used in our giant impact simulations. In Section 3, we show the collision outcomes, and investigate the transition between merging and hit-and-run collisions. We also perform a resolution test on the simulations. In Section 4, we derive the merging criteria as a function of the impact parameters and compare the results with those of previous studies. Using the derived criteria, we then discuss the merging probability of protoplanets during the giant impact stage in Section 5.

2. CALCULATION METHOD

2.1. Numerical Code

In order to perform impact simulations for protoplanets, we used the SPH method (e.g., Monaghan 1992), which is a flexible Lagrangian method of solving hydrodynamic equations and has been widely used in previous giant impact simulations. The SPH method can easily deal with large deformations and shock waves. Our numerical code is based on Canup (2004b); here, we briefly describe its essential points.

The equation of the motion for the ith SPH particle is given by

$$\frac{d\mathbf{v}_i}{dt} = -\sum_j^{\rm neighbor} \mathcal{F}_{ij} - \sum_j^{\rm all} \mathcal{G}_{ij}, \tag{1}$$

where $\mathbf{v}_i$ is the velocity of the ith SPH particle, t is the time, and $\mathcal{F}_{ij}$ and $\mathcal{G}_{ij}$ are the pressure gradient and mutual gravity terms between the ith and jth particles, respectively. Several forms have been used for the pressure gradient term, none of which appear to be clearly superior to the others. In this paper, we use the following symmetric expression,

$$\mathcal{F}_{ij} = m_j \left(\frac{P_i}{\rho_i^2} + \frac{P_j}{\rho_j^2} + \Pi_{ij} \right) \nabla_i W(r_{ij}, h_{ij}), \tag{2}$$

where m_j, P_j, and ρ_j are the mass, pressure, and density of the jth particle, respectively, Π_{ij} is the artificial viscosity, W is the kernel function, r_{ij} is the distance between the ith and jth particles, and h_{ij} is the average smoothing length of the ith and jth particles. For the artificial viscosity Π_{ij}, we use a Von Neumann–Richtmyer-type viscosity with parameters of $\alpha_{\rm vis} = 1.5$ and $\beta_{\rm vis} = 3.0$, as described in Monaghan (1992). For the kernel function W, we use the spherically symmetric spline kernel function proposed by Monaghan & Lattanzio (1985):

$$W(r,h) = \frac{1}{\pi h^3} \begin{cases} 1 - \frac{3}{2}\left(\frac{r}{h}\right)^2 + \frac{3}{4}\left(\frac{r}{h}\right)^3, & 0 \leqslant \frac{r}{h} < 1, \\ \frac{1}{4}\left(2 - \frac{r}{h}\right)^3, & 1 \leqslant \frac{r}{h} < 2, \\ 0, & 2 \leqslant \frac{r}{h}. \end{cases} \tag{3}$$

This function satisfies $\int W(|\mathbf{r}|, h) d\mathbf{r} = 1$ and has a zero value when $r \geqslant 2h$. In our code, h is variable for each particle and with time, and determined to satisfy the condition that the number of neighboring particles ($N_{\rm nei}$) within $2h$ is almost constant, $N_{\rm nei} = 64 \pm 2$. We used a maximum value of the smoothing length ($h_{\rm max}$) to save computational cost when searching for neighboring particles and calculating the pressure gradient term. The value of $h_{\rm max}$ is determined from

$$\frac{m}{\rho_{\rm min}} = \frac{4\pi}{3}(2h_{\rm max})^3, \tag{4}$$

where $\rho_{\rm min}$ is the minimum density, which is set to 5×10^{-3} kg m^{-3} in our simulations.

The mutual gravity term in Equation (1) can be written as

$$\mathcal{G}_{ij} = G \sum_j \hat{m}_j \frac{\mathbf{r}_i - \mathbf{r}_j}{r_{ij}^3}, \tag{5}$$

where G is the gravitational constant and $\hat{m}_j$ is the effective mass of the jth particle toward the ith particle defined by

$$\hat{m}_j = \int_0^{r_{ij}} 4\pi r^2 m_j W(r, h_j) dr. \tag{6}$$

This equation gives $\hat{m}_j = m_j$ when $r_{ij} \geqslant 2h_j$.

The mutual gravity term between all SPH particles was directly computed using a special-purpose computer for gravitational N-body systems named GRAPE-6A (Fukushige et al. 2005). GRAPE-6A can search for and produce lists of neighboring particles while simultaneously calculating their mutual gravity. This list of neighbors is used to compute the pressure gradient term in the equation of motion and the time derivative of the internal energy. In a simulation over a period of 10^5 s with 20,000 SPH particles, the typical CPU time was about 4 hr. Thus, GRAPE-6A allowed us to systematically explore a wide range of impact parameters. Time integration was performed using a PEC (predict, evaluate, and correct) scheme with variable time steps (e.g., Serna et al. 1996), which is second-order accurate in time.

2.2. Pre-impact Protoplanets

Here, we describe the modeling method for the pre-impact protoplanets. All the protoplanets are assumed to be differentiated, with a 30% iron core and 70% silicate mantle by mass. In our SPH simulations, we used the Tillotson equation of state (Tillotson 1962), which has been widely applied to giant impact simulations involving shock waves (e.g., Benz et al. 1987; Canup & Asphaug 2001; Agnor & Asphaug 2004a; Asphaug et al. 2006). The Tillotson equation of state contains ten material parameters, and the pressure is expressed as a function of the density and the specific internal energy, which is convenient for treating fluid dynamics. We used the parameter sets of granite for the silicate mantle and iron for the iron core, which are listed on page 234 of Melosh (1989).

Table 1
Parameter Sets for the Mass Ratio of Colliding Protoplanets

$\gamma = 1$	0.1 $M_\oplus$ vs. 0.1 $M_\oplus$	0.2 $M_\oplus$ vs. 0.2 $M_\oplus$	0.5 $M_\oplus$ vs. 0.5 $M_\oplus$
2/3	0.2 $M_\oplus$ vs. 0.3 $M_\oplus$	...	...
1/2	0.1 $M_\oplus$ vs. 0.2 $M_\oplus$	...	...
1/3	0.1 $M_\oplus$ vs. 0.3 $M_\oplus$	...	...
1/4	0.1 $M_\oplus$ vs. 0.4 $M_\oplus$	0.2 $M_\oplus$ vs. 0.8 $M_\oplus$	0.3 $M_\oplus$ vs. 1.2 $M_\oplus$
1/6	0.1 $M_\oplus$ vs. 0.6 $M_\oplus$	...	...
1/9	0.05 $M_\oplus$ vs. 0.45 $M_\oplus$	0.1 $M_\oplus$ vs. 0.9 $M_\oplus$	0.2 $M_\oplus$ vs. 1.8 $M_\oplus$

All SPH particles in the protoplanets were set to have the same mass, and the total number of particles used for impact simulations was fixed at 20,000. For example, in the case of a collision of protoplanets with a mass ratio of 1:9, the smaller protoplanet consisted of 2000 particles and the larger one 18,000 particles. To model the pre-impact protoplanets, we placed the SPH particles in a three-dimensional lattice (face-centered cubic) with iron particles on the inside and rocky particles outside. The internal energy of the SPH particles was set to $1.0 \times 10^6\,\mathrm{J\,kg^{-1}}$.

Beginning with this configuration, we calculated vibrations of the protoplanet until the particle velocities become slower than 100 m s^{-1}, which is much less than the impact velocity (order of km s^{-1}). After this operation, we used these relaxed objects as the protoplanets for impact simulation. As a first step, the protoplanets were assumed to have no spin.

In order to set impact parameters such as the impact velocity ($v_{\rm imp}$) and impact angle (θ), we need to determine the radius of the pre-impact protoplanets. Since the surface boundary of the protoplanets described by the SPH particles is obscure owing to the smoothing length (h), we determined the radius of the pre-impact protoplanet ($R_{\rm p}$) by the following equation:

$$\frac{4\pi}{3} R_{\rm p}^3 = \sum_i \frac{m_i}{\rho_i}. \tag{7}$$

2.3. Initial Conditions for Collisions

We prepared more than 1000 sets of initial conditions for the giant impact simulations. The parameters used were the mass ratio of the protoplanets ($\gamma = M_{\rm i}/M_{\rm t}$, where $M_{\rm t}$ and $M_{\rm i}$ are the mass of the target and impactor, respectively), the total mass of the two protoplanets ($M_{\rm T} = M_{\rm i} + M_{\rm t}$), the impact angle ($\theta$), and the impact velocity ($v_{\rm imp}$). We systematically varied the mass ratio as $\gamma = 1$, 2/3, 1/2, 1/3, 1/4, 1/6, and 1/9. For $\gamma = 1$, 1/4, and 1/9, we considered three different values of $M_{\rm T}$. In total, we used 13 different combinations for the two colliding protoplanets (see Table 1). For each mass combination, we varied the impact angle in the range $\theta = 0°$–$75°$ in 15° steps, and the impact velocity in the range $v_{\rm imp} = 1.0$–$3.0 v_{\rm esc}$ in $0.2 v_{\rm esc}$ steps, where $v_{\rm esc}$ is the two-body escape velocity defined as

$$v_{\rm esc} = \sqrt{\frac{2GM_{\rm T}}{R_{\rm t} + R_{\rm i}}}, \tag{8}$$

where $R_{\rm t}$ and $R_{\rm i}$ are the radius of the target (larger protoplanet) and the impactor (smaller protoplanet), respectively. To precisely determine the transition between merging and hit-and-run collisions, we varied $v_{\rm imp}$ with a smaller step size of $0.02 v_{\rm esc}$ near the transition. In total, we performed more than 1000 runs, consisting of 13 (mass combinations) × 6 (angles) × 16 (11 runs with $0.2 v_{\rm esc}$ steps and ~ 5 runs with $0.02 v_{\rm esc}$ steps).

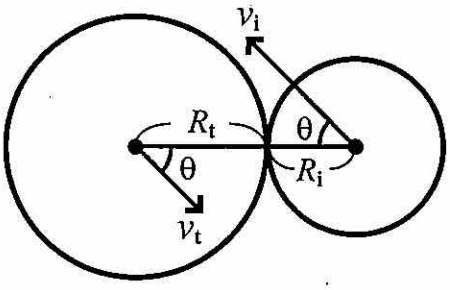

Figure 1. Geometry of the collision between a larger (target) and smaller (impactor) protoplanets with radii of $R_{\rm t}$ and $R_{\rm i}$, respectively. Since a center of mass coordinate system is used, the impact velocity, $v_{\rm imp}$, is given by $|v_{\rm i} - v_{\rm t}|$, where $v_{\rm t}$ and $v_{\rm i}$ are the velocities of the larger and smaller protoplanets, respectively. The impact angle is θ. A head-on collision corresponds to $\theta = 0°$.

The impact parameters $v_{\rm imp}$ and θ are defined when the two protoplanets are in contact with each other (see Figure 1). We assumed that the two protoplanets are mass points, and calculated backward the positions of two mass points until their distance was apart at a distance of 3 ($R_{\rm i}$+$R_{\rm t}$). Then, we performed the giant impact simulations over a period of 10^5 s.

3. COLLISION OUTCOMES

3.1. Merging and Hit-and-run Collisions

The outcomes of the collisions between the protoplanets are divided into two types: merging and hit-and-run collisions. According to the previous studies (Asphaug 2010; Leinhardt et al. 2010; Leinhardt & Stewart 2011), the collision outcomes are subdivided into several regimes (e.g., partial accretion, fragmentation, and so on). However, we classify collision outcomes into only two regimes of merging and hit-and-run collisions, because it is the most essential to the evolution of protoplanets during the giant impact stage that only one big body is left after the giant impact (i.e., merging collision) or two big bodies are left (i.e., hit-and-run collision). Additionally, we need to classify collision outcomes as simply as possible, in order to incorporate those into N-body simulation.

Figure 2 shows snapshots of two typical collisions. Panels (a)–(h) in Figure 2 show the time sequence for a relatively low velocity collision ($v_{\rm imp} = 1.3 v_{\rm esc}$) of same-sized protoplanets ($M_{\rm i} = M_{\rm t} = 0.1\,M_\oplus$) with $\theta = 30°$. After the first contact, the protoplanets become separated (see panel (e)), but remain gravitationally bound. Although some amount of mantle material is ejected, almost all parts of the colliding protoplanets finally merge. We refer to this type of collision as "a merging collision." On the other hand, a relatively high-velocity collision leads to a completely different result. Panels (i)–(l) show the time sequence of a collision with $v_{\rm imp} = 1.5 v_{\rm esc}$. The impact angle and protoplanet masses are the same as in panels (a)–(h). After the first contact, the protoplanets escape from each other and are no longer gravitationally bound. We refer to this type of collision as "a hit-and-run collision." By examining snapshots at $t = 10^5$ s, we could easily classify almost all the simulations performed in this study as either merging or hit-and-run collisions. However, in some cases, the protoplanets were separated but still gravitationally bound at $t = 10^5$ s. Since those protoplanets are expected to eventually merge, we classified such a case as a merging collision.

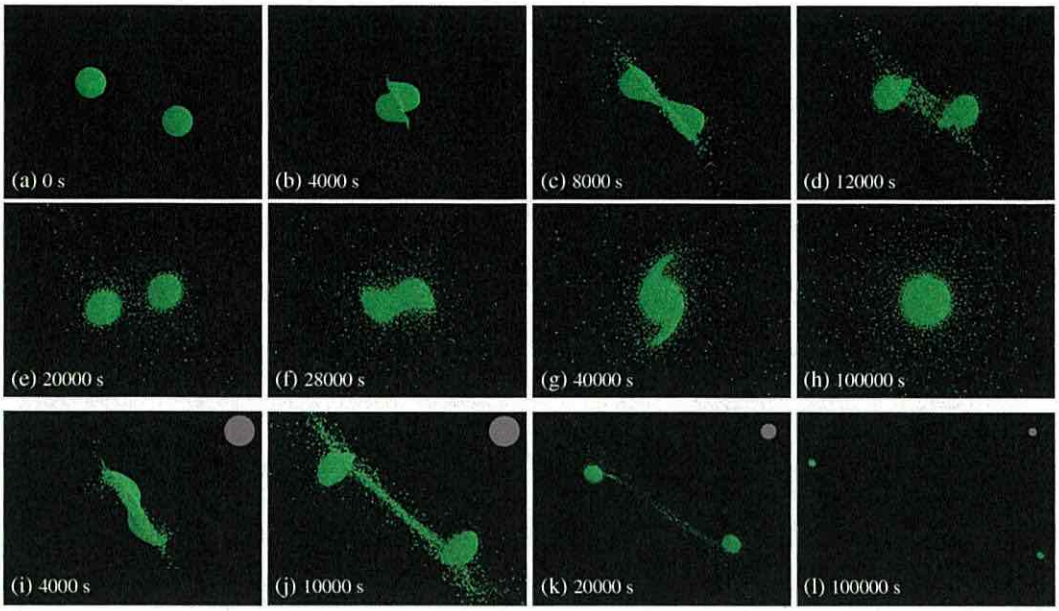

Figure 2. Snapshots of two typical giant impacts between equal-mass protoplanets with 0.1 $M_\oplus$. Panels (a)–(h) show the time sequence for a relatively low velocity collision of protoplanets ($v_{\rm imp} = 1.3 v_{\rm esc}$) with the impact angle 30°. The colliding protoplanets finally merge so that this type of collision is referred to as a merging collision. Panels (i)–(l) show the time sequence for a relatively high velocity collision ($v_{\rm imp} = 1.5 v_{\rm esc}$). The impact angle and mass of the protoplanets are the same as in (a)–(h), but the protoplanets do not merge. This type of collision is referred to as a hit-and-run collision. The dark gray circle at the top-right corner in panels (i)–(l) indicates the size of the initial protoplanets.

(A color version of this figure is available in the online journal.)

3.2. Mass of Protoplanet after a Collision

Here, we consider the mass of the protoplanet after the collision. We briefly describe the method to determine the mass of the gravitationally bound objects from the SPH particle data after $t = 10^5$ s. In the first step, we roughly identify clumps of SPH particles using a friends-of-friends algorithm (e.g., Huchra & Geller 1982). We then iteratively check whether or not any SPH particles not belonging to clumps are gravitationally bound to clumps. Finally, we iteratively identify pairs of clumps that are gravitationally bound. Such clumps should merge after $t = 10^5$ s, and we can thus regard them as a single object. We define the mass of the largest object as M_1 and the second largest object as M_2.

Figure 3 shows the mass of the largest object normalized by the total mass, $M_1/M_{\rm T}$, as a function of the impact velocity normalized by the escape velocity, $v_{\rm imp}/v_{\rm esc}$, for collisions of same-sized protoplanets with $\theta = 30°$. This figure also shows the numerical results of Agnor & Asphaug (2004a) for collisions of same-sized protoplanets with 0.1 $M_\oplus$, which are in good agreement with our results for total mass $M_{\rm T}$ of 0.2 $M_\oplus$. We also performed simulations for $M_{\rm T} = 0.4\,M_\oplus$ and $1.0\,M_\oplus$. As seen in Figure 3, $M_1/M_{\rm T}$ does not depend on the total mass, when the normalized impact velocity, $v_{\rm imp}/v_{\rm esc}$, is considered. The insensitivity to the total mass holds true to collisions between protoplanets, which has been predicted by Asphaug (2010). If the material properties such as strength dominates over gravity (typically collision between smaller bodies with less than 1 km in radius), the collision outcomes would depend on the total mass (Asphaug 2010).

3.3. Transition between Merging and Hit-and-run Collisions

Figure 3 indicates that $M_1/M_{\rm T}$ changes sharply around $1.4 v_{\rm esc}$. Collisions at impact velocities less than this velocity result in almost perfect accretion (i.e., $M_1/M_{\rm T} \simeq 1$), and thus are classified as merging collisions. For the case of a near head-on collision ($\theta \leqslant 15°$), $M_1/M_{\rm T}$ gradually decreases with the increase of $v_{\rm imp}$. Although such a collision should be classified as a partial accretion collision or a fragmentation collision according to Asphaug (2010) and Leinhardt & Stewart (2011), we here classify those as a merging collision because only one large body remains after the collision. Since the probability of a near head-on collision with high velocity is quite low during the giant impact stage, our treatment would not

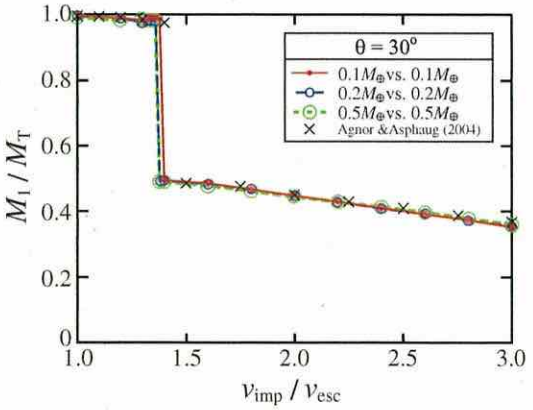

Figure 3. Normalized mass of the largest gravitationally bound object, $M_1/M_{\rm T}$, as a function of normalized impact velocity, $v_{\rm imp}/v_{\rm esc}$. Data for $\theta = 30°$ impacts between two equal-mass protoplanets with different total masses are plotted. Our collision outcomes are very similar to those obtained by Agnor & Asphaug (2004a) who performed simulations for collisions of same-sized protoplanets with masses of 0.1 $M_\oplus$.

(A color version of this figure is available in the online journal.)

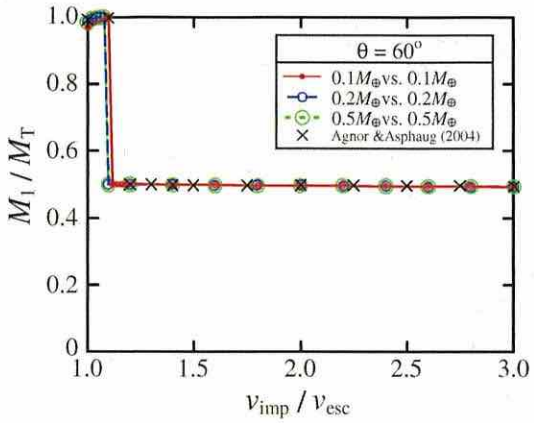

Figure 4. Same as Figure 3 but for $\theta = 60°$.
(A color version of this figure is available in the online journal.)

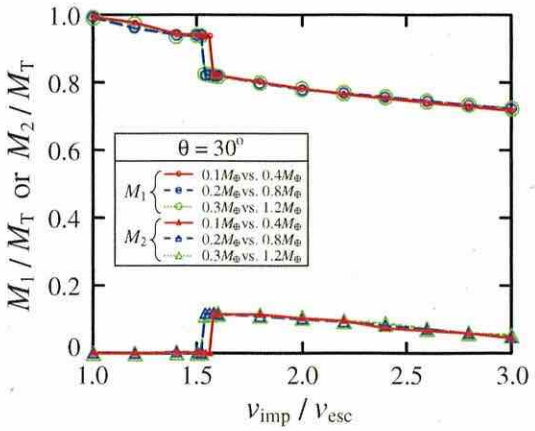

Figure 5. Same as Figure 3 but for collisions of different-sized protoplanets with the mass ratio of 1:4 ($\gamma = 1/4$). The mass of the second-largest object, M_2, is also plotted.
(A color version of this figure is available in the online journal.)

become a serious problem. On the other hand, Figure 3 indicates that the collisions at impact velocities higher than $1.4v_{\rm esc}$ result in $M_1/M_{\rm T} \simeq 0.5$. Some amount of material becomes stripped from the protoplanets, and the protoplanets escape from each other. These collisions are classified as hit-and-run collisions. We refer to the impact velocity at the transition between merging and hit-and-run collisions as the critical impact velocity, $v_{\rm cr}$. The normalized critical impact velocity, $v_{\rm cr}/v_{\rm esc}$, is not strongly dependent on the total mass, $M_{\rm T}$. We obtain $v_{\rm cr}/v_{\rm esc} = 1.39 \pm 0.01$, 1.37 ± 0.01, and 1.37 ± 0.01 for $M_{\rm T} = 0.2$, 0.4 and $1.0\,M_\oplus$, respectively.

The critical impact velocity is expected to depend on the impact angle. Figure 4 is similar to Figure 3, but for the collisions with $\theta = 60°$. As is the same in the case of $\theta = 30°$, $M_1/M_{\rm T}$ for $\theta = 60°$ does not depend on the total mass. However, collisions with $\theta = 60°$ result in lower $v_{\rm cr}/v_{\rm esc}$ values than the $\theta = 30°$ case. The calculated values are $v_{\rm cr}/v_{\rm esc} = 1.11 \pm 0.01$, 1.09 ± 0.01, and 1.09 ± 0.01 for $M_{\rm T} = 0.2$, 0.4, and $1.0\,M_\oplus$, respectively. This result implies that collisions at higher impact angles are more like to be hit-and-run collisions.

The critical impact velocity is also expected to depend on the mass ratio of the protoplanets (γ). Figure 5 shows the results for $\gamma = 1/4$ (mass ratio of 1:4) and $\theta = 30°$. It can be seen that in this case also, $M_1/M_{\rm T}$ does not depend on the total mass. This has also been verified for $\gamma = 1/9$ (mass ratio of 1:9), although the results are not shown here. As shown in Figure 5, $M_1/M_{\rm T}$ changes sharply around $1.5v_{\rm esc}$. The normalized critical impact velocities are $v_{\rm cr}/v_{\rm esc} = 1.57 \pm 0.01$, 1.53 ± 0.01, and 1.53 ± 0.01 for $M_{\rm T} = 0.5$, 1.0, and $1.5\,M_\oplus$, respectively, which are larger than for the case of collisions between same-sized protoplanets.

3.4. Dependence on Particle Number and Initial Internal Energy

In addition to the impact simulations with 20,000 SPH particles (standard case), we performed simulations with 3000 (low-resolution case), 60,000 and 100,000 particles (high-resolution cases) for certain impact parameters in order to check the dependence of convergence on particle number. Although we found that the critical impact velocity for the low-resolution case was slightly different from that for the standard case, the high-resolution cases yielded the same results. For example, for $\gamma = 1$, $M_{\rm T} = 0.2\,M_\oplus$, and $\theta = 30°$, we obtained $v_{\rm cr}/v_{\rm esc} = 1.39 \pm 0.01$ for both the standard and high-resolution

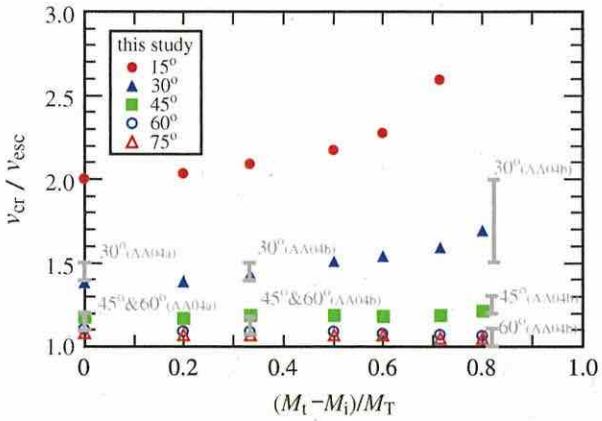

Figure 6. Critical impact velocities for the cases of the various impact angles and mass ratios of protoplanets. Note that $(M_{\rm t} - M_{\rm i})/M_{\rm T}$ is a function of γ, i.e., $(1-\gamma)/(1+\gamma)$. Data points represent our numerical results for $\theta = 15°$ (filled circles), 30° (filled triangles), 45° (filled squares), 60° (open circles), and 75° (open triangles). Bars labeled with AA04a and AA04b are the results obtained by Agnor & Asphaug (2004a) and Agnor & Asphaug (2004b), respectively.
(A color version of this figure is available in the online journal.)

cases. Therefore, using 20,000 SPH particles is enough for determining the critical impact velocity.

In Section 2.2, the initial internal energy of the SPH particles was set to $1.0 \times 10^6\,{\rm J\,kg^{-1}}$. To investigate the effect of the initial thermal state of the protoplanets, we prepared pre-impact protoplanets with an internal energies of 1.0×10^4 (cold-state case) and $3.0 \times 10^6\,{\rm J\,kg^{-1}}$ (hot-state case). We then performed simulations of collisions between same-sized protoplanets with impact parameters near the transition between merging and hit-and-run collisions. We found that although the results for the very low impact angle case ($\theta = 15°$) showed a very slight dependence on the initial thermal state, for all other cases no such dependence was observed.

4. MERGING CRITERIA FOR COLLIDING PROTOPLANETS

In the previous section, we determined the critical impact velocities for several impact parameters. In Figure 6, we

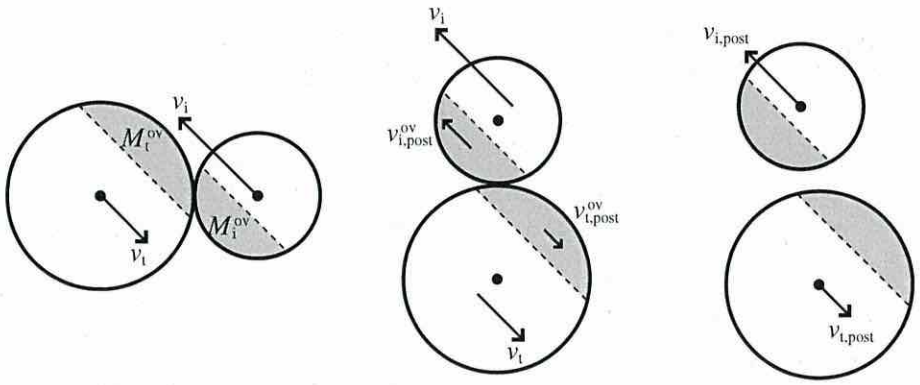

(a) pre-impact (b) momentum exchange (c) post-impact

Figure 7. Configuration of a target and an impactor for the simple physical model. (a) Before the impact, the velocities of the target and the impactor are v_t and v_i, respectively. (b) During the impact, the overlapping parts (shaded areas) exchange momentum, and the post-impact velocity of the overlapping area is reduced to $v_{t,post}^{ov}$ for the target and $v_{i,post}^{ov}$ for the impactor. (c) After the impact, the velocities of the target and impactor are $v_{t,post}$ and $v_{i,post}$, respectively.

summarize v_{cr}/v_{esc} for all parameter sets of the mass ratios (γ) and impact angles (θ). For $\gamma = 1$, 1/4, and 1/9, we performed simulations for three sets of M_T (see Table 1). In Figure 6, we plot the average of these three results.

The critical impact velocities estimated by Agnor & Asphaug (2004a) and Agnor & Asphaug (2004b) are also plotted in Figure 6. Agnor & Asphaug (2004a) investigated collisions between same-sized protoplanets with masses of 0.1 $M_\oplus$ and found that $v_{cr}/v_{esc} = 1.4$–1.5 for $\theta = 30°$ and $v_{cr}/v_{esc} = 1.1$–1.2 for $\theta = 45°$ or 60°. Our results are in good agreement with those of Agnor & Asphaug (2004a), since in our simulations, $v_{cr}/v_{esc} = 1.39 \pm 0.01$ for $\theta = 30°$, 1.19 ± 0.01 for $\theta = 45°$, and 1.11 ± 0.01 for $\theta = 60°$.

Agnor & Asphaug (2004b) investigated collisions between different-sized protoplanets with mass ratios of 1:2 and 1:10. Based on Figure 17 in Asphaug (2009), for a mass ratio of 1:2, $v_{cr}/v_{esc} = 1.4$–1.5 for $\theta = 30°$ and 1.1–1.2 for $\theta = 45°$ or 60°. In the present study, for a mass ratio of 1:2, we obtained $v_{cr}/v_{esc} = 1.43 \pm 0.01$ for $\theta = 30°$, 1.19 ± 0.01 for $\theta = 45°$, and 1.09 ± 0.01 for $\theta = 60°$, and these values are in good agreement with those of Agnor & Asphaug (2004b). Although we did not perform simulations for a mass ratio of 1:10, our data points for 1:9 ($\gamma = 1/9$) seem to fall within the range obtained by Agnor & Asphaug (2004b).

As shown in Figure 6, v_{cr}/v_{esc} increases with decreasing impact angle or mass ratio, which means that collisions with low impact angles or low mass ratios tend to be merging events. This can be explained in terms of the size of the overlapping volume of the colliding protoplanets. Since this is geometrically smaller for higher impact angles, the fraction of kinetic energy converted to thermal energy of protoplanets and kinetic energy of the fragments is small, resulting in a hit-and-run collision. In addition, in the case of a small impactor (i.e., small γ), most of the volume of the impactor tends to overlap with the target. Therefore, the impactor cannot easily be ejected, which leads to a merging collision.

In the following, we consider a simple physical model in order to express the critical impact velocity as a function of the impact angle and mass ratio. For two spheres with radii R_t and R_i colliding with an impact angle θ (see Figure 7), the mass fractions of the overlapping volumes for the target and impactor (β_t and β_i, respectively) are geometrically given by

$$\beta_t = \frac{M_t^{ov}}{M_t} = \left(\frac{R_t + R_i}{R_t}\right)^2 (1 - \sin\theta)^2 \times \left\{\frac{3}{4} - \frac{1}{4}\left(\frac{R_t + R_i}{R_t}\right)(1 - \sin\theta)\right\}, \quad (9)$$

$$\beta_i = \frac{M_i^{ov}}{M_i} = \begin{cases} \left(\frac{R_t + R_i}{R_i}\right)^2 (1 - \sin\theta)^2 \left\{\frac{3}{4} - \frac{1}{4}\left(\frac{R_t + R_i}{R_i}\right)(1 - \sin\theta)\right\}, \\ \qquad \text{if } \sin\theta \geqslant 1 - \frac{2R_t}{R_i + R_t}, \\ 1, \quad \text{otherwise}, \end{cases} \quad (10)$$

where M_t^{ov} and M_i^{ov} are the masses of the overlapping volumes for the target and impactor, respectively. A constant density is assumed for simplicity.

As illustrated in Figure 7, we divide the spheres into overlapping parts and non-overlapping parts, and consider the momentum exchange between the overlapping parts. Using the parameter of the degree of the momentum exchange (α), the post impact velocities of the overlapping parts ($v_{t,post}^{ov}$ and $v_{i,post}^{ov}$) are expressed as

$$\begin{cases} v_{t,post}^{ov} = (1 - \alpha)(v_t - v_{COM}^{ov}) + v_{COM}^{ov}, \\ v_{i,post}^{ov} = (1 - \alpha)(v_i - v_{COM}^{ov}) + v_{COM}^{ov}, \end{cases} \quad (11)$$

where v_{COM}^{ov} is the velocity of the center of mass of the overlapping parts and is written as

$$v_{COM}^{ov} = \frac{M_t^{ov} v_t + M_i^{ov} v_i}{M_t^{ov} + M_i^{ov}}. \quad (12)$$

For example, when $\alpha = 1$, the velocities of the overlapping parts ($v_{t,post}^{ov}$ and $v_{i,post}^{ov}$) become v_{COM}^{ov} owing to the complete momentum exchange.

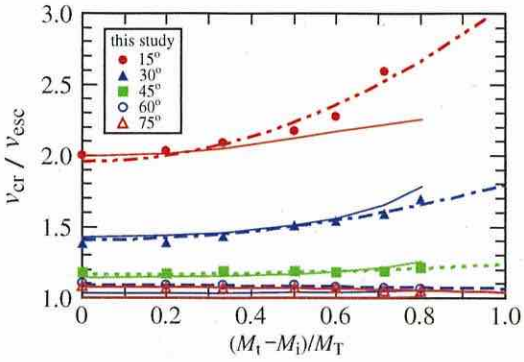

Figure 8. Fits to the normalized critical impact velocity data. Data points are our numerical results and the same as shown in Figure 3. Thin and thick curves represent fits using Equation (15) with $\alpha = 0.6$ and Equation (16), respectively. (A color version of this figure is available in the online journal.)

The post impact velocities of the entire target and impactor can be derived based on the conservation of momentum and written as

$$\begin{cases} M_t v_{t,post} = (M_t - M_t^{ov}) v_t + M_t^{ov} v_{t,post}^{ov}, \\ M_i v_{i,post} = (M_i - M_i^{ov}) v_i + M_i^{ov} v_{i,post}^{ov}, \end{cases} \quad (13)$$

where $v_{t,post}$ and $v_{i,post}$ are the velocities for the post-impact target and impactor, respectively. Combining Equations (11)–(13) gives

$$\begin{cases} v_{t,post} = \left(1 - \alpha\beta_t\beta_i \dfrac{M_t + M_i}{\beta_t M_t + \beta_i M_i}\right) v_t, \\ v_{i,post} = \left(1 - \alpha\beta_t\beta_i \dfrac{M_t + M_i}{\beta_t M_t + \beta_i M_i}\right) v_i. \end{cases} \quad (14)$$

If the relative velocity of post-impact objects is higher than the two-body escape velocity, a hit-and-run collision should occur. Therefore, to solve $v_{i,post} - v_{t,post} = v_{esc}$ using $v_{cr} = v_i - v_t$, the critical impact velocity is obtained as follows:

$$\frac{v_{cr}}{v_{esc}} = \left[1 - \alpha\beta_t\beta_i \frac{M_t + M_i}{\beta_t M_t + \beta_i M_i}\right]^{-1}. \quad (15)$$

The calculated results for $\alpha = 0.6$ are drawn as thin curves in Figure 8. We could roughly reproduce the dependence of v_{cr}/v_{esc} on θ and γ, but detailed features, especially the case for the low-impact angle and low-mass ratio, could not be reproduced. For such a collision, the role of fragmentation that has not been considered here may become important. It should be also noted that $\alpha = 0.6$ would not be applied to collisions other than giant impacts between rocky protoplanets.

In addition to the above physical model, we tried to mathematically fit the numerical data for the critical impact velocity. Of the many possibilities available, we found that the following simple formula with five fitting parameters, c_1 to c_5, was most effective,

$$\frac{v_{cr}}{v_{esc}} = c_1 \Gamma \Theta^{c_5} + c_2 \Gamma + c_3 \Theta^{c_5} + c_4, \quad (16)$$

where $\Gamma = (1-\gamma)/(1+\gamma) = (M_t - M_i)/M_T$ and $\Theta = 1 - \sin\theta$. The fitting parameters are $c_1 = 2.43$, $c_2 = -0.0408$, $c_3 = 1.86$, $c_4 = 1.08$, and $c_5 = 5/2$. The fitting curves produced by Equation (16) are shown in Figure 8 as thick curves and are in excellent agreement with numerical results. The value of the fitting parameters derived here is limited to the collision between protoplanets.

5. MERGING PROBABILITY OF PROTOPLANETS

Almost all previous N-body simulations of terrestrial planet formation during the giant impact stage have been performed based on the assumption of perfect accretion. In order to investigate the statistical properties of fully formed terrestrial planets, Kokubo et al. (2006) considered 10 sets of protoplanet initial conditions and performed 20 runs for each set under the assumption of perfect accretion. Subsequently, to investigate the spin state of the formed planets, Kokubo & Ida (2007) performed additional 30 runs each for seven sets of protoplanet initial conditions. Using the formula for the merging criteria (Equation (16)) derived in the present study, we can now determine whether each of giant impacts was a merging or a hit-and-run event.

Figure 9 shows the normalized impact velocity as a function of impact angle (left panel) and mass ratio (right panel) for 635 giant impact events during 50 runs under standard initial conditions (Model 1 in Kokubo & Ida (2007)). The symbols denoted by crosses represent hit-and-run events, as determined by Equation (16). In fact, 40% of all impact events (256 out of 635) are expected to be hit-and-run collisions. This result is consistent with a previous study by Agnor & Asphaug (2004a), who estimated a hit-and-run probability of roughly half.

6. SUMMARY AND DISCUSSION

During the giant impact stage of terrestrial planet formation in our solar system, a few tens of Mars-sized protoplanets collide with each other to form terrestrial planets. Almost all previous studies on N-body calculations of the giant impact stage have been based on the assumption of perfect accretion. However, recent impact simulations have shown that collisions of protoplanets are not always merging events.

As a first step toward studying the effects of such imperfect accretion on terrestrial planet formation, we investigated the merging criteria for a collision of rocky protoplanets. Using the SPH method, we performed more than 1000 simulations of giant impacts for various parameter sets, such as the mass ratio of colliding protoplanets (γ), the total mass of two protoplanets (M_T), the impact angle (θ), and the impact velocity (v_{imp}). We investigated the critical impact velocity (v_{cr}) at the transition between merging and hit-and-run collisions. We found that the normalized critical impact velocity, v_{cr}/v_{esc}, depends on γ and θ, but does not depend on M_T. We derived a simple formula for v_{cr}/v_{esc} as a function of γ and θ (see Equation (16)), and applied it to the giant impact events considered by Kokubo et al. (2006) and Kokubo & Ida (2007). We found that 40% of these events should not be merging events.

Kokubo & Genda (2010) was the first to performed N-body simulations of the giant impact stage taking into account the merging criteria shown in Equation (16), and investigated the effects of imperfect accretion on terrestrial planet formation. They found that some basic properties such as the final number, mass, orbital elements, and growth timescale of planets did not change very much, but the spin angular velocity of the fully formed planets was about 30% smaller than that for the perfect accretion model. They also determined that 49% of all impact events were hit-and-run collisions, which is also consistent with our estimate.

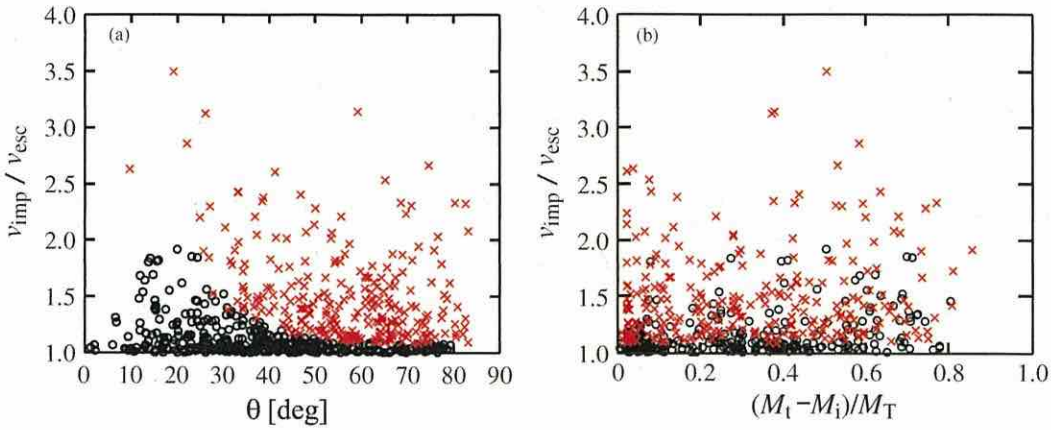

Figure 9. Normalized impact velocity for 635 giant impacts reported by Kokubo et al. (2006) and Kokubo & Ida (2007) as a function of the impact angle (a) and the mass ratio of protoplanets (b). Based on the critical impact velocity (Equation (16)), the giant impact events are distinguished as hit-and-run collisions (cross symbols) or merging collisions (circle symbols). Although Kokubo et al. (2006) and Kokubo & Ida (2007) assumed the perfect accretion of protoplanets in their *N*-body calculations, the present study reveals that 40% of the impact events (256 out of 635) are hit-and-run collisions.

(A color version of this figure is available in the online journal.)

In this paper, we focused on the merging criteria for protoplanet collisions. In the future, we plan to investigate additional collisional phenomena such as mantle stripping and ejection of small particles. Using our simulation data for more than 1000 collisional events, we can estimate the change in the core–mantle ratio during the giant impact stage. This is highly relevant to the formation of Mercury, and the formation probability of such planets with very large cores will be investigated.

The ejection of small particles during each collision in the giant impact stage may influence the orbital evolution of terrestrial planets. The ejected material may have damped the eccentricities of the terrestrial planets to their present low values, although it depends on the total amount of material ejected during the giant impact stage.

We thank Sarah T. Stewart for valuable comments on the manuscript. This research was partially supported by JSPS, the Grant-in-Aid for Young Scientists B (22740291), and MEXT, the Grant-in-Aid for Scientific Research on Priority Areas, and the Special Coordination Fund for Promoting Science and Technology.

REFERENCES

Agnor, C., & Asphaug, E. 2004a, ApJ, 613, L157
Agnor, C., & Asphaug, E. 2004b, American Geophysical Union, Fall Meeting, abstract #P32A-02
Agnor, C. B., Canup, R. M., & Levison, H. F. 1999, Icarus, 37, 219
Asphaug, E. 2009, Annu. Rev. Earth Planet. Sci., 37, 413
Asphaug, E. 2010, Chem. Erde, 70, 199
Asphaug, E., Agnor, C., & Williams, Q. 2006, Nature, 439, 155
Benz, W., Anic, A., & Whitby, J. A. 2007, Space Sci. Rev., 132, 189
Benz, W., Slattery, W. L., & Cameron, A. G. W. 1987, Icarus, 71, 30
Canup, R. M. 2004a, ARA&A, 42, 441
Canup, R. M. 2004b, Icarus, 168, 433
Canup, R. M., & Asphug, E. 2001, Nature, 412, 708
Chambers, J. E., & Wetherill, G. W. 1998, Icarus, 136, 304
Fukushige, T., Makino, J., & Kawai, A. 2005, PASJ, 57, 1009
Genda, H., & Abe, Y. 2005, Nature, 433, 842
Goldreich, P., & Ward, W. R. 1973, ApJ, 183, 1051
Huchra, J. P., & Geller, M. J. 1982, ApJ, 257, 423
Kokubo, E., & Genda, H. 2010, ApJ, 714, L21
Kokubo, E., & Ida, S. 1998, Icarus, 131, 171
Kokubo, E., & Ida, S. 2007, ApJ, 671, 2082
Kokubo, E., Kominami, J., & Ida, S. 2006, ApJ, 642, 1131
Leinhardt, Z. M., Marcus, R. A., & Stewart, S. T. 2010, ApJ, 714, 1789
Leinhardt, Z. M., & Stewart, S. T. 2011, MNRAS, submitted (arXiv:1106.6084)
Marcus, R. A., Sasselov, D., Stewart, S. T., & Hernquist, L. 2010, ApJ, 719, L45
Marcus, R. A., Stewart, S. T., Sasselov, D., & Hernquist, L. 2009, ApJ, 700, L118
Melosh, H. J. 1989, Impact Cratering: A Geologic Process (New York: Oxford Univ. Press)
Monaghan, J. J. 1992, ARA&A, 30, 543
Monaghan, J. J., & Lattanzio, J. C. 1985, A&A, 149, 135
Serna, A., Alimi, J.-M., & Chieze, J.-P. 1996, ApJ, 461, 884
Tillotson, J. H. 1962, Report No. GA-3216, July 18 (San Diego, CA: General Atomic)
Tonks, W. B., & Melosh, H. J. 1992, Icarus, 100, 326
Wetherill, G. W. 1985, Science, 228, 877
Youdin, A. N., & Shu, F. H. 2002, ApJ, 580, 494

The Astrophysical Journal, 738:141 (11pp), 2011 September 10 doi:10.1088/0004-637X/738/2/141

EVOLUTION OF SNOW LINE IN OPTICALLY THICK PROTOPLANETARY DISKS: EFFECTS OF WATER ICE OPACITY AND DUST GRAIN SIZE

Akinori Oka, Taishi Nakamoto, and Shigeru Ida
Department of Earth and Planetary Sciences, Tokyo Institute of Technology, Tokyo, Japan; akinorioka1@gmail.com, nakamoto@geo.titech.ac.jp
Received 2009 September 1; accepted 2011 June 13; published 2011 August 19

ABSTRACT

Evolution of a snow line in an optically thick protoplanetary disk is investigated with numerical simulations. The ice-condensing region in the disk is obtained by calculating the temperature and the density with the 1+1D approach. The snow line migrates as the mass accretion rate ($\dot{M}$) in the disk decreases with time. Calculations are carried out from an early phase with high disk accretion rates ($\dot{M} \sim 10^{-7}\,M_\odot\ \mathrm{yr}^{-1}$) to a later phase with low disk accretion rates ($\dot{M} \sim 10^{-12}\,M_\odot\ \mathrm{yr}^{-1}$) using the same numerical method. It is found that the snow line moves inward for $\dot{M} \gtrsim 10^{-10}\,M_\odot\ \mathrm{yr}^{-1}$, while it gradually moves outward in the later evolution phase with $\dot{M} \lesssim 10^{-10}\,M_\odot\ \mathrm{yr}^{-1}$. In addition to the silicate opacity, the ice opacity is taken into consideration. In the inward migration phase, the additional ice opacity increases the distance of the snow line from the central star by a factor of 1.3 for dust grains $\lesssim$10 μm in size and of 1.6 for $\gtrsim$100 μm. It is inevitable that the snow line comes inside Earth's orbit in the course of the disk evolution if the viscosity parameter α is in the range 0.001–0.1, the dust-to-gas mass ratio is higher than a tenth of the solar abundance value, and the dust grains are smaller than 1 mm. The formation of water-devoid planetesimals in the terrestrial planet region seems to be difficult throughout the disk evolution, which imposes a new challenge to planet formation theory.

Key words: accretion, accretion disks – planets and satellites: formation – protoplanetary disks – radiative transfer

Online-only material: color figures

1. INTRODUCTION

In a protoplanetary disk, a snow line, defined as the inner boundary of an ice-condensing region, is present. The snow line is considered to play an important role in planetary formation, since the solid mass density outside the snow line is high due to the condensation of water ice (water ice abundance is as large as silicate and iron in a protoplanetary disk with solar composition; Pollack et al. 1994). The snow line may also be related to the origin of the water distribution in our solar system. Water abundance in current solar system objects shows a clear variation; bodies in the inner part contain less, while bodies in the outer part have more. The terrestrial planets are significantly devoid of water. For example, Earth contains only 0.023 wt% water in its oceans, and Venus is considered to have contained an amount of water comparable with that of Earth (Lewis 2004). On the other hand, the outer planets and objects outside the asteroid belt contain a large amount of water. In the intermediate region, i.e., the asteroid belt, the radial distribution of asteroids also shows compositional zoning. From these facts, one may consider that the snow line might have been located in the asteroid belt when planetesimal formation occurred, since planetesimals that were formed outside the snow line would necessarily take in a large amount of icy materials.

The location of the snow line, which is used in many studies of planet formation, is the heliocentric distance where the temperature of the disk reaches about 170 K. In the solar nebula, the snow line location is estimated to be 2.7 AU, assuming that the solar nebula is optically thin (Hayashi 1981). Before planet formation takes place, however, protoplanetary disks are likely to be optically thick, since a large amount of fine dust particles is present. Thus, temperatures in optically thick disks should be obtained to determine the location of the snow line.

So far, the snow line location in an optically thick disk has been obtained theoretically from one-dimensional (1D) (radial) or 1+1D (radial and vertical) disk structure calculations (e.g., Cassen 1994; Stepinski 1998). The latest studies on the snow line location with a detailed disk structure calculation were made by Davis (2005) and Garaud & Lin (2007). They considered the stellar radiation flux and viscous dissipation of gas as the main heating sources in a disk, and obtained the disk temperature by solving the detailed radiative energy transfer. They revealed that the snow line migrates inward as the disk evolves and the mass accretion rate decreases, because viscous dissipation of gas, which is the main heating source in the disk, reduces as the disk evolves. Davis (2005) showed that the snow line reaches about 0.6 AU, which is the minimum radius in his calculations. Similarly, Garaud & Lin (2007) found that, in the later phase, the snow line migrates outward since stellar radiation penetrates deeper into the disk interior as the disk becomes optically thinner and its temperature rises.

One important point of their results is that the snow line comes inside the Earth's orbit; the minimum heliocentric distance of the snow line is about 0.6 AU (Davis 2005; Garaud & Lin 2007). If sufficiently large bodies like planetesimals were formed when the snow line was located at such a small heliocentric distance, Earth would have been formed with icy planetesimals. Then, Earth should presently contain comparable amounts of water, silicate, and iron. This conflicts with the current water content on Earth.

In order to make clear the important inconsistency in planet formation, we investigate the detailed thermal evolution of protoplanetary disks using precise radiative transfer calculations, taking into account the dependence of opacity on frequency, the scattering process of dust particles, and the ice opacity that previous studies did not consider. According to Inoue et al. (2009) and Dullemond et al. (2002), disk midplane temperature varies by a factor of at most about two due to the first two effects. Ice opacity may change the optical properties of a disk or disk temperature structure significantly, since ice is as abundant as silicate in a protoplanetary disk of solar composition. The effect of the dust grain size, which changes the snow line location as

well, has not received enough consideration in previous studies. These effects are examined carefully in this work to see the location of the snow line.

In this study, the snow line location is simulated numerically with the 1+1D disk model, taking into account the water ice opacity, the variety of dust grain sizes, and the scattering process in the radiative transfer. Then we discuss whether the snow line location obtained theoretically is consistent with the water distribution in the current solar system.

2. MODEL

2.1. Disk Structure

A geometrically thin axisymmetric disk revolving around a central star is considered. A plane symmetry with respect to the midplane is assumed. Cylindrical coordinates (R, ϕ, Z) are adopted. The origin and the $Z = 0$ plane are placed at the central star and the disk midplane.

The hydrodynamical and thermal structures of the disk are modeled in almost the same way as in Dullemond et al. (2002) and Inoue et al. (2009) except for the disk's gas surface density $\Sigma(R)$. The radiative cooling and two heating sources, irradiation by the central star and viscous dissipation, are considered. The temperature is determined with the radiative equilibrium condition. To obtain the whole disk structure, the 1+1D approach is adopted. The direct irradiation from the central star at the disk inner edge is ignored, and the disk structure is assumed to change gradually in the radial direction. This approach is justified if the snow line location is sufficiently far from the inner edge. The 2D structure of the inner disk region (the puffed-up inner rim and the adjacent shadowed region) seems to be important only in the innermost part of the disk around a T Tauri star, judging from results for Herbig Ae/Be stars of Dullemond (2002). Although the shadowed region extends to slightly large heliocentric distances, it does not matter for the scope of this study because it only lowers the disk temperature and does not shift the snow line location outward. Details are given in the Appendix.

The radial distribution of the gas surface density is modeled assuming that the disk is in the steady accretion state, i.e., the mass accretion rate $\dot{M}$ is constant along the radial direction R. The gas surface density in a region where $R \gg R_*$ (the stellar radius) is given as (e.g., Pringle 1981)

$$\Sigma(R) = \frac{\dot{M}}{3\pi \nu_t(R)}, \quad (1)$$

where $\nu_t(R)$ is the viscosity of the disk. The assumption of steady accretion is justified in the region around the snow line because the snow line is usually located within 10 AU, and the viscous diffusion timescale there is sufficiently smaller than the entire disk evolution timescale.

The viscosity ν_t is modeled with the α-prescription (Shakura & Sunyaev 1973) as $\nu_t = \alpha c_s^2/\Omega_K$, where α is a non-dimensional parameter, $c_s = \sqrt{kT/(\bar{\mu} m_u)}$ is the isothermal sound velocity of gas, k is the Boltzmann constant, T is the gas temperature, $\bar{\mu}$ is the mean molecular weight, m_u is the atomic mass unit, $\Omega_K = \sqrt{GM_*/R^3}$ is the Kepler angular velocity, G is the gravitational constant, and M_* is the stellar mass. The value of α ranges from 0.001 to 0.1 according to ideal MHD simulations (Hawley et al. 1995, 1996). The value of $\alpha = 0.01$ is adopted as a fiducial one throughout the disk in this study, except in Section 3.3. In the evaluation of ν_t, the sound velocity c_s at the midplane ($Z = 0$) is used. A value of $\bar{\mu} = 2.3$ is used for the mean molecular weight.

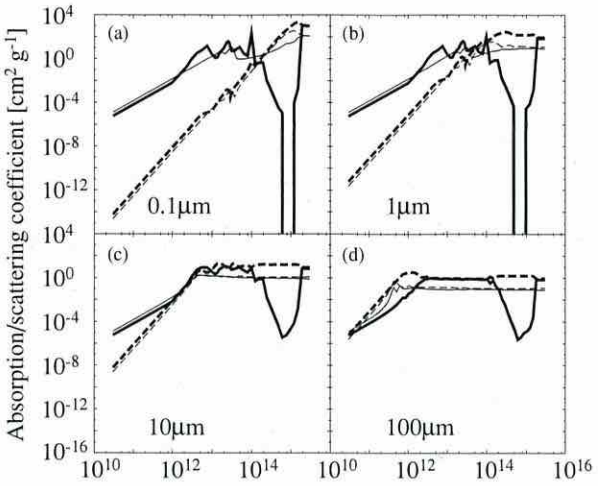

Figure 1. Absorption and scattering coefficients of the disk gas containing silicate and icy dust particles adopted in our calculation. These coefficients are taken from Miyake & Nakagawa (1993). Note that all the water molecules are condensed in the icy dust particles. In panels (a)–(d), the dust grain size is set to be 0.1, 1, 10, and 100 μm, respectively. The thick and thin curves represent the coefficients for icy and silicate dust particles, respectively, and the solid and dashed curves represent the absorption and scattering coefficients, respectively.

The frequency-dependent radiative transfer is solved numerically. Absorption and scattering by dust particles are taken into consideration as the opacity source in the disk. Isotropic scattering is assumed when the dust grain size is sufficiently smaller than the radiation wavelength. When the dust grain size is larger than the wavelength, the scattering coefficient is set to zero because forward scattering dominates in that case.

The steady-state disk structure is solved self-consistently as a function of the mass accretion rate. Although density, viscosity, and temperature are related to one another, they are numerically obtained consistently by iterative calculations.

2.2. Dust Abundance and Opacity

Only dust particles suspended in the disk are considered to be the opacity source because the gas opacity is negligibly small. Two kinds of dust particles, silicate and pure water ice particles, are assumed to be present separately. Effects of icy mantles on silicate cores will be discussed in Section 5.2. It is assumed that dust particles are uniformly sized spheres and mass ratios of the silicate and ice particles to the gas are constant throughout the disk. Radial transport, vertical mixing, and sedimentation of dust particles are neglected. Also, complete thermal coupling between dust particles and gas is assumed; this is valid in the disk considered in this study (Kamp & Dullemond 2004).

Absorption and scattering coefficients of dust particles and mass ratios to the gas are taken from Miyake & Nakagawa (1993); silicate and (maximum) ice mass ratios to the gas are $\zeta_{\rm sil} = 0.0043$ and $\zeta_{\rm ice} = 0.0094$, respectively, which are consistent with the solar elemental abundance given by Anders & Grevesse (1989). With this water ice abundance and the mean molecular weight of 2.3, the H_2O mole fraction in the disk gas becomes 1.2×10^{-3}. Figure 1 shows the absorption and scattering coefficients of a unit mass disk medium.

The ice abundance in the disk gas is determined with the thermal equilibrium condition under which the partial pressure

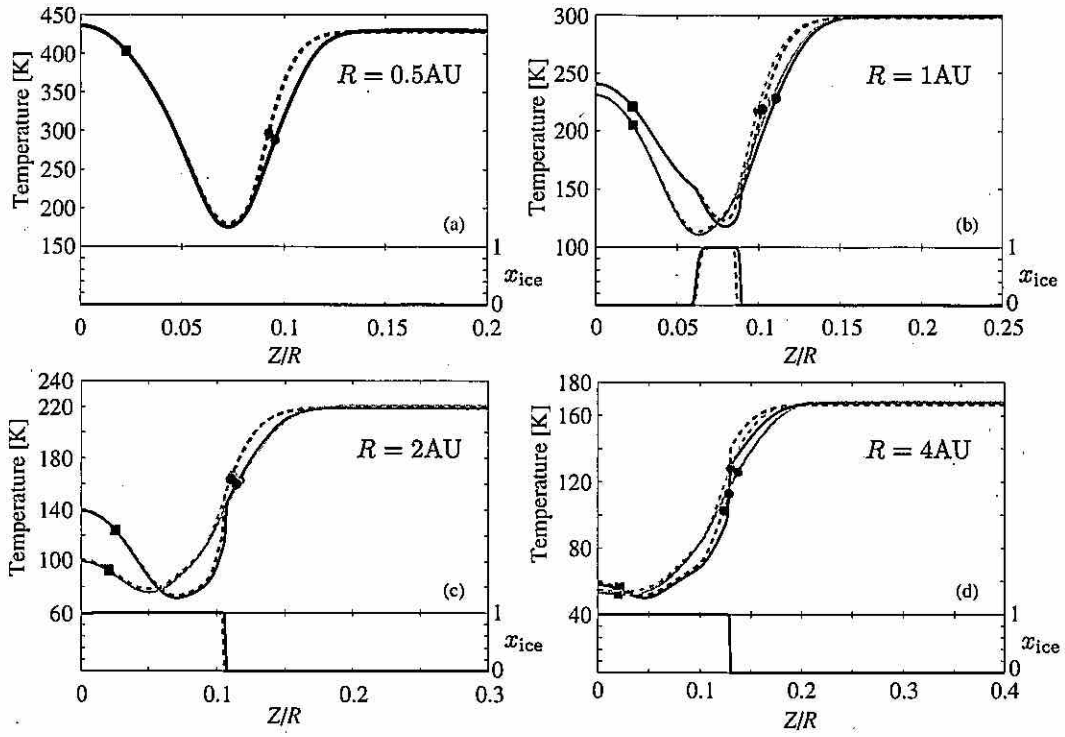

Figure 2. Vertical temperature profiles at various heliocentric distances. The mass accretion rate is fixed to be $10^{-8}\,M_\odot$ yr^{-1}. Other parameters are $M_* = 0.5\,M_\odot$, $R_* = 2\,R_\odot$, $T_{\rm eff} = 3000$ K, and $\alpha = 0.01$; the dust grain size is 0.1 μm. Panels (a)–(d) show the profiles at the heliocentric distances of 0.5, 1, 2, and 4 AU, respectively. The horizontal axis represents the height from the midplane normalized by the heliocentric distance. In each panel, the upper part shows the temperature profile and the lower part shows the vertical profile of the ice-condensing ratio. The solid and dotted curves show the results with and without scattering by dust particles, respectively. The black and gray curves show the results with and without ice opacity. The solid circle and the solid square on each curve show the height of H_s and the pressure scale height, respectively.

of water vapor is limited by the saturated vapor pressure (Bauer et al. 1997):

$$P_{\rm sat}(T) = \exp(-6070\ {\rm K}/T + 30.86)\ {\rm dyn\ cm^{-2}}. \quad (2)$$

The partial pressure of water vapor $P_{\rm H_2O}$ is given approximately by the product of the water vapor mole fraction $X_{\rm H_2O}$ and the total gas pressure:

$$P_{\rm H_2O} = X_{\rm H_2O} P. \quad (3)$$

The water vapor mole fraction $X_{\rm H_2O}$ is limited to 1.2×10^{-3}, so excess water molecules condense as water ice. Thus, $X_{\rm H_2O}$ is given by

$$X_{\rm H_2O} = \begin{cases} 1.2 \times 10^{-3} & (1.2 \times 10^{-3} P \leqslant P_{\rm sat}(T)), \\ P_{\rm sat}(T)/P & (1.2 \times 10^{-3} P > P_{\rm sat}(T)). \end{cases} \quad (4)$$

Then, the mass ratio of ice to the total water molecules in the disk gas, $x_{\rm ice}$, is given by

$$x_{\rm ice} = 1 - X_{\rm H_2O}/(1.2 \times 10^{-3}). \quad (5)$$

Using $x_{\rm ice}$, the absorption and scattering coefficients of the disk medium, $\kappa_{\rm abs}$ and $\kappa_{\rm sca}$, are given as

$$\kappa_{\rm abs} = \kappa_{\rm sil,abs} + x_{\rm ice}\kappa_{\rm ice,abs}, \quad (6)$$

$$\kappa_{\rm sca} = \kappa_{\rm sil,sca} + x_{\rm ice}\kappa_{\rm ice,sca}, \quad (7)$$

where $\kappa_{\rm sil,abs}$, $\kappa_{\rm sil,sca}$, $\kappa_{\rm ice,abs}$, and $\kappa_{\rm ice,sca}$ represent the absorption and scattering coefficients of the disk medium attributed to silicate and ice dust particles, respectively. Equations (6) and (7) are held for each frequency of the radiative transfer. The disk temperature depends on $x_{\rm ice}$; hence, the temperature and $x_{\rm ice}$ are solved consistently by iterative calculations.

3. RESULTS

3.1. Effects of Water Ice Opacity

Numerical results shown in this subsection are obtained by calculations with the following input parameters: $T_{\rm eff} = 3000$ K, $R_* = 2\,R_\odot$, and $M_* = 0.5\,M_\odot$. The dust grain size is 0.1 μm.

3.1.1. Disk Structure

Figures 2 and 3 show vertical temperature profiles at various radii with $\dot{M} = 10^{-8}\,M_\odot$ yr^{-1} and $10^{-10}\,M_\odot$ yr^{-1}, respectively, as typical cases for high and low mass accretion rates. In Figure 2, the temperature in the disk with ice opacity is higher than that in the one without it. The dominant heating source in this case is viscous dissipation, and the blanket effect of dust particles is enhanced due to the ice in the upper layers. On the other hand, in Figure 3, the midplane temperatures are not considerably different from each other, though ice condenses. In this case, the dominant heating source is the incident stellar radiation, so the midplane temperature does not depend so much on dust opacity. The temperature in the disk is lowered due to the ice condensation. The low temperature causes a slightly low altitude of the scale height and H_s as seen in Figure 3 (H_s is the

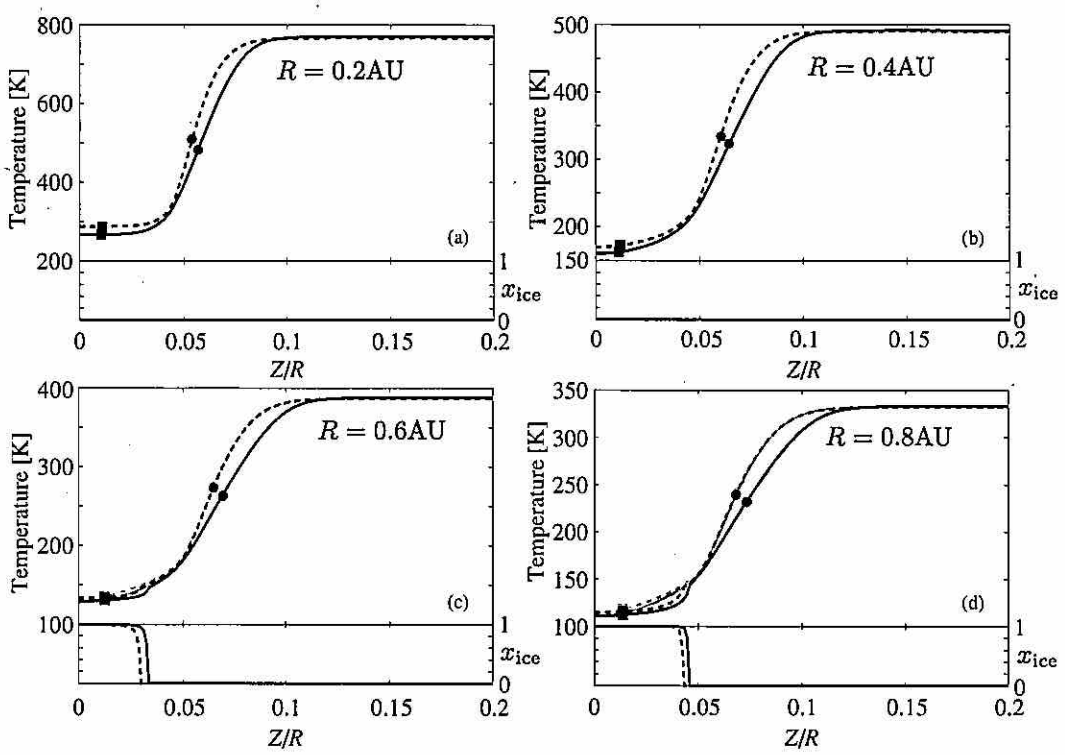

Figure 3. Same as in Figure 2 except for the mass accretion rate and the heliocentric distances. The mass accretion rate is $10^{-10}\ M_\odot\ \mathrm{yr}^{-1}$ and the heliocentric distances of the panels (a)–(d) are 0.2, 0.4, 0.6, and 0.8 AU, respectively.

height from the midplane where the incident stellar radiation energy flux is reduced by a factor of e).

The disk temperature is altered only a little by considering dust scattering, because a single scattering albedo dust particles of size 0.1 μm is small. Though small, the midplane temperature is increased slightly when viscous heating is dominant (Figure 2); the scattering by dust particles enhances the optical depth in the disk and increases the blanket effect. On the other hand, the midplane temperature is lowered slightly when stellar irradiation is the dominant heating source (Figure 3), since a large fraction of incident radiation is reflected toward space (Dullemond & Natta 2003; Inoue et al. 2009).

3.1.2. Evolution of the Ice-Condensing Region

Figure 4 shows the ice-condensing region in the (R, Z) sectional plane with various mass accretion rates.[1] A decrease in the mass accretion rate can be regarded as the time evolution of the disk.

When $\dot{M}$ is high ($\geqslant 10^{-9}\ M_\odot\ \mathrm{yr}^{-1}$), the condensation front has a two-branched structure, as found by Cassen (1994) and Davis (2005). The condensation front in the upper layer extends closer to the central star than to the snow line (hereafter, the snow line is defined as the condensation front at the midplane) irrespective of the presence of ice. The lower branch of the condensation front is formed by a high temperature caused by viscous dissipation, while the upper branch is formed by a high temperature caused by direct stellar radiation and a low partial pressure of water vapor. The snow line shifts outward by a factor of 1.3 due to the ice opacity independent of the mass accretion rate.

On the other hand, when $\dot{M}$ is low ($\leqslant 10^{-10}\ M_\odot\ \mathrm{yr}^{-1}$), the condensation front is a smooth curve and the snow line location is not shifted significantly by the ice opacity. This can be attributed to two reasons: when the disk is mainly heated by stellar irradiation (1) the midplane temperature does not depend so much on the opacity of the disk medium and (2) icy dust particles do not condense in the upper layer above the snow line due to the temperature increasing with height.

3.1.3. Evolution of the Snow Line

Figure 5 shows the snow line locations obtained with and without ice opacity as a function of the mass accretion rate. In both cases, the snow line migrates inward when $\dot{M}$ is high ($\gtrsim 10^{-10}\ M_\odot\ \mathrm{yr}^{-1}$) and outward when $\dot{M}$ is low ($\lesssim 10^{-10}\ M_\odot\ \mathrm{yr}^{-1}$). An inward migration is caused by the decrease of the midplane temperature due to the reduction of viscous heating and the decrease of the blanket effect. The inward migration ceases when stellar irradiation starts to dominate the heating around the midplane. Then, an outward migration is started by the decrease in the disk's optical thickness, which results in a higher temperature due to a deeper penetration of the stellar radiation into the disk interior. The snow line in this study migrates outward more slowly than the results of Garaud & Lin (2007) (see Section 3.3).

[1] The flaring index ξ is chosen to be zero at small heliocentric distances ($R \lesssim 4$ AU) for $\dot{M} \gtrsim 4 \times 10^{-8}\ M_\odot\ \mathrm{yr}^{-1}$ because the grazing angle in an inner region becomes negative due to the high temperature caused by viscous heating, and the grazing angle recipe becomes invalid. Though this operation is artificial, the disk structure around the midplane is not affected significantly by the operation due to the fact that the dominant heating source around the midplane is viscous dissipation. This operation is also done if the grazing angle becomes negative in the other calculations in this study.

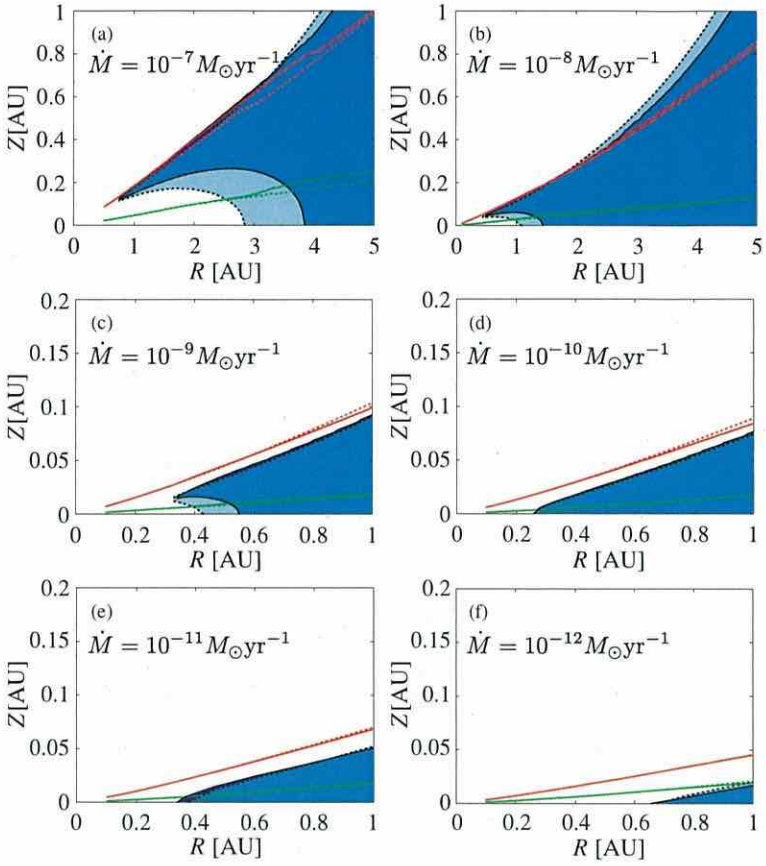

Figure 4. Ice-condensing region in the disk as a function of the mass accretion rate. Parameters are $M_* = 0.5\,M_\odot$, $R_* = 2\,R_\odot$, $T_{\rm eff} = 3000$ K, and $\alpha = 0.01$; the dust grain size is 0.1 μm. Panels (a)–(f) show the ice-condensing regions with $\dot{M}$ labeled in each pane. The horizontal and vertical axes represent the distance from the central star on the midplane and the altitude from the midplane, respectively. The blue and light blue regions represent the ice-condensing regions with and without ice opacity. The black, red, and green curves represent the condensation front, the altitude of H_s, and the pressure scale height, respectively. The solid and dotted curves with each color represent the results with and without ice opacity, respectively.

(A color version of this figure is available in the online journal.)

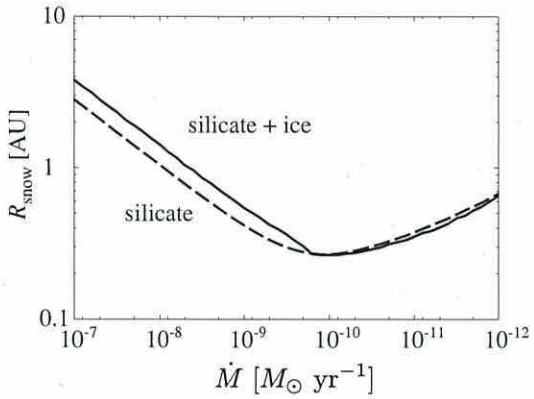

Figure 5. Heliocentric distance of the snow line as a function of the mass accretion rate. Parameters are $M_* = 0.5\,M_\odot$, $R_* = 2\,R_\odot$, $T_{\rm eff} = 3000$ K, and $\alpha = 0.01$; the dust grain size is 0.1 μm. The horizontal and vertical axes represent the mass accretion rate and the snow line location, respectively. The solid and dashed curves represent the results with and without ice opacity, respectively.

When $\dot{M}$ is high ($\gtrsim 10^{-10}\,M_\odot$ yr^{-1}), the ratio of the snow line distance with ice opacity ($R_{\rm SL,sil+ice}$) to that without ice opacity ($R_{\rm SL,sil}$), $f_{\rm SL} = R_{\rm SL,sil+ice}/R_{\rm SL,sil}$, is about 1.3 and almost constant. This constant ratio of the snow line shift factor $f_{\rm SL}$ originates from the assumptions that the disk is the steady accretion disk and the mass fraction of ice dust particles to silicate dust particles is uniform throughout the disk (see Section 4.1). On the other hand, when $\dot{M}$ is low ($\lesssim 10^{-10}\,M_\odot$ yr^{-1}), the snow line location is not substantially affected by ice opacity (i.e., $f_{\rm SL} \simeq 1$). This small difference in snow line location is caused by a small difference in the disk structure around the snow line.

3.2. Dependence of Snow Line Location on Dust Grain Size

The stellar parameters in this subsection are set as $L_* = 1\,L_\odot$, $M_* = 1\,M_\odot$, and $T_{\rm eff} = 4000$ K for comparison with the solar system. Figure 6 shows the heliocentric distance of the snow line as a function of the mass accretion rate. The different curves correspond to the different dust grain sizes assumed in each calculation. Calculations are stopped when the optical depth for stellar radiation in the region around the snow line becomes less than unity. When the grain size is $\geqslant 100\,\mu$m, the scattering coefficient is set to zero.

During the inward migration of the snow line, the snow line location is almost independent of the dust grain size if the grain

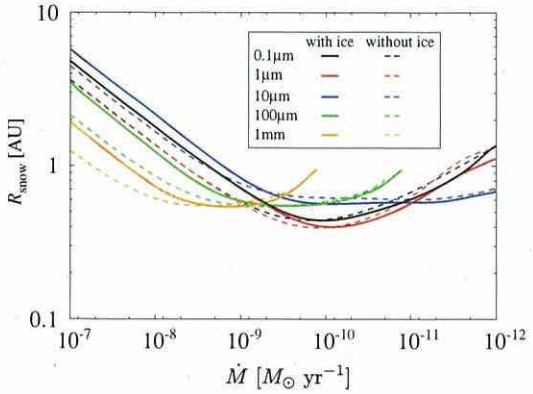

Figure 6. Heliocentric distance of the snow line as a function of the mass accretion rate with various dust grain sizes. Parameters are $M_* = 1\,M_\odot$, $T_{\rm eff} = 4000$ K, $L_* = 1\ L_\odot$, and $\alpha = 0.01$. The horizontal and vertical axes are the same as those in Figure 5. The black, red, blue, green, and orange curves represent the results with dust grain sizes of 0.1, 1, 10, and 100 μm, respectively. The solid and dashed curves represent the results with and without ice opacity, respectively.

(A color version of this figure is available in the online journal.)

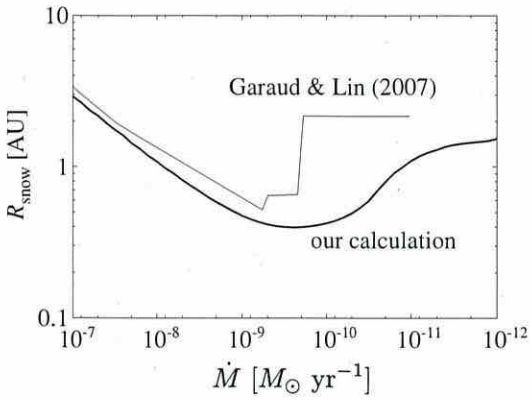

Figure 7. Comparison of the snow line location obtained in this study (thick curve) with that from Garaud & Lin (2007; thin curve). Parameters are $M_* = 1\,M_\odot$, $R_* = 1\,R_\odot$, $L_* = 1\ L_\odot$, and $\alpha = 0.001$; the dust opacity is similar to that of Garaud & Lin (2007). The horizontal and vertical axes are the same as those in Figure 5.

size is smaller than 10 μm. The wavelength of radiation from the disk interior at the condensation temperature ($T \simeq 170$ K) is longer than 10 μm, so the opacity of the dust particle is in the Rayleigh regime, dependent only on the total mass of the dust particles, and dominated by absorption. On the other hand, when the size is larger than 10 μm, i.e., in the geometrical optics regime, the opacity depends on the total cross section of the dust particles and decreases with the dust grain size; hence, the temperature enhancement by viscous heating becomes inefficient, although both absorption and scattering contribute in this case.

When the dust grain size is larger than 10 μm, the evolutional track of the snow line levels off at the minimum value, because the opacity of large grains is almost independent of the wavelength emitted from the disk. This implies that the snow line necessarily passes the heliocentric distance of 1 AU, unless the dust grain size exceeds a certain large value. This point will be considered in Section 4.4.

The shift ratio of the snow line $f_{\rm SL}$ is qualitatively the same as in Figure 5. The snow line shifts to a larger heliocentric distance in its inward migration phase, whereas it does not shift substantially in its outward migration and leveling-off phases.

The shift ratio of the snow line $f_{\rm SL}$ depends on the dust grain size: $f_{\rm SL} \simeq 1.3$ for dust grain sizes $\lesssim$10 μm, and $f_{\rm SL} \simeq 1.6$ for grain sizes $\gtrsim$100 μm. When the dust grain size is small, the total dust opacity increases in proportion to the total mass of the dust, while the total dust opacity increases in proportion to the total cross section of dust particles when the dust grain size is large. This different dependence of the opacity on the total amount of dust causes the different dependence of the shift ratio.

The critical mass accretion rate, that is the mass accretion rate with which the snow line starts to migrate outward, also depends on dust grain size. The snow line starts to migrate outward when the disk region around the snow line becomes transparent. When the dust grain size is sufficiently larger than the wavelength of the stellar radiation ($\sim$1 μm), the total opacity of the dust is inversely proportional to the grain size. Thus, the critical mass accretion rate is proportional to the dust grain size. Indeed, when the dust grain size is 10 μm, 100 μm, and 1 mm, the snow line starts to migrate outward at about $10^{-11}\,M_\odot$ yr^{-1}, $10^{-10}\,M_\odot$ yr^{-1}, and $10^{-9}\,M_\odot$ yr^{-1}, respectively (Figure 6).

3.3. Comparison with Garaud & Lin (2007)

The snow line evolution obtained from our numerical simulations is compared with that obtained from the semi-analytical model of Garaud & Lin (2007). The stellar parameters are $L_* = 1\ L_\odot$, $M_* = 1\,M_\odot$, and $R_* = 1\,R_\odot$, and the viscosity parameter is $\alpha = 0.001$. Other settings are almost the same as in Garaud & Lin (2007).

Garaud & Lin (2007) used the Planck mean opacity; thus, a new frequency-dependent opacity model of the mixture of disk gas and dust particles is developed so that its Planck mean agrees with that of Garaud & Lin (2007). The Planck mean opacity is proportional to temperature, so the absorption opacity is modeled as a linear function of frequency: $\kappa_\nu^{\rm abs} = C\nu$, where C is a constant determined by

$$\frac{\int_0^\infty \kappa_\nu^{\rm abs} B_\nu(T_{\rm eff})\,d\nu}{\int_0^\infty B_\nu(T_{\rm eff})\,d\nu} = \kappa_V, \tag{8}$$

where κ_V is the Planck mean opacity with the stellar effective temperature, and κ_V is set to be 2 cm^2 g^{-1} according to Garaud & Lin (2007).

The snow line location calculated as a function of $\dot{M}$ is shown in Figure 7, as is the result of Garaud & Lin (2007). Our result agrees well with that of Garaud & Lin (2007) for higher $\dot{M}$ ($>10^{-9}\,M_\odot$ yr^{-1}), though our result does not show an abrupt outward shift of the snow line at $\dot{M} \sim 10^{-9.5}\,M_\odot$ yr^{-1}. Garaud & Lin (2007) adopted a semi-analytical method to solve the temperature in the optically thin region. Although semi-analytical methods are much easier to use than numerical models, they may not be accurate enough for the evaluation of the disk midplane temperature in optically thin regions. (They are accurate enough and useful in optically thick regions.) The discontinuous evolution found by Garaud & Lin (2007) may come from the simplified treatment of the radiative transfer. Hereafter, the discontinuity is ignored and the overall features of the snow line evolution are discussed.

In order to obtain the midplane temperature, the estimation of the height of the superheated layer H_s is a key factor, because its radial dependence determines the grazing angle of the disk

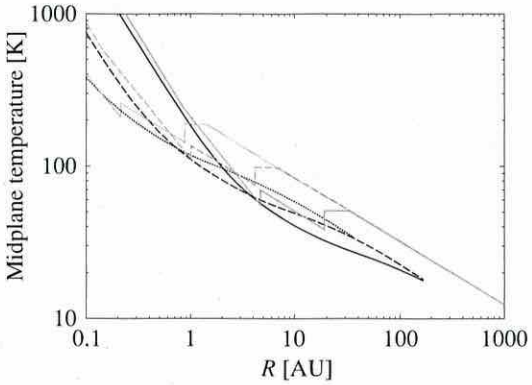

Figure 8. Comparison of the midplane temperature obtained in this study (black curves) with that from Garaud & Lin (2007; gray curves). Parameters are the same as those in Figure 7. The horizontal and vertical axes represent the heliocentric distance on the midplane and the midplane temperature, respectively. The solid, dashed, and dotted curves represent the results with mass accretion rates of 10^{-8}, 10^{-9}, and $10^{-10}\ M_\odot\ \mathrm{yr}^{-1}$, respectively.

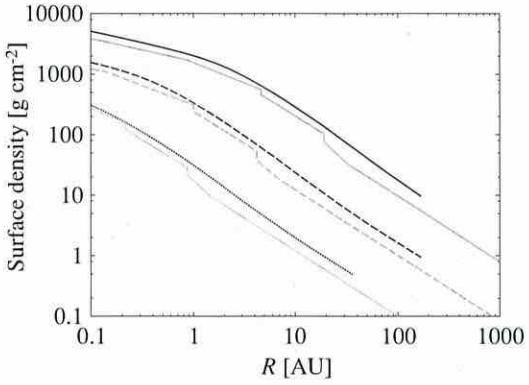

Figure 9. Comparison of the gas surface density obtained in this study (black curves) with that from Garaud & Lin (2007; gray curves). Parameters are the same as those in Figure 7. The horizontal and vertical axes represent the heliocentric distance on the midplane and the gas surface density, respectively. The solid, dashed, and dotted curves represent the results with mass accretion rates of 10^{-8}, 10^{-9}, and $10^{-10}\ M_\odot\ \mathrm{yr}^{-1}$, respectively.

for irradiation. When the midplane temperature in a region is increased, the surface density there is lowered according to the steady accretion assumption (Equation (1)). Then, the grazing angle decreases, the midplane temperature tends to fall, and the surface density tends to increase: a negative feedback takes place. Therefore, in our calculations, the disk does not become optically so thin and the snow line migrates outward more slowly than in the result of Garaud & Lin (2007), in which H_s is assumed to be proportional to the disk pressure scale height.

The minimum heliocentric distance of the snow line obtained from our calculations is slightly smaller than that of Garaud & Lin (2007). This may be attributed to the two-layer model (Chiang & Goldreich 1997) they adopted. Inoue et al. (2009) showed that the three-layer approach is necessary to obtain an accurate midplane temperature.

Figures 8 and 9 show the midplane temperature and the surface density profiles from our calculation and from Garaud & Lin (2007). These figures clearly show that the midplane temperatures of both models agree well in the inner optically thick region, whereas our result is lower than that of Garaud & Lin (2007) in the outer optically thin region. Similarly, the surface density distributions in both models agree in the inner region, whereas there is a difference in the outer region.

We conclude that if we are concerned with the detailed evolution of the snow line in the optically thin phases in which planet formation may proceed, we need to calculate the temperature numerically. (If we are concerned with optically thick phases or qualitative features of the snow line evolution in entire phases, semi-analytical calculations are sufficient.)

4. SEMI-ANALYTICAL ESTIMATES

4.1. Dependence on Water Ice Opacity

In the early phase in which the snow line migrates inward, the main heating source at the midplane around the snow line is viscous dissipation (Figure 2). Thus, the temperature is determined by viscous heating and radiative cooling. The diffusive radiative energy transfer gives the midplane temperature, T_c, as (e.g., Nakamoto & Nakagawa 1994)

$$T_c = \left[\left(\frac{3}{2}+\frac{9\tau_c}{16}\right)\left(\frac{GM_*\dot{M}}{4\pi\sigma R^3}\right)\right]^{\frac{1}{4}}, \tag{9}$$

where τ_c is the optical depth for the midplane and σ is the Stefan–Boltzmann constant. Substituting $\tau_c = \kappa\Sigma/2$ (κ is the Rosseland mean opacity of the disk medium) and noticing that τ_c is much larger than unity, we obtain

$$T_c \simeq \left[\left(\frac{9\kappa\Sigma}{32}\right)\left(\frac{GM_*\dot{M}}{4\pi\sigma R^3}\right)\right]^{\frac{1}{4}} \propto \left(\frac{\kappa\Sigma}{R^3}\right)^{\frac{1}{4}}. \tag{10}$$

The surface density of the steady accretion disk is given by $\Sigma = \dot{M}/(3\pi\alpha c_s^2/\Omega) \propto 1/(T_c R^{3/2})$. So, we have

$$T_c^5 \propto \kappa R^{-\frac{9}{2}}. \tag{11}$$

In the annulus located at the snow line, both silicate and ice particles contribute to the opacity κ (see Figure 4). This Rosseland mean opacity is denoted as $\kappa_{\mathrm{sil+ice}}$, whereas the Rosseland mean opacity due to silicate particles only is expressed as κ_{sil}. Since the ice condensation temperature at the midplane is almost independent of the heliocentric distance, the right-hand side of Equation (11) can be regarded as constant, and a relation between the snow line locations with and without water ice opacity, $R_{\mathrm{SL,sil+ice}}$ and $R_{\mathrm{SL,sil}}$, is obtained as

$$\kappa_{\mathrm{sil+ice}} R_{\mathrm{SL,sil+ice}}^{-\frac{9}{2}} = \kappa_{\mathrm{sil}} R_{\mathrm{SL,sil}}^{-\frac{9}{2}}. \tag{12}$$

The shift factor of the snow line location due to the additional ice is then written as

$$f_{\mathrm{SL}} = \frac{R_{\mathrm{SL,sil+ice}}}{R_{\mathrm{SL,sil}}} = \left(\frac{\kappa_{\mathrm{sil+ice}}}{\kappa_{\mathrm{sil}}}\right)^{\frac{2}{9}}. \tag{13}$$

Adopting the dust opacity model of Miyake & Nakagawa (1993), we have $\kappa_{\mathrm{sil+ice}}/\kappa_{\mathrm{sil}} \simeq 3$ for the thermal radiation at 170 K (the midplane temperature at the snow line) when the dust grain size is 0.1 μm. Then, f_{SL} is evaluated as $f_{\mathrm{SL}} = 3^{\frac{2}{9}} = 1.28$, which is consistent with our numerical results. Equation (13) implies that the snow line location is shifted outward in accordance with the water abundance around the snow line.

4.2. Dependence on Viscosity Parameter

The snow line location is considerably affected by α, because α relates to the disk's optical thickness and energy generation

rate by viscous dissipation. In the early phase of the disk evolution, the midplane temperature in the inner disk region is obtained in the same way as in Section 4.1. Then, we have $T_c^5 \propto \alpha^{-1} R^{-9/2}$. We then find the dependence of the snow line location $R_{\rm snow}$ on α as

$$R_{\rm snow} \propto \alpha^{-\frac{2}{9}}. \quad (14)$$

Taking into account the range of α ($0.001 \lesssim \alpha \lesssim 0.1$), the snow line location shifts inward or outward by at most 67% from the results with $\alpha = 0.01$ in the inward migration phase. Note that the minimum heliocentric distance of the snow line hardly changes, because it is determined not by viscous heating but by stellar radiation heating.

In the later phase of the disk evolution, a change in α changes the correlation between $R_{\rm snow}$ and $\dot{M}$. In the outward migration phase, $R_{\rm snow}$ is a function of Σ, and $\dot{M}$ is proportional to the product of ν_t and Σ. The viscosity ν_t is proportional to α, so $\dot{M}$ corresponding to each $R_{\rm snow}$ varies in proportion to α. Thus, $R_{\rm snow}$ in the later phase is shifted in proportion to α (Figure 6). This means that the $\dot{M}$ at which the disk becomes optically thin to the stellar radiation also decreases in proportion to α.

4.3. Dependence on Dust-to-Gas Mass Ratio

The dust-to-gas mass ratio, ζ_d, changes the opacity of the disk medium. Hence, it changes the disk temperature in the same way as ice opacity. In the inward migration phase, assuming that the opacity of the disk medium varies in proportion to ζ_d, a proportional relation between $R_{\rm snow}$ and ζ_d is obtained in the same way as in Sections 4.1 and 4.2:

$$R_{\rm snow} \propto \zeta_d^{\frac{2}{9}}. \quad (15)$$

In the outward migration phase, the correlation between $R_{\rm snow}$ and $\dot{M}$ depends on ζ_d. In this phase, $R_{\rm snow}$ is a function of solid mass surface density ($\zeta_d\Sigma$), and $\dot{M}$ is proportional to Σ, which is the product of solid mass surface density and the inverse of ζ_d. Thus, $\dot{M}$ corresponding to each $R_{\rm snow}$ varies in inverse proportion to ζ_d. Hence, $R_{\rm snow}$ is shifted in inverse proportion to ζ_d (Figure 6). The mass accretion rate with which the disk becomes optically thin to the stellar radiation increases in inverse proportion to ζ_d.

4.4. Possibility of the Snow Line Coming Inside Earth's Orbit

According to the results shown in Section 3, the snow line comes inside the Earth's current orbit in the course of the disk evolution. However, if planetesimals in the terrestrial planet region were icy, this is not consistent with current solar system bodies. Here, discussing the snow line evolution track on the ($\dot{M}$, $R_{\rm snow}$)-plane in Figure 6, we examine to what extent that conclusion is certain.

From Figure 6, we can see that if (α/ζ_d) is increased by more than a factor of 100 and if the dust grain size is 1 mm, the snow line would not come inside Earth's orbit. However, there are some caveats. Noticing that the range of α is from 0.001 to 0.1 and the fiducial value used in our calculations is $\alpha = 0.01$, we realize that ζ_d should be decreased by a factor of at least 10 from the value found by Miyake & Nakagawa (1993) to increase the value of (α/ζ_d) by more than a factor of 100. When $\alpha < 0.1$, ζ_d should be much smaller depending on the size of α. On the other hand, as the dust grain size becomes small, (α/ζ_d) should be large (or $\zeta_{\rm sil}$ should be small). Thus, it seems that the snow line necessarily comes inside Earth's orbit if the dust grain size is smaller than 1 mm, ζ_d is higher than a tenth of that of the solar abundance, and α ranges from 0.001 to 0.1.

Another possibility is an increase in ice abundance; this can prevent the snow line from coming inside Earth's orbit. An increase in ice abundance lowers the value of $\dot{M}$ at which the snow line migration levels off at the minimum distance or starts to move outward. For example, if the ratio of water ice mass to disk gas, $\zeta_{\rm ice}$, is increased by a factor of 10^4, it is expected that the snow line would not come inside Earth's orbit even in the case in which $\alpha = 0.01$, the dust grain size is 1 mm, and $\zeta_{\rm sil} = 0.0043$ (the solar abundance). When the dominant dust grain size or (α/ζ_d) is small, a greater increase in ice abundance is needed.

5. DISCUSSION

5.1. Comparison with the Current Solar System

In our solar system, the water distribution shows a drastic change at the asteroid belt; this may be a clue to the snow line. Terrestrial planets are thought to form from planetesimals that have formed inside the snow line, otherwise a large amount of water is inevitably accumulated into planets. Then, the timing of planetesimal formation may be restricted by the snow line evolution.

First, we consider the possibility that planetesimals form after the snow line migrates outward from the terrestrial planet region. When we look at the solid mass, planetesimal formation with dust grains of large size is favored because the gas surface density at which the snow line changes its direction of motion and moves outward increases as the dust grain size increases (Figure 6). The most favorable case from our numerical results is for dust grains of size 1 mm. Our numerical simulation shows that the surface density of solid material at the heliocentric distance of 1 AU is 1.1×10^{-2} g cm^{-2} when the outwardly moving snow line reaches 1 AU. This is much smaller than that of the minimum mass solar nebula model (about 10 g cm^{-2}). To match the minimum mass solar nebula model, or to match the current terrestrial planet's mass, the size of the dust particles would necessarily be larger than 1 m. This would be unrealistic, partly because complete depletion of fine dust particles smaller than 1 m would be difficult, and partly because dust particles of size 1 m are eliminated efficiently by accretion toward the central star due to gas drag. Thus, planetesimal formation during the snow line's outward migration would be unrealistic.

Next, let us consider the possibility of planetesimal formation during the snow line's inward migration. If planetesimal formation completes before the inwardly migrating snow line reaches the terrestrial planet region, planetesimals devoid of water can be formed. As for the solid mass, planetesimal formation in this phase is favorable. However, as the grain size grows, the snow line quickly migrates inward and eventually comes inside Earth's orbit; in Figure 6, at a fixed $\dot{M}$, we can see that $R_{\rm snow}$ is small if the grain size is large. Hence, the dust grain growth and planetesimal formation should be completed in a short period of time compared to the timescale with which the snow line moves inward. If not, a large amount of ice would necessarily accumulate deep within planetesimals. We are not sure if planetesimal formation is completed in such a short period of time.

In conclusion, the snow line location during disk evolution does not seem to match the current solar system. This inconsistency may originate from the following assumptions adopted in this study: (1) the continuous boundary condition at the inner

disk edge, (2) uniform dust grain size and uniform dust-to-gas mass ratio throughout the disk, and (3) neglecting the evolution of solid material and water distribution.

Here, we consider possible scenarios by relaxing the above assumptions.

1. *Continuous disk boundary.* The presence of the inner disk edge, where the disk is heated by direct stellar radiation and becomes hot, is ignored in this assumption. If the dust grain grows at the inner edge and the inner edge moves outward after planetesimal formation, dust grain growth would always proceed in a hot environment. Then the resulting planetesimals would be devoid of water.
2. *Uniform dust grain size and dust-to-gas mass ratio.* In a real disk, the dust grain size and the dust-to-gas mass ratio would be non-uniform. Dust particles grow mainly by collisions. Growth tends to proceed from the inner disk region, so the dust grain size in the inner disk is likely to be larger than that in the outer disk. When the dust grain is large enough, the height of the disk surface is lowered. Consequently, a disk region that is located just outside the dust grain region developed when dust grain growth is about to start can receive more stellar radiation flux. Then, dust grain growth may proceed at a hot temperature and water-deficit planetesimals may form.
3. *Solid material and water distribution evolution.* According to Ciesla & Cuzzi (2006) and Garaud (2007), large amounts of water vapor and fine dust particles are transported from the outer to the inner part of the disk during disk evolution. If fine dust particles or water vapor are supplied to the terrestrial planet region, and the snow line location is kept farther from the terrestrial planet region until planetesimal formation is completed, dust grain growth may proceed in a water-ice-free environment; consequently, water-devoid planetesimals may be formed. Whether or not this mechanism works may depend on the initial condition of the disk.

Yet another possible scenario may be the elimination of water from icy planetesimals after the snow line migrates outward from the terrestrial planet region. Future work on these points is needed.

5.2. Effects of the Ice Mantle on Silicate Dust Particles

In this study, it is assumed that ice condenses as pure ice particles and that no ice mantle forms on silicate particles. It would be more realistic, however, if H_2O molecules condense as ice mantles on silicate particles. Here, we discuss how ice mantle formation affects the snow line location. We consider its effects only in the inward migration phase, since ice opacity does not change the snow line location in the outward migration phase.

To evaluate the effects of the ice mantle, we consider to what extent the dust opacity changes due to the ice mantle. Dust opacity properties change as the ratio between the dust grain size and the wavelength of the thermal radiation ($\lambda \sim 10$–$20\,\mu$m) changes. When the dust grain size is sufficiently smaller than 10–20 μm (the Rayleigh regime), the total dust opacity is hardly affected by the ice mantle. On the other hand, when the dust grain size is sufficiently larger than 10–20 μm (the geometrical optics regime), the ice mantle changes the total dust opacity.

When the ice condenses, the opacity of dust particles generally increases. However, the opacity enhancement factor $g_{\rm ice}$ can be different between cases in which the ice condenses as independent ice particles and those in which the ice condenses as ice mantles on silicate cores, even though the amount of condensed ice is the same. In the geometrical optics regime, $g_{\rm ice}$ for the mantle case becomes smaller than that for the independent case, since the cross section of ice mantles is smaller than that of the independent particles. According to Miyake & Nakagawa (1993), the material densities of silicate and ice are 3.3 and 0.92 g cm^{-3}, respectively, and the mass fractions of silicate and water ice in the disk medium are 0.0043 and 0.0094, respectively. This means that ice has a volume about six times larger than that of silicate per unit mass at disk medium. As a result, if only pure ice particles are formed, the total cross section of the dust particles is increased by a factor of 7.9, while if ice mantles are formed on silicate cores, the total cross section of dust particles is increased only by a factor of 3.7. Thus, ice mantle formation reduces the opacity enhancement factor by ice condensation. Consequently, the snow line's shift ratio by ice condensation ($f_{\rm SL}$) would be reduced from 1.54 to 1.33 due to ice mantle formation (see Equation (13)).

Finally, we consider the non-uniformity of the dust grain size. When independent ice particles are formed, the opacity enhancement depends on the size distribution of ice particles. If all the ice particles are sufficiently small compared to the wavelength of the thermal radiation (the Rayleigh regime), the opacity enhancement depends only on the total mass of ice and is largest. When the dominant size of ice particles is larger than 10–20 μm, and as the dominant size increases, the opacity enhancement decreases. On the other hand, if ice mantles are formed on silicate particles, the opacity enhancement would be limited to a certain range. The real situation should be somewhere between the Rayleigh regime and the geometrical optics regime, so the enhancement of the dust opacity by ice condensation would be around 30%.

In summary, it is likely that the enhancement of the dust opacity would be limited to a range around 30% when ice mantles are formed around silicate dust particles. If pure ice particles are formed, the size distribution of ice particles is needed to evaluate the enhancement accurately.

6. CONCLUSIONS

The evolution of the snow line in an optically thick disk is simulated numerically and examined to see if it is consistent with the water distribution in the solar system. The evolution is examined from the early phase, in which the mass accretion rate in the disk is large and the optical depth of the disk is considerably high, to the later phase, in which the accretion rate is small and the optical depth is low with a single numerical scheme.

The snow line migrates as the mass accretion rate in the disk decreases (which is considered to be the evolution). Generally, in the early phase (high mass accretion phase), it moves inward because of the reduction in viscous heating, while in the later phase (low mass accretion phase), it moves outward due to stellar radiation. If the dust grain size is large ($\gtrsim 10\,\mu$m), the snow line stays at its minimum heliocentric distance for a wide range of mass accretion rates.

When the opacity of the condensed ice is taken into consideration, we find that the snow line location is shifted outward for the disk in the inward migration phase ($\dot{M} \gtrsim 10^{-10}\,M_\odot$ yr^{-1}). This is due to the additional blanket effect of the condensed ice particles in the upper layer of the disk. The shift ratio of the snow line ($f_{\rm SL} = R_{\rm SL,ice+sil}/R_{\rm SL,sil}$) varies with dust grain size: $f_{\rm SL} = 1.3$ for grains $\lesssim 10\,\mu$m and $f_{\rm SL} = 1.6$ for grains

$\gtrsim 100\,\mu$m. Our semi-analytical estimation has shown that $f_{\rm SL}$ increases with water abundance in the disk gas around the snow line. However, the snow line shift due to ice opacity is small compared to the total migration length during disk evolution, and is limited in the early phase of disk evolution.

The additional ice opacity does not change the snow line location of the disk in the outward migration phase. A vertically increasing temperature profile under irradiation by the central star prevents water molecules from condensing in the upper layer of the disk.

We also find that the snow line comes inside Earth's orbit as long as the dust-to-gas mass ratio is higher than about a tenth of the solar abundance, the viscosity parameter α is $0.001 \lesssim \alpha \lesssim 0.1$, and the dust grain size is smaller than 1 mm. Then, if one thinks that terrestrial planets should be formed from water-devoid planetesimals, dust grain growth should occur either before the snow line comes inside Earth's orbit or after the snow line passes out of Earth's orbit. In the latter case, the formation of water-devoid planetesimals is impossible because of the deficit of solid mass (Section 5.2). In the former case, dust grain growth should be completed within 1 yr because the snow line migrates inward on this timescale.

The inconsistency between the snow line evolution obtained in this study and the solar system originates from the following assumptions: (1) the continuous boundary condition at the inner disk edge, (2) uniform dust grain size and uniform dust-to-gas mass ratio throughout the disk, and (3) neglecting the evolution of solid material and water distribution. Future work on these points is needed.

We are grateful to Masahiro Ikoma and Hidekazu Tanaka for their fruitful discussions and useful comments. We also thank the anonymous reviewer for helpful comments.

APPENDIX

The density and temperature of the disk are obtained using the 1+1D approach. In this approach, one divides the disk into many annuli and solves the vertical structure of each annulus, and then adds them into the entire (radial and vertical) structure of the disk. Although we solve the dynamical and thermal equilibria separately, we calculate them iteratively to obtain a consistent solution.

A.1. Hydrostatic Equilibrium

The hydrostatic equilibrium along the vertical direction is expressed as

$$\frac{\partial P(R, Z)}{\partial Z} = -\rho(R, Z)\frac{GM_*}{R^3}Z, \tag{A1}$$

where P is the gas pressure and ρ is the mass density of the gas. The equation of the state of the gas is given as $P = \frac{\rho kT}{\bar{\mu} m_u} = c_s^2 \rho$, where $\bar{\mu}$ is the mean molecular weight, m_u is the atomic mass unit, and c_s is the sound velocity. Integrating the density over Z, the surface density Σ is given as $\Sigma = \int_{-\infty}^{\infty} \rho\, dZ$.

A.2. Radiative Transfer

Two heating sources are taken into consideration: viscous dissipation and irradiation of the central star. Balancing the heating sources and the radiative cooling, the following equilibrium temperature is obtained:

$$q_{\rm vis} + q_{\rm irr} + \int_0^\infty \rho\kappa_\nu(1-\varpi_\nu)\,d\nu \oint I_\nu(\Omega)\,d\Omega = 4\pi \int_0^\infty \rho\kappa_\nu(1-\varpi_\nu)B_\nu(T)\,d\nu, \tag{A2}$$

where $q_{\rm vis}$ is the heating rate by viscous dissipation, $q_{\rm irr}$ is the heating rate by irradiation of the central star, κ_ν is the extinction coefficient, ϖ_ν is the single scattering albedo, $I_\nu(\Omega)$ is the diffuse radiation field in the disk (intensity without including the direct radiation from the central star), and $B_\nu(T)$ is the Planck function. Quantities with subscript ν are a function of frequency ν. The integral $\oint d\Omega$ on the left-hand side of Equation (A2) represents the integral over the entire solid angle. The viscous heating rate $q_{\rm vis}$ is given by (e.g., D'Alessio et al. 1998) $q_{\rm vis} = \frac{9}{4}\rho\nu_t\Omega_K^2$.

The diffuse component of the intensity $I_{\mu,\nu}(\Omega)$ and $q_{\rm irr}$ are obtained by solving the radiative transfer. Assuming a plane-parallel structure along the Z-direction, the radiative transfer equation is written as

$$\mu\frac{dI_{\mu,\nu}(Z)}{dZ} = \rho\kappa_\nu(S_\nu(Z) - I_{\mu,\nu}(Z)), \tag{A3}$$

where μ is the cosine of the propagation direction of radiation and S_ν is the source function. The source function S_ν is given by

$$S_\nu(Z) = (1-\varpi_\nu(Z))B_\nu(T) + \varpi_\nu(Z) \times \frac{1}{2}\int_{-1}^{1} I_{\mu,\nu}d\mu + \varpi_\nu(Z)\frac{F_{{\rm irr},\nu}(Z)}{4\pi}, \tag{A4}$$

where $F_{{\rm irr},\nu}(Z)$ is the radiation energy flux from the central star. Therein, isotropic scattering is assumed. The energy flux $F_{{\rm irr},\nu}(Z)$ is evaluated using the so-called grazing angle recipe (e.g., Chiang & Goldreich 1997; Dullemond et al. 2002):

$$F_{{\rm irr},\nu}(Z) = \frac{L_\nu}{4\pi R^2}\exp\left(-\frac{\tau_\nu(R, Z)}{\beta}\right), \tag{A5}$$

where β, L_ν, and $\tau_\nu(R, Z)$ are the cosine of the penetrating angle of the radiation from the central star into the disk surface, the luminosity of the central star, and the optical depth between a point (R, Z) and infinity along the vertical direction (R, ∞), respectively. The optical depth τ_ν is defined as $\tau_\nu(R, Z) = \int_Z^\infty \kappa_\nu\rho(R, Z)dZ$. The central star is assumed to emit blackbody radiation with effective temperature $T_{\rm eff}$, so the luminosity is given by $L_\nu = 4\pi^2 R_*^2 B_\nu(T_{\rm eff})$. β is evaluated by (e.g., Kusaka et al. 1970; Chiang & Goldreich 1997; Dullemond et al. 2002)

$$\beta(R) = 0.4\frac{R_*}{R} + \xi(R)\frac{H_s}{R}, \tag{A6}$$

where H_s is the height from the midplane where the radiation from the central star loses its energy by $1-(1/e)$ and ξ is the so-called flaring index defined as $\xi = \frac{d\ln(H_s/R)}{d\ln R}$. Then, the heating rate by irradiation of the central star in Equation (A2) is given by

$$q_{\rm irr} = \int_0^\infty \rho(Z)\kappa_\nu(1-\varpi_\nu)F_{{\rm irr},\nu}(Z)\,d\nu. \tag{A7}$$

The boundary condition for Equation (A3) is

$$I_{\mu,\nu}(+\infty) = 0 \quad (\mu < 0), \tag{A8}$$

$$I_{\mu,\nu}(0) = I_{-\mu,\nu}(0) \quad (\mu \geqslant 0). \tag{A9}$$

This condition represents the mirror boundary at the $Z = 0$ plane and no incident diffuse radiation at the disk surface.

Vertical profiles of the diffuse radiation $I_{\mu,\nu}(\mathbf{\Omega})$ and the temperature T are obtained by solving Equations (A2)–(A4) iteratively. A straightforward way to solve these equations converges very slowly, so the variable Eddington factor (VEF) method, described in Dullemond et al. (2002) and Inoue et al. (2009), is employed. In this study, the VEF method is modified to deal with the heating by viscous dissipation.

REFERENCES

Anders, E., & Grevesse, N. 1989, Geochim. Cosmochim. Acta, 53, 197
Bauer, I., Finocchi, F., Duschl, W. J., Gail, H.-P., & Schloeder, J. P. 1997, A&A, 317, 273
Cassen, P. 1994, Icarus, 112, 405
Chiang, E. I., & Goldreich, P. 1997, ApJ, 490, 368
Ciesla, F. J., & Cuzzi, J. N. 2006, Icarus, 181, 178
D'Alessio, P., Canto, J., Calvet, N., & Lizano, S. 1998, ApJ, 500, 411
Davis, S. S. 2005, ApJ, 620, 994
Dullemond, C. P. 2002, A&A, 395, 853
Dullemond, C. P., & Natta, A. 2003, A&A, 408, 161
Dullemond, C. P., van Zadelhoff, G. J., & Natta, A. 2002, A&A, 389, 464
Garaud, P. 2007, ApJ, 671, 2091
Garaud, P., & Lin, D. N. C. 2007, ApJ, 654, 606
Hayashi, C. 1981, Prog. Theor. Phys. Suppl., 70, 35
Hawley, J. F., Gammie, C. F., & Balbus, S. A. 1995, ApJ, 440, 742
Hawley, J. F., Gammie, C. F., & Balbus, S. A. 1996, ApJ, 464, 690
Inoue, A. K., Oka, A., & Nakamoto, T. 2009, MNRAS, 393, 1377
Kamp, I., & Dullemond, C. P. 2004, ApJ, 615, 991
Kusaka, T., Nakano, T., & Hayashi, C. 1970, Prog. Theor. Phys., 44, 1580
Lewis, J. S. 2004, Physics and Chemistry of the Solar System (2nd ed.; San Diego, CA: Elsevier Academic Press), 550
Miyake, K., & Nakagawa, Y. 1993, Icarus, 106, 20
Nakamoto, T., & Nakagawa, Y. 1994, ApJ, 421, 640
Pollack, J. B., Hollenbach, D., Beckwith, S., et al. 1994, ApJ, 421, 615
Pringle, J. E. 1981, ARA&A, 19, 13
Shakura, N. I., & Sunyaev, R. A. 1973, A&A, 24, 337
Stepinski, T. F. 1998, Icarus, 132, 100

Development of the Savart-plate lateral-shearing interferometric nuller for exoplanet (SPLINE)

Naoshi Murakami *[a], Manabu Kida [b], Naoshi Baba [a], Taro Matsuo [c,d], Takayuki Kotani [d,e], Hajime Kawahara [f], Yuka Fujii [g], Motohide Tamura [d]
[a] Division of Applied Physics, Faculty of Engineering, Hokkaido University, Sapporo, Hokkaido 060-8628, Japan;
[b] Division of Applied Physics, Graduate School of Engineering, Hokkaido University, Sapporo, Hokkaido 060-8628, Japan;
[c] Department of Astronomy, Kyoto University, Sakyo-ku, Kyoto 606-8502, Japan;
[d] National Astronomical Observatory of Japan, Mitaka, Tokyo 181-8588, Japan;
[e] Institute of Space and Astronautical Science, Japan Aerospace Exploration Agency (ISAS/JAXA), 3-1-1 Yoshinodai, Chuo-ku, Sagamihara 252-0222, Japan
[f] Department of Physics, Tokyo Metropolitan University, Hachioji 192-0397, Japan;
[g] The Department of Physics, The University of Tokyo, Hongo, Bunkyo-ku, Tokyo 113-1133, Japan

ABSTRACT

The Savart-Plate Lateral-shearing Interferometric Nuller for Exoplanet (SPLINE) is a stable and fully achromatic nulling interferometer proposed for direct detection of extrasolar planets with segmented-mirror telescopes like the Thirty Meter Telescope (TMT). The SPLINE uses a Savart plate, a kind of polarizing beam splitter, to split a light beam into two orthogonally polarized ones with a lateral shift. The Savart plate placed between crossed polarizers causes fully achromatic destructive interference for an on-axis star light. On the other hand, planetary light from an off-axis direction does not destructively interfere due to the lateral shift. The SPLINE provides a stable interferometric output because of its simple common-path optical design without an optical-path difference control system. We carried out laboratory demonstrations of the SPLINE to evaluate its stability, achromaticity, and achievable contrast. As a result, a high contrast of $>10^4$ (peak-to-peak contrast) is achieved using a broadband light source as a star model. In addition, we also propose to apply a differential imaging technique to the SPLINE for improving achievable contrast. We report our recent activities and show the results of the laboratory demonstrations.

Keywords: high-contrast imaging, extrasolar planets, nulling interferometry, coronagraphy, TMT, polarization

1. INTRODUCTION

Ground-based extremely large telescopes (ELTs), such as the Thirty Meter Telescope (TMT) and the European Extremely Large Telescope (E-ELT), are attracting facilities for direct detection of exoplanets. Several high-contrast instruments have been proposed for the ELTs, such as the Planet Formation Imager (PFI) for the TMT [1], the Second-Earth Imager for the TMT (SEIT) [2], and the Exoplanet Imaging Camera and Spectrograph (EPICS) for the E-ELT [3].

These future-planned ELTs will use a large number of hexagonal segmented mirrors for constructing extremely large primary mirrors. For the ELTs, an entrance pupil will be complicated due to gaps between the segmented mirrors, a central obscuration of a secondary mirror and its support structure.

For suppressing light from a bright primary star, an infrared nulling interferometer has been proposed [4]. The infrared nulling interferometer uses two or more telescopes to receive the light and combine them. At the beam combination, optical-path difference (OPD) between the light beams is set to zero, and an additional π phase difference is introduced to cause destructive interference for starlight from an on-axis direction. A faint planetary light from an off-axis direction does not interfere destructively, and thus can be directly detected. A baseline, a distance between the telescopes, determines an angular resolution of the nulling interferometer.

*nmurakami@eng.hokudai.ac.jp; phone 81 11 706-6720; fax 81 11 706-7811

Ground-based and Airborne Instrumentation for Astronomy IV, edited by Ian S. McLean, Suzanne K. Ramsay, Hideki Takami, Proc. of SPIE Vol. 8446, 84468H · © 2012 SPIE · CCC code: 0277-786X/12/$18 · doi: 10.1117/12.925605

Several kinds of nulling interferometers have been proposed also for visible and near-infrared spectral range using a single telescope [5-9]. A visible nulling coronagraph (VNC) is one of the promising concepts [10]. The light received by the telescope is sent to a fully symmetric interferometer such as a modified Mach-Zehnder interferometer. The light beam is divided into two by a beam splitter. An achromatic π phase difference between the two light beams is introduced, and the phase-shifted light beams are recombined with a zero OPD. At the beam recombination, the light beams are laterally shifted. The lateral shift will be conducted by moving mirrors inside the interferometer [10], or by modified Fresnel rhomb retarders [11]. The lateral shift corresponds to the baseline of the infrared nulling interferometer and determines the angular resolution. For the VNC, a fine OPD control system and the achromatic π phase shifter are important key requisites.

In this paper, we report a recent progress of development of a novel type of the VNC, which we call the Savart-Plate Lateral-shearing Interferometric Nuller for Exoplanet (SPLINE) [12]. The SPLINE can obtain a stable and achromatic nulled output for the on-axis starlight due to the common-path optical configuration and the polarization-based phase modulation scheme. We carried out laboratory demonstration of the SPLINE by using a polychromatic light source as a model star. Preliminary results of the laboratory demonstration are shown in this paper.

2. PRINCIPLE

Figure 1 shows the principle of the SPLINE, in which a Savart plate (SP) is used for splitting an incoming light and introducing the lateral shift of the light beams. The Savart plate is composed of two crossed uniaxial plates cut at 45° with identical thicknesses [13,14]. The incoming light is split into two orthogonally polarized light beams by the Savart plate. The two light beams act as ordinary and extraordinary rays in the first plate, and vice versa in the second one. These two light beams ("*eo*" and "*oe*" rays) are orthogonally polarized, and emerge from the Savart plate parallel to each other with a lateral shift. The lateral shift s is written as

$$s = \sqrt{2}\,\frac{n_o^{\,2} - n_e^{\,2}}{n_o^{\,2} + n_e^{\,2}}\,t\,, \tag{1}$$

where t is a thickness of each plate, n_o and n_e is refractive indices for the ordinary and extraordinary rays, respectively. We note that the lateral shift s depends slightly on wavelength.

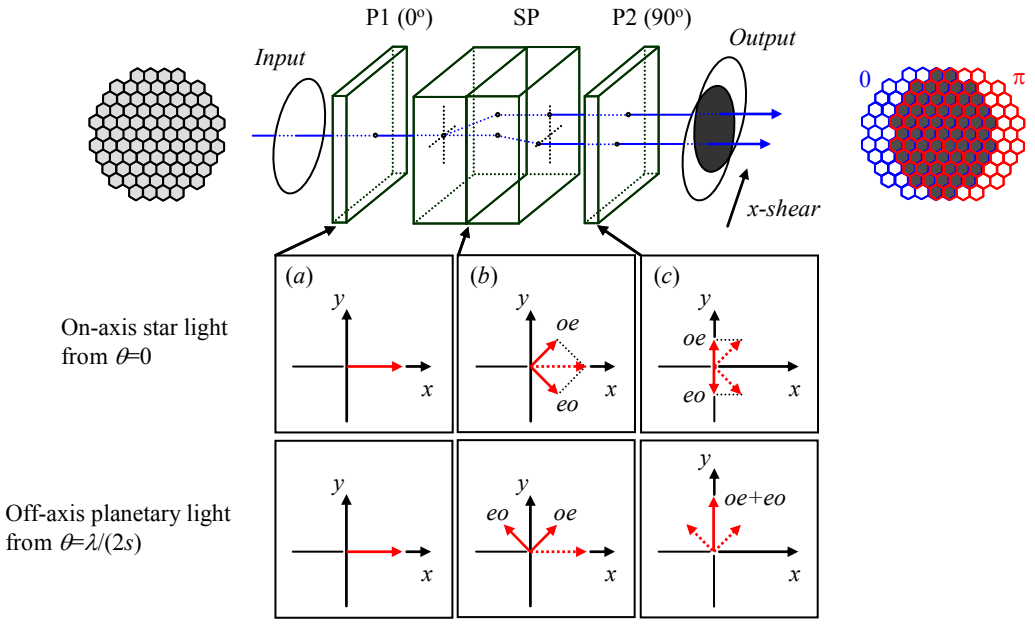

Figure 1. Principle of the two-beam SPLINE, in which a Savart plate (SP) is placed between two crossed polarizers (P). Achromatic destructive interference occurs for on-axis starlight over a region where two light beams are superposed. Schematic input and output light beams for a segmented-mirror telescope are also described.

The SPLINE is composed of a common-path lateral shearing interferometer, in which the Savart plate is placed between two crossed polarizers. We note that the common-path lateral shearing interferometers using the Savart plates have been used for measuring aberrations of optical systems [14]. The Savart plate divides 0° linearly polarized light from the first polarizer into ±45° linearly polarized one ("*eo*" and "*oe*" rays in fig. 1). The second polarizer analyzes these polarized light beams along 90°, resulting in oppositely directed polarization vectors for the on-axis starlight as described in fig. 1. The opposite polarization vectors of the output lights suggest that the phase difference between these two lights becomes π. This phase difference is introduced by the polarization control, and thus expected to be fully achromatic.

For planetary light from an off-axis direction, a non-zero phase difference between the two lights will be introduced by the lateral shift. When this additional phase becomes π, two polarization vectors would point to 45° and 135° directions as shown in fig. 1. A sum of these vectors becomes 90° linearly polarization ("*oe*+*eo*" rays in fig. 1), which can be extracted by the second polarizer without loss of intensity. We note that a 50% intensity loss will occur at the first polarizer, when the incoming planetary light is unpolarized and constructively interfered. We also note that this constructive condition will be satisfied when the planetary light comes from an off-axis direction $\theta=\lambda/(2s)$, where λ is a wavelength and s is the lateral shift.

For partially resolved stars with finite diameters, a four-beam nulling interferometer will be required for effectively suppressing the starlight. Figure 2 shows a scheme of the four-beam SPLINE, in which additional Savart plate (SP2) and polarizer (P3) are introduced behind the two-beam SPLINE. The four-beam SPLINE can also be realized by the simple common-path optical configuration.

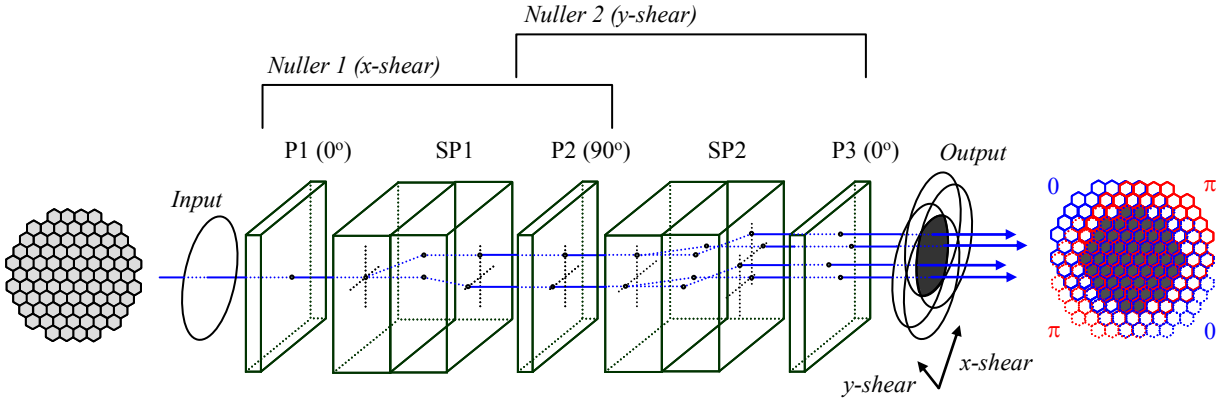

Figure 2. Principle of the four-beam SPLINE for effectively suppressing light from partially resolved stars with finite apparent sizes. Schematic input and output light beams for a segmented-mirror telescope are also described.

3. OPTICAL SETUP FOR LABORATORY DEMONSTRATION

We carried out laboratory demonstration of the four-beam SPLINE. Figure 3 shows an optical setup for the laboratory demonstration. A fiber-linked polychromatic light source (a xenon lamp) is used as a model star. The light from the single-mode fiber is collimated by a lens L1 and sent to the four-beam SPLINE. For simulating a telescope pupil, we use a clear circular aperture with a diameter of D=5 mm. Two Savart plates introduce lateral shifts to x and y directions with s=0.65 mm. A Lyot stop (D_L=4 mm) is placed behind the four-beam SPLINE to extract light from a superposed area on the pupil plane (corresponding to a dark area of the output beam drawn in fig. 2). Behind the Lyot stop, two lenses L4 and L5 are used for imaging the Lyot stop plane and the model star, respectively. These images are detected by an electron-multiplying CCD (EM-CCD) camera.

In fig. 3, we also show a spectrum of the model star measured by a commercial fiber-linked spectrometer placed just in front of the EM-CCD camera. The measured spectrum $I_{spe}(\lambda)$ suggests that the model star has a broad spectral range from 540 nm to 720 nm (FWHM), corresponding to a bandwidth of $\lambda/\Delta\lambda$~30%. We note that the measured spectrum corresponds to $I_{spe}(\lambda)=I(\lambda)QE_{spe}(\lambda)$, where $QE_{spe}(\lambda)$ is a quantum efficiency of the spectrometer, and $I(\lambda)$ is an intrinsic spectrum of the light source. For evaluating a spectrum of images detected by the EM-CCD camera $I_{ccd}(\lambda)= I(\lambda)QE_{ccd}(\lambda)$, it will be necessary to calibrate the spectrum as $I_{ccd}(\lambda)= I_{spe}(\lambda)QE_{ccd}(\lambda)/QE_{spe}(\lambda)$.

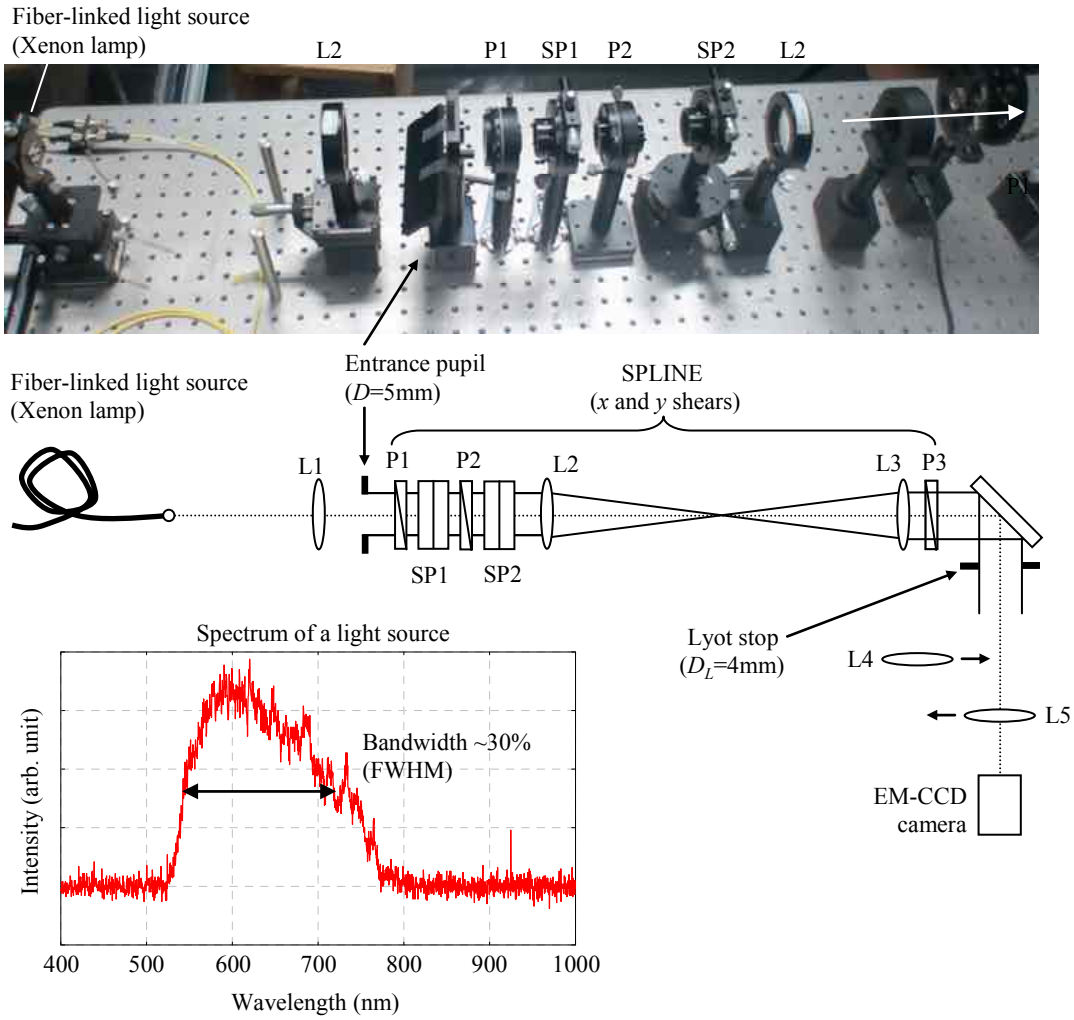

Figure 3. An optical setup of the four-beam SPLINE. A measured spectrum of a light source used for simulating a model star is also shown.

4. RESULTS OF LABORATORY DEMONSTRATION

Next, we report results of the laboratory demonstration of the four-beam SPLINE using the polychromatic light source. Figure 4a shows geometry on the reimaged pupil plane (a pupil diameter of D=5 mm, x and y lateral shifts of s=0.65 mm, and a Lyot stop diameter of D_L=4 mm as described in the previous section). The x and y lateral shifts s introduce a modulation of an interferometric transmittance for light from an on-sky position (θ_x, θ_y) as

$$T(\theta_x, \theta_y, \lambda) = \frac{1}{2}\sin^2\left(\frac{\pi s \theta_x}{\lambda}\right)\sin^2\left(\frac{\pi s \theta_y}{\lambda}\right) \quad (2)$$

for the wavelength λ. For example, when the light is coming from a pointing direction of a telescope (i.e., θ_x=θ_y=0), the transmittance becomes zero because of the destructive interference. When the light is coming from an off-axis direction θ_x=θ_y=λ/(2s), on the other hand, the constructive interference occurs and the transmittance becomes maximum (T=0.5). The coefficient 1/2 in eq. (2) comes from the intensity loss due to the first polarizer P1 as mentioned above. For a polychromatic light, the on-sky transmittance would be written as

$$T(\theta_x, \theta_y) = \frac{1}{2}\frac{\int I(\lambda)\sin^2\left(\frac{\pi s\theta_x}{\lambda}\right)\sin^2\left(\frac{\pi s\theta_y}{\lambda}\right)d\lambda}{\int I(\lambda)d\lambda}. \quad (3)$$

Figure 4b shows the on-sky transmission map, calculated from eq. (3), for a top-hat spectrum with a wavelength range from 540 nm to 720 nm.

Figures 4c, d show the acquired nulled and bright images on the Lyot stop plane when a light source is placed at the central null $\theta_x=\theta_y=0$ and the constructive position $\theta_x=\theta_y=\lambda/(2s)$ indicated by × and + on the on-sky transmission map, respectively. On these pupil images, we placed the Lyot stop with a diameter of D_L=4 mm as shown in fig. 4a.

Figure 5 shows an acquired nulled image on the final focal plane. The image exhibits a residual intensity of the four-beam SPLINE, normalized by a maximum intensity of the corresponding bright image. From the radial intensity profile of the nulled image, we can see that the model star light can be strongly suppressed, reaching an intensity level of 3×10^{-5} at the peak ("peak contrast" of 3×10^{4}), and 3×10^{-7} at $10\lambda/D$. We note that an inner working angle (IWA) of the four-beam SPLINE is about $\lambda/(2.2s)$, corresponding to $3.5\lambda/D$ for our SPLINE simulator.

We also measured temporal variation of the peak and halo (at $2.8\lambda/D$) contrasts to evaluate stability of the four-beam SPLINE. We note that the angular distance of $2.8\lambda/D$ corresponds to 0.8×IWA. The result shown in fig. 6 suggests that the halo contrast is highly stable over 3 hours, although the peak contrast is slightly degraded.

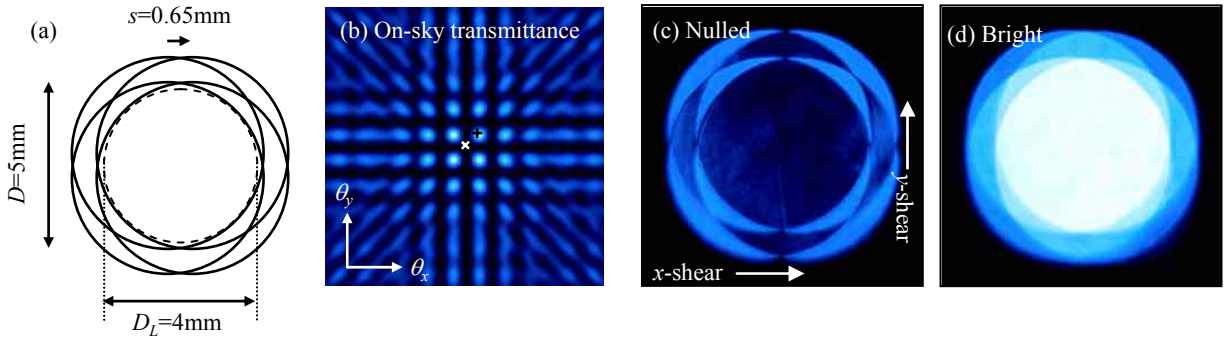

Figure 4. (a) Geometry on a reimaged pupil plane where the Lyot stop is placed. Four pupils with a diameter of D=5 mm are superposed with x and y lateral shifts of s=0.65 mm. A dashed circle shows the Lyot stop. (b) A corresponding on-sky transmission map of the four-beam SPLINE. (c,d) Acquired nulled and bright images on the Lyot stop plane. Four pupils are constructively and destructively interfered, respectively.

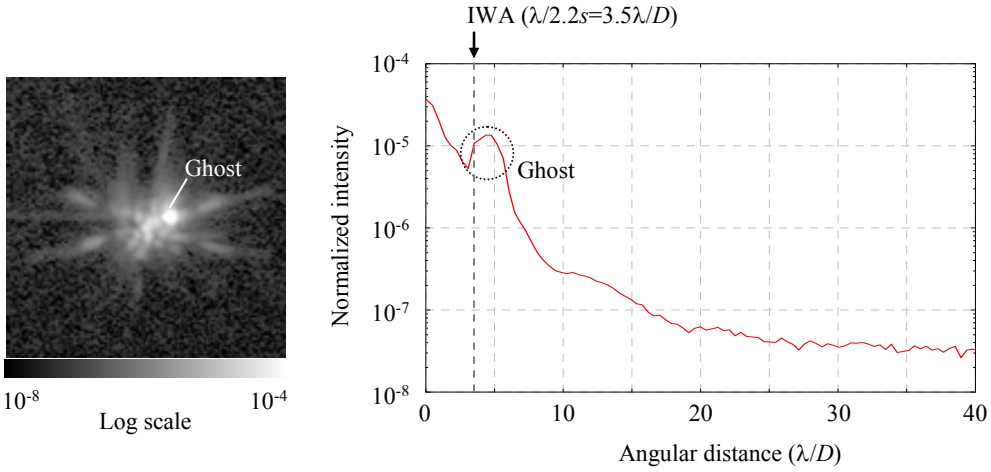

Figure 5. An acquired nulled image on the final focal plane and its radial intensity profile.

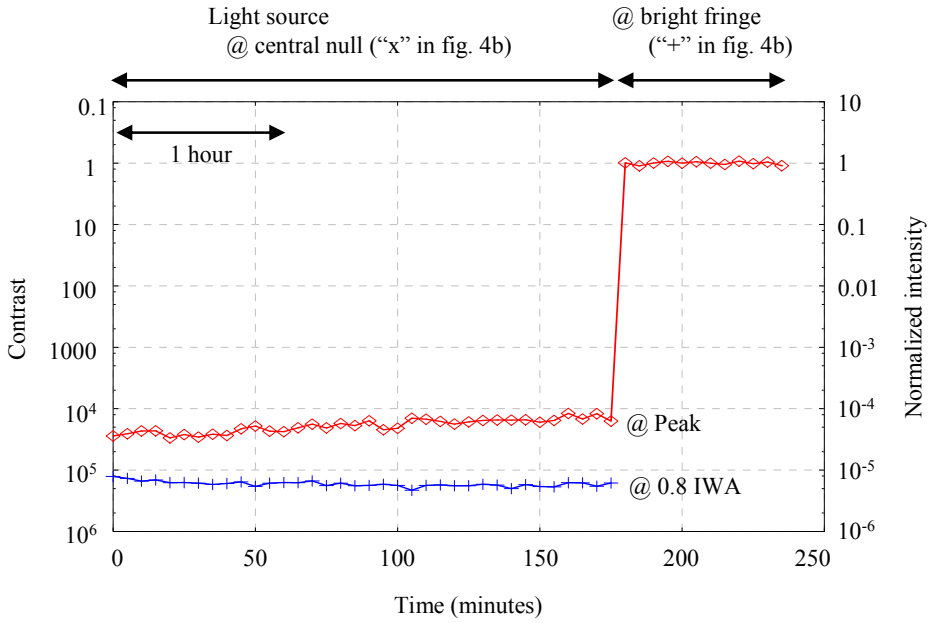

Figure 6. Measurements of a stability of the four-beam SPLINE. Two profiles show temporal variations of the contrasts at the peak and halo (at $2.8\lambda/D$, corresponding to 0.8×IWA). We note that any fringe-locking system, like an OPD control system for the nulling interferometer, is not necessary and not used during the measurements.

5. DISCUSSIONS

5.1 Combination with polarization differential imaging

For improving the achievable contrast, the SPLINE can be combined with differential techniques. Here we proposed to apply the polarization differential imaging (PDI) mode [15,16]. The PDI mode can be easily introduced to the SPLINE by inserting a polarization modulator (rotating wave plates, electrically controlled liquid crystal devices, and so on) in front of the first polarizer.

We carried out laboratory demonstration of the SPLINE/PDI mode. As the polarization modulator, we used a liquid-crystal variable retarder (LCVR). The optical setup is almost the same as fig. 3, but a pinhole illuminated by a He-Ne laser is used as model star and planet, instead of the single-mode optical fiber illuminated by the xenon lamp. We used the two-beam SPLINE with the single Savart plate.

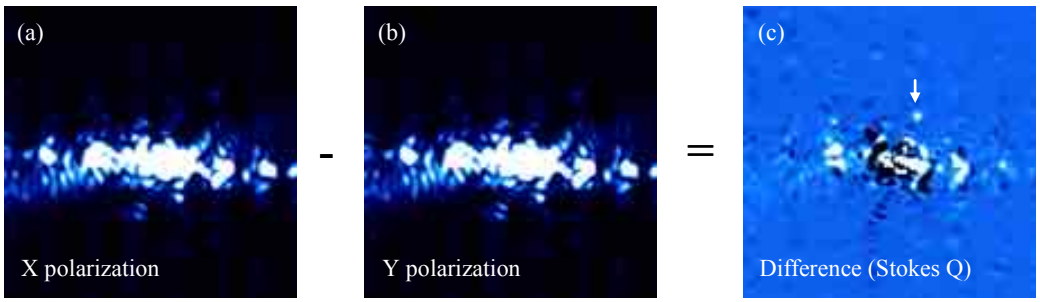

Figure 7. A preliminary result of the polarization-differential imaging mode of the two-beam SPLINE.

Figure 7 shows a preliminary result of the laboratory demonstration. We simulated unpolarized starlight and partially polarized planetary light (with a degree of polarization of about 50%) by 45° and 32° linearly polarized light, respectively. We set a planet/star intensity ratio to be about 1×10^{-6} and a star-planet separation to be $9\lambda/D$. We can see that the partially polarized model planet is clearly detected by the PDI mode as shown in fig. 7c.

5.2 Two-channel configuration for improving system throughput

As mentioned above, a system throughput of the SPLINE would be degraded by the intensity loss due to the first polarizer. For improving the system throughput, we propose a two-channel SPLINE configuration based on polarizing beam splitters (PBS). Figure 8 shows a scheme of the two-channel four-beam SPLINE configuration. The first polarizer P1 is replaced with the PBS1 to split unpolarized or partially polarized incoming light into two orthogonally polarized ones (p- and s polarizations, respectively). Behind the PBS1, Savart plates and polarizers are placed to build the four-beam SPLINE in each arm. Behind the SPLINE, half-wave plates (HWP) would be placed to convert the output p-polarized light to s-polarized one, and vise versa. These two lights are recombined by the PBS2. By the two-channel configuration, we can get rid of the coefficient 1/2 of the on-sky transmittance in eq. (2) as

$$T(\theta_x, \theta_y, \lambda) = \sin^2\left(\frac{\pi s \theta_x}{\lambda}\right)\sin^2\left(\frac{\pi s \theta_y}{\lambda}\right). \quad (4)$$

Thus the on-sky transmittance of the two-channel SPLINE will become unity for the constructive position $\theta_x=\theta_y=\lambda/(2s)$, and the system throughput will be improved.

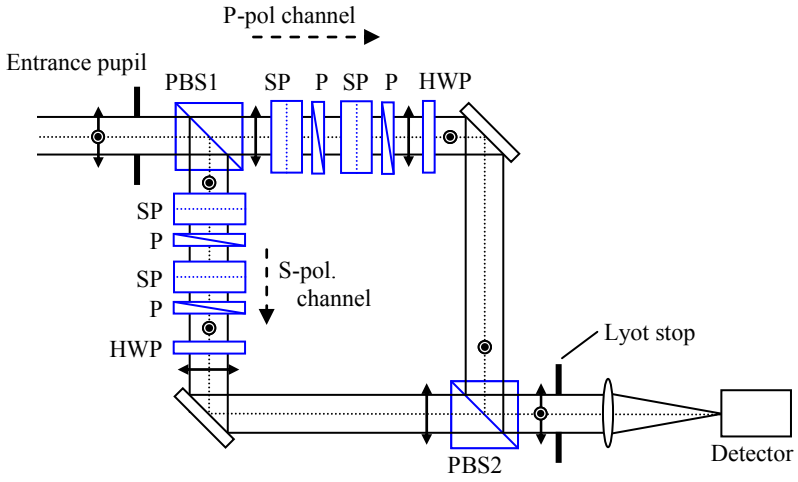

Figure 8. A scheme of the two-channel four-beam SPLINE configuration to improve the system throughput.

6. CONCLUSIONS

The SPLINE is a stable and achromatic lateral-shearing nulling interferometer for strongly suppressing bright starlight in visible and near-infrared spectral range. We constructed the four-beam SPLINE, and carried out laboratory demonstration using a polychromatic light source with a bandwidth of about 30% as a model star. As a result, a peak contrast of about 3×10^4 could be achieved. We also evaluated the stability of the four-beam SPLINE by measuring the peak and halo contrasts over 3 hours. The result demonstrated excellent stability of the SPLINE output.

The system throughput of the SPLINE will be degraded by the intensity loss due to the first polarizer. We also presented the two-channel four-beam SPLINE configuration based on the polarizing-beam splitters for improving the system throughput. By the two-channel SPLINE, we can avoid the intensity loss due to the first polarizer, and the system throughput will be improved.

The lateral shearing nulling interferometer is advantageous for the future-planned extremely large telescopes (ELTs), because its nulling performance does not suffer from complex pupil functions of the ELTs with segmented hexagonal mirrors. The SPLINE will be attractive for the future-planned high-contrast instruments such as the Second-Earth Imager for the TMT (SEIT) [2].

ACKNOWLEDGEMENTS

We acknowledge Kazuhiko Oka of the Hokkaido University for his many useful comments. This research was partially supported by the Japan Society for the Promotion of Science (JSPS) through KAKENHI (21340041, 23740139), and the Ministry of Education, Culture, Sports, Science and Technology (MEXT) through KAKENHI (24103501). MT is supported by KAKENHI (22000005).

REFERENCES

[1] Macintosh, B., Troy, M., Doyon, R., Graham, J., Baker, K., Bauman, B., Marois, C., Palmer, D., Phillion, D., Poyneer, L., Crossfield, I., Dumont, P., Levine, B. M., Shao, M., Serabyn, E., Shelton, C., Vasisht, G., Wallace, J. K., Lavigne, J.-F., Valee, P., Rowlands, N., Tam, K. and Hackett, D., "Extreme adaptive optics for the Thirty Meter Telescope," Proc. SPIE 6272, 62720N (2006).

[2] Matsuo, T. and Tamura, M., "Second-earth imager for TMT (SEIT): a proposal and concept description," Proc. SPIE 7735, 773584 (2010).

[3] Kasper, M., Beuzit, J.-L., Verinaud, C., Gratton, R. G., Kerber, F., Yaitskova, N., Boccaletti, A., Thatte, N., Schmid, H. M., Keller, C., Baudoz, P., Abe, L., Aller-Carpentier, E., Antichi, J., Bonavita, M., Dohlen, K., Fedrigo, E., Hanenburg, H., Hubin, N., Jager, R., Korkiakoski, V., Martinez, P., Mesa, D., Preis, O., Rabou, P., Roelfsema, R., Salter, G., Tecza, M. and Venema, L., "EPICS: direct imaging of exoplanets with the E-ELT," Proc. SPIE 7735, 77352E (2010).

[4] Bracewell, R. N., "Detecting nonsolar planets by spinning infrared interferometer," Nature 274, 780-781 (1978).

[5] Baudoz, P., Rabbia, Y. and Gay, J., "Achromatic interfero coronagraphy I. Theoretical capabilities for ground-based observations," Astron. Astrophys. Suppl. Ser. 141, 319-329 (2000).

[6] Tavrov, A. V., Kobayashi, Y., Tanaka, Y., Shioda, T., Otani, Y., Kurokawa, T. and Takeda, M., "Common-path achromatic interferometer-coronagraph: nulling of polychromatic light," Opt. Lett. 30, 2224-2226 (2005).

[7] Guyon, O. and Shao, M., "The pupil-swapping coronagraph," Publ. Astron. Soc. Pacific 118, 860-865 (2006).

[8] Murakami, N., Yokochi, K., Nishikawa, J., Tamura, M., Kurokawa, T., Takeda, M. and Baba, N., "Polarization interferometric nulling coronagraph for high-contrast imaging," Appl. Opt. 49, D106-D114 (2010).

[9] Aime, C., Ricort, G., Carlotti, A., Rabbia, Y. and Gay, J., "ARC: an achromatic rotation-shearing coronagraph," Astron. Astrophys. 517, A55 (2010).

[10] Mennesson, B. P., Shao, M., Levine, B. M., Wallace, J. K., Liu, D. T., Serabyn, E., Unwin, S. C. and Beichman, C. A., "Optical Planet Discoverer: how to turn a 1.5-m class space telescope into a powerful exo-planetary systems imager," Proc. SPIE 4860, 32-44 (2003).

[11] Baba, N., Kobayashi, K., Kogoma, Y. and Murakami, N., "Lateral shearing with a pair of double Fresnel rhombs for nulling interferometry," Opt. Lett. 36, 3611-3613 (2011).

[12] Murakami, N. and Baba, N., "Common-path lateral-shearing nulling interferometry with a Savart plate for exoplanet detection," Opt. Lett. 35, 3003-3005 (2010).

[13] Françon, M. and Mallick, S., [Polarization Interferometers], Wiley-Interscience, London, New York, Sydney, Toronto, 19-34 (1966).

[14] Mallick, S. and Malacara, D., [Optical Shop Testing], Wiley-Interscience, New Jersey, 97-121 (2007).

[15] Kuhn, J. R., Potter, D. and Parise, B., "Imaging polarimetric observations of a new circumstellar disk system," Astrophys. J. 553, L189-L191 (2001).

[16] Baba, N. and Murakami, N., "A method to image extrasolar planets with polarized light," Publ. Astron. Soc. Pacific 115, 1363-1366 (2003).

12.5-GHz-spaced laser frequency comb covering Y, J, and H bands for Infrared Doppler instrument

T. Kokubo[a], T. Mori[a], T. Kurokawa[b,a], K. Kashiwagi[a],
Y. Tanaka[a], T. Kotani[c,b], J. Nishikawa[b,c], and M. Tamura[d,b,c]

[a]Graduate School of Engineering, Tokyo University of Agriculture & Technology, 2-24-16 Nakamachi, Koganei, Tokyo, Japan 184-8588; [b]National Astronomical Observatory of Japan, 2-21-1 Osawa, Mitaka, Tokyo, Japan 181-8588; [c]Astrobiology Center, National Institute of Natural Sciences, 2-21-1 Osawa, Mitaka, Tokyo, Japan 181-8588; [d]Graduate School of Science, The University of Tokyo, 7-3-1 Hongo, Bunkyo-ku, Tokyo, Japan 113-0033

ABSTRACT

In order to detect Earth-like planets around nearby red dwarfs (in particular late-M stars), it is crucial to conduct precise radial velocity measurements at near-infrared wavelengths where these stars emit most of the light. We have been developing the Infrared Doppler (IRD) spectrograph which is a high dispersion spectrograph for the Subaru telescope. To achieve 1m/s RV measurement precision, we have developed a direct generation of laser frequency comb (LFC) that uses high-repetition-rate pump pulse synthesized by a line-by-line pulse-shaping technique. Our LFC generator has some advantages including simple and easy frequency stabilization, all fiber-optic configuration, and broadband calibration by the precise frequency shift of all modes in the LFC. We have successfully generated a 12.5-GHz-spaced comb spanning over 700 nm from 1040 to 1750 nm. The frequency stability was measured by optically heterodyning the comb with an acetylene-stabilized laser at 1542 nm as a reference light. The LFC showed a frequency stability of less than 0.2 MHz and an almost constant spectrum profile for 6 days. The original LFC that has just produced from highly nonlinear fibers needs some optical processing including spectrum shaping, depolarization, and a mode scramble in a multi-mode fiber before it is input into a spectrograph for the calibration. We have investigated the optical processing of the LFC which is necessary for the precise spectrograph calibration.

Keywords: laser frequency comb, infrared, spectrograph, Doppler shift

1. Introduction

In order to detect Earth-like planets around nearby red dwarfs (in particular late-M stars), it is crucial to conduct precise radial velocity measurements at near-infrared wavelengths where these stars emit most of the light. We have been developing the Infrared Doppler (IRD) spectrograph which is a high dispersion spectrograph for the Subaru telescope [1-2]. It aims at achieving measurement precision of 1 m/s in radial velocity and thus will be a powerful instrument for exoplanet searches around "red" stars. Our main astronomical targets using IRD are late-M dwarfs, which are too faint to observe at optical wavelengths even with such a large telescope. Because of their lower masses these stars cause a much larger velocity wobble than the Sun-like stars due to any orbiting planets, while their lower luminosities bring the potentially habitable zone (where water is liquid on the planet surface) closer to the star, making planets in shorter period orbits more interesting for the search of life outside our solar system.

To achieve 1m/s RV measurement precision, we employ our original laser frequency comb (LFC) with a wide-wavelength coverage in the near-infrared as an extremely stable wavelength standard. Traditional LFC has been produced by using a fiber-based femtosecond laser and a silica-based highly nonlinear fiber (HNF). The application of traditional LFC to spectrograph calibration in astrophysics is not easy because the line spacing is less than several hundred MHz. One approach for such LFC generation is to filter unwanted comb lines from a fine-spacing LFC [3-4].

We have developed a direct generation of LFC that uses high-repetition-rate pump pulse synthesized by a line-by-line pulse-shaping technique [5-6]. However, the direct generation method has some difficulties in making the comb spectrum

Advances in Optical and Mechanical Technologies for Telescopes and Instrumentation II,
edited by Ramón Navarro, James H. Burge, Proc. of SPIE Vol. 9912, 99121R
 · doi: 10.1117/12.2232221

broad since the pulse peak power is not quite high due to the high repetition rate. We have designed and fabricated solid silica-based HNFs with small zero-dispersion wavelengths to obtain strong spectral broadening. We have successfully generated a 12.5-GHz-spaced comb from 1040 to 1750 nm covering Y, J, and H bands as atmospheric windows [7]. The original LFC that has just produced from highly nonlinear fibers needs some optical processing including spectrum shaping, depolarization, and a mode scramble in a multi-mode fiber before it is input into a spectrograph for the calibration.

In this paper, we describe the latest characteristics of our LFC, and optical processing of the LFC including spectrum shaping, depolarization and a mode scramble in multimode fiber propagation.

2. Generation of 12.5-GHz-spaced broadband comb

Figure 1 shows a schematic of the experimental setup used to generate a 12.5-GHz-spaced broadband LFC. The LFC was generated from a pump pulse that was created by a frequency-stabilized continuous-wave laser diode (FSLD; wavelength 1549 nm) followed by two phase modulators and an optical pulse synthesizer (OPS). The OPS is composed of a silica-based array waveguide grating having an intensity and a phase modulator in each channel [8-10]. Due to such a high pulse repetition rate as 12.5 GHz, the pulse peak power is too small to make the comb spectrum broader. In order to increase its peak power, we amplified the average power to 4 W by an EDFA, and shortened the pulse width to 1/20 by a pulse compressor based on a comb-like-profiled fiber [11]. As a result, the peak power was enhanced to around 700W. The produced pulses were transmitted through dispersion-shifted highly nonlinear fibers (HNFs) to generate the 12.5-GHz-spaced frequency comb.

We numerically and experimentally investigated a configuration of the HNFs and found that two-stage broadening through different HNFs was required when using limited pulse energy at a high repetition rate. We designed and fabricated solid silica-based HNFs with small zero-dispersion wavelengths (ZDWs) to obtain strong spectral broadening, especially at the shorter wavelengths. We introduced two HNFs, each with a different ZDW, in a cascade configuration. Inserting a second HNF with a shorter ZDW than the first HNF further expanded the spectral edge at the shorter wavelengths [12].

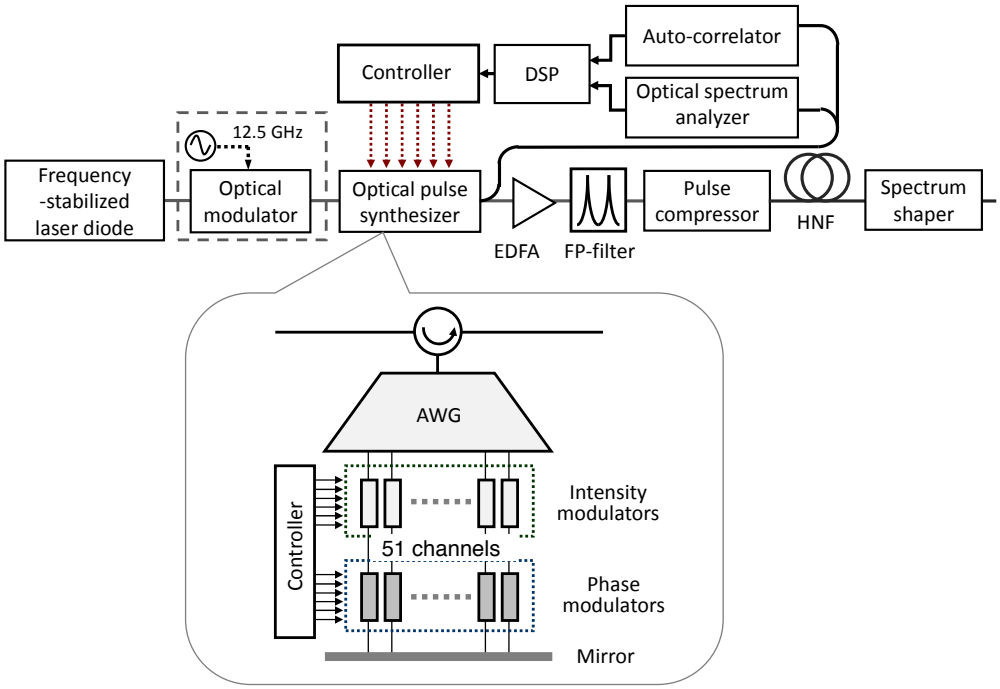

Fig. 1. Experimental setup for 12.5-GHz-spaced laser frequency comb generation.

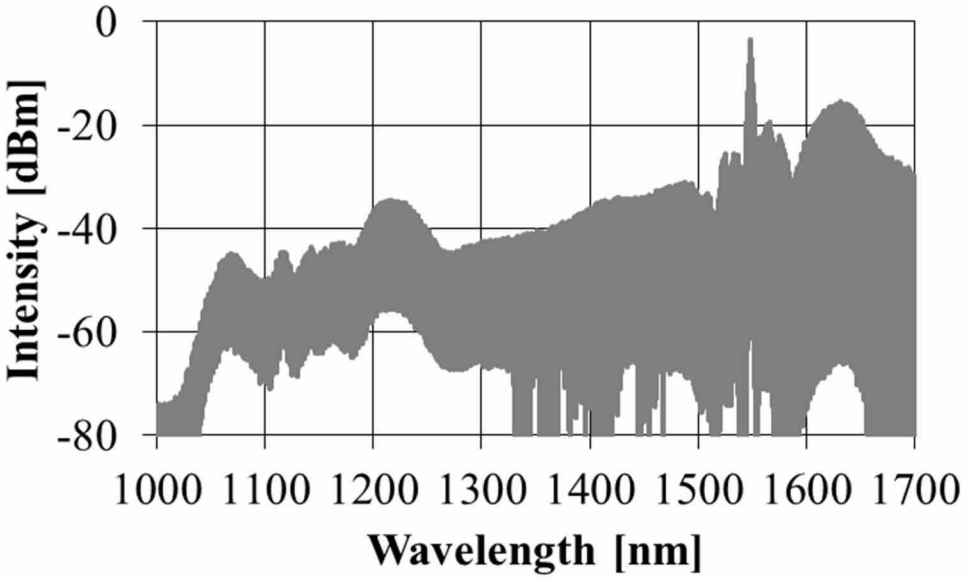

Fig. 2. Generated laser frequency comb spectrum. The wavelength range of the experimental spectrum is limited at 1700 nm in longer wavelength side because of the measurement range of the OSA. We confirmed resolvable comb-lines are spanning at least up to 1750 nm using a different type of OSA.

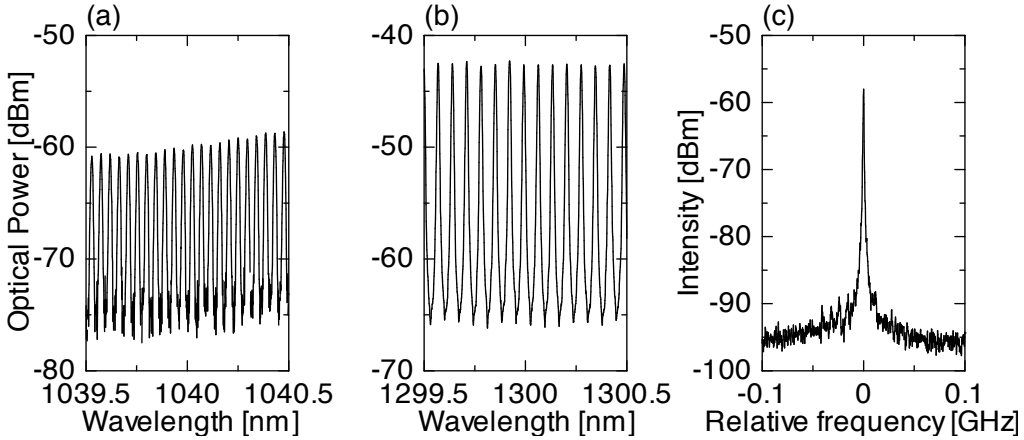

Fig. 3. Comb spectra expanded around (a) 1040 nm, (b) 1300 nm, and (c) spectrum of the heterodyne signal at 1565 nm.

Figure 2 shows the measured comb spectrum after the HNFs. Figure 3 (a) - (b) show comb spectra expanded around wavelength ranges of 1040 and 1300 nm, respectively, revealing clearly separated 12.5-GHz-spacing comb-modes. The LFC had over 15 dB contrast around wavelength range of 1040nm, although the contrast measurement was limited by the resolution of the optical spectrum analyzer (OSA), especially in the shorter-wavelength range. To verify the comb contrast free from the OSA resolution, we made heterodyne measurements at 1565 nm. Figure 3(c) shows the resulting heterodyne spectrum. The spectral component near the wavelength was filtered by a bandpass filter and combined with a beam from a local oscillator consisting of a semiconductor distributed-feedback laser. The linewidth of the local oscillator was less than 100 kHz. The combined beams were detected by a photodetector with a transimpedance amplifier and the spectrum of the beat signal was measured by an electric spectrum analyzer. The contrast of the beat signal exceeded 35 dB. The spectral width of the beat signal was ~1 MHz and linewidth of a line at 1565 nm was comparable to the FSLD line width.

It was confirmed that all individual lines were separated with high contrast over the entire wavelength range from 1040 to 1750 nm. The spectrum almost covers Y, J, and H bands as the atmospheric windows.

In order to evaluate the frequency stability of the comb spectrum, we made optical heterodyne measurement, where a frequency-stabilized laser by acetylene gas (wavelength: 1542 nm, frequency stability: less than 0.1 MHz) was used as a local oscillator. The beat frequency was measured continuously for 140 hours. As a result, the frequency stability was confirmed to be less than 0.2 MHz.

3. Optical processing of LFC before incidence to spectrograph

The original LFC that has just produced from HNFs has some problems to be solved before it is input into a spectrograph for the calibration. First, the LFC needs wavelength-independent attenuation over the broad bandwidth since it has much larger intensity than star light by over 4 orders of magnitude. We have developed a variable optical attenuator which has a rotating neutral density filter between fiber optic collimators.

Second, the spectrum of the LFC has full of ups and downs as shown in Fig. 2. It is needed to be flattened since the dynamic range of the detection camera is limited. Figure 4 shows the measured spectrum of the LFC, where the blue line indicates the spectrum of the original comb and the red line indicates the spectrum after a spectrum shaper. The spectrum shaper we developed consisted of a fiber Bragg grating, colored glass filters, and dielectric optical filters. Using the spectrum shaper, ups and downs of a spectrum of the LFC was improved to be about 15 dB.

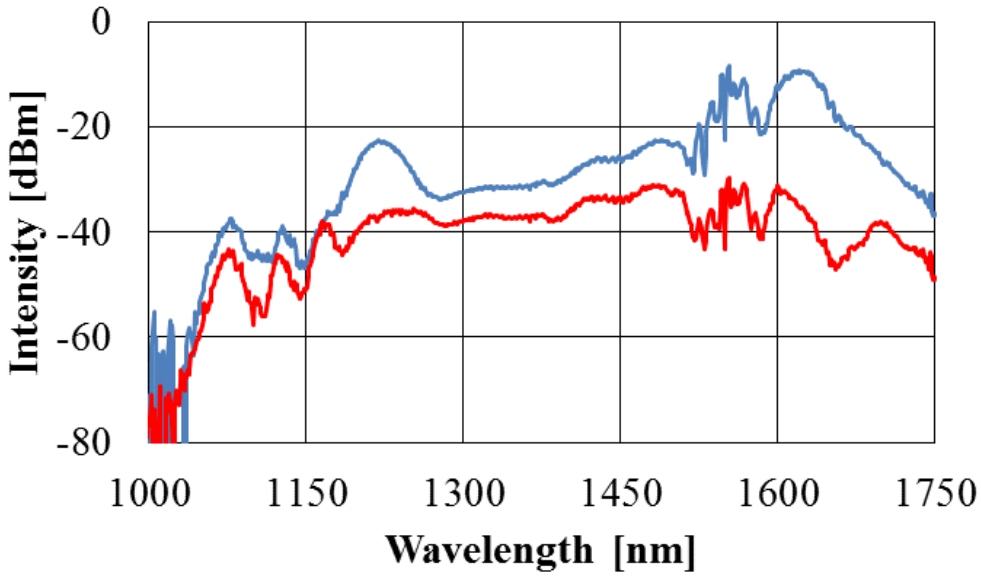

Fig. 4. Measured spectrum of the LFC. The blue and red lines indicate comb spectrum measured before and after a spectrum shaper, respectively.

Third issue is a high degree of polarization of the LFC. Since a spectrograph has some polarization dependence in the diffraction characteristics, the LFC needs to be depolarized. The depolarization means low degree of polarization in time average during star light exposure. Figure 5 shows a depolarizer which consists of rotating half and quarter wave plates (HWP and QWP) installed between fiber optic collimators. HWP and QWP have broadband characteristics covering the LFC spectrum and are rotated around the optical axis with a different rotational speed (HWP:180 rpm, QWP:80 rpm). We evaluated the depolarizer characteristics by measuring the Stokes parameters using laser diodes with the emission wavelength of 1.06, 1.31 and 1.55 μm. Table 1 shows the measurement results. The degree of polarization (DOP) of laser light propagated through the depolarizer was calculated from measured Stokes parameters. The DOPs were 0.01-0.04 at three wavelengths. It is confirmed that arbitrarily-polarized laser light can be fully depolarized by the depolarizer over the broad wavelength band.

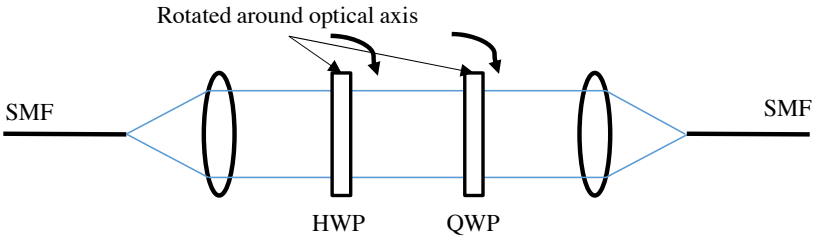

Fig. 5. Schematic of a depolarizer.

Table 1. Measurement results of Stokes parameters and the calculated DOP.

	Without depolarizer			With depolarizer		
	1.06μm	1.31μm	1.55μm	1.06μm	1.31μm	1.55μm
S1	0.721	-0.213	0.707	0.007	0.007	0.001
S2	-0.327	-0.490	-0.396	-0.003	-0.011	-0.014
S3	-0.650	0.841	-0.595	-0.035	0.003	0.003
DOP	1.02	1.00	1.00	0.04	0.01	0.01

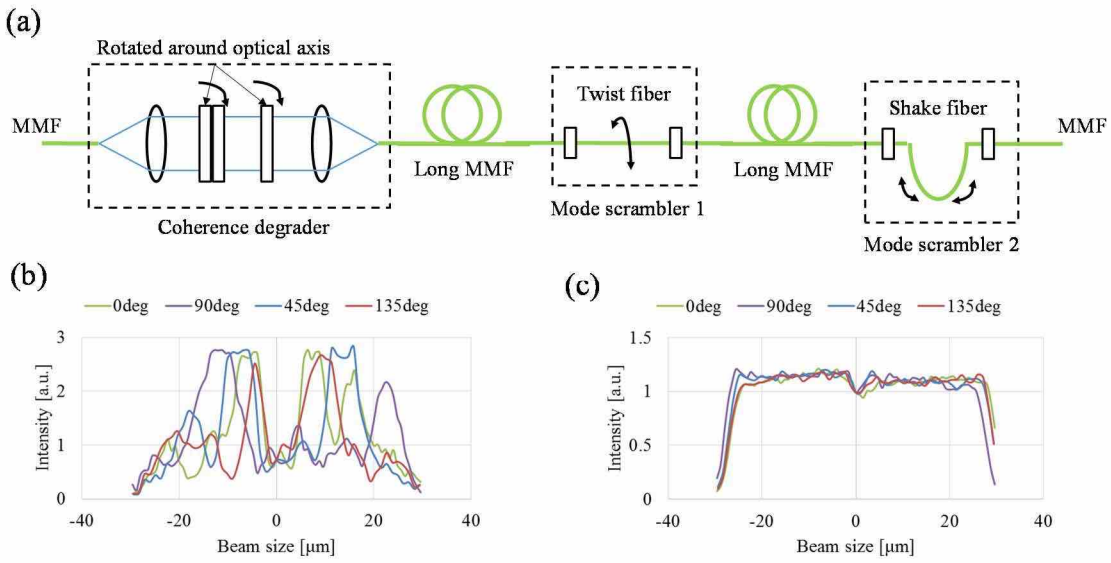

Fig. 6. (a) Schematic of a coherence degrader and mode scramblers. (b) and (c) show NFPs of laser light with a wavelength of 1.55 μm before and after coherence degrader and mode scramblers, respectively.

Final issue is a mode scramble of the comb light in a multimode fiber (MMF) [13]. As star light is coupled by an MMF between a telescope focus and a spectrograph, the coupling of the comb light with the spectrograph needs an MMF. The light intensity distribution in the fiber output installed at the slit position of the spectrograph, called modal noise, causes a fake RV shift and leads to poor precision of RV measurement because RV measurement is done by precise position determinations of stellar absorption lines and a laser frequency comb. Furthermore, high coherence of the comb light causes the speckle noise on the camera in the spectrograph. We developed a coherence degrader to reduce the speckle noise and a mode scrambler to reduce the modal noise, as shown in Fig. 6 (a). The MMF we used has a core diameter of 60 μm and a numerical aperture of 0.22. The coherence degrader has two kinds of rotating holographic diffuser with

different scattering angles (Edmund Optics, UV HLOGRAPHIC DIFFUSER 1 and 5 DEG) which are installed in MMF optic collimators. Two holographic diffusers is rotated around the optical axis with different rotational speeds (first:150 rpm, second: 96 rpm). We also used two kinds of mode scrambler. Mode scrambler 1 (GiGa Concept, GIG-6202-200) twists and Mode scrambler 2 shakes the MMFs, respectively. The near field pattern (NFP) of the laser light at the exit of the MMF was observed with an IR camera. Fig. 6 (b) and (c) show the NFPs before and after the coherence degrader and the mode scramblers. The experimental results showed that mode scramblers effectively suppressed modal noise.

4. Summary

We have successfully generated a 12.5-GHz-spaced comb spanning over 700 nm from 1040 to 1750 nm. The LFC showed a frequency stability of less than 0.2 MHz and an almost constant spectrum profile for 6 days. The noise of the comb modes was evaluated by optically heterodyning the comb with another continuous-wave laser. The comb showed a high contrast of about 35 dB.

The original LFC that has just produced from HNFs needs some optical processing including spectrum shaping, depolarization and mode scramble in the MMF coupling before it is input into a spectrograph for the calibration. We have investigated the optical processing of the LFC which makes spectrograph calibration effective.

REFERENCES

[1] M. Tamura et al., "Infrared Doppler instrument for the Subaru Telescope (IRD)," SPIE 8446, 84461T, August (2012).

[2] Kotani et al., “Infrared Doppler instrument (IRD) for the Subaru telescope to search for Earth-like planets around nearby M-dwarfs,” SPIE 9147, 914714 (2014).

[3] C. Li et al., "A laser frequency comb that enables radial velocity measurements with a precision of 1 cm s-1," Nature **452**, 610-612 (2008).

[4] F. Quinlan, G. Ycas, S. Osterman, and S. A. Diddams, "A 12.5 GHz-spaced optical frequency comb spanning >400 nm for near-infrared astronomical spectrograph calibration," Rev. Sci. Instrum. **81**, 063105 (2010).

[5] S. Choi, N. Tamura, K. Kashiwagi, T. Shioda, Y. Tanaka, and T. Kurokawa, "Supercontinuum Comb Generation Using Optical Pulse Synthesizer and Highly Nonlinear Dispersion-Shifted Fiber," Jpn. J. Appl. Phys. **48**, 09LF01 (2009).

[6] K. Kashiwagi, H. Ishizu, Y. Kodama, and T. Kurokawa, "Background suppression in synthesized pulse waveform by feedback control optimization for flatly broadened supercontinuum generation," Opt. Express **21**, 3001-3009 (2013).

[7] Y. Okuyama, K. Kashiwagi, T. Kotani, J. Nishikawa, M. Tamura, T. Kurokawa, “Broadband Multi-Gigahertz-Spaced Frequency Comb for Near Infrared Doppler Instrument,” Frontiers in Optics/Laser Science 2014 (FiO/LS 2014), no. FM3C.3, Tucson, Arizona, USA, 20th Oct. 2014.

[8] D. Miyamoto, K. Mandai, T. Kurokawa, S. Takeda, T. Shioda, and H. Tsuda, "Waveform-controllable optical pulse generation using an optical pulse synthesizer," IEEE Photonics Technol. Lett. **18**, 721-723 (2006).

[9] K. Mandai, D. Miyamoto, T. Suzuki, H. Tsuda, K. Aizawa, and T. Kurokawa, “Repetition rate and center wavelength-tunable optical pulse generation using an optical comb generator and a high-resolution arrayed-waveguide grating,” IEEE Photonics Technology Letters, vol. **18**, no. 5, pp. 679–681, Mar. 2006.

[10] H. Tsuda, Y. Tanaka, T. Shioda, and T. Kurokawa, “Analog and Digital Optical Pulse Synthesizers Using Arrayed-Waveguide Gratings for High-Speed Optical Signal Processing,” Journal of Lightwave Technology, vol. **26**, no. 6, pp. 670–677, Mar. 2008.

[11] T. Inoue and S. Namiki, "Pulse compression techniques using highly nonlinear fibers," Laser Photonics Rev. **2**, 83-99 (2008).

[12] K. Kashiwagi, T. Kurokawa, Y. Okuyama, T. Mori, Y. Tanaka, Y. Yamamoto, M. Hirano, Optics Express **24** (8), 8121-8131, 2016.

[13] S. Inoue, J. Nishikawa, T. Kotani, K. Kashiwagi, H. Suto, M. Tamura, T. Kurokawa, “Design and test of star light coupling to high precision Doppler spectrograph using multi-mode fiber,” FiO/LS 2012, FTh2F.2., Rochester, NY (USA), October 18, (2012).

Bull. Cent. Astron. Univ. Hyogo **3,** 1–20 (2015)

可視光分光撮像装置 LISS: 西はりま天文台 2.0-m なゆた望遠鏡への搭載と科学観測

小久保 充[1]、橋場 康人[1]、満田 和真[1]、酒向 重行[1]、諸隈 智貴[1]、土居 守[1]、Hanindyo Kuncarayakti[2,3]、森鼻 久美子[4]、伊藤 洋一[4]、新井 彰[5]

1) 東京大学大学院理学系研究科天文学教育研究センター
2) Millennium Institute of Astrophysics, Chile
3) Departamento de Astronomía, Universidad de Chile, Casilla 36-D, Santiago, Chile
4) 兵庫県立大学西はりま天文台
5) 京都産業大学神山天文台

Optical Imaging Spectrograph LISS: Development and Observations on the 2.0-m NAYUTA Telescope at NHAO

Mitsuru Kokubo[1], Yasuhito Hashiba[1], Kazuma Mitsuda[1], Shigeyuki Sako[1], Tomoki Morokuma[1], Mamoru Doi[1], Hanindyo Kuncarayakti[2,3], Kumiko Morihana[4], Yoichi Itoh[4], and Akira Arai[5]

1) Institute of Astronomy, University of Tokyo, 2-21-1 Osawa, Mitaka, Tokyo 181-0015, Japan
2) Millennium Institute of Astrophysics, Chile
3) Departamento de Astronomía, Universidad de Chile, Casilla 36-D, Santiago, Chile
4) Nishi-Harima Astronomical Observatory, Center for Astronomy, University of Hyogo, Sayo, Hyogo 679-5313, Japan
5) Koyama Astronomical Observatory, Kyoto Sangyo University, Motoyama, Kamigamo, Kita-ku, Kyoto 603-8555, Japan

E-mail: mkokubo@ioa.s.u-tokyo.ac.jp

(Received 2015 November 30)

概要

我々は、ファブリ・ペロー撮像 (R ∼200; 6000-9000 Å)、グリズム分光 (R ∼100、400; 4000-10000 Å)、および広/狭帯域フィルター撮像の 3 つの観測モードを搭載した可視光分光撮像装置 LISS (Line Imager and Slit Spectrograph) を開発してきた。2014 年 7 月からは兵庫県立大学西はりま天文台なゆた望遠鏡に PI 装置として搭載し、科学観測を行ってきた。本稿では、なゆた望遠鏡搭載時の LISS の性能について紹介するとともに、これまでに我々が行ってきた LISS を用いた科学観測について紹介する。

Abstract

We have developed LISS (Line Imager and Slit Spectrograph), an optical imaging spectrograph capable of Fabry-Perot imaging (R ∼200; 6000-9000 Å), slit spectroscopy (two grisms of R ∼100 and 400 available; 4000-10000 Å), and standard broad/narrow-band imaging. LISS has been installed to the NAYUTA telescope at Nishi-Harima Astronomical Observatory as a PI instrument, and we have been carrying out scientific observations with NAYUTA/LISS since July 2014. In this article, we describe the fundamental capabilities of NAYUTA/LISS and several scientific results obtained so far.

Key words: galaxies: ISM — galaxies: individual: M82, NGC7714, NGC4395 — instrumentation: spectrographs — quasars: general — supernovae: individual: 2014ec, 2014ed, 2015E, 2015aa

1. LISS (Line Imager and Slit Spectrograph) 装置概要

我々は、ファブリ・ペロー撮像 (R ∼200; 6000-9000 Å)、グリズム分光 (R ∼100、R ∼400)、 および広/狭帯域フィルター撮像の 3 つの観測モードを搭載した可視光分光撮像装置 LISS (Line Imager and Slit Spectrograph) の開発を行ってきた (Figure 1、 Figure 2)。長波長側で感度の高い浜松ホトニクス社 2k×1k 完全空乏型 CCD の特性を活かした、ファブリ · ペローエタロンや狭帯域フィルターを用いた近傍銀河の輝線の撮像観測、グリズムによる超新星 · クエーサーの分光観測などを主な目的として設計されている。

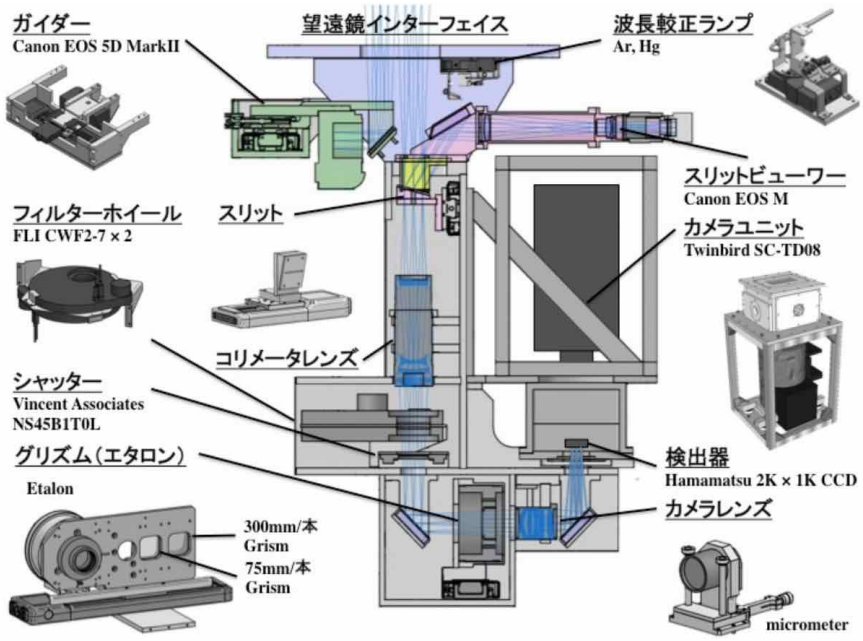

Fig. 1. LISS の光学系の断面図。カメラユニットを除く光学系 · 筐体の設計・製作はオプトクラフト社と共同で行った。望遠鏡の F 比が 9 以上の入射光学系に対応しており、2 対 1 の縮小光学系になっている。一部光学系部品は 15-band dichroic-mirror camera (DMC; Doi et al. 1998) の予備部品を使用している。

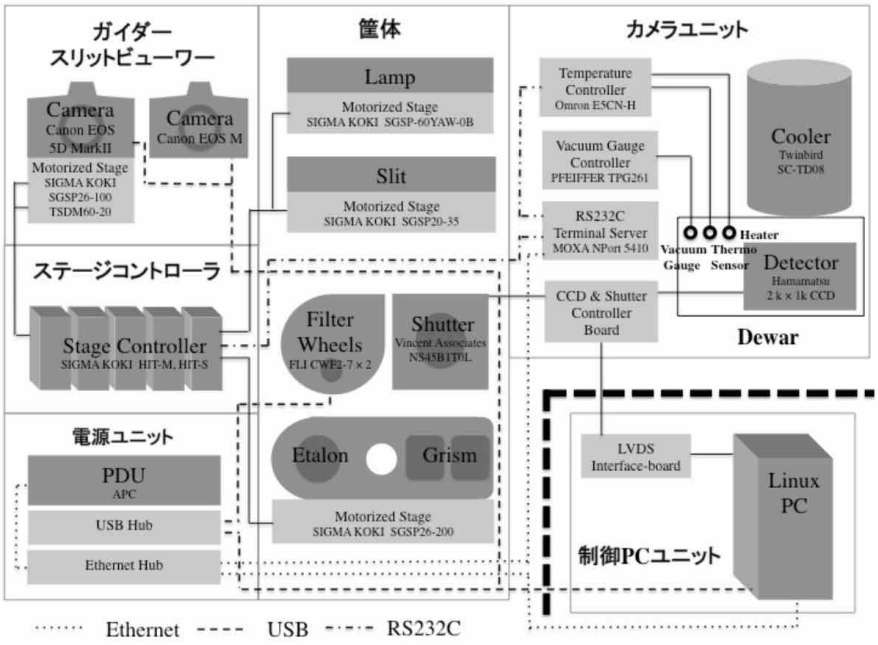

Fig. 2. LISS システム構成図

本装置は、2012 年に北海道大学 1.6-m ピリカ望遠鏡においてファーストライトを行い、その後 2012 年から 2013 年にかけてファブリ · ペローモードと低分散分光モードの立ち上げを行った。LISS の開発と、北海道大学 1.6-m ピリカ望遠鏡における立ち上げ、試験観測については Hashiba et al. (2014) において詳細が報告されている。その後 LISS は、2014 年 7 月に兵庫県立大学西はりま天文台に場所を移し、2.0-m なゆた望遠鏡カセグレン装置として再立ち上げが行われた。数回にわたる試験観測と装置の改良を経て、現在では定常的に科学観測を行うことができている。これまでに 2014 年 9 月、11 月、 2015 年 1 月、 2 月、5 月、9 月に、 なゆた望遠鏡公募観測時間を利用して科学観測を行ってきた。科学成果としてすでに 4 天体の超新星候補 (Kiso Supernova Survey; KISS) の分光同定に成功しており、特に 2015 年 5 月の観測で同定された Ia 型超新星 KISS15q=SN 2015aa (g ∼20.5mag、赤方偏移 ∼ 0.18; Morokuma et al. 2015d、2015e) は、日本国内の望遠鏡で分光同定された突発天体としては最も暗い天体である。さらに、科学観測と並行する形で、観測モードの設定やオートガイダーの操作などを統合した GUI の整備、測光フィルターの拡充、新たなグリズム (R∼400; 4000-8000 Å) と波長校正ランプの追加搭載等を行ってきている。本稿では、Hashiba et al. (2014) による報告以後の改良を経た LISS の最新の仕様や、なゆた望遠鏡搭載時の LISS の性能等について紹介する。

なゆた望遠鏡カセグレン焦点搭載時の LISS の装置特性を Table 1 にまとめた [1] [2]。なお本稿における LISS の機能 · 性能は 2015 年 11 月現在のものであり、今後さらなる変更/追加が行われる可能性がある。

1–1. CCD

検出器として浜松ホトニクス完全空乏型 2k×1k CCD (ピクセルサイズ=15μm×15μm) を採用している。検出器は独自に設計されたデュワー内におさめられ、 観測時には冷凍機 (ツインバード工業 スターリングクーラー

[1] オーバーヘッド領域、選択可能なビニングオプションについては 2015 年 1 月 16 日以降の仕様 (1200×2200 ピクセル → 1200×2240 ピクセル [オーバースキャン領域 =x、y 方向ともに 48 ピクセル] に変更
[2] 高分散分光モード (GRISM-H) の導入は 2015 年 2 月 17 日以降。

Table 1. LISS の装置特性 (なゆた望遠鏡カセグレン焦点搭載時)

CCD 素子	浜松ホトニクス完全空乏型 2k×1k CCD
データ領域	512x1152×4ch
オーバースキャン領域	48x1200×4ch + 512x48×4ch
ゲイン	2.0 e^-/ADU
読み出しノイズ:	$\sim$ 5.0-5.5 e^- (マルチサンプリング 3 回)
ビニング:	1×1, 2×2, 4×4
撮像モード	
ピクセルスケール	0.244 Å/pixel
視野	$\sim \phi$ 4 分角 (円形視野)
フィルター	B, V, Rc, Ic, g, r, i, z, Hα, Hβ, [SII], [SIII]
超低分散 (GRISM-L) 分光モード	
分散	12.4 Å/ pixel (1×1 binning)
観測波長域	4000-7000 Å(without LP filter)
	6000-10000 Å(with LP filter)
波長分解能 R	$\sim$100 (2 秒角スリット使用時)
低分散 (GRISM-H) 分光モード	
分散	2.9 Å/ pixel (1×1 binning)
観測波長域	4000-8400 Å
波長分解能 R	$\sim$400 (2 秒角スリット使用時)

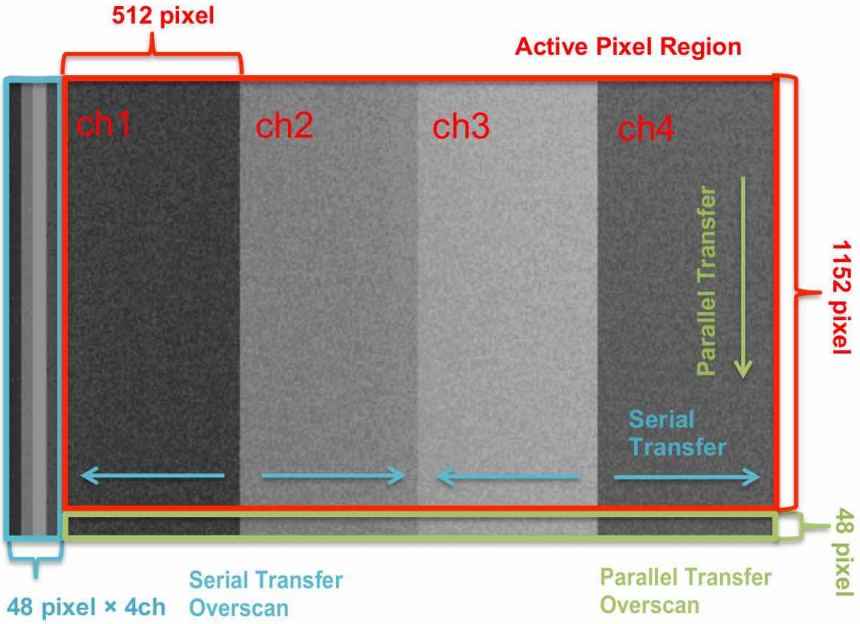

Fig. 3. 読み出される fits 画像のフォーマット。データ領域は 4 チャンネルで構成される。 48 pixel×4 チャンネル分の直列転送オーバースキャン領域、 48 pixel の並列転送オーバースキャン領域が存在する。

TD08) により-110 度まで冷却される。暗電流は-100 度程度 (173 K) の環境で $< 1\ e^-$/pixel/hour (Kamata et al. 2010) であるため、 通常の観測ではダーク画像を取得する必要はない。読み出しシステムには、 東京大学木曽観測所で開発された Kiso Array Controller (KAC; Sako et al. 2012) を用いている。1×1、2×2、4×4 の on-chip binning に対応しており、1×1 binning での取得 fits 画像のフォーマットは Figure 3 のようになっている。さらに、マルチサンプリング方式により、AD コンバータで生じるノイズを軽減することができる。サンプリング回数=1 での読み出し時間は約 13 秒であり、サンプリング回数が増えるごとに読み出し時間が約 3 秒ずつ増加する。なゆた望遠鏡搭載時の LISS の読み出しノイズについては、サンプリング回数 1 回の場合に $7e^-$、3 回の場合に 5.0-5.5e^- 程度に減少し、4 回以上のサンプリングを行っても $5e^-$ 以下に下がることはないことが分かっている。サンプリング回数の設定は、科学観測画像について 3 回、キャリブレーション画像については 1 回を標準設定としている。

1–2. フィルター撮像モード

LISS は撮像装置として使用することが可能であり、2k×1k CCD の中央の 2 チャンネル (1k×1k) を用いた視野 ϕ4 分角程度 (なゆた望遠鏡カセグレン焦点搭載時) のカメラとなる。なゆた望遠鏡のインストゥルメントローテータ角度が 0 度の状態で取得画像の上方向が北、左方向が東に対応するようになっており、インストゥルメントローテータ角度を調整することで任意のポジションアングル (天球面上) で撮像を行うことができる。フィルターホイール 2 個 (FLI CFW-2-7) が光路上に直列に配置されており、それぞれ 6 枚ずつフィルターを収納する (Figure 1)。Figure 4 に、2015 年 11 月現在 LISS が保有しているフィルターの透過曲線を示している。広帯域フィルター (B、V、Rc、Ic、g、r、i、z) に加え、いくつかの狭帯域フィルターも搭載している。2 枚のフィルターを組み合わせて使う場合もあり、例えば、A049 フィルターと F12 フィルターを組み合わせる

ことで [SII] 狭帯域フィルターとして機能させる。LISS に搭載されている Hβ、Hα、[SII]、[SIII] 狭帯域フィルターは主に系外銀河観測用に作成されているため、透過波長は輝線の静止系波長に対して少しレッドシフトした位置 (赤方偏移 0.002-0.008 程度) に最適化されていることに注意が必要である (ただし SII_{rest} フィルターは [SII] $\lambda\lambda$6717、6731 の静止系波長に最適化されている)。

1–3. グリズム分光モード

光路上にスリットとグリズムを挿入することで、スリット分光観測を行うことができる。スリット、グリズムはそれぞれ自動ステージ (シグマ光機 SGSP20-35、SGSP26-200) 上に固定されていて、ステージ位置を変更することで in/out を制御する (Figure 1、 2).

(a) スリット、グリズム

観測時のシーイング状況に応じて 1 秒角、2 秒角、3 秒角のスリット幅を選択できるように、 Figure 5 に示したようなロングスリットを採用している。なゆた望遠鏡のインストゥルメントローテータ角度が 0 度の状態でスリット長方向=南北方向になるが、撮像モードの場合と同様に、インストゥルメントローテータ角度を調整することで任意のポジションアングル (天球面上) 方向にスリットを当てて分光を行うことができる。CCD 画像上のスリット像の位置は固定されているため [3] 、スリット幅の選択は望遠鏡のポインティングをオフセットすることによって行う。

LISS には分散の異なる 2 つのグリズムが搭載されており、分光モードは “超低分散グリズムによる分光モード (GRISM-L)” と、“低分散グリズムによる分光モード (GRISM-H)” の 2 つの観測モードに細分化されている (Figure 11 参照)。ひとつは格子数 75 本/mm、頂角 4.3° の超低分散グリズムで、もともとは 15-band dichroic-mirror camera (DMC; Doi et al. 1998) のために製作したものを用いている。もうひとつは 2014 年度に新たに製作したもので、平面基板の透過型ブレーズド回折格子 (エドモンド VIS 300GPM 50 X 50) とプリズム (頂角 19.2°) をホルダー内で重ねて収納することで格子数 300 本/mm のグリズムとして機能させている。Figure 6 に超低分散グリズム (GRISM-L、実線)、低分散グリズム (GRISM-H、点線) それぞれの理論回折効率を示している。どちらのグリズムも Hβ、Hα 線両方をカバーするような波長域で最適化されている。

(b) 波長較正ランプ

LISS では、グリズム分光時の波長較正を行うための輝線ランプを内蔵している [4] 。輝線ランプとして ORIEL Instruments のペンシル型キャリブレーションランプを採用しており、6035 Hg (Ar) と 6030 Ar の 2 本のランプを同時に点灯して使用する [5] 。輝線ランプは、LISS-なゆた望遠鏡インターフェイス部分に備え付けてある自動回転ステージ (シグマ光機 SGSP-60YAW-0B; Figure 1) に 2 本まとめて並列に固定してあり、回転ステージを動作させることでスリット前面にランプ光を照射することができる。Figure 7、8 にはそれぞれ超低分散グリズム (GRISM-L)、低分散グリズム (GRISM-H) を用いた場合の分光ランプのスペクトルを図示している.。Figure 7 から明らかなように、超低分散グリズムを使用した際には、1 次光の長波長側に 2 次光の短波長側がオーバーラップしてくる (Figure 9)。超低分散グリズムを用いて長波長側 (>7000 $\mathring{\mathrm{A}}$) で高精度の分光スペクトルを取得したい場合には、Figure 4 にある LP(Long Pass) フィルターを用いて短波長側の透過を制限する必要がある。

[3] スリットはピクセル座標に対して約 0.3° の傾きがあり、1 秒角、2 秒角、3 秒角のスリット中心はそれぞれ (X, Y)=(1232,210)、(1233,530)、(1235,873) [pixel, pixel]。

[4] LISS の分光モードの波長分解能では夜光輝線はブレンドしてしまい、長波長側であっても夜光輝線を波長較正に用いることはできない。

[5] Hg(Ar) ランプを十分温めるため、点灯から約 10 秒程度待ち、Hg(Ar) ランプが十分温まってからデータを取得することを推奨する。

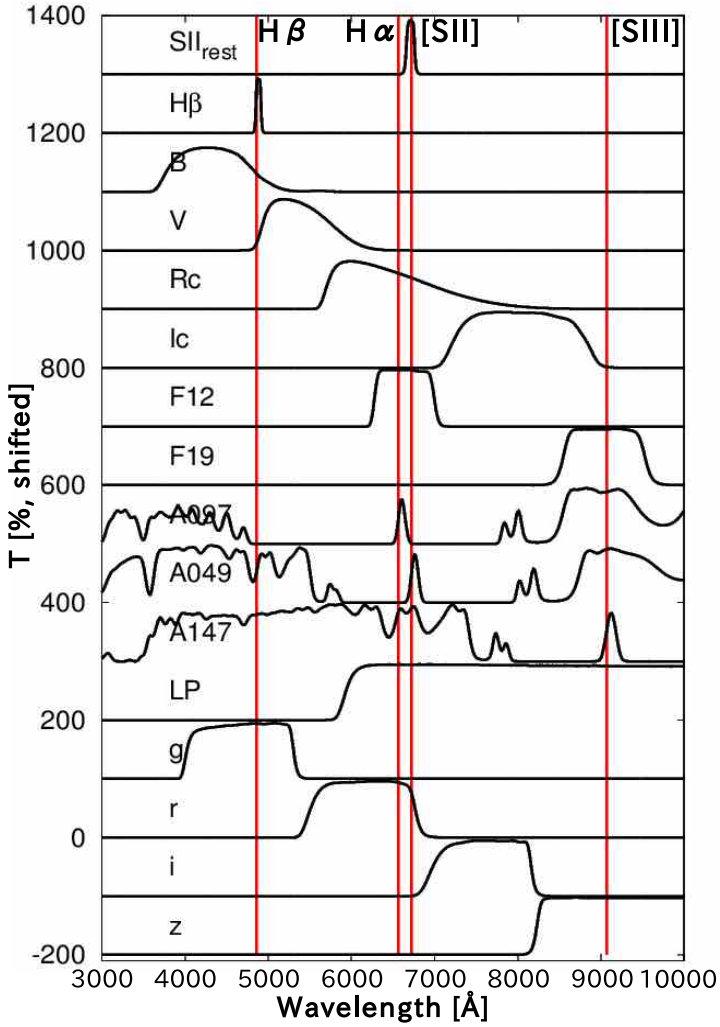

Fig. 4. 2015 年 11 月現在 LISS が保有しているフィルターの透過曲線。Hβ、Hα、[SII]、[SIII] 輝線の静止系波長に対応する位置を赤線で示している。 LISS に搭載されている Hβ、Hα、[SII]、[SIII] 狭帯域フィルターは近傍銀河の観測用に作成されているため、透過波長は輝線の静止系波長に対して少しレッドシフトした位置 (赤方偏移 0.002-0.008 程度) に最適化されている (ただし SII_{rest} フィルターは [SII] $\lambda\lambda$6717、6731 の静止系波長に最適化されている)。

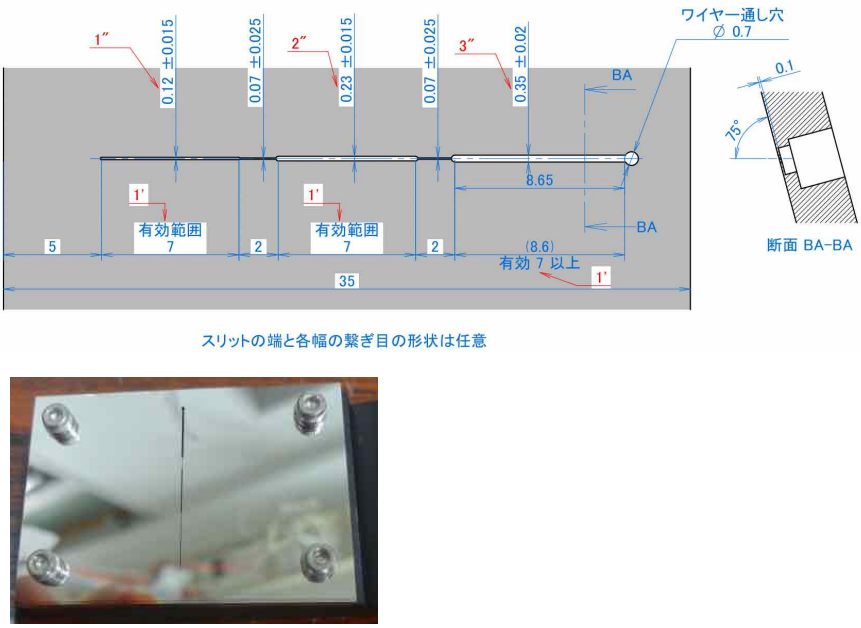

Fig. 5. 分光モードで使用されるスリットの設計図 (上) と実物 (下)。図中に示されている天球面上での角度スケールは、なゆた望遠鏡カセグレン焦点 (合成 F 比=12) 搭載時の値である。スリット表面は反射鏡になっており、反射された光はスリットビュワーで結像するように設計されている。

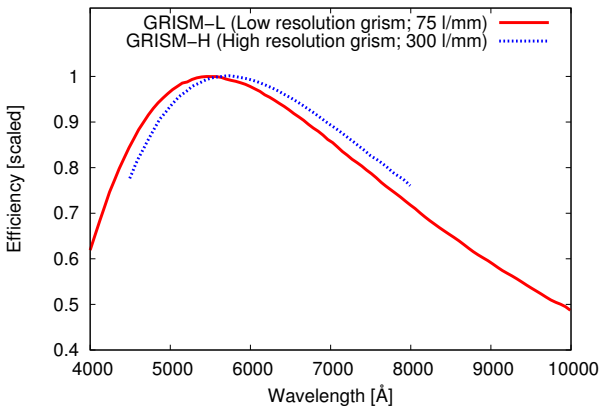

Fig. 6. 超低分散グリズム (GRISM-L、実線)、低分散グリズム (GRISM-H、点線) それぞれの理論回折効率。ただしここで示している効率はピーク値を 100%で規格化した相対値であり、実際の効率はより低い (GRISM-L は実測によると約 63%)。

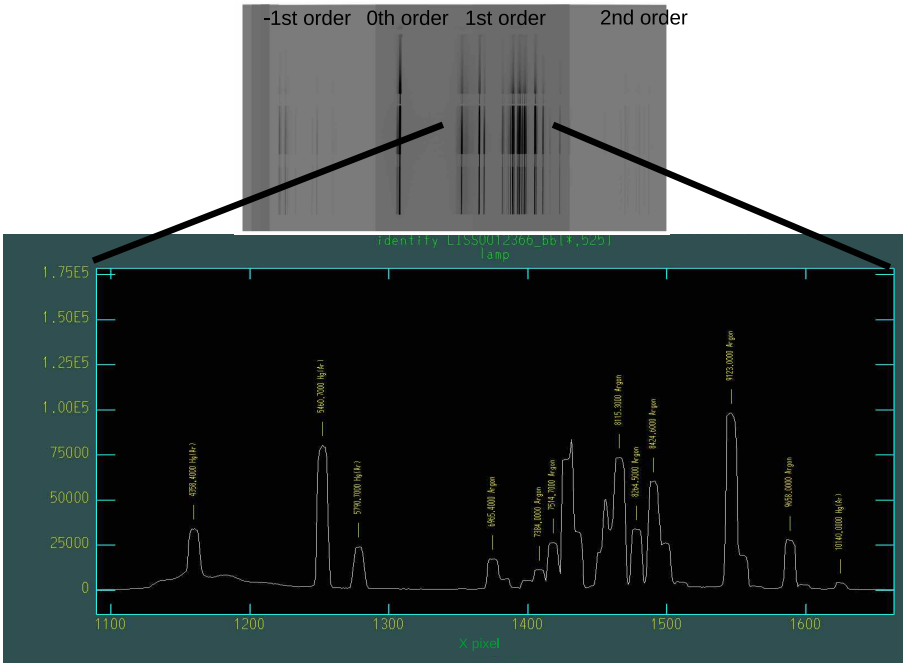

Fig. 7. 超低分散グリズム GRIMS-L ($R \sim 100$、フィルター無し) を用いた場合の分光ランプスペクトル。

(c) 波長分解能

Figure 9 に示したように、超低分散グリズム、低分散グリズムは、1×1 binning の場合に、おおまかにはそれぞれ 12.4 Å/ pixel、2.9 Å/ pixel の分散を持つ。2 秒角のスリット幅を用いる場合、波長分解能は 2/0.244/2 ∼ 4 pixel ∼49.6 Å(超低分散グリズム)、∼11.6 Å(低分散グリズム) になり、$R = \lambda/\Delta\lambda$ で表現すると $R \sim 100$ (超低分散グリズム)、∼ 400 (低分散グリズム) である。いずれのグリズムも一般的な天文観測用分光器としては低分散であり、LISS に搭載されている 2 つのグリズムを区別する際には便宜的に超低分散グリズム (GRISM-L)、低分散グリズム (GRISM-H) と呼んでいる。

(d) オートガイダー

LISS の分光観測では主に暗い天体をターゲットとするため、長時間露光が不可欠である。長時間のスリット分光を行う際には、望遠鏡のトラッキングエラーによって、 積分中にスリット上からターゲットが外れてしまうという問題が生じうる。なゆた望遠鏡では望遠鏡付属のオートガイダー機能 (圓谷 他 2006) が 2015 年 11 月現在稼働していないため、例えば 20 分の積分を行った場合、典型的に 2-3 秒角程度のトラッキングエラーが生じることを確認している。

望遠鏡トラッキングエラーを補正するため、LISS ではなゆた望遠鏡カセグレン焦点の視野の一部を用いたオフセット · オートガイダーを実装している (Figure 1)。オートガイダー用のカメラとして Canon EOS 5D MarkII を採用しており、 Figure 10 に示したように LISS 自身の CCD 視野から 7.6 分角オフセットした位置を視野にもつ。ガイダーカメラで取得される画像 (5634 pixel × 3753 pixel) の方向は、望遠鏡のインストゥルメントローテータ角度が 0 度のときに画像上方が西、画像左方向が北になっており、LISS 自身の CCD 画像の天球面上の方向に対して 90 度回転している (Figure 10)。

ガイダーカメラは、焦点合わせを行う Z 方向ステージと、視野を変更する X 方向ステージの 2 つの自動

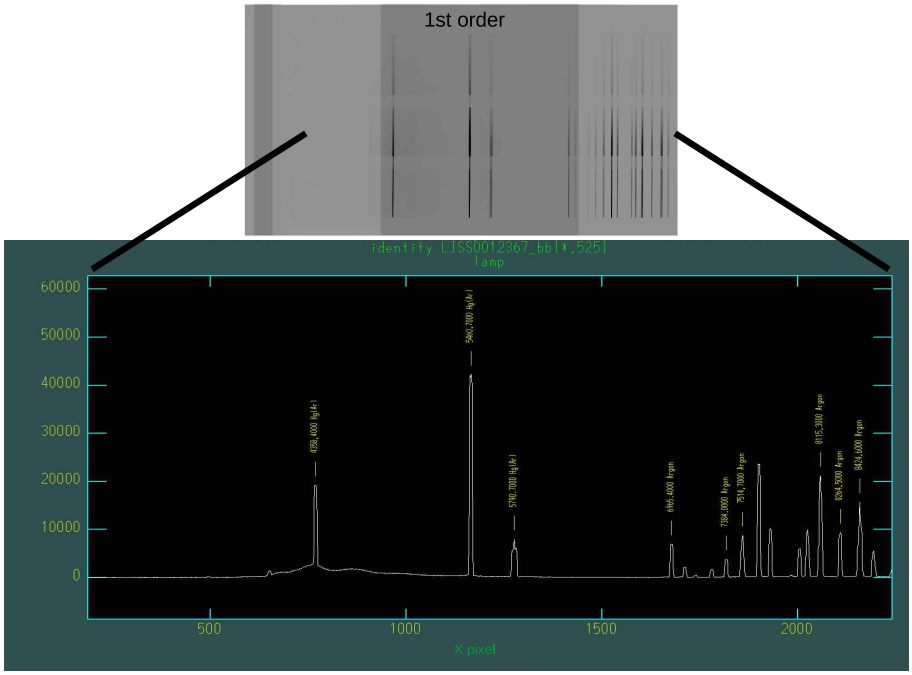

Fig. 8. 低分散グリズム GRISM-H ($R \sim 400$) を用いた場合の分光ランプスペクトル。

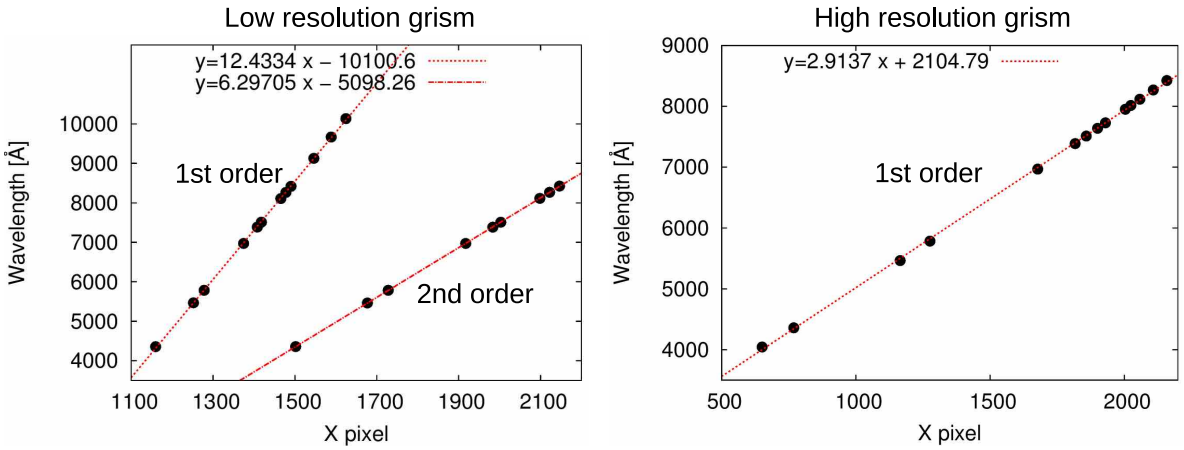

Fig. 9. 超低分散グリズム (左図)、低分散グリズム (右図) それぞれの pixel-波長対応。超低分散グリズムに関しては 2 次光の位置についてもプロットしてある。 1 次回帰直線 (点線) の傾きから、超低分散グリズム 1 次光の分散が約 12.4 Å/pixel、低分散グリズム 1 次光の分散が約 2.9 Å/pixel となっていることが分かる。

- **Guider stage x**： 視野方向のガイダー位置 (0 mm – Home)
- **Guider stage z**： 焦点方向のガイダー位置 (0 mm – Home)

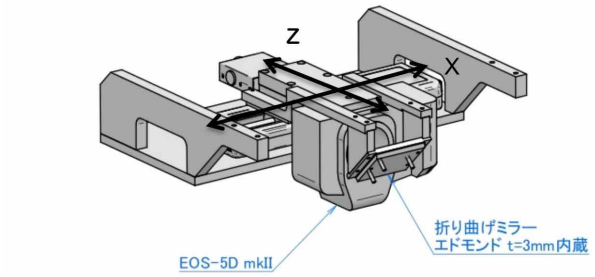

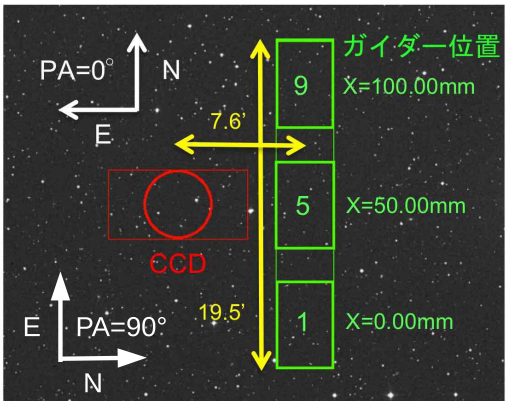

Fig. 10. 左図: オートガイダーを支持する 2 つの自動ステージ; ガイダーカメラ (EOS 5D MkII) の焦点合わせを行う Z 方向ステージ (TSDM60-20) と、視野を変更する X 方向ステージ (SGSP26-100)。 右図: CCD 画像 (赤枠) とオートガイダー画像 (緑枠) の天球面上での位置関係。X 方向ステージの位置 (1 から 9 までの 9 段階の位置を設定できる; 右図参照) を変化させることで視野位置を変えることができる。 右図中の PA は望遠鏡のインストゥルメントローテータ角度を表している。

ステージ (シグマ光機) に支持されている。ガイダーカメラの視野は 5.2 分角 ×3.4 分角であるが、X 方向ステージを動かして視野位置を変化させることで、合計で 19.5 分角 ×3.4 分角の範囲の中からガイド星を探すことができる。Z 方向ステージの位置は、 X 方向ステージ位置に対応して自動的に最適の位置に調整されるようになっている。なお、EOS 5D MarkII の機能的制限から、 オートガイダーの積分時間としては最長 30 秒 (V ∼15mag) までしか選べないことに注意して頂きたい。

オートガイダーを用いた観測を行う際には、オートガイダーの視野を考慮して前もってガイド星を選んでおき、必要ならば望遠鏡のインストゥルメントローテータ角度を調整してガイド星をガイダー視野内に導入してから、ガイダーソフトウェア [6] を起動する (Section 1–5. で述べる GUI から起動できる)。現在のガイダーソフトウェアではガイド星 1 つを用いてトラッキングエラーを補正しているが、今後は複数のガイド星を同時に用いてガイドを行うように改良したいと考えている。

1–4. ファブリ · ペロー狭帯域撮像モード

LISS は本来、Figure 1 にあるように、グリズムを搭載している可動ステージに液晶型エタロン (Scientific Solutions Inc.; フィネス ∼ 6) も搭載できるようになっており、撮像モード、分光モードと同様にファブリ · ペロー狭帯域撮像モードも選択できるように設計されている。実際、ファブリ · ペロー狭帯域撮像モードは過去に北海道大学ピリカ望遠鏡における試験観測時に使用実績があり、Hashiba et al. (2014) では惑星状星雲 M57 の [NII]λ6583、[SII]λλ6716/6731、[SIII]λ9069 の波長域での輝線と連続光のスキャンニング観測の結果が報告されている (R ∼450 at 6563 Å、R ∼330 at 9123 Å)。しかし現在、経年劣化による性能低下が主な原因で、上記のエタロンは LISS から取り外されている。修理を行う予定も現在のところ決定していないため、本稿ではファブリ · ペロー狭帯域撮像モードについては詳しく述べないことにする。

[6] gphoto2 v2.5.2、dcraw v9.26、Image-ExifTool v10.01、IRAF v2.16 を用いたシェルスクリプト

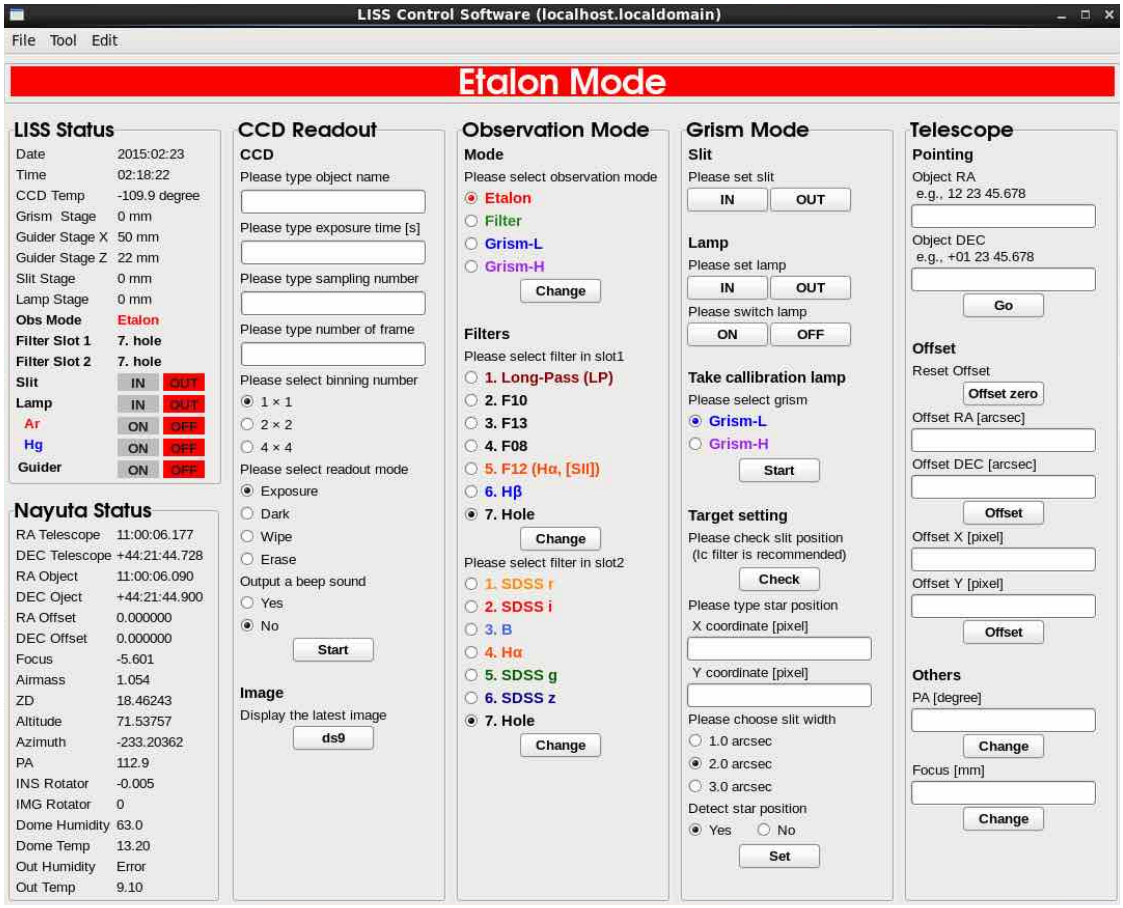

Fig. 11. LISS 制御 GUI (2015 年 2 月時点)。 製作には wxPython を使用している。

1–5. GUI による操作

なゆた望遠鏡において LISS を使用する際には、まずカセグレン可視撮像装置 MINT (尾崎 2005) を取り外し、MINT が接続されていた位置に LISS を搭載することになる。LISS 使用時の望遠鏡側の焦点の切り替え等は、MINT 使用時の設定スクリプトを統合制御計算機 (圓谷 他 2006) 上で実行すればよい。

望遠鏡のポインティングや副鏡 (フォーカス) 位置の調整をはじめとして、LISS の観測モードの切り替えや露光の実行などの操作は、LISS とともに望遠鏡に取り付けられている LISS 制御 PC(Figure 2) 上の GUI から行うことができるようになっている (Figure 11)。電算制御室に設置した LISS 用 PC から、ssh(+X11 転送) によって望遠鏡に取り付けられている LISS 制御 PC にリモートログインし、GUI を立ち上げる。Figure 11 にあるように、撮像 · 分光に必要なパラメータの設定は GUI のメイン画面で行うことができる。さらに左上のタブからガイダー制御 GUI やターゲットビジビリティー表示 GUI 等を呼び出すことができる。

1–6. 効率と限界等級

Figure 12 は標準星の測光によって測定された LISS 測光モードの効率 (大気減光+望遠鏡効率+LISS 光学系ロス+スリットロス+広帯域フィルター透過率を合わせた全透過率)、Figure 13 は標準星の分光によって測定された LISS 分光モードの効率 (大気減光+望遠鏡効率+LISS 光学系ロス+スリットロスを合わせた全透過率)

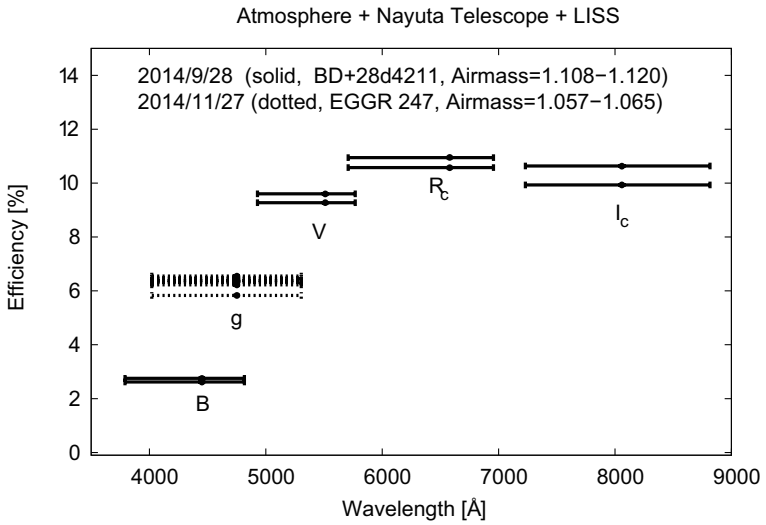

Fig. 12. 2 つの測光標準星 BD+28d4211 (B、V、R_c、I_c バンド; 2014 年 9 月 28 日観測)、EGGR 247 (g バンド; 2014 年 11 月 27 日観測) の観測から求めた、大気+望遠鏡+LISS 光学系ロス+広帯域フィルター透過率を含めた全透過効率。各測定点に付随する横線は各バンドの透過波長域 (FWHM) を表している。

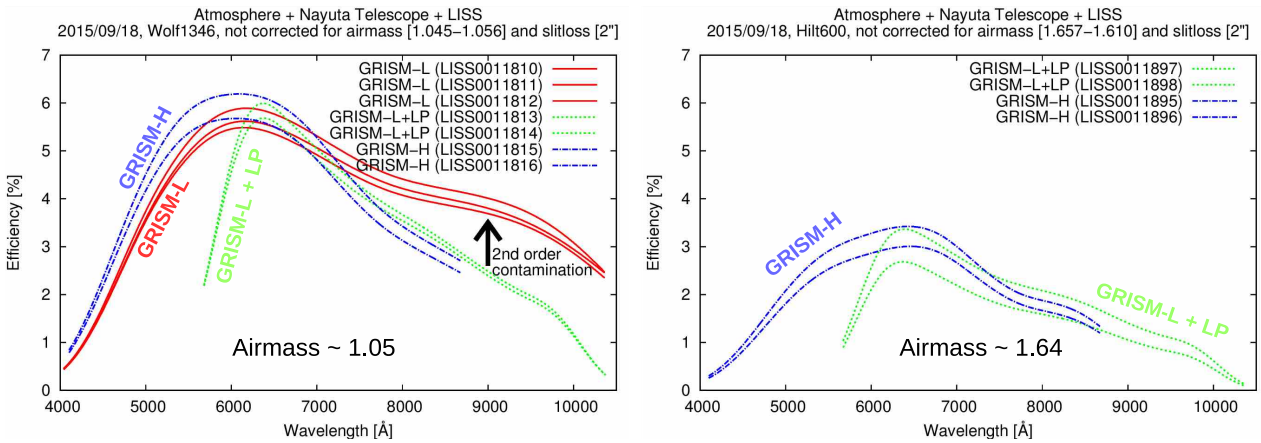

Fig. 13. 2015 年 9 月 18 日に観測した 2 つ分光標準星 (左図は Wolf1346、右図は Hilt600; シーイング FWHM は 2.5-3.0 秒角程度) から求めた、大気+望遠鏡+LISS 光学系ロス+スリットロスを含めた全透過効率。大気減光補正を行っていないため右図では効率が半減している。実線は超低分散グリズムをフィルター無しで使用した場合 (λ >7000 Å で 2 次光が混入)、点線は超低分散グリズムを LP フィルターと共に用いた場合、一点鎖線は低分散グリズムをフィルター無しで用いた場合の効率を表している。

を図示している。

測光モードの効率は、R_c バンドで最も高い効率を示しており、長波長側では高い効率が保たれていることが分かる。短波長側での効率の減少は、短波長側で大きくなる大気減光の影響と、浜松ホトニクス完全空乏型 CCD の量子効率特性の組み合わせによるものだと理解できる。分光モードについては、エアマス値が 1 に近い状態で測定された値 (Figure 13 左) を見てみると、6000 Å 付近で効率のピークを持ち (主にグリズムの回折効率のピークを反映している)、ピークの値は 5-6%程度になっていることがわかる。また、λ=10000Å 付近まで高い効率を保っており、ここに赤外線域で高い量子効率をもつ浜松ホトニクス完全空乏型 CCD の特長が現れている。なお、超低分散グリズム (GRISM-L) をフィルター無しで分光した場合の測定では、$\lambda > 7000$ Å において 2 次光の混入を強くうけている。

これらの透過効率の測定値に基づいて限界等級を評価すると、シーイング FWHM=1.5 秒角、夜光輝度 =20 等/arcsec^2 の仮定のもとで、$R_c = 20.1$ 等 (60 秒積分、S/N=10、1×1 binning)、6000Å のおける超低分散分光で 20.3 等 (1200 秒積分、S/N=10、2 秒角幅スリット、4×4 binning) となり、日本国内の撮像分光装置としては最高レベルの感度を持つことが分かる。

大気減光量についての定量的評価は行っていないが、以下のような報告が参考になる。大気減光について、後藤、松村、尾久土 (1993) は、西はりま天文台 60cm 望遠鏡で 1992 年 7 月 29 日に測定した V-band の天頂における減光量が $A_V = 0.7$ 等であったと報告している。このような大きな大気減光が我々の観測の時にも存在していたと考えると、大気減光を除いた合計効率は 5000 – 6000 Å 付近で 20% (撮像モード)、10% (分光モード) 程度であることになる。

また、Figure 12、Figure 13 に示した測定は、2016 年 1 月に予定 (本稿執筆時) されている主鏡の再蒸着の直前である 2015 年 9 月の観測データに基づいていることにも注意しなければならない。新井 他 (2013) は、なゆた望遠鏡の主鏡、副鏡、第 3 鏡の反射率の測定値を報告しており、可視光域 (6700 Å) における 2013 年 12 月 18 日 (鏡面清掃前) の主鏡の反射率は 68.0±0.4%程度まで落ちていたことが分かっている (同日の副鏡の反射率は 81.9±2.0%)。2009 年 3 月の再蒸着直後の可視光域での主鏡の反射率は 88%程度であった (新井 他 2013) ことから、2016 年 1 月の主鏡再蒸着後には、Figure 12、Figure 13 に示したような合計効率は 1.3 倍程度改善することが期待される。

2. 科学観測成果

以下では、我々LISS 開発グループがこれまでになゆた望遠鏡/LISS を用いて行ってきた科学観測の内容と初期成果について報告する。

2–1. 即時撮像 · 低分散分光追観測による超新星ショックブレイクアウト候補天体の同定

LISS の特長の一つとして、超低分散グリズムの採用によって、波長分解能は犠牲になるものの、非常に高感度の分光観測が可能になっている点を挙げることができる。このような装置の仕様は、比較的暗い ($g > 17$ 等) 超新星の分光同定を、1 時間程度の短時間分光観測で行うことを可能にする。このような LISS の特長を生かす観測として、西はりま天文台なゆた望遠鏡共同利用観測時間を利用して、木曽観測所 1.05-m 木曽シュミット望遠鏡に搭載された広視野カメラ KWFC を用いて 2012 年 4 月から行われている超新星サーベイ Kiso Supernova Survey[7] (KISS; Morokuma et al. 2014) で発見された超新星候補天体の超低分散分光追観測を行ってきた。本観測の最終目的は、KISS で発見されることが期待される重力崩壊型超新星ショックブレイクアウト現象の候補天体 (e.g., Tominaga et al. 2011) を即時撮像 · 分光追観測し、分光同定することである。こ

[7] http://www.ioa.s.u-tokyo.ac.jp/kisohp/KISS/

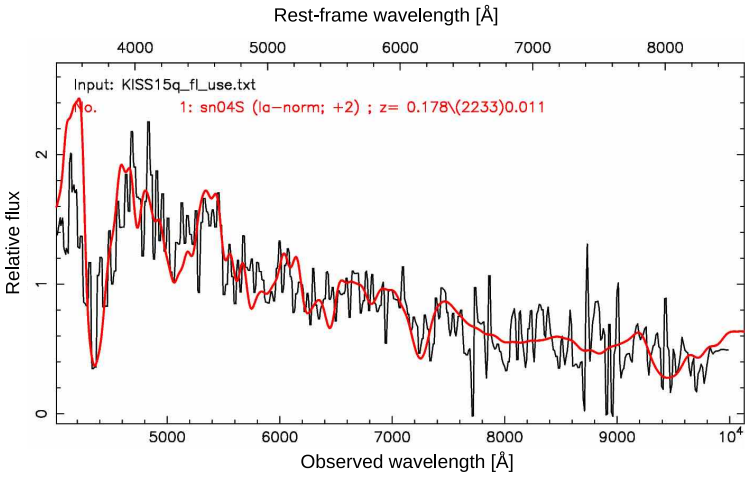

Fig. 14. なゆた/LISS 超低分散分光 ($R \sim 100$、10 分 × 5、2×2 ビニング) によって取得された Ia 型超新星 KISS15q=SN 2015aa ($g \sim 20.5$mag、赤方偏移 ~ 0.18) のスペクトル。SNID code (Blondin and Tonry 2007) によるベストフィットテンプレートスペクトルを重ねてプロットしている。この天体の場合、$\lambda > 7000$Å における 2 次光の混入はフィッティング結果に影響しない。分光観測は 2015 年 5 月 21 日 22 時 20 分-23 時 14 分に行われた。

れまでの KISS の観測ではまだショックブレイクアウト候補天体は見つかっていないが、その他の爆発初期以降の超新星候補天体については、なゆた望遠鏡/LISS の分光観測によって 4 天体の分光同定に成功している[8]。この 4 天体のうち、特に 2015 年 5 月の観測で同定された Ia 型超新星 KISS15q=SN 2015aa ($g \sim 20.5$mag; Morokuma et al. 2015d, 2015e) は、日本国内の望遠鏡で分光同定された突発天体としては最も暗い天体であり、2.0-m なゆた望遠鏡と LISS 超低分散分光の組み合わせによる高感度観測の威力が示された好例となっている (Figure 14)。

2–2. [SII]、[SIII] 狭帯域撮像観測を用いた近傍星形成銀河の電離パラメータの測定

我々は、LISS に搭載されている完全空乏型 CCD の長波長側での感度を活かし、[SIII] $\lambda\lambda$9069、9531 および [SII] $\lambda\lambda$6717、6731 輝線の狭帯域撮像観測を行い、近傍星形成銀河の電離パラメータの測定する研究を進めている。

星形成銀河の電離領域の状態を詳しく理解することは、銀河の形成 · 進化や宇宙再電離を理解する上で重要である。赤方偏移 $z \sim 0-3$ の星形成銀河において、電離パラメータは高赤方偏移になるにしたがって増大する傾向があり (Nakajima et al. 2013, Nakajima et al. 2014)、星形成率、星質量、金属量の関係 (Fundamental Metallicity Relation) に、電離パラメータを加えた四つの物理量が相関関係を示すことが報告されている (Nakajima et al. 2014)。また、宇宙再電離の電離光子源としては星形成銀河内の大質量星がひとつの候補として考えられているが、星形成銀河の宇宙再電離への寄与を考える上で、電離光子が銀河間空間に抜け出せる割合が重要である (e.g., Bouwens et al. 2010). この割合は星間物質の形態 (clumpiness 等) に依存しており、特に電離領域の広がり方や電離状態の空間分布が重要である (e.g., Zastrow et al. 2011)。本研究では電離パラメータに注目し、近傍の星形成銀河の電離パラメータの空間分布を調べる。

[8] KISS14ap=SN 2014ec (II 型; Morokuma et al. 2015a)、KISS14an=SN 2014ed (Ia 型; Morokuma et al. 2015b); KISS15a=SN 2015E (Ia 型; Morokuma et al. 2015c); KISS15q=SN 2015aa (Ia 型; Morokuma et al. 2015d, 2015e)

電離パラメーターは単位ガス密度あたりの平均電離光子フラックスとして定義され、電離状態と関係する量である。観測的には同じ元素についての異なる電離段階の輝線比、例えば [OIII]λ5007/[OII]λ3727 や [SIII]$\lambda\lambda$9069、9532/[SII] $\lambda\lambda$6717、6731 を用いて推定する (Kewley & Dopita 2002)。本研究では LISS を用いて [SIII] 及び [SII] 輝線の狭帯域撮像を行い、[SIII]/[SII] の輝線比を用いて電離パラメータを推定する。[OIII]/[OII] 輝線比が電離パラメータだけでなく金属量に依存するのに対し、[SIII]/[SII] の輝線比は金属量への依存性が小さいため、 [SIII]/[SII] の輝線比を測定することによって金属量と独立に電離パラメータを推定できるという利点がある (Kewley & Dopita 2002)。狭帯域フィルターを用いた撮像観測を行うことで、通常のスリット分光とは異なり、銀河内での電離パラメータの空間分布を調べることができる。さらに、LISS の狭帯域フィルターを用いた Hα、Hβ の狭帯域撮像観測を並行して行うことで、Hα/Hβ 輝線比からダスト減光を求めることができるため、 空間分解された局所的な電離パラメータとダスト減光の分布などの局所的な物理量との関係を調べることが可能となる。

先行研究 (Zastrow et al. 2013) では、[SII] と [SIII] の輝線を用いて、6 つの南天の近傍星形成銀河の電離領域の性質が調べられている。これらの銀河には、[SIII] の放射領域が [SII] のものと同程度まで広がっている、すなわち電離光子に対して光学的に薄いものと、[SIII] が銀河が広がっておらず、銀河から遠ざかるにつれて高い電離状態から低い電離状態に遷移する光学的に厚いものの両方が存在することが知られている。しかし、これらの性質が銀河の他のどのような性質と関係があるのか観測的にははっきりとはわかっていない。そこで本研究では、基本的な性質がよく調べられた近傍の星形成銀河の電離パラメータの空間分布を調べている。2014 年後期になゆた望遠鏡の公募観測として採択された観測時間では、近傍星形成銀河 M82 について [SIII]、[SII] の狭帯域撮像データを半分程度取得することができた。この観測時間で得られたデータから、予備的な結果ではあるが、[SII]、[SIII] のマップが得られた (Figure 15)。[SII] は銀河円盤の短軸方向に広がっている一方、[SIII] は中心に集中していることが見て取れる。2015 年後期公募観測において、積分時間が不足している分の [SII]、[SIII] の狭帯域撮像、また、Hα、Hβ の狭帯域撮像観測を行い、ダスト減光の補正やダスト減光分布との関係を議論していく予定である。さらに 2015 年前期の公募観測における観測時間では、近傍星形成銀河 NGC7714 の狭帯域撮像観測を、予定されていた積分時間に到達することはできなかったものの、[SIII]、[SII]、Hα、Hβ の 4 つすべての輝線について行うことができた。こちらの天体については現在データ解析中である。

2–3. 矮小 Seyfert 銀河 NGC4395 の多バンドモニタリング観測による 「熱的再放射モデル」の検証

ブラックホール降着円盤起源であると考えられている活動銀河中心核 (AGN) の可視光放射は、数日のタイムスケールで著しい光度変動を示すことが広く知られているが、変動を引き起こすメカニズムはいまだ謎に包まれている (e.g., Kokubo et al. 2014, Kokubo 2015)。本観測では、AGN の紫外-可視域の光度変動を説明するモデルとして「熱的再放射モデル」に着目する (例えば Cackett et al. 2007)。「熱的再放射モデル」では、ブラックホール極近傍の高温コロナ起源の高エネルギー光子によって降着円盤表面が加熱されている状況を考える。すなわち、高エネルギー光子放射量の激しい変動に伴って、高エネルギー光子に照らされている降着円盤表面の温度が時間変化することにより、可視-紫外域の光度変動が生じる、と考える。「熱的再放射モデル」における検証可能な予言の一つとして、円盤内縁部を起源とする短波長側の変動に対して、円盤外縁部を起源とする長波長側の変動が遅れて生じる、というものがある。本観測では、矮小 Seyfert 銀河 NGC 4395 (D =4.3 Mpc、赤方偏移 $\sim$0.001; Thim et al. 2004, Peterson et al. 2005) に対して密な V、i、z-band の 3 バンド光度曲線を取得することで、バンド間の変動の遅延時間を測定し、「熱的再放射モデル」の予言との比較を行うことで、AGN 可視光放射メカニズムに制限を与えることを目指している。

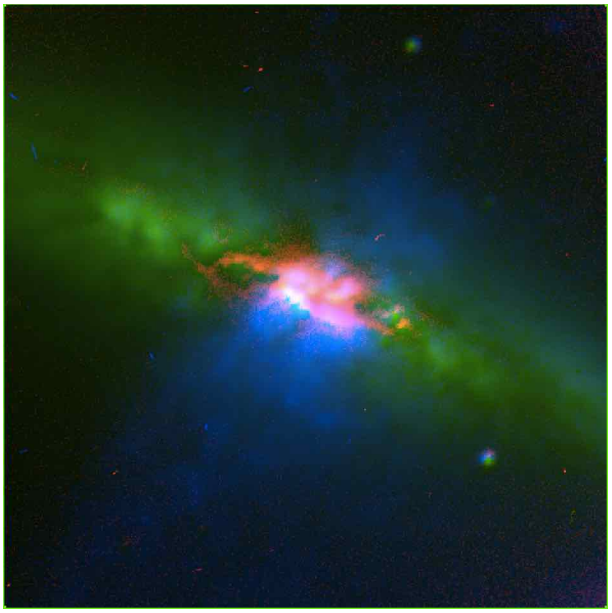

Fig. 15. 2014 年後期公募観測で得られた M82 の 3 色合成図。青が [SII]、赤が [SIII] で、0-2×10^{-15} erg/s/cm^2/$arcsec^2$ の範囲で平方根スケールで表示した。緑は 7000 Å 付近の連続光である。図の一辺は 3 分角に相当する。

これまでの先行研究から、NGC 4395 は数時間の間に 0.05 等程度の可視光度変動を示すことがわかっている (e.g, Minezaki et al. 2006)。なゆた/LISS を用いた本観測では、NGC 4395 を 1 晩にわたって、フィルターを交換しながら連続的に測光観測を行うことを提案した。これまでに、なゆた望遠鏡公募観測時間として、超新星分光観測 (Section 2–1.) とのシェアで、2015 年 5 月 17 日から 5 月 22 日の間の 0.75 夜 ×2 を割り当てられた。しかし、2015 年 5 月の観測ラン中は天候がすぐれず、予定していたような 1 晩 7-8 時間の多バンドモニタリング観測を行うことができなかった。Figure 16 には、データを取得できた時間帯における NGC 4395 の V-band と z-band の光度曲線 (NGC 4395 と近傍参照星とのフラックス比) を図示している。Figure 16 から明らかなように、今回の観測では残念ながら NGC 4395 の多バンド光度変動を捉えることができなかった。ただし、本観測によりなゆた/LISS を用いることによって (天候が良ければ) 十分な精度の測光値が得られることを確認できたので、次回のなゆた望遠鏡公募観測でも同様の観測を提案していきたいと考えている。

3. 今後の展望

最後に、LISS の今後の予定、展望について述べておく。

科学観測の予定としては、現在行っている狭帯域フィルター撮像観測による近傍星形成銀河の電離パラメータの測定、近傍 AGN の多バンド/低分散分光モニタリング観測などを継続していく予定である。また、系外惑星大気の組成を調べる観測的手法である transmission spectroscopy の実施についても、兵庫県立大学天文科学センタースタッフとの共同研究の形で検討を進めている。Transmission spectroscopy は、トランジットを起こしている天体を多バンド、あるいは分光観測によりモニタリングし、各波長でのトランジット光度曲線のプロファイルの違いから系外惑星大気の組成を調べる手法である (e.g., Bean et al. 2010, Gibson et al. 2013, Narita et al. 2015, and references therein)。LISS では、将来的にはマルチスリットマスクを制作してトランジット天体と複数参照星の同時分光モニタ観測による transmission spectroscopy を行うことを目指し

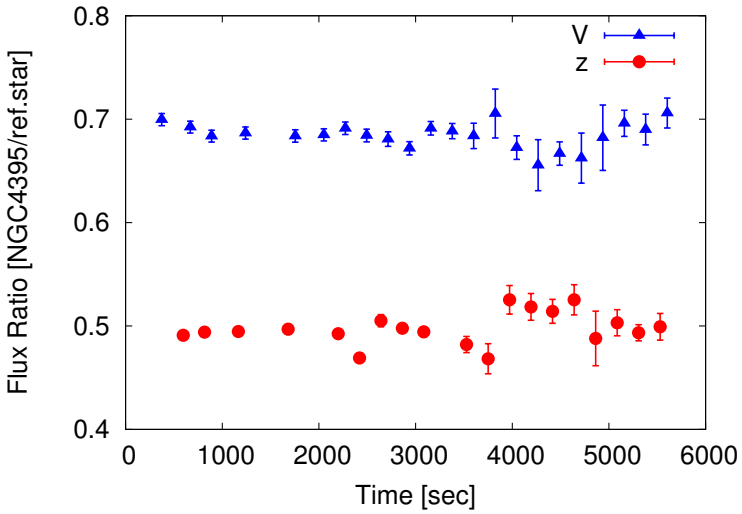

Fig. 16. なゆた/LISS で取得された、NGC 4395 と近傍参照星 [$\alpha = 12^h25^m50^s.91$、$\delta = +33°33'10".1$ (J2000)] とのフラックス比で表現した NGC 4395 の V-band と z-band の短時間スケールの光度曲線。各データ点の積分時間は 60 秒であり、V-band の最初の測光の開始時点が 2015 年 5 月 21 日 23 時 59 分 34 秒 (日本標準時) に対応している。後半では天候が崩れたため測光エラーが大きくなっている。

ているが、その前段階として本計画の実現可能性をテストするため、2015 年 12 月には専用の 10 秒角幅のロングスリット (Figure 17) を作成してトランジット天体 XO-3b と参照星 TYC 3727-339-1 の同時分光モニタを行うことを予定している。

以上、本稿で述べたように、2014 年 7 月からなゆた望遠鏡に搭載し観測/改良を行ってきた LISS は、現在では定常的に科学観測を行える安定した装置になっている。2.0-m なゆた望遠鏡との組み合わせにより、LISS は 現在日本国内で使用できる可視分光器 (ただし低分散) としては最も高感度の装置になっている。LISS は 2015 年度以降、PI 装置として西はりま天文台公募観測に供されており [9] 、LISS 開発メンバー以外の方々からの観測提案も受け入れ始めている。

謝辞

西はりま天文台のスタッフの皆様には、なゆた望遠鏡の使い方をご指導いただくのみならず、LISS 開発グループの天文台滞在及び観測ラン毎の LISS の望遠鏡への取り付けに際しては多大なるご協力をいただきました。ここに記して深く感謝致します。また、本研究は JSPS 科研費の助成を受けたものです。

《参考文献》

Bean et al. 2010, Nature, 468, 669

Blondin and Tonry 2007, ApJ, 666, 1024

[9] http://www.nhao.jp/ openuse/openuse.html

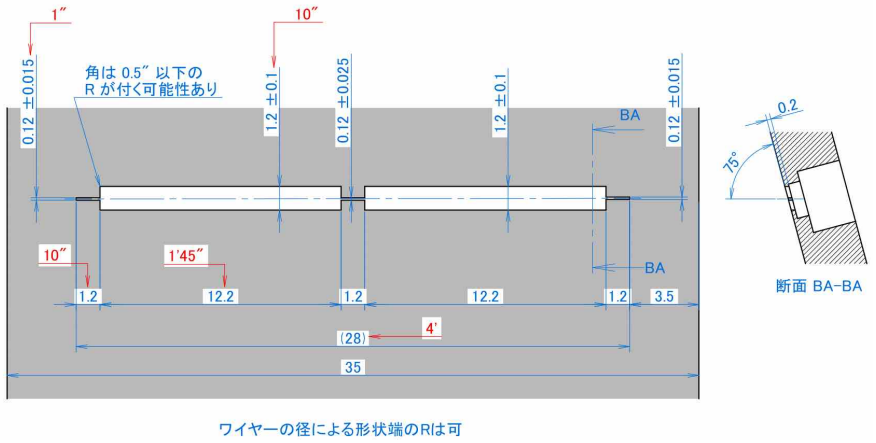

Fig. 17. 2015 年 12 月搭載予定の、系外惑星トランジット観測用スリット。ロングスリット上にターゲットと参照星を同時に導入し、分光する。シーイング変化によるスリットロスを低減するため、10 秒角のスリット幅を採用している。波長較正用に両端と中央に 1 秒角幅の領域を作っている。

Bouwens et al. 2010, ApJL, 708, L69

Cackett et al. 2007, MNRAS, 380, 669

Doi et al. 1998, SPIE, 3355, 646

Gibson et al. 2013, MNRAS, 428, 3680

Hashiba et al. 2014 SPIE, 9147, 2

Jones et al. 2013, A&A 560, 91

Kamata et al. 2010, SPIE, 7742, 29

Kewley & Dopita 2002, ApJS, 142, 35

Kokubo et al. 2014, ApJ, 783, 1, 46

Kokubo 2015, MNRAS, 449, 1, 94

Minezaki et al. 2006, ApJ, 643, 5

Morokuma et al. 2014, PASJ, 66, 114

Morokuma et al. 2015a, Central Bureau for Astronomical Telegrams, 4056, “Supernova 2014ec in UGC 6109 = PSN J11023520+5035094”

Morokuma et al. 2015b, Central Bureau for Astronomical Telegrams, 4057, “Supernova 2014ed”

Morokuma et al. 2015c, Central Bureau for Astronomical Telegrams, 4053, “Supernova 2015E”

Morokuma et al. 2015d, The Astronomer’s Telegram, 7562, “KISS: Discovery and Spectroscopic Classification of a Type Ia Supernova KISS15q”

Morokuma et al. 2015e, Central Bureau for Astronomical Telegrams, 4172, “Supernova 2015aa”

Nakajima et al. 2013, ApJ, 769, 3

Nakajima et al. 2014, MNRAS, 442, 900

Narita et al. 2015, J. Astron. Telesc. Instrum. Syst. 1(4), 045001

Noll et al. 2012, A&A, 543, 92

Peterson et al. 2005, ApJ, 632, 799

Sako et al. 2012, Proc. SPIE, 8446, 6

Thim et al. 2004, AJ, 127, 2322

Tominaga et al. 2011, ApJS, 193, 20

Zastrow et al. 2011, ApJL, 741, L17

Zastrow et al. 2013, ApJ, 779, 76

新井, 高木, 高橋, 本田, 森鼻, 伊藤 2013, Bull. Cent. Astron. Univ. Hyogo, 1, 11-16

尾崎 2005, Annu. Rep. Nishi-Harima Astron. Obs. 15, 6-14

五藤, 松村, 尾久土 1993, Annu, Rep. Nishi-Harima Astron. Obs., 3, 37-40

圓谷, 坂元, 尾崎, 高根, 井美, 江崎, 坂本, 西野, 森田, 三木, 倉津 2006, Annu. Rep. Nishi-Harima Astron. Obs. 16, 18-34

Infrared Doppler instrument (IRD) for the Subaru telescope to search for Earth-like planets around nearby M-dwarfs

Takayuki Kotani*[a], Motohide Tamura[a,b], Hiroshi Suto[a], Jun Nishikawa[a,c], Bun'ei Sato[d], Wak Aoki[a,c], Tomonori Usuda[a,c], Takashi Kurokawa[a,e], Ken Kashiwagi[e], Shogo Nishiyama[f], Yuji Ikeda[g], Donald B. Hall[h], Klaus W. Hodapp[h], Shane Jacobson[h], Jun Hashimoto[i], Jun-Ichi Morino[a], Yasushi Okuyama[e], Yoichi Tanaka[e], Shota Suzuki[e], Sadahiro Inoue[e], Jungmi Kwon[b], Takuya Suenaga[a], Dehyun Oh[c], Haruka Baba[a,c], Norio Narita[a], Eiichiro Kokubo[a], Yutaka Hayano[j], Hideyuki Izumiura[k], Eiji Kambe[k], Tomoyuki Kudo[j], Nobuhiko Kusakabe[a], Masahiro Ikoma[b] ,Yasunori Hori[l], Masashi Omiya[a], Hidenori Genda[d], Akihiko Fukui[k], Yuka Fujii[d], Olivier Guyon[j], Hiroki Harakawa[a], Masahiko Hayashi[a], Masahide Hidai[m], Teruyuki Hirano[d], Masayuki Kuzuhara[d], Masahiro Machida[n], Taro Matsuo[o], Tetsuya Nagata[o], Hirohi Onuki[a], Masahiro Ogihara[p], Hideki Takami[a], Naruhisa Takato[j], Yasuhiro H. Takahashi[a], Chihiro Tachinami[d], Hiroshi Terada[a], Hajime Kawahara[b], Tomoyasu Yamamuro[q], IRD team

[a]National Astronomical Observatory of Japan, 2-21-1 Osawa, Mitaka, 181-8588, Japan
[b]The University of Tokyo, Hongo, Tokyo 113-0033, Japan
[c]GUAS, 2-21-1, Osawa, Mitaka, Tokyo, 181-8588, Japan
[d]Tokyo Institute of technology, Meguro, Tokyo 152-8550, Japan
[e]Tokyo University of Agriculture and Technology, Koganei, Tokyo 184-8588, Japan
[f]Miyagi University of Education, 149, Aramaki-aza-Aoba,Aobaku, Sendai, 980-0845, Japan
[g]Photocoding, 460-102, Iwakura Nakamachi, Sakyo-ku, Kyoto 606-0025, Japan
[h]Institute for Astronomy, University of Hawaii, 640 North A'ohoku Place, Hilo, HI 96720, USA
[i]University of Oklahoma, 660 Parrington Oval, Norman, OK 73019, USA
[j]Subaru Telescope, 650 North A'ohoku Place, Hilo, HI 96720, USA
[k]OAO, National Astronomical Observatory, Okayama 719-0232, Japan
[l]University of California Santa Cruz, 1156 High Street, Santa Cruz, CA 95064, USA
[m]Tokai university, 4-1-1 Kitakaname, Hiratsuka-shi, Kanagawa, 259-1292 Japan
[n]Kyusyu University, Fukuoka, 812-8581, Japan
[o]Kyoto University, Kitashirakawa, Kyoto 606-8502, Japan
[p]Nagoya University, Furo-cho, Nagoya 464-8601, Japan
[q]Optocraft, 101, 3-16-8, Higashi-Hashimoto, Midori-ku, Sagamiha, 252-0144, Japan

ABSTRACT

We report the current status of the Infrared Doppler (IRD) instrument for the Subaru telescope, which aims at detecting Earth-like planets around nearby M darwfs via the radial velocity (RV) measurements. IRD is a fiber-fed, near infrared spectrometer which enables us to obtain high-resolution spectrum (R~70000) from 0.97 to 1.75 μm. We have been developing new technologies to achieve 1m/s RV measurement precision, including an original laser frequency comb as an extremely stable wavelength standard in the near infrared. To achieve ultimate thermal stability, very low thermal expansion ceramic is used for most of the optical components including the optical bench.

Keywords: exoplanet, infrared Doppler, M dwarf, laser frequency comb, high resolution spectrometer

* t.kotani@nao.ac.jp; Tel; +81 422 34 3900 (3249)

Ground-based and Airborne Instrumentation for Astronomy V, edited by
Suzanne K. Ramsay, Ian S. McLean, Hideki Takami, Proc. of SPIE Vol. 9147,
914714 · © 2014 SPIE · CCC code: 0277-786X/14/$18 · doi: 10.1117/12.2055075

1. INTRODUCTION

IRD is a near-infrared (NIR) high dispersion spectrograph being developed for the Subaru Telescope. It aims at achieving measurement precision of 1 m/s in radial velocity (RV) and thus will be a powerful instrument for exoplanet searches. Our main targets using IRD are late-M dwarfs. Focusing such planet searches on low mass stars offers several merits. The lower mass of these stars naturally causes a much stronger dynamical response to any orbiting planet and their lower luminosity brings the potentially habitable zone closer to the star, making planets in shorter period orbits more interesting for the search of life outside our own solar system. With the RV precision of 1 m/s, we can expect to detect Earths and Super-Earths in habitable zone around such low-mass stars. To realize the planet searches around low mass stars, a high spectral resolution instrument in NIR is needed because the flux distribution of late-M dwarfs has the peak in infrared wavelength regions (~1.0-1.8 μm), in contrast that they are very faint in the visible. The project started in 2010 and the instrument specifications were fixed after the conceptual design review held in 2012. The first light is planned in 2015. In this paper, the science case and survey plan is described in Section 2. The science case and survey plan, the expected performance is described in Section 3 and 4. The instrument description is shown in Section 5.

2. SCIENCE CASE

Although large number of exoplanets has been already discovered by both space and ground-based instruments (e.g. Kepler[1], HARPS[2], etc), our knowledge of the exoplanets around low-mass stars is still limited. Therefore, we do not know the variety of the planetary systems in our Galaxy in which low-mass stars are the main component. In addition, Kepler mission discovered many low-mass exoplanets but their distances are relatively large and therefore the follow-up of these interesting targets are very limited with the current instruments. Considering these situation, a survey of a sample of nearby M stars for Earth-mass planets is required. Once any Earth-mass planets have been discovered around nearby M stars, they will also be the best targets for the future direct imaging and characterization with the 30-m class telescopes with dedicated instruments, for example SEIT[3].

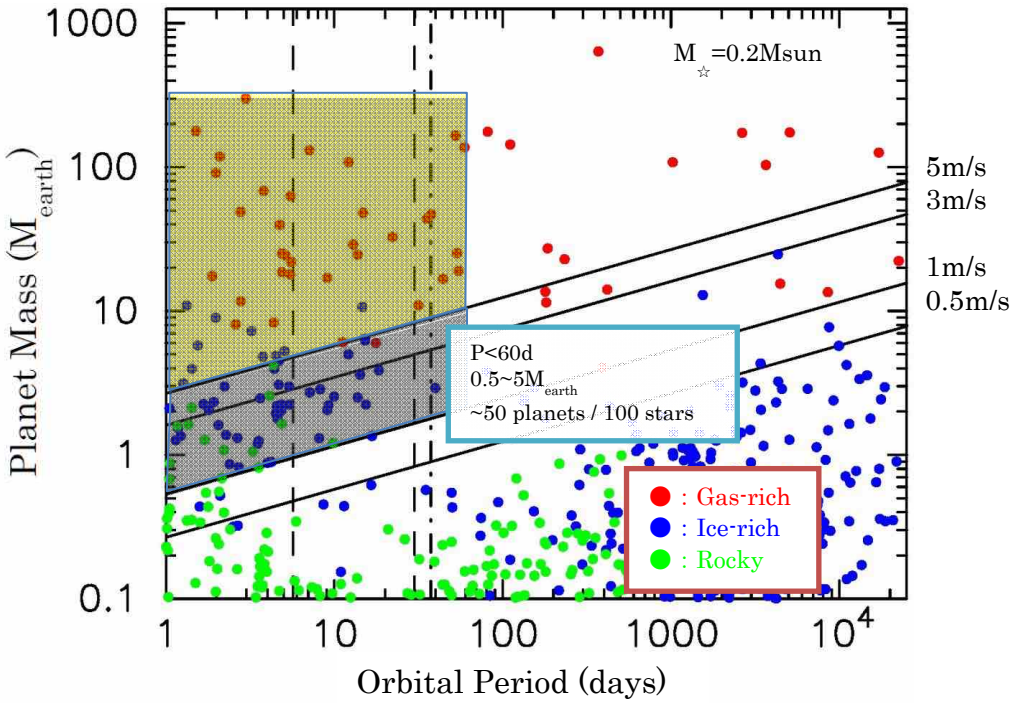

Figure 1. Planetary mass-semimajor axis distributions of extrasolar planets around 0.2 M_{sun} M dwarfs from population synthesis simulation (courtesy of Y. Hori). Detection limits with various RV measurement precisions are also plotted.

Survey of low-mass stars will also give us rich information for understandings of planet formation and evolution, in particular, for terrestrial, habitable planets. First, systems with no gas giants may be common, while Cool Jupiter (CJ)

mass planet harboring systems also exist. In the solar system, the presence of CJs should have played key roles in the accretion and dynamics of the terrestrial planets and also the habitability of the Earth through, for example, delivery of volatiles and organics. Thus, by comparing systems with and without CJs, we expect to appreciate the roles of CJs in forming terrestrial planets and making them habitable. These facts mean that we will be able to calibrate theories by comparing with observations and thereby develop accurate theories as to the formation and evolution of terrestrial planets. We simulate planetary growth directly by N-body simulations from planetesimals to planets. Such an approach is doable and crucial in building terrestrial planets around M stars. Adding to the mass-period plane, we synthesize planet populations on the density-period and density-mass planes (Figure 1). This enables us to improve theories from several perspectives by making use of observational results from Doppler and transit measurement.

3. TARGET STARS AND SURVEY PLAN

IRD survey focuses on late-M dwarfs, because early M dwarfs can be accessed with optical RV instruments. Furthermore, large aperture of the Subaru telescope can be a unique advantage for targeting faint late M dwarfs. We selected late M dwarfs with small rotational velocity and low stellar activity from available catalogs. Candidate target catalog includes about 250 stars which have J magnitude of 7-11.5 mag, stellar mass of 0.08-0.3 Msun, spectral type of M4-M9 (Figure 2). Further selection will be done by observations of stellar rotation period and activity with medium resolution spectroscopy and photometric variability measurements. After the careful selection, best 100 stars will be the final survey targets. To evaluate feasibility of our survey plan, we carried out survey simulation assuming that a total ~ 170 nights are available for 5 years. From the simulation, we found that ~ 40 Earth-mass planets including some of them in their habitable zone, as well as many Super-Earths and Neptunes.

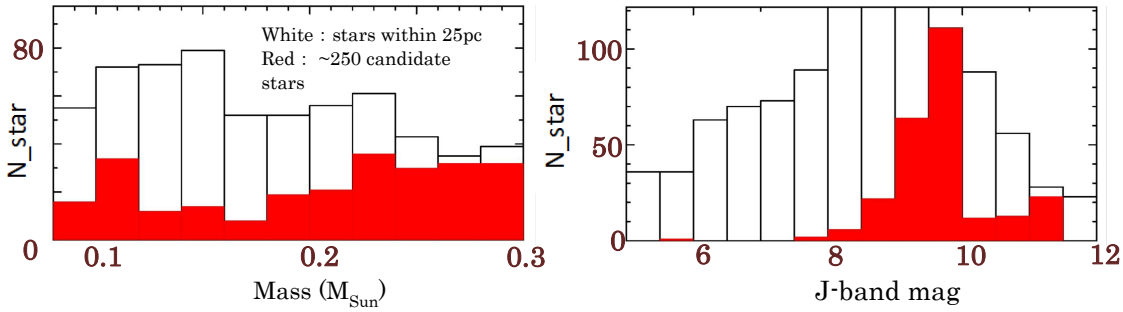

Figure 2. Distributions of stellar mass, J-band magnitude of candidate M-dwarfs (Courtesy of M. Omiya).

4. EXPECTED PERFORMANCE

To estimate achievable RV measurement precision, we carried out numerical simulations, taking account of an image quality of a spectrometer, photon noise, stellar rotational velocity, atmospheric transmission. We used PHOENIX code[5] to extract high-resolution spectrum of early to late type M dwarfs. Errors arising from modal noise, laser frequency comb, and instability of the instrument profile, etc are not taken into account for this simulation. S/N ratio of 200 for each pixel in simulated spectrum around 1μm is assumed. Figure 3 shows the simulation results. For a star with slow rotation period, IRD will be able to achieve 1 m/s precision, but as expected, a rapid rotator is a difficult target for precise RV measurement. It is interesting to see that RV precision of a late-type star relatively does not suffer from rapid rotation. IRD will focus on a late-type star as a survey target, therefore in terms of rotational velocity of a star is not a critical problem.

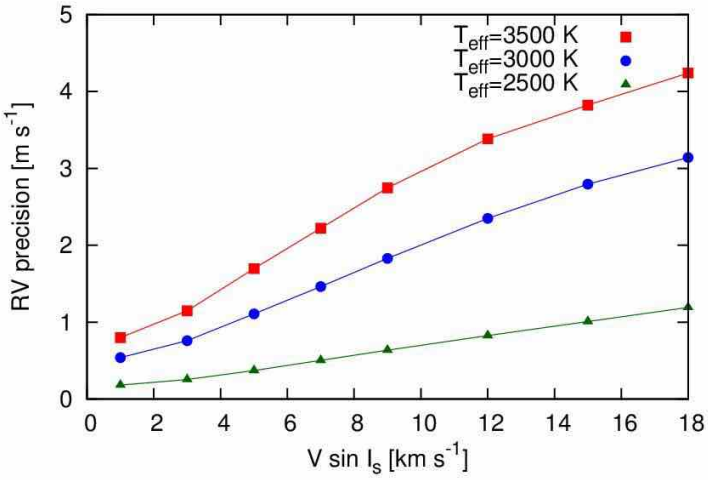

Figure 3. RV measurement precisions of early to late M dwarfs at various rotational velocities. S/N ratio of 200 for each pixel in simulated spectrum around 1.0 μm is assumed (courtesy of T. Hirano).

5. INSTRUMENT DESCRIPTION

The spectrometer is designed to cover wavelengths from 0.97 to 1.75 μm with a 70,000 spectral resolution and 3-pixel sampling. The instrument has a fore-optics part for star-light and laser frequency comb injection into fibers, and a backend spectrometer optics, detector unit. Table 1 shows the summary of the specifications of IRD. Figure 4 shows general schematic view of the instrument.

Table 1. Specifications of IRD instruments

Wavelength coverage	0.97-1.75 μm
Spectral resolution	70,000 (3-pixel sampling)
Detector	4096 × 4096 pixels HgCdTe (HAWAII4RG-15)
Detector controller	ASIC (Rockwell "sidecar")
Pixel scale	0.09 arcsec/pixel
Slit	0.27 arcsec × 2.2 arcsec
Fiber-fed	Star + Laser frequency comb
Dispersive optics	High Blaze angle Echelle grating + VPH-gratings (cross-disperser)
Detector temperature	~60K
Optics temperature	~180K
Cooler	2× Pulse-tube crycoolers
Platform	Subaru IR Nasmyth focus (Fiber injection) and coudé room (Spectrometer)
Adaptive optics	188-elements curvature sensing AO for tip/tilt correction

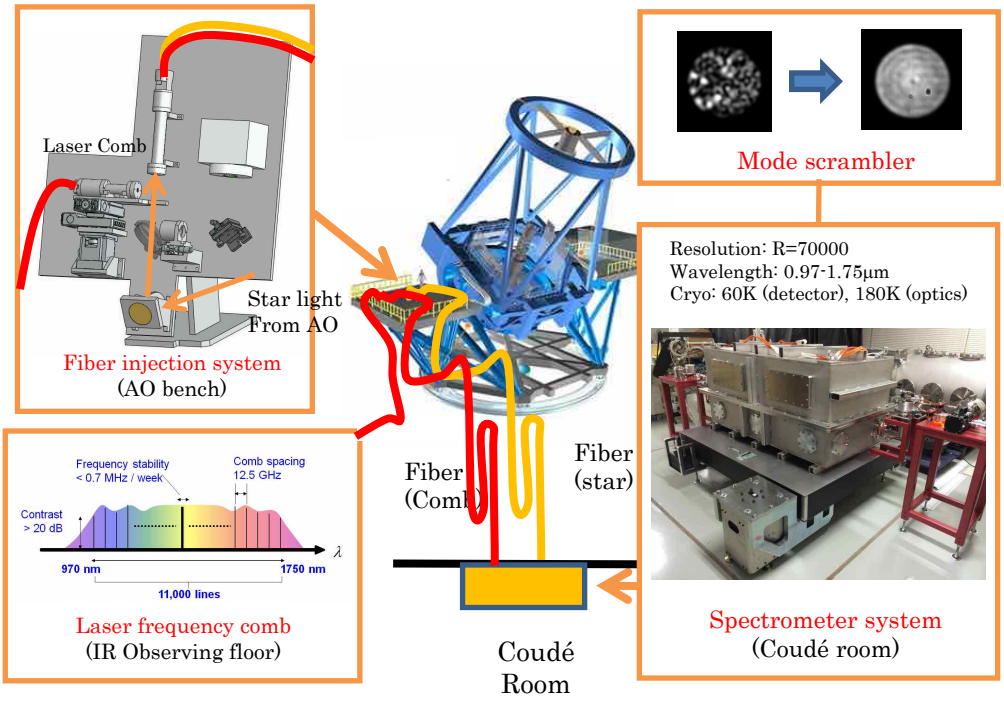

Figure 4. Schematic view of the IRD instruments.

5.1. Fiber injection module

A fiber injection module is located at the infrared Nasmyth platform to inject star light from Subaru's Adaptive Optics (AO) system[4] and a laser frequency comb into two fibers (Figure 5). The injection module is mounted on a motorized translation stage on the AO bench and it can be easily inserted into light path from AO, which is important to conduct efficient survey observation. Light coupling to a fiber is done on the image plane, not the pupil plane employed for some fiber-feed spectrometers (e.g. HARPS, etc.). The advantage of the image plane coupling is a good mode scrambling effect, which is especially important for a planet search NIR spectrometer. The disadvantage is a relatively low fiber coupling efficiency compared to the pupil plane coupling in general, but thanks to the AO system, 0".5 FOV of a 60 μm core fiber matches with an AO corrected image size, hence high coupling efficiency is possible. The F ratio of the input beams from AO and a laser comb fiber is converted from F/12.9 to F/3.33. Such a fast beam can mitigate focal ratio degradation (FRD) of a multi-mode fiber (MMF). Light of a laser frequency comb emerged from a MMF coming from observing floor in the telescope dome, is sent to a F-conversion lens system by a motorized pick-off mirror at the AO focus, after matching the F ratio to that of star light (F/12.9). Star light and a laser comb are injected into two fibers, separated by 18" at the focus of the F-conversion lens system. The pick-off mirror and the laser comb extraction optics are mounted on a motorized translation stage. This enables us to inject star and laser comb light into whichever two MMFs. Precise star light coupling into a fiber is important for high coupling efficiency. It is also crucial to prevent a drift of an image position which may introduce fake RV shift, if mode scrambling is not enough. Therefore, we use an NIR camera (Xeva 1.7-640-25, Xenics) to monitor an image position for real-time feedback correction by AO. The IR camera has 10" diameter FOV centered at each fiber and it can image star light or a laser comb reflected on the fiber head and their adjacent areas which is polished stainless steel plate. The fiber injection module can also inject star light into a single-mode fiber (SMF) which is located 3" from one of MMFs. To utilize a SMF is an attractive option because a SMF has no modal noise above the cut-off wavelength. On the other hand, it is difficulty to realize high coupling efficiency to a SMF if wavefront error (WFE) of the input beam is large. A SMF can be used for a very bright star, or the Subaru Coronagraphic Extreme AO (SCExAO) will enable us to achieve very high efficiency start light injection to a SMF[6]. A laboratory experiment has recently demonstrated high coupling efficiency.

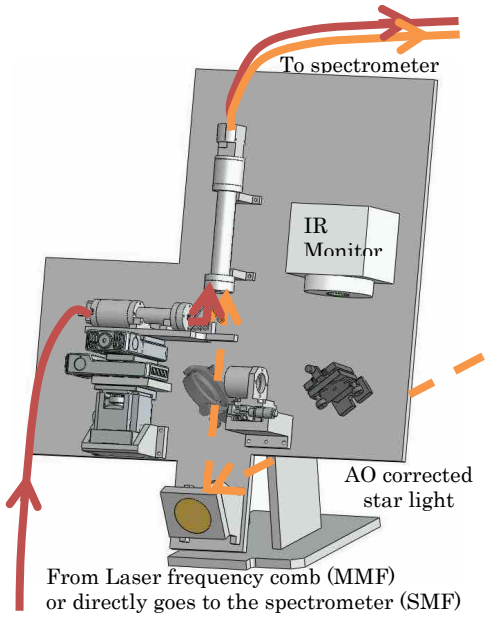

Figure 5. Fiber injection module mounted on a motorized translation stage on the AO bench.

5.2. Spectrometer

The spectrometer design is somewhat classical, i.e. it incorporates a high-blaze angle Echelle grating, collimator mirrors, a cross disperser grating and a camera lens system, and a 2D array detector. Figure 6 shows a top-view of the spectrometer system, including the ray-tracing model and the optical bench. Figure 7 shows the spot diagram and the echellogram of this optical design. The squares in the figure correspond to the 3-pixel detector size (45μm), which is similar to a slit width (~ 0.27"). The image size is mostly smaller than 3-pixels and it satisfies the requirement in most case. Thanks to a large format Hawaii4-RG detector, all spectrum from 0.97- 1.75 μm can be measured simultaneously.

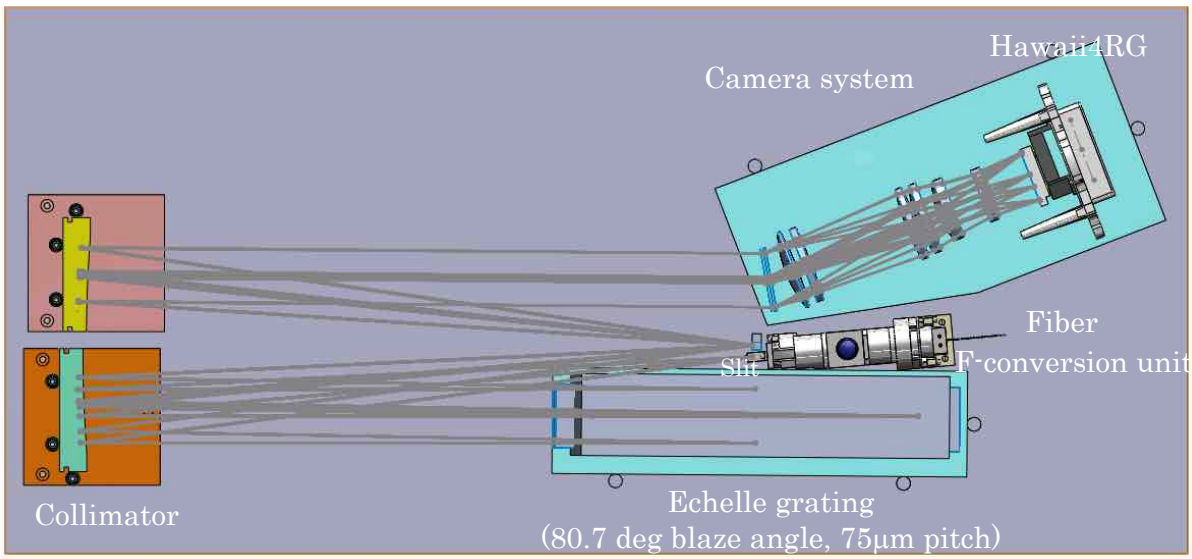

Figure 6. Top view of the spectrometer optics and the optical bench.

The spectrometer is composed of four parts: a fiber-feed system, a collimator optics, Echell and VPH cross-disperser grating, and a camera - detector system. These are all enclosed in a vacuum chamber and are cooled to ~ 180K (optics) and 60K (detector) for thermal background and dark noise reduction. The vacuum chamber will be placed in a temperature controlled coudé room of the Subaru to ensure a stable temperature environment.

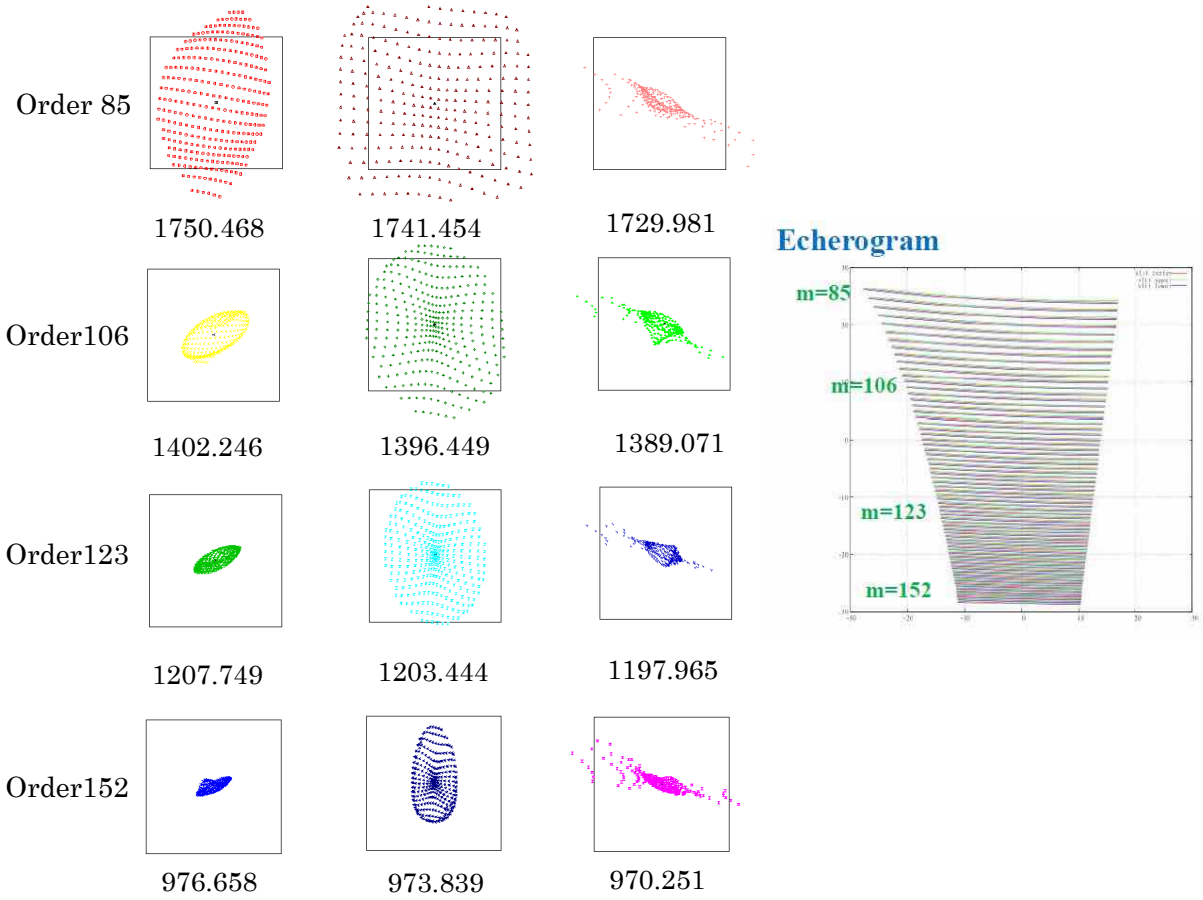

Figure 7. Left: Spot diagram of the optical design at some representative orders and wavelengths (shown in the bottom of the each panels). Right: Echellogram from 0.97-1.75μm (order 85 to 152). The rectangular frame corresponds to the size of Hawaii4-RG.

1) **Fiber-feed system:** 2 MMFs (60μm core OFS F8950) and 2 SMFs (Thorlabs 980HP) are introduced into the chamber by using a vacuum feed-through connector. In the chamber, the start light and the laser comb light are emerged from a linear array of MMFs and SMFs with 250 μm spacing. We can select any two of those as a star and a laser comb fiber (either MMF-MMF or MMF-SMF or SMF-SMF). The beams emerged from the fibers are imaged on a slit after F-conversion (3.33 to 12.65). The slit has 0".27 width × 2".2 long and the slit width corresponds to 64% of the size of the re-imaged 60 μm core fiber. This will increase the spectral resolution at the cost of 30% throughput loss. The light blocked by the slit edge will be used to monitor intensity fluctuation of the star light.

2) **Collimator and Gratings:** After the slit, the beams are sent to a collimator-grating module. The collimator consists of two off-axis parabola mirrors (f=741.1mm) with slightly shifted each other in order to reduce aberrations. After collimation, the beams are dispersed by a newly developed Echelle grating (Richardson grating).. The grating has 13.3 grooves/mm and its blaze angle is 80.7 degrees. The grating substrate is zerodur and the replicated grating surface is aluminum coated. The dimension is 410L × 90W × 74H mm. The dispersed beams are re-collimated by the collimator mirror system to make a re-imaged pupil at a Volume-Phase Holographic (VPH) grating (cross

disperser, 278 line/mm, Angle of Incidence = 10.9 degrees, Angle of Diffraction = -10.9 degrees, 102×79×6mm, Kaiser optical system inc.).

3) **Camera and detector assembly:** The spectrums are finally imaged on a 4K×4K HAWAII4-RG detector array through the camera optics. Thanks to a large format array, very wide spectral coverage (0.97-1.75 μm) can be achieved simultaneously. In most of the wavelength coverage, 3 pixel-sampling for each wavelength element is possible with this optical design. The VPH, the camera lens, and the detector unit will be cooled down to 60K by a pulse-tube cryocooler and the temperature of the other part of the optical system will be kept around 180K (for more detail about the vacuum chamber and the cooling system, see Section 5.3). The detector assembly is being developed at the Institute for Astronomy, University of Hawaii.

4) **Ultra-low CTE ceramic optics:** Most of the optics including the optical bench is made of ultra-low thermal expansion ceramic (cordierite from Kyocera. Coorp., CTE<$|0.05\times10^{-6}|$ at room temperature). The pore-less ceramic CO720 was used for off-axis parabolas, a flat mirrors and CO220 was used for the optical bench and a slit holder. The characteristics of CO220 and CO720 are almost same, except that CO720 has much less pore or void in its surface, hence it has better surface finish after polishing. The surface roughness of the off-axis parabolas and the flat mirror is less than 3 nm Ra and the surface figure error is < λ/4 PV at λ = 633nm, which means that there is no problem for near-infrared usage. Mirror surface was gold coated and reflectance is over 98% from 0.97-1.75 μm. The optical bench has 1300L×600W×25Hmm dimension and it is reinforced by 100mm height rib structures. These optical components are precisely machined and positioned by using a 3D coordinate-measuring machine. The same material used for the optics and the optical bench will ensure that optical alignment will be kept after cooling process. Figure 8 shows the ceramic optical bench, the mirrors and the slit holder.

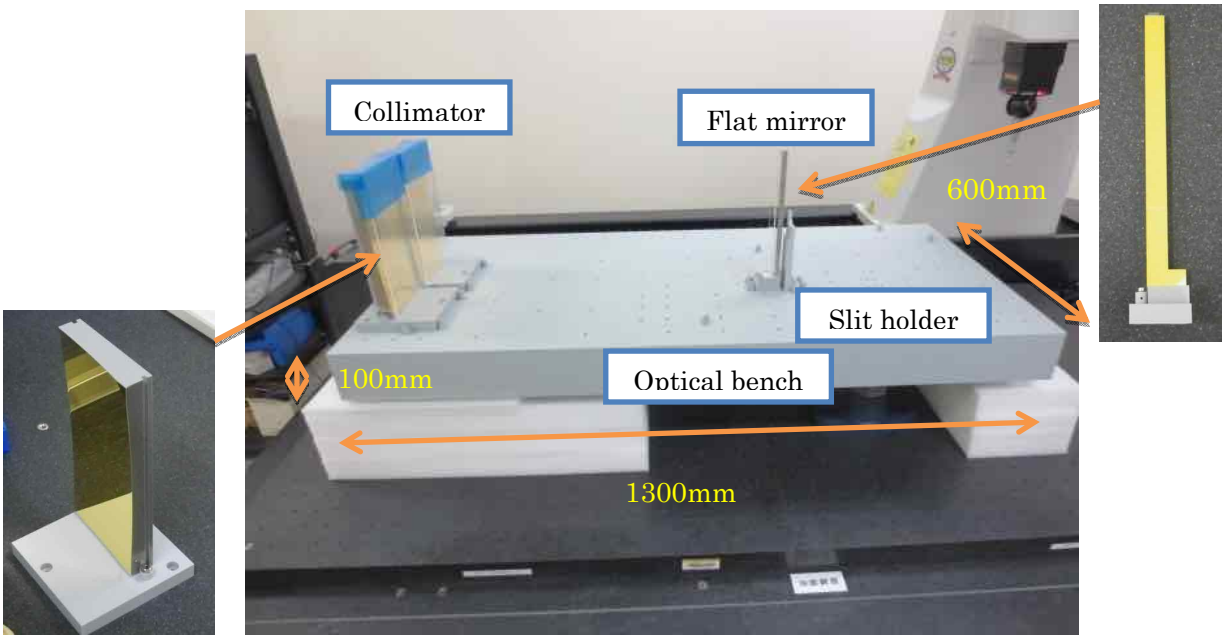

Figure 8. Optical bench, off-axis parabolas, flat mirror, and slit holder made of Kyocera's ultra-low CTE ceramic, cordierite CO720 (for the mirrors) and CO220 (for the optical bench, the slit holder). There is no moving part in the spectrometer and these ceramic optics are positioned by using a 3D coordinate-measuring machine.

5.3. Cryogenic and vibration damper system

The requirements to a cryogenic system are to keep temperatures of the optical bench and the reflective optics at 180K, and the VPH, the camera lens, the detector at 60K with a 0.01K stability. It is also important to minimize vibrations from any mechanical components like a cryo-cooler. After a careful thermal and mechanical design work, we found that a solution is to utilize a low-vibration, pulse-tube cryo-cooler. Furthermore, to avoid a break of ceramic components due to non-uniform thermal deformation during cooling phase, radiative cooling is used to cool the optical system. Figure 9 shows the cut-view of the vacuum chamber, the optical bench, and the radiation shield, etc. The optical bench is kinematically supported on an aluminum bench, in order to prevent deformation of the optical bench when temperature variation exists. A 5mm thickness aluminum enclosure is built on the aluminum bench, which is connected to the cry-cooler head (PC150U, Iwatani Gas corp.) by an oxygen-free copper plate and a copper strap to cool it to around 160K. The enclosure inner wall is painted in black for efficient radiative cooling. The VPH-camera lens-detector assembly is mounted on a small aluminum bench that is thermally isolated from the ceramic optical bench, and cooled to around 60K by using another pulse-tube cooler (PDC08W, Iwatani Gas corp.). The surface of the aluminum bench and the enclosure are finally covered with 10 layer MLI (multi-layer Insulation, COOLCAT2NW from RUAG corp.) to cut thermal radiation from the inner wall of the chamber. The aluminum bench is supported by 3 flexible glass fiber plates (NL-EG-TR, Nikkokasei) for thermal isolation and absorption of the thermal shrinkage of the aluminum bench. Temperatures of the cryo-cooler head are actively controlled by heaters and PID controllers (Lakeshore 335) to achieve a 0.01K stability.

Although pulse-tube cryocooler has no moving parts in a low-temperature part, vibrations may come from a compressor unit and from the ground. We employ a 3 stage vibration damping system to cut vibrations. First, the vacuum chamber is mounted on a low-frequency passive vibration isolators (2×1900SM-1, Minus-K technology inc.). Second, a rubber shock absorber and a flexible bellow are inserted between the pulse-tube coolers and the chamber wall. Third, a flexible cooper thermal strap is used to connect the cooler head to the aluminum bench and the detector assembly.

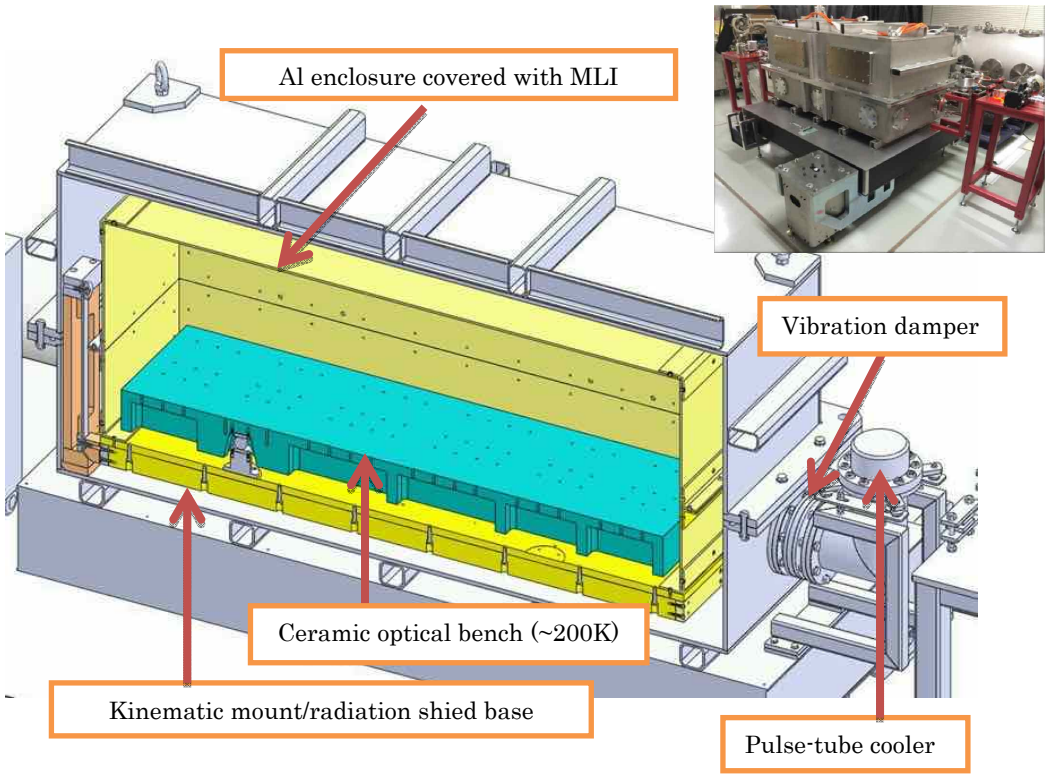

Figure 9. Cut view of the vacuum chamber, radiation shield, kinematic mount, and ceramic optical bench.

5.4. Laser frequency comb

Relievable wavelength calibration is a key to realize very high RV measurement precision. Traditionally a gas absorption cell like Thorium-Argon has been widely used for optical RV measurements[7]. In NIR, there is no such gas cell to cover wider wavelengths simultaneously. Recently, a laser frequency comb has attracted attention as a very precise, wideband wavelength standard for spectroscopy. A laser comb has many steep emission lines over some wavelengths with equally spaced frequency. Our original laser frequency comb, covering 0.97-1.75 μm eventually, has been developed based on a novel multi-gigahertz spaced comb generation technology employing a frequency stabilized laser diode, an optical pulse synthesizer and a highly nonlinear fiber[8]. The challenge for astronomical application of a laser comb is to realize the comb spacing wider than ~ 10 GHz (0.08nm at 1.55 μm), which is at least a few times larger than a spectral resolution of a typical high resolution spectrometer, because usual laser comb spacing is too narrow (100 MHz order) to be resolved by a spectrometer. A precisely controlled Fabry-Perrot filter with high finesse is required to filter out the unwanted comb lines and to increase the line spacing to multi-gigahertz[9,10], however in this case the system becomes large and complex, and it also requires precise and complicated control of the laser cavity and the FP-filter. We solved these problems by developing a novel optical spectral pulse synthesizer and several highly non-linear fibers. Figure 10 shows a schematic diagram of the astro-comb generator. The laboratory obtained laser frequency comb with 12.5 GHz spacing is shown in Figure 11. We already generated a laser comb almost covering Y, J, and H-band. Note that the shape of the each comb lines is not fully reliable due to the limited performance of the optical spectral analyzer used for the measurements. More precise, optical heterodyne based measurement is underway to characterize each comb lines.

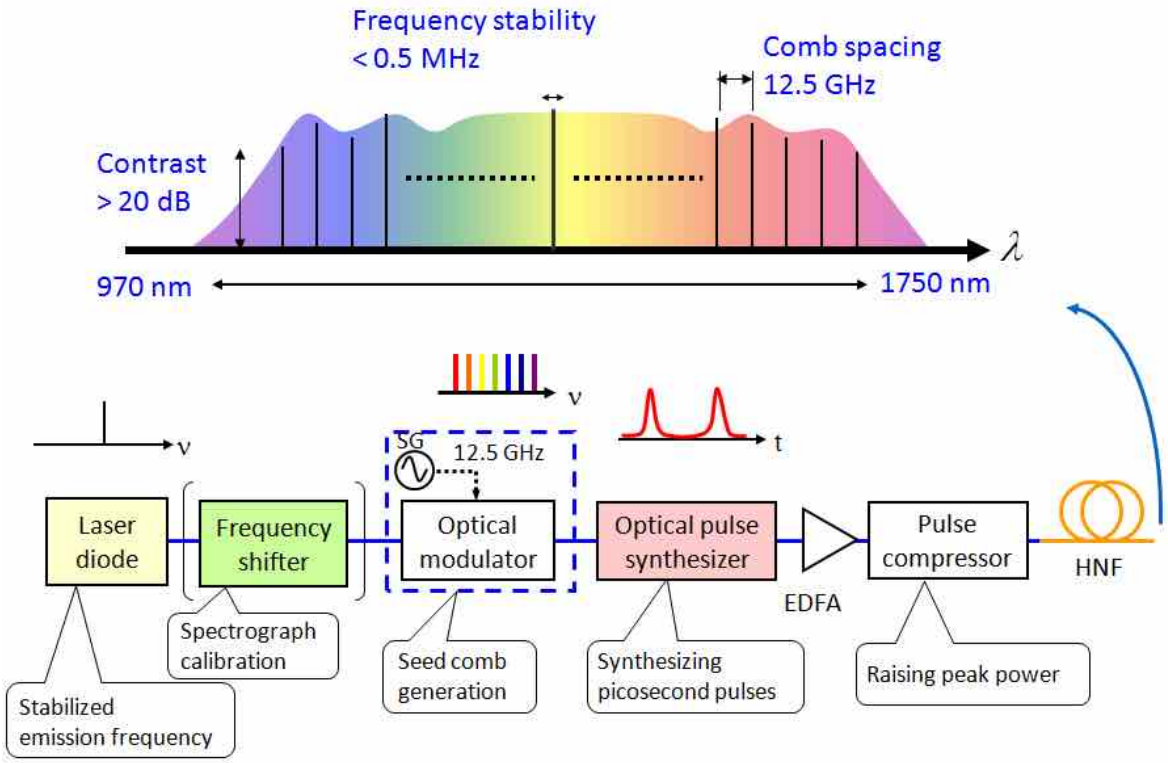

Figure 10. Schematic diagram of the laser frequency comb generator.

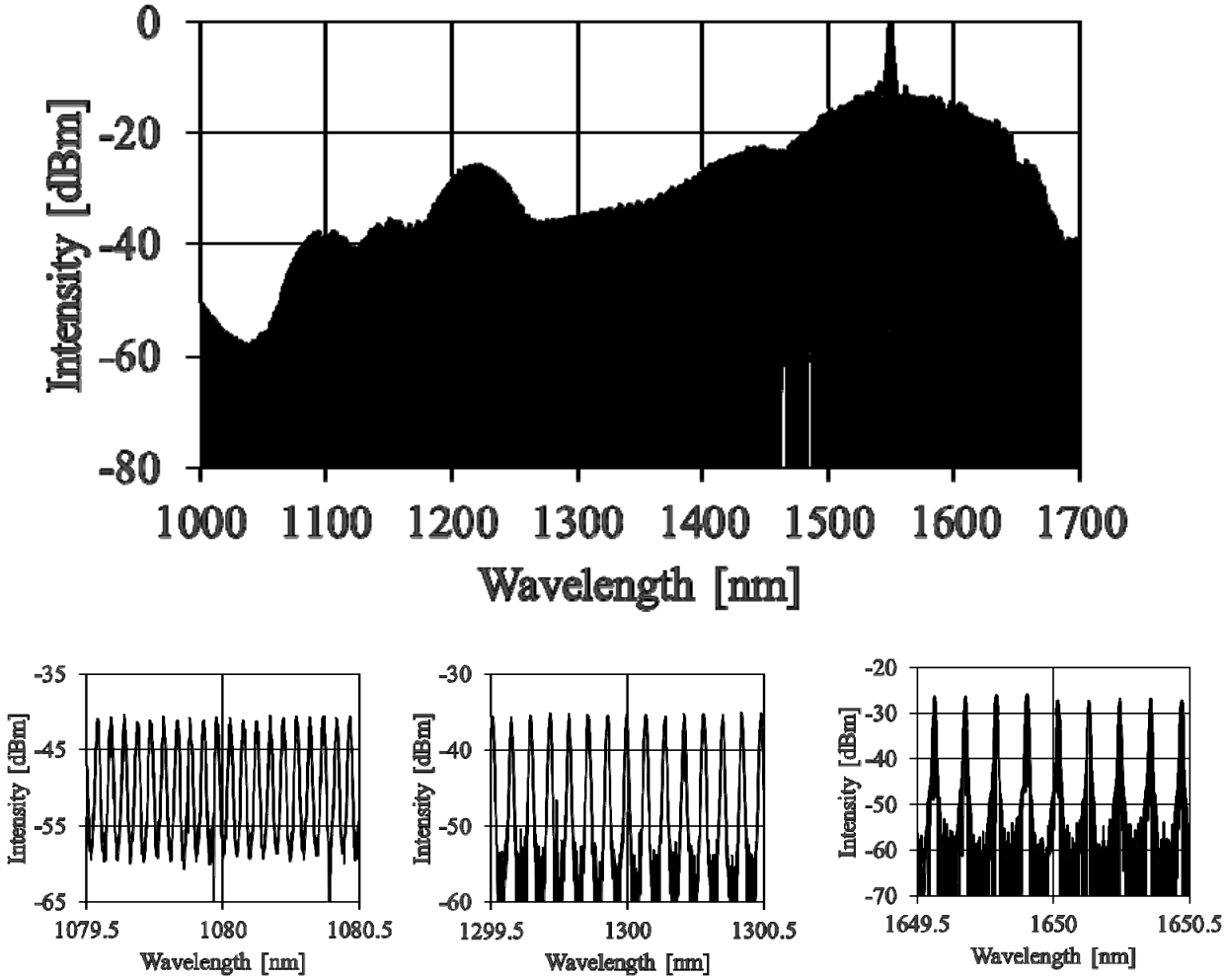

Figure 11. Laboratory obtained laser frequency comb spectrums. Bottom plots are magnified view of the plot in the upper panel.

5.5. Mode scrambler

Instability of a light intensity distribution in a slit or a fiber output in a spectrometer is known as modal noise which will limit achievable RV measurement precision. Because RV measurement is done by precise position determinations of stellar absorption lines and a laser frequency comb, which is convolved by intensity distribution of a slit image, modal noise may introduce fake RV shift which will lead to a poor precision. This effect is pronounced for a NIR spectrometer compared to the visible, because a number of propagating mode of electromagnetic wave is smaller. Some multi-mode fibers are known as a good mode scrambler. In the case of MMF, there are over 100 propagating modes of electromagnetic wave. Output image of a fiber head is a sum of mode patterns with different phase. When bandwidth of a light source is very narrow and coherent, it will cause interferences between different modes and it will result in very complex speckle pattern. These patterns are very sensitive to disturbance to a fiber for example stress, temperature change, bending, etc. In contrast, adding appropriate random disturbance to a fiber will yield time averaged, modal-noise free beam. This is so called “dynamic scrambler”.

We are now testing many static and dynamic scramblers in a laboratory. Because random seeing variation also acts as a mode scrambler, wavefront errors are introduce to an input beam by using Spatial Light Modulator (SLM) to simulate seeing condition on Mauna Kea and the AO system. As a static scrambler, we have tested various length of a fiber up to

1km, a fusion spliced step-index and graded-index fiber, a square and an octagonal core fiber. We are also testing a dynamic scrambler actively changing bending radius of a fiber. We found that, a dynamic scrambler yields best scrambling effect. Figure 12 shows Near Field Pattern (NFP) of a 60 μm core fiber with various scramblers. When there is no WFE and a scrambler, you can see that complex speckle patterns. Step-index-Graded-index fiber scrambler can be a good scrambler but a dynamic scrambler shows excellent scrambling effect and the output beam has very smooth intensity distribution.

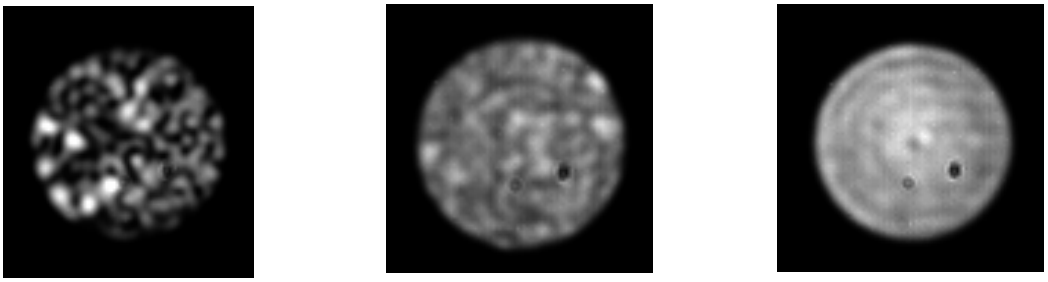

Without any scrambler, WFE

With SI+GI fiber mode scrambler + WFE

With dynamic mode scrambler +WFE

Figure 12. Near Field Pattern (NFP) of a 60 μm core fiber with various scramblers.

6. CONCLUSION

IRD is a NIR high resolution spectrometer mainly aiming for planet search around nearby M dwarfs. The goal precision in RV measurement of IRD is 1m/s which enable us to detect Earth-mass planets in their habitable zone. We have developed critical components like a laser frequency comb as wavelength standard, a high blaze angle Echelle grating, a cryogenic system etc. Currently the instruments are in integration and test phase, and the first light is planned in 2015.

REFERENCES

[1] Borucki, T. et al., "Kepler Planet-Detection Mission: Introduction and First Results," Science, 327, 977 (2010).
[2] Mayor, M. et al., "Setting New Standards with HARPS," The Messenger, 114, 20-24 (2003)
[3] Matsuo, T. et al., "Second-Earth imager for TMT (SEIT): concept and its numerical simulation," Proc. SPIE, 8446, 84461K (2012)
[4] Minowa, Y., et al., "Subaru laser guide adaptive optics system: performance and science operation," Proc. SPIE, 8447, 84471F (2012)
[5] Allard, F., Hauschildt, P. H., "Model atmospheres for M (sub) dwarf stars. 1: The base model grid", ApJ, 445, 433-450 (1995)
[6] Nemanja et al., "How to inject light efficiently into single-mode fibers", Proc. SPIE, this conference (2014)
[7] Lovis, C., & Pepe, F., "A new list of thorium and argon spectral lines in the visible", A&A, 468, 1115-1121 (2007)
[8] Choi, S., Tamura, N., Kashiwagi, K., Shioda, T., Tanaka, Y., Kurokawa, T., "Supercontinuum comb generation using optical pulse synthesizer and highly nonlinear dispersion-shifted fiber," Jpn. J. Appl. Phys., 48, pp. 09LF01-1-6 (2009)
[9] Li, C. et al., "A laser frequency comb that enables radial velocity measurements with a precision of 1cm s-1", Nature, 452, 610 (2008)
[10] Quinlan, F., Ycas, G., Osterman, S., Diddams, S. A., "A 12.5 GHz-spaced optical frequency comb spanning >400 nm for near-infrared astronomical spectrograph calibration", Review of Scientific Instruments, 81, 063105 (2010)

Geophysical Journal International

Geophys. J. Int. (2014) **197,** 119–134
Advance Access publication 2014 January 26

doi: 10.1093/gji/ggt518

Full sphere hydrodynamic and dynamo benchmarks

P. Marti,[1,2] N. Schaeffer,[3,4] R. Hollerbach,[1,5] D. Cébron,[1] C. Nore,[6,7] F. Luddens,[6] J.-L. Guermond,[8] J. Aubert,[9] S. Takehiro,[10] Y. Sasaki,[11] Y.-Y. Hayashi,[12] R. Simitev,[13,14,15] F. Busse,[14,16] S. Vantieghem[1] and A. Jackson[1]

[1]*Institute of Geophysics, ETH Zurich, Zurich* 8092, *Switzerland*
[2]*Department of Applied Mathematics, Engineering Center, Room ECOT* 521, *University of Colorado, Boulder, CO* 80309-0526, *USA. E-mail: philippe.marti@colorado.edu*
[3]*Univ. Grenoble Alpes, ISTerre, F-*38041 *Grenoble, France*
[4]*CNRS, ISTerre, F-*38041 *Grenoble, France*
[5]*Department of Applied Mathematics, University of Leeds, Leeds LS*2 9*JT, UK*
[6]*Laboratoire d'Informatique pour la Mécanique et les Sciences de l'Ingénieur, CNRS UPR* 3251, *BP* 133, 91403 *Orsay Cedex, France, and Université Paris-Sud* 11
[7]*Institut Universitaire de France,* 103, *bd Saint-Michel,* 75005 *Paris, France*
[8]*Department of Mathematics, Texas A&M University* 3368 *TAMU, College Station, TX* 77843-3368, *USA*
[9]*Dynamique des Fluides Géologiques, Institut de Physique du Globe de Paris, Sorbonne Paris Cité, Université Paris Diderot, UMR* 7154 *CNRS, F-*75005 *Paris, France*
[10]*Research Institute for Mathematical Sciences, Kyoto University, Japan*
[11]*Department of Mathematics, Kyoto University, Japan*
[12]*Center for Planetary Science/Department of Earth and Planetary Sciences, Kobe University, Japan*
[13]*Solar Physics, Hansen Experimental Physics Laboratory, Stanford University, CA* 94305, *USA*
[14]*Department of Earth and Space Sciences, University of California, Los Angeles, CA* 90095, *USA*
[15]*School of Mathematics and Statistics, University of Glasgow, Glasgow, G*12 8*QW, UK*
[16]*Institute of Physics, University of Bayreuth,* 95440 *Bayreuth, Germany*

Accepted 2013 December 19. Received 2013 December 12; in original form 2013 March 8

SUMMARY

Convection in planetary cores can generate fluid flow and magnetic fields, and a number of sophisticated codes exist to simulate the dynamic behaviour of such systems. We report on the first community activity to compare numerical results of computer codes designed to calculate fluid flow within a whole sphere. The flows are incompressible and rapidly rotating and the forcing of the flow is either due to thermal convection or due to moving boundaries. All problems defined have solutions that allow easy comparison, since they are either steady, slowly drifting or perfectly periodic. The first two benchmarks are defined based on uniform internal heating within the sphere under the Boussinesq approximation with boundary conditions that are uniform in temperature and stress-free for the flow. Benchmark 1 is purely hydrodynamic, and has a drifting solution. Benchmark 2 is a magnetohydrodynamic benchmark that can generate oscillatory, purely periodic, flows and magnetic fields. In contrast, Benchmark 3 is a hydrodynamic rotating bubble benchmark using no slip boundary conditions that has a stationary solution. Results from a variety of types of code are reported, including codes that are fully spectral (based on spherical harmonic expansions in angular coordinates and polynomial expansions in radius), mixed spectral and finite difference, finite volume, finite element and also a mixed Fourier–finite element code. There is good agreement between codes. It is found that in Benchmarks 1 and 2, the approximation of a whole sphere problem by a domain that is a spherical shell (a sphere possessing an inner core) does not represent an adequate approximation to the system, since the results differ from whole sphere results.

Key words: Numerical solutions; Non-linear differential equations; Dynamo: theories and simulations; Planetary interiors.

1 INTRODUCTION

The predominant theory for the generation mechanism of the Earth's magnetic field is that of magnetic field generation by thermal and compositional convection, creating the so-called self-excited dynamo mechanism. Beginning with the first 3-D self-consistent Boussinesq models of thermal convection (Glatzmaier & Roberts 1995; Kageyama *et al.* 1995), there has been burgeoning interest

in numerical solutions to the underlying equations of momentum conservation, magnetic field generation and heat transfer. Given the complexity and non-linearity of the physics, it has been of importance to verify that the codes used correctly calculate solutions to the underlying equations, and also to provide simple solutions that allow newly developed codes to be checked for accuracy. It is now over 11 yr since the undoubtedly successful numerical dynamo benchmark exercise of Christensen *et al.* (2001); Christensen *et al.* (2009), hereinafter B1. This benchmark exercise was set in the geometry of a spherical shell, with convection driven by a temperature difference between an inner core and the outer boundary of the spherical shell. In this respect, the computational domain is similar to that of the Earth, possessing as it does a small inner core. Three different benchmarks were devised, the first being purely thermal convection, and the second and third being dynamos (supporting magnetic fields). The latter two benchmarks differed in the treatment of the inner core: in one case the inner core was taken to be electrically insulating and fixed in the rotating frame, and in the other case the core was taken to be electrically conducting and free to rotate in response to torques that are applied to it, arising from the convection in the outer core. Central to these benchmarks was the fact that all of them possessed simple solutions, in the form of steadily drifting convection. As a result, energies are constant and, together with other diagnostics, these provide very clear solutions that could be reproduced by different numerical techniques. A measure of the success of this exercise is given by the fact that it has been used by numerous groups to check their codes.

The present benchmarking exercise is one of two brethren designed to broaden the scope of the original B1 and to provide further accurate solutions for a new generation of computer codes. The associated exercise by Jackson *et al.* (2013) is also set in a spherical shell as in B1; it is similar to B1 but has been designed to be particularly amenable to computer codes based on local (rather than spectral or global) descriptions of the temperature, magnetic and velocity fields. Thus, that benchmark allows comprehensive checking of finite element, finite volume and similar computer codes, as a result of the implementation of a local rather than global magnetic boundary condition. This paper treats a similar situation to B1 but differs in the removal of the inner core, and thus treats only a whole sphere. Flows in the first two benchmarks thus defined are driven by thermal convection, again under the Boussinesq approximation, and in the third by a boundary forcing. There are two reasons for defining benchmarks set in the whole sphere rather than the spherical shell. First, the whole sphere represents a canonical problem, surely a simpler geometry than the shell. There is one less degree of freedom, since the aspect ratio of the shell is no longer a defined parameter. Secondly, in the context of rapidly rotating fluid dynamics, there is likely to be a simplification in the flow structures generated because of the absence of an inner core. It is well known that the dynamics of rapidly rotating systems is dominated by the Coriolis force, thus leading to the Proudman–Taylor constraint, the alignment of flow structures with the rotation (z) axis. In a spherical shell when viscosity is reduced, as one moves from outside the so-called tangent cylinder (the cylinder that just encloses the inner core) to inside the tangent cylinder, a jump is present in the length of a column in the z-direction. Hence, there is the possibility of the need to resolve very fine shear layers in this region; for a recent discussion, see Livermore & Hollerbach (2012). The presence of very fine structures that need to be resolved can have very deleterious effects on a numerical method, particularly a spectral method based on spherical harmonics (again, for a discussion, see Livermore 2012). Thus, the choice of a full sphere is likely to be advantageous in the limit in which the viscosity is dropped to insignificant levels.

We note in passing that the whole sphere geometry is particularly relevant to the generation of magnetic fields in the early Earth, prior to the formation of the inner core. In this time period, the convection in the core was driven by secular cooling (and possibly internal heating), and this is precisely the scenario studied here in Benchmarks 1 and 2. Associated with this geometry is a possible numerical obstacle that has perhaps been responsible for the dearth of full-sphere calculations in the literature. Working in a spherical coordinate system (r, θ, ϕ), that is presumably convenient from the point of view of boundary conditions, the presence of the origin of the spherical coordinate system ($r = 0$) in the integration domain leads to additional numerical challenges. The results presented here show that the employed methods are able to correctly handle this singularity in coordinates.

The Benchmarks 1 and 2 set up here differ from those of B1 in their use of stress-free boundary conditions, rather than non-slip conditions. This arose purely as a result of our survey of parameter space while searching for whole-sphere dynamos that possess simple solutions with clear diagnostics suitable for a benchmark. In performing this survey, we did not find a dynamo that had a steady character similar to that in B1; this is not to say that one does not exist. The dynamo solution in Benchmark 2 shows an exact periodic character with energy conversion between kinetic and magnetic forms. It thus allows very precise comparison. The use of stress-free boundaries can cause problems with angular momentum conservation (see the discussion in Jones *et al.* 2011), but these were handled gracefully in the solutions we report.

We mention in passing the other benchmarks that have recently been provided to the community. A new benchmark for anelastic convection has recently been described by Jones *et al.* (2011) and already used as a comparison for the newly developed code of Zhan *et al.* (2012). This benchmark again is set in a spherical shell, but has a background state with a very large change in density across the shell. Three solutions are again compared, the first two (pure thermal convection and dynamo action, respectively) possessing simple drifting solutions with very precise diagnostics. A solar mean field benchmark has also recently been provided by Jouve *et al.* (2008).

The layout of the paper is as follows: in Section 2, we describe the physical problems to be addressed. Benchmarks 1 and 2 are driven by internal heating and Benchmark 3 by boundary forcing. In Section 3, we give a brief overview of the different numerical methods that have been employed by the different contributing teams. In Section 4, we present and discuss the results from the different codes.

2 TEST CASES

Three benchmarks for incompressible flows in a rapidly rotating whole sphere are considered. The first two test problems, Benchmarks 1 and 2, are subject to the thermal forcing of a homogeneous distribution of heat sources in the volume. Benchmark 1 is a purely hydrodynamic problem while Benchmark 2 consists of a self-sustained dynamo problem. Benchmark 3 extends the scope of these test cases by considering the mechanical forcing induced by moving boundaries. In all cases, the system consists of a whole sphere of radius r_o, filled with a fluid of density ρ and a kinematic viscosity ν. The system rotates at a rotation rate Ω. The fluid motion

is described by the velocity field $\boldsymbol{u}$ and, for Benchmarks 1 and 2, the temperature field is denoted by T.

2.1 Benchmark 1: thermal convection

Benchmark 1 is a purely hydrodynamic problem with the motion of the fluid described in the reference frame of the mantle. The system is described within the frame of the Boussinesq approximation, neglecting the density fluctuations except for the ones responsible for the buoyancy. Under the action of a gravitational field

$$\boldsymbol{g} = g\frac{\boldsymbol{r}}{r_o} \tag{1}$$

and in the presence of a homogeneous heat source distribution S, the basic state is given by

$$T_b = \frac{\beta}{2}\left(r_o^2 - r^2\right) \tag{2}$$

with $\beta = S/3\kappa$, where κ is the thermal diffusivity. The equations are non-dimensionalized using the radius r_o as length scale, the diffusion time r_o^2/ν as timescale and βr_o^2 as temperature scale. The three non-dimensional parameters are chosen to be the Ekman number E

$$E = \frac{\nu}{2\Omega r_o^2}, \tag{3}$$

the Prandtl number Pr

$$Pr = \frac{\nu}{\kappa} \tag{4}$$

and the modified Rayleigh number Ra

$$Ra = \frac{g\alpha\beta r_o^3}{2\Omega\kappa}, \tag{5}$$

with α the thermal expansion coefficient. The motion of the fluid is then described by the non-dimensional Navier–Stokes equation and the incompressibility condition for the velocity field $\boldsymbol{u}$

$$E\left(\partial_t - \nabla^2\right)\boldsymbol{u} = E\boldsymbol{u}\wedge(\nabla\wedge\boldsymbol{u}) + Ra\,Tr\,\boldsymbol{r} - \hat{\boldsymbol{z}}\wedge\boldsymbol{u} - \nabla\pi, \tag{6}$$

$$\nabla\cdot\boldsymbol{u} = 0 \tag{7}$$

with $\hat{\boldsymbol{z}}$ being the rotation axis. The evolution of the temperature T is described by the non-dimensional transport equation

$$\left(P_r\partial_t - \nabla^2\right)T = S - P_r\boldsymbol{u}\cdot\nabla T, \tag{8}$$

and the non-dimensional basic state is given by

$$T_b = \frac{1}{2}\left(1 - r^2\right). \tag{9}$$

The system is subject to stress-free and impenetrability mechanical boundary conditions and a fixed temperature at the outer boundary. Thus, while the radial velocity component has to vanish, a non-zero horizontal velocity component is possible at the boundary.

The benchmark solution is obtained for an Ekman number $E = 3\times10^{-4}$, a Prandtl number $Pr = 1$, a Rayleigh number $Ra = 95$ and a source term $S = 3$. This choice of parameters is close to the critical values for the onset of convection. More than one solution exists for this choice of parameters. To select the right solution branch, the following initial condition should be used for the temperature field:

$$T = \frac{1}{2}\left(1-r^2\right) + \frac{10^{-5}}{8}\sqrt{\frac{35}{\pi}}r^3\left(1-r^2\right)(\cos 3\phi + \sin 3\phi)\sin^3\theta. \tag{10}$$

For the sake of completeness, the second solution branch might be selected by replacing the spherical harmonic perturbation of degree and order 3 by a spherical harmonic perturbation of degree and order 4. The velocity field can safely be initialized to zero

$$\boldsymbol{u} = \boldsymbol{0}. \tag{11}$$

After the initial transient, the solution to Benchmark 1 settles in a quasi-stationary solution with a threefold symmetry. The alternative branch would lead to a similar solution with fourfold symmetry. To illustrate the solution, a few equatorial and meridional slices of the velocity field are provided in Figs 1 and 2.

Once the stable regime is reached, the solution exhibits a constant kinetic energy

$$E_\mathrm{k} = \frac{1}{2}\int_V \boldsymbol{u}^2\mathrm{d}V \tag{12}$$

providing an ideal diagnostic for the comparison among the different submissions (Fig. 3).

Furthermore, the whole solution is slowly drifting at a constant drift frequency. Similarly to what was done in B1, the velocity field of the solution can be described as

$$\boldsymbol{u} = \boldsymbol{u}(r,\theta,\varphi - 2\pi f_\mathrm{d}t), \tag{13}$$

where f_d is the drift frequency in units of s^{-1}. The drift frequency f_d is related to the angular velocity or drift rate ω_d in units of rad s^{-1} by

$$\omega_\mathrm{d} = 2\pi f_\mathrm{d}. \tag{14}$$

With this choice of definition, due to the threefold spatial symmetry (see Fig. 1a), the drift frequency f_d represents the frequency at which a given flow pattern will pass through a fixed point in space.

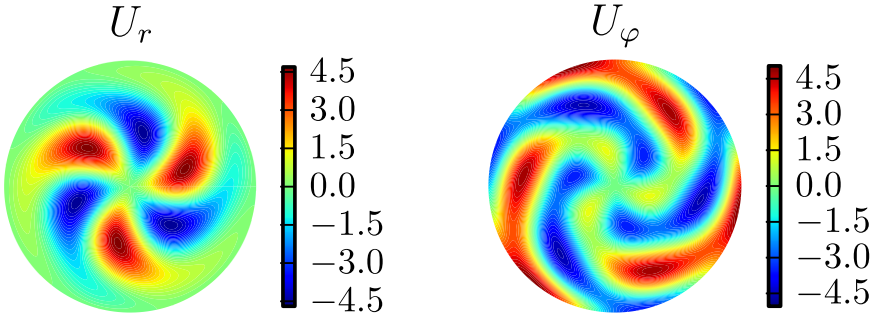

Figure 1. Equatorial slices of (a) the radial component u_r and (b) the azimuthal component u_φ of the velocity field for Benchmark 1. The velocity field is equatorially antisymmetric and thus the latitudinal component u_θ is zero in the equatorial plane.

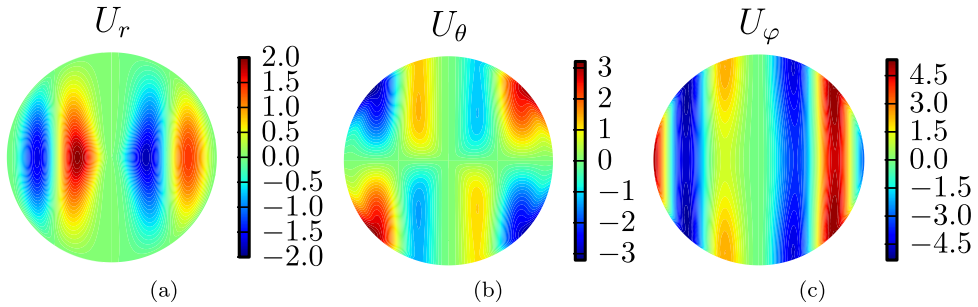

Figure 2. Meridional slices of the velocity field $\boldsymbol{u}$ for Benchmark 1: (a) radial component u_r, (b) latitudinal component u_θ and (c) azimuthal component u_φ. The slices are chosen such that they contain the maximal amplitude of the velocity field $|\boldsymbol{u}|$.

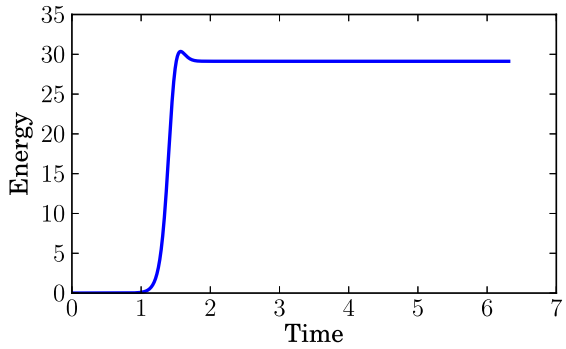

Figure 3. Typical time evolution of the kinetic energy E_k for Benchmark 1. After the initial transient, the kinetic energy reaches a constant value.

The whole solution pattern completes a full rotation at a frequency $\tilde{f}_\mathrm{d} = f_\mathrm{d}/3$.

To compare the results of the six participants in Benchmark 1, the constant kinetic energy E_k and the drift frequency f_d of their solution were requested.

2.2 Benchmark 2: thermally driven dynamo

Benchmark 2 extends the first benchmark by incorporating the generation and evolution of magnetic fields. While still working within the frame of the Boussinesq approximation, the sphere is now filled with a conducting fluid with magnetic diffusivity η and magnetic permeability μ. It is still thermally forced through the presence of a homogeneous distribution of heat sources resulting in the basic state given by eq. (2). The system of equations is extended by the induction equation to describe the evolution of the magnetic field **B**. The equations are non-dimensionalized using the radius r_o as length scale, the magnetic diffusion time r_o^2/η as timescale, βr_o^2 as the temperature scale and the magnetic field is rescaled by $\sqrt{2\Omega\rho\mu\eta}$. The four required parameters are the Ekman number E

$$E = \frac{\nu}{2\Omega r_o^2}, \tag{15}$$

the magnetic Rossby number (also referred to as the magnetic Ekman number) Ro

$$Ro = \frac{E}{Pm} = \frac{\eta}{2\Omega r_o^2}, \tag{16}$$

the Roberts number q

$$q = \frac{Pm}{Pr} = \frac{\kappa}{\eta}, \tag{17}$$

with κ the thermal diffusivity and the Rayleigh number Ra

$$Ra = \frac{g\alpha\beta r_o^3}{2\Omega\kappa}, \tag{18}$$

with α the thermal expansion coefficient. To ease the conversion to different choices of non-dimensionalizations, the Prandtl number Pr

$$Pr = \frac{\nu}{\kappa} = \frac{Pm}{q} = \frac{E}{qRo}, \tag{19}$$

and the magnetic Prandtl number Pm

$$Pm = \frac{\nu}{\eta} = \frac{E}{Ro}, \tag{20}$$

are also introduced. The motion of the conducting fluid is described by the non-dimensional Navier–Stokes equation and the incompressibility condition for the velocity field $\boldsymbol{u}$

$$\left(Ro\partial_t - E\nabla^2\right)\boldsymbol{u} = Ro\boldsymbol{u}\wedge(\nabla\wedge\boldsymbol{u}) + (\nabla\wedge\boldsymbol{B})\wedge\boldsymbol{B} + qRaT\boldsymbol{r} - \hat{\boldsymbol{z}}\wedge\boldsymbol{u} - \nabla\pi, \tag{21}$$

$$\nabla\cdot\boldsymbol{u} = 0. \tag{22}$$

The magnetic induction equation and the solenoidal condition for the magnetic field $\boldsymbol{B}$ read as

$$\left(\partial_t - \nabla^2\right)\boldsymbol{B} = \nabla\wedge(\boldsymbol{u}\wedge\boldsymbol{B}), \tag{23}$$

$$\nabla\cdot\boldsymbol{B} = 0, \tag{24}$$

and finally the transport equation for the temperature T is given by

$$\left(\partial_t - q\nabla^2\right)T = S - \boldsymbol{u}\cdot\nabla T. \tag{25}$$

As for Benchmark 1, the outer boundary is maintained at fixed temperature and a stress-free mechanical boundary condition is imposed. Furthermore, the outer region is considered to be a perfect insulator.

The thermal dynamo solution for Benchmark 2 is obtained for an Ekman number $E = 5\times10^{-4}$, a magnetic Rossby number $Ro = \frac{5}{7}\times10^{-4}$, a Roberts number $q = 7$, a Rayleigh number $Ra = 200$ and a source term $S = 3q = 21$. In terms of the Prandtl numbers, the Benchmark 2 is obtained for a Prandtl number $Pr = 1$ and a magnetic Prandtl $Pm = 7$. This parameter regime is approximately two times supercritical and a magnetic field is generated and sustained by the system. Although the solution for Benchmark 2 can be obtained by starting from a small initial perturbation, the convergence to the final state is extremely slow and requires prohibitively high computational resources. Furthermore, the presence

of several solution branches can not be excluded even if it was not seen during the computations. To reduce the computational load to a reasonable level, a special initial condition exhibiting a much faster convergence has been worked out.

The temperature field T should be initialized with the background conducting state with a small perturbation as a spherical harmonic of degree and order 3

$$T = \frac{1}{2}\left(1-r^2\right) + \frac{\epsilon}{8}\sqrt{\frac{35}{\pi}} r^3 \left(1-r^2\right)(\cos 3\varphi + \sin 3\varphi)\sin^3\theta \tag{26}$$

with $\epsilon = 10^{-5}$. The magnetic field should be initialized with a purely toroidal magnetic field given by

$$B_r = 0, \tag{27}$$

$$B_\theta = -\frac{3}{2} r \left(-1+4r^2-6r^4+3r^6\right)(\cos\varphi + \sin\varphi), \tag{28}$$

$$B_\varphi = -\frac{3}{4} r \left(-1+r^2\right)\cos\theta \left[3r\left(2-5r^2+4r^4\right)\sin\theta + 2\left(1-3r^2+3r^4\right)(\cos\varphi - \sin\varphi)\right]. \tag{29}$$

Finally, the velocity field should be initialized with a purely toroidal velocity given by

$$u_r = 0, \tag{30}$$

$$u_\theta = -\frac{10r^2}{7\sqrt{3}}\cos\theta\left[3\left(-147+343r^2-217r^4+29r^6\right)\cos\varphi + 14\left(-9-125r^2+39r^4+27r^6\right)\sin\varphi\right], \tag{31}$$

$$u_\varphi = -\frac{5r}{5544}\left\{7\left[\left(43\,700-58\,113r^2-15\,345r^4 + 1881r^6+20\,790r^8\right)\sin\theta + 1485r^2\left(-9+115r^2-167r^4+70r^6\right)\sin 3\theta\right] + 528\sqrt{3}r\cos 2\theta\left[14\left(-9-125r^2+39r^4+27r^6\right)\cos\varphi + 3\left(147-343r^2+217r^4-29r^6\right)\sin\varphi\right]\right\}. \tag{32}$$

For simulations using spherical harmonics and a toroidal/poloidal decomposition, the expression of the initial conditions can be written in a simpler form. Assuming that the magnetic field is decomposed as $\boldsymbol{B} = \boldsymbol{\nabla}\wedge\mathcal{T}\boldsymbol{r} + \boldsymbol{\nabla}\wedge\boldsymbol{\nabla}\wedge\mathcal{P}\boldsymbol{r}$, the initial field is given by the two scalars

$$\mathcal{T} = r\left[\left(\frac{3}{4}-3r^2+\frac{9}{2}r^4-\frac{9}{4}r^6\right)+\left(\frac{3}{4}-3r^2+\frac{9}{2}r^4-\frac{9}{4}r^6\right)\imath\right]\mathcal{Y}_1^1 + r^2\left(\frac{3}{2}-\frac{21}{4}r^2+\frac{27}{4}r^4-3r^6\right)\mathcal{Y}_2^0 + c.c., \tag{33}$$

$$\mathcal{P} = 0, \tag{34}$$

where $c.c.$ stands for the complex conjugate without the $m = 0$ modes and $\mathcal{Y}_l^m$ are Schmidt normalized complex spherical harmonics. Similarly assuming that the velocity field is decomposed as $\boldsymbol{u} = \boldsymbol{\nabla}\wedge T\boldsymbol{r} + \boldsymbol{\nabla}\wedge\boldsymbol{\nabla}\wedge P\boldsymbol{r}$, the initial condition is given by

$$T = r^2\left[\left(30+\frac{1250}{3}r^2-130r^4-90r^6\right) + \left(105-245r^2+155r^4-\frac{145}{7}r^6\right)\imath\right]\mathcal{Y}_2^1 + r\left(-\frac{54\,625}{198}+350r^2+\frac{625}{2}r^4-325r^6\right)\mathcal{Y}_1^0 + r^3\left(45-575r^2+835r^4-350r^6\right)\mathcal{Y}_3^0 + c.c., \tag{35}$$

$$P = 0. \tag{36}$$

Details of the definition and the normalization of the spherical harmonics $\mathcal{Y}_l^m$ are given in Appendix A.

The structure of the solution to Benchmark 2 is much more complicated than for Benchmark 1 and no longer exhibits a simple symmetry. Nevertheless, after the initial transient the system settles into a regime with periodic kinetic and magnetic energies. The amplitude and frequency of these oscillations provide a good diagnostic for Benchmark 2 (Fig. 4).

To illustrate the structure of the velocity field, a few equatorial slices are shown in Fig. 5. The time-dependent features of the solutions can be seen in the Hammer projection snapshots of the flow close to the outer boundary (Fig. 6) and the Hammer projections of the radial component of the magnetic field at the outer boundary (Fig. 7). The two comma shaped flux patches of opposite sign

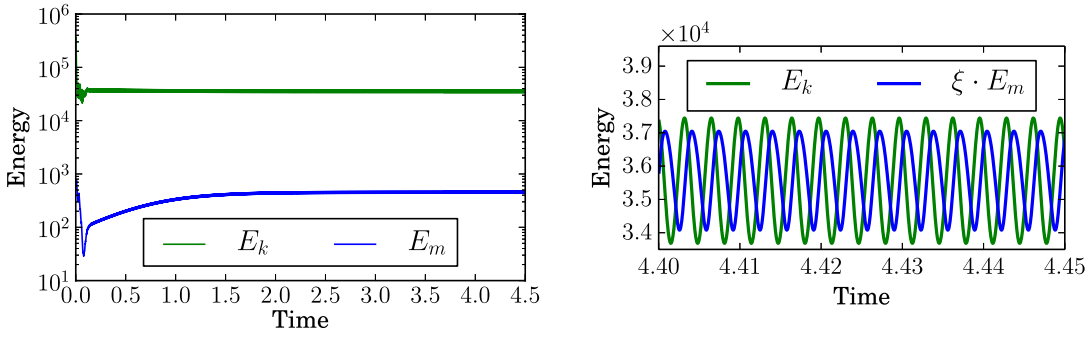

(a) (b)

Figure 4. Kinetic energy E_k and magnetic energy E_m for Benchmark 2. (a) Typical time evolution of E_k and E_m. After the initial transient, both energies settle into a periodic oscillation. (b) Detailed view of the oscillations in E_k and E_m. The magnetic energy has been rescaled by $\xi = \frac{C_\mathrm{k}}{C_\mathrm{m}} \approx 39$ (see eqs 37 and 40) to show the phase shift between E_k and E_m.

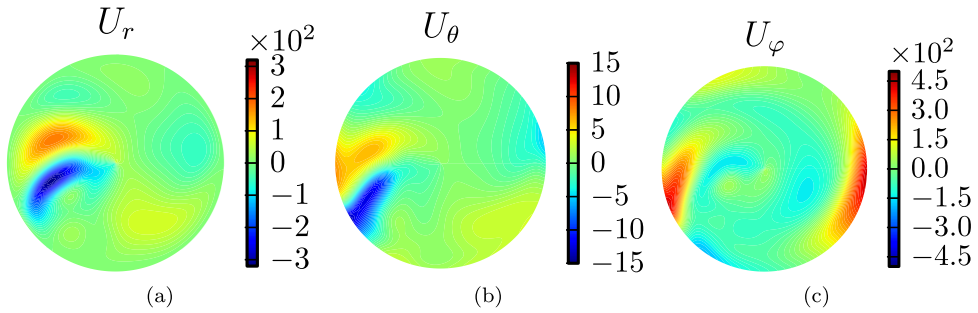

Figure 5. Equatorial slices of the velocity field $\boldsymbol{u}$ at $t = 4.43241$ for Benchmark 2: (a) radial component u_r, (b) latitudinal component u_θ and (c) azimuthal component u_φ.

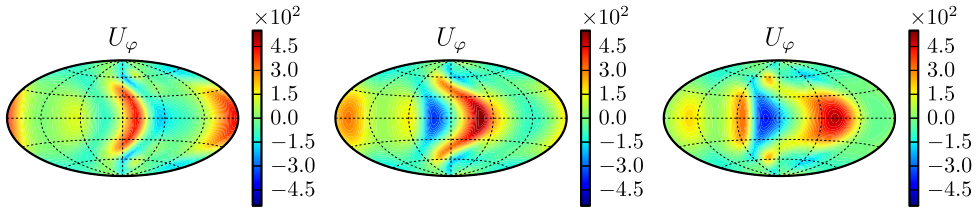

Figure 6. Hammer projections of three snapshots of the azimuthal velocity component u_φ at the outer boundary ($r = r_o$) for Benchmark 2.

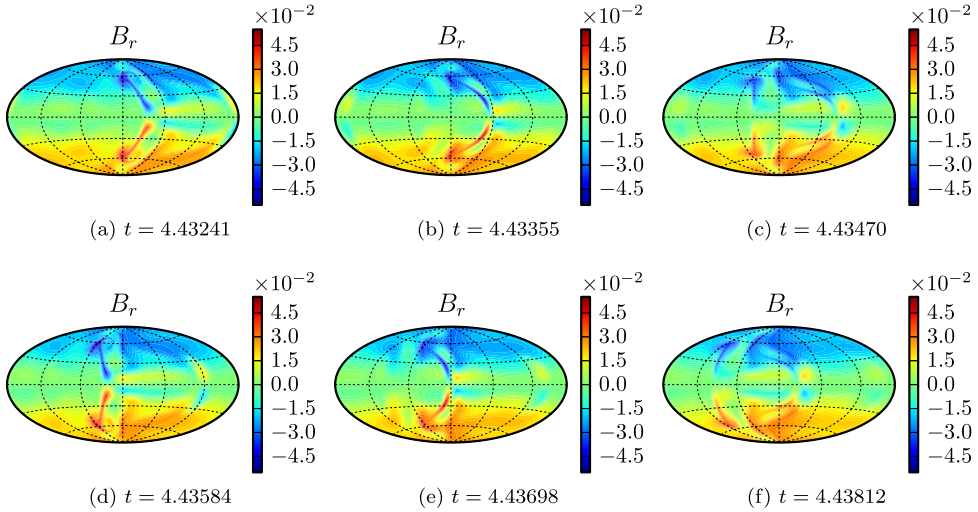

Figure 7. Hammer projections of six snapshots, spanning approximatively two periods, of the radial magnetic field B_r at the outer boundary $r = r_o$ for Benchmark 2.

emerge periodically. The lower part moves eastwards while rising to higher latitudes until they vanish. Fig 7 shows snapshots over approximately two periods.

The solution to Benchmark 2 will solely be characterized by the computed kinetic and magnetic energies. Their periodic behaviour allows us to define several diagnostic quantities used to compare the solutions from different simulations. The kinetic energy is decomposed into a constant component C_k, the amplitude of the leading oscillating term A_k, the frequency of this oscillation f_k and a phase shift ζ_k. Using these definitions,the kinetic energy E_k is written as

$$E_\mathrm{k} = \frac{1}{2}\int_V \boldsymbol{u}^2 \mathrm{d}V = C_\mathrm{k} + A_\mathrm{k}\cos(2\pi f_\mathrm{k} t + \zeta_\mathrm{k}) + \cdots \tag{37}$$

Furthermore, decomposing the velocity into its equatorially symmetric [labelled as (s)] and equatorially antisymmetric part [labelled as (a)], the velocity field was found to be purely equatorially symmetric

$$E_\mathrm{k}^{(s)} = E_\mathrm{k}, \tag{38}$$

$$E_\mathrm{k}^{(a)} = 0. \tag{39}$$

Using the same decomposition, the magnetic energy E_m can be written as

$$E_\mathrm{m} = \frac{1}{2Ro}\int_V \boldsymbol{B}^2 \mathrm{d}V = C_\mathrm{m} + A_\mathrm{m}\cos(2\pi f_\mathrm{m} t + \zeta_\mathrm{m}) + \cdots \tag{40}$$

Decomposing the magnetic field into its equatorially symmetric and antisymmetric parts, the magnetic field is found to be purely equatorially antisymmetric

$$E_\mathrm{m}^{(s)} = 0, \tag{41}$$

$$E_\mathrm{m}^{(a)} = E_\mathrm{m}. \tag{42}$$

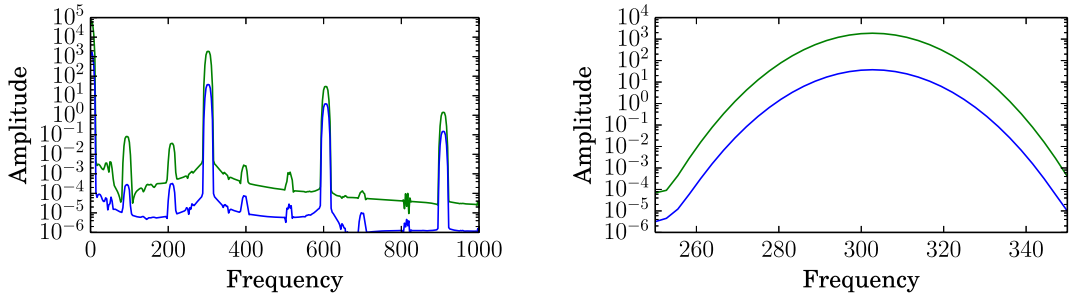

(a) (b)

Figure 8. (a) Frequency spectrum of the kinetic energy E_k and magnetic energy E_m for Benchmark 2 after a flat top window has been applied on the time-series. (b) Details of the peak of the main amplitude of the kinetic and magnetic energies after a Kaiser window with parameter $\beta = 14$ has been applied to the time-series. Note the use of a logarithmic scale for the ordinate, meaning that the frequency localization is extremely good. Both spectra have been obtained on a time-series over approximatively 0.35 diffusion times at a sampling rate of 1.75×10^5 obtained by (MJ) at $N = 31$ and $L = M = 63$ (see Section 3 for details).

It was found and confirmed by all participants that the oscillations in the magnetic energy and kinetic energy have the same frequency. In addition, as can be seen in Fig. 4(b), there is a phase shift between the magnetic and kinetic energy. This relative phase shift ($\zeta_\mathrm{k} - \zeta_\mathrm{m}$) is found to have value 1.91rad but is not included in the benchmark. The six constants C_k, A_k, f_k, C_m, A_m and f_m defined above are the diagnostic values that were requested from all submissions to Benchmark 2.

The computation of decompositions 37 and 40 requires some further explanations as several different approaches are possible. The first one involves computing the Fourier series. To reduce the spectral leakage, a flat top window (Oliphant 2007) is applied on the time-series. The amplitude of the different modes can then easily be extracted as shown in Fig. 8(a). Conversely, to compute an accurate frequency, a Kaiser window (Kaiser & Kuo 1966) with parameter $\beta = 14$ is applied to the time-series. The peaks in the spectrum are then well approximated with a parabolic fit allowing for interpolation between the available frequencies. The peak for the main oscillation is shown in Fig. 8(b). The frequencies can also be computed by counting the zero crossings. Both approaches provide the frequency within a relative error of 10^{-4} per cent. There is a simpler approach to obtain the requested data without using a Fourier transform. Assuming E_i^min, E_i^max are the minimum and maximum of the time-series for the energy, the constant component is approximatively given by

$$C_i \approx \frac{E_i^\mathrm{min} + E_i^\mathrm{max}}{2}, \tag{43}$$

and the amplitude of the main oscillation is approximatively given by

$$A_i \approx \frac{E_i^\mathrm{max} - E_i^\mathrm{min}}{2}. \tag{44}$$

These relations are not exact because the time-series do also include higher frequencies as shown in Fig. 8(a). Using the Fourier series, it is possible to bound the relative errors generated by the simplified approach. By including the second peak with a frequency of $2f_i$ and accounting for the phase shift, a comparison with the approximations 43 and 44 provides the relative errors ϵ_{C_k} and ϵ_{A_k} on C_k and A_k for the kinetic energy

$$\epsilon_{C_\mathrm{k}} = 3 \times 10^{-2} \text{ per cent}, \tag{45}$$

$$\epsilon_{A_\mathrm{k}} = 5 \times 10^{-2} \text{ per cent}. \tag{46}$$

The same analysis on the magnetic energy provides the relative errors ϵ_{C_m} and ϵ_{A_m} on C_m and A_m

$$\epsilon_{C_\mathrm{m}} = 0.4 \text{ per cent}, \tag{47}$$

$$\epsilon_{A_\mathrm{m}} = 0.6 \text{ per cent}. \tag{48}$$

These relative errors have been obtained by assuming that E_i^min and E_i^max are exact. An accurate value for the minimum and maximum requires a time-series sampled at a high frequency but it does in principle only require one cycle. On the other hand, an accurate Fourier series will require a long time-series. The errors made by using this simplified approach depend strongly on the relative magnitude of the higher frequencies. For the kinetic energy, the second oscillation with a frequency of $2f_\mathrm{k}$ has an approximatively 63 times smaller amplitude which leads to the rather small errors given in eqs (45) and (46). On the other hand, the second oscillation in the magnetic energy is only approximatively 10 times smaller leading to the larger errors given in eqs (47) and (48). In both cases, the third oscillation with a frequency $3f$ can be neglected as it is more than 20 times smaller than the second oscillation.

2.3 Benchmark 3: boundary forced rotating bubble

Benchmark 3 is again a purely hydrodynamic problem. It provides a simple test problem for boundary driven flows in a whole sphere as they might, for example, arise in precession or libration problems. The proposed system describes the motion of an incompressible fluid inside a spherical bubble rising in a rotating fluid. It is an important addition to the first two cases as it replaces the internal thermal forcing by a mechanical forcing due to an imposed tangential flow over the boundary. The bubble is assumed to be of unit radius $r_o = 1$ and is described by the Navier–Stokes equation and incompressibility condition

$$\partial_t \boldsymbol{u} + \boldsymbol{u} \cdot \nabla \boldsymbol{u} + 2\Omega \hat{\boldsymbol{z}} \wedge \boldsymbol{u} = -\nabla p + \nu \nabla^2 \boldsymbol{u}, \tag{49}$$

$$\nabla \cdot \boldsymbol{u} = 0 \tag{50}$$

with ν the viscosity of the fluid and Ω the rotation rate of the bubble. The rotation axis is parallel to $\hat{\boldsymbol{z}}$. The tangential flow over the boundary imposes a non-homogeneous boundary condition on the fluid at the surface of the bubble

$$u_\theta = -u_0 \cos\theta \cos\phi, \tag{51}$$

$$u_\phi = u_0 \sin\phi, \tag{52}$$

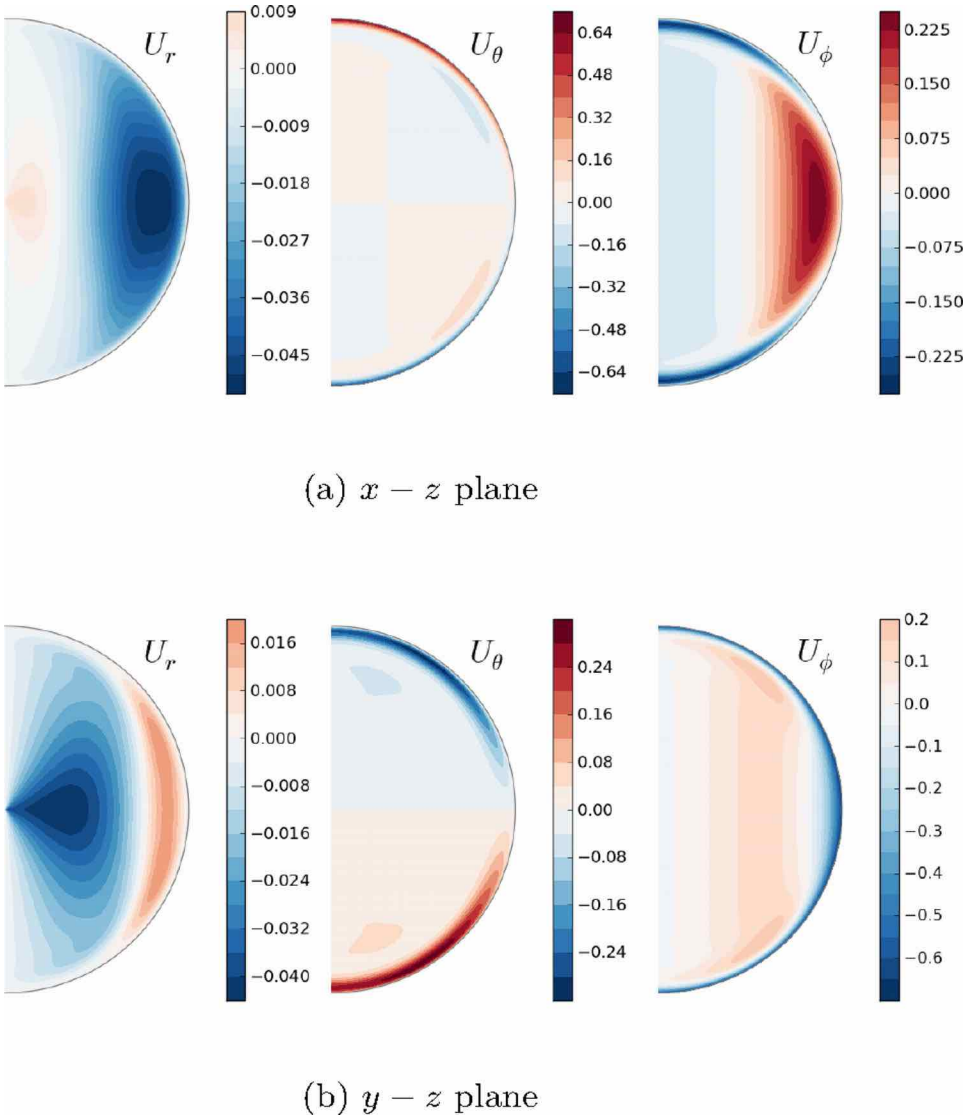

Figure 9. In the top row, velocity field in the x–z plane ($\phi = 0$) and in the bottom row, velocity field in the y–z plane ($\phi = \pi/2$) for Benchmark 3.

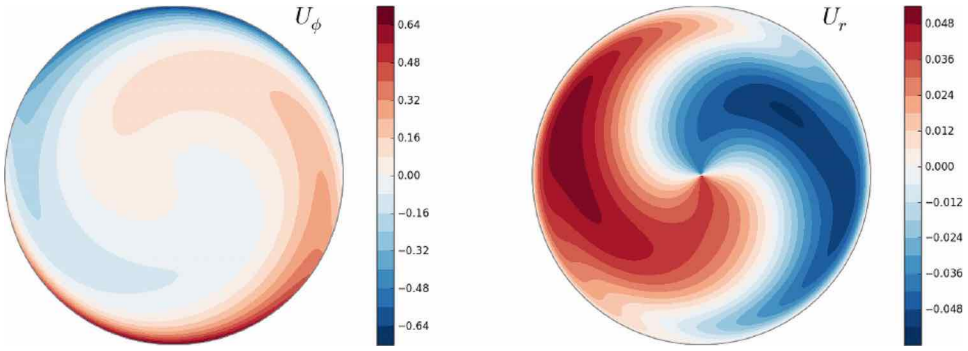

Figure 10. Velocity field in the x–y (equatorial) plane for Benchmark 3.

which is the gradient of a pure $l = 1$, $m = 1$ spherical harmonic $\mathcal{Y}_1^1(\theta, \phi)$.

The solution to Benchmark 3 is obtained for a boundary velocity $u_0 = \sqrt{\frac{3}{2\pi}}$, a viscosity $\nu = 10^{-2}$ and a rotation rate $\Omega = 10$. It does not require any particular initial condition and can be started with a zero initial velocity field.

The flow converges quickly to a stationary solution with a dominant $m = 1$ component. Interestingly, the solution contains an important and non-trivial flow through the centre of the bubble. As such, it provides a good diagnostic for this numerically challenging region. To illustrate the flow of the solution, the velocity field components in the $x - z$ and $y - z$ planes are shown in Fig. 9. The velocity field in the $x - y$ plane, which is orthogonal to the rotation axis (i.e. the equatorial plane) is shown in Fig. 10.

The solution to Benchmark 3 was characterized by five diagnostic values. The first diagnostic is the constant kinetic energy

$$E_\mathrm{k} = \frac{1}{2}\int_V \boldsymbol{u}^2 \mathrm{d}V \tag{53}$$

reached after the initial transient. When available, the energy in the spherical harmonic orders $m = 0$, $m = 1$ and $m = 2$ have also been collected. Secondly, the $\hat{\boldsymbol{z}}$ component of the angular momentum L_z is reported. The three components of the velocity field $\boldsymbol{u}$ at the centre of the bubble provide that last diagnostic data.

3 CONTRIBUTING NUMERICAL CODES

There was a total of nine contributors to the benchmark but each did not necessarily provide results for all three cases. A short description of the algorithm used by each simulation is provided below. Further references are given for a more detailed description.

Marti and Jackson (MJ): Spectral simulation using spherical harmonics for the angular component and polynomials developed by Worland (2004) and Livermore *et al.* (2007) in radius (see Marti 2012). The Worland polynomials satisfy exactly the parity and regularity conditions required at the origin of the spherical coordinate system. Specifically, the radial basis used is of the form $r^l P_n^{(-1/2,l-1/2)}(2r^2-1)$ for a given harmonic degree l, with $P_n^{(\alpha,\beta)}(x)$ the Jacobi polynomials. The incompressibility condition is guaranteed by the use of a toroidal/poloidal decomposition of the vector fields. A second-order predictor–corrector scheme is used for the time integration. No specific treatment is required to conserve angular momentum.

Hollerbach (H): An adaptation of the previous spherical shell code described by Hollerbach (2000), based on spherical harmonics and a toroidal/poloidal decomposition of the vector fields. Instead of expanding in the full set of Chebyshev polynomials in radius, regularity and parity conditions at the origin are now accommodated by expanding as $r \cdot T_{2k-1}(r)$ for odd harmonic degrees and $r^2 \cdot T_{2k-1}(r)$ for even harmonic degrees for the toroidal/poloidal scalars. The temperature is similarly expanded as $T_{2k-2}(r)$ for degree $l = 0$, $r \cdot T_{2k-2}(r)$ for odd degrees, and $r^2 \cdot T_{2k-2}(r)$ for even degrees. Angular momentum conservation is explicitly imposed by a modified stress-free boundary condition.

Aubert (A): Spectral simulation using the code PARODY-JA, which uses spherical harmonics for the angular component and a second-order finite differences in radius (see Dormy *et al.* 1998; Aubert *et al.* 2008). The time marching is done with a semi-implicit Crank–Nicolson/Adams–Bashforth scheme. The radial mesh includes a gridpoint exactly at the centre of the sphere. Spectral toroidal and poloidal components of order l behave like r^l at the centre. Angular momentum conservation is achieved by correcting for solid-body rotation at each time step.

Schaeffer (S): Spectral simulation using spherical harmonics for the angular component and second-order finite differences in radius (Monteux *et al.* 2012). The numerical instability near the origin is overcome by truncating the spherical harmonic expansion at $\ell_\mathrm{tr}(r)$ before computing the spatial fields that enter the non-linear terms. Specifically, the truncation is $\ell_\mathrm{tr}(r) = 1 + (\ell_\mathrm{max} - 1)\left(\frac{r}{r_o}\right)^\alpha$, where $\alpha = 0.5$ gives good results, and also saves some computation time. The time stepping uses a semi-implicit Crank–Nicolson scheme for the diffusive terms, while the non-linear terms can be handled either by an Adams–Bashforth or a predictor–corrector scheme (both second-order in time). The SHTns library (Schaeffer 2013) is used for efficient spherical harmonic transforms. Angular momentum conservation is achieved by adjusting the solid-body rotation component at each time step.

Takehiro, Sasaki and Hayashi (TSH): Spectral simulation using spherical harmonics for the angular components and the polynomials developed by Matsushima & Marcus (1995) and Boyd (2001) in radius (see Sasaki *et al.* 2012). The radial basis functions satisfy exactly the parity and regularity conditions at the origin of the spherical coordinate system. Specifically, the used radial basis is of the form $r^l P_n^{(\alpha,\beta)}(2r^2-1)$ for a given harmonic degree l, with $P_n(x)$ the Jacobi polynomials. The incompressibility condition is guaranteed by the use of a toroidal/poloidal decomposition of the vector fields. The time integration is performed with the Crank–Nicolson scheme for the diffusive terms and a second-order Adams–Bashforth scheme for the other terms. No specific treatment is required to conserve angular momentum.

Simitev and Busse (SB): Pseudospectral numerical code using spherical harmonics expansion in the angular variables and Chebyshev polynomials in radius. Time stepping is implemented by a combination of the implicit Crank–Nicolson scheme for the diffusion terms and the explicit Adams–Bashforth scheme for the Coriolis and the non-linear terms; both schemes are second-order accurate. Early versions of the code are described in Tilgner & Busse (1997) and Tilgner (1999). The code has been extensively modified and used for a number of years (Simitev & Busse 2005, 2009, 2012; Busse & Simitev 2006, 2008). This is a spherical shell code and no special effort was made to convert it to the full sphere geometry. Instead, the full sphere is approximated by placing a tiny inner core with radius ratio $r_i/r_o = 0.01$ at the centre of the shell. Angular momentum conservation is achieved by correcting for rigid-body rotation if required.

Cébron (C): Finite elements method simulation using the standard Lagrange element P2–P3, which is quadratic for the pressure field and cubic for the velocity field, and a Galerkin Least-Squares (GLS) stabilization method (Hauke & Hughes 1994). The (unstructured) mesh is made of prisms in the boundary layer and tetrahedrons in the bulk. The incompressibility is imposed using a penalty method. The time stepping uses the Implicit Differential-Algebraic solver (IDA solver), based on variable-coefficient Backward Differencing Formulae (e.g. Hindmarsh *et al.* 2005). The integration method in IDA is variable-order, the order ranging between 1 and 5. At each time step, the system is solved with the sparse direct linear solver PARDISO (www.pardiso-project.org) or a multigrid GMRES iterative solver. This is all implemented via the commercial code COMSOL Multiphysics®.

Nore, Luddens and Guermond (NLG): Hybrid Fourier and finite element method using a Fourier decomposition in the azimuthal direction and the standard Lagrange elements P1–P2 in the meridian section (with P1 for the pressure and P2 for the velocity field). The meridian mesh is made of quadratic triangles. The velocity and pressure are decoupled by using the rotational pressure-correction method. The time stepping uses the second-order Backward Difference Formula (BDF2). The non-linear terms are made explicit and approximated using second-order extrapolation in time. The code is parallelized in Fourier space and in meridian sections [domain decomposition with METIS (Karypis & Kumar 2009)] using MPI and PETSC (Portable, Extensible Toolkit for Scientific Computation; Balay *et al.* 1997, 2012a,b). This is implemented in the code SFEMaNS (for Spectral/Finite Element method for Maxwell and Navier–Stokes equations; Guermond *et al.* 2007, 2009, 2011).

Vantieghem (V): Unstructured finite-volume simulation (see Vantieghem 2011) using a grid of tetrahedral elements with smaller elements close to the wall. The spatial discretization is based on a centred-difference-like stencil that is second-order accurate for

regular tetrahedra. Time stepping is based on a canonical fractional-step method (Kim & Moin 1985), and the equations are integrated in time with a fourth order Runge–Kutta method. A BiCGstab(2) algorithm is used to solve the pressure Poisson equation. The reported Fourier components are obtained by an *a posteriori* interpolation of the results on a regular grid in terms of spherical coordinates ($N_r = 36$, $N_\theta = N_\varphi = 18$), which is subject to considerable additional numerical (interpolation) errors.

Table 1. Contributions to Benchmark 1. The labels used for the different codes are defined in Section 3. The values are shown with the number of significant digits provided by the authors. As all these codes are based on a spherical harmonics expansion for the angular component, the resolution is given as the radial resolution N, the highest harmonic degree L and the highest harmonic order M.

Code	E_k	f_d	N	L	M
(MJ)	29.08502	12.38841	8	15	15
(MJ)	29.07661	12.38860	8	23	23
(MJ)	29.12178	12.38604	12	23	23
(MJ)	29.12064	12.38619	16	23	23
(MJ)	29.12064	12.38619	16	31	31
(MJ)	29.12068	12.38619	23	47	47
(MJ)	29.12068	12.38619	31	63	63
(H)	29.11784	12.3862	12	23	23
(H)	29.12054	12.3862	16	31	31
(H)	29.12053	12.3862	23	31	31
(H)	29.12053	12.3862	23	47	47
(H)	29.12053	12.3862	31	63	63
(S)	29.219	12.388	120	31	31
(S)	29.1446	12.387	250	63	63
(S)	29.13501	12.38648	320	85	85
(TSH)	29.03074	12.3878	16	21	21
(TSH)	29.12878	12.3863	32	42	42
(TSH)	29.12878	12.3863	48	85	85
(SB)	29.00617	11.89445	33	42	42
(A)	29.12062	12.3931	1600	63	63

4 RESULTS

There is quite an important diversity in the type of simulations that took part in these benchmarks. All the diagnostics that have been considered for these benchmarks should be straightforward to obtain whenever the simulation code is based on some spectral expansion or on a local method. On the other hand, a direct comparison of the resolution used is a more subtle problem. The comparison will be done by comparing solutions based on the number of degrees of freedom present at the time stepping level. For local methods, the resolution R is computed as $R = N_{\rm grid}^{1/3}$ where $N_{\rm grid}$ is the number of gridpoints and for spherical harmonic–based codes $R = \left\{N_r \cdot \left[L_{\max}(2M_{\max}+1) - M_{\max}^2 + M_{\max} + 1\right]\right\}^{1/3}$. The same approach was used in B1.

4.1 Benchmark 1

There were six participants in Benchmark 1 and all of them used a spherical harmonics–based simulation . They agree qualitatively quite well and no important discrepancies were found. The details of all the solutions obtained by the participants is given in Table 1. At the quantitative level, a few interesting observations can be made. The results for the total kinetic energy are summarized in Fig. 11(a). The five codes (MJ), (H), (TSH), (S), (A) do all eventually converge to the same solution within 5×10^{-2} per cent. While using a completely different radial expansion, (MJ) and (H) even converge very rapidly within 5×10^{-4} per cent. The last code (SB) working in a spherical shell rather than a sphere comes within 0.4 per cent. Note that the results obtained with a very high radial resolution (1600 gridpoints) by (A) matches very closely to the solutions from the fully spectral codes. The other finite differences–based code (S) shows a clear convergence towards the same solution and would most likely have reached it at a higher resolution.

The picture is very similar for the drift frequency (Fig. 11b). The codes (MJ), (H) and (TSH) agree within 6×10^{-4} per cent , the solution by (S) is within 2×10^{-3} per cent and the solution by (A) is within 6×10^{-2} per cent. Finally, the solution by (SB) is within 4 per cent.

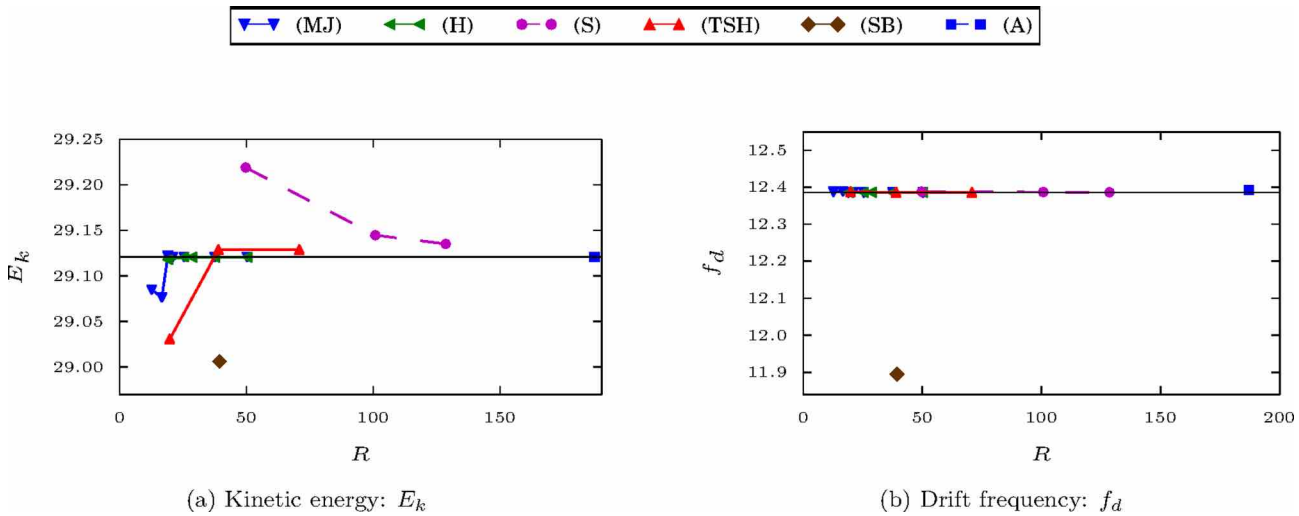

(a) Kinetic energy: E_k (b) Drift frequency: f_d

Figure 11. Summary of the solutions of the participants of Benchmark 1. (a) Constant kinetic energy E_k, as defined in eq. (12), reached after the initial transient. (b) Drift frequency f_d, defined in Section 2, of the threefold symmetric structure of the solution (see Fig. 1). The black horizontal line is the standard value given in Table 2. The error corridor for the standard values is represented by a greyed out area, but as the errors are very small it is only barely visible. The labels used for the different codes are defined in Section 3.

Table 2. Summary table and standard values obtained for Benchmark 1. The Ekman number E, the Prandtl number Pr and the modified Rayleigh number Ra as well as the governing equation for the velocity $\boldsymbol{u}$ and the temperature T are given in Section 2. The kinetic energy E_k is defined in eq. (12) and the drift frequency by eq. (13).

Benchmark 1: Thermal convection		
Parameters		
E	Pr	Ra
3×10^{-4}	1	95
Boundary conditions		
$\boldsymbol{u}$:	stress-free	
T:	fixed temperature	
	homogeneous heat sources	
Requested values		
E_k	29.1206	$\pm 1 \times 10^{-4}$
f_d	12.3862	$\pm 1 \times 10^{-4}$

A standard value for the kinetic energy and drift frequency for Benchmark 1 is derived from the three simulations showing the best convergence to a common result. The values as well as a short summary of the problem definition are given in Table 2. The very high convergence to a common solution allow to provide these with roughly six significant digits.

4.2 Benchmark 2

All the groups participating in Benchmark 1 also participated in Benchmark 2, except for (A). There are thus again only solutions from spherical harmonics–based simulations. The overall picture is very similar to Benchmark 1. The fully spectral simulations converge very rapidly to their final solution and which are in most cases very close to each other. The finite differences simulation, while requiring higher radial resolution, eventually reaches a similar solution. As was already observed in Benchmark 1, the simulation by (SB) which approximates the whole sphere as a shell with a tiny inner core, shows the largest discrepancy. The details of all the solutions to Benchmark 2 are given in Table 3.

The solutions obtained by the different simulations are summarized in Figs 12(a)–(e). For the constant part of the kinetic (C_k) and magnetic (C_m) energies, excluding the solution by (SB), all results lie within 2×10^{-2} and 0.3 per cent, respectively. A good convergence to a common solution was also observed for the amplitude of the oscillations in the kinetic energy. The solutions provided by (MJ), (H) and (S) lie within 7×10^{-3} per cent. The solution of (TSH) does not seem to converge to exactly the same value but remains within 0.4 per cent of the three other values. The convergence is not as good for the amplitude in the oscillation of the magnetic energy. All the results lie within 1 per cent. The solution by (MJ), (H) and (TSH) seem to show the clearest convergence trend and their solutions lie within 0.2 per cent. Finally, the frequency of the oscillations of the kinetic and magnetic energies have been compared. All groups reported the same frequency f for both energies. The summary of the solutions for the frequency is shown in Fig. 12(e). The results for (MJ), (H), (TSH) and (S) lie within 0.3 per cent while (SB) is a little bit further away with 0.6 per cent.

While the spread in the solutions is clearly more important for Benchmark 2, the general situation is very similar to Benchmark 1. The solutions by (MJ) and (H) do nearly overlap for all five diagnostic values and do exhibit a very fast convergence. As was explained in Section 3, the extraction of the different components of the energies requires some post-processing. The choice of methodology by each author, for example, to extract the oscillation amplitude, might explain a part of the somewhat larger discrepancies compared to Benchmark 1. The standard values given in Table 4 are obtained by taking the average of the highest resolution by (MJ) and (H). The error bars are chosen such that at least one additional solution is included in the error corridor. This choice is based on the fast convergence of both codes to essentially the same value for all the requested data.

While it was not part of the actual benchmark, the phase shift between the kinetic and magnetic energy (see Fig. 4b) is also reported in Table 4 to provide a more complete characterization of the solution. The reported value has been computed by (MJ) from

Table 3. Spectral method contributions to Benchmark 2. The labels used for the different codes are defined in Section 3. The values are shown with the number of significant digits provided by the authors. The decomposition of the kinetic energy E_k into C_k, A_k and f_k is defined in eq. (37) and the equivalent decomposition of the magnetic energy E_m into C_m, A_m and f_m is defined in eq. (40). As all these codes are based on a spherical harmonic expansion for the angular component, the resolution is given as the radial resolution N, the highest harmonic degree L and the highest harmonic order M.

Code	C_k	A_k	f_k	C_m	A_m	f_m	N	L	M
(MJ)	35 141.84	1836.287	302.2623	1153.695	51.77003	302.2623	12	23	23
(MJ)	35 548.95	1881.661	302.6947	922.3073	38.54002	302.6947	16	31	31
(MJ)	35 542.15	1880.460	302.6858	924.5757	38.48190	302.6858	23	31	31
(MJ)	35 551.33	1880.055	302.7018	908.9870	37.47705	302.7018	23	47	47
(MJ)	35 550.93	1879.837	302.7015	908.8059	37.45069	302.7015	31	63	63
(H)	35 378	1855	302.48	1043.77	46.16	302.48	12	23	23
(H)	35 588	1885	302.71	904.30	37.61	302.71	16	31	31
(H)	35 540	1881	302.66	925.64	38.50	302.66	23	31	31
(H)	35 551	1880	302.67	909.67	37.48	302.67	23	47	47
(H)	35 550	1880	302.67	909.46	37.47	302.67	31	63	63
(S)	35 544	1878.1	302.2	951.59	41.33	302.2	120	31	31
(S)	35 568	1881.0	302.65	908.69	37.951	302.65	250	63	63
(S)	35 552	1880.1	302.11	910.75	38.064	302.11	320	85	85
(TSH)	35 619.63	1887.200	303.0303	881.6272	36.97913	303.0303	32	42	42
(TSH)	35 564.30	1872.702	303.0303	905.8444	37.60794	303.0303	48	85	85
(SB)	35 951.5	1843.38	304.308	1046.12	38.08	304.308	41	96	96

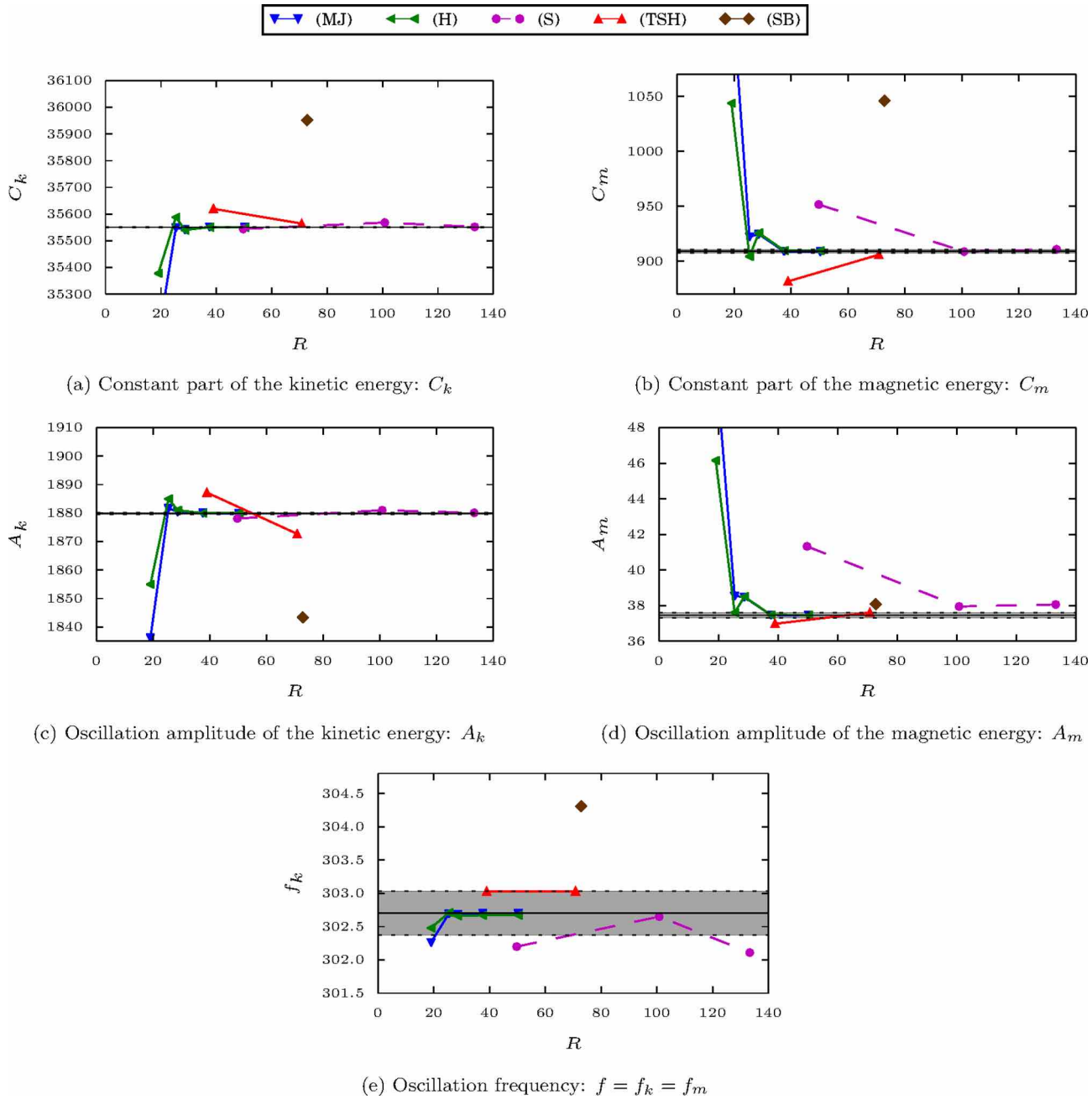

(a) Constant part of the kinetic energy: C_k

(b) Constant part of the magnetic energy: C_m

(c) Oscillation amplitude of the kinetic energy: A_k

(d) Oscillation amplitude of the magnetic energy: A_m

(e) Oscillation frequency: $f = f_k = f_m$

Figure 12. Summary of the solutions of the participants to Benchmark 2. The decomposition of the kinetic energy E_k into a constant part C_k, the amplitude of the main oscillation A_k and its frequency f_k is defined in eq. (37). The equivalent decomposition for the magnetic energy E_m, defining the three constants C_m, A_m and f_m is given in eq. (40). The black horizontal line is the standard value given in Table 4. The error corridor for the standard values, defined such that the three most converged solutions are included, is represented by a greyed out area. The labels used for the different codes are defined in Section 3.

time-series of the kinetic and magnetic energy at the highest reported resolution ($N = 31$, $L = M = 63$). The phase shift has been extracted from the Fourier series shown in Fig. 8.

4.3 Benchmark 3

Benchmark 3 had the highest number of participants with eight codes taking part. It is also the only case where results from local methods are available. The computation for Benchmark 3 does not require a very high horizontal resolution. For example, spherical harmonics–based codes exhibit a very good convergence at resolutions as low as $L_\mathrm{max} = 30$ and $M_\mathrm{max} = 10$. However, it is more demanding in the radial direction. The centre requires a sufficiently high resolution to describe flow crossing it properly as well as the moving outer boundary which is forcing the system.

The solutions obtained by the different groups are summarized in Figs 13(a)–(e). Note that some of the solutions obtained by spherical harmonics–based codes have been obtained with a reduced longitudinal resolution while a triangular truncation was used for Benchmarks 1 and 2. The details for each solution are given in Table 5 for the spectral methods and in Table 6 for the local methods. A good convergence of the kinetic energy E_k is observed. Surprisingly, it is the solution by (TSH) which shows the largest

Table 4. Summary table and standard values obtained for Benchmark 2. The Ekman number E, the magnetic Rossby number Ro, the Roberts number q and the modified Rayleigh number Ra, as well as the governing equations for the velocity $\boldsymbol{u}$, the magnetic field $\boldsymbol{B}$ and the temperature T are given in Section 2. The decomposition of the kinetic energy E_k into constant and oscillating components is defined in eq. (37) and the decomposition of the magnetic energy is defined in eq. (40).

Benchmark 2: Thermally driven dynamo			
Parameters			
E	Ro	q	Ra
5×10^{-4}	$5/7 \times 10^{-4}$	7	200
Boundary conditions			
$\boldsymbol{u}$:	stress-free		
$\boldsymbol{B}$:	insulating		
T:	fixed temperature		
	homogeneous heat sources		
Requested values			
Kinetic energy E_k			
	C_k	35 550.5	± 1.5
	A_k	1879.84	± 0.26
Magnetic energy E_m			
	C_m	909.133	± 1.62
	A_m	37.4603	± 0.1476
Frequency $f = f_k = f_m$		302.701	± 0.33
Additional characteristic			
Phase shift	$\lvert\zeta_k - \zeta_m\rvert$	1.91rad	

discrepancy (0.4 per cent) while all the other solutions agree within 0.1 per cent at least. (MJ), (H), (S), (C) and (NLG) show the clearest convergence with solutions within 8×10^{-3} per cent. The values obtained for the vertical component of the angular momentum show the largest discrepancies among the diagnostics for Benchmark 3. The solutions by (H), (S), (C), (NLG), (V) seem to converge to the same value within 7×10^{-2} per cent. While a very high agreement was achieved for the kinetic energy solutions, simulations by (MJ), (TSH) and (A) seem to converge to a lower value of L_z but still within 0.4 per cent. The last two diagnostic values involve the evaluation of the velocity field at the centre of the spherical domain. While all simulations lie within 0.15 per cent for the velocity along the y-axis, the velocity along the x-axis shows a larger discrepancy with values within 0.3 per cent.

Considering the very fast convergence it showed for all diagnostics, the standard value will be taken as the final solution by (H). As for the other two benchmarks, the error bars are chosen such that at least two additional solutions lie within the given bounds. These standard values and error bars for Benchmark 3 are given in Table 7.

5 DISCUSSION

The combination of the results for all three test cases paints a uniform and unambiguous picture of a successful benchmarking exercise. With the wide range of classes of problems covered by

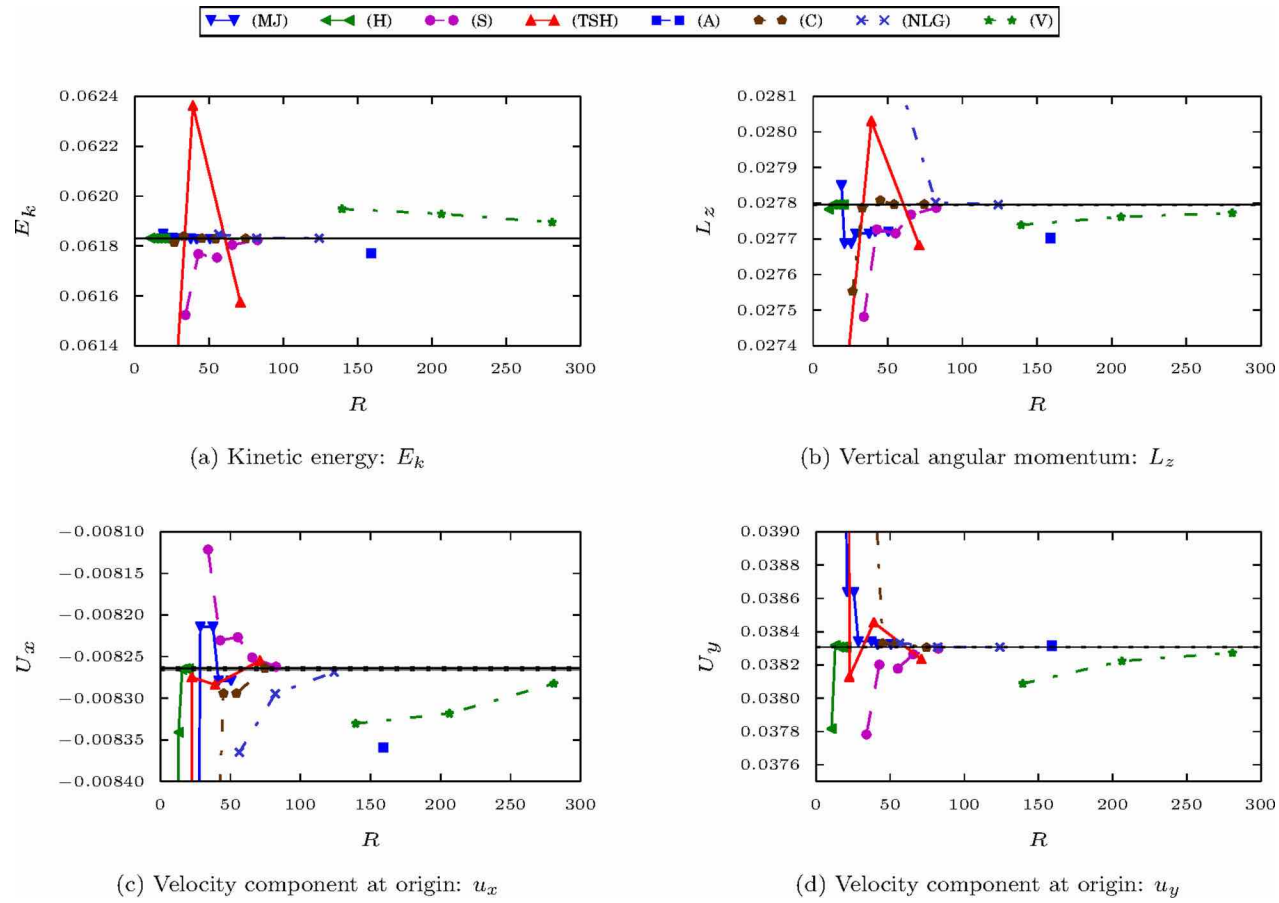

(a) Kinetic energy: E_k

(b) Vertical angular momentum: L_z

(c) Velocity component at origin: u_x

(d) Velocity component at origin: u_y

Figure 13. Summary of the solutions of the participants to Benchmark 3. The vertical velocity component u_z is not shown as it was consistently shown to be zero. The black horizontal line is the standard value given in Table 7. The error corridor for the standard values is represented by a greyed out area. Except for (c) which has larger errors, the error corridor is mostly hidden by the black line. The labels used for the different codes are defined in Section 3.

Table 5. Spectral method contributions to Benchmark 3. The labels used for the different codes are defined in Section 3. The values are shown with the number of significant digits provided by the authors. As all these codes are based on a spherical harmonics expansion for the angular component, the resolution is given as the radial resolution N, the highest harmonic degree L and the highest harmonic order M.

Code	E_k	E_k, $m=0$	E_k, $m=1$	E_k, $m=2$	L_z	U_x	U_y	N	L	M
(MJ)	6.18485e−2	4.35430e−4	6.12948e−2	1.17244e−4	2.78499e−2	−1.06714e−2	4.00811e−2	12	23	23
(MJ)	6.18338e−2	4.31265e−4	6.12841e−2	1.17319e−4	2.76877e−2	−8.91803e−3	3.86386e−2	16	23	23
(MJ)	6.18338e−2	4.31265e−4	6.12841e−2	1.17319e−4	2.76877e−2	−8.91803e−3	3.86386e−2	16	31	31
(MJ)	6.18291e−2	4.32506e−4	6.12783e−2	1.17195e−4	2.77151e−2	−8.21402e−3	3.83418e−2	23	31	31
(MJ)	6.18291e−2	4.32506e−4	6.12783e−2	1.17195e−4	2.77151e−2	−8.21402e−3	3.83418e−2	23	47	47
(MJ)	6.18286e−2	4.32813e−4	6.12776e−2	1.17118e−4	2.77204e−2	−8.27886e−3	3.83230e−2	31	47	47
(MJ)	6.18286e−2	4.32813e−4	6.12776e−2	1.17118e−4	2.77204e−2	−8.27885e−3	3.83230e−2	31	63	63
(H)	6.1832e−2	4.3521e−4	6.1278e−2	1.1762e−4	2.7783e−2	−1.0066e−2	3.7817e−2	12	12	4
(H)	6.1831e−2	4.3515e−4	6.1277e−2	1.1754e−4	2.7796e−2	−8.3410e−3	3.8318e−2	15	15	5
(H)	6.1831e−2	4.3514e−4	6.1277e−2	1.1754e−4	2.7796e−2	−8.2654e−3	3.8307e−2	18	18	6
(H)	6.1831e−2	4.3514e−4	6.1277e−2	1.1754e−4	2.7796e−2	−8.2644e−3	3.8307e−2	21	21	7
(H)	6.1831e−2	4.3514e−4	6.1277e−2	1.1754e−4	2.7796e−2	−8.2644e−3	3.8307e−2	24	24	8
(S)	6.15237e−2	4.25401e−4	6.09814e−2	1.15913e−4	2.748153e−2	−8.121293e−3	3.778225e−2	150	20	7
(S)	6.17682e−2	4.33033e−4	6.12169e−2	1.17198e−4	2.772647e−2	−8.230440e−3	3.820168e−2	300	20	7
(S)	6.17537e−2	4.32675e−4	6.12028e−2	1.17133e−4	2.771565e−2	−8.226658e−3	3.817840e−2	300	31	10
(S)	6.18047e−2	4.34295e−4	6.1252e−2	1.17400e−4	2.776804e−2	−8.251015e−3	3.826415e−2	500	31	10
(S)	6.18239e−2	4.34907e−4	6.12705e−2	1.17501e−4	2.778725e−2	−8.262105e−3	3.829847e−2	1000	31	10
(TSH)	5.98943e−2	3.63627e−4	5.94187e−2	1.10888e−4	2.53084e−2	−3.29031e−2	1.22471e−1	12	10	10
(TSH)	6.07755e−2	4.20777e−4	6.02401e−2	1.13600e−4	2.73295e−2	−8.27489e−3	3.81288e−2	24	21	21
(TSH)	6.23624e−2	4.42463e−4	6.17993e−2	1.19543e−4	2.80304e−2	−8.28375e−3	3.84550e−2	32	42	42
(TSH)	6.15750e−2	4.31638e−4	6.10257e−2	1.16576e−4	2.76827e−2	−8.25493e−3	3.82359e−2	48	85	85
(A)	6.1771e−2	4.3704e−4	6.1220e−2	1.1753e−4	2.7702e−2	−8.359e−3	3.8316e−2	200	63	63

Table 6. Local method contributions to Benchmark 3. The labels used for the different codes are defined in Section 3. The values are shown with the number of significant digits provided by the authors. The kinetic energy E_k in the $m=0$, $m=1$ and $m=2$ modes has to be computed in a post-processing step which is likely to introduce additional errors in the codes (C) and (V). For this reason, these values were not mandatory for Benchmark 3. The resolution R is given as the third root of the total number of gridpoints $N_{\rm grid}$.

Code	E_k	E_k, $m=0$	E_k, $m=1$	E_k, $m=2$	L_z	U_x	U_y	$N_{\rm grid}^{1/3}$
(C)	6.1814e−2	N/A	N/A	N/A	2.7553e−2	−8.8469e−3	4.0492e−2	26.4
(C)	6.1839e−2	N/A	N/A	N/A	2.7787e−2	−8.8469e−3	4.0492e−2	32.8
(C)	6.1831e−2	N/A	N/A	N/A	2.7808e−2	−8.2943e−3	3.8329e−2	45.0
(C)	6.1829e−2	N/A	N/A	N/A	2.7797e−2	−8.2943e−3	3.8329e−2	54.2
(C)	6.1830e−2	N/A	N/A	N/A	2.7797e−2	−8.2637e−3	3.8305e−2	74.5
(NLG)	6.1847e−2	4.4376e−4	6.1285e−2	1.1733e−4	2.8158e−2	−8.3649e−3	3.8332e−2	56.4
(NLG)	6.1831e−2	4.3534e−4	6.1277e−2	1.1754e−4	2.7803e−2	−8.2946e−3	3.8308e−2	82.0
(NLG)	6.1831e−2	4.3515e−4	6.1277e−2	1.1754e−4	2.7796e−2	−8.2686e−3	3.8307e−2	124.
(V)	6.19485e−2	4.2922e−4	5.6011e−2	1.1883e−4	2.77393e−2	−8.33047e−3	3.80877e−2	139.4
(V)	6.19288e−2	4.3333e−4	5.7559e−2	1.1808e−4	2.77620e−2	−8.31833e−3	3.82237e−2	206.3
(V)	6.18951e−2	4.3379e−4	5.7707e−2	1.1707e−4	2.77724e−2	−8.28240e−3	3.82734e−2	280.8

these three test cases, ranging from purely hydrodynamic problems with thermal or boundary forcing to non-linear dynamo simulations, these results do support the confidence that is put into numerical simulations in a full sphere geometry. The different codes used to compute numerical solutions, while based on wide range of numerical methods, all agreed very well with each other. As was observed in similar benchmarking exercises (e.g. Christensen *et al.* 2001; Jackson *et al.* 2013) in a spherical shell geometry, the fully spectral simulations showed the fastest convergence to the final solutions followed by the mixed spherical harmonics and finite difference codes. The simulations using local methods exhibited a very good agreement but required a much higher resolution to converge. However, one should keep in mind that the simple spherical geometry and solutions with a simple structure do favour spectral methods.

With at least five different implementations taking part in each benchmark case, the provided standard values and error bounds can be trusted to be accurate. Benchmark 1 showed the strongest convergence among all the solutions proposed. Maybe somewhat suprisingly, Benchmark 2 showed a somewhat larger discrepancy. Benchmark 3 showed also quite good convergence from all codes, except for the value of the angular momentum where a larger scatter in the solutions was observed also among the spectral codes that agreed well for Benchmarks 1 and 2. Interestingly, the two codes by (MJ) and (H) did exhibit a remarkably similar behaviour and produced nearly the same results for all values in Benchmarks 1 and 2. While both use a spherical harmonic expansion, the radial discretization is quite different. (H) uses a parity constrained Chebyshev expansion while (MJ) uses a basis set that satisfies the regularity conditions at the origin exactly.

Two physical issues have emerged as part of these calculations. The use of stress-free boundary conditions in Benchmarks 1 and 2 imply that angular momentum must be conserved. As was also discovered in Jones *et al.* (2011), it was not the case in all the codes. Several groups simply monitored the evolution of the angular momentum and reported no problem with the provided resolutions. On the other hand, some of the codes needed to correct every few time steps to avoid building up unphysical angular momentum. The relatively long integration time required to reach Benchmark 2 did

Table 7. Table of the standard values obtained for Benchmark 3. The viscosity ν, the rotation rate Ω and boundary velocity u_0 are used to parametrize Benchmark 3. The governing equation for the velocity $\boldsymbol{u}$ is given in Section 2. The kinetic energy E_k is defined in eq. (53). L_z is the $\hat{\boldsymbol{z}}$ component of the angular momentum. u_x and u_y are the $\hat{\boldsymbol{x}}$ and $\hat{\boldsymbol{y}}$ components of the velocity through the centre of the bubble.

Benchmark 3: Boundary forced rotating bubble		
Parameters		
ν	Ω	u_0
10^{-2}	10	$\sqrt{\frac{3}{2\pi}}$
Boundary conditions		
Tangential flow:	$\boldsymbol{u}_{bc} = u_0 \nabla \mathcal{Y}_1^1(\theta, \phi)$	
Requested values		
E_k	6.1831×10^{-2}	$\pm 1 \times 10^{-6}$
L_z	2.7796×10^{-2}	$\pm 1 \times 10^{-6}$
Velocity through centre		
u_x	-8.2644×10^{-3}	$\pm 2.3 \times 10^{-6}$
u_y	3.8307×10^{-2}	$\pm 2 \times 10^{-6}$

exacerbate the problem as even small errors do accumulate to a sizeable value over a large number of time steps. (H) did follow a different approach and imposed a modified boundary condition to explicitly impose conservation.

The full sphere dynamo problem is of great geophysical importance, as it accurately represents the Early Earth prior to the formation of the inner core (see Jacobs 1953). The results from Benchmarks 1 and 2 show that even a small inner core may result in solutions that strongly differ from the full sphere solutions. Indeed the use of a small inner core systematically produced less accurate solutions. Problems in a full sphere geometry, like the simulation of Early Earth's dynamo, should be addressed with specialized codes. It is expected that this issue will become even more important in more complex flows.

ACKNOWLEDGEMENTS

This work was partly funded by ERC grant 247303 'MFECE' to AJ. AJ and PM acknowledge SNF grant 200021-113466, and are grateful for the provision of computational resources by the Swiss National Supercomputing Centre (CSCS) under project ID s225. PM acknowledges the support of the NSF CSEDI Programme through award EAR-1067944. For this work, DC was supported by the ETH Zurich Post-doctoral fellowship programme as well as by the Marie Curie Actions for People COFUND Programme. JLG acknowledges support from the University Paris-Sud, the National Science Foundation (grants NSF DMS-1015984 and DMS-1217262), the Air Force Office of Scientific Research, (grant FA99550-12-0358) and the King Abdullah University of Science and Technology (Award No. KUS-C1-016-04). The computations using SFEMaNS were carried out on IBM SP6 of GENCI-IDRIS (project 0254).

REFERENCES

Aubert, J., Aurnou, J. & Wicht, J., 2008. The magnetic structure of convection-driven numerical dynamos, *Geophys. J. Int.,* **172**(3), 945–956.

Balay, S., Gropp, W.D., McInnes, L.C. & Smith, B.F., 1997. Efficient management of parallelism in object-oriented numerical software libraries, *Modern Software Tools in Scientific Computing,* pp. 163–202, eds Arge, E., Bruaset, A.M. & Langtangen, H. P., Birkhäuser, Boston.

Balay, S. *et al.*, 2012a. *PETSc Users Manual Revision 3.3*.

Balay, S. *et al.*, 2012b. PETSc Web page, available at: http://www.mcs.anl.gov/petsc, last accessed 12 January 2014.

Boyd, J.P., 2001. *Chebyshev and Fourier Spectral Methods, Courier Dover*.

Busse, F. & Simitev, R., 2008. Toroidal flux oscillation as possible cause of geomagnetic excursions and reversals, *Phys. Earth planet. Inter.,* **168**(3), 237–243.

Busse, F.H. & Simitev, R.D., 2006. Parameter dependences of convection-driven dynamos in rotating spherical fluid shells, *Geophys. astrophys. Fluid Dyn.,* **100**(4–5), 341–361.

Christensen, U. *et al.*, 2009. Erratum to a numerical dynamo benchmark [Phys. Earth planet. Inter. **128**(1–4) (2001) 25–34], *Phys. Earth planet. Inter.,* **172**(3–4), 356.

Christensen, U.R. *et al.*, 2001. A numerical dynamo benchmark, *Phys. Earth planet. Inter.,* **128,** 25–34.

Dormy, E., Cardin, P. & Jault, D., 1998. MHD flow in a slightly differentially rotating spherical shell, with conducting inner core, in a dipolar magnetic field, *Earth planet. Sci. Lett.,* **160**(1–2), 15–30.

Glatzmaier, G.A. & Roberts, P.H., 1995. A three-dimensional convective dynamo solution with rotating and finitely conducting inner core and mantle, *Phys. Earth planet. Inter.,* **91**(1–3), 63–75.

Guermond, J.-L., Laguerre, R., Léorat, J. & Nore, C., 2007. An interior penalty Galerkin method for the MHD equations in heterogeneous domains, *J. Comput. Phys.,* **221**(1), 349–369.

Guermond, J.-L., Laguerre, R., Léorat, J. & Nore, C., 2009. Nonlinear magnetohydrodynamics in axisymmetric heterogeneous domains using a Fourier/finite element technique and an interior penalty method, *J. Comput. Phys.,* **228**(8), 2739–2757.

Guermond, J.-L., Léorat, J., Luddens, F., Nore, C. & Ribeiro, A., 2011. Effects of discontinuous magnetic permeability on magnetodynamic problems, *J. Comput. Phys.,* **230**(16), 6299–6319.

Hauke, G. & Hughes, T., 1994. A unified approach to compressible and incompressible flows, *Comput. Methods Appl. Mech. Eng.,* **113**(3–4), 389–395.

Hindmarsh, A.C., Brown, P.N., Grant, K.E., Lee, S.L., Serban, R., Shumaker, D.E. & Woodward, C.S., 2005. Sundials: suite of nonlinear and differential/algebraic equation solvers, *ACM Trans. Math. Softw.,* **31**(3), 363–396.

Hollerbach, R., 2000. A spectral solution of the magneto-convection equations in spherical geometry, *Int. J. Numer. Methods Fluids,* **32**(7), 773–797.

Jackson, A. *et al.*, 2013. A spherical shell numerical dynamo benchmark with pseudo-vacuum magnetic boundary conditions, *Geophys. J. Int.,* **196**(2), 712–723.

Jacobs, J.A., 1953. The Earth's inner core, *Nature,* **172**(4372), 297–298.

Jones, C.A., Boronski, P., Brun, A.S., Glatzmaier, G.A., Gastine, T., Miesch, M.S. & Wicht, J., 2011. Anelastic convection-driven dynamo benchmarks, *Icarus,* **216**(1), 120–135.

Jouve, L. *et al.*, 2008. A solar mean field dynamo benchmark, *A&A,* **483**(3), 949–960.

Kageyama, A. & Sato, T. Complexity Simulation Group, 1995. Computer simulation of a magnetohydrodynamic dynamo. II, *Phys. Plasmas,* **2**(5), 1421–1431.

Kaiser, J. & Kuo, F., 1966. *Systems Analysis by Digital Computer,* Wiley.

Karypis, G. & Kumar, V., 2009. METIS: Unstructured Graph Partitioning and Sparse Matrix Ordering System, Version 4.0, University of Minnesota.

Kim, J. & Moin, P., 1985. Application of a fractional-step method to incompressible navier-stokes equations, *J. Comput. Phys.,* **59**(2), 308–323.

Livermore, P.W., 2012. The spherical harmonic spectrum of a function with algebraic singularities, *J. Fourier Anal. Appl.,* **18,** 1146–1166.

Livermore, P.W. & Hollerbach, R., 2012. Successive elimination of shear layers by a hierarchy of constraints in inviscid spherical-shell flows, *J. Math. Phys.,* **53**(7), 073104, doi:10.1063/1.4736990.

Livermore, P.W., Jones, C.A. & Worland, S.J., 2007. Spectral radial basis functions for full sphere computations, *J. Comput. Phys.,* **227**(2), 1209–1224.

Marti, P., 2012. Convection and boundary driven flows in a sphere, *PhD thesis,* ETH Zurich.

Matsushima, T. & Marcus, P., 1995. A spectral method for polar coordinates, *J. Comput. Phys.,* **120**(2), 365–374.

Monteux, J., Schaeffer, N., Amit, H. & Cardin, P., 2012. Can a sinking metallic diapir generate a dynamo? *J. geophys. Res. Planets,* **117,** E10005, doi:10.1029/2012JE004075.

Oliphant, T.E., 2007. Python for scientific computing, *Compu. Sci. Eng.,* **9**(3), 10–20.

Sasaki, Y., Takehiro, S. & Hayashi, Y.-Y. SPMODEL Development Group, 2012. Project of MHD Dynamo in rotating spheres and spherical shells. Available at: http://www.gfd-dennou.org/library/dynamo/, last accessed 9 January 2014.

Schaeffer, N., 2013. Efficient spherical harmonic transforms aimed at pseudo-spectral numerical simulations, *Geochem. Geophys. Geosyst.,* **14**(3), 751–758.

Simitev, R. & Busse, F., 2005. Prandtl-number dependence of convection-driven dynamos in rotating spherical fluid shells, *J. Fluid Mech.,* **532,** 365–388.

Simitev, R. & Busse, F., 2012. How far can minimal models explain the solar cycle? *Astrophys. J.,* **749**(1), 9, doi:10.1088/0004-637X/749/1/9.

Simitev, R.D. & Busse, F.H., 2009. Bistability and hysteresis of dipolar dynamos generated by turbulent convection in rotating spherical shells, *Europhys. Lett.,* **85**(1), 19001, doi:10.1209/0295-5075/85/19001.

Tilgner, A., 1999. Spectral methods for the simulation of incompressible flows in spherical shells, *Int. J. Numer. Methods Fluids,* **30**(6), 713–724.

Tilgner, A. & Busse, F., 1997. Finite-amplitude convection in rotating spherical fluid shells, *J. Fluid Mech.,* **332**(1), 359–376.

Vantieghem, S., 2011. Numerical simulations of quasi-static magnetohydrodynamics using an unstructured finite volume solver: development and applications, *PhD thesis,* Universitée Libre de Bruxelles.

Worland, S., 2004. Magnetoconvection in rapidly rotating spheres, *PhD thesis,* University of Exeter.

Zhan, X., Schubert, G. & Zhang, K., 2012. Anelastic convection-driven dynamo benchmarks: a finite element model, *Icarus,* **218**(1), 345–347.

APPENDIX A: SPHERICAL HARMONICS

The Schmidt quasi-normalized spherical harmonic basis was used to provide a simpler expression for the initial conditions. The spherical harmonic $\mathcal{Y}_l^m$ of degree l and order m is given by

$$\mathcal{Y}_l^m(\theta,\varphi) = P_l^m(\cos\theta)\mathrm{e}^{\mathrm{i}m\varphi}, \tag{A1}$$

where the $P_l^m(\cos\theta)$ are the Schmidt quasi-normalized associated Legendre functions. The above definition of the spherical harmonic can also be written as function of the normalized associated Legendre functions $\widehat{P}_l^m(\cos\theta)$ leading to the expression

$$\mathcal{Y}_l^m(\theta,\varphi) = \sqrt{\frac{(l-m)!}{(l+m)!}}\,\widehat{P}_l^m(\cos\theta)\mathrm{e}^{\mathrm{i}m\varphi}. \tag{A2}$$

The orthogonality relation for the $\mathcal{Y}_l^m$ defined above is given by

$$\int_0^{\pi}\int_0^{2\pi} \mathcal{Y}_l^m \mathcal{Y}_{l'}^{m'*}\,\mathrm{d}\Omega = \frac{4\pi(2-\delta_{m0})}{2l+1}\delta_{ll'}\delta_{mm'}, \tag{A3}$$

where the $*$ denotes the complex conjugate.

P-$\dot{\rho}$-T measurements of H_2O up to 260 GPa under laser-driven shock loading

T. Kimura, N. Ozaki, T. Sano, T. Okuchi, T. Sano, K. Shimizu, K. Miyanishi, T. Terai, T. Kakeshita, Y. Sakawa, and R. Kodama

Citation: J. Chem. Phys. **142**, 164504 (2015); doi: 10.1063/1.4919052
View online: http://dx.doi.org/10.1063/1.4919052
View Table of Contents: http://aip.scitation.org/toc/jcp/142/16
Published by the American Institute of Physics

P-ρ-T measurements of H_2O up to 260 GPa under laser-driven shock loading

T. Kimura,[1,2] N. Ozaki,[2,3] T. Sano,[4] T. Okuchi,[5] T. Sano,[2] K. Shimizu,[6] K. Miyanishi,[2] T. Terai,[2] T. Kakeshita,[2] Y. Sakawa,[4] and R. Kodama[2,3]
[1]*Geodynamics Research Center, Ehime University, 2-5 Bunkyo-cho, Matsuyama, Ehime 790-8577, Japan*
[2]*Graduate School of Engineering, Osaka University, Suita, Osaka 565-0871, Japan*
[3]*Photon Pioneers Center, Osaka University, Suita, Osaka 565-0871, Japan*
[4]*Institute of Laser Engineering, Osaka University, Suita, Osaka 565-0871, Japan*
[5]*Institute for Study of the Earth's Interior, Okayama University, Misasa, Tottori 682-0193, Japan*
[6]*KYOKUGEN, Center for Science and Technology under Extreme Conditions, Osaka University, Toyonaka, Osaka 560-8531, Japan*

(Received 15 December 2014; accepted 13 April 2015; published online 23 April 2015)

Pressure, density, and temperature data for H_2O were obtained up to 260 GPa by using laser-driven shock compression technique. The shock compression technique combined with the diamond anvil cell was used to assess the equation of state models for the *P-ρ-T* conditions for both the principal Hugoniot and the off-Hugoniot states. The contrast between the models allowed for a clear assessment of the equation of state models. Our *P-ρ-T* data totally agree with those of the model based on quantum molecular dynamics calculations. These facts indicate that this model is adopted as the standard for modeling interior structures of Neptune, Uranus, and exoplanets in the liquid phase in the multi-Mbar range. © *2015 AIP Publishing LLC.* [http://dx.doi.org/10.1063/1.4919052]

I. INTRODUCTION

H_2O is thought to be one of the most abundant compounds in ice giants such as Neptune and Uranus (e.g., Ref. 1). Therefore, the equation of state (EOS) for H_2O is critical for understanding the formation and composition of these planets and their temperature and pressure distributions. The ANEOS[2] and SESAME models[3] and the model based on quantum molecular dynamics (QMD) calculations[4,5] have been employed for modeling the interior structure of the ice giants. Recent shock experiments reported that their pressure and density data of H_2O are in good agreement with those of the QMD based EOS model,[6] indicating that this model is most suitable for modeling H_2O in the ice giants.

The QMD model predicted that a superionic conductor of H_2O exists in the deep interior of the icy planets above ~100 GPa.[4,7] Superionic H_2O is an ionic solid system that has high ionic conductivity well below the melting temperature.[8] Whether H_2O is in the superionic or liquid state in the planetary interior is of great importance to understanding the source of the planetary magnetic field.[9,10] Although some experimental studies reported the existence of the superionic phase,[11,12] recent measurements of the melting temperature of H_2O above the superionic phase show low melting temperatures and a quite gentle melting curve compared with those of the QMD prediction,[13] which implies that H_2O should remain in the liquid state even at deep interior conditions. This discrepancy between experimental and theoretical studies suggests that the QMD based EOS model is disputable for modeling the planetary interior. Indeed, the comparison between data obtained from the shock experiments and the QMD based EOS did not even cover the temperature.[6] Furthermore, the disagreement in the temperature of the kink of the melting curve between those of the experiments and the QMD based EOS is noteworthy. In fact, the temperature difference (T = 1000–1500 K) is larger than that of pressure (P = 35–47 GPa).[7,11] Taking into account these facts, EOS measurements covering pressure, density, and temperature (*P-ρ-T*) at extremely high pressures and temperatures are essential.

The laser-driven shock compression technique is useful for generating high pressure and temperature conditions comparable to the deep interiors of Neptune and Uranus. However, simultaneous measurements of *P-ρ-T* are challenging, especially temperature, because this requires absolute intensity measurements unlike the determination of the pressure or the density. In this study, we performed laser-driven shock experiments for H_2O up to 260 GPa and determined temperature from measured reflectivity and thermal emission, along with pressure and density. We also achieved temperature conditions lower than the principal Hugoniot states, which are comparably close to the planetary isentropes, by using the precompression cell applied for laser shock experiments.[14] The dataset of the principal and the off Hugoniot states can clarify the most validated EOS model.

II. EXPERIMENTAL PROCEDURE

The experiments were performed on the GEKKO/HIPER (High Intensity Plasma Experimental Research) laser facility at the Institute of Laser Engineering, Osaka University. In the experiments, we used nine beams of the system at a wavelength of 351 nm. A temporal profile of the laser pulse

was approximately a square shape in time with a full width at half maximum (FWHM) of 2.5 ns and the rise and fall times of 100 ps each. The focal-spot diameter was 600 μm with a flat top profile. Kinoform phase plates were used to achieve a uniform irradiation pattern. Spatially averaged intensities were 3.2×10^{13} to 6.9×10^{13} W/cm^2.[15]

A line-imaging velocity interferometer system for any reflector (VISAR) measured a shock velocity and a reflectivity in the sample.[16,17] An injection-seeded, Q-switched YAG laser was used as a probe-light source (532 nm/10 ns FWHM) in the VISAR, which irradiated the rear side of the target. Two VISARs with different velocity sensitivities were used to avoid the 2π phase-shift ambiguity due to the shock velocity jump at material interfaces. The velocity sensitivities were 4.78 and 11.3 (or 17.1) (km/s)/fringe in the water at ambient pressure with a density of 0.998 g/cm^3. The shock temperatures were measured with a different diagnostic tool. It consisted of a streaked optical pyrometer (SOP)[18,19] for a wavelength of 455 nm with 38 nm bandwidth. Spatially and temporally resolved temperatures were obtained from the self-emission of the shock-compressed matter with the absolutely calibrated SOP.

Ultra-pure water was loaded in the precompression cell for the laser-driven shock experiments. The diamond cell increased the initial pressure of the sample between 0.51 and 0.58 GPa. The samples at ambient pressure were also enclosed in the same cell. A detailed description of the cell was provided in our previous paper.[14] The thicknesses of thin (drive laser side) and thick (diagnostic side) diamonds were between 100 and 250 μm and 1000 μm, respectively. The thickness of the sample chamber was between 70 and 165 μm. The drive side of the thin diamond was coated with a gold x-ray preheat shield and a polypropylene ablator. The thickness of the Au shield and the CH ablator was 1.5 μm and 30 μm, respectively. On the sample chamber side, a z-cut α quartz was placed on the diamond and used as a reference standard for the impedance matching measurement.[20,21] The quartz thickness was 35 or 65 μm. There was an aluminum flash coating on the drive laser side of the quartz plate to clarify the breakout timing from the thin diamond. The thickness of the Al was 100 or 300 nm. Both sides of the thick rear diamond have antireflection coatings so that the VISAR does not detect spurious reflections from the stationary interfaces during shock loading. Initial pressure (P_0) was measured via the ruby fluorescence method.[22] The determination accuracy of the P_0 is better than ±50 MPa. The initial density (ρ_0) and refractive index (n_0) were derived from the EOS model for water at ambient pressure.[23,24]

III. RESULTS AND DISCUSSION

Figure 1 shows a velocity record extracted from the VISAR velocimetry image (inset in the Fig. 1). The time zero (t = 0) represents the shock breakout time from the Al coating. Both the shocked quartz and water are reflected during the transit across their layers, indicating that they transform to electronic conductors and the shock fronts reflect the 532 nm probe laser light of the VISAR diagnostic. Thus, the shock velocities of quartz and water (U_s^Q and U_s^w) were measured directly from the VISAR fringe shifts. The transit distance

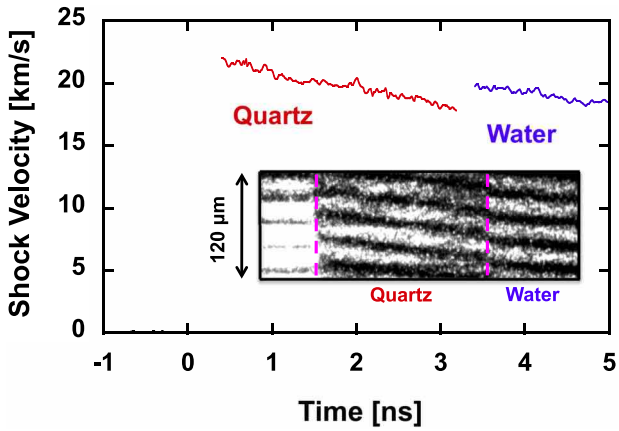

FIG. 1. Shock velocity in both quartz and water obtained from VISAR. The inset shows the corresponding raw VISAR image.

in both quartz and water determined from the time-integrated VISAR velocity is in agreement with the thicknesses measured before the experiments.

Figure 1 shows that the U_s^Q decays with time to a velocity of less than 80% of the maximum for ~2.5 ns. This velocity decay has to be taken into account for performing the impedance matching analysis (IMA). We adopted the U_s^Q and U_s^w immediately before and after the quartz–water interface for the IMA. A time gap found in the vicinity of where the shock transition from quartz to water was 70-150 ps, which is comparable to the temporal resolution of the streak camera of ~100 ps. To precisely determine the velocity at the interface time, we linearly fitted the velocities over 0.5 ns and extrapolated to forward or backward the impedance-matching time.[25] The velocities were calculated by averaging the shock profile over 100 ps. Here, we neglected the preheat effect, which was estimated to be less than 0.03 eV from radiation hydrodynamic simulations with the MULTI code.[26]

The particle velocity and pressure of quartz u_p^Q and P^Q were extracted from the measured U_s^Q and a Hugoniot U_s-u_p relation established by the Sandia Z-accelerator experiments; $U_s^Q = a + b\,u_p^Q - c\,u_p^Q e^{-d u_p^Q}$, where $a = 6.26 \pm 0.35$ km/s, $b = 1.20 \mp 0.02$, $c = 2.56 \mp 0.15$, and $d = 0.37 \pm 0.02$ (km/s).[21] In order to determine H_2O Hugoniot states, the knowledge of the release isentrope for quartz is required. In this work, we used the inverted quartz Hugoniot as an approximation of the release isentrope. The IMA provides the Hugoniot state of water, the intersection of the quartz release curve, and the water Rayleigh line ($P = \rho_0{}^W U_s{}^W u_p$) in the P-u_p plane.[27]

The results of the EOS data for the water are listed in Table I. U_s^Q and U_s^W are direct experimental observables, which are obtained as a fringe shift at the image of the VISAR. The velocity uncertainty ≦1.5% was achieved because the fringe position was determined to ~4% of a fringe and the shock velocities measured here correspond to 3–4 fringes. P^W and ρ^W were determined from U_s^W and u_p^W using the Rankine-Hugoniot conservations.[27] The random errors for P^W and ρ^W arising from the measurement uncertainties were estimated with a Monte Carlo algorithm based on the assumption of Gaussian distribution about each observable.[28]

TABLE I. Principal and off-Hugoniot data for water. Random and systematic uncertainties are listed in parentheses (ran and sys). NP means normal (i.e., ambient) pressure.

Shot no.	$P_0{}^W$ (GPa)	$\rho_0{}^W$ (g/cm^3)	$U_s{}^Q$ (km/s)	$U_s{}^W$ (km/s)	$u_p{}^W$ (km/s)	P^W (GPa)	ρ^W (g/cm^3)
33522	NP	0.998	17.77 ± 0.19	19.83 ± 0.22	13.05 ± (0.22, 0.25)	258.2 ± (4.9, 4.9)	2.92 ± (0.12, 0.11)
33687	NP	0.998	13.88 ± 0.20	15.10 ± 0.23	9.58 ± (0.21, 0.35)	144.4 ± (3.6, 5.3)	2.74 ± (0.14, 0.19)
33679	0.53 ± 0.04	1.16 ± 0.01	16.62 ± 0.21	18.75 ± 0.23	11.51 ± (0.22, 0.28)	250.4 ± (5.4, 6.0)	3.00 ± (0.12, 0.12)
33696	0.58 ± 0.05	1.17 ± 0.01	13.05 ± 0.21	14.57 ± 0.23	8.47 ± (0.21, 0.37)	144.7 ± (3.9, 6.2)	2.79 ± (0.12, 0.19)
33705	0.51 ± 0.03	1.15 ± 0.01	14.42 ± 0.21	15.80 ± 0.23	9.69 ± (0.21, 0.34)	176.7 ± (4.2, 6.1)	2.98 ± (0.14, 0.17)

Total error includes systematic uncertainties in the quartz EOS used in the analysis as well as the measurement uncertainties and was estimated as a quadrature sum of both random and systematic uncertainties.

Figure 2(a) shows the principal Hugoniot plots in the P-ρ plane for water together with the results of the previous works[6,29–31] as well as the EOS models.[3–5] Estimated total uncertainties of the density in the present study are between 5.6% and 8.5%. The shock densities exhibit significant differences between the data of Knudson *et al.*[6] and Celliers *et al.*[29] in the intermediate region between the available gas-gun and the nuclear explosion experiments. The data obtained in this study are in good agreement with the data of Knudson *et al.*[6] rather than Celliers *et al.*[29] It is likely that the use of the aluminum step for IMA by Celliers *et al.*[29] gives a comparatively high density because the apparent shock velocity of the standard should be slightly faster due to averaging the shock profile in this step. Although our approximation of the release isentrope of the quartz is different from that of Knudson *et al.*,[6] their data agree well with our data within the error. Indeed, a density shift estimated based on an assumption that the release isentrope predicted by the QMD method has confidence is only ~2%,[32] which is small enough compared to the density error. Fig. 2(b) shows the off-Hugoniot states together with the data from Lee *et al.*[33] of which the initial pressures are close to 0.5 GPa (0.4 and 0.68 GPa) and the states predicted by the QMD and SESAME models.[3–5] The densities obtained in this study are lower than the data of Lee *et al.*[33] for the same reason as for the case of Celliers *et al.*,[29] as described above. Our data for both the principal and the off-Hugoniot states are in good agreement with those of the QMD based EOS model, as well as with the results of the measurements obtained by Knudson *et al.*[6]

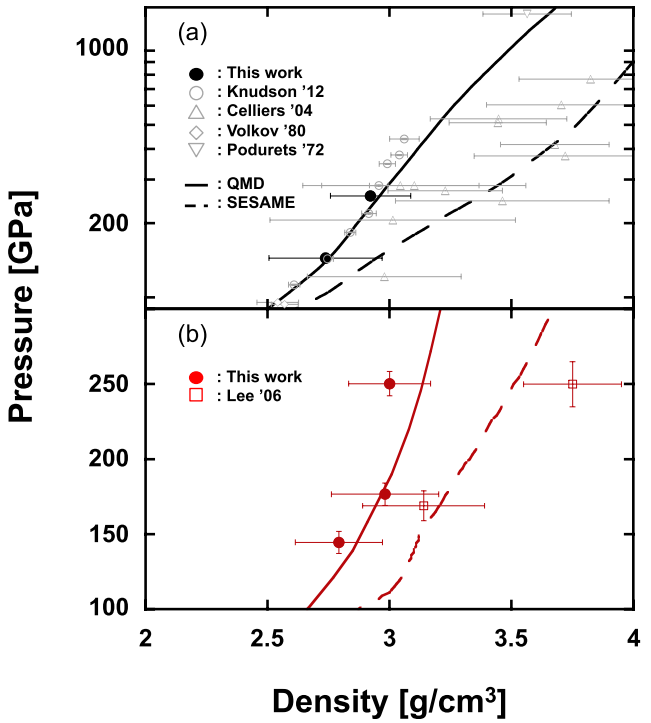

FIG. 2. (a) Principal Hugoniot plots in P-ρ plane for water. Data are from Celliers *et al.*[29] (triangle), Knudson *et al.*[6] (open circles), Volkov *et al.*[30] (diamonds), and this work (closed circles). Also, datum is from Podurets *et al.*[31] reanalyzed by Knudson *et al.*[6] using improved aluminum standard (inverted triangle). Also shown are the QMD based EOS model[4,5] (solid line) and SESAME model[3] (dashed line). (b) Off-Hugoniot plots obtained in this study (closed circles) together with data from *Lee et al.*[33] of which the initial pressures are near to 0.5 GPa (0.4 and 0.68 GPa) (open squares). Also shown are the EOS models same as in (a). Black and red colors represent the principal Hugoniot states and the off-Hugoniot states starting from 0.5 GPa, respectively.

The VISAR streak camera detected the intensities reflected from the observed shock fronts. In this work, the reflectivity of the shocked water was determined from the ratio of intensities just before and after the shock crossed the quartz–water interface.[34,35] The reflected intensity and the known reflectivity of quartz as a function of shock velocity provide the reflectivity of water.[34] The results of the reflectivity are listed in Table II. The total error includes measurement uncertainty and systematic uncertainty in quartz reflectivity. The reflectivities of the off-Hugoniot states are slightly lower than those of the principal Hugoniot, which indicate decreasing free carriers generated by thermal activation. The reflectivity data of the principal Hugoniot states are in good agreement with those of Knudson *et al.*,[6] as well as with the prediction from the QMD calculations of the Heyd, Scuseria, and Ernzerhof (HSE) exchange-correlation functional.[5]

The temperature T^W was measured using a SOP.[19] Recorded SOP intensities were modeled assuming a gray-body Planckian spectrum given by

$$I(\lambda,T) = \varepsilon(\lambda)\frac{2hc^2}{\lambda^5}\frac{1}{e^{hc/\lambda T}-1}, \quad (1)$$

where T is the temperature, ε is the emissivity, h is Planck's constant, and c is the speed of light. The emissivity is determined as $\varepsilon(\lambda) = 1 - R(\lambda)$, where $R(\lambda)$ is the reflectivity that is assumed to vary only slightly as a function of wavelength in the optical spectral range. We adopted the reflectivity at the VISAR wavelength assuming a weak dependence of R on the wavelength.[25] An example of the

TABLE II. Reflectivity and temperature data on the principal and the off-Hugoniot curves for water. The temperature of shot no. 33679 could not be estimated because the self-emission data were not obtained.

Shot no.	R^W (%)	T^W (10^3 K)
33522	24.0+4.0, −7.1	19.0+3.2, −3.3
33687	7.0+7.2, −3.8	9.6 ± 0.9
33679	17.3+5.1, −10.1	
33696	4.9+4.4, −2.9	7.2 ± 0.6
33705	8.2+3.8, −4.0	9.0 ± 0.9

emission intensity versus time data is shown in Fig. 3. The inset shows the raw image in the same shot. Clear intensity jumps are found in the aluminum–quartz and quartz–water interface. Shock arrival times in the interfaces from the SOP record are in agreement with those from the VISAR record. The temperature was obtained by averaging the profile of the time immediately after the quartz–water interface, over 170 ps corresponding to the temporal resolution of the streak camera.

The temperature results are listed in Table II. For shot no. 33679, the temperature could not be estimated because the self-emission data were not obtained. Estimated total uncertainty of the temperature is between 8% and 17%. This error arises from system calibration, measurements of self-emission, and the reflectivity of water. Taking into account changes in the optical property through the window due to, for instance, photo-excitation by low-level x-ray radiation generated by the ablation plasma,[34,36] we determined the sample temperature normalized to the quartz.[35] Fig. 4 shows the temperature data plotted against pressure together with the previous results[37] and Hugoniot curves predicted by the QMD based EOS and SESAME models. The temperatures of the off-Hugoniot states are significantly lower than those of the principal Hugoniot states, which is compatible with the reflectivity results. The difference in temperature between these two models significantly expands above 100 GPa. Our data of both the principal and the off-Hugoniot states are in very good agreement with those of the QMD based EOS, as well as the pressure and density results.

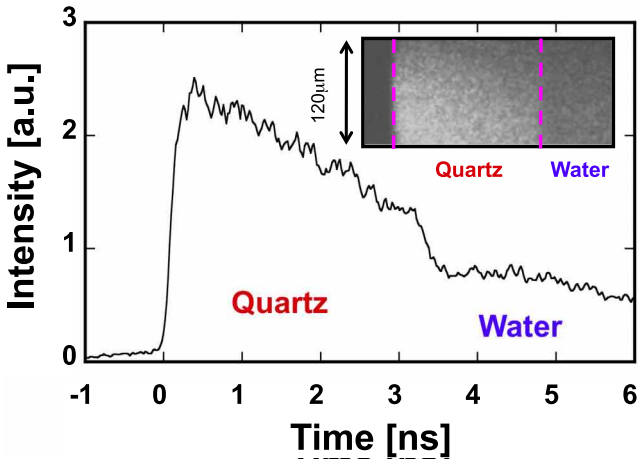

FIG. 3. Self-emission intensity in both quartz and water. The inset shows corresponding raw SOP image.

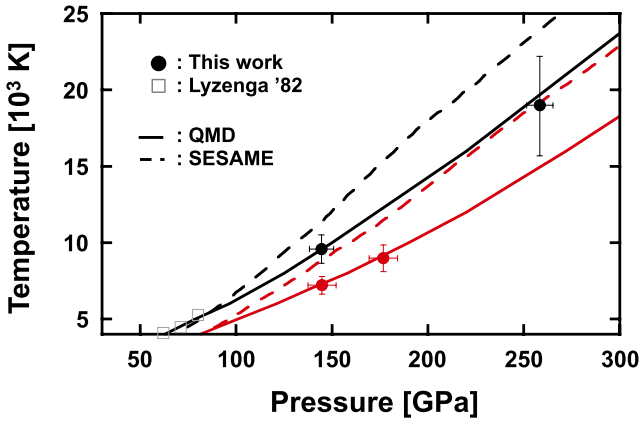

FIG. 4. Principal and off-Hugoniot data in P–T plane obtained in this study (closed circles) together with the previous results by Lyzenga *et al.*[37] (open squares). The temperature of shot no. 33679 could not be estimated because the self-emission data were not obtained. Also shown are the QMD based EOS model[4,5] (solid line) and SESAME model[3] (dashed line). Black and red colors represent the principal Hugoniot states and the off-Hugoniot states starting from 0.5 GPa, respectively.

Our data covering P-ρ-T agree well with those of the QMD based EOS. In addition, the QMD 300 K isotherm is also in good agreement with the measurements using diamond anvil cells.[38] Thus, the QMD model describes the EOS for water in solid and liquid states quite well. Moreover, the perfect agreement in reflectivity values between Knudson *et al.*,[6] the present experimental work shown here, and the QMD predictions[39] indicates that the QMD model reliably predicts electrical conductivity. The location of the superionic-to-plasma phase transition is important for understanding the dynamo source of Uranus and Neptune.[9,10] The boundary temperature estimated by the QMD calculation tends to be high compared with that obtained experimentally. For example, the predicted temperature at 70 GPa is about 2000 K,[7] on the other hand, the recent experimental study using a diamond anvil cell shows a lower temperature around 1400 K at 70 GPa.[13] A situation such as a disagreement in a melting curve though an agreement in EOS can happen since it is difficult to correlate EOS in the limited phases with the melting behavior. Especially, attention should be paid on the description for the melting from the superionic phase in which the proton has a high diffusivity. The phase transition in the QMD calculation is determined by observing the mean square displacements for oxygen ions.[4] Since melting can be thermodynamically defined in an approximate manner, the free energy comparison between solid and liquid states should be introduced in the QMD model in order to accurately determine the boundary (e.g., Ref. 40).

In addition to the fact that the experimental melting temperatures of H_2O are significantly lower than that of the QMD prediction,[13] the superionic-to-plasma phase boundary for the C–N–O–H mixture, which is a more realistic system for Uranus and Neptune, shifts downward.[41] Taking all of this into account, it is likely that the superionic ice is not present in deep interiors of their planets. Thus, the interior structure model including superionic ice is unrealistic.[10] Alternatively, the nonconvective layer in the deeper area of the icy region may be formed by a stable stratification due to the compositional

gradient.[1] The candidates as main components of the stratified layer can be C and N_2, according to some experimental studies[42–45] showing the dissociation of CH_4 and NH_3 at high pressures and temperatures. The precipitation and accretion of these heavier species may occur in the deeper region.

In summary, we have obtained P-ρ-T data for the EOS of not only the principal but also the off Hugoniot states up to 260 GPa. The dataset for the EOS on both the principal and the off Hugoniot curves is useful to assess the EOS models since it is possible to compare the states under the conditions that the contrast between the models clearly appears. We found that the QMD based model accurately describes the EOS for H_2O in the plasma phase along with the electrical property, while the location of superionic-to-plasma phase boundary is still disputable. Further work, such as EOS measurements of H_2O in the superionic phase are required for modeling the detailed structures of the icy giants as well as exoplanets. The laser-driven shock compression technique combined with the precompression cell allows us to approach such planetary internal conditions unreachable by conventional methods.

ACKNOWLEDGMENTS

We thank M. French for provision of the EOS of the off-principal Hugoniot where P_0 is 0.5 GPa and useful discussions about the *ab initio* calculations. We also thank Y. Hori, Y. Kuwayama, H. Dekura, Y. Tange, M. Nishi, and S. Whitaker for their helpful comments. We are deeply grateful to the GEKKO technical crew for their exceptional support during these experiments. This work was partially performed under the joint research project of the Institue of Laser Engineering, Osaka University. This work was supported by grants for the Global COE Program from the MEXT of Japan, and the CREST from JST. This work was also supported by grants from Grants-in-Aid for Scientific Research (Grant Nos. 25707041 and 22224012) and the Core-to-Core Program on International Alliance for Material Science in Extreme States with High Power Laser and XFEL of the Japan Society for the Promotion of Science.

[1]W. B. Hubbard, M. Podolak, and D. J. Stevenson, *The Interior of Neptune: Neptune and Triton* (University of Arizona Press, Tucson, 1995), pp. 109–138.
[2]S. P. Lyon and J. D. Johnson, Los Alamos Technical Report No. LA-UR-92-3407, 1992.
[3]National Technical Information Service Document No. DE94–011699 (J. D. Johnson, SESAME Tavles, 1994). Copies may be ordered from the National Technical Information Service, Springfield, VA 22161. For the water, we used SESAME Table 7150.
[4]M. French, T. R. Mattsson, N. Nettelmann, and R. Redmer, Phys. Rev. B **79**, 054107 (2009).
[5]M. French and R. Redmer, J. Phys.: Condens. Matter **21**, 375101 (2009).
[6]M. D. Knudson, M. P. Desjarlais, R. W. Lemke, T. R. Mattsson, M. French, N. Nettelmann, and R. Redmer, Phys. Rev. Lett. **108**, 091102 (2012).
[7]R. Redmer, T. R. Mattsson, N. Nettelmann, and M. French, Icarus **211**, 798 (2011).
[8]C. Cavazzoni, G. L. Chiarotti, S. Scandolo, E. Tosatti, M. Bernasconi, and M. Parrinello, Science **283**, 44 (1999).
[9]S. Stanley and J. Bloxham, Nature **428**, 151 (2004).
[10]B. Y. Tian and S. Stanley, Astrophys. J. **768**, 156 (2013).
[11]A. F. Goncharov, N. Goldman, L. E. Fried, J. C. Crowhurst, I. W. Kuo, C. J. Mundy, and J. M. Zaug, Phys. Rev. Lett. **94**, 125508 (2005).
[12]E. Sugimura, T. Komabayashi, K. Ohta, K. Hirose, Y. Ohishi, and L. S. Dubrovinsky, J. Chem. Phys. **137**, 194505 (2012).
[13]T. Kimura, T. Kuwayama, and T. Yagi, J. Chem. Phys. **140**, 074501 (2014).
[14]T. Kimura, N. Ozaki, T. Okuchi, T. Terai, T. Sano, K. Shimizu, T. Sano, M. Koenig, A. Hirose, T. Kakeshita, Y. Sakawa, and R. Kodama, Phys. Plasmas **17**, 054502 (2010).
[15]N. Ozaki, T. Sano, M. Ikoma, K. Shigemori, T. Kimura, K. Miyanishi, T. Vinci, F. H. Ree, H. Azechi, T. Endo, Y. Hironaka, Y. Hori, A. Iwamoto, T. Kadono, H. Nagatomo, M. Nakai, T. Norimatsu, T. Okuchi, K. Ohtani, T. Sakaiya, K. Shimizu, A. Shiroshita, A. Sunahara, H. Takahashi, and R. Kodama, Phys. Plasmas **16**, 062702 (2009).
[16]L. Barker and R. Hollenbach, J. Appl. Phys. **43**, 4669 (1972).
[17]P. M. Celliers, D. K. Bradley, G. W. Collins, D. G. Hicks, T. R. Boely, and W. J. Armstrong, Rev. Sci. Instrum. **75**, 4916 (2004).
[18]G. W. Collins, P. M. Celliers, L. B. Da Silva, R. Cauble, D. M. Gold, M. E. Foord, N. C. Holmes, B. A. Hammel, R. J. Wallace, and A. Ng, Phys. Rev. Lett. **87**, 165504 (2001).
[19]J. E. Miller, T. R. Boehly, A. Melchior, D. D. Meyerhofera, P. M. Celliers, J. H. Eggert, D. G. Hicks, C. M. Sorce, J. A. Oertel, and P. M. Emmel, Rev. Sci. Instrum. **78**, 034903 (2007).
[20]D. G. Hicks, T. R. Boehly, P. M. Celliers, J. H. Eggert, E. Vianello, D. D. Meyerhofer, and G. W. Collins, Phys. Plasmas **12**, 082702 (2005).
[21]M. D. Knudson and M. P. Desjarlais, Phys. Rev. Lett. **103**, 225501 (2009).
[22]H. K. Mao, P. M. Bell, J. W. Shaner, and D. J. Steinberg, J. Appl. Phys. **49**, 3276 (1978).
[23]W. Wagner and A. Pruß, J. Phys. Chem. Ref. Data **31**, 387 (2002).
[24]H. Shimizu, T. Nabetani, T. Nishiba, and S. Sasaki, Phys. Rev. B **53**, 6107 (1996).
[25]T. Sano, N. Ozaki, T. Sakaiya, K. Shigemori, M. Ikoma, T. Kimura, K. Miyanishi, T. Endo, A. Shiroshita, H. Takahashi, T. Jitsui, Y. Hori, Y. Hironaka, A. Iwamoto, T. Kadono, M. Nakai, T. Okuchi, K. Ohtani, K. Shimizu, T. Kondo, R. Kodama, and K. Mima, Phys. Rev. B **83**, 054117 (2011).
[26]R. Ramis, R. Schmalz, and J. Meyer-ter-Vehn, Comput. Phys. Commun. **49**, 475 (1988).
[27]Y. B. Zel'dovich and Y. P. Raizer, *Physics of Shock Waves and High—Temperature Hydrodynamic Phenomena* (Academic Press, New York, 1966).
[28]J. Eggert, S. Brygoo, P. Loubeyre, R. S. McWilliams, P. M. Celliers, D. G. Hicks, T. R. Boehly, R. Jeanloz, and G. W. Collins, Phys. Rev. Lett. **100**, 124503 (2008).
[29]P. M. Celliers, G. W. Collins, D. G. Hicks, M. Koenig, E. Henry, A. Benuzzi-Mounaix, D. Batani, D. K. Bradley, L. B. Da Silva, R. J. Wallace, S. J. Moon, J. H. Eggert, K. K. M. Lee, L. R. Benedetti, R. Jeanloz, I. Masclet, N. Dague, B. Marchet, M. Rabec le Gloahec, Ch. Reverdin, J. Pasley, O. Willi, D. Neely, and C. Danson, Phys. Plasmas **11**, L41 (2004).
[30]L. P. Volkov, N. P. Voloshin, R. A. Mangasarov, V. A. Simonenko, G. V. Sin'ko, and V. L. Sorokin, JETP Lett. **31**, 375 (1980).
[31]M. A. Podurets, G. V. Simakov, R. F. Trunin, L. V. Popov, and B. N. Moiseev, Sov. Phys. JETP **35**, 375 (1972).
[32]M. D. Knudson and M. P. Desjarlais, Phys. Rev. B **88**, 184107 (2013).
[33]K. K. M. Lee, L. R. Benedetti, R. Jeanloz, P. M. Celliers, J. H. eggert, D. G. Hicks, S. J. Moon, E. Henry, M. Koenig, and A. Benuzzi-Mounaix, J. Chem. Phys. **125**, 014701 (2006).
[34]P. M. Celliers, P. Loubeyre, J. H. Eggert, S. Brygoo, R. S. McWilliams, D. G. Hicks, T. R. Boehly, R. Jeanloz, and G. W. Collins, Phys. Rev. Lett. **104**, 184503 (2010).
[35]M. A. Barrios, D. G. Hicks, T. R. Boehly, D. E. Fratanduono, J. H. Eggert, P. M. Celliers, G. W. Collins, and D. D. Meyerhofer, Phys. Plasmas **17**, 056307 (2010).
[36]W. Theobald, J. E. Millerm, T. R. Boehly, E. Vianello, D. D. Meyerhofer, and T. C. Sangster, Phys. Plasmas **13**, 122702 (2006).
[37]G. A. Lyzenga, T. J. Ahrens, W. J. Nellis, and A. C. Mitchell, J. Chem. Phys. **76**, 12 (1982).
[38]E. Sugimura, T. Iitaka, K. Hirose, K. Kuwayama, N. Sata, and Y. Ohishi, Phys. Rev. B **77**, 214103 (2008).
[39]M. French, T. R. Mattsson, and R. Redmer, Phys. Rev. B **82**, 174108 (2010).
[40]L. Voadlo and D. Alfe, Phys. Rev. B **65**, 214105 (2002).
[41]R. Chau, S. Hamel, and W. Nellis, Nat. Commun. **2**, 203 (2010).
[42]L. R. Benedetti, J. H. Nguyen, W. A. Caldwell, H. Liu, M. Kruger, and R. Jeanloz, Science **286**, 100 (1999).
[43]H. Hirai, K. Konagai, T. Kawamura, Y. Yamamoto, and T. Yagi, Phys. Earth Planet. Inter. **174**, 242 (2009).
[44]S. S. Lobanov, P. N. Chen, X. J. Chen, C. S. Zha, K. D. Litasov, H. K. Mao, and A. F. Goncharov, Nat. Commun. **4**, 2446 (2013).
[45]J. G. O. Ojwang, R. S. McWilliams, X. Ke, and A. F. Goncharov, J. Chem. Phys. **137**, 064507 (2012).

J. Fluid Mech. (2015), *vol.* 774, *pp.* 224–244.
doi:10.1017/jfm.2015.262

Bifurcation structure of two-dimensional viscous zonal flows on a rotating sphere

Eiichi Sasaki[1,†], Shin-ichi Takehiro[2] and Michio Yamada[2]

[1]Graduate School of Informatics, Kyoto University, Kyoto 606-8501, Japan

[2]Research Institute for Mathematical Sciences, Kyoto University, Kyoto 606-8502, Japan

(Received 1 April 2014; revised 20 January 2015; accepted 1 May 2015;
first published online 5 June 2015)

We study the bifurcation structure of zonal flows on a rotating sphere. The setting of our problem is similar to the Kolmogorov problem on a flat torus, where the vorticity forcing is given by a single eigenfunction of the Laplacian. First we prove the global stability of two-jet zonal flow for arbitrary Reynolds number and the rotation rate of the sphere. Then we study the bifurcation structure of steady solutions arising from three-jet zonal flow. In the non-rotating case, we find that two steady travelling-wave solutions bifurcate from a three-jet zonal flow via Hopf bifurcation. As the Reynolds number increases, steady-travelling solutions arise via pitchfork bifurcation from the steady-travelling solutions. On the other hand, in the rotating case, we find saddle-node bifurcations and closed-loop branches. We carry out time integration to study the properties of unsteady solutions at high Reynolds numbers. In the non-rotating case, the unsteady solution is chaotic and it wanders around the steady-travelling solutions bifurcating from three-jet zonal flow. We show that a linear combination of the steady and steady-travelling solutions gives a good approximation of the zonal-mean zonal flow of the unsteady solution, suggesting that the chaotic solution at high Reynolds numbers exists mostly within a relatively low-dimensional space spanned by the steady and steady-travelling solutions, which become unstable at low Reynolds numbers.

Key words: bifurcation, chaos, rotating flows

1. Introduction

Stability of two-dimensional (2D) parallel flows is one of the fundamental problems in fluid dynamics, and bifurcation structures, as well as linear and nonlinear stabilities of many types of planar parallel flows, have been investigated in relation to various fluid phenomena in nature and engineering. In a plane, the 2D parallel flows are dependent only on a single coordinate of an orthogonal coordinate system. Similar problems arise for flows on a non-rotating and rotating sphere. Zonal flows on a sphere, often observed on planets and the sun, are in the azimuthal direction, sometimes making stripe patterns in planetary atmospheres. Note that the rotation has an effect on the 2D incompressible flows on a sphere, while it does not in a planar case.

† Present address: Graduate School of Engineering Science, Osaka University, Osaka 560-8531, Japan. Email address for correspondence: esasaki@me.es.osaka-u.ac.jp

Baines (1976) studied the inviscid linear stability of typical zonal flows on a sphere, the streamfunction of which is expressed by a single spherical harmonics Y_l^0. He solved the eigenvalue problem numerically by the spectral method. The inflection-point theorem, which gives a sufficient condition for linear stability, says that any zonal flow is linearly stabilized when the rotation rate is large enough (see Kuo 1949). Therefore the inviscid zonal flow has the critical rotation rate at which it is marginally stable. He obtained the critical rotation rate numerically, and found that it is only slightly different from the estimates obtained from the inflection-point theorem. Recently, Sasaki, Takehiro & Yamada (2012), however, re-studied the linear stability of the inviscid zonal flows in the same way as Baines (1976) but with a higher truncation wavenumber. They found that the numerical calculation is still problematic because of emergence of the critical layer, and obtained accurate values of the critical rotation rates with special attention to the critical layers. On the other hand, in the viscous case, Sasaki, Takehiro & Yamada (2013) studied the linear stability of the same type of zonal flow. They found that as the rotation rate increases, the critical Reynolds number, where zonal flow loses stability, increases rapidly, and zonal flow is linearly stable at Reynolds numbers less than 10^6 when the rotation rate is large enough. This stabilization by rotation appears to be consistent with the inviscid case described above.

In this paper we first study the nonlinear regime of the stability of viscous zonal flows on a rotating sphere, i.e. the bifurcation structure of zonal flows, with the Reynolds number and the rotation rate being the bifurcation parameters. We consider 2D incompressible viscous zonal flows driven by a forcing expressed by a single spherical harmonics Y_l^0. In a limited range of the rotation rate including the non-rotating case, we find that zonal flows are unstable when the Reynolds number is large enough. In order to find how the solution behaves in the unstable region, we carry out numerical time integration at high Reynolds numbers in the non-rotating case, and study the possibility of describing the chaotic solution with a linear combination of unstable steady and travelling solutions.

We should remark that our problem setting is similar to the Kolmogorov problem (Obukhov 1983). The Kolmogorov problem was first proposed by Kolmogorov in his seminar in the 1960s to study mathematical structures of solutions of the Navier–Stokes equations. The problem deals with a viscous incompressible 2D fluid in a double-periodic domain, a flat torus, with sine-type unidirectional external forcing, and gives a typical and fundamental example of transitions from laminar flow to turbulence. Iudovisch (1965) proved that two-jet parallel flow is globally stable for arbitrary Reynolds number, and Meshalkin & Sinai (1962) proved that the critical modes of the parallel flow are steady (not Hopf), while Iudovisch (1965) proved the existence of the bifurcation solution arising at the critical stability. The bifurcation diagram of steady solutions arising from the two-jet parallel flow was studied by Okamoto & Shōji (1993) for several aspect ratios of the flat torus. They found various types of bifurcation, including saddle-node bifurcation, Hopf bifurcation and secondary bifurcation. The inviscid limit of bifurcating steady solutions was studied by Kim & Okamoto (2010). They found that the flow field of nonlinear solutions becomes dominated by a pair of negative and positive vortices at high Reynolds numbers regardless of the forcing wavenumber, although those patterns are constructed by multiple vortices at low Reynolds numbers. They called this solution a unimodal solution, and suggested that at high Reynolds numbers there is at least one unimodal solution, independent of the number of jets of the original parallel flow. Note that the Kolmogorov problem has been studied from several

perspectives including transition to chaos (Platt, Sirovich & Fitzmaurice 1991), the orbital instability of chaotic flow (Inubushi *et al.* 2012) and the extraction of invariant sets from chaotic attractors (Lucas & Kerswell 2015). We will compare our results on a sphere with those of Kolmogorov flows in a planar domain. We note that a sphere (genus 0) is topologically simpler than a torus (genus 1), while a sphere has a non-zero curvature and is more complicated in the sense of differential geometry than the flat torus.

In the following, we discuss the bifurcation structure of 2D incompressible viscous zonal flows on a non-rotating/rotating sphere under zonal forcing. In § 2 we describe the governing equation, and in § 3 we prove the global stability of two-jet zonal flow. In § 4 we show bifurcation diagrams of the steady solutions arising from three-jet zonal flow, and in § 5 we discuss unsteady solutions at high Reynolds numbers. Section 6 is devoted to the discussions and conclusions.

2. Governing equations

We consider 2D incompressible viscous flow on a rotating sphere governed by the non-dimensional vorticity equation

$$\frac{\partial \Delta\psi}{\partial t} + J(\psi, \Delta\psi) + 2\Omega\frac{\partial \psi}{\partial \lambda} = \frac{1}{Re}\{(\Delta + 2)\Delta\psi + (l(l+1) - 2)Y_l^0(\mu)\}. \tag{2.1}$$

Here t represents the time, while λ and μ denote the longitude and the sine latitude, $\mu = \sin\phi$, where ϕ is the latitude. The streamfunction is denoted by ψ, and the vorticity is given by $\Delta\psi = \zeta$, where Δ is the horizontal Laplacian on the unit sphere. The longitudinal and latitudinal components of velocity (u_λ, u_μ) are expressed by $u_\lambda = -(1-\mu^2)^{1/2}(\partial\psi/\partial\mu)$ and $u_\mu = (1-\mu^2)^{-1/2}(\partial\psi/\partial\lambda)$, respectively. The parameter Re is the Reynolds number, Ω is the non-dimensional rotation rate of the sphere and $J(A, B)$ is the Jacobian $(\partial A/\partial\lambda)(\partial B/\partial\mu) - (\partial A/\partial\mu)(\partial B/\partial\lambda)$. The flow is driven by the vorticity forcing, $(l(l+1) - 2)Y_l^0(\mu)/Re$, where $Y_l^m(\lambda, \mu)$ is a 4π-normalized spherical harmonics with the total wavenumber l and the longitudinal wavenumber m. In addition, the term of $2\Delta\psi/Re$ in the viscosity term is necessary for the conservation of the total angular momentum of the system (see Silberman 1953).

The vorticity equation (2.1) has a steady l-jet zonal flow solution for arbitrary Reynolds number and the rotation rate, expressed by

$$\psi_0(\mu) = -\frac{1}{l(l+1)}Y_l^0(\mu), \quad \zeta_0(\mu) = Y_l^0(\mu). \tag{2.2a,b}$$

Note that this solution is independent of the Reynolds number. Here, the number of jets is defined as the number of extreme points of the longitudinal velocity, which is equivalent to the number of the nodes of the latitudinal distribution of the streamfunction. The steady l-jet solution (2.2) is the only steady solution independent of λ. Hereafter we call this solution the trivial solution.

We should note a similar problem named after Kolmogorov, who proposed to study solutions of 2D incompressible viscous flow on a doubly periodic domain (a flat torus). His school studied the problem under the vorticity forcing of $n^2\cos ny/Re$, yielding a $2n$-jet parallel flow with the streamfunction being $-\cos(ny)/n^2$. In the Kolmogorov problem, the flow becomes unstable as Re increases, and goes through several bifurcations to turbulent states. The sinusoidal forcing given by the single

sine function, which is the eigenfunction of the Laplacian on the flat torus, makes the nonlinear terms vanish for the $2n$-jet parallel flows. In our problem on a sphere, the forcing term is a single spherical harmonic function $Y_l^0(\mu)$, which is also an eigenfunction of the Laplacian on a sphere and makes the nonlinear terms vanish for the trivial steady l-jet solution. Thus our problem setting may be regarded as a spherical version of the Kolmogorov problem, and, from this point of view, it should be noted that the topology of the flow domain is simpler in our case (sphere of genus 0) than in the Kolmogorov problem (torus of genus 1).

3. Global stability of two-jet zonal flow

In the case of $l = 1$, the trivial solution is one-jet zonal flow. This is a special case in which the energy injection vanishes. Since the coefficient of Y_1^0 in the spherical harmonic expansion of the streamfunction is proportional to the total angular momentum along the rotation axis of the sphere, the amplitude of the Y_1^0 component remains constant over time. On the other hand, the Y_1^{-1} and Y_1^1 components keep oscillations with constant (complex) amplitudes. Therefore, under the viscous effect the disturbance to one-jet zonal flow decays to zero except for its $l = 1$ components, which stay on the constant amplitudes. In this sense, one-jet zonal flow is stable for any Reynolds number and any rotation rate. This conclusion is also obtained from another point of view when one-jet zonal flow corresponds to the rest state in an appropriate rotating frame of reference.

Next we consider the case of $l = 2$, where the energy injection does not vanish, but we can prove the global stability of the trivial zonal flow for arbitrary Reynolds number and the rotation rate.

Substituting $\psi(\lambda, \mu, t) = AY_2^0(\mu) + \tilde{\psi}(\lambda, \mu, t)$ $(A = -1/6)$ into (2.1) and omitting the tilde, we obtain

$$\partial_t \Delta\psi + J(AY_2^0, (\Delta + 6)\psi) + 2\Omega\partial_\lambda\psi + J(\psi, \Delta\psi) - \frac{1}{Re}(\Delta + 2)\Delta\psi = 0. \tag{3.1}$$

The inner products of ψ and $\Delta\psi$ yields

$$\frac{1}{2}\partial_t\|\nabla\psi\|^2 + \frac{1}{Re}(\|\Delta\psi\|^2 - 2\|\nabla\psi\|^2) + \int \mathrm{d}S\,\psi A(\partial_\mu Y_2^0)(\Delta\partial_\lambda\psi) = 0, \tag{3.2}$$

$$\frac{1}{2}\partial_t\|\Delta\psi\|^2 + \frac{1}{Re}(\|\nabla\Delta\psi\|^2 - 2\|\Delta\psi\|^2) + 6\int \mathrm{d}S\,\psi A(\partial_\mu Y_2^0)(\Delta\partial_\lambda\psi) = 0. \tag{3.3}$$

Here the norm $\|\cdot\|$ is defined as

$$\|f(\lambda, \mu)\|^2 := \int \mathrm{d}S f^2(\lambda, \mu) = \int_{-1}^{1} \mathrm{d}\mu \int_0^{2\pi} \mathrm{d}\lambda f^2(\lambda, \mu), \tag{3.4}$$

and we have used the periodic boundary condition with respect to λ, and

$$\int \mathrm{d}S J(f, g)h = \int \mathrm{d}S f J(g, h). \tag{3.5}$$

Equations (3.2) and (3.3) yield

$$\partial_t \left\{ \frac{1}{2} \left(\frac{1}{6} \|\Delta\psi\|^2 - \|\nabla\psi\|^2 \right) \right\} + \frac{1}{Re} \left\{ \frac{1}{6} \|\nabla\Delta\psi\|^2 - \|\Delta\psi\|^2 \right\} - \frac{2}{Re} \left\{ \frac{1}{6} \|\Delta\psi\|^2 - \|\nabla\psi\|^2 \right\} = 0. \tag{3.6}$$

We split the disturbance ψ into ψ_2 and ψ_{rest} defined as

$$\psi_2 = \sum_m \psi_2^m(t) Y_2^m(\lambda, \mu), \quad \psi_{rest} = \sum_{n \geqslant 3, m} \psi_n^m(t) Y_n^m(\lambda, \mu). \tag{3.7a,b}$$

Substituting $\psi(\lambda, \mu, t) = \psi_2 + \psi_{rest}$ into (3.6), we obtain

$$\partial_t \left\{ \frac{1}{2} \left(\frac{1}{6} \|\Delta\psi_{rest}\|^2 - \|\nabla\psi_{rest}\|^2 \right) \right\} + \frac{1}{Re} \left\{ \frac{1}{6} \|\nabla\Delta\psi_{rest}\|^2 - \|\Delta\psi_{rest}\|^2 \right\} - \frac{2}{Re} \left\{ \frac{1}{6} \|\Delta\psi_{rest}\|^2 - \|\nabla\psi_{rest}\|^2 \right\} = 0. \tag{3.8}$$

The second term of (3.8) is evaluated as

$$\begin{aligned} \frac{1}{6} \|\nabla\Delta\psi_{rest}\|^2 - \|\Delta\psi_{rest}\|^2 &\geqslant 12 \sum_{n \geqslant 3, m} n(n+1) \left(\frac{n(n+1)}{6} - 1 \right) |\psi_n^m|^2 \\ &= 12 \left(\frac{1}{6} \|\Delta\psi_{rest}\|^2 - \|\nabla\psi_{rest}\|^2 \right). \end{aligned} \tag{3.9}$$

Thus we obtain

$$\frac{1}{6} \|\Delta\psi_{rest}\|^2 - \|\nabla\psi_{rest}\|^2 \leqslant C_0 \exp\left(-\frac{20}{Re} t \right), \tag{3.10}$$

where C_0 is a constant depending on the initial condition of disturbance. Hereafter we denote other constants similarly, i.e. C_i $(i = 1, \ldots, 5)$. Using the obvious inequality

$$\|\Delta\psi_{rest}\|^2 \geqslant 12 \|\nabla\psi_{rest}\|^2 \geqslant 12^2 \|\psi_{rest}\|, \tag{3.11}$$

we have

$$\|\psi_{rest}\| \leqslant C_1 \exp\left(-\frac{10}{Re} t \right). \tag{3.12}$$

Next, taking the inner product of ψ_2 and (3.1), we obtain

$$\partial_t \|\psi_2\| + \frac{4}{Re} \|\psi_2\| = \frac{1}{6} \left\{ \int \frac{\psi_2}{\|\psi_2\|} J(AY_2^0, (\Delta + 6)\psi_{rest}) + \int \frac{\psi_2}{\|\psi_2\|} J(\psi_{rest}, \Delta\psi_{rest}) \right\}. \tag{3.13}$$

The first term on the right-hand side can be evaluated as

$$\left| \int \frac{\psi_2}{\|\psi_2\|} J(AY_2^0, (\Delta + 6)\psi_{rest}) \right| \leqslant \left| \int \frac{1}{\|\psi_2\|} J(\psi_2, AY_2^0) \Delta\psi_{rest} \right| + 6 \left| \int \frac{1}{\|\psi_2\|} \psi_2 J(AY_2^0, \psi_{rest}) \right|$$

$$\begin{aligned} &\leqslant \frac{1}{\|\psi_2\|}\|\nabla\psi_2 \times \nabla A Y_2^0\| \, \|\Delta\psi_{rest}\| \\ &\quad + 6\frac{1}{\|\psi_2\|}\|\psi_2\| \, \|\nabla A Y_2^0 \times \nabla\psi_{rest}\| \\ &\leqslant \|A\nabla Y_2^0\|(\sqrt{6}\|\Delta\psi_{rest}\| + 6\|\nabla\psi_{rest}\|) \\ &\leqslant C_2 \exp\left(-\frac{10}{Re}t\right), \end{aligned} \tag{3.14}$$

and the second term on the right-hand side becomes

$$\begin{aligned} \left|\int \frac{\psi_2}{\|\psi_2\|} J(\psi_{rest}, \Delta\psi_{rest})\right| &\leqslant \frac{1}{\|\psi_2\|}\|\nabla\psi_2 \times \nabla\psi_{rest}\| \, \|\Delta\psi_{rest}\| \\ &\leqslant \sqrt{6}\|\nabla\psi_{rest}\| \, \|\Delta\psi_{rest}\| \\ &\leqslant C_3 \exp\left(-\frac{20}{Re}t\right), \end{aligned} \tag{3.15}$$

where we have used the Cauchy–Schwarz inequality and (3.12). Therefore we have

$$\partial_t\|\psi_2\| + \frac{4}{Re}\|\psi_2\| \leqslant C_4 \exp\left(-\frac{10}{Re}t\right), \tag{3.16}$$

which with (3.12) leads to an upper bound on the disturbance $\psi = \psi_2 + \psi_{rest}$,

$$\|\psi(t)\| \leqslant C_5 \exp\left(-\frac{4}{Re}t\right) \to 0 \quad (t \to +\infty). \tag{3.17}$$

Thus we conclude that two-jet zonal flow is globally asymptotically stable for arbitrary Reynolds number and rotation rate. This conclusion is obtained under the assumption of a steady zonal forcing of Y_2^0, and we can make no reliable statement for the flow pattern when another type of forcing is employed. However, Obuse, Takehiro & Yamada (2010) showed numerically that a two-jet solution is one of the final states when a random high-wavenumber forcing is employed, suggesting global stability of two-jet zonal flow in a more general configuration.

4. Bifurcation structure of steady solutions arising from three-jet zonal flow

4.1. *Numerical method*

In the case of $l = 3$ a trivial zonal flow (three-jet flow, figure 1) has been found to be unstable when the Reynolds number is sufficiently large (Sasaki *et al.* 2013). A three-jet zonal flow becomes Hopf unstable at a critical Reynolds number which depends on the rotation rate Ω, for $\Omega_c^-(=-5.727) < \Omega < \Omega_c^+(=2.171)$. Outside this interval of Ω, three-jet flow is linearly stable for any Reynolds number. In this section we study nonlinear solutions of the vorticity equation, focusing on steady and travelling-wave solutions for $(\Omega_c^- <) -5.7 \leqslant \Omega \leqslant 2.1 (< \Omega_c^+)$ and $1 \leqslant Re \leqslant 10^4$.

In order to obtain the numerical solutions, a spectral method with a spherical harmonics expansion is employed, where the streamfunction ψ is expressed as

$$\psi(\lambda, \mu) = \sum_{n=1}^{T_N} \sum_{m=-n}^{n} \psi_n^m Y_n^m(\lambda, \mu), \tag{4.1}$$

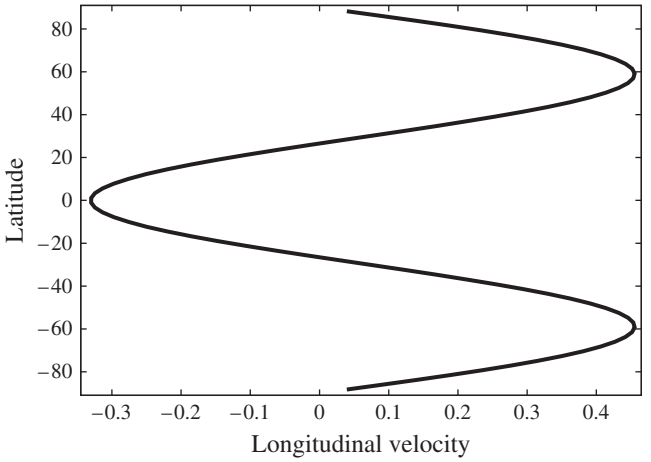

FIGURE 1. The longitudinal velocity of the three-jet trivial solution. The horizontal and vertical axes indicate longitudinal velocity and latitude.

where ψ_n^m is the expansion coefficient and T_N is the truncation wavenumber. We adopt the transform method to evaluate the nonlinear term in (2.1), eliminating the aliasing error. We have checked the accuracy by changing T_N up to 170. The Newton method is adopted to obtain the steady and travelling solutions.

4.2. *Bifurcation diagram in the non-rotating case*

We show the bifurcation diagram of the steady and travelling wave solutions for $\Omega = 0$, $1 \leqslant Re \leqslant 10^4$ in figure 2. Hereafter we denote the solutions in a systematic manner. For example, the solution $S_{12}^{(0)}$ means that it originates from the second bifurcation point on the solution branch $S_1^{(0)}$, where the superscript (0) shows the rotation rate of the sphere. The bifurcating points are expressed similarly: $B_{12}^{(0)}$ is the second bifurcation point on the solution branch $S_1^{(0)}$.

As for the symmetry of the streamfunctions, we focus on the following three types of operations. The first one is the longitudinal translation by $\alpha(\neq 0)$,

$$\sigma_\alpha : \psi(\lambda, \mu) \to \psi(\lambda - \alpha, \mu). \tag{4.2}$$

The second one is the sign inversion,

$$\sigma_- : \psi(\lambda, \mu) \to -\psi(\lambda, \mu). \tag{4.3}$$

The last one is the reflection with respect to the equator,

$$\sigma_r : \psi(\lambda, \mu) \to \psi(\lambda, -\mu). \tag{4.4}$$

We let Σ_α denote the symmetry group generated by σ_α. Similarly, Σ_α^+ denotes the group generated by $(\sigma_\alpha \sigma_r)$, and Σ_α^- denotes the group generated by $(\sigma_\alpha \sigma_r \sigma_-)$. We use the symbol Σ_* to express the group consisting of arbitrary longitudinal translations. We let E denote the trivial group consisting only of the identity transformation.

The streamfunction of the trivial zonal solution S_0 has symmetry group Σ_*^- and becomes Hopf unstable at $B_1^{(0)}(Re = 26.13)$. Then the travelling-wave solution $S_1^{(0)}$

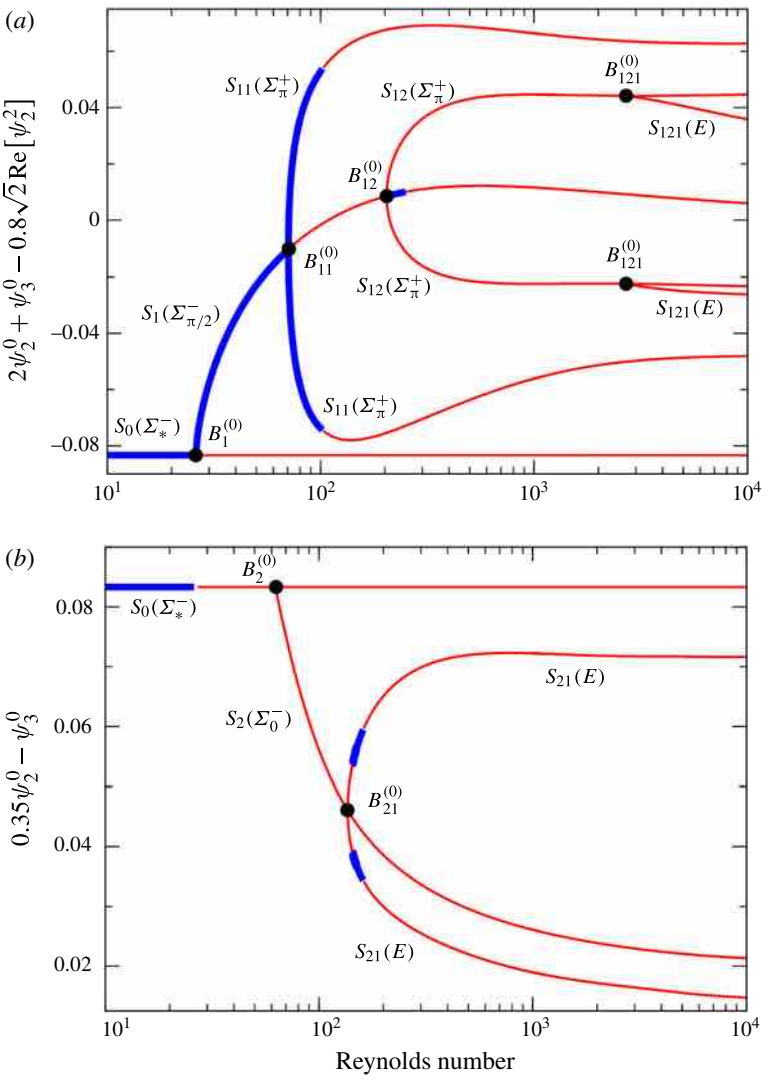

FIGURE 2. (Colour online) Bifurcation diagrams in the non-rotating case: (*a*) bifurcating branches from $B_1^{(0)}$, and (*b*) bifurcating branches from $B_2^{(0)}$. The notation of solutions and symmetries is described in the text. The blue (thick) and red (thin) lines denote linearly stable and unstable branches, respectively. The Reynolds numbers at $B_1^{(0)}$, $B_{11}^{(0)}$, $B_{12}^{(0)}$, $B_{121}^{(0)}$, $B_2^{(0)}$ and $B_{21}^{(0)}$, are 26.12, 70.66, 203.8, 2687, 62.51 and 136.2, respectively. Meanwhile, $S_1^{(0)}$ and $S_{11}^{(0)}$ become Hopf unstable at $Re = 249.4$ and 103.2, respectively. At these critical Reynolds numbers no steady or steady-travelling solution arises. In addition, $S_{21}^{(0)}$ is Hopf unstable except for the interval $143.5 \leqslant Re \leqslant 161.9$.

bifurcates with symmetry group $\Sigma_{\pi/2}^-$, losing the invariance to an arbitrary longitudinal translation. The $S_1^{(0)}$ again becomes unstable at $B_{11}^{(0)}$ with a new branch of $S_{11}^{(0)}$ which has symmetry group Σ_π, losing equatorial anti-symmetry. Note that the upper and lower branches of $S_{11}^{(0)}$ are related to each other by equatorial mirror symmetry. In the parameter range of our calculation, as depicted in figure 2, we found two Hopf

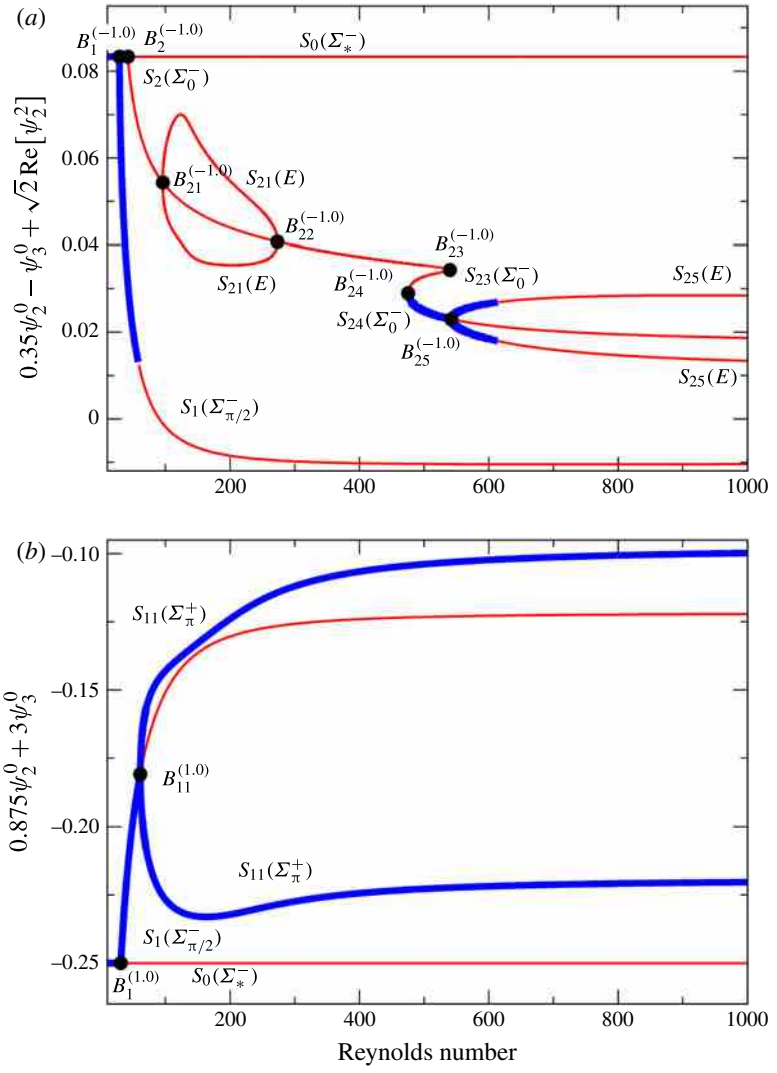

FIGURE 3. (Colour online) Bifurcation diagrams in the rotating cases: (*a*) $\Omega = -1.0$ and (*b*) $\Omega = 1.0$. In (*a*) the Reynolds numbers at bifurcating points are $Re = 28.94(B_1^{(-1.0)})$, $41.57(B_2^{(-1.0)})$, $95.72(B_{21}^{(-1.0)})$, $274.5(B_{22}^{(-1.0)})$, $540.05(B_{23}^{(-1.0)})$, $475.33(B_{24}^{(-1.0)})$, and $542.4(B_{25}^{(-1.0)})$. The solutions $S_1^{(-1.0)}$ and $S_{25}^{(-1.0)}$ become Hopf unstable at $Re = 58.29$ and 614.4, respectively. In (*b*) the Reynolds numbers at bifurcating points are $31.00(B_1^{(1.0)})$ and $61.11(B_{11}^{(1.0)})$.

bifurcation points and five pitchfork bifurcation points, and all the steady and steady-travelling solutions are found to be Hopf unstable in the range $249.4 \leqslant Re \leqslant 10^4$.

4.3. *Bifurcation diagrams in the rotating case*

The bifurcation structure of steady and steady-travelling wave solutions is varied by the rotation of the sphere. Numerical results at $\Omega = \pm 1.0$ are shown in figure 3.

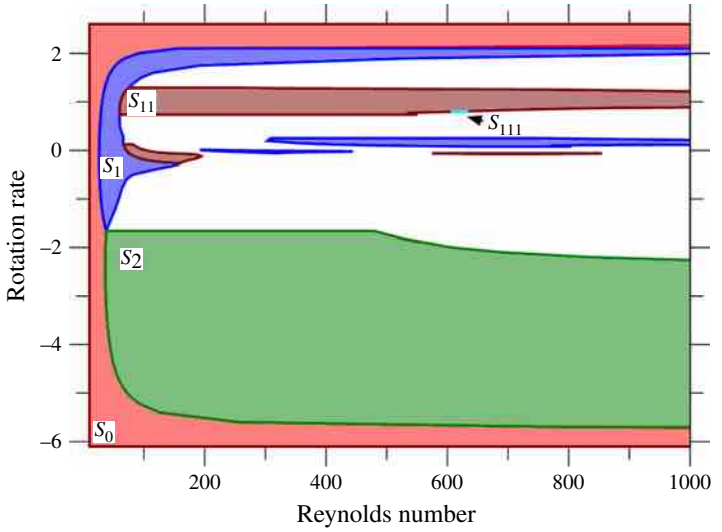

FIGURE 4. (Colour online) Linearly stable solutions which are connected to the trivial zonal flow S_0 through the stable branches of solutions. The red, blue, maroon, light blue and green regions represent the stable regions of the solutions S_0, S_1, S_{11}, S_{111} and S_2, respectively.

In the case of $\Omega = -1.0$, the trivial zonal solution S_0 becomes Hopf unstable at $B_1^{(-1.0)}$, where a new solution $S_1^{(-1.0)}$ arises which again becomes unstable at $Re = 58.29$. S_0 has the second bifurcation point $B_2^{(-1.0)}$, where an unstable branch arises and again has the bifurcation point $B_{21}^{(-1.0)}$. The upper and the lower branches of $S_{21}^{(-1.0)}$ contact each other at the next bifurcation point $B_{22}^{(-1.0)}$ on the branch of $S_2^{(-1.0)}$. Thus these upper and the lower branches make a closed loop connecting $B_{21}^{(-1.0)}$ and $B_{22}^{(-1.0)}$. Tracking the S_2 branch further, we find two saddle-node bifurcation points $B_{23}^{(-1.0)}$ and $B_{24}^{(-1.0)}$.

In the case of $\Omega = 1.0$, the bifurcation diagram is found to be quite simple compared to that of $\Omega = -1.0$. After a Hopf bifurcation at $B_1^{(1.0)}$, we find only one secondary pitchfork bifurcation point $B_{11}^{(1.0)}$ on the branch of $S_1^{(1.0)}$. The solution $S_{11}^{(1.0)}$ is found to be stable in the range of our calculation, $61.11 \leqslant Re \leqslant 10^4$. These results show that the bifurcation structure changes drastically by the effect of the rotation.

Figure 4 shows solutions which are linearly stable and realizable when the Reynolds number is gradually increased, i.e. the solutions in this figure are connected to the trivial zonal flow S_0 through the stable branches of solutions. There are other branches of stable solutions, but there is no stable branch connecting them to S_0. It should be remarked that we can find a linearly stable solution in most of the region except for small values of $|\Omega|$, even for large Reynolds numbers. Note also that the diagram is asymmetric with respect to $\Omega = 0$. The trivial zonal solution S_0 remains linearly stable even for large Reynolds number when $|\Omega|$ is sufficiently large, as already pointed out in the study of linear stability of S_0 by Sasaki *et al.* (2012).

4.4. *Flow fields of the nonlinear solutions at large Reynolds numbers*

Figure 5 shows the streamfunction of S_1 for $\Omega = 0.0$, 1.0 and -1.0. The solution S_1 has symmetry group $\Sigma^-_{\pi/2}$. In the non-rotating case, we find that, as the Reynolds

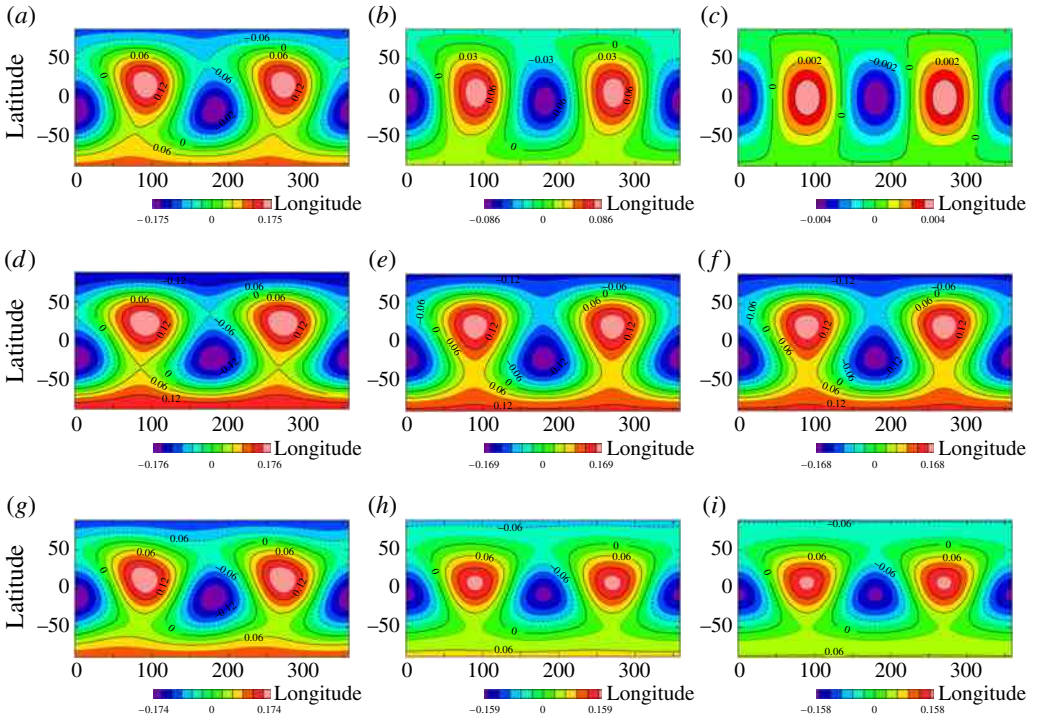

FIGURE 5. (Colour online) Streamfunctions of S_1: (*a*) $\Omega = 0$, $Re = 10^2$, (*b*) $\Omega = 0$, $Re = 10^3$, (*c*) $\Omega = 0$, $Re = 10^6$, (*d*) $\Omega = 1.0$, $Re = 10^2$, (*e*) $\Omega = 1.0$, $Re = 10^3$, (*f*) $\Omega = 1.0$, $Re = 10^6$, (*g*) $\Omega = -1.0$, $Re = 10^2$, (*h*) $\Omega = -1.0$, $Re = 10^3$, and (*i*) $\Omega = -1.0$, $Re = 10^6$, respectively.

number increases, the vorticity pattern, which is not symmetric with respect to the equator (figure 5*a*), approaches a symmetric pattern (figure 5*b*), and the streamfunction of S_1 at $Re = 10^6$ almost recovers the symmetry Σ^+ (figure 5*c*).

In the cases of $\Omega = \pm 1.0$, we find that the streamfunction of S_1 remains non-symmetric with respect to the equator and does not recover Σ^+ even at high Reynolds numbers. The flow field seems to change little as Re ($\gtrsim 10^3$) increases.

5. Properties of unsteady solutions at high Reynolds numbers

In this section we study numerically the unsteady solutions at high Reynolds numbers. We take as the initial condition a steady or steady-travelling solution superimposed by a disturbance which has the form

$$\delta\psi(\lambda, \mu) = \sum_{n=2}^{10} \sum_{m=-n}^{n} \delta\psi_n^m Y_n^m(\lambda, \mu). \tag{5.1}$$

The expansion coefficients $\delta\psi_n^m$ are given by the random number, with the (spatially averaged) energy of $\delta\psi$ being 10^{-4} times that of the steady or steady-travelling solution, where the energy of ψ is defined as

$$E = \frac{1}{8\pi} \int |\nabla\psi|^2 \, \mathrm{d}S = -\frac{1}{8\pi} \int \psi \Delta\psi \, \mathrm{d}S. \tag{5.2}$$

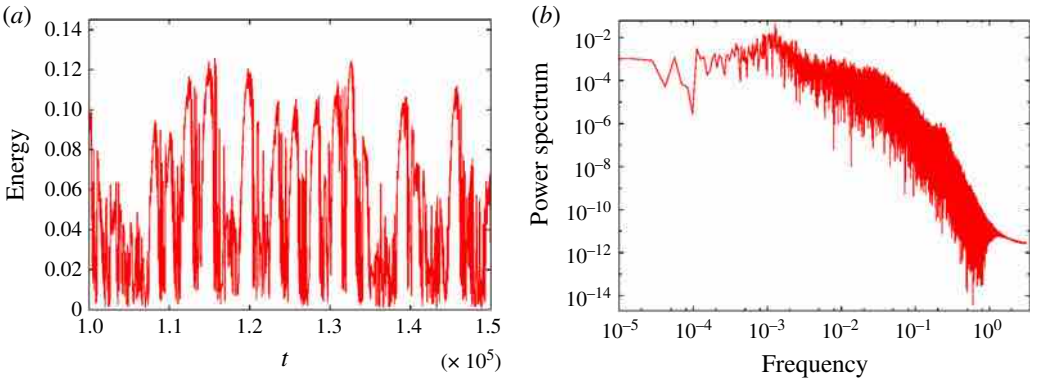

FIGURE 6. (Colour online) An example of the time development of the energy of the chaotic solutions (*a*) and its power spectrum (*b*). In (*a*) the horizontal and vertical axes indicate the time and the energy, while in (*b*) the horizontal and vertical axes indicate the frequency and the power spectrum.

In the non-rotating case, figure 6 shows the time development of the energy of the unsteady solutions and its power spectrum. The energy changes irregularly and its power spectrum is broad. The unsteady solution is seemingly chaotic, and the time-averages of some quantities in the time interval of $5 \times 10^4 \leqslant t \leqslant 5 \times 10^5$ are robust among some numerical solutions from different series of random numbers.

Figure 7 shows the time series of the streamfunction of the unsteady solution, while the streamfunction of the steady-travelling solutions at $Re = 10^4$ is represented in figure 8. The streamfunctions at some instants of the unsteady solution are similar to those of the unstable steady solutions. This observation suggests that the orbit of the unsteady solution wanders around the steady and steady-travelling solutions. Moreover, the unsteady solution is not highly but moderately turbulent, and therefore we expect that the orbit of the unsteady solution is mostly located in a low-dimensional space spanned by the steady and steady-travelling solutions.

However, because the system is invariant to the longitudinal translation, even the set of steady solutions constitutes an infinite-dimensional linear space, which is difficult to approximate by numerical calculations. Therefore we focus our attention on the zonal-mean zonal flows instead of the 2D flow field. The former flow is defined as

$$\boldsymbol{U}(\mu) = \frac{1}{2\pi} \int_0^{2\pi} u_\lambda(\lambda, \mu)\, \mathrm{d}\lambda, \tag{5.3}$$

which eliminates the infinite dimension arising from the longitudinal translation. In figure 9 we plot the zonal-mean zonal velocity of these solutions at $Re = 10^4$. The solution S_1 has a symmetry group generated by $\Sigma^-_{\pi/2}$, but S_1 and $\Sigma^-_{\pi/2} S_1$ give the same zonal-mean zonal velocity profile, and so does S_2. Each of the other solutions, however, gives two zonal-mean zonal velocity profiles when the symmetry is taken into account. In total, therefore, 11 independent velocity profiles, including the trivial zonal flow, are obtained from these solutions.

We try to reproduce the zonal-mean zonal velocity profile of the unsteady solution using a linear combination of the 11 unstable steady and steady-travelling solutions.

First, a linear space M spanned by the 11 unstable steady and steady-travelling solutions is introduced, and an orthogonal projection $P_M(\psi)$ from the unsteady

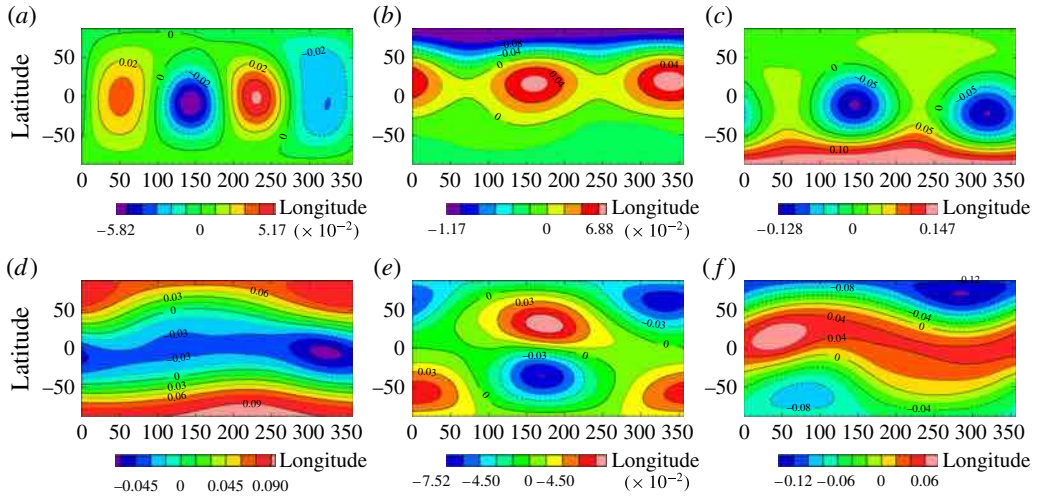

FIGURE 7. (Colour online) Snapshots of the streamfunction of a chaotic solution at $\Omega = 0$ and $Re = 10^4$: (*a*) $t = 107\,000$, (*b*) $t = 108\,000$, (*c*) $t = 146\,000$, (*d*) $t = 182\,000$, (*e*) $t = 237\,000$ and (*f*) $t = 313\,000$, respectively. The horizontal and vertical axes indicate longitude and latitude. Panels (*a–c*,*e*,*f*), respectively, resemble S_1, S^l_{11}, S^u_{12}, S^u_{21}, S_2 and S^l_{21} in figure 8.

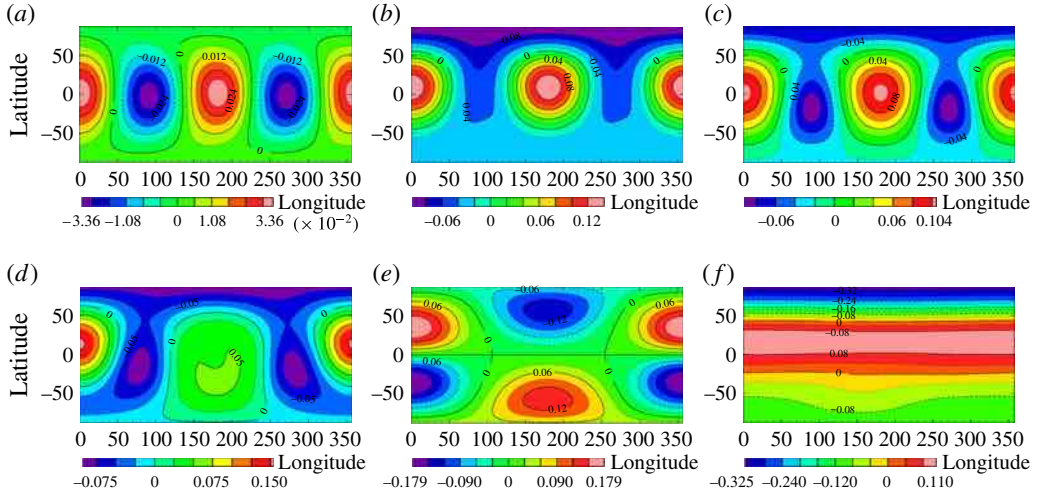

FIGURE 8. (Colour online) The streamfunctions of the steady-travelling solutions at $\Omega = 0$ and $Re = 10^4$: (*a*) S_1, (*b*) the lower branch of S_{11}, (*c*) the lower branch of S_{12}, (*d*) the lower branch of S_{121}, (*e*) S_2, and (*f*) the lower branch of S_{21}. The horizontal and vertical axes indicate longitude and latitude. The lower branches of S_{11}, S_{12}, S_{121} and S_{21} have the equatorial anti-symmetric relation with its upper branch.

solution ψ to M is defined. Further, $Z(\psi)$ is defined as a mapping from ψ to the zonal-mean zonal velocity of ψ. Therefore, when $Z(P_M(\cdot))$ operates on a general streamfunction, it gives a linear combination of the zonal-mean zonal velocity of the

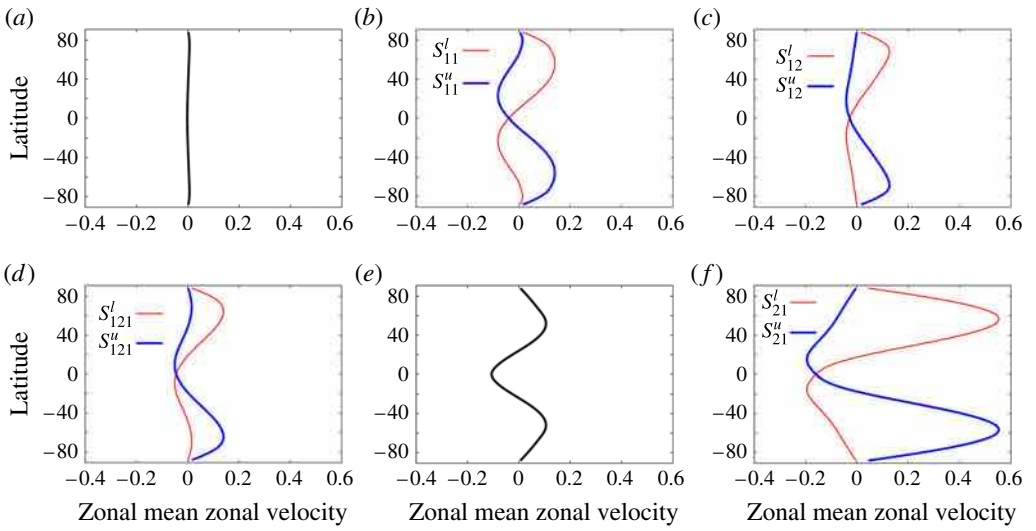

FIGURE 9. (Colour online) The zonal-mean zonal velocity of the steady-travelling solutions at $\Omega = 0$ and $Re = 10^4$: (*a*) S_1, (*b*) S_{11}, (*c*) S_{12}, (*d*) S_{121}, (*e*) S_2, and (*f*) S_{21}. Both these solutions are Hopf unstable at $Re = 249.5$.

11 solutions. The orthogonal projection, $P_M(\psi) = \hat{\psi}(\lambda, \mu, t)$, is expressed as

$$\hat{\psi}(\lambda, \mu, t) = \sum_{k=1}^{K} \int \frac{\mathrm{d}\theta}{2\pi} c_k(\theta, t)\psi_k(\lambda - \theta, \mu) + d(t)\psi^T(\mu), \tag{5.4}$$

where $\psi_k(\lambda, \mu)(k = 1, \ldots, K)$ are the unstable steady and steady-travelling solutions which depend on both the longitude and the latitude, $\psi^T(\mu)$ is the trivial solution and $c_k(\theta, t)$ and $d(t)$ are coefficients. The zonal velocity profile of the streamfunction projected on M, $Z(P_M(\psi)) = \hat{\boldsymbol{U}}(\mu, t)$, is then given by

$$\hat{\boldsymbol{U}}(\mu, t) = \sum_{k=1}^{K} \int \frac{\mathrm{d}\theta}{2\pi} c_k(\theta, t)\boldsymbol{U}_k(\mu) + d(t)\boldsymbol{U}^T(\mu), \tag{5.5}$$

where $\boldsymbol{U}_k(\mu) = Z(\psi_k)$ and $\boldsymbol{U}^T(\mu) = Z(\psi^T)$, respectively. The coefficients $\int (\mathrm{d}\theta/2\pi)c_k(\theta, t)$ and $d(t)$ are given by

$$\int \frac{\mathrm{d}\theta}{2\pi} c_k(\theta, t) = \int_{-1}^{1} \frac{\mathrm{d}\mu}{2} \boldsymbol{U}_k^{\dagger *}(\mu)\boldsymbol{U}(\mu, t), \quad d(t) = \int_{-1}^{1} \frac{\mathrm{d}\mu}{2} \boldsymbol{U}^{T\dagger *}(\mu)\boldsymbol{U}(\mu, t), \tag{5.6a,b}$$

where $\{\boldsymbol{U}_k^{\dagger}(\mu), \boldsymbol{U}^{T\dagger}(\mu)\}$ $(k = 1, \ldots, K)$ denotes the dual basis of $\{\boldsymbol{U}_k(\mu), \boldsymbol{U}^T(\mu)\}$ $(k = 1, \ldots, K)$, $\boldsymbol{U}(\mu, t) = Z(\psi)$, and * indicates complex conjugate.

The dual vectors $\{\boldsymbol{U}_i^{\dagger}(\mu)\}$ to a set of vectors $\{\boldsymbol{U}_i(\mu)\}$ are constructed so that the inner product of $\boldsymbol{U}_i(\mu)$ and $\boldsymbol{U}_j^{\dagger}(\mu)$ is δ_{ij}. The vectors $\{\boldsymbol{U}_i(\mu)\}$ are observed to be linearly independent, and therefore the dual vectors $\boldsymbol{U}_i^{\dagger}(\mu)$ are obtained by using Gram–Schmidt orthogonalization on the assumption that the dual vectors $\{\boldsymbol{U}_i^{\dagger}(\mu)\}$ belong to the linear space spanned by $\{\boldsymbol{U}_i(\mu)\}$.

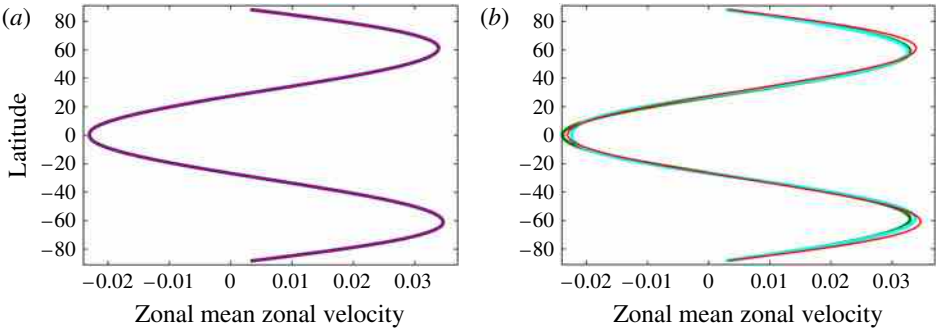

FIGURE 10. (Colour online) The reproduced zonal-mean zonal velocity by the linear mapping: (*a*) the 11 steady and steady-travelling solutions, and (*b*) the trivial solution/the single pair of S_{21}. The red lines show the time-averaged zonal-mean zonal velocity profile of the unsteady flow, the blue lines the reproduced profiles using 11 steady and steady-travelling solutions, the green lines using only the trivial solution and the light blue lines using the pair of S_{21} solutions. The reproduced profile agrees well with that of the unsteady solution.

Figure 10(*a*) shows the time-average of the reproduced zonal-mean zonal velocity. We find that the reproduced velocity profile agrees well with that of the unsteady solution within $\sim$1.1 % error. Further, figure 10(*b*) shows the time-averages of the reproduced zonal-mean zonal velocity using only the trivial solution and only the single pair of S_{21}. Even when only the single solution and the pair of S_{21} are employed, the reproduced velocity and the time-averaged zonal velocity profile agree well with each other.

Figure 11 shows the reproduced zonal-mean zonal velocity profiles and the unsteady flow at several times. There are significant errors between the zonal-mean zonal velocity profiles of the unsteady solutions and the reproduced profiles, unless the 11 solutions are employed for the reproduction of which the relative error is of the order of 0.01 %.

These results suggest that even at high Reynolds numbers ($\sim$40 times that of the critical Reynolds number of the laminar flow), the unsteady solution mostly lies within the relatively low-dimensional space spanned by the steady and steady-travelling solutions which bifurcate at low Reynolds numbers.

We examine each projected component of $\hat{\boldsymbol{U}}(\mu, t)$ to the steady and steady-travelling solution,

$$\int \frac{\mathrm{d}t}{T} \left(\int_{-1}^{1} e_i^*(\mu) \hat{\boldsymbol{U}}(\mu, t) \frac{\mathrm{d}\mu}{2} \right)^2, \tag{5.7}$$

where $e_i(\mu)$ is a normalized unit vector of the dual basis $\boldsymbol{U}_i^\dagger(\mu)$. This quantity represents the amount of the contribution of $\boldsymbol{U}_i(\mu)$ to $\hat{\boldsymbol{U}}(\mu, t)$. We exclude $\boldsymbol{U}_i(\mu)$ giving the smallest contribution and then again perform a reproduction using the remaining 10 solutions. By repeating this procedure, we successively reduce the number of the solutions $\boldsymbol{U}_i(\mu)$ for the reproduction. Figure 12 shows the absolute error

$$\int \frac{\mathrm{d}t}{T} \sqrt{\int_{-1}^{1} \frac{\mathrm{d}\mu}{2} (\boldsymbol{U}(\mu, t) - \hat{\boldsymbol{U}}(\mu, t))^2} \tag{5.8}$$

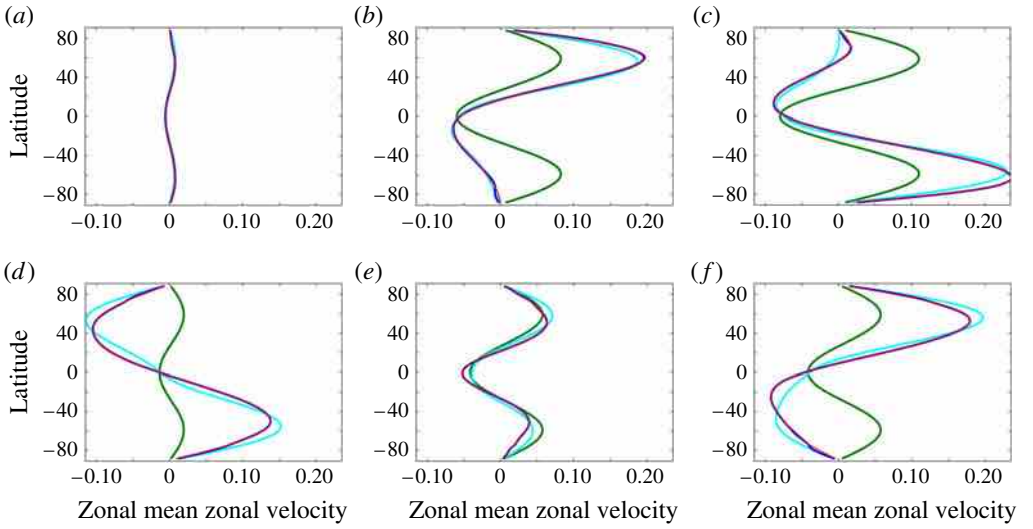

FIGURE 11. (Colour online) The instantaneous zonal-mean zonal velocity profiles and the reproduced profiles at the same times as in figure 7. The red lines show the zonal-mean zonal velocity profile of the unsteady flow, the blue lines the reproduced profiles using 11 steady and steady-travelling solutions, the green lines using only the trivial solution and the light blue lines using the pair of S_{21} solutions.

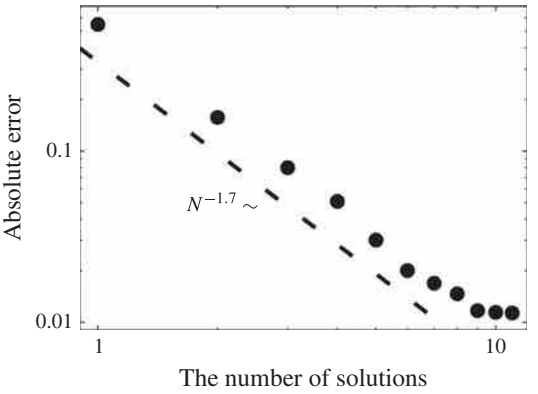

FIGURE 12. The absolute error and the number of solutions used for the reproduction. The dashed line shows $N^{-1.7}$, where the exponent -1.7 is obtained by the least-squares method in the range $1 \leqslant N \leqslant 8$.

against the number N of steady and steady-travelling solutions employed for the production. We see that when the 11 solutions are employed, the absolute error is smallest, but as the number of solutions decreases, the absolute error increases as $N^{-1.7}$.

Let us assume the attractor of the unsteady solution uniformly distributes in the M-dimensional sphere with radius r_c. The distance between this attractor and the subspace spanned by the N mutually orthogonal vectors ($N < M$) is then given by $d_N = \sqrt{\int_{V_M} (\mathrm{d}V/V_M) \sum_{i=1}^{M-N+1} x_i^2} = \sqrt{(M-N+1)/(M+2)}\, r_c$, where V_M is the volume

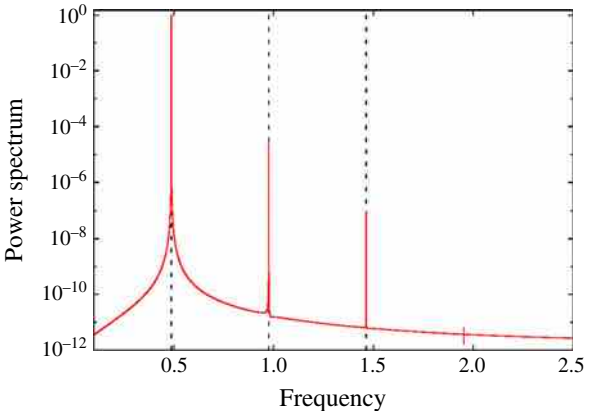

FIGURE 13. (Colour online) The power spectrum of the energy of the time-periodic solutions at $\Omega = -1.0$ and $Re = 10^3$. The horizontal and vertical axes indicate the frequency and the power spectrum. The vertical dashed lines indicate $\omega = 0.487$, 2ω and 3ω, respectively.

of the M-dimensional sphere. The absolute error is therefore proportional to $\sqrt{12 - N}$, which is in contrast with $N^{-1.7}$ in our case. This result suggests that the attractor of the unsteady solution distributes non-uniformly.

We also carried out the time integration in the rotating cases, $\Omega = \pm 1.0$, at high Reynolds numbers, and the unsteady solutions are either time-periodic or stable steady (not chaotic), suggesting the stabilizing effect of the rotation. Here we show the representative result of $\Omega = -1.0$ and $Re = 10^3$. Figure 13 shows the power spectrum in this case and the unsteady solution is time-periodic.

Figure 16 shows snapshots of streamfunction of the time-periodic solution. For comparison we show the streamfunctions of four steady-travelling solutions at $Re = 10^3$ in figure 14, while figure 15 shows their zonal-mean zonal velocity profiles. The flow field of the time-periodic solution is not similar to those of steady-travelling solutions. We reproduced the zonal-mean zonal velocity profiles using the five steady and steady-travelling solutions (figure 17). There are some discrepancies between the reproduced profiles and the time-periodic solution. However, the time-averaged zonal-mean zonal velocity can be successfully reproduced, as shown in figure 18. This result suggests that even the time-periodic solutions are not far from the unstable steady and steady-travelling solutions.

On the other hand, in the case of $\Omega = 1.0$, all the unsteady solutions converge to S_{11} at $Re = 10^3$, while most of the unsteady solutions except in a neighbourhood of S_{11} are time-periodic at $Re = 10^4$.

6. Discussion and conclusions

In this paper we have studied the bifurcation structure of viscous zonal flows on a rotating sphere under zonal forcings. Our problem could be considered as an extension of the Kolmogorov problem on a flat torus.

We prove rigorously that two-jet zonal flow is globally stable for an arbitrary Reynolds number and an arbitrary rotation rate. We note that in the flat torus case, Iudovisch (1965) proved that two-jet parallel flow is globally asymptotically stable for arbitrary Reynolds number.

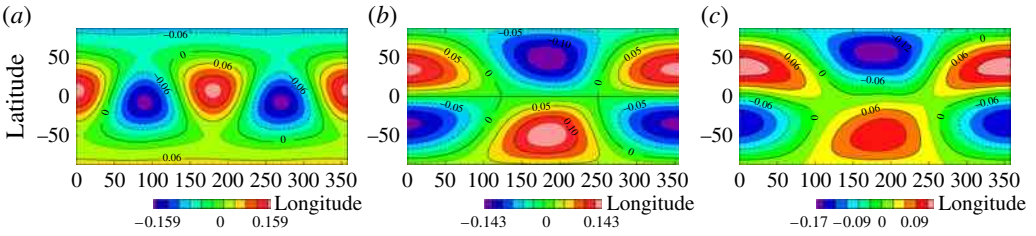

FIGURE 14. (Colour online) The streamfunction of the steady-travelling solutions at $\Omega = -1.0$ and $Re = 10^3$: (*a*) S_1, (*b*) S_2, (*c*) S^l_{25}. The horizontal and vertical axes indicate longitude and latitude.

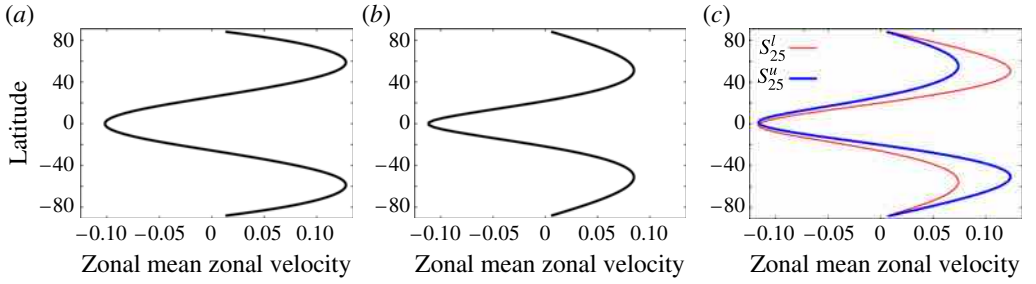

FIGURE 15. (Colour online) The zonal-mean zonal velocity of the steady-travelling solutions at $\Omega = -1.0$ and $Re = 10^3$: (*a*) S_1, (*b*) S_2, (*c*) S_{25}. The horizontal and vertical axes indicate amplitude and latitude.

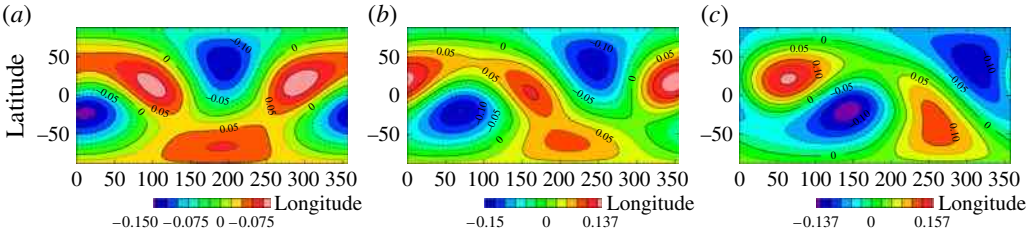

FIGURE 16. (Colour online) Snapshots of the streamfunction of the time-periodic solution at $\Omega = -1.0$ and $Re = 10^3$: (*a*) $t = 400\,291$, (*b*) $t = 400\,294$, (*c*) $t = 400\,298$. The horizontal and vertical axes indicate longitude and latitude.

Next we studied the bifurcation structure of nonlinear steady solutions arising from three-jet zonal flow. In the non-rotating case, as the Reynolds number increases, the steady-travelling solutions arise from three-jet zonal flow via Hopf bifurcations. As the Reynolds number increases further, several travelling solutions arise only via pitchfork bifurcation, and finally the steady-travelling solutions become Hopf unstable. In the rotating case, on the other hand, we find saddle-node bifurcations, closed-loop branches and linearly stable solutions at high Reynolds numbers. Thus the bifurcation structure changes drastically under the effect of rotation. On the flow field of the steady-travelling solutions, in the non-rotating case, we find equatorial symmetry restoration of the steady-travelling solution at high Reynolds numbers. In the flat torus case, Okamoto & Shōji (1993) and Kim & Okamoto (2010) found steady

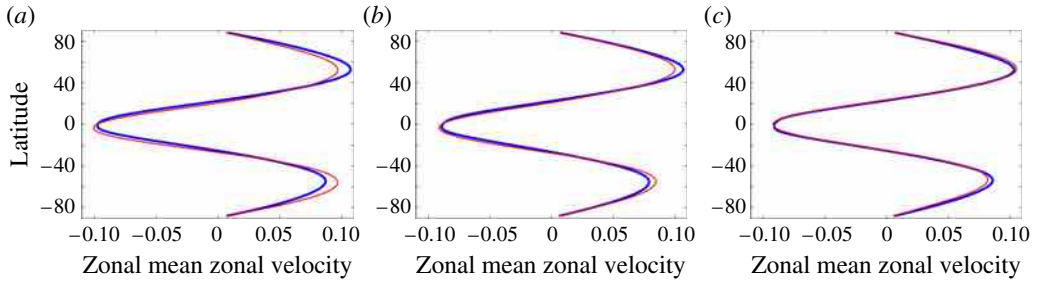

FIGURE 17. (Colour online) Snapshots of the zonal-mean zonal velocity of the time-periodic solution at $\Omega = -1.0$ and $Re = 10^3$. The distributions are shown at the same times as in figure 16. The red and blue (thin and thick) lines indicate the time-periodic solution and reproduced profiles using the linear mapping constructed with all four steady and steady-travelling solutions. The horizontal and vertical axes indicate velocity and latitude.

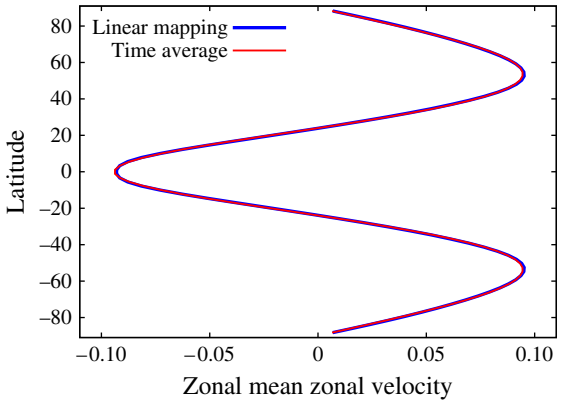

FIGURE 18. (Colour online) The time-averaged zonal-mean zonal velocity and reproduced profile at $\Omega = -1.0$ and $Re = 10^3$. The red and blue (thin and thick) lines represent the time-periodic solution velocity profiles reproduced by the linear mapping constructed with all four steady and steady-travelling solutions. The horizontal and vertical axes indicate velocity and latitude.

solutions for which the flow field is dominated only by one pair of negative and positive vortices at high Reynolds numbers. It should be noticed that the symmetries of those steady solutions are also restored as the Reynolds number increases. In the rotating cases, on the other hand, we do not find symmetry restoration of the steady-travelling solutions. We note that the rotation of the system further introduces the resonant interaction of the spherical harmonics, i.e. Rossby waves, in the flow system, and makes its analysis more complicated at moderate rotation rates, while the dynamics at extremely high rotation rates (Kartashova & L'vov 2008) would be modelled by taking into account only the resonant interaction of spherical harmonics. We also note that it would be interesting to make a low-dimensional model system of the turbulent state by taking appropriate spherical harmonics to get insight into the physical mechanism of the turbulence which appears to be a low dimension.

We carry out the time integration of the equation of motion at high Reynolds numbers where the steady and steady-travelling solutions are Hopf unstable. In the non-rotating case, we observed that the unsteady solutions goes around the unstable steady-travelling solutions. We reproduce the zonal-mean zonal velocity of the unsteady solution using a linear combination of those of the steady and steady-travelling solutions. We find that the reproduction of the zonal-mean zonal profiles approximates those of the unsteady solutions well. This result suggests that even at high Reynolds numbers the chaotic attractor exists mostly within a relatively low-dimensional space spanned by the steady and steady-travelling solutions.

Recently, low-dimensional ODE models of wall turbulence have been studied in order to understand the turbulence dynamics (Smith, Moehlis & Holmes 2005; Kim & Moehlis 2008). In this paper we show that a low-dimensional space constructed by the steady and steady-travelling solutions gives a good approximation in the case of 2D high-Reynolds number flows on a rotating sphere. It would be interesting to see if an attractor is found near steady or similar simple solutions in 3D cases.

Acknowledgements

We would like to express our deepest gratitude to Professor H. Okamoto for the fruitful discussions. In the numerical calculation of the spectrum method we use the spectral transformation library 'ISPACK' (Ishioka 2011) and the FORTRAN90 wrapper library 'SPMODEL' (Takehiro *et al.* 2011). This work was supported by JSPS KAKENHI grants 24340016, 15K13458 and 25610139 and MEXT KAKENHI grant 26103706.

REFERENCES

BAINES, P. G. 1976 The stability of planetary waves on a sphere. *J. Fluid Mech.* **73** (2), 193–213.

INUBUSHI, M., KOBAYASHI, M. U., TAKEHIRO, S. & YAMADA, M. 2012 Covariant Lyapunov analysis of chaotic Kolmogorov flows. *Phys. Rev.* E **85**, 016331.

ISHIOKA, K. 2011 ISPACK-0.96, http://www.gfd-dennou.org/arch/ispack/, GFD Dennou Club.

IUDOVISCH, V. I. 1965 Example of the generation of a secondary stationary or periodic flow when there is loss of stability of the laminar flow of a viscous incompressible fluid. *Z. Angew. Math. Mech.* **29**, 527–544.

KARTASHOVA, E. & L'VOV, V. S. 2008 Cluster dynamics of planetary waves. *Europhys. Lett.* **83**, 50012.

KIM, L. & MOEHLIS, J. 2008 Characterizing the edge of chaos for a shear flow model. *Phys. Rev.* E **78**, 036215.

KIM, S. C. & OKAMOTO, H. 2010 Stationary vortices of large scale appearing in 2D Navier–Stokes equations at large Reynolds numbers. *Japan J. Ind. Appl. Maths* **27**, 47–71.

KUO, H. 1949 Dynamic instability of two-dimensional nondivergent flow in a barotropic atmosphere. *J. Meteorol.* **6**, 105–122.

LUCAS, D. & KERSWELL, R. R. 2015 Recurrent flow analysis in spatiotemporally chaotic 2-dimensional Kolmogorov flow. *Phys. Fluids* **27**, 045106.

MESHALKIN, L. D. & SINAI, Y. G. 1962 Investigation of the stability of a stationary solution of a system of equations for the plane movement of an incompressible viscous liquid. *Z. Angew. Math. Mech.* **25**, 1700–1705.

OBUKHOV, A. M. 1983 Kolmogorov flow and laboratory simulation of it. *Russian Math. Surv.* **38** (4), 113–126.

OBUSE, K., TAKEHIRO, S. & YAMADA, M. 2010 Long-time asymptotic states of forced two-dimensional barotropic incompressible flows on a rotating sphere. *Phys. Fluids* **22**, 056601.

OKAMOTO, H. & SHŌJI, M. 1993 Bifurcation diagrams in Kolmogorov's problem of viscous incompressible fluid on 2-D flat tori. *Japan J. Ind. Appl. Maths* **10**, 191–218.

PLATT, N., SIROVICH, L. & FITZMAURICE, N. 1991 An investigation of chaotic Kolmogorov flows. *Phys. Fluids* **3**, 681–696.

SASAKI, E., TAKEHIRO, S. & YAMADA, M. 2012 A note on the stability of inviscid zonal jet flows on a rotating sphere. *J. Fluid Mech.* **710**, 154–165.

SASAKI, E., TAKEHIRO, S. & YAMADA, M. 2013 Linear stability of viscous zonal jet flows on a rotating sphere. *J. Phys. Soc. Japan* **82**, 094402.

SILBERMAN, I. 1953 Planetary waves in the atmosphere. *J. Meteorol.* **11**, 27–34.

SMITH, T. S., MOEHLIS, J. & HOLMES, P. 2005 Low-dimensional models for turbulent plane Couette flow in a minimal flow unit. *J. Fluid Mech.* **538**, 71–110.

TAKEHIRO, S., SASAKI, Y., MORIKAWA, Y., ISHIOKA, K., ODAKA, M., TAKAHASHI, Y. O., NISHIZAWA, S., NAKAJIMA, K., ISHIWATARI, M. & HAYASHI, Y.-Y. 2011 SPMODEL Development Group, 2011 Hierarchical Spectral Models for GFD (SPMODEL), http://www.gfd-dennou.org/library/spmodel/, GFD Dennou Club.

The Astrophysical Journal, 764:120 (11pp), 2013 February 20 doi:10.1088/0004-637X/764/2/120

EVAPORATION OF ICY PLANETESIMALS DUE TO BOW SHOCKS

Kyoko K. Tanaka[1], Tetsuo Yamamoto[1], Hidekazu Tanaka[1], Hitoshi Miura[2], Makiko Nagasawa[3], and Taishi Nakamoto[3]
[1] Institute of Low Temperature Science, Hokkaido University, Sapporo 060-0819, Japan
[2] Department of Earth Sciences, Tohoku University, Sendai 980-8578, Japan
[3] Earth and Planetary Sciences, Tokyo Institute of Technology, Tokyo 152-8551, Japan
Received 2012 April 11; accepted 2012 December 18; published 2013 January 30

ABSTRACT

We present the novel concept of evaporation of planetesimals as a result of bow shocks associated with planetesimals orbiting with supersonic velocities relative to the gas in a protoplanetary disk. We evaluate the evaporation rates of the planetesimals based on a simple model describing planetesimal heating and evaporation by the bow shock. We find that icy planetesimals with radius $\gtrsim$100 km evaporate efficiently even outside the snow line in the stage of planetary oligarchic growth, where strong bow shocks are produced by gravitational perturbations from protoplanets. The obtained results suggest that the formation of gas giant planets is suppressed owing to insufficient accretion of icy planetesimals onto the protoplanet within the $\lesssim$5 AU disk region.

Key words: comets: general – minor planets, asteroids: general – planets and satellites: formation – shock waves

1. INTRODUCTION

In protoplanetary disks, planetesimals grow to planets through mutual collisions and accumulations. The gravitational interactions among planetesimals increase the eccentricities of their orbits. When the relative velocity between a planetesimal and the disk gas exceeds the speed of sound of the gas, a bow shock is produced on the leading side of the planetesimal.

It has been demonstrated that heating of solid materials by planetesimal bow shocks in the nebular gas plays a key role in the formation of particles found in meteorites and interplanetary dust particles (IDPs; Hood 1998; Weidenschilling et al. 1998; Ciesla et al. 2004; Hood et al. 2005, 2009; Morris et al. 2012). For instance, the shock heating leads to the formation of chondrules, which are millimeter-scale igneous silicate spheres in chondrites, by melting dust in protoplanetary disks (Hood & Horanyi 1991, 1993; Iida et al. 2001; Ciesla & Hood 2002; Desch & Connolly 2002; Miura & Nakamoto 2005, 2006). Furthermore, shock heating causes some of the fine dust particles to evaporate (Miura et al. 2002; Miura & Nakamoto 2005, 2006) and recondensation of evaporated vapor results in the formation of a significant number of small dust particles. Miura et al. (2010) showed that it is possible for a planetesimal bow shock to form the various types of crystalline silicates observed in chondritic meteorites and IDPs.

Thus far, research has focused primarily on the thermal evolution of dust particles in the pre- and post-shock regions. However, we note the possibility that the bow shock also leads to heating and evaporation of the planetesimal itself. A similar process is found in the ablation of planetesimals penetrating through the thick atmosphere of protoplanets (e.g., Podolak et al. 1988; Pollack et al. 1986). Heating and resultant evaporation by the planetesimal bow shocks would shrink the planetesimals. Furthermore, cooling of the vapor produced in this manner would form fine dust particles by recondensation. These dust clouds in the disk may be found in the infrared spectra of protoplanetary disks in the late stage of their evolution.

Evaporation of planetesimals recalls that of comets, which release vapor gas and dust particles when they approach the Sun. Because of the strong head winds of the disk gas, however, the heating process of the planetesimals by bow shocks is different from that of comets.

According to the standard scenario, the formation of a planet passes through the so-called runaway growth stage (Wetherill & Stewart 1989). In this stage, large planetesimals grow faster than small ones, and the rate of mass growth of each object is an increasing function of its own mass. As a result, the planetary embryos grow to protoplanets by accumulating ambient planetesimals while maintaining their orbital separations of $\sim$10 Hill radii (Kokubo & Ida 1998, 2002). In this oligarchic growth stage, the orbital eccentricities and inclinations of the planetesimals are almost uniformly increased due to strong gravitational perturbations by the protoplanets. Strong bow shocks are always produced around planetesimals because of their large eccentricities ($e \sim 0.1$; see Figure 4 below) enhanced by massive protoplanets (Tanaka & Ida 1999; Kobayashi et al. 2010). Although energy dissipation rates by the bow shocks are high for such eccentric orbits, the strong perturbations by the protoplanets keep the eccentricities of the planetesimals large.

In the present study we focus on planetesimal heating and evaporation by these planetesimal bow shocks. Here we consider icy planetesimals, which evaporate more easily than rocky ones. If all of the energy flux, F, crossing the shock is used for evaporation of icy planetesimals, the timescale of the evaporation can be roughly estimated by $\tau = Lm/(\pi r^2 F)$, where L is the latent heat of evaporation of ice and r and m are the radius and mass of the planetesimal. Using the ambient gas density ρ_0 and the relative velocity $v_{\rm p}$ between the planetesimal and the gas, F is given by $\rho_0 v_{\rm p}^3/2$. The relative velocity $v_{\rm p}$ is approximately given by $ev_{\rm K}$, where $v_{\rm K}$ is the Keplerian rotation speed. Then the relative velocities of the planetesimals with $e \simeq 0.1$ are about 2 km s^{-1} at 3 AU. Accordingly, τ is evaluated to be

$$\tau = 1.0 \times 10^5 \left(\frac{r}{100\ \mathrm{km}}\right)\left(\frac{v_{\rm p}}{2\ \mathrm{km\ s^{-1}}}\right) \times \left(\frac{\rho_0}{10^{-10}\ \mathrm{g\ cm^{-3}}}\right)\ \mathrm{yr}, \quad (1)$$

where we have used $L = 2.7 \times 10^{10}$ erg g^{-1} and $\rho_{\rm p} (= 3m/4\pi r^3) = 2$ g cm^{-3}. Equation (1) shows that icy planetesimals with a radius of 100 km would evaporate and shrink within 10^5 yr. This evaporation time would be a significant

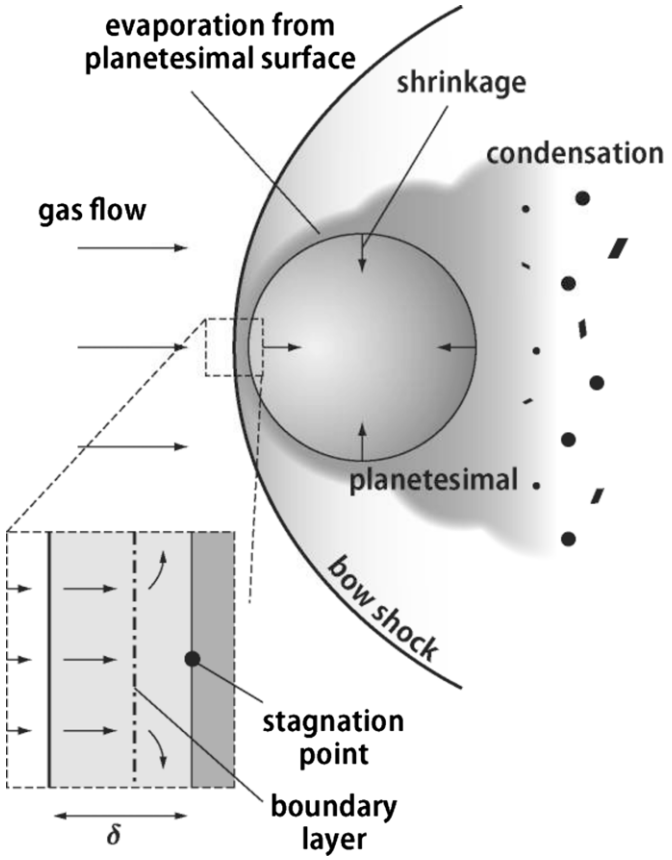

Figure 1. Illustration of planetesimal evaporation due to a planetesimal bow shock. A shock wave is generated in front of the planetesimal with respect to its direction of motion when the relative velocity between the disk gas and the planetesimal exceeds the sound velocity of the gas. The planetesimal surface is heated by a hot shocked gas and evaporates, which leads to planetesimal shrinkage. The evaporated vapor can recondense and form small dust particles. The box on the left is an enlargement of the area near the stagnation point. The distance from the shock front to the planetesimal surface, referred to as the stand-off distance, $\delta(\sim 0.1r)$, is known to be much smaller than the radius of the planetesimal (e.g., Wen & Hornung 1995). At the planetesimal surface, there is a boundary layer which is described in detail in Section 2.2.

underestimate because most of the thermal energy produced by the shock wave might be taken away by the ambient gas or the radiation. However, even if a few percent of the shock energy is used for the evaporation, the planetesimal evaporates effectively within the disk lifetime of $\sim 10^7$ yr. It is necessary to estimate accurately how much energy is used for the planetesimal evaporation.

In Section 2, we describe a model of planetesimal evaporation by a bow shock. In Section 3, we apply the evaporation model to planetesimals in the oligarchic growth stage. We show that icy planetesimals can evaporate efficiently in the oligarchic growth stage, where strong shocks are generated by the gravitational perturbations from the protoplanets. Sections 4 and 5 present a discussion and a summary.

2. THE MODEL

2.1. Evaporation Rate

As stated in Section 1, planetesimal bow shocks are frequently generated in protoplanetary disks. Figure 1 shows an illustration of a planetesimal bow shock. When the velocity of a planetesimal relative to the disk gas is supersonic, a bow shock forms on the leading side of the planetesimal. The gas is heated in the post-shock region as it passes through the shock front. Hot gas blows against the planetesimal and heats its surface. The materials on the planetesimal surface evaporate when the temperature rises above the evaporation temperature. As a result of the evaporation, the planetesimal shrinks and the vapor evaporating from the surface recondenses as it cools, and eventually forms fine dust particles if the evaporation produces a sufficient amount of vapor for their condensation.

The mass m of the planetesimal decreases with time t by evaporation. The rate of mass loss from the planetesimal is given by

$$-\frac{dm}{dt} = J, \tag{2}$$

where J is the evaporation rate of the planetesimal by mass. For a spherical planetesimal, this is given by

$$J = 2\pi r^2 \int_0^\pi j(\theta) \sin\theta d\theta, \tag{3}$$

where $j(\theta)$ is the evaporation flux and θ is the angle between the velocity vector of the planetesimal and the position vector from the center to the surface in question. The evaporation flux $j(\theta)$ is determined by the Hertz–Knudsen equation as a function of surface temperature $T_p(\theta)$, given by

$$j(\theta) = P_{\rm sat}(T_p)\sqrt{\frac{m_w}{2\pi k T_p}}, \tag{4}$$

where $P_{\rm sat}$ is the vapor pressure, m_w is the molecular mass of the evaporating materials, and k is the Boltzmann constant. Strictly speaking, Equation (4) is valid only for vaporization into a vacuum. However, this expression is sufficiently accurate in this case because molecules leaving the surface are quickly swept away by a strong gas flow around the planetesimal (Podolak et al. 1988).

The temperature of the planetesimal surface is determined by the energy balance on the planetesimal surface (Pollack et al. 1986), given by

$$F_e(\theta) - Lj(\theta) - \sigma\left[T_p(\theta)^4 - T_0^4\right] = 0, \tag{5}$$

where T_0 is the ambient radiation temperature and σ is the Stefan–Boltzmann constant. In Equation (5), $F_e(\theta)$ is the rate of heat transfer from the ambient gas; the second and third terms on the left-hand side indicate cooling due to the latent heat of evaporation and heat transfer due to radiation, respectively. Here, we neglected heat conduction into the planetesimal interior because of its low heat conductivity (Podolak et al. 1988). In Equation (5), we assumed that the planetesimal is a blackbody because absorption and emission efficiencies are high in the infrared compared with those in the visible (Irvine & Pollack 1968). Furthermore, absorption due to multiple scattering at the surface layer reduces the albedo.

As discussed in Appendix A, the evaporation rate can be approximated as $J = 4\pi f r^2 j(0)$, where f is a parameter measuring the homogeneity of the evaporation on the surface. We found that $f = 0.25$ provides a satisfactory fit to J, calculated taking into account the θ-dependence of $F_e(\theta)$, thus we hereafter approximate the evaporation rate of the planetesimal to be

$$J = \pi r^2 j(0). \tag{6}$$

The uncertainty in the f-values is very small compared to that in the rate of heat transfer from the gas, in particular in the Stanton number α, as will be discussed in Section 2.4.

2.2. Heat Transfer Rate

Due to the planetesimal bow shock, the gas is heated up in the post-shock region. The gas temperature behind the shock front is determined by the Rankine–Hugoniot relation (e.g., Landau & Lifshitz 1987), and is given by

$$T_{\rm s} = \frac{\{2\gamma\mathcal{M}^2 - (\gamma-1)\}\{(\gamma-1)\mathcal{M}^2+2\}}{(\gamma+1)^2\mathcal{M}^2}T_0, \quad (7)$$

where γ is the ratio of the specific heats and $\mathcal{M}$ is the Mach number of the pre-shocked gas whose velocity is measured relative to the planetesimal. The heated gas in the post-shock region flows onto the planetesimal surface.

There exists a thermal boundary layer near the surface of the planetesimal (see Figure 1). In this boundary layer, there is a large temperature gradient resulting from the low temperature of the surface and the thinness of the layer. Due to the large difference in the temperature between the outer edge of the boundary layer and the surface of the planetesimal, heat is transferred from the gas to the planetesimal surface. The heat transfer rate is determined by the state of the thermal boundary layer, as stated in the next section.

The distance from the shock front to the stagnation point at the planetesimal surface, referred to as the stand-off distance δ (see Figure 1), is known to be much smaller than the radius of the planetesimal. Wen & Hornung (1995) estimated $\delta \simeq 0.5(\rho_0/\rho_1)r$ from a mass balance using the gas density in the pre-shock region ρ_0 and that in the post-shock region ρ_1, which leads to $\delta \simeq r(\gamma-1)/[2(\gamma+1)] = 0.08r$ for $\mathcal{M} \gg 1$ and $\gamma = 1.4$. Because the stand-off distance is much smaller than r, we set the gaseous temperature at the outer edge of the boundary layer on the stagnation point to be $T_{\rm s}$, given by Equation (7), considering that the gas cooling is not effective in the region between the shock front and the planetesimal surface. Then, the rate of heat transfer at the stagnation point is expressed as (van Driest 1958; Schlichting 1979)

$$F_{\rm e}(0) = \alpha\rho_0 v_{\rm p} c_{\rm g}[T_{\rm s} - T_{\rm p}(0)], \quad (8)$$

where $c_{\rm g} = \gamma k/[(\gamma-1)\mu m_{\rm u}]$ is specific heat at constant pressure per unit mass of the disk gas with $m_{\rm u} = 1.66\times10^{-24}$ g being the atomic mass unit and $\mu = 2.24$ the mean molecular weight of the disk gas. α is a non-dimensional parameter, referred to as the Stanton number, expressing the efficiency of heat conduction (van Driest 1958; Schlichting 1979; Sarma 2000). $F_{\rm e}(0)$ in the limiting case of $\mathcal{M} \gg 1$, hence $T_{\rm s} \gg T_{\rm p}(0)$, is given by

$$F_{\rm e}(0) = \frac{2\gamma}{(\gamma+1)^2}\alpha\rho_0 v_{\rm p}^3 \quad (9)$$

using Equations (7) and (8) and $v_{\rm p} = \mathcal{M}c_{\rm s}$, where $c_{\rm s} = [\gamma kT_0/(\mu m_{\rm u})]^{1/2}$ is the sound speed in the gas. For $\gamma = 7/5$, the ratio of the specific heats for the disk gas mainly composed of H_2, the rate of heat transfer at the stagnation point is approximately given by $F_{\rm e} = 0.49\,\alpha\rho_0 v_{\rm p}^3$.

There is another heat source for planetesimals, that is, radiation from the ambient gas in addition to Equation (8). Heating due to line emissions from the gas molecules such as H_2O and CO may be effective (Miura & Nakamoto 2005); thermal radiation from the ambient gas is not effective because of the small optical depth in the region between the shock front and the planetesimal. The energy supply through collisions of large dust particles entrained in the gas may also be effective (Sekiya & Takeda 2005). Although the apparent expressions for these heat sources are different from that given by Equation (8), it is possible to take into account these effects by increasing the value of α (see Section 2.4).

2.3. Comparison with the Previous Formula of Heat Transfer

In previous studies on the ablation of planetesimals penetrating a thick planetary atmosphere, the rate of heat transfer from the gas such that

$$F'_{\rm e} = \frac{\Lambda\rho_0 v_{\rm p}^3}{2} \quad (10)$$

was adopted taking into account that a part of the kinetic energy of the relative motion of the gas to the planetesimal is converted into heating of the planetesimal (Pollack et al. 1986; Podolak et al. 1988). The conversion rate Λ was set to be 0.003 to 0.6; namely, $\Lambda = 0.3$ (Pollack et al. 1986; Inaba & Ikoma 2003), 0.5, 0.05 (Podolak et al. 1988), 0.6 (Sekanina 1993; Field & Ferrara 1995), 0.003 (Ahrens et al. 1994). $F'_{\rm e}$ can be compared with $F_{\rm e}$ given by Equation (9) for strong shocks, which was supposed in previous studies. The ratio of $F_{\rm e}(0)$ to $F'_{\rm e}$ is given by

$$\frac{F_{\rm e}(0)}{F'_{\rm e}} = 0.97\frac{\alpha}{\Lambda}. \quad (11)$$

Therefore, in the case of a strong shock wave, the two estimations of the rate of heat transfer are almost equal if $\Lambda \simeq \alpha$.

2.4. Stanton Number at the Planetesimal Bow Shock

The value of the Stanton number strongly depends on the state of the boundary layer. There are two states of this layer: laminar and turbulent (Schlichting 1979).

In the laminar case, the heat transfer from the gas to a spherical body has been investigated in detail (Sibulkin 1952; Baukal & Gebhart 1996). Based on analytical studies (Sibulkin 1952; Baukal & Gebhart 1996), the Stanton number is given by

$$\alpha = 1.22APr^{-0.6}\left(\frac{\rho_{\rm s}v_{\rm s}\eta_{\rm s}}{\rho_0 v_{\rm p}\eta_0}\right)^{1/2}\frac{1}{\sqrt{Re}}, \quad (12)$$

where Pr is the Prandtl number, $A \simeq 1$–2 is a constant (Sibulkin 1952; Baukal & Gebhart 1996), and η_0 is the viscosity of the gas in the pre-shock region. Here, $\rho_{\rm s}$, $v_{\rm s}$, and $\eta_{\rm s}$ are the gas density, velocity, and viscosity at the outer edge of the boundary layer. $Re \equiv \rho_0 v_{\rm p} r/\eta_0$ is the Reynolds number.

In the turbulent case, the thermal energy is transferred more easily from the gas to a body's surface than in the laminar case, by turbulent gas flow (Schlichting 1979; Baukal & Gebhart 1996; Isaev & Leont'ev 2003; Silva et al. 2007). In general, whether turbulence occurs or not is determined by the Reynolds number. The critical Reynolds number at the transition from a laminar boundary layer to a turbulent one is approximately 3×10^5 (Achenbach 1972; Schlichting 1979). When the surface is rough, the turbulent flows occur at smaller Reynolds numbers than the critical value. For example, an experiment in which "dimples" were artificially formed on the surface of the object revealed turbulent flows around the dimples (Mahmood et al. 2001; Mahmood & Ligrani 2002; Silva et al. 2007). In this case, a large increase in the rate of heat transfer was observed even though the Reynolds number was low ($Re \sim 10^4$) (Mahmood et al. 2001; Mahmood & Ligrani 2002). Mahmood & Ligrani

(2002) demonstrated an increase in the rate of heat transfer up to one order of magnitude, depending on the dimple features, such as its size and depth.

For planetesimals with a radius of 100 km, the Reynolds number is estimated to be $R_e \simeq 8 \times 10^6$ for $v_p = 3$ km s^{-1}, $\eta_0 \simeq 4 \times 10^{-5}$ poise (Kaye & Laby 1986), and $\rho_0 = 10^{-10}$ g cm^{-3}. Since this value is much higher than the critical value of 3×10^5, the boundary layer is fully turbulent. Roughness of the planetesimal surface also causes turbulence. Although the value of α obtained from Equation (12) is 0.2×10^{-2} for $Re \simeq 8 \times 10^6$ for a laminar flow, the true value of α could be much larger than this.

There is an additional heating due to line emissions from the gas molecules, as stated in Section 2.2. Here we estimate the heating rate. As will be shown in Section 3.3., the relative velocity of the planetesimal in the stage of the oligarchic growth is 1 km s^{-1} $\lesssim v_p \lesssim$ 5 km s^{-1}, which leads to an increase in gas temperature $\lesssim$1000 K in the post-shock region. In such a temperature region, line emissions due to the vibrational motions of H_2O and CO molecules become effective (Miura & Nakamoto 2005).

Because the optical depth in the stand-off distance is thin (Neufeld & Kaufman 1993), the radiative flux emitted from the gas in this region is given by $(\Lambda_{H2O} + \Lambda_{CO})\delta$, where Λ_{H2O} (or Λ_{CO}) is the rate of line emission per unit volume for the vibrational motions of H_2O (or CO) molecules and the thickness of the radiative region is assumed to be δ. If some fraction, say half, of the radiative flux is absorbed at the planetesimal surface, the ratio between the radiative flux F_{rad} and the heat transfer rate $F_e(0)$ from the gas at the stagnation point is estimated by

$$\frac{F_{rad}}{F_e(0)} = \frac{0.5(\Lambda_{H2O} + \Lambda_{CO})\delta}{\alpha \rho_0 v_p c_g (T_s - T_p(0))}. \quad (13)$$

To evaluate the ratio, we use timescales defined by Miura & Nakamoto (2005):

$$t_{cool,H2O} = \frac{n_H k T_s}{\Lambda_{H2O}} = 23 \left(\frac{T_s}{1000\,K}\right) \exp\left(\frac{2325\,K}{T_s}\right) \text{ s}, \quad (14)$$

$$t_{cool,CO} = \frac{n_H k T_s}{\Lambda_{CO}} = 140 \left(\frac{T_s}{1000\,K}\right) \exp\left(\frac{3080\,K}{T_s}\right) \text{ s}, \quad (15)$$

where $t_{cool,H2O}$ and $t_{cool,CO}$ are timescales to lose thermal energy of the gas via the line emissions of H_2O and CO molecules, respectively, and n_H is the total number density of hydrogen nuclei. Here, the abundances of H_2O and CO molecules are assumed to be solar (Miura & Nakamoto 2005). The line emission of H_2O is more effective than that of CO because $t_{cool,H2O} \lesssim t_{cool,CO}$ in the temperature range of $T \lesssim 1000$ K. For example, $t_{cool,H2O} = 336$ s (or 1200 s) at $T = 800$ K (or 500 K). Accordingly, we obtain

$$\frac{F_{rad}}{F_e(0)} \simeq \frac{1}{2\alpha} \frac{n_H k}{\rho_0 c_g} \left(\frac{\delta/v_p}{t_{cool,H2O}}\right) = 1.4 \left(\frac{\alpha}{0.01}\right)^{-1} \left(\frac{\rho_s/\rho_0}{6}\right) \times \left(\frac{r/v_p}{50\,s}\right) \left(\frac{t_{cool,H2O}}{300\,s}\right)^{-1}, \quad (16)$$

where we have assumed $T_s \gg T_p(0)$ and $\delta = 0.1r$. From Equation (16), we find that the radiative heating is comparable to the heat flux from the gas if $\alpha = 0.01$.

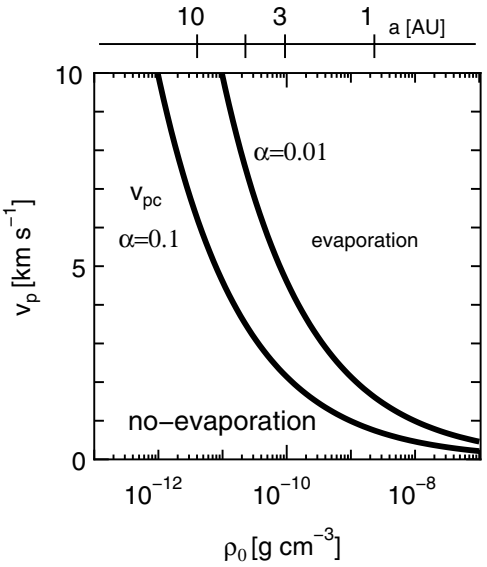

Figure 2. Threshold velocity for evaporation of icy planetesimals as a function of gas density. The top horizontal axis is the corresponding distance from the central star for the adopted disk model (Equations (23) and (24)).

In view of the highly turbulent state expected in the gas flow in the boundary layer around a planetesimal and the effect of the radiative heating, we consider the case of $\alpha = 0.01$ and 0.1 in the present study. From the above estimations, the large value of α ($\gtrsim 0.3$) would be overestimated. We discuss the dependence of the results on α in Section 3.

3. RESULTS

3.1. A Condition for Planetesimal Evaporation

Neglecting the radiation term in Equation (5), the evaporation flux of the planetesimal is estimated to be

$$j_{max} = \frac{\alpha \rho_0 v_p^3}{2L}, \quad (17)$$

for a strong shock. However, the evaporation flux given by Equation (17) is an overestimate because most of the thermal energy is taken away by thermal radiation from the surface of the planetesimal, resulting in an actual evaporation flux much smaller than that given by j_{max}. In order to induce active evaporation, the rate of heat transfer, $F_e(0)$, should be at least higher than the radiative energy loss at the evaporation temperature T_e($\simeq$ 170 K for ice), namely,

$$F_e(0) > \sigma T_e^4. \quad (18)$$

For a strong shock, this condition is expressed as

$$v_p > v_{pc}, \quad (19)$$

where the threshold velocity v_{pc} is given by

$$v_{pc} = \left[\frac{2\sigma T_e^4}{\alpha \rho_0}\right]^{1/3} \simeq 2 \left(\frac{T_e}{170\,K}\right)^{4/3} \left(\frac{\rho_0}{10^{-10}\,g\,cm^{-3}}\right)^{-1/3} \times \left(\frac{\alpha}{0.1}\right)^{-1/3} \text{ km s}^{-1}. \quad (20)$$

Figure 2 shows the threshold velocity for evaporation of icy planetesimals as a function of gas density. As can be seen, a

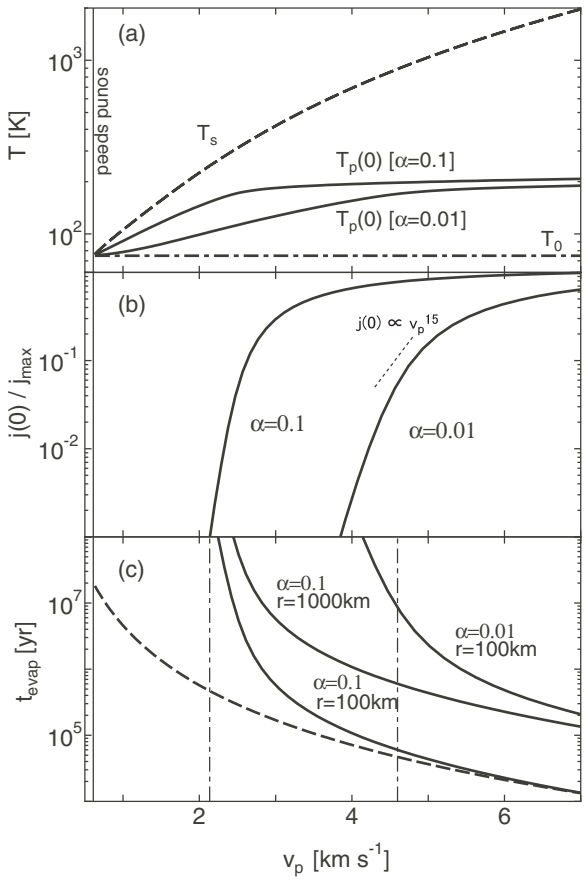

Figure 3. (a) Temperatures of the planetesimal surface at the stagnation point, $T_p(0)$, and of the gas in the post-shock region, T_s. Here, we set the Stanton number $\alpha = 0.1$ and 0.01 (solid curves). The disk gas temperature T_0 and the gas density are set to be 75 K and 1×10^{-10} g cm^{-3}, assuming that the distance from the central star is 3 AU (and using Equations (23) and (24)). (b) Ratio of the evaporation flux $j(0)$ to the maximum evaporation rate $j_{max}(= \alpha\rho_0 v_p^3/[2L])$. In the high-velocity case (strong shock), $j(0)$ is close to j_{max} while it is much smaller than j_{max} at low velocity. The rapid reduction of $j(0)$ occurs around the threshold velocities (vertical dashed-dotted lines, 2.1 km s^{-1} for $\alpha = 0.1$ and 4.6 km s^{-1} for $\alpha = 0.01$). For example, for $v_P = 4.6$ km s^{-1} and $\alpha = 0.01$, $j(0) \propto v_p^{15}$ (the slope is shown by the dotted line). (c) Evaporation time of planetesimals with $r = 100$ and 1000 km for $\alpha = 0.1$ and 0.01 (solid curves). The analytical estimation in Equation (22) is plotted with the dashed curve for $r = 100$ km and $\alpha = 0.1$.

large density as well as velocity leads to active evaporation of the planetesimals. The threshold velocity decreases with increasing α. For icy planetesimals, evaporation is possible because the relative velocities can exceed the threshold velocity, while evaporation of rocky planetesimals is difficult because of the large threshold velocity.

3.2. Evaporation Time of Icy Planetesimals

We calculate the temperature at the stagnation point of the planetesimal, $T_p(0)$, with the use of Equations (4), (5), (7), and (8). Figure 3(a) shows $T_p(0)$ together with the temperatures of the pre- and post-shock regions, T_0 and T_s, respectively, for the case of gas density $\rho_0 = 1.0 \times 10^{-10}$ g cm^{-3} and ambient radiation temperature $T_0 = 75$ K. The speed of sound in the disk gas is 0.61 km s^{-1}. For icy planetesimals, we use the vapor pressure of water ice (Kobayashi et al. 2008) and $m_w = 3.0 \times 10^{-23}$ g. In the calculations, we assume the ambient radiation temperature to be equal to the initial gas temperature. This assumption is valid if the optical depth between the shock front and the planetesimal surface is small.

As shown in Figure 3(a), the temperature of the planetesimal, $T_p(0)$, begins to increase when the relative velocity v_p exceeds 0.61 km s^{-1}, the speed of sound in the disk gas. Although T_s and T_p both increase as the relative velocity v_p increases, the increase in T_p is suppressed because of cooling due to the latent heat of evaporation. The increase in T_p stops at around 200 K, although T_s exceeds 1000 K when the relative velocity exceeds $\sim$5 km s^{-1}.

Figure 3(b) shows the ratio of evaporation flux $j(0)$ to j_{max}. In the high-velocity case (i.e., for very strong shocks) $j(0)$ is close to j_{max}. For relatively small velocities, on the other hand, the ratio is small and strongly dependent on v_p. This is because most of the thermal energy is taken away by the radiation. For example, $j(0) \propto v_p^{15}$ around $v_p = 4.6$ km s^{-1} (the threshold velocity for the effective evaporation for $\alpha = 0.01$) from the slope in Figure 3(b).

Evaporation reduces the mass of the planetesimal. We define the timescale of the planetesimal evaporation t_{evap} as

$$t_{evap} \equiv \left| \frac{1}{m} \frac{dm}{dt} \right|^{-1} = \frac{m}{J}, \quad (21)$$

where we have used Equations (2) and (6). Figure 3(c) shows t_{evap} of planetesimals of radii of 100 and 1000 km for $\alpha = 0.1$ and 100 km for $\alpha = 0.01$ (solid curves). The vertical dashed-dotted lines indicate the threshold velocities given by Equation (20). The threshold velocity is 2.1 kms^{-1} for $\alpha = 0.1$. For planetesimals with the threshold velocity, their evaporation time is larger than or comparable to the disk lifetime of $\sim 10^7$ yr. Around the threshold velocity, the evaporation time is strongly dependent on v_p as well as $j(0)$. Hence, we can say that the bow shock with the threshold velocity is the marginal shock for significant evaporation of planetesimals.

Active evaporation occurs when the rate of heat transfer is large. In active evaporation, heating and cooling by radiation is negligible, and the energy deposit is determined by the balance between heating due to the gas flow from the boundary layer and cooling due to the latent heat of evaporation. Ignoring the radiation term in Equation (5), we obtain the evaporation time t_{evap} from Equations (5) and (6) together with Equation (21), as

$$t_{evap} = \frac{2(\gamma+1)^2}{3\gamma} \frac{r\rho_p L}{\alpha\rho_0 c_s^3 \mathcal{M}^3} \quad (22)$$

in the limit $\mathcal{M} \gg 1$. Here, we set $m = 4\pi\rho_p r^3/3$, where ρ_p is the bulk density of the planetesimal. In Figure 3(c), we plot this approximate expression (22) by a dashed curve for $\alpha = 0.1$ and $r = 100$ km. Equation (22) agrees with the numerical result for high velocities of $v_p \gtrsim 2v_{pc}$. We see that, for such high velocities, the evaporation time is much shorter than the disk lifetime. It should be noted that even in the case of the marginal shock velocities, the effective evaporation occurs in the disk lifetime.

3.3. Planetesimal Evaporation in the Stage of Planetary Oligarchic Growth

As seen in the previous section, planetesimal evaporation due to a bow shock is strongly dependent on the shock velocity, which is determined by the orbital eccentricity and the inclination of the planetesimal. Here, we evaluate the eccentricities and the inclinations of planetesimals enhanced by

massive protoplanets based on the standard model of planetary formation, in order to estimate the evaporation time more accurately.

For the disk model, we assume the minimum-mass solar nebular model (Hayashi et al. 1985). The surface density distribution of the gaseous disk is given by

$$\Sigma_g = 1700 \left(\frac{a}{1\ \mathrm{AU}}\right)^{-3/2}\ \mathrm{g\ cm^{-2}}. \quad (23)$$

For the disk temperature, we adopt a relatively cold model proposed by Chiang & Goldreich (1997). In this model, the disk temperature is given by

$$T_0 = 120 \left(\frac{a}{1\ \mathrm{AU}}\right)^{-3/7}\ \mathrm{K}. \quad (24)$$

This model is valid for radially optically thick disks irradiated by solar-type stars (Chiang et al. 2001; Tanaka et al. 2005). The snow line is located at 0.5 AU in this model. The gas density ρ_0 is given by

$$\rho_0 = \frac{\Sigma_g \Omega_K}{\sqrt{2\pi}\, c_s} = 2.1 \times 10^{-9} \left(\frac{a}{1\ \mathrm{AU}}\right)^{-39/14}\ \mathrm{g\ cm^{-3}}, \quad (25)$$

where $\Omega_k = (GM_\odot/a^3)^{1/2}$, $M_\odot$ is the solar mass, and G is the gravitational constant.

In the oligarchic growth stage, the protoplanets stir up the planetesimals in the vicinity with their strong gravitational perturbations. On the other hand, the eccentricity e of the planetesimals is damped due to the shock wave or gas drag (Tanaka & Ida 1999). The equilibrium value of e is determined by the balance of the stirring by the gravitational perturbation and the damping by the shock wave, and is given (Kobayashi et al. 2010) by

$$e \simeq 0.16 \left(\frac{r}{100\ \mathrm{km}}\right)^{1/5} \left(\frac{a}{3\ \mathrm{AU}}\right)^{5/14} \left(\frac{M}{10\ M_E}\right)^{1/3}, \quad (26)$$

where M is the mass of the protoplanet, M_E is Earth mass, and the bulk density of the planetesimal is set as 2 g cm^{-3}. See Appendix B for the derivation of Equation (26).

The orbital inclination i is approximately given by $i = e/2$ (e.g., Kokubo & Ida 1998; Kobayashi et al. 2010). Since the disk gas is rotating with circular motion around the Sun, the relative velocity between the planetesimal and the disk gas is determined by the random velocity given by $v_p = (e^2 + i^2)^{1/2} a\Omega_K$ (Hayashi et al. 1985). Since the inclination is less than the eccentricity, we simply set $v_p \simeq ea\Omega_K$ in this study.

Figure 4 shows e and v_p of the planetesimals at $a = 3$ AU for $M = 5$ and 10 M_E. Note that e and v_p increase with increasing planetesimal radius r because the effect of gas drag becomes smaller for larger planetesimals. We find that strong bow shocks occur for planetesimals with radii $\gtrsim$10 km. Using the result in Appendix B, the damping time of the planetesimal eccentricity $t_{gas}(e)$ is given by $t_{gas}(e) = 5 \times 10^5$ yr for $r = 100$ km and $e = 0.1$ at 3 AU. Although the damping time of the eccentricities is shorter than the evaporation time, the planetesimal eccentricities remain high because of the strong perturbations by protoplanets.

In Figure 4, the dash-dotted lines are the threshold velocities determined by Equation (20). Figure 4 indicates that efficient evaporation occurs only for planetesimals having a radius larger than a threshold radius r_c defined by $v_p(r_c) = v_{pc}$. For the

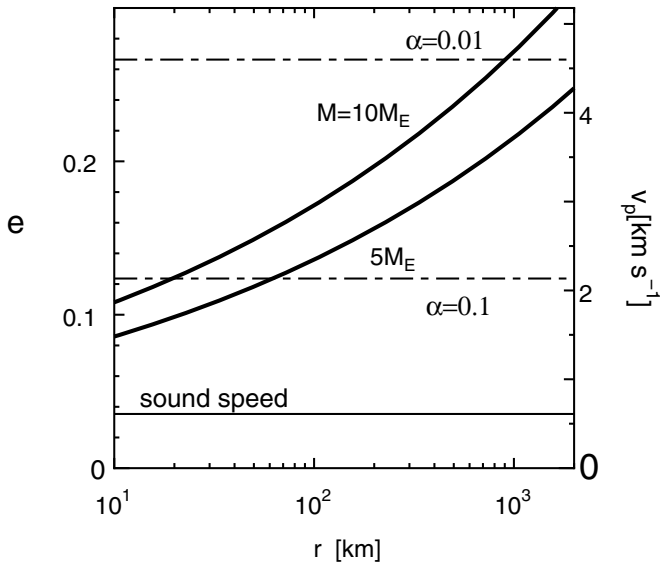

Figure 4. Eccentricities e and random velocities v_p of planetesimals as functions of planetesimal radius r at 3 AU. The mass M of the perturbing protoplanets is set to be 5 and 10 M_E. The dash-dotted lines are the threshold velocities given by Equation (20) for $\alpha = 0.1$ and 0.01. The sound speed is plotted with the thin solid line. Mach number ($=v_p/c_s$) is larger than 3 within the range of the velocity v_p shown in this figure.

adopted disk model (Equations (23) and (24)), the threshold radius is obtained as

$$r_c = 20 \left(\frac{M}{10 M_E}\right)^{-5/3} \left(\frac{a}{3\ \mathrm{AU}}\right)^{75/14} \times \left(\frac{T_e}{170\ \mathrm{K}}\right)^{20/3} \left(\frac{\alpha}{0.1}\right)^{-5/3}\ \mathrm{km} \quad (27)$$

using Equations (19) and (26). In the above estimation of the orbital eccentricities and inclinations, it is assumed that planetesimals stay inside the disk gas. This is valid only when their inclinations satisfy $i < H/a$, where $H(= c_s/\Omega_K)$ is the disk scale height. From Equation (26) and $i = e/2$, this could not be satisfied for planetesimals of $r \gtrsim 100$ km around protoplanets of $M = 10 M_E$. If planetesimals go out of the disk, the effect of gas drag is reduced and then their eccentricities and inclinations become larger than the estimation given by Equation (26). We discuss this effect on the planetesimal evaporation in Section 4. Furthermore, we note that Equation (26) gives mean eccentricities of the planetesimals. In other words, the eccentricities and inclinations are distributed around the mean values. Even for fixed eccentricity and inclination, the relative velocity between the planetesimal and the disk gas changes along a Keplerian orbit. The effect of these velocity fluctuations will also be discussed in the next section.

Using Equation (26), we can evaluate the evaporation time due to the planetesimal bow shocks in the planetary oligarchic stage. The evaporation time of the planetesimals is shown in Figure 5 as a function of the planetesimal radius for protoplanets with $M = 10\ M_E$ at $a = 3$ AU. Figure 5(a) corresponds to the case $\alpha = 0.1$.

In Figure 5(a), the evaporation time is much shorter than the disk lifetime of $\sim 10^7$ yr for large planetesimals with $r \gtrsim 100$ km because of their strong bow shock. In the strong shock case,

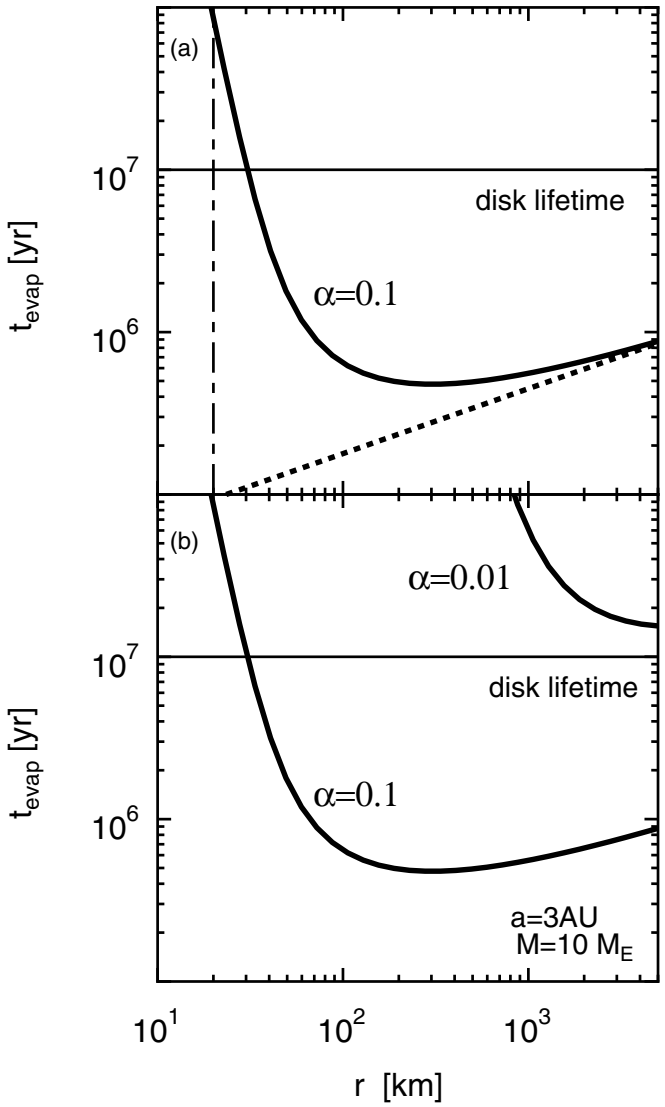

Figure 5. Evaporation time $t_{\rm evap}$ of planetesimals perturbed by protoplanets of $M = 10\,M_{\rm E}$ as functions of the planetesimal radius (solid curves). The distance from the central star is set to be 3 AU. Panel (a) shows the case of $\alpha = 0.1$ together with $r_{\rm c}$ (vertical dashed-dotted line) and the analytic estimation by Equation (22) (dotted line). Panel (b) shows the dependence of $t_{\rm evap}$ on α by plotting $t_{\rm evap}$ for $\alpha = 0.01$ and 0.1. The disk lifetime (of 10^7 yr) is plotted with thin solid lines in each panel.

using Equation (22), we can estimate the evaporation time to be

$$t_{\rm evap} = 1.2 \times 10^5 \left(\frac{r}{100\,{\rm km}}\right)^{2/5} \left(\frac{a}{3\,{\rm AU}}\right)^{45/14} \times \left(\frac{M}{10M_{\rm E}}\right)^{-1} \left(\frac{\alpha}{0.1}\right)^{-1} {\rm yr}. \quad (28)$$

This analytical expression is also plotted with a dotted line and we find that it is valid for planetesimals with $r \gtrsim 1000$ km. For small planetesimals with $r < 50$ km, on the other hand, the evaporation time is comparable with or longer than the disk lifetime. This is because their bow shock is weak and $j(0)$ is much smaller than $j_{\rm max}$.

For a fixed evaporation flux $j(0)$ (or a fixed random velocity $v_{\rm p}$), the evaporation time is proportional to the planetesimal radius, which comes from the ratio of mass to surface area of the planetesimals (see also Equation (28)). However, because of the strong dependence of $j(0)$ on $v_{\rm p}$ and the size dependence

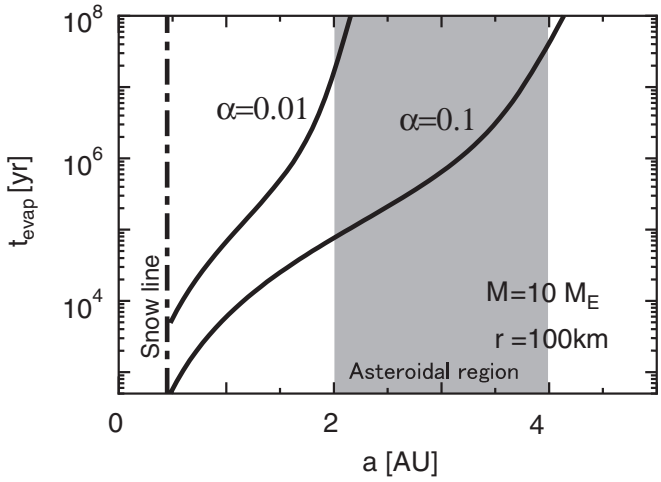

Figure 6. Evaporation time of planetesimals with $r = 100$ km as a function of the semi-major axis a. The mass of the protoplanet is set to be 10 $M_{\rm E}$.

of $v_{\rm p}$, the evaporation time rapidly decreases with radius up to 100 km. According to Equations (B1) and (B2), the random velocities of planetesimals are proportional to $r^{1/5}$. Although this size dependence of the random velocity is weak, due to the strong dependence of $j(0)$, larger planetesimals have a shorter evaporation time in spite of their large mass-to-area ratio for the marginal shock. For example, $t_{\rm evap} \propto r^{-2}$ using $j(0) \propto v_{\rm p}^{15}$, which is obtained around the threshold velocity, as shown in Section 3.2.

For the threshold radius of 20 km (Equation (27)), the evaporation time is much longer than the disk lifetime. Hence we can say that larger planetesimals shrink to 30 km size within the disk lifetime in the case of $\alpha = 0.1$. Figure 5(b) shows the dependence of the evaporation time on α. In the case of $\alpha = 0.01$, the planetesimal evaporation is inefficient at $a = 3$ AU.

In Figure 6, the evaporation time of planetesimals with $r = 100$ km is plotted as a function of the semi-major axis a for $\alpha = 0.1$ and 0.01. The evaporation time rapidly increases with distance a from the central star. The evaporation time is shorter than the disk lifetime in the region of $a < 4$ AU for $\alpha = 0.1$ (or $a < 2$ AU for $\alpha = 0.01$). With an increase in α, the disk region where the planetesimal evaporation is effective becomes wider.

4. DISCUSSION

4.1. Summary of Overall Scenario of Planetesimal Evaporation

In the previous section, we presented a scenario of planetesimal evaporation in the planetary oligarchic stage and examined it quantitatively. The scenario is summarized in Figure 7. As protoplanets become massive in the runaway growth stage, they start to gravitationally stir up the planetesimals (panels (a) and (b)). This gravitational stirring enhances the orbital eccentricities of the planetesimals, resulting in bow shocks on their leading side (panel (c)) of the planetesimals. The shock heating leads to evaporation of icy planetesimals. Planetesimals with radii larger than 100 km evaporate efficiently because of their relatively high eccentricities. The evaporation continues until they shrink below the critical radius, at which the eccentricities are too small for evaporation. The evaporated vapor recondenses and forms small dust particles. Finally, there remain large protoplanets, small icy planetesimals, and large amounts of fine dust particles (panel (d)). The kinetic energies of planetesimals are dissipated

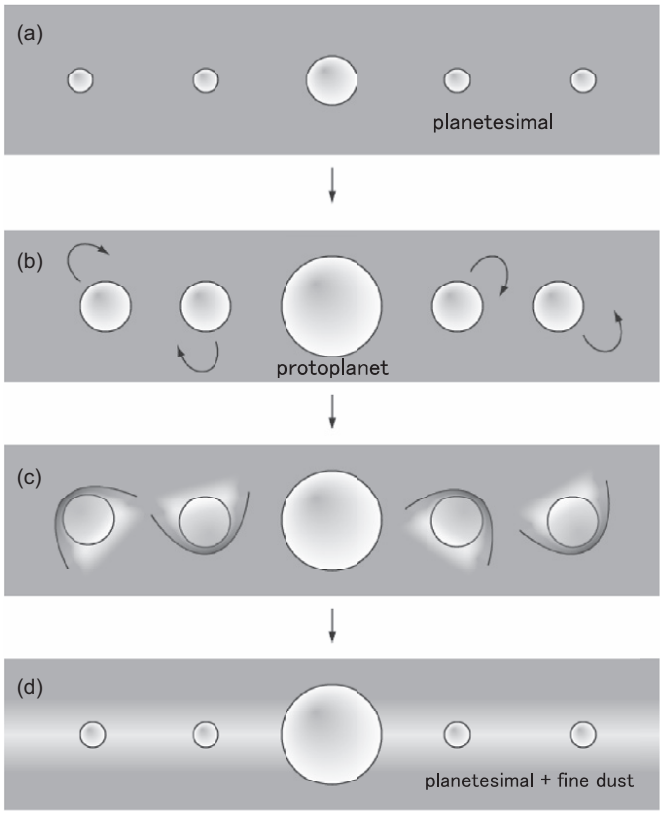

Figure 7. Illustrations showing the scenario of planetesimal evaporation in the planetary oligarchic stage: (a) runaway growth of planetesimals, (b) gravitational stirring by a protoplanet, (c) evaporation of icy planetesimals by bow shocks, and (d) a large protoplanet, small icy planetesimals, and remaining fine dust.

by their bow shocks at a high rate, which causes evaporation of icy planetesimals. Such kinetic energies are, on the other hand, continuously enhanced by the gravitational perturbations of protoplanets. This is the energy source for the strong bow shocks.

In the present study, we focused on the oligarchic growth stage of protoplanets, in which planetesimals have high velocities relative to the gas due to stirring by protoplanets. However, there is another stage in which e of the planetesimals increases. This stage follows the formation of gas giant planets. The planetesimals would be strongly affected by the gravitational perturbations of the gas giant planet (Weidenschilling et al. 1998). For example, secular resonances due to Jupiter cause strong perturbations on the asteroid region (Nagasawa et al. 2000, 2005). If a substantial amount of the gas remained in the disk after Jupiter has attained its final mass, stronger bow shocks would be generated in the disk. In such a stage, the evaporation of planetesimals would proceed much more strongly.

4.2. Effect of High Inclinations of Planetesimal Orbits

We ignored the possible effects of high inclinations of the planetesimal orbits in Section 3.3. Here we examine such effects. When the ratio defined by

$$I = \frac{ia}{H} \tag{29}$$

is larger than unity, the planetesimals go out of the gas disk twice during one Keplerian orbit. In this case, their time in the disk is reduced by a factor of $1/I$. Since the evaporation due to the shock stops outside the gas disk, one may simply expect that this effect might decrease the time-averaged evaporation flux and elongate the evaporation time of the planetesimals.

In the estimation of $t_{\rm evap}$, however, we have to take into account the velocity enhancement due to the high inclination (see below). The short time in the disk reduces the damping in the eccentricities due to gas drag by a factor of $1/I$, which increases the equilibrium eccentricities. According to Equation (B2), this reduction of the gas drag damping enhances the eccentricities (or relative velocities) of the planetesimals by a factor of $I^{1/5}$. (Note that this I-dependence is the same as its size dependence.) Because of strong dependence of $j(0)$ on the velocity, this enhancement of relative velocities can increase the time-averaged evaporation flux in spite of their short time in the disk. Indeed, we readily see that the dependence of the evaporation time on the factor I is completely the same as the size dependence shown in Figure 5. The random velocity depends on r and I in the same way as seen above, and the short time in the disk corresponds to the small area-to-mass ratio. This enables us to find the I-dependence of the evaporation time from Figure 5. Hence, it is concluded that the effect of high inclinations indeed enhances planetesimal evaporation for a marginal shock.

4.3. Effect of Velocity Fluctuations

The relative velocities of planetesimals to gas change along a Keplerian orbit and the orbital eccentricities e and inclinations i also fluctuate around their mean values in a long period. The distribution of e and i of planetesimals is a Rayleigh distribution (Ohtsuki & Ida 1990; Ida & Makino 1992). We briefly discuss the effect of these velocity fluctuations on planetesimal evaporation. We focus on the case of marginal shock where the evaporation time is comparable to or longer than the disk lifetime. For a marginal shock, since the evaporation flux rapidly increases with relative velocity, the major contribution of the planetesimal evaporation comes from the time period in which their relative velocities are close to maximum, although such a time period might be very short compared with the total time. For example, from Figure 3(b), we found that $j(0)$ increases by a factor five when $v_{\rm p}$ increases by 10% from the mean value of $v_{\rm p} = 4.6$ km s^{-1} for $\alpha = 0.01$. This means that the total evaporation flux doubles when the time period during which $v_{\rm p}$ increases 10% from the mean value is 1/5 of the total time. If the velocity fluctuation is larger, the evaporation flux becomes larger even for shorter time periods. This effect is also expected from the analogy to the high inclination case examined above. Accordingly, if we also include the effect of velocity fluctuations, the evaporation time would be further reduced compared with the case with constant velocity examined so far. A further quantitative estimation of this velocity fluctuation effect should be done in future work.

4.4. Dust Release by Planetesimal Bow Shocks

It is supposed that the dust particles composing the planetesimal consist not only of ice but also of refractory components such as silicates. During evaporation of the planetesimal, silicate grains may remain, forming a dark crust on the planetesimal surface as in comets. This would prevent further evaporation. However, silicate grains are also expected to be released from the planetesimal surface by the strong flow of the disk gas in the planetesimal evaporation. We discuss the possibility of such dust release below.

The critical velocity, u_*, required for the release of dust particles by the winds is determined by the balance between the dynamical force $\pi r_d^2 \rho_0 c_s u_*$ by the Epstein law (Adachi et al. 1976) and the gravitational force $\pi r_d^3 \rho_p g$, using the gravitational acceleration g and the radius of a dust particle r_d (Greeley & Iversen 1985). Then the critical velocity is approximately given by

$$u_* \simeq \frac{\rho_p g r_d}{\rho_0 c_s}. \quad (30)$$

For $r = 100$ km, $r_d = 1$ mm, and $\rho_0 = 10^{-10}$ g cm^{-3}, u_* is estimated to be 1 km s^{-1} from Equation (30), which is comparable with the gas velocity in the post-shock region. This indicates that dust grains smaller than 1 mm are removed by the gas flow. Since the primordial interstellar silicate grains are sub-micron size, we can expect in the present case that silicate grains might be easily removed from the surface.

4.5. Implications for Planetary Formation

The results of the present study suggest that the growth of a protoplanet is suppressed owing to insufficient accretion of planetesimals onto the protoplanet. In other words, evaporation of the planetesimals disturbs the growth of a Jupiter-type planet core. Recent research shows that its growth is suppressed by collisional destruction of the planetesimals (Kobayashi & Tanaka 2010; Kobayashi et al. 2010, 2011). Our results suggest that evaporation is another mechanism to suppress the growth of a Jupiter-type planet. Evaporation is more effective than destruction in the inner region of $a \lesssim 4$ AU in the disk if $\alpha = 0.1$.

Observations of the spectral energy distribution (SED) of protoplanetary disks have revealed a substantial amount of small dust remaining rich for up to several million years. This is in contradiction to the theoretical prediction that dust growth occurs from μm to meter size within a much shorter time, which depletes fine dust grains. In order to replenish fine dust grains, planetesimal destruction by their mutual collision is proposed (Dullemond & Dominik 2005; Birnstiel et al. 2009). But the amount of small dust grains $\sim\mu$m due to destruction is not so large (Kobayashi et al. 2010). The planetesimal evaporation that we discussed may provide clues to resolve this contradiction, because it provides dust even after the dust in the disk grows to planetesimals, in addition to planetesimal destruction (Dullemond & Dominik 2005; Birnstiel et al. 2009). The evaporated vapor recondenses and forms small dust particles, if the active evaporation supplies a sufficient amount of vapor for recondensation. Furthermore, planetesimal evaporation will exhibit features similar to cometary activity; dust particles composing the planetesimals are released to the disk along with the flow of evaporating vapor. These processes influence the SED of the protoplanetary disks in the late stage of their evolution.

There would be an influence on the formation of asteroids in the asteroidal belt. We note that active evaporation of planetesimal occurs in the vicinity of the asteroid belt (2–3.5 AU). Asteroids are considered to be surviving planetesimals. Significant amounts of icy substances should have been contained in the asteroids orbiting outside the snow line if there had been no change in the orbit of the planetesimals. In fact, however, a number of rocky asteroids are observed in the asteroid belt outside the snow line. Recent studies showed that a rocky core is formed by the settling of rocks after melting of ice depending on the abundance of radioactive elements such as ^{26}Al in the icy planetesimals (Schubert et al. 2007; Wakita & Sekiya 2011). The shock heating enables us to change icy planetesimals with a core–mantle structure to rocky planetesimals by evaporation of the icy mantle. This process may explain the presence of rocky asteroids outside the snow line. The loss of the icy component might also resolve the problem of overabundance of water in the terrestrial planets formed in the cold disk (Machida & Abe 2010). The quantitative predictions stated in this subsection are left as subjects of future study.

5. CONCLUSIONS

We investigated the novel concept of planetesimal evaporation in a protoplanetary disk. The eccentricities of planetesimals in the vicinity of a protoplanet increase in the stage of planetary oligarchic growth. As a result, heating and evaporation of the icy planetesimals occur even outside the snow line. For effective evaporation, the relative velocity between a planetesimal and the disk gas should exceed 2 km s^{-1} (or 4 km s^{-1}) for $\alpha = 0.1$ (or $\alpha = 0.01$). In the stage of planetary oligarchic growth, strong bow shocks are produced by gravitational perturbations by protoplanets. The evaporation of planetesimals is long-lasting because perturbations by protoplanets keep the planetesimal eccentricities high. The evaporation of icy planetesimals larger than 20 km occurs from the snow line to the vicinity of 2–4 AU in the disk for $\alpha = 0.1$. There are several important implications for planetary formation and observations, as shown in Section 4. The results of the present study suggest that growth of gas giant planets is suppressed owing to insufficient accretion of planetesimals onto the protoplanet in the inner disk region.

The evaporation time depends strongly on the efficiency α of heat conduction from the gas to the planetesimal surface. The dependence of the critical radius and the evaporation time on α is given by Equations (27) and (28), respectively. Precise evaluation of the Stanton number α in a turbulent boundary layer and the radiative heating due to the line emissions of gas molecules are important in future studies, in order to investigate planetesimal evaporation in more detail.

We are grateful to an anonymous reviewer for useful comments to improve the paper. This work was supported by the Grant-in-Aid Scientific Research on Innovative Areas (23103004) from JSPS.

APPENDIX A

θ-DEPENDENCE OF EVAPORATION RATE

We herein discuss the validity of the assumption that the evaporation rate is given by Equation (6). The heat transfer from the gas behind a shock wave has been investigated for many years. For a laminar boundary layer, Lees (1956) derived the rate of heat transfer over a hemisphere for a body moving at hypersonic speeds. Based on his results, the rate of heat transfer at "latitude" θ from the stagnation point ($\theta = 0$) is given by

$$\frac{F_e(\theta)}{F_e(0)} = \frac{2\theta \sin\theta}{\sqrt{D(\theta)}} \left\{ \left(1 - \frac{1}{\gamma \mathcal{M}^2}\right) \cos^2\theta + \left(\frac{1}{\gamma \mathcal{M}^2}\right) \right\}, \quad (A1)$$

where

$$D(\theta) = \left(1 - \frac{1}{\gamma \mathcal{M}^2}\right) \left(\theta^2 - \frac{\theta \sin 4\theta}{2} + \frac{1 - \cos 4\theta}{8}\right) + \frac{4}{\gamma \mathcal{M}^2} \left(\theta^2 - \theta \sin 2\theta + \frac{1 - \cos 2\theta}{2}\right). \quad (A2)$$

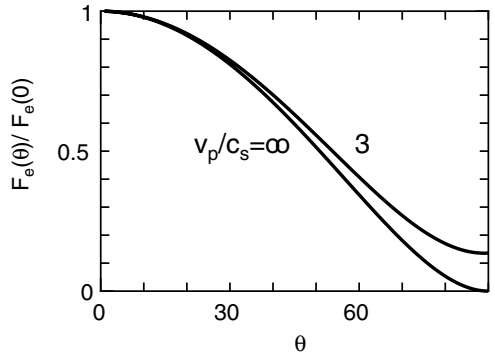

Figure 8. Ratio $F_e(\theta)/F_e(0)$ as a function of θ for $\mathcal{M} = 3$ and ∞ with $\gamma = 1.4$.

Figure 8 shows the ratio $F_e(\theta)/F_e(0)$ as a function of θ for $\mathcal{M} = 3$ and ∞ with $\gamma = 1.4$. Wen (1994) experimentally demonstrated that Equation (A1) holds for high Reynolds numbers ($Re \simeq 10^6$) as well, for which the flow is turbulent.

Using Equation (A1), we calculated T_p by solving Equation (5) and $j(\theta)$ from Equation (4), where we set $F_e(\theta) = 0$ for $\pi/2 \leqslant \theta \leqslant \pi$. Here, $F_e(0)$ is evaluated using Equation (8). The evaporation rate J given by Equation (3) is calculated numerically with the use of $j(\theta)$ obtained in this manner. The results are expressed as

$$J = 4\pi f r^2 j(0), \tag{A3}$$

where f is a parameter measuring the uniformity of the surface temperature. In fact, the value of f depends on the various parameters, such as the Mach number $\mathcal{M}$, the gas density, and the efficiency of heat conduction α, although the J-values are insensitive to these quantities. Figure 9 compares t_{evap} for $f = 0.25$ (solid curves) and that calculated taking into account θ-dependence of $F_e(\theta)$ given by Equation (A1) (dotted curves). Good agreement was found except in the case of large a. In the calculations described in the text, we set $f = 0.25$.

APPENDIX B

EQUILIBRIUM ECCENTRICITY

In the planetary oligarchic growth stage, the eccentricity e of a planetesimal is excited by gravitational scattering by a protoplanet and de-excited by shock wave or gas drag due to the disk gas. According to Kobayashi et al. (2010), the equilibrium value of e is given by

$$e = \left[\frac{C_{VS}\ln(\Lambda^2+1)\Omega_k\tau_{gas}}{25\pi C_{gas}}\right]^{1/5} h, \tag{B1}$$

where $C_{VS}(= 40)$ and $C_{gas}(= 2.1)$ are constants. Ω_K is the Keplerian angular velocity at the distance of the protoplanet. Here, τ_{gas} is the characteristic time of the gas drag defined by

$$\tau_{gas} = \frac{2m}{\pi r^2 C_D \rho_0 a \Omega_K}, \tag{B2}$$

where $C_D(\simeq 1)$ is the gas drag coefficient (Adachi et al. 1976) and h is the reduced Hill radius of the protoplanet given by

$$h = \left(\frac{M/M_\odot}{3}\right)^{1/3} = 0.014\left(\frac{M/M_E}{3}\right)^{1/3}, \tag{B3}$$

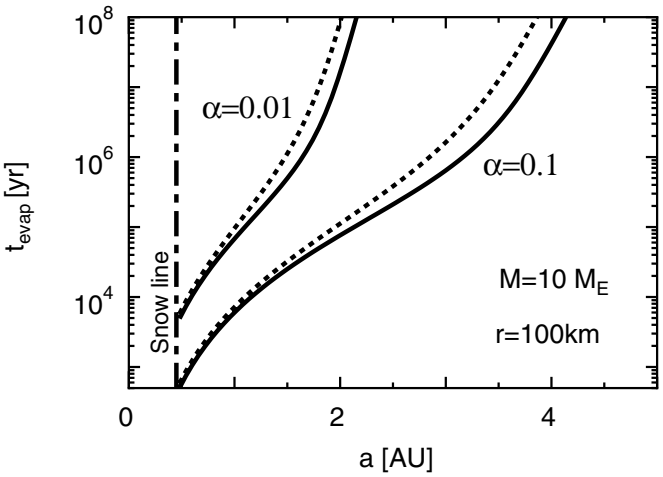

Figure 9. Same as Figure 6, together with the results (dotted curves) that take into account θ-dependence for the evaporation flux described in Appendix A.

using the mass of the protoplanet M. The time τ_{gas} corresponds to the damping time of the planetesimal eccentricity when $e \sim 1$. In the case of $e \ll 1$, the damping time of the planetesimal eccentricity, $t_{gas}(e)$ $(= e/[de/dt])$, is given by τ_{gas}/e. The factor Λ is expressed by Ohtsuki et al. (2002) as

$$\Lambda = \frac{i(e^2+i^2)}{3h^3}, \tag{B4}$$

where i is inclination of the planetesimal. For planetesimals with $r = 10$ to 100 km, we can set $e \simeq 2i \simeq 10h$, which yields $\ln(\Lambda^2+1) = 10.7$. Using these values, the equilibrium eccentricity is expressed as

$$e = 1.75\left(\frac{4r\rho_P}{3\pi C_D \rho_0 a}\right)^{1/5} h. \tag{B5}$$

REFERENCES

Achenbach, E. 1972, JFM, 54, 565
Adachi, I., Hayashi, C., & Nakazawa, K. 1976, PThPh, 56, 1756
Ahrens, T. J., Takata, T., O'Keefe, J. D., & Orton, G. S. 1994, Icar, 109, 3
Baukal, C. E., & Gebhart, B. 1996, IJHMT, 39, 2989
Birnstiel, T., Dullemond, C. P., & Brauer, F. 2009, A&A, 53, L5
Chiang, E. I., & Goldreich, P. 1997, ApJ, 490, 368
Chiang, E. I., Joung, M. K., Greech-Eakman, K. J. E., Blake, G. A., & van Dishoeck, E. F. 2001, ApJ, 547, 1077
Ciesla, F. J., & Hood, L. L. 2002, Icar, 158, 281
Ciesla, F. J., Hood, L. L., & Weidenschilling, S. J. 2004, M&PS, 39, 1809
Desch, S. J., & Connolly, H. C., Jr. 2002, M&PS, 37, 183
Dullemond, C. P., & Dominik, C. 2005, A&A, 434, 971
Field, G. B., & Ferrara, A. 1995, ApJ, 438, 957
Greeley, R., & Iversen, J. D. 1985, Wind as a Geological Process on Earth, Mars, Venus, and Titan (Cambridge: Cambridge Univ. Press)
Hayashi, C., Nakazawa, K., & Nakagawa, Y. 1985, in Protostars and Planets II, ed. D. C. Black & M. S. Matthews (Tucson, AZ: Univ. of Arizona Press), 1100
Hood, L. L. 1998, M&PS, 33, 97
Hood, L. L., Ciesla, F. J., Artemieva, N. A., Marzari, F., & Weidenschilling, S. J. 2009, M&PS, 44, 327
Hood, L. L., Ciesla, F. J., & Weidenschilling, S. J. 2005, in ASP Conf. Ser. 341, Chondrites and the Protoplanetary Disk, ed. A. N. Krot, E. R. D. Scott, & B. Reipurth (San Francisco, CA: ASP), 873
Hood, L. L., & Horanyi, M. 1991, Icar, 93, 259
Hood, L. L., & Horanyi, M. 1993, Icar, 106, 179
Ida, S., & Makino, J. 1992, Icar, 96, 107
Iida, A., Nakamoto, T., & Susa, H. 2001, Icar, 153, 430
Inaba, S., & Ikoma, M. 2003, A&A, 410, 711
Irvine, W. M., & Pollack, J. B. 1968, Icar, 8, 324

Isaev, S. A., & Leont'ev, A. I. 2003, High Temp., 41, 665
Kaye, G. W. C., & Laby, T. H. 1986, Physical constants; Physics; Chemistry; Tables (London: Longman)
Kobayashi, H., & Tanaka, H. 2010, Icar, 206, 735
Kobayashi, H., Tanaka, H., & Krivov, A. V. 2011, ApJ, 738, 35
Kobayashi, H., Tanaka, H., Krivov, A. V., & Inaba, S. 2010, Icar, 209, 836
Kobayashi, H., Watanabe, S., Kimura, H., & Yamamoto, T. 2008, Icar, 195, 871
Kokubo, E., & Ida, S. 1998, Icar, 131, 171
Kokubo, E., & Ida, S. 2002, ApJ, 581, 666
Landau, L. D., & Lifshitz, E. M. 1987, in Fluid Mechanics (2nd ed.; Oxford: Pergamon)
Lees, L. 1956, Jet Propulsion, 26, 259
Machida, R., & Abe, Y. 2010, ApJ, 716, 1252
Mahmood, G. I., Hill, M. L., Nelson, D. L., et al. 2001, J. Turbmach., 123, 115
Mahmood, G. I., & Ligrani, P. M. 2002, IJHMT, 45, 2011
Miura, H., & Nakamoto, T. 2005, Icar, 175, 289
Miura, H., & Nakamoto, T. 2006, ApJ, 651, 1272
Miura, H., Nakamoto, T., & Susa, H. 2002, Icar, 160, 258
Miura, H., Tanaka, K. K., Yamamoto, T., et al. 2010, ApJ, 719, 642
Morris, M. A., Boley, A. C., Desch, S. J., & Athanassiadou, T. 2012, ApJ, 752, 27
Nagasawa, M., Lin, D. N. C., & Thommes, E. 2005, ApJ, 634, 578
Nagasawa, M., Tanaka, H., & Ida, S. 2000, ApJ, 119, 1480
Neufeld, D. A., & Kaufman, M. J. 1993, ApJ, 418, 263
Ohtsuki, K., & Ida, S. 1990, Icar, 85, 499
Ohtsuki, K., Stewart, G. R., & Ida, S. 2002, Icar, 155, 436
Podolak, M., Pollack, J., & Reynolds, R. T. 1988, Icar, 73, 163
Pollack, J. B., Podolak, M., & Bodenheimer, P. 1986, Icar, 67, 409
Sarma, G. S. R. 2000, PrAeS, 36, 281
Schlichting, H. 1979, in Boundary-Layer Theory (7th ed.; New York: McGraw-Hill), 5
Schubert, G., Anderson, J. D., Travis, B. J., & Palguta, J. 2007, Icar, 188, 345
Sekanina, Z. 1993, Sci, 262, 382
Sekiya, M., & Takeda, H. 2005, Icar, 176, 220
Sibulkin, M. 1952, J. Aero. Sci., 19, 570
Silva, C., Marotta, E., & Fletcher, L. 2007, J. Electron. Packag., 129, 157
Tanaka, H., Himeno, Y., & Ida, S. 2005, ApJ, 625, 414
Tanaka, H., & Ida, S. 1999, Icar, 139, 350
van Driest, E. R. 1958, ZaMP, 9, 233
Wakita, S., & Sekiya, M. 2011, EP&S, 63, 1193
Weidenschilling, S. J., Marzari, F., & Hood, L. L. 1998, Sci, 279, 681
Wen, C.-Y. 1994, PhD thesis, California Institute of Technology
Wen, C.-Y., & Hornung, H. G. 1995, JFM, 299, 389
Wetherill, G. W., & Stewart, G. R. 1989, Icar, 77, 330

Submitted to ApJ

Final Masses of Giant Planets II: Jupiter Formation in a Gas-Depleted Disk

Takayuki Tanigawa

School of Medicine, University of Occupational and Environmental Health, Kita-Kyushu, 807-8555, Japan

t-tanigawa@med.uoeh-u.ac.jp

and

Hidekazu Tanaka

Institute of Low Temperature Science, Hokkaido University, Sapporo, 060-0819, Japan

ABSTRACT

Firstly, we study the final masses of giant planets growing in protoplanetary disks through capture of disk gas, by employing empirical formulas for the gas capture rate and a shallow disk gap model, which are both based on hydrodynamical simulations. We found that, for planets less massive than 10 Jupiter masses, their growth rates are mainly controlled by the gas supply through the global disk accretion, and the gap opening does not limit the accretion. The insufficient gas supply compared with the rapid gas capture causes a depletion of the gas surface density even at the outside of the gap, which can create a disk inner hole. Secondly, our findings are applied to the formation of our solar system. For the formation of Jupiter, a very low-mass gas disk with several Jupiter masses is required at the beginning of its gas capture because of the non-stopping capture. Such a low-mass gas disk with sufficient solid material can be formed through viscous evolution from an initially $\sim$10AU-sized compact disk. By the viscous evolution with a moderate viscosity of $\alpha \sim 10^{-3}$, most of disk gas accretes onto the sun and a widely spread low-mass gas disk remains when the solid core of Jupiter starts gas capture at $t \sim 10^7$yrs. A very low-mass gas disk also provides a plausible path where type I and II planetary migrations are both suppressed significantly. In particular, the type II migration of Jupiter-size planets becomes inefficient because of the additional gas depletion due to the rapid gas capture by themselves.

Subject headings: planets and satellites: formation — protoplanetary disks

1. Introduction

A leading hypothesis of giant planet formation is the core instability model (Mizuno 1980; Bodenheimer & Pollack 1986; Pollack et al. 1996; Ikoma, Nakazawa, & Emori 2000; Hubickyj et al. 2005). In a protoplanetary disk, a solid protoplanet attracts the disk gas and has a proto atmosphere. When the core solid is around 10 Earth masses, atmospheric mass becomes comparable to the core mass, and the atmosphere becomes gravitationally unstable, which triggers dynamical collapse of the atmosphere to become a giant planet. Since the gas accretion of the atmosphere onto the core is in an unstable and runaway manner, the growth continues as long as gas exists around the planet.

The gas-accretion growth of a giant planet is expected to terminate when the planet creates a gap, which is a low-density annulus region along the planet orbit, by its own strong gravity when the planet becomes massive. Two well-known gap-opening conditions have been widely used: the thermal condition and the viscous condition (Lin & Papaloizou 1993; Ida & Lin 2004; Crida, Morbidelli, & Masset 2006). The thermal condition is a condition that the (specific) gravitational energy at a distance of the disk scaleheight $\sim GM_{\rm p}/h$ is larger than the typical thermal energy $\sim c^2$, where G is the gravitational constant, $M_{\rm p}$ is the planet mass, h is the disk scale height, and c is the sound speed of disk gas. The viscous condition is a condition that planetary gravitational torque exerting on the gas disk is stronger than the viscous torque of the disk due to Keplerian shear motion (Lin & Papaloizou 1986). Since the thermal condition usually requires a larger planet mass for gap opening than that of the viscous condition and the required planet mass is consistent with Jupiter, the final masses of giant planets have been thought to be determined by the thermal condition.

Tanigawa & Ikoma (2007) (hereafter TI07) have constructed an analytic model for the gas accretion rate onto a planet embedded in a disk gap as a function of the planetary mass, viscosity, scale height, and unperturbed surface density. By using this, they systematically studied the long-term growth and the final masses of gas giant planets. To calculate the accretion rate, TI07 derived an analytic formula for surface density distribution in the gap region, where planet gravitational perturbation is significant. In addition to the gap formula that considers the balance between the viscous torque and the planetary gravitational torque (e.g., Lubow & D'Angelo 2006), TI07 also included the gap shallowing effect by the Rayleigh stable condition that inhibits a too steep radial gradient of surface density. The shallowing effect supplies a non-negligible amount of gas into the gap bottom, which enables the giant planet to keep on growing even after the gap opening. At the same time, TI07 also proposed that the gas accretion rate onto the planet can be limited by the disk viscous accretion rate. An insufficient gas supply by the disk accretion inevitably limits the gas accretion rate onto the planet even if the planet is capable of capturing the ambient gas at a higher rate. Such a

limited accretion rate onto a planet was also used in population synthesis calculations (e.g., Mordasini et al. 2009, 2012a). As a result, TI07 gave much larger final masses ($\gtrsim$ 10 Jupiter mass at 5AU) than the traditional prediction with the thermal condition for the minimum mass solar nebula (MMSN) disk.

Recent hydrodynamic simulations have extracted an empirical formula for surface density at the bottom of gap (Duffell & MacFadyen 2013; Fung, Shi, & Chiang 2014). This formula indicates that the gap is much shallower than the traditional prediction, and is even shallower than the analytic estimate given by TI07, which includes the shallowing effect by the Rayleigh stable condition. Kanagawa et al. (2015a) analytically derived this shallow gap formula, by including the effect of density wave propagation at the gap. Such a shallow gap model maintains high accretion rates onto planets and gives much larger final masses of giant planets than the prediction by TI07, leading to a possibility that Jupiter and Saturn formed in a much lighter disk than the MMSN model.

The rapid accretion onto a planet due to a shallow gap also causes a depletion of the disk gas over a wider radial region, in addition to the narrow gap. This gas depletion may alter the type II planetary migration as well as the planet growth. Lubow & D'Angelo (2006) examined this depletion mechanism due to the gas accretion onto a planet, by using their semi-analytical model and hydro-dynamical simulations. However, their estimations might suffer from large errors since the calculation time of their hydro-dynamical simulations is less than 1/10 of the characteristic viscous evolution time. It would be valuable to examine the gas depletion due to the gas accretion onto a planet, by using an updated formula for the accretion rate with the shallow gap model.

In this study, we update the growth model of giant planets proposed by TI07, by adopting the empirical shallow gap model, and demonstrate that the termination of giant planet growth by the gap opening is much harder than expected in the traditional prediction. From this result on the growth rate, we propose that a gas depleted disk is suitable for the formation of Jupiter-sized planets. We also estimate the gas depletion due to the rapid gas accretion onto the planet using the updated formula for the accretion rate, which enables us to quantitatively discuss the inner hole and its effect on the type II planetary migration. We first we describe the formulation of our model in section 2. We next shows examples of evolution of gas capturing growth and final mass of the giant planets in section 3. We discuss a plausible path for formation of Jupiter in section 4. The type II migration is also discussed there. Our results are summarized in section 5.

2. Formulation

2.1. Disk model

We consider a globally evolving protoplanetary disk. The protoplanetary disk has scale-height $h = c/\Omega$, where c and Ω are the sound speed and the Keplerian angular velocity around the central star, respectively. We set temperature distribution so that $h/r = 10^{-1.5}(r/1\mathrm{AU})^{1/4}$, where r is the distance from the star. This corresponds to the temperature profile $T \simeq 280$ K $(r/1\mathrm{AU})^{-1/2}$ for solar type stars. We use α-model for disk viscosity: $\nu = \alpha c h$, where α is a non-dimensional parameter and independent of the radius r and time (Shakura & Sunyaev 1973). For the above temperature profile, ν is proportional to r. We adopt a self-similar solution for global evolution of the protoplanetary disk (Hartmann et al. 1998; Lynden-Bell & Pringle 1974). The surface density of the solution is given by

$$\Sigma_{\rm ss}(r,t) = \frac{M_{\rm d,ini}}{2\pi R_{\rm o}^2}\left(\frac{r}{R_{\rm o}}\right)^{-1}\tilde{t}_{\rm ss}^{-3/2}\exp\left(-\frac{r}{\tilde{t}_{\rm ss}R_{\rm o}}\right), \tag{1}$$

$$\tilde{t}_{\rm ss} = \frac{t}{\tau_{\rm ss}} + 1, \tag{2}$$

where $M_{\rm d,ini}$ is the initial total mass of the protoplanetary disk and $R_{\rm o}$ is the disk outer radius at $t = 0$. Note that the initial time, $t = 0$, is set to be the onset time for the dynamical gas accretion onto the giant planet's core in our model. In Equation (2), we define $\tau_{\rm ss} = R_{\rm o}^2/3\nu_{\rm o}$, where $\nu_{\rm o}$ is the viscosity at $r = R_{\rm o}$. The total disk mass of this model is written as

$$M_{\rm d,ss}(t) = \int_0^\infty 2\pi r\Sigma_{\rm ss}(r,t)dr = M_{\rm d,ini}\tilde{t}_{\rm ss}^{-1/2}. \tag{3}$$

This means that disk mass decreases slowly with time as $\propto t^{-1/2}$. To avoid the unrealistic long lasting disk, we introduce an additional exponential decay for the disk

$$\Sigma_{\rm un}(r,t) = \Sigma_{\rm ss}(r,t)\exp\left(-\frac{t}{\tau_{\rm dep}}\right), \tag{4}$$

and the disk mass is written as a function of time: $M_{\rm d,ini}\tilde{t}_{\rm ss}^{-1/2}\exp(-t/\tau_{\rm dep})$. The additional exponential decay would correspond to some other mechanisms for disk dissipation, such as photoevaporation by ultraviolet radiation from the central star or disk wind (see discussion in section 5). We use $\Sigma_{\rm un}$ as the unperturbed disk surface density in this paper.

The global disk accretion rate of the self-similar solution with the additional exponential decay at an orbital radius r is given by

$$\begin{aligned}\dot{M}_{\rm d,global}(r,t) &= \frac{M_{\rm d,ini}}{2\tau_{\rm ss}}\left(1-\frac{r}{\tilde{t}_{\rm ss}R_{\rm o}/2}\right)\tilde{t}_{\rm ss}^{-3/2}\exp\left(-\frac{r}{\tilde{t}_{\rm ss}R_{\rm o}}\right)\exp\left(-\frac{t}{\tau_{\rm dep}}\right)\\ &= 3\pi\nu\Sigma_{\rm un}(r,t)\left(1-\frac{r}{\tilde{t}_{\rm ss}R_{\rm o}/2}\right),\end{aligned} \tag{5}$$

where the factor $\exp(-t/\tau_{\rm dep})$ is due to the additional exponential decay.

We put the initial total mass of the protoplanetary disk as

$$M_{\rm d,ini} = 1.1 \times 10^{-1} f_{\Sigma,5\rm AU} \left(\frac{R_{\rm o}}{200\rm AU}\right)^1 M_\odot, \tag{6}$$

where $f_{\Sigma,5\rm AU}$ is a parameter and $M_\odot$ is the mass of the Sun. When $f_{\Sigma,5\rm AU} = 1$, the initial total disk mass of Equation (6) makes the initial unperturbed surface density $\Sigma_{\rm un}(5\rm AU,\, t = 0)$ equal to that of the minimum mass solar nebula model at 5AU (i.e., $1.7 \times 10^{-5} M_\odot/\rm AU^2 = 1.4 \times 10^3$ kg/m^2, Hayashi et al. 1985).

It has been reported that photoevaporation by far-ultraviolet (FUV) radiation from a central star can considerably accelerate the dispersal of the circum-stellar disk (e.g., Gorti et al. 2009). Photoevaporation by FUV mainly removes the gas at the outer disk with $\gtrsim$100AU and decreases the disk mass exponentially with time at a relatively early stage ($\sim 10^6$yr). However, the mass loss rate by this mechanism is still uncertain at the order-of-magnitude level (e.g. Alexander et al. 2014). In this paper, thus, we do not include the effect of photoevaporation by FUV on the disk evolution for simplicity.

2.2. A new simple model for gas accretion onto a planet

We consider a protoplanet embedded in the evolving protoplanetary disk. The protoplanet with the mass $M_{\rm p}$ is rotating around the central star at a distance $r_{\rm p}$ from the star. The planet starts dynamical gas capturing, i.e., after gravitational instability of the protoatmosphere around a solid core with about 10 Earth masses (Mizuno 1980; Bodenheimer & Pollack 1986; Pollack et al. 1996; Ikoma, Nakazawa, & Emori 2000; Hubickyj et al. 2005).

We introduce a formula for gas accretion rate onto the protoplanet from the protoplanetary disk by an explicit function of parameters, which enables us to obtain time evolution of the planet mass and eventually the final mass. We basically follow the method of TI07, but we have improved some points, so we will re-summarize it below.

If sufficient gas is supplied toward the planet orbit by the disk accretion, the accretion rate onto the gas giant planet is determined by the hydrodynamics of the gas accretion flow onto the planet and denoted it by $\dot{M}_{\rm p,hydro}$. This accretion rate is given by a product of the two quantities:

$$\dot{M}_{\rm p,hydro} = D\Sigma_{\rm acc}, \tag{7}$$

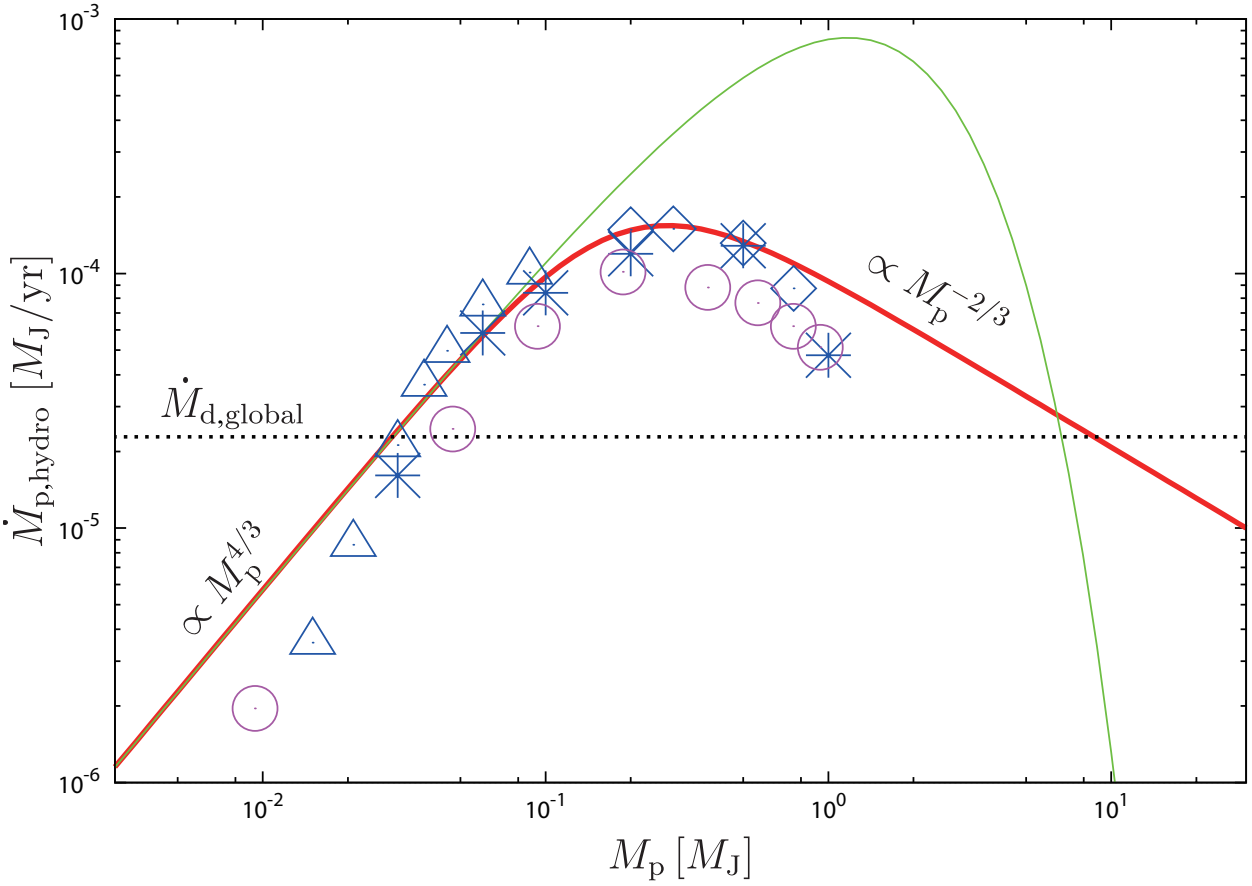

Fig. 1.— An example of gas accretion rate $\dot{M}_{\rm p,hydro}$ as a function of planet mass when $\alpha = 4 \times 10^{-3}$, $h/r_{\rm p} = 0.05$, $f_{\Sigma,5{\rm AU}} = 1$ and $r_{\rm p} = 5.2{\rm AU}$. The red thick curve is $\dot{M}_{\rm p,hydro}$ and the thin blue dashed curve is the corresponding accretion rate derived in Tanigawa & Ikoma (2007). The blue symbols show the accretion rates obtained by D'Angelo, Kley, & Henning (2003), where the three types of the marks correspond to different models of smoothing planet gravitational potentials. The purple circles plot the accretion rates obtained by Machida et al. (2010). As a reference, global disk accretion rate $\dot{M}_{\rm d,global}$ is also shown.

where D is the accretion *area* of the protoplanetary disk per unit time[1], and $\Sigma_{\rm acc}$ is the surface density at the accretion channel in the protoplanetary disk. Tanigawa & Watanabe (2002) performed two-dimensional hydrodynamic simulations of the accretion flow onto a planet and derived an empirical formula for the accretion rate. According to their result, D is given by

$$D = 0.29 \left(\frac{h_{\rm p}}{r_{\rm p}}\right)^{-2} \left(\frac{M_{\rm p}}{M_*}\right)^{4/3} r_{\rm p}^2 \Omega_{\rm p}, \tag{8}$$

where $M_{\rm p}$ and M_* are masses of the planet and central star, respectively, and $h_{\rm p}$ and $\Omega_{\rm p}$ are scaleheight and Keplerian angular velocity at the planet location, respectively. Note that the product form of D and $\Sigma_{\rm acc}$ in Equation (7) is valid when equation of state of gas around the Hill sphere can be approximated by isothermal.

TI07 gave the formula for the surface density $\Sigma_{\rm acc}$ purely in a theoretical manner, including the Rayleigh stable condition. This condition prevents unrealistically too steep surface density gradient and resultant too deep gap, which is a consequence of the simple assumption of the balance between viscous torque and gravitational torque by the planet. However, recent hydrodynamic simulations showed that the gap is even shallower than the prediction by TI07 (Duffell & MacFadyen 2013; Fung, Shi, & Chiang 2014), which are also supported by theoretical considerations (Fung, Shi, & Chiang 2014; Kanagawa et al. 2015a,b). In this study, we thus use an empirical formula for the gas surface density at the gap bottom obtained by these studies:

$$\Sigma_{\rm acc}(t) = \frac{1}{1+0.034K} \Sigma_{\rm un}(r_{\rm p}, t), \tag{9}$$

where

$$K = \left(\frac{h_{\rm p}}{r_{\rm p}}\right)^{-5} \left(\frac{M_{\rm p}}{M_*}\right)^{2} \alpha^{-1}. \tag{10}$$

In Equation (9), we assumed that the accretion band is located within the gap bottom. If the accretion band is located at the gap edge with a higher surface density, the accretion rate given by Equations (7) and (9) would be an underestimate. We set $M_{\rm p,ini} = 3.24 \times 10^{-5} M_*$ for initial mass of the protoplanet and $R_{\rm o} = 200$AU.

Figure 1 shows the accretion rate $\dot{M}_{\rm p,hydro}$ as a function of the planet mass. In the low-mass planet case where the parameter K is much less than $1/0.034$ (~ 30), there is no gas depletion due to the gap, so $\Sigma_{\rm acc}$ can be simply replaced by $\Sigma_{\rm un}$ (see Equation (9)). The

[1] D in this paper corresponds to $\dot{A}$ in TI07.

accretion rate in this regime is

$$\dot{M}_{\rm p,hydro} = \dot{M}_{\rm p,nogap} \equiv 0.29 \left(\frac{h_{\rm p}}{r_{\rm p}}\right)^{-2} \left(\frac{M_{\rm p}}{M_*}\right)^{4/3} \Sigma_{\rm un} r_{\rm p}^2 \Omega_{\rm p} \qquad \text{for } K \ll 1/0.034. \tag{11}$$

In the high-mass case where $K \gg 1/0.034$, on the other hand, $\Sigma_{\rm acc}$ is reduced to $\Sigma_{\rm un}/0.034K$ due to the gap opening and the accretion rate can be written as

$$\dot{M}_{\rm p,hydro} = \dot{M}_{\rm p,gap} \equiv 8.5 \left(\frac{h_{\rm p}}{r_{\rm p}}\right)^{1} \left(\frac{M_{\rm p}}{M_*}\right)^{-2/3} \Sigma_{\rm un} \nu_{\rm p} \qquad \text{for } K \gg 1/0.034. \tag{12}$$

Equation (12) shows that the accretion rate $\dot{M}_{\rm p,hydro}$ decreases gradually ($\propto M_{\rm p}^{-2/3}$) after the gap opening.

In Figure 1, we also plotted the accretion rates obtained by the previous hydrodynamical simulations to check the validity of our simple model. D'Angelo, Kley, & Henning (2003) examined the gas accretion rate onto a planet embedded in a protoplanetary disk, by performing three-dimensional global hydrodynamic simulations for various planet masses. We find that our model reproduces well their results. The results of three-dimensional local simulations by (Machida et al. 2010) are also plotted and their results are in good agreement with our model[2]. The accretion rate used in TI07 are also plotted. TI07's accretion rate declines rapidly with increasing mass because of its deeper gap model. The global disk accretion rate $\dot{M}_{\rm d,global}$ is also shown as a reference.

We also consider the case where the gas supply by the viscous disk accretion is insufficient. In such a case, the gas accretion onto the planet is regulated by the global disk accretion rate $\dot{M}_{\rm d,global}(r_{\rm p})$ rather than $\dot{M}_{\rm p,hydro}$. We need to take into account this effect since the gap opening cannot significantly slow down the gas accretion onto the planet. Furthermore, at an early stage of the gas capture by the planet, an additional treatment is required for the realistic gas supply to the planet orbit. At the early stage, a substantial amount of gas still exists near the planet orbit. The gas supply from the nearby part is

[2] Machida et al. (2010) claimed that the accretion rates in two-dimensional simulations (TW02), which our model is based on in this paper, are typically two orders of magnitude larger than those in three-dimensional cases. But their fitting formula (Equation (11) for $\tilde{r}_{\rm H}^3 < 0.3$ of their paper) is actually only a factor of 2 (or less) smaller than that in TW02 (Equation (18) of their paper). This can be confirmed by the fact that the width and position of the accretion bands in the two-dimensional (Fig. 8 of TW02) and three-dimensional (Fig. 3 of Tanigawa et al. 2012) cases are almost the same except near the midplane.

regulated by a local disk diffusion rather than the global disk accretion. The disk accretion rate due to the local diffusion is given by

$$\dot{M}_{\rm d,local} = \pi r_{\rm p} \Sigma_{\rm un}(r_{\rm p}) \sqrt{\frac{\nu_{\rm p}}{t - t_{\rm gap}}}, \tag{13}$$

(see Appendix A)[3]. In practice, the gas supply would be approximately given by the larger one of $\dot{M}_{\rm d,global}$ and $\dot{M}_{\rm d,local}$. In our model, therefore, by including the gas supply to the planet orbit, we give the gas accretion rate onto the planet, $\dot{M}_{\rm p}$, as

$$\dot{M}_{\rm p} = \min(\dot{M}_{\rm p,hydro}, \max(\dot{M}_{\rm d,global}, \dot{M}_{\rm d,local})). \tag{14}$$

Using this model for the gas accretion rate onto the planet, we can easily simulate evolution of the planet mass (or gas accretion rate) for a given set of disk parameters. To do that, we only need to numerically integrate the ordinary differential equation because the integrand is an explicit function of the disk parameters. The final mass of a planet is simply obtained by

$$M_{\rm p,final}(r_{\rm p}, \alpha, h_{\rm p}, M_{\rm d,ini}, R_{\rm o}) = \int_0^\infty \dot{M}_{\rm p}(M_{\rm p}, r_{\rm p}, \alpha, h_{\rm p}, M_{\rm d,ini}, R_{\rm o}, t) dt. \tag{15}$$

Note that Fung, Shi, & Chiang (2014) derives a more elaborate fitting formula by two-dimensional hydrodynamic simulations, which focus on cases for planets more massive than that of Duffell & MacFadyen (2013). But the difference between the two formula is much smaller than that between Duffell & MacFadyen (2013) and TI07, so we use the above equation for simplicity. In our model, we do not consider radial migration of planets, which will be discussed in Section 4.3.

[3]The coefficient of Equation (13) is a factor of two smaller than that in Appendix A. However this factor does not affect the final results because the accretion rate in Phase 2 (see Section 3) is not important for the final mass.

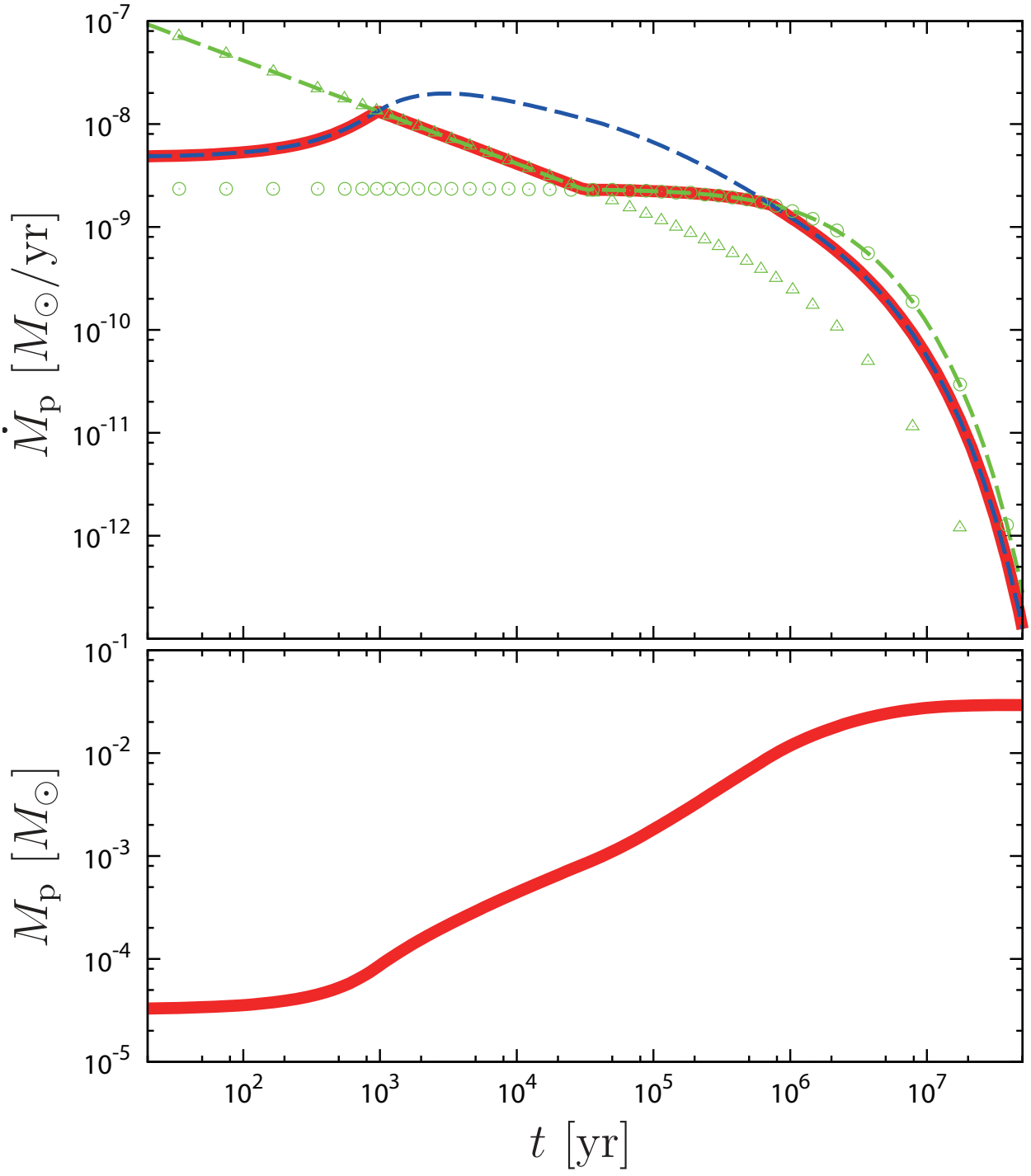

Fig. 2.— An example of time evolution for a protoplanet after the onset of dynamical gas capture in the case with $\alpha = 3.2 \times 10^{-3}$, $f_{\Sigma,5{\rm AU}} = 1$, $\tau_{\rm dep} = 10^7{\rm yr}$, $R_{\rm o} = 200{\rm AU}$, $r_{\rm p} = 5{\rm AU}$. Top panel shows the gas accretion rate onto the protoplanet. The thick red line shows that the accretion rate that we adopt (Equation (14)), which is a smaller one of $\dot{M}_{\rm p,hydro}$ (blue dashed line) or $\max(\dot{M}_{\rm d,global}, \dot{M}_{\rm d,local})$ (green dashed line). Open circles show $\dot{M}_{\rm d,global}$ and open triangles show $\dot{M}_{\rm d,local}$. Bottom panel shows the mass of the protoplanet.

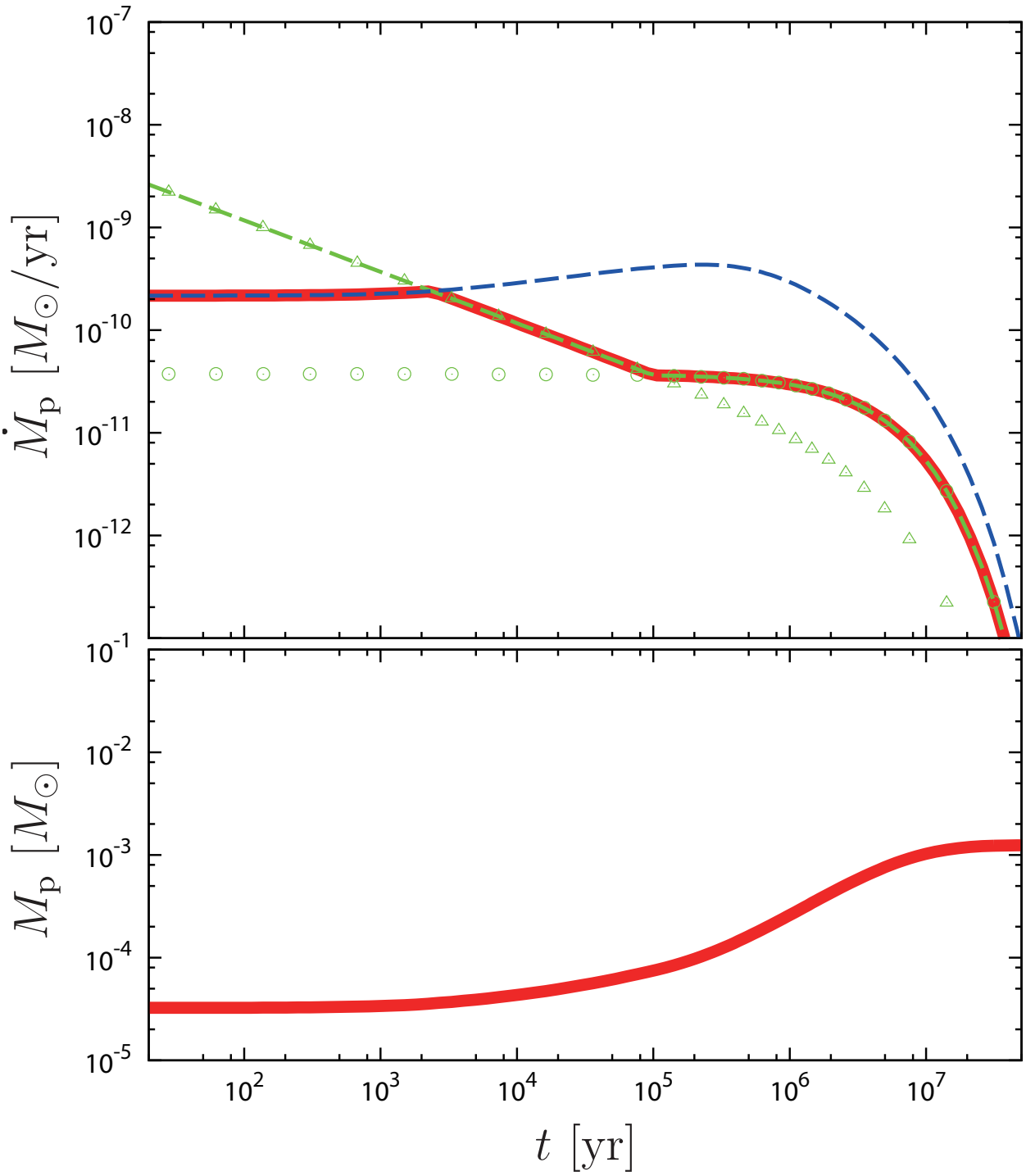

Fig. 3.— Same as Figure 2 but in the case with $\alpha = 10^{-3}$, $f_{\Sigma,5{\rm AU}} = 1/20$, $\tau_{\rm dep} = 10^7{\rm yr}$, $R_{\rm o} = 200{\rm AU}$, $r_{\rm p} = 5{\rm AU}$.

3. Results

3.1. Examples of time evolution

Figure 2 plots an example for time evolution of the gas accretion rate onto a proto-giant planet located at 5AU and that of planet mass. The parameters are set to be $\alpha = 3.2 \times 10^{-3}$, $f_{\Sigma,5\mathrm{AU}} = 1$, $\tau_{\mathrm{dep}} = 10^7$yr, $R_{\mathrm{o}} = 200$AU, $r_{\mathrm{p}} = 5$AU. This example illustrates that the evolution can be divided into four phases:

- Phase 1: after the onset of dynamical gas accretion, the gas accretion rate is regulated by the hydrodynamic accretion flow without a gap: $\dot{M}_{\mathrm{p,nogap}}$. In this case, there is abundant gas near the planet, and nothing to limit the accretion flow.
- Phase 2: the gas supply from the nearby part of the planet orbit, $\dot{M}_{\mathrm{d,local}}$, limits the accretion rate onto the planet because it is lower than $\dot{M}_{\mathrm{p,hydro}}$ and higher than the global disk accretion rate $\dot{M}_{\mathrm{d,global}}$.
- Phase 3: this is also the case where the gas supply toward the planet orbit limits the accretion rate, but the rate is given by $\dot{M}_{\mathrm{d,global}}$.
- Phase 4: this is again the case when gas supply is regulated by the hydrodynamic accretion flow, but with a deep gap: $\dot{M}_{\mathrm{p,gap}}$.

In this case, the final mass of the giant planet is as massive as $30M_{\mathrm{J}}$, which is about 1/3 of initial disk mass (see Equation (6)). The parameter set in this case is not very special (neither heavy nor highly viscous), but still results in forming a massive planet. This is because a gap does not significantly suppress gas accretion onto the planet.

The next example shown in Figure 3 is a case that produces a Jupiter-size planet. This case adopts a lower viscosity of $\alpha = 10^{-3}$ and a much lighter disk mass of $f_{\Sigma,5\mathrm{AU}} = 1/20$. Because of the lower surface density, accretion rate in phase 1 is lower and, as a result, accretion rate and planet mass do not significantly increase until the end of phase 1. In phases 2 and 3, sequence of the phase transition is basically the same as the previous example, but the absolute values of accretion rates are reduced because of the lower surface density and lower viscosity. Accretion rates in phase 2 and 3 are proportional to $\Sigma\alpha^{1/2}$ and $\Sigma\alpha$, respectively, thus comparing with the case of Figure 2, the accretion rates in this case are reduced by factors of 36 and 60, respectively. As a result of these low accretion rates, mass of the planet does not significantly increase, and the planet is not able to open a deep gap, which leads to no emergence of phase 4. When $r_{\mathrm{p}} \ll \tilde{t}_{\mathrm{ss}} R_{\mathrm{o}}/2$, we obtain from Equations (5)

and (12) as

$$\frac{\dot{M}_{\rm p,gap}}{\dot{M}_{\rm d,global}} \sim 0.90 \times \left(\frac{M_{\rm p}}{M_*}\right)^{-2/3} \left(\frac{h_{\rm p}}{r_{\rm p}}\right)^{1}. \tag{16}$$

The emergence of phase 4 requires $\dot{M}_{\rm p,gap} < \dot{M}_{\rm d,global}$, which gives

$$M_{\rm p} > 1.0 \times 10^{-2} \left(\frac{h_{\rm p}/r_{\rm p}}{0.05}\right)^{3/2} M_*, \tag{17}$$

which explains the presence or absence of phase 4 in the two cases. Thus, up to $\sim 10M_{\rm J}$, the reduction of the accretion rate by the gap is not effective. Even in phase 4 of Figure 2, $\dot{M}_{\rm p}$ is not so small compared with $\dot{M}_{\rm d,global}$ because the ratio $\dot{M}_{\rm p,gap}/\dot{M}_{\rm d,global}$ depends weakly on $M_{\rm p}$ as in Equation (16).

3.2. Final masses

Figure 4 plots the final mass of a gas-capturing planet as a function of orbital radius when $f_{\Sigma,5\rm AU} = 1$, $\alpha = 10^{-3}$, $R_{\rm out} = 200$ AU, $\tau_{\rm dep} = 10^7$yr. The solid line shows the final mass obtained in our model. We find that the final mass is 10-20 Jupiter masses in most of area and has only a slight radial dependence. Up to $\sim 10M_{\rm J}$, a giant planet grows mostly in phase 3 and the growth rate is regulated by global disk accretion rate $\dot{M}_{\rm d,global}$ at all radii. Thus the growth rate of giant planets is independent of their radial location. Even in phase 4 where $M_{\rm p} \gtrsim 10M_{\rm J}$, the growth rate is not much smaller than $\dot{M}_{\rm d,global}$. We also plot the final mass in the case of TI07 for comparison. In the case of TI07, $\Sigma_{\rm acc}$ uses a formula of TI07, while Equation (9) is used in this paper. Final mass with TI07's formula becomes larger than Jupiter mass for most of the region. This is mainly because TI07 considers the violation of the Rayleigh condition for steep radial density gradient, which limits the gradient, tends to fill the gap, and promotes gas capturing growth as a result. In this case, the final mass of a planet increases with its orbital radius $r_{\rm p}$. This is because gap opening is easier at the inner region in TI07. Thus the difference in the final mass between the two cases is originated from formulae for the gap depth.

The final mass can be estimated with a simple equation. Since the gap opening does not significantly affect $\dot{M}_{\rm p}$ up to $\sim 10M_{\rm J}$, the global disk accretion rate $\dot{M}_{\rm d,global}$ determines the final mass in most cases. Thus, using $\dot{M}_{\rm d,global}$ for a planet at $r_{\rm p} \ll R_{\rm o}$, final mass is

approximated by

$$\begin{aligned} M_{\rm p,final,p3} &\sim \int_0^\infty \dot{M}_{\rm d,global}\Big|_{r_{\rm p}\ll R_{\rm o}} dt \\ &\sim M_{\rm d,ini}\left[1-\left(\frac{\tau_{\rm dep}}{\tau_{\rm ss}}+1\right)^{-1/2}\right] = M_{\rm d,ini}-M_{\rm d,ss}(\tau_{\rm dep}). \end{aligned} \tag{18}$$

This means that all the mass lost from the disk is captured by the planet. In the case where $\tau_{\rm dep} \ll \tau_{\rm ss}$, the final mass of Equation (18) is approximately given by $(\tau_{\rm dep}/2\tau_{\rm ss})M_{\rm d,ini}$. When $r_{\rm p}$ is small, the deviation from Equation (18) becomes larger. This is because the accretion state is switched from phase 3 to 4 before the end of the growth. In this case, the final mass is roughly estimated by

$$M_{\rm p,final,p4} \sim M_{\rm p,final,p3}\frac{\dot{M}_{\rm p,gap}(M_{\rm p,final,p3})}{\dot{M}_{\rm d,global}}. \tag{19}$$

Note that $M_{\rm d,ini}$ is the disk mass at the time when the planet starts its gas capture and can be much smaller than the mass when the disk is formed. Time scale of global viscous evolution $\tau_{\rm ss}$ in our fiducial case is

$$\tau_{\rm ss} = \frac{R_{\rm o}^2}{3\nu_{\rm o}} = 1.1\times10^7\left(\frac{\alpha}{10^{-3}}\right)^{-1}\left(\frac{h_{\rm 1AU}/1{\rm AU}}{10^{-1.5}}\right)^{-2}\left(\frac{R_{\rm o}}{200{\rm AU}}\right)^{1}{\rm yr}. \tag{20}$$

Figure 5 plots final masses for various initial surface densities (or disk masses). The five curves, which correspond to five $f_{\Sigma,5{\rm AU}}$, show that final mass is proportional to $f_{\Sigma,5{\rm AU}}$ in general. This is simply because the growth rate in phase 3 $\dot{M}_{\rm d,global}$, which is proportional to surface density, mainly determines the final mass (see Equation (18)), and the gap effect is not significant. The final masses shown in this figure are close to possible maximum masses. In the case of Figure 5, $\tau_{\rm ss} \simeq \tau_{\rm dep}$, so $M_{\rm d,ini} - M_{\rm d,ss}(\tau_{\rm dep}) = M_{\rm d,ini}(1-1/\sqrt{2})$, which means that all the disk gas accreting inward is captured by the planet on the way toward the central star and gap has little effect on suppressing the gas capture. The final mass in the case of $f_{\Sigma,5{\rm AU}} = 1$ would be about $20M_{\rm J}$ around 5AU. For the formation of Jupiter-mass planets, the gas disk should be therefore much less massive than the MMSN disk at the onset of their gas capture.

Figure 6 plots $M_{\rm p,final}$ as a function of $r_{\rm p}$ in the cases with 10 times larger and smaller values of one of the three parameters: α, $\tau_{\rm dep}$, and $f_{\Sigma,5{\rm AU}}$. We can see that the final mass increases with both α and $\tau_{\rm dep}$ and depends only on the product $\alpha\tau_{\rm dep}$ in most range. For example, the degeneracy occurs at $r_{\rm p} \lesssim 10$AU in the cases with $(\alpha, \tau_{\rm dep}) = (10^{-3}, 10^8)$ and $(10^{-2}, 10^7)$ or the cases of $(10^{-3}, 10^6)$ and $(10^{-4}, 10^7)$. This is because the final mass is a

function of $(\tau_{\rm dep}/\tau_{\rm ss})$, which is proportional to $\alpha\tau_{\rm dep}$ (see Equation (18)). However, this dependency is weaker than that of $f_{\Sigma,5{\rm AU}}$ because the dependence of final mass on $(\tau_{\rm dep}/\tau_{\rm ss})$ is weaker than linear (see Equation (18)), while that on $f_{\Sigma,5{\rm AU}}$ is basically linear. Note that final masses for a pair of the degenerated cases ($\alpha\tau_{\rm dep} = 10^{-3}$ or 10^{-5}) are split at $r_{\rm p} \sim R_{\rm o}$. This is because most of gas accretion is done by $\dot{M}_{\rm d,local}$ (i.e., phase 2), which is proportional to $\alpha^{1/2}$, not like $\dot{M}_{\rm d,global} \propto \alpha^1$. This situation is realized in the case when $r_{\rm p} \sim R_{\rm o}$ and $\tau_{\rm dep} < \tau_{\rm ss}$.

3.3. Gas depletion due to the accretion onto the planet

In phase 3, the disk gas is further reduced, in addition to the effect of the gap produced by the planetary torque. In this phase, the gas supply by the global disk accretion is insufficient for the rapid gas capture, which causes an additional depletion of the gas surface density even at the outside of the narrow gap region. In this phase, the accretion rate, $D\Sigma_{\rm acc}$, cannot be larger than $\dot{M}_{\rm d,global}$. This indicates that $\Sigma_{\rm acc}$ should be depleted because D is independent of the surface density (see Equation (7)). The additional depletion factor due to the gas capture, f', is obtained from the balance of the mass fluxes (i.e., the mass conservation). Including this depletion factor, the disk surface density at the outside of the gap is given by $f'\Sigma_{\rm un}(r_{\rm p})$ and, thus the hydrodynamical capture rate should be evaluated to be $f'\dot{M}_{\rm p,hydro}$ instead of $\dot{M}_{\rm p,hydro}$. Assuming the quasi-steady flow in the disk, we obtain an equation of the mass flux balance, $f'\dot{M}_{\rm p,hydro} = \dot{M}_{\rm d,global}$. Hence the additional depletion factor is given by

$$\begin{aligned} f' &= \frac{\dot{M}_{\rm d,global}}{\dot{M}_{\rm p,hydro}} \\ &\simeq 1.1 \left(\frac{M_{\rm p}}{M_*}\right)^{2/3} \left(\frac{h_{\rm p}}{r_{\rm p}}\right)^{-1}, \end{aligned} \tag{21}$$

where we used Equation (16). From Equation (21), the additional depletion factor is unity for $M_{\rm p} = 0.01M_*$ and 0.2 for $M_{\rm p} = M_{\rm J}$ in a disk with $h_{\rm p}/r_{\rm p} = 0.05$. Note that this additional effect of gas depletion (or enhance) does not exist in phase 4 because of sufficient supply by the global disk accretion.

Lubow & D'Angelo (2006) also examined the gas depletion due to the accretion onto the planet and derived the radial distribution of the surface density, by considering a steady viscous accretion disk with a mass sink by the planet. From this accurate surface density distribution, the additional depletion factor is given by

$$f' = \frac{\dot{M}_{\rm d,global}}{(\dot{M}_{\rm p,hydro} + \dot{M}_{\rm d,global})}. \tag{22}$$

This agrees with Equation (21) when $\dot{M}_{\rm p,hydro} \gg \dot{M}_{\rm d,global}$. Since a detail derivation was not given in their paper, we presented the derivation of the surface density distribution in Appendix B. In Lubow & D'Angelo (2006), the ratio $\dot{M}_{\rm p,hydro}/\dot{M}_{\rm d,global}$ is called the accretion efficiency. They estimated the accretion efficiency from their two-dimensional hydrodynamical simulations. In Figure 7, we plot their results and our model (i.e., Equation (16)). The differences between theirs and our model are within the factor 2. Since the calculation time of their hydrodynamical simulations is less than 1/10 of the characteristic viscous evolution time, their values tends to be larger that those in the steady states. Thus we expect that the difference becomes smaller if the calculation time would be longer. Further investigation by long-term hydrodynamical simulations is necessary for checking our model.

This gas depletion would also create an inner hole, which is a depleted region inside a certain radius of a disk (e.g., Williams & Cieza 2011). Here we consider a possibility that the inner holes are formed by planets. We simply assume in Equation (21) that all the gas approaching to the planet orbit is captured by the planet when $\dot{M}_{\rm p,hydro} > \dot{M}_{\rm d,global}$ (i.e., in Phase 3), but Equation (22) means that all the gas is not necessarily captured even in such a case. This can be interpreted as the following. Gas capture by a planet reduces surface density in wide region, which reduces the gas capture rate in turn. When the reduced gas accretion rate is smaller than that of the global disk-viscous accretion, a fraction of gas that is not captured by the planet would need to pass through the planet orbit in a steady state. This inward flow creates a inner disk with a lower surface density, which would be a possible origin of the observed inner holes. The surface density at the inner hole would be given by $f'\Sigma_{\rm un}(r)$, whereas we neglected this small amount of mass loss through the inner hole in phase 3 in this paper. Note that the gas depletion considered here is different from that by gap formation, which is created by gravitational torque by the planet and is usually much narrower. The gas depletion considered here is a depletion in addition to that of the gap formation. Furthermore, the gas depletion due to the gas capture also affects the type II migration of the planet. This will be discussed in detail later.

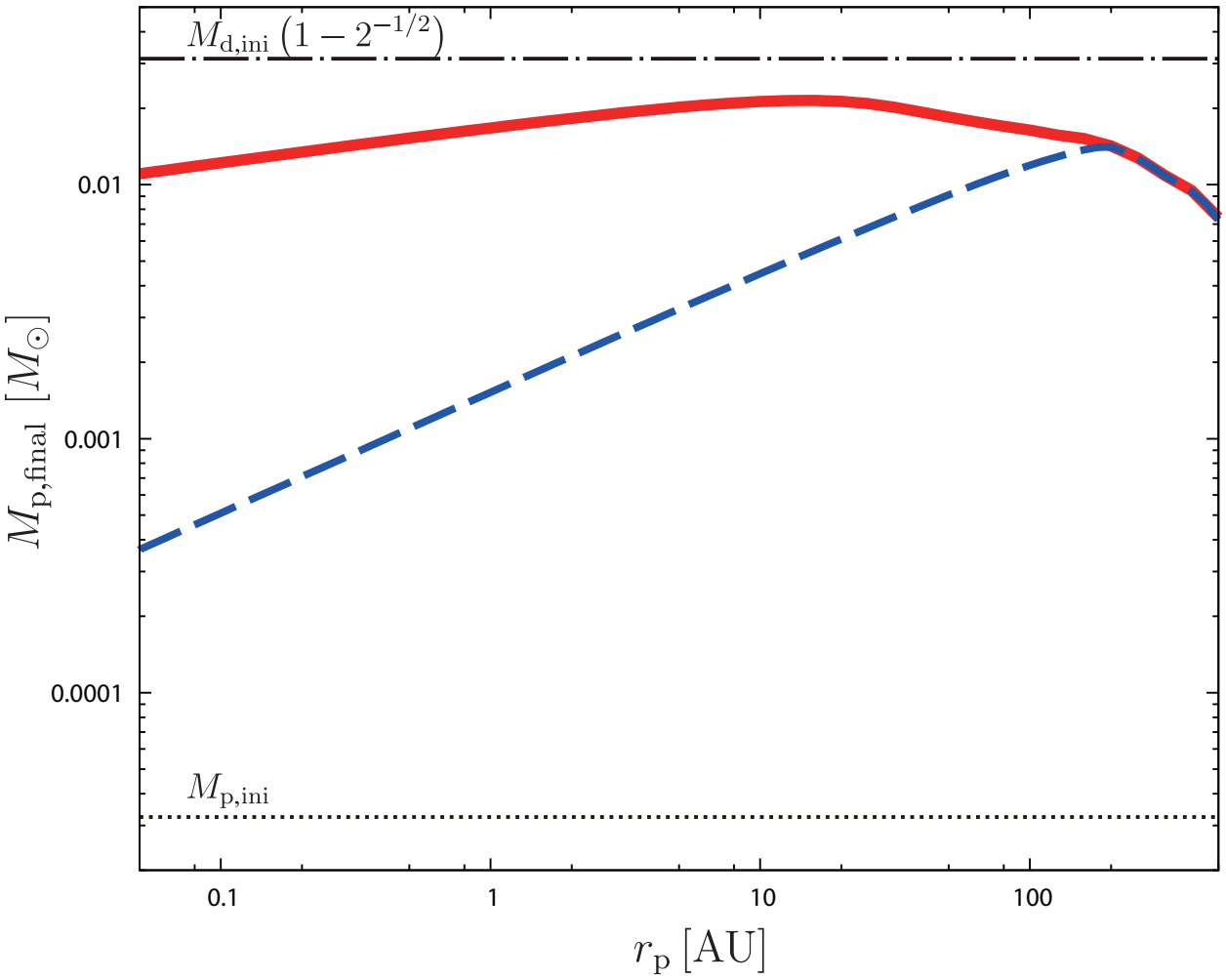

Fig. 4.— Final masses of giant planets as a function of orbital radius of the planets when $f_{\Sigma,5\rm AU} = 1$, $\alpha = 10^{-3}$, $R_{\rm out} = 200$ AU, $\tau_{\rm dep} = 10^7$yr. Red solid curves adopt the model in this paper, and the blue dashed curves shows the case when $\Sigma_{\rm acc}$ uses a formula of Tanigawa & Ikoma (2007), instead of Equation (9). The dot-dashed line corresponds to the final mass that assumes that all the gas accretion is done in phase 3 (see Equation (18)) and $\tau_{\rm dep} = \tau_{\rm ss}$, and the dotted line shows the initial mass of the protoplanet $M_{\rm p,ini}$.

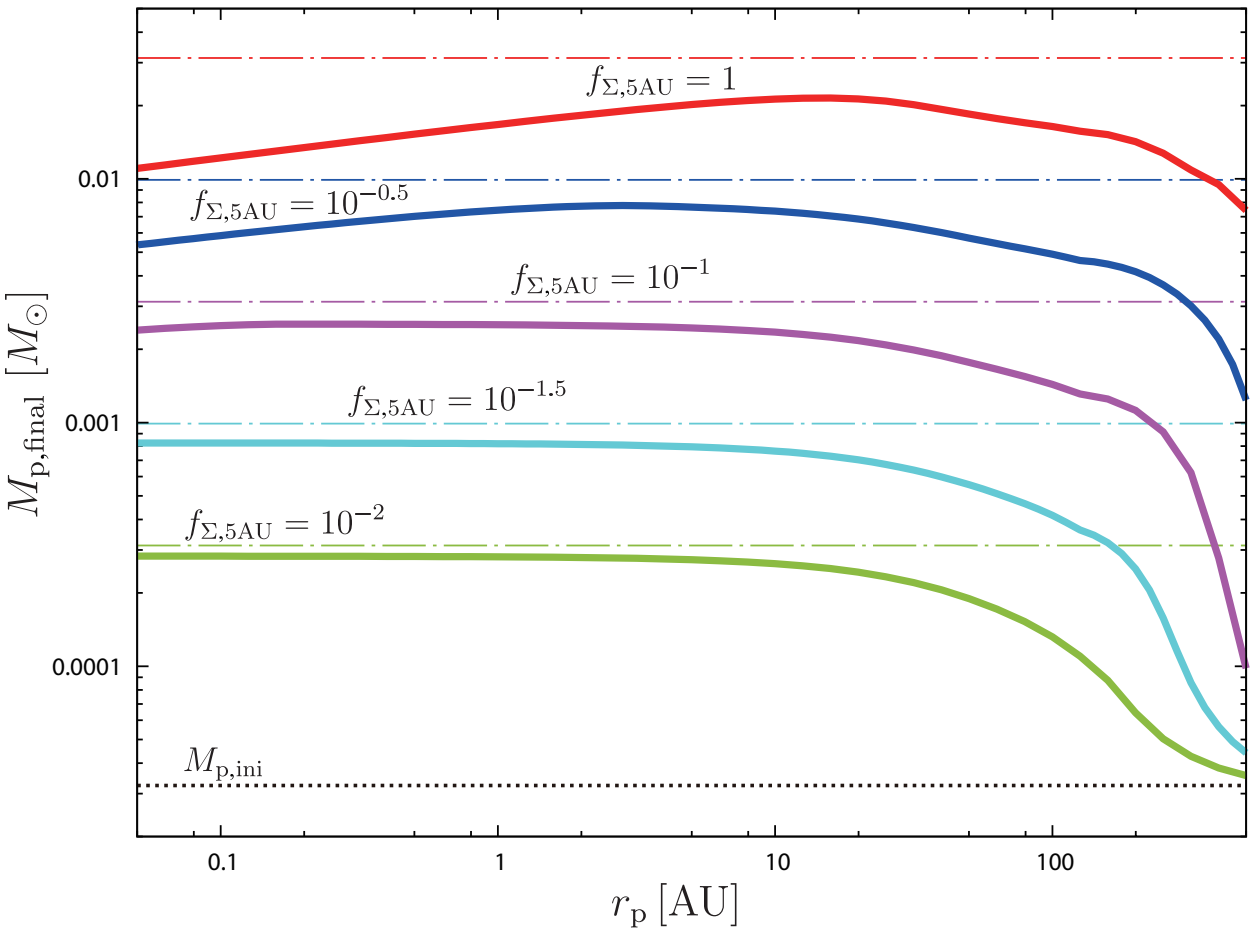

Fig. 5.— Final masses of giant planets as a function of orbital radius of the planets when $\alpha = 10^{-3}$, $R_{\mathrm{out}} = 200$ AU, $\tau_{\mathrm{dep}} = 10^7$yr. Five solid curves correspond to $f_{\Sigma,5\mathrm{AU}} = 1, 10^{-0.5}, 10^{-1}, 10^{-1.5}, 10^{-2}$ from top to bottom, and the dot-dashed line just above the each curve is the final mass estimated by Equation (18). The dotted line shows $M_{\mathrm{p,ini}}$.

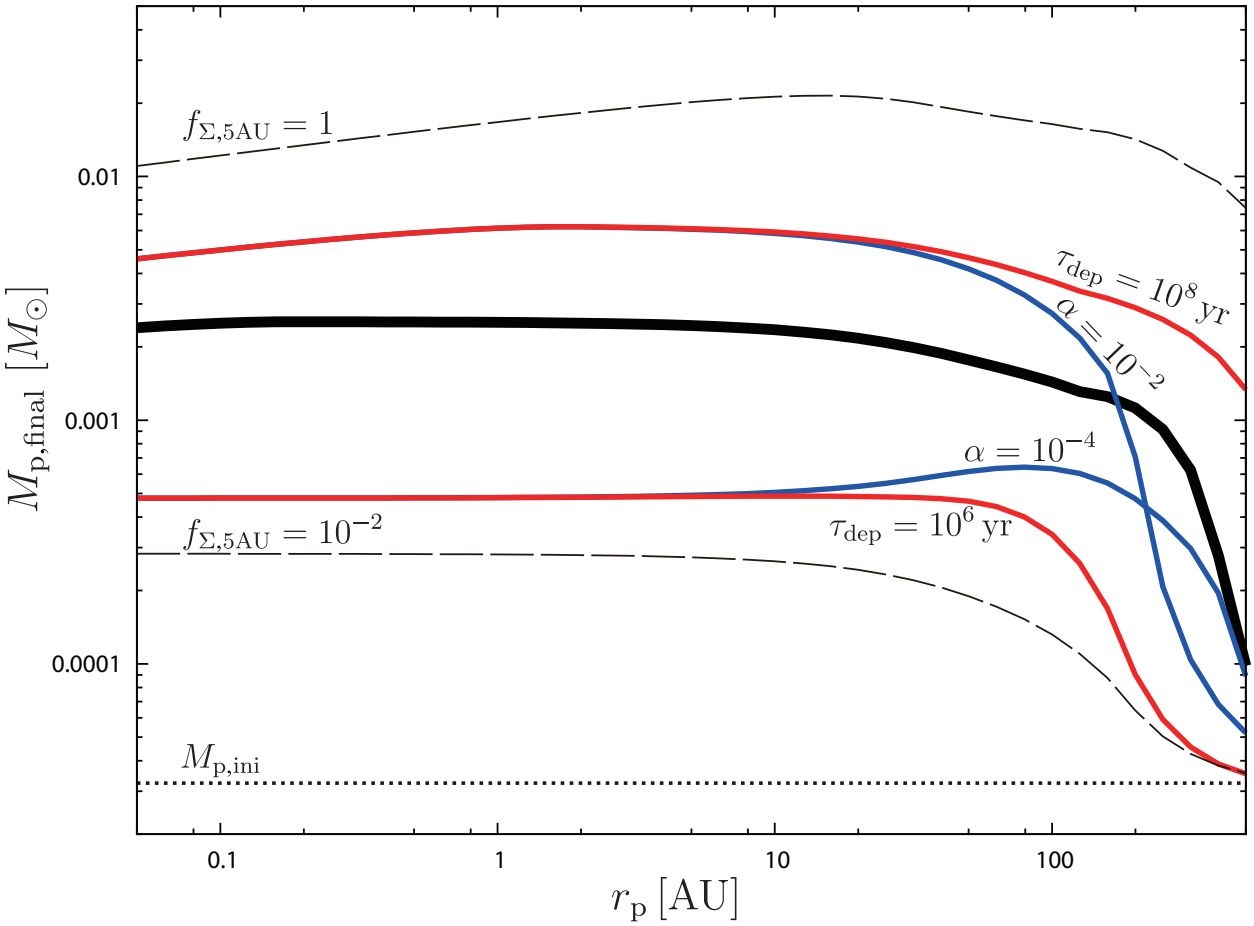

Fig. 6.— Final masses of giant planets as a function of orbital radius of the planets. The thick solid line is the same as the purple line in Figure 5 ($f_{\Sigma,5\mathrm{AU}} = 10^{-1}$, $\alpha = 10^{-3}$, $\tau_{\mathrm{dep}} = 10^7$yr, $R_{\mathrm{out}} = 200$AU). All the other lines correspond to cases with 10 times larger (or smaller) values for one of the three parameters: α, τ_{dep}, and $f_{\Sigma,5\mathrm{AU}}$. The two red lines show $\tau_{\mathrm{dep}} = 10^8$yr and 10^6yr cases, the two blue lines show $\alpha = 10^{-2}$ and 10^{-4} cases, and the two thin dashed lines show $f_{\Sigma,5\mathrm{AU}} = 1$ and 10^{-2} cases.

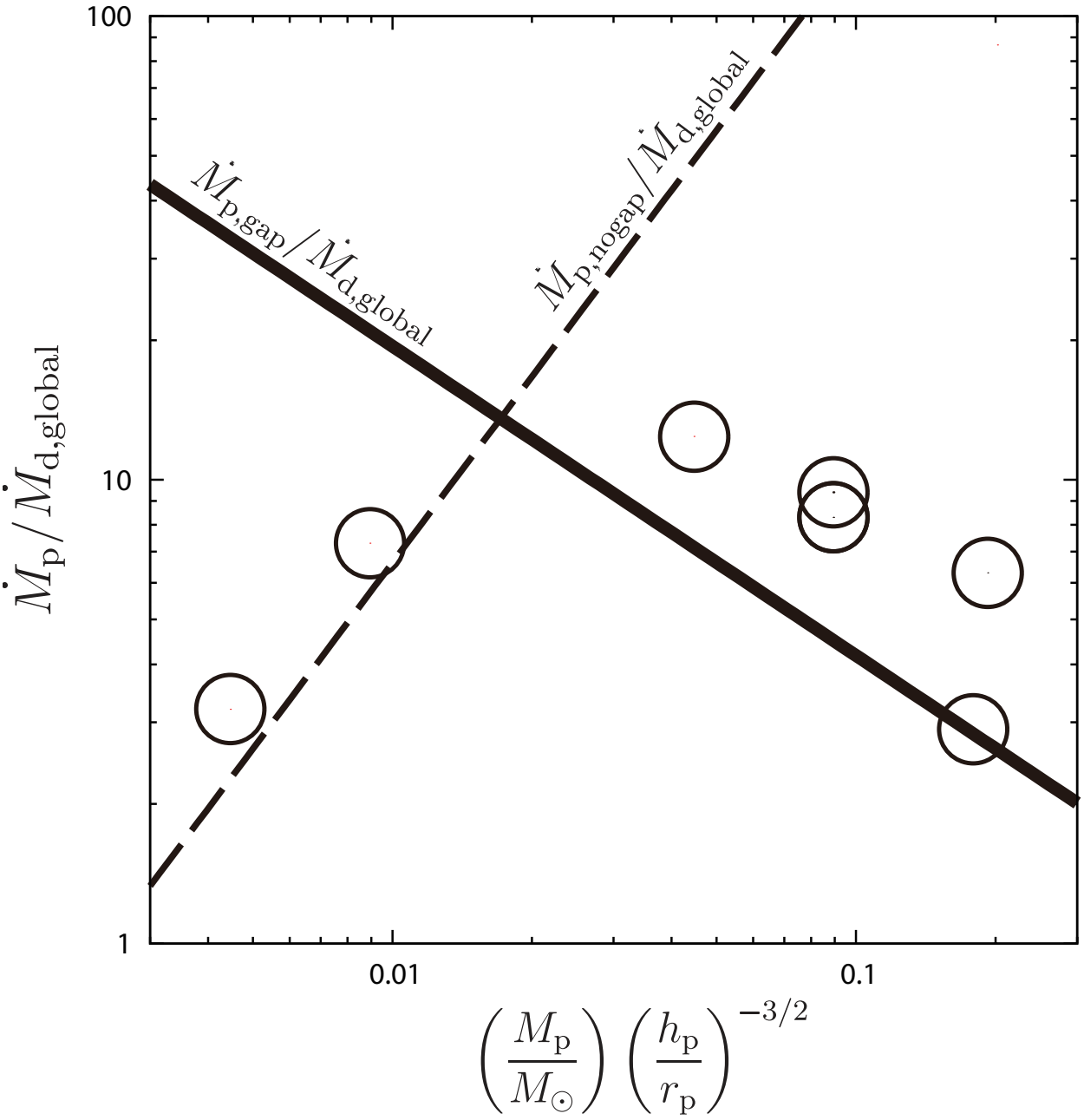

Fig. 7.— Accretion rate onto a planet normalized by disk viscous accretion rate. Circles show accretion efficiency E in Table 1 of Lubow & D'Angelo (2006), and the solid line shows $\dot{M}_{\rm p,gap}/\dot{M}_{\rm d,global}$. As a reference, $\dot{M}_{\rm p,nogap}/\dot{M}_{\rm d,global}$ is also shown by the dashed line.

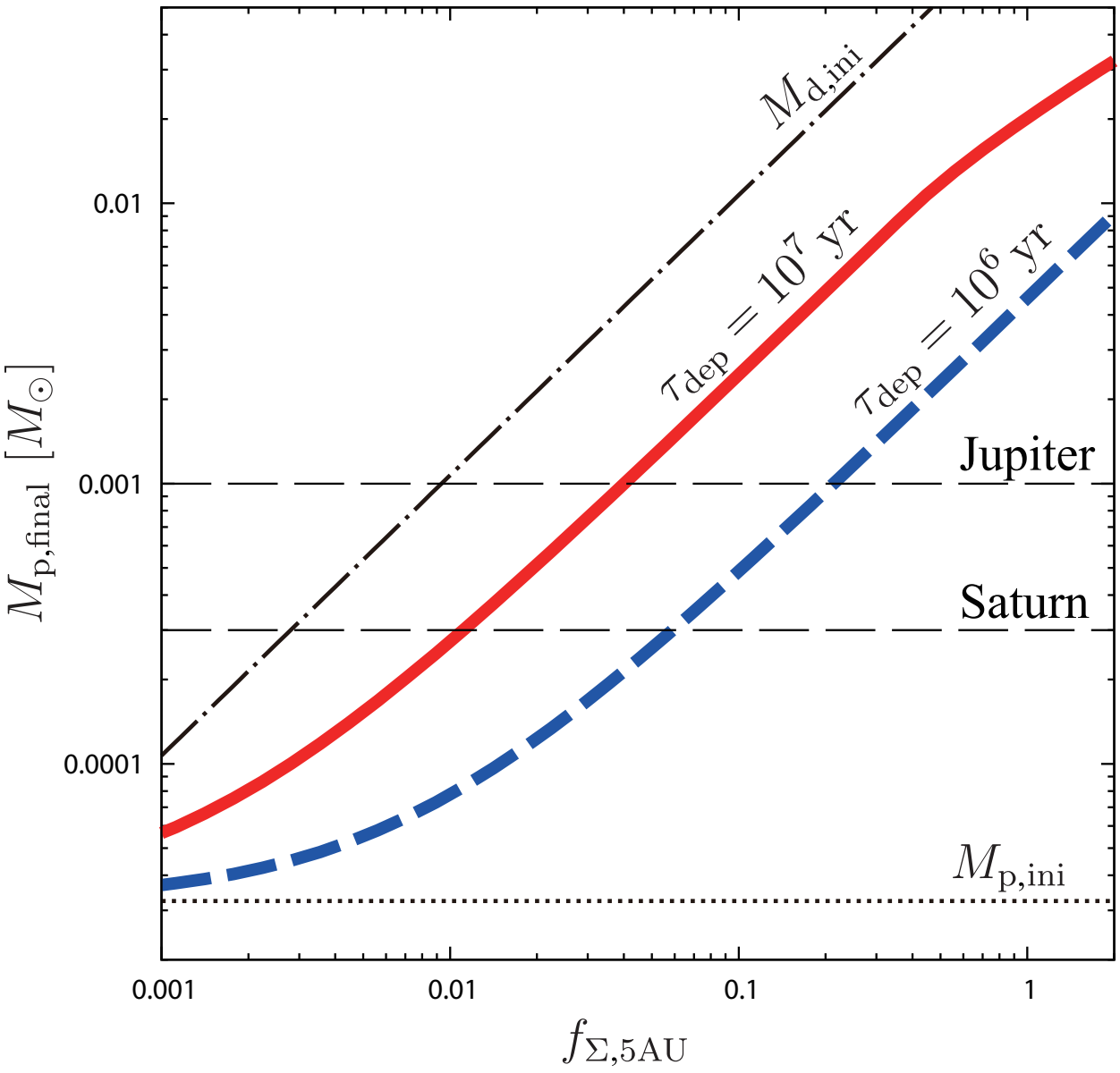

Fig. 8.— Final masses of giant planets at 5AU as a function of $f_{\Sigma,5\rm AU}$ when $\alpha = 10^{-3}$, $R_{\rm out} = 200$ AU in the cases of $\tau_{\rm dep} = 10^7$yr (red solid) and 10^6yr (blue dashed), respectively. Since α and $\tau_{\rm dep}$ is degenerated in most cases, the case with $\tau_{\rm dep} = 10^7$ corresponds to the case with $\tau_{\rm dep} = 10^6$ and $\alpha = 10^{-2}$, for example. The dot-dashed line shows $M_{\rm d,ini}$, which corresponds to possible maximum mass of the planet and the dotted line shows $M_{\rm p,ini}$.

4. Implication to the origin of our solar system

4.1. A suitable gas disk for Jupiter formation

In this paper, we updated the model for the growth of giant planets, by employing the shallow gap model revealed by the recent hydrodynamical simulations. The updated model showed that the formation of Jupiter-mass planets requires much less massive gas disks compared to the MMSN model at the stage of dynamical gas capturing by the planets. This is because the gap is not so deep to terminate the gas accretion to the planet.

Figure 8 plots $M_{\rm p,final}$ at 5AU as a function of $f_{\Sigma,5\rm AU}$, which indicates the depletion degree of the disk gas from the MMSN model at the beginning of the gas capture. The final mass is proportional to the depletion degree, $f_{\Sigma,5\rm AU}$, when the final mass is much larger than the initial core mass and smaller than $10M_{\rm J}$ (i.e., within phase 3). In the case of $\alpha = 10^{-3}$ and $\tau_{\rm dep} = 10^7$yr, a Jupiter-mass planet is formed in a gas disk with $f_{\Sigma,5\rm AU} = 0.04$. The total mass of this gas disk is about $4M_{\rm J}$. Such a very low-mass gas disk also has an advantage that type I and II planetary migrations are both suppressed significantly. In a less viscous case $\alpha = 10^{-4}$ (or equivalently a short disk lifetime case $\tau_{\rm dep} = 10^6$yr), $f_{\Sigma,5\rm AU} = 0.3$ is suitable. However, such a moderate-mass disk does not slow down the planetary migrations significantly. Hence we adopt the former case as a suitable gas disk for Jupiter formation. If we adopt a higher viscosity $\alpha > 10^{-3}$ or a longer depletion time ($\tau_{\rm dep} > 10^7$yr), the suitable disk mass further decreases. As mentioned in Section 3, the final mass depends on the product $\alpha\tau_{\rm dep}$. Thus, the case of $\alpha = 3 \times 10^{-3}$ and $\tau_{\rm dep} = 3 \times 10^6$yr also gives a suitable disk with $f_{\Sigma,5\rm AU} = 0.04$ as well as the former case. For the Saturn case, $f_{\Sigma,5\rm AU}$ should be an even lighter disk (~ 0.01 when $\tau_{\rm dep} = 10^7$ yr and $\alpha = 10^{-3}$), or later start (shorter duration) of the dynamical gas capture (ex. $f_{\Sigma,5\rm AU} \sim 0.06$ when $\tau_{\rm dep} = 10^6$yr).

4.2. Viscous evolution from a compact disk to a low-mass disk with high metallicity

Jupiter and Saturn have solid cores and also contains a considerable amount of heavy elements in their H/He envelopes. The two giant planets are expected to have solid components of 30-60$M_{\rm E}$ in total (e.g., Baraffe et al. (2014)). This shows that Jupiter and Saturn have much higher metallicity than the solar composition. If we also consider solids in other planets, the formation of our solar system requires solid materials of $\gtrsim 80M_{\rm E}$ in total, which is consistent with the amount of solid included within 50AU of the MMSN disk. However, the above low-mass disk with $4M_{\rm J}$ contains solid components of less than $20M_{\rm E}$ if it has the solar composition, in which heavy elements are 1.4% in mass. Hence, the low-mass disk

should have very high metallicity.

A low-mass disk with high metallicity can be formed through a viscous disk evolution from a compact size described by Equation (1). Consider an initially compact disk with radius of $\sim$ 10AU and with the solar composition. The disk mass is $\sim 18M_{\rm J}$, it thus contains solid material of $\sim 80M_{\rm E}$. Because of the compactness, the gas and solid surface densities of this disk are twice of the MMSN model at 5AU. Firstly, planetesimals are formed in-situ and decoupled with the gaseous disk before the disk evolution. Secondly, the compact gas disk suffers a viscous accretion and losses most of gas within a relatively short time. The gas disk spreads out to $\sim$ 200AU and reduces its mass to $\sim 4M_{\rm J}$ at $t = 10^7$yr in the case of $\alpha = 10^{-3}$ (see Equation (20)). During the disk evolution, planetary embryos grow, and finally a sufficient large solid core causes dynamical collapse of its envelope and starts to capture its surrounding disk gas rapidly. This scenario explains the suitable low-mass disk with high metallicity for Jupiter formation in a natural way. Saturn formation would also be reasonable if the onset of dynamical gas capture occurs at even later time. It can also naturally explain the high metallicity of Jupiter and Saturn of the factor ~ 10.

4.3. Type I and type II migration in gas-depleted disks

Here we discuss more in detail type I and type II migration in gas-depleted disks. In particular, we show below that the type II migration of Jupiter-size planets or smaller is inefficient because of the additional gas depletion due to the rapid gas capture described in Section 3.

Because of the problematic rapid type I migration (Tanaka et al. 2002), the studies on planet population synthesis prefer a gas-depleted (or high-metallicity) disk or a significant reduction of the type I migration speed (Daisaka et al. 2006; Ida & Lin 2008a; Mordasini et al. 2012b). In the gas depleted disk adopted in our scenario, the solid surface density is twice of the MMSN disk whereas the gas surface density is depleted to 4% at the end of the core-growth stage. This requires the solid-to-gas ratio to be 50 times as large as that of the solar composition. This enhancement is comparable to that required in the population synthesis calculations. Hence our scenario for Jupiter formation is a plausible and natural path which can overcome the type I migration problem. Mordasini et al. (2012c) also included the viscous disk evolution in their population synthesis calculations but they fixed the initial disk outer radius to be 30AU. Such an intermediate-size disk takes longer time to deplete the disk gas enough by disk accretion. More compact initial disks should also be examined in population synthesis calculations.

Next we examine type II migration in the gas-depleted disk. In our model of giant planet formation, we did not include the effect of type II migration. It is worthwhile to estimate the timescale of type II migration for our gas-depleted disk. Recently Duffell et al. (2014) have derived an empirical formula of migration speed in the classical type II regime from their hydrodynamical simulations and the revised timescale of type II migration is given by

$$\begin{aligned} t_{\rm migII} &= 0.14 \frac{2r_{\rm p}^2}{3\nu_{\rm p}} \frac{M_{\rm p}}{\Sigma_{\rm out} r_{\rm p}^2} \\ &= 0.089 \frac{M_{\rm p}}{\nu_{\rm p}\Sigma_{\rm out}}, \end{aligned} \tag{23}$$

where $\Sigma_{\rm out}$ is the gas surface density outside of the gap and corresponds to $\Sigma(r_{\rm p})$ in Appendix B. Equation (23) corresponds to the "planet-dominate" case where $M_{\rm p} > \Sigma_{\rm out} r_{\rm p}^2$. This condition is safely satisfied in the gas-depleted disk we consider. Equation (23) agrees well with the hydrodynamical simulations by Dürmann & Kley (2015) within a factor of ~ 2 in the "planet-dominate" case and is almost consistent with analytically derived formulae by Armitage (2007), which is used in population synthesis calculations.

As newly pointed out in this paper, for a giant planet smaller than $\sim 10 M_{\rm J}$, the gas surface density outside of the gap $\Sigma_{\rm out}$ suffers an additional depletion from the unperturbed disk because of the rapid gas capture by itself. The additional depletion factor f' is given by Equation (21). It gives 0.2 for Jupiter mass and $h_{\rm p}/r_{\rm p} = 0.05$. This additional depletion factor is derived from the mass-flux balance in the outer disk (see the subsection 3.1 and Appendix B). This effect slows down the type II migration and lengthen $t_{\rm migII}$ by the factor of $1/f'$. Also note that the additional depletion decreases the lower limit of $M_{\rm p}$ for the "planet-dominate" case. Any previous models of type II migration do not include the effect of this additional gas depletion. In fact, the gas capture rate, $\dot{M}_{\rm p,hydro}$, is not taken into account in population synthesis calculations and thus they cannot evaluate this depletion factor $f' = \dot{M}_{\rm d,global}/\dot{M}_{\rm p,hydro}$.

The growth time of giant planets less than $\sim 10 M_{\rm J}$ is given by

$$t_{\rm grow} = \frac{M_{\rm p}}{\dot{M}_{\rm p}} = \frac{M_{\rm p}}{3\pi\nu_{\rm p}\Sigma_{\rm un}}, \tag{24}$$

which is almost equal to $t_{\rm migII}$ if the unperturbed surface density $\Sigma_{\rm un}$ is replaced by $\Sigma_{\rm out}$. Hence the ratio $t_{\rm grow}/t_{\rm migII}$ is given by

$$\frac{t_{\rm grow}}{t_{\rm migII}} = f' \simeq 1.2 \times \left(\frac{M_{\rm p}}{M_*}\right)^{2/3} \left(\frac{h_{\rm p}}{r_{\rm p}}\right)^{-1}. \tag{25}$$

This indicates the Jupiter mass or smaller planets suffer only a small radial drift by type II migration during their growth. According to our growth model, the growth of giant planets

terminates only when the disk is depleted to a negligible mass. Hence our results indicate that type II migration is ineffective for Jupiter mass planets or smaller. On the other hand, since the previous models neglect this additional gas depletion, the growth time is always comparable to $t_{\rm migII}$, provided that the growth is controlled by the global disk accretion (Benz et al. 2014). Figure 9 shows growth-migration curves. Evolutions of our model shows growth without significant migration until $M_{\rm p} \sim M_{\rm J}$, while the case with traditional type II migration shows relatively rapid inward migration.

Calculations of planet population synthesis suggest that most giant planets fall to their host stars because of their rapid type II migration (e.g., Ida & Lin 2008b). This is inconsistent with the radial distribution of observed extra-solar planets, in which Jupiter-sized planets are piled up at ∼1AU and hot Jupiters are minor (Mayor et al. 2011; Ida et al. 2013). Hasegawa & Ida (2013) discussed possible mechanisms which slows down the type II migration but did not find any effective slowdown mechanisms. In the above and Figure 9, we showed that type II migration of giant planets smaller than $\sim 10M_{\rm J}$ slows down because of the additional gas depletion due to their rapid gas capture. Our slow down mechanism may resolve the problem of type II migration.

For giant planets larger than $\sim 10M_{\rm J}$ (i.e., in phase 4), the gap effect prolongs the growth time compared with Equation (24) and the additional gas depletion does not occur. Then we find that the time ratio is again given by Equation (25) but f' given by Equation (21) is larger than unity in this case. The time scale of type II migration is shorter than the growth time for $M_{\rm p} > 10M_{\rm J}$. This may explain that extra-solar planets more massive than $10M_{\rm J}$ are observed less frequently. A detail population synthesis calculation would be necessary, including our slowdown mechanism for type II migration.

5. Summary and Discussion

We examined the growth rates and the final masses of giant planets embedded in protoplanetary disks through capture of disk gas, by employing an empirical formula for the gas capture rate and a shallow disk gap model, which are both based on hydrodynamical simulations. Our findings are summarized as follows.

1. Because of the shallow gap revealed by recent hydrodynamical simulations, giant planets do not stop their gas-capturing growth. Only the depletion of the whole gas disk can terminate their growth. For planets less massive than $10M_{\rm J}$, their growth rates are mainly controlled by the gas supply through the global disk accretion, rather than their gaps. For such a mass range, the final planet mass is given by Equation (18). For

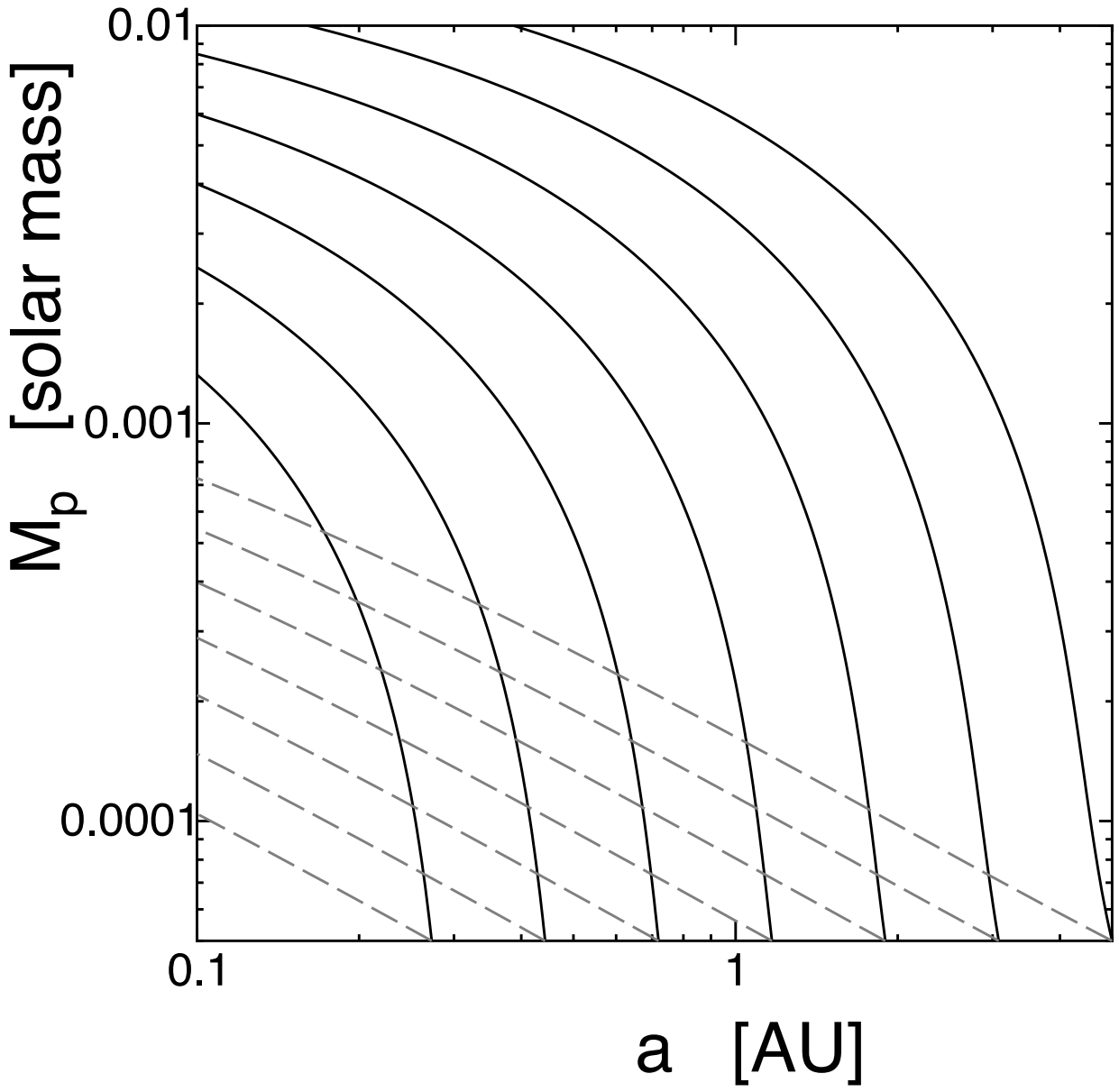

Fig. 9.— Growth-migration curves. Solid curves show evolution paths base on our result (Equation (25)), and dashed curves are the cases where the traditional type II migration is used.

the more massive planets, their growth rates are limited by deep gaps and their final mass is given by Equation (19).

2. For planets less massive than $10M_{\rm J}$, the gas supply to the planets by the disk accretion is insufficient. This also causes a depletion of the gas surface density even at the outside of the gap and create an inner hole in the protoplanetary disk The additional gas depletion factor is given by Equation (21) (see also Appendix B). Our result suggests that less massive giant planets can create deeper inner holes than more massive ones.

3. Because of the non-stopping growth, the Jupiter formation requires a very low-mass gas disk with a few or several $M_{\rm J}$, at least, at the beginning of its gas capture. This disk is much less massive than the MMSN model, whereas the solid material of ~ 80 Earth masses is also necessary for formation of the planets in our solar system. That is, we need a very low-mass disk with a high metallicity. These requirements can be achieved by the viscous evolution from an initially $\sim$ 10AU-sized compact disk with the solar composition. For a disk with a moderate viscosity of $\alpha \sim 10^{-3}$, most of disk gas accretes onto the central star and a widely-spread low-mass gas disk remains at $t \sim 10^7$ yrs. This scenario can explain the high metallicity in giant planets of our solar system.

4. A very low-mass gas disk also provides a plausible path where type I and II planetary migrations are both suppressed significantly. In particular, we also showed that the type II migration of Jupiter-size planets is inefficient because of the additional gas depletion due to their rapid gas capture. This slow type II migration is consistent with the radial distribution of observed extra-solar planets in which Jupiter-sized planets are piled up at $\sim$ 1AU.

In this paper, we proposed the formula that describes the gas accretion rate onto the planet, which combines an empirical formula of gas accretion rate obtained by a local hydrodynamic simulation (TW02) and another empirical formula of gap depth obtained by global hydrodynamical simulation (Duffell & MacFadyen 2013). Although the accretion rate is in good agreement with global hydrodynamic simulations, the function $\dot{M}_{\rm p,hydro}$ (or more specifically D) should be checked by making use of recent advancement of hydrodynamic simulations. We also proposed a formation of large-scale disk depletion created by gas capture of the planet based on analytic argument (see appendix B). This depletion arises also from long-term viscous evolution of the gas disk, which have not been studies so far. To check this, high-resolution hydrodynamic simulations with long-term evolution should be done in future work. Malik et al. (2015) have recently investigated the gap-opening criterion of migrating planets in protoplanetary disks and found that the gap opening is

more difficult than the traditional condition, which is based on the torque balance (e.g., Crida, Morbidelli, & Masset 2006; Lin & Papaloizou 1993). Other recent hydrodynamic simulations (Duffell & MacFadyen 2013; Fung, Shi, & Chiang 2014) also showed that the gap opening is less significant, although there are some differences on assumptions and purposes. Also, gas in the gap region tends to be turbulence by magneto-rotational instability (Gressel et al. 2013; Keith & Wardle 2015), which would lead to an even shallower gap. To quantify the gap deepening effect, further studies would be necessary.

In-situ formation of hot jupiters is thought to be difficult in general. This is because (1) a planet in inner region is easier to form a gap than that in outer region, which meant that the planet growth stops at a mass much less than that of Jupiter, (2) even if a hot jupiter forms, it is susceptible to type II migration and falls to the central star, and (3) there are not enough solid materials to trigger the dynamical gas capture of the protoplanet. Our model showed that the gap has little effect on suppressing gas accretion rate onto planets. In this sense, the first point is not a reason to prevent from in-situ formation anymore. We also showed that the type II migration is less effective than previously thought, which would not rule out the in-situ formation either. Although we have no claim that there are enough solid to form large solid cores, we should be noted that the difficulty of the in-situ formation of hot jupiters are greatly mitigated.

Our model assumes forced exponential decay with respect to time for the protoplanetary disk, but the way of disk dissipation would impact significantly on disk evolution and thus also on the planet formation scenario described above. Several mechanisms in addition to viscous disk accretion are proposed, such as photoevaporation (Hollenbach et al. 1994; Clarke et al. 2001; Owen et al. 2012), solar wind stripping (Horedt 1978; Matsuyama et al. 2009), solar wind induced accretion to the central star (Elmegreen 1978), disk wind (Suzuki & Inutsuka 2009, 2014). Among them, photoevaporation is thought to be the dominant mechanism to dissipate disks.

Photoevaporation has been actively studied recently and roles of X-ray and UV irradiation from the central star has been substantially understood. Since, however, luminosity of X-ray, EUV, and FUV and the time evolution has large uncertainty, the evolution of protoplanetary disks would have wide variety. If disk accretion rate toward the central star:

$$\dot{M}_{\rm d,global} = 5 \times 10^{-9} f_{\Sigma,5\rm AU} \left(\frac{\alpha}{10^{-3}}\right)^1 \left(\frac{h_{1\rm AU}/1\rm AU}{10^{-1.5}}\right)^2 M_\odot/\rm yr \tag{26}$$

is larger than mass-loss rate by photoevaporation, the effect of photoevaporation can be neglected. Our scenario suggests that $f_{\Sigma,5\rm AU} \sim 0.04$ is a plausible parameter, which gives $\dot{M}_{\rm d,global} = 2 \times 10^{-10} M_\odot/\rm yr$. According to Owen et al. (2012), mass-loss rate can be in a range from 10^{-12} to $10^{-7} M_\odot/\rm yr$ depending on X-ray luminosity, which means that our

scenario is realized when X-ray luminosity is not strong.

We are grateful to Masahiro Ikoma, Hiroshi Kobayashi, Satoshi Okuzumi, and Kazuhiro Kanagawa for valuable comments. This work was supported by JSPS KAKENHI Grant Numbers 24103503, 26800229, 15H02065, 26287101.

A. Derivation of Equation (13)

The diffusion equation of surface density $\Sigma(r,t)$ in a Keplerian disk with viscosity ν is

$$\frac{\partial \Sigma}{\partial t} = \frac{3}{r}\frac{\partial}{\partial r}\left[r^{1/2}\frac{\partial}{\partial r}(\Sigma \nu r^{1/2})\right]. \tag{A1}$$

Adopting the local approximation ($x = r - r_{\rm p} \ll 1$), we can rewrite the diffusion equation as

$$\frac{\partial \Sigma}{\partial t} = 3\nu_{\rm p}\frac{\partial^2 \Sigma}{\partial x^2}. \tag{A2}$$

Under the following initial and boundary conditions:

$$\Sigma(x, t=0) = \Sigma_{\rm un}, \tag{A3}$$

$$\Sigma(x=0, t) = 0, \tag{A4}$$

we obtain the exact solution (e.g., Landau & Lifshitz 1987):

$$\Sigma(x,t) = \Sigma_{\rm un}\,{\rm erf}\left(\frac{x}{2\sqrt{3\nu_{\rm p}t}}\right), \tag{A5}$$

where $\Sigma_{\rm un}$ is a constant.

Since the disk mass reduced from the initial condition equals to the mass sunk into the boundary at $x = 0$, we have

$$\begin{aligned}\int_0^t F(t')dt' &= 2\pi r_{\rm p}\int_0^\infty (\Sigma_{\rm un} - \Sigma(x,t)))dx \\ &= 2\pi r_{\rm p}\Sigma_{\rm un}\frac{2\sqrt{3\nu_{\rm p}t}}{\sqrt{\pi}},\end{aligned} \tag{A6}$$

where $F(t)$ is mass flux toward $x = 0$ from $x > 0$, and we use a mathematical formula: $\int_0^\infty {\rm erfc}(x)dx = 1/\sqrt{\pi}$. Differentiating Equation (A6) with respect to time yields the mass accretion rate to the boundary $x = 0$ as a function of time:

$$F(t) = 2\pi r_{\rm p}\Sigma_{\rm un}\sqrt{\frac{3\nu_{\rm p}}{\pi t}}. \tag{A7}$$

B. A solution of a steady accretion disk with a mass sink to an embedded planet

Lubow & D'Angelo (2006) obtained the radial gas distribution of a steady viscous accretion disk with a mass sink by a planet and showed that the mass sink causes a gas depletion in a wide region, but did not give a detailed derivation of it. Here, we present the derivation the solution of the surface density distribution in such a case.

In an accretion disk, the radial angular moment flux F_J is given by (Lynden-Bell & Pringle 1974)

$$F_J = jF_M + 3\pi r^2 \nu \Sigma \Omega, \tag{B1}$$

where F_M is the radial mass flux and the specific angular momentum j is given by $r^2\Omega$. For Ω, the Keplerian rotation is assumed. Thus, for given (constant) mass flux and angular momentum flux, the surface density of the quasi-steady disk is expressed as

$$\Sigma(r) = \frac{-F_M + F_J/j(r)}{3\pi\nu(r)}. \tag{B2}$$

We here consider an accretion disk having a mass sink with the rate of $\dot{M}_{\rm p}$ at $r = r_{\rm p}$ due of the accretion onto the planet. The disk angular momentum sinks into the planet with the rate of $j(r_{\rm p})\dot{M}_{\rm p}$. Then the mass and angular momentum fluxes are discontinuous at $r_{\rm p}$ and given by

$$F_M = \begin{cases} -(\dot{M}_* + \dot{M}_{\rm p}) & (r > r_{\rm p}), \\ -\dot{M}_* & (r < r_{\rm p}), \end{cases} \tag{B3}$$

and

$$F_J = \begin{cases} -(j_*\dot{M}_* + j_{\rm p}\dot{M}_{\rm p}) & (r > r_{\rm p}), \\ -j_*\dot{M}_* & (r < r_{\rm p}), \end{cases} \tag{B4}$$

where $\dot{M}_*$ is the mass accretion rate onto the central star and r_* is the radius of the inner disk edge. The specific angular momenta $j_{\rm p}$ and j_* are the values at $r_{\rm p}$ and r_*, respectively. Note that the sum $\dot{M}_{\rm p} + \dot{M}_*$ is equal to the global accretion rate $\dot{M}_{\rm d,global}$. The negative fluxes indicate the inward transport of the disk mass and angular momentum. Substituting Equations (B3) and (B4) into (B2), we obtain

$$\Sigma(r) = \begin{cases} \dfrac{\dot{M}_*}{3\pi\nu}\left(1 - \sqrt{\dfrac{r_*}{r}}\right) + \dfrac{\dot{M}_{\rm p}}{3\pi\nu}\left(1 - \sqrt{\dfrac{r_{\rm p}}{r}}\right) & \text{for} \quad r > r_{\rm p}, \\ \dfrac{\dot{M}_*}{3\pi\nu}\left(1 - \sqrt{\dfrac{r_*}{r}}\right) & \text{for} \quad r < r_{\rm p}. \end{cases} \tag{B5}$$

The ratio $\dot{M}_*/\dot{M}_{\rm p}$ is determined by the accretion formula of Equation (7). From Equation (B5), we obtain

$$\Sigma(r_{\rm p}) = \frac{\dot{M}_*}{3\pi\nu_{\rm p}}, \tag{B6}$$

where we omitted the term of $\sqrt{r_*/r_{\rm p}}$. This approximation would be valid for a planet with $r_{\rm p} \gtrsim 1$AU since r_* would be less than 0.1AU. Note that the solution given by Lubow & D'Angelo (2006) does not assume that $r_* \ll r_{\rm p}$. From Equations (7), (9) and (B6), we obtain

$$\dot{M}_{\rm p} = \frac{D'}{3\pi\nu_{\rm p}}\dot{M}_*, \tag{B7}$$

where D' is defined by

$$D' = \frac{1}{0.034K+1}D, \tag{B8}$$

$\nu_{\rm p} = \nu(r_{\rm p})$, and we equate $\Sigma(r_{\rm p})$ with $\Sigma_{\rm un}$ in Equation (9). Since the ratio $D'/3\pi\nu_{\rm p}$ is equal to $\dot{M}_{\rm p,hydro}/\dot{M}_{\rm d,global}$ by definition, the ratio is given by Equation (16):

$$\frac{D'}{3\pi\nu_{\rm p}} = 0.90\left(\frac{M_{\rm p}}{M_*}\right)^{-2/3}\left(\frac{h_{\rm p}}{r_{\rm p}}\right) = 4.5\left(\frac{M_{\rm p}}{M_J}\right)^{-2/3}\left(\frac{h_{\rm p}/r_{\rm p}}{0.05}\right). \tag{B9}$$

Noting $\dot{M}_{\rm p} + \dot{M}_* = \dot{M}_{\rm d,global}$ and using Equation (B7), we obtain the accretion rates as

$$\dot{M}_{\rm p} = \frac{D'/3\pi\nu_{\rm p}}{1+D'/3\pi\nu_{\rm p}}\dot{M}_{\rm d,global}, \qquad \dot{M}_* = \frac{1}{1+D'/3\pi\nu_{\rm p}}\dot{M}_{\rm d,global}. \tag{B10}$$

Substituting Equation (B10) into (B5), we finally obtain the expression of the surface density of the disk with a mass sink of the planetary gas capture as

$$\Sigma(r) = \begin{cases} \dfrac{\dot{M}_{\rm d,global}}{3\pi\nu(1+D'/3\pi\nu_{\rm p})}\left[\left(1-\sqrt{\dfrac{r_*}{r}}\right)+\dfrac{D'}{3\pi\nu_{\rm p}}\left(1-\sqrt{\dfrac{r_{\rm p}}{r}}\right)\right] & \text{for} \quad r > r_{\rm p}, \\ \dfrac{\dot{M}_{\rm d,global}}{3\pi\nu(1+D'/3\pi\nu_{\rm p})}\left(1-\sqrt{\dfrac{r_*}{r}}\right) & \text{for} \quad r < r_{\rm p}. \end{cases} \tag{B11}$$

From the expression, the additional gas depletion factor due to the gas capture is given by $(1+D'/3\pi\nu_{\rm p})^{-1}$, which is approximately equal to Equation (22) in the text. In Figure 10 we plot the obtained surface density distribution for a typical case. In the vicinity of the planet, the gap, which is an additional gas depletion due to the gravitational torque from the planet, should also exist. Even though the obtained surface density does not show this gap, the effect of the gap is included in this formulation through the parameter D' of Equation (B8).

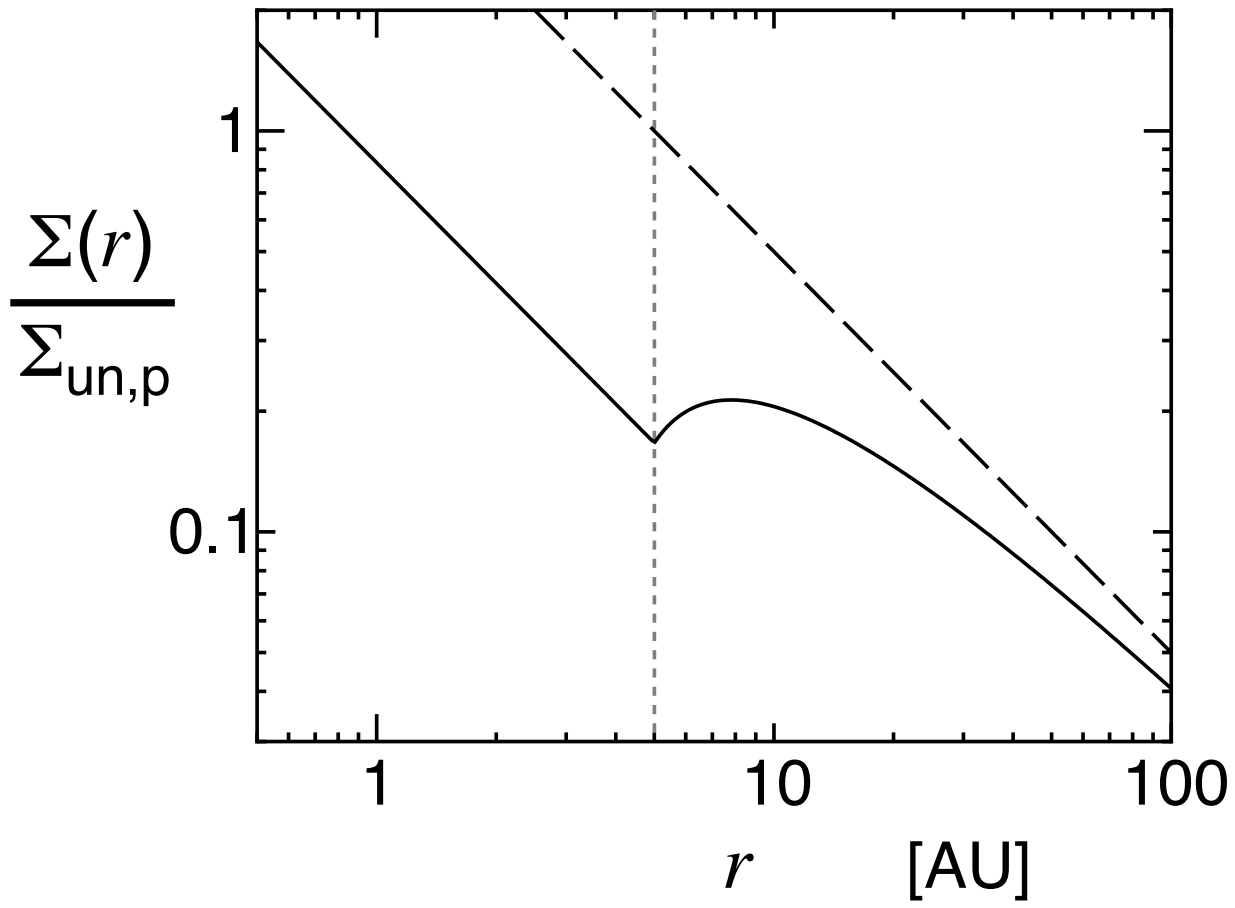

Fig. 10.— An example of the surface density distribution of the disk with a mass sink of the planetary gas capture (the solid line). The planet is located at 5AU (the vertical gray dotted line). The ratio $D/3\pi\nu_{\rm p}$ is set to be 5. It is also assumed that $r \gg r_*$. The unperturbed surface density Σ_{un} is also plotted by the dashed line for comparison. Because of the planetary gas capture, the gas surface density is further depleted and an inner hole is formed.

REFERENCES

Alexander, R., Pascucci, I., Andrews, S., Armitage, P., & Cieza, L. 2014, Protostars and Planets VI, Henrik Beuther, Ralf S. Klessen, Cornelis P. Dullemond, and Thomas Henning (eds.), University of Arizona Press, Tucson, 914 pp., p.475-496

Armitage, P. J. 2007, ApJ, 665, 1381

Baraffe, I., Chabrier, G., Fortney, J., & Sotin, C. 2014, Protostars and Planets VI, Henrik Beuther, Ralf S. Klessen, Cornelis P. Dullemond, and Thomas Henning (eds.), University of Arizona Press, Tucson, 914 pp., p.763-786

Benz, W., Ida, S., Alibert, Y., Lin, D., & Mordasini, C. 2014, Protostars and Planets VI, Henrik Beuther, Ralf S. Klessen, Cornelis P. Dullemond, and Thomas Henning (eds.), University of Arizona Press, Tucson, 914 pp., p.691-713

Bodenheimer, P., & Pollack, J. B. 1986, Icarus, 67, 391

Clarke, C. J., Gendrin, A., & Sotomayer, M. 2001, MNRAS, 328, 485

Crida, A., Morbidelli, A., & Masset, F. 2006, Icarus, 181, 587

Daisaka, J. K., Tanaka, H., & Ida, S. 2006, Icarus, 185, 492

D'Angelo, G., Kley, W., & Henning, T. 2003, ApJ, 586, 540

Duffell, P. C., & MacFadyen A. I. 2013, ApJ, 769, 41

Duffell, P. C., Haiman, Z., & MacFadyen, A. I., D'Orazio D. J., & Farris, B. D. 2014, ApJ, 792 10

Dürmann, C., & Kley, W. 2015, A&A, 574, A52

Elmegreen B. G. 1978, Moon Planets, 19, 261

Fung, J., Shi, J.-M., & Chiang, E., ApJ, 782, 88

Gorti, U, Dullemond, P., & Hollenbach, D. 2009, ApJ, 705, 1237

Gressel, O., Nelson, R. P., Turner, N. J., & Ziegler, U. 2013, ApJ, 779, 59

Hartmann, L., Calvet, N., Gullbring, E., & D'Alessio, P. 1998, ApJ, 495, 385

Hasegawa, Y. & Ida, S. 2013, ApJ, 774, 146

Hayashi, C., Nakazawa, K., & Nakagawa, Y. 1985, In Protostars and Planets II, eds. D. C. Black and M. S. Matthews, Univ. of Arizona Press, 1100

Hollenbach, D., Johnstone, D., Lizano, S., & Shu, F. 1994, ApJ, 428, 654

Horedt, G. P. 1978, A&A, 64, 173

Hubickyj, O., Bodenheimer, P., & Lissauer, J. J. 2005, Icarus, 179, 415

Ida, S., & Lin, D. N. C. 2004, ApJ, 604, 388

Ida, S., & Lin, D. N. C. 2008, ApJ, 673, 487

Ida, S., & Lin, D. N. C. 2008, ApJ, 685, 584

Ida, S., Lin, D. N. C., & Nagasawa, M. 2013, ApJ, 775, 42

Ikoma, M., Nakazawa, K., & Emori, H. 2000, ApJ, 537, 1013

Kanagawa, K. D., Muto, T., Tanaka, H., Tanigawa, T., & Takeuchi, T. 2015, MNRAS, 448, 994

Kanagawa, K. D., Tanaka, H., Muto, T., Tanigawa, T., Takeuchi, T., Tsukagoshi, T., & Momose, M. 2015, ApJ, 806, L15

Keith S. L., & Wardle, M. 2015, MNRAS, 451, 1104

Lin, D. N. C., & Papaloizou, J. 1986, ApJ, 309, 846

Lin, D. N. C., & Papaloizou, J. 1993, Protostars and planets III, 749

Lubow, S., H. & D'Angelo, G. 2006, ApJ, 641, 526

Lynden-Bell, D. & Pringle J. E. 1974, MNRAS, 168, 603

Malik, M., Meru, F., Mayer, L, & Meyer, M. 2015, ApJ, 802, 56

Matsuyama, I., Johnstone, D., & Hollenbach, D. 2009, ApJ, 700, 10

Machida, N. M., Kokubo, E., Inutsuka, S., & Matsumoto, T. 2010, MNRAS, 405, 1227

Mayor, M.; Marmier, M.; Lovis, C.; Udry, S.; Ségransan, D.; Pepe, F.; Benz, W.; Bertaux, J. -L.; Bouchy, F.; Dumusque, X.; Lo Curto, G.; Mordasini, C.; Queloz, D.; Santos, N. C. 2011, arXiv:1109.2497

Mizuno, H. 1980, Prog. Theor. Phys., 64, 544

Mordasini, C., Alibert, Y., Benz, W. 2009, A&A, 501, 1139

Mordasini, C., Alibert, Y., Klahr, H., & Henning, T. 2012, A&A, 547, A111

Mordasini, C., Alibert, Y., Benz, W., Klahr, H., & Henning, T. 2012, A&A, 541, 97

Mordasini, C., Alibert, Y., Klahr, H., & Henning, T. 2012, A&A, 547, A112

Owen, J. E., Clarke, C. J., & Ercolano, B. 2012, MNRAS, 422, 1880

Pollack, J. B., Hubickyj, O., Bodenheimer, P., Lissauer, J. J., Podolak, M., & Greenzweig, Y. 1996, Icarus, 124, 62

Landau, L. D., & Lifshitz, E. M. 1987, Fluid Mechanics, Second edition, U.S.S.R. Academy of Sciences

Shakura, N. I., & Sunyaev, R. A. 1973, A&A, 24, 337

Suzuki, T. K., & Inutsuka, S. 2009, ApJ, 691, L49

Suzuki, T. K., & Inutsuka, S. 2014, ApJ, 784, 121

Tanaka, H., Takeuchi, T., & Ward, W. R. 2002, ApJ, 565, 1257

Tanigawa, T., & Watanabe, S. 2002, ApJ, 586, 506

Tanigawa, T., & Ikoma, M. 2007, ApJ, 667, 557 (TI07)

Tanigawa, T., Ohtsuki, K., & Machida, M. N. 2012, ApJ, 747, 47

Williams, J. P., & Cieza, L. A. 2011, ARA&A, 49, 67

Draft version October 31, 2016
Preprint typeset using LaTeX style AASTeX6 v. 1.0

SUBMILLIMETER POLARIZATION OBSERVATION OF THE PROTOPLANETARY DISK AROUND HD 142527

Akimasa Kataoka[1,2], Takashi Tsukagoshi[3], Munetake Momose[3], Hiroshi Nagai[2], Takayuki Muto[4], Cornelis P. Dullemond[1], Adriana Pohl [1,5], Misato Fukagawa[6], Hiroshi Shibai[7], Tomoyuki Hanawa[8], Koji Murakawa[9]

[1]Zentrum für Astronomie der Universität Heidelberg, Institut für Theoretische Astrophysik, Albert-Ueberle-Str. 2, D-69120 Heidelberg, Germany
[2]National Astronomical Observatory of Japan, Mitaka, Tokyo 181-8588, Japan
[3]College of Science, Ibaraki University, 2-1-1 Bunkyo, Mito, Ibaraki 310-8512, Japan
[4]Division of Liberal Arts, Kogakuin University, 1-24-2 Nishi-Shinjuku, Shinjuku-ku, Tokyo 163-8677, Japan
[5]Max Planck Institute for Astronomy, Königstuhl 17, D-69117 Heidelberg, Germany
[6]Division of Particle and Astrophysical Science, Graduate School of Science, Nagoya University, Furo-cho, Chikusa-ku, Nagoya, Aichi 464-8602, Japan
[7]Graduate School of Science, Osaka University, 1-1 Machikaneyama, Toyonaka, Osaka 560-0043, Japan
[8]Center for Frontier Science, Chiba University, 1-33 Yayoi-cho, Inage, Chiba 263-8522, Japan
[9]College of General Education, Osaka Sangyo University, 3-1-1, Nakagaito, Daito, Osaka 574-8530, Japan

ABSTRACT

We present the polarization observations toward the circumstellar disk around HD 142527 by using Atacama Large Millimeter/submillimeter Array (ALMA) at the frequency of 343 GHz. The beam size is $0\farcs51 \times 0\farcs44$, which corresponds to the spatial resolution of $\sim 71 \times 62$ au. The polarized intensity displays a ring-like structure with a peak located on the east side with a polarization fraction of $P = 3.26 \pm 0.02\%$, which is different from the peak of the continuum emission from the northeast region. The polarized intensity is significantly weaker at the peak of the continuum where $P = 0.220 \pm 0.010\%$. The polarization vectors are in the radial direction in the main ring of the polarized intensity, while there are two regions outside at the northwest and northeast areas where the vectors are in the azimuthal direction. If the polarization vectors represent the magnetic field morphology, the polarization vectors indicate the toroidal magnetic field configuration on the main ring and the poloidal fields outside. On the other hand, the flip of the polarization vectors is predicted by the self-scattering of thermal dust emission due to the change of the direction of thermal radiation flux. Therefore, we conclude that self-scattering of thermal dust emission plays a major role in producing polarization at millimeter wavelengths in this protoplanetary disk. Also, this puts a constraint on the maximum grain size to be approximately 150 μm if we assume compact spherical dust grains.

Keywords: polarization — protoplanetary disks — stars: individual (HD 142527)

1. INTRODUCTION

Polarized emission at (sub)millimeter wavelengths has been observed from star-forming regions (e.g., Girart et al. 2006; Rao et al. 2009; Girart et al. 2009; Hull et al. 2013, 2014). As a direct extension, there have been several observations trying to detect (sub)millimeter-wave polarization of circumstellar disks. It has been difficult to detect (sub)millimeter polarization in protoplanetary disks with single-dish telescopes because of a lack of spatial resolution (e.g., Tamura et al. 1995). For cases of young circumstellar disks embedded in their envelopes, by using radio interferometry with high spatial resolution, there are some detections of (sub)millimeter-wave polarization toward IRAS 16293-2422 B (Rao et al. 2014), L 1527 (Segura-Cox et al. 2015), and HL Tau (Stephens et al. 2014). However, there has been no detection of millimeter-wave polarization signature from circumstellar disks in the later stages such as HD 163296, TW Hya (Hughes et al. 2009), GM Aur, DG Tau, and MWC 480 (Hughes et al. 2013).

Two possible mechanisms have been proposed for the polarization at millimeter wavelengths. One is the grain alignment with magnetic fields. If dust grains are elongated, they could align perpendicular to the magnetic fields (Davis & Greenstein 1951). Radiative torque can spin up the dust grains to help the alignment (Lazarian & Hoang 2007). Therefore, the polarization vectors have been used as a tracer of the magnetic fields. Particularly

in protoplanetary disks, the morphology of the magnetic fields is usually assumed to be toroidal (e.g., Brandenburg et al. 1995), and thus the polarization vectors are predicted to be directed radially (Cho & Lazarian 2007).

The other mechanism is the self-scattering of thermal dust emission. If dust grains grow to sizes as large as the observed wavelengths and if the radiation field at the same wavelengths has an anisotropy, the thermal dust emission can be scattered by the dust grains themselves and make the emission polarized (Kataoka et al. 2015). For example, the polarized emission from HL Tau disk can be explained either by the grain alignment with complex magnetic field morphology (Stephens et al. 2014) or by the self-scattering (Kataoka et al. 2016; Yang et al. 2016). In the case of face-on disks, the polarization vectors of disks are predicted to be in the radial direction at inner radii but in the azimuthal direction at outer radii (Kataoka et al. 2015).

In this Letter, we report the first detection of millimeter-wave polarization from a late-stage protoplanetary disk. The target is HD 142527, which is a Herbig Ae star (Waelkens et al. 1996). The associated circumstellar disk has a wide gap with spiral patterns in infrared observations (Fukagawa et al. 2006; Avenhaus et al. 2014) and a lopsided continuum structure with submillimeter-wave observations (Casassus et al. 2013; Fukagawa et al. 2013), which possibly show the trapping of dust by a vortex (e.g., Birnstiel et al. 2013; Zhu & Stone 2014).

2. OBSERVATIONS

HD142527 was observed by Atacama Large Millimeter / submillimeter Array (ALMA) on 2016 March 11, during its Cycle 3 operation. The antenna configuration was C36-2/3 and 38 antennas were operated during the observation period. The correlator processed four spectral windows centered at 336.5, 338.4, 348.5, and 350.5 GHz with a bandwidth of 1.875 GHz each. The bandpass and the complex gain were calibrated by observations of J1427-4206 and J1604-4441, respectively, and the polarization calibration was performed by observations of J1512-0905. The raw data were reduced by EA-ARC staff. A detailed description of the data reduction is given in Nagai et al. 2016.

We further perform the iterative CLEAN deconvolution imaging by using CASA with self-calibration to improve the image quality. We employ the Briggs weighting with a robust parameter of 0.5 and the multiscale option with scale parameters of 0, 0.3, and 0.9 arcsec. The beam size of the final product is $0''.51 \times 0''.44$, corresponding to $\sim 71 \times 62$ au at the distance to the target. The rms for each Stokes component is summarized in Table 1. The rms for the Stokes V image is 25.2 μJy, close to the thermal noise level of the integration time. Since the Stokes I, Q, and U images are dynamic range limited, the high rms on Stokes I, Q, and U images is not due to the lack of integration time nor the polarization calibration error.

Table 1. Observational Data of Each Stokes Component

	Total Flux (mJy)	Max, Min (mJy beam^{-1})	rms (μJy beam^{-1})
Stokes I	847	340	185
Stokes Q	...	1.99, -5.13	29.1
Stokes U	...	3.52, -2.88	29.5
Polarized Intensity	1.75	5.22	42.8

NOTE— The Stokes I and the polarized intensity show the maximum flux while the Stokes Q and U show both maximum and minimum values in the middle column.

3. RESULTS

The total and peak fluxes of each Stokes component are also summarized in Table 1. Here, the maximum flux is shown for the Stokes I while both maximum and minimum fluxes are shown for the Stokes Q and U. Spatially integrated Stokes Q and U components give the total polarized intensity $PI = \left((\sum Q)^2 + (\sum U)^2\right)^{0.5}$ to be 1.75 mJy with an rms of $\sigma_{\rm PI} = 42.8$ μJy beam^{-1}. Dividing the total polarized intensity by the total intensity, we derive the total polarization fraction to be 0.207 %. This low fraction of polarization is unlikely to be detected if the disk is spatially unresolved. Therefore, the high spatial resolution of this observation is essential to detect the polarization.

The left panel of Figure 1 shows the polarized intensity by colorscale overlaid with the solid contour of the continuum and the polarization vectors. The continuum emission well reproduces the previously observed

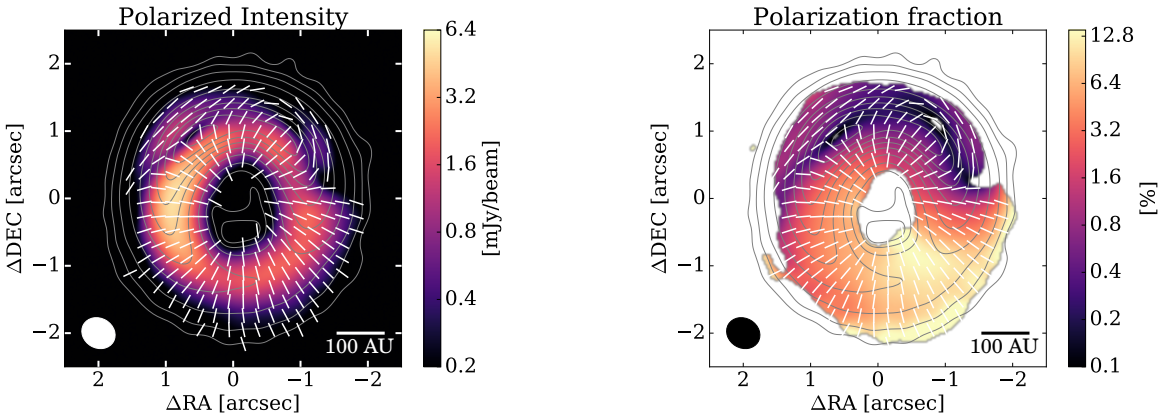

Figure 1. In the left panel, the colorscale represents the polarized intensity in units of mJy beam^{-1} with a log scale, the gray contours show the continuum emission, and the white vectors show the polarization vectors. Note that the lengths of the polarization vectors are set to be the same. The levels of the contours are $(3, 10, 30, 100, 300, 600, 900, 1200, 1500, 1800) \times \sigma_{\rm I} (= 185\ \mu$Jy beam$^{-1})$ for Stokes I. Polarization vectors are plotted where the polarized intensity is larger than $3\sigma_{\rm PI} = 0.128$ mJy beam^{-1}. In the right panel, the colorscale displays the polarization fraction overlaid with the polarization vectors. The gray contours display the continuum emission with the same levels of the left panel. The colorscale is only shown with the same threshold of the polarization vectors in the left panel.

lopsided structure (e.g., Casassus et al. 2013; Fukagawa et al. 2013). The polarized intensity shows a ring-like distribution with azimuthal asymmetry, for which the substructure is different from the continuum, and also shows two regions with azimuthal polarization. Although the continuum emission has a peak at the northeast region, the polarized intensity has a peak on the east side. The peak emission of the polarized emission is 5.22 mJy beam^{-1}. The ring of the polarized intensity is located slightly inside of the ring center of the continuum. The maps of each Stokes component are shown in Fig. 2.

The polarization vectors on the main ring of the polarized emission have a radial direction everywhere. However, the polarization vectors are rotated by 90° in two regions. The northeast region is $\sim 1\farcs3$ from the star toward the position angle of $\sim 42°$ while the northwest one is $\sim 1\farcs4$ from the star toward the position angle of $\sim -60°$. The two regions are clearly seen in Fig. 2 as a flip of the sign of Stokes Q or U from inside to outside.

Furthermore, the polarized intensity is relatively bright in the southwest direction, where Stokes I is the faintest. This causes high polarization fraction in the south region. The right panel of Fig. 1 shows the polarization fraction overlaid with the polarization vectors with the continuum as solid contours. The polarization fraction is 3.26 ± 0.02 % at the peak of the polarized intensity and as low as 0.220 ± 0.010 % at the peak of the continuum. The polarization fraction has a peak at the southwest region with a fraction of 13.9 ± 0.6 %, which corresponds to around the local minimum of the intensity of the main ring.

Here, we note that the polarization maps at low signal-to-noise ratio regions could be affected by the positive polarization bias (Vaillancourt 2006). The discussion in this Letter is concerning at the regions where the detection is larger than 3 $\sigma_{\rm PI}$ and thus the positive polarization bias does not affect the results.

4. DISCUSSIONS

We have detected spatially resolved polarized continuum emission from the disk around HD 142527. There are three distinct observational signatures - (1) difference of the locations of the brightest emission between Stokes I and PI, (2) 90° flip of the polarization vectors in the northeast and northwest region, and (3) the high fraction of polarization (13.9 ± 0.6%) in the southwest region. Two possible mechanisms to produce polarized emission in protoplanetary disks are suggested to date: grain alignment by the magnetic field or dust self-scattering. In this section, we qualitatively discuss which mechanism is more likely to take place in the disk around HD 142527.

4.1. *Grain alignment*

Here, we discuss the possibility that the polarization is due to the grain alignment with magnetic fields. The magnetic field direction is rotated by 90° from the polarization vectors in the thermal emission regime. Therefore, the morphology of the main polarization ring indicates the presence of toroidal magnetic fields, which is consistent with the common understanding of the magnetic field in disks (e.g., Brandenburg et al. 1995; Stone et al. 1996).

The difference between the peak position of the polarized intensity and the peak of the continuum could be explained with the depolarization due to the high

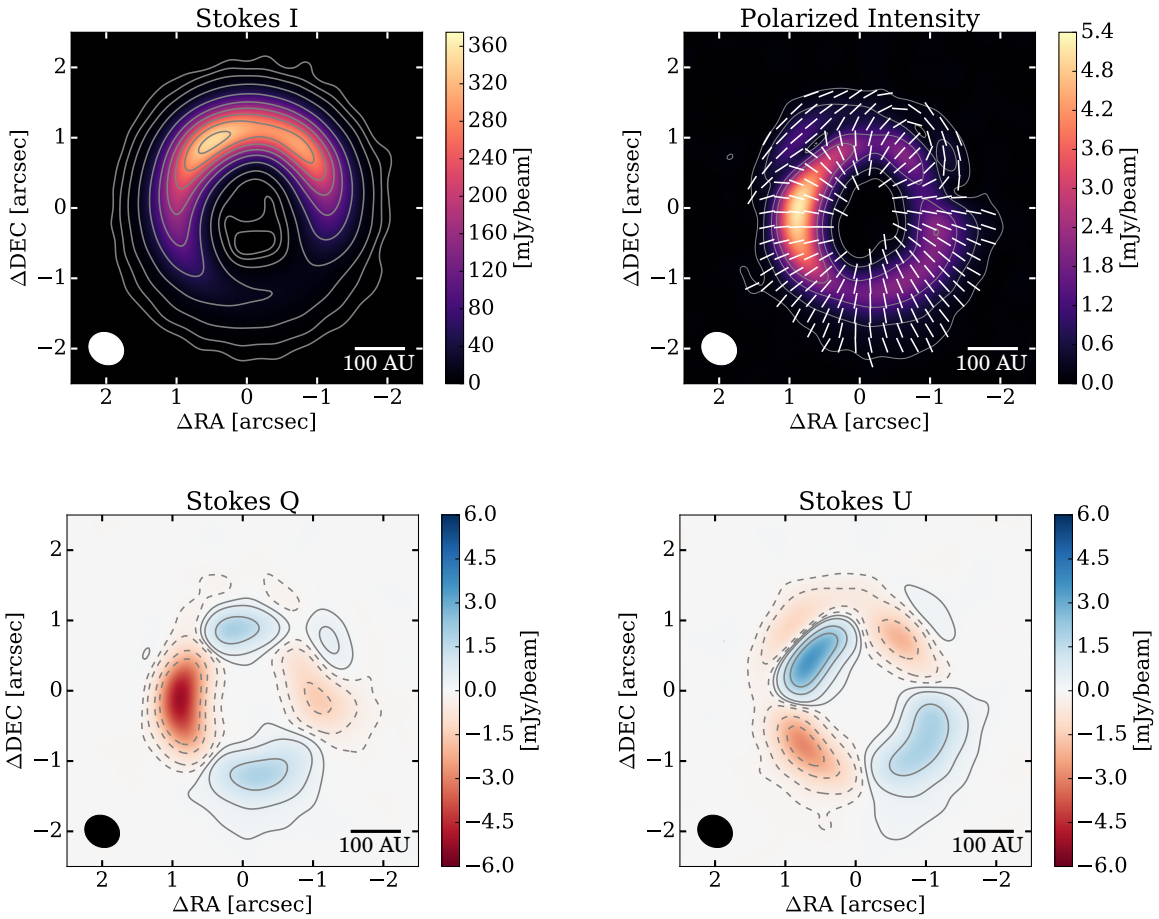

Figure 2. Four maps display the intensity of Stokes I, polarized intensity, Stokes Q, and Stokes U maps in a linear scale. Levels of contours are $(3, 10, 30, 100, 300, 600, 900, 1200, 1500, 1800) \times \sigma_{\rm I} (= 185\ \mu{\rm Jy\ beam^{-1}})$ for Stokes I, $(3, 10, 30, 50, 100) \times \sigma_{\rm PI} (= 42.8\ \mu{\rm Jy\ beam^{-1}})$ for the polarized intensity, and $(-50, -30, -10, -3, 3, 10, 30) \times \sigma_{\rm PI}$ for Stokes Q and $(-50, -30, -10, -3, 3, 10, 30, 50) \times \sigma_{\rm PI}$ for Stokes U. The solid contours in the Stokes Q and U maps represent plus components, and the dashed contours represent minus components.

optical depth at the peak of the continuum (e.g., Alves et al. 2014). We will also discuss the effects of the optical depth in the next section. Another possibility is the difference in the grain size and its effects on the alignment efficiency; the radiative torque efficiency decreases with decreasing grain size if the grain size is smaller than the wavelength. Therefore, if the peak emission of Stokes I is mainly coming from grains smaller than the wavelengths, it would decrease the alignment efficiency and thus the polarization fraction (e.g., Cho & Lazarian 2007; Lazarian & Hoang 2007).

The azimuthal direction of the polarization vectors as shown in the outer regions indicates the poloidal magnetic field configuration, while the radial direction on the inner ring indicates the toroidal magnetic field. There has been no mechanism locally to rotate the direction of the magnetic field by 90°. Therefore, at least at that position, the mechanism should be different from the grain alignment.

The polarization fraction in the south region is as high as 13.9 ± 0.7 %, which is higher than the predicted value (e.g., Cho & Lazarian 2007). The high fraction of polarization means that the alignment efficiency maybe higher than expected or the long-to-short axis ratio of elongated dust grains is larger than the assumed value (Cho & Lazarian 2007). Alternatively, the high polarization fraction observed in the southwest region could be due to interferometric filtering effects, where the Stokes I and the Stokes Q, U maps are resolved out differently.

Here, we also note that the high polarization fraction observed in the southwest region could be due to interferometric effects where the Stokes I and the Stokes Q, U maps are resolved out.

4.2. *Self-scattering*

4.2.1. *Model Prediction*

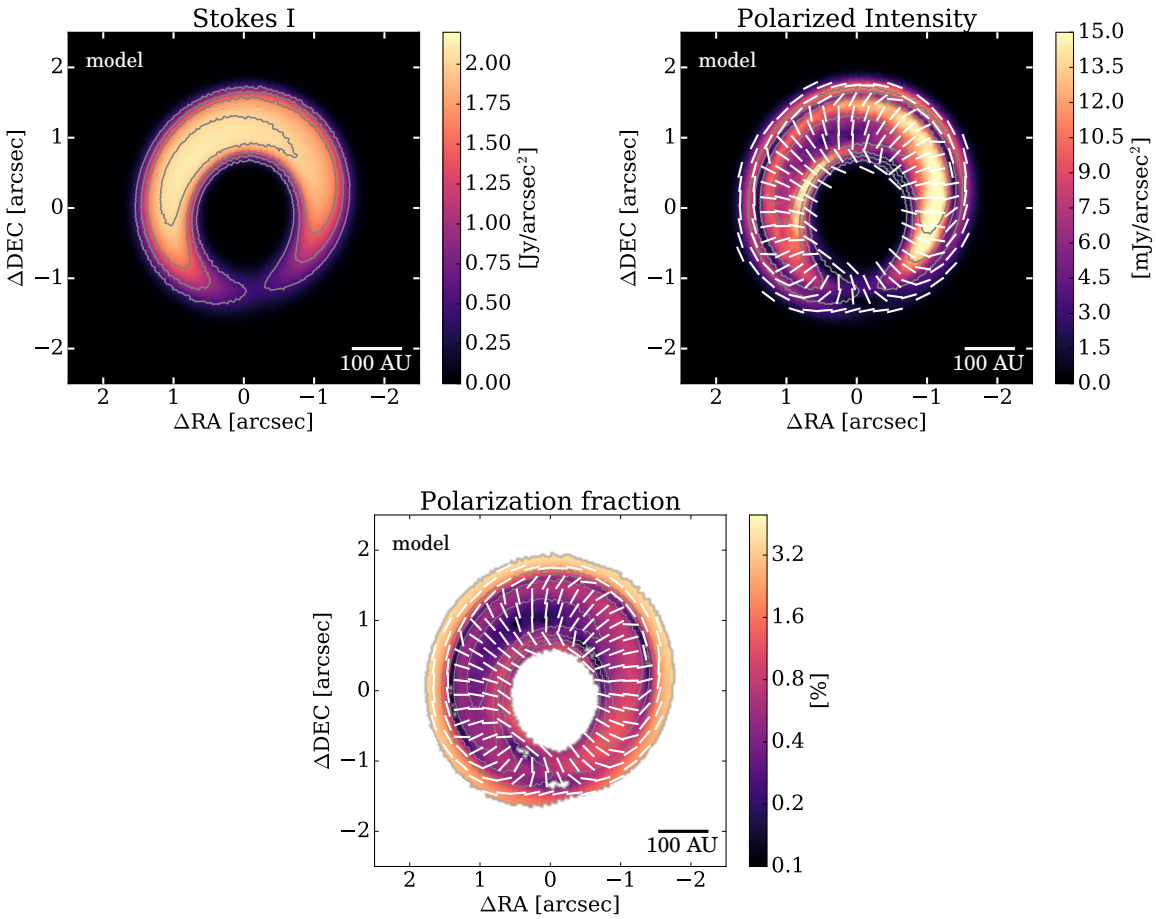

Figure 3. Colorscale of each figure displays the intensity, the polarized intensity, and the polarization fraction of the model calculations. The levels of the solid contours are $(5, 10, 15, 20) \times \sigma_{\rm I,sim} (= 0.1$ Jy arcsec$^{-2})$ of the intensity.

Another possible explanation for the millimeter-wave polarization is the self-scattering of the thermal dust emission at the observed wavelengths (Kataoka et al. 2015). We model the intensity with a simple model and perform radiative transfer calculations with RADMC-3D [1] to see the model prediction of the self-scattering. We assume that the dust grains have a power-law size distribution with a power of -3.5 and the maximum grain size 150 μm, which is the most efficient grain size to scatter the thermal emission and make it polarized at the observed wavelength of $\lambda = 0.87$ mm. The density distribution is based on a previous modeling of the continuum at the same wavelength (Muto et al. 2015). The density distribution of dust grains $\Sigma_{\rm d}$ is taken to be a Gaussian distribution in radial and azimuthal direction as

$$\Sigma_{\rm d} = \left[\Sigma_{0,\rm min} + (\Sigma_{0,\rm max} - \Sigma_{0,\rm min}) \exp\left(-\frac{(\theta-\theta_d)^2}{2\phi_d^2}\right)\right] \times \exp\left(-\frac{(r-r_c)^2}{2r_w^2}\right) \quad (1)$$

where r and θ are the radial and azimuthal coordinates $\Sigma_{0,\rm max}$ and $\Sigma_{0,\rm min}$ are the maximum and minimum surface density at the center of the ring, θ_d and ϕ_d represent the center and width of the vortex in the azimuthal direction, and r_c and r_w represent the center and width of the vortex in the radial direction. The values are taken to be $\Sigma_{0,\rm max} = 0.6$ g cm^{-2}, $\Sigma_{0,\rm min} = 0.008$ g cm^{-2}, $\theta_d = 30°$, $\phi_d = 60°$, $r_c = 170$ au, and $r_w = 27$ au. The dust temperature is set to 36 K. In the calculations of RADMC-3D, we set the inclination of the disk to be 27° (Fukagawa et al. 2013) and the position angle to be 71°. Here, we do not aim to model the intensity and the polarization perfectly, but to investigate the morphology and the strength of the polarization with a simple model of an inclined lopsided-disk to understand that feature can be explained with the simple model.

Here, we summarize the model prediction by the self-scattering model. Figure 3 shows the intensity, the polarized intensity, and the polarization fraction of the model. The polarized intensity shows the main ring in-

[1] RADMC-3D is an open code of radiative transfer calculations. The code is available online: http://www.ita.uni-heidelberg.de/~dullemond/software/radmc-3d/

side with radial polarization vectors and the ring outside with azimuthal polarization vectors. The polarization fraction is up to $\sim 2\%$ in the inner ring while $\sim 5\%$ in the outer ring. Also, the polarized intensity is weaker at the peak of the continuum than in other regions because the dust thermal emission is optically thick at the peak of the continuum. The reason is as follows. With the polarization observations, we are looking at the emission scattered by dust grains. Let us consider a dust grain as a scatterer. The polarization fraction is determined by the superposition of the scattered emission of all incoming fluxes from any direction. If the thermal dust emission is optically thin, the anisotropy of the radiation field causes difference of the incoming fluxes depending on its direction, that is why we can see the polarization as a residual. If the thermal dust emission is marginally optically thick, however, there is no difference in incoming fluxes depending on its direction, which causes no residual polarization because they are canceled. This is why we see less polarization fraction at the optically thick regions. These features have been predicted by Kataoka et al. 2015 as the face-on ring model. In the case of HD 142527, the emission from the peak of the continuum is shown to be optically thick at the observed wavelengths (Muto et al. 2015). Therefore, the depolarization due to the optical thickness is expected in the disk.

4.2.2. *Comparison with the Observation*

The flip of the polarization vectors of the observations is naturally explained with the self-scattering model. This flip is strong support for the self-scattering hypothesis. The peak difference between the PI and continuum can also be naturally explained by the effects of optical depth.

However, the simple model of the self-scattering with the constant maximum grain size does not explain the observed polarized intensity distribution qualitatively. The observation shows that the polarized intensity is the brightest at the position angle of $\sim 90^\circ$ while it is faint at the position angle of $\sim -45^\circ$. However, the model does not show the peak at the position angle of $\sim 90^\circ$. Also, the high polarization fraction of 13.9 ± 0.6 % at the south region has not been expected from the self-scattering model. The expected polarization fraction is a few percent for the main ring as shown in Fig. 3 (see also Kataoka et al. 2015).

4.2.3. *Possible Improvements of the Model*

We discuss further modeling in future publications to explain the observation. Including the spatial grain size distribution is essential to explain the peak difference between the intensity and the polarized intensity. If the maximum grain size is smaller or larger than ~ 150 μm, the polarization fraction decreases. The asymmetry of the polarized intensity between the leading and the trailing sides of the vortex could be correlated with the difference of the trapping size ahead of the vortex (Zhu & Baruteau 2016; Baruteau & Zhu 2016). Also, temperature distribution could also reduce or enhance the polarization fraction by changing the radiation field. Note that the temperature at the northwest region may be higher than other areas (e.g., Casassus et al. 2015). For explaining the high fraction of polarization, unresolved substructure such as a narrower ring should be added, which enhances the anisotropies of the radiation field and thus increases the polarization fraction.

4.2.4. *Indication on Dust Coagulation and Dynamics*

In this Letter, we have shown that the millimeter-wave polarization is explained with grains with the maximum size of 150 μm because the polarization is effective when the maximum grain size is $\sim \lambda/2\pi$. The available size range to explain the observations is roughly $\sim 40-300$ μm if we assume the compact spherical grains (Kataoka et al. 2015). This relatively small grain size is not consistent with the previous understanding of the dust trapping that requires larger grains of millimeter or centimeter.

The questions regarding the understanding of the continuum emission were how to trap the dust grains both radially and azimuthally. For the effective trapping of dust grains both radially and azimuthally, the grains should be partly decoupled from the gas, which suggests the grain size to be around millimeter to centimeter (e.g., Pinilla et al. 2012; Birnstiel et al. 2013). This theoretical explanation is supported by the observations at millimeter and centimeter wavelengths. The observations of the protoplanetary disk around HD 142527 by ALMA and ATCA exhibit the low spectral index and the spectral index is lower at the center of the vortex, which suggests that the grain size is around millimeter to centimeter and larger grains are more efficiently trapped (Casassus et al. 2015).

Furthermore, if dust grains are radially trapped by a pressure enhancement by a planet, the polarization rings should be radially narrower. The grain size is changing in radial direction, and the polarization should be detected only where the maximum grain size is around 150 μm, which are two rings radially separated as surrounding the dust trap (Pohl et al. 2016). Therefore, we are now at the stage to reconsider the interpretation of the emission of dust grains.

One possible idea to solve the problem that the spectral index and the polarization indicate the different grain sizes is to include the fluffiness of dust aggregates. Dust grains coagulate to form fluffy dust aggregates with a filling factor of 10^{-4} (e.g., Kataoka et al. 2013), and

they can also explain the absorption opacity but with large scattering opacity (Kataoka et al. 2014). If the dust grains are fluffy, then the scattering efficiency is expected to be much higher than compact grains (Min et al. 2016; Tazaki et al. 2016), and therefore it could explain the emission from everywhere in the disk. In this way, the millimeter-wave polarization due to the self-scattering raises new insights into our understanding of the grain growth.

5. CONCLUSIONS

We have observed the circumstellar disk around HD 142527 with the full polarization mode of ALMA. We have detected the linear polarization of the continuum at the wavelengths of 0.87 mm. This observation is the first successful polarization detection of a not-embedded protoplanetary disk with ALMA. The polarized intensity displays a ring structure with a peak on the east side, which is different from the peak position of the continuum. The polarized intensity has a local minimum at the peak of the continuum. The polarization vectors are in the radial direction on the main ring, while those are in the azimuthal direction at the outer regions of the disk. This change of orientation of polarization vectors is predicted in the self-scattering of the thermal emission (Kataoka et al. 2015) though it is hard to explain from the grain alignment with the magnetic fields because the magnetic fields are not expected to be rotated by 90° in protoplanetary disks. Therefore, we conclude that the self-scattering plays an important role in millimeter-wave polarization in the protoplanetary disk around HD 142527. The self-scattered polarization leads us to a new direction of observational tests on the grain growth: we can obtain the information of the absorption opacity from the continuum and the scattering opacity from the polarization, which have never been modeled at the (sub)millimeter wavelength range.

We acknowledge the fruitful discussions with Laura Perez, Leonardo Testi, Marco Tazzari, Carlo Manara, Til Birnstiel, and Paola Pinilla. This work is supported by MEXT KAKENHI No. 23103004 and by JSPS KAKENHI Nos. 15K17606 and 26800106. This work makes use of the Astropy (Astropy Collaboration et al. 2013) and Matplotlib (Hunter 2007) software packages. This Letter makes use of the following ALMA data: ADS/JAO.ALMA#2015.1.00425.S. ALMA is a partnership of ESO (representing its member states), NSF (USA) and NINS (Japan), together with NRC (Canada), NSC and ASIAA (Taiwan), and KASI (Republic of Korea), in cooperation with the Republic of Chile. The Joint ALMA Observatory is operated by ESO, AUI/NRAO and NAOJ.

REFERENCES

Alves, F. O., Frau, P., Girart, J. M., et al. 2014, A&A, 569, L1
Astropy Collaboration, Robitaille, T. P., Tollerud, E. J., et al. 2013, A&A, 558, A33
Avenhaus, H., Quanz, S. P., Schmid, H. M., et al. 2014, ApJ, 781, 87
Baruteau, C., & Zhu, Z. 2016, MNRAS, 458, 3927
Birnstiel, T., Dullemond, C. P., & Pinilla, P. 2013, A&A, 550, L8
Brandenburg, A., Nordlund, A., Stein, R. F., & Torkelsson, U. 1995, ApJ, 446, 741
Casassus, S., van der Plas, G., M, S. P., et al. 2013, Nature, 493, 191
Casassus, S., Wright, C. M., Marino, S., et al. 2015, ApJ, 812, 126
Cho, J., & Lazarian, A. 2007, ApJ, 669, 1085
Davis, Jr., L., & Greenstein, J. L. 1951, ApJ, 114, 206
Fukagawa, M., Tamura, M., Itoh, Y., et al. 2006, ApJL, 636, L153
Fukagawa, M., Tsukagoshi, T., Momose, M., et al. 2013, PASJ, 65, L14
Girart, J. M., Beltrán, M. T., Zhang, Q., Rao, R., & Estalella, R. 2009, Science, 324, 1408
Girart, J. M., Rao, R., & Marrone, D. P. 2006, Science, 313, 812
Hughes, A. M., Hull, C. L. H., Wilner, D. J., & Plambeck, R. L. 2013, AJ, 145, 115
Hughes, A. M., Wilner, D. J., Cho, J., et al. 2009, ApJ, 704, 1204
Hull, C. L. H., Plambeck, R. L., Bolatto, A. D., et al. 2013, ApJ, 768, 159
Hull, C. L. H., Plambeck, R. L., Kwon, W., et al. 2014, ApJS, 213, 13
Hunter, J. D. 2007, Computing in Science and Engineering, 9, 90
Kataoka, A., Muto, T., Momose, M., Tsukagoshi, T., & Dullemond, C. P. 2016, ApJ, 820, 54
Kataoka, A., Okuzumi, S., Tanaka, H., & Nomura, H. 2014, A&A, 568, A42
Kataoka, A., Tanaka, H., Okuzumi, S., & Wada, K. 2013, A&A, 557, L4
Kataoka, A., Muto, T., Momose, M., et al. 2015, ApJ, 809, 78
Lazarian, A., & Hoang, T. 2007, MNRAS, 378, 910
Min, M., Rab, C., Woitke, P., Dominik, C., & Ménard, F. 2016, A&A, 585, A13
Muto, T., Tsukagoshi, T., Momose, M., et al. 2015, PASJ, 67, 122
Nagai, H., Nakanishi, K., Paladino, R., et al. 2016, ApJ, 824, 132
Pinilla, P., Birnstiel, T., Ricci, L., et al. 2012, A&A, 538, A114
Pohl, A., Kataoka, A., Pinilla, P., et al. 2016, A&A, 593, A12
Rao, R., Girart, J. M., Lai, S.-P., & Marrone, D. P. 2014, ApJL, 780, L6
Rao, R., Girart, J. M., Marrone, D. P., Lai, S.-P., & Schnee, S. 2009, ApJ, 707, 921
Segura-Cox, D. M., Looney, L. W., Stephens, I. W., et al. 2015, ApJL, 798, L2
Stephens, I. W., Looney, L. W., Kwon, W., et al. 2014, Nature, 514, 597
Stone, J. M., Hawley, J. F., Gammie, C. F., & Balbus, S. A. 1996, ApJ, 463, 656
Tamura, M., Hough, J. H., & Hayashi, S. S. 1995, ApJ, 448, 346
Tazaki, R., Tanaka, H., Okuzumi, S., Kataoka, A., & Nomura, H. 2016, ApJ, 823, 70

Vaillancourt, J. E. 2006, PASP, 118, 1340

Waelkens, C., Waters, L. B. F. M., de Graauw, M. S., et al. 1996, A&A, 315, L245

Yang, H., Li, Z.-Y., Looney, L., & Stephens, I. 2016, MNRAS, 456, 2794

Zhu, Z., & Baruteau, C. 2016, MNRAS, 458, 3918

Zhu, Z., & Stone, J. M. 2014, ApJ, 795, 53

The Astrophysical Journal, 831:90 (13pp), 2016 November 1 doi:10.3847/0004-637X/831/1/90

FORMATION OF THE UNEQUAL-MASS BINARY PROTOSTARS IN L1551NE BY ROTATIONALLY DRIVEN FRAGMENTATION

Jeremy Lim[1,2], Tomoyuki Hanawa[3], Paul K. H. Yeung[1], Shigehisa Takakuwa[4], Tomoaki Matsumoto[5], and Kazuya Saigo[6]
[1] Department of Physics, The University of Hong Kong, Pokfulam Road, Hong Kong
[2] Laboratory for Space Research, Faculty of Science, The University of Hong Kong, Pokfulam Road, Hong Kong
[3] Center for Frontier Science, Chiba University, Inage-ku, Chiba 263-8522, Japan
[4] Department of Physics and Astronomy, Graduate School of Science and Engineering, Kagoshima University, 1-21-35 Korimoto, Kagoshima, Kagoshima, 890-0065, Japan
[5] Faculty of Humanity and Environment, Hosei University, Chiyoda-ku, Tokyo 102-8160, Japan
[6] Department of Physical Science, Graduate School of Science, Osaka Prefecture University, 1-1 Gakuen-cho, Naka-ku, Sakai, Osaka 599-8531, Japan
Received 2016 June 28; revised 2016 August 10; accepted 2016 August 10; published 2016 October 28

ABSTRACT

We present observations at 7 mm that fully resolve the two circumstellar disks and a reanalysis of archival observations at 3.5 cm that resolve along their major axes the two ionized jets of the Class I binary protostellar system L1551NE. We show that the two circumstellar disks are better fit by a shallow inner and steep outer power law than a truncated power law. The two disks have very different transition radii between their inner and outer regions of ∼18.6 au and ∼8.9 au, respectively. Assuming that they are intrinsically circular and geometrically thin, we find that the two circumstellar disks are parallel with each other and orthogonal in projection to their respective ionized jets. Furthermore, the two disks are closely aligned if not parallel with their circumbinary disk. Over an interval of ∼10 yr, source B (possessing the circumsecondary disk) has moved northward with respect to and likely away from source A, indicating an orbital motion in the same direction as the rotational motion of their circumbinary disk. All the aforementioned elements therefore share the same axis for their angular momentum, indicating that L1551NE is a product of rotationally driven fragmentation of its parental core. Assuming a circular orbit, the relative disk sizes are compatible with theoretical predictions for tidal truncation by a binary system having a mass ratio of ∼0.2, in agreement with the reported relative separations of the two protostars from the center of their circumbinary disk. The transition radii of both disks, however, are a factor of $\gtrsim$1.5 smaller than their predicted tidally truncated radii.

Key words: binaries: close – binaries: visual – circumstellar matter – stars: formation – stars: jets – stars: protostars

1. INTRODUCTION

Fragmentation—the internal breakup of a core into two or more fragments—is the leading contender for how the majority of multiple stars form (e.g., review by Goodwin et al. 2007). Fission and capture, two other hypotheses considered for the formation of multiple-star systems, have been ruled out or are disfavored in large part based on theoretical considerations. Two different mechanisms have been proposed to drive fragmentation: (i) bulk (large-scale ordered) rotation, and (ii) local (small-scale) turbulence (for a succinct description of how these mechanisms lead to fragmentation, see Lim et al. 2016; see also Section 6.4). Depending on the circumstances involved, these two mechanisms can predict very different geometries and dynamics for the resulting binary system: i.e., alignment between the circumstellar disks and/or spin axes of the binary components, as well as alignment between their circumstellar disks and orbital plane or between their spin and orbital axes. Comparisons between binary properties and model predictions for their formation, however, are complicated by possible internal or external interactions during or after the protostellar phase. Depending on the nature of the interaction, the binary system can be driven either toward or away from alignment, altering its original geometry and dynamics, thus masking its formation process.

Recently, we showed that the geometrical and dynamical relationship between the binary (protostellar) system and its surrounding bulk envelope (remnant parental core) provide the crucial distinction between the two possible modes of fragmentation (Lim et al. 2016). In the Class I system L1551 IRS 5, we found that the circumstellar disks of the binary protostars are not just closely parallel with each other, but also closely parallel with their surrounding flattened envelope. Furthermore, the protostars are orbiting each other in the same direction as the rotation of their surrounding envelope. The close relationship between all these different elements indicates that their angular momenta share a common axis, and points to large-scale ordered rotation for driving the fragmentation of the L1551 IRS 5 parental core. Orbital solutions to measurements of the relative proper motion between the binary protostars, omitting solutions for which their circumstellar disks are predicted to be tidally truncated to sizes smaller than are observed, favor a circular or low-eccentricity orbit tilted by up to ∼25° from the circumstellar disks. If the fragments that gave rise to the binary protostars in L1551 IRS 5 were produced at different heights or on opposite sides of the midplane in the flattened central region of a rotating core, the resulting protostars would then exhibit circumstellar disks parallel with each other and their surrounding flattened envelope but tilted from the orbital plane, as is observed. Early during their formation, tidal interactions between the individual protostars and their surrounding, much more massive, flattened envelope would have naturally given rise to an essentially circular orbit, which has presumably been (largely) preserved during the subsequent evolution (growth) of the binary protostars.

Here, we present observations that spatially resolve for the first time the circumstellar disks of the binary protostars in the Class I system L1551NE. Lying in the close vicinity of L1551 IRS 5, L1551NE is surrounded by a circumbinary disk (Takakuwa et al. 2012, 2014), which itself is embedded in a

Table 1
Map Parameters

Year	Wavelength	Map Weighting	Synthesized Beam						rms Noise (μJy)
			Major Axis (mas)	(au)	Minor Axis (mas)	(au)	Position Angle (deg)		
1994.89	3.5 cm	Natural	246.8	34.6	207.0	29.0	96.36		30
2002.30	3.5 cm	Natural	356.1	49.9	269.0	37.7	52.10		8
2012.91	7 mm	Natural	55.4	7.8	52.5	7.4	−1.20		12
		Robust (0.5)	44.9	6.3	41.8	5.9	−6.5		15
		Robust (−0.25)	36.3	5.1	33.8	4.7	−12.7		20

flattened infalling envelope (Takakuwa et al. 2013). The circumbinary disk exhibits clear deviations from Keplerian motion that we successfully modeled as the action of gravitational torques from the central binary system (Takakuwa et al. 2014). These torques force material in opposing segments of the circumbinary disk to orbit faster and collide with material upstream that is orbiting more slowly, resulting in a two-armed spiral pattern (comprising material compressed to higher density) imprinted onto the circumbinary disk. At opposing segments between the two spiral arms, torques from the binary prototellar system force material to orbit more slowly, resulting in inflows through the circumbinary disk. Successfully reproducing the observed spatial-kinematic structure of the circumbinary disk, the model assumes a coplanar binary system having an orbital motion in the same sense as the rotation of the circumbinary disk. In addition, based on the projected separation of the two protostars from the inferred kinematic center of the circumbinary disk, the model adopts a binary mass ratio of 0.19. The results presented here confirm that L1551NE is indeed a coplanar binary system, indicate an orbital motion for the binary protostars in the same sense as the rotational motion of their circumbinary disk, and provide entirely independent evidence in support of the inferred mass ratio of the binary system.

This paper is organized as follows. Our observations and data reduction are described in Section 2. To study the relative proper motion of the binary protostars, we reduced previously published archival data on the ionized jets in L1551NE dating back nearly 20 yr before our observations, as described also in Section 2. The results from all these data are presented in Section 3. In Section 4, we describe how we determined the physical parameters of the individual circumstellar disks. In Section 5, we present the relative proper motion of the binary protostars. In Section 6, we assemble all the available evidence (including that in the published literature) to infer the manner in which L1551NE formed. In Section 7, we provide a thorough summary of our results, analyses, and interpretation. Throughout this paper, we assume a distance to L1551NE of 140 pc (Kenyon et al. 1994; Bertout et al. 1999).

2. OBSERVATIONS

During our observations of L1551 IRS 5 with the Jansky Very Large Array (VLA) on 2012 November 16, 28, and 29 as reported in Lim et al. (2016), we also observed L1551NE. The observations of L1551NE were interleaved with those of L1551 IRS 5; i.e., employing the scan sequence J0431+1731 (the secondary calibrator) → L1551 IRS 5 → J0431+1731 → L1551NE → J0431+1731 → L1551 IRS 5 → J0431+1731 → L1551NE, etc. The observations spanned a total duration of ∼2.5 hr on each day. To mitigate against rapid changes in absorption and refraction by the Earth's atmosphere, causing rapid fluctuations in the measured visibility amplitude and phase of the target source, we switched between L1551NE and the nearby quasar J0431+1731 every 20 s. As a check of the quality of the amplitude and phase corrections, we performed similar observations of a quasar lying close to L1551NE, J0431+2037, every ∼30 minutes. This quasar also was used to check the pointing accuracy of the antennas, a task performed every ∼1 hr. The bright quasar J0510+1800 served as the bandpass calibrator, and the quasar 3C 48 as the flux calibrator.

We edited, calibrated, and made maps from the data using the Common Astronomy Software Applications (CASA) package. Considerable effort went into weeding out radio frequency interference (RFI), which can be very weak and difficult to find, to ensure that the actual data used for making the maps are as free of contamination as is possible. The calibration was performed in the standard manner (e.g., examples in https://casaguides.nrao.edu/index.php/Karl_G._Jansky_VLA_Tutorials) as recommended by the observatory. Maps were made using three different weighting schemes, natural (i.e., equal weights on all visibilities), robust = 0.5, and robust = −0.25 (robust utilizes unequal weights designed to provide a more uniform sampling in *uv*-space), to accentuate different features of interest. The synthesized beams and rms noise fluctuations (σ) of the maps thus made are summarized in Table 1. Notice that the synthesized beams obtained using the different weighting schemes are close to circular, making it easier to visually interpret as well as to analyze the maps. All subsequent analyses of the images obtained were made using the Astronomical Image Processing System (AIPS) and GALFIT (Peng et al. 2002, 2010) software packages.

For studying the relative proper motion of the binary protostars, we reduced data taken by Rodríquez et al. (1995) on 1994 April 10 and 22 and by Reipurth et al. (2002) on 2000 November 26–29, using also the VLA but at a wavelength of 3.5 cm. We edited, calibrated, and made maps from the 1994 and 2000 observations (combining the data taken in each year) using AIPS. The synthesized beams and rms noise fluctuations (σ) of the maps, both made with natural weighting, are summarized in Table 1. In the observation of Rodríquez et al. (1995) in 1994, the telescope was pointed at L1551 IRS5. L1551NE is located at an angular distance of 2.′5 from L1551 IRS5, almost at the half-power point of the telescope primary beam (FWHM of 5.′3 at 3.5 cm) in that observation. The map made was therefore corrected for the primary beam response of the antennas. In the observation of Reipurth et al. (2002) in 2002, the telescope was pointed at L1551NE.

In all subsequent analyses, the quoted uncertainties in flux densities correspond to statistical uncertainties only and thus do not include any systematic uncertainties (which are difficult to quantify) that arise in transferring the flux density of the

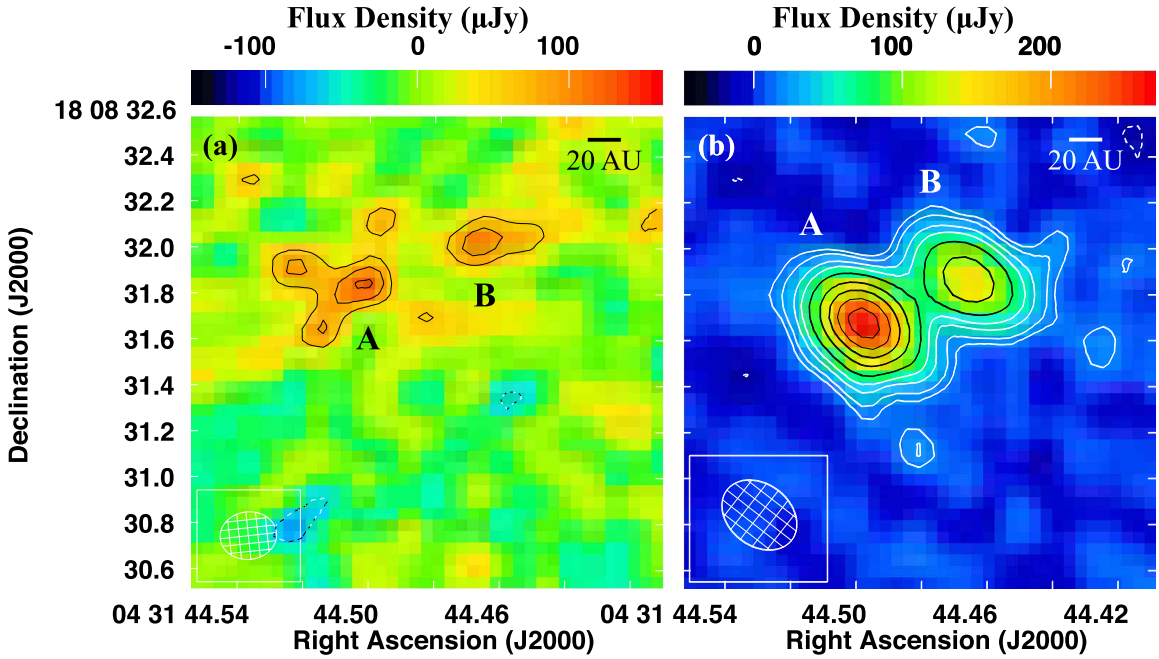

Figure 1. 3.5 cm images showing a pair of ionized jets from L1551NE in (a) 1994 and (b) 2002. The brighter source to the southeast is referred to as source A, and the dimmer source to the northwest as source B (Reipurth et al. 2002). Contour levels are plotted at −3, −2, 2, 3, and 5 × σ (where $\sigma = 30$ μJy beam^{-1}, the rms noise level) in panel (a) and −3, −2, 2, 3, 5, 7, 10, 15, 20, and 25 × σ ($\sigma = 8$ μJy beam^{-1}) in panel (b). The synthesized beam is indicated by the thatched ellipse at the lower left corner of each panel and has an FWHM of 264.8 mas × 207.0 mas (34.6 au × 29.0 au) and a position angle of 96.°36 in panel (a), and 356.1 mas × 269.0 mas (49.9 au × 37.7 au) and a position angle of 52.°1 in panel (b).

Table 2
Parameters of Ionized Jets

Year	Source	R.A. (J2000)	Decl. (J2000)	Flux Density (μJy)	Major Axis (mas)	Position Angle (deg)
1994.89	A	$04^h31^m44\overset{s}{.}4975 \pm 0.0038$	$+18°08'31\overset{''}{.}90 \pm 0.03$	269 ± 85	484^{+131}_{-138}	106^{+12}_{-14}
	B	$04^h31^m44\overset{s}{.}4625 \pm 0.0023$	$+18°08'32\overset{''}{.}10 \pm 0.02$	153 ± 54	252^{+97}_{-119}	108^{+40}_{-41}
2002.30	A	$04^h31^m44\overset{s}{.}49701 \pm 0.00048$	$+18°08'31\overset{''}{.}673 \pm 0.005$	348 ± 22	305^{+22}_{-20}	61^{+4}_{-3}
	B	$04^h31^m44\overset{s}{.}46643 \pm 0.00088$	$+18°08'31\overset{''}{.}864 \pm 0.009$	217 ± 23	359^{+34}_{-37}	69^{+4}_{-5}

Note. Flux densities listed are integrated quantities based on a two-dimensional Gaussian fit to each source.

primary calibrator to the secondary calibrator, and from the secondary calibrator to the target source.

3. RESULTS

3.1. Ionized Jets

Figure 1 shows images of L1551NE at 3.5 cm made from data taken by Rodríquez et al. (1995) in 1994 (Figure 1(a)) and Reipurth et al. (2002) in 2002 (Figure 1(b)). Two sources are detected in both maps: the stronger source, located to the southeast, was referred to by Reipurth et al. (2002) as source A, and the weaker source to the northwest as source B. We henceforth refer to these two sources in the same manner.

In Table 2, we list the parameters of the two sources based on a two-dimensional Gaussian fit to each source. In the 2002 map, which is far superior in sensitivity (a factor of nearly four lower noise) to the 1994 map, the results of the fits show that both sources are clearly resolved (at a significance level of 14σ for source A and 10σ for source B) along their major but not their minor axes. In this map, the major axes of both sources are aligned to within measurement uncertainties (difference of $8° \pm 6°$) along an average position angle of $65° \pm 3°$ (whereas the synthesized beam has a position angle for its major axis of 52.°1). We note that similar model fittings to the two sources in a robust-weighted map, which provides a higher angular resolution and hence in which the two sources are better separated, do not improve the precision of the fitting parameters. The position angle of the ionized jets as measured at 3.5 cm is identical to within the measurement uncertainties with the position angle of an [Fe II] jet detected by Reipurth et al. (2000) and Hayashi & Pyo (2009) originating from the vicinity of L1551NE, oriented along a position angle of 63° (Reipurth et al. 2000) or 64° (Hayashi & Pyo 2009). Herbig-Haro objects and a bipolar molecular outflow detected in CO, all driven by L1551NE, lie along approximately the same position angle as the [Fe II] jet (Moriarty-Schieven et al. 2000). Reipurth et al. (2000) found that the axis of the [Fe II] jet is offset from (lies to the south of) the apex of a cone-shaped nebula that is located just southwest of L1551NE. This nebula comprises scattered light from the nearer side of an outflow cavity evacuated by L1551NE. Based on the observed offset, Reipurth et al. (2000) attributed the [Fe II] jet to source A and associated the apex of the cone-shaped nebula with source B.

In the 1994 map, source A is formally resolved (at the 3.7σ confidence level) but not source B (only at the 2.6σ level). In this map, the major axis of source A is different by $45° \pm 15°$

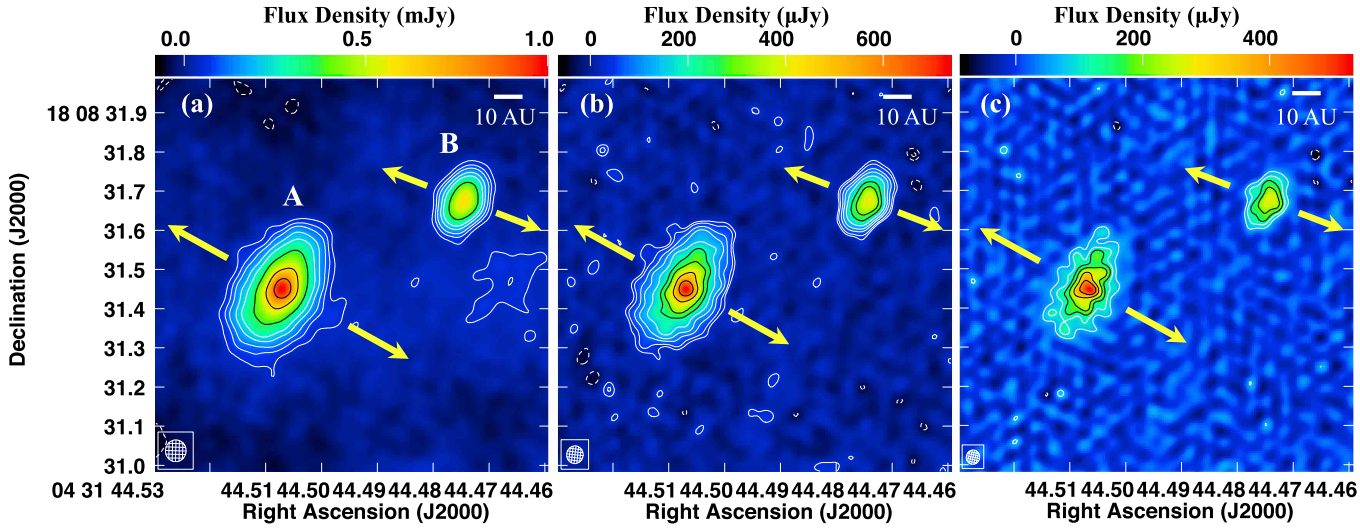

Figure 2. 7 mm images showing emission primarily from a pair of circumstellar dust disks in L1551NE made with (a) natural, (b) robust = 0.5, and (c) robust = −0.25 weighting of the data. Arrows indicate the position angles of ionized jets from sources A and B as derived by fitting a two-dimensional Gaussian to each source in Figure 1(b) (results listed in Table 2). Note the weak extension of source B along the direction of its ionized jet in all three panels. In panel (c), the central region of source A can be seen to be elongated along the direction of its ionized jet. Contour levels are plotted at −4, 4, 7, 10, 15, 20, 30, 50, 70, and 90 × σ (where $\sigma = 12$ μJy beam^{-1}, the rms noise level) in panel (a), −3, −2, 2, 3, 5, 7, 10, 20, and 25 × σ ($\sigma = 15$ μJy beam^{-1}) in panel (b), and −3, 3, 5, 7, 10, 15, and 20 × σ ($\sigma = 20$ μJy beam^{-1}) in panel (c). The synthesized beam in each weighting scheme is indicated by the thatched ellipse at the lower left corner of each panel and has an FWHM of 55.4 mas × 52.5 mas (7.8 au × 7.4 au) and a position angle of −1.20°36 in panel (a), 44.9 mas × 41.8 mas (6.3 au × 5.9 au) and a position angle of −6°.5 in panel (b), and 36.3 mas × 33.8 mas (5.1 au × 4.7 au) and a position angle of −12°.7 in panel (c).

from that of the same source in the 2002 map. Instead, in the 1994 map, the major axis of source A is aligned within measurement uncertainties to the major axis of the synthesized beam. Given that L1551NE was located close to the half-power point of the telescope primary beam in the 1994 observation and therefore subject to both bandwidth smearing and, perhaps even more detrimentally, telescope pointing errors, we place little weight on the measured source dimensions in this map.

3.2. Circumstellar Disks

Figure 2 show our images of L1551NE at 7 mm made with three different weightings, natural weighting that provides the lowest noise level but also the poorest angular resolution of 55.4 mas × 52.5 mas or 7.8 au × 7.4 au (Figure 2(a)), robust = 0.5 weighting that only slightly increases the noise level but significantly improves the angular resolution to 44.9 mas × 41.8 mas or 6.3 au × 5.9 au (Figure 2(b)), and robust = −0.25 weighting that provides close to the highest angular resolution possible with our data of 36.3 mas × 33.8 mas or 5.1 au × 4.7 au at the expense of a significantly higher noise level (Figure 2(c)). A simple visual inspection reveals that both sources A and B are clearly resolved along their major and minor axes. Source A is much larger and also has a higher peak and integrated flux density than source B. Both sources are elongated in a direction perpendicular to their ionized jets (indicated by arrows in Figure 2) as traced at 3.5 cm (Figure 1(b)), and so their emission must originate primarily from dust in their circumstellar disks. Emission from dust at larger spatial scales, namely, that in the circumbinary disk as imaged at 0.85 mm with Submillimeter Array (SMA; Takakuwa et al. 2012) and in follow-up observations also at 0.85 mm with the Atacama Large Millimeter and Submillimeter Array (ALMA; Takakuwa et al. 2014), as well as dust in the envelope around the circumbinary disk as imaged at 0.85 mm with the SMA (Takakuwa et al. 2013), is entirely resolved out in our observation (which has a much higher angular resolution and lacks relatively short baselines, compared with the ALMA and SMA observations).

In all the maps shown in Figure 2, source B exhibits an appreciable elongation along the northeast to southwest direction that extends beyond, and is perpendicular to the major axis of, its main body. This elongation is aligned with its ionized jet, so that, at 7 mm, the emission of source B along its minor axis must include a weak contribution from free–free emission associated with its ionized jet. This situation is similar to that found for both components of L1551 IRS5 at 7 mm, where the emission from each source is contributed by both ionized gas and dust (Lim & Takakuwa 2006; Lim et al. 2016). In the highest angular resolution map at 7 mm shown in Figure 2(c), the central peak in source A can be seen to be elongated in a direction perpendicular to its main body and aligned instead with its ionized jet. Thus, at 7 mm, the emission from the central region of source A must also include a contribution from free–free emission associated with its ionized jet.

4. PHYSICAL PARAMETERS OF CIRCUMSTELLAR DISKS

Because, in the images at 7 mm, the emission from both sources includes a weak contribution from their ionized jets, we first tried to remove the jets before fitting models to the disks. Using the task IMFIT in AIPS, we started by attempting to fit a two-component (one to represent the jet and the other the disk), two-dimensional, Gaussian function to sources A and B individually in the naturally weighted map (which provides the highest signal-to-noise ratio and hence traces the circumstellar disks farthest out). All such attempts either failed to converge or provided nonphysical results (e.g., negative intensities for one of the components) for both sources. This failure is in sharp contrast to our success using the same strategy for L1551 IRS 5, where a two-component, two-dimensional, Gaussian function provided a satisfactory fit to

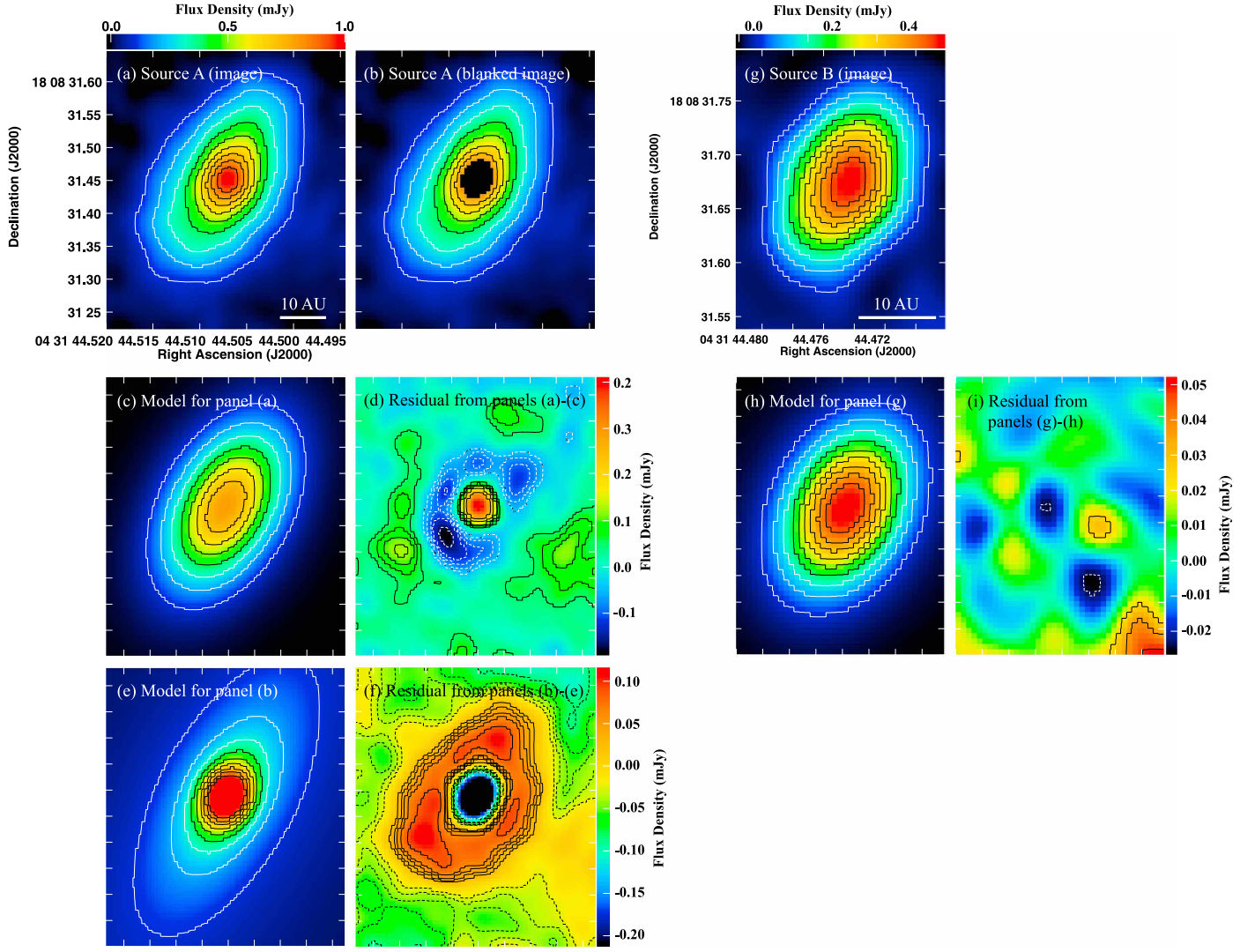

Figure 3. Two-dimensional Gaussian fits to the naturally weighted 7 mm images of (a) source A, (b) source A with its central region having a size of approximately the FWHM of the synthesized beam blanked out, and (g) source B. Panel (c) is the model fit to the unblanked image of source A in panel (a), and panel (d) the residuals (image − model). Panel (e) is the model fit to the centrally blanked image of source A in panel (b), and panel (f) the residuals. Panel (h) is the model fit to source B in panel (g), and panel (i) the residuals. Colors and contours in panels (c) and (e) are the same as in panels (a)–(b), where the contour levels are plotted at 10%, 20%, ..., and 90% of the peak intensity of source A, permitting a direct comparison between the model fits and the image of this source. Similarly, colors and contours in panels (h) are the same as in panel (g), where the contour levels are plotted at 10%, 20%, ..., and 90% of the peak intensity of source B, permitting a direct comparison between the model fit and the image of this source. Contour levels in residual maps plotted at −10, −7, −5, −4, −3, −2, 2, 3, 5, 7, and 10 × σ (where $\sigma = 12$ μJy beam^{-1}, the rms noise level). Unlike the less well resolved image of source B, the much better resolved image of source A cannot be satisfactorily fit by a two-dimensional Gaussian function.

each of the two sources in this system at 7 mm (Lim et al. 2016). Below, we explain why such a model fails to fit the image of either source in L1551NE.

GALFIT, unlike IMFIT (in AIPS), does not try to fit for the (spatially unresolved) central region of a source within an area spanned by the FWHM of the synthesized beam. This feature is convenient for our purpose so as to mitigate the contribution from the ionized jet emanating from the center of each source. (The model fitted by GALFIT therefore makes no statement about the radial intensity profile within a central area spanned by the FWHM of the synthesized beam.) We therefore started by fitting a 2D Gaussian function (i.e., one component only, corresponding to the circumstellar disk) to source A in the naturally weighted map. Figure 3(c) shows the resulting best-fit model (reduced-$\chi^2 = 6.50$). This model can be directly compared with the image of source A shown in Figure 3(a), where the contour levels are plotted at the same levels in flux density (from 10% to 90%, in steps of 10%, of the peak intensity of source A) and the colors span the same range in flux density (from the minimum to the maximum of the image shown in Figure 3(a)). Figure 3(d) shows the residuals (image − model) from the fit. The most prominent feature in the residual map is a strong central positive peak, encircled by a conspicuous negative ring and a fainter outer positive ring, indicating that a Gaussian function provides a poor fit to the circumstellar disk. As a check, we blanked different-sized areas at the center of source A and fitted a 2D Gaussian function to the remaining emission. Figure 3(b) shows an example where the central region of source A having a size of approximately the FWHM of the synthesized beam has been blanked out. The model fit of a 2D Gaussian function (reduced-$\chi^2 = 21.39$) is shown in Figure 3(e), and the residuals in Figure 3(f). The

residual map shows a negative ring around the central blanked area and a surrounding positive ring; the same pattern is seen no matter the size of the central area blanked out up to about twice the FWHM of the synthesized beam, the largest that we tried. Thus, the reason why a two-component, two-dimensional, Gaussian function fails to provide a satisfactory fit to source A is because its circumstellar disk simply does not have a Gaussian radial intensity profile.

Source B is, visually, much smaller and spanned by fewer resolution elements than source A. Unlike source A, source B can be satisfactorily fit (reduced-$\chi^2 = 1.15$) by a two-dimensional Gaussian function (corresponding to its circumstellar disk) as shown in Figure 3(h). The fitted Gaussian model can be directly compared with the image of source B shown in Figure 3(g), where the contour levels are plotted at the same levels in flux density (from 10% to 90%, in steps of 10%, of the peak intensity of source B) and the colors span the same range in flux density (from the minimum to the maximum of the image shown in Figure 3(g)). The residuals are shown in Figure 3(i), all of which are below 3σ within the detectable body of source B. Thus, the failure to fit a two-component, two-dimensional, Gaussian function to source B is because its jet is simply too weak to provide meaningful constraints.

The two-dimensional Gaussian function fitted to source B has an FWHM along its major axis of 0.″99, roughly comparable to the values found by fitting two-dimensional Gaussian functions to the two circumstellar disks in L1551 IRS5 of 0.″122 and 0.″092 (see Table 2 of Lim et al. 2016). The maps used for these fits have a similar FWHM for their synthesized beams of about 0.″055. On the other hand, the circumstellar disk of source A, which, as we show below, is over twice as large as that of source B, cannot be fit by a two-dimensional Gaussian function. Our ability to satisfactorily fit a two-dimensional Gaussian function to the circumstellar disk of source B, as well as to each of the two circumstellar disks in L1551 IRS5, is likely because their radial intensity profiles are dominated by their synthesized beams (which are Gaussian function) and not because these disks actually have Gaussian radial intensity profiles.

Physically motivated models (see brief review in Lim et al. 2016) such as power-law profiles, designed to mimic power-law surface density and temperature profiles, having an inner as well as an outer truncation radius or taper are usually fitted to images of circumstellar disks. Unlike optically revealed objects for which the spectral energy distributions in the near- to mid-infrared provide constraints on a central cavity in their circumstellar disks, no such constraints are possible for protostars. Conveniently, GALFIT does not attempt to fit for the centrally unresolved region where a cavity might be present. We started by fitting a two-dimensional power law, with no outer truncation, to sources A and B. Figure 4(c) shows the best fit of such a model (reduced-$\chi^2 = 25.16$) to the unblanked image of source A shown in Figures 4(a) and 4(d) shows the residuals. Figure 4(e) shows the corresponding model fit (reduced-$\chi^2 = 21.39$) and Figure 4(f) the residuals for the centrally blanked image of source A shown in Figure 4(b). In both cases, the residual map shows a negative central circular region or negative ring around the central blanked area and a surrounding positive ring, indicating that an untruncated two-dimensional power law provides a poor fit to the circumstellar disk of source A. The same is true for source B, where Figure 4(j) shows the fitted model (reduced-$\chi^2 = 10.97$) and Figure 4(k) the residuals. The residual map also shows a negative central circular region and a surrounding positive ring, just like the residual map of source A shown in Figure 4(d).

Given that circumstellar disks in binary systems are predicted to be truncated by tidal interactions with their neighboring companions, we then tried fitting a two-dimensional power law that is truncated at an outer radius. Figure 4(g) shows the model fit and Figure 4(h) the residuals for the unblanked image of source A (Figure 4(a)). The fit is much improved (reduced-$\chi^2 = 3.58$, versus a reduced-$\chi^2 = 6.50$ for a two-dimensional Gaussian and a reduced-$\chi^2 = 25.16$ for a two-dimensional power law with no outer truncation) as reflected by the relatively weak residuals, although a faint negative ring is visible, indicating a systematic deviation between the fitted model and the image. Figure 4(l) shows the corresponding model fit and Figure 4(m) the residuals for the unblanked image of source B (Figure 4(i)). Once again, the fit is much improved (reduced-$\chi^2 = 1.16$) over an untruncated two-dimensional power law (reduced-$\chi^2 = 10.97$), although in the case of source B providing no better a fit than a two-dimensional Gaussian function (reduced-$\chi^2 = 1.15$).

In L1551 IRS5, a NUKER function, comprising a relatively shallow inner power law and a very steep outer power law (i.e., a tapered rather than a truncated profile), was fitted to the two circumstellar disks (Lim et al. 2016). This function provides a smooth transition between the inner and outer power laws, a feature that was deemed to be more physical than a discontinuous transition. The NUKER function is parameterized as

$$I(r) = I_b\, 2^{\frac{\beta-\gamma}{\alpha}} \left(\frac{r}{r_b}\right)^{-\gamma} \left[1 + \left(\frac{r}{r_b}\right)^{\alpha}\right]^{\frac{\gamma-\beta}{\alpha}}, \quad (1)$$

where $I(r)$ is the intensity, I, as a function of radius, r, γ is the inner power-law slope, β is the outer power-law slope, α controls the sharpness of the transition between the two power laws (larger α indicating a sharper transition), r_b is the break radius at which the slope is the average of β and γ or, equivalently, the radius of maximum curvature in logarithmic units, and I_b is the intensity at r_b. Just like for the two circumstellar disks in L1551 IRS5, we found the central position, inclination (as determined from the ratio in dimensions of the minor to major axes), and position angle of the major axis of sources A and B to be essentially constant independent of α. As α increases (i.e., the transition between the inner and outer power law becomes sharper), the break radius r_b decreases somewhat and very rapidly converges. Likewise, both γ (the inner power-law index) and β (the outer power-law index) also rapidly converge with increasing α, such that $\beta \gg \gamma$ irrespective of α.

Fixing therefore the central location, inclination, and position angle of each source, we list in Table 3 the other parameters of the best-fit NUKER function at the largest value of α for which a solution is obtainable. In this way, we obtained a break radius of $r_b \sim 133$ mas (~18.6 au) for source A. Figure 5(c) shows the model fit to the unblanked image of source A (Figure 5(a)), and Figure 5(d) shows the residuals. This fit (reduced-$\chi^2 = 2.25$) is, by far, the best among all those considered (versus a reduced-$\chi^2 = 6.50$ for a two-dimensional Gaussian, a reduced-$\chi^2 = 25.16$ for a two-dimensional power law with no outer truncation, and a reduced-$\chi^2 = 3.58$ for a

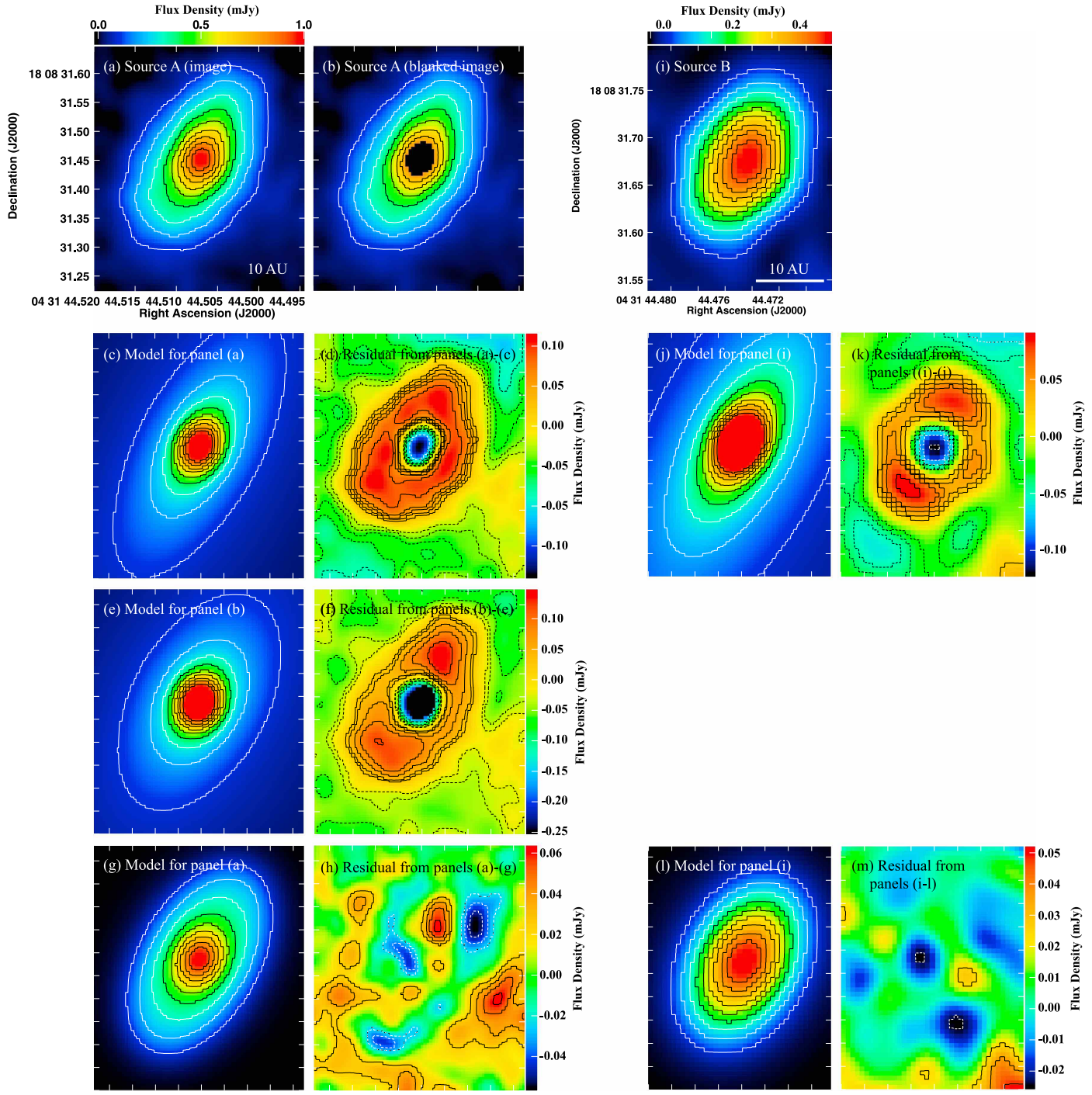

Figure 4. Same as in Figure 3, but now for two-dimensional power-law fits. Panel (c) is the model fit of a continuous power law to the unblanked image of source A in panel (a), and panel (d) the residuals (image-model). Panel (e) is the model fit of a continuous power law to the centrally blanked image of source A in panel (b), and panel (f) the residuals. Panel (g) is the model fit of a power law that is truncated at an outer radius to the unblanked image of source A, and panel (h) the residuals. Panel (j) is the model fit of a continuous power law to source B in panel (i), and panel (k) the residuals. Panel (l) is the model fit of a power law that is truncated at an outer radius to source B, and panel (m) the residuals. Colors and contours in panels (c), (e), and (g) are the same as in panels (a)–(b), where the contour levels are plotted at 10%, 20%, ..., and 90% of the peak intensity of source A, permitting a direct comparison between the model fits and the image of this source. Similarly, colors and contours in panels (j) and (l) are the same as in panel (i), where the contour levels are plotted at 10%, 20%, ..., and 90% of the peak intensity of source B, permitting a direct comparison between the model fit and the image of this source. Contour levels in residual maps plotted at -10, -7, -5, -4, -3, -2, 2, 3, 5, 7, and $10 \times \sigma$ (where $\sigma = 12$ μJy beam^{-1}, the rms noise level). Both sources are poorly fit by a continous power law, but quite well fit by a power law that is truncated at an outer radius.

two-dimensional power law truncated at an outer radius). Importantly, there are no clearly apparent systematic residuals indicating a systematic deviation between the fitted model and the image; nonetheless, there are low-level residuals in the outer regions that limit the goodness of the fit. Fitting a NUKER function to the image of source A where its central region is blanked out (Figure 5(b)), we obtained an essentially identical model fit (reduced-$\chi^2 = 2.24$) as shown in Figure 5(e)

Table 3
Parameters of Circumstellar Disks

Source	Inclination (deg)	Position Angle Major Axis (deg)	α	γ	β	r_b (mas)	r_b (au)
A	57.7	150.9	40.0	0.79	4.3	133.0	18.6
B	58.0	152.1	32.5	0.45	5.4	63.5	8.9

Note. NUKER fits to the naturally weighted images of sources A and B (Figure 2(a)) based on the largest value of α for which a solution is obtainable.

and residual map as shown in Figure 5(f). The position angle of the major axis thus derived for the circumstellar disk of source A is ~150.°9, accurately orthogonal in projection to the position angle inferred for the axis of its ionized jet of $61^{\circ}_{-3}^{+4}$. The corresponding model fit for source B (reduced-$\chi^2 = 1.07$) is shown in Figure 5(h) and the residual map in Figure 5(i). As for source A, this model provides a superior fit (lower reduced-χ^2) to source B than a two-dimensional Gaussian (reduced-$\chi^2 = 1.15$), a power law with no outer truncation (reduced-$\chi^2 = 10.97$), or a power law truncated at an outer radius (reduced-$\chi^2 = 1.16$). The position angle of the major axis thus derived for the circumstellar disk of source B is ~152.°1, closely orthogonal in projection to the position angle inferred for the axis of its ionized jet of $69^{\circ}_{-5}^{+4}$. Assuming both circumstellar disks to be circular and geometrically thin, the inclination derived for the circumstellar disk of source A is ~57.°7 and that of source B is ~58.°0. Their similar inclinations and position angles for their major axes imply that the two circumstellar disks are (closely) parallel.

GALFIT does not provide uncertainties for the model fitting parameters. As a measure of the uncertainties in the inclination and position angle for the circumstellar disk of source B, we also used IMFIT (which provides uncertainties in the model parameters) to fit a two-dimensional Gaussian function to this source. In this manner, we derived an inclination of 56.°3 ± 3.°8 deg (GALFIT reports 58.°2 for a two-dimensional Gaussian fit and 58.°0 for a NUKER fit) and a position angle of 154.°5 ± 4.°6 (GALFIT reports 152.°2 for a two-dimensional Gaussian fit and 152.°1 for a NUKER fit) for source B. With a position angle of $69^{\circ}_{-5}^{+4}$ for its ionized jet (Table 2), the circumstellar disk of source B is, within the uncertainties, orthogonal (85.°5 ± 6.°8) in projection to its ionized jet. As mentioned earlier, source A cannot be fit by a two-dimensional Gaussian function, and so we cannot provide corresponding uncertainties for the inclination and position angle for its circumstellar disk using this method. Nevertheless, based on the exercise conducted for source B, the uncertainties in the inclination and position angle of the major axis derived from fitting a NUKER function to source A are probably no larger than a few degrees.

5. ORBITAL MOTION

The 1994 observation of Rodríquez et al. (1995) was the first to show that L1551NE comprises two sources, as was subsequently confirmed in the 2002 observation of Reipurth et al. (2002). To date, only these and our observation in 2012 provide useful measurements of the relative proper motion of the binary protostars. Table 4 lists the positions (repeated, for convenience, from Table 2 for the 1994 and 2002 observations), relative separations, and relative orientations of the binary protostars on the aforementioned dates. The position for source B is derived from a two-dimensional Gaussian fit (using IMFIT) to the natural-weighted map of this source (as mentioned earlier, IMFIT reports uncertainties in the fitting parameters, unlike GALFIT) in Figure 2(a). The position of source A is derived from a two-dimensional Gaussian fit (also using IMFIT) to the ionized jet in the central region of this source in the robust = −0.25 image of Figure 2(c); the fitted Gaussian model shares a similar position angle ($67^{\circ}_{-4^{\circ}}^{+5^{\circ}}$) to that derived for the ionized jet at 3.5 cm ($61^{\circ}_{-3^{\circ}}^{+4^{\circ}}$), but is resolved also along the minor axes, suggesting a contribution from the circumstellar disk to the fit. Note that different secondary calibrators were used in the three observations of L1551NE, and so the positions listed in Table 4 are referenced with respect to a different position in the sky in each observation. The information listed in Table 4 should therefore be used with caution (i.e., the uncertainty in the position of the secondary calibrator needs to be included) for deriving the absolute proper motion of L1551NE (motion of the entire system across the sky).

Figure 6 shows the angular separation and orientation of source B with respect to source A over an interval spanning ~18.6 yr. As can be seen, there is no significant motion (i.e., difference in positions of $\geqslant 3\sigma$) of these two sources along the east–west direction, with their positions differing by 22.9 mas ± 14.6 mas in right ascension between 2002 and 2012. On the other hand, between 2002 and 2012, source B has moved northward with respect to source A by 33.6 mas ± 11.0 mas (a significance level of 3.1σ). Furthermore, source B is likely moving away (at a significance level of 2.5σ) from source A. The uncertainties in the measured source positions in 1994 are too large to detect any corresponding motion in source B between this and the later observations.

6. DISCUSSION

The circumstellar disks of the binary protostars in L1551NE are parallel to each other within measurement uncertainties of a few degrees. The close alignment between the circumstellar disks of binary protostars, however, does not by itself discriminate between different models for the formation of these systems. Even in those systems where the binary protostars are born with misaligned circumstellar disks, tidal interactions between the protostars can align their circumstellar disks with the orbital plane (Bate 2000; Lubow & Ogilvie 2000). In such situations, tidal interactions induce disk precession; viscosity in the disks acts on the shearing motion to dissipate energy, gradually aligning the disks with the orbital plane. Bate (2000) finds that such dissipative processes can align protostellar disks and their orbital plane on timescales of order 20 orbital periods, which for binary systems with a total mass of ~1 $M_{\odot}$ and an orbital separation of ~100 au correspond to an interval of just $\sim 10^4$ yr. Instead, as pointed out by Lim et al. (2016) and demonstrated for the binary protostellar system L1551 IRS5, the geometrical and dynamical relationships between the binary system and its surrounding bulk envelope provide the crucial distinction between different fragmentation models.

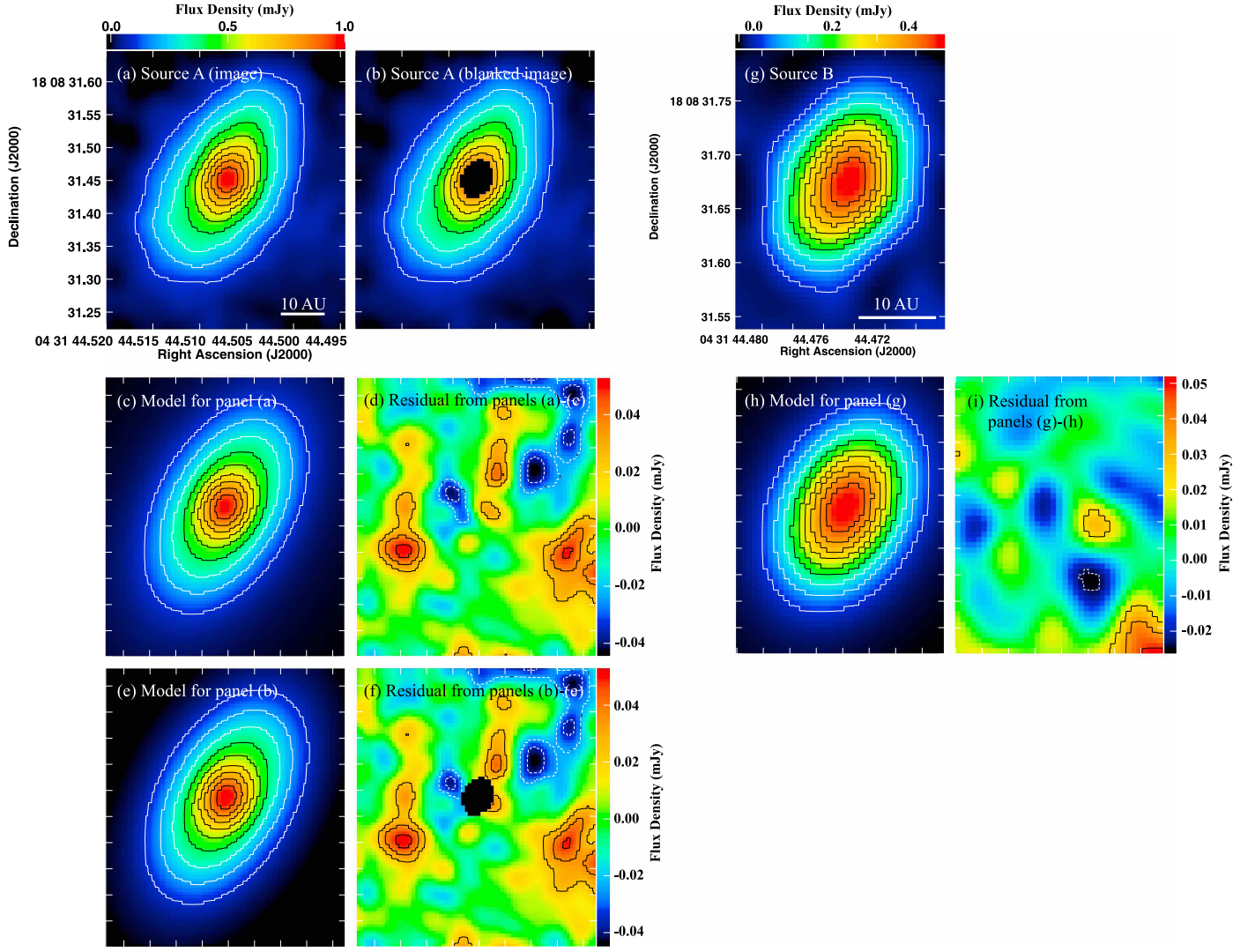

Figure 5. Same as in Figures 3 and 4, but now for two-dimensional NUKER (double power law with a smooth transition) fits. Panel (c) is the model fit to the unblanked image of source A in panel (a), and panel (d) the residuals (image – model). Panel (e) is the model fit to the centrally blanked image of source A in panel (b), and panel (f) the residuals. Panel (h) is the model fit to source B in panel (g), and panel (i) the residuals. Colors and contours in panels (c) and (e) are the same as in panels (a)–(b), where the contour levels are plotted at 10%, 20%, ..., and 90% of the peak intensity of source A, permitting a direct comparison between the model fits and the image of this source. Similarly, colors and contours in panels (h) are the same as in panel (g), where the contour levels are plotted at 10%, 20%, ..., and 90% of the peak intensity of source B, permitting a direct comparison between the model fit and the image of this source. Contour levels in residual maps plotted at −10, −7, −5, −4, −3, −2, 2, 3, 5, 7, and 10 $\times\ \sigma$ (where $\sigma = 12\ \mu$Jy beam^{-1}, the rms noise level). NUKER functions provide obviously better or statistically superior fits to both sources than either two-dimensional Gaussian (Figure 3) or single power-law (Figure 4) fits.

6.1. Relationship with Circumbinary Disk

Takakuwa et al. (2012) inferred the bulk properties of the circumbinary disk in L1551NE by fitting a circular and geometrically thin disk exhibiting Keplerian motion to channel maps in $C^{18}O$(3–2) as measured with the SMA. This simple model reproduces the global velocity behavior of the circumbinary disk and provides best-fit parameters of $62°^{+25°}_{-17°}$ for its inclination and $167°^{+23°}_{-27°}$ for the position angle of its major axis.

In observations at a higher angular resolution and sensitivity with the ALMA, Takakuwa et al. (2014) found clear deviations from Keplerian rotation in the circumbinary disk as measured also in $C^{18}O$(3–2). They were able to reproduce these deviations by including gravitational torques from the binary protostars, assumed to have a circular coplanar orbit, but otherwise retained the geometry inferred by Takakuwa et al. (2012) for the circumbinary disk. Based on the angular separation of the two sources from the inferred dynamic center of the circumbinary disk, they found a binary mass ratio of $m_B/m_A = 0.19$, where m_A is the mass of the protostar corresponding to source A and m_B that corresponding to source B. From the measured orientation of sources A and B and the assumed circular coplanar orbit, Takakuwa et al. (2014) inferred an orbital separation of ∼145 au for the binary system.

The inclination and position angle for the major axis of the circumbinary disk in the model proposed by Takakuwa et al. (2012) agree, to within their measurement uncertainties, with the corresponding values we derived for the circumstellar disks (Table 3). Although the uncertainties in these parameters for the circumbinary disk are much larger than the uncertainties in the corresponding parameters for the circumstellar disks, we note that their formal values agree to within ∼5° in inclination and ∼15° in position angle. Thus, the circumstellar disks are

Table 4
Relative Proper Motion

Year	Source	R.A. (J2000)	Decl. (J2000)	Δ(R.A.) (mas)	Δ(Decl.) (mas)	Separation (mas)	Position Angle (mas)
1994.89	A	$04^h31^m44\overset{s}{.}4975\pm0.0038$	$+18°08'31\overset{''}{.}90\pm0\overset{''}{.}03$				
	B	$04^h31^m44\overset{s}{.}4625\pm0.0023$	$+18°08'32\overset{''}{.}10\pm0\overset{''}{.}02$	-500.1 ± 62.9	200.0 ± 35.3	538.6 ± 59.9	291.8 ± 4.3
2002.30	A	$04^h31^m44\overset{s}{.}49701\pm0.00048$	$+18°08'31\overset{''}{.}673\pm0\overset{''}{.}005$				
	B	$04^h31^m44\overset{s}{.}46643\pm0.00088$	$+18°08'31\overset{''}{.}864\pm0\overset{''}{.}009$	-435.9 ± 14.4	191.1 ± 10.8	475.9 ± 13.9	293.7 ± 1.4
2012.91	A	$04^h31^m44\overset{s}{.}506729\pm0.000053$	$+18°08'31\overset{''}{.}4497\pm0\overset{''}{.}0010$				
	B	$04^h31^m44\overset{s}{.}474554\pm0.000160$	$+18°08'31\overset{''}{.}6744\pm0\overset{''}{.}0015$	-458.8 ± 2.4	224.7 ± 1.9	510.9 ± 2.3	296.1 ± 0.2

not only parallel with each other, but also closely (if not accurately) parallel with their surrounding circumbinary disk.

Assuming that the equatorial plane of the circumbinary disk is orthogonal to the outflow cavity so that its eastern side is the near side, Takakuwa et al. (2012, 2014) find that the circumbinary disk is rotating in an anticlockwise direction. For a coplanar binary system with a circular anticlockwise orbit, at their present orbital locations source B should be moving primarily northward and somewhat eastward with respect to source A, increasing in angular separation (see Figure 10 of Takakuwa et al. 2014). The northward motion and likely increasing separation that we measure for source B with respect to source A, but smaller (no detectable) motion along the east–west direction (Section 5), are therefore consistent with an orbital motion for the binary protostars in the same manner as the rotational motion of their surrounding circumbinary disk.

6.2. Binary Mass Ratio

If the binary protostars in L1551NE have a mass ratio of ∼0.19 and are in a circular orbit separated by ∼145 au as in the model described by Takakuwa et al. (2014), the circumstellar disk of source A is predicted to be tidally truncated at a radius of ∼58.4 au and that of source B at a radius of ∼23.5 au (derived from the calculations provided in Pichardo et al. 2005). By comparison, the inferred break radius (r_b) is ∼18.6 au for the circumstellar disk of source A and ∼8.9 au for the circumstellar disk of source B (Table 3), both a factor of ∼3 smaller than their predicted tidally truncated radii. Equating their break radii with their tidally truncated radii, then for a circular orbit, the predicted binary mass ratio is ∼0.23 and the orbital separation is ∼47 au. The binary mass ratio (which, for a given orbital eccentricity, solely determines the tidally truncated sizes of their constituent circumstellar disks) thus inferred is closely comparable to that inferred by Takakuwa et al. (2014) of ∼0.19. In this case, however, the predicted orbital separation is much smaller than the observed angular separation between the binary components in L1551NE of 71.5 ± 0.4 au. Thus, the binary components of this system cannot simultaneously have a circular orbit and break radii for their circumstellar disks corresponding to their tidally truncated radii.

In L1551 IRS5, the relative proper motions of the binary protostars have been measured with sufficient precision to make an exploration of orbital solutions meaningful (Lim et al. 2016). For circular orbits with orbital separations of up to ∼100 au, the (roughly comparable) break radii of the two circumstellar disks in this system can be closely comparable (somewhat smaller than) or at worse within a factor of ∼2 of their predicted tidally truncated radii. Thus, either the circumstellar disks of the binary protostars in both L1551 IRS5 and L1551NE do not extend to their tidally truncated radii, or observations at 7 mm do not trace the overall extents of these disks. Observations at shorter wavelengths, where the dust emissivity is larger and hence the dust emission stronger, may better define the overall extents of these circumstellar dust disks. Furthermore, such observations can reveal any dependence in disk sizes with wavelength, as has been found for the Class 0 source Per-emb-14 (also known as NGC 1333 IRAS 4C) and the pre-main-sequence (classical T Tauri) star AS 209. The circumstellar disk of Per-emb-14 is much smaller (by a factor of about three) at 8 mm (Segura-Cox et al. 2016) than at 1.3 mm (Tobin et al. 2015). Similarly, for AS 209, the measured size of its circumstellar disk decreases toward longer wavelengths, a behavior attributed to the radial drift of dust grains (Pérez et al. 2012). Alternatively, the orbit of both L1551 IRS5 and L1551NE may be highly eccentric, although Lim & Takakuwa (2006) found that even a moderate orbital eccentricity is highly unlikely in the case of L1551 IRS5.

6.3. Collimated Outflows

As mentioned in Section 3.1, Reipurth et al. (2000) argue that the apex of a cone-shaped reflection nebula—comprising an outflow cavity—associated with L1551NE is coincident with source B, and that the [Fe II] jet detected from L1551NE originates from source A. To be detectable in [Fe II], the jet from source A must have a higher density than that of source B at the same distance from their respective protostars (we rule out a much lower excitation for the jet from source B given that it, like the jet from source A, contains an ionized component detected in free–free emission at 3.5 cm). Thus, source A must have either a more powerful or a more highly collimated jet, or both (possibly related, perhaps indirectly, to the higher mass of this protostar and its larger circumstellar disk), than source B. A more highly collimated jet provides a natural explanation for why the refection nebula has its axis passing through source B rather than source A; i.e., the walls of the outflow cavity are carved out by the poorly collimated jet from source B. A more highly collimated jet also produces stronger free–free emission than a more poorly collimated jet for the same mass-loss rate (Reyholds 1986), adding to the reasons why the ionized jet from source A is brighter than that from source B.

Other scenarios cannot be ruled out, but are not supported by the available evidence or contrived. For example, perhaps source B grew more quickly in mass (i.e., it experienced a higher accretion rate) and drove a stronger outflow than source A, thus dominating the creation of the observed outflow cavity. In that case, source B ought to be more massive than source A, in contradiction with the evidence presented above. Alternatively, the jet from source A only turned on recently, and we

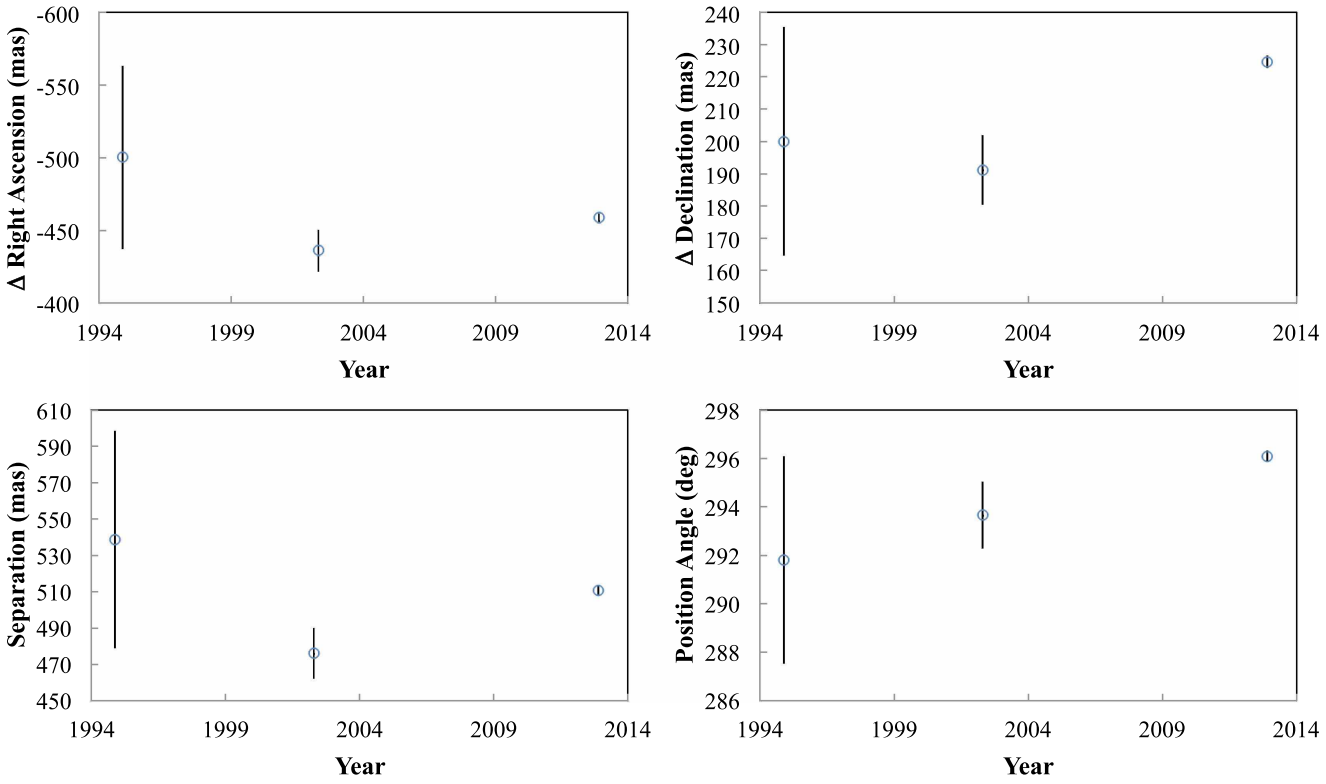

Figure 6. Angular separation and orientation of source B with respect to source A during the three observations reported in the text.

are fortunate to be observing L1551NE soon after this event, an unlikely situation.

6.4. Rotationally Driven Fragmentation of L1551NE Parental Core

Current models invoke either local (small-scale) turbulence in or the bulk (globally ordered) rotation of cores to drive fragmentation. In cores that have little or no bulk rotation, turbulence introduces velocity and density inhomogeneities that can seed and drive the growth of multiple density perturbations to become self-gravitating (e.g., Bate et al. 2002, 2003; Delgado-Donate et al. 2004a, 2004b; Goodwin et al. 2004a, 2004b, 2006; Bate & Bonnell 2005; Matsumoto et al. 2015). Multiple fragments produced in different turbulent cells are predicted to exhibit random orientations between the circumstellar disks of the binary components and no particular relationship between the circumstellar disks and surrounding circumbinary material. If multiple fragments are produced in a common region where turbulence conspires to create local angular momentum, however, the binary system thus assembled can exhibit quite well aligned circumstellar disks. Nevertheless, once again, the circumstellar disks should not bear any particular relationship with their surrounding circumbinary material.

Alternatively, the large-scale ordered rotation of the core can drive dynamical instabilities to induce fragmentation during collapse. In such models, conservation of angular momentum forces cores to become increasingly flattened as they collapse. As a result, a disequilibrium disk-like (i.e., flattened and rotating) structure forms at the center of the core. The central region of the core can become especially flattened if magnetic fields are invoked to direct infalling matter onto the midplane of the disk-like structure; the resulting structures closely resemble, at least morphologically, rotationally supported disks and are therefore referred to as pseudodisks (Galli & Shu 1993a, 1993b). By introducing an initial density or velocity perturbation, the large-scale ordered rotation of the core can drive dynamical instabilities in the form of a spiral, bar, or ring in its central flattened region (Cha & Whitworth 2003; Matsumoto & Hanawa 2003; Machida et al. 2008). Fragments form in localized regions of the resulting dynamical instabilities that are gravitationally unstable (according to the Toomre criterion) and have masses exceeding the local Jeans mass. Binary protostellar systems that form through rotational fragmentation of disk-like structures should naturally exhibit a close alignment between the circumstellar disks of the binary components and the surrounding circumbinary material and share the same sense in orbital motion. Such a close alignment and similar sense in orbital motion is what we find for L1551NE, as found also by Lim et al. (2016) for L1551 IRS5, arguing for the formation of L1551NE through rotational fragmentation just like in the case of L1551 IRS5.

In L1551 IRS5, the circumstellar disks of the binary components have comparable sizes (break radii of 12.2 au and 10.4 au, respectively; Lim et al. 2016), suggesting that the binary protostars have comparable masses. In L1551NE, one protostar is about five times more massive than the other. Evidently, rotationally driven fragmentation can lead to binary protostellar systems having either very similar or very different component masses.

6.5. Fragmentation of L1551 Cloud

Intriguingly, the spin axes of both the L1551NE and L1551 IRS5 systems are closely oriented in space. Specifically, the circumstellar disks of the binary protostars in L1551 IRS5 have inclinations of ~46° and position angles for their major axes of ~148° (Lim et al. 2016), compared with the circumstellar disks of the binary protostars in L1551NE that

have inclinations of ∼58° and position angles for their major axes of ∼151° (Section 4). Despite the close spatial orientation of their spin axes, however, the two systems exhibit opposite senses in spins. Specifically, as observed from Earth, the two components of L1551NE are orbiting in an anticlockwise direction (Section 6.1), whereas the two components in L1551 IRS5 are orbiting in a clockwise direction (Lim & Takakuwa 2006; Lim et al. 2016).

In theoretical simulations, an initial density or velocity perturbation is imprinted onto rotating cores to facilitate fragmentation driven by dynamical instablities. In molecular clouds, a ubiquitous source of perturbation is turbulence. Different turbulent cells may have been responsible for producing the parental cores of L1551NE and L1551 IRS5 and imparted on them opposite spins. If so, then the close alignment between the spin axes of these two binary protostellar systems is purely coincidental.

L1551NE and L1551 IRS5 make up one group of active star formation in the L1551 cloud. The other is the HL Tau group, which comprises HL Tau, XZ Tau, LkHα 358, and HH 30* (driving source of the Herbig-Haro object HH 30). HL Tau is classified as either a Class I object (protostar) or a Class II object (classical T Tauri star), and the others in the HL Tau group as Class II objects. The circumstellar disk of HL Tau has been very well resolved with ALMA. Based on a two-dimensional Gaussian fit to its image, ALMA Partnership et al. (2015) derive an inclination of $46\overset{\circ}{.}2 \pm 0\overset{\circ}{.}2$ and a position angle for its major axis of $138\overset{\circ}{.}2 \pm 0\overset{\circ}{.}2$. The ionized jet from HL Tau has its major axis at a position angle of ∼51° (Mundt et al. 1990; López et al. 1995; Moriarty-Schieven et al. 2006), closely orthogonal to the circumstellar disk of this object as projected onto the sky. Thus, surprisingly, the circumstellar disk of HL Tau also is closely aligned with the circumstellar disks of the binary protostars in L1551NE and L1551 IRS5.

The circumstellar disk of LkHα 358 has been resolved with ALMA. Based on a two-dimensional Gaussian fit to its image, ALMA Partnership et al. (2015) derive an inclination of 56° ± 2° and a position angle for its major axis of 170° ± 3°. LkHα 358 does not exhibit any known jet. HH 30* is a suspected binary based on wiggles in its optical jet (Anglada et al. 2007). The circumbinary disk of this system has an inclination of 81° ± 2° and a position angle for its major axis of 125° ± 1° (Guilloteau et al. 2008). The ionized jet from HH 30* has its major axis at a position angle of ∼31° (Mundt et al. 1990; López et al. 1995; Moriarty-Schieven et al. 2006), closely orthogonal to the circumbinary disk of this object as projected onto the sky. Although distributed over a wider range of angles, the circumstellar disk of LkHα 358 and the circumbinary disk of HH 30* do not appear to be randomly oriented with respect to, but instead are aligned to within a few tens of degrees of, the circumstellar disks of L1551NE, L1551 IRS5, and HL Tau. As a consequence, the outflows driven by all these objects, including the outflow from XZ Tau (Mundt et al. 1990; Krist et al. 1999; Moriarty-Schieven et al. 2006) (a binary system whose circumstellar disks have not been spatially resolved), are all oriented in the northeast–southwest direction as projected onto the sky.

If not for the counter-rotating spins of L1551NE and L1551 IRS5, it would have been natural to attribute the relatively close alignment between the spin axes of all the young stellar objects in the L1551 cloud to a large-scale ordered rotation of this cloud. Instead, we note that the spin axes of all these objects are approximately orthogonal, in projection, to the major axis of the filament that composes the L1551 cloud (Lin et al. 2016, whose measurements provide no evidence for any ordered rotation of this cloud); the L1551 cloud filament is itself aligned with the overall elongation of filamentary structures that make up the Taurus molecular cloud complex (Mizuno et al. 1995; Goldsmith et al. 2006). The close alignment in the spin axes of all the young stellar objects in the L1551 cloud may therefore reflect (faster) infall and the subsequent formation of cores that are flattened along the major axis of the cloud filament. Local turbulence may have imparted angular momentum to individual cores, thus giving rise to opposite spins between some cores.

7. SUMMARY AND CONCLUSIONS

Using the VLA, we have fully resolved (i.e., along both their major and minor axes) the two circumstellar disks in the Class I binary protostellar system L1551NE. We also reanalyzed archival observations at 3.5 cm that resolve along their major axes the two ionized jets in this system. These observations span nearly 2 decades, allowing us to study the relative proper motion of the binary protostars. We found the following:

1. The stronger ionized jet of source A has a position angle for its major axis of $61^{\circ}{}^{+4^{\circ}}_{-3^{\circ}}$, and the weaker ionized jet of source B a position angle for its major axis of $69^{\circ}{}^{+4^{\circ}}_{-5^{\circ}}$. Both jets are therefore aligned, as projected onto the sky, to within the measurement uncertainties (difference in position angles of 8° ± 6°).
2. The circumstellar disk of source A is much larger than that of source B. The images of both circumstellar disks are better fit by a double power law that exhibits a smooth transition between the inner and outer power laws than a single power law that is abruptly truncated. A single, untruncated power law is explicitly rejected for the circumstellar disks of both sources, as is a Gaussian for the circumstellar disk of source A.
3. Although we find no unique solution for a double power-law fit to either circumstellar disk, the ratio of their major to minor axes and the position angle of their major axes do not depend on other parameters. Assuming implicitly that the circumstellar disks are intrinsically circular and geometrically thin, we find that the circumstellar disk of source A has an inclination of $57\overset{\circ}{.}7$ and a position angle for its major axis of $150\overset{\circ}{.}9$, and the circumstellar disk of source B has an inclination of $58\overset{\circ}{.}0$ and a position angle for its major axis of $152\overset{\circ}{.}1$. With estimated uncertainties in these parameters of a few degrees, the two circumstellar disks are closely aligned if not parallel. Furthermore, the two circumstellar disks are accurately orthogonal in projection to their respective ionized jets.
4. For the sharpest transition between the inner and outer power laws as might be expected of tidally truncated disks, the radius of maximum curvature in this transition is ∼18.6 au for the circumstellar disk of source A and ∼8.9 au for the circumstellar disk of source B. Equating these transition radii with their theoretically predicted tidally truncated radii, then, for a circular orbit, the ratio in disk sizes implies a binary mass ratio of ∼0.23. This binary mass ratio is closely comparable with that inferred by Takakuwa et al. (2014) of ∼0.19 based on the projected angular separation between each protostar and

the inferred kinematic center of the circumbinary disk. Given the projected angular separation between the two protostars, however, the transition radii of both circumstellar disks are at least a factor of ∼1.5 times smaller than their predicted tidally truncated radii if the system has a binary mass ratio of ∼0.2 and a circular orbit.

5. Over an interval of 10 yr, source B has moved northward (at a significance level of 3.1σ) with respect to source A. By contrast, there is no detectable motion of these two sources along the east–west direction (significance level of only 1.6σ). Furthermore, source B is likely moving away (at a significance level of 2.5σ) from source A. All these measurements agree with the model proposed by Takakuwa et al. (2014) for the relative orientation of the two protostars at their inferred orbital locations for an anticlockwise and circular orbital motion.

The two circumstellar disks are closely aligned if not parallel not just with each other but also with their surrounding circumbinary disk, which has an inclination of $62^{\circ}_{-17^{\circ}}^{+25^{\circ}}$ and a position angle for its major axis of $167^{\circ}_{-27^{\circ}}^{+23^{\circ}}$. Furthermore, the two protostars appear to be orbiting each other in the same direction as the rotation of their circumbinary disk. Both the circumstellar and circumbinary disks, as well as the orbit, of this binary system therefore share the same axes for their angular momenta, indicating that L1551NE formed through the rotationally driven fragmentation of its parental core, as is the case for L1551 IRS5 (Lim et al. 2016). By contrast with L1551NE, where the two circumstellar disks have different sizes and their binary protostars different masses, the two circumstellar disks in L1551 IRS5 have roughly comparable sizes, suggesting that their binary protostars have comparable masses (for a given orbital eccentricity, the truncation radii of circumstellar disks in binary systems depend only on the binary mass ratio). Rotationally driven fragmentation can therefore lead to binary systems having comparable or very different component masses.

Finally, we pointed out that the circumstellar disks of the binary protostars in both L1551NE and L1551 IRS5, along with their circumbinary disks or flattened circumbinary envelopes, are closely oriented in space (i.e., similar inclinations, as well as position angles for their major axes). Indeed, all the young stellar objects in the L1551 cloud, including HL Tau, LkHα358, HH30*, and probably also XZ Tau, have spin axes that are approximately orthogonal in projection to the major axis of the filament that makes up the L1551 cloud, which itself is aligned with the major axes of the filamentary structures that make up the Taurus molecular cloud complex. This alignment may reflect (faster) infall along and the subsequent formation of cores that are flattened across the minor axes of these filaments. Local turbulence may have imparted angular momentum to individual cores, thus giving rise to opposite spins between some cores.

We thank the anonymous referee for constructive suggestions to improve the readability of the manuscript. J.L. acknowledges support from the Research Grants Council of Hong Kong through grants HKU 703512P and 17305115. Both T.H. and T.M. acknowledge the Japan Society for the Promotion of Science (JSPS) Grants-in-Aid for Scientific Research (KAKENHI) through, respectively, grant Nos. JP15K05017 and 26400233.

Facility: VLA.

Softwares: CASA, AIPS, GALFIT.

REFERENCES

ALMA Partnership et al. 2015, ApJL, 808, L3
Anglada, G., López, R., Estallela, R., et al. 2007, AJ, 133, 2799
Bate, M. R. 2000, MNRAS, 314, 33
Bate, M. R., & Bonnell, I. A. 2005, MNRAS, 356, 1201
Bate, M. R., Bonnell, I. A., & Bromm, V. 2002, MNRAS, 332, L65
Bate, M. R., Bonnell, I. A., & Bromm, V. 2003, MNRAS, 339, 577
Bertout, C., Robichon, N., & Arenou, F. 1999, A&A, 352, 574
Cha, S.-H., & Whitworth, A. P. 2003, MNRAS, 340, 91
Delgado-Donate, E. J., Clarke, C. J., & Bate, M. R. 2004a, MNRAS, 347, 759
Delgado-Donate, E. J., Clarke, C. J., Bate, M. R., & Hodgkin, S. T. 2004b, MNRAS, 351, 617
Galli, D., & Shu, F. H. 1993a, ApJ, 417, 220
Galli, D., & Shu, F. H. 1993b, ApJ, 417, 243
Goldsmith, P. F., Heyer, M., Narayanan, G., et al. 2006, ApJ, 680, 428
Goodwin, S. P., Kroupa, P., Goodman, A., & Burkert, A. 2007, in Protostars and Planets V, ed. B. Reipurth, D. Jewitt, & K. Keil (Tucson, AZ: Univ. Arizona Press), 133
Goodwin, S. P., Whitworth, A. P., & Ward-Thompson, D. 2004a, A&A, 414, 633
Goodwin, S. P., Whitworth, A. P., & Ward-Thompson, D. 2004b, A&A, 423, 169
Goodwin, S. P., Whitworth, A. P., & Ward-Thompson, D. 2006, A&A, 452, 487
Guilloteau, S., Dutrey, A., Pety, J., & Gueth, F. 2008, A&A, 478, L31
Hayashi, M., & Pyo, T.-S. 2009, ApJ, 694, 582
Kenyon, S. J., Dobrzycka, D., & Hartmann, L. 1994, AJ, 108, 1872
Krist, J. E., Stapelfeldt, K. R., Burrows, C. J., et al. 1999, ApJL, 515, L35
Lim, J., & Takakuwa, S. 2006, ApJ, 653, 425
Lim, J., Yeung, P. K. H., Hanawa, T., et al. 2016, ApJ, 826, 153
Lin, J., et al. 2016, ApJ, 826, 193
López, R., Raga, A., Riera, A., Anglada, G., & Estallela, R. 1995, MNRAS, 274, L19
Lubow, S. H., & Ogilvie, G. I. 2000, ApJ, 538, 326
Machida, M. N., Tomisaka, K., Matsumoto, T., & Inutsuka, S. 2008, ApJ, 677, 327
Matsumoto, T., & Hanawa, T. 2003, ApJ, 595, 913
Matsumoto, T., Onishi, T., Tokuda, K., & Inutsuka, S. 2015, MNRAS, 449, L123
Mizuno, A., Onishi, T., Yonekura, Y., et al. 1995, ApJL, 445, L161
Moriarty-Schieven, G. H., Johnstone, D., Bally, J., & Jenness, T. 2006, ApJ, 645, 357
Moriarty-Schieven, G. H., Powers, J. A., Butner, H. M., Wannier, P. G., & Keene, J. 2000, ApJL, 533, L143
Mundt, R., Ray, T. P., Bührke, T., Raga, A. C., & lf, J. 1990, A&A, 232, 37
Peng, C. Y., Ho, L. C., Impey, C. D., & Rix, H.-W. 2002, AJ, 124, 266
Peng, C. Y., Ho, L. C., Impey, C. D., & Rix, H.-W. 2010, AJ, 139, 2097
Pérez, L. M., Carpenter, J. M., Chandler, C. J., et al. 2012, ApJL, 760, L17
Pichardo, B., Sparke, L. S., & Aguilar, L. A. 2005, MNRAS, 359, 521
Reipurth, B., Chan, K. C., Heathcote, S., Bally, J., & Rodríquez, L. F. 2000, AJ, 120, 1449
Reipurth, B., Rodríquez, L. F., Anglada, G., & Bally, J. 2002, AJ, 124, 1054
Reyholds, S. P. 1986, ApJ, 304, 713
Rodríquez, L. F., Anglada, G., & Raga, A. 1995, ApJL, 454, L149
Segura-Cox, D. M., Harris, R. J., Tobin, J. J., et al. 2016, ApJL, 817, L14
Takakuwa, S., Saito, M., Lim, J., et al. 2012, ApJ, 754, 52
Takakuwa, S., Saito, M., Lim, J., & Saigo, K. 2013, ApJ, 776, 51
Takakuwa, S., Saito, M., Saigo, K., et al. 2014, ApJ, 776, 51
Tobin, J., Looney, L. W., Wilner, D. J., et al. 2015, ApJ, 805, 125

May 19, 2015

Mass Estimates of a Giant Planet in a Protoplanetary Disk from the Gap Structures

Kazuhiro D. KANAGAWA[1], Takayuki MUTO[2], Hidekazu TANAKA[1], Takayuki TANIGAWA[3], Taku TAKEUCHI[4], Takashi TSUKAGOSHI[5], Munetake MOMOSE[5],

kanagawa@lowtem.hokudai.ac.jp

ABSTRACT

A giant planet embedded in a protoplanetary disk forms a gap. An analytic relationship among the gap depth, planet mass M_p, disk aspect ratio h_p, and viscosity α has been found recently, and the gap depth can be written in terms of a single parameter $K = (M_p/M_*)^2 h_p^{-5} \alpha^{-1}$. We discuss how observed gap features can be used to constrain the disk and/or planet parameters based on the analytic formula for the gap depth. The constraint on the disk aspect ratio is critical in determining the planet mass so the combination of the observations of the temperature and the image can provide a constraint on the planet mass. We apply the formula for the gap depth to observations of HL Tau and HD 169142. In the case of HL Tau, we propose that a planet with $\gtrsim 0.3$ is responsible for the observed gap at 30 AU from the central star based on the estimate that the gap depth is $\lesssim 1/3$. In the case of HD 169142, the planet mass that causes the gap structure recently found by VLA is $\gtrsim 0.4 M_J$. We also argue that the spiral structure, if observed, can be used to estimate the lower limit of the disk aspect ratio and the planet mass.

Subject headings: protoplanetary disks — planet-disk interactions — stars:individual (HD 169142, HL Tau)

[1]Institute of Low Temperature Science, Hokkaido University, Sapporo 060-0819, Japan

[2]Division of Liberal Arts, Kogakuin University, 1-24-2, Nishi-Shinjuku, Shinjuku-ku, Tokyo, 163-8677, Japan

[3]School of Medicine, University of Occupational and Environmental Health, Yahatanishi-ku, Kitakyushu, Fukuoka 807-8555, Japan

[4]Department of Earth and Planetary Sciences, Tokyo Institute of Technology, Meguro-ku, Tokyo 152-8551, Japan

[5]College of Science, Ibaraki University, 2-1-1, Bunkyo, Mito, Ibaraki 310-851, Japan

1. Introduction

High resolution imaging observations of protoplanetary disks have revealed the presence of complex morphological structures in disks such as dips (e.g., Hashimoto et al. 2011), gap (e.g., Debes et al. 2013), or spirals (e.g., Muto et al. 2012; Grady et al. 2013) in near infrared (NIR) scattered light. At submillimeter wavelengths, ALMA has revealed the existence of non-axisymmetric structures in its early science operations (e.g., Casassus et al. 2013; Fukagawa et al. 2013; van der Marel 2013; Pérez et al. 2014) and now multiple ring-like structures are discovered in 2014 Long Baseline Campaign (ALMA Partnership 2015). It is now possible to obtain high spatial resolution data with the beam size less than $0\farcs04$ of multiple wavelengths.

One possible origin of the detail structures in protoplanetary disks is the disk–planet interaction. A giant planet creates a gap and spirals in the disk along its orbit, which are observable with high angular resolution observations. It is therefore important to understand what we can learn about the physical properties of the disk and planet once we can observe such structures.

In this letter, we present an estimation method of the planet mass from the gap depth which is potentially an observable quantity. The gap depth is related to the planet mass, the viscosity and the disk scale height (or disk temperature) (Duffell & MacFadyen 2013; Fung et al. 2014; Kanagawa et al. 2015, hereafter, K15). Using this relation, we can constrain the mass of a planet, if exists, by the combination of the disk image and observations of disk temperature and viscosity. The disk temperature can be obtained from the observation of optically thick gas/dust emissions. Alternatively, the spiral structure associated with the gap can be used to constrain the lower limit of the disk scale height. If the gap depth and the spiral structure are both observed, it enables us to derive the lower limit of the planet mass.

In Section 2, we present an analytic formula that describes the gap depth in terms of the physical parameters of the disk and the planet. In Section 3, we apply the gap depth formula to the observations of HL Tau by ALMA (ALMA Partnership 2015) and HD 169142 by VLA (Osorio et al. 2014). In Section 4, we discuss the constraints on the disk aspect ratio derived from spiral structure. Section 5 is for summary and discussion.

2. Gap model

In this section, we describe an analytic formula that relates the gap depth, planet mass and disk properties. A giant planet embedded in a protoplanetary disk creates a gap (e.g.,

Lin & Papaloizou 1979; Goldreich & Tremaine 1980), which has been investigated by many authors (e.g., Artymowicz & Lubow 1994; Kley 1999; Varnière et al. 2004; Crida et al. 2006). Recent hydrodynamic simulations by Duffell & MacFadyen (2013) and Fung et al. (2014) give an empirical formula for the relationship between planet mass and the gap depth, which is derived analytically by considering the angular momentum exchange processes between the disk and the planet (Fung et al. 2014, and K15). We briefly explain a more accurate derivation given by K15, below.

We assume a steady, axisymmetric, non–self–gravitating, geometrically thin disk. In a viscous accretion disk, the radial angular momentum flux F_J is given by the combination of the fluxes carried by advection and viscosity (Lynden-Bell & Pringle 1974),

$$F_J(R) = R^2 \Omega F_M - 2\pi R^3 \nu \Sigma \frac{\partial \Omega}{\partial R}, \tag{1}$$

where R, Ω, F_M, ν, and Σ denote the radial distance from the central star, the angular velocity of the disk, the mass flux, the kinetic viscosity, and the surface density, respectively. Adopting the α–prescription of kinematic viscosity (Shakura & Sunyaev 1973), we write $\nu = \alpha h^2 R^2 \Omega$, where $h = c/(R\Omega)$ denotes the disk aspect ratio and c is the sound speed, which are dependent on the disk temperature.

Because of a strong gravitational torque exerted by a planet on the disk, a gap opens along the planet orbit. We assume a sufficiently wide gap so that the torque is exerted mainly within a flat gap bottom with a constant surface density Σ_p. Then, using the WKB torque formula with a cutoff, the one–sided Lindblad torque, $T_{\rm LB}$, which is exerted by the planet on the outer disk, is approximately given by (see Lin & Papaloizou 1979, and K15)

$$\begin{aligned} T_{\rm LB} &= \int_{R_p+\Delta}^{\infty} 0.80\pi \left(\frac{M_p}{M_*}\right)^2 R_p^3 \Omega_p^2 \Sigma_p \left(\frac{R_p}{R-R_p}\right)^4 dR \\ &= 0.12\pi \left(\frac{M_p}{M_*}\right)^2 h_p^{-3} R_p^4 \Omega_{\rm p}^2 \Sigma_p, \end{aligned} \tag{2}$$

where M_p and M_* denotes the masses of the planet and the central star, respectively, and the subscript p denotes the values at the planet orbital radius R_p. In the above, we set the torque cutoff length $\Delta = 1.3 h_p R_p$ to match the one–sided torque with the results by detailed linear analyses of disk–planet interaction (Takeuchi & Miyama 1998; Tanaka et al. 2002; Muto & Inutsuka 2009). The above assumption that the planetary torque is exerted mainly within the gap can be valid when the gap width is much larger than the cutoff length.

In steady state, the mass flux is constant and the angular momentum flux radially changes due to the planetary torque. Thus, the angular momentum flux at the outside of

the gap, $R_e(> R_p)$ is equal to the sum of the angular momentum flux at R_p and the one–sided torque $T_{\rm LB}$,

$$F_J(R_e) = F_J(R_p) + T_{\rm LB}. \tag{3}$$

At the outside of the gap, the surface density is the unperturbed value Σ_0. The gap width is much smaller than R_p though the width is longer than the cutoff length. Then we can set $R_e \simeq R_p$, $h_e \simeq h_p$, and $\Omega_e \simeq \Omega_p$, and therefor $R_e^2\Omega_e F_{\rm M} \simeq R_p^2\Omega_p F_{\rm M}$. Under these approximations, substitution of Equations (1) and (2) into (3) yields

$$3\pi\alpha h_p^2 R_p^4\Omega_p^2\Sigma_0 = 3\pi\alpha h_p^2 R_p^4\Omega_p^2\Sigma_p + 0.12\pi\left(\frac{M_p}{M_*}\right)^2 h_p^{-3} R_p^4\Omega_p^2\Sigma_p. \tag{4}$$

From Equation (4), we obtain the gap depth Σ_p/Σ_0, as

$$\frac{\Sigma_p}{\Sigma_0} = \frac{1}{1+0.04K}, \tag{5}$$

where

$$K = \left(\frac{M_p}{M_*}\right)^2 h_p^{-5}\alpha^{-1}, \tag{6}$$

(see K15 for detail derivation). Although we adopt a simple expression for the one–sided torque, Equation (5) gives a good agreement with the results of hydrodynamic simulations as shown in Figure 1.

Equation (5) would be valid for $K \lesssim 10^4$. If K is appreciably large, the gap even becomes eccentric and non–steady, which breaks down our simple estimate (Kley & Dirksen 2006). In the eccentric state, the gap is shallower than the prediction by Equation (5) (Fung et al. 2014).

As seen in Equation (5), it is related to the planet mass, the viscosity and the aspect ratio. Solving Equation (5) for M_p/M_*, we obtain

$$\frac{M_p}{M_*} = 5\times10^{-4}\left(\frac{1}{\Sigma_p/\Sigma_0}-1\right)^{1/2}\left(\frac{h_p}{0.1}\right)^{5/2}\left(\frac{\alpha}{10^{-3}}\right)^{1/2}. \tag{7}$$

Figure 2 displays the planet mass given by Equation (7) as a function of the gap depth Σ_p/Σ_0 and the disk aspect ratio for several cases of α. The dependence of the planet mass on h_p is strong, though α–dependence is relatively weak. The planet mass varies from $\sim 10^{-5}$ to $\sim 10^{-2}$ if h_p changes from 0.01 to 0.2 for $\Sigma_p/\Sigma_0 = 1/10$ and $\alpha = 10^{-3}$. Therefore, the constraint on h_p, or equivalently disk temperature, is important in estimating the planet mass. In current observations, the constraints of the disk temperature can be given, for example, by emissions from optically thick gas (or sometimes dust) as discussed in Section 3.

As discussed in Section 4, we also show that the spiral structure can constrain the lower limit of the disk aspect ratio.

In application of our model to an observed gap, we assume that the distribution of dust is similar to the gas. Because of the dust filtration accompanied with the gap, however, the dust distribution can be significantly deviated from the gas , as reported by many theoretical studies (e.g., Paardekooper & Mellema 2004; Rice et al. 2006; Ward 2009; Zhu et al. 2012). The millimeter–sized or larger dust particles strongly suffer the dust filtration. They are piled up at the outer edge of the gap and have a much deeper gap than the gas. Smaller particles with radii of $\lesssim$ 0.1mm, on the other hand, are not much affected by the dust filtration and their distributions are similar to the gas for a gap created by a Jupiter mass planet (see Figure 3 of Zhu et al. 2012). Hence the above assumption in our model is valid for the case of such small dust particles. Also note that the critical dust size of filtration depends on the gas density and the turbulent viscosity. Zhu et al. (2012) did not take into account an additional diffusion of dust particles by the turbulence due to the Rossby wave instability and the Rayleigh unstable region (e.g., Zhu et al. 2014; Kanagawa et al. 2015), which occur at a deep gap. This additional diffusion can further increase the critical dust size for filtration. In application to an observed gap, it is also important to judge whether the filtration effect strongly alters the dust distribution at the gap or not. Such a judgement can be possible, by checking the dust pilling–up at the outer edge of the gap (see Section 3).

3. Application to Observations

In the actual observations of protoplanetary disks to date, there are several cases where the gap-like structures are observed. In this section, we consider two examples: HL Tau and HD 169142.

HL Tau was observed during the 2014 Long Baseline Campaign of ALMA (ALMA Partnership 2015). The observations show multiple rings but we focus on the ring residing at $\sim$ 30 AU, which is clearly seen and reasonably resolved.

We use the FITS image of the HL Tau that is publicly available from the ALMA archive site. We use the data of dust continuum emission in Band 6 and 7 in our analyses, and assume the distance of 140 pc. Figure 3–(a) and (b) show the radial profiles of the brightness temperature in Band 6 and 7 between 20 AU – 50 AU averaged over the position angles of $130^\circ <$ PA $< 140^\circ$, which is close to the major axis of the disk. We use the position of the central brightest pixel as the location of the disk center. Since the brightness temperatures in Band 6 and 7 are similar at $R \lesssim 25$ AU, the dust emission is likely to be

optically thick. Therefore, we use the ratio of the brightness temperature in the two bands to estimate the actual gap depth. The brightness temperatures in Band 6 and 7, T_{br6} and T_{br7}, are given by

$$T_{br6} = T\left(1 - e^{-\tau_6}\right) \tag{8}$$

and

$$T_{br7} = T\left(1 - e^{-\tau_7}\right) \tag{9}$$

where T is the disk temperature, τ_6 is the optical depth in Band 6 and τ_7 is that in Band 7. The optical depths of the Band 6 and 7 are related by $\tau_7 = \tau_6(\nu_7/\nu_6)^\beta$, where $\nu_6 = 233$ GHz is the central frequency at Band 6, $\nu_7 = 344$ GHz is that at Band 7, and β is the opacity index. We can derive τ_6 and T by using Equations (8) and (9) if we assume β. Figure 3–(c) shows the radial profiles of τ_6 in the cases of $\beta = 1$ and $\beta = 2$. By measuring the contrast of the maximum of τ at $R \sim 25$ AU and the minimum at $R \sim 30$ AU, we estimate the depth of the gap to be $\Sigma_p/\Sigma_0 \sim \tau_{\rm max}/\tau_{\rm min} \sim 1/3 - 1/7$.

Figure 3–(d) also shows the profile of T in the cases of $\beta = 1$ and 2. The temperature in the gap region strongly depends on the assumption of β, but that outside the gap is relatively insensitive to it. If we use $T = 55\ K$ at $R = 25$ AU, and assume that the sound speed is $c = 1$ km/s$(T/300\ {\rm K})^{1/2}$ and that the central star mass is 1 $M_\odot$, we derive $h \sim 0.07$ as an estimate of the disk aspect ratio. Adopting Equation (7), we derive

$$\frac{M_p}{M_*} = 3 - 5 \times 10^{-4} \left(\frac{h_p}{0.07}\right)^{5/2} \left(\frac{\alpha}{10^{-3}}\right)^{1/2}, \tag{10}$$

if this gap is created by a planet. Note that the error in the estimate of the stellar mass also increases the error in the planet-star mass-ratio through $h_p \propto c/(R_p\Omega_p) \propto M_*^{-1/2}$. In the above estimate, it is assumed that dust particles are gas have simular distributions. This assumption is vaild when dust particles are too samll to be much affected by the dust filtration, as mentioned in the end of Section 2. We can check the validity of the assumption, using the observed gap structure. According to the result by Zhu et al. (2012), the dust surface density at the outer edge of the gap is much larger than that at the inner edge when the dust filtration is effective. For the gap at 30 AU of HL Tau, on the other hand, the distribution of the dust optical depth (see Figure 3–[c]) does not show any enhance at the outer edge. Hence, we can judge that dust filtration is not so effective in this case.

The second example is the disk around HD 169142. Recent observations by Osorio et al. (2014) of 7 mm emission shows that there may exist a gap at ~ 50 AU from the central star. The observations also found a knot at 50 AU, which could be regarded as compact source with the mass of $\sim 0.6 M_J$. It is difficult to estimate the gap depth from their observation since the beam size is relatively large, but the radial profile given in the Figure 2 of Osorio

et al. (2014) suggests that the gap may be as shallow as $\Sigma_p/\Sigma_0 \simeq 0.5$. We consider this as the upper limit of the gap depth since the model with complete gap (i.e., $\Sigma_p/\Sigma_0 = 0$) seems to be consistent with observations. If we adopt the disk aspect ratio of ~ 0.1 and $\alpha = 5 \times 10^{-4}$, as indicated by Osorio et al. (2014), we obtain the lower limit of the planet mass as $\sim 0.4\ M_J$ from Equation (7).

4. The Constraint on Disk Temperature from Spiral Structures

We have seen that the constraint on disk temperature, or disk aspect ratio, is important in inferring the planet mass from the gap structure. As discussed above, the disk temperature is obtained from the disk emissions. Here, we discuss an alternative constraint on disk aspect ratio coming from a spiral density wave, which is a natural consequence of disk–planet interaction. The spiral structures have been observed in infrared observations so far (e.g., Muto et al. 2012; Grady et al. 2013; Currie et al. 2014). We expect such features may be observed at sub–millimeter wavelengths in near future when better sensitivity at higher spatial resolution is available.

This shape of the spiral density wave induced by disk–planet interaction is related to the disk aspect ratio (or temperature) and is given in an analytic form (Rafikov 2002; Muto et al. 2012). The shape of spiral waves excited by a planet is determined by four parameters, R_c, θ_0, δ and h_p (see eq. [1] Muto et al. 2012). The launching location of spiral waves (very close to the planet location) is denoted as (R_c, θ_0). The parameter δ denotes the profile of sound speed $c \propto R^{-\delta}$. The disk aspect ratio h changes as $h = h_p\,(R/R_p)^{-\delta+1/2}$.

For demonstration, we have performed two–dimensional hydrodynamic calculations using FARGO (Masset 2000) to obtain the gap and spiral structures caused by a Jupiter mass planet at $R_p = 40$ AU in a disk with $\alpha = 10^{-3}$, $h_p = 0.1$, and $\delta = 0.25$. Figure 4-(a) and (b) are the optically thin dust thermal emission at 230GHz obtained by the simulation (κ is assumed to be 2×10^{-2} cm^2/g per unit gas mass and the dust and gas are assumed to be well–mixed), and the radial cuts of the emission along the wave and in the direction opposite to the planet. Figure 4-(c) and (d) are the same as (a) and (b), but the emission is convolved with a circular Gaussian beam with an FWHM of 0.065" (the distance to the disk is set as 150 pc). Even in the convoluted image, the emission of wave is about 10% larger than the emission from non–wave region near the planet. Such spiral feature would be detectable with future ALMA or TMT observations. We fit the spiral structure, and the resulting χ^2–map (Figure 5) indicates that we can constrain the lower limit of h_p to be ~ 0.07. The gap depth can be estimated by $\Sigma_p/\Sigma_0 \sim 1/5$ from Figure 4. Therefore, from Equation (7), we derive the lower limit of the planet mass as $M_p/M_* \geq 4 \times 10^{-4}(\alpha/10^{-3})^{1/2}$. This lower limit actually

coincides with the actual planet mass within a factor of ~ 2.5 in this particular case.

5. Summary and Caveats

In this letter, we have shown an analytic derivation of the depth of the gap created by a planet embedded in a protoplanetary disk. Equation (7) gives the relationship between the gap depth, planet mass, disk temperature (aspect ratio) and viscosity. Since the gap depth strongly depends on the disk aspect ratio, the constraints on the disk temperature is critical in estimating the planet mass from the gap structure. The disk temperature is obtained by the emissions from optically thick gas/dust, as shown in Section 3. We have also argued that the spiral wave can constraint the disk temperature in the observation of optically thin emission. Our model assumed that dust particles and gas have similar distributions. This assumption is vaild when dust particles are too small to be much affected by the dust filtration. The assumption would be verified if the dust piling–up is not observed at the outer edge of the gap.

We have applied Equation (7) to the dust continuum observations of HL Tau and HD 169142 and derived the estimates of the mass of the planet, which could be responsible for the observed gaps (at 30 AU of HL Tau and at 50 AU of HD 169142). At the gap of HL Tau, the dust filtration does not seem so effective becasue no significant dust pilling–up is seen at outer edge of the gap.

We also note that in both the observations of HL Tau and HD 169142, the gaps we have focused on are only marginally resolved. Therefore, the gap depth quoted in this paper should be regarded as upper limit. Future high resolution observations by ALMA and/or TMT should put good constraints on the gap depth. When complex morphologies are found in protoplanetary disks, simple analytic formulae should be useful for interpreting (at least a part of) such structures and derive physical quantities.

KDK thanks Tatsuya Takekoshi for helpful comments. This paper makes use of the following ALMA data: ADS/JAO.ALMA#2011.0.00015.SV. ALMA is a partnership of ESO (representing its member states), NSF (USA) and NINS (Japan), together with NRC (Canada) and NSC and ASIAA (Taiwan), in cooperation with the Republic of Chile. The Joint ALMA Observatory is operated by ESO, AUI/NRAO and NAOJ. This work is partially supported by JSPS KAKENHI Grant Numbers 23103004, 26103701, 26800106. Numerical computations were carried out on Cray XC30 at Center for Computational Astrophysics, National Astronomical Observatory of Japan. This work is also greatly benefited from Workshop hosted by Institute of Low Temperature Science, Hokkaido University "Recent

Development in Studies of Protoplanetary Disks with ALMA".

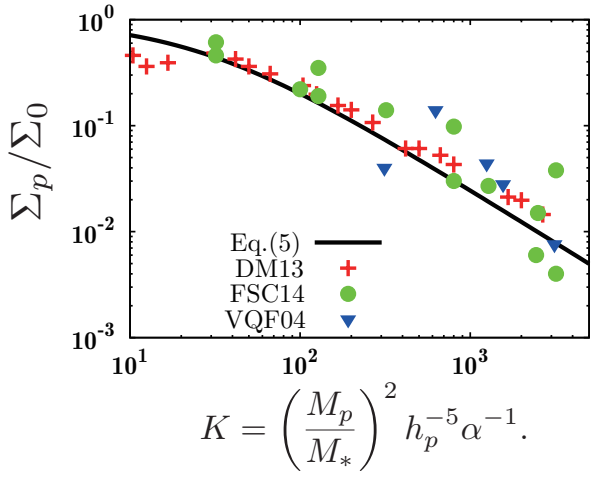

Fig. 1.— The gap depth as a function of the parameter K. The solid line denotes Equation (5). The crosses, circles and triangles represent the gep depth obtained by hydrodynamic simulations done by Duffell & MacFadyen (2013), Fung et al. (2014) and Varnière et al. (2004), respectively. (entire runs of $K < 8000$ in these papers are shown)

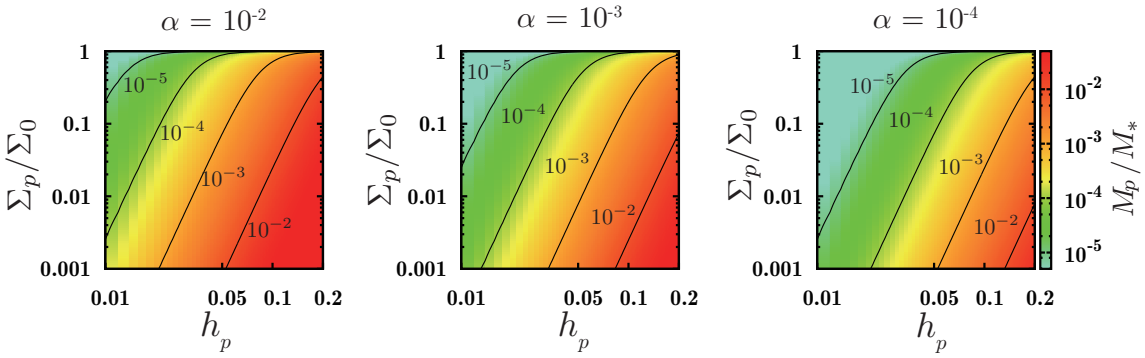

Fig. 2.— Planet mass as a function of the gap depth and the disk aspect ratio. The relationship between these values are given in Equation (7) and three panels correspond to the cases with $\alpha = 10^{-2}$ (left), 10^{-3} (center) and 10^{-4} (right).

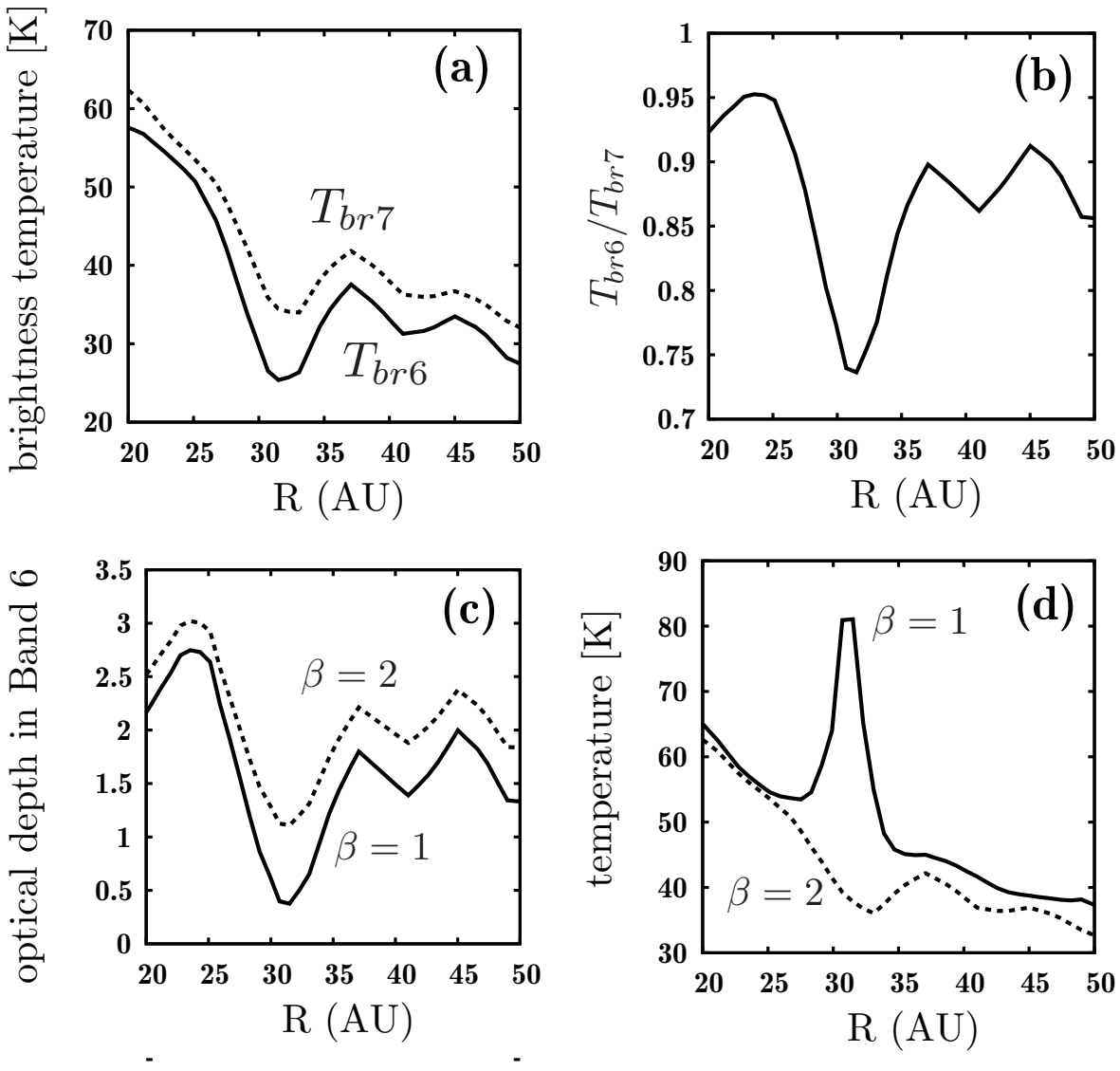

Fig. 3.— (a): Observed radial profile of the brightness temperature of dust continuum emission in HL Tau disk along the major axis. The data is averaged over PA=135° ± 5°. Solid line shows the Band 6 data and the dashed line shows the Band 7 data. (b): The ratio of brightness temperature in Band 6 and 7. (c): The radial profiles of the optical depth. (d): The temperature. The derivations of (c) and (d) are described in Section 3.

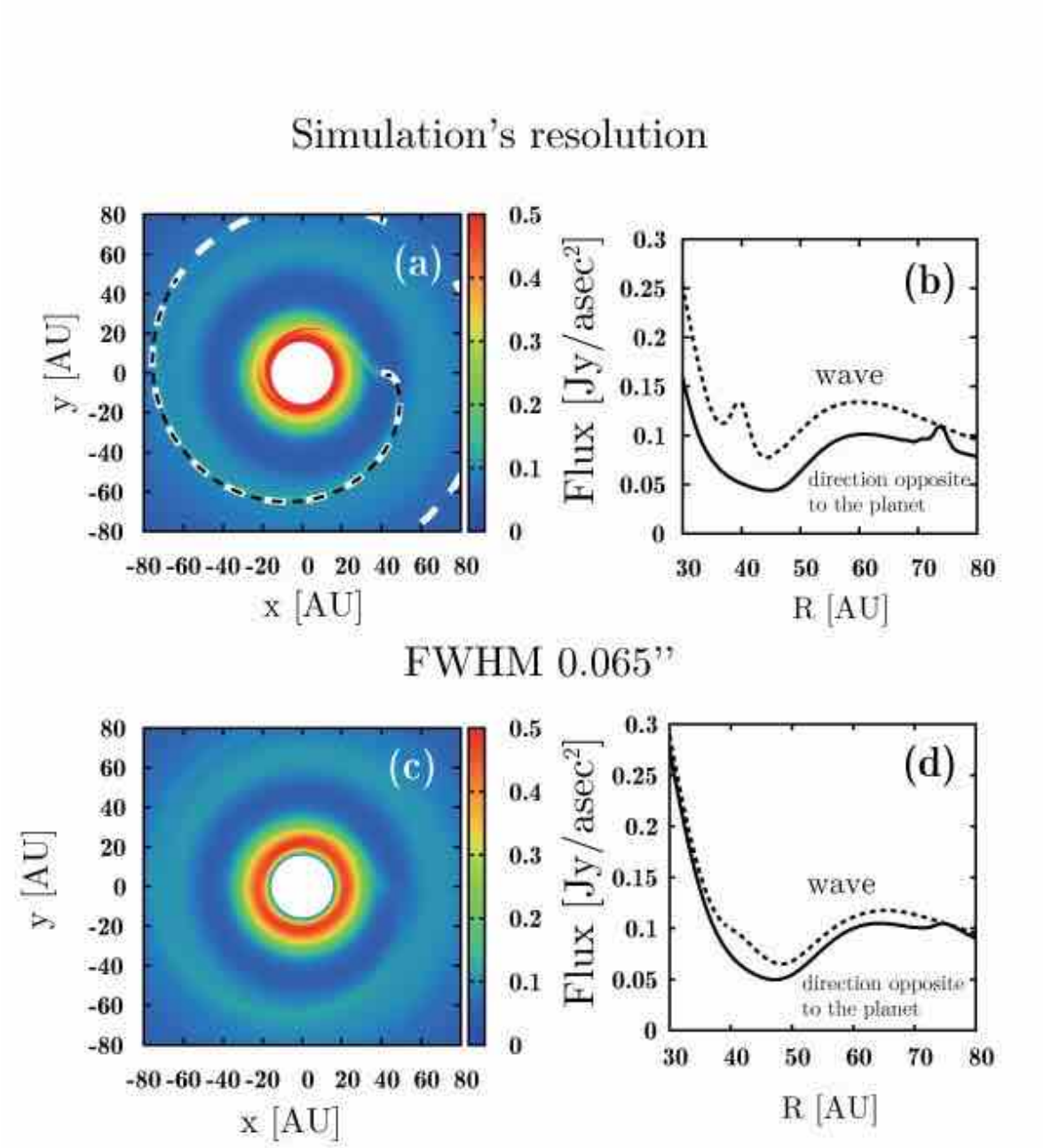

Fig. 4.— (a): The gap and spiral structure caused by a Jupiter mass planet in the disk with $\alpha = 10^{-3}$, $h_p = 0.1$ and $\delta = 0.25$. The black dashed line indicates the best-fit curve for the spiral shape and the white dashed line indicates the spiral used for fitting. (b): The radial cuts of emission along the spiral (dashed) and at a direction opposite to the planet (solid). (c) and (d): The same as (a) and (b), but the emission is convolved with a circular

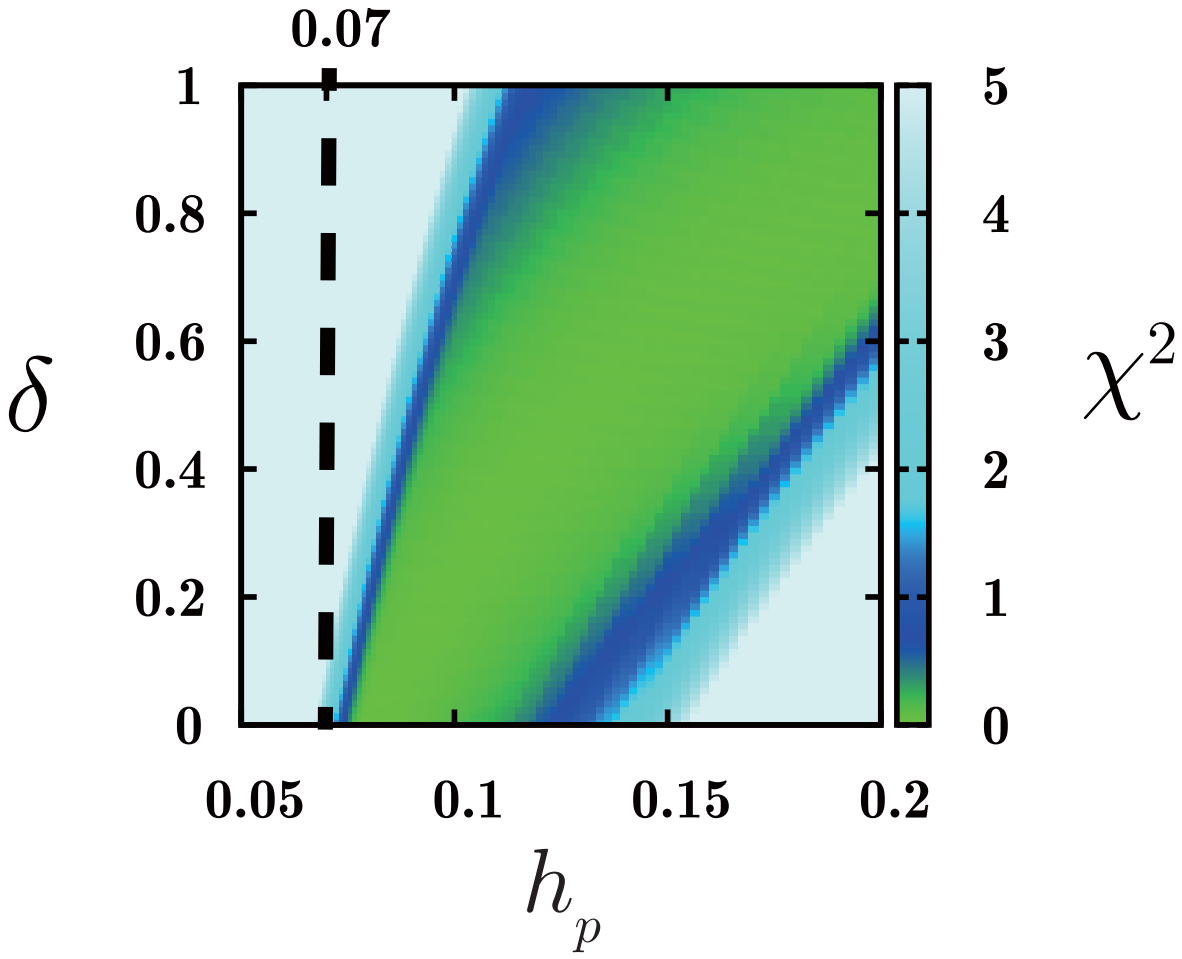

Fig. 5.— The χ^2-map of the fitting to the spiral structure.

REFERENCES

ALMA Partnership, arXiv:1503.02649

Artymowicz, P., & Lubow, S. H. 1994, ApJ, 421, 651

Casassus, S., van der Plas, G., M, S. P., et al. 2013, Nature, 493, 191

Crida, A., Morbidelli, A., & Masset, F. 2006, Icarus, 181, 587

Currie, T., Muto, T., Kudo, T., Honda, M., Brandt, T. D., Grady, C., Fukagawa, M., Burrows, A. et al. 2014, ApJ, 796, L30

Debes, J. H., Jang-Condell, H., Weinberger, A. J., Roberge, A., & Schneider, G. 2013, ApJ, 771, 45

Duffell, P. C., & MacFadyen, A. I. 2013, ApJ, 769, 41

Fukagawa, M., Tsukagoshi, T., Momose, M., et al. 2013, PASJ, 65, L14

Fung, J., Shi, J.-M., & Chiang, E. 2014, ApJ, 782, 88

Goldreich, P., & Tremaine, S. 1980, ApJ, 241, 425

Grady, C. A., Muto, T., Hashimoto, J., et al. 2013, ApJ, 762, 48

Hashimoto, J., Tamura, M., Muto, T., et al. 2011, ApJ, 729, L17

Kanagawa, K. D., Tanaka, H., Muto, T., Tanigawa, T., & Takeuchi, T., 2015, MNRAS, 558, 994

Kley, W. 1999, MNRAS, 303, 696

Kley, W., & Dirksen, G. 2006, A&A, 447, 369

Kwon, W., Looney, L. W., & Mundy, L. G. 2011, ApJ, 741, 3

Lin, D. N. C., & Papaloizou, J. 1979, MNRAS, 186, 799

Lynden-Bell, D., & Pringle, J. E. 1974, MNRAS, 168, 603

Masset, F. 2000, A&AS, 141, 165

van der Marel, N., et al. 2013, Science, 340, 1199

Muto, T., & Inutsuka, S.-i. 2009, ApJ, 701, 18

Muto, T., Grady, C. A., Hashimoto, J., et al. 2012, ApJ, 748, L22

Osorio, M., Anglada, G., Carrasco-González, C., et al. 2014, ApJ, 791, L36

Paardekooper, S.-J., & Mellema, G., 2004, A&A, 425, L9

Pérez, L. M., Isella, A., Carpenter, J. M., & Chandler, C. J. 2014, ApJ, 783, L13
766, L2

Rafikov, R. R., 2002, ApJ, 569, 997

Rice, W. K. M., Armitage, P. J., Wood, K., & Lodato, G. 2006, MNRAS, 373, 1619

Shakura, N. I., & Sunyaev, R. A. 1973, A&A, 24, 337

Takeuchi, T., & Miyama, S. M. 1998, PASJ, 50, 141

Tanaka, H., Takeuchi, T., & Ward, W. R. 2002, ApJ, 565, 1257

Varnière, P., Quillen, A. C., & Frank, A. 2004, ApJ, 612, 1152

Ward, W. R. 2009, in Lunar and Planetary Inst. Technical Report, Vol. 40, Lunar and Planetary Science Conference, 1477

Zhu, Z., Nelson, R. P., Dong, R., Espaillat, C., & Hartmann, L. 2012, ApJ, 755, 6

Zhu, Z., Stone, J. M., Rafikov, R. R., & Bai, X.-n. 2014, ApJ, 785, 122

ACCEPTED TO APJ
Preprint typeset using LaTeX style emulateapj v. 01/23/15

GIANT IMPACT: AN EFFICIENT MECHANISM FOR THE DEVOLATILIZATION OF SUPER-EARTHS

SHANG-FEI LIU (刘尚飞) [1], YASUNORI HORI (堀安範) [2,4], D.N.C. LIN [2,5,6] AND ERIK ASPHAUG [3]
[1] Department of Earth and Planetary Sciences, University of California, Santa Cruz, CA 95064, USA; sliu26@ucsc.edu
[2] Department of Astronomy and Astrophysics, University of California, Santa Cruz, CA 95064, USA; yahori@ucsc.edu, lin@ucolick.org
[3] School of Earth and Space Exploration, Arizona State University, Tempe, AZ 85287, USA; easphaug@asu.edu
[4] Astrobiology Center, National Institute of Natural Sciences and National Astronomical Observatory of Japan, Osawa 2-21-1, Mitaka, Tokyo 1818588, Japan
[5] Kavli Institute for Astronomy & Astrophysics, Peking University, Beijing, China
[6] Institute for Advanced Studies, Tsinghua University and National Astronomical Observatory of China, Beijing, China
Accepted to ApJ

ABSTRACT

Mini-Neptunes and volatile-poor super-Earths coexist on adjacent orbits in proximity to host stars such as Kepler-36 and Kepler-11. Several post-formation processes have been proposed for explaining the origin of the compositional diversity between neighboring planets: the mass loss via stellar XUV irradiation, degassing of accreted material, and in-situ accumulation of the disk gas. Close-in planets are also likely to experience giant impacts during the advanced stage of planet formation. This study examines the possibility of transforming volatile-rich super-Earths / mini-Neptunes into volatile-depleted super-Earths through giant impacts. We present the results of three-dimensional hydrodynamic simulations of giant impacts in the accretionary and disruptive regimes. Target planets are modeled with a three-layered structure composed of an iron core, silicate mantle and hydrogen/helium envelope. In the disruptive case, the giant impact can remove most of the H/He atmosphere immediately and homogenize the refractory material in the planetary interior. In the accretionary case, the planet is able to retain more than half of the original gaseous envelope, while a compositional gradient suppresses efficient heat transfer as the planetary interior undergoes double-diffusive convection. After the giant impact, a hot and inflated planet cools and contracts slowly. The extended atmosphere enhances the mass loss via both a Parker wind induced by thermal pressure and hydrodynamic escape driven by the stellar XUV irradiation. As a result, the entire gaseous envelope is expected to be lost due to the combination of those processes in both cases. Based on our results, we propose that Kepler-36b may have been significantly devolatilized by giant impacts, while a substantial fraction of Kepler-36c's atmosphere may remain intact. Furthermore, the stochastic nature of giant impacts may account for the observed large dispersion in the mass–radius relationship of close-in super-Earths and mini-Neptunes (at least to some extent).

Subject headings: equation of state — hydrodynamics — planets and satellites: formation — planets and satellites: interiors — stars: individual (Kepler-36, Kepler-11)

1. INTRODUCTION

Data obtained from the *Kepler* mission (Borucki et al. 2010) indicate an abundant population of close-in planets with radii of $R_p = 1 - 4\,R_\oplus$ (Petigura et al. 2013; Burke et al. 2014; Dressing & Charbonneau 2015). Although the masses of only a handful of those planets have been measured with radial-velocity or transit-timing variations (TTV) observations, a large range of their mean densities ρ_p indicates that they have diverse bulk compositions (e.g. see Fig.4 in Dressing et al. 2015). These kinematic and structural properties impose constraints on theories of planetary origin.

It has been suggested that these planets may have formed through the coagulation of grains and planetesimals at their present-day location (Hansen & Murray 2012; Chiang & Laughlin 2013). Although all volatile grains in their natal disks are sublimated in the proximity of their central stars, embryos may have formed prolifically from refractory grains (Li et al. submitted) and acquired or retained a modest amount of hydrogen/helium atmosphere *in situ* with relatively low apparent mean densities (Ikoma & Hori 2012).

Close-in planets are exposed to intense XUV (extreme UV and X-ray) irradiation from their host stars. Photoevaporation can significantly modify the structure of their atmosphere (e.g., Owen & Wu 2013). One possible cause for the apparent dispersion in ρ_p is the retention efficiency of H/He atmospheres among planets around host stars (Lissauer et al. 2013) with different XUV luminosities during their pre-main sequence stage. But around some host stars, high-density super-Earths and low-density hot-Neptunes with similar M_p and P (where M_p is the planetary mass and P is the orbital period) coexist. Their ρ_p diversity cannot be simply attributed to the XUV flux from their common host stars.

Around a particular sub-giant star, two planets, Kepler-36b and c, were found (Carter et al. 2012) with adjacent orbits (P = 13.8 and 16.2 days), comparable masses ($M_p = 4.46 \pm 0.3\,M_\oplus$ and $8.10 \pm 0.53\,M_\oplus$), and radii ($R_p = 1.48 \pm 0.03\,R_\oplus$ and $3.67 \pm 0.05\,R_\oplus$). The inferred ρ_p of the inner super-Earth (Kepler-36b) matches that of an Earth-like composition and that of the outer mini-Neptune (Kepler-36c) is consistent with an internal composition of a thick hydrogen/helium (H/He) envelope (8.6 ± 1.3 wt. %, assuming an Earth-like core) atop a rocky/iron core (Lopez & Fortney 2013). Although a fraction of Kepler 36c's atmosphere may be due to the degassing of accreted planetesimals (Elkins-Tanton & Seager 2008) or *in-situ* the accumulation of a residual disk gas onto its solid core (Ikoma & Hori 2012). However, such a large density contrast between these two closely-spaced planets is incompatible with either of these two accretion processes.

It is possible that these two planets may once have had a similar amount of atmospheric H/He and their compositional dichotomy could be caused by their different core masses (Lopez & Fortney 2013). Provided that the lost mass is a small fraction of M_p, their near 7:6 mean motion resonance (MMR) orbits would not be significantly affected by it (Teyssandier et al. 2015). However, Kepler 36c appears to have retained its atmosphere and Kepler 36b appears to have not, albeit the for-

mer has a smaller surface escape velocity and is expected to be more vulnerable to photoevaporation than the latter. Another system with a similar dichotomy is Kepler 11b and c (Lissauer et al. 2011).

Another scenario is that protoplanetary embryos formed throughout the disk, including the volatile-rich cold outer regions, and converged through type I migration to their present-day locations in the proximity of their host stars (Papaloizou & Terquem 2010; Ida et al. 2013). According to the conventional accretion scenario, protoplanetary embryos emerge through oligarchic growth and experience cohesive collisions with embryos with comparable masses (Kokubo & Ida 1998). The energy released in such catastrophic events intensely heats both the mantle and atmosphere and may induce substantial losses of planetary atmosphere (Schlichting 2014). The giant impact hypothesis is consistent with the chaotic dynamics exhibited in the Kepler-36 system (Deck et al. 2012). Hydrodynamic and N-body simulations have revealed that stochastic/convergent migration can lead to close encounters between the two planets and physical collisions with other embryos (Paardekooper et al. 2013; Quillen et al. 2013).

Due to the stochastic nature of these giant impact events, structural diversity among members of closely packed, multiple short-period planet systems is the hallmark of oligarchic growth, extensive migration, and giant impacts. This diversity takes the form of different levels of shock processing, different final material inventories and planetary densities (Asphaug 2010).

In this paper we explore the possibility that structural diversity is established by giant impacts during the formation of compact multiple-planet systems. Collisions and disruptions of differentiated super-Earths with terrestrial compositions (Marcus et al. 2009) or water : rock ratios of 1 : 1 (Marcus et al. 2010) have been previously simulated with the smoothed particle hydrodynamics (SPH) scheme (Reufer et al. 2012). However, there have been no systematic simulations of giant impacts between super-Earths with H/He atmospheres.

In §2, we outline the numerical method and the initial and boundary conditions used for these simulations. In our models, we adopt physical parameters similar to those of the Kepler 36 system and scrutinize the collisional origin of the compositional diversity between Kepler-36b and c. In §3, we present the results of two sets of numerical simulations to show that energetic giant impacts can cause strong shocks and lead to the ejection of a large amount of the H/He envelope. Shock dissipation also heats up the planetary atmosphere and interior, elevating the mass-loss rate induced by hydrodynamic escape and radiative evaporation (Hébrard et al. 2004). We summarize our results and discuss their implications in §4.

2. COMPUTATIONAL METHOD

Our three-dimensional hydrodynamic simulations are based on the framework of FLASH (Fryxell et al. 2000), an Eulerian code with an adaptive-mesh refinement (AMR) capability. This finite-volume scheme has advantages over most commonly-used SPH codes in terms of capturing shock waves as well as characterizing low-density and sparse regions. Besides, advection of different fluid species in a grid cell is allowed to obey their own advection equations, which is ideally suited for mixing problems. The main purpose of this work is to investigate the general aftermath of giant impacts, so our study here is on head-on collisions.

In order to minimize the artifact of artificial diffusivity (Tasker et al. 2008), collision simulations are performed in a pair of planets' center-of-mass frame rather than in the inertial reference frame in which they move through the numerical grids with a Keplerian speed. The width of the computational domain is 1×10^{13} cm on each side, and we choose an open boundary condition for our simulations. A multiple expansion with a large angular number ($L_{\rm max} = 60$) about the center of mass of the embryo pair is adopted in order to compute the self-gravity with a sufficient angular resolution.

Most hydrodynamic simulations of giant impacts ignore the presence of a central star and its tidal force. In the present context, the Hill radius of a planet, $r_{\rm H} = a\ \left(q/3\right)^{1/3}$ (where a is the semi-major axis of the planet and q is the mass ratio of the planet to its parent star) is only an order of magnitude larger than its physical size. Therefore, the tidal force of the central star may have a significant effect on the planet's post-impact evolution.

The orbit of the embryo pair around the host star is determined by solving a two-body problem that treats a central star and the embryo pair as two separate point masses (Guillochon et al. 2009). Here we consider giant impacts between a target planet $M_{\rm T}$ and an Earth-mass impactor $M_{\rm I}$ at 0.1 AU separation from a 1 $M_\odot$ star. Initially, the target and impactor are held apart from their center of mass by a few target's radii until they have relaxed into a hydrostatic equilibrium subjected to each other's tidal perturbation. They are released with their relative velocity gradually increased from rest to the values listed in Table 1. Further acceleration is determined by their mutual gravity.

Two simulations of head-on collisions in the accretionary and disruptive regimes are performed. In the accretionary model 1, $M_{\rm T} = 4.3\ M_\oplus$, i.e. close to the mass of Kepler-36b, and the impact velocity $v_{\rm imp} = v_{\rm esc}$, where $v_{\rm esc} = \sqrt{2G(M_{\rm T}+M_{\rm I})/(R_{\rm T}+R_{\rm I})}$ is the two-body escape velocity. In the disruptive model 2, $M_{\rm T} = 10\ M_\oplus$, i.e. the upper end of the mass spectrum that is commonly refer to super-Earths, and the impact velocity $v_{\rm imp} = 3v_{\rm esc}$ comparable to the local Keplerian speed. Our model 2 represents the largest scale of collisions that could happen to a close-in super-Earth with an atmosphere. Impacts onto a less massive super-Earth at the same speed lead to a more disruptive outcome.

In our models, the target is initially composed of an iron core, a silicate mantle, and an H/He gaseous envelope (7.5 wt %), while the impactor has the same layered structure except without an atmosphere. The mass ratio of an iron core to a silicate mantle is assumed to be 1 : 2 for all planets. We summarize the masses of each species in the targets and impactors in Table 1. The internal structure of all the target planets are resolved by a numerical mesh with $R_{\rm T}/\Delta d > 100$, where $R_{\rm T}$ is the target's initial radius and Δd is the width of the smallest grid cells.

Previously, Liu et al. (2015) have applied an early version of this scheme to investigate embryo impacts on gas giants. In those simulations, we approximated the internal structure of gas giants with a composite polytropic equation of state (EOS; Liu et al. 2013). We assume that the multi-species fluid obeys the Dalton's law, i.e. the total pressure of a mixture of gas equals the sum of the contributions of individual components. The current study focuses on collisions between smaller planets with compositions and internal structures similar to those of the Earth or Neptune. For 'terrestrial' types of planetary materials, we have incorporated the Tillotson EOS to model

TABLE 1
MASS AND ENERGY BUDGETS FOR THE LOW AND HIGH SPEED IMPACTS. [a]

v_{imp}	M_T			M_I		M			U_T	$E_{k,T}$	U_I	$E_{k,I}$	U		E_k	
(km/s)	Iron[b]	Rock[c]	H/He[d]	Iron	Rock	Iron	Rock	H/He					r_P[e]	r_H[f]	r_P	r_H
10.96	1.344	2.663	0.297	0.334	0.663	1.676	3.315	0.208	4.746	0.441	0.516	2.092	9.176	9.442	0.186	0.215
53.06	3.115	6.129	0.746	0.334	0.662	3.449	6.289	0.151	21.890	4.529	0.407	72.338	31.039	32.810	0.240	0.311

[a] Integral quantities M, U and E_k correspond to mass, internal energy and kinetic energy, respectively. Subscript T and I denote the target and the impactor. Integral quantities without additional subscripts are measured at the end point of our simulations. Mass data are in units of Earth mass and energy data are in units of 10^{39} erg.
[b, c, d] Mass of species iron, rock and H/He, respectively.
[e] The integral quantity is measured within the original radius of the target (cf. Figure 2 and 7).
[f] The integral quantity is measured within the Hill radius (2.62×10^{10} and 3.21×10^{10} cm, respectively).

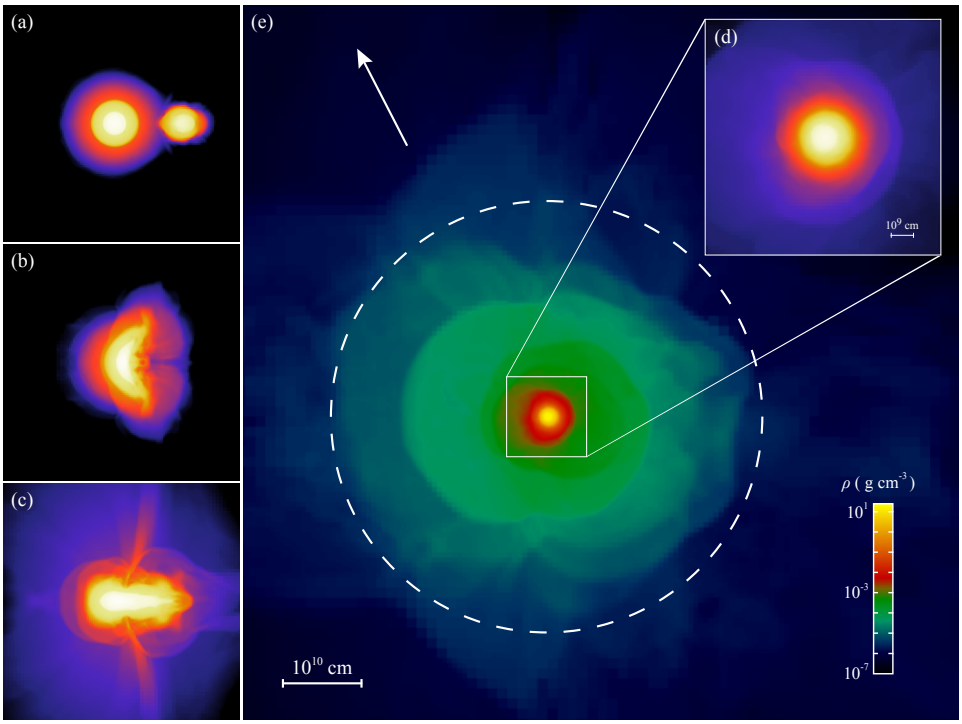

FIG. 1.— Snapshots of the giant impact simulation between a 4.3 $M_\oplus$ super-Earth and an Earth-mass planet at the escape velocity v_{esc}. The density distribution across slices in the planets' orbital plane with density range $[10^{-4}, 2.5 \times 10^{1}]$ g cm^{-3} (represented by colors ranging from purple to white) before the impact (panel a), immediately after (b), at 1.56 hours (c), and at 18 hours after the impact (d). Panel e shows an enlarged view of the panel d. With a radius 2.62×10^{10} cm, the dashed circle overplotted on the planet indicates its Hill sphere at a distance of 0.1 AU from a solar-mass star. The parent star is in the direction of the white arrow.

iron cores and silicate mantles (see Appendix I of Melosh 1989). We additionally model an H/He atmosphere (70 wt. % H_2 and 30 wt. % He) assuming a polytropic EOS ($P \propto \rho^\gamma$) with an adiabatic index of $\gamma = 5/3$. This simplified assumption can be validated for temperatures below the excitation temperature of the H_2 rotation band, 170K, and above H_2 dissociation temperature (~ 2000 K) but below that for the H and He atoms to be fully ionized. For the intermediate regime, our treatment underestimates the compressibility and heat capacity of hydrogen, which may exaggerate an impact-driven atmospheric escape. However, the atmosphere of the target is generally not sufficiently massive to stall the impactor and to prevent the dissipation of its kinetic energy near the target's core. We find that the computed turbulent mixing of material and the mass loss rate of the atmosphere are relatively insensitive to the specific H/He EOS model.

Giant impacts are violent and impulsive events. A new quasi-hydrostatic equilibrium within the planet's Hill's radius is generally established within a dynamical timescale (within a day). During the transitory phase, we can neglect the effect of stellar heating on the inflated atmosphere (see §4). After the impact, the efficiency of insolation due to stellar irradiation on the planet's surface and the efficiency of heat transfer in its interior determine the mass-loss rate from the inflated planet (Owen & Wu 2015). Here we must also consider that the giant impact has left behind a massive debris torus that can remain opaque for some time.

Part of the analysis and visualization presented in Section 3 is generated using the YT package (Turk et al. 2011) and the VisIt software (Childs et al. 2012).

3. RESULTS

3.1. *Low-speed model 1*

The compositional structure of a super-Earth after a low-speed collision with an Earth-mass impactor is shown in Figure 1. The initial mass of the target is 4.3 $M_\oplus$. The impactor's approaching speed is the escape velocity of the target-impactor system. Panels (a) – (c) show snapshots of density

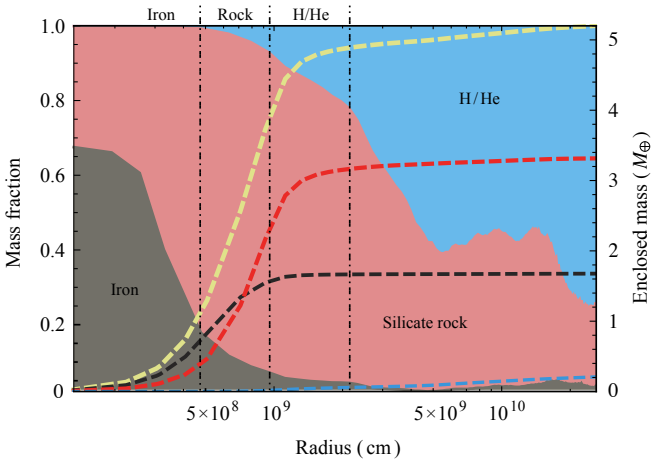

FIG. 2.— Each shaded area illustrates the mass fraction of each species as a function of radius at 18 hours after a low-speed giant impact. The grey, light coral, and blue regions represent iron, silicate rock and H/He gas, respectively. Three vertical dot-dashed lines indicate the initial compositional boundaries inside the target that has the three-layered structure. The dashed lines from top to bottom show the cumulative mass (yellow), the enclosed mass of silicate rock (red), iron (black), and H/He (blue) as a function of radius in units of Earth mass.

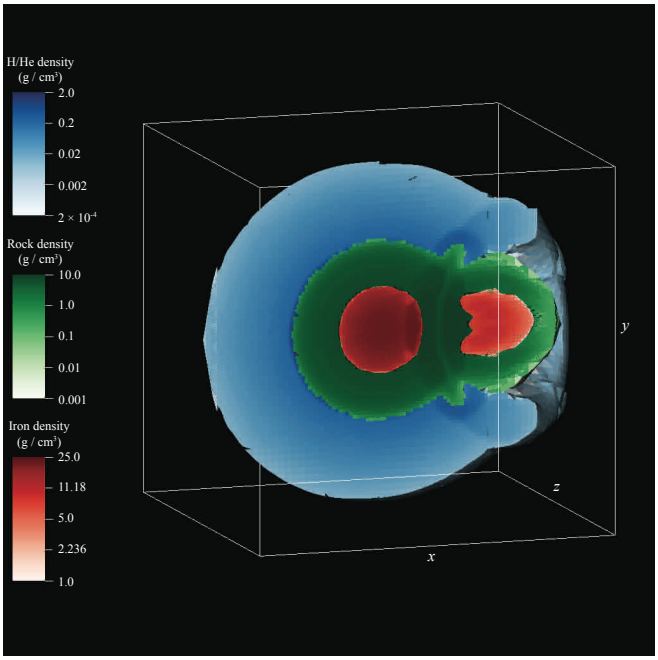

FIG. 3.— Cutaway view showing a snapshot after the contact between the rocky layers of the two planets and before the merger of their iron cores. The blue, green and red colors represent partial densities of H/He, rock and iron species, whichever is the dominant species of a grid cell. For the most part of the target, the total density of a grid cell is close to the partial density of the dominant species because mixing is not severe. However, a small fraction of H/He (less than 5 wt. %) being mixed with rock is responsible for the formation of a low-density arced structure between compressed rocky layers. The cubic box has a width of 4×10^9 cm.

contours before, during, and at 1.56 hr after the impact. The snapshots in panels (d) and (e) are taken at 18 hours after the impact. At this time, the central region of the post-impact target is mostly dynamically relaxed (see panel (d)), while the hot atmosphere extends well beyond the Hill radius and continues to lose its mass via Roche lobe overflow (see also §4).

Since the total orbital energy of the target-impactor system is nearly zero, this impact has an accretion efficiency close to but not quite one. The target gains mass after the impact (Table 1) but not all of it. The excess kinetic energy injected by the projectile drives an outflow as the planet approaches a hydrostatic equilibrium. As a result, the impact is not a perfect merger. The total mass loss (i.e. the mass that is failed to be accreted by the target) at 18 hours after the impact is $\sim 0.1\,M_\oplus$. This value is expected to increase slightly due to the slowly decaying oscillations in the tenuous outer part of the atmosphere over a prolonged period of time. Accretion efficiency in low-velocity collisions can be substantially lower than it is for the head-on cases considered here, because off-axis giant impacts can attempt to accrete too much angular momentum for a single planet or planet-satellite system to sustain. The so-called hit-and-run regime is relevant at velocities intermediate to those considered here (Asphaug 2010).

The gravitationally unbound mass, $\sim 0.1\,M_\oplus$, is mostly composed of H/He gas plus a minute contribution from iron and silicate material (see Table 1). The impact leads to the immediate ejection of nearly one-third of the target's initial H/He atmosphere. Most of the impactor's mass is added to that of the target. Consequently, the volatile fraction of the target is significantly reduced.

The enclosed mass as a function of radius inside the Hill sphere is plotted with a yellow dashed line in Figure 2. Most of the planetary mass is confined within its original radius, while the tenuous atmosphere spreads out by an order of magnitude, filling up the entire Hill sphere (see panel (e) of Figure 1). The grey, pink, and blue regions in Figure 2 illustrate iron, rock and H/He mass fractions as functions of planet's radius. The masses of the three components enclosed within a given spherical radius are overplotted with red (rock), black (iron), and blue (H/He) dashed lines, respectively.

When the intruding planet enters the target's envelope, a velocity shear is present at the interface between two species which triggers Kelvin-Helmholtz (K-H) instabilities. On the other hand, during the propagation of the impact-induced shock wave through the target, a denser fluid is accelerated by a less dense one at their interface and Rayleigh-Taylor (R-T) instabilities start to develop. However, since the impactor merges with the target in less than half an hour, only small-scale instabilities arise during such a short time span (see, e.g. Agertz et al. 2007), which can only be resolved with an extremely high resolution. Figure 3 shows a cutaway view of a snapshot when the impactor is about to merge with the target. We plot the partial density, i.e. the density times the mass fraction of the dominant species of a grid cell, to illustrate the interior structure. We note that only a little mixing occurs when the target's gaseous envelope gets crushed to its rocky layer, reducing the density of rocky material in a narrow region between the target and the impactor (see Figure 3). As during the short impact phase, both K-H and R-T instabilities are unable to cause large scale mixing, we identify that the impact-driven turbulence is responsible for the global mixing observed during the late stages (see Figure 4). Because a large amount of kinetic energy is released upon the coalescence of the target and the impactor, fluid motions become turbulent and a complex mixture of K-H and R-T instabilities can be triggered. The turbulent mixing, as well as hydrodynamic instabilities, destroy the original layered interior structure of the target – causing radial mixing between iron and rock near the center, and inducing a fraction of rock (and a much smaller fraction of iron) to diffuse into the H/He atmosphere (see Figure 4). Nevertheless, figure 2 shows that more than two-thirds of the mass at the center still consists of iron species. Besides,

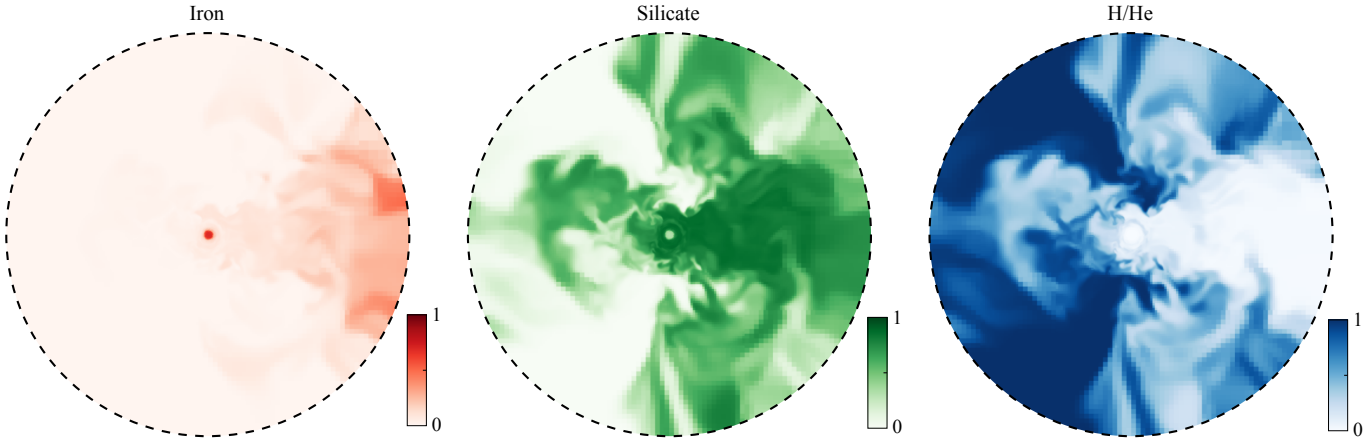

FIG. 4.— Mass fraction slices of each species through the orbital plane at 18 hr after the low-speed impact. A significant degree of mixing is established due to the turbulent mixing as well as hydrodynamic instabilities during the post-impact expansion phase. Dashed circles represent the the Hill sphere with a radius of 2.62×10^{10} cm.

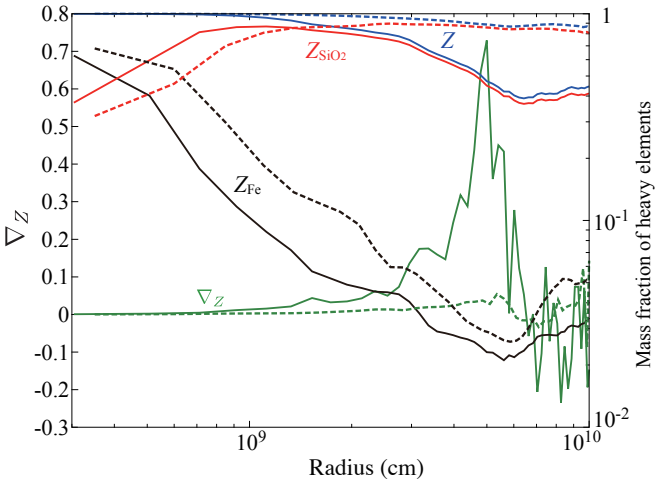

FIG. 5.— Compositional gradients inside the target planets after head-on collisions. The low-speed and high-speed impacts are represented by solid and dashed lines, respectively. Mass fractions of iron (black), rocky material (red), and heavy elements (blue) as functions of the radius are shown with labels on the right. The compositional gradient ∇_Z (green) increases with radius in the low-speed case. The small value of ∇_Z at radii indicates that the elements are well-mixed and homogenized. Fluctuation in ∇_Z reflects that the planet has not yet reached a relaxed state.

the iron mass fraction falls off rapidly with the radius, indicating that the planetary core survives from the impact and its mass grows in a coalescent manner.

In contrast, the rocky material is dredged up to the top of the atmosphere due to the turbulent motions driven by the impact. As shown in Figure 5, we note that the target's interior, i.e. within 6×10^9 cm, has a steep and positive compositional gradient, $\nabla_Z = \mathrm{d}\log Z/\mathrm{d}\log P$, which serves to stabilize thermal convection in the mantle. At least right after the giant impacts, a head-on collision develops a hot and inhomogeneous interior. Heat transport deep inside a post-impact planet may be suppressed by the effect of double diffusion convection (e.g. Rosenblum et al. 2011; Leconte & Chabrier 2012). Such an inefficient heat transfer mechanism would also prolong the presence of a magma ocean and delay the differentiation of iron material from a silicate-rich mantle. Off-axis collisions would lead to more efficient mixing, but also a less efficient kinetic energy contribution.

We summarize the energy budget in Table 1. Note that the planet's internal energy is almost doubled after the impact and it is larger than the sum of the internal and kinetic energies of the target and the impactor prior to the impact. This difference arises because the collision is accretionary, i.e. a large amount of the impactor's mass is delivered to the interior of the target. As a result, not only most of the kinetic energy but also some portion of the gravitational potential energy is converted into the post-impact internal energy. Therefore, one would expect that the temperature of the planet's interior to increase substantially after the impact.

3.2. *High-speed model 2*

The consequences of a high-speed impact is similar to that of the low-speed counterpart in terms of shock propagation throughout the target after the impact, mass loss via Roche lobe overflow, and gradually decaying oscillations inside the planet (Figure 6). Despite those general similarities, the high-speed impact differs from the low-speed one in three respects.

First, the high-speed impact is erosive. The mass of the target planet at 21.5 hr after the impact is about $9.9 M_\oplus$, i.e., $0.1 M_\oplus$ is stripped off from the target by the impactor. Thus, the total mass loss is $\sim 1.1 M_\oplus$. Besides, a significant amount of mass is levitated at the top of the atmosphere (see Figure 7). A breakdown of the mass budget in the Hill sphere (i.e., 3.21×10^{10} cm in this case) shows that the impactor successfully deposits all of its iron material into the target, while most of the impactor's rocky material is ejected (see also Table 1). And the target retains about $1/5$ of its original atmosphere after such an energetic impact.

Second, silicate rock material become the dominant species in the planet's atmosphere (Figure 7 and 8). As a result, the compositional gradient is nearly zero out to the Hill's radius, indicating a homogeneous distribution of the heavy material inside the bulk of the target (see Figure 5). In contrast to the low-velocity model, model 1, the negligible compositional gradient cannot suppress convection in the interior of the target planet. Nevertheless, iron material remains concentrated near the center of the planet as in the case of the low-speed model, model 1.

Third, the planet becomes less bound gravitationally. The mass contained within the target's original size is much smaller (see Figure 7). In terms of the energy budget, most of the kinetic energy is carried away by the unbound mass and only a fraction of it is directly converted to the planet's

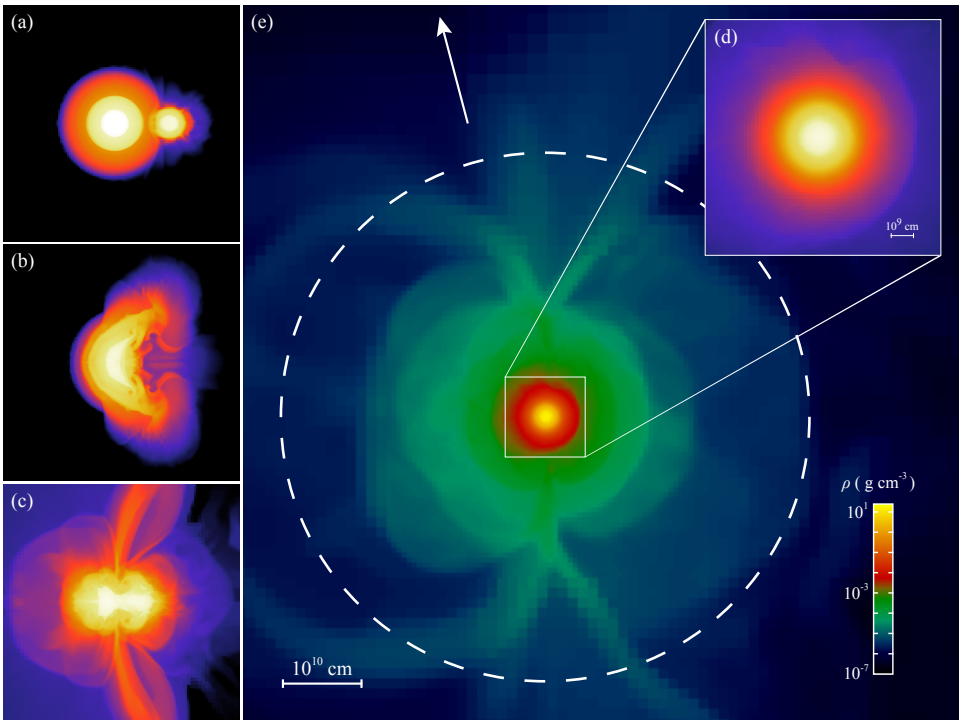

FIG. 6.— Snapshots of the giant impact simulation between a 10 $M_\oplus$ super-Earth and an Earth-mass planet at 3 v_{esc}. The colormaps and symbols are same as in Figure 1. Panels (a)–(d) are snapshots taken at the start of the impact, at 15 minutes, at 1.5 hr and at 21.5 hr after the impact, respectively. Panel (e) shows an enlarged view of the panel (d). The Hill sphere illustrated by the dashed circle has a radius of 3.21×10^{10} cm.

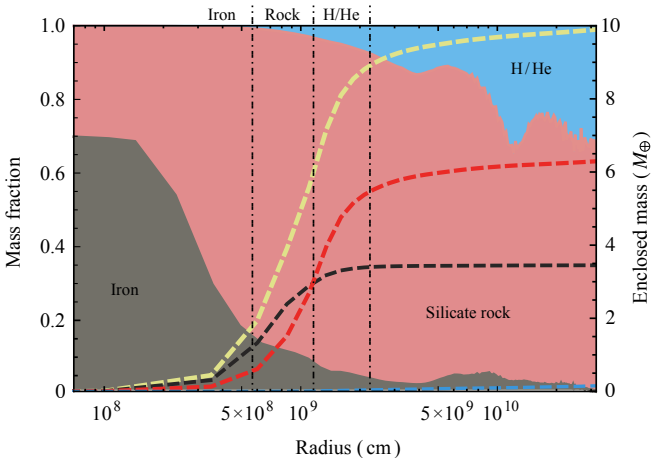

FIG. 7.— Mass fraction area plot and enclosed mass line plot at 21.5 hours after the high-speed impact. The symbols have the same meanings as in Figure 2.

internal energy. However, the gravitational potential energy released by the sedimentation of rock material in the atmosphere becomes an extra heat source for the target interior. Assuming that silicates in the H/He atmosphere establish a local thermal equilibrium with the turbulent gas, they condense into grains in cooler outer regions with $r \gtrsim 10^{10}$ cm. These silicate condensates grow through collisional coagulation (e.g. Podolak 2003). Relatively large silicate grains are expected to settle toward the planetary surface and sublimate along the way.

4. DISCUSSION AND CONCLUSIONS

The results presented in the previous sections show the planet's structure immediately after head-on giant impacts. Models 1 and 2 illustrate the possibility of diverse instantaneous outcomes depending on energy of collision, one at low velocity and the other at approximately the local Keplerian velocity, three times the planets' escape velocity. Whereas the initial gaseous envelope of a target super-Earth is mostly retained during the low-velocity impact, it is severely depleted shortly after the high-velocity impact. In this context, we suggest that giant impacts of varying energy can effectively devolatilize super-Earths/mini-Neptunes, and can diversify the compositions and interior structures of these mid-sized extrasolar planets, perhaps as occurred in our terrestrial system (see, e.g. Asphaug 2014).

The interior and atmosphere of a post-impact planet can achieve a thermal equilibrium state after a long-term evolution, which is difficult and not cost-effective to study by performing hydrodynamic simulations. Alternatively, the radiative cooling timescale (τ_{rad}) can be estimated from the rate of temperature change in an atmospheric layer via the outgoing infrared radiation: $\tau_{rad} \sim PC_p/(4g\sigma T^3)$, where P and T are the pressure and temperature near the photosphere obtained from the end state of hydrodynamic simulations, g is the surface gravity, and C_p is the specific heat capacity at a constant pressure, and σ is the Stefan-Boltzmann constant. Under the intense radiation from a $1\,M_\odot$ central star, an isothermal layer develops in the planet's residual upper atmosphere.

At the current location of Kepler 36b and c, the equilibrium temperature due to stellar irradiation is ~ 900 K. Adopting EOS of an ideal gas for H/He and the gas opacity of Freedman et al. (2008), we find that the H/He gas within the Hill sphere is optically thick. At the photosphere, we used $P \sim 2g/3\kappa$ and κ is the opacity to estimate τ_{rad} to be larger than several days. This estimate justifies, *a posteriori* the neglect of stellar irradiation in our impact simulations (see §2). Since this cooling time scale is much longer than the dynamical time scale, we can also assume that after a giant impact, a heated planet

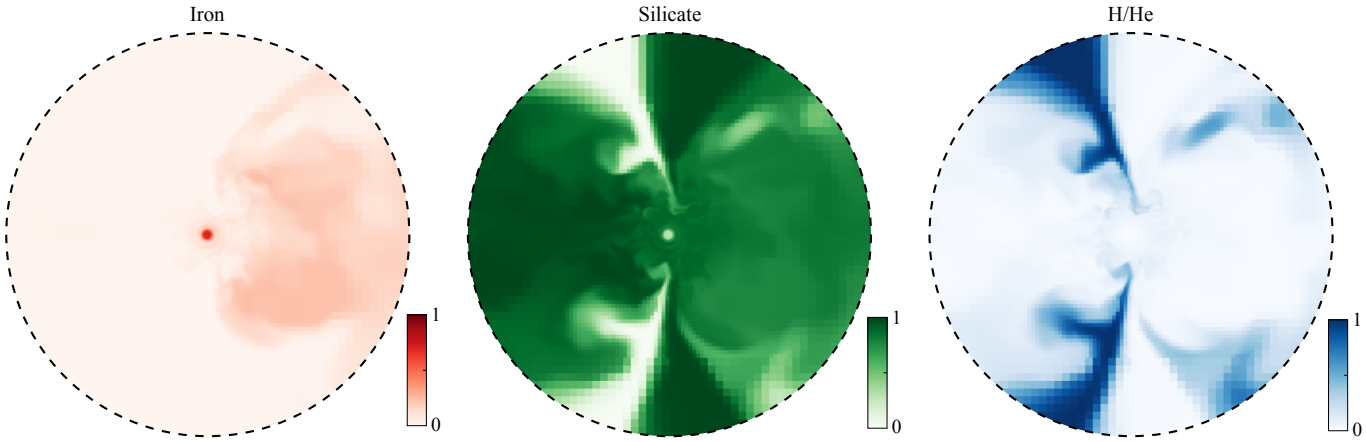

FIG. 8.— The mass fraction slices of each species through the orbital plane at 21.5 hours after the high-speed impact. Mixing becomes less efficient because most of the H/He envelope has been blown away by the impactor. Dashed circles represent the Hill sphere with a radius of 3.21×10^{10} cm.

evolves adiabatically into a hydrostatic equilibrium.

During the post-impact phase, the planet's atmosphere and interior contract as the planet cools. Above the photosphere, a highly-irradiated planet has an isothermal layer. We consider that an inflated planet after an impact radiates away heat from the photosphere. Owen & Wu (2015) estimated the Kelvin-Helmholtz timescale of a planet (3, 5, and $10\,M_\oplus$) with the equilibrium temperature of 900 K as a function of planetary radius in unit of the Bondi radius and envelope mass fraction based on a stellar evolution code, i.e., MESA (Paxton et al. 2011). We applied their results of 5 and $10\,M_\oplus$ shown in Figure 2 in Owen & Wu (2015) to our targets after giant impacts ($\sim 4.991\,M_\oplus$ and $9.738\,M_\oplus$ with the equilibrium temperature of ~ 900 K).

Following results of Owen & Wu (2015), we estimate the timescale of the Kelvin-Helmholtz contraction to be ~ 1 Myr for the low-speed case and < 10 kyr for the high-speed one. A protracted state of a hot and inflated atmosphere enhances its mass loss via a Parker wind. Based on Eq.(16) in Owen & Wu (2015), we estimate that the amount of mass loss for post-impact planets via a Parker wind for the two cases would be $\sim 88\%$ and $\sim 80\%$ of its envelope mass right after the impact.

As the planet cools down, silicate material sediments from its atmosphere and contracts within its interior. The release of gravitational energy provides a source of internal heat which prolongs the inflationary state of the planet's atmosphere and enhances mass loss via a Parker wind. The extended planetary atmosphere also intercepts a greater fraction of the stellar X-ray and UV irradiation and increases the rate of mass loss through photoevaporation.

We estimate the mass loss rate of an extended atmosphere via stellar XUV irradiation after giant impacts. Adopting analytical descriptions of a XUV energy flux from solar-type stars (Ribas et al. 2005), the incident XUV luminosity at the Hill radius is $1.0 \times 10^{-7}\,L_\odot$ and $1.5 \times 10^{-7}\,L_\odot$ in the low-speed and high-speed model, respectively. Given that the conversion efficiency from XUV photons to the kinetic energy of bulk atmospheric outflow is 10% as a fiducial value (Yelle 2004), the mass loss rate from the Roche lobe via stellar XUV irradiation right after giant impacts is estimated to be $\sim 3\,M_\oplus\,\mathrm{Myr}^{-1}$ for the former and $\sim 2\,M_\oplus\,\mathrm{Myr}^{-1}$ for the latter. If we consider a typical decay timescale of a XUV flux for Sun-like stars is ~ 0.1Gyr, the planet in the low-speed model may lose the entire envelope because its atmosphere shrinks in a few Myr. On the other hands, the planet in the high-speed model can contract more quickly (< 10 kyr), but it is unlikely for its tenuous post-impact atmosphere to survive a subsequent mass loss via stellar irradiation, either. Note that the stellar tidal field is crucial in this context because it can continuously remove planetary outer atmosphere that is beyond the Hill sphere. For giant impacts happen further away from the host star, tidal stripping becomes inefficient. And the outcome of a giant impact is determined by the mass ratio, impact speed and impact angle (Asphaug 2010; Leinhardt & Stewart 2012; Stewart & Leinhardt 2012).

To summarize, severe giant impacts can significantly devolatilize close-in super-Earths and mini-Neptunes. The compositional dichotomy between Kepler-36 b and c can be explained by their distinct impact histories along with the formation of the closely packed system, i.e. Kepler-36b experienced substantial giant impacts, and in the meanwhile Kepler-36c survived from being heavily bombarded. In addition, we speculate that giant impacts may have been imprinted in the large dispersion in the mass–radius relationship of close-in sub-Neptune-sized planets, as giant impacts occur stochastically and can diversify planetary interior and atmosphere otherwise well constrained.

In our solar system, there may be evidence for a similar though more subtle dichotomy. Despite their similar masses, radii, and compositions, thermal evolution models of Uranus and Neptune suggest that right after their formation, Neptune may have been relatively luminous but Uranus relatively faint (e.g. Hubbard & Macfarlane 1980; Fortney et al. 2011). Stevenson (1986) suggested that this dichotomy may be accounted for if a violent head-on collision yielded a hot and homogeneous interior of Neptune, whereas an oblique collision caused a tilted Uranus with a stably-stratified interior. The results presented here imply that the former scenario for Neptune may be possible.

We thank Jonathan Fortney, Pascale Garaud, James Guillochon, Don Korycansky, and Xiaojia Zhang for fruitful discussions. We also thank an anonymous referee for helpful suggestions to improve the clarity of this manuscript. S.-F.L. and E.A. are sponsored by the NASA grant NNX13AR66G. Y.H. is supported by a Grant-in-Aid for JSPS Fellows (No.25000465) and a Grant-in-Aid for Scientific Research on Innovative Areas (No. 26103711) from MEXT of Japan. Sup-

port from a UC/Lab Fee grant, an IGPPS grant, and the NSF grant 1211394 are also acknowledged. Numerical computations were carried out on the Laohu cluster at NAOC, on Cray XC30 at NAOJ, and on the Hyades cluster at UCSC. The FLASH code used in this work was in part developed by the DOE NNSA-ASC OASCR Flash Center at the University of Chicago. VisIt is supported by the Department of Energy with funding from the Advanced Simulation and Computing Program and the Scientific Discovery through Advanced Computing Program.

REFERENCES

Agertz, O., Moore, B., Stadel, J., et al. 2007, MNRAS, 380, 963
Asphaug, E. 2010, Chemie der Erde - Geochemistry, 70, 199
—. 2014, Annual Review of Earth and Planetary Sciences, 42, 551
Borucki, W. J., Koch, D., Basri, G., et al. 2010, Science, 327, 977
Burke, C. J., Bryson, S. T., Mullally, F., et al. 2014, ApJS, 210, 19
Carter, J. A., Agol, E., Chaplin, W. J., et al. 2012, Science, 337, 556
Chiang, E., & Laughlin, G. 2013, MNRAS, 431, 3444
Childs, H., Brugger, E., Whitlock, B., et al. 2012, in High Performance Visualization-Enabling Extreme-Scale Scientific Insight, 357
Deck, K. M., Deck, K. M., Holman, M. J., et al. 2012, ApJ, 755, L21
Dressing, C. D., & Charbonneau, D. 2015, ArXiv e-prints, 1501.01623
Dressing, C. D., Charbonneau, D., Dumusque, X., et al. 2015, ApJ, 800, 135
Elkins-Tanton, L. T., & Seager, S. 2008, ApJ, 685, 1237
Fortney, J. J., Ikoma, M., Nettelmann, N., et al. 2011, ApJ, 729, 32
Freedman, R. S., Marley, M. S., & Lodders, K. 2008, ApJS, 174, 504
Fryxell, B., Olson, K., Ricker, P., et al. 2000, ApJS, 131, 273
Guillochon, J., Ramirez-Ruiz, E., Rosswog, S., & Kasen, D. 2009, ApJ, 705, 844
Hansen, B. M. S., & Murray, N. 2012, ApJ, 751, 158
Hébrard, G., Lecavelier Des Étangs, A., Vidal-Madjar, A., Désert, J. M., & Ferlet, R. 2004, Extrasolar Planets: Today and Tomorrow, 321, 203
Hubbard, W. B., & Macfarlane, J. J. 1980, Journal of Geophysical Research, 85, 225
Ida, S., Lin, D. N. C., & Nagasawa, M. 2013, ApJ, 775, 42
Ikoma, M., & Hori, Y. 2012, ApJ, 753, 66
Kokubo, E., & Ida, S. 1998, Icarus, 131, 171
Leconte, J., & Chabrier, G. 2012, A&A 540, 20
Leinhardt, Z. M., & Stewart, S. T. 2012, ApJ, 745, 79
Li, R., Zhang, Y., Lin, D., & Dong, B. submitted
Lissauer, J. J., Fabrycky, D. C., Ford, E. B., et al. 2011, Nature, 470, 53
Lissauer, J. J., Jontof-Hutter, D., Rowe, J. F., et al. 2013, ApJ, 770, 131
Liu, S.-F., Agnor, C. B., Lin, D. N. C., & Li, S.-L. 2015, MNRAS, 446, 1685
Liu, S.-F., Guillochon, J., Lin, D. N. C., & Ramirez-Ruiz, E. 2013, ApJ, 762, 37
Lopez, E., & Fortney, J. J. 2013, ApJ, 776, 2
Marcus, R. A., Sasselov, D., Stewart, S. T., & Hernquist, L. 2010, ApJ, 719, L45
Marcus, R. A., Stewart, S. T., Sasselov, D., & Hernquist, L. 2009, ApJ, 700, L118
Melosh, H. J. 1989, Impact cratering: A geologic process (Research supported by NASA. New York, Oxford University Press (Oxford Monographs on Geology and Geophysics, No. 11), 1989, 253 p.)
Owen, J. E., & Wu, Y. 2013, ApJ, 775, 105
—. 2015, ArXiv e-prints, 1506.02049
Paardekooper, S.-J., Rein, H., & Kley, W. 2013, MNRAS, 434, 3018
Papaloizou, J. C. B., & Terquem, C. 2010, MNRAS, 405, 573
Paxton, B., Bildsten, L., Dotter, A., Herwig, F., Lesaffre, P., & Timmes, F. 2011, ApJS, 192, 3
Petigura, E. A., Marcy, G. W., & Howard, A. W. 2013, ApJ, 770, 69
Podolak, M. 2003, Icarus, 165, 428
Quillen, A. C., Bodman, E., & Moore, A. 2013, MNRAS, 435, 2256
Reufer, A., Meier, M. M. M., Benz, W., & Wieler, R. 2012, Icarus, 221, 296
Ribas, I., Guinan, E. F., Güdel, M., & Audard, M. 2005, ApJ, 622, 680
Rosenblum, E., Garaud, P., Traxler, A., & Stellmach, S. 2011, ApJ, 731, 66
Schlichting, H. E. 2014, ApJ, 795, L15
Stevenson, D. J. 1986, LUNAR AND PLANETARY SCIENCE XVII, 17, 1011
Stewart, S. T., & Leinhardt, Z. M. 2012, ApJ, 751, 32
Tasker, E. J., Brunino, R., Mitchell, N. L., et al. 2008, MNRAS, 390, 1267
Teyssandier, J., Owen, J. E., Adams, F. C., & Quillen, A. C. 2015, MNRAS, 452, 1743
Turk, M. J., Smith, B. D., Oishi, J. S., et al. 2011, ApJS, 192, 9
Yelle, R. V. 2004, Icarus, 170, 167